# Springer Handbook of Condensed Matter and Materials Data




*Martienssen*
*Warlimont*
*Editors*

Springer

# Springer Handbook of Condensed Matter and Materials Data

**Springer Handbook** provides a concise compilation of approved key information on methods of research, general principles, and functional relationships in physics and engineering. The world's leading experts in the fields of physics and engineering will be assigned by one or several renowned editors to write the chapters comprising each volume. The content is selected by these experts from Springer sources (books, journals, online content) and other systematic and approved recent publications of physical and technical information.

The volumes will be designed to be useful as readable desk reference book to give a fast and comprehensive overview and easy retrieval of essential reliable key information, including tables, graphs, and bibliographies. References to extensive sources are provided.

# Springer Handbook of Condensed Matter and Materials Data

W. Martienssen and H. Warlimont (Eds.)

With 1025 Figures and 914 Tables



Springer

Professor Werner Martienssen
Universität Frankfurt
Fachbereich 13, Physik
Robert-Mayer-Str. 2 – 4
60325 Frankfurt
Germany

Professor Hans Warlimont
IWF Dresden
Helmholzstr. 20
01069 Dresden
Germany

Library of Congress Control Number: 2004116537

ISBN 3-540-44376-2
Spinger Berlin Heidelberg New York

This work is subject to copyright. All rights reserved, whether the whole or part of the material is concerned, specifically the rights of translation, reprinting, reuse of illustrations, recitation, broadcasting, reproduction on microfilm or in any other way, and storage in data banks. Duplication of this publication or parts thereof is permitted only under the provisions of the German Copyright Law of September, 9, 1965, in its current version, and permission for use must always be obtained from Springer. Violations are liable for prosecution under the German Copyright Law.

Springer is a part of Springer Science+Business Media

springeronline.com

©Springer Berlin Heidelberg 2005
Printed in Germany

The use of designations, trademarks, etc. in this publication does not imply, even in the absence of a specific statement, that such names are exempt from the relevant protective laws and regulations and therefore free for general use.

Product liability: The publisher cannot guarantee the accuracy of any information about dosage and application contained in this book. In every individual case the user must check such information by consulting the relevant literature.

Production and typesetting: LE-TeX GbR, Leipzig
Handbook coordinator: Dr. W. Skolaut, Heidelberg
Typography, layout and illustrations: schreiberVIS, Seeheim
Cover design: eStudio Calamar Steinen, Barcelona
Cover production: *design&production* GmbH, Heidelberg
Printing and binding: Stürtz AG, Würzburg

Printed on acid-free paper
SPIN 10678245 62/3141/ 5 4 3 2 1 0

# Preface

The Springer Handbook of Condensed Matter and Materials Data is the realization of a new concept in reference literature, which combines introductory and explanatory texts with a compilation of selected data and functional relationships from the fields of solid-state physics and materials in a single volume. The data have been extracted from various specialized and more comprehensive data sources, in particular the Landolt–Börnstein data collection, as well as more recent publications. This Handbook is designed to be used as a desktop reference book for fast and easy finding of essential information and reliable key data. References to more extensive data sources are provided in each section. The main users of this new Handbook are envisaged to be students, scientists, engineers, and other knowledge-seeking persons interested and engaged in the fields of solid-state sciences and materials technologies.

The editors have striven to find authors for the individual sections who were experienced in the full breadth of their subject field and ready to provide succinct accounts in the form of both descriptive text and representative data. It goes without saying that the sections represent the individual approaches of the authors to their subject and their understanding of this task. Accordingly, the sections vary somewhat in character. While some editorial influence was exercised, the flexibility that we have shown is deliberate. The editors are grateful to all of the authors for their readiness to provide a contribution, and to cooperate in delivering their manuscripts and by accepting essentially all alterations which the editors requested to achieve a reasonably coherent presentation.

An onerous task such as this could not have been completed without encouragement and support from the publisher. Springer has entrusted us with this novel project, and Dr. Hubertus von Riedesel has been a persistent but patient reminder and promoter of our work throughout. Dr. Rainer Poerschke has accompanied and helped the editors constantly with his professional attitude and very personable style during the process of developing the concept, soliciting authors, and dealing with technical matters. In the later stages, Dr. Werner Skolaut became a relentless and hard-working member of our team with his painstaking contribution to technically editing the authors' manuscripts and linking the editors' work with the copy editing and production of the book.

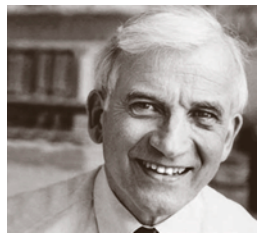

**Prof. Werner Martienssen**



**Prof. Hans Warlimont**

We should also like to thank our families for having graciously tolerated the many hours we have spent in working on this publication.

We hope that the users of this Handbook, whose needs we have tried to anticipate, will find it helpful and informative. In view of the novelty of the approach and any possible inadvertent deficiencies which this first edition may contain, we shall be grateful for any criticisms and suggestions which could help to improve subsequent editions so that they will serve the expectations of the users even better and more completely.

September 2004
Frankfurt am Main, Dresden

Werner Martienssen,
Hans Warlimont

## List of Authors

**Wolf Assmus**
Johann Wolfgang Goethe-University
Physics Department
Robert-Mayer-Str. 2 – 4
60054 Frankfurt am Main, Germany
e-mail: *assmus@physik.uni-frankfurt.de*

**Stefan Brühne**
Johann Wolfgang Goethe-University
Physics Department
Robert-Mayer-Str. 2 – 4
60054 Frankfurt am Main, Germany
e-mail: *bruehne@physik.uni-frankfurt.de*

**Fabrice Charra**
Commissariat à l'Énergie Atomique, Saclay
Département de Recherche sur l'État Condensé,
les Atomes et les Molécules
DRECAM-SPCSI, Centre d'Études de Saclay
91191 Gif-sur-Yvette, France
e-mail: *fabrice.charra@cea.fr*

**Gianfranco Chiarotti**
University of Rome "Tor Vergata"
Department of Physics
Via della Ricerca Scientifica 1
00133 Roma, Italy
e-mail: *chiarotti@roma2.infn.it*

**Claus Fischer**
Formerly Institute of Solid State and Materials
Research (IFW)
Georg-Schumann-Str. 20
01187 Dresden, Germany
e-mail: *A_C.FischerDD@t-online.de*

**Günter Fuchs**
Leibniz Institute for Solid State and Materials
Research (IFW) Dresden
Magnetism and Superconductivity in the Institute
of Metallic Materials
Helmholtzstraße 20
01171 Dresden, Germany
e-mail: *fuchs@ifw-dresden.de*

**Frank Goodwin**
International Lead Zinc Research Organization, Inc.
PO BOX 12036
Research Triangle Parc, NC 27709, USA
e-mail: *fgoodwin@ilzro.org*

**Susana Gota-Goldmann**
Commissariat à l'Energie Atomique (CEA)
Direction de la Recherche Technologique (DRT)
Centre de Fontenay aux Roses BP 6
92265 Fontenay aux Roses Cédex, France
e-mail: *susana.gota-goldmann@cea.fr*

**Sivaraman Guruswamy**
University of Utah
Metallurgical Engineering
135 South 1460 East RM 412
Salt Lake City, UT 84112-0114, USA
e-mail: *sguruswa@mines.utah.edu*

**Gagik G. Gurzadyan**
Technical University of Munich
Institute for Physical and Theoretical Chemistry
Lichtenbergstrasse 4
85748 Garching, Germany
e-mail: *gurzadyan@ch.tum.de*

**Hideki Harada**
High Tech Association Ltd.
3730-30 Higashikaya, Fukaya,Saitama, Japan
e-mail: *khb16457@nifty.com*

**Bernhard Holzapfel**
Leibniz Institute for Solid State and Materials
Research Dresden – Institute of Metallic Materials
Superconducting Materials
Helmholtzstr. 20
01069 Dresden, Germany
e-mail: *B.Holzapfel@ifw-dresden.de*

**Karl U. Kainer**
GKSS Research Center Geesthacht
Institute for Materials Research
Max-Planck-Str. 1
21502 Geesthacht, Germany
e-mail: *karl.kainer@gkss.de*

**Catrin Kammer**
METALL – Intl. Journal for Metallurgy
Kielsche Straße 43B
38642 Goslar, Germany
e-mail: *Kammer@metall-news.com*

**Wolfram Knabl**
Plansee AG
Technology Center
6600 Reutte, Austria
e-mail: *wolfram.knabl@plansee.com*

**Alfred Koethe**
Leibniz-Institut für Festkörper- und Werkstoffforschung
Institut für Metallische Werkstoffe (retired)
Lessingstrasse 11
01099 Dresden, Germany
e-mail: *alfred.koethe@web.de*

**Dieter Krause**
Schott AG
Research and Technology-Development
PO BOX 2480
55014 Mainz, Germany
e-mail: *dieter.krause@schott.com*

**Manfred D. Lechner**
Universität Osnabrück
Institut für Chemie – Physikalische Chemie
Barbarastraße 7
46069 Osnabrück, Germany
e-mail: *lechner@uni-osnabrueck.de*

**Gerhard Leichtfried**
Plansee AG
Technology Center
6600 Reutte, Austria
e-mail: *gerhard.leichtfried@plansee.com*

**Werner Martienssen**
Universität Frankfurt/Main
Physikalisches Institut
Robert-Mayer-Strasse 2 – 4
60054 Frankfurt/Main, Germany
e-mail: *Martienssen@Physik.uni-frankfurt.de*

**Toshio Mitsui**
Osaka University
Nakasuji-Yamate, 3-6-24
665-0875 Takarazuka, Japan
e-mail: *t-mitsui@jttk.zaq.ne.jp*

**Manfred Müller**
Dresden University of Technology
Institute of Materials Science
Leubnitzer Straße 26
01069 Dresden, Germany
e-mail: *m.mueller33@t-online.de*

**Sergei Pestov**
Moscow State Academy of Fine Chemical Technology
Department of Inorganic Chemistry
Vernadsky pr., 86
119571 Moscow, Russia
e-mail: *pestovsm@yandex.ru*

**Günther Schlamp**
Metallgesellschaft Ffm and Degussa
Demetron (retired)
Stettinerstr. 25
61449 Steinbach/Ts, Germany
e-mail:

**Barbara Schüpp-Niewa**
Leibniz-Institute for Solid State and Materials Research Dresden
Institute for Metallic Materials
Helmholtzstraße 20
01069 Dresden, Germany
e-mail: *b.schuepp@ifw-dresden.de*

**Roland Stickler**
University of Vienna
Department of Chemistry
Währingerstr. 42
1090 Vienna, Austria
e-mail: *roland.stickler@univie.ac.at*

**Pancho Tzankov**
Max Born Institute for Nonlinear Optics
and Short Pulse Spectroscopy
Max-Born-Str. 2A
12489 Berlin, Germany
e-mail: *tzankov@mbi-berlin.de*

**Volkmar Vill**
University of Hamburg
Department of Chemistry,
Institute of Organic Chemistry
Martin-Luther-King-Platz 6
20146 Hamburg, Germany
e-mail: *vill@chemie.uni-hamburg.de*

**Hans Warlimont**
DSL Dresden Material-Innovation GmbH
Helmholtzstrasse 20
01069 Dresden, Germany
e-mail: *warlimont@ifw-dresden.de*

# Contents

**List of Abbreviations** ..... XV

## Part 1 General Tables

1 **The Fundamental Constants**
*Werner Martienssen* ..... 3
1.1 What are the Fundamental Constants and Who Takes Care of Them? ..... 3
1.2 The CODATA Recommended Values of the Fundamental Constants ..... 4
References ..... 9

2 **The International System of Units (SI), Physical Quantities, and Their Dimensions**
*Werner Martienssen* ..... 11
2.1 The International System of Units (SI) ..... 11
2.2 Physical Quantities ..... 12
2.3 The SI Base Units ..... 13
2.4 The SI Derived Units ..... 16
2.5 Decimal Multiples and Submultiples of SI Units ..... 19
2.6 Units Outside the SI ..... 20
2.7 Some Energy Equivalents ..... 24
References ..... 25

3 **Rudiments of Crystallography**
*Wolf Assmus, Stefan Brühne* ..... 27
3.1 Crystalline Materials ..... 28
3.2 Disorder ..... 38
3.3 Amorphous Materials ..... 39
3.4 Methods for Investigating Crystallographic Structure ..... 39
References ..... 41

## Part 2 The Elements

1 **The Elements**
*Werner Martienssen* ..... 45
1.1 Introduction ..... 45
1.2 Description of Properties Tabulated ..... 46
1.3 Sources ..... 49
1.4 Tables of the Elements in Different Orders ..... 49
1.5 Data ..... 54
References ..... 158

## Part 3 Classes of Materials


1 **Metals**
*Frank Goodwin, Sivaraman Guruswamy, Karl U. Kainer, Catrin Kammer, Wolfram Knabl, Alfred Koethe, Gerhard Leichtfried, Günther Schlamp, Roland Stickler, Hans Warlimont* ..... 161
1.1 Magnesium and Magnesium Alloys ..... 162
1.2 Aluminium and Aluminium Alloys ..... 171
1.3 Titanium and Titanium Alloys ..... 206
1.4 Zirconium and Zirconium Alloys ..... 217
1.5 Iron and Steels ..... 221
1.6 Cobalt and Cobalt Alloys ..... 272
1.7 Nickel and Nickel Alloys ..... 279
1.8 Copper and Copper Alloys ..... 296
1.9 Refractory Metals and Alloys ..... 303
1.10 Noble Metals and Noble Metal Alloys ..... 329
1.11 Lead and Lead Alloys ..... 407
References ..... 422

2 **Ceramics**
*Hans Warlimont* ..... 431
2.1 Traditional Ceramics and Cements ..... 432
2.2 Silicate Ceramics ..... 433
2.3 Refractory Ceramics ..... 437
2.4 Oxide Ceramics ..... 437
2.5 Non-Oxide Ceramics ..... 451
References ..... 476

3 **Polymers**
*Manfred D. Lechner* ..... 477
3.1 Structural Units of Polymers ..... 480
3.2 Abbreviations ..... 482
3.3 Tables and Figures ..... 483
References ..... 522

4 **Glasses**
*Dieter Krause* ..... 523
4.1 Properties of Glasses – General Comments ..... 526
4.2 Composition and Properties of Glasses ..... 527
4.3 Flat Glass and Hollowware ..... 528
4.4 Technical Specialty Glasses ..... 530
4.5 Optical Glasses ..... 543
4.6 Vitreous Silica ..... 556
4.7 Glass-Ceramics ..... 558
4.8 Glasses for Miscellaneous Applications ..... 559
References ..... 572

## Part 4 Functional Materials

1 **Semiconductors**
*Werner Martienssen* ..... 575
1.1 Group IV Semiconductors and IV–IV Compounds ..... 578
1.2 III–V Compounds ..... 604
1.3 II–VI Compounds ..... 652
References ..... 691

2 **Superconductors**
*Claus Fischer, Günter Fuchs, Bernhard Holzapfel, Barbara Schüpp-Niewa, Hans Warlimont* ..... 695
2.1 Metallic Superconductors ..... 696
2.2 Non-Metallic Superconductors ..... 711
References ..... 749

3 **Magnetic Materials**
*Hideki Harada, Manfred Müller, Hans Warlimont* ..... 755
3.1 Basic Magnetic Properties ..... 755
3.2 Soft Magnetic Alloys ..... 758
3.3 Hard Magnetic Alloys ..... 794
3.4 Magnetic Oxides ..... 811
References ..... 814

4 **Dielectrics and Electrooptics**
*Gagik G. Gurzadyan, Pancho Tzankov* ..... 817
4.1 Dielectric Materials: Low-Frequency Properties ..... 822
4.2 Optical Materials: High-Frequency Properties ..... 824
4.3 Guidelines for Use of Tables ..... 826
4.4 Tables of Numerical Data for Dielectrics and Electrooptics ..... 828
References ..... 890

5 **Ferroelectrics and Antiferroelectrics**
*Toshio Mitsui* ..... 903
5.1 Definition of Ferroelectrics and Antiferroelectrics ..... 903
5.2 Survey of Research on Ferroelectrics ..... 904
5.3 Classification of Ferroelectrics ..... 906
5.4 Physical Properties of 43 Representative Ferroelectrics ..... 912
References ..... 936

## Part 5 Special Structures

1 **Liquid Crystals**
*Sergei Pestov, Volkmar Vill* ..... 941
1.1 Liquid Crystalline State ..... 941
1.2 Physical Properties of the Most Common Liquid Crystalline Substances 946

1.3 Physical Properties of Some Liquid Crystalline Mixtures ..... 975
References ..... 977

2 **The Physics of Solid Surfaces**
*Gianfranco Chiarotti* ..... 979
2.1 The Structure of Ideal Surfaces ..... 979
2.2 Surface Reconstruction and Relaxation ..... 986
2.3 Electronic Structure of Surfaces ..... 996
2.4 Surface Phonons ..... 1012
2.5 The Space Charge Layer at the Surface of a Semiconductor ..... 1020
2.6 Most Frequently Used Acronyms ..... 1026
References ..... 1029

3 **Mesoscopic and Nanostructured Materials**
*Fabrice Charra, Susana Gota-Goldmann* ..... 1031
3.1 Introduction and Survey ..... 1031
3.2 Electronic Structure and Spectroscopy ..... 1035
3.3 Electromagnetic Confinement ..... 1044
3.4 Magnetic Nanostructures ..... 1048
3.5 Preparation Techniques ..... 1063
References ..... 1066

**Acknowledgements** ..... 1073
**About the Authors** ..... 1075
**Detailed Contents** ..... 1081
**Subject Index** ..... 1091

# List of Abbreviations

| | |
|---|---|
| 2D-BZ | 2-dimensional Brillouin zone |
| 2P-PES | 2-photon photoemission spectroscopy |

## A

| | |
|---|---|
| AES | Auger electron spectroscopy |
| AFM | atomic force microscope |
| AISI | American Iron and Steel Institute |
| APS | appearance potential spectroscopy |
| ARUPS | angle-resolved ultraviolet photoemission spectroscopy |
| ARXPS | angle-resolved X-ray photoemission spectroscopy |
| ASTM | American Society for Testing and Materials |
| ATR | attenuated total reflection |

## B

| | |
|---|---|
| BBZ | bulk Brillouin zone |
| BIPM | Bureau International des Poids et Mesures |
| BZ | Brillouin zone |

## C

| | |
|---|---|
| CB | conduction band |
| CBM | conduction band minimum |
| CISS | collision ion scattering spectroscopy |
| CITS | current imaging tunneling spectroscopy |
| CMOS | complementary metal–oxide–semiconductor |
| CODATA | Committee on Data for Science and Technology |
| CVD | chemical vapour deposition |

## D

| | |
|---|---|
| DFB | distributed-feedback |
| DFG | difference frequency generation |
| DOS | density of states |
| DSC | differential scanning calorimetry |
| DTA | differential thermal analysis |

## E

| | |
|---|---|
| EB | electron-beam melting |
| ECS | electron capture spectroscopy |
| EELS | electron-energy loss spectroscopy |
| ELEED | elastic low-energy electron diffraction |
| ESD | electron-stimulated desorption |
| EXAFS | extended X-ray absorption fine structure |

## F

| | |
|---|---|
| FEM | field emission microscope/microscopy |
| FIM | field ion microscope/microscopy |

## G

| | |
|---|---|
| GMR | giant magnetoresistance |

## H

| | |
|---|---|
| HAS | helium atom scattering |
| HATOF | helium atom time-of-flight spectroscopy |
| HB | Brinell hardness number |
| HEED | high-energy electron diffraction |
| HEIS | high-energy ion scattering/high-energy ion scattering spectroscopy |
| HK | Knoop hardness |
| HOPG | highly oriented pyrolytic graphite |
| HPDC | high-pressure die casting |
| HR-EELS | high-resolution electron energy loss spectroscopy |
| HR-LEED | high-resolution LEED |
| HR-RHEED | high-resolution RHEED |
| HREELS | high-resolution electron energy loss spectroscopy |
| HRTEM | high-resolution transition electron microscopy |
| HT | high temperature |
| HTSC | high-temperature superconductor |
| HV | Vicker's Hardness |

## I

| | |
|---|---|
| IACS | International Annealed Copper Standard |
| IB | ion bombardment |
| IBAD | ion-beam-assisted deposition |
| ICISS | impact ion scattering spectroscopy |
| ICSU | International Council of the Scientific Unions |
| IPE | inverse photoemission |
| IPES | inverse photoemission spectroscopy |
| ISO | International Organization for Standardization |
| ISS | ion scattering spectroscopy |
| IUPAC | International Union of Pure and Applied Chemistry |

## J

| | |
|---|---|
| JDOS | joint density of states |

## K

| | |
|---|---|
| KRIPES | K-resolved inverse photoelectron spectroscopy |

## L

| | |
|---|---|
| LAPW | linearized augmented-plane-wave method |
| LB | Langmuir–Blodgett |
| LCM | liquid crystal material |
| LCP | liquid crystal polymer |
| LCs | liquid crystals |
| LDA | local-density approximation |
| LDOS | local density of states |
| LEED | low-energy electron diffraction |
| LEIS | low-energy ion scattering/low-energy ion scattering spectroscopy |
| LPE | liquid phase epitaxy |

## M

| | |
|---|---|
| MBE | molecular-beam epitaxy |
| MD | molecular dynamics |
| MEED | medium-energy electron diffraction |
| MEIS | medium-energy ion scattering/medium-energy ion scattering spectroscopy |
| MFM | magnetic force microscopy |
| ML | monolayer |
| MOCVD | metal-organic chemical vapor deposition |
| MOKE | magneto-optical Kerr effect |
| MOSFET | MOS field-effect transistor |
| MQW | multiple quantum well |

## N

| | |
|---|---|
| NICISS | neutral impact collision ion scattering spectroscopy |
| NIMs | National Institutes for Metrology |

## O

| | |
|---|---|
| OPO | optical parametric oscillation |

## P

| | |
|---|---|
| PDS | photothermal displacement spectroscopy |
| PED | photoelectron diffraction |
| PES | photoemission spectroscopy |
| PLAP | pulsed laser atom probe |
| PLD | pulsed laser deposition |
| PSZ | stabilized zirconia |
| PZT | piezoelectric material |

## R

| | |
|---|---|
| RAS | reflectance anisotropy spectroscopy |
| RE | rare earth |
| REM | reflection electron microscope/microscopy |
| RHEED | reflection high-energy electron diffraction |
| RIE | reactive ion etching |
| RPA | random-phase approximation |
| RT | room temperature |
| RTP | room temperaure and standard pressure |

## S

| | |
|---|---|
| SAM | self-assembled monolayer |
| SAM | scanning Auger microscope/microscopy |
| SARS | scattering and recoiling ion spectroscopy |
| SAW | surface acoustic wave |
| SBZ | surface Brillouin zone |
| SCLS | surface core level shift |
| SDR | surface differential reflectivity |
| SEM | scanning electron microscope |
| SEXAFS | surface-sensitive EXAFS |
| SFG | sum frequency generation |
| SH | second harmonic |
| SHG | second-harmonic generation |
| SI | Système International d'Unités |
| SIMS | secondary-ion mass spectroscopy |
| SNR | signal-to-noise ratio |
| SPARPES | spin polarized angle-resolved photoemission spectroscopy |
| SPIPES | spin-polarized inverse photoemission spectroscopy |
| SPLEED | spin-polarized |
| SPV | surface photovoltage spectroscopy |
| SQUIDS | superconducting quantum interference devices |
| SS | surface state |
| STM | scanning tunneling microscope/microscopy |
| STS | scanning tunneling spectroscopy |
| SXRD | surface X-ray diffraction |

## T

| | |
|---|---|
| TAFF | thermally activated flux flow |
| TEM | transmission electron microscope/microscopy |
| TFT | thin-film transistor |
| TMR | tunnel magnetoresistance |
| TMT | thermomechanical treatment |
| TOF | time of flight |
| TOM | torsion oscillation magnetometry |

| | |
|---|---|
| TRS | truncation rod scattering |
| TTT | time-temperature-transformation |

## U

| | |
|---|---|
| UHV | ultra-high vacuum |
| UPS | ultraviolet photoemission spectroscopy |
| UV | ultraviolet |

## V

| | |
|---|---|
| VBM | valence band maximum |
| VLEED | very low-energy electron diffraction |

## X

| | |
|---|---|
| XPS | X-ray photoemission spectroscopy |

# Part 1 General Tables


**1 The Fundamental Constants**
Werner Martienssen, Frankfurt/Main, Germany

**2 The International System of Units (SI), Physical Quantities, and Their Dimensions**
Werner Martienssen, Frankfurt/Main, Germany

**3 Rudiments of Crystallography**
Wolf Assmus, Frankfurt am Main, Germany
Stefan Brühne, Frankfurt am Main, Germany

# 1.1. The Fundamental Constants

In the quantitative description of physical phenomena and physical relationships, we find constant parameters which appear to be independent of the scale of the phenomena, independent of the place where the phenomena happen, and independent of the time when the phenomena is observed. These parameters are called fundamental constants. In Sect. 1.1.1, we give a qualitative description of these basic parameters and explain how "recommended values" for the numerical values of the fundamental constants are found. In Sect. 1.1.2, we present tables of the most recently determined recommended numerical values for a large number of those fundamental constants which play a role in solid-state physics and chemistry and in materials science.

1.1.1 **What are the Fundamental Constants and Who Takes Care of Them?** ..... 3

1.1.2 **The CODATA Recommended Values of the Fundamental Constants** ..... 4

1.1.2.1 The Most Frequently Used Fundamental Constants ..... 4

1.1.2.2 Detailed Lists of the Fundamental Constants in Different Fields of Application 5

1.1.2.3 Constants from Atomic Physics and Particle Physics ..... 7

**References** ..... 9

## 1.1.1 What are the Fundamental Constants and Who Takes Care of Them?

The fundamental constants are constant parameters in the laws of nature. They determine the size and strength of the phenomena in the natural and technological worlds. We conclude from observation that the numerical values of the fundamental constants are independent of space and time; at least, we can say that if there is any dependence of the fundamental constants on space and time, then this dependence must be an extremely weak one. Also, we observe that the numerical values are independent of the scale of the phenomena observed; for example, they seem to be the same in astrophysics and in atomic physics. In addition, the numerical values are quite independent of the environmental conditions. So we have confidence in the idea that the numerical values of the fundamental constants form a set of numbers which are the same everywhere in the world, and which have been the same in the past and will be the same in the future. Whereas the properties of all material objects in nature are more or less subject to continuous change, the fundamental constants seem to represent a constituent of the world which is absolutely permanent.

On the basis of this expected invariance of the fundamental constants in space and time, it appears reasonable to relate the units of measurement for physical quantities to fundamental constants as far as possible. This would guarantee that also the units of measurement become independent of space and time and of environmental conditions. Within the frame work of the International System of Units (Système International d'Unités, abbreviated to SI), the International Committee for Weights and Measures (Comité International des Poids et Mesures, CIPM) has succeeded in relating a large number of units of measurement for physical quantities to the numerical values of selected fundamental constants; however, several units for physical quantities are still represented by prototypes. For example, the unit of length 1 meter, is defined as the distance light travels in vacuum during a fixed time; so the unit of length is related to the fundamental constant $c$, i. e. the speed of light, and the unit of time, 1 second. The unit of mass, 1 kilogram, however, is still represented by a prototype, the mass of a metal cylinder made of a platinum–iridium alloy, which is carefully stored at the International Office for Weights and Measures (Bureau International des Poids et Mesures, BIPM), at Sèvres near Paris. In a few years, however, it might become possible also to relate the unit of mass to one or more fundamental constants.

The fundamental constants play an important role in basic physics as well as in applied physics and technology; in fact, they have a key function in the development of a system of reproducible and unchanging units for physical quantities. Nevertheless, there is, at present, no theory which would allow us to calculate the numerical values of the fundamental constants. Therefore, national institutes for metrology (NIMs), together with research institutes and university laboratories, are making efforts worldwide to determine the fundamental constants experimentally with the greatest possible accuracy and reliability. This, of course, is a continuous process, with hundreds of new publications every year.

The Committee on Data for Science and Technology (CODATA), established in 1966 as an interdisciplinary, international committee of the International Council of the Scientific Unions (ICSU), has taken the responsibility for improving the quality, reliability, processing, management, and accessibility of data of importance to science and technology. The CODATA task group on fundamental constants, established in 1969, has taken on the job of periodically providing the scientific and technological community with a self-consistent set of internationally recommended values of the fundamental constants based on all relevant data available at given points in time.

What is the meaning of "recommended values" of the fundamental constants?

Many fundamental constants are not independent of one another; they are related to one another by equations which allow one to calculate a numerical value for one particular constant from the numerical values of other constants. In consequence, the numerical value of a constant can be determined either by measuring it directly or by calculating it from the measured values of other constants related to it. In addition, there are usually several different experimental methods for measuring the value of any particular fundamental constant. This allows one to compute an adjustment on the basis of a least-squares fit to the whole set of experimental data in order to determine a set of best-fitting fundamental constants from the large set of all experimental data. Such an adjustment is done today about every four years by the CODATA task group mentioned above. The resulting set of best-fit values is then called the "CODATA recommended values of the fundamental constants" based on the adjustment of the appropriate year.

The tables in Sect. 1.1.2 show the CODATA recommended values of the fundamental constants of science and technology based on the 2002 adjustment. This adjustment takes into account all data that became available before 31 December 2002. A detailed description of the adjustment has been published by *Mohr* and *Taylor* of the National Institute of Standards and Technology, Gaithersburg, in [1.1].

The editors of this Handbook, H. Warlimont and W. Martienssen, would like to express their sincere thanks to Mohr and Taylor for kindly putting their data at our disposal prior to publication in Reviews of Modern Physics. These data first became available in December 2003 on the web site of the NIST fundamental constants data center [1.2].

## 1.1.2 The CODATA Recommended Values of the Fundamental Constants

### 1.1.2.1 The Most Frequently Used Fundamental Constants

Tables 1.1-1 – 1.1-9 list the CODATA recommended values of the fundamental constants based on the 2002 adjustment.

**Table 1.1-1** Brief list of the most frequently used fundamental constants

| Quantity | Symbol and relation | Numerical value | Units | Relative standard uncertainty |
|---|---|---|---|---|
| Speed of light in vacuum | $c$ | 299 792 458 | m/s | Fixed by definition |
| Magnetic constant | $\mu_0 = 4\pi \times 10^{-7}$ | $12.566370614\ldots \times 10^{-7}$ | $N/A^2$ | Fixed by definition |
| Electric constant | $\varepsilon_0 = 1/(\mu_0 c^2)$ | $8.854187817\ldots \times 10^{-12}$ | F/m | Fixed by definition |
| Newtonian constant of gravitation | $G$ | $6.6742(10) \times 10^{-11}$ | $m^3/(kg\,s^2)$ | $1.5 \times 10^{-4}$ |
| Planck constant | $h$ | $4.13566743(35) \times 10^{-15}$ | eV s | $8.5 \times 10^{-8}$ |
| Reduced Planck constant | $\hbar = h/2\pi$ | $6.58211915(56) \times 10^{-16}$ | eV s | $8.5 \times 10^{-8}$ |
| Elementary charge | $e$ | $1.60217653(14) \times 10^{-19}$ | C | $8.5 \times 10^{-8}$ |

**Table 1.1–1** Brief list of the most frequently used fundamental constants, cont.

| Quantity | Symbol and relation | Numerical value | Units | Relative standard uncertainty |
|---|---|---|---|---|
| Fine-structure constant | $\alpha = (1/4\pi\varepsilon_0)(e^2/\hbar c)$ | $7.297352568(24)\times10^{-3}$ | | $3.3\times10^{-9}$ |
| Magnetic flux quantum | $\Phi_0 = h/2e$ | $2.06783372(18)\times10^{-15}$ | Wb | $8.5\times10^{-8}$ |
| Conductance quantum | $G_0 = 2e^2/h$ | $7.748091733(26)\times10^{-5}$ | S | $3.3\times10^{-9}$ |
| Rydberg constant | $R_\infty = \alpha^2 m_e c/2h$ | 10 973 731.568525(73) | 1/m | $6.6\times10^{-12}$ |
| Electron mass | $m_e$ | $9.1093826(16)\times10^{-31}$ | kg | $1.7\times10^{-7}$ |
| Proton mass | $m_p$ | $1.67262171(29)\times10^{-27}$ | kg | $1.7\times10^{-7}$ |
| Proton–electron mass ratio | $m_p/m_e$ | 1836.15267261(85) | | $4.6\times10^{-10}$ |
| Avogadro number | $N_A, L$ | $6.0221415(10)\times10^{23}$ | | $1.7\times10^{-7}$ |
| Faraday constant | $F = N_A e$ | 96 485.3383(83) | C | $8.6\times10^{-8}$ |
| Molar gas constant | $R$ | 8.314472(15) | J/K | $1.7\times10^{-6}$ |
| Boltzmann constant | $k = R/N_A$ | $1.3806505(24)\times10^{-23}$<br>$8.617343(15)\times10^{-5}$ | J/K<br>eV/K | $1.8\times10^{-6}$<br>$1.8\times10^{-6}$ |
| Stefan–Boltzmann constant | $\sigma = (\pi^2/60)(k^4/(\hbar^3c^2))$ | $5.670400(40)\times10^{-8}$ | $W/(m^2\,K^4)$ | $7.0\times10^{-6}$ |

### 1.1.2.2 Detailed Lists of the Fundamental Constants in Different Fields of Application

**Table 1.1–2** Universal constants

| Quantity | Symbol and relation | Numerical value | Units | Relative standard uncertainty |
|---|---|---|---|---|
| Speed of light in vacuum | $c$ | 299 792 458 | m/s | Fixed by definition |
| Magnetic constant | $\mu_0 = 4\pi\times10^{-7}$ | $12.566370614\ldots\times10^{-7}$ | $N/A^2$ | Fixed by definition |
| Electric constant | $\varepsilon_0 = 1/(\mu_0 c^2)$ | $8.854187817\ldots\times10^{-12}$ | F/m | Fixed by definition |
| Characteristic impedance of vacuum | $Z_0 = (\mu_0/\varepsilon_0)^{1/2} = \mu_0 c$ | 376.730313461 ... | Ω | Fixed by definition |
| Newtonian constant of gravitation | $G$ | $6.6742(10)\times10^{-11}$ | $m^3/(kg\,s^2)$ | $1.5\times10^{-4}$ |
| Reduced Planck constant | $G/\hbar c$ | $6.7087(10)\times10^{-39}$ | $(GeV/c^2)^{-2}$ | $1.5\times10^{-4}$ |
| Planck constant | $h$ | $6.6260693(11)\times10^{-34}$<br>$4.13566743(35)\times10^{-15}$ | J s<br>eV s | $1.7\times10^{-7}$<br>$8.5\times10^{-8}$ |
| (Ratio) | $\hbar = h/2\pi$ | $1.05457168(18)\times10^{-34}$<br>$6.58211915(56)\times10^{-16}$ | J s<br>eV s | $1.7\times10^{-7}$<br>$8.5\times10^{-8}$ |
| (Product) | $\hbar c$ | 197.326968(17) | MeV fm | $8.5\times10^{-8}$ |
| (Product) | $c_1 = 2\pi hc^2$ | $3.74177138(64)\times10^{-16}$ | $W\,m^2$ | $1.7\times10^{-7}$ |
| (Product) | $(1/\pi)c_1 = 2hc^2$ | $1.19104282(20)\times10^{-16}$ | $W\,m^2/sr$ | $1.7\times10^{-7}$ |
| (Product) | $c_2 = h(c/k)$ | $1.4387752(25)\times10^{-2}$ | m K | $1.7\times10^{-6}$ |
| Stefan–Boltzmann constant | $\sigma = (\pi^2/60)(k^4/(\hbar^3c^2))$ | $5.670400(40)\times10^{-8}$ | $W/(m^2\,K^4)$ | $7.0\times10^{-6}$ |
| Wien displacement law constant | $b = \lambda_{max}T = c_2/4.965114231$ | $2.8977685(51)\times10^{-3}$ | m K | $1.7\times10^{-6}$ |
| Planck mass | $m_P = (\hbar c/G)^{1/2}$ | $2.17645(16)\times10^{-8}$ | kg | $7.5\times10^{-5}$ |
| Planck temperature | $T_P = (1/k)(\hbar c^5/G)^{1/2}$ | $1.41679(11)\times10^{32}$ | K | $7.5\times10^{-5}$ |
| Planck length | $l_P = \hbar/m_P c$<br>$= (\hbar G/c^3)^{1/2}$ | $1.61624(12)\times10^{-35}$ | m | $7.5\times10^{-5}$ |
| Planck time | $t_P = l_P/c = (\hbar G/c^5)^{1/2}$ | $5.39121(40)\times10^{-44}$ | s | $7.5\times10^{-5}$ |

**Table 1.1–3** Electromagnetic constants

| Quantity | Symbol and relation | Numerical value | Units | Relative standard uncertainty |
|---|---|---|---|---|
| Elementary charge | $e$ | $1.60217653(14)\times10^{-19}$ | C | $8.5\times10^{-8}$ |
| (Ratio) | $e/h$ | $2.41798940(21)\times10^{14}$ | A/J | $8.5\times10^{-8}$ |
| Fine-structure constant | $\alpha=(1/4\pi\varepsilon_0)(e^2/\hbar c)$ | $7.297352568(24)\times10^{-3}$ | | $3.3\times10^{-9}$ |
| Inverse fine-structure constant | $1/\alpha$ | 137.03599911(46) | | $3.3\times10^{-9}$ |
| Magnetic flux quantum | $\Phi_0=h/2e$ | $2.06783372(18)\times10^{-15}$ | Wb | $8.5\times10^{-8}$ |
| Conductance quantum | $G_0=2e^2/h$ | $7.748091733(26)\times10^{-5}$ | S | $3.3\times10^{-9}$ |
| Inverse of conductance quantum | $1/G_0$ | 12 906.403725(43) | Ω | $3.3\times10^{-9}$ |
| Josephson constant [a] | $K_J=2e/h$ | $483\,597.879(41)\times10^{9}$ | Hz/V | $8.5\times10^{-8}$ |
| von Klitzing constant [b] | $R_K=h/e^2=\mu_0c/2\alpha$ | 25 812.807449(86) | Ω | $3.3\times10^{-9}$ |
| Bohr magneton | $\mu_B=e\hbar/2m_e$ | $927.400949(80)\times10^{-26}$<br>$5.788381804(39)\times10^{-5}$ | J/T<br>eV/T | $8.6\times10^{-8}$<br>$6.7\times10^{-9}$ |
| (Ratio) | $\mu_B/h$ | $13.9962458(12)\times10^{9}$ | Hz/T | $8.6\times10^{-8}$ |
| (Ratio) | $\mu_B/hc$ | 46.6864507(40) | 1/(m T) | $8.6\times10^{-8}$ |
| (Ratio) | $\mu_B/k$ | 0.6717131(12) | K/T | $1.8\times10^{-6}$ |
| Nuclear magneton | $\mu_N=e\hbar/2m_p$ | $5.05078343(43)\times10^{-27}$<br>$3.152451259(21)\times10^{-8}$ | J/T<br>eV/T | $8.6\times10^{-8}$<br>$6.7\times10^{-9}$ |
| (Ratio) | $\mu_N/h$ | 7.62259371(65) | MHz/T | $8.6\times10^{-8}$ |
| (Ratio) | $\mu_N/hc$ | $2.54262358(22)\times10^{-2}$ | 1/(m T) | $8.6\times10^{-8}$ |
| (Ratio) | $\mu_N/k$ | $3.6582637(64)\times10^{-4}$ | K/T | $1.8\times10^{-6}$ |

[a] See Table 1.2-16 for the conventional value adopted internationally for realizing representations of the volt using the Josephson effect.
[b] See Table 1.2-16 for the conventional value adopted internationally for realizing representations of the ohm using the quantum Hall effect.

**Table 1.1–4** Thermodynamic constants

| Quantity | Symbol and relation | Numerical value | Units | Relative standard uncertainty |
|---|---|---|---|---|
| Avogadro number | $N_A$, $L$ | $6.0221415(10)\times10^{23}$ | | $1.7\times10^{-7}$ |
| Atomic mass constant | $u=(1/12)m(^{12}C)$<br>$=(1/N_A)\times10^{-3}$ kg | $1.66053886(28)\times10^{-27}$ | kg | $1.7\times10^{-7}$ |
| Energy equivalent of atomic mass constant | $m_uc^2$ | $1.49241790(26)\times10^{-10}$<br>931.494043(80) | J<br>MeV | $1.7\times10^{-7}$<br>$8.6\times10^{-8}$ |
| Faraday constant | $F=N_Ae$ | 96 485.3383(83) | C | $8.6\times10^{-8}$ |
| Molar Planck constant | $N_Ah$ | $3.990312716(27)\times10^{-10}$ | J s | $6.7\times10^{-9}$ |
| (Product) | $N_Ahc$ | 0.11962656572(80) | J m | $6.7\times10^{-9}$ |
| Molar gas constant | $R$ | 8.314472(15) | J/K | $1.7\times10^{-6}$ |
| Boltzmann constant | $k=R/N_A$ | $1.3806505(24)\times10^{-23}$<br>$8.617343(15)\times10^{-5}$ | J/K<br>eV/K | $1.8\times10^{-6}$<br>$1.8\times10^{-6}$ |
| (Ratio) | $k/h$ | $2.0836644(36)\times10^{10}$ | Hz/K | $1.7\times10^{-6}$ |
| (Ratio) | $k/hc$ | 69.50356(12) | 1/(m K) | $1.7\times10^{-6}$ |
| Molar volume of ideal gas at STP | $V_m=RT/p$<br>at $T=273.15$ K<br>and $p=101.325$ kPa | $22.413996(39)\times10^{-3}$ | $m^3$ | $1.7\times10^{-6}$ |
| Loschmidt constant | $n_0=N_A/V_m$ | $2.6867773(47)\times10^{25}$ | $1/m^3$ | $1.8\times10^{-6}$ |
| Stefan–Boltzmann constant | $\sigma=(\pi^2/60)(k^4/(\hbar^3c^2))$ | $5.670400(40)\times10^{-8}$ | $W/(m^2\,K^4)$ | $7.0\times10^{-6}$ |
| Wien displacement law constant | $b=\lambda_{max}T=c_2/4.965114231$ | $2.8977685(51)\times10^{-3}$ | m K | $1.7\times10^{-6}$ |

### 1.1.2.3 Constants from Atomic Physics and Particle Physics

**Table 1.1-5** Constants from atomic physics

| Quantity | Symbol and relation | Numerical value | Units | Relative standard uncertainty |
|---|---|---|---|---|
| Rydberg constant | $R_\infty = \alpha^2 m_e c/2h$ | 10 973 731.568525(73) | 1/m | $6.6\times10^{-12}$ |
| (Product) | $R_\infty c$ | $3.289841960360(22)\times10^{15}$ | Hz | $6.6\times10^{-12}$ |
| (Product) | $R_\infty hc$ | $2.17987209(37)\times10^{-18}$<br>13.6056923(12) | J<br>eV | $1.7\times10^{-7}$<br>$8.5\times10^{-8}$ |
| Bohr radius | $a_0 = \alpha/4\pi R_\infty$<br>$= 4\pi\varepsilon_0\hbar^2/m_e e^2$ | $0.5291772108(18)\times10^{-10}$ | m | $3.3\times10^{-9}$ |
| Hartree energy | $E_H = e^2/4\pi\varepsilon_0 a_0$<br>$= 2R_\infty hc = \alpha^2 m_e c^2$ | $4.35974417(75)\times10^{-18}$<br>27.2113845(23) | J<br>eV | $1.7\times10^{-7}$<br>$8.5\times10^{-8}$ |
| Quantum of circulation | $h/2m_e$ | $3.636947550(24)\times10^{-4}$ | $m^2/s$ | $6.7\times10^{-9}$ |
| (Product) | $h/m_e$ | $7.273895101(48)\times10^{-4}$ | $m^2/s$ | $6.7\times10^{-9}$ |

**Table 1.1-6** Properties of the electron

| Quantity | Symbol and relation | Numerical value | Units | Relative standard uncertainty |
|---|---|---|---|---|
| Electron mass | $m_e$ | $9.1093826(16)\times10^{-31}$<br>$5.4857990945(24)\times10^{-4}$ | kg<br>u | $1.7\times10^{-7}$<br>$4.4\times10^{-10}$ |
| Energy equivalent of electron mass | $m_e c^2$ | $8.1871047(14)\times10^{-14}$<br>0.510998918(44) | J<br>MeV | $1.7\times10^{-7}$<br>$8.6\times10^{-8}$ |
| Electron–proton mass ratio | $m_e/m_p$ | $5.4461702173(25)\times10^{-4}$ | | $4.6\times10^{-10}$ |
| Electron–neutron mass ratio | $m_e/m_n$ | $5.4386734481(38)\times10^{-4}$ | | $7.0\times10^{-10}$ |
| Electron–muon mass ratio | $m_e/m_\mu$ | $4.83633167(13)\times10^{-3}$ | | $2.6\times10^{-8}$ |
| Electron molar mass | $M(e) = N_A m_e$ | $5.4857990945(24)\times10^{-7}$ | kg | $4.4\times10^{-10}$ |
| Charge-to-mass ratio | $-e/m_e$ | $-1.75882012(15)\times10^{11}$ | C/kg | $8.6\times10^{-8}$ |
| Compton wavelength | $\lambda_C = h/m_e c$ | $2.426310238(16)\times10^{-12}$ | m | $6.7\times10^{-9}$ |
| (Ratio) | $\lambda_C/2\pi = \alpha a_0 = \alpha^2/(4\pi R_\infty)$ | $386.1592678(26)\times10^{-15}$ | m | $6.7\times10^{-9}$ |
| Classical electron radius | $r_e = \alpha^2 a_0$ | $2.817940325(28)\times10^{-15}$ | m | $1.0\times10^{-8}$ |
| Thomson cross section | $\sigma_e = (8\pi/3)r_e^2$ | $0.665245873(13)\times10^{-28}$ | $m^2$ | $2.0\times10^{-8}$ |
| Magnetic moment | $\mu_e$ | $-928.476412(80)\times10^{-26}$ | J/T | $8.6\times10^{-8}$ |
| Ratio of magnetic moment to Bohr magneton | $\mu_e/\mu_B$ | $-1.0011596521859(38)$ | | $3.8\times10^{-12}$ |
| Ratio of magnetic moment to nuclear magneton | $\mu_e/\mu_N$ | $-1838.28197107(85)$ | | $4.6\times10^{-10}$ |
| Ratio of magnetic moment to proton magnetic moment | $\mu_e/\mu_p$ | $-658.2106862(66)$ | | $1.0\times10^{-8}$ |
| Ratio of magnetic moment to neutron magnetic moment | $\mu_e/\mu_n$ | 960.92050(23) | | $2.4\times10^{-7}$ |
| Electron magnetic-moment anomaly | $a_e = \lvert\mu_e\rvert/(\mu_B - 1)$ | $1.1596521859(38)\times10^{-3}$ | | $3.2\times10^{-9}$ |
| $g$-factor | $g_e = -2(1 + a_e)$ | $-2.0023193043718(75)$ | | $3.8\times10^{-12}$ |
| Gyromagnetic ratio | $\gamma_e = 2\lvert\mu_e\rvert/\hbar$ | $1.76085974(15)\times10^{11}$ | 1/(s T) | $8.6\times10^{-8}$ |
| (Ratio) | $\gamma_e/2\pi$ | 28 024.9532(24) | MHz/T | $8.6\times10^{-8}$ |

**Table 1.1–7** Properties of the proton

| Quantity | Symbol and relation | Numerical value | Units | Relative standard uncertainty |
|---|---|---|---|---|
| Proton mass | $m_p$ | $1.67262171(29)\times10^{-27}$<br>$1.00727646688(13)$ | kg<br>u | $1.7\times10^{-7}$<br>$1.3\times10^{-10}$ |
| Energy equivalent of proton mass | $m_pc^2$ | $1.50327743(26)\times10^{-10}$<br>938.272029(80) | J<br>MeV | $1.7\times10^{-7}$<br>$8.6\times10^{-8}$ |
| Proton–electron mass ratio | $m_p/m_e$ | 1836.15267261(85) | | $4.6\times10^{-10}$ |
| Proton–neutron mass ratio | $m_p/m_n$ | 0.99862347872(58) | | $5.8\times10^{-10}$ |
| Proton molar mass | $M(\mathrm{p})=N_Am_p$ | $1.00727646688(13)\times10^{-3}$ | kg | $1.3\times10^{-10}$ |
| Charge-to-mass ratio | $e/m_p$ | $9.57883376(82)\times10^{7}$ | C/kg | $8.6\times10^{-8}$ |
| Compton wavelength | $\lambda_{C,p}=h/m_pc$ | $1.3214098555(88)\times10^{-15}$ | m | $6.7\times10^{-9}$ |
| (Ratio) | $(1/2\pi)\lambda_{C,p}$ | $0.2103089104(14)\times10^{-15}$ | m | $6.7\times10^{-9}$ |
| rms charge radius | $R_p$ | $0.8750(68)\times10^{-15}$ | m | $7.8\times10^{-3}$ |
| Magnetic moment | $\mu_p$ | $1.41060671(12)\times10^{-26}$ | J/T | $8.7\times10^{-8}$ |
| Ratio of magnetic moment to Bohr magneton | $\mu_p/\mu_B$ | $1.521032206(15)\times10^{-3}$ | | $1.0\times10^{-8}$ |
| Ratio of magnetic moment to nuclear magneton | $\mu_p/\mu_N$ | 2.792847351(28) | | $1.0\times10^{-8}$ |
| Ratio of magnetic moment to neutron magnetic moment | $\mu_p/\mu_n$ | −1.45989805(34) | | $2.4\times10^{-7}$ |
| $g$-factor | $g_p=2\mu_p/\mu_N$ | 5.585694701(56) | | $1.0\times10^{-8}$ |
| Gyromagnetic ratio | $\gamma_p=2\mu_p/\hbar$ | $2.67522205(23)\times10^{8}$ | 1/(s T) | $8.6\times10^{-8}$ |
| (Ratio) | $(1/2\pi)\gamma_p$ | 42.5774813(37) | MHz/T | $8.6\times10^{-8}$ |

**Table 1.1–8** Properties of the neutron

| Quantity | Symbol and relation | Numerical value | Units | Relative standard uncertainty |
|---|---|---|---|---|
| Neutron mass | $m_n$ | $1.67492728(29)\times10^{-27}$<br>$1.00866491560(55)$ | kg<br>u | $1.7\times10^{-7}$<br>$5.5\times10^{-10}$ |
| Energy equivalent | $m_nc^2$ | $1.50534957(26)\times10^{-10}$<br>939.565360(81) | J<br>MeV | $1.7\times10^{-7}$<br>$8.6\times10^{-8}$ |
| Neutron–electron mass ratio | $m_n/m_e$ | 1838.6836598(13) | | $7.0\times10^{-10}$ |
| Neutron–proton mass ratio | $m_n/m_p$ | 1.00137841870(58) | | $5.8\times10^{-10}$ |
| Molar mass | $M(\mathrm{n})=N_Am_n$ | $1.00866491560(55)\times10^{-3}$ | kg | $5.5\times10^{-10}$ |
| Compton wavelength | $\lambda_{C,n}=h/(m_nc)$ | $1.3195909067(88)\times10^{-15}$ | m | $6.7\times10^{-9}$ |
| (Ratio) | $(1/2\pi)\lambda_{C,n}$ | $0.2100194157(14)\times10^{-15}$ | m | $6.7\times10^{-9}$ |
| Magnetic moment | $\mu_n$ | $-0.96623645(24)\times10^{-26}$ | J/T | $2.5\times10^{-7}$ |
| Ratio of magnetic moment to Bohr magneton | $\mu_n/\mu_B$ | $-1.04187563(25)\times10^{-3}$ | | $2.4\times10^{-7}$ |
| Ratio of magnetic moment to nuclear magneton | $\mu_n/\mu_N$ | −1.91304273(45) | | $2.4\times10^{-7}$ |
| Ratio of magnetic moment to electron magnetic moment | $\mu_n/\mu_e$ | $1.04066882(25)\times10^{-3}$ | | $2.4\times10^{-7}$ |
| Ratio of magnetic moment to proton magnetic moment | $\mu_n/\mu_p$ | −0.68497934(16) | | $2.4\times10^{-7}$ |
| $g$-factor | $g_n=2\mu_n/\mu_N$ | −3.82608546(90) | | $2.4\times10^{-7}$ |
| Gyromagnetic ratio | $\gamma_n=2\lvert\mu_n\rvert/\hbar$ | $1.83247183(46)\times10^{8}$ | 1/(s T) | $2.5\times10^{-7}$ |
| (Ratio) | $(1/2\pi)\gamma_n$ | 29.1646950(73) | MHz/T | $2.5\times10^{-7}$ |

**Table 1.1-9** Properties of the alpha particle

| Quantity | Symbol and relation | Numerical value | Units | Relative standard uncertainty |
|---|---|---|---|---|
| Alpha particle mass [a] | $m_\alpha$ | $6.6446565(11)\times10^{-27}$<br>4.001506179149(56) | kg<br>u | $1.7\times10^{-7}$<br>$1.4\times10^{-11}$ |
| Energy equivalent of alpha particle mass | $m_\alpha c^2$ | $5.9719194(10)\times10^{-10}$<br>3727.37917(32) | J<br>MeV | $1.7\times10^{-7}$<br>$8.6\times10^{-8}$ |
| Ratio of alpha particle mass to electron mass | $m_\alpha/m_e$ | 7294.2995363(32) | | $4.4\times10^{-10}$ |
| Ratio of alpha particle mass to proton mass | $m_\alpha/m_p$ | 3.97259968907(52) | | $1.3\times10^{-10}$ |
| Alpha particle molar mass | $M(\alpha)=N_A m_\alpha$ | $4.001506179149(56)\times10^{-3}$ | kg/mol | $1.4\times10^{-11}$ |

[a] The mass of the alpha particle in units of the atomic mass unit u is given by $m_\alpha = A_r(\alpha)$ u; in words, the alpha particle mass is given by the relative atomic mass $A_r(\alpha)$ of the alpha particle, multiplied by the atomic mass unit u

## References


1.1 P. J. Mohr, B. N. Taylor: CODATA recommended values of the fundamental physical constants, Rev. Mod. Phys. (2004) (in press)

1.2 NIST Physics Laboratory: Web pages of the Fundamental Constants Data Center, http://physics.nist.gov/constants

# 1.2. The International System of Units (SI), Physical Quantities, and Their Dimensions



In this chapter, we introduce the International System of Units (SI) on the basis of the SI brochure "Le Système international d'unités (SI)" [2.1], supplemented by [2.2]. We give a short review of how the SI was worked out and who is responsible for the further development of the system. Following the above-mentioned publications, we explain the concepts of base physical quantities and derived physical quantities on which the SI is founded, and present a detailed description of the SI base units and of a large selection of SI derived units. We also discuss a number of non-SI units which still are in use, especially in some specialized fields. A table (Table 1.2-17) presenting the values of various energy equivalents closes the section.


1.2.1 **The International System of Units (SI)** ... 11
1.2.2 **Physical Quantities** ... 12
1.2.3 **The SI Base Units** ... 13
1.2.3.1 Unit of Length: the Meter ... 13
1.2.3.2 Unit of Mass: the Kilogram ... 14
1.2.3.3 Unit of Time: the Second ... 14
1.2.3.4 Unit of Electric Current: the Ampere ... 14
1.2.3.5 Unit of (Thermodynamic) Temperature: the Kelvin ... 14
1.2.3.6 Unit of Amount of Substance: the Mole ... 14
1.2.3.7 Unit of Luminous Intensity: the Candela ... 15
1.2.4 **The SI Derived Units** ... 16
1.2.5 **Decimal Multiples and Submultiples of SI Units** ... 19
1.2.6 **Units Outside the SI** ... 20
1.2.6.1 Units Used with the SI ... 20
1.2.6.2 Other Non-SI Units ... 20
1.2.7 **Some Energy Equivalents** ... 24
**References** ... 25


## 1.2.1 The International System of Units (SI)

All data in this handbook are given in the International System of Units (Système International d'Unités), abbreviated internationally to SI, which is the modern metric system of measurement and is acknowledged worldwide. The system of SI units was introduced by the General Conference of Weights and Measures (Conférence Générale des Poids et Mesures), abbreviated internationally to CGPM, in 1960. The system not only is used in science, but also is dominant in technology, industrial production, and international commerce and trade.

Who takes care of this system of SI units?

The Bureau International des Poids et Mesures (BIPM), which has its headquarters in Sèvres near Paris, has taken on a commitment to ensure worldwide unification of physical measurements. Its function is thus to:

- establish fundamental standards and scales for the measurement of the principal physical quantities and maintain the international prototypes;
- carry out comparison of national and international standards;
- ensure the coordination of the corresponding measuring techniques;
- carry out and coordinate measurements of the fundamental physical constants relevant to those activities.

The BIPM operates under the exclusive supervision of the Comité International des Poids et Mesures (CIPM), which itself comes under the authority of the

Conférence Générale des Poids et Mesures and reports to it on the work accomplished by the BIPM. The BIPM itself was set up by the Convention du Mètre signed in Paris in 1875 by 17 states during the final session of the Conference on the Meter. The convention was amended in 1921.

Delegates from all member states of the Convention du Mètre attend the Conférence Générale, which, at present, meets every four years. The function of these meetings is to:

- discuss and initiate the arrangements required to ensure the propagation and improvement of the International System of Units
- confirm the results of new fundamental metrological determinations and confirm various scientific resolutions with international scope
- take all major decisions concerning the finance, organization, and development of the BIPM.

The CIPM has 18 members, each from a different state; at present, it meets every year. The officers of this committee present an annual report on the administrative and financial position of the BIPM to the governments of the member states of the Convention du Mètre. The principal task of the CIPM is to ensure worldwide uniformity in units of measurement. It does this by direct action or by submitting proposals to the CGPM.

The BIPM publishes monographs on special metrological subjects and the brochure *Le Système international d'unités (SI)* [2.1, 2], which is periodically updated and in which all decisions and recommendations concerning units are collected together.

The scientific work of the BIPM is published in the open scientific literature, and an annual list of publications appears in the *Procès-Verbaux* of the CIPM.

Since 1965, *Metrologica*, an international journal published under the auspices of the CIPM, has printed articles dealing with scientific metrology, improvements in methods of measurements, and work on standards and units, as well as reports concerning the activities, decisions, and recommendations of the various bodies created under the Convention du Mètre.

## 1.2.2 Physical Quantities

Physical quantities are tools which allow us to specify and quantify the properties of physical objects and to model the events, phenomena, and patterns of behavior of objects in nature and in technology. The system of physical quantities used with the SI units is dealt by Technical Committee 12 of the International Organization for Standardization (ISO/TC 12). Since 1955, ISO/TC 12 has published a series of international standards on quantities and their units, in which the use of SI units is strongly recommended.

### How are Physical Quantities Defined?

It turns out that it is possible to divide the system of all known physical quantities into two groups:

- a small number of *base quantities*;
- a much larger number of other quantities, which are called *derived quantities*.

The derived quantities are introduced into physics unambiguously by a defining equation in terms of the base quantities; the relationships between the derived quantities and the base quantities are expressed in a series of equations, which contain a good deal of our knowledge of physics but are used in this system as the defining equations for new physical quantities. One might say that, in this system, physics is described in the rather low-dimensional space of a small number of base quantities.

Base quantities, on the other hand, cannot be introduced by a defining equation; they cannot be traced back to other quantities; this is what we mean by calling them "base". How can base quantities then be introduced unambiguously into physics at all?

Base physical quantities are introduced into physics in three steps:

- We borrow the qualitative meaning of the word for a base quantity from the meaning of the corresponding word in everyday language.
- We specify this meaning by indicating an appropriate method for measuring the quantity. For example, length is measured by a measuring rule, and time is measured by a clock.
- We fix a unit for this quantity, which allows us to communicate the result of a measurement. Length, for example, is measured in meters; time is measured in seconds.

On the basis of these three steps, it is expected that everyone will understand what is meant when the name of a base quantity is mentioned.

In fact, the number of base quantities chosen and the selection of the quantities which are considered as base quantities are a matter of expediency; in different fields and applications of physics, it might well be expedient to use different numbers of base quantities and different selections of base quantities. It should be kept in mind, however, that the number and selection of base quantities are only a matter of different representations of physics; physics itself is not affected by the choice that is made.

Today, many scientists therefore prefer to use the *conventional system* recommended by ISO. This system uses seven base quantities, which are selected according to the seven base units of the SI system. Table 1.2-1 shows the recommended names, symbols, and measuring devices for the conventional seven base quantities.

**Table 1.2-1** The ISO recommended base quantities

| Name of quantity | Symbol | Measured by |
|---|---|---|
| Length | $l$ | A measuring rule |
| Time | $t$ | A clock |
| Mass | $m$ | A balance |
| Electrical current | $I$ | A balance |
| Temperature | $T$ | A thermometer |
| Particle number | $N$ | Counting |
| Luminous intensity | $I_v$ | A photometer |

All other physical quantities can then be defined as derived quantities; this means they can be defined by equations in terms of the seven base quantities. Within this "conventional system", the set of all defining equations for the derived physical quantities also defines the units for the derived quantities in terms of the units of the base quantities. This is the great advantage of the "conventional system".

The quantity velocity $v$, for example, is defined by the equation

$$v = \frac{dl}{dt} .$$

In this way, velocity is traced back to the two base quantities length $l$ and time $t$. On the right-hand side of this equation, we have a differential of length $dl$ divided by a differential of time $dt$. The algebraic combination of the base quantities in the defining equation for a derived quantity is called the *dimensions* of the derived quantity. So velocity has the dimensions length/time, acceleration has the dimensions length/time squared, and so on.

Data for a physical quantity are always given as a product of a number (the *numerical value* of the physical quantity) and a unit in which the quantity has been measured.

## 1.2.3 The SI Base Units

Formal definitions of the seven SI base units have to be approved by the CGPM. The first such definition was approved in 1889. These definitions have been modified, however, from time to time as techniques of measurement have evolved and allowed more accurate realizations of the base units. Table 1.2-2 summarizes the present status of the SI base units and their symbols.

In the following, the current definitions of the base units adopted by the CGPM are shown in detail, together with some explanatory notes. Related decisions which clarify these definitions but are not formally part of them are also shown indented, but in a font of normal weight.

**Table 1.2-2** The seven SI base units and their symbols

| Base quantity | Symbol for quantity | Unit | Symbol for unit |
|---|---|---|---|
| Length | $l$ | metre | m |
| Time | $t$ | second | s |
| Mass | $m$ | kilogram | kg |
| Electrical current | $I$ | ampere | A |
| Temperature | $T$ | kelvin | K |
| Particle number | $n$ | mole | mol |
| Luminous intensity | $I_v$ | candela | cd |

### 1.2.3.1 Unit of Length: the Meter

The unit of length, the meter, was defined in the first CGPM approval in 1889 by an international prototype: the length of a bar made of a platinum–iridium alloy defined a length of 1 m. In 1960 this definition was replaced by a definition based upon a wavelength of krypton-86 radiation. Since 1983 (17th CGPM), the meter has been defined as:

> *The metre is the length of the path travelled by light in vacuum during a time interval of 1/299 792 458 of a second.*

As a result of this definition, the fundamental constant "speed of light in vacuum $c$" is fixed at exactly 299 792 458 m/s.

### 1.2.3.2 Unit of Mass: the Kilogram

Since the first CGPM in 1889, the unit of mass, the kilogram, has been defined by an international prototype, a metal block made of a platinum–iridium alloy, kept at the BIPM at Sèvres. The relevant declaration was modified slightly at the third CGPM in 1901 to confirm that:

> *The kilogram is the unit of mass; it is equal to the mass of the international prototype of the kilogram.*

### 1.2.3.3 Unit of Time: the Second

The unit of time, the second, was originally considered to be the fraction 1/86 400 of the mean solar day. Measurements, however, showed that irregularities in the rotation of the Earth could not be taken into account by theory, and these irregularities have the effect that this definition does not allow the required accuracy to be achieved. The same turned out to be true for other definitions based on astronomical data. Experimental work, however, had already shown that an atomic standard of time interval, based on a transition between two energy levels of an atom or a molecule, could be realized and reproduced much more precisely. Therefore, the 13th CGPM (1967 – 1968) replaced the definition of the second by:

> *The second is the duration of 9 192 631 770 periods of the radiation corresponding to the transition between the two hyperfine levels of the ground state of the caesium 133 atom.*

At its 1997 meeting, the CIPM affirmed that:

> This definition refers to a caesium atom at rest at a temperature of 0 K.

This note was intended to make it clear that the definition of the SI second is based on a Cs atom unperturbed by black-body radiation, that is, in an environment whose temperature is 0 K.

### 1.2.3.4 Unit of Electric Current: the Ampere

"International" electrical units for current and resistance were introduced by the International Electrical Congress in Chicago as early as in 1893 and were confirmed by an international conference in London in 1908. They were replaced by an "absolute" definition of the ampere as the unit for electric current at the 9th CGPM in 1948, which stated:

> *The ampere is that constant current which, if maintained in two straight parallel conductors of infinite length, of negligible circular cross-section, and placed 1 meter apart in vacuum, would produce between these conductors a force equal to $2 \times 10^{-7}$ newton per meter of length.*

As a result of this definition, the fundamental constant "magnetic field constant $\mu_0$" (also known as the permeability of free space) is fixed at exactly $4\pi \times 10^{-7}\ \mathrm{N/A^2}$.

### 1.2.3.5 Unit of (Thermodynamic) Temperature: the Kelvin

The definition of the unit of (thermodynamic) temperature was given in substance by the 10th CGPM in 1954, which selected the triple point of water as the fundamental fixed point and assigned to it the temperature 273.16 K, so defining the unit. After smaller amendments, made at the 13th CGPM in 1967–1968, the definition of the unit of (thermodynamic) temperature reads

> *The kelvin, unit of thermodynamic temperature, is the fraction 1/273.16 of the thermodynamic temperature of the triple point of water.*

Because of the way temperature scales used to be defined, it remains common practice to express a thermodynamic temperature, symbol $T$, in terms of its difference from the reference temperature $T_0 = 273.15$ K, the ice point. This temperature difference is called the Celsius temperature, symbol $t$, and is defined by the equation $t = T - T_0$. The unit of Celsius temperature is the degree Celsius, symbol °C, which is, by definition, equal in magnitude to the kelvin. A difference or interval of temperature may therefore be expressed either in kelvin or in degrees Celsius.

The numerical value of a Celsius temperature $t$ expressed in degrees Celsius is given by $t(°\mathrm{C}) = T(\mathrm{K}) - 273.15$.

### 1.2.3.6 Unit of Amount of Substance: the Mole

The "amount of substance" of a sample is understood as a measure of the number of elementary entities (for example atoms or molecules) that the sample consists of. Owing to the fact that on macroscopic scales this number cannot be counted directly in most cases, one has to relate this quantity "amount of substance" to a more easily measurable quantity, the mass of a sample of that substance.

On the basis of an agreement between the International Union of Pure and Applied Physics (IUPAP) and

the International Union of Pure and Applied Chemistry (IUPAC) in 1959/1960, physicists and chemists have ever since agreed to assign, by definition, the value 12, exactly, to the relative atomic mass (formerly called "atomic weight") of the isotope of carbon with mass number 12 (carbon-12, $^{12}C$). The scale of the masses of all other atoms and isotopes based on this agreement has been called, since then, the scale of relative atomic masses.

It remains to define the unit of the "amount of substance" in terms of the mass of the corresponding amount of the substance. This is done by fixing the mass of a particular amount of carbon-12; by international agreement, this mass has been fixed at 0.012 kg. The corresponding unit of the quantity "amount of substance" has been given the name "mole" (symbol mol).

On the basis of proposals by IUPAC, IUPAP, and ISO, the CIPM formulated a definition of the mole in 1967 and confirmed it in 1969. This definition was adopted by the 14th CGPM in 1971 in two statements:

> *1. The mole is the amount of substance of a system which contains as many elementary entities as there are atoms in* 0.012 *kilogram of carbon-12; its symbol is "mol".*
>
> *2. When the mole is used, the elementary entities must be specified and may be atoms, molecules, ions, electrons, other particles, or specified groups of such particles.*

In 1980, the CIPM approved the report of the Comité Consultatif des Unités (CCU), which specified that:

> In this definition, it is understood that unbound atoms of carbon-12, at rest and in their ground state, are referred to.

### 1.2.3.7 Unit of Luminous Intensity: the Candela

The base unit candela allows one to establish a quantitative relation between radiometric and photometric measurements of light intensities. In physics and chemistry, the intensities of radiation fields of various natures are normally determined by radiometry; in visual optics, in lighting engineering, and in the physiology of the visual system, however, it is necessary to assess the intensity of the radiation field by photometric means.

There are, in fact, three different ways to quantify the intensity of a radiation beam. One way is to measure the "radiant intensity" $I_e$, defined as the radiant flux $\Delta\Phi_e$ per unit solid angle $\Delta\Omega$ of the beam. The subscript "e" stands for "energetic". Here, the radiant flux $\Phi_e$ is defined as the energy of the radiation per unit time, and is accordingly measured in units of watts (W). The radiant intensity $I_e$, therefore, has the dimensions of energy per time per solid angle, and is measured in the derived unit "watt per steradian" (W/sr).

Another way to quantify the intensity of a beam of radiation is to measure the "particle intensity" $I_p$, which is defined as the particle flux $\Phi_p$ divided by the solid angle $\Delta\Omega$ of the beam. The subscript "p" stands for "particle". The particle flux $\Phi_p$ itself is measured by counting the number of particles per unit time in the beam; in the case of a light beam, for example, the particles are photons. The corresponding SI unit for the particle flux is seconds$^{-1}$ (1/s). The quantity particle intensity $I_p$ therefore has the dimensions of number per time per solid angle; the corresponding derived SI unit for the particle intensity $I_p$ is "seconds$^{-1}$ times steradian$^{-1}$" (1/(s sr)).

In addition to these two radiometric assessments of the beam intensity, for beams of visible light there is a third possibility, which is to quantify the intensity of the beam by the intensity of visual perception by the human eye. Physical quantities connected with this physiological type of assessment are called photometric quantities, in contrast to the two radiometric quantities described above. In photometry, the intensity of the beam is called the "luminous intensity" $I_v$. The subscript "v" stands for "visual". The luminous intensity $I_v$ is an ISO recommended base quantity; the corresponding SI base unit is the candela (cd). The luminous flux $\Phi_v$ is determined as the product of the luminous intensity and the solid angle. Its dimensions therefore are luminous intensity times solid angle, so that the SI unit of the luminous flux $\Phi_v$ turns out to be "candela times steradian" (cd sr). A derived unit, the lumen (lm), such that 1 lm = 1 cd sr, has been introduced for this product.

Table 1.2-3 summarizes the names, definitions, and SI units for the most frequently used radiometric and photometric quantities in radiation physics.

The history of the base unit candela is as follows. Before 1948, the units for photometric measurements were be based on flame or incandescent-filament standards. They were replaced initially by the "new candle" based on the luminance of a Planckian radiator (a blackbody radiator) at the temperature of freezing platinum. This modification was ratified in 1948 by the 9th CGPM, which also adopted the new international name for the base unit of luminous intensity, the candela, and its symbol cd. The 13th CGPM gave an amended version of the 1948 definition in 1967.

**Table 1.2-3** Radiometric and photometric quantities in radiation physics

| Quantity | Symbol and definition | Dimensions | SI unit | Symbol for unit |
|---|---|---|---|---|
| Radiant flux | $\Phi_e = \Delta E/\Delta t$ [a] | Power = energy/time | watt | W = J/s |
| Particle flux, activity | $\Phi_p = \Delta N_p/\Delta t$ | 1/time | second$^{-1}$ | 1/s |
| Luminous flux | $\Phi_v = I_v \Omega$ [b] | Luminous intensity times solid angle | lumen | lm = cd sr |
| Radiant intensity | $I_e = \Delta\Phi_e/\Delta\Omega$ | Power/solid angle | watt/steradian | W/sr |
| Particle intensity | $I_p = \Delta\Phi_p/\Delta\Omega$ | (Time times solid angle)$^{-1}$ | (second times steradian)$^{-1}$ | 1/(s sr) |
| Luminous intensity | $I_v$, basic quantity | Luminous intensity | candela | cd |
| Radiance [c] | $L_e = \Delta I_e(\varphi)/[\Delta A_1 g(\varphi)]$ [d] | Power per source area and solid angle | watt/(meter$^2$ times steradian) | W/(m$^2$ sr) = kg/(s$^3$ sr) |
| Particle radiance [c] | $L_p = \Delta I_p(\varphi)/[\Delta A_1 g(\varphi)]$ [d] | (Time times area times solid angle)$^{-1}$ | 1/(second times meter$^2$ times steradian) | 1/(s m$^2$ sr) |
| Luminance [c] | $L_v = \Delta I_v(\varphi)/[\Delta A_1 g(\varphi)]$ [d] | Luminous intensity/source area | candela/meter$^2$ | cd/m$^2$ |
| Irradiance | $E_e = \Delta\Phi_e/\Delta A_2$ [e] | Power/area | watt/meter$^2$ | W/m$^2$ |
| Particle irradiance | $E_p = \Delta\Phi_p/\Delta A_2$ [e] | Number of particles per (time times area) | 1/(second times meter$^2$) | 1/(s m$^2$) |
| Illuminance | $E_v = \Delta\Phi_v/\Delta A_2$ [e] | Luminous flux per area | lux = lumen/meter$^2$ | lx = lm/m$^2$ = cd sr/m$^2$ |

[a] The symbol $E$ stands for the radiant energy (see Table 1.2-5).

[b] $I_v$ stands for the luminous intensity, and $\Omega$ stands for the solid angle (see Table 1.2-5).

[c] The radiance $L_e$, particle radiance $L_p$, and luminance $L_v$ are important characteristic properties of sources, not radiation fields. For a blackbody source, the radiance $L_e$, for example, is dependent only on the frequency of the radiation and the temperature of the black body. The dependence is given by Planck's radiation law. In optical imaging, the radiance $L_e$ of an object turns out to show an invariant property. In correct imaging, the image always radiates with the same radiance $L_e$ as the object, independent of the magnification.

[d] $\varphi$ is the angle between the direction of the beam axis and the direction perpendicular to the source area; $A_1$ indicates the area of the source; and $g(\varphi)$ is the directional characteristic of the source.

[e] $A_2$ indicates the irradiated area or the area of the detector.

Because of experimental difficulties in realizing a Planckian radiator at high temperatures and because of new possibilities in the measurement of optical radiation power, the 16th CGPM in 1979 adopted a new definition of the candela as follows:

*The candela is the luminous intensity, in a given direction, of a source that emits monochromatic radiation of frequency* $540 \times 10^{12}$ *hertz and that has a radiant intensity in that direction of* 1/683 *watt per steradian.*

## 1.2.4 The SI Derived Units

The SI derived units are the SI units for derived physical quantities. In accordance with the defining equations for derived physical quantities in terms of the base physical quantities, the units for derived quantities can be expressed as products or ratios of the units for the base quantities. Table 1.2-4 shows some examples of SI derived units in terms of SI base units.

For convenience, certain derived units, which are listed in Table 1.2-5, have been given special names and symbols. Among these, the last four entries in Table 1.2-5 are of particular note, since they were accepted by the 15th (1975), 16th (1979), and 21st (1999) CGPMs specifically with a view to safeguarding human health.

In Tables 1.2-5 and 1.2-6, the final column shows how the SI units concerned may be expressed in terms of SI base units. In this column, factors such as m$^0$ and kg$^0$, etc., which are equal to 1, are not shown explicitly.

The special names and symbols for derived units listed in Table 1.2-5 may themselves be used to express other derived units: Table 1.2-6 shows some examples. The special names and symbols provide a compact form for the expression of units which are used frequently.

**Table 1.2-4** Examples of SI derived units (for derived physical quantities) in terms of base units

| Derived quantity | Defining equation | Name of SI derived unit | Symbol for unit |
|---|---|---|---|
| Area | $A = l_1 l_2$ | square meter | $m^2$ |
| Volume | $V = l_1 l_2 l_3$ | cubic meter | $m^3$ |
| Velocity | $v = dl/dt$ | meter per second | m/s |
| Acceleration | $a = d^2l/dt^2$ | meter per second squared | $m/s^2$ |
| Angular momentum | $L = \Theta\omega$ | meter squared kilogram/second | $m^2$ kg/s |
| Wavenumber | $k = 2\pi/\lambda$ | reciprocal meter | 1/m |
| Density | $\varrho = m/V$ | kilogram per cubic meter | $kg/m^3$ |
| Concentration (of amount of substance) | Concentration = amount/$V$ | mole per cubic meter | $mol/m^3$ |
| Current density | $j = I/A$ | ampere per square meter | $A/m^2$ |
| Magnetic exciting field | $H = I/l$ | ampere per meter | A/m |
| Radiance (of a radiation source) | $L_e = \Delta I_e(\varphi)/[\Delta A_1 g(\varphi)]$ [a] | watt per (square meter × steradian) | $W/(m^2\ sr) = kg/(s^3\ sr)$ |
| Luminance (of a light source) | $L_v = \Delta I_v(\varphi)/[\Delta A_1 g(\varphi)]$ [b] | candela per square meter | $cd/m^2$ |
| Refractive index | $n = c_{mat}/c$ | (number one) | 1 |

[a] $\varphi$ is the angle between the direction of the beam axis and the direction perpendicular to the source area; $I_e(\varphi)$ is the radiant intensity emitted in the direction $\varphi$; $A_1$ is the radiating area of the source; and $g(\varphi)$ is the directional characteristic of the source.

[b] $\varphi$ is the angle between the direction of the beam axis and the direction perpendicular to the source area; $I_v(\varphi)$ is the luminous intensity emitted in the direction $\varphi$; $A_1$ is the radiating area of the light source; and $g(\varphi)$ is the directional characteristic of the source.

**Table 1.2-5** SI derived units with special names and symbols

| Derived quantity | | SI derived unit | | | |
|---|---|---|---|---|---|
| Name | Symbol | Name | Symbol | Expressed in terms of other SI units | Expressed in terms of SI base units |
| Plane angle | $\alpha$, $\Delta\alpha$ | radian [a] | rad | | m/m = 1 [b] |
| Solid angle | $\Omega$, $\Delta\Omega$ | steradian [a] | sr [c] | | $m^2/m^2 = 1$ [b] |
| Frequency | $\nu$ | hertz | Hz | | 1/s |
| Force | $F$ | newton | N | | $m\,kg/s^2$ |
| Pressure, stress | $P$ | pascal | Pa | $N/m^2$ | $(1/m)\,kg/s^2$ |
| Energy, work, quantity of heat | $E$, $A$, $Q$ | joule | J | N m | $m^2\,kg/s^2$ |
| Power, radiant flux | $P$, $\Phi_e$ | watt | W | J/s | $m^2\,kg/s^3$ |
| Electric charge, quantity of electricity | $q$, $e$ | coulomb | C | | A s |
| Electric potential difference, electromotive force | $V$ | volt | V | W/A | $(1/A)\,m^2\,kg/s^3$ |
| Capacitance | $C$ | farad | F | C/V | $A^2\,(1/(m^2\,kg))\,s^4$ |
| Electrical resistance | $R$ | ohm | Ω | V/A | $(1/A^2)\,m^2\,kg/s^3$ |
| Electrical conductance | $1/R$ | siemens | S | A/V | $A^2\,(1/(m^2\,kg))s^3$ |
| Magnetic flux | $\Phi$ | weber | Wb | V s | $(1/A)\,m^2\,kg(1/s^2)$ |
| Magnetic field strength | $B$ | tesla | T | $Wb/m^2$ | $(1/A)\,kg/s^2$ |
| Inductance | $L$ | henry | H | Wb/A | $(1/A^2)\,m^2\,kg/s^2$ |
| Celsius temperature | $t$ | degree Celsius | °C | | K; $T/K = t/°C + 273.15$ |
| Luminous flux | $\Phi_v$ | lumen | lm | cd sr [c] | $(m^2/m^2)\,cd = cd$ |

**Table 1.2-5** SI derived units with special names and symbols, cont.

| Derived quantity | | SI derived unit | | | |
|---|---|---|---|---|---|
| **Name** | **Symbol** | **Name** | **Symbol** | **Expressed in terms of other SI units** | **Expressed in terms of SI base units** |
| Illuminance | $E_v = \Delta\Phi_v/\Delta A$ | lux | lx | $lm/m^2$ | $(m^2/m^4)\,cd = cd/m^2$ |
| Activity (referred to a radionuclide) | $A$ | becquerel | Bq | | $1/s$ |
| Absorbed dose | $D$ | gray | Gy | J/kg | $m^2/s^2$ |
| Dose equivalent | $H$ | sievert | Sv | J/kg | $m^2/s^2$ |
| Catalytic activity | | katal | kat | | $(1/s)\,mol$ |

[a] The units radian and steradian may be used with advantage in expressions for derived units to distinguish between quantities of different nature but the same dimensions. Some examples of their use in forming derived units are given in Tables 1.2-5 and 1.2-6.
[b] In practice, the symbols rad and sr are used where appropriate, but the derived unit "1" is generally omitted in combination with a numerical value.
[c] In photometry, the name steradian and the symbol sr are frequently retained in expressions for units.

**Table 1.2-6** Examples of SI derived units whose names and symbols include SI derived units with special names and symbols

| Derived quantity | | SI derived unit | | |
|---|---|---|---|---|
| **Name** | **Symbol** | **Name** | **Symbol** | **Expressed in terms of SI base units** |
| Dynamic viscosity | $\eta$ | pascal second | Pa s | $(1/m)\,kg/s$ |
| Moment of force | $M$ | newton meter | N m | $m^2\,kg/s^2$ |
| Surface tension | $\sigma$ | newton per meter | N/m | $kg/s^2$ |
| Angular velocity | $\omega$ | radian per second | rad/s | $m/(m\,s) = 1/s$ |
| Angular acceleration | $d\omega/dt$ | radian per second squared | $rad/s^2$ | $m/(m\,s^2) = 1/s^2$ |
| Heat flux density | $q_{th}$ | watt per square meter | $W/m^2$ | $kg/s^3$ |
| Heat capacity, entropy | $C$, $S$ | joule per kelvin | J/K | $m^2\,kg/(s^2\,K)$ |
| Specific heat capacity, specific entropy | $C_{mass}$, $S_{mass}$ | joule per (kilogram kelvin) | J/(kg K) | $m^2/(s^2\,K)$ |
| Specific energy | | joule per kilogram | J/kg | $m^2/s^2$ |
| Energy density | $w$ | joule per cubic meter | $J/m^3$ | $(1/m)\,kg/s^2$ |
| Thermal conductivity | $\lambda$ | watt per (meter kelvin) | W/(m K) | $m\,kg/(s^3\,K)$ |
| Electric charge density | $\rho$ | coulomb per cubic meter | $C/m^3$ | $(1/m^3)\,s\,A$ |
| Electric field strength | $E$ | volt per meter | V/m | $m\,kg/(s^3\,A)$ |
| Exciting electric field[b] | $D$ | coulomb per square meter | $C/m^2$ | $(1/m^2)\,s\,A$ |
| Molar energy | $E_{mol}$ | joule per mole | J/mol | $m^2\,kg/(s^2\,mol)$ |
| Molar heat capacity, molar entropy | $C_{mol}$, $S_{mol}$ | joule per (mole kelvin) | J/(mol K) | $m^2\,kg/(s^2\,K\,mol)$ |
| Exposure (X- and $\gamma$-rays) | | coulomb per kilogram | C/kg | $(1/kg)\,s\,A$ |
| Absorbed dose rate | $dD/dt$ | gray per second | Gy/s | $m^2/s^3$ |
| Radiant intensity | $I_\varepsilon$ | watt per steradian | W/sr | $(m^4/m^2)\,kg/s^3 = m^2\,kg/s^3$ |
| Radiance[a] | $L_e$ | watt per (square meter steradian) | $W/(m^2\,sr)$ | $(m^2/m^2)\,kg/s^3 = kg/s^3$ |
| Catalytic (activity) concentration | | katal per cubic meter | $kat/m^3$ | $(1/(m^3\,s))\,mol$ |

[a] The radiance is a property of the source of the radiation, not of the radiation field (see footnote c to Table 1.2-3).
[b] also called "electric flux density"

A derived unit can often be expressed in several different ways by combining the names of base units with special names for derived units. This, however, is an algebraic freedom whose use should be limited by common-sense physical considerations. The joule, for example, may formally be written "newton meter" or even "kilogram meter squared per second squared", but in a given situation some forms may be more helpful than others.

In practice, with certain quantities, preference is given to the use of certain special unit names or combinations of unit names, in order to facilitate making a distinction between different quantities that have the same dimensions. For example, the SI unit of frequency is called the hertz rather than the reciprocal second, and the SI unit of angular velocity is called the radian per second rather than the reciprocal second (in this case, retaining the word "radian" emphasizes that the angular velocity is equal to $2\pi$ times the rotational frequency). Similarly, the SI unit of moment of force is called the newton meter rather than the joule.

In the field of ionizing radiation, the SI unit of activity is called the becquerel rather than the reciprocal second, and the SI units of absorbed dose and dose equivalent are called the gray and the sievert, respectively, rather than the joule per kilogram. In the field of catalysis, the SI unit of catalytic activity is called the katal rather than the mole per second. The special names becquerel, gray, sievert, and katal were specifically introduced because of the dangers to human health which might arise from mistakes involving the units reciprocal second, joule per kilogram, and mole per second.

## 1.2.5 Decimal Multiples and Submultiples of SI Units

The 11th CGPM adopted, in 1960, a series of prefixes and prefix symbols for forming the names and symbols of the decimal multiples and submultiples of SI units ranging from $10^{12}$ to $10^{-12}$. Prefixes for $10^{-15}$ and $10^{-18}$ were added by the 12th CGPM in 1964, and for $10^{15}$ and $10^{18}$ by the 15th CGPM in 1975. The 19th CGPM extended the scale in 1991 from $10^{-24}$ to $10^{24}$. Table 1.2-7 lists all approved prefixes and symbols.

**Table 1.2-7** SI prefixes and their symbols

| Factor | Name | Symbol |
|---|---|---|
| $10^{24}$ | yotta | Y |
| $10^{21}$ | zeta | Z |
| $10^{18}$ | exa | E |
| $10^{15}$ | peta | P |
| $10^{12}$ | tera | T |
| $10^{9}$ | giga | G |
| $10^{6}$ | mega | M |
| $10^{3}$ | kilo | k |
| $10^{2}$ | hecto | h |
| $10^{1}$ | deca | da |
| $10^{-1}$ | deci | d |
| $10^{-2}$ | centi | c |
| $10^{-3}$ | milli | m |
| $10^{-6}$ | micro | μ |
| $10^{-9}$ | nano | n |
| $10^{-12}$ | pico | p |
| $10^{-15}$ | femto | f |
| $10^{-18}$ | atto | a |
| $10^{-21}$ | zepto | z |
| $10^{-24}$ | yocto | y |

## 1.2.6 Units Outside the SI

The SI base units and SI derived units, including those with special names, have the important advantage of forming a coherent set, with the effect that unit conversions are not required when one is inserting particular values for quantities into equations involving quantities.

Nonetheless, it is recognized that some non-SI units still appear widely in the scientific, technical, and commercial literature, and some will probably continue to be used for many years. Other non-SI units, such as the units of time, are so widely used in everyday life and are so deeply embedded in the history and culture of human beings that they will continue to be used for the foreseeable future. For these reasons, some of the more important non-SI units are listed.

### 1.2.6.1 Units Used with the SI

In 1996 the CIPM agreed upon a categorization of the units used with the SI into three groups: units accepted for use with the SI, units accepted for use with the SI whose values are obtained experimentally, and other units currently accepted for use with the SI to satisfy the needs of special interests. The three groups are listed in Tables 1.2-8 – 1.2-10.

Table 1.2-9 lists three non-SI units accepted for use with the SI, whose values expressed in SI units must be obtained by experiment and are therefore not known exactly. Their values are given with their combined standard uncertainties, which apply to the last two digits, shown in parentheses. These units are in common use in certain specialized fields.

Table 1.2-10 lists some other non-SI units which are currently accepted for use with the SI to satisfy the needs of commercial, legal, and specialized scientific interests. These units should be defined in relation to SI units in every document in which they are used. Their use is not encouraged.

### 1.2.6.2 Other Non-SI Units

Certain other non-SI units are still occasionally used. Some are important for the interpretation of older scientific texts. These are listed in Tables 1.2-11 – 1.2-16, but their use is not encouraged.

**Table 1.2-8** Non-SI units accepted for use with the International System

| Name | Symbol | Value in SI units |
|---|---|---|
| minute | min | $1\,\text{min} = 60\,\text{s}$ |
| hour | h | $1\,\text{h} = 60\,\text{min} = 3600\,\text{s}$ |
| day | d | $1\,\text{d} = 24\,\text{h} = 86\,400\,\text{s}$ |
| degree [a] | ° | $1° = (\pi/180)\,\text{rad}$ |
| minute of arc | ′ | $1′ = (1/60)° = (\pi/10\,800)\,\text{rad}$ |
| second of arc | ″ | $1″ = (1/60)′ = (\pi/648\,000)\,\text{rad}$ |
| litre [b] | l, L | $1\,\text{l} = 1\,\text{dm}^3 = 10^{-3}\,\text{m}^3$ |
| tonne [c] | t | $1\,\text{t} = 10^3\,\text{kg}$ |

[a] ISO 31 recommends that the degree be subdivided decimally rather than using the minute and second.

[b] Unfortunately, printers from all over the world seem not to be willing to admit that in some texts it would be very helpful to have distinguishable symbols for "the number 1" and "the letter l". Giving up any further discussion, the 16th CGPM therefore decided in 1979 that the symbol L should also be adopted to indicate the unit litre in order to avoid the risk of confusion between "the number 1" and "the letter l".

[c] This unit is also called the "metric ton" in some countries.

**Table 1.2-9** Non-SI units accepted for use with the International System, whose values in SI units are obtained experimentally

| Unit | Definition | Symbol | Value in SI units |
|---|---|---|---|
| Electron volt [a] | [b] | eV | $1\,\text{eV} = 1.60217653(14) \times 10^{-19}\,\text{J}$ |
| Unified atomic mass unit [a] | [c] | u | $1\,\text{u} = 1.66053886(28) \times 10^{-27}\,\text{kg}$ |
| Astronomical unit [d] | [e] | ua | $1\,\text{ua} = 1.49597870691(30) \times 10^{11}\,\text{m}$ |

[a] For the electron volt and the unified atomic mass unit, the values are quoted from the CODATA recommended values 2002 (see Chapt. 1.1).

[b] The electron volt is the kinetic energy acquired by an electron in passing through a potential difference of 1 V in vacuum.

[c] The unified atomic mass unit is equal to 1/12 of the mass of an unbound atom of the nuclide $^{12}C$, at rest and in its ground state. In the field of biochemistry, the unified atomic mass unit is also called the dalton, symbol Da.

[d] The value given for the astronomical unit is quoted from the IERS Convention (1996).

[e] The astronomical unit is a unit of length approximately equal to the mean Earth–Sun distance. Its value is such that, when it is used to describe the motion of bodies in the solar system, the heliocentric gravitational constant is $(0.01720209895)^2\,\text{ua}^3/\text{d}^2$.

**Table 1.2-10** Other non-SI units currently accepted for use with the International System

| Unit | Symbol | Value in SI units |
|---|---|---|
| nautical mile [a] | | 1 nautical mile = 1852 m |
| knot | | 1 knot = 1 nautical mile per hour = (1852/3600) m/s |
| are [b] | a | $1\,\mathrm{a} = 1\,\mathrm{dam}^2 = 10^2\,\mathrm{m}^2$ |
| hectare [b] | ha | $1\,\mathrm{ha} = 1\,\mathrm{hm}^2 = 10^4\,\mathrm{m}^2$ |
| Bar [c] | bar | 1 bar = 0.1 MPa = 100 kPa = 1000 hPa = $10^5$ Pa |
| angstrom | Å | $1\,\text{Å} = 0.1\,\mathrm{nm} = 10^{-10}\,\mathrm{m}$ |
| barn [d] | b | $1\,\mathrm{b} = 100\,\mathrm{fm}^2 = 10^{-28}\,\mathrm{m}^2$ |

[a] The nautical mile is a special unit employed for marine and aerial navigation to express distance. The conventional value given above was adopted by the First International Extraordinary Hydrographic Conference, Monaco, 1929, under the name "international nautical mile". As yet there is no internationally agreed symbol. This unit was originally chosen because one nautical mile on the surface of the Earth subtends approximately one minute of arc at the center.

[b] The units are and hectare and their symbols were adopted by the CIPM in 1879 and are used to express areas of land.

[c] The bar and its symbol were included in Resolution 7 of the 9th CGPM (1948).

[d] The barn is a special unit employed in nuclear physics to express effective cross sections.

Table 1.2-11 deals with the relationship between CGS units and SI units, and lists those CGS units that were assigned special names. In the field of mechanics, the CGS system of units was built upon three quantities and their corresponding base units: the centimeter, the gram, and the second. In the field of electricity and magnetism, units were expressed in terms of these three base units. Because this can be done in different ways, this led to the establishment of several different systems, for example the CGS electrostatic system, the CGS electromagnetic system, and the CGS Gaussian system. In those three systems, the system of quantities used and the corresponding system of defining equations for the derived quantities differ from those used with SI units.

**Table 1.2-11** Derived CGS units with special names

| Unit | Symbol | Value in SI units |
|---|---|---|
| erg [a] | erg | $1\,\mathrm{erg} = 10^{-7}\,\mathrm{J}$ |
| dyne [a] | dyn | $1\,\mathrm{dyn} = 10^{-5}\,\mathrm{N}$ |
| poise [a] | P | $1\,\mathrm{P} = 1\,\mathrm{dyn\,s/cm}^2 = 0.1\,\mathrm{Pa\,s}$ |
| stokes | St | $1\,\mathrm{St} = 1\,\mathrm{cm}^2/\mathrm{s} = 10^{-4}\,\mathrm{m}^2/\mathrm{s}$ |
| gauss [b] | G | $1\,\mathrm{G} \equiv 10^{-4}\,\mathrm{T}$ |
| oersted [b] | Oe | $1\,\mathrm{Oe} \equiv (1000/4\pi)\,\mathrm{A/m}$ |
| maxwell [b] | Mx | $1\,\mathrm{Mx} \equiv 10^{-8}\,\mathrm{Wb}$ |
| stilb [a] | sb | $1\,\mathrm{sb} = 1\,\mathrm{cd/cm}^2 = 10^4\,\mathrm{cd/m}^2$ |
| phot | ph | $1\,\mathrm{ph} = 10^4\,\mathrm{lx}$ |
| gal [c] | Gal | $1\,\mathrm{Gal} = 1\,\mathrm{cm/s}^2 = 10^{-2}\,\mathrm{m/s}^2$ |

[a] This unit and its symbol were included in Resolution 7 of the 9th CGPM (1948).

[b] This unit is part of the "electromagnetic" three-dimensional CGS system and cannot strictly be compared with the corresponding unit of the International System, which has four dimensions if only mechanical and electrical quantities are considered. For this reason, this unit is linked to the SI unit using the mathematical symbol for "equivalent to" (≡) here.

[c] The gal is a special unit employed in geodesy and geophysics to express the acceleration due to gravity.

Table 1.2-12 deals with the *natural units*, which are based directly on fundamental constants or combinations of fundamental constants. Like the CGS system, this system is based on mechanical quantities only. The numerical values in SI units are given here according to the 2002 CODATA adjustment.

Table 1.2-13 presents numerical values in SI units for some of the most frequently used *atomic units* (a.u.), again based on the 2002 CODATA adjustment.

Table 1.2-14 presents numerical values in SI units (based on the 2002 CODATA adjustment) for some X-ray-related quantities used in crystallography.

**Table 1.2-12** Natural units (n.u.)

| Unit | Symbol and definition | Value in SI units |
|---|---|---|
| n.u. of velocity: speed of light in vacuum | $c$ | 299 792 458 m/s |
| n.u. of action: reduced Planck constant | $\hbar = h/2\pi$ | $1.05457168(18) \times 10^{-34}$ J s<br>$6.58211915(56) \times 10^{-16}$ eV s |
| n.u. of mass: electron mass | $m_e$ | $9.1093826(16) \times 10^{-31}$ kg |
| n.u. of energy | $m_e c^2$ | $8.1871047(14) \times 10^{-14}$ J<br>0.510998918(44) MeV |
| n.u. of momentum | $m_e c$ | $2.73092419(47) \times 10^{-22}$ kg m/s<br>0.510998918(44) MeV/$c$ |
| n.u. of length | $\lambda\!\!\!^{-}_C = \hbar/m_e c$ | $386.1592678(26) \times 10^{-15}$ m |
| n.u. of time | $\hbar/m_e c^2$ | $1.2880886677(86) \times 10^{-21}$ s |

**Table 1.2-13** Atomic units (a.u.)

| Unit | Symbol and definition | Value in SI units |
|---|---|---|
| a.u. of charge: elementary charge | $e$ | $1.60217653(14) \times 10^{-19}$ C |
| a.u. of mass: electron mass | $m_e$ | $9.1093826(16) \times 10^{-31}$ kg |
| a.u. of action: reduced Planck constant | $\hbar = h/2\pi$ | $1.05457168(18) \times 10^{-34}$ J s |
| a.u. of length, 1 bohr: Bohr radius | $a_0 = \alpha/(4\pi R_\infty)$ | $0.5291772108(18) \times 10^{-10}$ m |
| a.u. of energy, 1 hartree: Hartree energy [a] | $E_H$ | $4.35974417(75) \times 10^{-18}$ J |
| a.u. of time | $\hbar/E_H$ | $2.418884326505(16) \times 10^{-17}$ s |
| a.u. of force | $E_H/a_0$ | $8.2387225(14) \times 10^{-8}$ N |
| a.u. of velocity | $\alpha c = a_0 E_H/\hbar$ | $2.1876912633(73) \times 10^{6}$ m/s |
| a.u. of momentum | $\hbar/a_0$ | $1.99285166(34) \times 10^{-24}$ kg m/s |
| a.u. of current | $eE_H/\hbar$ | $6.62361782(57) \times 10^{-3}$ A |
| a.u. of charge density | $e/a_0^3$ | $1.081202317(93) \times 10^{12}$ C/m$^3$ |
| a.u. of electric potential | $E_H/e$ | 27.2113845(23) V |
| a.u. of electric field | $E_H/(ea_0)$ | $5.14220642(44) \times 10^{11}$ V/m |
| a.u. of electric dipole moment | $ea_0$ | $8.47835309(73) \times 10^{-30}$ C m |
| a.u. of electric polarizability | $e^2a_0^2/E_H$ | $1.648777274(16) \times 10^{-41}$ C$^2$ m$^2$/J |
| a.u. of magnetic field $B$ | $\hbar/(ea_0^2)$ | $2.35051742(20) \times 10^{5}$ T |
| a.u. of magnetic dipole moment ($2\mu_B$) | $2\mu_B = \hbar e/m_e$ | $1.85480190(16) \times 10^{-23}$ J/T |
| a.u. of magnetizability | $e^2a_0^2/m_e$ | $7.89103660(13) \times 10^{-29}$ J/T$^2$ |
| a.u. of permittivity | $e^2/(a_0E_H)$ | Fixed by definition as: $10^7/c^2 = 1.112650056...10^{-10}$ F/m |

[a] The Hartree energy is defined as $E_H = e^2/(4\pi\varepsilon_0 a_0) = 2R_\infty hc = \alpha^2 m_e c^2$.

**Table 1.2-14** Units of some special X-ray-related quantities

| Unit | Definition | Symbol | Value in SI units |
|---|---|---|---|
| Cu X unit | $\lambda(\mathrm{CuK}\alpha_1)/1537.400$ | $\mathrm{xu(CuK}\alpha_1)$ | $1.00207710(29) \times 10^{-13}$ m |
| Mo X unit | $\lambda(\mathrm{MoK}\alpha_1)/707.831$ | $\mathrm{xu(MoK}\alpha_1)$ | $1.00209966(53) \times 10^{-13}$ m |
| angstrom star | $\lambda(\mathrm{WK}\alpha_1)/0.2090100$ | Å* | $1.00001509(90) \times 10^{-10}$ m |
| Lattice parameter [a] of Si (in vacuum, at 22.5 °C) | | $a$ | $543.102122(20) \times 10^{-12}$ m |
| (220) lattice spacing of Si (in vacuum, at 22.5 °C) | $d_{220} = a/\sqrt{8}$ | $d_{220}$ | $192.0155965(70) \times 10^{-12}$ m |
| Molar volume of Si (in vacuum, at 22.5 °C) | $V_m(\mathrm{Si}) = N_A a^3/8$ | $V_m(\mathrm{Si})$ | $12.0588382(24) \times 10^{-6}$ m$^3$/mol |

[a] This is the lattice parameter (unit cell edge length) of an ideal single crystal of naturally occurring silicon free from impurities and imperfections, and is deduced from measurements on extremely pure, nearly perfect single crystals of Si by correcting for the effects of impurities.

Table 1.2-15 lists some other units which are common in older texts. For current texts, it should be noted that if these units are used, the advantages of the SI are lost. The relation of these units to SI units should be specified in every document in which they are used.

For some selected quantities, there exists an international agreement that the numerical values of these quantities measured in SI units are fixed at the values given in Table 1.2-16.

**Table 1.2-15** Examples of other non-SI units

| Unit | Symbol | Value in SI units |
|---|---|---|
| curie [a] | Ci | $1\,\text{Ci} = 3.7\times10^{10}\,\text{Bq}$ |
| röntgen [b] | R | $1\,\text{R} = 2.58\times10^{-4}\,\text{C/kg}$ |
| rad [c,d] | rad | $1\,\text{rad} = 1\,\text{cGy} = 10^{-2}\,\text{Gy}$ |
| rem [d,e] | rem | $1\,\text{rem} = 1\,\text{cSv} = 10^{-2}\,\text{Sv}$ |
| X unit [f] | | $1\,\text{X unit} \cong 1.002\times10^{-4}\,\text{nm}$ |
| gamma [d] | $\gamma$ | $1\,\gamma = 1\,\text{nT} = 10^{-9}\,\text{T}$ |
| jansky | Jy | $1\,\text{Jy} = 10^{-26}\,\text{W}/(\text{m}^2\,\text{Hz})$ |
| fermi [d] | | $1\,\text{fermi} = 1\,\text{fm} = 10^{-15}\,\text{m}$ |
| metric carat [g] | | $1\,\text{metric carat} = 200\,\text{mg} = 2\times10^{-4}\,\text{kg}$ |
| torr | Torr | $1\,\text{Torr} = (101\,325/760)\,\text{Pa}$ |
| standard atmosphere | atm [h] | $1\,\text{atm} = 101\,325\,\text{Pa}$ |
| calorie | cal | [i] |
| micron [j] | $\mu$ | $1\,\mu = 1\,\mu\text{m} = 10^{-6}\,\text{m}$ |

[a] The curie is a special unit employed in nuclear physics to express the activity of radionuclides.

[b] The röntgen is a special unit employed to express exposure to X-ray or $\gamma$ radiation.

[c] The rad is a special unit employed to express absorbed dose of ionizing radiation. When there is a risk of confusion with the symbol for the radian, rd may be used as the symbol for $10^{-2}$ Gy.

[e] The rem is a special unit used in radioprotection to express dose equivalent.

[f] The X unit was employed to express wavelengths of X-rays. Its relationship to SI units is an approximate one.

[d] Note that this non-SI unit is exactly equivalent to an SI unit with an appropriate submultiple prefix.

[g] The metric carat was adopted by the 4th CGPM in 1907 for commercial dealings in diamonds, pearls, and precious stones.

[h] Resolution 4 of the 10th CGPM, 1954. The designation "standard atmosphere" for a reference pressure of 101 325 Pa is still acceptable.

[i] Several "calories" have been in use:
- the 15 °C calorie: $1\,\text{cal}_{15} = 4.1855\,\text{J}$ (value adopted by the CIPM in 1950);
- the IT (International Table) calorie: $1\,\text{cal}_{\text{IT}} = 4.1868\,\text{J}$ (5th International Conference on the Properties of Steam, London, 1956);
- the thermochemical calorie: $1\,\text{cal}_{\text{th}} = 4.184\,\text{J}$.

[j] The micron and its symbol, adopted by the CIPM in 1879 and repeated in Resolution 7 of the 9th CGPM (1948), were abolished by the 13th CGPM (1967–1968).

**Table 1.2-16** Internationally adopted numerical values for selected quantities

| Quantity | Symbol | Numerical value | Unit |
|---|---|---|---|
| Relative atomic mass [a] of $^{12}$C | $A_r(^{12}\text{C})$ | 12 | |
| Molar mass constant | $M_u$ | $1\times10^{-3}$ | kg/mol |
| Molar mass of $^{12}$C | $M(^{12}\text{C})$ | $12\times10^{-3}$ | kg/mol |
| Conventional value of the Josephson constant [b] | $K_{J\text{-}90}$ | 483 597.9 | GHz/V |
| Conventional value of the von Klitzing constant [c] | $R_{K\text{-}90}$ | 25 812.807 | Ω |
| Standard atmosphere | | 101 325 | Pa |
| Standard acceleration of free fall [d] | $g_n$ | 9.80665 | $\text{m/s}^2$ |

[a] The relative atomic mass $A_r(X)$ of a particle $X$ with mass $m(X)$ is defined by $A_r(X) = m(X)/m_u$, where $m_u = m(^{12}\text{C})/12 = M_u/N_A = 1\,\text{u}$ is the atomic mass constant, $M_u$ is the molar mass constant, $N_A$ is the Avogadro number, and u is the (unified) atomic mass unit. Thus the mass of a particle $X$ is $m(X) = A_r(X)\,\text{u}$ and the molar mass of $X$ is $M(X) = A_r(X)M_u$.

[b] This is the value adopted internationally for realizing representations of the volt using the Josephson effect.

[c] This is the value adopted internationally for realizing representations of the ohm using the quantum Hall effect.

[d] The value given was adopted by the 3rd General Conference on Weights and Measures (CGPM), 1903, and was the conventional value used to calculate the now obsolete unit kilogram force.

## 1.2.7 Some Energy Equivalents

In science and technology, energy is measured in many different units. Different units are used depending on the field of application, but owing to the different possible forms of the energy concerned, it is possible also to express the energy in terms of other quantities. All forms of the energy, however, are quantitatively related to one another and are therefore considered as being equivalent. Some of the most important equivalence relations are

$$E = eU = mc^2 = hc/\lambda = h\nu = kT \ .$$

These equations tell us that a given energy $E$, which is usually measured either in units of joule (J) or units of the Hartree energy ($E_\mathrm{H} = 1$ hartree), can also be specified by giving a voltage $U$, a mass $m$, a wavelength $\lambda$, a frequency $\nu$, or a temperature $T$. These equations contain, in addition to those variables, only well-known fundamental constants.

Table 1.2-17 gives the values of the energy equivalents of the joule and the hartree and for the SI units corresponding to the five quantities $U$, $m$, $\lambda$, $\nu$, and $T$. The equivalents have been calculated on the basis of the 2002 CODATA adjustment of the values of the constants.

**Table 1.2-17** Energy equivalents, expressed in the units joule (J), hartree ($E_\mathrm{H}$), volt (V), kilogram (kg), (unified) atomic mass unit (u), reciprocal meter ($\mathrm{m}^{-1}$), hertz (Hz), and kelvin (K)

| | Unit | | | |
|---|---|---|---|---|
| **Energy** | **Joule** | **Hartree** | **Volt** | **Kilogram** |
| 1 J | (1 J) $= 1$ J | (1 J) $= 2.29371257(39) \times 10^{17}\ E_\mathrm{H}$ | (1 J) $= 6.24150947(53) \times 10^{18}$ eV | (1 J)$/c^2$ $= 1.112650056 \times 10^{-17}$ kg |
| 1 $E_\mathrm{H}$ | (1 $E_\mathrm{H}$) $= 4.35974417(75) \times 10^{-18}$ J | (1 $E_\mathrm{H}$) $= 1\ E_\mathrm{H}$ | (1 $E_\mathrm{H}$) $= 27.2113845(23)$ eV | (1 $E_\mathrm{H}$)$/c^2$ $= 4.85086960(83) \times 10^{-35}$ kg |
| 1 eV | (1 eV) $= 1.60217653(14) \times 10^{-19}$ J | (1 eV) $= 3.67493245(31) \times 10^{-2}\ E_\mathrm{H}$ | (1 eV) $= 1$ eV | (1 eV)$/c^2$ $= 1.78266181(15) \times 10^{-36}$ kg |
| 1 kg | (1 kg) $c^2$ $= 8.987551787 \times 10^{16}$ J | (1 kg) $c^2$ $= 2.06148605(35) \times 10^{34}\ E_\mathrm{H}$ | (1 kg) $c^2$ $= 5.60958896(48) \times 10^{35}$ eV | (1 kg) $= 1$ kg |
| 1 u | (1 u) $c^2$ $= 1.49241790(26) \times 10^{-10}$ J | (1 u) $c^2$ $= 3.423177686(23) \times 10^{7}\ E_\mathrm{H}$ | (1 u) $c^2$ $= 931.494043(80) \times 10^{6}$ eV | (1 u) $= 1.66053886(28) \times 10^{-27}$ kg |
| 1 $\mathrm{m}^{-1}$ | (1 $\mathrm{m}^{-1}$) $hc$ $= 1.98644561(34) \times 10^{-25}$ J | (1 $\mathrm{m}^{-1}$) $hc$ $= 4.556335252760(30) \times 10^{-8}\ E_\mathrm{H}$ | (1 $\mathrm{m}^{-1}$) $hc$ $= 1.23984191(11) \times 10^{-6}$ eV | (1 $\mathrm{m}^{-1}$) $h/c$ $= 2.21021881(38) \times 10^{-42}$ kg |
| 1 Hz | (1 Hz) $h$ $= 6.6260693(11) \times 10^{-34}$ J | (1 Hz) $h$ $= 1.519829846006(10) \times 10^{-16}\ E_\mathrm{H}$ | (1 Hz) $h$ $= 4.13566743(35) \times 10^{-15}$ eV | (1 Hz) $h/c^2$ $= 7.3724964(13) \times 10^{-51}$ kg |
| 1 K | (1 K) $k$ $= 1.3806505(24) \times 10^{-23}$ J | (1 K) $k$ $= 3.1668153(55) \times 10^{-6}\ E_\mathrm{H}$ | (1 K) $k$ $= 8.617343(15) \times 10^{-5}$ eV | (1 K) $k/c^2$ $= 1.5361808(27) \times 10^{-40}$ kg |
| | **Unit** | | | |
| **Energy** | **Atomic mass unit** | **Reciprocal meter** | **Hertz** | **Kelvin** |
| 1 J | (1 J)$/c^2$ $= 6.7005361(11) \times 10^{9}$ u | (1 J)$/hc$ $= 5.03411720(86) \times 10^{24}\ \mathrm{m}^{-1}$ | (1 J)$/h$ $= 1.50919037(26) \times 10^{33}$ Hz | (1 J)$/k$ $= 7.242963(13) \times 10^{22}$ K |
| 1 $E_\mathrm{H}$ | (1 $E_\mathrm{H}$)$/c^2$ $= 2.921262323(19) \times 10^{-8}$ u | (1 $E_\mathrm{H}$)$/hc$ $= 2.194746313705(15) \times 10^{7}\ \mathrm{m}^{-1}$ | (1 $E_\mathrm{H}$)$/h$ $= 6.579683920721(44) \times 10^{15}$ Hz | (1 $E_\mathrm{H}$)$/k$ $= 3.1577465(55) \times 10^{5}$ K |
| 1 eV | (1 eV)$/c^2$ $= 1.073544171(92) \times 10^{-9}$ u | (1 eV)$/hc$ $= 8.06554445(69) \times 10^{5}\ \mathrm{m}^{-1}$ | (1 eV)$/h$ $= 2.41798940(21) \times 10^{14}$ Hz | (1 eV)$/k$ $= 1.1604505(20) \times 10^{4}$ K |
| 1 kg | (1 kg) $= 6.0221415(10) \times 10^{26}$ u | (1 kg) $c/h$ $= 4.52443891(77) \times 10^{41}\ \mathrm{m}^{-1}$ | (1 kg) $c^2/h$ $= 1.35639266(23) \times 10^{50}$ Hz | (1 kg) $c^2/k$ $= 6.509650(11) \times 10^{39}$ K |
| 1 u | (1 u) $= 1$ u | (1 u) $c/h$ $= 7.513006608(50) \times 10^{14}\ \mathrm{m}^{-1}$ | (1 u) $c^2/h$ $= 2.252342718(15) \times 10^{23}$ Hz | (1 u) $c^2/k$ $= 1.0809527(19) \times 10^{13}$ K |
| 1 $\mathrm{m}^{-1}$ | (1 $\mathrm{m}^{-1}$) $h/c$ $= 1.3310250506(89) \times 10^{-15}$ u | (1 $\mathrm{m}^{-1}$) $= 1\ \mathrm{m}^{-1}$ | (1 $\mathrm{m}^{-1}$) $c$ $= 299\,792\,458$ Hz | (1 $\mathrm{m}^{-1}$) $hc/k$ $= 1.4387752(25) \times 10^{-2}$ K |
| 1 Hz | (1 Hz) $h/c^2$ $= 4.439821667(30) \times 10^{-24}$ u | (1 Hz)$/c$ $= 3.335640951 \times 10^{-9}\ \mathrm{m}^{-1}$ | (1 Hz) $= 1$ Hz | (1 Hz) $h/k$ $= 4.7992374(84) \times 10^{-11}$ K |
| 1 K | (1 K) $k/c^2$ $= 9.251098(16) \times 10^{-14}$ u | (1 K) $k/hc$ $= 69.50356(12)\ \mathrm{m}^{-1}$ | (1 K) $k/h$ $= 2.0836644(36) \times 10^{10}$ Hz | (1 K) $= 1$ K |

## References

2.1 Bureau International des Poids et Mesures: *Le système international d'unités*, 7th edn. (Bureau International des Poids et Mesures, Sèvres 1998)

2.2 Organisation Intergouvernementale de la Convention du Mètre: *The International System of Units (SI), Addenda and Corrigenda to the 7th Edition* (Bureau International des Poids et Mesures, Sèvres 2000)

# 1.3. Rudiments of Crystallography

Crystallography deals basically with the question "Where are the atoms in solids?" The purpose of this section is to introduce briefly the basics of modern crystallography. The focus is on the description of periodic solids, which represent the major proportion of condensed matter. A coherent introduction to the formalism required to do this is given, and the basic concepts and technical terms are briefly explained. Paying attention to recent developments in materials research, we treat aperiodic, disordered, and amorphous materials as well. Consequently, besides the conventional three-dimensional (3-D) descriptions, the higher-dimensional crystallographic approach is outlined, and so is the atomic pair distribution function used to describe local phenomena. The section is concluded by touching on the basics of diffraction methods, the most powerful tool kit used by experimentalists dealing with structure at the atomic level in the solid state.

1.3.1 **Crystalline Materials** ..... 28
1.3.1.1 Periodic Materials ..... 28
1.3.1.2 Aperiodic Materials ..... 33
1.3.2 **Disorder** ..... 38
1.3.3 **Amorphous Materials** ..... 39
1.3.4 **Methods for Investigating Crystallographic Structure** ..... 39
**References** ..... 41



The structure of a solid material is very important, because the physical properties are closely related to the structure. In most cases solids are crystalline: they may consist of one single crystal, or be polycrystalline, consisting of many tiny single crystals in different orientations. All periodic crystals have a perfect translational symmetry. This leads to selection rules, which are very useful for the understanding of the physical properties of solids. Therefore, most textbooks on solid-state physics begin with some chapters on symmetry and structure. Today we know that other solids, which have no translational symmetry, also exist. These are amorphous materials, which have little order (in most cases restricted to the short-range arrangement of the atoms), and aperiodic crystals, which show perfect long-range order, but no periodicity – at least in 3-D space. In this chapter of the book, the basic concepts of crystallography – how the space of a solid can be filled with atoms – are briefly discussed. Readers who want to inform themselves in more detail about crystallography are referred to the classic textbooks [3.1–5].

Many crystalline materials, especially minerals and gems, were described more than 2000 years ago. The regular form of crystals and the existence of facets, which have fixed angles between them, gave rise to a belief that crystals were formed by a regular repetition of tiny, identical building blocks. After the discovery of X-rays by Röntgen, Laue investigated crystals in 1912 using these X-rays and detected interference effects caused by the periodic array of atoms. One year later, Bragg determined the crystal structures of alkali halides by X-ray diffraction.

Today we know that a crystal is a 3-D array of atoms or molecules, with various types of long-range order. A more modern definition is that all materials which show sharp diffraction peaks are crystalline. In this sense, aperiodic or quasicrystalline materials, as well as periodic materials, are crystals. A real crystal is never a perfect arrangement. Defects in the form of vacancies, dislocations, impurities, and other imperfections are often very important for the physical properties of a crystal. This aspect has been largely neglected in classical crystallography but is becoming more and more a topic of modern crystallographic investigations [3.6, 7].

As indicated in Table 1.3-1, condensed matter can be classified as either crystalline or amorphous. Both of these states and their formal subdivisions will be discussed in the following. The terms "matter", "structure", and "material" always refer to single-phase solids.

**Table 1.3-1** Classification of solids

| Condensed matter (solids) | | | | |
|---|---|---|---|---|
| Crystalline materials | | | | Amorphous materials |
| Periodic structures | Aperiodic structures | | | |
| | Modulated structures | Composite structures | Quasicrystals | |

## 1.3.1 Crystalline Materials

### 1.3.1.1 Periodic Materials



#### Lattice Concept

A periodic crystal is described by two entities, the *lattice* and the *basis*. The (translational) lattice is a perfect geometrical array of points. All lattice points are equivalent and have identical surroundings. This lattice is defined by three fundamental translation vectors $\boldsymbol{a}, \boldsymbol{b}, \boldsymbol{c}$. Starting from an arbitrarily chosen origin of the lattice, any other lattice point can be reached by a translation vector $\boldsymbol{r}$ that satisfies

$$\boldsymbol{r} = u\boldsymbol{a} + v\boldsymbol{b} + w\boldsymbol{c} \ ,$$

where $u$, $v$, and $w$ are arbitrary integers.

The lattice is an abstract mathematical construction; the description of the crystal is completed by attaching a set of atoms – the basis – to each lattice point. Therefore the crystal structure is formed by a lattice and a basis (see Fig. 1.3-1).

The parallelepiped that is defined by the axes $\boldsymbol{a}, \boldsymbol{b}, \boldsymbol{c}$ is called a *primitive cell* if this cell has the smallest volume out of all possible cells. It contains one lattice point per cell only (Fig. 1.3-2a). This cell is a type of unit cell which fills the space of the crystal completely under the application of the translation operations of the lattice, i. e. movements along the vectors $\boldsymbol{r}$.

Conventionally, the smallest cell with the highest symmetry is chosen. Crystal lattices can be transformed into themselves by translation along the fundamental vectors $\boldsymbol{a}, \boldsymbol{b}, \boldsymbol{c}$, but also by other symmetry operations. It can be shown that only onefold (rotation angle $\varphi = 2\pi/1$), twofold ($2\pi/2$), threefold ($2\pi/3$), fourfold ($2\pi/4$), and sixfold ($2\pi/6$) rotation axes are permissible. Other rotational axes cannot exist in a lattice, because they would violate the translational symmetry. For example, it is not possible to fill the space completely with a fivefold ($2\pi/5$) array of regular pentagons. Additionally, mirror planes and centers of inversion may exist. The restriction to high-symmetry cells may also lead to what is known as centering. Figure 1.3-2b illustrates a 2-D case. The centering types in 3-D are listed in Table 1.3-2.

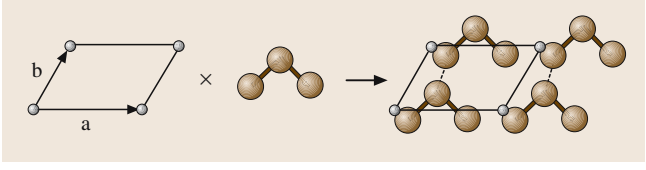


**Fig. 1.3-1** A periodic crystal can be described as a convolution of a mathematical point lattice with a basis (set of atoms). *Open circles*, mathematical points; *filled circles*, atoms

#### Planes and Directions in Lattices

If one peers through a 3-D lattice from various angles, an infinity of equidistant planes can be seen. The position and orientation of such a crystal plane are determined by three points. It is easy to describe a plane if all three points lie on crystal axes (i. e. the directions of unit cell vectors); in this case only the intercepts need to be used. It is common to use *Miller indices* to de-

**Table 1.3-2** Centering types for 3-D crystallographic unit cells

| Symbol | Description | Points per unit cell |
|---|---|---|
| $P$ | No centering (primitive) | 1 |
| $I$ | Body-centered (*innenzentriert*) | 2 |
| $F$ | All-face-centered | 4 |
| $S$; $A$, $B$, $C$ in specific cases | One-face-centered (*seitenzentriert*); $(\boldsymbol{b}, \boldsymbol{c})$, $(\boldsymbol{a}, \boldsymbol{c})$, and $(\boldsymbol{a}, \boldsymbol{b})$, respectively, in specific cases | 2 |
| $R$ | Hexagonal cell, rhombohedrally centered | 3 |

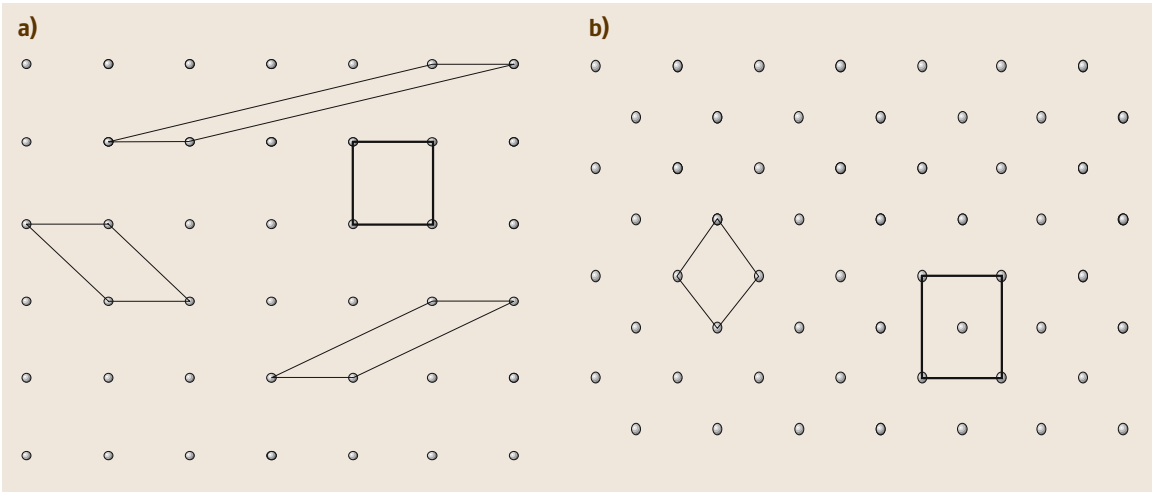


**Fig. 1.3-2a,b** Possible primitive and centered cells in 2-D lattices. *Open circles* denote mathematical points. **(a)** In this lattice, the conventional cell is the *bold square cell* because of its highest symmetry, 4*mm*. **(b)** Here, convention prefers 90° angles: a centered cell of symmetry 2*mm* is chosen. It contains two lattice points and is twice the area of the primitive cell

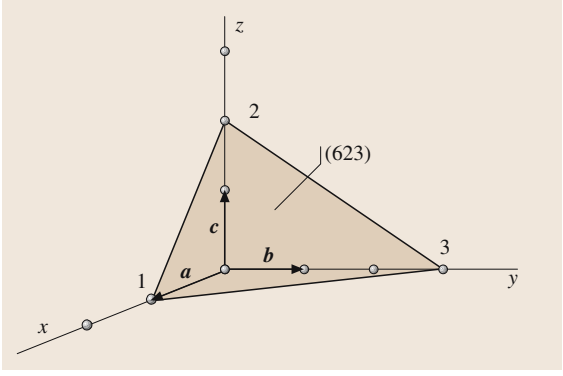


**Fig. 1.3-3** Miller indices: the intercepts of the (623) plane with the coordinate axes

scribe lattice planes. These indices are determined as follows:

1. For the plane of interest, determine the intercepts $x, y, z$ of the crystal axes $\boldsymbol{a}, \boldsymbol{b}, \boldsymbol{c}$.
2. Express the intercepts in terms of the basic vectors $\boldsymbol{a}, \boldsymbol{b}, \boldsymbol{c}$ of the unit cell, i. e. as $x/a$, $y/b$, $z/c$ (where $a = |\boldsymbol{a}|, \ldots$).
3. Form the reciprocals $a/x, b/y, c/z$.
4. Reduce this set to the smallest integers $h, k, l$. The result is written $(hkl)$.

The distance from the origin to the plane $(hkl)$ inside the unit cell is the interplanar spacing $d_{hkl}$. Negative intercepts, leading to negative Miller indices, are written as $\bar{h}$. Figure 1.3-3 shows a (623) plane and its construction.

A direction in a crystal is given as a set of three integers in square brackets $[uvw]$; $u$, $v$, and $w$ correspond to the above definition of the translation vector $\boldsymbol{r}$. A direction in a cubic crystal can be described also by Miller indices, as a plane can be defined by its normal. The indices of a direction are expressed as the smallest integers which have the same ratio as the components of a vector (expressed in terms of the axis vectors $\boldsymbol{a}, \boldsymbol{b}, \boldsymbol{c}$) in that direction. Thus the sets of integers 1, 1, 1 and 3, 3, 3 represent the same direction in a crystal, but the indices of the direction are [111] and not [333]. To give another example, the $x$ axis of an orthogonal $x$, $y$, $z$ coordinate system has Miller indices [100]; the plane perpendicular to this direction has indices (100).

For all crystals, except for the hexagonal system, the Miller indices are given in a three-digit system in the form $(hkl)$. However, for the hexagonal system, it is common to use four digits $(hkil)$. The four-digit hexagonal indices are based on a coordinate system containing four axes. Three axes lie in the basal plane of the hexagon, crossing at angles of 120°: $\boldsymbol{a}, \boldsymbol{b}$, and $-(\boldsymbol{a}+\boldsymbol{b})$. As the third vector in the basal plane can be expressed in terms of $\boldsymbol{a}$ and $\boldsymbol{b}$, the index can be expressed in terms of $h$ and $k$: $i = -(h+k)$. The fourth axis is the $\boldsymbol{c}$ axis normal to the basal plane.

### Crystal Morphology

The regular facets of a crystal are planes of the type described above. Here, the lattice architecture of the crystal is visible macroscopically at the surface. Figure 1.3-4 shows some surfaces of a cubic crystal. If the crystal had the shape or morphology of a cube, this would be described by the set of facets {(100), (010), (001), ($\bar{1}$00), (0$\bar{1}$0), (00$\bar{1}$)}. An octahedron would be described by {(111), ($\bar{1}$11), (1$\bar{1}$1), (11$\bar{1}$), ($\bar{1}\bar{1}\bar{1}$), (1$\bar{1}\bar{1}$), ($\bar{1}$1$\bar{1}$), ($\bar{1}\bar{1}$1)}. The morphology of a crystalline material may be of technological interest (in relation to the bulk density, flow properties, etc.) and can be influenced in various ways, for example by additives during the crystallization process.

### The 32 Crystallographic Point Groups

The symmetry of the space surrounding a lattice point can be described by the point group, which is a set of symmetry elements acting on the lattice. The crystallographic symbols for the symmetry elements of point groups compatible with a translational lattice are the rotation axes 1, 2, 3, 4, and 6, mirror planes $m$, and the center of inversion $\bar{1}$. Figure 1.3-5 illustrates, as an example, the point group $2/m$. The "2" denotes a twofold axis perpendicular ("/") to a mirror plane "$m$". Note that this combination of 2 and $m$ implies, or generates automatically, an inversion center $\bar{1}$. We have used the Hermann–Mauguin notation here; however, point groups of isolated molecules are more often denoted by the Schoenflies symbols. For a translation list, see Table 1.3-3.

No crystal can have a higher point group symmetry than the point group of its lattice, called the *holohedry*. In accordance with the various rotational symmetries,

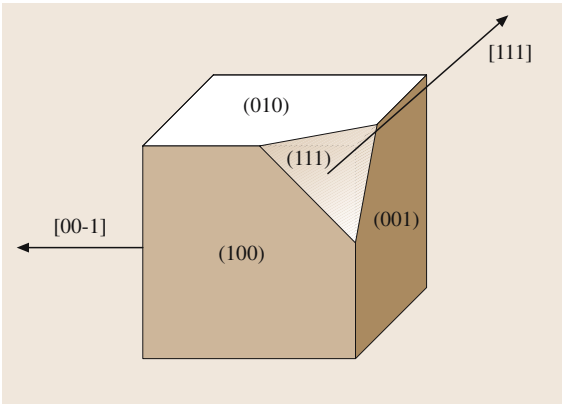


**Fig. 1.3-4** Some crystal planes and directions in a cubic crystal, and their Miller indices

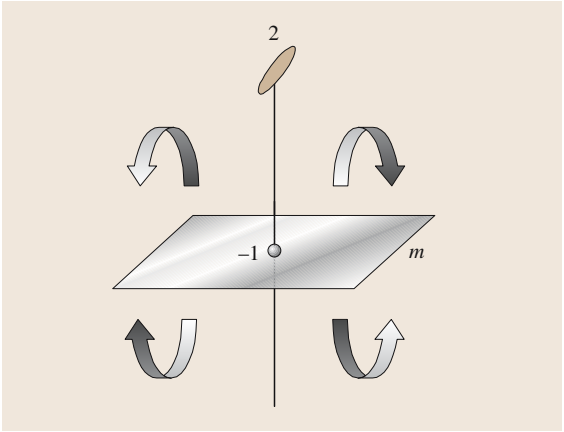


**Fig. 1.3-5** The point group $2/m$ ($C_{2h}$). Any object in space can be rotated by $\varphi = 2\pi/2$ around the twofold rotational axis 2 and reflected by the perpendicular mirror plane $m$, generating identical copies. The inversion center $\bar{1}$ is implied by the coupling of 2 and $m$

there are seven crystal systems (see Table 1.3-3), and the seven holohedries are $\bar{1}$, $2/m$, $mmm$, $4/mmm$, $\bar{3}m$, $6/mmm$, and $m\bar{3}m$. Other, less symmetric, point groups are also compatible with these lattices, leading to a total number of 32 crystallographic point groups (see Table 1.3-4). A lower symmetry than the holohedry can be introduced by a less symmetric basis in the unit cell.

Since $\bar{3}m$ and $6/mmm$ are included in the same point lattice, they are sometimes subsumed into the hexagonal crystal family. So there are seven crystal systems but six crystal families. Note further that rhombohedral symmetry is a special case of centering ($R$-centering) of the trigonal crystal system and offers two equivalent possibilities for selecting the cell parameters: hexagonal or rhombohedral axes (see Table 1.3-4 again).

It can be shown that in 3-D there are 14 different periodic ways of arranging identical points. These 14 3-D periodic point lattices are called the (translational) Bravais lattices and are shown in Fig. 1.3-6. Table 1.3-4 presents data related to some of the crystallographic terms used here. The 1-D and 2-D space groups can be classified analogously but are omitted here.

### The 230 Crystallographic Space Groups

Owing to the 3-D translational periodicity, symmetry operations other than point group operations are possible in addition: these are *glide planes* and *screw axes*. A glide plane couples a mirror operation and a translational shift. The symbols for glide planes

**Table 1.3-3** The 32 crystallographic point groups: translation list from the Hermann–Mauguin to the Schoenflies notation

| Crystal system | Hermann–Mauguin symbol | Schoenflies symbol | Crystal system | Hermann–Mauguin symbol | Schoenflies symbol |
|---|---|---|---|---|---|
| Triclinic | 1 | $C_1$ | Trigonal | 3 | $C_3$ |
| | $\bar{1}$ | $C_i$ | | $\bar{3}$ | $C_{3i}$ |
| Monoclinic | 2 | $C_2$ | | 32 | $D_3$ |
| | $m$ | $C_s$ | | $3m$ | $C_{3v}$ |
| | $2/m$ | $C_{2h}$ | | $\bar{3}m$ | $D_{3d}$ |
| Orthorhombic | 222 | $D_2$ | Hexagonal | 6 | $C_6$ |
| | $mm2$ | $C_{2v}$ | | $\bar{6}$ | $C_{3h}$ |
| | $mmm$ | $D_{2h}$ | | $6/m$ | $C_{6h}$ |
| Tetragonal | 4 | $C_4$ | | 622 | $D_6$ |
| | $\bar{4}$ | $S_4$ | | $6mm$ | $C_{6v}$ |
| | $4/m$ | $C_{4h}$ | | $\bar{6}2m$ | $D_{3h}$ |
| | 422 | $D_4$ | | $6/mmm$ | $D_{6h}$ |
| | $4mm$ | $C_{4v}$ | Cubic | 23 | $T$ |
| | $\bar{4}2m$ | $D_{2d}$ | | $m\bar{3}$ | $T_h$ |
| | $4/mmm$ | $D_{4h}$ | | 432 | $O$ |
| | | | | $\bar{4}3m$ | $T_d$ |
| | | | | $m\bar{3}m$ | $O_h$ |

are $a$, $b$, and $c$ for translations along the lattice vectors $\boldsymbol{a}, \boldsymbol{b}$, and $\boldsymbol{c}$, respectively, and $n$ and $d$ for some special lattice vector combinations. A screw axis is always parallel to a rotational axis. The symbols are $2_1, 3_1, 3_2, 4_1, 4_2, 4_3, 6_1, 6_2, 6_3, 6_4$, and $6_5$, where, for example, $6_3$ means a rotation through an angle $\varphi = 2\pi/6$ followed by a translation of $3/6\,(= 1/2)$ of a full translational period along the sixfold axis.

Thus the combination of 3-D translational and point symmetry operations leads to an infinite number of sets of symmetry operations. Mathematically, each of these sets forms a group, and they are called *space groups*. It can be shown that all possible periodic crystals can be described by only 230 space groups. These 230 space groups are described in tables, for example the *International Tables for Crystallography* [3.8].

In this formalism, a conventional space group symbol reflects the symmetry elements, arranged in the order of standardized *blickrichtungen* (symmetry directions). We shall confine ourselves here to explain one instructive example: $P4_2/mcm$, space group number 132 [3.8]. The full space group symbol is $P\,4_2/m\,2/c\,2/m$. The mean-

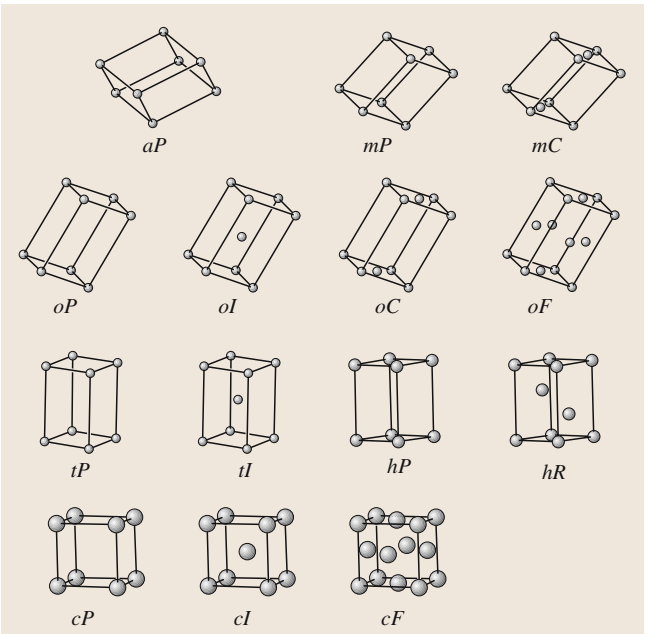


**Fig. 1.3-6** The 14 Bravais lattices

**Table 1.3-4** Crystal families, crystal systems, crystallographic point groups, conventional coordinate systems, and Bravais lattices in three dimensions. Lattice point symmetries (holohedries) are given in **bold**

| Crystal family | Symbol | Crystal system | Crystallographic point groups | No. of space groups | Conventional coordinate system | | Bravais lattice (Pearson symbol) |
|---|---|---|---|---|---|---|---|
| | | | | | Restrictions on cell parameters | Parameters to be determined | |
| Triclinic (*a*northic) | *a* | Triclinic | 1, $\bar{\mathbf{1}}$ | 2 | None | $a, b, c,$ $\alpha, \beta, \gamma$ | aP |
| *m*onoclinic | *m* | Monoclinic | 2, *m*, **2/*m*** | 13 | Setting with *b* unique: $\alpha = \gamma = 90°$ | $a, b, c,$ $\beta$ | mP, mS (mC, mA, mI) |
| | | | | | Setting with *c* unique: $\alpha = \beta = 90°$ | $a, b, c,$ $\gamma$ | mP, mS (mA, mB, mI) |
| *o*rthorhombic | *o* | Orthorhombic | 222, *mm*2, ***mmm*** | 59 | $\alpha = \beta = \gamma = 90°$ | $a, b, c$ | oP,oS, (oC, oA, oB) oI, oF |
| *t*etragonal | *t* | Tetragonal | 4, $\bar{4}$, 4/*m*, 422, 4*mm*, $\bar{4}2m$, **4/*mmm*** | 68 | $a = b$ $\alpha = \beta = \gamma = 90°$ | $a, c$ | tP, tI |
| *h*exagonal | *h* | Trigonal | 3, $\bar{3}$, 32, 3*m*, $\bar{\mathbf{3}}$***m*** | 18 | $a = b,$ $\alpha = \beta = 90°$ $\gamma = 120°$ (hexagonal axes) | $a, c$ | hP |
| | | | | 7 | $a = b = c$ $\alpha = \beta = \gamma \neq 90°$ (rhombohedral axes) | $a, \alpha$ | hR |
| | | Hexagonal | 6, $\bar{6}$, 6/*m*, 622, 6*mm*, $\bar{6}2m$, **6/*mmm*** | 27 | $a = b,$ $\alpha = \beta = 90°$ $\gamma = 120°$ | $a, c$ | hP |
| *c*ubic | *c* | Cubic | 23, $m\bar{3}$, 432, $\bar{4}3m$, $\boldsymbol{m\bar{3}m}$ | 36 | $a = b = c$ $\alpha = \beta = \gamma = 90°$ | $a$ | cP, cI,cF |



ing of the symbols is the following: *P* denotes a primitive Bravais lattice. It belongs to the tetragonal crystal system indicated by 4. Along the first standard *blickrichtung* [001] there is a $4_2$ screw axis with a perpendicular mirror plane *m*. Along [100] there is a twofold rotation axis, named 2, with a perpendicular glide plane *c* parallel to ***c***. Third, along [110] there is a twofold rotation axis 2, with a perpendicular mirror plane *m*.

### Decoration of the Lattice with the Basis

At this point we have to recall that in a real crystal structure we have not only the lattice, but also the basis. In [3.8], there are standardized sets of general and special positions (i. e. coordinates $x, y, z$) within the unit cell (Wyckoff positions). An atom placed in a general position is transformed into more than one atom by the action of all symmetry operators of the respective space group. Special positions are located on special points which are mapped onto themselves by one or more symmetry operations – for example a position in a mirror plane or exactly on a rotational axis. Reference [3.8] also provides information about symmetry relations between individual space groups (group–subgroup relations). These are often useful for describing relationships between crystal structures and for describing phase transitions of materials.

The use of the space group allows us to further reduce the basis to the *asymmetric unit*: this is the minimal set of atoms that needs to be given so that the whole crystal structure can be generated via the symmetry of the space group. This represents the main power of a crystallographically correct description of a material: just some 10 parameters are sufficient to describe an ensemble of some $10^{23}$ atoms.

Thus, a crystallographically periodic structure of a material is unambiguously characterized by

- the cell parameters;
- the space group;
- the coordinates of the atoms (and their chemical type) in the asymmetric unit;
- the occupation and thermal displacement factors of the atoms in the asymmetric unit.

For an example, the reader is referred to the crystallographic description of the spinel structure of $MgAl_2O_4$ given below under the heading "Structure Types".

To complete the information on space group symmetries given here, periodic magnetic materials should also be mentioned. Magnetic materials contain magnetic moments carried by atoms in certain positions in the unit cell. If we take into account the magnetic moments in the description of the structure, the classification by space groups (the 230 "gray" groups, described above) has to be extended to 1651 the "black and white", or Shubnikov, groups [3.9]. A magnetic periodic structure is then characterized by

- the crystallographic structure;
- the Shubnikov group;
- the cell parameters of the magnetic unit cell;
- the coordinates of the atoms carrying magnetic moments (the asymmetric unit in the magnetic unit cell);
- the magnitude and direction of the magnetic moments on these atoms.

#### Structure Types

It is useful to classify the crystal structures of materials by the assignment of *structure types*. The structure type is based on a representative crystal structure, the parameters of which describe the essential crystallographic features of other materials of the same type. As an example, we consider the structure of the spinel oxides $AB_2O_4$. The generic structure type is $MgAl_2O_4$, cF56. The *Pearson symbol*, here cF56, denotes the cubic crystal family and a face-centered Bravais lattice with 56 atoms per unit cell (see Table 1.3-5 and also the last column in Table 1.3-4).

Regarding the free parameters, for example $a$, the notation 8.174(1) in Table 1.3-5 means $8.174 \pm 0.001$. The chemical formula and the unit cell contents can easily be calculated from the site multiplicities (given by the Wyckoff positions) and the occupancies. So can the (crystallographic) density, using the appropriate atomic masses.

There is a huge variety of other materials belonging to the same structure type as in this example. The only parameters that differ (slightly) are the numerical value of $a$, the types of atoms in the positions, the numerical value of the parameter $x$ for Wyckoff position 32*e*, and the occupancies. Thus, for example, the crystal structure of the iron sulfide $Fe_3S_4$ can be characterized in its essential features via the information that it belongs to the same structure type.

### 1.3.1.2 Aperiodic Materials

In addition to the crystalline periodic state of matter, a class of materials exists that lacks 3-D translational symmetry and is called *aperiodic*. Aperiodic materials cannot be described by any of the 230 space groups mentioned above. Nevertheless, they show another type of long-range order and are therefore included in the term "crystal". This notion of long-range order is the major feature that distinguishes crystals from amorphous materials. Three types of aperiodic order may

**Table 1.3-5** Complete crystallographic parameter set for $MgAl_2O_4$, spinel structure type

| | |
|---|---|
| Material | $MgAl_2O_4$ |
| Structure type | $MgAl_2O_4$, spinel |
| Pearson symbol | cF56 |
| Space group | $Fd\bar{3}m$ (No. 227) |
| $a$ (Å) | 8.174(1) |

| Atom | Wyckoff position | $x$ | $y$ | $z$ | Occupancy |
|---|---|---|---|---|---|
| Mg | 8*a* | 0 | 0 | 0 | 1.0 |
| Al | 16*d* | 5/8 | 5/8 | 5/8 | 1.0 |
| O | 32*e* | 0.3863(2) | $x$ | $x$ | 1.0 |

be distinguished, namely modulated structures, composite structures, and quasicrystals. All aperiodic solids exhibit an essentially discrete diffraction pattern and can be described as atomic structures obtained from a 3-D section of a $n$-dimensional ($n$-D) ($n > 3$) periodic structure.

### Modulated Structures

In a modulated structure, periodic deviations of the atomic parameters from a reference or basic structure are present. The basic structure can be understood as a periodic structure as described above. Periodic deviations of one or several of the following atomic parameters are superimposed on this basic structure:

- atomic coordinates;
- occupancy factors;
- thermal displacement factors;
- orientations of magnetic moments.

Let the period of the basic structure be $a$ and the modulation wavelength be $\lambda$; the ratio $a/\lambda$ may be (1) a rational or (2) an irrational number (Fig. 1.3-7). In case (1), the structure is commensurately modulated; we observe a $qa$ superstructure, where $q = 1/\lambda$. This superstructure is periodic. In case (2), the structure is incommensurately modulated. Of course, the experimental distinction between the two cases is limited by the finite experimental resolution. $q$ may be a function of external variables such as temperature, pressure, or chemical composition, i. e. $q = f(T, p, X)$, and may adopt a rational value to result in a commensurate "lock-in" structure. On the other hand, an incommensurate charge-density wave may exist; this can be moved through a basic crystal without changing the internal energy $U$ of the crystal.

When a 1-D basic structure and its modulation function are combined in a 2-D hyperspace $\boldsymbol{R} = \boldsymbol{R}^{\text{parallel}} \oplus \boldsymbol{R}^{\text{perpendicular}}$, periodicity on a 2-D lattice results. The real atoms are generated by the intersection of the 1-D physical (external, parallel) space $\boldsymbol{R}^{\text{parallel}}$ with the hyperatoms in the complementary 1-D internal space $\boldsymbol{R}^{\text{perpendicular}}$. In the case of a modulated structure, the hyperatoms have the shape of the sinusoidal modulation function in $\boldsymbol{R}^{\text{perpendicular}}$.

Figure 1.3-8 illustrates this construction. We have to choose a basis $(\boldsymbol{a}_1, \boldsymbol{a}_2)$ in $\boldsymbol{R}$ where the slope of $\boldsymbol{a}_1$ with respect to $\boldsymbol{R}^{\text{parallel}}$ corresponds to the length of the modulation $\lambda$.

It is clear that real atomic structures are always manifestations of matter in 3-D real, physical space. The cutting of the 2-D hyperspace to obtain real 1-D atoms illustrated in Fig. 1.3-8 may serve as an instructive basic example of the concept of higher-dimensional ($n$-D, $n > 3$) crystallography. The concept is also called a superspace description; it applies to all aperiodic structures and provides a convenient finite set of variables that can be used to compute the positions of all atoms in the real 3-D structure.

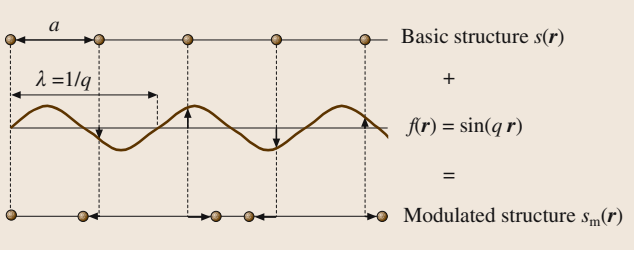


**Fig. 1.3-7** A 1-D modulated structure $s_{\text{m}}(\boldsymbol{r})$ can be described as a sum of a basic structure $s(\boldsymbol{r})$ and a modulation function $f(\boldsymbol{r})$ of its atomic coordinates. If $a/\lambda$ is irrational, the structure is incommensurately modulated. *Circles* denote atoms

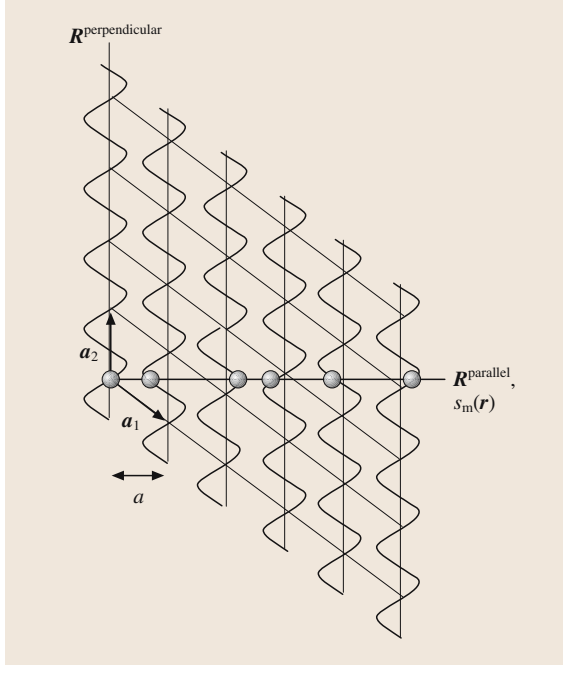


**Fig. 1.3-8** 2-D hyperspace description of the example of Fig. 1.3-7. The basis of the hyperspace $\boldsymbol{R} = \boldsymbol{R}^{\text{parallel}} \oplus \boldsymbol{R}^{\text{perpendicular}}$ is $(\boldsymbol{a}_1, \boldsymbol{a}_2)$; the slope of $\boldsymbol{a}_1$ with respect to $\boldsymbol{R}^{\text{parallel}}$ is proportional to $\lambda$. Atoms of the modulated structure $s_{\text{m}}(\boldsymbol{r})$ occur in the physical space $\boldsymbol{R}^{\text{parallel}}$ and are represented by *circles*

The modulation may occur in one, two, or three directions of the basic structure, yielding 1-D, 2-D, or 3-D modulated structures. If we introduce one additional dimension per modulation vector (the direction $\boldsymbol{r}$ that the modulation corresponding to $\lambda$ runs along), these structures can be described as periodic in 4-D, 5-D, or 6-D superspace, respectively.

### Composite Structures

Composite crystals are crystalline structures that consist of two or more periodic substructures, each one having its own 3-D periodicity to a first approximation. The symmetry of each of these subsystems is characterized by one of the 230 space groups. However, owing to their mutual interaction, the true structure consists of a collection of incommensurately modulated subsystems. All known composite structures to date have at least one lattice direction in common and consist of a maximum of three substructures. There are three main classes:

- channel structures;
- columnar packings;
- layer packings.

These composite structures are also known as intergrowth or host–guest structures. Figure 1.3-9 illustrates an example of a host with channels along $\boldsymbol{a}$, in which atoms of the substructure with a periodicity $\lambda\boldsymbol{a}$ reside as a guest.

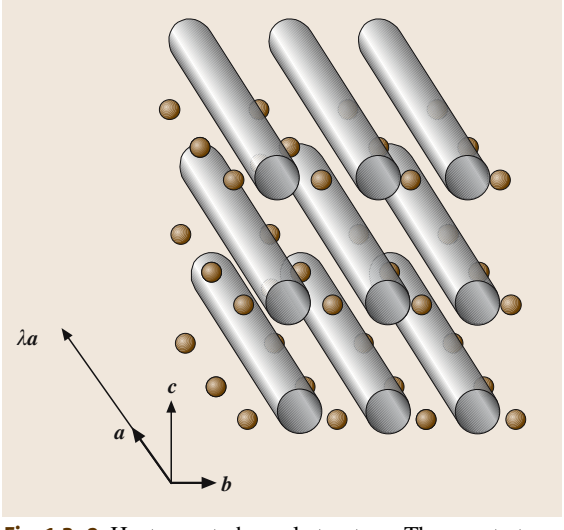


**Fig. 1.3-9** Host–guest channel structure. The guest atoms reside in channels parallel to $\boldsymbol{a}$, with a periodicity $\lambda\boldsymbol{a}$

The higher-dimensional $n$-D formalism ($n > 3$) used to describe composite structures is essentially the same as that which applies to modulated structures.

### Quasicrystals

Quasicrystals represent the third type of aperiodic materials. Quasiperiodicity may occur in one, two, or three dimensions of physical space and is associated with special irrational numbers such as the golden mean $\tau = (1+\sqrt{5})/2$, and $\xi = 2+\sqrt{3}$. The most remarkable feature of quasicrystals is the appearance of noncrystallographic point group symmetries in their diffraction patterns, such as $8/mmm$, $10/mmm$, $12/mmm$, and $2/m\bar{3}\bar{5}$. The golden mean is related to fivefold symmetry via the relation $\tau = 2\cos(\pi/5)$; $\tau$ can be considered as the "most irrational" number, since it is the irrational number that has the worst approximation by a truncated continued fraction,

$$\tau = 1 + \cfrac{1}{1 + \cfrac{1}{1 + \cfrac{1}{1 + \cfrac{1}{1 + \cfrac{1}{1+\ldots}}}}} \,.$$

This might be a reason for the stability of quasiperiodic systems where $\tau$ plays a role. A prominent 1-D example is the Fibonacci sequence, an aperiodic chain of short and long segments S and L with lengths $S$ and $L$, where the relations $L/S = \tau$ and $L + S = \tau L$ hold. A Fibonacci chain can be constructed by the simple substitution or inflation rule $\mathrm{L} \to \mathrm{LS}$ and $\mathrm{S} \to \mathrm{L}$ (Table 1.3-6, Fig. 1.3-10). Materials quasiperiodically modulated in 1-D along one direction may occur. Again, their structures are readily described using the superspace formalism as above.

The Fibonacci sequence can be used to explain the idea of a periodic rational approximant. If the sequence ...LSLLSLSLS... represents a quasicrystal, then the

**Table 1.3-6** Generation of the Fibonacci sequence using the inflation rule $\mathrm{L} \to \mathrm{LS}$ and $\mathrm{S} \to \mathrm{L}$. The ratio $F_{n+1}/F_n$ tends towards $\tau$ for $n \to \infty$. $F_n$ is a Fibonacci number; $F_{n+1} = F_n + F_{n-1}$. The sequence starts with $F_0 = 0$, $F_1 = 1$

| Sequence | $n$ | $F_{n+1}/F_n$ |
|---|---|---|
| L | 1 | $1/1 = 1$ |
| LS | 2 | $2/1 = 2$ |
| LSL | 3 | $3/2 = 1.5$ |
| LSLLS | 4 | $5/3 = 1.66666\ldots$ |
| LSLLSLSL | 5 | $8/5 = 1.6$ |
| ... | | |
| ... LSLLSLSLS ... | $\infty$ | $\tau = 1.61803\ldots$ |

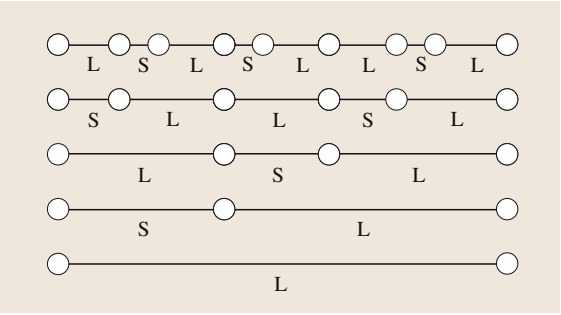


**Fig. 1.3-10** 1-D Fibonacci sequence. Moving downwards corresponds to an inflation of the self-similar chains, and moving upwards corresponds to a deflation



periodic sequence . . .LSLSLSLSLS. . ., consisting only of the word LS, is its 2/1 approximant (Table 1.3-6). In real systems, such approximants often exist as large-unit-cell (periodic!) structures with atomic arrangements locally very similar to those in the corresponding quasicrystal. When described in terms of superspace, they would result via cutting with a rational slope, in the above example $2/1 = 2$, instead of $\tau = 1.6180\ldots$.

To date, all known 2-D quasiperiodic materials exhibit noncrystallographic diffraction symmetries of $8/mmm$, $10/mmm$, or $12/mmm$. The structures of these materials are called octagonal, decagonal, and dodecagonal structures, respectively. Quasiperiodicity is present only in planes stacked along a perpendicular periodic direction. To index the lattice points in a plane, four basis vectors $\boldsymbol{a}_1, \boldsymbol{a}_2, \boldsymbol{a}_3, \boldsymbol{a}_4$ are needed; a fifth one, $\boldsymbol{a}_5$, describes the periodic direction. Thus a 5-D hypercrystal is appropriate for describing the solid periodically. In an analogous way to the 230 3-D space groups, the 5-D superspace groups (e.g. $P10_5/mmc$) provide

- the multiplicity and Wyckoff positions;
- the site symmetry;
- the coordinates of the hyperatoms.

Again, the quasiperiodic structure in 3-D can be obtained from an intersection with the external space.

On the atomic scale, these quasicrystals consist of units of some 100 atoms, called clusters. These clusters, of point symmetry $8/mmm$, $10/mmm$, or $12/mmm$ (or less), are fused, may interpenetrate partially, and can be considered to decorate quasiperiodic tilings. In a diffraction experiment, their superposition leads to an overall noncrystallographic symmetry. There are a number of different tilings that show such noncrystallographic symmetries. Figure 1.3-12 depicts four of them, as examples of the octagonal, decagonal, and dodecagonal cases.

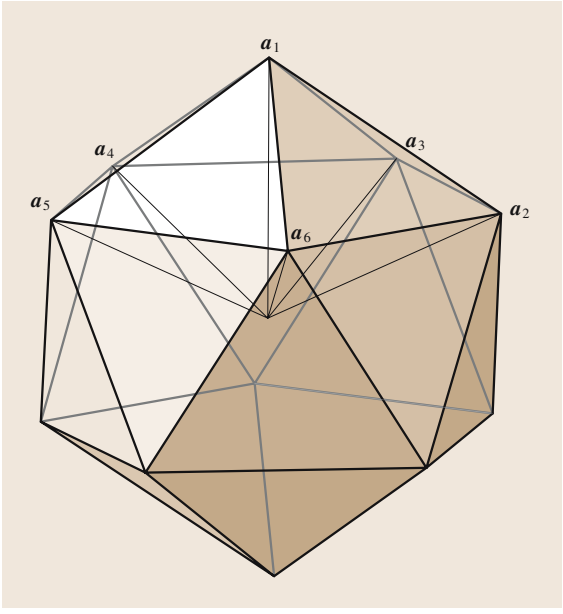


**Fig. 1.3-11** Unit vectors $\boldsymbol{a}_1, \ldots, \boldsymbol{a}_6$ of an icosahedral lattice

*Icosahedral quasicrystals* are also known. In 3-D, the icosahedral diffraction symmetry $2/m\bar{3}\bar{5}$ can be observed for these quasicrystals. Their diffraction patterns can be indexed using six integers, leading to a 6-D superspace description (see Fig. 1.3-11). On the atomic scale in 3-D, in physical space, clusters of some 100 atoms are arranged on the nodes of 3-D icosahedral tilings; the clusters have an icosahedral point group symmetry or less, partially interpenetrate, and generate an overall symmetry $2/m\bar{3}\bar{5}$. Many of their structures are still waiting to be determined completely. Figure 1.3-13 shows the two golden rhombohedra and the four Danzer tetrahedra that can be used to tile 3-D space icosahedrally.

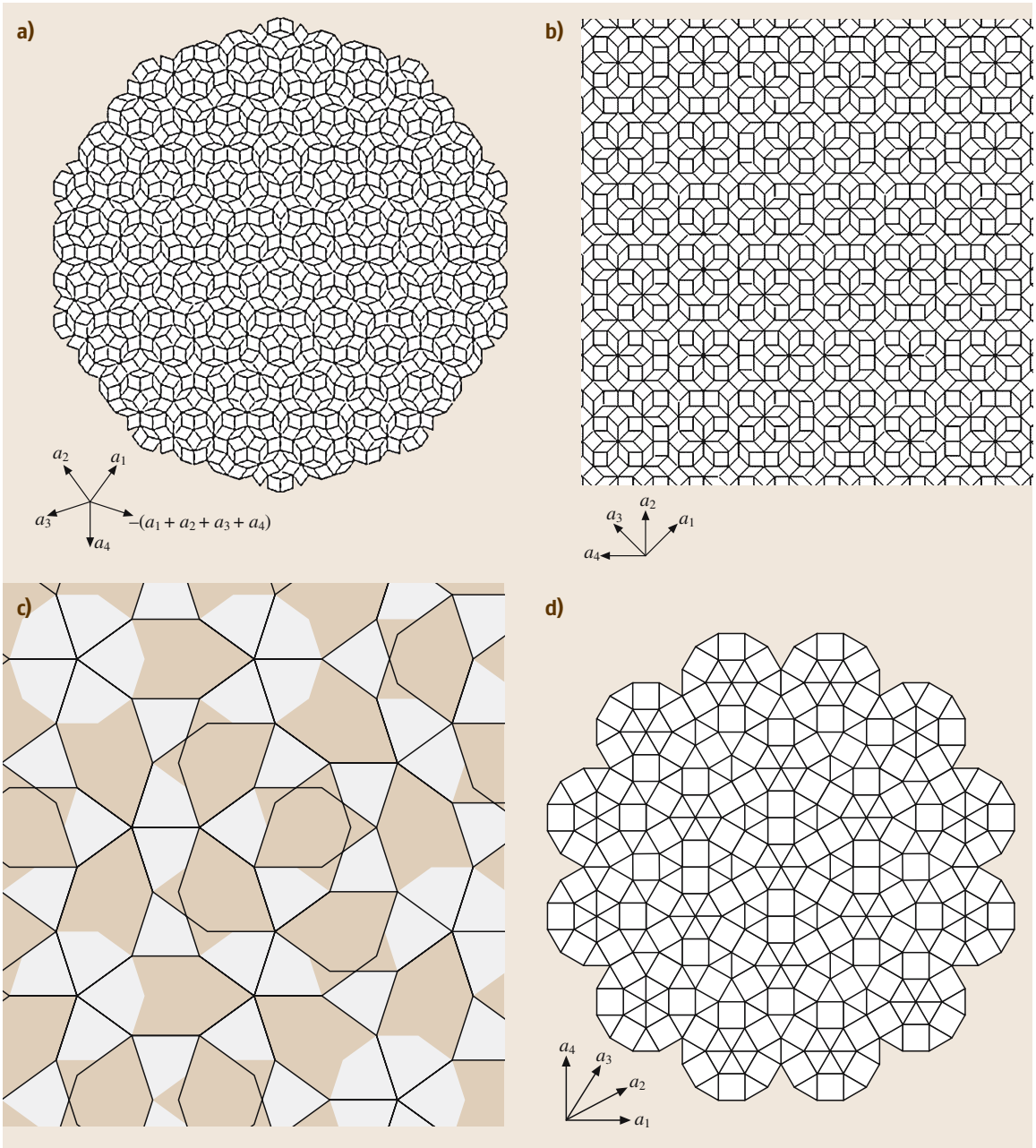


**Fig. 1.3-12a–d** Some 2-D quasiperiodic tilings; the corresponding four basis vectors $\boldsymbol{a}_1, \ldots, \boldsymbol{a}_4$ are shown. Linear combinations of $\boldsymbol{r} = \sum_i u_i \boldsymbol{a}_i$ reach all lattice points. **(a)** Penrose tiling with local symmetry $5mm$ and diffraction symmetry $10mm$, **(b)** octagonal tiling with diffraction symmetry $8mm$, **(c)** Gummelt tiling with diffraction symmetry $10mm$, and **(d)** dodecagonal Stampfli-type tiling with diffraction symmetry $12mm$

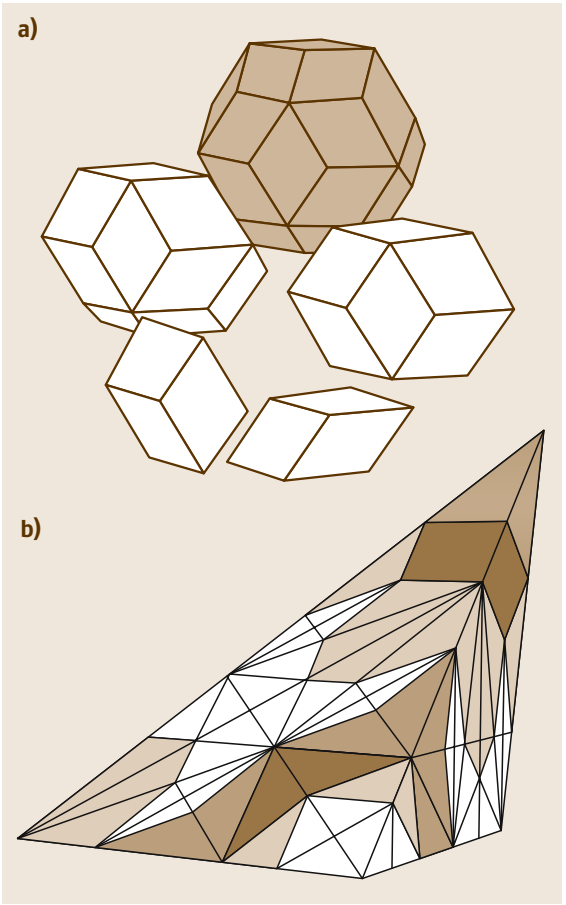


**Fig. 1.3-13** Icosahedral tilings. **(a)** The two golden rhombohedra (*bottom*) can be used to form icosahedral objects (the rhombic triacontahedron with point symmetry $m\bar{3}\bar{5}$ shown in *gray*). **(b)** Danzer's {ABCK} tiling: three inflation steps for prototile A

## 1.3.2 Disorder

In between the ideal crystalline and the purely amorphous states, most real crystals contain degrees of disorder. Two types of statistical disorder have to be distinguished: chemical disorder and displacive disorder (Fig. 1.3-14). Statistical disorder contributes to the entropy $S$ of the solid and is manifested by diffuse scattering in diffraction experiments. It may occur in both periodic and aperiodic materials.

### Chemical Disorder

Chemical disorder is observed, for example, in the case of solid solutions, say of $B$ in $A$, or $A_{1-x}B_x$ for short. Here, an average crystal structure exists. On the crystallographic atomic positions, different atomic species (the chemical elements $A$ and $B$) are distributed randomly. Generally, the cell parameter $a$ varies with $x$. For $x = 0$ or 1, the pure end member is present. A linear variation of $a(x)$ is predicted by Vegard's law. On the atomic scale, however, differences in the local structure, are present owing to the different contacts $A$–$A$, $B$–$B$, and $A$–$B$. These differences are usually represented by enlarged displacement factors, but can be investigated by analyzing the pair distribution function $G(r)$. $G(r)$ represents the probability of finding any atom at a distance $r$ from any other atom relative to an average density. Chemical disorder can also occur on only one or a few of the crystallographically different atomic positions (e.g. $A(X_{1-x}Y_x)_2$). This type of disorder is often intrinsic to a material and may be temperature-dependent.

### Displacive Disorder

The displacive type of disorder can be introduced by the presence of voids or vacancies in the structure or may exist for other reasons. Vacancies can be an important feature of a material: for example, they may leading to ionic conductivity or influence the mechanical properties.

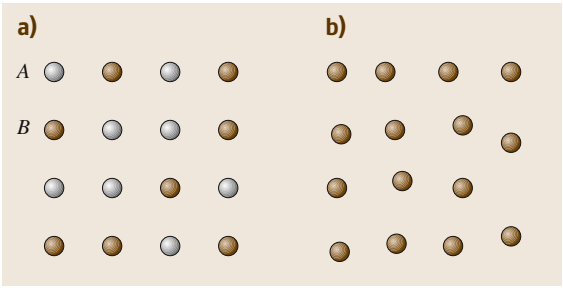


**Fig. 1.3-14** Schematic sketch of (a) chemical and (b) displacive disorder

## 1.3.3 Amorphous Materials

The second large group of condensed matter is classified as the amorphous or glassy state. No long-range order is observed. The atoms are more or less statistically distributed in space, but a certain short-range order is present.

This short-range order is reflected in the certain average coordination numbers or average coordination geometries. If there are strong (covalent) interactions between neighboring atoms, similar basic units may occur, which are in turn oriented randomly with respect to each other. The $SiO_4$ tetrahedron in silicate glasses is a well-known example. In an X-ray diffraction experiment on an amorphous solid, only isotropic diffuse scattering is observed. From this information, the radial atomic pair distribution function (Fig. 1.3-15) can be obtained. This function $G(r)$ can be interpreted as the probability of finding any atom at a distance $r$ from any other atom relative to an average density.

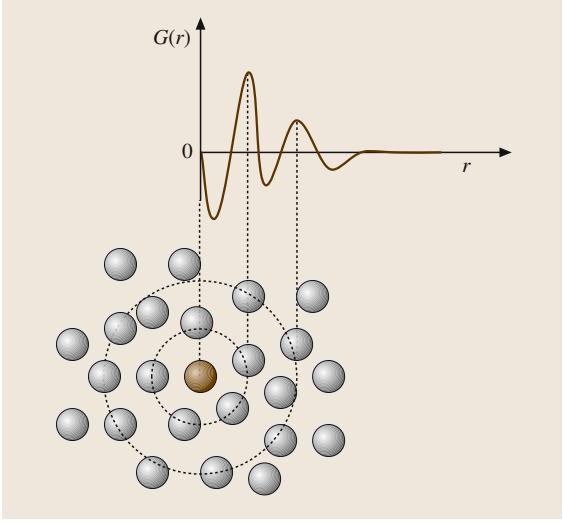


**Fig. 1.3-15** Radial atomic pair distribution function $G(r)$ of an amorphous material. Its shape can be deduced from diffuse scattering

## 1.3.4 Methods for Investigating Crystallographic Structure

So far, we have been dealing with the formal description of solids. To conclude this chapter, the tool kit that an experimentalist needs to obtain structural information about a material in front of him/her will be briefly described.

The major technique used to derive the atomic structure of solids is the diffraction method. To obtain the most comprehensive information about a solid, other techniques besides may be used to complement a model based on diffraction data. These techniques include scanning electron microscopy (SEM), wavelength-dispersive analysis of X-rays (WDX), energy-dispersive analysis of X-rays (EDX), extended X-ray atomic fine-structure analysis (EXAFS), transmission electron microscopy (TEM), high-resolution transmission electron microscopy (HRTEM), differential thermal analysis (DTA), and a number of other methods.

For diffraction experiments, three types of radiation with a wavelength $\lambda$ of the order of magnitude of

interatomic distances are used: X-rays, electrons, and neutrons. The shortest interatomic distances in solids are a few times $10^{-10}$ m. Therefore the non-SI unit the angstrom (1 Å $= 10^{-10}$ m) is often used in crystallography. In the case of electrons and neutrons, their energies have to be converted to de Broglie wavelengths:

$$\lambda = h/mv \,,$$
$$\lambda(\text{Å}) = 0.28/\sqrt{E(\text{eV})} \,.$$

Figure 1.3-16 compares the energies and wavelengths of the three types of radiation.

From wave optics, it is known that radiation of wavelength $\lambda$ is diffracted by a grid of spacing $d$. If we take a 3-D crystal lattice as such a grid, we expect diffraction maxima to occur at angles $2\theta$, given by the Bragg equation (Fig. 1.3-17)

$$\lambda = 2d_{hkl} \sin\theta_{hkl} \,.$$

For the aperiodic ($n$-D periodic crystal) case, $d_{hkl}$ has to be replaced by $d_{h_1 h_2 \ldots h_i \ldots h_n}$. To give a simple 3-D example, for the determination of the cell parameter $a$ in the cubic case, the Bragg equation can be rewritten in the form

$$(Q/2\pi)^2 = 4\sin^2\theta_{hkl}/\lambda^2 = (h^2+k^2+l^2)/a^2 \,.$$

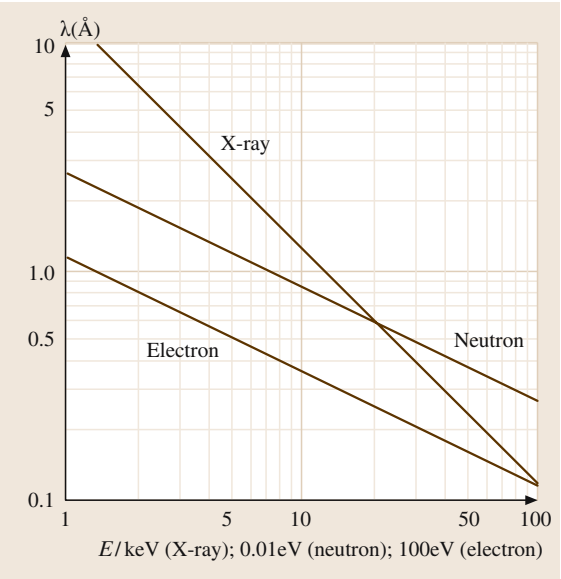


**Fig. 1.3-16** Wavelengths $\lambda$ in Å and particle energies $E$ for X-ray photons (energies in keV), neutrons (energies in 0.01 eV), and electrons (energies in 100 eV)

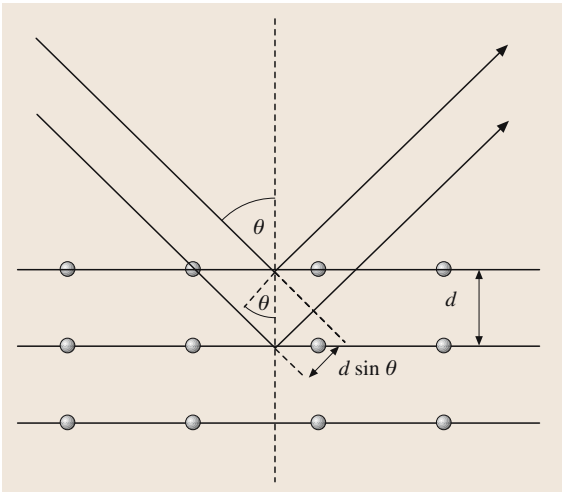


**Fig. 1.3-17** Geometrical derivation of the Bragg equation $n\lambda = 2d\sin\theta$. $n$ can be set to 1 when it is included in a higher-order $hkl$

Thus the crystal lattice is determined by a set of $\theta_{hkl}$. In the case of X-rays and neutrons, information about the atomic structure is contained in the set of diffraction intensities $I_{hkl}$. Here we have $I_{hkl} = F_{hkl}^2$ where $F_{hkl}$ are the structure factors.

To reconstruct the matter distribution $\rho(xyz)$ inside a unit cell of volume $V$, the crystallographic phase problem has to be solved. Once the phase factor $\phi$ for each $hkl$ is known, the crystal structure is solved.

$$\rho(xyz) = 1/V \times \sum_{\text{all } h,k,l}\sum\sum |F| \cos[2\pi(hx+ky+lz) - \phi] \,.$$

Non-Bragg diffraction intensities $I(Q)$ and therefore a normalized structure function $S(Q)$ can be obtained, for example, from an X-ray or neutron powder diffractogram. The sine Fourier transform of $S(Q)$ yields a normalized radial atomic pair distribution function $G(r)$:

$$G(r) = (2/\pi)\int_0^\infty Q[S(Q)-1]\sin(Qr)\,dQ \,.$$

For measurements at high $Q$, the 1-D function $G(r)$ contains detailed information about the local structure. This function therefore resolves, for example, disorder or vacancy distributions in a material. The method can be applied to 3-D diffuse scattering distributions as well and thus can include angular information with respect to $\boldsymbol{r}$.

### X-rays

X-rays can be produced in the laboratory using a conventional X-ray tube. Depending on the anode material, wavelengths $\lambda$ from 0.56 Å (Ag K$\alpha$) to 2.29 Å (Cr K$\alpha$) can be generated. Filtered or monochromatized radiation is usually used to collect diffraction data, from either single crystals or polycrystalline fine powders. A continuous X-ray spectrum, obtained from a tungsten anode, for example, is used to obtain Laue images to check the quality, orientation, and symmetry of single crystals.

X-rays with a higher intensity, a tunable energy, a narrower distribution, and higher brilliance are provided by synchrotron radiation facilities.

X-rays interact with the electrons in a structure and therefore provide information about the electron density distribution – mainly about the electrons near the atomic cores.

### Neutron Diffraction

Neutrons, generated in a nuclear reactor, are useful for complementing X-ray diffraction information. They interact with the atomic nuclei, and with the magnetic moments of unpaired electrons if they are present in a structure. Hydrogen atoms, which are difficult to locate using X-rays (the contain one electron, if at all, near the proton), give a far better contrast in neutron diffraction experiments. The exact positions of atomic nuclei permit "X minus N" structure determinations, so that the location of valence electrons can be made observable. Furthermore, the magnetic structure of a material can be determined.

### Electron Diffraction

The third type of radiation which can be used for diffraction purposes is an electron beam; this is usually done in combination with TEM or HRTEM. Because electrons have only a short penetration distance – electrons, being charged particles, interact strongly with the material – electron diffraction is mainly used for thin crystallites, surfaces, and thin films. In the TEM mode, domains and other features on the nanometer scale are visible. Nevertheless, crystallographic parameters such as unit cell dimensions, and symmetry and space group information can be obtained from selected areas.

In some cases, information about, for example, stacking faults or superstructures obtained from an electron diffraction experiment may lead to a revised, detailed crystal structure model that is "truer" than the model which was originally deduced from X-ray diffraction data. If only small crystals of a material are available, crystallographic models obtained from unit cell and symmetry information can be simulated and then adapted to fit HRTEM results.

The descriptions above provide the equipment needed to understand the structure of solid matter on the atomic scale. The concepts of crystallography, the technical terms, and the language used in this framework have been presented. The complementarities of the various experimental methods used to extract coherent, comprehensive information from a sample of material have been outlined. The "rudiments" presented here, however, should be understood only as a first step into the fascinating field of the atomic structure of condensed matter.



## References


3.1 L. V. Azaroff: *Elements of X-Ray Crystallography* (McGraw-Hill, New York 1968)

3.2 J. Pickworth Glusker, K. N. Trueblood: *Crystal Structure Analysis – A Primer* (Oxford Univ. Press, Oxford 1985)

3.3 E. R. Wölfel: *Theorie und Praxis der Röntgenstrukturanalyse* (Vieweg, Braunschweig 1987)

3.4 W. Kleber, H.-J. Bautsch, J. Bohm: *Einführung in die Kristallographie* (Verlag Technik, Berlin 1998)

3.5 C. Giacovazzo (Ed.): *Fundamentals of Crystallography*, IUCr Texts on Crystallography (Oxford Univ. Press., Oxford 1992)

3.6 C. Janot: *Quasicrystals – A Primer* (Oxford Univ. Press, Oxford 1992)

3.7 S. J. L. Billinge, T. Egami: *Underneath the Bragg Peaks: Structural Analysis of Complex Materials* (Elsevier, Amsterdam 2003)

3.8 T. Hahn (Ed.): *International Tables for Crystallography*, Vol. A (Kluwer, Dordrecht 1992)

3.9 A. V. Shubnikov, N. V. Belov: *Colored Symmetry* (Pergamon Press, Oxford 1964)

# Part 2 The Elements

## Part 2 The Elements

1 The Elements
Werner Martienssen, Frankfurt/Main, Germany

# 2.1. The Elements

This section provides tables of the physical and physicochemical properties of the elements. Emphasis is given to properties of the elements in the condensed state. The tables are structured according to the Periodic Table of the elements. Most of the tables deal with the properties of elements of one particular group (column) of the Periodic Table. Only the elements of the first period (hydrogen and helium), the lanthanides, and the actinides are arranged according to the periods (rows) of the Periodic Table. This synoptic representation is intended to provide an immediate overview of the trends in the data for chemically related elements.


2.1.1 **Introduction** ..... 45
2.1.1.1 How to Use This Section ..... 45
2.1.2 **Description of Properties Tabulated** ..... 46
2.1.2.1 Parts A of the Tables ..... 46
2.1.2.2 Parts B of the Tables ..... 46
2.1.2.3 Parts C of the Tables ..... 48
2.1.2.4 Parts D of the Tables ..... 49
2.1.3 **Sources** ..... 49
2.1.4 **Tables of the Elements in Different Orders** ..... 49
2.1.5 **Data** ..... 54
2.1.5.1 Elements of the First Period ..... 54
2.1.5.2 Elements of the Main Groups and Subgroup I to IV ..... 59
2.1.5.3 Elements of the Main Groups and Subgroup V to VIII ..... 98
2.1.5.4 Elements of the Lanthanides Period ..... 142
2.1.5.5 Elements of the Actinides Period 151
**References** ..... 158


## 2.1.1 Introduction

### 2.1.1.1 How to Use This Section

To find properties of a specific element or group of elements, start from one of Tables 2.1-1 – 2.1-5 and proceed in one of the following ways:

1. If you know the *name* of the element, refer to Table 2.1-1, where an alphabetical list of the elements is given, together with the numbers of the pages where the properties of these elements will be found.
2. If you know the *chemical symbol* of the element, refer to Table 2.1-2, where an alphabetical list of element symbols is given, together with the numbers of the pages where the properties of the corresponding elements will be found.
3. If you know the *atomic number Z* of the element, refer to Table 2.1-3, where a list of the elements in order of atomic number is given, together with the numbers of the pages where the properties of these elements will be found.
4. If you know the *group of the Periodic Table* that contains the element of interest, refer to Table 2.1-4, which gives the numbers of the pages where the properties of the elements of each group will be found.
5. If you wish to look up the element in the *Periodic Table*, refer to Table 2.1-5, where the element symbol and the atomic number will be found. Then use Table 2.1-2 or Table 2.1-3 to find the numbers of the pages where the properties of the element of interest are tabulated.
6. Alternatively you can also find the name and the chemical symbol of the element you are looking for in the alphabetic index at the end of the volume. The index again will give you the first number of those pages on which

you can find the properties of the element described.

The data-tables corresponding to the Periodes and Groups of the Periodic Table are subdivided in the following way:

A. Atomic, ionic, and molecular properties.
B. Materials data:
   (a) Crystallographic properties.
   (b) Mechanical properties.
   (c) Thermal and thermodynamic properties.
   (d) Electronic, electromagnetic, and optical properties.
C. Allotropic and high-pressure modifications.
D. Ionic radii.

## 2.1.2 Description of Properties Tabulated

### 2.1.2.1 Parts A of the Tables

The properties tabulated in parts A of the tables concern the atomic, ionic, and molecular properties of the elements:

- The relative atomic mass, or atomic weight, $A$.
- The abundance in the lithosphere and in the sea.
- The atomic radius: the radius $r_{\mathrm{cov}}$ for single covalent bonding (after Pauling), the radius $r_{\mathrm{met}}$ for metallic bonding with a coordination number of 12 (after Pauling), the radius $r_{\mathrm{vdW}}$ for van der Waals bonding (after Bondi), and, for some elements, the radius $r_{\mathrm{os}}$ of the outer-shell orbital are given.
- The completely and partially occupied electron shells in the atom.
- The symbol for the electronic ground state.
- The electronic configuration.
- The oxidation states.
- The electron affinity.
- The electronegativity $X_{\mathrm{A}}$ (after Allred and Rochow).
- The first, second, third, and fourth ionization energies and the standard electrode potential $E^0$.
- The internuclear distance in the molecule.
- The dissociation energy of the molecule.

### 2.1.2.2 Parts B of the Tables

Parts B of the tables contain data on the macroscopic properties of the elements. Most of the data concern the condensed phases. If not indicated otherwise, the data in this section apply to the standard state of the element, that is, they are valid at standard temperature and pressure (STP, i. e. $T = 298.15\,\mathrm{K}$ and $p = 100\,\mathrm{kPa} = 1\,\mathrm{bar}$). For those elements which are stable in the gas phase at STP, data are given for the macroscopic properties in the gas phase.

The quantities describing the physical and physicochemical properties of materials can be divided into two classes. The first class contains all those quantities which are not directly connected with external (generalized) forces, these quantities have well-defined values even in the absence of external forces. Some examples are the electronic ground-state configuration of the atom, the coordination number in the crystallized state and the surface tension in the liquid state. The second class contains those quantities which describe the response of the material to externally applied (generalized) forces $F$. Such a force might be a mechanical stress field, an electric or magnetic field, a field gradient, or a temperature gradient. The response of the material to the external force might be observed via a suitable observable $O$, such as a mechanical strain, an electric current density, a dielectric polarization, a magnetization, or a heat current density. Assuming homogeneous conditions, the dependence of the observable $O$ on the force $F$ can be used to define material-specific parameters $\chi$, which are also called physical properties of the material. Some examples are the elastic moduli or compliance constants, the electrical conductivity, the dielectric constant, the magnetic susceptibility, and the thermal conductivity.

In the *linear-response* regime, that is, under weak external forces $F$, these parameters $\chi$ are considered as being independent of the strength of the forces. The dependence of an observable $O$ on a force $F$ is then the simple proportionality

$$O = \chi F \,. \tag{1.1}$$

For strong external fields, the dependence of the response on the strength of the forces can be expressed by a power expansion in the forces, which then – in addition to the linear parameters $\chi$ – defines *nonlinear field-dependent* materials properties $\chi^{(\mathrm{nl})}(F)$, where

$$\chi^{(\mathrm{nl})}(F) = \chi + \chi^{(1)} F + \ldots \,. \tag{1.2}$$

In general, the class of materials properties that describe the response to externally applied forces have *tensor* character. The *rank* of the property tensor $\chi$ de-

pends on the rank of the external force $F$ and that of the observable $O$ considered. In the case of Ohm's law, $j = \sigma E$, in which the current density $j$ and the electric field strength $E$ are vectors, the conductivity tensor $\boldsymbol{\sigma}$ is of rank 2; in the case of the generalized Hooke's law, $\boldsymbol{\varepsilon} = \boldsymbol{s}\boldsymbol{\sigma}$, the strain tensor $\boldsymbol{\varepsilon}$ and the stress tensor $\boldsymbol{\sigma}$ both are of rank 2, so that the elastic compliance tensor $\boldsymbol{s}$ is of rank 4. A vector can be considered as a tensor of rank 1, and a scalar, correspondingly, as a tensor of rank 0. A second-rank tensor, such as the electrical conductivity $\boldsymbol{\sigma}$, in general has nine components in three-dimensional space; a tensor of rank $n$ in general has $3^n$ components in three-dimensional space. *Symmetry*, however, of both the underlying crystal lattice and the physical phenomenon (for example, action = reaction), may reduce the number of independent nonvanishing components in the tensor. The tensor components reflect the crystal symmetry by being invariant under those orthogonal transformations which are elements of the point group of the crystal. In cubic crystals, for example, physical properties described by tensors of rank 2 are characterized by only one nonvanishing tensor component. Therefore cubic crystals are isotropic with respect to their electrical conductivity, their heat conductivity, and their dielectric properties.

### Subdivisions B(a) of the Tables

These parts deal with the *crystallographic properties*. Here you will find the crystal system and the Bravais lattice in which the element is stable in its standard state; the structure type in which the element crystallizes; the lattice constants $a, b, c, \alpha, \beta, \gamma$ (symmetry reduces the number of independent lattice constants); the space group; the Schoenflies symbol; the *Strukturbericht* type; the Pearson symbol; the number $A$ of atoms per cell; the coordination number; and the shortest interatomic distance between atoms in the solid state and in the liquid state.

Basic concepts of crystallography are explained in Chapt. 1.3.

### Subdivisions B(b) of the Tables

These parts cover the *mechanical properties*. At the top of the table, you will find the density of the material in the solid state ($\varrho_s$) and in the liquid state ($\varrho_l$), and the molar volume $V_{mol}$ in the solid state. Here, one mole is the amount of substance which contains as many elementary particles (atoms or molecules) as there are atoms in 0.012 kg of the carbon isotope with a relative atomic mass of 12. This number of particles is called *Avogadro's number* and is approximately equal to $6.022 \times 10^{23}$. The next three rows present the viscosity $\eta$, the surface tension, and its temperature dependence, in the liquid state. The next properties are the coefficient of linear thermal expansion $\alpha$ and the sound velocity, both in the solid and in the liquid state. A number of quantities are tabulated for the presentation of the elastic properties. For isotropic materials, we list the volume compressibility $\kappa = -(1/V)(dV/dP)$, and in some cases also its reciprocal value, the bulk modulus (or compression modulus); the elastic modulus (or Young's modulus) $E$; the shear modulus $G$; and the Poisson number (or Poisson's ratio) $\mu$. Hooke's law, which expresses the linear relation between the strain $\varepsilon$ and the stress $\sigma$ in terms of Young's modulus, reads $\sigma = E\varepsilon$. For monocrystalline materials, the components of the elastic compliance tensor $\boldsymbol{s}$ and the components of the elastic stiffness tensor $\boldsymbol{c}$ are given. The elastic compliance tensor $\boldsymbol{s}$ and the elastic stiffness tensor $\boldsymbol{c}$ are both defined by the generalized forms of Hooke's law, $\boldsymbol{\sigma} = \boldsymbol{c}\boldsymbol{\varepsilon}$ and $\boldsymbol{\varepsilon} = \boldsymbol{s}\boldsymbol{\sigma}$. At the end of the list, the tensile strength, the Vickers hardness, and the Mohs hardness are given for some elements.

### Subdivisions B(c) of the Tables

The *thermal and thermodynamic properties* are tabulated in these subdivisions of the tables. The properties tabulated are:

- The thermal conductivity $\lambda$.
- The molar heat capacity at constant pressure, $c_p$.
- The standard entropy $S^0$, that is, the molar entropy of the element at 298.15 K and 100 kPa.
- The enthalpy difference $H_{298} - H_0$, that is, the difference between the molar enthalpies of the element at 298.15 K and at 0 K.
- The melting temperature $T_m$.
- The molar enthalpy change $\Delta H_m$ and molar entropy change $\Delta S_m$ at the melting temperature.
- The relative volume change $\Delta V_m = (V_l - V_s)/V_l$ on melting.
- The boiling temperature $T_b$.
- The molar enthalpy change $\Delta H_b$ of boiling, and, for some elements, the molar enthalpy of sublimation.

In addition, the critical temperature $T_c$, the critical pressure $p_c$, the critical density $\varrho_c$, the triple-point temperature $T_{tr}$, and the triple-point pressure $p_{tr}$ are given for some elements. For the element helium, the table also contains data for the $\lambda$ point, at which liquid helium passes from the normal-fluid phase helium I (above the $\lambda$ point) to the superfluid phase helium II (below the $\lambda$ point), for $^4$He and $^3$He.

Throughout Sect. 2.1, temperature is measured in units of kelvin (K), the unit of thermodynamic temperature. 1 K is defined as the fraction 1/273.16 of the thermodynamic temperature of the triple point of water. To convert data given in kelvin into degrees Celsius (°C), the following equation can be used:

$$T(^\circ\mathrm{C}) = (T(\mathrm{K}) - 273.15\,\mathrm{K})(^\circ\mathrm{C}/\mathrm{K})\,.$$

This can be expressed in words as follows: the Celsius scale is shifted towards higher temperatures by 273.15 K relative to the kelvin scale, such that the temperature 273.15 K becomes 0 °C and the temperature 0 K becomes −273.15 °C. To convert data given in kelvin into degrees Fahrenheit (°F), the following equation can be used:

$$T(^\circ\mathrm{F}) = (9/5)(T(\mathrm{K}) - 273.15\,\mathrm{K})(^\circ\mathrm{F}/\mathrm{K}) + 32\,^\circ\mathrm{F}\,.$$

This can be expressed approximately in words as follows: the Fahrenheit scale is shifted relative to the kelvin scale and also differs by a scaling so that its degrees are smaller than those of the kelvin scale by nearly a factor of 2.

#### Subdivisions B(d) of the Tables

These subdivisions of the tables present data on the *electronic, electromagnetic, and optical properties* of the elements. Data are given for the following:

- The electrical resistivity $\rho_\mathrm{s}$ in the solid state, and its temperature and pressure dependence.
- The electrical resistivity $\rho_\mathrm{l}$ in the liquid state, and the resistivity ratio $\rho_\mathrm{l}/\rho_\mathrm{s}$ at the melting temperature.
- The critical temperature $T_\mathrm{cr}$ and critical field strength $H_\mathrm{cr}$ for superconductivity.
- The electronic band gap $\Delta E$.
- The Hall coefficient $R$, together with the range of magnetic field strength $B$ over which it was measured.
- The thermoelectric coefficient.
- The electronic work function.
- The thermal work function.
- The intrinsic charge carrier concentration.
- The electron and hole mobilities.
- The static dielectric constant $\varepsilon$ of the element in the solid state, and in some cases also in the liquid state.
- The molar magnetic susceptibility $\chi_\mathrm{mol}$ and the mass magnetic susceptibility $\chi_\mathrm{mass}$ of the element in the solid state, and in some cases also in the liquid state. The susceptibilities are given in the definitions of both the SI system and the cgs system (see below).
- The refractive index $n$ in the solid and liquid states.

The magnetic susceptibility is the parameter that describes the response of the material to an externally applied magnetic field $H$, as measured by the observable magnetization $M$, in the linear regime, via $M = \chi H$. Three different forms of the term "magnetization" are in use, depending on the specific application: first, the volume magnetization $M_\mathrm{vol}$, equal to the magnetic dipole moment divided by the volume of the sample; second, the molar magnetization, or magnetization related to the number of particles, $M_\mathrm{mol}$, equal to the magnetic dipole moment divided by the number of particles measures in moles; and third, the mass magnetization $M_\mathrm{mass}$, equal to the magnetic dipole moment divided by the mass of the sample. Correspondingly, there are three different magnetic susceptibilities. The *volume susceptibility* $\chi_\mathrm{vol}$ is a dimensionless number because in this case $M$ and $H$ are both measured in the same units, namely A/m in the SI system and gauss in the cgs system. The dimensionless character of $\chi_\mathrm{vol}$ might be the reason why, in physics textbooks, mostly only this susceptibility is mentioned. The other two susceptibilities, the *molar susceptibility* $\chi_\mathrm{mol}$ and the *mass susceptibility* $\chi_\mathrm{mass}$, are more useful for practical applications. In both the SI system and the cgs system, the molar susceptibility is measured in units of $\mathrm{cm}^3/\mathrm{mol}$, and the mass susceptibility is measured in units of $\mathrm{cm}^3/\mathrm{g}$. In this Handbook, data are given for the molar and mass susceptibilities.

Although susceptibilities have the same dimensions in the SI and cgs systems, the numerical values in the cgs system are smaller than those in the SI system by a factor of $4\pi$. This is due to the different definitions of the quantities dipole moment and magnetization in the two systems. The difference can be seen most clearly in the general relations between the magnetization $M$ and the field strengths $B$ and $H$ in the two systems. In the SI system, this relation reads $B = \mu_0(H + M)$, whereas in the cgs system, it reads $B = H + 4\pi M$. Because of this difference, the magnetic-susceptibility data in Sect. 2.1.5 are given for both the SI and the cgs definitions.

### 2.1.2.3 Parts C of the Tables

Parts C of the tables present crystallographic data for allotropic and high-pressure modifications of the elements. The left-hand columns contain data for allotropic modifications that are stable at a pressure of 100 kPa over the temperature ranges indicated, and the right-hand columns contain data for modifications stable at higher pressures as indicated. The modifications stable at 100 kPa are denoted by Greek letters

in front of the chemical symbol of the element (normally starting with $\alpha$ for the modification stable over the lowest temperature range), and the high-pressure modifications are denoted by Roman numerals after the chemical symbol. In these parts of the tables, "RT" stands for "room temperature", and "RTP" stands for "room temperature and standard pressure", i. e. 100 kPa.

#### 2.1.2.4 Parts D of the Tables

Parts D of the tables contain data on *ionic radii* determined from crystal structures. The first row lists the elements, and the second row lists the positive and negative ions for which data are given. The remaining rows give the ionic radii of these ions for the most common coordination numbers.

## 2.1.3 Sources

Most of the data presented here have been taken from Landolt–Börnstein [1.1]. Additional data have been taken from the D'Ans-Lax series [1.2] and the *CRC Handbook of Chemistry and Physics* [1.3].

## 2.1.4 Tables of the Elements in Different Orders

**Table 2.1-1** The elements ordered by their names

| Element | Symbol | Atomic Number | Page | Element | Symbol | Atomic Number | Page | Element | Symbol | Atomic Number | Page |
|---|---|---|---|---|---|---|---|---|---|---|---|
| Actinium | Ac | 89 | 84 | Gold | Au | 79 | 65 | Praseodymium | Pr | 59 | 142 |
| Aluminium | Al | 13 | 78 | Hafnium | Hf | 72 | 94 | Promethium | Pm | 61 | 142 |
| Americium | Am | 95 | 151 | Hassium | Hs | 108 | 131 | Protactinium | Pa | 91 | 151 |
| Antimony | Sb | 51 | 98 | Helium | He | 2 | 54 | Radium | Ra | 88 | 68 |
| Argon | Ar | 18 | 128 | Holmium | Ho | 67 | 142 | Radon | Rn | 86 | 128 |
| Arsenic | As | 33 | 98 | Hydrogen | H | 1 | 54 | Rhenium | Re | 75 | 124 |
| Astatine | At | 85 | 118 | Indium | In | 49 | 78 | Rhodium | Rh | 45 | 135 |
| Barium | Ba | 56 | 68 | Iodine | I | 53 | 118 | Roentgenium | Rg | 111 | |
| Berkelium | Bk | 97 | 151 | Iridium | Ir | 77 | 135 | Rubidium | Rb | 37 | 59 |
| Beryllium | Be | 4 | 68 | Iron | Fe | 26 | 131 | Ruthenium | Ru | 44 | 131 |
| Bismuth | Bi | 83 | 98 | Krypton | Kr | 36 | 128 | Rutherfordium | Rf | 104 | 94 |
| Bohrium | Bh | 107 | 124 | Lanthanum | La | 57 | 84 | Samarium | Sm | 62 | 142 |
| Boron | B | 5 | 78 | Lawrencium | Lr | 103 | 151 | Scandium | Sc | 21 | 84 |
| Bromine | Br | 35 | 118 | Lead | Pb | 82 | 88 | Seaborgium | Sg | 106 | 114 |
| Cadmium | Cd | 48 | 73 | Lithium | Li | 3 | 59 | Selenium | Se | 34 | 108 |
| Calcium | Ca | 20 | 68 | Lutetium | Lu | 71 | 142 | Silicon | Si | 14 | 88 |
| Californium | Cf | 98 | 151 | Magnesium | Mg | 12 | 68 | Silver | Ag | 47 | 65 |
| Carbon | C | 6 | 88 | Manganese | Mn | 25 | 124 | Sodium | Na | 11 | 59 |
| Cerium | Ce | 58 | 142 | Meitnerium | Mt | 109 | 135 | Strontium | Sr | 38 | 68 |
| Cesium | Cs | 55 | 59 | Mendelevium | Md | 101 | 151 | Sulfur | S | 16 | 108 |
| Chlorine | Cl | 17 | 118 | Mercury | Hg | 80 | 73 | Tantalum | Ta | 73 | 105 |
| Chromium | Cr | 24 | 114 | Molybdenum | Mo | 42 | 114 | Technetium | Tc | 43 | 124 |
| Cobalt | Co | 27 | 135 | Neodymium | Nd | 60 | 142 | Tellurium | Te | 52 | 108 |
| Copper | Cu | 29 | 65 | Neon | Ne | 10 | 128 | Terbium | Tb | 65 | 142 |
| Curium | Cm | 96 | 151 | Neptunium | Np | 93 | 151 | Thallium | Tl | 81 | 78 |
| Darmstadtium | Ds | 110 | 139 | Nickel | Ni | 28 | 139 | Thorium | Th | 90 | 151 |
| Dubnium | Db | 105 | 105 | Niobium | Nb | 41 | 105 | Thulium | Tm | 69 | 142 |
| Dysprosium | Dy | 66 | 142 | Nitrogen | N | 7 | 98 | Tin | Sn | 50 | 88 |
| Einsteinium | Es | 99 | 151 | Nobelium | No | 102 | 151 | Titanium | Ti | 22 | 94 |
| Erbium | Er | 68 | 142 | Osmium | Os | 76 | 131 | Tungsten | W | 74 | 114 |
| Europium | Eu | 63 | 142 | Oxygen | O | 8 | 108 | Uranium | U | 92 | 151 |

**Table 2.1-1** The elements ordered by their names, cont.

| Element | Symbol | Atomic Number | Page | Element | Symbol | Atomic Number | Page | Element | Symbol | Atomic Number | Page |
|---|---|---|---|---|---|---|---|---|---|---|---|
| Fermium | Fm | 100 | 151 | Palladium | Pd | 46 | 139 | Vanadium | V | 23 | 105 |
| Fluorine | F | 9 | 118 | Phosphorus | P | 15 | 98 | Xenon | Xe | 54 | 128 |
| Francium | Fr | 87 | 59 | Platinum | Pt | 78 | 139 | Ytterbium | Yb | 70 | 142 |
| Gadolinium | Gd | 64 | 142 | Plutonium | Pu | 94 | 151 | Yttrium | Y | 39 | 84 |
| Gallium | Ga | 31 | 78 | Polonium | Po | 84 | 108 | Zinc | Zn | 30 | 73 |
| Germanium | Ge | 32 | 88 | Potassium | K | 19 | 59 | Zirconium | Zr | 40 | 94 |

[a] See Tungsten.

**Table 2.1-2** The elements ordered by their chemical symbols

| Element | Symbol | Atomic Number | Page | Element | Symbol | Atomic Number | Page | Element | Symbol | Atomic Number | Page |
|---|---|---|---|---|---|---|---|---|---|---|---|
| Actinium | Ac | 89 | 84 | Gadolinium | Gd | 64 | 142 | Polonium | Po | 84 | 108 |
| Silver | Ag | 47 | 65 | Germanium | Ge | 32 | 88 | Praseodymium | Pr | 59 | 142 |
| Aluminium | Al | 13 | 78 | Hydrogen | H | 1 | 54 | Platinum | Pt | 78 | 139 |
| Americium | Am | 95 | 151 | Helium | He | 2 | 54 | Plutonium | Pu | 94 | 151 |
| Argon | Ar | 18 | 128 | Mercury | Hg | 80 | 73 | Radium | Ra | 88 | 68 |
| Arsenic | As | 33 | 98 | Hafnium | Hf | 72 | 94 | Rubidium | Rb | 37 | 59 |
| Astatine | At | 85 | 118 | Holmium | Ho | 67 | 142 | Rhenium | Re | 75 | 124 |
| Gold | Au | 79 | 65 | Hassium | Hs | 108 | 131 | Rutherfordium | Rf | 104 | 94 |
| Boron | B | 5 | 78 | Iodine | I | 53 | 118 | Roentgenium | Rg | 111 | |
| Barium | Ba | 56 | 68 | Indium | In | 49 | 78 | Rhodium | Rh | 45 | 135 |
| Beryllium | Be | 4 | 68 | Iridium | Ir | 77 | 135 | Radon | Rn | 86 | 128 |
| Bohrium | Bh | 107 | 124 | Potassium | K | 19 | 59 | Ruthenium | Ru | 44 | 131 |
| Bismuth | Bi | 83 | 98 | Krypton | Kr | 36 | 128 | Sulfur | S | 16 | 108 |
| Berkelium | Bk | 97 | 151 | Lanthanum | La | 57 | 84 | Antimony | Sb | 51 | 98 |
| Bromine | Br | 35 | 118 | Lithium | Li | 3 | 59 | Scandium | Sc | 21 | 84 |
| Carbon | C | 6 | 88 | Lawrencium | Lr | 103 | 151 | Selenium | Se | 34 | 108 |
| Calcium | Ca | 20 | 68 | Lutetium | Lu | 71 | 142 | Seaborgium | Sg | 106 | 114 |
| Cadmium | Cd | 48 | 73 | Mendelevium | Md | 101 | 151 | Silicon | Si | 14 | 88 |
| Cerium | Ce | 58 | 142 | Magnesium | Mg | 12 | 68 | Samarium | Sm | 62 | 142 |
| Californium | Cf | 98 | 151 | Manganese | Mn | 25 | 124 | Tin | Sn | 50 | 88 |
| Chlorine | Cl | 17 | 118 | Molybdenum | Mo | 42 | 114 | Strontium | Sr | 38 | 68 |
| Curium | Cm | 96 | 151 | Meitnerium | Mt | 109 | 135 | Tantalum | Ta | 73 | 105 |
| Cobalt | Co | 27 | 135 | Nitrogen | N | 7 | 98 | Terbium | Tb | 65 | 142 |
| Chromium | Cr | 24 | 114 | Sodium | Na | 11 | 59 | Technetium | Tc | 43 | 124 |
| Cesium | Cs | 55 | 59 | Niobium | Nb | 41 | 105 | Tellurium | Te | 52 | 108 |
| Copper | Cu | 29 | 65 | Neodymium | Nd | 60 | 142 | Thorium | Th | 90 | 151 |
| Dubnium | Db | 105 | 105 | Neon | Ne | 10 | 128 | Titanium | Ti | 22 | 94 |
| Darmstadtium | Ds | 110 | 139 | Nickel | Ni | 28 | 139 | Thallium | Tl | 81 | 78 |
| Dysprosium | Dy | 66 | 142 | Nobelium | No | 102 | 151 | Thulium | Tm | 69 | 142 |
| Erbium | Er | 68 | 142 | Neptunium | Np | 93 | 151 | Uranium | U | 92 | 151 |
| Einsteinium | Es | 99 | 151 | Oxygen | O | 8 | 108 | Vanadium | V | 23 | 105 |
| Europium | Eu | 63 | 142 | Osmium | Os | 76 | 131 | Tungsten | W | 74 | 114 |
| Fluorine | F | 9 | 118 | Phosphorus | P | 15 | 98 | Xenon | Xe | 54 | 128 |
| Iron | Fe | 26 | 131 | Protactinium | Pa | 91 | 151 | Yttrium | Y | 39 | 84 |
| Fermium | Fm | 100 | 151 | Lead | Pb | 82 | 88 | Ytterbium | Yb | 70 | 142 |
| Francium | Fr | 87 | 59 | Palladium | Pd | 46 | 139 | Zinc | Zn | 30 | 73 |
| Gallium | Ga | 31 | 78 | Promethium | Pm | 61 | 142 | Zirconium | Zr | 40 | 94 |

**Table 2.1-3** The elements ordered by their atomic numbers

| Element | Symbol | Atomic Number | Page | Element | Symbol | Atomic Number | Page | Element | Symbol | Atomic Number | Page |
|---|---|---|---|---|---|---|---|---|---|---|---|
| Hydrogen | H | 1 | 54 | Strontium | Sr | 38 | 68 | Rhenium | Re | 75 | 124 |
| Helium | He | 2 | 54 | Yttrium | Y | 39 | 84 | Osmium | Os | 76 | 131 |
| Lithium | Li | 3 | 59 | Zirconium | Zr | 40 | 94 | Iridium | Ir | 77 | 135 |
| Beryllium | Be | 4 | 68 | Niobium | Nb | 41 | 105 | Platinum | Pt | 78 | 139 |
| Boron | B | 5 | 78 | Molybdenum | Mo | 42 | 114 | Gold | Au | 79 | 65 |
| Carbon | C | 6 | 88 | Technetium | Tc | 43 | 124 | Mercury | Hg | 80 | 73 |
| Nitrogen | N | 7 | 98 | Ruthenium | Ru | 44 | 131 | Thallium | Tl | 81 | 78 |
| Oxygen | O | 8 | 108 | Rhodium | Rh | 45 | 135 | Lead | Pb | 82 | 88 |
| Fluorine | F | 9 | 118 | Palladium | Pd | 46 | 139 | Bismuth | Bi | 83 | 98 |
| Neon | Ne | 10 | 128 | Silver | Ag | 47 | 65 | Polonium | Po | 84 | 108 |
| Sodium | Na | 11 | 59 | Cadmium | Cd | 48 | 73 | Astatine | At | 85 | 118 |
| Magnesium | Mg | 12 | 68 | Indium | In | 49 | 78 | Radon | Rn | 86 | 128 |
| Aluminium | Al | 13 | 78 | Tin | Sn | 50 | 88 | Francium | Fr | 87 | 59 |
| Silicon | Si | 14 | 88 | Antimony | Sb | 51 | 98 | Radium | Ra | 88 | 68 |
| Phosphorus | P | 15 | 98 | Tellurium | Te | 52 | 108 | Actinium | Ac | 89 | 84 |
| Sulfur | S | 16 | 108 | Iodine | I | 53 | 118 | Thorium | Th | 90 | 151 |
| Chlorine | Cl | 17 | 118 | Xenon | Xe | 54 | 128 | Protactinium | Pa | 91 | 151 |
| Argon | Ar | 18 | 128 | Cesium | Cs | 55 | 59 | Uranium | U | 92 | 151 |
| Potassium | K | 19 | 59 | Barium | Ba | 56 | 68 | Neptunium | Np | 93 | 151 |
| Calcium | Ca | 20 | 68 | Lanthanum | La | 57 | 84 | Plutonium | Pu | 94 | 151 |
| Scandium | Sc | 21 | 84 | Cerium | Ce | 58 | 142 | Americium | Am | 95 | 151 |
| Titanium | Ti | 22 | 94 | Praseodymium | Pr | 59 | 142 | Curium | Cm | 96 | 151 |
| Vanadium | V | 23 | 105 | Neodymium | Nd | 60 | 142 | Berkelium | Bk | 97 | 151 |
| Chromium | Cr | 24 | 114 | Promethium | Pm | 61 | 142 | Californium | Cf | 98 | 151 |
| Manganese | Mn | 25 | 124 | Samarium | Sm | 62 | 142 | Einsteinium | Es | 99 | 151 |
| Iron | Fe | 26 | 131 | Europium | Eu | 63 | 142 | Fermium | Fm | 100 | 151 |
| Cobalt | Co | 27 | 135 | Gadolinium | Gd | 64 | 142 | Mendelevium | Md | 101 | 151 |
| Nickel | Ni | 28 | 139 | Terbium | Tb | 65 | 142 | Nobelium | No | 102 | 151 |
| Copper | Cu | 29 | 65 | Dysprosium | Dy | 66 | 142 | Lawrencium | Lr | 103 | 151 |
| Zinc | Zn | 30 | 73 | Holmium | Ho | 67 | 142 | Rutherfordium | Rf | 104 | 94 |
| Gallium | Ga | 31 | 78 | Erbium | Er | 68 | 142 | Dubnium | Db | 105 | 105 |
| Germanium | Ge | 32 | 88 | Thulium | Tm | 69 | 142 | Seaborgium | Sg | 106 | 114 |
| Arsenic | As | 33 | 98 | Ytterbium | Yb | 70 | 142 | Bohrium | Bh | 107 | 124 |
| Selenium | Se | 34 | 108 | Lutetium | Lu | 71 | 142 | Hassium | Hs | 108 | 131 |
| Bromine | Br | 35 | 118 | Hafnium | Hf | 72 | 94 | Meitnerium | Mt | 109 | 135 |
| Krypton | Kr | 36 | 128 | Tantalum | Ta | 73 | 105 | Darmstadtium | Ds | 110 | 139 |
| Rubidium | Rb | 37 | 59 | Tungsten | W | 74 | 114 | Roentgenium | Rg | 111 | |

**Table 2.1–4** The elements ordered according to the Periodic Table

| | | | | | | | Page |
|---|---|---|---|---|---|---|---|
| **Elements of the first period** | | | | | | | **54** |
| 1 Hydrogen | 1 Deuterium | 1 Tritium | 2 Helium-4 | 2 Helium-3 | | | |
| **Elements of Group IA** | | | | | | | **59** |
| 3 Lithium | 11 Sodium | 19 Potassium | 37 Rubidium | 55 Cesium | 87 Francium | | |
| **Elements of Group IB** | | | | | | | **65** |
| 29 Copper | 47 Silver | 79 Gold | 111 Roentgenium | | | | |
| **Elements of Group IIA** | | | | | | | **68** |
| 4 Beryllium | 12 Magnesium | 20 Calcium | 38 Strontium | 56 Barium | 88 Radium | | |
| **Elements of Group IIB** | | | | | | | **73** |
| 30 Zinc | 48 Cadmium | 80 Mercury | | | | | |
| **Elements of Group IIIA** | | | | | | | **78** |
| 5 Boron | 13 Aluminium | 31 Gallium | 49 Indium | 81 Thallium | | | |
| **Elements of Group IIIB** | | | | | | | **84** |
| 21 Scandium | 39 Yttrium | 57 Lanthanum | 89 Actinium | | | | |
| **Elements of Group IVA** | | | | | | | **88** |
| 6 Carbon | 14 Silicon | 32 Germanium | 50 Tin | 82 Lead | | | |
| **Elements of Group IVB** | | | | | | | **94** |
| 22 Titanium | 40 Zirconium | 72 Hafnium | 104 Rutherfordium | | | | |
| **Elements of Group VA** | | | | | | | **98** |
| 7 Nitrogen | 15 Phosphorus | 33 Arsenic | 51 Antimony | 83 Bismuth | | | |
| **Elements of Group VB** | | | | | | | **105** |
| 23 Vanadium | 41 Niobium | 73 Tantalum | 105 Dubnium | | | | |
| **Elements of Group VIA** | | | | | | | **108** |
| 8 Oxygen | 16 Sulfur | 34 Selenium | 52 Tellurium | 84 Polonium | | | |
| **Elements of Group VIB** | | | | | | | **114** |
| 24 Chromium | 42 Molybdenum | 74 Tungsten | 106 Seaborgium | | | | |
| **Elements of Group VIIA** | | | | | | | **118** |
| 9 Fluorine | 17 Chlorine | 35 Bromine | 53 Iodine | 85 Astatine | | | |
| **Elements of Group VIIB** | | | | | | | **124** |
| 25 Manganese | 43 Technetium | 75 Rhenium | 107 Bohrium | | | | |
| **Elements of Group VIIIA** | | | | | | | **128** |
| 10 Neon | 18 Argon | 36 Krypton | 54 Xenon | 86 Radon | | | |
| **Elements of Group VIII(1)** | | | | | | | **131** |
| 26 Iron | 44 Ruthenium | 76 Osmium | 108 Hassium | | | | |
| **Elements of Group VIII(2)** | | | | | | | **135** |
| 27 Cobalt | 45 Rhodium | 77 Iridium | 109 Meitnerium | | | | |
| **Elements of Group VIII(3)** | | | | | | | **139** |
| 28 Nickel | 46 Palladium | 78 Platinum | 110 Darmstadtium | | | | |
| **Lanthanides** | | | | | | | **142** |
| 58 Cerium | 59 Praseodymium | 60 Neodymium | 61 Promethium | 62 Samarium | 63 Europium | 64 Gadolinium | |
| 65 Terbium | 66 Dysprosium | 67 Holmium | 68 Erbium | 69 Thulium | 70 Ytterbium | 71 Lutetium | |
| **Actinides** | | | | | | | **151** |
| 90 Thorium | 91 Protactinium | 92 Uranium | 93 Neptunium | 94 Plutonium | 95 Americium | 96 Curium | |
| 97 Berkelium | 98 Californium | 99 Einsteinium | 100 Fermium | 101 Mendelevium | 102 Nobelium | 103 Lawrencium | |

**Table 2.1-5** Periodic Table of the elements

## Periodic Table of the Elements

18 VIIIA — IUPAC Notation, CAS Notation
2 He — Atomic Number, Element Symbol
Unstable Nuclei

### Main Groups

| 1 IA | 2 IIA | 13 IIIA | 14 IVA | 15 VA | 16 VIA | 17 VIIA | 18 VIIIA | Shells |
|---|---|---|---|---|---|---|---|---|
| 1 H | | | | | | | 2 He | K |
| 3 Li | 4 Be | 5 B | 6 C | 7 N | 8 O | 9 F | 10 Ne | K–L |
| 11 Na | 12 Mg | 13 Al | 14 Si | 15 P | 16 S | 17 Cl | 18 Ar | K–L–M |
| 19 K | 20 Ca | 31 Ga | 32 Ge | 33 As | 34 Se | 35 Br | 36 Kr | –L–M–N |
| 37 Rb | 38 Sr | 49 In | 50 Sn | 51 Sb | 52 Te | 53 I | 54 Xe | –M–N–O |
| 55 Cs | 56 Ba | 81 Tl | 82 Pb | 83 Bi | 84 Po | 85 At | 86 Rn | –N–O–P |
| 87 Fr | 88 Ra | | | | | | | –O–P–Q |

### Subgroups

| 3 IIIB | 4 IVB | 5 VB | 6 VIB | 7 VIIB | 8 VIII (1) | 9 VIII (2) | 10 VIII (3) | 11 IB | 12 IIB | Shells |
|---|---|---|---|---|---|---|---|---|---|---|
| 21 Sc | 22 Ti | 23 V | 24 Cr | 25 Mn | 26 Fe | 27 Co | 28 Ni | 29 Cu | 30 Zn | –L–M–N |
| 39 Y | 40 Zr | 41 Nb | 42 Mo | 43 Tc | 44 Ru | 45 Rh | 46 Pd | 47 Ag | 48 Cd | –M–N–O |
| 57 La | 72 Hf | 73 Ta | 74 W | 75 Re | 76 Os | 77 Ir | 78 Pt | 79 Au | 80 Hg | –N–O–P |
| 89 Ac | 104 Rf | 105 Db | 106 Sg | 107 Bh | 108 Hs | 109 Mt | 110 Ds | 111 Rg | 112 | –O–P–Q |

**Lanthanides** (Shells –N–O–P)

| 58 Ce | 59 Pr | 60 Nd | 61 Pm | 62 Sm | 63 Eu | 64 Gd | 65 Tb | 66 Dy | 67 Ho | 68 Er | 69 Tm | 70 Yb | 71 Lu |
|---|---|---|---|---|---|---|---|---|---|---|---|---|---|

**Actinides** (Shells –O–P–Q)

| 90 Th | 91 Pa | 92 U | 93 Np | 94 Pu | 95 Am | 96 Cm | 97 Bk | 98 Cf | 99 Es | 100 Fm | 101 Md | 102 No | 103 Lr |
|---|---|---|---|---|---|---|---|---|---|---|---|---|---|

## 2.1.5 Data

### 2.1.5.1 Elements of the First Period

**Table 2.1-6A** Elements of the first period (hydrogen and helium). Atomic, ionic, and molecular properties

| **Element name** | **Hydrogen** | | | **Helium** | | | |
|---|---|---|---|---|---|---|---|
| **Special name** | **Hydrogen** | **Deuterium** | **Tritium** | **Helium 4** | **Helium 3** | | |
| **Chemical symbol** | **H** | **$^2$H or D** | **$^3$H or T** | **$^4$He** | **$^3$He** | | |
| **Atomic number $Z$** | **1** | **1** | **1** | **2** | **2** | | |
| | | | | | | **Units** | **Remarks** |
| Characteristics | | | Radioactive | | | | |
| Half-life | | | 12.32 | | | y | |
| Relative atomic mass $A$ (atomic weight) | 1.00794(7) | 2.01408 | 3.01605 | 4.002602(2) | | | |
| Abundance in lithosphere | $1400\times10^{-6}$ | $1.4\times10^{-4}$ | | $4.2\times10^{-7}$ | | | Mass ratio |
| Abundance in sea | $110\times10^{-3}$ | | | | | | Mass ratio |
| Atomic radius $r_{cov}$ | 30 | | | | | pm | Covalent radius |
| Atomic radius $r_{met}$ | | | | 140 | | pm | Metallic radius, CN[a] = 12 |
| Atomic radius $r_{vdW}$ | 140 | | | 140 | | pm | van der Waals radius |
| Electron shells | K | K | K | K | K | | |
| Electronic ground state | $^2S_{1/2}$ | $^2S_{1/2}$ | $^2S_{1/2}$ | $^1S_0$ | $^1S_0$ | | |
| Electronic configuration | $1s^1$ | $1s^1$ | $1s^1$ | $1s^2$ | $1s^2$ | | |
| Oxidation states | 1−, 1+ | | | | | | |
| Electron affinity | 0.754 | | | 0.19 | | eV | |
| Electronegativity $\chi_A$ | 2.20 | | | 3.20 | | | Allred and Rochow |
| 1st ionization energy | 13.59844 | | | 24.58741 | | eV | |
| 2nd ionization energy | | | | 54.41778 | | eV | |
| Standard electrode potential $E^0$ | 0.00000 | | | | | V | Reaction $2H^+ + 2e^- = H_2$ |
| Molecular form in gaseous state | $H_2$ | | | | | | |
| Internuclear distance in molecule | 74.166 | | | | | pm | |
| Dissociation energy | 4.475 | | | | | eV | Extrapolated to $T = 0$ K |

[a] Coordination number.

**Table 2.1-6B(a)** Elements of the first period (hydrogen and helium). Crystallographic properties (for allotropic and high-pressure modifications, see Table 2.1-6C)

| **Element name** | **Hydrogen** | | | **Helium** | | | |
|---|---|---|---|---|---|---|---|
| **Special name**<br>**Chemical symbol**<br>**Atomic number *Z*** | **Hydrogen**<br>**H**<br>**1** | **Deuterium**<br>**$^{2}$H or D**<br>**1** | **Tritium**<br>**$^{3}$H or T**<br>**1** | **Helium 4**<br>**$^{4}$He**<br>**2** | **Helium 3**<br>**$^{3}$He**<br>**2** | | |
| | | | | | | **Units** | **Remarks** |
| State | $H_2$ at 4.2 K | | | At 1.5 K | | | |
| Crystal system, Bravais lattice | hex | | | hex | | | |
| Structure type | Mg | | | Mg | | | |
| Lattice constant *a* | 377.1 | | | 357.7 | | pm | |
| Lattice constant *c* | 615.6 | | | 584.2 | | | |
| Space group | $P6_3/mmc$ | | | $P6_3/mmc$ | | | |
| Schoenflies symbol | $D_{6h}^4$ | | | $D_{6h}^4$ | | | |
| *Strukturbericht* type | A3 | | | AQ3 | | | |
| Pearson symbol | hP2 | | | hP2 | | | |
| Number *A* of atoms per cell | 2 | | | 2 | | | |
| Coordination number | 12 | | | 12 | | | |
| Shortest interatomic distance, solid | | | | 357 | | pm | |

**Table 2.1-6B(b)** Elements of the fist period (hydrogen and helium). Mechanical properties

| **Element name** | **Hydrogen** | | | **Helium** | | | |
|---|---|---|---|---|---|---|---|
| **Special name** | **Hydrogen** | **Deuterium** | **Tritium** | **Helium 4** | **Helium 3** | | |
| **Chemical symbol** | **H** | **$^{2}$H or D** | **$^{3}$H or T** | **$^{4}$He** | **$^{3}$He** | | |
| **Atomic number $Z$** | **1** | **1** | **1** | **2** | **2** | | |
| | | | | | | **Units** | **Remarks** |
| State | $H_2$ | $D_2$ | | | | | |
| Density $\varrho$, liquid | | 0.162 | 0.260 | | | g/cm$^3$ | Near $T_m$ |
| Density $\varrho$, gas | $0.0899\times10^{-3}$ | 0.0032 [a] | 0.0031 [a] | $0.1785\times10^{-3}$ | | g/cm$^3$ | At 273 K [b] |
| Molar volume $V_{mol}$, gas | 13.26 | | | 32.07 | | cm$^3$/mol | |
| Viscosity $\eta$, gas | 8.67 | | | | | mPa s | At 293 K, 101 kPa |
| Sound velocity, gas | 1237 | | | 969 (STP) | | m/s | STP |
| Sound velocity, liquid | 1340 | | | | | m/s | At $T_m$, 12 MHz |
| Elastic modulus $E$ | 0.2 | | | 0.1 | | GPa | Solid state, estimated |
| Elastic compliance $s_{11}$ | 2930 (4.2 K) | 1400 (4.2 K) | | $+226\times10^{3}$ (1.6 K) | $+202\times10^{3}$ (0.4 K) | 1/TPa | |
| Elastic compliance $s_{33}$ | 2000 (4.2 K) | 995 (4.2 K) | | | | | |
| Elastic compliance $s_{44}$ | 9090 (4.2 K) | 4350 (4.2 K) | | $+46\times10^{3}$ (1.6 K) | $+108\times10^{3}$ (0.4 K) | 1/TPa | |
| Elastic compliance $s_{12}$ | −1240 (4.2 K) | −490 (4.2 K) | | $-107\times10^{3}$ (1.6 K) | $-91.6\times10^{3}$ (0.4 K) | 1/TPa | |
| Elastic compliance $s_{13}$ | −166 (4.2 K) | −81 (4.2 K) | | | | | |
| Elastic stiffness $c_{11}$ | 0.042 (4.2 K) | 0.82 (4.2 K) | | $+31.1\times10^{-3}$ (1.6 K) | $+20.0\times10^{-3}$ (0.4 K) | GPa | |
| Elastic stiffness $c_{33}$ | 0.51 (4.2 K) | 1.02 (4.2 K) | | | | | |
| Elastic stiffness $c_{44}$ | 0.11 (4.2 K) | 0.23 (4.2 K) | | $+21.7\times10^{-3}$ (1.6 K) | $+9.2\times10^{-3}$ (0.4 K) | GPa | |
| Elastic stiffness $c_{12}$ | 0.18 (4.2 K) | 0.29 (4.2 K) | | $+28.1\times10^{-3}$ (1.6 K) | $+16.4\times10^{-3}$ (0.4 K) | GPa | |
| Elastic stiffness $c_{13}$ | 0.05 (4.2 K) | | | | | | |
| Solubility in water $\alpha_W$ | 0.0178 [b] | | | 0.0086 | | | |

[a] At 25 K.

[b] 101.3 kPa $H_2$ pressure.

**Table 2.1-6B(c)** Elements of the first period (hydrogen and helium). Thermal and thermodynamic properties

| **Element name** | **Hydrogen** | | | **Helium** | | | |
|---|---|---|---|---|---|---|---|
| **Special name**<br>**Chemical symbol**<br>**Atomic number *Z*** | **Hydrogen**<br>**H**<br>**1** | **Deuterium**<br>**$^2$H or D**<br>**1** | **Tritium**<br>**$^3$H or T**<br>**1** | **Helium 4**<br>**$^4$He**<br>**2** | **Helium 3**<br>**$^3$He**<br>**2** | | |
| | | | | | | **Units** | **Remarks** |
| State | $H_2$ gas | | | He gas | | | |
| Thermal conductivity $\lambda$ | 0.171 | | | $143.0 \times 10^{-3}$ | | W/(m K) | At 300 K |
| Molar heat capacity $c_p$ | 14.418 | | | 20.786 | | J/(mol K) | At 298 K |
| Standard entropy $S^0$ | 130.680 | | | 126.152 | | J/(mol K) | At 298 K and 100 kPa |
| Enthalpy difference $H_{298} - H_0$ | 8.4684 | | | 6.1965 | | kJ/mol | At 298 K |
| Melting temperature $T_m$ | 13.81 | 18.65 | 20.65 | 0.95 [a] | | K | |
| Enthalpy change $\Delta H_m$ | 0.12 | | | 0.021 | | kJ/mol | |
| Boiling temperature $T_b$ | 20.30 | 23.65 | 25.05 | 4.215 | 3.2 | K | |
| Enthalpy change $\Delta H_b$ | 0.46 | | | 0.082 | | kJ/mol | |
| Sublimation enthalpy | 0.376 | | | 0.060 | | kJ/mol | At 0 K |
| Critical temperature $T_c$ | 33.2 | 38.55 | 39.95 | 5.23 | | K | |
| Critical pressure $p_c$ | 1.297 | 1.645 | | 0.229 | | MPa | |
| Critical density $\varrho_c$ | 0.03102 | | | $69.3 \times 10^{-3}$ | | g/cm$^3$ | |
| Triple-point temperature $T_{tr}$ | 14.0 | | | [b] | | K | |
| Triple-point pressure $p_{tr}$ | 7.2 | | | | | kPa | |
| $\lambda$ point | | | | 2.184 | 0.0027 | K | |

[a] At 2.6 MPa.

[b] He does not have a triple point.

**Table 2.1-6B(d)** Elements of the first period (hydrogen and helium). Electronic, electromagnetic, and optical properties

| **Element name** | **Hydrogen** | | | **Helium** | | | |
|---|---|---|---|---|---|---|---|
| **Special name**<br>**Chemical symbol**<br>**Atomic number *Z*** | **Hydrogen**<br>**H**<br>**1** | **Deuterium**<br>**$^2$H or D**<br>**1** | **Tritium**<br>**$^3$H or T**<br>**1** | **Helium 4**<br>**$^4$He**<br>**2** | **Helium 3**<br>**$^3$He**<br>**2** | | |
| | | | | | | **Units** | **Remarks** |
| State | $H_2$ gas | | | He gas | | | |
| Characteristics | Light gas | | | Noble gas | | | |
| Dielectric constant $(\varepsilon - 1)$, gas | $+264 \times 10^{-6}$ | | | $+68 \times 10^{-6}$ | | | At 273 K |
| Dielectric constant $\varepsilon$, liquid | 1.225 | | | 1.048 (3.15 K) | | | At 20.30 K |
| Dielectric constant $\varepsilon$, solid | | | | | | | |
| Molar magnetic susceptibility $\chi_{mol}$, gas (SI system) | $-50.1 \times 10^{-6}$ | | | $-25.4 \times 10^{-6}$ | | $cm^3/mol$ | At 295 K |
| Molar magnetic susceptibility $\chi_{mol}$, gas (cgs system) | $-3.99 \times 10^{-6}$ | | | $-2.02 \times 10^{-6}$ | | $cm^3/mol$ | At 295 K |
| Mass magnetic susceptibility $\chi_{mass}$, liquid (SI system) | $-68.4 \times 10^{-6}$ | | | | | $cm^3/mol$ | At 20.3 K |
| Mass magnetic susceptibility $\chi_{mass}$, liquid (cgs system) | $-5.44 \times 10^{-6}$ | | | | | $cm^3/mol$ | At 20.3 K |
| Mass magnetic susceptibility $\chi_{mass}$, gas (SI system) | $-25 \times 10^{-6}$ | | | $-5.9 \times 10^{-6}$ | | $cm^3/g$ | At 295 K |
| Refractive index $(n - 1)$, gas | $132 \times 10^{-6}$ | | | $36 \times 10^{-6}$ | | | At 273.15 K, $101 \times 10^5$ Pa, $\lambda = 589.3$ nm |
| Refractive index $n$, liquid | 1.112 | | | 1.026 (3.7 K) | | | $\lambda = 589.3$ nm |

**Table 2.1-6C** Elements of the first period (hydrogen and helium). Allotropic and high-pressure modifications

| **Element** | **Hydrogen** | | **Helium** | | | |
|---|---|---|---|---|---|---|
| **Modification** | **α-H ($H_2$)** | **β-H ($H_2$)** | **α-He** | **β-He** | **γ-He** | |
| | | | | | | **Units** |
| Crystal system, Bravais lattice | cub, fc | hex, cp | hex, cp | cub, fc | cub, bc | |
| Structure type | Cu | Mg | Mg | Cu | W | |
| Lattice constant *a* | 533.4 | 377.1 | 357.7 | 4240 | 4110 | pm |
| Lattice constant *c* | | 615.6 | 584.2 | | | pm |
| Space group | $Fm\bar{3}m$ | $P6_3/mmc$ | $P6_3/mmc$ | $Fm\bar{3}m$ | $Im\bar{3}m$ | |
| Schoenflies symbol | $O_h^5$ | $D_{6h}^4$ | $D_{6h}^4$ | $O_h^5$ | $O_h^9$ | |
| *Strukturbericht* type | A1 | A3 | A3 | A1 | A2 | |
| Pearson symbol | cF4 | hP2 | hP2 | cF4 | cI2 | |
| Number *A* of atoms per cell | 4 | 2 | 2 | 4 | 2 | |
| Coordination number | 12 | 12 | 12 | 12 | 8 | |
| Shortest interatomic distance, solid | | | 357 | 300 | 356 | pm |
| Range of stability | < 1.25 K | < 13.81 K | < 0.95 K | 1.6 K; 0.125 GPa | 1.73 K; 0.03 GPa | |

**Table 2.1-7A** Elements of Group IA (CAS notation), or Group 1 (new IUPAC notation). Atomic, ionic, and molecular properties (see Table 2.1-7D for ionic radii)

| Element name | Lithium | Sodium | Potassium | Rubidium | Cesium | Francium | | |
|---|---|---|---|---|---|---|---|---|
| Chemical symbol<br>Atomic number $Z$ | Li<br>3 | Na<br>11 | K<br>19 | Rb<br>37 | Cs<br>55 | Fr<br>87 | | |
| | | | | | | | Units | Remarks |
| Characteristics | | | | | | Radioactive | | |
| Relative atomic mass $A$ (atomic weight) | 6.941(2) | 22.989770(2) | 39.0983(1) | 85.4678(3) | 132.90545(2) | [223] | | |
| Abundance in lithosphere | $65\times10^{-6}$ | $28\,300\times10^{-6}$ | $25\,900\times10^{-6}$ | $280\times10^{-6}$ | $3.2\times10^{-6}$ | | | Mass ratio |
| Abundance in sea | $0.18\times10^{-6}$ | $10\,770\times10^{-6}$ | $380\times10^{-6}$ | $0.12\times10^{-6}$ | $4\times10^{-10}$ | | | Mass ratio |
| Atomic radius $r_{cov}$ | 123 | 157 | 203 | 216 | 253 | | pm | Covalent radius |
| Atomic radius $r_{met}$ | 156 | 192 | 238 | 250 | 272 | | pm | Metallic radius, CN = 12 |
| Atomic radius $r_{os}$ | 158.6 | 171.3 | 216.2 | 228.7 | 251.8 | 244.7 | pm | Outer-shell orbital radius |
| Atomic radius $r_{vdW}$ | 180 | 230 | 280 | 244 | 262 | | pm | van der Waals radius |
| Electron shells | KL | KLM | –LMN | –MNO | –NOP | –OPQ | | |
| Electronic ground state | $^2S_{1/2}$ | $^2S_{1/2}$ | $^2S_{1/2}$ | $^2S_{1/2}$ | $^2S_{1/2}$ | $^2S_{1/2}$ | | |
| Electronic configuration | $[He]2s^1$ | $[Ne]3s^1$ | $[Ar]4s^1$ | $[Kr]5s^1$ | $[Xe]6s^1$ | $[Rn]7s^1$ | | |
| Oxidation states | 1+ | 1+ | 1+ | 1+ | 1+ | 1+ | | |
| Electron affinity | 0.618 | 0.548 | 0.501 | 0.486 | 0.472 | 0.46 | eV | |
| Electronegativity $\chi_A$ | 0.97 | 1.01 | 0.91 | 0.89 | 0.86 | (0.86) | | Allred and Rochow |
| 1st ionization energy | 5.39172 | 5.13908 | 4.34066 | 4.17713 | 3.89390 | 4.0727 | eV | |
| 2nd ionization energy | 75.64018 | 47.2864 | 31.63 | 27.285 | 23.15745 | | eV | |
| 3rd ionization energy | 122.45429 | 71.6200 | 45.806 | 40 | | | eV | |
| 4th ionization energy | | 98.91 | 60.91 | 52.6 | | | eV | |
| Standard electrode potential $E^0$ | −3.040 | −2.71 | −2.931 | −2.98 | −2.92 | | V | Reaction type<br>$Li^+ + e^- = Li$ |

**Table 2.1-7B(a)** Elements of Group IA (CAS notation), or Group 1 (new IUPAC notation). Crystallographic properties (see Table 2.1-7C for allotropic and high-pressure modifications)

| **Element name** | **Lithium** | **Sodium** | **Potassium** | **Rubidium** | **Cesium** | **Francium** | | |
|---|---|---|---|---|---|---|---|---|
| **Chemical symbol**<br>**Atomic number *Z*** | **Li**<br>**3** | **Na**<br>**11** | **K**<br>**19** | **Rb**<br>**37** | **Cs**<br>**55** | **Fr**<br>**87** | | |
| | | | | | | | **Units** | **Remarks** |
| Modification | $\beta$-Li | $\beta$-Na | | | | Cs -I | | |
| Crystal system, Bravais lattice | cub, bc | cub, bc | cub, bc | cub, bc | cub, bc | | | |
| Structure type | W | W | W | W | W | | | |
| Lattice constant *a* | 350.93 | 420.96 | 532.1 | 570.3 | 614.1 | | pm | |
| Space group | $Im\bar{3}m$ | $Im\bar{3}m$ | $Im\bar{3}m$ | $Im\bar{3}m$ | $Im\bar{3}m$ | | | |
| Schoenflies symbol | $O_h^9$ | $O_h^9$ | $O_h^9$ | $O_h^9$ | $O_h^9$ | | | |
| *Strukturbericht* type | A2 | A2 | A2 | A2 | A2 | | | |
| Pearson symbol | cI2 | cI2 | cI2 | cI2 | cI2 | | | |
| Number *A* of atoms per cell | 2 | 2 | 2 | 2 | 2 | | | |
| Coordination number | 8 | 8 | 8 | 8 | 8 | | | |
| Shortest interatomic distance, solid | 303 | 371 | 462 | 487 | 524 | | pm | |
| Shortest interatomic distance, liquid | | | | 497 (313 K) | | | pm | |

**Table 2.1-7B(b)** Elements of Group IA (CAS notation), or Group 1 (new IUPAC notation). Mechanical properties

| **Element name** | **Lithium** | **Sodium** | **Potassium** | **Rubidium** | **Cesium** | **Francium** | | |
|---|---|---|---|---|---|---|---|---|
| **Chemical symbol**<br>**Atomic number $Z$** | **Li**<br>**3** | **Na**<br>**11** | **K**<br>**19** | **Rb**<br>**37** | **Cs**<br>**55** | **Fr**<br>**87** | | |
| | | | | | | | **Units** | **Remarks** |
| Density $\varrho$, solid | 0.532 | 0.970 | 0.862 | 1.532 | 1.87 | 2.410 | g/cm$^3$ | |
| Density $\varrho$, liquid | 0.508 (453 K) | 0.927 | 0.827 | 1.470 | 1.847 | | g/cm$^3$ | Near $T_m$ |
| Molar volume $V_{mol}$ | 13.00 | 23.68 | 45.36 | 55.79 | 70.96 | 9.25 | cm$^3$/mol | |
| Viscosity $\eta$, liquid | 0.566 (473 K) | 0.565 (416 K) | 0.64 | 0.52 | | | mPa s | |
| Surface tension, liquid | 0.396 | 0.193 | 0.116 | 0.092 | 0.060 | | N/m | |
| Temperature coefficient | | $-0.05\times10^{-3}$ | $-0.06\times10^{-3}$ | | $-0.046\times10^{-3}$ | | N/(m K) | |
| Coefficient of linear thermal expansion $\alpha$ | $56\times10^{-6}$ | $70.6\times10^{-6}$ | $83\times10^{-6}$ | $90\times10^{-6}$ | $97\times10^{-6}$ | | 1/K | At 298 K |
| Sound velocity, liquid | | 2395 (371 K) | | 1260 | 967 | | m/s | At $T_m$,<br>At 12 MHz |
| Sound velocity, solid, transverse | 2820 | 1620 | 1230 | 770 | 590 | | m/s | |
| Sound velocity, solid, longitudinal | 6030 | 3310 | 2600 | 1430 | 1090 | | m/s | |
| Compressibility $\kappa$ | $8.93\times10^{-5}$ | $13.4\times10^{-5}$ | $23.7\times10^{-5}$ | $33.0\times10^{-5}$ | $0.75\times10^{-5}$ | | 1/MPa | Volume compressibility |
| Elastic modulus $E$ | 11.5 | 6.80 | 3.52 | 2.35 | 1.69 | | GPa | |
| Shear modulus $G$ | 4.24 | 2.94 | 1.28 | 0.91 | 0.65 | | GPa | |
| Poisson number $\mu$ | 0.36 | 0.34 | 0.35 | 0.29 | 0.30 | | | |
| Elastic compliance $s_{11}$ | 315 | 549 | 1339 | 1330 | 1190 (280 K) | | 1/TPa | |
| Elastic compliance $s_{44}$ | 104 | 233 | 526 | 625 | 690 (280 K) | | 1/TPa | |
| Elastic compliance $s_{12}$ | −144 | −250 | −620 | −600 | −450 (280 K) | | 1/TPa | |
| Elastic stiffness $c_{11}$ | 13.4 | 7.59 | 3.69 | 2.96 | 1.60 (280 K) | | GPa | |
| Elastic stiffness $c_{44}$ | 9.6 | 4.30 | 1.90 | 1.60 | 1.44 (280 K) | | GPa | |
| Elastic stiffness $c_{12}$ | 11.3 | 6.33 | 3.18 | 2.44 | 0.99 (280 K) | | GPa | |
| Tensile strength | 0.6 | | | | | | MPa | |
| Vickers hardness | | | | 0.37 | 0.15 | | | |
| Mohs hardness | 0.6 | | | | | | | |

**Table 2.1-7B(c)** Elements of Group IA (CAS notation), or Group 1 (new IUPAC notation). Thermal and thermodynamic properties

| **Element name** | **Lithium** | **Sodium** | **Potassium** | **Rubidium** | **Cesium** | **Francium** | | |
|---|---|---|---|---|---|---|---|---|
| **Chemical symbol**<br>**Atomic number $Z$** | **Li**<br>**3** | **Na**<br>**11** | **K**<br>**19** | **Rb**<br>**37** | **Cs**<br>**55** | **Fr**<br>**87** | | |
| | | | | | | | **Units** | **Remarks** |
| Thermal conductivity $\lambda$ | 84.7 | 141 | 102.4 | 58.2 | 35.9 | | W/(m K) | At 300 K |
| Molar heat capacity $c_p$ | 24.77 | 28.24 | 29.58 | 31.062 | 32.18 | | J/(mol K) | At 298 K |
| Standard entropy $S^0$ | 29.120 | 51.300 | 64.680 | 76.776 | 85.230 | 101.00 | J/(mol K) | At 298 K and 100 kPa |
| Enthalpy difference $H_{298} - H_0$ | 4.6320 | 6.4600 | 7.0880 | 7.4890 | 7.7110 | 10.000 | kJ/mol | |
| Melting temperature $T_m$ | 453.69 | 370.87 | 336.86 | 312.47 | 301.59 | 300 | K | |
| Enthalpy change $\Delta H_m$ | 3.0000 | 2.5970 | 2.3208 | 2.1924 | 2.0960 | | kJ/mol | |
| Entropy change $\Delta S_m$ | 6.612 | 7.002 | 6.890 | 7.016 | 6.950 | | J/(mol K) | |
| Relative volume change $\Delta V_m$ | 0.0151 | 0.027 | 0.0291 | 0.0228 | 0.0263 | | | $(V_l - V_s)/V_l$ at $T_m$ |
| Boiling temperature $T_b$ | 1620 | 1156 | 1040 | 970 | 947 | 950 (estimated) | K | |
| Enthalpy change $\Delta H_b$ | 147.7 | 99.2 | 79.1 | 75.7 | 67.7 | | kJ/mol | |
| Critical temperature $T_c$ | | 2500 | 2280 | | 2010 | | K | |
| Critical pressure $p_c$ | | 25.3 | 16.1 | | 11.3 | | MPa | |
| Critical density $\varrho_c$ | | 0.210 | 0.190 | | 0.410 | | g/cm$^3$ | |

**Table 2.1-7B(d)** Elements of Group IA (CAS notation), or Group 1 (new IUPAC notation). Electronic, electromagnetic, and optical properties

| **Element name** | **Lithium** | **Sodium** | **Potassium** | **Rubidium** | **Cesium** | **Francium** | | |
|---|---|---|---|---|---|---|---|---|
| **Chemical symbol**<br>**Atomic number *Z*** | **Li**<br>**3** | **Na**<br>**11** | **K**<br>**19** | **Rb**<br>**37** | **Cs**<br>**55** | **Fr**<br>**87** | | |
| | | | | | | | **Units** | **Remarks** |
| Characteristics | Very reactive metal | Reactive metal | Soft, reactive metal | Soft, reactive metal | Alkali metal | Alkali metal | | |
| Electrical resistivity $\rho_s$ | 85.5 | 42 | 61 | 116 | 188 | | nΩ m | Solid, at 293 K |
| Temperature coefficient | $48.9\times10^{-4}$ | $54.6\times10^{-4}$ | $67.3\times10^{-4}$ | $63.7\times10^{-4}$ | $50.3\times10^{-4}$ | | 1/K | Solid |
| Pressure coefficient | $-2.1\times10^{-9}$ | $-38.3\times10^{-9}$ | $-69.7\times10^{-9}$ | $-62.9\times10^{-9}$ | $0.5\times10^{-9}$ | | 1/hPa | Solid |
| Electrical resistivity $\rho_l$ | 240 at $T_m$ | | 129.7 | 220 | 367 | | nΩ m | Liquid |
| Resistivity ratio at $T_m$ | 1.68 | 1.44 | 1.56 | 1.612 | 1.66 | | | $\rho_l/\rho_s$ at $T_m$ |
| Hall coefficient $R^a$ | $-1.70\times10^{-10}$ | $-2.1\times10^{-10}$ | $-4.2\times10^{-10}$ | $-5.92\times10^{-10}$ | $-7.8\times10^{-10}$ | | $m^3/(A\,s)$ | At 300 K |
| Thermoelectric coefficient | 14.37 | | 12 | −8.26 | 0.2 | | μV/K | |
| Electronic work function | 2.28 | 2.75 | 2.30 | 2.05 | 1.94 | | V | |
| Thermal work function | 2.39 | | 2.15 | 2.13 | 1.87 | | V | |
| Molar magnetic susceptibility $\chi_{mol}$, solid (SI) | $178\times10^{-6}$ | $201\times10^{-6}$ | $261\times10^{-6}$ | $214\times10^{-6}$ | $364\times10^{-6}$ | | $cm^3/mol$ | At 295 K |
| Molar magnetic susceptibility $\chi_{mol}$, solid (cgs) | $14.2\times10^{-6}$ | $16\times10^{-6}$ | $20.8\times10^{-6}$ | $17\times10^{-6}$ | $29\times10^{-6}$ | | $cm^3/mol$ | At 295 K |
| Mass magnetic susceptibility $\chi_{mass}$, solid (SI) | $25.6\times10^{-6}$ | $8.8\times10^{-6}$ | $6.7\times10^{-6}$ | $2.49\times10^{-6}$ | $2.8\times10^{-6}$ | | $cm^3/g$ | At 295 K |
| Mass magnetic susceptibility $\chi_{mass}$, liquid (SI) | | | | | $2.6\times10^{-6}$ | | $cm^3/g$ | |
| Refractive index $n$, solid | | 4.22 | 0.024 (134 nm) | | | | | $\lambda = 589.3$ nm |
| Refractive index $n$, liquid | | 0.0045 | | | | | | $\lambda = 589.3$ nm |

[a] $B = 1$–$3\ T$

**Table 2.1-7C** Elements of Group IA (CAS notation), or Group 1 (new IUPAC notation). Allotropic and high-pressure modifications

| Element | Lithium | | | Sodium | | Cesium | | | |
|---|---|---|---|---|---|---|---|---|---|
| **Modification** | **α-Li** | **β-Li** | **γ-Li** | **α-Na** | **β-Na** | **Cs-I** | **Cs-II** | **Cs-III** | |
| | | | | | | | | | **Units** |
| Crystal system, Bravais lattice | hex, cp | cub, bc | cub, fc | hex, cp | cub, bc | cub, bc | cub, fc | cub, fc | |
| Structure type | Mg | W | Cu | Mg | W | W | Cu | Cu | |
| Lattice constant *a* | 311.1 | 309.3 | | 376.7 | 420.96 | 614.1 | 598.4 | 580.0 | pm |
| Lattice constant *c* | 509.3 | | | 615.4 | | | | | |
| Space group | $P6_3/mmc$ | $Im\bar{3}m$ | $Fm\bar{3}m$ | $P6_3/mmc$ | $Im\bar{3}m$ | $Im\bar{3}m$ | $Fm\bar{3}m$ | $Fm\bar{3}m$ | |
| Schoenflies symbol | $D_{6h}^4$ | $O_h^9$ | $O_h^5$ | $D_{6h}^4$ | $O_h^9$ | $O_h^9$ | $O_h^5$ | $O_h^5$ | |
| *Strukturbericht* type | A3 | A2 | A1 | A3 | A2 | A2 | A1 | A1 | |
| Pearson symbol | hP2 | cI2 | cF4 | hP2 | cI2 | cI2 | cF4 | cF4 | |
| Number *A* of atoms per cell | 2 | 2 | 4 | 2 | 2 | 2 | 4 | 4 | |
| Coordination number | 6+6 | 8 | 12 | 12 | 8 | 8 | 12 | 12 | |
| Shortest interatomic distance, solid | 310 | 303 | 310 | 377 | 371 | 524 | 457 | 410 | pm |
| Range of stability | < 72 K | RT | | < 36 K | RT | RTP | > 2.37 GPa | > 4.22 GPa | |

**Table 2.1-7D** Elements of Group IA (CAS notation), or Group 1 (new IUPAC notation). Ionic radii (determined from crystal structures)

| Element | Lithium | Sodium | Potassium | Rubidium | Cesium | Francium | |
|---|---|---|---|---|---|---|---|
| **Ion** | **$Li^+$** | **$Na^+$** | **$K^+$** | **$Rb^+$** | **$Cs^+$** | **$Fr^+$** | |
| **Coordination number** | | | | | | | **Units** |
| 4 | 59 | 99 | 137 | | | | pm |
| 6 | 76 | 102 | 138 | 152 | 167 | 180 | pm |
| 8 | 92 | 118 | 151 | 161 | 174 | | pm |
| 9 | | 124 | | | | | pm |
| 10 | | | | 166 | 181 | | pm |
| 12 | | 139 | 164 | 172 | 188 | | pm |

**Table 2.1-8A** Elements of Group IB (CAS notation), or Group 11 (new IUPAC notation). Atomic, ionic, and molecular properties (see Table 2.1-8D for ionic radii)

| **Element name** | **Copper** | **Silver** | **Gold** | | |
|---|---|---|---|---|---|
| **Chemical symbol**<br>**Atomic number *Z*** | **Cu**<br>**29** | **Ag**<br>**47** | **Au**<br>**79** | | |
| | | | | **Units** | **Remarks** |
| Relative atomic mass $A_r$ (atomic weight) | 63.546(3) | 107.8682(2) | 196.96655(2) | | |
| Abundance in lithosphere | $70\times10^{-6}$ | $2.0\times10^{-6}$ | $3\times10^{-9}$ | | Mass ratio |
| Abundance in sea | $5\times10^{-10}$ | $4\times10^{-11}$ | $4\times10^{-12}$ | | Mass ratio |
| Atomic radius $r_{cov}$ | 117 | 134 | 134 | pm | Covalent radius |
| Atomic radius $r_{met}$ | 128 | 144 | 144 | pm | Metallic radius, CN = 12 |
| Atomic radius $r_{vdW}$ | 140 | 170 | 170 | pm | van der Waals radius |
| Electron shells | –LMN | –MNO | –NOP | | |
| Electronic ground state | $^2S_{1/2}$ | $^2S_{1/2}$ | $^2S_{1/2}$ | | |
| Electronic configuration | $[Ar]3d^{10}4s^1$ | $[Kr]4d^{10}5s^1$ | $[Xe]4f^{14}5d^{10}\ 6s^1$ | | |
| Oxidation states | 2+, 1+ | 1+ | 3+, 1+ | | |
| Electron affinity | 1.24 | 1.30 | 2.309 | eV | |
| Electronegativity $\chi_A$ | 1.75 | 1.42 | (1.42) | | Allred and Rochow |
| 1st ionization energy | 7.72638 | 7.57624 | 9.22567 | eV | |
| 2nd ionization energy | 20.29240 | 21.49 | 20.5 | eV | |
| 3rd ionization energy | 36.841 | 34.83 | | eV | |
| 4th ionization energy | 57.38 | | | eV | |
| Standard electrode potential $E^0$ | +0.521 | +0.7996 | +1.692 | V | Reaction type $Cu^+ + e^- = Cu$ |
| | +0.342 | | | V | Reaction type $Cu^{2+} + 2e^- = Cu$ |
| | +0.153 | | | V | Reaction type $Cu^{2+} + e^- = Cu^+$ |
| | | | +1.498 | V | Reaction type $Au^{3+} + 3e^- = Au$ |
| | | | +1.401 | V | Reaction type $Au^{3+} + 2e^- = Au^+$ |

**Table 2.1-8B(a)** Elements of Group IB (CAS notation), or Group 11 (new IUPAC notation). Crystallographic properties

| **Element name** | **Copper** | **Silver** | **Gold** | | |
|---|---|---|---|---|---|
| **Chemical symbol**<br>**Atomic number *Z*** | **Cu**<br>**29** | **Ag**<br>**47** | **Au**<br>**79** | | |
| | | | | **Units** | **Remarks** |
| Crystal system, Bravais lattice | cub, fc | cub, fc | cub, fc | | |
| Structure type | Cu | Cu | Cu | | |
| Lattice constant *a* | 361.49 | 408.61 | 407.84 | pm | At 298 K |
| Space group | $Fm\bar{3}m$ | $Fm\bar{3}m$ | $Fm\bar{3}m$ | | |
| Schoenflies symbol | $O_h^5$ | $O_h^5$ | $O_h^5$ | | |
| *Strukturbericht* type | A1 | A1 | A1 | | |
| Pearson symbol | cF4 | cF4 | cF4 | | |
| Number *A* of atoms per cell | 4 | 4 | 4 | | |
| Coordination number | 12 | 12 | 12 | | |
| Shortest interatomic distance, solid | 255.6 | 288 | 288 | pm | At 293 K |
| Shortest interatomic distance, liquid | 257 (1363 K) | | | pm | |

**Table 2.1-8B(b)** Elements of Group IB (CAS notation), or Group 11 (new IUPAC notation). Mechanical properties

| Element name | Copper | Silver | Gold | | |
|---|---|---|---|---|---|
| Chemical symbol<br>Atomic number $Z$ | Cu<br>29 | Ag<br>47 | Au<br>79 | | |
| | | | | Units | Remarks |
| Density $\varrho$, solid | 8.960 | 10.50 | 19.30 | g/cm$^3$ | |
| Density $\varrho$, liquid | 8.000 | 9.345 | 17.300 | g/cm$^3$ | |
| Molar volume $V_{mol}$ | 7.09 | 10.27 | 10.19 | cm$^3$/mol | |
| Viscosity $\eta$, liquid | 3.36 | 3.62 | 5.38 | mPa s | At $T_m$ |
| Surface tension, liquid | 1.300 | 0.923 | 1.128 | N/m | |
| Temperature coefficient | $-0.18\times10^{-3}$ | $-0.13\times10^{-3}$ | $-0.10\times10^{-3}$ | N/(m K) | |
| Coefficient of linear thermal expansion $\alpha$ | $16.5\times10^{-6}$ | $19.2\times10^{-6}$ | $14.16\times10^{-6}$ | 1/K | At 298 K |
| Sound velocity, solid, transverse | 2300 | 1690 | 1190 | m/s | |
| Sound velocity, solid, longitudinal | 4760 | 3640 | 3280 | m/s | |
| Compressibility $\kappa$ | $0.702\times10^{-5}$ | $0.95\times10^{-5}$ | $0.563\times10^{-5}$ | 1/MPa | Volume compressibility |
| Elastic modulus $E$ | 128 | 80.0 | 78.0 | GPa | |
| Shear modulus $G$ | 46.8 | 29.5 | 26.0 | GPa | |
| Poisson number $\mu$ | 0.34 | 0.38 | 0.42 | | |
| Elastic compliance $s_{11}$ | 15.0 | 23.0 | 23.4 | 1/TPa | |
| Elastic compliance $s_{44}$ | 13.3 | 22.0 | 23.8 | 1/TPa | |
| Elastic compliance $s_{12}$ | −6.3 | −9.8 | −10.8 | 1/TPa | |
| Elastic stiffness $c_{11}$ | 169 | 122 | 191 | GPa | |
| Elastic stiffness $c_{44}$ | 75.3 | 45.5 | 42.2 | GPa | |
| Elastic stiffness $c_{12}$ | 122 | 92 | 162 | GPa | |
| Tensile strength | 209 | 125 | 110 | MPa | At 293 K |
| Vickers hardness | 369 | 251 | 216 | | At 293 K |

**Table 2.1-8B(c)** Elements of Group IB (CAS notation), or Group 11 (new IUPAC notation). Thermal and thermodynamic properties

| Element name | Copper | Silver | Gold | | |
|---|---|---|---|---|---|
| Chemical symbol<br>Atomic number $Z$ | Cu<br>29 | Ag<br>47 | Au<br>79 | | |
| | | | | Units | Remarks |
| Thermal conductivity $\lambda$ | 1401 | 429 | 317 | W/(m K) | At 300 K |
| Molar heat capacity $c_p$ | 24.443 | 25.36 | 25.42 | J/(mol K) | At 298 K |
| Standard entropy $S^0$ | 33.150 | 42.551 | 47.488 | J/(mol K) | At 298 K and 100 kPa |
| Enthalpy difference $H_{298} - H_0$ | 5.0040 | 5.7446 | 6.0166 | kJ/mol | |
| Melting temperature $T_m$ | 1357.77 | 1234.93 | 1337.33 | K | |
| Enthalpy change $\Delta H_m$ | 13.263 | 11.297 | 12.552 | kJ/mol | |
| Entropy change $\Delta S_m$ | 9.768 | 9.148 | 9.386 | J/(mol K) | |
| Relative volume change | +0.0415 | 0.038 | 0.051 | | $(V_l - V_s)/V_l$ at $T_m$ |
| Boiling temperature $T_b$ | 2843 | 2436 | 3130 | K | |
| Enthalpy change $\Delta H_b$ | 300.7 | 250.6 | 334.4 | kJ/mol | |

**Table 2.1-8B(d)** Elements of Group IB (CAS notation), or Group 11 (new IUPAC notation). Electronic, electromagnetic, and optical properties. There is no Table 2.1-8C, because no allotropic or high-pressure modifications are known

| **Element name** | **Copper** | **Silver** | **Gold** | | |
|---|---|---|---|---|---|
| **Chemical symbol**<br>**Atomic number $Z$** | **Cu**<br>**29** | **Ag**<br>**47** | **Au**<br>**79** | | |
| | | | | **Units** | **Remarks** |
| Characteristics | Metal | Noble metal | Noble metal | | |
| Electrical resistivity $\rho_s$ | 16.78 | 147 | 20.5 | nΩ m | At 293 K |
| Temerature coefficient | $43.8\times10^{-4}$ | $43\times10^{-4}$ | $40.2\times10^{-4}$ | 1/K | |
| Pressure coefficient | $-1.86\times10^{-9}$ | $-3.38\times10^{-9}$ | $-2.93\times10^{-9}$ | 1/hPa | |
| Electrical resistivity $\rho_l$ | 21.5 | | 312 | nΩ m | |
| Resistivity ratio | 2.07 | | 2.28 | | $\rho_l/\rho_s$ at $T_m$ |
| Hall coefficient $R$ | $-0.536\times10^{-10}$ | $-0.84\times10^{-10}$ | $-0.704\times10^{-10}$ | $m^3/(A\,s)$ | $B = 0.3–2.2$ T, 298 K |
| Thermoelectric coefficient | 1.72 | 1.42 | 1.72 | μV/K | |
| Electronic work function | 4.65 | 4.26 | 5.1 | V | |
| Thermal work function | 4.39 | 4.31 | 4.25 | V | |
| Molar magnetic susceptibility $chi_{mol}$, solid (SI) | $-68.6\times10^{-6}$ | $-245\times10^{-6}$ | $-352\times10^{-6}$ | $cm^3/mol$ | At 295 K |
| Molar magnetic susceptibility $\chi_{mol}$, solid (cgs) | $-5.46\times10^{-6}$ | $-19.5\times10^{-6}$ | $-28\times10^{-6}$ | $cm^3/mol$ | At 295 K |
| Mass magnetic susceptibility $\chi_{mass}$, solid (SI) | $-1.081\times10^{-6}$ | $-2.27\times10^{-6}$ | $-1.78\times10^{-6}$ | $cm^3/g$ | At 295 K |
| Mass magnetic susceptibility $\chi_{mass}$, liquid (SI) | $-1.2\times10^{-6}$ | $-2.83\times10^{-6}$ | $-2.16\times10^{-6}$ | $cm^3/g$ | |

**Table 2.1-8D** Elements of Group IB (CAS notation), or Group 11 (new IUPAC notation). Ionic radii (determined from crystal structures)

| **Element** | **Copper** | | **Silver** | | **Gold** | | |
|---|---|---|---|---|---|---|---|
| **Ion** | **$Cu^+$** | **$Cu^{2+}$** | **$Ag^+$** | **$Ag^{2+}$** | **$Au^+$** | **$Au^{3+}$** | |
| **Coordination number** | | | | | | | **Units** |
| 2 | 46 | | | | | | pm |
| 4 | 60 | 57 | 100 | 79 | | 64 | pm |
| 6 | 77 | 73 | 115 | 94 | 137 | 85 | pm |
| 8 | | | 128 | | | | pm |

**Table 2.1-9A** Elements of Group IIA (CAS notation), or Group 2 (new IUPAC notation). Atomic, ionic, and molecular properties (see Table 2.1-9D for ionic radii)

| **Element name** | **Beryllium** | **Magnesium** | **Calcium** | **Strontium** | **Barium** | **Radium** | | |
|---|---|---|---|---|---|---|---|---|
| **Chemical symbol**<br>**Atomic number *Z*** | **Be**<br>**4** | **Mg**<br>**12** | **Ca**<br>**20** | **Sr**<br>**38** | **Ba**<br>**56** | **Ra**<br>**88** | | |
| | | | | | | | **Units** | **Remarks** |
| Characteristics | | | | | | Radioactive | | |
| Relative atomic mass $A$ (atomic weight) | 9.012182(3) | 24.3050(6) | 40.078(4) | 87.62(1) | 137.327(7) | [226] | | |
| Abundance in lithosphere | $6\times10^{-6}$ | $20\,900\times10^{-6}$ | $26\,300\times10^{-6}$ | $150\times10^{-6}$ | $430\times10^{-6}$ | | | Mass ratio |
| Abundance in sea | $6\times10^{-13}$ | $1290\times10^{-6}$ | $412\times10^{-6}$ | $8.0\times10^{-6}$ | $2\times10^{-9}$ | | | Mass ratio |
| Atomic radius $r_{cov}$ | 89 | 136 | 174 | 191 | 198 | | pm | Covalent radius |
| Atomic radius $r_{met}$ | 112 | 160 | 197 | 215 | 224 | 230 | pm | Metallic radius, CN = 12 |
| Atomic radius $r_{vdW}$ | | 170 | | | | | pm | van der Waals radius |
| Electron shells | KL | KLM | –LMN | –MNO | –NOP | –OPQ | | |
| Electronic ground state | $^1S_0$ | $^1S_0$ | $^1S_0$ | $^1S_0$ | $^1S_0$ | $^1S_0$ | | |
| Electronic configuration | $[He]2s^2$ | $[Ne]2s^2$ | $[Ar]4s^2$ | $[Kr]5ss^2$ | $[Xe]6s^2$ | $[Rn]7s^2$ | | |
| Oxidation states | 2+ | 2+ | 2+ | 2+ | 2+ | 2+ | | |
| Electron affinity | Not stable | Not stable | 0.0246 | 0.048 | 0.15 | | eV | |
| Electronegativity $\chi_A$ | 1.47 | 1.23 | 1.04 | 0.99 | 0.97 | (0.97) | | Allred and Rochow |
| 1st ionization energy | 9.32263 | 7.64624 | 6.11316 | 5.69484 | 5.21170 | 5.27892 | eV | |
| 2nd ionization energy | 18.21116 | 15.03528 | 11.87172 | 11.03013 | 10.00390 | 10.14716 | eV | |
| 3rd ionization energy | 153.89661 | 80.1437 | 50.9131 | 42.89 | | | eV | |
| 4th ionization energy | 217.71865 | 109.2655 | 67.27 | 57 | | | eV | |
| Standard electrode potential $E^0$ | −1.847 | −2.372 | −2.868 | −2.89 | −2.90 | | V | Reaction type<br>$Be^{++}+2e^-=Be$ |

**Table 2.1-9B(a)** Elements of Group IIA (CAS notation), or Group 2 (new IUPAC notation). Crystallographic properties (see Table 2.1-9C for allotropic and high-pressure modifications)

| **Element name** | **Beryllium** | **Magnesium** | **Calcium** | **Strontium** | **Barium** | **Radium** | | |
|---|---|---|---|---|---|---|---|---|
| **Chemical symbol**<br>**Atomic number *Z*** | **Be**<br>**4** | **Mg**<br>**12** | **Ca**<br>**20** | **Sr**<br>**38** | **Ba**<br>**56** | **Ra**<br>**88** | | |
| | | | | | | | **Units** | **Remarks** |
| Modification | $\alpha$-Be | | $\alpha$-Ca | $\alpha$-Sr | | | | |
| Crystal system, Bravais lattice | hex | hex | cub, fc | cub, fc | cub, bc | cub, bc | | |
| Structure type | Mg | Mg | Cu | Cu | W | W | | |
| Lattice constant *a* | 228.57 | 320.93 | 558.84 | 608.4 | 502.3 | 514.8 | pm | |
| Lattice constant *c* | 358.39 | 521.07 | | | | | pm | |
| Space group | $P6_3/mmc$ | $P6_3/mmc$ | $Fm\bar{3}m$ | $Fm\bar{3}m$ | $Im\bar{3}m$ | $Im\bar{3}m$ | | |
| Schoenflies symbol | $D_{6h}^4$ | $D_{6h}^4$ | $O_h^5$ | $O_h^5$ | $O_h^9$ | $O_h^9$ | | |
| *Strukturbericht* type | A3 | A3 | A1 | A1 | A2 | A2 | | |
| Pearson symbol | hP2 | hP2 | cF4 | cF4 | cI2 | cI2 | | |
| Number *A* of atoms per cell | 2 | 2 | 4 | 4 | 2 | 2 | | |
| Coordination number | 12 | 6+6 | 12 | 12 | 8 | 8 | | |
| Shortest interatomic distance, solid | 222 | 319 | 393 | 430 | 434 | 446 | pm | |

**Table 2.1-9B(b)** Elements of Group IIA (CAS notation), or Group 2 (new IUPAC notation). Mechanical properties

| Element name | Beryllium | Magnesium | Calcium | Strontium | Barium | Radium | | |
|---|---|---|---|---|---|---|---|---|
| Chemical symbol<br>Atomic number $Z$ | Be<br>4 | Mg<br>12 | Ca<br>20 | Sr<br>38 | Ba<br>56 | Ra<br>88 | | |
| | | | | | | | Units | Remarks |
| Density $\varrho$, solid | 1.85 | 1.74 | 1.55 | 2.60 | 3.50 | 5.000 | g/cm$^3$ | |
| Density $\varrho$, liquid | 1.420 (1770 K) | 1.590 | 1.365 | 2.375 | 3.325 | | g/cm$^3$ | |
| Molar volume $V_{mol}$ | 4.88 | 13.98 | 25.86 | 34.50 | 38.21 | 45.2 | cm$^3$/mol | |
| Viscosity $\eta$, liquid | | 1.23 | 1.06 | | | | mPa s | |
| Surface tension $\gamma$, liquid | 1.1 (1770 K) | 0.563 (954 K) | 0.361 | 0.303 | 0.276 | 0.45 | N/m | |
| Temperature coefficient | | | $-0.068\times10^3$ | | $-0.095$ | | N/(m K) | |
| Coefficient of linear thermal expansion $\alpha$ | $11.5\times10^{-6}$ | $26.1\times10^{-6}$ | $22\times10^{-6}$ | $23\times10^{-6}$ | $20.7\times10^{-6}$ | $20.2\times10^{-6}$ | 1/K | |
| Sound velocity, solid, transverse | 8330 | 3170 | 2210 | 1520 | 1160 | | m/s | |
| Sound velocity, solid, longitudinal | 12 720 | 5700 | 4180 | 2780 | 2080 | | m/s | |
| Compressibility $\kappa$ | $0.765\times10^{-5}$ | $2.88\times10^{-5}$ | $5.73\times10^{-5}$ [a] | $7.97\times10^{-5}$ | $10.0\times10^{-5}$ | | 1/MPa | Volume compressibility |
| Elastic modulus $E$ | 286 | 44.4 | 19.6 [a] | 15.7 | 12.8 | 13.2 [b] | GPa | |
| Shear modulus $G$ | 133 | 16.9 | 7.85 [a] | 6.03 | 4.84 | | GPa | |
| Poisson number $\mu$ | 0.12 | 0.28 | 0.31 [a] | 0.28 | 0.28 | | | |
| Elastic compliance $s_{11}$ | 3.45 | 22.0 | 104 | 218 | 157 | | 1/TPa | |
| Elastic compliance $s_{33}$ | 2.87 | 19.7 | | | | | 1/TPa | |
| Elastic compliance $s_{44}$ | 6.16 | 60.9 | 71 | 135 | 105 | | 1/TPa | |
| Elastic compliance $s_{12}$ | $-0.28$ | $-7.8$ | $-42$ | $-90$ | $-61$ | | 1/TPa | |
| Elastic compliance $s_{13}$ | $-0.05$ | $-5.0$ | | | | | 1/TPa | |
| Elastic stiffness $c_{11}$ | 292 | 59.3 | 22.8 | 10.94 | 12.6 | | GPa | |
| Elastic stiffness $c_{33}$ | 349 | 61.5 | | | | | GPa | |
| Elastic stiffness $c_{44}$ | 163 | 16.4 | 14 | 7.41 | 9.5 | | GPa | |
| Elastic stiffness $c_{12}$ | 24 | 25.7 | 16.0 | 7.69 | 8.0 | | GPa | |
| Elastic stiffness $c_{13}$ | 6 | 21.4 | | | | | GPa | |
| Tensile strength | 228–352 | 90 | | | | | GPa | |
| Vickers hardness | 1670 | | 130 | 140 | 42 | | | |
| Brinell hardness | 1060–1300 | 300–500 | | | | | | At 293 K |

[a] At 348 K.
[b] Estimated.

**Table 2.1-9B(c)** Elements of Group IIA (CAS notation), or Group 2 (new IUPAC notation). Thermal and thermodynamic properties

| Element name | Beryllium | Magnesium | Calcium | Strontium | Barium | Radium | | |
|---|---|---|---|---|---|---|---|---|
| Chemical symbol<br>Atomic number $Z$ | Be<br>4 | Mg<br>12 | Ca<br>20 | Sr<br>38 | Ba<br>56 | Ra<br>88 | | |
| | | | | | | | Units | Remarks |
| Thermal conductivity $\lambda$ | 200 | 171 | 200 | 35.3 | 18.4 | 18.6 | W/(m K) | |
| Molar heat capacity $c_p$ | 16.44 | 24.895 | 25.940 | 26.4 | 28.09 | | J/(mol K) | At 298 K |
| Standard entropy $S^0$ | 9.500 | 32.671 | 41.588 | 55.694 | 62.500 | 69.000 | J/(mol K) | At 298 K and 100 kPa |
| Enthalpy difference $H_{298} - H_0$ | 1.9500 | 4.9957 | 5.7360 | 6.5680 | 6.9100 | 7.2000 | kJ/mol | |
| Melting temperature $T_m$ | 1560.0 | 923.00 | 1115.0 | 1050.0 | 1000.0 | 969.00 | K | |
| Enthalpy change $\Delta H_m$ | 7.8950 | 8.4768 | 8.5395 | 7.4310 | 7.1190 | 7.7000 | kJ/mol | |
| Entropy change $\Delta S_m$ | 5.061 | 9.184 | 7.659 | 7.077 | 7.119 | 7.946 | J/(mol K) | |
| Relative volume change $\Delta V_m$ | | 0.042 | 0.047 | | | | | $(V_l - V_s)/V_l$ at $T_m$ |
| Boiling temperature $T_b$ | 2741 | 1366 | 1773 | 1685 | 2118 | | K | |
| Enthalpy change $\Delta H_b$ | 291.58 | 127.4 | 153.6 | 137.19 | 141.5 | 136.7 | kJ/mol | |

**Table 2.1-9B(d)** Elements of Group IIA (CAS notation), or Group 2 (new IUPAC notation). Electronic, electromagnetic, and optical properties

| Element name | Beryllium | Magnesium | Calcium | Strontium | Barium | Radium | | |
|---|---|---|---|---|---|---|---|---|
| Chemical symbol<br>Atomic number $Z$ | Be<br>4 | Mg<br>12 | Ca<br>20 | Sr<br>38 | Ba<br>56 | Ra<br>88 | | |
| | | | | | | | Units | Remarks |
| Characteristics | Light metal | Light metal | Metal | Soft metal | Soft metal | Metal | | |
| Electrical resistivity $\rho_s$ | 28 | 39.4 | 31.6 | 303 | 500 | | nΩ m | At RT |
| Temperature coefficient | $90.0 \times 10^{-4}$ | $41.2 \times 10^{-4}$ | $41.7 \times 10^{-4}$ | $38.2 \times 10^{-4}$ | $64.9 \times 10^{-4}$ | | 1/K | |
| Pressure coefficient | $-1.6 \times 10^{-9}$ | $-4.7 \times 10^{-9}$ | $15.2 \times 10^{-9}$ | $5.56 \times 10^{-9}$ | $-3.0 \times 10^{-9}$ | | 1/hPa | |
| Electrical resistivity $\rho_l$ | 27.4 | | | | | | nΩ m | |
| Resistivity ratio | | 1.78 | | | | | | $\rho_l/\rho_s$ at $T_m$ |
| Hall coefficient $R$ | $2.4 \times 10^{-10}$ | $-0.83 \times 10^{-10}$ | | | | | $m^3/(A\,s)$ | At 300 K, $B = 1$ T |
| Thermoelectric coefficient | | −0.4 | −8.2 | | | | μV/K | |
| Electronic work function | 4.98 | 3.97 | 2.87 | 2.74 | 2.56 | | V | |
| Thermal work function | 3.37 | 3.46 | 2.76 | 2.35 | 2.29 | | V | |
| Molar magnetic susceptibility $\chi_{mol}$, solid (SI) | $-113 \times 10^{-6}$ | $165 \times 10^{-6}$ | $503 \times 10^{-6}$ | $1.16 \times 10^{-3}$ | $259 \times 10^{-6}$ | | $cm^3/mol$ | At 295 K |
| Molar magnetic susceptibility $\chi_{mol}$, solid (cgs) | $-9.0 \times 10^{-6}$ | $13.1 \times 10^{-6}$ | $40.0 \times 10^{-6}$ | $92.0 \times 10^{-6}$ | $20.6 \times 10^{-6}$ | | $cm^3/mol$ | At 295 K |
| Mass magnetic susceptibility $\chi_{mass}$, solid (SI) | $-13 \times 10^{-6}$ | $6.8 \times 10^{-6}$ | $14 \times 10^{-6}$ | $13.2 \times 10^{-6}$ | $1.9 \times 10^{-6}$ | | $cm^3/g$ | At 295 K |
| Refractive index $n$, solid | | 0.37 | | | | | | $\lambda = 589$ nm |

**Table 2.1-9C** Elements of Group IIA (CAS notation), or Group 2 (new IUPAC notation). Allotropic and high-pressure modifications

| **Element** | **Beryllium** | | **Calcium** | | **Strontium** | | | | |
|---|---|---|---|---|---|---|---|---|---|
| **Modification** | **α-Be** | **β-Be** | **α-Ca** | **γ-Ca** | **α-Sr** | **β-Sr** | **γ-Sr** | **Sr-II** | |
| | | | | | | | | | **Units** |
| Crystal system, Bravais lattice | hex, cp | cub, bc | cub, fc | cub, bc | cub, fc | hex, cp | cub, bc | cub, bc | |
| Structure type | Mg | W | Cu | W | Cu | Mg | W | W | |
| Lattice constant *a* | 228.57 | 255.15 | 558.84 | 448.0 | 608.4 | 428 | 487 | 443.7 | pm |
| Lattice constant *c* | 358.39 | | | | | 705 | | | pm |
| Space group | $P6_3/mmc$ | $Im\bar{3}m$ | $Fm\bar{3}m$ | $Im\bar{3}m$ | $Fm\bar{3}m$ | $P6_3/mmc$ | $Im\bar{3}m$ | $Im\bar{3}m$ | |
| Schoenflies symbol | $D_{6h}^4$ | $O_h^9$ | $O_h^5$ | $O_h^9$ | $O_h^5$ | $D_{6h}^4$ | $O_h^9$ | $O_h^9$ | |
| *Strukturbericht* type | A3 | A2 | A1 | A2 | A1 | A3 | A2 | A2 | |
| Pearson symbol | hP2 | cI2 | cF4 | cI2 | cF4 | hP2 | cI2 | cI2 | |
| Number *A* of atoms per cell | 2 | 2 | 4 | 2 | 4 | 2 | 2 | 2 | |
| Coordination number | 12 | 8 | 12 | 8 | 12 | 12 | 8 | 8 | |
| Shortest interatomic distance, solid | 222 | 221 | 393 | 388 | 430 | | 422 | | pm |
| Range of stability | RT | > 1523 K | RT | > 1010 K | RT | > 486 K | > 878 K | > 3.5 GPa | |

**Table 2.1-9D** Elements of Group IIA (CAS notation), or Group 2 (new IUPAC notation). Ionic radii (determined from crystal structures)

| **Element** | **Beryllium** | **Magnesium** | **Calcium** | **Strontium** | **Barium** | **Radium** | |
|---|---|---|---|---|---|---|---|
| **Ion** | **$Be^{2+}$** | **$Mg^{2+}$** | **$Ca^{2+}$** | **$Sr^{2+}$** | **$Ba^{2+}$** | **$Ra^{2+}$** | |
| **Coordination number** | | | | | | | **Units** |
| 4 | 27 | 57 | | | | | pm |
| 6 | 45 | 72 | 100 | 118 | 135 | | pm |
| 8 | | 89 | 112 | 126 | 142 | 148 | pm |
| 10 | | | 123 | 136 | | | pm |
| 12 | | | 134 | 144 | 161 | 170 | pm |

**Table 2.1-10A** Elements of Group IIB (CAS notation), or Group 12 (new IUPAC notation). Atomic, ionic, and molecular properties (see Table 2.1-10D for ionic radii)

| **Element name** | **Zinc** | **Cadmium** | **Mercury** | | |
|---|---|---|---|---|---|
| **Chemical symbol**<br>**Atomic number *Z*** | **Zn**<br>**30** | **Cd**<br>**48** | **Hg**<br>**80** | | |
| | | | | **Units** | **Remarks** |
| Relative atomic mass $A$ (atomic weight) | 65.39(2) | 112.411(8) | 200.59(2) | | |
| Abundance in lithosphere | $80\times10^{-6}$ | $0.18\times10^{-6}$ | $0.5\times10^{-6}$ | | Mass ratio |
| Abundance in sea | $4.9\times10^{-9}$ | $1\times10^{-10}$ | $3\times10^{-11}$ | | Mass ratio |
| Atomic radius $r_{cov}$ | 125 | 141 | 144 | pm | Covalent radius |
| Atomic radius $r_{met}$ | 134 | 149 | 162 | pm | Metallic radius, CN = 12 |
| Atomic radius $r_{vdW}$ | 140 | 160 | 150 | pm | van der Waals radius |
| Electron shells | –LMN | –MNO | –NOP | | |
| Electronic ground state | $^1S_0$ | $^1S_0$ | $^1S_0$ | | |
| Electronic configuration | $[Ar]3d^{10}4s^2$ | $[Kr]4d^{10}5s^2$ | $[Xe]4f^{14}5d^{10}6s^2$ | | |
| Oxidation states | 2+ | 2+ | 2+, 1+ | | |
| Electron affinity | Not stable | Not stable | Not stable | eV | |
| Electronegativity $\chi_A$ | 1.66 | 1.46 | (1.44) | | Allred and Rochow |
| 1st ionization energy | 9.39405 | 8.99367 | 10.43750 | eV | |
| 2nd ionization energy | 17.96440 | 16.90832 | 18.756 | eV | |
| 3rd ionization energ | 39.723 | 37.48 | 34.2 | eV | |
| 4th ionization energy | 59.4 | | | eV | |
| Standard electrode potential $E^0$ | −0.7618 | −0.403 | +0.7973 | V<br>V | Reaction type $Hg^{2+}+2e^-=2Hg$<br>Reaction type $Cu^{2+}+2e^-=Cu$ |

**Table 2.1-10B(a)** Elements of Group IIB (CAS notation), or Group 12 (new IUPAC notation). Crystallographic properties (see Table 2.1-10 for allotropic and high-pressure modifications)

| **Element name** | **Zinc** | **Cadmium** | **Mercury** | | |
|---|---|---|---|---|---|
| **Chemical symbol**<br>**Atomic number *Z*** | **Zn**<br>**30** | **Cd**<br>**48** | **Hg**<br>**80** | | |
| | | | | **Units** | **Remarks** |
| Modification | | | $\alpha$-Hg | | |
| Crystal system, Bravais lattice | hex | hex | trig, R | | |
| Structure type | Mg | Mg | $\alpha$-Hg | | |
| Lattice constant $a$ | 266.44 | 297.88 | 300.5 (225 K) | pm | At 298 K |
| Lattice constant $c$ | 494.94 | 561.67 | | pm | At 298 K |
| Lattice angle $\alpha$ | | | 70.53 (225 K) | deg | |
| Space group | $P6_3/mmc$ | $P6_3/mmc$ | $R\bar{3}m$ | | |
| Schoenflies symbol | $D^4_{6h}$ | $D^4_{6h}$ | $D^5_{3d}$ | | |
| *Strukturbericht* type | A3 | A3 | A 10 | | |
| Pearson symbol | hP2 | hP2 | hR1 | | |
| Number $A$ of atoms per cell | 2 | 2 | 1 | | |
| Coordination number | 6+6 | 6+6 | 6+6 | | |
| Shortest interatomic distance, solid | 266 | 297 | 299<br>(at 234 K) | pm | At 293 K |

**Table 2.1-10B(b)** Elements of Group IIB (CAS notation), or Group 12 (new IUPAC notation). Mechanical properties

| **Element name** | **Zinc** | **Cadmium** | **Mercury** | | |
|---|---|---|---|---|---|
| **Chemical symbol**<br>**Atomic number *Z*** | **Zn**<br>**30** | **Cd**<br>**48** | **Hg**<br>**80** | | |
| | | | | **Units** | **Remarks** |
| Density $\varrho$, solid | 7.14 | 8.65 | | $g/cm^3$ | |
| Density $\varrho$, liquid | 6.570 | 8.02 | 13.53 (25 °C) | $g/cm^3$ | |
| Molar volume $V_{mol}$ | 9.17 | 13.00 | 14.81 | $cm^3/mol$ | |
| Viscosity $\eta$, liquid | 2.95 | 2.29 | 1.55 | mPa s | At $T_m$ |
| Surface tension, liquid | 0.816 | 0.564 | 0.476 | N/m | |
| Temperature coefficient | $0.25\times10^{-3}$ | $0.39\times10^{-3}$ | $-0.20\times10^{-3}$ | N/(m K) | |
| Coefficient of linear thermal expansion $\alpha$ | $25.0\times10^{-6}$ | $29.8\times10^{-6}$ | 18.1 | 1/K | At 298.15 K |
| Sound velocity, liquid | 2790 | 2200[a] | 1451 | m/s | 12 MHz[a] |
| Sound velocity, solid, transverse | 2290 | 1690 | | m/s | |
| Sound velocity, solid, longitudinal | 3890 | 2980 | | m/s | |
| Compressibility $\kappa$ | $1.65\times10^{-5}$ | $2.14\times10^{-5}$ | $3.77\times10^{-5}$ | 1/MPa | Volume compressibility |
| Elastic modulus $E$ | 92.7 | 62.3 | 25 | GPa | |
| Shear modulus $G$ | 34.3 | 24.5 | | GPa | |
| Poisson number $\mu$ | 0.29 | 0.30 | | | |
| Elastic compliance $s_{11}$ | 8.22 | 12.4 | 154 (83 K) | 1/TPa | |
| Elastic compliance $s_{33}$ | 27.7 | 34.6 | 45 (83 K) | 1/TPa | |
| Elastic compliance $s_{44}$ | 25.3 | 53.1 | 151 (83 K) | 1/TPa | |
| Elastic compliance $s_{12}$ | 0.60 | −1.2 | −119 (83 K) | 1/TPa | |
| Elastic compliance $s_{13}$ | −7.0 | −9.1 | −21 (83 K) | 1/TPa | |
| Elastic compliance $s_{14}$ | | | −100 (83 K) | 1/TPa | |
| Elastic stiffness $c_{11}$ | 165 | 114.1 | 36.0 (83 K) | GPa | |
| Elastic stiffness $c_{33}$ | 61.8 | 49.9 | 50.5 (83 K) | GPa | |
| Elastic stiffness $c_{44}$ | 39.6 | 19.0 | 12.9 (83 K) | GPa | |
| Elastic stiffness $c_{12}$ | 31.1 | 41.0 | 28.9 (83 K) | GPa | |
| Elastic stiffness $c_{13}$ | 50.0 | 40.3 | 30.3 (83 K) | GPa | |
| Elastic stiffness $c_{14}$ | | | 4.7 (83 K) | GPa | |
| Tensile strength | 20–40 | 71 | | MPa | 293 K |
| Brinell hardness | 280–330 | 180–230 | | | |

[a] At 594 K

**Table 2.1-10B(c)** Elements of Group IIB (CAS notation), or Group 12 (new IUPAC notation). Thermal and thermodynamic properties

| **Element name** | **Zinc** | **Cadmium** | **Mercury** | | |
|---|---|---|---|---|---|
| **Chemical symbol**<br>**Atomic number $Z$** | **Zn**<br>**30** | **Cd**<br>**48** | **Hg**<br>**80** | | |
| | | | | **Units** | **Remarks** |
| State | Solid | Solid | Liquid | | |
| Thermal conductivity $\lambda$ | 121 | 96.8 | 8.34 | W/(m K) | At 300 K |
| Molar heat capacity $c_p$ | 25.44 | 25.98 | 27.983 | J/(mol K) | At 298 K |
| Standard entropy $S^0$ | 41.631 | 51.800 | 75.900 | J/(mol K) | At 298 K and 100 kPa |
| Enthalpy difference $H_{298} - H_0$ | 5.6570 | 6.2470 | 9.3420 | kJ/mol | |
| Melting temperature $T_m$ | 692.68 | 594.22 | 234.32 | K | |
| Enthalpy change $\Delta H_m$ | 7.3220 | 6.1923 | 2.2953 | kJ/mol | |
| Entropy change $\Delta S_m$ | 10.571 | 10.421 | 9.796 | J/(mol K) | |
| Relative volume change | 0.0730 | 0.0474 | 0.037 | | $(V_l - V_s)/V_l$ at $T_m$ |
| Boiling temperature $T_b$ | 1180 | 1040 | 629 | K | |
| Enthalpy change $\Delta H_b$ | 115.3 | 97.40 | 59.2 | kJ/mol | |
| Critical temperature $T_c$ | | | 1750 | K | |
| Critical pressure $p_c$ | | | 167 | MPa | |
| Critical density $\varrho_c$ | | | 5.700 | g/cm$^3$ | |

**Table 2.1-10B(d)** Elements of Group IIB (CAS notation), or Group 12 (new IUPAC notation). Electronic, electromagnetic, and optical properties

| **Element name** | **Zinc** | **Cadmium** | **Mercury** | | |
|---|---|---|---|---|---|
| **Chemical symbol**<br>**Atomic number *Z*** | **Zn**<br>**30** | **Cd**<br>**48** | **Hg**<br>**80** | | |
| | | | | **Units** | **Remarks** |
| Characteristics | Ductile metal | Soft metal | Noble metal | | |
| Electrical resistivity $\rho_s$ | 54.3 | 68 | | nΩ m | At 293 K |
| Temperature coefficient | $41.7\times10^{-4}$ | $46.2\times10^{-4}$ | | 1/K | |
| Pressure coefficient | $-6.3\times10^{-9}$ | $-7.32\times10^{-9}$ | | 1/hPa | |
| Electrical resistivity $\rho_l$ | 326 | 337 | 958 (298 K) | nΩ m | |
| Resistivity ratio | 2.1 | 1.97 | 3.74–4.94 | | $\rho_l/\rho_s$ at $T_m$ |
| Superconducting critical temperature $T_{crit}$ | 0.88 | 0.55 | 4.15 K | K | $\alpha$-Hg |
| Superconducting critical field $H_{crit}$ | 53 | 30 | 412 | Oe | $\alpha$-Hg |
| Hall coefficient $R$ | $0.63\times10^{-10}$ | $0.589\times10^{-10}$ | $-0.73\times10^{-10}$ | $m^3/(A\,s)$ | $B = 0.3$–$2.2$ T<br>298 K |
| Thermoelectric coefficient | 2.9 | 2.8 | −3.4 | μV/K | |
| Electronic work function | 4.22 | 4.04 | | V | |
| Thermal work function | 3.74 | 3.92 | | V | |
| Molar magnetic susceptibility $\chi_{mol}$, solid (SI) | $-115\times10^{-6}$ | $-248\times10^{-6}$ | $-303\times10^{-6}$<br>(234 K) | $cm^3/mol$ | At 295 K |
| Molar magnetic susceptibility $\chi_{mol}$, solid (cgs) | $-9.15\times10^{-6}$ | $-19.7\times10^{-6}$ | $-24.1\times10^{-6}$<br>(234 K) | $cm^3/mol$ | At 295 K |
| Molar magnetic susceptibility $\chi_{mol}$, liquid (SI) | | | $-421\times10^{-6}$ | $cm^3/mol$ | At 295 K |
| Molar magnetic susceptibility $\chi_{mol}$, liquid (cgs) | | | $-33.5\times10^{-6}$ | $cm^3/mol$ | At 295 K |
| Mass magnetic susceptibility $\chi_{mass}$, solid (SI) | $-1.38\times10^{-6}$ | $-2.21\times10^{-6}$ | | $cm^3/g$ | At 295 K |
| Mass magnetic susceptibility $\chi_{mass}$, liquid (SI) | $-1.32\times10^{-6}$ | $-1.83\times10^{-6}$ | | $cm^3/g$ | |
| Refractive index $(n-1)$, gas | | | $+1882\times10^{-6}$<br>($Hg_2$ vapor) | | |
| Refractive index $n$, solid | 1.19 ($\lambda = 550$ nm) | 1.8 (578 nm) | | | |

**Table 2.1-10C** Elements of Group IIB (CAS notation), or Group 12 (new IUPAC notation). Allotropic and high-pressure modifications

| **Element** | **Mercury** | | |
|---|---|---|---|
| **Modification** | **α-Hg** | **β-Hg** | |
| | | | **Units** |
| Crystal system, Bravais lattice | trig, R | tetr | |
| Structure type | α-Hg | In | |
| Lattice constant *a* | 300.5 (225 K) | 399.5 | pm |
| Lattice constant *c* | | 282.5 | pm |
| Lattice angle α | 70.53 (225 K) | | |
| Space group | $R\bar{3}m$ | $14/mmm$ | |
| Schoenflies symbol | $D_{3d}^5$ | $D_{4h}^{17}$ | |
| *Strukturbericht* type | A10 | | |
| Pearson symbol | hR1 | tI2 | |
| Number *A* of atoms per cell | 1 | 2 | |
| Coordination number | 6 + 6 | 2 + 8 | |
| Shortest interatomic distance, solid | 299 | 283 | pm |
| Range of stability | < 234.2 K | 77 K, high pressure | |

**Table 2.1-10D** Elements of Group IIB (CAS notation), or Group 12 (new IUPAC notation). Ionic radii (determined from crystal structures)

| **Element** | **Zinc** | **Cadmium** | **Mercury** | | |
|---|---|---|---|---|---|
| **Ion** | **$Zn^{2+}$** | **$Cd^{2+}$** | **$Hg^{+}$** | **$Hg^{2+}$** | |
| **Coordination number** | | | | | **Units** |
| 2 | | | | 69 | pm |
| 4 | 60 | 78 | | 96 | pm |
| 6 | 74 | 95 | 119 | 102 | pm |
| 8 | 90 | 110 | | 114 | pm |
| 12 | | 131 | | | pm |

**Table 2.1-11A** Elements of Group IIIA (CAS notation), or Group 13 (new IUPAC notation). Atomic, ionic, and molecular properties (see Table 2.1-11D for ionic radii)

| **Element name** | **Boron** | **Aluminium** | **Gallium** | **Indium** | **Thallium** | | |
|---|---|---|---|---|---|---|---|
| **Chemical symbol**<br>**Atomic number *Z*** | **B**<br>**5** | **Al**<br>**13** | **Ga**<br>**31** | **In**<br>**49** | **Tl**<br>**81** | | |
| | | | | | | **Units** | **Remarks** |
| Relative atomic mass *A* (atomic weight) | 10.811(7) | 26.981538(2) | 69.723(1) | 114.818(3) | 204.3833(2) | | |
| Abundance in lithosphere | $10\times10^{-6}$ | $81\,300\times10^{-6}$ | $15\times10^{-6}$ | $0.06\times10^{-6}$ | $0.3\times10^{-6}$ | | Mass ratio |
| Abundance in sea | $4.4\times10^{-6}$ | $0.002\times10^{-6}$ | $3\times10^{-11}$ | $1\times10^{-13}$ | $1\times10^{-11}$ | | Mass ratio |
| Atomic radius $r_{cov}$ | 81 | 125 | 125 | 150 | 155 | pm | Covalent radius |
| Atomic radius $r_{met}$ | 89 | 143 | 153 | 167 | 170 | pm | Metallic radius, CN = 12 |
| Atomic radius $r_{vdW}$ | | 205 | 190 | 190 | 200 | pm | van der Waals radius |
| Electron shells | KL | KLM | –LMN | –MNO | –NOP | | |
| Electronic ground state | $^2P_{1/2}$ | $^2P_{1/2}$ | $^2P_{1/2}$ | $^2P_{1/2}$ | $^2P_{1/2}$ | | |
| Electronic configuration | $[He]2s^22p^1$ | $[Na]3s^23p^1$ | $[Ar]3d^{10}4s^24p^1$ | $[Kr]4d^{10}5s^25p^1$ | $[Xe]4f^{14}5d^{10}6s^26p^1$ | | |
| Oxidation states | 3+ | 3+ | 3+ | 3+ | 3+, 1+ | | |
| Electron affinity | 0.277 | 0.441 | 0.3 | 0.3 | 0.2 | eV | |
| Electronegativity $\chi_A$ | 2.01 | 1.47 | 1.82 | 1.49 | 1.44 | | Allred and Rochow |
| 1st ionization energy | 8.29803 | 5.98577 | 5.99930 | 5.78636 | 6.10829 | eV | |
| 2nd ionization energy | 25.15484 | 18.82856 | 20.5142 | 18.8698 | 20.428 | eV | |
| 3rd ionization energy | 37.93064 | 28.44765 | 30.71 | 28.03 | 29.83 | eV | |
| 4th ionization energy | 259.37521 | 119.992 | 64 | 54 | | eV | |
| Standard electrode potential $E^0$ | | | | | −0.336 | V | Reaction type $Tl^+ + e^- = Tl$ |
| | | −1.662 | −0.560 | −0.338 | | V | Reaction type $Al^{3+} + 3e^- = Al$ |
| | | | | | +1.252 | V | Reaction type $Tl^{3+} + 2e^- = Tl^+$ |

**Table 2.1-11B(a)** Elements of Group IIIA (CAS notation), or Group 13 (new IUPAC notation). Crystallographic properties (see Table 2.1-11C for allotropic and high-pressure modifications)

| **Element name** | **Boron** | **Aluminium** | **Gallium** | **Indium** | **Thallium** | | |
|---|---|---|---|---|---|---|---|
| **Chemical symbol**<br>**Atomic number *Z*** | **B**<br>**5** | **Al**<br>**13** | **Ga**<br>**31** | **In**<br>**49** | **Tl**<br>**81** | | |
| | | | | | | **Units** | **Remarks** |
| Modification | $\beta$-B | $\alpha$-Al | $\alpha$-Ga | | | | |
| Crystal system, Bravais lattice | trig, R | cub, fc | orth, C | tetr, I | hex | | |
| Structure type | $\beta$-B | Cu | $\alpha$-Ga | In | Mg | | |
| Lattice constant *a* | | 361.49 | 451.92 | 459.90 | 345.63 | pm | |
| Lattice constant *b* | | | 765.86 | | | pm | |
| Lattice constant *c* | | | 452.58 | 494.70 | 552.63 | pm | |
| Space group | $R\bar{3}m$ | $Fm\bar{3}m$ | $Cmca$ | $I4/mmm$ | $P6_3/mmc$ | | |
| Schoenflies symbol | $D_{3d}^5$ | $O_h^5$ | $D_{2h}^{18}$ | $D_{4h}^{17}$ | $D_{6h}^4$ | | |
| *Strukturbericht* type | | A1 | A11 | A6 | A3 | | |
| Pearson symbol | hR105 | cF4 | oC8 | tI2 | hP2 | | |
| Number *A* of atoms per cell | 105 | 4 | 8 | 2 | 2 | | |
| Coordination number | | 12 | 1+2+2+2 | 4+8 | | | |
| Shortest interatomic distance, solid | 162–192 | 286 | 247 | 325 | | pm | |

**Table 2.1-11B(b)** Elements of Group IIIA (CAS notation), or Group 13 (new IUPAC notation). Mechanical properties

| **Element name** | **Boron** | **Aluminium** | **Gallium** | **Indium** | **Thallium** | | |
|---|---|---|---|---|---|---|---|
| **Chemical symbol**<br>**Atomic number *Z*** | **B**<br>**5** | **Al**<br>**13** | **Ga**<br>**31** | **In**<br>**49** | **Tl**<br>**81** | | |
| | | | | | | **Units** | **Remarks** |
| Density $\varrho$, solid | 2.46 | 2.70 | 5.91 | 7.31 | 11.85 | g/cm$^3$ | |
| Density $\varrho$, liquid | | 2.39 | 6.200 | 6.990 | 11.29 | g/cm$^3$ | At $T_m$ |
| Molar volume $V_{mol}$ | 4.62 | 10.00 | 11.81 | 15.71 | 17.24 | cm$^3$/mol | |
| Viscosity $\eta$, liquid | | 1.38 | 1.70 | 1.65 | | mPa s | At $T_m$ |
| Surface tension $\gamma$, liquid | | 0.860 | 0.718 | 0.556 | 0.447 | N/m | At $T_m$ |
| Temperature coefficient | | $-0.135\times10^{-3}$ | | $-0.09\times10^{-3}$ | $-0.07\times10^{-3}$ | N/(m K) | |
| Coefficient of linear thermal expansion $\alpha$ | $5\times10^{-6}$ | $23.03\times10^{-6}$ | $18.3\times10^{-6}$ | $33\times10^{-6}$ | $28\times10^{-6}$ | 1/K | |
| Sound velocity, liquid | | 4650 | 2740 | 2215 | | m/s | At 12 MHz |
| Sound velocity, solid, transverse | | 3130 | 750 | 710 | 480 | m/s | |
| Sound velocity, solid, longitudinal | | 6360 | 3030 | 2460 | 1630 | m/s | |
| Compressibility $\kappa$ | $0.539\times10^{-5}$ | $1.33\times10^{-5}$ | $1.96\times10^{-5}$ | $2.70\times10^{-5}$ | $3.41\times10^{-5}$ | 1/MPa | Volume compressibility |
| Elastic modulus $E$ | 178[a] | 70.2 | 9.81 | 10.6 | 7.89 | GPa | |
| Shear modulus $G$ | | 27.8 | 6.67 | 3.68 | 2.67 | GPa | |
| Poisson number $\mu$ | | 0.34 | 0.47 | 0.45 | 0.45 | | |
| Elastic compliance $s_{11}$ | | 16.0 | 12.2 | 148.8 | 104 | 1/TPa | |
| Elastic compliance $s_{22}$ | | | 14.0 | | | 1/TPa | |
| Elastic compliance $s_{33}$ | | | 8.49 | 196.2 | 31.1 | 1/TPa | |
| Elastic compliance $s_{44}$ | | 35.3 | 28.6 | 153.7 | 139 | 1/TPa | |
| Elastic compliance $s_{55}$ | | | 23.9 | | | 1/TPa | |
| Elastic compliance $s_{66}$ | | | 24.8 | 83.2 | | 1/TPa | |
| Elastic compliance $s_{12}$ | | −5.8 | −4.4 | −46.0 | −83 | 1/TPa | |
| Elastic compliance $s_{13}$ | | | −1.7 | −94.5 | −11.6 | 1/TPa | |
| Elastic compliance $s_{23}$ | | | −2.4 | | | 1/TPa | |

[a] Estimated.

**Table 2.1-11B(b)** Elements of Group IIIA (CAS notation), or Group 13 (new IUPAC notation). Mechanical properties , cont.

| Element name | Boron | Aluminium | Gallium | Indium | Thallium | | |
|---|---|---|---|---|---|---|---|
| Chemical symbol<br>Atomic number $Z$ | B<br>5 | Al<br>13 | Ga<br>31 | In<br>49 | Tl<br>81 | | |
| | | | | | | Units | Remarks |
| Elastic stiffness $c_{11}$ | 467 | 108 | 100 | 45.1 | 41.9 | GPa | |
| Elastic stiffness $c_{22}$ | | | 90.2 | | | GPa | |
| Elastic stiffness $c_{33}$ | 473 | | 135 | 44.6 | 54.9 | GPa | |
| Elastic stiffness $c_{44}$ | 198 | 28.3 | 35.0 | 6.51 | 7.20 | GPa | |
| Elastic stiffness $c_{55}$ | | | 41.8 | | | GPa | |
| Elastic stiffness $c_{66}$ | | | 40.3 | 12.0 | | GPa | |
| Elastic stiffness $c_{12}$ | 241 | 62 | 37 | 40.0 | 36.6 | GPa | |
| Elastic stiffness $c_{13}$ | | | 33 | 41.0 | 29.9 | GPa | |
| Elastic stiffness $c_{23}$ | | | 31 | | | GPa | |
| Elastic stiffness $c_{14}$ | 15.1 | | | | | GPa | |
| Tensile strength | 16–24[a] | 90–100 | | | 8.9 | MPa | |
| Vickers hardness | 49 000 | 167 | | | 9 | | At 293 K |
| Brinell hardness | | | | 0.9 | | | |
| Mohs hardness | 9.3 | | 1.5–2.5 | | | | |

[a] Amorphous.

**Table 2.1-11B(c)** Elements of Group IIIA (CAS notation), or Group 13 (new IUPAC notation). Thermal and thermodynamic properties

| Element name | Boron | Aluminium | Gallium | Indium | Thallium | | |
|---|---|---|---|---|---|---|---|
| Chemical symbol<br>Atomic number $Z$ | B<br>5 | Al<br>13 | Ga<br>31 | In<br>49 | Tl<br>81 | | |
| | | | | | | Units | Remarks |
| State | Crystalline | | | | | | |
| Thermal conductivity $\lambda$ | 27.0 | 237 | 33.5 | 81.6 | 46.1 | W/(m K) | |
| Thermal conductivity (liquid) $\lambda_l$ | | 90 | | | | W/(m K) | At $T_m$ |
| Molar heat capacity $c_p$ | 11.20 | 24.392 | 26.15 | 26.732 | 26.32 | J/(mol K) | At 298 K |
| Standard entropy $S^0$ | 5.900 | 28.300 | 40.727 | 57.650 | 64.300 | J/(mol K) | At 298 K and 100 kPa |
| Enthalpy difference $H_{298} - H_0$ | 1.2220 | 4.5400 | 5.5720 | 6.6100 | 6.832 | kJ/mol | |
| Melting temperature $T_m$ | 2348.00 | 933.47 | 302.91 | 429.75 | 577.00 | K | |
| Enthalpy change $\Delta H_m$ | 50.200 | 10.7110 | 5.5898 | 3.2830 | 4.1422 | kJ/mol | |
| Entropy change $\Delta S_m$ | 21.380 | 11.474 | 18.454 | 7.639 | 7.179 | J/(mol K) | |
| Volume change $\Delta V_m$ | | 0.065 | −0.034 | 0.025 | 0.0323 | | $(V_l - V_s)/V_l$ at $T_m$ |
| Boiling temperature $T_b$ | 4138 | 2790 | 2478 | 2346 | 1746 | K | |
| Enthalpy change $\Delta H_b$ | 480.5 | 294.0 | 258.7 | 231.45 | 164.1 | kJ/mol | |

**Table 2.1-11B(d)** Elements of Group IIIA (CAS notation), or Group 13 (new IUPAC notation). Electronic, electromagnetic, and optical properties

| **Element name** | **Boron** | **Aluminium** | **Gallium** | **Indium** | **Thallium** | | |
|---|---|---|---|---|---|---|---|
| **Chemical symbol**<br>**Atomic number *Z*** | **B**<br>**5** | **Al**<br>**13** | **Ga**<br>**31** | **In**<br>**49** | **Tl**<br>**81** | | |
| | | | | | | **Units** | **Remarks** |
| Characteristics | Semiconductor | Light metal | Soft metal | Soft metal | Soft metal, toxic | | |
| Electrical resistivity $\rho_s$ | $6500\times10^{9}$ [a] | 25.0 | 136 | 80.0 | 150 | nΩ m | [a] At 300 K |
| Temperature coefficient | | $46\times10^{-4}$ | $39.6\times10^{-4}$ | $49.0\times10^{-4}$ | $51.7\times10^{-4}$ | 1/K | |
| Pressure coefficient | | $-4.06\times10^{-9}$ | $-2.47\times10^{-9}$ | $-12.2\times10^{-9}$ | $-3.4\times10^{-9}$ | 1/hPa | |
| Electrical resistivity $\rho_l$ | | 200 | 258 | 331 | 740 | nΩ m | |
| Resistivity ratio at $T_m$ | | 1.64 | 1.9 | 2.18 | | | $\rho_l/\rho_s$ at $T_m$ |
| Superconducting critical temperature $T_{cr}$ | | 1.2 | 1.09 | 3.4 | 2.4 | K | |
| Superconducting critical field $H_{cr}$ | | 99 | 51 | 293 | 171 | Oe | |
| Electronic band gap $\Delta E$ | 1.5 | | | | | eV | |
| Electronic work function | 4.79 | 4.28 | 4.35 | 4.08 | 4.05 | V | |
| Thermal work function | 5.71 | 3.74 | 4.12 | 4.0 | 3.76 | V | |
| Intrinsic charge carrier concentration | $+5\times10^{14}$ | | | | | $1/cm^3$ | At 430 K |
| Electron mobility | 1 | | | | | $cm^2/(V\,s)$ | |
| Hole mobility | 55 | | | | | $cm^2/(V\,s)$ | |
| Hall coefficient $R$ | | $-0.343\times10^{-10}$ | $-0.63\times10^{-10}$ | $-0.24\times10^{-10}$ | $0.240\times10^{-10}$ | $m^3/(A\,s)$ | $B=1.0-1.8$ T<br>300 K |
| Thermoelectric coefficient | | −0.6 | | 2.4 | 0.4 | μV/K | |
| Dielectric constant $\varepsilon$, solid | 13 (0.5 MHz) | | | | | | |
| Molar magnetic susceptibility $\chi_{mol}$, solid (SI) | $-84.2\times10^{-6}$ | $207\times10^{-6}$ | $-271\times10^{-6}$ | $-128\times10^{-6}$ | $-628\times10^{-6}$ | $cm^3/mol$ | At 295 K |
| Molar magnetic susceptibility $\chi_{mol}$, solid (cgs) | $-6.7\times10^{-6}$ | $16.5\times10^{-6}$ | $-21.6\times10^{-6}$ | $-10.2\times10^{-6}$ | $-50.0\times10^{-6}$ | $cm^3/mol$ | At 295 K |
| Mass magnetic susceptibility $\chi_{mass}$, solid (SI) | | $+7.9\times10^{-6}$ | $-3.9\times10^{-6}$ | $-1.4\times10^{-6}$ | $-3.13\times10^{-6}$ | $cm^3/g$ | At 295 K |
| Mass magnetic susceptibility $\chi_{mass}$, liquid (SI) | | | | | $-1.72\times10^{-6}$ | $cm^3/g$ | At $T_m$ |
| Refractive index $n$, solid | 3.2 (λ=1 μm) | | | | | | |

[a] At 300 K.

**Table 2.1-11C** Elements of Group IIIA (CAS notation), or Group 13 (new IUPAC notation). Allotropic and high-pressure modifications

| Element | Aluminium | | Gallium | | | Thallium | | | |
|---|---|---|---|---|---|---|---|---|---|
| **Modification** | **α-Al** | **β-Al** | **α-Ga** | **β-Ga** | **γ-Ga** | **α-Tl** | **β-Tl** | **γ-Tl** | |
| | | | | | | | | | Units |
| Crystal system, Bravais lattice | cub, fc | hex, cp | orth, C | tetr | orth | hex, cp | cub, bc | cub, fc | |
| Structure type | Cu | Mg | α-Ga | In | γ-Ga | Mg | W | Cu | |
| Lattice constant *a* | 404.96 | 269.3 | 451.92 | 280.8 | 1059.3 | 345.63 | 387.9 | | pm |
| Lattice constant *b* | | | 765.86 | | 1352.3 | | | | pm |
| Lattice constant *c* | | 439.8 | 452.58 | 445.8 | 520.3 | 552.63 | | | pm |
| Space group | $Fm\bar{3}m$ | $P6_3/mmc$ | $Cmca$ | $I4/mmm$ | $Cmcm$ | $P6_3/mmc$ | $Im\bar{3}m$ | $Fm\bar{3}m$ | |
| Schoenflies symbol | $O_h^5$ | $D_{6h}^4$ | $D_{2h}^{18}$ | | $D_{2h}^{17}$ | $D_{6h}^4$ | $O_h^9$ | $O_h^5$ | |
| *Strukturbericht* type | A1 | A3 | A11 | A6 | | A3 | A2 | A1 | |
| Pearson symbol | cF4 | hP2 | oC8 | tI2 | oC40 | hP2 | cI2 | cF4 | |
| Number *A* of atoms per cell | 4 | 2 | 8 | 2 | 40 | 2 | 2 | 4 | |
| Coordination number | 12 | 12 | 1+2+2+2 | 4+8 | | | 8 | 12 | |
| Shortest interatomic distance, solid | 286 | | 247 | 281 | 260–308 | | 336 | | |
| Range of stability | RTP | > 20.5 GPa | RTP | > 1.2 GPa | 220 K, > 3.0 GPa | RTP | > 503 K | High pressure | |

**Table 2.1-11D** Elements of Group IIIA (CAS notation), or Group 13 (new IUPAC notation). Ionic radii (determined from crystal structures)

| Element | Aluminium | Gallium | Indium | Thallium | | |
|---|---|---|---|---|---|---|
| **Ion** | **$Al^{3+}$** | **$Ga^{3+}$** | **$In^{3+}$** | **$Tl^{+}$** | **$Tl^{3+}$** | |
| **Coordination number** | | | | | | **Units** |
| 4 | 39 | 47 | 62 | | 75 | pm |
| 5 | 48 | | | | | pm |
| 6 | 54 | 62 | 80 | 150 | 89 | pm |
| 8 | | | | 159 | 98 | pm |
| 12 | | | | 170 | | pm |

**Table 2.1-12A** Elements of Group IIIB (CAS notation), or Group 3 (new IUPAC notation). Atomic, ionic, and molecular properties (see Table 2.1-12D for ionic radii)

| **Element name** | **Scandium** | **Yttrium** | **Lanthanum** | **Actinium** | | |
|---|---|---|---|---|---|---|
| **Chemical symbol**<br>**Atomic number *Z*** | **Sc**<br>**21** | **Y**<br>**39** | **La**<br>**57** | **Ac**<br>**89** | | |
| | | | | | **Units** | **Remarks** |
| Characteristics | | | | Radioactive | | |
| Relative atomic mass $A$ (atomic weight) | 44.955910(8) | 88.90585(2) | 138.9055(2) | [227] | | |
| Abundance in lithosphere | $5\times10^{-6}$ | $28.1\times10^{-6}$ | $18.3\times10^{-6}$ | | | Mass ratio |
| Abundance in sea | $6\times10^{-13}$ | $3\times10^{-12}$ | $3\times10^{-12}$ | | | Mass ratio |
| Atomic radius $r_{cov}$ | 144 | 162 | 169 | | pm | Covalent radius |
| Atomic radius $r_{met}$ | 166 | 178 | 187 | 188 | pm | Metallic radius, CN = 12 |
| Electron shells | –LMN | –MNO | –NOP | –OPQ | | |
| Electronic ground state | $^2D_{3/2}$ | $^2D_{3/2}$ | $^2D_{3/2}$ | $^2D_{3/2}$ | | |
| Electronic configuration | $[Ar]3d^14s^2$ | $[Kr]4d^15s^2$ | $[Xe]5d^16s^2$ | $[Rn]6d^17s^2$ | | |
| Oxidation states | 3+ | 3+ | 3+ | 3+ | | |
| Electron affinity | 0.188 | 0.307 | 0.5 | | eV | |
| Electronegativity $\chi_A$ | 1.20 | 1.11 | 1.08 | (1.00) | | Allred and Rochow |
| 1st ionization energy | 6.56144 | 6.217 | 5.5770 | 5.17 | eV | |
| 2nd ionization energy | 12.79967 | 12.24 | 11.060 | 12.1 | eV | |
| 3rd ionization energy | 24.75666 | 20.52 | 19.1773 | | eV | |
| 4th ionization energy | 73.4894 | 60.597 | 49.95 | | eV | |
| Standard electrode potential $E^0$ | | | −2.522 | | V | Reaction type $La^{3+} + 3e^- = La$ |

**Table 2.1-12B(a)** Elements of Group IIIB (CAS notation), or Group 3 (new IUPAC notation). Crystallographic properties (see Table 2.1-12C for allotropic and high-pressure modifications)

| **Element name** | **Scandium** | **Yttrium** | **Lanthanum** | **Actinium** | | |
|---|---|---|---|---|---|---|
| **Chemical symbol**<br>**Atomic number *Z*** | **Sc**<br>**21** | **Y**<br>**39** | **La**<br>**57** | **Ac**<br>**89** | | |
| | | | | | **Units** | **Remarks** |
| Modification | $\alpha$-Sc | $\alpha$-Y | $\alpha$-La | | | |
| Crystal system, Bravais lattice | hex | hex | hex | | | |
| Structure type | Mg | Mg | $\alpha$-La | | | |
| Lattice constant $a$ | 330.88 | 364.82 | 377.40 | | pm | |
| Lattice constant $c$ | 526.80 | 573.18 | 1217.1 | | pm | |
| Space group | $P6_3/mmc$ | $P6_3/mmc$ | $P6_3/mmc$ | | | |
| Schoenflies symbol | $D^4_{6h}$ | $D^4_{6h}$ | $D^4_{6h}$ | | | |
| *Strukturbericht* type | A3 | A3 | A3′ | | | |
| Pearson symbol | hP2 | hP2 | hP4 | | | |
| Number $A$ of atoms per cell | 2 | 2 | 4 | | | |
| Coordination number | 12 | 6+6 | 12 | | | |
| Shortest interatomic distance, solid | 166 | | 364 | | pm | |

**Table 2.1-12B(b)** Elements of Group IIIB (CAS notation), or Group 3 (new IUPAC notation). Mechanical properties

| **Element name** | **Scandium** | **Yttrium** | **Lanthanum** | **Actinium** | | |
|---|---|---|---|---|---|---|
| **Chemical symbol**<br>**Atomic number *Z*** | **Sc**<br>**21** | **Y**<br>**39** | **La**<br>**57** | **Ac**<br>**89** | | |
| | | | | | **Units** | **Remarks** |
| Density $\varrho$, solid | 2.989 | 4.50 | 6.70 | 10.07 | g/cm$^3$ | |
| Molar volume $V_{mol}$ | 15.04 | 19.89 | 22.60 | | cm$^3$/mol | |
| Surface tension, liquid | 0.9 | 0.9 | 0.71 | | N/m | |
| Coefficient of linear thermal expansion $\alpha$ | $10.0\times10^{-6}$ | $10.6\times10^{-6}$ | $4.9\times10^{-6}$ | | 1/K | |
| Sound velocity, solid, transverse | | 2420 | 1540 | | m/s | |
| Sound velocity, solid, longitudinal | | 4280 | 2770 | | m/s | |
| Compressibility $\kappa$ | $2.22\times10^{-5}$ | $2.62\times10^{-5}$ | $3.96\times10^{-5}$ | | 1/MPa | Volume compressibility |
| Elastic modulus $E$ | 75.2 | 66.3 | 39.2 | 25[a] | GPa | |
| Shear modulus $G$ | 29.7 | 25.5 | 14.9 | | GPa | |
| Poisson number $\mu$ | 0.28 | 0.27 | 0.28 | | | |
| Elastic compliance $s_{11}$ | 12.5 | 15.4 | 51.7 [b] | | 1/TPa | |
| Elastic compliance $s_{33}$ | 10.6 | 14.4 | | | 1/TPa | |
| Elastic compliance $s_{44}$ | 36.1 | 41.1 | 55.7 [b] | | 1/TPa | |
| Elastic compliance $s_{12}$ | −4.3 | −5.1 | −19.2 [b] | | 1/TPa | |
| Elastic compliance $s_{13}$ | −2.2 | −2.7 | | | 1/TPa | |
| Elastic stiffness $c_{11}$ | 99.3 | 77.9 | 34.5 [b] | | GPa | |
| Elastic stiffness $c_{33}$ | 107 | 76.9 | | | GPa | |
| Elastic stiffness $c_{44}$ | 27.7 | 24.3 | 18.0 [b] | | GPa | |
| Elastic stiffness $c_{12}$ | 39.7 | 29.2 | 20.4 [b] | | GPa | |
| Elastic stiffness $c_{13}$ | 29.4 | 20 | | | GPa | |
| Tensile strength | 256 | 250–380 | | | MPa | |
| Vickers hardness | 350 | 40 | 491 | | | |

[a] Estimated.

[b] For lanthanum in its metastable fcc phase at room temperature.

**Table 2.1-12B(c)** Elements of Group IIIB (CAS notation), or Group 3 (new IUPAC notation). Thermal and thermodynamic properties

| **Element name** | **Scandium** | **Yttrium** | **Lanthanum** | **Actinium** | | |
|---|---|---|---|---|---|---|
| **Chemical symbol**<br>**Atomic number *Z*** | **Sc**<br>**21** | **Y**<br>**39** | **La**<br>**57** | **Ac**<br>**89** | | |
| | | | | | **Units** | **Remarks** |
| Thermal conductivity $\lambda$ | 15.8 | 17.2 | 13.5 | | W/(m K) | |
| Molar heat capacity $c_p$ | 25.52 | 26.53 | 27.11 | 27.2 | J/(mol K) | At 298 K |
| Standard entropy $S^0$ | 34.644 | 44.788 | 56.902 | 62.000 | J/(mol K) | At 298 K and 100 kPa |
| Enthalpy difference $H_{298} - H_0$ | 5.2174 | 5.9835 | 6.6651 | 6.7000 | kJ/mol | |
| Melting temperature $T_m$ | 1814.00 | 1795.15 | 1193.00 | 1323.00 | K | |
| Enthalpy change $\Delta H_m$ | 14.0959 | 11.3942 | 6.1965 | 12.000 | kJ/mol | |
| Entropy change $\Delta S_m$ | 7.771 | 6.347 | 5.194 | 9.070 | J/(mol K) | |
| Relative volume change $\Delta V_m$ | | | 0.006 | | | $(V_l - V_s)/V_l$ at $T_m$ |
| Boiling temperature $T_b$ | 3104 | 3611 | 3730 | 3473 | K | |
| Enthalpy change $\Delta H_b$ | 314.2 | 363.3 | 413.7 | 293 | kJ/mol | |

**Table 2.1-12B(d)** Elements of Group IIIB (CAS notation), or Group 3 (new IUPAC notation). Electronic, electromagnetic, and optical properties

| **Element name** | **Scandium** | **Yttrium** | **Lanthanum** | **Actinium** | | |
|---|---|---|---|---|---|---|
| **Chemical symbol**<br>**Atomic number *Z*** | **Sc**<br>**21** | **Y**<br>**39** | **La**<br>**57** | **Ac**<br>**89** | | |
| | | | | | **Units** | **Remarks** |
| Characteristics | Soft metal | Reactive metal | Very reactive metal | | | |
| Electrical resistivity $\rho_s$<br>Temperature coefficient<br>Pressure coefficient | 505<br>$28.2\times10^{-4}$ | 550<br>$27.1\times10^{-4}$ | 540<br>$21.8\times10^{-4}$<br>$-1.7\times10^{-9}$ | | nΩ m<br>1/K<br>1/hPa | At RT |
| Electrical resistivity $\rho_l$ | | | 1350 | | nΩ m | |
| Superconducting critical temperature $T_{crit}$ | | | 5.0 | | K | |
| Superconducting critical field $H_{crit}$ | | | | | | |
| Hall coefficient $R$ | $-0.67\times10^{-10}$ | $-0.770\times10^{-10}$ | $-0.8\times10^{-10}$ | | $m^3/(A\,s)$ | At 293 K, $B = 0.5$–$1.0$ T |
| Thermoelectric coefficient | −3.6 | 2.2 | | | μV/K | |
| Electronic work function | 3.5 | 3.1 | 3.5 | | V | |
| Thermal work function | 3.23 | 3.07 | 3.3 | | V | |
| Molar magnetic susceptibility $\chi_{mol}$, solid (SI) | $3710\times10^{-6}$ | $2359\times10^{-6}$ | $+1205\times10^{-6}$ | | $cm^3/mol$ | At 295 K |
| Molar magnetic susceptibility $\chi_{mol}$, solid (cgs) | $295\times10^{-6}$ | $188\times10^{-6}$ | $+95.9\times10^{-6}$ | | $cm^3/mol$ | At 295 K |
| Mass magnetic susceptibility $\chi_{mass}$, solid (SI) | $88\times10^{-6}$ | $27.0\times10^{-6}$ | $+11\times10^{-6}$ | | $cm^3/g$ | |

**Table 2.1-12C** Elements of Group IIIB (CAS notation), or Group 3 (new IUPAC notation). Allotropic and high-pressure modifications

| **Element** | **Scandium** | | **Yttrium** | | **Lanthanum** | | | | |
|---|---|---|---|---|---|---|---|---|---|
| **Modification** | **α-Sc** | **β-Sc** | **α-Y** | **β-Y** | **α-La** | **β-La** | **γ-La** | **β′-La** | |
| | | | | | | | | | **Units** |
| Crystal system, Bravais lattice | hex, cp | cub, bc | hex, cp | cub, bc | hex | cub, fc | cub, bc | cub, fc | |
| Structure type | Mg | W | Mg | W | α-La | Cu | W | Cu | |
| Lattice constant *a* | 330.88 | | 364.82 | | 377.40 | 530.45 | 426.5 | 517 | pm |
| Lattice constant *c* | 526.80 | | 573.18 | | 1217.1 | | | | pm |
| Space group | $P6_3/mmc$ | $Im\bar{3}m$ | $P6_3/mmc$ | $Im\bar{3}m$ | $P6_3/mmc$ | $Fm\bar{3}m$ | $Im\bar{3}m$ | $Fm\bar{3}m$ | |
| Schoenflies symbol | $D_{6h}^4$ | $O_h^9$ | $D_{6h}^4$ | $O_h^9$ | $D_{6h}^4$ | $O_h^5$ | $O_h^9$ | $O_h^5$ | |
| *Strukturbericht* type | A3 | A2 | A3 | A2 | A3′ | A1 | A2 | A1 | |
| Pearson symbol | hP2 | cI2 | hP2 | cI2 | hP4 | cF4 | cI2 | cF4 | |
| Number *A* of atoms per cell | 2 | 2 | 2 | 2 | 4 | 4 | 2 | 4 | |
| Coordination number | 12 | 8 | 6+6 | 8 | 12 | 12 | 8 | 12 | |
| Shortest interatomic distance, solid | | | | 356 | 374 | 375 | 369 | | pm |
| Range of stability | RT | > 1607 K | RT | > 1752 K | RTP | > 613 K | > 1141 K | > 2.0 GPa | |

**Table 2.1-12D** Elements of Group IIIB (CAS notation), or Group 3 (new IUPAC notation). Ionic radii (determined from crystal structures)

| Element | Scandium | Yttrium | Lanthanum | Actinium | |
|---|---|---|---|---|---|
| Ion | $Sc^{3+}$ | $Y^{3+}$ | $La^{3+}$ | $Ac^{3+}$ | |
| Coordination number | | | | | Units |
| 6 | 75 | 90 | 103 | 112 | pm |
| 8 | 87 | 102 | 116 | | pm |
| 9 | | 108 | | | pm |
| 10 | | | 127 | | pm |
| 12 | | | 136 | | pm |

**Table 2.1-13A** Elements of Group IVA (CAS notation), or Group 14 (new IUPAC notation). Atomic, ionic, and molecular properties (see Table 2.1-13D for ionic radii)

| Element name | Carbon | Silicon | Germanium | Tin | Lead | | |
|---|---|---|---|---|---|---|---|
| Chemical symbol<br>Atomic number $Z$ | C<br>6 | Si<br>14 | Ge<br>32 | Sn<br>50 | Pb<br>82 | | |
| | | | | | | Units | Remarks |
| Relative atomic mass $A$ (atomic weight) | 12.0107(8) | 28.0855(3) | 72.61(2) | 118.710(7) | 207.2(1) | | |
| Abundance in lithosphere | $320\times10^{-6}$ | $277\,200\times10^{-6}$ | $7\times10^{-6}$ | $40\times10^{-6}$ | $16\times10^{-6}$ | | Mass ratio |
| Abundance in sea | $28\times10^{-6}$ | $2\times10^{-6}$ | $5\times10^{-11}$ | $1\times10^{-11}$ | $3\times10^{-11}$ | | Mass ratio |
| Atomic radius $r_{cov}$ | 77 | 117 | 122 | 140 | 154 | pm | Covalent radius |
| Atomic radius $r_{met}$ | 91 | 132 | 137 | 220 | 175 | pm | Metallic radius, CN = 12 |
| Atomic radius $r_{vdW}$ | 170 | 210 | 234 | 158 | 200 | pm | van der Waals radius |
| Electron shells | KL | KLM | –LMN | –MNO | –NOP | | |
| Electronic ground state | $^3P_0$ | $^3P_0$ | $^3P_0$ | $^3P_0$ | $^3P_0$ | | |
| Electronic configuration | $1s^2 2s^2 2p^2$ | $[Ne]3s^2 3p^2$ | $[Ar]3d^{10}4s^2 4p^2$ | $[Kr]4d^{10}5s^2 5p^2$ | $[Xe]4f^{14}5d^{10}6s^2 6p^2$ | | |
| Oxidation states | 4+, 4−, 2+ | 4+ | 4+ | 4+, 2+ | 4+, 2+ | | |
| Electron affinity | 1.26 | 1.39 | 1.23 | 1.11 | 0.364 | eV | |
| Electronegativity $\chi_A$ | 2.50 | 1.74 | 2.02 | 1.72 | 1.55 | | Allred and Rochow |
| 1st ionization energy | 11.26030 | 8.15169 | 7.900 | 7.34381 | 7.41666 | eV | |
| 2nd ionization energy | 24.38332 | 16.34585 | 15.93462 | 14.63225 | 15.0322 | eV | |
| 3rd ionization energy | 47.8878 | 33.49302 | 34.2241 | 30.50260 | 31.9373 | eV | |
| 4th ionization energy | 64.4939 | 45.14181 | 45.7131 | 40.73502 | 42.32 | eV | |
| 5th ionization energy | 392.087 | 166.767 | 93.5 | 72.28 | 68.8 | eV | |
| Standard electrode potential $E^0$ | | | | −0.137 | −0.126 | V | Reaction type $Sn^{2+} + 2e^- = Sn$ |
| | | | | +0.151 | | V | Reaction type $Sn^{4+} + 2e^- = Sn^{2+}$ |

**Table 2.1-13B(a)** Elements of Group IVA (CAS notation), or Group 14 (new IUPAC notation). Crystallographic properties (see Table 2.1-13C for allotropic and high-pressure modifications)

| **Element name** | **Carbon** | | **Silicon** | **Germanium** | **Tin** | **Lead** | | |
|---|---|---|---|---|---|---|---|---|
| **Chemical symbol**<br>**Atomic number *Z*** | **C**<br>**6** | | **Si**<br>**14** | **Ge**<br>**32** | **Sn**<br>**50** | **Pb**<br>**82** | | |
| | | | | | | | **Units** | **Remarks** |
| Modification | Diamond | Graphite | | | $\beta$-Sn,[a]<br>white tin, Sn I | | | |
| Crystal system, Bravais lattice | cub | hex | cub, fc | cub, fc | tetr, I | cub, fc | | |
| Structure type | Diamond | C | Diamond | Diamond | $\beta$-Sn | Cu | | |
| Lattice constant *a* | 356.71 | 246.12 | 543.102<br>(22.5 °C) | 565.9(1)<br>RT | 581.97<br>(300 K) | 495.02 | pm | |
| Lattice constant *c* | | 670.90 | | | 317.49 | | pm | |
| Space group | $Fd3m$ | $P6_3/mmc$ | $Fd3m$ | $Fd3m$ | $I4_1/amd$ | $Fm3m$ | | |
| Schoenflies symbol | $O_h^7$ | $D_{6v}^4$ | $O_h^7$ | $O_h^7$ | $D_{4h}^{19}$ | $O_h^5$ | | |
| *Strukturbericht* type | | A9 | A4 | A4 | A5 | A1 | | |
| Pearson symbol | | hP4 | cF8 | cF8 | tI4 | cF4 | | |
| Number *A* of atoms per cell | 8 | 4 | 8 | 8 | 4 | 4 | | |
| Coordination number | 4 | 3 | 4 | 4 | | 12 | | |
| Shortest interatomic distance, solid | 154.45 | 142.10<br>335.45 | 235 | 244 | 302 | 349 | pm<br>pm | Graphite, within layers<br>Graphite, between layers |
| Range of stability | RT, > 60 GPa | RTP | | | | | | |

[a] At ambient pressure Sn crystallizes in the diamond structure (gray tin, $\alpha$-Sn) and below 17 °C in the $\beta$-tin structure (white tin, $\beta$-Sn, Sn-I) at room temperature. If it is alloyed with In or Hg, the simple hexagonal $\gamma$-Sn structure is observed

**Table 2.1-13B(b)** Elements of Group IVA (CAS notation), or Group 14 (new IUPAC notation). Mechanical properties

| **Element name** | **Carbon** | | **Silicon** | **Germanium** | **Tin** | **Lead** | | |
|---|---|---|---|---|---|---|---|---|
| **Chemical symbol**<br>**Atomic number $Z$** | **C**<br>**6** | | **Si**<br>**14** | **Ge**<br>**32** | **Sn**<br>**50** | **Pb**<br>**82** | | |
| | | | | | | | **Units** | **Remarks** |
| Modification | Diamond | Graphite | | | $\beta$-Sn (white) | | | |
| Density $\varrho$, solid | 3.513 | 2.266 | 2.33 | 5.32 | 7.30 | 11.4 | g/cm$^3$ | At 293 K |
| Density $\varrho$, liquid | | | 2.525 | 5.500 | 6.978 | 10.678 | g/cm$^3$ | |
| Molar volume $V_{mol}$ | 3.42 | 5.3 | 12.06 | 13.64 | 16.24 | 18.26 | cm$^3$/mol | |
| Viscosity $\eta$, liquid | | | 2.0 | | 2.71 | 1.67 | mPa s | |
| Surface tension $\gamma$, liquid | | | 0.735 | 0.650 | 0.545 | 0.470 | N/m | |
| Temperature coefficient | | | $-0.5\times10^{-3}$ | $-0.20\times10^{-3}$ | $-0.075\times10^{-3}$ | $-0.26\times10^{-3}$ | N/(m K) | |
| Coefficient of linear thermal expansion $\alpha$ | $1.06\times10^{-6}$ | $1.9\times10^{-6}$ [a] | $2.56\times10^{-6}$ | $5.57\times10^{-6}$ | $21.2\times10^{-6}$ | $29.1\times10^{-6}$ | 1/K | At 293 K |
| Sound velocity, liquid | | | | | 2270 | 1790 | m/s | At $T_m$, 12 MHz |
| Sound velocity, solid, transverse | | | 5845 | 2420 | 1650 | 710 | m/s | At 298 K |
| Sound velocity, solid, longitudinal | 11 220 | 3450 | 8433 | 4580 | 3300 | 2050 | m/s | |
| Compressibility $\kappa$ | $2.25\times10^{-6}$ | $1.56\times10^{-6}$ | $10.2\times10^{-6}$ | $13.4\times10^{-6}$ | $18.3\times10^{-6}$ | $23.7\times10^{-6}$ | 1/MPa | Volume compressibility |
| Bulk modulus $B_0$ | 444 | | 98.0 | 74.9 | 56.6 | | GPa | At 295 K |
| Elastic modulus $E$ | 545 | | 112 | 79.9 | 52.9 | 15.8 | GPa | |
| Shear modulus $G$ | | | 80.5 | 29.6 | 19.9 | 5.54 | GPa | |
| Poisson number $\mu$ | | | | 0.34 | 0.33 | 0.44 | | |
| Elastic compliance $s_{11}$ | 0.951 | 0.98 | 7.73 | 9.73 | 41.6 | 93.7 | 1/TPa | |
| Elastic compliance $s_{33}$ | | 27.5 | | | 14.9 | | 1/TPa | |
| Elastic compliance $s_{44}$ | 1.732 | 250 | 12.7 | 14.9 | 45.6 | 68.0 | 1/TPa | |
| Elastic compliance $s_{66}$ | | | | | 42.8 | | 1/TPa | |
| Elastic compliance $s_{12}$ | −0.0987 | −0.16 | −2.15 | −2.64 | 31.2 | −43.0 | 1/TPa | |
| Elastic compliance $s_{13}$ | | −0.33 | | | 4.6 | | 1/TPa | |
| Elastic stiffness $c_{11}$ | 1079 | 1060 | 165.6 | 129 | 72.30 | 48.8 | GPa | At 300 K |
| Elastic stiffness $c_{33}$ | | 36.5 | | | 88.40 | | GPa | At 300 K |
| Elastic stiffness $c_{44}$ | 578 | 4 | 79.6 | 67.1 | 22.03 | 14.8 | GPa | At 300 K |
| Elastic stiffness $c_{66}$ | | | | | 24.00 | | GPa | At 300 K |
| Elastic stiffness $c_{12}$ | 124.5 | 180 | 63.9 | 48.3 | 59.40 | 41.4 | GPa | At 300 K |
| Elastic stiffness $c_{13}$ | | 15 | | | 35.78 | | GPa | At 300 K |
| Tensile strength | | | 690 | | | 700 | MPa | |
| Vickers hardness | | | 2350 | | | 39 | | |
| Mohs hardness | 10 | | | | | | | |

[a] At 298 K, parallel to layer planes. The corresponding value perpendicular to the layer planes is $2.9\times10^{-6}$/K

**Table 2.1-13B(c)** Elements of Group IVA (CAS notation), or Group 14 (new IUPAC notation). Thermal and thermodynamic properties

| **Element name** | **Carbon** | | **Silicon** | **Germanium** | **Tin** | **Lead** | | |
|---|---|---|---|---|---|---|---|---|
| **Chemical symbol**<br>**Atomic number Z** | **C**<br>**6** | | **Si**<br>**14** | **Ge**<br>**32** | **Sn**<br>**50** | **Pb**<br>**82** | | |
| | | | | | | | **Units** | **Remarks** |
| Modification | Diamond | Graphite | | | $\beta$-Sn (white) | | | |
| Thermal conductivity $\lambda$ | 1000–2320 | 5.7[a]<br>1960[b] | 83.7 | 58.6 | 66.6 | 35.2 | W/(m K)<br>W/(m K) | At 300 K<br>At 300 K |
| Molar heat capacity $c_p$ | 6.11 | 8.519 | 20.00 | 33.347 | 27.17 | 26.51 | J/(mol K) | At 298 K |
| Standard entropy $S^0$ | 2.360 | 5.742 | 18.810 | 31.090 | 51.180 | 64.800 | J/(mol K) | At 298 K and 100 kPa |
| Enthalpy difference $H_{298} - H_0$ | 0.5188 | 1.0540 | 3.2170 | 4.6360 | 6.3230 | 6.8700 | kJ/mol | |
| Melting temperature $T_m$ | | 4765.30 | 1687.00 | 1211.0 | 505.08 | 600.61 | K | |
| Enthalpy change $\Delta H_m$ | | 117.3690 | 50.208 | 36.9447 | 7.01940 | 4.7739 | kJ/mol | |
| Entropy change $\Delta S_m$ | | 24.630 | 29.762 | 30.498 | 14.243 | 7.948 | J/(mol K) | |
| Relative volume change $\Delta V_m$ | | | −0.10 | −0.054 | 0.028 | 0.032 | | $(V_l - V_s)/V_l$ at $T_m$ |
| Boiling temperature $T_b$ | | 3915 | 3505 | 3107 | 2876 | 2019 | K | |
| Enthalpy change $\Delta H_b$ | | 710.9 | 383.3 | 331 | 295.8 | 177.58 | kJ/mol | |
| Transformation temperature | 1900–2100 | | | | | | K | Transforms to graphite |

[a] Perpendicular to layer planes.

[b] Parallel to layer planes.

**Table 2.1-13B(d)** Elements of Group IVA (CAS notation), or Group 14 (new IUPAC notation). Electronic, electromagnetic, and optical properties

| **Element name** | **Carbon** | | **Silicon** | **Germanium** | **Tin** | **Lead** | | |
|---|---|---|---|---|---|---|---|---|
| **Chemical symbol**<br>**Atomic number $Z$** | **C**<br>**6** | | **Si**<br>**14** | **Ge**<br>**32** | **Sn**<br>**50** | **Pb**<br>**82** | | |
| | | | | | | | **Units** | **Remarks** |
| Modification | Diamond | Graphite | | | $\beta$-Sn(white) | | | |
| Characteristics | Very hard insulator | Soft conductor | Hard semicondor | Semicondor | Ductile metal | Soft metal | | |
| Electrical resistivity $\rho_s$<br>Temperature coefficient<br>Pressure coefficient | $10^{11}$ | $1.4\times10^{-5}$ | | 0.45 | $110\times10^{-9}$<br>$46.5\times10^{-4}$<br>$-9.2\times10^{-9}$ | $192\times10^{-9}$<br>$42.8\times10^{-4}$<br>$-12.5\times10^{-9}$ | $\Omega$ m<br>1/K<br>1/hPa | At 293 K |
| Electrical resistivity $\rho_l$ | | | | 710 | | | n$\Omega$ m | |
| Resistivity ratio | | | | 0.071 | | 1.94 | | $\rho_l/\rho_s$ at $T_m$ |
| Superconducting critical temperature $T_{crit}$ | | | | | 3.72 | 7.2 | K | |
| Superconducting critical field $H_{crit}$ | | | | | 309 | 803 | Oe | |
| Hall coefficient $R$ [a] | | $-487\times10^{-10}$ | $-100$ | 0.1 | $0.041\times10^{-10}$ | $0.09\times10^{-10}$ | $m^3/(A\,s)$ | At 300 K |
| Thermoelectric coefficient | | 11.06 | | 302.5 | 0.1 | $-0.1$ | $\mu$V/K | |
| Electronic band gap $\Delta E$<br>Temperature dependence | 5.4 | | 1.107<br>$-2.3\times10^{-4}$ | 0.6642 | | | eV<br>eV/K | At 300 K<br>At 300 K |
| Electronic work function | | 4.81 | 4.95 | 5.0 | 4.42 | 4.25 | V | |
| Thermal work function | | 4.00 | 4.1 | 4.56 | 4.11 | 3.83 | V | |
| Electron mobility | 1800 | | 1900 | 3800 | | | $cm^2/(V\,s)$ | |
| Hole mobility | 1400 | | 480 | 1820 | | | $cm^2/(V\,s)$ | |
| Dielectric constant $\varepsilon$, static, solid | 5.68 | | 11.7[b] | 16.0 | | | | |
| Dielectric constant $\varepsilon$, high-frequency, solid | 5.9(1) | | 12.0 | 16 | 24 | | | |
| Molar magnetic susceptibility $\chi_{mol}$, solid [c] (SI) | $-74.1\times10^{-6}$ | $-75.4\times10^{-6}$ | $-39.2\times10^{-6}$ | $-146\times10^{-6}$ | $-470\times10^{-6}$ | $-289\times10^{-6}$ | $cm^3/mol$ | At 295 K |
| Molar magnetic susceptibility $\chi_{mol}$, solid [c] (cgs) | $-5.88\times10^{-6}$ | $-6.0\times10^{-6}$ | $-3.12\times10^{-6}$ | $-11.6\times10^{-6}$ | $-37.4\times10^{-6}$ | $-23\times10^{-6}$ | $cm^3/mol$ | At 295 K |
| Mass magnetic susceptibility $\chi_{mass}$, solid (SI) | $-6.17\times10^{-6}$ | $-6.3\times10^{-6}$ | $-1.8\times10^{-6}$ | $-1.328\times10^{-6}$ | $-3.3\times10^{-6}$ | $-1.39\times10^{-6}$ | $cm^3/g$ | At 295 K |
| Mass magnetic susceptibility $\chi_{mass}$, liquid (SI) | | | | | $-4.4\times10^{-6}$ | | $cm^3/g$ | |
| Refractive index $n$, solid | 2.4173 | | 4.24 | 4.00 (25 $\mu$m) | 1.0 | 2.01 | | $\lambda = 589$ nm |
| Refractive index $n$, liquid | | | | | 1.7 | | | |

[a] $B = 1.0$–$1.6$ T.

[b] At 11 K and 1 MHz.

[c] The values for Sn apply to gray Sn.

**Table 2.1-13C** Elements of Group IVA (CAS notation), or Group 14 (new IUPAC notation). Allotropic and high-pressure modifications

| Element | Silicon | | | | Germanium | | | | |
|---|---|---|---|---|---|---|---|---|---|
| **Modification** | **α-Si** | **β-Si** | **γ-Si** | **δ-Si** | **α-Ge** | **β-Ge** | **γ-Ge** | **δ-Ge** | |
| | | | | | | | | | **Units** |
| Crystal system, Bravais lattice | cub, fc | tetr | cub | hex | cub, fc | tetr | tetr | cub, bc | |
| Structure type | Diamond | β-Sn | | α-La | Diamond | β-Sn | | γ-Si | |
| Lattice constant *a* | 543.06 | 468.6 | 636 | 380 | 565.74 | 488.4 | 593 | 692 | pm |
| Lattice constant *c* | | 258.5 | | 628 | | 269.2 | 698 | | pm |
| Space group | $Fd\bar{3}m$ | $I4_1/amd$ | $Im3m$ | $P6_3/mmc$ | $Fd\bar{3}m$ | $I4_1/amd$ | $P4_32_12$ | $Im\bar{3}m$ | |
| Schoenflies symbol | $O_h^7$ | $D_{4h}^{19}$ | $O_h^9$ | $D_{6v}^4$ | $O_h^7$ | $D_{4h}^{19}$ | $D_4^8$ | | |
| *Strukturbericht* type | A4 | A5 | | A3′ | A4 | A5 | | | |
| Pearson symbol | cF8 | tI4 | cI16 | hP4 | cF8 | tI4 | tP12 | cI16 | |
| Number *A* of atoms per cell | 8 | 4 | | 4 | 8 | 4 | 12 | 16 | |
| Coordination number | 4 | 4+2 | | | 4 | 4+2 | 4+2+2 | | |
| Shortest interatomic distance, solid | 235 | 243 | | | 245 | 253 | 249 | | |
| Range of stability | RTP | > 9.5 GPa | > 16.0 GPa | [a] | RTP | > 12.0 GPa | [b] | > 12.0 GPa | |

[a] Decompressed β-Si.
[b] Decompressed β-Ge.

**Table 2.1-13C** Elements of Group IVA (CAS notation), or Group 14 (new IUPAC notation). Allotropic and high-pressure modifications, cont.

| Element | Tin | | | Lead | | |
|---|---|---|---|---|---|---|
| **Modification** | **α-Sn (gray tin)** | **β-Sn (white tin)** | **γ-Sn** | **Pb I** | **Pb II** | |
| | | | | | | **Units** |
| Crystal system, Bravais lattice | cub, fc | tetr, I | tetr | cub, fc | hex, cp | |
| Structure type | Diamond | β-Sn | In | Cu | Mg | |
| Lattice constant *a* | 648.92 | 583.16 | 370 | 495.02 | 326.5 | pm |
| Lattice constant *c* | | 318.15 | 337 | | 538.7 | pm |
| Space group | $Fd\bar{3}m$ | $I4_1/amd$ | | $Fm\bar{3}m$ | $P6_3/mmc$ | |
| Schoenflies symbol | $O_h^7$ | $D_{4h}^{19}$ | | $O_h^5$ | $D_{6h}^4$ | |
| *Strukturbericht* type | A4 | A5 | | A1 | A3 | |
| Pearson symbol | c8 | tI4 | tI2 | cF4 | hP2 | |
| Number *A* of atoms per cell | 8 | 4 | 2 | 4 | 2 | |
| Coordination number | 4 | | | 12 | | |
| Shortest interatomic distance, solid | 281 | 302 | | 349 | | |
| Range of stability | < 291 K | RT | > 9 GPa | RTP | > 10.3 GPa | |

**Table 2.1-13D** Elements of Group IVA (CAS notation), or Group 14 (new IUPAC notation). Ionic radii (determined from crystal structures)

| Element | Carbon | Silicon | Germanium | | Tin | Lead | | |
|---|---|---|---|---|---|---|---|---|
| Ion | $C^{4+}$ | $Si^{4+}$ | $Ge^{2+}$ | $Ge^{4+}$ | $Sn^{4+}$ | $Pb^{2+}$ | $Pb^{4+}$ | |
| Coordination number | | | | | | | | Units |
| 4 | 15 | 26 | | 39 | 55 | | 65 | pm |
| 6 | 16 | 40 | 73 | 53 | 69 | 119 | 78 | pm |
| 8 | | | | | 81 | 129 | 94 | pm |
| 10 | | | | | | 140 | | |
| 12 | | | | | | 149 | | pm |

**Table 2.1-14A** Elements of Group IVB (CAS notation), or Group 4 (new IUPAC notation). Atomic, ionic, and molecular properties (see Table 2.1-14D for ionic radii)

| Element name | Titanium | Zirconium | Hafnium | Rutherfordium | | |
|---|---|---|---|---|---|---|
| Chemical symbol<br>Atomic number $Z$ | Ti<br>22 | Zr<br>40 | Hf<br>72 | Rf<br>104 | | |
| | | | | | Units | Remarks |
| Characteristics | | | | Radioactive | | |
| Relative atomic mass $A$ (atomic weight) | 47.867(1) | 91.224(2) | 178.49(2) | [261] | | |
| Abundance in lithosphere | $4400\times10^{-6}$ | $220\times10^{-6}$ | $4.5\times10^{-6}$ | | | Mass ratio |
| Abundance in sea | $1\times10^{-9}$ | $3\times10^{-11}$ | $7\times10^{-12}$ | | | Mass ratio |
| Atomic radius $r_{cov}$ | 132 | 145 | 144 | | pm | Covalent radius |
| Atomic radius $r_{met}$ | 147 | 160 | 156 | | pm | Metallic radius, CN = 12 |
| Electron shells | –LMN | –MNO | –NOP | –OPQ | | |
| Electronic ground state | $^3F_2$ | $^3F_2$ | $^3F_2$ | $^3F_2$ | | |
| Electronic configuration | $[Ar]3d^24s^2$ | $[Kr]4d^25s^2$ | $[Xe]4f^{14}5d^26s^2$ | | | |
| Oxidation states | 4+, 3+ | 4+ | 4+ | | | |
| Electron affinity | 0.079 | 0.426 | near 0 | | eV | |
| Electronegativity $\chi_A$ | 1.32 | 1.22 | (1.23) | | | Allred and Rochow |
| 1st ionization energy | 6.8282 | 6.63390 | 6.82507 | | eV | |
| 2nd ionization energy | 13.5755 | 13.13 | 14.9 | | eV | |
| 3rd ionization energy | 27.4917 | 22.99 | 23.3 | | eV | |
| 4th ionization energy | 43.2672 | 34.34 | 33.33 | | eV | |
| Standard electrode potential $E^0$ | −1.630 | −1.553[a] | | | V | Reaction type $Ti^{2+} + 2e^- = Ti$ |
| | −0.368 | | | | V | Reaction type $Ti^{3+} + e^- = Ti^{2+}$ |
| | −0.04 | | | | V | Reaction type $Ti^{4+} + e^- = Ti^{3+}$ |

[a] Reaction type $ZrO_2 + 4H^+ + 4e^- = Zr + 2H_2O$.

**Table 2.1-14B(a)** Elements of Group IVB (CAS notation), or Group 4 (new IUPAC notation). Crystallographic properties (see Table 2.1-14C for allotropic and high-pressure modifications)

| **Element name** | **Titanium** | **Zirconium** | **Hafnium** | **Rutherfordium** | | |
|---|---|---|---|---|---|---|
| **Chemical symbol**<br>**Atomic number *Z*** | **Ti**<br>**22** | **Zr**<br>**40** | **Hf**<br>**72** | **Rf**<br>**104** | | |
| | | | | | **Units** | **Remarks** |
| Modification | $\alpha$-Ti | $\alpha$-Zr | $\alpha$-Hf | | | |
| Crystal system, Bravais lattice | hex | hex | hex | | | |
| Structure type | Mg | Mg | Mg | | | |
| Lattice constant $a$ | 295.03 | 323.17 | 319.46 | | pm | |
| Lattice constant $c$ | 468.36 | 514.76 | 505.11 | | pm | |
| Space group | $P6_3/mmc$ | $P6_3/mmc$ | $P6_3/mmc$ | | | |
| Schoenflies symbol | $D^4_{6h}$ | $D^4_{6h}$ | $D^4_{6h}$ | | | |
| *Strukturbericht* type | A3 | A3 | A3 | | | |
| Pearson symbol | hP2 | hP2 | hP2 | | | |
| Number $A$ of atoms per cell | 2 | 2 | 2 | | | |
| Coordination number | 12 | 6+6 | 12 | | | |
| Shortest interatomic distance, solid | 291 | | 318 | | pm | |

**Table 2.1-14B(b)** Elements of Group IVB (CAS notation), or Group 4 (new IUPAC notation). Mechanical properties

| **Element name** | **Titanium** | **Zirconium** | **Hafnium** | **Rutherfordium** | | |
|---|---|---|---|---|---|---|
| **Chemical symbol**<br>**Atomic number *Z*** | **Ti**<br>**22** | **Zr**<br>**40** | **Hf**<br>**72** | **Rf**<br>**104** | | |
| | | | | | **Units** | **Remarks** |
| Density $\varrho$, solid | 4.50 | 6.49 | 13.10 | | g/cm$^3$ | |
| Density $\varrho$, liquid | 4.110 | 5.80 | 12.00 | | g/cm$^3$ | |
| Molar volume $V_{mol}$ | 10.55 | 14.02 | 13.41 | | cm$^3$/mol | |
| Surface tension, liquid | 1.65 | 1.48 | 1.63 | | N/m | Near $T_m$ |
| Temperature coefficient | $0.26\times10^{-3}$ | $-0.2\times10^{-3}$ | $-0.21\times10^{-3}$ | | N/(m K) | |
| Coefficient of linear thermal expansion $\alpha$ | $8.35\times10^{-6}$ | $5.78\times10^{-6}$ | $5.9\times10^{-6}$ | | 1/K | |
| Sound velocity, solid, transverse | 2920 | 1950 | 2000 | | m/s | |
| Sound velocity, solid, longitudinal | 6260 | 4360 | 3671 | | m/s | |
| Compressibility $\kappa$ | $0.779\times10^{-5}$ | $1.08\times10^{-5}$ | $0.80\times10^{-5}$ | | 1/MPa | Volume compressibility |
| Elastic modulus $E$ | 102 | 68.0 | 138 | | GPa | |
| Shear modulus $G$ | 37.3 | 24.8 | 53.0 | | GPa | |
| Poisson number $\mu$ | 0.35 | 0.37 | 0.29 | | | |
| Elastic compliance $s_{11}$ | 9.69 | 10.1 | 7.16 | | 1/TPa | |
| Elastic compliance $s_{33}$ | 6.86 | 8.0 | 6.13 | | 1/TPa | |
| Elastic compliance $s_{44}$ | 21.5 | 30.1 | 18.0 | | 1/TPa | |
| Elastic compliance $s_{12}$ | −4.71 | −4.0 | −2.48 | | 1/TPa | |
| Elastic compliance $s_{13}$ | −1.82 | −2.4 | −1.57 | | 1/TPa | |
| Elastic stiffness $c_{11}$ | 160 | 144 | 181 | | GPa | |
| Elastic stiffness $c_{33}$ | 181 | 166 | 197 | | GPa | |
| Elastic stiffness $c_{44}$ | 46.5 | 33.4 | 55.7 | | GPa | |
| Elastic stiffness $c_{12}$ | 90 | 74 | 77 | | GPa | |
| Elastic stiffness $c_{13}$ | 66 | 67 | 66 | | GPa | |
| Tensile strength | 235 | 150–450 | 400 | | MPa | |
| Vickers hardness | 2000–3500 | 903 | 1760 | | | |

**Table 2.1-14B(c)** Elements of Group IVB (CAS notation), or Group 4 (new IUPAC notation). Thermal and thermodynamic properties

| **Element name** | **Titanium** | **Zirconium** | **Hafnium** | **Rutherfordium** | | |
|---|---|---|---|---|---|---|
| **Chemical symbol**<br>**Atomic number $Z$** | **Ti**<br>**22** | **Zr**<br>**40** | **Hf**<br>**72** | **Rf**<br>**104** | | |
| | | | | | **Units** | **Remarks** |
| Modification | | $\alpha$-Zr | | | | |
| Thermal conductivity $\lambda$ | 21 | 22.7 | 23.0 | | W/(m K) | |
| Molar heat capacity $c_p$ | 25.02 | 25.36 | 25.3 | | J/(mol K) | At 298 K |
| Standard entropy $S^0$ | 30.720 | 39.181 | 43.560 | | J/(mol K) | At 298 K and 100 kPa |
| Enthalpy difference $H_{298} - H_0$ | 4.8240 | 5.5663 | 5.8450 | | kJ/mol | |
| Melting temperature $T_m$ | 1941.00 | 2127.85 | 2506.00 | | K | |
| Enthalpy change $\Delta H_m$ | 14.1460 | 20.9978 | 27.1960 | | kJ/mol | |
| Entropy change $\Delta S_m$ | 7.288 | 9.868 | 10.852 | | J/(mol K) | |
| Volume change $\Delta V_m$ | | | | | | $(V_l - V_s)/V_l$ at $T_m$ |
| Boiling temperature $T_b$ | 3631 | 4203 | 4963 | | K | |
| Enthalpy change $\Delta H_b$ | 410.0 | 561.3 | 575.5 | | kJ/mol | |

**Table 2.1-14B(d)** Elements of Group IVB (CAS notation), or Group 4 (new IUPAC notation). Electronic, electromagnetic, and optical properties

| **Element name** | **Titanium** | **Zirconium** | **Hafnium** | **Ruther-fordium** | | |
|---|---|---|---|---|---|---|
| **Chemical symbol**<br>**Atomic number $Z$** | **Ti**<br>**22** | **Zr**<br>**40** | **Hf**<br>**72** | **Rf**<br>**104** | | |
| | | | | | **Units** | **Remarks** |
| Modification | | $\alpha$-Zr | | | | |
| Characteristics | Hard, light metal | Resistant metal | Metal | | | |
| Electrical resistivity $\rho_s$ | 390 | 410 | 296 | | n$\Omega$ m | At 293 K |
| Temperature coefficient | $54.6\times10^{-4}$ | $44.0\times10^{-4}$ | $44\times10^{-4}$ | | 1/K | |
| Pressure coefficient | $-1.118\times10^{-9}$ | $0.33\times10^{-9}$ | $-0.87\times10^{-9}$ | | 1/hPa | |
| Superconducting critical temperature $T_{crit}$ | 0.39 | 0.55 | 0.35 | | K | |
| Superconducting critical field $H_{crit}$ | 100 | 47 | | | Oe | |
| Hall coefficient $R$ | $-1.2\times10^{-10}$ | $0.212\times10^{-10}$ | $0.43\times10^{-10}$ | | $m^3/(A\,s)$ | At 300 K, $B = 0.4$–$2.8$ T |
| Electronic work function | 4.31 | 4.05 | 3.9 | | V | |
| Thermal work function | 4.16 | 4.12 | 3.53 | | V | |
| Molar magnetic susceptibility $\chi_{mol}$, solid (SI) | $1898\times10^{-6}$ | $1508\times10^{-6}$ | $892\times10^{-6}$ | | $cm^3$/mol | At 295 K |
| Molar magnetic susceptibility $\chi_{mol}$, solid (cgs) | $151\times10^{-6}$ | $120\times10^{-6}$ | $71\times10^{-6}$ | | $cm^3$/mol | At 295 K |
| Mass magnetic susceptibility $\chi_{mass}$, solid (SI) | $40.1\times10^{-6}$ | $16.8\times10^{-6}$ | $5.3\times10^{-6}$ | | $cm^3$/g | At 295 K |

**Table 2.1-14C** Elements of Group IVB (CAS notation), or Group 4 (new IUPAC notation). Allotropic and high-pressure modifications

| **Element** | **Titanium** | | **Zirconium** | | **Hafnium** | | | |
|---|---|---|---|---|---|---|---|---|
| **Modification** | **α-Ti** | **β-Ti** | **α-Zr** | **β-Zr** | **α-Hf** | **β-Hf** | **Hf-II** | |
| | | | | | | | | **Units** |
| Crystal system, Bravais lattice | hex, cp | cub, bc | hex, cp | cub, bc | hex, cp | cub, bc | hex | |
| Structure type | Mg | W | Mg | W | Mg | W | | |
| Lattice constant *a* | 295.03 | 330.65 | 323.17 | 360.9 | 319.46 | 361.0 | | pm |
| Lattice constant *c* | 468.36 | | 514.76 | | 505.11 | | | pm |
| Space group | $P6_3/mmc$ | $Im\bar{3}m$ | $P6_3/mmc$ | $Im\bar{3}m$ | $P6_3/mmc$ | $Im\bar{3}m$ | | |
| Schoenflies symbol | $D_{6h}^4$ | $O_h^9$ | $D_{6h}^4$ | $O_h^9$ | $D_{6h}^4$ | $O_h^9$ | | |
| *Strukturbericht* type | A3 | A2 | A3 | A2 | A3 | A2 | | |
| Pearson symbol | hP2 | cI2 | hP2 | cI2 | hP2 | cI2 | | |
| Number *A* of atoms per cell | 2 | 2 | 2 | 2 | 2 | 2 | | |
| Coordination number | 12 | 8 | 6+6 | 8 | 12 | 8 | | |
| Shortest interatomic distance, solid | 291 | 286 | | 313 | 318 | 313 | | |
| Range of stability | RT | >1173 K | RT | >1138 K | RTP | >2268 K | >38.8 GPa | |

**Table 2.1-14D** Elements of Group IVB (CAS notation), or Group 4 (new IUPAC notation). Ionic radii (determined from crystal structures)

| **Element** | **Titanium** | | | **Zirconium** | **Hafnium** | |
|---|---|---|---|---|---|---|
| **Ion** | **$Ti^{2+}$** | **$Ti^{3+}$** | **$Ti^{4+}$** | **$Zr^{4+}$** | **Hf $^{4+}$** | |
| **Coordination number** | | | | | | **Units** |
| 4 | | | 42 | 59 | 58 | pm |
| 6 | 86 | 67 | 61 | 72 | 71 | pm |
| 8 | | | 74 | 84 | 83 | pm |
| 9 | | | | 89 | | pm |

**Table 2.1-15A** Elements of Group VA (CAS notation), or Group 15 (new IUPAC notation). Atomic, ionic, and molecular properties (see Table 2.1-15D for ionic radii)

| **Element name** | **Nitrogen** | **Phosphorus** | **Arsenic** | **Antimony** | **Bismuth** | | |
|---|---|---|---|---|---|---|---|
| **Chemical symbol**<br>**Atomic number *Z*** | **N**<br>**7** | **P**<br>**15** | **As**<br>**33** | **Sb**<br>**51** | **Bi**<br>**83** | | |
| | | | | | | **Units** | **Remarks** |
| Relative atomic mass *A* (atomic weight) | 14.00674(7) | 30.973761(2) | 74.92160(2) | 121.760(1) | 208.98038(2) | | |
| Abundance in lithosphere | $20\times10^{-6}$ | $1200\times10^{-6}$ | $5\times10^{-6}$ | $0.2\times10^{-6}$ | $0.2\times10^{-6}$ | | Mass ratio |
| Abundance in sea | $150\times10^{-6}$ | $0.06\times10^{-6}$ | $3.7\times10^{-9}$ | $2.4\times10^{-10}$ | $2\times10^{-11}$ | | Mass ratio |
| Atomic radius $r_{cov}$ | 70 | 110 | 121 | 141 | 146 | pm | Covalent radius |
| Atomic radius $r_{met}$ | 92 | 128 | 139 | 159 | 182 | pm | Metallic radius, CN = 12 |
| Atomic radius $r_{vdW}$ | 155 | 190 | 200 | 220 | 240 | pm | van der Waals radius |
| Electron shells | KL | KLM | –LMN | –MNO | –NOP | | |
| Electronic ground state | $^4S_{3/2}$ | $^4S_{3/2}$ | $^4S_{3/2}$ | $^4S_{3/2}$ | $^4S_{3/2}$ | | |
| Electronic configuration | $[He]2s^22p^3$ | $[Ne]3s^23p^3$ | $[Ar]3d^{10}4s^24p^3$ | $[Kr]4d^{10}5s^25p^3$ | $[Xe]4f^{14}5d^{10}6s^26p^3$ | | |
| Oxidation states | 5+, 3+, 3– | 5+, 3+, 3– | 5+, 3+, 3– | 5+, 3+, 3– | 5+, 3+ | | |
| Electron affinity | Not stable | 0.747 | 0.81 | 1.046 | 0.946 | eV | |
| Electronegativity $\chi_A$ | 3.07 | 2.06 | 2.20 | 1.82 | (1.67) | | Allred and Rochow |
| 1st ionization energy | 14.53414 | 10.48669 | 9.8152 | 8.64 | 7.289 | eV | |
| 2nd ionization energy | 29.6013 | 19.7694 | 18.633 | 16.53051 | 16.69 | eV | |
| 3rd ionization energy | 47.44924 | 30.2027 | 28.351 | 25.3 | 25.56 | eV | |
| 4th ionization energy | 77.4735 | 51.4439 | 50.13 | 44.2 | 45.3 | eV | |
| 5th ionization energy | 97.8902 | 65.0251 | 62.63 | 56 | 56.0 | eV | |
| 6th ionization energy | 552.0718 | 220.421 | 127.6 | 108 | 88.3 | eV | |

**Table 2.1-15B(a)** Elements of Group VA (CAS notation), or Group 15 (new IUPAC notation). Crystallographic properties (see Table 2.1-15C for allotropic and high-pressure modifications)

| **Element name** | **Nitrogen** | **Phosphorus** | **Arsenic** | **Antimony** | **Bismuth** | | |
|---|---|---|---|---|---|---|---|
| **Chemical symbol**<br>**Atomic number *Z*** | **N**<br>**7** | **P**<br>**15** | **As**<br>**33** | **Sb**<br>**51** | **Bi**<br>**83** | | |
| | | | | | | **Units** | **Remarks** |
| State | $N_2$, 4.2 K | P, black | | | | | |
| Crystal system, Bravais lattice | cub, sc | orth, C | trig, R | trig, R | trig, R | | |
| Structure type | $\alpha$-N | P, black | $\alpha$-As | $\alpha$-As | $\alpha$-As | | |
| Lattice constant *a* | 565.9 | 331.36 | 413.20 | 450.65 | 474.60 | pm | |
| Lattice constant *b* | | 1047.8 | | | | pm | |
| Lattice constant *c* | | 43 763 | | | | pm | |
| Lattice angle $\alpha$ | | | 54.12 | 57.11 | 57.23 | deg | |
| Space group | *Pa*3 | *Cmca* | $R\bar{3}m$ | $R\bar{3}m$ | $R\bar{3}m$ | | |
| Schoenflies symbol | $T_h^6$ | $D_{2h}^{18}$ | $D_{3d}^5$ | $D_{3d}^5$ | $D_{3d}^5$ | | |
| *Strukturbericht* type | | A11 | A7 | A7 | A7 | | |
| Pearson symbol | cP8 | oC8 | hR2 | hR2 | hR2 | | |
| Number *A* of atoms per cell | 4×2 | 8 | 2 | 2 | 2 | | |
| Coordination number | | 2+1 | 3 | 3 | 3 | | |
| Shortest interatomic distance, solid | | 222 | 252 | 291 | 307 | pm | |

**Table 2.1-15B(b)** Elements of Group VA (CAS notation), or Group 15 (new IUPAC notation). Mechanical properties

| **Element name** | **Nitrogen** | **Phosphorus** | **Arsenic** | **Antimony** | **Bismuth** | | |
|---|---|---|---|---|---|---|---|
| **Chemical symbol**<br>**Atomic number $Z$** | **N**<br>**7** | **P**<br>**15** | **As**<br>**33** | **Sb**<br>**51** | **Bi**<br>**83** | | |
| | | | | | | **Units** | **Remarks** |
| State | $N_2$ gas | P, black | | | | | |
| Density $\varrho$, solid | | 2.690 | 5.72 | 6.68 | 9.80 | g/cm$^3$ | |
| Density $\varrho$, liquid | | | | | 10.05 | g/cm$^3$ | |
| Density $\varrho$, gas | $1.2506\times10^{-3}$ | | | | | g/cm$^3$ | At 273 K |
| Molar volume $V_{mol}$ | 13.65 | | 12.95 | 18.20 | 21.44 | cm$^3$/mol | |
| Viscosity $\eta$, gas | 18.9 | | | | | µPa s | At 323 K |
| Viscosity $\eta$, liquid | | | | 1.50 | 1.65 | mPa s | Near $T_m$ |
| Surface tension $\gamma$, liquid | | | | 0.384 | 0.376 | N/m | |
| Coefficient of linear thermal expansion $\alpha$ | | | $4.7\times10^{-6}$ | $8.5\times10^{-6}$ | $13.4\times10^{-6}$ | 1/K | |
| Sound velocity, gas | 336.9 | | | | | m/s | |
| Sound velocity, liquid | 929 (70 K) | | | | 1635 | m/s | |
| Sound velocity, solid, transverse | | | | 1800 | 1140 | m/s | |
| Sound velocity, solid, longitudinal | | | | 3140 | 2298 | m/s | |
| Compressibility $\kappa$ | | | | $2.6\times10^{-5}$ | $2.86\times10^{-5}$ | 1/MPa | Volume compressibility |
| Elastic modulus $E$ | 1.2 [a,b] | 30.4 [b] | 22 | 54.4 | 34.0 | GPa | |
| Shear modulus $G$ | | | | 20.6 | 12.8 | GPa | |
| Poisson number $\mu$ | | | | 0.25 | 0.33 | | |
| Elastic compliance $s_{11}$ | | | 46.71 | 16.1 | 26.0 | 1/TPa | |
| Elastic compliance $s_{33}$ | | | 202.9 | 29.9 | 42.0 | 1/TPa | |
| Elastic compliance $s_{44}$ | | | 44.91 | 38.9 | 114 | 1/TPa | |
| Elastic compliance $s_{12}$ | | | 36.94 | −6.1 | −7.9 | 1/TPa | |
| Elastic compliance $s_{13}$ | | | −88.2 | −6.2 | −11.9 | 1/TPa | |
| Elastic compliance $s_{14}$ | | | 1.80 | −12.3 | −21.2 | 1/TPa | |

[a] Solid.
[b] Estimated.

**Table 2.1-15B(b)** Elements of Group VA (CAS notation), or Group 15 (new IUPAC notation). Mechanical properties, cont.

| **Element name** | **Nitrogen** | **Phosphorus** | **Arsenic** | **Antimony** | **Bismuth** | | |
|---|---|---|---|---|---|---|---|
| **Chemical symbol**<br>**Atomic number Z** | **N**<br>**7** | **P**<br>**15** | **As**<br>**33** | **Sb**<br>**51** | **Bi**<br>**83** | | |
| | | | | | | **Units** | **Remarks** |
| State | $N_2$ gas | P, black | | | | | |
| Elastic stiffness $c_{11}$ | | 73.9 | 123.6 | 101 | 63.4 | GPa | |
| Elastic stiffness $c_{22}$ | | 277 | | | | GPa | |
| Elastic stiffness $c_{33}$ | 53.7 | 53.7 | 59.1 | 44.9 | 37.9 | GPa | |
| Elastic stiffness $c_{44}$ | | 15.6 | 22.6 | 39.5 | 11.5 | GPa | |
| Elastic stiffness $c_{55}$ | | 11.5 | | | | GPa | |
| Elastic stiffness $c_{66}$ | | 56.7 | | | | GPa | |
| Elastic stiffness $c_{12}$ | | | 19.7 | 32.2 | 24.5 | GPa | |
| Elastic stiffness $c_{13}$ | | | 62.3 | 27.6 | 24.9 | GPa | |
| Elastic stiffness $c_{14}$ | | | −4.16 | 21.8 | 7.3 | GPa | |
| Brinell hardness | | | | | 200 | | |
| Mohs hardness | | | 3.5 | | | | |
| Solubility in water $\alpha_W$, 293 K | 0.01557 | | | | | | $\alpha_W$ = vol (gas)/vol (water) |

**Table 2.1-15B(c)** Elements of Group VA (CAS notation), or Group 15 (new IUPAC notation). Thermal and thermodynamic properties

| **Element name** | **Nitrogen** | **Phosphorus** | **Arsenic** | **Antimony** | **Bismuth** | | |
|---|---|---|---|---|---|---|---|
| **Chemical symbol**<br>**Atomic number $Z$** | **N**<br>**7** | **P**<br>**15** | **As**<br>**33** | **Sb**<br>**51** | **Bi**<br>**83** | | |
| | | | | | | **Units** | **Remarks** |
| State | $N_2$ gas | P, white [a] | $\alpha$-As | | | | |
| Thermal conductivity $\lambda$ | 0.02598 | | 50.0 | 25.9 | 7.87 | W/(m K) | |
| Molar heat capacity $c_p$ | 14.560 | 23.824 | 24.65 | 25.23 | 25.52 | J/(mol K) | At 298 K |
| Standard entropy $S^0$ | 191.611 | 41.090 | 35.689 | 45.522 | 56.735 | J/(mol K) | At 298 K and 100 kPa |
| Enthalpy difference $H_{298} - H_0$ | 8.6692 | 5.3600 | 5.1170 | 5.8702 | 6.4266 | kJ/mol | |
| Melting temperature $T_m$ | 63.1458 | 317.30 | 1090.00 | 903.78 | 544.55 | K | |
| Enthalpy change $\Delta H_m$ | 0.720 | 0.6590 | 24.4429 | 19.8740 | 11.2968 | kJ/mol | |
| Entropy change $\Delta S_m$ | | 2.077 | 22.425 | 21.990 | 20.745 | J/(mol K) | |
| Volume change $\Delta V_m$ | | | 0.10 | −0.008 | −0.33 | | $(V_l - V_s)/V_l$ at $T_m$ |
| Boiling temperature $T_b$ | 77.35 | 550 | | 1860 | 1837 | K | |
| Enthalpy change $\Delta H_b$ | 5.577 | 51.9 | 34.8 | 165.8 | 174.1 | kJ/mol | |
| Critical temperature $T_c$ | 126.25 | | 1089 | | | K | |
| Critical pressure $p_c$ | 3.40 | | 36 | | | MPa | |
| Critical density $\varrho_c$ | 0.311 | | | | | g/cm$^3$ | |
| Triple-point temperature $T_{tr}$ | 63.14 | | | | | K | |
| Triple-point pressure $p_{tr}$ | 12.5 | | | | | kPa | |

[a] In Landolt–Börnstein, Group IV, Vol. 19A, Part 1 [1.4], the white form of phosphorus has been chosen as the reference phase for all phosphides because the more stable red form is difficult to characterize.

**Table 2.1-15B(d)** Elements of Group VA (CAS notation), or Group 15 (new IUPAC notation). Electronic, electromagnetic, and optical properties

| Element name | Nitrogen | Phosphorus | Arsenic | Antimony | Bismuth | | |
|---|---|---|---|---|---|---|---|
| Chemical symbol<br>Atomic number $Z$ | N<br>7 | P<br>15 | As<br>33 | Sb<br>51 | Bi<br>83 | | |
| | | | | | | Units | Remarks |
| State | $N_2$ gas | P, black | | | | | |
| Characteristics | Gas | Semiconductor | Semiconductor | Semimetal | Brittle metal | | |
| Electrical resistivity $\rho_s$ | | | 260 | 370 | 1068 | n$\Omega$ m | Solid, at RT |
| Temperature coefficient | | | $42\times10^{-4}$ | $51.1\times10^{-4}$ | $45.4\times10^{-4}$ | 1/K | |
| Pressure coefficient | | | | $6.0\times10^{-9}$ | $15.2\times10^{-9}$ | 1/hPa | |
| Electrical resistvity $\rho_l$ | | | | 1135 | 1280 | n$\Omega$ m | Liquid |
| Resistivity ratio | | | | 0.61 | 0.43 | | $\rho_l/\rho_s$ at $T_m$ |
| Electronic band gap $\Delta E$ | | 0.57 | 1.14 | | | eV | At 300 K |
| Temperature coefficient | | $8\times10^{-4}$ | | | | eV/K | |
| Electronic work function | | | 4.79 | 4.56 | 4.36 | V | |
| Thermal work function | | | 5.71 | 4.08 | 4.28 | V | |
| Electron mobility | | 220 | | | | $cm^2/(V\,s)$ | |
| Hole mobility | | 350 | | | | $cm^2/(V\,s)$ | |
| Hall coefficient $R$ | | | $0.45\times10^{-7}$ | $0.27\times10^{-7}$ | $-6.33\times10^{-7}$ | $m^3/(A\,s)$ | $B = 0.4-1.0$ T |
| Thermoelectric coefficient | | | | 35 | −70 | $\mu$V/K | |
| Dielectric constant $(\varepsilon - 1)$, gas | $580\times10^{-6}$ | | | | | | At 293 K |
| Dielectric constant $\varepsilon$, liquid | 1.45 | | | | | | At 74.8 K |
| Dielectric constant $\varepsilon$, solid | | | 11.2 (optical) | | | | |
| Molar magnetic susceptibility $\chi_{mol}$, (SI) | $-151\times10^{-6}$ | [a,b] | $-70.4\times10^{-6}$ [c] | $-1244\times10^{-6}$ | $-3520\times10^{-6}$ | $cm^3/mol$ | At 295 K |
| Molar magnetic susceptibility $\chi_{mol}$, (cgs) | $-12.0\times10^{-6}$ | [a,b] | $-5.60\times10^{-6}$ [c] | $-99\times10^{-6}$ | $-280.1\times10^{-6}$ | $cm^3/mol$ | At 295 K |
| Mass magnetic susceptibility $\chi_{mass}$, (SI) | $-5.4\times10^{-6}$ | | $-3.9\times10^{-6}$ | $-10\times10^{-6}$ | $-16.8\times10^{-6}$ | $cm^3/g$ | At 295 K |
| Refractive index $(n - 1)$, gas | $297\times10^{-6}$ | | | | | | 589.3 nm |
| Refractive index $n$, liquid | 1.929 (78 K) | | | | | | 589.3 nm |
| Refractive index $n$, solid | | | 3.35 (0.8 $\mu$m) | | | | |

[a] White P: molar magnetic susceptibility: $-26.7\times10^{-6}$ (cgs) and $-335\times10^{-6}$ (SI) $cm^3/mol$.

[b] Red P: molar magnetic susceptibility: $-20.8\times10^{-6}$ (cgs) and $-261\times10^{-6}$ (SI) $cm^3/mol$.

[c] Yellow As: molar magnetic susceptibility: $-292\times10^{-6}$ (SI) and $-23.2\times10^{-6}$ (cgs) $cm^3/mol$.

**Table 2.1-15C** Elements of Group VA (CAS notation), or Group 15 (new IUPAC notation). Allotropic and high-pressure modifications

| Element | Nitrogen | | | Arsenic | | Antimony | | | | |
|---|---|---|---|---|---|---|---|---|---|---|
| **Modification** | **α-N** | **β-N** | **γ-N** | **α-As** | **ε-As** | **Sb-I** | **Sb-II** | **Sb-III** | **Sb-IV** | |
| | | | | | | | | | | **Units** |
| Crystal system, Bravais lattice | cub, P | hex | tetr | trig, R | orth | trig, R | cub | hex, cp | mon | |
| Structure type | α-N | La | | As | α-Ga | α-As | | Mg | | |
| Lattice constant *a* | 565.9 | 404.6 | 395.7 | 413.20 | 362 | 450.65 | 299.2 | 337.6 | 556 | pm |
| Lattice constant *b* | | | | | 1085 | | | | 404 | pm |
| Lattice constant *c* | | 662.9 | 510.1 | | 448 | | | 534.1 | 422 | pm |
| Lattice angle α | | | | 54.12 | | 57.11 | | | | deg |
| Lattice angle β | | | | | | | | | 86.0 | deg |
| Space group | $Pa3$ | $P6_3/mmc$ | $P4_2/mnm$ | $R\bar{3}m$ | $Cmca$ | $R\bar{3}m$ | $Pm3m$ | $P6_3/mmc$ | | |
| Schoenflies symbol | $T_h^6$ | $D_{6v}^4$ | $D_{4h}^{12}$ | $D_{3d}^5$ | $D_{2h}^{18}$ | $D_{3d}^5$ | $O_h^1$ | $D_{6h}^4$ | | |
| *Strukturbericht* type | | A9 | | A7 | A11 | A7 | | | | |
| Pearson symbol | cP8 | hP4 | tP4 | hR2 | oC8 | hR2 | cP1 | A3 | | |
| Number *A* of atoms per cell | 4×2 | 4 | 4 | 2 | 8 | 2 | 1 | hP2 | | |
| Coordination number | | 3 | | 3 | | 3 | | 2 | | |
| Shortest interatomic distance, solid | | | | 252 | | 291 | | | | pm |
| Range of stability | < 20 K | > 35.6 K | 20 K, > 3.3 GPa | | > 721 K | RTP | > 5.0 GPa | > 7.5 GPa | 14.0 GPa | |

**Table 2.1-15C** Elements of Group VA (CAS notation), or Group 15 (new IUPAC notation). Allotropic and high-pressure modifications, cont.

| Element | Bismuth | | | | | | |
|---|---|---|---|---|---|---|---|
| **Modification** | **α-Bi** | **β-Bi** | **γ-Bi** | **δ-Bi** | **ε-Bi** | **ζ-Bi** | |
| | | | | | | | **Units** |
| Crystal system, Bravais lattice | trig, R | mon | mon | | | cub, bc | |
| Structure type | α-As | | | | | W | |
| Lattice constant *a* | 474.60 | | 605 | | | 3800 | pm |
| Lattice constant *b* | | | 420 | | | | pm |
| Lattice constant *c* | | | 465 | | | | pm |
| Lattice angle α | 57.23 | | | | | | deg |
| Space group | $R\bar{3}m$ | $C2/m$ | | | | $Im\bar{3}m$ | |
| Schoenflies symbol | $D_{3d}^5$ | $C_{2h}^3$ | | | | $O_h^9$ | |
| *Strukturbericht* type | A7 | | | | | A2 | |
| Pearson symbol | hR2 | mC4 | mP3 | | | cI2 | |
| Number *A* of atoms per cell | 2 | 4 | 3 | | | 2 | |
| Coordination number | 3 | | | | | | |
| Shortest interatomic distance, solid | 307 | | | | | | pm |
| Range of stability | RTP | > 0.28 GPa | > 3.0 GPa | > 4.3 GPa | > 6.5 GPa | > 9.0 GPa | |

**Table 2.1-15D** Elements of Group VA (CAS notation), or Group 15 (new IUPAC notation). Ionic radii (determined from crystal structures)

| Element | Nitrogen | | Phosphorus | Arsenic | | Antimony | | Bismuth | | |
|---|---|---|---|---|---|---|---|---|---|---|
| Ion | $N^{3+}$ | $N^{5+}$ | $P^{5+}$ | $As^{3+}$ | $As^{5+}$ | $Sb^{3+}$ | $Sb^{5+}$ | $Bi^{3+}$ | $Bi^{5+}$ | |
| Coordination number | | | | | | | | | | Units |
| 4 | | | 17 | | 34 | 76 | | | | pm |
| 5 | | | | | | | | 96 | | pm |
| 6 | 16 | 13 | 38 | 58 | 46 | 76 | 60 | 103 | 76 | pm |
| 8 | | | | | | | | 117 | | pm |

**Table 2.1-16A** Elements of Group VB (CAS notation), or Group 5 (new IUPAC notation). Atomic, ionic, and molecular properties (see Table 2.1-16D for ionic radii)

| Element name | Vanadium | Niobium | Tantalum | Dubnium | | |
|---|---|---|---|---|---|---|
| Chemical symbol<br>Atomic number $Z$ | V<br>23 | Nb<br>41 | Ta<br>73 | Db<br>105 | | |
| | | | | | Units | Remarks |
| Relative atomic mass $A$ (atomic weight) | 50.9415(1) | 92.90638(2) | 180.9479(1) | [262] | | |
| Abundance in lithosphere | $150\times10^{-6}$ | $20\times10^{-6}$ | $2.1\times10^{-6}$ | | | Mass ratio |
| Abundance in sea | $2.5\times10^{-9}$ | $1\times10^{-11}$ | $2\times10^{-12}$ | | | Mass ratio |
| Atomic radius $r_{cov}$ | 122 | 134 | 134 | | pm | Covalent radius |
| Atomic radius $r_{met}$ | 135 | 147 | 147 | | pm | Metallic radius, CN = 12 |
| Electron shells | –LMN | –MNO | –NOP | –OPQ | | |
| Electronic ground state | $^4F_{3/2}$ | $^6D_{1/2}$ | $^4F_{3/2}$ | | | |
| Electronic configuration | $[Ar]3d^34s^2$ | $[Kr]4d^45s^1$ | $[Xe]4f^{14}5d^36s^2$ | | | |
| Oxidation states | 5+, 4+, 3+, 2+ | 5+, 3+ | 5+ | | | |
| Electron affinity | 0.525 | 0.893 | 0.322 | | eV | |
| Electronegativity $\chi_A$ | 1.45 | 1.23 | (1.33) | | | Allred and Rochow |
| 1st ionization energy | 6.7463 | 6.75885 | 7.89 | | eV | |
| 2nd ionization energy | 14.66 | 14.32 | | | eV | |
| 3rd ionization energy | 29.311 | 25.04 | | | eV | |
| 4th ionization energy | 46.709 | 38.3 | | | eV | |
| 5th ionization energy | 65.282 | 50.55 | | | eV | |
| Standard electrode potential $E^0$ | −1.175 | | | | V | Reaction type $V^{2+}+2e^-=V$ |
| | −0.255 | | | | V | Reaction type $V^{3+}+e^-=V^{2+}$ |

**Table 2.1-16B(a)** Elements of Group VB (CAS notation), or Group 5 (new IUPAC notation). Crystallographic properties

| Element name | Vanadium | Niobium | Tantalum | Dubnium | | |
|---|---|---|---|---|---|---|
| Chemical symbol<br>Atomic number $Z$ | V<br>23 | Nb<br>41 | Ta<br>73 | Db<br>105 | | |
| | | | | | Units | Remarks |
| Crystal system, Bravais lattice | cub, bc | cub, bc | cub, bc | | | |
| Structure type | W | W | W | | | |
| Lattice constant $a$ | 302.38 | 330.07 | 330.31 | | pm | |
| Space group | $Im\bar{3}m$ | $Im\bar{3}m$ | $Im\bar{3}m$ | | | |
| Schoenflies symbol | $O_h^9$ | $O_h^9$ | $O_h^9$ | | | |
| *Strukturbericht* type | A2 | A2 | A2 | | | |
| Pearson symbol | cI2 | cI2 | cI2 | | | |
| Number $A$ of atoms per cell | 2 | 2 | 2 | | | |
| Coordination number | 8 | 8 | 8 | | | |
| Shortest interatomic distance, solid | 263 | 285 | 285 | | pm | |

**Table 2.1-16B(b)** Elements of Group VB (CAS notation), or Group 5 (new IUPAC notation). Mechanical properties

| Element name | Vanadium | Niobium | Tantalum | Dubnium | | |
|---|---|---|---|---|---|---|
| Chemical symbol<br>Atomic number $Z$ | V<br>23 | Nb<br>41 | Ta<br>73 | Db<br>105 | | |
| | | | | | Units | Remarks |
| Density $\varrho$, solid | 5.80 | 8.35 | 16.60 | | $g/cm^3$ | |
| Density $\varrho$, liquid | 5.55 | 7.830 | 15,00 | | $g/cm^3$ | |
| Molar volume $V_{mol}$ | 8.34 | 10.84 | 10.87 | | $cm^3/mol$ | |
| Surface tension, liquid | 1.95 | 2.0 | 2.15 | | N/m | |
| Temperature coefficient | $0.3\times10^{-3}$ | $-0.24\times10^{-3}$ | $-0.25\times10^{-3}$ | | N/(m K) | |
| Coefficient of linear thermal expansion $\alpha$ | $8.3\times10^{-6}$ | $7.34\times10^{-6}$ | $6.64\times10^{-6}$ | | 1/K | 300 K |
| Sound velocity, solid, transverse | 2780 | 2100 | 2900 | | m/s | |
| Sound velocity, solid, longitudinal | 6000 | 4900 | 4100 | | m/s | |
| Compressibility $\kappa$ | $0.63\times10^{-5}$ | $0.56\times10^{-5}$ | $0.465\times10^{-5}$ | | 1/MPa | Volume compressibility |
| Elastic modulus $E$ | 127 | 104 | 185 | | GPa | |
| Shear modulus $G$ | 46.6 | 59.5 | 64.7 | | GPa | |
| Poisson number $\mu$ | 0.36 | 0.38 | 0.35 | | | |
| Elastic compliance $s_{11}$ | 6.75 | 6.56 | 6.89 | | 1/TPa | |
| Elastic compliance $s_{44}$ | 23.2 | 35.2 | 12.1 | | 1/TPa | |
| Elastic compliance $s_{12}$ | −2.31 | −2.29 | −2.58 | | 1/TPa | |
| Elastic stiffness $c_{11}$ | 230 | 245 | 264 | | GPa | |
| Elastic stiffness $c_{44}$ | 43.1 | 28.4 | 82.6 | | GPa | |
| Elastic stiffness $c_{12}$ | 120 | 132 | 158 | | GPa | |
| Vickers hardness | 630 | 70–250<br>(HV 10) | 80–300<br>(HV 10) | | | At 293 K |

**Table 2.1-16B(c)** Elements of Group VB (CAS notation), or Group 5 (new IUPAC notation). Thermal and thermodynamic properties

| Element name | Vanadium | Niobium | Tantalum | Dubnium | | |
|---|---|---|---|---|---|---|
| Chemical symbol<br>Atomic number $Z$ | V<br>23 | Nb<br>41 | Ta<br>73 | Db<br>105 | | |
| | | | | | Units | Remarks |
| Thermal conductivity $\lambda$ | 30.7 | 59.0 | 60.7 | | W/(m K) | At 300 K |
| Molar heat capacity $c_p$ | 24.90 | 24.69 | 25.30 | | J/(mol K) | At 298 K |
| Standard entropy $S^0$ | 30.890 | 36.270 | 41.472 | | J/(mol K) | At 298 K and 100 kPa |
| Enthalpy difference $H_{298} - H_0$ | 4.5070 | 5.2200 | 5.6819 | | kJ/mol | |
| Melting temperature $T_m$ | 2183.00 | 2750.00 | 3290.00 | | K | |
| Enthalpy change $\Delta H_m$ | 21.5000 | 30.0000 | 36.5682 | | kJ/mol | |
| Entropy change $\Delta S_m$ | 9.849 | 10.909 | 11.115 | | J/(mol K) | |
| Relative volume change $\Delta V_m$ | | | | | | $(V_l - V_s)/V_l$ at $T_m$ |
| Boiling temperature $T_b$ | 3690 | 5017 | 5778 | | K | |
| Enthalpy change $\Delta H_b$ | 451.8 | 683.2 | 743.1 | | kJ/mol | |

**Table 2.1-16B(d)** Elements of Group VB (CAS notation), or Group 5 (new IUPAC notation). Electronic, electromagnetic, and optical properties. There is no Table 2.1-16C, because no allotropic or high-pressure modifictions are known

| Element name | Vanadium | Niobium | Tantalum | Dubnium | | |
|---|---|---|---|---|---|---|
| Chemical symbol<br>Atomic number $Z$ | V<br>23 | Nb<br>41 | Ta<br>73 | Db<br>105 | | |
| | | | | | Units | Remarks |
| Electrical resistivity $\rho_s$ | 248 | 152 | 125 | | n$\Omega$ m | At RT |
| Temperature coefficient | $39.0\times10^{-4}$ | $25.8\times10^{-4}$ | $38.2\times10^{-4}$ | | 1/K | |
| Pressure coefficient | $-1.6\times10^{-9}$ | $-1.37\times10^{-9}$ | $-1.62\times10^{-9}$ | | 1/hPa | |
| Superconducting critical temperature $T_{crit}$ | 5.3 | 9.13 | 4.49 | | K | |
| Superconducting critical field $H_{crit}$ | 1020 | 1980 | 830 | | Oe | |
| Hall coefficient $R$ | $0.82\times10^{-10}$ | $0.88\times10^{-10}$ | $1.01\times10^{-10}$ | | $m^3/(A\,s)$ | At 273 K, $B = 0.5$–$2.9$ T |
| Thermoelectric coefficient | | | $-5.0$ | | $\mu$V/K | |
| Electronic work function | 4.3 | 4.3 | 4.3 | | V | |
| Thermal work function | 4.09 | 3.99 | 4.25 | | V | |
| Molar magnetic susceptibility, solid $\chi_{mol}$, (SI) | $3581\times10^{-6}$ | $2614\times10^{-6}$ | $1935\times10^{-6}$ | | $cm^3$/mol | At 295 K |
| Molar magnetic susceptibility, solid $\chi_{mol}$, (cgs) | $285\times10^{-6}$ | $208\times10^{-6}$ | $154\times10^{-6}$ | | $cm^3$/mol | At 295 K |
| Mass magnetic susceptibility, solid $\chi_{mass}$, (SI) | $62.8\times10^{-6}$ | $27.6\times10^{-6}$ | $10.7\times10^{-6}$ | | $cm^3$/g | At 295 K |

**Table 2.1-16D** Elements of Group VB (CAS notation), or Group 5 (new IUPAC notation). Ionic radii (determined from crystal structures)

| Element | Vanadium | | | | Niobium | | | Tantalum | | | |
|---|---|---|---|---|---|---|---|---|---|---|---|
| Ion | $V^{2+}$ | $V^{3+}$ | $V^{4+}$ | $V^{5+}$ | $Nb^{3+}$ | $Nb^{4+}$ | $Nb^{5+}$ | $Ta^{3+}$ | $Ta^{4+}$ | $Ta^{5+}$ | |
| Coordination number | | | | | | | | | | | Units |
| 4 | | | | 36 | | | 48 | | | | pm |
| 5 | | | 53 | 46 | | | | | | | pm |
| 6 | 79 | 64 | 58 | 54 | 72 | 68 | 64 | 72 | 68 | 64 | pm |
| 8 | | | 72 | | 79 | | 74 | | | | pm |

**Table 2.1-17A** Elements of Group VIA (CAS notation), or Group 16 (new IUPAP notation). Atomic, ionic and molecular properties (see Table 2.1-17D for ionic radii)

| Element name | Oxygen | Sulfur | Selenium | Tellurium | Polonium | | |
|---|---|---|---|---|---|---|---|
| Chemical symbol<br>Atomic number $Z$ | O<br>8 | S<br>16 | Se<br>34 | Te<br>52 | Po<br>84 | | |
| | | | | | | Units | Remarks |
| Characteristics | | | | | Radioactive | | |
| Relative atomic mass $A$ (atomic weight) | 15.9994(3) | 32.066(6) | 78.96(3) | 127.60(3) | [209] | | |
| Abundance in lithosphere | $464\,000 \times 10^{-6}$ | $520 \times 10^{-6}$ | $0.09 \times 10^{-6}$ | $2 \times 10^{-9}$ | | | Mass ratio |
| Abundance in sea | $880\,000 \times 10^{-6}$ | $905 \times 10^{-6}$ | $2 \times 10^{-10}$ | | | | Mass ratio |
| Atomic radius $r_{cov}$ | 66 | 104 | 117 | 137 | 146 | pm | Covalent radius |
| Atomic radius $r_{met}$ | | 127 | 140 | 160 | 176 | pm | Metallic radius, CN = 12 |
| Atomic radius $r_{vdW}$ | 150 | 185 | 200 | 220 | | | van der Waals radius |
| Electron shells | KL | KLM | –LMN | –MNO | –NOP | | |
| Electronic ground state | $^3P_2$ | $^3P_2$ | $^3P_2$ | $^3P_2$ | $^3P_2$ | | |
| Electronic configuration | $[He]2s^2 2p^4$ | $[Ne]3s^2 3p^4$ | $[Ar]3d^{10}4s^2 4p^4$ | $[Kr]4d^{10}5s^2 5p^4$ | $[Xe]4f^{14}5d^{10}6s^2 6p^4$ | | |
| Oxidation states | 2– | 6+, 4+, 2+, 2– | 6+, 4+, 2+, 2– | 6+, 4+, 2+, 2– | 4+, 2+ | | |
| Electron affinity | 1.46<br><br>–8.75 | 2.08<br><br>–5.51 | 2.02 | 1.97 | 1.9 | eV<br>Reaction type $O + e^- = O^-$<br>eV | Reaction type $O^- + e^- = O^{2-}$ |
| Electronegativity $\chi_A$ | 3.50 | 2.44 | 2.48 | 2.01 | (1.76) | | Allred and Rochow |
| 1st ionization energy | 13.61806 | 10.36001 | 9.75238 | 9.0096 | 8.41671 | eV | |
| 2nd ionization energy | 35.11730 | 23.3379 | 21.19 | 18.6 | | eV | |
| 3rd ionization energy | 54.9355 | 34.79 | 30.8204 | 27.96 | | eV | |
| 4th ionization energy | 77.41353 | 47.222 | 42.9450 | 37.41 | | eV | |
| Standard electrode potential $E^0$ | | –0.476 | –0.924 | –1.143<br><br><br><br>+0.568 | <br><br>+0.56 | V<br>V<br>V | Reaction type $Te^{2-} = Te + 2e^-$<br>Reaction type $Po^{3+} + 3e^- = Po$<br>Reaction type $Te^{4+} + 4e^- = Te$ |

**Table 2.1-17B(a)** Elements of Group VIA (CAS notation), or Group 16 (new IUPAC notation). Crystallographic properties (see Table 2.1-17C for allotropic and high-pressure modifications)

| **Element name** | **Oxygen** | **Sulfur** | **Selenium** | **Tellurium** | **Polonium** | | |
|---|---|---|---|---|---|---|---|
| **Chemical symbol**<br>**Atomic number *Z*** | **O**<br>**8** | **S**<br>**16** | **Se**<br>**34** | **Te**<br>**52** | **Po**<br>**84** | | |
| | | | | | | **Units** | **Remarks** |
| State | $\alpha$-O,<br>$T < 23$ K | $S_8$, $\alpha$-S | Gray Se,<br>Se chains | | $\alpha$-Po | | |
| Crystal system, Bravais lattice | mon, C | orth, F | hex | hex | cub, sc | | |
| Structure type | $\alpha$-O | $\alpha$-S | $\gamma$-Se | $\gamma$-Se | $\alpha$-Po | | |
| Lattice constant *a* | 540.3 | 1046.4 | 436.55 | 445.61 | 336.6 | pm | |
| Lattice constant *b* | 342.9 | 1286.60 | | | | pm | |
| Lattice constant *c* | 508.6 | 2448.60 | 495.76 | 592.71 | | pm | |
| Lattice angle $\gamma$ | 132.53 | | | | | deg | |
| Space group | $C2/m$ | $Fddd$ | $P3_121$ | $P3_121$ | $Pm3m$ | | |
| Schoenflies symbol | $C_{2h}^3$ | $D_{2h}^{24}$ | $D_3^4$ | $D_3^4$ | $O_h^1$ | | |
| *Strukturbericht* type | | A16 | A8 | A8 | $A_h$ | | |
| Pearson symbol | mC4 | oF128 | hP3 | hP3 | cP1 | | |
| Number *A* of atoms per cell | 2×2 | 128 | 3 | 3 | 1 | | |
| Coordination number | | 2 | 2 | 2+4 | 6 | | |
| Shortest interatomic distance, solid | | 204 | 237 | 283 | 337 | pm | |

**Table 2.1-17B(b)** Elements of Group VIA (CAS notation), or Group 16 (new IUPAC notation). Mechanical properties

| **Element name** | **Oxygen** | **Sulfur** | **Selenium** | **Tellurium** | **Polonium** | | |
|---|---|---|---|---|---|---|---|
| **Chemical symbol**<br>**Atomic number Z** | **O**<br>**8** | **S**<br>**16** | **Se**<br>**34** | **Te**<br>**52** | **Po**<br>**84** | | |
| | | | | | | **Units** | **Remarks** |
| State | $O_2$ gas | $\alpha$-S | Gray Se | | | | |
| Density $\varrho$, solid | | 2.037 | 4.79 | 6.24 | 9.40 | $g/cm^3$ | At 293 K |
| Density $\varrho$, liquid | | 1.819 | 3.990 | 5.797 | | $g/cm^3$ | |
| Density $\varrho$, gas | $1.429 \times 10^{-3}$ | | | | | $g/cm^3$ | |
| Molar volume $V_{mol}$ | 8.00 | 15.49 | 16.48 | 20.45 | 22.4 | $cm^3/mol$ | |
| Viscosity $\eta$, gas | 19.5 | | | | | µPa s | |
| Viscosity $\eta$, liquid | | 11.5 | 1260 | | | mPa s | At $T_m$ |
| Surface tension, liquid | | 0.061 | 0.106 | 0.186 | | N/m | At $T_m$ |
| Coefficient of linear thermal expansion $\alpha$ | | $74.33 \times 10^{-6}$ | $36.9 \times 10^{-6}$ | $16.75 \times 10^{-6}$ | $23 \times 10^{-6}$ | 1/K | |
| Sound velocity, gas | 336.95 (70 K) | | | | | m/s | |
| Sound velocity, liquid | 1079 (70 K) | | | | | m/s | |
| Compressibility $\kappa$ | | $13.0 \times 10^{-5}$ | $11.6 \times 10^{-5}$ | $4.8 \times 10^{-5}$ | | 1/MPa | Volume compressibilty |
| Elastic modulus $E$ | | 17.8 [a] | 58.0 | 47.1 | 26 [a] | GPa | |
| Shear modulus $G$ | | | 6.46 | 16.7 | | GPa | |
| Poisson number $\mu$ | | | 0.45 | 0.23 | | | |
| Elastic compliance $s_{11}$ | 1280 [b] | 74.6 | | | | 1/TPa | |
| Elastic compliance $s_{22}$ | | 111 | | | | 1/TPa | |
| Elastic compliance $s_{33}$ | | 75.4 | | | | 1/TPa | |
| Elastic compliance $s_{44}$ | 3640 [b] | 121 | | | | 1/TPa | |
| Elastic compliance $s_{55}$ | | 234 | | | | 1/TPa | |
| Elastic compliance $s_{66}$ | | 229 | | | | 1/TPa | |
| Elastic compliance $s_{12}$ | −570 [b] | −13.1 | | | | 1/TPa | |
| Elastic compliance $s_{13}$ | | −7.1 | | | | 1/TPa | |
| Elastic compliance $s_{23}$ | | −45.8 | | | | 1/TPa | |
| Elastic stiffness $c_{11}$ | 2.60 [b] | 14.22 | | | | GPa | |
| Elastic stiffness $c_{22}$ | | 12.68 | | | | GPa | |
| Elastic stiffness $c_{33}$ | | 18.30 | | | | GPa | |
| Elastic stiffness $c_{44}$ | 0.275 [b] | 8.27 | | | | GPa | |
| Elastic stiffness $c_{55}$ | | 4.28 | | | | GPa | |
| Elastic stiffness $c_{66}$ | | 4.37 | | | | GPa | |
| Elastic stiffness $c_{12}$ | 2.06 [b] | 2.99 | | | | GPa | |
| Elastic stiffness $c_{13}$ | | 3.14 | | | | GPa | |
| Elastic stiffness $c_{23}$ | | 7.95 | | | | GPa | |
| Tensile strength | | | | 10.8–12.25 | | MPa | |
| Brinell hardness | | | | 250 | | | |
| Mohs hardness | | | 2.0 | | | | |
| Solubility in water $\alpha_W$ [c] | 0.0310 | | | | | | At 293 K and 1013 hPa |

[a] Estimated. [b] $\gamma$-Oxygen, $T = 54.4$ K. [c] $\alpha_W$ = vol (gas)/vol (water).

**Table 2.1-17B(c)** Elements of Group VIA (CAS notation), or Group 16 (new IUPAC notation). Thermal and thermodynamic properties

| **Element name** | **Oxygen** | **Sulfur** | **Selenium** | **Tellurium** | **Polonium** | | |
|---|---|---|---|---|---|---|---|
| **Chemical symbol**<br>**Atomic number $Z$** | **O**<br>**8** | **S**<br>**16** | **Se**<br>**34** | **Te**<br>**52** | **Po**<br>**84** | | |
| | | | | | | **Units** | **Remarks** |
| State | $O_2$ gas | $\alpha$-S | $\alpha$-Se | $\alpha$-Te | $\alpha$-Po | | |
| Thermal conductivity $\lambda$ | 0.0245 | 0.269 | 2.48 | 1.7 | 20 | W/(m K) | At STP |
| Molar heat capacity $c_p$ | 14.690 | 22.70 | 25.04 | 25.73 | | J/(mol K) | At 298 K |
| Standard entropy $S^0$ | 205.147 | 32.070 | 41.966 | 49.221 | 62.000 | J/(mol K) | At 298 K and 100 kPa |
| Enthalpy difference $H_{298} - H_0$ | 8.6800 | 4.4120 | 5.5145 | 6.0800 | 6.700 | kJ/mol | |
| Melting temperature $T_m$ | 54.361 | 388.36 | 494 | 722.66 | 527.00 | K | |
| Enthalpy change $\Delta H_m$ | 0.444 | 1.7210 | 6.6944 | 17.3760 | 10.000 | kJ/mol | |
| Entropy change $\Delta S_m$ | | 4.431 | 13.551 | 24.045 | 18.975 | J/(mol K) | |
| Relative volume change $\Delta V_m$ | | 0.515 | +0.168 | 0.05 | | | $(V_l - V_s)/V_l$ at $T_m$ |
| Boiling temperature $T_b$ | 90.18 | 882 | 958 | 1261 | 1335 | K | |
| Enthalpy change $\Delta H_b$ | 6.2 | 9.62 | 90 | 104.6 | 100.8 | kJ/mol | |
| Critical temperature $T_c$ | 154.58 | | 1863 | | | K | |
| Critical pressure $p_c$ | 5.4 | | 38 | | | MPa | |
| Critical density $\varrho_c$ | 0.419 | | | | | g/cm$^3$ | |
| Triple-point temperature $T_{tr}$ | 54.4 | | | | | K | |
| Triple-point pressure $p_{tr}$ | 1.52 | | | | | hPa | |

**Table 2.1-17B(d)** Elements of Group VIA (CAS notation), or Group 16 (new IUPAC notation). Electronic, electromagnetic, and optical properties

| **Element name** | **Oxygen** | **Sulfur** | **Selenium** | **Tellurium** | **Polonium** | | |
|---|---|---|---|---|---|---|---|
| **Chemical symbol**<br>**Atomic number** $Z$ | O<br>**8** | S<br>**16** | Se<br>**34** | Te<br>**52** | Po<br>**84** | | |
| | | | | | | **Units** | **Remarks** |
| State | $O_2$ gas | | Gray Se | | | | |
| Characteristics | | Solid insulator | Semiconductor | Semiconductor | Volatile metal | | |
| Electrical resistivity $\rho_s$ | | | 100 | 1–50 | | MΩ m | At RT |
| Electrical resistivity $\rho_l$ | | | 20 | 6.0 μΩ m | | MΩ m | |
| Resistivity ratio at $T_m$ | | | 1.0 | 0.048–0.091 | | | |
| Hall coefficient $R$ | | | | $0.24\times10^{-10}$ | | $m^3/(A\,s)$ | At 298 K |
| Thermoelectric coefficient | | | | 400 | | μV/K | |
| Electronic band gap $\Delta E$<br>Temperature coefficient | | 3.6<br>$-6.8\times10^{-4}$ | 1.79<br>$-9\times10^{-4}$ | 0.33 | | eV<br>eV/K | |
| Electronic work function | | | 5.9 | 4.95 | | V | |
| Thermal work function | | | 4.72 | 4.73 | | V | |
| Electron mobility | | | | 1100 | | $cm^2/(V\,s)$ | |
| Hole mobility | | | | 560 | | $cm^2/(V\,s)$ | |
| Dielectric constant $(\varepsilon-1)$, gas | $525\times10^{-6}$ | | | | | | At 373 K |
| Dielectric constant $\varepsilon$, liquid | 1.505 | | | | | | At 81 K |
| Dielectric constant $\varepsilon$, solid | | | 8.5<br>($\lambda = 3.3$ cm) | 5.0 $\parallel c$<br>2.2 $\perp c$ | | | |
| Molar magnetic susceptibility $\chi_{mol}$ (SI) | $43\,341\times10^{-6}$ [a] | $-195\times10^{-6}$ | $-314\times10^{-6}$ | $-478\times10^{-6}$ | | $cm^3/mol$ | At 295 K |
| Molar magnetic susceptibility $\chi_{mol}$ (cgs) | $3449\times10^{-6}$ [b] | $-15.5\times10^{-6}$ | $-25\times10^{-6}$ | $-38\times10^{-6}$ | | $cm^3/mol$ | At 295 K |
| Mass magnetic susceptibility $\chi_{mass}$ (SI) | $1.34\times10^{-6}$ [c] | $-6.09\times10^{-6}$ | $-4.0\times10^{-6}$ | $-3.9\times10^{-6}$ | | $cm^3/g$ | At 295 K |
| Mass magnetic susceptibility $\chi_{mass}$, liquid (SI) | | | | $-0.6\times10^{-6}$ | | $cm^3/g$ | |
| Refractive index $(n-1)$, gas | $270.6\times10^{-6}$ | | | | | | $\lambda = 589.3$ nm |
| Refractive index $n$, liquid | 1.221 (92 K) | | | | | | $\lambda = 589.3$ nm |
| Refractive index $n$, solid | | | 4.0 | | | | $\lambda = 589.3$ nm |

[a] Liquid $O_2$, 90 K, 96 748 $cm^3/mol$; solid $O_2$, 54 K, 128 177 $cm^3/mol$. [b] Liquid $O_2$, 90 K, 7699 $cm^3/mol$; solid $O_2$, 54 K, 10 200 $cm^3/mol$.
[c] At 280 K.

**Further remarks**

Liquid $O_3$ has a molar magnetic susceptibility of $84.2\times10^{-6}$ $cm^3/mol$ (SI) and $6.7\times10^{-6}$ $cm^3/mol$ (cgs).

The values given for the molar magnetic susceptibility $\chi_{mol}$ of sulfur apply to rhombic sulfur. The corresponding values for monoclinic sulfur are $-187\times10^{-6}$ $cm^3/mol$ (SI) and $-14.9\times10^{-6}$ $cm^3/mol$ (cgs).

**Table 2.1-17c** Elements of Group VIA (CAS notation), or Group 16 (new IUPAC notation). Allotropic and high-pressure modifications

| Element | Oxygen | | | Selenium | | | |
|---|---|---|---|---|---|---|---|
| **Modification** | **α-O** | **β-O** | **γ-O** | **γ-Se** | **α-Se** | **β-Se** | |
| | | | | | | | **Units** |
| Crystal system, Bravais lattice | mon, C | trig, R | cub, P | hex | mon | mon | |
| Structure type | α-O | α-As | γ-O | γ-Se | | | |
| Lattice constant *a* | 540.3 | 421.0 | 683 | 436.55 | 905.4 | 1501.8 | pm |
| Lattice constant *b* | 342.9 | | | | 908.3 | 1471.3 | pm |
| Lattice constant *c* | 508.6 | | | 495.76 | 233.6 | 887.9 | pm |
| Lattice angle α | | 46.27 | | | | | deg |
| Lattice angle γ | 132.53 | | | | 90.82 | 93.6 | deg |
| Space group | $C2/m$ | $R\bar{3}m$ | $Pm\bar{3}m$ | $P3_121$ | $P2_1/m$ | $P2_1/b$ | |
| Schoenflies symbol | $C_{2h}^3$ | $D_{3d}^5$ | $O_h^3$ | $D_3^4$ | $C_{2h}^2$ | $C_{2h}^5$ | |
| *Strukturbericht* type | | A7 | A15 | A8 | | | |
| Pearson symbol | mC4 | hR2 | cP16 | hP3 | | mP32 | |
| Number *A* of atoms per cell | 2×2 | 2 | 16 | 3 | | 32 | |
| Coordination number | | | | 2 | 2 | 2 | |
| Shortest interatomic distance, solid | | | | 237 | 233–235 | 233–236 | |
| Range of stability | < 23 K | > 23.9 K | > 43.6 K | RT | RT | RT | |
| Characteristics | | | | Gray, Se chains | Red, $Se_8$ rings; | Red, $Se_8$ rings | |

**Table 2.1-17c** Elements of Group VIA, or Group 16. Allotropic and high-pressure modifications, cont.

| Element | Tellurium | | | Polonium | | |
|---|---|---|---|---|---|---|
| **Modification** | **α-Te** | **β-Te** | **γ-Te** | **α-Po** | **β-Po** | |
| | | | | | | **Units** |
| Crystal system, Bravais lattice | hex | trig, R | trig, R | cub, P | trig, R | |
| Structure type | γ-Se | α-As | α-Hg | α-Po | α-Hg | |
| Lattice constant *a* | 445.61 | 469 | 300.2 | 336.6 | 337.3 | pm |
| Lattice constant *c* | 592.71 | | | | | pm |
| Lattice angle α | | 53.30 | 103.3 | | 98.08 | deg |
| Space group | $P3_121$ | $R\bar{3}m$ | $R\bar{3}m$ | $Pm\bar{3}m$ | $R\bar{3}m$ | |
| Schoenflies symbol | $D_3^4$ | $D_{3d}^5$ | $D_{3d}^5$ | $O_h^1$ | $D_{3d}^5$ | |
| *Strukturbericht* type | A8 | A7 | A10 | $A_h$ | A10 | |
| Pearson symbol | hP3 | hR2 | hR1 | cP1 | hR1 | |
| Number *A* of atoms per cell | 3 | 2 | 1 | 1 | 1 | |
| Coordination number | 2+4 | | | 6 | 6 | |
| Shortest interatomic distance, solid | 283 | | | 337 | 337 | |
| Range of stability | RTP | > 2 GPa | > 7.0 GPa | RTP | > 327 K | |

**Table 2.1-17d** Elements of Group VIA (CAS notation), or Group 16 (new IUPAC notation). Ionic radii (determined from crystal structures)

| Element | Oxygen | Sulfur | | | Selenium | | | Tellurium | | | Polonium | |
|---|---|---|---|---|---|---|---|---|---|---|---|---|
| **Ion** | **$O^{2-}$** | **$S^{2-}$** | **$S^{4+}$** | **$S^{6+}$** | **$Se^{2-}$** | **$Se^{4+}$** | **$Se^{6+}$** | **$Te^{2-}$** | **$Te^{4+}$** | **$Te^{6+}$** | **$Po^{4+}$** | |
| **Coordination number** | | | | | | | | | | | | **Units** |
| 2 | 121 | | | | | | | | | | | pm |
| 4 | | | | 12 | | | 28 | | 66 | 43 | | pm |
| 6 | 140 | 184 | 37 | 29 | 198 | 50 | 42 | 221 | 97 | 56 | 97 | pm |
| 8 | 142 | | | | | | | | | | | pm |

**Table 2.1-18A** Elements of Group VIB (CAS notation), or Group 6 (new IUPAC notation). Atomic, ionic, and molecular properties (see Table 2.1-18D for ionic radii)

| **Element name** | **Chromium** | **Molybdenum** | **Tungsten** | **Seaborgium** | | |
|---|---|---|---|---|---|---|
| **Chemical symbol**<br>**Atomic number *Z*** | **Cr**<br>**24** | **Mo**<br>**42** | **W**<br>**74** | **Sg**<br>**106** | | |
| | | | | | **Units** | **Remarks** |
| Characteristics | | | | Radioactive | | |
| Relative atomic mass $A$ (atomic weight) | 51.9961(6) | 95.94(1) | 183.84(1) | | | |
| Abundance in lithosphere | $200\times10^{-6}$ | $2.3\times10^{-6}$ | $1\times10^{-6}$ | | | Mass ratio |
| Abundance in sea | $3\times10^{-10}$ | $0.01\times10^{-6}$ | $1\times10^{-10}$ | | | Mass ratio |
| Atomic radius $r_{cov}$ | 118 | 130 | 130 | | pm | Covalent radius |
| Atomic radius $r_{met}$ | 129 | 140 | 141 | | pm | Metallic radius, CN = 12 |
| Electron shells | –LMN | –MNO | –NOP | –OPQ | | |
| Electronic ground state | $^7S_3$ | $^7S_3$ | $^5D_0$ | | | |
| Electronic configuration | $[Ar]3d^54s^1$ | $[Kr]4d^55s^1$ | $[Xe]4f^{14}5d^46s^2$ | | | |
| Oxidation states | 6+, 3+, 2+ | 6+, 5+, 4+, 3+, 2+, 1+, 2– | 6+, 5+, 4+, 3+, 2+, 1–, 2– | | | |
| Electron affinity | 0.666 | 0.748 | 0.815 | | eV | |
| Electronegativity $\chi_A$ | 1.56 | 1.30 | (1.40) | | | Allred and Rochow |
| 1st ionization energy | 6.76664 | 7.09243 | 7.98 | | eV | |
| 2nd ionization energy | 16.4857 | 16.16 | | | eV | |
| 3rd ionization energy | 30.96 | 27.13 | | | eV | |
| 4th ionization energy | 49.16 | 46.4 | | | eV | |
| Standard electrode potential $E^0$ | –0.913 | | | | V | Reaction type $Cr^{2+} + 2e^- = Cr$ |
| | –0.744 | –0.2 | | | V | Reaction type $Cr^{3+} + 3e^- = Cr$ |
| | –0.407 | | | | V | Reaction type $Cr^{3+} + e^- = Cr^{2+}$ |

**Table 2.1-18B(a)** Elements of Group VIB (CAS notation), or Group 6 (new IUPAC notation). Crystallographic properties (see Table 2.1-18C for allotropic and high-pressure modifications)

| **Element name** | **Chromium** | **Molybdenum** | **Tungsten** | **Seaborgium** | | |
|---|---|---|---|---|---|---|
| **Chemical symbol**<br>**Atomic number *Z*** | **Cr**<br>**24** | **Mo**<br>**42** | **W**<br>**74** | **Sg**<br>**106** | | |
| | | | | | **Units** | **Remarks** |
| Crystal system, Bravais lattice | cub, bc | cub, bc | cub, bc | | | |
| Structure type | W | W | W | | | |
| Lattice constant $a$ | 288.47 | 314.70 | 316.51 | | pm | |
| Space group | $Im\bar{3}m$ | $Im\bar{3}m$ | $Im\bar{3}m$ | | | |
| Schoenflies symbol | $O_h^9$ | $O_h^9$ | $O_h^9$ | | | |
| *Strukturbericht* type | A2 | A2 | A2 | | | |
| Pearson symbol | cI2 | cI2 | cI2 | | | |
| Number $A$ of atoms per cell | 2 | 2 | 2 | | | |
| Coordination number | 8 | 8 | 8 | | | |
| Shortest interatomic distance, solid | 249 | 272 | 273 | | pm | |

**Table 2.1-18B(b)** Elements of Group VIB (CAS notation), or Group 6 (new IUPAC notation). Mechanical properties

| **Element name** | **Chromium** | **Molybdenum** | **Tungsten** | **Seaborgium** | | |
|---|---|---|---|---|---|---|
| **Chemical symbol**<br>**Atomic number *Z*** | **Cr**<br>**24** | **Mo**<br>**42** | **W**<br>**74** | **Sg**<br>**106** | | |
| | | | | | **Units** | **Remarks** |
| Density $\varrho$, solid | 7.19 | 10.220 | 19.30 | | $g/cm^3$ | |
| Density $\varrho$, liquid | 6.460 | | 17.60 | | $g/cm^3$ | |
| Molar volume $V_{mol}$ | 7.23 | 9.39 | 9.53 | | $cm^3/mol$ | |
| Surface tension, liquid<br>Temperature coefficient | 1.6 | 2.25<br>$-0.3\times10^{-3}$ | 2.31<br>$-0.29\times10^{-3}$ | | N/m<br>N/(m K) | |
| Coefficient of linear thermal expansion $\alpha$ | $6.2\times10^{-6}$ | $5.35\times10^{-6}$ | $4.31\times10^{-6}$ | | 1/K | 300 K |
| Sound velocity, solid, transverse | 3980 | 3350 | 2870 | | m/s | |
| Sound velocity, solid, longitudinal | 6850 | 6250 | 5180 | | m/s | |
| Compressibility $\kappa$ | $0.78\times10^{-5}$ | $0.338\times10^{-5}$ | $0.28\times10^{-5}$ | | 1/MPa | Volume compressibility |
| Elastic modulus $E$ | 145 | 330 | 407 | | GPa | |
| Shear modulus $G$ | 71.6 | 123 | 152 | | GPa | |
| Poisson number $\mu$ | 0.31 | 0.31 | 0.28 | | | |
| Elastic compliance $s_{11}$ | 3.05 | 2.63 | 2.45 | | 1/TPa | |
| Elastic compliance $s_{44}$ | 9.98 | 9.20 | 6.24 | | 1/TPa | |
| Elastic compliance $s_{12}$ | −0.49 | −0.68 | −0.69 | | 1/TPa | |
| Elastic stiffness $c_{11}$ | 348 | 465 | 523 | | GPa | |
| Elastic stiffness $c_{44}$ | 100.0 | 109 | 160 | | GPa | |
| Elastic stiffness $c_{12}$ | 67 | 163 | 203 | | GPa | |
| Tensile strength | Strongly dependent on microstructure | | | | | |
| Vickers hardness | 1060 | 160–400<br>(HV 10) | 360–600<br>(HV 30) | | | |

**Table 2.1-18B(c)** Elements of Group VIB (CAS notation), or Group 6 (new IUPAC notation). Thermal and thermodynamic properties

| Element name | Chromium | Molybdenum | Tungsten | Seaborgium | | |
|---|---|---|---|---|---|---|
| Chemical symbol<br>Atomic number $Z$ | Cr<br>24 | Mo<br>42 | W<br>74 | Sg<br>106 | | |
| | | | | | Units | Remarks |
| Thermal conductivity $\lambda$ | 93.7 | 142 | 164 | | W/(m K) | At 293 K |
| Molar heat capacity $c_p$ | 23.44 | 23.932 | 24.27 | | J/(mol K) | At 298 K |
| Standard entropy $S^0$ | 23.543 | 28.560 | 32.618 | | J/(mol K) | At 298 K and 100 kPa |
| Enthalpy difference $H_{298} - H_0$ | 4.0500 | 4.5890 | 4.9700 | | kJ/mol | |
| Melting temperature $T_m$ | 2180.00 | 2893 | 3693 | | K | |
| Enthalpy change $\Delta H_m$ | 21.0040 | 37.4798 | 52.3137 | | kJ/mol | |
| Entropy change $\Delta S_m$ | 9.635 | 12.942 | 14.158 | | J/(mol K) | |
| Relative volume change $\Delta V_m$ | | | | | | $(V_l - V_s)/V_l$ at $T_m$ |
| Boiling temperature $T_b$ | 2952 | 4952 | 5828 | | K | |
| Enthalpy chnage $\Delta H_b$ | 344.3 | 582.2 | 806.8 | | kJ/mol | |
| Critical temperature $T_c$ | | 11 000 | | | K | |
| Critical pressure $p_c$ | | 540 | | | MPa | |
| Critical density $\varrho_c$ | | 2.630 | | | g/cm$^3$ | |

**Table 2.1-18B(d)** Elements of Group VIB (CAS notation), or Group 6 (new IUPAC notation). Electronic, electromagnetic, and optical properties

| Element name | Chromium | Molybdenum | Tungsten | Seaborgium | | |
|---|---|---|---|---|---|---|
| Chemical symbol<br>Atomic number $Z$ | Cr<br>24 | Mo<br>42 | W<br>74 | Sg<br>106 | | |
| | | | | | Units | Remarks |
| Electrical resistivity $\rho_s$ | 127 | 52 | 54.9 | | n$\Omega$ m | At 293 K |
| Temperature coefficient | $30.1 \times 10^{-4}$ | $43.3 \times 10^{-4}$ | $51 \times 10^{-4}$ | | 1/K | |
| Pressure coefficient | $-17.3 \times 10^{-9}$ | $-1.29 \times 10^{-9}$ | $-1.333 \times 10^{-9}$ | | 1/hPa | |
| Superconducting critical temperature $T_{crit}$ | | 0.92 | 0.005 | | K | |
| Superconducting critical field $H_{crit}$ | | 98 | | | Oe | |
| Hall coefficient $R$ | $3.63 \times 10^{-10}$ | $1.26 \times 10^{-10}$ | $0.856 \times 10^{-10}$ | | m$^3$/(A s) | $B = 0.5$–$2.0$ T, $T = 293$ K |
| Thermoelectric coefficient | | 5.9 | 1.5 | | $\mu$V/K | |
| Electronic work function | 4.5 | 4.39 | 4.54 | | eV | |
| Thermal work function | 4.6 | 4.26 | 4.50 | | V | |
| Molar magnetic susceptibility $\chi_{mol}$ (SI) | $2099 \times 10^{-6}$ | $905 \times 10^{-6}$ | $666 \times 10^{-6}$ | | cm$^3$/mol | At 295 K |
| Molar magnetic susceptibility $\chi_{mol}$ (cgs) | $167 \times 10^{-6}$ | $72 \times 10^{-6}$ | $53 \times 10^{-6}$ | | cm$^3$/mol | At 295 K |
| Mass magnetic susceptibility $\chi_{mass}$ (SI) | $44 \times 10^{-6}$ | $12 \times 10^{-6}$ | $4.0 \times 10^{-6}$ | | cm$^3$/g | At 295 K |

**Table 2.1-18C** Elements of Group VIB (CAS notation), or Group 6 (new IUPAC notation). Allotropic and high-pressure modifications

| **Element** | **Chromium** | | |
|---|---|---|---|
| **Modification** | **α-Cr** | **α′-Cr** | |
| | | | **Units** |
| Crystal system, Bravais lattice | cub, bc | cub, bc | |
| Structure type | W | W | |
| Lattice constant *a* | 288.47 | 288.2 | pm |
| Space group | $Im\bar{3}m$ | $Im\bar{3}m$ | |
| Schoenflies symbol | $O_h^9$ | $O_h^9$ | |
| *Strukturbericht* type | A2 | A2 | |
| Pearson symbol | cI2 | cI2 | |
| Number *A* of atoms per cell | 2 | 2 | |
| Coordination number | 8 | 8 | |
| Shortest interatomic distance, solid | 249 | | |
| Range of stability | RTP | High pressure | |

**Table 2.1-18D** Elements of Group VIB (CAS notation), or Group 6 (new IUPAC notation). Ionic radii (determined from crystal structures)

| **Element** | **Chromium** | | | | **Molybdenum** | | | | **Tungsten** | | | |
|---|---|---|---|---|---|---|---|---|---|---|---|---|
| **Ion** | **$Cr^{2+}$** | **$Cr^{3+}$** | **$Cr^{4+}$** | **$Cr^{6+}$** | **$Mo^{3+}$** | **$Mo^{4+}$** | **$Mo^{5+}$** | **$Mo^{6+}$** | **$W^{4+}$** | **$W^{5+}$** | **$W^{6+}$** | |
| **Coordination number** | | | | | | | | | | | | **Units** |
| 4 | | | 41 | 26 | | | 46 | 41 | | | 42 | pm |
| 5 | | | | | | | | | | | 51 | pm |
| 6 | 73 | 62 | 55 | 44 | 69 | 65 | 61 | 59 | 66 | 62 | 60 | pm |
| 7 | | | | | | | | 73 | | | | pm |

**Table 2.1-19A** Elements of Group VIIA (CAS notation), or Group 17 (new IUPAC notation). Atomic, ionic, and molecular properties (see Table 2.1-19D for ionic radii)

| **Element name** | **Fluorine** | **Chlorine** | **Bromine** | **Iodine** | **Astatine** | | |
|---|---|---|---|---|---|---|---|
| **Chemical symbol**<br>**Atomic number *Z*** | **F**<br>**9** | **Cl**<br>**17** | **Br**<br>**35** | **I**<br>**53** | **At**<br>**85** | | |
| | | | | | | **Units** | **Remarks** |
| Characterization | | | | | Radioactive | | |
| Relative atomic mass $A$ (atomic weight) | 18.9984032(5) | 35.4527(9) | 79.904(1) | 126.90447(3) | [210] | | |
| Abundance in lithosphere | $800\times10^{-6}$ | $480\times10^{-6}$ | $2.5\times10^{-6}$ | $0.3\times10^{-6}$ | | | Mass ratio |
| Abundance in sea | $1.3\times10^{-6}$ | $18\,800\times10^{-6}$ | $67\times10^{-6}$ | $0.06\times10^{-6}$ | | | Mass ratio |
| Atomic radius $r_{cov}$ | 64 | 99 | 114 | 133 | 145 | pm | Covalent radius |
| Atomic radius $r_{vdW}$ | 150–160 | 175 | 200 | 210 | | pm | van der Waals radius |
| Electron shells | KL | KLM | –LMN | –MNO | –NOP | | |
| Electronic ground state | $^2P_{3/2}$ | $^2P_{3/2}$ | $^2P_{3/2}$ | $^2P_{3/2}$ | $^2P_{3/2}$ | | |
| Electronic configuration | $[He]2s^22p^5$ | $[Ne]3s^23p^5$ | $[Ar]3d^{10}4s^24p^5$ | $[Kr]4d^{10}5s^25p^5$ | $[Xe]4f^{14}5d^{10}6s^26p^5$ | | |
| Oxidation states | | 1+, 3+, 5+, 7+, 1−, 3−, 5−, 7− | | | | | |
| Electron affinity | 3.40 | 3.61 | 3.36 | 3.06 | 2.8 | eV | Reaction type $F+e^-=F^-$ |
| Electronegativity $\chi_A$ | 4.10 | 2.83 | 2.74 | 2.21 | (1.90) | | Allred and Rochow |
| 1st ionization energy | 17.42282 | 12.96764 | 11.81381 | 10.45126 | | eV | |
| 2nd ionization energy | 34.97082 | 23.814 | 21.8 | 19.1313 | | eV | |
| 3rd ionization energy | 62.7084 | 39.61 | 36 | 33 | | eV | |
| 4th ionization energy | 87.1398 | 53.4652 | 47.3 | | | eV | |
| Standard electrode potential $E^0$ | +2.866 | +1.358 | +1.066 | +0.536 | | V | Reaction type $2Cl^-=Cl_2+2e^-$ |
| Molecular form in gaseous state | $F_2$ | $Cl_2$ | $Br_2$ | $I_2$ | | | |
| Internuclear distance in molecule | | 198.8 | | | | pm | |
| Dissociation energy | | 2.475 | | 1.5417 | | eV | Extrapolated to $T=0\,K$ |

**Table 2.1-19B(a)** Elements of Group VIIA (CAS notation), or Group 17 (new IUPAC notation). Crystallographic properties (see Table 2.1-19C for allotropic and high-pressure modifications)

| **Element name** | **Fluorine** | **Chlorine** | **Bromine** | **Iodine** | **Astatine** | | |
|---|---|---|---|---|---|---|---|
| **Chemical symbol**<br>**Atomic number *Z*** | **F**<br>**9** | **Cl**<br>**17** | **Br**<br>**35** | **I**<br>**53** | **At**<br>**85** | | |
| | | | | | | **Units** | **Remarks** |
| State | $F_2$, $< 45.6$ K | $Cl_2$, 113 K | $Br_2$, 123 K | $I_2$ | | | |
| Crystal system, Bravais lattice | mon, C | orth, C | orth, C | orth, C | | | |
| Structure type | | | | Ga | | | |
| Lattice constant $a$ | 550 | 624 | 668 | 726.8 | | pm | |
| Lattice constant $b$ | 328 | 448 | 449 | 479.7 | | pm | |
| Lattice constant $c$ | 728 | 826 | 874 | 979.7 | | pm | |
| Lattice angle $\beta$ | 102.17 | | | | | deg | |
| Space group | $C2/m$ | $Cmca$ | $Cmca$ | $Cmca$ | | | |
| Schoenflies symbol | $C_{2h}^3$ | $D_{2h}^{18}$ | $D_{2h}^{18}$ | $D_{2h}^{18}$ | | | |
| *Strukturbericht* type | C34 | A11 | A11 | A11 | | | |
| Pearson symbol | mC6 | oC8 | oC8 | oC8 | | | |
| Number $A$ of atoms per cell | 6 | 2×4 | 2×4 | 2×4 | | | |
| Coordination number | 1 | 1 | 1 | 1 | | | |
| Shortest interatomic distance, solid | 149 | 198.0 | 227 | 269 | | pm | |

**Table 2.1-19B(b)** Elements of Group VIIA (CAS notation), or Group 17 (new IUPAC notation). Mechanical properties

| **Element name** | **Fluorine** | **Chlorine** | **Bromine** | **Iodine** | **Astatine** | | |
|---|---|---|---|---|---|---|---|
| **Chemical symbol**<br>**Atomic number $Z$** | **F**<br>**9** | **Cl**<br>**17** | **Br**<br>**35** | **I**<br>**53** | **At**<br>**85** | | |
| | | | | | | **Units** | **Remarks** |
| State | $F_2$, gas | $Cl_2$, gas | $Br_2$, crystalline | $I_2$, crystalline | | | |
| Density $\varrho$, solid | | | | 4.92 | | $g/cm^3$ | |
| Density $\varrho$, liquid | | | 3.119 (293 K) | | | | |
| Density $\varrho$, gas | $1.696 \times 10^{-3}$ | $3.17 \times 10^{-3}$ | | | | $g/cm^3$ | At 273 K, 1 bar |
| Molar volume $V_{mol}$ | 18.05 | 17.46 | 19.73 | 25.74 | | $cm^3/mol$ | |
| Viscosity $\eta$, gas | $209.3 \times 10^2$ | | | | | µPa s | |
| Viscosity $\eta$, liquid | | | 0.916 (299 K) | 2.27 | | mPa s | |
| Surface tension, liquid | | | 0.0441 (286 K) | 0.0557 | | N/m | |
| Sound velocity, gas | 336 (375 K) | 206 | | | | m/s | STP |
| Elastic compliance $s_{11}$ | | | | 328 | | 1/TPa | |
| Elastic compliance $s_{22}$ | | | | 103 | | 1/TPa | |
| Elastic compliance $s_{33}$ | | | | 132 | | 1/TPa | |
| Elastic compliance $s_{44}$ | | | | 303 | | 1/TPa | |
| Elastic compliance $s_{55}$ | | | | 67.7 | | 1/TPa | |
| Elastic compliance $s_{66}$ | | | | 170 | | 1/TPa | |
| Elastic compliance $s_{12}$ | | | | −97 | | 1/TPa | |
| Elastic compliance $s_{13}$ | | | | −173 | | 1/TPa | |
| Elastic compliance $s_{23}$ | | | | 49 | | 1/TPa | |
| Elastic stiffness $c_{11}$ | | | 11.5 | | | GPa | |
| Elastic stiffness $c_{22}$ | | | 13.5 | | | GPa | |
| Elastic stiffness $c_{33}$ | | | 25.0 | | | GPa | |
| Elastic stiffness $c_{44}$ | | | 3.30 | | | GPa | |
| Elastic stiffness $c_{55}$ | | | 14.8 | | | GPa | |
| Elastic stiffness $c_{66}$ | | | 5.88 | | | GPa | |
| Elastic stiffness $c_{12}$ | | | 4.50 | | | GPa | |
| Elastic stiffness $c_{13}$ | | | 13.5 | | | GPa | |
| Elastic stiffness $c_{23}$ | | | 0.93 | | | GPa | |

**Table 2.1-19B(c)** Elements of Group VIIA (CAS notation), or Group 17 (new IUPAC notation). Thermal and thermodynamic properties

| **Element name** | **Fluorine** | **Chlorine** | **Bromine** | **Iodine** | **Astatine** | | |
|---|---|---|---|---|---|---|---|
| **Chemical symbol**<br>**Atomic number *Z*** | **F**<br>**9** | **Cl**<br>**17** | **Br**<br>**35** | **I**<br>**53** | **At**<br>**85** | | |
| | | | | | | **Units** | **Remarks** |
| State | $F_2$, gas | $Cl_2$, gas | $Br_2$, liquid | $I_2$, crystalline | $At_2$, crystalline | | |
| Thermal conductivity $\lambda$ | $2.43 \times 10^{-2}$ | $9.3 \times 10^{-3}$ | | 0.4 | 1.7 | W/(m K) | STP |
| Molar heat capacity $c_p$ | 15.66 | 16.974 | 37.84 | 27.21 | | J/(mol K) | At 298 K |
| Standard entropy $S^0$ | 202.789 | 223.079 | 152.210 | 116.139 | 54.000 | J / (mol K) | At 298 K and 100 kPa |
| Enthalpy difference $H_{298} - H_0$ | 8.8250 | 9.1810 | | 13.1963 | 13.4000 | kJ/mol | |
| Melting temperature $T_m$ | 53.48 | 172.18 | 265.90 | 386.75 | 575 | K | |
| Enthalpy change $\Delta H_m$ | | 6.41 | 10.8 | 15.5172 | 23.8 | kJ/mol | |
| Entropy change $\Delta S_m$ | | | | 40.122 | 40.0 | J/(mol K) | |
| Volume change $\Delta V_m$ | | | | | | | $(V_l - V_s)/V_l$ at $T_m$ |
| Boiling temperature $T_b$ | 84.95 | 239.1 | 332.3 | 458.4 | | K | |
| Enthalpy change $\Delta H_b$ | | 20.40 | 29.56 | 41.96 | 91 | kJ/mol | |
| Critical temperature $T_c$ | 144.3 | 417 | | 819 | | K | |
| Critical pressure $p_c$ | 5.22 | 7.98 | | | | MPa | |
| Critical density $\varrho_c$ | 0.630 | 0.573 | | | | g/cm$^3$ | |
| Triple-point temperature $T_{tr}$ | 55 | 162 | | | | K | |
| Triple-point pressure $p_{tr}$ | 0.221 | 1.39 | | | | kPa | |
| Solubility in water[a] | | 4.610 | | | | | At 273 K and 101 kPa |

[a] $m^3$ gas/$m^3$ water.

**Table 2.1-19B(d)** Elements of Group VIIA (CAS notation), or Group 17 (new IUPAC notation). Electronic, electromagnetic, and optical properties

| **Element name** | **Fluorine** | **Chlorine** | **Bromine** | **Iodine** | **Astatine** | | |
|---|---|---|---|---|---|---|---|
| **Chemical symbol**<br>**Atomic number *Z*** | **F**<br>**9** | **Cl**<br>**17** | **Br**<br>**35** | **I**<br>**53** | **At**<br>**85** | | |
| | | | | | | **Units** | **Remarks** |
| State | $F_2$, gas | $Cl_2$, gas | $Br_2$, liquid | $I_2$, crystalline | | | |
| Characteristics | Yellow gas, very reactive | Yellow-green gas | Liquid halogen | Solid semiconductor | | | |
| Electronic work function | | | | 2.8 | | eV | |
| Dielectric constant $\varepsilon$, liquid | 1.517(83.2 K) | 2.15 (213 K) | | | | | |
| Molar magnetic susceptibility $\chi_{mol}$, gas (SI) | | | −924 | | | $cm^3/mol$ | |
| Molar magnetic susceptibility $\chi_{mol}$, gas (cgs) | | | $-73.5\times10^{-6}$ | | | $cm^3/mol$ | |
| Molar magnetic susceptibility $\chi_{mol}$, liquid (SI) | | $-508\times10^{-6}$ | −709 | | | $cm^3/mol$ | |
| Molar magnetic susceptibility $\chi_{mol}$, liquid (cgs) | | $-40.4\times10^{-6}$ | $-56.4\times10^{-6}$ | | | $cm^3/mol$ | |
| Molar magnetic susceptibility $\chi_{mol}$, solid (SI) | | | | $-1131\times10^{-6}$ | | $cm^3/mol$ | |
| Molar magnetic susceptibility $\chi_{mol}$, solid (cgs) | | | | $-90\times10^{-6}$ | | $cm^3/mol$ | |
| Mass magnetic susceptibility $\chi_{mass}$, solid (SI) | | $-7.2\times10^{-6}$ | $-11.1\times10^{-6}$ | $-4.40\times10^{-6}$ | | $cm^3/g$ | |
| Refractive index $(n-1)$, gas [a] | $206\times10^{-6}$ | $773\times10^{-6}$ | | | | | At 273 K and 101 kPa |
| Refractive index $n$, liquid [a] | | 1.367 [b] | 1.659 | | | | |

[a] $\lambda = 589$ nm. [b] At 92 K, $\varrho = 1.330\ g/cm^3$.

**Table 2.1-19C** Elements of Group VIIA (CAS notation), or Group 17 (new IUPAC notation). Allotropic and high-pressure modifications

| **Element** | **Fluorine** | | |
|---|---|---|---|
| **Modification** | **α-F ($F_2$)** | **β-F** | |
| | | | **Units** |
| Crystal system, Bravais lattice | mon, C | cub, P | |
| Structure type | | $\gamma$-O | |
| Lattice constant $a$ | 550 | 667 | pm |
| Lattice constant $b$ | 328 | | pm |
| Lattice constant $c$ | 728 | | pm |
| Lattice angle $\gamma$ | 102.17 | | deg |
| Space group | $C2/m$ | $Pm\bar{3}m$ | |
| Schoenflies symbol | $C_{2h}^3$ | $O_h^3$ | |
| *Strukturbericht* type | C34 | A15 | |
| Pearson symbol | mC6 | cP16 | |
| Number $A$ of atoms per cell | 6 | 16 | |
| Coordination number | 1 | | |
| Shortest interatomic distance, solid | 149 | | pm |
| Range of stability | $< 45.6$ K | $> 45.6$ K | |

**Table 2.1-19D** Elements of Group VIIA (CAS notation), or Group 17 (new IUPAC notation). Ionic radii (determined from crystal structures)

| **Element** | **Fluorine** | | **Chlorine** | | | **Bromine** | | | **Iodine** | | | |
|---|---|---|---|---|---|---|---|---|---|---|---|---|
| **Ion** | **$F^-$** | **$F^{7+}$** | **$Cl^-$** | **$Cl^{5+}$** | **$Cl^{7+}$** | **$Br^-$** | **$Br^{5+}$** | **$Br^{7+}$** | **$I^-$** | **$I^{5+}$** | **$I^{7+}$** | |
| **Coordination number** | | | | | | | | | | | | **Units** |
| 3 | | | | 12 | | | 31 | | | 44 | | pm |
| 3 | | | | | 8 | | | 25 | | | 42 | pm |
| 6 | 133 | 8 | 181 | | | 196 | | 39 | 220 | 95 | 53 | pm |

**Table 2.1-20A** Elements of Group VIIB (CAS notation), or Group 7 (new IUPAC notation). Atomic, ionic, and molecular properties (see Table 2.1-20D for ionic radii)

| **Element name** | **Manganese** | **Technetium** | **Rhenium** | **Bohrium** | | |
|---|---|---|---|---|---|---|
| **Chemical symbol**<br>**Atomic number *Z*** | **Mn**<br>**25** | **Tc**<br>**43** | **Re**<br>**75** | **Bh**<br>**107** | | |
| | | | | | **Units** | **Remarks** |
| Characteristics | | Radioactive | | | | |
| Relative atomic mass $A$ (atomic weight) | 54.938049(9) | [98] | 186.207(1) | | | |
| Abundance in lithosphere | $1000\times10^{-6}$ | | $1\times10^{-9}$ | | | Mass ratio |
| Abundance in sea | $2\times10^{-10}$ | | | | | Mass ratio |
| Atomic radius $r_{cov}$ | 118 | 127 | 128 | | pm | Covalent radius |
| Atomic radius $r_{met}$ | 137 | 137 | 137 | | pm | Metallic radius, CN = 12 |
| Electron shells | –LMN | –MNO | –NOP | –OPQ | | |
| Electronic ground state | $^6S_{5/2}$ | $^6S_{5/2}$ | $^6S_{5/2}$ | | | |
| Electronic configuration | $[Ar]3d^5 4s^2$ | $[Kr]4d^5 5s^2$ | $[Xe]4f^{14}5d^5 6s^2$ | | | |
| Oxidation states | 7+, 6+, 4+<br>3+, 2+ | 7+ | 7+, 6+, 4+,<br>2+, 1− | | | |
| Electron affinity | Not stable | 0.55 | 0.15 | | eV | Reaction type $Tc + e^- = Tc^-$ |
| Electronegativity $\chi_A$ | 1.60 | 1.36 | (1.46) | | | Allred and Rochow |
| 1st ionization energy | 7.43402 | 7.28 | 7.88 | | eV | |
| 2nd ionization energy | 15.63999 | 15.26 | | | eV | |
| 3rd ionization energy | 33.668 | 29.54 | | | eV | |
| 4th ionization energy | 51.2 | | | | eV | |
| Standard electrode potential $E^0$ | −1.185 | | | | V | Reaction type $Mn^{2+} + 2e^- = Mn$ |

**Table 2.1-20B(a)** Elements of Group VIIB (CAS notation), or Group 7 (new IUPAC notation). Crystallographic properties (see Table 2.1-20C for allotropic and high-pressure modifications)

| **Element name** | **Manganese** | **Technetium** | **Rhenium** | **Bohrium** | | |
|---|---|---|---|---|---|---|
| **Chemical symbol**<br>**Atomic number *Z*** | **Mn**<br>**25** | **Tc**<br>**43** | **Re**<br>**75** | **Bh**<br>**107** | | |
| | | | | | **Units** | **Remarks** |
| State | $\alpha$-Mn | | | | | |
| Crystal system, Bravais lattice | cub, bc | hex | hex | | | |
| Structure type | $\alpha$-Mn | Mg | Mg | | | |
| Lattice constant $a$ | 892.19 | 273.8 | 276.08 | | pm | |
| Lattice constant $c$ | | 439.4 | 445.80 | | pm | |
| Space group | $Im\bar{3}m$ | $P6_3/mmc$ | $P6_3/mmc$ | | | |
| Schoenflies symbol | $T_d^3$ | $D_{6h}^4$ | $D_{6h}^4$ | | | |
| *Strukturbericht* type | A12 | A3 | A3 | | | |
| Pearson symbol | cI58 | hP2 | hP2 | | | |
| Number $A$ of atoms per cell | 58 | 2 | 2 | | | |
| Coordination number | | 12 | 12 | | | |
| Shortest interatomic distance, solid | 226–293 | 274 | | | pm | |

**Table 2.1-20B(b)** Elements of Group VIIB (CAS notation), or Group 7 (new IUPAC notation). Mechanical properties

| **Element name** | **Manganese** | **Technetium** | **Rhenium** | **Bohrium** | | |
|---|---|---|---|---|---|---|
| **Chemical symbol**<br>**Atomic number *Z*** | **Mn**<br>**25** | **Tc**<br>**43** | **Re**<br>**75** | **Bh**<br>**107** | | |
| | | | | | **Units** | **Remarks** |
| Density $\varrho$, solid | 7.470 | 11.50 | 21.00 | | $g/cm^3$ | |
| Density $\varrho$, liquid | 6.430 | | 18.80 | | $g/cm^3$ | |
| Molar volume $V_{mol}$ | 7.38 | 8.6 | 8.86 | | $cm^3/mol$ | |
| Surface tension, liquid | 1.10 | | 2.65 | | N/m | |
| Temperature coefficient | 0 | | $-0.34\times10^{-3}$ | | N/(m K) | |
| Coefficient of linear thermal expansion $\alpha$ | $23\times10^{-6}$ | $8.06\times10^{-6}$ | $6.63\times10^{-6}$ | | 1/K | |
| Sound velocity, solid, transverse | 3280 | 50.6 | 2930 | | m/s | |
| Sound velocity, solid, longitudinal | 5560 | 3270 | 5360 | | m/s | |
| Compressibility $\kappa$ | $0.716\times10^{-5}$ | $3.22\times10^{-5}$ | $0.264\times10^{-5}$ | | 1/MPa | Volume compressibility |
| Elastic modulus $E$ | 196 | 407 | 520 | | GPa | At 293 K |
| Shear modulus $G$ | 79.4 | 162 | 180 | | GPa | |
| Poisson number $\mu$ | 0.24 | 0.26 | 0.26 | | | |
| Elastic compliance $s_{11}$ | | 3.2 | 2.11 | | 1/TPa | |
| Elastic compliance $s_{33}$ | | 2.9 | 1.70 | | 1/TPa | |
| Elastic compliance $s_{44}$ | | 5.7 | 6.21 | | 1/TPa | |
| Elastic compliance $s_{12}$ | | −1.1 | −0.80 | | 1/TPa | |
| Elastic compliance $s_{13}$ | | −0.9 | −0.40 | | 1/TPa | |
| Elastic stiffness $c_{11}$ | | 433 | 616 | | GPa | |
| Elastic stiffness $c_{33}$ | | 470 | 683 | | GPa | |
| Elastic stiffness $c_{44}$ | | 177 | 161 | | GPa | |
| Elastic stiffness $c_{12}$ | | 199 | 273 | | GPa | |
| Elastic stiffness $c_{13}$ | | 199 | 206 | | GPa | |
| Tensile strength | | 0.40–0.74 | 1.16 | | GPa | |
| Vickers hardness | 9.81 | 1.510 | 2.45–8.00 | | | |

**Table 2.1-20B(c)** Elements of Group VIIB (CAS notation), or Group 7 (new IUPAC notation). Thermal and thermodynamic properties

| Element name | Manganese | Technetium | Rhenium | Bohrium | | |
|---|---|---|---|---|---|---|
| Chemical symbol<br>Atomic number $Z$ | Mn<br>25 | Tc<br>43 | Re<br>75 | Bh<br>107 | | |
| | | | | | Units | Remarks |
| State | $\alpha$-Mn | | | | | |
| Thermal conductivity $\lambda$ | 29.7 | 185 | 71.2 | | W/(m K) | |
| Molar heat capacity $c_p$ | 26.28 | | 25.31 | | J/(mol K) | At 298 K |
| Standard entropy $S^0$ | 32.220 | 32.985 | 36.482 | | J/(mol K) | At 298 K and 100 kPa |
| Enthalpy difference $H_{298} - H_0$ | 4.9957 | | 5.3330 | | kJ/mol | |
| Melting temperature $T_m$ | 1519.00 | 2430.01 | 3458.00 | | K | |
| Transition | $\delta$–liquid | $\alpha$–liquid | $\alpha$–liquid | | | |
| Enthalpy change $\Delta H_m$ | 12.9089 | 33.2912 | 34.0750 | | kJ/mol | |
| Entropy change $\Delta S_m$ | 8.498 | 13.700 | 9.854 | | J/(mol K) | |
| Relative volume change $\Delta V_m$ | 0.017 | | | | | $(V_l - V_s)/V_l$ at $T_m$ |
| Boiling temperature $T_b$ | 2335 | 4538 | 5869 | | K | |
| Enthalpy change $\Delta H_b$ | 226.7 | 592.9 | 714.8 | | kJ/mol | |
| Critical temperature $T_c$ | | | 2090 | | K | |
| Critical pressure $p_c$ | | | 14.5 | | MPa | |
| Critical density $\varrho_c$ | | | 0.320 | | g/cm$^3$ | |

**Table 2.1-20B(d)** Elements of Group VIIB (CAS notation), or Group 7 (new IUPAC notation). Electronic, electromagnetic, and optical properties

| Element name | Manganese | Technetium | Rhenium | Bohrium | | |
|---|---|---|---|---|---|---|
| Chemical symbol<br>Atomic number $Z$ | Mn<br>25 | Tc<br>43 | Re<br>75 | Bh<br>107 | | |
| | | | | | Units | Remarks |
| Characteristics | Brittle metal | Metal | Metal | | | |
| Electrical resistivity $\rho_s$ | 1380 | 1510 | 172 | | n$\Omega$ m | At RT |
| Temperature coefficient | $5.0 \times 10^{-4}$ | | $44.8 \times 10^{-4}$ | | 1/K | |
| Pressure coefficient | $-3.54 \times 10^{-9}$ | | | | 1/hPa | |
| Electrical resistivity $\rho_l$ | 400 | | | | n$\Omega$ m | |
| Resistivity ratio at $T_m$ | 0.61 | | | | | |
| Superconducting critical temperature $T_{crit}$ | | | 1.70 | | K | |
| Superconducting critical field $H_{crit}$ | | | 198 | | Oe | |
| Hall coefficient $R$ | $0.84 \times 10^{-10}$ | | $3.15 \times 10^{-10}$ | | m$^3$/(A s) | At 297 K,<br>$B = 0.5$–$5.0$ T |
| Electronic work function | 4.08 | | About 5.0 | | V | |
| Thermal work function | 3.91 | | 4.96 | | V | |
| Molar magnetic susceptibility $\chi_{mol}$ (SI) | $6421 \times 10^{-6}$ | $1445 \times 10^{-6}$ | $842 \times 10^{-6}$ | | cm$^3$/mol | At 295 K |
| Molar magnetic susceptibility $\chi_{mol}$ (cgs) | $511 \times 10^{-6}$ | $115 \times 10^{-6}$ | $67 \times 10^{-6}$ | | cm$^3$/mol | At 295 K |
| Mass magnetic susceptibility $\chi_{mass}$ (SI) | $121 \times 10^{-6}$ | $31 \times 10^{-6}$ | $4.56 \times 10^{-6}$ | | cm$^3$/g | At 295 K |

**Table 2.1-20C** Elements of Group VIIB (CAS notation), or Group 7 (new IUPAC notation). Allotropic and high-pressure modifications

| **Element** | **Manganese** | | | | |
|---|---|---|---|---|---|
| **Modification** | **α-Mn** | **β-Mn** | **γ-Mn** | **δ-Mn** | |
| | | | | | **Units** |
| Crystal system, Bravais lattice | cub, bc | cub, P | cub, fc | cub, bc | |
| Structure type | α-Mn | β-Mn | Cu | W | |
| Lattice constant *a* | 892.19 | 631.52 | 386.24 | 308.06 | pm |
| Lattice constant *c* | | | | | pm |
| Space group | $Im\bar{3}m$ | $P4_132$ | $Fm\bar{3}m$ | $Im\bar{3}m$ | |
| Schoenflies symbol | $T_d^3$ | $O'$ | $O_h^5$ | $O_h^9$ | |
| *Strukturbericht* type | A12 | A13 | A1 | A2 | |
| Pearson symbol | cI58 | cP20 | cF4 | cI2 | |
| Number *A* of atoms per cell | 58 | 20 | 4 | 2 | |
| Coordination number | | | 12 | 8 | |
| Shortest interatomic distance, solid | 226–293 | | 273 | 267 | pm |
| Range of stability | RTP | > 1000 K | > 1368 K | > 1408 K | |

**Table 2.1-20D** Elements of Group VIIB (CAS notation), or Group 7 (new IUPAC notation). Ionic radii (determined from crystal structures)

| **Element** | **Manganese** | | | | | | **Technetium** | **Rhenium** | | | | |
|---|---|---|---|---|---|---|---|---|---|---|---|---|
| **Ion** | **$Mn^{2+}$** | **$Mn^{3+}$** | **$Mn^{4+}$** | **$Mn^{5+}$** | **$Mn^{6+}$** | **$Mn^{7+}$** | **$Tc^{4+}$** | **$Re^{4+}$** | **$Re^{5+}$** | **$Re^{6+}$** | **$Re^{7+}$** | |
| **Coordination number** | | | | | | | | | | | | **Units** |
| 4 | 66 | | 39 | 33 | 26 | 25 | | | | | 38 | pm |
| 6 | 83 | 58 | 53 | | | | 65 | 63 | 58 | 55 | | pm |
| 8 | 96 | | | | | | | | | | | pm |

**Table 2.1-21A** Elements of Group VIIIA (CAS notation), or Group 18 (new IUPAC notation). Atomic, ionic, and molecular properties

| **Element name** | **Neon** | **Argon** | **Krypton** | **Xenon** | **Radon** | | |
|---|---|---|---|---|---|---|---|
| **Chemical symbol**<br>**Atomic number *Z*** | **Ne**<br>**10** | **Ar**<br>**18** | **Kr**<br>**36** | **Xe**<br>**54** | **Rn**<br>**86** | | |
| | | | | | | **Units** | **Remarks** |
| Characteristics | | | | | Radioactive | | |
| Relative atomic mass $A$ (atomic weight) | 20.1797(6) | 39.948(1) | 83.80(1) | 131.29(2) | [222] | | |
| Atomic radius $r_{cov}$ | (69) | (97) | 110 | 130 | | pm | Covalent radius |
| Atomic radius $r_{met}$ | 154 | 188 | 202 | 216 | 240 | pm | Metallic radius, CN = 12 |
| Atomic radius $r_{vdW}$ | 160 | 188 | 200 | 220 | 240 | pm | van der Waals radius |
| Electron shells | KL | KLM | –LMN | –MNO | –NOP | | |
| Electronic ground state | $^1S_0$ | $^1S_0$ | $^1S_0$ | $^1S_0$ | $^1S_0$ | | |
| Electronic configuration | $[He]2s^22p^6$ | $[Ne]3s^23p^6$ | $[Ar]3d^{10}4s^24p^6$ | $[Kr]4d^{10}5s^25p^6$ | $[Xe]4f^{14}5d^{10}6s^26p^6$ | | |
| Electron affinity | Not stable | Not stable | Not stable | Not stable | Not stable | eV | Reaction type<br>$He + e^- = He^-$ |
| Electronegativity $\chi_A$ | 5.10 | 3.30 | 3.10 | 2.40 | (2.06) | | Allred and Rochow |
| 1st ionization energy | 21.56454 | 15.75962 | 13.99961 | 12.12987 | 10.74850 | eV | |
| 2nd ionization energy | 40.96328 | 27.62967 | 24.35985 | 21.20979 | | eV | |
| 3rd ionization energy | 63.45 | 40.74 | 36.950 | 32.1230 | | eV | |
| 4th ionization energy | 97.12 | 59.81 | 52.5 | | | eV | |

**Table 2.1-21B(a)** Elements of Group VIIIA (CAS notation), or Group 18 (new IUPAC notation). Crystallographic properties (see Table 2.1-21C for allotropic and high-pressure modifications)

| **Element name** | **Neon** | **Argon** | **Krypton** | **Xenon** | **Radon** | | |
|---|---|---|---|---|---|---|---|
| **Chemical symbol**<br>**Atomic number *Z*** | **Ne**<br>**10** | **Ar**<br>**18** | **Kr**<br>**36** | **Xe**<br>**54** | **Rn**<br>**86** | | |
| | | | | | | **Units** | **Remarks** |
| State | At 4.2 K | At 4.2 K | At 4.2 K | At 4.2 K | | | |
| Crystal system, Bravais lattice | cub, fc | cub, fc | cub, fc | cub, fc | | | |
| Structure type | Cu | Cu | Cu | Cu | | | |
| Lattice constant $a$ | 446.22 | 531.2 | 564.59 | 613.2 | | pm | |
| Space group | $Fm\bar{3}m$ | $Fm\bar{3}m$ | $Fm\bar{3}m$ | $Fm\bar{3}m$ | | | |
| Schoenflies symbol | $O_h^5$ | $O_h^5$ | $O_h^5$ | $O_h^5$ | | | |
| *Strukturbericht* type | A1 | A1 | A1 | A1 | | | |
| Pearson symbol | cF4 | cF4 | cF4 | cF4 | | | |
| Number $A$ of atoms per cell | 4 | 4 | 4 | 4 | | | |
| Coordination number | 12 | 12 | 12 | 12 | | | |
| Shortest interatomic distance, solid | 320 | 383 | 405 | 441 | | pm | |

**Table 2.1-21B(b)** Elements of Group VIIIA (CAS notation), or Group 18 (new IUPAC notation). Mechanical properties

| **Element name** | **Neon** | **Argon** | **Krypton** | **Xenon** | **Radon** | | |
|---|---|---|---|---|---|---|---|
| **Chemical symbol**<br>**Atomic number *Z*** | **Ne**<br>**10** | **Ar**<br>**18** | **Kr**<br>**36** | **Xe**<br>**54** | **Rn**<br>**86** | | |
| | | | | | | **Units** | **Remarks** |
| Characterics | Noble gas | Noble gas | Noble gas | Noble gas | Noble gas | | |
| Density $\varrho$, solid | | 1.736 (40 K) | | | | $g/cm^3$ | |
| Density $\varrho$, gas | $0.8994 \times 10^{-3}$ | | $3.7493 \times 10^{-3}$ | $5.8971 \times 10^{-3}$ | $9.73 \times 10^{-3}$ | $g/cm^3$ | At 273 K |
| Molar volume $V_{mol}$ | 13.97 | | 29.68 | 37.09 | 50.5 | $cm^3/mol$ | |
| Viscosity $\eta$, gas | 29.8 | 21 | 23.4 | 21.2 | | µPa s | At 293 K |
| Sound velocity, gas | 461 | 308 | 213 | 168 | | m/s | At STP |
| Sound velocity, liquid | | 855 (85 K) | | | | m/s | |
| Elastic modulus $E$ | 1.0 | 1.6 | 1.8 | | | GPa | Low temperature, estimated values |
| Elastic compliance $s_{11}$ | 1020 (4.7 K) | 593 (80 K) | 618 (115 K) | 690 (160.5 K) | | 1/TPa | |
| Elastic compliance $s_{44}$ | 1000 (4.7 K) | 1073 (80 K) | 744 (115 K) | 708 (160.5 K) | | 1/TPa | |
| Elastic compliance $s_{12}$ | −370 (4.7 K) | −205 (80 K) | −226 (115 K) | −271 (160.5 K) | | 1/TPa | |
| Elastic stiffness $c_{11}$ | 1.69 (4.7 K) | 2.77 (80 K) | 2.85 (115 K) | 2.93 (160.5 K) | | GPa | |
| Elastic stiffness $c_{44}$ | 1.00 (4.7 K) | 0.98 (80 K) | 1.35 (115 K) | 1.41 (160.5 K) | | GPa | |
| Elastic stiffness $c_{12}$ | 0.97 (4.7 K) | 1.37 (80 K) | 1.60 (115 K) | 1.89 (160.5 K) | | GPa | |
| Solubility in water $\alpha_W$ | 0.010 | 0.0340 | 0.059 | 0.108 | | | At 293 K, $\alpha_W$ = vol(gas)/vol(water) |

**Table 2.1-21B(c)** Elements of Group VIIIA (CAS notation), or Group 18 (new IUPAC notation). Thermal and thermodynamic properties

| **Element name** | **Neon** | **Argon** | **Krypton** | **Xenon** | **Radon** | | |
|---|---|---|---|---|---|---|---|
| **Chemical symbol**<br>**Atomic number *Z*** | **Ne**<br>**10** | **Ar**<br>**18** | **Kr**<br>**36** | **Xe**<br>**54** | **Rn**<br>**86** | | |
| | | | | | | **Units** | **Remarks** |
| State | Ne gas | Ar gas | Kr gas | Xe gas | Rn gas | | |
| Thermal conductivity $\lambda$ | $49.3 \times 10^{-3}$ | $18.0 \times 10^{-3}$ | $9.49 \times 10^{-3}$ | $5.1 \times 10^{-3}$ | $3.64 \times 10^{-3}$ | W/(m K) | |
| Molar heat capacity $c_p$ | 20.786 | 20.87 | 20.786 | 20.744 | 20.786 | J/(mol K) | At 298.15 K |
| Standard entropy $S^0$ | 146.328 | 154.842 | 164.085 | 169.575 | 176.234 | J/(mol K) | At 298.15 K and 100 kPa |
| Enthalpy difference $H_{298} - H_0$ | 6.1965 | 6.1965 | 6.1965 | 6.1970 | 6.1970 | kJ/mol | At 298.15 K |
| Melting temperature $T_m$ | 24.563 | 83.8 | 115.765 | 161.391 | 202 | K | |
| Transition | α–liquid | α–liquid | | α–liquid | α–liquid | | |
| Enthalpy change $\Delta H_m$ | 27.0 | 1.21 | 1.64 | 3.10 | 2.7 | kJ/mol | |
| Boiling temperature $T_b$ | 27.10 | 87.30 | 119.80 | 165.03 | 211 | K | |
| Enthalpy change $\Delta H_b$ | 0.324 | 6.3 | 9.05 | 12.65 | 18.1 | kJ/mol | |
| Critical temperature $T_c$ | 44.0 | 150.75 | 209.4 | 289.74 | | K | |
| Critical pressure $p_c$ | 2.75 | 4.86 | 5.50 | 5.840 | | MPa | |
| Critical density $\varrho_c$ | 0.4835 | 0.307 | 0.9085 | 1.105 | | $g/cm^3$ | |
| Triple-point temperature $T_{tr}$ | 24.5 | 83.85 | 115.95 | 161.25 | | K | |
| Triple-point pressure $p_{tr}$ | 43.3 | 68.75 | 73.19 | 81.6 | | kPa | |

**Table 2.1-21B(d)** Elements of Group VIIIA (CAS notation), or Group 18 (new IUPAC notation). Electronic, electromagnetic, and optical properties

| **Element name** | **Neon** | **Argon** | **Krypton** | **Xenon** | **Radon** | | |
|---|---|---|---|---|---|---|---|
| **Chemical symbol**<br>**Atomic number Z** | **Ne**<br>**10** | **Ar**<br>**18** | **Kr**<br>**36** | **Xe**<br>**54** | **Rn**<br>**86** | | |
| | | | | | | **Units** | **Remarks** |
| State | Ne gas | Ar gas | Kr gas | Xe gas | Rn gas | | |
| Dielectric constant $\varepsilon - 1$, gas | $130 \times 10^{-6}$ | $545 \times 10^{-6}$ | $7 \times 10^{-6}$ | $1238 \times 10^{-6}$ | | | At STP |
| Dielectric constant $\varepsilon$, liquid | | 1.516 (89 K) | | | | | |
| Molar magnetic susceptibility $\chi_{mol}$, gas (SI) | $-87.5 \times 10^{-6}$ | $-243 \times 10^{-6}$ | $-364 \times 10^{-6}$ | $-572 \times 10^{-6}$ | | $cm^3/mol$ | At 295 K |
| Molar magnetic susceptibility $\chi_{mol}$, gas (cgs) | $-6.96 \times 10^{-6}$ | $-19.3 \times 10^{-6}$ | $-29.0 \times 10^{-6}$ | $-45.5 \times 10^{-6}$ | | $cm^3/mol$ | At 295 K |
| Mass magnetic susceptibility $\chi_{mass}$, gas (SI) | $-4.2 \times 10^{-6}$ | $-6.16 \times 10^{-6}$ | $-4.32 \times 10^{-6}$ | $-4.20 \times 10^{-6}$ | | $cm^3/g$ | At 293 K |
| Refractive index $(n - 1)$, gas | $7.25 \times 10^{-6}$ | $281 \times 10^{-6}$ | | $706 \times 10^{-6}$ | | | $\lambda = 589.3$ nm |
| Refractive index $n$, liquid | | 1.233 (84 K) | | | | | $\lambda = 589.3$ nm |

**Table 2.1-21C** Elements of Group VIIIA (CAS notation), or Group 18 (new IUPAC notation). Allotropic and high-pressure modifications. There is no Table 2.1-21D, because no data on ionic radii are available

| **Element** | **Argon** | | |
|---|---|---|---|
| **Modification** | **α-Ar** | **β-Ar** | |
| | | | **Units** |
| Crystal system, Bravais lattice | cub, fc | hex, cp | |
| Structure type | Cu | Mg | |
| Lattice constant $a$ | 531.2 | 376.0 | pm |
| Lattice constant $c$ | | 614.1 | pm |
| Space group | $Fm\bar{3}m$ | $P6_3/mmc$ | |
| Schoenflies symbol | $O_h^5$ | $D_{6h}^4$ | |
| *Strukturbericht* type | A1 | A3 | |
| Pearson symbol | cF4 | hP2 | |
| Number $A$ of atoms per cell | 4 | 2 | |
| Coordination number | 12 | 12 | |
| Shortest interatomic distance, solid | 383 | | pm |
| Range of stability | < 83.8 K | > 83.8 K | |

**Table 2.1-22A** Elements of Group VIII(1) (CAS notation), or Group 8 (new IUPAC notation). Atomic, ionic, and molecular properties (see Table 2.1-22D for ionic radii)

| **Element name** | **Iron** | **Ruthenium** | **Osmium** | **Hassium** | | |
|---|---|---|---|---|---|---|
| **Chemical symbol**<br>**Atomic number Z** | **Fe**<br>**26** | **Ru**<br>**44** | **Os**<br>**76** | **Hs**<br>**108** | | |
| **Quantity** | | | | | **Units** | **Remarks** |
| Relative atomic mass $A$ (atomic weight) | 55.845(2) | 101.07(2) | 190.23(3) | | | |
| Abundance in lithosphere | $50\,000 \times 10^{-6}$ | | | | | Mass ratio |
| Abundance in sea | $2 \times 10^{-9}$ | | | | | Mass ratio |
| Atomic radius $r_{cov}$ | 116 | 125 | 126 | | pm | Covalent radius |
| Atomic radius $r_{met}$ | 126 | 132.5 | 134 | | pm | Metallic radius, CN = 12 |
| Electron shells | –LMN | –MNO | –NOP | –OPQ | | |
| Electronic ground state | $^5D_4$ | $^5F_5$ | $^5D_4$ | | | |
| Electronic configuration | $[Ar]3d^6 4s^2$ | $[Kr]4d^7 5s^1$ | $[Xe]4f^{14} 5d^6 6s^2$ | | | |
| Oxidation states | 3+, 2+ | 8+, 6+, 4+, 3+, 2+ | 8+, 6+, 4+, 3+, 2+ | | | |
| Electron affinity | 0.151 | 1.05 | 1.1 | | eV | Reaction type $Fe + e^- = Fe^-$ |
| Electronegativity $\chi_A$ | 1.64 | 1.42 | (1.52) | | | Allred and Rochow |
| 1st ionization energy | 7.9024 | 7.36050 | 8.7 | | eV | |
| 2nd ionization energy | 16.1878 | 16.76 | | | eV | |
| 3rd ionization energy | 30.652 | 28.47 | | | eV | |
| 4th ionization energy | 54.8 | | | | eV | |
| 5th ionization energy | 75.0 | | | | eV | |
| Standard electrode potential $E^0$ | −0.447 | | | | V | Reaction type $Fe^{2+} + 2e^- = Fe$ |
| | −0.037 | | | | V | Reaction type $Fe^{3+} + 3e^- = Fe$ |
| | +0.771 | | | | V | Reaction type $Fe^{3+} + e^- = Fe^{2+}$ |

**Table 2.1-22B(a)** Elements of Group VIII(1) (CAS notation), or Group 8 (new IUPAC notation). Crystallographic properties (see Table 2.1-22C for allotropic and high-pressure modifications)

| Element name | Iron | Ruthenium | Osmium | Hassium | | |
|---|---|---|---|---|---|---|
| Chemical symbol<br>Atomic number $Z$ | Fe<br>26 | Ru<br>44 | Os<br>76 | Hs<br>108 | | |
| | | | | | Units | Remarks |
| Modification | $\alpha$-Fe | | | | | |
| Crystal system, Bravais lattice | cub, bc | hex | hex | | | |
| Structure type | W | Mg | Mg | | | |
| Lattice constant $a$ | 286.65 | 270.53 | 273.48 | | pm | |
| Lattice constant $c$ | | 428.14 | 439.13 | | pm | |
| Space group | $Im\bar{3}m$ | $P6_3/mmc$ | $P6_3/mmc$ | | | |
| Schoenflies symbol | $O_h^9$ | $D_{6h}^4$ | $D_{6h}^4$ | | | |
| *Strukturbericht* type | A2 | A3 | A3 | | | |
| Pearson symbol | cI2 | hP2 | hP2 | | | |
| Number $A$ of atoms per cell | 2 | 2 | 2 | | | |
| Coordination number | 8 | 6+6 | 6+6 | | | |
| Shortest interatomic distance, solid | 248 | 265 | 267 | | pm | |

**Table 2.1-22B(b)** Elements of Group VIII(1) (CAS notation), or Group 8 (new IUPAC notation). Mechanical properties

| Element name | Iron | Ruthenium | Osmium | Hassium | | |
|---|---|---|---|---|---|---|
| Chemical symbol<br>Atomic number $Z$ | Fe<br>26 | Ru<br>44 | Os<br>76 | Hs<br>108 | | |
| | | | | | Units | Remarks |
| Density $\varrho$, solid | 7.86 | 12.20 | 22.4 | | $g/cm^3$ | |
| Density $\varrho$, liquid | 7.020 | 10.90 | 20.100 | | $g/cm^3$ | |
| Molar volume $V_{mol}$ | 7.09 | 8.14 | 8.43 | | $cm^3/mol$ | |
| Viscosity $\eta$, liquid | 5.53 | | | | mPa s | |
| Surface tension, liquid | 1.65 | 2.25 | 2.5 | | N/m | |
| Temperature coefficient | | $-0.31\times10^{-3}$ | $-0.33\times10^{-3}$ | | N/(m K) | |
| Coefficient of linear thermal expansion $\alpha$ | $12.3\times10^{-6}$ | $9.1\times10^{-6}$ | $6.1\times10^{-6}$ | | 1/K | |
| Sound velocity, solid, transverse | 3220 | 3740 | 3340 | | m/s | |
| Sound velocity, solid, longitudinal | 5920 | 6530 | 5480 | | m/s | |
| Compressibility $\kappa$ | $0.56\times10^{-5}$ | $0.331\times10^{-5}$ | $0.261\times10^{-5}$ | | 1/MPa | Volume compressibility |
| Elastic modulus $E$ | 211 | 432 | 559 | | GPa | |
| Shear modulus $G$ | 80.4 | 173 | 223 | | GPa | |
| Poisson number $\mu$ | 0.29 | 0.25 | 0.25 | | | |
| Elastic compliance $s_{11}$ | 7.67 | 2.09 | | | 1/TPa | |
| Elastic compliance $s_{33}$ | | 1.82 | | | 1/TPa | |
| Elastic compliance $s_{44}$ | 8.57 | 5.53 | | | 1/TPa | |
| Elastic compliance $s_{12}$ | −2.83 | −0.58 | | | 1/TPa | |
| Elastic compliance $s_{13}$ | | −0.41 | | | 1/TPa | |
| Elastic stiffness $c_{11}$ | 230 | 563 | | | GPa | |
| Elastic stiffness $c_{33}$ | | 624 | | | GPa | |
| Elastic stiffness $c_{44}$ | 117 | 181 | | | GPa | |
| Elastic stiffness $c_{12}$ | 135 | 188 | | | GPa | |
| Elastic stiffness $c_{13}$ | | 168 | | | GPa | |
| Tensile strength | 193–206 [a] | 540 | | | MPa | |
| Vickers hardness | 608 [a] | $2-5\times10^3$ | 800 | | | |

[a] Strongly dependent on microstructure

**Table 2.1-22B(c)** Elements of Group VIII(1) (CAS notation), or Group 8 (new IUPAC notation). Thermal and thermodynamic properties

| **Element name** | **Iron** | **Ruthenium** | **Osmium** | **Hassium** | | |
|---|---|---|---|---|---|---|
| **Chemical symbol**<br>**Atomic number $Z$** | **Fe**<br>**26** | **Ru**<br>**44** | **Os**<br>**76** | **Hs**<br>**108** | | |
| | | | | | **Units** | **Remarks** |
| Modification | $\alpha$-Fe | | | | | |
| Thermal conductivity $\lambda$ | 80.2 | 117 | 87.6 | | W/(m K) | |
| Molar heat capacity $c_p$ | 25.10 | 24.06 | 24.7 | | J/(mol K) | At 298.2 K |
| Standard entropy $S^0$ | 27.280 | 28.614 | 32.635 | | J/(mol K) | At 298.15 K and 100 kPa |
| Enthalpy difference $H_{298} - H_0$ | 4.4890 | 4.6024 | | | kJ/mol | At 298.15 K |
| Melting temperature $T_m$ | 1811.0 | 2607.0 | 3306.0 | | K | |
| Transition | $\delta$–liquid | $\alpha$–liquid | $\delta$–liquid | | | |
| Enthalpy change $\Delta H_m$ | 13.8060 | 38.5890 | 57.8550 | | kJ/mol | |
| Entropy change $\Delta S_m$ | 7.623 | 14.802 | 17.500 | | J/(mol K) | |
| Relative volume change $\Delta V_m$ | 0.034 | | | | | $(V_l - V_s)/V_l$ at $T_m$ |
| Boiling temperature $T_b$ | 3139 | 4423 | 5285 | | K | |
| Enthalpy change $\Delta H_b$ | 349.6 | 595.5 | 746 | | kJ/mol | |

**Table 2.1-22B(d)** Elements of Group VIII(1) (CAS notation), or Group 8 (new IUPAC notation). Electronic, electromagnetic, and optical properties

| **Element name** | **Iron** | **Ruthenium** | **Osmium** | **Hassium** | | |
|---|---|---|---|---|---|---|
| **Chemical symbol**<br>**Atomic number $Z$** | **Fe**<br>**26** | **Ru**<br>**44** | **Os**<br>**76** | **Hs**<br>**108** | | |
| | | | | | **Units** | **Remarks** |
| Characteristics | Soft metal | Metal | Brittle metal | | | |
| Electrical resistivity $\rho_s$ | 89 | 76 | 81 | | n$\Omega$ m | At RT |
| Temperature coefficient | $65.1 \times 10^{-4}$ | $45.8 \times 10^{-4}$ | $42 \times 10^{-4}$ | | 1/K | |
| Pressure coefficient | $-2.34 \times 10^{-9}$ | $-2.48 \times 10^{-9}$ | | | 1/hPa | |
| Superconducting critical temperature $T_{crit}$ | | 0.49 | 0.66 | | K | |
| Superconducting critical field $H_{crit}$ | | 66 | 65 | | Oe | |
| Hall coefficient $R$ | $8 \times 10^{-10}$ | $2.2 \times 10^{-10}$ | | | $m^3/(A\,s)$ | At 300 K,<br>$B = 4$–5 T |
| Thermoelectric coefficient | −51.34 | | | | $\mu$V/K | |
| Electronic work function | 4.70 | 4.71 | | | V | |
| Thermal work function | 4.50 | 4.73 | 4.83 | | V | |
| Molar magnetic susceptibility $\chi_{mol}$ (SI) | Ferromagnetic | 490 | 138 | | $cm^3$/mol | At 295 K |
| Molar magnetic susceptibility $\chi_{mol}$ (cgs) | Ferromagnetic | 39 | 11 | | $cm^3$/mol | At 295 K |
| Mass magnetic susceptibility $\chi_{mass}$ (SI) | Ferromagnetic | $5.37 \times 10^{-6}$ | $0.65 \times 10^{-6}$ | | $cm^3$/g | At 295 K |

**Table 2.1-22C** Elements of Group VIII(1) (CAS notation), or Group 8 (new IUPAC notation). Allotropic and high-pressure modifications

| **Element** | **Iron** | | | | |
|---|---|---|---|---|---|
| **Modification** | **α-Fe** | **γ-Fe** | **δ-Fe** | **ε-Fe** | |
| | | | | | **Units** |
| Crystal system, Bravais lattice | cub, bc | cub, fc | cub, bc | hex, cp | |
| Structure type | W | Cu | W | Mg | |
| Lattice constant *a* | 286.65 | 364.67 | 291.35 | 248.5 | pm |
| Lattice constant *c* | | | | 399.0 | pm |
| Space group | $Im\bar{3}m$ | $Fm\bar{3}m$ | $Im\bar{3}m$ | $P6_3/mmc$ | |
| Schoenflies symbol | $O_h^9$ | $O_h^5$ | $O_h^9$ | $D_{6h}^4$ | |
| *Strukturbericht* type | A2 | A1 | A2 | A3 | |
| Pearson symbol | cI2 | cF4 | cI2 | hP2 | |
| Number *A* of atoms per cell | 2 | 4 | 2 | 2 | |
| Coordination number | 8 | 12 | 8 | 6 + 6 | |
| Shortest interatomic distance, solid | 248 | 258 | 254 | 241 | pm |
| Range of stability | RTP | > 1183 K | > 1663 K | > 13.0 GPa | |

**Table 2.1-22D** Elements of Group VIII(1) (CAS notation), or Group 8 (new IUPAC notation). Ionic radii (determined from crystal structures)

| **Element** | **Iron** | | **Ruthenium** | | | | | **Osmium** | | | | |
|---|---|---|---|---|---|---|---|---|---|---|---|---|
| **Ion** | **$Fe^{2+}$** | **$Fe^{3+}$** | **$Ru^{3+}$** | **$Ru^{4+}$** | **$Ru^{5+}$** | **$Ru^{7+}$** | **$Ru^{8+}$** | **$Os^{4+}$** | **$Os^{5+}$** | **$Os^{6+}$** | **$Os^{8+}$** | |
| **Coordination number** | | | | | | | | | | | | **Units** |
| 4 | 63 | 49 | | | | 38 | 36 | | | | 39 | pm |
| 6 | 61 | 55 | 68 | 62 | 57 | | | 63 | 58 | 55 | | pm |
| 8 | 92 | 78 | | | | | | | | | | pm |

**Table 2.1-23A** Elements of Group VIII(2) (CAS notation), or Group 9 (new IUPAC notation). Atomic, ionic, and molecular properties (see Table 2.1-23D for ionic radii)

| **Element name** | **Cobalt** | **Rhodium** | **Iridium** | **Meitnerium** | | |
|---|---|---|---|---|---|---|
| **Chemical symbol**<br>**Atomic number Z** | **Co**<br>**27** | **Rh**<br>**45** | **Ir**<br>**77** | **Mt**<br>**109** | | |
| | | | | | **Units** | **Remarks** |
| Relative atomic mass $A$ (atomic weight) | 58.933200(9) | 102.90550(2) | 192.217(3) | | | |
| Abundance in lithosphere | $40\times10^{-6}$ | $0.001\times10^{-6}$ | $1\times10^{-9}$ | | | Mass ratio |
| Abundance in sea | $5\times10^{-11}$ | | | | | Mass ratio |
| Atomic radius $r_{cov}$ | 116 | 125 | 127 | | pm | Covalent radius |
| Atomic radius $r_{met}$ | 125 | 134.5 | 136 | | pm | Metallic radius, CN = 12 |
| Electron shells | –LMN | –MNO | –NOP | –OPQ | | |
| Electronic ground state | $^4F_{9/2}$ | $^4F_{9/2}$ | $^4F_{9/2}$ | | | |
| Electronic configuration | $[Ar]3d^74s^2$ | $[Kr]4d^85s^1$ | $[Xe]4f^{14}5d^76s^2$ | | | |
| Oxidation states | 3+, 2+ | 4+, 3+, 2+ | 6+, 4+, 3+, 2+ | | | |
| Electron affinity | 0.662 | 1.14 | 1.57 | | eV | Reaction type $Co + e^- = Co^-$ |
| Electronegativity $\chi_A$ | 1.75 | 1.35 | (1.44) | | | Allred and Rochow |
| 1st ionization energy | 7.8810 | 7.45890 | 9.1 | | eV | |
| 2nd ionization energy | 17.083 | 18.08 | | | eV | |
| 3rd ionization energy | 33.50 | 31.06 | | | eV | |
| 4th ionization energy | 51.3 | | | | eV | |
| Standard electrode potential $E^0$ | −0.28 | +0.6 | | | V | Reaction type $Co^{2+} + 2e^- = Co$ |
| | | | +1.156 | | V | Reaction type $Ir^{3+} + 3e^- = Ir$ |

**Table 2.1-23B(a)** Elements of Group VIII(2) (CAS notation), or Group 9 (new IUPAC notation). Crystallographic properties (see Table 2.1-23C for allotropic and high-pressure modifications)

| **Element name** | **Cobalt** | **Rhodium** | **Iridium** | **Meitnerium** | | |
|---|---|---|---|---|---|---|
| **Chemical symbol**<br>**Atomic number *Z*** | **Co**<br>**27** | **Rh**<br>**45** | **Ir**<br>**77** | **Mt**<br>**109** | | |
| | | | | | **Units** | **Remarks** |
| Modifaction | $\varepsilon$-Co | | | | | |
| Crystal system, Bravais lattice | hex, cp | cub, fc | cub, fc | | | |
| Structure type | Mg | Cu | Cu | | | |
| Lattice constant $a$ | 250.71 | 280.32 | 383.91 | | pm | |
| Lattice constant $c$ | 406.94 | | | | pm | |
| Space group | $P6_3/mmc$ | $Fm\bar{3}m$ | $Fm\bar{3}m$ | | | |
| Schoenflies symbol | $D_{6h}^4$ | $O_h^5$ | $O_h^5$ | | | |
| *Strukturbericht* type | A3 | A1 | A1 | | | |
| Pearson symbol | hP2 | cF4 | cF4 | | | |
| Number $A$ of atoms per cell | 2 | 4 | 4 | | | |
| Coordination number | $6+6$ | 12 | 12 | | | |
| Shortest interatomic distance, solid | 250 | 269 | 271 | | pm | |

**Table 2.1-23B(b)** Elements of Group VIII(2) (CAS notation), or Group 9 (new IUPAC notation). Mechanical properties

| **Element name** | **Cobalt** | **Rhodium** | **Iridium** | **Meitnerium** | | |
|---|---|---|---|---|---|---|
| **Chemical symbol**<br>**Atomic number *Z*** | **Co**<br>**27** | **Rh**<br>**45** | **Ir**<br>**77** | **Mt**<br>**109** | | |
| | | | | | **Units** | **Remarks** |
| Modification | $\varepsilon$-Co | | | | | |
| Density $\varrho$, solid | 8.90 | 12.40 | 22.50 | | g/cm$^3$ | |
| Density $\varrho$, liquid | 7.670 | 10.800 | 20.000 | | g/cm$^3$ | |
| Molar volume $V_{mol}$ | 6.62 | 8.29 | 8.57 | | cm$^3$/mol | |
| Viscosity $\eta$, liquid | 4.8 | | | | mPa s | Near $T_m$ |
| Coefficient of linear thermal expansion $\alpha$ | $13.36\times10^{-6}$ | $8.40\times10^{-6}$ | $6.8\times10^{-6}$ | | 1/K | |
| Surface tension, liquid | 1.520 | 1.97 | 2.250 | | N/m | |
| Temperature coefficient | $-0.92\times10^{-3}$ | $-0.3\times10^{-3}$ | $-0.31\times10^{-3}$ | | N/(m K) | |
| Sound velocity, solid, transverse | 3000 | 3470 | 3050 | | m/s | |
| Sound velocity, solid, longitudinal | 5730 | 6190 | 5380 | | m/s | |
| Compressibility $\kappa$ | $0.525\times10^{-5}$ | $0.350\times10^{-5}$ | $0.258\times10^{-5}$ | | 1/MPa | Volume compressibility |
| Elastic modulus $E$ | 204 | 379 | 528 | | GPa | |
| Shear modulus $G$ | 77.3 | 149 | 209 | | GPa | |
| Poisson number $\mu$ | 0.32 | 0.27 | 0.26 | | | |
| Elastic compliance $s_{11}$ | 5.11 | 3.46 | 2.28 | | 1/TPa | |
| Elastic compliance $s_{33}$ | 3.69 | | | | 1/TPa | |
| Elastic compliance $s_{44}$ | 14.1 | 5.43 | 3.90 | | 1/TPa | |
| Elastic compliance $s_{12}$ | −2.37 | −1.10 | −0.67 | | 1/TPa | |
| Elastic compliance $s_{13}$ | −0.94 | | | | 1/TPa | |
| Elastic stiffness $c_{11}$ | 295 | 413 | 580 | | GPa | |
| Elastic stiffness $c_{33}$ | 335 | | | | GPa | |
| Elastic stiffness $c_{44}$ | 71.0 | 184 | 256 | | GPa | |
| Elastic stiffness $c_{12}$ | 159 | 194 | 242 | | GPa | |
| Elastic stiffness $c_{13}$ | 111 | | | | GPa | |
| Tensile strength | 255 | 951 | $623\times10^3$ | | MPa | |
| Vickers hardness | 1043 | 1246 | 1760 | | | |

**Table 2.1-23B(c)** Elements of Group VIII(2) (CAS notation), or Group 9 (new IUPAC notation). Thermal and thermodynamic properties

| **Element name** | **Cobalt** | **Rhodium** | **Iridium** | **Meitnerium** | | |
|---|---|---|---|---|---|---|
| **Chemical symbol**<br>**Atomic number $Z$** | **Co**<br>**27** | **Rh**<br>**45** | **Ir**<br>**77** | **Mt**<br>**109** | | |
| | | | | | **Units** | **Remarks** |
| Modification | $\varepsilon$-Co | | | | | |
| Thermal conductivity $\lambda$ | 100 | 150 | 147 | | W/(m K) | |
| Molar heat capacity $c_p$ | 24.811 | 24.98 | 24.98 | | J/(mol K) | At 298 K |
| Standard entropy $S^0$ | 30.040 | 31.556 | 35.505 | | J/(mol K) | At 298 K and 100 kPa |
| Enthalpy difference $H_{298} - H_0$ | 4.7655 | | 5.2677 | | kJ/mol | |
| Melting temperature $T_m$ | 1768.0 | 2237.0 | 2719.0 | | K | |
| Transition | $\alpha$–liquid | $\alpha$–liquid | $\alpha$–liquid | | | |
| Enthalpy change $\Delta H_m$ | 16.200 | 26.5935 | 41.124 | | kJ/mol | |
| Entropy change $\Delta S_m$ | 9.163 | 11.888 | 15.125 | | J/(mol K) | |
| Relative volume change $\Delta V_m$ | | 0.12 | | | 1 | $(V_l - V_s)/V_l$ at $T_m$ |
| Boiling temperature $T_b$ | 3184 | 3970 | 4701 | | K | |
| Enthalpy change $\Delta H_b$ | 376.6 | 493.3 | 604.1 | | kJ/mol | |

**Table 2.1-23B(d)** Elements of Group VIII(2) (CAS notation), or Group 9 (new IUPAC notation). Electronic, electromagnetic, and optical properties

| **Element name** | **Cobalt** | **Rhodium** | **Iridium** | **Meitnerium** | | |
|---|---|---|---|---|---|---|
| **Chemical symbol**<br>**Atomic number $Z$** | **Co**<br>**27** | **Rh**<br>**45** | **Ir**<br>**77** | **Mt**<br>**109** | | |
| | | | | | **Units** | **Remarks** |
| Modification | $\alpha$-Co | | | | | |
| Characteristics | Hard metal | Metal | Brittle metal | | | |
| Electrical resistivity $\rho_s$ | 56 | 43.0 | 47 | | n$\Omega$ m | At RT |
| Temperature coefficient | $6.04\times10^{-3}$ | $4.62\times10^{-3}$ | $4.11\times10^{-3}$ | | 1/K | |
| Pressure coefficient | $-0.904\times10^{-9}$ | $-1.62\times10^{-9}$ | $-1.37\times10^{-9}$ | | 1/hPa | |
| Electrical resistivity $\rho_l$ | 1020 | | | | n$\Omega$ m | |
| Resistivity ratio at $T_m$ | 1.05 | | | | | |
| Superconducting critical temperature $T_{crit}$ | | | 0.14 | | K | |
| Superconducting critical field $H_{crit}$ | | | 77 | | Oe | |
| Hall coefficient $R$ | $360\times10^{-12}$ | $50.5\times10^{-12}$ | $31.8\times10^{-12}$ | | $m^3/(A\,s)$ | At 300 K, $B = 4.5$–$5.0$ T |
| Thermoelectronic coefficient | 17.5 | 1.0 | 1.2 | | $\mu$V/K | |
| Electronic work function | 4.97 | 4.98 | | | V | |
| Thermal work function | 4.37 | 4.68 | 5.03 | | V | |
| Molar magnetic susceptibility $\chi_{mol}$ (SI) | Ferromagnetic | $1282\times10^{-6}$ | $314\times10^{-6}$ | | $cm^3$/mol | At 295 K |
| Molar magnetic susceptibility $\chi_{mol}$ (cgs) | Ferromagnetic | $102\times10^{-6}$ | $25\times10^{-6}$ | | $cm^3$/mol | At 295 K |
| Mass magnetic susceptibility $\chi_{mass}$ (SI) | Ferromagnetic | $13.6\times10^{-6}$ | $1.67\times10^{-6}$ | | $cm^3$/g | At 295 K |

**Table 2.1-23C** Elements of Group VIII(2) (CAS notation), or Group 9 (new IUPAC notation). Allotropic and high-pressure modifications

| **Element** | **Cobalt** | | |
|---|---|---|---|
| **Modification** | **ε-Co** | **α-Co** | |
| | | | **Units** |
| Crystal system, Bravais lattice | hex, cp | cub, fc | |
| Structure type | Mg | Cu | |
| Lattice constant *a* | 250.71 | 354.45 | pm |
| Lattice constant *c* | 406.94 | | pm |
| Space group | $P6_3/mmc$ | $Fm\overline{3}m$ | |
| Schoenflies symbol | $D_{6h}^4$ | $O_h^5$ | |
| *Strukturbericht* type | A3 | A1 | |
| Pearson symbol | hP2 | cF4 | |
| Number *A* of atoms per cell | 2 | 4 | |
| Coordination number | 6 + 6 | 12 | |
| Shortest interatomic distance, solid | 250 | 251 | pm |
| Range of stability | RTP | > 661 K | |

**Table 2.1-23D** Elements of Group VIII(2) (CAS notation), or Group 9 (new IUPAC notation). Ionic radii (determined from crystal structures)

| **Element** | **Cobalt** | | **Rhodium** | | | **Iridium** | | | |
|---|---|---|---|---|---|---|---|---|---|
| **Ion** | **$Co^{2+}$** | **$Co^{3+}$** | **$Rh^{3+}$** | **$Rh^{4+}$** | **$Rh^{5+}$** | **$Ir^{3+}$** | **$Ir^{4+}$** | **$Ir^{5+}$** | |
| **Coordination number** | | | | | | | | | **Units** |
| 4 | 56 | | | | | | | | pm |
| 6 | 65 | 55 | 67 | 60 | 55 | 68 | 63 | 57 | pm |
| 8 | 90 | | | | | | | | pm |

**Table 2.1-24A** Elements of Group VIII(3) (CAS notation) or Group 10 (new IUPAC notation). Atomic, ionic, and molecular properties (see Table 2.1-24D for ionic radii)

| **Element name** | **Nickel** | **Palladium** | **Platinum** | | | |
|---|---|---|---|---|---|---|
| **Chemical symbol**<br>**Atomic number *Z*** | **Ni**<br>**28** | **Pd**<br>**46** | **Pt**<br>**78** | **Uun**<br>**110** | | |
| | | | | | **Units** | **Remarks** |
| Relative atomic mass $A$ (atomic weight) | 58.6934(2) | 106.42(1) | 195.078(2) | | | |
| Abundance in lithosphere | $100\times10^{-6}$ | $0.01\times10^{-6}$ | $5\times10^{-9}$ | | | Mass ratio |
| Abundance in sea | $1.7\times10^{-9}$ | | | | | Mass ratio |
| Atomic radius $r_{cov}$ | 115 | 128 | 130 | | pm | Covalent radius |
| Atomic radius $r_{met}$ | 125 | 138 | 137 | | pm | Metallic radius, CN = 12 |
| Atomic radius $r_{vdW}$ | 160 | 160 | 170–180 | | pm | van der Waals radius |
| Electron shells | –LMN | –MNO | –NOP | –OPQ | | |
| Electronic ground state | $^3F_4$ | $^1S_0$ | $^3D_3$ | | | |
| Electronic configuration | $[Ar]3d^84s^2$ | $[Kr]4d^{10}$ | $[Xe]4f^{14}5d^96s^1$ | | | |
| Oxidation states | 3+, 2+ | 4+, 2+ | 4+, 2+ | | | |
| Electron affinity | 1.16 | 0.562 | 2.13 | | eV | Reaction type $Ni + e^- = Ni^-$ |
| Electronegativity $\chi_A$ | 1.75 | 1.35 | (1.44) | | | Allred and Rochow |
| 1st ionization energy | 7.6398 | 8.3369 | 9.0 | | eV | |
| 2nd ionization energy | 18.16884 | 19.43 | 18.563 | | eV | |
| 3rd ionization energy | 35.19 | 32.93 | | | eV | |
| 4th ionization energy | 54.9 | | | | eV | |
| Standard electrode potential $E^0$ | −0.257 | +0.951 | +1.118 | | V | Reaction type $Ni^{2+} + 2e^- = Ni$ |

**Table 2.1-24B(a)** Elements of Group VIII(3) (CAS notation) or Group 10 (new IUPAC notation). Crystallographic properties

| **Element name** | **Nickel** | **Palladium** | **Platinum** | | | |
|---|---|---|---|---|---|---|
| **Chemical symbol**<br>**Atomic number *Z*** | **Ni**<br>**28** | **Pd**<br>**46** | **Pt**<br>**78** | **Uun**<br>**110** | | |
| | | | | | **Units** | **Remarks** |
| Crystal system, Bravais lattice | cub, fc | cub, fc | cub, fc | | | |
| Structure type | Cu | Cu | Cu | | | |
| Lattice constant $a$ | 352.41 | 389.01 | 392.33 | | pm | |
| Space group | $Fm\bar{3}m$ | $Fm\bar{3}m$ | $Fm\bar{3}m$ | | | |
| Schoenflies symbol | $O_h^5$ | $O_h^5$ | $O_h^5$ | | | |
| *Strukturbericht* type | A1 | A1 | A1 | | | |
| Pearson symbol | cF4 | cF4 | cF4 | | | |
| Number $A$ of atoms per cell | 4 | 4 | 4 | | | |
| Coordination number | 12 | 12 | 12 | | | |
| Shortest interatomic distance, solid | 249 | 274 | 277 | | pm | |

**Table 2.1-24B(b)** Elements of Group VIII(3) (CAS notation), or Group 10 (new IUPAC notation). Mechanical properties

| **Element name** | **Nickel** | **Palladium** | **Platinum** | | | |
|---|---|---|---|---|---|---|
| **Chemical symbol**<br>**Atomic number $Z$** | **Ni**<br>**28** | **Pd**<br>**46** | **Pt**<br>**78** | **Uun**<br>**110** | | |
| | | | | | **Units** | **Remarks** |
| Density $\varrho$, solid | 8.90 | 12.00 | 21.40 | | $g/cm^3$ | |
| Density $\varrho$, liquid | 7.910 | 10.700 | 19.700 | | $g/cm^3$ | |
| Molar volume $V_{mol}$ | 6.59 | 8.85 | 9.10 | | $cm^3/mol$ | |
| Viscosity $\eta$, liquid | 5.0 | | | | mPa s | |
| Surface tension, liquid | 1.725 | 1.50 | 1.866 | | N/m | |
| Temperature coefficient | $-0.98\times10^{-3}$ | $-0.22\times10^{-3}$ | $-0.17\times10^{-3}$ | | N/(m K) | |
| Coefficient of linear thermal expansion $\alpha$ | $13.3\times10^{-6}$ | $11.2\times10^{-6}$ | $9.0\times10^{-6}$ | | 1/K | |
| Sound velocity, solid, transverse | 3080 | 1900 | 1690 | | m/s | |
| Sound velocity, solid, longitudinal | 5810 | 4540 | 4080 | | m/s | |
| Compressibility $\kappa$ | $0.513\times10^{-5}$ | $0.505\times10^{-5}$ | $0.351\times10^{-5}$ | | 1/MPa | Volume compressibility |
| Elastic modulus $E$ | 220 | 121 | 170 | | GPa | |
| Shear modulus $G$ | 78.5 | 43.5 | 60.9 | | GPa | |
| Poisson number $\mu$ | 0.31 | 0.39 | 0.39 | | | |
| Elastic compliance $s_{11}$ | 7.67 | 13.7 | 7.35 | | 1/TPa | |
| Elastic compliance $s_{44}$ | 8.23 | 14.1 | 13.1 | | 1/TPa | |
| Elastic compliance $s_{12}$ | −2.93 | −6.0 | −3.08 | | 1/TPa | |
| Elastic stiffness $c_{11}$ | 247 | 221 | 347 | | GPa | |
| Elastic stiffness $c_{44}$ | 122 | 70.8 | 76.5 | | GPa | |
| Elastic stiffness $c_{12}$ | 153 | 171 | 251 | | GPa | |
| Tensile strength | 317 | | 134 | | MPa | At 293 K |
| Vickers hardness | 640 | 461 | 560 | | | At 293 K |

**Table 2.1-24B(c)** Elements of Group VIII(3) (CAS notation), or Group 10 (new IUPAC notation). Thermal and thermodynamic properties

| **Element name** | **Nickel** | **Palladium** | **Platinum** | | | |
|---|---|---|---|---|---|---|
| **Chemical symbol**<br>**Atomic number $Z$** | **Ni**<br>**28** | **Pd**<br>**46** | **Pt**<br>**78** | **Uun**<br>**110** | | |
| | | | | | **Units** | **Remarks** |
| Thermal conductivity $\lambda$ | 83 | 71.8 | 71.6 | | W/(m K) | |
| Molar heat capacity $c_p$ | 26.07 | 25.98 | 25.85 | | J/(mol K) | At 298 K |
| Standard entropy $S^0$ | 29.796 | 37.823 | 41.631 | | J/(mol K) | At 298 K and 100 kPa |
| Enthalpy difference $H_{298}-H_0$ | 4.7870 | 5.4685 | 5.7237 | | kJ/mol | |
| Melting temperature $T_m$ | 1728.30 | 1828.0 | 2041.50 | | K | |
| Transition | $\alpha$–liquid | $\alpha$–liquid | $\alpha$–liquid | | | |
| Enthalpy change $\Delta H_m$ | 17.4798 | 16.736 | 22.1750 | | kJ/mol | |
| Entropy change $\Delta S_m$ | 10.114 | 9.155 | 10.862 | | J/(mol K) | |
| Relative volume change $\Delta V_m$ | | | | | | $(V_l-V_s)/V_l$ at $T_m$ |
| Boiling temperature $T_b$ | 3157 | 3237 | 4100 | | K | |
| Enthalpy change $\Delta H_b$ | 369.24 | 357.6 | 509.8 | | kJ/mol | |

**Table 2.1-24B(d)** Elements of Group VIII(3) (CAS notation), or Group 10 (new IUPAC notation). Electronic, electromagnetic, and optical properties. There is no Table 2.1-24C, because no allotropic or high-pressure modifications are known

| **Element name** | **Nickel** | **Palladium** | **Platinum** | | | |
|---|---|---|---|---|---|---|
| **Chemical symbol**<br>**Atomic number *Z*** | **Ni**<br>**28** | **Pd**<br>**46** | **Pt**<br>**78** | **Uun**<br>**110** | | |
| | | | | | **Units** | **Remarks** |
| Characteristics | Ductile metal | Ductile metal | Ductile metal | | | |
| Electrical resistivity $\rho_s$ | 59.0 | 101 | 98.1 | | nΩ m | At RT |
| Temperature coefficient | $69.2\times10^{-4}$ | $37.7\times10^{-4}$ | $39.6\times10^{-4}$ | | 1/K | |
| Pressure coefficient | $1.82\times10^{-9}$ | $-2.1\times10^{-9}$ | $-1.88\times10^{-9}$ | | 1/hPa | |
| Electrical resistivity $\rho_l$ | 850 | | | | nΩ m | |
| Resistivity ratio at $T_m$ | 1.3 | | | | | |
| Hall coefficient $R$ | $-60\times10^{-12}$ | $-86\times10^{-12}$ | $-24.4\times10^{-12}$ | | $m^3/(A\,s)$ | At 298 K, $B = 0.3$–$4.6$ T |
| Thermoelectronic coefficient | −18 | −9.54 | −3.50 | | μV/K | |
| Electronic work function | 5.15 | 5.12 | 5.65 | | V | |
| Thermal work function | 4.60 | 4.99 | 5.30 | | V | |
| Molar magnetic susceptibility $\chi_{mol}$ (SI) | Ferromagnetic | $6786\times10^{-6}$ | $2425\times10^{-6}$ | | $cm^3/mol$ | At 295 K |
| Molar magnetic susceptibility $\chi_{mol}$ (cgs) | Ferromagnetic | $540\times10^{-6}$ | $193\times10^{-6}$ | | $cm^3/mol$ | At 295 K |
| Mass magnetic susceptibility $\chi_{mass}$ (SI) | Ferromagnetic | $67.0\times10^{-6}$ | $13.0\times10^{-6}$ | | $cm^3/g$ | At 295 K |

**Table 2.1-24D** Elements of Group VIII(3) (CAS notation), or Group 10 (new IUPAC notation). Ionic radii (determined from crystal structures)

| **Element** | **Nickel** | | **Palladium** | | | **Platinum** | | |
|---|---|---|---|---|---|---|---|---|
| **Ion** | **$Ni^{2+}$** | **$Ni^{3+}$** | **$Pd^{2+}$** | **$Pd^{3+}$** | **$Pd^{4+}$** | **$Pt^{2+}$** | **$Pt^{4+}$** | |
| **Coordination number** | | | | | | | | **Units** |
| 4 | 49 | | 64 | | | 60 | | pm |
| 6 | 69 | 56 | 86 | 76 | 62 | 80 | 63 | pm |

**Table 2.1-25A** Lanthanides. Atomic, ionic, and molecular properties (see Table 2.1-25D for ionic radii)

| Element name | Cerium | Praseodymium | Neodymium | Promethium | Samarium | Europium | Gadolinium | |
|---|---|---|---|---|---|---|---|---|
| Chemical symbol<br>Atomic number $Z$ | Ce<br>58 | Pr<br>59 | Nd<br>60 | Pm<br>61 | Sm<br>62 | Eu<br>63 | Gd<br>64 | |
| | | | | | | | | Units |
| Characteristics | | | | Radioactive | | | | |
| Relative atomic mass $A$ (atomic weight) | 140.116(1) | 140.90765(2) | 144.24(3) | [145] | 150.36(3) | 151.964(1) | 157.25(3) | |
| Abundance in lithosphere [a] | $41.6\times10^{-6}$ | $5.5\times10^{-6}$ | $23.9\times10^{-6}$ | | $6.5\times10^{-6}$ | $1.1\times10^{-6}$ | $6.4\times10^{-6}$ | |
| Abundance in sea [a] | $1\times10^{-12}$ | $6\times10^{-13}$ | $3\times10^{-12}$ | | $5\times10^{-14}$ | $1\times10^{-14}$ | $7\times10^{-13}$ | |
| Atomic radius $r_{cov}$ | 165 | 165 | 164 | 165 | 162 | 185 | 161 | pm |
| Atomic radius $r_{met}$ | 182 | 183 | 182 | 181 | 180 | 200 | 179 | pm |
| Electron shells | –NOP | –NOP | –NOP | –NOP | –NOP | –NOP | –NOP | |
| Electronic ground state | $^3H_4$ | $^4I_{9/2}$ | $^5I_4$ | $^6H_{5/2}$ | $^7F_0$ | $^8S_{7/2}$ | $^9D_2$ | |
| Electronic configuration | $[Xe]4f^1 5d^1 6s^2$ | $[Xe]4f^3 6s^2$ | $[Xe]4f^4 6s^2$ | $[Xe]4f^5 6s^2$ | $[Xe]4f^6 6s^2$ | $[Xe]4f^7 6s^2$ | $[Xe]4f^7 5d^1 6s^2$ | |
| Oxidation states | 4+, 3+ | 4+, 3+ | 3+ | 3+ | 3+, 2+ | 3+, 2+ | 3+ | |
| Electronegativity $\chi_A$ [b] | (1.08) | (1.07) | (1.07) | (1.07) | (1.07) | (1.01) | 1.11 | |
| 1st ionization energy | 5.5387 | 5.464 | 5.5250 | 5.55 | 5.6437 | 5.6704 | 6.1500 | eV |
| 2nd ionization energy | 10.85 | 10.55 | 10.73 | 10.90 | 11.07 | 11.241 | 12.09 | eV |
| 3rd ionization energy | 20.198 | 21.624 | 22.1 | 22.3 | 23.4 | 24.92 | 20.63 | eV |
| 4th ionization energy | 36.758 | 38.98 | 40.4 | 41.1 | 41.4 | 42.7 | 44.0 | eV |

[a] Mass ratio. [b] According to Allred and Rochow.

| Element name | Terbium | Dysprosium | Holmium | Erbium | Thulium | Ytterbium | Lutetium | |
|---|---|---|---|---|---|---|---|---|
| Chemical symbol<br>Atomic number $Z$ | Tb<br>65 | Dy<br>66 | Ho<br>67 | Er<br>68 | Tm<br>69 | Yb<br>70 | Lu<br>71 | |
| | | | | | | | | Units |
| Relative atomic mass $A$ (atomic weight) | 158.92534(2) | 162.50(3) | 164.93032(2) | 167.26(3) | 168.93421(2) | 173.04(3) | 174.967(1) | |
| Abundance in lithosphere [a] | $1\times10^{-6}$ | $4.5\times10^{-6}$ | $1.2\times10^{-6}$ | $2.5\times10^{-6}$ | $0.2\times10^{-6}$ | $2.7\times10^{-6}$ | $0.8\times10^{-6}$ | |
| Abundance in sea [a] | $1\times10^{-13}$ | $9\times10^{-13}$ | $2\times10^{-13}$ | $8\times10^{-13}$ | $2\times10^{-13}$ | $8\times10^{-13}$ | $2\times10^{-13}$ | |
| Atomic radius $r_{cov}$ | 159 | 159 | 158 | 157 | 156 | 174 | 156 | pm |
| Atomic radius $r_{met}$ | 176 | 175 | 174 | 173 | 172 | 194 | 172 | pm |
| Electron shells | –NOP | –NOP | –NOP | –NOP | –NOP | –NOP | –NOP | |
| Electronic ground state | $^6H_{15/2}$ | $^5I_8$ | $^4I_{15/2}$ | $^3H_6$ | $^2F_{7/2}$ | $^1S_0$ | $^2D_{3/2}$ | |
| Electronic configuration | $[Xe]4f^6 6s^2$ | $[Xe]4f^{10} 6s^2$ | $[Xe]4f^{11} 6s^2$ | $[Xe]4f^{12} 6s^2$ | $[Xe]4f^{13} 6s^2$ | $[Xe]4f^{14} 6s^2$ | $[Xe]4f^{14} 5d^1 6s^2$ | |
| Oxidation states | 4+, 3+ | 3+ | 3+ | 3+ | 3+, 2+ | 3+, 2+ | 3+ | |
| Electronegativity $\chi_A$ [b] | (1.10) | (1.10) | (1.10) | (1.11) | (1.11) | (1.06) | (1.14) | |
| 1st ionization energy | 5.8639 | 5.9389 | 6.0216 | 6.1078 | 6.18431 | 6.25416 | 5.42585 | eV |
| 2nd ionization energy | 11.52 | 11.67 | 11.80 | 11.93 | 12.05 | 12.1761 | 13.9 | eV |
| 3rd ionization energy | 21.91 | 22.8 | 22.84 | 22.74 | 23.68 | 25.05 | 20.9594 | eV |
| 4th ionization energy | 39.79 | 41.4 | 42.5 | 42.7 | 42.7 | 43.56 | 45.25 | eV |

[a] Mass ratio. [b] According to Allred and Rochow.

**Table 2.1-25B(a)** Lanthanides. Crystallographic properties (see Table 2.1-25C for allotropic and high-pressure modifications)

| Element name | Cerium | Praseodymium | Neodymium | Promethium | Samarium | Europium | Gadolinium | |
|---|---|---|---|---|---|---|---|---|
| **Chemical symbol**<br>**Atomic number *Z*** | **Ce**<br>**58** | **Pr**<br>**59** | **Nd**<br>**60** | **Pm**<br>**61** | **Sm**<br>**62** | **Eu**<br>**63** | **Gd**<br>**64** | |
| | | | | | | | | **Units** |
| Modification | | | | | $\alpha$-Sm | | | |
| Crystal system, Bravais lattice | cub, fc | hex | hex | hex | hex | cub, bc | hex | |
| Structure type | Cu | $\alpha$-La | $\alpha$-La | $\alpha$-La | Se | W | Mg | |
| Lattice constant *a* | 516.10 | 367.21 | 365.82 | 365 | 362.90 | 458.27 | 363.36 | pm |
| Lattice constant *c* | | 1183.26 | 1179.66 | 1165 | 2620.7 | | 578.10 | pm |
| Space group | $Fm\bar{3}m$ | $P6_3/mmc$ | $P6_3/mmc$ | $P6_3/mmc$ | | $Im\bar{3}m$ | $P6_3/mmc$ | |
| Schoenflies symbol | $O_h^5$ | $D_{6h}^4$ | $D_{6h}^4$ | $D_{6h}^4$ | | $O_h^9$ | $D_{6h}^4$ | |
| *Strukturbericht* type | A1 | A3′ | A3′ | A3′ | | A2 | A3 | |
| Pearson symbol | cF4 | hP4 | hP4 | hP4 | | cI2 | hP2 | |
| Number *A* of atoms per cell | 4 | 4 | 4 | 4 | | 2 | 2 | |
| Coordination number | 12 | 12 | 12 | 12 | | | 12 | |
| Shortest interatomic distance, solid | 364 | | 364 | 362 | | 397 | 360 | pm |

| Element name | Terbium | Dysprosium | Holmium | Erbium | Thulium | Ytterbium | Lutetium | |
|---|---|---|---|---|---|---|---|---|
| **Chemical symbol**<br>**Atomic number *Z*** | **Tb**<br>**65** | **Dy**<br>**66** | **Ho**<br>**67** | **Er**<br>**68** | **Tm**<br>**69** | **Yb**<br>**70** | **Lu**<br>**71** | |
| | | | | | | | | **Units** |
| Crystal system, Bravais lattice | hex | hex | hex | hex | hex | cub, fc | hex | |
| Structure type | Mg | Mg | Mg | Mg | Mg | Cu | Mg | |
| Lattice constant *a* | 360.55 | 359.15 | 357.78 | 355.92 | 353.75 | 548.48 | 350.52 | pm |
| Lattice constant *c* | 569.66 | 565.01 | 561.78 | 558.50 | 555.40 | | 554.94 | pm |
| Space group | $P6_3/mmc$ | $P6_3/mmc$ | $P6_3/mmc$ | $P6_3/mmc$ | $P6_3/mmc$ | $Fm\bar{3}m$ | $P6_3/mmc$ | |
| Schoenflies symbol | $D_{6h}^4$ | $D_{6h}^4$ | $D_{6h}^4$ | $D_{6h}^4$ | $D_{6h}^4$ | $O_h^5$ | $D_{6h}^4$ | |
| *Strukturbericht* type | A3 | A3 | A3 | A3 | A3 | A1 | A3 | |
| Pearson symbol | hP2 | hP2 | hP2 | hP2 | hP2 | cF4 | hP2 | |
| Number *A* of atoms per cell | 2 | 2 | 2 | 2 | 2 | 4 | 2 | |
| Coordination number | 12 | 12 | 12 | 12 | 12 | 12 | 12 | |
| Shortest interatomic distance, solid | 357 | 355 | 353 | 351 | 349 | 388 | 347 | pm |

**Table 2.1-25B(b)** Lanthanides. Mechanical properties

| Element name | Cerium [a] | Praseodymium | Neodymium | Promethium | Samarium | Europium | Gadolinium | |
|---|---|---|---|---|---|---|---|---|
| Chemical symbol<br>Atomic number $Z$ | Ce<br>58 | Pr<br>59 | Nd<br>60 | Pm<br>61 | Sm<br>62 | Eu<br>63 | Gd<br>64 | |
| | | | | | | | | Units |
| Density $\varrho$, solid | 6.78 | 6.77 | 7.00 | 6.48 | 7.54 | 5.26 | 7.89 | $g/cm^3$ |
| Density $\varrho$, liquid | | 6.609 | | | | | | $g/cm^3$ |
| Molar volume $V_{mol}$ | 17.00 | 20.80 | 20.59 | 20.1 | 20.00 | 28.29 | 19.90 | $cm^3/mol$ |
| Viscosity $\eta$, liquid | | 0.431 | | | | | | mPa s |
| Surface tension, liquid | 0.72 | 0.7 | 0.688 | 0.65 | 0.6 | 0.450 | 0.816 | N/m |
| Coefficient of linear thermal expansion $\alpha$ | $6.3\times10^{-6}$ | $6.79\times10^{-6}$ | $9.6\times10^{-6}$ | $11\times10^{-6}$ | $10.4\times10^{-6}$ | $32\times10^{-6}$ | $9.4\times10^{-6}$ | 1/K |
| Sound velocity, solid, transverse | 1230 | 1410 | 1440 | | 1290 | | 1680 | m/s |
| Sound velocity, solid, longitudinal | 3060 | 2660 | 2720 | | 2700 | | 2950 | m/s |
| Volume compressibility $\kappa$ | $5.06\times10^{-5}$ | $3.15\times10^{-5}$ | $2.94\times10^{-5}$ | $2.9\times10^{-5}$ | $3.27\times10^{-5}$ | $8.13\times10^{-5}$ | $2.47\times10^{-5}$ | 1/MPa |
| Elastic modulus $E$ | 44.1 | 35.2 | 37.9 | 46 | 53.9 | 18.2 | 56.3 | GPa |
| Shear modulus $G$ | 12.1 | 13.2 | 14.3 | 18 | 12.7 | 7.8 | 22.4 | GPa |
| Poisson number $\mu$ | 0.25 | 0.31 | 0.31 | 0.28 | 0.35 | 0.17 | 0.26 | |
| Elastic compliance $s_{11}$ | 62.8 | 26.6 | 23.7 | | | | 18.0 | 1/TPa |
| Elastic compliance $s_{33}$ | | 19.3 | 18.5 | | | | 16.1 | 1/TPa |
| Elastic compliance $s_{44}$ | 57.8 | 73.6 | 66.5 | | | | 48.1 | 1/TPa |
| Elastic compliance $s_{12}$ | −22.3 | −11.3 | −9.5 | | | | −5.7 | 1/TPa |
| Elastic compliance $s_{13}$ | | −3.8 | −3.9 | | | | −3.6 | 1/TPa |
| Elastic stiffness $c_{11}$ | 26.0 | 49.4 | 54.8 | | | | 67.8 | GPa |
| Elastic stiffness $c_{33}$ | | 57.4 | 60.9 | | | | 71.2 | GPa |
| Elastic stiffness $c_{44}$ | 17.3 | 13.6 | 15.0 | | | | 20.8 | GPa |
| Elastic stiffness $c_{12}$ | 14.3 | 23.0 | 24.6 | | | | 25.6 | GPa |
| Elastic stiffness $c_{13}$ | | 14.3 | 16.6 | | | | 20.7 | GPa |
| Tensile strength | 117 | 169 | 169 | 170 | 157 | | 122 | MPa |
| Vickers hardness | 275 | 400 | 348 | | 412 | 167 | 510–638 | |

[a] The data for the elastic behavior of cerium concern $\gamma$-cerium.

**Table 2.1-25B(b)** Lanthanides. Mechanical properties, cont.

| Element name | Terbium | Dysprosium | Holmium | Erbium | Thulium | Ytterbium | Lutetium | |
|---|---|---|---|---|---|---|---|---|
| Chemical symbol<br>Atomic number $Z$ | Tb<br>65 | Dy<br>66 | Ho<br>67 | Er<br>68 | Tm<br>69 | Yb<br>70 | Lu<br>71 | |
| | | | | | | | | Units |
| Density $\varrho$, solid | 8.27 | 8.54 | 8.80 | 9.05 | 9.33 | 6.98 | 9.840 | $g/cm^3$ |
| Density $\varrho$, liquid | | | | | | 6.292 | | $g/cm^3$ |
| Molar volume $V_{mol}$ | 19.31 | 19.00 | 18.75 | 18.44 | 18.12 | 24.84 | 17.78 | $cm^3/mol$ |
| Viscosity $\eta$, liquid | | | | | | 0.424 | | mPa s |
| Surface tension, liquid | 0.65 | 0.650 | 0.650 | 0.620 | 0.62 | 0.85 | | N/m |
| Coefficient of linear thermal expansion $\alpha$ | $7.0\times10^{-6}$ | $10.0\times10^{-6}$ | $11.2\times10^{-6}$ | $9.2\times10^{-6}$ | $13.3\times10^{-6}$ | $25.0\times10^{-6}$ | $8.12\times10^{-6}$ | 1/K |
| Sound velocity, solid, transverse | 1060 | 1720 | 1740 | 1810 | | 1000 | | m/s |
| Sound velocity, solid, longitudinal | 2920 | 2960 | 3040 | 3080 | | 1820 | | m/s |
| Volume compressibility $\kappa$ | $2.40\times10^{-5}$ | $2.50\times10^{-5}$ | $2.42\times10^{-5}$ | $2.34\times10^{-5}$ | $2.42\times10^{-5}$ | $7.24\times10^{-5}$ | $2.33\times10^{-5}$ | 1/MPa |
| Elastic modulus $E$ | 57.5 | 63.1 | 67.1 | 73.3 | 74.0 | 18.4 | 68.4 | GPa |
| Shear modulus $G$ | 22.8 | 25.5 | 26.7 | 29.6 | 30.4 | 7.16 | 27.1 | GPa |
| Poisson number $\mu$ | 0.26 | 0.24 | 0.26 | 0.24 | 0.27 | 0.28 | 0.27 | |
| Elastic compliance $s_{11}$ | 17.4 | 16.0 | 15.3 | 14.1 | | 89.2 | 14.3 | 1/TPa |
| Elastic compliance $s_{33}$ | 15.6 | 14.5 | 14.0 | 13.2 | | | 14.8 | 1/TPa |
| Elastic compliance $s_{44}$ | 46.0 | 41.2 | 38.6 | 36.4 | | 56.4 | 37.3 | 1/TPa |
| Elastic compliance $s_{12}$ | −5.2 | −4.6 | −4.3 | −4.2 | | −31.9 | −4.2 | 1/TPa |
| Elastic compliance $s_{13}$ | −3.6 | −3.2 | −2.9 | −2.6 | | | −3.5 | 1/TPa |
| Elastic stiffness $c_{11}$ | 69.2 | 74.0 | 76.5 | 84.1 | | 18.6 | 86.2 | GPa |
| Elastic stiffness $c_{33}$ | 74.4 | 78.6 | 79.6 | 84.7 | | | 80.9 | GPa |
| Elastic stiffness $c_{44}$ | 21.8 | 24.3 | 25.9 | 27.4 | | 17.7 | 26.8 | GPa |
| Elastic stiffness $c_{12}$ | 25.0 | 25.5 | 25.6 | 29.4 | | 10.4 | 32.0 | GPa |
| Elastic stiffness $c_{13}$ | 21.8 | 21.8 | 21.0 | 22.6 | | | 28.0 | GPa |
| Tensile strength | About 122 | | About 132 | 139 | About 140 | 72.5 | 139 | MPa |
| Vickers hardness | 863 | 544 | 481 | 589 | 520 | 206 | 1160 | |

**Table 2.1-25B(c)** Lanthanides. Thermal and thermodynamic properties

| Element name | Cerium | Praseodymium | Neodymium | Promethium | Samarium | Europium | Gadolinium | | |
|---|---|---|---|---|---|---|---|---|---|
| Chemical symbol<br>Atomic number $Z$ | Ce<br>58 | Pr<br>59 | Nd<br>60 | Pm<br>61 | Sm<br>62 | Eu<br>63 | Gd<br>64 | | |
| | | | | | | | | Units | Remarks |
| Thermal conductivity $\lambda$ | 11.4 | 12.5 | 16.5 | 17.9 | 13.3 | 13.9 | 10.6 | W/(m K) | |
| Molar heat capacity $c_p$ | 26.4 | 27.20 | 27.45 | | 29.54 | 27.6 | 37.02 | J/(mol K) | At 298.2 K |
| Standard entropy $S^0$ | 69.454 | 73.931 | 71.086 | 72.00 | 69.496 | 80.793 | 68.089 | J/(mol K) | At 298.15 K and 100 kPa |
| Enthalpy difference $H_{298} - H_0$ | 7.2802 | 7.4182 | 7.1337 | 7.3000 | 7.5730 | 8.0040 | 9.0876 | kJ/mol | At 298.15 K |
| Melting temperature $T_m$ | 1072.0 | 1204.0 | 1289.0 | 1315.0 | 1345.0 | 1095.0 | 1586.15 | K | |
| Transition | $\delta$–liquid | $\beta$–liquid | $\beta$–liquid | $\beta$–liquid | $\gamma$–liquid | $\alpha$–liquid | $\beta$–liquid | | |
| Enthalpy change $\Delta H_m$ | 5.4601 | 6.8869 | 7.1421 | 7.7000 | 8.6190 | 9.2132 | 9.6680 | kJ/mol | |
| Entropy change $\Delta S_m$ | 5.093 | 5.720 | 5.541 | 5.856 | 6.408 | 8.414 | 6.095 | J/(mol K) | |
| Relative volume change $\Delta V_m$ | 0.011 | 0.02 | 0.09 | | 0.036 | 0.048 | 0.02 | | $(V_l - V_s)/V_l$ at $T_m$ |
| Boiling temperature $T_b$ | 3699 | 3785 | 3341 | 3785 | 2064 | 1870 | 3569 | K | |
| Enthalpy change $\Delta H_b$ | 414.2 | 296.8 | 273.0 | | 166.4 | 144.7 | 359.4 | kJ/mol | |

**Table 2.1-25B(c)** Lanthanides. Thermal and thermodynamic properties, cont.

| Element name | Terbium | Dysprosium | Holmium | Erbium | Thulium | Ytterbium | Lutetium | | |
|---|---|---|---|---|---|---|---|---|---|
| Chemical symbol<br>Atomic number $Z$ | Tb<br>65 | Dy<br>66 | Ho<br>67 | Er<br>68 | Tm<br>69 | Yb<br>70 | Lu<br>71 | | |
| | | | | | | | | Units | Remarks |
| Thermal conductivity $\lambda$ | 11.1 | 10.7 | 16.2 | 14 | 16.8 | 38.5 | 16.4 | W/(m K) | |
| Molar heat capacity $c_p$ | 28.91 | 28.16 | 27.15 | 28.12 | 27.03 | 26.74 | 26.86 | J/(mol K) | At 298.2 K |
| Standard entropy $S^0$ | 73.8 | 74.956 | 75.019 | 73.178 | 74.015 | 59.831 | 50.961 | J/(mol K) | At 298.15 K and 100 kPa |
| Enthalpy difference $H_{298} - H_0$ | 9.4266 | 8.8659 | 7.9956 | 7.3923 | 7.3973 | 6.7111 | 6.3890 | kJ/mol | At 298.15 K |
| Melting temperature $T_m$ | 1632 | 1685.15 | 1745.0 | 1802.0 | 1818.0 | 1097 | 1936.0 | K | |
| Transition | $\beta$–liquid | $\beta$–liquid | $\beta$–liquid | $\alpha$–liquid | $\alpha$–liquid | $\gamma$–liquid | $\alpha$–liquid | | |
| Enthalpy change $\Delta H_m$ | 10.1504 | 11.3505 | 11.7570 | 19.9033 | 16.8406 | 7.6567 | 18.6481 | kJ/mol | |
| Entropy change $\Delta S_m$ | 6.220 | 6.736 | 6.738 | 11.045 | 9.263 | 6.980 | 9.632 | J/(mol K) | |
| Relative volume change $\Delta V_m$ | 0.031 | 0.45 | 0.074 | 0.09 | 0.069 | 0.051 | 0.036 | | $(V_l - V_s)/V_l$ at $T_m$ |
| Boiling temperature $T_b$ | 3496 | 2835 | 2968 | 3136 | 2220 | 1467 | 3668 | K | |
| Enthalpy change $\Delta H_b$ | 330.9 | 230 | 242.50 | 261.4 | 190.7 | 128.83 | 355.9 | kJ/mol | |

**Table 2.1-25B(d)** Lanthanides. Electronic, electromagnetic, and optical properties

| Element name | Cerium | Praseodymium | Neodymium | Promethium | Samarium | Europium | Gadolinium | | |
|---|---|---|---|---|---|---|---|---|---|
| Chemical symbol<br>Atomic number $Z$ | Ce<br>58 | Pr<br>59 | Nd<br>60 | Pm<br>61 | Sm<br>62 | Eu<br>63 | Gd<br>64 | | |
| | | | | | | | | Units | Remarks |
| Characteristics | Metal | Ductile reactive metal | Reactive metal | Metal | Metal | Soft metal very reactive | Soft metal | | |
| Electrical resistivity $\rho_s$ | 730 | 650 | 610 | 500 | 914 | 890 | 1260 | nΩ m | At RT |
| Temperature coefficient | $9.7\times10^{-4}$ | $17.1\times10^{-4}$ | $21.3\times10^{-4}$ | $28\times10^{-4}$ | $14.8\times10^{-4}$ | $81.3\times10^{-4}$ | $17.6\times10^{-4}$ | 1/K | |
| Pressure coefficient | $-45.2\times10^{-9}$ | $-0.4\times10^{-9}$ | $-1.5\times10^{-9}$ | | $-3.57\times10^{-9}$ | | $-4.5\times10^{-9}$ | 1/hPa | |
| Electrical resistivity $\rho_l$ | | 1130 | 1550 | | | 2440 | 1950 | nΩ m | |
| Hall coefficient $R$ | $1.92\times10^{-10}$ | $0.709\times10^{-10}$ | $0.971\times10^{-10}$ | | $-0.2\times10^{-10}$ | | $0.95\times10^{-10}$ | $m^3/(A\,s)$ | At 293 K, $B < 1$ T |
| Thermoelectric coefficient | 4.39 | | | | | | | μV/K | |
| Electronic work function | 2.88 | | 3.2 | | 2.7 | 2.5 | 3.1 | V | |
| Thermal work function | 2.6 | 2.7 | 3.3 | | 3.2 | 2.54 | 3.07 | V | |
| Molar magnetic susceptibility $\chi_{mol}$ (SI) | $31.4\times10^{-3}$ | $69.5\times10^{-3}$ | $74.5\times10^{-3}$ | | $16.1\times10^{-3}$ | $388\times10^{-3}$ | 2.324 | $cm^3/mol$ | At 295 K |
| Molar magnetic susceptibility $\chi_{mol}$ (cgs) | $2.5\times10^{-3}$ | $5.53\times10^{-3}$ | $5.93\times10^{-3}$ | | $1.28\times10^{-3}$ | $30.9\times10^{-3}$ | $185\times10^{-3}$ | $cm^3/mol$ | At 295 K |
| Mass magnetic susceptibility $\chi_{mass}$ (SI) | $217\times10^{-6}$ | $474\times10^{-6}$ | $490\times10^{-6}$ | | $106\times10^{-6}$ | $2.81\times10^{-3}$ | $14.9\times10^{-3}$ | $cm^3/g$ | At 295 K |

| Element name | Terbium | Dysprosium | Holmium | Erbium | Thulium | Ytterbium | Lutetium | | |
|---|---|---|---|---|---|---|---|---|---|
| Chemical symbol<br>Atomic number $Z$ | Tb<br>65 | Dy<br>66 | Ho<br>67 | Er<br>68 | Tm<br>69 | Yb<br>70 | Lu<br>71 | | |
| | | | | | | | | Units | Remarks |
| Characteristics | Ductile metal | Metal | Soft metal | Soft metal | Ductile metal | Ductile metal | Metal | | |
| Electrical resistivity $\rho_s$ | 1130 | 890 | 814 | 810 | 670 | 250 | 540 | nΩ m | At RT |
| Temperature coefficient | $11.9\times10^{-4}$ | $11.9\times10^{-4}$ | $17.1\times10^{-4}$ | $20.1\times10^{-4}$ | $19.5\times10^{-4}$ | $13\times10^{-4}$ | $24\times10^{-4}$ | 1/K | |
| Pressure coefficient | | $-2.3\times10^{-9}$ | $-2.2\times10^{-9}$ | $-27\times10^{-9}$ | $-2.6\times10^{-9}$ | $9.7\times10^{-9}$ | $-1.31\times10^{-9}$ | 1/hPa | |
| Electrical resistivity $\rho_l$ | 1930 | 2100 | 2210 | 2260 | | 1080 | | nΩ m | |
| Hall coefficient $R$ | | | | $-0.34\times10^{-10}$ | | $-0.53\times10^{-10}$ | | $m^3/(A\,s)$ | At 293 K, $B < 1$ T |
| Electronic work function | | | | | | | 3.3 | V | |
| Thermal work function | 3.4 | 3.09 | 3.09 | 3.12 | 3.12 | 2.50 | 3.14 | V | |
| Molar magnetic susceptibility $\chi_{mol}$ (SI) | 2.136 [a] | 1.232 [a] | $916\times10^{-3}$ | $603\times10^{-3}$ | $329\times10^{-3}$ | $842\times10^{-6}$ | $2.30\times10^{-3}$ | $cm^3/mol$ | At 295 K |
| Molar magnetic susceptibility $\chi_{mol}$ (cgs) | $170\times10^{-3}$ [a] | $98\times10^{-3}$ [a] | $72.9\times10^{-3}$ | $48\times10^{-3}$ | $26.2\times10^{-3}$ | $67\times10^{-6}$ | $183\times10^{-6}$ | $cm^3/mol$ | At 295 K |
| Mass magnetic susceptibility $\chi_{mass}$ (SI) | $15.3\times10^{-3}$ | $8.00\times10^{-3}$ | $5.49\times10^{-3}$ | $3.33\times10^{-3}$ | $1.90\times10^{-3}$ | $4.9\times10^{-6}$ | $13\times10^{-6}$ | $cm^3/g$ | At 295 K |

[a] The molar magnetic susceptibility is given for Tb and Dy for the $\alpha$-phase [1.3].

**Table 2.1-25C** Lanthanides. Allotropic and high-pressure modifications

| Element | Cerium | | | | | Praseodymium | | | |
|---|---|---|---|---|---|---|---|---|---|
| Modification | α-Ce | β-Ce | γ-Ce | α′-Ce | Ce-III | α-Pr | β-Pr | γ-Pr | |
| | | | | | | | | | Units |
| Crystal system, Bravais lattice | cub, fc | hex | cub, fc | cub, fc | orth | hex | cub, bc | cub, fc | |
| Structure type | Cu | α-La | Cu | Cu | α-U | α-La | W | Cu | |
| Lattice constant *a* | 516.10 | 367.3 | | 482 | | 367.21 | 413 | 488 | pm |
| Lattice constant *c* | | 1180.2 | | | | 1183.26 | | | pm |
| Space group | $Fm\bar{3}m$ | $P6_3/mmc$ | $Fm\bar{3}m$ | $Fm\bar{3}m$ | $Cmcm$ | $P6_3/mmc$ | $Im\bar{3}m$ | $Fm\bar{3}m$ | |
| Schoenflies symbol | $O_h^5$ | $D_{6h}^4$ | $O_h^5$ | $O_h^5$ | $D_{2h}^{17}$ | $D_{6h}^4$ | $O_h^9$ | $O_h^5$ | |
| *Strukturbericht* type | A1 | A3′ | A1 | A1 | A20 | A3′ | A2 | A1 | |
| Pearson symbol | cF4 | hP4 | cF4 | cF4 | oC4 | hP4 | cI2 | cF4 | |
| Number *A* of atoms per cell | 4 | 4 | 4 | 4 | 4 | 4 | 2 | 4 | |
| Coordination number | 12 | 12 | 12 | 12 | 2+2 +4+4 | 12 | 8 | 12 | |
| Shortest interatomic distance, solid | 364 | | | | | | 358 | 345 | pm |
| Range of stability | RTP | > 263 K | < 95 K | > 1.5 GPa | 5.1 GPa | RTP | > 1094 K | > 4.0 GPa | |

| Element | Neodymium | | | Promethium | | |
|---|---|---|---|---|---|---|
| Modification | α-Nd | β-Nd | γ-Nd | α-Pm | β-Pm | |
| | | | | | | Units |
| Crystal system, Bravais lattice | hex | cub, bc | cub, fc | hex | cub, bc | |
| Structure type | α-La | W | Cu | α-La | W | |
| Lattice constant *a* | 365.82 | 413 | 480 | 365 | | pm |
| Lattice constant *c* | 1179.66 | | | 1165 | | pm |
| Space group | $P6_3/mmc$ | $Im\bar{3}m$ | $Fm\bar{3}m$ | $P6_3/mmc$ | $Im\bar{3}m$ | |
| Schoenflies symbol | $D_{6h}^4$ | $O_h^9$ | $O_h^5$ | $D_{6h}^4$ | $O_h^9$ | |
| *Strukturbericht* type | A3′ | A2 | A1 | A3′ | A2 | |
| Pearson symbol | hP4 | cI2 | cF4 | hP4 | cI2 | |
| Number *A* of atoms per cell | 4 | 2 | 4 | 4 | 2 | |
| Coordination number | 12 | 8 | 12 | 12 | 8 | |
| Shortest interatomic distance, solid | 364 | 358 | 339 | 362 | | pm |
| Range of stability | RTP | > 1135 K | > 5.0 GPa | RTP | > 1163 K | |

| Element | Samarium | | | Gadolinium | | | |
|---|---|---|---|---|---|---|---|
| Modification | α-Sm | β-Sm | γ-Sm | α-Gd | β-Gd | γ-Gd | |
| | | | | | | | Units |
| Crystal system, Bravais lattice | trig | cub, bc | hex | hex, cp | cub, bc | trig | |
| Structure type | α-Sm | W | α-La | Mg | W | α-Sm | |
| Lattice constant *a* | 362.90 | | 361.8 | 363.36 | 406 | 361 | pm |
| Lattice constant *c* | 2620.7 | | 1166 | 578.10 | | 2603 | pm |
| Space group | $R\bar{3}m$ | $Im\bar{3}m$ | $P6_3/mmc$ | $P6_3/mmc$ | $Im\bar{3}m$ | $R\bar{3}m$ | |
| Schoenflies symbol | $D_{3d}^5$ | $O_h^9$ | $D_{6h}^4$ | $D_{6h}^4$ | $O_h^9$ | $D_{3d}^5$ | |
| *Strukturbericht* type | A7 | A2 | A3′ | A3 | A2 | A7 | |
| Pearson symbol | hR3 | cI2 | hP4 | hP2 | cI2 | hR3 | |
| Number *A* of atoms per cell | 3 | 2 | 4 | 2 | 2 | 3 | |
| Coordination number | 12 | 8 | 12 | 12 | 8 | | |
| Shortest interatomic distance, solid | 361 | 353 | 360 | 360 | 351 | | pm |
| Range of stability | RTP | > 1190 K | > 4.0 GPa | RTP | > 1535 K | > 3.0 GPa | |

**Table 2.1–25C** Lanthanides. Allotropic and high-pressure modifications, cont.

| Element | Terbium | | | Dysprosium | | | | |
|---|---|---|---|---|---|---|---|---|
| **Modification** | **α-Tb** | **β-Tb** | **Tb-II** | **α-Dy** | **β-Dy** | **α′-Dy** | **γ-Dy** | |
| | | | | | | | | **Units** |
| Crystal system, Bravais lattice | hex, cp | cub, bc | trig | hex, cp | cub, bc | orth | trig | |
| Structure type | Mg | W | α-Sm | Mg | W | | α-Sm | |
| Lattice constant *a* | 360.55 | | 341 | 359.15 | | 359.5 | 343.6 | pm |
| Lattice constant *b* | | | | | | 618.4 | | pm |
| Lattice constant *c* | 569.66 | | 2450 | 565.01 | | 567.8 | 2483.0 | pm |
| Space group | $P6_3/mmc$ | $Im\bar{3}m$ | $R\bar{3}m$ | $P6_3/mmc$ | $Im\bar{3}m$ | $Cmcm$ | $R\bar{3}m$ | |
| Schoenflies symbol | $D_{6h}^4$ | $O_h^9$ | $D_{3d}^5$ | $D_{6h}^4$ | $O_h^9$ | $D_{2h}^{17}$ | $D_{3d}^5$ | |
| *Strukturbericht* type | A3 | A2 | A7 | A3 | A2 | | | |
| Pearson symbol | hP2 | cI2 | hR3 | hP2 | cI2 | oC4 | hR3 | |
| Number *A* of atoms per cell | 2 | 2 | 3 | 2 | 2 | 4 | 3 | |
| Coordination number | 12 | | | 12 | 8 | | | |
| Shortest interatomic distance, solid | 357 | | | 355 | 345 | | | pm |
| Range of stability | RTP | > 1589 K | > 6.0 GPa | RTP | > 1243 K | < 86 K | > 7.5 GPa | |

| Element | Holmium | | | Erbium | | Thulium | | | |
|---|---|---|---|---|---|---|---|---|---|
| **Modification** | **α-Ho** | **β-Ho** | **γ-Ho** | **α-Er** | **β-Er** | **α-Tm** | **β-Tm** | **Tm-II** | |
| | | | | | | | | | **Units** |
| Crystal system, Bravais lattice | hex, cp | cub, bc | trig | hex, cp | cub, bc | hex, cp | cub, bc | trig | |
| Structure type | Mg | W | α-Sm | Mg | W | Mg | W | α-Sm | |
| Lattice constant *a* | 357.78 | | 334 | 355.92 | | 353.75 | | | pm |
| Lattice constant *c* | 561.78 | | 2450 | 558.50 | | 555.40 | | | pm |
| Space group | $P6_3/mmc$ | $Im\bar{3}m$ | $R\bar{3}m$ | $P6_3/mmc$ | $Im\bar{3}m$ | $P6_3/mmc$ | $Im\bar{3}m$ | $R\bar{3}m$ | |
| Schoenflies symbol | $D_{6h}^4$ | $O_h^9$ | $D_{3d}^5$ | $D_{6h}^4$ | $O_h^9$ | $D_{6h}^4$ | $O_h^9$ | $D_{3d}^5$ | |
| *Strukturbericht* type | A3 | A2 | A7 | A3 | A2 | A3 | A2 | | |
| Pearson symbol | hP2 | cI2 | hR3 | hP2 | cI2 | hP2 | cI2 | hR3 | |
| Number *A* of atoms per cell | 2 | 2 | 3 | 2 | 2 | 2 | 2 | 3 | |
| Coordination number | 12 | 8 | | 12 | 8 | 12 | 8 | | |
| Shortest interatomic distance, solid | 353 | 343 | | 351 | | 349 | | | pm |
| Range of stability | RTP | High temperature | > 4.0 GPa | RTP | High temperature | RTP | High temperature | > 6.0 GPa | |

| Element | Ytterbium | | | Lutetium | | | |
|---|---|---|---|---|---|---|---|
| **Modification** | **α-Yb** | **β-Yb** | **γ-Yb** | **α-Lu** | **β-Lu** | **Lu-II** | |
| | | | | | | | **Units** |
| Crystal system, Bravais lattice | cub, fc | cub, bc | hex, cp | hex, cp | cub, bc | trig | |
| Structure type | Cu | W | Mg | Mg | W | α-Sm | |
| Lattice constant *a* | 548.48 | 444 | 387.99 | 350.52 | | | pm |
| Lattice constant *c* | | | 638.59 | 554.94 | | | pm |
| Space group | $Fm\bar{3}m$ | $Im\bar{3}m$ | $P6_3/mmc$ | $P6_3/mmc$ | $Im\bar{3}m$ | $R\bar{3}m$ | |
| Schoenflies symbol | $O_h^5$ | $O_h^9$ | $D_{6h}^4$ | $D_{6h}^4$ | $O_h^9$ | $D_{3d}^5$ | |
| *Strukturbericht* type | A1 | A2 | A3 | A3 | A2 | | |
| Pearson symbol | cF4 | cI2 | hP2 | hP2 | cI2 | hR3 | |
| Number *A* of atoms per cell | 4 | 2 | 2 | 2 | 2 | 3 | |
| Coordination number | 12 | 8 | 6 + 6 | 12 | 8 | 12 | |
| Shortest interatomic distance, solid | 388 | 385 | 388 | 347 | 385 | | pm |
| Range of stability | RTP | > 1005 K | < 270 K | RTP | > 1005 K | > 23 GPa | |

**Table 2.1-25D** Lanthanides. Ionic radii (determined from crystal structures)

| Element | Cerium | | Praseodymium | | Neodymium | Promethium | Samarium | | Europium | | Gadolinium | |
|---|---|---|---|---|---|---|---|---|---|---|---|---|
| Ion | $Ce^{3+}$ | $Ce^{4+}$ | $Pr^{3+}$ | $Pr^{4+}$ | $Nd^{3+}$ | $Pm^{3+}$ | $Sm^{2+}$ | $Sm^{3+}$ | $Eu^{2+}$ | $Eu^{3+}$ | $Gd^{3+}$ | |
| Coordination number | | | | | | | | | | | | Units |
| 6 | 101 | 87 | 99 | 85 | 98 | | 119 | 96 | 117 | 95 | 94 | pm |
| 8 | 114 | 97 | 113 | 96 | 112 | 109 | 127 | 108 | 125 | 107 | 105 | pm |
| 9 | | | | | 116 | | | | | | | pm |
| 10 | 125 | 107 | | | | | | | 135 | | | pm |
| 12 | 134 | 114 | | | 127 | | | 124 | | | | pm |

| Element | Terbium | | Dysprosium | | Erbium | Thulium | | Ytterbium | | Lutetium | |
|---|---|---|---|---|---|---|---|---|---|---|---|
| Ion | $Tb^{3+}$ | $Tb^{4+}$ | $Dy^{2+}$ | $Dy^{3+}$ | $Er^{3+}$ | $Tm^{2+}$ | $Tm^{3+}$ | $Yb^{2+}$ | $Yb^{3+}$ | $Lu^{3+}$ | |
| Coordination number | | | | | | | | | | | Units |
| 6 | 92 | 76 | 107 | 91 | 89 | 101 | 88 | 102 | | 86 | pm |
| 7 | | | | | | 109 | | | | | pm |
| 8 | 104 | 88 | 119 | 103 | 100 | | 99 | 114 | 99 | 97 | pm |
| 9 | | | | | | | | | 104 | | pm |

**Table 2.1-26A** Actinides. Atomic, ionic, and molecular properties (see Table 2.1-26D for ionic radii)

| Element name | Thorium | Protactinium | Uranium | Neptunium | Plutonium | Americium | Curium | |
|---|---|---|---|---|---|---|---|---|
| Chemical symbol<br>Atomic number $Z$ | Th<br>90 | Pa<br>91 | U<br>92 | Np<br>93 | Pu<br>94 | Am<br>95 | Cu<br>96 | |
| | | | | | | | | Units |
| Characteristics | Radioactive | Radioactive | Radioactive | Radioactive | Radioactive | Radioactive | Radioactive | |
| Relative atomic mass $A$ (atomic weight) | 232.0381(1) | 231.03588(2) | 238.0289(1) | [237] | [244] | [243] | [247] | |
| Abundance in lithosphere [a] | $11.5\times10^{-6}$ | | $4\times10^{-6}$ | | | | | |
| Atomic radius $r_{cov}$ | 165 | | 142 | | | | | pm |
| Atomic radius $r_{met}$ | 180 | 164 | 154 | 150 | 164 | 173 | 174 | pm |
| Electron shells | –OPQ | –OPQ | –OPQ | –OPQ | –OPQ | –OPQ | –OPQ | |
| Electronic ground state | $^3F_2$ | $^4K_{11/2}$ | $^5L_6$ | $^6L_{11/2}$ | $^7F_0$ | $^8S_{7/2}$ | $^9D_2$ | |
| Electronic configuration | $[Rn]6d^27s^2$ | $[Rn]5f^26d^17s^2$ | $[Rn]5f^36d^17s^2$ | $[Rn]5f^46d^17s^2$ | $[Rn]5f^67s^2$ | $[Rn]5f^77s^2$ | $[Rn]5f^76d^17s^2$ | |
| Oxidation states | 4+ | 5+, 4+ | 6+, 5+, 4+, 3+ | 6+, 5+, 4+, 3+ | 6+, 5+, 4+, 3+ | 6+, 5+, 4+, 3+ | 3+ | |
| Electronegativity $\chi_A$ [b] | (1.11) | (1.14) | (1.22) | (1.22) | (1.22) | (1.2) | (1.2) | |
| 1st ionization energy | 6.08 | 5.89 | 6.19405 | 6.2657 | 6.06 | 5.993 | 6.02 | eV |
| 2nd ionization energy | 11.5 | | | | | | | eV |
| 3rd ionization energy | 20.0 | | | | | | | eV |
| 4th ionization energy | 28.8 | | | | | | | eV |
| Standard electrode potential $E^0$ [c] | −1.899 | | | | | | | V |

[a] Mass ratio. [b] According to Allred and Rochow. [c] Reaction type $Th^{4+} + 4e^- = Th$

| Element name | Berkelium | Californium | Einsteinium | Fermium | Mendelevium | Nobelium | Lawrencium | |
|---|---|---|---|---|---|---|---|---|
| Chemical symbol<br>Atomic number $Z$ | Bk<br>97 | Cf<br>98 | Es<br>99 | Fm<br>100 | Md<br>101 | No<br>102 | Lr<br>103 | |
| | | | | | | | | Units |
| Characteristics | Radioactive | Radioactive | Radioactive | Radioactive | Radioactive | Radioactive | Radioactive | |
| Relative atomic mass $A$ (atomic weight) | [247] | [251] | [252] | [257] | [258] | [259] | [262] | |
| Atomic radius $r_{met}$ | 170 | 186 | 186 | | | | | pm |
| Electron shells | –OPQ | –OPQ | –OPQ | –OPQ | –OPQ | –OPQ | –OPQ | |
| Electronic ground state | $^6H_{15/2}$ | $^5I_8$ | $^5I_{15/2}$ | $^3H_6$ | $^2F_{7/2}$ | $^1S_0$ | $^2D_{5/2}$ | |
| Electronic configuration | $[Rn]5f^97s^2$ | $[Rn]5f^{10}7s^2$ | $[Rn]5f^{11}7s^2$ | $[Rn]5f^{12}7s^2$ | $[Rn]5f^{13}7s^2$ | $[Rn]5f^{14}7s^2$ | $[Rn]5f^{14}6d^17s^2$ | |
| Oxidation states | 4+, 3+ | 3+ | | | | | 3+ | |
| Electronegativity $\chi_A$ [a] | (1.2) | (1.2) | (1.2) | (1.2) | (1.2) | | | |
| 1st ionization energy | 6.23 | 6.30 | 6.42 | 6.50 | 6.58 | 6.65 | | eV |

[a] According to Allred and Rochow.

**Table 2.1-26B(a)** Actinides. Crystallographic properties (see Table 2.1-26C for allotropic and high-pressure modifications)

| Element name | Thorium | Protactinium | Uranium | Neptunium | Plutonium | Americium | Curium | |
|---|---|---|---|---|---|---|---|---|
| **Chemical symbol**<br>**Atomic number Z** | **Th**<br>**90** | **Pa**<br>**91** | **U**<br>**92** | **Np**<br>**93** | **Pu**<br>**94** | **Am**<br>**95** | **Cu**<br>**96** | |
| | | | | | | | | **Units** |
| Modification | | | α-U | | α-Pu | | | |
| Crystal system, Bravais lattice | cub, fc | tetr, I | orth, C | orth, P | mon, P | hex | hex | |
| Structure type | Cu | α-Pa | α-U | α-Np | α-Pu | α-La | α-La | |
| Lattice constant *a* | 508.51 | 394.5 | 285.38 | 666.3 | 618.3 | 346.8 | 349.6 | pm |
| Lattice constant *b* | | | 586.80 | 472.3 | 482.2 | | | pm |
| Lattice constant *c* | | 324.2 | 495.57 | 488.7 | 1096.8 | 1124.1 | 1133.1 | pm |
| Lattice angle γ | | | | | 101.78 | | | deg |
| Space group | $Fm3m$ | $I4/mmm$ | $Cmcm$ | $Pnma$ | $P2_1/m$ | $P6_3/mmc$ | $P6_3/mmc$ | |
| Schoenflies symbol | $O_h^5$ | $D_{4h}^{17}$ | $D_{2h}^{17}$ | $D_{2h}^{16}$ | $C_{2h}^2$ | $D_{6h}^4$ | $D_{6h}^4$ | |
| *Strukturbericht* type | A1 | A6 | A20 | $A_c$ | | A3′ | A3′ | |
| Pearson symbol | cF4 | tI2 | oC4 | oP8 | mP16 | hP4 | hP4 | |
| Number *A* of atoms per cell | 4 | 2 | 4 | 8 | 16 | 4 | 4 | |
| Coordination number | 12 | 8+2 | 2+2+4+4 | 8+6 | | 6+6 | 6+6 | |
| Shortest interatomic distance, solid | 360 | 321 | 276 | 259–335 | 257–278 | 347 | 349 | pm |

| Element name | Berkelium | Californium | Einsteinium | Fermium | Mendelevium | Nobelium | Lawrencium | |
|---|---|---|---|---|---|---|---|---|
| **Chemical symbol**<br>**Atomic number Z** | **Bk**<br>**97** | **Cf**<br>**98** | **Es**<br>**99** | **Fm**<br>**100** | **Md**<br>**101** | **No**<br>**102** | **Lr**<br>**103** | |
| | | | | | | | | **Units** |
| Crystal system, Bravais lattice | hex | hex | hex | | | | | |
| Structure type | α-La | α-La | α-La | | | | | |
| Lattice constant *a* | 341.6 | | | | | | | pm |
| Lattice constant *c* | 1106.9 | | | | | | | pm |
| Space group | $P6_3/mmc$ | $P6_3/mmc$ | $P6_3/mmc$ | | | | | |
| Schoenflies symbol | $D_{6h}^4$ | $D_{6h}^4$ | $D_{6h}^4$ | | | | | |
| *Strukturbericht* type | A3′ | A3′ | A3′ | | | | | |
| Pearson symbol | hP4 | hP4 | hP4 | | | | | |
| Number *A* of atoms per cell | 4 | 4 | 4 | | | | | |

**Table 2.1-26B(b)** Actinides. Mechanical properties

| Element name | Thorium | Protactinium | Uranium | Neptunium | Plutonium | Americium | Curium | |
|---|---|---|---|---|---|---|---|---|
| Chemical symbol<br>Atomic number $Z$ | Th<br>90 | Pa<br>91 | U<br>92 | Np<br>93 | Pu<br>94 | Am<br>95 | Cu<br>96 | |
| | | | | | | | | Units |
| Modification | | | | | $\alpha$-Pu | | | |
| Density $\varrho$, solid | 11.70 | 15.40 | 18.90 | 20.40 | 19.80 | 13.60 | 13.510 | g/cm$^3$ |
| Density $\varrho$, liquid | 10.35 | | 17.907 | | 16.623 | | | |
| Molar volume $V_{mol}$ | 19.80 | 15.0 | 12.56 | 11.71 | 12.3 | 17.78 | 18.3 | cm$^3$/mol |
| Viscosity $\eta$, liquid | | | | | 7.4 | | | mPa s |
| Surface tension, liquid<br>Temperature coefficient | 1.05 | | 1.53<br>$-0.14\times10^{-3}$ | | 0.55 | | | N/m<br>N/(m K) |
| Coefficient of linear thermal expansion $\alpha$ | $12.5\times10^{-6}$ | $7.3\times10^{-6}$ | $12.6\times10^{-6}$ | $27.5\times10^{-6}$ | $55\times10^{-6}$ | | | 1/K |
| Sound velocity, solid, transverse | 1630 | | 1940 | | | | | m/s |
| Sound velocity, solid, longitudinal | 2850 | | 3370 | | | | | m/s |
| Volume compressibility $\kappa$ | $1.86\times10^{-5}$ | | $0.785\times10^{-5}$ | | | | | 1/MPa |
| Elastic modulus $E$ | 78.3 | 76 | 177 | 68 | 92.7 | | | GPa |
| Shear modulus $G$ | 30.8 | | 70.6 | | 45 | | | GPa |
| Poisson number $\mu$ | 0.26 | | 0.25 | | 0.18 | | | |
| Elastic compliance $s_{11}$ | 27.4 | | 4.91 | | | | | 1/TPa |
| Elastic compliance $s_{22}$ | | | 6.73 | | | | | 1/TPa |
| Elastic compliance $s_{33}$ | | | 4.79 | | | | | 1/TPa |
| Elastic compliance $s_{44}$ | 22.0 | | 8.04 | | | | | 1/TPa |
| Elastic compliance $s_{55}$ | | | 13.6 | | | | | 1/TPa |
| Elastic compliance $s_{66}$ | | | 13.4 | | | | | 1/TPa |
| Elastic compliance $s_{12}$ | −10.9 | | −1.19 | | | | | 1/TPa |
| Elastic compliance $s_{13}$ | | | 0.08 | | | | | 1/TPa |
| Elastic compliance $s_{23}$ | | | −2.61 | | | | | 1/TPa |
| Elastic stiffness $c_{11}$ | 77.0 | | 215 | | | | | GPa |
| Elastic stiffness $c_{22}$ | | | 199 | | | | | GPa |
| Elastic stiffness $c_{33}$ | | | 267 | | | | | GPa |
| Elastic stiffness $c_{44}$ | 45.5 | | 124 | | | | | GPa |
| Elastic stiffness $c_{55}$ | | | 73.4 | | | | | GPa |
| Elastic stiffness $c_{66}$ | | | 74.3 | | | | | GPa |
| Elastic stiffness $c_{12}$ | 50.9 | | 46 | | | | | GPa |
| Elastic stiffness $c_{13}$ | | | 22 | | | | | GPa |
| Elastic stiffness $c_{23}$ | | | 108 | | | | | GPa |
| Tensile strength | 0.219 | | 0.585 | | 0.525 | | | GPa |
| Vickers hardness | 294–687 | | 1960 | | 2500–2800 | | | |

**Table 2.1-26B(b)** Actinides. Mechanical properties, cont.

| Element name | Berkelium | Californium | Einsteinium | Fermium | Mendelevium | Nobelium | Lawrencium | |
|---|---|---|---|---|---|---|---|---|
| **Chemical symbol**<br>**Atomic number Z** | **Bk**<br>**97** | **Cf**<br>**98** | **Es**<br>**99** | **Fm**<br>**100** | **Md**<br>**101** | **No**<br>**102** | **Lr**<br>**103** | |
| | | | | | | | | **Units** |
| Density $\varrho$, solid | 14.790 | 9.310 | 8.840 | | | | | $g/cm^3$ |
| Molar volume $V_{mol}$ | 16.70 | 26.96 | 28.5 | | | | | $cm^3/mol$ |

**Table 2.1-26B(c)** Actinides. Thermal and thermodynamic properties

| Element name | Thorium | Protactinium | Uranium | Neptunium | Plutonium | Americium | Curium | | |
|---|---|---|---|---|---|---|---|---|---|
| **Chemical symbol**<br>**Atomic number Z** | **Th**<br>**90** | **Pa**<br>**91** | **U**<br>**92** | **Np**<br>**93** | **Pu**<br>**94** | **Am**<br>**95** | **Cu**<br>**96** | | |
| | | | | | | | | **Units** | **Remarks** |
| Modification | $\alpha$-Th | $\alpha$-Pa | $\alpha$-U | $\alpha$-Np | $\alpha$-Pu | | | | |
| Thermal conductivity $\lambda$ | 77.0 | About 47 | 22.0 | 6.3 | 6.74 | About 10 | About 10 | W/(m K) | |
| Molar heat capacity $c_p$ | 27.32 | (27.61) | 27.66 | 29.62 | 32.84 | 25.9 | (27.70) | J/(mol K) | At 298 K |
| Standard entropy $S^0$ | 51.800 | 51.882 | 50.200 | 50.459 | 54.461 | 55.396 | 71.965 | J/(mol K) | At 298.15 K and 100 kPa |
| Enthalpy difference $H_{298} - H_0$ | 6.3500 | 6.4392 | 6.3640 | 6.6065 | 6.9023 | 6.4070 | 6.1337 | kJ/mol | |
| Melting temperature $T_m$ | 2022.99 | 1844.78 | 1408.0 | 917.0 | 913.0 | 1449.0 | 1618.0 | K | |
| Transition | $\beta$–liquid | $\beta$–liquid | $\gamma$–liquid | $\gamma$–liquid | $\varepsilon$–liquid | $\gamma$–liquid | $\beta$–liquid | | |
| Enthalpy change $\Delta H_m$ | 13.8072 | 12.3412 | 9.1420 | 3.1986 | 2.8240 | 14.3930 | 14.6440 | kJ/mol | |
| Entropy change $\Delta S_m$ | 6.825 | 6.690 | 6.493 | 3.488 | 3.093 | 9.933 | 9.051 | J/(mol K) | |
| Relative volume change $\Delta V_m$ | 0.05 | | 0.022 | | | | | | $(V_l - V_s)/V_l$ at $T_m$ |
| Boiling temperature $T_b$ | 5061 | | 4407 | | 3503 | 2880 | | K | |
| Enthalpy change $\Delta H_b$ | 514.1 | 481 | 464.1 | 423.4 | 260.0 | 238.5 | 395.7 | kJ/mol | |

| Element name | Berkelium | Californium | Einsteinium | Fermium | Mendelevium | Nobelium | Lawrencium | | |
|---|---|---|---|---|---|---|---|---|---|
| **Chemical symbol**<br>**Atomic number Z** | **Bk**<br>**97** | **Cf**<br>**98** | **Es**<br>**99** | **Fm**<br>**100** | **Md**<br>**101** | **No**<br>**102** | **Lr**<br>**103** | | |
| | | | | | | | | **Units** | **Remarks** |
| Thermal conductivity $\lambda$ | About 10 | About 10 | About 10 | | | | | W/(m K) | |
| Standard entropy $S^0$ | (76.15) | 80.542 | 89.471 | 87.236 | | | | J/(mol K) | At 298.15 K and 100 kPa |
| Melting temperature $T_m$ | 1256 | 1213 | 1133.0 | 1800 | 1100 | 1100 | 1900 | K | |
| Transition | | | $\beta$–liquid | | | | | | |
| Enthalpy change $\Delta H_m$ | | | 9.4056 | 1.02 | | | | kJ/mol | |
| Entropy change $\Delta S_m$ | | | 8.302 | | | | | J/(mol K) | |
| Enthalpy of boiling $\Delta H_b$ | | | | 3.26 | | | | kJ/mol | |

**Table 2.1-26B(d)** Actinides. Electronic, electromagnetic, and optical properties

| Element name | Thorium | Protactinium | Uranium | Neptunium | Plutonium | Americium | Curium | | |
|---|---|---|---|---|---|---|---|---|---|
| **Chemical symbol**<br>**Atomic number *Z*** | **Th**<br>**90** | **Pa**<br>**91** | **U**<br>**92** | **Np**<br>**93** | **Pu**<br>**94** | **Am**<br>**95** | **Cu**<br>**96** | | |
| | | | | | | | | **Units** | **Remarks** |
| Characteristics | Soft metal | Toxic metal | Ductile metal | Reactive metal | Metal, very toxic | Metal | Metal, very reactive | | |
| Electrical resistivity $\rho_s$ | 147 | 177 | 280 | | 1414 | 680 | 860 | nΩ m | At RT |
| Temperature coefficient | $27.5\times10^{-4}$ | | $28.2\times10^{-4}$ | | | $33\times10^{-4}$ | | 1/K | |
| Pressure coefficient | $-3.4\times10^{-9}$ | | | | | | | 1/Pa | |
| Superconducting critical temperature $T_{crit}$ | 1.37 | | | | | | | K | |
| Superconducting critical field $H_{crit}$ | 162 | | | | | | | Oe | |
| Hall coefficient $R$ [a] | $-1.2\times10^{-10}$ | | $0.34\times10^{-10}$ | | $0.69\times10^{-6}$ | | | $m^3/(A\,s)$ | |
| Thermoelectronic coefficient | | | 5.0 | | | | | μV/K | |
| Electronic work function | 3.67 | | 3.47 | | | | | V | |
| Thermal work function | 3.42 | 4.8 | 3.47 | | | | | V | |
| Molar magnetic susceptibility $\chi_{mol}$ (SI) | $1.22\times10^{-3}$ | $3.48\times10^{-3}$ | $5.14\times10^{-3}$ | $7.23\times10^{-3}$ | $6.60\times10^{-3}$ | | | $cm^3/mol$ | |
| Molar magnetic susceptibility $\chi_{mol}$ (cgs) | $97\times10^{-6}$ | $277\times10^{-6}$ | $409\times10^{-6}$ | $575\times10^{-6}$ | $525\times10^{-6}$ | | | $cm^3/mol$ | |
| Mass magnetic susceptibility $\chi_{mol}$ (SI) | $7.2\times10^{-6}$ | | $21.6\times10^{-6}$ | | $31.7\times10^{-6}$ | $50\times10^{-6}$ | | $cm^3/g$ | |

[a] At 298 K, $B = 0.3$–$0.7$ T.

| Element name | Berkelium | Californium | Einsteinium | Fermium | Mendelevium | Nobelium | Lawrencium | |
|---|---|---|---|---|---|---|---|---|
| **Chemical symbol**<br>**Atomic number *Z*** | **Bk**<br>**97** | **Cf**<br>**98** | **Es**<br>**99** | **Fm**<br>**100** | **Md**<br>**101** | **No**<br>**102** | **Lr**<br>**103** | |
| Characteristics | Metal | Metal | Metal | | Metal | | | |

**Table 2.1-26C** Actinides. Allotropic and high-pressure modifications

| Element | Thorium | | Protactinium | | Uranium | | | |
|---|---|---|---|---|---|---|---|---|
| **Modification** | **α-Th** | **β-Th** | **α-Pa** | **β-Pa** | **α-U** | **β-U** | **γ-U** | |
| | | | | | | | | **Units** |
| Crystal system, Bravais lattice | cub, fc | cub, bc | tetr, I | cub, bc | orth, C | tetr | cub, bc | |
| Structure type | Cu | W | In | W | α-U | | W | |
| Lattice constant *a* | 508.51 | 411 | 394.5 | | 285.38 | 1075.9 | 352.4 | pm |
| Lattice constant *b* | | | | | 586.80 | | | pm |
| Lattice constant *c* | | | 324.2 | | 495.57 | 565.4 | | pm |
| Space group | $Fm\bar{3}m$ | $Im\bar{3}m$ | $I4/mmm$ | $Im\bar{3}m$ | $Cmcm$ | $P4_2/mmm$ | $Im\bar{3}m$ | |
| Schoenflies symbol | $O_h^5$ | $O_h^9$ | $D_{4h}^{17}$ | $O_h^9$ | $D_{2h}^{17}$ | $C_{2h}^{14}$ | $O_h^9$ | |
| *Strukturbericht* type | A1 | A2 | A6 | A2 | A20 | | A2 | |
| Pearson symbol | cF4 | cI2 | tI2 | cI2 | oC4 | tP30 | cI2 | |
| Number *A* of atoms per cell | 4 | 2 | 2 | 2 | 4 | 30 | 2 | |
| Coordination number | 12 | 8 | 8+2 | 2+2+4+4 | 2+2+4+4 | 12 | 8 | |
| Shortest interatomic distance, solid | 360 | 356 | 321 | | 276 | 287–353 | 347 | pm |
| Range of stability | RTP | > 1673 K | RTP | > 1443 K | RTP | > 935 K | > 1045 K | |

| Element | Neptunium | | | Plutonium | | | | | | |
|---|---|---|---|---|---|---|---|---|---|---|
| **Modification** | **α-Np** | **β-Np** | **γ-Np** | **α-Pu** | **β-Pu** | **γ-Pu** | **δ-Pu** | **δ′-Pu** | **ε-Pu** | |
| | | | | | | | | | | **Units** |
| Crystal system, Bravais lattice | orth, P | tetr | cub, bc | mon, P | mon | orth | cub, fc | tetr | cub, bc | |
| Structure type | α-Np | | W | | | | Cu | In | W | |
| Lattice constant *a* | 666.3 | 489.6 | 352 | 618.3 | 928.4 | 315.87 | 463.71 | 332.61 | 570.3 | pm |
| Lattice constant *b* | 472.3 | | | 482.2 | 1046.3 | 576.82 | | | | pm |
| Lattice constant *c* | 488.7 | 338.7 | | 1096.8 | 785.9 | 1016.2 | | 446.30 | | pm |
| Lattice angle $\gamma$ | | | | 101.78 | 92.13 | | | | | deg |
| Space group | $Pnma$ | $P42_12$ | $Im\bar{3}m$ | $P2_1/m$ | $I2/m$ | $Fddd$ | $Fm\bar{3}m$ | $I4/mmm$ | $Im\bar{3}m$ | |
| Schoenflies symbol | $D_{2h}^{16}$ | $D_{4h}^{7}$ | $O_h^9$ | $C_{2h}^{2}$ | $C_{2h}^{3}$ | $D_{2h}^{24}$ | $O_h^5$ | $D_{4h}^{17}$ | $O_h^9$ | |
| *Strukturbericht* type | $A_c$ | $A_d$ | A2 | | | | A1 | A6 | A2 | |
| Pearson symbol | oP8 | tP4 | cI2 | mP16 | mI34 | oF8 | cF4 | tI2 | cI2 | |
| Number *A* of atoms per cell | 8 | 4 | 2 | 16 | 34 | 8 | 4 | 2 | 2 | |
| Coordination number | 8+6 | 8+6 | 8+6 | | | 4+2+4 | 12 | 4+8 | 8+6 | |
| Shortest interatomic distance, solid | 260–336 | 275–356 | 305 | 257–278 | 259–310 | 303 | 328 | 333 | 315 | pm |
| Range of stability | RTP | > 553 K | > 850 K | RTP | > 395 K | > 508 K | > 592 K | > 726 K | > 744 K | |

**Table 2.1-26C** Actinides. Allotropic and high-pressure modifications, cont.

| Element | Americium | | | Curium | | |
|---|---|---|---|---|---|---|
| **Modification** | **α-Am** | **β-Am** | **γ-Am** | **α-Cm** | **β-Cm** | |
| | | | | | | **Units** |
| Crystal system, Bravais lattice | hex | cub, fc | orth | hex | cub, fc | |
| Structure type | α-La | Cu | α-U | α-La | Cu | |
| Lattice constant *a* | 346.8 | 489.4 | 306.3 | 349.6 | 438.1 | pm |
| Lattice constant *b* | | | 596.8 | | | pm |
| Lattice constant *c* | 1124.1 | | 516.9 | 1133.1 | | pm |
| Space group | $P6_3/mmc$ | $Fm\bar{3}m$ | $Cmcm$ | $P6_3/mmc$ | $Fm\bar{3}m$ | |
| Schoenflies symbol | $D_{6h}^4$ | $O_h^5$ | $D_{2h}^{17}$ | $D_{6h}^4$ | $O_h^5$ | |
| *Strukturbericht* type | A3′ | A1 | A20 | A3′ | A1 | |
| Pearson symbol | hP4 | cF4 | oC4 | hP4 | cF4 | |
| Number *A* of atoms per cell | 4 | 4 | 4 | 4 | 4 | |
| Coordination number | 6 + 6 | 12 | | 6 + 6 | 12 | |
| Shortest interatomic distance, solid | 347 | 346 | | 350 | 310 | pm |
| Range of stability | RTP | > 878 K | > 15.0 GPa | RTP | > 1449 K | |

| Element | Berkelium | | Californium | | Einsteinium | | |
|---|---|---|---|---|---|---|---|
| **Modification** | **α-Bk** | **β-Bk** | **α-Cf** | **β-Cf** | **α-Es** | **β-Es** | |
| | | | | | | | **Units** |
| Crystal system, Bravais lattice | hex | cub, fc | hex | cub, fc | hex | cub, fc | |
| Structure type | α-La | Cu | α-La | Cu | α-La | Cu | |
| Lattice constant *a* | 341.6 | 499.7 | | | | | pm |
| Lattice constant *c* | 1106.9 | | | | | | pm |
| Space group | $P6_3/mmc$ | $Fm\bar{3}m$ | $P6_3/mmc$ | $Fm\bar{3}m$ | $P6_3/mmc$ | $Fm\bar{3}m$ | |
| Schoenflies symbol | $D_{6h}^4$ | $O_h^5$ | $D_{6h}^4$ | $O_h^5$ | $D_{6h}^4$ | $O_h^5$ | |
| *Strukturbericht* type | A3′ | A1 | A3′ | A1 | A3′ | A1 | |
| Pearson symbol | hP4 | cF4 | hP4 | cF4 | hP4 | cF4 | |
| Number *A* of atoms per cell | 4 | 4 | 4 | 4 | 4 | 4 | |
| Coordination number | | 12 | | 12 | | | |
| Shortest interatomic distance, solid | | 353 | | 406 | | | pm |
| Range of stability | RTP | > 1183 K | | > 1213 K | RTP | > 1093 K | |

**Table 2.1-26D** Actinides. Ionic radii (determined from crystal structures)

| Element | Thorium | Protactinium | | | Uranium | | | | Neptunium | | | | |
|---|---|---|---|---|---|---|---|---|---|---|---|---|---|
| **Ion** | **$Th^{4+}$** | **$Pa^{3+}$** | **$Pa^{4+}$** | **$Pa^{5+}$** | **$U^{3+}$** | **$U^{4+}$** | **$U^{5+}$** | **$U^{6+}$** | **$Np^{3+}$** | **$Np^{4+}$** | **$Np^{5+}$** | **$Np^{6+}$** | |
| **Coordination number** | | | | | | | | | | | | | **Units** |
| 2 | | | | | | | | 45 | | | | | pm |
| 4 | | | | | | | | 52 | | | | | pm |
| 6 | 94 | 104 | 90 | 78 | 103 | 89 | 76 | 73 | 101 | 87 | 75 | 72 | pm |
| 8 | 105 | | | | | 100 | | 86 | | | | | pm |
| 10 | 113 | | | | | | | | | | | | pm |
| 12 | 121 | | | | | 117 | | | | | | | pm |

**Table 2.1-26D** Actinides. Ionic radii (determined from crystal structures), cont.

| Element | Plutonium | | | | Americium | | Curium | | |
|---|---|---|---|---|---|---|---|---|---|
| Ion | $Pu^{3+}$ | $Pu^{4+}$ | $Pu^{5+}$ | $Pu^{6+}$ | $Am^{3+}$ | $Am^{4+}$ | $Cm^{3+}$ | $Cm^{4+}$ | |
| Coordination number | | | | | | | | | Units |
| 6 | 100 | 86 | 74 | 71 | 98 | 85 | 97 | 85 | pm |
| 8 | | | | | 109 | 95 | | 95 | pm |

| Element | Berkelium | | Californium | | |
|---|---|---|---|---|---|
| Ion | $Bk^{3+}$ | $Bk^{4+}$ | $Cf^{3+}$ | $Cf^{4+}$ | |
| Coordination number | | | | | Units |
| 6 | 96 | 83 | 95 | 82 | pm |
| 8 | | 93 | | 92 | pm |

## References


1.1 W. Martienssen (Ed.): *Numerical Data and Functional Relationships in Science and Technology*, Landolt–Börnstein, New Series III and IV (Springer, Berlin, Heidelberg 1970–2003)

1.2 R. Blachnik (Ed.): *Elemente, anorganische Verbindungen und Materialien, Minerale*, D'Ans-Lax, Taschenbuch für Chemiker und Physiker, Vol. 3, 4th edn. (Springer, Berlin, Heidelberg 1998)

1.3 D. R. Lide (Ed.): *CRC Handbook of Chemistry and Physics*, 80th edn. (CRC Press, Boca Raton 1999)

1.4 Lehrstuhl für Werkstoffchemie, T.H. Aachen: *Thermodynamic Properties of Inorganic Materials*, Landolt–Börnstein, New Series IV/19 (Springer, Berlin, Heidelberg 1999)

# Part 3 Classes of Materials


**1 Metals**

Frank Goodwin, Research Triangle Parc, USA
Sivaraman Guruswamy, Salt Lake City, USA
Karl U. Kainer, Geesthacht, Germany
Catrin Kammer, Goslar, Germany
Wolfram Knabl, Reutte, Austria
Alfred Koethe, Dresden, Germany
Gerhard Leichtfried, Reutte, Austria
Günther Schlamp, Steinbach/Ts, Germany
Roland Stickler, Vienna, Austria
Hans Warlimont, Dresden, Germany

**2 Ceramics**

Hans Warlimont, Dresden, Germany

**3 Polymers**

Manfred D. Lechner, Osnabrück, Germany

**4 Glasses**

Dieter Krause, Mainz, Germany

# Metals

# 3.1. Metals

hereas the fundamental properties of all metallic elements are covered systematically and comprehensively in Chapt. 2.1, this section chapter treats those metals that are applied as base and alloying elements of metallic materials. According to common usage, the section is subdivided into treatments of metallic materials based on a single elements (Mg, Al, Ti, Zr, Fe, Co, Ni, Cu, Pb), and treatments of groups of metals with common dominating features (refractory metals, noble metals). The term metal is used indiscriminately for pure metals and for multicomponent metallic materials, i. e., alloys.

The properties of metallic materials depend sensitively not only on their chemical composition and on the electronic and crystal structure of the phases formed, but also to a large degree on their microstructure including the kind and distribution of lattice defects. The phase composition and microstructure of metallic materials are strongly dependent, in turn, on the thermal and mechanical treatments, which are applied under well-controlled conditions to achieve the desired properties. Accordingly, the production of metallic semifinished products and final parts on one hand, and the properties in the final state on the other hand, are usually intricately linked. This also applies to metallic materials treated in other chapters (Chapt. 4.2 on superconductors and Chapt. 4.3 on magnetic materials), as well as to the majority of other inorganic and organic materials.

According to the complexity of the interrelations between fundamental (intrinsic) and microstructure-dependent (extrinsic) properties of metallic materials, this section provides a substantial amount of explanatory text. By the same token, the data given are mostly typical examples indicating characteristic ranges of properties achievable rather than providing complete listings. More comprehensive databases are indicated by way of reference.


3.1.1 **Magnesium and Magnesium Alloys** ..... 162
3.1.1.1 Magnesium Alloys ..... 163
3.1.1.2 Melting and Casting Practices, Heat Treatment ..... 168
3.1.1.3 Joining ..... 169
3.1.1.4 Corrosion Behavior ..... 169
3.1.1.5 Recent Developments ..... 170

3.1.2 **Aluminium and Aluminium Alloys** ..... 171
3.1.2.1 Introduction ..... 171
3.1.2.2 Production of Aluminium ..... 171
3.1.2.3 Properties of Pure Al ..... 172
3.1.2.4 Aluminium Alloy Phase Diagrams ..... 174
3.1.2.5 Classification of Aluminium Alloys ..... 179
3.1.2.6 Structure and Basic Mechanical Properties of Wrought Work-Hardenable Aluminium Alloys ... 180
3.1.2.7 Structure and Basic Mechanical Properties of Wrought Age-Hardenable Aluminium Alloys ... 182
3.1.2.8 Structure and Basic Mechanical Properties of Aluminium Casting Alloys ..... 184
3.1.2.9 Technical Properties of Aluminium Alloys ..... 186
3.1.2.10 Thermal and Mechanical Treatment ..... 194
3.1.2.11 Corrosion Behavior of Aluminium ..... 202

3.1.3 **Titanium and Titanium Alloys** ..... 206
3.1.3.1 Commercially Pure Grades of Ti and Low-Alloy Ti Materials ..... 207
3.1.3.2 Ti-Based Alloys ..... 208
3.1.3.3 Intermetallic Ti–Al Materials ..... 209
3.1.3.4 TiNi Shape-Memory Alloys ..... 216

3.1.4 **Zirconium and Zirconium Alloys** ..... 217
3.1.4.1 Technically-Pure and Low-Alloy Zirconium Materials ..... 217
3.1.4.2 Zirconium Alloys in Nuclear Applications ..... 218
3.1.4.3 Zirconium-Based Bulk Glassy Alloys ..... 218

3.1.5 **Iron and Steels** ..... 221
3.1.5.1 Phase Relations and Phase Transformations ..... 222
3.1.5.2 Carbon and Low-Alloy Steels ..... 227
3.1.5.3 High-Strength Low-Alloy Steels 240
3.1.5.4 Stainless Steels ..... 240
3.1.5.5 Heat-Resistant Steels ..... 257
3.1.5.6 Tool Steels ..... 262
3.1.5.7 Cast Irons ..... 268

3.1.6 **Cobalt and Cobalt Alloys** ..... 272
3.1.6.1 Co-Based Alloys ..... 272
3.1.6.2 Co-Based Hard-Facing Alloys and Related Materials ..... 274
3.1.6.3 Co-Based Heat-Resistant Alloys, Superalloys ..... 274
3.1.6.4 Co-Based Corrosion-Resistant Alloys ..... 276
3.1.6.5 Co-Based Surgical Implant Alloys ..... 277
3.1.6.6 Cemented Carbides ..... 277

3.1.7 **Nickel and Nickel Alloys** ..... 279
3.1.7.1 Commercially Pure and Low-Alloy Nickels ..... 279
3.1.7.2 Highly Alloyed Ni-Based Materials ..... 279
3.1.7.3 Ni-Based Superalloys ..... 284
3.1.7.4 Ni Plating ..... 288

3.1.8 **Copper and Copper Alloys** ..... 296
3.1.8.1 Unalloyed Coppers ..... 296
3.1.8.2 High Copper Alloys ..... 297
3.1.8.3 Brasses ..... 298
3.1.8.4 Bronzes ..... 298
3.1.8.5 Copper–Nickel and Copper–Nickel–Zinc Alloys ..... 300

3.1.9 **Refractory Metals and Alloys** ..... 303
3.1.9.1 Physical Properties ..... 306
3.1.9.2 Chemical Properties ..... 308
3.1.9.3 Recrystallization Behavior ..... 311
3.1.9.4 Mechanical Properties ..... 314

3.1.10 **Noble Metals and Noble Metal Alloys** ..... 329
3.1.10.1 Silver and Silver Alloys ..... 330
3.1.10.2 Gold and Gold Alloys ..... 347
3.1.10.3 Platinum Group Metals and Alloys ..... 363
3.1.10.4 Rhodium, Iridium, Rhutenium, Osmium, and their Alloys ..... 386

3.1.11 **Lead and Lead Alloys** ..... 407
3.1.11.1 Pure Grades of Lead ..... 407
3.1.11.2 Pb–Sb Alloys ..... 411
3.1.11.3 Pb–Sn Alloys ..... 414
3.1.11.4 Pb–Ca Alloys ..... 416
3.1.11.5 Pb–Bi Alloys ..... 419
3.1.11.6 Pb–Ag Alloys ..... 420
3.1.11.7 Pb–Cu, Pb–Te, and Pb–Cu–Te Alloys ..... 421
3.1.11.8 Pb–As Alloys ..... 421
3.1.11.9 Lead Cable Sheathing Alloys ..... 421
3.1.11.10 Other Lead Alloys ..... 421

**References** ..... 422


## 3.1.1 Magnesium and Magnesium Alloys

Magnesium is the lightest structural metal with a density of 1.74 g cm$^{-3}$. It is produced by two basic processes. One is the electrolysis of fused anhydrous magnesium chloride ($MgCl_2$) derived from magnesite, brine, or seawater, and recently from serpentine ores. The other one is the thermal reduction of magnesium oxide (MgO) by ferrosilicon derived from carbonate ores [1.1]. The use of primary Mg is shown in Fig. 3.1-1. Only one third is used for structural parts, mainly for castings, while the major amount of Mg is still used as an alloying element in Al alloys.

Pure Mg is rarely used for structural applications due to its poor mechanical properties. Therefore, Al and Zn have been introduced as major alloying elements for high-pressure die casting alloys. The main reason for using magnesium alloys is to lower the weigh load, predominantly in transportation industries. The weight reduction amounts to about 30% compared to Al alloys and to about 75% compared to steel. Magnesium has a hexagonal close-packed crystal structure (hcp). Therefore its deformation properties are poor. At room temperature slip occurs on the basal plane {0001} in the $\langle 11\bar{2}0\rangle$ direction only. In addition to slip on basal planes the deformation by twinning is also possible, the twinning system is $\{10\bar{1}2\}\langle 10\bar{1}1\rangle$. Twin formation leads to different behavior of Mg alloys under tensile and compressive load. With increasing temperature above 200–225 °C, prismatic slip planes are activated in addition. This is of main importance for the processing wrought magnesium alloys.

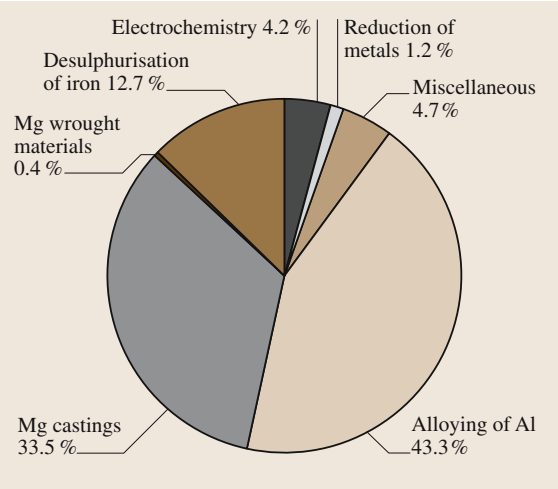


**Fig. 3.1-1** World consumption of Mg in 2001 (329 480 t) [1.2]

Alloying elements used in Mg alloys and their abbreviations applied in the designation of Mg materials are listed in Table 3.1-1. General data, maximum solubility data, and compounds formed in major binary magnesium alloy systems are given in Table 3.1-2 [1.4]. Since Al is one of the most important alloying elements, Fig. 3.1-2 [1.3] shows an example of an Al–Mg binary alloy system. The effect of alloying elements in Mg materials is given in Table 3.1-3 [1.3, 4].

### 3.1.1.1 Magnesium Alloys

The major alloying elements are manganese, aluminium, zinc, zirconium, silicon, thorium, and rare earth metals (E). At present E elements are the most promising candidates for magnesium alloys, with high temperature stability as well as improved corrosion behavior. E metals are forming stable intermetallic compounds at high temperature and therefore they decrease castability. Aluminium and zinc are introduced mainly to

**Table 3.1-1** Alloying elements and abbreviations used for Mg materials [1.3]

| | | | | | | | | | |
|---|---|---|---|---|---|---|---|---|---|
| A | C | E | K | L | M | Q | S | W | Z |
| Al | Cu | Rare earth | Zr | Li | Mn | Ag | Si | Y | Zn |

**Table 3.1-2** Solubility data and intermetallic phases in binary magnesium alloys [1.4]

| Solute element | Maximum solubility | | Adjacent intermetallic phase | Melting point of intermetallic phase (°C) | Type of equilibrium |
|---|---|---|---|---|---|
| | (wt%) | (at%) | | | |
| Lithium | 5.5 | 17.0 | – | – | Eutectic |
| Aluminium | 12.7 | 11.8 | $Mg_{17}Al_{12}$ | 402 | Eutectic |
| Silver | 15.0 | 3.8 | $Mg_3Ag$ | 492 | Eutectic |
| Yttrium | 12.5 | 3.75 | $Mg_{24}Y_5$ | 620 | Eutectic |
| Zinc | 6.2 | 2.4 | MgZn | 347 | Eutectic |
| Neodymium | ≈ 3 | ≈ 1 | $Mg_{41}Nd_5$ | 560 | Eutectic |
| Zirconium | 3.8 | 1.0 | Zr | 1855 | Peritectic |
| Manganese | 2.2 | 1.0 | Mn | 1245 | Peritectic |
| Thorium | 4.75 | 0.52 | $Mg_{23}Th_6$ | 772 | Eutectic |
| Cerium | 0.5 | 0.1 | $Mg_{12}Ge$ | 611 | Eutectic |
| Indium | 53.2 | 19.4 | $Mg_3In$ | 484 | Peritectic |
| Thallium | 60.5 | 15.4 | $Mg_5Tl_2$ | 413 | Eutectic |
| Scandium | ≈ 24.5 | ≈ 15 | MgSc | – | Peritectic |
| Lead | 41.9 | 7.75 | $Mg_2Pb$ | 538 | Eutectic |
| Thulium | 31.8 | 6.3 | $Mg_{24}Tm_6$ | 645 | Eutectic |
| Terbium | 24.0 | 4.6 | $Mg_{24}Tb_5$ | – | Eutectic |
| Tin | 14.5 | 3.35 | $Mg_2Sn$ | 770 | Eutectic |
| Gallium | 8.4 | 3.1 | $Mg_5Ga_2$ | 456 | Eutectic |
| Bismuth | 8.9 | 1.1 | $Mg_3Bi_2$ | 821 | Eutectic |
| Calcium | 1.35 | 0.82 | $Mg_2Ca$ | 714 | Eutectic |
| Samarium | ≈ 6.4 | ≈ 1.0 | $Mg_{6.2}Sm$ | – | Eutectic |

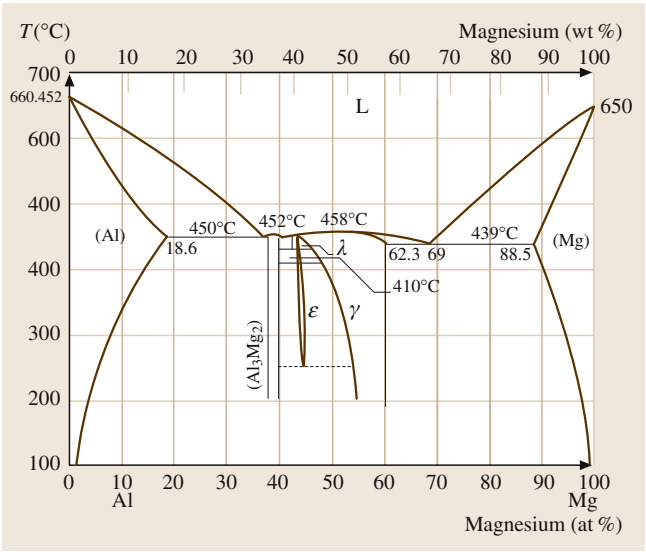


**Fig. 3.1-2** Al−Mg phase equilibria [1.3]

increase castability. However, Al forms an intermetallic phase $Mg_{17}Al_{12}$ which is brittle and limits ductility and, thus, the use of Al-containing alloys such as AZ91 above 120 °C. Manganese has been introduced to increase ductility. It is replacing Zn in several cast alloys. Moreover, Mn is binding Fe in intermetallic phases. These can be separated before casting and therefore Mn can be used to purify the alloys. Silicon was also thought to increase high temperature stability by forming the intermetallic compound $Mg_2Si$. Due to the typical needle shape of this precipitate (so-called chinese script microstructure) it has only limited use because it acts like a notch, leading to crack formation at higher stress levels. Zirconium is not used in Al-containing alloys but it is added to other alloys acting as grain refiner.

Wrought magnesium alloys are not used widely. The application of AZ31 is most common for forgings, extrusions, as well as for sheetmetal. There is an increasing demand for the use of wrought magnesium alloys, especially in the automotive industries, in the form of sheet

**Table 3.1-3** General effects of alloying elements in magnesium materials [1.3–5]

| Series | Alloying elements | Melting and casting behavior | Mechanical and technological properties |
|---|---|---|---|
| AZ | Al, Zn | Improve castability; tendency to microporosity; increase fluidity of the melt; refine weak grain | Solid solution hardener; precipitation hardening at low temperatures (< 120 °C); improve strength at ambient temperatures; tendency to brittleness and hot shortness unless Zr is refined |
| QE | Ag, rare earths | Improve castability; reduce microporosity | Solid solution and precipitation hardening at ambient and elevated temperatures; improve elevated temperature tensile and creep properties in the presence of rare earth metals |
| AM | Al, Mn | Improve castability; tendency to microporosity; control of Fe content by precipitating Fe–Mn compound; refinement of precipitates | Solid solution hardener; precipitation hardening at low temperatures (< 120 °C); increase creep resistivity |
| AE | Al, rare earth | Improve castability; reduce microporosity | Solid solution and precipitation hardening at ambient and elevated temperatures; improve elevated temperature tensile and creep properties; increase creep resistivity |
| AS | Al, Si | Tendency to microporosity; decreased castability; formation of stable silicide alloying elements; compatible with Al, Zn, and Ag; refine week grain | Solid solution hardener, precipitation hardening at low temperatures (< 120 °C); improved creep properties |
| WE | Y, rare earths | Grain refining effect; reduce microporosity | Improve elevated temperature tensile and creep properties; solid solution and precipitation hardening at ambient and elevated temperatures; improve elevated temperature tensile and creep properties |

material. Therefore, a number of processes, which are introduced for the processing of aluminium and steel are under research to find out the economic boundary conditions for the processing of magnesium alloys. Beside the investigations on processing routes, there is ongoing research on alloy development since AZ31 does not meet the given aims in most requirements. The compositions of selected cast and wrought magnesium alloys are given in Tables 3.1-4 and 3.1-5. The mechanical properties of the cast and wrought magnesium alloys are listed in Tables 3.1-6 and 3.1-7 [1.3, 4].

The system to denote Mg alloys is generally showing major alloying elements and their content in wt%. The first two letters are key letters and are used for the major alloying elements (Table 3.1-1). The two letters are followed by a number, which represents the nominal composition of the major alloying elements in wt%. The number indicates the content rounded to

**Table 3.1-4** Nominal composition of selected cast Mg alloys [1.3, 4]

| ASTM designation | Nominal composition (wt%) | | | | | | | | | | |
|---|---|---|---|---|---|---|---|---|---|---|---|
| | Al | Zn | Mn | Si | Cu | Zr | RE (MM) | RE (Nd) | Th | Y | Ag |
| AZ63 | 6 | 3 | 0.3 | | | | | | | | |
| AZ81 | 8 | 0.5 | 0.3 | | | | | | | | |
| AZ91 | 9.5 | 0.5 | 0.3 | | | | | | | | |
| AM50 | 5 | | 0.3 | | | | | | | | |
| AM20 | 2 | | 0.5 | | | | | | | | |
| AS41 | 4 | | 0.3 | 1 | | | | | | | |
| AS21 | 2 | | 0.4 | 1 | | | | | | | |
| ZK51 | | 4.5 | | | | 0.7 | | | | | |
| ZK61 | | 6 | | | | 0.7 | | | | | |
| ZE41 | | 4.2 | | | | 0.7 | 1.3 | | | | |
| ZC63 | | 6 | 0.5 | | 3 | | | | | | |
| EZ33 | | 2.7 | | | | 0.7 | 3.2 | | | | |
| HK31 | | | | | | 0.7 | | | 3.2 | | |
| HZ32 | | 2.2 | | | | 0.7 | | | 3.2 | | |
| QE22 | | | | | | 0.7 | | 2.5 | | | 2.5 |
| QH21 | | | | | | 0.7 | | 1 | 1 | | 2.5 |
| WE54 | | | | | | 0.5 | | 3.25 | | 5.1 | |
| WE43 | | | | | | 0.5 | | 3.25 | | 4 | |

**Table 3.1-5** Nominal composition of selected wrought Mg alloys [1.3, 4]

| ASTM designation | Nominal composition (wt%) | | | | | | |
|---|---|---|---|---|---|---|---|
| | Al | Zn | Mn | Zr | Th | Cu | Li |
| M1 | | | | 1.5 | | | |
| AZ31 | 3 | 1 | 0.3 (0.20 min.) | | | | |
| AZ61 | 6.5 | 1 | 0.3 (0.15 min.) | | | | |
| AZ80 | 8.5 | 0.5 | 0.2 (0.12 min.) | | | | |
| ZM 21 | | 2 | 1 | | | | |
| ZMC711 | | 6.5 | 0.75 | | | 1.25 | |
| LA141 | 1.2 | | 0.15 (min.) | | | | 14 |
| ZK61 | | 6 | | 0.8 | | | |
| HK31 | | | | | 0.7 | 3.2 | |
| HM21 | | | 0.8 | | 2 | | |
| HZ11 | | 0.6 | | 0.6 | 0.8 | | |

**Table 3.1-6** Typical tensile properties and characteristics of selected cast Mg alloys [1.3–5]

| ASTM designation | Condition | Tensile properties | | | Characteristics |
|---|---|---|---|---|---|
| | | 0.2%proof stress (MPa) | Tensile strength (MPa) | Elongation to fracture (%) | |
| AZ63 | As-sand cast | 75 | 180 | 4 | Good room-temperature strength and ductility |
| | T6 | 110 | 230 | 3 | |
| AZ81 | As-sand cast | 80 | 140 | 3 | Tough, leak-tight casting with 0.0015 Be, used for pressure die casting |
| | T4 | 80 | 220 | 5 | |
| AZ91 | As-sand cast | 95 | 135 | 2 | General-purpose alloy used for sand and die casting |
| | T4 | 80 | 230 | 4 | |
| | T6 | 120 | 200 | 3 | |
| | As-chill cast | 100 | 170 | 2 | |
| | T4 | 80 | 215 | 5 | |
| | T6 | 120 | 215 | 2 | |
| AM50 | As-die cast | 125 | 200 | 7 | High-pressure die casting |
| AM20 | As-die cast | 105 | 135 | 10 | Good ductility and impact strength |
| AS41 | As-die cast | 135 | 225 | 4.5 | Good creep properties up to 150 °C |
| AS21 | As-die cast | 110 | 170 | 4 | Good creep properties up to 150 °C |
| ZK51 | T5 | 140 | 253 | 5 | Sand casting, good room-temperature strength and ductility |
| ZK61 | T5 | 175 | 275 | 5 | As for ZK51 |
| ZE41 | T5 | 135 | 180 | 2 | Sand casting, good room-temperature strength, improved castability |
| ZC 63 | T6 | 145 | 240 | 5 | Pressure-tight casting, good elevated temperature strength, weldable |
| EZ33 | Sand cast T5 | 95 | 140 | 3 | Good castability, pressure tight, weldable, creep resistant up to 250 °C |
| | Chill cast T5 | 100 | 155 | 3 | |
| HK31 | Sand cast T6 | 90 | 185 | 4 | Sand casting, good castability, weldable, creep resistant up to 350 °C |
| HZ32 | Sand or chill cast T5 | 90 | 185 | 4 | As for HK31 |
| QE22 | Sand or chill cast T6 | 185 | 240 | 2 | Pressure tight and weldable, high proof stress up to 250 °C |
| QH21 | As-sand cast T6 | 185 | 240 | 2 | Pressure tight, weldable, good creep resistance and stress-proof to 300 °C |
| WE54 | T6 | 200 | 285 | 4 | High strength at room and elevated temperatures, good corrosion resistance |
| WE43 | T6 | 190 | 250 | 7 | Weldable |

the nearest digit for the range of that element. For variation within this range suffix letters A, B, C, etc., are used to indicate the stage of development of the alloy, and X is used for alloys which are still experimental. For example, AZ91D indicates that the two major alloying elements are 9 wt% Al and 1 wt% Zn. The letter D signifies that it is the fourth stage in development. The designations of the tempers are identical to those used for Al alloys and are given in Table 3.1-8 [1.3].

**Table 3.1-7** Typical tensile properties and characteristics of selected wrought Mg alloys [1.3–5]. (For temper designations see Table 3.1-8)

| ASTM designation | Condition | Tensile properties | | | Characteristics |
|---|---|---|---|---|---|
| | | 0.2% proof stress (MPa) | Tensile strength (MPa) | Elongation to fracture (%) | |
| M1 | Sheet, plate F | 70 | 200 | 4 | Low to medium strength alloy, |
| | Extrusion F | 130 | 230 | 4 | weldable, corrosion-resistant |
| | Forgings F | 105 | 200 | 4 | |
| AZ31 | Sheet, plate O | 120 | 240 | 11 | Medium-strength alloy |
| | H24 | 160 | 250 | 6 | weldable, good formability |
| | Extrusion F | 130 | 230 | 4 | |
| | Forging F | 105 | 200 | 4 | |
| AZ61 | Extrusion F | 105 | 260 | 7 | High-strength alloy, |
| | Forging F | 160 | 275 | 7 | weldable |
| AZ80 | Forging T6 | 200 | 290 | 6 | High-strength alloy |
| ZM 21 | Sheet, plate O | 120 | 240 | 11 | Medium-strength alloy, |
| | H24 | 165 | 250 | 6 | good formability, good |
| | Extrusions | 155 | 235 | 8 | damping capacity |
| | Forgings | 125 | 200 | 9 | |
| ZMC711 | Extrusions T6 | 300 | 325 | 3 | High-strength alloy |
| LA141 | Sheet, plate T7 | 95 | 115 | 10 | Ultra-light weight (S.G. 1.35) |
| ZK61 | Extrusion F | 210 | 185 | 6 | High strength alloy |
| | T5 | 240 | 305 | 4 | |
| | Forging T5 | 160 | 275 | 7 | |
| HK31 | Sheet, plate H24 | 170 | 230 | 4 | High-creep resistance to 350 °C, weldable |
| | Extrusion T5 | 180 | 255 | 4 | |
| HM21 | Sheet, plate T8 | 135 | 215 | 6 | High-creep resistance to 350 °C, |
| | T81 | 180 | 255 | 4 | weldable after short time exposure to 425 °C |
| | Forging T5 | 175 | 225 | 3 | |
| HZ11 | Extrusion F | 120 | 215 | 7 | Creep resistance to 350 °C, weldable |

**Table 3.1-8** Temper designations [1.3]

| General Designations | | | |
|---|---|---|---|
| F | As fabricated. | | |
| O | Annealed, recrystallized (Wrought products only). | | |
| H | Strain-hardened. | | |
| T | Thermally treated to produce stable tempers other than F, O, or H. | | |
| W | Solution heat-treated (unstable temper). | | |
| **Subdivisions of H** | | **Subdivisions of T** | |
| H1, Plus one or more digits | Strained only | T2 | Annealed (Cast products only) |
| H2, Plus one or more digits | Strain-hardened and then partially annealed. | T3 | Solution heat-treated and cold-worked |
| H3, Plus one or more digits | Strain-hardened and then stabilized. | T4 | Solution heat-treated |
| | | T5 | Artificially aged only |
| | | T6 | Solution heat-treated and artificially aged |
| | | T7 | Solution heat-treated and stabilized |
| | | T8 | Solution heat-treated, cold-worked and artificially aged |
| | | T9 | Solution heat-treated, artificially aged, and cold-worked |
| | | T10 | Artificially aged and cold-worked |

### 3.1.1.2 Melting and Casting Practices, Heat Treatment

Due to the relatively low melting temperature of Mg, casting is the preferred processing route of Mg materials. The addition of Al and Zn are known to improve castability. All processing operations such as melting, alloying, refining, and the cleaning of melts can be carried out in plain carbon steel crucibles. The use of protective gases or fluxes is a recommended practice during melting. Fluxes consist of salts such as KCl, $MgCl_2$, $BaCl_2$, and $CaCl_2$ [1.6]. Gases are used in different combinations, also forming a stable film during melting. Combinations of argon and/or nitrogen with additions of $SF_6$ or $SO_2$ are in use. The application of vacuum during melting cannot be recommended due to the high vapor pressure of liquid Mg at low pressure.

During melting, a control of impurities is also necessary. The elements Fe, Ni, Co, and Cu are critical due to their effect of decreasing the corrosion resistance. The Fe content can be controlled by adding Mn, forming intermetallic compounds which are settling at the bottom of the melting crucible. But in general the amount of these critical elements has to be controlled during the primary production of Mg itself. Fortunately Cu is not part of any feedstock material used for primary production. Therefore only master alloys or alloying elements for producing the diverse alloys have to be controlled for Co and also for Fe, which is a major impurity in a number of master alloys and alloying elements.

Any casting process can be used to manufacture parts from Mg alloys. But in view of the low liquidus temperatures, the broad melting ranges, and the excellent fluidity of Mg casting alloys, high-pressure die casting (HPDC) is used most frequently at present. Mainly alloys from the AZ or AM series are used in HPDC but alloys from the AS or AE series are also useable when cast with cold chamber HPDC machines. Alloys from the QE or WE series are not suitable for HPDC but for sand casting or permanent mold casting.

The mechanical properties of the Mg alloys can be improved by heat treatment. Mainly T4, T5, and T6 heat treatments are in use. A T4 treatment means dissolution of precipitates. In general, a T4 treatment is followed by an artificial aging (T6). Stress relieving can also be applied to the cast alloys. Major variables which affect the heat-treatments are section size and heating time, annealing time and temperature, and the protective atmosphere. Welded parts made of Mg alloys can be stress relieved. In general, the heat treatments can be applied to castings with the exception of HPDCs. It is not rec-

ommended to heat-treat HPDCs materials because of the entrapment of gases during casting. The absorption of gases can be avoided by applying vacuum during casting. In this case all heat treatments can be applied as well. Table 3.1-9 shows Mg alloys with their respective useful heat treatments.

### 3.1.1.3 Joining

Brazing and soldering are not praticable due to corrosion problems and the formation of brittle phases. Similar problems occur during welding processes such as metal inert gas welding, laser welding, or even electron beam welding. As with brazing or soldering, the formation of brittle phases leads to failures, drastically decreasing the reliability of welded joints. Riveting and mechanical joining using screws are well introduced. Especially when the joint is supported with adhesives for sealing and for adding additional forces for bonding, riveting and screwing can still be viewed as state of the art in the joining of Mg alloys. Mg alloys are seldom used as rivets or screws due to their limited mechanical properties. But it was proven that Al alloys (5052, 5056, or 6061) for rivets and surface coated steel for screws can be used to fasten Mg alloys due to similarity in corrosion potentials. Moreover, the use of inert washers or layers to minimize contact between different materials is recommended [1.3, 7]. Due to the increasing demand for Mg wrought materials, especially in sheet form, new joining processes are under investigation. These processes are friction stir welding or clinching, often combined with the use of adhesives. While a certain degree of ductility ($A > 12\%$) is necessary in clinching processes, friction stir welding appears to be independent of that requirement. Experiments have shown that even cast magnesium alloys can be joined using this process.

### 3.1.1.4 Corrosion Behavior

In general only poor corrosion behavior is attributed to Mg and its alloys. This is mainly true when Mg is in contact with other metals and alloys in accordance with the electrochemical potential series of metals. Therefore, special care has to be taken to avoid conductive contact between Mg alloys and other metals with different electrochemical potentials. When joining Mg parts with other materials, insulating washers, surface-coated screws or nonconducting films and surface coatings can be applied. When investigating a Mg

**Table 3.1-9** Heat treatments applied to magnesium alloys [1.3]

| Alloy | Heat Treatment | | | |
|---|---|---|---|---|
| **Cast Alloy** | **F** | **T4** | **T5** | **T6** |
| AM100A | | × | × | × |
| AZ63A | | × | × | × |
| AZ81A | | × | | |
| AZ91C | | × | | × |
| AZ92A | | × | | × |
| EZ33A | | | × | |
| EQ21A | | | | × |
| QE22A | | | | × |
| WE43A | | | | × |
| WE54A | | | | × |
| ZC63A | | | | × |
| ZE41A | | | × | |
| ZE63A | | | | × |
| ZK51A | | | × | |
| ZK61A | | × | | × |
| **Wrought Alloys** | | | | |
| AZ80A | | | × | |
| ZC71A | × | | × | × |
| ZK60A | | | × | |

alloy by itself the material shows similar behavior as plain cabon steels, even in different environments. The main reason for an increase in corrosion rate could be found in the presence of impurities such as Fe, Ni, Co, and Cu. In order to improve the stand-alone corrosion properties these impurities have to be controlled regarding their content. While Co will normally not pose a problem since it is not part of any material used for the primary production of Mg, the content of the other elements needs to be controlled from the beginning in the production of primary Mg. According to the influence of Fe, Ni, and Cu, limits have been defined for high purity alloys which are mainly used today in the production of Mg parts (Fe/Mn < 0.0232, Cu < 0.04 wt%, Ni < 0.005 wt% for AZ91 hp). But it should be mentioned that these limits depend on the contents of other alloying elements as well as the casting processes applied [1.3, 8]. Figure 3.1-3 shows the influence of alloying elements on the rate of corrosion [1.7].

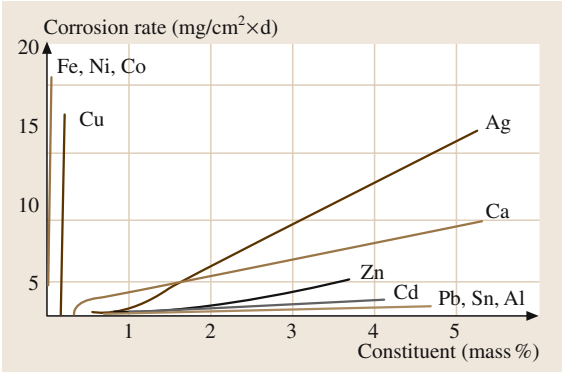


**Fig. 3.1-3** Influence of alloying elements on the corrosion rate of Mg [1.7]

### 3.1.1.5 Recent Developments

Squeeze casting and semi-solid metal processing (SSMP) are recent developments in casting technology by which high quality castings can be produced. Almost all Mg alloys can be subjected to SSMP if they have a broad melting interval [1.3]. First trials using AZ91 led also to the development of different processes which are making use of processing in the semi-solid state. Recently Thixomolding® was introduced, a technique similar to processing techniques for polymers. Thixomolding is in use mainly for the production of housings for handheld devices such as laptops or cameras. It is under research to investigate the capability of this technology for processing alloys which are showing limited castability mainly in HPDC. Another process using the semi-solid behavior of some magnesium alloys is thixocasting which is still a topic of research, not of production. The New RheoCast process (NRC) which is well introduced in Al industries can, also, be applied to casting semi-solid materials based on Mg.

Beyond monolithic alloys the investigation of Mg matrix composites is still in progress. They can be processed using either the ingot metallurgy route or the powder metallurgy route. There are promising candidates that may be introduced to applications but the production routes are quite expensive and, moreover, the corrosion behavior is not well known.

Apart from cast or powder metallurgical products, the use of wrought Mg materials is thought to increase in the future. To support the demands stemming mainly from the automotive industry the total production route is under investigation right now. This means that the developments of new wrought magnesium alloys as well as the development of suitable deformation processes in combination with appropriate joining techniques are underway. These studies are accompanied by developing modeling and simulation tools to ensure high quality and accurate prediction of properties and lifetime behavior of magnesium-based materials.

Controlling corrosion is the most pressing problem under research at the moment. Since Mg alloys are about to be widely used in several applications, the corrosion problem, i. e., mainly contact corrosion in combination with other metals and alloys is receiving more and more attention. Therefore, the influence of alloying elements, mainly in combination with each other, is investigated intensively. Aside from alloying, different kinds of surface protection such as surface layers and coatings are under investigation. While castings are normally showing sufficient volume to withstand corrosion attack, this is not the case for magnesium sheet materials even for a long time.

## 3.1.2 Aluminium and Aluminium Alloys

### 3.1.2.1 Introduction

Aluminium alloys are the second most widely used metallic materials after steels. Comprehensive treatments and data of Al-based materials are given in [1.9, 10]. Their most important properties are: *low density* ($2.7\,g/cm^{-3}$); alloying can result in significant further density reductions in Al-Li alloys; the low density can lead to significant energy savings, especially in applications in transportation; *good mechanical properties* offering optimum tensile strength ranging from 60 to 530 MPa; *good workability* permitting most varied shapes to be produced; *good castability* with a variety of casting techniques: sand, mould, die-casting; *good machinability*; *ease of joining* using all commonly applied techniques; *comparatively high corrosion resistance* thanks to the spontaneous formation of a strongly-adherent passivating surface film in air; *different surface treatments* are applicable; *high electrical and thermal conductivity*, especially of unalloyed aluminium; *good optical properties* depending on the degree of purity; *non-magnetic*; *low absorption cross section* for thermal neutrons; *non-combustible*, not causing sparking; *no health risk* is associated with the use of aluminium and its alloys; excellent *recycling* properties.

### 3.1.2.2 Production of Aluminium

The production of aluminium is based on the electrolysis of molten alumina $Al_2O_3$ using the Hall–Herault process. Alumina is extracted in the Bayer process form the bauxite ore which contains 20 to 30 wt% Al. In 2002 the main producers of the ore are Australia (28%), Guinea (20%), Brazil (14%), Jamaica (7%), India (4%), and Guyana (3%) [1.9].

After milling, the ore is first broken down using an Al-containing NaOH solution which is seeded to precipitate aluminium hydroxide $Al(OH)_3$. This is dehydrated at about 1100 °C according to $2Al(OH)_3 \rightarrow Al_2O_3 + 3H_2O$.

An electrolytic reduction is carried out in a cell as shown in Fig. 3.1-4. Cryolithe $Na_3AlF_6$ is used as an additive to decrease the high melting point of pure $Al_2O_3$ (about 2050 °C) since the two compounds form a eutectic near 10 wt% of $Al_2O_3$ in $Na_3AlF_6$, Fig. 3.1-5 [1.11, 12]. The electrolysis is carried out in a cell lined with carbon, which serves as the cathode. Carbon anodes are suspended from above the cell into the electrolyte. Two main reactions occur: $2Al^{3+} + 6e^- \rightarrow 2Al$, and oxygen ions react with the carbon of the cathode to form $CO_2$ (consumption of the cathode). A primary aluminium smelter requires on average 13 to 14 kW h per kg of Al. The main power used is hydro-electric (52.5% in 2001 [1.13]). In recent decades

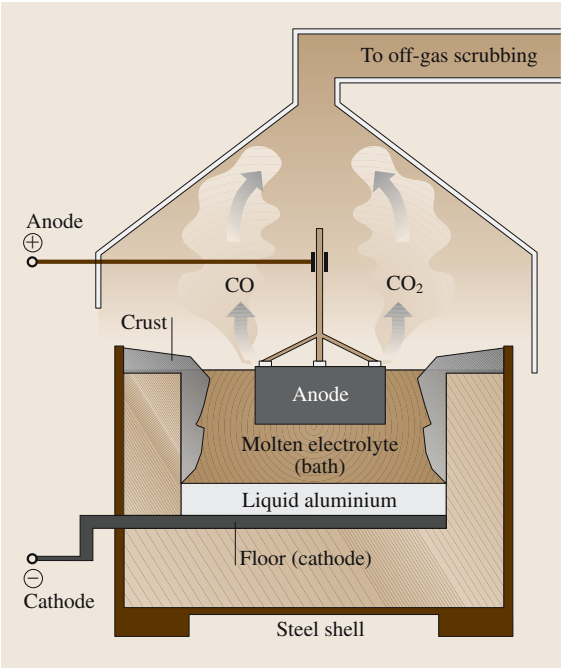


**Fig. 3.1-4** Schematic representation of an electrolytic cell for Al winning [1.9]

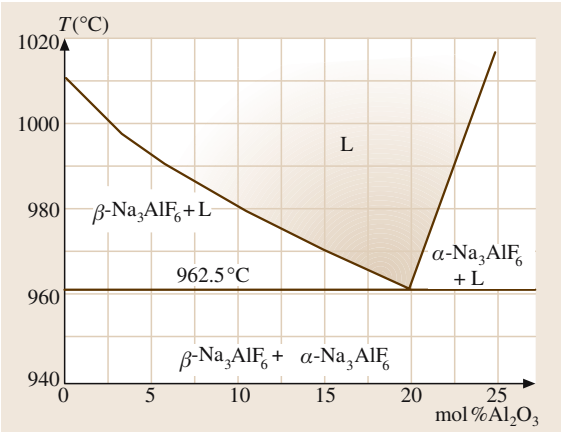


**Fig. 3.1-5** Phase diagram of cryolithe $Na_3AlF_6$-alumina $Al_2O_3$ [1.9]

secondary production, i. e., recycling of scrap and waste material, has reached 30% of the total production, with high regional variations. Up to 95% less energy is needed to produce Al via secondary production.

### 3.1.2.3 Properties of Pure Al

Aluminium can be classified as "unalloyed," "pure," or "refined," depending on its degree of purity. The Al from conventional electrolysis is 99.5 to 99.9 wt% pure. Higher purity is produced by "triple-layer refining electrolysis" that can reach ≥ 99.99 wt% purity. The latter grade is used, for example, in the electronics sector.

#### Physical Properties

The physical properties of pure Al are given in Chapt. 2.1,Table 2.1-11. The temperature dependence of its density is shown in Fig. 3.1-6. The contraction of 6.5% upon solidification corresponds to an increase in density from 2.37 g cm$^{-3}$ in the liquid state to 2.55 g cm$^{-3}$ in the solid state. The temperature dependence of the coefficient of thermal expansion is given in Table 3.1-10.

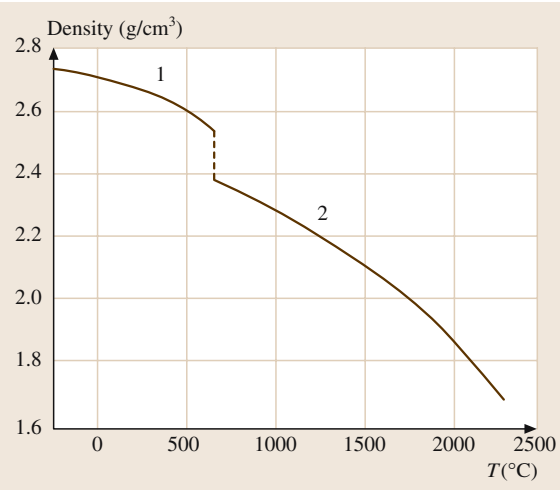


**Fig. 3.1-6** Density of solid and liquid aluminium as a function of temperature [1.9]

The specific heat in the solid state increases with temperature from 720 kJ at −100 °C, to 900 at 20 °C, and 1110 at 500 °C. At its melting point Al has a specific heat of 1220 (solid) and 1040 (liquid). In the liquid state the specific heat rises further, e.g., to 1060 kJ at 800 °C. Aluminium has a high reflectivity for light, heat, and for electromagnetic radiation. The Youngs's modulus $E$ of aluminium materials is usually taken to be 70 GPa; it varies between 60 and 78 GPa depending on alloy composition. The shear modulus $G$ varies between 22 and 28 GPa, the value for refined aluminium is 25.0 GPa. Poisson's ratio $\nu$ varies between 0.32 and 0.40 (0.35 for refined aluminium).

Unalloyed aluminium has an electrical conductivity of 34 to 38 m Ω$^{-1}$ mm$^{-2}$. Due to this relatively high conductivity, a large fraction of unalloyed Al and Al−Mg−Si alloys are used for electrical conductors. The temperature dependence of the electrical conductivity depends on alloying additions, impurities, and microstructure (Figs. 3.1-7 – 3.1-9). Superconductivity occurs at $T_c = 1.2$ K in refined grades of aluminium (≥ 99.99 wt% Al). The electrical conductivity of high-purity aluminium is still high at 4.2 K.

#### Mechanical Properties

The ultimate tensile strength of pure aluminium increases markedly with increasing amounts of alloying or impurity additions, as shown in Fig. 3.1-10. Unalloyed aluminium is soft (tensile strength 10–30 MPa, Table 3.1-11) and, like all fcc metals, shows a low rate of work hardening.

#### Chemical Properties

Aluminium, as a relatively reactive element, is a very strong base, as shown by its position in the electrochemical series and its low standard potential ($V_H = -1.66$ V). Therefore, it is not possible to obtain the element from aqueous solutions by electrolysis. Similarly, it is not possible to obtain aluminium by a carbother-

**Table 3.1-10** Coefficient of thermal expansion of Al 99.99 as a function of temperature [1.9]

| Temperature range (°C) | Average linear coefficient of thermal expansion ($10^{-6}$/K$^{-1}$) |
|---|---|
| (−200) – 20 | 18.0 |
| (−200) – 20 | 21.0 |
| 20–100 | 23.6 |
| 20–200 | 24.5 |
| 20–400 | 26.4 |
| 20–600 | 28.5 |

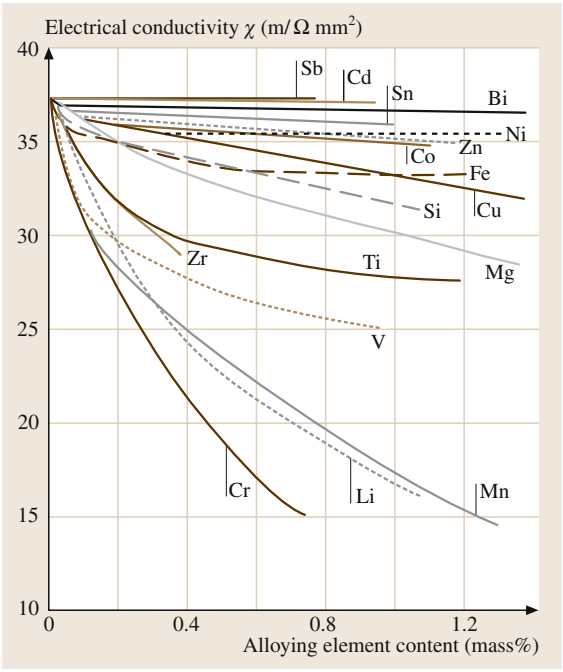


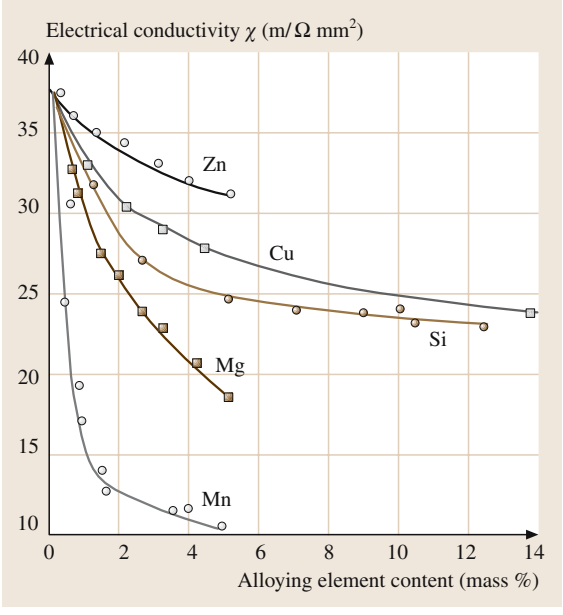


**Fig. 3.1-8** Electrical conductivity of as-cast binary aluminium alloys (containing larger amounts of the alloying additions) as a function of concentration of the alloying element [1.14, 15]

**Fig. 3.1-7** Electrical conductivity of as-cast binary alloys based on high-purity aluminium as a function of the alloying element concentration [1.14, 15]

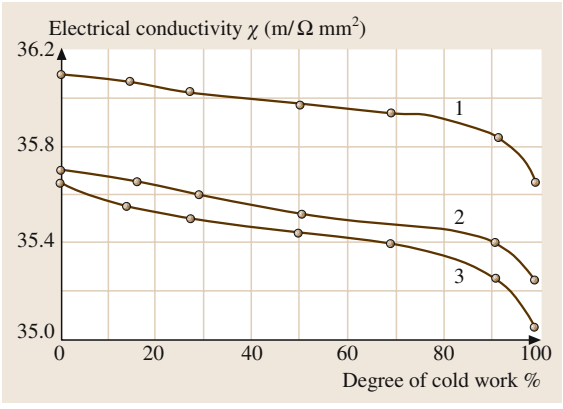


**Fig. 3.1-9** Electrical conductivity of unalloyed Al (0.21 wt% Fe; 0.11 wt% Si) as a function of the degree of cold work and the degree of supersaturation and/or intermediate annealing temperature [1.14]; (1) intermediate annealing temperature 350 °C; (2) intermediate annealing temperature 500 °C; (3) as extruded

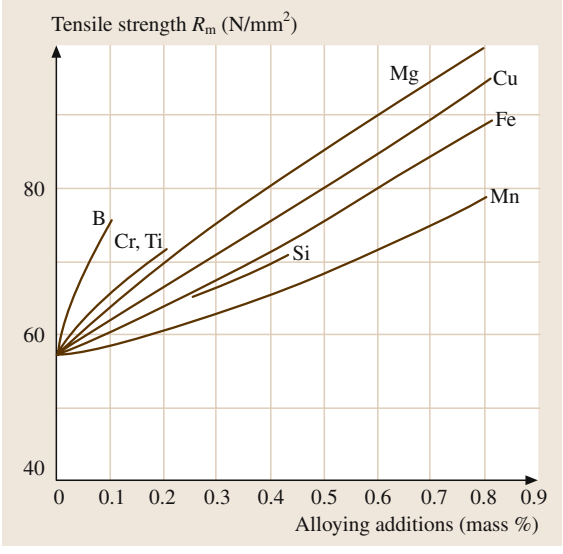


**Fig. 3.1-10** Effect of small additions of alloying elements or impurities on the ultimate tensile strength of aluminium of high-purity (99.98 wt% Al, soft condition, 5 h, 360 °C) [1.14]

**Table 3.1-11** Typical mechanical properties of refined aluminium (Al 99.98) [1.9]

| Condition | Proof stress $R_{p0.2}$ (MPa) | Ultimate tensile strength $R_m$ (MPa) | Elongation at fracture $A_{10}$ (%) | Brinell hardness number HB |
|---|---|---|---|---|
| Soft | 10–25 | 39–49 | 30–45 | 15 |
| Hard | 69–98 | 88–118 | 1–3 | 25 |

mic reaction. In chemical compounds, aluminium is positively charged and trivalent ($Al^{3+}$). It reacts readily with hydrochloric acid and caustic soda, but less readily with sulfuric acid; dilute sulfuric acid does not attack aluminium. It is not attacked by cold nitric acid at any concentration, and hardly so when heated. The reaction with sodium hydroxide is given by: $2Al + 2NaOH + 3H_2O \rightarrow 2Na[Al(OH)_4] + 3H_2$.

Aluminium-based materials are non-flammable. Even turnings and chippings do not ignite. Extremely fine aluminium particles can undergo spontaneous combustion and thus cause explosions. The heat of formation of the aluminium oxide $Al_2O_3$ is about 1590 kJ mol$^{-1}$, making aluminium a very effective deoxidiser for the steel industry and in metalothermic metal reduction processes (aluminothermy; e.g., $3V_2O_5 + 10Al \rightarrow 6V + 5Al_2O_3$ and aluminothermic welding, "thermit process" $3Fe_3O_4 + 8Al \rightarrow 9Fe + 4Al_2O_3$).

Important aluminium compounds include aluminium oxide $Al_2O_3$, which is commonly called alumina (in powder form) or corundum (in coarse crystalline structure), and aluminium hydroxide $Al(OH)_3$ ("hydrated alumina," usually extracted from bauxite in the Bayer process).

### 3.1.2.4 Aluminium Alloy Phase Diagrams

The properties of aluminium strongly depend on the concentration of alloying additions and impurities. Even the low residual contents of Fe and Si in unalloyed aluminium (Al99 to Al99.9) have a marked effect.

The main alloying elements of Al materials are Cu, Si, Mg, and Zn while Mn, Fe, Cr, and Ti are frequently present in small quantities, either as impurities or additives. Ni, Co, Ag, Li, Sn, Pb, and Bi are added to produce special alloys. Be, B, Na, Sr, and Sb may be added as important trace elements. All of these elements affect the structure and thus the properties of an alloy. The compositions of the more important aluminium materials are discussed below, using the relevant phase diagram. All alloying components are completely soluble in liquid aluminium if the temperature is sufficiently high. However, these elements have only limited solubility in solid solution. Continuous solid solubility does not occur in any of the alloy systems of Al.

Aluminium-rich solid solutions are often formed and are referred to as $\alpha$-phase, $\alpha_{Al}$-phase, or $\alpha$-Al solid solution. Most of the phases occurring in equilibrium with $\alpha$-Al are hard. They consist of elements or intermetallic compounds such as $Al_2Cu$, $Al_8Mg_5$, $Al_6Mn$, $Al_3Fe$, and AlLi.

#### Binary Al-Based Systems

*Aluminium–Copper.* Al–Cu forms a simple eutectic system in the range from 0 to 53 wt% Cu, as shown in Fig. 3.1-11. The $\alpha$-Al solid solution and the intermetallic compound $Al_2Cu$ ($\theta$ phase) are in equilibrium. At intermediate temperatures, metastable transition phases may form and precipitate from the supersaturated solid solution. These metastable phases may be characterised according to their crystal structure, the nature of the phase boundary they form, and their size:

- From room temperature up to ≈ 150 °C the coherent Cu-rich Guinier-Preston zones I (GP I phase) form; they are only one to two {001} layers thick and have a highly strained, coherent phase boundary with the $\alpha$-Al matrix phase.

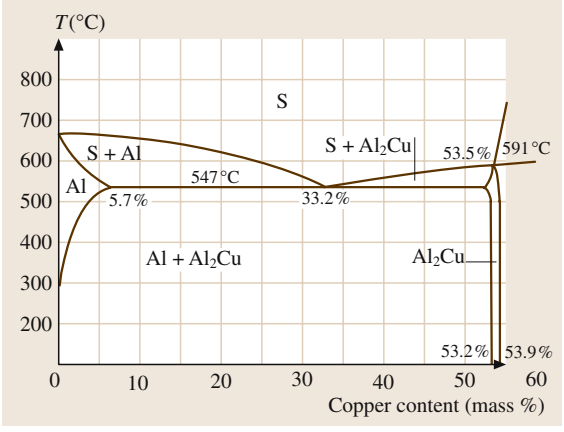


**Fig. 3.1-11** Al–$Al_2Cu$ section of the Al–Cu system [1.16]

- At ≈ 80 to ≈ 200 °C the GP II phase, also called $\theta''$ phase, forms; it has a superlattice structure of the Al fcc lattice and has a coherent interface also, but the particle size grows larger than that of GP I.
- Above ≈ 150 °C the $\theta'$ phase forms; it is only partially coherent.
- Above ≈ 300 °C the incoherent, stable $\theta$-phase $Al_2Cu$ is formed (over-ageing).

These phase transformations are decisive for the precipitation-hardening behavior of Al–Cu-based technical Al alloys.

*Aluminium–Silicon.* Al–Si forms a simple eutectic system (Fig. 3.1-12). At room temperature the solubility of Si in Al is negligible. Thanks to the good casting properties of the Al−Si eutectic, this alloy system is the basis of a major part of the Al-based casting alloys. However, when slowly cooled (e.g., in sand casting), a degenerate form of eutectic, microstructure may occur. Instead of the desired fine eutectic array, the alloy develops a structure that is characterised by larger, plate-like primary Si crystals, leading to very brittle behavior. This degenerate behavior can be suppressed by the addition of small amounts of Na, Sb, or Sr to the melt at about 720 to 780 °C. This "modification" causes a lowering of the eutectic temperature and a shift in concentration of the eutectic point, as indicated in Fig. 3.1-12; the extent of the shift is dependent on the rate of solidification.

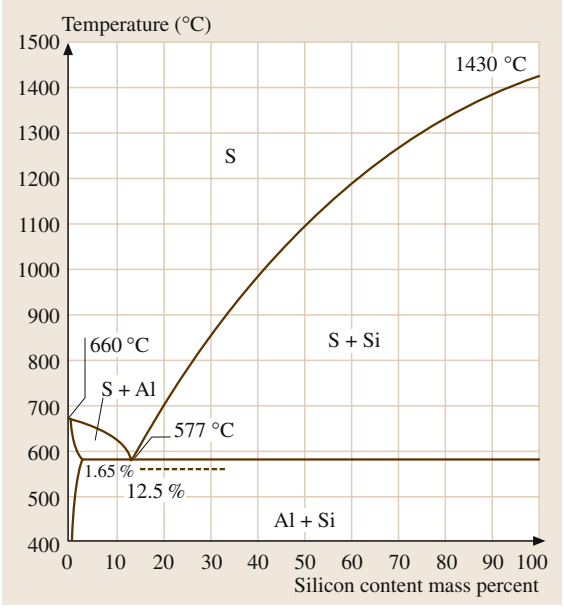


**Fig. 3.1-12** Al−Si system; the *dotted line* shows the extent to which alloys can be supercooled

*Aluminium–Iron.* Figure 3.1-13 shows the Al-rich part of this system. The solubility of Fe in Al is very low. In the range shown $Al_3Fe$ is formed by a peritectic reaction at 1160 °C. The eutectic between the Al phase and $Al_3Fe$ crystallises in a degenerate manner to form brittle needles of $Al_3Fe$. The formation of $Al_3Fe$ needles is also occurring in Al−Fe−Si alloys such as commercially (available) pure aluminium (Fig. 3.1-14).

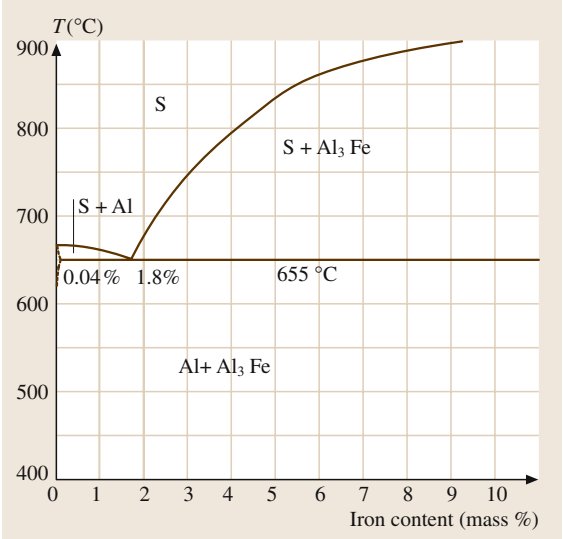


**Fig. 3.1-13** Al−Fe system up to 10 wt% Fe

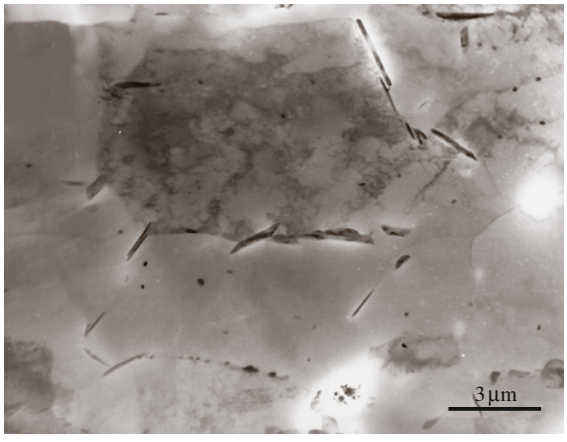


**Fig. 3.1-14** $Al_3Fe$ needles formed after annealing commercially pure aluminium sheet (Al99.5) for 65 h at 590 °C, 800X [1.17]

**Table 3.1-12** Solubility of some elements in aluminium solid solutions [1.16, 18]

| Element | Temperature of eutectic (E) or peritectic (P) eqilibrium °C | Phase in equilibrium with Al solid solution | $T_E$ or $T_P$ (wt%) | Solubility (wt%) 500 °C | 400 °C | 300 °C | 200 °C |
|---|---|---|---|---|---|---|---|
| Cu | 547 (E) | $Al_2Cu$ | 5.7 | 4.4 | 1.6 | 0.6 | 0.2 |
| Fe | 655 (E) | $AL_3Fe$ | ~ 0.04 | 0.005 | < 0.001 | | |
| Li | 602 (E) | AlLi | 4.7 | 2.8 | 2.0 | 1.5 | 1.0 |
| Mg | 450 (E) | $Al_8Mg_5$ | 17.4 | ~ 12.0 | 12.2 | 6.6 | 3.5 |
| Mn | 657 (E) | $Al_6Mn$ | 1.82 | 0.36 | 0.17 | 0.02 | |
| Si | 577 (E) | Si | 1.65 | 0.8 | 0.3 | 0.07 | 0.01 |
| Zn | 275 Eutectoid equilibrium | Zn | 31.6 | | | | 14.5 |

*Aluminium–Lithium.* The Al-rich part of this system is shown in Fig. 3.1-15. The Al(Li) solid solution and the $\eta$ ($Al_3Li$) phase are in equilibrium. Al–Li-based alloys are used for their low density.

*Aluminium–Magnesium.* This system is shown in Fig. 3.1-16. The solid phases are the $\alpha$-Al solid solution and the $\beta$-$Al_8Mg_5$ intermetallic compound. The high solubility of Mg in Al can be put to practical use for solid solution hardening. The $\beta$ phase precipitates preferentially at grain boundaries, forming a continuous network at the grain boundaries of the Al-rich $\alpha$ solid solution, e.g., after slow cooling from temperatures above 400 °C, especially in alloys containing more than 3 wt% Mg. Precipitates of the $\beta$ phase are less noble electrochemically than the $\alpha$ phase and are thus subject to preferential attack by corrosive media. Accordingly the disadvantage of Al−Mg alloys is their potentially high susceptibility to intergranular corrosion.

*Aluminium–Manganese.* The Al-rich part of this system includes the intermetallic phases $Al_4Mn$ (above 710 °C) and $Al_6Mn$ (Fig. 3.1-17). The $\alpha$-Al solid solution and the $Al_6Mn$ phase form a eutectic (Fig. 3.1-17). The solubility of Mn in Al at room temperature is negligibly small. In hypereutectic Al−Mn alloys, pre-

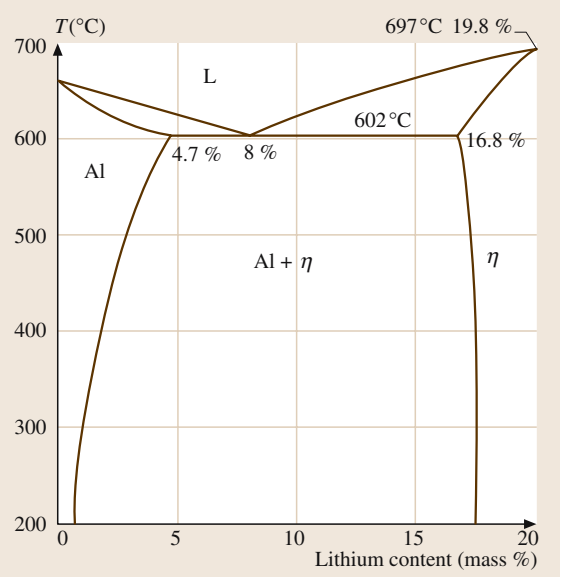


**Fig. 3.1-15** Al−Li system for up to 20 wt% Li [1.18]

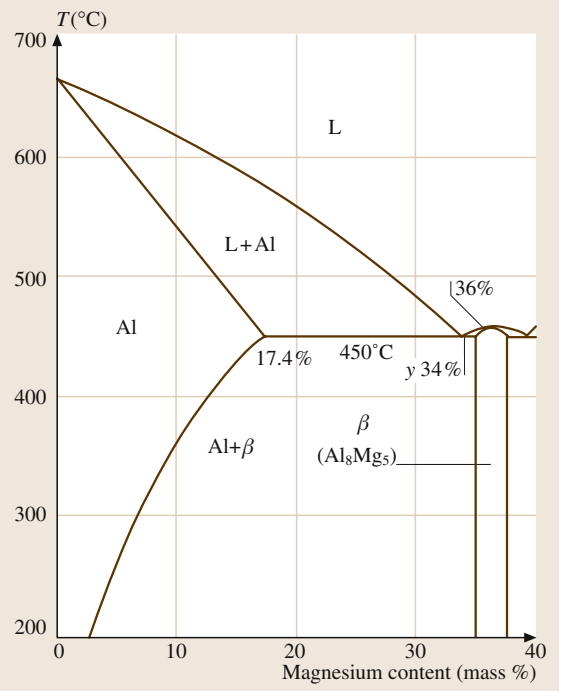


**Fig. 3.1-16** Al−$Al_8Mg_5$ section of Al−Mg system

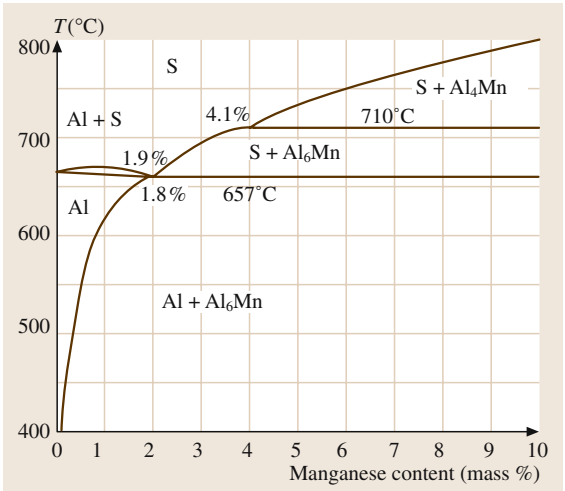


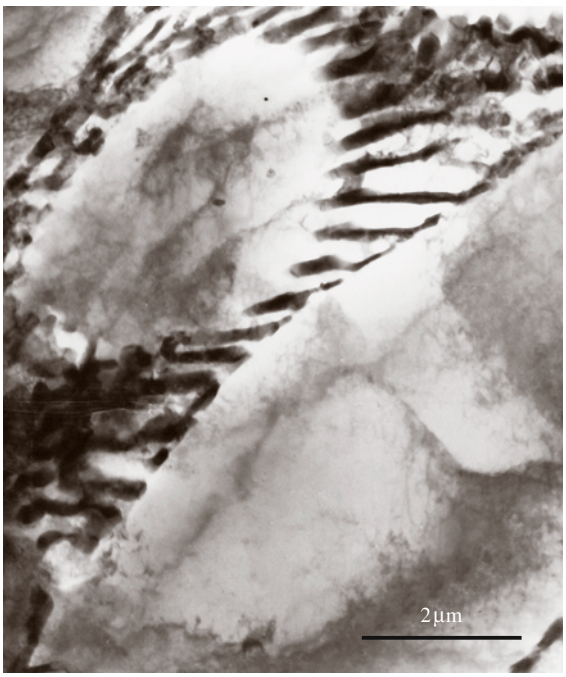


**Fig. 3.1-17** **(a)** Al−Mn equilibrium system up to 10 wt% Mn. **(b)** Microstructure of an as-cast Al-1 wt% Mn alloy (TEM micrograph, 7000X) [1.17]

cipitation of primary, bar-shaped $Al_2Mn$ crystals occurs in the eutectic structure. These have a marked embrittling effect. Therefore, the maximum Mn content is limited to 2 wt% in commercial Al–Mn alloys.

*Aluminium–Titanium.* Intermetallic phases with a significantly higher melting point (dissociation temperature) than Al exist in this system: $Al_3Ti$ (1340 °C) and AlTi (1460 °C) (Fig. 3.1-18). The structure of Al-rich Al–Ti alloys consists of $Al_3Ti$ and an Al-rich solid solution.

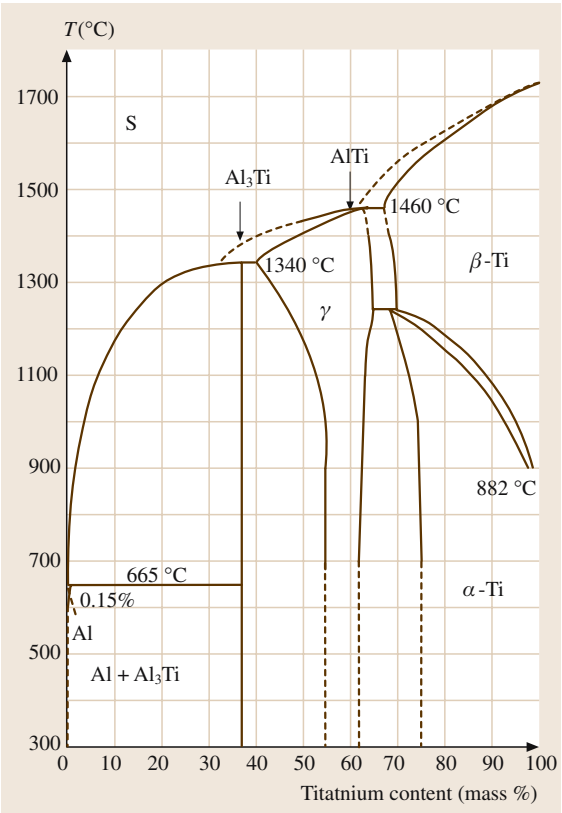


**Fig. 3.1-18** Al−Ti system

*Aluminium–Zinc.* Zn is highly soluble in Al. The eutectic point occurs at Zn-rich concentration (Fig. 3.1-19). The liquidus and solidus temperatures depend markedly on temperature.

### Ternary Al-Based Systems

Most technical Al alloys contain more than two components because of the presence of impuritiy and alloying elements.

*Aluminium–Iron–Silicon.* Figure 3.1-20 shows the Al-rich corner as a section for 0.5 wt% Fe. This concentration range is of particular interest for commercially pure, unalloyed Al. Apart from the solid solution and the AlFe and Si phases there are two ternary phases, i. e., $\alpha$-$Al_{12}Fe_3Si$ and $\beta$-$Al_9Fe_2Si_2$. The exact

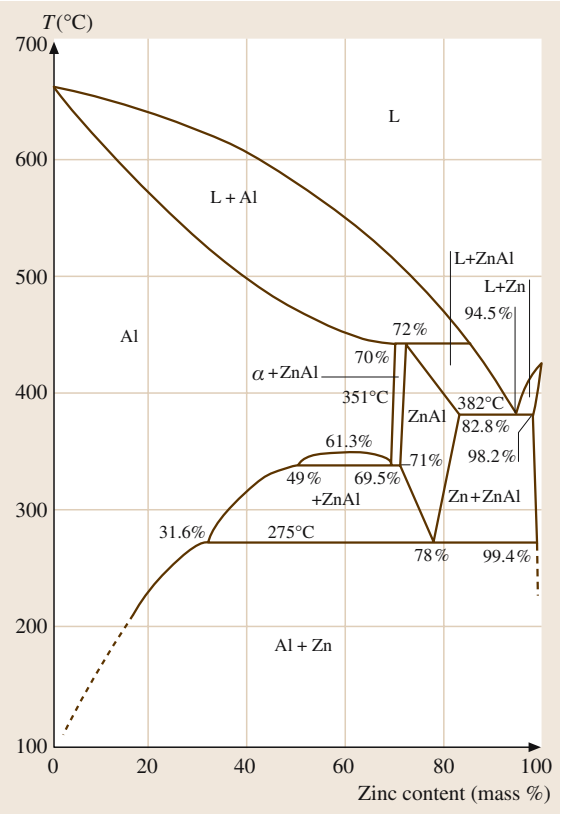


**Fig. 3.1-19** Al−Zn system

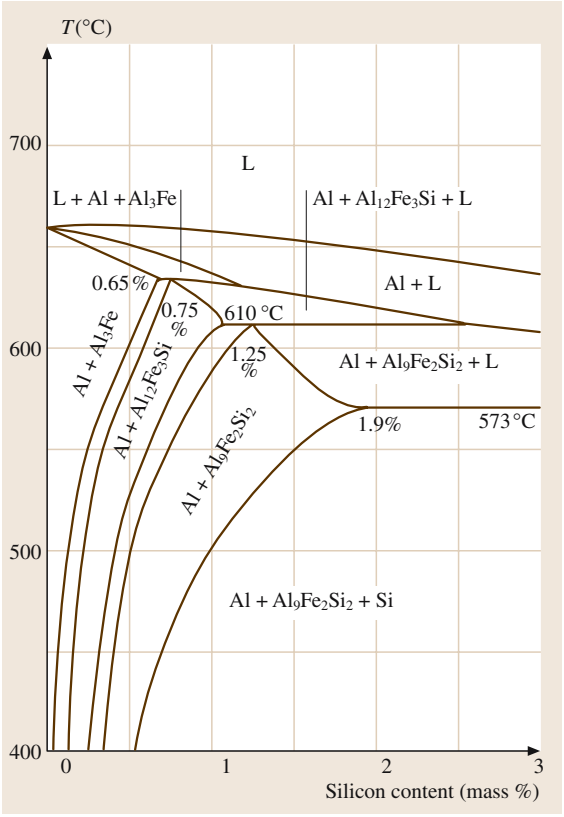


**Fig. 3.1-20** Section through the Al−Fe−Si phase diagram at 0.5 wt% Fe [1.11]

compositions are subject to discussion and there are corresponding differences in the description of the solidification and precipitation processes. At the level of Fe and Si contents found in commercially pure aluminium (Al + Si ≤ 1 wt%), $\alpha$-$Al_{12}Fe_3Si$ will form as a result of the transformation of the $\alpha$-solid solution and AlFe with decreasing temperature, as shown in Fig. 3.1-14. If the temperature further decreases, precipitation of $\beta$-$Al_9Fe_2Si_2$ and even Si will occur. Due to the low rate of diffusion at low temperatures it is possible that all four phases coexist with the Al-rich solid solution phase. The solid solution becomes supersaturated in Fe and Si at the cooling rates used in industrial practice. Moreover, non-equilibrium ternary phases form, often locally at the grain boundaries of the as-cast microstructure. Fe and Si are in solution inside the grains. For a given cooling rate, the maximum Fe solubility decreases with increasing Si content of the alloy, whereas the Si solubility is independent of Fe content [1.19–21]. Thermodynamically, such non-equilibrium microstructures are very stable. The primary non-equilibrium ternary phases only decompose to the secondary equilibrium phases $Al_3Fe$ and Si at about 600 °C [1.22].

*Aluminium–Magnesium–Silicon.* Figures 3.1-21a and 3.1-21b show the Al-rich corner as a quasi-binary section Al−$Mg_2Si$ (Mg/Si ratio 1:0.58). It divides the system into the two simple ternary eutectic systems shown. The fine-grained microstructure of Al−Mg−Si alloys consists of $\alpha$-Al(Mg,Si) and numerous intermetallic compounds, such as $Mg_2Si$ (forming a characteristic particle shape called "Chinese script"), $Al_6Mn$, and $Al_3Fe$. $Mg_2Si$ has an important effect on properties. Its solid solubility in the aluminium matrix is temperature-dependent and, thus, leads to hardening effects, which are exploited in technical alloys. A coarse network of intermetallic phases impairs forming behavior, but annealing before further processing produces finely-dispersed precipitates. These improve workability but are, also, effective in retarding recrystallization.

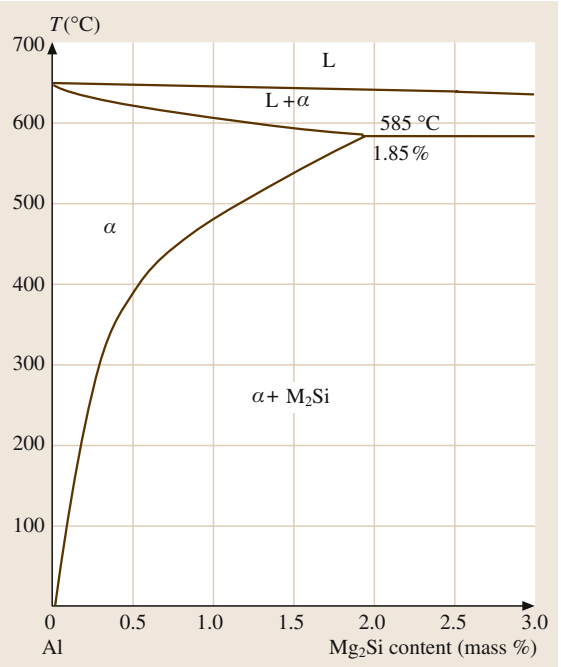


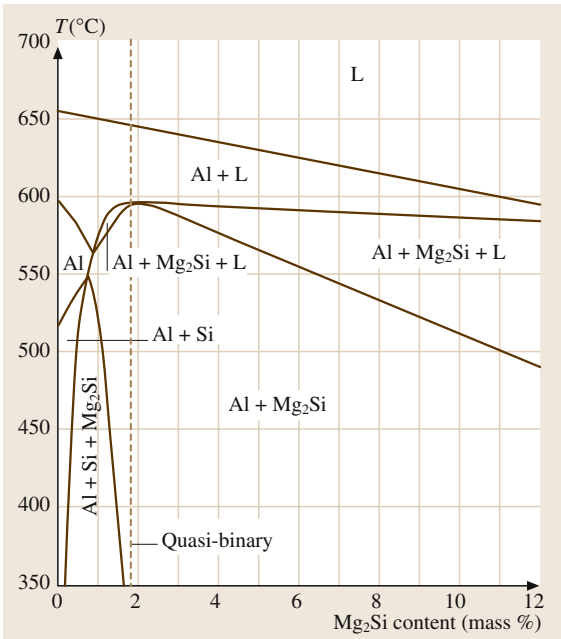


**Fig. 3.1-21a,b** Al−Mg−Si system **(a)** Quasi-binary section Al−$Mg_2Si$; **(b)** Section at a constant Si content of 1 wt% [1.11]

*Aluminium–Copper–Magnesium.* In addition to the two binary phases, $Al_8Mg_5$ ($\beta$) and $Al_2Cu$ ($\theta$), there are two ternary phases, $Al_2CuMg$ (S) and $Al_6Mg_4Cu$ (T), in equilibrium with the Al-rich solid solution. The microstructure of castings shows various ternary eutectics which, in addition to $Al_2Cu$, also contain $Mg_2Si$, resulting from Si as an impurity, and AlCuMg [1.9].

*Aluminium–Copper–Lithium.* In addition to binary phases between all three elements, three ternary phases, $Al_7Cu_4Li$, $Al_2CuLi$, and $Al_5Li_3Cu$, occur in equilibrium with the Al-rich solid solution in the aluminium-rich corner of this system.

*Aluminium–Zinc–Magnesium.* The Al-rich corner consists of two binary phases, $Al_8Mg_5$ and $MgZn_2$, and a ternary phase T with a nominal composition $Al_2Mg_2Zn_3$ having a wide range of homogeneity. The Al−$MgZn_2$ and Al−T sections may be regarded as quasi-binary systems with eutectic temperatures at 475 and 489 °C, respectively. The Al−$Al_8Mg_5$−T range constitutes a ternary eutectic, $T_E = 450$ °C. In the Al−T−Zn range there is a four-phase reaction in which the T phase transforms to $Mg_2Zn$. At high Zn contents, $Mg_2Zn_{11}$ transforms to $MgZn_2$ in another four-phase reaction at 365 °C. $MgZn_2$ subsequently solidifies eutectically at 343 °C together with Al and Zn. There is evidence of eutectic solidification in the as-cast structure of these alloys. If ternary Al−Zn−Mg alloys are solution-treated at temperatures above 450 °C they, consist of a homogeneous $\alpha$ phase solid solution which is supersaturated with respect to one phase at least, corresponding to its composition [1.9].

### 3.1.2.5 Classification of Aluminium Alloys

Technical aluminium alloys are subdivided first into the two main groups of cast and wrought alloys (Fig. 3.1-22). Typically, the alloying content of casting alloys is 10 to 12 wt%. This is significantly higher than the value for wrought alloys, most of which contain only a total of 1 to 2 wt% alloying elements; their content may be as high as 6 or even 8 wt% in individual cases.

Aluminium alloys are further subdivided, depending on whether or not an alloy can be hardened by the addition of alloying elements, as is the case with

- Precipitation-hardenable alloys which can be strengthened by aging and
- Non-precipitation-hardenable alloys which can be strengthened by work-hardening only.

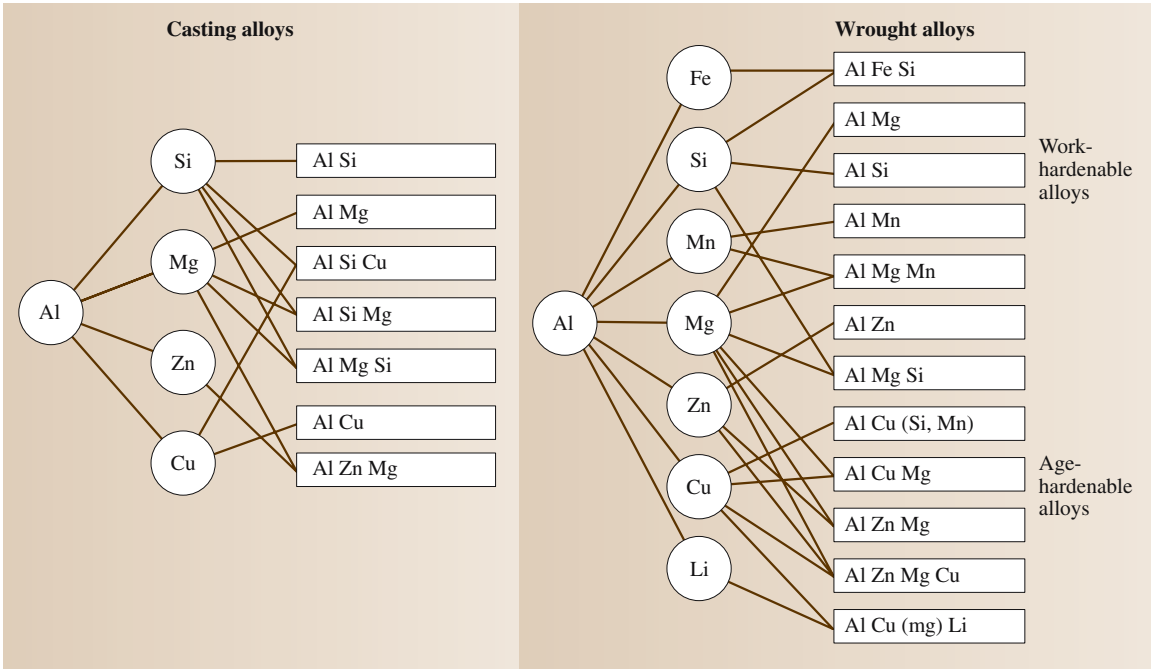


**Fig. 3.1-22** Schematic array of cast and wrought aluminium alloys. The numbers are given according to European standardization. In the case of wrought alloys the numbers are the same as those used in North-American standardization

The addition of further alloying elements will always cause hardening, but not all elements have the same hardening effect. Hardening will also depend on whether the solute atoms are present in solid solution or as particles. Alloy hardening can be divided into

- Solid-solution hardening (as with non-precipitation hardening, work-hardenable alloys) and
- Hardening due to elements that are initially in solid solution and are precipitating as second phases (as is the case with age-hardenable alloys).

It should be noted that age-hardenable alloys can be strengthened by the use of a suitable heat treatment whereas the same heat treatment of alloys which are not age-hardenable leads to a loss in strength.

### 3.1.2.6 Structure and Basic Mechanical Properties of Wrought Work-Hardenable Aluminium Alloys

#### Al–Fe–Si and Unalloyed Aluminium (1xxx)

Al–Fe–Si contains about 0.6 wt% Fe and 0.8 wt% Si that has been added deliberately. The properties of Al–Fe–Si alloys, and of unalloyed aluminium, are strongly influenced by the elements which are in solid solution and the binary and higher phases that form. Increasing amounts of alloying additions lead to a marked increase in strength but there is a decrease in electrical conductivity since transition elements have a high effective scattering power for electrons.

#### Wrought Al–Mn (3xxx)

Manganese additions increase the strength of unalloyed aluminium (Fig. 3.1-23). The chemical resistance is not impaired. These alloys have very good forming properties, when the Mn content is below the maximum solubility of Mn in the Al-rich $\alpha$-phase, i. e., practically below 1.5 wt%. At higher Mn content, brittle $Al_6Mn$ crystals form and impair workability.

If Al–Mn alloys are rapidly solidified as in continuous casting, considerable supersaturation of Mn occurs. Fe reduces the solubility for Mn and promotes its precipitation in the form of multicomponent phases. Fe is often added to counteract supersaturation and for an increase of the tensile strength (Fig. 3.1-24). Depending on the amount of precipitation, Mn can inhibit recrystallization.

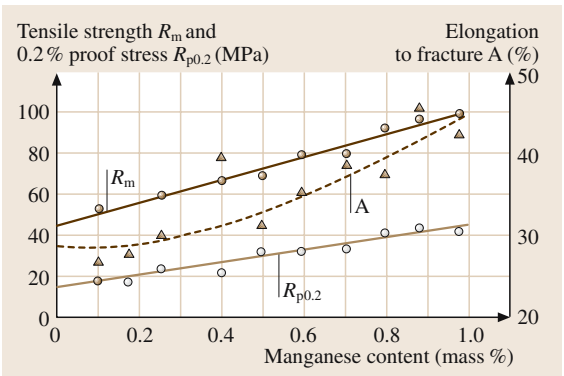


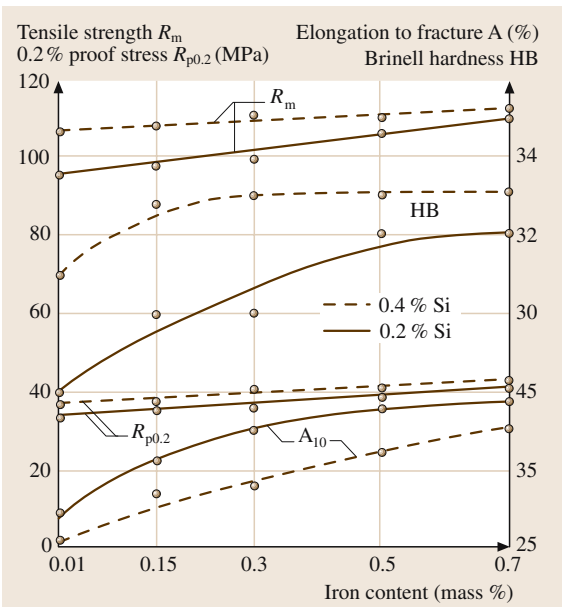


**Fig. 3.1-24** Effect of iron and silicon on the strength of an Al−Mn alloy containing 1.2 wt% Mn; soft condition, sheet sample [1.24]

### Wrought Al–Si (4xxx)

Aside from 1 to 12.5 wt% Si, wrought Al−Si alloys contain other elements such as Mg, Fe, Mn or Cu.

### Wrought Al–Mg and Al–Mg–Mn (5xxx)

The two non-age-hardening alloy systems Al−Mg and Al−Mg−Mn cover the entire compositional range from 0.5 to 5.5 wt% Mg, 0 to 1.1 wt% Mg, and 0 to 0.35 wt% Cr. Alloys with more than 5.6 wt% Mg are of no significance as wrought alloys.

In Al−Mg alloys both tensile strength and 0.2% proof stress increase with increasing Mg content,

**Fig. 3.1-23** Effect of manganese additions on the strength of aluminium; alloys based on 99.5 wt% Al, quenched from 565 °C, sheet samples, 1.6 mm thick [1.23]

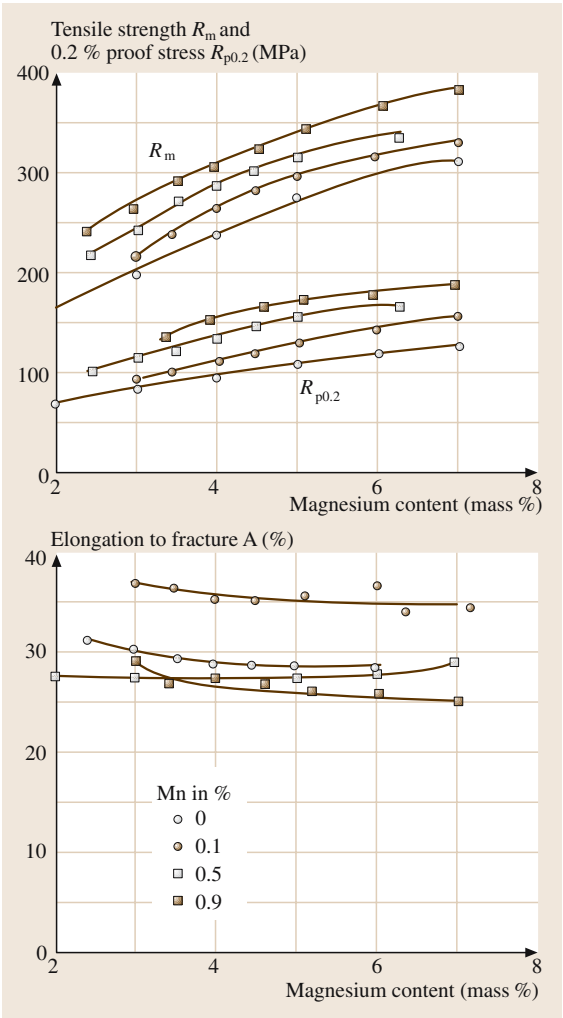


**Fig. 3.1-25** Effect of Mn content on the mechanical properties of Al−Mg alloys [1.23]

whereas elongation shows a steady decrease up to about 3 wt% Mg, beyond which it increases again slightly. Embrittlement does not occur at low temperatures. The solubility of Mg in the Al-rich solid solution decreases rapidly with decreasing temperature. Thus most Al−Mg alloys are effectively supersaturated at room temperature. This is of practical significance in alloys containing more than 3 wt% Mg, where precipitation of the $\beta$-$Al_8Mg_5$ can occur, especially after prior

cold working. This is not associated with any beneficial increases in strength but leads to deterioration in the corrosion resistance by intergranular corrosion (Fig. 3.1-16). It is necessary to avoid the formation of continuous networks of $\beta$ particles at the grain boundaries. Individual $\beta$ particles can be obtained by a globulization treatment (200–250 °C), followed by slow cooling.

Another means to increase strength is the addition of Mn. Al–Mn–Mg alloys show an additional increase in tensile strength, which is significantly higher than for binary Al–Mn alloys (Fig. 3.1-26). The alloys show good toughness and can be used at low temperatures. If the Mn content exceeds 0.6 wt%, the recrystallization temperature can be increased to such an extent that recrystallization does not occur during extrusion. With extruded sections, there is an increase in tensile strength and proof stress in the longitudinal direction termed "press effect."

### 3.1.2.7 Structure and Basic Mechanical Properties of Wrought Age-Hardenable Aluminium Alloys

#### Wrought Al–Cu–Mg and Al–Cu–Si–Mn (2xxx) Alloys

The 2xxx series alloys usually contain 3.5 to 5.5 wt% Cu and additions of Mg, Si and Mn and residual Fe. They show a significant increase in tensile strength by aging (310 to 440 MPa). Natural (room temperature) or artificial aging (at elevated temperature) may be preferable, depending on the alloy composition (Fig. 3.1-26). Additions of up to 1.5 wt% Mg increase both tensile strength and proof stress. At these Mg contents, the Al-rich solid solution is in equilibrium with the ternary $Al_2CuMg$ phase which, together with the $\theta$ phase ($Al_2Cu$), is responsible for hardening. Mn additions increase the strength (Fig. 3.1-27) and can also cause a press effect. For achieving good ductility, the Mn content is limited to $\approx$ 1 wt%.

#### Wrought Al–Mg–Si (6xxx)

Al–Mg–Si alloys are the most widely used wrought age-hardenable alloys. Hardening is attributable to the formation of the $Mg_2Si$ phase. The compositional range of interest is 0.30 to 1.5 wt% Mg, 0.20 to 1.6 wt% Si, up to 1.0 wt% Mn, and up to 0.35 wt% Cr. This is equivalent to about 0.40 to 1.6 vol% $Mg_2Si$ and varying amounts of free Si and/or Mg. Some alloys are close to the pseudo-binary section Al–$Mg_2Si$, in others there is a significant excess of Si. This affects the maximum

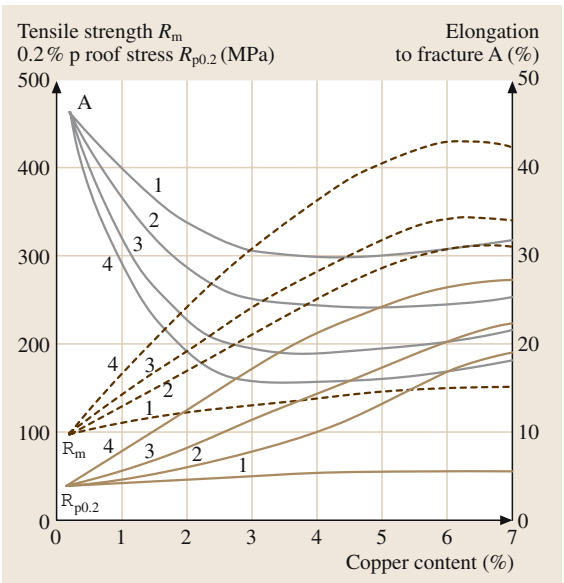


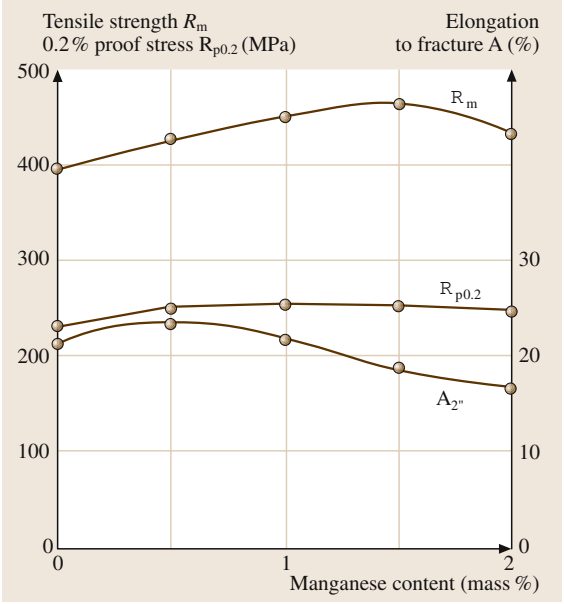


**Fig. 3.1-26a,b** Behavior of wrought Al–Cu-alloys **(a)** Effect of copper on the strength of binary Al–Cu alloys; base material 99.95 wt% Al, 1.6 mm thick sheet [1.23]. (1) Soft annealed; (2) Solution annealed and quenched; (3) Naturally aged; (4) Artificially aged. **(b)** Effect of Mn on the strength of an Al–Cu–Mg alloy with approx. 4 wt% Cu and 0.5 wt% Mg; naturally aged [1.23]

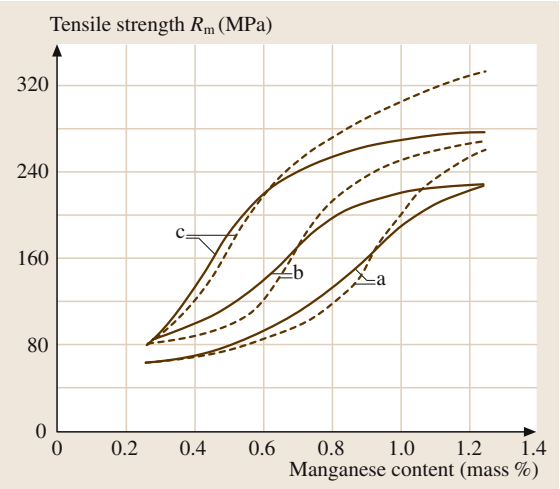


**Fig. 3.1-27** Effect of $Mg_2Si$ on tensile strength [1.9] (1) stoichiometric composition, (2) 0.3 wt% excess Mg, (3) 0.3 wt% excess Si. The *solid line* refers to alloys that were quenched + immediate ageing at 160 °C, the *dotted line* represents data for alloys that were quenched + intermediate ageing for 24 h at 20 °C + ageing at 160 °C

attainable strength values because of the resulting variations in the amount of $Mg_2Si$, as shown in Fig. 3.1-28 for the quenched and artificially aged condition. Additions of 0.2 to 1.0 wt% Mn lead to an increase in the notch impact toughness of Al−Mg−Si alloys (Fig. 3.1-29), and affect the recrystallization behavior. Additions of Cr cause similar effects.

### Wrought Al–Zn–Mg- and Al–Zn–Mg–Cu Alloys (7xxx)

Additions of Zn to Al lead to an insignificant increase in strength. Combined additions of Zn and Mg cause age hardening and thus an increase in strength (Fig. 3.1-28). The sum of the Zn and Mg contents is limited to about 6–7% because of the risk of stress corrosion cracking at higher levels in Cu-free Al−Zn−Mg alloys; this results in medium strength. Zr, Mn, and Cr are added to reduce the tendency to recrystallize. If suitably heat-treated, such alloys have adequate corrosion resistance. It is important that cooling after solution treatment is not too rapid and that the proper precipitation treatment, usually step ageing, should be used. The alloys are of interest for welded structures because of their low quench

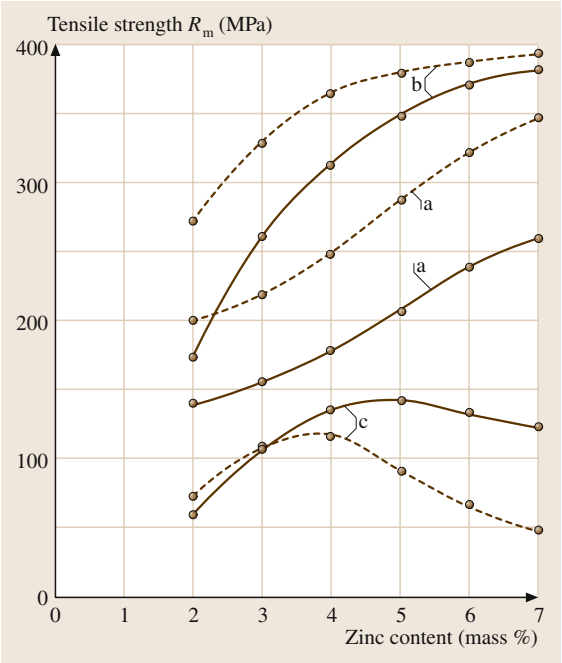


**Fig. 3.1-28** Effect of Zn and Mg on the strength and aging effect of Al–Zn–Mg alloys [1.24] (1) Solution treatment at 450 °C and quenching. (2) Solution treatment at 450 °C and quenching plus natural aging for 3 months. (3) Ageing effect i. e., the increase in strength attributable to natural ageing; difference between (1) and (2)

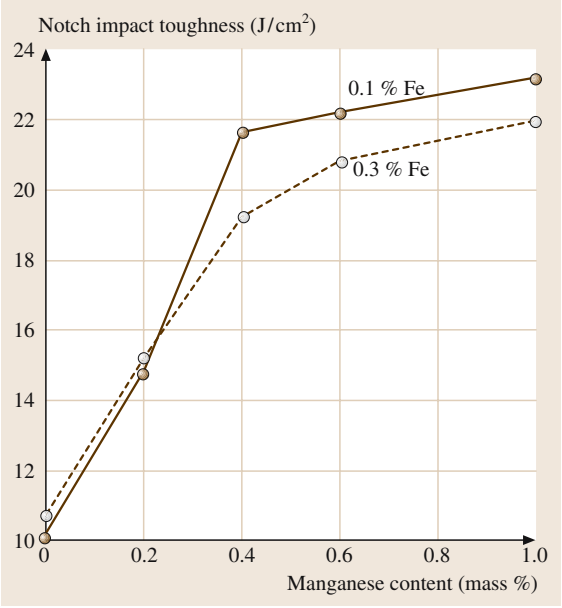


**Fig. 3.1-29** Effect of Mn and Fe on the notch impact toughness of AlMgSi1 alloy 1 wt% Si and 0.75 wt% Mg; artificially aged, flat bars, $60 \times 10 mm^2$ [1.24]

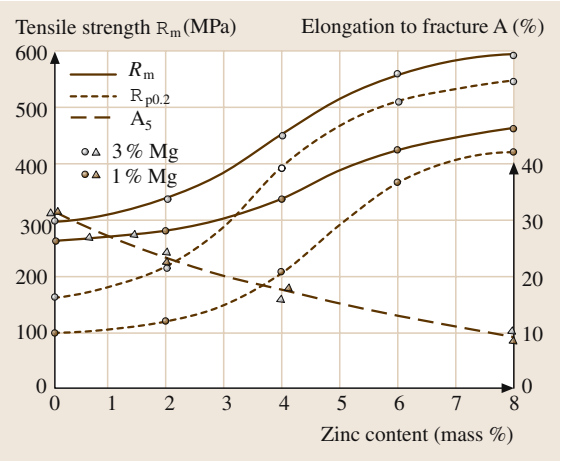


**Fig. 3.1-30** Effect of zinc on the tensile properties of Al–Zn–Mg–Cu alloys; solution treated at 460 °C, quenched, aged for 12 h at 135 °C, 1.5 wt% Cu [1.23]

sensitivity. The low-strength heat-affected zone formed during welding is restored to full hardness without the need for renewed solution treatment. Al−Zn−Mg alloys usually contain 0.1 to 0.2 wt% Zr and some Ti in order to improve their weldability and resistance to stress corrosion cracking. Cu additions are avoided, despite their favourable effect on stress corrosion cracking, because they increase susceptibility to weld cracking.

#### Al–Zn–Mg–Cu Alloys

The addition of 0.5 to 2.0 wt% Cu strengthens Al−Zn−Mg alloys. Cu also reduces the tendency for stress corrosion cracking so that the upper limit for (Zn + Mg) can be increased to 9 wt%, provided additions of Cr are also made. The Zn/Mg ratio should preferably lie between 2 and 3. Al−Zn−Mg−Cu alloys can be aged both naturally and artificially. They attain the highest strength levels of all aluminium alloys. The actual hardening mechanism is attributable to Mg and Zn. Cu increases the rate of aging and acts as a nucleus for the hardening phases. Figure 3.1-30 shows some properties as a function of the Zn content at constant Cu content and two different Mg contents.

### 3.1.2.8 Structure and Basic Mechanical Properties of Aluminium Casting Alloys

#### Al–Si Casting Alloys

Due to the Al−Si eutectic (Fig. 3.1-12), these alloys, containing 5 to ≤ 20 wt% Si, have good casting

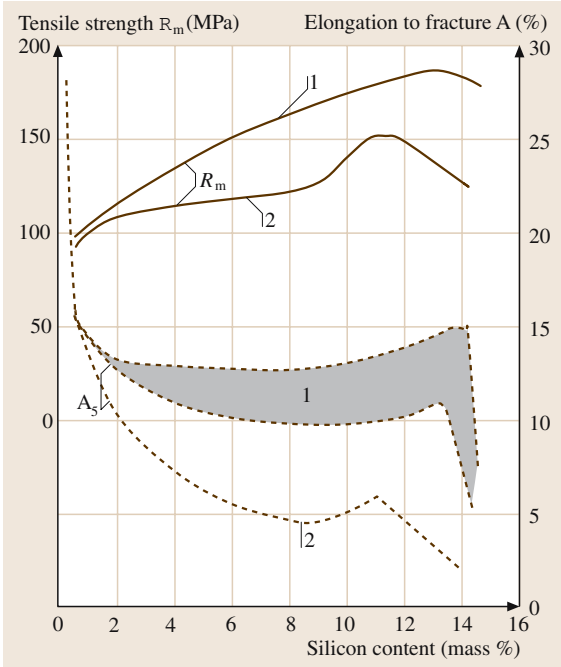


**Fig. 3.1-31** Effect of Si on the strength and ductility of Al−Si casting alloys; modified and unmodified sand castings. [1.9] (1) modified; (2) unmodified

properties. The tensile strength increases with the Si content (Fig. 3.1-31). Apart from Si other elements may be added, e.g., for the modification of the eutectic. Cu is present in residual amounts and impairs chemical resistance if levels exceed 0.05 wt%. Additions of about 1 wt% Cu yield an increase in solid solution hardening and thus reduce the tendency for smearing during machining. Residual Fe reduces sticking tendency, but leads to the formation of $\beta$-AlFeSi needles which reduce strength and ductility. Therefore the Fe content must be limited. An addition of Mn has a favorable effect on the sticking tendency. Mn leads to the formation of a quaternary phase; but it poses no problem because of its globular shape. "Piston alloys" have hypereutectic compositions of up to 25 wt% Si. During solidification, primary Si crystals are formed which increase wear strength and reduce thermal expansion.

#### Al–Si–Mg Casting Alloys

These alloys contain about 5 wt%, 7 wt%, or 10 wt% Si and between 0.3 and 0.5 wt% Mg. The optimum amount of Mg decreases with increasing Si content. Mg causes high strength and a moderate ductility depending on the

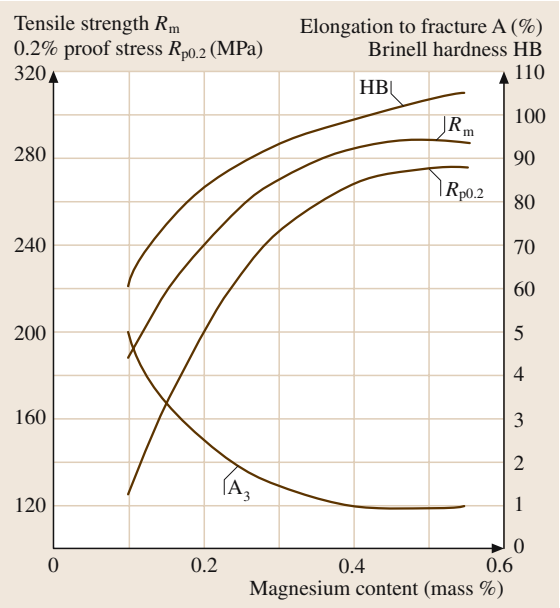


**Fig. 3.1-32** Effect of Mg on the mechanical properties of G-AlSi10Mg casting alloy (with 9.5 wt% Si, 0.45 wt% Fe and 0.3 wt% Mn), sand cast and artificially aged [1.25–27]

temper (Fig. 3.1-32). The alloys can be age hardened both naturally and artificially. Fe leads to a reduction in sticking tendency, but also to a drastic reduction in ductility.

### Al–Mg Casting Alloys

These alloys contain 3–12 wt% Mg. Strength increases with increasing Mg content (Fig. 3.1-33). Above about 7 wt% Mg, the alloy has to be heat-treated to homogenise the structure and thus obtain good tensile properties. With Mg contents of up to 5 wt%, Si additions of up to 1 wt% are possible, and these lead mainly to improvements in the casting properties. The addition of Si causes hardening due to the formation of $Mg_2Si$.

### Al–Zn–Mg Casting Alloys

They contain 4 to 7 wt% Zn and 0.3 to 0.7 wt% Mg. They can be naturally or artificially age hardened in the as-cast condition, without the need for prior solution treatment. Mg has a significant effect on the mechanical properties in the aged condition (Fig. 3.1-34). If the Mg content is limited, Al–Zn–Mg casting alloys can exhibit particularly good elongation to fracture.

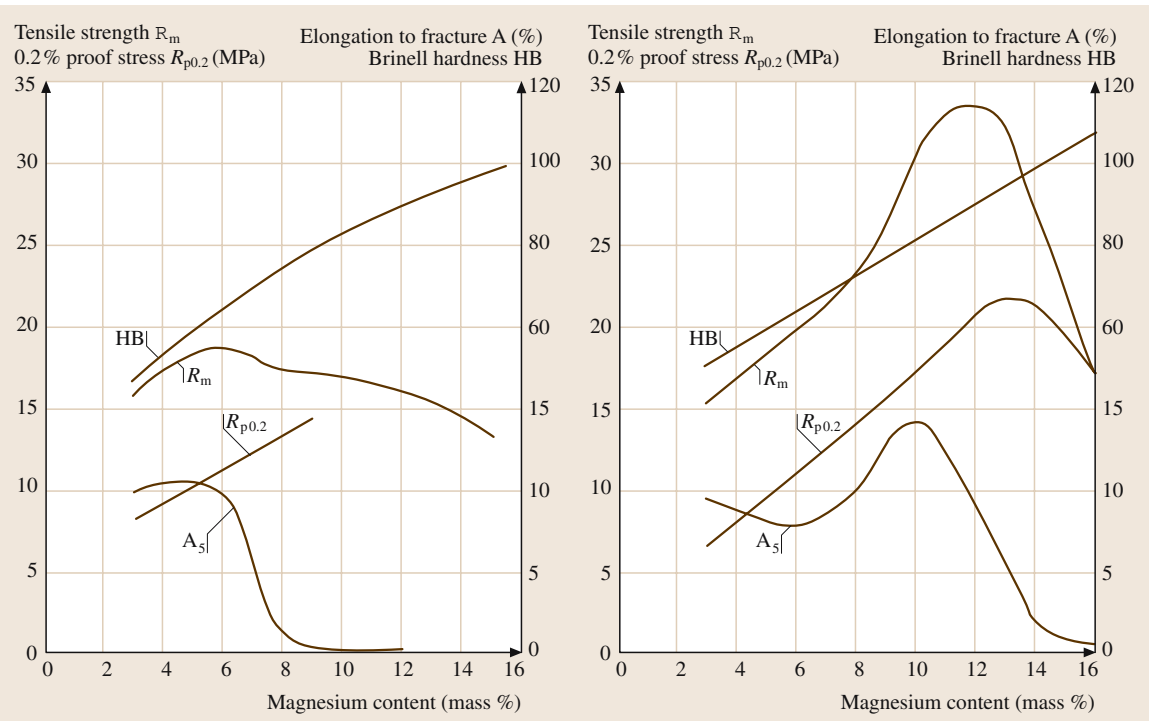


**Fig. 3.1-33a,b** Effect of Mg on the mechanical properties of Al–Mg casting alloys, sand cast, untreated and homogenised [1.9]. **(a)** As-cast condition. **(b)** Homogenized

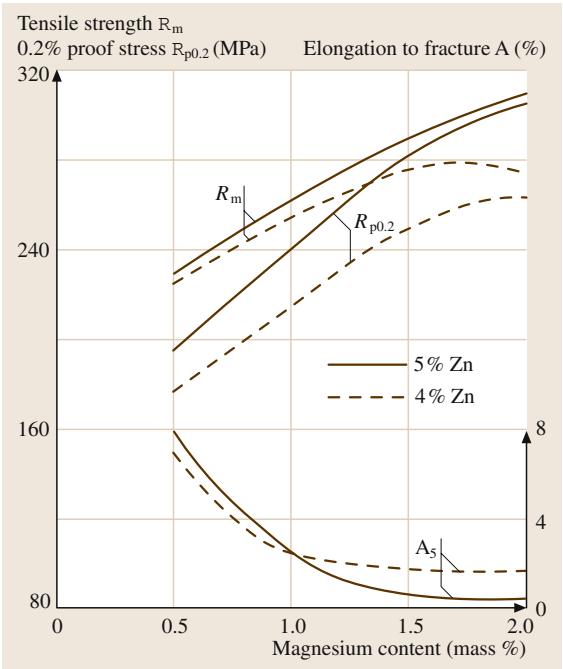


**Fig. 3.1-34** Effect of Mg on the strength of cast Al–Zn–Mg alloys; sand casting, artificially aged [1.9]

### 3.1.2.9 Technical Properties of Aluminium Alloys

The applications of aluminium and its alloys are depending on the properties. In most cases, mechanical properties are an important criterion for assessing the suitability of an Al alloy for a specific application. Other properties, such as electrical conductivity or corrosion resistance, may also be included in the assessment process.

#### Mechanical Properties

*Hardness.* The Brinell hardness number HB ranges from 15 for unalloyed Al in the soft temper to about 140 for an artificially aged Al−Zn−Mg−1.5 wt%Cu alloy.

*Tensile Strength.* Figures 3.1-35 and 3.1-36 indicate the typical levels of strength attainable with wrought and cast aluminium alloys, respectively. There will be a range of tensile strengths in specific alloying systems because of possible additional increases in strength due to hardening by cold work or precipitation. The different alloying elements cause differing degrees of strengthening.

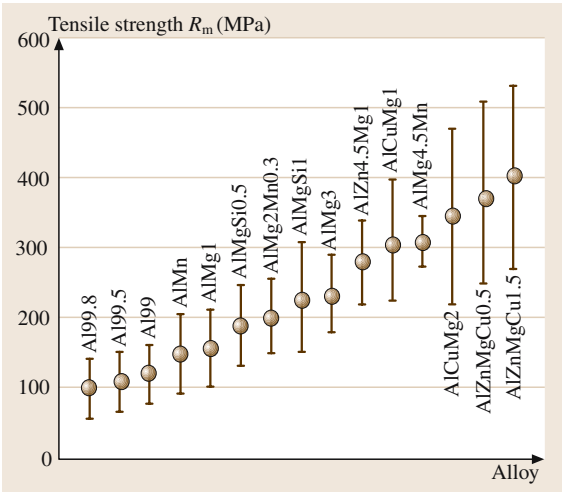


**Fig. 3.1-35** Ranges of tensile strength for some important wrought aluminium alloys [1.9]

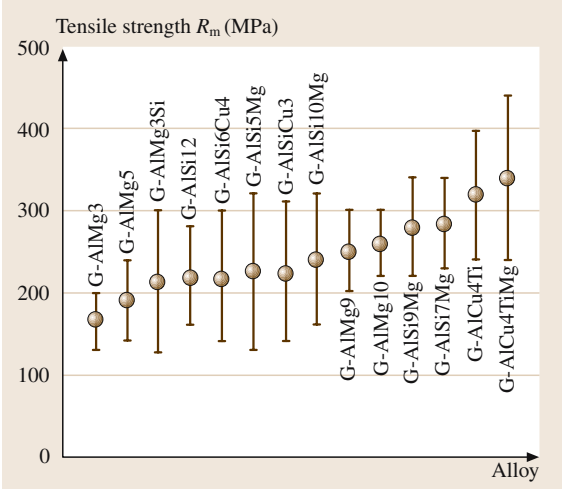


**Fig. 3.1-36** Ranges of tensile strength for some important aluminium casting alloys [1.9]

*Strength at Elevated Temperatures.* An example of the temperature and time dependence of the different mechanical properties is given in Fig. 3.1-37. With regard to the resistance to softening the materials can be classified as follows, depending on their temper:

- Wrought alloys in the soft temper and as-cast non-age-hardenable casting alloys are all practically thermally stable.
- For cold worked wrought alloys, partially annealed to obtain an intermediate temper, the increase in

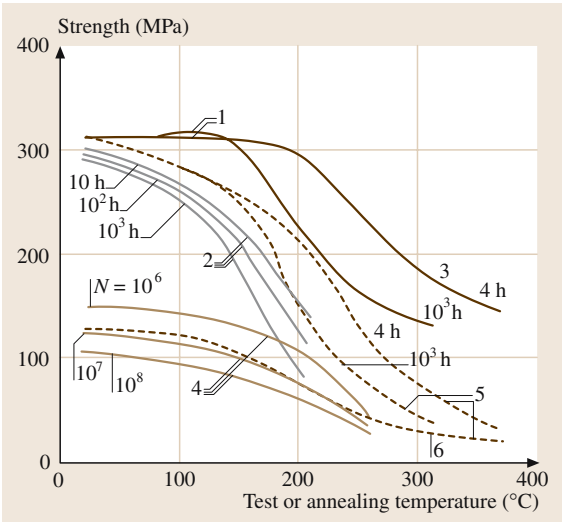


**Fig. 3.1-37** Properties of 6061-T6 at elevated temperatures; 1.0 wt% Mg, 0.6 wt% Si, 0.3 wt% Cu, 0.25 wt% Cr, artificially aged [1.9]. (1) tensile strength $R_m$ at 20 °C, (2) stress rupture strength, (3) duration of exposure, (4) fatigue strength, (5) tensile strength at test temperature, (6) solution treated

strength due to forming is diminished with increasing temperature and exposure time.

- Artificially aged alloys do not undergo any permanent changes on annealing up to approaching the ageing temperature. At higher temperatures, aging continues from the point where it was interrupted during the aging process (Figs. 3.1-38 and 3.1-39).
- Naturally aged alloys usually exhibit increased hardening when exposed to higher temperatures as a result of artificial ageing. At higher temperatures, the behavior is similar to that of artificially aged alloys.

*High Temperature Mechanical Properties in Short-Term Tests.* In materials that are not thermally stable, there will be an effect due to irreversible changes in properties. Its magnitude depends on the temperature and duration of exposure, Figs. 3.1-40 and 3.1-41.

*Creep Behavior.* Creep of Al alloys starts to play an important role at temperatures above 100 to 150 °C (Figs. 3.1-42 and 3.1-43). Material, amount of cold work

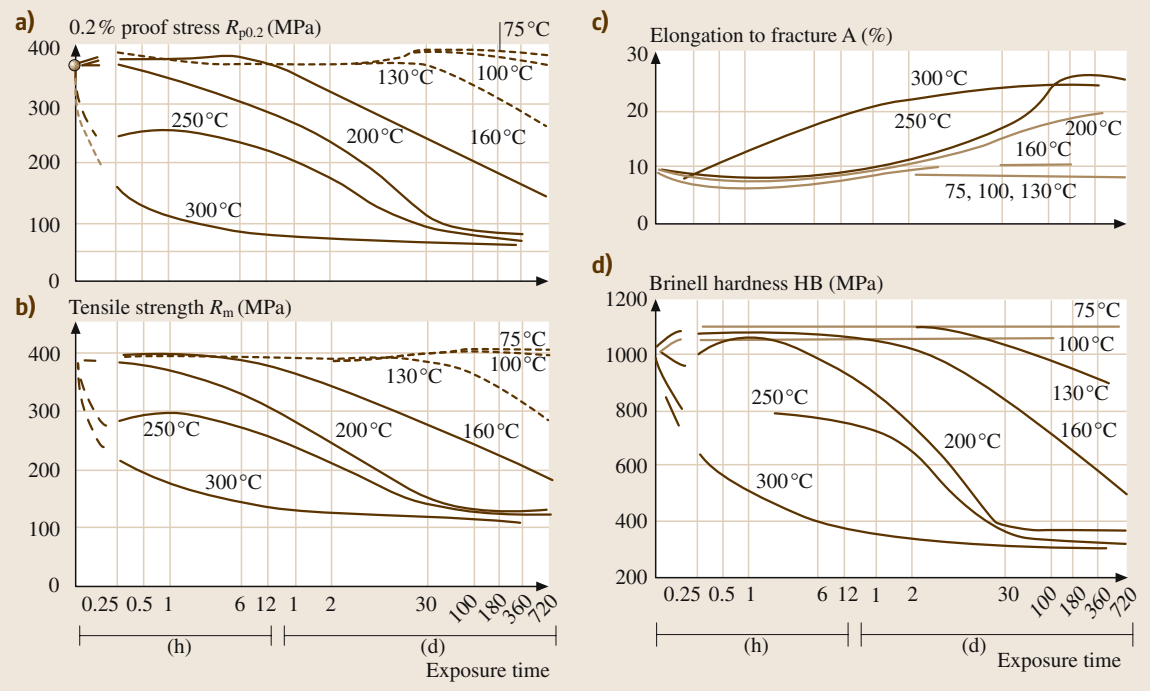


**Fig. 3.1-38a–d** Effect of temporary exposure to elevated temperature on the mechanical properties of artificially aged AlSi1MgMn [6082] at 20 °C [1.9]. **(a)** tensile strength; **(b)** 0.2% proofstress $R_P0.2$; **(c)** elongation to fracture A; **(d)** Brinell hardness

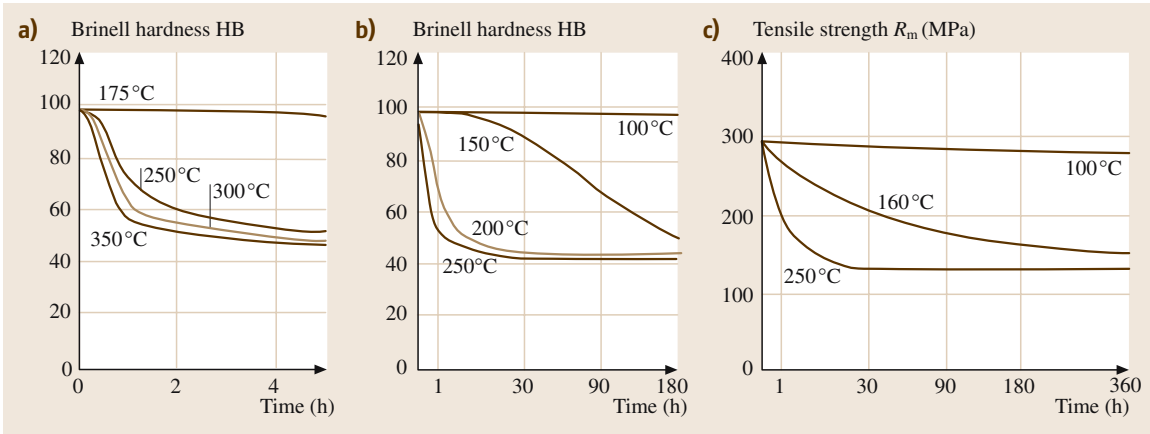


**Fig. 3.1-39a–c** Effect of temporary exposure to elevated temperature on the hardness and tensile strength at 20 °C of cast G-AlSi10Mg [43000, AlSi10Mg(a)] alloy, artificially aged [1.28]. **(a)** 0–4 h; **(b)** 1–180 d; **(c)** 1–360 d

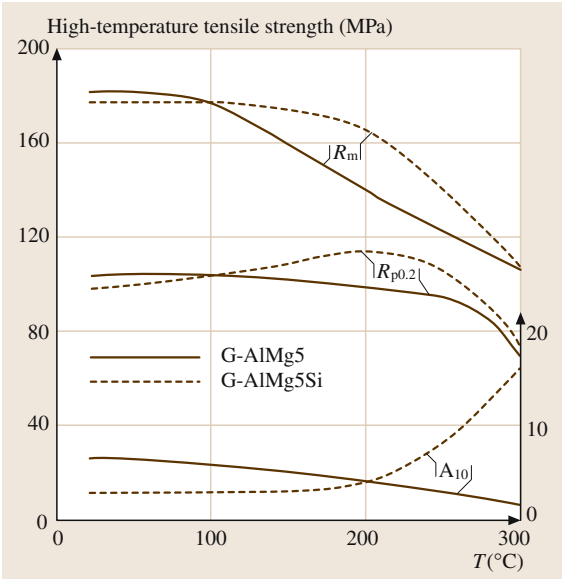


**Fig. 3.1-40** High-temperature tensile strength of G-AlMg5 [51300] and G-AlMg5Si [51400] casting alloys, sand cast, after 30 min prior exposure to the test temperature [1.29]

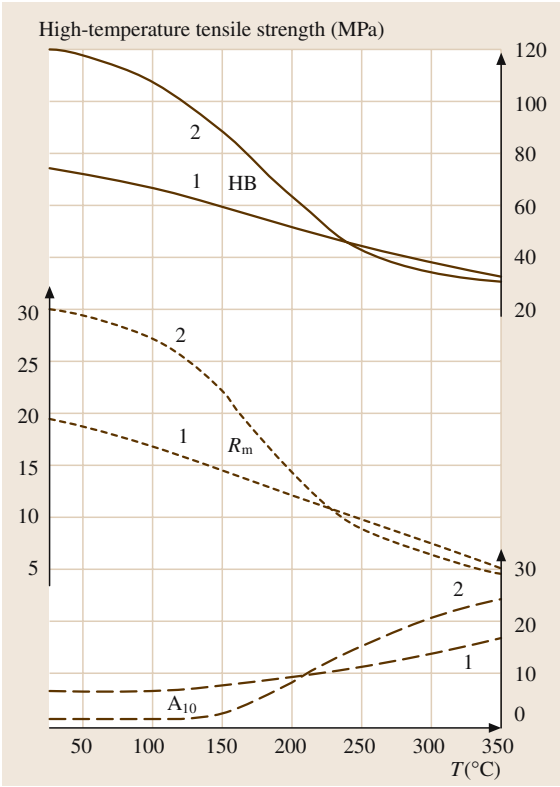


**Fig. 3.1-41** High-temperature tensile strength of casting alloys [1.28]. (1) As-cast G-AlSi12 alloy [44300, AlSi12(Fe)]. (2) G-AlSi10Mg alloy [43000, AlSi10Mg(a)] after preheating for 8 days at the test temperature

and degree of age-hardening can affect creep behavior in various ways. With non-age-hardenable alloys, the effect of cold working is more pronounced at low temperatures, below about 150 °C. At higher temperatures, the behavior rapidly approaches that of the softened material. Thus, more highly alloyed materials in the soft temper may exhibit better creep properties than cold worked alloys that are less highly alloyed. Artificially

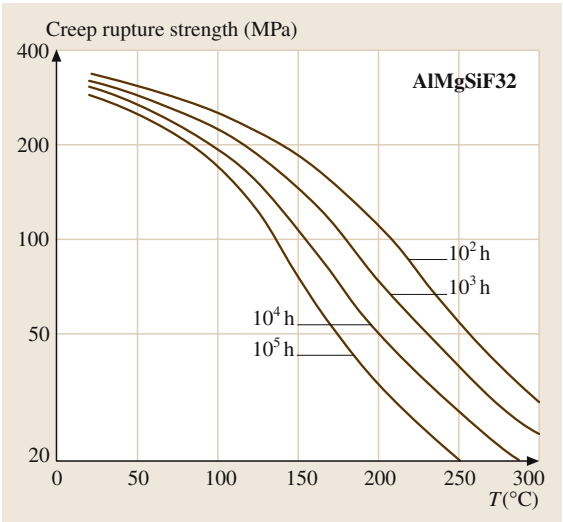


**Fig. 3.1-42** Creep rupture behavior of 6082, AlSi1MgMn, T6 alloy, strain-hardened, min. tensile strength 320 MPa; extruded rods, 25 mm diameter [1.30, 31]

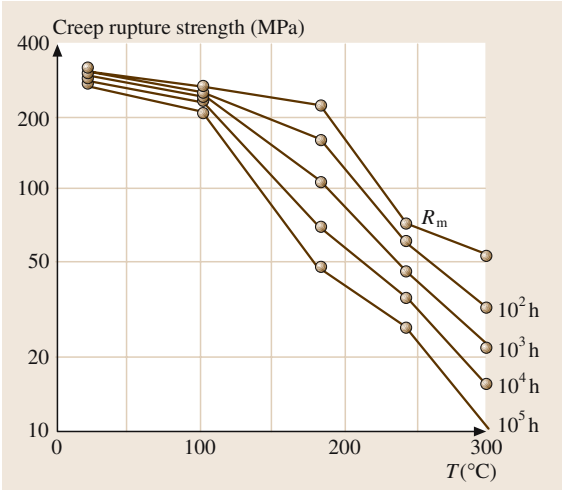


**Fig. 3.1-43** Creep rupture behavior of AlSi10MgCa [43000] casting alloy, artificially aged, 100 h prior exposure to the test temperature [1.30, 31]

aged alloys should only be exposed for prolonged periods to temperatures that are significantly lower than the temperature of artificial ageing, otherwise over-ageing will lead to a complete loss of strength.

*Mechanical Properties at Low Temperatures.* Based on its fcc crystal structure, Al and its alloys show neither a rapid increase in yield stress nor a rapid decrease in fracture toughness with decreasing temperature (Figs. 3.1-44 – 3.1-46). Tests carried out on Al–Mn, Al–Mg, Al–Mg–Si, Al–Cu–Mg, and Al–Zn–Mg wrought alloys at −268 °C showed that the values of elongation to fracture at extremely low temperatures were even higher than at room temperature. In most cases, tensile strength and 0.2% proof stress increased weakly with decreasing temperature. Casting alloys behave similar to wrought alloys at low temperatures. The behavior will depend on composition, temper (especially size, shape and distribution of precipitates), and on the casting process used (Fig. 3.1-47).

*Fatigue.* There is a marked effect of composition, heat treatment, and method of processing on fatigue strength. Solid solution hardening, cold work, and age hardening all lead to an increase in fatigue strength. For a given alloy composition, extruded sections usually have a higher fatigue strength than sheet or forgings. Fine grains are generally beneficial whereas coarse grains and coarse intermetallic phase particles can lead to a reduction in fatigue strength. Often there is an increase in fatigue strength with decreasing sample thickness, especially with bending stresses. Moreover, the effect of roughness or surface defects in thin specimens is usually less than that in thicker samples. With wrought aluminium alloys, there is a marked difference between age-hardenable alloys and non-age-hardenable alloys. It manifests itself in the shape of the S–N curve (Fig. 3.1-47), which is almost horizontal after about $10^6$ cycles for non-age-hardenable alloys and after about $10^8$ cycles for age-hardenable alloys. Fig-

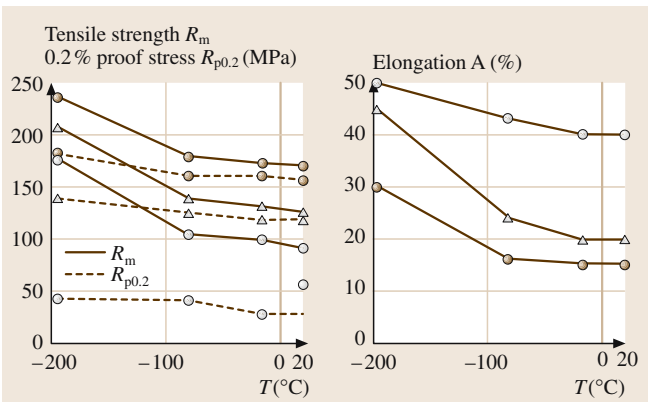


**Fig. 3.1-44a,b** Mechanical properties of unalloyed aluminium AA 1100 (Al99) at low temperatures [1.9]. **(a)** Tensile strength $R_m$; **(b)** Elongation A

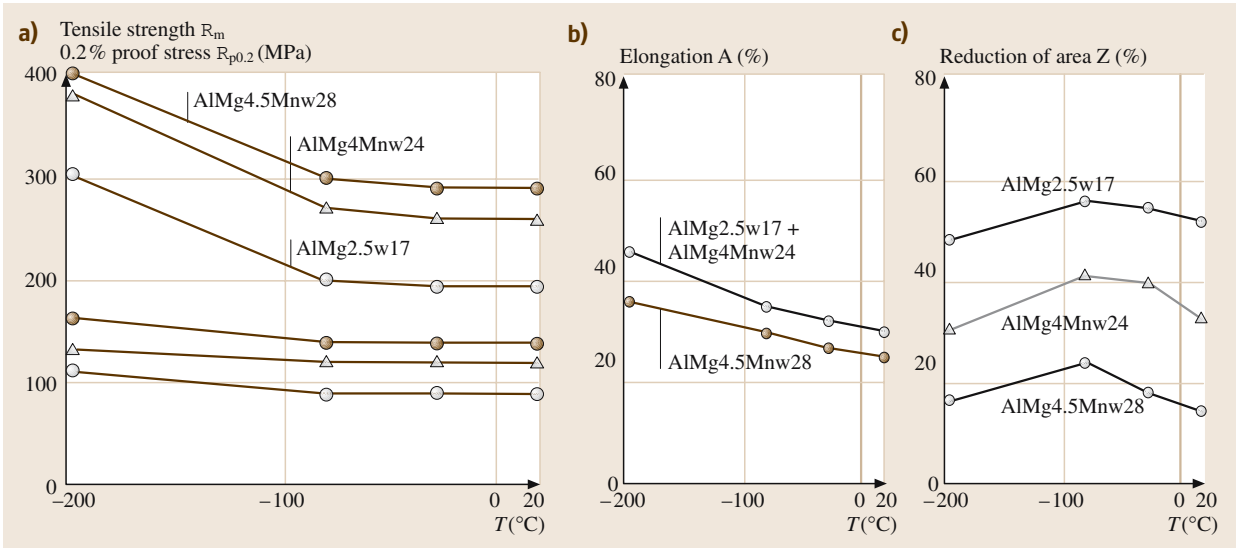


**Fig. 3.1-45a–c** Mechanical properties at low temperatures for some Al−Mg and Al−Mg−Mn alloys in the soft temper [1.9]. **(a)** Tensile strength $R_m$ and 0.2 proof stress $R_{p0.2}$; **(b)** Elongation $A_2''$; **(c)** reduction of area AlMg4Mn (≈ 5086, AlMg4), W24 ∼O/H111; AlMg2.5 (≈ 5052, AlMg2.5), W17 ∼O/H111; AlMg4.5Mn (≈ 5083, AlMg4.5Mn), W28 ∼O/H111

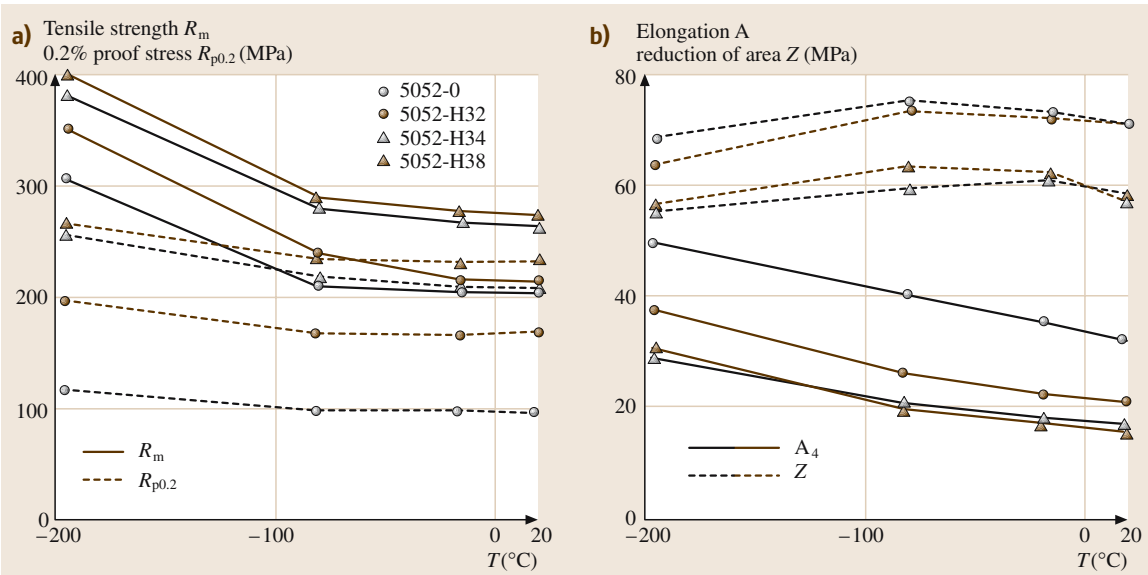


**Fig. 3.1-46a,b** Effect of cold working on the tensile properties of AlMg2.5 (5052) at low temperatures [1.9]. **(a)** Tensile strength and 0.2 proof stress; **(b)** Elongation and reduction of area

ure 3.1-48 illustratesthat the choice of $10^8$ cycles as the ultimate number of stress cycles is regarded as adequate. Figure 3.1-49 shows fatigue curves for a number of casting alloys.

### Technological Properties

*Abrasion Resistance.* The wear resistance of Al alloys is low, especially in the absence of lubricants. There is no relation between hardness, strength and

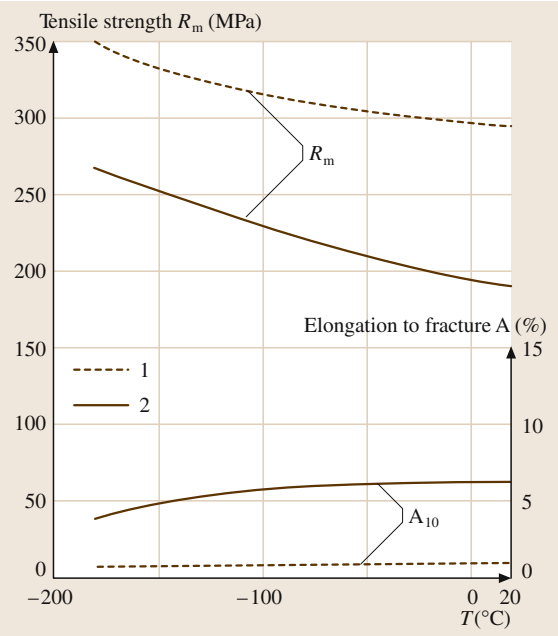


**Fig. 3.1-47** Mechanical properties of artificially aged G-AlSi12 and G-AlSi10Mg casting alloys at low temperatures [1.28]. The *solid line* represents G-AlSi10Mg, artificially aged; the *dotted line* represents G-AlSi12, as-cast

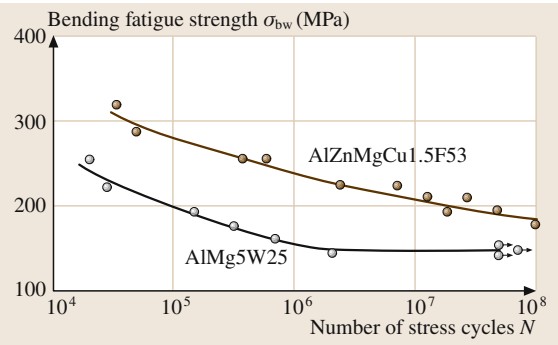


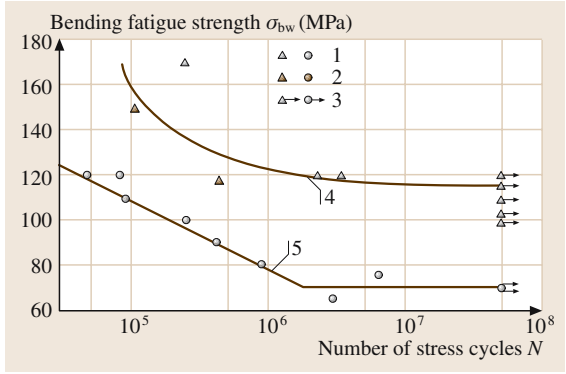


**Fig. 3.1-49** Bending fatigue strength of two aluminium pressure die-casting alloys; flat samples with cast skin [1.9]. (1) Fracture; (2) Fracture, with evidence of defect; (3) No fracture; (4) GD-AlSi6Cu3; (not in EN); (5) GD-AlSi12 [≈ 44300, AlSi12(Fe)]

abrasion resistance. Under suitable conditions of lubrication, aluminium alloys can be safely used where they will encounter friction, as shown by their widespread use in the fabrication of pistons and sliding bearings. Wear can be drastically reduced by the suitable surface treatments.

*Sheet Formability.* Typical values for deep-drawing indices for commonly used sheet materials are shown in Fig. 3.1-50, whereas typical values of strain-hardening exponent $n$ and degree of anisotropy $r$ are given in Table 3.1-13. The $r$ value is strongly dependent on the manufacturing process in particular, as is the case with all texture-dependent properties. In general, materials with high $n$ and $r$ values are deep-drawable.

**Fig. 3.1-48** Typical S-Ncurves for reverse bending tests on an age-hardenable and a non-age-hardenable alloy [1.9], AlZnMgCu1.5 F53 (≈ 7075, AlZn5.5MgCu, T651) and AlMg5 (≈ 5019, AlMg5), W25

**Table 3.1-13** Typical values of strain-hardening exponent $n$ and degree of anisotropy $r$ for some aluminium-base materials based on data from various sources [1.9]; n.a. – not available

| Material, Alloy | | Temper | $n$ | $r$ |
|---|---|---|---|---|
| Al99.5 | 1050A | O/H111 | 0.25 | 0.62 |
| AlMn1 | 3103 | O/H111 | 0.15 | n.a. |
| AlMg3 | 5754 | O/H111 | 0.20 | 0.64 |
| AlMg3 | 5754 | H14 | 0.16 | 0.75 |
| AlMg3 | 5754 | H18 | 0.12 | 1.10 |
| AlMg2Mn0.8 | 5049 | O/H111 | 0.20 | 0.66 |
| AlMg2Mn0.8 | 5049 | H112 | 0.20 | 0.92 |
| AlMg4.5Mn | 5063 | O/H111 | 0.15 | n.a. |

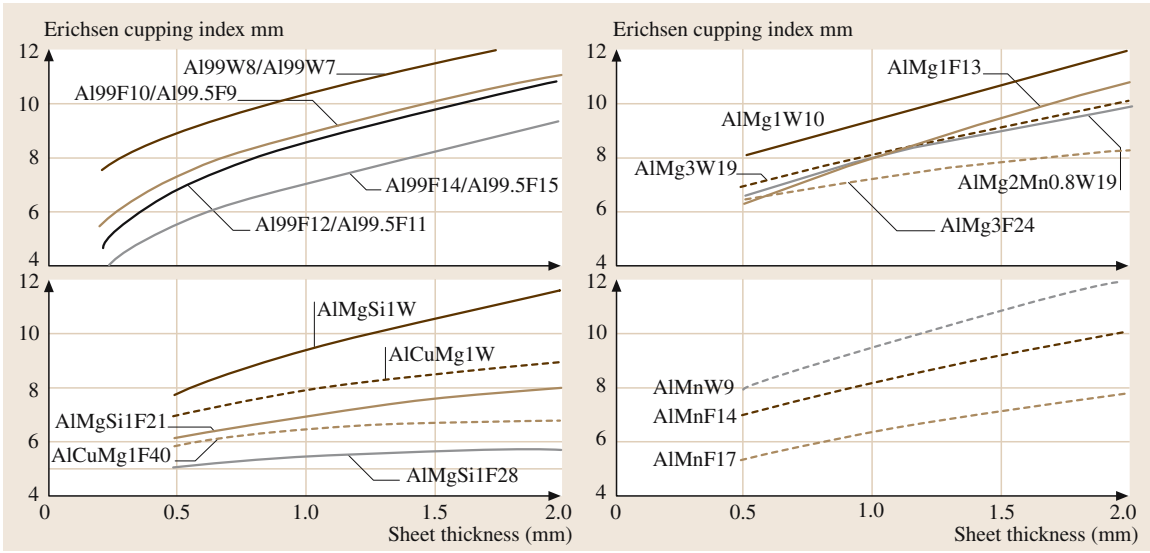


**Fig. 3.1-50** Dependence of deep-drawing index on sheet thickness for different aluminium sheet alloys [1.9]

*Machinability.* There are difficulties to classify aluminium alloys according to their machinability. In general, soft wrought alloys perform worse than other materials regardless of the machining conditions because of chip shape. Harder wrought alloys perform somewhat better and special machining alloys and casting alloys perform best of all. In Si-containing alloys, including wrought alloys, there is a marked increase in tool wear with increasing Si content if the relatively hard Si is present in its elemental form.

### Physical Properties

The most important physical properties of pure Al are listed in Chapt. 2.1,Table 3.1-11 Characteristic ranges of property variations with the amount of impurities or alloying elements are compiled in Table 3.1-14.

*Coefficient of Thermal Expansion.* Values of the average linear coefficient of thermal expansion for some Al-based materials at temperatures of practical significance are given in Table 3.1-15. Alloying leads to

**Table 3.1-14** Examples for physical properties of aluminium alloys [1.9][a]

| Designation EN | EN former designation | | Density ($g\,cm^{-3}$) | Freezing range [b] (°C) | Electrical conductivity ($m\,\Omega^{-1}\,mm^{-2}$) | Thermal conductivity ($W\,m^{-1}\,K^{-1}$) | Coefficient of linear expansion ($10^{-6}/K$) |
|---|---|---|---|---|---|---|---|
| **Wrought alloys** | | | | | | | |
| 1098 | Al99.98 | Al99.98R | 2.70 | 660 | 37.6 | 232 | 23.6 |
| 1050A | Al99.5 | Al99.5 | 2.70 | 646–657 | 34–36 | 210–220 | 23.5 |
| 1200 | Al99 | Al99 | 2.71 | 644–657 | 33–34 | 205–210 | 23.5 |
| 8011A | AlFeSi(A) | AlFeSi | 2.71 | 640–655 | 34–35 | 210–220 | 23.5 |
| 3103 | AlMn1 | AlMn | 2.73 | 645–655 | 22–28 | 160–200 | 23.5 |
| 3003 | AlMn1Cu | AlMnCu | 2.73 | 643–654 | 23–29 | 160–200 | 23.2 |
| 3105 | AlMn0.5Mg0.5 | AlMn0.5Mg0.5 | 2.71 | 635–654 | 25–27 | 180–190 | 23.2 |
| 3004 | AlMn1Mg1 | AlMnlMg1 | 2.72 | 629–654 | 23–25 | 160–190 | 23.2 |
| 5005A | AlMn1(C) | AlMg1 | 2.69 | 630–650 | 23–31 | 160–220 | 23.6 |
| 5052 | AlMg2.5 | AlMg2.5 | 2.68 | 607–649 | 19–21 | 130–150 | 23.8 |
| 5754 | AlMg3 | AlMg3 | 2.66 | 610–640 | 20–23 | 140–160 | 23.9 |
| 5019 | AlMg5 | AlMg5 | 2.64 | 575–630 | 15–19 | 110–140 | 24.1 |
| 5049 | AlMg2Mn0.8 | AlMg2Mn0.8 | 2.71 | 620–650 | 20–25 | 140–180 | 23.7 |

**Table 3.1-14** Examples for physical properties of aluminium alloys [1.9][a], cont.

| Designation EN | EN former designation | | Density ($g\,cm^{-3}$) | Freezing range [b] (°C) | Electrical conductivity ($m\,\Omega^{-1}\,mm^{-2}$) | Thermal conductivity ($W\,m^{-1}\,K^{-1}$) | Coefficient of linear expansion ($10^{-6}/K$) |
|---|---|---|---|---|---|---|---|
| 5454 | AlMg2.7Mn | AlMg2.7Mn | 2.68 | 602–646 | 19–21 | 130–150 | 23.6 |
| 5086 | AlMg4 | AlMg4Mn | 2.66 | 585–641 | 17–19 | 120–140 | 23.8 |
| 5083 | AlMg4.5Mn0.7 | AlMg4.5Mn | 2.66 | 574–638 | 16–19 | 110–140 | 24.2 |
| 6060 | AlMgSi | AlMgSi0.5 | 2.70 | 585–650 | 28–34 | 200–220 | 23.4 |
| 6181 | AlSi1Mg0.8 | AlMgSi0.8 | 2.70 | 585–650 | 24–32 | 170–220 | 23.4 |
| 6082 | AlSi1MgMn | AlMgSi1 | 2.70 | 585–650 | 24–32 | 170–220 | 23.4 |
| 6012 | AlMgSiPb | AlMgSiPb | 2.75 | 585–650 | 24–32 | 170–220 | 23.4 |
| 2011 | AlCu6BiPb | AlCuBiPb | 2.82 | 535–640 | 22–26 | 160–180 | 23.1 |
| 2007 | AlCu4PbMgMn | AlCuMgPb | 2.85 | 507–650 | 18–22 | 130–160 | 23 |
| 2117 | AlCu2.5Mg0.5 | AlCu2.5Mg0.5 | 2.74 | 554–650 | 21–25 | 150–180 | 23.8 |
| 2017A | AlCu4MgSi(A) | AlCuMg1 | 2.80 | 512–650 | 18–28 | 130–200 | 23.0 |
| 2024 | AlCu4Mg1 | AlCuMg2 | 2.78 | 505–640 | 18–21 | 130–150 | 22.9 |
| 2014 | AlCu4SiMg | AlCuSiMn | 2.80 | 507–638 | 20–29 | 140–200 | 22.8 |
| 7020 | AlZn4.5Mg1 | AlZn4.5Mg1 | 2.77 | 600–650 | 19–23 | 130–160 | 23.1 |
| 7022 | AlZn5Mg3Cu | AlZnMgCu0.5 | 2.78 | 485–640 | 19–23 | 130–160 | 23.6 |
| 7075 | AlZn5.5MgCu | AlZnMgCul.5 | 2.80 | 480–640 | 19–23 | 130–160 | 23.4 |
| **Casting alloys** | | | | | | | |
| 44100 | AlSi12(b) | G-AlSi12 | 2.65 | 575–585 | 17–27 | 120–190 | 20 |
| 47000 | AlSi12(Cu) | G-AlSil2(Cu) | 2.65 | 570–585 | 16–23 | 110–160 | 20 |
| 43000 | AlSi10Mg(a) | G-AlSil0Mg | 2.65 | 575–620 | 17–26 | 120–180 | 20 |
| 43200 | AlSi10Mg(Cu) | G-AlSil0Mg(Cu) | 2.65 | 570–620 | 16–20 | 110–140 | 20 |
| 42000 | AlSi7Mg | G-AlSi7Mg | 2.70 | 550–625 | 21–32 | 150–220 | 22 |
| 51000 | AlMg3(b) | G-AlMg3 | 2.70 | 580–650 | 16–24 | 110–170 | 23 |
| 51300 | AlMg5 | G-AlMg5 | 2.60 | 560–630 | 15–22 | 100–160 | 23 |
| 51400 | AlMg5(Si) | G-AlMg5Si | 2.60 | 560–630 | 16–21 | 110–150 | 23 |
| 51200 | AlMg9 | GD-AlMg9 | 2.60 | 510–620 | 11–15 | 80–110 | 24 |
| 46200 | AlSi8Cu3 | G-AlSi8Cu3 | 2.75 | 510–610 | 14–18 | 100–130 | 22 |
| 45000 | AlSi6Cu4 | G-AlSi6Cu4 | 2.75 | 510–620 | 15–18 | 110–130 | 22 |
| 21100 | AlCu4Ti | G-AlCu4Ti | 2.75 | 550–640 | 16–20 | 110–140 | 23 |
| 21000 | AlCu4MgTi | G-AlCu4TiMg | 2.75 | 540–640 | 16–20 | 110–140 | 23 |

[a] The actual values will depend on the material composition within the permitted range; electrical and thermal conductivity will also depend on the material structure

[b] Where a eutectic structure is expected to form because of segregation, this will solidify at the lowest temperature given

**Table 3.1-15** Linear coefficient of thermal expansion of some Al alloys for different ranges of temperature [1.9]

| Designation (according to EN 573.3 and EN 1706) | | Average coefficient of linear expansion ($10^{-6}\,K^{-1}$), for the range | | | |
|---|---|---|---|---|---|
| | | −50 to 20 °C | 20 to 100 °C | 20 to 200 °C | 20 to 300 °C |
| 1098 | Al99.98 | 21.8 | 23.6 | 24.5 | 25.5 |
| 1050A | Al99.5 | 21.7 | 23.5 | 24.4 | 25.4 |
| 3003 | AlMn1Cu | 21.5 | 23.2 | 24.1 | 25.2 |
| 3004 | AlMn1Mg1 | 21.5 | 23.2 | 24.1 | 25.1 |
| 5005A | AlMg1(C) | 21.8 | 23.6 | 24.5 | 25.5 |
| 5019 | AlMg5 | 22.5 | 24.1 | 25.1 | 26.1 |
| 5474 | AlMg3Mn | 21.9 | 23.7 | 24.6 | 25,6 |
| 6060 | AlMgSi0.5 | 21.8 | 23.4 | 24.5 | 25,6 |
| 2011 | AlCu6BiPb | 21.4 | 23.1 | 24.0 | 25,0 |
| 44100 | AlSi12(b) | – | 20.0 | 21.0 | 22.0 |

only small changes in the coefficient of thermal expansion (Tables 3.1-14 and 3.1-15). Si additions with 1.2% reduction in the coefficient of thermal expansion for each wt% Si have the greatest effect of the alloying elements commonly used. This effect is applied to the manufacture of piston alloys.

*Specific Heat.* The specific heat of aluminium in the solid state increases continuously from 0 at 0 K to a maximum at the melting point. This is only the case with alloys when there are no solid state reactions. The effect of alloying elements in solution is not very marked.

*Elastic Properties.* The Young's modulus of Al and its alloys is usually taken to be about 70 GPa. Values given in the literature for aluminium of all grades of purity and aluminium alloys range from about 60 GPa to 78 GPa. Unalloyed and low-alloyed materials are found in the lower part of the range. The age-hardenable alloys are in the middle to upper part. The Young's modulus is dependent on texture, because the elastic anisotropy as expressed by the ratio of the elastic moduli for single crystals with [111] and [100] orientations is 1.17. Furthermore, there is a marked effect of cold working and test temperature (Fig. 3.1-51).

*Electrical Conductivity.* The electrical conductivity is influenced largely by alloying or impurities and the

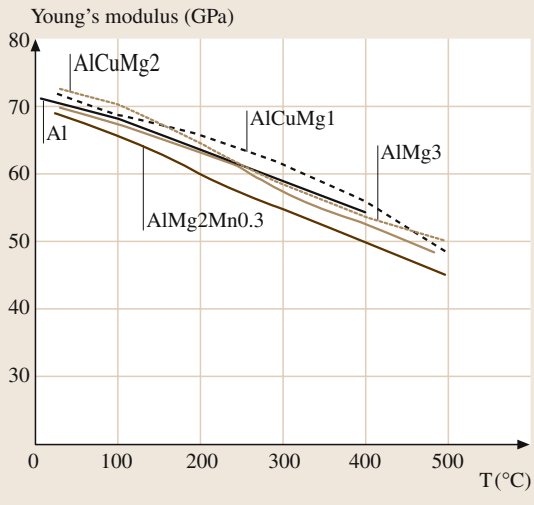


**Fig. 3.1-51** Dependence of Young's modulus $E$ of different Al alloys on temperature; determined using 9 mm thick plate [1.32]

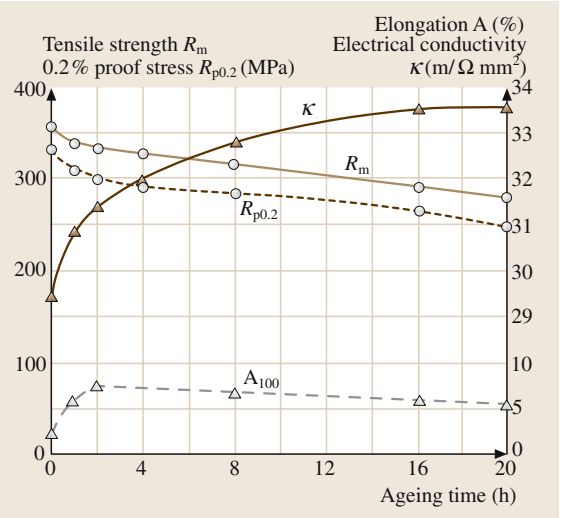


**Fig. 3.1-52** Changes in the mechanical properties and electrical conductivity of electrical grade E-AlMgSi (≈ 6101) alloy wire during artificial ageing at 160 °C; solution treated at 525 °C, water quenched, naturally aged for 14 days, 95% cold-worked and then artificially aged [1.14]

structure. Elements present in solid solution lead to a greater reduction in electrical conductivity than precipitates (Figs. 3.1-7 and 3.1-8). By use of a suitable combination of heat treatment and cold working, it is possible to obtain microstructures with an adequate combination of tensile strength and electrical conductivity. This is shown in Fig. 3.1-52, using E-AlMgSi wire as an example.

*Behavior in Magnetic Fields.* Aluminium is weakly paramagnetic. The specific susceptibility of Al and its alloys is about $7.7 \times 10^{-9}$ m$^3$ kg$^{-1}$ at room temperature.

*Nuclear Properties.* Thanks to its small absorption cross section for thermal neutrons, aluminium is often used in reactor components requiring low neutron absorption.

*Optical Properties.* The integral reflection is almost independent of the technical brightening process applied, but it depends on the purity of the metal. It is 84–85% for high-purity aluminium Al99.99 and 83–84% for unalloyed aluminium Al99.9. Higher amounts of diffuse reflection can be obtained by mechanical or chemical pre-treatment, such as sand blasting or strong pickling before brightening.

### 3.1.2.10 Thermal and Mechanical Treatment

Thermal and mechanical treatments have a great influence on the properties of aluminium and its alloys. Moreover these treatments influence some physical properties, for example the electrical conductivity. Thus these treatments are used to obtain a material with an optimum of properties required.

#### Work Hardening

Strengthening by work hardening can be achieved by both cold- and warm working. Figures 3.1-53 – 3.1-56 illustrate the effect of cold working. During hot working, strengthening and softening processes occur simultaneously; with aluminium-based materials, this will be above about 150–200 °C. Therefore hardness decreases with increasing hot-working temperature (Fig. 3.1-57). The formation of subgrains occurs in the microstructure; their size increases with increasing rolling temperature. Alloying atoms, such as Mg, impede growth or coarsening of the subgrains.

#### Thermal Softening

Figures 3.1-57a and 3.1-57b show typical softening curves for aluminium alloys in three characteristic stages: recovery, recrystallization, and grain-growth. In the case of the untreated continuously cast and rolled strip shown in Fig. 3.1-57a, recrystallization will occur at temperatures between about 260 and 290 °C. In Fig. 3.1-57b, recrystallization starts after about half an hour and is complete after about an hour. The

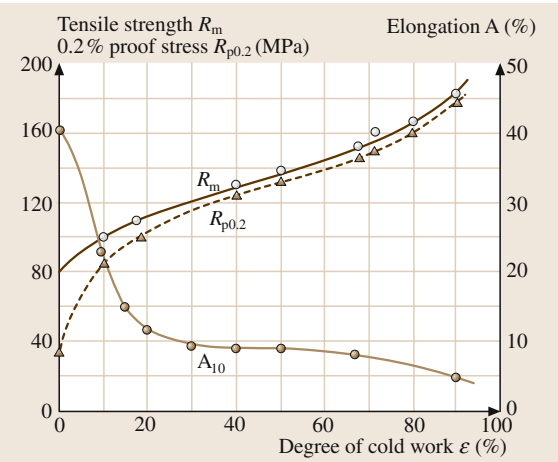


**Fig. 3.1-53** Hardening of Al99.5 strip (0.15 wt% Si, 0.28 wt% Fe) after recrystallization annealing and subsequent cold-rolling [1.33]

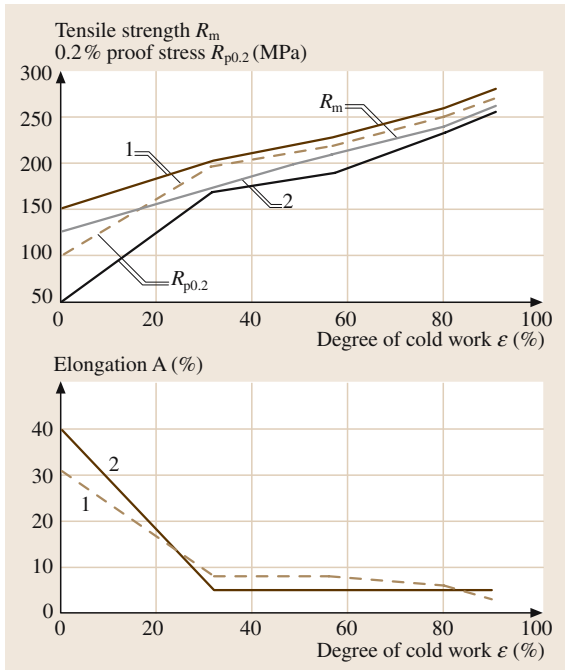


**Fig. 3.1-54** Typical mechanical properties of (1) continuously cast and rolled strip and (2) strip produced conventionally by hot-rolling and then cold-rolling cast billets of AlMn1 (3103) [1.34]

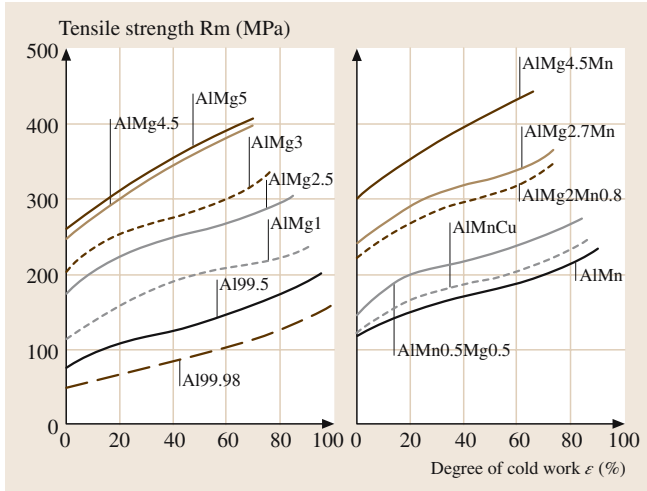


**Fig. 3.1-55** Tensile strength of various wrought non-age-hardenable aluminium alloys as a function of the degree of cold work [1.33]: AlMg4.5 – 5082; AlMg5 – 5019; AlMg3 – 5754; AlMg2.5 – 5052; AlMg1 – 5005; Al99.5 – 1050A; Al99.8 – 1080°; AlMg4.5Mn – 5083; AlMg2.7Mn – 5454; AlMg2Mn0.8 – 5049; AlMn0.5Mg0.5 – 3105; AlMn – 3103; AlMnCu – 3003

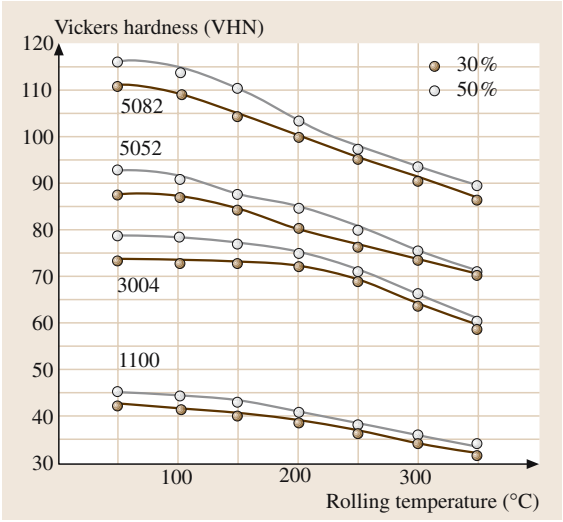


**Fig. 3.1-56** Effect of rolling temperature on hardness; specimens quenched after hot-rolling: Al99.0Cu – 1100; AlMn1Mg2 – 3004; AlMg2.5 – 5052; AlMg4.5 – 5082

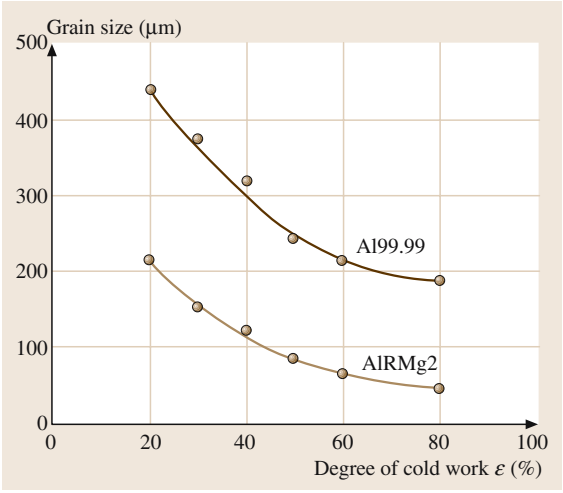


**Fig. 3.1-58** Grain size after complete recrystallization of Al99.99 and AlRMg2 as a function of degree of cold work (annealed at 350 to 415 °C until complete recrystallization) [1.9]

softening curves depend not only on the alloy composition but also on the degree of prior cold working to a marked extent. Further factors are the content of alloying and impurity elements, annealing time, heating rate, the microstructure prior to deformation and prior thermomechanical treatment, which can also include the casting process used to produce the starting material.

The softening due to recovery or partial recrystallization is very important when producing semi-finished products of medium hardness (e.g., half hard). The relationship between the degree of cold work and grain size is apparent in Fig. 3.1-58. If the degree of cold work is below a critical value, no recrystallization will occur. This threshold depends on material and prior thermo-

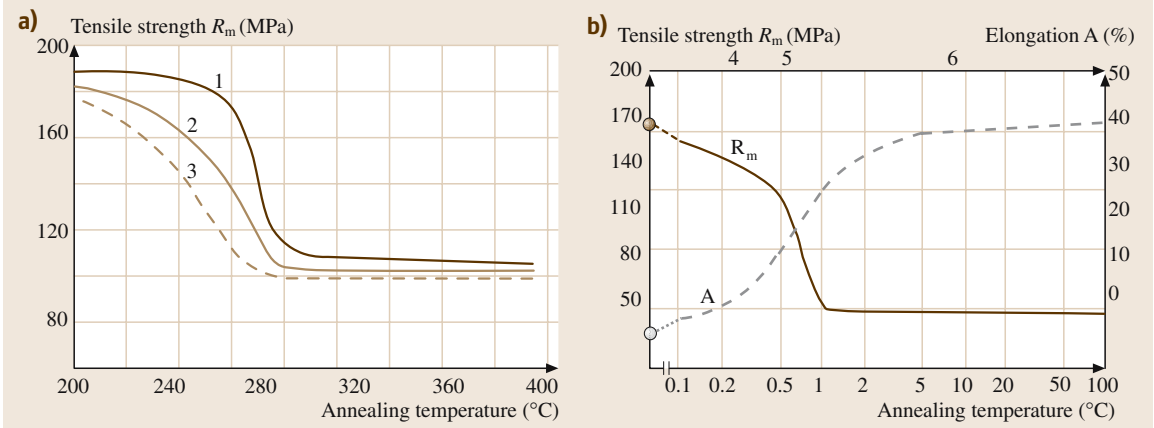


**Fig. 3.1-57a,b** Typical softening curves for cold-rolled Al99.5 [1.35, 36]. **(a)** Recrystallization after different initial tempers to 90% cold work and subsequent annealing for 1 h at different temperatures: (1) Continuously cast and rolled strip, subsequently cold-worked without an intermediate annealing treatment; (2) as 1 but with an intermediate annealing treatment for 1 h at 580 °C; (3) Strip conventionally produced using permanent mould casting and hot-rolling. **(b)** Continuously cast and rolled strip, cold-worked 90% and then annealed at 320 °C for time shown: (4) Recovery; (5) Recrystallization; (6) Grain growth

mechanical treatment, and is about 2–15%. If the degree of cold work is near the critical value, coarse grains can form during recrystallization, as clearly shown in the three-dimensional diagram in Fig. 3.1-59.

Other elements can affect the recrystallization temperature and the grain size after recrystallization. Mg does not have a marked effect (Fig. 3.1-60), while Mn, Fe, Cr, Ti, V, and Zr increase the recrystallization temperature (Fig. 3.1-61 delaying effect = plateau).

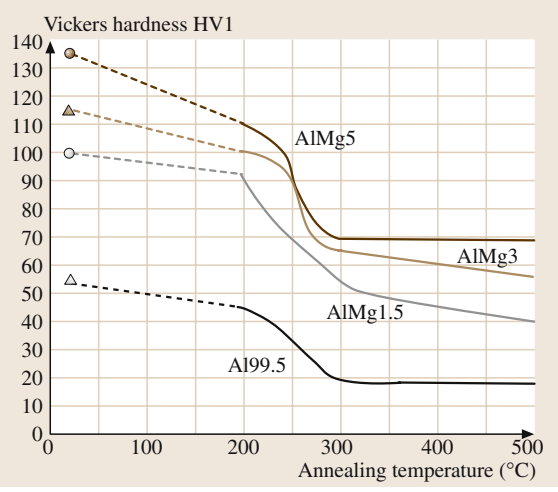


**Fig. 3.1-60** Effect of Al−Mg alloy composition on the softening behavior; the material was 90% cold-worked and annealed for 1 h at temperature shown [1.36]

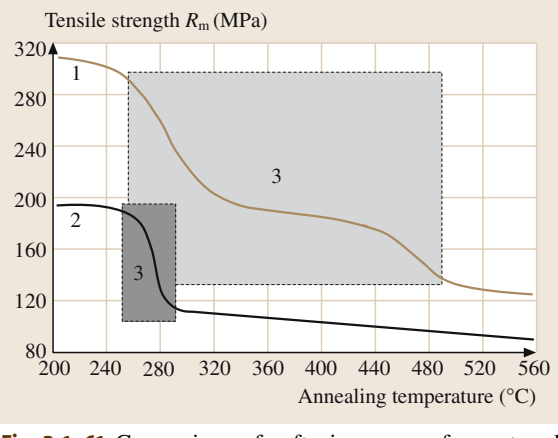


**Fig. 3.1-61** Comparison of softening curves for cast and hot-rolled Al99.5 and AlMn1 strip; material cold-worked 90% and annealed for 1 h at the temperature shown [1.36]: (1) Cast and hot-rolled AlMn1 (3103) strip; (2) Cast and hot-rolled Al99.5 (1050A) strip; (3) Recrystallization range

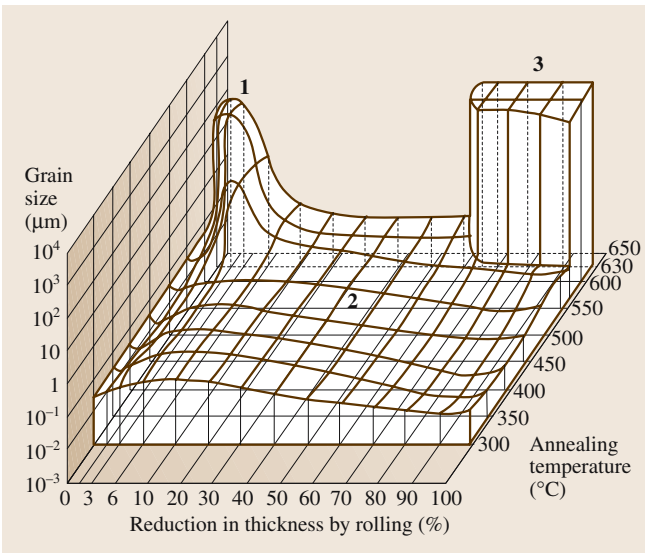


**Fig. 3.1-59** Recrystallization diagram showing grain size of Al99.6 (1060) as a function of cold work and annealing for 2 h at the temperatures shown [1.9]: (1) Coarse grains in the region of critical degree of cold work (primary recrystallization); (2) Area of primary recrystallization with fine and medium-sized grains, (3) Coarse grains as a result of secondary recrystallization

This is dependent on the amount and distribution of these elements, i. e., whether they are present as precipitates or in supersaturated solid solution, and/or whether they form intermetallic phases. In Fig. 3.1-62 it is clearly apparent that solution treatment reduces the degree of supersaturation and that the range over which tensile strength and 0.2% proof stress decrease rapidly with temperature is thus shifted to significantly lower temperatures. Interactions between the various elements present can also affect recrystallization behavior.

### Soft Annealing, Stabilization

With cold-worked materials, soft annealing consists of recrystallization annealing. The duration of the treatment, degree of cold work, and intermediate annealing treatments need to be selected with grain size in mind. In age-hardenable alloys, soft annealing permits most of the supersaturated components to precipitate out in coarse form or coherent or partially coherent phases to transform to incoherent stable phases. Soft annealing of casting alloys involves annealing the as-cast structure at 350 to 450 °C. With age-hardenable alloys, this is also possible using a solution treatment followed by furnace cooling

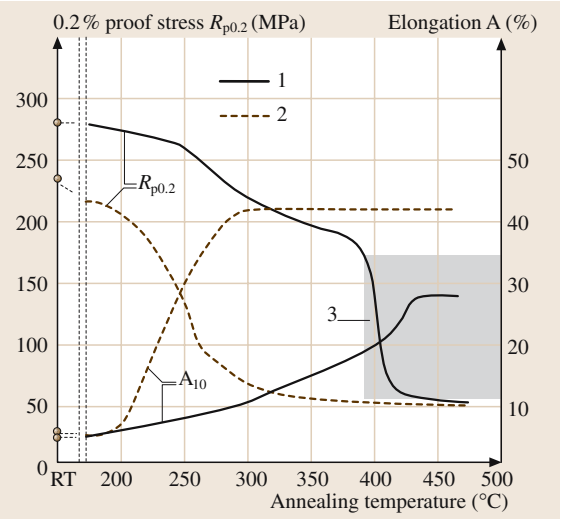


**Fig. 3.1-62** Softening curves for continuously cast and rolled AlMn1 strip after annealing for 4 h at elevated temperatures [1.37,38]: (1) Untreated material, as-cast condition; (2) Homogenised at 540 °C after cold working; (3) Coarse grains

or nonforced air cooling. Al−Mg alloys with more than 4 wt% Mg may have to be stabilized to produce a structure that is not susceptible to intergranular corrosion.

### Stress-Relieving

The temperatures used for thermal stress relief are relatively low, i. e., at the lower end of the recovery range, or even lower, and between 200 and 300 °C for non-age-hardenable alloy castings, otherwise there will be an unacceptably large loss of strength.

### Homogenization

This treatment is used for the elimination of residual casting stresses and segregation, for dissolution of eutectoid components at grain boundaries, or for producing a more uniform precipitation of supersaturated elements (e.g., Mn and Fe). Additionally, the elements which are responsible for hardening in age-hardenable alloys are taken into solid solution. A homogenization is carried out at temperatures which are composition-dependent and close to the solidus temperature of the alloy in question. Long exposure times are required, typically about 10–12 hr but possibly even longer, depending on the relevant diffusion coefficients and microstructure.

### Aging

Age hardening treatments require the three steps of solution treatment, quenching, and aging (Fig. 3.1-63). The purpose of solution treatment is to produce a homogenous $\alpha$-Al solid solution. The annealing temperature is determined by the relevant phase. It should be as high as possible in order to avoid excessively long annealing times, but lower than the solidus of $\alpha$ and the melting point of the lowest melting phase (Table 3.1-16). It should be noted that segregation effects tend to displace the effective phase boundaries to lower temperatures and incipient melting may occur. In addition, the effect of the selected solution treatment temperature on strength levels attained after aging will vary with alloy (Figs. 3.1-64 and 3.1-65). The annealing time depends

**Fig. 3.1-64** Effect of solution treatment temperature on the tensile strength of wrought aluminium alloys [1.9]: AlZnMgCu1.5 (≈ 7075, AlZn5.5MgCu), 24 h at 120 °C; AlCuMg1 [≈ 2017A, AlCu4MgSi(A)], 5 days at room temperature; AlZn4.5Mg1 7020, (≈ AlZn4.5Mhg1), 1 month at room temperature; AlMgSi1 (≈ 6082, AlSi1MgMn), 16 h at 160 °C ▶

**Table 3.1-16** Conditions for aging treatments [a]

| Alloy | Annealing Temperature [b] (°C) | Quenching medium | Natural aging time (d) | Artificial aging Temperature (°C) | Time (h) |
|---|---|---|---|---|---|
| E-AlMgSi | 525–540 | Water | 5–8 | 155–190 | 4–16 |
| AlMgSi0.5 | 525–540 | Air/water | 5–8 | 155–190 | 4–16 |
| AlMgSi1 | 525–540 | Water/air | 5–8 | 155–190 | 4–16 |
| AlMg1SiCu | 525–540 | Water/air | 5–8 | 155–190 | 4–16 |
| AlCuBiPb | 515–525 | Water up to 65 °C | 5–8 | 165–185 | 8–16 |
| AlCuMg1 | 495–505 | Water | 5–8 | [d] | 4[d] |
| AlCuMg2 | 495–505 | Water | | 180–195[d] | 16–24[d] |
| AlZn4.5Mg | 460–485 | Air At least | 90 | I 90–100/ II 140–160[c] | I 8–12/ II 16–24[c] |

[a] Recommendations only; exact specification as per agreement with semi-finishing plant
[b] Metal temperature
[c] Stages I and II of step annealing
[d] Usually only naturally aged

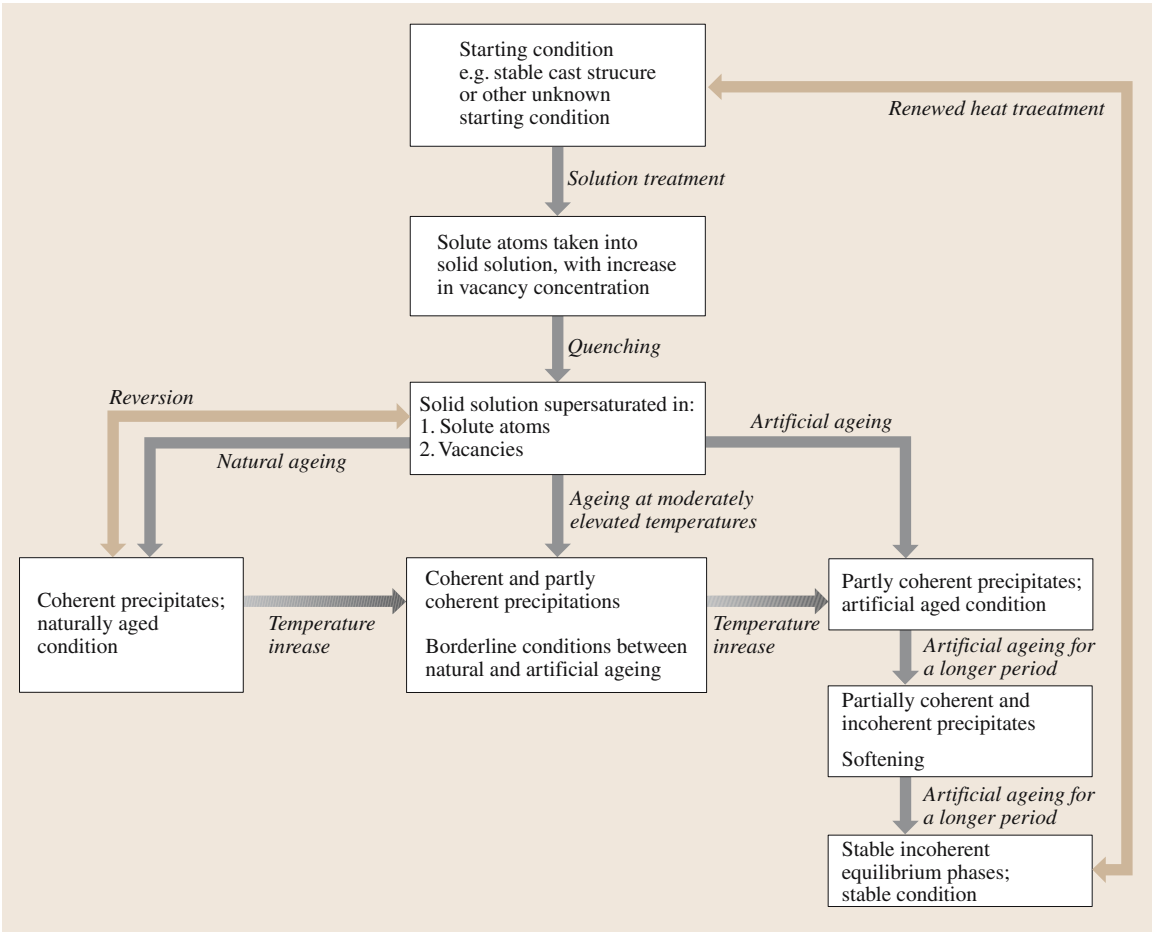


**Fig. 3.1-63** Schematic of the age hardening process

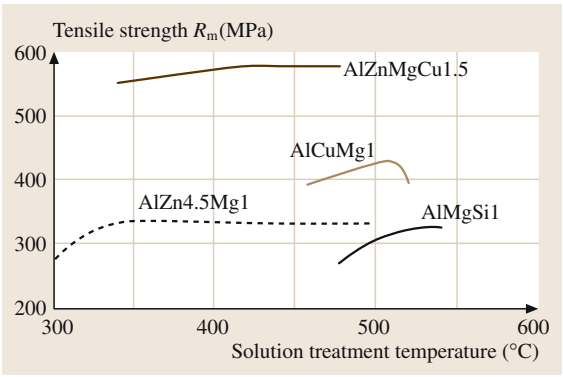


**Fig. 3.1-65** Effect of solution treatment temperature on the mechanical properties of G-AlSi10Mg casting alloy after subsequent aging [≈ 43 000, AlSi10Mg(a)] [1.9] ▶

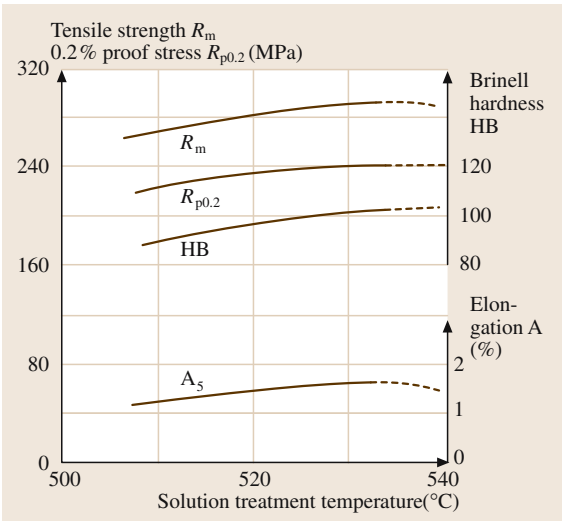

mainly on the initial condition of the semi-finished material, type of semi-finished product, and the wall thickness (Figs. 3.1-66 and 3.1-67).

During quenching, it is important to pass through the temperature range around 200 °C as quickly as possible, in order to prevent premature precipitation of the elements in supersaturated solid solution.

Some alloys require high cooling rates, such as those obtained by quenching in water. For others, especially with thinner sections, cooling in a forced draft of air or a mist spray suffices. In this case, quenching takes place immediately after hot working or even directly in the extrusion press. With most alloys it is important that the annealed material is rapidly transferred to the quenching bath as any delay (incipient cooling) can have a detrimental effect on strength and corrosion resistance.

After the first two stages of the hardening process, the solid solution will be supersaturated in both vacancies and solute atoms. It will tend to attain equilibrium conditions by precipitation of the supersaturated solute atoms. As the process is both temperature- and time-dependent, precipitation is basically possible either by natural or artificial aging, i. e., at room or elevated temperature respectively.

Aging at room temperature, or slightly elevated temperature, is accompanied by the formation of metastable Guinier–Preston zones (GP zones). These metastable phases increase the strength by differing amounts depending on their type, size, volume fraction, and distribution. With fully coherent precipitates, the crystal lattice is strongly strained locally, resulting in a marked increase in hardness and strength, while ductility and electrical conductivity decreases (Figs. 3.1-68 and 3.1-69).

At higher aging temperatures of about 100 °C to 200 °C, metastable phases form that are partially coherent. The local coherency strain is less pronounced

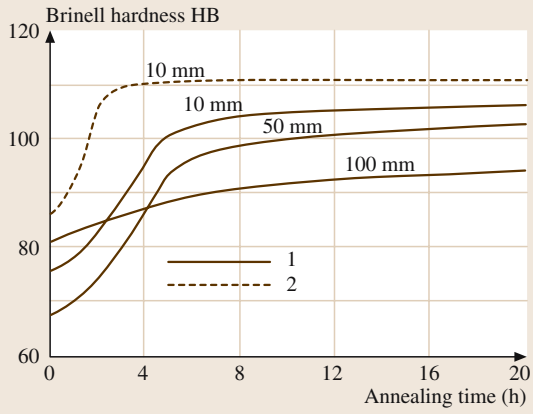


**Fig. 3.1-66** Effect of annealing time on the hardness of artificially aged G-AlSi10Mg casting alloy for different casting techniques and specimen diameters [1.9]: (1) Sand cast; (2) Permanent mould cast

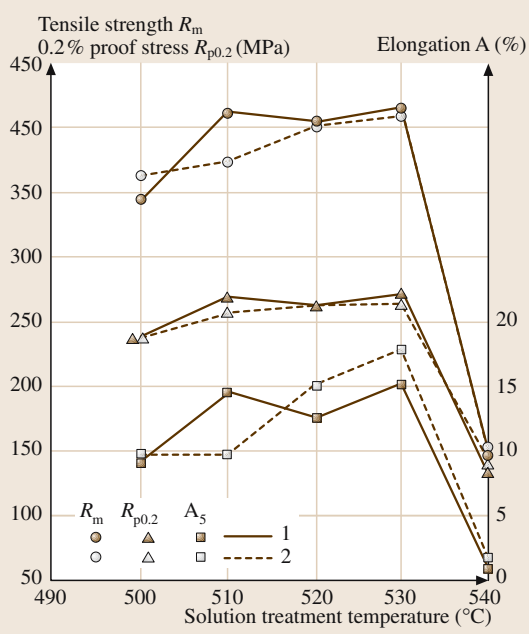


**Fig. 3.1-67** Dependence of mechanical properties of naturally aged G-AlCu4TiMg casting alloy on the maximum solution treatment temperature: (1) Step annealing; (2) Single step annealing

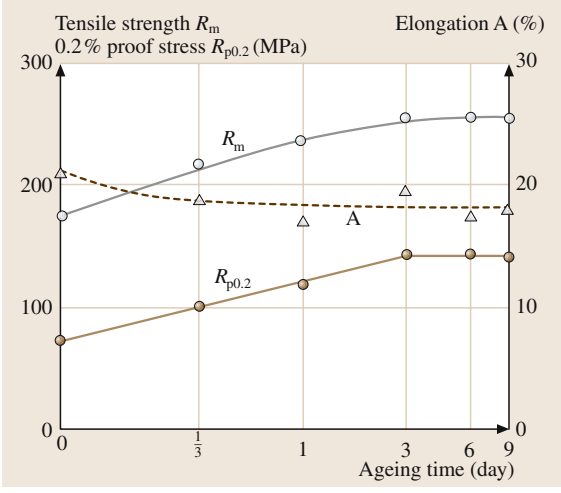


**Fig. 3.1-68** Natural aging of AlMgSi1 alloy [1.39]

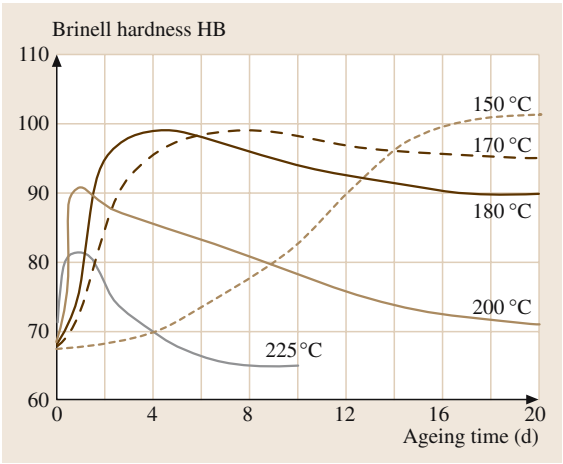


**Fig. 3.1-69** Artificial aging of G-AlSi10Mg casting alloy [1.9]

because the stresses are partly reduced by the formation of interfacial dislocations. This would lead to a lower increase in strength in principle. However, since the particle size of the metastable phases formed in this range is often larger than that of the coherent phases which result from natural aging, there is a marked increase in strength (Figs. 3.1-70 and 3.1-71).

Higher temperatures and longer aging times lead to the formation of incoherent equilibrium phases (e.g., $Al_2Cu$, $Mg_2Si$, and $MgZn_2$) and there is a reduction in the hardening effect. This is called over-aging.

### Effects of Plastic Deformation on Age-Hardening Behavior

For wrought age-hardenable aluminium alloys, the combination of heat treatments with hot and/or cold working (thermo-mechanical treatment) is of great practical significance. It can be a method to obtain a better combination of mechanical properties, such as moderate ductility and higher strength. The effects of thermo-mechanical treatments can be attributed to the fact that all processes occurring during heat treatment are influenced by the concentration of defects introduced during working. It is not necessary to carry out both steps simultaneously; the heat treatment can be carried out after forming [1.40]. As far as precipitation is concerned, lattice defects facilitate diffusion and at the same time act as nucleation sites. Thus, by deforming a material by a certain amount *prior* to aging and thereby obtaining the desired defect concentration, one can influence the size, quantity and distribution of the precipitates that form subsequently. It is important, however, that the

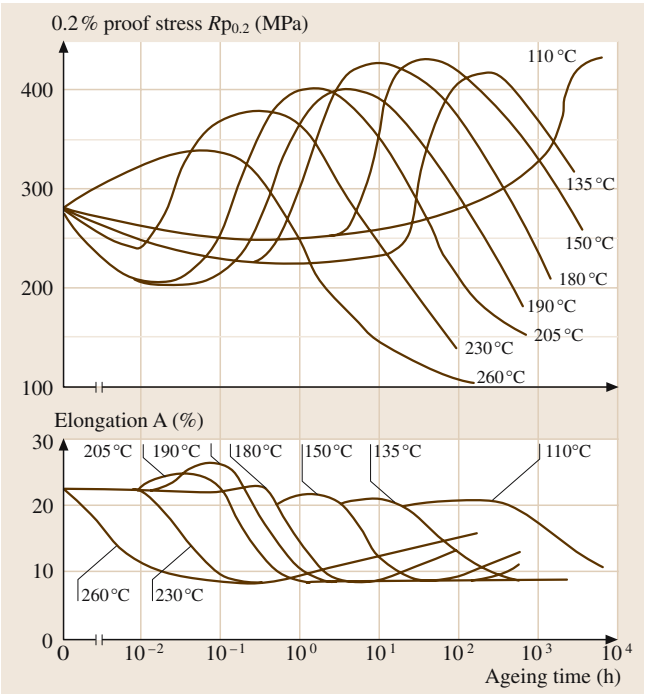


**Fig. 3.1-70** Artificial aging curves for AlCuSiMn alloy [1.9]

final ageing treatment is carried out at a temperature below the recrystallization temperature, as the lattice defect concentration that is generated is fully effective only then.

Controlled hot working, often in combination with additional heat treatments, is another form of thermo-mechanical treatment and is used to improve fracture toughness, creep strength and fatigue strength. One tries to obtain a suitable recrystallized grain size and an optimum distribution of lattice defects and precipitates. Such treatments are very often used with high strength Al−Zn−Mg−Cu alloys. They usually consist of a series of solution treatments with controlled cooling and hot-rolling under well defined conditions. Cold working carried out between the various stages of a step-aging treatment is also referred to as thermomechanical treatment. Examples are shown in Fig. 3.1-72 and Fig. 3.1-73.

### Simultaneous Softening and Precipitation

One of the factors that influence the softening of an alloy is the possible supersaturation by alloying of impurity elements. Supersaturation can be achieved deliberately, e.g., by solution treatment and subsequent quenching, or, as is often the case, it may be the result of rapid cool-

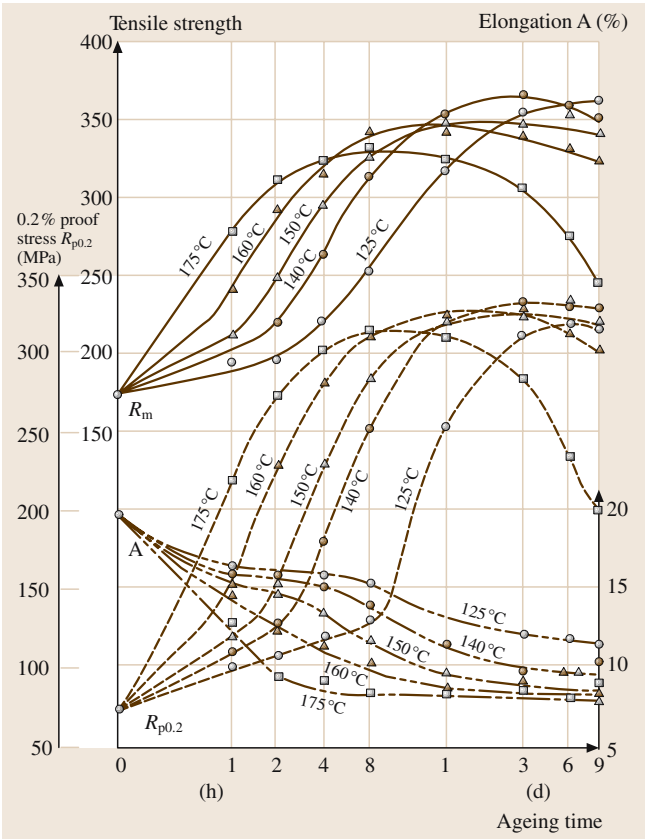


**Fig. 3.1-71** Artificial aging curves for AlMgSi1 alloy after solution treatment at 520 °C and water quenching

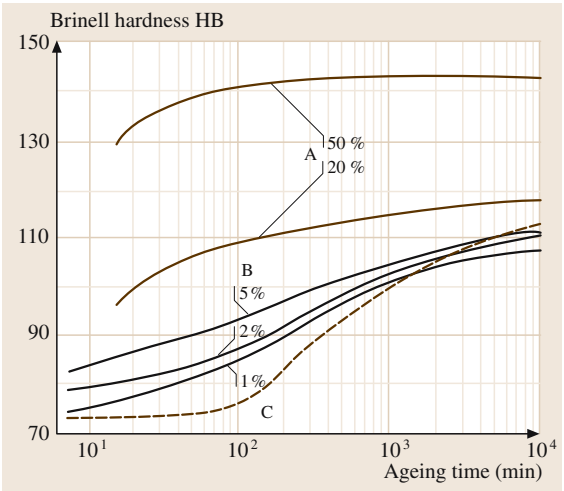


**Fig. 3.1-72** Effect of cold work on the natural aging of AlCuMg1 (2017A) [1.9]; A – Rolled; B – Stretched; C – Without cold work

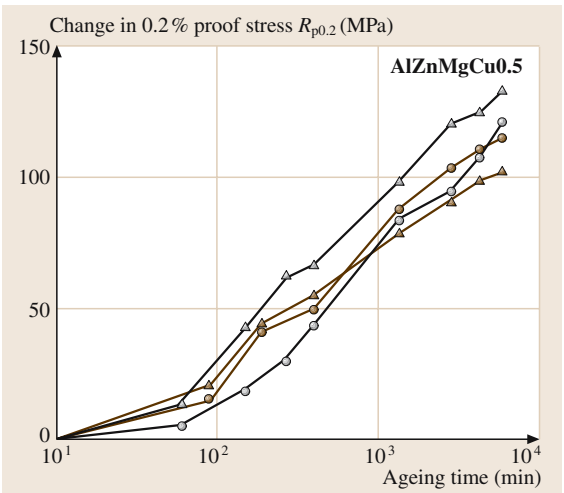


**Fig. 3.1-73** Changes in the 0.2% proof stress during natural aging of 0.5 mm diameter wire specimens AlZnMgCu0.5 (7022) alloys after different degrees of cold working. The alloys were first solution-treated at 490 °C and then immediately subjected to cold working as indicated below [1.41]

ing, e.g., of castings. If such a supersaturated material is cold-worked and then aged, it reveals markedly different softening behavior because solute atom clusters or precipitates are formed during recovery at lattice defects in the deformed or recovered structure which pin lattice defects and the formation of solute atom clusters or of precipitates during recrystallization at the recrystallization front, which pin down the recrystallization front. There is a slowing down of the softening process as a result of these pinning effects (Figs. 3.1-74a and 3.1-74b).

The Stage III area in Fig. 3.1-74b is of particular interest, as by definition this is a thermomechanical treatment because the lattice defects introduced by working are fully effective during the formation of the precipitates. Dislocations, which are present in large quantities, act as nuclei for precipitation and this results in the formation of numerous finely-dispersed precipitates. These impair subsequent recrystallization at every stage – the formation of recrystallization nuclei, the moving of boundaries and the subsequent grain growth. These effects increase the thermal resistance and delay the loss of strength that occurs after prolonged exposure because of grain growth. The Figs. 3.1-77 to 3.1-79 show some examples of TTT-Diagrams for unalloyed aluminium and for alloys.

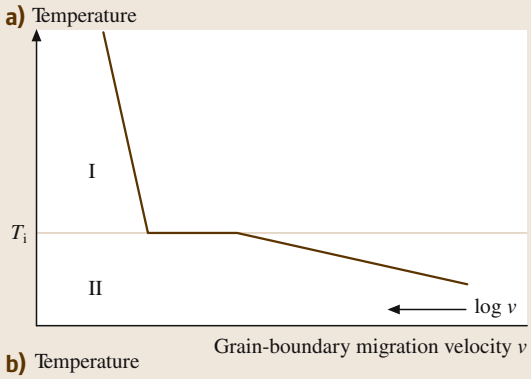


**Fig. 3.1-74a,b** Effect of segregation and precipitation on recrystallization (grain-boundary migration): (1) Start of recrystallization; (2) Start of precipitation. **(a)** Basic effects of solute atom clusters on the grain boundary migration velocity [1.42]. Region I, high temperatures: The grain boundary migration velocity is only weakly dependent on temperature because it is unaffected by the clustering (→ high velocity). Region II: Below $T_i$, the mobility of the boundaries is reduced because atom clusters have to be dragged along by the boundary, and the diffusion rate of these atoms determines the migration velocity of the boundary (→ low velocity). **(b)** Interrelationship between recrystallization and precipitation as TTT (time-temperature-transformation) diagram [1.43]. Region I: Recrystallization as a homogenous stable solid solution, unaffected by precipitation processes, i. e., at these temperatures there is no longer any supersaturation. Region II: Recrystallization in a supersaturated solid solution; the number of potential precipitation nuclei (dislocations) decreases. Result: Fewer but larger precipitations. Region III: Precipitation prior to recrystallization, or simultaneously ($T_i$) the precipitates delay recrystallization significantly

**Fig. 3.1-77** TTT diagram for Al-0.5 wt%Fe-0.15 wt% Si alloy Harvey cast strip after 80% cold work [1.45] (1) Start of precipitation; (2) Recrystallization zone

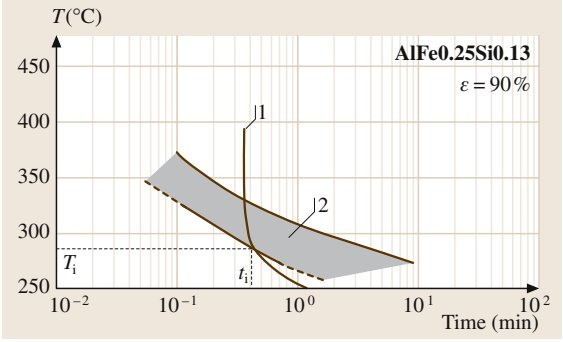


**Fig. 3.1-75** TTT diagram for Al-0.25 wt% Fe-0.13 wt% Si alloy Hunter-Engineering cast strip after 90% cold work [1.35]. (1) First signs of precipitation; (2) Recrystallization zone

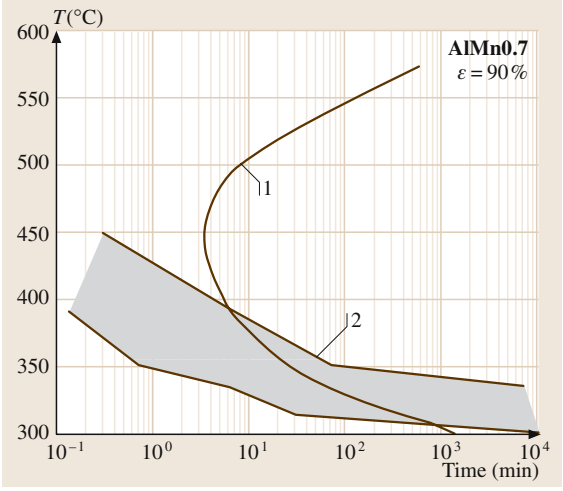


**Fig. 3.1-76** TTT diagram showing precipitation and recrystallization in 90% cold-rolled, high-purity AlMn0.7 alloy, strip produced by permanent mould casting, hot-rolling, and then cold-rolling [1.44]. (1) Start of precipitation; (2) Recrystallization zone

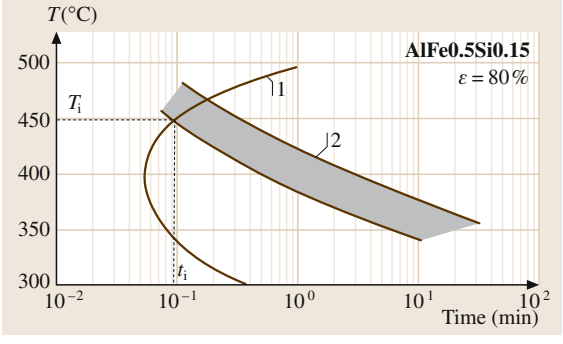

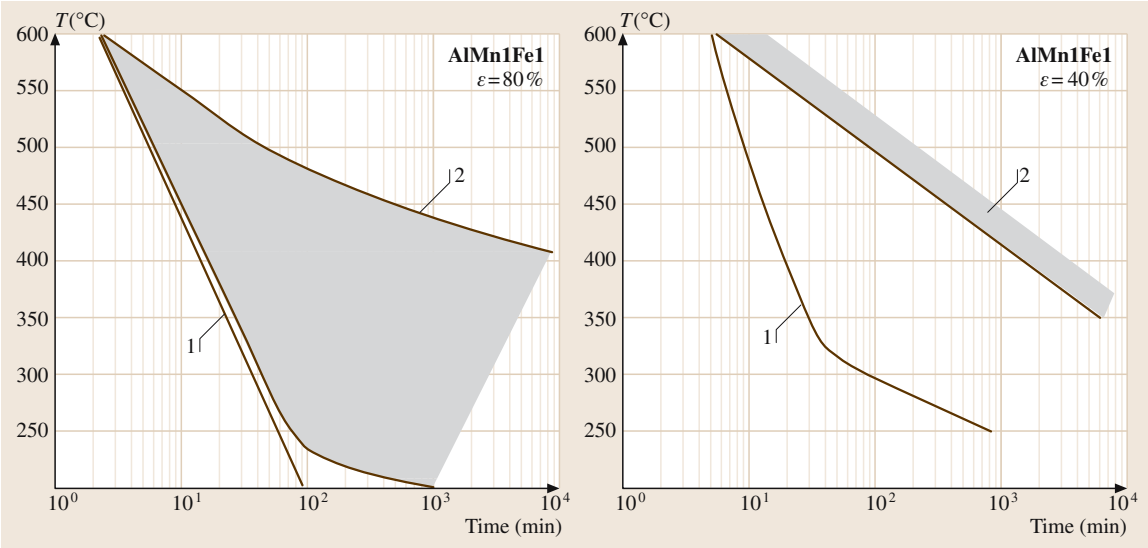


**Fig. 3.1-79a,b** TTT diagrams for precipitation and recrystallization in commercially pure AlMn1Fe1 (0.16 wt% Si), Hunter-Engineering cast strip after varying degrees of cold-rolling [1.49]. (1) Start of precipitation; (2) Recrystallization zone. **(a)** 90%. **(b)** 40%

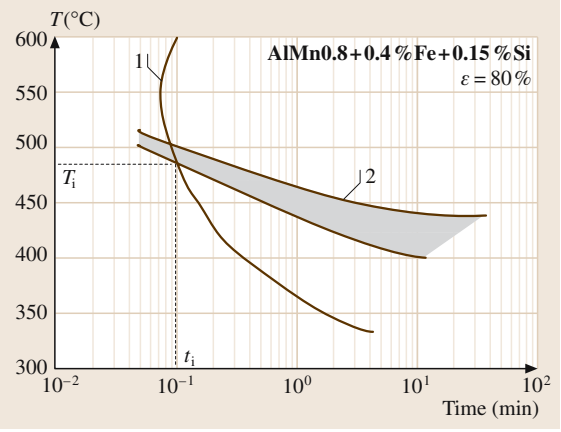


**Fig. 3.1-78** TTT diagram showing precipitation and recrystallization in commercially pure AlMn0.8 alloy strip (0.4 wt% Fe and 0.15 wt% Si) produced by strip casting and 85% cold-rolled [1.46–48]. (1) Start of precipitation; (2) Recrystallization zone

## 3.1.2.11 Corrosion Behavior of Aluminium

From a thermodynamic point of view, aluminium would have to react with water to form hydrogen. However, Al and Al alloys have proven to be very corrosion-resistant in a wide range of practical applications. This corrosion resistance is attributable to the reaction of Al with oxygen or water vapor and the formation of a thin but compact natural oxide film when it is exposed to air, i. e. Al is passivated. In contrast to the oxide layers formed on many other materials, this oxide layer is strongly adherent and thus protects the underlying metal against further oxidation. This property explains the good resistance of aluminium when exposed to the weather or a large number of organic and inorganic substances. The corrosion resistance can be increased further by various surface treatments.

Aluminium and all standardized aluminium alloys are non-toxic. Aluminium products are easy to clean, can be sterilized and meet all hygienic and antitoxic requirements.

### Surface Layers

Aluminium and Al alloys react with oxygen and water vapor in the air to produce a thin, compact surface oxide film which protects the underlying metal from further attack (Fig. 3.1-80). The surface layer contains mainly amorphous $Al_2O_3$ in several layers. The so-called barrier layer has an extremely low conductivity for electrons and ions and thus acts as an insulator in any interfacial electrochemical reactions. It thus affords effective protection against corrosion. If mechanical damage of the protective layer occurs, or if the layer is removed by pickling, it re-forms immediately. Aluminium and Al alloys thus exhibit good corrosion resistance to chemicals, seawater, and the weather.

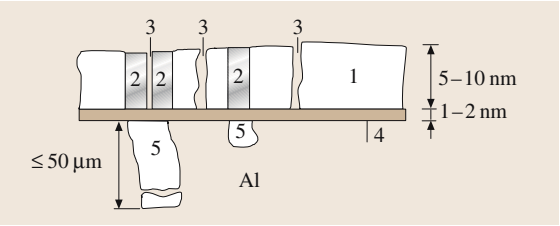


**Fig. 3.1-80** Schematic representation of the structure of the oxide film formed on unalloyed aluminium in dry air; the total thickness is typically 0.005 to 0.02 mm [1.50]. Al = Aluminium; 1 = Surface layer; 2 = Mixed oxides; 3 = Pores; 4 = Barrier layer; 5 = Heterogeneous components

The oxide film which forms on bare aluminium in dry air at room temperature grows to a thickness of a few µm in a few minutes. It then grows to about two or three times this thickness in a few days at a continuously decreasing rate, so-called self-protection. Higher temperatures, such as those during heat treatments, accelerate the rate of growth of the natural oxide layer and lead to the growth of thicker films (Fig. 3.1-81). In moist air, the oxide films grow rapidly at first but then more slowly, and they are markedly thicker than the films formed in dry air.

The composition of the atmosphere has a significant effect on the behavior of the oxide layer. The aggressiveness of the atmosphere is particularly dependent on the amounts of sulfur dioxide, sulfur trioxide, dust, soot, and salts present. Rain water hitting the surface and running off flushes away these substances and thus reduces their influence.

Tap water or natural waters cause growth of the outer layer on top of the barrier layer of the oxide. The growth will depend on the alloy composition, the nature of the water and temperature. In aggressive waters, especially those containing chlorides and heavy metals, pitting corrosion can occur if oxygen from the air or other oxidizing media are introduced into the water. Traces of Cu (from copper piping or fittings containing copper) are particularly aggressive. Copper ions enter the oxide layer on the aluminium surface via defects and precipitate out as metallic Cu. Copper then acts as a cathode in the resulting local galvanic element such that Al is dissolved anodically.

### Corrosion

If Al is exposed to acids or bases these dissolve the oxide film. The pH value of the electrolyte strongly influences corrosion in aqueous media. The protective film on aluminium is practically insoluble in the pH range from 4.5

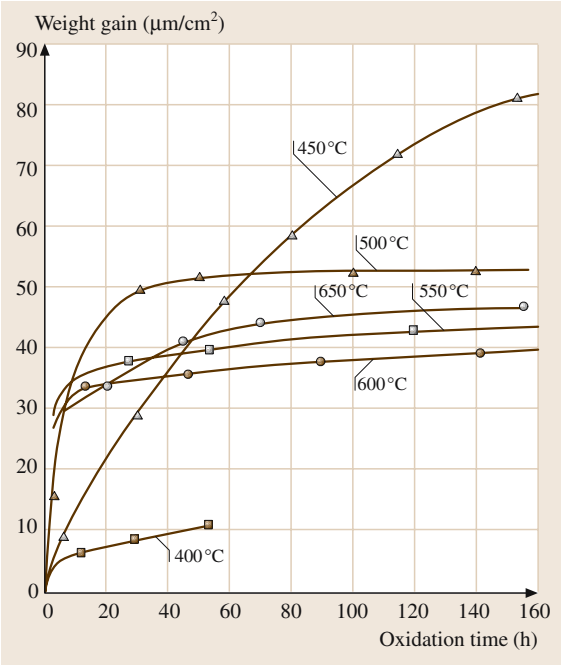


**Fig. 3.1-81** Growth of the oxide film on super-purity aluminium in dry oxygen during the first 160 h [1.22]

to 8.5, which explains why aluminium is usually only used in this range.

Aluminium alloys have heterogeneous microstructural components such as intermetallic phases and resulting oxides in the surface and barrier layers. This explains why unalloyed aluminium and aluminium alloys have lower corrosion resistance than high-purity aluminium.

Apart from the effects of alloying and impurities, there are some other factors affecting corrosion, for example, changes in microstructure by thermal or mechanical treatments and ensuing changes of the surface condition.

Corrosion protection covers any measure aimed at modifying a corrosion system in order to mitigate corrosion damage. This can involve influencing the properties of the metal or the corrosive medium, or separating the metal from the medium by the use of protective layers. One can differentiate between active and passive measures. Passive measures, such as the use of organic polymer coatings (paints), will provide temporary protection, the level of which will depend on the nature, thickness, and quality of the layer. Active measures, such as the use of sacrificial magnesium or zinc anodes, offer long-term protection.

## 3.1.3 Titanium and Titanium Alloys

Titanium and its alloys are used as technical materials mainly because of the low density ($\varrho = 4.5\,\mathrm{g\,cm^{-3}}$) of Ti at technically useful levels of mechanical properties, and the formation of a passivating, protective oxide layer in air, which leads to a pronounced stability in corrosive media and at elevated temperatures. Further useful properties to be noted are its paramagnetic behavior, low temperature ductility, low thermal conductivity ($\kappa = 21\,\mathrm{W\,m^{-1}\,K^{-1}}$), low thermal expansion coefficient ($\lambda = 8.9\times10^{-6}\,\mathrm{K^{-1}}$), and its biocompatibility which is essentially due to its passivating oxide layer.

Five groups of materials based on Ti may be distinguished [1.51–53]: commercially pure (i. e., commercially available) Ti (cp-Ti), low-alloy Ti materials, Ti-base alloys, intermetallic Ti-Al materials, and highly alloyed functional materials: TiNi shape memory alloys, Nb–Ti superconducting materials (Sect. 4.2.1), and Ti-Fe-Mn materials for hydrogen storage.

Titanium undergoes a structural phase transformation at 882 °C. Like in steels, this transformation is crucial for the microstructural design and the mechanical properties of Ti-based alloys. The low temperature phase $\alpha$-Ti has an almost close packed hexagonal (A3) structure that is somewhat compressed along the $c$ axis. Its lattice parameters are $c = 0.4679$ nm and $a = 0.2951$ nm at room temperature. The high-temperature phase $\beta$-Ti has a body-centered cubic (A2) structure. The lattice parameter of $\beta$-Ti at room temperature can be obtained as $a = 0.3269$ nm by extrapolation from alloy solid solutions.

The binary phase diagrams of Ti [1.54] indicate that several interstitial components such as O, N, C, and H form extended solid solutions with $\alpha$-Ti. As an example Fig. 3.1-82 shows the Ti-rich part of the Ti–O phase diagram. The high local lattice strains caused by the interstitial atoms lead to pronounced solid solution strengthening which is exploited, in particular, to harden commercially pure Ti by O additions. On average, the interstitials lead to a pronounced elongation of both the $a$ and $c$ axes of the $\alpha$-Ti lattice, as shown in Fig. 3.1-83.

Figure 3.1-84 shows the influence of the concentration of residual impurity elements O, N, C, Fe, and Si on the increase of hardness HB.

Commercially pure grades of Ti, cp-Ti, are produced via the reduction of $TiCl_4$ by Mg (Kroll process). The product is Ti sponge. Table 3.1-17 gives typical concentration levels of the main impurity components and corresponding hardness values of the Ti sponge. Impu-

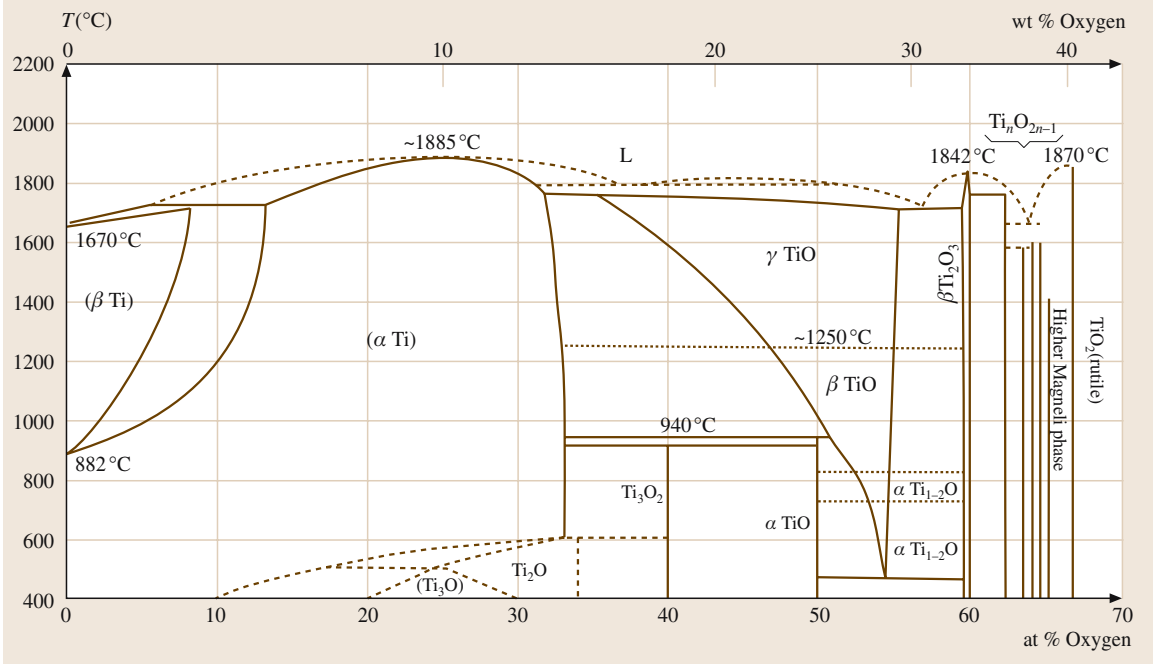


**Fig. 3.1-82** Ti−O phase diagram

**Table 3.1-17** Chemical composition of titanium sponge [1.53]

| Reduction process/ element | (wt%) | | | | | | | | Maximum hardness (HB) |
|---|---|---|---|---|---|---|---|---|---|
| | C | N | O | H | Fe | Mg | Na | Cl | |
| Magnesium | 0.006 | 0.003 | 0.045 | 0.002 | 0.02 | 0.03 | | 0.10 | 95 |
| | 0.008 | 0.005 | 0.05 | 0.002 | 0.04 | | | 0.09 | 100 |
| | 0.008 | 0.005 | 0.06 | 0.002 | 0.05 | 0.03 | | 0.08 | 110 |
| | 0.008 | 0.005 | 0.07 | 0.002 | 0.06 | 0.03 | | 0.09 | 120 |
| Sodium electrolysis | 0.009 | 0.004 | 0.07 | 0.01 | 0.016 | | 0.08 | 0.13 | 120 |
| | 0.003 | 0.002 | 0.01 | 0.003 | 0.001 | | | 0.08 | 60 |
| | 0.013 | 0.004 | 0.03 | 0.004 | 0.004 | | | 0.09 | 75 |
| | 0.018 | 0.004 | 0.04 | 0.004 | 0.020 | | | 0.16 | 90 |

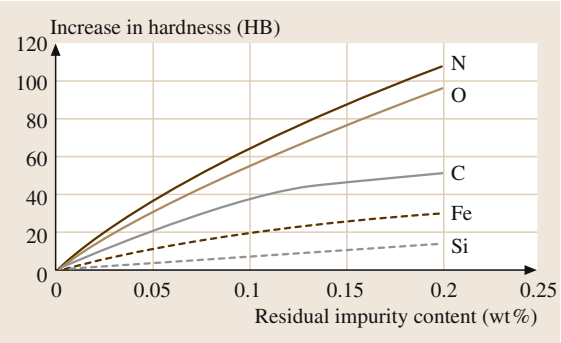


**Fig. 3.1-84** Increase of hardness HB of Ti as a function of concentration of residual impurities O, N, C, Fe, and Si

rity levels resulting from earlier reduction processes by Na and electrolysis are also listed. The concentration of the residual content of the reducing elements Mg, Na, and their chlorides is lowered by the subsequent melting processes. High purity levels (5N) of Ti can be obtained by the iodide reduction process. These grades are used for electronic devices.

### 3.1.3.1 Commercially Pure Grades of Ti and Low-Alloy Ti Materials

Materials designated as commercially pure grades of Ti are interstitial solid solutions of O, N, C, and H in Ti. Oxygen is the only element added deliberately for solid solution strengthening. The other interstitial solutes are impurities resulting from the production process as indicated. Table 3.1-18 shows the chemical compositions and mechanical properties of commercially pure grades of Ti. The temperature dependence of their mechanical properties is shown in Fig. 3.1-85. Low-alloy Ti materials containing Pd, Ru, and Ni + Mo, respectively, are providing increased corrosion resistance at

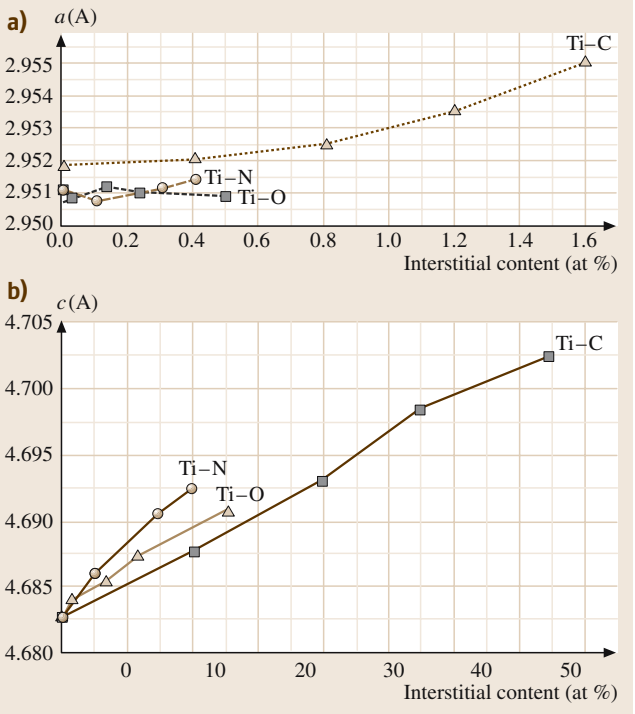


**Fig. 3.1-83a,b** Lattice parameters $a$ (**a**) and $c$ (**b**) of $\alpha$-Ti as a function of interstitial content

identical levels of mechanical properties as those of the corresponding cp-Ti grades. The compositions and mechanical properties of typical alloys are also shown in Table 3.1-18. All commercially pure and low-alloy Ti materials may be strengthened by cold work. The tensile strength $R_m$ is about doubled by cold work, which amounts to 80 to 90% reduction in area, and the fracture strain $A_5$ and the reduction in area are about halved.

**Table 3.1-18** Chemical composition (maximum contents) and mechanical properties of commercially pure and low-alloy grades of Ti

| O wt% | Tensile strength $R_m$ (MPa) | Yield strength $R_{p0.2}$ (MPa) | Fracture strain $A_{10}$ (%) | Standard grade [a] cp | Standard grade [a] low alloyed |
|---|---|---|---|---|---|
| 0.12 | 290–410 | > 180 | > 30 | Grade 1 | Pd: grade 11 |
| 0.18 | 390–540 | > 250 | > 22 | Grade 2 | Pd: grade 7<br>Ru: grade 27 |
| 0.25 | 460–590 | > 320 | > 18 | Grade 3 | Ru: grade 26 |
| 0.35 | 540–740 | > 390 | > 16 | Grade 4 | |
| 0.25 | > 480 | > 345 | > 18 | | Ni+Mo: grade 12 |

[a] ASTM B265, ed. 2001; $N_{max}$: 0.03 wt%; $C_{max}$: 0.08 wt%; $H_{max}$: 0.015 wt%

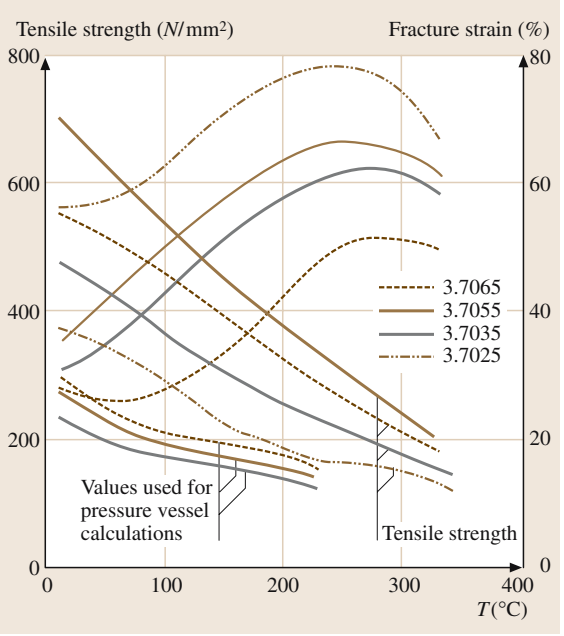


**Fig. 3.1-85** High-temperature tensile strength and fracture strain of titanium, and values used for titanium pressure vessel calculations (105 h)

Most applications of cp-Ti and low-alloy Ti materials are based on their high corrosion resistance, such as components in chemical plants, heat exchangers, offshore technology, seawater desalination plants, Ni winning, electroplating plants, medical applications such as heart pacer casings, surgical implants including ear implants [1.55], and automotive applications. Applications of unalloyed Ti in architecture and jewellery are based on coloring the surface by oxide growth upon heat treatment in air. Unalloyed Ti grades are, also, applied at elevated temperature because of their favorable mechanical properties and oxidation resistance at high temperature. Figure 3.1-86 shows the creep date for grade 4 Ti.

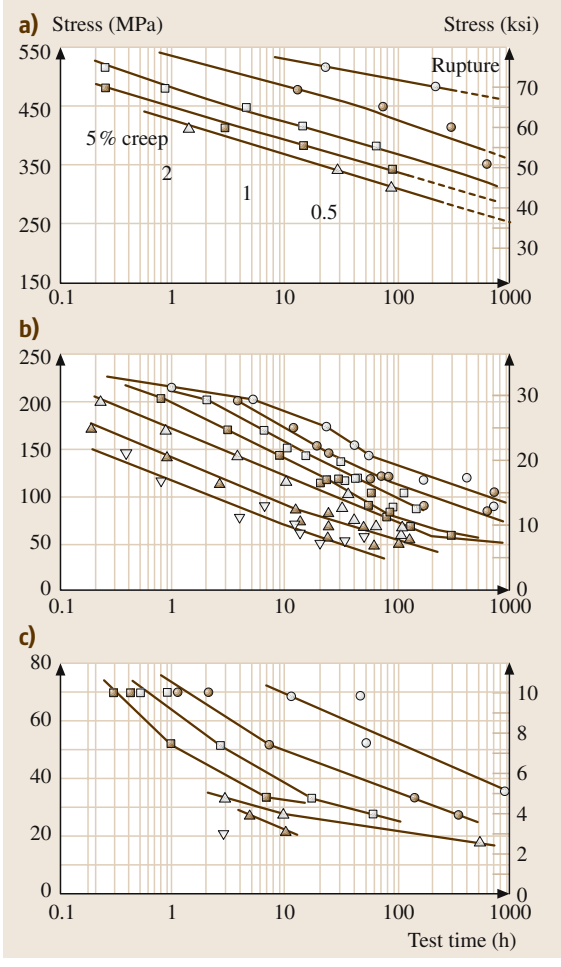


**Fig. 3.1-86a–c** Creep behavior of commercially pure Ti grade 4, mill annealed with a minimum yield stress of 480 MPa [1.56]. **(a)** 25 °C; **(b)** 425 °C; **(c)** 540 °C

### 3.1.3.2 Ti-Based Alloys

Alloying elements are added to Ti to improve its mechanical properties. Based on the phase transformation of pure Ti, alloying elements influence the phase equilibria and, thus, the transformations and the resulting microstructural states. The phase composition of the microstructure may be varied from pure $\alpha$ through $(\alpha + \beta)$ to pure $\beta$, depending on the alloy content [1.54]. The $\alpha$ phase is stabilized by O, N, C, and Al. The $\beta$ phase range is expanded by H, V, Mo, Fe, Cr, Cu, Pd, and Si. High solubility in $\alpha$ and $\beta$ is exhibited by Zr and Sn. The alloy variants are characterized by the phases present in the annealed state at room temperature, as shown in Table 3.1-19. Alloys consisting partially or fully of the $\beta$ phase are more easily deformed because of the larger number of slip systems in the bcc structure of the $\beta$ phase compared to those in the hcp $\alpha$ phase. The alloying elements provide, also, solid solution strengthening. A further increase in yield strength may be attained by quenching and aging of $\beta$-phase alloys which leads to the coherent precipitation of the $\alpha$ and $\omega$ phases. However, the strength increase is moderate (10–20%) compared to that caused by precipitation hardening effects in Al and Cu-based alloys.

Based on their high specific strength, Ti alloys are widely used in aerospace applications, furthermore for high-speed moving parts, corrosion resistant pressure vessels and pipes, and for sports gear. The high-temperature strength has been increased by alloying for elevated temperature applications, as shown in Table 3.1-20. The densely packed hcp structure of the $\alpha$ phase is more creep-resistant than the more open bcc structure of the $\beta$ phase. Accordingly the creep strength of the $\alpha$- and near-$\alpha$-phase alloys is clearly higher than that of $\alpha + \beta$-phase alloys, as shown in Fig. 3.1-87.

Titanium alloys may be processed like stainless steel. This leads to a cost effective production of a wide range of semi-finished and finished products and parts. If the tendency to oxidation and welding above approximately 350 °C and the low thermal conductivity are taken into account, parts can be manufactured from Ti alloys, quite similar to manufacturing from stainless steels. A wide variety of working, joining, and coating processes is well established.

**Table 3.1-19** Chemical composition and mechanical properties of Ti-base alloys at room temperature (minimum values)

| Alloy composition [a] | Alloy type | Tensile strength $R_m$ (MPa) | Yield strength $R_{p0.2}$ (MPa) | Density $\varrho$ (g/cm$^3$) | Young's modulus $E$ (GPa) | Main property | Standard grade [b] |
|---|---|---|---|---|---|---|---|
| Ti5Al2.5Sn | $\alpha$ | 830 | 780 | 4.48 | 110 | High strength | |
| Ti6Al2Sn4Zr2MoSi | near $\alpha$ | 900 | 830 | 4.54 | 114 | High-temperature strength | 3.7145 |
| Ti6Al5Zr0.5MoSi | near $\alpha$ | 950 | 880 | 4.45 | 125 | High-temperature strength | 3.7155 |
| Ti5.8Al4Sn3.5Zr0.7Nb 0.5Mo0.2Si0.05C | near $\alpha$ | 1030 | 910 | 4.55 | 120 | High-temperature strength | |
| Ti6Al4V | $\alpha + \beta$ | 900 | 830 | 4.43 | 114 | High strength | |
| Ti4Al4Mo2Sn | $\alpha + \beta$ | 1100 | 960 | 4.60 | 114 | High strength | 3.7185 |
| Ti6Al6V2Sn | $\alpha + \beta$ | 1030 | 970 | 4.54 | 116 | High strength | 3.7175 |
| Ti10V2Fe3Al | near $\beta$ | 1250 | 1100 | 4.65 | 103 | High strength | |
| Ti15V3Cr3Sn3Al | $\beta$ | 1000 | 965 | 4.76 | 103 | High strength; cold formability | |
| Ti3Al8V6Cr4Zr4Mo | $\beta$ | 1170 | 1100 | 4.82 | 103 | High corrosion; resistance | |
| Ti15Mo3Nb3AlSi | $\beta$ | 1030 | 965 | 4.94 | 96 | High corrosion; resistance | |

[a] Figure before chemical symbol denotes nominal wt%

[b] according to DIN 17851, ASTM B 265 ed. 2001

**Table 3.1-20** Upper temperature limit for Ti alloys developed for elevated-temperature applications

| Alloy | Alloy type | Year of introduction | Useful maximum °C |
|---|---|---|---|
| Ti-6Al-4V (Ti-64) | $\alpha+\beta$ | 1954 | 300 |
| Ti-4Al-2Sn-4Mo-0.5Si (IMI-550) | $\alpha+\beta$ | 1956 | 400 |
| Ti-8Al-1Mo-1V (Ti-811) | near-$\alpha$ | 1961 | 425 |
| Ti-2Al-11Sn-5Zr-1Mo-0.2Si (IMI-679) | near-$\alpha$ | 1961 | 450 |
| Ti-6Al-2Sn-4Zr-6Mo (Ti-6246) | $\alpha+\beta$ | 1966 | 450 |
| Ti-6Al-2Sn-4Zr-2Mo (Ti-6242) | near-$\alpha$ | 1967 | 450 |
| Ti-3Al-6Sn-4Zr-0.5Mo-0.5Si (Hylite 65) | near-$\alpha$ | 1967 | 520 |
| Ti-6Al-5Zr-0.5Mo-0.25Si (IMI-685) | near-$\alpha$ | 1969 | 520 |
| Ti-5Al-5Sn-2Zr-2Mo-0.2Si (Ti5522S) | near-$\alpha$ or $\alpha+\beta$ | 1972 | 520 |
| Ti-6Al-2Sn-1.5Zr-1Mo-0.1Si-0.3Bi (Ti-11) | near-$\alpha$ | 1972 | 540 |
| Ti-6Al-2Sn-4Zr-2Mo-0.1Si (Ti-6242S) | near-$\alpha$ | 1974 | 520 |
| Ti-5Al-5Sn-2Zr-4Mo-0.1Si (Ti-5524S) | near-$\alpha$ or $\alpha+\beta$ | 1976 | 500 |
| Ti-5.5Al-3.5Sn-3Zr-0.3Mo-1Nb-0.3Si (IMI-829) | near-$\alpha$ | 1976 | 580 |
| Ti-5.5Al-4Sn-4Zr-0.3Mo-1Nb-0.5Si-0.06C (IMI-834) | near-$\alpha$ | 1984 | 590 |
| Ti-6Al-2.75Sn-4Zr-0.4Mo-0.45Si (Ti-1100) | near-$\alpha$ | 1987 | 590 |
| Ti-15Mo-3Al-2.75Nb-0.25Si (Beta-21S) | $\beta$ | 1988 | 590 |

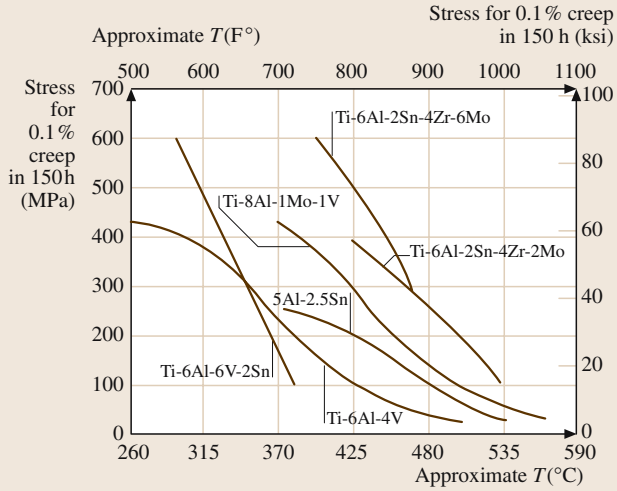


**Fig. 3.1-87** Creep strength for $\alpha$ (Ti-5Al-2.5Sn), near-$\alpha$ (Ti-8Al-1Mo-1V and Ti-6Al-2Sn-4Zr-2Mo), and $\alpha+\beta$ (Ti-6Al-4V and Ti-6Al-2Sn-4Zr-6Mo) alloys

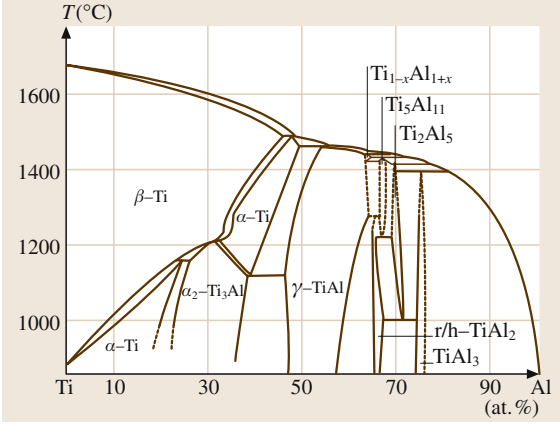


**Fig. 3.1-88** Ti−Al phase diagram

### 3.1.3.3 Intermetallic Ti–Al Materials

The intermetallic compounds $Ti_3Al$ and TiAl are studied for high-temperature materials developments. Extensive accounts [1.52, 57] are the sources of the data presented here. In Table 3.1-21 the property ranges of $Ti_3Al$- and TiAl-based alloys are compared to those of conventional Ti alloys and Ni-based superalloys.

Various versions of the binary Ti–Al phase diagram are available [1.54] and are still under discussion because of conflicting results. The phase diagram shown in Fig. 3.1-88 incorporates recent results.

#### $Ti_3Al$-Based Alloys

Various $Ti_3Al$-based alloys have been developed with niobium as a major alloying element and further components for obtaining an optimised balance of strength, formability, toughness, and oxidation resistance. The alloys are two-phase or three-phase. Current $Ti_3Al$-based alloys with engineering significance are listed in Table 3.1-23.

**Table 3.1-21** Properties of alloys based on the titanium aluminides $Ti_3Al$ and TiAl [1.50] and of conventional titanium alloys and nickel based superalloys

| Property | Ti-based alloys | $Ti_3Al$-based intermetallic materials | TiAl-based intermetallic materials | Ni-based superalloys |
|---|---|---|---|---|
| Structure | A3/A2 | $D0_{19}$/A2/B2 | $L1_0/D0_{19}$ | $A1/L1_2$ |
| Density ($g/cm^3$) | 4.5–4.6 | 4.1–4.7 | 3.7–3.9 | 7.9–9.1 |
| Thermal conductivity (W/m K) | 21 | 7 | 22 | 11 |
| Young's modulus at room temperature ($GN/m^2$) | 95–115 | 100–145 | 160–180 | 195–220 |
| Yield strength at room temperature ($MN/m^2$) | 380–1150 | 700–990 | 400–650 | 250–1310 |
| Tensile strength at room temperature ($MN/m^2$) | 480–1200 | 800–1140 | 450–800 | 620–1620 |
| Temperature limit due to creep (°C) | 600 | 760 | 1000 | 1090 |
| Temperature limit due to oxidation (°C) | 600 | 650 | 900 | 1090 |
| Tensile strain to fracture at room temperature (%) | 10–25 | 2–26 | 1–4 | 3–50 |
| Tensile strain to fracture at high temperature (%) | 12–50 | 10–20 | 10–60 | 8–125 |
| Fracture toughness $K_{Ic}$ at room temperature ($MN/m^{3/2}$) | High | 13–42 | 10–20 | 25 |

**Table 3.1-22** Crystal structure data

| Phase designation | Composition | Strukturbericht designation (prototype) |
|---|---|---|
| $\alpha$-Ti(Al) | 0–45 at.% Al | A3 (Mg) |
| $\beta$-Ti(Al) | 0–47.5 at.% Al | A2 (W) |
| $\beta_1$ | | B2 (CsCl) |
| $\alpha_2$-$Ti_3Al$ | 22–39 at.% Al | $DO_{19}$ ($Ni_3Sn$) |
| $\gamma$-TiAl | 48–69.5 at.% Al | $L1_0$ (AuCu) |
| O | $Ti_2AlNb$ | |
| $\omega$ | $Ti_4Al_3Nb$ | $B8_2$ |

**Table 3.1-23** Major $Ti_3Al$-based alloys [1.50]

| Alloy composition (at.%) | Phases | Designation |
|---|---|---|
| Ti-24Al-11Nb | $\alpha_2+\beta$ | 24-11 |
| Ti-25Al-11Nb | $\alpha_2+\beta$ | 25-11 |
| Ti-25Al-8Nb-2Mo-2Ta | $\alpha_2+\beta$ | 8-2-2 |
| Ti-25Al-16Nb | $\alpha_2+\beta+O$ | 25-16 |
| Ti-25Al-17Nb | $\alpha_2+\beta+O$ | 25-17 |
| Ti-27Al-15Nb | $\alpha_2+\beta+O$ | 27-15 |
| Ti-27Al-15Nb-1Mo | $\alpha_2+\beta+O$ | 27-15-1 |
| Ti-22Al-17Nb-1Mo | $\alpha_2+\beta+O$ | 22-17-1 |
| Ti-25Al-17Nb-1Mo | $\alpha_2+\beta+O$ | 25-17-1 |
| Ti-25Al-10Nb-3V-1Mo | $\alpha_2+\beta+O$ | 10-3-1 |
| Ti-25Al-24Nb | $O+\beta$ | 25-24 |
| Ti-22Al-27Nb | $O+\beta$ | 22-27 |
| Ti-30Al-20Nb | $O+\omega$ | 30-20 (1986) |
| SCS/6Ti-24Al-11Nb | $\alpha_2+\beta+SiC$ | SCS-6/24-11 |
| Alloy 24-11 and alloy 10-3-1 have already been produced on a production mill scale. | | |

*Mechanical Properties.* The elastic properties of selected alloys are presented in Table 3.1-24. Strength, ductility, and toughness of the $Ti_3Al$-based alloys are sensitive functions of both composition and microstructure which are controlled by prior processing. Characteristic data are shown in Table 3.1-25 for various alloys. Different property data for the same alloy composition indicate the effect of different prior thermomechanical treatments. The effect of microstructure on toughness is exemplified by Table 3.1-26. Particularly high strengths can be obtained in intermetallic $Ti_3Al$-based matrix composites.

**Table 3.1-26** Effect of microstructure variation on fracture toughness $K_{Ic}$ at room temperature for a Ti-25Al-10Nb-3V-1Mo alloy

| Microstructure | $K_{Ic}$ [MPa m$^{1/2}$] |
|---|---|
| Coarse globular | 11 |
| Fine globular | 10 |
| Coarse bimodal | 11 |
| Fine bimodal | 14 |
| Fine lamellar | 8 |
| Coarse lamellar | 50 |

**Table 3.1-24** Elastic moduli $E$, $G$, $K$, and Poisson's ratio $\nu$ at various temperatures $T$ for selected simple $Ti_3Al$-based alloys

| Alloy (at.%) | $T$ (°C) | $E$ (GPa) | $G$ (GPa) | $\nu$ | $K$ (GPa) |
|---|---|---|---|---|---|
| Ti-25.5Al | 27 | 144 | 56.2 | 0.283 | |
| Ti-25.5Al | −270 | 151 | 59.0 | 0.280 | |
| Ti-25Al-10Nb-3V-1Mo (coarse globular) | 23 | 72 | | | |
| Ti-25Al-10Nb-3V-1Mo (fine lamellar) | 23 | 120 | | | |
| Ti-25Al-10Nb-3V-1Mo (coarse lamellar) | 23 | 159 | | | |
| Ti-26.6Al-4.9Nb | 26–883 | 134.47–0.0482$T$ | 53.56–0.0180$T$ | 0.257–0.00004$T$ | |
| Ti-27.4Al-20.3Nb | 25 | 128.8 | 48.8 | 0.32 | 118.4 |
| Ti-22Al-23Nb/Ultra-SCS | 25 | 201 ± 8 | | | |
| Ti-22Al-23Nb/Ultra-SCS | 649 | 173 | | | |
| Ti-22Al-23Nb/Ultra-SCS | 760 | 135 ± 8 | | | |

**Table 3.1-25** Selected tensile data for yield stress $R_p$, fracture stress $R_m$, total elongation $A$, fracture toughness $K_{Ic}$ at room temperature, and creep time to rupture $t_r$ at 650 °C and 380 MPa for various $Ti_3Al$-based alloys

| Alloy (at.%) | $R_p$ (MPa) | $R_m$ (MPa) | $A$ (%) | $K_{Ic}$ (MPa m$^{1/2}$) | $t_r$ (h) |
|---|---|---|---|---|---|
| Ti-25Al | 538 | 538 | 0.3 | | |
| Ti-24Al-11Nb | 787 | 824 | 0.7 | | 44.7 |
| Ti-24Al-11Nb | 510 | | 2.0 | 20.7 | |
| Ti-24Al-11Nb | 761 | 967 | 4.8 | | |
| Ti-24Al-14Nb | 831 | 977 | 2.1 | | 59.5 |
| Ti-24Al-14Nb | 790 | | 3.3 | 15.8 | 60.4 |
| Ti-15Al-22.5Nb | 860 | 963 | 6.7 | 42.3 | 0.9 |
| Ti-25Al-10Nb-3V-1Mo | 825 | 1042 | 2.2 | 13.5 | 360 |
| Ti-25Al-10Nb-3V-1Mo | 823 | 950 | 0.8 | | |
| Ti-25Al-10Nb-3V-1Mo | 745 | 907 | 1.1 | | |
| Ti-25Al-10Nb-3V-1Mo | 759 | 963 | 2.6 | | |
| Ti-25Al-10Nb-3V-1Mo | 942 | 1097 | 2.7 | | |
| Ti-24.5Al-17Nb | 952 | 1010 | 5.8 | 28.3 | 62 |
| Ti-24.5Al-17Nb | 705 | 940 | 10.0 | | |
| Ti-25Al-17Nb-1Mo | 989 | 1133 | 3.4 | 20.9 | 476 |
| Ti-22Al-23Nb | 863 | 1077 | 5.6 | | |
| Ti-22Al-27Nb | 1000 | | 5.0 | 30.0 | |
| Ti-22Al-20Nb-5V | 900 | 1161 | 18.8 | | |
| Ti-22Al-20Nb-5V | 1092 | 1308 | 8.8 | | |

*Chemical Properties.* The oxidation resistance of the $Ti_3Al$-based alloys is higher than that of conventional Ti alloys with $TiO_2$ formation, but lower than that of $Al_2O_3$-forming alloys. The rate controlling mechanisms are complex and change with atmosphere, temperature, and time. Oxidation is moderate with porous scales up to 800 °C whereas spallation occurs at higher temperatures. The addition of Nb to the $Ti_3Al$-based alloys is beneficial to the oxidation resistance as well as nitrogen in the atmosphere [1.58]. Table 3.1-27 presents characteristic data for oxidation at 800 °C.

It should be noted that H is easily dissolved in $Ti_3Al$-based alloys, leading to embrittlement and stress corrosion cracking. Furthermore, the thermal stability of intermetallic $Ti_3Al$-based matrix composites – in particular SCS-6 SiC/Ti-25Al-10Nb-3V-1Mo – is affected by chemical reactions between the matrix and the strengthening phase.

### TiAl-Based Alloys

Alloys based on $\gamma$-TiAl, also called gamma titanium aluminides, excel due to their high strength per unit density. These alloys contain the $\alpha_2$-phase $Ti_3Al$ as a second phase and are further alloyed with other elements for property optimization. The composition range is Ti-(45–48)Al-(0–2)(Cr, Mn, V)-(0–5)(Nb, Ta, W)-(0–2)(Si, B, Fe, N) (at.%). Further components such as Hf, Sn, C, and/or 0.8–7 vol.% $TiB_2$ are added for dispersion strengthening [1.59]. Table 3.1-28 shows the standard microstructures and Table 3.1-29 lists the alloys of primary interest.

Various jet engine and car engine components have been identified for application of TiAl-based alloys. It is particularly noteworthy that large sheets, which are suitable for superplastic forming and joining by diffusion bonding, can be produced from these intrinsically brittle intermetallic compound alloys.

*Physical Properties.* Some thermal data for single crystalline and polycrystalline TiAl alloys are shown in Tables 3.1-30 and 3.1-31.

*Mechanical Properties.* Elastic properties of TiAl-based materials are compiled in Table 3.1-32. Strength, ductility, and toughness of the TiAl-based alloys are sensitive functions of both composition and microstructure which is controlled by prior processing [1.59]. Characteristic data are shown in Table 3.1-33 for various alloys. Different property data for the same alloy composition indicate the effect of different prior thermo-mechanical treatments. It is noted that TiAl-based alloys are prone to hydrogen/environmental embrittlement depending on the amount of $\alpha_2$ from $Ti_3Al$ [1.60]. Creep and fatigue data are available [1.59, 61].

**Table 3.1-27** Characteristic oxidation data for various $Ti_3Al$-based alloys at 800 °C. Apparent parabolic rate constant $k_p$ and apparent activation energy $Q$ [1.58]

| Alloy (at.%) | Atmosphere | Test duration (h) | $k_p$ ($10^{-12}$ g$^2$ cm$^{-4}$ s$^{-1}$) | $Q$ (kJ mol$^{-1}$) |
|---|---|---|---|---|
| Ti-25Al | $O_2$ | 9 | 19 | 289 |
| Ti-25Al-11Nb | $O_2$ | 4 | 2.0 | 330 |
| Ti-24Al-15Nb | $O_2$ | 6 | 2.2 | 329 |
| Ti-24Al-15Nb | 20% $O_2$ + 80% $N_2$ | 5 | 0.25 | 274 |
| Ti-24Al-10Nb-3V-1Mo | 20% $O_2$ + 80% $N_2$ | 15 | 1150 | 217 |
| Ti-25Al-10Nb-3V-1Mo | Air | 24 | 2.4 | 248 |

**Table 3.1-28** Standard microstructures of TiAl-based alloys [1.59]

| Type | Phase distribution |
|---|---|
| Near-gamma (NG) | $\gamma$ grains + $\alpha_2$ particles |
| Duplex (DP) | $\gamma$ grains + $\alpha_2$ plates or particles |
| Nearly lamellar (NL) | Lamellar $\gamma + \gamma$ grains |
| Fully lamellar (FL) | Lamellar $\gamma$ + residual $\gamma$ grains on grain boundaries |
| Modified NL (MNL) | Lamellar $\gamma$ + fine $\gamma$ grains |
| Modified FL (MFL) | Lamellar $\gamma$ |

**Table 3.1-29** Important TiAl-based alloys with microstructures according to Table 3.1-28 [1.59]

| Composition (at.%) | Microstructure type | Designation |
|---|---|---|
| Ti-48Al-1V-0.3C-0.2O | DP | 48-1-(0.3C) |
| Ti-48Al-1V-0.2C-0.14O | DP/NL | 48-1-(0.2C) |
| Ti-48Al-2Cr-2Nb | DP, NL, DP/FL | 48-2-2 |
| Ti-47Al-1Cr-1V-2.6Nb | DP/FL | G1 |
| Ti-45Al-1.6Mn | NL | Sumitomo |
| Ti-47.3Al-0.7V-1.5Fe-0.7B | – | IHI Alloy |
| Ti-47Al-2W-0.5Si | DP | ABB Alloy |
| Ti-47Al-2Mn-2Nb-0.8$TiB_2$ | NL + $TiB_2$ | 47XD |
| Ti-45Al-2Mn-2Nb-0.8$TiB_2$ | MFL + $TiB_2$ | 45XD |
| Ti-46.2Al-xCr-y(Ta,Nb) | NL | GE Alloy 204b |
| Ti-47Al-2Nb-2Cr-1Ta | DP | Ti-47Al-2Nb-2Cr-1Ta |
| Ti-46Al-4Nb-1W | NL | Alloy 7 |
| Ti-46.5Al-2Cr-3Nb-0.2W | DP/MFL | Alloy K5 |
| Ti-48Al-2Cr | NG, DP, FL | Ti-48Al-2Cr |
| Ti-47Al-1.5Nb-1Cr-1Mn-0.7Si-0.5B | MFL | $\gamma$-TAB |
| Ti-46.5Al-4(Cr, Nb, Ta, B) | MFL | $\gamma$-Met |

**Table 3.1-30** Temperature dependence of the thermal expansion coefficient $\alpha$ for single crystalline TiAl

| Alloy (at.%) | $T$ (°C) | $\alpha_{[100]}$ ($K^{-1}$) | $\alpha_{[001]}$ ($K^{-1}$) |
|---|---|---|---|
| Ti-56Al | 25–500 | $9.77\times10^{-6}+4.46\times10^{-9}(T+273)$ | $9.26\times10^{-6}+3.76\times10^{-9}(T+273)$ |

**Table 3.1-31** Thermal expansion coefficient $\alpha$, thermal conductivity $\lambda$ and specific heat $c_p$ at various temperatures $T$ for polycrystalline TiAl alloys [1.62]

| Alloy (at.%) | $T$ (°C) | $\alpha$ ($K^{-1}$) | $\lambda$ ($W\,K^{-1}\,m^{-1}$) | $c_p$ ($J\,g^{-1}\,K^{-1}$) |
|---|---|---|---|---|
| Ti-50Al | 27 | $11\times10^{-6}$ | 11 | 0.4 |
| Ti-50Al | 850 | $13\times10^{-6}$ | 19 | 0.5 |
| Ti-48Al-2Cr | 100 | $9.1\times10^{-6}$ | – | – |
| Ti-48Al-2Cr | 700 | $11.8\times10^{-6}$ | – | – |

**Table 3.1-32** Young's modulus $E$, shear modulus $G$, Poisson's ratio $\nu$ and bulk modulus $K$ for single-phase TiAl and a TiAl composite

| Alloy (at.%) | $T$ (°C) | $E$ (GPa) | $G$ (GPa) | $\nu$ | $K$ (GPa) |
|---|---|---|---|---|---|
| Ti-49.4Al | 25–935 | $173.59-0.0342T$ | $70.39-0.0141T$ | 0.234 | |
| Ti-50Al | 25 | 185 | 75.7 | | 110 |
| Ti-50Al | −273 | 190 | 78.3 | | 112 |
| Ti-47Al-2V-7 vol.%$TiB_2$ | 27 | 180 | | | |
| Ti-47Al-2V-7 vol.%$TiB_2$ | 647 | 162 | | | |

**Table 3.1-33** Selected tensile data for yield stress $R_p$, fracture stress $R_m$, total elongation $A$, toughness $K_{Ic}$ at room temperature (RT) or higher temperature $T$ for the TiAl-based alloys of Table 3.1-29 with microstructures of Table 3.1-28 [1.59, 61]

| Alloy designation | Alloy condition, processing, microstructure | $T$ [°C] | $R_p$ (MPa) | $R_m$ (MPa) | $A$ (%) | $K_{Ic}$ (MPa m$^{1/2}$) |
|---|---|---|---|---|---|---|
| 48-1-(0.3C) | Forging + HT | RT | 392 | 406 | 1.4 | 12.3 |
| | | 760 | 320 | 470 | 10.8 | – |
| | Casting-duplex | RT | 490 | – | – | 24.3 |
| 48-1-(0.2C) | Forging + HT | RT | 480 | 530 | 1.5 | – |
| | | 815 | 360 | 450 | 720 | – |
| 48-2-2 | Casting + HIP + HT | RT | 331 | 413 | 2.3 | 20–30 |
| | | 760 | 310 | 430 | – | – |
| | Extrusion + HT: DP/FL | RT | 480/454 | – | 3.1/0.5 | – |
| | | 870 | 330/350 | – | 53/19 | – |
| | PM extrusion + HT | RT | 510 | 597 | 2.9 | – |
| | | 700 | 421 | 581 | 5.2 | – |
| G1 | Forging + HT: DP/FL | RT | 480/330 | 548/383 | 2.3/0.8 | 12/30-36 |
| | | 600 | 383/– | 507/– | 3.1/– | 16/ – |
| | | 800 | 324/290 | 492/378 | 55/1.5 | –/40-70 |
| Sumitomo | Reactive sintering | RT | 465 | 566 | 1.4 | – |
| | | 800 | 370 | 540 | 14 | – |
| IHI Alloy | Casting | RT | – | 520 | 0.6 | – |
| | | 800 | – | 424 | 40 | – |
| ABB Alloy | Casting + HT | RT | 425 | 520 | 1.0 | 22 |
| | | 760 | 350 | 460 | 2.5 | – |
| 47XD | Casting + HIP + HT | RT | 402 | 482 | 1.5 | 15–16 |
| | | 760 | 344 | 458 | – | – |
| 45XD | Casting + HIP + HT | RT | 550–590 | 670–720 | 1.5 | 15–19 |
| | | 760 | 415 | 510 | 19 | – |
| GE Alloy 204b | Casting + HIP + HT | RT | 442 | 575 | 1.5 | 34.5 |
| | | 840 | 381 | 549 | 12.2 | – |
| Ti-47Al-2Nb-2Cr-1Ta | Casting + HIP + HT | RT | 430 | 515 | 1.0 | – |
| | | 870 | 334 | 403 | 14.6 | – |
| Alloy 7 | Extrusion + HT | RT | 648 | 717 | 1.6 | – |
| | | 760 | 517 | 692 | – | – |
| Alloy K5 | Forging + HT: DP/MFL | RT | 462/473 | 579/557 | 2.8/1.2 | 11/20-22 |
| | | 870 | –/362 | –/485 | –/12.0 | – |
| Ti-48Al-2Cr | Casting + HIP + HT | RT | 390 | 405 | 1.5 | – |
| | | 700 | 340 | 395 | 2.7 | – |
| $\gamma$-TAB | Casting + HIP + HT | RT | 475 | – | 1.6 | – |
| | | 700 | 385 | – | 6.0 | – |

*Chemical Properties.* The oxidation behavior of TiAl alloys is complex as both $Al_2O_3$ and/or $TiO_2$ are formed at parabolic rate constants ranging from $3\times10^{-13}$ to $3\times10^{-9}$ g$^2$ cm$^{-4}$ s$^{-1}$ at 950 °C, depending not only on alloy composition, atmosphere, and temperature, but also on alloy surface quality. The oxidation rate is higher in air than in pure oxygen. Alloying additions of Nb, W, Ta, or Si generally improve the oxidation resistance. Additions of V and Mo promote $Al_2O_3$ formation above 900 °C, which is beneficial, but accelerates scale growth at lower temperatures, i. e., at possible service temperatures. Small additions of Cr reduce the oxidation resistance whereas larger amounts improve it. Small additions of P or Cl have been found to increase the oxidation resistance. Some characteristic data are shown in Table 3.1-34.

**Table 3.1-34** Characteristic oxidation data for some TiAl-based alloys of Table 3.1-29. Apparent parabolic rate constant $k_p$ at 800 °C in air

| Alloy designation | Test duration (h) | $k_p$ ($10^{-12}$ g$^2$ cm$^{-4}$ s$^{-1}$) |
|---|---|---|
| 48-2-2 | 500 | 2 |
| Alloy K5 | 1000 | 0.5 |
| Alloy 7 (5 at.% Nb) | 1000 | 0.1 |

Usually $\gamma$-TiAl-based alloys contain $\alpha_2$-$Ti_3Al$ as a second phase and are, therefore, subject to hydrogen uptake and hydrogen/environmental embrittlement depending on the amount of $\alpha_2$-$Ti_3Al$.

### 3.1.3.4 TiNi Shape-Memory Alloys

The shape-memory effect is based on martensitic transformations of intermetallic phases with a high degree of reversibility [1.63]. The alloy TiNi is the most advanced and has widespread shape memory. The present state of development and applications is summarized in [1.63, 64]. The high-temperature TiNi phase, having a cubic B2 (CsCl type) structure, is transformed martensitically, i. e., by a combination of transformation shears, into a low-temperature phase with a monoclinic $DO_{19}$ structure upon cooling or upon applying a stress and strain. The transformation can be associated with a macroscopic shape change. The transformation and the associated shape change are reversed on heating (shape-memory effect) or on releasing the stress and strain isothermally (superelasticity). The range of transformation start temperatures $M_s$ varies between −200 °C and 110 °C depending on the alloy composition, as shown in Fig. 3.1-89.

Further reversible, diffusionless, but non-martensitic transformation phenomena occur in the TiNi high temperature phase on approaching the temperature range of martensitic transformation. Microscopically, these transformation phenomena are associated with phonon softening. Crystallographically, they are observable as localised rhombohedral distortions of the B2 structure. Furthermore, these localized displacements appear to be stabilized by annealing. Annealing treatments in the temperature range of 300 to 800 °C are increasing the $M_s$ temperature. Figure 3.1-90 shows a characteristic example.

The shape-memory effect is a complex function of composition, martensite start temperature $M_s$, stress, strain, microstructure, texture, and aging treatment. It consists essentially of a reversible transformation strain and the associated macroscopic shape change. At low numbers of transformation cycles (e.g., up to 100), the reversible transformation strain decreases from a typical initial value 8% to about 6%; even after ≥ 100 000 transformation cycles it stays at a technically useful level of ≅ 2%. A considerable number and variety of technical and medical applications of the shape-memory effect and of the closely related effect of superelasticity have been developed [1.65, 66].

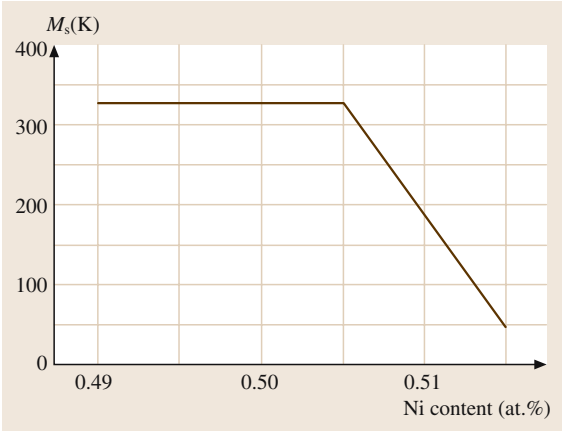


**Fig. 3.1-89** Martensite start temperature $M_s$ of the TiNi phase as a function of Ni content

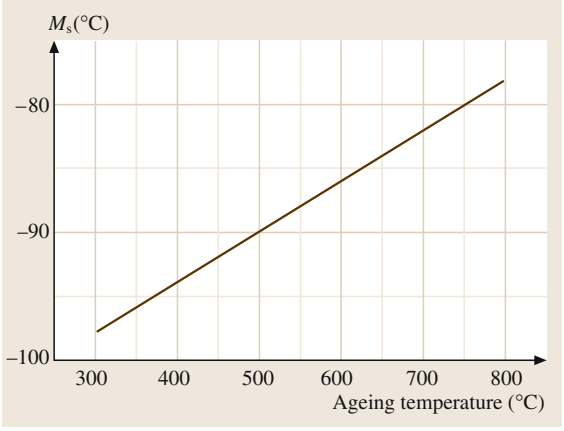


**Fig. 3.1-90** Effect of aging temperature on the $M_s$ temperature of an $Ni_{47.3}Ti_{43.8}Nb_{8.9}$ alloy

## 3.1.4 Zirconium and Zirconium Alloys

Zirconium is used – similarly to titanium but less extensively so – as a special structural material of high corrosion resistance due to its highly stable protective oxide layer. This oxide layer forms in air at ambient temperature spontaneously and can be increased in thickness and stability by heat treatment in air. More extensive treatments are found in [1.51, 67]. Technically-pure and low-alloy Zr materials are especially used in applications requiring structural parts of high chemical stability. The processing is closely analogous to that of Ti. Another main application of Zr is in high-purity Zr alloys used as cladding and structural materials in nuclear applications due to the low thermal neutron capture cross section of Zr. A third group of Zr-based materials with application potential is due to the fact that some Zr-based alloys form the amorphous state easily upon cooling at a comparatively low rate. They are suitable for the production of bulk glassy alloys.

At 1138 K, Zr undergoes a structural phase transformation from low-temperature, hexagonal close-packed $\alpha$-Zr to high-temperature, body-centered cubic $\beta$-Zr. Alloying elements such as Nb stabilize the $\beta$ phase. On slow cooling and annealing of the $\beta$ phase, a metastable $\omega$ phase can be obtained which forms by coherent precipitation.

### 3.1.4.1 Technically-Pure and Low-Alloy Zirconium Materials

Only two zirconium materials are standardised: Zr 702 which is essentially technically-pure Zr and consists of the $\alpha$ phase only, and Zr 705 which contains 2 to 3 wt% Nb, has an $\alpha + \beta$ microstructure and a higher yield stress. Their composition ranges and mechanical properties are listed in Tables 3.1-35 and 3.1-36. Since Hf is usually contained in the Zr ore zircon ($ZrSiO_4$) and is difficult to separate, the Zr materials are specified to contain Hf up to 4.5 wt%. The presence of Hf in Zr alloys up to this level of composition does not affect the mechanical and corrosion properties significantly.

The Zr–Nb phase diagram (Fig. 3.1-91) indicates that $\alpha + \beta$ microstructures can be obtained at the 2–3 wt% Nb level. This leads to both substitutional solid solution strengthening and dual phase strengthening effects. Oxygen has a high interstitial solubility in $\alpha$-Zr. Fig. 3.1-92 shows the Zr–O phase diagram. It is inter-

**Table 3.1-35** Composition of technically-pure and low-alloy Zr materials

| Common designation<br>ASTM/UNS designation | Zr 702<br>R 60702 | Zr 705<br>R 60705 |
|---|---|---|
| **Alloying, elements (wt%)** | | |
| Zr+Hf, min | 99.2 | 95.5 |
| Hf, max | 4.5 | 4.5 |
| Fe+Cr, max | 0.20 | 0.20 |
| Nb | – | 2.0–3.0 |
| O, max | 0.16 | 0.18 |
| H, max | 0.005 | 0.005 |
| N, max | 0.025 | 0.025 |
| C, max | 0.05 | 0.05 |

**Table 3.1-36** Mechanical properties of technically-pure and low-alloy Zr materials

| Alloy | Property | Test temperature (°C) | | | | |
|---|---|---|---|---|---|---|
| | | 20 | 95 | 150 | 260 | 370 |
| Zr 702 | $R_{p0.2}$ (MPa) | 321 | 267 | 196 | 129 | 82 |
| | $R_m$ (MPa) | 468 | 364 | 304 | 201 | 157 |
| | $A$ (%) | 28.9 | 31.5 | 42.5 | 49.0 | 44.1 |
| Zr 705 | $R_{p0.2}$ (MPa) | 506 | | 272 | 196 | |
| | $R_m$ (MPa) | 615 | | 389 | 326 | |
| | $A$ (%) | 18.8 | | 31.7 | 28.9 | |

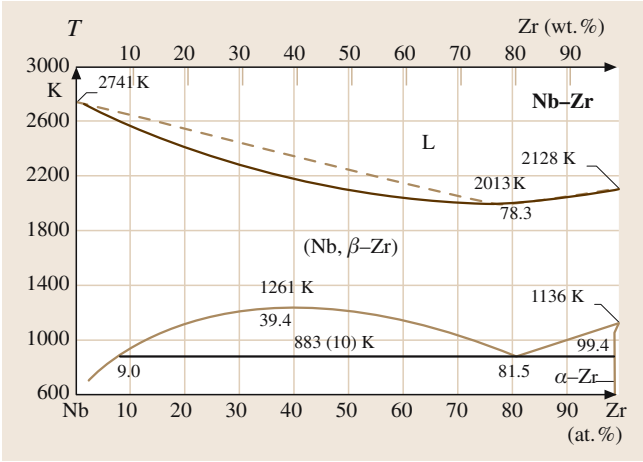


**Fig. 3.1-91** Zr–Nb phase diagram

esting to note that the O atoms undergo ordering on the interstitial lattice sites of the $\alpha$-Zr solid solution above about 10 at.% O. These interstitially ordered phases are termed suboxides. The interstitial O content leads to a strong interstitial solid solution strengthening effect: about 0.01 wt% O increases the yield stress by about 150 MPa.

Extensive data and references are available on the corrosion behavior of Zr in many types of media and under various conditions of exposure [1.67].

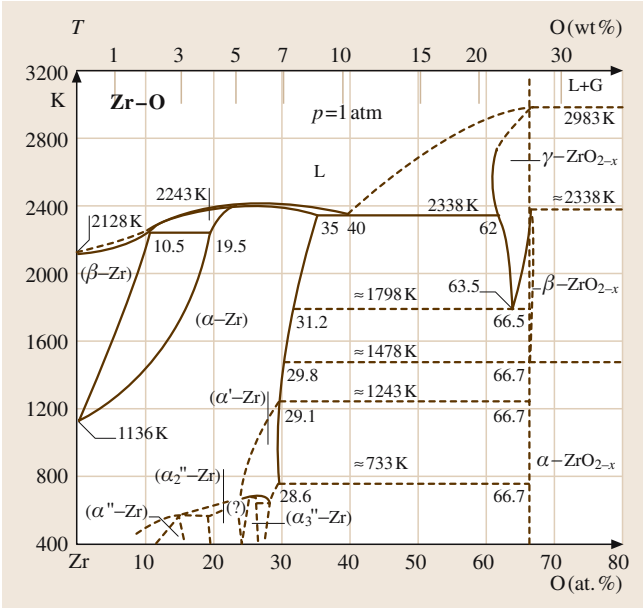


**Fig. 3.1-92** Zr–O phase diagram

### 3.1.4.2 Zirconium Alloys in Nuclear Applications

Based on its low cross section for thermal neutrons and its high corrosion resistance in water, Zr is the preferred material for structural parts and cladding in pressurized and boiling water nuclear reactors. An extensive account of these materials and of their behavior under irradiation is given in [1.68]. Designations and composition ranges of the 4 standardized alloys are listed in Table 3.1-37. The addition of Sn gives rise to a strengthening contribution and increases corrosion resistance by reducing the deleterious effect of nitrogen. The metals Fe, Cr, and Ni, which are highly soluble in the $\beta$ phase, have very low solubility in $\alpha$-Zr (maximum solubility: Fe 120 ppm, Cr 200 ppm). This is the basis of a heat treatment involving a high-temperature solution annealing and a low-temperature precipitation treatment. The resulting precipitates are the Laves phases $Zr_2(Ni, Fe)$ and $Zr(Cr, Fe)_2$. In their presence the corrosion resistance is increased by reducing forms of localized corrosion. A specified O content serves to adjust the yield stress due to interstitial solid solution strengthening. Hafnium is removed and its upper limit is specified in Zr alloys for nuclear applications because of its high cross section for thermal neutrons.

The irradiation effects on the mechanical properties are significant. The interstitial atoms and vacancies resulting from irradiation-induced atomic displacements give rise to the formation of dislocation loops of interstitial and vacancy type. These dislocation loops act as obstacles to slip dislocations and lead to an increase in yield stress and decrease in elongation upon fracture as a function of dose, as shown in Fig. 3.1-93. The effect saturates at about $10^{24}$ nm$^{-2}$.

### 3.1.4.3 Zirconium-Based Bulk Glassy Alloys

Zirconium-based alloys were among the first non-noble metal-based alloys found to solidify in the amorphous state upon cooling from the melt at comparatively low rates $R$, such as 10 K s$^{-1}$ [1.69,70]. The term bulk glassy alloys refers to the fact that this solidification behavior permits us to obtain bulky parts with an amorphous structure by conventional casting procedures, e.g., in rod form, up to 30 mm. Data are given in [1.71,72].

The tendency to solidification in the amorphous state is due to a low rate of nucleation of the equilibrium phase(s) at a particular alloy composition. An empirical method to determine the ease of glass formation has proved to be an evaluation of the glass-transition tem-

**Table 3.1-37** Designations and compositions of the standardized Zr alloys for nuclear applications [1.68]

| Common designation<br>ASTM/UNS designation | Zircaloy-2<br>R 60802 | Zircaloy-4<br>R 60804 | Zr–Nb<br>R 60901 | Zr–Nb<br>R 60904 |
|---|---|---|---|---|
| **Alloying elements (wt%)** | | | | |
| Sn | 1.2–1.7 | 1.2–1.7 | – | – |
| Fe | 0.07–0.2 | 0.18–0.24 | – | – |
| Cr | 0.05–0.15 | 0.07–0.13 | – | – |
| Ni | 0.03–0.08 | – | – | – |
| Nb | – | – | 2.4–2.8 | 2.5–2.8 |
| O | 0.010–0.014 (t.b.s.)[a] | | 0.09–0.13 | (t.b.s.)[a] |
| **Impurity elements, maximum permissible content (wt ppm)** | | | | |
| Al | 75 | 75 | 75 | 75 |
| C | 270 | 270 | 270 | 150 |
| Cu | 50 | 50 | 50 | 50 |
| Hf | 100 | 100 | 100 | 50 |
| Mn | 50 | 50 | 50 | 50 |
| Mo | 50 | 50 | 50 | 50 |
| Ni | – | 80 | 80 | 65 |
| Si | 120 | 120 | 120 | 120 |
| Ti | 50 | 50 | 50 | 50 |
| W | 100 | 100 | 100 | 100 |

[a] t.b.s. – to be specified

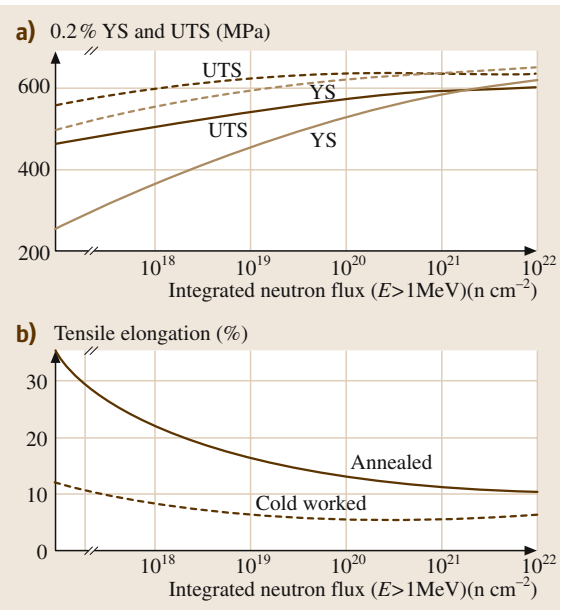


**Fig. 3.1-93** Irradiation effects on mechanical properties of a zircaloy [1.68]. YS – yield stress; UTS – ultimate tensile strength. *Solid lines*: irradiation in the annealed state. *Dashed lines*: irradiation in the 10% cold worked state

perature $T_g$ and the crystallization temperature $T_x$, which can be determined by thermal analysis of the amorphous alloy in question upon heating. For a great number of alloys which form the amorphous state upon cooling, it has been shown that the critical cooling rate $R_c$, i. e., lowest rate which is sufficient for complete glass formation, decreases strongly with two parameters:

- The relative glass-transition temperature $T_{rg} = T_g/T_{l/el}$, where $T_{l/el}$ is the liquidus temperature, and
- The magnitude of the temperature range $\Delta T_x = T_x - T_g$.

Figures 3.1-94 – 3.1-97 show characteristic data for Zr alloys which have been investigated in a wide range of compositions.

It is impossible to date to derive from first principles which alloy compositions are prone to easy glass formation. It has been found empirically that multi-component alloys with components of significantly different ionic radii are suitable candidates in principle. Examples of Zr-based systems that show bulk glassy solidification behavior are listed in Table 3.1-38.

Empirical findings have been subjected to a systematic treatment involving a mismatch entropy term $S_\sigma$ and the enthalpy of mixing $\Delta H$ [1.73]. Such re-

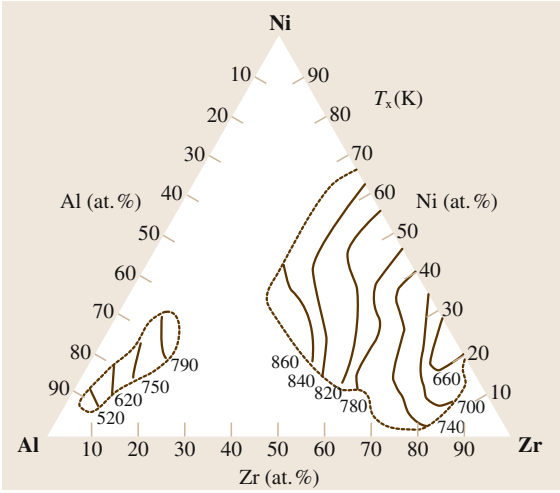


**Fig. 3.1-94** Dependence of crystallization temperature $T_x$ on composition in amorphous Zr−Al−Ni alloys [1.72]

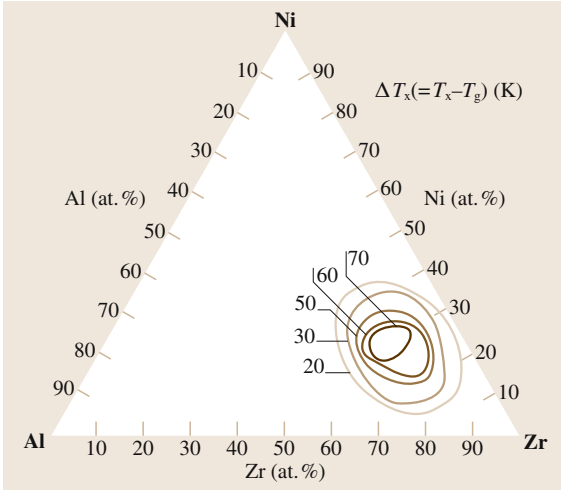


**Fig. 3.1-96** Dependence of $\Delta T_x$ on composition in amorphous Zr−Al−Ni alloys [1.72]

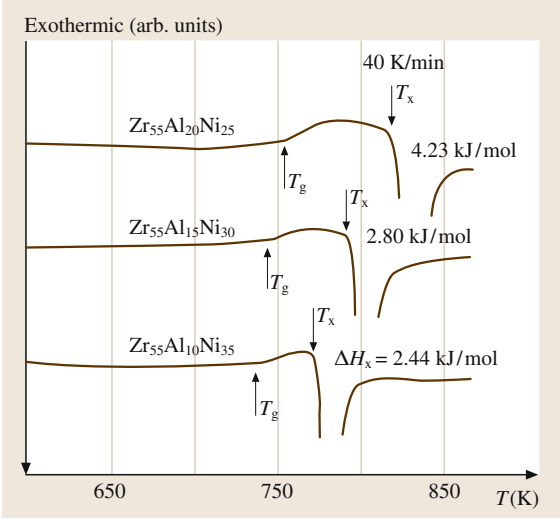


**Fig. 3.1-95** Dependence of $\Delta T_x$ on composition as determined by differential thermal analysis of amorphous Zr−Al−Ni alloys [1.72]

**Table 3.1-38** Zr-based alloy systems exhibiting bulk glassy behavior

| Alloy system | Reference |
|---|---|
| Zr–Al–TM | [1.72] |
| Zr–Al–Ni–Cu–(Ti, Nb, Pd) | [1.72] |
| Zr–Al–Co | [1.74] |
| Zr–Ti–Ni–Cu–(Be) | [1.75] |
| Zr–Cu–Ni–(Al, Ti, Ta) | [1.76] |

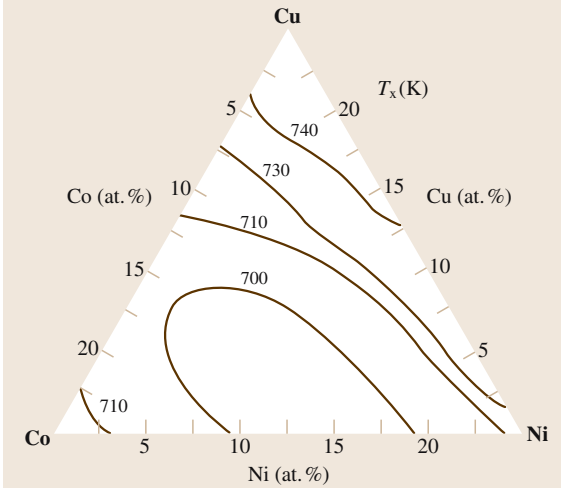


**Fig. 3.1-97** Dependence of $T_x$ on composition in amorphous $Zr_{65}Al_{7.5}Cu_{2.5}(Co_{1-x-y}Ni_xCu_y)_{25}$ alloys [1.72]

lations are based on systematic investigations of the effects of individual alloying elements on the characteristic properties $T_g$, $T_x$, and $\Delta T_x$, as shown in Fig. 3.1-98 for a characteristic example.

There are no tabulated data of the properties of Zr-based bulk glassy alloys available yet. A typical set of data is given in Table 3.1-39 [1.75].

**Table 3.1-39** Properties of amorphous $Zr_{41.2}Ti_{13.8}Cu_{12.5}Ni_{10}Be_{22.5}$

| $E$ (GPa) | $G$ (GPa) | $\nu$ | Elastic strain limit % | $R_{p0.2}$ (GPa) | HV | $\varrho$ g/cm$^3$ | $R_{p0.2}/\varrho$ (GPa cm$^3$ g$^{-1}$) | $A_e^a$ (%) | $A_c^b$ (%) | $K_{1c}$ (MN m$^{1/2}$) |
|---|---|---|---|---|---|---|---|---|---|---|
| 90±1 | 33±1 | 0.354 | 2.0–2.2 | 1.9±0.05 | 590 | 5.9 | 0.32 | ~1 | 1–20 | 20–40 |

[a] Plastic strain to failure in tension
[b] Plastic strain to failure in compression

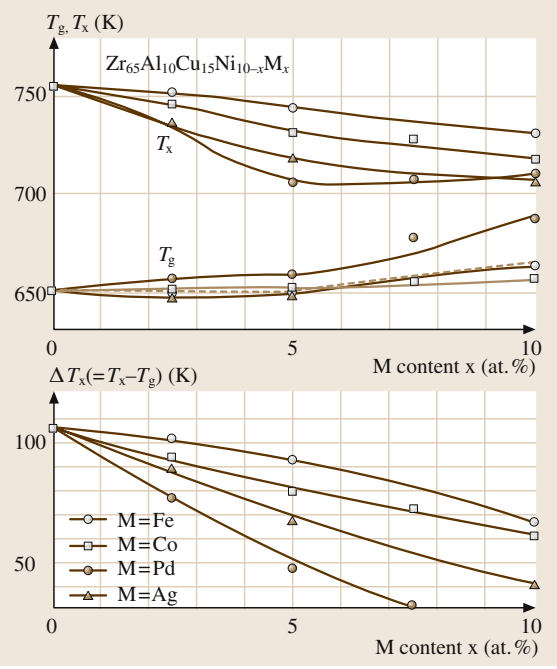


**Fig. 3.1-98** Variation of $T_g$, $T_x$, and $\Delta T_x$ with M content for melt-spun $Zr_{65}Al_{10}Cu_{15}Ni_{10-x}M_x$ (M = Fe, Co, Pd, Ag) amorphous alloys

## 3.1.5 Iron and Steels

Iron is technically the most versatile and economically the most important base metal for a great variety of structural and magnetic materials, most of which are called steels. With increasing temperature, iron undergoes two structural phase transitions,

$$\alpha\ (\text{bcc}) \leftrightarrow \gamma\ (\text{fcc})\ \text{at}\ 911\,^{\circ}\text{C}$$

and

$$\gamma\ (\text{fcc}) \leftrightarrow \delta\ (\text{bcc})\ \text{at}\ 1392\,^{\circ}\text{C},$$

and a magnetic phase transition,

$$\alpha_{\text{ferromagnetic}} \leftrightarrow \alpha_{\text{paramagnetic}}\ \text{at}\ 769\,^{\circ}\text{C},$$

at ambient pressure. At elevated pressure levels, Fe forms a third structural phase $\varepsilon$ (hcp). These phase transitions, their variation upon alloying, and the concomitant phase transformations are the thermodynamic, structural and microstructural basis for the unique variety of iron-based alloys and of their properties [1.52, 77–80].

The wide variety of standards for steels which have developed from national standards and efforts of international standardization are compiled in [1.81]. In the present section we are using different standard designations as provided by the sources used. In the following sections, the SAE (Society of Automotive Engineers), AISI (American Iron and Steel Institute), and UNS (Unified Numbering System) designations are the dominating ones.

### 3.1.5.1 Phase Relations and Phase Transformations

#### Iron–Carbon Alloys

The most frequent alloying element of iron is carbon. The Fe–C phase diagram (Fig. 3.1-99) shows the important metastable phase equilibria involving the metastable carbide $Fe_3C$, called cementite, in dashed lines, whereas the stable equlibria with graphite C are shown in solid lines. The formation of $Fe_3C$ predominates in most carbon and low-alloy steels because the activation energy of its nucleation is considerably lower than that of graphite. At higher carbon contents (2.5–4.0 wt% C) and in the presence of Si (1.0–3.0 wt% Si), graphite formation is favored. This is the basis of alloying and microstructure of gray cast iron (see Sect. 3.1.5.7).

The Fe–C phase forms interstitial solid solutions of $\alpha$- and $\gamma$-Fe. The solid solution phase of $\alpha$-Fe is called ferrite, the solid solution phase based on $\gamma$-Fe is called austenite in the binary Fe–C system. These terms for the solid solutions phases of $\alpha$- and $\gamma$-Fe are applied to all other Fe-based alloy systems as well. Since phase transformations induced by cooling from the austenite phase field play a major role to induce particular microstructures and properties, some resulting microstructures have also been given particular terms and form the basis of the nomenclature in steels. Cooling of Fe–C alloys from the austenite phase field can lead to three different phase transformations below the eutectoid temperature of 1009 K (736 °C). Their kinetics of formation depends on composition and cooling rate. The transformation products are:

- Pearlite, a lamellar product of ferrite and cementite. It is formed by a discontinuous (pearlitic) transformation, i. e., both phases are formed side by side in the reaction front. The lamellar spacing decreases with decreasing temperature of formation. The maximum rate of formation occurs at about 500 °C.

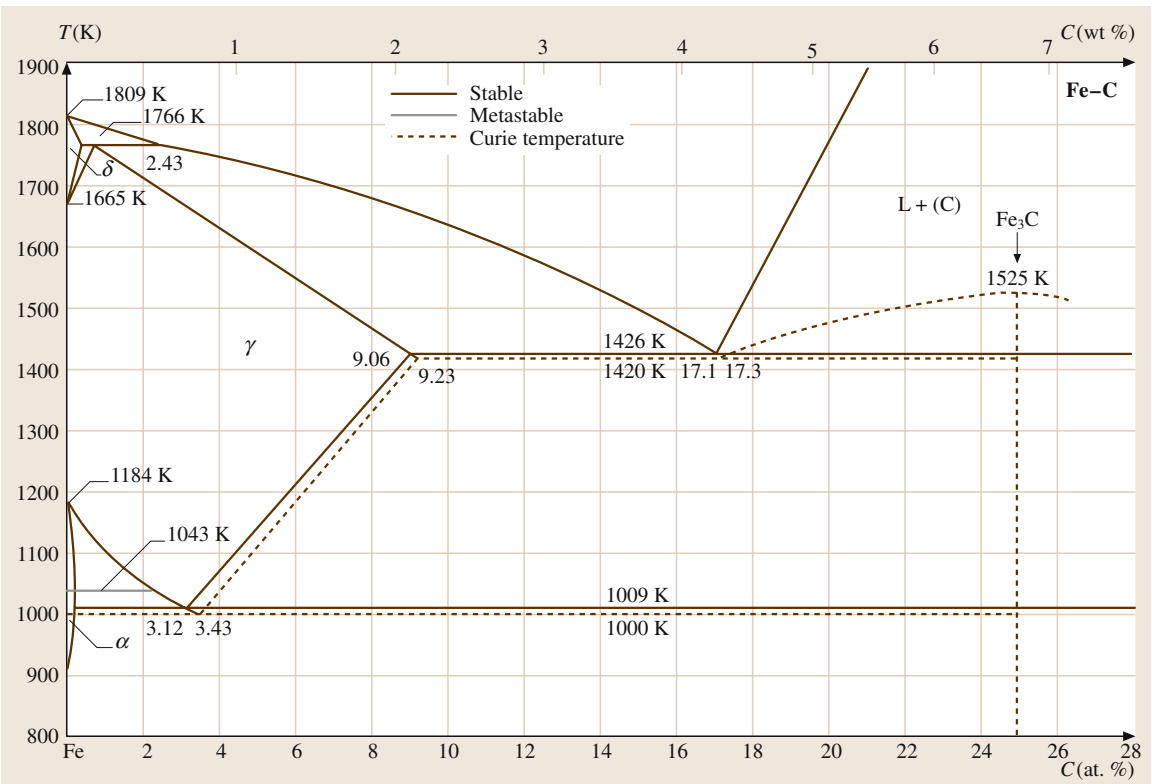


**Fig. 3.1-99** Fe–C phase diagram. Metastable equilibria involving cementite $Fe_3C$ are shown in *dashed lines*, stable equilibria with graphite C are shown in *solid lines* [1.82] (*dotted lines* – Curie temperature)

- Bainite, a plate- or spearhead-shaped product consisting of a ferrite matrix in which carbide particles are dispersed. The bainitic transformation mechanism depends sensitively on alloy composition and the temperature of transformation, yielding essentially two microstructural variants. A somewhat coarser transformation product formed at about 450 °C is called upper bainite and a finer transformation product formed at about 350 °C is termed lower bainite.
- Martensite, a plate-shaped product formed by a diffusionless, athermal transformation. Thermodynamically it is a metastable ferrite, designated as $\alpha'$ and supersatured in carbon. But by the displacive mechanism of the transformation, the distribution of the C atoms in the martensite lattice is anisotropic such that is has a body-centered tetragonal crystal structure and its $c$ and $a$ parameters vary with the C content accordingly (Fig. 3.1-100). The temperature below which martensite begins to form upon quenching is termed martensite start temperature $M_s$ and depends strongly on the C concentration (Fig. 3.1-101). $M_f$ designates the temperature at which the transformation is complete. In order to promote the diffusionless martensitic transformation, the diffusion-dependent transformations to pearlite and bainite have to be suppressed by rapid cooling, usually termed quenching.

Since martensite formation is used as a main hardening mechanism in steels, the hardenability is a main concern of alloy design and consequence of alloy composition. The lower the rate of formation of the diffusion-dependent transformations, the higher is the fraction of martensite formed upon cooling from the austenite range, i. e., the hardenability (see Sect. 3.1.5.2). The rates of pearlite and bainite formation are reduced by alloying with carbon and all substitutional alloying elements except by Co. But the decrease of $M_s$ with increasing alloy content has, also, to be taken into account.

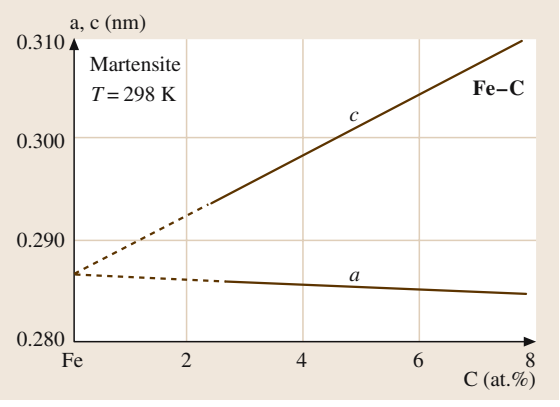


**Fig. 3.1-100** Lattice parameters of Fe−C martensite as a function of composition [1.82]

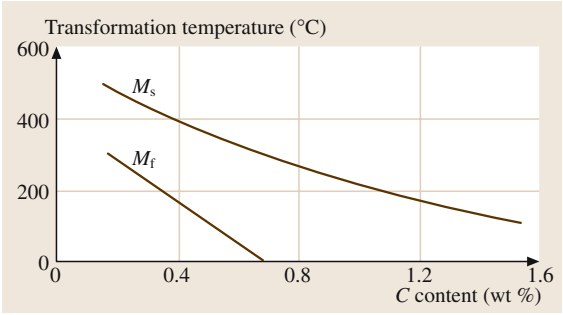


**Fig. 3.1-101** Concentration dependence of the martensite transformation temperatures. $M_s$ – martensite start; $M_f$ – martensite finish, i. e., austenite is transformed completely

Subsequent heat treatment of the phases formed is termed annealing with regard to ferrite and bainite, and tempering with regard to martensite. These heat treatments play a major role in optimizing the microstructure to obtain specific properties. Upon subsequent heat treatment the transformation products listed above undergo the following reactions:

- Pearlite is coarsened by the transition of the cementite lamellae into spherical particles, thus reducing the interfacial free energy per unit volume. The process is called spheroidization and consequently the resulting microstructural constituent is termed spheroidite.
- Bainite is coarsened as well both by recovery of the ferrite plates and by coarsening of the carbide particles.
- Martensite is essentially transformed into bcc ferrite by the precipitation of carbide particles during tempering. The tempering treatment usually leads to the precipitation of metastable carbides from the martensite phase. Different metastable carbides may be formed depending on alloy composition (including substitutional alloying elements), temperature, and time of annealing. A compilation of all metastable carbides occurring in Fe−C(−X) alloys is given in Table 3.1-40.

**Table 3.1-40** Metastable and stable carbide phases occurring in the Fe−C(−X) alloy system [1.82]

| Phase | Structure | Type | *a* (nm) | *b* (nm) | *c* (nm) |
|---|---|---|---|---|---|
| $Fe_4C$ | cub | | 0.3878 | | |
| $Fe_3C$ | orth | $Fe_3C$ | 0.50889 | 0.67433 | 0.452353 |
| $\varepsilon$-$Fe_3C$ | hex | | 0.273 | | 0.433 |
| $Fe_{2-3}C$ | hex | | 0.4767 | | 0.4354 |
| $Fe_5C_2$ | mon | $Mn_5C_2$ | 1.1563 | 0.4573<br>$\beta = 97.73°$ | 0.5058 |
| $Fe_7C_3$ | hex | $Th_7Fe_3$ | 0.6882 | | 0.4540 |
| $Fe_{20}C_9$ | orth | | 0.9061 | 1.5695 | 0.7937 |

### Heat Treatments

The heat treatments referred to above need to be specified rather succinctly such that they can be correlated with the ensuing microstructures and properties. Furthermore, the specifications of heat treatments require taking the cross section and form of the part to be heat treated into account (at least if the cross sections get larger than, say, 0.5 mm). The finite thermal conductivity and the heat capacity of the material will cause any temperature change applied to the surface to occur at a decreasing rate with increasing depth in the heat-treated part. Thus, not only the time and temperature of an isothermal treatment but also the rate of cooling or the rate of heating are common parameters to be specified. Beyond those referred to above, the following treatments are widely applied to steels:

*Austenitizing.* Heating to and holding in the range of the austenite phase is commonly the first stage of transformation heat treatments. The higher the austenitizing temperature, the more lattice defects such as dislocations and grain boundaries are annihilated. This lowers the rate of nucleation of subsequent phase transformations.

*Soft Annealing.* This term is used for heat treatment of hardenable steels containing $\geq 0.4$ wt% C at temperatures closely below the eutectoid temperature for a duration of $\leq 100$ h. It results in a microstructure of coarse grained, ductile ferrite, and coarsened cementite.

*Normalizing.* This heat treatment is applied to obtain a uniform, fine-grained microstructure. The first step consists of heating the metal rapidly to, and holding it at a temperature 30–50 K above the $(\alpha+\gamma)/\gamma$ phase boundary (also referred to as the $A_{c3}$ line) for hypo-eutectoid steels, and heating rapidly to and holding at about 50 K above the eutectoid temperature (also referred to as $A_{c1}$ line). This step results in the formation of a fairly fine-grained austenite and ferrite structure in the hypo-eutectoid and in a fine-grained austenite with coagulated grain boundary cementite in the hyper-eutectoid compositions. Upon cooling, the austenite transforms into pearlite and this microstructural state has a favorable combination of strength, ductility, and machinability.

### Substitutional Iron-Based Alloys

For the phase diagrams with substitutional alloying components shown in later sections, a major aspect pertaining to both the binary alloys shown and the steels alloyed with these components is whether the $\alpha$ or the $\gamma$ phase of Fe is stabilized. i. e., which phase field is expanded or contracted upon alloying.

Fe−Ni. Figure 3.1-102 shows the Fe−Ni phase equilibria indicating that Ni stabilizes the fcc $\gamma$ phase. If Fe-rich alloys are quenched from the $\gamma$ phase field they transform martensitically to bcc $\alpha'$ martensite. The transformation temperatures are shown in Fig. 3.1-103. The Fe−Ni phase diagram is particularly relevant for the controlled thermal expansion and constant-modulus alloys as well as for the soft magnetic Fe−Ni based materials at higher Ni contents. These, in turn, derive their magnetic properties in part from the occurrence of the superlattice phase $FeNi_3$.

Nickel is added to Fe−C alloys to increase the hardenability and to increase the yield strength of ferrite by solid solution hardening.

Fe−Mn. Figure 3.1-104 shows the Fe−Mn phase equilibria indicating that Mn is stabilizing the fcc $\gamma$ phase similar to Ni. It should be noted that quenching Fe-rich alloys from the $\gamma$-phase field leads to two different martensitic transformations which may result in a bcc structure ($\alpha'$ martensite) or an hcp structure ($\varepsilon'$ martensite). The transformation temperatures are shown in Fig. 3.1-105. The martensitic transformation can also be induced by deformation. This property is exploited

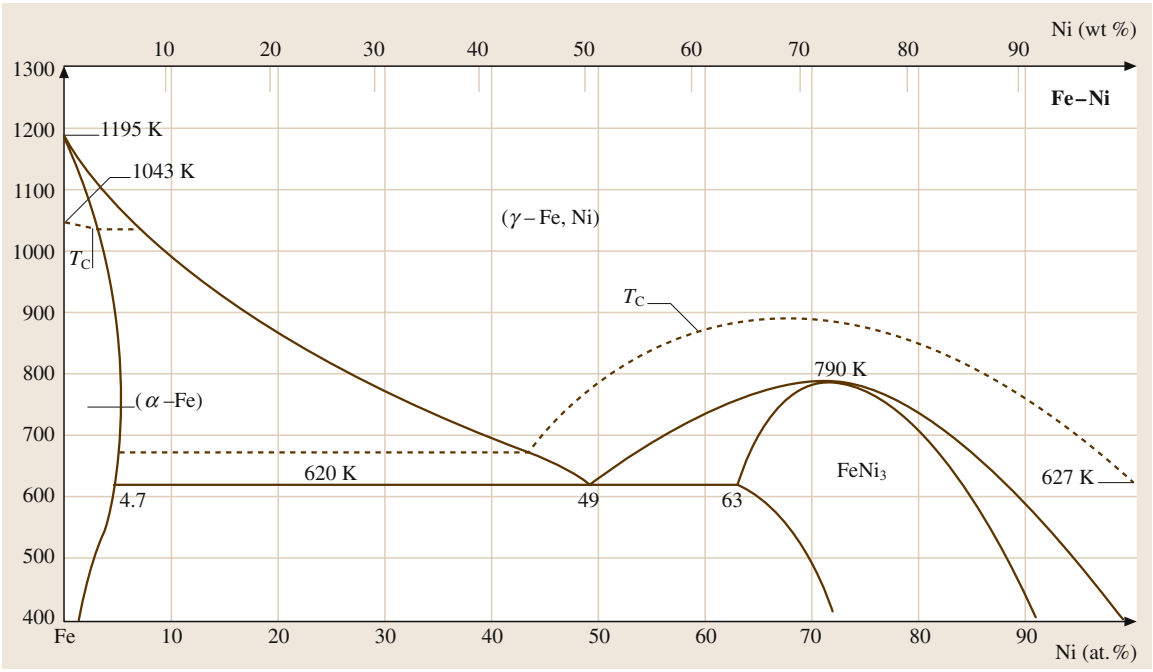


**Fig. 3.1-102** Fe–Ni phase diagram. $T_C$ – Curie temperature [1.82]

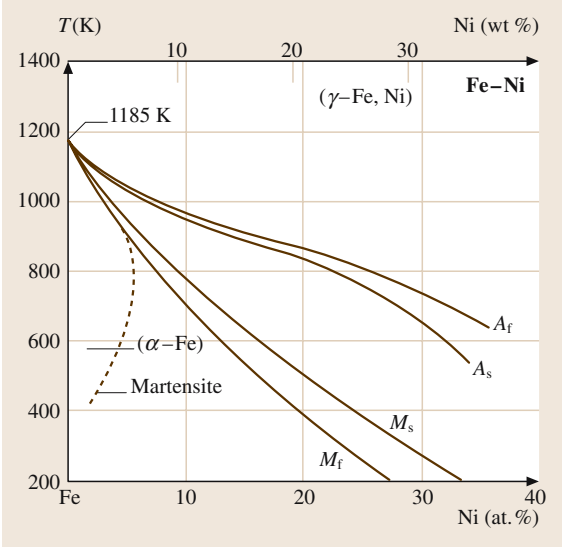


**Fig. 3.1-103** Martensitic transformation temperatures of Fe-rich Fe–Ni alloys. The reverse transformation is characterized by the $A_s$ (austenite start) and $A_f$ (austenite finish) temperatures [1.82]

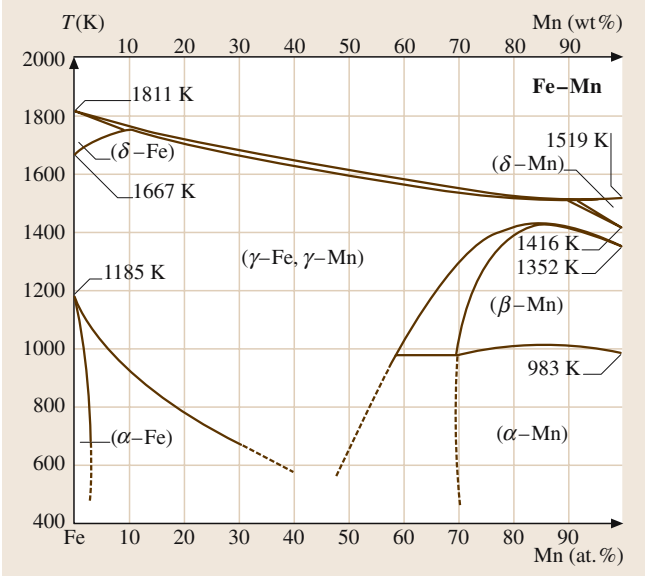


**Fig. 3.1-104** Fe–Mn phase diagram [1.82]

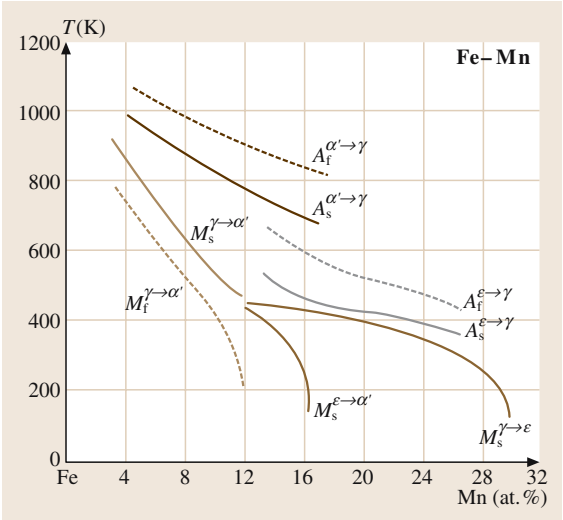


**Fig. 3.1-105** Martensitic transformation temperatures of Fe-rich Fe−Mn alloys. The superscripts indicate the transforming phases [1.82]

in the design of wear-resistant steels (Hatfield steel: 12 wt% Mn, 1 wt% C).

Manganese is contained in practically all commercial steels because it is used for deoxidation of the melt. Typical contents are 0.3–0.9 wt% Mn. Manganese increases the hardenability of steels and contributes moderately to the yield strength by solid solution hardening.

Fe−Cr. The Fe−Cr phase diagram, Fig. 3.1-106, is the prototype of the case of an iron-based system with an $\alpha$-phase stabilizing component. Chromium is the most important alloying element of corrosion resistant, ferritic stainless steels and ferritic heat-resistant steels. If $\alpha$-Fe−Cr alloys are quenched from above 1105 K and subsequently annealed, they decompose according to a metastable miscibility gap shown in Fig. 3.1-107. This decomposition reaction can cause severe embrittlement which is called "475 °C-embrittlement" in ferritic chromium steels. Embrittlement can also occur upon formation of the $\sigma$ phase.

In carbon steels, Cr is added to increase corrosion and oxidation resistance because it promotes the formation of stable passivating and protective oxide layers. Moreover, Cr is a strong carbide former which modifies and delays the formation of pearlite and bainite, thus increasing the hardenability. In heat-resistant steels Cr contributes to the high-temperature yield strength.

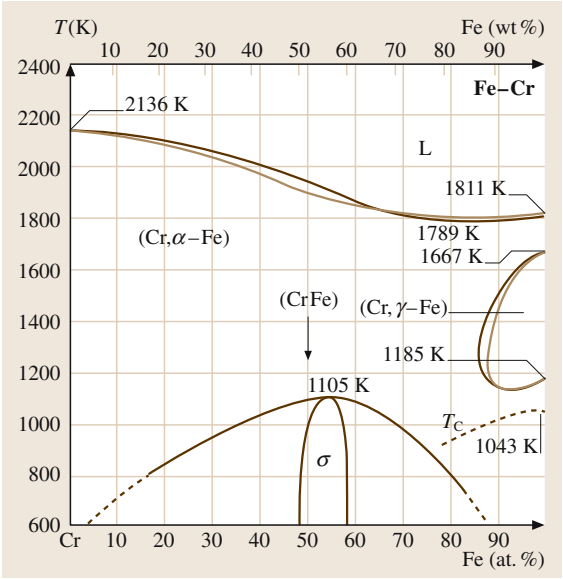


**Fig. 3.1-106** Fe−Cr phase diagram [1.82]

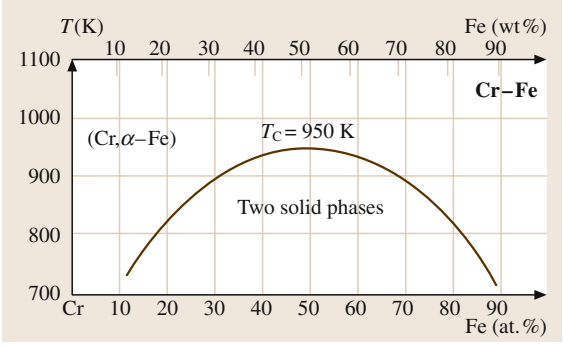


**Fig. 3.1-107** Metastable miscibility gap in the Fe−Cr alloy system [1.82]

Fe−Si. The phase diagram Fe−Si, Fig. 3.1-108, shows that Si is a strong ferrite former. The main application of binary Fe−Si alloys is in the form of steels with $\leq 3.5$ wt% Si which have an optimum combination of high magnetic moment, low magnetostriction, and low magnetocrystalline anisotropy such that they are the ideal material for high induction and low magnetic power loss applications such as power transformers. Data are given in Sect. 4.3.2.3.

In Fe−C steelmaking, Si is one of the principal deoxidizers. It may amount to 0.05–0.3 wt% Si in the steel depending on the deoxidizing treatment and the amount of other deoxidants used. At these levels of concentration Si contributes only moderately to the strength of ferrite and causes no significant loss of ductility.

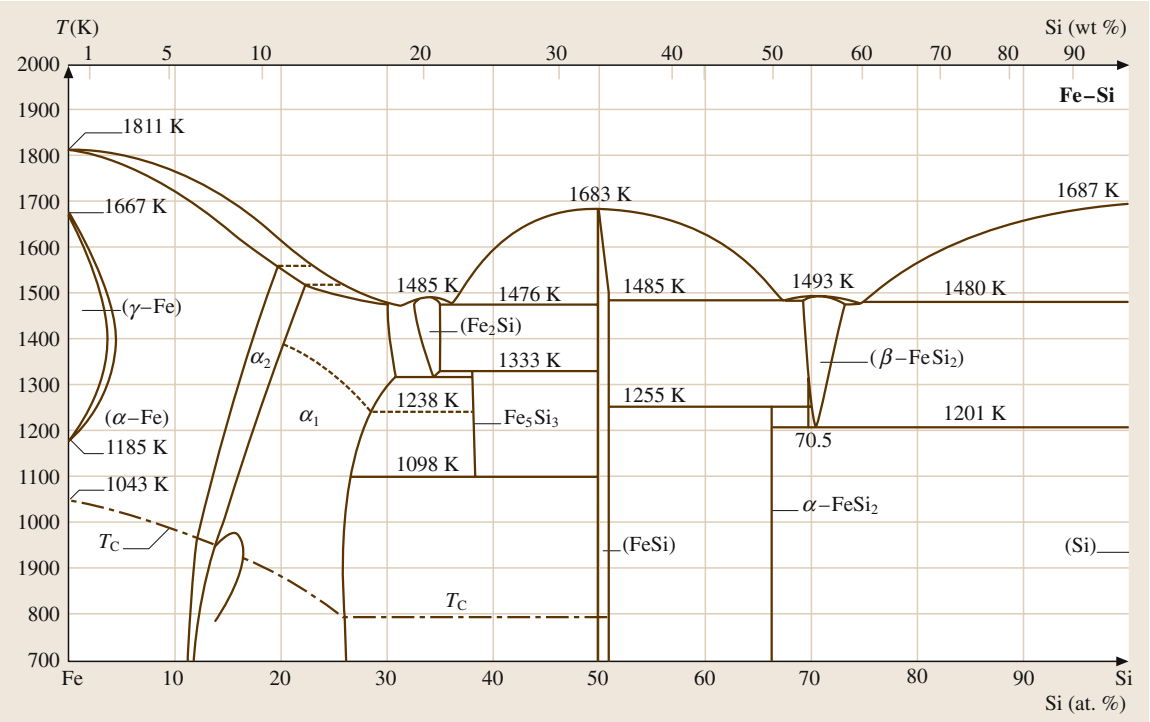


**Fig. 3.1-108** Fe−Si phase diagram [1.82]

### 3.1.5.2 Carbon and Low-Alloy Steels

The largest group of steels produced both by number of variants and by volume is that of carbon and low-alloy steels. It is characterized by the fact that most of the phase relations and phase transformations may be referred to the binary Fe−C phase diagram or comparatively small deviations from it. These steels are treated extensively in [1.80].

#### Compositions and Properties of Carbon Steels

According to the effect of carbon concentration on the phases formed and on their properties, Fig. 3.1-109 shows the variation of the effective average mechanical properties of as-rolled 25-mm bars of plain carbon steels as an approximate survey of the typical concentration dependence.

Carbon steels are defined as containing up to 1 wt% C and a total of 2 wt% alloying elements. Apart from the deoxidizing alloying elements Mn and Si, two impurity elements are always present in carbon steels: phosphorous and sulfur. Phosphorus increases strength and hardness significantly by solid solution hardening, but severely decreases ductility and toughness. Only in exceptional cases may P be added deliberately to increase machinability and corrosion resistance. Sulfur has essentially no effect on the strength properties since it is practically insoluble in ferrite. However, it decreases the ductility and fracture toughness. But S is added deliberately along with an increased Mn content to promote the formation of MnS. This compound is formed in small particles which are comparatively soft and serve as effective chip breakers in free-cutting steel grades, thus increasing machinability. On the basis of these effects of the most common alloying and impurity elements, carbon steel compositions are specified as listed in Table 3.1-41 and free-cutting carbon steel compositions are specified as listed in Table 3.1-42.

A survey of the alloying elements used and of the ranges of composition applied in carbon and low-alloy steels may be gained from the SAE–AISI system of designations for carbon and alloy steels listed in Table 3.1-43. Extensive cross references to other standards may be found in [1.81].

**Table 3.1-41** Standard carbon steel compositions applicable to semi-finished products for forging, hot-rolled and cold-finished bars, wire rods, and seamless tubing [1.80]. Selected grades

| Designation | | Cast or heat chemical ranges and limits[a] (wt%) | | | |
|---|---|---|---|---|---|
| UN number | SAE-AISI number | C | Mn | $P_{max}$ | $S_{max}$ |
| G10050 | 1005 | 0.06 max | 0.35 max | 0.040 | 0.050 |
| G10100 | 1010 | 0.08–0.13 | 0.30–0.60 | 0.040 | 0.050 |
| G10200 | 1020 | 0.18–0.23 | 0.30–0.60 | 0.040 | 0.050 |
| G10300 | 1030 | 0.28–0.34 | 0.60–0.90 | 0.040 | 0.050 |
| G10400 | 1040 | 0.37–0.44 | 0.60–0.90 | 0.040 | 0.050 |
| G10500 | 1050 | 0.48–0.55 | 0.60–0.90 | 0.040 | 0.050 |
| G10600 | 1060 | 0.55–0.65 | 0.60–0.90 | 0.040 | 0.050 |
| G10700 | 1070 | 0.65–0.75 | 0.60–0.90 | 0.040 | 0.050 |
| G10800 | 1080 | 0.75–0.88 | 0.60–0.90 | 0.040 | 0.050 |
| G10900 | 1090 | 0.85–0.98 | 0.60–0.90 | 0.040 | 0.050 |

[a] When silicon ranges or limits are required for bar and semifinished products, the following ranges are commonly used: 0.10% max; 0.10 to 0.20%; 0.15 to 0.35%; 0.20 to 0.40%; or 0.30 to 0.60%. For rods the following ranges are commonly used: 0.10 max; 0.07–0.15%; 0.10–0.20%; 0.15–0.35%; 0.20–0.40%; and 0.30–0.60%. Steels listed in this table can be produced with additions of leaf or boron. Leaded steels typically contain 0.15–0.40% Pb and are identified by inserting the letter L in the desingnation (10L45); boron steels can be expected to contain 0.0005–0.003% B and are identified by inserting the letter B in the desingnation (10B46)

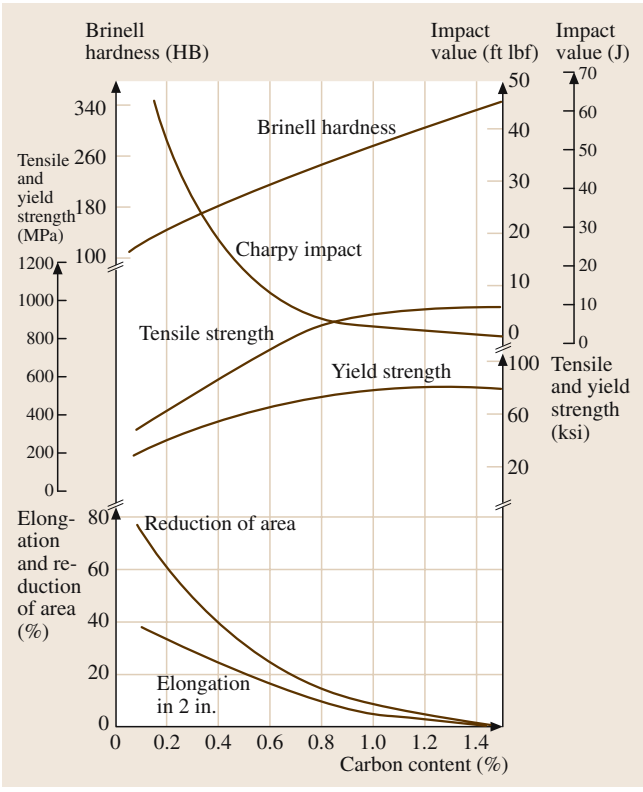


**Fig. 3.1-109** Variations in average mechanical properties of as-rolled 25-mm-diam. bars of plain carbon steels as a function of carbon content [1.80]

**Table 3.1-42** Standard free-cutting (re-sulfurized) carbon steel compositions applicable to semi-finished products for forging, hot-rolled and cold-finished bars, and seamless tubing [1.80]

| Designation | | Cast or heat chemical ranges and limits[a] (wt%) | | | |
|---|---|---|---|---|---|
| UN number | SAE-AISI number | C | Mn | $P_{max}$ | S |
| G11080 | 1108 | 0.08–0.13 | 0.85–0.98 | 0.040 | 0.08–0.13 |
| G11100 | 1110 | 0.08–0.13 | 0.30–0.60 | 0.040 | 0.08–0.13 |
| G11170 | 1117 | 0.14–0.20 | 1.00–1.30 | 0.040 | 0.08–0.13 |
| G11180 | 1118 | 0.14–0.20 | 1.30–1.60 | 0.040 | 0.08–0.13 |
| G11370 | 1137 | 0.32–0.39 | 1.35–1.65 | 0.040 | 0.08–0.13 |
| G11390 | 1139 | 0.35–0.43 | 1.35–1.65 | 0.040 | 0.13–0.20 |
| G11400 | 1140 | 0.37–0.44 | 0.70–1.00 | 0.040 | 0.08–0.13 |
| G11410 | 1141 | 0.37–0.45 | 1.35–1.65 | 0.040 | 0.08–0.13 |
| G11440 | 1144 | 0.40–0.48 | 1.35–1.65 | 0.040 | 0.24–0.33 |
| G11460 | 1146 | 0.42–0.49 | 0.70–1.00 | 0.040 | 0.08–0.13 |
| G11510 | 1151 | 0.48–0.55 | 0.70–1.00 | 0.040 | 0.08–0.13 |

[a] When lead ranges or limits are required or when silicon or limits are required for bars or semifinished products, the values in Table 5 apply. For rods, the following ranges and limits for silicon are commonly used: up to SAE 1110 inclusive, 0.10% max; SAE 1117 and over, 0.10%, 0.10–0.20%, or 0.15–0.35%

**Table 3.1-43** SAE–AISI system of designations for carbon and low-alloy steels [1.80]

| Numerals and digits | Type of steel and nominal alloy content (wt%) |
|---|---|
| **Carbon steels** | |
| 10xx[a] | Plain carbon (Mn 100 max) |
| 11xx | Resulfurized |
| 12xx | Resulfurized and rephosphorized |
| 15xx | Plain carbon (max Mn range: 1.00–1.65) |
| **Manganese steels** | |
| 13xx | Mn 1.75 |
| **Nickel steels** | |
| 23xx | Ni 3.50 |
| 25xx | Ni 5.00 |
| **Nickel–chromium steels** | |
| 31xx | Ni 1.25; Cr 0.65 and 0.80 |
| 32xx | Ni 1.75; Cr 1.07 |
| 33xx | Ni 3.50; Cr 1.50 and 1.57 |
| 34xx | Ni 3.00; Cr 0.77 |
| **Molybdenum steels** | |
| 40xx | Mo 0.20 and 0.25 |
| 44xx | Mo 0.40 and 0.52 |
| **Chromium–molybdenum steels** | |
| 41xx | Cr 0.50, 0.80, and 0.95; Mo 0.12, 0.20, 0.25, and 0.30 |
| **Nickel–chromium–molybdenum steels** | |
| 43xx | Ni 1.82; Cr 0.50 and 0.80; Mo 0.25 |
| 43BVxx | Ni 1.82; Cr 0.50; Mo 0.12 and 0.25; V 0.03 min |
| 47xx | Ni 1.05; Cr 0.45; Mo 0.20 and 0.35 |
| 81xx | Ni 0.30; Cr 0.40; Mo 0.12 |
| 86xx | Ni 0.55; Cr 0.50; Mo 0.20 |

**Table 3.1-43** SAE–AISI system of designations for carbon and low-alloy steels [1.80] , cont.

| Numerals and digits | Type of steel and nominal alloy content (wt%) |
|---|---|
| 87xx | Ni 0.55; Cr 0.50; Mo 0.25 |
| 88xx | Ni 0.55; Cr 0.50; Mo 0.35 |
| 93xx | Ni 3.25; Cr 1.20; Mo 0.12 |
| 94xx | Ni 0.45; Cr 0.40; Mo 0.12 |
| 97xx | Ni 0.55; Cr 0.20; Mo 0.20 |
| 98xx | Ni 1.00; Cr 0.80; Mo 0.25 |
| **Nickel–molybdenum steels** | |
| 46xx | Ni 0.85 and 1.82; Mo 0.20 and 0.25 |
| 48xx | Ni 3.50; Mo 0.25 |
| **Chromium steels** | |
| 50xx | Cr 0.27, 0.40, 0.50, and 0.65 |
| 51xx | Cr 0.80, 0.87, 0.92, 0.95, 1.00, and 1.05 |
| 50xxx | Cr 0.50; C 1.00 min |
| 51xxx | Cr 1.02; C 1.00 min |
| 52xxx | Cr 1.45; C 1.00 min |
| **Chromium–vanadium steels** | |
| 61xx | Cr 0.60, 0.80, and 0.95; V 0.10 and 0.15 min |
| **Tungsten–chromium steels** | |
| 72xx | W 1.75; Cr 0.75 |
| **Silicon–manganese steels** | |
| 92xx | Si 1.40 and 2.00; Mn 0.65, 0.82, and 0.85; Cr 0 and 0.65 |
| **Boron steels** | |
| xxBxx | B denotes boron steel |
| **Leaded steels** | |
| xxLxx | L denotes leaded steel |
| **Vanadium steels** | |
| xxVxx | V denotes vanadium steel |

[a] The xx in the last two digits of these designations indicates that the carbon content (in hundredths of a weight percent) is to be inserted

Turning to the mechanical properties, it should be emphasized that the microstructure has a decisive influence on the properties of all steels. Therefore the composition and the prior thermal, mechanical, or thermomechanical treatments which determine the phase transformations and ensuing microstructural state of a steel will always have to be taken into account. Accordingly, tabulated property data will invariably be given with reference to mechanical and thermal treatments applied. The terms used and their specific definitions are outlined in Sect. 3.1.5.1.

In plain carbon steels the C content and microstructure are determining the mechanical properties. Manganese is providing moderate solid solution strengthening and increases the hardenability. The properties of plain carbon steels are also affected by the other common residual elements Si, P, and S. Furthermore, the gasses O, N, and H and their reaction products may play a role. Their content depends largely on the melting, deoxidizing and pouring practice. While Fig. 3.1-109 illustrates the general effect of C content on the mechanical properties if the austenite grain size and transformation microstructure are held essentially constant. Tables 3.1-44 and 3.1-45 list the mechanical properties of representative carbon and low alloy steels in specified states as a function of deformation and heat treatment.

**Table 3.1-44** Mechanical properties of selected carbon and low-alloy steels in the hot-rolled, normalized, and annealed conditions [1.80]

| AISI No.[a] | Treatment | Austenitizing temperature (°C) | Tensile strength (MPa) | Yield strength (MPa) | Elongation (%) | Reduction in area (%) | Hardness (HB) |
|---|---|---|---|---|---|---|---|
| 1015 | As-rolled | – | 420.6 | 313.7 | 39.0 | 61.0 | 126 |
| | Normalized | 925 | 424.0 | 324.1 | 37.0 | 69.6 | 121 |
| | Annealed | 870 | 386.1 | 284.4 | 37.0 | 69.7 | 111 |
| 1020 | As-rolled | – | 448.2 | 330.9 | 36.0 | 59.0 | 143 |
| | Normalized | 870 | 441.3 | 346.5 | 35.8 | 67.9 | 131 |
| | Annealed | 870 | 394.7 | 294.8 | 36.5 | 66.0 | 111 |
| 1022 | As-rolled | – | 503.3 | 358.5 | 35.0 | 67.0 | 149 |
| | Normalized | 925 | 482.6 | 358.5 | 34.0 | 67.5 | 143 |
| | Annealed | 870 | 429.2 | 317.2 | 35.0 | 63.6 | 137 |
| 1030 | As-rolled | – | 551.6 | 344.7 | 32.0 | 57.0 | 179 |
| | Normalized | 925 | 520.6 | 344.7 | 32.0 | 60.8 | 149 |
| | Annealed | 845 | 463.7 | 341.3 | 31.2 | 57.9 | 126 |
| 1040 | As-rolled | – | 620.5 | 413.7 | 25.0 | 50.0 | 201 |
| | Normalized | 900 | 589.5 | 374.0 | 28.0 | 54.9 | 170 |
| | Annealed | 790 | 518.8 | 353.4 | 30.2 | 57.2 | 149 |
| 1050 | As-rolled | – | 723.9 | 413.7 | 20.0 | 40.0 | 229 |
| | Normalized | 900 | 748.1 | 427.5 | 20.0 | 39.4 | 217 |
| | Annealed | 790 | 636.0 | 365.4 | 23.7 | 39.9 | 187 |
| 1060 | As-rolled | – | 813.6 | 482.6 | 17.0 | 34.0 | 241 |
| | Normalized | 900 | 775.7 | 420.6 | 18.0 | 37.2 | 229 |
| | Annealed | 790 | 625.7 | 372.3 | 22.5 | 38.2 | 179 |
| 1080 | As-rolled | – | 965.3 | 586.1 | 12.0 | 17.0 | 293 |
| | Normalized | 900 | 1010.1 | 524.0 | 11.0 | 20.6 | 293 |
| | Annealed | 790 | 615.4 | 375.8 | 24.7 | 45.0 | 174 |
| 1095 | As-rolled | – | 965.3 | 572.3 | 9.0 | 18.0 | 293 |
| | Normalized | 900 | 1013.5 | 499.9 | 9.5 | 13.5 | 293 |
| | Annealed | 790 | 656.7 | 379.2 | 13.0 | 20.6 | 192 |
| 1117 | As-rolled | – | 486.8 | 305.4 | 33.0 | 63.0 | 143 |
| | Normalized | 900 | 467.1 | 303.4 | 33.5 | 63.8 | 137 |
| | Annealed | 855 | 429.5 | 279.2 | 32.8 | 58.0 | 121 |
| 1118 | As-rolled | – | 521.2 | 316.5 | 32.0 | 70.0 | 149 |
| | Normalized | 925 | 477.8 | 319.2 | 33.5 | 65.9 | 143 |
| | Annealed | 790 | 450.2 | 284.8 | 34.5 | 66.8 | 131 |
| 1137 | As-rolled | – | 627.4 | 379.2 | 28.0 | 61.0 | 192 |
| | Normalized | 900 | 668.8 | 396.4 | 22.5 | 48.5 | 197 |
| | Annealed | 790 | 584.7 | 344.7 | 26.8 | 53.9 | 174 |
| 1141 | As-rolled | – | 675.7 | 358.5 | 22.0 | 38.0 | 192 |
| | Normalized | 900 | 706.7 | 405.4 | 22.7 | 55.5 | 201 |
| | Annealed | 815 | 598.5 | 353.0 | 25.5 | 49.3 | 163 |
| 1144 | As-rolled | – | 703.3 | 420.6 | 21.0 | 41.0 | 212 |
| | Normalized | 900 | 667.4 | 399.9 | 21.0 | 40.4 | 197 |
| | Annealed | 790 | 584.7 | 346.8 | 24.8 | 41.3 | 167 |
| 1340 | Normalized | 870 | 836.3 | 558.5 | 22.0 | 62.9 | 248 |
| | Annealed | 800 | 703.3 | 436.4 | 25.5 | 57.3 | 207 |
| 3140 | Normalized | 870 | 891.5 | 599.8 | 19.7 | 57.3 | 262 |
| | Annealed | 815 | 689.5 | 422.6 | 24.5 | 50.8 | 197 |

**Table 3.1-44** Mechanical properties of selected carbon and low-alloy steels [1.80], cont.

| AISI No.[a] | Treatment | Austenitizing temperature (°C) | Tensile strength (MPa) | Yield strength (MPa) | Elongation (%) | Reduction in area (%) | Hardness (HB) |
|---|---|---|---|---|---|---|---|
| 4130 | Normalized | 870 | 668.8 | 436.4 | 25.5 | 59.5 | 197 |
| | Annealed | 865 | 560.5 | 360.6 | 28.2 | 55.6 | 156 |
| 4140 | Normalized | 870 | 1020.4 | 655.0 | 17.7 | 46.8 | 302 |
| | Annealed | 815 | 655.0 | 417.1 | 25.7 | 56.9 | 197 |
| 4150 | Normalized | 870 | 1154.9 | 734.3 | 11.7 | 30.8 | 321 |
| | Annealed | 815 | 729.5 | 379.2 | 20.2 | 40.2 | 197 |
| 4320 | Normalized | 895 | 792.9 | 464.0 | 20.8 | 50.7 | 235 |
| | Annealed | 850 | 579.2 | 609.5 | 29.0 | 58.4 | 163 |
| 4340 | Normalized | 870 | 1279.0 | 861.8 | 12.2 | 36.3 | 363 |
| | Annealed | 810 | 744.6 | 472.3 | 22.0 | 49.9 | 217 |
| 4620 | Normalized | 900 | 574.3 | 366.1 | 29.0 | 66.7 | 174 |
| | Annealed | 855 | 512.3 | 372.3 | 31.3 | 60.3 | 149 |
| 4820 | Normalized | 860 | 75.0 | 484.7 | 24.0 | 59.2 | 229 |
| | Annealed | 815 | 681.2 | 464.0 | 22.3 | 58.8 | 197 |
| 5140 | Normalized | 870 | 792.9 | 472.3 | 22.7 | 59.2 | 229 |
| | Annealed | 830 | 572.3 | 293.0 | 28.6 | 57.3 | 167 |
| 5150 | Normalized | 870 | 870.8 | 529.0 | 20.7 | 58.7 | 255 |
| | Annealed | 825 | 675.7 | 357.1 | 22.0 | 43.7 | 197 |
| 5160 | Normalized | 855 | 957.0 | 530.9 | 17.5 | 44.8 | 269 |
| | Annealed | 815 | 722.6 | 275.8 | 17.2 | 30.6 | 197 |
| 6150 | Normalized | 815 | 722.6 | 275.8 | 17.2 | 30.6 | 197 |
| | Annealed | 815 | 667.4 | 412.3 | 23.0 | 48.4 | 197 |
| 8620 | Normalized | 915 | 632.9 | 357.1 | 26.3 | 59.7 | 183 |
| | Annealed | 870 | 536.4 | 385.4 | 31.3 | 62.1 | 149 |
| 8630 | Normalized | 870 | 650.2 | 429.5 | 23.5 | 53.5 | 187 |
| | Annealed | 845 | 564.0 | 372.3 | 29.0 | 58.9 | 156 |
| 8650 | Normalized | 870 | 1023.9 | 688.1 | 14.0 | 40.4 | 302 |
| | Annealed | 795 | 715.7 | 386.1 | 22.5 | 46.4 | 212 |
| 8740 | Normalized | 870 | 929.4 | 606.7 | 16.0 | 47.9 | 269 |
| | Annealed | 815 | 695.0 | 415.8 | 22.2 | 46.4 | 201 |
| 9255 | Normalized | 900 | 932.9 | 579.2 | 19.7 | 43.4 | 269 |
| | Annealed | 845 | 774.3 | 486.1 | 21.7 | 41.1 | 229 |
| 9310 | Normalized | 890 | 906.7 | 570.9 | 18.8 | 58.1 | 269 |
| | Annealed | 845 | 820.5 | 439.9 | 17.3 | 42.1 | 241 |

[a] All grades are fine-grained except for those in the 1100 series, which are coarse-grained. Heat-treated specimens were oil quenched unless otherwise indicated

**Table 3.1-45** Mechanical properties of selected carbon and alloy steels in the quenched-and-tempered condition, heat treated as 25 mm rounds [1.80]

| AISI No.[a] | Tempering temperature (°C) | Tensile strength (MPa) | Yield strength (MPa) | Elongation (%) | Reduction in area (%) | Hardness HB |
|---|---|---|---|---|---|---|
| 1030[b] | 205 | 848 | 648 | 17 | 47 | 495 |
| | 315 | 800 | 621 | 19 | 53 | 401 |
| | 425 | 731 | 579 | 23 | 60 | 302 |
| | 540 | 669 | 517 | 28 | 65 | 255 |
| | 650 | 586 | 441 | 32 | 70 | 207 |
| 1040[b] | 205 | 896 | 662 | 16 | 45 | 514 |
| | 315 | 889 | 648 | 18 | 52 | 444 |
| | 425 | 841 | 634 | 21 | 57 | 352 |
| | 540 | 779 | 593 | 23 | 61 | 269 |
| | 650 | 669 | 496 | 28 | 68 | 201 |
| 1040 | 205 | 779 | 593 | 19 | 48 | 262 |
| | 315 | 779 | 593 | 20 | 53 | 255 |
| | 425 | 758 | 552 | 21 | 54 | 241 |
| | 540 | 717 | 490 | 26 | 57 | 212 |
| | 650 | 634 | 434 | 29 | 65 | 192 |
| 1050[b] | 205 | 1124 | 807 | 9 | 27 | 514 |
| | 315 | 1089 | 793 | 13 | 36 | 444 |
| | 425 | 1000 | 758 | 19 | 48 | 375 |
| | 540 | 862 | 655 | 23 | 58 | 293 |
| | 650 | 717 | 538 | 28 | 65 | 235 |
| 1050 | 205 | – | – | – | – | – |
| | 315 | 979 | 724 | 14 | 47 | 321 |
| | 425 | 938 | 655 | 20 | 50 | 277 |
| | 540 | 876 | 579 | 23 | 53 | 262 |
| | 650 | 738 | 469 | 29 | 60 | 223 |
| 1060 | 205 | 1103 | 779 | 13 | 40 | 321 |
| | 315 | 1103 | 779 | 13 | 40 | 321 |
| | 425 | 1076 | 765 | 14 | 41 | 311 |
| | 540 | 965 | 669 | 17 | 45 | 277 |
| | 650 | 800 | 524 | 23 | 54 | 229 |
| 1080 | 205 | 1310 | 979 | 12 | 35 | 388 |
| | 315 | 1303 | 979 | 12 | 35 | 388 |
| | 425 | 1289 | 951 | 13 | 36 | 375 |
| | 540 | 1131 | 807 | 16 | 40 | 321 |
| | 650 | 889 | 600 | 21 | 50 | 255 |
| 1095[b] | 205 | 1489 | 1048 | 10 | 31 | 601 |
| | 315 | 1462 | 1034 | 11 | 33 | 534 |
| | 425 | 1372 | 958 | 13 | 35 | 388 |
| | 540 | 1138 | 758 | 15 | 40 | 293 |
| | 650 | 841 | 586 | 20 | 47 | 235 |
| 1095 | 205 | 1289 | 827 | 10 | 30 | 401 |
| | 315 | 1262 | 813 | 10 | 30 | 375 |
| | 425 | 1213 | 772 | 12 | 32 | 363 |
| | 540 | 1089 | 676 | 15 | 37 | 321 |
| | 650 | 896 | 552 | 21 | 47 | 269 |

**Table 3.1–45** Mechanical properties of selected carbon and alloy steels, cont.

| AISI No.[a] | Tempering temperature (°C) | Tensile strength (MPa) | Yield strength (MPa) | Elongation (%) | Reduction in area (%) | Hardness (HB) |
|---|---|---|---|---|---|---|
| 1137 | 205 | 1082 | 938 | 5 | 22 | 352 |
| | 315 | 986 | 841 | 10 | 33 | 285 |
| | 425 | 876 | 731 | 15 | 48 | 262 |
| | 540 | 758 | 607 | 24 | 62 | 229 |
| | 650 | 655 | 483 | 28 | 69 | 197 |
| 1137[b] | 205 | 1496 | 1165 | 5 | 17 | 415 |
| | 315 | 1372 | 1124 | 9 | 25 | 375 |
| | 425 | 1103 | 986 | 14 | 40 | 311 |
| | 540 | 827 | 724 | 19 | 60 | 262 |
| | 650 | 648 | 531 | 25 | 69 | 187 |
| 1141 | 205 | 1634 | 1213 | 6 | 17 | 461 |
| | 315 | 1462 | 1282 | 9 | 32 | 415 |
| | 425 | 1165 | 1034 | 12 | 47 | 331 |
| | 540 | 896 | 765 | 18 | 57 | 262 |
| | 650 | 710 | 593 | 23 | 62 | 217 |
| 1144 | 205 | 876 | 627 | 17 | 36 | 277 |
| | 315 | 869 | 621 | 17 | 40 | 262 |
| | 425 | 848 | 607 | 18 | 42 | 248 |
| | 540 | 807 | 572 | 20 | 46 | 235 |
| | 650 | 724 | 503 | 23 | 55 | 217 |
| 1330[b] | 205 | 1600 | 1455 | 9 | 39 | 459 |
| | 315 | 1427 | 1282 | 9 | 44 | 402 |
| | 425 | 1158 | 1034 | 15 | 53 | 335 |
| | 540 | 876 | 772 | 18 | 60 | 263 |
| | 650 | 731 | 572 | 23 | 63 | 216 |
| 1340 | 205 | 1806 | 1593 | 11 | 35 | 505 |
| | 315 | 1586 | 1420 | 12 | 43 | 453 |
| | 425 | 1262 | 1151 | 14 | 51 | 375 |
| | 540 | 965 | 827 | 14 | 58 | 295 |
| | 650 | 800 | 621 | – | 66 | 252 |
| 4037 | 205 | 1027 | 758 | 6 | 38 | 310 |
| | 315 | 951 | 765 | 14 | 53 | 295 |
| | 425 | 876 | 731 | 20 | 60 | 270 |
| | 540 | 793 | 655 | 23 | 63 | 247 |
| | 650 | 696 | 421 | 29 | 60 | 220 |
| 4042 | 205 | 1800 | 1662 | 12 | 37 | 516 |
| | 315 | 1613 | 1455 | 13 | 42 | 455 |
| | 425 | 1289 | 1172 | 15 | 51 | 380 |
| | 540 | 986 | 883 | 20 | 59 | 300 |
| | 650 | 793 | 689 | 28 | 66 | 238 |
| 4130[b] | 205 | 1627 | 1462 | 10 | 41 | 467 |
| | 315 | 1496 | 1379 | 11 | 43 | 435 |
| | 425 | 1282 | 1193 | 13 | 49 | 380 |
| | 540 | 1034 | 910 | 17 | 57 | 315 |
| | 650 | 814 | 703 | 22 | 64 | 245 |

**Table 3.1-45** Mechanical properties of selected carbon and alloy steels, cont.

| AISI No.[a] | Tempering temperature (°C) | Tensile strength (MPa) | Yield strength (MPa) | Elongation (%) | Reduction in area (%) | Hardness (HB) |
|---|---|---|---|---|---|---|
| 4140 | 205 | 1772 | 1641 | 8 | 38 | 510 |
| | 315 | 1551 | 1434 | 9 | 43 | 445 |
| | 425 | 1248 | 1138 | 13 | 49 | 370 |
| | 540 | 951 | 834 | 18 | 58 | 258 |
| | 650 | 758 | 655 | 22 | 63 | 230 |
| 4150 | 205 | 1931 | 1724 | 10 | 39 | 530 |
| | 315 | 1765 | 1593 | 10 | 40 | 495 |
| | 425 | 1517 | 1379 | 12 | 45 | 440 |
| | 540 | 1207 | 1103 | 15 | 52 | 370 |
| | 650 | 958 | 841 | 19 | 60 | 290 |
| 4340 | 205 | 1875 | 1675 | 10 | 38 | 520 |
| | 315 | 1724 | 1586 | 10 | 40 | 486 |
| | 425 | 1469 | 1365 | 10 | 44 | 430 |
| | 540 | 1172 | 1076 | 13 | 51 | 360 |
| | 650 | 965 | 855 | 19 | 60 | 280 |
| 5046 | 205 | 1744 | 1407 | 9 | 25 | 482 |
| | 315 | 1413 | 1158 | 10 | 37 | 401 |
| | 425 | 1138 | 931 | 13 | 50 | 336 |
| | 540 | 938 | 765 | 18 | 61 | 282 |
| | 650 | 786 | 655 | 24 | 66 | 235 |
| 50B46 | 205 | – | – | – | – | 560 |
| | 315 | 1779 | 1620 | 10 | 37 | 505 |
| | 425 | 1393 | 1248 | 13 | 47 | 405 |
| | 540 | 1082 | 979 | 17 | 51 | 322 |
| | 650 | 883 | 793 | 22 | 60 | 273 |
| 50B60 | 205 | – | – | – | – | 600 |
| | 315 | 1882 | 1772 | 8 | 32 | 525 |
| | 425 | 1510 | 1386 | 11 | 34 | 435 |
| | 540 | 1124 | 1000 | 15 | 38 | 350 |
| | 650 | 896 | 779 | 19 | 50 | 290 |
| 5130 | 205 | 1613 | 1517 | 10 | 40 | 475 |
| | 315 | 1496 | 1407 | 10 | 46 | 440 |
| | 425 | 1275 | 1207 | 12 | 51 | 379 |
| | 540 | 1034 | 938 | 15 | 56 | 305 |
| | 650 | 793 | 689 | 20 | 63 | 245 |
| 5140 | 205 | 1793 | 1641 | 9 | 38 | 490 |
| | 315 | 1579 | 1448 | 10 | 43 | 450 |
| | 425 | 1310 | 1172 | 13 | 50 | 365 |
| | 540 | 1000 | 862 | 17 | 58 | 280 |
| | 650 | 758 | 662 | 25 | 66 | 235 |
| 5150 | 205 | 1944 | 1731 | 5 | 37 | 525 |
| | 315 | 1737 | 1586 | 6 | 40 | 475 |
| | 425 | 1448 | 1310 | 9 | 47 | 410 |
| | 540 | 1124 | 1034 | 15 | 54 | 340 |
| | 650 | 807 | 814 | 20 | 60 | 270 |

**Table 3.1–45** Mechanical properties of selected carbon and alloy steels, cont.

| AISI No.[a] | Tempering temperature (°C) | Tensile strength (MPa) | Yield strength (MPa) | Elongation (%) | Reduction in area (%) | Hardness (HB) |
|---|---|---|---|---|---|---|
| 5160 | 205 | 2220 | 1793 | 4 | 10 | 627 |
| | 315 | 1999 | 1772 | 9 | 30 | 555 |
| | 425 | 1606 | 1462 | 10 | 37 | 461 |
| | 540 | 1165 | 1041 | 12 | 47 | 341 |
| | 650 | 896 | 800 | 20 | 56 | 269 |
| 51B60 | 205 | – | – | – | – | 600 |
| | 315 | – | – | – | – | 540 |
| | 425 | 1634 | 1489 | 11 | 36 | 460 |
| | 540 | 1207 | 1103 | 15 | 44 | 355 |
| | 650 | 965 | 869 | 20 | 47 | 290 |
| 6150 | 205 | 1931 | 1689 | 8 | 38 | 538 |
| | 315 | 1724 | 1572 | 8 | 39 | 483 |
| | 425 | 1434 | 1331 | 10 | 43 | 420 |
| | 540 | 1158 | 1069 | 13 | 50 | 345 |
| | 650 | 945 | 841 | 17 | 58 | 282 |
| 81B45 | 205 | 2034 | 1724 | 10 | 33 | 550 |
| | 315 | 1765 | 1572 | 8 | 42 | 475 |
| | 425 | 1407 | 1310 | 11 | 48 | 405 |
| | 540 | 1103 | 1027 | 16 | 53 | 338 |
| | 650 | 896 | 793 | 20 | 55 | 280 |
| 8630 | 205 | 1641 | 1503 | 9 | 38 | 465 |
| | 315 | 1482 | 1392 | 10 | 42 | 430 |
| | 425 | 1276 | 1172 | 13 | 47 | 375 |
| | 540 | 1034 | 896 | 17 | 54 | 310 |
| | 650 | 772 | 689 | 23 | 63 | 240 |
| 8640 | 205 | 1862 | 1669 | 10 | 40 | 505 |
| | 315 | 1655 | 1517 | 10 | 41 | 460 |
| | 425 | 1379 | 1296 | 12 | 45 | 400 |
| | 540 | 1103 | 1034 | 16 | 54 | 340 |
| | 650 | 896 | 800 | 20 | 62 | 280 |
| 86B45 | 205 | 1979 | 1641 | 9 | 31 | 525 |
| | 315 | 1696 | 1551 | 9 | 40 | 475 |
| | 425 | 1379 | 1317 | 11 | 41 | 395 |
| | 540 | 1103 | 1034 | 15 | 49 | 335 |
| | 650 | 903 | 876 | 19 | 58 | 280 |
| 8650 | 205 | 1937 | 1675 | 10 | 38 | 525 |
| | 315 | 1724 | 1551 | 10 | 40 | 490 |
| | 425 | 1448 | 1324 | 12 | 45 | 420 |
| | 540 | 1172 | 1055 | 15 | 51 | 340 |
| | 650 | 965 | 827 | 20 | 58 | 280 |
| 8660 | 205 | – | – | – | – | 580 |
| | 315 | – | – | – | – | 535 |
| | 425 | 1634 | 1551 | 13 | 37 | 460 |
| | 540 | 1310 | 1213 | 17 | 46 | 370 |
| | 650 | 1068 | 951 | 20 | 53 | 315 |

**Table 3.1-45** Mechanical properties of selected carbon and alloy steels, cont.

| AISI No.[a] | Tempering temperature (°C) | Tensile strength (MPa) | Yield strength (MPa) | Elongation (%) | Reduction in area (%) | Hardness (HB) |
|---|---|---|---|---|---|---|
| 8740 | 205 | 1999 | 1655 | 10 | 41 | 578 |
| | 315 | 1717 | 1551 | 11 | 46 | 495 |
| | 425 | 1434 | 1358 | 13 | 50 | 415 |
| | 540 | 1207 | 1138 | 15 | 55 | 363 |
| | 650 | 986 | 903 | 20 | 60 | 302 |
| 9255 | 205 | 2103 | 2048 | 1 | 3 | 601 |
| | 315 | 1937 | 1793 | 4 | 10 | 578 |
| | 425 | 1606 | 1489 | 8 | 22 | 477 |
| | 540 | 1255 | 1103 | 15 | 32 | 352 |
| | 650 | 993 | 814 | 20 | 42 | 285 |
| 9260 | 205 | – | – | – | – | 600 |
| | 315 | – | – | – | – | 540 |
| | 425 | 1758 | 1503 | 8 | 24 | 470 |
| | 540 | 1324 | 1131 | 12 | 30 | 390 |
| | 650 | 979 | 814 | 20 | 43 | 295 |
| 94B30 | 205 | 1724 | 1551 | 12 | 46 | 475 |
| | 315 | 1600 | 1420 | 12 | 49 | 445 |
| | 425 | 1344 | 1207 | 13 | 57 | 382 |
| | 540 | 1000 | 931 | 16 | 65 | 307 |
| | 650 | 827 | 724 | 21 | 69 | 250 |

[a] All grades are fine-grained except for those in the 1100 series, which are coarse-grained. Heat-treated specimens were oil quenched unless otherwise indicated

[b] Water quenched

### Hardenability

Hardening of steels is the heat treatment consisting of heating to the range of austenite, cooling in water, oil, or air, and subsequent tempering. The term hardenability refers to the suitability of a steel to be transformed partially or completely from austenite to martensite to a specified depth below the free surface of a workpiece when cooled under specified conditions. This definition reflects that the term hardenability does not only refer to the magnitude of hardness which can be attained for a particular steel, but it relates the extent of hardening achievable to the macroscopic or local cooling rate or isothermal holding time in the transformation range and, thus, to the mechanisms, kinetic phase transformations, and their effects on the mechanical properties.

The amount of martensite formed upon cooling is a function of C content and total steel composition. This behavior is due to two decisive factors of influence:

- The temperature range of transformation of austenite to martensite depends on the C content, as shown in Fig. 3.1-101 of Sect. 3.1.5.1, and
- The diffusion-dependent transformations of austenite (to ferrite, pearlite, and bainite) compete with the martensitic transformation such that the volume fraction available for the latter will decrease as the volume transformed by the former increases. This transformation kinetics of the diffusional phase transformations is strongly dependent on alloy composition.

The lower the cooling rate may be while still permitting one to obtain a high fraction of martensite, the higher the hardenability of steel. This can best be tested by varying the cooling rate and analyzing the resulting microstructure and its hardness (and other mechanical properties). The method used most widely is an ingeniously simple testing procedure, the Jominy end-quench test illustrated in Fig. 3.1-110. The mater-

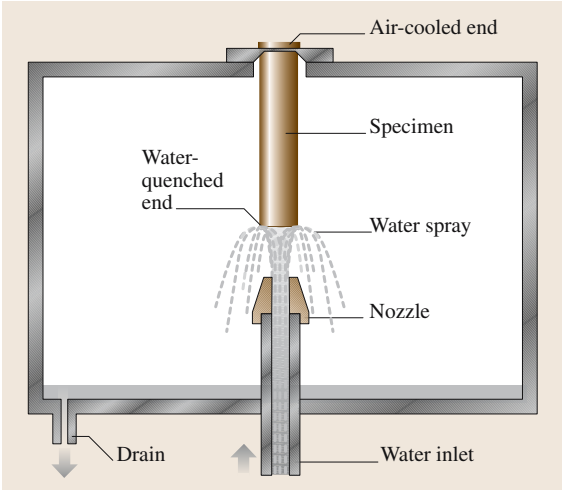


**Fig. 3.1-110** Jominy end-quench apparatus

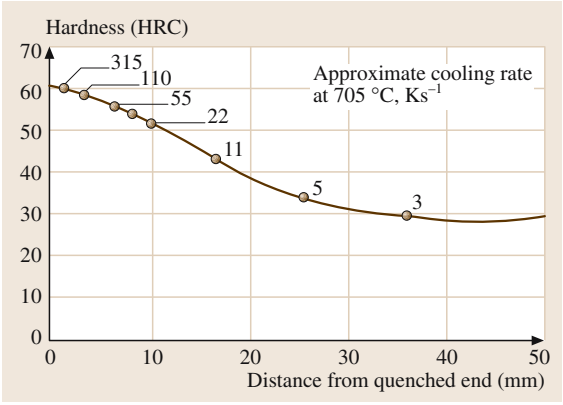


**Fig. 3.1-111** Plot of end-quench hardenability data of an AISI 8650 steel (0.49 wt% C, 0.98 wt% Mn, 0.29 wt% Si, 0.59 wt% Ni, 0.47 wt% Cr, 0.19 wt% Mo) [1.80]

ial to be tested is normalized and a test bar 100 mm long and 25 mm in diameter is machined. This specimen is austenitized and transferred to the fixture (shown in Fig. 3.1-110) holding it vertically 13 mm above the nozzle through which water is directed against the bottom face of the specimen. While the bottom end is quenched by water, the top end is slowly cooled in air and intermediate cooling rates occur at intermediate positions. After the test, hardness readings and microstructural analyses may be taken along the bar. They can be correlated to the pre-determined approximate cooling rate at a given temperature, as shown for a characteristic example in Fig. 3.1-111.

The hardenability of numerous commonly used steels has been characterised quantitatively by extensive investigations of their transformation behavior as a function of temperature and time. These investigations have been carried out in two modes of heat treatment:

- Quenching from the austenite range to a temperature in the transformation range at which the specimen is held isothermally in a salt or a lead bath for different times, and finally quenched to room temperature to be investigated regarding the transformation products by microstructural and supplementary measurements. The resulting plots of the beginning of formation of the different transformation products (sometimes including the fractional amounts and end of transformation) are termed time-temperature-transformation (TTT) or isothermal transformation (IT) diagrams. An example is shown as Fig. 3.1-112.
- Cooling from the austenite range through the transformation range at different cooling rates, and investigating the temperature of onset of transformation of the different products for different cooling rates by microstructural and supplementary measurements, e.g., dilatometry. The resulting plot is called a continuous-cooling-transformation (CCT) diagram. An example is shown in Fig. 3.1-113. The critical cooling rate means the lowest rate for which a fully martensitic state can be obtained.

Apart from empirical determinations of these transformation diagrams, methods of prediction based on nucleation theory and phenomenological growth theory using the Johnson–Mehl–Avrami equation have been devised to estimate TTT diagrams [1.83].

The hardenability increases with increasing carbon and metallic alloy element concentration (with the exception of Co). The transformation kinetics and ensuing hardenability properties are documented extensively in compilations of TTT and CCT diagrams such as [1.84].

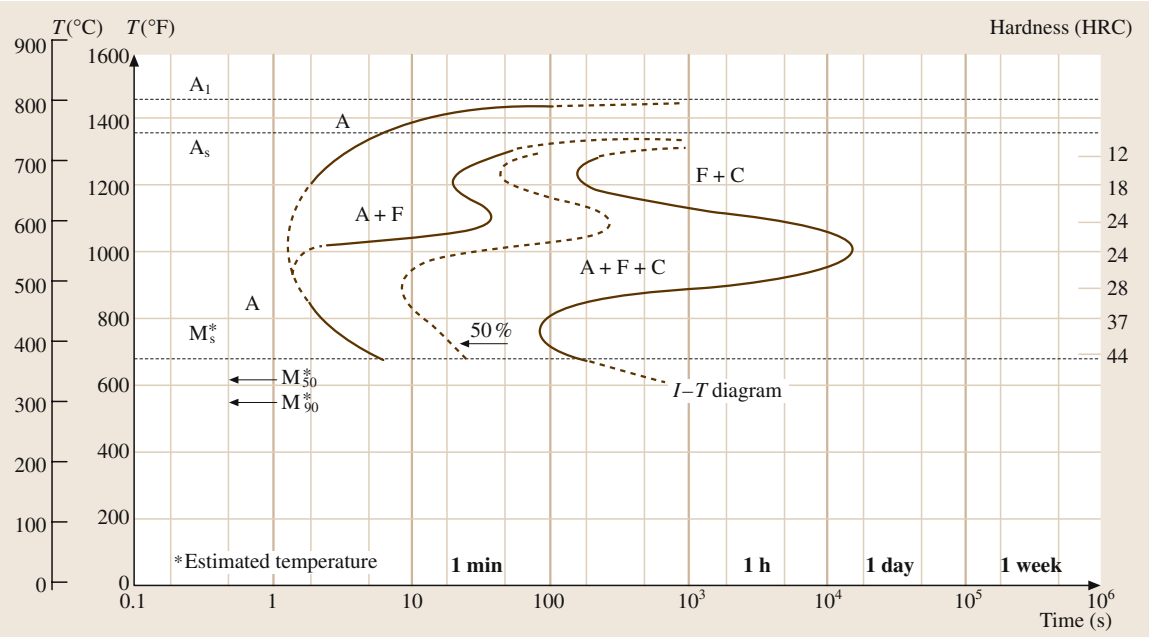


**Fig. 3.1-112** Time-temperature-transformation (TTT) diagram of a 4130 grade low-alloy steel. A – austenite; F – ferrite; C – cementite; M – Martensite (the suffix indicates the amount of martensite formed in vol.%)

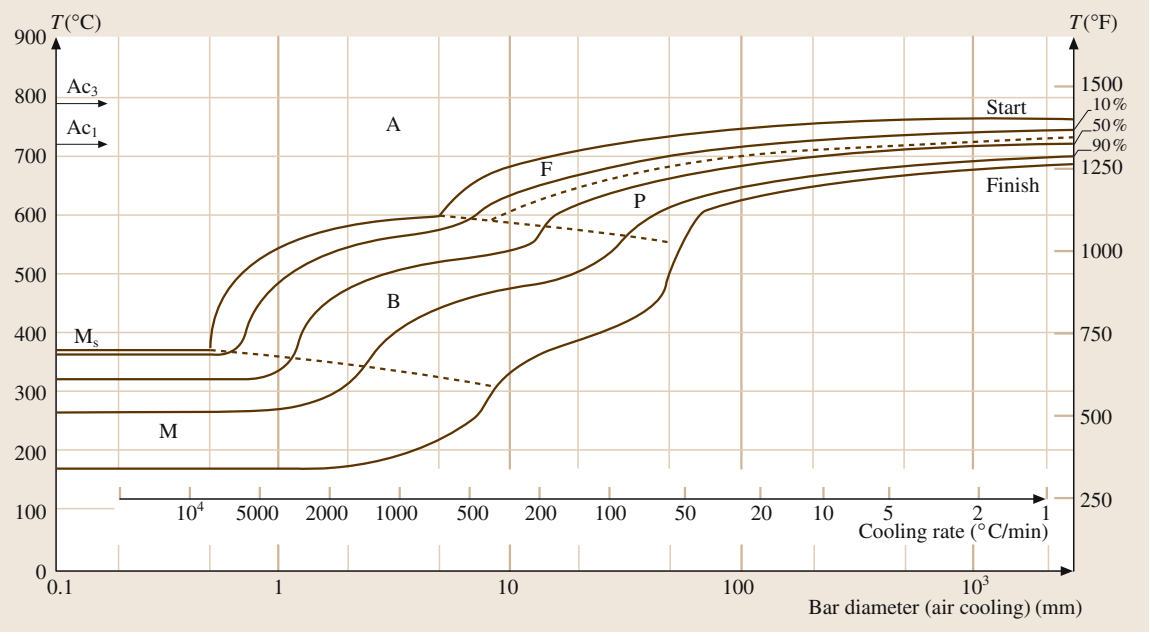


**Fig. 3.1-113** Continuous-cooling-transformation (CCT) diagram for a 4130 grade low-alloy steel. $Ac_3$ and $Ac_1$ signify the temperatures of the $\gamma/(\gamma+\alpha)$ and eutectoid reation, respectively. A – austenite, F – ferrite, B – bainite, P – pearlite, M – martensite. The cooling rate is measured at 705 °C. The calculated critical cooling rate is 143 K/s [1.80]

### 3.1.5.3 High-Strength Low-Alloy Steels

High-strength low-alloy (HSLA) steels are designed to provide higher mechanical property values and/or higher resistance to atmospheric corrosion than conventional low-alloy steels of comparable level of alloy content. Higher yield stress is achieved by adding $\leq 0.1$ wt% N, Nb, V, Ti, and/or Zr (micro-alloying) which form carbide or carbonitrite precipitates, and by special, closely-controlled processing which yields mostly fine-grained microstructures.

HSLA steels contain 0.05 to 0.25 wt% C, $\leq 2$ wt% Mn and mainly Cr, Ni, Mo, and Cu as further alloying elements. Their yield stress is in the range $\geq 275$ MPa. They are primarily hot-rolled into usual wrought product forms and commonly delivered in the as-rolled condition.

The particular processing methods of HSLA steels include [1.80]:

- *Controlled rolling* of micro-alloyed, precipitation hardening variants to obtain fine equiaxial and/or highly deformed, pancake-shaped austenite grains. During cooling these austenite grains transform into fine ferrite grains, providing an optimum combination of high yield strength and ductility.
- *Accelerated cooling* of controlled-rolled steels to enhance the formation of fine ferrite grains.
- *Quenching of steels containing* $\leq 0.08$ wt% C such that acicular ferrite or low-carbon bainite is formed. This microstructural state provides an excellent combination of high yield strengths of 275 to 690 MPa, ductility, formability, and weldability.
- *Normalizing of V-alloyed steel*, thus increasing yield strength and ductility.
- *Intercritical annealing*, i. e., annealing in the $\gamma + \alpha$ phase field to obtain a dual-phase microstructure which, after cooling, consists of martensite islands dispersed in a ferrite matrix. This microstructure exhibits a somewhat lower yield strength but a high rate of work-hardening, providing a better combination of tensile strength, ductility, and formability than conventional HSLA steels.

HSLA steels include numerous standard and proprietary grades designed to provide specific desirable combinations of properties such as strength, ductility, weldability, and atmospheric corrosion resistance. Table 3.1-46 lists characteristic compositions and Table 3.1-47 lists mechanical properties of these characteristic variants.

In view of the multitude of compositional and processing variants of HSLA steels it is useful to have a summarizing overview as provided in Table 3.1-48.

### 3.1.5.4 Stainless Steels

Stainless steels are treated extensively in [1.79]. Compared to carbon or low-alloy steels, they are characterized by an increased resistance against corrosion in aggressive media. The corrosion resistance is achieved basically by an alloy content of at least 11–12 wt% Cr. This content is required to form a dense, pore-free protective surface layer consisting mainly of chromium oxides and hydroxides. The corrosion resistance can be further increased by additional alloying with elements such as Ni, Mo, W, Mn, Si, Cu, Co, Al, or N.

Since chromium has a high affinity to carbon, the formation of chromium carbides may reduce the local concentration of Cr in solution and thus deteriorate the corrosion resistance. This can be avoided by

- Low carbon content of the steel.
- Suitable heat treatment.
- Bonding of carbon by other elements with higher carbon affinity, such as Ti and Nb, so-called stabilization.

Similar effects can be attained by the formation of chromium nitrides. Thus, in addition to the chemical composition of the steel, its corrosion properties are strongly influenced by its heat treatment condition.

Depending on the intended field of application, the corrosion resistance of the steel must often be combined with other useful properties such as high strength or hardness, high temperature strength, good formability, low temperature fracture toughness, weldability or machinability. However, since optimization of one property is generally only possible at the expense of others, the property spectrum of a stainless steel is often the result of a compromise. Consequently, a large number of steel grades has been developed to meet different property requirements. Some steels have been developed just for a single application. The following section gives typical representatives of the various types of stainless steel grades.

Depending on alloy composition and cooling conditions from elevated temperature, stainless steels may occur in different types of microstructure: ferritic (bcc), austenitic (fcc), martensitic, or mixtures of two or all three of these phases. The bcc structure is promoted by the ferrite forming elements Cr, Mo, W, Ti, V, Nb, Al, and Si, whereas the fcc structure is promoted by the austenite

**Table 3.1-46** Compositional limits of HSLA steel grades according to ASTM standards [1.80]

| ASTM specification [a] | Type or grade | UNS designation | Heat compositional limits (wt%) [b] | | | | | | | | | |
|---|---|---|---|---|---|---|---|---|---|---|---|---|
| | | | C | Mn | P | S | Si | Cr | Ni | Cu | V | Other |
| A 242 | Type 1 | K11510 | 0.15 | 1.00 | 0.45 | 0.05 | – | – | – | 0.20 min | – | – |
| A 572 | Grade 42 | – | 0.21 | 1.35 [c] | 0.04 | 0.05 | 0.30 [c] | – | – | 0.20 min [d] | – | [e] |
| | Grade 50 | – | 0.23 | 1.35 [c] | 0.04 | 0.05 | 0.30 [c] | – | – | 0.20 min [d] | – | [e] |
| | Grade 60 | – | 0.26 | 1.35 [c] | 0.04 | 0.05 | 0.30 | – | – | 0.20 min [d] | – | [e] |
| | Grade 65 | – | 0.23 [c] | 1.65 [c] | 0.04 | 0.05 | 0.30 | – | – | 0.20 min [d] | – | [e] |
| A 588 | Grade A | K11430 | 0.10–0.19 | 0.90–1.25 | 0.04 | 0.05 | 0.15–0.30 | 0.40–0.65 | – | 0.25–0.40 | 0.02–0.10 | – |
| | Grade B | K12043 | 0.20 | 0.75–1.25 | 0.04 | 0.05 | 0.15–0.30 | 0.40–0.70 | 0.25–0.50 | 0.20–0.40 | 0.01–0.10 | – |
| | Grade C | K11538 | 0.15 | 0.80–1.35 | 0.04 | 0.05 | 0.15–0.30 | 0.30–0.50 | 0.25–0.50 | 0.20–0.50 | 0.01–0.10 | – |
| | Grade D | K11552 | 0.10–0.20 | 0.75–1.25 | 0.04 | 0.05 | 0.50–0.90 | 0.50–0.90 | – | 0.30 | – | 0.04 Nb, 0.05–0.35 Zr |
| | Grade K | – | 0.17 | 0.50–1.20 | 0.04 | 0.05 | 0.25–0.50 | 0.40–0.70 | 0.40 | 0.30–0.50 | – | 0.10 Mo, 0.005–0.05 Nb |
| A 606 | – | – | 0.22 | 1.25 | – | 0.05 | – | – | – | – | – | – |
| A 607 | Grade 45 | – | 0.22 | 1.35 | 0.04 | 0.05 | – | – | – | 0.20 min [d] | – | [e] |
| | Grade 50 | – | 0.23 | 1.35 | 0.04 | 0.05 | – | – | – | 0.20 min [d] | – | [e] |
| | Grade 55 | – | 0.25 | 1.35 | 0.04 | 0.05 | – | – | – | 0.20 min [d] | – | [e] |
| | Grade 60 | – | 0.26 | 1.50 | 0.04 | 0.05 | – | – | – | 0.20 min [d] | – | [e] |
| | Grade 65 | – | 0.26 | 1.50 | 0.04 | 0.05 | – | – | – | 0.20 min [d] | – | [e] |
| | Grade 70 | – | 0.26 | 1.65 | 0.04 | 0.05 | – | – | – | 0.20 min [d] | – | [e] |
| A 618 | Grade Ia | – | 0.15 | 1.00 | 0.15 | 0.05 | – | – | – | 0.20 min | – | – |
| | Grade Ib | – | 0.20 | 1.35 | 0.04 | 0.05 | – | – | – | 0.20 min [f] | – | – |
| | Grade II | K12609 | 0.22 | 0.85–1.25 | 0.04 | 0.05 | 0.30 | – | – | – | 0.02 min | – |
| | Grade III | K12700 | 0.23 | 1.35 | 0.04 | 0.05 | 0.30 | – | – | – | 0.02 min | 0.005 Nb min [g] |
| A 633 | Grade A | K01802 | 0.18 | 1.00–1.35 | 0.04 | 0.05 | 0.15–0.30 | – | – | – | – | 0.05 Nb |
| | Grade C | K12000 | 0.20 | 1.15–1.50 | 0.04 | 0.05 | 0.15–0.50 | – | – | – | – | 0.05–0.05 Nb |
| | Grade D | K02003 | 0.20 | 0.70–1.60 [c] | 0.04 | 0.05 | 0.15–0.50 | 0.25 | 0.25 | 0.35 | – | 0.08 Mo |
| | Grade E | K12202 | 0.22 | 1.15–1.50 | 0.04 | 0.05 | 0.15–0.50 | – | – | – | 0.04–0.11 | 0.01–0.05 Nb [d], 0.01–0.03 N |
| A 656 | Type 3 | – | 0.18 | 1.65 | 0.025 | 0.035 | 0.60 | – | – | – | 0.08 | 0.020 N, 0.005–0.15 Nb |
| | Type 7 | – | 0.18 | 1.65 | 0.025 | 0.035 | 0.60 | – | – | – | 0.005–0.15 | 0.020 N, 0.005–0.10 Nb |

**Table 3.1-46** Compositional limits of HSLA steel grades according to ASTM standards [1.80], cont.

| ASTM specification [a] | Type or grade | UNS designation | Heat compositional limits (wt%) [b] | | | | | | | | | |
|---|---|---|---|---|---|---|---|---|---|---|---|---|
| | | | C | Mn | P | S | Si | Cr | Ni | Cu | V | Other |
| A 690 | – | K12249 | 0.22 | 0.60–0.90 | 0.08–0.15 | 0.05 | 0.10 | – | 0.40–0.75 | 0.50 min | – | – |
| A 709 | Grade 50, type 1 | – | 0.23 | 1.35 | 0.04 | 0.05 | 0.40 | – | – | – | – | 0.005–0.05 Nb |
| | Grade 50, type 2 | – | 0.23 | 1.35 | 0.04 | 0.05 | 0.40 | – | – | – | 0.01–0.15 | – |
| | Grade 50, type 3 | – | 0.23 | 1.35 | 0.04 | 0.05 | 0.40 | – | – | – | [h] | 0.05 Nb max |
| | Grade 50, type 4 | – | 0.23 | 1.35 | 0.04 | 0.05 | 0.40 | – | – | – | [i] | 0.015 Nb max |
| A 715 | – | – | 0.15 | 1.65 | 0.025 | 0.035 | – | – | – | – | Added as necessary | Ti, Nb added as necessary |
| A 808 | – | – | 0.12 | 1.65 | 0.04 | 0.05 max or 0.010 max | 0.15–0.50 | – | – | – | 0.10 | 0.02–0.10 Nb, V + Nb = 0.15 max |
| A 812 | 65 | – | 0.23 | 1.40 | 0.035 | 0.04 | 0.15–0.50 [j] | – | – | – | V + Nb = 0.02–0.15 | 0.05 Nb max |
| | 80 | – | 0.23 | 1.50 | 0.035 | 0.04 | 0.15–0.50 | 0.35 | – | – | V + Nb = 0.02–0.15 | 0.05 Nb max |
| A 841 | – | – | 0.20 | [k] | 0.030 | 0.030 | 0.15–0.50 | 0.25 | 0.25 | 0.35 | 0.06 | 0.08 Mo, 0.03 Nb, 0.02 Al total |
| A 871 | – | – | 0.20 | 1.50 | 0.04 | 0.05 | 0.90 | 0.90 | 1.25 | 1.00 | 0.10 | 0.25 Mo, 0.15 Zr, 0.05 Nb, 0.05 Ti |

[a] For characteristics and intended uses, see Table 3.1-48; for mechanical properties, see Table 3.1-47.

[b] If a single value is shown, it is a maximum unless otherwise stated.

[c] Values may vary, or minimum value may exist, depending on product size and mill form.

[d] Optional or when specified

[e] May purchased as type 1 (0.005–0.05 Nb), type 2 (0.01–0.15 V), type 3 (0.05 Nb, max, plus 0.02–0.15 V) or type 4 (0.015 N, max, plus V ≥ 4 N).

[f] If chromium and silicon are each 0.50% min, the copper minimum does not apply.

[g] May be substituted for all or part of V.

[h] Niobium plus vanadium, 0.02 to 0.15%.

[i] Nitrogen with vanadium content of 0.015% (max) with a minimum vanadium-to-nitrogen ratio of 4:1.

[j] When silicon-killed steel is specified.

[k] For plate under 40 mm (1.5 in.), manganese contents are 0.70 to 1.35% or up to 1.60% if carbon equivalents do not exceed 0.47%. For plate thicker than 40 mm (1 to 5 in.), ASTM A 841 specifies manganese contents of 1.00 to 1.60%

**Table 3.1-47** Tensile properties of HSLA steel grades specified in ASTM standards [1.80]

| ASTM specification[a] | Type, grade or condition | Product thickness[b] (mm) | Minimum tensile strength[c] (MPa) | Minimum yield strength[c] (MPa) | Minimum elongation (%)[c] in 200 mm | in 50 mm | Bend radius[c] Longitudinal | Transverse |
|---|---|---|---|---|---|---|---|---|
| A242 | Type 1 | 20 | 480 | 345 | 18 | – | – | – |
| | | 20–40 | 460 | 315 | 18 | 21 | – | – |
| | | 40–100 | 435 | 290 | 18 | 21 | – | – |
| A572 | Grade 42 | 150 | 415 | 290 | 20 | 24 | [d] | – |
| | Grade 50 | 100 | 450 | 345 | 18 | 21 | [d] | – |
| | Grade 60 | 32 | 520 | 415 | 16 | 18 | [d] | – |
| | Grade 65 | 32 | 550 | 450 | 15 | 17 | [d] | – |
| A588 | Grades A–K | 100 | 485 | 345 | 18 | 21 | [d] | – |
| | | 100–125 | 460 | 315 | – | 21 | [d] | – |
| | | 125–200 | 435 | 290 | – | 21 | [d] | – |
| A606 | Hot rolled | sheet | 480 | 345 | – | 22 | $t$ | $2t-3t$ |
| | Hot rolled and annealed or normalized | sheet | 450 | 310 | – | 22 | $t$ | $2t-3t$ |
| | Cold rolled | sheet | 450 | 310 | – | 22 | $t$ | $2t-3t$ |
| A607 | Grade 45 | sheet | 410 | 310 | – | 22–25 | $t$ | $1.5t$ |
| | Grade 50 | sheet | 450 | 345 | – | 20–22 | $t$ | $1.5t$ |
| | Grade 55 | sheet | 480 | 380 | – | 18–20 | $1.5t$ | $2t$ |
| | Grade 60 | sheet | 520 | 415 | – | 16–18 | $2t$ | $3t$ |
| | Grade 65 | sheet | 550 | 450 | – | 15–16 | $2.5t$ | $3.5t$ |
| | Grade 70 | sheet | 590 | 485 | – | 14 | $3t$ | $4t$ |
| A618 | Ia, Ib, II | 19 | 485 | 345 | 19 | 22 | $t-2t$ | – |
| | Ia, Ib, II, III | 19–38 | 460 | 315 | 18 | 22 | $t-2t$ | – |
| A633 | A | 100 | 430–570 | 290 | 18 | 23 | [d] | – |
| | C, D | 65 | 485–620 | 345 | 18 | 23 | [d] | – |
| | C, D | 65–100 | 450–590 | 315 | 18 | 23 | [d] | – |
| | E | 100 | 550–690 | 415 | 18 | 23 | [d] | – |
| | E | 100–150 | 515–655 | 380 | 18 | 23 | [d] | – |
| A656 | 50 | 50 | 415 | 345 | 20 | – | [d] | – |
| | 60 | 40 | 485 | 415 | 17 | – | [d] | – |
| | 70 | 25 | 550 | 485 | 14 | – | [d] | – |
| | 80 | 20 | 620 | 550 | 12 | – | [d] | – |
| A690 | – | 100 | 485 | 345 | 18 | – | $2t$ | – |
| A709 | 50 | 100 | 450 | 345 | 18 | 21 | – | – |
| | 50W | 100 | 450 | 345 | 18 | 21 | – | – |
| A715 | Grade 50 | sheet | 415 | 345 | – | 22–24 | 0 | $t$ |
| | Grade 60 | sheet | 485 | 415 | – | 20–22 | 0 | $t$ |
| | Grade 70 | sheet | 550 | 485 | – | 18–20 | $t$ | $1.5t$ |
| | Grade 80 | sheet | 620 | 550 | – | 16–18 | $t$ | $1.5t$ |
| A808 | – | 40 | 450 | 345 | 18 | 22 | – | – |
| | | 40–50 | 450 | 315 | 18 | 22 | – | – |
| | | 50–65 | 415 | 290 | 18 | 22 | – | – |

**Table 3.1-47** Tensile properties of HSLA steel grades specified in ASTM standards [1.80], cont.

| ASTM specification[a] | Type, grade or condition | Product thickness[b] (mm) | Minimum tensile strength[c] (MPa) | Minimum yield strength[c] (MPa) | Minimum elongation (%)[c] in 200 mm | in 50 mm | Bend radius[c] Longitudinal | Transverse |
|---|---|---|---|---|---|---|---|---|
| A812 | 65 | sheet | 585 | 450 | – | 13–15 | – | – |
| | 80 | sheet | 690 | 550 | – | 11–13 | – | – |
| A841 | – | 65 | 485–620 | 345 | 18 | 22 | – | – |
| | | 65–100 | 450–585 | 310 | 18 | 22 | – | – |
| A871 | 60, as-hot-rolled | 5–35 | 520 | 415 | 16 | 18 | – | – |
| | 65, as-hot-rolled | 5–20 | 550 | 450 | 15 | 17 | – | – |

[a] For characteristics and intended uses, see Table 3.1-48; for specified composition limits, see Table 3.1-46
[b] Maximum product thickness exept when a range is given. No thickness are specified for sheet products.
[c] May vary with product size and mill form
[d] Optional supplementary requierement given in ASTM A6

**Table 3.1-48** Summary of characteristics and uses of HSLA steels according to ASTM standards [1.80]

| ASTM specification[a] | Title | Alloying elements[b] | Avalible mill forms | Special characteristics | Intended uses |
|---|---|---|---|---|---|
| A 242 | High-strength low-alloy structural steel | Cr, Cu, N, Ni, Si, Ti, V, Zr | Plate, bar, and shapes $\leq$ 100 mm in thickness | Atmospheric-corrosion resistance four times of carbon steel | Structural members in welded, bolted, or riveted construction |
| A 572 | High-strength low-alloy niobium-vanadium steels of structural quality | Nb, V, N | Plate, bar, and sheet piling $\leq$ 150 mm in thickness | Yield strength of 290 to 450 MPa in six grades | Welded, bolted, or riveted structures, but many bolted or riveted bridges and buildings |
| A 588 | High-strength low-alloy structural steel with 345 MPa minimum yield point $\leq$ 100 mm in thickness | Nb, V, Cr, Ni, Mo, Cu, Si, Ti, Zr | Plate, bar, and shapes $\leq$ 200 mm in thickness | Atmospheric-corrosion resistance four times of carbon steel; nine grades of similar stregth | Welded, bolted, or riveted structures, but primarily welded bridges and buildings in which weight savings or added durability is important |
| A 606 | Steel sheet and strip hot-rolled steel and cold-rolled, high-strength low-alloy with improved corrosion resistance | Not specified | Hot-rolled and cold-rolled sheet and strip | Atmospheric-corrosion twice that of carbon steel (type 2) or four times of carbon steel (type 4) | Structural and miscellaneous purposes for which weight savings or added durability is important |
| A 607 | Steel sheet and strip hot-rolled steel and cold-rolled, high-strength low-alloy niobium and/or vanadium | Nb, V, N, Cu | Hot-rolled and cold-rolled sheet and strip | Atmospheric-corrosion twice that of carbon steel, but only when copper content is specified; yield strength of 310 to 485 MPa in six grades | Structural and miscellaneous purposes for which greater strength or weight savings is important |
| A 618 | Hot formed welded and seamless high-strength low-alloy structural tubing | Nb, V, Si, Cu | Square, rectangular round and special-shape structural welded or seamless tubing | Three grades of similar yield strength; may be purchased with atmospheric-corrosion resistance twice that of carbon steel | General structural purposes include welded, bolted or riveted bridges and buildings |

**Table 3.1-48** Summary of characteristics and uses of HSLA steels according to ASTM standards [1.80], cont.

| ASTM specification[a] | Title | Alloying elements[b] | Avalible mill forms | Special characteristics | Intended uses |
|---|---|---|---|---|---|
| A 633 | Normalized high-strength low-alloy structural steel | Nb, V, Cr, Ni, Mo, Cu, N, Si | Plate, bar, and shapes ≤ 150 mm in thickness | Enhanced notch toughness; yield strength of 290 to 415 MPa in five grades | Welded, bolted, or riveted structures for service at temperatures at or above −45 °C |
| A 656 | High strength low-alloy, hot rolled structural vanadium-aluminium-nitrogen and titanium-aluminium steels | V, Al, N, Ti, Si | Plate, normally ≤ 16 mm in thickness | Yield strength of 552 MPa | Truck frames, brackets, crane booms, rail cars and other applications for witch weight savings is important |
| A 690 | High-strength low-alloy steel H-piles and sheet piling | Ni, Cu, Si | Structural-quality H-pills and sheet piling | Corrosion resistance two to three times greater than that of carbon steel in the splash zone of marine marine structures | Dock walls, sea walls Bulkheads, excavations and similar structures exposed to seawater |
| A 709, grade 50 and 50W | Structural steel | V, Nb, N, Cr, Ni, Mo | All structural-shape groups and plate ≤ 100 mm in thickness | Minimum yield strength of 345 MPa, Grade 50W is a weathering steel | Bridges |
| A 714 | High-strength low-alloy welded and seamless steel pipe | V, NI, Cr, Mo, Cu, Nb | Pipe with nominal pipe size diameters of 13 to 660 mm | Minimum yield strength of ≤ 345 MPa and corrosion resistance two or four times that of carbon steel | Piping |
| A 715 | Steel sheet and strip hot-rolled. high-strength low-alloy with improved formability | Nb, V, Cr, Mo, N, Ti, Zr, B | Hot-rolled sheet and strip | Improved formability[c] compared to a A 606 and A 607; yield strength of 345 to 550 MPa in four grades | Structural and miscellaneous applications for which high strength, weight savings, improved formability and good weldability are important |
| A 808 | High-strength low-alloy steel with improved notch toughness | V, Nb | Hot-rolled plate ≤ 65 mm in thickness | Charpy V-notch impact energies of 40–60 J (40–60 ft lfb) at −45 °C | Railway tank cars |
| A 812 | High-strength low-alloy steels | V, Nb | Steel sheet in coil form | Yield strength of 450–550 MPa | Welded layered pressure vesels |
| A 841 | Plate produced by themomechanical controlled processes | V, Nb, Cr Mo, Ni | Plates ≤ 100 mm in thickness | Yield strength of 310–345 MPa | Welded pressure vessels |
| A 847 | Cold formed welded and seamless high-strength low-alloy structural rubing with improved atmospheric corrosion resistance | Cu, Cr, Ni, Si, V, Ti, Zr, Nb | Welded rubing with maximum periphery of 1625 mm and wall thickness of 16 mm or seamless tubing with maximum periphery of 810 mm and wall thickness of 13 mm | Minimum yield strength ≤ 345 MPa with atmosphieric-corrosion twice that of carbon steel | Round, square, or specially shaped structural tubing for welded, riveted or bolted construction of bridges and buildings |

**Table 3.1-48** Summary of characteristics and uses of HSLA steels according to ASTM standards [1.80], cont.

| ASTM specification[a] | Title | Alloying elements[b] | Avalible mill forms | Special characteristics | Intended uses |
|---|---|---|---|---|---|
| A 860 | High-strength butt-welding fittings of wrought high-strength low-alloy steel | Cu, Cr, Ni, Mo, V, Nb, Ti | Normalized or quenched-and-tempered wrought fittings | Minimum yield strength ≤ 485 MPa | High-pressure gas and oil transmission lines |
| A 871 | High-strength low-alloy steel with atmospheric corrosion resistance | V, Nb, Ti Cu, Mo, Cr | As-rolled plate ≤ 35 mm in thickness | Atmosperic-corrosion resistance four times that of carbon structural steel | Tubular structures and poles |

[a] For grades and mechanical properties, see Table 3.1-47.
[b] In addition to carbon, manganese, phosphorus, and sulfur. A given grade may contain one or more of the listed elements, but not necessarily all of them; for specified compositional limits, see Table 3.1-46.
[c] Obtained by producing killed steel, made to fine grain practice, and with microalloying elements such as niobium, vanadium titanium, and zirconium in the composition.

forming elements C, N, Ni, Mn, Cu, and Co. All alloying elements suppress the austenite to martensite transformation by reducing the $M_s$ temperature, so that the steel may remain fcc at and below room temperature at a sufficiently high alloy content. For a rough estimate of the structural components of a stainless steel as a function of alloy composition, the so-called Schaeffler diagram (initially determined by M. Strauss and E. Maurer in 1920) can be used (see Fig. 3.1-114 [1.77]). It relates the equivalent Cr and Ni content to the observed fractions of martensite, austenite, and ferrite. One of the formulas of the Ni and Cr equivalent used most frequently is that of Schneider [1.85] (in wt%):

$$\mathrm{Cr_{equ}} = \mathrm{Cr} + 2\,\mathrm{Si} + 1.5\,\mathrm{Mo} + 5\,\mathrm{V} + 5.5\,\mathrm{Al} + 1.5\,\mathrm{Ti} + 0.7\,\mathrm{W}$$

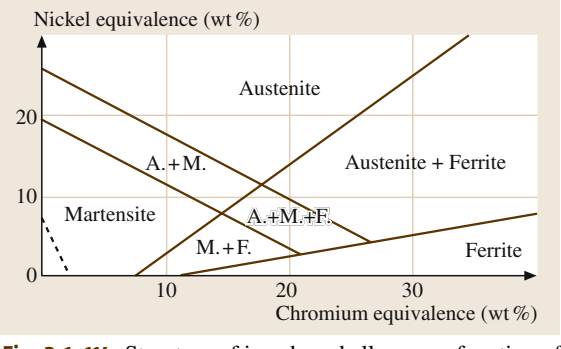


**Fig. 3.1-114** Structure of iron-based alloys as a function of the concentrations of the chromium and nickel equivalent elements. A: austenite (face centered cubic); F: ferrite (body centered cubic); M: martensite (tetragonal-body centered cubic) [1.77]

and

$$\mathrm{Ni_{equ}} = \mathrm{Ni} + \mathrm{Co} + 0.5\,\mathrm{Mn} + 0.3\,\mathrm{Cu} + 25\,\mathrm{N} + 30\,\mathrm{C}\,.$$

### Ferritic Chromium Steels

High chromium (≥ 18 wt% Cr) and low carbon concentrations result in a fully ferritic structure of the steels at all temperatures, i. e., with a bcc delta ferrite structure and no phase transformations. Therefore these steels cannot be strengthened by quenching and tempering. The possibility to increase strength by cold deformation is limited since it decreases ductility and toughness. Steels containing < 18 wt% Cr form some austenite during heating which can be transformed into martensite by fast cooling, thus strengthening the steel. A tempering treatment just below $Ar_1$ results in a mixture of $\delta$-ferrite, $\alpha$-ferrite, and carbides formed from tempered martensite.

In general the toughness of the conventional stainless ferritic chromium steels is not very high, the impact transition temperature often being at or above room temperature and reaching 100 °C after welding (see curve (e) in Fig. 3.1-115). This is due to (i) the tendency of the ferritic stainless steels to pronounced grain coarsing on heat treatments, leading to a relatively large grain size (which cannot be refined by phase transformation) and (ii) the precipitation of chromium carbides at the grain boundaries. Both effects render the steel rather brittle after welding. Furthermore, precipitation of chromium carbides at the grain boundaries causes susceptibility to intergranular corrosion due to the formation of zones with local chromium depletion along the grain boundaries. Some improvement can be achieved

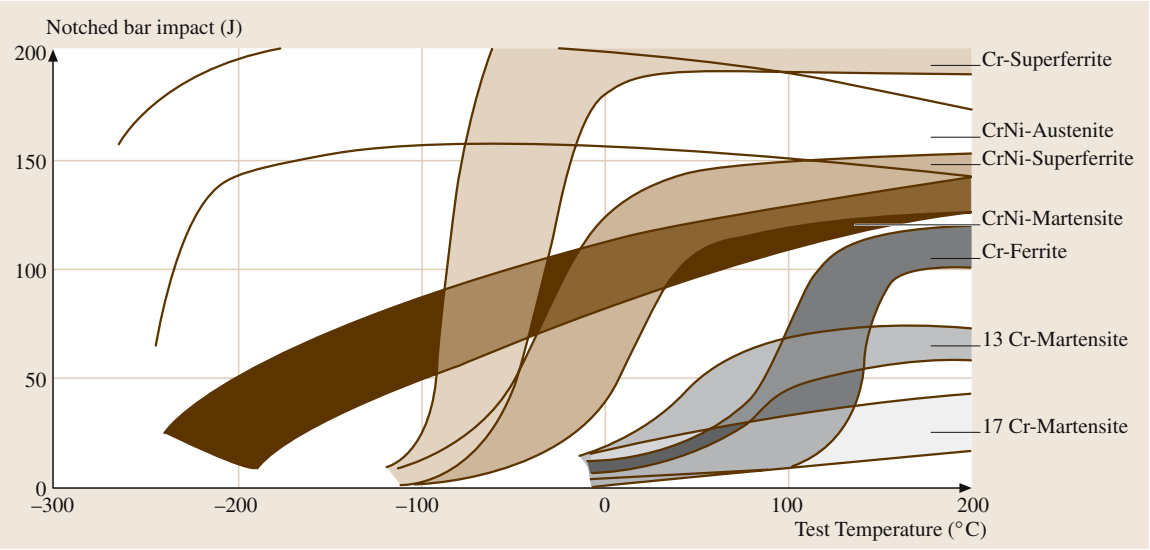


**Fig. 3.1-115** Notched bar impact energy as a function of test temperature of various types of stainless steels (DVM samples: dimension $10 \times 10 \times 55\ mm^3$, notch depth 3 mm, notch root radius 1 mm)

(i) by quenching or a suitable diffusion heat treatment for equilibration of the chromium distribution, and (ii) by a stabilization of the steels with small amounts of Ti and/or Nb which are added to bind the carbon and nitrogen in more stable compounds. In unstabilized steels the carbon content is generally restricted to $\leq 0.1$ wt%. Up to 2 wt% Mo improves the corrosion resistance of ferritic chromium steels, especially in chloride-containing media.

In Table 3.1-49 the chemical composition of a number of ferritic stainless steels is given. The most common representative is the grade X6Cr17/AISI 430. Table 3.1-50 presents some information on hot deformation and recommended heat treatment parameters. Tables 3.1-51 and 3.1-52 show typical data of the mechanical and physical properties, respectively, and Table 3.1-53 reviews the weldability of these steels.

Good ductility and toughness at sub-zero temperatures can be achieved when the carbon and nitrogen content in ferritic steels is reduced to very low concentrations (below 100 ppm) (see curve (a) in Fig. 3.1-115). With higher alloy concentrations on the order of 26–30 wt% Cr, up to 2 wt% Mo, and up to 4 wt% Ni, these so-called superferritic steels exhibit excellent corrosion properties, i. e., high resistance against transcrystalline stress corrosion cracking and chloride-induced pitting corrosion, as well as intercrystalline and general corrosion. However, in order to maintain the low C and N contents even after welding, an effective inert gas shielding is required during welding as it is known for welding of Ti. Obviously, the high purity requirements which have to be observed during melting, hot forming and welding, and some embrittling effects which occur in high Cr steels after lengthy high temperature exposure (475° embrittlement and $\sigma$-phase formation) have precluded as yet a wider application of these steels, in spite of their attractive properties. In addition to their good corrosion resistance these steels possess a higher thermal conductivity than austenitic stainless steels, which is of special interest in heat exchanger applications, and a lower rate of work hardening on cold deformation.

**Table 3.1-49** Chemical composition of ferritic stainless steels

| Grade no. (EN 10088) | Steel designation | ASTM A 276/ AISI grade | Chemical composition (wt%) C | Si | Mn | S | P | Cr | Mo | Others |
|---|---|---|---|---|---|---|---|---|---|---|
| 1.4016 | X6Cr17 | 430 | ≤0.08 | ≤1 | ≤1 | ≤0.03 | | 15.5–17.5 | | |
| 1.4104 | X12CrMoS17 | 430F | 0.10–0.17 | ≤1.5 | ≤1 | 0.15–0.35 | ≤0.06 | 15.5–17.5 | 0.2–0.6 | |
| 1.4105 | X4CrMoS18 | | ≤0.06 | ≤1.5 | ≤1 | 0.15–0.35 | ≤0.06 | 16.5–18.5 | 0.2–0.6 | |
| 1.4509 | X2CrTiNb18 | 441 | ≤0.03 | ≤1 | ≤1 | ≤0.015 | | 17.5–18.5 | | Ti 0.1–0.6 Nb 9$x$% C+ 0.3–1.0 |
| 1.4510 | X3CrTi17 | 430Ti | ≤0.08 | ≤1 | ≤1 | ≤0.03 | ≤0.045 | 16–18 | | Ti ≥ 7$x$% C up to 1.20% |
| 1.4511 | X3CrNb17 | | ≤0.08 | ≤1 | ≤1 | ≤0.03 | ≤0.045 | 16–18 | | Nb ≥ 12$x$% C up to 1.20% |
| 1.4113 | X6Cr Mo17-1 | 434 | ≤0.08 | ≤1 | ≤1 | ≤0.03 | ≤0.045 | 16–18 | 0.9–1.3 | |
| 1.4520 | X2CrTi15 | | ≤0.015 | ≤0.5 | ≤0.5 | ≤0.020 | ≤0.025 | 14–16 | | Ti 0.25–0.40 |
| 1.4521 | X2CrMoTi18-2 | 444 | ≤0.025 | ≤1 | ≤1 | ≤0.03 | ≤0.045 | 17–19 | 1.8–2.3 | Ti ≥ 7$x$% (C+N) up to 0.8, (C+N) ≤ 0.04 |
| | X20Cr20 | 442 | ≤0.2 | ≤1 | ≤1 | ≤0.03 | ≤0.04 | 18–23 | | |
| 1.3810 | X20Cr25 | 446 | ≤0.25 | ≤0.5–2.0 | ≤0.5 | ≤0.03 | ≤0.04 | 23–27 | | |
| [a] | X1CrMo26-1 | | 0.002 | 0.1 | 0.3 | 0.015 | 0.01 | 26 | 1 | N 0.006 |
| [a] | X1CrMo29-4 | | 0.003 | 0.1 | 0.04 | 0.01 | 0.01 | 29.5 | 4 | |
| [a] | X1CrMoNi29-4-2 | | 0.002 | 0.1 | 0.1 | 0.01 | 0.01 | 29.5 | 4 | Ni 2.2 |
| [a] | X2CrMoNiTi25-4-4 | | 0.012 | 0.04 | 0.3 | 0.006 | | 25 | 4 | Ni 4, Ti 0.4 |

[a] Typical values

**Table 3.1-50** Heat treatment conditions of ferritic stainless steels

| Grade no. | Rolling and forging (°C) | Soft annealing Temperature (°C) | Time (min) | Cooling |
|---|---|---|---|---|
| 1.4016 | 1100–800 | 750–850 | 20–30 | Air/water |
| 1.4104 | 1100–800 | 750–850 | 120–180 | Air/furnace |
| 1.4105 | 1100–800 | 750–850 | | Air/water |
| 1.4510 | 1100–800 | 750–850 | 20–30 | Air/water |
| 1.4511 | 1050–750 | 750–850 | 20–30 | Air/water |
| 1.4113 | 1050–750 | 750–850 | 20–30 | Air/water |
| 1.4521 | 1150–750 | 750–900 | | Air/water |
| X1CrMo26-1 | 1150–750 | 750–900 | | Air/water |
| X1CrMo29-4 | 1100–800 | 750–800 | 120–360 | Air/furnace |
| X1CrMoNi29-4-2 | 1150–750 | 750–800 | 15–30 | Air |
| X2CrMoNiTi25-4-4 | 1100–800 | 730–780 | 120–360 | Air/furnace |

**Table 3.1-51** Mechanical properties of ferritic stainless steels

| Grade no. | Heat treatment condition | Tensile properties of flat products ≤ 25 mm in thickness | | |
|---|---|---|---|---|
| | | Min. yield strength or 0.2% proof strength (MPa) | Ultimate tensile strength (MPa) | Min. fracture elongation $A_5$ (%) |
| 1.4016 | Annealed | 270 | 450–600 | 20 |
| 1.4104 | Annealed | 300 | 540–740 | 16 |
| 1.4105 | Annealed | 270 | 450–650 | 20 |
| 1.4510 | Annealed | 270 | 450–600 | 20 |
| 1.4511 | Annealed | 250 | 450–600 | 20 |
| 1.4113 | Annealed | 260 | 480–630 | 20 |
| 1.4521 | Annealed | 320 | 450–650 | 20 |
| X1CrMo26-1 | Annealed | 275 [a] | 450 [a] | 22 [a] |
| X1CrMo29-4 | Annealed | 415 [a] | 550 [a] | 20 [a] |
| X1CrMoNi29-4-2 | Annealed | 415 [a] | 550 [a] | 20 [a] |
| X2CrMoNiTi25-4-4 | Annealed | 550 [a] | 650 [a] | 20 [a] |

[a] Typical values

**Table 3.1-52** Physical properties of ferritic stainless steels

| Grade no. | Mean thermal expansion coefficient between 20 °C and $T$ (°C) in $10^{-6}$ $K^{-1}$ | | | | Density ($kg/dm^3$) | Thermal conductivity at 20 °C (W/K m) | Specific heat at 20 °C (J/g K) | Electrical resistvity at 20 °C (Ω $mm^2/m$) | Modulus of elasticity ($kN/mm^2$) | Magnetizable |
|---|---|---|---|---|---|---|---|---|---|---|
| | 100 | 200 | 300 | 400 | | | | | | |
| 1.4016 | 10.0 | 10.0 | 10.5 | 10.5 | 7.7 | 25 | 0.46 | 0.60 | 220 | yes |
| 1.4104 | 10.0 | 10.5 | 10.5 | 10.5 | 7.7 | 25 | 0.46 | 0.70 | 216 | yes |
| 1.4105 | 10.0 | 10.5 | 10.5 | 10.5 | 7.7 | 25 | 0.46 | 0.70 | 216 | yes |
| 1.4510 | 10.0 | 10.0 | 10.5 | 10.5 | 7.7 | 25 | 0.46 | 0.60 | 220 | yes |
| 1.4511 | 10.0 | 10.0 | 10.5 | 10.5 | 7.7 | 25 | 0.46 | 0.60 | 220 | yes |
| 1.4113 | 10.0 | 10.0 | 10.5 | 10.5 | 7.7 | 25 | 0.46 | 0.70 | 216 | yes |
| 1.4521 | 10.4 | 10.8 | 11.2 | 11.6 | 7.7 | 15 | 0.43 | 0.80 | 220 | yes |

**Table 3.1-53** Weldability of ferritic stainless steels

| Grade no. | Weldable | Welding method | | | | Preheating (°C) | After-treatment | |
|---|---|---|---|---|---|---|---|---|
| | | SAW/MIG/TIG welding | Arc welding | Resistance welding | Autogenous welding | | Annealing | at $T$ (°C) |
| 1.4016 | Yes | + | + | + | (+) | 200 | (+) | 700 |
| 1.4104 | No | – | – | – | – | – | – | – |
| 1.4105 | No | – | – | – | – | – | – | – |
| 1.4510 | Yes | + | + | + | – | 200 | (+) | 750 |
| 1.4511 | Yes | + | + | + | – | 200 | (+) | 750 |
| 1.4113 | Yes | + | + | – | – | – | + | 750 |
| 1.4521 | Yes | + | – | – | – | – | – | – |
| X2CrMoTi29-4 | Yes | + | – | – | – | | | |
| X1CrMo26-1 | Yes | + | – | – | – | | | |
| X1CrMo29-4 | Yes | + | – | – | – | | | |
| X1CrMoNi29-4-2 | Yes | + | – | – | – | | | |

### Martensitic and Martensitic-Ferritic Chromium Steels

Steels with 11.5 to 18 wt% Cr and up to 1.2 wt% C are austenitic at high temperatures and can be transformed into martensite by fast cooling. Due to the high chromium content, the hardenability of these steels is relatively high, so a fully martensitic transformation can be achieved even with relatively large cross sections and moderate cooling rates. They are normally used for applications requiring a combination of high hardness with good corrosion and wear resistance. With carbon contents below about 0.35 wt% C the steels are hypo-eutectic, and some ferrite will be present after heat treatment. They can be austenitized at $\geq$ 960 °C. Steels with $\geq$ 0.40 wt% C and 13 wt% Cr are already hyper-eutectic and will contain some undissolved primary carbides after quenching. To dissolve more carbon, these steels are usually quenched from a higher austenitization temperature around 1050 °C. The steels cannot be hardened if the carbon concentration is below 0.12 wt% C and the chromium content $\geq$ 16 wt% Cr.

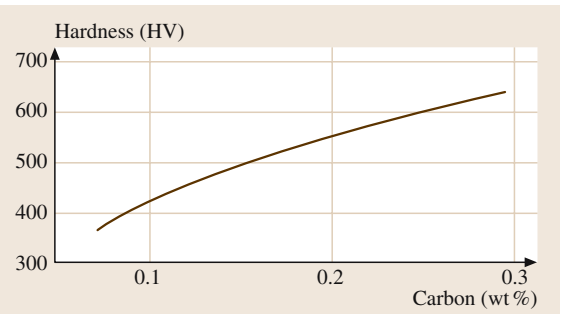


**Fig. 3.1-116** As-quenched hardness as a function of the carbon content of a martensitic 12 wt% Cr steel

In some grades a small content of 0.5–1 wt% Mo (and sometimes some W, V, or Nb) is used to increase the tempering resistance, i. e., to retain higher hardness on tempering by means of precipitation reactions. Increased S contents or Se additions improve the machinability of the steels. About 1–2.5 wt% Ni together with reduced carbon content is applied if hardenabilty of higher cross sections and an improved weldability are required.

The hardness after quenching depends on the carbon content, as illustrated in Fig. 3.1-116 for a 12 wt% Cr steel [1.77]. In the as-quenched state the steels are hard but very brittle. Thus a tempering treatment is necessary to adjust toughness and strength to the level required for a specific application. For high hardness, annealing temperatures of about 100–300 °C are applied, whereas increases in ductility and toughness require tempering at or above 650 °C.

The chemical composition for a number of martensitic Cr steels is given in Table 3.1-54. Tables 3.1-55 – 3.1-58 review data on recommended heat treatment conditions, mechanical properties, physical properties, and weldability, respectively.

It should be noted that a different way to produce stainless steels with high hardness is by precipitation hardening. Such steels have a low carbon content and contain in addition to chromium a few wt% of Ni and Cu. The hardening is caused by Cu precipitates. Others use precipitation hardening by intermetallic phases such as NiTi, TiAl, or NiAl.

**Table 3.1-54** Chemical composition of martensitic and martensitic-ferritic chromium steels

| Grade no. (EN 10088) | Steel designation | ASTM A 276/ AISI grade | Chemical composition (wt%) | | | | | | | |
|---|---|---|---|---|---|---|---|---|---|---|
| | | | C | Si | Mn | P | S | Cr | Mo | Ni |
| 1.4006 | X12Cr13 | 410 | 0.08–0.12 | ≤1.0 | ≤1.0 | ≤0.045 | ≤0.030 | 12.0–14.0 | – | – |
| 1.4005 | X12CrS13 | 416 | ≤0.15 | ≤1.0 | ≤1.0 | 0.15–0.25 | ≤0.045 | 12.0–13.0 | – | – |
| 1.4021 | X20Cr13 | 420 | 0.17–0.25 | ≤1.0 | ≤1.0 | ≤0.045 | ≤0.030 | 12.0–14.0 | – | – |
| 1.4028 | X30Cr13 | 420 | 0.28–0.35 | ≤1.0 | ≤1.0 | ≤0.045 | ≤0.030 | 12.0–14.0 | – | – |
| 1.4104 | X12CrMoS17-2 | 430F | 0.10–0.17 | ≤1.0 | ≤1.5 | ≤0.060 | 0.15–0.35 | 15.5–17.5 | 0.2–0.6 | |
| 1.4057 | X20CrNi17-2 | 431 | 0.14–0.23 | ≤1.0 | ≤1.0 | ≤0.045 | ≤0.030 | 15.5–17.5 | – | 1.50–2.50 |
| 1.4109 | X70CrMo15 | 440A | 0.60–0.75 | ≤1.0 | ≤1.0 | ≤0.045 | ≤0.030 | 13.0–15.0 | 0.50–0.60 | – |
| 1.4125 | X105CrMo17 | 440C | 0.95–1.20 | ≤1.0 | ≤1.0 | ≤0.045 | ≤0.030 | 16.0–18.0 | 0.40–0.80 | |

**Table 3.1-55** Heat treatment conditions of martensitic and martensitic-ferritic chromium steels

| Grade no. | Rolling and forging | Soft annealing | | | Quenching | | | Annealing |
|---|---|---|---|---|---|---|---|---|
| | $T$ (°C) | $T$ (°C) | Time (min) | Cooling | $T$ (°C) | Medium | Hardness HRC ca. | $T$ (°C) |
| 1.4006 | 1100–800 | 750–800 | 120–360 | Air/furnace | 950–1000 | Air/oil | 31 | 780–680 |
| 1.4005 | 1150–750 | 750–800 | 15–30 | Air | 950–1000 | Oil | 31 | 700–600 |
| 1.4021 | 1100–800 | 730–780 | 120–360 | Air/furnace | 980–1030 | Air/oil | 47 | 750–650 |
| 1.4028 | 1100–800 | 730–780 | | Air/furnace | 980–1030 | Air/oil | | 740–640 |
| 1.4104 | 1100–800 | 750–850 | 120–180 | Air/furnace | 980–1030 | Air/oil | 27 | 650–550 |
| 1.4057 | 1100–800 | 650–750 | 180–240 | Air/furnace | 980–1030 | Air/oil | 47 | 720–620 |
| 1.4109 | 1100–900 | 790–840 | 120–360 | Furnace | 1020–1060 | Oil | 59 | 200–150 |
| 1.4125 | 1100–900 | 800–850 | 160–240 | Furnace | 1000–1050 | Oil | 61 | 300–100 |

**Table 3.1-56** Mechanical properties of martensitic and martensitic-ferritic chromium steels

| Grade no. | Heat treatment condition | Tensile properties of flat products ≤25 mm thickness | | | CVN impact energy at room temperature (J) longitudinal/ transversal | Min. yield strength or 0.2% proof strength at $T$ (°C) in MPa | | | |
|---|---|---|---|---|---|---|---|---|---|
| | | Min. yield strength or 0.2% proof strength (MPa) | Ultimate tensile strength (MPa) | Fracture elongation $A_5$ (%) long./transv. | | 100 | 200 | 300 | 400 |
| 1.4006 | Annealed | 250 | 450–650 | 20/15 | –/– | 235 | 225 | 220 | 195 |
| | Quenched and tempered | 420 | 600–800 | 16/12 | –/– | 420 | 400 | 365 | 305 |
| 1.4005 | Quenched and tempered | 440 | 590–780 | 12/– | –/– | – | – | – | – |
| 1.4021 | Annealed | – | ≤740 | – | –/– | | | | |
| | Quenched | 450 | 650–800 | 15/11 | 30/– | 420 | 400 | 365 | 305 |
| | and tempered | 550 | 750–950 | 13/10 | 25/– | | | | |
| 1.4028 | Annealed | – | ≤780 | – | –/– | | | | |
| | Quenched and tempered | 600 | 800–1000 | – | 11/– | | | | |
| 1.4104 | Annealed | 300 | 540–740 | – | –/– | | | | |
| | Quenched and tempered | 450 | 640–840 | – | –/– | | | | |
| 1.4057 | Annealed | – | ≤950 | – | –/– | | | | |
| | Quenched and tempered | 550 | 750–950 | 14/10 | 20/– | 495 | 460 | 430 | 345 |

**Table 3.1-57** Physical properties of martensitic and martensitic-ferritic chromium steels

| Grade no. | Mean thermal expansion coefficient between 20 °C and $T$ (°C) in $10^{-6}$ K$^{-1}$ | | | | Density (kg/dm$^3$) | Thermal conductivity at 20 °C (W/K m) | Specific heat at 20 °C (J/g K) | Electrical resistvity at 20 °C (Ω mm$^2$/m) | Modulus of elasticity (kN/mm$^2$) | Magnetizable |
|---|---|---|---|---|---|---|---|---|---|---|
| | 100 | 200 | 300 | 400 | | | | | | |
| 1.4006 | 10.5 | 11.0 | 11.5 | 12.0 | 7.7 | 30 | 0.46 | 0.60 | 216 | yes |
| 1.4005 | 10.5 | 11.0 | 11.5 | 12.0 | 7.7 | 30 | 0.46 | 0.60 | 216 | yes |
| 1.4021 | 10.0 | 10.0 | 10.5 | 10.5 | 7.7 | 30 | 0.46 | 0.60 | 216 | yes |
| 1.4028 | 10.5 | 11.0 | 11.5 | 12.0 | 7.7 | 30 | 0.46 | 0.65 | 220 | yes |
| 1.4104 | 10.0 | 10.5 | 10.5 | 10.5 | 7.7 | 25 | 0.46 | 0.70 | 216 | yes |
| 1.4057 | 10.0 | 10.5 | 11.0 | 11.0 | 7.7 | 25 | 0.46 | 0.70 | 216 | yes |
| 1.4109 | 10.5 | 11.0 | 11.0 | 11.5 | 7.7 | 30 | 0.46 | 0.65 | 210 | yes |
| 1.4125 | 10.4 | 10.8 | 11.2 | 11.6 | 7.7 | 15 | 0.43 | 0.80 | 220 | yes |

**Table 3.1-58** Weldability of martensitic and martensitic-ferritic chromium steels

| Grade no. | Weldable | Welding method | | | | Pre-heating (°C) | After-treatment | | |
|---|---|---|---|---|---|---|---|---|---|
| | | SAW/MIG TIG welding | Arc welding | Resistance welding | Autogenous welding | | Annealing | at $T$ (°C) | Q+T anew |
| 1.4006 | Yes | + | + | + | (+) | 250 | + | 750 | – |
| 1.4005 | No | – | – | – | – | – | – | – | – |
| 1.4021 | Condit. | + | + | – | – | 350 | + | 720 | (+) |
| 1.4028 | Yes | – | + | – | – | – | + | 720 | – |
| 1.4104 | No | – | – | – | – | – | – | – | – |
| 1.4057 | Condit. | + | + | – | – | 200 | + | 700 | (+) |
| 1.4109 | No | – | – | – | – | – | – | – | – |
| 1.4125 | No | – | – | – | – | – | – | – | – |

### Austenitic Stainless Steels

By adding of austenite forming elements, mainly Ni, the range of stability of the fcc phase is extended down to and below room temperature. The favorable combinations of ductility, toughness, hot and cold formability, weldability, and corrosion resistance have made the austenitic CrNi steels by far the most important and popular stainless steels. The most widespread representatives are the steel grades AISI 304 (X5CrNi18-10, 1.4301) and AISI 316 (X5CrNiMo17-12-2, 1.4401). The austenitic steels are applied in the solution-annealed (at 1000–1100 °C) and fast-cooled state which yields a microstructure that is free of carbide precipitates and has a homogeneous distribution of the alloying elements necessary for good corrosion resistance.

Compared to the bcc ferrite phase the fcc austenite phase is characterized by a higher solubility but a lower diffusivity of almost all alloying elements. The first fact allows the production of single phase fcc alloys with a broad composition spectrum. This permits adjustment of the properties of the steel to specific requirements of corrosion and oxidation resistance, cold and hot strength etc. The low diffusivity makes precipitation processes rather sluggish.

The austenite of the quenched steels can be unstable and can transform into martensite as a result of cold deformation or cooling to sub-zero temperatures, especially if these steels are relatively weakly-alloyed. This transformation leads to increased strength and reduced ductility. Martensite can be detected by magnetization measurements because the austenite is paramagnetic whereas the martensite is ferromagnetic. Since the fcc austenitic steels do not exhibit the ductile-brittle transition characteristic of ferritic alloys, the austenitic steels stay sufficiently ductile even at liquid He temperature (4.2 K) and are thus preferred materials for cryogenic applications. Their yield strength of 200–250 MPa is lower than that of the ferritic steels, but due to their pronounced work hardening by cold deformation (making extensive cold-forming operations difficult and often requiring intermediate soft annealing heat treatments), they have a higher tensile strength and fracture elon-

gation. A pronounced solid solution strengthening is possible, especially by higher concentrations of nitrogen (up to about 0.4 wt% N). The nitrogen-alloyed CrNi steels are characterized by particularly favorable combinations of mechanical and corrosion properties.

As mentioned above, after fast cooling from $\geq 1000\,^{\circ}C$, the austenitic stainless steels are free of carbide precipitates. But since steels with $\geq 0.05$ wt% C are already carbon-supersaturated at temperatures below 900 °C, holding the material at temperatures between about 400 and 900 °C will lead to preciptation of chromium carbides (mainly $M_{23}C_6$ type), preferentially at the grain boundaries. This will result in an increased susceptibility to intergranular corrosion due to local chromium depletion. The means to avoid this undesirable effect are the same as for the ferritic steels: bonding of the carbon (and nitrogen) atoms by an overstoichiometric alloying with Nb, Ta, or Ti (so-called stabilization of the steels), or the reduction of the carbon content to below 0.03 wt% C resulting in the development of the extra low carbon (ELC) steels. However, in strongly oxidative media (such as concentrated nitric acid) even steels that have been sufficiently stabilized by Ti may exhibit intergranular corrosion due to selective dissolution of the TiC. Under less severe corrosion conditions, the Ti stabilized steels are as stable as the Nb stabilized grades but at somewhat lower costs.

Chemical compositions, heat treatment conditions, physical properties, and hints to weldability of austenitic stainless steels are presented in Tables 3.1-59 – 3.1-63.

**Table 3.1-59** Heat treatment conditions of austenitic stainless steels

| Grade no. | Rolling and forging temperature (°C) | Cooling | Quenching temperature (°C) | Cooling |
|---|---|---|---|---|
| 1.4541<br>1.4401<br>1.4402<br>1.4406<br>1.4436<br>1.4571<br>1.4580 | 1150–750 | Air | 1020–1100 | Air, > 2 mm water |
| 1.4301<br>1.4303<br>1.4305<br>1.4306<br>1.4311 | 1150–750 | Air | 1000–1080 | Air, > 2 mm water |
| 1.4550 | 1150–750 | Air | 1050–1150 | Air, > 2 mm water |
| 1.4429<br>1.4438<br>1.4439 | 1150–750 | Air | 1040–1120 | Air, > 2 mm water |
| 1.4435 | 1150–750 | Air, below 600 °C furnace | 1020–1100 | Air, > 2 mm water |

**Table 3.1-60** Chemical composition of austenitic stainless steels

| Grade no. (EN 10088) | Steel designation | ASTM A 276/ AISI grade | Chemical composition (wt%) C | Si | Mn | P | S | Cr | Ni | Mo | Others |
|---|---|---|---|---|---|---|---|---|---|---|---|
| 1.4310 | X12CrNi17-7 | 301 | ≤0.12 | ≤1.5 | ≤2.0 | ≤0.045 | 0.030 | 16.0–18.0 | 6.0–9.0 | | |
| 1.4301 | X5CrNi18-10 | 304 | ≤0.07 | ≤1.0 | ≤2.0 | ≤0.045 | ≤0.030 | 17.0–19.0 | 8.5–10.5 | | |
| 1.4303 | X5CrNi18-12 | 305, 308 | ≤0.07 | ≤1.0 | ≤2.0 | 0.15–0.25 | ≤0.045 | 17.0–19.0 | 11.0–13.0 | | |
| 1.4305 | X10CrNiS18-9 | 303 | ≤0.12 | ≤1.0 | ≤2.0 | ≤0.060 | 0.15–0.35 | 17.0–19.0 | 8.0–10.0 | | |
| 1.4306 | X2CrNi19-11 | 304L | ≤0.03 | ≤1.0 | ≤2.0 | ≤0.045 | ≤0.030 | 18.0–20.0 | 10.0–12.5 | | |
| 1.4311 | X2CrNiN18-10 | 304LN | ≤0.03 | ≤1.0 | ≤2.0 | ≤0.060 | 0.15–0.35 | 17.0–19.0 | 8.5–11.5 | | N 0.12–0.22 |
| 1.4541 | X6CrNiTi18-10 | 321 | ≤0.08 | ≤1.0 | ≤2.0 | ≤0.045 | ≤0.030 | 17.0–19.0 | 9.0–12.0 | | Ti 5$x$% C up to 0.80 |
| 1.4550 | X6CrNiNb18-10 | 347 | ≤0.08 | ≤1.0 | ≤2.0 | ≤0.045 | ≤0.030 | 17.0–19.0 | 9.0–12.0 | | Nb 10$x$% C up to 1.0 |
| 1.4401 | X5CrNiMo17-12-2 | 316 | ≤0.07 | ≤1.0 | ≤2.0 | ≤0.045 | ≤0.030 | 16.5–18.5 | 10.5–13.5 | 2.0–2.5 | |
| 1.4404 | X2CrNiMo17-13-2 | 316L | ≤0.03 | ≤1.0 | ≤2.0 | ≤0.045 | ≤0.030 | 16.5–18.5 | 11.0–14.0 | 2.0–2.5 | |
| 1.4406 | X2CrNiMoN17-12-2 | 316LN | ≤0.03 | ≤1.0 | ≤2.0 | ≤0.045 | ≤0.030 | 16.5–18.5 | 10.5–13.5 | 2.0–2.5 | N 0.12–0.22 |
| 1.4571 | X6CrNiMoTi17-12-2 | 316Ti | ≤0.08 | ≤1.0 | ≤2.0 | ≤0.045 | ≤0.030 | 16.5–18.5 | 10.5–13.5 | 2.0–2.5 | Ti 5$x$% C up to 0.80 |
| 1.4580 | X6CrNiMoNb17-12-2 | 316Cb | ≤0.08 | ≤1.0 | ≤2.0 | ≤0.045 | ≤0.030 | 16.5–18.5 | 10.5–13.5 | 2.0–2.5 | Nb 10$x$% C up to 1.0 |
| 1.4429 | X2CrNiMoN17-13-3 | 316LN | ≤0.03 | ≤1.0 | ≤2.0 | ≤0.045 | ≤0.025 | 16.5–18.5 | 11.5–14.5 | 2.5–3.0 | N 0.14–0.22 |
| 1.4435 | X2CrNiMo18-14-3 | 316L<br>317L | ≤0.03 | ≤1.0 | ≤2.0 | ≤0.045 | ≤0.025 | 17.0–18.5 | 12.5–15.0 | 2.5–3.0 | |
| 1.4436 | X5CrNiMo17-13-3 | 316 | ≤0.07 | ≤1.0 | ≤2.0 | ≤0.045 | ≤0.025 | 16.5–18.5 | 11.0–14.0 | 2.5–3.0 | |
| 1.4438 | X2CrNiMo18-16-4 | 317L | ≤0.03 | ≤1.0 | ≤2.0 | ≤0.045 | ≤0.025 | 17.5–19.5 | 14.0–17.0 | 3.0–4.0 | |
| 1.4439 | X2CrNiMoN17-13-5 | F48<br>201<br>202 | ≤0.03<br>≤0.15<br>≤0.15 | ≤1.0<br>≤1.0<br>≤1.0 | ≤2.0<br>5.5–7.5<br>7.5–10.0 | ≤0.045<br>≤0.06<br>≤0.06 | ≤0.025<br>≤0.03<br>≤0.03 | 16.5–18.5<br>16.8–18.0<br>17.0–19.0 | 12.5–14.5<br>3.5–5.5<br>4.0–6.0 | 4.0–5.0 | N 0.12–0.22<br>N 0.25<br>N 0.25 |
| (1.4828) | (X15CrNiSi20-12) | 309 | ≤0.20 | ≤1.0 | ≤2.0 | ≤0.045 | ≤0.03 | 22.0–24.0 | 12.0–15.0 | | |
| (1.4845) | (X12CrNi25-21) | 310 | ≤0.25 | ≤1.5 | ≤2.0 | ≤0.045 | ≤0.03 | 24.0–26.0 | 19.0–22.0 | | |

**Table 3.1-61** Mechanical properties of austenitic stainless steels

| Grade no. | Heat treatment condition | Tensile properties of flat products ≤ 25 mm thickness | | | Min. CVN impact energy at room temperarture (J) | Min. yield strength or 0.2% proof strength at $T$ (°C) in MPa | | | | |
|---|---|---|---|---|---|---|---|---|---|---|
| | | Min. yield strength or 0.2% proof strength (MPa) | Ultimate tensile strength (MPa) | Min. fracture elongation $A_5$ (%) | | 100 | 200 | 300 | 400 | 500 |
| 1.4310 | Quenched | 260 | 600–950 | 35 | 105 | – | – | – | – | – |
| 1.4301 | Quenched | 195 | 500–700 | 45 | 85 | 157 | 127 | 110 | 98 | 92 |
| 1.4303 | Quenched | 185 | 490–690 | 45 | 85 | 155 | 127 | 110 | 98 | 92 |
| 1.4305 | Quenched | 195 | 500–700 | 35 | – | – | – | – | – | – |
| 1.4306 | Quenched | 180 | 460–680 | 45 | 85 | 147 | 118 | 100 | 89 | 81 |
| 1.4311 | Quenched | 270 | 550–760 | 40 | 85 | 205 | 157 | 136 | 125 | 119 |
| 1.4541 | Quenched | 200 | 500–730 | 40 | 85 | 176 | 157 | 136 | 125 | 119 |
| 1.4550 | Quenched | 205 | 510–740 | 40 | 85 | 177 | 157 | 136 | 125 | 119 |
| 1.4401 | Quenched | 205 | 510–710 | 40 | 85 | 177 | 147 | 127 | 115 | 110 |
| 1.4404 | Quenched | 190 | 490–690 | 40 | 85 | 166 | 137 | 118 | 108 | 100 |
| 1.4406 | Quenched | 280 | 580–800 | 40 | 85 | 211 | 167 | 145 | 135 | 129 |
| 1.4571 | Quenched | 210 | 500–730 | 35 | 85 | 185 | 167 | 145 | 135 | 129 |
| 1.4580 | Quenched | 215 | 510–740 | 35 | 85 | 186 | 167 | 145 | 135 | 129 |
| 1.4429 | Quenched | 295 | 580–800 | 40 | 85 | 225 | 178 | 155 | 145 | 138 |
| 1.4435 | Quenched | 190 | 490–690 | 35 | 85 | 166 | 137 | 118 | 108 | 100 |
| 1.4436 | Quenched | 205 | 510–710 | 40 | 85 | 177 | 147 | 127 | 115 | 110 |
| 1.4438 | Quenched | 195 | 490–690 | 35 | 85 | 172 | 147 | 127 | 115 | 110 |
| 1.4439 | Quenched | 285 | 580–800 | 35 | 85 | 225 | 185 | 165 | 150 | – |
| AISI 201 | | 370[a] | 1125[a] | 57[a] | | | | | | |
| AISI 202 | | 359[a] | 1110[a] | 55[a] | | | | | | |
| AISI 309 | | 334[a] | 691[a] | 48[a] | | | | | | |
| AISI 310 | | 319[a] | 678[a] | 50[a] | | | | | | |

[a] Typical values

**Table 3.1-62** Physical properties of austenitic stainless steels

| Grade no. | Mean thermal expansion coefficient between 20 °C and $T$ (°C) in $10^{-6}$ $K^{-1}$ | | | | | | | | Density (kg/dm$^3$) | Thermal conductivity at 20 °C (W/K m) | Specific heat at 20 °C (J/g K) | Electrical resistivity at 20 °C (Ω mm$^2$/m) | Modulus of elasticity at 20 °C (kN/mm$^2$) | Magnetizable |
|---|---|---|---|---|---|---|---|---|---|---|---|---|---|---|
| | 100 | 200 | 300 | 400 | 500 | 600 | 700 | 800 | | | | | | |
| 1.4310 | 16.4 | 16.9 | 17.4 | 17.8 | 18.2 | | | | 8.0 | 15 | 0.45 | 0.80 | 198 | No |
| 1.4301 | 16.0 | 17.0 | 17.0 | 18.0 | 18.0 | 18.5 | 18.5 | 19.0 | 7.9 | 15 | 0.50 | 0.73 | 200 | No |
| 1.4303 | 16.0 | 17.0 | 17.0 | 18.0 | 18.0 | | | | 7.9 | 15 | 0.50 | 0.73 | 200 | No |
| 1.4305 | 16.0 | 17.0 | 17.0 | 18.0 | 18.0 | 18.5 | 18.5 | 19.0 | 7.9 | 15 | 0.50 | 0.73 | 200 | No |
| 1.4306 | | | | | | | | | | | | | | |
| 1.4311 | | | | | | | | | | | | | | |
| 1.4541 | | | | | | | | | | | | | | |
| 1.4550 | | | | | | | | | | | | | | |

**Table 3.1-62** Physical properties of austenitic stainless steels, cont.

| Grade no. | Mean thermal expansion coefficient between 20 °C and $T$ (°C) in $10^{-6}$ $K^{-1}$ | | | | | | | | Density ($kg/dm^3$) | Thermal conductivity at 20 °C (W/K m) | Specific heat at 20 °C (J/g K) | Electrical resistivity at 20 °C ($\Omega$ $mm^2/m$) | Modulus of elasticity at 20 °C ($kN/mm^2$) | Magnetizable |
|---|---|---|---|---|---|---|---|---|---|---|---|---|---|---|
| | 100 | 200 | 300 | 400 | 500 | 600 | 700 | 800 | | | | | | |
| 1.4401<br>1.4404<br>1.4406<br>1.4435<br>1.4436<br>1.4571<br>1.4580 | 16.5 | 17.5 | 17.5 | 18.5 | 18.5 | 19.0 | 19.5 | 19.5 | 7.98 | 15 | 0.50 | 0.75 | 200 | No |
| 1.4429 | 16.5 | 17.5 | 17.5 | 18.5 | 18.5 | | | | 7.98 | 15 | 0.50 | 0.75 | 200 | No |
| 1.4438 | 16.5 | 17.5 | 18.0 | 18.5 | 19.0 | 19.0 | 19.5 | 19.5 | 8.0 | 14 | 0.50 | 0.85 | 200 | No |
| 1.4439 | 16.5 | 17.5 | 17.5 | 18.5 | 18.5 | | | | 8.02 | 14 | 0.50 | 0.85 | 200 | No |

**Table 3.1-63** Weldability of austenitic stainless steels welding methods not in parentheses are to be preferred

| Grade no. | Weldable | Welding method | | | | Preheating (°C) | After-treatment |
|---|---|---|---|---|---|---|---|
| | | SAW/MIG/TIG welding | Arc welding | Resistance welding | Autogenous welding | | |
| 1.4310 | Yes | + | + | + | + | – | – |
| 1.4301<br>1.4303<br>1.4306<br>1.4438<br>1.4541<br>1.4550<br>1.4401<br>1.4404<br>1.4406<br>1.4571<br>1.4580 | Yes | + | + | + | (+) | – | – |
| 1.4305 | No | – | – | – | – | – | – |
| 1.4311<br>1.4429<br>1.4435<br>1.4436<br>1.4439 | Yes | + | + | + | – | – | – |

### Duplex Stainless Steels

Duplex steels have a mixed structure of ferrite and austenite. They contain the ferrite-forming elements Cr and Mo at levels of 20–29 wt% Cr and up to 4 wt% Mo, respectively, and the austenite-forming elements of about 4–9 wt% Ni and up to 0.3 wt% N. Typical examples are presented in Table 3.1-64. These steels solidify as $\delta$-ferrite which will partly transform into austenite upon cooling. Thus, the phase fractions of ferrite and austenite depend not only on the chemical composition, but also on the annealing and cooling conditions.

The advantages of the duplex steels compared to the austenitic steels are a substantially higher yield and tensile strength (cf. Table 3.1-66) and a better resistance against stress corrosion cracking. A few data on heat treatment conditions, physical properties, and weldability are given in Tables 3.1-65, 3.1-67, and 3.1-68. In comparison with ferritic stainless steels, the duplex steels have a better weldability, a higher low temperature toughness, and a lower susceptibility to general and intergranular corrosion. With respect to optimum toughness, the $\delta$-ferrite content of duplex steels should be below 60 vol%. The influence of annealing temperature and cooling conditions on the ferrite content of a steel with 0.05 wt% C, 25 wt% Cr, 8 wt% Ni, 2.5 wt% Mo, and 1.5 wt% Cu is illustrated in Table 3.1-69 [1.78]. During the partial phase transformation of ferrite into austenite below 1350 °C, a redistribution of the alloying elements occurs with the ferrite-forming elements Cr, Mo, and Ti enriched in the $\alpha$-phase and the austenite-forming elements C, N, Ni, and Mn enriched in the $\gamma$-phase. The reduced C content in the $\alpha$-phase delays the formation of chromium carbides. The relatively high Mo and N contents ensure good resistance against pitting corrosion.

The formation of the brittle Cr-rich $\sigma$-phase, which can form in the temperature range of 1000–500 °C and can lead to a drastic reduction of toughness and corrosion resistance, requires special attention. Therefore, duplex steels are usually water quenched from a solution treatment at 1100–1150 °C.

**Table 3.1-64** Chemical composition of duplex stainless steels

| Grade no. (EN 10088) | Steel designation | ASTM A 276/ AISI grade | Chemical composition (wt%) C | Si | Mn | S | P | Cr | Ni | Mo | N |
|---|---|---|---|---|---|---|---|---|---|---|---|
| 1.4460 | X4CrNiMoN27-5-2 | 329 | ≤0.05 | ≤1 | ≤2 | ≤0.03 | ≤0.045 | 25.0–28.0 | 4.5–6.0 | 1.3–2.0 | 0.05–0.20 |
| 1.4462 | X2CrNiMoN22-5-3 | F51 | ≤0.03 | ≤1 | ≤2 | ≤0.02 | ≤0.03 | 21.0–23.0 | 4.5–6.5 | 2.5–3.5 | 0.08–0.20 |

**Table 3.1-65** Heat treatment conditions of duplex stainless steels

| Grade no. | Rolling and forging temperature (°C) | Cooling | Quenching temperature (°C) | Cooling |
|---|---|---|---|---|
| 1.4460 | 1150–900 | Air | 1020–1100 | Air, water |
| 1.4462 | 1150–900 | Air | 1020–1100 | Air, water |

**Table 3.1-66** Mechanical properties of duplex stainless steels

| Grade no. | Heat treatment condition | Tensile properties of flat products ≤ 25 mm thickness: Min. yield strength or 0.2% proof strength (MPa) | Ultimate tensile strength (MPa) | Min. fracture elongation $A_5$ (%) | Min. CVN impact energy at room temp. (J) | Min. yield strength or 0.2% proof strength at $T$ (°C) in MPa: 100 | 200 | 300 | 400 | 500 |
|---|---|---|---|---|---|---|---|---|---|---|
| 1.4460 | Quenched | 450 | 600–800 | 20 | 55 | 360 | 310 | – | – | – |
| 1.4462 | Quenched | 450 | 640–900 | 30 | 120 | 360 | 310 | 280 | – | – |

**Table 3.1-67** Physical properties of duplex stainless steels

| Grade no. | Mean thermal expansion coefficient between 20 °C and $T$ (°C) in $10^{-6}$ $K^{-1}$ | | | | | | | | Density ($kg/dm^3$) | Thermal conductivity at 20 °C (W/K m) | Specific heat at 20 °C (J/g | Electrical resistivity at 20 °C (Ω $mm^2$/m) | Modulus of elasticity at 20 °C ($kN/mm^2$) | Magnetizable |
|---|---|---|---|---|---|---|---|---|---|---|---|---|---|---|
| | 100 | 200 | 300 | 400 | 500 | 600 | 700 | 800 | | | | | | |
| 1.4460 | 12.0 | 12.5 | 13.0 | 13.5 | – | – | – | – | 7.8 | 15 | 0.45 | 0.80 | 200 | Yes |
| 1.4462 | 12.0 | 12.5 | 13.0 | – | – | – | – | – | 7.8 | 15 | 0.45 | 0.80 | 200 | Yes |

**Table 3.1-68** Weldability of duplex stainless steels

| Grade no. | Weldable | Welding method | | | | Preheating (°C) | Aftertreatment |
|---|---|---|---|---|---|---|---|
| | | SAW/MIG/TIG welding | Arc welding | Resistance welding | Autogenous welding | | |
| 1.4460 | Yes | + | + | + | + | – | 1020 °C |
| 1.4462 | Yes | + | + | + | – | – | – |

**Table 3.1-69** Influence of annealing temperature and cooling conditions on the ferrite content of a steel with 0.05 wt% C, 25 wt% Cr, 8 wt% Ni, 2.5 wt% Mo and 1.5 wt% Cu [1.10]

| Annealing temperature (°C) (holding time 15 min) | Ferrite content (vol.%) after | |
|---|---|---|
| | water quenching | air cooling |
| 1350 | 93.0 | 78.8 |
| 1300 | 70.2 | 61.8 |
| 1250 | 43.5 | 37.5 |
| 1150 | 35.7 | 34.2 |
| 1050 | 24.0 | 23.7 |
| 1000 | 7.6 | 7.6 |

### 3.1.5.5 Heat-Resistant Steels

Heat-resistant steels are treated extensively in [1.52], creep data are compiled in [1.86]. Steels are considered heat-resistant if they possess–in addition to good mechanical properties at ambient temperature–special resistance against short or long term exposure to hot gases, combustion products and melts of metals or salts at temperatures above about 550 °C where non- or low-alloyed steels are no longer applicable due to extensive scaling and creep.

Thus, heat-resistant steels are characterized by a combination of good high temperature strength, scaling resistance, a sufficient hot and cold formabilty, and weldability. They are sufficiently stable against embrittling processes at the high application temperatures. The resistance against scaling and hot gas corrosion is affected by the formation of a protective dense, pore-free, and tightly adherent oxide layer at the surface. The main alloying elements leading to such an oxide layer are Cr, Al, and Si. The oxidation and scaling resistance increases with increasing Cr content between about 6 and 25 wt% Cr. Higher Cr concentrations do not lead to further improvement. Additions of up to 2 wt% Al and up to 3 wt% Si enhance the effect of Cr. Small additions of rare earth metals, e.g., of Ce, can improve the adherence and the ductility of the oxide layer. In order to keep the protective oxide layer intact during temperature changes, the steels should exhibit low volume changes and, if possible, no phase transformations during heating and cooling. Consequently, there are two main groups of heat resistant steels: ferritic and austenitic steels, both showing no phase transformations.

The *ferritic* Cr (or Cr−Al−Si) steels are less expensive but have a lower creep strength above 800 °C. They may suffer from three embrittling mechanisms:

- The "475 °C embrittlement" due to decomposition in the metastable miscibility gap of the Fe−Cr solid solution, occuring between about 350 and 550 °C at Cr contents above 15 wt% Cr (Fig. 3.1-107);
- The formation of the brittle intermetallic FeCr $\sigma$-phase at temperatures between about 550 and 900 °C (Sect. 3.1.5.1, Fig. 3.1-106);
- Grain coarsening at temperatures above about 900 °C.

However, these embrittling mechanisms will not impair the behavior at high operating temperatures if taken into account properly, but will deteriorate the toughness after cooling to room temperature. Heating to temperatures above the range of occurrence of the embrittling phases followed by sufficiently fast cooling will suppress the embrittling effects.

The Cr and Ni alloyed *austenitic* steels possess a higher temperature strength and better ductility, toughness, and weldability. The susceptibility to embrittling effects is considerably lower. At Ni contents above 30 wt% Ni, they are outside the stability region of the brittle $\sigma$-phase.

The properties of the *ferritic-austenitic* steels lie between those of the ferritic and austenitic steels. They are characterized by a higher fracture toughness, cold formability, high temperature strength, and weldability than the fully ferritic grades, and by a higher chemical resistance in sulphurous gases than the austenitic grades.

It is obvious that the scaling resistance of the heat-resisting steels will be detrimentally influenced by any other corrosion mechanism which may be destroying the oxide layer, e.g., by chemical reactions with other metal oxides, chlorine, or chlorides. Thus in general, the heat resistance cannot be characterized by a single test method or measuring parameter but will depend on the specific environmental conditions.

In Table 3.1-70 chemical compositions of the most important grades of heat resistant steels are presented [1.87]. Table 3.1-71 contains some information about recommended temperature ranges for heat treatment and hot forming. In Tables 3.1-72 and 3.1-73 the mechanical properties at room temperature and at high temperatures are listed, respectively. Table 3.1-74 shows some physical properties. The ferritic and ferritic-austenitic steels are magnetisable while the austenitic grades are nonmagnetic. Qualitative data on the high temperature behavior in special gas atmospheres are given in Table 3.1-75. In carburizing atmospheres carbon can diffuse into the steel, reacting with the chromium to form chromium carbides which can lead to embrittlement and reduced scaling resistance due to chromium depletion in the matrix. Higher Ni and Si contents reduce the carburization susceptibility. In sulfur-containing atmospheres, which contain the sulfur mostly in the form of $SO_2$ or $H_2S$, the formation of sulfides at the surface may inhibit the formation of the protecting oxide layer. Under oxidizing conditions this process will proceed rather slowly, but under reducing conditions the pick-up of sulfur occurs very

**Table 3.1-70** Chemical composition of heat-resistant steels according to SEW [1.87]

| Grade[a] | Steel designation | ASTM/ AISI grade | Chemical composition (wt%) | | | | | | | | |
|---|---|---|---|---|---|---|---|---|---|---|---|
| | | | C | Si | Mn | P | S | Al | Cr | Ni | Others |
| **Ferritic steels** | | | | | | | | | | | |
| 1.4713 | X10CrAlSi7 | – | ≤0.12 | 0.5–1.0 | ≤1 | ≤0.04 | ≤0.03 | 0.5–1.0 | 6.0–8.0 | – | – |
| 1.4720 | X7CrTi12 | – | ≤0.08 | ≤1.0 | ≤1 | ≤0.04 | ≤0.03 | – | 10.5–12.5 | – | Ti ≥ 6x wt% C up to 1.0 |
| 1.4724 | X10CrAlSi13 | 405 | ≤0.12 | 0.7–1.4 | ≤1 | ≤0.04 | ≤0.03 | 0.7–1.2 | 12.0–14.0 | – | – |
| 1.4742 | X10CrAlSi18 | 430 | ≤0.12 | 0.7–1.4 | ≤1 | ≤0.04 | ≤0.03 | 0.7–1.2 | 17.0–19.0 | – | – |
| 1.4762 | X10CrAlSi25 | 446 | ≤0.12 | 0.7–1.4 | ≤1 | ≤0.04 | ≤0.03 | 1.2–1.7 | 23.0–26.0 | – | – |
| **Ferritic–austenitic steels** | | | | | | | | | | | |
| 1.4821 | X15CrNiSi25-4 | 327 | 0.10–0.20 | 0.8–1.5 | 2.0 | ≤0.04 | ≤0.03 | – | 24.0–27.0 | 3.5–5.5 | – |
| **Austenitic steels** | | | | | | | | | | | |
| 1.4878 | X10CrNiTi18-10 | 321 | ≤0.12 | ≤1 | ≤2.0 | ≤0.045 | ≤0.03 | – | 17.0–19.0 | 9.0–12.0 | Ti ≥ 4x wt% C up to 0.8 |
| 1.4828 | X15CrNiSi20-12 | 309 | ≤0.20 | 1.5–2.5 | ≤2.0 | ≤0.045 | ≤0.03 | – | 19.0–21.0 | 11.0–13.0 | – |
| 1.4833 | X12CrNi23-12 | 309S | ≤0.08 | ≤1 | ≤2.0 | ≤0.045 | ≤0.03 | – | 21.0–23.0 | 12.0–15.0 | – |
| 1.4845 | X8CrNi25-21-12 | 310S | ≤0.15 | ≤0.75 | ≤2.0 | ≤0.045 | ≤0.03 | – | 24.0–26.0 | 19.0–22.0 | – |
| 1.4841 | X15CrNiSi25-20 | 310/314 | ≤0.20 | 1.5–2.5 | ≤2.0 | ≤0.045 | ≤0.03 | – | 24.0–26.0 | 19.0–22.0 | |
| 1.4864 | X12NiCrSi36-18 | 330 | ≤0.15 | 1.0–2.0 | ≤2.0 | ≤0.030 | ≤0.02 | – | 15.0–17.0 | 33.0–37.0 | – |
| 1.4876 | X10NiCrAlTi32-21 | B163 | ≤0.12 | ≤1 | ≤2.0 | 0.030 | ≤0.02 | 0.15–0.6 | 19.0–23.0 | 30.0–34.0 | Ti 0.15–0.6 |

[a] According to SEW [1.87]

**Table 3.1-71** Recommended conditions for heat treatment and hot forming of heat-resistant steels

| Grade[a] | Hot forming temperature (°C) | Soft annealing (°C) Cooling in air (water) | Quenching temperature (°C) Cooling in water (air) | Limiting scaling temperature in air (°C) |
|---|---|---|---|---|
| **Ferritic steels** | | | | |
| 1.4713 | 1100–750 | 750–800 | – | 620 |
| 1.4720 | 1050–750 | 750–850 | – | 800 |
| 1.4724 | 1100–750 | 800–850 | – | 850 |
| 1.4742 | 1100–750 | 800–850 | – | 1000 |
| 1.4762 | 1100–750 | 800–850 | – | 1150 |
| **Ferritic–austenitic steels** | | | | |
| 1.4821 | 1150–800 | – | 1000–1050 | 1100 |
| **Austenitic steels** | | | | |
| 1.4878 | 1150–800 | – | 1020–1070 | 850 |
| 1.4828 | 1150–800 | – | 1050–1100 | 1000 |
| 1.4833 | 1150–900 | – | 1050–1100 | 1000 |
| 1.4845 | 1150–800 | – | 1050–1100 | 1050 |
| 1.4841 | 1150–800 | – | 1050–1100 | 1150 |
| 1.4864 | 1150–800 | – | 1050–1100 | 1100 |
| 1.4876 | 1150–800 | 900–980 (recrystallization annealing) | 1100–1150 (solution annealing) | 1100 |

[a] According to SEW [1.87]

**Table 3.1-72** Mechanical properties of heat-resistant steels at 20 °C

| Grade[a] | Heat treatment condition | Hardness (HB) max. | 0.2% proof stress (MPa) min. | Ultimate tensile strength (MPa) | Elongation $L_o = 5d_o$ min. (%) long. | transv. |
|---|---|---|---|---|---|---|
| **Ferritic steels** | | | | | | |
| 1.4713 | Annealed | 192 | 220 | 420–620 | 20 | 15 |
| 1.4720 | Annealed | 179 | 210 | 400–600 | 25 | 20 |
| 1.4724 | Annealed | 192 | 250 | 450–650 | 15 | 11 |
| 1.4742 | Annealed | 212 | 270 | 500–700 | 12 | 9 |
| 1.4762 | Annealed | 223 | 280 | 520–720 | 10 | 7 |
| **Ferritic–austenitic steels** | | | | | | |
| 1.4821 | Quenched | 235 | 400 | 600–850 | 16 | 12 |
| **Austenitic steels** | | | | | | |
| 1.4878 | Quenched | 192 | 210 | 500–750 | 40 | 30 |
| 1.4828 | Quenched | 223 | 230 | 500–750 | 30 | 22 |
| 1.4833 | Quenched | 192 | 210 | 500–750 | 35 | 26 |
| 1.4845 | Quenched | 192 | 210 | 500–750 | 35 | 26 |
| 1.4841 | Quenched | 223 | 230 | 550–800 | 30 | 22 |
| 1.4864 | Quenched | 223 | 230 | 550–800 | 30 | 22 |
| 1.4876 | Recryst. annealed | 192 | 210 | 500–750 | 30 | 22 |
| | Solution annealed | 192 | 170 | 450–700 | 30 | 22 |

[a] According to SEW [1.87]

**Table 3.1-73** Long-term mechanical properties of heat-resistant steels at high temperatures; average values of scatter bands

| Grade[a] | Temperature (°C) | 1% creep limit (MPa) at $t$ = | | Creep rupture strength (MPa) at $t$ = | | |
|---|---|---|---|---|---|---|
| | | 1000 h | 10 000 h | 1000 h | 10 000 h | 100 000 h |
| **Ferritic and ferritic-austenitic steels** | | | | | | |
| 1.4713<br>1.4720<br>1.4724<br>1.4742<br>1.4762<br>1.4821 | 500 | 80 | 50 | 160 | 100 | 55 |
| | 600 | 27.5 | 17.5 | 55 | 35 | 20 |
| | 700 | 8.5 | 4.7 | 17 | 9.5 | 5 |
| | 800 | 3.7 | 2.1 | 7.5 | 4.3 | 2.3 |
| | 900 | 1.8 | 1.0 | 3.6 | 1.9 | 1.0 |
| **Austenitic steels** | | | | | | |
| 1.4878 | 600 | 110 | 85 | 185 | 115 | 65 |
| | 700 | 45 | 30 | 80 | 45 | 22 |
| | 800 | 15 | 10 | 35 | 20 | 10 |
| 1.4828<br>1.4833 | 600 | 120 | 80 | 190 | 120 | 65 |
| | 700 | 50 | 25 | 75 | 36 | 16 |
| | 800 | 20 | 10 | 35 | 18 | 7.5 |
| | 900 | 8 | 4 | 15 | 8.5 | 3.0 |
| 1.4845<br>1.4841 | 600 | 150 | 105 | 230 | 160 | 80 |
| | 700 | 53 | 37 | 80 | 40 | 18 |
| | 800 | 23 | 12 | 35 | 18 | 7 |
| | 900 | 10 | 5.7 | 15 | 8.5 | 3.0 |
| 1.4864 | 600 | 105 | 80 | 180 | 125 | 75 |
| | 700 | 50 | 35 | 75 | 45 | 25 |
| | 800 | 25 | 15 | 35 | 20 | 7 |
| | 900 | 12 | 5 | 15 | 8 | 3 |
| 1.4876 (solution annealed) | 600 | 130 | 90 | 200 | 152 | 114 |
| | 700 | 70 | 40 | 90 | 68 | 47 |
| | 800 | 30 | 15 | 45 | 30 | 19 |
| | 900 | 13 | 5 | 20 | 11 | 4 |

[a] According to SEW [1.87]

**Table 3.1-74** Physical properties of heat-resistant steels

| Grade[a] | Density at 20 °C ($g\,cm^3$) | Average coefficient of thermal expansion between 20 °C and $T$ (°C) ($\times 10^{-6}\ K^{-1}$) | | | | | | Thermal conductivity at $T$ (°C) ($W\,m^{-1}\,K^{-1}$) | | Specific heat at 20 °C ($J\,g^{-1}\,K^{-1}$) | Specific electrical resistivity at 20 °C ($\Omega\,mm^2\,m^{-1}$) |
|---|---|---|---|---|---|---|---|---|---|---|---|
| | | 200 | 400 | 600 | 800 | 1000 | 1200 | 20 | 500 | | |
| **Ferritic steels** | | | | | | | | | | | |
| 1.4713 | 7.7 | 11.5 | 12.0 | 12.5 | 13.0 | – | – | 23 | 25 | 0.45 | 0.70 |
| 1.4720 | 7.7 | 11.0 | 12.0 | 12.5 | 13.0 | – | – | 25 | 28 | 0.45 | 0.60 |
| 1.4724 | 7.7 | 11.0 | 11.5 | 12.0 | 12.5 | 13.5 | – | 21 | 23 | 0.45 | 0.90 |
| 1.4742 | 7.7 | 10.5 | 11.5 | 12.0 | 12.5 | 13.5 | – | 19 | 25 | 0.45 | 0.95 |
| 1.4762 | 7.7 | 10.5 | 11.5 | 12.0 | 12.5 | 13.5 | 15.0 | 17 | 23 | 0.45 | 1.10 |
| **Ferritic–austenitic steels** | | | | | | | | | | | |
| 1.4821 | 7.7 | 13.0 | 13.5 | 14.0 | 14.5 | 15.0 | 15.5 | 17 | 23 | 0.50 | 0.90 |

**Table 3.1-74** Physical properties of heat-resistant steels, cont.

| Grade [a] | Density at 20 °C ($g\,cm^3$) | Average coefficient of thermal expansion between 20 °C and $T$ (°C) ($\times 10^{-6}\ K^{-1}$) | | | | | | Thermal conductivity at $T$ (°C) ($W\,m^{-1}\,K^{-1}$) | | Specific heat at 20 °C ($J\,g^{-1}\,K^{-1}$) | Specific electrical resistivity at 20 °C ($\Omega\,mm^2\,m^{-1}$) |
|---|---|---|---|---|---|---|---|---|---|---|---|
| | | 200 | 400 | 600 | 800 | 1000 | 1200 | 20 | 500 | | |
| **Austenitic steels** | | | | | | | | | | | |
| 1.4878 | 7.9 | 17.0 | 18.0 | 18.5 | 19.0 | – | – | 15 | 21 | 0.50 | 0.75 |
| 1.4828 | 7.9 | 16.5 | 17.5 | 18.0 | 18.5 | 19.5 | – | 15 | 21 | 0.50 | 0.85 |
| 1.4833 | 7.9 | 16.0 | 17.5 | 18.0 | 18.5 | 19.5 | – | 15 | 19 | 0.50 | 0.80 |
| 1.4845 | 7.9 | 15.5 | 17.0 | 17.5 | 18.0 | 19.0 | – | 14 | 19 | 0.50 | 0.85 |
| 1.4841 | 7.9 | 15.5 | 17.0 | 17.5 | 18.0 | 19.0 | 19.5 | 15 | 19 | 0.50 | 0.90 |
| 1.4864 | 8.0 | 15.0 | 16.0 | 17.0 | 17.5 | 18.5 | – | 13 | 19 | 0.50 | 1.00 |
| 1.4876 | 8.0 | 15.0 | 16.0 | 17.0 | 17.5 | 18.5 | – | 12 | 19 | 0.50 | 1.00 |

[a] According to SEW [1.87]

**Table 3.1-75** Resistance of heat-resistant steels in various media

| Grade [a] | Resistance to Carburization | Sulphurous gases | | Nitrogenous and low-oxygen gases | Maximum operating temperature in air (°C) |
|---|---|---|---|---|---|
| | | Oxidizing | Reducing | | |
| **Ferritic steels** | | | | | |
| 1.4713 | Medium | Very high | Medium | Low | 800 |
| 1.4762 | Medium | Very high | High | Low | 1150 |
| **Ferritic–austenitic steels** | | | | | |
| 1.4821 | Medium | High | Medium | Medium | 1100 |
| **Austenitic steels** | | | | | |
| 1.4878 | Low | Medium | Low | High | 850 |
| 1.4828 | Low | Medium | Low | High | 1000 |
| 1.4841 | Low | Medium | Low | High | 1150 |
| 1.4864 | High | Medium | Low | High | 1100 |

[a] According to SEW [1.87]

fast. This is especially true with Ni-alloyed steels due to the formation at about 650 °C of a low-melting Ni/NiS eutectic. Thus under such conditions the ferritic steels are more stable than the austenitic grades. In sulfur-containing atmospheres the maximum service temperatures will be about 100 to 200 °C lower than in air.

The heat-resistant steels are weldable by the usual processes, with arc welding preferred over gas fusion welding. For the ferritic steels, the tendency to grain coarsening in the heat affected zone has to be kept in mind. The application of austenitic filler metals will lead to better mechanical properties of the weld connection than those of the base metal (however, with respect to the scaling resistance, different thermal expansions of the ferritic and austenitic materials may be a problem). Filler materials should be at least as highly alloyed as the base metal. In sulfurizing atmospheres it is advisable to use ferritic electrodes for the cap passes only in order to ensure a tough weld. Post-weld heat treatments are generally not necessary.

### 3.1.5.6 Tool Steels

Tool steels are the largest group of materials used to make tools for cutting, forming, or otherwise shaping a material into a part or component. An extensive account is given in [1.88]. Other major groups of tool materials are cemented carbides (Sect. 3.1.6.6), and ceramics including diamond (Chapt. 3.2).

The most commonly used materials are wrought tool steels, which are either carbon, alloy, or high-speed steels capable of being hardened by quenching and tempering to hardness levels $\leq 70$ HRC. High-speed tool steels are so named because of their suitability to machine materials at high cutting speed. Other steels used for metalworking applications include steels produced by powder metallurgy, medium-carbon alloy steels,

high-carbon martensitic stainless steels, and maraging steels.

Wrought tool steels are essentially hardenable alloy steels with relatively high contents of the carbide forming elements Cr, Mo, W, and V. If the steels are quenched and tempered, the dependence of their hardness on tempering temperature indicates the level of hardening achieved as well as its temperature stability, (Fig. 3.1-117). The rate of effective softening at tempering temperatures up to about 300 °C is mainly due to the competing effects of recovery and the precipitation of iron carbides (Table 3.1-40). The hardening at higher temperatures is associated with the precipitation of alloy carbides which can form at elevated temperatures only because of their high melting points and transformation kinetics. They give rise to a second maximum on isothermal tempering curves, as curves 3 and 4 in Fig. 3.1-117, which is referred to as secondary hardening.

The alloy carbide phases which precipitate and give rise to secondary hardening are listed in Table 3.1-76.

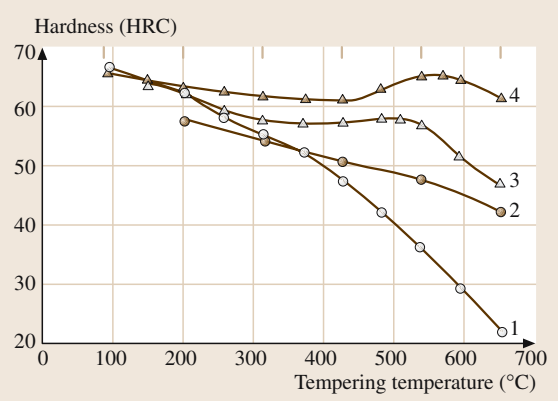


**Fig. 3.1-117** Isothermal (1 h) tempering curves of 4 typical tool steels. Curves 1 and 2: softening of AISI grade W (water-hardening) and O (oil-hardening) steels; Curves 3 and 4: softening and secondary hardening of AISI grade A2 (air-hardening medium alloy) and M2 (Mo high-speed) steels [1.88]

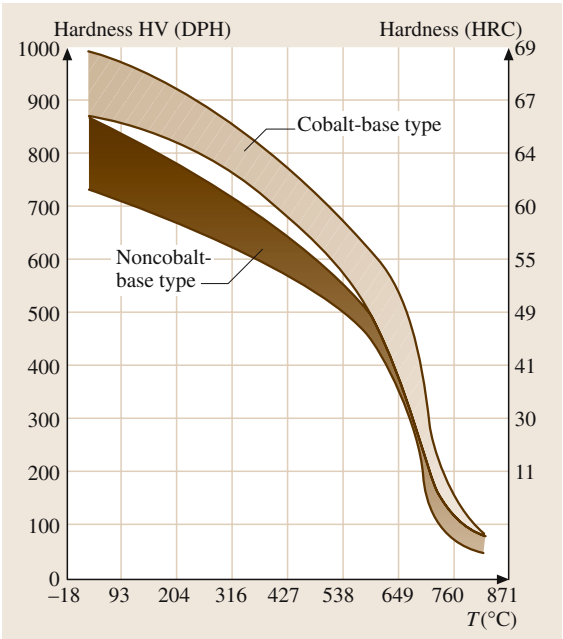


**Fig. 3.1-118** Comparison of the hot hardness of Co-bearing versus non-Co bearing high-speed tool steels [1.88]

Co is an alloying element which raises the high temperature stability of tool steels by raising their melting temperature. Figure 3.1-118 shows this effect by a comparison of the hardness vs. temperature data for non-Co-based and Co-based high-speed tool steels.

Table 3.1-77 gives composition ranges for the tool steels most commonly used. According to the AISI classification, each group of similar composition and properties is given a capital letter, somewhat related to the major alloying element. Thus, high-speed steels are classified by M for molybdenum and T for tungsten. Within each group individual types are assigned code numbers.

The basic properties of tool steels that determine their performance in service are hardness, wear

**Table 3.1-76** Alloy carbides occurring in tool steels

| Type of carbide | Prototype | Lattice type | Occurrence, composition [a] |
|---|---|---|---|
| $M_7C_3$ | $Cr_7C_3$ | Hexagonal | In Cr alloy steels M = **Cr** |
| $M_{23}C_6$ | $Cr_{23}C_6$ | Face-centered cubic | In high-Cr steels M = **Cr**, Fe, W, Mo |
| $M_6C$ | $W_6C$ | Face-centered cubic | M = **W**, **Mo**, Cr, V, Co |
| $M_2C$ | $W_2C$ | Hexagonal | M = **W**, **Mo**, Cr |
| MC | VC | Face-centered cubic | VC |

[a] Bold letters indicate major components

**Table 3.1-77** Composition ranges of principle types of tool steels according to AISI and UNS classifications [1.88]

| Designation | | Composition[b] (wt%) | | | | | | | | |
|---|---|---|---|---|---|---|---|---|---|---|
| AISI | UNS No. | C | Mn | Si | Cr | Ni | Mo | W | V | Co |
| **Molybdenum high-speed steels** | | | | | | | | | | |
| M1 | T11301 | 0.78–0.88 | 0.15–0.40 | 0.20–0.50 | 3.50–4.00 | 0.30 max | 8.20–9.20 | 1.40–2.10 | 1.00–1.35 | – |
| M2 | T11302 | 0.78–0.88; 0.95–1.05 | 0.15–0.40 | 0.20–0.45 | 3.75–4.50 | 0.30 max | 4.50–5.50 | 5.50–6.75 | 1.75–2.20 | – |
| M3, class 1 | T11313 | 1.00–1.10 | 0.15–0.40 | 0.20–0.45 | 3.75–4.50 | 0.30 max | 4.75–6.50 | 5.00–6.75 | 2.25–2.75 | – |
| M3, class 2 | T11323 | 1.15–1.25 | 0.15–0.40 | 0.20–0.45 | 3.75–4.50 | 0.30 max | 4.75–6.50 | 5.00–6.75 | 2.75–3.75 | – |
| M4 | T11304 | 1.25–1.40 | 0.15–0.40 | 0.20–0.45 | 3.75–4.75 | 0.30 max | 4.25–5.50 | 5.25–6.50 | 3.75–4.50 | – |
| M7 | T11307 | 0.97–1.05 | 0.15–0.40 | 0.20–0.55 | 3.50–4.00 | 0.30 max | 8.20–9.20 | 1.40–2.10 | 1.75–2.25 | – |
| M10 | T11310 | 0.84–0.94; 0.95–1.05 | 0.10–0.40 | 0.20–0.45 | 3.75–4.50 | 0.30 max | 7.75–8.50 | – | 1.80–2.20 | – |
| M30 | T11330 | 0.75–0.85 | 0.15–0.40 | 0.20–0.45 | 3.50–4.25 | 0.30 max | 7.75–9.00 | 1.30–2.30 | 1.00–1.40 | 4.50–5.50 |
| M33 | T11333 | 0.85–0.92 | 0.15–0.40 | 0.15–0.50 | 3.50–4.00 | 0.30 max | 9.00–10.00 | 1.30–2.10 | 1.00–1.35 | 7.75–8.75 |
| M34 | T11334 | 0.85–0.92 | 0.15–0.40 | 0.20–0.45 | 3.50–4.00 | 0.30 max | 7.75–9.20 | 1.40–2.10 | 1.90–2.30 | 7.75–8.75 |
| M35 | T11335 | 0.82–0.88 | 0.15–0.40 | 0.20–0.45 | 3.75–4.50 | 0.30 max | 4.50–5.50 | 5.50–6.75 | 1.75–2.20 | 4.50–5.50 |
| M36 | T11336 | 0.80–0.90 | 0.15–0.40 | 0.20–0.45 | 3.75–4.50 | 0.30 max | 4.50–5.50 | 5.50–6.50 | 1.75–2.25 | 7.75–8.75 |
| M41 | T11341 | 1.05–1.15 | 0.20–0.60 | 0.15–0.50 | 3.75–4.50 | 0.30 max | 3.25–4.25 | 6.25–7.00 | 1.75–2.25 | 4.75–5.75 |
| M42 | T11342 | 1.05–1.15 | 0.15–0.40 | 0.15–0.65 | 3.50–4.25 | 0.30 max | 9.00–10.00 | 1.15–1.85 | 0.95–1.35 | 7.75–8.75 |
| M43 | T11343 | 1.15–1.25 | 0.20–0.40 | 0.15–0.65 | 3.50–4.25 | 0.30 max | 7.50–8.50 | 2.25–3.00 | 1.50–1.75 | 7.75–8.75 |
| M44 | T11344 | 1.10–1.20 | 0.20–0.40 | 0.30–0.55 | 4.00–4.75 | 0.30 max | 6.00–7.00 | 5.00–5.75 | 1.85–2.20 | 11.00–12.25 |
| M46 | T11346 | 1.22–1.30 | 0.20–0.40 | 0.40–0.65 | 3.70–4.20 | 0.30 max | 8.00–8.50 | 1.90–2.20 | 3.00–3.30 | 7.80–8.80 |
| M47 | T11347 | 1.05–1.15 | 0.15–0.40 | 0.20–0.45 | 3.50–4.00 | 0.30 max | 9.25–10.00 | 1.30–1.80 | 1.15–1.35 | 4.75–5.25 |
| M48 | T11348 | 1.42–1.52 | 0.15–0.40 | 0.15–0.40 | 3.50–4.00 | 0.30 max | 4.75–5.50 | 9.50–10.50 | 2.75–3.25 | 8.00–10.00 |
| M62 | T11362 | 1.25–1.35 | 0.15–0.40 | 0.15–0.40 | 3.50–4.00 | 0.30 max | 10.00–11.00 | 5.75–6.50 | 1.80–2.10 | – |
| **Tungsten high-speed steels** | | | | | | | | | | |
| T1 | T12001 | 0.65–0.80 | 0.10–0.40 | 0.20–0.40 | 3.75–4.50 | 0.30 max | – | 17.25–18.75 | 0.90–1.30 | – |
| T2 | T12002 | 0.80–0.90 | 0.20–0.40 | 0.20–0.40 | 3.75–4.50 | 0.30 max | 1.0 max | 17.50–19.00 | 1.80–2.40 | – |
| T4 | T12004 | 0.70–0.80 | 0.10–0.40 | 0.20–0.40 | 3.75–4.50 | 0.30 max | 0.40–1.00 | 17.50–19.00 | 0.80–1.20 | 4.25–5.75 |
| T5 | T12005 | 0.75–0.85 | 0.20–0.40 | 0.20–0.40 | 3.75–5.00 | 0.30 max | 0.50–1.25 | 17.50–19.00 | 1.80–2.40 | 7.00–9.50 |
| T6 | T12006 | 0.75–0.85 | 0.20–0.40 | 0.20–0.40 | 4.00–4.75 | 0.30 max | 0.40–1.00 | 18.50–21.00 | 1.50–2.10 | 11.00–13.00 |
| T8 | T12008 | 0.75–0.85 | 0.20–0.40 | 0.20–0.40 | 3.75–4.50 | 0.30 max | 0.40–1.00 | 13.25–14.75 | 1.80–2.40 | 4.25–5.75 |
| T15 | T12015 | 1.50–1.60 | 0.15–0.40 | 0.15–0.40 | 3.75–5.00 | 0.30 max | 1.00 max | 11.75–13.00 | 4.50–5.25 | 4.75–5.25 |
| **Intermediate high-speed steels** | | | | | | | | | | |
| M50 | T11350 | 0.78–0.88 | 0.15–0.45 | 0.20–0.60 | 3.75–4.50 | 0.30 max | 3.90–4.75 | – | 0.80–1.25 | – |
| M52 | T11352 | 0.85–0.95 | 0.15–0.45 | 0.20–0.60 | 3.50–4.30 | 0.30 max | 4.00–4.90 | 0.75–1.50 | 1.65–2.25 | – |

**Table 3.1-77** Composition ranges of principle types of tool steels according to AISI and UNS classifications [1.88], cont.

| Designation | | Composition[b] (wt%) | | | | | | | | |
|---|---|---|---|---|---|---|---|---|---|---|
| AISI | UNS No. | C | Mn | Si | Cr | Ni | Mo | W | V | Co |
| **Chromium hot-worked steels** | | | | | | | | | | |
| H10 | T20810 | 0.35–0.45 | 0.25–0.70 | 0.80–1.20 | 3.00–3.75 | 0.30 max | 2.00–3.00 | – | 0.25–0.75 | – |
| H11 | T20811 | 0.33–0.43 | 0.20–0.50 | 0.80–1.20 | 4.75–5.50 | 0.30 max | 1.10–1.60 | – | 0.30–0.60 | – |
| H12 | T20812 | 0.30–0.40 | 0.20–0.50 | 0.80–1.20 | 4.75–5.50 | 0.30 max | 1.25–1.75 | 1.00–1.70 | 0.50 max | – |
| H13 | T20813 | 0.32–0.45 | 0.20–0.50 | 0.80–1.20 | 4.75–5.50 | 0.30 max | 1.10–1.75 | – | 0.80–1.20 | – |
| H14 | T20814 | 0.35–0.45 | 0.20–0.50 | 0.80–1.20 | 4.75–5.50 | 0.30 max | – | 4.00–5.25 | – | – |
| H19 | T20819 | 0.32–0.45 | 0.20–0.50 | 0.20–0.50 | 4.00–4.75 | 0.30 max | 0.30–0.55 | 3.75–4.50 | 1.75–2.20 | 4.00–4.50 |
| **Tungsten hot-worked steels** | | | | | | | | | | |
| H21 | T20821 | 0.26–0.36 | 0.15–0.40 | 0.15–0.50 | 3.00–3.75 | 0.30 max | – | 8.50–10.00 | 0.30–0.60 | – |
| H22 | T20822 | 0.30–0.40 | 0.15–0.40 | 0.15–0.40 | 1.75–3.75 | 0.30 max | – | 10.00–11.75 | 0.25–0.50 | – |
| H23 | T20823 | 0.25–0.45 | 0.15–0.40 | 0.15–0.60 | 11.00–12.75 | 0.30 max | – | 11.00–12.75 | 0.75–1.25 | – |
| H24 | T20824 | 0.42–0.53 | 0.15–0.40 | 0.15–0.40 | 2.50–3.50 | 0.30 max | – | 14.00–16.00 | 0.40–0.60 | – |
| H25 | T20825 | 0.22–0.32 | 0.15–0.40 | 0.15–0.40 | 3.75–4.50 | 0.30 max | – | 14.00–16.00 | 0.40–0.60 | – |
| H26 | T20826 | 0.45–0.55[b] | 0.15–0.40 | 0.15–0.40 | 3.75–4.50 | 0.30 max | – | 17.25–19.00 | 0.75–1.25 | – |
| **Molybdenum hot-worked steels** | | | | | | | | | | |
| H42 | T20842 | 0.55–0.70[b] | 0.15–0.40 | – | 3.75–4.50 | 0.30 max | 4.50–5.50 | 5.50–6.75 | 1.75–2.20 | – |
| **Air-hardening, medium-alloy, cold-worked steels** | | | | | | | | | | |
| A2 | T30102 | 0.95–1.05 | 1.00 max | 0.50 max | 4.75–5.50 | 0.30 max | 0.90–1.40 | – | 0.15–0.50 | – |
| A3 | T30103 | 1.20–1.30 | 0.40–0.60 | 0.50 max | 4.75–5.50 | 0.30 max | 0.90–1.40 | – | 0.80–1.40 | – |
| A4 | T30104 | 0.95–1.05 | 1.80–2.20 | 0.50 max | 0.90–2.20 | 0.30 max | 0.90–1.40 | – | – | – |
| A6 | T30106 | 0.65–0.75 | 1.80–2.50 | 0.50 max | 0.90–1.20 | 0.30 max | 0.90–1.40 | – | – | – |
| A7 | T30107 | 2.00–2.85 | 0.80 max | 0.50 max | 5.00–5.75 | 0.30 max | 0.90–1.40 | 0.50–1.50 | 3.90–5.15 | – |
| A8 | T30108 | 0.50–0.60 | 0.50 max | 0.75–1.10 | 4.75–5.50 | 0.30 max | 1.15–1.65 | 1.00–1.50 | – | – |
| A9 | T30109 | 0.45–0.55 | 0.50 max | 0.95–1.15 | 4.75–5.50 | 1.25–1.75 | 1.30–1.80 | – | 0.80–1.40 | – |
| A10 | T30110 | 1.25–1.50[b] | 1.60–2.10 | 1.00–1.50 | – | 1.55–2.05 | 1.25–1.75 | – | – | – |
| **High-carbon, high-chromium, cold-worked steels** | | | | | | | | | | |
| D2 | T30402 | 1.40–1.60 | 0.60 max | 0.60 max | 11.00–13.00 | 0.30 max | 0.70–1.20 | – | 1.10 max | – |
| D3 | T30403 | 2.00–2.35 | 0.60 max | 0.60 max | 11.00–13.50 | 0.30 max | – | 1.00 max | 1.00 max | – |
| D4 | T30404 | 2.05–2.40 | 0.60 max | 0.60 max | 11.00–13.00 | 0.30 max | 0.70–1.20 | – | 1.00 max | – |
| D5 | T30405 | 1.40–1.60 | 0.60 max | 0.60 max | 11.00–13.00 | 0.30 max | 0.70–1.20 | – | 1.00 max | 2.50–3.50 |
| D7 | T30407 | 2.15–2.50 | 0.60 max | 0.60 max | 11.50–13.50 | 0.30 max | 0.70–1.20 | – | 3.80–4.40 | – |

**Table 3.1-77** Composition ranges of principle types of tool steels according to AISI and UNS classifications [1.88], cont.

| Designation | | Composition[b] (wt%) | | | | | | | | |
|---|---|---|---|---|---|---|---|---|---|---|
| AISI | UNS No. | C | Mn | Si | Cr | Ni | Mo | W | V | Co |
| **Oil-hardening cold-worked steels** | | | | | | | | | | |
| O1 | T31501 | 0.85–1.00 | 1.00–1.40 | 0.50 max | 0.40–0.60 | 0.30 max | – | 0.40–0.60 | 0.30 max | – |
| O2 | T31502 | 0.85–0.95 | 1.40–1.80 | 0.50 max | 0.50 max | 0.30 max | 0.30 max | – | 0.30 max | – |
| O6 | T31506 | 1.25–1.55[c] | 0.30–1.10 | 0.55–1.50 | 0.30 max | 0.30 max | 0.20–0.30 | – | – | – |
| O7 | T31507 | 1.10–1.30 | 1.00 max | 0.60 max | 0.35–0.85 | 0.30 max | 0.30 max | 1.00–2.00 | 0.40 max | – |
| **Shock-resisting steels** | | | | | | | | | | |
| S1 | T41901 | 0.40–0.55 | 0.10–0.40 | 0.15–1.20 | 1.00–1.80 | 0.30 max | 0.50 max | 1.50–3.00 | 0.15–0.30 | – |
| S2 | T41902 | 0.40–0.55 | 0.30–0.50 | 0.90–1.20 | – | 0.30 max | 0.30–0.60 | – | 0.50 max | – |
| S5 | T41905 | 0.50–0.65 | 0.60–1.00 | 1.75–2.25 | 0.50 max | – | 0.20–1.35 | – | 0.35 max | – |
| S6 | T41906 | 0.40–0.50 | 1.20–1.50 | 2.00–2.50 | 1.20–1.50 | – | 0.30–0.50 | – | 0.20–0.40 | – |
| S7 | T41907 | 0.45–0.55 | 0.20–0.90 | 0.20–1.00 | 3.00–3.50 | – | 1.30–1.80 | – | 0.20–0.30[d] | – |
| **Low-alloy special-purpose tool steels** | | | | | | | | | | |
| L2 | T61202 | 0.45–1.00[b] | 0.10–0.90 | 0.50 max | 0.70–1.20 | – | 0.25 max | – | 0.10–0.30 | – |
| L6 | T61206 | 0.65–0.75 | 0.25–0.80 | 0.50 max | 0.60–1.20 | 1.25–2.00 | 0.50 max | – | 0.20–0.30[d] | – |
| **Low-carbon mold steels** | | | | | | | | | | |
| P2 | T51602 | 0.10 max | 0.10–0.40 | 0.10–0.40 | 0.75–1.25 | 0.10–0.50 | 0.15–0.40 | – | – | – |
| P3 | T51603 | 0.10 max | 0.20–0.60 | 0.40 max | 0.40–0.75 | 1.00–1.50 | – | – | – | – |
| P4 | T51604 | 0.12 max | 0.20–0.60 | 0.10–0.40 | 4.00–5.25 | – | 0.40–1.00 | – | – | – |
| P5 | T51605 | 0.10 max | 0.20–0.60 | 0.40 max | 2.00–2.50 | 0.35 max | – | – | – | – |
| P6 | T51606 | 0.05–0.15 | 0.35–0.70 | 0.10–0.40 | 1.25–1.75 | 3.25–3.75 | – | – | – | – |
| P20 | T51620 | 0.28–0.40 | 0.60–1.00 | 0.20–0.80 | 1.40–2.00 | – | 0.30–0.55 | – | – | – |
| P21 | T51621 | 0.18–0.22 | 0.20–0.40 | 0.20–0.40 | 0.50 max | 3.90–4.25 | – | – | 0.15–0.25 | 1.05–1.25Al |
| **Water-hardening tool steels** | | | | | | | | | | |
| W1 | T72301 | 0.70–1.50[e] | 0.10–0.40 | 0.10–0.40 | 0.15 max | 0.20 max | 0.10 max | 0.15 max | 0.10 max | – |
| W2 | T72302 | 0.85–1.50[e] | 0.10–0.40 | 0.10–0.40 | 0.15 max | 0.20 max | 0.10 max | 0.15 max | 0.15–0.35 | – |
| W3 | T72303 | 1.05–1.15 | 0.10–0.40 | 0.10–0.40 | 0.40–0.60 | 0.20 max | 0.10 max | 0.15 max | 0.10 max | – |

[a] All steels except group W contain 0.25 max Cu, 0.03 max P, and 0.03 max S; group W steels contain 0.20 max Cu, 0.025 max P, and 0.025 max S. Where specified, sulfur may be increased to 0.06 to 0.15% to improve machinability of group A, D, H, M and T steels.

[b] Available in several carbon ranges.

[c] Contains free graphite in the microstructure.

[d] Optional.

[e] Specified carbon ranges are designated by suffix numbers.

resistance, ductility and fracture toughness, and in many applications stability against softening at elevated temperatures. Characteristic mechanical properties at room temperature as a function of hardening treatment are listed for group L and group S steels in Table 3.1-78.

**Table 3.1-78** Mechanical properties of group L and group S tool steels at room temperature as a function of hardening treatment [1.88]

| Type | Condition | Tensile strength (MPa) | 0.2% yield strength (MPa) | Elongation[a] (%) | Reduction in area (%) | Hardness (HRC) |
|---|---|---|---|---|---|---|
| L2 | Annealed | 710 | 510 | 25 | 50 | 96 HRB |
| | Oil quenched from 855 °C and single tempered at: | | | | | |
| | 205 °C | 2000 | 1790 | 5 | 15 | 54 |
| | 315 °C | 1790 | 1655 | 10 | 30 | 52 |
| | 425 °C | 1550 | 1380 | 12 | 35 | 47 |
| | 540 °C | 1275 | 1170 | 15 | 45 | 41 |
| | 650 °C | 930 | 760 | 25 | 55 | 30 |
| L6 | Annealed | 655 | 380 | 25 | 55 | 93 HRB |
| | Oil quenched from 845 °C and single tempered at: | | | | | |
| | 315 °C | 2000 | 1790 | 4 | 9 | 54 |
| | 425 °C | 1585 | 1380 | 8 | 20 | 46 |
| | 540 °C | 1345 | 1100 | 12 | 30 | 42 |
| | 650 °C | 965 | 830 | 20 | 48 | 32 |
| S1 | Annealed | 690 | 415 | 24 | 52 | 96 HRB |
| | Oil quenched from 925 °C and single tempered at: | | | | | |
| | 205 °C | 2070 | 1895 | – | – | 57.5 |
| | 315 °C | 2025 | 1860 | 4 | 12 | 54 |
| | 425 °C | 1790 | 1690 | 5 | 17 | 50.5 |
| | 540 °C | 1680 | 11 525 | 9 | 23 | 47.5 |
| | 650 °C | 1345 | 1240 | 12 | 37 | 42 |
| S5 | Annealed | 725 | 440 | 25 | 50 | 96 HRB |
| | Oil quenched from 870 °C and single tempered at: | | | | | |
| | 205 °C | 2345 | 1930 | 5 | 20 | 59 |
| | 315 °C | 2240 | 1860 | 7 | 24 | 58 |
| | 425 °C | 1895 | 1690 | 9 | 28 | 52 |
| | 540 °C | 1515 | 1380 | 10 | 30 | 48 |
| | 650 °C | 1035 | 1170 | 15 | 40 | 37 |
| S7 | Annealed | 640 | 380 | 25 | 55 | 95 HRB |
| | Oil quenched from 940 °C and single tempered at: | | | | | |
| | 205 °C | 2170 | 1450 | 7 | 20 | 58 |
| | 315 °C | 1965 | 1585 | 9 | 25 | 55 |
| | 425 °C | 1895 | 1410 | 10 | 29 | 53 |
| | 540 °C | 1820 | 1380 | 10 | 33 | 51 |
| | 650 °C | 1240 | 1035 | 14 | 45 | 39 |

[a] In 50 mm

### 3.1.5.7 Cast Irons

The term cast iron pertains to a large family of multi-component Fe−C−Si alloys which solidify according to the eutectic of the Fe−C system (Sect. 3.1.5.1; Fig. 3.1-99). They are treated extensively in [1.89]. Their comparatively high C and Si contents lead to solidification either according to the metastable equilibria involving $Fe_3C$ or according to the stable equilibria involving graphite, depending, also, on the content of further alloying elements, melt treatment, and rate of cooling. Since, in addition, the metallic phases can be alloyed and their microstructures varied by annealing and transformation treatments as in other ferrous alloys, a multitude of microstructural states and associated properties result.

#### Classification

The C rich phases determine the basic classification of cast irons. According to the color of their facture surfaces, $Fe_3C$-containing grades are called white, graphite-containing grades are called gray, and alloys which solidify in mixed states are called mottled. In addition, the shape of the graphite phase particles and the microstructure of the metallic matrix phases are taken into account since they are also characterizing the mechanical properties.

*Shape of Graphite Phase Particles.* Lamellar (flake) graphite (FG) is characteristic of cast irons with near-zero ductility; spheroidal (nodular) graphite (SG) is characteristic of ductile cast iron; compacted (vermicular) graphite (CG) is a transition form between flake and nodule shape; temper graphite (TG) results from a tempering treatment and consists of small clusters of branched graphite lamellae.

*Microstructure of Metallic Matrix Phases.* Ferritic, pearlitic, austenitic, bainitic (austempered). More details are presented in Fig. 3.1-119 and Table 3.1-79.

#### Iron–Carbon–Silicon Equilibria and Carbon Equivalent

Since C and Si are the alloying elements which dominate the solidification behavior and the resulting microstructures of cast irons, their phase equilibria need to be taken into account. Figure 3.1-120 shows a section through the metastable ternary Fe−C−Si diagram at 2 wt% Si which approximates the Si content of many cast irons. Compared to the binary Fe−C system, the addition of Si decreases the stability of $Fe_3C$ and increases the stability of ferrite, as indicated by the expansion of the $\alpha$-phase field. With increasing Si concentration, the C concentrations of the eutectic and the eutectoid equilibria decrease while their temperatures increase.

These relations are the basis for correlating the C and Si concentrations with the ranges of formation of steels and of the main groups of cast irons as shown in Fig. 3.1-121. The relations are expressed in terms of the carbon equivalent CE = (wt% C) + (1/3) (wt% Si). The concentration of the eutectic (upper dashed line) is given by $CE_e = 4.3$. Accordingly, alloys with $CE < 4.3$ are hypoeutectic and alloys with $CE > 4.3$ are hypereutectic. In P-containing cast irons the relation is CE = (wt% C) + (1/3) (wt% Si + wt% P). In addition, Fig. 3.1-121 shows the limit of solubility of C in austenite (lower dashed line), which is the upper limit of the range of steels. It is given by $CE_{\gamma_{max}} = 2.1 = (\text{wt\% C}) + (1/6)\ (\text{wt\% Si})$.

#### Grades of Cast Irons

Table 3.1-80 lists the composition ranges of typical unalloyed cast irons, indicating that they are classified mainly by the type of carbon-rich phase formed and by the basic mechanical behavior.

**Table 3.1-79** Classification of cast irons according to commercial designation, microstructure and color of fracture surface [1.89]

| Commercial designation | Carbon-rich phase | Matrix[a] | Fracture | Final structure after |
|---|---|---|---|---|
| Gray iron | Lamellar graphite | P | Gray | Solidification |
| Ductile iron | Spheriodal graphite | F, P, A | Silver-gray | Solidification or heat treatment |
| Compacted graphite iron | Compacted (vermicular) graphite | F, P | Gray | Solidification |
| White iron | $Fe_3C$ | P, M | White | Solidification and heat treatment[b] |
| Mortled iron | Lamellar Gr + $Fe_3C$ | P | Mottled | Solidification |
| Malleable iron | Temper graphite | F, P | Silver-gray | Heat treatment |
| Austempered ductile iron | Spheroidal graphite | At | Silver-gray | Heat treatment |

[a] F, ferrite; P, pearlite; A, austenite; M, martensite; At, austempered (bainite)

[b] White irons are not usually heat treated, exept for stress relief and to continue austenite transformation

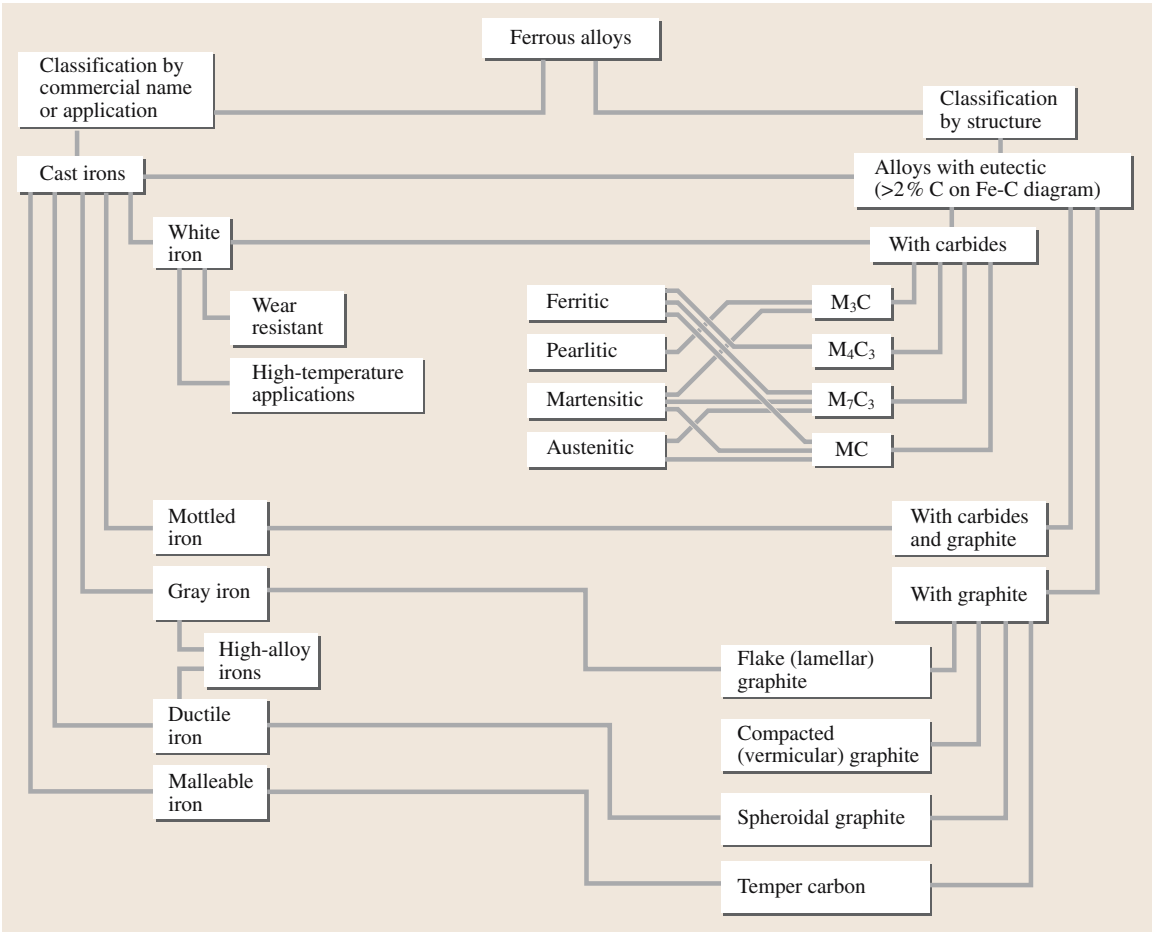


**Fig. 3.1-119** Classification of cast irons [1.89]

**Table 3.1-80** Range of composition, microstructural and mechanical characteristics of typical unalloyed cast irons [1.89]

| Type | Carbon phase | Concentration range (wt%) C | Si | Mn | P | S |
|---|---|---|---|---|---|---|
| Gray | FG | 2.5–4.0 | 1.0–3.0 | 0.2–1.0 | 0.002–1.0 | 0.02–0.25 |
| Compacted graphite | CG | 2.5–4.0 | 1.0–3.0 | 0.2–1.0 | 0.01–0.1 | 0.01–0.03 |
| Ductile | SG | 3.0–4.0 | 1.8–2.8 | 0.1–1.0 | 0.01–0.1 | 0.01–0.03 |
| White | $Fe_3C$ | 1.8–3.6 | 0.5–1.9 | 0.25–0.8 | 0.06–0.2 | 0.06–0.2 |
| Malleable | $Fe_3C$/TG | 2.2–2.9 | 0.9–1.9 | 0.15–1.2 | 0.02–0.2 | 0.02–0.2 |

*Gray Iron.* This most common type of cast iron is characterised by flake graphite and requires a high CE to ensure a sufficient graphitization potential which is also increased by Al addition. Gray irons may be moderately alloyed, e.g., by 0.2–0.6 wt% Cr, 0.2–1 wt% Mo, and 0.1–0.2 wt% V which promote the formation of alloy carbides and pearlite. Upon plastic deformation the flake form of graphite promotes early internal crack formation and, thus, causes the low ductility of gray iron.

*Ductile Iron.* This cast iron is characterized by the spheroidal graphite phase (SG) in its microstructure. Spheroidal graphite is formed during solidification if the melt has been treated by the addition of a component which promotes the particular nucleation and

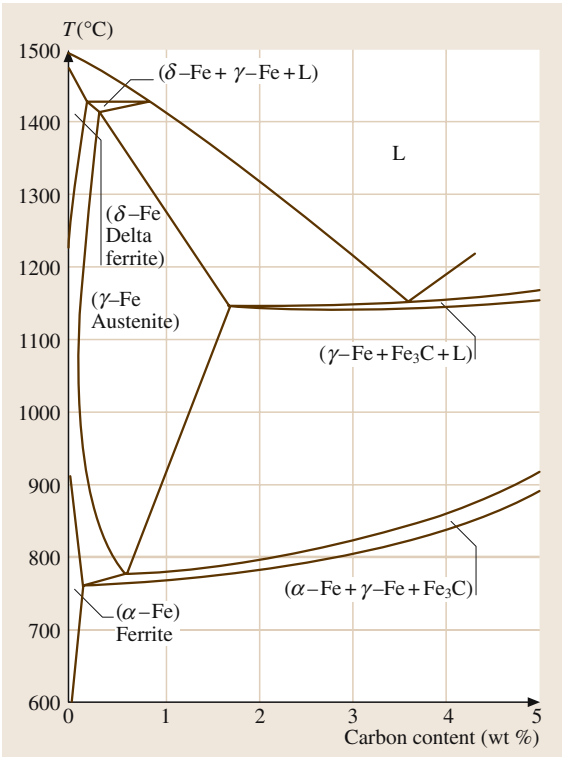


**Fig. 3.1-120** Section through the metastable Fe−C−Si phase diagram at 2 wt% Si [1.89]

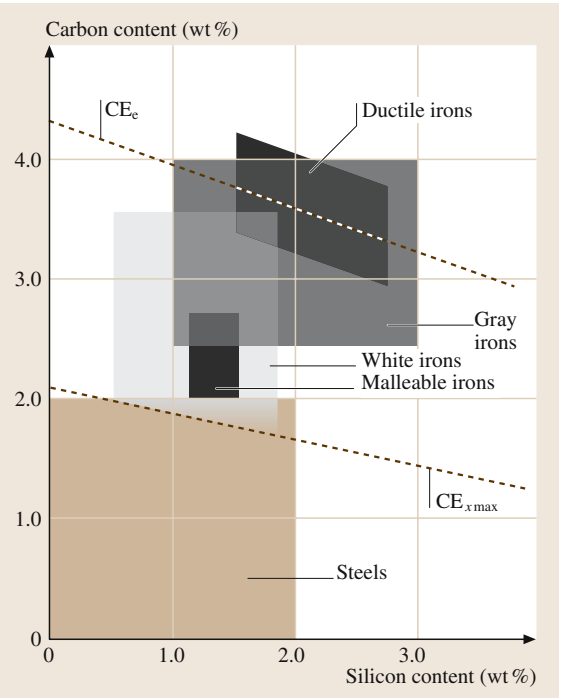


**Fig. 3.1-121** Approximate C and Si concentrations for the composition ranges of steels and different grades of cast irons [1.89]

growth behavior of graphite in the form of nodules. The most common alloying component added to nucleate spheroidal graphite is Mg, but Ca, Ce, La, and Y have also been found to favour spheroidal graphite formation. Basically this microstructural modification leads to higher yield strength and higher ductility because the plastic deformation of the metallic matrix phases can be extended to higher strains than in gray iron before fracture sets in.

*Malleable Irons.* The melt treatment of malleable cast irons involves Mg, Ca, Bi, or Te additions. But malleable irons have an as-cast structure consisting of $Fe_3C$ in a pearlitic matrix. By heat treatment in the range of 800–970 °C the cementite phase is transformed into graphite (TG). The cooling is controlled in such a way as to promote pearlite formation, ferrite formation, or a mixture of the two.

*Alloy Cast Irons.* Alloying elements beyond the levels mentioned above are added to cast irons almost exclusively to enhance resistance to abrasive wear or chemical corrosion, or to extend their stability for application at elevated temperature. The function of the alloying elements is essentially the same as in steels. Table 3.1-81 lists the groups of grades with typical compositions and the microstructural constituents present in the as-cast state.

### Mechanical Properties of Cast Irons

Due to the multitude of as-cast structures as a function of alloy composition, melt treatment, cooling rate (as influenced by the cooling conditions and the cross section of the work piece), and subsequent heat treatment, there is a wide range of mechanical properties which can be achieved according to the requirements of the application. Table 3.1-82 gives a survey in terms of characteristic examples.

**Table 3.1-81** Ranges of alloy content of typical alloy cast irons [1.89]

| Description | Composition (wt%) [a] | | | | | | | | | Matrix structure as-cast [c] |
|---|---|---|---|---|---|---|---|---|---|---|
| | TC [b] | Mn | P | S | Si | Ni | Cr | Mo | Cu | |
| **Abrasion-resistant white irons** | | | | | | | | | | |
| Low-carbon white iron [d] | 2.2–2.8 | 0.2–0.6 | 0.15 | 0.15 | 1.0–1.6 | 1.5 | 1.0 | 0.5 | [e] | CP |
| High-carbon, low-silicon white iron | 2.8–3.6 | 0.3–2.0 | 0.30 | 0.15 | 0.3–1.0 | 2.5 | 3.0 | 1.0 | [e] | CP |
| Martensitic nickel-chromium iron | 2.5–3.7 | 1.3 | 0.30 | 0.15 | 0.8 | 2.7–5.0 | 1.1–4.0 | 1.0 | – | M, A |
| Martensitic nickel, high-chromium iron | 2.5–3.6 | 1.3 | 0.10 | 0.15 | 1.0–2.2 | 5.0–7.0 | 7.0–11.0 | 1.0 | – | M, A |
| Martensitic chromium-molybdenum iron | 2.0–3.6 | 0.5–1.5 | 0.10 | 0.06 | 1.0 | 1.5 | 11.0–23.0 | 0.5–3.5 | 1.2 | M, A |
| High-chromium iron | 2.3–3.0 | 0.5–1.5 | 0.10 | 0.06 | 1.0 | 1.5 | 23.0–28.0 | 1.5 | 1.2 | M |
| **Corrosion-resistant irons** | | | | | | | | | | |
| High-silicon iron [f] | 0.4–1.1 | 1.5 | 0.15 | 0.15 | 14.0–17.0 | – | 5.0 | 1.0 | 0.5 | F |
| High-chromium iron | 1.2–4.0 | 0.3–1.5 | 0.15 | 0.15 | 0.5–3.0 | 5.0 | 12.0–35.0 | 4.0 | 3.0 | M, A |
| Nickel-chromium gray iron [g] | 3.0 | 0.5–1.5 | 0.08 | 0.12 | 1.0–2.8 | 13.5–36.0 | 1.5–6.0 | 1.0 | 7.5 | A |
| Nickel-chromium ductile iron [h] | 3.0 | 0.7–4.5 | 0.08 | 0.12 | 1.0–3.0 | 18.0–36.0 | 1.0–5.5 | 1.0 | – | A |
| **High-resistant gray iron** | | | | | | | | | | |
| Medium-silicon iron [i] | 1.6–2.5 | 0.4–0.8 | 0.30 | 0.10 | 4.0–7.0 | – | – | – | – | F |
| Nickel-chromium iron [g] | 1.8–3.0 | 0.4–1.5 | 0.15 | 0.15 | 1.0–2.75 | 13.5–36.0 | 1.8–6.0 | 1.0 | 7.5 | A |
| Nickel-chromium-silicon iron [j] | 1.8–2.6 | 0.4–1.0 | 0.10 | 0.10 | 5.0–6.0 | 13.0–43.0 | 1.8–5.5 | 1.0 | 10.0 | A |
| High-aluminium iron | 1.3–2.0 | 0.4–1.0 | 0.15 | 0.15 | 1.3–6.0 | – | 20.0–25.0 Al | – | – | F |
| **Heat resistant ductile irons** | | | | | | | | | | |
| Medium-silicon ductile iron | 2.8–3.8 | 0.2–0.6 | 0.08 | 0.12 | 2.5–6.0 | 1.5 | – | 2.0 | – | F |
| Nickel-chromium ductile iron [h] | 3.0 | 0.7–2.4 | 0.08 | 0.12 | 1.75–5.5 | 18.0–36.0 | 1.75–3.5 | 1.0 | – | A |
| Heat-resistant white irons | | | | | | | | | | |
| Ferritic grade | 1.0–2.5 | 0.3–1.5 | – | – | 0.5–2.5 | – | 30.0–35.0 | – | – | F |
| Austenitic grade | 1.0–2.0 | 0.3–1.5 | – | – | 0.5–2.5 | 10.0–15.0 | 15.0–30.0 | – | – | A |

[a] Where a single value is given rather than a range, that value is a maximum limit
[b] Total carbon
[c] CP, coarse pearlite; M, martensite; A, austenite; F, ferrite
[d] Can be produced from a malleable-iron base composition
[e] Copper can replace all or part of the nickel
[f] Such as Durion, Durichlor 51, Superchlor
[g] Such as Ni-Resist austenitic iron (ASTM A 436)
[h] Such as Ni-Resist austenitic ductile iron (ASTM A 439)
[i] Such as Silal
[j] Such asd Nicrosilal

**Table 3.1-82** Mechanical properties of cast irons

| Material | $R_{p0.2}$ ($N\,mm^{-2}$) (min.) | $R_m$ ($N\,mm^{-2}$) (min.) | $A_5$ (%) (min.) | Matrix microstructure Unspecified | Material number [a] | Short code [a] |
|---|---|---|---|---|---|---|
| Gray cast | | 100 [b] | | Mainly ferritic | 0.6010 | GG-10 |
| irons (FG) | | 200 [b] | | | 0.6020 | GG-20 |
| DIN 1691 | | 350 [b] | | | 0.6035 | GG-35 |
| Ductile cast | 250 [c] | 390 [c] | 15 [d] | Pearlitic-ferritic | 0.7040 | GGG-40 |
| irons (SG) | 360 [c] | 600 [c] | 2 [d] | Mainly pearlitic | 0.7060 | GGG-60 |
| DIN 1693 | 400 [c] | 700 [c] | 2 [d] | Wide variation permissable | 0.7070 | GGG-70 |

**Table 3.1-82** Mechanical properties of cast irons, cont.

| Material | $R_{p0.2}$ ($N\,mm^{-2}$) (min.) | $R_m$ ($N\,mm^{-2}$) (min.) | $A_5$ (%) (min.) | Matrix microstructure<br>Unspecified | Material number[a] | Short code[a] |
|---|---|---|---|---|---|---|
| White malleable | | 350[d] | 4 | Core: ganular pearlite | 0.8035 | GTW-35-04 |
| irons (TG) | 260[b] | 450[d] | 7 | Core: lamellar to granular pearlite | 0.8045 | GTW-45-07 |
| DIN 1692 | 220[b] | 400[d] | 5 | Ferrite | 0.8040 | GTW-40-05 |
| Black malleable | 200[c] | 350[d] | 10 | Pearlite, ferrite | 0.8135 | GTS-35-10 |
| irons (TG) | 270[c] | 450[d] | 6 | Pearlite | 0.8145 | GTS-45-06 |
| DIN 1692 | 430[c] | 650[d] | 2 | Hardened | 0.8165 | GTS-65-02 |
| | 530[c] | 700[d] | 2 | | 0.8170 | GTS-70-02 |
| Austenitic alloy | | 140/220 | – | | 0.6652 | GGL-NiMn13-7 |
| cast irons (FG) | | 190/240 | 12 | | 0.6661 | GGL NiCr20-3 |
| DIN 1694 | | 170/240 | – | | 0.6680 | GGL-NiSiCr30-5-5 |
| Austenitic cast | 210 | 390 | 15[d] | | 0.7652 | GGG-NiMn13-7 |
| iron (SG) | 210 | 390 | 7[d] | | 0.7661 | GGG NiCr20-3 |
| DIN 1694 | 240 | 390 | – | | 0.7680 | GGG-NiSiCr30-5-5 |
| | 210 | 370 | 7[d] | | 0.7685 | GGG-NiCr35-3 |

[a] According to German Materials Standard

[b] The values refer to a cylindrical test specimen of 30 mm in diameter corresponding to a wall thickness of 15 mm. The tensile strength values to be expected depend on the wall thickness Example: GG-20.

| Wall thickness (mm) | 2.5–5.5 | 5.5–10 | 10–20 | 20–40 | 40–80 | 80–150 |
|---|---|---|---|---|---|---|
| $R_m$ ($N/mm^2$) | 230 | 205 | 180 | 155 | 130 | 115 |

[c] Diameter of the test rod: 12 or 15 mm. For cast parts with a thickness < 6 mm tensile test specimens.

[d] For a cylindrical test specimen of 12 mm in diameter. The mechanical properties depend on the diameter of the test specimen Example: GTW-45-07

| Diameter of the test rod (mm) | 9 | 12 | 15 |
|---|---|---|---|
| $R_m$ ($N/mm^2$) | 400 | 450 | 480 |
| $R_{p0.2}$ ($N/mm^2$) | 230 | 260 | 280 |

## 3.1.6 Cobalt and Cobalt Alloys

Cobalt is applied as a base metal for a number of alloys, as an alloying element, and as a component of numerous inorganic compounds. Table 3.1-83 lists its major applications. Cobalt and cobalt-based materials are treated extensively in [1.90, 91].

Data on the electronic structure of Co and Co alloys may be found in [1.92]. Phase diagrams, crystal structures, and thermodynamic data of binary Co alloys may be found in [1.93].

### 3.1.6.1 Co-Based Alloys

Cobalt-based alloys with a carbon content in the range of 1 to 3 wt% C are widely used as wear-resistant solid materials and weld overlays. Depending on the alloy composition and heat treatment, $M_{23}C_6$, $M_6C$, and MC carbides are formed. Materials with lower carbon content are mostly designed for corrosion resistance and for heat resistance, sometimes combined with wear resistance. The metals W, Mo, and Ta are essentially added for solid solution strengthening. In a few alloys Ti and Al are added. They serve to form a coherent ordered $Co_3(Ti, Al)$ phase which precipitates and leads to strengthening by age hardening. The Cr content is generally rather high to provide oxidation and hot corrosion resistance. Table 3.1-84 presents a survey of Co-based alloys.

**Table 3.1-83** Applications of cobalt [1.91]

| Application | Co consumption (%) | Form | Section |
|---|---|---|---|
| Co-based alloys, Co-based superalloys, steels | 24.3 | Base and alloying element | Sects. 3.1.5, 3.1.6, 3.1.7 |
| Hard facing and related materials | 6.9 | Base and alloying element | Sect. 3.1.6 |
| Soft and hard magnetic materials, and controlled thermal expansion alloys | 8.5 | Base and alloying element, oxide | Chapt. 4.3 |
| Cemented carbides, diamond tooling | 15.2 | Metal, binder | Sect. 3.1.6 |
| Catalysts | 8.0 | Metal, sulfates | – |
| Colorizer for glass, enamel, ceramics, plastics, fabrics | 11.6 | Oxides, salts | – |
| Batteries | 9.5 | Powder, hydroxide, $LiCoO_2$ | – |
| Tire adhesives, soaps, driers | 11.0 | Soaps, complexes made from metal powder | – |
| Feedstuff, anodizing, electrolysis, copper winning | 5.0 | Sulphate, carbonate, hydroxide | – |

**Table 3.1-84** Compositions of Co-based alloys

| Alloy tradename | UNS No. | Nominal composition (wt%) Co | Cr | W | Mo | C | Fe | Ni | Si | Mn | Others |
|---|---|---|---|---|---|---|---|---|---|---|---|
| **Cast, P/M and weld overlay wear-resistant alloys** | | | | | | | | | | | |
| Stellite 1 | R30001 | bal | 30 | 13 | 0.5 | 2.5 | 3 | 1.5 | 1.3 | 0.5 | – |
| Stellite 3 (P/M) | R30103 | bal | 30.5 | 12.5 | – | 2.4 | 5 (max) | 3.5 (max) | 2 (max) | 2 (max) | 1 B (max) |
| Stellite 4 | R30404 | bal | 30 | 14 | 1 (max) | 0.57 | 3 (max) | 3 (max) | 2 (max) | 1 (max) | – |
| Stellite 6 | R30006 | bal | 29 | 4.5 | 1.5 (max) | 1.2 | 3 (max) | 3 (max) | 1.5 (max) | 1 (max) | – |
| Stellite 6 (P/M) | R30106 | bal | 28.5 | 4.5 | 1.5 (max) | 1 | 5 (max) | 3 (max) | 2 (max) | 2 (max) | 1 B (max) |
| Stellite 12 | R30012 | bal | 30 | 8.3 | – | 1.4 | 3 (min) | 1.5 | 0.7 | 2.5 | – |
| Stellite 21 | R30021 | bal | 27 | – | 5.5 | 0.25 | 3 (max) | 2.75 | 1 (max) | 1 (max) | 0.007 B (max) |
| Stellite 98M2 (P/M) | – | bal | 30 | 18.5 | 0.8 (max) | 2 | 5 (max) | 3.5 | 1 (max) | 1 (max) | 4.2 V, 1 B (max) |
| Stellite 703 | – | bal | 32 | – | 12 | 2.4 | 3 (max) | 3 (max) | 1.5 (max) | 1.5 (max) | – |
| Stellite 706 | – | bal | 29 | – | 5 | 1.2 | 3 (max) | 3 (max) | 1.5 (max) | 1.5 (max) | – |
| Stellite 712 | – | bal | 29 | – | 8.5 | 2 | 3 (max) | 3 (max) | 1.5 (max) | 1.5 (max) | – |
| Stellite 720 | – | bal | 33 | – | 18 | 2.5 | 3 (max) | 3 (max) | 1.5 (max) | 1.5 (max) | 0.3 B |
| Stellite F | R30002 | bal | 25 | 12.3 | 1 (max) | 1.75 | 3 (max) | 22 | 2 (max) | 1 (max) | – |
| Stellite Star J (P/M) | R30102 | bal | 32.5 | 17.5 | – | 2.5 | 3 (max) | 2.5 (max) | 2 (max) | 2 (max) | 1 B (max) |
| Stellite Star J | R31001 | bal | 32.5 | 17.5 | – | 2.5 | 3 (max) | 2.5 (max) | 2 (max) | 2 (max) | – |
| Tantung G | – | bal | 29.5 | 16.5 | – | 3 | 3.5 | 7 (max) | – | 2 (max) | 4.5 Ta/Nb |
| Tantung 144 | – | bal | 27.5 | 18.5 | – | 3 | 3.5 | 7 (max) | – | | 5.5 Ta/Nb |
| **Laves-phase wear-resistant alloys** | | | | | | | | | | | |
| Tribaloy T-400 | R30400 | bal | 9 | – | 29 | – | – | – | 2.5 | – | – |
| Tribaloy T-800 | – | bal | 18 | – | 29 | – | – | – | 3.5 | – | – |
| **Wrought wear-resistant alloys** | | | | | | | | | | | |
| Stellite 6B | R30016 | bal | 30 | 4 | 1.5 (max) | 1 | 3 (max) | 2.5 | 0.7 | 1.4 | – |
| Stellite 6K | – | bal | 30 | 4.5 | 1.5 (max) | 1.6 | 3 (max) | 3 (max) | 2 (max) | 2 (max) | – |

**Table 3.1-84** Compositions of Co-based alloys, cont.

| Alloy tradename | UNS No. | Nominal composition (wt%) Co | Cr | W | Mo | C | Fe | Ni | Si | Mn | Others |
|---|---|---|---|---|---|---|---|---|---|---|---|
| **Wrought heat-resistant alloys (see Table 3.1-86 for cast alloy compositions)** | | | | | | | | | | | |
| Haynes 25 (L605) | R30605 | bal | 20 | 15 | – | 0.1 | 3 (max) | 10 | 0.4 (max) | 1.5 | – |
| Haynes 188 | R30188 | bal | 22 | 14 | – | 0.1 | 3 (max) | 22 | 0.35 | 1.25 | 0.03 La |
| Inconel 783 | R30783 | bal | 3 | – | – | 0.03 (max) | 25.5 | 28 | 0.5 (max) | 0.5 (max) | 5.5 Al, 3 Nb, 3.4 Ti (max) |
| UMCo-50 | – | bal | 28 | – | – | 0.02 (max) | 21 | – | 0.75 | 0.75 | – |
| S-816 | R30816 | 40 (min) | 20 | 4 | 4 | 0.37 | 5 (max) | 20 | 1 (max) | 1.5 | 4 Nb |
| **Corrosion-resistant alloys** | | | | | | | | | | | |
| Ultimet (1233) | R31233 | bal | 26 | 2 | 5 | 0.06 | 3 | 9 | 0.3 | 0.8 | 0.08 N |
| MP 159 | R30159 | bal | 19 | – | 7 | – | 9 | 25.5 | – | – | 3 Ti, 0.6 Nb, 0.2 Al |
| MP35N | R30035 | 35 | 20 | – | 10 | – | – | 35 | – | – | – |
| Duratherm 600 | R30600 | 41.5 | 12 | 3.9 | 4 | 0.05 (max) | 8.7 | bal | 0.4 | 0.75 | 2 Ti, 0.7 Al, 0.05 Be |
| Elgiloy | R30003 | 40 | 20 | – | 7 | 0.15 (max) | bal | 15.5 | – | 2 | 1 Be (max) |
| Havar | R30004 | 42.5 | 20 | 2.8 | 2.4 | 0.2 | bal | 13 | – | 1.6 | 0.06 Be (max) |

P/M: powder metallurgy; bal: balance

### 3.1.6.2 Co-Based Hard-Facing Alloys and Related Materials

The behavior of Co-based wear resistant alloys is based on a coarse dispersion of hard carbide phases embedded in a tough Co-rich metallic matrix. The volume fraction of the hard carbide phase is comparatively high: e.g., at 2.4 wt% C the carbide content is 30 wt%. The carbide phases are $M_7C_3$ ($Cr_7C_3$ type) and $M_6C$ ($W_6C$ type). Table 3.1-85 lists characteristic properties of Co-based hard facing alloys the compositions of which are listed Table 3.1-83.

### 3.1.6.3 Co-Based Heat-Resistant Alloys, Superalloys

Both wrought and cast Co-based heat resistant alloys, listed in Tables 3.1-84 and 3.1-86, respectively, are also referred to as Co superalloys. They are based on the face-centered cubic high temperature phase of Co which is stabilized between room temperature and the solidus temperature by alloying with $\geq$ 10 wt% Ni. They are solid-solution strengthened by alloying with W, Ta, and Mo. Furthermore, they are dispersion strengthened by carbides.

**Table 3.1-85** Properties of selected Co-based hard-facing alloys

| Property | Stellite 21 | Stellite 6 | Stellite 12 | Stellite 1 | Tribaloy T-800 |
|---|---|---|---|---|---|
| Density, g cm$^{-3}$ (lb in$^{-3}$) | 8.3 (0.30) | 8.3 (0.30) | 8.6 (0.31) | 8.6 (0.31) | 8.6 (0.31) |
| Ultimate compressive strength, MPa (ksi) | 1295 (188) | 1515 (220) | 1765 (256) | 1930 (280) | 1780 (258) |
| Ultimate tensile strength, MPa (ksi) | 710 (103) | 834 (121) | 827 (120) | 620 (90) | 690 (100) |
| Elongation, % | 8 | 1.2 | 1 | 1 | <1 |
| Coefficient of thermal expansion, °C$^{-1}$ (°F$^{-1}$) | $14.8\times10^{-6}$ ($8.2\times10^{-6}$) | $15.7\times10^{-6}$ ($8.7\times10^{-6}$) | $14\times10^{-6}$ ($7.8\times10^{-6}$) | $13.1\times10^{-6}$ ($7.3\times10^{-6}$) | $12.3\times10^{-6}$ ($6.8\times10^{-6}$) |
| Hot hardness, HV, at: | | | | | |
| 445 °C (800 °F) | 150 | 300 | 345 | 510 | 659 |
| 540 °C (1000 °F) | 145 | 275 | 325 | 465 | 622 |
| 650 °C (1200 °F) | 135 | 260 | 285 | 390 | 490 |
| 760 °C (1400 °F) | 115 | 185 | 245 | 230 | 308 |

**Table 3.1–85** Properties of selected Co-based hard-facing alloys, cont.

| Property | Stellite 21 | Stellite 6 | Stellite 12 | Stellite 1 | Tribaloy T-800 |
|---|---|---|---|---|---|
| Unlubricated sliding wear[a], $mm^3$ ($in^3 \times 10^{-3}$) at: | | | | | |
| 670 N (150 lbf) | 5.2 (0.32) | 2.6 (0.16) | 2.4 (0.15) | 0.6 (0.04) | 1.7 (0.11) |
| 1330 N (300 lbf) | 14.5 (0.90) | 18.8 (1.17) | 18.4 (1.14) | 0.8 (0.05) | 2.1 (0.13) |
| Abrasive wear[b], $mm^3$ ($in^3 \times 10^{-3}$) | | | | | |
| OAW | – | 29 (1.80) | 12 (0.75) | 8 (0.50) | – |
| GTAW | 86 (5.33) | 64 (3.97) | 57 (3.53) | 52 (3.22) | 24 (1.49) |
| Unnotched Charpy impact strength, J (ft × lbf) | 37 (27) | 23 (17) | 5 (4) | 5 (4) | 1.4 (1) |
| Corrosion resistance[c]: | | | | | |
| 65% nitric acid at 65 °C (150 °F) | U | U | U | U | S |
| 5% sulfuric acid at 65 °C (150 °F) | E | E | E | E | – |
| 50% phosphoric acid at 400 °C (750 °F) | E | E | E | E | E |

[a] Wear measured from tests conducted on Dow-Corning LFW-1 against 4620 steel ring at 80 rev/min for 2000 rev varying the applied load

[b] Wear measured from dry sand rubber wheel abrasion tests. Tested for 2000 rev at a load of 135 N (30 lbf) using a 230 mm (9 in) diam rubber wheel and American Foundrymen's Society test sand. OAW, oxyacetylene welding; GTAW, gas-tungsten arc welding

[c] E, less than 0.05 mm/yr (2 mils/year); S, 0.5 to less than 1.25 mm/yr (over 20 to less than 50 mils/year); U, more than 1.25 mm/year (50 mils/year)

**Table 3.1–86** Nominal compositions of cast cobalt-based heat-resistant alloys

| Alloy designation | Nominal composition (wt%) | | | | | | | | | | | | |
|---|---|---|---|---|---|---|---|---|---|---|---|---|---|
| | C | Ni | Cr | Co | Mo | Fe | Al | B | Ti | Ta | W | Zr | Other |
| AiResist 13 | 0.45 | – | 21 | 62 | – | – | 3.4 | – | – | 2 | 11 | – | 0.1 Y |
| AiResist 213 | 0.20 | 0.5 | 20 | 64 | – | 0.5 | 3.5 | – | – | 6.5 | 4.5 | 0.1 | 0.1 Y |
| AiResist 215 | 0.35 | 0.5 | 19 | 63 | – | 0.5 | 4.3 | – | – | 7.5 | 4.5 | 0.1 | 0.1 Y |
| FSX-414 | 0.25 | 10 | 29 | 52.5 | – | 1 | – | 0.010 | – | – | 7.5 | – | – |
| Haynes 25 (L-605) | 0.1 | 10 | 20 | 54 | – | 1 | – | – | – | – | 15 | – | – |
| J-1650 | 0.20 | 27 | 19 | 36 | – | – | – | 0.02 | 3.8 | 2 | 12 | – | – |
| MAR-M 302 | 0.85 | – | 21.5 | 58 | – | 0.5 | – | 0.005 | – | 9 | 10 | 0.2 | – |
| MAR-M 322 | 1.0 | – | 21.5 | 60.5 | – | 0.5 | – | – | 0.75 | 4.5 | 9 | 2 | – |
| MAR-M 509 | 0.6 | 10 | 23.5 | 54.5 | – | – | – | – | 0.2 | 3.5 | 7.5 | 0.5 | – |
| NASA (Co–W–Re) | 0.40 | – | 3 | 67.5 | – | – | – | – | 1 | – | 25 | 1 | 2Re |
| S-816 | 0.4 | 20 | 20 | 42 | – | 4 | – | – | – | – | 4 | – | 4 Mo, 4 Nb, 1.2 Mn, 0.4 Si |
| V-36 | 0.27 | 20 | 25 | 42 | – | 3 | – | – | – | – | 2 | – | 4 Mo, 2 Nb, 1 Mn, 0.4 Si |
| WI-52 | 0.45 | – | 21 | 63.5 | – | 2 | – | – | – | – | 11 | – | 2 Nb + Ta |
| Stellite 23 | 0.40 | 2 | 24 | 65.5 | – | 1 | – | – | – | – | 5 | – | 0.3 Mn, 0.6 Si |
| Stellite 27 | 0.40 | 32 | 25 | 35 | 5.5 | 1 | – | – | – | – | – | – | 0.3 Mn, 0.6 Si |
| Stellite 30 | 0.45 | 15 | 26 | 50.5 | 6 | 1 | – | – | – | – | – | – | 0.6 Mn, 0.6 Si |
| Stellite 31 (X-40) | 0.50 | 10 | 22 | 57.5 | – | 1.5 | – | – | – | – | 7.5 | – | 0.5 Mn, 0.5 Si |

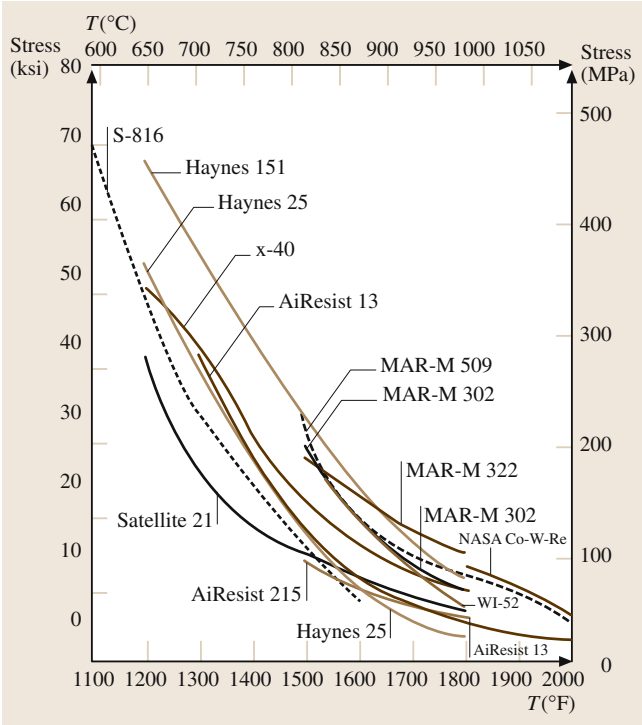


**Fig. 3.1-122** Stress–rupture curves for 1000-h life of cast Co-based superalloys

Differences of the high-temperature mechanical behavior of these materials are shown in terms of stress-rupture curves in Fig. 3.1-122.

Investment-cast Co alloys are generally used for parts of complex shape such as first- and second-stage vanes and nozzles in gas turbine engines.

### 3.1.6.4 Co-Based Corrosion-Resistant Alloys

Compared to the heat resistant Co-based alloys, the corrosion-resistant alloys have low C concentrations and are alloyed with higher Mo contents rather than with W since Mo contributes to their corrosion and oxidation resistance. Table 3.1-87 shows the compositions of various Co-based corrosion-resistant alloys.

The multiphase (MP) alloys MP35N and MP159 combine ultra-high strength, high ductility, and corrosion resistance, including resistance to stress-corrosion cracking in the work-hardened state. The prime strengthening is based on the deformation-induced martensitic transformation of the fcc matrix phase into the hcp phase which has been termed a multiphase reaction. The multiphase microstructure provides an increased density of barriers for slip dislocations. Subsequent annealing leads to a stabilization of the two-phase structure by solute partitioning. Figures 3.1-123 and 3.1-124 show the increase in strength and decrease in ductility for alloys MP35N and Duratherm 600 with work hardening and aging.

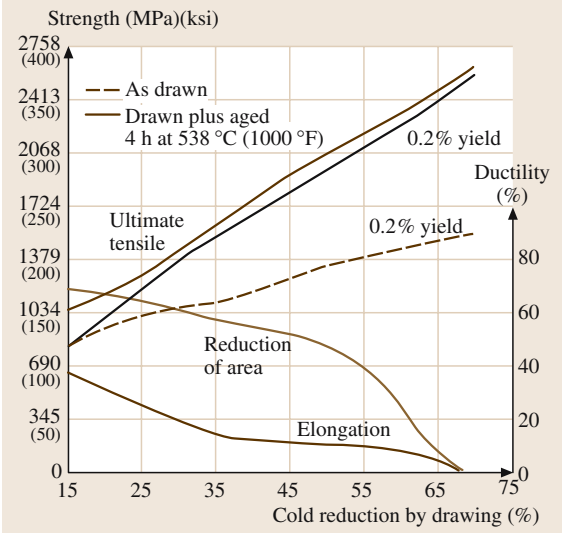


**Fig. 3.1-123** Tensile properties of cold-drawn and aged MP35N

**Table 3.1-87** Co-based corrosion resistant alloys

| Alloy tradename | UNS No. | Nominal Composition (wt%) Co | Cr | W | Mo | C | Fe | Ni | Si | Mn | Others |
|---|---|---|---|---|---|---|---|---|---|---|---|
| Ultimet (1233) | R31233 | bal | 26 | 2 | 5 | 0.06 | 3 | 9 | 0.3 | 0.8 | 0.08 N |
| MP 159 | R30159 | bal | 19 | – | 7 | – | 9 | 25.5 | – | – | 3 Ti, 0.6 Nb, 0.2 Al |
| MP35N | R30035 | 35 | 20 | – | 10 | – | – | 35 | – | – | – |
| Duratherm 600 | R30600 | 41.5 | 12 | 3.9 | 4 | 0.05 (max) | 8.7 | bal | 0.4 | 0.75 | 2 Ti, 0.7 Al, 0.05 Be |
| Elgiloy | R30003 | 40 | 20 | – | 7 | 0.15 (max) | bal | 15.5 | – | 2 | 1 Be (max) |
| Havar | R30004 | 42.5 | 20 | 2.8 | 2.4 | 0.2 | bal | 13 | – | 1.6 | 0.06 Be (max) |

bal: balance

### 3.1.6.5 Co-Based Surgical Implant Alloys

Co-based surgical implant alloys (see Table 3.1-88 for compositions) are used to fabricate a variety of implant parts and devices. These are predominantly implants for hip and knee joint replacements, implants that fix bone fractures such as bone screws, staples, plates, support structures for heart valves, and dental implants. The mechanical properties (shown in Table 3.1-89) depend sensitively on the thermal and thermomechanical treatments of the materials.

### 3.1.6.6 Cemented Carbides

The term cemented carbides, also called hardmetals, refers to powder-composite materials consisting of carbide particles bonded with metals or alloys. Extensive treatments are given in [1.94,95]. The most common cemented carbide is WC bonded with Co. Cobalt is used as a binder since it wets the angular WC particles particularly well. Nickel is added to increase corrosion and oxidation resistance of the Co binder phase. The metals Ta, Nb, and Ti may be added to form a (W, Ta, Nb, or Ti) C solid solution carbide phase which is an additional microstructural constituent in the form of rounded particles in the so-called complex grade, multigrade, or steel-cutting grade cemented carbides. Table 3.1-90 lists representative materials.

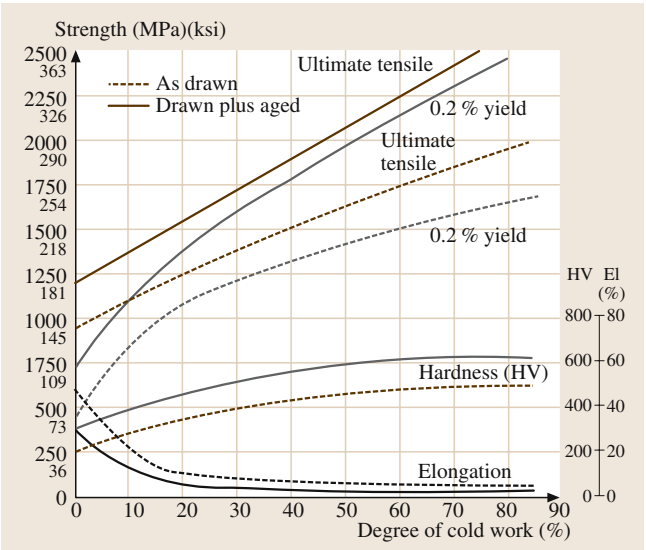


**Fig. 3.1-124** Tensile properties of cold-drawn and aged Duratherm 600

**Table 3.1-88** Compositions of Co-based surgical implant alloys

| ASTM specification | Composition (wt%) Co | Cr | Ni | Mo | Fe | C | Mn | Si | Other |
|---|---|---|---|---|---|---|---|---|---|
| F75 | bal | 27.0–30.0 | 1.0 | 5.0–7.0 | 0.75 | 0.35 | 1.0 | 1.0 | – |
| F90 | bal | 19.0–21.0 | 9.0–11.0 | – | 3 (max) | 0.05–0.15 | 1.0–2.0 | 0.4 | 14.0–16.0 W |
| F562 | bal | 19.0–21.0 | 33.0–37.0 | 9.0–10.5 | 1 (max) | 0.025 (max) | 0.15 (max) | 0.15 (max) | 1.0 Ti (max) |

bal: balance

**Table 3.1-89** Mechanical properties of Co-based surgical implant alloys

| ASTM specification | Alloy system | Condition | Yield strength (MPa) | (ksi) | Tensile strength (MPa) | (ksi) | Elongation (%) | Elastic modulus (GPa) | ($10^6$ ksi) |
|---|---|---|---|---|---|---|---|---|---|
| F75 | Co–Cr–Mo | Cast | 450 | 65 | 655 | 95 | 8 | 248 | 36 |
| F799 | Co–Cr–Mo | Thermomechanically processed | 827 | 120 | 1172 | 170 | 12 | – | – |
| F90 | Co–Cr–W–Ni | Wrought | 379 | 55 | 896 | 130 | – | 242 | 35 |
| F562 | Co–Ni–Cr–Mo | Annealed, | 241–448 | 35–65 | 793–1000 | 115–145 | 50 | 228 | 33 |
| | | cold-worked and aged | 1586 | 230 | 1793 | 260 | 8 | – | – |

**Table 3.1-90** Compositions, microstructures and properties of representative Co-bonded cemented carbides

| Nominal composition | Grain size | Hardness (HRA) | Density | | Transverse strength | | Compressive strength | | Modulus of elasticit | | Relative abrasion resistance[a] | Coefficient of thermal expansion (μm/m K) | | Thermal conductivity |
|---|---|---|---|---|---|---|---|---|---|---|---|---|---|---|
| | | | ($g\,cm^{-3}$) | ($oz\,in^{-3}$) | (MPa) | (ksi) | (MPa) | (ksi) | (GPa) | ($10^6$ psi) | | at 200 °C (390 °F) | at 1000 °C (1830 °F) | (W/m K) |
| 97WC–3Co | Medium | 92.5–93.2 | 15.3 | 8.85 | 1590 | 230 | 5860 | 850 | 641 | 93 | 100 | 4.0 | – | 121 |
| 94WC–6Co | Fine | 92.5–93.1 | 15.0 | 8.67 | 1790 | 260 | 5930 | 860 | 614 | 89 | 100 | 4.3 | 5.9 | – |
| | Medium | 91.7–92.2 | 15.0 | 8.67 | 2000 | 290 | 5450 | 790 | 648 | 94 | 58 | 4.3 | 5.4 | 100 |
| | Coarse | 90.5–91.5 | 15.0 | 8.67 | 2210 | 320 | 5170 | 750 | 641 | 93 | 25 | 4.3 | 5.6 | 121 |
| 90WC–10Co | Fine | 90.7–91.3 | 14.6 | 8.44 | 3100 | 450 | 5170 | 750 | 620 | 90 | 22 | – | – | – |
| | Coarse | 87.4–88.2 | 14.5 | 8.38 | 2760 | 400 | 4000 | 580 | 552 | 80 | 7 | 5.2 | – | 112 |
| 84WC–16Co | Fine | 89 | 13.9 | 8.04 | 3380 | 490 | 4070 | 590 | 524 | 76 | 5 | – | – | – |
| | Coarse | 86.0–87.5 | 13.9 | 8.04 | 2900 | 420 | 3860 | 560 | 524 | 76 | 5 | 5.8 | 7.0 | 88 |
| 75WC–25Co | Medium | 83–85 | 13.0 | 7.52 | 2550 | 370 | 3100 | 450 | 483 | 70 | 3 | 6.3 | – | 71 |
| 71WC–12.5TiC –12TaC–4.5Co | Medium | 92.1–92.8 | 12.0 | 6.94 | 1380 | 200 | 5790 | 840 | 565 | 82 | 11 | 5.2 | 6.5 | 35 |
| 72WC–8TiC –11.5TaC–8.5Co | Medium | 90.7–91.5 | 12.6 | 7.29 | 1720 | 250 | 5170 | 750 | 558 | 81 | 13 | 5.8 | 6.8 | 50 |

[a] Based on a value of 100 for the most abrasion-resistant material

## 3.1.7 Nickel and Nickel Alloys

Nickel is the base element for a variety of Ni alloys. But it is mainly used as a major alloying element in Fe- and Cu-based alloys, especially in stainless steels. A further major use is Ni plating. A survey of its applications is given in Table 3.1-91. It also indicates where Ni bearing alloys are covered in this handbook. Nickel materials are treated extensively in [1.96] and the special group of heat resistant alloys and superalloys in [1.97]. Alloys of Ni−Fe show ferromagnetism in a wide range of compositions. This, in combination with other intrinsic magnetic properties, is the basis for the Ni−Fe based alloys with soft magnetic and controlled thermal expansion properties, respectively, covered in Chapt. 3.4.3. NiTi shape memory alloys are treated in Sect. 3.1.3.4.

Data on the electronic structure of Ni and Ni alloys may be found in [1.98, 99], phase diagrams, crystal structures and thermodynamic data of binary Ni alloys are contained in [1.100].

### 3.1.7.1 Commercially Pure and Low-Alloy Nickels

Commercially pure and low-alloy nickels are used as corrosion-resistant materials with very good formability. Some Ni-based alloys are precipitation hardened; Ni–2 wt% Be (Duranickel 301) shows pronounced precipitation hardening. Commonly used, commercially pure and low-alloy nickels are listed in Table 3.1-92. Room-temperature mechanical properties of these and

**Table 3.1-91** Uses of nickel

| Use | Fraction of total Ni consumption (%) | Section |
|---|---|---|
| Stainless steels | 63 | Sect. 3.1.5.4 |
| Nickel-based alloys | 12 | Sect. 3.1.7 |
| Nickel plating | 10 | Sect. 3.1.7 |
| Nickel in alloy steels | 9 | Sect. 3.1.5 |
| Nickel in foundry products | 3.5 | Sect. 3.1.5.7 |
| Nickel in copper alloys | 1.5 | Sect. 3.1.8 |
| Others | 1 | – |

**Table 3.1-92** Nominal compositions of corrosion-resistant nickels and nickel-base alloys

| Alloy | UNS No. | Composition (wt%) Ni | Cu | Fe | Mn | C | Si | S | Other |
|---|---|---|---|---|---|---|---|---|---|
| **Commercially pure nickels** | | | | | | | | | |
| Nickel 200 | N02200 | 99.0 (min) | 0.25 | 0.40 | 0.35 | 0.15 | 0.35 | 0.01 | – |
| Nickel 201 | N02201 | 99.0 (min) | 0.25 | 0.40 | 0.35 | 0.02 | 0.35 | 0.01 | – |
| Nickel 205 | N02205 | 99.0 (min(b)) | 0.15 | 0.20 | 0.35 | 0.15 | 0.15 | 0.008 | 0.01–0.08 Mg, 0.01–0.05 Ti |
| Nickel 212 | – | 97.0 (min) | 0.20 | 0.25 | 1.5–2.5 | 0.10 | 0.20 | – | 0.20 Mg |
| Nickel 220 | N02220 | 99.0 (min) | 0.10 | 0.10 | 0.20 | 0.15 | 0.01–0.05 | 0.008 | 0.01–0.08 Mg |
| Nickel 225 | N02225 | 99.0 (min) | 0.10 | 0.10 | 0.20 | 0.15 | 0.15–0.25 | 0.008 | 0.01–0.08 Mg, 0.01–0.05 Ti |
| Nickel 230 | N02230 | 99.0 (min) | 0.10 | 0.10 | 0.15 | 0.15 | 0.01–0.035 | 0.008 | 0.04–0.08 Mg, 0.005 Ti |
| Nickel 270 | N02270 | 99.97 (min) | 0.001 | 0.005 | 0.02 | 0.02 | 0.001 | 0.001 | 0.001 Co, 0.001 Cr, 0.001 Ti |
| **Low-alloy nickels** | | | | | | | | | |
| Nickel 211 | N02211 | 93.7 (min) | 0.25 | 0.75 | 4.25–5.25 | 0.20 | 0.15 | 0.015 | – |
| Duranickel 301 | N03301 | 93.00 (min) | 0.25 | 0.60 | 0.50 | 0.30 | 1.00 | 0.01 | 4.00–4.75 Al, 0.25–1.00 Ti |
| Alloy 360 | N03360 | bal | – | – | – | – | – | – | 1.85–2.05 Be, 0.4–0.6 Ti |

bal: balance

**Table 3.1-93** Mechanical properties of nickel-based alloys at room temperature

| Alloy | Ultimate tensile strength | | Yield strength (0.2% offset) | | Elongation in 50 mm (2 in) | Elastic modulus (tension) | | Hardness |
|---|---|---|---|---|---|---|---|---|
| | (MPa) | (ksi) | (MPa) | (ksi) | (%) | (GPa) | ($10^6$ psi) | |
| Nickel 200 | 462 | 67 | 148 | 21.5 | 47 | 204 | 29.6 | 109 HB |
| Nickel 201 | 403 | 58.5 | 103 | 15 | 50 | 207 | 30 | 129 HB |
| Nickel 205 | 345 | 50 | 90 | 13 | 45 | – | – | – |
| Nickel 211 | 530 | 77 | 240 | 35 | 40 | – | – | – |
| Nickel 212 | 483 | 70 | – | – | – | – | – | – |
| Nickel 222 | 380 | 55 | – | – | – | – | – | – |
| Nickel 270 | 345 | 50 | 110 | 16 | 50 | – | – | 30 HRB |
| Duranickel 301 (precipitation hardened) | 1170 | 170 | 862 | 125 | 25 | 207 | 30 | 30–40 HRC |
| Alloy 400 | 550 | 80 | 240 | 35 | 40 | 180 | 26 | 110–150 HB |
| Alloy 401 | 440 | 64 | 134 | 19.5 | 51 | – | – | – |
| Alloy R-405 | 550 | 80 | 240 | 35 | 40 | 180 | 26 | 110–140 HB |
| Alloy K-500 (precipitation hardened) | 1100 | 160 | 790 | 115 | 20 | 180 | 26 | 300 HB |
| Alloy 600 | 655 | 95 | 310 | 45 | 40 | 207 | 30 | 75 HRB |
| Alloy 601 | 620 | 90 | 275 | 40 | 45 | 207 | 30 | 65–80 HRB |
| Alloy 617 (solution annealed) | 755 | 110 | 350 | 51 | 58 | 211 | 30.6 | 173 HB |
| Alloy 625 | 930 | 135 | 517 | 75 | 42.5 | 207 | 30 | 190 HB |
| Alloy 690 | 725 | 105 | 348 | 50.5 | 41 | 211 | 30.6 | 88 HRB |
| Alloy 718 (precipitation hardened) | 1240 | 180 | 1036 | 150 | 12 | 211 | 30.6 | 36 HRC |
| Alloy C-22 | 785 | 114 | 372 | 54 | 62 | – | – | 209 HB |
| Alloy C-276 | 790 | 115 | 355 | 52 | 61 | 205 | 29.8 | 90 HRB |
| Alloy G3 | 690 | 100 | 320 | 47 | 50 | 199 | 28.9 | 79 HRB |
| Alloy 800 | 600 | 87 | 295 | 43 | 44 | 193 | 28 | 138 HB |
| Alloy 825 | 690 | 100 | 310 | 45 | 45 | 206 | 29.8 | – |
| Alloy 925[a] | 1210 | 176 | 815 | 118 | 24 | – | – | 36.5 HRC |

Properties are for annealed sheet unless otherwise indicated.

[a] Annealed at 980 °C (1800 °F) for 30 min, air cooled, and aged at 760 °C (1400 °F) for 8 h, furnace at a rate of 55 °C (1150 °F) for 8 h, air cooled

some further Ni alloys which are dealt with in the next section are listed in Table 3.1-93.

### 3.1.7.2 Highly Alloyed Ni-Based Materials

Nickel forms extensive solid solutions with many alloying elements: complete solid solutions with Fe and Cu, and limited solid solutions with $\leq 35$ wt% Cr, $\leq 20$ wt% Mo, $\leq 5-10$ wt% Al, Ti, and Mn; and V. Nickel and its alloys are providing favorable properties for uses in corrosive environments and at elevated temperatures.

The extensive solubility of several of the alloying elements is the basis of solid solution hardening which scales roughly with the atomic-size difference of the solute and is, therefore, pronounced with W, Mo, Nb, Ta, and Al. Based on the face-centered cubic structure, Ni-based solid solutions show high ductility, fracture toughness, and formability. The basic corrosion resistance of Ni is strongly increased by alloying additions of Cr, Mo, and W.

On the basis of these possibilities of materials design, a number of corrosion-resistant materials have been developed according to the criteria shown in

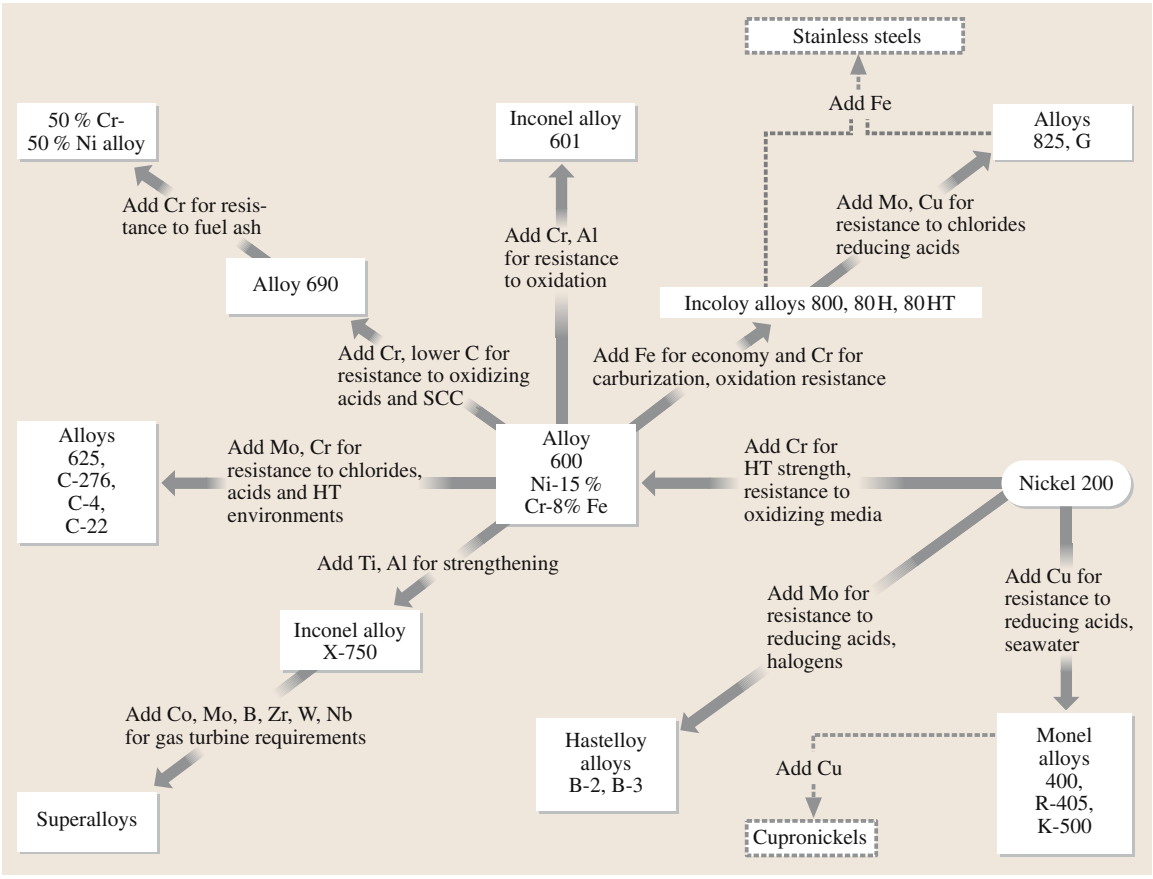


**Fig. 3.1-125** Effects of alloying additions on the corrosion resistance of nickel alloys. (HT denotes high temperature)

Fig. 3.1-125. The materials listed in Table 3.1-94 are the main representatives of high-Ni alloys.

Mechanical properties are listed in Table 3.1-93. Characteristic creep data are shown in Fig. 3.1-126.

**Table 3.1-94** Nominal compositions of highly-alloyed Ni

| Designation | UNS Nr | (wt%) Ni | Cr | Fe | Co | Mo | |
|---|---|---|---|---|---|---|---|
| **Nickel-molybdenum alloys** | | | | | | | |
| Hastelloy B | N10001 | bal | 1.0 | 6.0 | 2.5 | 26.0–33.0 | |
| Hastelloy B-2 | N10665 | bal | 1.0 | 2.0 | 1.0 | 26.0–30.0 | |
| Hastelloy B-3 | N10675 | 65.0 | 1.0–3.0 | 1.0–3.0 | 3.0 | 27.0–32.0 | |
| Nicrofer 6629 (B-4) | N10629 | bal | 0.5–1.5 | 1.0–6.0 | 2.5 | 26.0–30.0 | |
| **Nickel-chromium-iron alloys** | | | | | | | |
| Inconel 600 | N06600 | 72.0 (min(b)) | 14.0–17.0 | 6.0–10.0 | – | – | |
| Inconel 601 | N06601 | 58.0–63.0 | 21.0–25.0 | bal | – | – | |
| Inconel 690 | N06690 | 58.0 (min) | 27.0–31.0 | 7.0–11.0 | – | – | |
| Haynes 214 | N07214 | bal | 15.0–17.0 | 2.0–4.0 | 2.0 | 0.5 | |
| **Iron-nickel-chromium alloys** | | | | | | | |
| Incoloy 800 | N08800 | 30.0–35.0 | 19.0–23.0 | 39.5 (min) | – | – | |
| Incoloy 800HT | N08811 | 30.0–35.0 | 19.0–23.0 | 39.5 (min) | – | – | |
| Incoloy 801 | N08801 | 30.0–34.0 | 19.0–22.0 | bal | – | – | |
| Incoloy 803 | S35045 | 32.0–37.0 | 25.0–29.0 | 37.0 (min) | – | – | |
| **Nickel-chromium-molybdenum alloys** | | | | | | | |
| Hastelloy C | N10002 | bal | 14.5–16.50 | 4.0–7.0 | 2.5 | 15.0–17.0 | |
| Hastelloy C-4 | N06455 | bal | 14.0–18.0 | 3.0 | 2.0 | 14.0–17.0 | |
| Hastelloy C-22 | N06022 | bal | 20.0–22.5 | 2.0–6.0 | 2.5 | 12.5–14.5 | |
| Hastelloy C-276 | N10276 | bal | 14.5–16.50 | 4.0–7.0 | 2.5 | 15.0–17.0 | |
| Hastelloy C-2000 | N06200 | bal | 22.0–24.0 | 3.0 | 2.0 | 15.0–17.0 | |
| Nicrofer 5923 (Alloy 59) | N06059 | bal | 22.0–24.0 | 1.5 | 0.3 | 15.0–16.5 | |
| Inconel 617 | N06617 | 44.5 (min) | 20.0–24.0 | 3.0 | 10.0–15.0 | 8.0–10.0 | |
| Inconel 625 | N06625 | 58.0 (min) | 20.0–23.0 | 5.0 | 1.0 | 8.0–10.0 | |
| Inconel 686 | N06686 | bal | 19.0–23.0 | 5.0 | – | 15.0–17.0 | |
| Hastelloy S | N06635 | bal | 14.5–17.0 | 3.0 | 2.0 | 14.0–16.5 | |
| Allcorr | N06110 | bal | 27.0–33.0 | – | 12.0 | 8.0–12.0 | |
| **Nickel-chromium-iron-molybdenum alloys** | | | | | | | |
| Incoloy 825 | N08825 | 38.0–46.0 | 19.5–23.5 | bal | – | 2.5–3.5 | |
| Hastelloy G | N06007 | bal | 21.0–23.5 | 18.0–21.0 | 2.5 | 5.5–7.5 | |
| Hastelloy G-2 | N06975 | 47.0–52.0 | 23.0–26.0 | bal | – | 5.0–7.0 | |
| Hastelloy G-3 | N06985 | bal | 21.0–23.5 | 18.0–21.0 | 5.0 | 6.0–8.0 | |
| Hastelloy G-30 | N06030 | bal | 28.0–31.5 | 13.0–17.0 | 5.0 | 4.0–6.0 | |
| Hastelloy G-50 | N06950 | 50.0 (min) | 19.0–21.0 | 15.0–20.0 | 2.5 | 8.0–10.0 | |
| Hastelloy D-205 | – | 65.0 | 20.0 | 6.0 | – | 2.5 | |
| Hastelloy N | N10003 | bal | 6.0–8.0 | 5.0 | 0.2 | 15.0–18.0 | |
| Hastelloy X | N06002 | bal | 20.5–23.0 | 17.0–20.0 | 0.5–2.5 | 8.0–10.0 | |
| Nicrofer 3033 (Alloy 33) | R20033 | 30.0–33.0 | 31.0–35.0 | bal | – | 0.5–2.0 | |
| **Nickel-chromium-tungsten, nickel-iron-chromium, and nickel-cobalt-chromium-silicon alloys** | | | | | | | |
| Haynes 230 | N06230 | bal | 20.0–24.0 | 3.0 | – | 1.0–3.0 | |
| Haynes HR-120 | N08120 | 35.0–39.0 | 23.0–27.0 | bal | 3.0 | 2.5 | |
| Haynes HR-160 | N12160 | bal | 26.0–30.0 | 3.5 | 27.0–33.0 | 1.0 | |
| **Precipitation-hardening alloys** | | | | | | | |
| Alloy 625 Plus | N07716 | 57.0–63.0 | 19.0–22.0 | bal | – | 7.0–9.50 | |
| Inconel 718 | N07718 | 50.0–55.0 | 17.0–21.0 | bal | 1.0 | 2.80–3.30 | |
| Inconel 725 | N07725 | 55.0–59.0 | 19.0–22.5 | bal | – | 7.0–9.50 | |
| Inconel 925 | N09925 | 38.0–46.0 | 19.5–23.5 | 22.0 (min) | – | 2.50–3.50 | |

(a) Single values are maximum unless otherwise indicated; (b) Nickel plus cobalt content; bal: balance

**Table 3.1–94** Nominal compositions of highly alloyed Ni alloys, cont.

| | (wt%) | | | | | | | |
|---|---|---|---|---|---|---|---|---|
| | W | Nb | Ti | Al | C | Mn | Si | B | Others |
| **Nickel-molybdenum alloys** | | | | | | | | | |
| | – | – | – | – | 0.12 | 1.0 | 1.0 | – | 0.60 V |
| | – | – | – | – | 0.02 | 1.0 | 0.10 | – | – |
| | 3.0 | 0.20 | 0.20 | 0.50 | 0.01 | 3.0 | 0.10 | – | 0.20 Ta |
| | – | – | – | 0.1–0.5 | 0.01 | 1.5 | 0.05 | – | – |
| **Nickel-chromium-iron alloys** | | | | | | | | | |
| | – | – | – | – | 0.15 | 1.0 | 0.5 | – | 0.5 Cu |
| | – | – | – | 1.0–1.7 | 0.10 | 1.0 | 0.50 | – | 1.0 Cu |
| | – | – | – | – | 0.05 | 0.50 | 0.50 | – | 0.50 Cu |
| | 0.5 | – | 0.5 | 4.0–5.0 | 0.05 | 0.5 | 0.2 | 0.006 | 0.05 Zr, 0.002–0.040 Y |
| **Iron-nickel-chromium alloys** | | | | | | | | | |
| | – | – | 0.15–0.60 | 0.15–0.60 | 0.10 | 1.5 | 1.0 | – | – |
| | – | – | 0.15–0.60 | 0.15–0.60 | 0.06–0.10 | 1.5 | 1.0 | – | 0.895–1.20 Al + Ti |
| | – | – | 0.75–1.5 | – | 0.10 | 1.5 | 1.0 | – | 0.5 Cu |
| | – | – | 0.15–0.60 | 0.15–0.60 | 0.06–0.10 | 1.5 | 1.0 | – | 0.75 Cu |
| **Nickel-chromium-molybdenum alloys** | | | | | | | | | |
| | 3.0–4.5 | – | – | – | 0.08 | 1.0 | 1.0 | – | 0.35 V |
| | – | – | 0.70 | – | 0.015 | 1.0 | 0.08 | – | – |
| | 2.5–3.5 | – | – | – | 0.015 | 0.5 | 0.08 | – | 0.35 V |
| | 3.0–4.5 | – | – | – | 0.02 | 1.0 | 0.08 | – | 0.35 V |
| | – | – | – | 0.5 | 0.010 | 0.5 | 0.08 | – | 1.3–1.9 Cu |
| | – | – | – | 0.1–0.4 | 0.010 | 0.5 | 0.10 | – | – |
| | – | – | 0.6 | 0.8–1.5 | 0.05–0.15 | 1.0 | 1.0 | 0.006 | 0.5 Cu |
| | – | 3.15–4.15 | 0.40 | 0.40 | 0.10 | 0.50 | 0.50 | – | – |
| | 3.0–4.4 | – | 0.02–0.25 | – | 0.010 | 0.75 | 0.08 | – | – |
| | 1.0 | – | – | 0.1–0.50 | 0.02 | 0.3–1.0 | 0.20–0.75 | 0.015 | 0.35 Cu, 0.01–0.10 La |
| | 4.0 | 2.0 | 1.50 | 1.50 | 0.15 | – | – | – | – |
| **Nickel-chromium-iron-molybdenum alloys** | | | | | | | | | |
| | – | – | 0.6–1.2 | 0.2 | 0.05 | 1.0 | 0.5 | – | – |
| | 1.0 | 1.75–2.5 | – | – | 0.05 | 1.0–2.0 | 1.0 | – | – |
| | – | – | 0.70–1.5 | – | 0.03 | 1.0 | 1.0 | – | 0.7–1.20 Cu |
| | 1.5 | – | – | – | 0.015 | 1.0 | 1.0 | – | 1.5–2.5 Cu, 0.50 Nb + Ta |
| | 1.5–4.0 | 0.3–1.5 | – | – | 0.03 | 1.5 | 0.8 | – | 1.0–2.4 Cu |
| | 1.0 | 0.5 | – | – | 0.015 | 1.0 | 1.0 | – | 0.5 Cu |
| | – | – | – | – | 0.03 | – | 5.0 | – | 2.0 Cu |
| | 0.5 | – | – | – | 0.010 | 1.0 | 1.0 | 0.010 | 0.50 V, 0.35 Cu |
| | 0.20–1.0 | – | – | – | 0.05–0.15 | 1.0 | 1.0 | – | – |
| | – | – | – | – | 0.015 | 2.0 | 0.5 | – | 0.3–1.2 Cu |
| **Nickel-chromium-tungsten, nickel-iron-chromium, and nickel-cobalt-chromium-silicon alloys** | | | | | | | | | |
| | 13.0–15.0 | – | – | 0.20–0.50 | 0.05–0.15 | 0.3–1.0 | 0.25–0.75 | 0.015 | 0.005–0.05 La |
| | 2.5 | 0.4–0.9 | 0.20 | 0.40 | 0.02–0.1 | 1.5 | 1.0 | 0.010 | 0.5 Cu |
| | 1.0 | – | 0.20–0.80 | – | 0.15 | 1.5 | 2.4–3.0 | – | – |
| **Precipitation-hardening alloys** | | | | | | | | | |
| | – | 2.75–4.0 | 1.0–1.60 | 0.35 | 0.03 | 0.20 | 0.20 | – | – |
| | – | 4.75–5.50 | 0.35 | 0.20–0.80 | 0.08 | 0.35 | 0.35 | 0.06 | 0.3 Cu |
| | – | 2.75–4.0 | 1.0–1.70 | 0.35 | 0.03 | 0.35 | 0.50 | – | – |
| | – | 0.50 | 1.9–2.40 | 0.10–0.50 | 0.03 | 1.0 | 0.50 | – | 1.5–3.0 Cu |

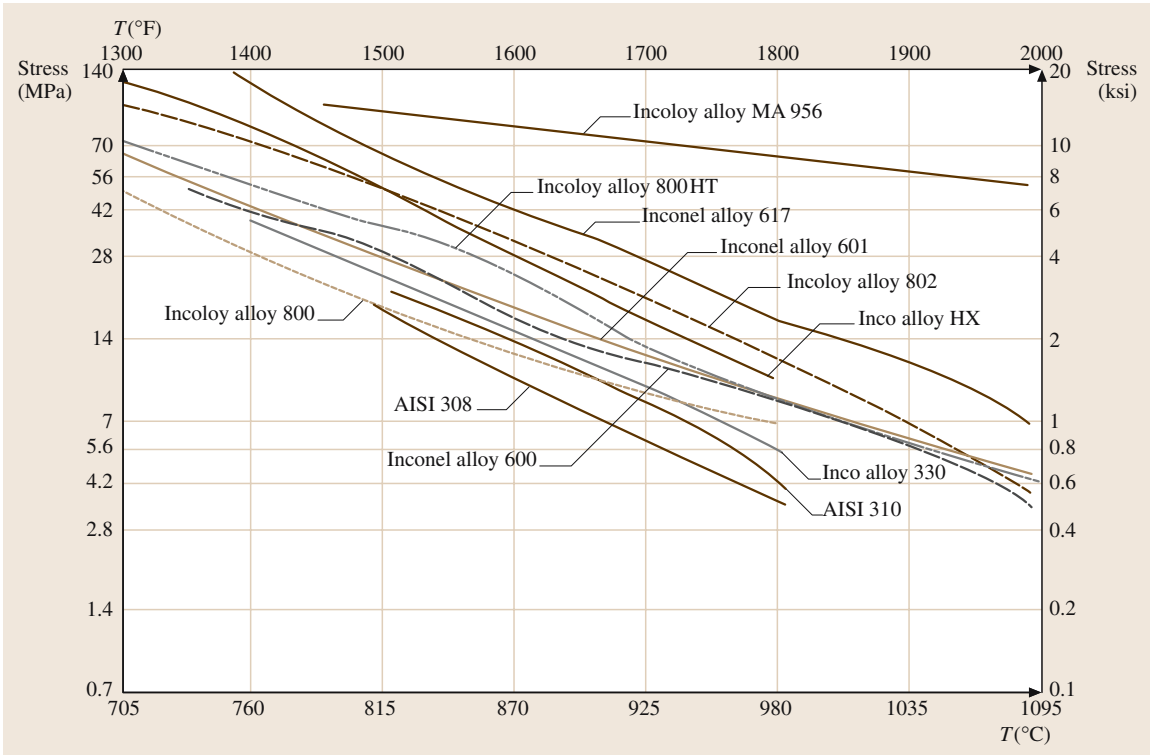


**Fig. 3.1-126** Rupture strength (10 000 h) of Ni-based alloys and stainless steels

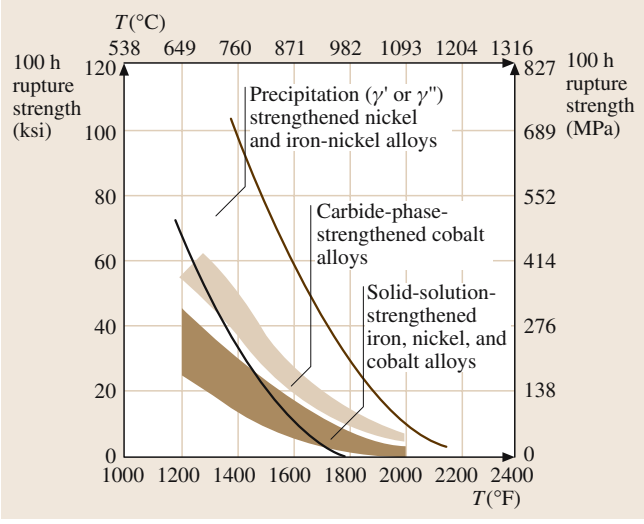


**Fig. 3.1-127** Stress–rupture characteristics of wrought superalloys

### 3.1.7.3 Ni-Based Superalloys

The term superalloy is used for a group of nickel-, iron–nickel-, and cobalt-based high-temperature materials for applications at temperatures $\geq 540\,^{\circ}\mathrm{C}$. It is useful to compare the main subgroups in terms of the strengthening mechanisms applied and stress–rupture characteristics achieved, as shown in Fig. 3.1-127. In this section iron–nickel- and nickel-based superalloys are covered whereas cobalt-based superalloys are dealt with in Sect. 3.1.6.3. Nickel-based superalloys are among the most complex metallic materials with numerous alloying elements serving particular functions, as briefly outlined here.

All Ni and Fe−Ni-based superalloys are alloyed with Al. This leads to a two-phase matrix consisting of the $\gamma$-(Ni, Fe, Al) solid solution phase (fcc, A1 structure) and the intermetallic $\gamma'$-$Ni_3Al$ phase ($L1_2$ structure), which has a superlattice structure relative to the fcc structure of the $\gamma$ phase. The binary Al−Ni phase diagram in Fig. 3.1-128 shows clearly that the $\gamma'$ phase is stable up to the melting range. The matrix phase $\gamma$ is solid solution strengthened by alloying additions of Cr, Mo, W, and

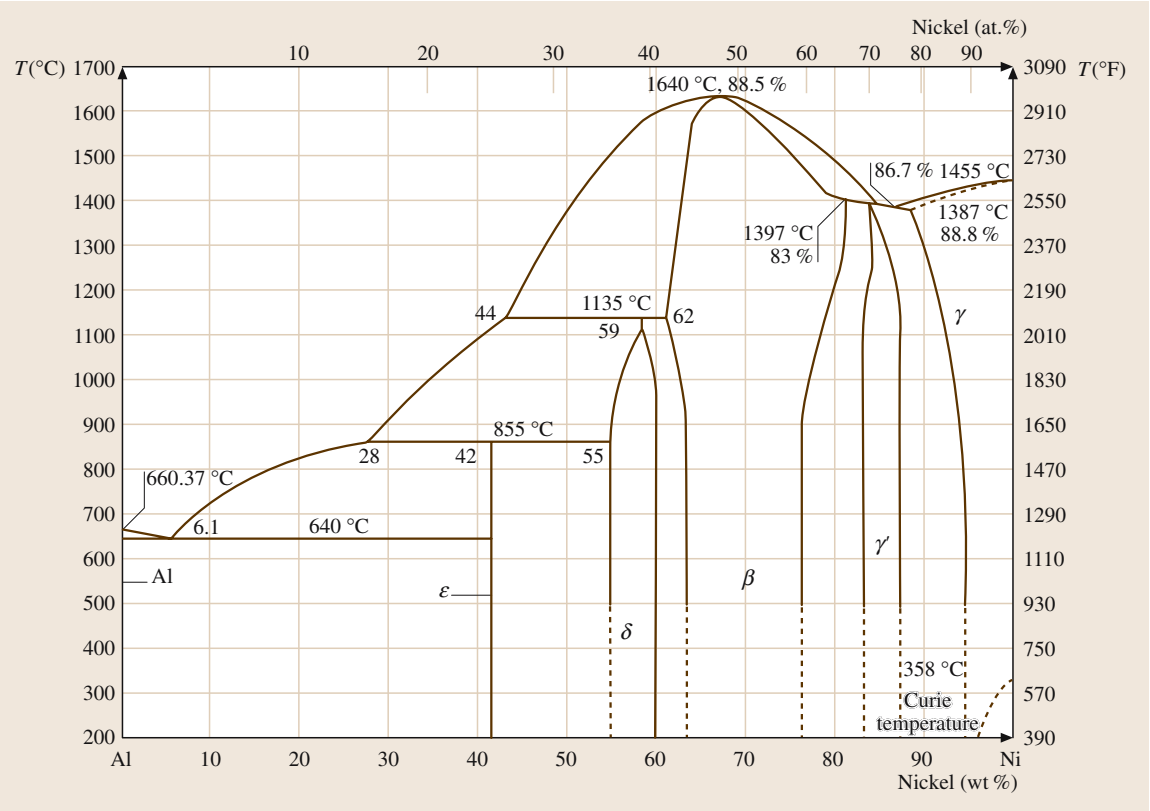


**Fig. 3.1-128** Al–Ni phase diagram indicating the high thermal stability of the $\gamma'$ phase

Ta. The $\gamma'$-$Ni_3Al$ phase is precipitated coherently from the $\gamma$ phase by appropriate heat treatment in amounts ranging from 20 to 45 vol% $\gamma'$ in wrought superalloys and about 60 vol% $\gamma'$ in cast superalloys. The hardening effect of $\gamma'$ in these alloys is due to its high yield stress which increases with increasing temperature to a maximum at about 650 °C, as shown in Fig. 3.1-129. The anomalous temperature dependence is due to the fact that the plastic deformation is associated with the formation and motion of partial dislocations, giving rise to local disordering of the ordered structure. Figure 3.1-129 shows also that alloying additions such as Cr, Ti, and Nb increase the yield stress and tend to shift its maximum to higher temperatures. This is because several alloying elements substitute Ni (Fe, Co, Cr) or Al (Ti, Nb) in the $Ni_3Al$ structure and raise its critical resolved shear stress. Another major alloying addition is carbon in combination with carbide forming alloy components such as Ti, Cr, Mo, W, and Nb (which are partly added to achieve hardening of the metallic phases as well, as described above). The carbides (MC, $M_7C_3$, $M_{23}C_6$, and $M_6C$) are precipitated or formed by secondary reactions as intragrain or grain boundary precipitates further stabilizing the microstructure against creep deformation.

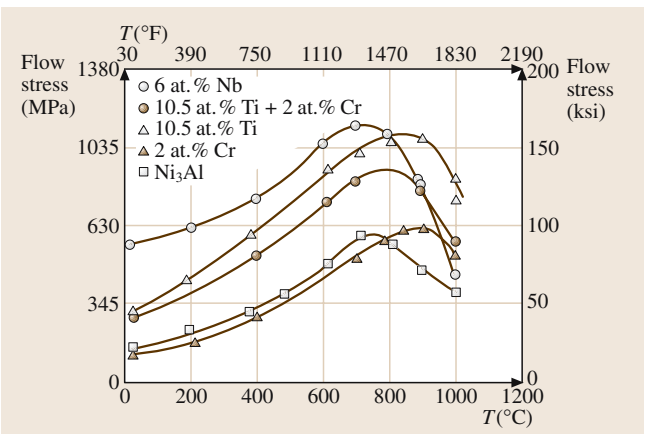


**Fig. 3.1-129** Temperature dependence of the flow stress of the $\gamma'$-$Ni_3Al$ phase and effects of Nb, Ti, and Cr alloying additions

Taking these factors of influence into account the wrought superalloys listed in Table 3.1-95 and the cast superalloys listed in Table 3.1-96 have been developed.

**Table 3.1-95** Nominal compositions of Fe–Ni-based and Ni-based wrought superalloys

| Alloy | UNS No. | Composition (wt%) Cr | Ni | Co | Mo | W | Nb | Ti | Al | Fe | C | Other |
|---|---|---|---|---|---|---|---|---|---|---|---|---|
| **Solid-solution alloys Iron-nickel-based** | | | | | | | | | | | | |
| Alloy N-155 (Multimet) | R30155 | 21.0 | 20.0 | 20.0 | 3.00 | 2.5 | 1.0 | – | – | 32.2 | 0.15 | 0.15 N, 0.2 La, 0.02 Zr |
| Haynes 556 | R30556 | 22.0 | 21.0 | 20.0 | 3.0 | 2.5 | 0.1 | – | 0.3 | 29.0 | 0.10 | 0.50 Ta, 0.02 La, 0.002 Zr |
| 19-9 DL | S63198 | 19.0 | 9.0 | – | 1.25 | 1.25 | 0.4 | 0.3 | – | 66.8 | 0.30 | 1.10 Mn, 0.60 Si |
| Incoloy 800 | N08800 | 21.0 | 32.5 | – | – | – | – | 0.38 | 0.38 | 45.7 | 0.05 | – |
| Incoloy 800H | N08810 | 21.0 | 33.0 | – | – | – | – | – | – | 45.8 | 0.08 | – |
| Incoloy 800HT | N08811 | 21.0 | 32.5 | – | – | – | – | 0.4 | 0.4 | 46.0 | 0.08 | 0.8 Mn, 0.5 Si, 0.4 Cu |
| Incoloy 801 | N08801 | 20.5 | 32.0 | – | – | – | – | 1.13 | – | 46.3 | 0.05 | – |
| Incoloy 802 | – | 21.0 | 32.5 | – | – | – | – | 0.75 | 0.58 | 44.8 | 0.35 | – |
| **Nickel-based** | | | | | | | | | | | | |
| Haynes 214 | – | 16.0 | 76.5 | – | – | – | – | – | 4.5 | 3.0 | 0.03 | |
| Haynes 230 | N06230 | 22.0 | 55.0 | 5.0 (max) | 2.0 | 14.0 | – | – | 0.35 | 3.0 (max) | 0.10 | 0.015 (max) B, 0.02 La |
| Inconel 600 | N06600 | 15.5 | 76.0 | – | – | – | – | – | – | 8.0 | 0.08 | 0.25 Cu |
| Inconel 601 | N06601 | 23.0 | 60.5 | – | – | – | – | – | 1.35 | 14.1 | 0.05 | 0.5 Cu |
| Inconel 617 | N06617 | 22.0 | 55.0 | 12.5 | 9.0 | – | – | – | 1.0 | – | 0.07 | – |
| Inconel 625 | N06625 | 21.5 | 61.0 | – | 9.0 | – | 3.6 | 0.2 | 0.2 | 2.5 | 0.05 | – |
| RA 333 | N06333 | 25.0 | 45.0 | 3.0 | 3.0 | 3.0 | – | – | – | 18.0 | 0.05 | – |
| Hastelloy B | N01001 | 1.0 (max) | 63.0 | 2.5 (max) | 28.0 | – | – | – | – | 5.0 | 0.05 (max) | 0.03 V |
| Hastelloy N | N01003 | 7.0 | 72.0 | – | 16.0 | – | – | 0.5 (max) | – | 5.0 (max) | 0.06 | |
| Hastelloy S | N06635 | 15.5 | 67.0 | – | 15.5 | – | – | – | 0.2 | 1.0 | 0.02 (max) | 0.02 La |
| Hastelloy W | N10004 | 5.0 | 61.0 | 2.5 (max) | 24.5 | – | – | – | – | 5.5 | 0.12 (max) | 0.6 V |
| Hastelloy X | N06002 | 22.0 | 49.0 | 1.5 (max) | 9.0 | 0.6 | – | – | 2.0 | 15.8 | 0.15 | – |
| Hastelloy C-276 | N10276 | 15.5 | 59.0 | – | 16.0 | 3.7 | – | – | – | 5.0 | 0.02 (max) | – |
| Haynes HR-120 | N08120 | 25.0 | 37.0 | 3.0 | 2.5 | 2.5 | 0.7 | – | 0.1 | 33.0 | 0.05 | 0.7 Mn, 0.6 Si, 0.2 N, 0.004 B |
| Haynes HR-160 | N12160 | 28.0 | 37.0 | 29.0 | – | – | – | – | – | 2.0 | 0.05 | 2.75 Si, 0.5 Mn |
| Nimonic 75 | N06075 | 19.5 | 75.0 | – | – | – | – | 0.4 | 0.15 | 2.5 | 0.12 | 0.25 (max) Cu |
| Nimonic 86 | – | 25.0 | 65.0 | – | 10.0 | – | – | – | – | – | 0.05 | 0.03 Ce, 0.015 Mg |
| **Precipitation-hardening alloys Iron-nickel-based** | | | | | | | | | | | | |
| A-286 | S66286 | 15.0 | 26.0 | – | 1.25 | – | – | 2.0 | 0.2 | 55.2 | 0.04 | 0.005 B, 0.3 V |
| Discaloy | S66220 | 14.0 | 26.0 | – | 3.0 | – | – | 1.7 | 0.25 | 55.0 | 0.06 | – |
| Incoloy 903 | N19903 | 0.1 (max) | 38.0 | 15.0 | 0.1 | – | 3.0 | 1.4 | 0.7 | 41.0 | 0.04 | – |
| Pyromet CTX-1 | – | 0.1 (max) | 37.7 | 16.0 | 0.1 | – | 3.0 | 1.7 | 1.0 | 39.0 | 0.03 | – |
| Incoloy 907 | N19907 | – | 38.4 | 13.0 | – | – | 4.7 | 1.5 | 0.03 | 42.0 | 0.01 | 0.15 Si |
| Incoloy 909 | N19909 | – | 38.0 | 13.0 | – | – | 4.7 | 1.5 | 0.03 | 42.0 | 0.01 | 0.4 Si |
| Incoloy 925 | N09925 | 20.5 | 44.0 | – | 2.8 | – | – | 2.1 | 0.2 | 29 | 0.01 | 1.8 Cu |
| V-57 | – | 14.8 | 27.0 | – | 1.25 | – | – | 3.0 | 0.25 | 48.6 | 0.08 (max) | 0.01 B, 0.5 (max) V |
| W-545 | S66545 | 13.5 | 26.0 | – | 1.5 | – | – | 2.85 | 0.2 | 55.8 | 0.08 (max) | 0.05 B |

**Table 3.1–95** Nominal compositions of Fe–Ni-based and Ni-based wrought superalloys, cont.

| Alloy | UNS No. | Composition (wt%) Cr | Ni | Co | Mo | W | Nb | Ti | Al | Fe | C | Other |
|---|---|---|---|---|---|---|---|---|---|---|---|---|
| **Nickel-based** | | | | | | | | | | | | |
| Astroloy | N13017 | 15.0 | 56.5 | 15.0 | 5.25 | – | – | 3.5 | 4.4 | <0.3 | 0.06 | 0.03 B, 0.06 Zr |
| Custom Age 625 PLUS | N07716 | 21.0 | 61.0 | – | 8.0 | – | 3.4 | 1.3 | 0.2 | 5.0 | 0.01 | – |
| Haynes 242 | – | 8.0 | 62.5 | 2.5 (max) | 25.0 | – | – | – | 0.5 (max) | 2.0 (max) | 0.10 (max) | 0.006 (max) B |
| Haynes 263 | N07263 | 20.0 | 52.0 | – | 6.0 | – | – | 2.4 | 0.6 | 0.7 | 0.06 | 0.6 Mn, 0.4 Si, 0.2 Cu |
| Haynes R-41 | N07041 | 19.0 | 52.0 | 11.0 | 10.0 | – | – | 3.1 | 1.5 | 5.0 | 0.09 | 0.5 Si, 0.1 Mn, 0.006 B |
| Inconel 100 | N13100 | 10.0 | 60.0 | 15.0 | 3.0 | – | – | 4.7 | 5.5 | <0.6 | 0.15 | 1.0 V, 0.06 Zr, 0.015 B |
| Inconel 102 | N06102 | 15.0 | 67.0 | – | 2.9 | 3.0 | 2.9 | 0.5 | 0.5 | 7.0 | 0.06 | 0.005 B, 0.02 Mg, 0.03 Zr |
| Incoloy 901 | N09901 | 12.5 | 42.5 | – | 6.0 | – | – | 2.7 | – | 36.2 | 0.10 (max) | – |
| Inconel 702 | N07702 | 15.5 | 79.5 | – | – | – | – | 0.6 | 3.2 | 1.0 | 0.05 | 0.5 Mn, 0.2 Cu, 0.4 Si |
| Inconel 706 | N09706 | 16.0 | 41.5 | – | – | – | – | 1.75 | 0.2 | 37.5 | 0.03 | 2.9 (Nb + Ta), 0.15 (max) Cu |
| Inconel 718 | N07718 | 19.0 | 52.5 | – | 3.0 | – | 5.1 | 0.9 | 0.5 | 18.5 | 0.08 (max) | 0.15 (max) Cu |
| Inconel 721 | N07721 | 16.0 | 71.0 | – | – | – | – | 3.0 | – | 6.5 | 0.04 | 2.2 Mn, 0.1 Cu |
| Inconel 722 | N07722 | 15.5 | 75.0 | – | – | – | – | 2.4 | 0.7 | 7.0 | 0.04 | 0.5 Mn, 0.2 Cu, 0.4 Si |
| Inconel 725 | N07725 | 21.0 | 57.0 | – | 8.0 | – | 3.5 | 1.5 | 0.35 (max) | 9.0 | 0.03 (max) | |
| Inconel 751 | N07751 | 15.5 | 72.5 | – | – | – | 1.0 | 2.3 | 1.2 | 7.0 | 0.05 | 0.25 (max) Cu |
| Inconel X-750 | N07750 | 15.5 | 73.0 | – | – | – | 1.0 | 2.5 | 0.7 | 7.0 | 0.04 | 0.25 (max) Cu |
| M-252 | N07252 | 19.0 | 56.5 | 10.0 | 10.0 | – | – | 2.6 | 1.0 | <0.75 | 0.15 | 0.005 B |
| Nimonic 80A | N07080 | 19.5 | 73.0 | 1.0 | – | – | – | 2.25 | 1.4 | 1.5 | 0.05 | 0.10 (max) Cu |
| Nimonic 90 | N07090 | 19.5 | 55.5 | 18.0 | – | – | – | 2.4 | 1.4 | 1.5 | 0.06 | – |
| Nimonic 95 | – | 19.5 | 53.5 | 18.0 | – | – | – | 2.9 | 2.0 | 5.0 (max) | 0.15 (max) | +B, +Zr |
| Nimonic 100 | – | 11.0 | 56.0 | 20.0 | 5.0 | – | – | 1.5 | 5.0 | 2.0 (max) | 0.30 (max) | +B, +Zr |
| Nimonic 105 | – | 15.0 | 54.0 | 20.0 | 5.0 | – | – | 1.2 | 4.7 | – | 0.08 | 0.005 B |
| Nimonic 115 | – | 15.0 | 55.0 | 15.0 | 4.0 | – | – | 4.0 | 5.0 | 1.0 | 0.20 | 0.04 Zr |
| C-263 | N07263 | 20.0 | 51.0 | 20.0 | 5.9 | – | – | 2.1 | 0.45 | 0.7 (max) | 0.06 | – |
| Pyromet 860 | – | 13.0 | 44.0 | 4.0 | 6.0 | – | – | 3.0 | 1.0 | 28.9 | 0.05 | 0.01 B |
| Pyromet 31 | N07031 | 22.7 | 55.5 | – | 2.0 | – | 1.1 | 2.5 | 1.5 | 14.5 | 0.04 | 0.005 B |
| Refractaloy 26 | – | 18.0 | 38.0 | 20.0 | 3.2 | – | – | 2.6 | 0.2 | 16.0 | 0.03 | 0.015 B |
| René 41 | N07041 | 19.0 | 55.0 | 11.0 | 10.0 | – | – | 3.1 | 1.5 | <0.3 | 0.09 | 0.01 B |
| René 95 | – | 14.0 | 61.0 | 8.0 | 3.5 | 3.5 | 3.5 | 2.5 | 3.5 | <0.3 | 0.16 | 0.01 B, 0.05 Zr |
| René 100 | – | 9.5 | 61.0 | 15.0 | 3.0 | – | – | 4.2 | 5.5 | 1.0 (max) | 0.16 | 0.015 B, 0.06 Zr, 1.0 V |
| Udimet 500 | N07500 | 19.0 | 48.0 | 19.0 | 4.0 | – | – | 3.0 | 3.0 | 4.0 (max) | 0.08 | 0.005 B |
| Udimet 520 | – | 19.0 | 57.0 | 12.0 | 6.0 | 1.0 | – | 3.0 | 2.0 | – | 0.08 | 0.005 B |
| Udimet 630 | – | 17.0 | 50.0 | – | 3.0 | 3.0 | 6.5 | 1.0 | 0.7 | 18.0 | 0.04 | 0.004 B |
| Udimet 700 | – | 15.0 | 53.0 | 18.5 | 5.0 | – | – | 3.4 | 4.3 | <1.0 | 0.07 | 0.03 B |
| Udimet 710 | – | 18.0 | 55.0 | 14.8 | 3.0 | 1.5 | – | 5.0 | 2.5 | – | 0.07 | 0.01 B |
| Unitemp AF2-1DA | N07012 | 12.0 | 59.0 | 10.0 | 3.0 | 6.0 | – | 3.0 | 4.6 | <0.5 | 0.35 | 1.5 Ta, 0.015 B, 0.1 Zr |
| Waspaloy | N07001 | 19.5 | 57.0 | 13.5 | 4.3 | – | – | 3.0 | 1.4 | 2.0 (max) | 0.07 | 0.006 B, 0.09 Zr |

**Table 3.1-96** Nominal compositions of Ni-based cast superalloys

| Alloy designation | Nominal composition (wt%) | | | | | | | | | | | | |
|---|---|---|---|---|---|---|---|---|---|---|---|---|---|
| | C | Ni | Cr | Co | Mo | Fe | Al | B | Ti | Ta | W | Zr | Other |
| **Nickel-based** | | | | | | | | | | | | | |
| B-1900 | 0.1 | 64 | 8 | 10 | 6 | – | 6 | 0.015 | 1 | 4[a] | – | 0.10 | – |
| CMSX-2 | – | 66.2 | 8 | 4.6 | 0.6 | – | 56 | – | 1 | 6 | 8 | 6 | – |
| Hastelloy X | 0.1 | 50 | 21 | 1 | 9 | 18 | – | – | – | – | 1 | – | – |
| Inconel 100 | 0.18 | 60.5 | 10 | 15 | 3 | – | 5.5 | 0.01 | 5 | – | – | 0.06 | 1 V |
| Inconel 713C | 0.12 | 74 | 12.5 | – | 4.2 | – | 6 | 0.012 | 0.8 | 1.75 | – | 0.1 | 0.9 Nb |
| Inconel 713LC | 0.05 | 75 | 12 | – | 4.5 | – | 6 | 0.01 | 0.6 | 4 | – | 0.1 | – |
| Inconel 738 | 0.17 | 61.5 | 16 | 8.5 | 1.75 | – | 3.4 | 0.01 | 3.4 | – | 2.6 | 0.1 | 2 Nb |
| Inconel 792 | 0.2 | 60 | 13 | 9 | 2.0 | – | 3.2 | 0.02 | 4.2 | – | 4 | 0.1 | 2 Nb |
| Inconel 718 | 0.04 | 53 | 19 | – | 3 | 18 | 0.5 | – | 0.9 | – | – | – | 0.1 Cu, 5 Nb |
| X-750 | 0.04 | 73 | 15 | – | – | 7 | 0.7 | – | 2.5 | – | – | – | 0.25 Cu, 0.9 Nb |
| M-252 | 0.15 | 56 | 20 | 10 | 10 | – | 1 | 0.005 | 2.6 | – | – | – | – |
| MAR-M 200 | 0.15 | 59 | 9 | 10 | – | 1 | 5 | 0.015 | 2 | – | 12.5 | 0.05 | 1 Nb[b] |
| MAR-M 246 | 0.15 | 60 | 9 | 10 | 2.5 | – | 5.5 | 0.015 | 1.5 | 1.5 | 10 | 0.05 | – |
| MAR-M 247 | 0.15 | 59 | 8.25 | 10 | 0.7 | 0.5 | 5.5 | 0.015 | 1 | 3 | 10 | 0.05 | 1.5 Hf |
| PWA 1480 | – | bal | 10 | 5.0 | – | – | 5.0 | – | 1.5 | 12 | 4.0 | – | – |
| René 41 | 0.09 | 55 | 19 | 11.0 | 10.0 | – | 1.5 | 0.01 | 3.1 | – | – | – | – |
| René 77 | 0.07 | 58 | 15 | 15 | 4.2 | – | 4.3 | 0.015 | 3.3 | – | – | 0.04 | – |
| René 80 | 0.17 | 60 | 14 | 9.5 | 4 | – | 3 | 0.015 | 5 | – | 4 | 0.03 | – |
| René 80 Hf | 0.08 | 60 | 14 | 9.5 | 4 | – | 3 | 0.015 | 4.8 | – | 4 | 0.02 | 0.75 Hf |
| René 100 | 0.18 | 61 | 9.5 | 15 | 3 | – | 5.5 | 0.015 | 4.2 | – | – | 0.06 | 1 V |
| René N4 | 0.06 | 62 | 9.8 | 7.5 | 1.5 | – | 4.2 | 0.004 | 3.5 | 4.8 | 6 | – | 0.5 Nb, 0.15 Hf |
| Udimet 500 | 0.1 | 53 | 18 | 17 | 4 | 2 | 3 | – | 3 | – | – | – | – |
| Udimet 700 | 0.1 | 53.5 | 15 | 18.5 | 5.25 | – | 4.25 | 0.03 | 3.5 | – | – | – | – |
| Udimet 710 | 0.13 | 55 | 18 | 15 | 3 | – | 2.5 | – | 5 | – | 1.5 | 0.08 | – |
| Waspaloy | 0.07 | 57.5 | 19.5 | 13.5 | 4.2 | 1 | 1.2 | 0.005 | 3 | – | – | 0.09 | – |
| WAX-20 (DS) | 0.20 | 72 | – | – | – | – | 6.5 | – | – | – | 20 | 1.5 | – |

[a] B-1900 + Hf also contains 1.5% Hf

[b] MAR-M 200 + Hf also contains 1.5% Hf

bal: balance

The mechanical properties as a function of temperature of the wrought superalloys are listed in Tables 3.1-97 and 3.1-98, those for the cast alloys in Table 3.1-99. The temperature dependence of the mechanical properties is essentially dependent on the volume fraction, composition, and resulting flow stress of the $\gamma'$ phase.

Figure 3.1-126 shows some typical results of stress rupture tests characterising the time-dependent high temperature behavior dominated by creep deformation. A compilation of creep data may be found in [1.101].

### 3.1.7.4 Ni Plating

Nickel plating is used extensively for decorative applications (80%) and for engineering and electroforming purposes (20%).

Electroless Ni coatings are produced by autocatalytical reduction of Ni ions from aqueous solution. Three electroless coatings are applied most frequently: nickel–phosphorus (6–12 wt% P), nickel–boron (≈ 5 wt% B), and composite coatings (Ni−P with SiC, fluorocarbons, and diamond). A more extensive account is given in [1.96].

**Table 3.1-97** Effect of temperature on the ultimate tensile strength of wrought Ni-based superalloys

| Alloy | Form | Ultimate tensile strength at: | | | | | | | | | | Condition of test material[a] |
|---|---|---|---|---|---|---|---|---|---|---|---|---|
| | | 21 °C (70 °F) | | 540 °C (1000 °F) | | 650 °C (1200 °F) | | 760 °C (1400 °F) | | 870 °C (1600 °F) | | |
| | | (MPa) | (ksi) | (MPa) | (ksi) | (MPa) | (ksi) | (MPa) | (ksi) | (MPa) | (ksi) | |
| **Nickel-based** | | | | | | | | | | | | |
| Astroloy | Bar | 1415 | 205 | 1240 | 180 | 1310 | 190 | 1160 | 168 | 775 | 112 | 1095 °C (2000 °F)/4 h/OQ + 870 °C (1600 °F)/8 h/AC + 980 °C (1800 °F)/4 h/AC + 650 °C (1200 °F)/24 h/AC + 760 °C (1400 °F)/8 h/AC |
| Cabot 214 | – | 915 | 133 | 715 | 104 | 675 | 98 | 560 | 84 | 440 | 64 | 1120 °C (2050 °F) |
| D-979 | Bar | 1410 | 204 | 1295 | 188 | 1105 | 160 | 720 | 104 | 345 | 50 | 1040 °C (1900 °F)/1 h/OQ + 845 °C (1550 °F)/6 h/AC + 705 °C (1300 °F)/16 h/AC |
| Hastelloy C-22 | Sheet | 800 | 116 | 625 | 91 | 585 | 85 | 525 | 76 | – | – | 1120 °C (2050 °F)/RQ |
| Hastelloy G-30 | Sheet | 690 | 100 | 490 | 71 | – | – | – | – | – | – | 1175 °C (2150 °F)/RAC-WQ |
| Hastelloy S | Bar | 845 | 130 | 775 | 112 | 720 | 105 | 575 | 84 | 340 | 50 | 1065 °C (1950 °F)/AC |
| Hastelloy X | Sheet | 785 | 114 | 650 | 94 | 570 | 83 | 435 | 63 | 255 | 37 | 1175 °C (2150 °F)/RAC |
| Haynes230 | – | 870 | 126 | 720 | 105 | 675 | 98 | 575 | 84 | 385 | 56 | 1230 °C (2250 °F)/AC |
| Inconel 587[b] | Bar | 1180 | 171 | 1035 | 150 | 1005 | 146 | 830 | 120 | 525 | 76 | – |
| Inconel 597[b] | Bar | 1220 | 177 | 1140 | 165 | 1060 | 154 | 930 | 135 | – | – | – |
| Inconel 600 | Bar | 660 | 96 | 560 | 81 | 450 | 65 | 260 | 38 | 140 | 20 | 1120 °C (2050 °F)/2 h/AC |
| Inconel 601 | Sheet | 740 | 107 | 725 | 105 | 525 | 76 | 290 | 42 | 160 | 23 | 1150 °C (2100 °F)/2 h/AC |
| Inconel 617 | Bar | 740 | 107 | 580 | 84 | 565 | 82 | 440 | 64 | 275 | 40 | 1175 °C (2150 °F)/AC |
| Inconel 617 | Sheet | 770 | 112 | 590 | 86 | 590 | 86 | 470 | 68 | 310 | 45 | 1175 °C (2150 °F)/0.2 h/AC |
| Inconel 625 | Bar | 965 | 140 | 910 | 132 | 835 | 121 | 550 | 80 | 275 | 40 | 1150 °C (2100 °F)/1 h/WQ |
| Inconel 706 | Bar | 1310 | 190 | 1145 | 166 | 1035 | 150 | 725 | 105 | – | – | 980 °C (1800 °F)/1 h/AC + 845 °C (1550 °F)/3 h/AC + 720 °C (1325 °F)/8 h/FC + 620 °C (1150 °F)/8 h/AC |
| Inconel 718 | Bar | 1435 | 208 | 1275 | 185 | 1228 | 178 | 950 | 138 | 340 | 49 | 980 °C (1800 °F)/1 h/AC + 720 °C (1325 °F)/8 h/FC + 620 °C (1150 °F)/18 h/AC |
| Inconel 718 Direct Age | Bar | 1530 | 222 | 1350 | 196 | 1235 | 179 | – | – | – | – | 735 °C (1325 °F)/8 h/SC + 620 °C (1150 °F)/8 h/AC |
| Inconel 718 Super | Bar | 1530 | 196 | 1200 | 174 | 1130 | 164 | – | – | – | – | 925 °C (1700 °F)/1 h/AC + 735 °C (1325 °F)/8 h/SC + 620 °C (1150 °F)/8 h/AC |

**Table 3.1–97** Effect of temperature on the ultimate tensile strength of wrought Ni-based superalloys, cont.

| Alloy | Form | Ultimate tensile strength at: | | | | | | | | | | Condition of test material[a] |
|---|---|---|---|---|---|---|---|---|---|---|---|---|
| | | 21 °C (70 °F) | | 540 °C (1000 °F) | | 650 °C (1200 °F) | | 760 °C (1400 °F) | | 870 °C (1600 °F) | | |
| | | (MPa) | (ksi) | (MPa) | (ksi) | (MPa) | (ksi) | (MPa) | (ksi) | (MPa) | (ksi) | |
| **Nickel-based** | | | | | | | | | | | | |
| Inconel X750 | Bar | 1200 | 174 | 1050 | 152 | 940 | 136 | – | – | – | – | 1150 °C (2100 °F)/2 h/AC + 845 °C (1550 °F)/24 h/AC + 705 °C (1300 °F)/20 h/AC |
| M-252 | Bar | 1240 | 180 | 1230 | 178 | 1160 | 168 | 945 | 137 | 510 | 74 | 1040 °C (1900 °F)/4 h/AC + 760 °C (1400 °F)/16 h/AC |
| Nimonic 75 | Bar | 745 | 108 | 675 | 98 | 540 | 78 | 310 | 45 | 150 | 22 | 1050 °C (1925 °F)/1 h/AC |
| Nimonic 80A | Bar | 1000 | 145 | 875 | 127 | 795 | 115 | 600 | 87 | 310 | 45 | 1080 °C (1975 °F)/8 h/AC + 705 °C (1300 °F)/16 h/AC |
| Nimonic 90 | Bar | 1235 | 179 | 1075 | 156 | 940 | 136 | 655 | 95 | 330 | 48 | 1080 °C (1975 °F)/8 h/AC + 705 °C (1300 °F)/16 h/AC |
| Nimonic 105 | Bar | 1180 | 171 | 1130 | 164 | 1095 | 159 | 930 | 135 | 660 | 96 | 1150 °C (2100 °F)/4 h/AC + 1060 °C (1940 °F)/16 h/AC + 850 °C (1560 °F)/16 h/AC |
| Nimonic 115 | Bar | 1240 | 180 | 1090 | 158 | 1125 | 163 | 1085 | 157 | 830 | 120 | 1190 °C (2175 °F)/1.5 h/AC + 1100 °C (2010 °F)/6 h/AC |
| Nimonic 263 | Sheet | 970 | 141 | 800 | 116 | 770 | 112 | 650 | 94 | 280 | 40 | 1150 °C (2100 °F)/0.2 h/WQ + 800 °C (1470 °F)/8 h/AC |
| Nimonic 942 | Bar | 1405 | 204 | 1300 | 189 | 1240 | 180 | 900 | 131 | – | – | – |
| Nimonic PE.11 | Bar | 1080 | 157 | 1000 | 145 | 940 | 136 | 760 | 110 | – | – | – |
| Nimonic PE.16 | Bar | 885 | 128 | 740 | 107 | 660 | 96 | 510 | 74 | 215 | 31 | 1040 °C (1900 °F)/4 h/AC + 800 °C (1470 °F)/2 h/AC + 1100–1115 °C (2010–2040 °F)/0.25 h/AC + 850 °C (1500 °F)/4 h/AC |
| Nimonic PK.33 | Sheet | 1180 | 171 | 1000 | 145 | 1000 | 145 | 885 | 128 | 510 | 74 | 1100–1115 °C (2010–2040 °F)/0.25 h/AC + 850 °C (1500 °F)/4 h/AC |
| Pyromet 860 | Bar | 1295 | 188 | 1255 | 182 | 1110 | 161 | 910 | 132 | – | – | 1095 °C (2000 °F)/2 h/WQ + 830 °C (1525 °F)/2 h/AC + 760 °C (1400 °F)/24 h/AC |
| René 41 | Bar | 1420 | 206 | 1400 | 203 | 1340 | 194 | 1105 | 160 | 620 | 90 | 1065 °C (1950 °F)/4 h/AC + 760 °C (1400 °F)/16 h/AC |
| René 95 | Bar | 1620 | 235 | 1550 | 224 | 1460 | 212 | 1170 | 170 | – | – | 900 °C (1650 °F)/24 h + 1105 °C (2025 °F)/1 h/OQ + 730 °C (1350 °F)/64 h/AC |
| Udimet 400 | Bar | 1310 | 190 | 1185 | 172 | – | – | – | – | – | – | – |
| Udimet 500 | Bar | 1310 | 190 | 1240 | 180 | 1215 | 176 | 1040 | 151 | 640 | 93 | 1080 °C (1975 °F)/4 h/AC + 845 °C (1550 °F)/24 h/AC + 760 °C (1400 °F)/16 h/AC |
| Udimet 520 | Bar | 1310 | 190 | 1240 | 180 | 1175 | 170 | 725 | 105 | 515 | 75 | 1105 °C (2025 °F)/4 h/AC + 845 °C (1550 °F)/24 h/AC + 760 °C (1400 °F)/16 h/AC |
| Udimet 630 | Bar | 1520 | 220 | 1380 | 200 | 1275 | 185 | 965 | 140 | – | – | – |
| Udimet 700 | Bar | 1410 | 204 | 1275 | 185 | 1240 | 180 | 1035 | 150 | 690 | 100 | 1175 °C (2150 °F)/4 h/AC + 1080 °C (1975 °F)/4 h/AC + 845 °C (1550 °F)/24 h/AC + 760 °C (1400 °F)/16 h/AC |

**Table 3.1–97** Effect of temperature on the ultimate tensile strength of wrought Ni-based superalloys, cont.

| Alloy | Form | Ultimate tensile strength at: 21 °C (70 °F) (MPa) | (ksi) | 540 °C (1000 °F) (MPa) | (ksi) | 650 °C (1200 °F) (MPa) | (ksi) | 760 °C (1400 °F) (MPa) | (ksi) | 870 °C (1600 °F) (MPa) | (ksi) | Condition of test material [a] |
|---|---|---|---|---|---|---|---|---|---|---|---|---|
| **Nickel-based** | | | | | | | | | | | | |
| Udimet 710 | Bar | 1185 | 172 | 1150 | 167 | 1290 | 187 | 1020 | 148 | 705 | 102 | 1175 °C (2150 °F)/4 h/AC + 1080 °C (1975 °F)/4 h/AC + 845 °C (1550 °F)/24 h/AC + 760 °C (1400 °F)/16 h/AC |
| Udimet 720 | Bar | 1570 | 228 | – | – | 1455 | 211 | 1455 | 211 | 1150 | 167 | 1115 °C (2035 °F)/2 h/AC + 1080 °C (1975 °F)/4 h/OQ + 650 °C (1200 °F)/24 h/AC + 760 °C (1400 °F)/8 h/AC |
| Unitemp AF2-1DA6 | Bar | 1560 | 226 | 1480 | 215 | 1400 | 203 | 1290 | 187 | – | – | 1150 °C (2100 °F)/4 h/AC + 760 °C (1400 °F)/16 h/AC |
| Waspaloy | | 1275 | 185 | 1170 | 170 | 1115 | 162 | 650 | 94 | 275 | 40 | 1080 °C (1975 °F)/4 h/AC + 845 °C (1550 °F)/24 h/AC + 760 °C (1400 °F)/16 h/AC |
| **Iron base** | | | | | | | | | | | | |
| A-286 | Bar | 1005 | 146 | 905 | 131 | 720 | 104 | 440 | 64 | – | – | 980 °C (1800 °F)/1 h/OQ + 720 °C (1325 °F)/16 h/AC |
| Alloy 901 | Bar | 1205 | 175 | 1030 | 149 | 960 | 139 | 725 | 105 | – | – | 1095 °C (2000 °F)/2 h/WQ + 790 °C (1450 °F)/2 h/AC + 720 °C (1325 °F)/24 h/AC |
| Discaloy | Bar | 1000 | 145 | 865 | 125 | 720 | 104 | 485 | 70 | – | – | 1010 °C (1850 °F)/2 h/OQ +730 °C (1350 °F)/20 h/AC + 650 °C (1200 °F)/20 h/AC |
| Haynes 556 | Sheet | 815 | 118 | 645 | 93 | 590 | 85 | 470 | 69 | 330 | 48 | 1175 °C (2150 °F)/AC |
| Incoloy 800 | Bar | 595 | 86 | 510 | 74 | 405 | 59 | 235 | 34 | – | – | – |

[a] OQ, oil quench; AC, air cool; RQ, rapid quench; RAC-WQ, rapid air cool-water quench; FC, furnace cool; SC, slow cool; CW, cold worked

[d] Annealed

[e] Precipitation hardened

[f] Ref 15.

[g] Ref 1.

[h] Work strengthened and aged

[i] At 700 °C(1290 °F)

[j] At 900 °C (1650 °F). Source: Ref 12, except as noted

**Table 3.1-98** Effect of temperature on the mechanical properties of wrought Ni-based superalloys

| Alloy | Form | Yield strength at 0.2% offset at | | | | | | | | | | Tensile elongation (%) at | | | | |
|---|---|---|---|---|---|---|---|---|---|---|---|---|---|---|---|---|
| | | 21 °C (70 °F) | | 540 °C (1000 °F) | | 650 °C (1200 °F) | | 760 °C (1400 °F) | | 870 °C (1600 °F) | | 21 °C (70 °F) | 540 °C (1000 °F) | 650 °C (1200 °F) | 760 °C (1400 °F) | 870 °C (1600 °F) |
| | | (MPa) | (ksi) | (MPa) | (ksi) | (MPa) | (ksi) | (MPa) | (ksi) | (MPa) | (ksi) | | | | | |
| **Nickel-based** | | | | | | | | | | | | | | | | |
| Astroloy | Bar | 1050 | 152 | 965 | 140 | 965 | 140 | 910 | 132 | 690 | 100 | 16 | 16 | 18 | 21 | 25 |
| Cabot 214 | – | 560 | 81 | 510 | 74 | 505 | 73 | 495 | 72 | 310 | 45 | 38 | 19 | 14 | 9 | 11 |
| D-979 | Bar | 1005 | 146 | 925 | 134 | 980 | 129 | 655 | 95 | 305 | 44 | 15 | 15 | 21 | 17 | 18 |
| Hastelloy C-22 | Sheet | 405 | 59 | 275 | 40 | 250 | 36 | 240 | 35 | – | – | 57 | 61 | 65 | 63 | – |
| Hastelloy G-30 | Sheet | 315 | 46 | 170 | 25 | – | – | – | – | – | – | 64 | 75 | – | – | – |
| Hastelloy S | Bar | 455 | 65 | 340 | 49 | 320 | 47 | 310 | 45 | 220 | 32 | 49 | 50 | 56 | 70 | 47 |
| Hastelloy X | Sheet | 360 | 52 | 290 | 42 | 275 | 40 | 260 | 38 | 180 | 26 | 43 | 45 | 37 | 37 | 50 |
| Haynes 230 | [a] | 390 | 57 | 275 | 40 | 270 | 39 | 285 | 41 | 225 | 32 | 48 | 56 | 55 | 46 | 59 |
| Inconel 587 | Bar | 705 | 102 | 620 | 90 | 615 | 89 | 605 | 88 | 400 | 58 | 28 | 22 | 21 | 20 | 16 |
| Inconel 597 | Bar | 760 | 110 | 720 | 104 | 675 | 98 | 665 | 96 | – | – | 15 | 15 | 15 | 16 | – |
| Inconel 600 | Bar | 285 | 41 | 220 | 32 | 205 | 30 | 180 | 26 | 40 | 6 | 45 | 41 | 49 | 70 | 80 |
| Inconel 601 | Sheet | 455 | 66 | 350 | 51 | 310 | 45 | 220 | 32 | 55 | 8 | 40 | 34 | 33 | 78 | 128 |
| Inconel 617 | Bar | 295 | 43 | 200 | 29 | 170 | 25 | 180 | 26 | 195 | 28 | 70 | 68 | 75 | 84 | 118 |
| Inconel 617 | Sheet | 345 | 50 | 230 | 33 | 220 | 32 | 230 | 33 | 205 | 30 | 55 | 62 | 61 | 59 | 73 |
| Inconel 625 | Bar | 490 | 71 | 415 | 60 | 420 | 61 | 415 | 60 | 275 | 40 | 50 | 50 | 34 | 45 | 125 |
| Inconel 706 | Bar | 1005 | 146 | 910 | 132 | 860 | 125 | 660 | 96 | – | – | 20 | 19 | 24 | 32 | – |
| Inconel 718 | Bar | 1185 | 172 | 1065 | 154 | 1020 | 148 | 740 | 107 | 330 | 48 | 21 | 18 | 19 | 25 | 88 |
| Inconel 718 Direct Age | Bar | 1365 | 198 | 1180 | 171 | 1090 | 158 | – | – | – | – | 16 | 15 | 23 | – | – |
| Inconel 718 Super | Bar | 1105 | 160 | 1020 | 148 | 960 | 139 | – | – | – | – | 16 | 18 | 14 | – | – |
| Inconel X750 | Bar | 815 | 118 | 725 | 105 | 710 | 103 | – | – | – | – | 27 | 26 | 10 | – | – |
| M-252 | Bar | 840 | 122 | 765 | 111 | 745 | 108 | 720 | 104 | 485 | 70 | 16 | 15 | 11 | 10 | 18 |
| Nimonic 75 | Bar | 285 | 41 | 200 | 29 | 200 | 29 | 160 | 23 | 90 | 13 | 40 | 40 | 46 | 67 | 68 |
| Nimonic 80A | Bar | 620 | 90 | 530 | 77 | 550 | 80 | 505 | 73 | 260 | 38 | 39 | 37 | 21 | 17 | 30 |
| Nimonic 90 | Bar | 810 | 117 | 725 | 105 | 685 | 99 | 540 | 78 | 260 | 38 | 33 | 28 | 14 | 12 | 23 |
| Nimonic 105 | Bar | 830 | 120 | 775 | 112 | 765 | 111 | 740 | 107 | 490 | 71 | 16 | 22 | 24 | 25 | 27 |
| Nimonic 115 | Bar | 865 | 125 | 795 | 115 | 815 | 118 | 800 | 116 | 550 | 80 | 27 | 18 | 23 | 24 | 16 |
| Nimonic 263 | Sheet | 580 | 84 | 485 | 70 | 485 | 70 | 460 | 67 | 180 | 26 | 39 | 42 | 27 | 21 | 25 |
| Nimonic 942 | Bar | 1060 | 154 | 970 | 141 | 1000 | 145 | 860 | 125 | – | – | | | | | |
| Nimonic PE.11 | Bar | 720 | 105 | 690 | 100 | 670 | 97 | 560 | 81 | – | – | | | | | |
| Nimonic PE.16 | Bar | 530 | 77 | 485 | 70 | 485 | 70 | 370 | 54 | 140 | 20 | 37 | 26 | 30 | 42 | 80 |
| Nimonic 860 | Sheet | 780 | 113 | 725 | 105 | 725 | 105 | 670 | 97 | 420 | 61 | 30 | 30 | 26 | 18 | 24 |
| Pyromet 860 | Bar | 835 | 121 | 840 | 122 | 850 | 123 | 835 | 121 | – | – | 22 | 15 | 17 | 18 | – |
| René 41 | Bar | 1060 | 154 | 1020 | 147 | 1000 | 145 | 940 | 136 | 550 | 80 | 14 | 14 | 14 | 11 | 19 |
| René 95 | Bar | 1310 | 190 | 1255 | 182 | 1220 | 177 | 1100 | 160 | – | – | 15 | 12 | 14 | 15 | – |

**Table 3.1–98** Effect of temperature on the mechanical properties of wrought Ni-based superalloys, cont.

| Alloy | Form | Yield strength at 0.2% offset at | | | | | | | | | | Tensile elongation (%) at | | | | |
|---|---|---|---|---|---|---|---|---|---|---|---|---|---|---|---|---|
| | | 21 °C (70 °F) | | 540 °C (1000 °F) | | 650 °C (1200 °F) | | 760 °C (1400 °F) | | 870 °C (1600 °F) | | 21 °C (70 °F) | 540 °C (1000 °F) | 650 °C (1200 °F) | 760 °C (1400 °F) | 870 °C (1600 °F) |
| | | (MPa) | (ksi) | (MPa) | (ksi) | (MPa) | (ksi) | (MPa) | (ksi) | (MPa) | (ksi) | | | | | |
| Udimet 400 | Bar | 930 | 135 | 830 | 120 | – | – | – | – | – | – | 30 | 26 | – | – | – |
| Udimet 500 | Bar | 840 | 122 | 795 | 115 | 760 | 110 | 730 | 106 | 495 | 72 | 32 | 28 | 28 | 39 | 20 |
| Udimet 520 | Bar | 860 | 125 | 825 | 120 | 795 | 115 | 725 | 105 | 520 | 75 | 21 | 20 | 17 | 15 | 20 |
| Udimet 630 | Bar | 1310 | 190 | 1170 | 170 | 1105 | 160 | 860 | 125 | – | – | 15 | 15 | 7 | 5 | – |
| Udimet 700 | Bar | 965 | 140 | 895 | 130 | 855 | 124 | 825 | 120 | 635 | 92 | 17 | 16 | 16 | 20 | 27 |
| Udimet 710 | Bar | 910 | 132 | 850 | 123 | 860 | 125 | 815 | 118 | 635 | 92 | 7 | 10 | 15 | 25 | 29 |
| Udimet 720 | Bar | 1195 | 173 | – | – | 1130 | 164 | 1050 | 152 | – | – | 13 | – | 17 | 9 | – |
| Unitemp AF2-1DA6 | Bar | 1015 | 147 | 1040 | 151 | 1020 | 148 | 995 | 144 | – | – | 20 | 19 | 18 | 16 | – |
| Waspaloy | Bar | 795 | 115 | 725 | 105 | 690 | 100 | 675 | 98 | 520 | 75 | 25 | 23 | 34 | 28 | 35 |
| **Iron-based** | | | | | | | | | | | | | | | | |
| A-286 | Bar | 725 | 105 | 605 | 88 | 605 | 88 | 430 | 62 | – | – | 25 | 19 | 13 | 19 | – |
| Alloy 901 | Bar | 895 | 130 | 780 | 113 | 760 | 110 | 635 | 92 | – | – | 14 | 14 | 13 | 19 | – |
| Discaloy | Bar | 730 | 106 | 650 | 94 | 630 | 91 | 430 | 62 | – | – | 19 | 16 | 19 | – | – |
| Haynes 556 | Sheet | 410 | 60 | 240 | 35 | 225 | 33 | 220 | 32 | 195 | 29 | 48 | 54 | 52 | 49 | 53 |
| Incoloy 800 | Bar | 250 | 36 | 180 | 26 | 180 | 26 | 150 | 22 | – | – | 44 | 38 | 51 | 83 | – |
| Incoloy 801 | Bar | 385 | 56 | 310 | 45 | 305 | 44 | 290 | 42 | – | – | 30 | 28 | 26 | 55 | – |
| Incoloy 802 | Bar | 290 | 42 | 195 | 28 | 200 | 29 | 200 | 29 | 150 | 22 | 44 | 39 | 25 | 15 | 38 |
| Incoloy 807 | Bar | 380 | 55 | 255 | 37 | 240 | 35 | 225 | 32.5 | 185 | 26.5 | 48 | 40 | 35 | 34 | 71 |
| Incoloy 825 | – | 310 | 45 | ≈234 | ≈34 | ≈220 | ≈32 | 180 | ≈26 | ≈105 | ≈15 | 45 | ≈44 | ≈35 | ≈86 | ≈100 |
| Incoloy 903 | Bar | 1105 | 160 | – | – | 895 | 130 | – | – | – | – | 14 | – | 18 | – | – |
| Incoloy 907 | – | ≈1110 | ≈161 | ≈960 | ≈139 | ≈895 | ≈130 | ≈565 | ≈82 | – | – | ≈12 | ≈11 | ≈10 | ≈20 | – |
| Incoloy 909 | Bar | 1020 | 148 | 945 | 137 | 870 | 126 | 540 | 78 | – | – | 16 | 14 | 24 | 34 | – |
| N-155 | Bar | 400 | 58 | 340 | 49 | 295 | 43 | 250 | 36 | 175 | 25 | 40 | 33 | 32 | 32 | 33 |
| V-57 | Bar | 830 | 120 | 760 | 110 | 745 | 108 | 485 | 70 | – | – | 26 | 19 | 22 | 34 | – |
| 19-9 DL | – | 570 | 83 | 395 | 57 | 360 | 52 | – | – | – | – | 43 | 30 | 30 | – | – |
| 16-25-6 | – | 770 | 112 | – | – | 517 | 75 | 345 | 50 | 255 | 37 | 23 | – | 12 | 11 | 9 |

[a] Cold-rolled and solution-annealed sheet, 1.2 to 1.6 mm thick

**Table 3.1-99** Effect of temperature on the mechanical properties of cast Ni-based superalloys

| Alloy | Ultimate tensile strength at: | | | | | | 0.2% yield strength at: | | | | | |
|---|---|---|---|---|---|---|---|---|---|---|---|---|
| | 21 °C (70 °F) | | 538 °C (1000 °F) | | 1093 °C (2000 °F) | | 21 °C (70 °F) | | 538 °C (1000 °F) | | 1093 °C (2000 °F) | |
| | MPa | ksi | MPa | ksi | MPa | ksi | MPa | ksi | MPa | ksi | MPa | ksi |
| **Nickel-base** | | | | | | | | | | | | |
| IN-713 C | 850 | 123 | 860 | 125 | – | – | 740 | 107 | 705 | 102 | – | – |
| IN-713 LC | 895 | 130 | 895 | 130 | – | – | 750 | 109 | 760 | 110 | – | – |
| B-1900 | 970 | 141 | 1005 | 146 | 270 | 38 | 825 | 120 | 870 | 126 | 195 | 28 |
| IN-625 | 710 | 103 | 510 | 74 | – | – | 350 | 51 | 235 | 34 | – | – |
| IN-718 | 1090 | 158 | – | – | – | – | 915 | 133 | – | – | – | – |
| IN-100 | 1018 | 147 | 1090 | 150 | (380) | (55) | 850 | 123 | 885 | 128 | (240) | (35) |
| IN-162 | 1005 | 146 | 1020 | 148 | – | – | 815 | 118 | 795 | 115 | – | – |
| IN-731 | 835 | 121 | – | – | 275 | 40 | 725 | 105 | – | – | 170 | 25 |
| IN-738 | 1095 | 159 | – | – | – | – | 950 | 138 | – | – | – | – |
| IN-792 | 1070 | 170 | – | – | – | – | 1060 | 154 | – | – | – | – |
| IN-22 | 730 | 106 | 780 | 113 | – | – | 685 | 99 | 730 | 106 | – | – |
| MAR-M 200 | 930 | 135 | 945 | 137 | 325 | 47 | 840 | 122 | 880 | 123 | – | – |
| MAR-M 246 | 965 | 140 | 1000 | 145 | 345 | 50 | 860 | 125 | 860 | 125 | – | – |
| MAR-M 247 | 965 | 140 | 1035 | 150 | – | – | 815 | 118 | 825 | 120 | – | – |
| MAR-M 421 | 1085 | 157 | 995 | 147 | – | – | 930 | 135 | 815 | 118 | – | – |
| MAR-M 432 | 1240 | 180 | 1105 | 160 | – | – | 1070 | 155 | 910 | 132 | – | – |
| MC-102 | 675 | 98 | 655 | 95 | – | – | 605 | 88 | 540 | 78 | – | – |
| Nimocast 75 | 500 | 72 | – | – | – | – | 179 | 26 | – | – | – | – |
| Nimocast 80 | 730 | 106 | – | – | – | – | 520 | 75 | – | – | – | – |
| Nimocast 90 | 700 | 102 | 595 | 86 | – | – | 520 | 75 | 420 | 61 | – | – |
| Nimocast 242 | 460 | 67 | – | – | – | – | 300 | 44 | – | – | – | – |
| Nimocast 263 | 730 | 106 | – | – | – | – | 510 | 74 | – | – | – | – |
| René 77 | – | – | – | – | – | – | – | – | – | – | – | – |
| René 80 | – | – | – | – | – | – | – | – | – | – | – | – |
| Udimet 500 | 930 | 135 | 895 | 130 | – | – | 815 | 118 | 725 | 105 | – | – |
| Udimet 710 | 1075 | 156 | – | – | 240 | 35 | 895 | 130 | – | – | 170 | 25 |
| CMSX-2[a] | 1185 | 172 | 1295[b] | 188[b] | – | – | 1135 | 165 | 1245[b] | 181[b] | – | – |
| GMR-235 | 710 | 103 | – | – | – | – | 640 | 93 | – | – | – | – |
| IN-939 | 1050 | 152 | 915[b] | 133[b] | 325[c] | 47[c] | 800 | 116 | 635[b] | 92[b] | 205[c] | 30[c] |
| MM 002[d] | 1035 | 150 | 1035[b] | 150[b] | 550[c] | 80[c] | 825 | 120 | 860[b] | 125[b] | 345[c] | 50[c] |
| IN-713 Hf[e] | 1000 | 145 | 895[b] | 130[b] | 380[c] | 55[c] | 760 | 110 | 620[b] | 90[b] | 240[c] | 35[c] |
| René 125 Hf[f] | 1070 | 155 | 1070[b] | 155[b] | 550[c] | 80[c] | 825 | 120 | 860[b] | 125[b] | 345[c] | 50[c] |
| MAR-M 246 Hf[g] | 1105 | 160 | 1070[b] | 155[b] | 565[c] | 82[c] | 860 | 125 | 860[b] | 125[b] | 345[c] | 50[c] |
| MAR-M 200 Hf[h] | 1035 | 150 | 1035[b] | 150[b] | 540[c] | 78[c] | 825 | 120 | 860[b] | 125[b] | 345[c] | 50[c] |
| PWA-1480[a] | – | – | 1130[b] | 164[b] | 685[c] | 99[c] | 895 | 130 | 905[b] | 131[b] | 495[c] | 72[c] |
| SEL | 1020 | 148 | 875[b] | 127[b] | – | – | 905 | 131 | 795[b] | 115[b] | – | – |
| UDM 56 | 945 | 137 | 945[b] | 137[b] | – | – | 850 | 123 | 725[b] | 105[b] | – | – |
| SEL 15 | 1060 | 154 | 1090[b] | 158[b] | – | – | 895 | 130 | 815[b] | 118[b] | – | – |

(a) Single-crystal [001]
[b] At 760 °C (1400 °F)
[c] At 980 °C (1800 °F)
[d] RR-7080
[e] MM 004

**Table 3.1–99** Effect of temperature on the mechanical properties of cast Ni-base superalloys, cont.

| Tensile elongation % at: | | | Dynamic modulus of elasticity at: | | | | | |
|---|---|---|---|---|---|---|---|---|
| 21 °C (70 °F) | 538 °C (1000 °F) | 1093 °C (2000 °F) | 21 °C (70 °F) | | 538 °C (1000 °F) | | 1093 °C (2000 °F) | |
| | | | GPa | $10^6$ psi | GPa | $10^6$ psi | GPa | $10^6$ psi |
| **Nickel-base** | | | | | | | | |
| 8 | 10 | – | 206 | 29.9 | 179 | 26.2 | – | – |
| 15 | 11 | – | 197 | 28.6 | 172 | 25.0 | – | – |
| 8 | 7 | 11 | 214 | 31.0 | 183 | 27.0 | – | – |
| 48 | 50 | – | – | – | – | – | – | – |
| 11 | – | – | – | – | – | – | – | – |
| 9 | 9 | – | 215 | 31.2 | 187 | 27.1 | – | – |
| 7 | 6.5 | – | 197 | 28.5 | 172 | 24.9 | – | – |
| 6.5 | – | – | – | – | – | – | – | – |
| – | – | – | 201 | 29.2 | 175 | 25.4 | – | – |
| 4 | – | – | – | – | – | – | – | – |
| 5.5 | 4.5 | – | – | – | – | – | – | – |
| 7 | 5 | – | 218 | 31.6 | 184 | 26.7 | – | – |
| 5 | 5 | – | 205 | 29.8 | 178 | 25.8 | 145 | 21.1 |
| 7 | – | – | – | – | – | – | – | – |
| 4.5 | 3 | – | 203 | 29.4 | – | – | 141 | 20.4 |
| 6 | – | – | – | – | – | – | – | – |
| 5 | 9 | – | – | – | – | – | – | – |
| 39 | – | – | – | – | – | – | – | – |
| 15 | – | – | – | – | – | – | – | – |
| 14 | 15 | – | – | – | – | – | – | – |
| 8 | – | – | – | – | – | – | – | – |
| 18 | – | – | – | – | – | – | – | – |
| – | – | – | – | – | – | – | – | – |
| – | – | – | 208 | 30.2 | – | – | – | – |
| 13 | 13 | – | – | – | – | – | – | – |
| 8 | – | – | – | – | – | – | – | – |
| 10 | 17[b] | – | – | – | – | – | – | – |
| 3 | – | 18[c] | – | – | – | – | – | – |
| 5 | 7[b] | 25[c] | – | – | – | – | – | – |
| 7 | 5[b] | 12[c] | – | – | – | – | – | – |
| 11 | 6[b] | 20[c] | – | – | – | – | – | – |
| 5 | 5[b] | 12[c] | – | – | – | – | – | – |
| 6 | 7[b] | 14[c] | – | – | – | – | – | – |
| 5 | 5[b] | 10[c] | – | – | – | – | – | – |
| 4 | 8[b] | 20[c] | – | – | – | – | – | – |
| 6 | 7[b] | – | – | – | – | – | – | – |
| 3 | 5[b] | – | – | – | – | – | – | – |
| 9 | 5[b] | – | – | – | – | – | – | – |

[f] M 005
[g] MM 006
[h] MM 009
[i] Data from Metals Handbook,9th edn.,Vol.3, 1980
[j] At 650 °C (1200 °F)
Source: Nickel Development institute, except as noted

## 3.1.8 Copper and Copper Alloys

Copper and copper alloys are used as materials mainly because of the high electrical and thermal conductivity of Cu and because of the variability and favorable combination of electrical, mechanical, and corrosion properties and of color (from copper red to silver white) by alloying and heat treatment. The basic properties of Cu are covered in Sect. 2.2.3. The electrical resistivity of Cu, $\sigma = 16.78\,\mathrm{n\Omega\,m}$ (293 K), is the highest among the metals of moderate cost. The corresponding high thermal conductivity $\lambda = 397\,\mathrm{W\,m^{-1}K^{-1}}$ of Cu gives rise to numerous applications in heat exchangers. Its high corrosion resistance and good formability are the basis of its use as gas and water pipes, in the chemical and food industries, and – combined with its color – in architecture.

The alloying of Cu with group IIB to IVB metals results in a series of alloy systems with a characteristic sequence of intermetallic phases characterised by their outer electron to atom ratio (e/a), as first recognised by and named after Hume-Rothery. This behavior is attributed to the fact that the electronic structure rather than ionic radius, directed bonds, or other factors of influence for alloy formation is dominating the and crystal structure formation of the intermetallic phases. The same is true for Ag- and Au-based alloy systems. A survey is given in Table 3.1-100.

The solid solution phase $\alpha$ of Cu, dominating in most Cu materials, is hardened by the solute elements s through solid solution hardening which is proportional to the misfit parameter $\eta_s$, given by the relative difference in atomic radius $r_s$ to $r_{Cu}$: $\eta_s = 2(r_s - r_{Cu})/(r_s + r_{Cu})$. Since $r_{Cu} = 1.28$, $r_{Ni} = 1.25$, $r_{Zn} = 1.33$, and $r_{Sn} = 1.51$, it follows that the increase in yield stress per at.% of solute increases in the order Ni < Zn < Sn.

The materials on copper basis may be subdivided into the groups shown in Table 3.1-101. Standards for copper and copper materials have been issued by ASTM, DIN, DKE, CEN, CENELEC, ISO, and IEC. In the USA, the Unified Numbering System for Metals and Alloys (UNS) applied to Cu materials consists of the letter C and a 5 digit number. More extensive accounts of Cu and Cu alloys as materials are given in [1.102–104].

**Table 3.1-100** Characteristics of Hume-Rothery phases in Cu-, Ag- and Au-based alloy systems

| e/a | Phase designation | Crystal structure | Example |
|---|---|---|---|
| 3/2 | $\beta$ | bcc | CuZn |
| 3/2 | $\zeta$ | hcp | CuGa, CuGe |
| 21/13 | $\gamma$ | $\gamma$ brass structure | $Cu_5Zn_8$ |
| 7/4 | $\varepsilon$ | hcp | $CuZn_3$ |

### 3.1.8.1 Unalloyed Coppers

Cu is used as the technical standard for the conductivity of metals and alloys. The International Annealed Copper Standard (IACS) is defined by a Cu wire, 1 m long and weighing 0.1 kg, the resistance of which is 0.15327 Ω at 20 °C. Accordingly, a conductivity of 100% IACS = 58.00 MS m$^{-1}$ (or m Ω$^{-1}$ mm$^{-2}$), which corresponds to a resistivity of 1.7243793 (μΩ cm). The electrical conductivity is specifically and strongly dependent on the kind and concentration of impurities (Fig. 3.1-130).

**Table 3.1-101** Groups of copper materials according to ASTM

| Designation | Maximum alloying range, wt%, further alloying elements | Wrought alloys | Cast alloys alloys | Particular alloying range for castings |
|---|---|---|---|---|
| Coppers | – | + | + | – |
| High copper alloys | 1.2Cd, 2Be, 3Fe, 2.7Co, 3Ni, 2.5Sn, 1.5Cr, 0.7Zn, 0.25Si, 3.4Ti, 1Zr, 3.5Pb | + | + | |
| Brasses | 43Zn, 3Pb, 2Al, Co, Si, Mn, Fe | + | + | |
| Bronzes | 8Sn, Zn | + | + | 12Sn, 2Pb, 2Ni |
| Cu–Pb–Sn | – | – | + | 10Sn, 20Pb |
| Copper–Nickels | 30Ni, 1Fe, 1Mn, 2Sn | + | + | |
| Nickel–Silvers | 18Ni, 39Zn, 3Pb, 2Mn | + | – | – |
| Cu–Sn–Zn | – | – | + | 7Sn, 8Zn, 7Pb |
| Cu–Al | 8Al | + | + | |

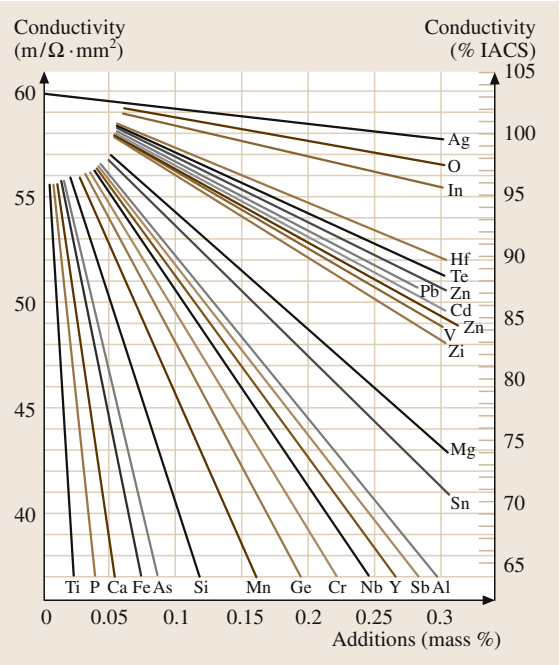


**Fig. 3.1-130** Effect of solute elements on the conductivity of Cu

Unalloyed coppers contain ≥ 99.3 wt% Cu. The elements O, P, and/or As are deliberate additions. Small oxygen additions to Cu in the range of 0.005 to 0.04 wt% O are used to oxidize the metallic impurities which may be dissolved in small $Cu_2O$ particles or form their own oxides. Thus the conductivity of the Cu is increased. Alternatively ultra-high purity cathodes from the electrolytic copper refining process are used as raw material. Oxygen-bearing Cu is unsuitable for applications requiring exposure to hydrogen, or requiring bonding by soldering or by brazing, because reactions between oxygen and hydrogen or between oxygen and the braze or solder components, respectively, lead to embrittlement. Gas evolution may occur in ultra-high-vacuum equipment if the Cu applied contains oxygen additions or higher contents of other impurities with a higher vapor pressure. Therefore, use of oxygen-free high purity copper is mandatory in these cases. In less critical cases, deoxidation by phosphorus is applied to the copper with an ensuing loss in conductivity. These measures lead to the different technical coppers ranging from about 40 to 58 MS $m^{-1}$ in conductivity and from 99.90 to 99.99 wt% in purity. Table 3.1-102 lists major unalloyed coppers.

### 3.1.8.2 High Copper Alloys

This group of materials comprises essentially a number of age-hardenable alloys which are listed in Table 3.1-103.

**Table 3.1-102** Composition and properties of characteristic unalloyed coppers

| Material | UNS No. | Purity; other elements (wt%) | Yield stress $R_{po.2}$ (MPa) | Ultimate tensile strength $R_m$ (MPa) | Fracture strain $A_f$ (%) | Thermal conductivity $\kappa$ (W $m^{-1}$ $K^{-1}$) | Electrical resistivity $\rho$ (μΩ cm) |
|---|---|---|---|---|---|---|---|
| Pure Cu (oxygen-free electronic) | C10100 | 99.99 Cu | 69–365 | 221–455 | 4–55 | 392 | 1.741 |
| Pure Cu (oxygen-free) | C10200 | 99.95 Cu | 69–365 | 221–455 | 4–55 | 397 | 1.741 |
| Electrolytic tough pitch Cu | C11000 | 99.90 Cu–0.04 O | 69–365 | 224–455 | 4–55 | 397 | 1.707 |
| Oxygen-free low phosphorus Cu | C10800 | 99.95 Cu–0.009 P | 69–345 | 221–379 | 4–50 | 397 | 2.028 |
| Phosphorus deoxidized arsenical Cu | C14200 | 99.68 Cu–0.35 As –0.02 P | 69–345 | 221–379 | 8–45 | 397 | 3.831 |

**Table 3.1-103** Composition of high copper alloys

| Basic alloy system | UNS No. | Major alloying elements (mass%) | Minor elements |
|---|---|---|---|
| Cu–Cd | C16200 | 0.7–1.2 Cd | |
| Cu–Be | C17000–C17300 | 1.6–2.0 Be | Al, Pb |
| Cu–Ni–Be | C17450–C17460 | 0.5–1.4 Ni, 0.15–0.50 Be | Al, Zr |
| Cu–Co–Be | C17500 | 2.4–2.7 Co, 0.4–0.7 Be | |
| Cu–Ni–Cr–Si | C18000 | 1.8–3.0 Ni, 0.1–0.8 Cr, 0.4–0.8 Si | |
| Cu–Sn–Cr | C18030–C18040 | 0.08–0.3 Sn, 0.1–0.35 Cr | P |

**Table 3.1-104** Properties of high copper alloys

| Material | UNS No. | Yield stress $R_{po.2}$ (MPa) | Ultimate tensile strength $R_m$ (MPa) | Fracture strain $A_f$ (%) | Brinell Hardness (HB) | Thermal conductivity $\kappa$ ($W\,m^{-1}\,K^{-1}$) | Electrical resistivity $\rho$ ($\mu\Omega$ cm) |
|---|---|---|---|---|---|---|---|
| Beryllium copper | C17200 | 172–1344 | 469–1462 | 1–48 | 100–363 | ≤95 | 4.009 |
| Beryllium copper | C17000 | 221–1172 | 483–1310 | 3–45 | 100–363 | ≤95 | 2.053 |
| Cadmium copper | C16200 | 600 | 649 | n.a. | n.a. | 376 | 2.028 |
| Chromium copper | C18200 | 479–531 | 232–593 | 14–60 | 58–140 | 188 | 3.831 |
| Cobalt beryllium copper | C17500 | 172–758 | 310–793 | 5–28 | 67–215 | 84 | 7.496 |
| Lead copper | C18700 | 69–345 | 221–379 | 8–45 | n.a. | n.a. | n.a. |
| Silver-bearing copper | C11300 | 69–365 | 221–455 | 4–55 | 55–90 | 397 | 1.741 |
| Sulfur copper | C14700 | 69–379 | 221–393 | 8–52 | 55–85 | 373 | 1.815 |
| Tellurium copper | C14500 | 69–352 | 221–386 | 8–45 | 49–80 | 382 | 1.759 |
| Zirconium copper | C15000 | 41–496 | 200–524 | 2–54 | n.a. | n.a. | n.a. |

n.a. not available

The age-hardening behavior is based on the fact that the solubility of Cd, Be, and Cr in Cu decreases with decreasing temperature. On this basis a heat treatment is applied, that leads to age-hardening. A high-temperature solution treatment is followed by a low-temperature annealing, or aging, treatment. This serves to precipitate a dispersion of small metastable or stable particles which give rise to hardening by several hardening mechanisms that depend in detail on the microstructural, chemical, crystallographic and mechanical properties of the precipitated particles (see Table 3.1-104).

### 3.1.8.3 Brasses

The term brass was originally applied to binary Cu−Zn alloys (Fig. 3.1-131) but was extended to Cu−Zn-based multi-component alloys, mainly containing Fe, Al, Ni, and Si.

The phases of technical interest are the fcc $\alpha$ phase and the bcc $\beta$ phase. The high-temperature $\beta$ phase transforms to its ordered (CsCl type) variant $\beta'$ at temperatures below 727 to 741 K depending on composition, as shown in Fig. 3.1-131. The intermetallic phases with higher Zn content are brittle and have no technical relevance.

Brasses and other Cu-based alloys are mainly supplied as wrought alloys which designate the state of the final material which is obtained by a final shaping operation (rolling, rod, and wire drawing etc.) with a controlled degree of cold work. The work-hardening behavior of the alloys is, thus, exploited to vary the final mechanical properties in comparatively wide limits (see Table 3.1-105). By way of an example, Fig. 3.1-132 shows the mechanical properties of CuZn15 as a function of the degree of cold work.

The dependence of the mechanical properties on the effect of annealing is similarly important. Figure 3.1-133 shows the changes upon isothermal annealing for the same alloy as in Fig. 3.1-132. Table 3.1-105 lists the nominal compositions and property ranges of brasses.

### 3.1.8.4 Bronzes

Bronze is the original term for Cu−Sn alloys, Fig. 3.1-134. The term bronze has, also, been extended to Cu−Al and Cu−Si based alloys. Table 3.1-106 lists the composition and properties of charactristic bronzes. As referred to in the introduction the $\alpha$ solid solution of Cu−Sn is increasing in yield stress as a function of solute content most strongly of all common Cu alloys because of the high misfit of Sn in Cu.

Aluminium bronzes, especially ternary alloys containing Ni and Mn, have an increased high temperature oxidation resistance due to the formation of a protective $Al_2O_3$ layer upon exposure to higher temperature. The Cu−Al alloys and the related systems have been studied extensively as prototype systems which show martensitic transformations upon cooling and upon plastic deformation [1.105]. This transformation behavior is, also, the basis of shape memory and superplastic properties. Table 3.1-106 lists the nominal compositions and property ranges of bronzes. Figure 3.1-135 shows a phase diagram of Cu−Al.

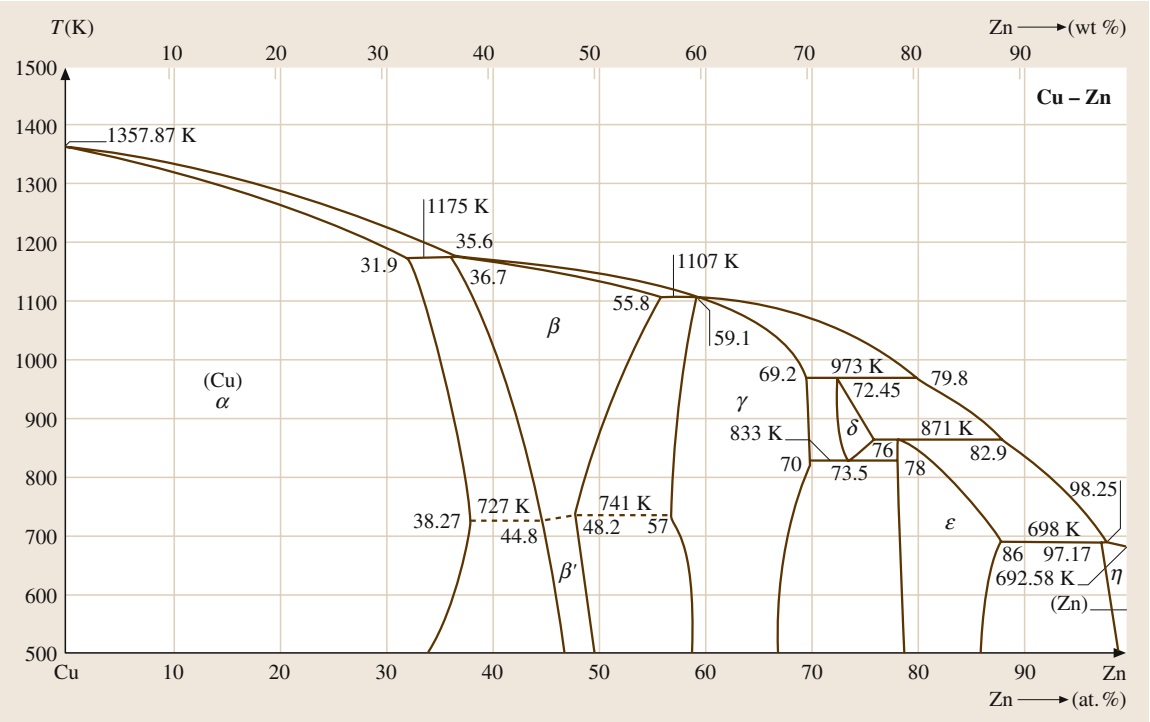


**Fig. 3.1-131** Cu−Zn phase diagram [1.106]

**Table 3.1-105** Composition and properties of characteristic brasses

| Material | UNS No. | Composition (wt%) | Yield stress $R_{po.2}$ (MPa) | Ultimate tensile strength $R_m$ (MPa) | Fracture strain $A_f$ (%) | Thermal conductivity $\kappa$ ($W\,m^{-1}\,K^{-1}$) | Electrical resistivity $\rho$ ($\mu\Omega$ cm) |
|---|---|---|---|---|---|---|---|
| Admiralty brass | C44300 | 71 Cu–28 Zn –1 Sn | 124–152 | 331–379 | 60–65 | | |
| Aluminium brass | C68700 | 77.5 Cu–20.5 Zn –2 Al | 186 | 414 | 55 | 101 | 7.496 |
| Cartridge brass | C68700 | 70 Cu–30 Zn | 76–448 | 303–896 | 3–66 | 121 | 6.152 |
| Free-cutting brass | C36000 | 61.5 Cu–35.5 Zn –3 Pb | 124–310 | 338–469 | 18–53 | 109 | 6.631 |
| Gilding metal (cap copper) | C21000 | 95.0 Cu–5.0 Zn | 69–400 | 234–441 | 8–45 | 234 | 3.079 |
| High tensile brass (architectural bronze) | C38500 | 57 Cu–40 Zn –3 Pb | 138 | 414 | 30 | 88–109 | 8.620 |
| Hot stamping brass (forging) | C37700 | 59 Cu–39 Zn –2 Pb | 138 | 359 | 45 | 109 | 6.631 |
| Low brass | C24000 | 80 Cu–20 Zn | 83–448 | 290–862 | 3–55 | 138 | 4.660 |
| Muntz metal | C28000 | 60 Cu–40 Zn | 145–379 | 372–510 | 10–52 | 126 | 6.157 |
| Naval brass | C46400 | 60 Cu–39.25 Zn –0.75 Sn | 172–455 | 379–607 | 17–50 | 117 | 6.631 |
| Red brass | C23000 | 85 Cu–15 Zn | 69–434 | 269–724 | 3–55 | 159 | 3.918 |
| Yellow brass | C26800 | 65 Cu–35 Zn | 97–427 | 317–883 | 3–65 | 121 | 6.631 |

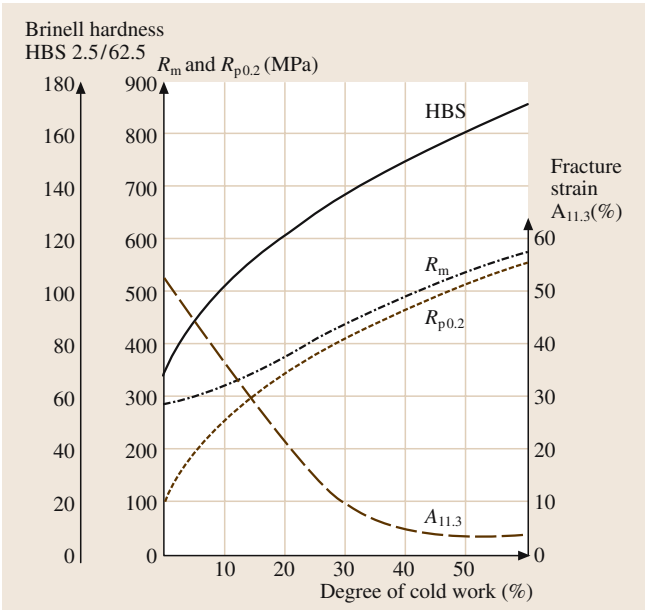


**Fig. 3.1-132** Effect of work hardening, expressed as % reduction in thickness by rolling, on the mechanical properties of CuZn15 brass. This relation is a typical example for the control of the mechanical properties of wrought copper alloys by work hardening

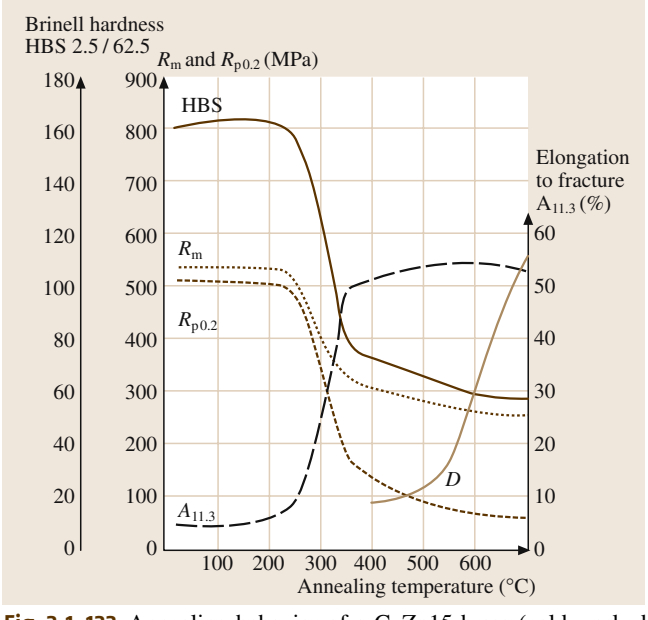


**Fig. 3.1-133** Annealing behavior of a CuZn15 brass (cold worked 50%; Annealing time 3 h)

## 3.1.8.5 Copper–Nickel and Copper–Nickel–Zinc Alloys

### Copper–Nickel Alloys

Figure 3.1-136 shows the Cu–Ni phase diagram which is characterized by a continuous solid solution which extends to room temperature. The metal Cu is solution-hardened only weakly by alloying with Ni because of the low misfit between the two components. But Cu–Ni alloys show an excellent corrosion resistance against seawater and are used, e.g., in desalination plants, accordingly. Another outstanding effect of Ni in Cu is the drastic decrease in electrical and thermal conductivity with increasing Ni content, as shown in Figs. 3.1-137 and 3.1-138. The interrelation through the Wiedemann–Franz law is obvious. A prominent application of the low thermal conductivity of Cu–Ni material is its use in equipment for operation at cryogenic temperature where heat loss by conduction is a major concern.

### Copper–Nickel–Zinc Alloys. Nickel-Silvers

The designation of these Cu–Ni–Zn alloys is based on the silver-like color. Their composition ranges from 45 to 49 wt% Cu, 10 to 12 wt% Ni, with the balance composing Zn. Up to 2 wt% Pb is added for better drilling and turning behavior. Ni increases the yield stress and decreases the electrical and thermal conductivity (see Table 3.1-107).

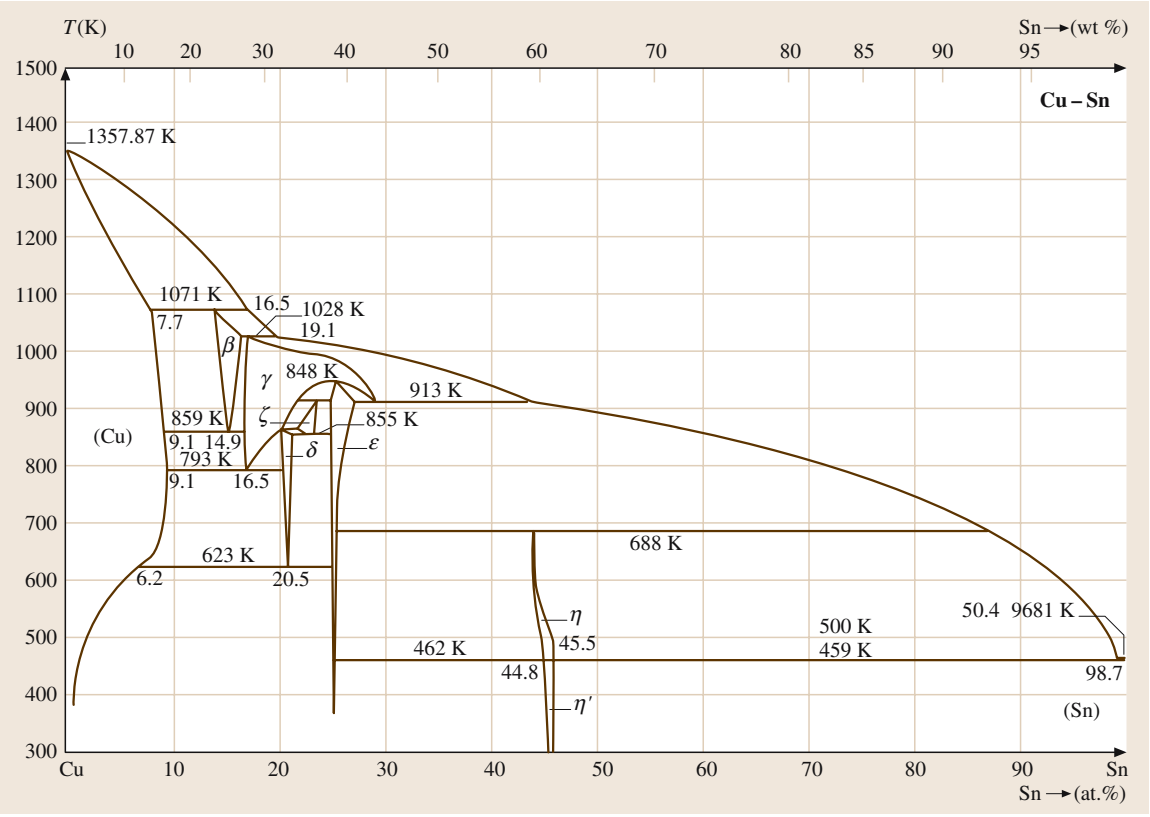


**Fig. 3.1-134** Cu–Sn phase diagram [1.106]

**Table 3.1-106** Composition and properties of characteristic bronzes

| Material | UNS No. | Purity; other elements (wt%) | Yield stress $R_{p0.2}$ (MPa) | Ultimate tensile strength $R_m$ (MPa) | Fracture strain $A_f$ (%) | Thermal conductivity $\kappa$ ($W\,m^{-1}\,K^{-1}$) | Electrical resistivity $\rho$ ($\mu\Omega$ cm) |
|---|---|---|---|---|---|---|---|
| Phosphor bronze | C51100 | 96 Cu–3.5 Sn –0.12 P | 345–552 | 317–710 | 2–48 | 85 | 9.171 |
| Phosphor bronze A | C51000 | 95 Cu–5 Sn –0.09 P | 131–552 | 324–965 | 2–64 | 75 | 10.26 |
| Phosphor bronze C | C52100 | 92 Cu–7 Sn –0.12 P | 165–552 | 379–965 | 2–70 | 67 | 12.32 |
| Phosphor bronze D | C52400 | 90 Cu–10 Sn | 193 | 455–1014 | 3–70 | 63 | 12.32 |
| Silicon bronze A | C65500 | 97 Cu–3.0 Si | 145–483 | 386–1000 | 3–63 | 50 | 21.29 |
| Silicon bronze B | C65100 | 98.5 Cu–1.5 Si | 103–476 | 276–655 | 11–55 | not available | not available |
| Aluminium bronze D | C61400 | 91 Cu–7 Al–2 Fe | 228–414 | 524–614 | 32–45 | not available | 12.32 |
| Aluminium bronze | C60800 | 95 Cu–5 Al | 186 | 414 | 55 | 85 | 9.741 |
| Aluminium bronze | C63000 | Cu–9.5 Al–4 Fe –5 Ni–1 Mn | 345–517 | 621–814 | 15–20 | 62 | 13.26 |

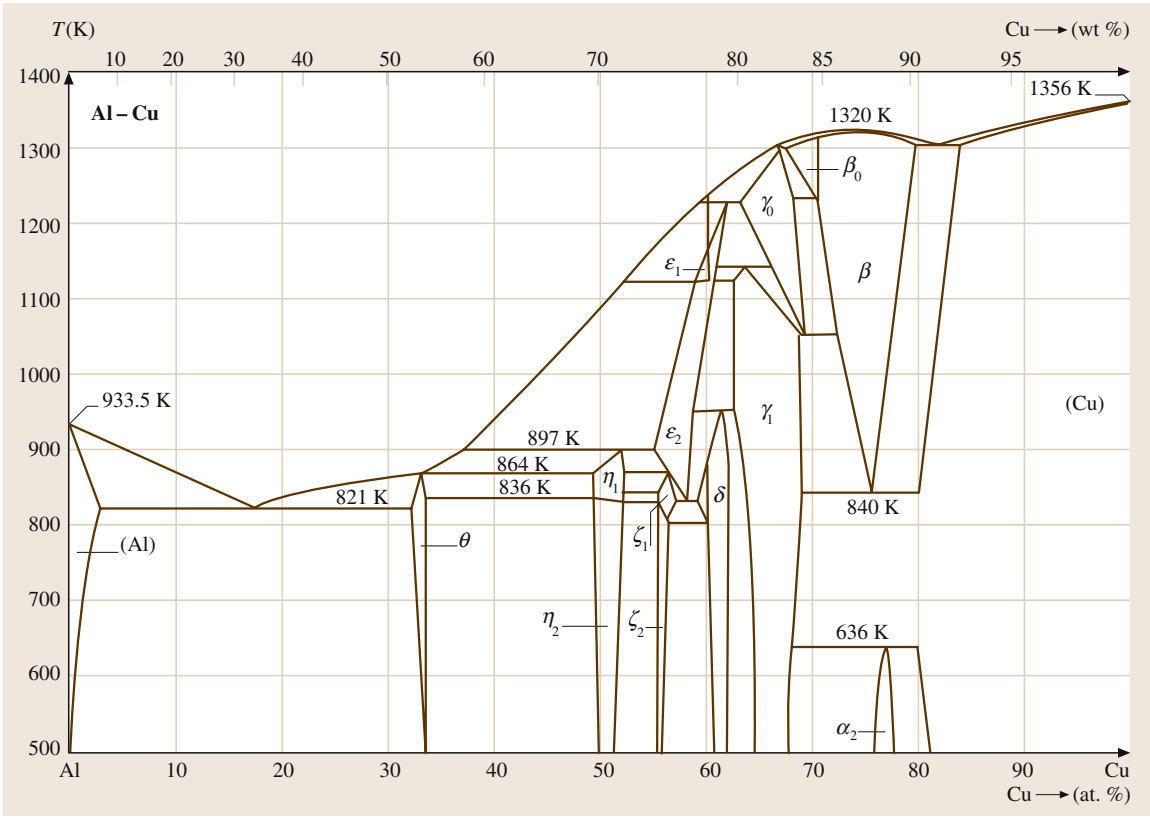


**Fig. 3.1-135** Cu−Al phase diagram [1.106]

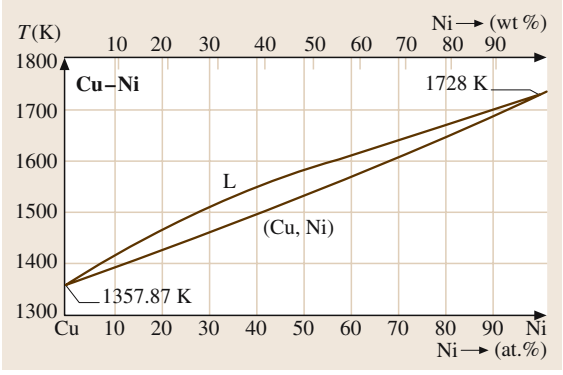


**Fig. 3.1-136** Cu−Ni phase diagram [1.106]

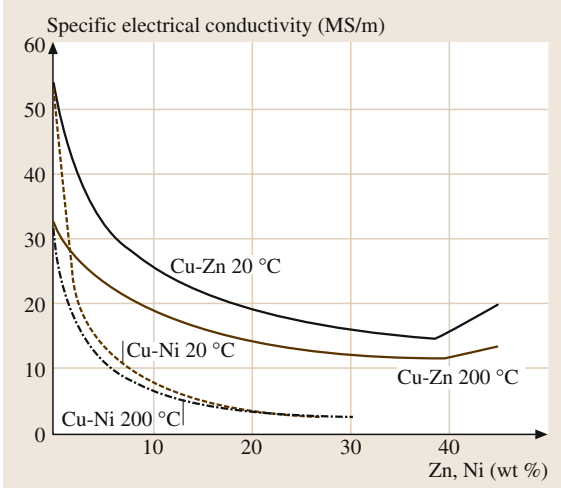


**Fig. 3.1-137** Electrical conductivity of Cu−Ni and Cu−Zn alloys [1.103]

**Table 3.1-107** Composition and properties of characteristic copper–nickel and copper–nickel–zinc alloys

| Material | UNS No. | Purity; other elements (wt%) | Yield stress $R_{po.2}$ (MPa) | Ultimate tensile strength $R_m$ (MPa) | Fracture strain $A_f$ (%) | Thermal conductivity $\kappa$ ($W\,m^{-1}\,K^{-1}$) | Electrical resistivity $\rho$ ($\mu\Omega$ cm) |
|---|---|---|---|---|---|---|---|
| Copper nickel | C70400 | 92.4 Cu–5.5 Ni –1.5 Fe–0.6 Mn | 276–524 | 262–531 | 2–46 | 67 | 13.79 |
| Copper nickel | C70600 | 87.7 Cu–10 Ni –1.5 Fe–0.6 Mn | 110–393 | 303–414 | 10–42 | 42 | 21.55 |
| Copper nickel | C71500 | 67 Cu–31 Ni –0.7 Fe–0.5 Be | 138–483 | 372–517 | 15–45 | 21 | 38.31 |
| Nickel silver 10% | C74500 | 65 Cu–25 Zn–10 Ni | 124–524 | 338–896 | 1–50 | 37 | 20.75 |
| Nickel silver 12% | C74500 | 65 Cu–23 Zn–12 Ni | 124–545 | 359–641 | 2–48 | 30 | 22.36 |
| Nickel silver 15% | C75200 | 65 Cu–20 Zn–15 Ni | 124–545 | 365–634 | 2–43 | 27 | 24.59 |
| Nickel silver 18% | C74500 | 65 Cu–17 Zn–18 Ni | 172–621 | 386–710 | 3–45 | 28 | 27.37 |

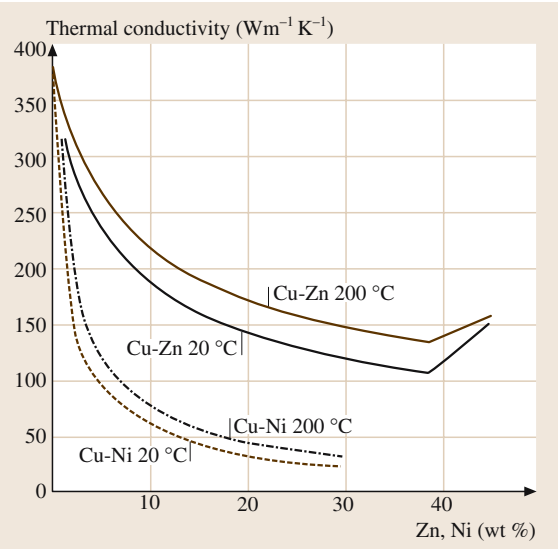


**Fig. 3.1-138** Thermal conductivity of Cu−Ni and Cu−Zn alloys [1.103]

## 3.1.9 Refractory Metals and Alloys

Several books and reviews have been published on the technology and properties of refractory metals and their alloys [1.107–116]. According to the most common definition, refractory metals comprise elements of the Group VB and VIB with a melting point higher than 2000 °C; these are niobium, tantalum, molybdenum, and tungsten. In some publications the VIIB metal rhenium is also included, as it does not fit in any other classification. Less common definitions describe a refractory metal as metal with a melting point equal to or greater than that of chromium, thus additionally including vanadium, technetium, the reactive metal hafnium, and the noble metals ruthenium, osmium, ruthenium, and iridium. This chapter will give data on molybdenum, tungsten, tantalum, niobium, and their alloys. Powder metallurgy (P/M) is the only production route for commercial W and W alloys and for 97% of Mo, the remainder is processed by electron-beam melting (EB) and vacuum-arc casting (VAC) [1.117]. The finer grain structure of P/M-material is advantageous for both the further processing and the mechanical properties of the finished product. For some alloys such as those doped with potassium silicate, $La_2O_3$, and $Y_2O_3$, P/M is the only possible production technique.

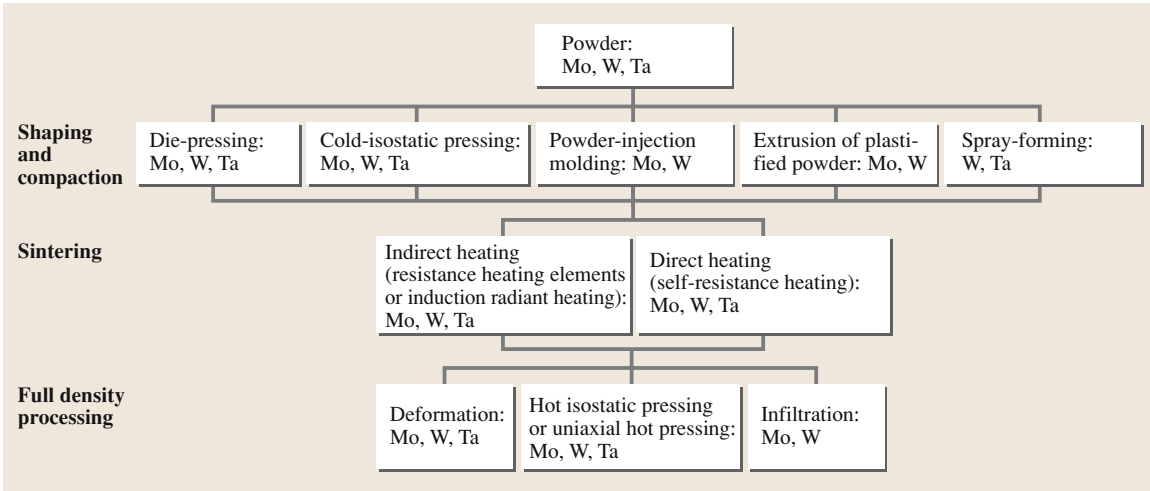


**Fig. 3.1-139** Large-scale P/M production routes for Mo, W and Ta [1.118]

The mechanical properties and homogenous microstructure required are again the reasons to apply P/M in producing Ta wire as employed extensively in the manufacture of capacitors. The larger fraction of the Ta sheet production is based on the use of EB sheet bars, as this is more economical. The techniques of VAC and EB dominate in the production of Nb and Nb alloys. The industrial P/M production routes of Mo, W, Ta, and their alloys are given in Fig. 3.1-139.

Net shape techniques such as powder injection molding and spraying on a lost core (vacuum-plasma-spraying, chemical vapor deposition) are limited to some specific applications in the field of electronic devices and aerospace products. Less than 10% of the production quantity is delivered in the as-sintered state. The most common fully-dense-processing techniques are deformation by rolling, forging, swaging, and drawing.

Initially refractory metals were applied mainly in the pure state. Extensive developments mainly driven by US aerospace programs led to a wide variety of alloys now commercially available. The compositions of solid-solution, precipitation- and dispersion-strengthened alloys are given in Table 3.1-108. Tungsten heavy metals and refractory-metal-based composite materials are not included here.

Carbide precipitation hardening (in TZM, MHC) is effective up to 1400 °C. The addition of the deformable oxides $La_2O_3$ (in ML) and $xK_2O \cdot ySiO_2$ (in K–Si–Mo), respectively, results in oxide refinement by deformation and in the possibility of tailoring the mechanical properties. This is the main alloying mechanism for Mo applied in lamps [1.119].

The tungsten alloy which is commercially most important is Al–K-silicate doped W (AKS–W). It is a dispersion-strengthened, micro-alloyed metal with a directionally recrystallized microstructure. Spherical bubbles stabilized by containing K gas are interacting with dislocations, sub-boundaries and high-angle boundaries [1.120, 121]. The high stability of these bubbles can be explained by the low solubility of K in W, even at operating temperatures up to 3200 °C.

A current task is to reduce the low-temperature brittleness of Mo and W, which is essentially due to a rigid covalent component of the interatomic bond along the edges of the bcc unit cell. This causes a low solubility for interstitial elements which occupy the octahedral sites of the lattice and give rise to its tetragonal distortion and a strong interaction of dislocations with the elastic strain field surrounding the interstitial solutes, thus impeding the dislocation movement [1.122]. One possibility to increase the low-temperature ductility is alloying with Re which lowers the brittle-to-ductile-transition temperature of both W and Mo [1.123–125]. But the insufficient supply and the high price of Re limit the application of these alloys.

The addition of oxides such as $ThO_2$, BaO, SrO, $Y_2O_3$, and $Sc_2O_3$ lowers the electron work function of W, which is important for its application in electrodes. The production quantities of W–$La_2O_3$ and W–$Ce_2O_3$ as electron emitting materials are increasing at the expense of the slightly radioactive W–$ThO_2$ material.

The production of capacitors, the dominating application of Ta, requires material in its purest

**Table 3.1–108** Typical compositions of commercial refractory metal alloys (in weight percent, analyses of base-metal correspond to metallic purity) [1.118]

| Alloy designation | Mo | W | Ta | Nb | Re | C | O | Si | K | Y | La | Ce | Th | Ti | Zr | Hf |
|---|---|---|---|---|---|---|---|---|---|---|---|---|---|---|---|---|
| **Molybdenum alloys** | | | | | | | | | | | | | | | | |
| Pure Mo | 99.97 | | | | | | | | | | | | | | | |
| UHP-Mo | 99.9995 | | | | | | | | | | | | | | | |
| TZM | 99.3 | | | | | 0.025 | 0.02 | | | | | | | 0.5 | 0.08 | |
| MHC | 98.6 | | | | | 0.08 | 0.035 | | | | | | | | | 1.2 |
| Mo–$La_2O_3$ (ML) | 99.2–99.6 | | | | | | 0.048–0.1 | | | | 0.27–0.6 | | | | | |
| Mo–$Y_2O_3$ (MY) | 99.42 | | | | | | 0.10–0.12 | | | 0.37–0.43 | | 0–0.06 | | | | |
| K–Si–Mo | 99.8–99.9 | | | | | | 0.01–0.07 | 0.013–0.07 | 0.005–0.03 | | | | | | | |
| Mo50Re | 52.4 | | | | 47.5 | | | | | | | | | | | |
| Mo30W | 69.7 | 30 | | | | | | | | | | | | | | |
| **Tungsten alloys** | | | | | | | | | | | | | | | | |
| Pure W | | 99.99 | | | | | | | | | | | | | | |
| UHP-W | | 99.9995 | | | | | | | | | | | | | | |
| AKS-W | | 99.98 | | | | | | | 0.004–0.01 | | | | | | | |
| W–$La_2O_3$ (WL) | | 97.9–98.9 | | | | | 0.015–0.03 | | | | 0.85–1.7 | | | | | |
| W–$Ce_2O_3$ (WC) | | 98.0 | | | | | 0.28 | | | | | 1.62 | | | | |
| W–$ThO_2$ (WT) | | 98.0 | | | | | 0.24 | | | | | | 1.71 | | | |
| AKS-W–$ThO_2$ | | 98.0–99.0 | | | | | 0.12–0.24 | | 0.001–0.005 | | | | 0.86–1.71 | | | |
| W5Re | | 94.9 | | | 5.0 | | | | | | | | | | | |
| W26Re | | 73.9 | | | 26 | | | | | | | | | | | |
| AKS-W3Re | | 96.9 | | | 3.0 | | | | 0.004 | | | | | | | |
| **Tantalum alloys** | | | | | | | | | | | | | | | | |
| Pure Ta | | | 99.95 | | | | | | | | | | | | | |
| Ta2.5W | | 2.5 | 97.4 | | | | | | | | | | | | | |
| Ta10W | | 10.0 | 89.9 | | | | | | | | | | | | | |
| **Niobium alloys** | | | | | | | | | | | | | | | | |
| Pure Nb | | | | 99.9 | | | | | | | | | | | | |
| Nb1Zr | | | | 98.9 | | | | | | | | | | | 1.0 | |
| C-103 | | | | 88.8 | | | | | | | | | | 1 | | 10 |
| FS-85 | | 10 | 28 | 60.8 | | | | | | | | | | | 1 | |
| WC-3009 | | 9 | | 60.8 | | | 0.1 | | | | | | | | | 30 |
| Nb – 46.5Ti | | | | | | | | | | | | | | 46.5 | | |

state. Solid-solution-strengthened Ta2.5W is used for components in chemical apparatus. Superconducting Nb46.5Ti accounts for more than half of all Nb alloys produced. Hafnium is the main addition for niobium-based alloys used by the aerospace industry.

Refractory metals and their alloys are used in a wide variety of fields of application and products such as electrical and electronic devices; light sources; medical equipment; automotive, aerospace, and defense industry; chemical and pharmaceutical industry; or premium and sporting goods.

The producers of electrical and electronic devices, including the lighting industry, are the largest consumers of refractory metal products. In 1998, 1850 t of W products was used for filaments and electrodes in lamps only. Significant quantities of Mo are used for semiconductor base-plates for power rectifiers and in various products for lamps, such as dipped beam shields or support wires. Rapid growth in multimedia and wireless communication networks systems has boosted the need for W−Cu and Mo−Cu heat sink materials. These materials possess a high thermal conductivity combined with a low thermal expansion, close to those of Si and GaAs semiconductors or certain packaging materials. Also, the amount of Mo sputtering targets applied in the production of wiring for large format thin-film transistor LCDs and PDPs has risen significantly owing to the unique combination of low resistivity and high resistance against hillock formation. The electronic industry is the largest market (around 70%) for Ta products, employing the metal mainly in the manufacture of capacitors.

Refractory metals are also widely used by the materials processing industry. Molybdenum glass melting electrodes, TZM and MHC isothermal forging tools, weighing several tons per part, TZM piercing plugs for the production of stainless steel tubes, Mo and Ta crucibles for synthesizing artificial diamond, or TIG-welding electrodes are examples of products in this field. In order to improve the tribological properties of transmission and engine components for automobiles they are coated with Mo.

Recent products in the field of aerospace and defense industry are shaped charge liners made of Mo and Ta penetrators formed explosively. The X-ray anode, a composite product made of W5Re or W10Re, TZM and optionally graphite, is the essential item of computer-tomography equipment, a very demanding application that critically depends on the users' expertise.

**Fig. 3.1-141** Thermal conductivity versus temperature of molybdenum [1.126], tungsten [1.129], niobium [1.127], and tantalum [1.127]

### 3.1.9.1 Physical Properties

The atomic and structural properties of the pure refractory metals are listed in Chapt. 2.1, Tables 2.1-16 and 2.1-18. Special features of refractory metals are their low vapor pressure, low coefficient of thermal expansion, and the high thermal and electrical conductivity of Mo and W. This combination of physical properties has opened up a wide range of new applications during the last decade, especially in the field of electronics.

The coefficient of linear thermal expansion, the thermal conductivity, the specific heat, and the electrical resistivity as function of temperature are shown in Figs. 3.1-140 – 3.1-143. The vapor pressure and rate of evaporation are shown in Fig. 3.1-144. In the case of precipitation- and dispersion-strengthened Mo alloys, such as TZM, MHC, ML, MY, and K−Si−Mo,

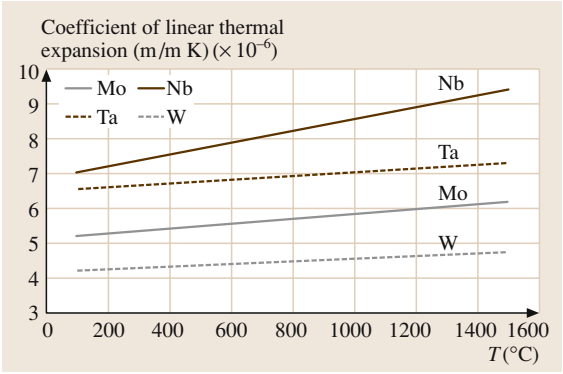


**Fig. 3.1-140** Coefficient of linear thermal expansion versus temperature of molybdenum [1.126], tungsten [1.126], niobium [1.127], and tantalum [1.128]

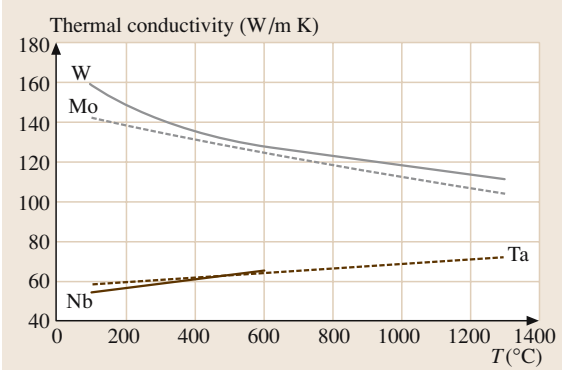

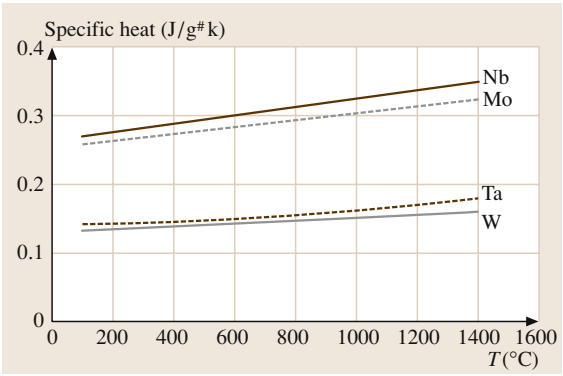


**Fig. 3.1-142** Specific heat versus temperature of molybdenum, tungsten, niobium, and tantalum [1.126]

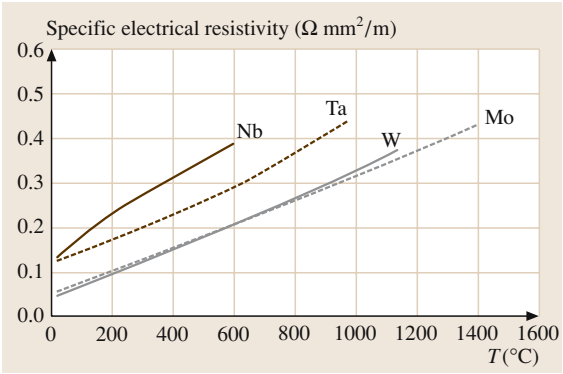


**Fig. 3.1-143** Specific electrical resistivity versus temperature of molybdenum [1.126], tungsten [1.126], niobium [1.127], and tantalum [1.127]

as well as the tungsten based alloys AKS–W, WL, WC, and WT, the physical properties do not differ significantly from those of the pure metals. Values for the Young's modulus and its temperature dependence are plotted in Fig. 3.1-145. The Young's moduli of the Group VA metals are considerably lower than those of the Group VIA metals due to the differences in electronic structure.

The strong influence of the surface conditions on the emissivity and lack of information in the literature concerning pre-treatment make it difficult to interpret emissivity data. An overview of emissivity measurements for W, Nb, and Ta at 684.5 nm from 1500 °C up to the liquid phase using laser polarimetry is given in [1.130].

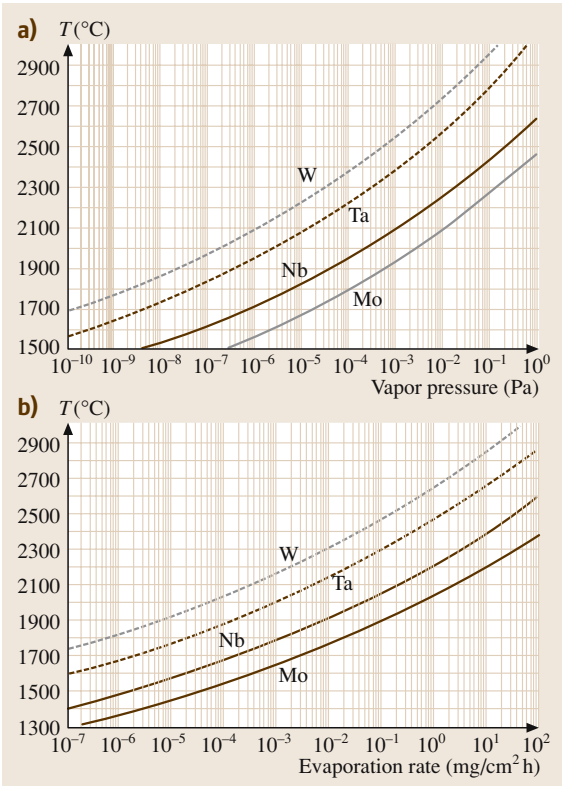


**Fig. 3.1-144a,b** Vapor pressure **(a)** and evaporation rate **(b)** versus temperature of molybdenum, tungsten, niobium, and tantalum [1.129]

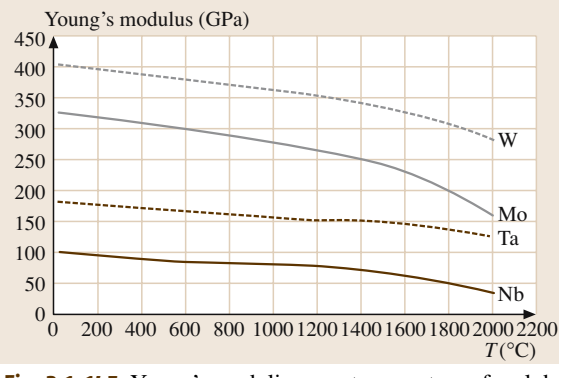


**Fig. 3.1-145** Young's moduli versus temperature of molybdenum, tungsten, niobium, and tantalum [1.128]

### 3.1.9.2 Chemical Properties

Refractory metals are highly resistant to many chemical agents. Tantalum is outstanding in its performance as it is inert to all concentrations of hydrochloric and nitric acid, 98% sulphuric acid, 85% phosphoric acid, and aqua regia below 150 °C. Tantalum is attacked by hydrofluoric acid and strong alkalis, however. The excellent corrosion resistance of Ta is attributed to dense natural oxide layers which prevent the chemical attack of the metal. Niobium is less resistant than Ta and embrittles more easily. Nevertheless the more economical Nb has replaced Ta in some applications. Molybdenum and W are highly resistant to many molten glasses and metals as long as free oxygen is absent.

The interaction with H, N, and O is widely different for Mo and W on the one hand, and Nb and Ta on the other. Molybdenum and W have almost no solubility, whereas Nb and Ta can dissolve a considerable amount of these elements. Hydrogen can be removed from Nb at 300 °C to 1600 °C and from Ta at 800 °C to 1800 °C without metal loss by degassing in high vacuum. For the removal of N, temperatures higher than 1600 °C are recommended. The evaporation of volatile oxides at temperatures above 1600 °C in high vacuum leads to a reduction of the oxygen content in Nb and Ta. But during such heat treatments, metal is evaporated simultaneously.

An overview on the resistance of pure Mo, W, Nb, and Ta against different media is given in Tables 3.1-109 to 3.1-111. In accordance with the definition given in [1.131], a material is considered "stable" against a corrosive medium if the metal loss is $< 0.1$ mm per year. If the loss of material is between 0.1 and 1.0 mm per year, the material is "considerably stable;" and it is "fairly unstable" if the loss of material is between 1.0 and 3.0 mm. The material is "unsuitable" in an environment if the metal loss is $> 3.0$ mm per year.

#### Oxidation Behavior

Refractory metals require protection from oxidizing environment as they do not form protective oxide layers. Oxidation of Mo and W leads to a loss of material by the formation of volatile oxides above 600 °C in case of Mo and 750 °C in case of W, respectively, but without any significant impact on the mechanical properties.

The low temperature oxidation of Mo and W often causes problems in practical use as thin corrosion films are formed during storage in moist air. The surface topography of Mo has a strong impact on the reaction rate. The corrosion film contains oxygen but also chemically-bonded nitrogen, which is incorporated in the film during film growth. $C_xH_y$ residues are the nuclei for the oxidative attack in the early stage of film growth [1.132].

There is extensive evidence that between 300 and 500 °C, oxide-dispersion-strengthened (ODS) refractory metal alloys (e.g., Mo−$La_2O_3$ and Mo−$Y_2O_3$ grades) possess markedly reduced oxidation rates compared to the pure metals [1.133]. In-situ oxidation and evaluation of the binding state reveal that $MoO_2$ dominates over $MoO_3$ both for Mo and Mo–

**Table 3.1-109** Metal loss of Mo, W, Nb and Ta in millimeter per year (mm/yr) in acids, alkalis and salt solutions

| Corroding agent (aqueous solution) | Temperature | Metal loss (mm/yr) | | | |
|---|---|---|---|---|---|
| | | Mo | W | Nb | Ta |
| 10% HCl | 20 °C | < 0.003 | 0.002 | 0 | < 0.001 |
| 10% $H_2SO_4$ | 20 °C | < 0.005 | < 0.1 | < 0.1 | < 0.1 |
| 10% $HNO_3$ | 20 °C | 18.6 | < 0.25 | < 0.013 | < 0.013 |
| 3% HF | 20 °C | < 0.001 | < 0.1 | > 3.0 | > 3.0 |
| 10% $CH_3COOH$ | 20 °C | 0.07 | < 0.05 | < 0.1 | < 0.013 |
| 10% KOH | 20 °C | < 0.1 | < 0.1 | < 0.2 | < 0.1 |
| 3% NaCl | 20 °C | < 0.1 | < 0.1 | < 0.1 | < 0.1 |
| 10% HCl | 100 °C | < 0.025 | 0.005 | 0.005 (embrittlement) | < 0.025 |
| 10% $H_2SO_4$ | 100 °C | 0.17 | < 0.25 | < 0.001 | 0 |
| 10% $HNO_3$ | 100 °C | 150 | < 0.25 | < 0.076 | < 0.025 |
| 3% HF | 100 °C | 0.18 | 0.15 | > 3.0 | > 3.0 |
| 10% $CH_3COOH$ | 100 °C | 0.033 | < 0.05 | < 0.1 | < 0.013 |
| 10% KOH | 100 °C | 0.054 | 0.01 | 1.2 (embrittlement) | < 0.003 (embrittlement) |
| 3% NaCl | 100 °C | < 0.1 | < 0.1 | < 0.1 | < 0.1 |

**Table 3.1-110** Maximum temperatures for the resistance of Mo, W, Nb, and Ta against metal melts (up to the stated temperatures the solubility of the refractory metal in the metal melts and vice versa is negligible)

| Metal melt | Maximum resistance temperature (°C) | | | |
|---|---|---|---|---|
| | Mo | W | Nb | Ta |
| Al | Not resistant | 680 | Not resistant | Not resistant |
| Pb | 1100 | 1100 | 850 | 1000 |
| Fe | Not resistant | Not resistant | Not resistant | Not resistant |
| Ga | 300 | 800 | 400 | 450 |
| K | 1200 | 900 | 1000 | 1000 |
| Cu | 1300 | Resistant | Resistant | Resistant |
| Mg | 1000 | 600 | 950 | 1150 |
| Na | 1030 | 900 | 1000 | 1000 |
| Hg | 600 | 600 | 600 | 600 |
| Zn | 500 | 750 | Not resistant | 500 |
| Sn | 550 | 980 | Not resistant | 260 |
| Ag | Resistant | Resistant | Resistant | 1200 |

**Table 3.1-111** Maximum temperatures for the resistance of Mo, W, Nb, and Ta against gaseous media at atmospheric pressure

| Gaseous media | Maximum resistance temperature | | | |
|---|---|---|---|---|
| | Mo | W | Nb | Ta |
| Air and oxygen | see Sect. 3.1.9.2 | | | |
| Hydrogen | Resistant | Resistant | 250 °C ($T > 250$ °C embrittlement owing to dissolved hydrogen) | 300 °C ($T > 300$ °C embrittlement owing to dissolved hydrogen) |
| Nitrogen | Resistant | Resistant | 300 °C ($T > 300$ °C embrittlement owing to dissolved nitrogen) | 400 °C ($T > 400$ °C embrittlement owing to dissolved nitrogen) |
| Ammonia | Resistant (except 1000–1100 °C: nitration) | Resistant (except 700–1150 °C: nitration) | 300 °C ($T > 300$ °C embrittlement owing to dissolved nitrogen) | 700 °C ($T > 700$ °C embrittlement owing to dissolved nitrogen) |
| Water vapor | 700 °C | 700 °C | 200 °C | 200 °C |
| Carbon monoxide | 800 °C ($T > 800$ °C carburization) | 1000 °C ($T > 800$ °C carburization) | 800 °C | 1100 °C |
| Carbon dioxide | 1200 °C ($T > 1200$ °C oxidation) | 1200 °C ($T > 1200$ °C oxidation) | 400 °C | 500 °C |

0.47 wt%$Y_2O_3$–0.08 wt%$Ce_2O_3$ (Fig. 3.1-146). These results are confirmed when comparing the thickness of the oxide layer formed at 500 °C in air (Fig. 3.1-147). The enhanced oxidation resistance of doped samples cannot be attributed to a chemical but rather to a morphological-mechanical effect. Investigations of the surface of pure Mo samples subjected to long-term oxidation reveal a network of cracks in the $MoO_2$ layer which drastically diminishes the passivating effect of this layer by facilitating a further attack by O. Such cracks cannot be found on the surface of oxidized Mo−$La_2O_3$ and Mo−$Y_2O_3$ samples [1.133].

Above 700 °C for Mo and approximately 900 °C for W, evaporation of the volatile oxides $MoO_3$ and $WO_3$ is the rate-controlling process and the oxidation follows a linear time dependence. Above 2000 °C for Mo and 2400 °C for W, the metal loss increases because of the increasing vapor pressure of the pure metals. The time

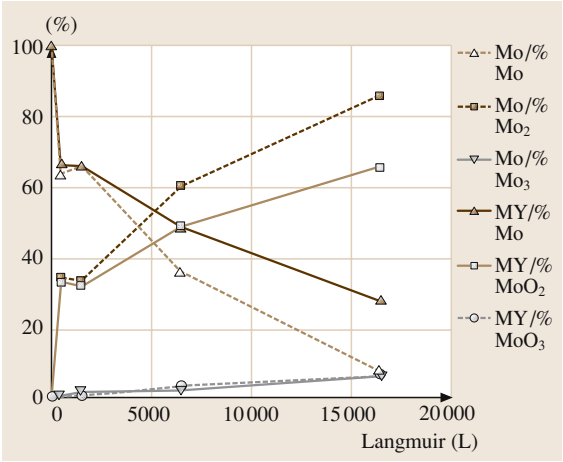


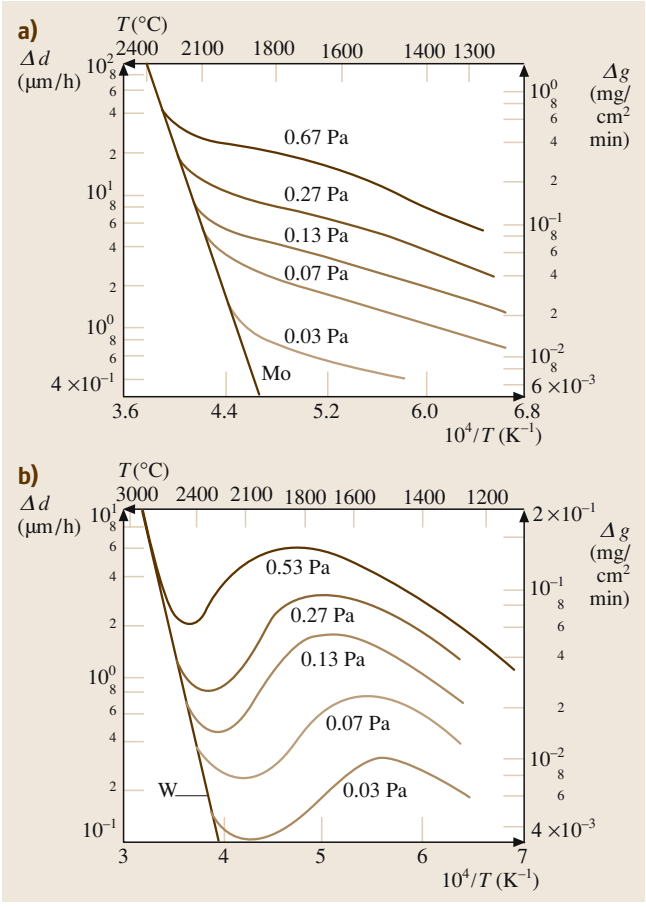


**Fig. 3.1-148a,b** Metal loss in air for Mo **(a)** and W **(b)** at $T \geq 1200\,°C$ [1.134]

**Fig. 3.1-146** ESCA measurements and evaluation of $Mo/MoO_2/MoO_3$ fraction versus in-situ oxidation conditions in Langmuir ($1\,L = 10^{-6}$ Torr s). Mo: 4N5 Mo ribbon, electro-polished surface; MY: Mo–0.47 wt%$Y_2O_3$–0.08 wt%$Ce_2O_3$ ribbon, electro-polished surface, test conditions: 500 °C/air [1.133]

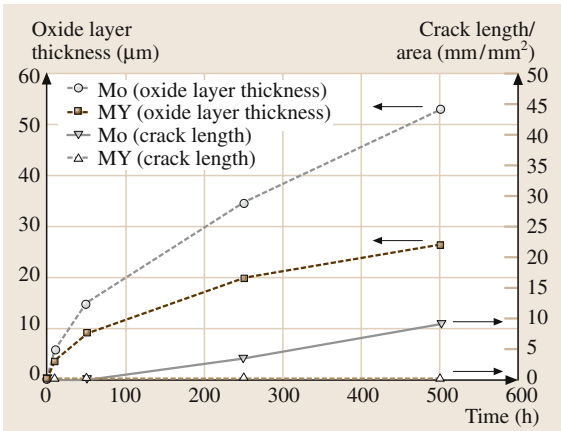


**Fig. 3.1-147** Thickness of oxide layer and crack length per area versus testing time. Mo: 4N5 Mo ribbon, electropolished surface; MY: Mo–0.47 wt%$Y_2O_3$–0.08 wt%$Ce_2O_3$ ribbon, electropolished surface, test conditions: 500 °C/air [1.133]

dependence of metal loss for Mo and W at $T \geq 1200\,°C$ is shown in Fig. 3.1-148 [1.134].

The oxidation rates of Nb and Ta strongly depend on temperature, pressure, and time. Different mechanisms causing different oxidation rates can be observed and metastable sub-oxides are formed during use in O-containing atmospheres [1.131, 134]. Oxygen is dissolved in the metal matrix which leads to significant changes of the mechanical properties. A poorly adherent, porous pentoxide is formed on the metal surface which does not protect the metal from further attack. Oxygen which has penetrated the porous oxide layer diffuses along the grain boundaries of the metal, leading to drastic embrittlement.

The metal loss at 1100 °C due to oxidation in air is shown for Mo, W, Nb, and Ta in Fig. 3.1-149 [1.135]. The embrittled zone caused by oxygen diffusion into the substrate is not considered in this diagram.

Only a few coating systems have been found to prevent the refractory metals from oxidation. In the case of Mo, Pt-cladded components with a diffusion barrier interlayer on the basis of alumina, which prevents the formation of brittle intermetallic molybdenum–platinum

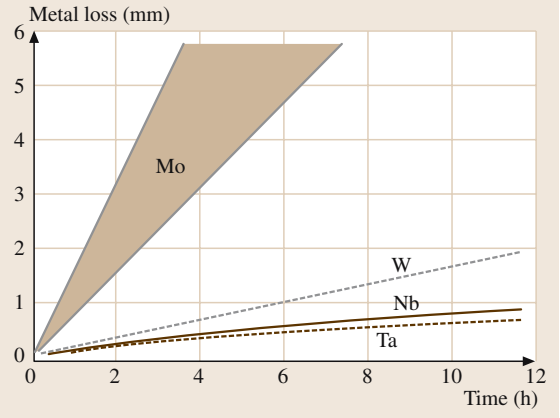


**Fig. 3.1-149** Oxidation behavior of Mo, W, Nb, and Ta at 1100 °C [1.135]

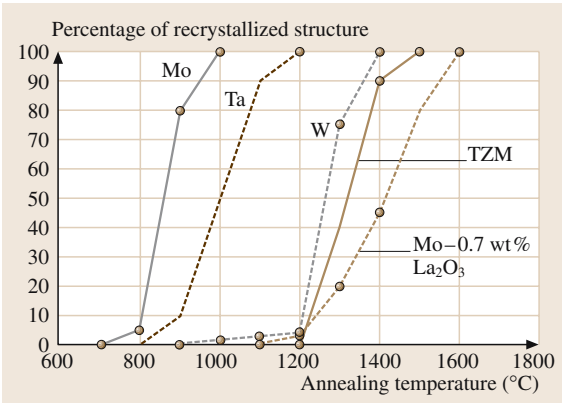


**Fig. 3.1-150** Fraction of recrystallized structure versus annealing temperature (annealing time $t_a = 1$ h) for Mo, P/M Ta, W, TZM, and Mo–0.7 wt% $La_2O_3$ sheets with a thickness of 1 mm, degree of deformation, $\varphi = \frac{th_p - th_s}{th_p} 100[\%]$, where $th_p =$ thickness of sintered plate, and $th_s =$ thickness of rolled sheet. Mo: $\varphi = 94\%$, P/M Ta: $\varphi = 98\%$, W: $\varphi = 94\%$, TZM: $\varphi = 98\%$, Mo–0.7 wt% $La_2O_3$: $\varphi = 99\%$ [1.126]

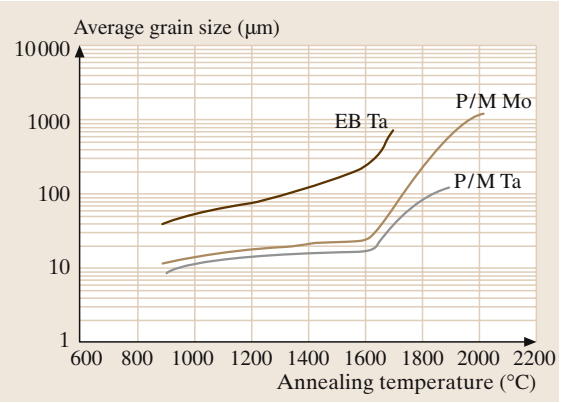


**Fig. 3.1-151** Grain size versus annealing temperature (annealing time $t_a = 1$ h) for Mo, P/M Ta, and EB Ta sheets with a thickness of 1 mm. Mo: $\varphi = 94\%$, P/M Ta: $\varphi = 98\%$, EB Ta: $\varphi = 98\%$ [1.126, 140]

phases, are used; e.g., for stirrers used to homogenize special glasses. Mo components for glass tanks and glass melting electrodes are protected from oxidation by coatings based on silicides, such as Si−B [1.136]. Silicon–boron and other silicide based coatings, such as Si−Cr−Fe or Si−Cr−Ti, are also used to protect Mo and Nb based alloys from oxidation in aerospace applications [1.135, 137–139]

### 3.1.9.3 Recrystallization Behavior

The mechanisms and kinetics of recovery and recrystallization processes significantly affect the processing and application of refractory metals. The homologous temperatures ($T/T_M$ in K) for obtaining 50% recrystallized structure during annealing for one hour, range from 0.39 for Mo, 0.41 for W, 0.42 for Nb, to 0.43 for P/M Ta. The fraction of recrystallized structure as a function of the annealing temperature of Mo, W, P/M Ta, TZM, and Mo–0.7 wt%$La_2O_3$ sheets of 1 mm thickness is shown in Fig. 3.1-150. Experimental data on the evolution of grain size with the annealing temperature for pure Mo and Ta sheets of 1 mm thickness are shown in Fig. 3.1-151 [1.126, 140]. A recrystallization diagram for Mo is published in [1.141], and for P/M Ta in [1.142].

Compared to pure Mo, the recrystallization temperature of the carbide-precipitation-hardened alloy TZM is increased by 450 °C and that of Mo–0.7 wt%$La_2O_3$ by 550 °C. The data listed in Table 3.1-112 show that all those alloys containing particles, which deform together with the matrix metal (ML, K−Si−Mo, WL10, WL15, WT20, and AKS−W−$ThO_2$), reveal a significantly increased recrystallization temperature in the highly deformed state. Increasing the degree of deformation from $\varphi = 90\%$ to $\varphi = 99.99\%$ leads to a further increase of the recrystallization temperature (100% recrystallized structure, 1 h annealing time) ranging from 600 °C for K−Si−Mo, 700 °C for ML, 950 °C for WT20, 1000 °C for WL10, to 1050 °C for WL15 and WC20. This can be explained by particle refinement. During the deformation process the particles are elongated. During annealing they break up and rows of smaller particles

**Table 3.1-112** Typical recrystallization temperature and ultimate tensile strength of commercial Mo and W based rod and wire materials with a defined degree of total deformation $\varphi$ [1.118]

| Alloy designation | Composition (wt%) | Temperature for 100% recrystallized structure ($t = 1$ h) (°C) | Typical ultimate tensile strength at 1000 °C (MPa) |
|---|---|---|---|
| Pure Mo | | 1100 ($\varphi = 90\%$) | 250 ($\varphi = 90\%$) |
| TZM | Mo, 0.5% Ti, 0.08% Zr, 0.025% C | 1400 ($\varphi = 90\%$) | 600 ($\varphi = 90\%$) |
| MHC | Mo, 1.2% Hf, 0.08% C | 1550 ($\varphi = 90\%$) | 800 ($\varphi = 90\%$) |
| ML | Mo, 0.3% $La_2O_3$ | 1300 ($\varphi = 90\%$), 2000 ($\varphi = 99.99\%$) | 300 ($\varphi = 90\%$) |
| MY | Mo, 0.48% $La_2O_3$, 0.07% $Ce_2O_3$ | 1100 ($\varphi = 90\%$), 1350 ($\varphi = 99.99\%$) | 300 ($\varphi = 90\%$) |
| K–Si–Mo | Mo, 0.05% Si, 0.025% K | 1200 ($\varphi = 90\%$), 1800 ($\varphi = 99.99\%$) | 300 ($\varphi = 90\%$) |
| Mo50Re | Mo, 47.5% Re | 1300 ($\varphi = 90\%$) | 600 ($\varphi = 90\%$) |
| Mo30W | Mo, 30% W | 1200 ($\varphi = 90\%$) | 350 ($\varphi = 90\%$) |
| Pure W | | 1350 ($\varphi = 90\%$) | 350 ($\varphi = 90\%$) |
| AKS-W | W, 0.005% K | 2000 ($\varphi = 99.9\%$) | 800 ($\varphi = 99.9\%$) |
| WL10 | W, 1.0% $La_2O_3$ | 1500 ($\varphi = 90\%$), 2500 ($\varphi = 99.99\%$) | 400 ($\varphi = 90\%$) |
| WL15 | W, 1.5% $La_2O_3$ | 1550 ($\varphi = 90\%$), 2600 ($\varphi = 99.99\%$) | 420 ($\varphi = 90\%$) |
| WC20 | W, 1.9% $Ce_2O_3$ | 1550 ($\varphi = 90\%$), 2600 ($\varphi = 99.99\%$) | 420 ($\varphi = 90\%$) |
| WT20 | W, 2% $ThO_2$ | 1450 ($\varphi = 90\%$), 2400 ($\varphi = 99.99\%$) | 400 ($\varphi = 90\%$) |
| AKS-W–$ThO_2$ | W, 1% $ThO_2$, 0.004% K | 2400 ($\varphi = 99.9\%$) | 1000 ($\varphi = 99.9\%$) |
| W5Re | W, 5 Re | 1700 ($\varphi = 90\%$) | 500 ($\varphi = 90\%$) |
| W26Re | W, 26 Re | 1750 ($\varphi = 90\%$) | 900 ($\varphi = 90\%$) |

are formed. With the increase in number of particles, the subgrain boundaries are pinned more effectively, resulting in an increase of the recrystallization temperature [1.119].

Experiments with various oxide-dispersion-strengthened (ODS) Mo materials with 2 vol.% of oxide, mean oxide particle sizes in the as-sintered state of around 0.8 µm, and a degree of deformation $\ln(A_0/A) = 8.5$ ($A_0$ = cross section as-sintered, $A$ = cross section as-deformed), revealed differences in the recrystallization temperature of up to 750 °C depending on the oxide used. It could be shown that this effect is caused by particle refinement during deformation and subsequent heat treatment. Particles which increase the recrystallization temperature very effectively, as is the case with $La_2O_3$, show a high particle deformability [1.143].

Whether oxide particles deform in a pseudo-plastic manner or not depends on a multitude of parameters, such as the yield stress of the particles, the yield stress of the matrix, the particle/matrix bonding strength, the crystallite size, the defect density, or the state of stresses. Most of these parameters are unknown or difficult to measure. Good correlation could be found between the particle deformability, with its effect on the increase of the recrystallization temperature, and the fraction of ionic bonding character of the oxide, following the definition of Pauling [1.143]. Figure 3.1-152 shows that compounds with a high fraction of ionic bonding character, such as $La_2O_3$ or SrO, raise the recrystallization temperature very effectively. Slight particle multiplication could also be found for $Al_2O_3$, $ZrO_2$, and $HfO_2$ compounds with a marked covalent bonding character, but because of breakage of the particles during the deformation process.

The recrystallization temperature can be tailored by varying both the type and the content of the oxide, the lat-

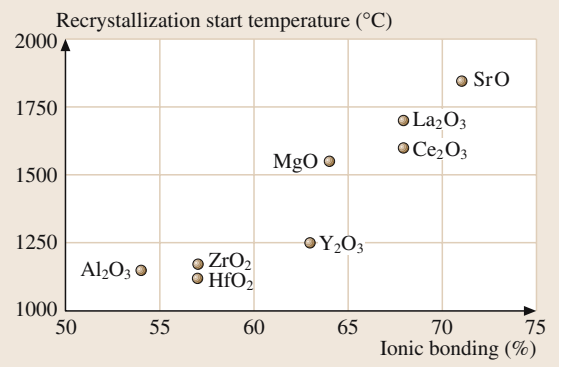


**Fig. 3.1-152** Recrystallization start temperature of various ODS Mo materials versus fraction of ionic bonding (according to Pauling) of the respective oxides. Oxide content = 2 vol.%, wire diameter = 0.6 mm [1.143]

ter shown in Fig. 3.1-153 for Mo–0.03 wt%$La_2O_3$ (ILQ) and Mo–0.3 wt%$La_2O_3$ (ML).

AKS–W shows a similar effect where the K-containing bubbles are effective pinning centers. The recovery and recrystallization mechanisms of AKS–W as a function the annealing temperature are summarized in Table 3.1-113.

The recrystallization temperature of AKS–W is determined by the relation of the driving to dragging forces. The driving forces are determined by the thermomechanical treatment (TMT), the dragging forces depend on the number, size, and distribution of the K bubbles. With increasing degree of deformation, both the driving forces (increasing dislocation density and low-angle/high-angle boundary volume) and dragging forces (increasing length of stringers of K-filled pores and, as a consequence, increasing number of K bubbles formed) become larger. During the first deformation

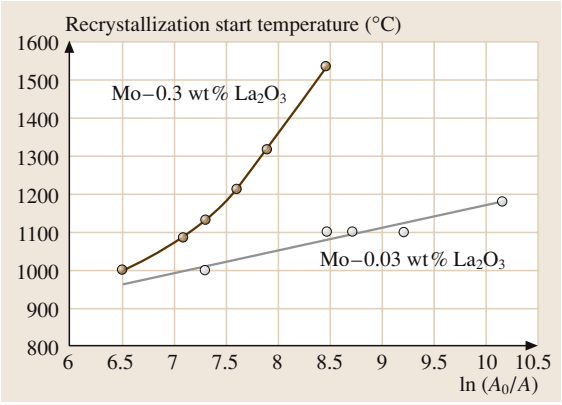


**Fig. 3.1-153** Recrystallization start temperature of Mo–0.03 wt% $La_2O_3$ and Mo–0.3 wt% $La_2O_3$ wires versus degree of deformation $\ln(A_0/A)$ [1.133]

**Table 3.1-113** Recrystallization mechanisms for AKS-W wires [1.120, 144, 145]

| Microstructural state | Processes |
|---|---|
| **Evolution of the microstructure during wire drawing** | • Formation of a dislocation cell structure by static and dynamic recovery processes |
| **Coarsening of the microstructure during annealing** | • Annealing temperature 800 to 1400 °C:<br>– Reduction of the dislocation density within the cell walls;<br>– Break-up of the K-containing stringers into pearl rows of bubbles;<br>– Migration of longitudinal grain boundaries is strongly reduced by pearl rows of bubbles;<br>– Similar ⟨110⟩ texture as in the as-worked state.<br>• For low heating rates, partial or even entire bubble rows can be dragged by the boundaries moving in the transverse direction. As a result, row/row collision and bubble coalescence can occur<br>• The temperature up to which the coarsened substructure remains stable depends on the degree of deformation (e.g., diameter 0.18 mm: 2100 °C/15 min). The coarsened substructure has a significant portion of high-angle grain boundaries (misorientation angles higher than 15°) |
| **Exaggerated grain growth** | Nucleation and growth of large interlocking grains occur by primary recrystallization, whereby a subgrain begins to grow laterally at the expense of neighboring polygonized subgrains.<br>• Because of the pearl row of bubbles, the rate of grain boundary movement is higher in the axial, than in the transverse direction<br>• Because of the interaction between the bubbles and the growing grains, the grain boundaries possess a wave-like, interlocking structure<br>• The grain aspect ratio of the recrystallized structure increases with increasing number of K bubbles. The number of K bubbles is a function of the K-content, the degree of deformation and the TMT.<br>• Highly deformed, recrystallized wires reveal a ⟨531⟩ texture. |

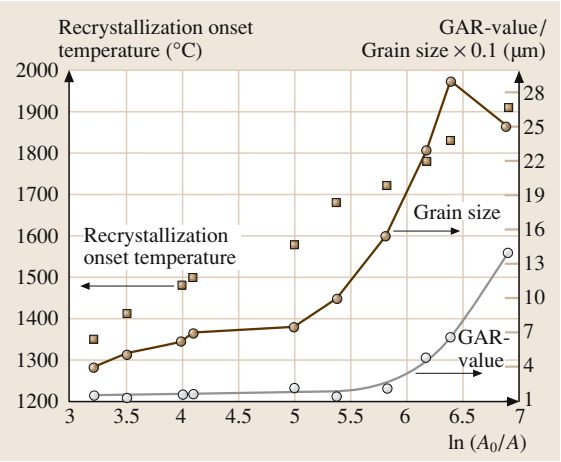


**Fig. 3.1-154** Recrystallization onset temperature, grain size, and grain aspect ratio (GAR) versus $\ln(A_0/A)$. AKS-W grade with K content of 42 μg/g; deformation temperature below the onset temperature of recrystallization; no intermediate heat treatments above recrystallization temperature; annealing time = 15 min; heating rate = 3 K/s; annealing atmosphere = hydrogen; annealing temperature for GAR evaluation = 2200 °C ($t_a$ = 5 min); grain size measured in transverse direction [1.133]

steps the increase of the driving forces outweighs that of the dragging forces. Then the rise of the dragging forces starts to dominate, resulting in an increase of the recrystallization temperature (see Fig. 3.1-154). With increasing length of the K stringers/number of K bubbles, the significance of the dragging effect in the transverse direction increases, resulting in an increase of the grain aspect ratio (GAR) in the recrystallized state. A marked increase of the GAR starts at a degree of deformation that coincides with a pronounced increase of the transverse grain size, as illustrated in Fig. 3.1-154.

### 3.1.9.4 Mechanical Properties

#### Influence of Thermomechanical Treatment (TMT) and Impurities

*Molybdenum and Tungsten Alloys [1.133].* The formation of a cellular dislocation structure increases both strength and fracture toughness [1.146, 147]. Additionally, the mechanical properties depend on the type of deformation process, purity, and heat treatment. The thermomechanical treatment (TMT) serves to obtain the specified shape, to eliminate the porosity, and to adjust the mechanical and structural properties. In particular, the evolution of the density distribution, pore size and shape, and its interaction with the mechanical properties are of high importance [1.120, 148–150].

During hot deformation which is usually the primary working step for both Mo and W, high-angle grain boundaries are formed and migrate, grains are subdivided by low-angle boundaries, and new large-angle boundaries are formed by coarsening of the substructure [1.151]. Grains with an aspect ratio close to one and a low dislocation density are formed.

Following this hot deformation, the material is processed at temperatures below the recrystallization onset temperature, but above the onset temperature of polygonization, leading to a cellular dislocation structure. The cell boundaries become impenetrable for slip dislocations and behave like grain boundaries, when the misorientation between neighboring cells is higher than a critical value of about 4° for Mo and W [1.146]. The formation of a misoriented cellular dislocation structure results both in an increase of strength and a decrease of the ductile-brittle-transition temperature (DBTT). Both effects become more and more significant with increasing degree of deformation which results in a smaller effective grain size [1.146]. The size of the misoriented cellular dislocation structure depends sensitively on the deformation temperature. A high deformation temperature implies large grains [1.152]. It is essential to control the deformation temperature carefully. The control of the microstructure at intermediate steps has also been recommended [1.153].

The production yield is mainly decreased by the formation of grain boundary cracks. The cohesion of the grain boundaries is believed to be the controlling factor limiting the ductility of Mo and W [1.154]. Impurities segregated at the grain boundaries can lead to a strong decrease in ductility. Based on both semi-empirical and first principle modeling of the energetics and the electronic structures of impurities on a Σ3 (111) grain boundary in W, it was concluded that the impurities N, O, P, S, and Si weaken the intergranular cohesion, while B and C enhance the interatomic interaction across the grain boundary [1.154].

The amount of O in Mo (≈ 10 μg/g) and W (≈ 5 μg/g) is sufficient to form a monolayer of O on the grain boundaries as long as the grain size is not smaller than 10 μm. During recrystallization a migrating grain boundary can be saturated by collecting impurities while sweeping the volume. Based on the investigation of arc-cast Mo samples, a beneficial effect of C was found and attributed to the following mechanisms [1.155]:

- Suppression of oxygen segregation
- Precipitation of carbides, acting as dislocation sources
- Formation of an epitaxial relationship between precipitates and bulk crystals at grain boundaries

From these findings it was proposed that a C/O atomic ratio of >2 should improve the mechanical properties of Mo. The results obtained with arc-cast samples published in [1.155] could not be reproduced for samples produced by a P/M route [1.157].

As a consequence of the above mentioned effects, but in contrast to many other metallic materials, the fracture toughness of Mo and W is strongly reduced with increasing degree of recrystallization. With increasing plastic deformation, the fracture toughness increases (see Sect. 3.1.9.4), combined with a transition from intercrystalline to transcrystalline cleavage and to a transcrystalline ductile fracture [1.147, 158, 159].

With increasing degree of deformation the working temperature can be progressively reduced. In particular, products with a high degree of deformation such as wires, thin sheets, and foils can be subjected to a high degree of deformation at a temperature below the polygonization temperature. The reduction of grain boundaries oriented transversely to the drawing direction increases the bending ductility of W [1.160]. Tungsten wire with an optimum ductility can only be obtained, when deformed in such a way that dynamic recovery processes occur without polygonization [1.161]. Other recovery phenomena, besides polygonization, are described in [1.162]. However a high degree of deformation below the onset temperature for dynamic polygonization favors the formation of longitudinal cracks.

Thin sheets and foils, annealed under conditions resulting in a small fraction of primarily recrystallized grains, can show a very specific fracture behavior, i. e., cracks running at an angle of 45° to the rolling direction [1.163, 164]. Such 45° embrittlement is caused by the nucleation of critical cracks at isolated grains formed by recrystallization of weak secondary components of the texture. Cracks propagate under 45° to the rolling direction owing to the alignment of the cleavage planes in the rolling texture.

*Niobium and Tantalum Alloys.* Contrary to Mo and W, pure Nb and Ta are deformed at room temperature. Only highly-alloyed materials require breaking down the ingot microstructure either by forging or extrusion at elevated temperatures. In these cases the ingot has to be protected to prevent an interaction with the atmosphere. The mechanical behavior of pure annealed Nb and Ta is characterized by a high ductility and low work-hardening rate. The influence of deformation on the yield strength and fracture elongation of pure Ta is shown in Fig. 3.1-155.

Mechanical properties of Nb- and Ta-based alloys are strongly influenced by interstitial impurities, e.g., oxygen, nitrogen, carbon, and hydrogen. The generally lower content of impurities and the larger grain size are the reasons why melt-processed Nb and Ta have a lower room-temperature tensile strength compared to sintered material. As an example, the influence of oxygen on the mechanical properties of Ta is presented in Fig. 3.1-156.

After deformation both Nb- and Ta-based alloys are usually heat treated in high vacuum before delivering in order to achieve a fine grained primarily recrystallized microstructure.

### Static Mechanical Properties

*Properties at Low Temperatures and Low Strain Rates.* The flow stress of the transition metals Mo, W, Nb, and Ta is strongly dependent on temperature and a strain rate below a characteristic transition temperature $T_K$ ("knee" temperature) (corresponding to 0.1 to 0.2 of the absolute melting temperature) and plastic strain rates below $1 \times 10^{-5}\,s^{-1}$ [1.165]. As an example, experimental data on the temperature dependence of the flow stress of recrystallized Ta are shown in Fig. 3.1-157. This dependence has

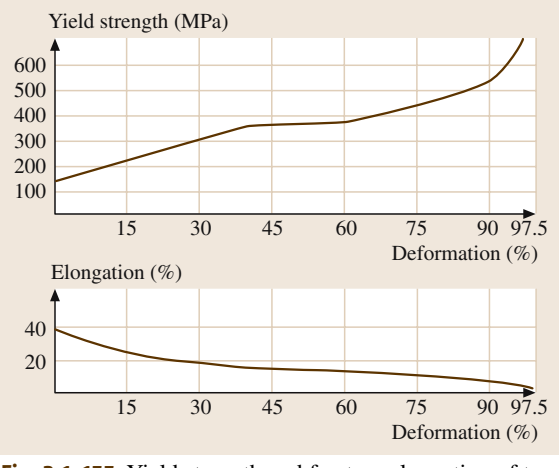


**Fig. 3.1-155** Yield strength and fracture elongation of tantalum versus degree of deformation [1.156]

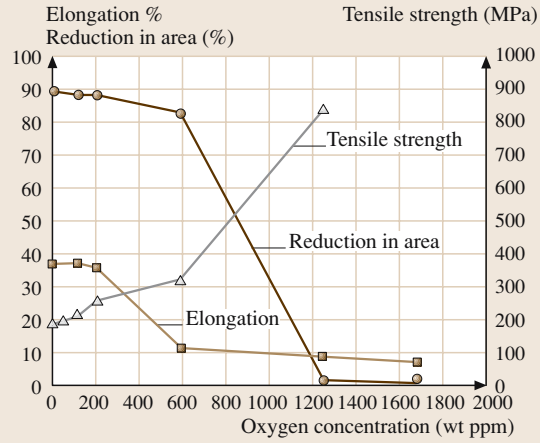


**Fig. 3.1-156** Tensile strength, fracture elongation, and reduction in area versus oxygen concentration of tantalum specimens tested at room temperature [1.168]

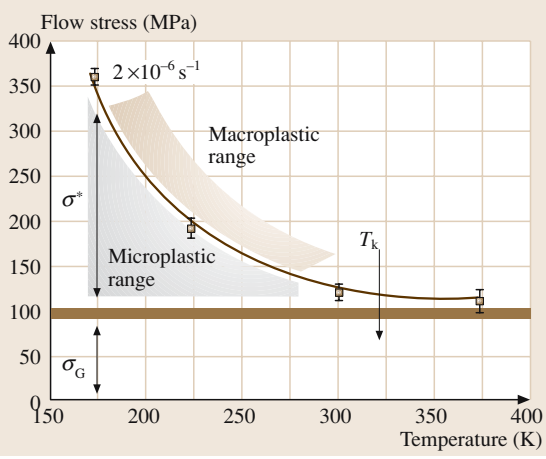


**Fig. 3.1-157** Temperature dependence of the flow stress (at $\varepsilon_{pl} = 1\times10^{-5}$) of recrystallized Ta under monotonic loading and $d\varepsilon/dt = 2\times10^{-6}\,s^{-1}$, $T_K$ = "knee" temperature, $\sigma_G$ = athermal range, $\sigma^*$ = thermal range [1.140]

been attributed to the characteristic behavior of screw dislocations [1.166]. The transition temperature $T_K$ was shown to depend on the strain rate (Fig. 3.1-158) [1.140, 167].

For test temperatures $T < T_K$ the flow stress increases markedly. Borderlines between elastic/anelastic strain ($\sigma_A$) and microstrain/macrostrain deformation ranges can be deduced, subdivided into athermal ($\sigma_G$) and thermal ($\sigma^*$) ranges. The lower borderline of the microplastic region is almost independent of temperature and may be called the intrinsic flow stress which is much lower than the conventionally determined flow stress (technical flow stress). In the stress range between the intrinsic and the technical flow stress below $T_K$, strains of up to several percent were observed after extended loading times for Mo and Ta [1.169, 170]. The effect of temperature and strain rate on the monotonic microflow behavior of bcc metals as functions of temperature and strain rate was presented schematically [1.171]. Experimental data for Mo and Ta in constant load tests (low temperature creep tests) for stresses considerably below the technical flow stress are shown in Figs. 3.1-159 and 3.1-160. After a considerable incubation period, depending on the test temperature and stress, a rapid increase in strain can be noticed approaching a saturation strain which depends on the stress level. The effect of the loading rate on the instantaneous plas-

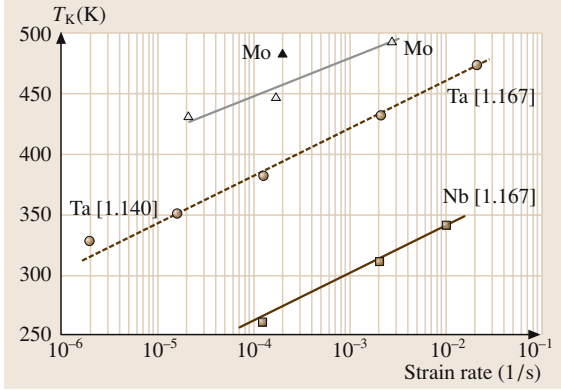


**Fig. 3.1-158** Dependence of $T_K$ on strain rate [1.140, 167]

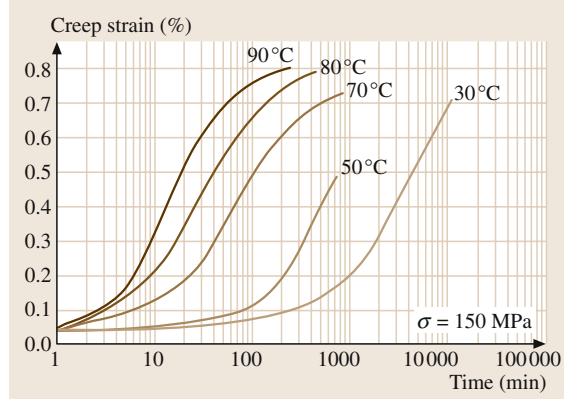


**Fig. 3.1-159** Creep elongation of recrystallized Mo at $\sigma$ = 150 MPa for 30 °C ≤ $T$ ≤ 90 °C [1.126]

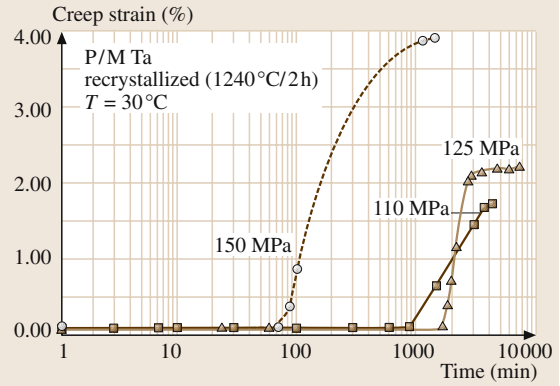


**Fig. 3.1-160** Creep elongation of recrystallized Ta sheets (thickness = 2 mm) at 30 °C for 110 MPa $\leq \sigma \leq$ 150 MPa [1.126]

tic strain can be revealed with high resolution in loading–unloading tests under various constant loading rates [1.140, 170]. This microflow behavior may be significant for components at low temperatures and low loads, e.g., under storage conditions. Internal stresses in semi-finished products may be reduced even at room temperature to levels corresponding to the intrinsic flow stress [1.170].

A significant influence of the strain rate on the tensile properties at room temperature was determined for recrystallized Mo and Ta (Fig. 3.1-161) [1.140], in close agreement with literature data [1.172]. This strain rate effect makes it imperative for comparison of test data to list the test conditions.

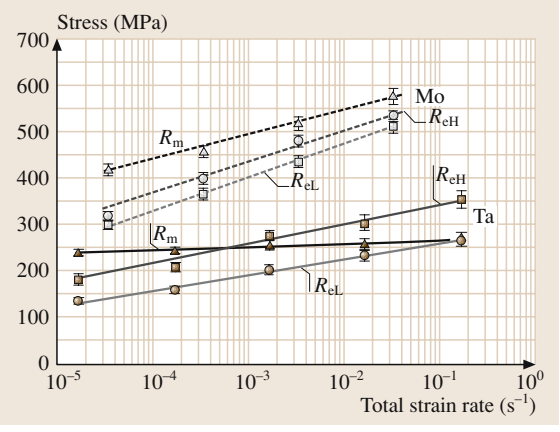


**Fig. 3.1-161** Effect of strain rate on tensile properties at room temperature of recrystallized Mo and recrystallized Ta [1.140]

*Properties at Elevated Temperatures.* A rough ranking of the high temperature strength of Mo and W alloys can be obtained from the comparison presented in Table 3.1-112 (Sect. 3.1.9.3). Carbide-precipitation-strengthened Mo-based alloys (MHC, TZM) and alloys high in Re (Mo–50 wt%Re, W–26 wt%Re) have the highest tensile strength. Alloys containing K (AKS–W, AKS−W−$ThO_2$) exhibit high strength only in the case of a high preceding plastic deformation.

A comparison of the high-temperature strength of rods made of Mo, W, Nb, and Ta in their usual state of delivery is given in Fig. 3.1-162. The typical microstructure of stress-relieved Mo is a highly polygonized structure with up to 5% recrystallized grains. Depending on the product shape W is delivered in the as-worked state, especially in case of sheet material and wires, or stress-relieved with a polygonized microstructure.

The decrease of tensile strength and the increase of reduction in area with increasing test temperature can be related to changes in the fracture mode (Fig. 3.1-163), i. e., cleavage fracture, brittle grain boundary failure, and ductile transcrystalline failure [1.158].

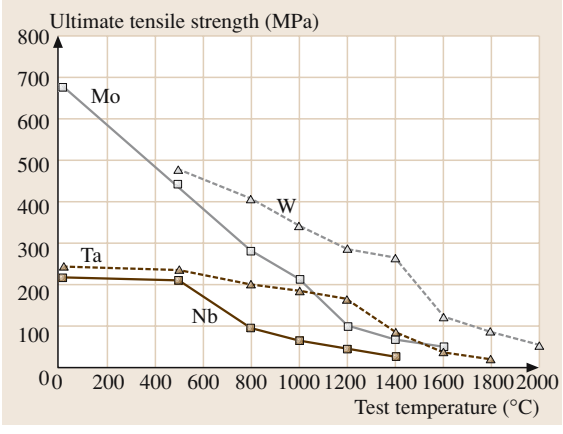


**Fig. 3.1-162** Ultimate tensile strength versus test temperature for Mo, W, Ta, and Nb rods in their usual delivering condition. Mo, W: diameter = 25 mm (stress relieved); Ta, Nb: diameter = 12 mm (recrystallized); technical strain rates = $1.0\times10^{-4}\,s^{-1}$ up to the 0.2% yield strength followed by $3.3\times10^{-3}\,s^{-1}$ (Mo, room temperature), $1.7\times10^{-3}\,s^{-1}$ (Mo, elevated temperatures), $8.3\times10^{-4}\,s^{-1}$ (W, elevated temperatures), $6.7\times10^{-4}\,s^{-1}$ up to the 0.2% yield strength followed by $3.3\times10^{-3}\,s^{-1}$ (Nb, Ta for all test temperatures) [1.118]

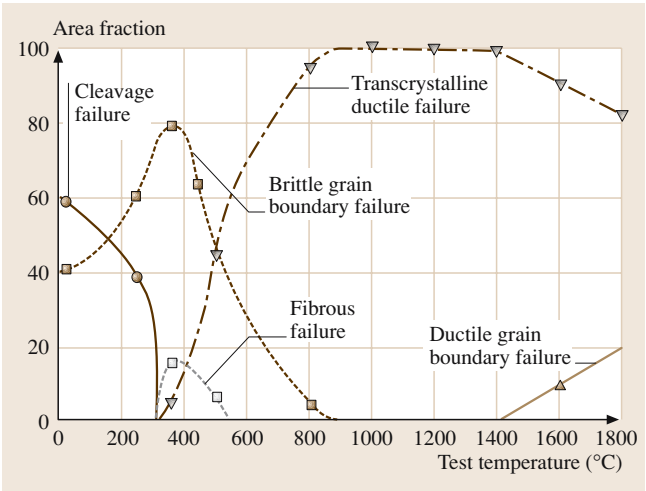


**Fig. 3.1-163** Effect of test temperature on fracture modes of pure W, stress relieved at 1000 °C/6 h [1.158]

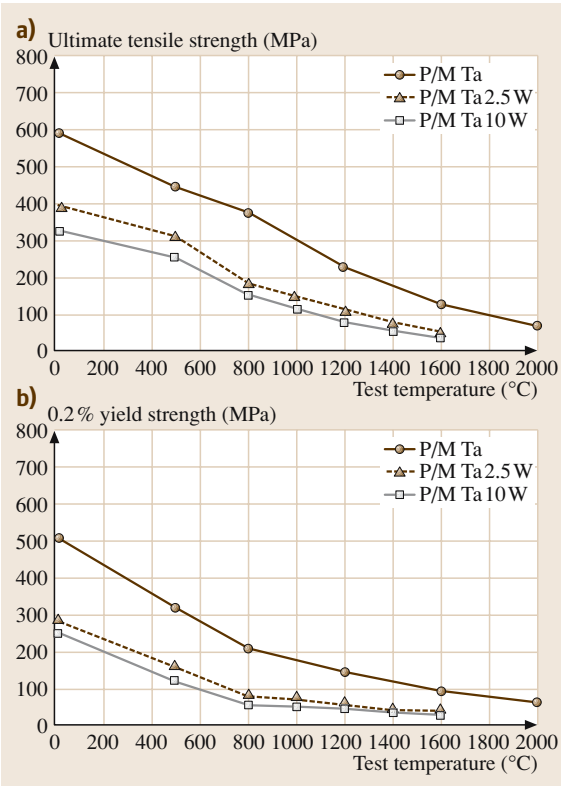


**Fig. 3.1-164a,b** The ultimate tensile strength $R_m$ **(a)** and the yield strength $R_{p0.2}$ **(b)** versus test temperature of P/M Ta, P/M Ta2.5W, and P/M Ta10W sheets that are 1 mm thick, with impurity content (μg/g) Ta: O = 60, N = 10, H = 1.8, C < 5; Ta2.5W: O = 70, N = 12, H = 2.4, C = 5; Ta10W: O = 31, N < 5, H < 1, C = 21; material condition = recrystallized, technical strain rates = $6.7\times10^{-4}\,s^{-1}$ up to $R_{p0.2}$, followed by $3.3\times10^{-3}\,s^{-1}$ [1.126]

The influence of alloying Ta with W is illustrated in Fig. 3.1-164 for Ta2.5W and Ta10W, which are the main commercial Ta-based alloys.

Figure 3.1-165 summarizes values of $R_{p0.2}$ of the most common Nb-based alloys at elevated temperatures. All of these alloys are hardened primarily by solid solution strengthening; however, small amounts of precipitates are present.

For comparison, the high-temperature strength of stress-relieved 1 mm sheets made of Mo- and W-based materials is shown in Fig. 3.1-166. For short-term application under high stresses, the precipitation-strengthened Mo alloys TZM and MHC offer the best performance up to a service temperature of 1500 °C. For higher temperatures, W-based materials should be applied. Tantalum-based alloys are used only if additional high ductility is required after cooling to room temperature.

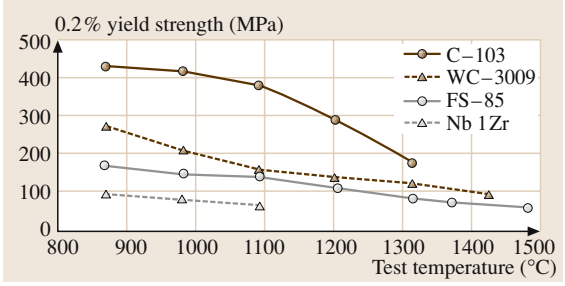


**Fig. 3.1-165** Effect of temperature on $R_{p0.2}$ for common Nb-based alloys [1.173]

## Dynamic Properties

*Microplasticity Effects under Cyclic Loading at Low Temperatures.* Microplasticity effects under monotonic loading have been reported in the literature for single- and polycrystalline Mo and Ta [1.171, 174]; information regarding effects of strain rate and temperature on the cyclic stress–strain response is given in [1.140, 170]. Most experiments on cyclic stress–strain behavior have

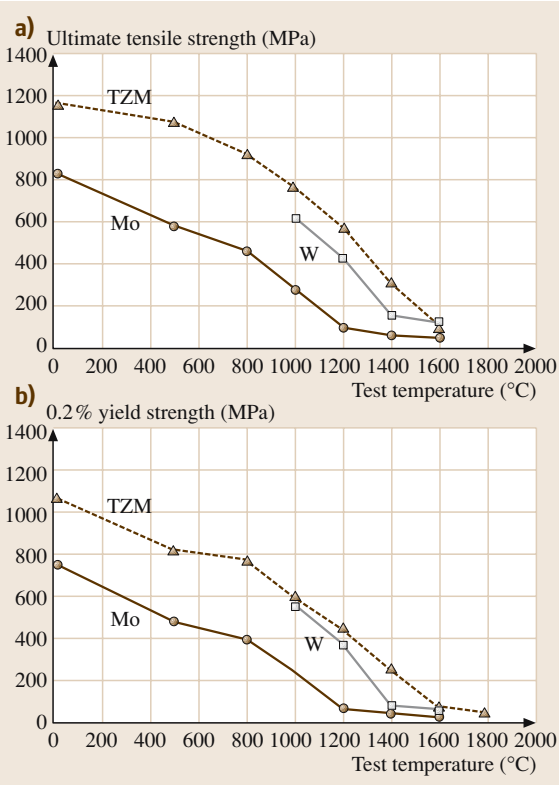


**Fig. 3.1-166a,b** The ultimate tensile strength $R_m$ **(a)** and the yield strength $R_{p0.2}$ **(b)** versus test temperature for Mo, TZM, and W sheets that are 1 mm thick. Material condition = stress relieved, technical strain rates = $2.0\times10^{-3}\,s^{-1}$ (Mo, TZM, room temperature), $1.3\times10^{-3}\,s^{-1}$ (Mo, TZM, elevated temperatures), $3.3\times10^{-4}\,s^{-1}$ up to $R_{p0.2}$, followed by $6.7\times10^{-4}\,s^{-1}$ (W, elevated temperatures) [1.126]

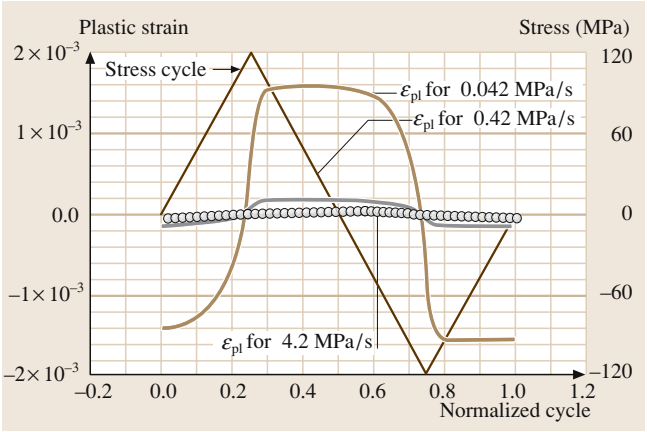


**Fig. 3.1-167** Effect of loading rate on cyclic plastic strain of recrystallized Ta during a tension-compression cycle ($R=-1$). Stress amplitude = 120 MPa; test temperature = 25 °C; duration of a cycle at 0.042 MPa/s = 190 min, at 4.2 MPa/s = 1.9 min; maximum plastic strain rate at all loading rates = approx. $3\times10^{-6}\,s^{-1}$ [1.140]

been carried out at room temperature. When bcc metals are deformed at $T < 0.2\,T_m$, microstrain ($\varepsilon_{pl} < 10^{-3}$) is characterized as the plastic strain, accommodated by the motion of non-screw dislocations [1.166, 169]. These differences are manifested in the temperature and strain-rate dependence of the flow behavior [1.171, 175]. Investigations of Mo and Ta showed that a true microplastic deformation can only be considered at plastic strains of less than $5\times10^{-4}$ [1.140]. The critical temperature below which the marked increase in the cyclic flow stress occurs is in the range of 25 °C to 80 °C for Ta and between 200 °C and 280 °C for Mo, depending on the strain rate. The experimental results for Ta showed that the highest cyclic plastic strains are obtained under strain rates between $1\times10^{-8}\,s^{-1}$ and $2\times10^{-6}\,s^{-1}$. As an example, the effect of the loading rate on the cyclic plastic strain of recrystallized tantalum during tension–compression cycles at loading rates between 0.042 MPa/s (duration of one cycle = 190 min) and 4.2 MPa/s (duration of one cycle = 1.9 min) is shown in Fig. 3.1-167 [1.140].

*High-Cycle Fatigue Properties.* Most of the fatigue data are reported in form of stress vs. number of cycles to failure (S–N) curves. For Mo a fatigue limit may be approached for $N > 10^7$ under stress-controlled conditions [1.176]. Experiments were conducted at test frequencies up to 20 kHz. The results of such tests should be considered with caution, taking into account the temperature and strain-rate sensitivity of bcc metals. Representative S–N curves for as-worked and recrystallized Mo, and a comparison of push–pull- and bending–fatigue-tested Mo sheet specimens are shown in Figs. 3.1-168 [1.126] and 3.1-169 [1.126].

The reported fatigue test data for various test methods are summarized in Table 3.1-114 with the fatigue limit ($S_e$) and the ratio of fatigue limit to tensile–stress ($S_e/R_m$) as characteristic parameters. Methods of statistical evaluation of test data were published [1.176, 177]. A decrease in fatigue limits with decreasing cyclic frequency was found.

Cyclic hardening/softening was deduced and cyclic stress–strain curves over wide ranges of plastic strain amplitudes were published in [1.178, 179] for Mo, in [1.172, 180, 181] for Ta, and in [1.182] for Nb and

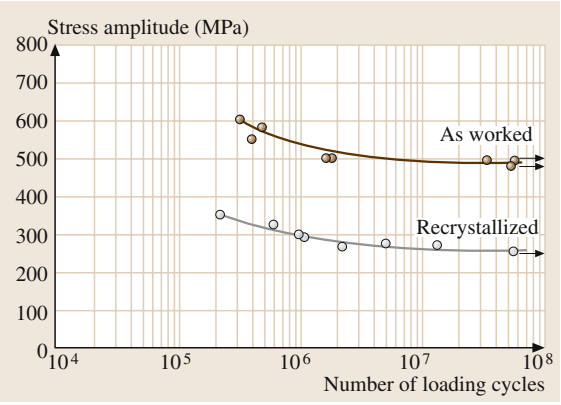


**Fig. 3.1-168** Rotating–bending fatigue test results for as-received and recrystallized Mo rods (diameter = 25 mm) at room temperature [1.126]

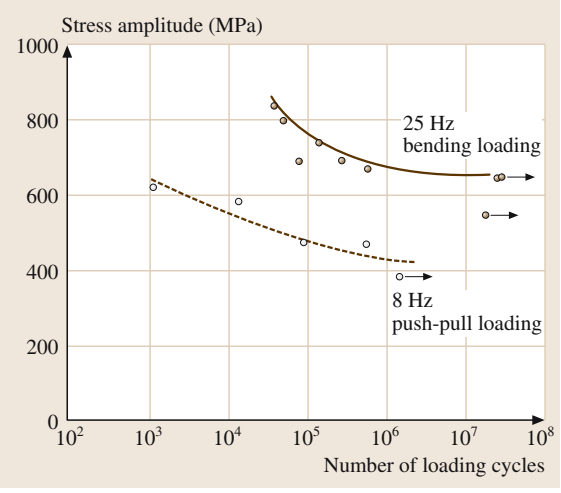


**Fig. 3.1-169** Comparison of test results of bending (at 25 Hz) and push–pull fatigue (at 8 Hz) tests of stress-relieved Mo sheet specimens (800 °C/6 h) [1.126] at room temperature

Nb1Zr. Cyclic stress–plastic-strain curves are given in Figs. 3.1-170 and 3.1-171 for Mo and Ta at various test temperatures. The ranges of microplastic and macroplastic strain can be differentiated, based on the different slopes.

The elevated temperature fatigue behavior of TZM was investigated for test temperatures between 300 °C and 500 °C [1.183]. Brittle failure under high cycle fatigue conditions was found over the entire temperature range, with a significant decrease in fatigue strength with increasing temperature.

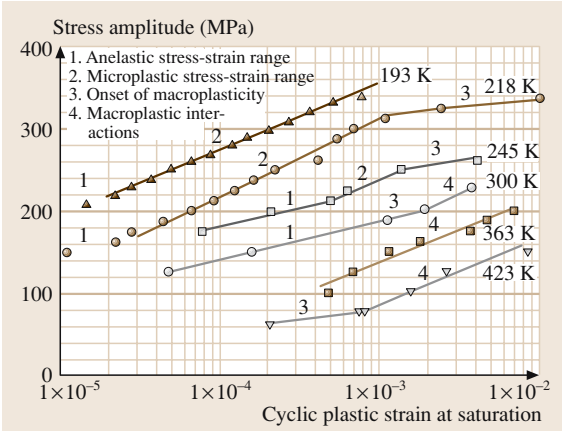


**Fig. 3.1-170** Cyclic-stress–plastic-strain curves of recrystallized Mo at different temperatures at a loading rate of 60 MPa/s [1.140]

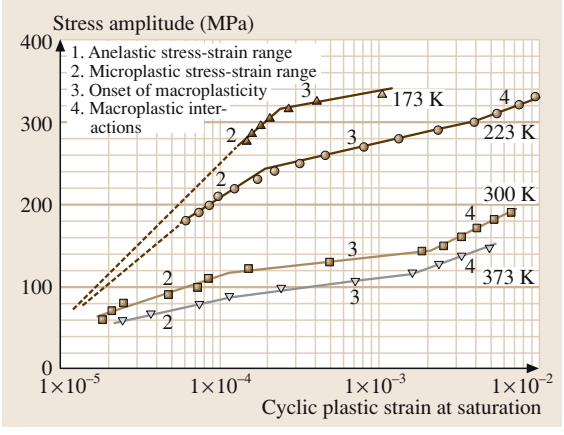


**Fig. 3.1-171** Cyclic-stress–plastic-strain curves of recrystallized Ta at different temperatures at a loading rate of 0.42 MPa/s [1.140]

*Low-Cycle Fatigue Properties.* Results of low-cycle fatigue experiments under strain control on as-worked W plate material at 815 °C are shown in Fig. 3.1-172. Low-cycle fatigue tests of pure W were performed in the temperature range between 1650 °C and 3300 °C [1.184]. A relationship $N_{\text{failure}} \approx \exp(-\alpha T)$ was found to be valid up to test temperatures of 2700 °C [1.185]. In all cases the failure mode was intercrystalline. Similar results were also obtained at a test temperature of 1232 °C [1.186]. The deformation behavior of Nb and Nb1Zr under plastic-strain control at room temperature was investigated and cyclic stress–strain curves published [1.182].

**Table 3.1-114** Summary of fatigue data of refractory metals, pretreatment: Aw = as worked, Sr = stress relieved, Rxx = recrystallized. RT = room temperature

| Test mode | Material | Production process | Dimension (mm) (plate: thickness, bar: diameter) | Pretreatment $T$(°C)/$t_a$ (h) | Test conditions, temperature, frequency | $S_e$ (MPa) | $S_e/R_m$ | Ref. |
|---|---|---|---|---|---|---|---|---|
| Rotating bending fatigue, $R = -1$, fatigue limit $S_e$ for 50% probability at $N = 5 \times 10^7$ | Mo | P/M | bar 12 | Aw<br>Rxx 1200/1 | RT, 100 Hz<br>RT, 100 Hz | 450<br>220 | 0.68<br>0.44 | [1.126] |
| | Mo5Re | P/M | bar 12 | Aw<br>Sr 900/6<br>Rxx 1300/1 | RT, 100 Hz<br>RT, 100 Hz<br>RT, 100 Hz | 450<br>400<br>230 | 0.68<br>0.68<br>0.48 | [1.126] |
| | Mo41Re | P/M | bar 12 | Aw<br>Sr 1050/6<br>Rxx 1400/1 | RT, 100 Hz<br>RT, 100 Hz<br>RT, 100 Hz | 690<br>620<br>320 | 0.62<br><br>0.36 | [1.126] |
| | TZM | P/M | bar 12 | Aw<br>Sr<br>Rxx 1500/1 | RT, 100 Hz<br>RT, 100 Hz<br>RT, 100 Hz | 550<br>560<br>340 | 0.62<br><br>0.57 | [1.126] |
| | W | P/M | bar 12 | Aw<br>Rxx 1600/1 | RT, 100 Hz<br>RT, 100 Hz | 760<br>310 | 0.48<br>0.70 | [1.126] |
| | W5Re | P/M | bar 12 | Aw<br>Rxx 1800/1 | RT, 100 Hz<br>RT, 100 Hz | 770<br>440 | 0.71<br>0.65 | [1.126] |
| | W26Re | P/M | bar 12 | Aw<br>Rxx 1700/1 | RT, 100 Hz<br>RT, 100 Hz | 820<br>450 | 0.54<br>0.39 | [1.126] |
| | W2ThO$_2$ | P/M | bar 12 | Rxx 1900/1 | RT, 100 Hz | 365 | 0.64 | [1.126] |
| | Nb | P/M | bar 5.9 | Aw<br>Rxx | RT, 100 Hz<br>RT, 100 Hz | 225<br>220 | 0.42<br>0.51 | [1.190] |
| | Ta | P/M | bar 5.9 | Aw<br>Rxx | RT, 100 Hz<br>RT, 100 Hz | 290<br>270 | 0.92<br>0.95 | [1.190] |
| Push-pull fatigue, $R = -1$, fatigue limit $S_e$ for $N = 1 \times 10^7$ | Mo | P/M | plate 1 | Rxx 1200/1 | RT, 0.05 Hz | 195 | | [1.179] |
| | TZM | P/M | bar 50 | Aw<br>Aw | RT, 25 Hz<br>850 °C, 25 Hz | 440<br>250 | | [1.191] |
| | Ta | | plate 2 | Aw<br>Aw<br>Rxx 1200/2<br>Rxx 1200/2 | RT, 0.05 Hz<br>RT, 10 Hz<br>RT, 0.05 Hz<br>RT, 10 Hz | 205<br>225<br>180<br>210 | | [1.179] |
| Bending fatigue, $R = -1$, fatigue limit $S_e$ for 50% fracture probability at $N = 1 \times 10^7$ | Mo | P/M | plate 2 | Aw<br>Sr 780/6<br>Rxx 1200/1 | RT, 25 Hz<br>RT, 25 Hz<br>RT, 25 Hz | 520<br>540<br>280 | | [1.126] |
| | Mo5Re | P/M | plate 1.6 | Sr | RT, 25 Hz | 460 | 0.56 | [1.126] |
| | Mo41Re | P/M | plate 1.6 | Sr | RT, 25 Hz | 680 | 0.61 | [1.126] |
| | TZM | P/M | plate 2 | Aw<br>Sr 1150/6<br>Rxx 1500/1 | RT, 25 Hz<br>RT, 25 Hz<br>RT, 25 Hz | 650<br>750<br>460 | | [1.126] |
| | W | P/M | plate 2 | Aw<br>Rxx 1600/1 | RT, 25 Hz<br>RT, 25 Hz | 520<br>225 | | [1.126] |
| | Ta | P/M | plate 1 | Aw<br>Rxx 1200/1 | RT, 25 Hz<br>RT, 25 Hz | 335<br>240 | 0.56<br>0.75 | [1.126] |
| | Ta | EB | plate 1 | Aw<br>Rxx 1200/1 | RT, 25 Hz<br>RT, 25 Hz | 270<br>220 | 0.61<br>0.96 | [1.126] |
| | Ta2.5W | P/M | plate 1 | Rxx 1300/1 | RT, 25 Hz | 310 | 0.79 | [1.126] |
| | Ta2.5W | EB | plate 1 | Rxx 1300/1 | RT, 25 Hz | 270 | 0.69 | [1.126] |
| | Ta10W | EB | plate 0.64 | Aw | RT, 25 Hz | 480 | | [1.168] |

**Table 3.1-114** (cont.) Summary of fatigue data of refractory metals, pretreatment: Aw = as worked, Sr = stress relieved, Rxx = recrystallized

| Test mode | Material | Production process | Dimension (mm) plate: thickness, bar: diameter | Pretreatment $T$(°C)/$t_a$ (h) | Test conditions, temperature, frequency | $S_e$ (MPa) | $S_e/R_m$ | Ref. |
|---|---|---|---|---|---|---|---|---|
| High-frequency push–pull fatigue, $R = -1$, fatigue limit $S_e$ for 50% fracture probability at $N = 10^8$ | Mo | P/M | bar 11 | Rxx 1300/4 | RT, 20 kHz | 278 | 0.56 | [1.176] |
| | TZM | P/M | bar 11 | Rxx 1600/2 | RT, 20 kHz | 383 | 0.69 | [1.176] |
| | Ta | EB | bar 3 | Aw<br>Sr | RT, 20 kHz<br>RT, 20 kHz | 383<br>286 | 0.72<br>0.92 | [1.126] |
| | Ta2.5W | P/M | plate 2 | Rxx | RT, 20 kHz | 300 | | [1.126] |
| | Ta10W | P/M | bar 12 | Rxx | RT, 20 kHz | 580 | | [1.126] |
| | Nb | | bar 3 | Aw<br>Rxx | RT, 20 kHz<br>RT, 20 kHz | 230<br>220 | 0.80<br>0.65 | [1.177] |

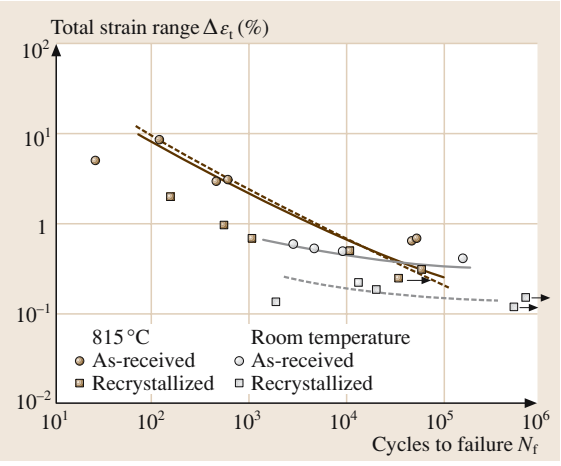


**Fig. 3.1-172** Low-cycle fatigue data of as-received and recrystallized W at room temperature and 815 °C [1.186]

Low-cycle fatigue test data of Mo at high test temperatures were reported in [1.187]. The influence of microstructural changes in cold-worked Mo on the low-cycle fatigue behavior was reported for test temperatures between 300 °C and 950 °C [1.188]. Deformation experiments under low-cycle fatigue conditions between room temperature and 100 °C showed that recrystallized Mo, in spite of the low temperature and stress level, exhibits considerable plastic strains which depend sensitively on the loading frequency [1.189]. Data on the high temperature (350 °C and 500 °C) isothermal mechanical fatigue behavior of TZM were reported and a model for lifetime prediction was proposed [1.183].

**Fig. 3.1-173** $K_{Ic}$ of forged Mo rods ($\varphi = 74\%$) versus degree of recrystallization [1.147]

## Fracture Mechanics Properties

*Fracture Toughness.* Fracture toughness properties are affected by many parameters (thermomechanical pretreatments, microstructure, specimen and crack plane orientation; testing procedures as well as the preparation of the starting notch and of the fatigue precrack). Due to the peculiarities of the P/M production process, it is frequently not possible to introduce sufficient deformation into products of larger dimension in order to completely eliminate sinter pores which may affect the dynamic properties. The increase of fracture toughness with increasing degree of hot working of disc-shaped compact tension specimens, cut from a hot forged Mo bar is shown in Fig. 3.1-173 and the decrease of fracture toughness with increasing fraction of recrystallized microstructure in Fig. 3.1-174 [1.147].

Fracture toughness data for Mo, TZM, and W materials are summarized in Table 3.1-115. Data taken at elevated temperature for Mo and W are shown in Fig. 3.1-175 [1.192], and for TZM in Fig. 3.1-176 [1.193]. Data for Nb could only

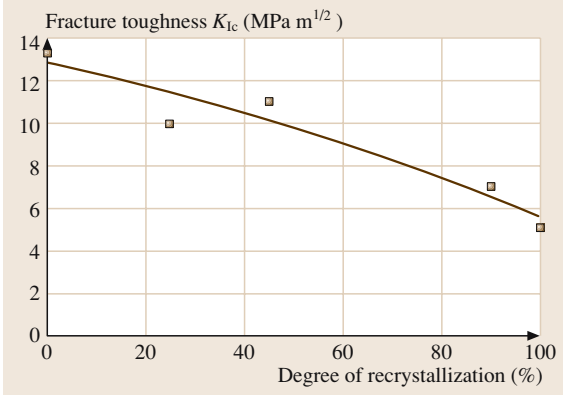

**Table 3.1-115** Fracture mechanical data for various refractory metals, pretreatment: Aw = as worked, Sr = stress relieved, Rxx = recrystallized. RT = room temperature

| Fracture toughness data | | | | Specimen type: CT compact tension, SCT center surface cracked tension, DCT disk-shaped compact tension, SNB side notched bend, CNT center through-thickness notched tension | | | | |
|---|---|---|---|---|---|---|---|---|
| **Material** | **Production process** | **Dimension (mm) plate: thickness, bar: diameter** | **Pretreatment $T$ (°C)/$t_a$ (h)** | **Specimen type** | **Crack plane ASTM 399** | **Test temperature** | **Fracture toughness (MPa m$^{1/2}$)** | **Ref.** |
| Mo | P/M | plate 6.5 | Rxx 1300/2 | CNT | L-T | RT | 9.5 | [1.126] |
| Mo | P/M | bar 50 | Sintered<br>Hot forged<br>Rxx 1400/2 | DCT<br>DCT<br>DCT | R-C<br>R-C<br>R-C | RT<br>RT<br>RT | 6<br>12<br>5 | [1.147] |
| Mo | VAC | plate 6.4 | Sr<br>Rxx<br>Sr<br>Rxx | CT<br>CT<br>CT<br>CT | L-T/T-L<br>L-T/T-L<br>L-T/T-L<br>L-T/T-L | RT<br>RT<br>300 °C<br>300 °C | 20/21<br>18/19<br>74/70<br>60/67 | [1.195] |
| Mo5Re | | bar 54 | Rxx 1300/1 | DCT | R-C | RT/450 °C | 18/27 | [1.193] |
| Mo–0.3 wt% $La_2O_3$ | P/M | plate | Sintered | CT | L-T | RT | 25 | [1.196] |
| TZM | VAC | plate 6.4 | Sr<br>Rxx<br>Sr<br>Rxx | CT<br>CT<br>CT<br>CT | T-L/L-T<br>T-L/L-T<br>T-L/L-T<br>T-L/L-T | RT<br>RT<br>300 °C<br>300 °C | 19/15<br>15/18<br>85/89<br>59/68 | [1.195] |
| TZM | P/M | bar 54<br>Machined to 12<br>Swaged to 12 | Aw<br>Aw<br>Rxx 1400/2 | DCT<br>SCT<br>SCT | R-C<br>L-C<br>L-C | RT<br>RT<br>RT | 19<br>37<br>19 | [1.159, 197] |
| W | | bar 10 | | SNB<br>SNB | C-R/L-R<br>C-R/L-R | −196 °C<br>RT | 11/6<br>13/8 | [1.198] |
| W | | bar 25 | Aw | SNB | R-L | RT/150 °C/<br>300 °C/500 °C | 9/10/13/14 | [1.199] |
| W | Single crystal | bar 16 (111)[011]<br>bar 16 (011)[100]<br>bar 16 (100)[001] | | SNB<br>SNB<br>SNB | | −196 °C/RT<br>−196 °C/RT<br>−196 °C/RT | 9/31<br>4/20<br>3/9 | [1.198] |
| W | | | Aw | SNB | | RT/400/600/<br>800 | 15/21/26/39 | [1.200] |
| W5Re | | | Aw | SNB | | RT/400 °C/<br>600 °C | 11/26/58 | [1.200] |
| W-1 wt% $La_2O_3$ | P/M | bar 25 | Aw | SNB | R-L | RT/150 °C/<br>300 °C/500 °C | 9/10/11/13 | [1.199] |
| Nb | | plate 1.25 | Sr<br>Rxx | CNT<br>CNT | L-T<br>L-T | −253 °C<br>−253 °C | 40<br>72 | [1.192] |
| Nb | | | Rxx<br>Rxx | SNB<br>SNB | | −196 °C<br>RT | 37<br>37 | [1.194] |

be determined below −200 °C [1.192]. Data on the impact and dynamic toughness of Nb between −196 °C and 25 °C were reported in [1.194]. The dynamic cleavage fracture toughness was shown to be 37 MPa m$^{1/2}$, relatively independent on grain size and test temperature.

**Table 3.1-115** Fracture mechanical data for various refractory metals, pretreatment: Aw = as worked, Sr = stress relieved, Rxx = recrystallized. RT = room temperature, cont.

| Fatigue crack growth and threshold data | | | | | Specimen type: CNT center through-thickness notched tension CCT corner cracked tension | | | | | SCT center surface cracked tension SNT side notched tension | | |
|---|---|---|---|---|---|---|---|---|---|---|---|---|
| Material | Production process | Dimension (mm) plate: thickness, bar: diameter | Pretreatment $T$ (°C)/$t_a$ (h) | | Specimen type | Crack plane ASTM 399 | Test conditions, temperature, frequency | Stress ratio $R$ | $da/dN$-range, (m/cycle) | $\Delta K_{th}$ | $\Delta K_{th,eff}$ | ASTM | Ref. |
| Mo | P/M | plate 6.5 | Rxx | 1300/2 | CNT | L-T | RT, 20 kHz | −1 | $10^{-13}$–$10^{-9}$ | 5.8 | | E647 | [1.126] |
| Mo | P/M | bar 12 | Aw | | SCT | L-C | RT, 20 kHz | −1 | $10^{-13}$–$10^{-9}$ | 11.3 | 11 | E647 | [1.159] |
| | | | Rxx | 1400/2 | | | | | | 10.7 | 11 | | |
| Mo | P/M | bar 12 | Sr | 850/1 | SNT | C-R | RT, 20 kHz | −1 | $10^{-13}$–$10^{-9}$ | 10.3 | 7.0 | E647 | [1.201] |
| | | | Rxx | 1400/2 | | | | | | 8.5 | 6.6 | | |
| TZM | P/M | bar 12 | Rxx | 1700/2 | SNT | C-R | RT, 20 kHz | −1 | $10^{-13}$–$10^{-9}$ | 10.1 | 6.3 | E647 | [1.201] |
| Mo5Re | P/M | bar 12 | Rxx | 1300/1 | SCT | L-C | RT, 20 kHz | −1 | $10^{-13}$–$10^{-9}$ | 11.4 | 9.9 | E647 | [1.126] |

20 kHz resonance test method, crack growth monitored by traveling light microscope,
$\Delta K_{th}$ corresponding to a crack growth rate of $da/dN < 10^{-13}$ m/cycle,
$\Delta K_{th,eff}$ calculated from crack closure measurements based on strain gauge method

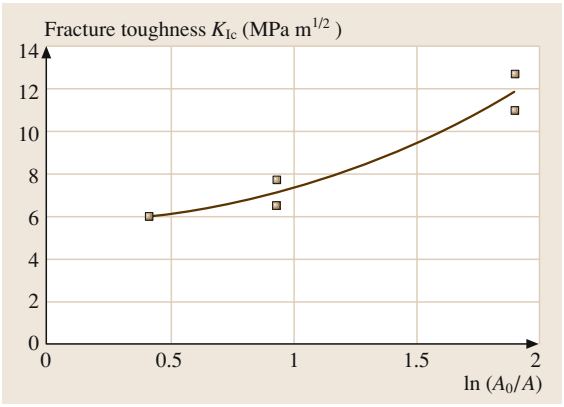


**Fig. 3.1-174** $K_{Ic}$ of forged Mo rods versus $\ln(A_0/A)$ [1.147]

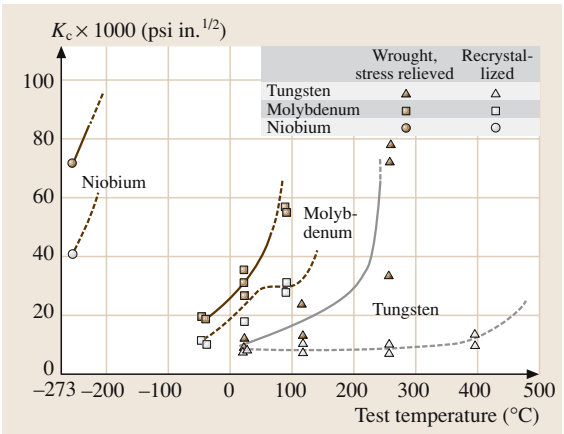


**Fig. 3.1-175** Effect of test temperature on fracture toughness of unalloyed W, Mo, and Nb sheet specimens [1.192]

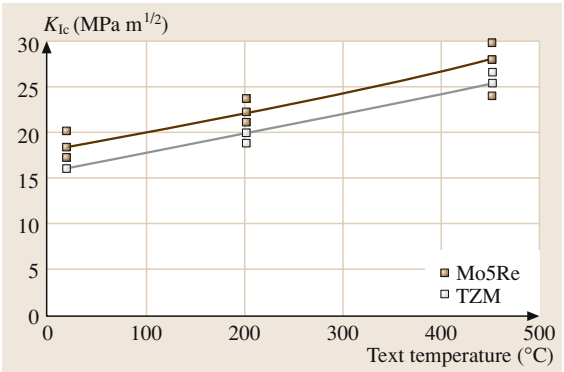


**Fig. 3.1-176** Effect of test temperature on static fracture toughness of TZM and Mo5Re specimens [1.193]

*Fatigue Crack Growth.* Few data on the linear region of crack growth were published for Ta10W (Fig. 3.1-177), and a Nb−W−Zr alloy [1.202, 203].

*Threshold Stress Intensity for Fatigue Crack Growth.* The fatigue crack growth behavior of Mo, TZM, and W in the region near the threshold stress intensity, $\Delta K_{th}$, considered to correspond to fatigue crack growth rates of $da/dN < 10^{-13}$ m/cycle, is shown in Fig. 3.1-178 [1.126]. The available crack growth and threshold data are included in Table 3.1-115.

An effective threshold value for fatigue crack growth, $\Delta K_{th,eff}$, can be computed. Methods for the determination of this effective threshold stress intensity range are described in [1.197]. The available data on $\Delta K_{th,eff}$ of Mo and TZM are listed in Table 3.1-115.

*Short Fatigue Crack Growth Behavior.* The nucleation and growth behavior of short fatigue cracks is of considerable practical and theoretical significance. Differences in the growth behavior exist between initial short cracks (length comparable with microstructural features) and long cracks of macroscopic dimensions. The irregular growth rate of such short cracks

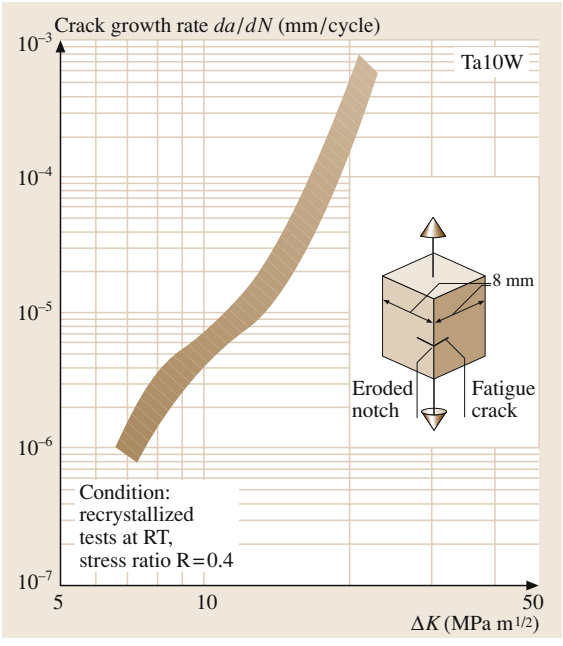


**Fig. 3.1-177** Crack propagation behavior of recrystallized P/M Ta10W specimens at room temperature at a stress ratio of $R = 0.4$ [1.202]

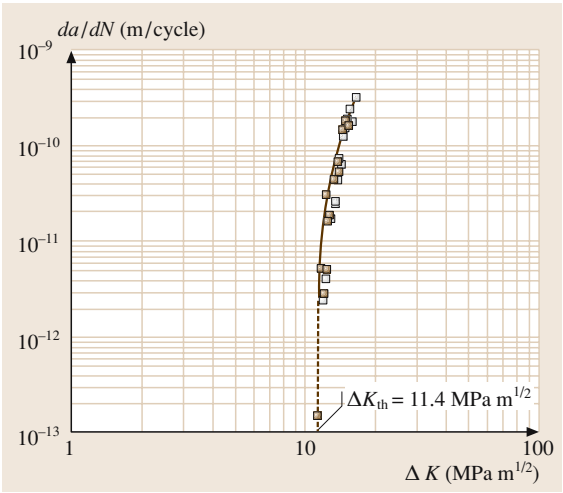


**Fig. 3.1-178** Crack growth curve near threshold stress intensity of a center surface cracked specimen machined from a recrystallized Mo5Re rod, tested at a stress ratio of $R = -1$, test temperature = 50 °C, and 20 kHz cyclic frequency; *open symbols* test under increasing load, *solid symbols* tests under decreasing load [1.126]

(Fig. 3.1-179) may pose problems for a conservative prediction of fatigue life [1.201]. Microscopic observations during fatigue exposure of specimens, loaded at stress amplitudes slightly above the fatigue limit, show initially a surface deformation very early in fatigue life, followed by short crack initiation and growth up to the final long crack growth. The number of fatigue cycles of the various stages depends on the microstructure and the presence of second phase particles (Fig. 3.1-180) [1.204].

It is known that fatigue failures occur in defect-containing materials after a high number of loading cycles ($N > 10^8$) at stresses considerably below the fatigue limit determined by conventional test procedures ($N < 10^7$). A fracture mechanics approach to this problem was proposed by *Kitagawa* et al. [1.205]. Based on a diagram relating a cyclic stress amplitude with crack length, a critical defect size ($a_t$) can be deduced which, when exceeded, causes a reduction of the fatigue strength. A modification of this diagram by introducing the value of the effective stress intensity range is shown in Fig. 3.1-181 [1.201]. Good agreement between predicted values and experimental results are obtained for hemispherical surface notches of various sizes [1.206, 207].

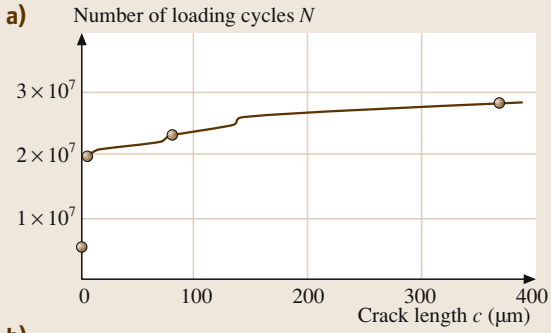


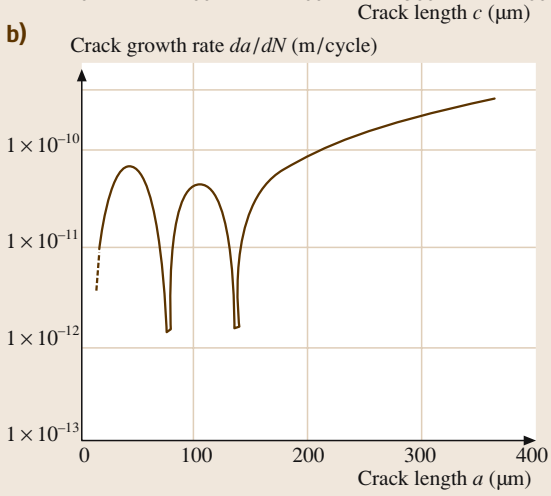


**Fig. 3.1-179a,b** Growth behavior of short surface cracks in a TZM specimen, tested at a stress amplitude of 375 MPa [1.201,204]. **(a)** Crack length as function of number of loading cycles. **(b)** Crack growth rate as function of crack length

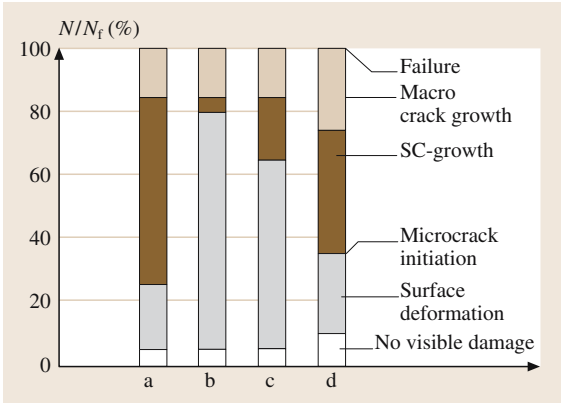


**Fig. 3.1-180** Fraction of total fatigue life spent on damage accumulation and crack growth in specimens of stress relieved Mo (a), recrystallized Mo (b), TZM with fine particles (c), and TZM with coarse particles (d) [1.204]

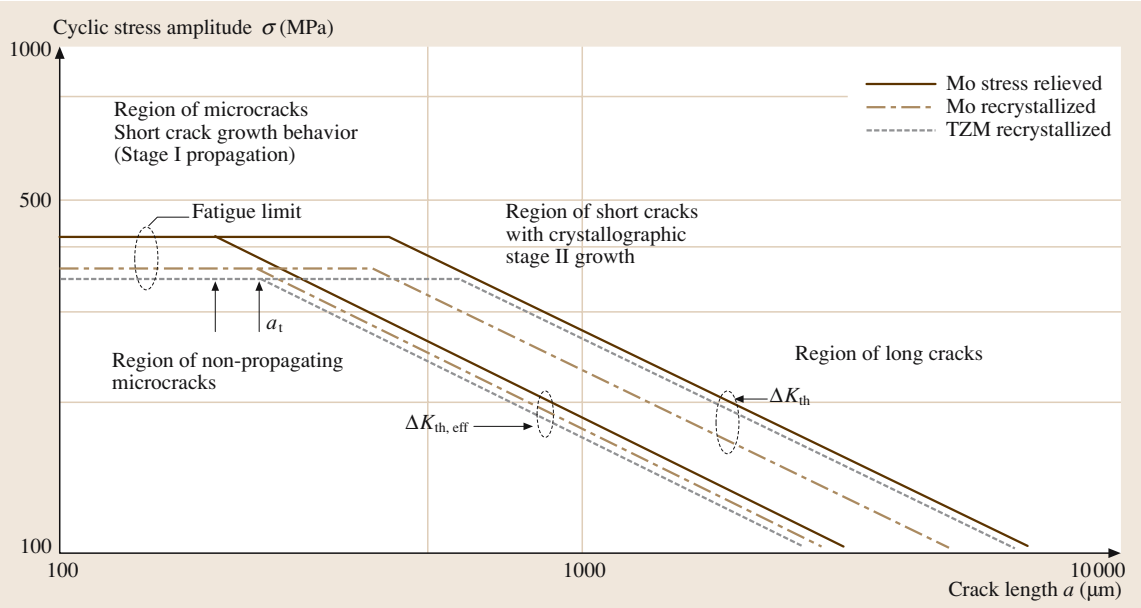


**Fig. 3.1-181** Effect of crack length on stress amplitude for crack growth in specimens of stress relieved Mo, recrystallized Mo, and recrystallized TZM (modified Kitagawa diagram) [1.201]

### Creep Properties

Creep-rupture data available up to 1970 were collected in [1.107]. The fairly wide scatter results from minor differences in microstructure, thermomechanical pretreatment, and impurity levels, but possibly also from impurities picked up from the environment in the high-temperature test systems. A summary of 10 000 h/1% creep data for Mo, W, and TZM is given in Fig. 3.1-182; the 100 h creep-rupture data for Mo, W, Nb, Ta, W25Re and TZM are given in Fig. 3.1-183, based on [1.107]. Up to 1100 °C the carbide-precipitation-hardened material TZM reveals the highest creep strength, only outperformed by Mo and W alloys precipitation hardened with hafnium carbide, which are not considered in these figures. Comparing the stress causing a steady state creep rate of $1 \times 10^{-4}$ /h, as illustrated in Fig. 3.1-184, it can be concluded that precipitation hardening is effective up to 1600 °C. At higher temperatures, the creep strength of TZM deteriorates to the level of Mo or even below. Above 1600 °C, W-based materials offer the best performance.

The influence of the microstructure on the creep mechanisms of Mo is illustrated in Fig. 3.1-185 for 1450 °C [1.208]. For a test stress of 35 MPa the steady state creep rate is almost independent of the grain size. In this stress regime a stress exponent of 5.4 was obtained, indicating dislocation creep as the rate-controlling mechanism. Lowering the test stress to 14 MPa and 7 MPa, grain-size-dependent creep mechanisms, such as diffusion creep and grain boundary sliding, become active, and as a consequence, the steady state creep rate increases with decreasing grain size [1.208].

The steady state creep rates of Mo rods made of VAC ingots, VAC and P/M Mo sheets, and P/M Mo–0.7 wt%$La_2O_3$ sheets are summarized in Fig. 3.1-186. Stress exponents of 4.3 (P/M Mo sheet/1800 °C), 4.5–4.7 (VAC Mo sheet/1600 °C), 4.6 (VAC Mo rod/1600 °C), 5.0 (Mo–0.7 wt% $La_2O_3$/1800 °C), and 5.5 (VAC Mo sheet/2200 °C) indicate that dislocation-controlled creep is rate-controlling in the stress regime investigated.

For AKS–W wires, used as lamp filaments, creep resistance is one of the most important requirements. The fine, K filled bubbles act as an effective barrier against dislocation movement, thereby reducing the deformation rate in the power-law creep

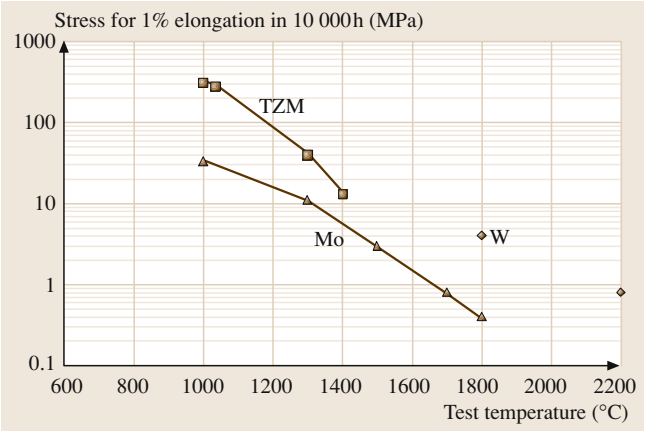


**Fig. 3.1-182** Comparison of 10 000 h/1% creep data for Mo, TZM, and W based on [1.107]

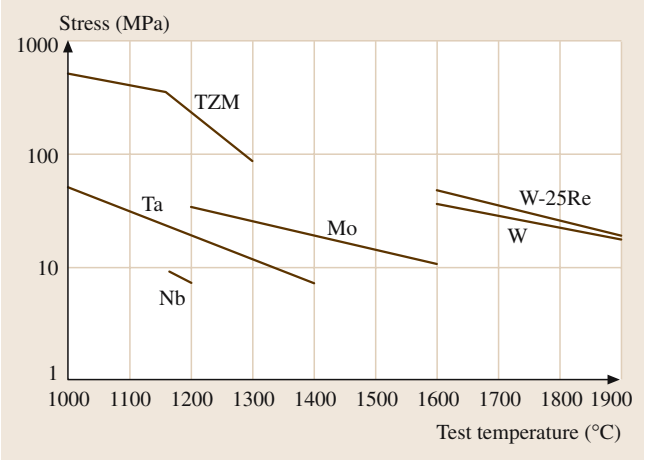


**Fig. 3.1-183** Comparison of 100 h of rupture data for selected refractory metals based on [1.107]

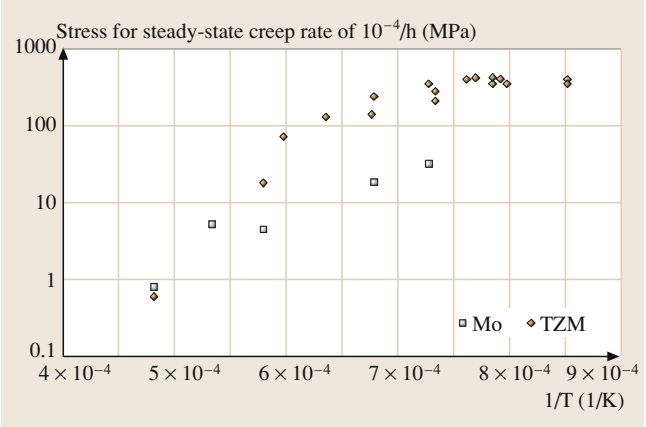


**Fig. 3.1-184** Stress for steady state creep rate of $1 \times 10^{-4}$ /h versus $1/T$ for Mo and TZM, deformed samples, various shapes [1.208]

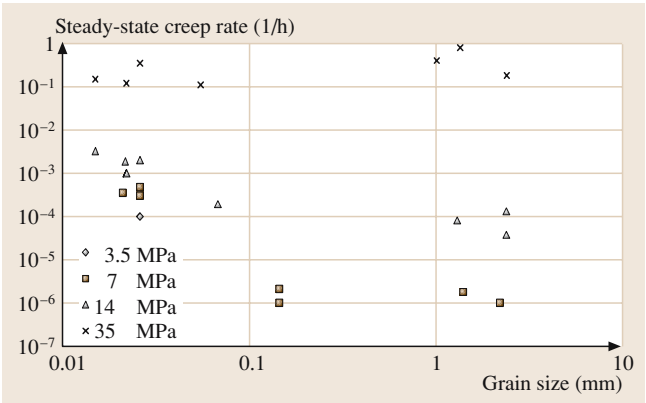


**Fig. 3.1-185** Steady state creep rate of molybdenum sheets versus grain size. Sheet thickness = 2 mm/6 mm; test temperature = 1450 °C; test atmosphere = hydrogen [1.208]

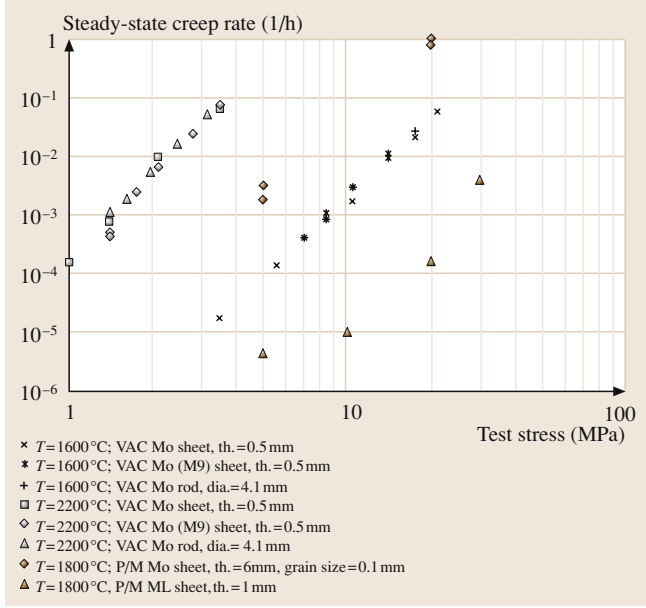


**Fig. 3.1-186** Steady state creep rate at various test temperatures of vacuum-arc-cast (VAC) Mo sheet (thickness = 0.5 mm), VAC Mo rod (diameter = 4.1 mm), P/M Mo sheet (thickness = 6 mm), and P/M ML (Mo–0.7 wt% $La_2O_3$) sheet, recrystallized (thickness = 1 mm) versus test stress [1.107, 208]

regime. Nabarro–Herring and/or Coble creep is suppressed because of the large diffusion distances in a structure with large, highly elongated grains. Grain boundaries resist sliding because of the interlocking structure. A comparison of creep rupture data of pure tungsten and two AKS–W grades with different grain aspect ratios (GAR) is given in Fig. 3.1-187.

In the high stress regime (> 60 MPa) and at temperatures between 2500 °C and 3000 °C, stress exponents between 8 and 25 were found [1.162,209,210]. This high stress dependence led to the introduction of a threshold stress ($\sigma_{th}$) below which a component does not reveal any measurable creep deformation under usual service conditions. For this threshold stress, which is lower than the Orowan stress, the detachment of the dislocations from the second phase particles or bubbles is the controlling factor [1.211,212].

In the second phase particle/metal matrix interface, the dislocation line energy is lower compared to the dislocation line energy in the metal matrix. Of all dispersion strengthened materials investigated, potassium bubbles in AKS–W exert the most attractive interaction on dislocations [1.213].

For material produced in the 1970s with a mean, but strongly scattered, grain aspect ratio of around 35, dislocation creep dominated at stresses > 60 MPa (stress exponent = 25), as can be seen in Fig. 3.1-188. For material produced 20 years later with a similar grain aspect ratio of 31, a stress exponent of 1.2 was found in the stress regime from 30 to 80 MPa, indicating a diffusion-controlled creep process [1.214]. The evaluation of the strain rate/stress dependence of the values

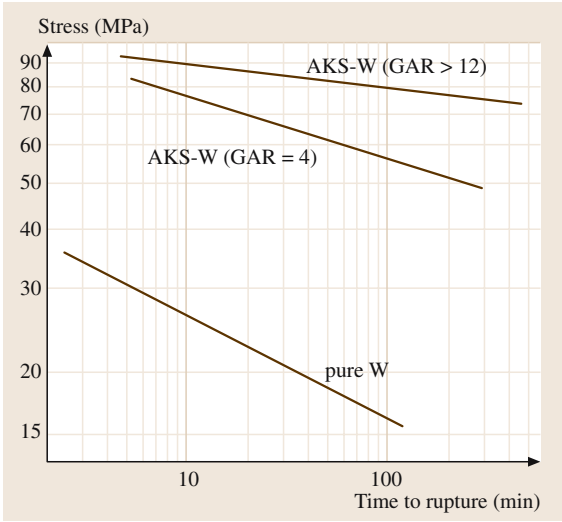


**Fig. 3.1-187** Creep rupture data for AKS–W wires in comparison with pure tungsten. Wire diameter = 0.183 mm; test temperature = 2527 °C; atmosphere = vacuum better than $7 \times 10^{-5}$ Pa; heating rate = approximately 2000 °C/s [1.162]

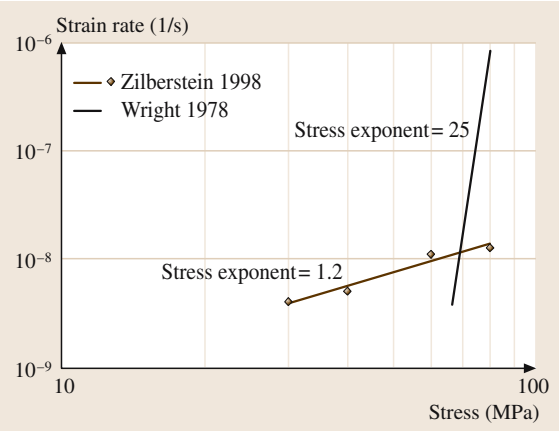


**Fig. 3.1-188** Strain rate versus stress for AKS–W wires tested at 2527 °C. *Wright* 1978 [1.162]: AKS–W wire with a diameter of 0.183 mm; atmosphere = vacuum better than $7 \times 10^{-5}$ Pa; heating rate = approximately 2000 °C/s; GAR = 35±10; pre-recrystallized at 2527 °C/10 min. *Zilberstein* 1998 [1.215]: AKS–W wire with a diameter of 0.178 mm; atmosphere = vacuum; GAR = 31±1; pre-recrystallized at 2527 °C/15 min

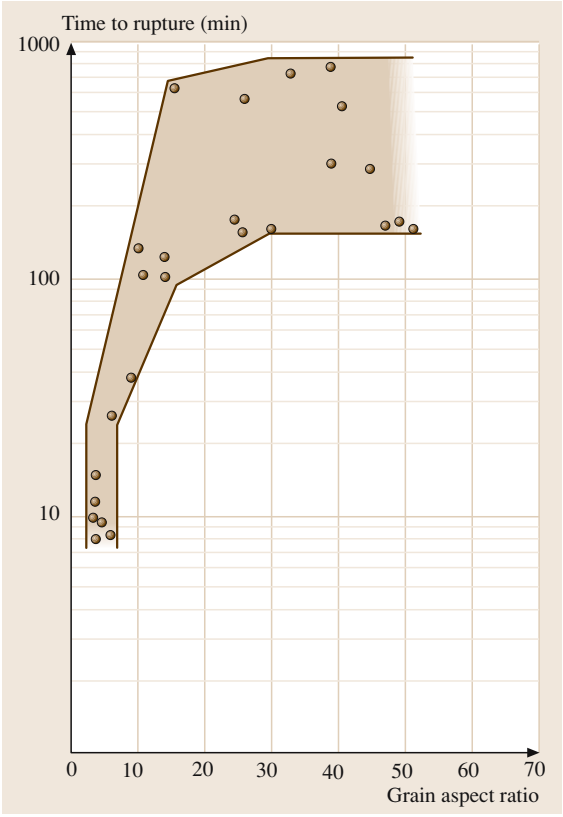


**Fig. 3.1-189** Time-to-rupture versus grain aspect ratio for AKS–W wires with a diameter of 0.183 mm. Test temperature = 2527 °C; test stress = 73.6 MPa; atmosphere = vacuum better than $7 \times 10^{-5}$ Pa; heating rate = approximately 2000 °C/s [1.162]

generated under vacuum also reveals a stress exponent close to 1 [1.215]. Data for the stress exponents are summarized in [1.113].

By lowering the grain aspect ratio, the transition temperature between dislocation and diffusion creep is shifted towards lower stresses. In the low GAR regime a strong dependence of the creep resistance on microstructural features can be observed, as grain boundary related phenomena, such as grain boundary sliding and diffusion creep resulting in cavitations become rate-controlling. The influence of the GAR on time to creep rupture is demonstrated in Fig. 3.1-189.

## 3.1.10 Noble Metals and Noble Metal Alloys

The noble metals Ag, Au, Pd, Pt, Rh, Ir, Ru, and Os are characterized by their positive reduction potentials against hydrogen, high densities, high melting temperatures, high vapor pressures (Fig. 3.1-190), high electrical and thermal conductivities, optical reflectivity (Fig. 3.1-191), and catalytic properties. The electronic density of states (DOS) near the Fermi surface is nearly the same for all noble metals. Individual differences of electrical conductivity, magnetic, and optical behavior are related to different positions of the Fermi level relative to the DOS function (Fig. 3.1-192). Small energy differences between their outer s and d electronic states result in multiple oxidation states.

Silver, Au, Pd, and Pt are comparatively soft and ductile. Their hardness increases in the order Rh < Ir < Ru < Os. Strengthening of the alloys is affected by solid solution and dispersion hardening. The corrosion resistance against different agents decreases in the order Ir > Ru > Rh > Os > Au > Pt > Pd > Ag.

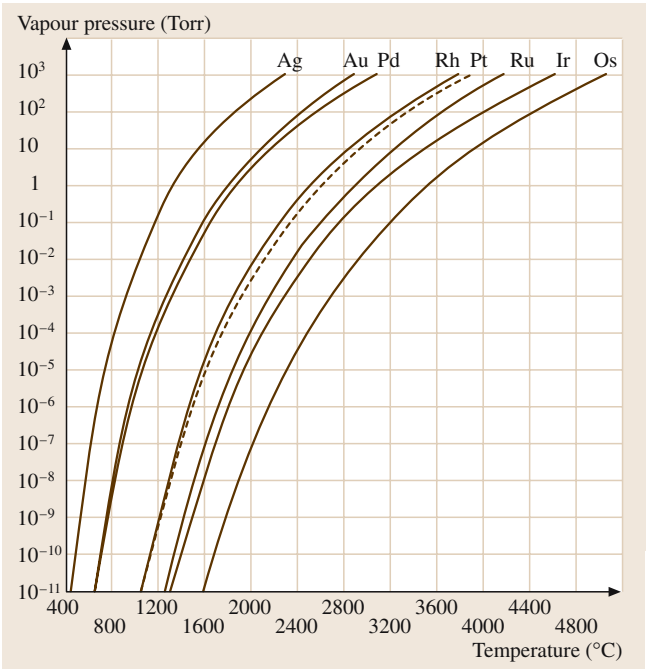


**Fig. 3.1-190** Vapour pressures of the noble metals [1.216, p. 43]

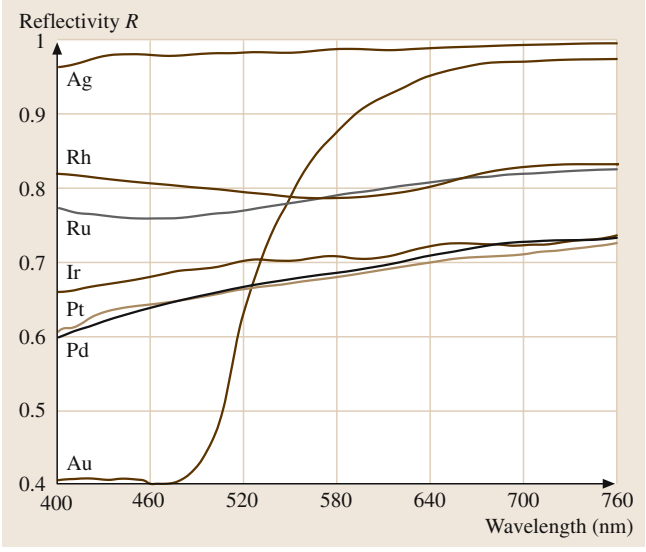


**Fig. 3.1-191** Optical reflectivity in the visible spectral range [1.217, p. 173]

The purity grades of the elements are standardized according to ASTM (American Society for Testing and Materials) standards from 99.8 to 99.999 wt%: Ag (B 413–69), Au (B 562–86), Pd (B 589–82), Pt (B 561–86), Rh (B 616–78), Ir (B 671–91), Ru (B 717).

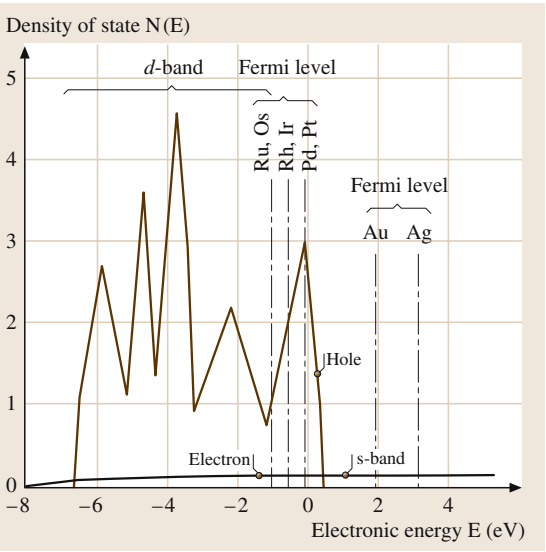


**Fig. 3.1-192** Schematic density of states (DOS) curve of the noble metals [1.218, p. 30]

The pure elements and their alloys are key materials in electronics and electrical engineering (Ag, Au, Pd, Pt, and Ru) and serve to manufacture high strength, corrosion-resistant, high temperature, and highly oxidation-resistant structural parts (Pt, Au, Rh, and Ir). The platinum group metals, Ag, and Au, in both the metallic state and in the form of chemical compounds are effective heterogeneous or homogeneous catalysts for a wide variety of chemical reactions. Traditional applications of noble metals and their alloys are in dentistry (Au, Pt, Ag, Pd, and Ir), jewellery (Au, Ag, Pt, Pd, Rh, and Ir), and in coins and medals (Au and Ag).

### 3.1.10.1 Silver and Silver Alloys

#### Application

Silver and silver alloys are used for electrical contacts, connecting leads in semiconductor devices, solders and brazes, corrosion-resistant structural parts, batteries, oxidation catalysts, optical and heat reflecting mirrors, table ware, jewellery, dentistry, and coins. Silver halides are base components in photographic emulsions.

#### Production

Silver is extracted from ores through lead melts and precipitation with zinc by the Parkes process. Zinc is removed by distillation, while the remaining lead

and base metals are removed by oxidation (cupellation) up to ≈ 99% Ag. True silver ores are extracted by cyanide leaching. High purity grades are produced by electrolysis. Bars, sheets, and wires are produced by classical metallurgical processing, powder by chemical and by electrolytic precipitation from solutions, and nano-crystalline powder grades by dispersion in organic solutions. Coatings and laminate structures are produced by cladding, by electroplating, in thick film layers by applying pastes of silver or in silver alloy powder with organic binder and glass frits onto ceramic surfaces and firing, in thin film coatings by evaporation, and by sputtering Composite materials are made by powder technology, or by infiltration of liquid Ag into sintered refractory metals skeletons. Commercial grades of Ag are listed in Table 3.1-116. Standard purities of crystal powder and bars range from 99.9% to 99.999 wt% (ASTM B 413-69) [1.217].

### Phases and Phase Equilibria

Selected phase diagrams are shown in Figs. 3.1-193–3.1-198 [1.219, 220]. Silver forms continuous solid solutions with Au and Pd, with miscibility gaps occuring in alloy systems with Mn, Ni, Os, P, Rh. Data for the solubility of oxygen are given in Table 3.1-117 [1.216]. Thermodynamic data are given in Tables 3.1-118–3.1-121. The entropy of fusion $(L/T)$ of completely disordered intermetallic phases can generally be calculated by fractional addition from those of the components. For the completely ordered state the term $-19.146\ (N_1 \log N_1 + N_2 \log N_2)$ is to be added to the calculated entropy of fusion [1.216–218, 221, 222]. The molar heat capacity of the homogeneous alloy phases and intermetallic compounds, as calculated approximately from the atomic heat capacities of the components using Neumann–Kopps' rule, is obeyed to within ±3% in the temperature range 0–500 °C in the Ag−Au, Ag−Al, Ag−Al, and Ag−Mg alloy systems. The heat capacities of heterogeneous alloys may be calculated by fractional addition from those of the components by the empirical relation $c_p = 4.1816(a + 10^{-3}bT + 10^5 cT^{-2})\,\mathrm{J/(K\,mol)}$ to satisfactory accuracy.

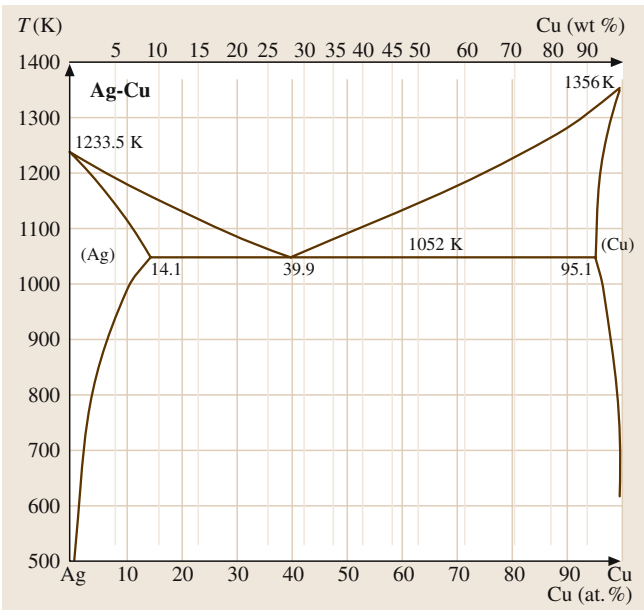


**Fig. 3.1-193** Binary phase diagram: Ag−Cu [1.219, p. 38]

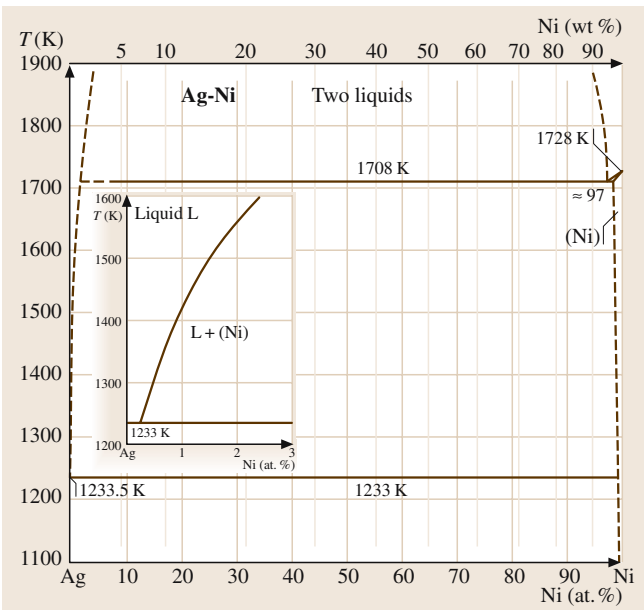


**Fig. 3.1-194** Binary phase diagram: Ag−Ni [1.219, p. 88]

**Table 3.1-116** Specifications of fine silver grades [1.217, p. 51]

| Designation | Grade (wt%) | Impurity | Maximum content (ppm) |
|---|---|---|---|
| "Good delivery" | > 99.9 | any, Cu | 1000 |
| Fine silver | > 99.97 | Cu/Pb/Bi/Se/Te | 300/10/10/5/5 |
| Fine silver 999.9 | > 99.99 | Cu/Pb/Bi/Se/Te | 100/10/10/5/5 |
| F. silver high pure | < 99.999 | Fe/Pb/Au/Cu/Cd/Bi/Se/Te | 2/1/1/1/0.5/0.5/0.5/0.5/0.5 |

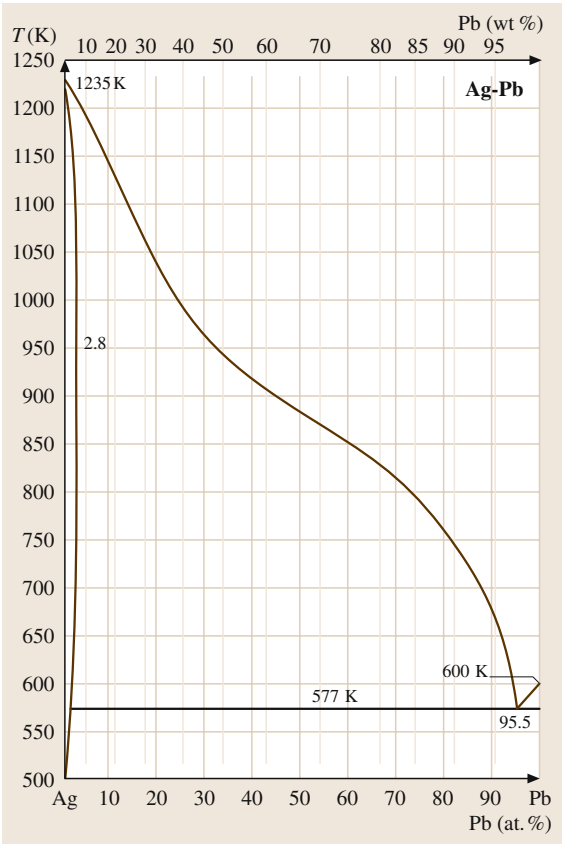


**Fig. 3.1-195** Binary phase diagram: Ag−Pb [1.219, p. 92]

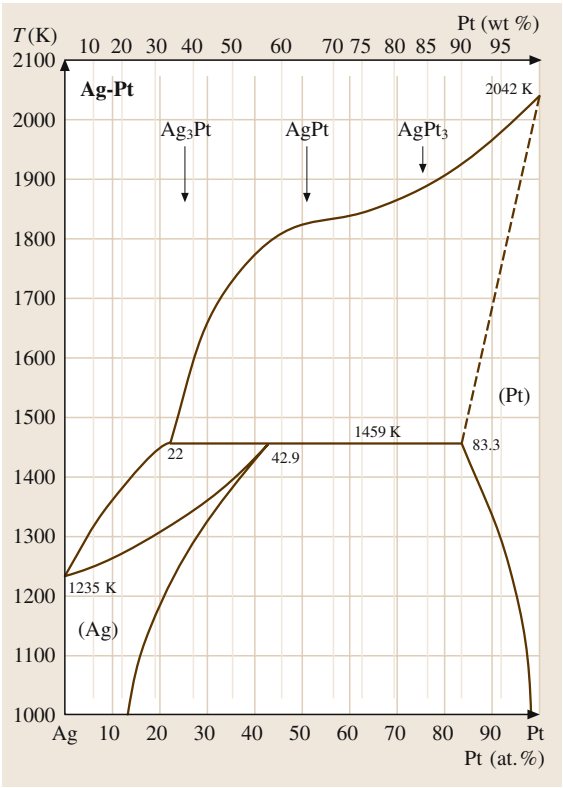


**Fig. 3.1-196** Binary phase diagram: Ag−Pt [1.219, p. 101]

**Table 3.1-117** Solubility $L$ (ppm) of oxygen in solid and liquid Ag ($O_2$ pressure 1 bar) [1.216, p. 57]

| $T$ (°C) | 200 | 400 | 600 | 800 | 973 | 1000 | 1200 |
|---|---|---|---|---|---|---|---|
| $L_{ppm}$ | 0.03 | 1.4 | 10.6 | 38.1 | 3050 | 3000 | 2500 |

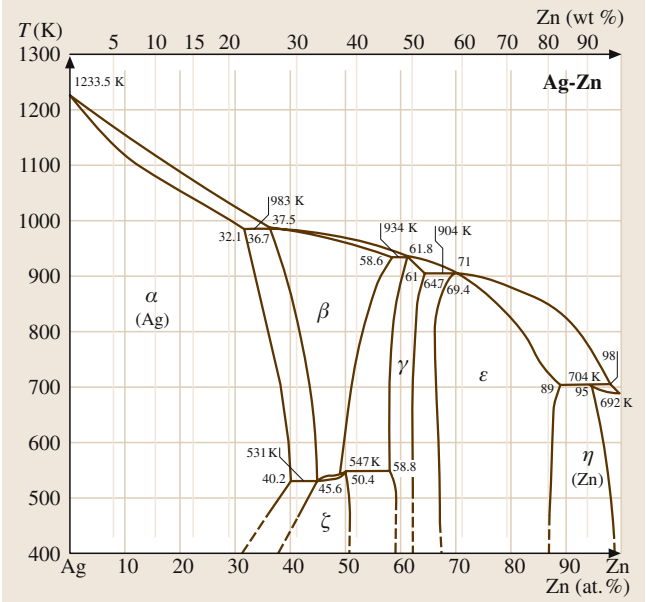


**Fig. 3.1-197** Binary phase diagram: Ag−Zn [1.219, p. 144]

**Table 3.1-119** Molar heat capacities of solid Ag and Au, $c_p = 4.1868\ (a + 10^{-3}bT + 10^{-5}T^{-2})$ J/K [1.222, p. 219]

| Element | *a* | *b* | *c* | Temperature range (K) |
|---|---|---|---|---|
| Ag | 5.09 | 2.04 | 0.36 | 298–mp* |
| Au | 5.66 | 1.24 | – | 298–mp* |

* = melting point

**Table 3.1-120** Latent heat and temperatures of transition of Ag and Au intermediate compounds [1.222, p. 189]

| Phase | $N_2$ | Transition | $T_t$ | $L_t$ |
|---|---|---|---|---|
| $\beta$-AgCd | 50 | $\beta'$–$\beta$ | 211 | 712 |
| AgZn | 50 | order–disorder | 258 | 2449 |
| AuCu | 50 | order–disorder | 408 | 1779 |
| $AuCu_3$ | 75 | order–disorder | 390 | 1214 |
| $AuSb_2$ | 66.7 | $\beta$–$\gamma$ | 355 | 335 |

$T_t$ = transition temperature, $L_t$ = latent heat of transition, $N_2$ = mole fraction of the second component

**Table 3.1-121** Latent heats and temperatures of fusion of Ag and Au intermediate compounds [1.222, p. 188]

| Phase | $N_2$ | $T_m$ (°C) | $L_m$ (hJ/g-at.) | |
|---|---|---|---|---|
| $\beta$-AgCd | 67.5 | 592 | 8.46 | 0.42 |
| $\gamma$-AgZn | 61.8 | 664 | 7.79 | 0.33 |
| AgZn | 72.1 | 632 | 8.75 | 0.42 |
| $\delta$-AuCd | 50.0 | 627 | 8.96 | 0.50 |
| AuSn | 50.0 | 418 | 12.81 | 0.33 |
| $\beta$-AuZn | 50.0 | 760 | 12.31 | 0.54 |

$N_2$ = mole fraction of the second component, $T_m$ = melting point, $L_m$ = Latent heat of fusion.

For compositions and crystal structures, see Tables 3.1-122–3.1-124 [1.217, 218, 223, 224]. Primary solid solutions have the fcc structure of Ag and the lattice parameters correspond roughly to Vegard's rule with a few exceptions. Alloys with Pt, In, Mg, Cd, and Zn form superlattice phases with tetrahedral and rhombohedral symmetry. A characteristic series of structures of intermetallic phases are formed with B-metals at compositions corresponding to e/a values (valence electrons per atom) of 3/2, 21/13, and 7/4 (Hume-Rothery phases) [1.225].

**Table 3.1-118** Thermodynamic data of Ag [1.217, p. 107]

| *T* (K) | $c_p$ (J/K mol) | *H* (J/K mol) | *S* (J/mol) | *G* (J/mol) | *p* (at) |
|---|---|---|---|---|---|
| 298.15 | 25.397 | 42.551 | 0 | −12.687 | $1.09 \times 10^{-43}$ |
| 400 | 25.812 | 50.069 | 2.606 | −17.421 | $5.02 \times 10^{-31}$ |
| 800 | 28.279 | 68.661 | 13.392 | −41.537 | $1.45 \times 10^{-12}$ |

$T$ = Temperature, $c_p$ = specific heat capacity, $S$ = Entropy, $H$ = Enthalpy, $G$ = free Enthalpy, $p$ = partial pressure of the pure elements

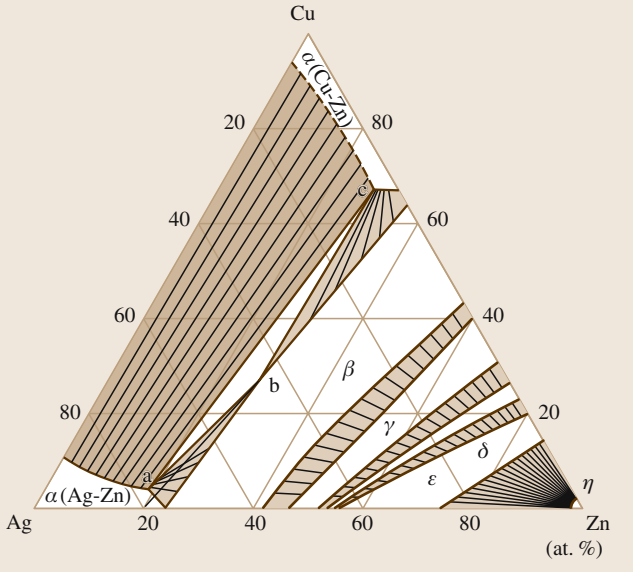


**Fig. 3.1-198** Ternary phase diagram: Ag−Cu−Zn [1.220, p. 153]

| Phase | Pearson symbol | *a* (nm) | *b* (nm) | *c* (nm) | *c*/*a* | Remarks | Concentration *x*: A(1 − *x*)B(*x*) |
|---|---|---|---|---|---|---|---|
| Ag–Al | cF4 | 0.4064 | | | | | 0.18 |
| $Ag_2Al$ | hP2 | 0.28777 | | 0.46223 | 1.6062 | | |
| Ag–Cd | hP2 | 0.2987 | | 0.553 | 1.8514 | | 0.97 |
| AgCd | cP2 | 0.3332 | | | | 293 K | 0.5 |
| AgCd | hP2 | 0.3016 | | 0.4863 | 1.6124 | 673 K | 0.5 |
| Ag–Cu | cF4 | 0.3603 | | | | | 0.95 |
| Ag–Mg | cF4 | 0.4116 | | | | | 0.26 |
| Ag–Mg | hP2 | 0.3197 | | 0.51838 | 1.6215 | | 0.98 |
| AgO | cF8 | 0.4816 | | | | | |
| AgO | mP8 | 0.5852 | 0.3478 | 0.5495 | | | |
| Ag–O | cP6 | 0.4728 | | | | | |
| Ag–O | hP3 | 0.3072 | | 0.4941 | 1.6084 | HP/HT | |
| Ag–Zn | hP2 | 0.28227 | | 0.44274 | 1.5685 | | 0.775 |
| Ag–Zn | hP9 | 0.7636 | | 0.28179 | 0.369 | | 0.38–0.52 |

HT = High-temperature modification, HP = High-pressure modification

**Table 3.1-122** Structure and lattice parameter of intermediate Ag compounds [1.217, p. 112]

| Atomic ratio | Composition | | | | Superlattice structure | Fundamental structure |
|---|---|---|---|---|---|---|
| 3:1 or 1:3 | $Pd_3Fe$ | $PdCu_3$ | $Au_3Cu$ | $AuCu_3$ | | |
| | $Pt_3Fe$ | $PtCu_3$ | $Au_3Pd$ | | | |
| | $Pt_3Ti$ | $PtNi_3$ | $Ag_3Pt$ | | $L1_2$ | fcc |
| | | $PtMn_3$ | | | | |
| | $Rh_3Mo$ | | $Ag_3In$ | | | |
| | $Rh_3W$ | | | | $DO_{14}$ | |
| | $Ir_3Mo$ | | | | | |
| | $Ir_2W$ | | $(Au_2Mn)$ | | $DO_{22}$ | fcc |
| | $Pd_3V$ | | | | | |
| | $Pd_3Nb$ | | | | | |
| | $Pt_3V$ | | | | | |
| | | | $Au_3Cd$ | | $DO_{23}$ | fcc |
| | | | $Au_3Zn$ | | | |
| | | | $Ag_3Mg$ | | | |
| 2:1 | $Pd_2V$ | | | | $Ni_2Cr$ | fcc |
| | $Pt_2V$ | | | | | |
| | $Pt_2Mo$ | | | | | |
| 1:1 | PdFe | | AuCu | | | |
| | PtFe | | | | $L1_0$ | fcc |
| | PtV | | | | | |
| | PtNi | | | | | |
| | PtCo | | | | | |
| | PtCu | | | | | fcc |
| | PdCu | | AuMn | | $L1_1$ | bcc |
| | | | AgCd | | $L2_0$ or B2 | |
| | | | AgZn | | | |
| | RhMo | | | | | hcp |
| | IrMo | | | | B19 | |
| | PtMo | | | | | |
| | IrW | | | | | |
| | PtNb | | | | | |

**Table 3.1-123** Composition and structures of superlattices in NM-alloy systems [1.218, p. 105]

**Table 3.1-124** Compositions and structures of $e/a$ (Hume-Rothery) compounds [1.225, p. 197]

| Electron: atom ratio = 3:2 | | | Electron: atom ratio = 21:13 | Electron: atom ratio = 7:4 |
|---|---|---|---|---|
| Body-centered cubic structure | Complex cubic ($\beta$-manganese) structure | Close-packed hexagonal structure | $\gamma$-brass structure | Close packed hexagonal structure |
| AgMg | AgHg | AgZn | $Ag_5Zn_8$ | $AgZn_3$ |
| AgZn | $Ag_3Al$ | AgCd | $Ag_5Cd_8$ | $AgCd_3$ |
| AgCd | $Au_3Al$ | $Ag_3Al$ | $Ag_5Hg_8$ | $Ag_3Sn$ |
| $Ag_3Al$ | | $Ag_3Ga$ | $Ag_9In_4$ | $Ag_5Al_3$ |
| $Ag_3In$ | | $Ag_3In$ | $Au_3Zn_8$ | $AuZn_3$ |
| AuMg | | $Ag_5Sn$ | $Au_5Cd_8$ | $AuCd_3$ |
| AuZn | | $Ag_7Sb$ | $Au_9In_4$ | $Au_3Sn$ |
| AuCd | | $Au_3In$ | $Rh_5Zn_{21}$ | $Au_5Al_3$ |
| | | $Au_5Sn$ | $Pd_5Zn_{21}$ | |
| | | | $Pt_5Be_{21}$ | |
| | | | $Pt_5Zn_{21}$ | |

### Mechanical Properties

In Tables 3.1-125–3.1-135 and Figs. 3.1-199–3.1-204 characteristic data are shown [1.217,220,225–229]. References for data of elastic constants of Ag alloys are given in [1.222]. Pure silver is very soft. Strengthening is affected by solid solution and by dispersion hardening [1.216,230]. Alloying with 0.15 wt% Ni affects grain refinement and stabilizes against recrystallization. The high solubility of oxygen in silver (Table 3.1-117) permits the inducement of dispersion hardening by internal oxidation of Ag alloys containing Al, Cd, Sn, and/or Zr.

**Table 3.1-125** Module of elasticity of Ag in crystal directions (GPa) [1.217, p. 204]

| $E\langle 100\rangle$ | $E\langle 110\rangle$ | $E\langle 111\rangle$ |
|---|---|---|
| 44 | 82 | 115 |

**Table 3.1-126** Elastic constants of Ag (GPa) [1.217, p. 204]

| $T$ (°C) | c11 | c12 | c14 |
|---|---|---|---|
| −273 | 131.4 | 97.3 | 51.1 |
| +20 | 124.0 | 93.4 | 46.1 |

**Table 3.1-127** Mechanical properties of Ag (99.97%) at different temperatures (°C) [1.217, p. 204]

| $T$ (°C) | $E$ (GPa) | $R_m$ (MPa) | $A$ (%) | $R_{p0.2}$ (MPa) | HV |
|---|---|---|---|---|---|
| 20 | 82 | 150 | 50 | 28 | 26 |
| 200 | 77 | 130 | – | 25 | 22 |
| 400 | 67 | 100 | 30 | 20 | 17 |
| 800 | 46 | 35 | – | 17 | 5 |

$A$ = Elongation, $E$ = Module of elasticity, $R_p$ = Limit of proportionality, HV = Vickers hardness, $R_m$ = Tensile strength

**Table 3.1-128** Tensile strength $R_m$ (MPa) of binary Ag alloys [1.217, p. 207]

| Content (wt%) | 2 | 5 | 10 | 20 |
|---|---|---|---|---|
| Alloying elements | $R_m$ (MPa) | | | |
| Au | 160 | 170 | 180 | 200 |
| Cd | 160 | 170 | 180 | 210 |
| Cu | 190 | 240 | 280 | 310 |
| Pd | 160 | 180 | 21 | |
| Sb | 190 | 240 | 300 | |
| Sn | 190 | 240 | 300 | |

**Table 3.1-129** Hardness of Ag–Mn alloys [1.226, p. 473]

| wt% Mn | 0.5 | 4.9 | 6.2 | 12.0 |
|---|---|---|---|---|
| HV (kg/mm$^2$) | 31 | 39 | 40 | 58 |

**Table 3.1-130** Mechanical properties of Ag–Cu–P alloys [1.226, p. 477]

| Composition (wt%) | | | BS[a] | Density | Melting range | Tensile strength | Elongation |
|---|---|---|---|---|---|---|---|
| Ag | Cu | P | 1845 | (g/cm$^3$) | (°C) | (kg/mm$^2$) | (%) |
| 15 | 80 | 5 | CP1 | 8.40 | 645–719 | 25 | 10 |
| 5 | 89 | 6 | CP4 | 8.20 | 645–750 | 25 | 5 |
| 2 | 91 | 7 | CP3 | 8.15 | 645–770 | 25 | 5 |

[a] = British standard (1966/1971) designation

| Composition (wt%) Cu | Zn | Ag | Specific weight (cast) | Tensile strength (kg/mm²) | Elongation (%) | Electrical conductivity (% of Cu) |
|---|---|---|---|---|---|---|
| 36 | 24 | 40 | 9.11 | 40.5 | 6.2 | 19.7 |
| 25 | 15 | 60 | 9.52 | 45.0 | 7.7 | 20.5 |
| 22 | 3.0 | 75 | 10.35 | 29.3 | 5.3 | 53.4 |
| 16 | 4.0 | 80 | 10.05 | 35.1 | 16.0 | 45.8 |

**Table 3.1-131** Mechanical properties of Ag–Cu–Zn alloys [1.220, p. 154]

| Alloy Ag–X (wt%) | HV5 s | h | $R_{p0.2}$ (MPa) s | h | $R_{on}$ (MPa) s | h | $A$ (%) s | h |
|---|---|---|---|---|---|---|---|---|
| Pd27.5 | 55 | | 80 | | 230 | | 33 | |
| Pd27.4Cu10.5 | 140 | 310 | 320 | 940 | 510 | 950 | 31 | 3 |
| Pd39.9Zn4 | 160 | 270 | 285 | 595 | 560 | 790 | 18 | 6 |

s = soft, h = hard

**Table 3.1-132** Mechanical properties of Ag–Pd alloys in annealed (s) and hard (h) condition [1.217, p. 208]

| Alloy AgX (wt%) | Temperature (°C) 20 | 200 | 400 | 600 | 800 |
|---|---|---|---|---|---|
| | $R_m/A$ | | | | |
| Cd 4 | 170/60 | 150/50 | – | – | – |
| Cd 8 | 480/5 | 260/20 | 200/55 | – | – |
| Cu 3 | 190/35 | 170/40 | 140/40 | 90/80 | 30/150 |
| Cu 7.5 | 250.46 | 220/48 | 180/47 | 120/55 | 60/78 |
| Ni 0.3 | 190/60 | 170/60 | 130/65 | 100/65 | 60/50 |
| Si 3 | 260/39 | 220/33 | 180/35 | 90/52 | 20/55 |

**Table 3.1-133** Tensile strength $R_m$ (MPa) and elongation $A$ (%) of Ag alloys at different temperatures [1.217, p. 207]

**Table 3.1-134** Strengthening of Ag (99.975%) by cold forming as a function of reduction in cross section in % [1.217, p. 204]

| $V$ (%) | | $R_m$ (MPa) | $A$ (%) | HV |
|---|---|---|---|---|
| 0 | | 150 | 50 | 26 |
| 10 | | 180 | 30 | 54 |
| 30 | | 260 | 5 | 70 |
| 80 | 2 | 90 | | |

$V$ = reduction of cross section

**Table 3.1-135** Strengthening of Ag alloys by cold forming (HV 10) (reduction in % of thickness) [1.217, p. 207]

| Reduction (%) Alloying element | 0 | 40 | 80 |
|---|---|---|---|
| Cu 5 | 58 | 108 | 134 |
| Cu 15 | 76 | 126 | 158 |
| Cu 28 | 98 | 136 | 177 |
| Cu 50 | 84 | 130 | 166 |
| Ni 0.15 | 40 | 86 | 100 |
| Pd 30 | 70 | 132 | 164 |
| Pd 30 Cu 5 | 92 | 174 | 2165 |

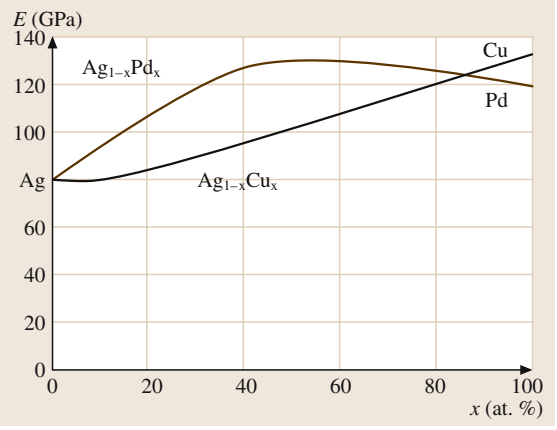


**Fig. 3.1-199** Module of elasticity of Ag–Pd and Ag–Cu alloys [1.217, p. 206]

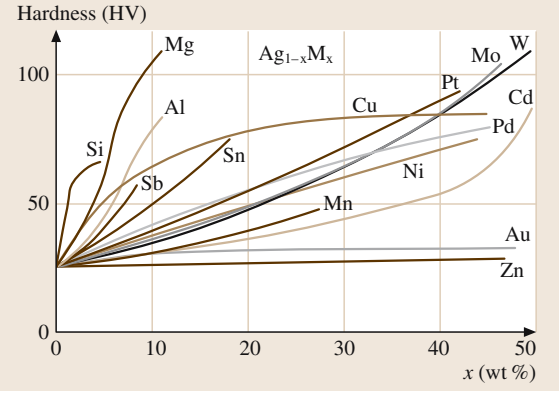


**Fig. 3.1-200** Influence of alloying elements on the hardness of binary Ag alloys [1.217, p. 206]

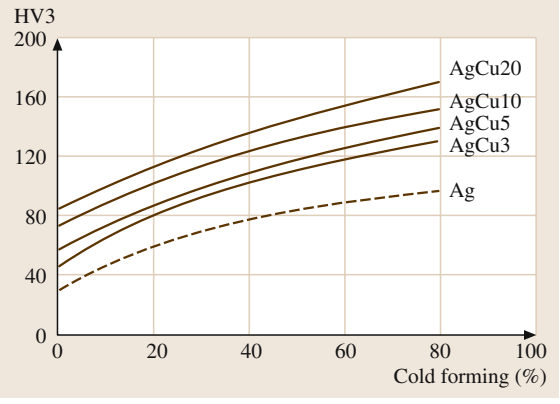


**Fig. 3.1-201** Hardening of Ag–Cu alloys by cold forming [1.217, p. 432]

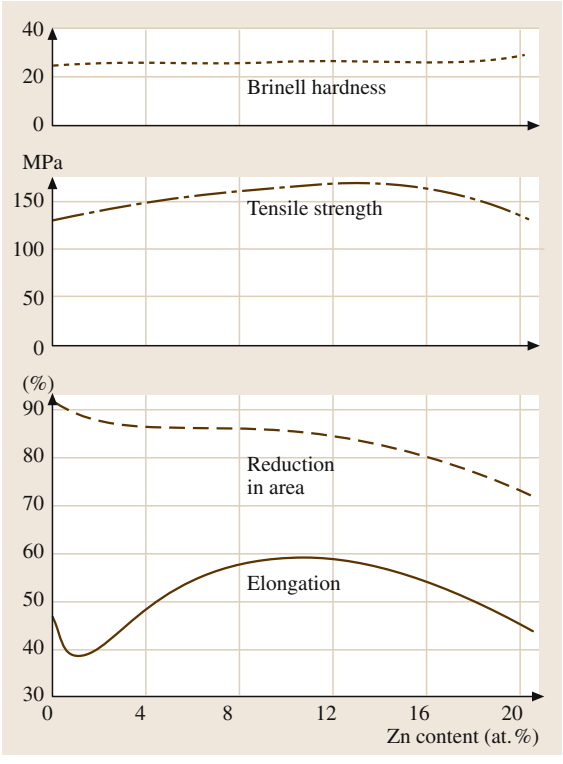


**Fig. 3.1-202** Plastic properties of Ag–Zn crystals [1.220, p. 135]

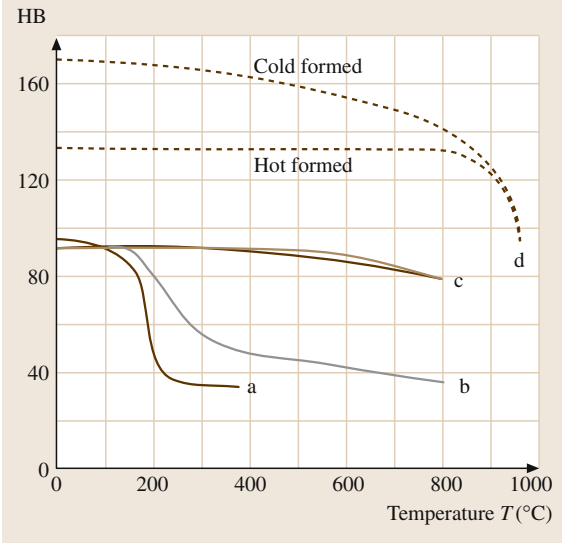


**Fig. 3.1-203** Hardness of fine grain and dispersion-hardened Ag [1.216, p. 36]

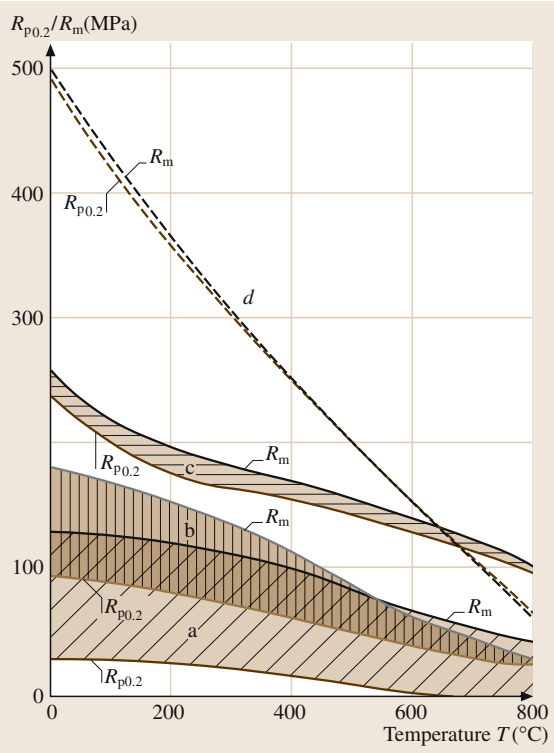


**Fig. 3.1-204** Tensile strength and 0.2% proof stress of silver grades at different temperatures [1.216, p. 37]

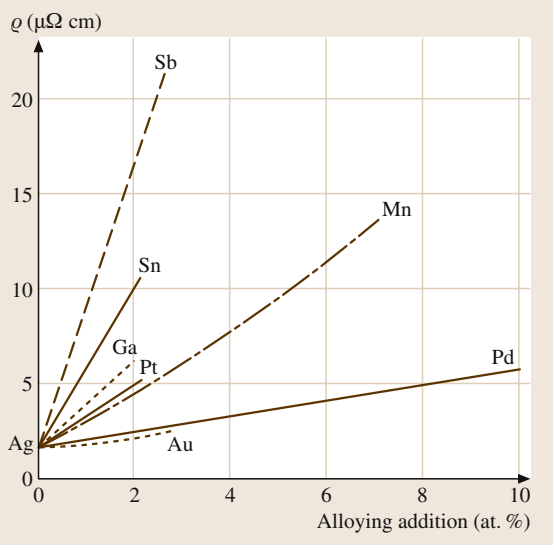


**Fig. 3.1-205** Influence of alloying elements on the electrical conductivity of binary Ag alloys [1.231, p. 20]

## Electrical Properties

Tables 3.1-136–3.1-139 and Fig. 3.1-205 [1.217, 231–233] show characteristic data. The residual resistivity ratio (RRR) of pure Ag ranges up to 2100. Ag alloys with Pb and Sn show superconductivity in the composition ranges: $Ag_{0.95-0.66}Pb_{0.05-0.34}$ with $T_c = 6.6–7.3$ K and $Ag_{0.72-0.52}Sn_{0.28-0.48}$ with $T_c = 3.5–3.65$ K [1.234].

**Table 3.1-136** Specific electrical resistivity $\rho(T) = \rho_0 + \rho_i(T)$ of Ag ($\rho_0 = 0.0008\ \mu\Omega\,\text{cm}$) at different temperatures [1.217, p. 156]

| $T$ (K) | $\rho(T)$ (μΩ cm) |
|---|---|
| 10 | 0.0001 |
| 50 | 0.1032 |
| 120 | 0.5448 |
| 273 | 1.470 |
| 500 | 2.860 |
| 700 | 4.172 |
| 900 | 5.562 |
| 1100 | 7.031 |

**Table 3.1-137** Increase of atomic electrical resistivity of Ag by alloying elements $\Delta\rho/C$ (μΩ cm/at.%) [1.217, p. 157]

| Base element | Alloying elements |
|---|---|
| Ag | Al 1.87, As 8, Au 0.36, Cd 0.35, Cr 6.5, Cu 0.07, Fe 3.2, Ga 2.3, Ge 5, Hg 0.8, In 1.6, Pb 4.6, Pd 0.44, Pt 1.5, Sn 4.5, Zn 0.63 |

**Table 3.1-138** Specific electrical resistivity $\rho_i$ and coefficient of electrical resistivity (TCR) of noble metal solid solution alloy phases [1.217, p. 158]

| Base/ solute-metal | | Solute content 20 | 40 | 60 | 80 |
|---|---|---|---|---|---|
| Rh/Ni | $\rho_i$ | 21 | 37 | 51 | 50 |
| | TCR | 3.8 | 1.8 | < 0.1 | 3 |
| Ag/Au | $\rho_i$ | 8.3 | 11.0 | 11.0 | 8.1 |
| | TCR | 0.93 | 0.83 | 0.84 | 1.1 |
| Ag/Pd | $\rho_i$ | 11 | 22 | 41 | 34 |
| | TCR | 0.58 | 0.40 | – | 0.75 |
| Ag/Pt | $\rho_i$ | 33 | 60 | 46 | 35 |
| Au/Pd | $\rho_i$ | 9.8 | 17 | 30 | 26 |
| | TCR | 0.88 | 0.61 | 0.45 | 1.2 |
| Au/Pt | $\rho_i$ | 28 | 44 | 0.82 | 0.8 |
| | TCR | 0.28 | 0.26 | 0.82 | 0.8 |

**Table 3.1-139** Specific electrical resistivity $\rho_{25}$ of annealed (8 h at 550 °C) Ag–Cu wire at 25 °C and 100 °C ($\rho_{100}$) and temperature coefficient of resistivity (TCR) $\alpha$ for 25–100 °C [1.226, p. 380]

| at.% Ag | 5 | 15 | 45 | 75 | 96 |
|---|---|---|---|---|---|
| $\rho_{25} \times 10^{-6}$ (μΩ cm) | 1.832 | 1.895 | 1.913 | 1.645 | 1.822 |
| $\rho_{100} \times 10^{-6}$ (μΩ cm) | 2.369 | 2.320 | 2.411 | 2.308 | 2.297 |
| TCR $\times 10^5$ | 389 | 387 | 380 | 365 | 381 |

## Thermoelectric Properties

In Tables 3.1-140–3.1-142 and Fig. 3.1-206, characteristic data are shown: absolute thermoelectric power, thermo-electromotive force of pure Ag as well as Ag–Au, Ag–Pd, and Ag–Pt alloys at different temperatures against a reference junction at 0 °C [1.217, 235, 236].

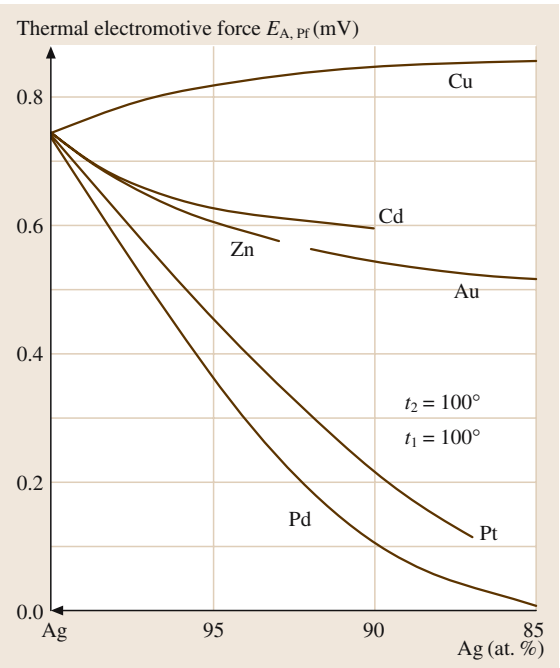


**Fig. 3.1-206** Thermal electromotive force of binary Ag alloys [1.216, p. 98]

**Table 3.1-140** Thermal electromotive force $E_{Ag,Pt}$ (mV) force of Ag at different temperatures; reference junction at 0 °C [1.217, p. 159]

| T (°C) | −200 | −100 | −50 | +100 | +200 | +400 | +800 |
|---|---|---|---|---|---|---|---|
| $E_{Ag,Pt}$ (mV) | −0.39 | −0.21 | −0.10 | 0.74 | 1.77 | 4.57 | 13.36 |

**Table 3.1-142** Thermal electromotive force of Ag–Au alloys in mV at 100 °C and 700 °C reference junction at 0 °C [1.217, p. 160]

| T (°C) | Composition (wt%) | | | | | |
|---|---|---|---|---|---|---|
| | 0 | 20 | 40 | 60 | 80 | 100 |
| 100 | 0.74 | 0.47 | 0.42 | 0.42 | 0.49 | 0.78 |
| 700 | 10.75 | 7.7 | 6.7 | 6.8 | 7.3 | 10.15 |

## Magnetic Properties

Silver is diamagnetic (Table 3.1-143). The magnetic susceptibility remains constant from 0 K to the melting point. Alloying with B metals causes only minor variations compared to pure Ag. In the continuous solid solution range the molar susceptibilities remain negative and the alloys are diamagnetic. Ni, Pd, and Pt dissolve up to 25 at.% diamagnetically. Cr, Fe, and Mn give rise to paramagnetism, while Co causes ferromagnetism [1.216, 217].

**Table 3.1-143** Atom susceptibility of Ag and Au alloys at room temperature [1.216, p. 90]

| Base metal | Alloying element | Base metal content (at.%) | | | | |
|---|---|---|---|---|---|---|
| | | 100 | 99 | 95 | 90 | 80 |
| Ag | Au | −19 | | −20.2 | −20.8 | −22.2 |
| | Pd | −20 | | | −21 | −22 |
| Au | Cu | −26 | | −25.2 | −24.2 | −22.4 |
| | Ni | −28 | −22 | ±0 | +16 | – |
| | Pd | −28 | | | −20 | −15 |
| | Pt | −28 | | | −6 | ±0 |

**Table 3.1-141** Absolute thermoelectric power of Ag at different temperatures [1.216, p. 94]

| Temperature (°C) | −255 | −200 | −100 | −20 | 0 | 100 | 300 | 500 | 800 |
|---|---|---|---|---|---|---|---|---|---|
| Thermoelectric power (μV/°C) | +0.62 | +0.82 | +1.00 | – | +1.4 | +1.9 | +3.0 | +4.6 | +8.3 |

### Thermal Properties

Selected data of thermal expansion, thermal conductivity, and melting temperatures of Ag alloys are given in Tables 3.1-144–3.1-150 and in Fig. 3.1-207 [1.216, 220].

**Table 3.1-144** Recrystallization temperatures (°C) of Ag 99.95 and 99.995% purity after different degrees of deformation $V$; annealing time 1 h [1.217, p. 205]

| $V$ (%) | $T_{recryst.}$ Purity | |
|---|---|---|
| | 99.95% | 99.995% |
| 40 | 190 | 125 |
| 60 | 160 | 100 |
| 99 | 127 | 70 |

**Table 3.1-145** Mean coefficients of thermal expansion $\alpha$ ($10^{-6}\,K^{-1}$) of Ag and Au [1.217, p. 154]

| $T$ (K) | $\alpha$ ($10^{-6}\,K^{-1}$) | |
|---|---|---|
| | Ag | Au |
| 373 | 17.9 | 13.9 |
| 473 | 19.1 | 14.8 |
| 673 | 19.9 | 15.3 |
| 873 | 21.1 | 15.7 |
| 1073 | 23.6 | 16.2 |

**Table 3.1-146** Mean coefficients of thermal expansion $\alpha$ ($10^{-6}\,K^{-1}$) of Ag and Au alloys [1.217, p. 154]

| Base metal | Au | Au | Au | Au | Ag |
|---|---|---|---|---|---|
| 2nd metal | Ag | Ag | Cu | Ni | Pd |
| Temp. range (K) | 273 373 | 293 1073 | 273 593 | 273 373 | 373 473 |
| wt% of 2nd metal | $\alpha$ ($10^{-6}\,K^{-1}$) | | | | |
| 20 | 15.5 | 17.0 | 14.9 | 14.4 | 16.2 |
| 40 | 16.5 | 18.7 | – | 13.9 | – |
| 50 | 17.0 | – | 15.7 | 14.0 | 14.7 |
| 60 | 17.5 | 20.1 | 15.8 | 13.9 | – |
| 80 | 18.2 | 20.8 | 15.9 | 13.4 | 12.4 |

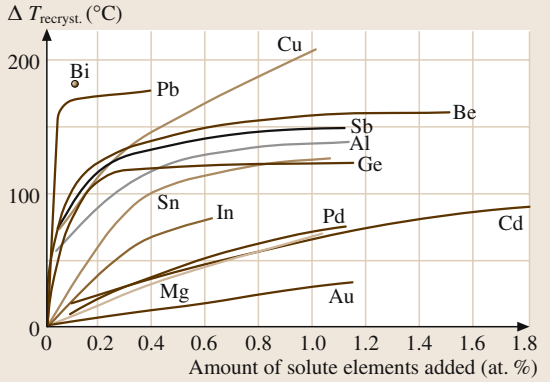


**Fig. 3.1-207** Increase of the recrystallization temperature of Ag by solute elements [1.218, p. 452]

**Table 3.1-149** Thermal conductivity λ (W/m K) of Ag and Au at different temperatures [1.217, p. 153]

| $T$ (K) | λ (W/m K) | |
|---|---|---|
| | Ag | Au |
| 40 | 1050 | 420 |
| 100 | 475 | 360 |
| 273 | 435 | 318 |
| 600 | 411 | 296 |
| 800 | 397 | 284 |

**Table 3.1-150** Melting range of Ag–Cu–Sn and Ag–Cu–In solder alloys

| Composition (wt%) | | | | Melting range (°C) |
|---|---|---|---|---|
| Ag | Cu | Sn | In | |
| 60 | 23 | 17 | | 557–592 |
| 50 | 30 | 20 | | 555–578 |
| 47 | 20 | 33 | | 472–515 |
| 50 | 10 | 40 | | 435–456 |
| 49 | 19 | | 32 | 549–556 |
| 50 | 25 | | 25 | 594–601 |
| 45 | 17 | | 38 | 534–548 |
| 25 | 45 | | 30 | 581–610 |

**Table 3.1-147** Specific heat of Ag at different temperatures [1.220, p. 9]

| $T$ (°C) | −259.46 | −240.86 | −141.93 | −67.90 | +98.7 | +249.0 | +399.5 | +652.2 |
|---|---|---|---|---|---|---|---|---|
| $c_p$ (cal/g) | 0.001177 | 0.01259 | 0.04910 | 0.05334 | 0.0569 | 0.0583 | 0.0600 | 0.0635 |

**Table 3.1-148** Vapor pressure of liquid Ag [1.220, p. 8]

| $T$ (°C) | 1550 | 1611 | 1742 | 1838 | 1944 | 2152 |
|---|---|---|---|---|---|---|
| Vapour pressure (mm Hg) | 8.5 | 15.7 | 54 | 100 | 190 | 760 (extrapol.) |

### Optical Properties

Table 3.1-151 and Figs. 3.1-208, 3.1-209 [1.237] show characteristic data of optical properties. Ag has the highest reflectivity of all noble metals. An interband transition takes place in the ultraviolet range at 3.9 eV. Ag−Al alloys between 10 at.% and 28 at.% Ag show higher reflectance in the low wavelength range than the pure elements. In Ag−Pd alloys, the threshold energy at 3.9 eV for the interband transition remains constant up to ≈ 34 at.% Pd. Examples of colored Ag alloys are given in Table 3.1-152 [1.237].

**Table 3.1-151** Spectral emissivity of Ag and Au at different temperatures [1.217, p. 171]

| | Surface | Temperature (°C) | Spectral degree of emission |
|---|---|---|---|
| Ag | Solid | 940 | 0.044 |
| | Liquid | 1060 | 0.0722 |
| Au | Solid | 1000 | 0.154 |
| | Liquid | 1067 | 0.222 |

**Table 3.1-152** Colored noble metal alloys [1.237, p. 178]

| Alloy | Color | Remarks |
|---|---|---|
| Ag−Zn ($\beta$-phase) | Rose | |
| Ag−Au(70) | Green-yellow | |
| $Al_2Au$ | Violet | |
| $KAu_2$ | Violet | |
| Au−Zn−Cu−Ag | Green | |
| $AuIn_2$ | Blue | |
| *Zintl Phases* | | |
| $Li_2AgAl$ | Yellow-rose | VEC 1.5 |
| $Li_2AgGa$ | Yellowish | VEC 1.5 |
| $Li_2AgIn$ | Gold-yellow | VEC 1.5 |
| $Li_2AgTl$ | Violet-rose | VEC 1.5 |
| $Li_2AuTl$ | Green-yellow | VEC 1.5 |
| $Li_2AgSi$ | Rose-violet | VEC 1.75 |
| $Li_2AgGe$ | Rose-violet | VEC 1.75 |
| $Li_2AgSn$ | Violet | VEC 1.75 |
| $Li_2AgPb$ | Blue-violet | VEC 1.75 |
| $Li_2AuPb$ | Violet | VEC 1.75 |

VEC = Valence electron concentration

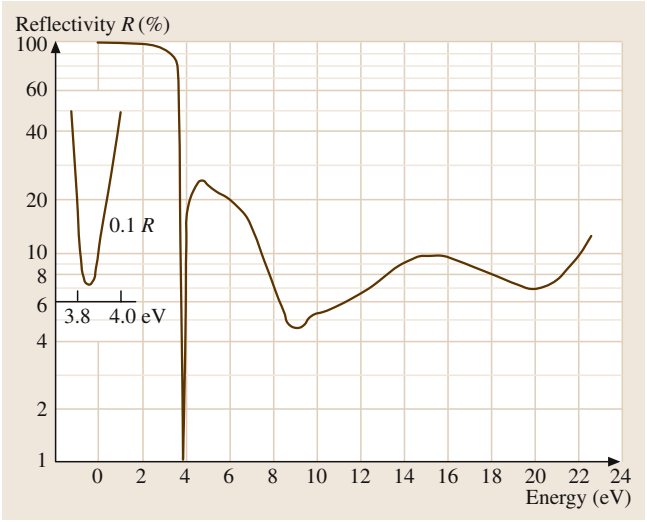


**Fig. 3.1-208** Reflectance versus radiation energy of Ag [1.237, p. 158]

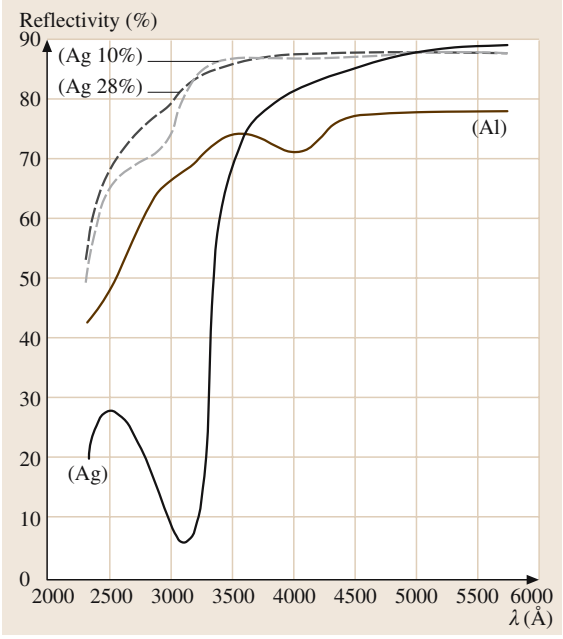


**Fig. 3.1-209** Reflectivity of Ag−Al alloys [1.220, p. 142]

### Diffusion

Data for self-diffusion of Ag in Ag alloys and diffusion of tracer impurity elements are shown in Tables 3.1-153–3.1-158 and Figs. 3.1-210–3.1-212. Diffusion of H and O is of importance for annealing treatments and dispersion hardening [1.217, 220, 226, 235].

**Table 3.1-153** Self-diffusion in binary homogeneous Ag–Au alloys [1.217, p. 150]

| Au (at.%) | $\Delta T$ (K) | $D^0$ ($10^4$ m$^2$/s) | $Q$ (kJ/mol) |
|---|---|---|---|
| Ag–Au ($^{110m}$Ag diffusion) | | | |
| 8 | 927–1218 | 0.52 | 187.5 |
| 17 | 908–1225 | 0.32 | 184.4 |
| 83 | 923–1284 | 0.09 | 171.7 |
| 94 | 936–1234 | 0.072 | 168.5 |
| Ag–Au ($^{198}$Au diffusion) | | | |
| 8 | 991–1213 | 0.82 | 202.2 |
| 17 | 991–1220 | 0.48 | 198.0 |
| 83 | 985–1274 | 0.12 | 180.2 |
| 94 | 991–1283 | 0.09 | 176.1 |

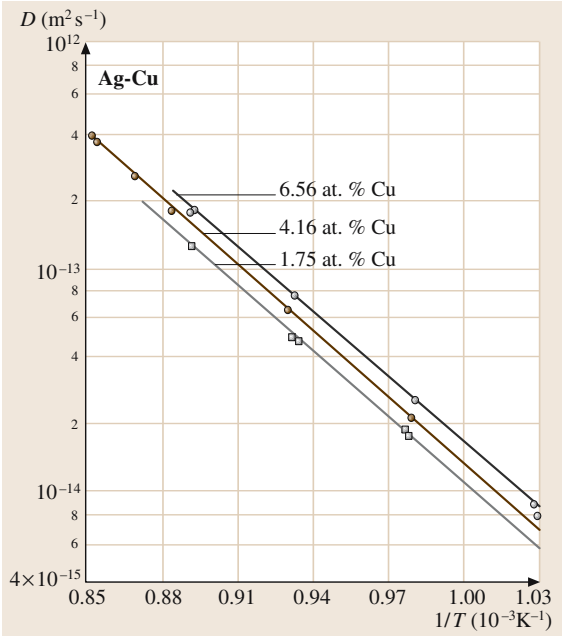


**Fig. 3.1-210** Self-diffusion of Ag(110w) in Ag–Cu (1.75–6.56 at.% Cu) alloys [1.238, p. 189]

| | Element | $D^0$ (m$^2$/s) | $Q$ (kJ/mol) | $T$ (K) |
|---|---|---|---|---|
| Lattice | Ag | 0.278 | 181.7 | 1038–1218 |
| | Ag(s)[a] | 0.67 | 190.1 | 913–1221 |
| | Au | 0.107 | 176.9 | 623–733 |
| | Au(s)[a] | 0.027 | 165 | 603–866 |
| Surface | Ag | $1\times10^4$ | 264 | 873–1173 ($H_2$) |
| | Ag | $3\times10^{-5}$ | 49 | 580–730 (Vac.) |
| | Au(110) | $1\times10^2$ | 227 | 1138–1329 ($H_2$) |
| | Au | $8\times10^2$ | 272 | 1200–1300 (Vac.) |
| Grain-boundary | Ag | $7.24\times10^{-5}$ | 190.4 | ~790–680 |
| | Au | $9.10\times10^{-6}$ | 174.6 | 625–521 |

[a] (s) = single crystal

**Table 3.1-154** Self-diffusion in pure Ag and Au [frequency factor $D^0$ ($10^{-4}$ m$^2$/s)], activation energy $Q$ (kJ/mol) [1.217, p. 149]

**Table 3.1-155** Diffusion of Ag in Cu and Cu in Ag [1.226, p. 365f.]

| **Ag in Cu** | | | | | |
|---|---|---|---|---|---|
| $T$ (°C) | 485 | 574 | 625 | 731 | 794 |
| $D_{Ag}$ | $4.9\times10^{-14}$ | $8.2\times10^{-13}$ | $2.91\times10^{-12}$ | $7.7\times10^{-11}$ | $1.65\times10^{-10}$ |
| | ±0.1 | ±0.6 | ±0.08 | | |
| $D = D_0 \exp(-E_A/RT)$ with $D_0 = 0.61$ cm$^2$/s, $E_A = 46.5$ kcal/g-at. | | | | | |
| **Cu in Ag** | | | | | |
| $T$ (°C) | 498 | 597 | 760 | 800 | 895 |
| $D_{Cu}$ | $2.87\times10^{-13}$ | $5.08\times10^{-12}$ | $3.55\times10^{-10}$ | $5.9\times10^{-10}$ | $9.4\times10^{-10}$ |
| | ±0.45 | ±0.54 | | | |
| $D_0 = 1.23$ cm$^2$/s, $E_A = (46.1 \pm 0.9)$ kcal/g-at. | | | | | |

**Table 3.1-156** Diffusion of impurities in Ag, Au, Pt and Pd [1.217, p. 151]

| Tracer | $D^0$ ($10^{-4}$ m$^2$/s) | $Q$ (kJ/mol) | ΔT (K) | Tracer | $D^0$ ($10^{-4}$ m$^2$/s) | $Q$ (kJ/mol) | ΔT (K) |
|---|---|---|---|---|---|---|---|
| Matrix: Silver (Ag) | | | | Matrix: Gold (Au) | | | |
| Cu | 1.23 | 193.0 | 990–1218 | Pd | 0.076 | 195.1 | 973–1273 |
| | 0.029 | 164.1 | 699–897 | Pt | 0.095 | 201.4 | 973–1273 |
| Au | 0.262 | 190.5 | 923–1223 | Ag | 0.072 | 168.3 | 943–1281 |
| | 0.41 | 194.3 | 929–1178 | | 0.08 | 169.1 | 1046–1312 |
| | 0.85 | 202.1 | 991–1198 | | 0.086 | 169.3 | 1004–1323 |
| | 0.62 | 199.0 | | Hg | 0.116 | 156.5 | 877–1300 |
| Pd | 9.57 | 237.6 | 1009–1212 | Matrix: Platin (Pt) | | | |
| Pt | 6.0 | 238.2 | 923–1223 | Ag | 0.13 | 258.1 | 1473–1873 |
| | 1.9 | 235.7 | 1094–1232 | Au | 0.13 | 252.0 | 850–1265 |
| Ru | 180 | 275.5 | 1066–1219 | Matrix: Palladium (Pd) | | | |
| | | | | Fe | 0.18 | 260 | 1373–1523 |

**Table 3.1-157** Grain boundary tracer diffusion in pure Ag [1.217, p. 150]

| Matrix metal | Tracer | $D^0$ (m$^2$/s) | $Q$ (kJ/mol) | $T$ (K) |
|---|---|---|---|---|
| Ag | Cd | $5.04\times10^{4}$ | 176.6 | 772–557 |
| | In | $5.50\times10^{4}$ | 174.8 | 764–469 |
| | Sb | $2.34\times10^{4}$ | 163.5 | 771–471 |
| | Sn | $4.72\times10^{4}$ | 170.9 | 776–527 |
| | Te | $2.10\times10^{4}$ | 154.7 | 970–650 |

**Table 3.1-158** Diffusion of hydrogen and oxygen in Ag, Pd, Pt, and Au [1.217, p. 151]

| Matrix | Gas | $D^0$ ($10^{-4}$ m$^2$/s) | $Q$ (kJ/mol) | ΔT (K) |
|---|---|---|---|---|
| Ag | H | $8.55\times10^{-3}$ | 30.11 | 947–1123 |
| Ag | O | $3.66\times10^{-3}$ | 46.1 | 680–1140 |
| Pd | H | $2.9\times10^{-3}$ | 22.19 | 473–1548 |
| | D | $1.7\times10^{-3}$ | 19.88 | 218–233 |
| | T | $7.2\times10^{-3}$ | 23.8 | 273–323 |
| Pt | H | $6\times10^{-3}$ | 24.70 | 600–900 |
| Au | H | $5.6\times10^{-4}$ | 23.61 | 773–1213 |

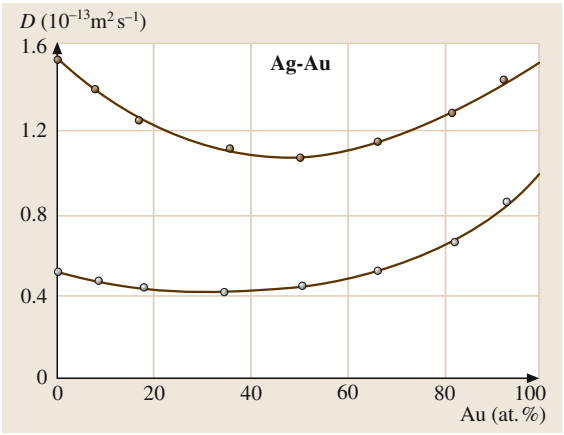


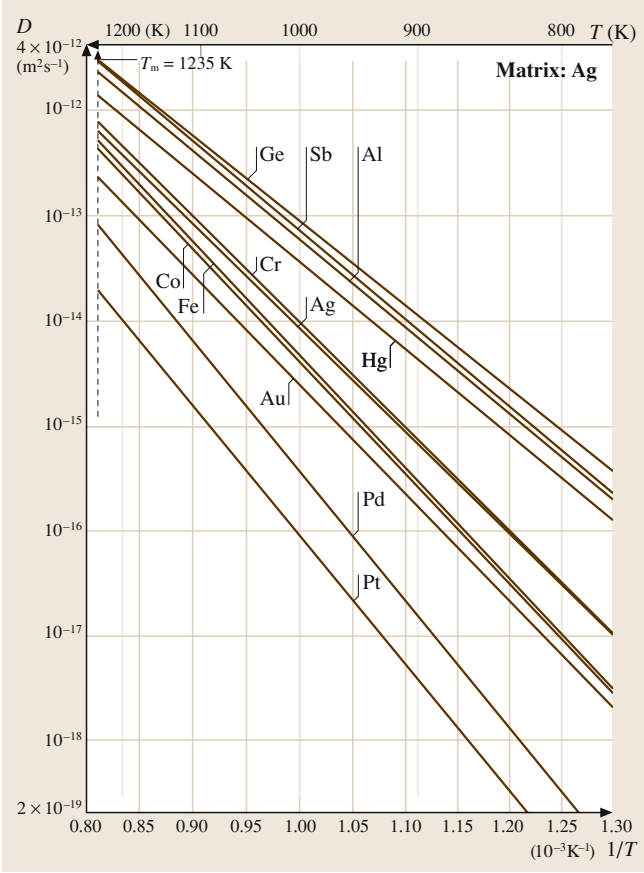


**Fig. 3.1-211** Diffusion of impurities in Ag [1.238, p. 244]

**Fig. 3.1-212** Self-diffusion of Ag(110w) (*brown circles*) and Au(198) (*gray circles*) in Ag–Au (8–94 at.%) Ag–Au alloys [1.238, p. 190]

### Chemical Properties

Silver has the reduction potential of $E_0 = +0.8\,V$ for $Ag/Ag^+$. It is resistant against dry oxygen, air, non-oxidizing acids, organic acids, and alkali. Water and water vapor do not attack Ag up to 600 °C. Ag is dissolved in alkaline cyanidic solutions in the presence of oxidizing agents, air, and oxygen. $H_2S$ attacks Ag readily at room temperature, forming black $Ag_2S$ layers (tarnish) [1.217].

Metallic Ag and Ag−Au alloys are heterogeneous catalysts for oxidation processes, e.g., in the production of ethylene oxide and formaldehyde applied as grids or as powder preparations on $Al_2O_3$ or carbon substrates [1.217].

### Ag-Based Materials

Binary alloys (Tables 3.1-159–3.1-161) [1.218]: Ag−Ni alloys are grain-stabilized materials usually containing 0.15 wt% Ni. Ag−Cu alloys have manifold applications in jewelry, silverware, brazes, and solders. Jewelry, sil-

**Table 3.1-161** Physical properties of noble-metal-containing vacuum braze alloys [1.217, p. 560]

| | Composition | Solidus (°C) | Liquidus (°C) |
|---|---|---|---|
| Ag−Cu | Ag40Cu19Zn21Cd20 | 595 | 630 |
| | Ag60Cu27In13 | 605 | 710 |
| | Ag44Cu30Zn26 | 675 | 735 |
| | Ag72Cu28 | 779 *E* [a] | |
| Ag−Mn | Ag85Mn15 | 950 | 950 |
| Ag−Pd | Ag68.4Pd5Cu26.6 | 807 | 810 |
| | Ag54Pd25Cu21 | 901 | 950 |
| | Ag75Pd20Mn5 | 100 | 1120 |
| Pd−Cu | Pd18Cu72 | 1080 | 1090 |
| Pd−Ni | Pd60Ni40 | 1237 | 1237 |
| Au−Cu | Au80Cu20 | 890 | 890 |
| | Au33Cu65 | 990 | 1010 |
| Au−Ni | Au82Ni18 | 950 | 950 |

[a] *E* = Eutectic composition

**Table 3.1-159** Noble metal containing soft solders [1.217]

| Alloy (wt%) | Melting range (°C) | Density ($g/cm^3$) | Tensile strength ($N/mm^2$) | Elongation (%) | Eleasticity module ($N/mm^2$) | Thermal expansion ($10^{-6}\,K^{-1}$) | Electrical conductivity ($m/\Omega\,mm^2$) | Thermal conductivity (W/m K) |
|---|---|---|---|---|---|---|---|---|
| AuSn20 | 280 | 14.57 | 275 | < 1 | 59 200 | 16 | < 5 | 57.3 |
| AuGe12 | 356 | 14.70 | 150–200 | < 1 | 69 300 | 13.4 | 7 | 44.4 |
| AuSi2 | 363–740 | 14.50 | 500–600 [a] | 0.5–3 [a] | | 12.6 | 33 | 50 |
| SnAg25Sb10 | 228–395 | 7.86 | 80–120 | 1–4 | 23 000 | 19 | 6.5 | 55 |
| SnAg3.5 | 221 | 7.38 | 25–35 | 20–30 | 41 100 | 27.9 | 7.5 | 57 |
| PbSn5Ag2.5 | 280 | 11.70 | 25–35 | 20–30 | 21 300 | 29 | < 5 | 44 |
| PbIn5Ag2.5 | 307 | 11.60 | 35–40 | 28–34 | 19 900 | 29 | < 5 | 42 |

[a] Hard rollded condition

**Table 3.1-160** Noble-metal-containing brazing alloys [1.217, p. 560]

| Alloy (wt%) | Melting range (°C) | Density ($g/cm^3$) | Tensile strength ($N/mm^2$) | Elongation (%) | E-Modul. ($N/mm^2$) | Thermal expansn. ($10^{-6}\,K^{-1}$) | Electrical condct. ($m/\Omega\,mm^2$) | Thermal condct. (W/m K) | ISO Type 3677 |
|---|---|---|---|---|---|---|---|---|---|
| AgCu28 | 779 | 10.00 | 250–350 | 20–28 | 100 000 | 19.8 | 10 | | B Ag72 Cu780 |
| AgCu27In13 | 605–710 | 9.70 | 400–500 | 20–30 | 85 000 | 17.8 | 46.1 | 352 | B Ag60CuIn 695-710 |
| AgCu26.6Pd5 | 807–810 | 10.10 | 370–410 | 12–20 | 120 000 | 22 | 26 | 215 | B Ag68CuPd 807-810 |
| AgCu31.5Pd10 | 824–852 | 10.10 | 500–540 | 2–5 | 140 000 | 17.5 | 19 | 150 | B Ag58CuPd 824-852 |
| AgCu20Pd15 | 850–900 | 10.40 | 510–550 | 5–9 | 140 000 | 22 | 15 | 100 | B Ag65CuPd 850-900 |
| AgCu21Pd25 | 910–950 | 10.50 | 540–580 | 13–21 | 140 000 | 17.5 | 8 | 80 | B Ag54PdCu 901-950 |
| AgPd5 | 970–1010 | 10.50 | 180–220 | 26–34 | 40 000 | 22 | 25 | 220 | B Ag95Pd 970-1010 |
| CuPd18 | 1080–1090 | 9.40 | 380–420 | 31–39 | 135 000 | 18.9 | 9.1 | 100 | B Cu82Pd 1080-1090 |
| AgCu28Pd20 | 879–898 | 10.30 | 580–620 | 6–10 | 100 000 | 18.6 | 9.5 | 95 | B Ag52CuPd 879-898 |
| AuNi18 | 950 | 15.96 | 550–650 | 8 | | 14.6 | 5.9 | | B Au82Ni 950 |

**Table 3.1-162** Typical powder grades of Ag, Pd, and Ag−Pd preparations for capacitors

| Metal | Manufacturing method | Grain shape | Grain size (μm) | Tap density ($g/cm^3$) | Specific surface[a] ($m^2/g$) |
|---|---|---|---|---|---|
| Ag | Chemical reduction | Microcrystalline | 0.5–2.0 | 0.8–5.0 | 0.1–2.0 |
| | Electrolytic deposition | Dendritic | 1–200 | 4.5–4 | 0.1–0.5 |
| | | ↓ | | | |
| | Ball milling | Flakes | 2–40 | 2.5–5 | 0.2–1.8 |
| Pd | Chemical reduction | Crystalline | < 20 | 0.8 | 2.5 |
| | | spheres | < 1.2 | 4.0 | 2.3 |
| Ag−Pd30 | Coprecipitation | Spheres | < 1.2 | 3.3 | 2.2 |
| | | ↓ | | | |
| | | Flakes | < 9 | 3.4 | 3.3 |

[a] BET in $N_2$ adsorption

ver ware alloys, and coins usually contain between 7.5 wt% Cu ("sterling silver") and 20 wt% Cu. The material Ag–28 wt% Cu is the most common silver brazing alloy. Alloys of Ag−Mn are special solders for hard metal and refractory metals (Mo, W). The alloy Ag–1 wt% Pt is applied in thick film layers for conductor paths in passive electronic devices. Ag−Pd powder preparations containing 10 to 30 wt% Pd form the conductor layers in multilayer capacitors (Table 3.1-162) [1.217].

### Ternary and Higher Alloys

Alloys of the systems Ag−Cu−Sn, Ag−Cu−Zn, and Ag−Cu−$Cu_3P$ are used as solders and brazes. Ag−Cu−P solder alloys can be applied without flux. Ti-containing solder alloys (active solders) allow direct bonding to ceramics (Table 3.1-162) [1.239]. Alloys of the systems Ag−Au−Cu, Ag−Au−Ni, and Ag−Cu−Pd are applied in jewelry and dentistry (Tables 3.1-186, 3.1-187).

The oxide AgO forms the cathode of AgO/Zn button type batteries with a cell voltage of 1.55 V and with energy densities in the range of 80–250 W h/$dm^2$ [1.218, 240–242].

Composite materials with $SnO_2$, CdO, carbon, Ni, and refractory carbides as dispersoids are base materials of electrical (Tables 3.1-163, 3.1-164, and Fig. 3.1-213) [1.226, 231, 243]. Extruded powder composites show preferred alignment of the dispersoid particles along the rod axes. Silver–nickel fiber composites are magnetic. Their coercivity increases with decreasing diameter of the Ni fibers [1.244].

**Table 3.1-163** Hardness and electrical conductivity of Ag−Ni−C (contact) alloys [1.226, p. 436]

| | | | | | |
|---|---|---|---|---|---|
| Alloy content wt% C | 3 | 2 | 2.5 | 2.5 | 2.5 |
| Alloy content wt% Ni0.5 | 0.5 | 0.5 | 1 | 5 | 10 |
| HV $(kg/mm^2)^{40.5}$ | 43 | 53 | 50 | 53 | 56–57 |
| Electrical conductivity in % of standard Cu | 63.7 | 74.8 | 69.8 | 67.3 | 64.5 |

**Table 3.1-164** Silver bearing composite contact materials [1.243, p. 156]

| Type | Composition (at.%) | Hardness HV | Electrical conductivity (m/Ω mm²) |
|---|---|---|---|
| Alloys | AgNi(0.15) | 100 | 58 |
| | AgCu(3) | 120 | 52 |
| | ↓ | | |
| | AgCu(20) | 150 | 49 |
| Composites with: | | | |
| Metals | Ag−Ni(10) | 90 | 54 |
| | ↓ | | |
| | Ag−Ni(40) | 115 | 37 |
| Oxides | Ag−CdO(10) | 80 | 48 |
| | ↓ | | |
| | Ag−CdO(15) | 115 | 45.5 |
| | Ag−ZnO(88) | 95 | 49 |
| | Ag−$SnO_2$(8) | 92 | 51 |
| | Ag−$SnO_2$(12) | 100 | 42 |
| Carbon | Ag−C(2) | 40 | 48 |
| | Ag−C(5) | 40 | 43.5 |
| Refractory metal compounds | Ag−W(20) | 240 | 26–28 |
| | ↓ | | |
| | Ag−W(80) | 80 | 42 |
| | Ag−WC(40) | 130 | 24–30 |
| | ↓ | | |
| | Ag−WC(80) | 470 | |

[a] Composite made by infiltration of liquid silver into a tungsten skeleton

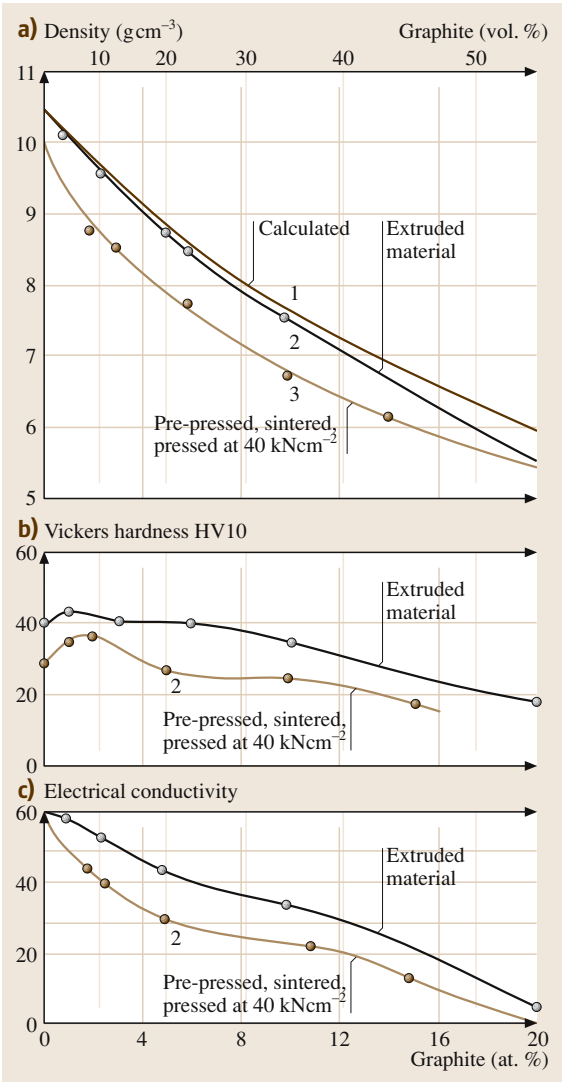


**Fig. 3.1-213** (a) Density, (b) hardness, and (c) electrical conductivity of Ag−C alloys [1.231, p. 44f.]

## 3.1.10.2 Gold and Gold Alloys

### Application

Gold and gold alloys are used for electrical contacts, bonding wires and conductor paths in semiconductor devices, chemical and corrosion resistant materials, thin surface coatings for optical and heat reflecting mirrors, special thermocouples, and catalysts for organic chemical reactions. Classical applications are jewelry, dentistry, monetary bars, and coins. Commercial grades: Table 3.1-165. The purity grades of gold bars are standardized in the range of 99.9 to 99.999 wt% (ASTM B 562-86), Tables 3.1-165, and 3.1-166 [1.217].

### Production

Elementary gold is extracted from ores by cyanide leaching and precipitated with zinc, and by electrolysis. Refining is achieved by application of chlorine gas up to 99.5%, and to 99.9% and higher by electrolysis. Bars, sheets and wires are made by casting, rolling and drawing; powder is formed by chemical and by electrolytic precipitation from solutions; and nanocrystalline powders are formed by dispersion in organic solutions. Coatings are produced by cladding; electroplating; and applying powder preparations followed by firing. Thin films are produced by evaporation and cathode sputtering. Very fine gold leaves are made by traditional hammering to a thickness of $\sim 0.2\,\mu m$, or by cathode sputtering.

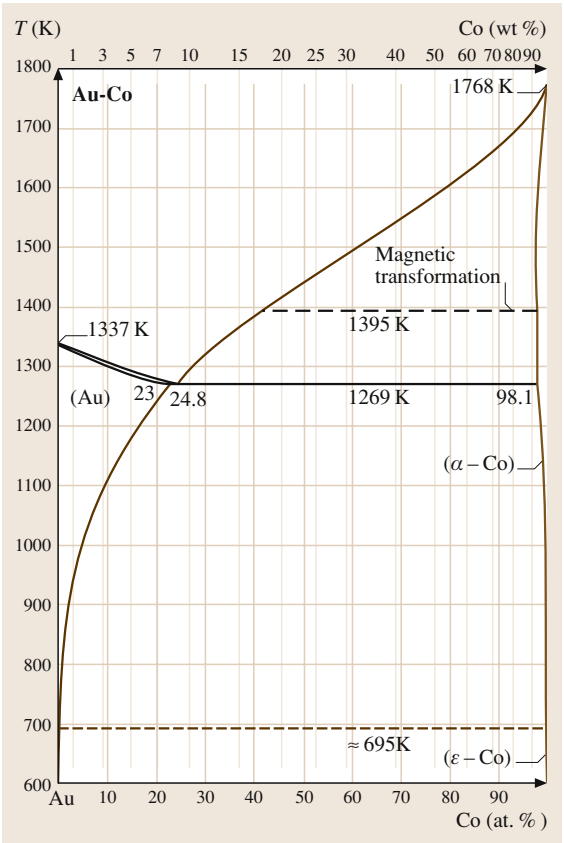


**Fig. 3.1-214** Binary phase diagram of Au–Co [1.245]

### Phases and Phase Equilibria

Selected phase diagrams are shown in Figs. 3.1-214–3.1-223 [1.245, 246]. Continuous solid solutions are formed with Ag, Co, Cu, Fe, Ni, Pd, and Pt. Miscibility gaps occur with Be, Ni, Pt, Rh, and Ru. Thermochemical data are listed in Tables 3.1-167,

**Table 3.1-165** Specifications of fine gold [1.217, p. 52]

| Designation | Grade (wt%) | Impurity | Maximum content (ppm) |
|---|---|---|---|
| "Good delivery" gold | 99.5 | any, total | 5000 |
| Fine gold | 99.99 | Ag/Cu/others/total | 100/20/30/100 |
| Fine gold, chemically pure | 99.995 | Ag/others/total | 25/25/50 |
| Fine gold, high purity | 99.999 | Ag/Fe/Bi/Al/Cu/Ni/Pd + Pt/total | 3/3/2/0.5/0.5/0.5/5/10 |

**Table 3.1-166** Standard fineness of noble metal alloys and corresponding carat of jewelry [1.217, p. 52]

| | Fineness (wt‰) | | | | | |
|---|---|---|---|---|---|---|
| Au | | 375 | 585 | 750 | 916,999 | |
| Ag | | | | | 800,925,999 | |
| Pd | | | 500 | | 850,900,950,999 | |
| Pt | | | 500 | | 950,999 | |
| | 333 | 375 | 585 | 750 | | 1000 |
| Carat | 8 | 9 | 14 | 18 | | 24 |

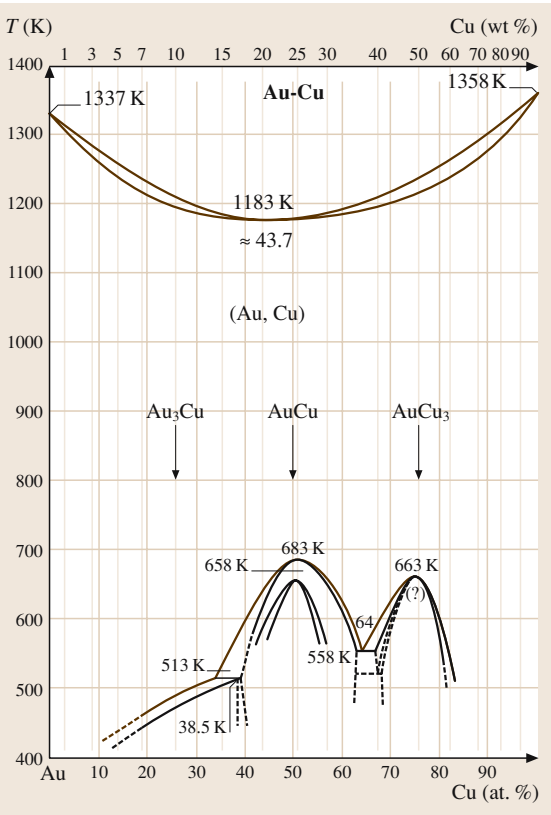


**Fig. 3.1-215** Binary phase diagram of Au−Cu [1.245]

and 3.1-168 [1.217, 222]. Compositions, crystal structures and lattice parameters of selected intermetallic compounds are given in Table 3.1-169 [1.217] and in Figs. 3.1-224 and 3.1-225 [1.245]. Primary solid solutions have the fcc structure of Au. The lattice parameters of the substitutional solid solutions correspond roughly to Vegard's law with a few exceptions [1.247].

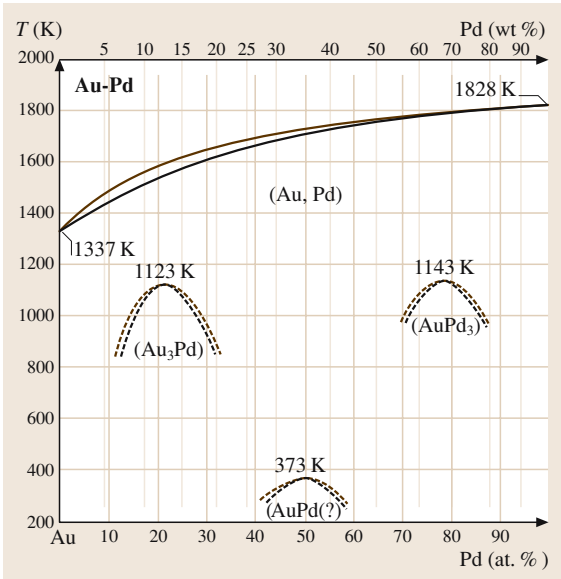


**Fig. 3.1-217** Binary phase diagram of Au−Pd [1.245]

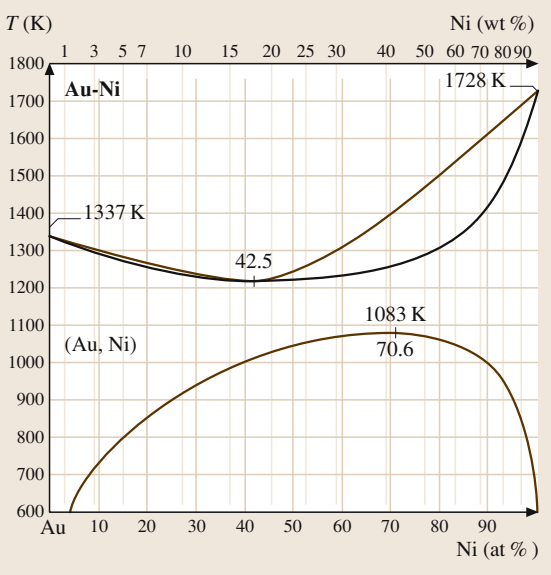


**Fig. 3.1-216** Binary phase diagram of Au−Ni [1.245]

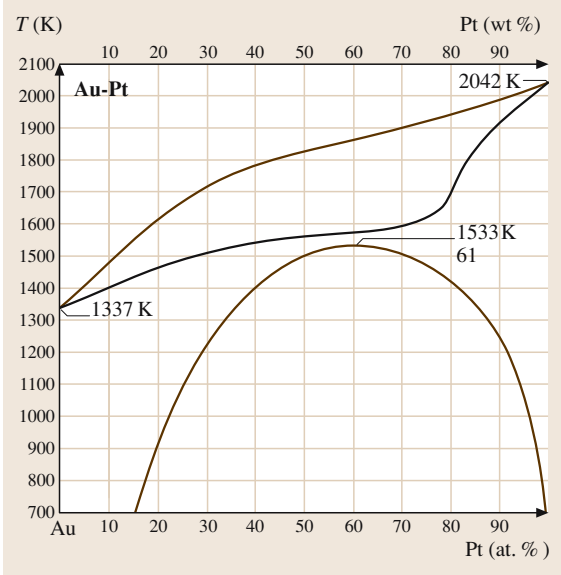


**Fig. 3.1-218** Binary phase diagram of Au−Pt [1.245]

**Table 3.1-167** Thermodynamic data of Au [1.217, p. 107]

| $T$ (K) | $c_p$ (J/K mol) | $S$ (J/K mol) | $H$ (J/mol) | $G$ (J/mol) | $p$ (at) |
|---|---|---|---|---|---|
| 300 | 25.303 | 47.645 | 0.047 | − 14.247 | $6.87\times10^{-58}$ |
| 500 | 26.158 | 60.757 | 5.188 | − 25.191 | $2.82\times10^{-32}$ |
| 700 | 27.028 | 69.701 | 10.509 | − 38.282 | $2.49\times10^{-21}$ |

$T$ = Temperature, $c_p$ = specific heat capacity, $S$ = Entropy, $H$ = Enthalpy, $p$ = partial pressure of the pure elements

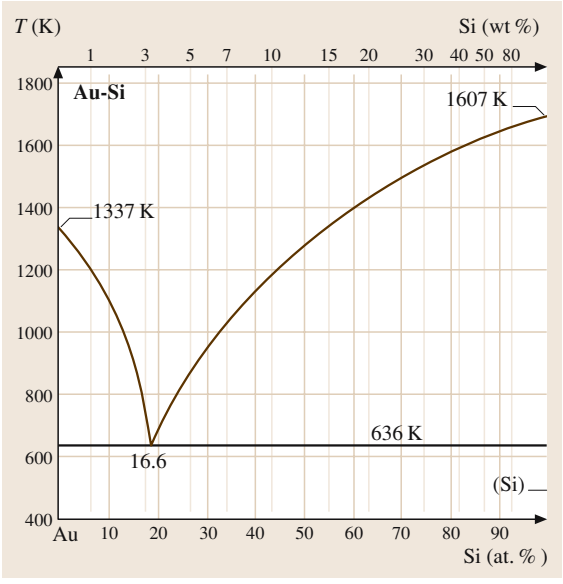


**Fig. 3.1-219** Binary phase diagram of Au−Si [1.245]

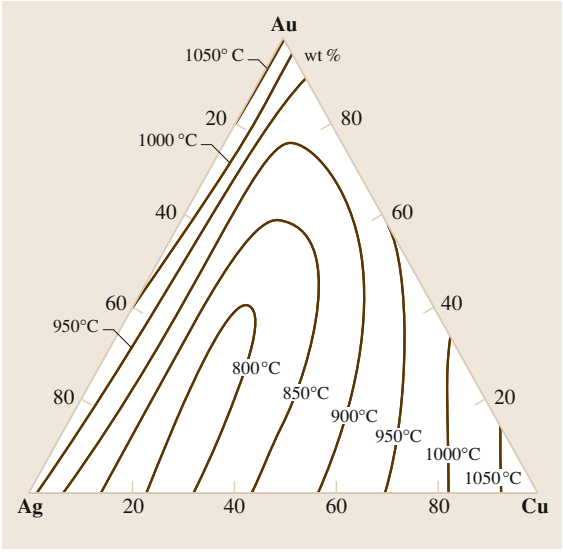


**Fig. 3.1-220** Liquidus sections through the miscibility gap of the Au−Ag−Cu system [1.246]

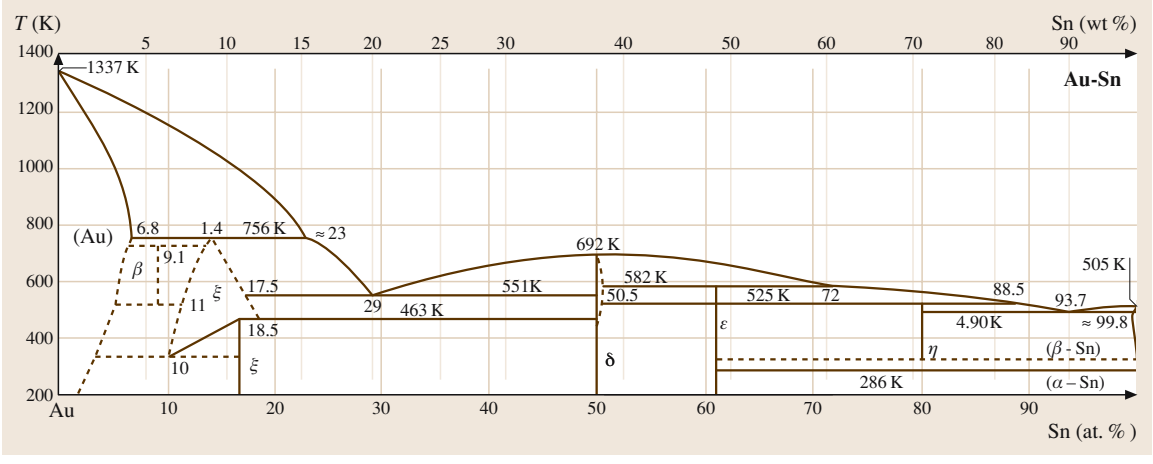


**Fig. 3.1-221** Binary phase diagram of Au−Sn [1.245]

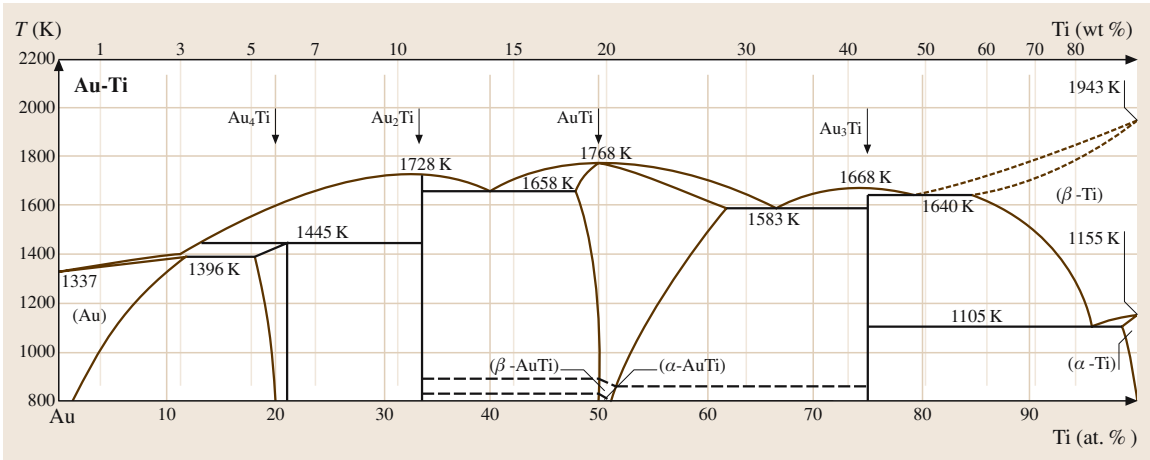


**Fig. 3.1-222** Binary phase diagram of Au−Ti [1.245]

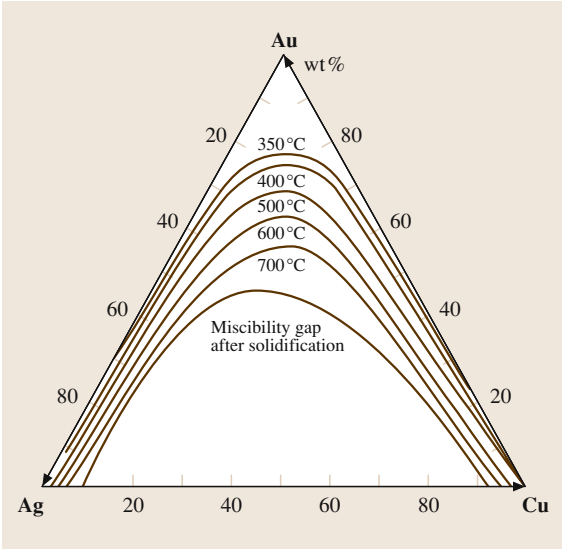


**Fig. 3.1-223** Isothermal sections through the miscibility gap of the Au−Ag−Cu system [1.246]

Superlattice phases occur in alloys with Cd, Cu, Mn, Pd, Pt, Rh, Ru, and Zn. The superlattice structures have tetrahedral or rhombohedral symmetry. Typical compositions are $AB_3$ and $A_3B$ [1.218]. If they are not precipitated as second phases, superlattice phases form antiphase domains on different sublattices separated by antiphase domain boundaries. Intermetallic compounds are formed with numerous elements with different and complex crystal structures [1.225]. Metastable phases exist with Ni and Pt. Alloys with B-metals form intermetallic phases at compositions corresponding to e/a values of 3/2, 21/13, and 7/4 (Hume-Rothery phases). Structural types of intermetallic compounds of gold with rare earth metals are listed in [1.248].

**Table 3.1-168** Heats, entropies and free energies of formation of Au compounds [1.222, p. 196]

| Phase | $N_2$ | $T$ (°C) | $H$ (J/mol) | $G$ (J/mol) | $S$ (J/K mol) |
|---|---|---|---|---|---|
| AuCu s.s. | 0.58 | 500 | 5.32 | 9.67 | 5.65 |
| $Au_3Cu$ | 0.26 | 25 | 4.03 | 4.90 | 2.97 |
| AuCu I | 0.50 | 25 | 8.96 | 8.96 | – |
| AuCu II | 0.50 | 400 | 6.03 | 8.79 | 4.10 |
| $AuCu_3$ | 0.75 | 25 | 6.87 | 7.24 | 1.26 |
| AuNi s.s. | 0.53 | 877 | −7.5 | – | 8.71 |
| AuSn | 0.50 | 25 | 14.24 | – | −0.4 |

$N_2$ = mole fraction of second compound,
$\Delta S$ = entropy of formation, s.s. = solid solution
s.s. = solid solution

**Table 3.1-169** Structure and lattice parameters of selected intermediate Au compounds [1.217, p. 113]

| Phase | Pearson Symbol | *a* (nm) | *b* (nm) | *c* (nm) | *c*/*a* | Remarks | Concentration (A/1 − *x*)B(*x*) |
|---|---|---|---|---|---|---|---|
| AuAl | mPs | 0.6415 | 0.3331 | 0.6339 | | | |
| $Au_2Al$ | oP30 | 0.8801 | 1.6772 | 0.3219 | | LT | 0.664–0.667 |
| $Au_5Al$ | cP20 | 0.69208 | | | | LT | |
| $Au-Al_2$ | cF12 | 0.59973 | | | | | 0.334 |
| AuCu | oI40 | 0.3676 | 0.3972 | | | 773 K | |
| AuCu | oP8 | 0.456 | 0.892 | 0.283 | | | |
| AuCu | tP4 | 0.3966 | | 0.3673 | 0.9261 | | 0.46–0.54 |
| $Au_3Cu$ | cP4 | 0.39853 | | | | | |
| Au–Pd | cP4 | 0.3991 | | | | | 0.552 |
| Au–Pt | cF4 | 0.3996 | | | | | 0.5 |
| Au–Sn | hP2 | 0.29228 | | 0.47823 | 1.6329 | | 0.14 |
| AuSn | hP4 | 0.43218 | | 0.5523 | 1.2779 | | |
| $AuSn_4$ | oC20 | 0.6502 | 0.6543 | 1.1705 | | 475 K | |
| $Au_4Ti$ | tI10 | 0.6485 | | 0.4002 | 0.6171 | | |

LT = low-temperature modification

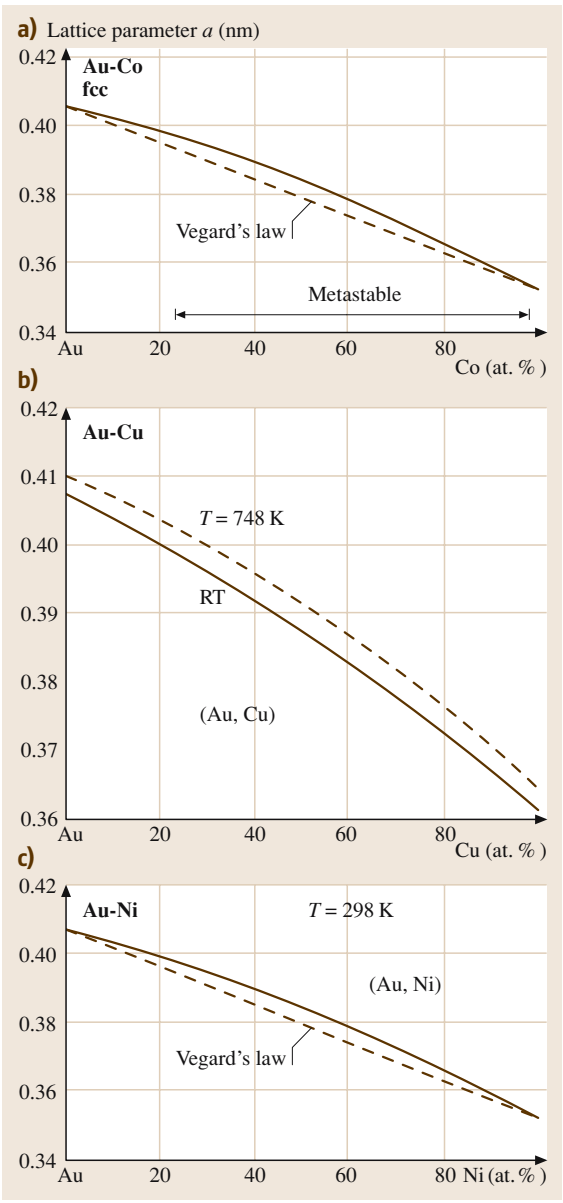


**Fig. 3.1-224a–c** Lattice parameter versus composition in the systems (**a**) Au–Co, (**b**) Au–Cu, (**c**) Au–Ni [1.245]

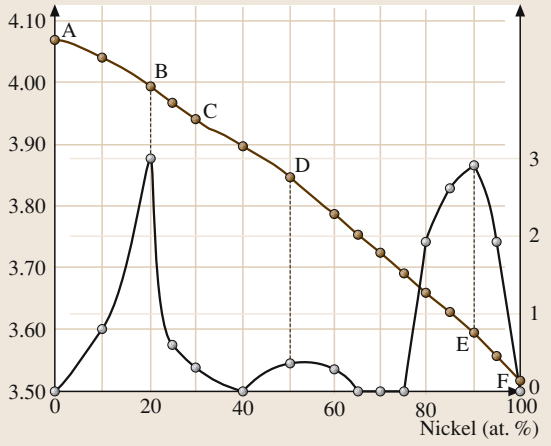


**Fig. 3.1-225** Vacant lattice sites in Au–Ni alloys [1.225, p. 141]

### Mechanical Properties

The mechanical properties of gold are given in Tables 3.1-170–3.1-176 and Figs. 3.1-226–3.1-237 [1.216, 217]. References for data of elastic constants of Au alloys are given in [1.217]. Pure gold is very soft. It can be cold-worked to more than 90% by

**Table 3.1-170** Modulus of elasticity of Au in crystal directions (GPa) [1.217, p. 208]

| *E* ⟨100⟩ | *E* ⟨110⟩ | *E* ⟨111⟩ |
|---|---|---|
| 42 | 81 | 114 |

**Table 3.1-171** Elastic constants of Au (GPa) [1.217, p. 209]

| *T* (°C) | *c*11 | *c*12 | *c*14 |
|---|---|---|---|
| −273 | 131.4 | 97.3 | 51.1 |
| 20 | 124.0 | 93.4 | 46.1 |

**Table 3.1-172** Mechanical properties of Au (99.99%) at different temperatures [1.217, p. 209]

| *T* (°C) | *E* (GPa) | $R_m$ (MPa) | $R_{p\,0.2}$ (MPa) | HV |
|---|---|---|---|---|
| 20 | 79 | 125 | 30 | 28 |
| 200 | 75 | 110 | 20 | 19 |
| 400 | 70 | 92 | – | 16 |
| 700 | 58 | 40 | – | 5 |

*E* = Modul of elasticity, $R_m$ = Tensile strength, $R_p$ = Limit of proportionality, HV = Vickers hardness

**Table 3.1-176** Mechanical properties of AuPt alloys in annealed and aged condition, Pt in wt% [1.217, p. 211] ▶

**Table 3.1-173** Tensile strength $R_m$ (MPa) of binary Au alloys [1.217, p. 210]

| Content (wt%) Alloying element | 2 | 5 | 10 | 20 |
|---|---|---|---|---|
| Ag | 140 | 150 | 170 | 190 |
| Co | 240 | – | – | – |
| Cr | 200 | – | – | – |
| Cu | 190 | 290 | 400 | 500 |
| Fe | 190 | – | – | – |
| Ni | 220 | 350 | 470 | 680 |
| Pd | 150 | 170 | 220 | 290 |
| Pt | 150 | 189 | 240 | 370 |

**Table 3.1-174** Mechanical properties of Au (99.99%) as a function of the reduction *V* (%) in thickness by cold forming [1.217, p. 209]

| *V* (%) | $R_m$ (MPa) | *A* (%) | HV |
|---|---|---|---|
| 0 | 120 | 45 | 28 |
| 10 | 140 | 22 | 55 |
| 30 | 180 | 75 | 63 |
| 50 | 220 | 4 | 65 |

$R_m$ = Tensile strength, *A* = Elongation of rupture, HV = Vickers hardness

**Table 3.1-175** Change of hardness (HV 10) of Au alloys by cold forming (Degree of reduction in thickness in %) [1.217, p. 210]

| Degree of reduction in thickness (%) Alloying element | 0 | 40 | 80 |
|---|---|---|---|
| Ag20 | 40 | 95 | 1141 |
| Ag25Cu5 | 92 | 160 | 188 |
| Ag20Cu10 | 120 | 190 | 240 |
| Co5 | 92 | 126 | 154 |
| Ni5 | 120 | 162 | 188 |
| Pt10 | 78 | 102 | 118 |
| Pd30Cu5 | 92 | 174 | 216 |

| Alloy | $R_m$ (MPa) | *A* (%) | HV |
|---|---|---|---|
| Pt10 [a] | 250 | 38 | 42 |
| Pt30 [a] | 430 | 12 | 120 |
| Pt30 [b] | 740 | – | 300 |
| Pt50 [a] | 900 | 3 | 240 |
| Pt50 [c] | 1460 | 2 | 420 |

[a] annealed at 1000–11 150 °C and quenched
[b] stored 70 h at 500 °C,
[c] stored 25 h at 500 °C

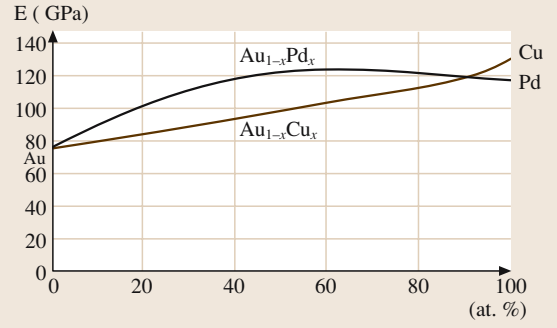


**Fig. 3.1-226** Modulus of elasticity of Au−Cu and Au−Pd alloys [1.217, p. 219]

**Fig. 3.1-227** Influence of alloying elements on the hardness of binary Au alloys [1.217, p. 211] ▶

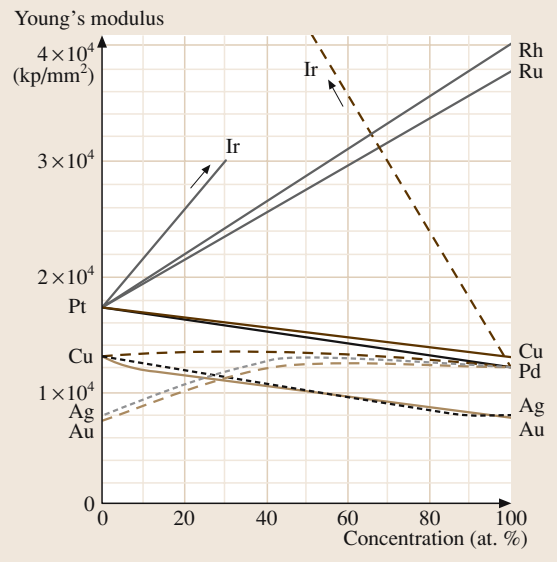


**Fig. 3.1-228** Modulus of elasticity versus composition of binary noble-metal alloys [1.216, p. 77]

rolling or drawing. Cold hard drawn wires (about 90% deformation) have predominantly ⟨111⟩ fiber texture, which is converted by annealing into ⟨100⟩ orientation [1.249]. Strengthening of pure gold is affected by alloying (solid solution hardening, precipitation hardening) or by dispersion hardening. Ternary Au−Ag−Cu

**Fig. 3.1-229a,b** Hardness of Au−Co alloys by annealing; **(a)** influence of time, **(b)** influence of temperature $T$ [1.231, p. 62]

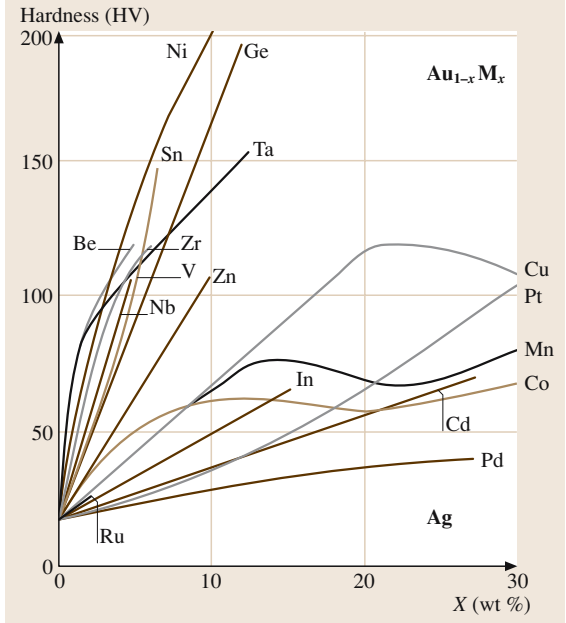


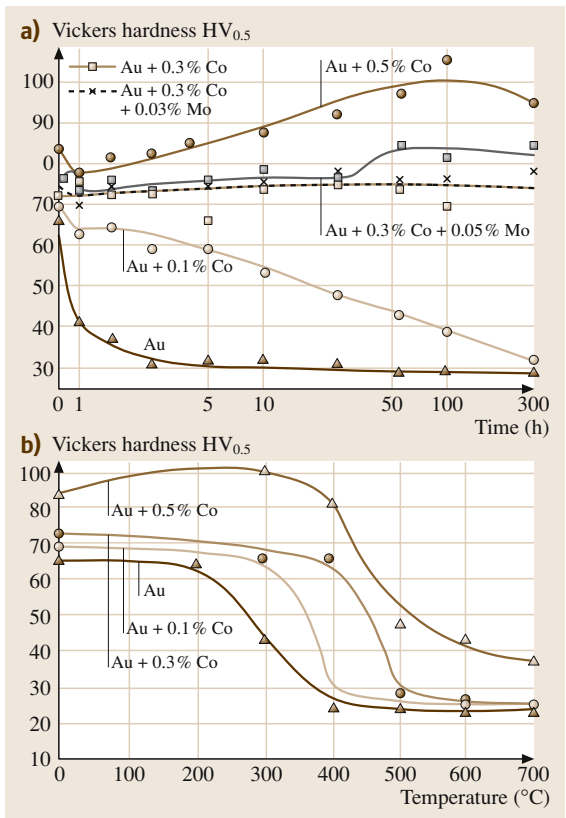

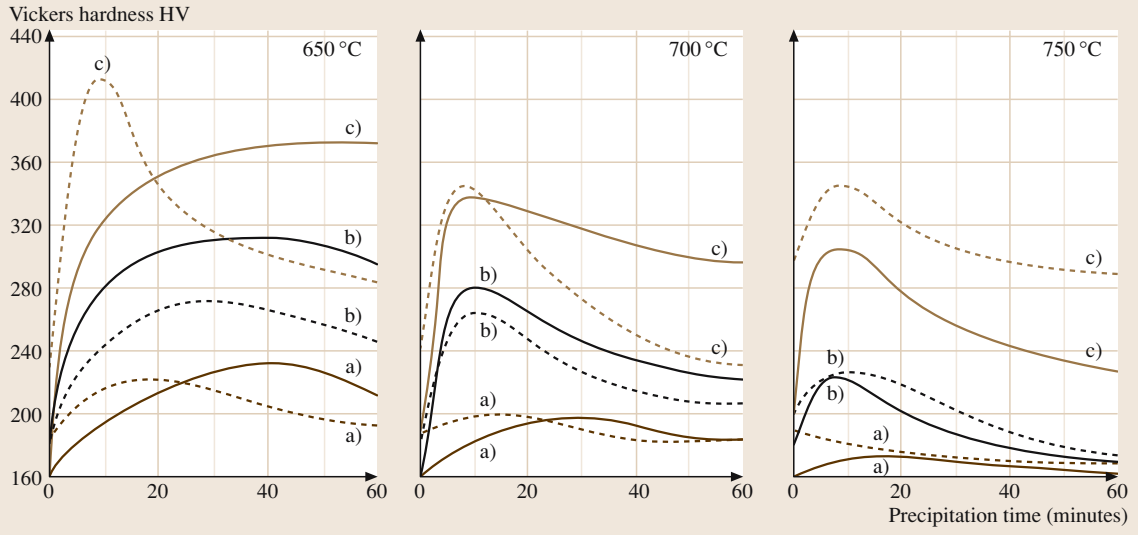


**Fig. 3.1-230** Precipitation hardening of Au/Pt-40 (*solid curve*) and Au/Pt-50 (*broken curve*): solution treatment 15 min at a) 950 °C, b) 1050 °C and c) 1150 °C. Precipitation hardening performed at 650 °C, 700 °C, and 750 °C [1.218, p. 610]

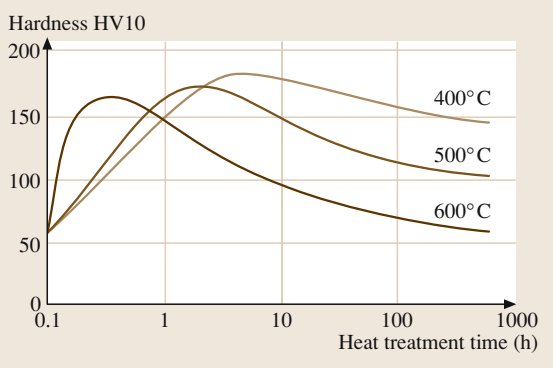


**Fig. 3.1-231** Precipitation-hardening characteristic of Au-1% Ti alloy by annealing [1.252, p. 139]

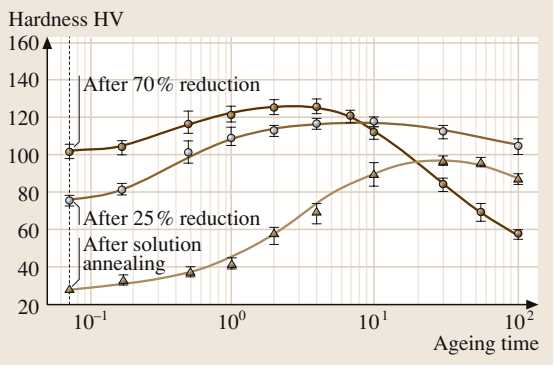


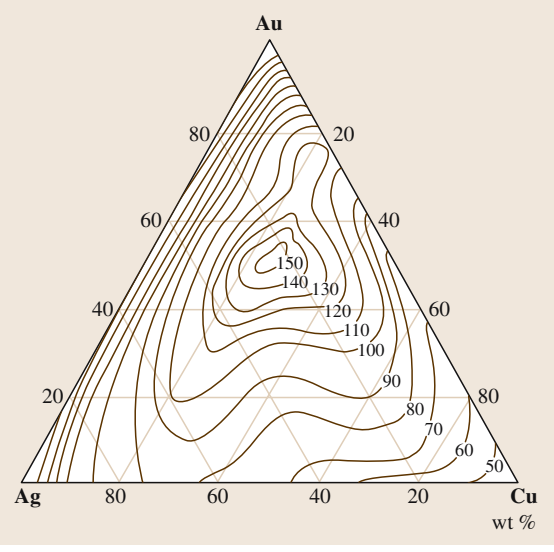


**Fig. 3.1-232** Hardness of annealed and quenched Au–Ag–Cu alloys [1.253, p. 517]

alloys can be hardened by decomposition into Cu-rich Cu–Au and Ag-rich Ag–Au phases during annealing below the critical temperature of the miscibility gap and

**Fig. 3.1-233** Hardness of the alloy AuSb0.3Co0.2 as a function of the reduction in thickness and of annealing time [1.254, p. 49]

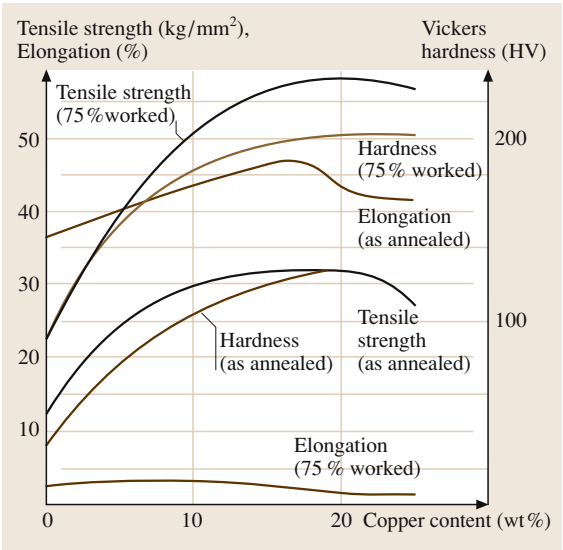


**Fig. 3.1-235** Tensile strength and hardness of 18 carat Au–Ag–Cu alloys as a function of Cu content [1.218, p. 437]

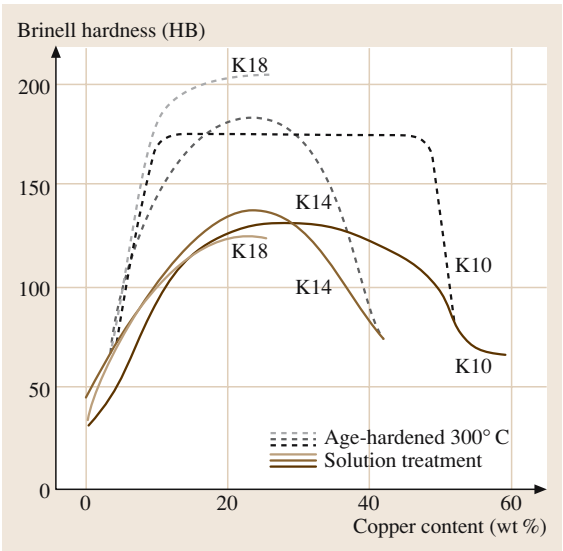


**Fig. 3.1-236** Influence of Cu content on age hardening of 14 carat and 18 carat Au–Ag–Cu alloys [1.218, p. 437]

by formation of the ordered Au–Cu-phase at more than 75 wt% Au. Hardening of Au by alloying with rare-earth metals is described in detail in [1.248]. Grain refinement, applied especially to jewelry and dentistry alloys, is affected by the addition of 0.05–1 at.% of Ir, Ru, or Co [1.250, 251].

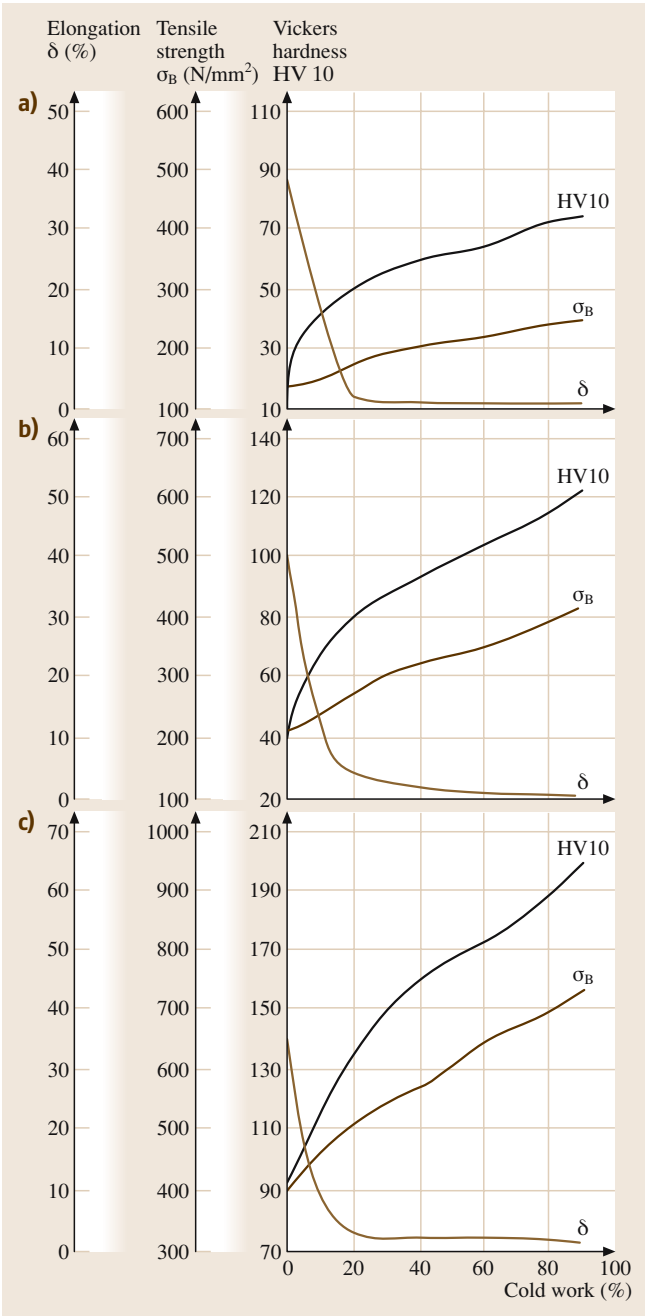


**Fig. 3.1-234a–c** Mechanical properties of (a) Au, (b) AuAg30, and (c) AuAg25Cu5 as a function of the reduction in thickness (%) [1.231, p. 58f.]

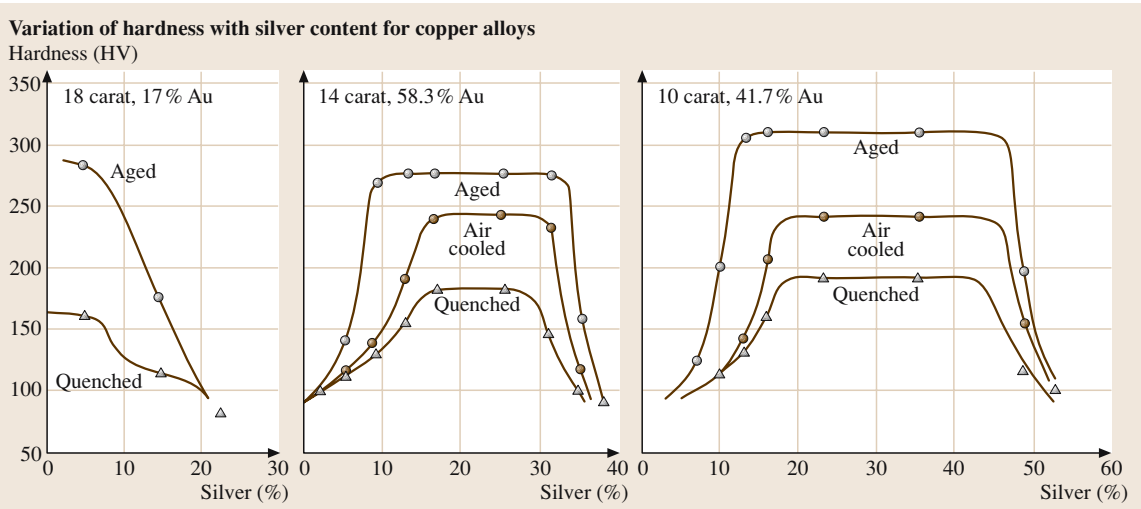


**Fig. 3.1-237** Variation of hardness with silver content for Au−Ag−Cu alloys [1.217]

### Electrical Properties

Tables 3.1-177–3.1-179 and Figs. 3.1-238, 3.1-239 [1.217, 231, 255] summarize the electrical properties of gold and gold alloys. The residual resistivity ratio for high purity gold amounts to 300. The electrical conductivity of gold alloys decreases in the low concentration range roughly linearly with the atomic concentration of the solute. Au alloys with 1.15 at.% Mn show increasing temperature coefficients of the electrical resistivity (positive TCR) due to the Kondo effect. This behavior is applied in resistance thermometers for temperature measurements below 20 K. Superconductivity occurs in intermetallic phases of Au−Ge with $2.99 < T_c < 3.16$ K and Au−Sn with $T_c = 1.25$ K [1.256, 257].

**Table 3.1-177** Specific electrical resistivity $\rho = \rho_0 + \rho_i(T)$ of Au at different temperatures ($\rho_0 = 0.0222\ \mu\Omega$ cm) [1.217, p. 157]

| $T$ (K) | 20 | 60 | 120 | 273.2 | 400 | 800 | 1000 | 1200 |
|---|---|---|---|---|---|---|---|---|
| $\rho(\mu\Omega\,\text{cm})$ | 0.0138 | 0.287 | 0.796 | 2.031 | 3.094 | 6.742 | 8.871 | 11.299 |

at $T < 400$ K, $\rho_0 = 0.014\ \mu\Omega$ cm at $T > 400$ K

**Table 3.1-178** Specific electrical resistivity ($\rho_{25}$) and temperature coefficient of resistivity (TCR) of Au−Pd and Au−Pt alloys [1.217, p. 158]

| Solute | Content | Content | | | |
|---|---|---|---|---|---|
| Content | | 80 | 60 | 40 | 30 |
| Pd | $\rho_{25}$ | 9.8 | 17 | 30 | 26 |
| | TCR | 0.88 | 0.61 | 0.45 | 1.2 |
| Pt | $\rho_{25}$ | 28 | 44 | 37 | 34 |
| | TCR | 0.28 | 0.26 | 0.82 | 0.8 |

$$\text{TCR}_{T_1\,T_2} = \frac{1}{\rho_1}\,\frac{\rho_{T_2} - \rho_{T_1}}{T_2 - T_1}$$

**Table 3.1-179** Increase of atomic electrical resistivity of Au by alloying elements $\Delta\rho/C$ (μΩ cm/at.%) [1.217, p. 157]

| Base element | Alloying elements | Δ ρ /C (μΩ cm/at.%) |
|---|---|---|
| Au | Ag | 0.35 |
| | Al | 1.9 |
| | Cd 0.60 | |
| | Co | 6.2 |
| | Cr | 4.5 |
| | Cu | 0.4 |
| | Fe | 8 |
| | Ga | 2.2 |
| | Ge | 5.5 |
| | Hg | 0.4 |
| | In | 1.4 |
| | Mn | 2.4 |
| | Mo | 4 |
| | Ni | 0.8 |
| | Pb | 3.9 |
| | Pt | 1 |
| | Rh | 3.3 |
| | Ru | 1.6 |
| | Sn | 3.5 |
| | Ti | 13 |
| | V | 13 |
| | Zn | 0.94 |

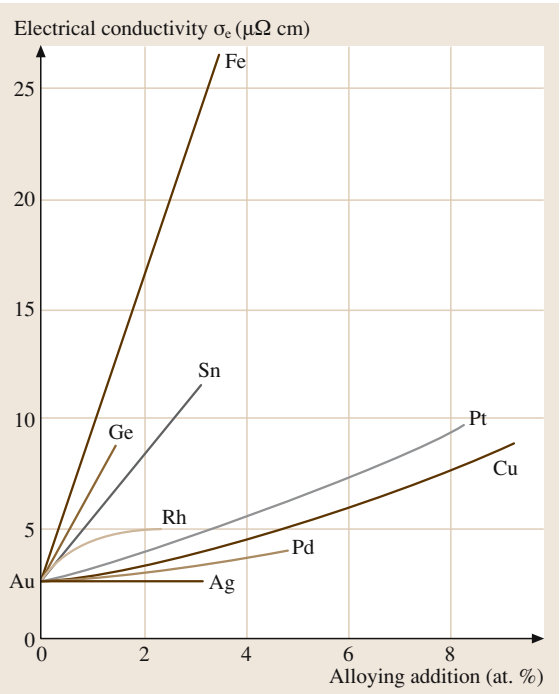


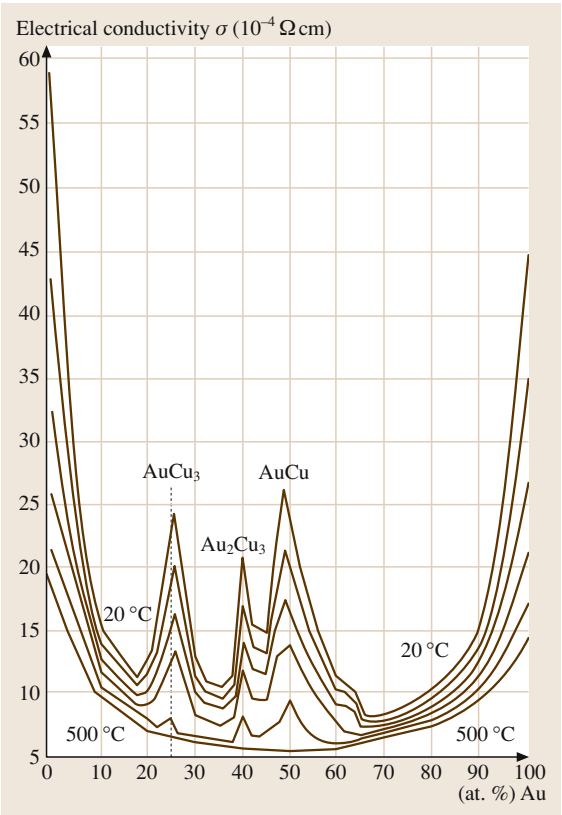


**Fig. 3.1-238** Specific electrical conductivity of Au–Cu alloy phases [1.255, p. 619]

**Fig. 3.1-239** Influence of alloying elements on the electrical conductivity of binary Au alloys [1.231, p. 50]

### Thermoelectric Properties

Tables 3.1-180–3.1-183 [1.216] and Figs. 3.1-240–3.1-242 [1.216, 218] list the thermoelectric properties of gold and its alloys. Au−Fe and Au−Co-alloys are used in thermocouples for measuring very low temperatures [1.258], Au−Pd and Au−Pd−Pt alloys in thermocouples working under highly corrosive conditions.

### Magnetic Properties

Figure 3.1-243 [1.217] illustrates the metal's magnetic properties. Gold is diamagnetic. The magnetic susceptibility remains constant from 0 K to the melting point. Alloying of gold with B metals causes only weak variations compared to pure gold. In the range of continuous solid solutions, the molar susceptibilities remain negative, the alloys are diamagnetic. Ni, Pd, and Pt dissolve diamagnetically up to 25 at.%. Cr, Fe, and Mn give rise to paramagnetism. Magnetic transformations are reported

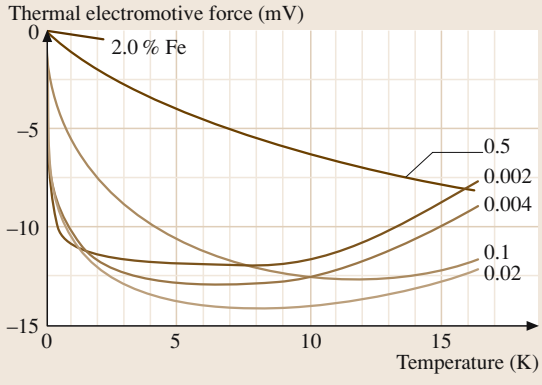


**Fig. 3.1-240** Thermal electromotive force of Au−Fe alloys [1.218, p. 58]

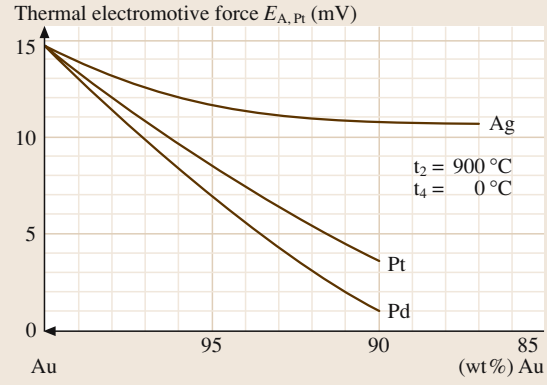


**Fig. 3.1-241** Thermal electromotive force of Au alloys [1.216, p. 97]

**Table 3.1-180** Absolute thermoelectric power of gold [1.216, p. 94]

| Temperature (°C) | −255 | −200 | −160 | −100 | 0 | 100 | 300 | 500 | 700 |
|---|---|---|---|---|---|---|---|---|---|
| Thermoelectr. power (μV/K) | −0.93 | −0.78 | +0.80 | +1.00 | +1.1 | +1.8 | +3.1 | +3.3 | +3.7 |

**Table 3.1-181** Thermal electromotive force $E$ of Au and Pt (mV) at different temperatures; reference junction at 0 °C [1.216, p. 159]

| $T$ (°C) | −200 | −100 | −50 | +100 | +200 | +400 | +800 |
|---|---|---|---|---|---|---|---|
| $E_{Au,Pt}$ (mV) | −0.39 | −0.21 | −0.10 | 0.77 | 1.834 | 4.623 | 12.288 |

**Table 3.1-182** Thermal electromotive force of Au−Fe and Au−Co-alloys [1.216, p. 100]

| $T_1$ (K) | $T_2$ (K) | Au−$Co_{2.1}$Cu (at.%) | Au−$Fe_{0.02}$Cu (at.%) |
|---|---|---|---|
| 4.2 | 10 | 0.044 | 0.093 |
| | 20 | 0.173 | 0.208 |
| 4.2 | 40 | 0.590 | 0.423 |

**Table 3.1-183** Thermocouples for very low temperatures [1.216, p. 97, 99]

- AuFe(0.03 at.% Fe)−chromel from 4.2 to 273 K
- AuCo(2.11 at.% Co)−AuAg (0.37 at.% Ag) or Cu from −240 to 0 °C
- AuFe(0.02 at.% Fe)−Cu from −270 to −230 °C

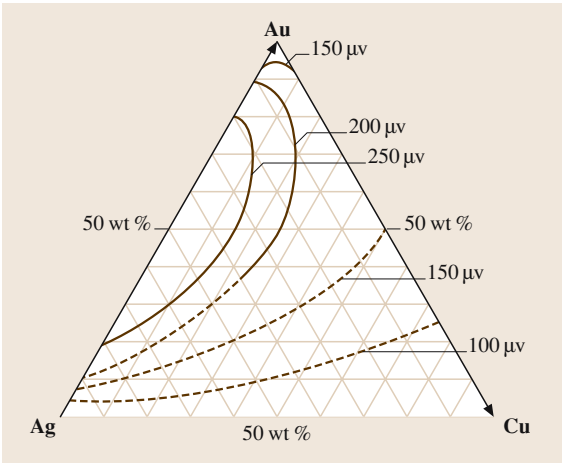


**Fig. 3.1-242** Thermal electromotive force of Au−Ag−Cu alloys [1.216, p. 99]

for Au−Co alloys between ≈ 18 and 92 wt% Co at 1122 °C and for Au−Ni alloys between ≈ 3 and 95 wt% at ≈ 340 °C [1.259].

### Thermal Properties

Data for thermal expansion and thermal conductivity of Au and Au alloys are listed in Tables 3.1-145–3.1-149. Table 3.1-184 [1.217] shows the recrystallization temperatures of gold of different purity. After 90% cold work, the hardness decreases by about 50%.

### Optical Properties

For the optical properties of colored Au alloys, see Tables 3.1-151, 3.1-152 and Figs. 3.1-244–3.1-247 [1.260–263]. The reflectivity of gold shows a marked decrease at ≈ 550 nm in the visible range with a minimum of $R \approx 0.25$ in the near ultraviolet. Interband transitions occur at ≈ 2.17 eV. The reflected light contains all wavelengths above 550 nm, which accounts for the typical gold color.

**Table 3.1-184** Recrystallization temperatures of Au 3N, 4N and 5N purity [1.217, p. 210]

| Purity (%) | Decrease of hardness | |
|---|---|---|
| | 50% $T_{recryst.}$ | 100% $T_{recryst.}$ |
| 99.9 (3N) | 200 | |
| 99.99 (4N) | 160 | 200 |
| 99.999 (5N) | 112 | 149 |

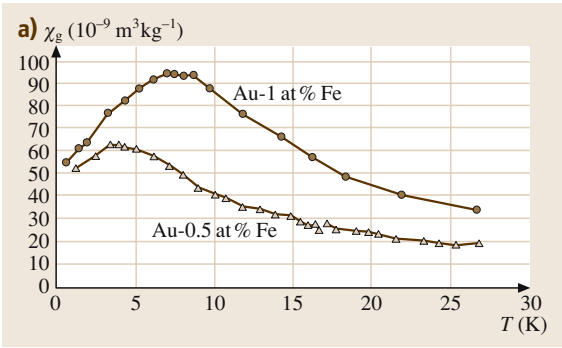


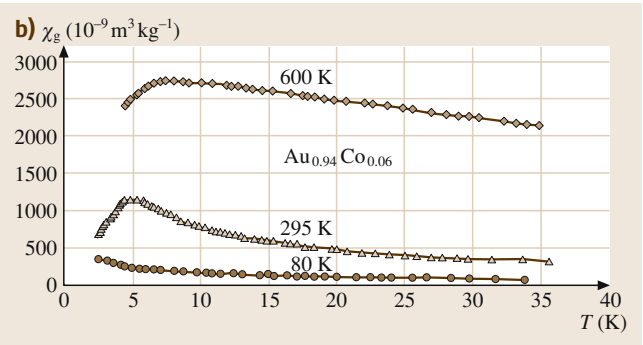


**Fig. 3.1-243a,b** Magnetic susceptibility of **(a)** Au−Fe and **(b)** Au−Co alloys [1.217, p. 169]

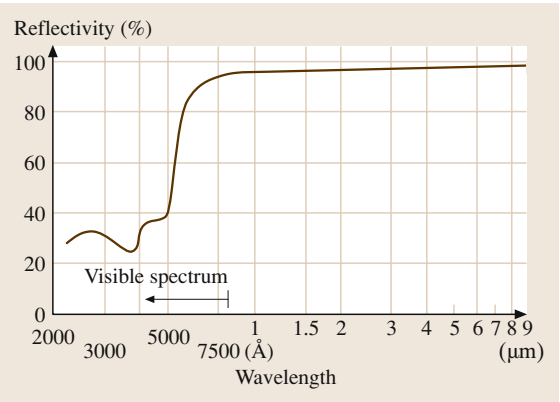


**Fig. 3.1-244** Reflectance as a function of wavelength of pure Au [1.260, p. 53]

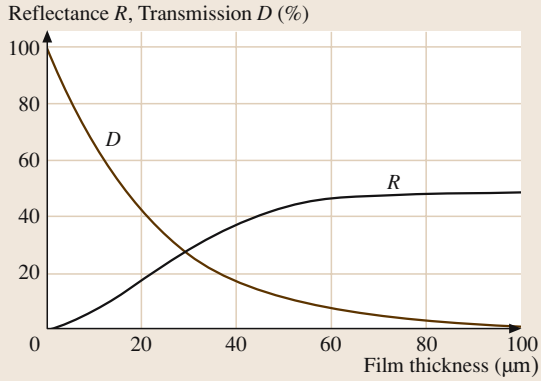


**Fig. 3.1-245** Reflectance and transmission of thin Au films at $\lambda = 492\,\mu m$ [1.260]

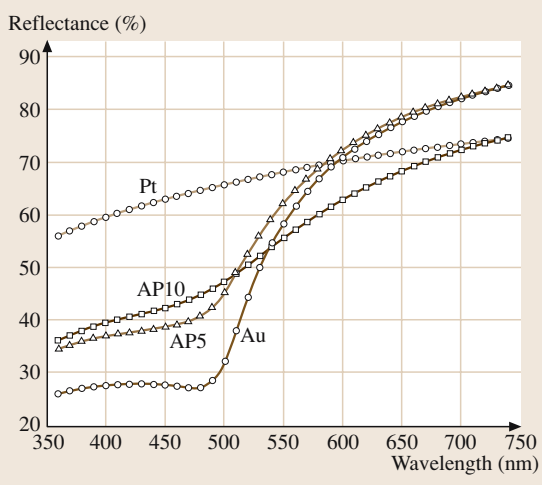


**Fig. 3.1-246** Reflectance-wavelength curves for Au−Pt and binary Au−Pt alloys [1.261, p. 130]

### Diffusion

Characteristic data are shown on Tables 3.1-153–3.1-156, 3.1-158 and Figs. 3.1-212, and 3.1-248 [1.217, 238].

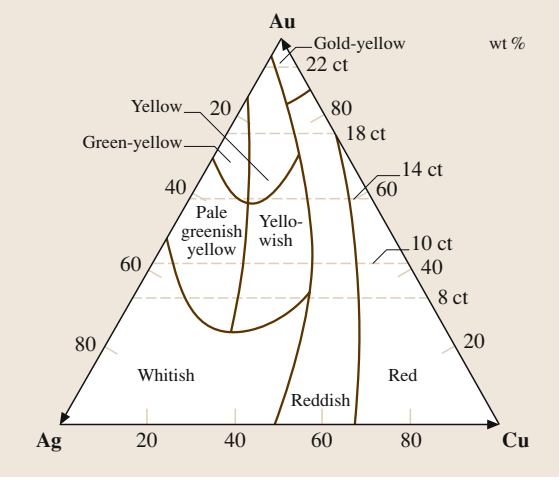


**Fig. 3.1-247** Color ranges of Au−Ag−Cu alloys [1.262, p. 37]

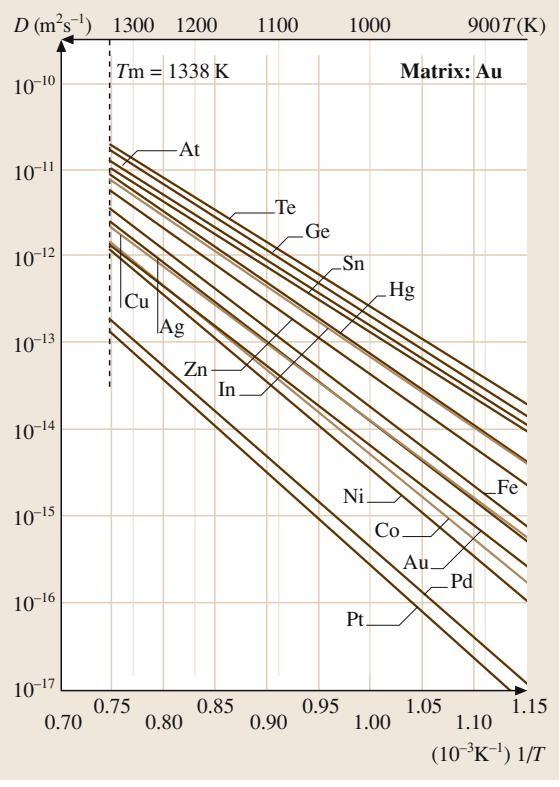


**Fig. 3.1-248** Diffusion of impurities in Au [1.238, p. 191]

### Chemical Properties

Figures 3.1-249 and 3.1-250 show that gold has the reduction potential of $E_0 = +1.42\,V$ for $Au/Au^{3+}$. At room temperature it is resistant against dry and wet atmospheres, $H_2O$, $O_2$, F, I, S, alkali, non-oxidizing acids, and ozone below 100 °C. It is dissolved in 3 HCl + 1 $HNO_3$, HCl + $Cl_2$ in acid concentration above 6 mol/l, in $NaCN/H_2O/O_2$, and other oxidizing solutions. Halogens generally attack gold, except for dry fluorine below 300 °C. Gold alloys are corrosion-resistant against acids if the base metal content is lower than 50% and also if each base metal present contains more than 50% of noble metal. Detailed information of chemical properties of Au and Au alloys are given in [1.217].

Gold and gold alloys (with Ag, Ir, Pt) and cationic gold (I) phosphines act as selective catalysts in hydrogenation, oxidation, and reduction reactions [1.264–266]. Nanometer-sized Au particles (≈ 5 nm) in the presence of ceria or a transition-metal oxide have superior catalytic activities [1.267–269, 269].

### Special Alloys

*Binary Alloys.* The material Au–20 wt% Ag is used for low-voltage electrical contacts. Gold–copper alloys form the ordered phases $Au_3Cu$ [60748-60-9], AuCu [12006-51-8], and $AuCu_3$ [12044-96-1]. Gold–nickel alloys decompose into gold-rich and nickel-rich solid solution phases in a miscibility gap below 800 °C. The alloy Au–18 wt% Ni is a structural material for turbine blades in jet engines and nuclear and space technology materials.

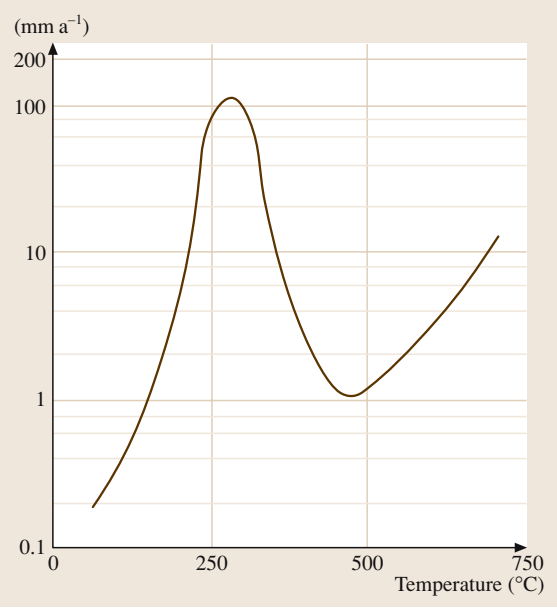


**Fig. 3.1-249** Corrosion of gold in dry chlorine gas [1.217, p. 183]

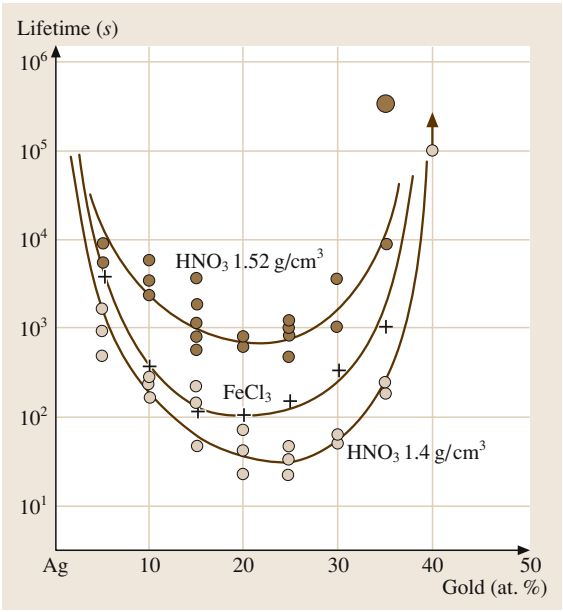


**Fig. 3.1-250** Lifetime of Ag−Au solid solutions in $HNO_3$ and $FeCl_3$ solution [1.217, p. 197]

Alloys of Au−Co(Fe, Ni) with 1–3 wt% Co, Fe, or Ni serve as hard and wear-resistant surface coatings on electrical contacts. The gold-cobalt alloy of Au–5 wt% Co is resistant against silver migration. The gold-platinum alloy of Au–10 wt% Pt is used for electrical contacts working under highly corrosive conditions. The high Pt content alloy Au–30 wt% Pt serves as a material for spinnerets for rayon and as a high-melting platinum solder ($T_{liquidus} = 1450\,°C$, $T_{solidus} = 1228\,°C$), additions ≈ 0.5% of Rh, Ru, or Ir suppress segregation. Gold-Platinum alloys containing 40 to 65 wt% Au harden by quenching from 1100 °C and annealing at 500 °C to yield strengths up to ≈ 1400 $N/mm^2$. Au–1 wt% Ti (Figs. 3.1-222, 3.1-231 [1.246, 252, 270, 271]) is of importance for bonding wires, electrical conductors, and as hard high-carat gold alloy for jewelry. Strengthening can be induced by precipitation of the intermetallic compound $Au_4Ti$ and by formation of highly-dispersed Ti oxide on annealing in an oxidizing atmosphere. The alloys Au–12 wt% Ge, Au–3.1 wt% Si, and Au–20 wt% Sn are low melting eutectic solders of high strength, corrosion resistance and stability against temperature cycling,

**Table 3.1-185** Physical properties of the eutectic alloys Au−20Sn, Au−12Ge, and Au−3Si [1.272, p. 194]

| Composition (wt%) | Melting point (°C) | Young's modulus versus temperature (GPa) −60 °C | 23 °C | 100 °C | 150 °C | Thermal conductivity (W/m K) | Coefficient of thermal expansion (ppm/°C) |
|---|---|---|---|---|---|---|---|
| Au−20Sn | 280 | 59.5 | 59.2 | 48.5 | 35.8 | 57.3 | 15.93 ± 0.88 (−50 to 170) |
| Au−12Ge | 356 | 69.8 | 69.3 | 68.2 | 62.7 | 44.4 | 13.35 ± 3.13 (10 to 250) |
| Au−3Si | 363 | 77.0 | 83.0 | 82.8 | 83.0 | 27.2 | 12.33 ± 0.86 (10 to 250) |

used for the hermetic sealing of electronic devices (Table 3.1-185 [1.272]).

*Ternary and Higher Alloys.* Au−Ag−Cu, Au−Ag−Ni and Au−Ag−Pd alloys are of major importance for jewelry and dentistry (Tables 3.1-186, 3.1-187) [1.250,251]. The microstructures and thus the mechanical properties are determined by wide miscibility gaps. Additions of Zn and In serve to adjust the melting ranges. The high-carat Au alloy AuSb0.3Co0.2 can be hardened by cold working and precipitation annealing to 142 HV5 (Fig. 3.1-233) [1.254].

AuAg25Pt5, AuAg26Ni3, and AuCu14Pt9Ag4 are used for electrical contacts working under highly corrosive conditions. AuNi22Cr6 is a hard solder of high mechanical stability [1.231]. Au−Ag−Ge alloys of various compositions are solders applicable under $H_2$, Ar, or vacuum in melting ranges between 400 and 600 °C. Additions of 0.5–2 wt% Pd, Cd, or Zn improve their ductility [1.273–275].

**Table 3.1-186** Basic compositions (wt%) of gold-based jewellery alloys [1.250, p. 271]

| Jewelry alloys | | | |
|---|---|---|---|
| **Colored gold fineness** | **Ag (wt%)** | **Cu (wt%)** | |
| 750 | 0–20 | 5–25 | |
| 585 | 5–35 | 5–35 | |
| 375 | 5–15 | 45–50 | |
| (333) | 5–40 | 25–60 | |
| **White gold fineness** | **Ag (wt%)** | **Cu (wt%)** | **Pd(Ni) (wt%)** |
| 750 | 0–10 | 0–10 | 10–20 |
| 585 | 0–25 | 5–30 | 5–20 |
| 375 | 0–35 | 5–50 | 5–20 |
| (333) | 0–35 | 10–50 | 5–25 |
| Zinc max. 20%. Tin, indium, gallium each max. 4% | | | |

**Table 3.1-187** Basic compositions of noble-metal-based dental alloys [1.251, p. 251]

| Noble metal base | Most common alloying elements |
|---|---|
| **Crown and bridge alloys** | |
| Au | Ag, Cu, Pt, Zn |
| Au−Ag | Pd, Cu, Zn, In |
| Ag−Pd | Cu, In, Au, Zn |
| **Porcelain fused to metal alloys** | |
| Au | Pt, Pd, In, Sn |
| Au−Pd | Sn, In, Ga, Ag |
| Pd | Cu, Ga, Sn, In |
| Pd−Ag | Sn, In, Zn |

### 3.1.10.3 Platinum Group Metals and Alloys

Characteristic properties of the platinum-group metals (PGM) Pd, Pt, Rh, Ir, Ru, and Os are their high chemical stability; mechanical strength; thermoelectric and magnetic behavior; and their catalytic activities in heterogeneous and homogeneous chemical reactions, automobile exhaust gas purification, and the stereospecific synthesis of enantiomeric compounds. Their melting temperatures, $T_m(\mathrm{Os}) = 3045\,^\circ\mathrm{C}$, $T_m(\mathrm{Pd}) = 1554\,^\circ\mathrm{C}$, hardness, brittleness, and the recrystallization temperatures decrease with increasing nuclear charge, while their thermal expansion and ductility increase.

The catalytic properties of the PGM in the heterogeneous catalysis are based on the moderate values of the heats of adsorption which correspond to the dissociation energies of the reactant molecules. Figure 3.1-251 [1.276] and Table 3.1-188 [1.218] give some values of the heat of adsorption and binding energies between adsorbates and surface atoms on various noble metal single crystals. The heat of adsorption increases for different orientations of the crystal surface planes of the fcc crystals in the order [111] < [100] < [110] (Table 3.1-189 [1.218]). The catalytic activities are element-specific for different reactions. Reactivity and selectivity of the reactions are presumably controlled by the dimensional fit between adsorbed molecules and catalyst surface, and the alloy composition. A survey of PGM catalyst activities is given in [1.217, 218, 243].

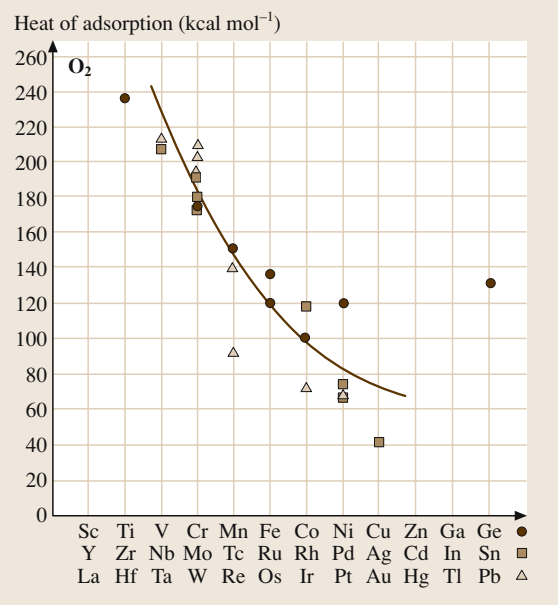


**Fig. 3.1-251** Heat of adsorption of molecular oxygen on polycrystaline transition metal surfaces [1.218, p. 265]

**Table 3.1-188** Binding energies (kcal/mol) between adsorbates and surface atoms on noble metal single crystals [1.218, p. 267]

| Precious metals | N | O | H | CO | NO |
|---|---|---|---|---|---|
| | Binding energy (kcal/mol) | | | | |
| Ru (0001) | | | 61 | 29 | |
| Ir (111) | 127 | 93 | 63 | 34 | 20 |
| Pd (111) | 130 | 87 | 62 | 34 | 31 |
| Pt (111) | 127 | | 57 | 30 | 27 |
| Ag (111) | | 80 | | 6.5 | 25 |

**Table 3.1-189** Heat of adsorption of diatomic molecules on different single crystals planes of various transition metals (kcal/mol) [1.218, p. 267]

| Adsorption system | (111) | (100) | (110) |
|---|---|---|---|
| | Heat of adsorption (kcal/mol) | | |
| $O_2Pd$ | 50 | 55 | 80 |
| Co/Ni | 27 | 30 | 30 |
| Co/Pd | 34 | 37 | 40 |
| Co/Pt | 30 | 32 | 32 |
| $H_2$/Pd | 21 | | 24 |
| $H_2$/W | 37 | 33 | 35 |
| $N_2$/Fe | 51 | 53 | 49 |

All platinum metals are paramagnetic ($\chi > 0$). The magnetic susceptibilities of palladium and platinum decrease with increasing temperature, the magnetic susceptibilities of rhodium, iridium, ruthenium, and osmium increase with increasing temperature (Fig. 3.1-272 [1.218]).

The platinum group metals occur jointly as alloys and as mineral compounds in placer deposits of varying compositions. Ru and Os are separated from the PGM mix by distillation of their volatile oxides, whereas platinum, iridium, palladium, and rhodium are separated by repeated solution and precipitation as complex PGM chlorides, or by solvent extraction and thermal decomposition to sponge or powder. PGM scrap is recycled by melting with collector metals (lead, iron, or copper) followed by element-specific extraction.

### Palladium and Palladium Alloys

*Applications.* Palladium and palladium alloys are important constituents of catalysts of chemical reactions and automobile exhaust gas cleaning, of electrical contacts, capacitors, permanent magnetic alloys, thermocouples, and for the production of high purity hydrogen. The low thermal neutron cross section permits their use in solders and brazes of nuclear structural parts. Classical applications are jewelry and dentistry alloys.

Commercial grades of palladium are sponge and powder in purities of 99.9 wt% to 99.95–99.98 wt% (ASTM (B 589-82)). High purity electronic grade is 99.99 wt%.

*Production.* Palladium sponge or powder are compacted by pressing and sintering. Melting and alloying is performed in electrical heated furnaces, vacuum arc, or by electron beam melting. Crucible materials are $Al_2O_3$ and MgO.

*Phases and Phase Equilibria.* Selected phase diagrams are shown in Figs. 3.1-252 – 3.1-257 [1.219]. Pd forms continuous solid solutions with all other noble metals and with Co, Cu, Fe, and Ni. Miscibility gaps exist in alloys with C, Co, Ir, Pt, Rh, and ternary Pd–Ag–Cu alloys (Fig. 3.1-257) [1.220]. All platinum-group metals (PGM) lower the $\gamma$–$\alpha$ transition temperature in Fe-alloys considerably (Fig. 3.1-343). Thermodynamic data are given in Tables 3.1-190 – 3.1-194. Numerous intermediate phases exist also in alloys with rare earth metals [1.216, 217, 217, 222]. The solubility of

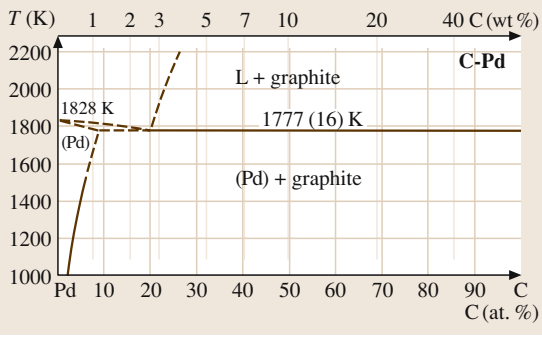


**Fig. 3.1-252** Binary phase diagram Pd–C [1.219]

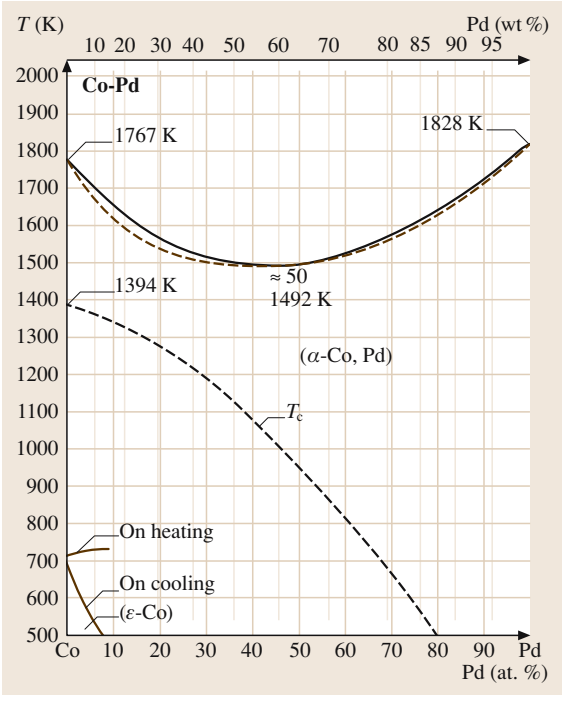


**Fig. 3.1-253** Binary phase diagram Pd–Co [1.219]

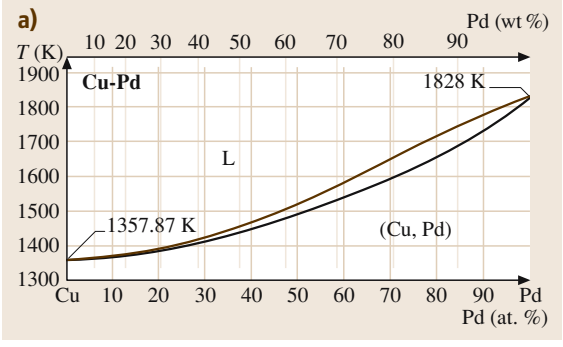


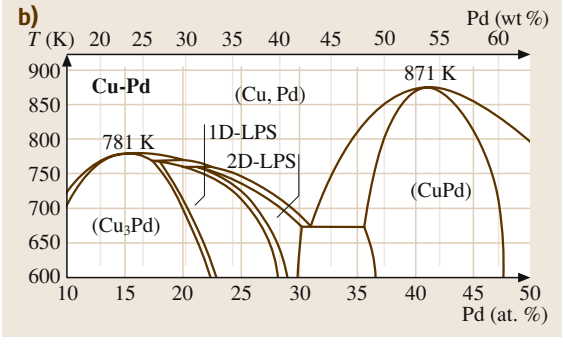


**Fig. 3.1-254a,b** Binary phase diagrams: Pd–Cu. **(a)** liquid–solid equilibrium; **(b)** low temperature (600–900 °C). 1-D LPS = one-dimensional long-period superstructure; 2-D LPS = two-dimensional long-period superstructure [1.219]

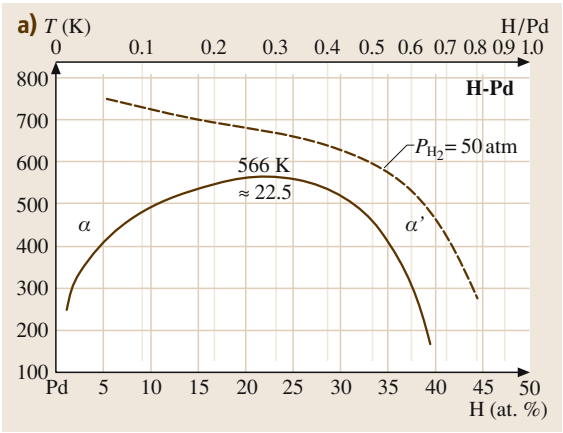


**Fig. 3.1-255a,b** Binary phase diagrams: Pd–H. **(a)** Phase diagram; **(b)** low temperature phase [1.219]

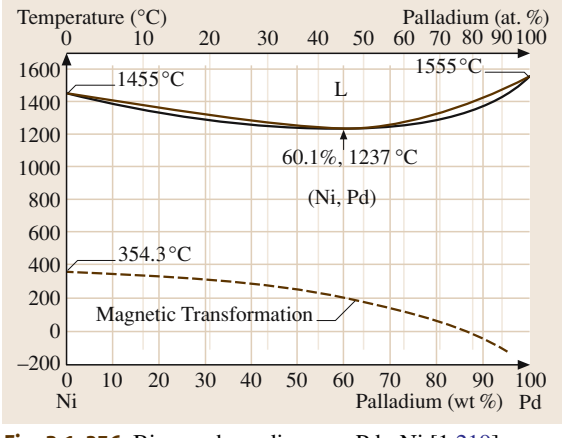


**Fig. 3.1-256** Binary phase diagram: Pd–Ni [1.219]

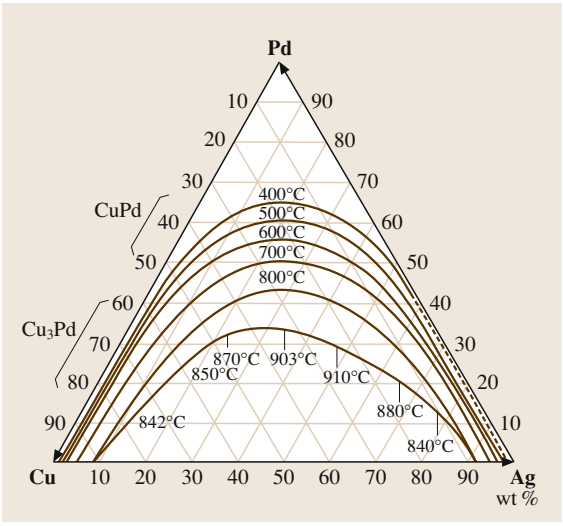


**Fig. 3.1-257** Miscibility gap in the Pd–Ag–Cu alloy system [1.220]

**Table 3.1-190** Molar heat capacities of solid PGMs [1.222, p. 219]

| Element | $c_p = 4.1868\left(a + 10^{-3}bT + 10^{-5}T^2\right)$ J/K | | | |
|---|---|---|---|---|
| | *a* | *b* | *c* | Temperature range (K) |
| Ir | 5.56 | 1.42 | – | 298–1800 |
| Os | 5.69 | 0.88 | – | 298–1900 |
| Pd | 5.80 | 1.38 | – | 298–1828 |
| Pt | 5.80 | 1.28 | – | 298–2043 |
| Rh | 5.49 | 2.06 | – | 298–1900 |
| Ru | 5.20 | 1.50 | – | 298–1308 |
| Ru | 7.20 | – | – | 1308–1773 |
| Ru | 7.50 | – | – | 1773–1900 |

**Table 3.1-191** Latent heat and temperatures of transition of Pd and Pt intermediate compounds [1.222, p. 189]

| Phase | $N_2$ | Transition | $T_t$ | $L_t$ |
|---|---|---|---|---|
| CuPt | 50 | order-disorder | 800 | 3810 |
| $Cu_3Pt$ | 20 | order-disorder | 610 | 1968 |
| $Pd_3Sb$ | 25 | order-disorder | 950 | 10 300 |

$T_t$ = transition temperature, $L_t$ = latent heat of transition

carbon rises from 0.04 wt% at 800 °C to 0.45 wt% at 1400 °C, with the hardness increasing from 80 to 180 $HV_{25\,g}$ [1.277]. The continuous series of solid solutions of Pd–H-alloys (Fig. 3.1-258) [1.277] splits up below 295 °C into a fcc palladium-rich $\beta$ phase and an fcc hydrogen-rich phase, forming a miscibil-

**Table 3.1-192** Thermodynamic data of Pd [1.217, p. 108]

| $T$ (K) | $c_p$ (J/K mol) | $S$ (J/K mol) | $H$ (J/mol) | $G$ (J/mol) | $p$ (at) |
|---|---|---|---|---|---|
| 298.15 | 25.99 | 37.823 | 0 | −11.277 | $5.97\times10^{-60}$ |
| 400 | 26.706 | 45.568 | 2.686 | −13.541 | $3.65\times10^{-43}$ |
| 600 | 27.768 | 56.602 | 8.136 | −25.825 | $8.92\times10^{-27}$ |
| 800 | 28.827 | 64.733 | 13.704 | −37.903 | $1.11\times10^{-18}$ |

$T$ = Temperature, $c_p$ = specific heat capacity, $S$ = Entropy, $H$ = Enthalpy, $G$ = free Enthalpy, $p$ = partial pressure of the pure elements

**Table 3.1-193** Enthalpy of formation $H_T$ of Pd and Pt alloys at temperatures of reaction [1.216, p. 89]

| Base metal | Concentration of alloying metal in at.% [ETA 89] Alloy comp. | Temp. (K) | 20 at.% | 40 at.% | 60 at.% | 80 at.% |
|---|---|---|---|---|---|---|
| Enthalpy of formation $H_T$ | | | | | | |
| Pd | Ag | 915 | | | | 1050 |
| | | 1200 | 283 | 897 | 1290 | 887 |
| Pt | Co | 914 | 1680 | 2580 | | |
| | Cu | 1625 | (30%):3110 | | 3375 | (90%):1950 |
| | Fe | 1123 | −680 | 0 | 1600 | 1800 |

**Table 3.1-194** Maximum hydrogen inclusion by platinum-group metals in ml/g (elements) [1.217, p. 616]

| Element | Max $H_2$ (ml/g) | Composition |
|---|---|---|
| Ru | 123 | $RuH_{1.1}$ |
| Rh | 24 | $RhH_{0.2}$ |
| Pd | 75 | $PdH_{0.7}$ |
| Os | 75 | $OsH_{1.2}$ |
| Ir | 35 | $IrH_{0.6}$ |
| Pt | 2.4 | $PtH_{0.04}$ |

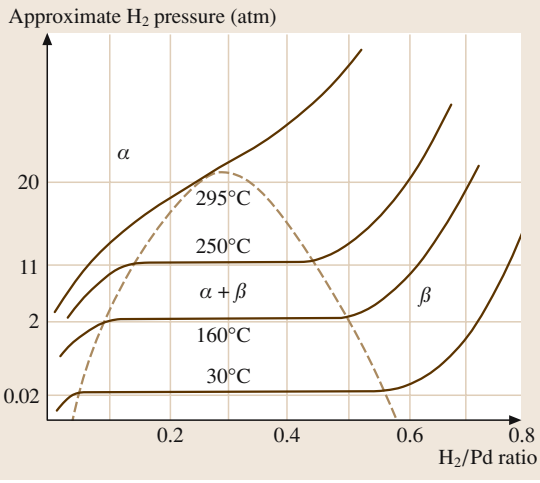


**Fig. 3.1-258** Hydrogen pressure in the Pd−H system [1.278, p. 130]

ity gap which broadens with decreasing temperature. The equilibrium hydrogen-pressure at 295 °C amounts to 19.87 atm with 21 at.% hydrogen. The $\alpha$-phase takes hydrogen up to 1300 times of the volume of palladium, corresponding 50 at.% hydrogen. Further quantities up to 2800 times of the Pd-volume can be loaded by cathodic deposition. The lattice parameters increase with increasing hydrogen content from 3.891 A to 4.06 A at 75 at.% hydrogen. The dissolved hydrogen moves easily and diffuses quickly through thin Pd-membranes. This effect is used for the production of high-purity Pd and for the separation of H isotopes.

Thermal cycling of Pd−H-alloys in the duplex phase causes brittleness due to stresses generated by changes of the lattice dimensions for different quantities of dissolved hydrogen. Palladium-silver alloys with 20–25 wt% silver dissolve higher amounts of hydrogen than pure palladium (Fig. 3.1-259).

For composition and crystal structures, see Tables 3.1-195 and 3.1-196 [1.217, 219, 277]. Primary solid solutions have the fcc structure of Pd. The lattice parameters correspond with few exceptions roughly to Vegard's law. Superlattices occur in alloys with Cu, Fe, Nb, V, in atomic ratios from 1:1, 2:1, and 3:1 (Tables 3.1-123, 3.1-197).

Ordered $A_3B$-phases of Pd−Mn and Pd−Fe alloys show higher solubility for hydrogen than the disordered phases. In Pd−Mn alloys, hydrogen uptake lowers the temperature of the ordering process.

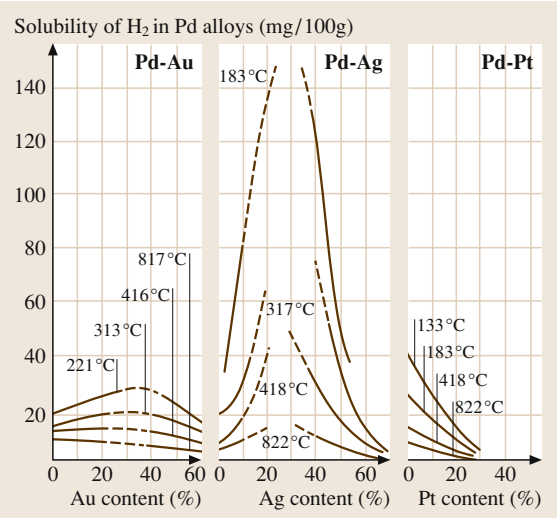


**Fig. 3.1-259** Solubility of hydrogen at 1 atm in Pd−Au, Pd−Ag, and Pd−Pt alloys [1.279, p. 44]

**Table 3.1-196** Structures of platinum-group metal oxides [1.219, 277]

| Oxide | Structure type | Unit cell dimensions (Å) | | |
|---|---|---|---|---|
| | | *a* | *b* | *c* |
| $\alpha$-$PtO_2$ | primitive hexagonal | 3.08 | | 4.19 |
| $\beta$-$PtO_2$ | primitive othorhombic | 4.486 | 4.537 | 3.138 |
| $Pt_3O_4$ | primitive cubic | 5.585 | | |
| PdO | tetragonal | 3.043 | | |
| PdRhO | hexagonal | 5.22 | | 6.0 |
| $Rh_2O_3$ (LT) | hexagonal (corundum) | 5.108 | | 13.87 |
| $Rh_2O_2$ | tetragonal (rutile) | 4.4862 | 3.0884 | |
| PdO | tetragonal PdO | 3.03 | | 5.33 |
| $PdO_2$ | tetragonal $TiO_2$ (rutile) | 4.483 | | 3.101 |

LT = low temperature modification

**Table 3.1-195** Structure and lattice parameters of selected intermediate Pd compounds [1.217, p. 118]

| Phase | Pearson Symbol | *a* (nm) | *b* (nm) | *c* (nm) | *c*/*a* | Remarks | Concentration *x* A(1 − *x*)B(*x*) |
|---|---|---|---|---|---|---|---|
| C−Pd | cF4 | 0.3735 | | | | | 0.97 |
| Co−Pd | cF4 | 0.3735 | | | | | |
| Cu−Pd | cF4 | 0.377 | | | | HT | 0.5 |
| $Cu_3Pd$ | tP4 | 0.3701 | 0.3666 | 0.9905 | | | |
| $Cu_3Pd$ | tP28 | 0.371 | 2.5655 | 6.9151 | | | 0.19 |
| Fe−Pd | cF4 | 0.38873 | | | | | 0.936 |
| FePd | tP4 | 0.386 | | 0.3731 | 0.9666 | | |
| $FePd_3$ | cP4 | 0.3851 | | | | | |
| $H_3Pd_5$ | cF* | 0.4018 | | | | | |
| $H_4Pd_3$ | cP* | 0.2995 | | | | HT > 923 K | |
| $H_4Pd_3$ | tP4 | 0.2896 | | 0.333 | 1.1499 | | |
| Ni−Pd | cF4 | 0.373 | | | | 298 K | 0.474 |
| $Pd_3Zr$ | hP16 | 0.5612 | | 0.9235 | 1.6456 | | |

HT = high temperature modification

| Ordered structure type | Examples |
|---|---|
| Tetragonal ($L1_0$-type) | CdPt, CoPt, $Cu_4Pd$, FePd, FePt, MnPt, NiPt |
| Face-centered cubic ($L1_2$-type) | $CoPt_3$, $Cu_3Pt$, $FePd_3$, $FePt_3$, $Fe_3Pt$, $MnPt_3$, $Ni_3Pt$ |
| Body-centered cubic (B2-type) | BePd, CuPd, FeRh, RhSc, RhTi |
| Rhombohedral ($L1_1$-type) | CuPt (unique) |
| Close-packed hexagonal ($DO_{19}$-type) | $Pt_3U$ |

**Table 3.1-197** Superlattice structures of the platinum-group metals [1.280, p. 22]

*Mechanical Properties.* Characteristic data are shown in Tables 3.1-198 – 3.1-202 and Figs. 3.1-260 – 3.1-266 [1.217, 220, 231, 277]. At room temperature Pd is very ductile and can be easily rolled or drawn to form a sheet, foil, and wire. The recrystallization temperatures (Table 3.1-212) depend on purity grade, degree of cold forming and annealing time. Strengthening is affected by solid solution and by order hardening in alloys, forming superlattice structures. Solid solution hardening is also effected by alloying with rare earth metals in concentrations of 0.1 – 0.6 at.%.

**Table 3.1-198** Modulus of elasticity in crystal directions (GPa) [1.217, p. 214]

| *E*⟨100⟩ | *E*⟨110⟩ | *E*⟨111⟩ |
|---|---|---|
| 65 | 129 | 186 |

**Table 3.1-199** Elastic constants of Pd [1.217, p. 216]

| *T* (°C) | *c*11 | *c*12 | *c*14 |
|---|---|---|---|
| −273 | 234.1 | 176.1 | 71.2 |
| 7 | 226.2 | 175.2 | 71.5 |

**Table 3.1-200** Mechanical properties of Pd (99.9%) at different temperatures (°C) [1.217, p. 215]

| *T* (°C) | *E* (GPa) | $R_m$ (MPa) | *A* (%) | $R_{p0.2}$ (MPa) | HV |
|---|---|---|---|---|---|
| 20 | 124 | 190 | 25 | 50 | 50 |
| 250 | 121 | 180 | 16 | 90 | 47 |
| 500 | 117 | 68 | 94 | 50 | 39 |
| 750 | 98 | 28 | 42 | 20 | 17 |

$A$ = Elongation, $E$ = Modul of elasticity,
$R_p$ = Limit of proportionality, HV = Vickers hardness,
$R_m$ = Tensile strengh

**Table 3.1-201** Tensile strength (MPa) of binary Pd and Pt alloys [1.217, p. 223]

| Alloying element | Weight % of alloying element 2 | | 5 | | 10 | |
|---|---|---|---|---|---|---|
| | Pd | Pt | Pd | Pt | Pd | Pt |
| Ag | 230 | 370 | 270 | 550 | 310 | 830 |
| Au | 200 | 200 | 220 | 320 | 230 | 540 |
| Co | 190 | 360 | 210 | – | 270 | – |
| Cu | 240 | 290 | 280 | 400 | 300 | – |
| Fe | 200 | 360 | 230 | – | 340 | – |
| Ni | 190 | 260 | 219 | 450 | 270 | 640 |
| Pd | – | 170 | – | 190 | – | 200 |
| Pt | 200 | – | 220 | – | 240 | – |
| Rh | 230 | 170 | 290 | 230 | 380 | 330 |
| Ru | 230 | 250 | 350 | 380 | – | 550 |

**Table 3.1-202** Mechanical properties of Pd by cold forming as a function of reduction in thickness *V* in % [1.217, p. 215]

| *V* (%) | $R_m$ (MPa) | *A* (%) | HV |
|---|---|---|---|
| 0 | 220 | 60 | 50 |
| 20 | 250 | 170 | 80 |

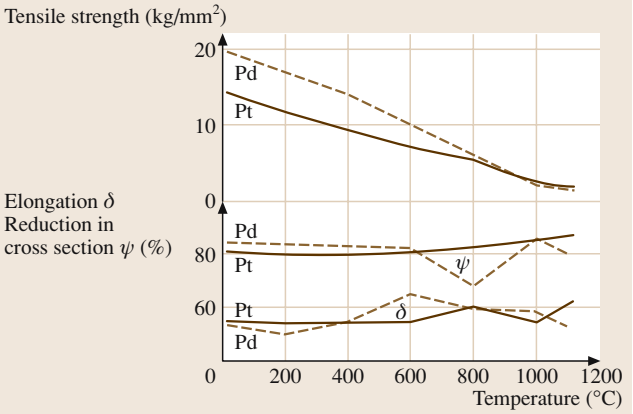


**Fig. 3.1-261** Tensile strength of Pd and Pt at different temperatures [1.220, p. 82]

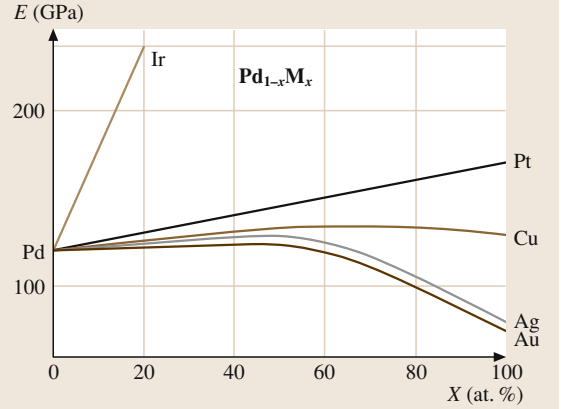


**Fig. 3.1-260** Modulus of elasticity of Pd alloys [1.217, p. 216]

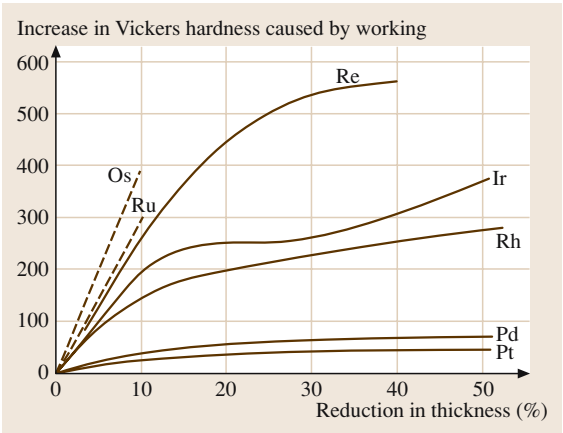


**Fig. 3.1-262** Work hardening of the platinum group metals [1.277, p. 93]

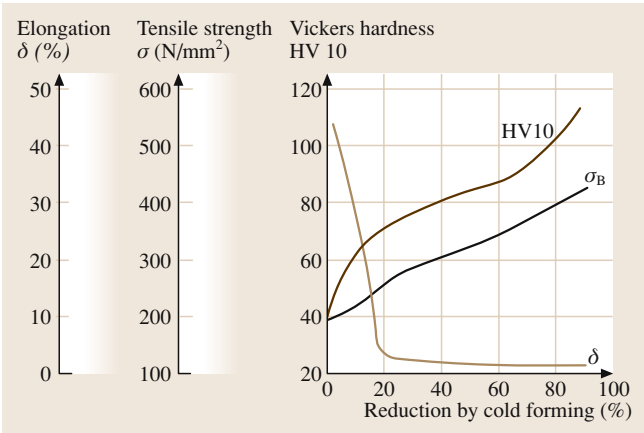


**Fig. 3.1-263** Work hardening of Pd (99.99%) (% reduction by cold forming) [1.231, p. 71]

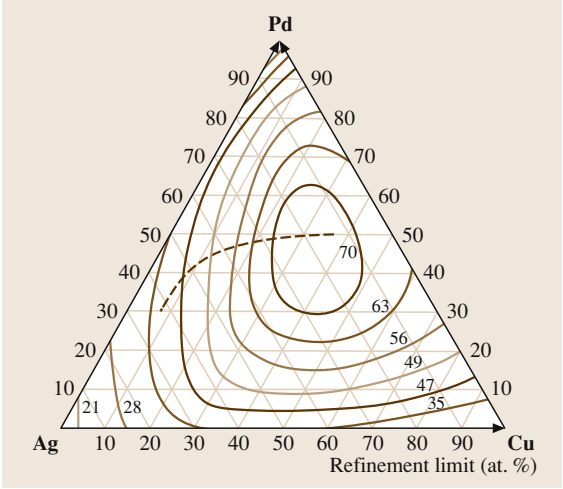


**Fig. 3.1-265** Tensile strength of Pd−Ag−Cu alloys. *Dashed line*: refinement limit [1.220, p. 268]

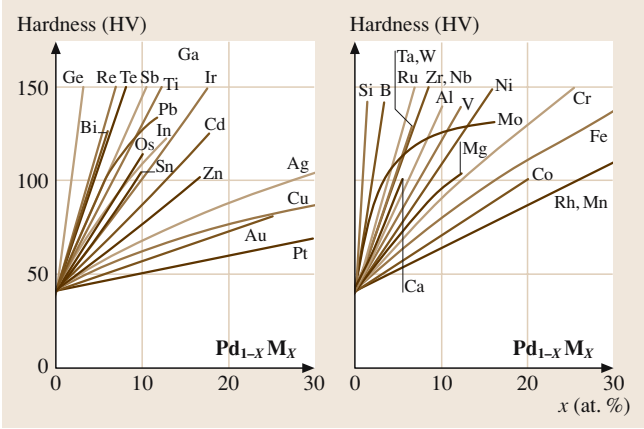


**Fig. 3.1-264** Solid solution hardening of Pd by various elements [1.217, p. 217]

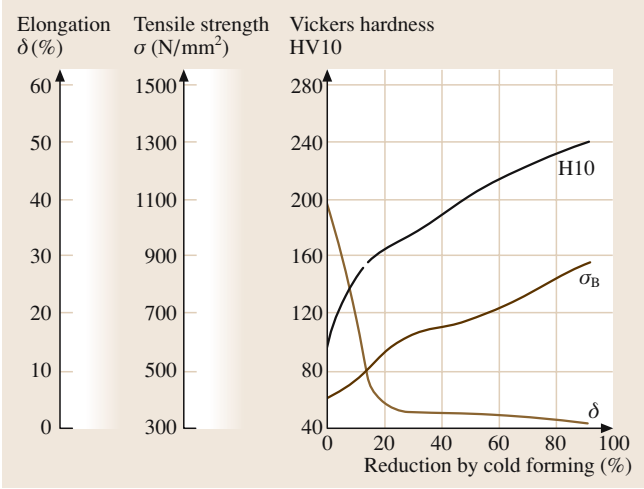


**Fig. 3.1-266** Work hardening of PdCu15 alloys (% reduction by cold forming) [1.231, p. 72]

*Electrical Properties.* In Tables 3.1-203 – 3.1-205 [1.217] and Figs. 3.1-267, 3.1-268 [1.228, 231] characteristic data are shown. Pure Pd shows no superconductivity, PdH and some intermetallic compounds are superconducting at low critical temperatures, e.g., $T_c(Bi_2Pd) = 3.7\,K$.

**Table 3.1-203** Residual electrical resistivity ratio (RRR) of pure noble metals [1.217, p. 156]

| 273.2 K/4.2 K | | | | | | | |
|---|---|---|---|---|---|---|---|
| **Ru** | **Rh** | **Pd** | **Ag** | **Os** | **Ir** | **Pt** | **Au** |
| 25 000 | 570 | 570 | 2100 | 400 | 85 | 5000 | 300 |

**Table 3.1-204** Increase of atomic resistivity of Pd and Pt [1.217, p. 158]

| Basic element | $\Delta\rho/C$ (μΩ cm/at.%) |
|---|---|
| Pd | Ag 1.17 Al 2.17 Au 0.65 B 1.43 Bi 5.45 Cd 1.36 Co 2.04 Cr 2.98 Cu 1.35 Fe 2.06 Ga 2.25 Ge 4.13 In 1.96 Ir 7.0 Mn 167 Mo 4.49 Ni 0.72 Pb 3.5 Pt 0.88 Rh 1.67 Ru 3.3 Sn 2.89 V 3.2 Zn 1.73 Zr 2.49 |
| Pt | Ag 2.2 Au 1.3 Be 3 Co 1.7 Cr 6.8 Cu 3 Fe 3.9 In 3.4 Mn 2.95 Mo 6.2 Nb 5.4 Ni 0.9 Os 2.4 Pd 0.6 Rh 1.0 Ru 2.4 Sn 3.9 W 5.7 Zr 4.7 |

**Table 3.1-205** Specific electrical resistivity (μΩ cm) of Pd at different temperatures (K) [1.217, p. 156]

| $T$ (K) | 90 | 175 | 273 | 500 | 800 | 1300 |
|---|---|---|---|---|---|---|
| | 2.147 | 5.821 | 9.725 | 17.848 | 26.856 | 38.061 |

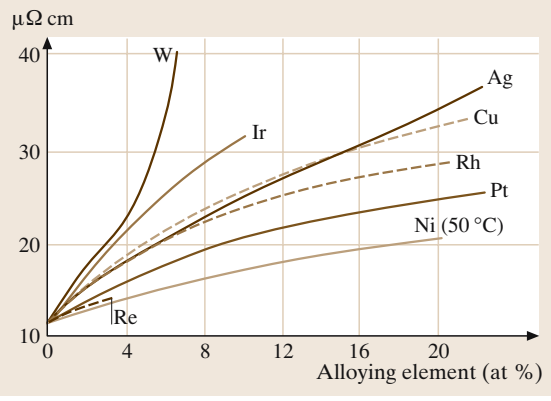


**Fig. 3.1-267** Influence of alloying elements on the electrical conductivity of Pd [1.231, p. 67]

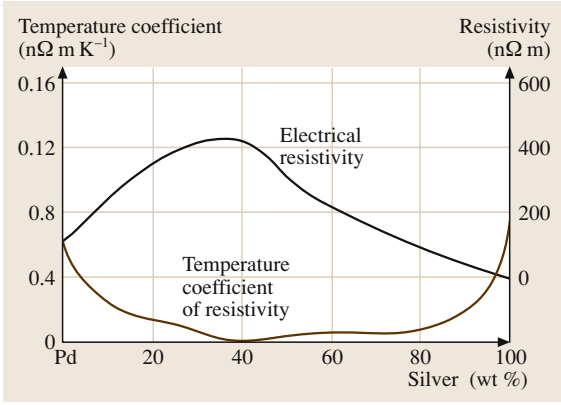


**Fig. 3.1-268** Electrical resistivity and temperature coefficient of resistivity of Pd−Ag alloys as a function of Ag content [1.228, p. 702]

*Thermoelectric Properties.* Tables 3.1-206 – 3.1-209 [1.216, 217] and Figs. 3.1-269, 3.1-270 [1.216, 218] give data of absolute thermoelectric power, thermal electromotive force of pure Pd and Pd alloys at different temperatures. Special alloys for thermocouples with high corrosion resistance are shown in Table 3.1-210 [1.217].

| | Absolute thermoelectric power (μV/grd) | | | | | | | | |
|---|---|---|---|---|---|---|---|---|---|
| | *T* (°C) | | | | | | | | |
| Metal | −255 | −200 | −100 | −20 | 0 | 100 | 300 | 500 | 800 |
| Pd | +1.02 | +3.96 | −3.16 | −7.94 | −9.6 | −13.4 | −18.8 | – | −35 |
| Pt | +1.8 | +5.9 | +0.1 | −3.6 | −4.4 | −7.3 | −10.9 | −14.0 | −18.6 |
| Rh | +1.6 | +1.8 | – | +1.7 | – | +1.2 | +0.3 | −0.3 | – |
| Ir | – | – | +1.8 | – | +1.5 | +0.9 | −0.3 | −1.3 | – |
| Ru | – | – | – | – | – | – | −32.5 | −42 | −43 |

**Table 3.1-206** Absolute thermoelectric power (μV/grd) of the platinum-group metals at different temperatures [1.216, p. 89]

| Thermal electromotive force $E_{A,Pt}$ (mV) | | | | | | |
|---|---|---|---|---|---|---|
| *T* (°C) | Ru | Rh | Ir | Pd | Ag | Au |
| −100 | | −0.32 | −0.35 | 0.48 | −0.21 | −0.21 |
| 0 | 0 | 0 | 0 | 0 | 0 | 0 |
| 100 | 0.684 | 0.70 | 0.660 | 0.570 | 0.740 | 0.770 |
| 300 | 2.673 | 2.68 | 2.522 | −1.990 | 3.050 | 3.127 |
| 600 | 6.485 | 6.77 | 6.201 | −5.030 | 8.410 | 8.115 |
| 900 | 11.229 | 12.04 | 10.943 | −9.720 | 10.943 | 14.615 |
| 1200 | 16.864 | 18.42 | 16.665 | – | – | – |
| 1400 | – | 22.56 | 20.819 | −20.41 | – | – |

**Table 3.1-207** Thermal electromotive force $E_{A,Pt}$ (mV) of the thermocouples of noble metals and pure Pt at different temperatures, reference junction at 0 °C [1.217, p. 159]

**Table 3.1-208** Thermal electromotive force $E_{A,Pt}$ (mV) of Pd alloys at different temperatures, reference junction at 0 °C [1.217, p. 160]

| Alloying element | *T* (°C) | Composition (wt% Ir) | | | | |
|---|---|---|---|---|---|---|
| | | 10 | 30 | 50 | 70 | 90 |
| Ag | 100 | −1.1 | −2.4 | −3.3 | −0.5 | 0.1 |
| | 1000 | −23.5 | −44.4 | −45.8 | −11.5 | – |
| Au | 100 | −1.0 | −1.7 | −2.7 | −2.7 | 0 |
| | 1000 | −14.5 | −24.1 | −38.5 | −33.5 | 3.0 |
| | 1300 | −22.0 | −34.0 | −52.0 | −48.0 | – |
| Cu | 100 | −1.05 | −1.49 | | | |
| Ir | 100 | 2.01 | 2.02 | | | |
| | 1000 | 22.1 | 26.1 | | | |
| Ni | 100 | −0.80 | −1.47 | −1.75 | −1.75 | −1.65 |
| | 1000 | −9.4 | −9.4 | −10.2 | −11.6 | −11.5 |
| Pt | 100 | 0.32 | 0.83 | 0.75 | 0.53 | 0.22 |
| | 1000 | −2.1 | 7.8 | 9.4 | 7.8 | 4.6 |
| | 1300 | −5.2 | 8.0 | 11.7 | 10.7 | 5.3 |

**Table 3.1-209** Basic data of thermal electromotive force of thermocouples according to Table 3.1-210 [1.217, p. 474]

| *T* (°C) | Th.-C.1 (mV) | Th.-C.2 (mV) | Th.-C.3 (mV) |
|---|---|---|---|
| 100 | 3.31 | 4.6 | 3.3 |
| 400 | 15.70 | 21.5 | 15.4 |
| 600 | 24.70 | 34.2 | 24.6 |
| 800 | 33.50 | 46.9 | 33.4 |
| 1000 | 41.65 | 59.6 | 41.3 |

**Table 3.1-210** Palladium alloys for thermocouples (Th.-C.) of high corrosion resistance [1.217, p. 472]

| | | | |
|---|---|---|---|
| Th.-C. | 1.: | AuPd40 | Pd38Pt14Au3 |
| Th.-C. | 2.: | AuPd46 | PtIr10 |
| Th.-C. | 3.: | AuPd35 | PtPd12.5 |

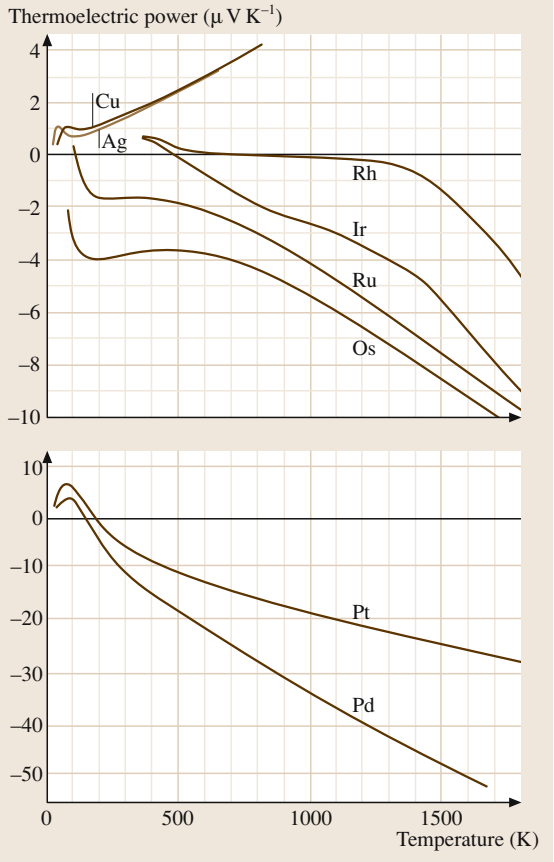


**Fig. 3.1-269** Thermoelectric power of the platinum group metals [1.218, p. 58]

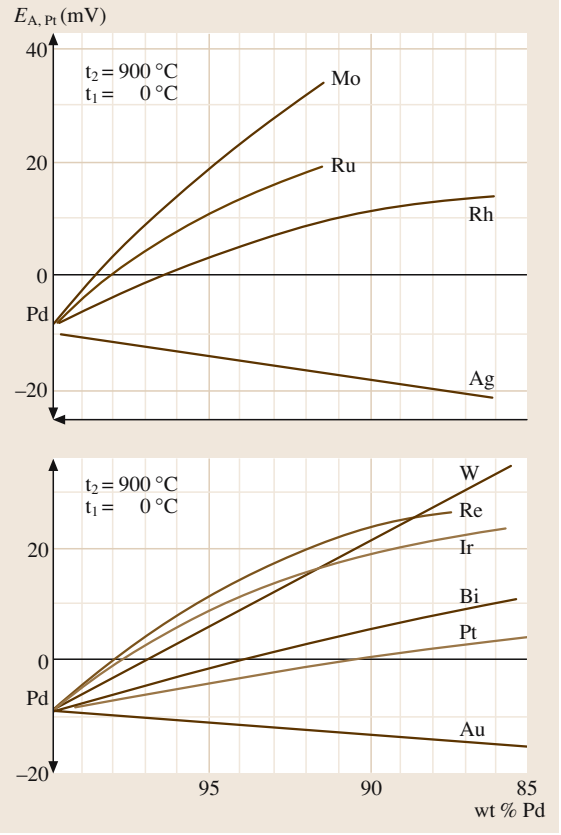


**Fig. 3.1-270** Thermal electromotive force of Pd alloys at 900 °C (reference junction at 0 °C) [1.216, p. 97]

*Magnetic Properties.* All PGMs show magnetostriction in a magnetic field. The reversible change of length is proportional to the square of the applied magnetic field (Table 3.1-211) [1.217, 218]. The paramagnetic susceptibilities of Pd and Pd alloys decrease with increasing temperature (Figs. 3.1-271, 3.1-272) [1.217, 218]. Alloying with 0.05 wt% Rh raises the susceptibility from $88 \times 10^{-10}$ m$^3$/mol to $160 \times 10^{-10}$ m$^3$/mol. Pd–Cu alloys are diamagnetic up to 50 at.% Pd. The susceptibilities of the ordered phases in this system are higher than those of the disordered solid solution phase. The paramagnetism of Pd decreases by dissolution of $H_2$ to reach zero at $PdH_{0.66}$ and above. Partial ordering within FePd raises its coercive field from the disordered value of 2 to 260 Oe [1.281, 282].

| Metal | $S_l$ |
|---|---|
| Ru | −1.4 |
| Rh | 11 |
| Pd | −39.4 |
| Ir | 3.8 |
| Pt | −32 |
| $Rh_{0.50}Ir_{0.50}$ | 9.5 |
| $Rh_{0.50}Pd_{0.50}$ | 27 |
| $Ir_{0.60}Pd_{0.40}$ | 13.4 |
| $Pd_{0.67}Pt_{0.33}$ | −17.4 |
| $Pd_{0.33}Pt_{0.67}$ | −79 |

**Table 3.1-211** Magnetostriction of platinum-group metal and platinum-group metal alloys, expressed by the factor $S_l$ of proportionality according to $\Delta l/l = S_l H^2$ [1.217, p. 161]

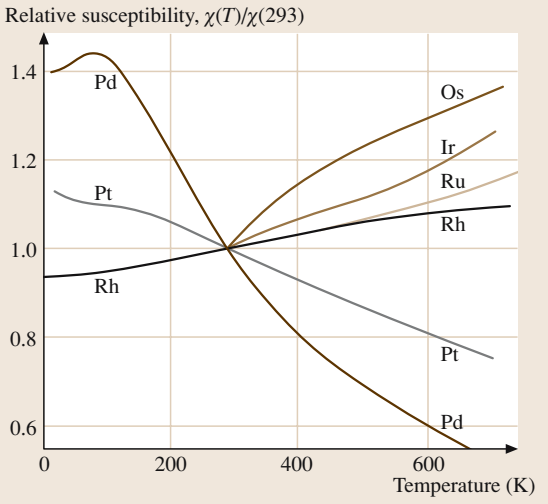


**Fig. 3.1-271** Temperature dependence of the magnetic susceptibility of the platinum group metals [1.218, p. 98]

*Thermal Properties.* Selected data of thermal conductivity and thermal expansion of PGM and PgAg alloys are given in Tables 3.1-212–3.1-215, Fig. 3.1-273. FePd-alloys exhibit around the $Fe_3Pd$ stoechiometry in the disordered state zero coefficient of thermal expansion (Invar effect) [1.281, 282].

**Table 3.1-212** Recrystallization temperatures of platinum-group metal (0 °C) (Depending on purity, degree of cold forming an annealing time) [1.217, p. 216]

| Metal | Recryst. temperature (°C) |
|---|---|
| Ir | 1200–1400 |
| Pd | 485–600 |
| Pt | 350–600 |
| Rh | 700–800 |
| Ru | 1200–1300 |

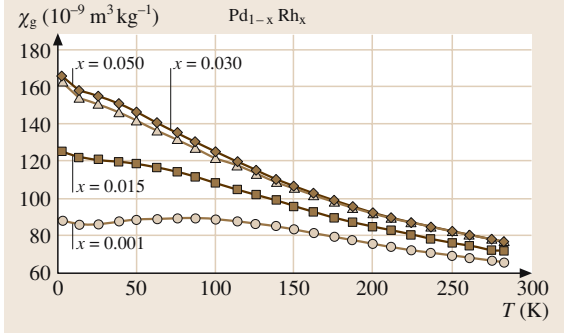


**Fig. 3.1-272** Temperature dependence of the magnetic mass susceptibility of Pd−Rh alloys [1.217, p. 169]

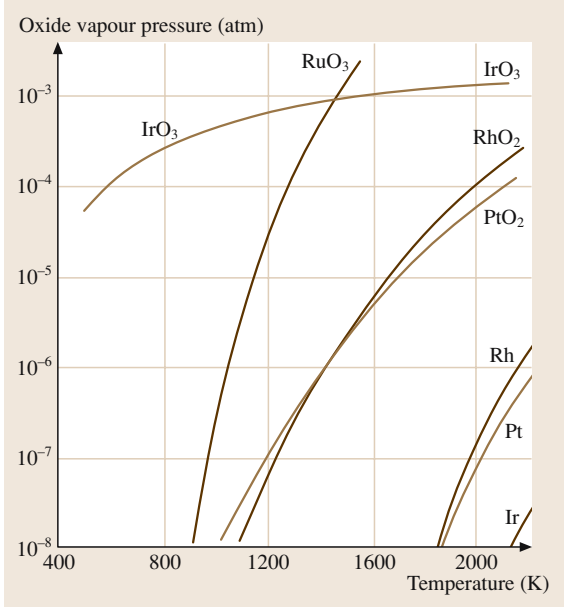


**Fig. 3.1-273** Vapor pressures of platinum group metal oxides [1.277, p. 178]

| Temperature (°C) | Thermal conductivity (W/m K) | | | | | | | |
|---|---|---|---|---|---|---|---|---|
| | Pd | Pt | Rh | Ir | Ru[a] | Ru[b] | Ru[p] | Os |
| 100 | 76 | 85.6 | 185 | – | 140 | 180 | 150 | – |
| 273 | 75.6 | 75.0 | 153 | 149 | 110 | 134 | 119 | 88 |
| 600 | 79.0 | 73.0 | 135 | 130 | 95 | 129 | 105 | 85 |
| 800 | 83.0 | 74.8 | 126 | 125 | 87 | 112 | 96 | – |
| 1200 | 88.2 | 83.2 | 118 | 117 | 77 | 101 | 83 | – |

[a] vertical to the crystal $c$ axis,
[b] parallel to the crystal $c$ axis
[p] polycrystalline

**Table 3.1-213** Thermal conductivity of platinum-group metal at different temperatures [1.217, p. 153]

**Table 3.1-214** Thermal expansion coefficient of the platinum-group metals [1.217, p. 154]

| Temperature (°C) | Thermal expansion coefficients ($10^{-6}$ K$^{-1}$) | | | | | | | | | |
|---|---|---|---|---|---|---|---|---|---|---|
| Metal | Pd | Pt | Rh | Ir | Ru[a] | Ru[b] | Ru[p] | Os[a] | Os[b] | Os[p] |
| 323 | – | – | – | – | 5.9 | 8.8 | 6.9 | 4.0 | 5.8 | 4.8 |
| 373 | 11.9 | 9.1 | 8.5 | 6.7 | – | – | – | – | – | – |
| 423 | | | | | 6.1 | 9.3 | 7.2 | 4.3 | 6.2 | 5.0 |
| 473 | 12.1 | 9.2 | 9.0 | – | – | – | – | – | – | – |
| 623 | | | | | 6.8 | 10.5 | 8.0 | 4.0 | 7.1 | 5.7 |
| 673 | 12.6 | 9.5 | 9.6 | – | – | – | | – | – | |
| 723 | | | | | 7.2 | 11.0 | 8.4 | 5.3 | 7.6 | 62 |
| 823 | – | – | 9.6 | – | | 11.7 | 8.8 | 5.8 | 8.3 | 6.9 |
| 1073 | 13.4 | 10.0 | 10.3 | – | – | – | – | – | – | |

[a] vertical to the crystal $c$ axis,
[b] parallel to the crystal $c$ axis
[p] polycrystalline

**Table 3.1-215** Thermal expansion coefficient of Pd–Ag alloys [1.217, p. 154]

| Temp. range (K) 373–473 | |
|---|---|
| Pd-content (%) | Thermal expansion coefficient ($10^{-6}$ K$^{-1}$) |
| 20 | 16.2 |
| 50 | 14.7 |
| 80 | 12.4 |

*Optical Properties.* In Table 3.1-216 and Fig. 3.1-274 characteristic data are given. The optical reflectance of Pd is increased by alloying with Ru (Fig. 3.1-275).

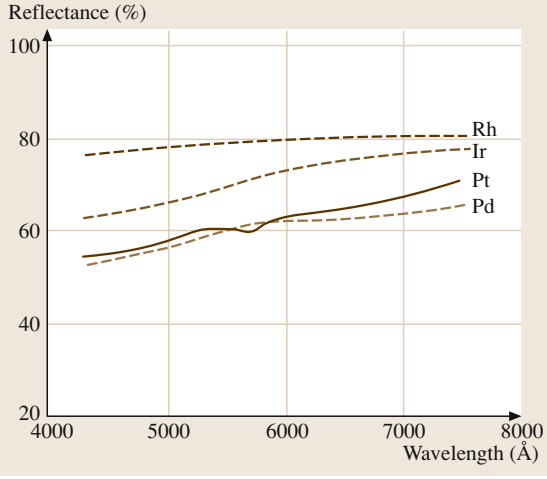


**Fig. 3.1-274** Optical reflectance of the platinum group metals [1.220, p. 78]

**Table 3.1-216** Spectral degree of emission $\varepsilon$ of the platinum-group metals at different temperatures [1.217, p. 171]

| | Surface | Temperature (°C) | Spectral emission $\epsilon$ |
|---|---|---|---|
| Ru[b] | solid | 1000 | 0.421 |
| | solid | 2000 | 0.314 |
| Os[b] | solid | 1000 | 0.526 |
| | solid | 2000 | 0.383 |
| Rh[a] | solid | < 1966 | 0.29 |
| | liquid | > 1966 | 0.3 |
| Ir[a] | solid | 927–2027 | 0.3 |
| | solid | 2000 | 0.383 |
| Pd[a] | solid | 900–1530 | 0.33 |
| | liquid | 1555 | 0.37 |
| Pt[a] | solid | 1000 | 0.371 |
| | solid | 1400 | 0.421 |
| | liquid | 1800 | 0.38 |

[a] 650 nm; [b] 655 nm

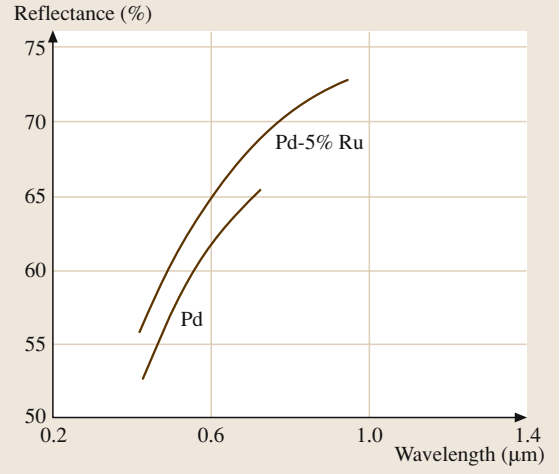


**Fig. 3.1-275** Optical reflectance (%) of PdRu5 alloy [1.228, p. 700]

*Diffusion.* Data for selfdiffusion, diffusion of tracer elements and of hydrogen and oxygen are shown in Tables 3.1-156, 3.1-158, 3.1-217.

Carbon diffuses very rapidly through Pd at elevated temperatures in presence of a concentration gradient on the surface.

**Table 3.1-217** Self-diffusion in pure platinum-group metals [1.217, p. 149]

| | Element | $D^0$ | $O$ | $T$ (K) |
|---|---|---|---|---|
| Lattice diffusion | Ir(S) | 0.36 | 438.8 | 2092–2664 |
| | Pd(S) | 0.205 | 266.3 | 1323–1773 |
| | Pt | 0.33 | 285.6 | 1598–1837 |
| | Pt(S) | 0.05 | 257.6 | 850–1265 |
| Surface diffusion | Rh(111) | $4\times10^{-6}$ | 174 | 1200–1500 (Vac.) |
| | Pt | $4\times10^{-7}$ | 108 | 1160–1580 (Vac.) |

*Chemical Properties.* Pd has the reduction potential of $E_0 = 0.951$ for $Pd/Pd^{2+}$. It is resisant against reducing acids and in oxydizing media above *p*H 2. Alkali melts attack above ~ 400 °C. In oxygen atmosphere between 400 and 800 °C are thin PdO-surface layers formed, which dissociate above 800 °C. Above 1100 °C occur increasing weight losses by evaporation (Fig. 3.1-276).

Catalysis: Pd and Pd alloys are effective catalysts in numerous chemical reactions. In heterogenous catalysis,

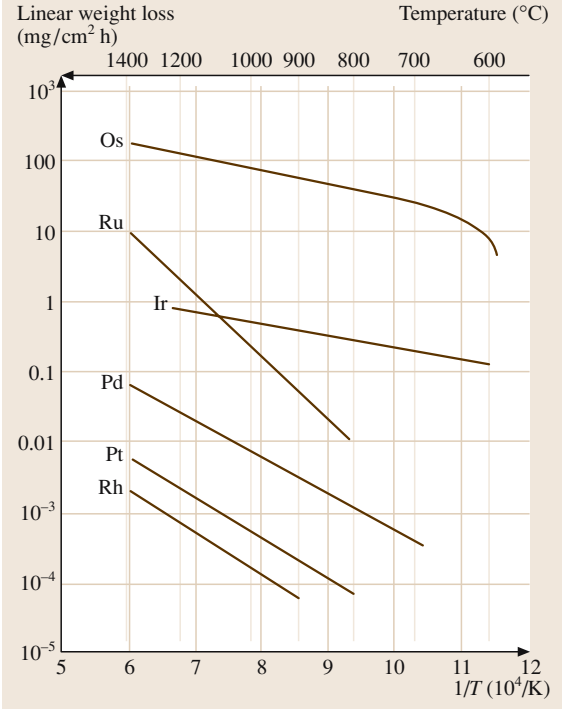


**Fig. 3.1-276** Weight losses of the platinum group metals at annealing on air [1.217, p. 183]

PGM are applied in form of wire nets and of powders with high specific surfaces (20 to 1000 $m^2/g$, "platinum black", "palladium black") on carbon or $Al_2O_3$ supports. Automotive gas cleaning catalysts use of Pd–Pt–Rh alloys in different compositions.

*Special Alloys.* Tables 3.1-159, 3.1-160, 3.1-218 show typical compositions of Pd containing brazing alloys, Table 3.1-219 Pd containing jewelry alloys. PdAg40 has a very low temperature coefficient of resistivity (0.00003/°C between 0 and 100 °C, electrical resistivity 42 μ cm). It is used for precision resistance wires (Fig. 3.1-268). Pd60Ni35Cr5 is corrosion resistant against molten salt mixtures up to 700 °C, suited for brazing graphit, Mo and W.

Ti−Pd−Ni and Fe−Pd alloys show shape memory effects. Partial replacement of Pd in the alloy Fe30 at.% Pd by > 4 at.% Pt decreases the temperature of the f.c.c./f.c.t. martensite transformation and effects strengthening.

**Table 3.1-218** Physical properties of some technical Pd and Pt alloys [1.231, p. 67]

| Material | Density ($g/cm^3$) | Melting point (interval) (°C) | Electrical conductivity ($m/\Omega\ mm^2$) | Temperature coefficient of electrical resistance ($10^3\ K^{-1}$) | Modulus of elasticity ($kN/mm^2$) |
|---|---|---|---|---|---|
| Pt(99.9) | 21.45 | 1773 | 9.4 | 3.92 | 16–17 |
| PtIr5 | 21.5 | 1774–1776 | 4.5 | – | 18.5–19.5 |
| PtIr10 | 21.6 | 1780–1785 | 5.6 | 2.0 | ca. 22 |
| PtRu10 | 20.6 | ca. 1800 | 3.0 | 0.83 | ca. 23.5 |
| PtNi8 | 19.2 | 1670–1710 | 3.3 | 1.5 | ca. 18 |
| PtW5 | 21.3 | 1830–1850 | 2.3 | 0.7 | ca. 18.5 |
| Pd(99.99) | 12.0 | 1552 | 9.3 | 3.77 | ca. 12.5 |
| PdCu15 | 11.3 | 1370–1410 | 2.6 | 0.49 | ca. 17.5 |
| FdCu40 | 10.4 | 1200–1230 | 3.0 | 0.28 | ca. 17.5 |
| PdNi5 | 11.8 | 1455–1485 | 5.9 | 2.47 | ca. 17.5 |

**Table 3.1-219** Composition and melting temperature range of selected Pd-jewellery alloys [1.217, p. 511]

| Alloy | Melting temperature range (°C) |
|---|---|
| Pd95Cu3Ga2 | 1340–1400 |
| Pd95Cu5 | 1400–1460 |
| Pd95Ni5 | 1450–1490 |
| Pd50Ag47.5Cu2.5 | 1200–1280 |

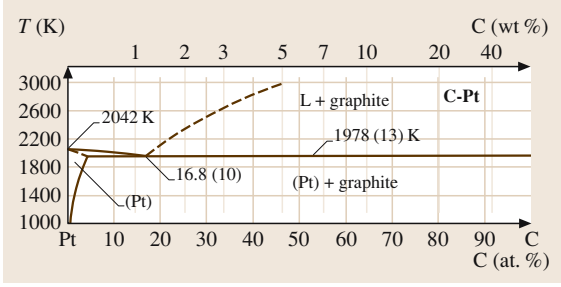


**Fig. 3.1-277** Binary phase diagram Pt–C [1.219]

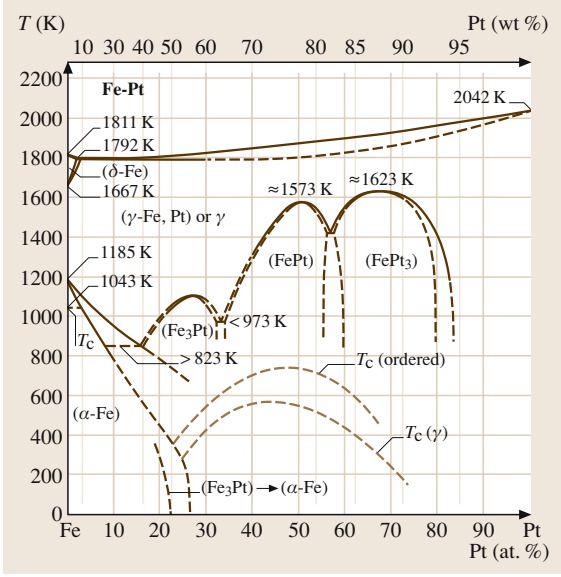


**Fig. 3.1-278** Binary phase diagram Pt–Fe (*dash-dotted line*: Curie temperature) [1.219]

## Platinum and Platinum Alloys

*Applications.* Platinum and platinum alloys are important constituents of catalysts (chemistry, automotive exhaust gas cleaning, fuel cells), sensor materials (thermocouples, resistance thermometers), strong permanent magnet alloys, magnetic and magnetooptical (memory) devices, high temperature and corrosion resistant structural parts, and electrical contacts and connecting elements. Classical applications are jewelry and dentistry alloys.

Commercial grades are sponge and powder in purities varying from minimum 99.9% to 99.95% (ASTM B 561-86). High purity electronic grade is 99.99%.

*Production.* Platinum sponge or powder are compacted by pressing and sintering. Melting and alloying is done in electrical heated furnaces in $Al_2O_3$ or MgO crucibles, by vacuum arc and by electron beam melting 99.98%.

*Phases and Phase Equilibria.* Selected phase diagrams are shown in Figs. 3.1-277–3.1-281 [1.219]. Thermodynamic data are given in Tables 3.1-190 – 3.1-193 and 3.1-220 [1.216, 217, 222]. For compositions and crystal structures, see Tables 3.1-196, 3.1-219, 3.1-222, 3.1-221 [1.217, 219]. Platinum forms continuous solid

**Table 3.1-220** Thermodynamic data of Pt [1.217, p. 109]

| $T$ (K) | $c_p$ (J/K mol) | $S$ (J/K mol) | $H$ (J/mol) | $G$ (J/mol) | $p$ (at) |
|---|---|---|---|---|---|
| 298.15 | 25.857 | 41.631 | 0 | 12.412 | $8.26\times10^{-92}$ |
| 400 | 26.451 | 49.314 | 2.664 | −17.961 | $1.30\times10^{-66}$ |
| 800 | 28.593 | 68.313 | 13.677 | −40.973 | $9.75\times10^{-30}$ |
| 1400 | 31.731 | 85.111 | 31.776 | −87.38 | $5.84\times10^{-14}$ |

$T$ = Temperature, $c_p$ = specific heat capacity, $S$ = Entropy, $H$ = Enthalpy, $G$ = free Enthalpy, $p$ = partial pressure of the pure elements

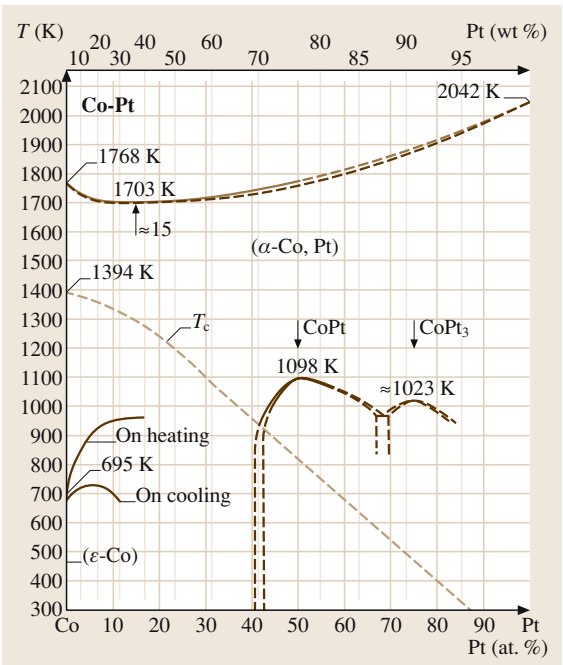


**Fig. 3.1-279** Binary phase diagram Pt–Co [1.219]

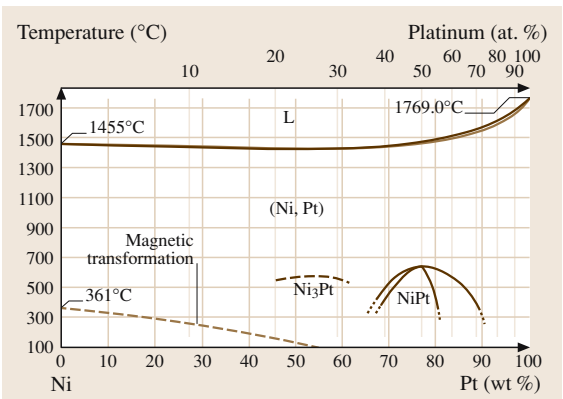


**Fig. 3.1-281** Binary phase diagram Pt–Ni [1.219]

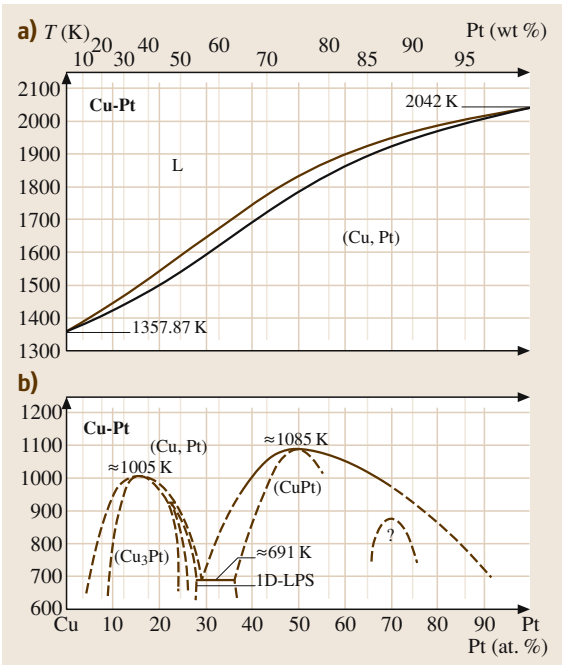


**Fig. 3.1-280a,b** Binary phase diagrams Pt–Cu. **(a)** Liquid–solid. **(b)** Solid–solid (1-D LPS = one-dimensional long-period superstructure) [1.219]

**Table 3.1-221** Crystal structure and lattice parameters of intermediate phases of Pt oxides [1.219]

| Phase | Structure | Type | $a$ (nm) | $b$ (nm) | $c$ (nm) |
|---|---|---|---|---|---|
| PtO | tetragonal | PtO | 0.304 | | 0.534 |
| $Pt_3O_4$ | cubic | $Pt_3O_4$ | 0.6226 | | |
| $PtO_2$ | orthorhombic | $Fe_2O_3$ | 0.4533 | 0.4488 | 0.3138 |
| $PtO_2$ | hexagonal | | 0.310 | | 0.435 |

solutions with all other noble metals and with Co, Cu, Fe, and Ni. Miscibility gaps exist with C, Co, Ir, Pt, and Rh. Primary solid solutions have fcc structure and the lattice parameters correspond with few exceptions roughly to Vegard's law. Numerous intermediate phases exist in al-

**Table 3.1-222** Structure and lattice parameter of selected intermediate Pt compounds [1.217, p. 119]

| Phase | Pearson Symbol | $a$ (nm) | $b$ (nm) | $c$ (nm) | $c/a$ | Remarks | Concentration $x$ A$(1-x)$B$(x)$ |
|---|---|---|---|---|---|---|---|
| CoPt | tP4 | 0.3806 | 0.3684 | 0.9679 | | | |
| $CoPt_3$ | cP4 | 0.3831 | | | | | |
| CuPt | hR32 | 0.7589 | | | | | 0.5 |
| $CuPt_3$ | cF4 | 0.3849 | | | | | |
| $Cu_3Pt$ | o** | 0.7596 | 0.2745 | 0.777 | | | |
| $Cu_3Pt$ | cP4 | 0.3682 | | | | | |
| Fe−Pt | cF4 | 0.376 | | | | | 0.245 |
| FePt | tP4 | 0.3861 | | 0.3788 | 0.9811 | | |
| $Fe_3Pt$ | cP4 | 0.3727 | | | | | |
| NiPt | tP4 | 0.3823 | | 0.3589 | 0.9388 | | |
| PtZr | oC8 | 0.3409 | 1.0315 | 0.4277 | | | |
| $Pt_3Zr$ | hP16 | 0.5624 | | 0.9213 | 1.6328 | | |

loy systems with rare earth metals. The formation and crystal structures of the intermediate phases have been related to the electron configuration of the alloy components (Engel–Brewer correlation) [1.283, 284]. Phases with superlattice structures are formed with Co, Cu, Fe, Nb, and V in atomic ratios of 1:1, 2:1, and 3:1 (Tables 3.1-123, 3.1-197). The ordered CuPt phase has a long-range ordered rhombohedral structure.

*Mechanical Properties.* Characteristic data are shown in Tables 3.1-223 – 3.1-226 [1.217], Figs. 3.1-282 – 3.1-290 [1.217, 228, 228, 231]. For elastic properties of PGMs at different temperatures, see [1.217]. Strengthening is affected by solid solution hardening, order hardening (Pt−Co, Pt−Cu), and dispersion hardening. Dispersion-strengthened Pt and Pt alloys are remarkably resistant to creep at high temperatures. They are produced either by co-precipitation with refractory oxides (e.g., 0.16 vol% $ZrO_2$) or by internal oxidation of alloys with 0.2 wt% Cr or 0.8 wt% Zr. Rh additions improve the solubility for oxygen. TiC powder affects dispersion strengthening in concentrations of 0.04–0.08 wt% (Fig. 3.1-291) [1.277].

**Table 3.1-223** Elastic constants of Pt [1.217, p. 219]

| $c_{11}$ | $c_{12}$ | $c_{44}$ |
|---|---|---|
| 347 | 173 | 76.5 |

**Table 3.1-224** Mechanical properties of Pt (99.9%) at different temperatures (°C) [1.217, p. 220]

| $T$ (°C) | $E$ (GPa) | $R_m$ (MPa) | $A$ (%) | $R_{p0.2}$ (MPa) | HV |
|---|---|---|---|---|---|
| 20 | 173 | 135 | 41 | 50 | 55 |
| 250 | 169 | 110 | 40 | 40 | 53 |
| 500 | 159 | 78 | 42 | 30 | 50 |
| 750 | 140 | 44 | 46 | 20 | 35 |
| 900 | 126 | 34 | 44 | 17[a] | 23 |

[a] interpolation
$A$ = Elongation, $E$ = Modulus of elasticity, $R_p$ = Limit of proportionality, HV = Vickers hardness, $R_m$ = Tensile strength

**Table 3.1-225** Mechanical properties of Pt as function of reduction in thickness (%) by cold rolling [1.217, p. 220]

| Reduction (%) | $R_m$ (MPa) | $R_p$ (MPa) | HV | |
|---|---|---|---|---|
| | | | a | b |
| 0 | 250 | 140 | 50 | 40 |
| 20 | 350 | 310 | 70 | 63 |
| 59 | 400 | 380 | 84 | 73 |

a = Pt > 99.5%, b = Pt > 99.99%

**Table 3.1-226** Tensile strength $R_m$ (MPa) and elongation $A$ (%) of binary Pt alloys at different temperatures [1.217, p. 217, 220]

| Alloy compound | Temperature (°C) | | |
|---|---|---|---|
| | 20 | 400 | 600 |
| (wt%) | $R_m/A$ | | |
| Au5 | 340/18 | 290/10 | 250/10 |
| Ir10 | 260/33 | 240/27 | 180/33 |
| Ni5 | 470/26 | 420/26 | 320/25 |
| Pd20Rh5 | 370/30 | 290/18 | 240/23 |
| Rh5 | 225/44 | 150/40 | 120/43 |
| Rh10 | 287/39 | 200/33 | 170/38 |

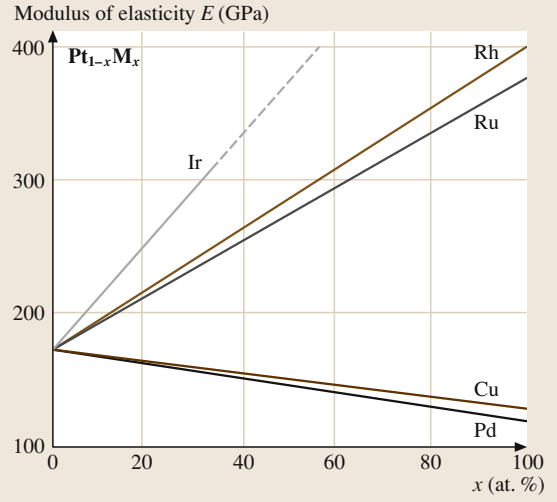


**Fig. 3.1-282** Modulus of elasticity of binary Pt alloys [1.217, p. 222]

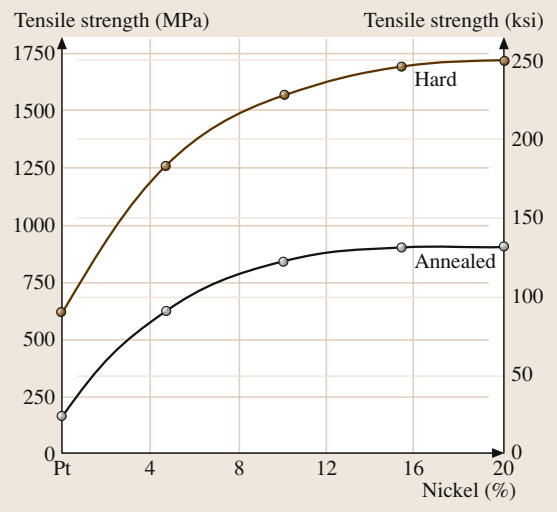


**Fig. 3.1-284** Tensile strength of Pt–Ni alloys as a function of Ni content [1.228, p. 695]

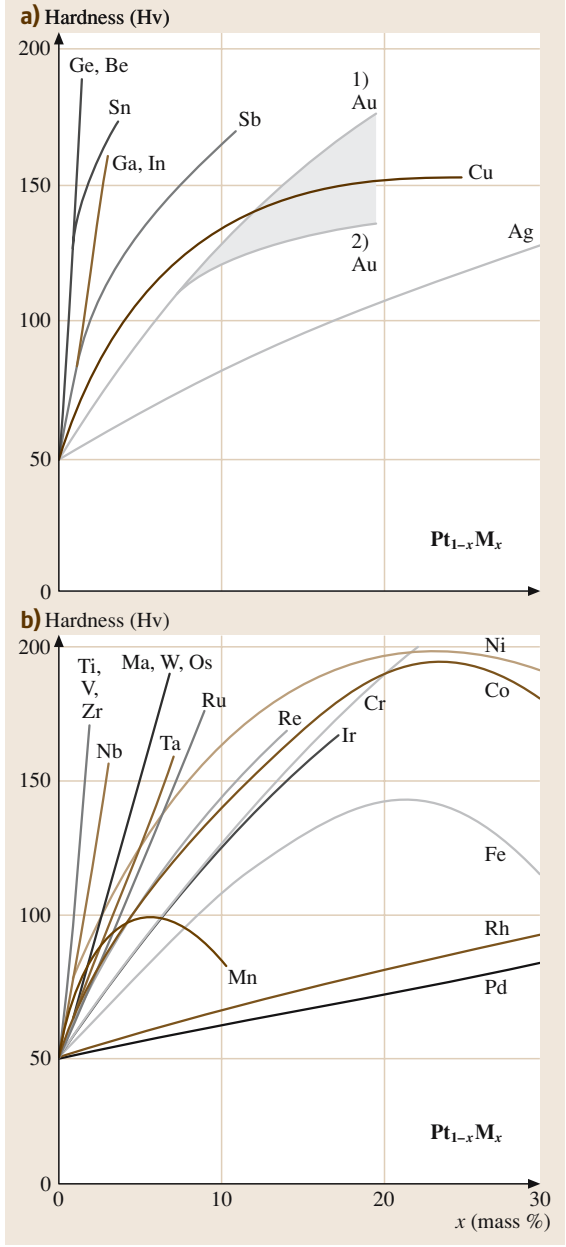


**Fig. 3.1-283a,b** Solid solution hardening of binary Pt alloys **(a)** de-alloyed at 900 °C; **(b)** solution annealed at 1200 °C [1.217, p. 223]

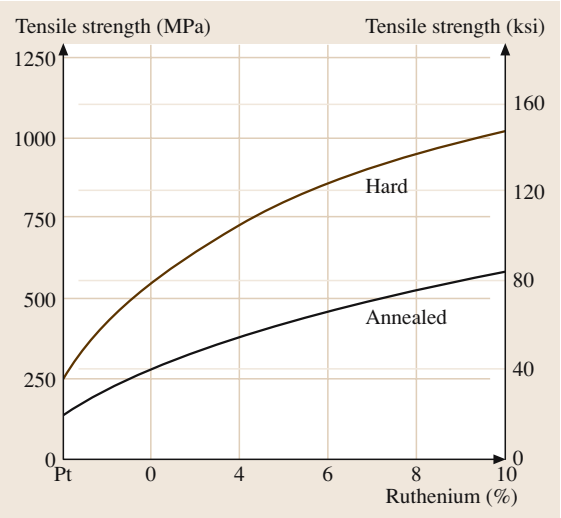


**Fig. 3.1-285** Tensile strength of Pt−Ru alloys as a function of Ru content [1.228, p. 694]

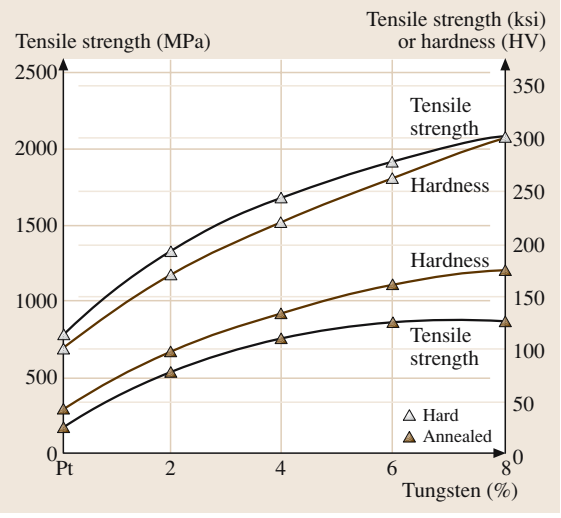


**Fig. 3.1-286** Tensile strength of Pt−W alloys as a function of W content [1.228, p. 697]

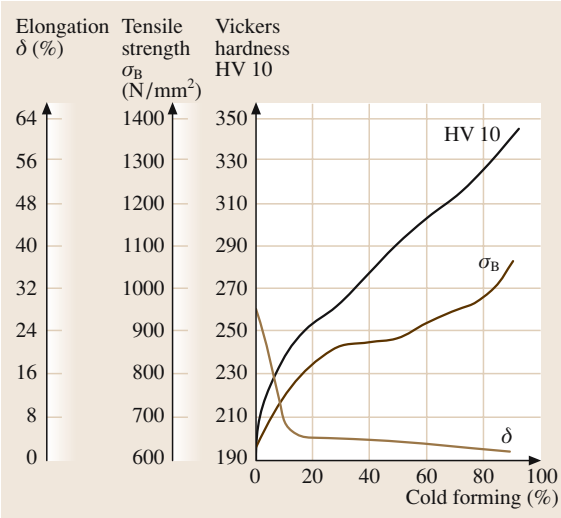


**Fig. 3.1-287** Mechanical properties of PtNi8 by cold forming as a function of reduction of cross section [1.231, p. 69]

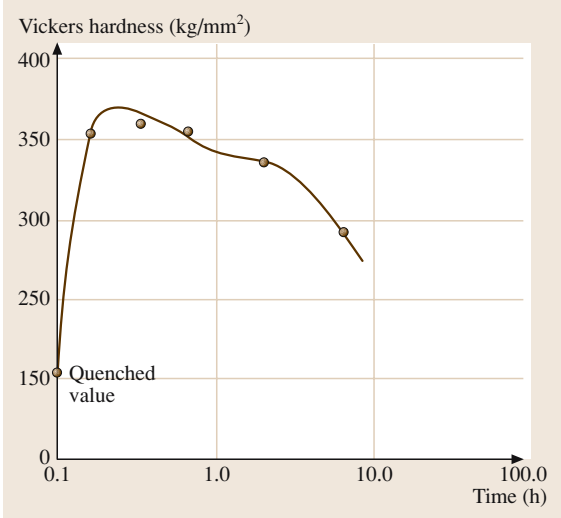


**Fig. 3.1-288** Order hardening of stoichiometrc CuPt alloy [1.285, p. 49]

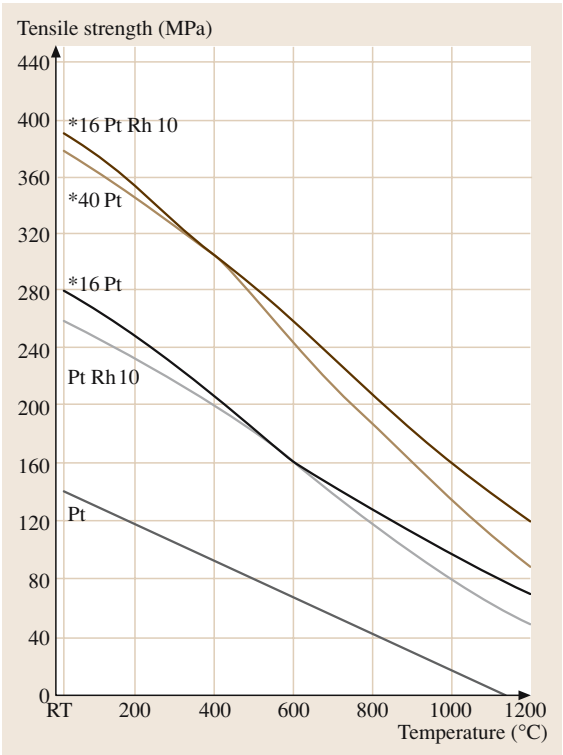


**Fig. 3.1-289** Tensile strength of dispersion hardened Pt and PtRh10 (∗ grain stabilized with 0.16 and 0.40 vol.% $ZrO_2$, respectively) [1.217, p. 222]

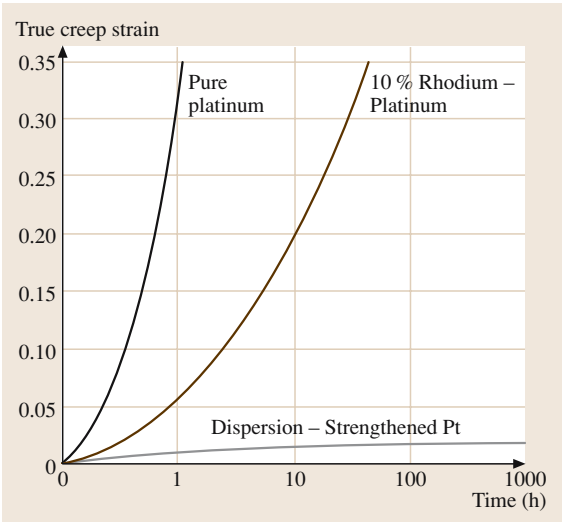


**Fig. 3.1-290** Creep curves of TiC-dispersion-strengthened Pt and PtRh wire at 1400 °C in air [1.277]

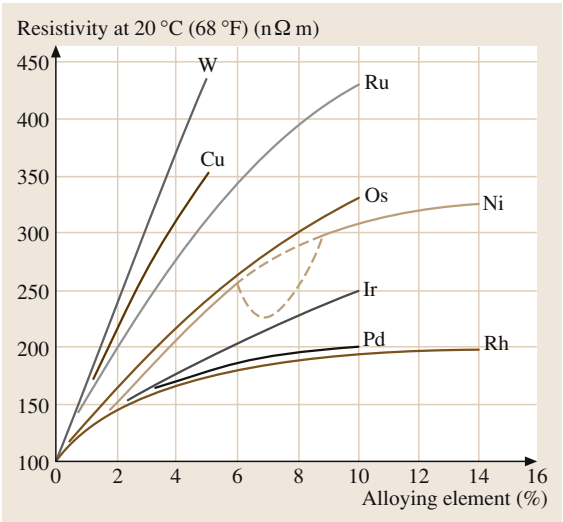


**Fig. 3.1-291** Effect of various alloying additions on the electrical resistivity of binary Pt alloys [1.231, p. 67]

*Electrical Properties.* Characteristic data are shown in Tables 3.1-203, 3.1-205, 3.1-227 [1.217], and Figs. 3.1-292 – 3.1-294 [1.217,228,231]. Mo–28 at.% Pt (A15 structure) shows superconductivity at $T_c \approx 4.2–5.6$ K [1.286].

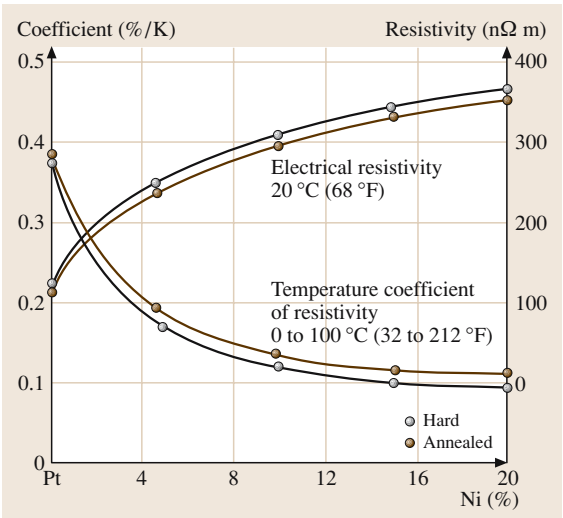


**Fig. 3.1-292** Electrical resistivity and temperature coefficient of resistivity (TCR) of Pt−Ni alloys as a function of composition [1.228, p. 696]

**Table 3.1-227** Specific electrical resistivity (μΩ cm) of Pt at temperature (K) [1.217, p. 157]

| $T$ (K) | 10 | 50 | 120 | 273 | 673 | 1273 | 1673 |
|---|---|---|---|---|---|---|---|
| $\rho$ (μΩ cm) | 0.0029 | 0.719 | $3.56_5$ | 9.83 | 24.57 | 37.45 | 53.35 |

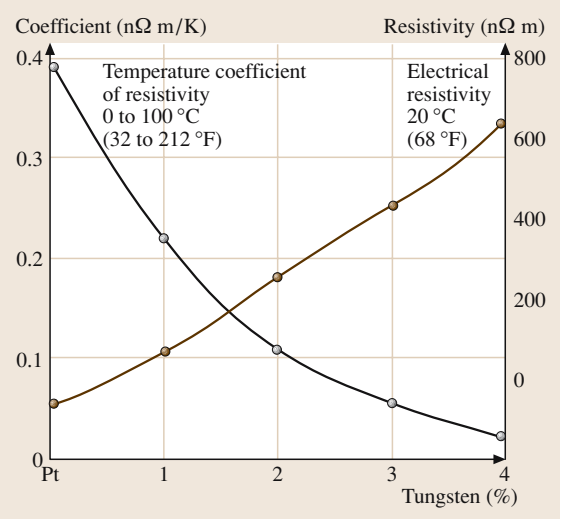


**Fig. 3.1-293** Electrical resistivity and temperature coefficient of resistivity (TCR) of Pt−W alloys as a function of composition [1.228, p. 697]

*Thermoelectric Properties.* Selected values of thermal electromotive force of Pt and Pt alloys are given in Tables 3.1-206, 3.1-207, 3.1-228 – 3.1-231 [1.216, 217, 222], and Fig. 3.1-295 [1.216]. Thermocouples that are Pt−Rh-based are especially suited for high temperatures (see Fig. 3.1-296).

**Table 3.1-228** Pt−Rh thermocouples according IEC 5845 (see Fig. 3.1-296) [1.217, p. 472]

| Class | Alloy | Maximum applicable temperature (°C) |
|---|---|---|
| Type R: | PtRh(87/13)–Pt | 1500 – 1600 |
| Type S: | PtRh(90/10)–Pt | 1500 – 1600 |
| Type B: | PtRh(70/30)–Pt | 1750 – 1800 |

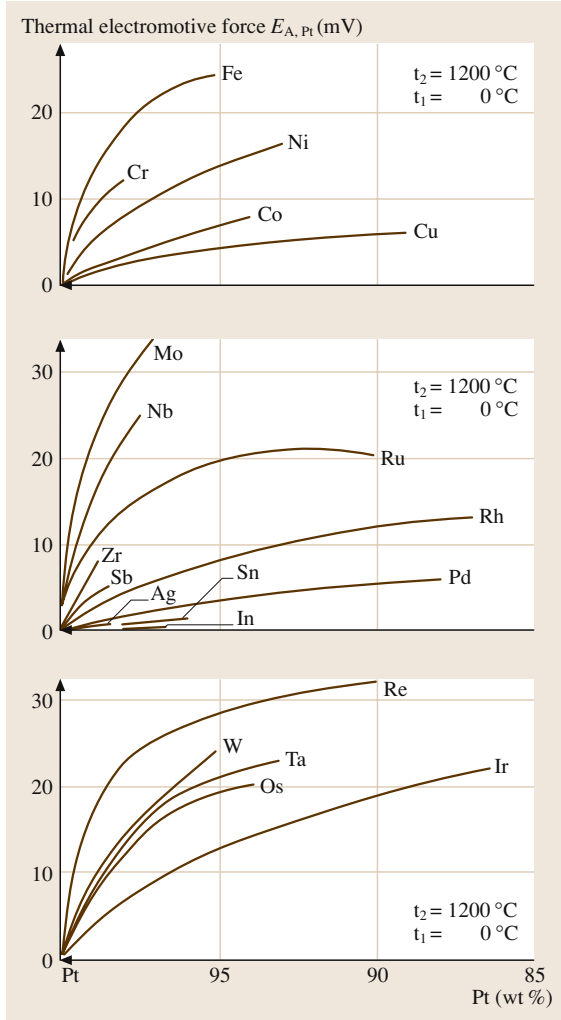


**Fig. 3.1-294** Thermal electromotive force of binary Pt alloys [1.216, p. 97]

**Table 3.1-229** Absolute thermoelectric power of Pt [1.222, p. 1009]

| Temperature (K) | 300 | 400 | 500 | 600 | 700 | 800 | 900 | 1000 | 1100 | 1200 |
|---|---|---|---|---|---|---|---|---|---|---|
| Thermoelectric power (μV/K) | −5.05 | −7.66 | −9.69 | −11.33 | −12.87 | −14.38 | −15.97 | −17.58 | −19.03 | −20.56 |

| Alloy const. | $T$ (°C) | Composition (wt% Ir) 10 | 30 | 40 | 70 | 80 | 90 |
|---|---|---|---|---|---|---|---|
| Ag | 100 | | | | −0.4 | −0.1 | 0.2 |
| | 900 | | | | 6.8 | 4.0 | 4.5 |
| Au | 100 | | | | | 0.8 | 0.4 |
| | 900 | | | | | 11.9 | 13.5 |
| Ir | 100 | 1.3 | 1.2 | | | | |
| | 1000 | 15.7 | 19.1 | 19.4 | | | |
| Rh | 100 | 0.64 | 0.62 | 0.60 | | | |
| | 1000 | 9.57 | 12.3 | 13.3 | | | |
| | 1300 | 13.1 | 17.9 | 19.0 | | | |

**Table 3.1-230** Thermal electromotive force of Pt alloys (mV) at different temperatures, reference junction at 0 °C [1.217, p. 160]

**Table 3.1-231** Basic values of thermal electromotive force (mV) of common PGM-based thermocouples [1.216, p. 100]

| $T_1$ (°C) | $T_2$ (°C) | Pt – Rh10/Pt | Pt – Rh20/Pt – Rh5 | Rh – Ir60 | Pt-el[b] | Pd-or[c] |
|---|---|---|---|---|---|---|
| 0 | 100 | 0.643 | 0.074 | 0.371 | 3.31 | 4.6 |
| | 500 | 4.221 | 1.447 | 2.562 | 20.20 | 27.9 |
| | 1000 | 9.570 | 4.921 | 5.495 | 41.65 | 59.6 |
| $T_1$ (K) | $T_2$ (K) | Au – Co2.1/Cu[d] | Au – Fe0.02/Cu[d] | | | |
| 4.2 | 10 | 0.044 | 0.093 | | | |
| | 20 | 0.173 | 0.208 | | | |
| | 40 | 0.590 | 0.423 | | | |

[b] Pt-el = Platinel, Pd83Pt14Au3/AuPd35
[c] Pd-or = Pallador, PtIr10/AuPd40
[d] at.%

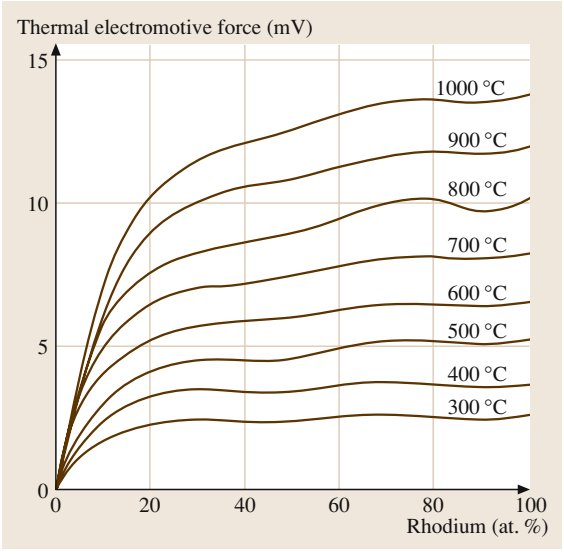


**Fig. 3.1-295** Influence of the Rh content on the thermal emf of Pt−Rh alloys against Pt [1.217, p. 473]

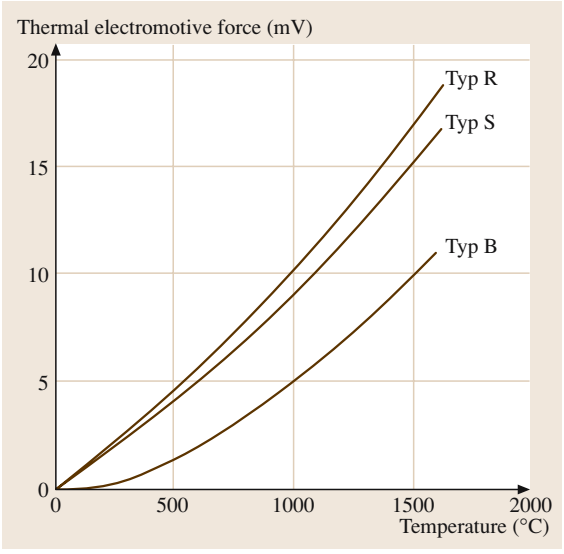


**Fig. 3.1-296** Thermal electromotive force of Pt−Rh thermocouples according to IEC 5845 (Type R: PtRh(87/13)–Pt; type S: PtRh(90/10)–Pt; type B: PtRh(70/30)–PtRh(94/6)) [1.217, p. 473]

*Magnetic Properties.* Selected data are shown in Tables 3.1-211, 3.1-232 [1.217, 222], and Figs. 3.1-297 [1.220] and 3.1-298. The paramagnetic susceptibility of Pt ($25.2\times10^{-10}$ m$^3$ mol$^{-1}$ at 0 K) rises by alloying with 0.1 at.% Rh to $42.5\times10^{-10}$ m$^3$ mol$^{-1}$. CoPt is a hard magnetic material ($H_c = 3500–4700$ Oe) but has been replaced by rare-earth transition metal magnetic materials in recent years. Superlattice phases in PtCr-alloys in the composition ranges of 17–65 wt% Cr are ferromagnetic, with the maximum of $T_c$ at ~ 30 at.% Cr. The superlattice structure in FePt and CoPt with tetragonal crystal symmetry gives rise to high values of magnetic anisotropy. The coercivity of sputtered Pt−Co multilayers is increased by annealing in air, caused by the formation of cobalt oxide at the grain boundaries. The oxide layer gives rise to domain pinning and to magnetic isolation of the grains, thus leading to a high perpendicular anisotropy [1.217].

**Table 3.1-232** Characteristic properties of technical permanent magnet alloys [1.222, p. 1053]

| Alloy (wt%) | $H_{max}$ (kJ/m$^3$) | $H_c$ (kA/m) | $B_r$ (T) |
|---|---|---|---|
| Pt77Co23 | 75.0 | 380 | 0.60 |
| Sm34Co66 | 110–160 | 560 | 0.80 |
| Co52Fe35V$_{13}$ | 22.4 | 36 | 1.00 |

$B$ = magnetic flux density, $H$ = magnetic field, $B_r$ = Remanence

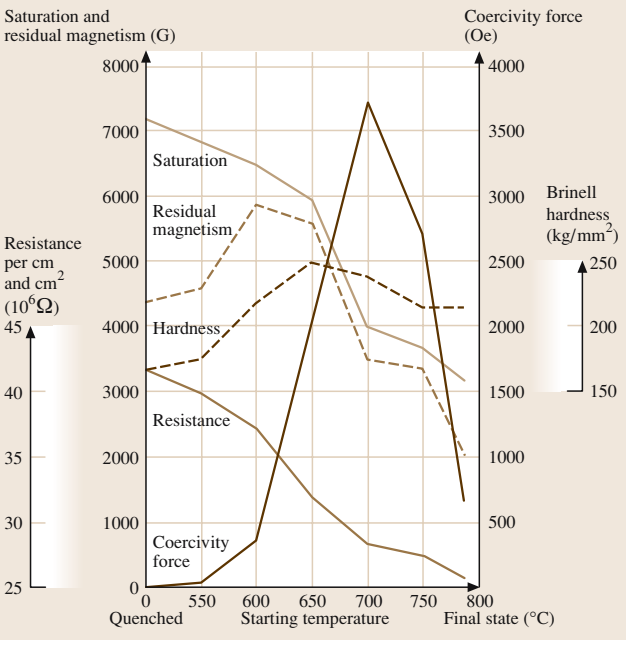


**Fig. 3.1-297** Change of magnetic properties of PtCo50 alloy by annealing [1.220, p. 263]

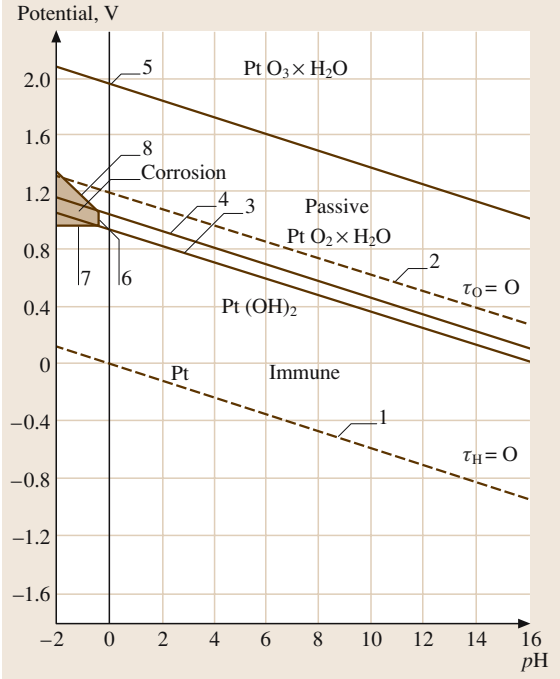


**Fig. 3.1-298** Potential *p*H-diagram of the system Pt/$H_2O$ at 25 °C (see Table 3.1-232) [1.217, p. 201]

**Table 3.1-233** Thermal conductivity λ of Pt–(Au, Rh, Ir) alloys (W/m K) [1.217, p. 153]

| PtAu5 | PtRh5 | PtRh10 | PtRh20 | PtIr5 | PtIr10 |
|---|---|---|---|---|---|
| 43 | 33 [a] | 30 | 28 [a] | 42 | 31 |

[a] = calculated with Wiedemann-Franz' law $\lambda = L\sigma T$, Lorenz number $L = 2.45\times10^{-6}$ W/K from λ(PtRh10) and the specific electrical conductivity of PtRh-alloys

**Table 3.1-234** Thermal expansion coefficient α ($10^{-6}$ K$^{-1}$) of Pt−Rh alloys at different temperature ranges [1.217, p. 155]

| Temperature range (K) Rh-content (wt%) | α ($10^{-6}$/K) 273–983 ($10^{-6}$/K) | 293–1473 ($10^{-6}$/K) |
|---|---|---|
| 6 | 10.7 | 11.3 |
| 10 | 10.7 | 11.2 |
| 20 | 10.9 | 11.5 |
| 30 | 10.8 | 11.4 |

*Thermal Properties.* Tables 3.1-212 – 3.1-215, 3.1-233, and 3.1-234 [1.217,217] provide selected data of thermal conductivity and thermal expansion. In the disordered state the Fe–Pt alloy system exhibits a negative thermal expansion coefficient at room temperature near $Fe_3Pt$ (Invar effect) [1.281, 282].

*Optical Properties.* Values of the spectral degree of emission and the optical reflectivity are given in Table 3.1-216 [1.217] and Fig. 3.1-275 [1.220].

*Diffusion.* Data for self-diffusion, diffusion of tracer elements and of hydrogen and oxygen are shown in Tables 3.1-158, 3.1-216, 3.1-217 [1.217].

*Chemical Properties.* Platinum has the reduction potential of $E_0 = +1.118$ for $Pt/Pt^{2+}$. It is resistant against reducing acids in all *p*H ranges, but is attacked by alkali and oxidizing media. Alloying with 30 at.% Rh improves the corrosion resistance against alkali hydroxides. Figure 3.1-298 and Table 3.1-235 [1.217] give the potential *p*H diagram of the system $Pt/H_2O$ at 25 °C. Dry Chlorine attacks with rising temperature (Fig. 3.1-299 [1.217]). Detailed information about chemical behavior is given in [1.217].

Platinum reacts with ZrC to form $Pt_3Zr$. It also reacts in the presence of hydrogen with $ZrO_2$, $Al_2O_3$, and rare earth oxides at temperatures between 1200 and 1500 °C [1.283, 284]. The solubility of oxygen in platinum is very low. Thin coatings of Pt on reactive materials are an effective protection against oxidation. Alloying of Pt with 2 wt% or higher Al improves the oxidation resistance up to 1400 °C by forming protective dense oxide coatings [1.287]. Superalloys that are Pt–Al-based have high compression strength at high temperatures. Third alloying elements (e.g., Ru) stabilize the high-temperature phase down to room temperature and affects solid-solution strengthening [1.288].

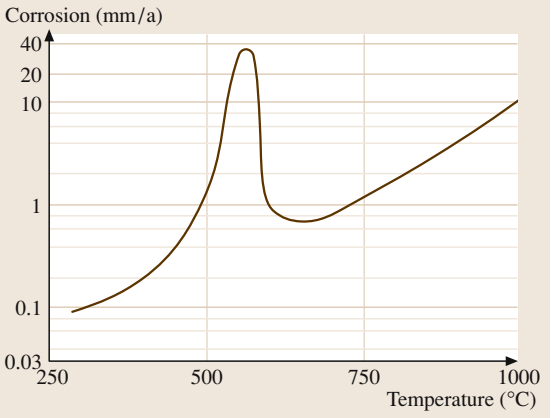


**Fig. 3.1-299** Corrosion of Pt in dry $Cl_2$ gas [1.217, p. 186]

*Catalysis.* Platinum and Pt alloys are preferably applied in heterogeneous catalysis as wire nets or powders with a high specific surface area ranging from 20 to 1000 $m^2/g$ ("platinum black," "palladium black") on carbon or $Al_2O_3$ supports. The catalytic effectivity is structure-sensitive. Figure 3.1-300 show an example of the catalytic action of Pt for the reaction rate and the product selectivity on different crystal planes [1.218]. Pt–Pd–Rh alloys are the main active constituents of catalytic converters for automobile exhaust gas cleaning.

*Special Alloys.* Molybdenum clad with Pt serves as glass handling equipment up to 1200 °C. Binary Pt alloys with Cu(4), Co(5), W(5), and Ir(10) at.%; and ternary alloys of Pt–Pd–Cu and Pt–Pd–Co are standard jewelry alloys. Alloys of Pt–Au and Pt–Au–Rh surpass the strength of pure Pt at 1000 °C and resist wetting of molten glass. The materials PtIr3, PtAu5 are suitable for laboratory crucibles and electrodes with high mechanical stability.

| Number | Reaction equation | Potential $E_0$ (V) |
|---|---|---|
| 1 | $2H^+ + 2e^- \rightarrow H_2$ | $0.000 - 0.0591\,pH$ |
| 2 | $2H_2O \rightarrow O_2 + 4H^+ + 4e^-$ | $1.228 - 0.0591\,pH$ |
| 3 | $Pt + 2H_2O \rightarrow Pt(OH_2) + 2H^+ + 2e^-$ | $0.980 - 0.0591\,pH$ |
| 4 | $Pt(OH)_2 \rightarrow PtO_2 + 2H^+ + 2e^-$ | $1.045 - 0.0591\,pH$ |
| 5 | $PtO_2 + H_2O \rightarrow PtO_3 + 2H^+ + 2e^-$ | $2.000 - 0.0591\,pH$ |
| 6 | $Pt + H_2O \rightarrow PtO + 2H^+$ | $\log[Pt^{++}] = -7.06 - 2\,pH$ |
| 7 | $Pt \rightarrow Pt^{++} + 2e^-$ | $1.188 + 0.0259\log[Pt^{++}]$ |
| 8 | $Pt^{++} + 2H_2O \rightarrow PtO_2 + 4H^+ + 2e^-$ | $0.837 - 0.1182\,pH - 0.0259\log[Pt^{++}]$ |

**Table 3.1-235** Reaction and potentials corresponding to graphs of Fig. 3.1-298 [1.217, p. 200]

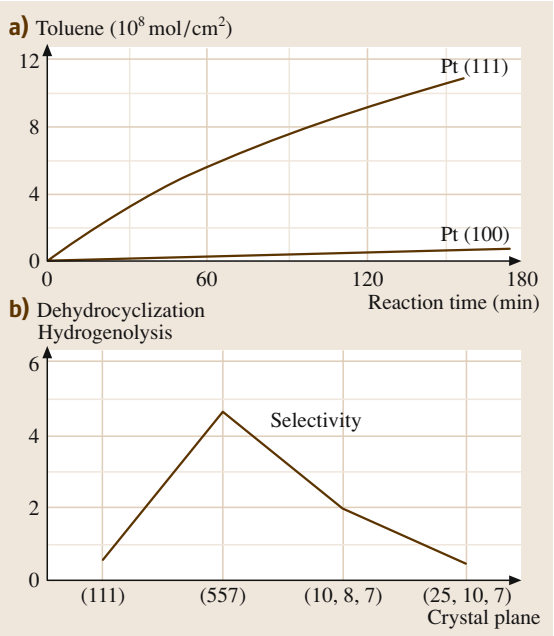


**Fig. 3.1-300** (a) Rate of reaction of n-heptane dehydrocyclization to toluol on Pt(111) and Pt(100). (b) Variation of selectivity at different crystal planes [1.218, p. 279]

### 3.1.10.4 Rhodium, Iridium, Rhutenium, Osmium, and their Alloys

#### Rhodium and Rhodium Alloys

*Applications.* Rhodium is an essential component of catalysts in numerous chemical reactions and automobile exhaust-gas cleaning. In heterogeneous catalysis it is applied in alloyed form, in homogeneous catalysis as complex organic compounds. Rhodium is an alloy component of corrosion- and wear-resistant tools in the glass industry and a constituent in platinum-group-metal-based thermocouples. Rhodium coatings on silverware and mirrors protect them against corrosion. Commercial grades available are powder, shot, foil, rod, plate, and wires with purity from 98–99.5% (ASTM B 616-78; reappraised 1983).

*Production.* Rhodium is produced as powder and sponge by chemical reduction or thermal decomposition of the chloro–ammonia complex $(NH_4)_3[RHCl_6]$. Bars, rods, and wires are produced by powder compacting and extrusion, while coatings are produced galvanically, by evaporation or by sputtering.

*Phases and Phase Equilibria.* Selected phase diagrams of Rh are shown in Fig. 3.1-301a–c. Rhodium forms continuous solid solutions with Fe, Co, Ni, Ir, Pd, and Pt. Miscibility gaps exist in alloys with Fe, Co, Ni, Cu, Ag, Au, Pd, Pt, Ru, and Os. Thermodynamic data are given in Table 3.1-236 (see also

**Table 3.1-236** Thermodynamic data of Rh [1.217, p. 110]

| $T$ (K) | $c_p$ (J/K mol) | $S$ (J/K mol) | $H$ (J/mol) | $G$ (J/mol) | $p$ (atm.) |
|---|---|---|---|---|---|
| 298.15 | 24.978 | 31.506 | 0 | −9.393 | $1.43\times10^{-89}$ |
| 400 | 26.044 | 38.993 | 2.598 | −13 | $6.59\times10^{-65}$ |
| 800 | 39.155 | 58.333 | 13.853 | −32.813 | $7.21\times10^{-29}$ |
| 1400 | 35.195 | 76.556 | 33.532 | −73.646 | $1.71\times10^{-13}$ |

$T$ = Temperature, $c_p$ = specific heat capacity, $S$ = Entropy, $H$ = Enthalpy, $G$ = free Enthalpy, $p$ = partial pressure of the pure elements

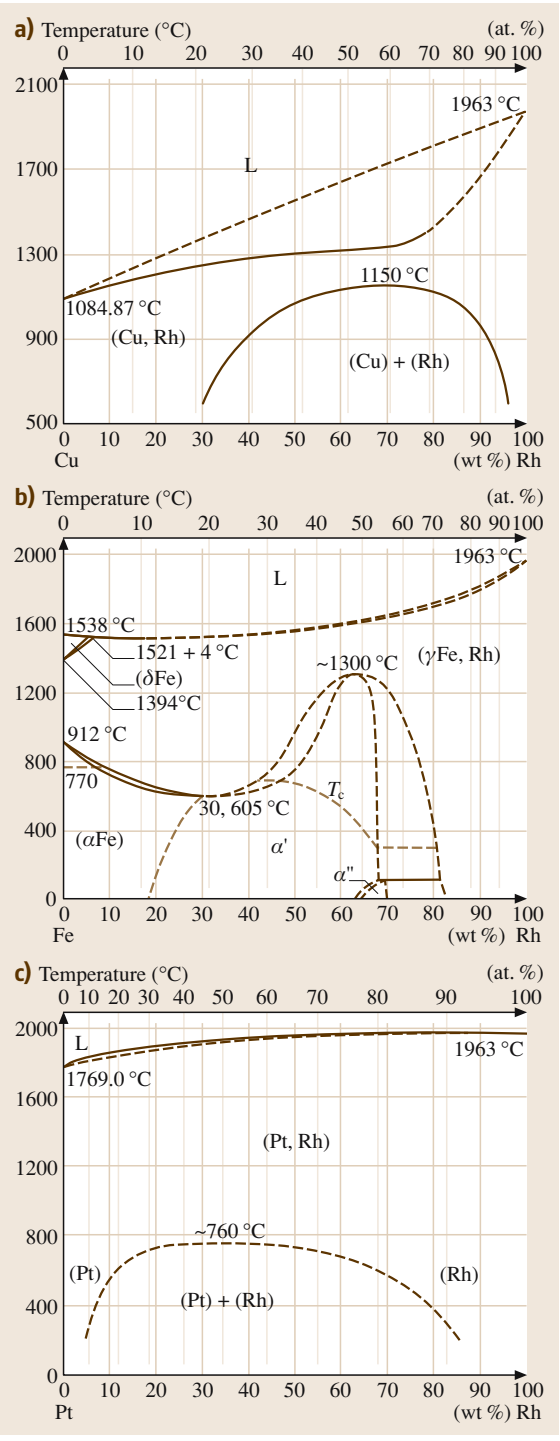


**Fig. 3.1-301a–c** Phase diagrams of Rh alloys with **(a)** Cu, **(b)** Fe, and **(c)** Pt [1.216, p. 101, 104]

Table 3.1-190) and the maximum hydrogen inclusion is listed in Table 3.1-194.

The compositions and crystal structures of intermediate compounds are shown in Table 3.1-237 (see Table 3.1-197 for superlattice structures).

*Mechanical Properties.* Characteristic mechanical data of Rh are given in Tables 3.1-238–3.1-241 and Figs. 3.1-302–3.1-307. The modulus of rigidity $G = 153$ GPa; Poisson's ratio is 0.26; the elastic constants are $c_0 = 413$, $c_{12} = 194$, and $c_{44} = 184$.

Rhodium is very hard but can be deformed at temperatures above 200 °C. For strong hardening by deformations, repeated annealing is needed at temperatures higher than 1000 °C. Rh is an effective hardener in Pd and Pt alloys.

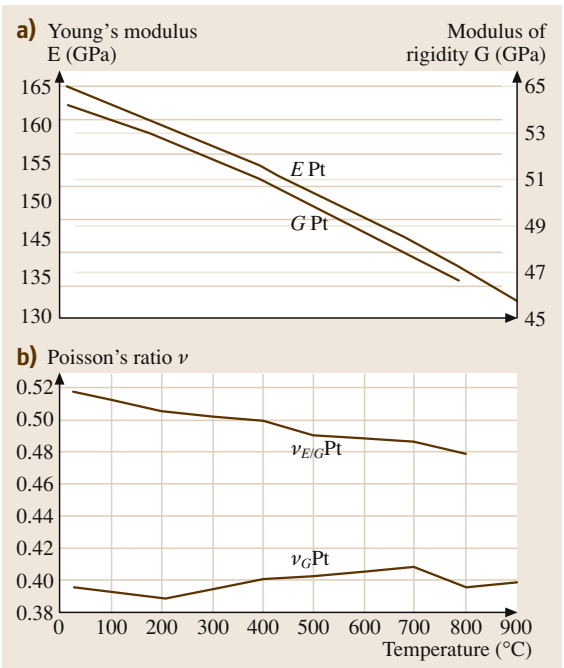


**Fig. 3.1-302 (a)** Young's modulus $E$ (GPa) and modulus of rigidity $G$ (GPa) of Pt at different temperatures. **(b)** Poisson's ratio for Pt at different temperatures [1.289, p. 76]

**Table 3.1-237** Structure and lattice parameter of selected Rh compounds [1.217, p. 117ff.]

| Phase | Pearson symbol | *a* (nm) | *b* (nm) | *c* (nm) | Concentration *x* A(1 − *x*)B(*x*) |
|---|---|---|---|---|---|
| Cu−Rh | cF4 | 0.3727 | | | 0.5 |
| Fe−Rh | cI2 | 0.288885 | | | |
| Fe−Rh | cF4 | 0.374 | | | 0.5 |
| FeRh | cP2 | 0.2998 | | | |
| Fe−Ru | hP2 | 0.258 | | 0.414 | 0.2 |
| Ni−Rh | cF4 | 0.36845 | | | 0.494 |

**Table 3.1-238** Mechanical properties of Rh (99%) at different temperatures [1.217, p. 227]

| *T* (°C) | *E* (GPa) | $R_m$ (MPa) | *A* (%) | $R_{p0.2}$ (MPa) | HV |
|---|---|---|---|---|---|
| 20 | 386 | 420 | 9 | 70 | 130 |
| 500 | 336 | 370 | 19 | 80 | 91 |
| 700 | 315 | 340 | 16 | 40 | 73 |
| 1000 | – | 120 | 10 | 30 | 52 |

*A* = elongation of rupture, *E* = modul of elasticity, $R_p$ = limit of proportionality, HV = Vickers hardness, $R_m$ = tensile strength

**Table 3.1-239** Increase of Rh hardness by cold forming [1.217, p. 227]

| V (%) | HV |
|---|---|
| 0 | 130 |
| 10 | 275 |
| 30 | 50 |
| 50 | 400 |

**Table 3.1-240** Hardness of Pd/Rh and Pt/Rh alloys as a funtion of composition [1.217, p. 218]

| 2nd metal | HV 5 Content (mass%) | | | | |
|---|---|---|---|---|---|
| | 0 | 20 | 40 | 60 | 80 |
| Pd | 130 | 178 | 235 | 229 | 138 |
| Pt | 130 | 165 | 164 | 145 | 123 |

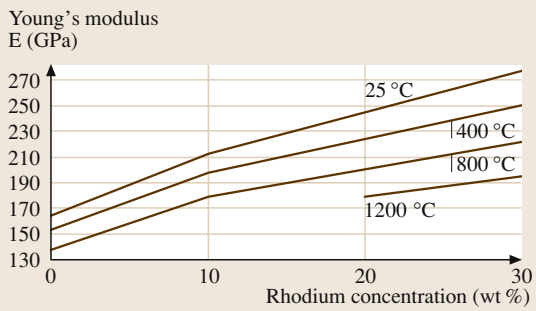


**Fig. 3.1-303** Young's modulus of as cast Pt/Rh-alloys at various temperatures [1.289, p. 80]

**Table 3.1-241** Hardness of Rh−Ni alloys at 300 K [1.217, p. 228]

| Alloy | HV 5 |
|---|---|
| RhNi27 | 275 |
| RhNi40 | 220 |
| RhPd20 | 178 |
| RhPt20 | 165 |

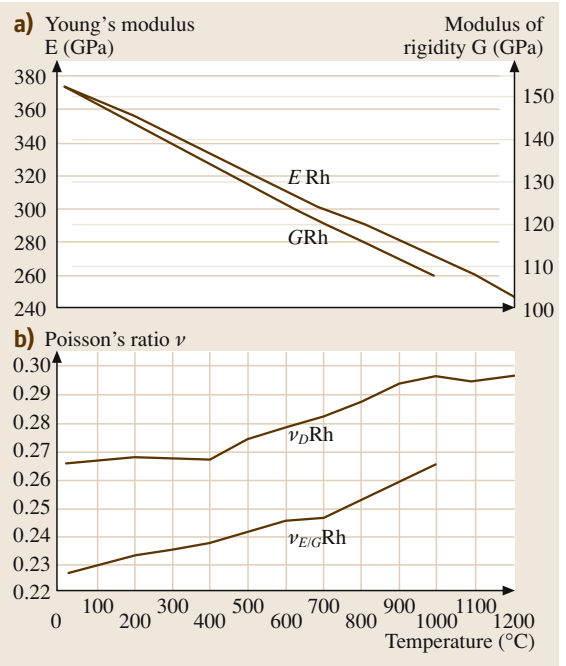

**Fig. 3.1-305** Vickers hardness of Pt/Rh-10 as a function of reduction (%) and various annealing temperatures [1.218, p. 608]

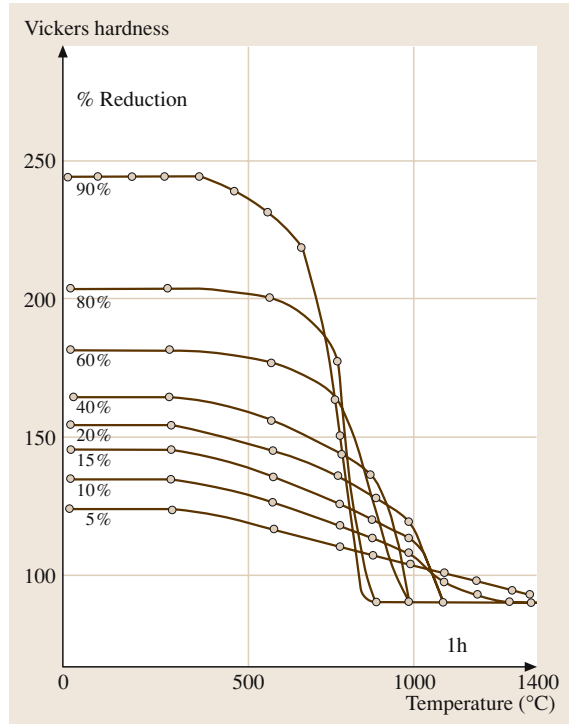


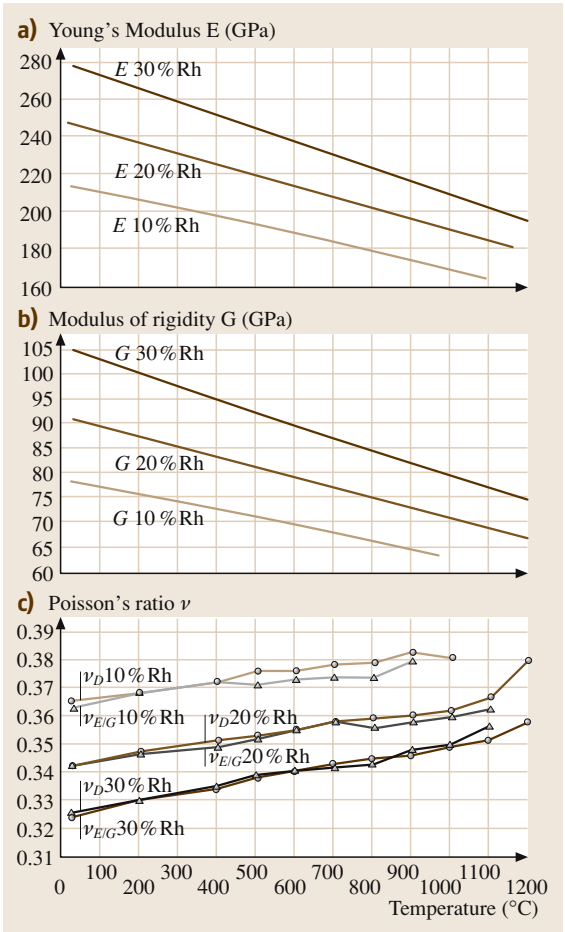


**Fig. 3.1-306** **(a)** Young's modulus $E$ (GPa) of Pt/Rh-10, Pt/Rh-20 and Pt/Rh-30 alloys at different temperatures. **(b)** Modulus of rigidity $G$ (GPa) of Pt/Rh-10,Pt/Rh-20 and Pt/Rh-30 alloys at different temperatures. **(c)** Poisson's ratio of Pt/Rh 10, Pt/Rh 20 and Pt/Rh-30 alloys at different temperatures [1.289, p. 79]

◀ **Fig. 3.1-304** **(a)** Young's modulus $E$ (GPa) and the modulus of rigidity $G$ (GPa) of forged Rh at different temperatures. **(b)** Poissons ratio for forged Rh at different temperatures [1.289, p. 77]

**Fig. 3.1-307** Mechanical properties of Pt/Rh-10 alloy [1.218, p. 609]

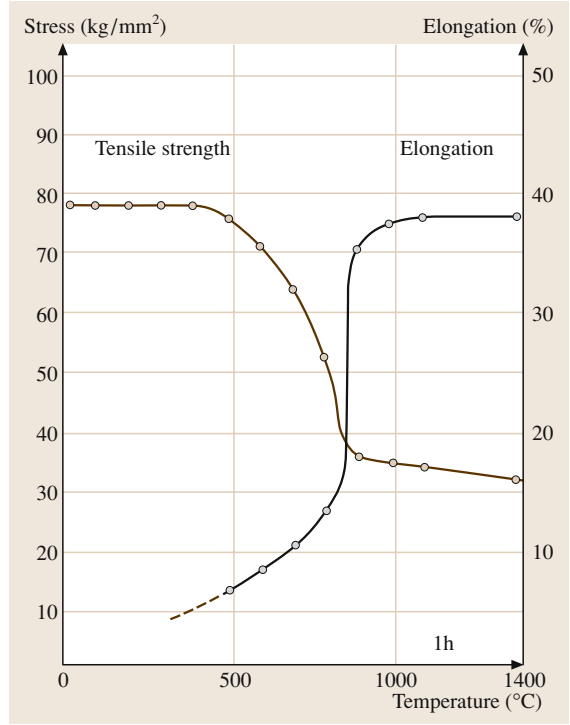

*Electrical Properties.* Characteristic electrical properties are given in Tables 3.1-242 and 3.1-243 (see also Table 3.1-203). Rhodium shows superconductivity below 0.9 K [1.216]. Superconducting Rh alloys are shown in Table 3.1-244. Among the three-element alloys containing precious metals there exists a special group known as magnetic superconductors [1.218]. Figure 3.1-308shows as example the alloy $ErRh_4B_4$ with the coexistence of superconductivity and magnetic order changing in the region below the critical temperature of beginning superconductivity [1.218]. Data for light and thermoelectric emission are given in Table 3.1-245 [1.290].

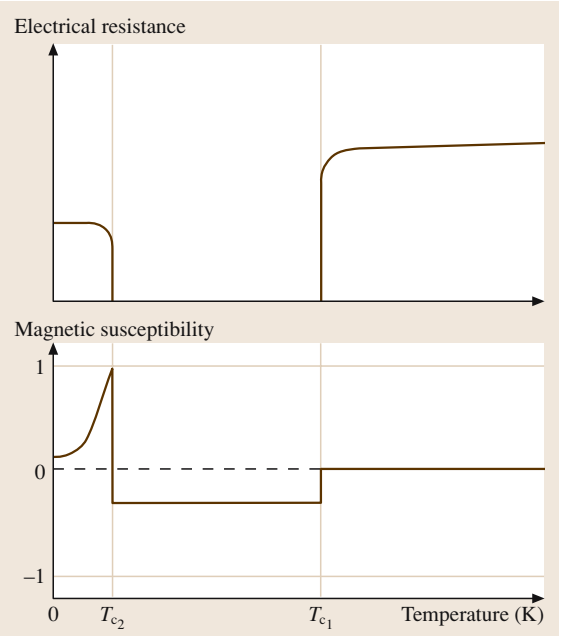


**Fig. 3.1-308** Coexistence of superconductivity and magnetic order in ErRh4B4 [1.218, p. 637]

**Table 3.1-242** Increase of atomic resistivity $\Delta\rho/C$ of Rh [1.217, p. 158]

| Base element | $\Delta\rho/C$ (μΩ cm/at.%) |
|---|---|
| Rh | Co 0.34, Cr 4, Fe 0.6, Mn 1.4 |

**Table 3.1-243** Specific electric resistivity $\rho_i(T)$ (μΩ cm) of Rh at temperature $T$ ($\rho_0 = 0.0084$) [1.217, p. 156]

| $T$ (K) | 25 | 70 | 160 | 273 | 500 | 1250 | 1750 |
|---|---|---|---|---|---|---|---|
| $\rho_i(T)$ | 0.0049 | 0.34 | 2.12 | 4.3 | 9.20 | 26.7 | 40.9 |

**Table 3.1-244** Superconducting Pd, Pt, and Rh alloys [1.218, p. 636]

| Pd, Pt Compound | $T_c$ (K) | Rh Compound | $T_c$ (K) |
|---|---|---|---|
| PtNb3 | 10.6 | Rh2P | 1.3 |
| Pd1.1Te | 4.07 | Rh4P3 | 2.5 |
| PdTe1.02 | 2.56 | ErRhB4 | 8.5 |
| PdTe2 | 1.69 | | |

**Table 3.1-245** Light and thermoelectric emission of Rh, Pd, and Pt [1.220, p. 79]

| Metal | Light-electric constants | | Temperature (°C) | Thermoelectric work function (V) |
|---|---|---|---|---|
| | Wavelength limit (Å) | Work function (V) | | |
| Rh | 2500 | 4.57 | 20 | 4.58 (at 1550° abs.) |
| | 2700 | – | 240 | |
| Pd | 2490 | 4.96 | RT | 4.99 (at 1550° abs.) |
| Pt | 1962 | 6.30 | RT | 6.37 (at 1550° abs.) |

*Thermoelectrical Properties.* Tables 3.1-206 and 3.1-207 give data for the absolute thermoelectric power; Tables 3.1-246 and 3.1-247 give the thermal electromotive force of Rh and of Rh/Ni alloys at different temperatures. Rh is also used as a component in Pt-based thermocouples (Tables 3.1-230–3.1-228, Fig. 3.1-295).

*Magnetical Properties.* Data of the magnetic susceptibility of Rh and Rh alloys are given in Figs. 3.1-271, 3.1-272, and 3.1-309–3.1-312. For magnetostriction data see Table 3.1-211. The superlattice alloy FeRh shows a transition from the antiferro- to the ferromagnetic state near room temperature Fig. 3.1-312 [1.218] where small additions of Pd, Pt, Ir, Ru, or Os enhance this effect.

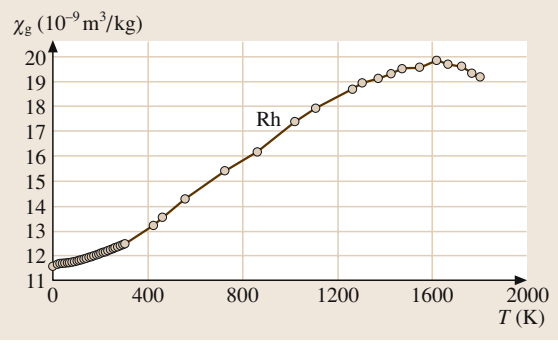


**Fig. 3.1-309** Temperature dependence of the mass susceptibility of Rh [1.217, p. 163]

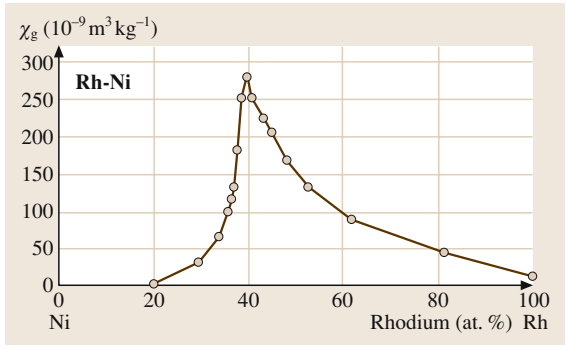


**Fig. 3.1-310** Mass susceptibility of Rh–Ni alloys as a function of alloy composition at 4.2 K [1.217, p. 166]

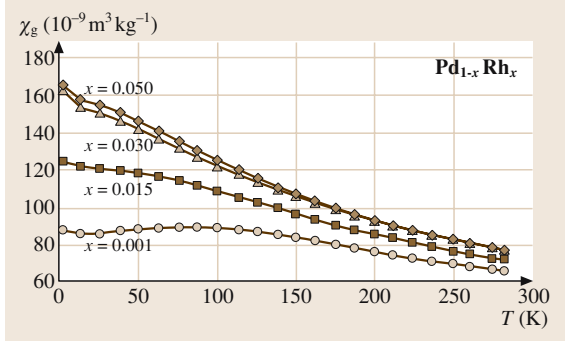


**Fig. 3.1-311** Mass susceptibility of Pd–Rh alloys as a function of alloy composition [1.217, p. 169]

**Table 3.1-246** Thermal electromotive force of Rh at different temperatures [1.217, p. 159]

| $T$ (°C) | −200 | −100 | +100 | +400 | +800 | +1000 | +1300 |
|---|---|---|---|---|---|---|---|
| $E_{Rh/Pt}$ | −0.23 | −0.32 | +0.70 | +3.92 | +10.16 | +14.05 | +20.34 |

**Table 3.1-247** Thermal electromotive force of Rh/Ir alloys at different temperatures [1.217, p. 160]

| $T$ (°C) | Composition (wt% Ir) | | | | | |
|---|---|---|---|---|---|---|
| | 10 | 30 | 50 | 70 | 90 | |
| 1000 | | 15.15 | 17.40 | 18.40 | 17.75 | 15.45 |

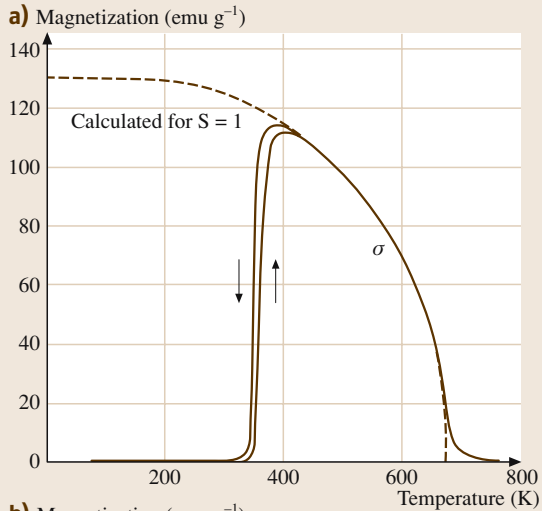


**Fig. 3.1-312a,b** Metamagnetic behavior of **(a)** FeRh superlattice alloy [1.218, p. 102]. **(b)** Variation by addition of small amounts of Pd, Ru, Ir, Pt, Os [1.218, p. 102]

*Thermal Properties.* Tables 3.1-212–3.1-214 show the recrystalization temperature, thermal conductivity and thermal expansion at different temperatures. Vapor pressure at different temperatures is shown in Fig. 3.1-273.

*Optical Properties.* Rhodium has the highest optical reflectivity of all platinum-group metals (Fig. 3.1-274), ranging about 20% below the reflectivity of Ag. It is used as hard and corrosion-resistant coating on silver jewelry and for optical reflectors. Data of the spectral emissivity are given in Table 3.1-216.

*Diffusion.* Data for self-diffusion are given in Table 3.1-217 (see [1.216] for further data).

*Chemical Properties.* Rhodium is not attacked by acids or alkali even under oxidizing conditions (aqua regia) (Fig. 3.1-313). Sodium hypochlorite attacks in the order of increasing strength: Pt = Rh = Ir = Ru < Pd < Os. Heating in air causes the formation of thin oxide layers above 600 °C which decompose above 1100 °C (Fig. 3.1-314). Pt alloys with 5–40 wt% Rh are corrosion-resistant against $H_2F_2$. A detailed survey about these chemical properties is given in [1.216].

Rhodium is the effective component of the three-way Pt/Pd/Rh alloy autocatalyst for the reduction of

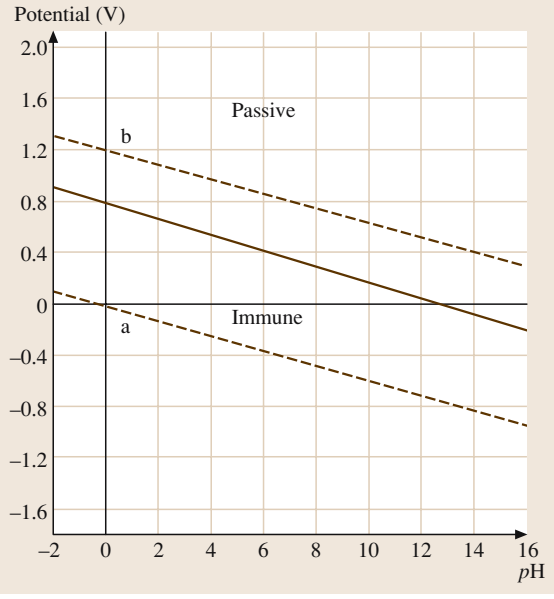


**Fig. 3.1-313** Potential *p*H diagram for the system Rh–$H_2O$ [1.217, p. 202]

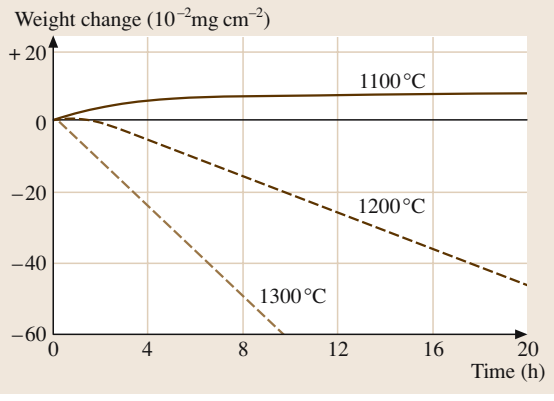


**Fig. 3.1-314** Weight change of Rh in oxygen [1.217, p. 185]

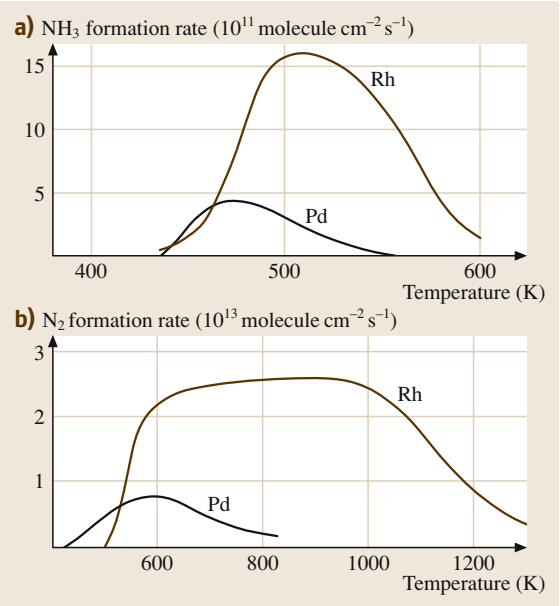


**Fig. 3.1-315a,b** Product formation rates in $N = -H_2$ reactions on Pd- and Rh-catalyst foils. **(a)** $NH_3$ formation rates $p(NO) = 9.4 \times 10^{-5}$ Pa, $p(H_2) = 4.9 \times 10^{-5}$ Pa. **(b)** $N_2$ formation rates $p(NO) = 1.1 \times 10^{-5}$ Pa, $p(H_2) = 1.9 \times 10^{-5}$ Pa [1.218, p. 287]

$NO_x$ of exhaustion gases (Figs. 3.1-315a,b). Rhatalysts surpass the group homolog, Co-based catalysts, with lower reaction pressures and temperatures and higher yields [1.216]. Complex organic rhodium compounds on the basis of RhCl ($PPH_3$) with different substitute ligands are important homogeneous catalysts in the technical production processes for hydrogenation and hydroformulation ("oxo"-processes, e.g., synthesis of aldehydes and acetic acid). Replacement of $PPH_3$ by complex chiral phosphan ligands enables the synthesis of asymmetric compounds, e.g., L-DOPA and L-menthol (Fig. 3.1-316a,b) [1.291].

### Iridium and Iridium Alloys

*Applications.* Iridium is used for crucibles to grow high-purity crystals for lasers, medical scanners etc., anodes to prevent corrosion of shipping vessels and under-water structures, coatings of electrodes for the manufacturing of chlorine and caustic soda, as an alloy component of automotive exhaust catalysts, and as alloy component and compounds of chemical process catalysts for the production of acetic acid and complex organic compounds. Iridium is an effective hardener for materials used at high temperature, high wear, and high corrosion conditions (e.g., spark plugs). It is also used as fine-grain forming addition in jewelry and dental gold alloys. Commercial grades available are powder, shot, ingot, and wire in a purity ranging from 98–99.9% (ASTM 671-81, reappraised 1987).

*Production.* Iridium is produced as powder and sponge by chemical reduction or thermal decomposition of the chloro–ammonia compound $(NH_4)_2[IrCl_6]$. Bars, rods, ingot, and wires are produced by compacting of powder followed by extrusion. Coatings are produced galvanically, by evaporation, or by sputtering.

*Phases and Phase Equilibria.* Figures 3.1-317–3.1-319 [1.216] show the binary phase diagrams of Ir alloys with Pt, Rh, and Ru. Miscibility gaps exist in the solid state also in the alloy systems with Cu, Os, Re, and Ru. Iridium alloyed in Fe lowers the $\alpha$–$\lambda$ transition temperature consider-

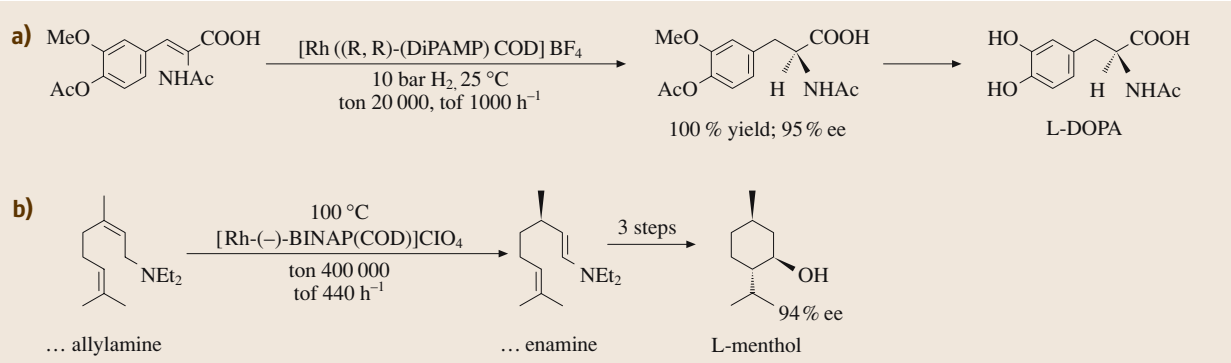


**Fig. 3.1-316a,b** Examples of organic synthesis of chiral compounds catalysed by complex Rh compounds. **(a)** L-DOPA. **(b)** L-menthol [1.291, p. 83]

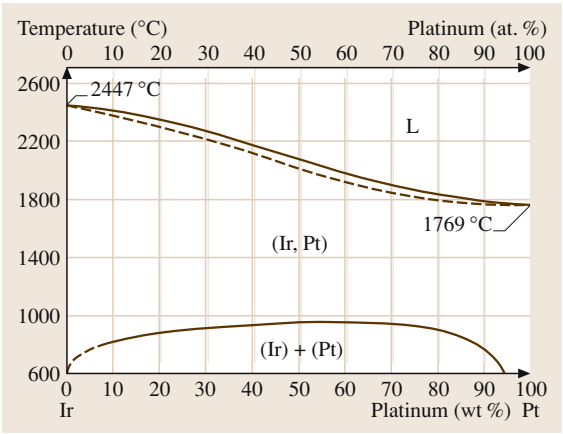


**Fig. 3.1-317** Phase diagram of Ir–Pt [1.217, p. 88]

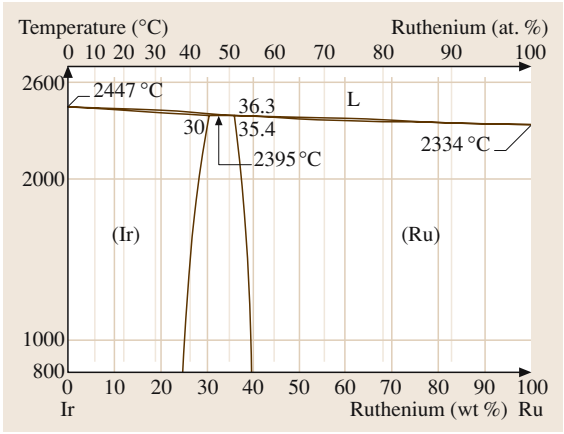


**Fig. 3.1-319** Phase diagram of Ir–Ru [1.217, p. 89]

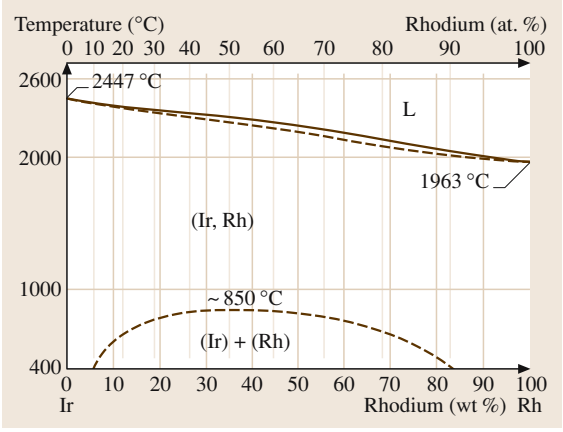


**Fig. 3.1-318** Phase diagram of Ir–Rh [1.217, p. 89]

ably (Fig. 3.1-343). Thermodynamic data are given in Table 3.1-248 [1.216].

Structure and lattice parameters of selected intermediate compounds are given in Table 3.1-249 [1.216].

**Table 3.1-248** Thermodynamic data of Ir [1.217, p. 109]

| $T$ (K) | $c_p$ (J/K mol) | $S$ (J/K mol) | $H$ (J/mol) | $G$ (J/mol) | $p$ (atm) |
|---|---|---|---|---|---|
| 298.15 | 24.979 | 35.505 | 0 | −10.586 | |
| 400 | 25.695 | 42.946 | 2.581 | −14.598 | $6.70\times10^{-80}$ |
| 800 | 28.51 | 61.62 | 13.442 | −35.875 | $2.81\times10^{-36}$ |
| 1400 | 32.733 | 78.647 | 31.795 | −78.311 | $1.15\times10^{-17}$ |

$T$ = Temperature, $c_p$ = specific heat capacity, $S$ = Entropy, $H$ = Enthalpy, $G$ = free Enthalpy, $p$ = partial pressure of the pure elements

**Table 3.1-249** Structure and lattice parameter of intermediate compounds [1.217, p. 117ff,]

| Phase | Pearson symbol | $a$ (nm) | $b$ (nm) | $c$ (nm) | Concentration $x$ A(1 − $x$)B($x$) |
|---|---|---|---|---|---|
| Cu–Ir | cF4 | 0.3629 | | | |
| Ir–Os | hP2 | 0.27361 | | 0.43417 | 0.65 |
| Ir–Os | cF4 | 0.38358 | | | 0.2 |
| Ir–Rh | cF4 | 0.3824 | | | 0.5 |
| Ir–Ru | hP2 | 0.2718 | | 0.4331 | 0.56 |
| Ir–Ru | cF4 | 0.3818 | | | 0.47 |

HT = high temperature modification, LT = low temperature modification

*Mechanical Properties.* Iridium is extremely hard and can only be deformed at temperatures above 600 °C, with repeated annealing steps at temperatures higher than 1200 °C. The Young's modulus is different for different crystal directions (Table 3.1-250) [1.216], the modulus of rigidity is 214 GPa, and the Poisson's ratio amounts to 0.26.

Characteristic data of mechanical properties of Ir and Pt/Ir alloys are given in Tables 3.1-251–3.1-253 [1.216] and Figs. 3.1-320–3.1-322 [1.289]. Two-phase Ir-based refractory superalloys with fcc and $L1_2$ structure of the components (Ir−12Zr and Ir−17Nb, Ir−15Nb−5Ni) have resist temperatures up to 1200 °C and exhibit marked creep resistance (Figs. 3.1-323–3.1-325) [1.292, 293].

**Table 3.1-250** Modulus of elasticity in crystal direction [1.217, p. 212]

| $E\langle 110\rangle$ | $E\langle 111\rangle$ |
|---|---|
| 47.4 GPa | 662 GPa |

**Table 3.1-251** Elastic constants of Ir [1.217, p. 212]

| | | | |
|---|---|---|---|
| $T = 300$ K | $c_{11} = 580$ | $c_{12} = 242$ | $c_{44} = 256$ |

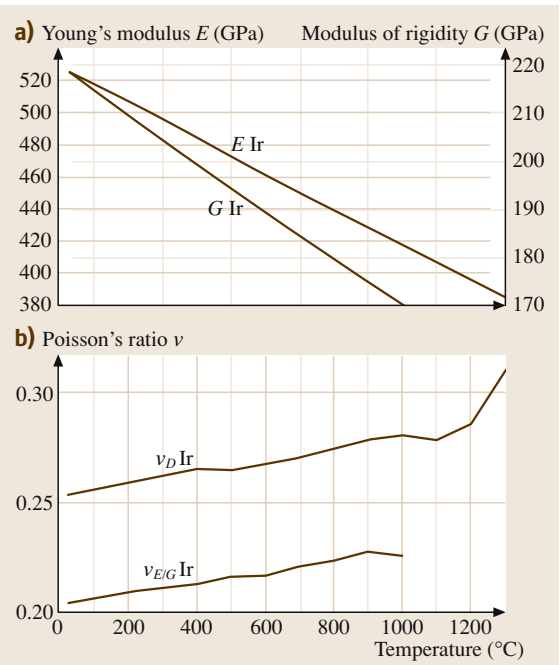


**Fig. 3.1-320** **(a)** Young's modulus of Ir at different temperatures. **(b)** Poisson's ratio for as cast Ir at different temperatures [1.289]

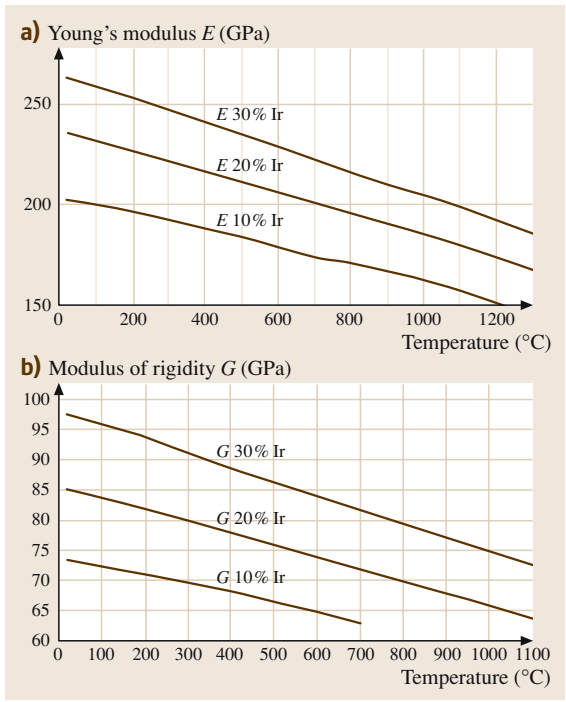


**Fig. 3.1-321** **(a)** Young's modulus of Pt−Ir alloys at different temperatures. **(b)** Modulus of rigidity of as cast Pt−Ir alloys at different temperatures [1.289]

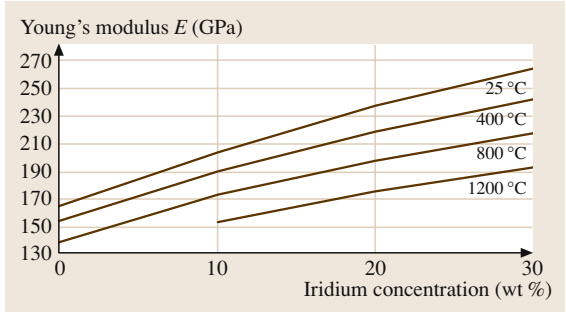


**Fig. 3.1-322** Young's modulus of as cast Pt−Ir alloys at different temperatures [1.289]

**Table 3.1-252** Mechanical properties of Ir at different temperatures [1.217, p. 213]

| $T$ (°C) | $E$ (GPa) | $R_m$ (MPa) | $A$ (%) | $R_{p0.2}$ (MPa) | HV |
|---|---|---|---|---|---|
| 20 | 538 | 623 | 6.8 | 234 | 200 |
| 500 | 488 | 530 | 9 | 12.7 234 | 138 |
| 800 | 456 | 450 | 18 | 51 142 | 112 |
| 1000 | 434 | 331 | – | 80.6 43.4 | 97 |

$A$ = elongation of rupture, $E$ = modul of elasticity, $R_p$ = limit of proportionality, HV = Vickers hardness, $R_m$ = tensile strength

**Table 3.1-253** Change of hardness of Ir by degree cold forming V (%) [1.217, p. 312]

| $V$ (%) | HV |
|---|---|
| 0 | 240 |
| 10 | 425 |
| 20 | 485 |
| 30 | 475 |
| 59 | 590 |

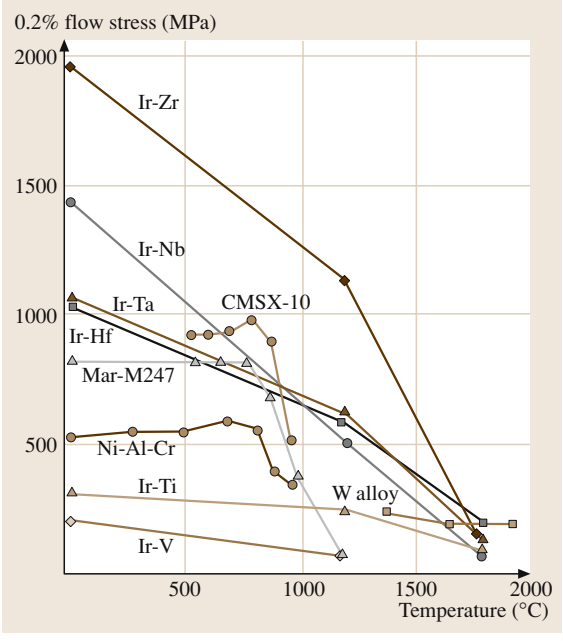


**Fig. 3.1-323** High-temperature compression strength of selected Ir-based alloys [1.292, p. 159]

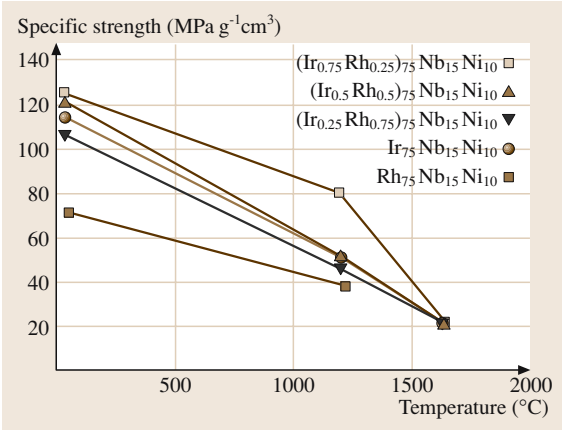


**Fig. 3.1-324** Specific strength of Ir–Rh–Nb alloys [1.293, p. 78]

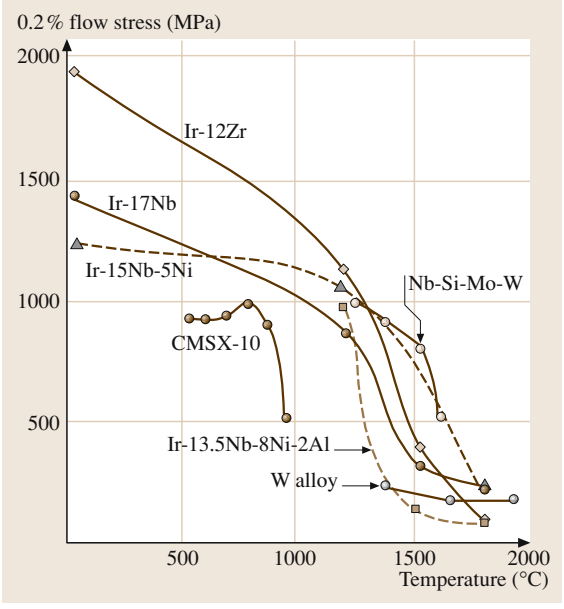


**Fig. 3.1-325** Comparison of compressive strength of Ir alloys versus W and Nb/Mo alloys at various temperatures [1.293, p. 77]

**Table 3.1-254** Specific electrical resisitivity $[\rho_i(T) = \rho_0 + \rho_i(T)]$ of Ir at temperatures $T$ ($\rho_0 = 0.10\,\mu\Omega\,\text{cm}$) [1.217, p. 157]

| $T$ (K) | 15 | 40 | 140 | 273 | 700 | 1100 | 1500 |
|---|---|---|---|---|---|---|---|
| $\rho_i(T)$ | 0.0013 | 0.10 | 1.96 | 4.65 | 13.90 | 23.20 | 34.02 |

*Electrical Properties.* The residual resistance ratio (RRR) amounts to 85 (Table 3.1-203). The specific electrical resistivity at different temperatures and the dependence of the atomic resistivity are given in Tables 3.1-254, and 3.1-255 [1.216]. The RRR is listed in Table 3.1-203.

Iridium becomes superconducting below 0.11 K. Some ternary alloys show critical transition temperatures between 3 K and above 8 K (Table 3.1-256) [1.218

*Thermoelectrical Properties.* Data for the absolute thermoelectric power and the thermoelectric voltage of Ir, and the thermoelectric voltage of Ir/Rh alloys are shown in Tables 3.1-206–3.1-208, 3.1-257 [1.216] and Fig. 3.1-326 [1.217].

*Magnetic Properties.* Iridium is paramagnetic. Figures 3.1-271, 3.1-327, 3.1-328 [1.216] show the mass susceptibility of Ir and Pt/Ir alloys at different temperatures. Iridium exhibits magnetostriction according the equation $\Delta l/l = S_l H^2$, with $S_l = +3.8$ (Table 3.1-211).

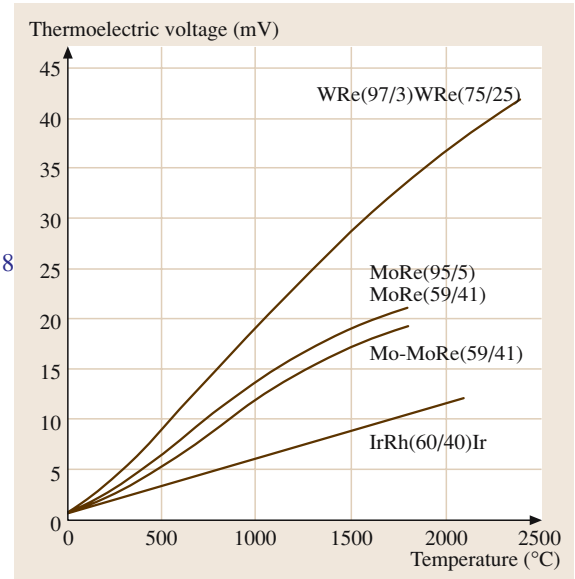


**Fig. 3.1-326** Thermoelectric voltage of Ir−Rh alloys compared to Mo−Re and W−Re alloys [1.217, p. 474]

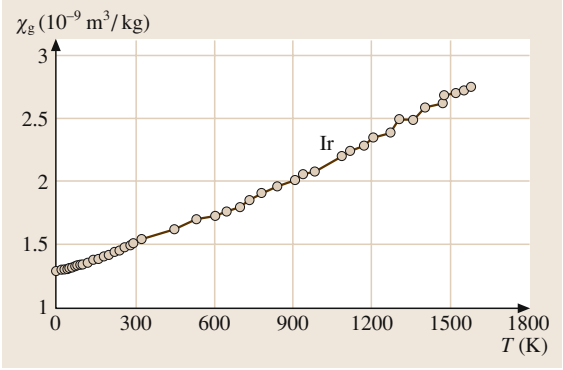


**Fig. 3.1-327** Mass susceptibility of Ir at different temperatures [1.217, p. 164]

**Table 3.1-255** Increase of atomic resistivity [1.217, p. 158]

| Base element | $\Delta\rho/C$ (μΩ cm/at.%) |
|---|---|
| Ir | Pt 1.33, Re 2.7, Cr 2, Mo 3.65, W 3, Fe 0.6 |

**Table 3.1-256** Superconducting Ir alloys [1.218, p. 636]

| Ir Compound | $T_c$ (K) |
|---|---|
| IrTe3 | 1.18 |
| Sc5Ir4Si10 | 8.46–8.38 |
| Y5Ir4Si10 | 3.0–2.3 |
| Lu5Ir4Si10 | 3.76–3.72 |

**Table 3.1-257** Thermoelectric voltage of Ir at different temperatures [1.216, p. 95]

| $T$ (°C) | −200 | −100 | −50 | +100 | +200 | +400 | +800 |
|---|---|---|---|---|---|---|---|
| $E_{\text{Ir,Pt}}$ (mV) | −0.20 | −0.35 | −0.20 | 0.66 | 1.525 | 3.636 | 9.246 |

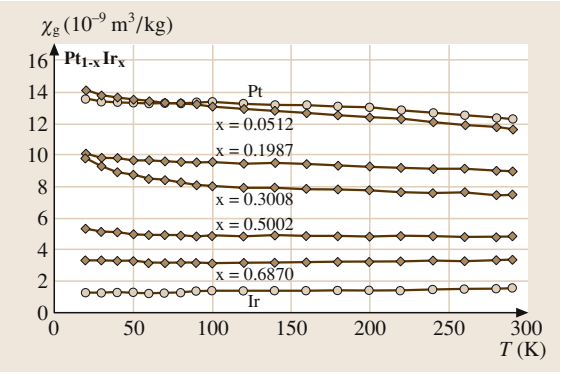


**Fig. 3.1-328** Mass susceptibility of Pt–Ir alloys at different temperatures [1.217, p. 68]

*Thermal Properties.* Tables 3.1-212–3.1-214 give selected data for the recrystallization temperature (varying by purity, degree of cold forming, and annealing time), thermal conductivity, and thermal expansion coefficient.

*Optical Properties.* The optical reflectivity of Ir is markedly lower than that of Rh increasing in the wavelength range from 0.4 to 0.8 µm (Figs. 3.1-191 and 3.1-274). Data of the spectral emissivity are given in Table 3.1-216.

*Diffusion.* Table 3.1-217 gives only one value for self diffusion of iridium but further information may be obtained from Landolt–Börnstein [1.238].

*Chemical Properties.* Iridium is not attacked by acids or alkali even under oxidizing conditions (aqua regia). It forms volatile oxides in air above 1000 °C but it can be heated up to 2300 °C without danger of catastrophic oxidation. Pt alloys with 1–30 wt% Ir are corrosion-resistant against $H_2F_2$. Figures 3.1-329 and 3.1-330 [1.216, 294] show data of the evaporation and oxidation behavior of Ir alloys. A detailed survey on the chemical properties is given in [1.216, 294].

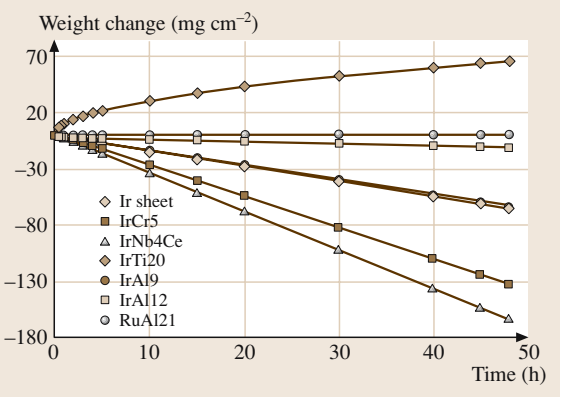


**Fig. 3.1-330** Oxidation behavior of various Ir alloys at 1000 °C in air [1.294, p. 100]

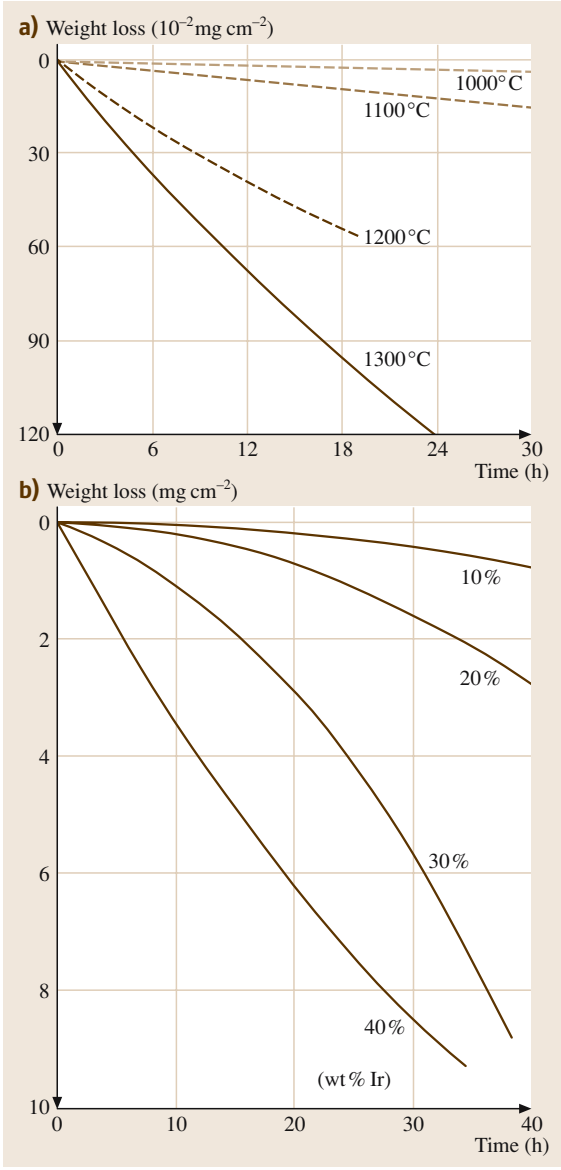


**Fig. 3.1-329a,b** Evaporation losses. **(a)** Pt loss in oxygen. **(b)** Pt–Ir clad loss in oxygen at 900 °C [1.217, p. 184]

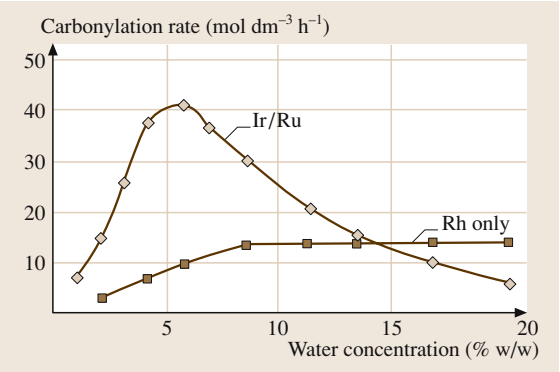


**Fig. 3.1-331** Carbonylation rates for Ir–Ru and Rh catalysts in methylacetat reactions [1.295, p. 100]

Metal-organic Ir compounds are effective homogeneous catalysts for organo-chemical reactions such as hydrogenation and carbonylation. The technical production of acetic acid ("Cativa" process). Figure 3.1-331 shows an example for different carbonylation rates of Rh- and Ir/Ru-based catalysts [1.295]. Complex organic Ir catalysts have high stereoselectivity in hydrating cyclic alcohols [1.216].

### Ruthenium and Ruthenium Alloys

*Applications.* Ruthenium is a component of alloys and compounds of chemical process catalysts, and Pt-based catalysts for proton-exchange fuel cells (PEFC). Because of its corrosion resistance, it is used for corrosion-preventing anodes in shipping vessels and under-water structures, pipelines, in geothermal industries, and as coating of electrodes in chlorine and caustic soda production. Ruthenium oxide ($RuO_2$) and complex Bi/Ba/Pt oxides are materials for electrical resistors. Ruthenium layers on computer hard discs are used for high density data storage improvement of data-storage densities. Ruthenium is an effective hardener of Pd and Pt. Commercial grades available are sponge, powder, grains, and pellets in purity ranging from 99–99.95% (ASTM B 717).

*Production.* Production of ruthenium starts with chemical reduction of chloro compounds to powder, followed by compacting to pellets. Coatings are produced by galvanic processing, evaporation or sputtering.

*Phases and Phase Equilibria.* Selected phase diagrams are shown in Figs. 3.1-332–3.1-334, thermodynamic data are listed in Table 3.1-258, and molar heat capacities can be found in Table 3.1-190. Ruthenium alloyed

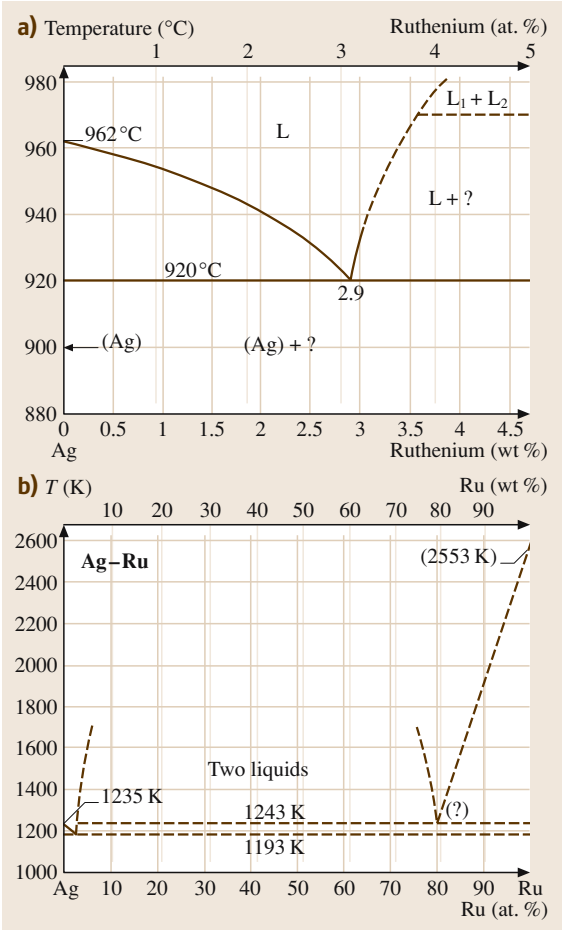


**Fig. 3.1-332a,b** Phase diagram of Ag–Ru **(a)** and phase diagram of Ag–Ru in the high-temperature range **(b)** [1.217, 245]

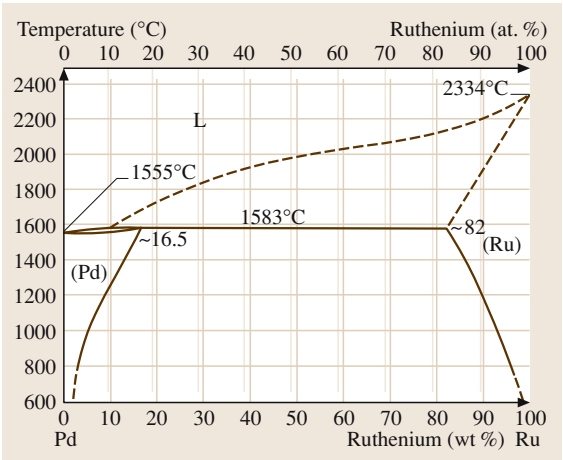


**Fig. 3.1-333** Phase diagram of Pd/Ru [1.217]

**Table 3.1-258** Thermodynamic data of Ru [1.217, p. 110]

| $T$ (K) | $c_p$ (J/K mol) | $S$ (J/K mol) | $H$ (J/mol) | $G$ (J/mol) | $p$ (at) |
|---|---|---|---|---|---|
| 298.15 | 23.705 | 28.535 | 0 | − 8.508 | |
| 400 | 24.345 | 35.595 | 2.449 | − 11.79 | $1.50 \times 10^{-77}$ |
| 800 | 26.516 | 53.121 | 12.611 | − 29.885 | $4.83 \times 10^{-35}$ |
| 1400 | 30.97 | 69.01 | 29.77 | − 66.844 | $7.73 \times 10^{-17}$ |

$T$ = Temperature, $c_p$ = specific heat capacity, $S$ = Entropy, $H$ = Enthalpy, $G$ = free Enthalpy,
$p$ = partial pressure of the pure elements

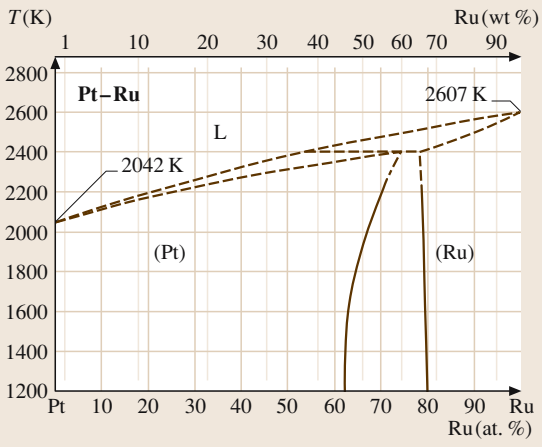


**Fig. 3.1-334** Phase diagram of Pt/Ru [1.245]

to Fe lowers the $\gamma$–$\alpha$ transition temperature considerably (Fig. 3.1-343). Table 3.1-259 gives the structure and lattice parameters of intermediate Co and Fe compounds. The superlattice structures can be found in Table 3.1-197.

**Table 3.1-261** Hardness (HV 5) of Pd/Ru and Pt/Ru alloys at 300 K [1.217, p. 230]

| Alloying metal | HV 5 alloy conc. (wt%) | | | | |
|---|---|---|---|---|---|
| | 0 | 20 | 40 | 60 | 80 |
| Pd | 350 | 412 | 425 | 284 | 243 |
| Pt | 350 | 330 | 446 | 293 | 253 |

*Mechanical Properties.* Ruthenium has a Young's modulus of 485 GPa, the Poisson's ratio amounts to 0.29, and the modulus of rigidity is 172 GPa. Characteristic properties of Ru are given in Tables 3.1-260 and 3.1-261. The mechanical properties are marked anisotropic. The hardness of different single crystal faces varies between 100 HV and 250 HV [1.216]. High compression-strength alloys are formed by two-phase Ru−Al intermetallic structures. Figure 3.1-335 gives

**Table 3.1-259** Structure and lattice parameter of intermediate compounds [1.217, p. 117ff.]

| Phase | Pearson symbol | $a$ (nm) | $b$ (nm) | $c$ (nm) | Concentration $x$ A$(1-x)$B$(x)$ |
|---|---|---|---|---|---|
| Co−Ru | hP2 | 0.261 | | 0.4181 | 0.5 |
| Co−Ru | cF4 | 0.3592 | | | 0.2 |
| Fe−Ru | cI2 | 0.2883 | | | 0.06 |
| Fe−Ru | hP2 | 0.258 | | 0.414 | 0.2 |
| Os−Ru | hP2 | 0.27193 | | 0.4394 | 0.5 |

**Table 3.1-260** Mechanical properties of Ru at different temperatures [1.217, p. 229], [1.216, p. 31]

| $T$(°C) | $R_m$ (MPa) | $A$ (%) | $R_{p0.2}$ (MPa) | HV |
|---|---|---|---|---|
| 20 | 500 | 3 | 380 | 250–500 [a] |
| 750 | 300 | 15 | 230 | 160–280 [b] |
| 1000 | 220 (430) | 14 | 190 | 100–200 [a] |

[a] at different crystal planes,
[b] at 600 °C
$A$ = Elongation of rupture, $R_p$ = Limit of proportionality,
HV = Vickers hardness, $R_m$ = Tensile strength

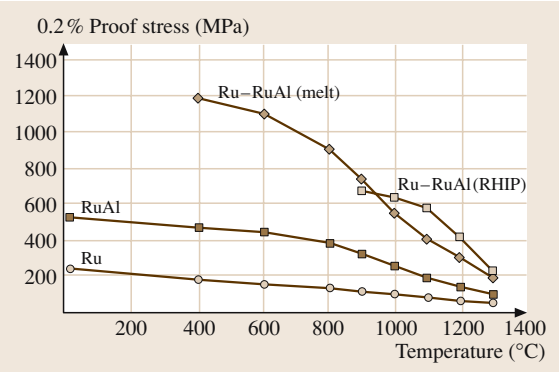


**Fig. 3.1-335** High-temperature compression strength of eutectic Ru-70/Al-30 in relation to its constituent phases [1.288, p. 164]

an example of molten and hot isostatic-pressed eutectic Ru (Ru-70/Al-30) in relation to the constituent phases [1.296].

*Electrical Properties.* The residual resistance ratio (RRR) amounts to 25 000 (Table 3.1-203). Characteristic electrical properties of Ru are given in Tables 3.1-203, 3.1-262, and 3.1-263. The specific electrical resistivity of $RuO_2$ is $3.5 \times 10^{-5}\,\Omega\,\mathrm{cm}$ ($1\,\Omega\,\mathrm{cm}$ for PdO for comparison). Together with its low temperature dependence of the coefficient of resistance, Ru is suited for the production of resistors in sintered form or as thick-film layers covering resistors ranging from $\approx 1.5 to 10\,\mathrm{M}\Omega$. Conductive components are either $RuO_2$, $Pb_2Ru_2O_6$, or $Bi_2Ru_2O_7$ together with additions of doping oxides [1.218].

Ruthenium shows superconductivity below 0.47 K [1.218]. Ternary alloys have critical transition temperatures up to 12.7 K (Table 3.1-264).

*Thermoelectric Properties.* Data of thermoelectric properties of Ru are given in Tables 3.1-206 and 3.1-265.

*Magnetic Properties.* Figures 3.1-271, 3.1-337, and 3.1-336 present data of the magnetic mass susceptibility of Ru and of Ru/Cr alloy at different temperatures.

**Table 3.1-263** Increase of atomic resistivity by alloying ($\Delta\rho/C$ ($\mu\Omega\,\mathrm{cm/at.\%}$)) [1.217, p. 158]

| Base element | $\Delta\rho/C$ ($\mu\Omega$ cm/at.%) |
|---|---|
| Ru | Fe 0.21, Re 2, Y 1.5 |
| Os | Y 10 |

**Table 3.1-264** Critical transition temperature of superconducting Ru alloys [1.218, p. 636]

| Ru | |
|---|---|
| **Composit** | **$T_c$ (K)** |
| TiRuP | 1.33 |
| ZrRuP | 12.34–10.56 |
| HrRuP | 12.70–11.08 |
| TiRuAs | >0.35 |
| ZrRuAs | 11.90–1.03 |
| HfRuAs | 4.93–4.37 |
| Y3Ru4Ge13 | 1.7–1.4 |
| Lu3Ru4Ge13 | 2.3–2.2 |

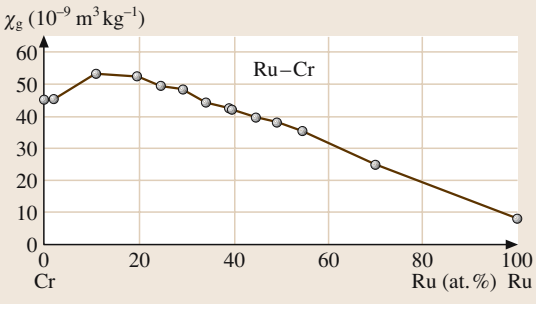


**Fig. 3.1-336** Temperature dependence of the mass susceptibility of Ru/Cr alloy [1.217, p. 166]

**Table 3.1-262** Specific electrical resistivity $\rho_i(T)$ ($\mu\Omega\,\mathrm{cm}$) of Ru at different temperatures ($\rho_0 = 0.016\,\mu\Omega\,\mathrm{cm}$) $\rho(T) = \rho_0 + \rho_i(T)$ [1.217, p. 156]

| $T$ (K) | 25 | 50 | 100 | 200 | 273 | 300 | 500 |
|---|---|---|---|---|---|---|---|
| $\rho_i(T)$ | 0.005 | 0.105 | 1.25 | 4.38 | 6.69 | 7.43 | 13.2 |

**Table 3.1-265** Thermal electromotive force of Ru at different temperatures [1.217, p. 159]

| $T$ (°C) | +100 | +200 | +300 | +500 | +800 | +1000 | +1200 |
|---|---|---|---|---|---|---|---|
| $E_{\mathrm{Ru/Pt}}$ | 0.684 | 1.600 | 2.673 | 5.119 | 9.519 | 13.003 | 16.864 |

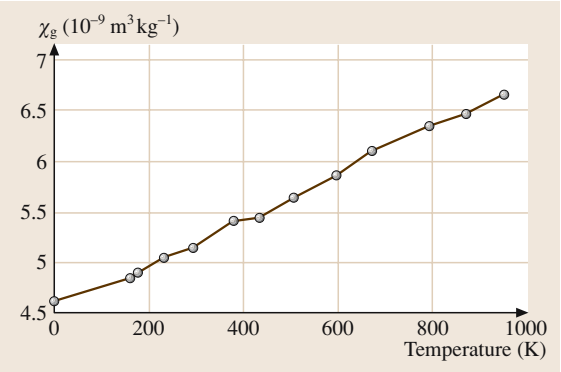


**Fig. 3.1-337** Temperature dependence of the mass susceptibility of Ru [1.217, p. 163]

*Thermal Properties.* Characteristic data of thermal expansion and thermal conductivity are given in Tables 3.1-213 and 3.1-266. Figure 3.1-273 shows the vapor pressure data for Ru.

*Optical Properties.* The optical reflectivity of Ru is near that of Rh (Fig. 3.1-333). Ruthenium alloyed to Pd enhances the optical reflectivity by 4–5% (Fig. 3.1-275).

*Diffusion.* Table 3.1-217 gives some values for self diffusion of Ru.

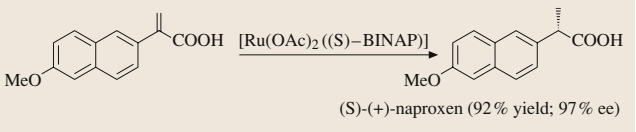


**Fig. 3.1-338** Synthesis of (S)-(+)-Naproxen catalysed by Ru-cplx compound [1.291, p. 83]

*Chemical Properties.* Ruthenium is not attacked by acids or alkali even under oxidizing conditions (aqua regia). By heating in air above 800 °C Ru forms the oxides RuO and $RuO_2$; above 1100 °C Ru forms $RuO_3$ which vaporizes. Detailed survey about the chemical properties is given in [1.218, 218].

Complex organic Ru compounds are catalysts for the enantioselective hydrogenation of unsaturated carboxylic acids, used in pharmaceutical, agrochemical, flavors and fine chemicals (Fig. 3.1-338) [1.291].

### Osmium and Osmium Alloys

*Applications.* Osmium is used as a component in hard, wear- and corrosion-resistant alloys, as surface coatings of W-based filaments of electric bulbs, cathodes of electron tubes, and thermo-ionic sources. Osmium itself, Os alloys, and Os compounds are strong and selective oxidation catalysts. Commercial grades available are powder in 99.6% and 99.95% purity, $OsO_4$, and chemical compounds.

*Production.* The production of Os starts from the mineral osmiridium via soluble compounds and the reduction to metal powder followed by powder-metallurgical compacting.

*Phases and Phase Equilibria.* Selected phase diagrams are shown in Figs. 3.1-339–3.1-342 [1.216]. Continuous series of solid solution are formed with Re and Ru. Miscibility gaps exist with Ir, Pd and Pt. The solid solubility in the Os−W system are 48.5 at.% for W and ≈ 5 at.% for Os. Osmium alloyed to Fe lowers the $\gamma$–$\alpha$ transition temperature considerably (Fig. 3.1-343 [1.297]). Thermodynamic data are given in Table 3.1-267 [1.216] and molar heat capacities in Table 3.1-190. Table 3.1-268 gives structures and lattice parameters of intermediate compounds with Ir, Ru, Pt, and W [1.216].

**Table 3.1-266** Thermal expansion coefficients of Ru and Os at different temperatures [1.217, p. 154]

| Temperature (°C) | ($10^{-6}$ $K^{-1}$) Ru[a] | Ru[b] | Ru[p] | Os[a] | Os[b] | Os[p] |
|---|---|---|---|---|---|---|
| 323 | 5.9 | 8.8 | 6.9 | 4.0 | 5.8 | 4.8 |
| 423 | 6.1 | 9.3 | 7.2 | 4.3 | 6.2 | 5.0 |
| 623 | 6.8 | 10.5 | 8.0 | 4.0 | 7.1 | 5.7 |
| 723 | 7.2 | 11.0 | 8.4 | 5.3 | 7.6 | 6.2 |
| 823 | 7.6 | 11.7 | 8.8 | 5.8 | 8.3 | 6.9 |

[a] vertical to the crystal ***c*** axis
[b] parallel to the crystal ***c*** axis
[p] polycrystalline

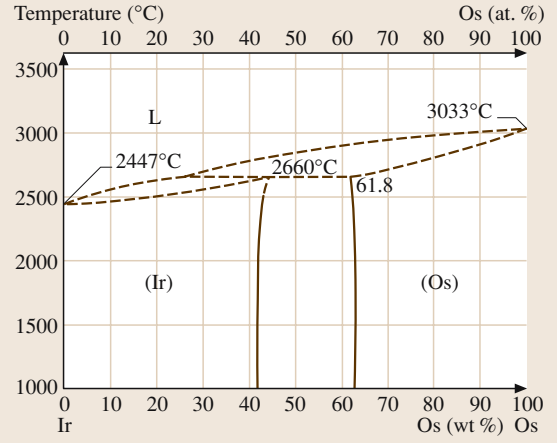


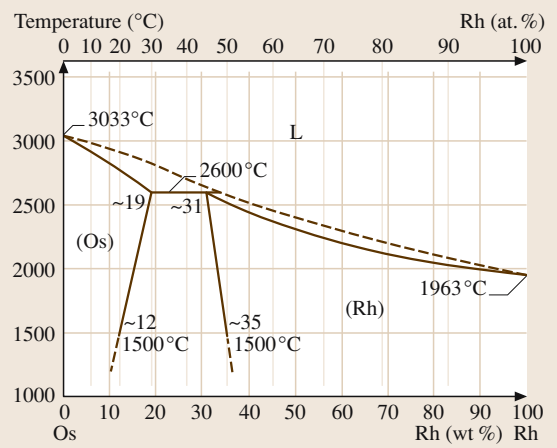


**Fig. 3.1-340** Phase diagram of Os–Rh [1.217, p. 90]

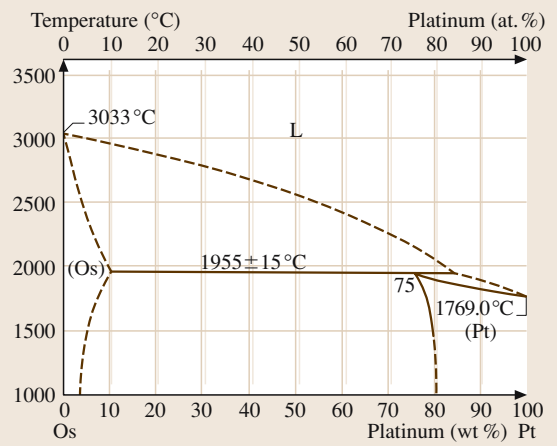


**Fig. 3.1-341** Phase diagram of Os–Pt [1.217, p. 90]

**Fig. 3.1-339** Phase diagram of Os–Ir [1.217, p. 87]

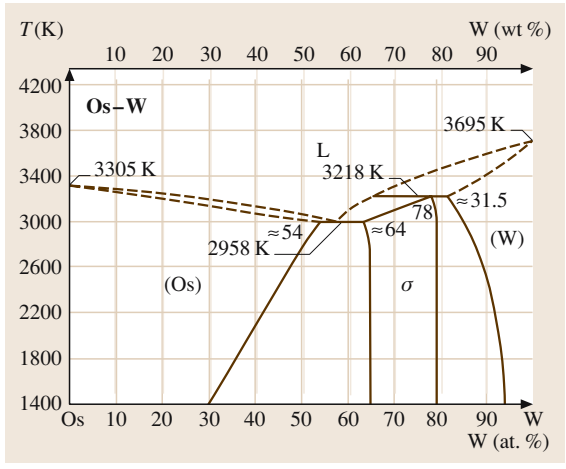


**Fig. 3.1-342** Phase diagram of Os–W [1.245]

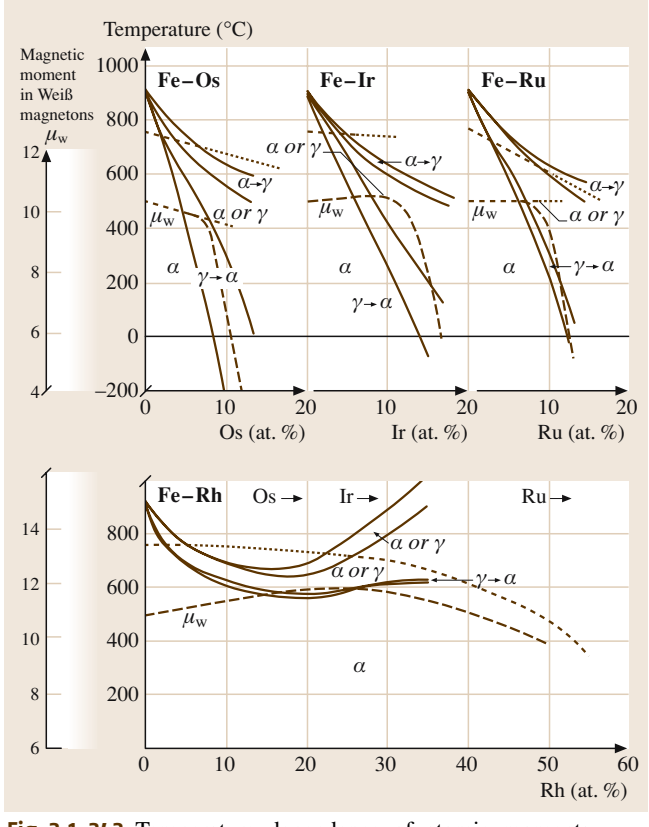


**Fig. 3.1-343** Temperature dependence of atomic moments, $\gamma$–$\alpha$ transition and magnetic transition of iron alloys [1.220, p. 259]

**Table 3.1-267** Thermodynamic data of Os [1.217, p. 110]

| $T$ (K) | $c_p$ (J/K mol) | $S$ (J/K mol) | $H$ (J/mol) | $G$ (J/mol) | $p$ (at) |
|---|---|---|---|---|---|
| 298.15 | 24.707 | 32.635 | 0 | −9.73 | |
| 400 | 25.094 | 39.95 | 2.536 | −13.444 | $2.95\times10^{-95}$ |
| 800 | 26.618 | 57.811 | 12.879 | −33.371 | $6.31\times10^{-44}$ |
| 1400 | 28.903 | 73.287 | 29.535 | −73.067 | $5.81\times10^{-22}$ |

$T$ = Temperature, $c_p$ = specific heat capacity, $S$ = Entropy, $H$ = Enthalpy, $G$ = free Enthalpy, $p$ = partial pressure of the pure elements

**Table 3.1-268** Structure and lattice parameter of selected Os alloy phases [1.217, p. 118]

| Phase | Pearson symbol | $a$ (nm) | $c$ (nm) | Remarks | Concentration $x$ A$(1-x)$ B$(x)$ |
|---|---|---|---|---|---|
| Os | hP2 | 0.27353 | 0.43191 | 293 K | |
| Os−Ir | hP2 | 0.27361 | 0.43417 | | 0.35 |
| Os−Ir | cF4 | 0.38358 | | | 0.8 |
| Os−Pt | hP2 | 0.27361 | 0.43247 | | 0.1 |
| Os−Pt | cF4 | 0.39094 | | | 0.8 |
| Os−Ru | hP2 | 0.27193 | 0.4394 | | 0.5 |
| $Os_3W_7$ | tP30 | 0.9650 | 0.4990 | | 0.78 |

*Mechanical Properties.* Osmium is very hard and brittle. The hardness is, as in the case of Ru, strongly anisotropic. Characterisitic properties for hardness of the element at different temperatures, as well as work hardening and hardness of Os−Pt alloys are given in Tables 3.1-269 and 3.1-270 [1.216, 217] and Fig. 3.1-262. Osmium exhibits a Young's modulus of 570 GPa, a modulus of rigidity of 220 GPa, and the Poisson's ratio is 0.25.

*Electrical Properties.* The residual electrical resistivity ratio (273.2 K/4.2 K) is 400 [1.216] (Table 3.1-203).

**Table 3.1-269** Hardness of Os at different temperatures [1.216]

| $T$ (°C) | HV |
|---|---|
| 20 | 300–680 [a] |
| 200 | 260–580 [a] |
| 600 | 200–410 [a] |
| 1200 | 130–400 [a] |

[a] all values depending on crystal orientation

**Table 3.1-270** Hardness of Os−Pt alloys [1.217]

| Pt content (wt%) | HV |
|---|---|
| 0 | 560 |
| 20 | 578 |
| 40 | 555 |

**Table 3.1-271** Specific electrical resistivity $\rho_i(T)$ (μΩ cm) of Os at temperature $T$ $[\rho(T)=\rho_0+\rho_i(T)]$; $(\rho_0 = 0.09\,\mu\Omega\,\text{cm}$ [a]) [1.216]

| $T$ (K) | $\rho_i$ (μΩ cm) |
|---|---|
| 25 | 0.012 |
| 100 | 1.90 |
| 273 | 8.30 |
| 900 | 26.0 |
| 1300 | 38.0 |

At $T < 273$ K; $\rho_0 = 0.8\,\mu\Omega$ cm at $T > 273$ K

Table 3.1-271 [1.216] gives the specific electric resistivity of Os at different temperatures. The increase of atomic resistivity is shown in Table 3.1-263. Osmium coatings on W-based dispenser cathodes lower its work function (source Ba−Ca aluminate). It enhances the secondary electron emission (Fig. 3.1-344) and enables the operation at higher current densities in high power klystron and magnetron valves. Osmium shows superconductivity below 0.71 K and Table 3.1-272 gives some examples of superconducting Os alloys [1.218].

*Thermoelectric Properties.* Figure 3.1-269 shows a comparison of the thermoelectric power of the different noble metals of the platinum group as a function of temperature.

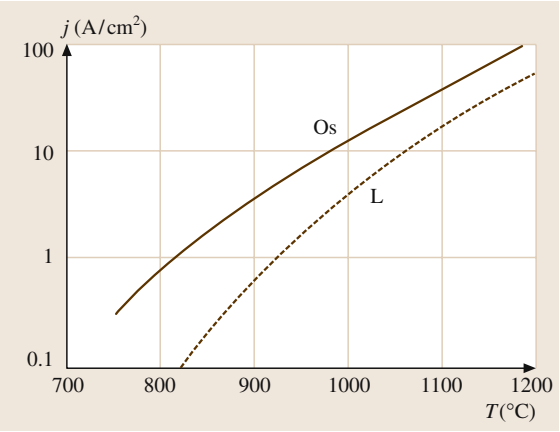


**Fig. 3.1-344** Current density as a function of cathodic temperature for a normal cathode (*dashed curve*) and a cathode with a 5 μm thick Os coating [1.298]

*Magnetic Properties.* Figures 3.1-271 and 3.1-345–3.1-347 [1.216] give a survey and present selected data of the magnetic mass susceptibility for the element and for Os−Cr alloys. This alloy system exhibits antiferromagnetism in compositions from 0.3 to 2.2 at.% Os in the temperature range on the left-hand side of the bold vertical bars in Fig. 3.1-347. In Fe−Os alloys the temperature of the magnetic transitionand the atomic magnetic moment decrease with increasing Os content (see Fig. 3.1-343).

**Table 3.1-272** Superconducting Os-alloys [1.218]

| Os | |
|---|---|
| **Compound** | **$T_c$ (K)** |
| Ce3Os4Ge13 | 6.1 |
| Pr3Os4Ge13 | 16 |
| Nd3Os4Ge13 | 1.9 |
| Eu3Os4Ge13 | 10.1 |
| Tb3Os4Ge13 | 14.1 |
| Dy3Os4Ge13 | 2.1 |
| Er3Os4Ge13 | 1.9 |
| ZrOsAs | 8 |
| HfOsAs | 3.2 |
| Y3Os4Ge13 | 3.9–3.7 |
| Lu3Os4Ge13 | 3.6–3.1 |
| Y5Os4Ge10 | 8.68–8.41 |
| TiOsP | <1.2 |
| ZrOsP | 7.44–7.1 |
| HfOsP | 6.10–4.96 |

*Thermal Properties.* Data for the thermal expansion coefficient at different temperatures are given in Table 3.1-266.

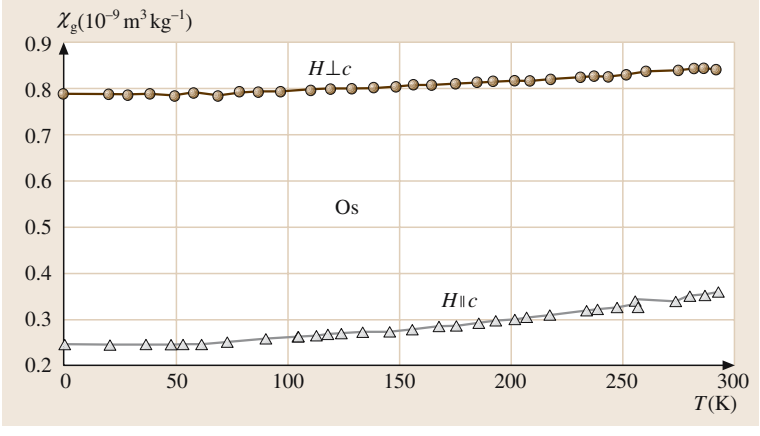


**Fig. 3.1-345** Temperature dependence of the mass susceptibility of Os (single crystal) at applied magnet field of 795–700 A/m [1.217, p. 164]

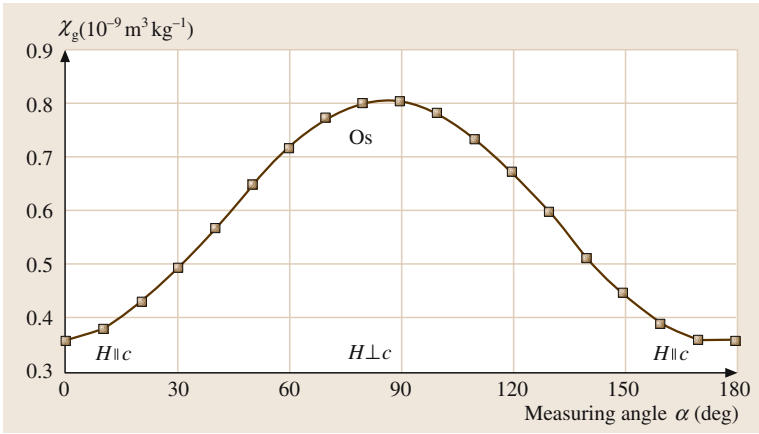


**Fig. 3.1-346** Mass susceptibility of an Os single crystal at room temperature as a function of measuring angle [1.217, p. 164]

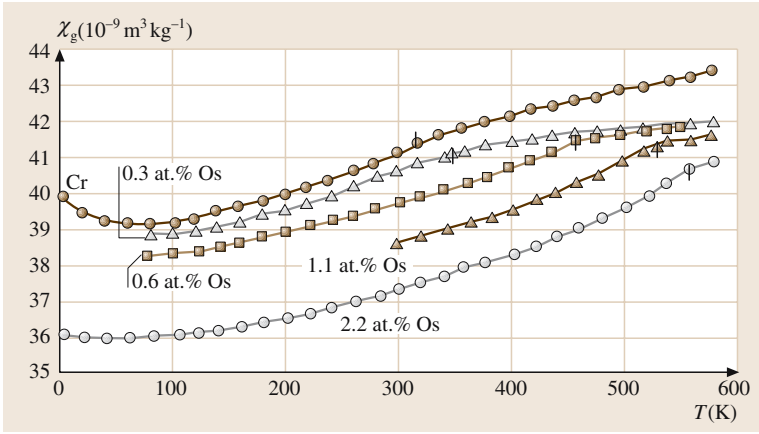


**Fig. 3.1-347** Temperature dependence of the mass susceptibilty of Os−Cr alloys. Small marks indicate the Neel temperature $T_N$ [1.217, p. 167]

*Chemical Properties.* Osmium is resistant against HCl but is attacked by $HNO_3$ and aqua regia. The element oxidizes in powder form readily at room temperature, forming $OsO_4$ which vaporizes above 130 °C. A detailed survey about chemical properties is given in [1.216]. The oxide $OsO_4$ serves as a catalyst for the synthesis of asymmetric organic compounds. Figure 3.1-348 shows an example for a ligand-supported chiral dihydroxylation [1.291].

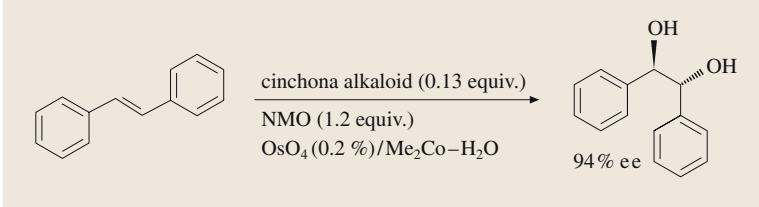


**Fig. 3.1-348** Chiral dihydroxylation using $OsO_4$ as catalyst component [1.291, p. 83]

## 3.1.11 Lead and Lead Alloys

Lead constitutes only about 12.5 wtppm (weight part per million) of the earth's crust, but concentrated lead ore deposits make it easy to mine. Lead and its alloys are used in a wide range of technical applications because of their low melting point, ease of casting, high density, softness and high formability at room temperature, excellent resistance to corrosion in acidic environments, attractive electrochemical behavior in many chemical environments, chemical stability in air, water and soil, and the high atomic number and stable nuclear structure. Despite their known toxicity, lead and its alloys can be handled safely and it ranks fifth in tonnage consumed (6 Mt/yr), after Fe, Cu, Al, and Zn. The type of data available on different alloys depends to a great extent on the areas of application [1.299].

The most important Pb ore mineral is galena, (87 wt% Pb). The lead ore concentrate is roasted to form Pb oxide. Smelting to reduce the oxide by CO produces Pb. The lead bullion thus obtained contains Sb, As, Te, Sn, Cu, Ni, Co, and Bi besides noble metals, and is further refined to produce various grades of lead. Commercial grade pure lead is produced by the removal of impurities through selective gas phase oxidation, precipitation from molten lead phase as pure elements, and through the formation of intermetallic compounds with low solubility (removal of Fe, Ni, Co, As, Te, and Sb as oxides; precipitation of Cu as elemental Cu, CuS, and Cu arsenates and antimonides; precipitation of Fe as Fe arsenates and antimonides; precipitation of Ag and Au as intermetallic compounds of Zn with Au and Ag; Bi precipitation through the formation of a compound $CaMg_2Bi_2$). Electrolytic refining of commercial purity lead is used to obtain lead with purity to levels down to 99.99 to 99.9995 wt%. Zone melting is used to produce ultrapure grades of Pb.

### 3.1.11.1 Pure Grades of Lead

The commercial grades of pure lead (Table 3.1-273) are used in chemical plants, sound attenuation, roof-

**Table 3.1-273** Impurity levels of commercial lead grades [1.299]

| Impurities, additions | Low Bi, low Ag, pure Pb [a,d] L50006 | Refined pure Pb [b,d] L50021 | Corroding lead [e] L50042 | Pure lead (common lead) [e] L50049 | Chemical lead [c,e] L51120 | Copper bearing lead [e] L51121 | Tellurium lead [e] L51123 |
|---|---|---|---|---|---|---|---|
| (wt%) | max. | max. | | | | | |
| Ag, max. | 0.0010 | 0.0025 | 0.0015 | 0.005 | 0.020 | 0.020 | 0.020 |
| Ag, min. | – | – | – | – | 0.002 | – | – |
| Cu, max. | 0.0010 | 0.0010 | 0.0015 | 0.0015 | 0.080 | 0.080 | 0.080 |
| Cu, min. | – | – | – | – | 0.040 | 0.040 | 0.040 |
| Ag + Cu, max. | – | – | 0.0025 | – | – | – | – |
| SbAs, Sn each | 0.0005 | 0.0005 | – | – | – | – | – |
| As + Sb + Sn, max. | – | – | 0.002 | 0.002 | 0.002 | 0.002 | 0.002 |
| Zn, max. | 0.0005 | 0.0005 | 0.001 | 0.001 | 0.001 | 0.001 | 0.001 |
| Fe, max. | 0.0002 | 0.001 | 0.002 | 0.002 | 0.002 | 0.002 | 0.002 |
| Bi, max. | 0.0015 | 0.025 | 0.050 | 0.050 [c] | 0.005 | 0.025 | 0.025 |
| Te | 0.0001 | 0.0001 | – | – | – | – | 0.035–0.060 |
| Ni, max. | 0.0002 | 0.0002 | – | – | – | – | |
| Pb (by difference) min. | 99.995 | 99.97 | 99.94 | 99.94 | 99.90 | 99.90 | 99.85 |

[a] For chemical applications where low Ag and low Bi contents are required

[b] For lead acid battery applications

[c] For applications requiring corrosion protection and formability, as per ASTM B29-92

[d] As per ASTM B29-92

[e] As per ASTM 749-85 (re-approved 1991)

**Table 3.1-274** Mechanical properties of pure grades of lead [1.299–301]

| Lead grade | Hardness HB | Yield strength (0.125) (MPa) | Tensile strength (MPa) | Comp. strength (25%) (MPa) | Elongation (%) | Fatigue strength at $10^7$ cycles (MPa) | Creep strength (0.2%/yr) (MPa) |
|---|---|---|---|---|---|---|---|
| Pure lead (c) | 4.0 | 5.9 | 13.1 | 15.2 | 45 | 2.7 | |
| Corroding lead, Pb > 99.94 | 3.2–4.5 | 5.5 | 12–13 | | 30 | 3.2 | |
| Refined pure (r) | 3.8 | | 12.1 | | 53 | 3.2 | 1.2 |
| Chemical (c) | 5.2 | 11.3 | 17.9 | 20.0 | 45 | | |
| Chemical (r) | 5.5 | | 19.3 | | 47 | 6.9 | |
| Undesilverized (e) | | | 17.2 | | 50 | | |
| Undesilverized (r) | 4.7 | 8.6 | 16.5 | 17.9 | 51 | 5.0 | 15.8 |

(r) - rolled; (c) - cast; (e) - extruded

ing, flashings and weather stripping, water-proofing, and radiation shielding.

The mechanical properties of pure grades of lead are listed in Table 3.1-274 [1.299–301]. The near ambient temperatures at which lead and its alloys are used correspond to high homologous temperatures ($T/T_M \sim 0.5$ or higher) for lead and therefore significant diffusion can occur. Consequently, the mechanical properties are affected by dynamic and static recovery, recrystallization effects, and creep deformation. Therefore, caution is advised in the use of short-term mechanical properties. The recrystallization temperatures of different lead grades are shown as a function cold work and grain size in Fig. 3.1-349 [1.303]. The lowest reported value of recrystallization temperature for 99.9999 wt% purity lead is $\sim -59\,^{\circ}C$; for lead of not very high purity it is $\sim -33\,^{\circ}C$. The fatigue behavior of 99.99 wt% pure lead in a Haigh push–pull test at a test cycle frequency of 33.67 Hz is presented in the form of S–N (stress to failure versus number of cycles) curves in Fig. 3.1-350 [1.303].

Coefficients of internal friction of relevance to acoustic damping are given in Table 3.1-275 [1.299, 302]. As lead is used in sound attentuation applications, acoustic transmission data of selected single-skin and double-skin partitions with and without lead are given in Table 3.1-276 [1.299]. The sound reduction versus frequency is given in [1.299, 304].

Corrosion rates of lead in $H_2SO_4$ and HF acids are presented in Figs. 3.1-351 and 3.1-352 [1.301]. Corrosion behavior of chemical lead in some common environments is presented in Table 3.1-277 [1.301]. Corrosion rates of the different lead grades normally fall in the same category.

As lead is extensively used in radiation shielding, the gamma-ray mass-absorption data for lead are presented in Fig. 3.1-353 [1.299, 305].

**Table 3.1-275** Experimental values of coefficient of internal friction $Q^{-1}$. Values in single crystal and polycrystalline lead [1.299, 302] (RT = room temperature)

| Material | Frequency (kHz) | $Q^{-1}$ |
|---|---|---|
| Pure polycrystalline lead | 0.016–2 | $0.35\times10^{-2}$–$4\times10^{-2}$ |
| | 17–28 | $0.2\times10^{-2}$–$0.8\times10^{-2}$ |
| Single-crystal line lead | 4–64 | $0.2\times10^{-2}$–$0.7\times10^{-2}$ |
| Single-crystal Pb–0.033 wt% Sn | 30 | $0.11\times10^{-2}$ (max. deformation of $10^{-7}$, RT) |
| Single-crystal Pb–0.035 wt% Bi | 30 | $0.22\times10^{-3}$ (max. deformation of $10^{-7}$, RT) |
| Single-crystal Pb–0.0092 wt% Cd | 30 | $0.9\times10^{-3}$ (max. deformation of $10^{-7}$, RT) |
| Single-crystal Pb–0.0022 wt% In | 4 | $2\times10^{-3}$ (max. deformation of $10^{-7}$) |

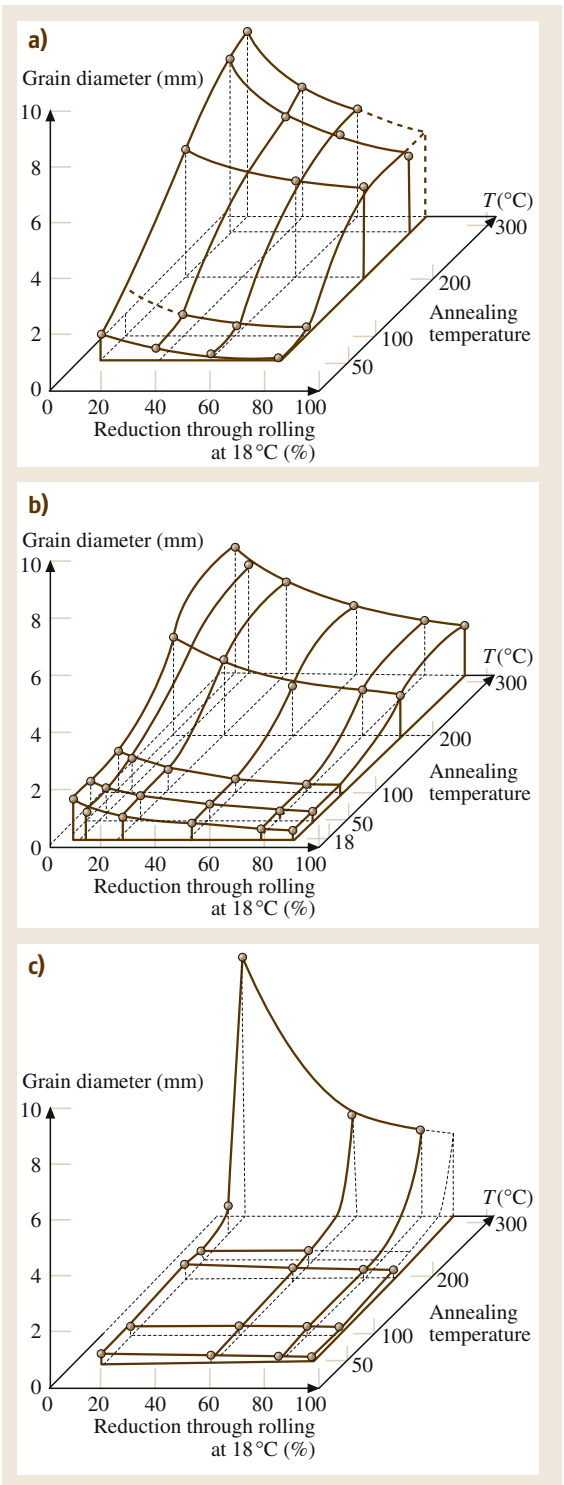


**Fig. 3.1-349a–c** Recrystallization diagrams: **(a)** Electrolytic Pb. **(b)** Parkes Pb. **(c)** Pattinson Pb [1.303]

**Table 3.1-276** Acoustic transmission data of selected single skin and double skin partitions with and without lead [1.299, 304]

| Description of test partition | Thickness (mm) | Surface weight ($kg/m^2$) | Average SRI (dB) | RW (dB) | STC (dB) |
|---|---|---|---|---|---|
| Single skin – code 1 lead sheet | 0.5 | 5.65 | 22.7 | 25 | 25 |
| Single skin – code 3 lead sheet | 1.52 | 17.16 | 31.8 | 35 | 35 |
| Single skin – 0.5 mm lead equivalent lead impregnated PVC sheet | 2.17 | 7.94 | 27.4 | 30 | 30 |
| Double skin – 12.4 mm Gyproc plasterboard – no infill | 117.76 | 19.04 | 40.2 | 42 | 41 |
| Double skin – code 3 lead sheet bonded to 12.4 mm Gyproc plasterboard – no infill | 121.88 | 52.20 | 51.8 | 52 | 52 |

SRI: sound reduction index; RW: weighted sound reduction; STC: sound transmission classification

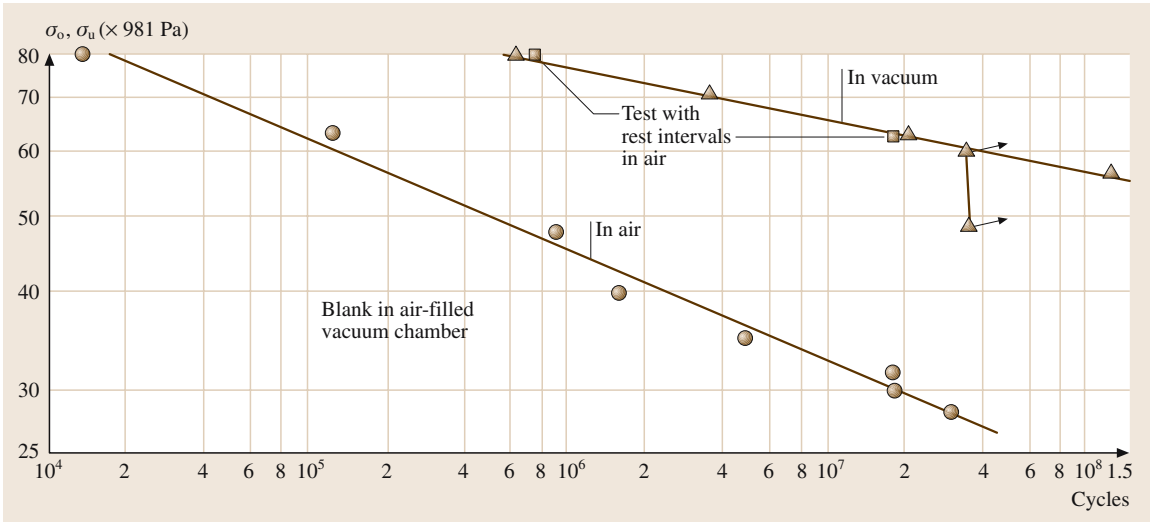


**Fig. 3.1-350** *S–N* (stress vs. number of cycles) curves for Pb in air and vacuum [1.303]

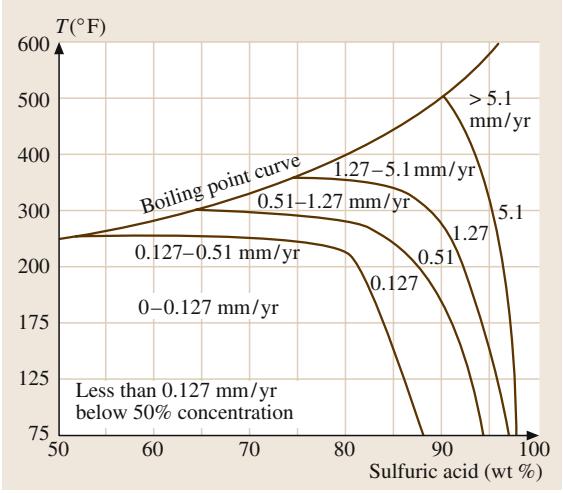


**Fig. 3.1-351** Corrosion rates of lead in $H_2SO_4$ [1.301]

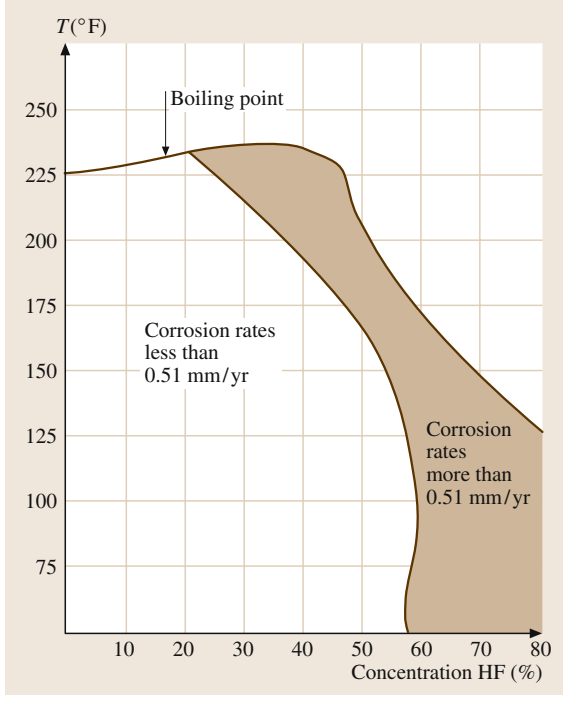


**Fig. 3.1-352** Corrosion rates of lead in HF [1.301]

**Table 3.1-277** Classifying corrosion behavior of Pb in selected environments [1.301]

| Chemical | Temperature (°C) | Concentration (wt%) | Corrosion class |
|---|---|---|---|
| Acetic acid | 24 | Glacial | B |
| Acetone | 24–100 | 10–90 | A |
| Acetylene, dry | 24 | – | A |
| Ammonia | 24–100 | 10–30 | B |
| Ammonium azide | 24 | – | B |
| Ammonium carbonate | 24–100 | 10 | B |
| Ammonium chloride | 24 | 0–10 | B |
| Ammonium hydroxide | 27 | 3.5–40 | A |
| Ammonium nitrate | 20–52 | 10–30 | D |
| Ammonium phosphate | 66 | – | A |
| Ammonium sulfate | 24 | – | B |
| Arsenic acid | 24 | 10 | B |
| Benzene | 24 | – | B |
| Boric acid | 24–149 | 10–100 | B |
| Bromine | 24 | – | B |
| Butane | 24 | – | A |
| Carbon tetrachloride (dry) | BP | 100 | A |
| Chlorine | 38 | – | B |
| Citric acid | 24–79 | 10–30 | B |
| DDT | 24 | – | B |
| Fluorine | 24–100 | – | A |
| Hydrochloric acid | 24 | 0–10 | C |
| Hydrogen chloride (anh HCl) | 24 | 100 | A |
| Mercury | 24 | 100 | D |
| Methanol | 30 | – | B |
| Methyl ethyl ketone | 24–100 | 10–100 | B |
| Phosphoric acid | 24–93 | – | B |
| Sodium carbonate | 24 | 10 | B |
| Sodium chloride | 25 | 0.5–24 | A |
| Sodium hydroxide | 26 | 0–30 | B |
| Sodium nitrate | 24 | 10 | D |
| Sodium sulfate | 24 | 2–20 | A |
| Sulfur dioxide | 24–204 | 90 | B |
| Natural outdoor atmospheres | 24 | | –A |
| Industrial, natural and domestic waters | 24 | | –A |
| Soils | 24 | | –A |

Data mostly correspond to chemical lead. The four corrosion performance categories:
A < 0.051 mm/yr: Negligible corrosion – lead recommended for use;
B < 0.51 mm/yr: Practically resistant – lead recommended for use;
C = 0.51–1.27 mm/yr: Lead may be used where this effect on service life can be tolerated;
D > 1.27 mm/yr: Corrosion rate too high to merit any consideration of lead

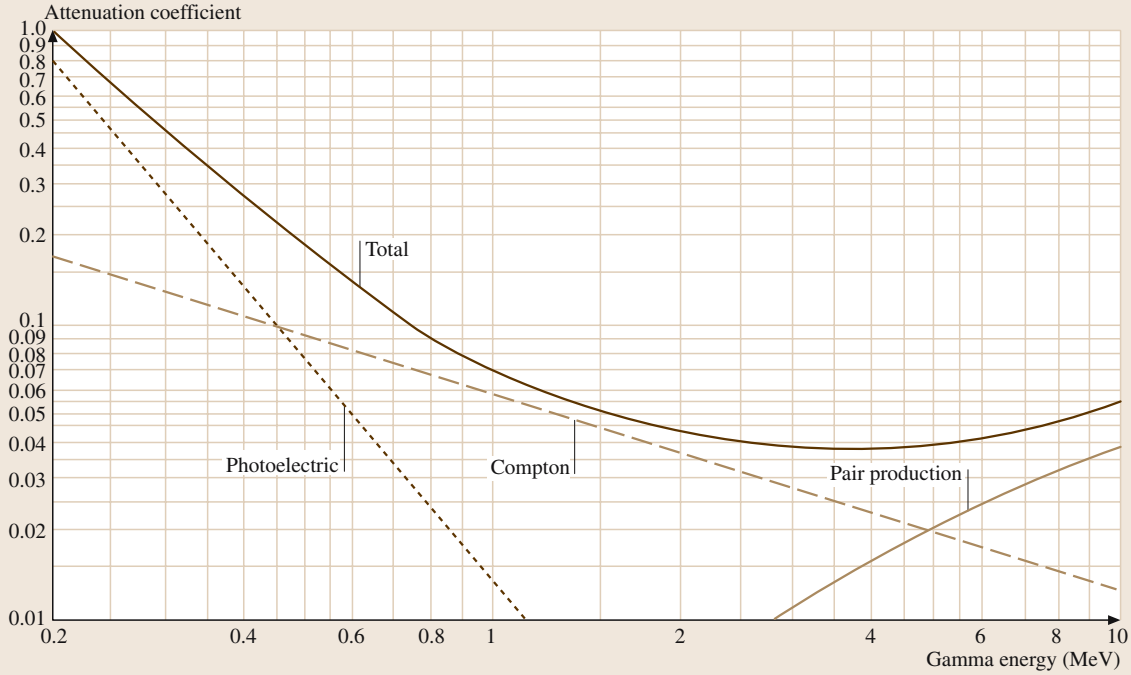


**Fig. 3.1-353** Gamma-ray mass-absorption coefficients for lead [1.299, 305]

### 3.1.11.2 Pb–Sb Alloys

#### Pb–Sb Binary Alloys

Lead–antimony alloys are widely used for pipe, cable sheathing, collapsible tubes, storage battery grids, anodes, sulfuric acid fittings, and X-ray and gamma ray shielding (in the absence of neutron irradiation). The addition of 1 to 13 wt% Sb to Pb increases tensile strength, fatigue strength, and hardness compared to pure lead (99.99). Lead and Sb form a eutectic system as shown in Fig. 3.1-354 [1.303]. The maximum solubility of Sb in Pb is 3.45 wt% at the eutectic temperature and decreases to 0.3 wt% at 50 °C. Thus considerable age-hardening can be obtained in these alloys. Small additions of As (0.05–0.1 wt%) dramatically increase the rate of aging and final strength. The microstructure at higher Sb contents consists of proeutectic lead-rich phase surrounded by a network of eutectic phase that contributes to enhanced as-cast and high temperature strength. Shrinkage on solidification varies from 3.85% for Pb to 2.06% for a Pb–16 wt% Sb alloy. These alloys have high corrosion resistance in most environments. They form a protective and impermeable film faster than pure lead and, in some cases, even faster than chemical lead. Table 3.1-278 lists the physical properties of selected Pb–Sb alloys [1.300]. Table 3.1-279 lists the mechanical properties of cast

**Table 3.1-278** Physical properties of Pb–Sb alloys [1.300]

| Alloy composition (wt%) | Solidification range (°C) | Coefficient of thermal expansion ($10^{-6}$ K$^{-1}$) | Specific heat (J kg$^{-1}$ K$^{-1}$) | Thermal conductivity (W m$^{-1}$ K$^{-1}$) | Resistivity (nΩ m) | Density (g cm$^{-3}$) | Volume change on freezing[a] (%) |
|---|---|---|---|---|---|---|---|
| Pb–1 Sb | 322–317 | 28.8 | 131 | 33 | | 11.27 | −3.75 |
| Pb–3 Sb | 310–269 | 28.1 | | | | 11.19 | |
| Pb–6 Sb | 285–252 | 27.2 | 135 (solid) | 29 | 253 | 10.88 | −3.11 |
| Pb–9 Sb | 265–252 | 26.4 | 137 (solid) | 27 | 271 | 10.60 | −2.76 |

[a] Negative values show contraction

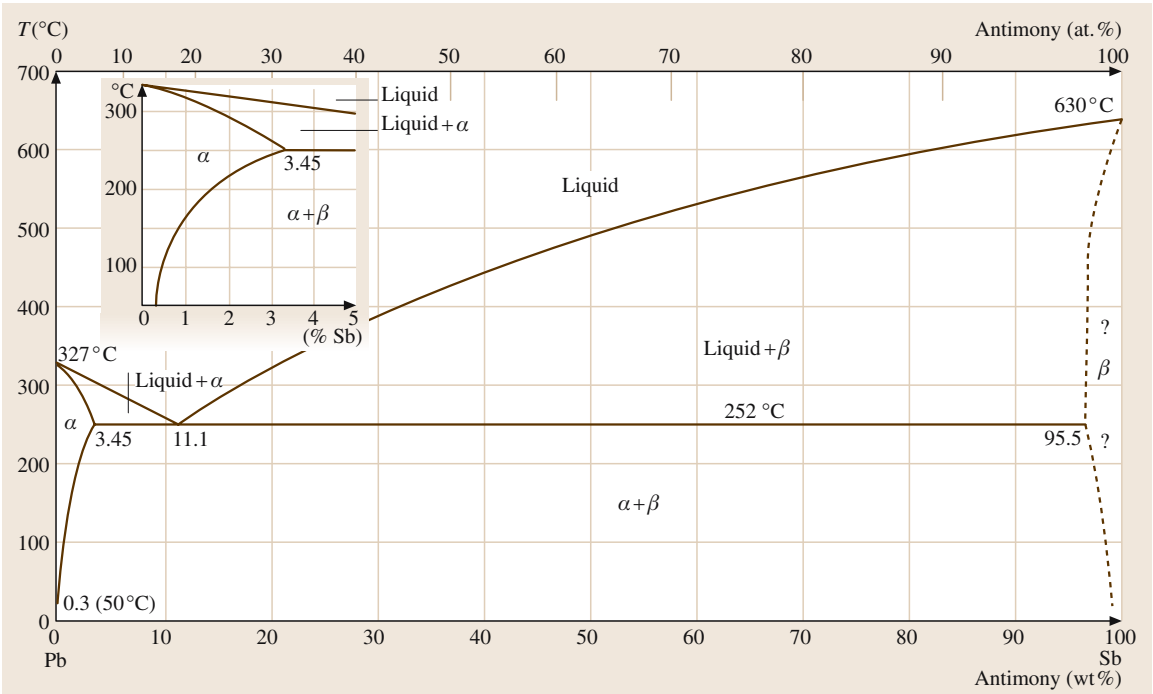


**Fig. 3.1-354** Pb–Sb phase diagram [1.303]

**Table 3.1-279** Mechanical properties of Pb–Sb alloys [1.299–301, 306]

| Sb content (wt%) | | Tensile strength (MPa) | Elongation at fracture (%) | Hardness HB | Yield strength $R_{p0.125}$ (MPa) | Fatigue strength for $2 \times 10^7$ cycles (MPa) | Creep strength | Young's modulus (GPa) |
|---|---|---|---|---|---|---|---|---|
| 1 | (a) | 37.9 | 20 | | 19.3 | 7.6 | 190 h at 20.7 MPa | – |
| 1 | (c) | 20 | 50 | 7.0 | – | 7.6 | | – |
| 3 | (a) | 65.5 | 10 | | 55.2 | – | 630 h at 27.6 MPa | – |
| 3 | (c) | 32.43 | 15 | 9.1 | | | | – |
| 6 | (a) | 73.8 | 8 | | 71.0 | | 1000 h at 27.6 MPa | |
| 6 | (c) | 47 | 24 | 13 | | 17.2 | | 24.15 |
| 6 | (r) | 29.6 | 42 | 8.7 | 15.2 | 10.3 | – | – |

(c) cast; (a) cast and stored 30 days at room temperature; (r) rolled

alloys [1.299–301, 306]. Data for one of the rolled alloys are also given to indicate that they exhibit poorer properties.

### Pb–Sb-Based Lead Acid Battery Grid Alloys

Lead–acid batteries are the most widely used secondary battery type in current automotive and industrial applications due to the relatively low cost and high availability of the raw materials, room temperature operation, ease of manufacture, long life cycle, versatility, and the excellent reversibility of the electrochemical system. Lead alloys are used as electrode grids, connectors, and grid posts. The two classes of alloys that are in extensive use are (i) Pb–Sb based ternary and multi-component alloys with As, Sn, Ag, Se, Cu, S, and Cd and (ii) Pb–Ca based ternary alloys and multi-component alloys with Sn, Ag, and Al. In the Pb–Sb based alloys, Sb addition to Pb enhances castability, tensile strength, creep strength, corrosion resistance under battery operating conditions, and resistance to structural changes during deep charge–

discharge cycling. However, Sb migration from Pb−Sb based positive grid alloys to negative electrode results in the reduction of hydrogen over-voltage and consequent decrease in cell voltage. This led to increased degassing and water loss. To minimize this poisoning of negative plates, lower Sb contents (1–3 wt% Sb) are now used in battery grids. The posts and straps use about 3 wt% Sb. Low Sb content promotes the formation of solidification shrinkage porosity and cracking but the cracking tendency is overcome by the use of grain-refining additions of S, Cu, and Se. Arsenic additions to Pb−Sb alloys increase the rate of age-hardening and reduce the time of grid storage required after casting. Arsenic addition also increases the creep resistance which is very beneficial in deep cycling conditions. The addition of tin is used to act synergistically with As and Sb to improve fluidity and castability. It also increases cycle life of deep cycling batteries containing thin plates. Silver additions increases both the corrosion and creep resistance in Pb−Sb alloy grids. Cast Pb−Sb based alloys are typically used in grid alloys as the Pb−Sb based wrought alloys have lower yield strength, tensile strength, and creep strength. The corrosion behavior of wrought alloys is inferior due to the nature of distribution of the PbSb eutectic phase and lower creep resistance. Corrosion of cast Pb−Sb occurs by the attack of Pb−Sb eutectic. It solubilizes some Sb and stresses of corrosion product are accommodated. In rolled alloys the eutectic phase is isolated, which leads to stresses in the grid. The current choice of alloy composition is Pb−1.6Sb−0.2As−0.2Sn−0.2Se. Table 3.1-280 lists the compositions of common lead–antimony battery grid alloys [1.300, 307].

**Table 3.1-280** Alloying components of common lead–antimony battery grid alloys [1.300, 307]

| Alloy concentration (wt%) | | | | |
|---|---|---|---|---|
| Sb | Sn | As | Cu | Se |
| 2.75 | 0.2 | 0.18 | 0.075 | – |
| 2.75 | 0.3 | 0.3 | 0.075 | – |
| 2.9 | 0.3 | 0.15 | 0.04 | – |
| 2.9 | 0.3 | 0.15 | 0.05 | – |
| 1.6 | 0.2 | 0.2 | – | 0.2 |

Lead–antimony alloys containing 0.2 to 1 wt% Sb are used to form barrier sheaths in high voltage cables. Properties of Pb−0.85Sb cable sheathing alloy are presented in the section on cable sheathing alloys. Lead alloys with 6–8 wt% Sb are used to fabricate a wide variety of equipment such as tank linings, pipe and one type of anode used in chromium plating. Alloys with 13 wt% Sb are used to make castings when hardness is of key importance. About 6% of the Pb produced in the world was used in the production of sports and military ammunition due to its high density and low cost. Lead containing up to 8 wt% Sb and 2 wt% As is used.

### Pb−Sb−Sn Alloys

These alloys have low melting points, high hardness, and excellent high temperature strength and fluidity. These characteristics together with its applicability for the replication of detail make them suitable as printing types. Table 3.1-281 lists the characteristics of selected type-metal alloys [1.300].

The Pb-rich ternary Pb−Sb−Sn white metal alloys are also used in journal bearings due to the excellent anti-friction (and anti-seizure) characteristics and hardness. These Pb-rich white metal alloys, also referred to as Babbit alloys, contain 9–15 wt% Sb, 1–20 wt% Sn, and small amounts of Cu and As. Table 3.1-282 lists the physical properties of different bearing alloys [1.299, 300]. The mechanical property data for some of these alloys are presented in Table 3.1-283 [1.299, 308]. Most of the alloys lie in the primary crystallization field of Sb or SbSn of the ternary system. They contain primary crystals of Sb (or SbSn) in a binary (or ternary) eutectic matrix apart from the high-melting Cu-rich phases. Copper contents above 1.5 wt% also increase the hardness. Arsenic addition leads to a fine and uniform structure, improves fatigue strength, and minimizes softening. Arsenic is present in solid solution in Pb, Sb, and Sb-containing phases such as SbSn. The lead–alkali alloys, e.g., Bahnmetall, or the Pb−Sn−alkali alloys, also have a limited significance as bearing metals.

**Table 3.1-281** Typical compositions and properties of selected type metals [1.299, 300]

| Alloy | Composition (wt%) | | | Hardness HB | Liquidus temperature (°C) | Solidus temperature (°C) |
|---|---|---|---|---|---|---|
| | Pb | Sn | Sb | | | |
| Electrotype – General | 94 | 3 | 3 | 14 | 299 | 245 |
| Linotype – Special | 84 | 5 | 11 | 22 | 246 | 239 |
| Stereotype – Flat | 80 | 6 | 14 | 23 | 256 | 239 |
| Monotype – Ordinary | 78 | 7 | 15 | 24 | 262 | 239 |

**Table 3.1-282** Composition and physical properties of selected lead-based white metal bearing alloys [1.299, 300]

| Alloy composition (wt%) | | Freezing range | Density | Volume change on freezing[a] | Coefficient of thermal expansion | Specific heat | Latent heat of fusion | Electrical resistivity | Thermal conductivity |
|---|---|---|---|---|---|---|---|---|---|
| Sb | Sn | (°C) | (g cm$^{-3}$) | (%) | ($10^{-6}$ K$^{-1}$) | (J kg$^{-1}$ K$^{-1}$) | (kJ kg$^{-1}$) | (nΩ m) | (W m$^{-1}$ K$^{-1}$) |
| 9.5–10.5 | 5.5–6.5 | 256–240 | 10.50 | −2 | | 150 | 0.9 | 287 | |
| 14–16 | 4.5–5.5 | 272–240 | 9.96 | −2 | 24 | 150 | 0.1 | 282 | |
| 14–16 | 9.3–9.7 | 268–240 | 9.70 | −2.3 | 19.6 | 160 | | 286 | 24 |
| 14.5–17.5 | 0.8–1.2 | 353–247 | 10.10 | −2.5 | | | | | |

[a] Negative values show contraction

**Table 3.1-283** Composition and mechanical properties of ASTM B23 Pb-based white metal bearing alloys [1.299, 308]

| Alloy no. | Nominal alloy content (wt%) | | | | Yield stress (MPa) | | Elongation at fracture (%) | Ultimate strength in compression (MPa) | | Hardness HB 500/30 | | Melting range | Fatigue strength $2\times10^7$ cycles (MPa) |
|---|---|---|---|---|---|---|---|---|---|---|---|---|---|
| | Sb | Sn | Cu | As | 20 °C | 100 °C | 20 °C | 20 °C | 100 °C | 20 °C | 100 °C | (°C) | |
| 7 | 15 | 10.0 | <0.5 | 0.45 | 24.5 | 11.0 | 4 | 107.9 | 42.4 | 22.5 | 10.5 | 240–268 | 28 |
| 8 | 15 | 5.0 | <0.5 | 0.45 | 23.4 | 12.1 | 5 | 107.6 | 42.4 | 20.0 | 9.5 | 237–272 | 27 |
| 15 | 16 | 1.0 | <0.5 | 0.8–1.4 | | | 2 | | | 21.0 | 13.0 | 248–281 | 30 |

### 3.1.11.3 Pb–Sn Alloys

Lead-tin alloys serve as materials for a number of applications as summarized in Table 3.1-284.

The Pb−Sn system (Fig. 3.1-355) shows an extended and strongly temperature-dependent solid solubility of Sn in Pb decreasing from 19.2 wt% at the eutectic temperature to about 1.3 wt% Sn at room temperature. This can lead to significant age-hardening on rapid cooling from the range of the homogeneous $\alpha$ phase. Streaky and granular Sn precipitates lead to hardness increases from about HB = 4 in pure lead to around HB = 12 at the solid solubility limit. In the stable $\alpha+\beta$ range hardness increases less rapidly to about HB = 18 at the eutectic composition.

#### Pb–Sn-Based Solder Alloys

Lead–tin alloys in the Pb-rich hypoeutectic region are the most widely used of all solders. In the melt, the surface tension increases with Sn content. Table 3.1-285 gives the melting characteristics of some Pb−Sn solders and lists their typical applications. When referring to Pb−Sn solders, the Sn content is customarily given first, for example 40/60 refers to 40 wt% Sn and 60 wt% Pb. Table 3.1-286 summarizes the mechanical and physical properties of different soft solders [1.309]. Further alloying additions are Cd, Bi, Sb, and Ag. Silver is added to increase tensile, creep, fatigue, and shear strengths, and to reduce the dissolution of Ag from Ag alloy coatings. Addition of 5 to 6% in Sn content increases the tensile and creep strengths. Addition

**Table 3.1-284** Applications and typical compositions of Pb−Sn materials

| Application | Alloying elements (wt%) | | Remarks |
|---|---|---|---|
| | Sn | Others | |
| Cable sheathing | <0.5 | Sb (0.2), Ca (0.33) or Cd (0.15) | |
| Solders | 2–63 | | See below |
| Pressure die castings | ~62 (near eutectic) | | |
| Organ pipes | (45) 55–74 | | |
| Sliding layer on bearings | 10–20 | 5 Cu | Electroplated |
| Type metals | 3–12 | Sb (3–25) | See Table 3.1-281 |
| Terne steel coatings | 12–20 | | Corrosion protection |
| Anodes | 7 | | Cr plating |

**Table 3.1-285** Melting characteristics and applications of Sn–Pb solders [1.309]

| Solder alloy Sn/Pb | Composition (wt%) Sn | Pb | Temperature (°C) Solidus | Liquidus | Pasty range | Uses |
|---|---|---|---|---|---|---|
| 2/98 | 2 | 98 | 316 | 322 | 10 | Side seams for can manufacture |
| 5/95 | 5 | 95 | 305 | 312 | 13 | For coating and joining metals |
| 10/90 | 10 | 90 | 268 | 302 | 62 | For coating and joining metals |
| 15/85 | 15 | 85 | 227 | 288 | 110 | For coating and joining metals |
| 20/80 | 20 | 80 | 183 | 277 | 170 | For coating and joining metals. For filling dents or seams in automobile bodies |
| 25/75 | 25 | 75 | 183 | 266 | 150 | For machine and torch soldering |
| 30/70 | 30 | 70 | 183 | 255 | 130 | For machine and torch soldering |
| 35/65 | 35 | 65 | 183 | 247 | 116 | General purpose and wiping solder |
| 40/60 | 40 | 60 | 183 | 238 | 99 | Wiping solder for joining lead pipes and cable sheaths. For automobile radiator cores and heating units |
| 45/55 | 45 | 55 | 183 | 227 | 80 | For automobile radiator cores and roofing seams |
| 50/50 | 50 | 50 | 183 | 216 | 60 | For general purpose. Most popular of all |
| 60/40 | 60 | 40 | 183 | 190 | 13 | Primarily used in electronic soldering applications where low soldering temperatures are required |
| 3/37 | 63 | 37 | 183 | 183 | 0 | Lowest melting (Eutectic) solder for electronic applications |

**Table 3.1-286** Physical and mechanical property data on Pb–Sn solders [1.309]

| Material (wt%) | Tensile strength (MPa) | Shear strength (MPa) | Density ($g\,cm^{-3}$) | Brinell hardness HB | Electrical conductivity (% of $\sigma_{Cu}$) | Young's modulus (GPa) | Surface tension (290 °C) ($10^{11}\,N\,m^{-1}$) |
|---|---|---|---|---|---|---|---|
| Pb | 12.30 | 12.44 | 11.34 | 4.0 | 7.9 | 18.04 | |
| 5/95 Sn/Pb | 28.96 | 20.73 | 11.06 | 9.0 | 8.0 | | |
| 10/90 Sn/Pb | 32.48 | 26.96 | 10.44 | 11.0 | 8.2 | 19.08 | |
| 15/85 Sn/Pb | 34.56 | 30.89 | 10.50 | 11.3 | 8.4 | | |
| 20/80 Sn/Pb | 35.94 | 32.76 | 10.23 | 11.5 | 8.7 | 20.04 | 467 |
| 25/75 Sn/Pb | 37.32 | 36.70 | 10.00 | 11.5 | 8.9 | | |
| 30/70 Sn/Pb | 39.74 | 38.01 | 9.74 | 11.3 | 9.3 | 21.08 | 470 |
| 35/65 Sn/Pb | 41.82 | 38.64 | 9.50 | 11.0 | 9.8 | | |
| 40/60 Sn/Pb | 42.85 | 39.26 | 9.29 | 10.5 | 10.1 | 23.08 | 474 |
| 45/55 Sn/Pb | 42.85 | 39.53 | 9.08 | 10.6 | 10.4 | | |
| 50/50 Sn/Pb | 44.58 | 40.57 | 8.88 | 11.0 | 10.9 | | 476 |
| 60/40 Sn/Pb | 44.23 | 39.40 | 8.51 | 12.0 | 11.3 | 30.07 | |
| 63/37 Sn/Pb | 46.31 | 41.88 | 8.41 | 12.0 | 11.5 | | 490 |
| 62Sn/36Pb/2Ag | 46.31 | 43.20 | 8.42 | 16.0 | 11.6 | 23.57 | |
| 10Sn/88Pb/2Ag | 33.87 | 29.72 | 10.75 | 12.0 | 8.4 | 19.35 | |
| 1Sn/97.5Pb/1.5Ag | 24.88 | 24.88 | 11.28 | 11.0 | 8.8 | | |

of 0.18 wt% Cu causes a further increase. Bismuth-containing solders, the so-called fusible alloys, are used for low temperature soldering and are discussed in the section on fusible alloys. Alloys of Pb–In are primarily used for soldering at low temperatures and where reduction in gold-scavenging is desired. They are also extremely ductile, making them suitable for use in areas where there is a thermal mismatch. Compositions of other commonly used Pb solders are given in Table 3.1-287 [1.309].

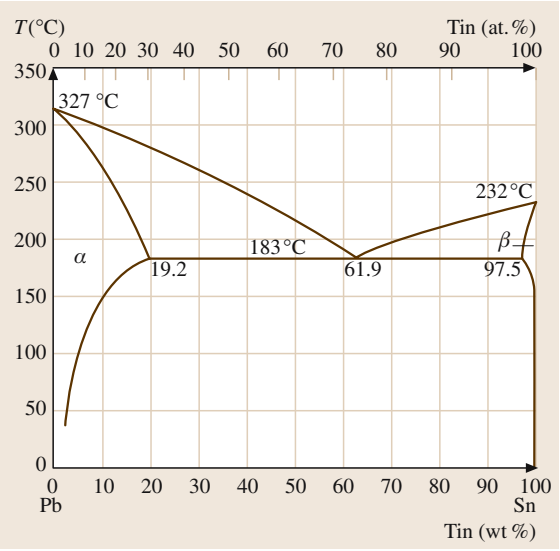


**Fig. 3.1-355** The Pb−Sn binary phase diagram [1.303]

### 3.1.11.4 Pb–Ca Alloys

The Pb−Ca and Pb−Ca−Sn alloys are used in storage battery grid, pipe, wire, cable sheathing, anodes, chemical handling equipment, radiation shielding, and other applications [1.299]. Calcium is also used as a secondary additive in hardened lead-bearing metals. Its solubility in Pb decreases from 0.1 wt% Ca at 328.3 °C to ~ 0.01 wt% Ca at room temperature (Fig. 3.1-356) and pronounced age-hardening can be obtained. A peritectic reaction involving liquid Pb−Ca and $Pb_3Ca$ to form the α-Pb–0.1 wt% Ca phase occurs at 328.3 °C [1.303]. At > 0.07 wt% Ca, $Pb_3Ca$ crystallizes directly on solidification. At > 0.1 wt% Ca, the microstructure consists of primary crystals of $Pb_3Ca$ and a Pb matrix with finer $Pb_3Ca$ precipitates. The two-phase structure present at these higher Ca contents leads to grain refinement. Supersaturated solid solutions of Ca in Pb at room temperature can be obtained at high cooling rates upto about 0.13 wt% Pb. The hardness increase observed on aging increases with Ca content. Upon aging, the hardness of a 0.07 wt% Ca alloy at room temperature increases from HB = 4 to HB = 8.25 (10 mm-31.2 kg-120 s) in 6 h. Electrical resistivity drops from 22.63 to $22.25 \times 10^{-6}$ Ω cm. Maximum in hardness for quenched alloys occurs at 0.13 wt% Ca and in air-cooled alloys at 0.085 wt% Ca.

Further additions of Li, Ba, and Na increase the hardness. The addition of Sn to Pb−Ca alloys increases the hardness, tensile strength, and stress rupture properties. The hardness decreases as Sb and Bi form

**Table 3.1-287** Other common Pb-alloy solders [1.309]

| Composition (wt%) | | | | Temperature (°C) | | |
|---|---|---|---|---|---|---|
| Pb | Sn | Ag | In | Solidus | Liquidus | Pasty range |
| 97.5 | 1 | 1.5 | – | 309 | 309 | Eutectic |
| 36.0 | 62 | 2.0 | – | 179 | 189 | 18 |
| 97.5 | – | 2.5 | – | 304 | 304 | 62 |
| 50 | – | | 50 | 124 | 209 | 52 |
| 92.5 | – | 2.5 | 5 | 285 | 305 | 36 |

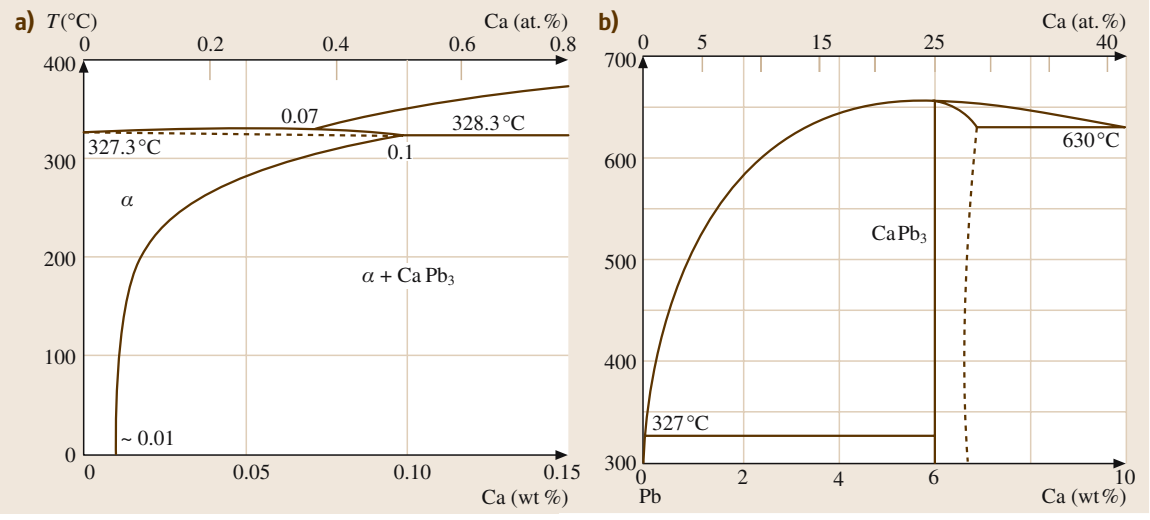


**Fig. 3.1-356** Pb-rich portion of the Pb−Ca phase diagram [1.303]

intermetallic compounds with Ca and segregate from the melt. Due to the presence of finely distributed precipitate phase, the age-hardened alloys show a high resistance to recrystallization after room temperature working. The creep rate increases with Ca content, mainly due to the smaller grain size. The mechanical properties of binary Pb−Ca and Pb−Ca−Sn alloys are presented in Table 3.1-288 [1.299, 306]. The fine-grained wrought Pb−Ca and Pb−Ca−Sn alloys possess improved material integrity and also exhibit improved corrosion performance, as they tend to undergo uniform corrosion. The corrosion resistance of these alloys is higher than that of Pb−Sb alloys in many applications.

### Pb−Ca−Sn Battery Grid Alloys

Most batteries produced currently use Pb−Ca alloys for grids and connectors and the use of Pb−Sb based alloys is declining [1.307]. The Ca content varies from 0.03 to 0.13 wt%. The narrow freezing range of a few degrees allows continuous casting and grid production. The mechanical properties in Pb−Ca binary alloys peak at 0.07 wt%. Above 0.06 wt% Ca, cellular precipitation of $Pb_3Ca$ leads to fine grain size. Increasing Ca contents above 0.07 wt% level accelerate corrosion and this is believed to be due to fine grains and primary $Pb_3Ca$. Addition of Sn dramatically improves the properties by promoting the formation of the more effective and stable $Sn_3Ca$. The phase relations of Pb rich Pb−Ca−Sn alloys according to [1.310] are shown in Fig. 3.1-357. Tin additions also improve the corrosion resistance and the charge–discharge process by Sn enrichment of the corrosion product layer. Aluminium acts as a deoxidant and prevents drossing loss of Ca. The addition of Sn aids electrochemical properties by preventing passivation of the grid and permitting recharge of batteries from a deeply discharged condition. Additions of Ag to Pb−Ca and Pb−Ca−Sn alloys increase the creep and corrosion resistance. However, Sn and Ag additions are not re-

**Table 3.1-288** Mechanical properties of Pb−Ca−Sn alloys and corrosion rates in battery environments [1.299, 306]

| Composition (wt%) | | Tensile strength (MPa) | Yield stress ($R_{p0.125}$) (MPa) | Elongation (%) | Creep to failure, at 20.7 MPa (h) | Corrosion rate in battery service (mm yr$^{-1}$) |
|---|---|---|---|---|---|---|
| Ca | Sn | | | | | |
| **Cast** | | | | | | |
| 0.025 | | 25.1 | 17.7 | | 1 | 0.279 |
| 0.050 | | 37.2 | 29.0 | | 30 | 0.345 |
| 0.075 | | 46.4 | 35.3 | | 40 | 0.358 |
| 0.100 | | 47.8 | 32.5 | | 10 | 0.411 |
| 0.025 | 0.5 | 25.5 | 19.3 | | 10 | 0.256 |
| 0.050 | 0.5 | 48.2 | 38.5 | | 70 | 0.310 |
| 0.065 | 0.5 | 48.9 | 40.0 | | 200 | 0.325 |
| 0.075 | 0.5 | 50.3 | 40.2 | | 300 | 0.325 |
| 0.100 | 0.5 | 51.7 | 38.7 | | 70 | 0.343 |
| 0.025 | 1.5 | 45.8 | 34.3 | | 30 | 0.246 |
| 0.050 | 1.5 | 55.1 | 46.8 | | 100 | 0.271 |
| 0.075 | 1.5 | 60.1 | 49.2 | | 1000 | 0.297 |
| 0.100 | 1.5 | 57.9 | 43.7 | | 250 | 0.345 |
| **Wrought** | | | | | | |
| 0.050 | 0.5 | 55.2 | 45.3 | 30 | 10[a] | |
| 0.07 | 0.5 | 62.1 | 45.0 | 30 | 20[a] | |
| 0.05 | 1.0 | 61.4 | 52.8 | 25 | 150[a] | |
| 0.07 | 1.0 | 68.9 | 64.0 | 15 | 400[a] | |
| 0.050 | 1.5 | 63.8 | 57.4 | 15 | 300[a] | |
| 0.07 | 1.5 | 71.0 | 65.3 | 14 | 1000[a] | |

[a] At 27.6 MPa

**Table 3.1-289** Currently preferred compositions of automotive battery-grid alloys [1.307]

| Manufacturing process; grid type | Composition (wt%) Ca | Sn | Ag | Al |
|---|---|---|---|---|
| Book mold cast; positive | 0.03–0.06 | 0.5–0.9 | 0.010–0.045 | 0.01–0.02 |
| Book mold cast; negative | 0.09–0.13 | 0–0.3 | Trace | 0.015–0.03 |
| Rolled, expanded; positive | 0.06–0.08 | 1.2–1.6 | Trace | 0.003–0.008 |
| Rolled, expanded; negative | 0.06–0.08 | 0–0.5 | Trace | 0.003–0.008 |
| Concast strip, expanded; positive | 0.03–0.06 | 0.4–0.6 | 0.03–0.045 | 0.005–0.010 |
| Concast strip, expanded; negative | 0.07–0.1 | 0–0.2 | Trace | 0.005–0.010 |
| Continuously cast; negative | 0.07–0.1 | 0–0.3 | Trace | 0.005–0.010 |

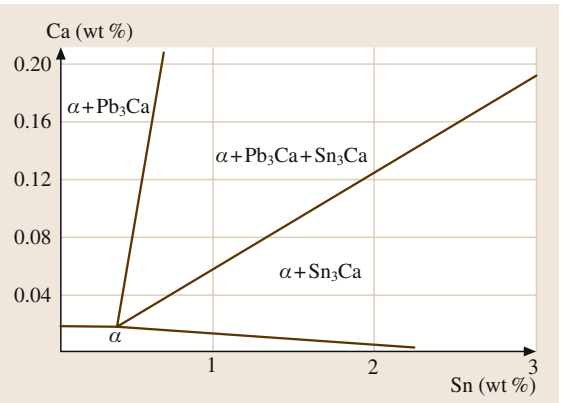


**Fig. 3.1-357** Suggested phase relations of Pb-rich Pb–Ca–Sn alloys [1.310]

quired in negative grids to provide the corrosion and creep resistance. The Ca content in positive grids is lower than in negative grids to reduce corrosion. Table 3.1-289 presents the compositions of Pb–Ca–Sn alloys currently preferred in lead acid automotive batteries [1.307]. Table 3.1-290 presents mechanical and properties of commonly used Pb–Ca–Sn battery alloys [1.299, 306].

### 3.1.11.5 Pb–Bi Alloys

#### Pb–Bi Binary Alloys

Even though the relative difference of atomic radii of Bi (1.56) and Pb (1.75) amounts to about 12%, the solubility of Bi reaches 23.5 wt% at 184 °C and 7.5 wt% at room temperature. While Bi addition has very little influence on mechanical properties, Pb–Bi alloys' excellent wetting properties make them valuable as solders for glass-to-metal joints. Their desirable solidification shrinkage characteristics and casting properties (that provide an ability to reproduce surface details) make them useful in printing and prototyping applications.

The Pb–Bi alloy system exhibits behavior of an eutectic between an hcp intermetallic $\beta$ phase and the Bi terminal phase at 56.5 wt% Bi and 125 °C. Both Pb and Bi have low cross sections for neutron absorption such that these alloys are attractive in heat transfer applications in nuclear reactor systems [1.299].

#### Fusible Alloys

Lead forms a number of extremely useful low-melting alloys when combined with Bi, Sn, Cd, or a combination of these metals. The metals In, Sb, and Ag are also

**Table 3.1-290** Properties of some of selected Pb–Ca–Sn battery-grid alloys [1.299, 300]

| Alloy composition (wt%) | Liquidus (°C) | Solidus (°C) | Ultimate tensile strength (MPa) | Elongation (%) | Hardness (HR) | Coefficient of thermal expansion ($10^{-6}$ K$^{-1}$) | Resistivity (nΩ m) |
|---|---|---|---|---|---|---|---|
| Pb–0.065Ca–0.7Sn | | 327 | | | | | 219 |
| Pb–0.065Ca–1.3Sn | | 323 | | | | 26.6 | 220 |
| Pb–0.07Ca | | 328 | 36–39 | 35–40 | 70–80 | 30.2 | 218 |
| Pb–0.1Ca–0.3Sn | 338 | 328 | 41–45 | 20–35 | 90–95 | | 219 |
| Pb–0.1Ca–0.5Sn | 336 | 327 | 44.8–51.7 | 25–35 | 85–90 | | 219 |
| Pb–0.1Ca–1Sn | 332 | 325 | 52–55 | 20–35 | 90–95 | | 212 |

added in some of the alloys. Some of these alloys melt at a temperature lower than the boiling point of water, and those containing appreciable amounts of Bi (> 55 wt%) expand slightly upon solidification.

The melting point of the Pb−Sn−Cd ternary eutectic is only 145 °C. By the addition of Zn, a quaternary eutectic can be obtained with a melting point of 138 °C at a composition of Pb–16.7 wt% Cd–52.45 wt% Sn–2.25 wt% Zn. A further effective decrease in the melting point is obtained by additions of Bi to Pb−Cd−Sn alloys. The quaternary Bi−Pb−Cd−Sn eutectic has a melting point of about 70 °C and a composition of Pb–50 wt% Bi–12.5 wt% Cd–12.5 wt% Sn (Wood's metal). The phases of the quaternary eutectic are solid solutions corresponding to the Pb, Sn, and Cd phases, as well as and the $\beta$-phase of the Pb−Bi system. The quaternary Pb−Bi−Sn−Cd eutectic alloy is brittle when cast, and becomes ductile on storage for two to three hours. The melting point of the quaternary eutectic alloy can be further lowered to 47 °C by additions of In. Addition of Hg instead of In could also lower the melting point of Pb−Bi−Sn−Ca eutectic but is not used due to its high vapor pressure and toxicity. In addition to the above quaternary eutectic alloys, alloys of the ternary-Pb−Bi−Sn system are also of great technical importance. One of these alloys is the Newton-metal (Pb–50 wt% Bi–20 wt% Sn) that has approximately the ternary eutectic composition. The melting temperature of this eutectic alloy is 90 °C. Another important alloy is Rose's metal, with a composition Pb–50 wt% Bi–25 wt% Sn and a melting temperature of 100 °C. Table 3.1-291 presents the compositions and properties of selected fusible alloys [1.299, 300].

Low melting alloys are employed in safety devices such as sprinkler systems and boiler plugs, as special solders where high temperatures cannot be used, hermetic seals for molds, patterns, punches and dies, for anchoring punches in punch plates, and for bending tubing (Table 3.1-292).

### 3.1.11.6 Pb−Ag Alloys

The addition of Ag to Pb in the range of 0.01–0.1 wt% provides high resistance to recrystallization, grain refinement, and high creep strength. Eutectic Pb−Ag

**Table 3.1-291** Compositions and properties of selected fusible alloys [1.299, 300]

| Alloy composition [a] (wt%) | Liquidus (°C) | Solidus (°C) | Volume change on freezing (vol.%) [b] | Density ($g\,cm^{-3}$) | Conductivity (% of IACS) | Coefficient of thermal expansion ($10^{-6}\,K^{-1}$) | Specific heat ($J\,kg^{-1}\,K^{-1}$) | Latent heat of fusion ($kJ\,kg^{-1}$) | Thermal conductivity ($W\,m^{-1}\,K^{-1}$) |
|---|---|---|---|---|---|---|---|---|---|
| Pb−42Bi−11Sn−9Cd | 88 | 70 | 2 | 9.45 | 4 | 24 | 168 | 23 | 21 |
| Pb−42.9Bi−5.1Cd−7.9Sn−4Hg−18.3In | 43 | 38 | | | | | | | |
| Pb−44.7Bi−5.3Cd−8.3Sn−9.1In ASTM Alloy 117 | 47 | 47 | 1.4 | 8.85 | 4.5 | | 147 | 14 | |
| Pb−48Bi−14.5Sn−9Sb | 227 | 103 | 1.5 | 9.50 | 3 | 22 | 189 | | |
| Pb−49Bi−21In−12Sn ASTM Alloy 136 | 58 | 58 | 1.5 | 8.60 | 3 | | 134.4 | | 21 |
| Pb−50Bi−9.3Sn−6.2Cd | 70 | 78 | | | | | | | |
| Pb−50Bi−10Cd−13.3Sn ASTM Alloy 158 | 70 | 70 | 1.7 | 9.40 | 4 | 22 | 168 | 32 | |
| Pb−51.7Bi−8.1Cd | 92 | 92 | | 10.25 | | | | | |
| Pb−52.5Bi−15.5Sn ASTM Alloy 203 | 96 | 96 | | 9.71 | | | | | |
| Pb−55Bi ASTM Alloy 255 | 124 | 124 | 1.5 | 10.30 | 3 | | 126 | 16 | 16.8 |

[a] Alloys may contain small amounts of Ag, Cu, Sb and Zn

[b] Positive values indicate expansion on freezing

**Table 3.1-292** Typical applications of some common fusible alloys [1.299, 300]

| Alloy | Melting temperature (°C) | Typical applications |
|---|---|---|
| ASTM 117 | 47 | Dental models, part anchoring, and lens chucking |
| ASTM 158 (Woods metal) | 70 | Bushings and locators in jigs and fixtures, lens chucking, reentrant tooling, founding cores and patterns, light sheet-metal embossing dies, tube bending, and Wood's metal-sprinkler heads |
| ASTM 255 | 124 | Inserts in wood, plastics, bolt anchors, founding cores and patterns, embossing dies, press-form blocks, duplicating plaster patterns, tube bending, and hobbyist pans |
| ASTM 281 | 138 | Locator members in tools and fixtures, electroforming cores, dies for lost-wax patterns, plastic casting molds, prosthetic development work, encapsulating avionic components, spray metalizing, and pantograph tracer molds |
| Pb–48 wt% Bi–14.5 wt% Sn–9 wt% Sb | 103–217 | Punch and die assemblies, small bearings, anchoring for machinery, tooling, forming blocks, and stripper plates in stamping dies |

alloys containing about 2.5 wt% Ag are used as soft solders of high melting point. The alloy Pb–0.1 wt% Ag is used as a precoat to metallurgically bond lead to steel. Alloys of Pb–0.8–1 wt% Ag are used as insoluble anodes for electrowinning of metals from leach solutions and for electrogalvanizing. The alloys Pb–6 wt% Sb–1 wt% Ag, Pb–1 wt% Ag, Pb–2 wt% Ag, and Pb–1 wt% Ag–1 wt% Sn are used as anodes for cathodic protection.

### 3.1.11.7 Pb–Cu, Pb–Te, and Pb–Cu–Te Alloys

Maximum solubility in Pb is very low for both Cu (< 0.007%) and Te (< 0.005%). Copper contents of less than 0.1% provide considerable grain refinement and structural stability at high temperature. Pb–Cu alloys are used in cable sheathing and chemical applications. A Te content of 0.01% refines and stabilizes the grain size and increases the work-hardening in Pb–Te alloys. Significant age-hardening is also obtained from supersaturated solid solutions containing up to 0.1 wt% Te. The optimal Te content is 0.04–0.05% with Cu addition of 0.06%. Alloys of Pb–Te have very high fatigue strengths and are used in cable sheathing, radiation shielding, and steam-heating coil applications.

### 3.1.11.8 Pb–As Alloys

The alloy Pb–0.85 wt% As has very low volume shrinkage on solidification and pore free castings obtained with this alloy are used in radiation protection applications. Arsenic is added in Pb–Sb alloys to accelerate age hardening. It is also used in Pb cable sheathing alloys to enhance the bending and creep resistance.

### 3.1.11.9 Lead Cable Sheathing Alloys

Lead alloys are used as cable sheath in the construction of electrical cables for communication and high voltage transmission. The cable sheath serves as an impermeable barrier to prevent access of moisture to the insulated core, a containment of the oil or gas in oil- or gasfilled cables, and a ground to the power cables under short circuit conditions. The sheaths need to be easily applied in long lengths and should have good creep resistance, fatigue resistance, corrosion resistance, and microstructural stability. Table 3.1-293 lists some of cable sheathing alloys and their typical applications.

### 3.1.11.10 Other Lead Alloys

Alloys of Pb–Li are attractive in some nuclear shielding applications due to their ability to thermalize neutrons. Lead containing more than 0.5 wt% In wets glass, and Pb–In alloys with up to 5 wt% In can be used for soldering glass over a narrow temperature range. Additions over 25 wt% of In are made to Pb–Sn solders to increase their alkali resistance. An addition of 1–2 wt% In in Pb–Ag solders increases their strength. Indium is also used in multi-component fusible alloy systems.

**Table 3.1-293** Compositions of commonly-used cable sheathing alloys [1.299]

| Alloy name | Nominal composition (wt%) | Fatigue strength (MPa) at $10^7$ cycles 37–50 Hz | Applications |
|---|---|---|---|
| Alloy B | Pb-0.8-0.95 Sb | 9.6 | Solid type cables and telecommunication cables subjected to severe vibrations |
| Alloy 1/2B | Pb-0.5 Sb | 7.5 | Solid type cables and telecommunication cables subjected to severe vibrations |
| Alloy C | Pb-0.35–0.45 Sn-0.12–0.18 Cd | 5.4 | Power cables in ships. Acceptable for most types of cables |
| Alloy 1/2C | Pb-0.18–0.22% Sb-0.06–0.09 Cd | 4.2 0.07%[a] | Oil-filled and submarine power cables. Power cables subjected to severe vibrations in service. Acceptable for most types of reinforced cables |
| Alloy E | Pb-0.35–0.45 Sn-0.15–0.25 Sb | 6.3 | Solid type power cables, telecommunication cables, and reinforced gas or oil pressurized power cables under moderate vibrations |
| Pb–Cu | Pb-0.06 Cu | 3.34 | Gas or oil pressurized power cables |
| Cu–Te | Pb-0.06 Cu-0.045 Te | 6.9 | Cables subjected to high vibrations and oil-filled cables |
| F3 | Pb-0.15 As-0.15 Sn-0.1% Bi | 6.1 | PILC cables, submarine cables, power cables subjected to severe bending or vibration conditions |
| Pb–Ca–Sn | Pb-0.033 Ca-0.38 Sn | 0.11%[a] | High-voltage DC and AC submarine cables |

[a] Reversible strain for $10^7$ cycle at 30 Hz in reversible cantilever bending

## References


1.1 E. G. Emley: *Principles of Magnesium Technology* (Pergamon, New York 1966)
1.2 IMA: *Annual Report* (Int. Magnesium Association, Washington, DC 2001)
1.3 M. M. Avedesian, H. Baker: *Magnesium and Magnesium Alloys*, ASM Specialty Handbook (ASM, Metals Park 1999)
1.4 I. J. Polmear: *Light Metals, Metallurgy of the Light Metals* (Wiley, New York 1995)
1.5 G. Neite: Structure and properties of nonferrous alloys. In: *Materials Science and Technologie*, Vol. 8, ed. by K. H. Matucha (Verlag Chemie, Weinheim 1996)
1.6 C. S. Roberts: *Magnesium and Its Alloys* (Wiley, Chichester 1960)
1.7 C. Kammer: *Magnesium Taschenbuch* (Aluminium Verlag, Düsseldorf 2000)
1.8 G. L. Song, A. Atrens: Corrosion mechanisms of magnesium alloys, Adv. Eng. Mater. **1** (1999)
1.9 C. Kammer: *Aluminium Handbook 1, Fundamentals and Materials* (Aluminium Verlag, Düsseldorf 2002)
1.10 J. R. Davis (Ed.): *Aluminium and Aluminium Alloys*, ASM Specialty Handbook (ASM, Metals Park 1993)
1.11 H. W. L. Phillips: *Equilibrium Diagrams of Aluminium Alloy System* (The Aluminium Development Association, London 1961)
1.12 J. Thonstad, P. Fellner, G. M. Haarberg, J. Hives, H. Kvande, A. Sterten: *Aluminium Electrolysis – Fundamentals of the Hall-H'eroult Process*, 3rd edn. (Aluminium Verlag, Düsseldorf 2001)
1.13 International Aluminium Institute (AIA, London 2003), www.world-aluminium.org and www.world-aluminum.org
1.14 E. Nachtigall, H. Landerl: The treatment of the conductor alloy E-AlMgSi, Aluminium Ranshofen Mitteilungen **2**, 40–43 (in German) (1955)
1.15 E. Nachtigall, G. Lang: Electrical conductivity of aluminium castings, Mitt. Verein. Metallwerke Ranshofen-Berndorf , 16–19 (in German) (1965)
1.16 L. F. Mondolfo: *Aluminium Alloys – Structure and Properties* (Butterworths, London 1976)
1.17 C. Kammer: Thermomechanical treatment of Al strip casting. Ph.D. Thesis (TU Bergakademie Freiberg, Freiberg 1989) (in German)
1.18 E. Schürmann, I. K. Geissler: Solid-state phase equilibria in the Al and Mg rich areas of the Al-Mg-Li system, Giessereiforschung **32**, 163–174 (in German) (1981)
1.19 A. Dons: AlFeSi-Particles in industrially cast aluminium alloys, Z. Metallkunde **76**, 609–612 (1985)

1.20 A. Cziraki, B. Fogarassy, I. Szábo: Structure of high purity Al-Fe-Si-cast with different cooling rates, Cryst. Res. Technol. Berlin **20**, 279–281 (1985)

1.21 H. Westengen: Structure inhomogenities in direct chill cast sheet ingots of commercial pure aluminium, Z. Metallkunde **73**, 360–368 (1982)

1.22 H. P. Godard, W. B. Jepson, M. R. Bothwell, R. L. Kane: *The Corrosion of Light Metals* (Wiley, New York 1967)

1.23 K. R. Van Horn: *Aluminium. Bd. 1, Properties, Physical Metallurgy and Phase Diagrams* (ASM, Metals Park 1967)

1.24 D. Altenpohl: *Aluminium and Aluminium-Alloys* (Springer, Berlin, Heidelberg 1965 (in German))

1.25 U. Hielscher, H. Arbenz, H. Diekmann: Properties of AlSi-casting alloys with low iron content, Giesserei **53**, 125–133 (in German) (1966)

1.26 U. Hielscher: Ductile aluminium-silicon casting alloys for safety components in cars, Schweiz. Alum. Rundsch. **29**, 13–15 (in German) (1979)

1.27 U. Hielscher, R. Klos: A new low iron diecasting alloy, Aluminium **71**, 676–685 (in German) (1995)

1.28 W. Jung-König, U. Zwicker: Behaviour of light metal alloys on heating, Aluminium **34**, 337–345 (in German) (1958)

1.29 H. Vosskühler: Aluminium-Gusslegierungen hoher Dauerstandfestigkeit mit Magnesium und Silicium, Aluminium **31**, 219–222 (1955)

1.30 K. Wellinger, E. Keil, G. Maier: Strength of aluminium and its alloys up to 300 °C, Aluminium **34**, 458–463 (in German) (1958)

1.31 K. Wellinger, E. Keil et al.: On the mechanical properties of aluminium and aluminium alloys at elevated temperatures, Aluminium **39**, 372–377 (in German) (1963)

1.32 E. Richter, E. Hanitzsch: Elastic modulus and other physical properties of aluminium-base materials. Part 1., Aluminium **70**, 570–574 (in German) (1994)

1.33 D. Lenz, G. M. Renouard: Definition of cold rolled tempers by means of flow curves and energy of deformation, Aluminium **46**, 694–699 (in German) (1970)

1.34 A. Odok, G. Thym: The technical and economic advantages of continuous strip casting, Aluminium Engl. Suppl. **50**, E9–E11 (English transl.) (1974)

1.35 C. Kammer, M. Krumnacker et al.: Thermomechanical treatment of continuously cast and rolled Al99.5 alloy, Neue Hütte **35**, 418–421 (in German) (1990)

1.36 C. Kammer, M. Krumnacker et al.: Comparison of the strengthening effects in strip cast Al99.5, AlMn1 and AlMn1Fe1, Metall **45**, 135–138 (in German) (1991)

1.37 J. Althoff: Properties and uses of a new heat-resistant Al-Mn alloy, Metall **31**, 263–267 (in German) (1977)

1.38 J. Althoff: Examples of the application-orientated development of high-strength aluminium manganese alloys, Aluminium Engl. Suppl. **56**, E37–E39 (English transl.) (1982)

1.39 P. Brenner, H. Kostron: Treatment of AlMgSi-alloys, Z. Metallkunde **31**, 89–97 (1939)

1.40 I. Novikov: *Theory of Heat Treatment of Metals*, 1st edn. (Metalurgija, Moscow 1978)

1.41 Y. Takeuchi: Effect of plastic deformation on the natural ageing of AlCuMg1, AlCuMg2 and AlZnMgCu0.5, Aluminium **47**, 665–670 (in German) (1971)

1.42 K. Lücke, P. Stüwe: On the theory of impurity cotrolled grain boundary motion, Acta Met. **19**, 1067–1099 (1971)

1.43 H. Warlimont: Effect of segregation and precipitation on the recrystallisation and grain size of non-ferrous metals, Freiberg. Forschungsh. B **200**, 31–57 (in German) (1979)

1.44 D. B. Goel, P. Furrer, H. Warlimont: Precipitation behaviour of AlMnCuFe-alloys, Aluminium **50**, 511–516 (in German) (1974)

1.45 E. Nes, S. Slevolden: Casting and annealing structures in strip cast alloy, Aluminium **55**, 319–324 (1979)

1.46 E. Nes, J. D. Embury: The influence of a fine particle dispersion on the recrystallisation behaviour of a two phase aluminium alloy, Z. Metallkunde **66**, 589–593 (1975)

1.47 E. Nes, S. Slevolden: The concept of a grain size diagramm in the analysis of the recrystallisation behaviour of AlMn-alloys, Aluminium **52**, 560–563 (1976)

1.48 E. Nes: The effect of a fine particle dispersion on heterogeneous recrystallisation, Acta Met. **24**, 391–398 (1976)

1.49 C. Kammer, M. Krumnacker et al.: Thermomechanical treatment of strip cast AlMn1Fe1 alloy, Metall **43**, 1162–1168 (in German) (1993)

1.50 W. Huppatz: The fundamentals of corrosion protection of aluminium alloys used as structural materials. Part 1, Metall **49**, 505–509 (in German) (1995)

1.51 K. H. Matucha: Structure and properties of nonferrous alloys. In: *Materials Science and Technology*, Vol. 8, ed. by R. W. Cahn, P. Haasen, E. J. Kramer (VCH, Weinheim 1996)

1.52 J. R. Davis (Ed.): *Heat-Resistant Materials*, ASM Specialty Handbook (ASM, Metals Park 1997)

1.53 H. Sibum, G. Volker, O. Roidl, H. U. Wolf: Titanium and titanium alloys. In: *Ullmann's Encyclopedia of Industrial Chemistry*, Vol. A27 (VCH, Weinheim 1996) pp. 95–122

1.54 J. L. Murray: *Phase Diagrams of Binary Titanium Alloys* (ASM, Metals Park 1990)

1.55 D. F. Williams: Medical and dental materials. In: *Materials Science and Technology*, Vol. 14, ed. by R. W. Cahn, P. Haasen, E. J. Kramer (VCH, Weinheim 1992)

1.56 S. Steiner: *Properties and Selection: Irons, Steels and High Performance Alloys*, Metals Handbook, Vol. 1, 8th edn. (ASM, Metals Park 1961)

1.57 G. Sauthoff: *Intermetallic Materials*, Landolt–Börnstein, New Series VIII/2, ed. by P. Beiss, R. Ruthardt, H. Warlimont (Springer, Berlin, Heidelberg 2002)

1.58 T. K. Roy, R. Balasubramanian, A. Ghosh: Metall. Mater. Trans. Trans. A **27**, 3993–4003 (1996)

1.59 Y. W. Kim: JOM-J. Min. Met. Mater. Soc. **46** (1994)

1.60 N. S. Stoloff, V. K. Sikka: *Pysical Metallurgy and Processing of Intermetallic Compounds*, 1st edn. (Chapman & Hall, London 1996)

1.61 Y. W. Kim, R. Wagner, M. Yamaguchi: Gamma titanium aluminides, Proc. ISGTA'95 (TMS, Warrendale 1995)

1.62 R. Darolia, J. J. Lewandowski, C. T. Liu, P. L. Martin, D. B. Miracle, M. V. Nanthal: Structural intermetallics, Proc. First Intl. Symp. (TMS, Warrendale 1993)

1.63 K. Otsuka, C. M. Wayman (Eds.): *Shape Memory Materials* (Cambridge University Press, Cambridge 1998)

1.64 K. Otsuka, T. Kakeshita (Guest Eds.): Science and technology of shape-memory alloys: New developments, Mater. Res. Soc. Bull. **27**, 91–129 (2002)

1.65 H. Horikawa: , Proc. 1st Europ. Conf. on Shape Memory and Superelastic Technologies, Antwerp 1999) 256

1.66 A. E. Pelton, S. M. Russell, J. DiCello: The physical metallurgy of nitinol for medical applications, JOM-J. Min. Met. Mater. Soc. **55**, 33–37 (2003)

1.67 W. Chang: Zirconium products: Technical data sheet (Allegheny Technologies Inc. Pittsburgh, PA), www.alleghenytechnologies.com/wahchang

1.68 C. Lemaignan, A. T. Motta: Zirconium alloys in nuclear applications. In: *Materials Science and Technology*, Vol. 10B/II, ed. by B. R. T. Frost (VCH, Weinheim 1994)

1.69 A. Inoue, T. Zhang, T. Masumoto: Production of amorphous cylinder and sheet of $La_{55}Al_{25}Ni_{20}$ alloy by a metallic mold casting method, JIM **31**, 425 (1990)

1.70 A. Peker, W. L. Johnson: Appl. Phys. Lett. **63**, 2342 (1993)

1.71 W. L. Johnson: Fundamental aspects of bulk metallic glass formation in multicomponent alloys, Mater. Sci. Forum **225–227**, 35 (1996)

1.72 A. Inoue: *Bulk Amorphous Alloys* (Trans Tech, Uetikon-Zurich 1998)

1.73 A. Takeuchi, A. Inoue: Mater. Sci. Eng. A **304-306**, 446 (2001)

1.74 T. Wada, T. Zhang, A. Inoue: Mater. Trans. **43**, 2843 (2002)

1.75 C. C. Hays, J. Schroers, U. Geyer, S. Bossuyt, N. Stein, W. L. Johnson: Glass forming ability in the Zr-Nb-Ni-Cu-Al bulk metallic glasses. In: *Metastable, Mechanically Alloyed and Nanocrystalline Materials*, ed. by H. Eckert, H. Schlörb, L. Schultz (Trans Tech, Uetikon-Zurich 1995)

1.76 G. He, W. Löser, J. Eckert, L. Schultz: Mater. Sci. Eng. A **352**, 179 (2003)

1.77 J. E. Truman: Stainless steels. In: *Constitution and Properties of Steels*, Materials Science and Technology, Vol. 7, ed. by F. B. Pickerling (VCH, Weinheim 1992) p. 527

1.78 W. Dahl (Ed.): *Eigenschaften und Anwendungen von Stählen* (Institut für Eisenhüttenkunde IEHK, RWTH Aachen, Aachen 1993) p. 727 in German

1.79 J. R. Davis (Ed.): *Stainless Steels*, ASM Speciality Handbook (ASM, Metals Park 1994)

1.80 J. R. Davis (Ed.): *Carbon and Alloy Steels*, ASM Speciality Handbook (ASM, Metals Park 1996)

1.81 J. E. Bringas (Ed.): *Handbook of Comparative World Steel Standards* (ASTM, West Conshohocken 2001)

1.82 B. Predel (Ed.): *Phase Equilibria, Crystallographic and Thermodynamic Data of Binary Alloys*, Landolt–Börnstein, New Series IV/5 (Springer, Berlin, Heidelberg 1991 – 1998)

1.83 J. L. Lee, H. K. D. H. Bhadeshia: Mater. Sci. Eng. A **171**, 223–230 (1993)

1.84 G. Vander Voort: *Atlas of Time Temperature Diagrams*, Vol. 1, 2 (ASM, Materials Park 1991)

1.85 H. Schneider: Investment casting of high-hot strength 12% chrome steel, Foundry Trade J. **108**, 562 (1960)

1.86 K. Yagi, G. Merkling, H. Irie, H. Warlimont (Eds.): *Creep Properties of Heat Resistant Steels and Superalloys*, Landolt–Börnstein, New Series VIII (Springer, Berlin, Heidelberg 2004)

1.87 VDEh (Ed.): Stahl-Eisen-Werkstoffblatt (SEW) no. 470, Feb. 1976 (Verlag Stahleisen GmbH, Düsseldorf 1976)

1.88 J. R. Davis (Ed.): *Tool Materials*, ASM Speciality Handbook (ASM, Metals Park 1995)

1.89 J. R. Davis (Ed.): *Cast Irons*, ASM Speciality Handbook (ASM, Metals Park 1996)

1.90 W. Betteridge: *Cobalt and Its Alloys* (Ellis Horwood, New York 1982)

1.91 J. R. Davis (Ed.): *Nickel, Cobalt and Their Alloys*, ASM Specialty Handbook (The Materials Information Society, Materials Park 2000)

1.92 W. Gudat, O. Rader (Eds.): *Electronic Structure of Solids. Photoemission Spectra and Related Data. Magnetic Transition Metals*, Landolt–Börnstein, New Series III/23 (Springer, Berlin, Heidelberg 1999)

1.93 B. Predel: *Phase Equilibria*, Landolt–Börnstein, New Series IV/5 (Springer, Berlin, Heidelberg 1991–1998)

1.94 J. R. Davis (Ed.): *Tool Materials*, ASM Specialty Handbook (The Materials Information Society, Materials Park 1995)

1.95 P. Beiss, R. Ruthardt, H. Warlimont (Eds.): *Powder Metallurgy Data*, Landolt–Börnstein, New Series VIII/2 (Springer, Berlin, Heidelberg 2002)

1.96 J. R. Davis (Ed.): *Nickel, Cobalt and Their Alloys*, ASM Specialty Handbook (ASM International, Materials Park 2000)

1.97 J. R. Davis (Ed.): *Heat-Resistant Materials*, ASM Specialty Handbook (ASM International, Materials Park 1997)

1.98 J. C. Fuggle, U. Hillebrecht, R. Zeller, Z. Zolonierek, P. Bennet, C. Freiburg: Phys. Rev. B **27**, 719 (1982)

1.99 W. Gudat, O. Rader (Eds.): *Electronic Structure of Solids. Photoemission Spectra and Related Data. Magnetic Transition Metals*, Landolt–Börnstein, New Series III/23 (Springer, Berlin, Heidelberg 1999)

1.100 B. Predel: *Phase Equilibria, Crystallographic and Thermodynamic Data of Binary Alloys*, Landolt–Börnstein, New Series IV/5 (Springer, Berlin, Heidelberg 1991–1998)

1.101 K. Yagi, G. Merckling, H. Irie, H. Warlimont (Eds.): *Creep Properties of Heat Resistant Steels and Superalloys*, Landolt–Börnstein, New Series VIII (Springer, Berlin, Heidelberg 2004)

1.102 G. Joseph, K. J. A. Kundig: *Copper, Its Trade, Manufacture, Use, and Environmental Status* (ASM International, Materials Park 1998)

1.103 Wieland-Werke AG: *Wieland-Kupferwerkstoffe* (Ulm, Germany 1999)

1.104 J. R. Davis (Ed.): *Copper and Copper Alloys*, ASM Specialty Handbook (ASM, Metals Park 2001)

1.105 H. Warlimont, L. Delay: *Martensitic Transformations in Copper-, Silver-, and Gold-Based Alloys* (Pergamon, Oxford 1974)

1.106 B. Predel: *Cr-Cs-Cu-Zr*, Landolt–Börnstein, New Series IV/5 (Springer, Berlin, Heidelberg 1991–1998)

1.107 J. B. Conway, B. N. Flagella: *Creep Rupture Data for the Refractory Metals to High Temperatures* (Gordon Breach, New York 1971)

1.108 R. Kieffer, G. Jangg, P. Ettmayer: *Sondermetalle* (Springer, Vienna 1971) in German

1.109 American Society for Metals: *Properties and Selection: Nonferrous Alloys and Pure Metals*, Metals Handbook, Vol. 2, 9th edn. (American Society for Metals, Metals Park 1979)

1.110 W. C. Hagel, J. A. Shields, S. M. Tuominen: Processing and production of molybdenum and tungsten alloys, Proc. Symp. on Refractory Technology for Space Nuclear Power Applications, CONF-8308130 (Oak Ridge National Laboratory 1983) 98

1.111 K. H. Miska, M. Semchyshen, E. P. Whelan (Eds.): *Physical Metallurgy and Technology of Molybdenum and its Alloys* (AMAX, Michigan 1985)

1.112 J. Wadsworth, T. G. Nieh, J. J. Stephens: Recent advances in aerospace refractory metal alloys, Inter. Mater. Rev. **33**(3), 131 (1988)

1.113 E. Pink, I. Gaal: Mechanical properties and deformation mechanisms of non-sag tungsten wires. In: *The Metallury of Doped, Non-Sag Tungsten*, ed. by E. Pink, L. Bartha (Elsevier, New York 1989) p. 209

1.114 T. G. Nieh, J. Wadsworth: Recent advances and developments in refractory alloys, Mat. Res. Soc. Symp. Proc. **322**, 315 (1994), ISBN: 1-55899-221-9

1.115 E. Pink, R. Eck: Refractory metals and their alloys. In: *Materials Science and Technology – A Comprehensive Treatment*, Vol. 8, ed. by R. W. Cahn, P. Haasen, E. J. Kramer (VCH Verlag, Weinheim 1997) p. 589

1.116 E. Lassner, W. D. Schubert: *Tungsten: Properties, chemistry, technology of the element, alloys, and chemical compounds* (Kluwer/Plenum, New York 1999)

1.117 G. Leichtfried: *Handbook of Extractive Metallurgy* (Wiley-VCH, Weinheim 1997) p. 1371

1.118 G. Leichtfried: *Powder Metallurgy Data*, Landolt–Börnstein, New Series VIII/2A (Springer, Berlin, Heidelberg, New York 2002)

1.119 G. Leichtfried: Molybdenum lanthanum oxide: Special material properties by dispersoid refining during deformation. In: *Advances in Powder Metallurgy and Particulate Materials*, Vol. 9 (MPIF, Princeton 1992) p. 123

1.120 D. M. Moon, R. C. Koo: Mechanism and kinetics of bubble formation in doped W, Metall. Trans. **2**, 2125 (1971)

1.121 H. G. Sell, D. F. Stein, R. Stickler, A. Joshi, E. Berkey: The identification of bubble forming impurities in doped tungsten, J. Inst. Met. **100**, 275 (1972)

1.122 P. Makarov, K. Povarova: Principles of the alloying of tungsten and development of the manufacturing technology for the tungsten alloys, Proc. 15th Plansee Seminar, Vol. 3 (Plansee AG, Reutte 2001) p. 464

1.123 G. A. Geach, J. E. Hughes: The alloy of rhenium with molybdenum or with tungsten and having good high temperature properties, Proc. 2nd Plansee Seminar (Plansee AG, Reutte 1955) p. 245

1.124 R. I. Jaffee, C. T. Sims, J. J. Harwood: The effect of rhenium on the fabricability and ductility of molybdenum and tungsten, Proc. 3rd Plansee Seminar (Plansee AG, Reutte 1958) p. 380

1.125 J. G. Booth, R. I. Jaffee, E. I. Salkovitz: The mechanisms of the rhenium-alloying effect in group VI-A metals, Proc. 5th Plansee Seminar (Plansee AG, Reutte 1964) p. 547

1.126 Plansee Aktiengesellschaft: Material Data Base, Reutte (2000)

1.127 H. Borchers, E. Schmidt (Eds.): *Stoffwerte und Verhalten von metallischen Werkstoffen*, Landolt–Börnstein IV/2b, 6th edn. (Springer, Berlin, Heidelberg 1964)

1.128 T. E. Tietz, J. W. Wilson: *Behavior and Properties of Refractory Metals* (Stanford Univ. Press, Stanford 1965) p. 325

1.129 Plansee Aktiengesellschaft: Tungsten Brochure, Reutte (1997)

1.130 C. Cagran, C. Brunner, A. Seifter, G. Pottlacher: Liquid-phase behaviour of normal spectral emissivity at 684.5 nm of some selected metals, High Temp.-High Press. **34**, 669 (2002)

1.131 Dechema-Werkstoff-Tabelle: *Oxidierende Heißgase* (Dechema, Frankfurt 1981)

1.132 A. Schintlmeister, H.-P. Martinz, P. Wilhartitz, F. P. Netzer: Low-temperature oxidation of industrial molybdenum surfaces, Powder Metallurgy

World Congress & Exhibition, Granada 1998 (EPMA 1998) 526
1.133 G. Leichtfried: Powder metallurgical components for light sources, Habilitation Thesis (Montanuniversität, Leoben 2003)
1.134 E. Fromm, E. Gebhardt: *Gase und Kohlenstoff in Metallen* (Springer, Berlin, Heidelberg 1976) p. 747 in German
1.135 R. Speiser, G. R. St. Pierre: Proc. AGARD (Advisory Group for Aerospace Research and Development) Conf. on refractory metals, Oslo 1963
1.136 J. Disam, H.-P. Martinz, M. Sulik: European Patent Specification EP798402
1.137 C. A. Krier: *Coatings for the Protection of Refractory Metals from Oxidation*, Defense Metals Information Center Report 162 (Battelle Memorial Institute, Columbus 1961)
1.138 W. Knabl: Oxidationsschutz von Refraktärmetallen auf der Basis von Silizid- und Aluminidschichten. Ph.D. Thesis (Montanuniversität, Leoben 1995) in German
1.139 H.-P. Martinz, M. Sulik: Oxidation protection of refractory metals in the glass industry, Glastechnische Berichte, Glas Sci. Technol. **73**(C2) (2000)
1.140 C. Stickler: Mikroplastizität und zyklisches Spannungs-Dehnungsverhalten von Ta und Mo bei Temperaturen unter 0.2 $T_m$. Ph.D. Thesis (University of Vienna, Vienna 1998) in German
1.141 F. Benesovsky: *Pulvermetallurgie und Sinterwerkstoffe* (Plansee AG, Reutte 1982) p. 95, in German
1.142 E. Pink, H. Kärle: Zum Rekristallisationsverhalten von Sintertantal, Planseeberichte für Pulvermetallurgie **16**, 105 (1968) in German
1.143 G. Leichtfried, G. Thurner, R. Weirather: Molybdenum alloys for glass-to-metal seals, Proc. 14th Plansee Seminar, Vol. 4 (Plansee AG, Reutte 1997) p. 26
1.144 H. H. R. Jansen: The recrystallization texture of non-sag wire. In: *The Metallurgy of Doped, Non-Sag Tungsten*, ed. by E. Pink, L. Bartha (Elsevier, New York 1989) p. 203
1.145 D. B. Snow: The recrystallization of non-sag tungsten wire. In: *The Metallurgy of Doped, Non-Sag Tungsten* (Elsevier, New York 1989) p. 189
1.146 V. I. Trefilov, Y. V. Milman: Physical basis of thermomechanical treatment of refractory metals, Proc. 12th Plansee Seminar, Vol. 1 (Plansee AG ,Reutte 1989) p. 107
1.147 E. Parteder, W. Knabl, R. Stickler, G. Leichtfried: Bruchzähigkeit und Porenverteilung von Molybdän Stabmaterial in Abhängigkeit des Reckgrades und des Rekristallisationsgrades, Proc. 14th Plansee Seminar, Vol. 1 (Plansee AG, Reutte 1997) p. 984, in German
1.148 E. Parteder, H. Riedel, R. Kopp: Densification of sintered molybdenum during hot upsetting: Experiments and modeling, Mat. Sci. Eng. A **264**, 17 (1999)
1.149 E. Parteder: Ein Modell zur Simulation von Umformprozessen pulvermetallurgisch hergestellter hochschmelzender Metalle. Ph.D. Thesis (RWTH, Aachen 2000) in German
1.150 E. Parteder, H. Riedel: Simulating of hot forming processes of refractory metals using porous metal plasticicty models, Proc. 15th Plansee Seminar, Vol. 3 (Plansee AG, Reutte 2001) p. 60
1.151 B. P. Bewlay, C. L. Briant: Discussion of "Evidence for the Existence of Potassium Bubbles in AKS-Doped Tungsten Wire" and Reply, Met. Trans. A **22A**, 2153 (1991)
1.152 C. L. Briant: The effect of thermomechanical processing on the microstructure of tungsten rod, Proc. 13th Plansee Seminar, Vol. 1 (Plansee AG, Reutte 1993) p. 321
1.153 J. L. Walter, C. L. Briant: Tungsten wire for incandescent lamps, J. Mat. Res. **5**, 2004 (1990)
1.154 G. L. Krasko: Effect of impurities on the electronic structure of grain boundaries and intergranular cohesion in tungsten, Proc. 13th Plansee Seminar, Vol. 1 (Plansee AG, Reutte 1993) p. 27
1.155 A. Kumar, B. L. Eyre: Grain boundary segregation and intergranular fracture in molybdenum, Proc. R. Soc. London A **370**, 431 (1980)
1.156 St. M. Cardonne: Tantalum and its alloys, Advanced Mat. & Processes **9**, 16 (1992)
1.157 P. Wilhartitz, G. Leichtfried, H. P. Martinz, H. Hutter, A. Virag, M. Grasserbauer: Applications of 3D-SIMS for the development of refractory metal products, Proc. 2nd Europ. Conf. on Advanced Materials and Processes, ed. by T. W. Clyne, P. J. Withers, London 1992) 323
1.158 J. Femböck, R. Stickler, A. Vinckier: The effect of strain rate and heating rate on the tensile behavior of W and W—$ThO_2$ between room temperature and 1400 °C, Proc. 11th Plansee Seminar, Vol. 1 (Plansee AG, Reutte 1985) p. 361
1.159 D. L. Chen, B. Weiss, R. Stickler, M. Witwer, G. Leichtfried, H. Hödl: Fracture toughness of high melting point materials, Proc. 13th Plansee Seminar, Vol. 1 (Plansee AG, Reutte 1993) p. 621
1.160 E. S. Meiren, D. A. Thomas: Effect of grain boundaries on the bending ductility of tungsten, Metall. Trans. **233**, 937 (1965)
1.161 P. F. Browning, C. L. Briant, B. A. Knudsen: Dependence of material properties on processing history during wire drawing of commercially doped tungsten lamp wire, Proc. 13th Plansee Seminar, Vol. 1 (Plansee AG, Reutte 1993) p. 336
1.162 P. K. Wright: High temperature creep behavior of doped tungsten wire, Metall. Trans. **9**, 955 (July 1978)
1.163 J. Neges, B. Ortner, G. Leichtfried, H. P. Stüwe: On the 45° embrittlement of tungsten sheets, Mat. Sci. Eng. A **196**, 129 (1995)
1.164 Y. V. Milman: unpublished results

1.165 A. Seeger: The temperature dependence of the critical shear stress and of work hardening of metal crystals, Philos. Mag. **7**, 771 (1954)

1.166 J. W. Christian: Plastic deformation of bcc metals, Proc. International Conference on the Strength of Materials (ICSMA-2), Asilomar (ASTM, Philadelphia 1970) 31

1.167 H. Mughrabi: unpublished results

1.168 H. Ullmaier: Design properties of tantalum or everything you always wanted to know about tantalum but were afraid to ask, ESS (European Spallation Source) report ISSN 1433-559X, 03-131-T (2003)

1.169 W. Rinnerthaler, F. Benesovsky: Untersuchungen über das Mikrodehnungsverhalten von Molybdän, Planseeberichte für Pulvermetallurgie **21**, 253 (1973) in German

1.170 C. Stickler, D. L. Chen, B. Weiss, R. Stickler: Time dependent microplastic deformation of Mo and Ta at low temperatures, Proc. 14th Plansee Seminar, Vol. 1 (Plansee AG, Reutte 1997) p. 1004

1.171 K. J. Bowman, R. Gibala: Cyclic deformation of W single crystals, Scripta Met. **20**, 1451 (1986)

1.172 M. A. Meyers, Y.-J. Chen, F. D. S. Marquis, J. B. Isaacs: High strain rate behavior of Ta, The Univ. of Cal., Inst. for Mechanics and Materials, Report **94-25** (1994)

1.173 C. C. Wojcik: Thermomechanical processing and properties of niobium alloys, Proc. of the Internat. Symposium Niobium 2001 (Niobium 2001 Limited, Orlando 2001) 163

1.174 H. Mughrabi, K. Herz, X. Stark: Cyclic deformation and fatigue behavior of $\alpha$-Fe mono- and polycrystals, Int. J. Fracture **17**, 193 (1981)

1.175 M. Werner: Temperature and strain rate dependence of the flow stress of Ta single crystals in cyclic deformation, Revue de Physique Appliquee **23**, 672 (1988)

1.176 J. Femböck, K. Pfaffinger, B. Weiss, R. Stickler: Verhalten von Mo-Werkstoffen unter zyklischer Beanspruchung, Proc. 10th Plansee Seminar, Vol. 2 (Plansee AG, Reutte 1981) p. 27

1.177 K. Pfaffinger, J. Femböck: Versuchsplanung und statistische Auswertung von Schwingfestigkeitsdaten von Mo-Werkstoffen, Proc. 10th Plansee Seminar, Vol. 2 (Plansee AG, Reutte 1981) p. 233

1.178 K. Mecke, C. Holste, W. F. Terentjev: Dislocation arrangement in cyclically deformed Mo, Krist. Tech. **15**, 83 (1980)

1.179 S. Kong, B. Weiss, R. Stickler, M. Witwer, H. Ödl: Cyclic stress strain behavior of high melting point metals, Proc. 13th Plansee Seminar, Vol. 1 (Plansee AG, Reutte 1993) p. 720

1.180 D. R. Helebrand, R. I. Stephens: Cyclic yield behavior of Ta, J. Mater. Sci. **7**, 530 (1972)

1.181 C. Stickler, W. Knabl, R. Stickler, B. Weiss: Cyclic behavior of Ta at low temperatures under low stresses and strain rates, Proc. 15th Plansee Seminar, Vol. 3 (Plansee AG, Reutte 2001) p. 34

1.182 J. M. Meiniger, J. C. Gibeling: LCF of Nb and Nb-1Zr alloys, Met. Trans. **23A**, 3077 (1992)

1.183 H. J. Shi, L. S. Niu, C. Korn, G. Pluvinage: High temperature fatigue behavior of Mo-TZM alloy under mechanical and thermomechanical cyclic load, J. Nuclear Mat. **278**, 328 (2000)

1.184 R. F. Brodrick: LCF-data of P/M-W between 1650 and 3300 °C, Proc. ASTM **64**, 505 (1965)

1.185 S. S. Manson: *Thermal Stress and Low Cycle Fatigue* (McGraw-Hill, New York 1981) p. 187

1.186 R. E. Schmunk, G. E. Korth, M. Ulrickson: Tensile and LCF measurements on cross rolled tungsten, J. Nuclear Mat. **103**, 943 (1981)

1.187 T. Kimishima, M. Sukekawa, K. Owada, M. Shimizu: Fatigue data of Mo, 9th Symp. on Engineering Problems of Fusion Research 1981 (IEEE, New York 1981) 255

1.188 H. Nishi, T. Oku, T. Kodeira: Influence of microstructural change caused by cyclic strain on the LCF strength of sintered Mo, Fusion-Engineering-Design **9**, 123 (1989)

1.189 Z. M. Sun, Z. G. Wang, H. Ödl, R. Stickler, B. Weiss: Low cycle fatigue and creep behavior of recrystallized Mo near room temperature, Materialwissenschaft und Werkstofftechnik **26**, 483 (1995)

1.190 M. Papakyriacou, H. Mayer, C. Pypen, H. Plenk, S. Stanzl-Tschegg: Influence of loading frequency on high cycle fatigue properties of bcc and hcp metals, Mat. Sci. Eng. A **A308**, 143 (2001)

1.191 H. A. Calderon, G. Kostorz: Microstructure and plasticity of two molybdenum-base alloys (TZM), Mat. Sci. Eng. A **A160**, 189 (1993)

1.192 C. W. Marschall, F. C. Holden: Fracture toughness of refractory metals and alloys. In: *High Temperature Refractory Metals*, ed. by L. Richardson (Gordon Breach, New York 1964) p. 129

1.193 M. Rödig, H. Derz, G. Pott, B. Werner: Fracture mechanics investigations of TZM and Mo5Re, Proc. 14th Plansee Seminar, Vol. 1 (Plansee AG, Reutte 1997) p. 781

1.194 D. Padhi, J. J. Lewandowski: Effects of test temperature and grain size on the charpy impact toughness and dynamic toughness (KID) of polycrystalline niobium, Met. Mat. Trans. A **34**, 967 (2003)

1.195 J. A. Shields, P. Lipetzly, A. J. Mueller: Fracture toughness of 6.4 mm arc cast Mo and TZM Plate at RT and 300 °C, Proc. 15th Plansee Seminar, Vol. 4 (Plansee AG, Reutte 2001) p. 187

1.196 J. X. Zhang, L. Liu, M. L. Zhou, Y. C. Hu, T. Y. Zuo: Fracture toughness of sintered Mo$-La_2O_3$, Internat. J. Refract. Met. Hard Mat. **17**, 405 (1999)

1.197 D. L. Chen, B. Weiss, R. Stickler: The effective fatigue threshold: Significance of the loading cycle below the crack opening load, Internat. J. Fatigue **16**, 485 (1994)

1.198 J. Riedle: Bruchwiderstand in Wolfram-Einkristallen: Einfluß der kristallographischen Orientierung, der Temperatur und der Lastrate. In: *Fortschrittsberichte VDI*, Reihe 18, Mechanik/Bruchmechanik, Vol. 184 (VDI, Düsseldorf 1995) in German

1.199 R. Pippan: *Bruchzähigkeitsuntersuchungen an W Proben* (Erich Schmid Institut, Leoben 1999) Report in German

1.200 Y. Mutoh, K. Ichikawa, K. Nagata, M. Takeuchi: Effect of Re addition on fracture toughness of W at elevated temperatures, J. Mat. Sci. **30**, 770 (1995)

1.201 A. Fathulla, B. Weiss, R. Stickler: Short fatigue cracks in technical P/M-Mo alloys. In: *The Behavior of Short Fatigue Cracks, Mechanical Engineering Publications*, Vol. 1 (EGF Pub., Suffolk 1986) p. 115

1.202 R. Grill, H. Clemens, P. Rödhammer, A. Voiticek: P/M processing, characterization and application of Ta-10W, Proc. 14th Plansee Seminar, Vol. 4 (Plansee AG, Reutte 1997) p. 211

1.203 R. Heidenreich, R. Schäfer, H. Clemens, M. Witwer: Mechanical properties of high-temperature fasteners from refractory alloys, Proc. 13th Plansee Seminar, Vol. 1 (Plansee AG, Reutte 1993) p. 664

1.204 A. Fathulla, B. Weiss, R. Stickler, J. Femböck: The initiation and growth of short cracks in pm-Mo, Proc. 11th Plansee Seminar, Vol. 1 (Plansee AG, Reutte 1985) p. 45

1.205 H. Kitagawa, S. Takahashi: Applicability of fracture mechanics to very small cracks or the cracks in the early stage, Proc. second international conference on mechanical behavior of materials (ASM, Metals Park 1976) 627

1.206 B. Weiss, R. Stickler: Methods for predicting the fatigue strength of P/M-materials, Proc. International Powder Metallurgy Conf. PM'88, Orlando 1988, 3

1.207 B. Weiss, R. Stickler, A. F. Blom: A model for the description of the influence of small 3-dimensional defects on the HCF limit, Proc. Conf.: Short Fatigue Cracks, Sheffield 1990 (Mechanical Engineering Publications Limited, Suffolk 1992) 423

1.208 G. Leichtfried: Die Entwicklung von kriechfesten Molybdän – Seltenerdoxid – Werkstoffen für Hochtemperaturanwendungen. Ph.D. Thesis (Montanuniversität, Leoben 1997) in German

1.209 D. M. Moon, R. Stickler: Creep behavior of fine wires of P/M pure, doped and thoriated tungsten, High Temp. High Press. **3**, 503 (1971)

1.210 J. W. Pugh: On the short time creep rupture properties of lamp wire, Metall. Trans. **4**, 533 (1973)

1.211 J. H. Schröder, E. Arzt: Weak beam studies of dislocation/dispersoid interaction in an ODS superalloy, Scripta Met. **19**, 1129 (1985)

1.212 J. Rössler, E. Arzt: Kinetics of dislocation climb over hard particles – Climb without attractive particle-dislocation interaction, Acta Met. **36**, 1043 (1988)

1.213 J. Rössler, E. Arzt: A new model-based creep equation for dispersion strengthened materials, Acta Met. Mat. **38**(4), 671 (1990)

1.214 G. Zilberstein, J. Selverian: Creep deformation of non-sag tungsten in argon doped with low oxygen concentrations, Proc. 13th Plansee Seminar, Vol. 1 (Plansee AG, Reutte 1993) p. 132

1.215 G. Zilberstein: Creep properties of non-sag tungsten recrystallized in stagnant oxygen-doped argon, Int. J. Refract. Met. Hard Mat. **16**, 71 (1998)

1.216 Degussa AG (Ed.): *Edelmetall-Taschenbuch* (Degussa, Frankfurt 1967)

1.217 Degussa AG (Ed.): *Edelmetall-Taschenbuch*, 2nd edn. (Hüthig, Heidelberg 1995)

1.218 L. S. Benner, T. Suzuki, K. Meguro, S. Tanaka (Eds.): *Precious Metals, Science, Technology* (Int. Precious Metals Institute, Allentown 1991)

1.219 B. Predel (Ed.): *Phase Equilibria, Crystallographic, Thermodynamic Data of Binary Alloys*, Landolt-Börnstein, New Series IV/5 (Springer, Berlin, Heidelberg 1991–1998)

1.220 E. Raub: *Die Edelmetalle und ihre Legierungen* (Springer, Berlin, Heidelberg 1940)

1.221 P. J. Spencer, K. Hack: Swiss Materials **2**, 69–73 (1990)

1.222 C. J. Smithells, E. A. Brandes: *Metals Reference Book*, 5th edn. (Butterworth, London 1977)

1.223 P. Villars, L. D. Calvert: *Pearson's Handbook of Crystallographic Data for Intermetallic Phases*, Vol. 2, 3 (American Society for Metals, Metals Park 1985)

1.224 Landolt-Börnstein: *Technik*, Landolt-Börnstein, New Series IV/4, 6th edn. (Springer, Berlin, Heidelberg 1967)

1.225 W. Hume-Rothery, G. V. Raynor: *The Structure of Metals and Alloys* (Institute of Metals, London 1956)

1.226 Gmelin: *Handbuch der anorganischen Chemie*, Syst. Nr. 61 (Springer, Berlin, Heidelberg 1970–1975)

1.227 V. Behrens, K. H. Schröder: *Werkstoffe für elektrische Kontakte und ihre Anwendungen*, Kontakt u. Studium, Vol. 366 (Expert, Ehningen 1992)

1.228 W. H. Cubberly, H. Baker, D. Benjamin (Eds.): *Metals Handbook*, Vol. 2, 9th edn. (American Society for Metals, Metals Park 1979) pp. 671–678

1.229 E. M. Savitskii, A. Prince: *Handbook of Precious Metals* (Hemisphere, New York 1989) pp. 117–128

1.230 K.-H. Hellwege, A. M. Hellwege (Eds.): *Elastics, Piezolelectric, Pyroelectric, Electrooptic Constants, Nonlinear Dielectric Susceptibilities of Crystals*, Landolt-Börnstein, New Series III/18 (Springer, Berlin, Heidelberg 1984) p. 66

1.231 Doduco: *Datenbuch, Handbuch für Techniker*, 2. Aufl. (Doduco, Pforzheim 1977)

1.232 H. Spengler: Metall **18**, 36 (1964)

1.233 K.-H. Hellwege, J. L. Olsen: *Metals – Electronic Transport Phenomena*, Landolt-Börnstein, New Series III/15 (Springer, Berlin, Heidelberg 1982) p. 167

1.234 D. D. Pollok: Trans. Metall. Soc. AIME **230**, 753 (1964)

1.235 H. Flükiger, W. Klose (Eds.): *Superconductors Ac-Na*, Landolt-Börnstein, New Series III/21 (Springer, Berlin, Heidelberg 1990)

1.236 Chr. Raub: Z. Metallkde. **55**, 195 (1964)

1.237 R. E. Hummel: *Optische Eigenschaften von Metallen und Legierungen* (Springer, Berlin, Heidelberg pp. 158,178

1.238 H. Mehrer (Ed.): *Diffusion in Solid Metals and Alloys*, Landolt–Börnstein, New Series III/26 (Springer, Berlin, Heidelberg 1990)
1.239 G. Schlamp: Mater. Sci. Technol. **8**, 471–587 (1996)
1.240 D. Lee: *Modern Chlor-Alkali Technology*, Vol. 2, ed. by C. Jackson (Horwood, Chichester 1983)
1.241 S. U. Falk, A. J. Salkind: *Alkaline Storage Batteries* (Wiley, New York 1971)
1.242 A. Fleischer, J. J. Lander: *Zinc-Silver-Oxide Batteries* (Wiley, New York 1971)
1.243 H. Renner: *Ullmann's Encyclopedia of Industrial Chemistry* (Wiley-VCH, Weinheim 2002)
1.244 D. Z. Stöckel: Z. Werkstofftechnik **10**, 238 (1979)
1.245 B. Predel: *Phase Equilibria, Crystallophic and Thermodynamik Data of Binary Alloys*, Landolt–Börnstein, New Series IV/5 (Springer, Berlin, Heidelberg 1991–1998)
1.246 H. Renner: *Ullmann's Encyclopedia of Industrial Chemistry*, 6th edn. (Wiley-VCH, Weinheim 2001)
1.247 R. Forro: Gold Bull. **36**(2), 39–58 (2003)
1.248 N. Yuantao: Gold Bull. **34**(3), 77–87 (2001)
1.249 H. Ahlborn, G. Wassermann: Z. Metallkde. **55**, 685 (1964)
1.250 E. Drost, J. H. Hausselt: Interdisc. Sci. Rev. **17**, 271–280 (1992)
1.251 B. Kempf, J. Hausselt: Interdisc. Sci. Rev. **17**, 251–260 (1992)
1.252 G. Humpston: Gold Bull. **26**, 139 (1993)
1.253 C. J. Raub D. Ott: Z. Metallkde. **25**(4), 629 (1992)
1.254 M. Du Toit, E. van der Lingen, L. Glaner, R. Süss: *Gold Bulletin*, quarterly reviews, Vol. 35, ed. by C. Corti, D. Thompson (World gold council, London 2002) p. 49
1.255 Gmelin: *Gmelin Handbuch der anorganischen Chemie*, Vol. 62 (Springer, Berlin, Heidelberg 1970–1975) p. 619
1.256 H. R. Khan, Ch. R. Raub: *Gold Bulletin*, quarterly reviews, Vol. 8, ed. by C. Corti, D. Thompson (World gold council, London 1975) pp. 114–118
1.257 H. R. Khan: *Gold Bulletin*, quarterly reviews, Vol. 17, ed. by C. Corti, D. Thompson (World gold council, London 1984) pp. 94–100
1.258 J. Kopp: *Gold Bulletin*, quarterly reviews, Vol. 9, ed. by C. Corti, D. Thompson (World gold council, London 1976) p. 55
1.259 M. Hansen, K. Anderko: *Constitution of Binary Alloys*, 2nd edn. (McGraw-Hill, New York 1958) pp. 195, 221
1.260 E. Raub: *Die Edelmetalle und ihre Legierungen*, Reine angewandte Metallkunde, Vol. 5, ed. by W. Köster (Springer, Berlin, Heidelberg 1955) Chap. II, A5, pp. 53,54
1.261 T. Shiraishi, K. Hisatsune, Y. Tanaka, E. Miura, Y. Takuma: Gold Bull. **34**, 130 (2001)
1.262 W. S. Rapson, T. Groenewald: *Gold Usage* (Academic Press, New York 1978) p. 37
1.263 D. Compton et al.: *Gold Bulletin*, quarterly reviews, Vol. 10, ed. by C. Corti, D. Thompson (World gold council, London 1977) p. 51
1.264 G. C. Bond: *Gold Bulletin*, quarterly reviews, Vol. 34, ed. by C. Corti, D. Thompson (World gold council, London 2001) p. 117
1.265 A. St. K. Hashmi: *Gold Bulletin*, quarterly reviews, Vol. 36, ed. by C. Corti, D. Thompson (World gold council, London 2003) p. 3
1.266 M. Gupta, A. K. Tripathi: *Gold Bulletin*, quarterly reviews, Vol. 34, ed. by C. Corti, D. Thompson (World gold council, London 2001) p. 120
1.267 C. Corti, R. J. Holliday, D. T. Thompson: *Gold Bulletin*, quarterly reviews, Vol. 35 (World gold council, London 2002) p. 111
1.268 R. Grisel, K. J. Weststrate, A. Gluhoi, B. E. Nieuwenhuys: Gold Bull. **35**, 39–45 (2002)
1.269 H. Knosp, R. J. Holliday, Ch. W. Corti: *Gold in dentistry*, Vol. 36 2003) pp. 93–102
1.270 G. Gafner: *Gold Bulletin*, quarterly reviews, Vol. 22, ed. by C. Corti, D. Thompson (World gold council, London 1989) p. 112
1.271 G. Humston, D. M. Jacobson: *Gold Bulletin*, quarterly reviews, Vol. 25, ed. by C. Corti, D. Thompson (World gold council, London 1992) p. 139
1.272 D. R. Olsen, H. M. Berg: , Proc. 27th Electronic Components Conf. (IEEE, Piscataway 1977)
1.273 G. Zwingmann: Z. Metall. **34**(18), 726 (1964)
1.274 G. Petzow, G. Effenberg: *Ternary Alloys* (Verlag Chemie, Weinheim 1988)
1.275 W. Müller: *Metallische Lotwerkstoffe* (DVS, Düsseldorf 1990)
1.276 K. Toyoshima, Somorjai: Cat. Rev. Sci. Eng. **19** (1979)
1.277 A. S. Darling: , Review 175 (Institute of Metals, London 1973)
1.278 J. B. Hunter: Platinum Met. Rev. **4**(4), 130 (1960)
1.279 A. G. Knapton: Platinum Met. Rev. **21**(2), 44 (1977)
1.280 R. S. Irani: Metals Rev. **17**, 22 (1973)
1.281 A. Kussmann, G. Von Rittberg: Ann. Phys. **7**, 173 (1950)
1.282 A. Kussmann, K. Jesson: J. Phys. Soc. Jpn. **17**, 272 (1962)
1.283 A. S. Darling: Platinum Met. Rev. **11**, 138 (1967)
1.284 A. S. Darling: Platinum Met. Rev. **13**, 53 (1969)
1.285 R. S. Irani, R. W. Cahn: Met. Rev. **16**, 49 (1972)
1.286 H. Ocken, J. H. N. Van Vucht: J. Less-Comm. Met. **15**, 196–199 (1968)
1.287 I. Gurappa: Platinum Met. Rev. **45**(3), 124 (2001)
1.288 I. Wolff, P. J. Hill: Platinum Met. Rev. **44**(4), 161 (2000)
1.289 J. Merker, D. Lupton, M. Töpfer, H. Knake: Platinum Met. Rev. **45**, 76–80 (2001)
1.290 G. Borelius et al.: Proc. K. Acad. Wet. **33**, 17 (1930)
1.291 Th. J. Colacot: Platinum Met. Rev. **46**(2), 83 (2002)
1.292 I. M. Wolff, P. J. Hill: Platinum Met. Rev. **44**(4), 159 (2000)
1.293 Y. Yamabe-Mitarai, Y. F. Gu, H. Harada: Platinum Met. Rev. **46**(2), 77, 78 (2002)
1.294 M. Graff, B. Kempf, J. Breme: Metall **53**, 616–621 (1999)
1.295 J. H. Jones: Platinum Met. Rev. **44**(3), 100 (2000)

1.296 I. M. Wolff, P. J. Hill: Platinum Met. Rev. **44**(4), 164 (2000)
1.297 M. Fallot: Ann. Phys. (Paris) **10**, 29 (1938)
1.298 Philips AG: Philips Techn. Rev. , 73 (1966)
1.299 S. Guruswamy: *Engineering Properties and Applications of Lead Alloys* (Dekker, New York 2000) pp. 1–635
1.300 Lead Industries Association: *Properties of Lead and Lead Alloys*, Booklet No. 5M (Lead Industries Association, New York 1983) pp. 12–83
1.301 Lead Industries Association: *Lead for Corrosion Resistant Applications – A Guide* (Lead Industries Association, New York 1974)
1.302 G. Baralis, I. Tangerini: A study of some dynamic properties of lead and its alloys, Proc. 3rd Intl. Lead Conference, Venice, ed. by European Lead Development Committee and Lead Development Association (Pergamon, London 1968) 309–319
1.303 W. Hofmann: *Lead and Lead Alloys* (Springer, Berlin, Heidelberg 1970)
1.304 G. Kerry, P. Lord: *Project Report LM-375*, International Lead Zinc Research Organization (ILZRO) (University Salford, Salford 1990)
1.305 Lead Industries Association: *Lead Shielding for the Nuclear Industry* (Lead Industries Association, New York 1985)
1.306 R. D. Prengaman: Wrought lead–calcium–tin alloys for tubular lead/acid battery grids, J. Power Sources **53**, 207–214 (1995)
1.307 A. Siegmund, R. D. Prengaman: Grid alloys for automobile batteries in the new millenium, J. Metals **53**, 38 (2001)
1.308 ASTM: *Standard Specification for White Metal Bearing Alloys*, ASTM B23 (American Society for Testing Materials, West Conshohocken 1996)
1.309 Lead Industries Association: *Solders and Soldering – A Primer* (Lead Industries Association, Sparta 1996)
1.310 P. Adeva, G. Caruana, M. Aballe, M. Torralba: The lead-rich corner of the Pb–Ca–Sn phase diagram, Mater. Sci. Eng. **54**, 229–236 (1982)

# 3.2. Ceramics



Ceramics have various definitions, because of their long history of development as one of the oldest and most versatile groups of materials and because of the different ways in which materials can be classified, such as by chemical composition (silicates, oxides and non-oxides), properties (mechanical and physical), or applications (building materials, high-temperature materials and functional materials). The most widely used, minimal definition of ceramics is that they are inorganic nonmetallic materials. The broadest subdivision is into traditional, and technical or engineering ceramics. Detailed groupings and definitions of technical ceramics are given in DIN EN 60672. In the present section we differentiate between traditional ceramics and cements, silicate ceramics, refractory ceramics, oxide ceramics, and non-oxide ceramics, being aware that there are overlaps. It should also be noted that other sections of this Handbook cover particular groups of ceramics: glasses (Chapt. 3.4), semiconductors (Chapt. 4.1), nonmetallic superconductors (Sect. 4.2.2), magnetic oxides (Sect. 4.3.4), dielectrics and electrooptics (Chapt. 4.4) and ferroelectrics and related materials, (Chapt. 4.5).


3.2.1 **Traditional Ceramics and Cements** ..... 432
3.2.1.1 Traditional Ceramics ..... 432
3.2.1.2 Cements ..... 432

3.2.2 **Silicate Ceramics** ..... 433

3.2.3 **Refractory Ceramics** ..... 437

3.2.4 **Oxide Ceramics** ..... 437
3.2.4.1 Magnesium Oxide ..... 444
3.2.4.2 Alumina ..... 445
3.2.4.3 Al–O–N Ceramics ..... 447
3.2.4.4 Beryllium Oxide ..... 447
3.2.4.5 Zirconium Dioxide ..... 447
3.2.4.6 Titanium Dioxide, Titanates, etc. 450

3.2.5 **Non-Oxide Ceramics** ..... 451
3.2.5.1 Non-Oxide High-Temperature Ceramics ..... 451
3.2.5.2 Borides ..... 451
3.2.5.3 Carbides ..... 458
3.2.5.4 Nitrides ..... 467
3.2.5.5 Silicides ..... 473

**References** ..... 476


Detailed treatments of ceramics are given in [2.1–3]. Reference [2.4] is a comprehensive handbook on materials, emphasizing ceramics and minerals. Structural ceramics are treated in [2.5]. Reference [2.6] is a hands-on practical reference book for technical ceramics, and recent data on technical ceramics can be found in conference proceedings such as [2.7].

## 3.2.1 Traditional Ceramics and Cements

### 3.2.1.1 Traditional Ceramics

Traditional ceramics are obtained by the firing of clay-based materials. They are commonly composed of a clay mineral (kaolinite, montmorillonite, or illite), fluxing agents (orthoclase and plagioclase), and filler materials ($SiO_2$, $Al_2O_3$, and MgO). The processing steps are mixing, forming, drying, firing (high-temperature treatment in air), and finishing (enameling, cleaning, and machining). The main classes of traditional ceramics are fired bricks, whiteware (china, stoneware, and porcelain), glazes, porcelain enamels, high-temperature refractories, cements, mortars, and concretes. Table 3.2-1 lists some of main groups of traditional ceramics, with some of their properties and applications.

### 3.2.1.2 Cements

Cement is the common binder of traditional building ceramics. It is produced by mixing about 80 wt% of low-magnesium (< 3 wt% MgO) calcium carbonate ($CaCO_3$) (limestone, marl, or chalk) with about 20 wt% clay (which may be obtained from clays, shale, or slag). In terms of oxide content, this corresponds to a ratio of CaO to $SiO_2$ of 3:1 by weight. The common term "Portland cement" is based on the early use of a particular limestone called Portland stone. The processing steps are milling and mixing, heating to 260 °C, precalcining at 900 °C, and calcining in a rotary kiln at temperatures ≤ 1450 °C. The resulting product is termed "clinker" and consists of a vitreous nodular material composed of calcium silicates and aluminates. This is mixed with 2 to 4 wt% gypsum ($CaSO_4 \cdot 2H_2O$) to adjust the setting time, and ground to the final product. The ranges of the percentages of the constituents are given in Table 3.2-2.

Some standardized grades of Portland cement and their uses are listed in Table 3.2-3. Mortars and concretes are mixtures of cement with specified amounts of sand, gravel, or crushed stones with specified particle sizes.

**Table 3.2-2** Chemical composition of Portland cement [2.4]

| Component | Average mass fraction (wt%) |
|---|---|
| $SiO_2$ | 21.8 – 21.9 |
| $Al_2O_3$ | 4.9 – 6.9 |
| $Fe_2O_3$ | 2.4 – 2.9 |
| CaO | 63.0 – 65.0 |
| MgO | 1.1 – 2.5 (max. 3.0) |
| $SO_3$ | 1.7 – 2.6 |
| $Na_2O$ | 0.2 |
| $K_2O$ | 0.4 |
| $H_2O$ | 1.4 – 1.5 |

**Table 3.2-1** Examples of traditional ceramics [2.4]

| Type | Properties | Applications |
|---|---|---|
| Fired brick | Porosity 15 – 30%<br>Firing temperature 950 – 1050 °C<br>May be enameled or not | Bricks, pipes, ducts, walls, floor tiles |
| China | Porosity 10 – 15%<br>Firing temperature 950 – 1200 °C<br>Enameled, opaque | Sanitary, tiles |
| Stoneware | Porosity 0.5 – 3%<br>Firing temperature 1100 – 1300 °C<br>Glassy surface | Crucibles, labware, pipes |
| Porcelain | Porosity 0 – 2%<br>Firing temperature 1100 – 1400 °C<br>Glassy, translucent | Insulators, labware, cookware |

**Table 3.2-3** ASTM Portland cement types [2.4]

| ASTM type | Name | Compressive strength after 28 days (MPa) | Applications |
|---|---|---|---|
| Type I | Normal or ordinary Portland cement (NPC) | 42 | General uses, and hence used when no special properties are required. |
| Type II | Modified Portland cement (MPC) | 47 | Low heat generation during the hydration process. Most useful in structures with large cross sections and for drainage pipes where sulfate levels are low. |
| Type III | Rapid-hardening Portland cement (RHPC) | 52 | Used when high strength is required after a short period of curing. |
| Type IV | Low-heat Portland cement (LHPC) | 34 | Less heat generation during hydration than for Type II. Used for mass concrete construction where large heat generation could create problems. The tricalcium aluminate content must be maintained below 7 wt%. |
| Type V | Sulfate-resisting Portland cement (SRPC) | 41 | Has high sulfate resistance. It is a special cement used when severe attack is possible. |

## 3.2.2 Silicate Ceramics

Silicates are the salts or esters of orthosilicic acid ($H_4SiO_4$) and of its condensation products. The silicates are categorized according to the arrangement of the [$SiO_4$] tetrahedra in their crystal structure. Figure 3.2-1 shows some simple, planar arrangements. In the tectosilicates, the array of the $SiO_4$ tetrahedra is three-dimensional. Typical examples are talc, feldspar, and the zeolites.

As silicates are the most important constituents of the earth's crust, they became the basis of the traditional

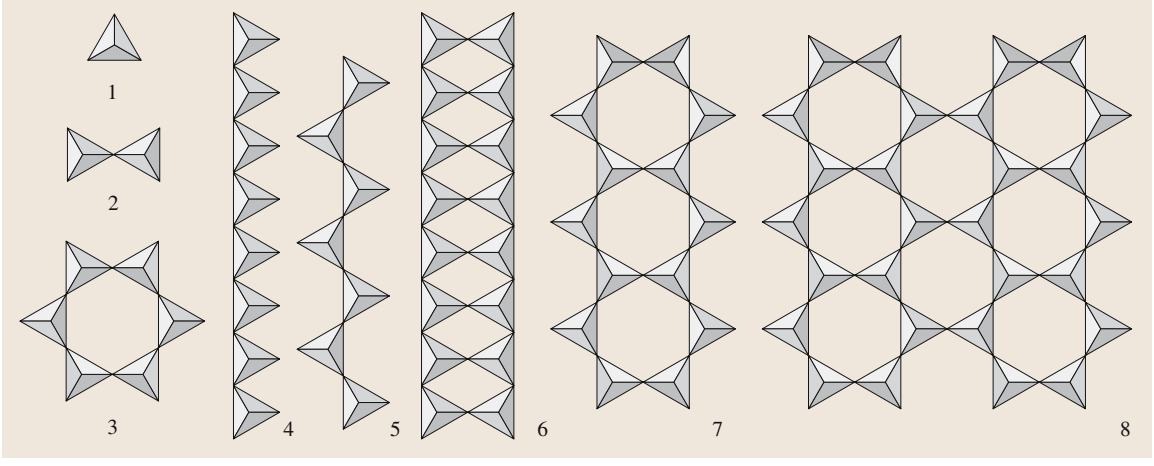


**Fig. 3.2-1** Schematic representation of the arrangement of the [$SiO_4$] tetrahedra in planar silicate crystal structures: 1, nesosilicate; 2, sorosilicate; 3, cyclosilicate; 4 and 5, inosilicates; 6 and 7, ribbon silicates; 8, layered silicate or phyllosilicate

ceramics, from which a variety of technical ceramic materials have been developed, particularly for electrotechnical and electronic applications. Some silicate ceramics are also used for high-temperature applications in the processing of materials. Silicate ceramics are composed essentially of porcelain, steatite, cordierite, and mullite ($3Al_2O_3 \cdot 2SiO_2$).

Recent standards that classify and characterize technical silicate ceramics are listed in Tables 3.2-4 – 3.2-7.

**Table 3.2-4** Properties of Alkali aluminium silicates according to DIN EN 60672 [2.6]

| | | | Designation | | | | | |
|---|---|---|---|---|---|---|---|---|
| | | | C 110 | C 111 | C 112 | C 120 | C 130 | C 140 |
| **Mechanical properties** | **Symbol** | **Units** | **Quartz porcelain, plastically formed** | **Quartz porcelain, pressed** | **Cristobalite porcelain** | **Alumina porcelain** | **Alumina porcelain, high-strength** | **Lithium porcelain** |
| Density, minimum | $\varrho$ | $t/m^3$ | 2 | 2.2 | 2.3 | 2.3 | 2.5 | 2.0 |
| Bending strength, unglazed | $\sigma_{ft}$ | MPa | 50 | 40 | 80 | 90 | 140 | 50 |
| Bending strength, glazed | $\sigma_{fg}$ | MPa | 60 | – | 100 | 110 | 160 | 60 |
| Young's modulus | $E$ | GPa | 60 | – | 70 | – | 100 | – |
| **Electrical properties** | | | | | | | | |
| Breakdown strength | $E_d$ | kV/mm | 20 | – | 20 | 20 | 20 | 15 |
| Withstand voltage | $U$ | kV | 30 | – | 30 | 30 | 30 | 20 |
| Permittivity at 48 – 62 Hz | $\varepsilon_r$ | | 6 – 7 | – | 5 – 6 | 6 – 7 | 6 – 7.5 | 5 – 7 |
| Loss factor at 20 °C, 1 kHz | $\tan \delta_{pf}$ | $10^{-3}$ | 25 | – | 25 | 25 | 30 | 10 |
| Loss factor at 20 °C, 1 MHz | $\tan \delta_{1M}$ | $10^{-3}$ | 12 | – | 12 | 12 | 15 | 10 |
| Resistivity at 20 °C | $\rho_{20}$ | Ω m | $10^{11}$ | $10^{10}$ | $10^{11}$ | $10^{11}$ | $10^{11}$ | $10^{11}$ |
| Resistivity at 600 °C | $\rho_{600}$ | Ω m | $10^2$ | $10^2$ | $10^2$ | $10^2$ | $10^2$ | $10^2$ |
| **Thermal properties** | | | | | | | | |
| Average coefficient of thermal expansion at 30 – 600 °C | $\alpha_{30-600}$ | $10^{-6}\,K^{-1}$ | 4 – 7 | 4 – 7 | 6 – 8 | 4 – 7 | 5 – 7 | 1 – 3 |
| Specific heat capacity at 30 – 600 °C | $c_{p,30-600}$ | $J\,kg^{-1}K^{-1}$ | 750 – 900 | 800 – 900 | 800 – 900 | 750 – 900 | 800 – 900 | 750 – 900 |
| Thermal conductivity | $\lambda_{30-100}$ | $W\,m^{-1}K^{-1}$ | 1 – 2.5 | 1.0 – 2.5 | 1.4 – 2.5 | 1.2 – 2.6 | 1.5 – 4.0 | 1.0 – 2.5 |
| Thermal fatigue resistance | | (Rated) | Good | Good | Good | Good | Good | Good |

**Table 3.2-5** Properties of magnesium silicate according to DIN EN 60672 [2.6]

| | | | Designation | | | | | |
|---|---|---|---|---|---|---|---|---|
| | | | C 210 | C 220 | C 221 | C 230 | C 240 | C 250 |
| **Mechanical properties** | **Symbol** | **Units** | **Steatite for low voltage** | **Steatite, standard** | **Steatite, low-loss** | **Steatite, porous** | **Forsterite, porous** | **Forsterite, dense** |
| Open porosity | | vol. % | 0.5 | 0.0 | 0.0 | 35.0 | 30.0 | 0.0 |
| Density, minimum | $\varrho$ | $t/m^3$ | 2.3 | 2.6 | 2.7 | 1.8 | 1.9 | 2.8 |
| Bending strength | $\sigma_B$ | MPa | 80 | 120 | 140 | 30 | 35 | 140 |
| Young's modulus | $E$ | GPa | 60 | 80 | 110 | – | – | – |
| **Electrical properties** | | | | | | | | |
| Breakdown strength | $E_d$ | kV/mm | – | 15 | 20 | – | – | 20 |
| Withstand voltage | $U$ | kV | – | 20 | 30 | – | – | 20 |
| Permittivity at 48–62 Hz | $\varepsilon_r$ | | 6 | 6 | 6 | – | – | 7 |
| Loss factor at 20 °C, 1 kHz | $\tan\delta_{pf}$ | $10^{-3}$ | 25 | 5 | 1.5 | – | – | 1.5 |
| Loss factor at 20 °C, 1 MHz | $\tan\delta_{1M}$ | $10^{-3}$ | 7 | 3 | 1.2 | – | – | 0.5 |
| Resistivity at 20 °C | $\rho_{20}$ | Ω m | $10^{10}$ | $10^{11}$ | $10^{11}$ | – | – | $10^{11}$ |
| Resistivity at 600 °C | $\rho_{600}$ | Ω m | $10^3$ | $10^3$ | $10^5$ | $10^5$ | $10^5$ | $10^5$ |
| **Thermal properties** | | | | | | | | |
| Average coefficient of thermal expansion at 30–600 °C | $\alpha_{30-600}$ | $10^{-6}\,K^{-1}$ | 6–8 | 7–9 | 7–9 | 8–10 | 8–10 | 9–11 |
| Specific heat capacity at 30–100 °C | $c_{p,30-600}$ | $J\,kg^{-1}K^{-1}$ | 800–900 | 800–900 | 800–900 | 800–900 | 800–900 | 800–900 |
| Thermal conductivity | $\lambda_{30-100}$ | $W\,m^{-1}K^{-1}$ | 1–2.5 | 2–3 | 2–3 | 1.5–2 | 1.4–2 | 3–4 |
| Thermal fatigue resistance | | (Rated) | Good | Good | Good | Good | Good | Good |

**Table 3.2-6** Properties of alkaline-earth aluminium silicates according to DIN EN 60672 [2.6]

| | | | Designation | | | |
|---|---|---|---|---|---|---|
| | | | C 410 | C 420 | C 430 | C 440 |
| **Mechanical properties** | **Symbol** | **Units** | **Cordierite, dense** | **Celsians, dense** | **Calcium-based, dense** | **Zirconium-based, dense** |
| Open porosity | | vol. % | 0.5 | 0.5 | 0.5 | 0.5 |
| Density, minimum | $\varrho$ | $t/m^3$ | 2.1 | 2.7 | 2.3 | 2.5 |
| Bending strength | $\sigma_B$ | MPa | 60 | 80 | 80 | 100 |
| Young's modulus | $E$ | GPa | – | – | 80 | 130 |

**Table 3.2-6** Properties of alkaline-earth aluminium silicates according to DIN EN 60672 [2.6], cont.

| | | | Designation C 410 | C 420 | C 430 | C 440 |
|---|---|---|---|---|---|---|
| **Electrical properties** | **Symbol** | **Units** | **Cordierite, dense** | **Celsians, dense** | **Calcium-based, dense** | **Zirconium-based, dense** |
| Breakdown strength | $E_d$ | kV/mm | 10 | 20 | 15 | 15 |
| Withstand voltage | $U$ | kV | 15 | 30 | 20 | 20 |
| Permittivity at 48–62 Hz | $\varepsilon_r$ | | 5 | 7 | 6–7 | 8–12 |
| Loss factor at 20 °C, 1 kHz | $\tan \delta_{pf}$ | $10^{-3}$ | 25 | 10 | 5 | 5 |
| Loss factor at 20 °C, 1 MHz | $\tan \delta_{1M}$ | $10^{-3}$ | 7 | 0.5 | 5.0 | 5 |
| Resistivity at 20 °C | $\rho_{20}$ | Ω m | $10^{10}$ | $10^{12}$ | $10^{11}$ | $10^{11}$ |
| Resistivity at 600 °C | $\rho_{600}$ | Ω m | $10^3$ | $10^7$ | $10^2$ | $10^2$ |
| **Thermal properties** | | | | | | |
| Average coefficient of thermal expansion at 30–600 °C | $\alpha_{30-600}$ | $10^{-6}$ K$^{-1}$ | 2–4 | 3.5–6 | – | – |
| Specific heat capacity at 30–100 °C | $c_{p,30-600}$ | J kg$^{-1}$K$^{-1}$ | 800–1200 | 800–1000 | 700–850 | 550–650 |
| Thermal conductivity | $\lambda_{30-100}$ | W m$^{-1}$K$^{-1}$ | 1.2–2.5 | 1.5–2.5 | 1–2.5 | 5–8 |
| Thermal fatigue resistance | | (Rated) | Good | Good | Good | Good |

**Table 3.2-7** Properties of porous aluminium silicates and magnesium silicates according to DIN EN 60672 [2.6]

| | | | Designation C 510 | C 511 | C 512 | C 520 | C 530 |
|---|---|---|---|---|---|---|---|
| **Mechanical properties** | **Symbol** | **Units** | **Aluminosilicate-based** | **Magnesia–alumino-silicate-based** | **Magnesia–alumino-silicate-based** | **Cordierite-based** | **Aluminosilicate-based** |
| Open porosity | | vol. % | 30 | 20 | 40 | 20 | 30 |
| Density, minimun | $\varrho$ | t/m$^3$ | 1.9 | 1.9 | 1.8 | 1.9 | 2.1 |
| Bending strength | $\sigma_B$ | MPa | 25 | 25 | 15 | 30 | 30 |
| Young's modulus | $E$ | GPa | – | – | – | 40 | – |
| **Electrical properties** | | | | | | | |
| Resistivity at 600 °C | $\rho_{600}$ | Ω m | $10^3$ | $10^3$ | $10^3$ | $10^3$ | $10^4$ |
| **Thermal properties** | | | | | | | |
| Average coefficient of thermal expansion at 30–600 °C | $\alpha_{30-600}$ | $10^{-6}$K$^{-1}$ | 3–6 | 4–6 | 3–6 | 2–4 | 4–6 |
| Specific heat capacity at 30–100 °C | $c_{p,30-600}$ | J kg$^{-1}$K$^{-1}$ | 750–850 | 750–850 | 750–900 | 750–900 | 800–900 |
| Thermal conductivity | $\lambda_{30-100}$ | W m$^{-1}$K$^{-1}$ | 1.2–1.7 | 1.3–1.8 | 1–1.5 | 1.3–1.8 | 1.4–2.0 |
| Thermal fatigue resistance | | Rated | Good | Good | Good | Good | Good |

## 3.2.3 Refractory Ceramics

Traditional refractory ceramics are produced as bricks from a broad variety of materials for various applications, ranging from building bricks used at ambient and moderately elevated temperatures to high-temperature refractory grades with particularly high melting temperatures and refractory stability, such as magnesite, silicon carbide, stabilized zirconia, and chrome-magnesite. Table 3.2-8 gives a survey of fired refractory brick materials.

It should be noted that these refractory ceramics in brick form differ from materials classified as technical refractory ceramics in the amounts of material used and in the composition, including the impurity content, but they rely basically on the same oxide or non-oxide ceramic compounds. These compounds are used in technical ceramics and are treated in more detail below.

**Table 3.2-8** Properties of fired refractory brick materials [2.4]

| Brick (major chemical components) | Density $\varrho$ (kg/m$^3$) | Melting temperature (°C) | Thermal conductivity $\kappa$ (W/m K) |
|---|---|---|---|
| Alumina brick (6–65 wt% $Al_2O_3$) | 1842 | 1650 – 2030 | 4.67 |
| Building brick | 1842 | 1600 | 0.72 |
| Carbonbrick (99 wt% graphite) | 1682 | 3500 | 3.6 |
| Chromebrick (100 wt% $Cr_2O_3$) | 2900 – 3100 | 1900 | 2.3 |
| Crome–magnesite brick (52 wt% MgO, 23 wt% $Cr_2O_3$) | 3100 | 3045 | 3.5 |
| Fireclay brick (54 wt% $SiO_2$, 40 wt% $Al_2O_3$) | 2146 – 2243 | 1740 | 0.3 – 1.0 |
| Fired dolomite (55 wt% CaO, 37 wt% MgO) | 2700 | 2000 | – |
| High-alumina brick (90–99 wt% $Al_2O_3$) | 2810 – 2970 | 1760 – 2030 | 3.12 |
| Magnesite brick (95.5 wt% MgO) | 2531 – 2900 | 2150 | 3.7 – 4.4 |
| Mullite brick (71 wt% $Al_2O_3$) | 2450 | 1810 | 7.1 |
| Silica brick (95–99 wt% $SiO_2$) | 1842 | 1765 | 1.5 |
| Silicon carbide brick (80–90 wt% SiC) | 2595 | 2305 | 20.5 |
| Zircon (99 wt% $ZrSiO_4$) | 3204 | 1700 | 2.6 |
| Zirconia (stabilized) brick | 3925 | 2650 | 2.0 |

## 3.2.4 Oxide Ceramics

Oxides are the most common constituents of all ceramics, traditional and technical. An extensive account is given in [2.8]. They are used for their physical as well as refractory properties. Table 3.2-9 presents a systematic listing of their composition, structure and properties. Some of the more important oxides are dealt with in more detail further below.

**Table 3.2-9** Physical properties of oxides and oxide-based high-temperature refractories [2.4]

| IUPAC name (synonyms and common trade names) | Theoretical chemical formula, [CASRN], relative molecular mass ($^{12}C = 12.000$) | Crystal system, lattice parameters, *Strukturbericht* symbol, Pearson symbol, space group, structure type, $Z$ | Density ($\varrho$, kg m$^{-3}$) | Electrical resistivity ($\rho$, $\mu\Omega$ cm) | Melting point (°C) | Thermal conductivity ($\kappa$, W m$^{-1}$ K$^{-1}$) | Specific heat capacity ($c_p$, J kg$^{-1}$ K$^{-1}$) | Coefficient linear thermal expansion ($\alpha$, $10^{-6}$K$^{-1}$) | |
|---|---|---|---|---|---|---|---|---|---|
| Aluminium sesquioxide (alumina, corundum, sapphire) | $\alpha$-$Al_2O_3$ [1344-28-1] [1302-74-5] 101.961 | Trigonal (rhombohedral) $a = 475.91$ pm $c = 1298.4$ pm D5$_1$, $hR10$, $R\bar{3}c$, corundum type ($Z = 2$) | 3987 | $2 \times 10^{23}$ | 2054 | 35.6–39 | 795.5 – 880 | 7.1 – 8.3 | |
| Beryllium monoxide (beryllia) | BeO [1304-56-9] 25.011 | Trigonal (hexagonal) $a = 270$ pm $c = 439$ pm B4, $hP4$, $P6_3mc$, wurtzite type ($Z = 2$) | 3008 – 3030 | $10^{22}$ | 2550 – 2565 | 245 – 250 | 996.5 | 7.5–9.7 | |
| Calcium monoxide (calcia, lime) | CaO [1305-78-8] 56.077 | Cubic $a = 481.08$ pm B2, $cP2$, $Pm3m$, CsCl type ($Z = 1$) | 3320 | $10^{14}$ | 2927 | 8 – 16 | 753.1 | 3.88 | |
| Cerium dioxide (ceria, cerianite) | $CeO_2$ [1306-38-3] 172.114 | Cubic $a = 541.1$ pm Cl, $cF12$, $Fm3m$, fluorite type ($Z = 4$) | 7650 | $10^{10}$ | 2340 | – | 389 | 10.6 | |
| Chromium oxide (eskolaite) | $Cr_2O_3$ [1308-38-9] 151.990 | Trigonal (rhombohedral) $a = 538$ pm $\alpha = 54°50'$ D5$_1$, $hR10$, $R\bar{3}c$, corundum type ($Z = 2$) | 5220 | $1.3 \times 10^9$ (346 °C) | 2330 | – | 921.1 | 10.9 | |
| Dysprosium oxide (dysprosia) | $Dy_2O_3$ [1308-87-8] 373.00 | Cubic D5$_3$, $c180$, $Ia\bar{3}$, $Mn_2O_3$ type ($Z = 16$) | 8300 | – | 2408 | – | – | 7.74 | |
| Europium oxide (europia) | $Eu_2O_3$ [1308-96-9] 351.928 | Cubic D5$_3$, $c180$, $Ia\bar{3}$, $Mn_2O_3$ type ($Z = 16$) | 7422 | – | 2350 | – | – | 7.02 | |
| Hafnium dioxide (hafnia) | $HfO_2$ [12055-23-1] 210.489 | Monoclinic (1790°C) $a = 511.56$ pm $b = 517.22$ pm $c = 529.48$ pm C43, $mP12$, $P2_1c$, baddeleyite type ($Z = 4$) | 9680 | $5 \times 10^{15}$ | 2900 | 1.14 | 121 | 5.85 | |
| Gadolinium oxide (gadolinia) | $Gd_2O_3$ [12064-62-9] 362.50 | Cubic D5$_3$ , $c180$, $Ia\bar{3}$, $Mn_2O_3$ type ($Z = 16$) | 7630 | – | 2420 | – | 276 | 10.44 | |
| Lanthanum dioxide (lanthana) | $La_2O_3$ [1312-81-8] 325.809 | Trigonal (hexagonal) D5$_2$, $hP5$, $P\bar{3}m1$, lanthana type ($Z = 1$) | 6510 | $10^{14}$ (550 °C) | 2315 | – | 288.89 | 11.9 | |

**Table 3.2-9** Physical properties of oxides and oxide-based high-temperature refractories [2.4], cont.

| | Young's modulus ($E$, GPa) | Flexural strength ($\tau$, MPa) | Compressive strength ($\alpha$, MPa) | Vickers hardness HV (Mohs hardness HM) | Other physicochemical properties, corrosion resistance,[a] and uses | IUPAC name (synonyms and common trade names) |
|---|---|---|---|---|---|---|
| | 365 – 393 | 282 | 2549 – 3103 | 2100 – 3000 (HM 9) | White and translucent; hard material used as abrasive for grinding. Excellent electrical insulator and also wear-resistent. Insoluble in water, insoluble in strong mineral acids, readily soluble in strong solutions of alkali metal hydroxides, attacked by HF and $NH_4HF_2$. Owing to its corrosion resistance under an inert atmosphere in molten metals such as Mg, Ca, Sr, Ba, Mn, Sn, Pb, Ga, Bi, As, Sb, Hg, Mo, W, Co, Ni, Pd, Pt, and U, it is used for crucibles for these liquid metals. Alumina is readily attacked under an inert atmosphere by molten metals such as Li, Na, Be, Al, Si, Ti, Zr, Nb, Ta, and Cu. Maximum service temperature 1950 °C. | Aluminium sesquioxide (alumina, corundum, sapphire) |
| | 296.5 – 345 | 241 – 250 | 1551 | 1500 (HM 9) | | Beryllium monoxide (beryllia) |
| | – | – | – | 560 (HM 4.5) | Forms white or grayish ceramics. It is readily absorbs $CO_2$ and water from air to form calcium carbonate and slaked lime. It reacts readily with water to give $Ca(OH)_2$. Volumetric expansion coefficient $0.225 \times 10^{-9}\ K^{-1}$. It exhibits outstanding corrosion resistance in the following liquid metals: Li and Na. | Calcium monoxide (calcia, lime) |
| | 181 | – | 589 | (HM 6) | Pale yellow cubic crystals. Abrasive for polishing glass; used in interference filters and antireflection coatings. Insoluble in water, soluble in $H_2SO_4$ and $HNO_3$, but insoluble in dilute acids. | Cerium dioxide (ceria, Cerianite) |
| | – | – | – | (HM > 8) | | Chromium oxide (eskolaite) |
| | – | – | – | – | | Dysprosium oxide (dysprosia) |
| | – | – | – | – | | Europium oxide (europia) |
| | 57 | – | – | 780 – 1050 | | Hafnium dioxide (hafnia) |
| | 124 | – | – | 480 | | Gadolinium oxide (gadolinia) |
| | – | – | – | – | Insoluble in water, soluble in dilute strong mineral acids. | Lanthanum dioxide (lanthana) |

**Table 3.2-9** Physical properties of oxides and oxide-based high-temperature refractories [2.4], cont.

| IUPAC name (synonyms and common trade names) | Theoretical chemical formula, [CASRN], relative molecular mass ($^{12}C = 12.000$) | Crystal system, lattice parameters, *Strukturbericht* symbol, Pearson symbol, space group, structure type, $Z$ | Density ($\varrho$, kg m$^{-3}$) | Electrical resistivity ($\rho$, μΩ cm) | Melting point (°C) | Thermal conductivity ($\kappa$, W m$^{-1}$ K$^{-1}$) | Specific heat capacity ($c_p$, J kg$^{-1}$ K$^{-1}$) | Coefficient of linear thermal expansion ($\alpha$, $10^{-6}$ K$^{-1}$) | |
|---|---|---|---|---|---|---|---|---|---|
| Magnesium monoxide (magnesia, periclase) | MgO [1309-48-4] 40.304 | Cubic $a = 420$ pm B1, $cF8$, $Fm\bar{3}m$, rock salt type ($Z = 4$) | 3581 | $1.3 \times 10^{15}$ | 2852 | 50 – 75 | 962.3 | 11.52 | |
| Niobium pentoxide (columbite, niobia) | $Nb_2O_5$ [1313-96-8] 265.810 | Numerous polytypes | 4470 | $5.5 \times 10^{12}$ | 1520 | – | 502.41 | – | |
| Samarium oxide (samaria) | $Sm_2O_3$ [12060-58-1] 348.72 | Cubic $D5_3$, $c180$, $Ia\bar{3}$, $Mn_2O_3$ type ($Z = 16$) | 7620 | – | 2350 | 2.07 | 331 | 10.3 | |
| Silicon dioxide (silica, α-quartz) | α-$SiO_2$ [7631-86-9] [14808-60-7] 60.085 | Trigonal (rhombohedral) $a = 491.27$ pm $c = 540.46$ pm C8, $hP9$, $R\bar{3}c$, α-quartz type ($Z = 3$) | 2202 – 2650 | $10^{20}$ | 1710 | 1.38 | 787 | 0.55 | |
| Tantalum pentoxide (tantalite, tantala) | $Ta_2O_5$ [1314-61-0] 441.893 | Trigonal (rhombohedral) columbite type | 8200 | $10^{12}$ | 1882 | – | 301.5 | – | |
| Thorium dioxide (thoria, thorianite) | $ThO_2$ [1314-20-1] 264.037 | Cubic $a = 559$ pm Cl, $cF12$, $Fm\bar{3}m$, fluorite type ($Z = 4$) | 9860 | $4 \times 10^{19}$ | 3390 | 14.19 | 272.14 | 9.54 | |
| Titanium dioxide (anatase) | $TiO_2$ [13463-67-7] [1317-70-0] 79.866 | Tetragonal $a = 378.5$ pm $c = 951.4$ pm C5, $tI12$, $I4_1amd$, anatase type ($Z = 4$) | 3900 | – | 700 °C (rutile) | – | – | – | |
| Titanium dioxide (brookite) | $TiO_2$ [13463-67-7] 79.866 | Orthorhombic $a = 916.6$ pm $b = 543.6$ pm $c = 513.5$ pm C21, $oP24$, $Pbca$, brookite type ($Z = 8$) | 4140 | – | 1750 | – | – | – | |

**Table 3.2-9** Physical properties of oxides and oxide-based high-temperature refractories [2.4], cont.

| | Young's modulus ($E$, GPa) | Flexural strength ($\tau$, MPa) | Compressive strength ($\alpha$, MPa) | Vickers hardness HV (Mohs hardness HM) | Other physicochemical properties, corrosion resistance,[a] and uses | IUPAC name (synonyms and common trade names) |
|---|---|---|---|---|---|---|
| | 303.4 | 441 | 1300 – 1379 | 750 (HM 5.5 – 6) | Forms ceramics with a high reflection coefficient in the visible and near-UV region. Used in linings for steelmaking furnaces and in crucibles for fluoride melts. Very slowly soluble in pure water; but soluble in dilute strong mineral acids. It exhibits outstanding corrosion resistance in the following liquid metals: Mg, Li, and Na. It is readily attacked by molten metals such as Be, Si, Ti, Zr, Nb, and Ta. MgO reacts with water, $CO_2$, and dilute acids. Maximum service temperature 2400 °C. Transmittance of 80 % and refractive index of 1.75 in the IR region from 7 to 300 μm. | Magnesium monoxide (magnesia, periclase) |
| | – | – | – | 1500 | Dielectric used in film supercapacitors. Insoluble in water; soluble in HF and in hot concentrated $H_2SO_4$. | Niobium pentoxide (columbite, niobia) |
| | 183 | – | – | 438 | | Samarium oxide (samaria) |
| | 72.95 | 310 | 680 – 1380 | 550 – 1000 (HM 7) | Colorless amorphous (fused silica) or crystalline (quartz) material having a low thermal expansion coefficient and excellent optical transmittance in the far UV. Silica is insoluble in strong mineral acids and alkalis except HF, concentrated $H_3PO_4$, $NH_4HF_2$ and concentrated alkali metal hydroxides. Owing to its good corrosion resistance to liquid metals such as Si, Ge, Sn, Pb, Ga, In, TI, Rb, Bi, and Cd, it is used in crucibles for melting these metals. Silica is readily attacked under an inert atmosphere by molten metals such as Li, Na, K, Mg, and Al. Quartz crystals are piezoelectric and pyroelectric. Maximum service temperature 1090 °C. | Silicon dioxide (silica, α-quartz) |
| | – | – | – | – | Dielectric used in film supercapacitors. Tantalum oxide is a high-refractive index, low-absorption material usable for making optical coatings from the near-UV (350 nm) to the IR (8 μm). Insoluble in most chemicals except HF, HF–$HNO_3$ mixtures, oleum, fused alkali metal hydroxides (e.g. NaOH and KOH) and molten pyrosulfates. | Tantalum pentoxide (tantalite, tantala) |
| | 144.8 | – | 1475 | 945 (HM 6.5) | Corrosion-resistant container material for the following molten metals: Na, Hf, Ir, Ni, Mo, Mn, Th, U. Corroded by the following liquid metals: Be, Si, Ti, Zr, Nb, Bi. Radioactive. | Thorium dioxide (thoria, thorianite) |
| | – | – | – | (HM 5.5–6) | | Titanium dioxide (anatase) |
| | – | – | – | (HM 5.5–6) | | Titanium dioxide (brookite) |

**Table 3.2–9** Physical properties of oxides and oxide-based high-temperature refractories [2.4], cont.

| IUPAC name (synonyms and common trade names) | Theoretical chemical formula, [CASRN], relative molecular mass ($^{12}C = 12.000$) | Crystal system, lattice parameters, Strukturbericht, symbol, Pearson symbol, space group, structure type, $Z$ | Density ($\varrho$, kg m$^{-3}$) | Electrical resistivity ($\rho$, $\mu\Omega$ cm) | Melting point (°C) | Thermal conductivity ($\kappa$, W m$^{-1}$ K$^{-1}$) | Specific heat capacity ($c_p$, J kg$^{-1}$ K$^{-1}$) | Coefficient of linear thermal expansion ($\alpha$, $10^{-6}$K$^{-1}$) | |
|---|---|---|---|---|---|---|---|---|---|
| Titanium dioxide (rutile, titania) | $TiO_2$ [13463-67-7] [1317-80-2] 79.866 | Tetragonal $a = 459.37$ pm $c = 296.18$ pm C4, $tP6$, $P4/mnm$, rutile type ($Z = 2$) | 4240 | $10^{19}$ | 1855 | 10.4 (∥ c) 7.4 (⊥ c) | 711 | 7.14 | |
| Uranium dioxide (uraninite) | $UO_2$ [1344-57-6] 270.028 | Cubic $a = 546.82$ pm Cl, $cF12$, $Fm3m$, fluorite type ($Z = 4$) | 10 960 | $3.8 \times 10^{10}$ | 2880 | 10.04 | 234.31 | 11.2 | |
| Yttrium oxide (yttria) | $Y_2O_3$ [1314-36-9] 225.81 | Trigonal (hexagonal) $D5_2$, $hP5$, $P\bar{3}m1$, lanthana type ($Z = 1$) | 5030 | – | 2439 | – | 439.62 | 8.10 | |
| Zirconium dioxide (baddeleyite) | $ZrO_2$ [1314-23-4] [12036-23-6] 123.223 | Monoclinic $a = 514.54$ pm $b = 520.75$ pm $c = 531.07$ pm $\alpha = 99.23°$ C43, $mP12$, $P2_1c$, baddeleyite type ($Z = 4$) | 5850 | – | 2710 | – | 711 | 7.56 | |
| Zirconium dioxide PSZ (stabilized with MgO) (zirconia > 2300 °C) | $ZrO_2$ [1314-23-4] [64417-98-7] 123.223 | Cubic Cl, $cF12$, $Fm3m$, fluorite type ($Z = 4$) | 5800 – 6045 | – | 2710 | 1.8 | 400 | 10.1 | |
| Zirconium dioxide TTZ (stabilized with $Y_2O_3$) (zirconia > 2300 °C) | $ZrO_2$ [1314-23-4] [64417-98-7] 123.223 | Cubic Cl, $cF12$, $Fm3m$, fluorite type ($Z = 4$) | 6045 | – | 2710 | – | – | – | |
| Zirconium dioxide TZP (zirconia > 1170 °C) | $ZrO_2$ [1314-23-4] 123.223 | Tetragonal C4, $tP6$, $P4_2/mnm$, rutile type ($Z = 2$) | 5680 – 6050 | $7.7 \times 10^7$ | 2710 | – | – | 10 – 11 | |
| Zirconium dioxide (stabilized with 10–15% $Y_2O_3$) (zirconia > 2300 °C) | $ZrO_2$ [1314-23-4] [64417-98-7] 123.223 | Cubic Cl, $cF12$, $Fm3m$, fluorite type ($Z = 4$) | 6045 | – | 2710 | – | – | – | |

[a] Corrosion data in molten salts from [2.9].

**Table 3.2-9** Physical properties of oxides and oxide-based high-temperature refractories [2.4], cont.

| | Young's modulus ($E$, GPa) | Flexural strength ($\tau$, MPa) | Compressive strength ($\alpha$, MPa) | Vickers hardness HV (Mohs hardness HM) | Other physicochemical properties, corrosion resistance,[a] and uses | IUPAC name (synonyms and common trade names) |
|---|---|---|---|---|---|---|
| | 248 – 282 | 340 | 800 – 940 | (HM 7 – 7.5) | White, translucent, hard ceramic material. Readily soluble in HF and in concentrated $H_2SO_4$, and reacts rapidly with molten alkali hydroxides and fused alkali carbonates. Owing to its good corrosion resistance to liquid metals such as Ni and Mo, it is used in crucibles for melting these metals. Titania is readily attacked under an inert atmosphere by molten metals such as Be, Si, Ti, Zr, Nb, and Ta. | Titanium dioxide (rutile, titania) |
| | 145 | – | – | 600 (HM 6 – 7) | Used in nuclear power reactors in sintered nuclear-fuel elements containing either natural or enriched uranium. | Uranium dioxide (uraninite) |
| | 114.5 | – | 393 | 700 | Yttria is a medium-refractive-index, low-absorption material usable for optical coating, in the near-UV (300 nm) to the IR (12 μm) regions. Hence used to protect Al and Ag mirrors. Used for crucibles containing molten lithium. | Yttrium oxide (yttria) |
| | 241 | – | 2068 | (HM 6.5) 1200 | Zirconia is highly corrosion-resistant to molten metals such as Bi, Hf, Ir, Pt, Fe, Ni, Mo, Pu, and V, while is strongly attacked by the following liquid metals: Be, Li, Na, K, Si, Ti, Zr, and Nb. Insoluble in water, but slowly soluble in HCl and $HNO_3$; soluble in boiling concentrated $H_2SO_4$ and alkali hydroxides and readily attacked by HF. Monoclinic (baddeleyite) below 1100 °C, tetragonal between 1100 and 2300 °C, cubic (fluorite type) above 2300 °C. Maximum service temperature 2400 °C. | Zirconium dioxide (baddeleyite) |
| | 200 | 690 | 1850 | 1600 | | Zirconium dioxide PSZ (stabilized with MgO) (zirconia > 2300 °C) |
| | – | – | – | – | | Zirconium dioxide TTZ (stabilized with $Y_2O_3$) (zirconia > 2300 °C) |
| | 200 – 210 | > 800 | > 2900 | – | | Zirconium dioxide TZP (zirconia > 1170 °C) |
| | – | – | – | – | | Zirconium dioxide (stabilized 10 – 15% $Y_2O_3$) (zirconia > 2300 °C) |

### 3.2.4.1 Magnesium Oxide

Table 3.2-10 lists the properties of the magnesium oxide rich raw material used in the production of oxide ceramics. MgO occurs rarely, as the mineral periclase, but is abundant as magnesite ($MgCO_3$) and dolomite ($(Mg,Ca)CO_3$).

Magnesium oxide is mainly processed into a high-purity single-phase ceramic material, in either porous or gas-tight form. Some properties of porous MgO are listed in Table 3.2-11. The properties of MgO ceramics that are of particular benefit in applications are their high electrical insulation capability and their high thermal conductivity. Typical examples of their application are for insulation in sheathed thermocouples and in resistive heating elements.

**Table 3.2-10** Physical properties of MgO-rich raw materials used in the production of refractory ceramics [2.3]

| Composition (wt%) | Sintered MgO clinker | Sintered doloma clinker | Fused MgO |
|---|---|---|---|
| MgO | 96 – 99 | 39 – 40 | 97 – 98 |
| $Al_2O_3$ | 0.05 – 0.25 | 0.3 – 0.8 | 0.1 – 0.2 |
| $Fe_2O_3$ | 0.05 – 0.2 | 0.6 – 1.0 | 0.1 – 0.5 |
| CaO | 0.6 – 2.4 | 57.5 – 58.5 | 0.9 – 2.5 |
| $SiO_2$ | 0.1 – 0.5 | 0.6 – 1.1 | 0.3 – 0.9 |
| $B_2O_3$ | 0.005 – 0.6 | | 0.004 – 0.01 |
| Bulk density ($g/cm^3$) | 3.4 – 3.45 | 3.15 – 3.25 | 3.5 |
| Grain porosity (vol.%) | 2 – 3 | 5.5 – 7 | 0.5 – 2 |

**Table 3.2-11** Properties of MgO according to DIN EN 60672 [2.6]

| | | | Designation C 820 |
|---|---|---|---|
| **Mechanical properties** | **Symbol** | **Units** | **Porous** |
| Open porosity | | vol. % | 30 |
| Density, minimum | $\varrho$ | $Mg/m^3$ | 2.5 |
| Bending strength | $\sigma_B$ | MPa | 50 |
| Young's modulus | $E$ | GPa | 90 |
| **Electrical properties** | | | |
| Permittivity at 48 – 62 Hz | $\varepsilon_r$ | | 10 |
| **Thermal properties** | | | |
| Average coefficient of thermal expansion at 30 – 600 °C | $\alpha_{30-600}$ | $10^{-6}\,K^{-1}$ | 11 – 13 |
| Specific heat capacity at 30 – 100 °C | $c_{p,30-600}$ | $J\,kg^{-1}\,K^{-1}$ | 850 – 1050 |
| Thermal conductivity | $\lambda_{30-100}$ | $W\,m^{-1}\,K^{-1}$ | 6 – 10 |
| Thermal fatigue resistance | | (Rated) | Good |

### 3.2.4.2 Alumina

The properties of commercial grades of alumina (corundum) are closely related to the microstructure. Pure $\alpha$-$Al_2O_3$ is denser, harder, stiffer, and more refractory than most silicate ceramics so that increasing the proportion of the second phase in an alumina ceramic tends to decrease the density, Young's modulus, strength, hardness, and refractoriness. Sintered alumina is produced from high-purity powders, which densify to give single-phase ceramics with a uniform grain size. Table 3.2-12 gives typical examples of properties of high-density alumina, and Table 3.2-13 lists further properties of various alumina ceramics.

Alumina is widely applied both as an electronic ceramic material and in cases where its nonelectronic properties, such as fracture toughness, wear and high-temperature resistance, are required. Some typical applications are in insulators in electrotechnical equipment; substrates for electronic components; wear-resistant machine parts; refractory materials in the chemical industry, where resistance against vapors, melts, and slags is important; insulating materials in sheathed thermocouples and heating elements; medical implants; and high-temperature parts such as burner nozzles.

**Table 3.2-12** Typical properties of high-density alumina [2.3]

| | $Al_2O_3$ content (wt%) | | | |
|---|---|---|---|---|
| | > 99.9 | > 99.7[a] | > 99.7[b] | 99 – 99.7 |
| Density ($g/cm^3$) | 3.97 – 3.99 | 3.6 – 3.85 | 3.65 – 3.85 | 3.89 – 3.96 |
| Hardness (GPa), HV 500 g | 19.3 | 16.3 | 15 – 16 | 15 – 16 |
| Fracture toughness $K_{IC}$ at room temperature ($MPa\,m^{1/2}$) | 2.8 – 4.5 | – | – | 5.6 – 6 |
| Young's modulus (GPa) | 366 – 410 | 300 – 380 | 300 – 380 | 330 – 400 |
| Bending strength (MPa) at room temperature | 550 – 600 | 160 – 300 | 245 – 412 | 550 |
| Thermal expansion coefficient ($10^{-6}$/K) at 200 – 1200 °C | 6.5 – 8.9 | 5.4 – 8.4 | 5.4 – 8.4 | 6.4 – 8.2 |
| Thermal conductivity at room temperature (W/m K) | 38.9 | 28 – 30 | 30 | 30.4 |
| Firing temperature range (°C) | 1600 – 2000 | 1750 – 1900 | 1750 – 1900 | 1700 – 1750 |

[a] "Recrystallized" without MgO.
[b] With MgO.

**Table 3.2-13** Properties of $Al_2O_3$ according to DIN EN 60672 [2.6]

| | | | Designation | | | | | | | |
|---|---|---|---|---|---|---|---|---|---|---|
| | | | C 780 | C 786 | C 795 | C 799 | $Al_2O_3$ | $Al_2O_3$ | $Al_2O_3$ | $Al_2O_3$ |
| **Mechanical properties** | **Symbol** | **Units** | **Alumina 80–86%** | **Alumina 86–95%** | **Alumina 95–99%** | **Alumina >99%** | **Alumina <90%** | **Alumina 92–96%** | **Alumina 99%** | **Alumina >99%** |
| Open porosity | | vol. % | 0.0 | 0.0 | 0.0 | 0.0 | 0 | 0 | 0 | 0 |
| Density, min. | $\varrho$ | $Mg/m^3$ | 3.2 | 3.4 | 3.5 | 3.7 | > 3.2 | 3.4 – 3.8 | 3.5 – 3.9 | 3.75 – 3.98 |
| Bending strength | $\sigma_B$ | MPa | 200 | 250 | 280 | 300 | > 200 | 230 – 400 | 280 – 400 | 300 – 580 |
| Young's modulus | $E$ | GPa | 200 | 220 | 280 | 300 | > 200 | 220 – 340 | 220 – 350 | 300 – 380 |
| Vickers hardness | HV | 100 | – | – | – | – | 12 – 15 | 12 – 15 | 12 – 20 | 17 – 23 |
| Fracture toughness | $K_{IC}$ | MPa $\sqrt{m}$ | – | – | – | – | 3.5 – 4.5 | 4 – 4.2 | 4 – 4.2 | 4 – 5.5 |

**Table 3.2–13** Properties of $Al_2O_3$ according to DIN EN 60672 [2.6], cont.

| | | | Designation | | | | | | | |
|---|---|---|---|---|---|---|---|---|---|---|
| | | | C 780 | C 786 | C 795 | C 799 | $Al_2O_3$ | $Al_2O_3$ | $Al_2O_3$ | $Al_2O_3$ |
| **Thermal properties Electrical properties** | **Symbol** | **Units** | **Alumina 80–86%** | **Alumina 86–95%** | **Alumina 95–99%** | **Alumina >99%** | **Alumina <90%** | **Alumina 92–96%** | **Alumina 99%** | **Alumina >99%** |
| Breakdown strength | $E_d$ | kV/mm | 10 | 15 | 15 | 17 | 10 | 15 – 25 | 15 | 17 |
| Withstand voltage | $U$ | kV | 15 | 18 | 18 | 20 | 15 | 18 | 18 | 20 |
| Permittivity at 48 – 62 Hz | $\varepsilon_r$ | – | 8 | 9 | 9 | 9 | 9 | 9 – 10 | 9 | 9 |
| Loss factor at 20 °C, 1 kHz | $\tan \delta_{pf}$ | $10^{-3}$ | 1.0 | 0.5 | 0.5 | 0.2 | 0.5 – 1.0 | 0.3 – 0.5 | 0.2 – 0.5 | 0.2 – 0.5 |
| Loss factor at 20 °C, 1 MHz | $\tan \delta_{1M}$ | $10^{-3}$ | 1.5 | 1 | 1 | 1 | 1 | 1 | 1 | 1 |
| Resistivity at 20 °C | $\rho_{20}$ | Ω m | $10^{12}$ | $10^{12}$ | $10^{12}$ | $10^{12}$ | $10^{12} – 10^{13}$ | $10^{12} – 10^{14}$ | $10^{12} – 10^{15}$ | $10^{12} – 10^{15}$ |
| Resistivity at 600 °C | $\rho_{600}$ | Ω m | $10^5$ | $10^6$ | $10^6$ | $10^6$ | $10^6$ | $10^6$ | $10^6$ | $10^6$ |
| Ave. coeff. of thermal expansion at 30 – 600 °C | $\alpha_{30-600}$ | $10^{-6}K^{-1}$ | 6 – 8 | 6 – 8 | 6 – 8 | 7 – 8 | 6 – 8 | 6 – 8 | 6 – 8 | 7 – 8 |
| Specific heat at 30 – 100 °C | $c_{p,30-600}$ | $J\,kg^{-1}K^{-1}$ | 850 – 1050 | 850 – 1050 | 850 – 1050 | 850 – 1050 | 850 – 1050 | 850 – 1050 | 850 – 1050 | 850 – 1050 |
| Thermal conductivity | $\lambda_{30-100}$ | $W\,m^{-1}K^{-1}$ | 10 – 16 | 14 – 24 | 16 – 28 | 19 – 30 | 10 – 16 | 14 – 25 | 16 – 28 | 19 – 30 |
| Thermal fatigue resistance | | (Rated) | Good | Good | Good | Good | Good | Good | Good | Good |
| Typ. max. application temperature | $T$ | °C | – | – | – | – | 1400 – 1500 | 1400 – 1500 | 1400 – 1500 | 1400 – 1700 |

### 3.2.4.3 Al–O–N Ceramics

A class of variants of the ceramics related to alumina is based on the ternary Al–O–N system, which forms 13 different compounds, some of which are polytypes of aluminium nitride based on the wurtzite structure. Table 3.2-14 lists some typical properties compiled from various publications. Al–O–N ceramics have optical and dielectric properties which make them suitable, for use, for example, in windows for elctromagnetic radiation.

**Table 3.2-14** Selected properties of Al−O−N ceramics [2.3]

| Property | Value |
|---|---|
| Refractive index at $\lambda = 0.55\,\mu m$ | 1.77 – 1.88 |
| IR cutoff | 5.12 μm |
| UV cutoff | 0.27 μm |
| Dielectric constant at 20 °C, 100 Hz | 8.5 |
| Dielectric constant at 500 °C, 100 Hz | 14.0 |
| Loss tangent at 20 °C, 100 Hz | 0.002 |
| Loss tangent at 500 °C, 100 Hz | 1.0 |
| Thermal conductivity at 20 °C | 10.89 $W\,m^{-1}\,K^{-1}$ |
| Thermal expansion coefficient at 25 – 1000 °C | $7.6 \times 10^6\,K^{-1}$ |
| Flexural strength at 20 °C | 306 MPa |
| Flexural strength at 1000 °C | 267 MPa |
| Fracture toughness | 2.0–2.9 $MPa\,m^{1/2}$ |

### 3.2.4.4 Beryllium Oxide

Beryllium oxide (BeO, beryllia) is the only material apart from diamond which combines high thermal-shock resistance, high electrical resistivity, and high thermal conductivity at a similar level. Hence its major application is in heat sinks for electronic components. BeO is highly soluble in water, but dissolves slowly in concentrated acids and alkalis. It is highly toxic. It is highly corrosion-resistant in several liquid metals, such as Li, Na, Al, Ga, Pb, Ni, and Ir. Its maximum service temperature is 2400 °C. Some properties are listed in Table 3.2-15.

**Table 3.2-15** Properties of BeO according to DIN EN 60672 [2.6]

| | | | Designation C 810 |
|---|---|---|---|
| **Mechanical properties** | **Symbol** | **Units** | **Beryllium oxide, dense** |
| Open porosity | | vol. % | 0.0 |
| Density, minimum | $\varrho$ | $Mg/m^3$ | 2.8 |
| Bending strength | $\sigma_B$ | MPa | 150 |
| Young's modulus | $E$ | GPa | 300 |

**Table 3.2-15** Properties of BeO according to DIN EN 60672 [2.6], cont.

| | | | Designation C 810 |
|---|---|---|---|
| **Electrical properties** | **Symbol** | **Units** | **Beryllium oxide, dense** |
| Breakdown strength | $E_d$ | kV/mm | 13 |
| Withstand voltage | $U$ | kV | 20 |
| Permittivity at 48–62 Hz | $\varepsilon_r$ | | 7 |
| Loss factor at 20 °C, 1 kHz | $\tan \delta_{pf}$ | $10^{-3}$ | 1 |
| Loss factor at 20 °C, 1 MHz | $\tan \delta_{1M}$ | $10^{-3}$ | 1 |
| Resistivity at 20 °C | $\rho_{20}$ | Ω m | $10^{12}$ |
| Resistivity at 600 °C | $\rho_{600}$ | Ω m | $10^{7}$ |
| **Thermal properties** | | | |
| Average coefficient of thermal expansion at 30–600 °C | $\alpha_{30-600}$ | $10^{-6}$ K$^{-1}$ | 7–8.5 |
| Specific heat capacity at 30–100 °C | $c_{p,30-100}$ | J kg$^{-1}$K$^{-1}$ | 1000–1250 |
| Thermal conductivity | $\lambda_{30-100}$ | W m$^{-1}$K$^{-1}$ | 150–220 |
| Thermal fatigue resistance | | (Rated) | Good |

### 3.2.4.5 Zirconium Dioxide

Zirconium dioxide ($ZrO_2$), commonly called zirconium oxide, forms three phases, with a monoclinic, a tetragonal, and a cubic crystal structure. Dense parts may be obtained by sintering of the cubic or tetragonal phase only. In order to stabilize the cubic phase, "stabilizers" such as MgO, CaO, $Y_2O_3$, and $CeO_2$ are added.

An important class of zirconium dioxide ceramics is known as partially stabilized zirconia (PSZ), and Table 3.2-16 gives typical property data for several different grades. Further properties of PSZ are listed in Table 3.2-17. It should be noted that, as with most ceramic materials, the $K_{1C}$ data depend on the test method applied, and all the other mechanical properties are strongly affected by the microstructure (grain size, stabilizer content, etc.) and further variables such as temperature and atmospheric conditions.

**Table 3.2-16** Physical properties reported for commercial grades of partially stabilized zirconia (PSZ) [2.3]

| | Mg-PSZ | Ca-PSZ | Y-PSZ | Ca/Mg-PSZ |
|---|---|---|---|---|
| wt% stabilizer | 2.5–3.5 | 3–4.5 | 5–12.5 | 3 |
| Hardness (GPa) | 14.4[a] | 17.1[b] | 13.6[c] | 15 |
| Fracture toughness $K_{IC}$ at room temperature (MPa m$^{1/2}$) | 7–15 | 6–9 | 6 | 4.6 |
| Young's modulus (GPa) | 200[a] | 200–217 | 210–238 | – |
| Bending strength (MPa) at room temperature | 430–720 | 400–690 | 650–1400 | 350 |
| Thermal expansion coefficient ($10^{-6}$ /K) at 1000 °C | 9.2[a] | 9.2[b] | 10.2[c] | – |
| Thermal conductivity at room temperature (W m$^{-1}$K$^{-1}$) | 1–2 | 1–2 | 1–2 | 1–2 |

[a] 2.8% MgO.
[b] 4% CaO.
[c] 5% $Y_2O_3$.

**Table 3.2-17** Properties of PSZ according to DIN EN 60672 [2.6]

| | | | **Designation** PSZ |
|---|---|---|---|
| **Mechanical properties** | **Symbol** | **Units** | **Partially stabilized $ZrO_2$** |
| Open porosity | | vol. % | 0 |
| Density, minimum | $\varrho$ | $Mg/m^3$ | 5 – 6 |
| Bending strength | $\sigma_B$ | MPa | 500 – 1000 |
| Young's modulus | $E$ | GPa | 200 – 210 |
| Vickers hardness | HV | 100 | 11 – 12.5 |
| Fracture toughness | $K_{IC}$ | MPa $\sqrt{m}$ | 5.8 – 10.5 |
| **Electrical properties** | | | |
| Permittivity at 48 – 62 Hz | $\varepsilon_r$ | | 22 |
| Resistivity at 20 °C | $\rho_{20}$ | Ω m | $10^8 – 10^{13}$ |
| Resistivity at 600 °C | $\rho_{600}$ | Ω m | $10^3 – 10^6$ |
| **Thermal properties** | **Symbol** | **Units** | **Partially stabilized $ZrO_2$** |
| Average coefficient of thermal expansion at 30 – 600 °C | $\alpha_{30-1000}$ | $10^{-6}\,K^{-1}$ | 10 – 12.5 |
| Specific heat capacity at 30 – 100 °C | $c_{p,30-1000}$ | $J\,kg^{-1}K^{-1}$ | 400 – 550 |
| Thermal conductivity | $\lambda_{30-100}$ | $W\,m^{-1}K^{-1}$ | 1.5 – 3 |
| Thermal fatigue resistance | | (Rated) | Good |
| Typical maximum application temperature | $T$ | °C | 900 – 1600 |

### 3.2.4.6 Titanium Dioxide, Titanates, etc.

Titanium dioxide ($TiO_2$) is widely used in powder form as a pigment and filler material and in optical and catalytic applications. Technical ceramics made from titanium dioxide or titanates have the characteristic feature that their permittivity and its temperature coefficient can be adjusted over a wide range. Furthermore, they have a low loss factor. Some properties are listed in Table 3.2-18.

**Table 3.2-18** Properties of titanium dioxide, titanates etc. according to DIN EN 60672 [2.6]

| | | | Designation | | | | | |
|---|---|---|---|---|---|---|---|---|
| | | | C 310 | C 320 | C 330 | C 331 | C 340 | C 350 |
| **Mechanical properties** | **Symbol** | **Units** | **Titanium dioxide chief constituent** | **Magnesium titanate** | **Titanium dioxide with other oxides** | **Titanium dioxide with other oxides** | **Bismuth titanate, basic** | **Perovskites, middle $\varepsilon_r$** |
| Open porosity | | vol. % | 0.0 | 0.0 | 0.0 | 0.0 | 0.0 | 0.0 |
| Density, minimum | $\varrho$ | $Mg/m^3$ | 3.5 | 3.1 | 4.0 | 4.5 | 3.0 | 4.0 |
| Bending strength | $\sigma_B$ | MPa | 70 | 70 | 80 | 80 | 70 | 50 |
| Breakdown strength | $E_d$ | kV/mm | 8 | 8 | 10 | 10 | 6 | 2 |
| Withstand voltage | $U$ | kV | 15 | 15 | 15 | 15 | 8 | 2 |
| Permittivity at 48–62 Hz | $\varepsilon_r$ | | 40–100 | 12–40 | 25–50 | 30–70 | 100–700 | 350–3000 |
| Loss factor at 20 °C, 1 kHz | $\tan\delta_{1k}$ | $10^{-3}$ | 6.5 | 2 | 20.0 | 7 | – | – |
| Loss factor at 20 °C, 1 MHz | $\tan\delta_{1M}$ | $10^{-3}$ | 2 | 1.5 | 0.8 | 1 | 5 | 35.0 |
| Resistivity at 20 °C | $\rho_{20}$ | Ω m | $10^{10}$ | $10^9$ | $10^9$ | $10^9$ | $10^9$ | $10^8$ |
| **Thermal properties** | | | | | | | | |
| Average coefficient of thermal expansion at 30–600 °C | $\alpha_{30-600}$ | $10^{-6}\,K^{-1}$ | 6–8 | 6–10 | – | – | – | – |
| Specific heat capacity at 30–100 °C | $c_{p,30-100}$ | $J\,kg^{-1}K^{-1}$ | 700–800 | 900–1000 | – | – | – | – |
| Thermal conductivity | $\lambda_{30-100}$ | $W\,m^{-1}K^{-1}$ | 3–4 | 3.5–4 | – | – | – | – |

## 3.2.5 Non-Oxide Ceramics

The non-oxide ceramics comprise essentially borides, carbides, nitrides, and silicides. Like oxide ceramics they have two kinds of uses, which frequently overlap: application of their physical properties and of their refractory high-temperature properties. Extensive accounts can be found in [2.1–3, 8, 10].

### 3.2.5.1 Non-Oxide High-Temperature Ceramics

The two dominating design variables to be considered for high-temperature materials are hardness and thermal conductivity as a function of temperature. Figure 3.2-2 gives a survey. It is obvious that borides and carbides are superior to most oxide ceramics. Depending upon the microstructure, SiC has a higher hardness than that of $\beta$-$Si_3N_4$, but it decreases somewhat more rapidly, with increasing temperature. Both $Si_3N_4$ and SiC ceramics possess a high thermal conductivity and thus excellent thermal-shock resistance.

### 3.2.5.2 Borides

Borides and boride-based high-temperature refractories are treated extensively in [2.2, 3, 10]. Some properties are listed in Table 3.2-19.

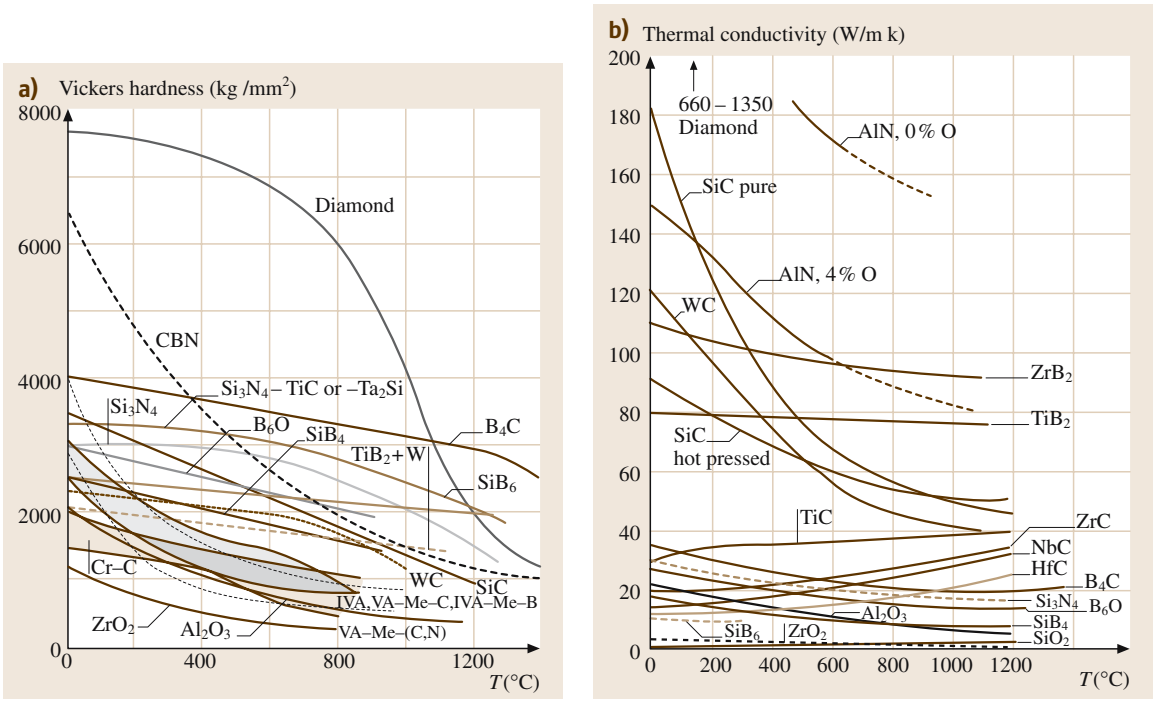


**Fig. 3.2-2a,b** Temperature dependence of (a) the hardness and (b) the thermal conductivity of ceramic materials in comparison with diamond and cubic boron nitride (CBN) [2.3]

**Table 3.2-19** Physical properties of borides and boride-based high-temperature refractories [2.4]

| IUPAC name | Theoretical chemical formula, [CASRN], relative molecular mass ($^{12}C = 12.000$) | Crystal system, lattice parameters, *Strukturbericht* symbol, Pearson symbol, space group, structure type, $Z$ | Density ($\varrho$, kg m$^{-3}$) | Electrical resistivity ($\rho$, $\mu\Omega$ cm) | Melting point (°C) | Thermal conductivity ($\kappa$, W m$^{-1}$ K$^{-1}$) | Specific heat capacity ($c_p$, J kg$^{-1}$ K$^{-1}$) | Coefficient of linear thermal expansion ($\alpha$, $10^{-6}$K$^{-1}$) | |
|---|---|---|---|---|---|---|---|---|---|
| Aluminium diboride | $AlB_2$ [12041-50-8] 48.604 | Hexagonal $a = 300.50$ pm $c = 325.30$ pm C32, $hP3$, $P/6mmm$, $AlB_2$ type ($Z = 1$) | 3190 | – | 1654 | – | 897.87 | – | |
| Aluminium dodecaboride | $AlB_{12}$ [12041-54-2] 156.714 | Tetragonal $a = 1016$ pm $c = 1428$ pm | 2580 | – | 2421 | – | 954.48 | – | |
| Beryllium boride | $Be_4B$ [12536-52-6] 46.589 | – | – | – | 1160 | – | – | – | |
| Beryllium diboride | $BeB_2$ [12228-40-9] 30.634 | Hexagonal $a = 979$ pm $c = 955$ pm | 2420 | 10 000 | 1970 | – | – | – | |
| Beryllium hemiboride | $Be_2B$ [12536-51-5] | Cubic $a = 467.00$ pm Cl, $cF12$, $Fm3m$, $CaF_2$ type ($Z = 4$) | 1890 | 1000 | 1520 | – | – | – | |
| Beryllium hexaboride | $BeB_6$ [12429-94-6] | Tetragonal $a = 1016$ pm $c = 1428$ pm | 2330 | $10^{13}$ | 2070 | – | – | – | |
| Beryllium monoboride | BeB [12228-40-9] | – | – | – | 1970 | – | – | – | |
| Boron | $\beta$-B [7440-42-8] 10.811 | Trigonal (rhombohedral) $a = 1017$ pm $\alpha = 65° 12'$ $hR105$, $R3m$, $\beta$-B type | 2460 | 18 000 | 2190 | – | – | – | |
| Chromium boride | $Cr_5B_3$ [12007-38-4] 292.414 | Orthorhombic $a = 302.6$ pm $b = 1811.5$ pm $c = 295.4$ pm $D8_1$, $ti32$, $I4/mcm$, $Cr_5B_3$ type ($Z = 4$) | 6100 | – | 1900 | 15.8 | – | 13.7 | |
| Chromium diboride | $CrB_2$ [12007-16-8] 73.618 | Hexagonal $a = 292.9$ pm $c = 306.6$ pm C32, $hP3$, $P6/mmm$, $AlB_2$ type ($Z = 1$) | 5160 – 5200 | 21 | 1850 – 2100 | 20 – 32 | 712 | 6.2 – 7.5 | |
| Chromium monoboride | CrB [12006-79-0] 62.807 | Tetragonal $a = 294.00$ pm $c = 1572.00$ pm $B_f$, $oC8$, $Cmcm$, CrB type ($Z = 4$) | 6200 | 64.0 | 2000 | 20.1 | – | 12.3 | |

**Table 3.2-19** Physical properties of borides and boride-based high-temperature refractories [2.4], cont.

| | Young's modulus ($E$, GPa) | Flexural strength ($\tau$, MPa) | Compressive strength ($\alpha$, MPa) | Vickers hardness HV (Mohs hardness HM) | Other physicochemical properties, corrosion resistance,[a] and uses | IUPAC name |
|---|---|---|---|---|---|---|
| | – | – | – | 2500 | Phase transition to $AlB_{12}$ at 920 °C. Soluble in dilute HCl. Nuclear shielding material. | Aluminium diboride |
| | – | – | – | – | Soluble in hot $HNO_3$, insoluble in other acids and alkalis. Neutron-shielding material. | Aluminium dodecaboride |
| | – | – | – | – | | Beryllium boride |
| | – | – | – | – | | Beryllium diboride |
| | – | – | – | 870 | | Beryllium hemiboride |
| | – | – | – | – | | Beryllium hexaboride |
| | – | – | – | – | | Beryllium monoboride |
| | 320 | – | – | 2055 (11) | Brown or dark powder, unreactive to oxygen, water, acids and alkalis. $\Delta H_{vap} = 480\,kJ\,mol^{-1}$. | Boron |
| | – | – | – | – | | Chromium boride |
| | 211 | 607 | 1300 | 1800 | Strongly corroded by molten metals such as Mg, Al, Na, Si, V, Cr, Mn, Fe, and Ni. It is corrosion-resistant to the following liquid metals: Cu, Zn, Sn, Rb, and Bi. | Chromium diboride |
| | – | – | – | – | | Chromium monoboride |

**Table 3.2–19** Physical properties of borides and boride-based high-temperature refractories [2.4], cont.

| IUPAC name | Theoretical chemical formula, [CASRN], relative molecular mass ($^{12}C = 12.000$) | Crystal system, lattice parameters, *Strukturbericht* symbol, Pearson symbol, space group, structure type, $Z$ | Density ($\varrho$, kg m$^{-3}$) | Electrical resistivity ($\rho$, $\mu\Omega$ cm) | Melting point (°C) | Thermal conductivity ($\kappa$, W m$^{-1}$ K$^{-1}$) | Specific heat capacity ($c_p$, J kg$^{-1}$ K$^{-1}$) | Coefficient of linear thermal expansion ($\alpha$, $10^{-6}$K$^{-1}$) | |
|---|---|---|---|---|---|---|---|---|---|
| Hafnium diboride | $HfB_2$ [12007-23-7] 200.112 | Hexagonal $a = 314.20$ pm $c = 347.60$ pm C32, $hP3$, $P6/mmm$, $AlB_2$ type ($Z = 1$) | 11 190 | 8.8 – 11 | 3250 – 3380 | 51.6 | 247.11 | 6.3 – 7.6 | |
| Lanthanum hexaboride | $LaB_6$ [12008-21-8] 203.772 | Cubic $a = 415.7$ pm $D2_1$, $cP7$, $Pm3m$, $CaB_6$ type ($Z = 1$) | 4760 | 17.4 | 2715 | 47.7 | – | 6.4 | |
| Molybdenum boride | $Mo_2B_5$ [12007-97-5] 245.935 | Trigonal $a = 301.2$ pm $c = 2093.7$ pm $D8_1$, $hR7$, $R\bar{3}m$, $Mo_2B_5$ type ($Z = 1$) | 7480 | 22 – 55 | 1600 | 50 | – | 8.6 | |
| Molybdenum diboride | $MoB_2$ 117.59 | Hexagonal $a = 305.00$ pm $c = 311.30$ pm C32, $hP3$, $P6/mmm$, $AlB_2$ type ($Z = 1$) | 7780 | 45 | 2100 | – | 527 | 7.7 | |
| Molybdenum hemiboride | $Mo_2B$ [12006-99-4] 202.691 | Tetragonal $a = 554.3$ pm $c = 473.5$ pm C16, $tI2$, $I4/mcm$, $CuAl_2$ type ($Z = 4$) | 9260 | 40 | 2280 | – | 377 | 5 | |
| Molybdenum monoboride | MoB 106.77 | Tetragonal $a = 311.0$ $c = 169.5$ $B_g$, $t14$, $I4_1/amd$, MoB type ($Z = 2$) | 8770 – – | $\alpha$-MoB 45, $\beta$-MoB 24 | 2180 | – | 368 | – | |
| Niobium diboride | $\epsilon$-$NbB_2$ [12007-29-3] 114.528 | Hexagonal $a = 308.90$ pm $c = 330.03$ pm C32, $hP3$, $P6/mmm$, $AlB_2$ type ($Z = 1$) | 6970 | 26 – 65 | 2900 | 17 – 23.5 | 418 | 8.0 – 8.6 | |
| Niobium monoboride | $\delta$-NbB [12045-19-1] 103.717 | Orthorhombic $a = 329.8$ pm $b = 316.6$ pm $c = 87.23$ pm $B_f$, $oC8$, $Cmcm$, CrB type ($Z = 4$) | 7570 | 40 – 64.5 | 2270 – 2917 | 15.6 | – | 12.9 | |
| Silicon hexaboride | $SiB_6$ [12008-29-6] | Trigonal (rhombohedral) | 2430 | 200 000 | 1950 | – | – | – | |
| Silicon tetraboride | $SiB_4$ [12007-81-7] 71.330 | – | 2400 | – | – (dec.) | – | – | – | |
| Tantalum diboride | $TaB_2$ [12077-35-1] 202.570 | Hexagonal $a = 309.80$ pm $c = 324.10$ pm $C_{32}$, $hP3$, $P6/mmm$, $AlB_2$ type ($Z = 1$) | 12 540 | 33 | 3037 – 3200 | 10.9 – 16.0 | 237.55 | 8.2 – 8.8 | |

**Table 3.2-19** Physical properties of borides and boride-based high-temperature refractories [2.4], cont.

| | Young's modulus ($E$, GPa) | Flexural strength ($\tau$, MPa) | Compressive strength ($\alpha$, MPa) | Vickers hardness HV (Mohs hardness HM) | Other physicochemical properties, corrosion resistance,[a] and uses | IUPAC name |
|---|---|---|---|---|---|---|
| | 500 | 350 | – | 2900 | Gray crystals, attacked by HF, otherwise highly resistant. | Hafnium diboride |
| | 479 | 126 | – | – | Wear-resistant, semiconducting, thermoionic-conductor films. | Lanthanum hexaboride |
| | 672 | 345 | – | – | Corroded by the following molten metals: Al, Mg, V, Cr, Mn, Fe, Ni, Cu, Nb, Mo, and Ta. It is corrosion resistant to molten Cd, Sn, Bi, and Rb. | Molybdenum boride |
| | – | – | – | 1280 | | Molybdenum diboride |
| | – | – | – | – (HM 8 – 9) | Corrosion-resistant films. | Molybdenum hemiboride |
| | – | – | – | 1570 | | Molybdenum monoboride |
| | 637 | – | – | 3130 (HM > 8) | Corrosion-resistant to molten Ta; corroded by molten Re. | Niobium diboride |
| | – | – | – | – | Wear-resistant, semiconducting films; neutron-absorbing layers on nuclear fuel pellets. | Niobium monoboride |
| | – | – | – | – | | Silicon hexaboride |
| | – | – | – | – | | Silicon tetraboride |
| | 257 | – | – | (HM > 8) | Gray metallic powder. Severe oxidation in air above 800 °C. Corroded by the following molten metals: Nb, Mo, Ta, and Re. | Tantalum diboride |

**Table 3.2–19** Physical properties of borides and boride-based high-temperature refractories [2.4], cont.

| IUPAC name | Theoretical chemical formula, [CASRN], relative molecular mass ($^{12}C = 12.000$) | Crystal system, lattice parameters, *Strukturbericht* symbol, Pearson symbol, space group, structure type, $Z$ | Density ($\varrho$, kg m$^{-3}$) | Electrical resistivity ($\rho$, $\mu\Omega$ cm) | Melting point (°C) | Thermal conductivity ($\kappa$, W m$^{-1}$ K$^{-1}$) | Specific heat capacity ($c_p$, J kg$^{-1}$ K$^{-1}$) | Coefficient of linear thermal expansion ($\alpha$, $10^{-6}$K$^{-1}$) | |
|---|---|---|---|---|---|---|---|---|---|
| Tantalum monoboride | TaB [12007-07-7] 191.759 | Orthorhombic $a = 327.6$ pm $b = 866.9$ pm $c = 315.7$ pm $B_f$, $oC8$, $Cmcm$, CrB type ($Z = 4$) | 14 190 | 100 | 2340 – 3090 | – | 246.85 | – | |
| Thorium hexaboride | $ThB_6$ [12229-63-9] 296.904 | Cubic $a = 411.2$ pm $D2_1$, $cP7$, $Pm3m$, $CaB_6$ type ($Z = 1$) | 6800 | – | 2149 | 44.8 | – | 7.8 | |
| Thorium tetraboride | $ThB_4$ [12007-83-9] 275.53 | Tetragonal $a = 725.6$ pm $c = 411.3$ pm $D1_e$, $tP20$, $P4/mbm$, $ThB_4$ type ($Z = 4$) | 8450 | – | 2500 | 25 | 510 | 7.9 | |
| Titanium diboride | $TiB_2$ [12045-63-5] 69.489 | Hexagonal $a = 302.8$ pm $c = 322.8$ pm C32, $hP3$, $P6/mmm$, $AlB_2$ type ($Z = 1$) | 4520 | 16 – 28.4 | 2980 – 3225 | 64.4 | 637.22 | 7.6 – 8.6 | |
| Tungsten hemiboride | $W_2B$ [12007-10-2] 378.491 | Tetragonal $a = 556.4$ pm $c = 474.0$ pm C16, $tI12$, $I4/mcm$, $CuAl_2$ type ($Z = 4$) | 16 720 | – | 2670 | – | 168 | 6.7 | |
| Tungsten monoboride | WB [12007-09-9] 194.651 | Tetragonal $a = 311.5$ pm $c = 1692$ pm | 15 200 16 000 | 4.1 | 2660 | – | – | 6.9 | |
| Uranium diboride | $UB_2$ [12007-36-2] 259.651 | Hexagonal $a = 313.10$ pm $c = 398.70$ pm C32, $hP3$, $P6/mmm$, $AlB_2$ type | 12 710 | – | 2385 | 51.9 | – | 9 | |
| Uranium dodecaboride | $UB_{12}$ 367.91 | Cubic $a = 747.3$ pm $D2_f$, $cF52$, $Fm3m$, $UB_{12}$ type ($Z = 4$) | 5820 | – | 1500 | – | – | 4.6 | |
| Uranium tetraboride | $UB_4$ [12007-84-0] 281.273 | Tetragonal $a = 707.5$ pm $c = 397.9$ pm $D1_e$, $tP20$, $P4/mbm$, $ThB_4$ type ($Z = 4$) | 5350 | – | 2495 | 4.0 | – | 7.0 | |
| Vanadium diboride | $VB_2$ [12007-37-3] 72.564 | Hexagonal $a = 299.8$ pm $c = 305.7$ pm C32, $hP3$, $P6/mmm$, $AlB_2$ type ($Z = 1$) | 5070 | 23 | 2450 – 2747 | 42.3 | 647.43 | 7.6 – 8.3 | |

**Table 3.2-19** Physical properties of borides and boride-based high-temperature refractories [2.4], cont.

| | Young's modulus ($E$, GPa) | Flexural strength ($\tau$, MPa) | Compressive strength ($\alpha$, MPa) | Vickers hardness HV (Mohs hardness HM) | Other physicochemical properties, corrosion resistance,[a] and uses | IUPAC name |
|---|---|---|---|---|---|---|
| | – | – | – | 2200 (HM > 8) | Severe oxidation above 1100–1400 °C in air. | Tantalum monoboride |
| | – | – | – | – | | Thorium hexaboride |
| | 148 | 137 | – | – | | Thorium tetraboride |
| | 372–551 | 240 | 669 | 3370 (HM > 9) | Gray crystals, superconducting at 1.26 K. High-temperature electrical conductor, used in the form of a cermet as a crucible material for handling molten metals such as Al, Zn, Cd, Bi, Sn, and Rb. It is strongly corroded by liquid metals such as Tl, Zr, V, Nb, Ta, Cr, Mn, Fe, Co, Ni, and Cu. Begins to be oxidized in air above 1100–1400 °C. Corrosion-resistant in hot concentrated brines. Maximum operating temperature 1000 °C (reducing environment) and 800 °C (oxidizing environment). | Titanium diboride |
| | – | – | – | 2420 (HM 9) | Black powder. | Tungsten hemiboride |
| | – | – | – | (HM 9) | Black powder. | Tungsten monoboride |
| | – | – | – | 1390 | | Uranium diboride |
| | – | – | – | – | | Uranium dodecaboride |
| | 440 | 413 | – | 2500 | | Uranium tetraboride |
| | 268 | – | – | (HM 8–9) | Wear-resistant, semiconducting films. | Vanadium diboride |

**Table 3.2-19** Physical properties of borides and boride-based high-temperature refractories [2.4], cont.

| IUPAC name | Theoretical chemical formula, [CASRN], relative molecular mass ($^{12}C = 12.000$) | Crystal system, lattice parameters, *Strukturbericht* symbol, Pearson symbol, space group, structure type, $Z$ | Density ($\varrho$, kg m$^{-3}$) | Electrical resistivity ($\rho$, μΩ cm) | Melting point (°C) | Thermal conductivity ($\kappa$, W m$^{-1}$ K$^{-1}$) | Specific heat capacity ($c_p$, J kg$^{-1}$ K$^{-1}$) | Coefficient of linear thermal expansion ($\alpha$, $10^{-6}$K$^{-1}$) | |
|---|---|---|---|---|---|---|---|---|---|
| Zirconium diboride | $ZrB_2$ [12045-64-6] 112.846 | Hexagonal $a = 316.9$ pm $c = 353.0$ pm C32, $hP3$, $P6/mmm$, $AlB_2$ type ($Z = 1$) | 6085 | 9.2 | 3060 – 3245 | 57.9 | 392.54 | 5.5 – 8.3 | |
| Zirconium dodecaboride | $ZrB_{12}$ 283.217 | Cubic $a = 740.8$ pm D2$_f$, $cF52$, $Fm3m$, $UB_{12}$ type ($Z = 4$) | 3630 | 60 – 80 | 2680 | – | 523 | – | |

### 3.2.5.3 Carbides

Carbides are treated extensively in [2.1–3].Some properties of carbides and carbide-based high-temperature refractories are listed in Table 3.2-20 and Table 3.2-21. It should be noted that carbides also play a major role as hardening constituents in all carbon-containing steels (Sect. 3.1.5).

**Table 3.2-20** Physical properties of carbides and carbide-based high-temperature refractories [2.4]

| IUPAC name (synonyms and common trade names) | Theoretical chemical formula, [CASRN], relative molecular mass ($^{12}C = 12.000$) | Crystal system, lattice parameters, *Strukturbericht* symbol, Pearson symbol, space group, structure type, $Z$ | Density ($\varrho$, kg m$^{-3}$) | Electrical resistivity ($\rho$, μΩ cm) | Melting point (°C) | Thermal conductivity ($\kappa$, W m$^{-1}$ K$^{-1}$) | Specific heat capacity ($c_p$, J kg$^{-1}$ K$^{-1}$) | Coefficient of linear thermal expansion ($\alpha$, $10^{-6}$ K$^{-1}$) | |
|---|---|---|---|---|---|---|---|---|---|
| Aluminium carbides | $Al_4C_3$ [1299-86-1] 143.959 | Numerous polytypes | 2360 | – | 2798 | n.a | n.a | n.a | |
| Beryllium carbide | $Be_2C$ [506-66-1] 30.035 | Cubic $a = 433$ pm Cl, $cF12$, $Fm3m$, $CaF_2$ type ($Z = 4$) | 1900 | – | 2100 | 21.0 | 1397 | 10.5 | |
| Boron carbide (Norbide®) | $B_4C$ [12069-32-8] 55.255 | Hexagonal $a = 560$ pm $c = 1212$ pm DI$_g$, $hR15$, $R\bar{3}m$, $B_4C$ type | 2512 | 4500 | 2350 – 2427 | 27 | 1854 | 2.63 – 5.6 | |

**Table 3.2-19** Physical properties of borides and boride-based high-temperature refractories [2.4], cont.

| | Young's modulus ($E$, GPa) | Flexural strength ($\tau$, MPa) | Compressive strength ($\alpha$, MPa) | Vickers hardness HV (Mohs hardness HM) | Other physicochemical properties, corrosion resistance,[a] and uses | IUPAC name |
|---|---|---|---|---|---|---|
| | 343 – 506 | 305 | – | 1900 – 3400 (HM 8) | Gray metallic crystals, excellent thermal-shock resistance, greatest oxidation inertness of all refractory hard metals. Hot-pressed material is used in crucibles for handling molten metals such as Zn, Mg, Fe, Cu, Zn, Cd, Sn, Pb, Rb, Bi, Cr, brass, carbon steel, and cast iron, and also molten cryolite, yttria, zirconia, and alumina. It is readily corroded by liquid metals such as Si, Cr, Mn, Co, Ni, Nb, Mo, and Ta, and attacked by molten salts such as $Na_2O$, alkali carbonates, and NaOH. Severe oxidation in air occurs above 1100 – 1400 °C. Stable above 2000 °C under inert or reducing atmosphere. | Zirconium diboride |
| | – | – | – | – | | Zirconium dodecaboride |

[a] Corrosion data in molten salts from [2.9].

**Table 3.2-20** Physical properties of carbides and carbide-based high-temperature refractories [2.4], cont.

| | Young's modulus ($E$, GPa) | Flexural strength ($\tau$, MPa) | Compressive strength ($\alpha$, MPa) | Vickers hardness HV (Mohs hardness HM) | Other physicochemical properties, corrosion resistance,[a] and uses | IUPAC name (synonyms and common trade names) |
|---|---|---|---|---|---|---|
| | n.a | n.a | n.a | n.a | Decomposed in water with evolution of $CH_4$. | Aluminium carbides |
| | 314.4 | – | 723 | 2410 HK | Brick-red or yellowish-red octahedra. Used in nuclear-reactor cores. | Beryllium carbide |
| | 440 – 470 | – | 2900 | 3200 – 3500 HK (HM 9) | Hard, black, shiny crystals, the fourth hardest material known after diamond, cubic boron nitride, and boron oxide. It does not burn in an $O_2$ flame if the temperature is maintained below 983 °C. Maximum operating temperature 2000 °C (inert or reducing environment) or 600 °C (oxidizing environment). It is not attacked by hot HF or chromic acid. Used as abrasive, and in crucibles for molten salts, except molten alkalimetal hydroxides. In the form of molded shapes, it is used for pressure blast nozzles, wire-drawing dies, and bearing surfaces for gauges. For grinding and lapping applications, the available mesh sizes cover the range 240 to 800. | Boron carbide (Norbide®) |

**Table 3.2-20** Physical properties of carbides and carbide-based high-temperature refractories [2.4], cont.

| IUPAC name (synonyms and common trade names) | Theoretical chemical formula, [CASRN], relative molecular mass ($^{12}C = 12.000$) | Crystal system, lattice parameters, *Strukturbericht* symbol, Pearson symbol, space group, structure type, $Z$ | Density ($\varrho$, kg m$^{-3}$) | Electrical resistivity ($\rho$, $\mu\Omega$ cm) | Melting point (°C) | Thermal conductivity ($\kappa$, W m$^{-1}$ K$^{-1}$) | Specific heat capacity ($c_p$, J kg$^{-1}$ K$^{-1}$) | Coefficient of linear thermal expansion ($\alpha$, $10^{-6}$K$^{-1}$) | |
|---|---|---|---|---|---|---|---|---|---|
| Chromium carbide | $Cr_7C_3$ 400.005 | Hexagonal $a = 1389.02$ pm $c = 453.20$ pm | 6992 | 109.0 | 1665 | – | – | 11.7 | |
| Chromium carbide | $Cr_3C_2$ [12012-35-0] 180.010 | Orthorhombic $a = 282$ pm $b = 553$ pm $c = 1147$ pm $D5_{10}$, $oP20$, $Pbnm$, $Cr_3C_2$ type ($Z = 4$) | 6680 | 75.0 | 1895 | 19.2 | – | 10.3 | |
| Diamond | C [7782-40-3] 12.011 | Cubic $a = 356.683$ pm A4, $cF8$, $Fd3m$, diamond type ($Z = 8$) | 3515.24 | $>10^{16}$ (types I and IIa) $>10^3$ (type IIb) | 3550 | 900 (type I) 2400 (type IIa) | – | 2.16 | |
| Graphite | C [7782-42-5] 12.011 | Hexagonal $a = 246$ pm $b = 428$ pm $c = 671$ pm A9, $hP4$, $P6_3/mmc$, graphite type ($Z = 4$) | 2250 | 1385 | 3650 | – | – | 0.6 – 4.3 | |
| Hafnium monocarbide | HfC [12069-85-1] 190.501 | Cubic $a = 446.0$ pm B1, $cF8$, $Fm3m$, rock salt type ($Z = 4$) | 12 670 | 45.0 | 3890 – 3950 | 22.15 | – | 6.3 | |
| Lanthanum dicarbide | $LaC_2$ [12071-15-7] 162.928 | Tetragonal $a = 394.00$ pm $c = 657.20$ pm C11a, $tI6$, $I4/mmm$, $CaC_2$ type ($Z = 2$) | 5290 | 68.0 | 2360 – 2438 | – | – | 12.1 | |
| Molybdenum hemicarbide | $\beta$-$Mo_2C$ [12069-89-5] 203.891 | Hexagonal $a = 300.20$ pm $c = 427.40$ pm L′3, $hP3$, $P6_3/mmc$, $Fe_2N$ type ($Z = 1$) | 9180 | 71.0 | 2687 | – | 29.4 | 7.8 | |
| Molybdenum monocarbide | MoC [12011-97-1] 107.951 | Hexagonal $a = 290$ pm $c = 281$ pm $B_k$, $P6_3$/mmc, BN type ($Z = 4$) | 9159 | 50.0 | 2577 | – | – | 5.76 | |
| Niobium hemicarbide | $Nb_2C$ [12011-99-3] 197.824 | Hexagonal $a = 312.70$ pm $c = 497.20$ pm L′3, $hP3$, $P6_3/mmc$, $Fe_2N$ type ($Z = 1$) | 7800 | – | 3090 | – | – | – | |
| Niobium monocarbide | NbC [12069-94-2] 104.917 | Cubic $a = 447.71$ pm B1, $cF8$, $Fm3m$, rock salt type ($Z = 4$) | 7820 | 51.1 – 74.0 | 3760 | 14.2 | – | 6.84 | |

**Table 3.2-20** Physical properties of carbides and carbide-based high-temperature refractories [2.4], cont.

| | Young's modulus ($E$, GPa) | Flexural strength ($\tau$, MPa) | Compressive strength ($\alpha$, MPa) | Vickers hardness HV (Mohs hardness HM) | Other physicochemical properties, corrosion resistance,[a] and uses | IUAPC name (synonyms and common trade names) |
|---|---|---|---|---|---|---|
| | – | – | – | 1336 | Resists oxidation in the range 800–1000 °C. Corroded by the following molten metals: Ni and Zn. | Chromium carbide |
| | 386 | – | 1041 | 2650 | Corroded by the following molten metals: Ni, Zn, Cu, Cd, Al, Mn, and Fe. Corrosion-resistant in molten Sn and Bi. | Chromium carbide |
| | 930 | – | 7000 | 8000 HK (HM 10) | Type I contains 0.1–0.2% N, type IIa is N-free, and type IIb is very pure, generally blue in color. Electrical insulator ($E_g = 7$ eV). Burns in oxygen. | Diamond |
| | 6.9 | – | – | (HM 2) | High-temperature lubricant, used in crucibles for handling molten metals such as Mg, Al, Zn, Ga, Sb, and Bi. | Graphite |
| | 424 | – | – | 1870–2900 | Dark, gray, brittle solid, the most refractory binary material known. Used in control rods in nuclear reactors and in crucibles for melting $HfO_2$ and other oxides. Corrosion-resistant to liquid metals such as Nb, Ta, Mo, and W. Severe oxidation in air above 1100–1400 °C, but stable up to 2000 °C in helium. | Hafnium monocarbide |
| | – | – | – | – | Decomposed by $H_2O$. | Lanthanum dicarbide |
| | 221 | – | n.a | 1499 (HM > 7) | Gray powder. Wear-resistant film. Oxidized in air at 700–800 °C. Corroded in the following molten metals: Al, Mg, V, Cr, Mn, Fe, Ni, Cu, Zn, and Nb. Corrosion-resistant in molten Cd, Sn, and Ta. | Molybdenum hemicarbide |
| | 197 | n.a. | n.a. | 1800 (HM > 9) | Oxidized in air at 700–800 °C. | Molybdenum monocarbide |
| | n.a. | n.a. | n.a. | 2123 | | Niobium hemicarbide |
| | 340 | n.a. | n.a. | 2470 (HM > 9) | Lavender-gray powder, soluble in HF-$HNO_3$ mixture. Wear-resistant film, used for coating graphite in nuclear reactors. Oxidation in air becomes severe only above 1000 °C. | Niobium monocarbide |

**Table 3.2-20** Physical properties of carbides and carbide-based high-temperature refractories [2.4], cont.

| IUPAC name (synonyms, and common trade names) | Theoretical chemical formula, [CASRN], relative molecular mass ($^{12}C = 12.000$) | Crystal system, lattice parameters, *Strukturbericht* symbol, Pearson symbol, space group, structure type ($Z$) | Density ($\varrho$, kg m$^{-3}$) | Electrical resistivity ($\rho$, $\mu\Omega$ cm) | Melting point (°C) | Thermal conductivity ($\kappa$, W m$^{-1}$ K$^{-1}$) | Specific heat capacity ($c_p$, J kg$^{-1}$ K$^{-1}$) | Coefficient of linear thermal expansion ($\alpha$, $10^{-6}$K$^{-1}$) | |
|---|---|---|---|---|---|---|---|---|---|
| Silicon monocarbide (moissanite, Carbolon®, Crystolon®, Carborundum®) | $\alpha$-SiC [409-21-2] 40.097 | Hexagonal $a = 308.10$ pm $c = 503.94$ pm B4, $hP4$, $P6_3/mmc$, wurtzite type ($Z = 2$) | 3160 | $4.1 \times 10^5$ | 2093 transformation temperature | 42.5 | 690 | 4.3 – 4.6 | |
| Silicon monocarbide (Carbolon®, Crystolon®, Carborundum®) | $\beta$-SiC [409-21-2] 40.097 | Cubic $a = 435.90$ pm B3, $cF8$, $F43m$, ZnS type ($Z = 4$) | 3160 | 107 – 200 | ~ 2700, subl. | 135 | 1205 | 4.5 | |
| Tantalum hemicarbide | $Ta_2C$ [12070-07-4] 373.907 | Hexagonal $a = 310.60$ pm $c = 493.00$ pm L′3, $hP3$, $P6_3/mmc$, $Fe_2N$ type ($Z = 2$) | 15 100 | 80.0 | 3327 | – | – | – | |
| Tantalum monocarbide | TaC [12070-06-3] 194.955 | Cubic $a = 445.55$ pm B1, $cF8$, $Fm3m$, rock salt type ($Z = 4$) | 14 800 | 30 – 42.1 | 3880 | 22.2 | 190 | 6.64 – 8.4 | |
| Thorium dicarbide | $\alpha$-$ThC_2$ [12071-31-7] 256.060 | Tetragonal $a = 585$ pm $c = 528$ pm C11a, $tI6$, $I4mmm$, $CaC_2$ type ($Z = 2$) | 8960 – 9600 | 30.0 | 2655 | 23.9 | – | 8.46 | |
| Thorium monocarbide | ThC [12012-16-7] 244.089 | Cubic $a$=534.60 pm B1, $cF8$, $Fm3m$, rock salt type ($Z$=4) | 10 670 | 25.0 | 2621 | 28.9 | – | 6.48 | |
| Titanium monocarbide | TiC [12070-08-5] 59.878 | Cubic $a = 432.8$ pm B1, $cF8$, $Fm3m$, rock salt type ($Z = 4$) | 4938 | 52.5 | 3140 ± 90 | 17 – 21 | – | 7.5 – 7.7 | |
| Tungsten hemicarbide | $W_2C$ [12070-13-2] 379.691 | Hexagonal $a = 299.82$ pm $c = 472.20$ pm L′3, $hP3$, $P6_3/mmc$, $Fe_2N$ type ($Z = 1$) | 17 340 | 81.0 | 2730 | – | – | 3.84 | |
| Tungsten monocarbide (Widia®) | WC [12070-12-1] 195.851 | Hexagonal $a = 290.63$ pm $c = 283.86$ pm L′3, $hP3$, $P6_3/mmc$, $Fe_2N$ type ($Z = 1$) | 15 630 | 19.2 | 2870 | 121 | – | 6.9 | |

**Table 3.2-20** Physical properties of carbides and carbide-based high-temperature refractories [2.4], cont.

| | Young's modulus ($E$, GPa) | Flexural strength ($\tau$, MPa) | Compressive strength ($\alpha$, MPa) | Vickers hardness HV (Mohs hardness HM) | Other physicochemical properties, corrosion resistance,[a] and uses | IUPAC name (synonyms and common trade names) |
|---|---|---|---|---|---|---|
| | 386 – 414 | – | 500 | 2400 – 2500 (HM 9.2) | Semiconductor ($E_g = 3.03$ eV). Soluble in fused alkalimetal hydroxides. | Silicon monocarbide (moissanite, Carbolon®, Crystolon®, Carborundum®) |
| | 262 – 468 | – | 1000 | 2700 – 3350 (HM 9.5) | Green to bluish-black, iridescent crystals. Soluble in fused alkalimetal hydroxides. Abrasives made from this material are best suited to the grinding of low-tensile-strength materials such as cast iron, brass, bronze, marble, concrete, stone, glass, optical, structural, and wear-resistant components. Corroded by molten metals such as Na, Mg, Al, Zn, Fe, Sn, Rb, and Bi. Resistant to oxidation in air up to 1650 °C. Maximum operating temperature of 2000 °C in reducing or inert atmosphere. | Silicon monocarbide (Carbolon®, Crystolon®, Carborundum®) |
| | – | – | – | 1714 – 2000 | | Tantalum hemicarbide |
| | 364 | – | – | 1599 – 1800 (HM 9 – 10) | Golden-brown crystals, soluble in HF-$HNO_3$ mixture. Used in crucibles for melting $ZrO_2$ and similar oxides with high melting points. Corrosion-resistant to molten metals such as Ta, and Re. Readily corroded by liquid metals such as Nb, Mo, and Sn. Burning occurs in pure oxygen above 800 °C. Severe oxidation in air above 1100–1400 °C. Maximum operating temperature of 3760 °C under helium. | Tantalum monocarbide |
| | – | – | – | 600 | $\alpha - \beta$ transition at 1427 °C and $\beta - \gamma$ transition at 1497 °C. Decomposed by $H_2O$ with evolution of $C_2H_6$. | Thorium dicarbide |
| | – | – | – | 1000 | Readily hydrolyzed in water, evolving $C_2H_6$. | Thorium monocarbide |
| | 310 – 462 | – | 1310 | 2620 – 3200 (HM 9 – 10) | Gray crystals. Superconducting at 1.1 K. Soluble in $HNO_3$ and aqua regia. Resistant to oxidation in air up to 450 °C. Maximum operating temperature 3000 °C under helium. Used in crucibles for handling molten metals such as Na, Bi, Zn, Pb, Sn, Rb, and Cd. Corroded by the following liquid metals: Mg, Al, Si, Ti, Zr, V, Nb, Ta, Cr, Mo, Mn, Fe, Co, and Ni. Attacked by molten NaOH. | Titanium monocarbide |
| | 421 | – | – | 3000 | Black. Resistant to oxidation in air up to 700 °C. Corrosion-resistant to Mo. | Tungsten hemicarbide |
| | 710 | – | 530 | 2700 (HM > 9) | Gray powder, dissolved by HF-$HNO_3$ mixture. Cutting tools, wear-resistant semiconductor films. Corroded by the following molten metals: Mg, Al, V, Cr, Mn, Ni, Cu, Zn, Nb, and Mo. Corrosion-resistant to molten Sn. | Tungsten monocarbide (Widia®) |

**Table 3.2-20** Physical properties of carbides and carbide-based high-temperature refractories [2.4], cont.

| IUPAC name (synonyms, and common trade names) | Theoretical chemical formula, [CASRN], relative molecular mass ($^{12}C = 12.000$) | Crystal system, lattice parameters, *Strukturbericht* symbol, Pearson symbol, space group, structure type ($Z$) | Density ($\varrho$, kg m$^{-3}$) | Electrical resistivity ($\rho$, $\mu\Omega$ cm) | Melting point (°C) | Thermal conductivity ($\kappa$, W m$^{-1}$ K$^{-1}$) | Specific heat capacity ($c_p$, J kg$^{-1}$ K$^{-1}$) | Coefficient of linear thermal expansion ($\alpha$, $10^{-6}$K$^{-1}$) | |
|---|---|---|---|---|---|---|---|---|---|
| Uranium carbide | $U_2C_3$ [12076-62-9] 512.091 | Cubic $a = 808.89$ pm D5c, $cI40$, $I\bar{4}3d$, $Pu_2C_3$ type ($Z = 8$) | 12 880 | – | 1777 | – | – | 11.4 | |
| Uranium dicarbide | $UC_2$ [12071-33-9] 262.051 | Tetragonal $a = 352.24$ pm $c = 599.62$ pm C11a, $ti6$, $I4/mmm$, $CaC_2$ type ($Z = 2$) | 11 280 | – | 2350 – 2398 | 32.7 | 147 | 14.6 | |
| Uranium monocarbide | UC [12070-09-6] 250.040 | Cubic $a = 496.05$ pm B1, $cF8$, $Fm3m$, rock salt type ($Z = 4$) | 13 630 | 50.0 | 2370 – 2790 | 23.0 | – | 11.4 | |
| Vanadium hemicarbide | $V_2C$ [2012-17-8] 113.89 | Hexagonal $a = 286$ pm $c = 454$ pm L′3, $hP3$, $P6_3mmc$, $Fe_2N$ type ($Z = 2$) | 5750 | – | 2166 | – | – | – | |
| Vanadium monocarbide | VC [12070-10-9] 62.953 | Cubic $a = 413.55$ pm B1, $cF8$, $Fm3m$, rock salt type ($Z = 4$) | 5770 | 65.0 – 98.0 | 2810 | 24.8 | – | 4.9 | |
| Zirconium monocarbide | ZrC [12020-14-3] 103.235 | Cubic $a = 469.83$ pm B1, $cF8$, $Fm3m$, rock salt type ($Z = 4$) | 6730 | 68.0 | 3540 – 3560 | 20.61 | 205 | 6.82 | |

[a] Corrosion data in molten salts from [2.9].

**Table 3.2-20** Physical properties of carbides and carbide-based high-temperature refractories [2.4], cont.

| | Young's modulus ($E$, GPa) | Flexural strength ($\tau$, MPa) | Compressive strength ($\alpha$, MPa) | Vickers hardness HV (Mohs hardness HM) | Other physicochemical properties, corrosion resistance,[a] and uses | IUPAC name (synonyms and common trade names) |
|---|---|---|---|---|---|---|
| | 179 – 221 | – | 434 | – | | Uranium carbide |
| | – | – | – | 600 | Transition from tetragonal to cubic at 1765 °C. Decomposed in $H_2O$, slightly soluble in alcohol. Used in microsphere pellets to fuel nuclear reactors. | Uranium dicarbide |
| | 172.4 | – | 351.6 | 750 – 935 (HM > 7) | Gray crystals with metallic appearance, reacts with oxygen. Corroded by the following molten metals: Be, Si, Ni, and Zr. | Uranium monocarbide |
| | – | – | – | 3000 | Corroded by molten Nb, Mo, and Ta. | Vanadium hemicarbide |
| | 614 | – | 613 | 2090 | Black crystals, soluble in $HNO_3$ with decomposition. Used in wear-resistant films and cutting tools. Resistant to oxidation in air up to 300 °C. | Vanadium monocarbide |
| | 345 | – | 1641 | 1830 – 2930 (HM > 8) | Dark gray, brittle solid, soluble in HF solutions containing nitrates or peroxide ions. Used in nuclear power reactors and in crucibles for handling molten metals such as Bi, Cd, Pb, Sn, and Rb, and molten zirconia ($ZrO_2$). Corroded by the following liquid metals: Mg, Al, Si, V, Nb, Ta, Cr, Mo, Mn, Fe, Co, Ni, and Zn. In air, oxidized rapidly above 500 °C. Maximum operating temperature of 2350 °C under helium. | Zirconium monocarbide |

**Table 3.2-21** Properties of carbides according to DIN EN 60672 [2.6]

| | | | Designation | | | | |
|---|---|---|---|---|---|---|---|
| | | | SSIC | SISIC | RSIC | NSIC | BC |
| **Mechanical properties** | **Symbol** | **Units** | **Silicon carbide, sintered** | **Silicon carbide, silicon-infiltrated** | **Silicon carbide, recrystallized** | **Silicon carbide, nitride-bonded** | **Boron carbide** |
| Open porosity | | vol. % | 0 | 0 | 0 – 15 | – | 0 |
| Density, minimum | $\varrho$ | $Mg/m^3$ | 3.08 – 3.15 | 3.08 – 3.12 | 2.6 – 2.8 | 2.82 | 2.50 |
| Bending strength | $\sigma_B$ | MPa | 300 – 600 | 180 – 450 | 80 – 120 | 200 | 400 |
| Young's modulus | $E$ | GPa | 370 – 450 | 270 – 350 | 230 – 280 | 150 – 240 | 390 – 440 |
| Hardness | HV | 100 | 25 – 26 | 14 – 25 | 25 | – | 30 – 40 |
| Fracture toughness | $K_{IC}$ | MPa $\sqrt{m}$ | 3.0 – 4.8 | 3.0 – 5.0 | 3.0 | – | 3.2 – 3.6 |
| **Electrical properties** | | | | | | | |
| Resistivity at 20 °C | $\rho_{20}$ | Ω m | $10^3 - 10^4$ | $2 \times 10^1 - 10^3$ | – | – | – |
| Resistivity at 600 °C | $\rho_{600}$ | Ω m | 10 | 5 | – | – | – |
| **Thermal properties** | | | | | | | |
| Average coefficient of thermal expansion at 30 – 600 °C | $\alpha_{30-1000}$ | $10^{-6}\,K^{-1}$ | 4 – 4.8 | 4.3 – 4.8 | 4.8 | 4.5 | 6 |
| Specific heat capacity at 30 – 100 °C | $c_{p,30-1000}$ | $J\,kg^{-1}K^{-1}$ | 600 – 1000 | 650 – 1000 | 600 – 900 | 800 – 900 | – |
| Thermal conductivity | $\lambda_{30-100}$ | $W\,m^{-1}K^{-1}$ | 40 – 120 | 110 – 160 | 20 | 14 – 15 | 28 |
| Thermal fatigue resistance | | (Rated) | Very good | Very good | Very good | Very good | – |
| Typical maximum application temperature | $T$ | °C | 1400 – 1750 | 1380 | 1600 | 1450 | 700 – 1000 |

### 3.2.5.4 Nitrides

Nitrides are treated extensively in [2.1–3]. Some properties are listed in Tables 3.2-22 and 3.2-23.

#### Silicon Nitride

$Si_3N_4$ is the dominant nitride ceramic material because of its favorable combination of properties. The preparation of powders for the formation of dense silicon nitride materials requires the use of precursors. Four routes for the production of $Si_3N_4$ powders are used in practice: nitridation of silicon, chemical vapor deposition from $SiCl_4 + NH_3$, carbothermal reaction of $SiO_2$, and precipitation of silicon diimide $Si(NH)_2$ followed by decomposition. Table 3.2-24 gives examples of the properties of the resulting powders.

**Table 3.2-22** Properties of nitrides according to DIN EN 60672 [2.6]

| | | | Designation | | | | |
|---|---|---|---|---|---|---|---|
| | | | SSN | RBSN | HPSN | SRBSN | AlN |
| **Mechanical properties** | **Symbol** | **Units** | **Silicon nitride, sintered** | **Silicon nitride, reaction-bonded** | **Silicon nitride, hot-pressed** | **Silicon nitride, reaction-bonded** | **Aluminium nitride** |
| Open porosity | | vol. % | – | – | 0 | – | 0 |
| Density, minimum | $\varrho$ | $Mg/m^3$ | 3 – 3.3 | 1.9 – 2.5 | 3.2 – 3.4 | 3.1 – 3.3 | 3.0 |
| Bending strength | $\sigma_B$ | MPa | 700 – 1000 | 200 – 330 | 600 – 800 | 700 – 1200 | 200 |
| Young's modulus | $E$ | GPa | 250 – 330 | 80 – 180 | 600 – 800 | 150 – 240 | 320 |
| Hardness | HV | 100 | 4 – 18 | 8 – 10 | 15 – 16 | – | 11 |
| Fracture toughness | $K_{IC}$ | MPa $\sqrt{m}$ | 5 – 8.5 | 1.8 – 4.0 | 6.0 – 8.5 | 3.0 – 6? | 3.0 |
| **Electrical properties** | | | | | | | |
| Resistivity at 20 °C | $\rho_{20}$ | Ω m | $10^{11}$ | $10^{13}$ | $10^{13}$ | – | $10^{13}$ |
| Resistivity at 600 °C | $\rho_{600}$ | Ω m | $10^{2}$ | $10^{10}$ | $10^{9}$ | – | $10^{12}$ |
| **Thermal properties** | | | | | | | |
| Average coefficient of thermal expansion at 30–600 °C | $\alpha_{30-1000}$ | $10^{-6}\,K^{-1}$ | 2.5 – 3.5 | 2.1 – 3 | 3.1 – 3.3 | 3.0 – 3.4 | 4.5 – 5 |
| Specific heat capacity at 30–100 °C | $c_{p,30-1000}$ | $J\,kg^{-1}K^{-1}$ | 700 – 850 | 700 – 850 | 700 – 850 | 700 – 850 | – |
| Thermal conductivity | $\lambda_{30-100}$ | $W\,m^{-1}K^{-1}$ | 15 – 45 | 4 – 15 | 15 – 40 | 14 – 15 | > 100 |
| Thermal fatigue resistance | | (Rated) | Very good | Very good | Very good | Very good | Very good |
| Typical maximum application temperature | $T$ | °C | 1250 | 1100 | 1400 | 1250 | – |

**Table 3.2-23** Physical properties of nitrides and nitride-based high-temperature refractories [2.4]

| IUPAC name (synonyms and common trade names) | Theoretical chemical formula, [CASRN], relative molecular mass ($^{12}C = 12.000$) | Crystal system, lattice parameters, *Strukturbericht* symbol, Pearson symbol, space group, structure type, $Z$ | Density ($\varrho$, kg m$^{-3}$) | Electrical resistivity ($\rho$, $\mu\Omega$ cm) | Melting point (°C) | Thermal conductivity ($\kappa$, W m$^{-1}$ K$^{-1}$) | Specific heat capacity ($c_p$, J kg$^{-1}$ K$^{-1}$) | Coefficient of linear thermal expansion ($\alpha$, $10^{-6}$K$^{-1}$) | |
|---|---|---|---|---|---|---|---|---|---|
| Aluminium mononitride | AlN [24304-00-5] 40.989 | Hexagonal $a = 311.0$ pm $c = 497.5$ pm B4, $hP4$, $P6_3mc$, wurtzite type ($Z = 2$) | 3050 | $10^{17}$ | 2230 | 29.96 | 820 | 5.3 | |
| Beryllium nitride | $\alpha$-$Be_3N_2$ [1304-54-7] 55.050 | Cubic $a = 814$ pm $D5_3$, $cI80$, $Ia3$, $Mn_2O_3$ type ($Z = 16$) | 2710 | – | 2200 | – | 1221 | – | |
| Boron mononitride | BN [10043-11-5] 24.818 | Hexagonal $a = 250.4$ pm $c = 666.1$ pm $B_k$, $hP8$, $P6_3/mmc$, BN type ($Z = 4$) | 2250 | $10^{19}$ | 2730 (dec.) | 15.41 | 711 | 7.54 | |
| Boron mononitride (Borazon®, CBN) | BN 24.818 | Cubic $a = 361.5$ pm | 3430 | 1900 (200°C) | 1540 | – | – | – | |
| Chromium heminitride | $Cr_2N$ [12053-27-9] 117.999 | Hexagonal $a = 274$ pm $c = 445$ pm L′3, $hP3$, $P6_3/mmc$, $Fe_2N$ type ($Z = 1$) | 6800 | 76 | 1661 | 22.5 | 630 | 9.36 | |
| Chromium mononitride | CrN [24094-93-7] 66.003 | Cubic $a = 415.0$ pm B1, $cF8$, $Fm3m$, rock salt type ($Z = 4$) | 6140 | 640 | 1499 (dec.) | 12.1 | 795 | 2.34 | |
| Hafnium mononitride | HfN [25817-87-2] 192.497 | Cubic $a = 451.8$ pm B1, $cF8$, $Fm3m$, rock salt type ($Z = 4$) | 13 840 | 33 | 3310 | 21.6 | 210 | 6.5 | |
| Molybdenum heminitride | $Mo_2N$ [12033-31-7] 205.887 | Cubic $a = 416$ pm L′1, $cP5$, $Pm3m$, $Fe_4N$ type ($Z = 2$) | 9460 | 19.8 | 760 – 899 | 17.9 | 293 | 6.12 | |
| Molybdenum mononitride | MoN [12033-19-1] 109.947 | Hexagonal $a = 572.5$ pm $c = 560.8$ pm $B_h$, $hP2$, $P6/mmm$, WC type ($Z = 1$) | 9180 | – | 1749 | – | – | – | |
| Niobium mononitride | NbN [24621-21-4] 106.913 | Cubic $a = 438.8$ pm B1, $cF8$, $Fm3m$, rock salt type ($Z = 4$) | 8470 | 78 | 2575 | 3.63 | – | 10.1 | |
| Silicon nitride | $\beta$-$Si_3N_4$ [12033-89-5] 140.284 | Hexagonal $a = 760.8$ pm $c = 291.1$ pm $P6/3m$ | 3170 | $10^6$ | 1850 | 28 | 713 | 2.25 | |

**Table 3.2-23** Physical properties of nitrides and nitride-based high-temperature refractories [2.4], cont.

| | Young's modulus (E, GPa) | Flexural strength (τ, MPa) | Compressive strength (α, MPa) | Vickers hardness HV (Mohs hardness HM) | Other physicochemical properties, corrosion resistance,[a] and uses | IUPAC name (synonyms and common trade names) |
|---|---|---|---|---|---|---|
| | 346 | – | 2068 | 1200 (HM 9 – 10) | Insulator ($E_g = 4.26$ eV). Decomposed by water, acids, and alkalis to $Al(OH)_3$ and $NH_3$. Used in crucibles for GaAs crystal growth. | Aluminium mononitride |
| | – | – | – | – | Hard white or grayish crystals. Oxidized in air above 600 °C. Slowly decomposed in water, quickly in acids and alkalis, with evolution of $NH_3$. | Beryllium nitride |
| | 85.5 | – | 310 | 230 (HM 2.0) | Insulator ($E_g = 7.5$ eV). Used in crucibles for molten metals such as Na, B, Fe, Ni, Al, Si, Cu, Mg, Zn, In, Bi, Rb, Cd, Ge, and Sn. Corroded by these molten metals: U, Pt, V, Ce, Be, Mo, Mn, Cr, V, and Al. Attacked by the following molten salts: $PbO_2$, $Sb_2O_3$, $Bi_2O_3$, KOH, and $K_2CO_3$. Used in furnace insulation, diffusion masks, and passivation layers. | Boron mononitride |
| | – | – | 7000 | 4700 – 5000 (HM 10) | Tiny reddish to black grains. Used as an abrasive for grinding tool and die steels and high-alloy steels when chemical reactivity of diamond is a problem. | Boron mononitride (Borazon®, CBN) |
| | – | – | – | 1200 – 1571 | | Chromium heminitride |
| | – | – | – | 1090 | | Chromium mononitride |
| | – | – | – | 1640 (HM > 8–9) | Most refractory of all nitrides. | Hafnium mononitride |
| | – | – | – | 1700 | Phase transition at 5.0 K. | Molybdenum heminitride |
| | – | – | – | 650 | | Molybdenum mononitride |
| | – | – | – | 1400 (HM > 8) | Dark gray crystals. Transition temperature 15.2 K. Insoluble in HCl, $HNO_3$, and $H_2SO_4$, but attacked by hot caustic solutions, lime, or strong alkalis, evolving $NH_3$. | Niobium mononitride |
| | 55 | – | – | (HM > 9) | | Silicon nitride |

**Table 3.2-23** Physical properties of nitrides and nitride-based high-temperature refractories [2.4], cont.

| IUPAC name (synonyms and common trade names) | Theoretical chemical formula, [CASRN], relative molecular mass ($^{12}C = 12.000$) | Crystal system, lattice parameters, *Strukturbericht* symbol, Pearson symbol, space group, structure type, $Z$ | Density ($\varrho$, kg m$^{-3}$) | Electrical resistivity ($\rho$, $\mu\Omega$ cm) | Melting point (°C) | Thermal conductivity ($\kappa$, W m$^{-1}$ K$^{-1}$) | Specific heat capacity ($c_p$, J kg$^{-1}$ K$^{-1}$) | Coefficient of linear thermal expansion ($\alpha$, $10^{-6}$K$^{-1}$) | |
|---|---|---|---|---|---|---|---|---|---|
| Silicon nitride (Nitrasil®) | $\alpha$-$Si_3N_4$ [12033-89-5] 140.284 | Hexagonal $a = 775.88$ pm $c = 561.30$ pm $P31c$ | 3184 | $10^{19}$ | 1900 (sub.) | 17 | 700 | 2.5 – 3.3 | |
| Tantalum heminitride | $Ta_2N$ 375.901 | Hexagonal $a = 306$ pm $c = 496$ pm L′3, $hP3$, $P6_3/mmc$, $Fe_2N$ type ($Z = 1$) | 15 600 | 263 | 2980 | 10.04 | 126 | 5.2 | |
| Tantalum mononitride ($\epsilon$) | TaN [12033-62-4] 194.955 | Hexagonal $a = 519.1$ pm $c = 290.6$ pm | 13 800 | 128 – 135 | 3093 | 8.31 | 210 | 3.2 | |
| Thorium mononitride | ThN [12033-65-7] 246.045 | Cubic $a = 515.9$ B1, $cF8$, $Fm3m$, rock salt type ($Z = 4$) | 11 560 | 20 | 2820 | – | – | 7.38 | |
| Thorium nitride | $Th_2N_3$ [12033-90-8] | Hexagonal $a = 388$ pm $c = 618$ pm $D5_2$, $hP5$, $\bar{3}ml$, $La_2O_3$ type ($Z = 1$) | 10 400 | – | 1750 | – | – | – | |
| Titanium mononitride | TiN [25583-20-4] 61.874 | Cubic $a = 424.6$ pm B1, $cF8$, $Fm3m$, rock salt type ($Z = 4$) | 5430 | 21.7 | 2930 (dec.) | 29.1 | 586 | 9.35 | |
| Tungsten dinitride | $WN_2$ [60922-26-1] 211.853 | Hexagonal $a = 289.3$ pm $c = 282.6$ pm | 7700 | – | 600 (dec.) | – | – | – | |
| Tungsten heminitride | $W_2N$ [12033-72-6] 381.687 | Cubic $a = 412$ pm L′1, $cP5$, $Pm3m$, $Fe_4N$ type ($Z = 2$) | 17 700 | – | 982 | – | – | – | |
| Tungsten mononitride | WN [12058-38-7] | Hexagonal | 15 940 | – | 593 | – | – | – | |
| Uranium nitride | $U_2N_3$ [12033-83-9] 518.259 | Cubic $a = 1070$ pm $D5_3$, $c180$, $Ia3$, $Mn_2O_3$ type ($Z = 16$) | 11 240 | – | – | – | – | – | |
| Uranium mononitride | UN [25658-43-9] 252.096 | Cubic $a = 489.0$ pm B1, $cF8$, $Fm3m$, rock salt type ($Z = 4$) | 14 320 | 208 | 2900 | 12.5 | 188 | 9.72 | |
| Vanadium mononitride | VN [24646-85-3] 64.949 | Cubic $a = 414.0$ pm B1, $cF8$, $Fm3m$, rock salt type ($Z = 4$) | 6102 | 86 | 2360 | 11.25 | 586 | 8.1 | |
| Zirconium mononitride | ZrN [25658-42-8] 105.231 | Cubic $a = 457.7$ pm B1, $cF8$, $Fm3m$, rock salt type ($Z = 4$) | 7349 | 13.6 | 2980 | 20.90 | 377 | 7.24 | |

**Table 3.2-23** Physical properties of nitrides and nitride-based high-temperature refractories [2.4], cont.

| | Young's modulus ($E$, GPa) | Flexural strength ($\tau$, MPa) | Compressive strength ($\alpha$, MPa) | Vickers hardness HV (Mohs hardness HM) | Other physicochemical properties, corrosion resistance,[a] and uses | IUAPC name (synonyms and common trade names) |
|---|---|---|---|---|---|---|
| | 304 | – | – | (HM > 9) | Gray amorphous powder or crystals. Corrosion-resistant to molten metals such as Al, Pb, Zn, Cd, Bi, Rb, and Sn, and molten salts NaCl-KCl, NaF, and silicate glasses. Corroded by molten Mg, Ti, V, Cr, Fe, Co, cryolite, KOH, and $Na_2O$. | Silicon nitride (Nitrasil®) |
| | – | – | – | 3200 | Decomposed by KOH with evolution of $NH_3$. | Tantalum heminitride |
| | – | – | – | 1110 (HM > 8) | Bronze-colored or black crystals. Transition temperature 1.8 K. Insoluble in water, slowly attacked by aqua regia, HF, and $HNO_3$. | Tantalum mononitride ($\epsilon$) |
| | – | – | – | 600 | Gray solid. Slowly hydrolyzed by water. | Thorium mononitride |
| | – | – | – | – | | Thorium nitride |
| | 248 | – | 972 | 1900 (HM 8 – 9) | Bronze-colored powder. Transition temperature 4.2 K. Corrosion-resistant to molten metals such as Al, Pb, Mg, Zn, Cd, and Bi. Corroded by molten Na, Rb, Ti, V, Cr, Mn, Sn, Ni, Cu, Fe, and Co. Dissolved by boiling aqua regia; decomposed by boiling alkalis, evolving $NH_3$. | Titanium mononitride |
| | – | – | – | – | Brown crystals. | Tungsten dinitride |
| | – | – | – | – | Gray crystals. | Tungsten heminitride |
| | – | – | – | – | Gray solid. Slowly hydrolyzed by water. | Tungsten mononitride |
| | – | – | – | – | | Uranium nitride |
| | 149 | – | – | 455 | | Uranium mononitride |
| | – | – | – | 1520 (HM 9 – 10) | Black powder. Transition temperature 7.5 K. Soluble in aqua regia. | Vanadium mononitride |
| | – | – | 979 | 1480 (HM > 8) | Yellow solid. Transition temperature 9 K. Corrosion-resistant to steel, basic slag, and cryolite, and molten metals such as Al, Pb, Mg, Zn, Cd, and Bi. Corroded by molten Be, Na, Rb, Ti, V, Cr, Mn, Sn, Ni, Cu, Fe, and Co. Soluble in concentrated HF, slowly soluble in hot $H_2SO_4$. | Zirconium mononitride |

[a] Corrosion data in molten salts from [2.9].

**Table 3.2-24** Characteristics of $Si_3N_4$ powders processed by different preparation techniques [2.3]

| | Technique | | | | | | |
|---|---|---|---|---|---|---|---|
| | Nitridation of Si | | Chemical vapor deposition | | Carbothermal reduction | Diimide precipitation | |
| **Sample no.** | **1** | **2** | **1** | **2** | | **1** | **2** |
| Specific surface area ($m^2/g$) | 23 | 11 | 4 | 10 | 10 | 11 | 13 |
| O (wt%) | 1.4 | 1.0 | 1.0 | 3.0 | 2.0 | 1.4 | 1.5 |
| C (wt%) | 0.2 | 0.25 | – | – | 0.9 | 0.1 | 0.1 |
| Fe, Al, Ca (wt%) | 0.07 | 0.4 | 0.005 | 0.005 | 0.22 | 0.01 | 0.015 |
| Other impurities (wt%) | | | Cl 0.04<br>Mo + Ti 0.02 | | | Cl 0.1 | Cl 0.005 |
| Crystallinity (%) | 100 | 100 | 60 | 0 | 100 | 98 | – |
| $\alpha/(\alpha+\beta)$ (%) | 95 | 92 | 95 | – | 98 | 86 | 95 |
| Morphology[a] | E | E | E + R | E + R | E + R | E | E |

[a] E, equiaxed; R, rod-like.

**Table 3.2-25** Physical properties of silicides and silicide-based high-temperature refractories [2.4]

| IUPAC name | Theoretical chemical formula, [CASRN], relative molecular mass ($^{12}C = 12.000$) | Crystal system, lattice parameters, *Strukturbericht* symbol, Pearson symbol, space group, structure type, $Z$ | Density ($\varrho$, kg m$^{-3}$) | Electrical resistivity ($\rho$, $\mu\Omega$ cm) | Melting point (°C) | Thermal conductivity ($\kappa$, W m$^{-1}$ K$^{-1}$) | Specific heat capacity ($c_p$, J kg$^{-1}$ K$^{-1}$) | Coefficient of linear thermal expansion ($\alpha$, $10^{-6}$K$^{-1}$) | |
|---|---|---|---|---|---|---|---|---|---|
| Chromium disilicide | $CrSi_2$<br>[12018-09-6]<br>108.167 | Hexagonal<br>$a = 442$ pm<br>$c = 635$ pm<br>C40, *hP*9, $P6_222$,<br>$CrSi_2$ type ($Z = 3$) | 4910 | 1400 | 1490 | 106 | – | 13.0 | |
| Chromium silicide | $Cr_3Si$<br>[12018-36-9]<br>184.074 | Cubic<br>$a = 456$ pm<br>A15, *cP*8, $Pm3n$,<br>$Cr_3Si$ type ($Z = 2$) | 6430 | 45.5 | 1770 | – | – | 10.5 | |
| Hafnium disilicide | $HfSi_2$<br>[12401-56-8]<br>234.66 | Orthorhombic<br>$a = 369$ pm<br>$b = 1446$ pm<br>$c = 346$ pm<br>C49, *oC*12, *Cmcm*,<br>$ZrSi_2$ type ($Z = 4$) | 8030 | – | 1699 | – | – | – | |
| Molybdenum disilicide | $MoSi_2$<br>[12136-78-6]<br>152.11 | Tetragonal<br>$a = 319$ pm<br>$c = 783$ pm<br>C11b, *tI*6, *I*4/*mmm*,<br>$MoSi_2$ type ($Z = 2$) | 6260 | 21.5 | 1870 | 58.9 | – | 8.12 | |
| Niobium disilicide | $NbSi_2$<br>[12034-80-9]<br>149.77 | Hexagonal<br>$a = 479$ pm<br>$c = 658$ pm<br>C40, *hP*9, $P6_222$,<br>$CrSi_2$ type ($Z = 3$) | 5290 | 50.4 | 2160 | – | – | – | |
| Tantalum disilicide | $TaSi_2$<br>[12039-79-1]<br>237.119 | Hexagonal<br>$a = 477$ pm<br>$c = 655$ pm<br>C40, *hP*9, $P6_222$,<br>$CrSi_2$ type ($Z = 3$) | 9140 | 8.5 | 2299 | – | – | 8.8 – 9.54 | |

### 3.2.5.5 Silicides

Silicides, being compounds of silicon with metals, mostly show a metallic luster. Like intermetallic phases the silicides of a metal may occur in different stoichiometric variants, e.g. $Ca_2Si$, $Ca_5Si_3$, and CaSi. Silicides of the non-noble metals are unstable in contact with water and oxidizing media. Silicides of transition metals are highly oxidation-resistant. Silicides are used as ceramic materials mainly in high-temperature applications. $MoSi_2$ is used in resistive heating elements. Some properties are listed in Table 3.2-25.



**Table 3.2-25** Physical properties of silicides and silicide-based high-temperature refractories [2.4], cont.

| | Young's modulus ($E$, GPa) | Flexural strength ($\tau$, MPa) | Compressive strength ($\alpha$, MPa) | Vickers hardness HV (Mohs hardness HM) | Other physicochemical properties, corrosion resistance and uses | IUPAC name |
|---|---|---|---|---|---|---|
| | – | – | – | 1000 – 1130 | | Chromium disilicide |
| | – | – | – | 1005 | | Chromium silicide |
| | – | – | – | 865 – 930 | | Hafnium disilicide |
| | 407 | – | 2068 – 2415 | 1260 | The compound is thermally stable in air up to 1000 °C. Corrosion-resistant to molten metals such as Zn, Pd, Ag, Bi, and Rb. It is corroded by the following liquid metals: Mg, Al, Si, V, Cr, Mn, Fe, Ni, Cu, Mo, and Ce. | Molybdenum disilicide |
| | – | – | – | 1050 | | Niobium disilicide |
| | – | – | – | 1200 – 1600 | Corroded by molten Ni. | Tantalum disilicide |

**Table 3.2-25** Physical properties of silicides and silicide-based high-temperature refractories [2.4], cont.

| IUPAC name | Theoretical chemical formula, [CASRN], relative molecular mass ($^{12}C = 12.000$) | Crystal system, lattice parameters, *Strukturbericht* symbol, Pearson symbol, space group, structure type, $Z$ | Density ($\varrho$, kg m$^{-3}$) | Electrical resistivity ($\rho$, $\mu\Omega$ cm) | Melting point (°C) | Thermal conductivity ($\kappa$, W m$^{-1}$ K$^{-1}$) | Specific heat capacity ($c_p$, J kg$^{-1}$ K$^{-1}$) | Coefficient of linear thermal expansion ($\alpha$, $10^{-6}$K$^{-1}$) | |
|---|---|---|---|---|---|---|---|---|---|
| Tantalum silicide | $Ta_5Si_3$ [12067-56-0] 988.992 | Hexagonal | 13 060 | – | 2499 | – | – | – | |
| Thorium disilicide | $ThSi_2$ [12067-54-8] 288.209 | Tetragonal $a = 413$ pm $c = 1435$ pm Cc, $tI12$, $I4amd$, $ThSi_2$ type ($Z = 4$) | 7790 | – | 1850 | – | – | – | |
| Titanium disilicide | $TiSi_2$ [12039-83-7] 104.051 | Orthorhombic $a = 360$ pm $b = 1376$ pm $c = 360$ pm C49, $oC12$, $Cmcm$, $ZrSi_2$ type ($Z = 4$) | 4150 | 123 | 1499 | – | – | 10.4 | |
| Titanium trisilicide | $Ti_5Si_3$ [12067-57-1] 323.657 | Hexagonal $a = 747$ pm $c = 516$ pm $D8_8$, $hP16$, $P6_3mcm$, $Mn_5Si_3$ type ($Z = 2$) | 4320 | 55 | 2120 | – | – | 110 | |
| Tungsten disilicide | $WSi_2$ [12039-88-2] 240.01 | Tetragonal $a = 320$ pm $c = 781$ pm C11b, $tI6$, $I4/mmm$, $MoSi_2$ type ($Z = 2$) | 9870 | 33.4 | 2165 | – | – | 8.28 | |
| Tungsten silicide | $W_5Si_3$ [12039-95-1] 1003.46 | | 12 210 | – | 2320 | – | – | – | |
| Uranium disilicide | $USi_2$ 294.200 | Tetragonal $a = 397$ pm $c = 1371$ pm Cc, $tI12$, $I4/amd$, $ThSi_2$ type ($Z = 4$) | 9250 | – | 1700 | – | – | – | |
| Uranium silicide | $\beta$-$U_3Si_2$ 770.258 | Tetragonal $a = 733$ pm $c = 390$ pm D5a, $tP10$, $P4/mbm$, $U_3Si_2$ type ($Z = 2$) | 12 200 | 150 | 1666 | 14.7 | – | 14.8 | |
| Vanadium disilicide | $VSi_2$ [12039-87-1] 107.112 | Hexagonal $a = 456$ pm $c = 636$ pm C40, $hP9$, $P6_222$, $CrSi_2$ type ($Z = 3$) | 5100 | 9.5 | 1699 | – | – | 11.2 | |
| Vanadium silicide | $V_3Si$ [12039-76-8] 147.9085 | Cubic $a = 471$ pm A15, $cP8$, $Pm3n$, $Cr_3Si$ type ($Z = 2$) | 5740 | 203 | 1732 | – | – | 8.0 | |
| Zirconium disilicide | $ZrSi_2$ [12039-90-6] 147.395 | Orthorhombic $a = 372$ pm $b = 1469$ pm $c = 366$ pm C49, $oC12$, $Cmcm$, $ZrSi_2$ type ($Z = 4$) | 4880 | 161 | 1604 | – | – | 8.6 | |

**Table 3.2-25** Physical properties of silicides and silicide-based high-temperature refractories [2.4], cont.

| | Young's modulus ($E$, GPa) | Flexural strength ($\tau$, MPa) | Compressive strength ($\alpha$, MPa) | Vickers hardness HV (Mohs hardness HM) | Other physicochemical properties, corrosion resistance, and uses | IUPAC name |
|---|---|---|---|---|---|---|
| | – | – | – | 1200 – 1500 | The compound is thermally stable in air up to 400 °C. | Tantalum silicide |
| | – | – | – | 1120 | Corrosion-resistant to molten Cu, while corroded by molten Ni. | Thorium disilicide |
| | – | – | – | 890 – 1039 | | Titanium disilicide |
| | – | – | – | 986 | | Titanium trisilicide |
| | – | – | – | 1090 | | Tungsten disilicide |
| | – | – | – | 770 | Corroded by molten Ni. | Tungsten silicide |
| | – | – | – | 700 | | Uranium disilicide |
| | 77.9 | – | – | 796 | | Uranium silicide |
| | – | – | – | 1400 | | Vanadium disilicide |
| | – | – | – | 1500 | | Vanadium silicide |
| | – | – | – | 1030 – 1060 | | Zirconium disilicide |

## References


2.1 L. E. Toth: *Transition Metals, Carbides and Nitrides* (Academic Press, New York 1971)

2.2 R. Freer: *The Physics and Chemistry of Carbides, Nitrides and Borides* (Kluwer, Boston 1989)

2.3 M. V. Swain (Ed.): Structure and properties of ceramics. In: *Materials Science and Technology*, Vol. 11 (Verlag Chemie, Weinheim 1994)

2.4 F. Cardarelli: *Materials Handbook* (Springer, London 2000)

2.5 J. R. Davis (Ed.): *Heat-Resistant Materials*, ASM Specialty Handbook (ASM International, Materials Park 1997)

2.6 Verband der keramischen Industrie: *Brevier Technische Keramik* (Fahner Verlag, Lauf 1999) (in German)

2.7 P. Otschick (Ed.): *Langzeitverhalten von Funktionskeramiken* (Werkstoff-Informationsgesellschaft, Frankfurt 1997) (in German)

2.8 G. V. Samsonov: *The Oxides Handbook* (Plenum, New York 1974)

2.9 G. Geirnaert: Céramiques et mètaux liquides: Compatibilitiés et angles de mouillages, Bull. Soc. Fr. Ceram **106**, 7 (1970)

2.10 V. I. Matkovich (Ed.): *Boron and Refractory Borides* (Springer, Berlin, Heidelberg 1977)

# 3.3. Polymers

The physical properties of polymers depend not only on the kind of material but also on the molar mass, the molar-mass distribution, the kind of branching, the degree of branching, the crystallinity (amorphous or crystalline), the tacticity, the end groups, any superstructure, and any other kind of molecular architecture. In the case of copolymers, the physical properties are additionally influenced by the type of arrangement of the monomers (statistical, random, alternating, periodic, block, or graft). Furthermore, the properties of polymers are influenced if they are mixed with other polymers (polymer blends), with fibers (glass fibers, carbon fibers, or metal fibers), or with other fillers (cellulose, inorganic materials, or organic materials).

The tables and figures include the physical and physicochemical properties of those polymers, copolymers, and polymer blends which are widely used for scientific applications and in industry. The figures include mainly the following physical properties: stress versus strain, viscosity versus shear rate, and creep modulus versus time. However, other physical properties are also included. Additionally, the most relevant applications of the materials are given.

3.3.1 **Structural Units of Polymers** ..... 480
3.3.2 **Abbreviations** ..... 482
3.3.3 **Tables and Figures** ..... 483
3.3.3.1 Polyolefines ..... 483
3.3.3.2 Vinyl Polymers ..... 489
3.3.3.3 Fluoropolymers ..... 492
3.3.3.4 Polyacrylics and Polyacetals ..... 497
3.3.3.5 Polyamides ..... 501
3.3.3.6 Polyesters ..... 503
3.3.3.7 Polysulfones and Polysulfides ..... 506
3.3.3.8 Polyimides and Polyether Ketones ..... 508
3.3.3.9 Cellulose ..... 509
3.3.3.10 Polyurethanes ..... 511
3.3.3.11 Thermosets ..... 512
3.3.3.12 Polymer Blends ..... 515
**References** ..... 522



The tables and figures include the physical and physicochemical properties of the most important polymers, copolymers, and polymer blends. "Most important" here means that these materials are widely used for scientific applications and in industry. The values in the main tables are given for room temperature, that is, ≈25 °C; otherwise, the temperature is given in parentheses. The tables and figures include the following physical properties:

Melting temperature $T_m$: heating rate 10 K/min (ISO 11357).

Enthalpy of fusion $\Delta H_u$: the amount of enthalpy (given per monomer unit of the polymer) needed for the transition of the polymer from the solid state to the molten state.

Entropy of fusion $\Delta S_u$: amount of entropy (given per monomer unit of the polymer) which is needed for the transition of a polymer from the solid state to the molten state.

Heat capacity $c_p = (\partial H/\partial T)_p \approx \Delta H/\Delta T$; $\Delta H$ = quantity of heat per mass unit, $\Delta T$ = temperature increase.

Enthalpy of combustion $\Delta H_c$: amount of enthalpy released in flaming combustion per unit mass of the polymer.

Glass transition temperature $T_g$: heating rate 10 K/min (ISO 11357).

Vicat softening temperature : $T_V$ 10/50, force 10 N, heating rate 50 K/h; $T_V$ 50/50, force 50 N, heating rate 50 K/h (ISO 306).

Thermal conductivity $\lambda$: $dq/dt = A\lambda\, dT/dx$; $dq/dt$ = heat flux, $A$ = area, $dT/dx$ = temperature gradient.

Density $\varrho = m/V$ (ISO 1183).

Coefficient of expansion $\alpha = (1/V_0)(\partial V/\partial T)_p$: $T = 23$–$55\,^{\circ}\mathrm{C}$ (ISO 11359).

Compressibility $\kappa = -(1/V)(\partial V/\partial p)_T$.

Elastic modulus $E = \sigma/\varepsilon$ ($\sigma$ = stress, $\varepsilon$ = strain (elongation)); elongation rate 1 mm/min (ISO 527).

Shear modulus $G = \tau/\gamma$ ($\tau$ = shear stress, $\gamma$ = shear angle).

Poisson's ratio $\mu = 0.5[1 - (E/\sigma)(\Delta V/V)]$; $\Delta V/V$ = relative volume change.

Stress at yield $\sigma_y$, strain (elongation) at yield $\varepsilon_y$: see Fig. 3.3-1; elongation rate 50 mm/min (ISO 527).

Stress at 50% strain (elongation) $\sigma_{50}$: see Fig. 3.3-1; elongation rate 50 mm/min (ISO 527).

Stress at fracture $\sigma_b$, strain (elongation) at fracture $\varepsilon_b$: see Fig. 3.3-1; elongation rate 5 mm/min (ISO 527).

Impact strength, and notched impact strength (Charpy) (ISO 179).

Sound velocity $v_s$, longitudinal (long) and transverse (trans).

Shore hardness A, $D$ (ISO 868).

Volume resistivity $\rho_e$, surface resistivity $\sigma_e$: contact electrodes, voltage 500 V (DIN 0303 T30, ISO 93, IEC 60093).

Electric strength $E_B$: specimen of thickness $1.0 \pm 0.1$ mm (ISO 10350, IEC 60243).

Relative permittivity $\varepsilon_r$, dielectric loss (dissipation factor) $\tan\delta$ (IEC 60250).

Refractive index $n_D$, temperature coefficient of refractive index $dn_D/dT$.

Steam permeation: 20–25 °C, 85% relative humidity gradient (DIN 53122, ISO 15106).

Gas permeation: 20–25 °C, reduced to 23 °C, 1 bar (ISO 2556, DIN 53380, ISO 15105).

Melt-viscosity–molar-mass relation.

Viscosity–molar-mass relation: $[\eta] = KM^a$ means $[\eta]/[\eta_0] = K(M/M_0)^a$, where $[\eta_0] = 1\,\mathrm{cm}^3/\mathrm{g}$, $M_0 = 1\,\mathrm{g/mol}$, and $[\eta]$ = intrinsic viscosity number at concentration $C = 0\,\mathrm{g/cm}^3$ [3.1] (DIN 53726, DIN 53727).

Stress $\sigma(\varepsilon, T)$; $\varepsilon$ = strain (elongation), $T$ = temperature (ISO 527).

Viscosity $\eta(d\gamma/dt, T)$; $d\gamma/dt$ = shear rate, $T$ = temperature (ISO 11443).

Creep modulus $E_{tc}(t, p, T)$; $t$ = time, $p$ = pressure, $T$ = temperature; $E_{tc} = \sigma_{tc}/\varepsilon(t)$ ($\sigma_{tc}$ = creep stress, $\varepsilon(t)$ = creep strain (creep elongation)); strain $\leq 0.5\%$ (ISO 899).

For selected polymers, the temperature dependence of some physical properties is given. Additionally, the most relevant applications of the materials are given. The tables and figures include the physical properties given in the table below (see [3.1–3]).

As the physical and physicochemical properties of each polymer vary with its molecular architecture, the tables show the ranges of the physical and physicochemical properties, whereas the diagrams show the functional relationships for a typical species of the polymer, copolymer, or polymer blend. The table on page 479 shows the selected 77 polymers, copolymers and polymer blends.

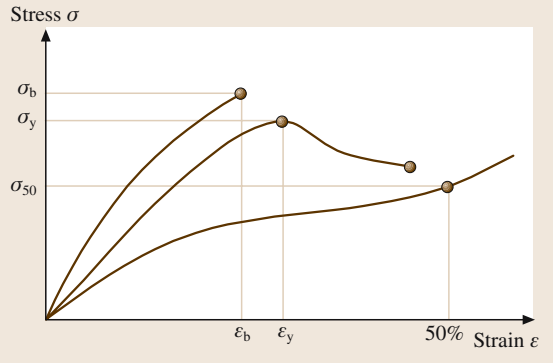


**Fig. 3.3-1** Stress $\sigma$ as a function of the strain $\varepsilon$ for different kinds of polymers (see page 478)

| |
|---|
| **3.3.3.1 Polyolefines** |
| **Polyolefines I** |
| Polyethylene: high density HDPE, medium density MDPE, low density LDPE, linear low density LLDPE, ultra high molecular weight UHMWPE |
| **Polyolefines II** |
| Poly(ethylene-co-vinylacetate) EVA, Polyethylene ionomer EIM, Cycloolefine copolymer COC [Poly(ethylene-co-norbornene)], Poly(ethylene-co-acrylic acid) EAA |
| **Polyolefines III** |
| Polypropylene PP, Polybutene-1 PB, Polyisobutylene PIB, Poly(4-methylpentene-1) PMP |
| **3.3.3.2 Vinylpolymers** |
| **Vinylpolymers I** |
| Polystyrene PS, Poly(styrene-co-butadiene) SB, Poly(styrene-co-acrylonitrile) SAN |
| **Vinylpolymers II** |
| Poly(vinyl carbazole) PVK, Poly(acrylonitrile-co-butadiene-co-styrene) ABS, Poly(acrylonitrile-co-styrene-co-acrylester) ASA |
| **Vinylpolymers III** |
| Poly(vinyl chloride): unplastisized PVC-U, plastisized (75/25) PVC-P1, plastisized (60/40) PVC-P2 |
| **3.3.3.3 Fluoropolymers** |
| Polytetrafluoroethylene PTFE, Polychlorotrifluoroethylene PCTFE, Poly(tetrafluoroethylene-co-hexafluoropro- pylene) FEP, Poly(ethylene-co-tetrafluoroethylene) ETFE, Poly(ethylene-co-chlorotrifluoroethylene), ECTFE |
| **3.3.3.4 Polyacrylics, Polyacetals** |
| Poly(methyl methacrylate) PMMA; Poly(oxymethylene) POM-H, Poly(oxymethylene-co-ethylene) POM-R |
| **3.3.3.5 Polyamides** |
| Polyamide 6 PA6, Polyamide 66 PA66, Polyamide 11 PA11, Polyamide 12 PA12, Polyamide 610 PA610 |
| **3.3.3.6 Polyesters** |
| Polycarbonate PC, Poly(ethylene terephthalate) PET, Poly(butylene terephthalate) PBT, Poly(phenylene ether) PPE |
| **3.3.3.7 Polysulfones, Polysulfides** |
| Polysulfon PSU, Poly(phenylene sulfide) PPS, Poly(ether sulfone) PES |
| **3.3.3.8 Polyimides, Polyether ketones** |
| Poly(amide imide), PAI; Poly(ether imide), PEI; Polyimide, PI; Poly(ether ether ketone), PEEK |
| **3.3.3.9 Cellulose** |
| Cellulose acetate CA, Cellulose propionate CP, Cellulose acetobutyrate CAB, Ethyl cellulose EC, Vulcanized fiber VF |
| **3.3.3.10 Polyurethanes** |
| Polyurethane PUR, Thermoplastic polyurethane elastomer TPU |
| **3.3.3.11 Thermosets** |
| **Thermosets I** |
| Phenol formaldehyde PF, Urea formaldehyde UF, Melamine formaldehyde MF |
| **Thermosets II** |
| Unsaturated polyester UP, Diallylphthalat DAP, Silicone resin SI, Epoxy resin EP |
| **3.3.3.12 Polymer Blends** |
| **Polymer Blends I** |
| Polypropylene + Ethylene/propylene/diene-rubber PP + EPDM, Poly(acrylonitrile-co-butadiene-co-styrene) + Polycarbonate ABS + PC, Poly(acrylonitrile-co-butadiene-co-styrene) + Polyamide ABS + PA, Poly(acrylonitrile-co-butadiene-co-acrylester) + Polycarbonate ASA + PC |

| Polymer Blends II |
|---|
| Poly(vinyl chloride) + Poly(vinylchloride-co-acrylate) PVC + VC/A, Poly(vinyl chloride) + chlorinated Polyethylene PVC + PE-C, Poly(vinyl chloride) + Poly(acrylonitrile-co-butadiene-co-acrylester) PVC + ASA |
| **Polymer Blends III** |
| Polycarbonate + Poly(ethylene terephthalate) PC + PET, Polycarbonate + Liquid crystall polymer PC + LCP, Polycarbonate + Poly(butylene terephthalate) PC + PBT, Poly(ethylene terephthalate) + Polystyrene PET + PS, Poly(butylene terephthalate) + Polystyrene PBT + PS |
| **Polymer Blends IV** |
| Poly(butylene terephthalate) + Poly(acrylonitrile-co-butadiene-co-acrylester) PBT + ASA, Polysulfon + Poly(acrylonitrile-co-butadiene-co-styrene) PSU + ABS, Poly(phenylene ether) + Poly(styrene-co-butadiene) PPE + SB, Poly(phenylene ether) + Polyamide 66 PPE + PA66, Poly(phenylene ether) + Polystyrene PPE + PS |



## 3.3.1 Structural Units of Polymers

The polymers given in this chapter are divided into polyolefines, vinyl polymers, fluoropolymers, polyacrylics, polyacetals, polyamides, polyesters, polysulfones, polysulfides, polyimides, polyether ketones, cellulose, polyurethanes, and thermosets. The structural units of the polymers are as follows:

### Polyolefines

Polyethylene, PE: $-CH_2-CH_2-$

Polypropylene, PP: $-CH_2-CH(CH_3)-$

Poly(butene-1), PB: $-CH_2-CH(CH_2CH_3)-$

Poly(isobutylene), PIB: $-CH_2-C(CH_3)_2-$

Poly(4-methylpentene-1), PMP: $-CH_2-CH(CH_2CH(CH_3)_2)-$

Polynorbornene:

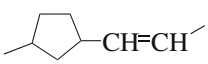

Poly(1,4-butadiene), BR: $-CH_2-CH=CH-CH_2-$

### Vinyl Polymers

Polystyrene, PS:

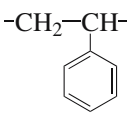

Poly(acrylonitrile), PAN: $-CH_2-CH(CN)-$

Poly(vinyl acetate), PVAC: $-CH_2-CH(OCOCH_3)-$

Poly(vinyl chloride), PVC: $-CH_2-CHCl-$

Poly(vinyl carbazole), PVK:

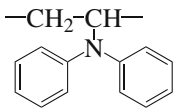

### Fluoropolymers

Poly(tetrafluoroethylene), PTFE: $-CF_2-CF_2-$

Poly(chlorotrifluoroethylene), PCTFE: $-CFCl-CF_2-$

Poly(hexafluoropropylene): $-CF_2-CF(CF_3)-$

### Polyacrylics and Polyacetals

Poly(methyl methacrylate), PMMA: $-CH_2-C(CH_3)(COOCH_3)-$

Poly(acrylic acid), PAA: $-CH_2-CH(COO^-)-$

Poly(oxymethylene), POM: $-CH_2-O-$

### Polyamides

Polyamide 6, PA6: $-CO-(CH_2)_5-NH-$

Polyamide 66, PA66:
—NH—$(CH_2)_6$—NH—CO—$(CH_2)_4$—CO—

Polyamide 11, PA11: —CO—$(CH_2)_{10}$—NH—

Polyamide 12, PA12: —CO—$(CH_2)_{11}$—NH—

Polyamide 610, PA610:
—NH—$(CH_2)_6$—NH—CO—$(CH_2)_8$—CO—

Polyamide 612, PA612:
—NH—$(CH_2)_6$—NH—CO—$(CH_2)_{10}$—CO—

### Polyesters

Polycarbonate, PC:

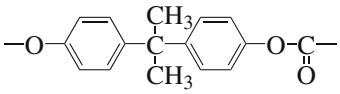

Poly(ethylene terephthalate), PET:

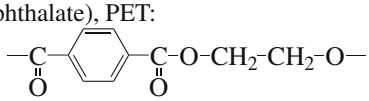

Poly(butylene terephthalate), PBT:

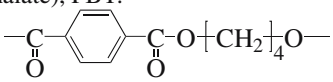

Poly(phenylene ether), PPE:

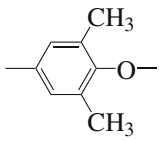

### Polysulfones and Polysulfides

Polysulfone, PSU:

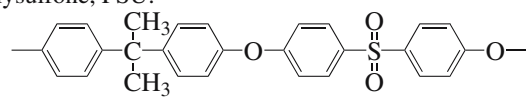

Poly(phenylene sulfide), PPS:

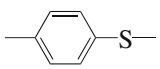

Poly(ether sulfone), PES:

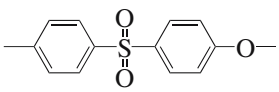

### Polyimides and Polyether Ketones

Poly(amide imide), PAI:

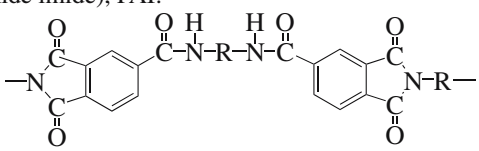

Poly(ether imide), PEI:

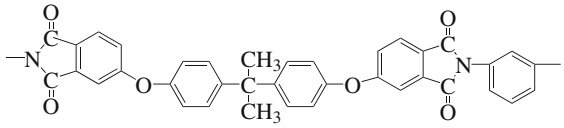

Polyimide, PI:

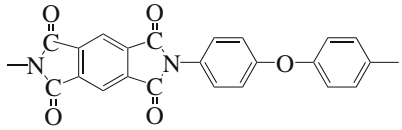

Poly(ether ether ketone), PEEK:

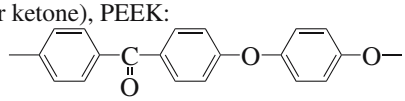

### Cellulose

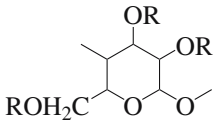

Cellulose acetate, CA: R = $-COCH_3$

Cellulose propionate, CP: R = $-COCH_2CH_3$

Cellulose acetobutyrate, CAB: R = $-COCH_3$ and
R = $-COCH_2CH_2CH_3$

Ethyl cellulose, EC: R = $-CH_2CH_3$

### Polyurethanes

Polyurethane, PUR, TPU:
—CO-NH—$(CH_2)_6$—NH-CO-O—$(CH_2)_4$-O—

### Thermosets

Phenol formaldehyde, PF:

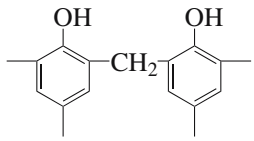

Urea formaldehyde, UF:

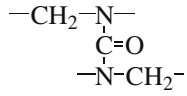

Melamine formaldehyde, MF:

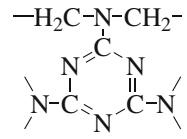

## 3.3.2 Abbreviations

The following abbreviations are used in this chapter. The abbreviations are in accordance with international rules.

| | |
|---|---|
| am | amorphous |
| C | chlorinated |
| co | copolymer |
| cr | crystalline |
| DOP | dioctyl phthalate |
| HI | high impact (modifier) |
| iso | isotactic |
| long | longitudinal |
| LCP | liquid crystal polymer |
| mu | monomer unit |
| pcr | partially crystalline |
| syn | syndiotactic |
| str | strained |
| THF | tetrahydrofuran |
| trans | transverse |

| | |
|---|---|
| DSC | differential scanning calorimetry |
| DTA | differential thermal analysis |

| | |
|---|---|
| CF*a* | carbon fiber content = *a* mass%, e.g. PS-CF20 means polystyrene with 20% carbon fiber |
| GB*a* | content of glass beads, spheres, or balls = *a* mass%, e.g. PS-GB20 means polystyrene with 20% glass beads |
| GF*a* | glass fiber content = *a* mass%, e.g. PS-GF20 means polystyrene with 20% glass fiber |
| MeF*a* | metal fiber content = *a* mass% |

| Abbreviated notations for polymer names | | | |
|---|---|---|---|
| ABS | Poly(acrylonitrile-co-butadiene-co-styrene) | PEI | Poly(ether imide) |
| ASA | Poly(acrylonitrile-co-styrene-co-acrylester) | PES | Poly(ether sulfone) |
| CA | Cellulose acetate | PET | Poly(ethylene terephthalate) |
| CAB | Cellulose acetobutyrate | PF | Phenol formaldehyde |
| COC | Cycloolefine copolymer | PI | Polyimide |
| CP | Cellulosepropionate | PIB | Poly(isobutylene) |
| DAP | Diallylphthalat | PMMA | Poly(methyl methacrylate) |
| EAA | Poly(ethylene-co-acrylic acid) | PMP | Poly(4-methylpenten-1) |
| EC | Ethylcellulose | POM | Poly(oxymethylene) |
| ECTFE | Poly(ethylene-co-chlorotrifluoroethylene) | PP | Polypropylene |
| EPDM | Ethylene/propylene/diene-rubber | PPE | Poly(phenylene ether) |
| EIM | Polyethylene ionomer | PPS | Poly(phenylene sulfide) |
| EP | Epoxide; epoxy | PTFE | Poly(tetrafluoro ethylene) |
| ETFE | Poly(ethylene-co-tetrafluoroethylene) | PVC-P | Poly(vinyl chloride), plastisized with DOP |
| EVA | Poly(ethylene-co-vinylacetate) | PVC-U | Poly(vinyl chloride), unplastisized |
| FEP | Poly(tetrafluoroethylene-co-hexafluoropropylene) | PVK | Poly(vinyl carbazole) |
| HDPE | High density polyethylene | PS | Polystyrene |
| LDPE | Low density polyethylene | PSU | Polysulfone |
| LLDPE | Linear low density polyethylene | PUR | Polyurethane |
| MDPE | Medium density polyethylene | SAN | Poly(styrene-co-acrylonitrile) |
| MF | Melamine formaldehyde | SB | Poly(styrene-co-butadiene) |

| | | | |
|---|---|---|---|
| PA | Polyamide | SI | Silicone resin |
| PAI | Poly(amide imide) | TPU | Thermoplastic polyurethane elastomer |
| PB | Polybutene-1 | UF | Urea formaldehyde |
| PBT | Poly(butylene terephthalate) | UHMWPE | Ultra high molecular weight polyethylene |
| PC | Polycarbonate | UP | Unsaturated polyester |
| PCTFE | Poly(trifluorochloroethylene) | VC/A | Poly(vinyl chloride-co-acrylate) |
| PE | Polyethylene | VF | Vulcanized fiber |
| PEEK | Poly(ether ether ketone) | | |



## 3.3.3 Tables and Figures

The following tables and diagrams contain physical and physicochemical properties of common polymers, copolymers, and polymer blends. The materials are arranged according to increasing number of functional groups, i. e. polyolefines, vinyl polymers, fluoropolymers, polyacrylics, polyacetals, polyamides, polyesters, and polymers with special functional groups [3.2–16].

### 3.3.3.1 Polyolefines

*Polyethylene, HDPE, MDPE.* Applications: injection molding for domestic parts and industrial parts; blow molding for containers and sports goods; extrusion for pressure pipes, pipes, electrical insulating material, bags, envelopes, and tissue.

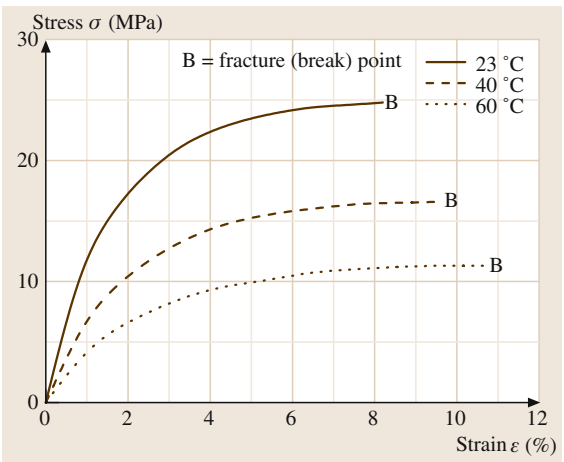


**Fig. 3.3-2** Polyethylene, HDPE: stress versus strain

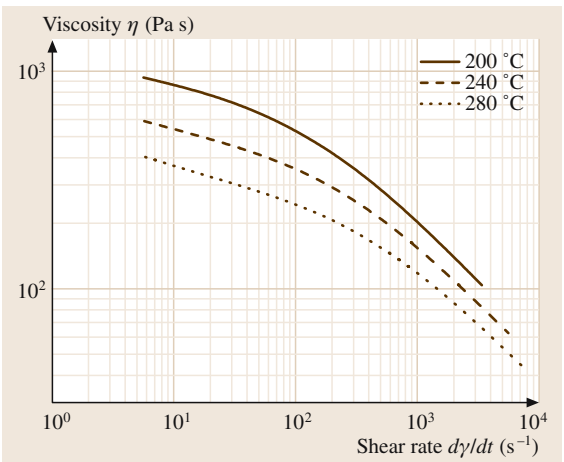


**Fig. 3.3-3** Polyethylene, HDPE: viscosity versus shear rate

**Table 3.3-1** Polyethylene: high-density, HDPE; medium-density, MDPE; low-density, LDPE; linear low-density, LLDPE; ultrahigh-molecular-weight, UHMWPE

| | HDPE | MDPE | LDPE | LLDPE | UHMWPE |
|---|---|---|---|---|---|
| Melting temperature $T_m$ (°C) | 126–135 | 120–125 | 105–118 | 126 | 130–135 |
| Enthalpy of fusion $\Delta H_u$ (kJ/mol) (mu) | 3.9–4.1 | | 3.9–4.1 | | |
| Entropy of fusion $\Delta S_u$ (J/(K mol)) (mu) | 9.6–9.9 | | 9.6–9.9 | | |
| Heat capacity $c_p$ (kJ/(kg K))<br>Temperature coefficient $dc_p/dT$ (kJ/(kg K$^2$)) | 2.1–2.7 | | 2.1–2.5 | | 1.7–1.8 |
| Enthalpy of combustion $\Delta H_c$ (kJ/g) | −46.4 | −46.5 | −46.5 | | |
| Glass transition temperature $T_g$ (°C) | −110 | −110 | | −110 | −110 |
| Vicat softening temperature $T_V$50/50 (°C) | 60–80 | | 45–60 | | 74 |
| Thermal conductivity λ (W/(m K)) | 0.38–0.51 | | 0.32–0.40 | | 0.41 |
| Density $\varrho$ (g/cm$^3$) | 0.94–0.96 | 0.925–0.935 | 0.915–0.92 | ≈ 0.935 | 0.93–0.94 |
| Coefficient of thermal expansion $\alpha$ ($10^{-5}$/K) (linear) (296–328 K) | 14–18 | 18–23 | 23–25 | 18–20 | 15–20 |
| Compressibility $\kappa$ ($10^{-4}$/MPa) (cubic) | | | 2.2 | | |
| Elastic modulus $E$ (GPa) | 0.6–1.4 | 0.4–0.8 | 0.2–0.4 | 0.3–0.7 | 0.7–0.8 |
| Shear modulus $G$ (GPa) | 0.85 | 0.66 | 0.16–0.25 | | |
| Poisson's ratio $\mu$ | | | | | |
| Stress at yield $\sigma_y$ (MPa) | 18–30 | 11–18 | 8–10 | 20–30 | ≈ 22 |
| Stress at 50% strain $\sigma_{50}$ (MPa) | | | | | |
| Strain at yield $\varepsilon_y$ (%) | 8–12 | 10–15 | ≈ 20 | ≈ 15 | ≈ 15 |
| Stress at fracture $\sigma_b$ (MPa) | 18–35 | | 8–23 | | |
| Strain at fracture $\varepsilon_b$ (%) | 100–1000 | | 300–1000 | | |
| Impact strength (Charpy) (kJ/m$^2$) | | | 13–25 | | |
| Notched impact strength (Charpy) (kJ/m$^2$) | | | 3–5 | | |
| Sound velocity $v_s$ (m/s) (longitudinal) | 2430 | | 2400 | | |
| Sound velocity $v_s$ (m/s) (transverse) | 950 | | 1150 | | |
| Shore hardness $D$ | 58–63 | 45–60 | 45–51 | 38–60 | 62 |
| Volume resistivity $\rho_e$ (Ω m) > $10^{15}$ | > $10^{15}$ | > $10^{15}$ | > $10^{15}$ | > $10^{15}$ | |
| Surface resistivity $\sigma_e$ (Ω) | > $10^{14}$ | > $10^{14}$ | > $10^{14}$ | > $10^{14}$ | > $10^{14}$ |
| Electric strength $E_B$ (kV/mm) | 30–40 | 30–40 | 30–40 | 30–40 | 30–40 |
| Relative permittivity $\varepsilon_r$ (100 Hz) | 2.4 | 2.3 | 2.3 | 2.3 | 2–2.4 |
| Dielectric loss tan $\delta$ ($10^{-4}$) (100 Hz) | 1–2 | 2 | 2–2.4 | 2 | 2 |
| Refractive index $n_D$ (589 nm)<br>Temperature coefficient $dn_D/dT$ ($10^{-4}$/K) | 1.53 | | 1.51–1.42 | | |
| Steam permeation (g/(m$^2$ d)) | 0.9 (40 µm) | | 1 (100 µm) | | |
| Gas permeation (cm$^3$/(m$^2$ d bar)), 23 °C, 100 µm | 700 ($N_2$)<br>1800 ($O_2$)<br>10 000 ($CO_2$)<br>1100 (air) | | 700 ($N_2$)<br>2000 ($O_2$)<br>10 000 ($CO_2$)<br>1100 (air) | | |
| Melt viscosity–molar-mass relation | | | | | |
| Viscosity–molar-mass relation | $[\eta] = 62 \times 10^{-3} M^{0.70}$ (decalin, 135 °C)<br>$[\eta] = 51 \times 10^{-3} M^{0.725}$ (tetralin, 130 °C) | | | | |

**Table 3.3-2** Polyethylene, HDPE: heat capacity, thermal conductivity, and coefficient of thermal expansion

| Temperature $T$ (°C) | −200 | −150 | −100 | −50 | 0 | 20 | 50 | 100 | 150 |
|---|---|---|---|---|---|---|---|---|---|
| Heat capacity $c_p$ (kJ/(kg K)) | 0.55 | 0.84 | 1.10 | 1.34 | 1.64 | | 2.05 | 2.86 | |
| Thermal conductivity λ (W/(m K)) | | 0.62 | 0.56 | 0.50 | 0.44 | | 0.38 | 0.32 | 0.25 |
| Coefficient of thermal expansion $\alpha$ ($10^{-5}$/K) (linear) | 4.5 | 6.8 | 9.5 | 12.4 | | 16.9 | 33.0 | 69.0 | |

**Table 3.3-3** Polyethylene, LDPE: heat capacity and thermal conductivity

| Temperature $T$ (°C) | −200 | −150 | −100 | −50 | 0 | 20 | 50 | 100 | 150 |
|---|---|---|---|---|---|---|---|---|---|
| Heat capacity $c_p$ (kJ/(kg K)) | 0.55 | 0.84 | 1.10 | 1.43 | 1.90 | | 2.73 | | |
| Thermal conductivity λ (W/(m K)) | | 0.36 | 0.38 | 0.38 | 0.35 | | 0.31 | 0.24 | 0.25 |

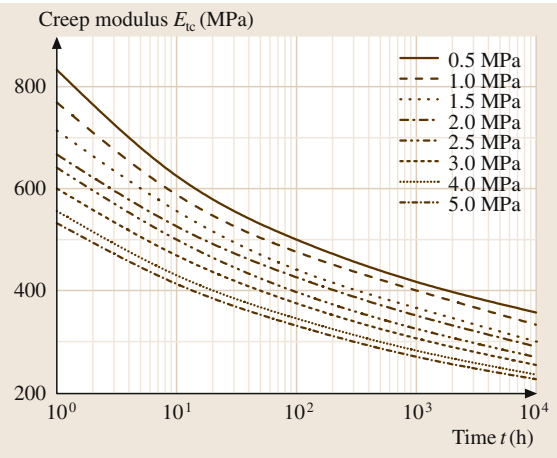


**Fig. 3.3-4** Polyethylene, HDPE: creep modulus versus time, at 23 °C

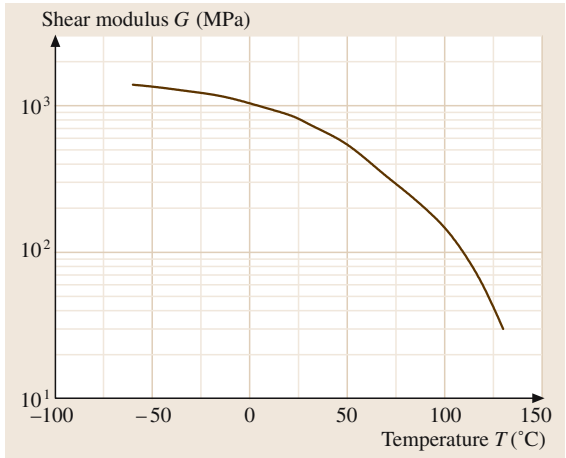


**Fig. 3.3-5** Polyethylene, HDPE: shear modulus versus temperature

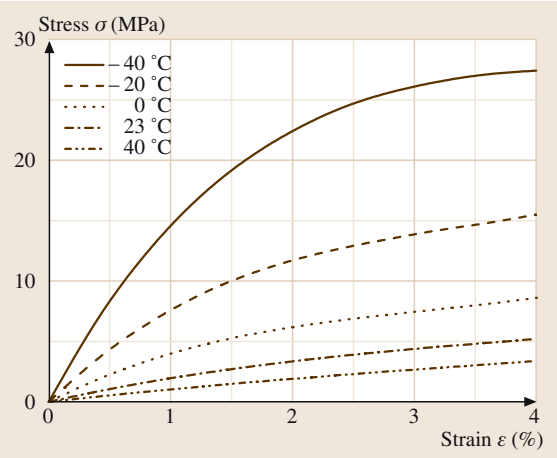


**Fig. 3.3-6** Polyethylene, LDPE: stress versus strain

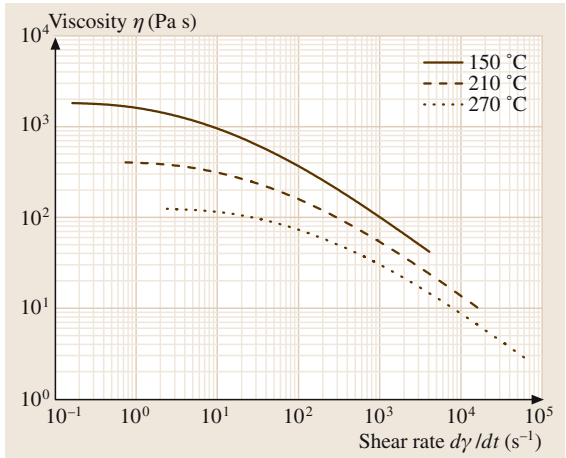


**Fig. 3.3-7** Polyethylene, LDPE: viscosity versus shear rate

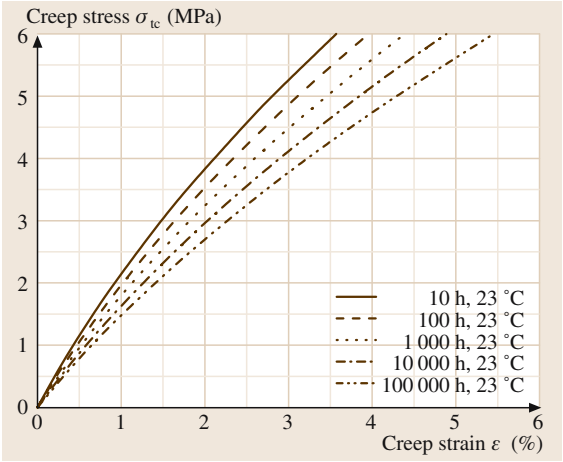


**Fig. 3.3-8** Polyethylene, UHMWPE: isochronous stress versus strain

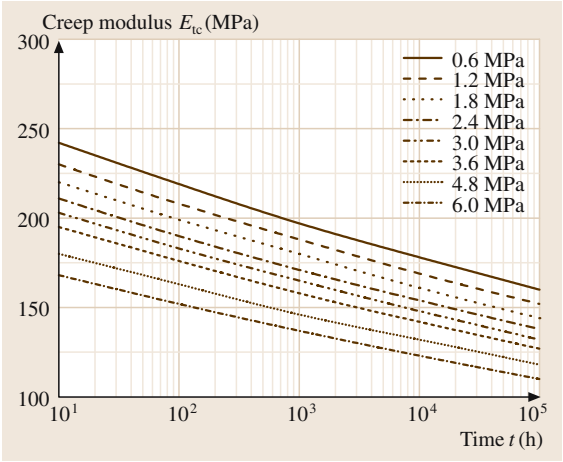


**Fig. 3.3-9** Polyethylene, UHMWPE: creep modulus versus time

*Polyethylene, LDPE*. Applications: all kinds of sheeting, bags, insulating material, hollow bodies, bottles, injection-molded parts.

*Polyethylene, LLDPE*. Applications: foils, bags, waste bags, injection-molded parts, rotatory-molded parts.

*Polyethylene UHMWPE, Applications*: mechanical engineering parts, food wrapping, commercial packaging, textile industry parts, electrical engineering parts, paper industry parts, low temperature materials, medical parts, chemical engineering parts, electroplating.

*Poly(ethylene-co-vinyl acetate), EVA*. Applications: films, deep-freeze packaging, laminates, fancy leather, food packaging, closures, ice trays, bags, gloves, fittings, pads, gaskets, plugs, toys.

*Polyethylene ionomer, EIM*. Applications: transparent tubes for water and liquid foods, transparent films, bottles, transparent coatings, adhesion promoters.

*Cycloolefine copolymer, COC*. Applications: precision optics, optical storage media, lenses, medical and labware applications.

*Poly(ethylene-co-acrylic acid), EAA*. Applications: packaging foils, sealing layers, tubing.

*Polypropylene, PP*. Applications: injection molding for domestic parts, car parts, electric appliances, packing materials, and pharmaceutical parts; blow

**Table 3.3-4** Poly(ethylene-co-vinyl acetate), EVA; polyethylene ionomer, EIM; cycloolefine copolymer, COC (poly-(ethylene-co-norbornene)); poly(ethylene-co-acrylic acid), EAA

| | EVA | EIM | COC | EAA |
|---|---|---|---|---|
| Melting temperature $T_m$ (°C) | 90–110 | 95–110 | | 92–103 |
| Enthalpy of fusion $\Delta H_u$ (kJ/mol) (mu) | | | | |
| Entropy of fusion $\Delta S_u$ (J/(K mol)) (mu) | | | | |
| Heat capacity $c_p$ (kJ/(kg K))<br>Temperature coefficient $dc_p/dT$ (kJ/(kg $K^2$)) | | 2.2 | | |
| Enthalpy of combustion $\Delta H_c$ (kJ/g) | | | | |
| Glass transition temperature $T_g$ (°C) | 66 | | 80–180 | |
| Vicat softening temperature $T_V$50/50 (°C) | 63–96 VST/A50 | | | |
| Thermal conductivity λ (W/(m K)) | 0.28–0.35 | 0.24 | 0.16 | |
| Density $\varrho$ (g/$cm^3$) | 0.93–0.94 | 0.94–0.95 | 1.02 | 0.925–0.935 |
| Coefficient of thermal expansion $\alpha$ ($10^{-5}$/K) (linear) | ≈ 25 | 10–15 | 6–7 | ≈ 20 |

**Table 3.3-4** Poly(ethylene-co-vinyl acetate), EVA; polyethylene ionomer, EIM; . . . , cont.

| | EVA | EIM | COC | EAA |
|---|---|---|---|---|
| Compressibility $\kappa$ ($10^{-4}$/MPa) (cubic) | | | | |
| Elastic modulus $E$ (GPa) | 0.03–0.1 | 0.15–0.2 | 2.6–3.2 | 0.04–0.13 |
| Shear modulus $G$ (GPa) | 0.04–0.14 | | | |
| Poisson's ratio $\mu$ | | | | |
| Stress at yield $\sigma_y$ (MPa) | 5–8 | 7–8 | 66 | 4–7 |
| Strain at yield $\varepsilon_y$ (%) | | > 20 | 3.5–10 | > 20 |
| Stress at 50% strain $\sigma_{50}$ (MPa) | 4–9 | | | |
| Stress at fracture $\sigma_b$ (MPa) | 16–23 | 21–35 | 66 | |
| Strain at fracture $\varepsilon_b$ (%) | 700 | 250–500 | 3–10 | |
| Impact strength (Charpy) (kJ/m$^2$) | | | 13–20 | |
| Notched impact strength (Charpy) (kJ/m$^2$) | | | 1.7–2.6 | |
| Sound velocity $v_s$ (m/s) (longitudinal) | | | | |
| Sound velocity $v_s$ (m/s) (transverse) | | | | |
| Shore hardness $D$ | 34–44 | | | |
| Volume resistivity $\rho_e$ (Ω m) | > $10^{14}$ | > $10^{15}$ | > $10^{13}$ | > $10^{14}$ |
| Surface resistivity $\sigma_e$ (Ω) | > $10^{13}$ | > $10^{13}$ | $10^{14}$ | > $10^{13}$ |
| Electric strength $E_B$ (kV/mm) | 30–35 | 40 | | 30–40 |
| Relative permittivity $\varepsilon_r$ (100 Hz) | 2.5–3 | ≈ 2.4 | 2.35 | 2.5–3 |
| Dielectric loss tan $\delta$ ($10^{-4}$) (100 Hz) | 20–40 | ≈ 30 | 0.2 | 30–130 |
| Refractive index $n_D$ (589 nm) | | 1.51 | 1.53 | |
| Temperature coefficient $dn_D/dT$ ($10^{-4}$/K) | | | | |
| Steam permeation (g/(m$^2$ d)) (25 µm) | | 25 | 1–1.8 | |
| Gas permeation (cm$^3$/(m$^2$ d bar)) (25 µm) | | 9300 ($O_2$) | | |
| Melt viscosity–molar-mass relation | | | | |
| Viscosity–molar-mass relation | | | | |

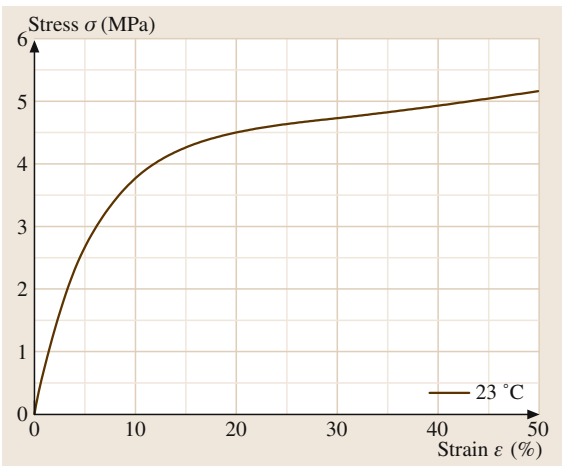


**Fig. 3.3-10** Poly(ethylene-co-vinylacetate), EVA: stress versus strain

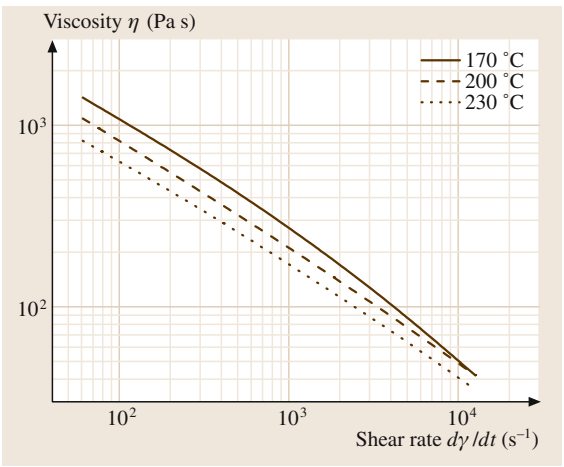


**Fig. 3.3-11** Poly(ethylene-co-vinylacetate), EVA: viscosity versus shear rate

**Table 3.3-5** Polypropylene, PP; polybutene-1, PB; polyisobutylene, PIB; poly(4-methylpentene-1), PMP

| | PP | PB | PIB | PMP |
|---|---|---|---|---|
| Melting temperature $T_m$ (°C) | 160–170 | 126 | | 230–240 |
| Enthalpy of fusion $\Delta H_u$ (kJ/mol) (mu) | 7–10 | | | |
| Entropy of fusion $\Delta S_u$ (J/(K mol)) (mu) | 15–20 | | | |
| Heat capacity $c_p$ (kJ/(kg K))<br>Temperature coefficient $dc_p/dT$ (kJ/(kg K$^2$)) | 1.68 | | | |
| Enthalpy of combustion $\Delta H_c$ (kJ/g) | −44 | | −45 | |
| Glass transition temperature $T_g$ (°C) | 0 to −10 | 78 | −70 | |
| Vicat softening temperature $T_V$50/50 (°C) | 60–102 | 108–113 | | |
| Thermal conductivity $\lambda$ (W/(m K)) | 0.22 | 0.22 | 0.12–0.20 | 0.17 |
| Density $\varrho$ (g/cm$^3$) | 0.90–0.915 | 0.905–0.920 | 0.91–0.93 | 0.83 |
| Coefficient of thermal expansion $\alpha$ ($10^{-5}$/K) (linear) | 12–15 | 13 | 8–12 | 12 |
| Compressibility $\kappa$ ($10^{-4}$/MPa) (cubic) | 2.2 | | | |
| Elastic modulus $E$ (GPa) | 1.3–1.8 | 0.21–0.26 | | 1.1–2.0 |
| Shear modulus $G$ (GPa) | | | | |
| Poisson's ratio $\mu$ | | | | |
| Stress at yield $\sigma_y$ (MPa) | 25–40 | 16–24 | | |
| Strain at yield $\varepsilon_y$ (%) | 8–18 | 24 | | |
| Stress at 50% elongation $\sigma_{50}$ (MPa) | | | | |
| Stress at fracture $\sigma_b$ (MPa) | | 30–38 | 2–6 | 25–28 |
| Strain at fracture $\varepsilon_b$ (%) | > 50 | 300–380 | > 1000 | 10–50 |
| Impact strength (Charpy) (kJ/m$^2$) | 60–140 | | | |
| Notched impact strength (Charpy) (kJ/m$^2$) | 3–10 | | | |
| Sound velocity $v_s$ (m/s) (longitudinal) | 2650 | | 1950 | 2180 |
| Sound velocity $v_s$ (m/s) (transverse) | 1300 | | | 1080 |
| Shore hardness $D$ | 69–77 | | | |
| Volume resistivity $\rho_e$ ($\Omega$ m) | > $10^{14}$ | > $10^{14}$ | > $10^{13}$ | > $10^{14}$ |
| Surface resistivity $\sigma_e$ ($\Omega$) | > $10^{13}$ | | | |
| Electric strength $E_B$ (kV/mm) | 30–70 | 18–40 | 23–25 | |
| Relative permittivity $\varepsilon_r$ (100 Hz) | 2.3 | 2.5 | 2.3 | 2.1 |
| Dielectric loss tan $\delta$ ($10^{-4}$) (100 Hz) | 2.5 | 20–50 | < 4 | 15 |
| Refractive index $n_D$ (589 nm)<br>Temperature coefficient $dn_D/dT$ ($10^{-4}$/K) | 1.50 | | | 1.46 |
| Steam permeation (g/(m$^2$ d)) (40 µm) | 2.1 | | | |
| Gas permeation (cm$^3$/(m$^2$ d bar)) (40 µm) | 430 ($N_2$)<br>1900 ($O_2$)<br>6100 ($CO_2$)<br>700 (air) | | | |
| Melt viscosity–molar-mass relation | | | | |
| Viscosity–molar-mass relation | $[\eta] = 20 \times 10^{-3} M^{0.67}$ (PIB, toluene, 30 °C) | | | |

**Table 3.3-6** Polypropylene, PP: heat capacity, thermal conductivity, and coefficient of thermal expansion

| Temperature $T$ (°C) | −200 | −150 | −100 | −50 | 0 | 20 | 50 | 100 | 150 |
|---|---|---|---|---|---|---|---|---|---|
| Heat capacity $c_p$ (kJ/(kg K)) | 0.46 | 0.77 | 1.03 | 1.28 | 1.57 | 1.68 | 1.92 | 2.35 | |
| Thermal conductivity λ (W/(m K)) | 2.3 | 0.17 | 0.19 | 0.21 | 0.22 | 0.22 | 0.22 | 0.20 | |
| Coefficient of thermal expansion $\alpha$ ($10^{-5}$/K) (linear) | | 5.8 | 6.9 | 7.6 | 19.1 | 19.4 | 14.3 | 22.6 | 29.4 |

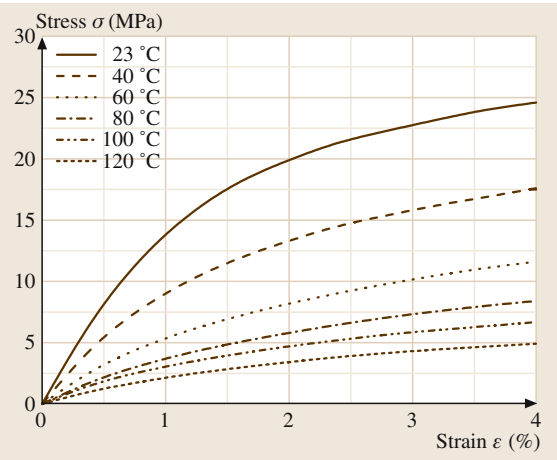


**Fig. 3.3-12** Polypropylene, PP: stress versus strain

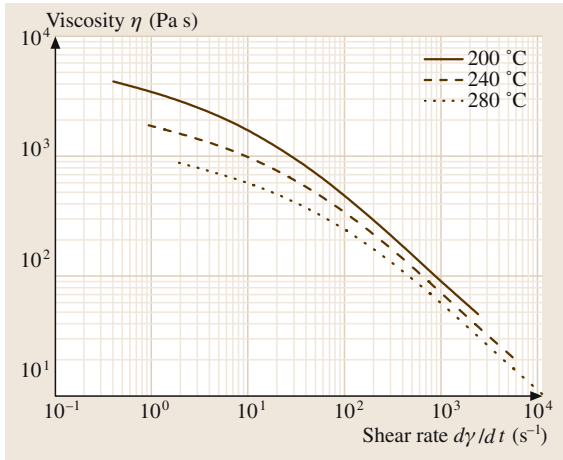


**Fig. 3.3-13** Polypropylene, PP: viscosity versus shear rate

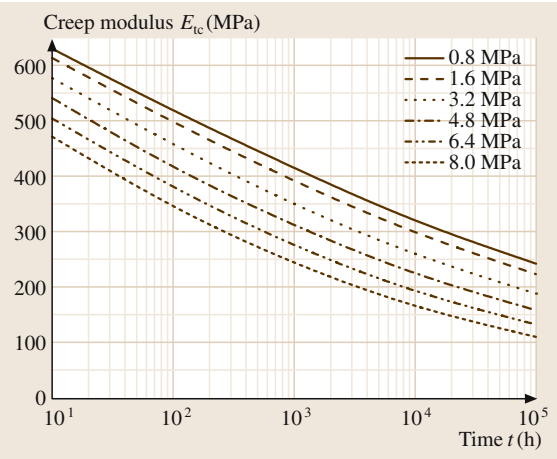


**Fig. 3.3-14** Polypropylene, PP: creep modulus versus time, at 23 °C

molding for cases, boxes, and bags; pressure molding for blocks and boards; tissue coating; extrusion for pressure pipes, pipes, semiproducts, flexible tubing, textile fabrics, fibers, sheets; foamed polymers for sports goods, boxes, cases, handles, and domestic parts.

*Polybutene-1, PB*. Applications: tubing, pipes, fittings, hollow bodies, cables, foils, packing.

*Polyisobutylene, PIB*. Applications: adhesives, sealing compounds, electrical insulating oils, viscosity improvers.

*Poly(4-methylpentene-1), PMP*. Applications: glasses, light fittings, molded parts, foils, packing, rings, tubes, fittings, cable insulation.

### 3.3.3.2 Vinyl Polymers

*Polystyrene, PS*. Applications: packaging, expanded films, toys, artificial wood, food holders, housings, plates, cases, boxes, glossy sheets, containers, medical articles, panels.

*Poly(styrene-co-butadiene), SB*. Applications: flame-retardant articles, housings.

*Poly(styrene-co-acrylnitrile), SAN*. Applications: food holders, cases, shelves, covers, automotive and electrical parts, sheets, profiles, containers, plastic windows, doors, cosmetic items, medical items, pharmaceutical items, fittings, components, musical items, toys, displays, lighting, food compartments, cassettes, tableware, engineering parts, housings.

**Table 3.3-7** Polystyrene, PS; poly(styrene-co-butadiene), SB; poly(styrene-co-acrylonitrile), SAN

| | PS | SB | SAN |
|---|---|---|---|
| Melting temperature $T_m$ (°C) | > 243.2 (iso), > 287.5 (syn) | | |
| Enthalpy of fusion $\Delta H_u$ (KJ/mol) (mu) | 8.682 (iso), 8.577 (syn) | | |
| Entropy of fusion $\Delta S_u$ (J/(K mol)) (mu) | 16.8 (iso), 15.3 (syn) | | |
| Heat capacity $c_p$ (kJ/(kg K))<br>Temperature coefficient $dc_p/dT$ (kJ/(kg K$^2$)) | 1.2–1.4<br>$4.04\times10^{-3}$ (323 K) | 1.3 | 1.3 |
| Enthalpy of combustion $\Delta H_c$ (kJ/g) | −41.6 | −36 to −38 | −36 to −38 |
| Glass transition temperature $T_g$ (°C) | 95–100 | 90–95 | 110 |
| Vicat softening temperature $T_V$50/50 (°C) | 80–100 | 80–110 | 105–120 |
| Thermal conductivity λ (W/(m K)) | 0.16 | 0.18 | 0.18 |
| Density $\varrho$ (g/cm$^3$) | 1.05 | 1.05–1.06 | 1.07–1.08 |
| Coefficient of thermal expansion $\alpha$ ($10^{-5}$/K) (linear) | 6–8 | 8–10 | 7–8 |
| Compressibility $\kappa$ ($10^{-4}$/MPa) (cubic) | 2.2 | | |
| Elastic modulus $E$ (GPa) | 3.1–3.3 | 2.0–2.8 | 3.5–3.9 |
| Shear modulus $G$ (GPa) | 1.2 | 0.6 | 1.5 |
| Poisson's ratio $\mu$ | 0.38 | | |
| Stress at yield $\sigma_y$ (MPa) | 50 | 25–45 | |
| Strain at yield $\varepsilon_y$ (%) | | 1.1–2.5 | |
| Stress at 50% elongation $\sigma_{50}$ (MPa) | | | |
| Stress at fracture $\sigma_b$ (MPa) | 30–55 | 26–38 | 65–85 |
| Strain at fracture $\varepsilon_b$ (%) | 1.5–3 | 25–60 | 2.5–5 |
| Impact strength (Charpy) (kJ/m$^2$) | 13–25 | 50–105 | |
| Notched impact strength (Charpy) (kJ/m$^2$) | 3–5 | 5–10 | 2–4 |
| Sound velocity $v_s$ (m/s) (longitudinal) | 2400 | | |
| Sound velocity $v_s$ (m/s) (transverse) | 1150 | | |
| Shore hardness $D$ | 78 | | |
| Volume resistivity $\rho_e$ (Ω m) | > $10^{14}$ | > $10^{14}$ | $10^{14}$ |
| Surface resistivity $\sigma_e$ (Ω) | > $10^{14}$ | > $10^{13}$ | $10^{14}$ |
| Electric strength $E_B$ (kV/mm) | 30–70 | 45–65 | 30–60 |
| Relative permittivity $\varepsilon_r$ (100 Hz) | 2.4–2.5 (am); 2.61 (cr) | 2.4–2.6 | 2.8–3 |
| Dielectric loss tan δ ($10^{-4}$) (100 Hz) | 1–2 | 1–3 | 40–50 |
| Refractive index $n_D$ (589 nm)<br>Temperature coefficient $dn_D/dT$ ($10^{-4}$/K) | 1.58–1.59<br>−1.42 | | 1.57 |
| Steam permeation (g/(m$^2$ d)) (100 µm) | 12 | | |
| Gas permeation (cm$^3$/(m$^2$ d bar)) (100 µm) | 2500 ($N_2$)<br>1000 ($O_2$)<br>5200 ($CO_2$) | | |
| Melt viscosity–molar-mass relation | $\eta = 13.04M^{3.4}$ (217 °C) | | |
| Viscosity–molar-mass relation | $[\eta] = 11.3\times10^{-3}M^{0.73}$ (PS, toluene, 25 °C) | | |

**Table 3.3-8** Polystyrene, PS: heat capacity, thermal conductivity, and coefficient of thermal expansion

| Temperature $T$ (°C) | −200 | −150 | −100 | −50 | 0 | 20 | 50 | 100 | 150 | 200 |
|---|---|---|---|---|---|---|---|---|---|---|
| Heat capacity $c_p$ (kJ/(kg K)) | | | | 0.89 | 1.09 | | 1.34 | 1.68 | 2.03 | 2.19 |
| Thermal conductivity λ (W/(m K)) | | 0.13 | 0.14 | 0.14 | 0.16 | 0.16 | 0.16 | 0.16 | 0.16 | |
| Coefficient of thermal expansion $\alpha$ ($10^{-5}$/K) (linear) | 3.9 | 5.1 | 6.1 | 6.7 | | 7.1 | 10.0 | 17.6 | 18.0 | 17.4 |

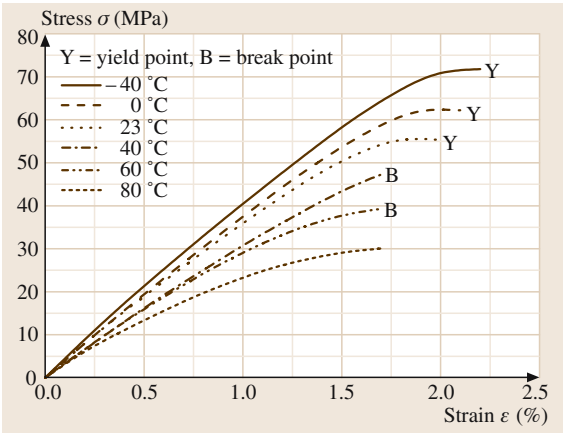


**Fig. 3.3-15** Polystyrene, PS: stress versus strain

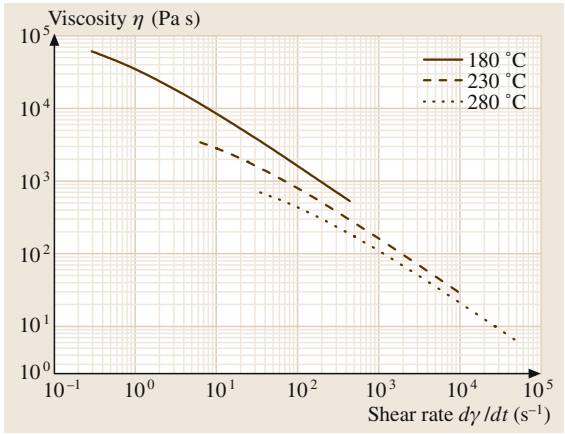


**Fig. 3.3-16** Polystyrene, PS: viscosity versus shear rate

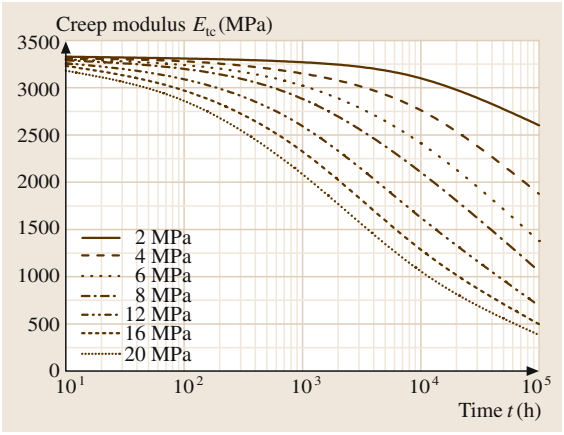


**Fig. 3.3-17** Polystyrene, PS: creep modulus versus time, at 23 °C

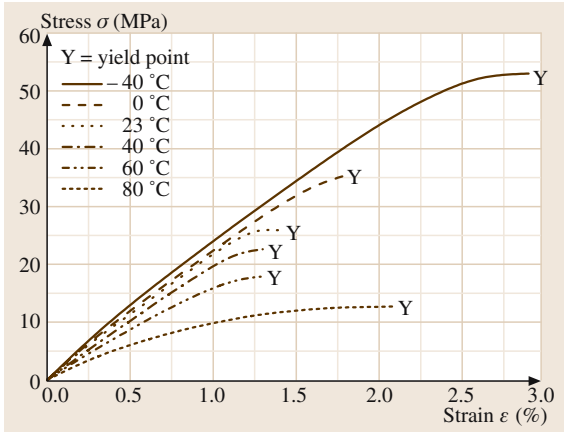


**Fig. 3.3-18** Poly(styrene-co-butadiene), SB: stress versus strain

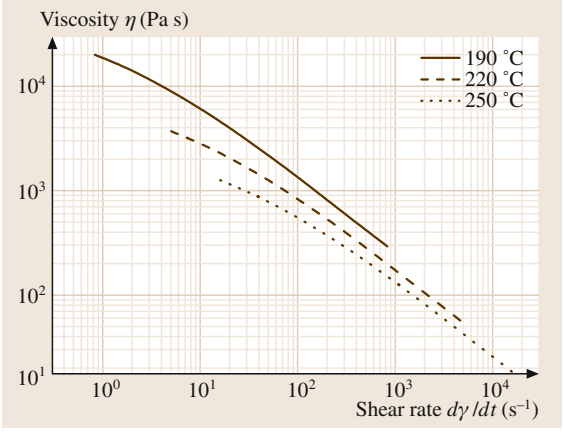


**Fig. 3.3-19** Poly(styrene-co-butadiene), SB: viscosity versus shear rate

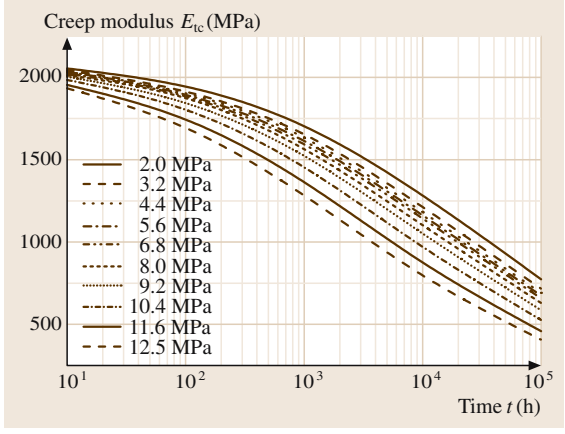


**Fig. 3.3-20** Poly(styrene-co-butadiene), SB: creep modulus versus time

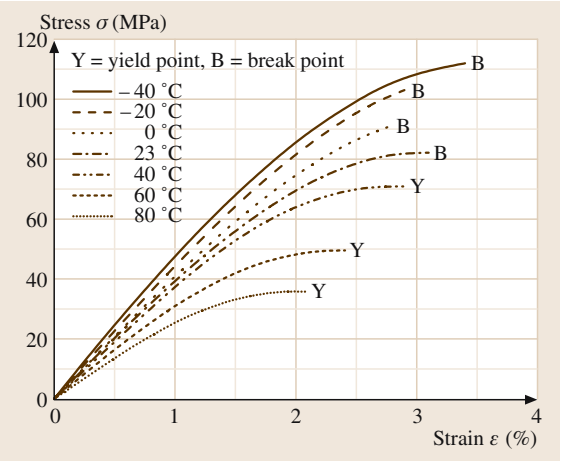


**Fig. 3.3-21** Poly(styrene-co-acrylonitrile), SAN: stress versus strain

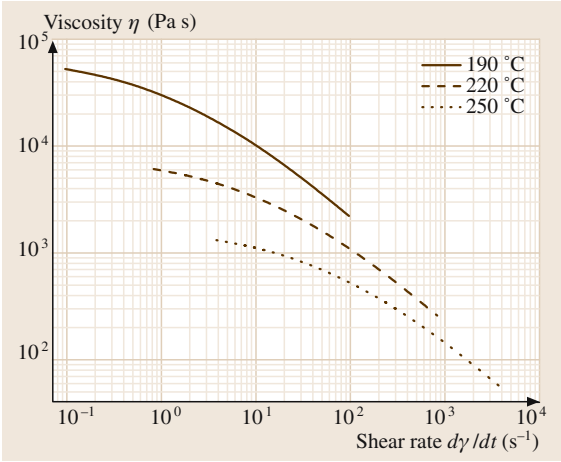


**Fig. 3.3-22** Poly(styrene-co-acrylonitrile), SAN: viscosity versus shear rate

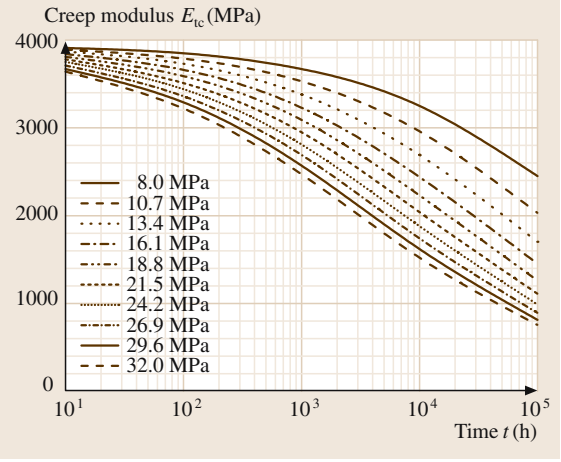


**Fig. 3.3-23** Poly(styrene-co-acrylonitrile), SAN: creep modulus versus time

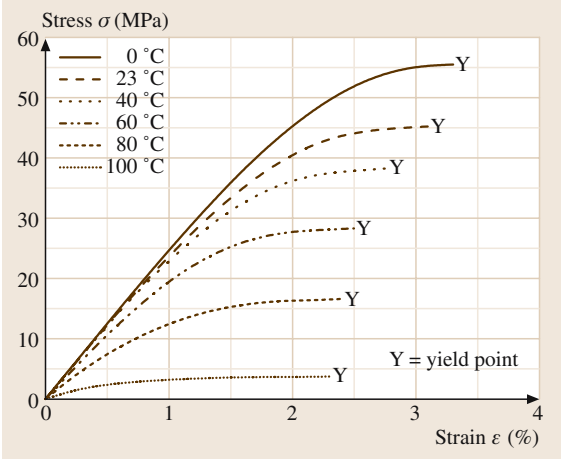


**Fig. 3.3-24** Poly(acrylonitrile-co-butadiene-co-styrene), ABS: stress versus strain

*Poly(vinyl carbazole), PVK*. Applications: electrical insulating materials.

*Poly(acrylonitrile-co-butadiene-co-styrene), ABS*. Applications: housings, boxes, cases, tools, office equipment, helmets, pipes, fittings, frames, toys, sports equipment, housewares, packaging, panels, covers, automotive interior parts, food packaging, furniture, automobile parts.

*Poly(acrylonitrile-co-styrene-co-acrylester), ASA*. Applications: outdoor applications, housings, covers, sports equipment, fittings, garden equipment, antennas.

*Poly(vinyl chloride), PVC-U*. Applications: extruded profiles, sealing joints, jackets, furniture, claddings, roller shutters, fences, barriers, fittings, injection-molded articles, sheets, films, plates, bottles, coated fabrics, layers, toys, bumpers, buoys, car parts, cards, holders, sleeves, pipes, boxes, inks, lacquers, adhesives, foams.

*Poly(vinyl chloride), PVC-P1, PVC-P2*. Applications: flexible tubes, technical items, compounds for insulation and jacketing, joints, seals, pipes, profiles, soling, tubes, floor coverings, wall coverings, car undersealing, mastics, foams, coatings, cap closures,

**Table 3.3-9** Poly(vinyl carbazole), PVK; poly(acrylonitrile-co-butadiene-co-styrene), ABS; poly(acrylonitrile-co-styrene-co-acrylester), ASA

| | PVK | ABS | ASA |
|---|---|---|---|
| Melting temperature $T_m$ (°C) | | | |
| Enthalpy of fusion $\Delta H_u$ (kJ/mol) (mu) | | | |
| Entropy of fusion $\Delta S_u$ (J/(K mol)) (mu) | | | |
| Heat capacity $c_p$ (kJ/(kg K))<br>Temperature coefficient $dc_p/dT$ (kJ/(kg K$^2$)) | | 1.3 | 1.3 |
| Enthalpy of combustion $\Delta H_c$ (kJ/g) | | −35 | |
| Glass transition temperature $T_g$ (°C) | 173 | 80–110 | 100 |
| Vicat softening temperature $T_V$50/50 (°C) | | 95–105 | 90–102 |
| Thermal conductivity $\lambda$ (W/(m K)) | 0.29 | 0.18 | 0.18 |
| Density $\varrho$ (g/cm$^3$) | | 1.03–1.07 | 1.07 |
| Coefficient of thermal expansion $\alpha$ ($10^{-5}$/K) (linear) | 1.19 | 8.5–10 | 9.5 |
| Compressibility $\kappa$ (1/MPa) (cubic) | | | |
| Elastic modulus $E$ (GPa) | 3.5 | 2.2–3.0 | 2.3–2.9 |
| Shear modulus $G$ (GPa) | | 0.7–0.9 | 0.7–0.9 |
| Poisson's ratio $\mu$ | | | |
| Stress at yield $\sigma_y$ (MPa) | | 45–65 | 40–55 |
| Strain at yield $\varepsilon_y$ (%) | | 2.5–3 | 3.1–4.3 |
| Stress at 50% elongation $\sigma_{50}$ (MPa) | | | |
| Stress at fracture $\sigma_b$ (MPa) | 20–30 | 15–30 | |
| Strain at fracture $\varepsilon_b$ (%) | | 55–80 | |
| Impact strength (Charpy) (kJ/m$^2$) | | 40–1000 | 105–118 |
| Notched impact strength (Charpy) (kJ/m$^2$) | | | |
| Sound velocity $v_s$ (m/s) (longitudinal) | | 2040–2160 | |
| Sound velocity $v_s$ (m/s) (transverse) | | 830–930 | |
| Shore hardness $D$ | | | |
| Volume resistivity $\rho_e$ (Ω m) | $> 10^{14}$ | $10^{12}$–$10^{13}$ | $10^{12}$–$10^{14}$ |
| Surface resistivity $\sigma_e$ (Ω) | $10^{14}$ | $> 10^{13}$ | $10^{13}$ |
| Electric strength $E_B$ (kV/mm) | | 30–40 | |
| Relative permittivity $\varepsilon_r$ (100 Hz) | | 2.8–3.1 | 3.4–4 |
| Dielectric loss tan $\delta$ ($10^{-4}$) (100 Hz) | 6–10 | 90–160 | 90–100 |
| Refractive index $n_D$ (589 nm)<br>Temperature coefficient $dn_D/dT$ (1/K) | | 1.52 | |
| Steam permeation (g/(m$^2$ d)) (100 µm) | | 27–33 | 30–35 |
| Gas permeation (cm$^3$/(m$^2$ d bar)) (100 µm) | | 100–200($N_2$)<br>400–900 ($O_2$) | 60–70 ($N_2$)<br>150–180 ($O_2$)<br>6000–8000 ($CO_2$) |
| Melt viscosity–molar-mass relation | | | |
| Viscosity–molar-mass relation | | | |

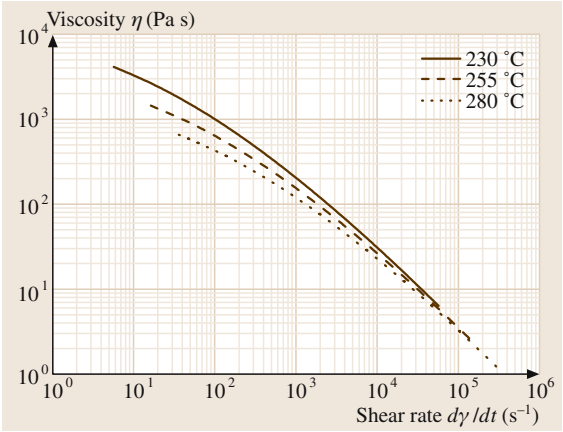


**Fig. 3.3-25** Poly(acrylonitrile-co-butadiene-co-styrene), ABS: viscosity versus shear rate

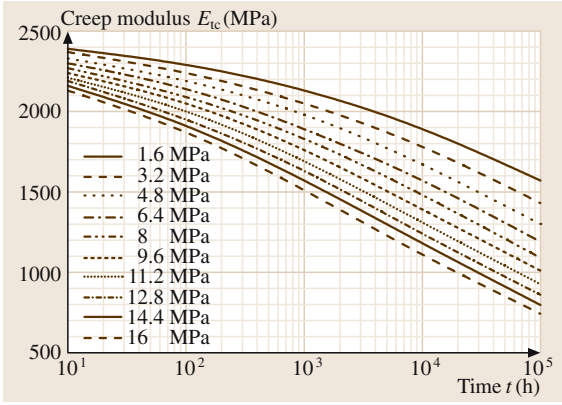


**Fig. 3.3-26** Poly(acrylonitrile-co-butadiene-co-styrene), ABS: creep modulus versus time

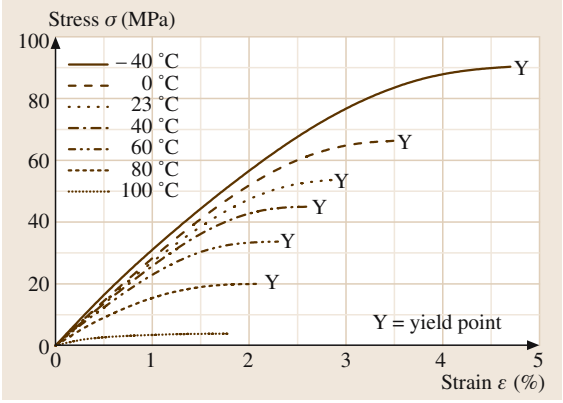


**Fig. 3.3-27** Poly(acrylonitrile-co-styrene-co-acrylester), ASA: stress versus strain

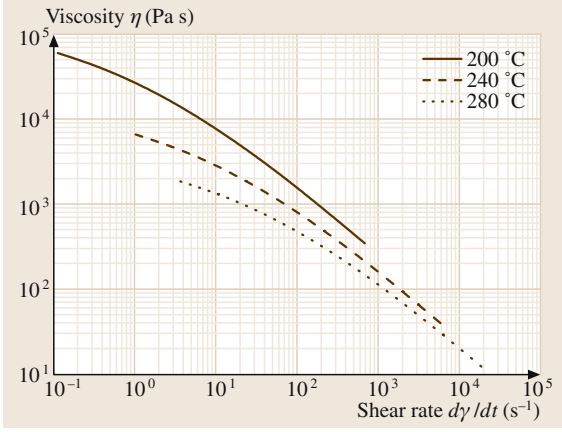


**Fig. 3.3-28** Poly(acrylonitrile-co-styrene-co-acrylester), ASA: viscosity versus shear rate

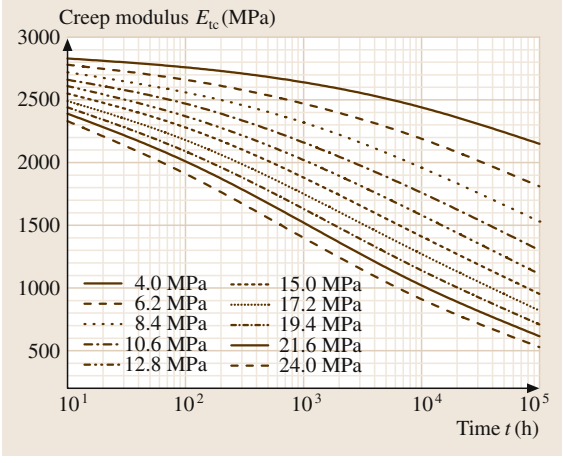


**Fig. 3.3-29** Poly(acrylonitrile-co-styrene-co-acrylester), ASA: creep modulus versus time

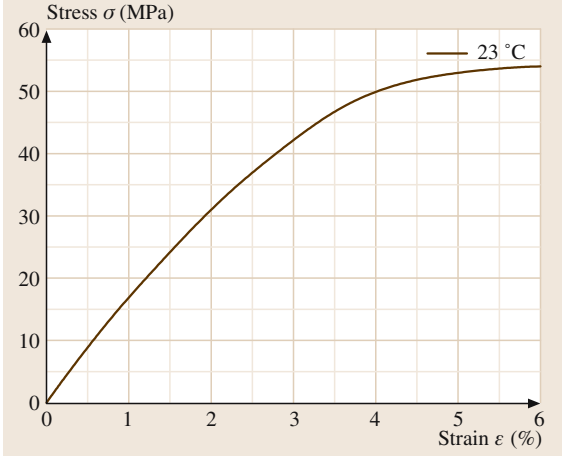


**Fig. 3.3-30** Poly(vinyl chloride), PVC-U: stress versus strain

**Table 3.3-10** Poly(vinyl chloride): unplasticized, PVC-U; plasticized (75/25), PVC-P1; plasticized (60/40), PVC-P2

| | PVC-U | PVC-P1 | PVC-P2 |
|---|---|---|---|
| Melting temperature $T_m$ (°C) | 175 | | |
| Enthalpy of fusion $\Delta H_u$ (kJ/mol) (mu) | 3.28 | | |
| Entropy of fusion $\Delta S_u$ (J/(K mol)) (mu) | | | |
| Heat capacity $c_p$ (kJ/(kg K))<br>Temperature coefficient $dc_p/dT$ (kJ/(kg K$^2$)) | 0.85–0.9 | 0.9–1.8 | 0.9–1.8 |
| Enthalpy of combustion $\Delta H_c$ (kJ/g) | −18 to −19 | | |
| Glass transition temperature $T_g$ (°C) | 85 | ≈ 80 | ≈ 80 |
| Vicat softening temperature $T_V$50/50 (°C) | 63–82 | ≈ 42 | |
| Thermal conductivity λ (W/(m K)) | 0.16 | 0.15 | 0.15 |
| Density $\varrho$ (g/cm$^3$) | 1.38–1.4 | 1.24–1.28 | 1.15–1.20 |
| Coefficient of thermal expansion $\alpha$ ($10^{-5}$/K) (linear) | 7–8 | 18–22 | 23–25 |
| Compressibility $\kappa$ (1/MPa) (cubic) | | | |
| Elastic modulus $E$ (GPa) | 2.7–3.0 | 2.9–37 | |
| Shear modulus $G$ (GPa) | 0.12 | 0.07 | |
| Poisson's ratio $\mu$ | | | |
| Stress at yield $\sigma_y$ (MPa) | 50–60 | | |
| Strain at yield $\varepsilon_y$ (%) | 4–6 | | |
| Stress at 50% elongation $\sigma_{50}$ (MPa) | | | |
| Stress at fracture $\sigma_b$ (MPa) | 40–80 | 10–25 | 10–25 |
| Strain at fracture $\varepsilon_b$ (%) | 10–50 | 170–400 | 170–400 |
| Impact strength (Charpy) (kJ/m$^2$) | 13–25 | | |
| Notched impact strength (Charpy) (kJ/m$^2$) | 3–5 | | |
| Sound velocity $v_s$ (m/s) (longitudinal) | 2330 | 2126 | |
| Sound velocity $v_s$ (m/s) (transverse) | 1070 | | |
| Shore hardness $D$ | 74–94 | | |
| Volume resistivity $\rho_e$ (Ω m) | > $10^{13}$ | $10^{12}$ | $10^{11}$ |
| Surface resistivity $\sigma_e$ (Ω) | $10^{14}$ | $10^{11}$ | $10^{10}$ |
| Electric strength $E_B$ (kV/mm) | 20–40 | 30–35 | ≈ 25 |
| Relative permittivity $\varepsilon_r$ (100 Hz) | 3.5 | 4–5 | 6–7 |
| Dielectric loss tan $\delta$ ($10^{-4}$) (100 Hz) | 110–140 | 0.05–0.07 | 0.08–0.1 |
| Refractive index $n_D$ (589 nm)<br>Temperature coefficient $dn_D/dT$ (1/K) | 1.52–1.54 | | |
| Steam permeation (g/(m$^2$ d)) (100 µm) | 2.5 | 20 | 20 |
| Gas permeation (cm$^3$/(m$^2$ d bar)) (100 µm) | 2.7–3.8 ($N_2$)<br>33–45 ($O_2$)<br>120–160 ($CO_2$)<br>28 (air) | 350 ($N_2$)<br>1500 ($O_2$)<br>8500 ($CO_2$)<br>550 (air) | 350 ($N_2$)<br>1500 ($O_2$)<br>8500 ($CO_2$)<br>550 (air) |
| Melt viscosity–molar-mass relation | | | |
| Viscosity–molar-mass relation | $[\eta] = 14.5 \times 10^{-3} M^{0.851}$ (PVC-U, THF, 25 °C) | | |

**Table 3.3-11** Poly(vinyl chloride), PVC-U: heat capacity and thermal conductivity

| Temperature $T$ (°C) | −150 | −100 | −50 | 0 | 20 | 50 | 100 |
|---|---|---|---|---|---|---|---|
| Heat capacity $c_p$ (kJ/(kg K)) | 0.47 | 0.61 | 0.75 | 0.92 | | 1.04 | 1.53 |
| Thermal conductivity λ (W/(m K)) | 0.13 | 0.15 | 0.15 | 0.16 | 0.16 | 0.17 | 0.17 |

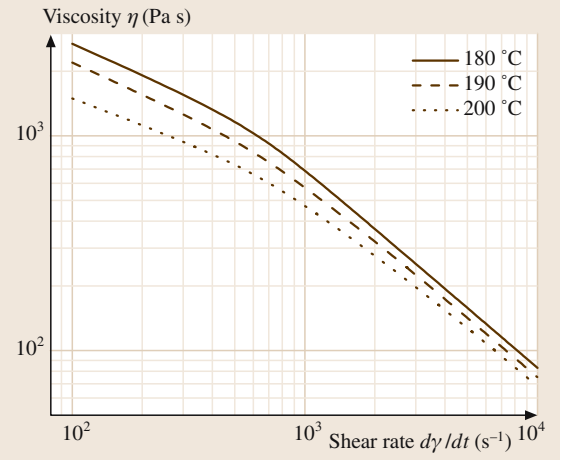


**Fig. 3.3-31** Poly(vinyl chloride), PVC-U: viscosity versus shear rate

protective clothes, cable insulation, fittings, leads, films, artificial leathers.

### 3.3.3.3 Fluoropolymers

*Polytetrafluoroethylene, PTFE.* Applications: molded articles, foils, flexible tubing, coatings, jackets, sealings, bellows, flasks, machine parts, semifinished goods, printed networks.

*Polychlorotrifluoroethylene, PCTFE.* Applications: fittings, flexible tubing, membranes, printed networks, bobbins, insulating foils, packings.

*Poly(tetrafluoroethylene-co-hexafluoropropylene), FEP.* Applications: cable insulation, coatings, coverings, printed networks, injection-molded parts, packaging foils, impregnations, heat-sealing adhesives.

**Table 3.3-12** Polytetrafluoroethylene, PTFE; polychlorotrifluoroethylene, PCTFE; poly(tetrafluoroethylene-co-hexafluoro-propylene), FEP; poly(ethylene-co-tetrafluoroethylene), ETFE; poly(ethylene-co-chlorotrifluoroethylene), ECTFE

| | PTFE | PCTFE | FEP | ETFE | ECTFE |
|---|---|---|---|---|---|
| Melting temperature $T_m$ (°C) | 325–335 | 210–215 | 255–285 | 265–270 | 240 |
| Enthalpy of fusion $\Delta H_u$ (kJ/kg) | | 1.2 | 24.3 | | |
| Entropy of fusion $\Delta S_u$ (J/(kg K)) | | | | | |
| Heat capacity $c_p$ (kJ/(kg K)) Temperature coefficient $dc_p/dT$ (kJ/(kg K²)) | 1.0 | 0.9 | 1.12 | 0.9 | |
| Enthalpy of combustion $\Delta H_c$ (kJ/g) | −5.1 | | | | |
| Glass transition temperature $T_g$ (°C) | 127 | | | | |
| Vicat softening temperature $T_V50/50$ (°C) | 110 | | | 134 | |
| Thermal conductivity λ (W/(m K)) | 0.25 | 0.22 | 0.25 | 0.23 | |
| Density $\varrho$ (g/cm³) | 2.13–2.23 | 2.07–2.12 | 2.12–2.18 | 1.67–1.75 | 1.68–1.70 |
| Coefficient of thermal expansion $\alpha$ ($10^{-5}$/K) (linear) | 11–18 | 6–7 | 8–12 | 7–10 | 7–8 |
| Compressibility $\kappa$ (1/MPa) (cubic) | | | | | |
| Elastic modulus $E$ (GPa) | 0.40–0.75 | 1.30–1.50 | 0.40–0.70 | 0.8–1.1 | 1.4–1.7 |
| Shear modulus $G$ (GPa) | | | | | |
| Poisson's ratio $\mu$ | | | | | |
| Stress at yield $\sigma_y$ (MPa) | 11.7 | | | 25–35 | |
| Strain at yield $\varepsilon_y$ (%) | | | | 15–20 | |

**Table 3.3-12** Polytetrafluoroethylene, PTFE; polychlorotrifluoroethylene, PCTFE; . . . , cont.

| | PTFE | PCTFE | FEP | ETFE | ECTFE |
|---|---|---|---|---|---|
| Stress at 50% elongation $\sigma_{50}$ (MPa) | | | | | |
| Stress at fracture $\sigma_b$ (MPa) | 25–36 | 32–40 | 22–28 | 35–54 | |
| Strain at fracture $\varepsilon_b$ (%) | 350–550 | 120–175 | 250–330 | 400–500 | |
| Impact strength (Charpy) (kJ/m$^2$) | | | | | |
| Notched impact strength (Charpy) (kJ/m$^2$) | | | | | |
| Sound velocity $v_s$ (m/s) (longitudinal) | 1410 | | | | |
| Sound velocity $v_s$ (m/s) (transverse) | 730 | | | | |
| Shore hardness $D$ | 50–60 | 78 | 55–58 | 67–75 | |
| Volume resistivity $\rho_e$ (Ω m) | $> 10^{16}$ | $> 10^{16}$ | $> 10^{16}$ | $> 10^{14}$ | $> 10^{13}$ |
| Surface resistivity $\sigma_e$ (Ω) | $> 10^{16}$ | $> 10^{16}$ | $> 10^{16}$ | $> 10^{14}$ | $10^{12}$ |
| Electric strength $E_B$ (kV/mm) | 48 | 55 | 55 | 40 | |
| Relative permittivity $\varepsilon_r$ (100 Hz) | 2.1 | 2.5–2.7 | 2.1 | 2.6 | 2.3–2.6 |
| Dielectric loss tan $\delta$ ($10^{-4}$) (100 Hz) | 0.5–0.7 | 90–140 | 0.5–0.7 | 5–6 | 10–15 |
| Refractive index $n_D$ (589 nm)<br>Temperature coefficient $dn_D/dT$ ($10^{-5}$/K) | 1.35 | 1.43 | 1.344 | 1.403 | |
| Steam permeation (g/(m$^2$ d)) | 0.03 (300 µm) | 0.4–0.9 (25 µm) | | 0.6 (25 µm) | 9 (25 µm) |
| Gas permeation (cm$^3$/(m$^2$ d bar)) | 60–80 ($N_2$)<br>160–250 ($O_2$)<br>450–700 ($CO_2$)<br>80–100 (air) | 39 ($N_2$)<br>110–230 ($O_2$)<br>250–620 ($CO_2$) | | 470 ($N_2$)<br>1560 ($O_2$)<br>3800 ($CO_2$) | 150 ($N_2$)<br>39 ($O_2$)<br>1700 ($CO_2$) |
| Melt viscosity–molar-mass relation | | | | | |
| Viscosity–molar-mass relation | | | | | |

**Table 3.3-13** Polytetrafluoroethylene, PTFE: heat capacity, thermal conductivity, and coefficient of thermal expansion

| Temperature $T$ (°C) | −200 | −150 | −100 | −50 | 0 | 20 | 50 | 100 | 150 | 200 | 250 |
|---|---|---|---|---|---|---|---|---|---|---|---|
| Heat capacity $c_p$ (kJ/(kg K)) | | | | 0.8 | 0.96 | 1.0 | 1.06 | 1.10 | 1.15 | 1.23 | |
| Thermal conductivity λ (W/(m K)) | | 0.23 | 0.24 | 0.25 | 0.25 | 0.25 | 0.26 | 0.26 | 0.26 | | |
| Coefficient of thermal expansion $\alpha$ ($10^{-5}$/K) (linear) | 3.4 | 4.5 | 7.0 | 9.5 | 11.6 | | 11.9 | 13.1 | 16.7 | 22.2 | 30.5 |

*Poly(ethylene-co-tetrafluoroethylene), ETFE*. Applications: gear wheels, pump parts, packaging, laboratory articles, coverings, cable insulation, blown films.

*Poly(ethylene-co-chlorotrifluoroethylene), ECTFE*. Applications: cable coverings, coverings, molded articles, packaging, printed networks, foils, fibers.

### 3.3.3.4 Polyacrylics and Polyacetals

*Poly(methyl methacrylate), PMMA*. Applications: extruded articles, injection-molded parts, injection blow-molded parts, houseware, medical devices, sanitary ware, automotive components, lighting, tubes, sheets, profiles, covers, panels, fiber optics, optical lenses, displays, disks, cards.

*Poly(oxymethylene), POM-H*. Applications: molded parts, extruded parts, gears, bearings, snap-fits, fuel system components, cable ties, automotive components, seatbelt parts, pillar loops, tubes, panels.

*Poly(oxymethylene-co-ethylene), POM-R*. Applications: extruded articles, injection-molded articles, gear wheels, bushes, bearings, rollers, guide rails, tubing, films, clips, zippers, boards, pipes.

**Table 3.3-14** Poly(methyl methacrylate), PMMA; poly(oxymethylene), POM-H; poly(oxymethylene-co-ethylene), POM-R

| | PMMA | POM-H | POM-R |
|---|---|---|---|
| Melting temperature $T_m$ (K) | 175 | 175 | 164–172 |
| Enthalpy of fusion $\Delta H_u$ (kJ/kg) | | 222 | 211 |
| Entropy of fusion $\Delta S_u$ (J/(kg K)) | | 1.49 | 1.44 |
| Heat capacity $c_p$ (kJ/(kg K))<br>Temperature coefficient $dc_p/dT$ (kJ/(kg K$^2$)) | 1.255 | 1.46 | 1.47 |
| Enthalpy of combustion $\Delta H_c$ (kJ/g) | −26.2 | −16.7 | −17 |
| Glass transition temperature $T_g$ (°C) | 104–105 | 25 | |
| Vicat softening temperature $T_V$50/50 (°C) | 85–110 | 160–170 | 151–162 |
| Thermal conductivity $\lambda$ (W/(m K)) | 0.193 | 0.25–0.30 | 0.31 |
| Density $\varrho$ (g/cm$^3$) | 1.17–1.19 | 1.40–1.42 | 1.39–1.41 |
| Coefficient of thermal expansion $\alpha$ ($10^{-5}$/K) (linear) | 7–8 | 11–12 | 10–11 |
| Compressibility $\kappa$ ($10^{-4}$/MPa) (cubic) | 2.45 | 1.5 | |
| Elastic modulus $E$ (GPa) | 3.1–3.3 | 3.0–3.2 | 2.8–3.2 |
| Shear modulus $G$ (GPa) | 1.7 | 0.7–1.0 | |
| Poisson's ratio $\mu$ | | | |
| Stress at yield $\sigma_y$ (MPa) | 50–77 | 60–75 | 65–73 |
| Strain at yield $\varepsilon_y$ (%) | | 8–25 | 8–12 |
| Stress at 50% elongation $\sigma_{50}$ (MPa) | | | |
| Stress at fracture $\sigma_b$ (MPa) | 60–75 | 62–70 | 59 |
| Strain at fracture $\varepsilon_b$ (%) | 2–6 | 25–70 | |
| Impact strength (Charpy) (kJ/m$^2$) | 18–23 | 180 | |
| Notched impact strength (Charpy) (kJ/m$^2$) | 2 | 9 | 6.5 |
| Sound velocity $v_s$ (m/s) (longitudinal) | 2690 | 2440 | |
| Sound velocity $v_s$ (m/s) (transverse) | 1340 | 1000 | |
| Shore hardness $D$ | 85 | 80 | |
| Volume resistivity $\rho_e$ (Ω m) | $> 10^{13}$ | $> 10^{13}$ | $> 10^{13}$ |
| Surface resistivity $\sigma_e$ (Ω) | $> 10^{13}$ | $> 10^{14}$ | $> 10^{13}$ |
| Electric strength $E_B$ (kV/mm) | 30 | 25–35 | 35 |
| Relative permittivity $\varepsilon_r$ (100 Hz) | 3.5–3.8 | 3.5–3.8 | 3.6–4 |
| Dielectric loss tan $\delta$ ($10^{-4}$) (100 Hz) | 500–600 | 30–50 | 30–50 |
| Refractive index $n_D$ (589 nm)<br>Temperature coefficient $dn_D/dT$ ($10^{-4}$/K) | 1.492<br>−1.2 | 1.49 | |
| Steam permeation (g/(m$^2$ d)) (80 µm) | 12 | 12 | |
| Gas permeation (cm$^3$/(m$^2$ d bar)) | 2500 ($N_2$)<br>1000 ($O_2$)<br>5200 ($CO_2$) | 5 ($N_2$)<br>24 ($O_2$)<br>470 ($CO_2$)<br>8 (air) | |
| Melt viscosity–molar-mass relation | | | |
| Viscosity–molar-mass relation | $[\eta] = 10.4 \times 10^{-3} M^{0.70}$ (PMMA, THF, 25 °C)<br>$[\eta] = 11.3 \times 10^{-3} M^{0.76}$ (POM-H, Phenol, 90 °C) | | |

**Table 3.3-15** Poly(methyl methacrylate), PMMA: heat capacity, thermal conductivity, and coefficient of thermal expansion

| Temperature $T$ (°C) | −200 | −150 | −100 | −50 | 0 | 20 | 50 | 100 | 150 | 200 |
|---|---|---|---|---|---|---|---|---|---|---|
| Heat capacity $c_p$ (kJ/(kg K)) | | 0.67 | 0.90 | 1.06 | 1.26 | 1.26 | 1.42 | 1.85 | | |
| Thermal conductivity $\lambda$ (W/(m K)) | | 0.16 | 0.18 | 0.19 | 0.19 | 0.19 | 0.19 | 0.20 | 0.19 | 0.18 |
| Coefficient of thermal expansion $\alpha$ ($10^{-5}$/K) (linear) | | 3.0 | 3.7 | 4.5 | 5.7 | 6.9 | 7.5 | 12.0 | 18.4 | |

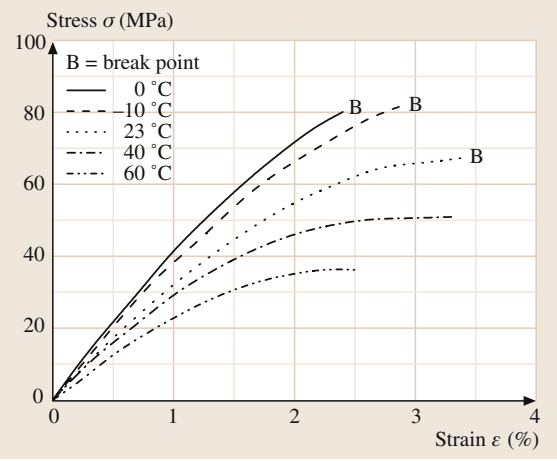


**Fig. 3.3-32** Poly(methyl methacrylate), PMMA: stress versus strain

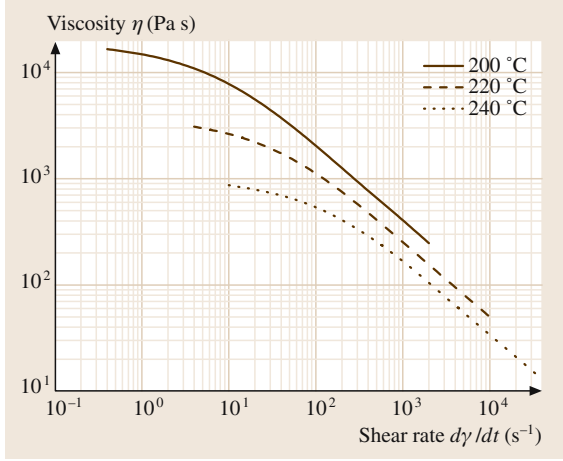


**Fig. 3.3-33** Poly(methyl methacrylate), PMMA: viscosity versus shear rate

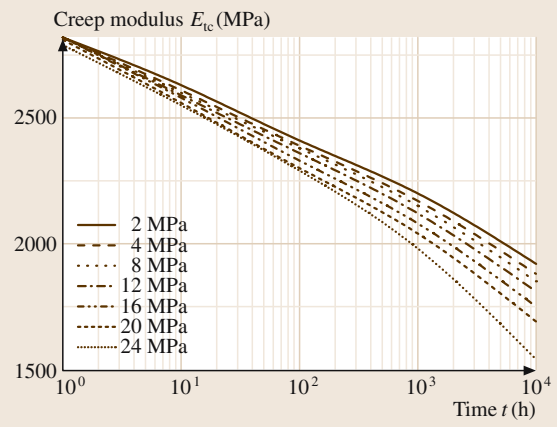


**Fig. 3.3-34** Poly(methyl methacrylate), PMMA: creep modulus versus time, at 23 °C

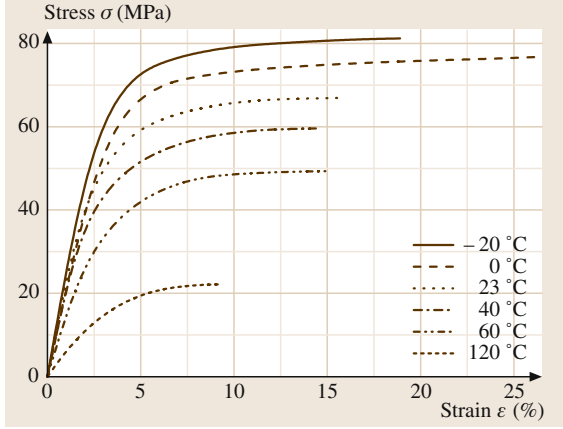


**Fig. 3.3-35** Poly(oxymethylene), POM-H: stress versus strain

**Table 3.3-16** Poly(oxymethylene), POM-H: heat capacity, thermal conductivity, and coefficient of thermal expansion

| Temperature $T$ (°C) | −200 | −150 | −100 | −50 | 0 | 20 | 50 | 100 | 150 | 200 |
|---|---|---|---|---|---|---|---|---|---|---|
| Heat capacity $c_p$ (kJ/(kg K)) | 0.47 | 0.65 | 0.82 | 1.08 | 1.27 | | 1.46 | 1.85 | | |
| Thermal conductivity λ (W/(m K)) | | 0.47 | 0.45 | 0.43 | 0.42 | | 0.41 | | | |
| Coefficient of thermal expansion $\alpha$ ($10^{-5}$/K) (linear) | | | | | 9.0 | 9.5 | 10.0 | 16.5 | 41.0 | 23.0 |

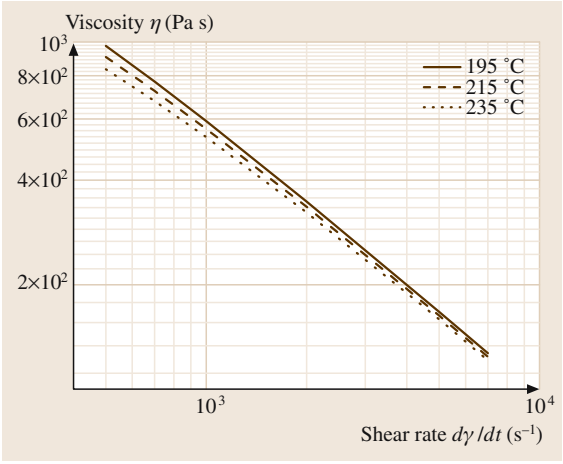


**Fig. 3.3-36** Poly(oxymethylene), POM-H: viscosity versus shear rate

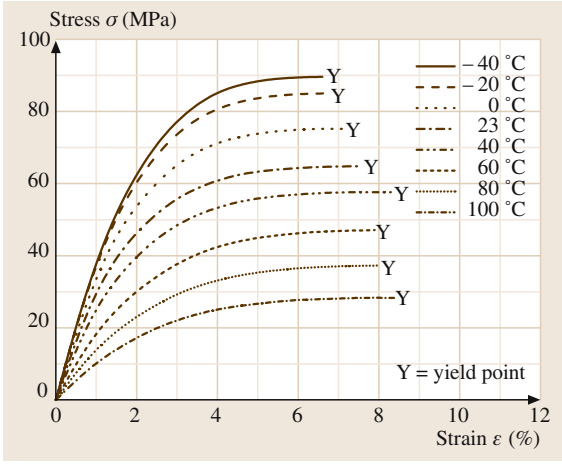


**Fig. 3.3-37** Poly(oxymethylene-co-ethylene), POM-R: stress versus strain

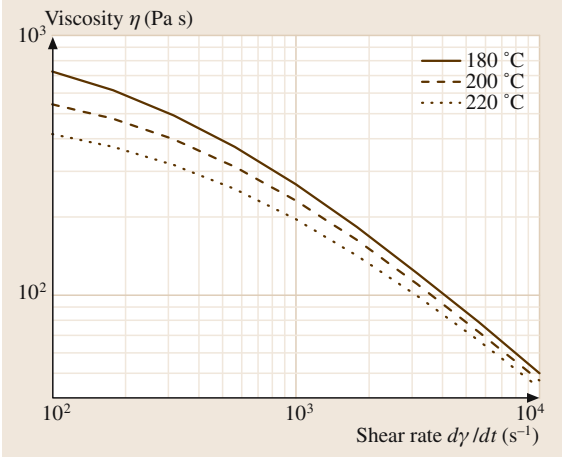


**Fig. 3.3-38** Poly(oxymethylene-co-ethylene), POM-R: viscosity versus shear rate

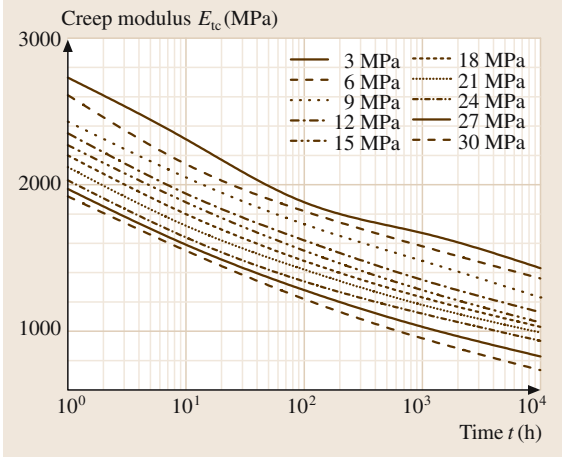


**Fig. 3.3-39** Poly(oxymethylene-co-ethylene), POM-R: creep modulus versus time at 23 °C

### 3.3.3.5 Polyamides

*Polyamide 6, PA6; polyamide 66, PA66; polyamide 11, PA11; polyamide 12, PA12; polyamide 610, PA610.* Applications: technical parts, bearings, gear wheels, rollers, screws, gaskets, fittings, coverings, housings, automotive parts, houseware, semifinished goods, sports goods, membranes, foils, packings, blow-molded parts, fibers, tanks.

**Table 3.3-17** Polyamide 6, PA6; polyamide 66, PA66; polyamide 11, PA11; polyamide 12, PA12; polyamide 610, PA610

| | PA6 | PA66 | PA11 | PA12 | PA610 |
|---|---|---|---|---|---|
| Melting temperature $T_m$ (°C) | 220–225 | 255–260 | 185 | 175–180 | 210–220 |
| Enthalpy of fusion $\Delta H_u$ (J/mol) (mu) | | | | | |
| Entropy of fusion $\Delta S_u$ (J/(K mol)) (mu) | | | | | |
| Heat capacity $c_p$ (kJ/(kg K))<br>Temperature coefficient $dc_p/dT$ (kJ/(kg K$^2$)) | 1.7 | 1.7 | 1.26 | 1.26 | 1.7 |
| Enthalpy of combustion $\Delta H_c$ (kJ/g) | −31.4 | −31.4 | | | |
| Glass transition temperature $T_g$ (°C) | 55 | 80 | 50 | 50 | 55–60 |
| Vicat softening temperature $T_V$50/50 (°C) | 180–220 | 195–220 | 180–190 | 140–160 | 205–215 |
| Thermal conductivity λ (W/(m K)) | 0.29 | 0.23 | 0.23 | 0.23 | 0.23 |
| Density $\varrho$ (g/cm$^3$) | 1.12–1.14 | 1.13–1.15 | 1.04 | 1.01–1.03 | 1.06–1.09 |
| Coefficient of thermal expansion $\alpha$ ($10^{-5}$/K) (linear) | 7–10 | 7–10 | 13 | 10–12 | 8–10 |
| Compressibility $\kappa$ (1/MPa) (cubic) | | | | | |
| Elastic modulus $E$ (GPa) | 2.6–3.2 | 2.7–3.3 | 1.0 | 1.3–1.6 | 2.0–2.4 |
| Shear modulus $G$ (GPa) | 1.1–1.5 | 1.3–1.7 | 0.4–0.5 | 0.5 | 0.8 |
| Poisson's ratio $\mu$ | | | | | |
| Stress at yield $\sigma_y$ (MPa) | 70–90 | 75–100 | | 45–60 | 60–70 |
| Strain at yield $\varepsilon_y$ (%) | 4–5 | 4.5–5 | | 4–5 | 4 |
| Stress at 50% elongation $\sigma_{50}$ (MPa) | | | | | |
| Stress at fracture $\sigma_b$ (MPa) | 70–85 | 77–84 | 56 | 56–65 | 40 |
| Strain at fracture $\varepsilon_b$ (%) | 200–300 | 150–300 | 500 | 300 | 500 |
| Impact strength (Charpy) (kJ/m$^2$) | | | | | |
| Notched impact strength (Charpy) (kJ/m$^2$) | 3–6 | 2–3 | | | 4–10 |
| Sound velocity $v_s$ (m/s) (longitudinal) | 2700 | 2710 | | | |
| Sound velocity $v_s$ (m/s) (transverse) | 1120 | 1120 | | | |
| Shore hardness $D$ | 72 | 75 | | | |
| Volume resistivity $\rho_e$ (Ω m) | $> 10^{13}$ | $> 10^{12}$ | $10^{11}$ | $> 10^{13}$ | $> 10^{13}$ |
| Surface resistivity $\sigma_e$ (Ω) | $> 10^{12}$ | $> 10^{10}$ | $10^{11}$ | $> 10^{13}$ | $> 10^{12}$ |
| Electric strength $E_B$ (kV/mm) | 30 | 25–35 | 42.5 | 27–29 | |
| Relative permittivity $\varepsilon_r$ (100 Hz) | 3.5–4.2 | 3.2–4 | 3.7 | 3.7–4 | 3.5 |
| Dielectric loss tan $\delta$ tan $\delta$ ($10^{-4}$) (100 Hz) | 60–150 | 50–150 | 600 | 300–700 | 70–150 |
| Refractive index $n_D$ (589 nm)<br>Temperature coefficient $dn_D/dT$ (1/K) | 1.52–1.53 | 1.52–1.53 | 1.52–1.53 | 1.52–1.53 | 1.53 |
| Steam permeation (g/(m$^2$ d)) (100 µm) | 10–20 | 10–20 | 2.4–4 | 2.4–4 | |
| Gas permeation (cm$^3$/(m$^2$ d bar)) (100 µm) | 1–2 ($N_2$)<br>2–8 ($O_2$)<br>80–120 ($CO_2$) | 1–2 ($N_2$)<br>2–8 ($O_2$)<br>80–120 ($CO_2$) | 0.5–0.7 ($N_2$)<br>2–3.5 ($O_2$)<br>6–13 (CO) | 0.5–0.7 ($N_2$)<br>2–3.5 ($O_2$)<br>6–13 (CO) | |
| Melt viscosity–molar-mass relation | | | | | |
| Viscosity–molar-mass relation | | | | | |

**Table 3.3-18** Polyamide 6, PA6; polyamide 66, PA66; polyamide 610, PA610: heat capacity, thermal conductivity, and coefficient of thermal expansion

| Temperature $T$ (°C) | −200 | −150 | −100 | −50 | 0 | 20 | 50 | 100 | 150 | 200 |
|---|---|---|---|---|---|---|---|---|---|---|
| Heat capacity $c_p$ (kJ/(kg K)), PA | 0.47 | 0.73 | 0.93 | 1.15 | 1.38 | | 1.68 | 2.15 | 2.60 | |
| Thermal conductivity λ (W/(m K)), PA6 | | 0.29 | 0.31 | 0.32 | 0.32 | | 0.29 | 0.27 | 0.25 | |
| Thermal conductivity λ (W/(m K)), PA66 | | 0.32 | 0.33 | 0.33 | 0.33 | | 0.33 | | | |
| Thermal conductivity λ (W/(m K)), PA610 | | 0.31 | 0.32 | 0.33 | 0.33 | | 0.32 | 0.31 | | |
| Coefficient of thermal expansion $\alpha$ ($10^{-5}$/K) (linear), PA6 | | | 5.0 | 6.6 | 8.0 | 9.1 | 40.1 | 15.1 | 14.0 | 34.6 |



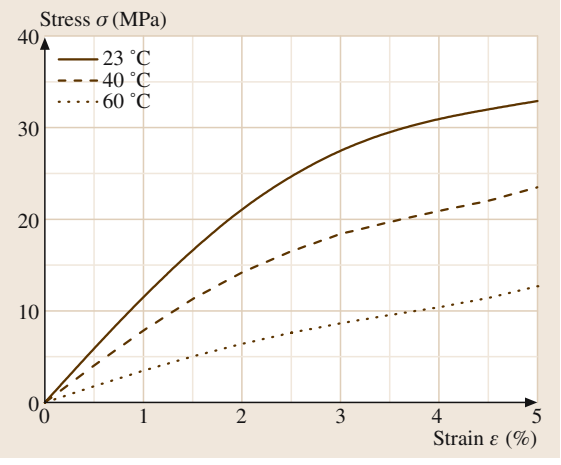


**Fig. 3.3-40** Polyamide 6, PA6: stress versus strain

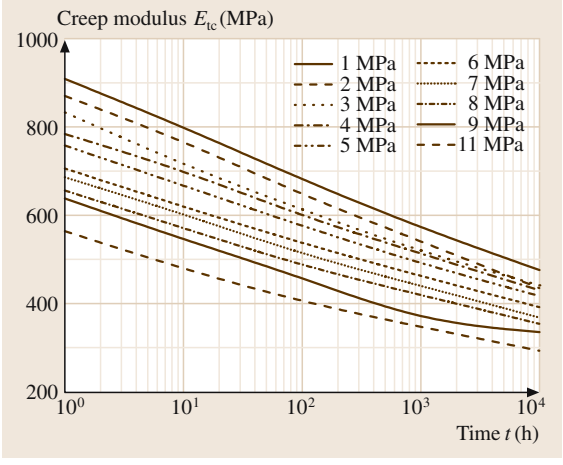


**Fig. 3.3-41** Polyamide 6, PA6: creep modulus versus time

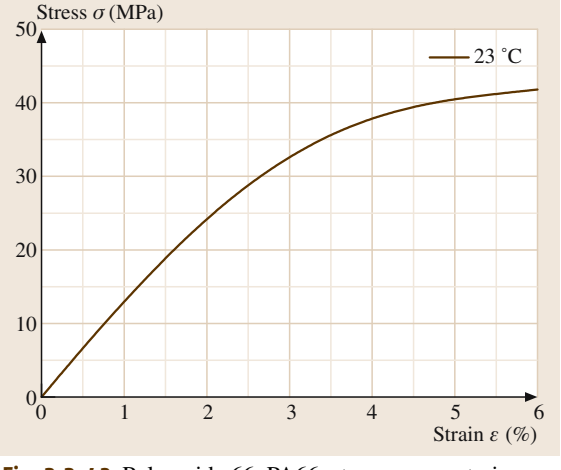


**Fig. 3.3-42** Polyamide 66, PA66: stress versus strain

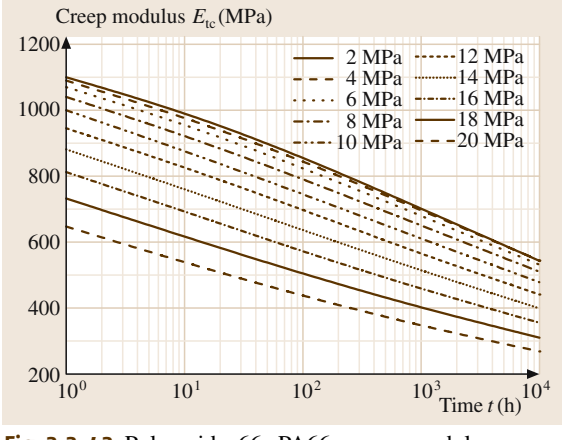


**Fig. 3.3-43** Polyamide 66, PA66: creep modulus versus time

### 3.3.3.6 Polyesters

*Polycarbonate, PC*. Applications: injection-molded parts, extruded parts, disks, lamp housings, electronic articles, optical articles, houseware, foils.

*Poly(ethylene terephthalate), PET*. Applications: bearings, gear wheels, shafts, couplings, foils, ribbons, flexible tubing, fibers.

*Poly(butylene terephthalate), PBT*. Applications: bearings, valve parts, screws, plugs, housings, wheels, houseware.

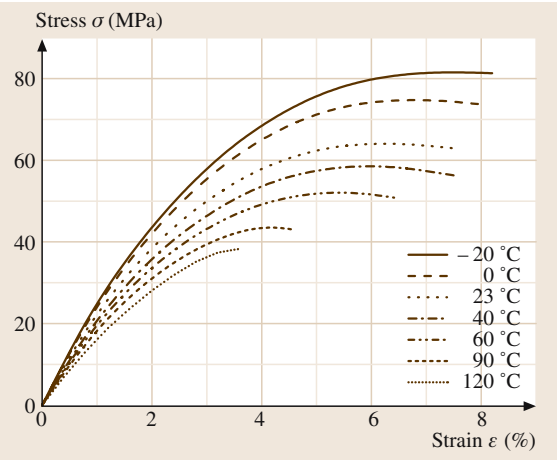


**Fig. 3.3-44** Polycarbonate, PC: stress versus strain

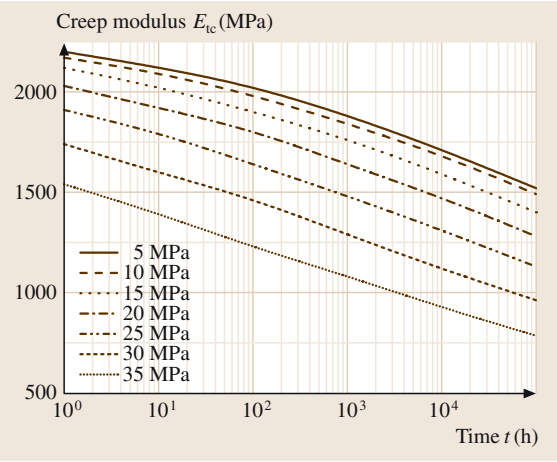


**Fig. 3.3-46** Polycarbonate, PC: creep modulus versus time

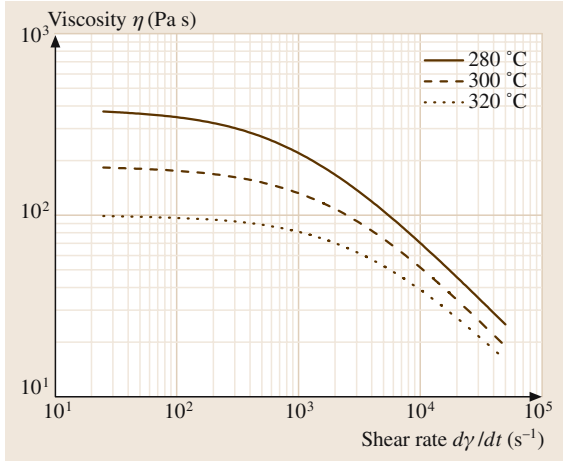


**Fig. 3.3-45** Polycarbonate, PC: viscosity versus shear rate

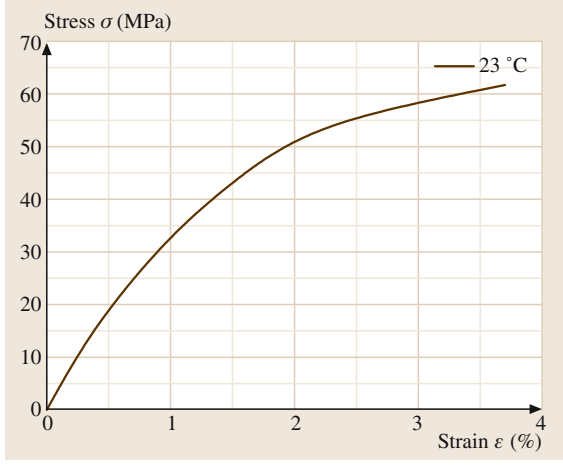


**Fig. 3.3-47** Poly(ethylene terephthalate), PET: stress versus strain

**Table 3.3-19** Polycarbonate, PC: heat capacity and thermal conductivity

| Temperature $T$ (°C) | −200 | −150 | −100 | −50 | 0 | 20 | 50 | 100 | 150 |
|---|---|---|---|---|---|---|---|---|---|
| Heat capacity $c_p$ (kJ/(kg K)) | 0.34 | 0.50 | 0.70 | 0.90 | 1.10 | 1.17 | 1.30 | 1.50 | 1.70 |
| Thermal conductivity λ (W/(m K)) | | 0.17 | 0.19 | 0.21 | 0.23 | | 0.24 | 0.24 | 0.24 |

**Table 3.3-20** Polycarbonate, PC; poly(ethylene terephthalate), PET; poly(butylene terephthalate), PBT; poly(phenylene ether), PPE

| | PC | PET | PBT | PPE |
|---|---|---|---|---|
| Melting temperature $T_m$ (°C) | 220–260 | 250–260 (pcr) | 220–225 | |
| Enthalpy of fusion $\Delta H_u$ (kJ/mol) (mu) | 8.682 (iso), 8.577 (syn) | 2.69 | 54 kJ/kg | |
| Entropy of fusion $\Delta S_u$ (J/(K mol)) (mu) | 16.8 (iso), 15.3 (syn) | 48.6 | | |
| Heat capacity $c_p$ (kJ/(kg K))<br>Temperature coefficient $dc_p/dT$ (kJ/(kg $K^2$)) | 1.17<br>$4.04\times10^{-3}$ | 1.223 | 1.35 | |
| Enthalpy of combustion $\Delta H_c$ (kJ/g) | −30.7 | −21.6 | | |
| Glass transition temperature $T_g$ (°C) | 150 | 98 | 60 | 110–150 |
| Vicat softening temperature $T_V$50/50 (°C) | 83 | 79 | 165–180 | 105–132 |
| Thermal conductivity λ (W/(m K)) | 0.21 | 0.11 | 0.21 | 0.17–0.22 |
| Density $\varrho$ (g/$cm^3$) | 1.2<br>1.38–1.40 (pcr) | 1.33–1.35 (am) | 1.30–1.32 | 1.04–1.10 |
| Coefficient of thermal expansion $\alpha$ ($10^{-5}$/K) (linear) | 6.5–7 | 8 (am), 7(pcr) | 8–10 | 8–9 |
| Compressibility $\kappa$ (1/MPa) (cubic) | $2.2\times10^{-4}$ | $6.99\times10^{-6}$ (melt) | | |
| Elastic modulus $E$ (GPa) | 2.3–2.4 | 2.1–2.4 (am)<br>2.8–3.1 (pcr) | 2.5–2.8 | 2.0–3.1 |
| Shear modulus $G$ (GPa) | 0.72 | 1.2 | 1.0 | |
| Poisson's ratio $\mu$ | | 0.38 | | |
| Stress at yield $\sigma_y$ (MPa) | 55–65 | 55 (am), 60–80 (pcr) | 50–60 | 45–70 |
| Strain at yield $\varepsilon_y$ (%) | 6–7 | 4 (am), 5–7 (pcr) | 3.5–7 | 3–6 |
| Stress at 50% elongation $\sigma_{50}$ (MPa) | | | | |
| Stress at fracture $\sigma_b$ (MPa) | 69–72 | 30–55 | 52 | 35–55 |
| Strain at fracture $\varepsilon_b$ (%) | 120–125 | 1.5–3 | | 15–40 |
| Impact strength (Charpy) (kJ/$m^2$) | | 13–25 | | |
| Notched impact strength (Charpy) (kJ/$m^2$) | | 3–5 | | 6–16 |
| Sound velocity $v_s$ (m/s) (longitudinal) | 2220 | 2400 | | 2220 |
| Sound velocity $v_s$ (m/s) (transverse) | 909 | 1150 | | 1000 |
| Shore hardness $D$ | | | 80 | |
| Volume resistivity $\rho_e$ (Ω m) | $> 10^{14}$ | $> 10^{13}$ | $> 10^{13}$ | $10^{14}-10^{15}$ |
| Surface resistivity $\sigma_e$ (Ω) | $> 10^{14}$ | $> 10^{14}$ | $> 10^{14}$ | $10^{16}-10^{17}$ |
| Electric strength $E_B$ (kV/mm) | 30–75 | 42 | 42 | 25–35 |
| Relative permittivity $\varepsilon_r$ (100 Hz) | 2.8–3.2 | 3.4–3.6 | 3.3–4.0 | 2.6–2.9 |
| Dielectric loss tan $\delta$ ($10^{-4}$) (100 Hz) | 7–20 | 20 | 15–20 | 10–40 |
| Refractive index $n_D$ (589 nm)<br>Temperature coefficient $dn_D/dT$ (1/K) | 1.58–1.59<br>$-1.42\times10^{-4}$ | 1.57–1.64 | 1.58 | |
| Steam permeation (g/($m^2$ d)) | 4 | 4.5–5.5, 0.6 (str) | | |
| Gas permeation ($cm^3$/($m^2$ d bar)) | 680 ($N_2$), 4000 ($O_2$)<br>14 500 ($CO_2$) | 6.6 ($N_2$), 30 ($O_2$)<br>140 ($CO_2$), 12 (air)<br>9–15 (str, $N_2$)<br>80–110 (str, $O_2$)<br>200–340 (str, $CO_2$) | | |
| Melt viscosity–molar-mass relation | | | | |
| Viscosity–molar-mass relation | $[\eta] = 4.25\times10^{-3} M^{0.69}$ (PET) | | | |

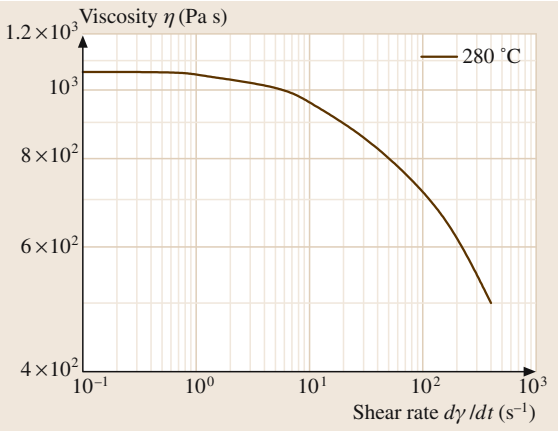


**Fig. 3.3-48** Poly(ethylene terephthalate), PET: viscosity versus shear rate

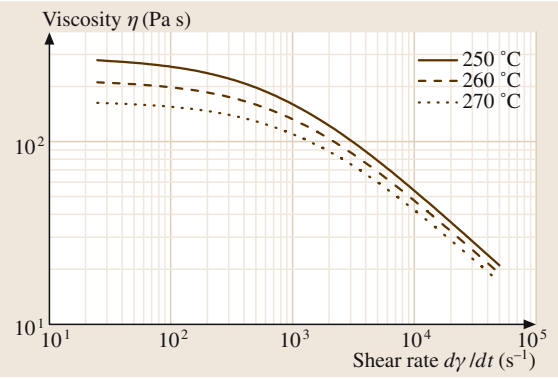


**Fig. 3.3-50** Poly(butylene terephthalate), PBT: viscosity versus shear rate

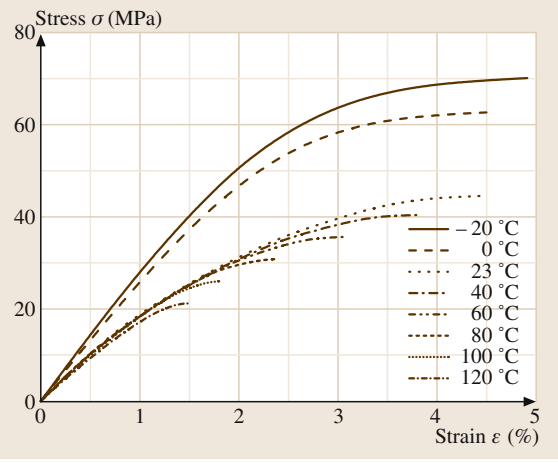


**Fig. 3.3-52** Poly(phenylene ether), PPE: stress versus strain

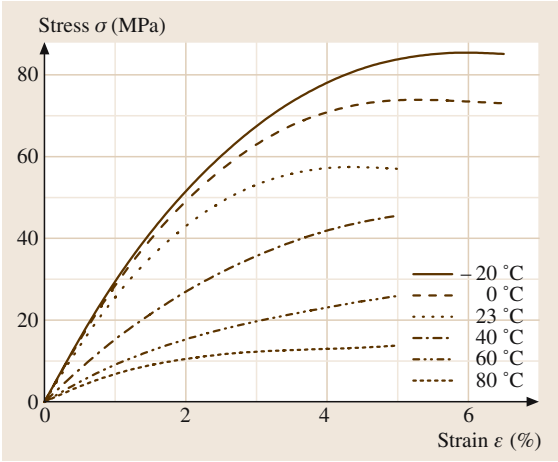


**Fig. 3.3-49** Poly(butylene terephthalate), PBT: stress versus strain

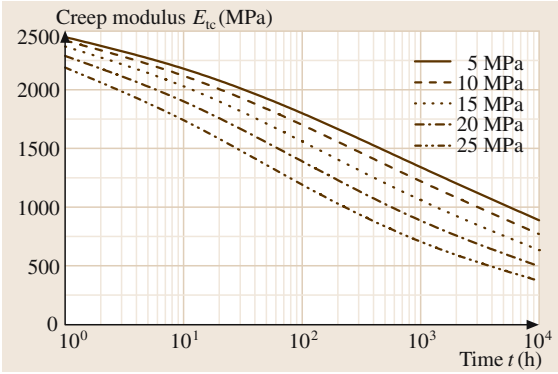


**Fig. 3.3-51** Poly(butylene terephthalate), PBT: creep modulus versus time

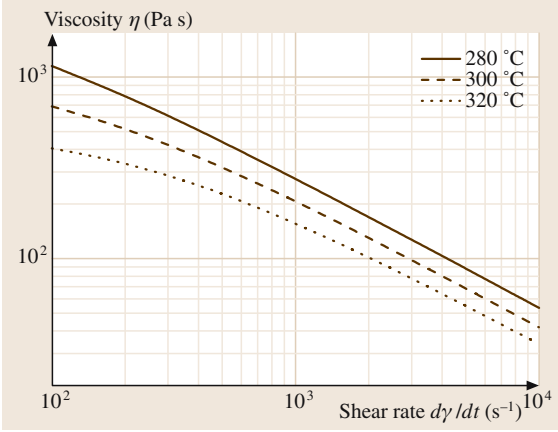


**Fig. 3.3-53** Poly(phenylene ether), PPE: viscosity versus shear rate

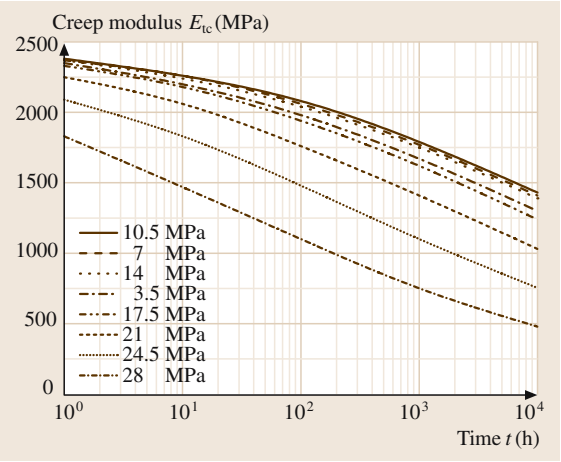


**Fig. 3.3-54** Poly(phenylene ether), PPE: creep modulus versus time

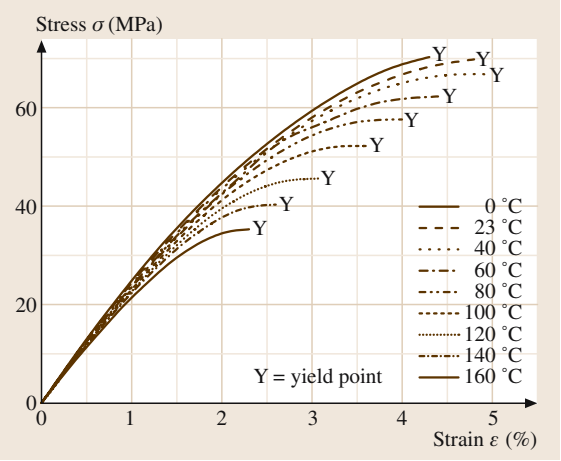


**Fig. 3.3-55** Polysulfone, PSU: stress versus strain

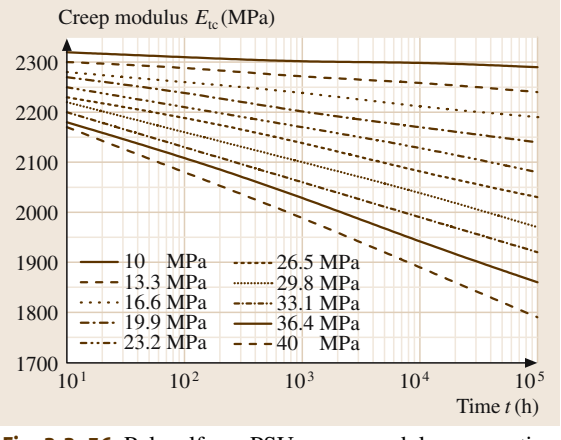


**Fig. 3.3-56** Polysulfone, PSU: creep modulus versus time

## 3.3.3.7 Polysulfones and Polysulfides

*Polysulfone, PSU; Poly(ether sulfone), PES.* Applications: injection-molded parts, coatings, electronic articles, printed circuits, houseware, medical devices, membranes, lenses, optical devices.

*Poly(phenylene sulfide), PPS.* Applications: injection-molded parts, sintered parts, foils, fibers, housings, sockets, foams.

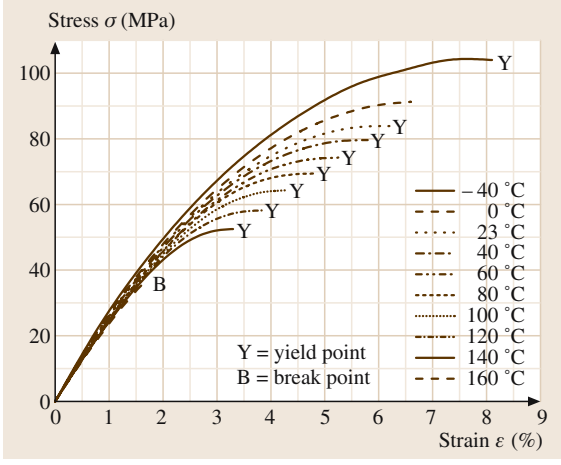


**Fig. 3.3-57** Poly(ether sulfone), PES: stress versus strain

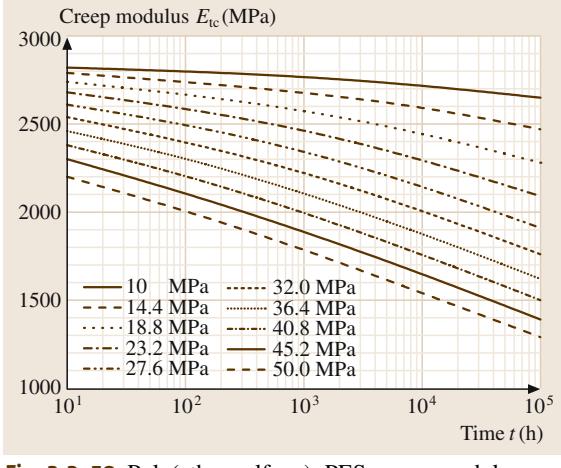


**Fig. 3.3-58** Poly(ether sulfone), PES: creep modulus versus time

**Table 3.3-21** Polysulfone, PSU; poly(phenylene sulfide), PPS; poly(ether sulfone), PES

| | PSU | PPS | PES |
|---|---|---|---|
| Melting temperature $T_m$ (°C) | | 285 | |
| Enthalpy of fusion $\Delta H_u$ (J/mol) (mu) | | | |
| Entropy of fusion $\Delta S_u$ (J/(K mol)) (mu) | | | |
| Heat capacity $c_p$ (kJ/(kg K))<br>Temperature coefficient $dc_p/dT$ (kJ/(kg K$^2$)) | 1.30 | | 1.10 |
| Enthalpy of combustion $\Delta H_c$ (kJ/g) | 17 | | 36 |
| Glass transition temperature $T_g$ (°C) | 190 | 85 | 225 |
| Vicat softening temperature $T_V50/50$ (°C) | 175–210 | 200 | 215–225 |
| Thermal conductivity $\lambda$ (W/(m K)) | 0.28 | 0.25 | 0.18 |
| Density $\varrho$ (g/cm$^3$) | 1.24–1.25 | 1.34 | 1.36–1.37 |
| Coefficient of thermal expansion $\alpha$ ($10^{-5}$/K) (linear) | 5.5–6 | 5.5 | 5–5.5 |
| Compressibility $\kappa$ (1/MPa) (cubic) | | | |
| Elastic modulus $E$ (GPa) | 2.5–2.7 | 3.4 | 2.6–2.8 |
| Shear modulus $G$ (GPa) | | | |
| Poisson's ratio $\mu$ | | | |
| Stress at yield $\sigma_y$ (MPa) | 70–80 | | 80–90 |
| Strain at yield $\varepsilon_y$ (%) | 5.5–6 | | 5.5–6.5 |
| Stress at 50% elongation $\sigma_{50}$ (MPa) | | | |
| Stress at fracture $\sigma_b$ (MPa) | 50–100 | 75 | 85 |
| Strain at fracture $\varepsilon_b$ (%) | 25–30 | 3 | 30–80 |
| Impact strength (Charpy) (kJ/m$^2$) | | | |
| Notched impact strength (Charpy) (kJ/m$^2$) | | | |
| Sound velocity $v_s$ (m/s) (longitudinal) | 2260 | | 2260 |
| Sound velocity $v_s$ (m/s) (transverse) | 920 | | |
| Shore hardness $D$ | | | |
| Volume resistivity $\rho_e$ (Ω m) | $> 10^{13}$ | $> 10^{13}$ | $10^{13}$ |
| Surface resistivity $\sigma_e$ (Ω) | $> 10^{15}$ | | $> 10^{13}$ |
| Electric strength $E_B$ (kV/mm) | 20–30 | 59.5 | 20–30 |
| Relative permittivity $\varepsilon_r$ (100 Hz) | 3.2 | 3.1 | 3.5–3.7 |
| Dielectric loss tan $\delta$ ($10^{-4}$) (100 Hz) | 8–10 | 4 | 10–20 |
| Refractive index $n_D$ (589 nm)<br>Temperature coefficient $dn_D/dT$ (1/K) | 1.63 | | 1.65 |
| Steam permeation (g/(m$^2$ d)) (25 µm) | 6 | | |
| Gas permeation (cm$^3$/(m$^2$ d bar)) (25 µm) | 630 ($N_2$)<br>3600 ($O_2$)<br>15 000 ($CO_2$) | | |
| Melt viscosity–molar-mass relation | | | |
| Viscosity–molar-mass relation | | | |

### 3.3.3.8 Polyimides and Polyether Ketones

*Poly(amide imide), PAI.* Applications: constructional parts, wheels, rotors, bearings, housings, slip fittings, lacquers.

*Poly(ether imide), PEI.* Applications: electrical housings, sockets, microwave parts, bearings, gear wheels, automotive parts.

*Polyimide, PI.* Applications: foils, semifinished goods, sintered parts.

**Table 3.3-22** Poly(amide imide), PAI; poly(ether imide), PEI; polyimide, PI; poly(ether ether ketone), PEEK

| | PAI | PEI | PI | PEEK |
|---|---|---|---|---|
| Melting temperature $T_m$ (°C) | | | 335–345 | |
| Enthalpy of fusion $\Delta H_u$ (J/mol) (mu) | | | | |
| Entropy of fusion $\Delta S_u$ (J/(K mol)) (mu) | | | | |
| Heat capacity $c_p$ (kJ/(kg K))<br>Temperature coefficient $dc_p/dT$ (kJ/(kg $K^2$)) | | 1.1 | | |
| Enthalpy of combustion $\Delta H_c$ (kJ/g) | | | | |
| Glass transition temperature $T_g$ (°C) | 240–275 | 215 | 250–270 | 145 |
| Vicat softening temperature $T_V$50/50 (°C) | | 220 | 260 | |
| Thermal conductivity λ (W/(m K)) | 0.26 | 0.22 | 0.29–0.35 | 0.25 |
| Density $\varrho$ (g/$cm^3$) | 1.38–1.40 | 1.27 | 1.43 | 1.32 |
| Coefficient of thermal expansion $\alpha$ ($10^{-5}$/K) (linear) | 3.0–3.5 | 5.5–6.0 | 5–6 | 4.7 |
| Compressibility $\kappa$ (1/MPa) (cubic) | | | | |
| Elastic modulus $E$ (GPa) | 4.5–4.7 | 2.9–3.0 | 3.0–3.2 | 4.7 |
| Shear modulus $G$ (GPa) | | | | |
| Poisson's ratio $\mu$ | | | 0.41 | |
| Stress at yield $\sigma_y$ (MPa) | | | | |
| Strain at yield $\varepsilon_y$ (%) | | | | 5 |
| Stress at 50% elongation $\sigma_{50}$ (MPa) | | | | |
| Stress at fracture $\sigma_b$ (MPa) | 150–160 | 105 | 75–100 | 100 |
| Strain at fracture $\varepsilon_b$ (%) | 7–8 | 60 | 88 | 50 |
| Impact strength (Charpy) (kJ/$m^2$) | | | | |
| Notched impact strength (Charpy) (kJ/$m^2$) | | | | |
| Sound velocity $v_s$ (m/s) (longitudinal) | | | | |
| Sound velocity $v_s$ (m/s) (transverse) | | | | |
| Shore hardness $D$ | | | | |
| Volume resistivity $\rho_e$ (Ω m) | $10^{15}$ | $10^{16}$ | $> 10^{14}$ | $10^{14}$ |
| Surface resistivity $\sigma_e$ (Ω) | $> 10^{16}$ | $> 10^{16}$ | $> 10^{15}$ | |
| Electric strength $E_B$ (kV/mm) | 25 | 25 | 200 | |
| Relative permittivity $\varepsilon_r$ (100 Hz) | 3.5–4.2 | 3.2–3.5 | 3.4 | 3.2 |
| Dielectric loss tan $\delta$ ($10^{-4}$) (100 Hz) | 10 | 10–15 | 52 | 30 |
| Refractive index $n_D$ (589 nm)<br>Temperature coefficient $dn_D/dT$ (1/K) | | 1.66 | | |
| Steam permeation (g/($m^2$ d)) (25 µm) | | | 25 | |
| Gas permeation ($cm^3$/($m^2$ d bar)) (25 µm) | | | 94 ($N_2$)<br>390 ($O_2$)<br>700 ($CO_2$) | |
| Melt viscosity–molar-mass relation | | | | |
| Viscosity–molar-mass relation | | | | |

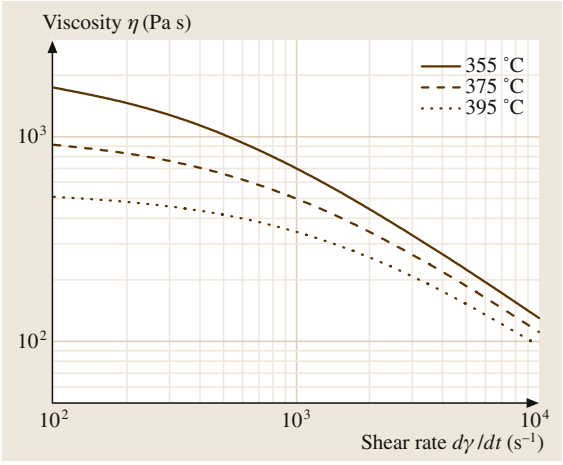


**Fig. 3.3-59** Poly(ether imide), PEI: viscosity versus shear rate

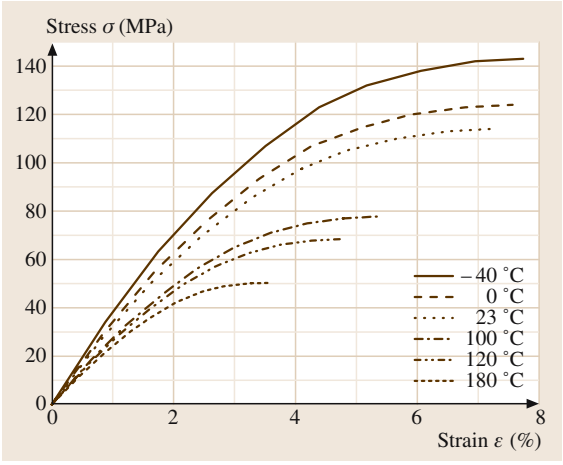


**Fig. 3.3-60** Poly(ether imide), PEI: stress versus strain

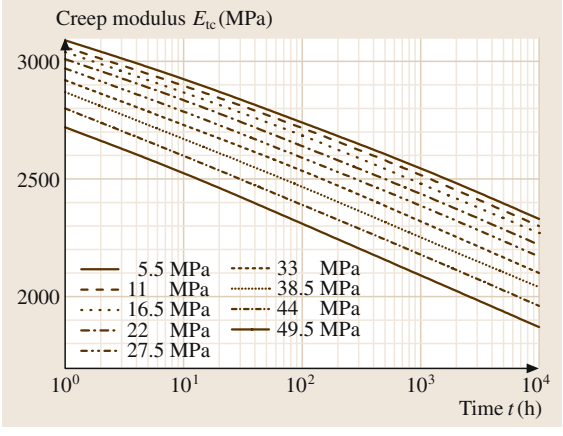


**Fig. 3.3-61** Poly(ether imide), PEI: creep modulus versus time

*Poly(ether ether ketone), PEEK*. Applications: injection-molded parts, automotive parts, aircraft parts, electronic parts, cable insulation, foils, fibers, tapes, plates.

### 3.3.3.9 Cellulose

*Cellulose acetate, CA*. Applications: tool handles, pens, combs, buckles, buttons, electronic parts, spectacles, hollow fibers, fibers, foils, lacquers, resin adhesives, sheet molding compounds (SMCs), bulk molding compounds (BMCs).

*Cellulose propionate, CP*. Applications: fibers, foils, lacquers, resin adhesives, sheet molding compounds, bulk molding compounds (BMC), spectacles, houseware goods, boxes.

**Table 3.3-23** Cellulose acetate, CA; cellulose propionate, CP; cellulose acetobutyrate, CAB; ethylcellulose, EC; vulcanized fiber, VF

| | CA | CP | CAB | EC | VF |
|---|---|---|---|---|---|
| Melting temperature $T_m$ (°C) | | | | | |
| Enthalpy of fusion $\Delta H_u$ (J/mol) (mu) | | | | | |
| Entropy of fusion $\Delta S_u$ (J/(K mol)) (mu) | | | | | |
| Heat capacity $c_p$ (kJ/(kg K))<br>Temperature coefficient $dc_p/dT$ (kJ/(kg K$^2$)) | 1.6 | 1.7 | 1.6 | | |
| Enthalpy of combustion $\Delta H_c$ (kJ/g) | | | | | |
| Glass transition temperature $T_g$ (°C) | | | | | |
| Vicat softening temperature $T_V$50/50 (°C) | 77–110 | 70–100 | 65–100 | | |

**Table 3.3-23** Cellulose acetate, CA; cellulose propionate, CP; cellulose acetobutyrate, CAB; . . . , cont.

| | CA | CP | CAB | EC | VF |
|---|---|---|---|---|---|
| Thermal conductivity $\lambda$ (W/(m K)) | 0.22 | 0.21 | 0.21 | | |
| Density $\varrho$ (g/cm$^3$) | 1.26–1.32 | 1.17–1.24 | 1.16–1.22 | 1.12–1.15 | 1.1–1.45 |
| Coefficient of thermal expansion $\alpha$ ($10^{-5}$/K) (linear) | 10–12 | 11–15 | 10–15 | 10 | |
| Compressibility $\kappa$ (1/MPa) (cubic) | | | | | |
| Elastic modulus $E$ (GPa) | 1.0–3.0 | 1.0–2.4 | 0.8–2.3 | 1.2–1.3 | |
| Shear modulus $G$ (GPa) | | 0.75 | 0.85 | | |
| Poisson's ratio $\mu$ | | | | | |
| Stress at yield $\sigma_y$ (MPa) | 25–55 | 20–50 | 20–55 | 35–40 | |
| Strain at yield $\varepsilon_y$ (%) | 2.5–4 | 3.5–4.5 | 3.5–5 | | |
| Stress at 50% elongation $\sigma_{50}$ (MPa) | | | | | |
| Stress at fracture $\sigma_b$ (MPa) | 38 | 14–55 | 26 | | 85–100 |
| Strain at fracture $\varepsilon_b$ (%) | 3 | 30–100 | 4 | | |
| Impact strength (Charpy) (kJ/m$^2$) | | | | | |
| Notched impact strength (Charpy) (kJ/m$^2$) | | | | | |
| Sound velocity $v_s$ (m/s) (longitudinal) | | | | | |
| Sound velocity $v_s$ (m/s) (transverse) | | | | | |
| Shore hardness $D$ | | | | | |
| Volume resistivity $\rho_e$ ($\Omega$ m) | $10^{10}$–$10^{14}$ | $10^{10}$–$10^{14}$ | $10^{10}$–$10^{14}$ | $10^{11}$–$10^{13}$ | |
| Surface resistivity $\sigma_e$ ($\Omega$) | $10^{10}$–$10^{14}$ | $10^{12}$–$10^{14}$ | $10^{12}$–$10^{14}$ | $10^{11}$–$10^{13}$ | |
| Electric strength $E_B$ (kV/mm) | 25–35 | 30–35 | 32–35 | $\approx$ 30 | |
| Relative permittivity $\varepsilon_r$ (100 Hz) | 5–6 | 4.0–4.2 | 3.7–4.2 | $\approx$ 4 | |
| Dielectric loss tan $\delta$ ($10^{-4}$) (100 Hz) | 70–100 | 50 | 50–70 | 100 | |
| Refractive index $n_D$ (589 nm)<br>Temperature coefficient $dn_D/dT$ (1/K) | 1.47–1.50 | 1.47–1.48 | 1.48 | | |
| Steam permeation (g/(m$^2$ d)) (25 µm) | 150–600 | | 460–600 | | |
| Gas permeation (cm$^3$/(m$^2$ d bar)) (25 µm) | 470–630 ($N_2$)<br>13 000–15 000 ($O_2$)<br>14 000 ($CO_2$)<br>1800–2300 (air) | | 3800 ($N_2$)<br>15 000 ($O_2$)<br>94 000 ($CO_2$) | | |
| Melt viscosity–molar-mass relation | | | | | |
| Viscosity–molar-mass relation | | | | | |

*Cellulose acetobutyrate, CAB*. Applications: fibers, foils, lacquers, resin adhesives, sheet molding compounds, bulk molding compounds, automotive parts, switches, light housings, spectacles.

*Ethylcellulose, EC*. Applications: foils, injection-molded parts, lacquers, adhesives.

*Vulcanized fiber, VF*. Applications: gear wheels, abrasive wheels, case plates.

### 3.3.3.10 Polyurethanes

*Polyurethane, PUR; thermoplastic polyurethane elastomer, TPU.* Applications: blocks, plates, formed pieces, cavity forming, composites, coatings, impregnations, films, foils, fibers, molded foam plastics, insulation boards, sandwich boards, installation boards, reaction injection molding (RIM), automotive parts, houseware goods, sports goods.

**Table 3.3-24** Polyurethane, PUR; thermoplastic polyurethane elastomer, TPU

| | PUR | TPU |
|---|---|---|
| Melting temperature $T_m$ (°C) | | |
| Enthalpy of fusion $\Delta H_u$ (J/mol) (mu) | | |
| Entropy of fusion $\Delta S_u$ (J/(K mol)) (mu) | | |
| Heat capacity $c_p$ (kJ/(kg K))<br>Temperature coefficient $dc_p/dT$ (kJ/(kg K$^2$)) | 1.76 | 0.5 |
| Enthalpy of combustion $\Delta H_c$ (kJ/mol) (mu) | | |
| Glass transition temperature $T_g$ (K) | 15–90 | −40 |
| Vicat softening temperature $T_V50/50$ (°C) | 100–180 | |
| Thermal conductivity $\lambda$ (W/(m K)) | 0.58 | 1.70 |
| Density $\varrho$ (g/cm$^3$) | 1.05 | 1.1–1.25 |
| Coefficient of thermal expansion $\alpha$ ($10^{-5}$/K) (linear) | 1.0–2.0 | 15 |
| Compressibility $\kappa$ (1/MPa) (cubic) | | |
| Elastic modulus $E$ (GPa) | 4.0 | 0.015–0.7 |
| Shear modulus $G$ (GPa) | | 0.006–0.23 |
| Poisson's ratio $\mu$ | | |
| Stress at yield $\sigma_y$ (MPa) | | |
| Strain at yield $\varepsilon_y$ (%) | | |
| Stress at 50% elongation $\sigma_{50}$ (MPa) | | |
| Stress at fracture $\sigma_b$ (MPa) | 70–80 | 30–50 |
| Strain at fracture $\varepsilon_b$ (%) | 3–6 | 300–500 |
| Impact strength (Charpy) (kJ/m$^2$) | | |
| Notched impact strength (Charpy) (kJ/m$^2$) | | |
| Sound velocity $v_s$ (m/s) (longitudinal) | 1550–1750 | |
| Sound velocity $v_s$ (m/s) (transverse) | | |
| Shore hardness $D$ | 60–90 | 30–70 |
| Volume resistivity $\rho_e$ (Ω m) | $10^{14}$ | $10^{10}$ |
| Surface resistivity $\sigma_e$ (Ω) | $10^{14}$ | $10^{11}$ |
| Electric strength $E_B$ (kV/mm) | 24 | 30–60 |
| Relative permittivity $\varepsilon_r$ (100 Hz) | 3.6 | 6.5 |
| Dielectric loss tan $\delta$ ($10^{-4}$) (100 Hz) | 500 | 300 |
| Refractive index $n_D$ (589 nm)<br>Temperature coefficient $dn_D/dT$ (1/K) | | |
| Steam permeation (g/(m$^2$ d)) (25 µm) | | 13–25 |
| Gas permeation (cm$^3$/(m$^2$ d bar)) (25 µm) | | 550–1600 ($N_2$)<br>1000–4500 ($O_2$)<br>6000–22 000 ($CO_2$) |
| Melt viscosity–molar-mass relation | | |
| Viscosity–molar-mass relation | | |

**Table 3.3-25** Polyurethane, PUR: thermal conductivity and coefficient of thermal expansion

| Temperature $T$ (°C) | −200 | −150 | −100 | −50 | 0 | 20 | 50 | 100 |
|---|---|---|---|---|---|---|---|---|
| Thermal conductivity λ (W/(m K)) | | 0.20 | 0.21 | 0.22 | 0.21 | | 0.20 | 0.20 |
| Average coefficient of thermal expansion $\alpha^*$ ($10^{-5}$/K) (linear)[a] | 9.9 | 12.7 | 16.0 | 26.0 | 20.0 | | | |

[a] $\alpha^*(T) = (1/(T-20)) \int_{T=20}^{T'} \alpha(T)\, dT$, $T$ in °C

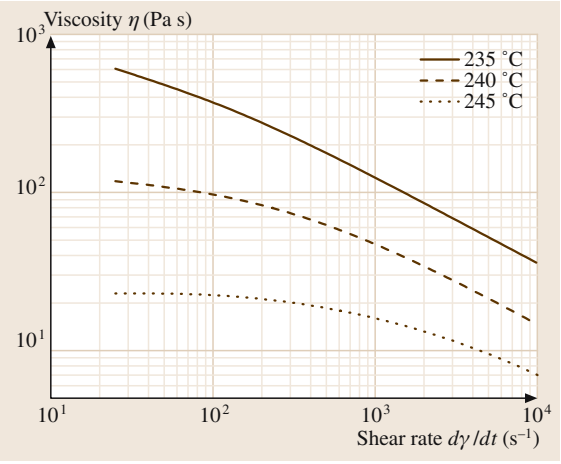


**Fig. 3.3-62** Thermoplastic polyurethane elastomer, TPU: viscosity versus shear rate

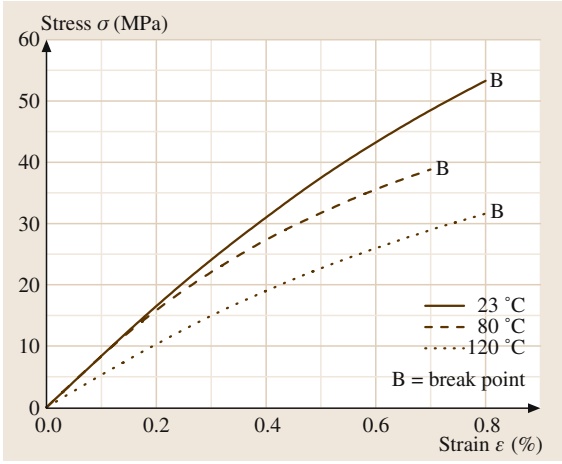


**Fig. 3.3-63** Phenol formaldehyde, PF: stress versus strain

### 3.3.3.11 Thermosets

*Phenol formaldehyde, PF; urea formaldehyde, UF; melamine formaldehyde, MF*. Applications: molded pieces, granulated molding compounds (GMCs), bulk molding compounds, dough molding compounds (DMCs), sheet molding compounds, plates, gear wheels, abrasive wheels, lacquers, coatings, chipboards, adhesives, foams, fibers.

*Unsaturated polyester, UP; diallyl phthalate, DAP*. Applications: molding compounds, cast resins, electronic parts, automotive parts, containers, tools, housewares goods, sports goods.

**Table 3.3-26** Phenol formaldehyde, PF; urea formaldehyde, UF; melamine formaldehyde, MF

| | PF | UF | MF |
|---|---|---|---|
| Melting temperature $T_m$ (°C) | | | |
| Enthalpy of fusion $\Delta H_u$ (J/mol) (mu) | | | |
| Entropy of fusion $\Delta S_u$ (J/(K mol)) (mu) | | | |
| Heat capacity $c_p$ (kJ/(kg K))<br>Temperature coefficient $dc_p/dT$ (kJ/(kg K$^2$)) | 1.30 | 1.20 | 1.20 |
| Enthalpy of combustion $\Delta H_c$ (kJ/g) | | | |
| Glass transition temperature $T_g$ (°C) | | | |
| Vicat softening temperature $T_V$50/50 (°C) | | | |
| Thermal conductivity λ (W/(m K)) | 0.35 | 0.40 | 0.50 |
| Density ϱ (g/cm$^3$) | 1.4 | 1.5 | 1.5 |
| Coefficient of thermal expansion α ($10^{-5}$/K) (linear) | 3–5 | 5–6 | 5–6 |

**Table 3.3-26** Phenol formaldehyde, PF; urea formaldehyde, UF; melamine formaldehyde, MF, cont.

| | PF | UF | MF |
|---|---|---|---|
| Compressibility $\kappa$ (1/MPa) (cubic) | | | |
| Elastic modulus $E$ (GPa) | 5.6–12 | 7.0–10.5 | 4.9–9.1 |
| Shear modulus $G$ (GPa) | | | |
| Poisson's ratio $\mu$ | | | |
| Stress at yield $\sigma_y$ (MPa) | | | |
| Strain at yield $\varepsilon_y$ (%) | | | |
| Stress at 50% elongation $\sigma_{50}$ (MPa) | | | |
| Stress at fracture $\sigma_b$ (MPa) | 25 | 30 | 30 |
| Strain at fracture $\varepsilon_b$ (%) | 0.4–0.8 | 0.5–1.0 | 0.6–0.9 |
| Impact strength (Charpy) (kJ/m$^2$) | 4.5–10 | | |
| Notched impact strength (Charpy) (kJ/m$^2$) | 1.5–3 | | |
| Sound velocity $v_s$ (m/s) (longitudinal) | | | |
| Sound velocity $v_s$ (m/s) (transverse) | | | |
| Shore hardness $D$ | 82 | | 90 |
| Volume resistivity $\rho_e$ ($\Omega$ m) | $10^9$ | $10^9$ | $10^9$ |
| Surface resistivity $\sigma_e$ ($\Omega$) | $> 10^8$ | $> 10^{10}$ | $> 10^8$ |
| Electric strength $E_B$ (kV/mm) | 30–40 | 30–40 | 29–30 |
| Relative permittivity $\varepsilon_r$ (100 Hz) | 6 | 8 | 9 |
| Dielectric loss tan $\delta$ ($10^{-4}$) (100 Hz) | 1000 | 400 | 600 |
| Refractive index $n_D$ (589 nm)<br>Temperature coefficient $dn_D/dT$ (1/K) | 1.63 | | |
| Steam permeation (g/(m$^2$ d)) (40 µm) | 43 | | 400 |
| Gas permeation (cm$^3$/(m$^2$ d bar)) | | | |
| Melt viscosity–molar-mass relation | | | |
| Viscosity–molar-mass relation | | | |

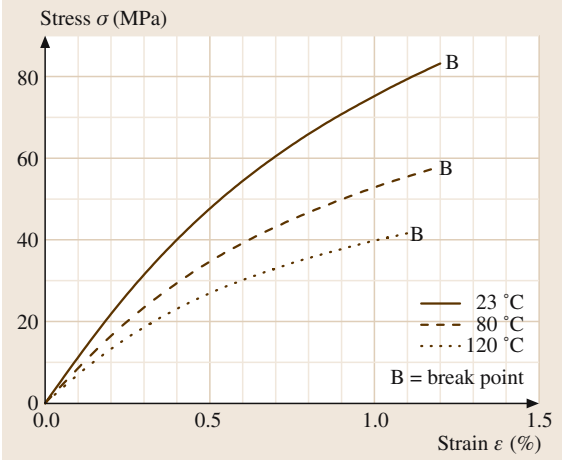


**Fig. 3.3-64** Melamine formaldehyde, MF: stress versus strain

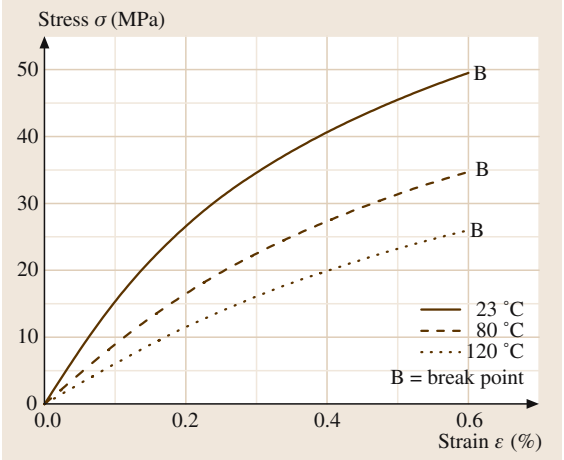


**Fig. 3.3-65** Unsaturated polyester, UP: stress versus strain

**Table 3.3-27** Unsaturated polyester, UP; diallyl phthalate, DAP; silicone resin, SI; epoxy resin, EP

| | UP | DAP | SI | EP |
|---|---|---|---|---|
| Melting temperature $T_m$ (°C) | | | | |
| Enthalpy of fusion $\Delta H_u$ (J/mol) (mu) | | | | |
| Entropy of fusion $\Delta S_u$ (J/(K mol)) (mu) | | | | |
| Heat capacity $c_p$ (kJ/(kg K))<br>Temperature coefficient $dc_p/dT$ (kJ/(kg $K^2$)) | 1.20 | | 0.8–0.9 | 0.8–1.0 |
| Enthalpy of combustion $\Delta H_c$ (kJ/g) | | | | |
| Glass transition temperature $T_g$ (°C) | 70–120 | | | |
| Vicat softening temperature $T_V$50/50 (°C) | | | | |
| Thermal conductivity λ (W/(m K)) | 0.7 | 0.6 | 0.3–0.4 | 0.88 |
| Density $\varrho$ (g/$cm^3$) | 2.0 | 1.51–1.78 | 1.8–1.9 | 1.9 |
| Coefficient of thermal expansion $\alpha$ ($10^{-5}$/K) (linear) | 2–4 | 1–3.5 | 2–5 | 1.1–3.5 |
| Compressibility $\kappa$ (1/MPa) (cubic) | | | | |
| Elastic modulus $E$ (GPa) | 14–20 | 9.8–15.5 | 6–12 | 21.5 |
| Shear modulus $G$ (GPa) | | | | |
| Poisson's ratio $\mu$ | | | | |
| Stress at yield $\sigma_y$ (MPa) | | | | |
| Strain at yield $\varepsilon_y$ (%) | | | | |
| Stress at 50% elongation $\sigma_{50}$ (MPa) | | | | |
| Stress at fracture $\sigma_b$ (MPa) | 30 | 40–75 | 28–46 | 30–40 |
| Strain at fracture $\varepsilon_b$ (%) | 0.6–1.2 | | | 4 |
| Impact strength (Charpy) (kJ/$m^2$) | | | | |
| Notched impact strength (Charpy) (kJ/$m^2$) | | | | |
| Sound velocity $v_s$ (m/s) (longitudinal) | | | | |
| Sound velocity $v_s$ (m/s) (transverse) | | | | |
| Shore hardness $D$ | 82 | | | |
| Volume resistivity $\rho_e$ (Ω m) | $> 10^{10}$ | $10^{11}$–$10^{14}$ | $10^{12}$ | $> 10^{12}$ |
| Surface resistivity $\sigma_e$ (Ω) | $> 10^{10}$ | $10^{13}$ | $10^{12}$ | $> 10^{12}$ |
| Electric strength $E_B$ (kV/mm) | 25–53 | 40 | 20–40 | 30–40 |
| Relative permittivity $\varepsilon_r$ (100 Hz) | 6 | 5.2 | 4 | 3.5–5 |
| Dielectric loss tan $\delta$ ($10^{-4}$) (100 Hz) | 400 | 400 | 300 | 10 |
| Refractive index $n_D$ (589 nm)<br>Temperature coefficient $dn_D/dT$ (1/K) | 1.54–1.58 | | | 1.47 |
| Steam permeation (g/($m^2$ d)) | | | | |
| Gas permeation ($cm^3$/($m^2$ d bar)) | | | | |
| Melt viscosity–molar-mass relation | | | | |
| Viscosity–molar-mass relation | | | | |

**Table 3.3-28** Unsaturated polyester, UP: coefficient of thermal expansion

| Temperature $T$ (°C) | −200 | −150 | −100 | −50 | 0 | 20 | 50 | 100 |
|---|---|---|---|---|---|---|---|---|
| Coefficient of thermal expansion $\alpha$ ($10^{-5}$/K) (linear) | 3.0 | 4.1 | 4.9 | 5.8 | 7.3 | 8.4 | 10.7 | 15.0 |

**Table 3.3-29** Epoxy resin, EP: thermal conductivity and coefficient of thermal expansion

| Temperature $T$ (°C) | −200 | −150 | −100 | −50 | 0 | 20 | 50 | 100 | 150 |
|---|---|---|---|---|---|---|---|---|---|
| Thermal conductivity $\lambda$ (W/(m K)) | | | | | 0.20 | 0.20 | 0.20 | 0.20 | |
| Coefficient of thermal expansion $\alpha$ ($10^{-5}$/K) (linear) | 1.8 | 2.8 | 3.8 | 4.9 | 6.1 | 6.2 | 6.3 | 7.5 | 13.0 |

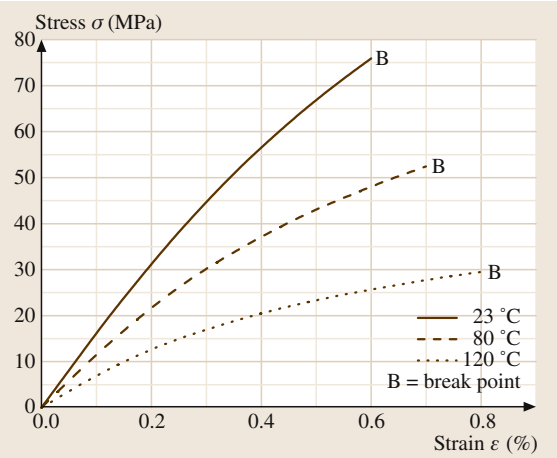


**Fig. 3.3-66** Epoxy resin, EP: stress versus strain

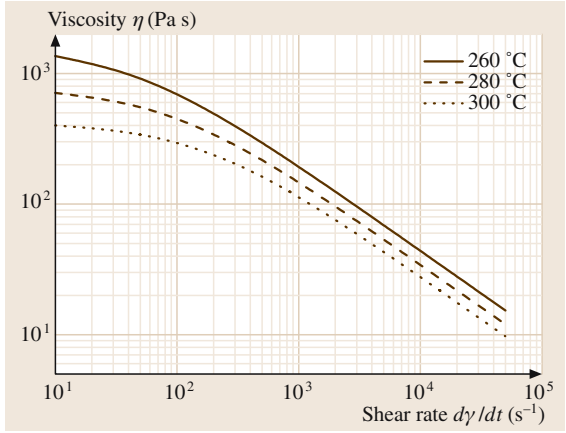


**Fig. 3.3-67** Poly(acrylonitrile-co-butadiene-co-styrene) + polycarbonate, ABS + PC: viscosity versus shear rate

*Silicone resin, SI*. Applications: molding compounds, laminates.

*Epoxy resin EP, Applications*: moulding compounds.

### 3.3.3.12 Polymer Blends

*Polypropylene + ethylene/propylene/diene rubber, PP + EPDM*. Applications: automotive parts, flexible tubes, sports goods, toys.

*Poly(acrylonitrile-co-butadiene-co-styrene) + polycarbonate, ABS + PC; Poly(acrylonitrile-co-butadiene-co-acrylester) + polycarbonate ASA + PC; poly(acrylonitrile-co-butadiene-co-styrene) + polyamide, ABS + PA*. Applications: semifinished goods, automotive parts, electronic parts, optical parts, houseware goods.

*Poly(vinyl chloride) + poly(vinyl chloride-co-acrylate), PVC + VC/A; poly(vinyl chloride) + chlorinated polyethylene, PVC + PE-C, poly(vinyl chloride) + poly(acrylonitrile-co-butadiene-co-acrylester), PVC + ASA*. Applications: semifinished goods, foils, plates, profiles, pipes, fittings, gutters, window frames, door frames, panels, housings, bottles, blow molding, disks, blocking layers, fibers, fleeces, nets.

*Polycarbonate + poly(ethylene terephthalate), PC + PET; polycarbonate + liquid crystal polymer, PC + LCP; polycarbonate + poly(butylene terephthalate), PC + PBT*. Applications: optical devices, covering devices, panes, safety glasses, semifinished goods, houseware goods, compact discs, bottles.

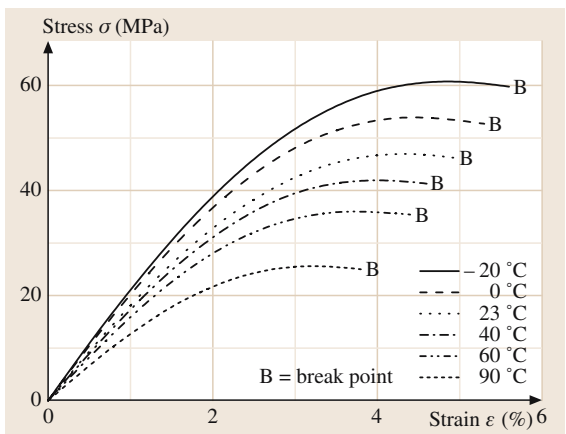


**Fig. 3.3-68** Poly(acrylonitrile-co-butadiene-co-styrene) + polycarbonate, ABS + PC: stress versus strain

*Poly(ethylene terephthalate) + polystyrene, PET + PS; poly(butylene terephthalate) + polystyrene, PBT + PS*. Applications: same as for PET, PBT, and PS.

**Table 3.3-30** Polypropylene + ethylene/propylene/diene rubber, PP + EPDM; poly(acrylonitrile-co-butadiene-co-styrene) + polycarbonate, ABS + PC; poly(acrylonitrile-co-butadiene-co-styrene) + polyamide, ABS + PA; poly(acrylonitrile-co-butadiene-co-acrylester) + polycarbonate, ASA + PC

| | PP + EPDM | ABS + PC | ABS + PA | ASA + PC |
|---|---|---|---|---|
| Melting temperature $T_m$ (°C) | 160–168 | | | |
| Enthalpy of fusion $\Delta H_u$ (J/mol) (mu) | | | | |
| Entropy of fusion $\Delta S_u$ (J/(K mol)) (mu) | | | | |
| Heat capacity $c_p$ (kJ/(kg K))<br>Temperature coefficient $dc_p/dT$ (kJ/(kg K$^2$)) | | | | |
| Enthalpy of combustion $\Delta H_c$ (kJ/g) | | | | |
| Glass transition temperature $T_g$ (°C) | | | | |
| Vicat softening temperature $T_V$50/50 (°C) | | | | |
| Thermal conductivity $\lambda$ (W/(m K)) | | | | |
| Density $\varrho$ (g/cm$^3$) | 0.89–0.92 | 1.08–1.17 | 1.07–1.09 | 1.15 |
| Coefficient of thermal expansion $\alpha$ ($10^{-5}$/K) (linear) | 15–18 | 7–8.5 | 9 | 7–9 |
| Compressibility $\kappa$ (1/MPa) (cubic) | | | | |
| Elastic modulus $E$ (GPa) | 0.5–1.2 | 2.0–2.6 | 1.2–1.3 | 2.3–2.6 |
| Shear modulus $G$ (GPa) | | | | |
| Poisson's ratio $\mu$ | | | | |
| Stress at yield $\sigma_y$ (MPa) | 10–25 | 40–60 | 30–32 | 53–63 |
| Strain at yield $\varepsilon_y$ (%) | 10–35 | 3–3.5 | | 4.6–5 |
| Stress at 50% elongation $\sigma_{50}$ (MPa) | | | | |
| Stress at fracture $\sigma_b$ (MPa) | | | | |
| Strain at fracture $\varepsilon_b$ (%) | > 50 | > 50 | > 50 | > 50 |
| Impact strength (Charpy) (kJ/m$^2$) | | | | |
| Notched impact strength (Charpy) (kJ/m$^2$) | | | | |
| Sound velocity $v_s$ (m/s) (longitudinal) | | | | |
| Sound velocity $v_s$ (m/s) (transverse) | | | | |
| Shore hardness $D$ | | | | |
| Volume resistivity $\rho_e$ (Ω m) | > $10^{14}$ | > $10^{14}$ | $2\times10^{12}$ | $10^{11}$–$10^{13}$ |
| Surface resistivity $\sigma_e$ (Ω) | > $10^{13}$ | $10^{14}$ | $3\times10^{14}$ | $10^{13}$–$10^{14}$ |
| Electric strength $E_B$ (kV/mm) | 35–40 | 24 | 30 | |
| Relative permittivity $\varepsilon_r$ (100 Hz) | 2.3 | 3 | | 3–3.5 |
| Dielectric loss tan $\delta$ ($10^{-4}$) (100 Hz) | 2.5 | 30–60 | | 20–160 |
| Refractive index $n_D$ (589 nm)<br>Temperature coefficient $dn_D/dT$ (1/K) | | | | |
| Steam permeation (g/(m$^2$ d)) | | | | |
| Gas permeation (cm$^3$/(m$^2$ d bar)) | | | | |
| Melt viscosity–molar-mass relation | | | | |
| Viscosity–molar-mass relation | | | | |

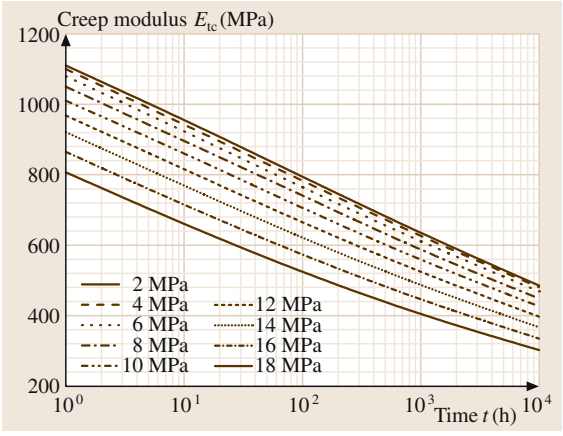


**Fig. 3.3-69** Poly(acrylonitrile-co-butadiene-co-styrene) + polycarbonate, ABS + PC: creep modulus versus time

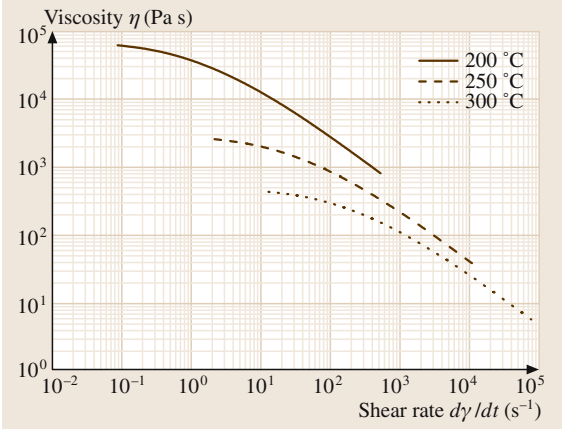


**Fig. 3.3-71** Poly(acrylonitrile-co-butadiene-co-acrylester) + polycarbonate, ASA + PC: viscosity versus shear rate

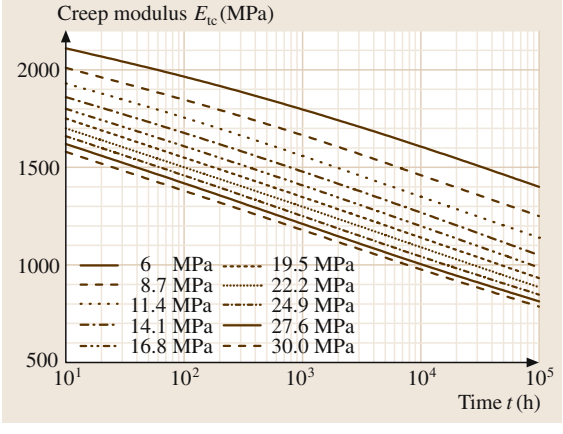


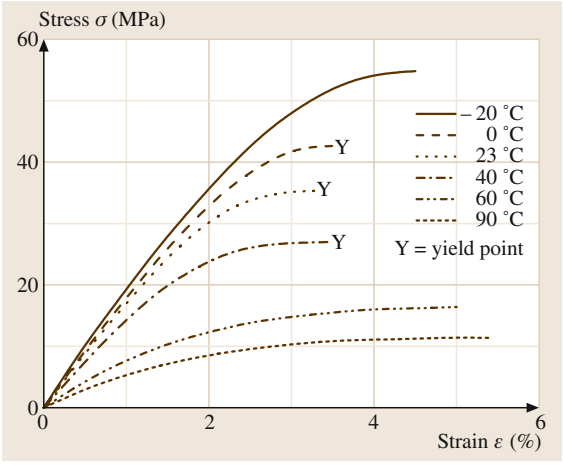


**Fig. 3.3-70** Poly(acrylonitrile-co-butadiene-co-styrene) + polyamide, ABS + PA: stress versus strain

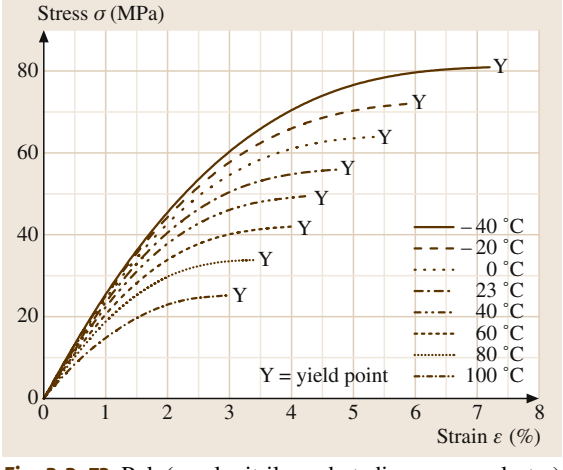


**Fig. 3.3-72** Poly(acrylonitrile-co-butadiene-co-acrylester) + polycarbonate, ASA + PC: stress versus strain

*Poly(butylene terephthalate) + poly(acrylonitrile-co-butadiene-co-acrylester), PBT + ASA*. Applications: same as for PBT and ASA.

*Polysulfone + poly(acrylonitrile-co-butadiene-co-styrene), PSU + ABS*. Applications: same as for PSU.

*Poly(styrene-co-butadiene), PPE + SB*. Applications: same as for PPE.

*Poly(phenylene ether) + polyamide 66, PPE + PA66*. Applications: automotive parts, semifinished goods.

**Fig. 3.3-73** Poly(acrylonitrile-co-butadiene-co-acrylester) + polycarbonate, ASA + PC: creep modulus versus time

**Table 3.3-31** Poly(vinyl chloride) + poly(vinyl chloride-co-acrylate), PVC + VC/A; poly(vinyl chloride) + chlorinated polyethylene, PVC + PE-C; poly(vinyl chloride) + poly(acrylonitrile-co-butadiene-co-acrylester), PVC + ASA

| | PVC + VC/A | PVC + PE-C | PVC + ASA |
|---|---|---|---|
| Melting temperature $T_m$ (°C) | | | |
| Enthalpy of fusion $\Delta H_u$ (J/mol) (mu) | | | |
| Entropy of fusion $\Delta S_u$ (J/(K mol)) (mu) | | | |
| Heat capacity $c_p$ (kJ/(kg K))<br>Temperature coefficient $dc_p/dT$ (kJ/(kg K$^2$)) | | | |
| Enthalpy of combustion $\Delta H_c$ (kJ/g) | | | |
| Glass transition temperature $T_g$ (°C) | | | |
| Vicat softening temperature $T_V$50/50 (°C) | | | |
| Thermal conductivity $\lambda$ (W/(m K)) | | | |
| Density $\varrho$ (g/cm$^3$) | 1.42–1.44 | 1.36–1.43 | 1.28–1.33 |
| Coefficient of thermal expansion $\alpha$ ($10^{-5}$/K) (linear) | 7–7.5 | 8 | 7.5–10 |
| Compressibility $\kappa$ (1/MPa) (cubic) | | | |
| Elastic modulus $E$ (GPa) | 2.5–2.7 | 2.6 | 2.6–2.8 |
| Shear modulus $G$ (GPa) | | | |
| Poisson's ratio $\mu$ | | | |
| Stress at yield $\sigma_y$ (MPa) | 45 | 40–50 | 45–55 |
| Strain at yield $\varepsilon_y$ (%) | 4–5 | 3 | 3–3.5 |
| Stress at 50% elongation $\sigma_{50}$ (MPa) | | | |
| Stress at fracture $\sigma_b$ (MPa) | | | |
| Strain at fracture $\varepsilon_b$ (%) | > 50 | 10 to >50 | ≈ 8 |
| Impact strength (Charpy) (kJ/m$^2$) | | | |
| Notched impact strength (Charpy) (kJ/m$^2$) | | | |
| Sound velocity $v_s$ (m/s) (longitudinal) | | | |
| Sound velocity $v_s$ (m/s) (transverse) | | | |
| Shore hardness $D$ | | | |
| Volume resistivity $\rho_e$ (Ω m) | $10^{13}$ | $10^{12}$ to >$10^{13}$ | $10^{12}$ to >$10^{14}$ |
| Surface resistivity $\sigma_e$ (Ω) | > $10^{13}$ | > $10^{13}$ | $10^{12}$–$10^{14}$ |
| Electric strength $E_B$ (kV/mm) | | | |
| Relative permittivity $\varepsilon_r$ (100 Hz) | 3.5 | 3.1 | 3.7–4.3 |
| Dielectric loss tan $\delta$ ($10^{-4}$) (100 Hz) | 120 | 140 | 100–120 |
| Refractive index $n_D$ (589 nm)<br>Temperature coefficient $dn_D/dT$ (1/K) | | | |
| Steam permeation (g/(m$^2$ d)) | | | |
| Gas permeation (cm$^3$/(m$^2$ d bar)) | | | |
| Melt viscosity–molar-mass relation | | | |
| Viscosity–molar-mass relation | | | |

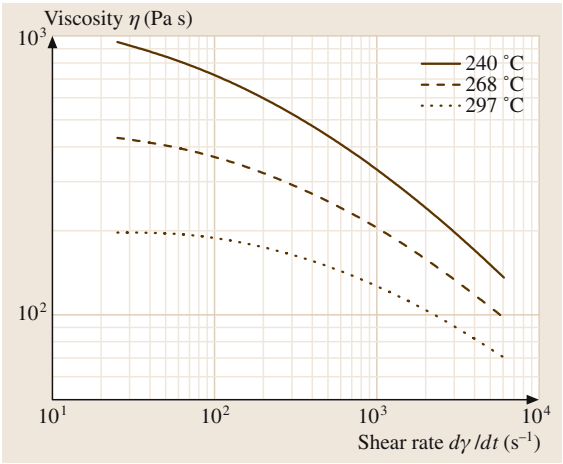


**Fig. 3.3-74** Polycarbonate + poly(butylene terephthalate), PC + PBT: viscosity versus shear rate

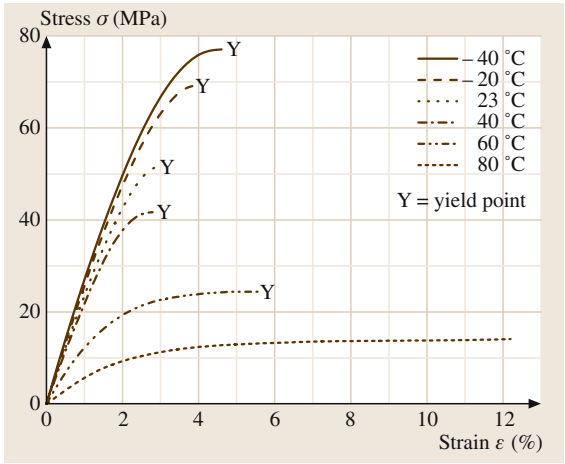


**Fig. 3.3-75** Polycarbonate + poly(butylene terephthalate), PC + PBT: stress versus strain

**Table 3.3-32** Polycarbonate + poly(ethylene terephthalate), PC + PET; polycarbonate + liquid crystall polymer, PC + LCP; polycarbonate + poly(butylene terephthalate), PC + PBT; poly(ethylene terephthalate) + polystyrene, PET + PS; poly(butylene terephthalate) + polystyrene, PBT + PS

| | PC + PET | PC + LCP | PC + PBT | PET + PS | PBT + PS |
|---|---|---|---|---|---|
| Melting temperature $T_m$ (°C) | | | | | |
| Enthalpy of fusion $\Delta H_u$ (J/mol) (mu) | | | | | |
| Entropy of fusion $\Delta S_u$ (J/(K mol)) (mu) | | | | | |
| Heat capacity $c_p$ (kJ/(kg K))<br>Temperature coefficient $dc_p/dT$ (kJ/(kg K$^2$)) | | | | 1.05 | 1.30 |
| Enthalpy of combustion $\Delta H_c$ (kJ/g) | | | | | |
| Glass transition temperature $T_g$ (°C) | | | | | |
| Vicat softening temperature $T_V$50/50 (°C) | | | | | |
| Thermal conductivity $\lambda$ (W/(m K)) | | | | 0.24 | 0.21 |
| Density $\varrho$ (g/cm$^3$) | 1.22 | | 1.2–1.26 | 1.37 | 1.31 |
| Coefficient of thermal expansion $\alpha$ ($10^{-5}$/K) (linear) | 9–10 | | 8–9 | 7 | 6.0 |
| Compressibility $\kappa$ (1/MPa) (cubic) | | | | | |
| Elastic modulus $E$ (GPa) | 2.1–2.3 | 2.6–4.0 | 2.3 | 3.1 | 2.0 |
| Shear modulus $G$ (GPa) | | | | | |
| Poisson's ratio $\mu$ | | | | | |
| Stress at yield $\sigma_y$ (MPa) | 50–55 | 66 | 50–60 | 47 | 40 |
| Strain at yield $\varepsilon_y$ (%) | 5 | 5.6–6.9 | 4–5 | | |
| Stress at 50% elongation $\sigma_{50}$ (MPa) | | | | | |
| Stress at fracture $\sigma_b$ (MPa) | | 74–82 | | | 15 |
| Strain at fracture $\varepsilon_b$ (%) | > 50 | | 25 to > 50 | 50 | |
| Impact strength (Charpy) (kJ/m$^2$) | | | | | |
| Notched impact strength (Charpy) (kJ/m$^2$) | | | | | |
| Sound velocity $v_s$ (m/s) (longitudinal) | | | | | |

**Table 3.3-32** Polycarbonate + poly(ethylene terephthalate), PC + PET; polycarbonate + liquid crystall polymer, PC + LCP; polycarbonate + poly(butylene terephthalate), PC + PBT; poly(ethylene terephthalate) + polystyrene, PET + PS; poly(butylene terephthalate) + polystyrene, PBT + PS, cont.

| | PC + PET | PC + LCP | PC + PBT | PET + PS | PBT + PS |
|---|---|---|---|---|---|
| Sound velocity $v_s$ (m/s) (transverse) | | | | | |
| Shore hardness $D$ | | | | | |
| Volume resistivity $\rho_e$ ($\Omega$ m) | $> 10^{13}$ | | $10^{14}$ | $> 10^{12}$ | |
| Surface resistivity $\sigma_e$ ($\Omega$) | $> 10^{15}$ | | $10^{14}$ | $> 10^{12}$ | |
| Electric strength $E_B$ (kV/mm) | 30 | | 35 | | |
| Relative permittivity $\varepsilon_r$ (100 Hz) | 3.3 | | 3.3 | | |
| Dielectric loss tan $\delta$ ($10^{-4}$) (100 Hz) | 200 | | 20–40 | | |
| Refractive index $n_D$ (589 nm) | | | | | |
| Temperature coefficient $dn_D/dT$ (1/K) | | | | | |
| Steam permeation (g/(m$^2$ d)) | | | | | |
| Gas permeation (cm$^3$/(m$^2$ d bar)) | | | | | |
| Melt viscosity–molar-mass relation | | | | | |
| Viscosity–molar-mass relation | | | | | |

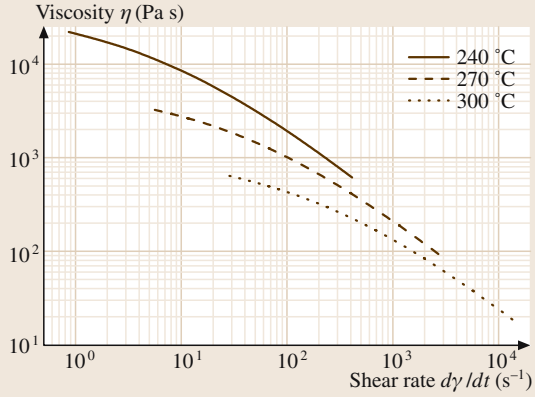


**Fig. 3.3-76** Poly(phenylene ether) + poly(styrene-co-butadiene), PPE + SB: viscosity versus shear rate

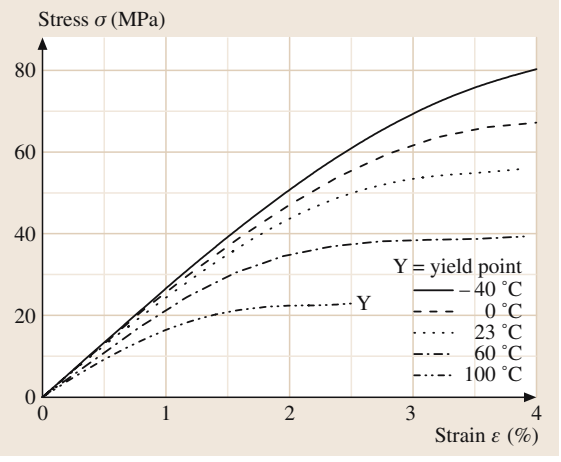


**Fig. 3.3-77** Poly(phenylene ether) + poly(styrene-co-butadiene), PPE + SB: stress versus strain

*Poly(phenylene ether) + polystyrene, PPE + PS.* Applications: automotive parts, foams, office goods, electrical parts, houseware goods.

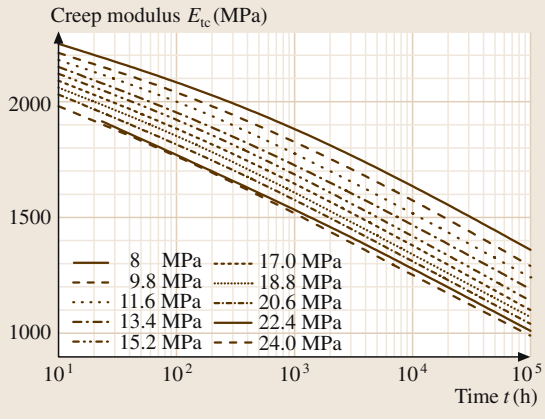


**Fig. 3.3-78** Poly(phenylene ether) + poly(styrene-co-butadiene), PPE + SB: creep modulus versus time

**Table 3.3-33** Poly(butylene terephthalate) + poly(acrylonitrile-co-butadiene-co-acrylester), PBT + ASA; polysulfon + poly(acrylonitrile-co-butadiene-co-styrene), PSU + ABS; poly(phenylene ether) + poly(styrene-co-butadiene), PPE + SB; poly(phenylene ether) + polyamide 66, PPE + PA66; poly(phenylene ether) + polystyrene PPE + PS

| | PBT + ASA | PSU + ABS | PPE + SB | PPE + PA66 | PPE + PS |
|---|---|---|---|---|---|
| Melting temperature $T_m$ (°C) | 225 | | | | |
| Enthalpy of fusion $\Delta H_u$ (J/mol) (mu) | | | | | |
| Entropy of fusion $\Delta S_u$ (J/(K mol)) (mu) | | | | | |
| Heat capacity $c_p$ (kJ/(kg K))<br>Temperature coefficient $dc_p/dT$ (kJ/(kg K$^2$)) | | | | | 1.40 |
| Enthalpy of combustion $\Delta H_c$ (kJ/g) | | | | | |
| Glass transition temperature $T_g$ (°C) | | | | | |
| Vicat softening temperature $T_V50/50$ (°C) | | | | | |
| Thermal conductivity $\lambda$ (W/(m K)) | | | | | 0.23 |
| Density $\varrho$ (g/cm$^3$) | 1.21–1.22 | 1.13 | 1.04–1.06 | 1.09–1.10 | 1.06 |
| Coefficient of thermal expansion $\alpha$ ($10^{-5}$/K) (linear) | 10 | 6.5 | 6.0–7.5 | 8–11 | 6.0 |
| Compressibility $\kappa$ (1/MPa) (cubic) | | | | | |
| Elastic modulus $E$ (GPa) | 2.5 | 2.1 | 1.9–2.7 | 2.0–2.2 | 2.5 |
| Shear modulus $G$ (GPa) | | | | | |
| Poisson's ratio $\mu$ | | | | | |
| Stress at yield $\sigma_y$ (MPa) | 53 | 50 | 45–65 | 50–60 | 55 |
| Strain at yield $\varepsilon_y$ (%) | 3.6 | 4 | 3–7 | 5 | |
| Stress at 50% elongation $\sigma_{50}$ (MPa) | | | | | |
| Stress at fracture $\sigma_b$ (MPa) | | | 20 to >50 | > 50 | |
| Strain at fracture $\varepsilon_b$ (%) | > 50 | > 50 | | | 50 |
| Impact strength (Charpy) (kJ/m$^2$) | | | | | |
| Notched impact strength (Charpy) (kJ/m$^2$) | | | | | |
| Sound velocity $v_s$ (m/s) (longitudinal) | | | | | |
| Sound velocity $v_s$ (m/s) (transverse) | | | | | |
| Shore hardness $D$ | | | | | |
| Volume resistivity $\rho_e$ (Ω m) | > $10^{14}$ | > $10^{13}$ | > $10^{14}$ | > $10^{11}$ | $10^{12}$ |
| Surface resistivity $\sigma_e$ (Ω) | > $10^{15}$ | > $10^{14}$ | > $10^{14}$ | > $10^{12}$ | $10^{12}$ |
| Electric strength $E_B$ (kV/mm) | 30 | 20–30 | 35–40 | 95 | |
| Relative permittivity $\varepsilon_r$ (100 Hz) | 3.3 | 3.1–3.3 | 2.6–2.8 | 3.1–3.4 | |
| Dielectric loss tan $\delta$ ($10^{-4}$) (100 Hz) | 200 | 40–50 | 5–15 | 450 | |
| Refractive index $n_D$ (589 nm)<br>Temperature coefficient $dn_D/dT$ (1/K) | | | | | |
| Steam permeation (g/(m$^2$ d)) | | | | | |
| Gas permeation (cm$^3$/(m$^2$ d bar)) | | | | | |
| Melt viscosity–molar-mass relation | | | | | |
| Viscosity–molar-mass relation | | | | | |

## References


3.1 M. D. Lechner, K. Gehrke, E. H. Nordmeier: *Makromolekulare Chemie* (Birkhäuser, Basel 2003)

3.2 G. W. Becker, D. Braun (Eds.): *Kunststoff Handbuch* (Hanser, Munich 1969 – 1990)

3.3 Kunststoffdatenbank CAMPUS, M-Base, Aachen (www.m-base.de)

3.4 J. Brandrup, E. H. Immergut, E. A. Grulke (Eds.): *Polymer Handbook* (Wiley, New York 1999)

3.5 J. E. Mark (Ed.): *Physical Properties of Polymers Handbook* (AIP, Woodbury 1996)

3.6 C. C. Ku, R. Liepins: *Electrical Properties of Polymers* (Hanser, Munich 1987)

3.7 H. Saechtling: *Kunststoff Taschenbuch* (Hanser, Munich 1998)

3.8 W. Hellerich, G. Harsch, S. Haenle: *Werkstoff-Führer Kunststoffe* (Hanser, Munich 1996)

3.9 B. Carlowitz: *Kunststoff Tabellen* (Hanser, Munich 1995)

3.10 G. Allen, J. C. Bevington (Eds.): *Comprehensive Polymer Science* (Pergamon, Oxford 1989)

3.11 H. Dominghaus: *Die Kunststoffe und ihre Eigenschaften* (VDI, Düsseldorf 1992)

3.12 H. J. Arpe (Ed.): *Ullmann's Encyclopedia of Industrial Chemistry*, 5th edn. (VCH, Weinheim 1985 – 1996)

3.13 R. E. Kirk, D. F. Othmer (Eds.): *Encyclopedia of Chemical Technology*, 4th edn. (Wiley, New York 1978 – 1984)

3.14 H. F. Mark, N. Bikales, C. G. Overberger, G. Menges, J. I. Kroschwitz: *Encyclopedia of Polymer Science and Engineering* (Wiley, New York 1985 – 1990)

3.15 Werkstoff-Datenbank POLYMAT, Deutsches Kunststoff-Institut, Darmstadt

3.16 M. Neubronner: Stoffwerte von Kunststoffen. In: *VDI-Wärmeatlas*, 8th edn. (VDI, Düsseldorf 1997)

# Glasses

# 3.4. Glasses

This chapter has been conceived as a source of information for scientists, engineers, and technicians who need data and commercial-product information to solve their technical task by using glasses as engineering materials. It is not intended to replace the comprehensive scientific literature. The fundamentals are merely sketched, to provide a feeling for the unique behavior of this widely used class of materials.

The properties of glasses are as versatile as their composition. Therefore only a selection of data can be listed, but their are intended to cover the preferred glass types of practical importance. Wherever possible, formulas, for example for the optical and thermal properties, are given with their correct constants, which should enable the reader to calculate the data needed for a specific situation by him/herself.

For selected applications, the suitable glass types and the main instructions for their processing are presented. Owing to the availability of the information, the products of Schott AG have a certain preponderance here. The properties of glass types from other manufacturers have been included whenever available.

3.4.1 **Properties of Glasses – General Comments** ..... 526

3.4.2 **Composition and Properties of Glasses** . 527

3.4.3 **Flat Glass and Hollowware** ..... 528
3.4.3.1 Flat Glass ..... 528
3.4.3.2 Container Glass ..... 529

3.4.4 **Technical Specialty Glasses** ..... 530
3.4.4.1 Chemical Stability of Glasses ..... 530
3.4.4.2 Mechanical and Thermal Properties ..... 533
3.4.4.3 Electrical Properties ..... 537
3.4.4.4 Optical Properties ..... 539

3.4.5 **Optical Glasses** ..... 543
3.4.5.1 Optical Properties ..... 543
3.4.5.2 Chemical Properties ..... 549
3.4.5.3 Mechanical Properties ..... 550
3.4.5.4 Thermal Properties ..... 556

3.4.6 **Vitreous Silica** ..... 556
3.4.6.1 Properties of Synthetic Silica ..... 556
3.4.6.2 Gas Solubility and Molecular Diffusion ..... 557

3.4.7 **Glass-Ceramics** ..... 558

3.4.8 **Glasses for Miscellaneous Applications** . 559
3.4.8.1 Sealing Glasses ..... 559
3.4.8.2 Solder and Passivation Glasses .. 562
3.4.8.3 Colored Glasses ..... 565
3.4.8.4 Infrared-Transmitting Glasses ... 568

**References** ..... 572



Glasses are very special materials that are formed only under suitable thermodynamic conditions; these conditions may be natural or man-made. Most glass products manufactured on a commercial scale are made by quenching a mixture of oxides from the melt (Fig. 3.4-1).

For some particular applications, glasses are also made by other technologies, for example by chemical vapor deposition to achieve extreme purity, as required in optical fibers for communication, or by roller chilling in the case of amorphous metals, which need extremely high quenching rates. The term "amorphous" is a more general, generic expression in comparison with the term "glass". Many different technological routes are described in [4.1].

Glasses are also very universal engineering materials. Variation of the composition results in a huge variety of glass types, families, or groups, and a corresponding variety of properties. In large compositional areas, the properties depend continuously on composition, thus allowing one to design a set of properties to fit a specific application. In narrow ranges, the properties depend linearly on composition; in wide ranges, nonlinearity and step-function behavior have to be con-

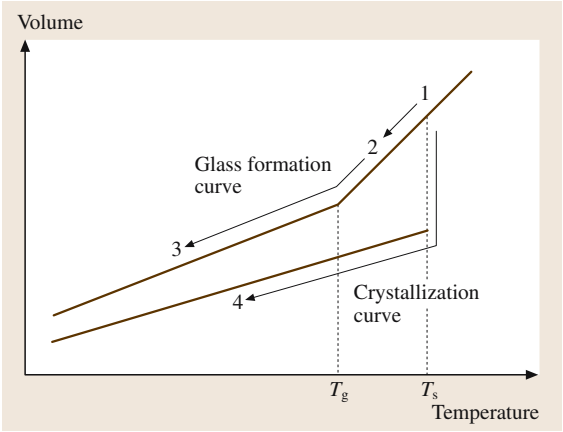


**Fig. 3.4-1** Schematic volume–temperature curves for glass formation along path 1–2–3 and crystallization along path 1–4. $T_s$, melting temperature; $T_g$, transformation temperature. 1, liquid; 2, supercooled liquid; 3, glass; 4, crystal

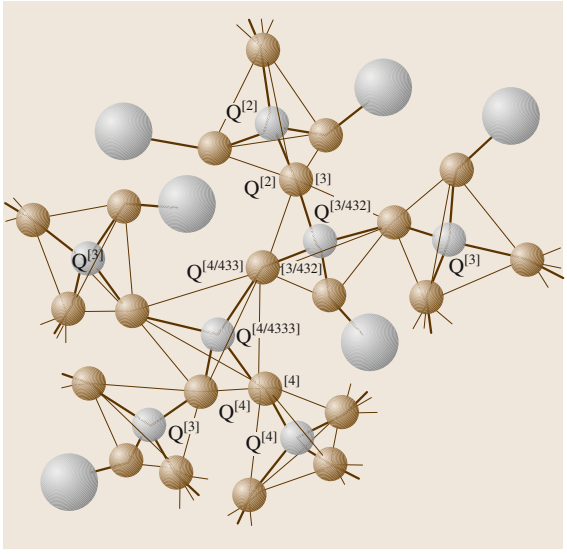


**Fig. 3.4-2** Fragment of a sodium silicate glass structure. The $SiO_2$ tetrahedra are interconnected by the bridging oxygen atoms, thus forming a three-dimensional network. $Na_2O$ units form nonbridging oxygen atoms and act as network modifiers which break the network. The $Q^{[i/klmn]}$ nomenclature describes the connectivity of different atom shells around a selected central atom (after [4.2])



sidered. The most important engineering glasses are mixtures of oxide compounds. For some special requirements, for example a particular optical transmission window or coloration, fluorides, chalcogenides, and colloidal (metal or semiconductor) components are also used.

A very special glass is single-component silica, $SiO_2$,which is a technological material with extraordinary properties and many important applications.

On a quasi-macroscopic scale (> 100 nm), glasses seem to be homogeneous and isotropic; this means that all structural effects are, by definition, seen only as average properties. This is a consequence of the manufacturing process. If a melt is rapidly cooled down, there is not sufficient time for it to solidify into an ideal, crystalline structure. A structure with a well-defined short-range order (on a scale of less than 0.5 nm, to fulfill the energy-driven bonding requirements of structural elements made up of specific atoms) [4.2] and a highly disturbed long-range order (on a scale of more than 2 nm, disturbed by misconnecting lattice defects and a mixture of different structural elements) (Fig. 3.4-2).

Crystallization is bypassed. We speak of a frozen-in, supercooled, liquid-like structure. This type of quasi-static solid structure is thermodynamically controlled but not in thermal equilibrium and thus is not absolutely stable; it tends to relax and slowly approach an "equilibrium" structure (whatever this may be in a complex multicomponent composition, it represents a minimum of the Gibbs free enthalpy). This also means that all properties change with time and temperature, but in most cases at an extremely low rate which cannot be observed under the conditions of classical applications (in the range of ppm, ppb, or ppt per year at room temperature). However, if the material is exposed to a higher temperature during processing or in the final application, the resulting relaxation may result in unacceptable deformation or internal stresses that then limit its use.

If a glass is reheated, the quasi-solid material softens and transforms into a liquid of medium viscosity in a continuous way. No well-defined melting point exists. The temperature range of softening is called the "transition range". By use of standardized measurement techniques, this imprecise characterization can be replaced by a quasi-materials constant, the "transformation temperature" or "glass temperature" $T_g$, which depends on the specification of the procedure (Fig. 3.4-3).

As illustrated in Fig. 3.4-4, the continuous variation of viscosity with temperature allows various technologies for hot forming to be applied, for example casting, floating, rolling, blowing, drawing, and pressing, all of which have a specific working point.

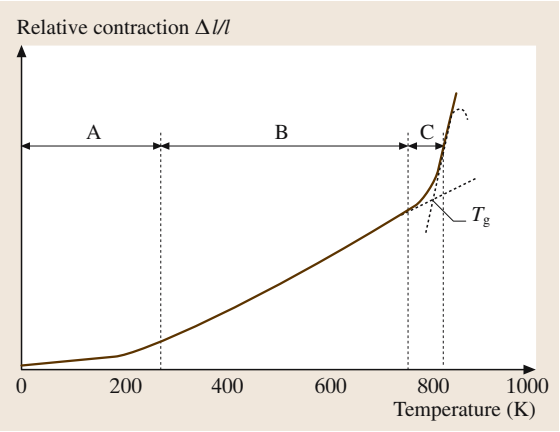


**Fig. 3.4-3** Definition of the glass transition temperature $T_g$ by a diagram of length versus temperature during a measurement, as the intersection of the tangents to the elastic region B and to the liquid region to the right of C. In the transformation range C, the glass softens

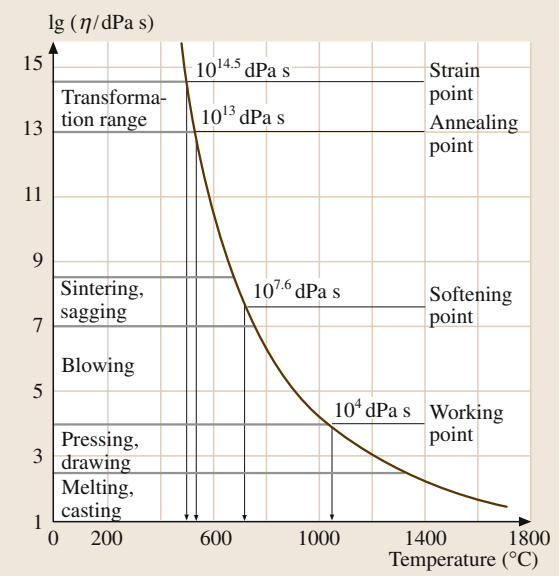


**Fig. 3.4-4** Typical viscosity–temperature curve: viscosity ranges for the important processing technologies, and definitions of fixed viscosity points

The liquid-like situation results in thermodynamically induced density and concentration fluctuations, with a tendency toward phase separation and crystallization, which starts via a nucleation step. This can also be used as a technological route to produce unconventional, i. e. inhomogeneous, glasses. Some examples are

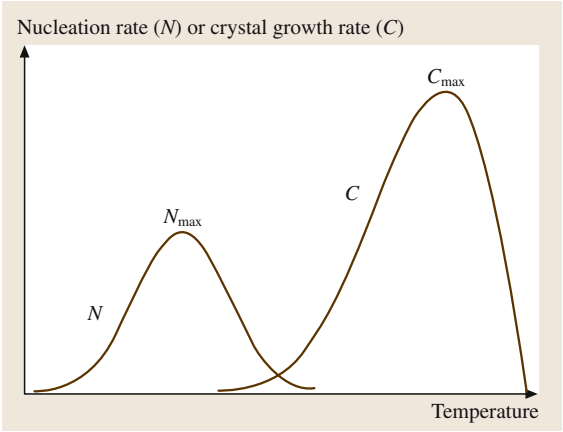


**Fig. 3.4-5** Nucleation rate ($N$) and crystal growth rate ($C$) of glass as a function of temperature

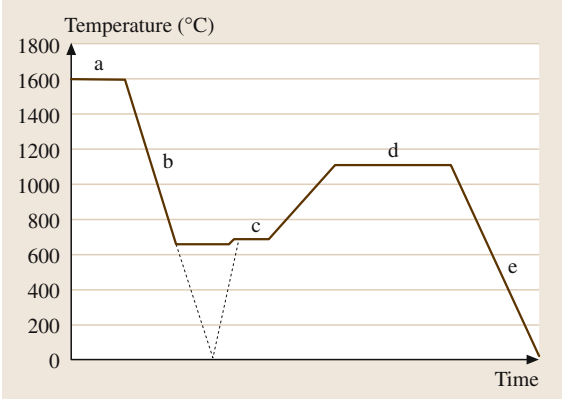


**Fig. 3.4-6** Temperature–time schedule for glass-ceramic production: a, melting; b, working; c, nucleation; d, crystallization; e, cooling to room temperature

colored glasses with colloidal inclusions, porous glasses, and glass-ceramics, to name just a few.

The commercially important glass-ceramics consist of a mixture of 30–90% crystallites (< 50 nm in diameter) and a residual glass phase, without any voids. The material is melted and hot-formed as a glass, cooled down, then annealed for nucleation, and finally tempered to allow crystal growth to a percentage that depends on the desired properties [4.3, 4]. Some characteristic features of the manufacturing process are shown in Figs. 3.4-5 and 3.4-6. As the melt is cooled, a region of high velocity of crystal growth has to be passed through, but no nuclei exist in that region. The nuclei are formed at a much lower temperature, where the crystallization is slow again. Thus the material solidifies as a glass in the

first process step. In a second process step, the glass is reheated, annealed in the range of maximum nucleation rate $N_{max}$, and then annealed at a higher temperature in the range of maximum crystal growth rate $C_{max}$. The overall bulk properties are the averages of the properties of the components. One of the major properties of commercially important glass-ceramics is a near-zero coefficient of thermal expansion.

## 3.4.1 Properties of Glasses – General Comments

As for all materials, there are many properties for every type of glass described in the literature. In this section only a limited selection can be given. We also restrict the presentation to commercially important glasses and glass-ceramics. For the huge variety of glasses that have been manufactured for scientific purposes only, the original literature must be consulted. Extensive compilations of data of all kind may be found in books, e.g. [4.5–7], and in software packages [4.8, 9], which are based upon these books and/or additional original data from literature, patents, and information from manufacturers worldwide.

Almost all commercially important glasses are silicate-based. For practical reasons, these glasses are subdivided into five major groups which focus on special properties. These groups are:

1. Mass-production glasses, such as window and container glasses, which are soda–lime–silicate glasses. Besides the application-dependant properties such as transparency, chemical resistance, and mechanical strength, the main concern is cost.
2. Technical specialty glasses, such as display or television glasses, glasses for tubes for pharmaceutical packaging, glasses for industrial ware and labware, glasses for metal-to-glass sealing and soldering, and glasses for glassware for consumers. The dominant properties are chemical inertness and corrosion resistance, electrical insulation, mechanical strength, shielding of X-ray or UV radiation, and others. To fulfill these specifications, the glass composition may be complex and even contain rare components.
3. Optical glasses have the greatest variety of chemical components and do not exclude even the most exotic materials, such as rare earth and non-oxide compounds. The dominant properties are of optical origin: refraction and dispersion with extremely high homogeneity, combined with low absorption and light scattering within an extended transmission range, including the infrared and ultraviolet parts of the electromagnetic spectrum. They are produced in comparably small volumes but with raw materials of high purity, and are thus quite expensive.
4. Vitreous silica, as a single-component material, has some extraordinary properties: high transparency from 160 nm to 1800 nm wavelength, high electrical insulation if it is of low hydrogen content, high chemical and corrosion resistance, and quite low thermal expansion with high thermal-shock resistance. A technological handicap is the high glass temperature $T_g \approx 1250\,°C$, depending on the water content.
5. Glass-ceramics are glassy in the first production step. An important property is the final (after ceramization) coefficient of thermal expansion, often in combination with a high elastic modulus and low specific weight. High thermal stability and thermal-shock resistance are a prerequisite for the major applications. This group has the potential for many other applications which require different property combinations [4.3].

This separation into groups seems to be somewhat artificial, in view of the material properties alone, and is justified only by the very different technological conditions used for manufacturing and processing. It corresponds to the specialization of the industry and to a traditional structuring in the literature.

For all these groups, various classes of product defects exist, and these defects may occur in varying concentration. Among these defects may be bubbles, striations, crystalline inclusions, and metal particles, which are relics of a nonideal manufacturing process. There may also be inclusions of foreign components which were introduced with the raw materials as impurities or contamination. If a three-dimensional volume of glass is cooled down, the finite heat conductivity causes the volume elements to have nonidentical histories in time and temperature. As a consequence, the time- and temperature-dependent relaxation processes produce internal mechanical stress, which results in optical birefringence. These "technical" properties are often very important for the suitability of a piece of glass for a specific application, but they are not "intrinsic" properties of the material, and are not considered in this section.

## 3.4.2 Composition and Properties of Glasses

A very common method for describing the composition of a glass is to quote the content of each component (oxide) by weight fraction ($w_i$ in wt%) or mole fraction ($m_i$ in mol%). If $M_i$ is the molar mass of the component $i$, the relationship between the two quantities is given by

$$m_i = \frac{100 w_i}{M_i \sum_{j=1}^{n} w_j / M_j}, \quad 1 \le i \le n, \tag{4.1}$$

and

$$w_i = \frac{100 m_i M_i}{\sum_{j=1}^{n} m_j M_j}, \quad 1 \le i \le n, \tag{4.2}$$

with the side conditions

$$\sum_{i=1}^{n} m_i = 1 \quad \text{and} \quad \sum_{i=1}^{n} w_i = 1. \tag{4.3}$$

If components other than oxides are used, it is advantageous to define fictitious components, for example the component $F_2{-}O$ (= fluorine–oxygen, with $M = 2\times19 - 16 = 22$); this can be used to replace a fluoride with an oxide and this hypothetical oxide component, for example $CaF_2 = CaO + F_2{-}O$. This reduces the amount of data required

**Table 3.4-1** Factors $\varrho_{w_i}$ for the calculation of glass densities [4.10]

| Component $i$ | $\varrho_{w_i}$ (g/cm³) |
|---|---|
| $Na_2O$ | 3.47 |
| MgO | 3.38 |
| CaO | 5.0 |
| $Al_2O_3$ | 2.75 |
| $SiO_2$ | 2.20 |

**a)**

| 1a | 2a | 3b | 4b | 5b | 6b | 7b | 8 | | | 1b | 2b | 3a | 4a | 5a | 6a | 7a | 0 |
|---|---|---|---|---|---|---|---|---|---|---|---|---|---|---|---|---|---|
| H | | | | | | | | | | | | | | | | | He |
| Li | Be | | | | | | | | | | | B | C | N | O | F | Ne |
| Na | Mg | | | | | | | | | | | Al | Si | P | S | Cl | Ar |
| K | Ca | Sc | Ti | V | Cr | Mn | Fe | Co | N | Cu | Zn | Ga | Ge | As | Se | Br | Kr |
| Rb | Sr | Y | Zr | Nb | Mo | Tc | Ru | Rh | Pd | Ag | Cd | In | Sn | Sb | Te | I | Xe |
| Cs | Ba | La | Hf | Ta | W | Re | Os | Ir | Pt | Au | Hg | Te | Pb | Bi | Po | At | Rn |

**b)**

| 1a | 2a | 3b | 4b | 5b | 6b | 7b | 8 | | | 1b | 2b | 3a | 4a | 5a | 6a | 7a | 0 |
|---|---|---|---|---|---|---|---|---|---|---|---|---|---|---|---|---|---|
| H | | | | | | | | | | | | | | | | | He |
| Li | Be | | | | | | | | | | | B | C | N | O | F | Ne |
| Na | Mg | | | | | | | | | | | Al | Si | P | S | Cl | Ar |
| K | Ca | Sc | Ti | V | Cr | Mn | Fe | Co | Ni | Cu | Zn | Ga | Ge | As | Se | Br | Kr |
| Rb | Rb | Y | Zr | Nb | Mo | Tc | Ru | Rh | Pd | Ag | Cd | In | Sn | Sb | Te | I | Xe |
| Cs | Ba | La | Hf | Ta | W | Re | Os | Ir | Pt | Au | Hg | Te | Pb | Bi | Po | At | Rn |

**Fig. 3.4-7** **(a)** Elements whose oxides act as glass-formers (*gray*) and conditional glass-formers (*brown*) in oxide systems (after [4.11]). **(b)** Elements whose fluorides act as glass-formers (*gray*) and conditional glass-formers (*brown*) in fluoride glass systems (after [4.12])

**Table 3.4-2** Composition of selected technical glasses

| Glass type | Code[a] | Main components (wt%) | | | | | Minor components |
|---|---|---|---|---|---|---|---|
| | | $SiO_2$ | $B_2O_3$ | $Al_2O_3$ | $Na_2O$ | PbO | < 10% |
| Lead glass | S 8095 | 57 | | | | 28 | $Al_2O_3$, $Na_2O$, $K_2O$ |
| Low dielectric loss glass | S 8248 | 70 | 27 | | | | $Al_2O_3$, $Li_2O$, $Na_2O$, $K_2O$, BaO |
| Sealing glass | S 8250 | 69 | 19 | | | | $Al_2O_3$, $Li_2O$, $Na_2O$, $K_2O$, ZnO |
| Duran® | S 8330 | 80 | 13 | | | | $Al_2O_3$, $Na_2O$, $K_2O$ |
| Supremax® | S 8409 | 52 | | 22 | | | $B_2O_3$, CaO, MgO, BaO, $P_2O_5$ |
| Sealing glass | S 8465 | | 11 | 11 | | 75 | $SiO_2$ |
| Sealing glass | S 8487 | 75 | 16.5 | | | | $Al_2O_3$, $Na_2O$, $K_2O$ |
| Vycor™ | C 7900 | 96 | | | | | $Al_2O_3$, $B_2O_3$, $Na_2O$ |

[a] Code prefix: S = Schott AG, Mainz; C = Corning, New York.

to handle the different cation–anion combinations (Fig. 3.4-7).

With given weight or mole fractions, a property $P$ can be calculated (or approximated) via a linear relation of the type

$$P = \frac{1}{100}\sum_{i=1}^{n} p_{w_i} w_i \quad \text{or} \quad P = \frac{1}{100}\sum_{i=1}^{n} p_{m_i} m_i \; . \tag{4.4}$$

The component-specific factors $p_i$ were first systematically determined by *Winckelmann* and *Schott* [4.13], and are listed in detail in the standard literature, e.g. [4.14].

As an example, the density $\varrho$ can be calculated via (4.4) from: $P = 1/\varrho$, $p_{w_i} = 1/\varrho_{w_i}$, and the data in Table 3.4-1.

The composition of selected technical glasses is given in Table 3.4-2.

## 3.4.3 Flat Glass and Hollowware

By far the highest glass volume produced is for windows and containers. The base glass is a soda–lime composition, which may be modified for special applications. Owing to the Fe content of the natural raw materials, a green tint is observed for thicknesses that are not too small.

If the product is designed to have a brown or green color (obtained by the use of reducing or oxidizing melting conditions), up to 80% waste glass can be used as a raw material.

### 3.4.3.1 Flat Glass

Plate glass for windows is mainly produced by floating the melt on a bath of molten tin. All manufacturers worldwide use a soda–lime-type glass, with the average composition given in Table 3.4-3. For some other applications, this base glass may be modified by added coloring agents, for example Cr and Fe oxides.

For architectural applications, the surface(s) may be modified by coatings or grinding to achieve specific



**Table 3.4-3** Average composition in wt% and viscosity data, for soda–lime glass, container glass, and Borofloat glass

| | Soda–lime glass | Container glass | Borofloat®33 |
|---|---|---|---|
| Composition (wt%) | | | |
| $SiO_2$ | 71–73 | 71–75 | 81 |
| $CaO + MgO$ | 9.5–13.5 | 10–15 | |
| $Na_2O + K_2O$ | 13–16 | 12–16 | 4 |
| $B_2O_3$ | 0–1.5 | | 13 |
| $Al_2O_3$ | 0.5–3.5 | | 2 |
| Other | 0–3 | 0–3 | |
| Temperature (°C) | | | |
| at viscosity of $10^{14.5}$ dPa s | | | 518 |
| at viscosity of $10^{13}$ dPa s | 525–545 | | 560 |
| at viscosity of $10^{7.6}$ dPa s | 717–735 | | 820 |
| at viscosity of $10^{4}$ dPa s | 1015–1045 | | 1270 |
| Density (g/cm$^3$) | 2.5 | | 2.2 |
| Young's modulus (GPa) | 72 | | 64 |
| Poisson's ratio | | | 0.2 |
| Knoop hardness | | | 480 |
| Bending strength (MPa) | 30 | | 25 |
| Thermal expansion coefficient $\alpha$, 20–300 °C ($10^{-6}$/K) | 9.0 | | 3.25 |
| Specific heat capacity $c_p$, 20–100 °C (kJ/kg K) | | | 0.83 |

**Table 3.4-3** Average composition in wt% and viscosity data for soda–lime glass, cont.

| | Soda–lime glass | Container glass | Borofloat®33 |
|---|---|---|---|
| Heat conductivity $\lambda$ at 90 °C (W/m kg) | | | 1.2 |
| Chemical resistance | | | |
| Water | | | HGB1/HGA1 |
| Acid | | | 1 |
| Alkali | | | A2 |
| Refractive index $n_d$ | | | 1.47140 |
| Abbe value $\nu_e$ | | | 65.41 |
| Stress-optical constant $K$ ($10^{-6}$ mm$^2$/N) | | | 4.0 |
| Dielectric constant $\varepsilon_r$ | | | 4.6 |
| Dielectric loss tan $\delta$ at 25 °C, 1 MHz | | | $37 \times 10^{-4}$ |
| Volume resistivity $\rho$ | | | |
| at 250 °C ($\Omega$ cm) | | | $10^8$ |
| at 350 °C ($\Omega$ cm) | | | $10^{6.5}$ |

optical effects, such as decorative effects, a higher reflectivity in certain spectral regions (e.g. the IR), or an opaque but translucent appearance. Some other applications require antireflection coatings.

If steel wires are embedded as a web into rolled glass, the resulting product can be used as a window glass for areas where improved break-in protection is required.

Fire-protecting glasses are designed to withstand open fire and smoke for well-defined temperature–time programs, for example from 30 min to 180 min with a maximum temperature of more than 1000 °C (test according to DIN 4102, Part 13). The main goal is to avoid the glass breaking under thermal load. There are various ways to achieve this, such as mechanical wire reinforcement, prestressing the plate by thermal or surface-chemical means, or reducing the thermal expansion by using other glass compositions, for example the floated borosilicate glass Pyran® (Schott).

In automotive applications, flat glass is used for windows and mirrors. Single-pane safety glass is produced by generating a compressive stress near to the surface by a special tempering program: a stress of 80–120 MPa is usual. In the case of a breakage the window breaks into small pieces, which greatly reduces the danger of injuries.

Windshields are preferably made of laminated compound glass. Here, two (or more) layers are joined under pressure with a tough plastic foil.

The compound technique is also used for armorplate glass: here, at least four laminated glass layers with a total thickness of at least 60 mm are used.

For plasma and LCD displays and photovoltaic substrates, extremely smooth, planar, and thin sheets of glass are needed which fit the thermal expansion of the electronic materials in direct contact with them. These panes must remain stable in geometry (no shrinkage) when they are processed to obtain the final product.

### 3.4.3.2 Container Glass

For packaging, transportation, storage of liquids, chemicals, pharmaceuticals, etc., a high variety of hollowware is produced in the shape of bottles and tubes. Most of the products are made from soda–lime glass (Table 3.4-3) directly from the glass melt. Vials and ampoules are manufactured from tubes; for pharmaceuticals these are made from chemically resistant borosilicate glass.

Clear glass products have to be made from relatively pure raw materials. To protect the contents from light, especially UV radiation, the glass may be colored brown or green by the addition of Fe or Cr compounds. For other colors, see Sect. 3.4.8.3.

## 3.4.4 Technical Specialty Glasses

Technical glasses are special glasses manufactured in the form of tubes, rods, hollow vessels, and a variety of special shapes, as well as flat glass and granular form. Their main uses are in chemistry, pharmaceutical packaging, electronics, and household appliances. A list of typical applications of different glass types is given in Table 3.4-10, and a list of their properties is given in Table 3.4-11.

The multitude of technical glasses can be roughly arranged in the following four groups, according to their oxide composition (in weight percent). However, certain glass types fall between these groups or even completely outside.

*Borosilicate Glasses.* The network formers are substantial amounts of silica ($SiO_2$) and boric oxide ($B_2O_3$ > 8%). The following subtypes can be differentiated:

- *Non-alkaline-earth borosilicate glass*: with $SiO_2$ > 80% and $B_2O_3$ at 12–13%, these glasses show high chemical durability and low thermal expansion (about $3.3 \times 10^{-6}\,K^{-1}$).
- *Alkaline-earth-containing glasses*: with $SiO_2 \approx$ 75%, $B_2O_3$ at 8–12%, and alumina ($Al_2O_3$) and alkaline earths up to 5%, these glasses are softer in terms of viscosity, and have high chemical durability and a thermal expansion in the range of $4.0–5.0 \times 10^{-6}\,K^{-1}$.
- *High-borate glasses*: with 65–70% $SiO_2$, 15–25% $B_2O_3$, and smaller amounts of $Al_2O_3$ and alkalis, these glasses have a low softening point and a thermal expansion which is suitable for glass-to-metal seals.

*Alkaline-Earth Aluminosilicate Glasses.* These glasses are free from alkali oxides, and contain 52–60% $SiO_2$, 15–25% $Al_2O_3$, and about 15% alkaline earths. A typical feature is a very high transformation temperature.

*Alkali-Lead Silicate Glasses.* These glasses contain over 10% lead oxide (PbO). Glasses with 20–30% PbO, 54–58% $SiO_2$, and about 14% alkalis are highly insulating and provide good X-ray shielding. They are used in cathode-ray tube components.

*Alkali-Alkaline-Earth Silicate Glasses (Soda-Lime Glasses).* This is the oldest glass type, which is produced in large batches for windows and containers (see Sect. 3.4.3). Such glasses contain about 71% $SiO_2$, 13–16% alkaline earths CaO + MgO, about 15% alkali (usually $Na_2O$), and 0–2% $Al_2O_3$.

Variants of the basic composition can contain significant amounts of BaO with reduced alkali and alkaline-earth oxides: these are used for X-ray shielding of cathode-ray tube screens.

### 3.4.4.1 Chemical Stability of Glasses

Characteristically, glasses are highly resistant to water, salt solutions, acids, and organic substances. In this respect, they are superior to most metals and plastics. Glasses are attacked to a significant degree only by hydrofluoric acid, strongly alkaline solutions, and concentrated phosphoric acid; this occurs particularly at higher temperatures.

Chemical reactions with glass surfaces, induced by exchange, erosion, or adsorption processes, can cause the most diverse effects, ranging from virtually invisible surface modifications to opacity, staining, thin films with interference colors, crystallization, holes, and rough or smooth ablation, to name but a few such effects. These changes are often limited to the glass surface, but in extreme cases they can completely destroy or dissolve the glass. The glass composition, stress medium, and operating conditions will decide to what extent such chemical attacks are technically significant.

#### Chemical Reaction Mechanisms with Water, Acid, and Alkaline Solutions

Chemical stability is understood as the resistance of a glass surface to chemical attack by defined agents; here, temperature, exposure time, and the condition of the glass surface play important roles.

Every chemical attack on glass involves water or one of its dissociation products, i. e. $H^+$ or $OH^-$ ions. For this reason, we differentiate between hydrolytic (water), acid, and alkali resistance. In water or acid attack, small amounts of (mostly monovalent or divalent) cations are leached out. In resistant glasses, a very thin layer of silica gel then forms on the surface, which normally inhibits further attack (Fig. 3.4-8a,b). Hydrofluoric acid, alkaline solutions, and in some cases phosphoric acid, however, gradually destroy the silica framework and thus ablate the glass surface in total (Fig. 3.4-8c). In contrast, water-free (i. e. organic) solutions do not react with glass.

Chemical reactions are often increased or decreased by the presence of other components. Alkali attack on glass is thus hindered by certain ions, particularly those

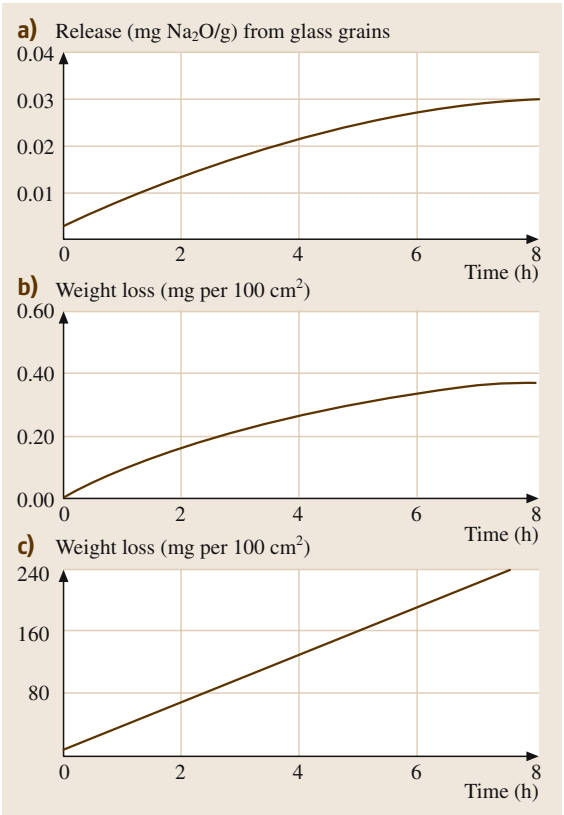


**Fig. 3.4-8a–c** Attack by **(a)** water, **(b)** acid, and **(c)** alkaline solution on chemically resistant glass as a function of time

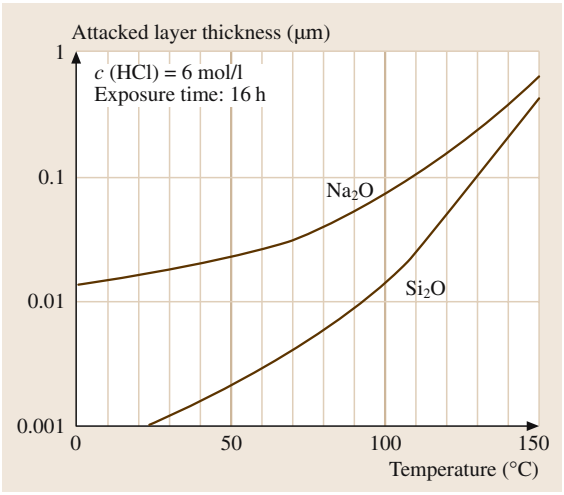


**Fig. 3.4-9** Acid attack on Duran® 8330 as a function of temperature, determined from leached amounts of $Na_2O$ and $SiO_2$

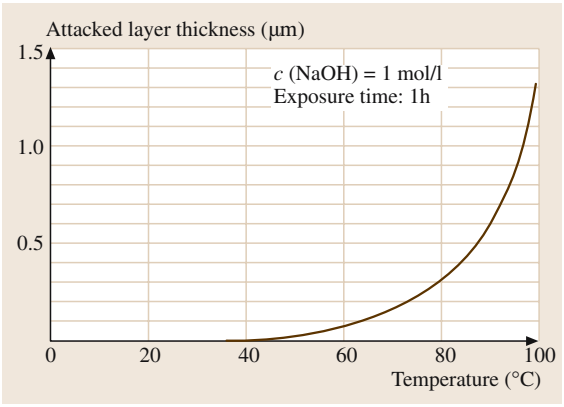


**Fig. 3.4-10** Alkali attack on Duran® 8330 as a function of temperature, determined from weight loss

of aluminium. On the other hand, complex-forming compounds such as EDTA, tartaric acid, and citric acid can increase the solubility. In general terms, the glass surface reacts with solutions which induce small-scale exchange reactions and/or adsorption. Such phenomena are observed, for example, in high-vacuum technology when residual gases are removed, and in certain inorganic-chemical operations, when small amounts of adsorbed chromium, resulting from treatment with chromic acid, are removed.

Because acid and alkali attacks on glass are fundamentally different, silica-gel layers produced by acid attack obviously are not necessarily effective against alkali solutions and may be destroyed. Conversely, the presence of ions that inhibit alkali attack does not necessarily represent protection against acids and water. The most severe chemical exposure is therefore an alternating treatment with acids and alkaline solutions. As in all chemical reactions, the intensity of the interaction increases rapidly with increasing temperature (Figs. 3.4-9 and 3.4-10).

In the case of truly ablative solutions such as hydrofluoric acid, alkaline solutions, and hot concentrated phosphoric acid, the rate of attack increases rapidly with increasing concentration (Fig. 3.4-11). As can be seen in Fig. 3.4-12, this is not true for the other frequently used acids.

### Determination of the Chemical Stability

In most cases, either is the glass surface is analyzed in its "as delivered" condition (with the original fire-polished surface), or the basic material is analyzed with its fire-

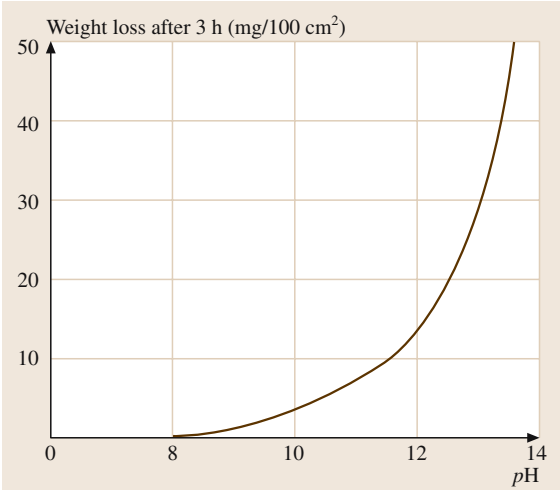


**Fig. 3.4-11** Alkali attack on Duran® 8330 at 100 °C as a function of pH value

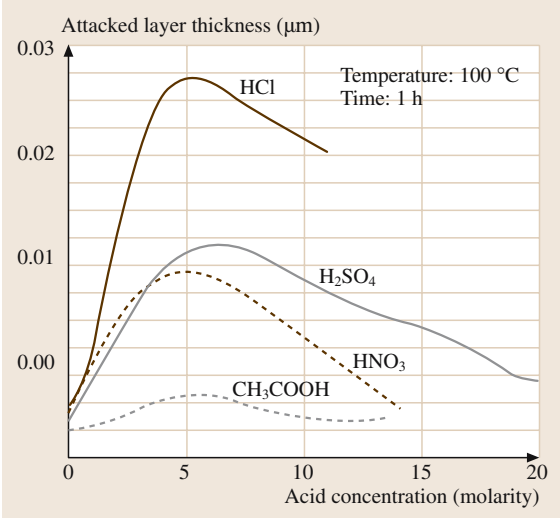


**Fig. 3.4-12** Acid attack on Duran® 8330 as a function of concentration

polished surface removed by mechanical or chemical ablation, or after crushing.

The standardized DIN (Deutsches Institut für Normung, German Institute for Standardization) test methods, which are universally and easily applicable, are the most reliable analysis methods. They include the determination of hydrolytic resistance (by two grain-titration methods and one surface method), of acid resistance to hydrochloric acid, and of alkali resistance to a mixture of alkaline solutions. Details are described in [4.2, 15] and summarized in Tables 3.4-4–3.4-6. The DIN classes of hydrolytic, acid, and alkali resistance of technical glasses are also listed Table 3.4-11, second page, last three colums.

### Significance of the Chemical Stability

*Release of Glass Constituents.* In various processes in chemical technology, pharmaceutical manufacture, and laboratory work, the glass material used is expected to release no constituents (or a very minimal amnount) into reacting solutions or stored specimens.

Because even highly resistant materials such as non-alkaline-earth and alkaline-earth borosilicate glasses do react to a very small degree with the surrounding media, the fulfillment of this requirement is a question of quantity and of detection limits. Concentrations of $10^{-6}$–$10^{-9}$ (i. e. trace amounts), which are measurable today with highly sophisticated analytical instruments, can be released even from borosilicate glasses in the form of $SiO_2$, $B_2O_3$, and $Na_2O$, depending on the conditions. However, solutions in contact with high-grade colorless Duran® laboratory glass will not be contaminated by Fe, Cr, Mn, Zn, Pb, or other heavy-metal ions.

*Undesirable Glass Surface Modifications.* When an appreciable interaction between a glass surface and an aqueous solution occurs, there is an ion exchange in which the easily soluble glass components are replaced by $H^+$ or $OH^-$ ions. This depletion of certain glass components in the surface leads to a corresponding enrichment in silica, which is poorly soluble, and thus to the formation of a silica-gel layer. This layer proves, in most cases, to be more resistant than the base glass. When its thickness exceeds about 0.1–0.2 µm, interference colors caused by the different refractive indices of the layer and the base glass make this silica-gel layer visible to the unaided eye. With increasing layer thickness it becomes opaque and finally peels off, destroying the glass. Between these stages there is a wide range of possible surface modifications, some of which, although optically visible, are of no practical significance, whereas others must be considered.

In the case of less resistant glasses, small amounts of water (from air humidity and condensation) in the presence of other agents such as carbon dioxide or sulfur oxides can lead to surface damage. In the case of sensitive glasses, hand perspiration or impurities left by detergents can sometimes induce strongly adhering surface defects, mostly recognizable as stains. If a contaminated glass surface is reheated (> 350–400 °C), the

**Table 3.4-4** Hydrolytic classes according to DIN 12111 (ISO 719)

| Hydrolytic class | Acid consumption of 0.01 mol/l hydrolytic acid per g glass grains (ml/g) | Base equivalent as $Na_2O$ per g glass grains (µg/g) | Possible designation |
|---|---|---|---|
| 1 | Up to 0.10 | Up to 31 | Very high resistance |
| 2 | Above 0.10, up to 0.20 | Above 31, up to 62 | High resistance |
| 3 | Above 0.20, up to 0.85 | Above 62, up to 264 | Medium resistance |
| 4 | Above 0.85, up to 2.0 | Above 264, up to 620 | Low resistance |
| 5 | Above 2.0, up to 3.5 | Above 620, up to 1085 | Very low resistance |

**Table 3.4-5** Acid classes according to DIN 12116

| Acid class | Designation | Half loss in weight after 6 h (mg/100 cm²) |
|---|---|---|
| 1 | High acid resistance | Up to 0.7 |
| 2 | Good acid resistance | Above 0.7, up to 1.5 |
| 3 | Medium acid attack | Above 1.5, up to 15 |
| 4 | High acid attack | Above 15 |

**Table 3.4-6** Alkali classes according to DIN ISO 695

| Alkali class | Designation | Loss in weight after 3 h (mg/100 cm²) |
|---|---|---|
| 1 | Low alkali attack | Up to 75 |
| 2 | Medium alkali attack | Above 75, up to 175 |
| 3 | High alkali attack | Above 175 |

contaminants or some of their components may burn in. Normal cleaning processes will then be ineffective and the whole surface layer has to be removed (e.g. by etching).

*Desirable Chemical Reactions with the Glass Surface (Cleaning and Etching).* Very strong reactions between aqueous agents and glass can be used for the thorough cleaning of glass. The complete ablation of a glass layer leads to the formation of a new surface.

Hydrofluoric acid reacts most strongly with glass. Because it forms poorly soluble fluorides with a great number of glass constituents, it is mostly used only in diluted form. The best etching effect is usually achieved when another acid (e.g. hydrochloric or nitric acid) is added. A mixture of seven parts by volume of water, two parts of concentrated hydrochloric acid ($c = 38\%$) and one part of hydrofluoric acid ($c = 40\%$) is recommended for a moderate surface ablation of highly resistant borosilicate glasses. When chemically less resistant glasses (e.g. Schott 8245 and 8250) are exposed for 5 min to a stirred solution at room temperature, a surface layer with a thickness of 1–10 µm is ablated, and a transparent, smooth, completely new surface is produced.

Glasses can also be ablated with alkaline solutions, but the alkaline etching process is much less effective.

### 3.4.4.2 Mechanical and Thermal Properties

#### Viscosity

As described earlier, the viscosity of glasses increases by 15–20 orders of magnitude during cooling. Within this viscosity range, glasses are subject to three different thermodynamic states:

- the melting range, above the liquidus temperature $T_s$;
- the range of the supercooled melt, between the liquidus temperature $T_s$ and the transformation temperature $T_g$, which is defined by ISO 7884-8;
- the frozen-in, quasi-solid melt range ("glass range"), below the transformation temperature $T_g$.

The absence of any significant crystallization in the range of the supercooled melt (see Fig. 3.4-1, line segment 2) is of the utmost importance for glass formation. Hence a basically steady, smooth variation in the viscosity in all temperature regions is a fundamental characteristic of glasses (Fig. 3.4-4) and a crucial property for glass production. Figure 3.4-13 shows the strongly differing temperature dependences of the viscosity for some glasses. The best mathematical expression for practical purposes is the VFT (Vogel, Fulcher, and Tammann) equation,

$$\log \eta(T) = A + B/(T - T_0)\,, \qquad (4.5)$$

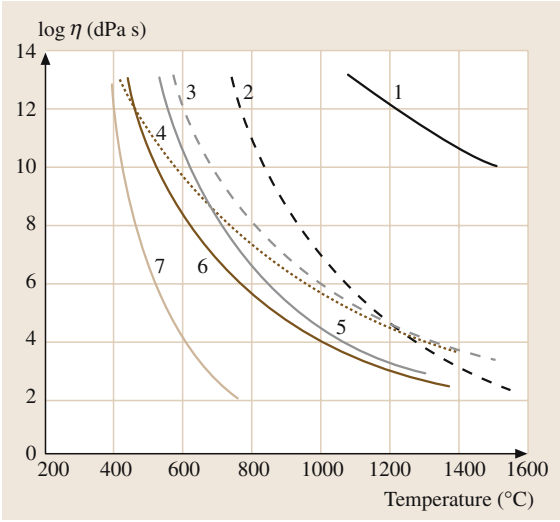


**Fig. 3.4-13** Viscosity–temperature curves for some important technical glasses. 1, fused silica; 2, 8405; 3, 8330; 4, 8248; 5, 8350; 6, 8095; 7, 8465. Glasses with steep gradients (such as 7) are called "short" glasses, and those with relatively shallow gradients (such as 4) are called "long" glasses

where $A$, $B$, and $T_0$ are glass-specific constants (Table 3.4-7).

Somewhat above $10^{10}$ dPa s, the viscosity becomes increasingly time-dependent. With increasing viscosity (i. e. with decreasing temperature), the delay in establishing structural equilibrium finally becomes so large that, under normal cooling conditions, the glass structure at $10^{13}$ dPa s can be described as solidified or "frozen-in". This temperature (for which a method of measurement is specified by ISO 7884-4) is called the "annealing point". At this viscosity, internal stresses in the glass are released after ≈15 min annealing time, while the dimensional stability of the glass is sufficient for many purposes, and its brittleness (susceptibility to cracking) is almost fully developed.

The lower limit of the annealing range is indicated by the "strain point", at which the glass has a viscosity of $10^{14.5}$ dPa s (determined by extrapolation from the viscosity–temperature curve). For most glasses, the strain point lies about 30–40 K below the annealing point. Relaxation of internal stresses here takes 3–5 h. The strain point marks the maximum value for short-term heat load. Thermally prestressed glasses, in contrast, show significant stress relaxation even at 200–300 K below $T_g$. For glass objects with precisely defined dimensions (e.g. etalons and gauge blocks) and in the case of extreme demands on the stability of certain properties of the glass, application temperatures of 100–200 °C can be the upper limit.

### Strength

The high structural (theoretical) strength of glasses and glass-ceramics ($> 10^4$ N/mm$^2$ = 10 GPa) is without practical significance, because the strength of glass articles is determined by surface defects induced by wear, such as tiny chips and cracks (Griffith flaws), at whose tips critical stress concentrations may be induced by a mechanical load, especially if the load is applied perpendicular to the plane of the flaw (fracture mode I). Glasses and glass-ceramics, in contrast to ductile materials such as metals, show no plastic flow and behave under a tensile stress $\sigma$ in as brittle a manner as ceramics. A flaw will result in a fracture if the "stress intensity factor"

$$K_I = 2\sigma\sqrt{a} > K_{Ic}\,, \qquad (4.6)$$

where $a$ is the depth of the flaw and $K_{Ic}$ is the "critical stress intensity factor", a material constant which is temperature- and humidity-dependent: see Table 3.4-8.

For $K_{Ic} = 1$ MPa $\sqrt{\text{m}}$ and a stress $\sigma = 50$ MPa, the critical flaw depth $a_c$ is 100 µm. Thus very small flaws

**Table 3.4-7** Parameters of the VFT equation (4.5) for the glasses in Fig. 3.4-13

| Glass | $A$ | $B$ (°C) | $T_0$ (°C) |
|---|---|---|---|
| 8095 | −1.5384 | 4920.68 | 96.54 |
| 8248 | −0.2453 | 4810.78 | 126.79 |
| 8330 | −1.8500 | 6756.75 | 105.00 |
| 8350 | −1.5401 | 4523.85 | 218.10 |
| 8405 | −2.3000 | 5890.50 | 65.00 |
| 8465 | −1.6250 | 1873.73 | 256.88 |
| Fused silica | −7.9250 | 31 282.9 | −415.00 |
| Soda–lime glass | −1.97 | 4912.5 | 475.4 |

can cause cracking at a comparatively low stress level, and the practical strength of a glass is not a materials constant!

*Surface Condition.* As a result of wear-induced surface defects, glass and glass-ceramic articles have practical tensile strengths of $20–200\,N/mm^2 = 20–200\,MPa$, depending on the surface condition and the atmospheric-exposure condition. To characterize the strength, a Weibull distribution for the cumulative failure probability $F$ is assumed:

$$F(\sigma) = 1 - \exp\left[-(\sigma/\sigma_c)^m\right] , \qquad (4.7)$$

where $0 \le F(\sigma) \le 1$ is the probability of a fracture if the applied stress is less than $\sigma$; $\sigma_c$ denotes the characteristic value (approximately the mean value of the distribution), and $m$ is the Weibull modulus of the distribution (which determines the standard deviation). To obtain reproducible measurements, the surface is predamaged by grinding with a narrow grain-size distribution (Fig. 3.4-14).

Only a slight – as a rule with neglible – dependence on the chemical composition is found for silicate glasses (Table 3.4-8).

*Stress Rate.* The rate of increase of the stress and the size of the glass area exposed to the maximum stress have to be considered for the specification of a strength value. In contrast to the rapid stress increase occurring in an impact, for example, a slowly increasing tensile stress or continuous stress above a certain critical limit may – as a result of stress corrosion cracking – cause the propagation of critical surface flaws and cracks and thus enhance their effect. Hence the tensile strength is time- and stress-rate-dependent (this is mainly important for test loads), as shown in Fig. 3.4-15. Independent of surface damage or the initial tensile strength, increasing

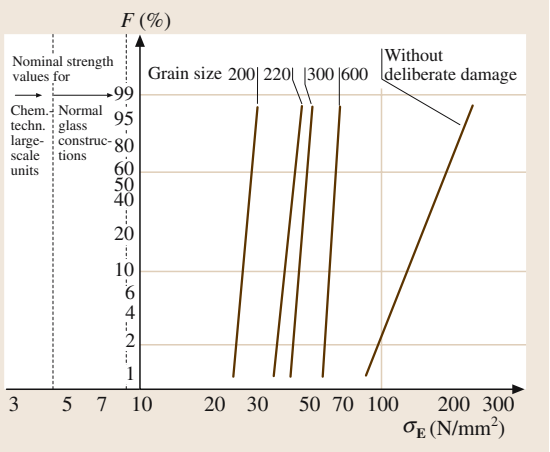


**Fig. 3.4-14** Failure probability $F$ for samples abraded by variously sized grains. Predamaged surface area $100\,mm^2$, rate of stress increase $d\sigma/dt = 10\,MPa\,s^{-1}$. A, range of nominal strength for large-scale units in chemical technology; B, range of nominal strength for normal glass structures

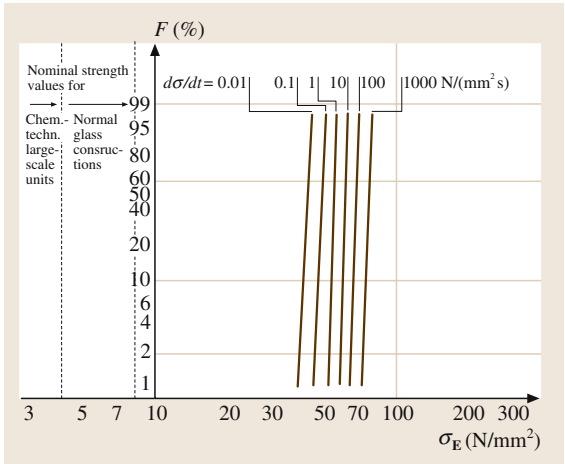


**Fig. 3.4-15** Failure probability $F$ of a predamaged surface ($100\,mm^2$; grain size 600) for various rates of increase of stress $d\sigma/dt$. A, range of nominal strength for large-scale units in chemical technology; B, range of nominal strength for normal glass structures

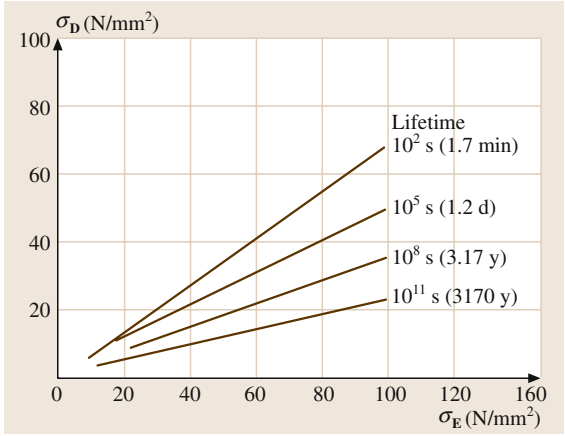


**Fig. 3.4-16** Time-related strength $\sigma_D$ (strength under constant loading) of soda–lime glass compared with the experimental strength $\sigma_E$ at $d\sigma/dt = 10\,N/mm^2\,s$ for various lifetimes, in a normal humid atmosphere

the rate of increase of the stress by a factor of 10 results in an increase in the strength level of about 15%.

*Constant Loading.* Fracture analysis of the effect and behavior of cracks in glasses and glass-ceramics yield further information about the relationship between the experimentally determined tensile strength $\sigma_E$ (usually measured for a rapidly increasing load) and the tensile strength $\sigma_D$ expected under constant loading (= fatigue strength), as shown in Fig. 3.4-16. Such analyses show that, depending on the glass type, the tensile strength under constant loading $\sigma_D$ (for years of loading) may amount to only about 1/2 to 1/3 of the experimental tensile strength $\sigma_E$.

*Area Dependence.* The larger the stressed area, the higher is the probability of large defects (large crack depths) within this area. This relationship is important for the transfer of experimental tensile strengths, which are mostly determined with relatively small test samples, to practical glass applications such as pipelines, where many square meters of glass can be uniformly stressed (Fig. 3.4-17).

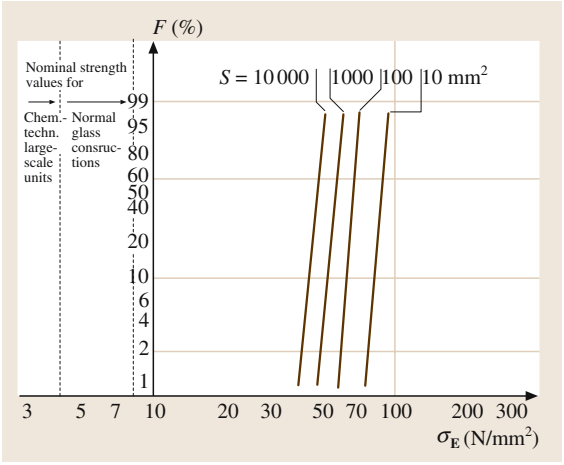


**Fig. 3.4-17** Failure probability $F$ for differently sized stressed areas $S$. All samples abraded with 600 mesh grit, stress rate $d\sigma/dt = 10\,N/mm^2\,s$. A, range of nominal strength for large-scale units in chemical technology; B, range of nominal strength for normal glass structures

## Elasticity

The ideal brittleness of glasses and glass-ceramics is matched by an equally ideal elastic behavior up to breaking point. The elastic moduli for most technical glasses lie within a range of 50–90 $kN/mm^2$. The mean value of 70 $kN/mm^2$ is about equal to the Young's modulus of aluminium (see Table 3.4-11, first page, column 7).

## Coefficient of Linear Thermal Expansion

With few exceptions, the length and the volume of glasses increase with increasing temperature (positive coefficient).

The typical curve begins with a zero gradient at absolute zero (Fig. 3.4-3) and increases slowly. At about room temperature (section A in Fig. 3.4-3), the curve shows a distinct bend and then gradually increases (section B, the quasi-linear region) up to the beginning of the experimentally detectable plastic behavior. Another distinct bend in the expansion curve characterizes the transition from a predominantly elastic to a more plastic behavior of the glass (section C, the transformation range). As a result of increasing structural mobility, the temperature dependence of almost all glass properties changes distinctly in this range. Figure 3.4-18 shows the linear thermal expansion curves of five glasses; 8330 and 4210 roughly define the normal range of technical glasses, with expansion coefficients

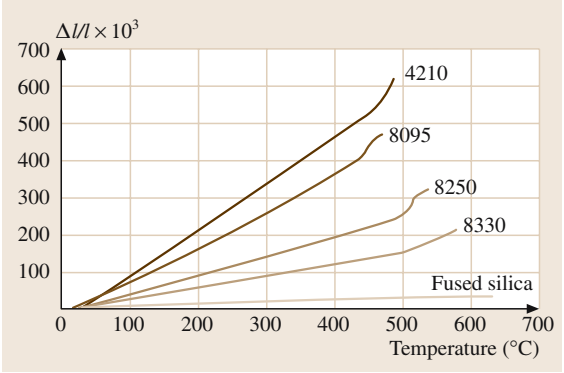


**Fig. 3.4-18** Linear thermal expansion coefficients of various technical glasses and of fused silica

$\alpha_{(20\,°C/300\,°C)} = 3.3–12.0 \times 10^{-6}\,/K$ (see Table 3.4-11, first page, third column).

The linear thermal expansion is an essential variable in determining the sealability of glasses to other materials and in determining thermally induced stress formation, and is therefore of prime importance for applications of glasses.

*Thermal Stresses.* Owing to the low thermal conductivity of glasses (typically 0.9–1.2 W/m K at 90 °C, and a minimum of 0.6 W/m K for high-lead-content glasses), temperature changes produce relatively high temperature differences $\Delta T$ between the surface and

the interior, which, depending on the elastic properties $E$ (Young's modulus) and $\mu$ (Poisson's ratio) and on the coefficient of linear thermal expansion $\alpha$, can result in stresses

$$\sigma = \frac{\Delta T \alpha E}{(1-\mu)} \quad \mathrm{N/mm^2}\,. \tag{4.8}$$

In addition to the geometric factors (shape and wall thickness), the material properties $\alpha$, $E$, and $\mu$ decisively influence the thermal strength of glasses subjected to temperature variations and/or thermal shock. Thermal loads in similar articles made from different glasses are easily compared by means of the characteristic material value

$$\varphi = \frac{\sigma}{\Delta T} = \frac{\alpha E}{(1-\mu)} \quad \mathrm{N/(mm^2\,K)}\,, \tag{4.9}$$

which indicates the maximum thermally induced stress to be expected in a flexure-resistant piece of glass for a local temperature difference of 1 K. Because cracking originates almost exclusively from the glass surface and is caused there by tensile stress alone, cooling processes are usually much more critical than the continuous rapid heating of glass articles.

### 3.4.4.3 Electrical Properties

Glasses are used as electrically highly insulating materials in electrical engineering and electronics, in the production of high-vacuum tubes, lamps, electrode seals, hermetically encapsulated components, high-voltage insulators, etc. Moreover, glasses may be used as insulating substrates for electrically conducting surface layers (in surface heating elements and data displays).

#### Volume Resistivity

Electrical conductivity in technical silicate glasses is, in general, a result of the migration of ions – mostly alkali ions. At room temperature, the mobility of these ions is usually so small that the volume resistivity, with values above $10^{15}\ \Omega\,\mathrm{cm}$, is beyond the range of measurement. The ion mobility increases with increasing temperature. Besides the number and nature of the charge carriers, the structural effects of other components also influence the volume resistivity and its relationship to temperature. The Rasch and Hinrichsen law applies to this relationship at temperatures below the transformation range:

$$\log \rho = A - B/T\,, \tag{4.10}$$

where $\rho$ is the electrical volume resistivity in $\Omega$ cm, $A$, $B$ are constants specific to the particular glass, and $T$ is the absolute temperature in K.

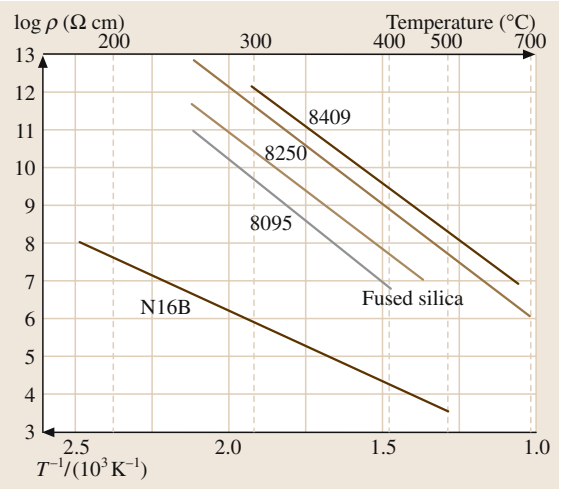


**Fig. 3.4-19** Electrical volume resistivity of various technical glasses and fused silica as a function of reciprocal absolute temperature

A plot of $\log \rho = f(1/T)$ thus yields straight lines (Fig. 3.4-19). Because of the relatively small differences in slope for most glasses, the electrical insulation of glasses is often defined only by the temperature at which the resistivity is $10^8\ \Omega\,\mathrm{cm}$. According to DIN 52326, this temperature is denoted by $T_{k100}$. The international convention is to quote volume resistivities at 250 °C and 350 °C (Table 3.4-11, second page, second column), from which the constants $A$ and $B$

**Table 3.4-8** Fracture toughness of some glasses

| Glass | $K_{Ic}$ (MPa $\sqrt{\mathrm{m}}$) |
|---|---|
| BK7 | 1.08 |
| F5 | 0.86 |
| SF6 | 0.74 |
| K50 | 0.77 |
| Duran® | 0.85 |

**Table 3.4-9** Parameters of the volume resistivity (4.10) of the glasses in Fig. 3.4-19

| Glass | $A$ | $B$ (K) |
|---|---|---|
| 8095 | − 2.863 | − 6520.0 |
| 8250 | − 0.594 | − 5542.0 |
| 8409 | − 0.463 | − 6520.0 |
| N16B | − 1.457 | − 3832.4 |
| Fused silica | − 0.394 | − 6222.4 |

(Table 3.4-9) and various other values below $T_g$ can be calculated.

### Surface Resistivity

The generally very high volume resistivity of glasses at room temperature has superimposed on it in a normal atmosphere a surface resistivity which is several orders of magnitude lower. The all-important factor is the adsorption of water on the glass surface. Depending on the glass composition, surface resistivities of $10^{13}-10^{15}\ \Omega$ occur at low relative humidities, and $10^{8}-10^{10}\ \Omega$ at high relative humidities. Above 100 °C, the effect of this hydrated layer disappears almost completely. (Treatment with silicones also considerably reduces this effect.)

### Dielectric Properties

With dielectric constants generally between 4.5 and 8, technical glasses behave like other electrically insulating materials. The highest values are obtained for lead glasses such as 8531 ($\varepsilon_r = 9.5$) and for ultra-high-lead-content solder glasses ($\varepsilon_r \sim 20$). The dependence of the dielectric constants $\varepsilon_r$ on frequency and temperature is relatively small (Fig. 3.4-20). For a frequency range of $50-10^9$ Hz, $\varepsilon_r$ values generally do not vary by more than 10%.

The dielectric dissipation factor $\tan\delta$ is frequency- and temperature-dependent. Owing to the diverse mechanisms which cause dielectric losses in glasses, there is a minimum of $\tan\delta$ in the region of $10^6-10^8$ Hz, and increasing values at lower and higher frequencies (Fig. 3.4-21).

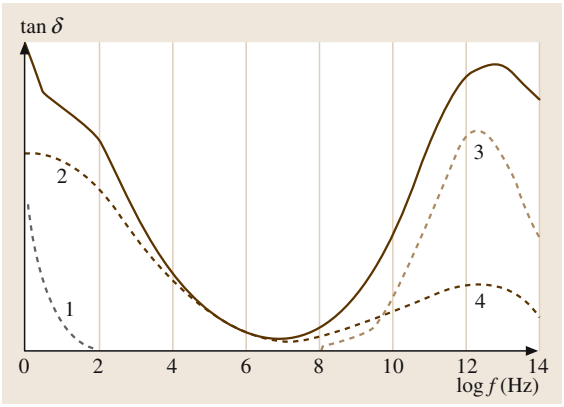


**Fig. 3.4-21** Schematic representation of the frequency spectrum of dielectric losses in glasses at room temperature. The *solid curve* gives the total losses, made up of (1) conduction loss, (2) relaxation loss, (3) vibration loss, and (4) deformation loss

At $10^6$ Hz, the dissipation factors $\tan\delta$ for most glasses lie between $10^{-2}$ and $10^{-3}$; fused silica, with a value of $10^{-5}$, has the lowest dissipation factor of all glasses. The special glass 8248 has relatively low losses, and in this cases $\tan\delta$ increases only slightly up to 5.5 GHz (where $\tan\delta = 3\times10^{-3}$).

The steep increase in dielectric losses with increasing temperature (Fig. 3.4-22) can lead to instability, i. e. overheating of the glass due to dielectric loss energy in the case of restricted heat dissipation and corresponding electrical power.

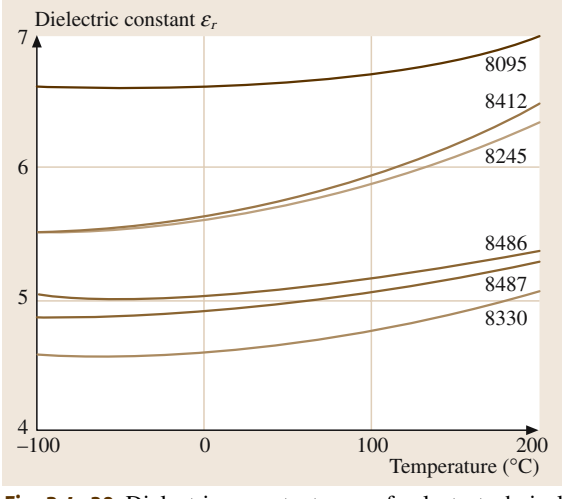


**Fig. 3.4-20** Dielectric constant $\varepsilon_r$ of electrotechnical glasses as a function of temperature, measured at 1 MHz

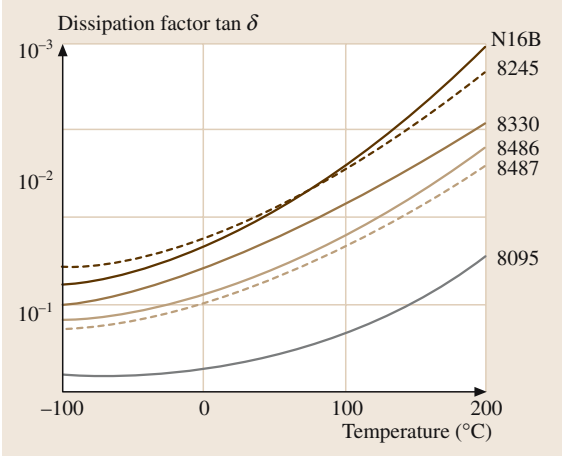


**Fig. 3.4-22** Dissipation factor $\tan\delta$ as a function of temperature in the range $-100\,°C < T < +200\,°C$, measured at 1 MHz

### Dielectric Strength

Some approximate values for the dielectric strength of glasses are a field strength of 20–40 kV/mm for a glass thickness of 1 mm at 50 Hz at 20 °C, and 10–20 kV/mm for greater thicknesses. At higher temperatures and frequencies, decreasing values can be expected.

## 3.4.4.4 Optical Properties

### Refraction of Light

The refractive indices $n_d$ of technical glasses at a wavelength of $\lambda_d = 587.6$ nm generally lie within the range 1.47–1.57. The exceptions to this rule are lead glasses with PbO contents of over 35% (e.g. glass 8531, which has $n_d = 1.7$; see Table 3.4-11, second page, fourth column). The principal dispersion $n_F - n_C$ ($\lambda_F = 486.1$ nm, $\lambda_C = 656.3$ nm) of technical glasses lies between 0.007 and 0.013.

At perpendicular incidence, the reflectance $R_d$ of a glass–air interface is 3.6% to 4.9%.

The transmittance $\tau_d$ and the reflectance $\rho_d$ of a non-absorbing, planar, parallel-sided glass plate with two glass–air interfaces, with multiple reflections taken into account, can be calculated from the refractive index as

$$\tau_d = \frac{2n_d}{n_d^2 + 1} \qquad (4.11)$$

and

$$\rho_d = \frac{(n_d - 1)^2}{n_d + 1} \,. \qquad (4.12)$$

The transmittance $\tau_d$ at perpendicular incidence has values between 90.6% and 93.1%.

### Stress Birefringence

Owing to its structure, glass is an isotropic material. Mechanical stress causes anisotropy, which manifests itself as stress-induced birefringence. A light beam, after passing through a plate of thickness $d$ which is subjected to a principal-stress difference $\Delta\sigma$, shows an optical path difference $\Delta s$ between the two relevant polarization directions. This path difference can either be estimated by means of the birefrigence colors or be measured with a compensator, and is given by

$$\Delta s = Kd\Delta\sigma \text{ nm} \,, \qquad (4.13)$$

where $K$ is the stress-optical coefficient of the glass (determined according to DIN 52314),

$$K = \frac{\Delta s}{d}\frac{1}{\Delta\sigma} \text{ mm}^2/\text{N} \,. \qquad (4.14)$$

Many glasses have stress-optical coefficients of about $3 \times 10^{-6}$ mm$^2$/N, and borosilicate glasses have values of up to $4 \times 10^{-6}$ mm$^2$/N. High-lead-content glasses can have values down to nil or even negative (Table 3.4-11, second page, fifth column).

### Light Transmittance

The transmittance due to the refractive index can be further reduced by coloring agents (oxides of transition elements or colloids) or by fine particles in the glass which have a different refractive index (in this case light scattering occurs, giving opal glasses).

Absorption caused by impurities such as $Fe_2O_3$ and by some major glass components such as PbO strongly reduces transparency in the UV range. Particularly good UV-transmitting multicomponent glasses have a cutoff

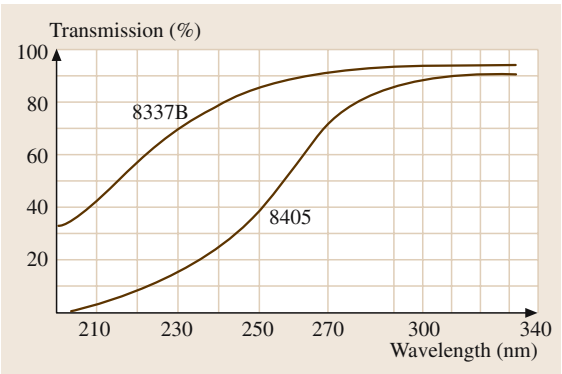


**Fig. 3.4-23** UV transmission of highly UV-transparent glasses 8337B and 8405 for 1 mm glass thickness

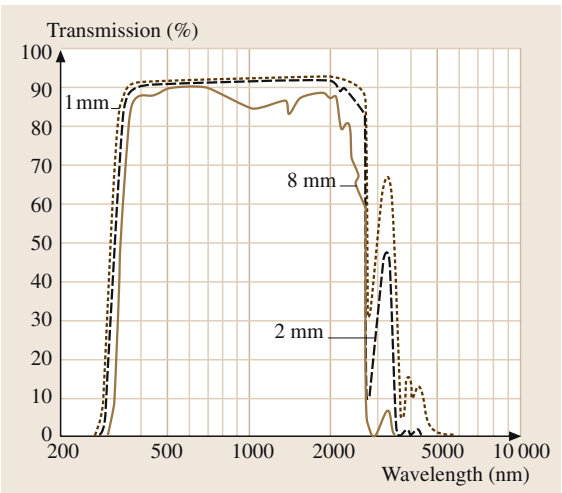


**Fig. 3.4-24** Transmission of Duran® 8330 for thicknesses of 1, 2, and 8 mm

(50% value) at a wavelength of 220 nm (Fig. 3.4-23); normal technical glasses already absorb considerably at 300 nm.

In the IR range, absorption caused by impurities such as $H_2O$ and by lattice vibrations limits the transmittance (Fig. 3.4-24).

**Table 3.4-10** Schott technical specialty glasses and their typical applications

| | |
|---|---|
| 8095 | Lead glass (28% PbO), electrically highly insulating, for general electrotechnical applications |
| 8245 | Sealing glass for Fe–Ni–Co alloys and molybdenum, minimum X-ray absorption, chemically highly resistant |
| 8248 | Borosilicate glass (of high $B_2O_3$ content), minimum dielectric losses up to the GHz range, electrically highly insulating |
| 8250 | Sealing glass for Ni–Fe–Co alloys and molybdenum, electrically highly insulating |
| 8252 | Alkaline-earth aluminosilicate glass for high-temperature applications, for sealing to molybdenum |
| 8253 | Alkaline-earth aluminosilicate glass for high-temperature applications, for sealing to molybdenum |
| 8321 | Alumino-borosilicate glass for TFT displays |
| 8326 | SBW glass, chemically highly resistant |
| 8330 | Duran®, borosilicate glass, general-purpose glass for apparatus for the chemical industry, pipelines, and laboratory glassware |
| 8337B | Borosilicate glass, highly UV-transmitting, for sealing to glasses and to metals of the Kovar and Vacon-10 ranges and tungsten |
| 8350 | AR glass®, soda–lime silicate glass tubing |
| 8405 | Highly UV-transmitting soft glass |
| 8409 | Supremax® (black identification line), alkali-free, for high application temperatures in thermometry, apparatus construction, and electrical engineering |
| 8412 [a] | Fiolax®, clear (blue identification line), neutral, glass tubing (chemically highly resistant) for pharmaceutical packaging |
| 8414 | Fiolax®, amber (blue identification line), neutral, glass tubing (chemically highly resistant) for pharmaceutical packaging |
| 8415 | Illax®, amber tubing glass for pharmaceutical packaging |
| 8421 | Sealing glass for seals to NiFe45 (DIN 17745) and compression seals |
| 8422 | Sealing glass for seals to NiFe47 or 49 (DIN 17745) and compression seals |
| 8436 | Particularly resistant to sodium vapor and alkaline solutions, suitable for sealing to sapphire |
| 8486 | Suprax®, borosilicate glass, chemically and thermally resistant, suitable for sealing to tungsten |
| 8487 | Sealing glass for tungsten, softer than 8486 |
| 8488 | Borosilicate glass, chemically and thermally resistant |
| 8490 | Black glass, light-transmitting in the UV region, highly absorbing in the visible region |
| 8512 | IR-absorbing sealing glass for Fe–Ni, lead-free (reed switches) |
| 8516 | IR-absorbing sealing glass for NiFe, lead-free, slow-evaporating (reed switches) |
| 8531 | Soft glass, Na-free, high lead-content, for low temperature encapsulation of semiconductor components (diodes) |
| 8532 | Soft glass, Na-free, high lead-content, for low-temperature encapsulation of semiconductor components (diodes) |
| 8533 | IR-absorbing sealing glass for Ni–Fe, lead- and potassium-free, slow-evaporating (reed switches) |
| 8625 | IR-absorbing biocompatible glass for (implantable) transponders |
| 8650 | Alkali-free sealing glass for molybdenum, especially for implosion diodes; high lead content |
| 8651 | Tungsten sealing glass for power diodes |
| 8652 | Tungsten sealing glass, low-melting, for power diodes |
| 8656 | Borofloat® 40, borosilicate float glass adapted for prestressing |

[a] Also known as 8258, Estax®, low-potassium glass tubing for the manufacture of counting vials.

**Table 3.4-11** Characteristic data of technical specialty glasses

| Glass No. | Shapes produced[a] | Thermal expansion coefficient $\alpha_{(20/300)}$ ($10^{-6}$ /K) | Transformation temperature $T_g$ (°C) | Temperature at viscosity $10^{13}$ dPa s (°C) | $10^{7.6}$ dPa s (°C) | $10^{4}$ dPa s (°C) | Density at 25 °C (g/cm³) | Young's modulus ($10^3$ N/mm²) | Poisson's ratio $\mu$ | Heat conductivity $\lambda$ at 90 °C (W/m K) |
|---|---|---|---|---|---|---|---|---|---|---|
| **8095** | TP | 9.2 | 435 | 435 | 635 | 985 | 3.01 | 60 | 0.22 | 0.9 |
| **8245** | MTRP | 5.1 | 505 | 515 | 720 | 1040 | 2.31 | 68 | 0.22 | 1.2 |
| **8248** | BP | 3.1 | 445 | 490 | 740 | 1260 | 2.12 | 44 | 0.22 | 1.0 |
| **8250** | MTBPC | 5.0 | 490 | 500 | 720 | 1055 | 2.28 | 64 | 0.21 | 1.2 |
| **8252** | TP | 4.6 | 725 | 725 | 935 | 1250 | 2.63 | 81 | 0.24 | 1.1 |
| **8253** | TP | 4.7 | 785 | 790 | 1000 | 1315 | 2.65 | 83 | 0.23 | 1.1 |
| **8261** | SP | 3.7 | 720 | 725 | 950 | 1255 | 2.57 | 79 | 0.24 | 1.1 |
| **8326** | MTP | 6.6 | 560 | 565 | 770 | 1135 | 2.46 | 75 | 0.20 | 1.2 |
| **8330** | MSTRPC | 3.3 | 525 | 560 | 820 | 1260 | 2.23 | 63 | 0.20 | 1.12 |
| **8337B** | TP | 4.1 | 430 | 465 | 715 | 1090 | 2.21 | 51 | 0.22 | 1.0 |
| **8350** | TRP | 9.1 | 525 | 530 | 715 | 1040 | 2.50 | 73 | 0.22 | 1.1 |
| **8405** | MTP | 9.8 | 460 | 450 | 660 | 1000 | 2.51 | 65 | 0.21 | 1.0 |
| **8409** | MTRP | 4.1 | 745 | 740 | 950 | 1230 | 2.57 | 85 | 0.24 | 1.2 |
| **8412** | TP | 4.9 | 565 | 565 | 780 | 1165 | 2.34 | 73 | 0.20 | 1.2 |
| **8414** | TP | 5.4 | 560 | 560 | 770 | 1155 | 2.42 | 71 | 0.19 | 1.2 |
| **8415** | TP | 7.8 | 535 | 530 | 720 | 1050 | 2.50 | 74 | 0.21 | 1.1 |
| **8421** | P | 9.7 | 525 | 535 | 705 | 1000 | 2.59 | 74 | 0.22 | 1.0 |
| **8422** | P | 8.7 | 540 | 535 | 715 | 1010 | 2.46 | 76 | 0.21 | 1.1 |
| **8436** | TRP | 6.7 | 630 | 630 | 830 | 1110 | 2.76 | 85 | 0.22 | 1.1 |
| **8486** | MP | 4.1 | 555 | 580 | 820 | 1220 | 2.32 | 66 | 0.20 | 1.1 |
| **8487** | TRP | 3.9 | 525 | 560 | 775 | 1135 | 2.25 | 66 | 0.20 | 1.2 |
| **8488** | M | 4.3 | 545 | 560 | 800 | 1250 | 2.30 | 67 | 0.20 | 1.2 |
| **8490** | MP | 9.6 | 475 | 480 | 660 | 1000 | 2.61 | 70 | 0.22 | 1.0 |
| **8512** | TP | 9.0 | 445 | 460 | 665 | 980 | 2.53 | 68 | 0.22 | 1.0 |
| **8516** | TP | 8.9 | 440 | 445 | 650 | 990 | 2.56 | 72 | 0.21 | 1.1 |
| **8531** | TP | 9.0 | 440 | 430 | 590 | 830 | 4.34 | 52 | 0.24 | 0.57 |
| **8532** | TP | 8.8 | 430 | 425 | 565 | 760 | 4.47 | 56 | 0.24 | 0.7 |
| **8533** | TP | 8.7 | 475 | 480 | 645 | 915 | 2.57 | 79 | 0.21 | 1.1 |
| **8625** | TP | 9.0 | 510 | 520 | 710 | 1030 | 2.53 | 73 | 0.22 | 1.1 |
| **8650** | TP | 5.2 | 475 | 475 | 620 | 880 | 3.57 | 62 | 0.23 | 0.5 |
| **8651** | TP | 4.5 | 540 | 540 | 735 | 1040 | 2.87 | 59 | 0.24 | 0.9 |
| **8652** | TP | 4.5 | 495 | 490 | 640 | 915 | 3.18 | 58 | 0.25 | 0.9 |
| **8656** | SP | 4.1 | 590 | 600 | 850 | 1270 | 2.35 | – | – | – |

[a] Shapes produced: B = block glass; C = capillaries; M = molded glass (blown or pressed); P = powder, spray granulates, or sintered parts; R = rods; S = sheet glass; T = tubing

**Table 3.4–11** Characteristic data of technical specialty glasses, cont.

| $T_{k100}$ (°C) | Logarithm of electrical volume resistivity (Ω cm) at 250 °C | 350 °C | Dielectric properties at 1 MHz and 25 °C $\varepsilon_r$ | $\tan\delta$ ($10^{-4}$) | Refractive index $n_d$ ($\lambda_d = 587.6$ nm) | Stress-optical coefficient $K$ ($10^{-6}$ mm$^2$/N) | Classes of chemical stability against Water | Acid | Alkaline solution |
|---|---|---|---|---|---|---|---|---|---|
| 330 | 9.6 | 7.6 | 6.6 | 11 | 1.556 | 3.1 | 3 | 2 | 3 |
| 215 | 7.4 | 5.9 | 5.7 | 80 | 1.488 | 3.8 | 3 | 4 | 3 |
| – | 12 | 10 | 4.3 | 10 | 1.466 | 5.2 | 3 | 3 | 3 |
| 375 | 10 | 8.3 | 4.9 | 22 | 1.487 | 3.6 | 3 | 4 | 3 |
| 660 | – | 12 | 6.1 | 11 | 1.538 | 3.3 | 1 | 3 | 2 |
| 630 | – | 11 | 6.6 | 15 | 1.547 | 2.7 | 1 | 2 | 2 |
| 585 | – | – | 5.8 | 14 | 1.534 | 3.1 | 1 | 4 | 2 |
| 210 | 7.3 | 6.0 | 6.4 | 65 | 1.506 | 2.8 | 1 | 1 | 2 |
| 250 | 8.0 | 6.5 | 4.6 | 37 | 1.473 | 4.0 | 1 | 1 | 2 |
| 315 | 9.2 | 7.5 | 4.7 | 22 | 1.476 | 4.1 | 3 | 4 | 3 |
| 200 | 7.1 | 5.7 | 7.2 | 70 | 1.514 | 2.7 | 3 | 1 | 2 |
| 280 | 8.5 | 6.9 | 6.5 | 45 | 1.505 | 2.8 | 5 | 3 | 2 |
| 530 | 12 | 10 | 6.1 | 23 | 1.543 | 2.9 | 1 | 4 | 3 |
| 215 | 7.4 | 6.0 | 5.7 | 80 | 1.492 | 3.4 | 1 | 1 | 2 |
| 200 | 7.1 | 5.6 | 6.3 | 107 | 1.523 | 2.2 | 1 | 2 | 2 |
| 180 | 6.7 | 5.3 | 7.1 | 113 | 1.521 | 3.2 | 2 | 2 | 2 |
| 255 | 8.1 | 6.4 | 7.4 | 43 | 1.526 | 2.7 | 3 | 3 | 2 |
| 205 | 7.3 | 5.8 | 7.3 | 60 | 1.509 | 2.9 | 2 | 3 | 3 |
| 245 | 7.9 | 6.5 | 7.9 | 75 | 1.564 | 2.9 | 1–2 | 1–2 | 1 |
| 230 | 7.5 | 6.1 | 5.1 | 40 | 1.487 | 3.8 | 1 | 1 | 2 |
| 300 | 8.3 | 6.9 | 4.9 | 36 | 1.479 | 3.6 | 4 | 3 | 3 |
| 200 | 7.1 | 5.8 | 5.4 | 96 | 1.484 | 3.2 | 1 | 1 | 2 |
| 235 | 7.7 | 6.1 | 6.7 | 32 | 1.52 | – | 3 | 2 | 2 |
| 320 | 9.5 | 7.5 | 6.5 | 21 | 1.510 | 3.0 | 3 | 1–2 | 2 |
| 250 | 8.1 | 6.4 | 6.5 | 25 | 1.516 | 3.0 | 3 | 1 | 2 |
| 450 | 11 | 9.8 | 9.5 | 9 | 1.700 | 2.2 | 1 | 4 | 3 |
| 440 | 11 | 9.4 | 10.2 | 9 | 1.724 | 1.7 | 1 | 4 | 3 |
| 200 | 7.0 | 5.5 | 6.9 | 55 | 1.527 | 3.0 | 1 | 2 | 2 |
| 210 | 7.2 | 5.8 | 7.1 | 68 | 1.525 | – | 3 | 1 | 2 |
| – | – | – | 7.6 | 33 | 1.618 | 2.8 | 1 | 4 | 3 |
| – | 11.2 | 10.0 | 6.0 | 31 | 1.552 | 3.6 | 1 | 4 | 3 |
| – | – | – | 6.9 | 35 | 1.589 | 3.4 | 1 | 4 | 3 |
| 265 | 8.3 | 6.8 | 5.5 | 51 | 1.493 | 3.6 | 1 | 1 | 1 |

## 3.4.5 Optical Glasses

Historically, optical glasses were developed to optimize imaging refractive optics in the visible part of the spectrum. With new mathematical tools, new light sources, and new detectors, the resulting lens systems, which used a combination of different glasses (or even sometimes crystalline materials), changed the requirement from high versatility in terms of material properties to homogeneity, precision, and reproducibility, and an extended spectral range in the ultraviolet and infrared regions; environmental aspects also became important. Consequently, the high number of glass types has been reduced.

### 3.4.5.1 Optical Properties

#### Refractive Index, Abbe Value, Dispersion, and Glass Designation

The most common identifying features used for characterizing an optical glass are the refractive index $n_d$ in the middle range of the visible spectrum, and the Abbe value $\nu_d = (n_d - 1)/(n_F - n_C)$ as a measure of the dispersion. The difference $n_F - n_C$ is called the principal dispersion. The symbols have subscripts that identify spectral lines that are generally used to determine refractive indices; these spectral lines are listed in Table 3.4-12.

The quantities $n_e$ and $\nu_e = (n_e - 1)/(n_{F'} - n_{C'})$ based on the e-line are usually used for specifying optical components.

For the comparison of glass types from different manufacturers, an abbreviated glass code is defined in the following way: the first three digits correspond to $n_d - 1$, the second three digits represent the Abbe value $\nu_d$, and, after a dot, three more digits characterize the density (see Table 3.4-13).

Glasses can be grouped into families in an $n_d/\nu_d$ Abbe diagram (Fig. 3.4-25). These glass families differ in chemical composition as shown in Fig. 3.4-26.

**Table 3.4-12** Wavelengths of a selection for frequently used spectral lines

| Wavelength (nm) | Designation | Spectral line used | Element |
|---|---|---|---|
| 2325.42 | | Infrared mercury line | Hg |
| 1970.09 | | Infrared mercury line | Hg |
| 1529.582 | | Infrared mercury line | Hg |
| 1060.0 | | Neodymium glass laser | Nd |
| 1013.98 | t | Infrared mercury line | Hg |
| 852.11 | s | Infrared cesium line | Cs |
| 706.5188 | r | Red helium line | He |
| 656.2725 | C | Red hydrogen line | H |
| 643.8469 | C′ | Red cadmium line | Cd |
| 632.8 | | Helium–neon gas laser | He–Ne |
| 589.2938 | D | Yellow sodium line (center of the double line) | Na D |
| 587.5618 | d | Yellow helium line | He |
| 546.0740 | e | Green mercury line | Hg |
| 486.1327 | F | Blue hydrogen line | H |
| 479.9914 | F′ | Blue cadmium line | Cd |
| 435.8343 | g | Blue mercury line | Hg |
| 404.6561 | h | Violet mercury line | Hg |
| 365.0146 | i | Ultraviolet mercury line | Hg |
| 334.1478 | | Ultraviolet mercury line | Hg |
| 312.5663 | | Ultraviolet mercury line | Hg |
| 296.7278 | | Ultraviolet mercury line | Hg |
| 280.43 | | Ultraviolet mercury line | Hg |
| 248.00 | | Excimer laser | KrF |
| 248.35 | | Ultraviolet mercury line | Hg |
| 194.23 | | | |
| 193.00 | | Excimer laser | ArF |

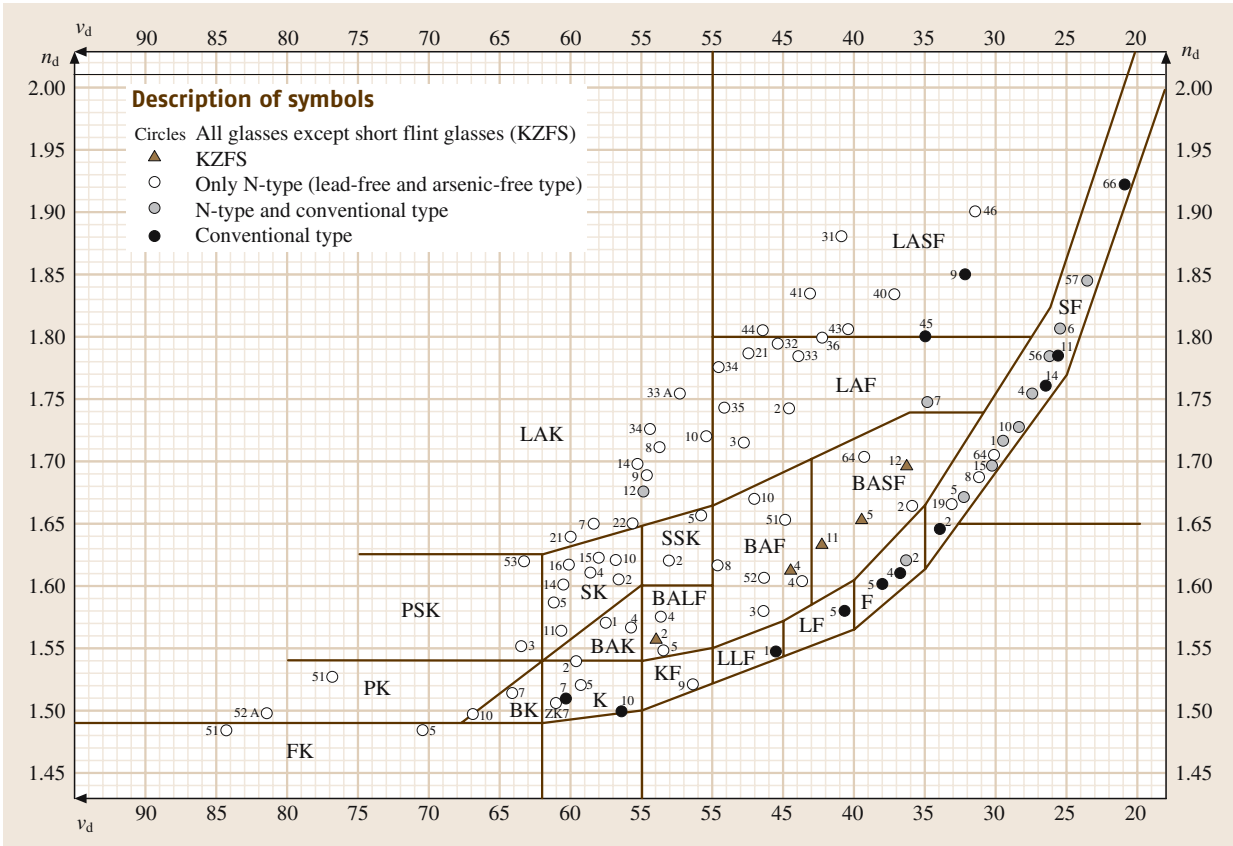


**Fig. 3.4-25** Abbe diagram of glass families

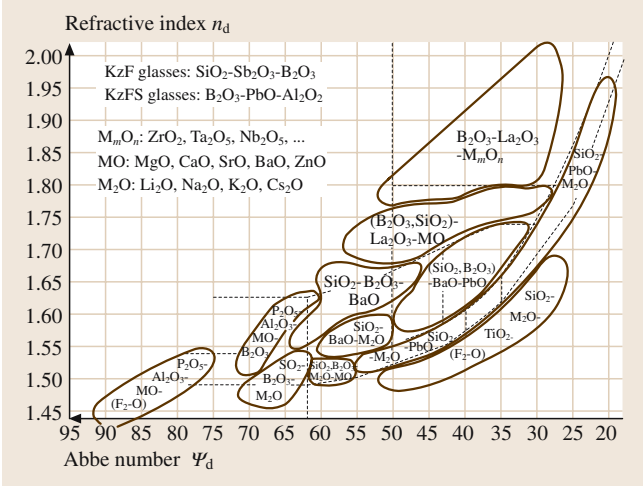


**Fig. 3.4-26** Abbe diagram showing the chemical composition of the glass families

**Table 3.4-13** Examples of glass codes

| Glass type | $n_d$ | $\nu_d$ | Density $\varrho$ (g cm$^{-3}$) | Glass code | Remarks |
|---|---|---|---|---|---|
| N-SF6 | 1.80518 | 25.36 | 3.37 | 805 254.337 | Lead- and arsenic-free glass |
| SF6 | 1.80518 | 25.43 | 5.18 | 805 254.518 | Classical lead silicate glass |

The designation of each glass type here is composed of an abbreviated family designation and a number. The glass families are arranged by decreasing Abbe value in the data tables (Table 3.4-14).

Table 3.4-14 gives an overview of the preferred optical glasses from Schott, Hoya, and Ohara. The glass types are listed in order of increasing refractive index $n_d$.

**Table 3.4-14** Comparison of the preferred optical glasses from different manufacturers

| Schott | | Hoya | | Ohara | |
|---|---|---|---|---|---|
| Code | Glass type | Code | Glass type | Code | Glass type |
| 434950 | N-FK56 | | | | |
| | | | | 439950 | S-FPL53 |
| | | | | 456903 | S-FPL52 |
| 487704 | N-FK5 | 487704 | FC5 | 487702 | S-FSL5 |
| 487845 | N-FK51 | | | | |
| 497816 | N-PK52 | 497816 | FCD1 | 497816 | S-FPL51 |
| 498670 | N-BK10 | | | | |
| 501564 | K10 | | | | |
| 508612 | N-ZK7 | | | | |
| 511604 | K7 | | | | |
| | | 517522 | CF6 | | |
| | | 517524 | E-CF6 | 517524 | S-NSL36 |
| 517642 | N-BK7 | 517642 | BSC7 | 516641 | S-BSL7 |
| | | | | 517696 | S-APL1 |
| | | 518590 | E-C3 | 518590 | S-NSL3 |
| | | | | 521526 | SSL5 |
| 522595 | N-K5 | | | | |
| | | | | 522598 | S-NSL5 |
| 523515 | N-KF9 | | | | |
| | | | | 529517 | SSL2 |
| 529770 | N-PK51 | | | | |
| 532488 | N-LLF6 | 532488 | FEL6 | | |
| | | 532489 | E-FEL6 | 532489 | S-TIL6 |
| 540597 | N-BAK2 | | | 540595 | S-BAL12 |
| | | 541472 | E-FEL2 | 541472 | S-TIL2 |
| | | 541472 | FEL2 | | |
| 547536 | N-BALF5 | | | | |
| 548458 | LLF1 | 548458 | FEL1 | | |
| 548458 | N-LLF1 | 548458 | E-FEL1 | 548458 | S-TIL1 |
| | | 551496 | SbF1 | | |
| 552635 | N-PSK3 | | | | |
| 558542 | N-KZFS2 | | | | |
| | | | | 560612 | S-BAL50 |
| 564608 | N-SK11 | 564607 | EBaCD11 | 564607 | S-BAL41 |
| | | 567428 | FL6 | 567428 | PBL26 |
| 569561 | N-BAK4 | 569563 | BaC4 | 569563 | S-BAL14 |
| 569713 | N-PSK58 | | | | |
| | | | | 571508 | S-BAL2 |
| | | | | 571530 | S-BAL3 |
| 573576 | N-BAK1 | | | 573578 | S-BAL11 |

| Schott | | Hoya | | Ohara | |
|---|---|---|---|---|---|
| Code | Glass type | Code | Glass type | Code | Glass type |
| | | | | 575415 | S-TIL27 |
| 580537 | N-BALF4 | | | | |
| 581409 | N-LF5 | 581407 | E-FL5 | 581407 | S-TIL25 |
| 581409 | LF5 | 581409 | FL5 | | |
| 583465 | N-BAF3 | | | 583464 | BAM3 |
| | | 583594 | BaCD12 | 583594 | S-BAL42 |
| 589613 | N-SK5 | 589613 | BaCD5 | 589612 | S-BAL35 |
| 592683 | N-PSK57 | | | | |
| | | | | 593353 | S-FTM16 |
| | | 594355 | FF5 | | |
| | | 596392 | E-F8 | 596392 | S-TIM8 |
| | | 596392 | F8 | | |
| | | 603380 | E-F5 | 603380 | S-TIM5 |
| 603380 | F5 | | | 603380 | F5 |
| 603606 | N-SK14 | 603606 | BaCD14 | 603607 | S-BSM14 |
| | | | | 603655 | S-PHM53 |
| 606439 | N-BAF4 | | | 606437 | S-BAM4 |
| 607567 | N-SK2 | 607568 | BaCD2 | 607568 | S-BSM2 |
| 609464 | N-BAF52 | | | | |
| | | 613370 | F3 | 613370 | PBM3 |
| 613443 | KZFSN4 | 613443 | ADF10 | 613443 | BPM51 |
| 613445 | N-KZFS4 | | | | |
| 613586 | N-SK4 | 613587 | BaCD4 | 613587 | S-BSM4 |
| | | | | 614550 | BSM9 |
| 617366 | F4 | | | | |
| | | | | 617628 | S-PHM51 |
| 618498 | N-SSK8 | | | 618498 | S-BSM28 |
| | | 618634 | PCD4 | 618634 | S-PHM52 |
| 620364 | N-F2 | 620363 | E-F2 | 620363 | S-TIM2 |
| 620364 | F2 | 620364 | F2 | | |
| 620603 | N-SK16 | 620603 | BaCD16 | 620603 | S-BSM16 |
| | | 620622 | ADC1 | | |
| 620635 | N-PSK53 | | | | |
| | | | | 621359 | TIM11 |
| 621603 | SK51 | | | | |
| 622532 | N-SSK2 | | | 622532 | BSM22 |
| | | | | | |
| 623569 | N-SK10 | 623570 | EBaCD10 | 623570 | S-BSM10 |
| 623580 | N-SK15 | 623582 | BaCD15 | 623582 | S-BSM15 |
| | | 624470 | BaF8 | | |

**Table 3.4–14** Comparison of the preferred optical glasses from different manufacturers, cont.

| Schott | | Hoya | | Ohara | |
|---|---|---|---|---|---|
| Code | Glass type | Code | Glass type | Code | Glass type |
| | | 626357 | F1 | | |
| | | 626357 | E-F1 | 626357 | S-TIM1 |
| 639421 | N-KZFS11 | | | | |
| | | | | 639449 | S-BAM12 |
| 639554 | N-SK18 | 639554 | BaCD18 | 639554 | S-BSM18 |
| | | 640345 | E-FD7 | 640345 | S-TIM27 |
| 640601 | N-LAK21 | 640601 | LaCL60 | 640601 | S-BSM81 |
| | | | | 641569 | S-BSM93 |
| | | | | 643584 | S-BSM36 |
| 648339 | SF2 | 648339 | FD2 | | |
| | | 648338 | E-FD2 | 648338 | S-TIM22 |
| | | 649530 | E-BaCED20 | 649530 | S-BSM71 |
| 651559 | N-LAK22 | | | | |
| | | 651562 | LaCL2 | 651562 | S-LAL54 |
| 652449 | N-BAF51 | | | | |
| 652585 | N-LAK7 | 652585 | LaC7 | 652585 | S-LAL7 |
| 654396 | KZFSN5 | 654396 | ADF50 | 654397 | BPH5 |
| 658509 | N-SSK5 | 658509 | BaCED5 | 658509 | S-BSM25 |
| | | | | 658573 | S-LAL11 |
| 664360 | N-BASF2 | | | | |
| | | | | 667330 | S-TIM39 |
| | | 667484 | BaF11 | 667483 | S-BAH11 |
| | | | | 670393 | BAH32 |
| 670471 | N-BAF10 | 670473 | BaF10 | 670473 | S-BAH10 |
| | | | | | |
| | | | | 670573 | S-LAL52 |
| 673322 | N-SF5 | 673321 | E-FD5 | 673321 | S-TIM25 |
| 673322 | SF5 | 673322 | FD5 | | |
| | | 678507 | LaCL9 | 678507 | S-LAL56 |
| 678549 | LAKL12 | | | | |
| 678552 | N-LAK12 | 678553 | LaC12 | 678553 | S-LAL12 |
| 689312 | N-SF8 | 689311 | E-FD8 | 689311 | S-TIM28 |
| | | 689312 | FD8 | | |
| 691547 | N-LAK9 | 691548 | LaC9 | 691548 | S-LAL9 |
| | | 694508 | LaCL5 | 694508 | LAL58 |
| 694533 | LAKN13 | 694532 | LaC13 | 694532 | S-LAL13 |
| | | | | 695422 | S-BAH54 |
| | | 697485 | LaFL2 | 697485 | LAM59 |
| 697554 | N-LAK14 | 697555 | LaC14 | 697555 | S-LAL14 |
| | | | | 697565 | S-LAL64 |

| Schott | | Hoya | | Ohara | |
|---|---|---|---|---|---|
| Code | Glass type | Code | Glass type | Code | Glass type |
| 699301 | N-SF15 | 699301 | E-FD15 | 699301 | S-TIM35 |
| 699301 | SF15 | 699301 | FD15 | | |
| | | | | 700481 | S-LAM51 |
| | | 702412 | BaFD7 | 702412 | S-BAH27 |
| 704394 | NBASF64 | | | | |
| 706303 | N-SF64 | | | | |
| 713538 | N-LAK8 | 713539 | LaC8 | 713539 | S-LAL8 |
| 717295 | N-SF1 | 717295 | E-FD1 | | |
| 717295 | SF1 | 717295 | FD1 | 717295 | PBH1 |
| 717480 | N-LAF3 | 717480 | LaF3 | 717479 | S-LAM3 |
| | | | | 720347 | BPH8 |
| | | | | 720420 | LAM58 |
| | | | | 720437 | S-LAM52 |
| | | | | 720460 | LAM61 |
| 720506 | N-LAK10 | 720504 | LaC10 | 720502 | S-LAL10 |
| | | | | 722292 | S-TIH18 |
| 724381 | NBASF51 | | | 723380 | S-BAH28 |
| 724381 | BASF51 | 724381 | BaFD8 | | |
| | | | | 726536 | S-LAL60 |
| 728284 | SF10 | 728284 | FD10 | | |
| 728285 | N-SF10 | 728285 | E-FD10 | 728285 | S-TIH10 |
| 729547 | N-LAK34 | 729547 | TaC8 | 729547 | S-LAL18 |
| | | 734515 | TaC4 | 734515 | S-LAL59 |
| | | | | 740283 | PBH3W |
| | | 741276 | FD13 | 740283 | PBH3 |
| | | 741278 | E-FD13 | 741278 | S-TIH13 |
| | | 741527 | TaC2 | 741527 | S-LAL61 |
| 743492 | N-LAF35 | 743493 | NbF1 | 743493 | S-LAM60 |
| 744447 | N-LAF2 | 744447 | LaF2 | 744448 | S-LAM2 |
| 750350 | LaFN7 | 750353 | LaF7 | 750353 | LAM7 |
| 750350 | N-LAF7 | | | | |
| 754524 | N-LAK33 | 755523 | TaC6 | 755523 | S-YGH51 |
| 755276 | N-SF4 | 755275 | E-FD4 | 755275 | S-TIH4 |
| 755276 | SF4 | 755276 | FD4 | | |
| | | | | 756251 | TPH55 |
| | | 757478 | NbF2 | 757478 | S-LAM54 |
| 762265 | N-SF14 | 762265 | FD140 | 762265 | S-TIH14 |
| 762265 | SF14 | 762266 | FD14 | | |
| | | | | 762401 | S-LAM55 |
| 772496 | N-LAF34 | 772496 | TaF1 | 772496 | S-LAH66 |

**Table 3.4-14** Comparison of preferred optical glasses, cont.

| Schott | | Hoya | | Ohara | |
|---|---|---|---|---|---|
| Code | Glass type | Code | Glass type | Code | Glass type |
| 785258 | SF11 | 785258 | FD11 | | |
| | | 785258 | FD110 | 785257 | S-TIH11 |
| 785261 | SF56A | | | | |
| 785261 | N-SF56 | 785261 | FDS30 | 785263 | S-TIH23 |
| 786441 | N-LAF33 | 786439 | NBFD11 | 786442 | S-LAH51 |
| | | | | 787500 | S-YGH52 |
| 788475 | N-LAF21 | 788475 | TAF4 | 788474 | S-LAH64 |
| 794454 | N-LAF32 | | | 795453 | S-LAH67 |
| 800423 | N-LAF36 | 800423 | NBFD12 | 800422 | S-LAH52 |
| 801350 | N-LASF45 | | | 801350 | S-LAM66 |
| | | | | 804396 | S-LAH63 |
| 804466 | N-LASF44 | 804465 | TAF3 | 804466 | S-LAH65 |
| 805254 | N-SF6 | 805254 | FD60 | 805254 | S-TIH6 |
| 805254 | SF6 | 805254 | FD6 | | |
| | | 805396 | NBFD3 | | |
| | | 806333 | NBFD15 | | |
| 806407 | N-LASF43 | 806407 | NBFD13 | 806409 | S-LAH53 |
| | | | | 808228 | S-NPH1 |
| | | 816445 | TAFD10 | 816444 | S-LAH54 |
| | | 816466 | TAF5 | 816466 | S-LAH59 |
| 834374 | N-LASF40 | 834373 | NBFD10 | 834372 | S-LAH60 |
| 835430 | N-LASF41 | 835430 | TAFD5 | 835427 | S-LAH55 |
| 847238 | N-SF57 | 847238 | FDS90 | 847238 | S-TIH53 |
| 847236 | SFL57 | | | | |
| 847238 | SF57 | 847238 | FDS9 | 847238 | TIH53 |
| 850322 | LASFN9 | | | | |
| | | | | 874353 | S-LAH75 |
| 881410 | N-LASF31 | | | | |
| | | 883408 | TAFD30 | 883408 | S-LAH58 |
| 901315 | N-LASF46 | | | 901315 | LAH78 |
| 923209 | SF66 | 923209 | E-FDS1 | | |
| | | | | 923213 | PBH71 |
| | | | | 1003283 | S-LAH79 |
| 1022291 | N-LASF35 | | | | |

### Formulas for Optical Characterization

The characterization of optical glasses through the refractive index and Abbe value alone is insufficient for high-quality optical systems. A more accurate description of the properties of a glass can be achieved with the aid of the relative partial dispersion.

*Relative Partial Dispersion.* The relative partial dispersion $P_{x,y}$ for the wavelengths $x$ and $y$ based on the blue F hydrogen line and red C hydrogen line is given by

$$P_{x,y} = (n_x - n_y)/(n_F - n_C) \,. \tag{4.15}$$

The corresponding value based on the blue F′ cadmium line and red C′ cadmium line is given by

$$P'_{x,y} = (n_x - n_y)/(n_{F'} - n_{C'}) \,. \tag{4.16}$$

*Relationship Between the Abbe Value and the Relative Partial Dispersion.* A linear relationship exists between the Abbe value and the relative partial dispersion for what are known as "normal glasses":

$$P_{x,y} \approx a_{xy} + b_{xy}\nu_d \,. \tag{4.17}$$

*Deviation from the "Normal Line".* All other glasses deviate from the "normal line" defined by $\Delta P_{x,y}$. For the selected wavelength pairs the $\Delta P$-value are calculated from the following equations:

$$P_{x,y} = a_{xy} + b_{xy}\nu_d + \Delta P_{x,y} \,, \tag{4.18}$$

$$\Delta P_{C,t} = (n_C - n_t)/(n_F - n_C) - (0.5450 + 0.004743\nu_d) \,, \tag{4.19}$$

$$\Delta P_{C,s} = (n_C - n_s)/(n_F - n_C) - (0.4029 + 0.002331\nu_d) \,, \tag{4.20}$$

$$\Delta P_{F,e} = (n_F - n_e)/(n_F - n_C) - (0.4884 - 0.000526\nu_d) \,, \tag{4.21}$$

$$\Delta P_{g,F} = (n_g - n_F)/(n_F - n_C) - (0.6438 - 0.001682\nu_d) \,, \tag{4.22}$$

$$\Delta P_{i,g} = (n_i - n_g)/(n_F - n_C) - (1.7241 - 0.008382\nu_d) \,. \tag{4.23}$$

The "normal line" has been determined based on value pairs of glasses types K7 and F2. The term $\Delta P_{x,y}$ quantitatively describes the deviation of the behavior of the dispersion from that of "normal glasses".

The Sellmeier dispersion formula for the refractive index,

$$n^2(\lambda) - 1 = B_1\lambda^2/(\lambda^2 - C_1) + B_2\lambda^2/(\lambda^2 - C_2) + B_3\lambda^2/(\lambda^2 - C_3) \,, \tag{4.24}$$

can be derived from classical dispersion theory with the assumption of three resonance wavelengths. It is valid only for interpolation within a spectral region in which the refractive index has been measured. The vacuum wavelength $\lambda$ in µm has to be used. The precision of the calculation achievable is generally better than $1 \times 10^{-5}$.

*Temperature Dependence of the Refractive Index.* The refractive index is also dependent on temperature. This temperature dependence is represented by $\Delta n_{rel}/\Delta T$ for an air pressure of 1013.3 hPa and $\Delta n_{abs}/\Delta T$ in vacuum. The following equation is derived from the Sellmeier formula and is valid with the given coefficients in the temperature range $-40\,°C < T < +80\,°C$ and within the wavelength range $435.8\,nm < \lambda < 643.8\,nm$:

$$\frac{dn_{abs}(\lambda, T)}{dT} = \frac{n^2(\lambda, T_0) - 1}{2n(\lambda, T_0)} \times \left( D_0 + 2D_1\Delta T + 3D_2\Delta T^2 + \frac{E_0 + 2E_1\Delta T}{\lambda^2 - \lambda_{TK}^2} \right), \quad (4.25)$$

where $\Delta T$ is the temperature difference in °C from 20 °C, and $\lambda_{TK}$ is an effective resonance wavelength.

The changes in the refractive index and Abbe value caused by a change in the annealing rate are given by

$$n_d(h_x) = n_d(h_0) + m_{nd}\log(h_x/h_0)\,, \quad (4.26)$$

$$\nu_d(h_x) = \nu_d(h_0) + m_{\nu d}\log(h_x/h_0)\,, \quad (4.27)$$

$$m_{\nu d} = \frac{m_{nd} - \nu_d(h_0)m_{nF-nC}}{(n_F - n_C) + 2m_{nF-nC}\log(h_x/h_0)}\,, \quad (4.28)$$

where $h_0$ is the original annealing rate in °C/h, $h_x$ is the new annealing rate in °C/h, $m_{nd}$ is the annealing coefficient for the refractive index (Table 3.4-15), $m_{\nu d}$ is the annealing coefficient for the Abbe value and $m_{nF-nC}$ is the annealing coefficient for the principal dispersion. The last three quantities depend on the glass type.

The measurement accuracy of the Abbe value can be calculated using

$$\sigma(\nu_d) \approx \sigma(n_F - n_C)\nu_d/(n_F - n_C)\,. \quad (4.29)$$

The accuracy of precision measurements of the refractive indices is better than $\pm 1\times10^{-5}$, and the accuracy of the dispersion is $\pm 3\times10^{-6}$. In the infrared wavelength range above 2 µm, the corresponding accuracies are $\pm 2\times10^{-5}$ and $\pm 5\times10^{-6}$.

**Table 3.4-15** Annealing coefficients for selected glass types

| Glass type | $m_{nd}$ | $m_{nF-nC}$ | $m_{\nu d}$ |
|---|---|---|---|
| N-BK7 | −0.00087 | −0.000005 | −0.0682 |
| N-FK51 | −0.00054 | −0.000002 | −0.0644 |
| SF6 | −0.00058 | +0.000035 | −0.0464 |
| N-SF6 | −0.0025 | −0.000212 | +0.0904 |

*Transmission.* The transmittance of glasses is limited by electronic excitiations and light scattering in the UV, by vibronic excitations in the IR, and by reflections and impurity absorptions within the transmission window (in the visible part of the spectrum): Fig. 3.4-27. The UV absorption edge is temperature dependent. An example is shown in Fig. 3.4-28.

*Spectral Internal Transmittance.* The spectral internal transmittance is given by

$$\tau_{i\lambda} = \Phi_{e\lambda}/\Phi_{i\lambda}\,, \quad (4.30)$$

where $\Phi_{i\lambda}$ is the incident light intensity and $\Phi_{e\lambda}$ is the intensity at the exit.

*Spectral Transmission.* The spectral transmission is given by

$$\tau_\lambda = \tau_{i\lambda}P_\lambda\,, \quad (4.31)$$

where $P_\lambda$ is the reflection factor.

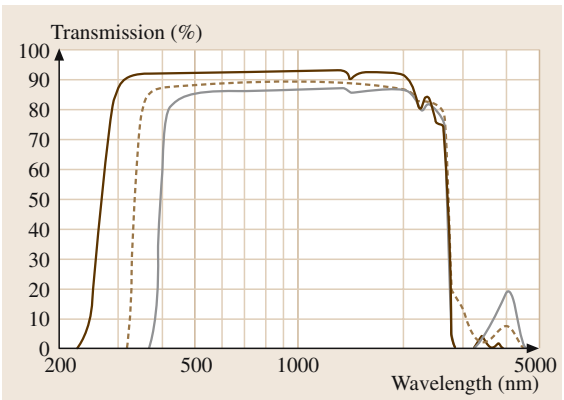


**Fig. 3.4-27** Transmission of three glasses for a thickness of 5 mm: *Brown line* FK5; *dashed line* SF2; *gray line* SF11

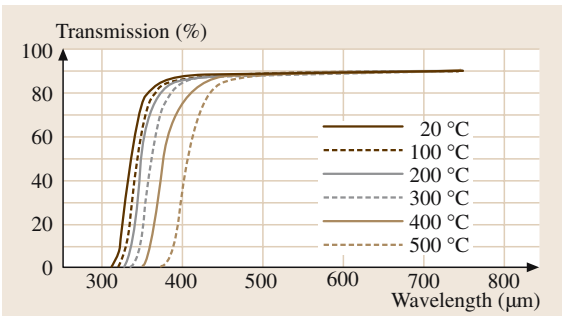


**Fig. 3.4-28** Influence of temperature on the UV transmission of glass F2 for a thickness of 10 mm

*Fresnel Reflectivity.* For a light beam striking the surface perpendicularly, the Fresnel reflectivity is, independent of polarization,

$$R = (n-1)^2/(n+1)^2 \,. \tag{4.32}$$

*Reflection Factor.* The reflection factor, taking account of multiple reflection, is given by

$$P = (1-R)^2/(1-R^2) = 2n/(n^2+1) \,, \tag{4.33}$$

where $n$ is the refractive index for the wavelength $\lambda$.

*Conversion of Internal Transmittance to Another Layer Thickness.* The conversion of data for internal transmittance to another sample thickness is accomplished by the use of the equation

$$\log \tau_{i1} / \log \tau_{i2} = d_1/d_2 \tag{4.34}$$

$$\text{or } \tau_{i2} = \tau_{i1}^{(d_2/d_1)} \,, \tag{4.35}$$

where $\tau_{i1}$ and $\tau_{i2}$ are the internal transmittances for the thicknesses $d_1$ and $d_2$, respectively.

*Stress Birefringence.* The change in optical path length for existing stress birefringence can be calculated from

$$\Delta s = (n_\parallel - n_\perp)d = (K_\parallel - K_\perp)d\sigma = Kd\sigma \,, \tag{4.36}$$

where $K$ is the stress optical coefficient, dependent on the glass type, $d$ is the length of the light path in the sample, and $\sigma$ is the mechanical stress (positive for tensile stress). If $K$ is given in $10^{-6}$ mm$^2$/N, $d$ is given in mm, and $\sigma$ is measured in MPa = N/mm$^2$, $\Delta s$ comes out in mm.

For the Pockels glass SF57, the stress optical coefficient $K$ is close to 0 in the visible wavelength range.

*Homogeneity.* The homogeneity of the refractive index of a sample can be measured from the interferometrically measured wavefront deformation using the equation

$$\Delta n = \Delta W/2d$$

$$= \Delta W(\lambda) \times 633 \times 10^{-6}/(2d[\text{mm}]) \,, \tag{4.37}$$

where the wavefront deformation is in units of the wavelength and is measured using a test wavelength of 633 nm (He–Ne laser); $\Delta W$ is the wavefront deformation for double beam passage; and $d$ is the thickness of the test piece. With special effort during melting and careful annealing, it is possible to produce pieces of glass having high homogeneity. The refractive-index homogeneity achievable for a given glass type depends on the volume and the form of the individual glass piece. Values of $\pm 5 \times 10^{-7}$ (class H5) cannot be achieved for all dimensions and glass types.

The properties of a selection of optical glasses are collected together in Table 3.4-16.

#### Internal Transmittance and Color Code

The internal transmittance, i. e. the light transmission excluding reflection losses, is closely related to the optical position of the glass type, according to general dispersion theory. This can be achieved, however, only by using purest raw materials and costly melting technology.

The internal transmittance of lead- and arsenic-free glasses, in which lead has been replaced by other elements, is markedly less than in the lead-containing predecessor glasses.

The limit of the transmission range of optical glasses towards the UV area is of special interest and is characterized by the position and slope of the UV absorption curve, which is described by a color code. The color code gives the wavelengths $\lambda_{80}$ and $\lambda_5$, at which the transmission (including reflection losses) is 0.80 and 0.05, respectively, at 10 mm thickness. The color code 33/30 means, for example, $\lambda_{80} = 330$ nm and $\lambda_5 = 300$ nm.

### 3.4.5.2 Chemical Properties

The composition of optical glasses includes elements that reduce chemical resistance. For these glasses, five test methods are used to assess the chemical behavior of polished glass surfaces in typical applications. The test methods and classification numbers take the place of those described for technical glasses in Sect. 3.4.4. Data for optical properties are found in Table 3.4-16c.

#### Climatic Resistance (ISO/WD 13384): Division into Climatic Resistance Classes CR 1–4

Climatic resistance describes the behavior of optical glasses at high relative humidity and high temperatures. In the case of sensitive glasses, a cloudy film can appear that generally cannot be wiped off.

The classifications are based on the increase in transmission haze $\Delta H$ after a 30 h test period. The glasses in class CR 1 display no visible attack after being subjected to 30 h of climatic change.

Under normal humidity conditions, no surface attack should be expected during the fabrication and storage of

optical glasses in class CR 1. On the other hand, the fabrication and storage of optical glasses in class CR 4 should be done with caution because these glasses are very sensitive to climatic influences.

#### Stain Resistance: Division into Stain Resistance Classes FR 0–5

The test procedure gives information about possible changes in the glass surface (stain formation) under the influence of lightly acidic water (for example perspiration and acidic condensates) without vaporization. Two test solutions are used. Test solution I is a standard acetate solution with pH = 4.6, for classes FR 0 to 3. Test solution II is a sodium acetate buffer solution with pH = 5.6, for classes FR 4 and FR 5.

Interference color stains develop as a result of decomposition of the surface of the glass by the test solution. The measure used for classifying the glasses is the time that elapses before the first brown–blue stain occurs at a temperature of 25 °C.

Stain resistance class FR 0 contains all glasses that exhibit virtually no interference colors even after 100 h of exposure to test solution I.

Glasses in classification FR 5 must be handled with particular care during processing.

#### Acid Resistance (ISO 8424: 1987): Division into Acid Resistance Classes SR 1–4, 5, and 51–53

Acid resistance classifies the behavior of optical glasses that come into contact with large quantities of acidic solutions (from a practical standpoint, these may be perspiration, laminating substances, carbonated water, etc.).

The time $t$ required to dissolve a layer with a thickness of 0.1 µm serves as a measure of acid resistance. Two aggressive solutions are used in determining acid resistance. A strong acid (nitric acid, $c = 0.5$ mol/l, pH = 0.3) at 25 °C is used for the more resistant glass types. For glasses with less acid resistance, a weakly acidic solution with a pH value of 4.6 (standard acetate) is used, also at 25 °C.

#### Alkali Resistance (ISO 10629) and Phosphate Resistance (ISO 9689): Division into Alkali Resistance Classes AR 1–4 and Phosphate Resistance Classes PR 1–4

These two test methods indicate the resistance to aqueous alkaline solutions in excess and use the same classification scheme. The alkali resistance indicates the sensitivity of optical glasses when they are in contact with warm, alkaline liquids, such as cooling liquids used in grinding and polishing processes. The phosphate resistance describes the behavior of optical glasses during cleaning with phosphate-containing washing solutions (detergents).

The alkali resistance class AR is based on the time required to remove a layer of glass of thickness 0.1 µm in an alkaline solution (sodium hydroxide, $c = 0.01$ mol/l, pH = 12) at a temperature of 50 °C.

The phosphate resistance class PR is based on the time required to remove a layer of glass of thickness 0.1 mm in an alkaline phosphate-containing solution (pentasodium triphosphate, $Na_5P_3O_{10}$, $c = 0.01$ mol/l, pH = 10) at a temperature of 50 °C. The thickness is calculated from the weight loss per unit surface area and the density of the glass.

### 3.4.5.3 Mechanical Properties

#### Young's Modulus and Poisson's Ratio

The adiabatic Young's modulus $E$ (in units of $10^3$ N/mm$^2$) and Poisson's ratio $\mu$ have been determined at room temperature and at a frequency of 1 kHz using carefully annealed test samples. Data are listed in Table 3.4-16c. In most cases, the values decrease slightly with temperature.

The torsional modulus can be calculated from

$$G = E/[2(1+\mu)] \,. \tag{4.38}$$

The longitudinal sound velocity is

$$v_{\text{long}} = \sqrt{\frac{E(1-\mu)}{\varrho(1+\mu)(1-2\mu)}} \,, \tag{4.39}$$

where $\varrho$ is the density.

#### Knoop Hardness

The Knoop hardness (HK) of a material is a measure of the residual surface changes after the application of pressure with a test diamond. The standard ISO 9385 describes the measurement procedure for glasses. In accordance with this standard, values for Knoop hardness HK are listed in the data sheets for a test force of 0.9807 N (corresponds to 0.1 kp) and an effective test period of 20 s. The test was performed on polished glass surfaces at room temperature. The data for hardness values are rounded to 10 HK 0.1/20. The microhardness is a function of the magnitude of the test force and decreases with increasing test force.

**Table 3.4-16a** Properties of optical glasses. Refractive index and Sellmeier constants

| Glass type | Refractive index | | Abbe value | | Constants of the Sellmeier dispersion formula | | | | | |
|---|---|---|---|---|---|---|---|---|---|---|
| | $n_d$ | $n_e$ | $v_d$ | $v_e$ | $B_1$ | $B_2$ | $B_3$ | $C_1$ | $C_2$ | $C_3$ |
| F2 | 1.62004 | 1.62408 | 36.37 | 36.11 | $1.34533359\times10^{+00}$ | $2.09073176\times10^{-01}$ | $9.37357162\times10^{-01}$ | $9.97743871\times10^{-03}$ | $4.70450767\times10^{-02}$ | $1.11886764\times10^{+02}$ |
| K10 | 1.50137 | 1.50349 | 56.41 | 56.15 | $1.15687082\times10^{+00}$ | $6.42625444\times10^{-02}$ | $8.72376139\times10^{-01}$ | $8.09424251\times10^{-03}$ | $3.86051284\times10^{-02}$ | $1.04747730\times10^{+02}$ |
| LASF35 | 2.02204 | 2.03035 | 29.06 | 28.84 | $2.45505861\times10^{+00}$ | $4.53006077\times10^{-01}$ | $2.38513080\times10^{+00}$ | $1.35670404\times10^{-02}$ | $5.45803020\times10^{-02}$ | $1.67904715\times10^{+02}$ |
| LF5 | 1.58144 | 1.58482 | 40.85 | 40.57 | $1.28035628\times10^{+00}$ | $1.63505973\times10^{-01}$ | $8.93930112\times10^{-01}$ | $9.29854416\times10^{-03}$ | $4.49135769\times10^{-02}$ | $1.10493685\times10^{+02}$ |
| LLF1 | 1.54814 | 1.55098 | 45.89 | 45.60 | $1.23326922\times10^{+00}$ | $1.16923839\times10^{-01}$ | $8.62645379\times10^{-01}$ | $8.85396812\times10^{-03}$ | $4.36875155\times10^{-02}$ | $1.04992168\times10^{+02}$ |
| N-BAF10 | 1.67003 | 1.67341 | 47.11 | 46.83 | $1.58514950\times10^{+00}$ | $1.43559385\times10^{-01}$ | $1.08521269\times10^{+00}$ | $9.26681282\times10^{-03}$ | $4.24489805\times10^{-02}$ | $1.05613573\times10^{+02}$ |
| N-BAF52 | 1.60863 | 1.61173 | 46.60 | 46.30 | $1.43903433\times10^{+00}$ | $9.67046052\times10^{-02}$ | $1.09875818\times10^{+00}$ | $9.07800128\times10^{-03}$ | $5.08212080\times10^{-02}$ | $1.05691856\times10^{+02}$ |
| N-BAK4 | 1.56883 | 1.57125 | 55.98 | 55.70 | $1.28834642\times10^{+00}$ | $1.32817724\times10^{-01}$ | $9.45395373\times10^{-01}$ | $7.79980626\times10^{-03}$ | $3.15631177\times10^{-02}$ | $1.05965875\times10^{+02}$ |
| N-BALF4 | 1.57956 | 1.58212 | 53.87 | 53.59 | $1.31004128\times10^{+00}$ | $1.42038259\times10^{-01}$ | $9.64929351\times10^{-01}$ | $7.96596450\times10^{-03}$ | $3.30672072\times10^{-02}$ | $1.09197320\times10^{+02}$ |
| N-BASF64 | 1.70400 | 1.70824 | 39.38 | 39.12 | $1.65554268\times10^{+00}$ | $1.71319770\times10^{-01}$ | $1.33664448\times10^{+00}$ | $1.04485644\times10^{-02}$ | $4.99394756\times10^{-02}$ | $1.18961472\times10^{+02}$ |
| N-BK7 | 1.51680 | 1.51872 | 64.17 | 63.96 | $1.03961212\times10^{+00}$ | $2.31792344\times10^{-01}$ | $1.01046945\times10^{+00}$ | $6.00069867\times10^{-03}$ | $2.00179144\times10^{-02}$ | $1.03560653\times10^{+02}$ |
| N-FK56 | 1.43425 | 1.43534 | 94.95 | 94.53 | $9.11957171\times10^{-01}$ | $1.28580417\times10^{-01}$ | $9.83146162\times10^{-01}$ | $4.50933489\times10^{-03}$ | $1.53515963\times10^{-02}$ | $2.23961126\times10^{+02}$ |
| N-KF9 | 1.52346 | 1.52588 | 51.54 | 51.26 | $1.19286778\times10^{+00}$ | $8.93346571\times10^{-02}$ | $9.20819805\times10^{-01}$ | $8.39154696\times10^{-03}$ | $4.04010786\times10^{-02}$ | $1.12572446\times10^{+02}$ |
| N-KZFS2 | 1.55836 | 1.56082 | 54.01 | 53.83 | $1.23697554\times10^{+00}$ | $1.53569376\times10^{-01}$ | $9.03976272\times10^{-01}$ | $7.47170505\times10^{-03}$ | $3.08053556\times10^{-02}$ | $7.01731084\times10^{+01}$ |
| N-LAF2 | 1.74397 | 1.74791 | 44.85 | 44.57 | $1.80984227\times10^{+00}$ | $1.57295550\times10^{-01}$ | $1.09300370\times10^{+00}$ | $1.01711622\times10^{-02}$ | $4.42431765\times10^{-02}$ | $1.00687748\times10^{+02}$ |
| N-LAK33 | 1.75398 | 1.75740 | 52.43 | 52.20 | $1.45796869\times10^{+00}$ | $5.55403936\times10^{-01}$ | $1.19938794\times10^{+00}$ | $6.80545280\times10^{-03}$ | $2.25253283\times10^{-02}$ | $8.27543327\times10^{+01}$ |
| N-LASF31 | 1.88067 | 1.88577 | 41.01 | 40.76 | $1.71317198\times10^{+00}$ | $7.18575109\times10^{-01}$ | $1.72332470\times10^{+00}$ | $8.19172228\times10^{-03}$ | $2.97801704\times10^{-02}$ | $1.38461313\times10^{+02}$ |
| N-PK51 | 1.52855 | 1.53019 | 76.98 | 76.58 | $1.15610775\times10^{+00}$ | $1.53229344\times10^{-01}$ | $7.85618966\times10^{-01}$ | $5.85597402\times10^{-03}$ | $1.94072416\times10^{-02}$ | $1.40537046\times10^{+02}$ |
| N-PSK57 | 1.59240 | 1.59447 | 68.40 | 68.01 | $9.88511414\times10^{-01}$ | $5.10855261\times10^{-01}$ | $7.58837122\times10^{-01}$ | $4.78397680\times10^{-03}$ | $1.58020289\times10^{-02}$ | $1.29709222\times10^{+02}$ |
| N-SF1 | 1.71736 | 1.72308 | 29.62 | 29.39 | $1.60865158\times10^{+00}$ | $2.37725916\times10^{-01}$ | $1.51530653\times10^{+00}$ | $1.19654879\times10^{-02}$ | $5.90589722\times10^{-02}$ | $1.35521676\times10^{+02}$ |
| N-SF56 | 1.78470 | 1.79179 | 26.10 | 25.89 | $1.73562085\times10^{+00}$ | $3.17487012\times10^{-01}$ | $1.95398203\times10^{+00}$ | $1.29624742\times10^{-02}$ | $6.12884288\times10^{-02}$ | $1.61559441\times10^{+02}$ |
| N-SK16 | 1.62041 | 1.62286 | 60.32 | 60.08 | $1.34317774\times10^{+00}$ | $2.41144399\times10^{-01}$ | $9.94317969\times10^{-01}$ | $7.04687339\times10^{-03}$ | $2.29005000\times10^{-02}$ | $9.27508526\times10^{+01}$ |
| N-SSK2 | 1.62229 | 1.62508 | 53.27 | 52.99 | $1.43060270\times10^{+00}$ | $1.53150554\times10^{-01}$ | $1.01390904\times10^{+00}$ | $8.23982975\times10^{-03}$ | $3.33736841\times10^{-02}$ | $1.06870822\times10^{+02}$ |
| SF1 | 1.71736 | 1.72310 | 29.51 | 29.29 | $1.55912923\times10^{+00}$ | $2.84246288\times10^{-01}$ | $9.68842926\times10^{-01}$ | $1.21481001\times10^{-02}$ | $5.34549042\times10^{-02}$ | $1.12174809\times10^{+02}$ |
| SF11 | 1.78472 | 1.79190 | 25.76 | 25.55 | $1.73848403\times10^{+00}$ | $3.11168974\times10^{-01}$ | $1.17490871\times10^{+00}$ | $1.36068604\times10^{-02}$ | $6.15960463\times10^{-02}$ | $1.21922711\times10^{+02}$ |
| SF2 | 1.64769 | 1.65222 | 33.85 | 33.60 | $1.40301821\times10^{+00}$ | $2.31767504\times10^{-01}$ | $9.39056586\times10^{-01}$ | $1.05795466\times10^{-02}$ | $4.93226978\times10^{-02}$ | $1.12405955\times10^{+02}$ |
| SF66 | 1.92286 | 1.93325 | 20.88 | 20.73 | $2.07842233\times10^{+00}$ | $4.07120032\times10^{-01}$ | $1.76711292\times10^{+00}$ | $1.80875134\times10^{-02}$ | $6.79493572\times10^{-02}$ | $2.15266127\times10^{+02}$ |
| SK51 | 1.62090 | 1.62335 | 60.31 | 60.02 | $1.44112715\times10^{+00}$ | $1.43968387\times10^{-01}$ | $8.81989862\times10^{-01}$ | $7.58546975\times10^{-03}$ | $2.87396017\times10^{-02}$ | $9.46838154\times10^{+01}$ |
| K7 | 1.51112 | 1.51314 | 60.41 | 60.15 | $1.12735550\times10^{+00}$ | $1.24412303\times10^{-01}$ | $8.27100531\times10^{-01}$ | $7.20341707\times10^{-03}$ | $2.69835916\times10^{-02}$ | $1.00384588\times10^{+02}$ |
| N-SF6 | 1.80518 | 1.81266 | 25.36 | 25.16 | $1.77931763\times10^{+00}$ | $3.38149866\times10^{-01}$ | $2.08734474\times10^{+00}$ | $1.33714182\times10^{-02}$ | $6.17533621\times10^{-02}$ | $1.74017590\times10^{+02}$ |
| SF6 | 1.80518 | 1.81265 | 25.43 | 25.24 | $1.72448482\times10^{+00}$ | $3.90104889\times10^{-01}$ | $1.04572858\times10^{+00}$ | $1.34871947\times10^{-02}$ | $5.69318095\times10^{-02}$ | $1.18557185\times10^{+02}$ |
| N-FK51 | 1.48656 | 1.48794 | 84.47 | 84.07 | $9.71247817\times10^{-01}$ | $2.16901417\times10^{-01}$ | $9.04651666\times10^{-01}$ | $4.72301995\times10^{-03}$ | $1.53575612\times10^{-02}$ | $1.68681330\times10^{+02}$ |
| Lithosil™Q | 1.45843 | 1.46004 | 67.87 | 67.67 | $6.69422575\times10^{-01}$ | $4.34583937\times10^{-01}$ | $8.71694723\times10^{-01}$ | $4.48011239\times10^{-03}$ | $1.32847049\times10^{-02}$ | $9.53414824\times10^{+01}$ |

**Table 3.4-16b** Data for $dn/dT$

| Glass type | Data for $dn/dT$ | | | | | |
|---|---|---|---|---|---|---|
| | $10^6 D_0$ | $10^8 D_1$ | $10^{11} D_2$ | $10^7 E_0$ | $10^{10} E_1$ | $\lambda_{TK}$ (µm) |
| F2 | 1.51 | 1.56 | −2.78 | 9.34 | 10.4 | 0.250 |
| K10 | 4.86 | 1.72 | −3.02 | 3.82 | 4.53 | 0.260 |
| LASF35 | 0.143 | 0.871 | −2.71 | 10.2 | 15.0 | 0.263 |
| LF5 | −2.27 | 0.971 | −2.83 | 8.36 | 9.95 | 0.228 |
| LLF1 | 0.325 | 1.74 | −6.12 | 6.53 | 2.58 | 0.233 |
| N-BAF10 | 3.79 | 1.28 | −1.42 | 5.84 | 7.60 | 0.220 |
| N-BAF52 | 1.15 | 1.27 | −0.508 | 5.64 | 6.38 | 0.238 |
| N-BAK4 | 3.06 | 1.44 | −2.23 | 5.46 | 6.05 | 0.189 |
| N-BALF4 | 5.33 | 1.47 | −1.58 | 5.75 | 6.58 | 0.195 |
| N-BASF64 | 1.60 | 1.02 | −2.68 | 7.87 | 9.65 | 0.229 |
| N-BK7 | 1.86 | 1.31 | −1.37 | 4.34 | 6.27 | 0.170 |
| N-FK56 | −20.4 | −1.03 | 0.243 | 3.41 | 4.37 | 0.138 |
| N-KF9 | −1.66 | 0.844 | −1.01 | 6.10 | 6.96 | 0.217 |
| N-KZFS2 | 6.77 | 1.31 | −1.23 | 3.84 | 5.51 | 0.196 |
| N-LAF2 | −3.64 | 0.920 | −0.600 | 6.43 | 6.11 | 0.220 |
| N-LAK33 | 2.57 | 1.16 | −7.29 | 6.01 | 1.59 | 0.114 |
| N-LASF31 | 2.29 | 0.893 | −1.59 | 6.52 | 8.09 | 0.236 |
| N-PK51 | −19.8 | −0.606 | 1.60 | 4.16 | 5.01 | 0.134 |
| N-PSK57 | −22.3 | −0.560 | 0.997 | 4.47 | 5.63 | – |
| N-SF1 | −3.72 | 0.805 | −1.71 | 8.98 | 13.4 | 0.276 |
| N-SF56 | −4.13 | 0.765 | −1.12 | 9.90 | 15.7 | 0.287 |
| N-SK16 | −0.0237 | 1.32 | −1.29 | 4.09 | 5.17 | 0.170 |
| N-SSK2 | 5.21 | 1.34 | −1.01 | 5.21 | 5.87 | 0.199 |
| SF1 | 4.84 | 1.70 | −4.52 | 13.8 | 12.6 | 0.259 |
| SF11 | 11.2 | 1.81 | −5.03 | 14.6 | 15.8 | 0.282 |
| SF2 | 1.10 | 1.75 | −1.29 | 10.8 | 10.3 | 0.249 |
| SF66 | – | – | – | – | – | – |
| SK51 | −5.63 | 0.738 | −6.20 | 3.91 | 2.64 | 0.230 |
| K7 | −1.67 | 0.880 | −2.86 | 5.42 | 7.81 | 0.172 |
| N-SF6 | −4.93 | 0.702 | −2.40 | 9.84 | 15.4 | 0.290 |
| SF6 | 6.69 | 1.78 | −3.36 | 17.7 | 17.0 | 0.272 |
| N-FK51 | −18.3 | −0.789 | −0.163 | 3.74 | 3.46 | 0.150 |
| Lithosil™Q | 20.6 | 2.51 | −2.47 | 3.12 | 4.22 | 0.160 |

**Table 3.4-16c** Chemical and physical data

| Glass type | Stress-optical coefficient $K$ | Chemical properties | | | | | Density | Viscosity (dPa s) | | | Thermal properties | | | | Mechanical properties | | |
|---|---|---|---|---|---|---|---|---|---|---|---|---|---|---|---|---|---|
| | | | | | | | | $10^{14.5}$ | $10^{13}$ | $10^{7.6}$ | Heat capacity | Heat conductivity | Thermal expansion | | Young's modulus $E$ | Poisson's ratio $\mu$ | Knoop hardness |
| | | CR | FR | SR | AR | PR | | at temperature | | | $c_p$ | $\lambda$ | $\alpha_{(30/70)}$ | $\alpha_{(20/300)}$ | | | |
| | ($10^{-6}$ mm$^2$/N) | | | | | | (g/cm$^3$) | (°C) | (°C) | (°C) | (J/g K) | (W/m K) | ($10^{-6}$/K) | ($10^{-6}$/K) | ($10^3$ N/mm$^2$) | | HK |
| F2 | 2.81 | 1 | 0 | 1 | 2.3 | 1.3 | 3.61 | 432 | 421 | 593 | 0.557 | 0.780 | 8.20 | 9.20 | 57 | 0.220 | 420 |
| K10 | 3.12 | 1 | 0 | 1 | 1 | 1.2 | 2.52 | 459 | 453 | 691 | 0.770 | 1.120 | 6.50 | 7.40 | 65 | 0.190 | 470 |
| LASF35 | 0.73 | 1 | 0 | 1.3 | 1 | 1.3 | 5.41 | 774 | – | – | 0.445 | 0.920 | 7.40 | 8.50 | 132 | 0.303 | 810 |
| LF5 | 2.83 | 2 | 0 | 1 | 2.3 | 2 | 3.22 | 419 | 411 | 585 | 0.657 | 0.866 | 9.10 | 10.60 | 59 | 0.223 | 450 |
| LLF1 | 3.05 | 1 | 0 | 1 | 2 | 1 | 2.94 | 448 | 426 | 628 | 0.650 | – | 8.10 | 9.20 | 60 | 0.208 | 450 |
| N-BAF10 | 2.37 | 1 | 0 | 4.3 | 1.3 | 1 | 3.75 | 660 | 652 | 790 | 0.560 | 0.780 | 6.18 | 7.04 | 89 | 0.271 | 620 |
| N-BAF52 | 2.42 | 1 | 0 | 1 | 1.3 | 1 | 3.05 | 594 | 596 | 723 | 0.680 | 0.960 | 6.86 | 7.83 | 86 | 0.237 | 600 |
| N-BAK4 | 2.90 | 1 | 0 | 1.2 | 1 | 1 | 3.05 | 581 | 569 | 725 | 0.680 | 0.880 | 6.99 | 7.93 | 77 | 0.240 | 550 |
| N-BALF4 | 3.01 | 1 | 0 | 1 | 1 | 1 | 3.11 | 578 | 584 | 661 | 0.690 | 0.850 | 6.52 | 7.41 | 77 | 0.245 | 540 |
| N-BASF64 | 2.38 | 1 | 0 | 3.2 | 1.2 | 1 | 3.20 | 582 | 585 | 712 | – | – | 7.30 | 8.70 | 105 | 0.264 | 650 |
| N-BK7 | 2.77 | 2 | 0 | 1 | 2 | 2.3 | 2.51 | 557 | 557 | 719 | 0.858 | 1.114 | 7.10 | 8.30 | 82 | 0.206 | 610 |
| N-FK56 | 0.68 | 1 | 0 | 52.3 | 4.3 | 4.3 | 3.54 | 422 | 416 | – | 0.750 | 0.840 | – | 16.16 | 70 | 0.293 | 350 |
| N-KF9 | 2.74 | 1 | 0 | 1 | 1 | 1 | 2.50 | 476 | 476 | 640 | 0.860 | 1.040 | 9.61 | 10.95 | 66 | 0.225 | 480 |
| N-KZFS2 | 4.02 | 1 | 4 | 52.3 | 4.3 | 4.2 | 2.55 | 491 | 488 | 600 | 0.830 | 0.810 | 4.43 | 5.43 | 66 | 0.266 | 490 |
| N-LAF2 | 1.42 | 2 | 3 | 52.2 | 1 | 2.2 | 4.30 | 653 | 645 | 742 | 0.510 | 0.670 | 8.06 | 9.10 | 94 | 0.288 | 530 |
| N-LAK33 | 1.49 | 1 | 1 | 51.3 | 1 | 2.3 | 4.26 | 652 | 648 | – | 0.554 | 0.900 | 6.00 | 7.00 | 124 | 0.291 | 780 |
| N-LASF31 | 1.10 | 1 | 0 | 2 | 1 | 1 | 5.41 | 758 | 756 | – | – | 0.910 | 6.80 | 7.70 | 124 | 0.299 | 770 |
| N-PK51 | 0.54 | 2 | 0 | 51.2 | 3.3 | 4.3 | 3.96 | 496 | 486 | – | – | – | 12.70 | 14.40 | 74 | 0.295 | 400 |
| N-PSK57 | 0.13 | 1 | 0 | 51.3 | 1.2 | 4.3 | 4.48 | 497 | 499 | – | 0.490 | 0.560 | 13.17 | 14.75 | 69 | 0.298 | 370 |
| N-SF1 | 2.72 | 1 | 0 | 1 | 1 | 1 | 3.03 | 553 | 554 | 660 | 0.750 | 1.000 | 9.13 | 10.54 | 90 | 0.250 | 540 |
| N-SF56 | 2.87 | 1 | 0 | 1 | 1.3 | 1 | 3.28 | 592 | 585 | 691 | 0.700 | 0.940 | 8.70 | 10.00 | 91 | 0.255 | 560 |
| N-SK16 | 1.90 | 4 | 4 | 53.3 | 3.3 | 3.2 | 3.58 | 636 | 633 | 750 | 0.578 | 0.818 | 6.30 | 7.30 | 89 | 0.264 | 600 |
| N-SSK2 | 2.51 | 1 | 0 | 1.2 | 1 | 1 | 3.53 | 653 | 655 | 801 | 0.580 | 0.810 | 5.81 | 6.65 | 82 | 0.261 | 570 |
| SF1 | 1.80 | 2 | 1 | 3.2 | 2.3 | 3 | 4.46 | 417 | 415 | 566 | – | – | 8.10 | 8.80 | 56 | 0.232 | 390 |
| SF11 | 1.33 | 1 | 0 | 1 | 1.2 | 1 | 4.74 | 503 | 500 | 635 | 0.431 | 0.737 | 6.10 | 6.80 | 66 | 0.235 | 450 |
| SF2 | 2.62 | 1 | 0 | 2 | 2.3 | 2 | 3.86 | 441 | 428 | 600 | 0.498 | 0.735 | 8.40 | 9.20 | 55 | 0.227 | 410 |
| SF66 | – 1.20 | 2 | 5 | 53.4 | 2.3 | 4.2 | 6.03 | 384 | 385 | 482 | 0.340 | 0.530 | 9.01 | 11.48 | 51 | 0.258 | 310 |
| SK51 | 1.47 | 2 | 3 | 52.3 | 1.3 | 4.3 | 3.52 | 597 | 579 | 684 | – | – | 8.90 | 10.10 | 75 | 0.291 | 450 |
| K7 | 2.95 | 3 | 0 | 2 | 1 | 2.3 | 2.53 | 513 | – | 712 | – | – | 8.4 | 9.7 | 69 | 0.214 | 520 |
| N-SF6 | 2.82 | 1 | 0 | 2 | 1 | 1 | 3.37 | 594 | 591 | 694 | 0.69 | 0.96 | 9.03 | 10.39 | 93 | 0.262 | 550 |
| SF6 | 0.65 | 2 | 3 | 51.3 | 2.3 | 3.3 | 5.18 | 423 | 410 | 538 | 0.389 | 0.673 | 8.1 | 9 | 55 | 0.244 | 370 |
| N-FK51 | 0.70 | 2 | 0 | 52.3 | 2.2 | 4.3 | 3.73 | 420 | 403 | – | 0.636 | 0.911 | 13.3 | 15.3 | 81 | 0.293 | 430 |
| Lithosil™Q | 3.40 | 1 | – | 1 | 1 | – | 2.20 | 980 | 1080 | 1600 | 0.790 | 1.310 | 0.50 | – | 72 | 0.170 | 580 |

**Table 3.4-16d** Internal transmission and color code

| Glass type | Color code | Internal transmission measured for 25 mm sample thickness at wavelength λ (nm) | | | | | | | | | | | | |
|---|---|---|---|---|---|---|---|---|---|---|---|---|---|---|
| | | 2500 | 2325 | 1970 | 1530 | 1060 | 700 | 660 | 620 | 580 | 546 | 500 | 460 | 436 |
| F2 | 35/32 | 0.610 | 0.700 | 0.890 | 0.990 | 0.998 | 0.998 | 0.996 | 0.997 | 0.997 | 0.997 | 0.996 | 0.993 | 0.991 |
| K10 | 33/30 | 0.520 | 0.630 | 0.850 | 0.983 | 0.996 | 0.997 | 0.994 | 0.993 | 0.993 | 0.992 | 0.991 | 0.990 | 0.988 |
| LASF35 | –/37 | 0.690 | 0.880 | 0.972 | 0.992 | 0.990 | 0.978 | 0.970 | 0.962 | 0.950 | 0.920 | 0.810 | 0.630 | 0.470 |
| LF5 | 34/31 | – | 0.660 | 0.870 | 0.992 | 0.998 | 0.998 | 0.998 | 0.998 | 0.997 | 0.997 | 0.996 | 0.995 | 0.994 |
| LLF1 | 33/31 | 0.500 | 0.610 | 0.840 | 0.990 | 0.996 | 0.997 | 0.996 | 0.996 | 0.997 | 0.997 | 0.996 | 0.996 | 0.996 |
| N-BAF10 | 39/35 | 0.450 | 0.680 | 0.920 | 0.980 | 0.994 | 0.994 | 0.990 | 0.991 | 0.990 | 0.990 | 0.981 | 0.967 | 0.954 |
| N-BAF52 | 39/35 | 0.390 | 0.630 | 0.890 | 0.975 | 0.994 | 0.993 | 0.990 | 0.989 | 0.990 | 0.989 | 0.980 | 0.967 | 0.954 |
| N-BAK4 | 36/33 | 0.540 | 0.710 | 0.900 | 0.982 | 0.995 | 0.997 | 0.995 | 0.995 | 0.996 | 0.996 | 0.994 | 0.989 | 0.988 |
| N-BALF4 | 37/33 | 0.580 | 0.740 | 0.920 | 0.984 | 0.993 | 0.997 | 0.995 | 0.995 | 0.996 | 0.995 | 0.993 | 0.986 | 0.983 |
| N-BASF64 | 40/35 | 0.450 | 0.670 | 0.900 | 0.970 | 0.985 | 0.970 | 0.955 | 0.949 | 0.949 | 0.950 | 0.940 | 0.920 | 0.900 |
| N-BK7 | 33/29 | 0.360 | 0.560 | 0.840 | 0.980 | 0.997 | 0.996 | 0.994 | 0.994 | 0.995 | 0.996 | 0.994 | 0.993 | 0.992 |
| N-FK56 | 33/28 | – | – | 0.979 | 0.991 | 0.996 | 0.996 | 0.996 | 0.996 | 0.996 | 0.996 | 0.996 | 0.996 | 0.995 |
| N-KF9 | 37/34 | 0.300 | 0.430 | 0.740 | 0.981 | 0.995 | 0.997 | 0.995 | 0.994 | 0.996 | 0.996 | 0.994 | 0.990 | 0.988 |
| N-KZFS2 | 34/30 | 0.040 | 0.260 | 0.800 | 0.940 | 0.991 | 0.996 | 0.994 | 0.994 | 0.994 | 0.994 | 0.992 | 0.987 | 0.981 |
| N-LAF2 | 40/34 | 0.400 | 0.690 | 0.930 | 0.990 | 0.997 | 0.996 | 0.993 | 0.992 | 0.993 | 0.994 | 0.983 | 0.962 | 0.940 |
| N-LAK33 | 39/32 | 0.090 | 0.400 | 0.850 | 0.975 | 0.995 | 0.991 | 0.990 | 0.990 | 0.990 | 0.990 | 0.987 | 0.977 | 0.967 |
| N-LASF31 | 45/32 | 0.540 | 0.810 | 0.960 | 0.992 | 0.993 | 0.994 | 0.994 | 0.993 | 0.993 | 0.990 | 0.973 | 0.940 | 0.910 |
| N-PK51 | 35/29 | 0.890 | 0.920 | 0.965 | 0.985 | 0.992 | 0.991 | 0.991 | 0.992 | 0.994 | 0.995 | 0.993 | 0.989 | 0.987 |
| N-PSK57 | 34/29 | – | – | 0.950 | 0.970 | 0.982 | 0.996 | 0.996 | 0.996 | 0.996 | 0.996 | 0.992 | 0.991 | 0.991 |
| N-SF1 | 41/36 | 0.460 | 0.580 | 0.850 | 0.973 | 0.995 | 0.990 | 0.986 | 0.987 | 0.990 | 0.986 | 0.968 | 0.940 | 0.910 |
| N-SF56 | 44/37 | 0.590 | 0.680 | 0.900 | 0.981 | 0.996 | 0.986 | 0.981 | 0.981 | 0.983 | 0.976 | 0.950 | 0.910 | 0.860 |
| N-SK16 | 36/30 | 0.260 | 0.540 | 0.880 | 0.973 | 0.995 | 0.996 | 0.994 | 0.993 | 0.994 | 0.994 | 0.991 | 0.984 | 0.981 |
| N-SSK2 | 37/33 | 0.500 | 0.720 | 0.930 | 0.981 | 0.992 | 0.996 | 0.994 | 0.993 | 0.995 | 0.995 | 0.992 | 0.985 | 0.980 |
| SF1 | 39/34 | 0.650 | 0.730 | 0.900 | 0.985 | 0.996 | 0.996 | 0.995 | 0.995 | 0.996 | 0.996 | 0.993 | 0.984 | 0.976 |
| SF11 | 44/39 | 0.610 | 0.700 | 0.930 | 0.982 | 0.997 | 0.993 | 0.991 | 0.991 | 0.991 | 0.989 | 0.976 | 0.940 | 0.860 |
| SF2 | 37/33 | 0.620 | 0.710 | 0.880 | 0.985 | 0.996 | 0.996 | 0.994 | 0.995 | 0.995 | 0.995 | 0.993 | 0.988 | 0.982 |
| SF66 | 48/38 | 0.700 | 0.740 | 0.920 | 0.990 | 0.995 | 0.990 | 0.989 | 0.989 | 0.988 | 0.985 | 0.965 | 0.890 | 0.770 |
| SK51 | 36/31 | 0.270 | 0.520 | 0.830 | 0.959 | 0.993 | 0.993 | 0.993 | 0.993 | 0.993 | 0.993 | 0.990 | 0.981 | 0.975 |
| K7 | 33/30 | 0.340 | 0.500 | 0.790 | 0.980 | 0.994 | 0.996 | 0.995 | 0.995 | 0.994 | 0.994 | 0.993 | 0.990 | 0.990 |
| N-SF6 | 45/37 | 0.850 | 0.880 | 0.962 | 0.994 | 0.994 | 0.987 | 0.980 | 0.979 | 0.980 | 0.970 | 0.940 | 0.899 | 0.850 |
| SF6 | 42/36 | 0.730 | 0.780 | 0.930 | 0.990 | 0.996 | 0.996 | 0.995 | 0.995 | 0.995 | 0.994 | 0.989 | 0.972 | 0.940 |
| N-FK51 | 34/28 | 0.750 | 0.840 | 0.940 | 0.980 | 0.994 | 0.995 | 0.995 | 0.996 | 0.997 | 0.997 | 0.996 | 0.993 | 0.992 |
| Lithosil™Q | 17/16 | 0.780 | – | – | – | – | – | – | – | – | – | – | – | – |

| Internal transmission measured for 25 mm sample thickness at wavelength λ (nm) | | | | | | | | | | | | | | | | |
|---|---|---|---|---|---|---|---|---|---|---|---|---|---|---|---|---|
| | **420** | **405** | **400** | **390** | **380** | **370** | **365** | **350** | **334** | **320** | **310** | **300** | **290** | **248** | **200** | **193** |
| | 0.990 | 0.986 | 0.984 | 0.977 | 0.963 | 0.940 | 0.920 | 0.780 | 0.210 | – | – | – | – | – | – | – |
| | 0.988 | 0.987 | 0.986 | 0.982 | 0.973 | 0.966 | 0.958 | 0.910 | 0.720 | 0.310 | 0.130 | 0.020 | – | – | – | – |
| | 0.320 | 0.170 | 0.120 | 0.050 | 0.010 | – | – | – | – | – | – | – | – | – | – | – |
| | 0.993 | 0.992 | 0.992 | 0.984 | 0.973 | 0.961 | 0.954 | 0.880 | 0.570 | 0.040 | – | – | – | – | – | – |
| | 0.995 | 0.994 | 0.993 | 0.992 | 0.988 | 0.984 | 0.981 | 0.955 | 0.810 | 0.300 | 0.010 | – | – | – | – | – |
| | 0.940 | 0.900 | 0.880 | 0.800 | 0.660 | 0.440 | 0.310 | 0.010 | – | – | – | – | – | – | – | – |
| | 0.938 | 0.900 | 0.880 | 0.800 | 0.650 | 0.370 | 0.210 | – | – | – | – | – | – | – | – | – |
| | 0.987 | 0.983 | 0.980 | 0.967 | 0.940 | 0.890 | 0.840 | 0.550 | 0.070 | – | – | – | – | – | – | – |
| | 0.981 | 0.970 | 0.964 | 0.940 | 0.900 | 0.820 | 0.750 | 0.380 | – | – | – | – | – | – | – | – |
| | 0.880 | 0.840 | 0.820 | 0.750 | 0.610 | 0.370 | 0.220 | – | – | – | – | – | – | – | – | – |
| | 0.993 | 0.993 | 0.992 | 0.989 | 0.983 | 0.977 | 0.971 | 0.920 | 0.780 | 0.520 | 0.250 | 0.050 | – | – | – | – |
| | 0.994 | 0.996 | 0.996 | 0.995 | 0.992 | 0.985 | 0.975 | 0.920 | 0.760 | 0.460 | 0.210 | 0.060 | 0.010 | – | – | – |
| | 0.985 | 0.975 | 0.965 | 0.940 | 0.880 | 0.770 | 0.680 | 0.210 | – | – | – | – | – | – | – | – |
| | 0.975 | 0.967 | 0.963 | 0.950 | 0.930 | 0.910 | 0.890 | 0.800 | 0.590 | 0.240 | 0.030 | – | – | – | – | – |
| | 0.915 | 0.865 | 0.840 | 0.760 | 0.630 | 0.430 | 0.310 | 0.025 | – | – | – | – | – | – | – | – |
| | 0.954 | 0.928 | 0.910 | 0.860 | 0.790 | 0.690 | 0.630 | 0.400 | 0.140 | 0.020 | – | – | – | – | – | – |
| | 0.880 | 0.840 | 0.820 | 0.750 | 0.650 | 0.530 | 0.460 | 0.210 | 0.040 | 0.020 | – | – | – | – | – | – |
| | 0.986 | 0.985 | 0.984 | 0.977 | 0.965 | 0.940 | 0.910 | 0.750 | 0.430 | 0.120 | 0.030 | – | – | – | – | – |
| | 0.991 | 0.991 | 0.992 | 0.992 | 0.989 | 0.975 | 0.965 | 0.880 | 0.680 | 0.380 | 0.130 | 0.020 | – | – | – | – |
| | 0.870 | 0.760 | 0.700 | 0.520 | 0.250 | 0.030 | – | – | – | – | – | – | – | – | – | – |
| | 0.780 | 0.640 | 0.570 | 0.370 | 0.130 | – | – | – | – | – | – | – | – | – | – | – |
| | 0.979 | 0.974 | 0.970 | 0.956 | 0.930 | 0.890 | 0.860 | 0.700 | 0.400 | 0.110 | 0.020 | – | – | – | – | – |
| | 0.975 | 0.963 | 0.954 | 0.920 | 0.860 | 0.750 | 0.670 | 0.250 | – | – | – | – | – | – | – | – |
| | 0.961 | 0.930 | 0.920 | 0.870 | 0.790 | 0.640 | 0.500 | 0.030 | – | – | – | – | – | – | – | – |
| | 0.700 | 0.340 | 0.200 | 0.010 | – | – | – | – | – | – | – | – | – | – | – | – |
| | 0.975 | 0.962 | 0.954 | 0.920 | 0.870 | 0.790 | 0.720 | 0.370 | – | – | – | – | – | – | – | – |
| | 0.610 | 0.340 | 0.240 | 0.050 | – | – | – | – | – | – | – | – | – | – | – | – |
| | 0.971 | 0.963 | 0.958 | 0.940 | 0.910 | 0.850 | 0.800 | 0.600 | 0.300 | 0.100 | 0.030 | – | – | – | – | – |
| | 0.990 | 0.990 | 0.990 | 0.988 | 0.983 | 0.976 | 0.971 | 0.940 | 0.780 | 0.420 | 0.100 | – | – | – | – | |
| | 0.780 | 0.640 | 0.570 | 0.370 | 0.140 | – | – | – | – | – | – | – | – | – | – | – |
| | 0.900 | 0.810 | 0.760 | 0.620 | 0.370 | 0.100 | 0.020 | – | – | – | – | – | – | – | – | – |
| | 0.992 | 0.993 | 0.993 | 0.992 | 0.988 | 0.976 | 0.963 | 0.875 | 0.630 | 0.300 | 0.120 | 0.035 | 0.010 | – | – | – |
| | – | – | – | – | – | – | – | – | – | – | – | – | – | 0.995 | 0.990 | 0.980 |

#### Viscosity

As explained in the introduction, glasses pass through three viscosity ranges between the melting temperature and room temperature: the melting range, the supercooled melt range, and the solidification range. The viscosity increases during the cooling of the melt, starting from $10^0$–$10^4$ dPa s. A transition from a liquid to a plastic state is observed between $10^4$ and $10^{13}$ dPa s.

The softening point, i. e. the temperature where the viscosity is $10^{7.6}$ dPa s, identifies the plastic range in which glass parts rapidly deform under their own weight. The glass structure can be described as solidified or "frozen" above $10^{13}$ dPa s. At this viscosity, the internal stresses in glass anneal out equalize in approximately 15 min. The temperature at which the viscosity is $10^{13}$ dPa s is called the upper annealing point, and is important for the annealing of glasses.

In accordance with ISO 7884-8, the rate of change of the relative linear thermal expansion can be used to determine the transformation temperature $T_g$, which is close to the temperature at which the viscosity is $10^{13}$ dPa s.

Precision optical surfaces may deform and refractive indices may change if a temperature of $T_g - 200\,K$ is exceeded during any thermal treatment.

#### Coefficient of Linear Thermal Expansion

The typical curve of the linear thermal expansion of a glass begins with an increase in slope from absolute zero to approximately room temperature. Then a nearly linear increase to the beginning of the plastic behavior follows. The transformation range is distinguished by a distinct bending of the expansion curve, which results from the increasing structural rearrangement in the glass. Above this range, the expansion again exhibits a nearly linear increase, but with a noticeably greater slope.

Two averaged coefficients of linear thermal expansion $\alpha$ are usually given: $\alpha_{30/70}$, averaged from −30 °C to +70 °C, which is the relevant value for room temperature; and $\alpha_{20/300}$, averaged from +20 °C to +300 °C, which is the standard international value. These values are listed in Table 3.4-16.

### 3.4.5.4 Thermal Properties

#### Thermal Conductivity

The range of values for the thermal conductivity of glasses at room temperature extends from 1.38 W/m K (pure vitreous silica) to about 0.5 W/m K (high-lead-content glasses). The most commonly used silicate glasses have values between 0.9 and 1.2 W/m K. All data in Table 3.4-16c are given for a temperature of 90 °C, with an accuracy of ±5%.

#### Specific Thermal Capacity

The mean isobaric specific heat capacities $c_p$ (20 °C; 100 °C) listed in Table 3.4-16c were measured from the heat transfer from a hot glass sample at 100 °C into a liquid calorimeter at 20 °C. The values of $c_p$(20 °C; 100 °C) and also of the true thermal capacity $c_p$(20 °C) for silicate glasses range from 0.42 to 0.84 J/g K.

## 3.4.6 Vitreous Silica

Vitreous silica has a unique set of properties. It is produced either from natural quartz by fusion or, if extreme purity is required, by chemical vapor deposition or via a sol–gel routes. Depending on the manufacturing process, variable quantities impurities are incorporated in the ppm or ppb range, such as Fe, Mg, Al, Mn, Ti, Ce, OH, Cl, and F. These impurities and radiation-induced defects, as well as complexes of impurities and defects, and also overtones, control the UV and IR transmittance. In the visible part of the spectrum, Rayleigh scattering from thermodynamically caused density fluctuations dominates. Defects are also responsible for the damage threshold under radiation load, and for fluorescence. The refractive index $n$ and the absorption constant $K$ as a function of wavelength are found in Fig. 3.4-29.

The highest transmittance is required for applications in optical communication networks, in optics for lithography, and in high-power laser physics. For certain applications, for example to increase the refractive index in the IR in fiber optics, the silica is "doped" with $GeO_2$, $P_2O_5$, $B_2O_3$, etc. in the range of 5–10%. In such cases the scattering loss increases owing to concentration fluctuations.

There are also many technical applications which make use of the chemical inertness, light weight, high temperature stability, thermal-shock resistance, and low thermal expansion of vitreous silica. A very low thermal

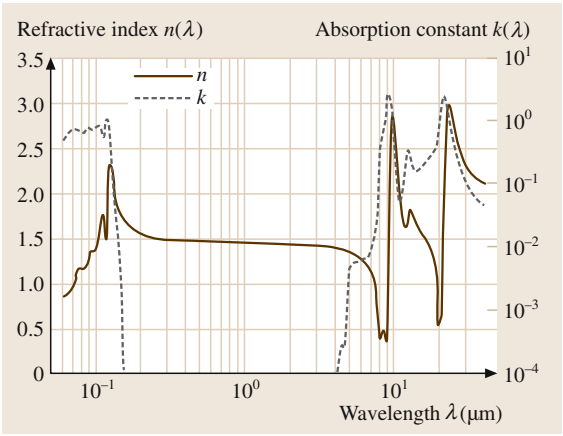


**Fig. 3.4-29** Measured optical constants $n(\lambda)$ and $k(\lambda)$ of vitreous silica according to [4.16]

expansion is obtained in ULE glass (Corning "ultralow expansion" glass) by doping with ≈ 9% $TiO_2$.

### 3.4.6.1 Properties of Synthetic Silica

The precise data for materials from various suppliers differ slightly, depending on the thermal history and impurity concentration. The data listed in Table 3.4-16a–d and in Table 3.4-17, are for Lithosil$^{TM}$Q0 (Schott Lithotec). The various quantities are defined in the same way as for optical glasses, as described in Sect. 3.4.5.

**Table 3.4-17** Electrical properties of vitreous silica (Lithosil$^{TM}$)

| | |
|---|---|
| Dielectric constant $\varepsilon_r$ | $3.8 \pm 0.2$ |
| Dielectric loss angle $\varphi$ | $89.92° \pm 0.03°$ at 25 °C and 1 MHz |
| $\tan\delta$ ($\delta = 90° - \varphi$) | $14 \pm 5 \times 10^{-4}$ |
| Electrical resistivity | $1.15 \times 10^{18}$ (Ω cm) at 20 °C |

### 3.4.6.2 Gas Solubility and Molecular Diffusion

The relatively open structure of vitreous silica provides space for the incorporation and diffusion of molecular species. The data in the literature are not very consistent; Table 3.4-18 should serve as an orientation.

The pressure dependence of the solubility is small up to about 100 atm.

The diffusion coefficient depends on temperature as

$$D = D_0 T \exp(-Q/RT) . \quad (4.40)$$

Water can react with the silica network:

$$H_2O + Si{-}O{-}Si = 2\,Si{-}OH . \quad (4.41)$$

The reaction has a strong influence on the concentration and apparent diffusion of dissolved molecular water.

**Table 3.4-18** Solubility and diffusion of molecular gases in vitreous silica (Lithosil$^{TM}$)

| Gas | Molecular diameter (nm) | $c_{glass}/c_{gas}$ at 200–1000 °C | Dissolved molecules $S$ ($cm^{-3}\,atm^{-1}$) at 200 °C | Diffusion coefficient $D_0$ ($cm^2/s$) 25 °C | 1000 °C | Activation energy $Q$ (kJ/mole) |
|---|---|---|---|---|---|---|
| Helium | 0.20 | 0.025 | $3.9 \times 10^{-17}$ | $2.4 \times 10^{-8}$ | $5.5 \times 10^{-5}$ | 20 |
| Neon | 0.24 | 0.019 | $3.1 \times 10^{-17}$ | $5.0 \times 10^{-12}$ | $2.5 \times 10^{-6}$ | 37 |
| Hydrogen | 0.25 | 0.03 | $4.7 \times 10^{-17}$ | $2.2 \times 10^{-11}$ | $7.3 \times 10^{-6}$ | 36 |
| Argon | 0.32 | 0.01 | $1.5 \times 10^{-17}$ | – | $1.4 \times 10^{-9}$ | 111 |
| Oxygen | 0.32 | 0.01 | $1.5 \times 10^{-17}$ | – | $6.6 \times 10^{-9}$ | 105 |
| Water | 0.33 | – | – | – | $\approx 3.0 \times 10^{-7}$ | 71 |
| Nitrogen | 0.34 | – | – | – | – | 110 |
| Krypton | 0.42 | – | – | – | – | ≈ 190 |
| Xenon | 0.49 | – | – | – | – | ≈ 300 |

## 3.4.7 Glass-Ceramics

Glass-ceramics are distinguished from glasses and from ceramics by the characteristics of their manufacturing processes (see introduction to this chapter 3.4) as well as by their physico-chemical properties.

They are manufactured in two principal production steps. In the first step, a batch of exactly defined composition is melted (as for a conventional glass). The composition is determined by the desired properties of the endproduct and by the necessary working properties of the glass. After melting, the product is shaped by pressing, blowing, rolling, or casting, and then annealed. In this second step, "glassy" articles are partly crystallized by use of a specific temperature–time program between 800 and 1200 °C (this program must be defined for each composition). Apart from the crystalline phase, with crystals 0.05–5 μm in size, this material contains a residual glass phase that amounts to 5–50% of the volume.

In the temperature range between 600 and 700 °C, small amounts of nucleating agents (e.g. $TiO_2$, $ZrO_2$, or F) induce precipitation of crystal nuclei. When the temperature is increased, crystals grow on these nuclei. Their type and properties, as well as their number and size, are predetermined by the glass composition and the annealing program. By selection of an appropriate program, either transparent, slightly opaque, or highly opaque, nontransparent glass-ceramics can be produced. Unlike conventional ceramics, these glass ceramics are fully dense and pore-free.

Like the composition of glasses, the composition of glass-ceramics is highly variable. Some well-known compositions lie within the following systems: $Li_2O-Al_2O_3-SiO_2$, $MgO-Al_2O_3-SiO_2$, and $CaO-P_2O_5-Al_2O_3-SiO_2$.

Glass-ceramics of the $Li_2O-Al_2O_3-SiO_2$ system, which contain small amounts of alkali and alkaline-earth oxides, as well as $TiO_2$ and $ZrO_2$ as nucleating agents, have achieved the greatest commercial importance. On the basis of this system, glass-ceramics with coefficients of linear thermal expansion near to zero can be produced (Fig. 3.4-30 and Table 3.4-19). This exceptional property results from the bonding of crystalline constituents (such as solid solutions of *h*-quartz, *h*-eucryptite, or *h*-spodumene) which have negative coefficients of thermal expansion with the residual glass phase of the system, which has a positive coefficient of thermal expansion.

Such "$\alpha = 0$ glass-ceramics" can be subjected to virtually any thermal shock or temperature variation below 700 °C. Wall thickness, wall thickness differences, and complicated shapes are of no significance.

Another technical advantage is the exceptionally high dimensional and shape stability of objects made from these materials, even when the objects are subjected to considerable temperature variations.

The Zerodur® glass-ceramic, whose coefficient of linear thermal expansion at room temperature can be kept at $\leq 0.05 \times 10^{-6}$ /K (Table 3.4-19), was especially developed for the production of large mirror blanks for astronomical telescopes. Zerodur® has further applications in optomechanical precision components such as length standards, and mirror spacers in lasers. With

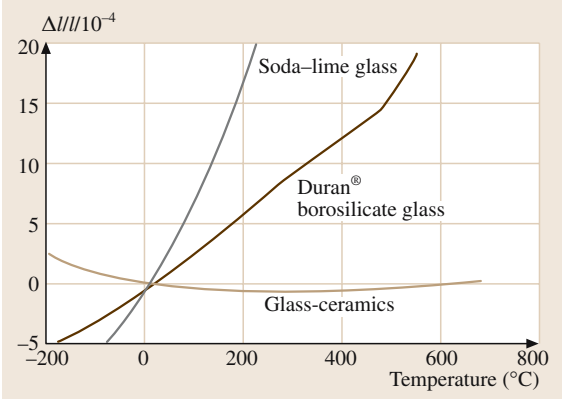


**Fig. 3.4-30** Thermal expansion of glass-ceramics compared with borosilicate glass 3.3 and soda–lime glass

**Table 3.4-19** Coefficient of linear thermal expansion $\alpha$, density, and elastic properties of Zerodur® and Ceran® glass-ceramics

| | Zerodur® | Ceran® | Units | Product class |
|---|---|---|---|---|
| $\alpha_{0/50}$ | $0 \pm 0.05$ | – | $10^{-6}$/K | 1 |
| | $0 \pm 0.1$ | – | $10^{-6}$/K | 2 |
| | $0 \pm 0.15$ | – | $10^{-6}$/K | 3 |
| $\alpha_{20/300}$ | $+0.1$ | $-0.2$ | $10^{-6}$/K | |
| $\alpha_{20/500}$ | – | $-0.01$ | $10^{-6}$/K | |
| $\alpha_{20/600}$ | $+0.2$ | – | $10^{-6}$/K | |
| $\alpha_{20/700}$ | – | $+0.15$ | $10^{-6}$/K | |
| Density | 2.53 | 2.56 | g/cm³ | |
| Young's modulus $E$ | $91 \times 10^3$ | $92 \times 10^3$ | N/mm² | |
| Poisson's ratio $\mu$ | 0.24 | 0.24 | | |

a length aging coefficient $A$ (where $L = L_0(1 + A\Delta t)$, $\Delta t$ = time span) below $1 \times 10^{-7}$/y, Zerodur® has excellent longitudinal stability.

The Ceran® glass-ceramic is colored and is designed for applications in cooker surface panels.

As in glasses, the variability of the composition can be used to design very different sets of properties of glass-ceramics. Some examples are:

- photosensitive, etchable glass-ceramics based on Ag doping: Foturan (Schott), and Fotoform and Fotoceram (Corning);
- machinable glass-ceramics based on mica crystals, for example for electronic packaging: Macor and Dicor (Corning), and Vitronit (Vitron and Jena);
- glass-ceramics used as substrates for magnetic disks, based on spinel or gahnite crystals, resulting in a very high elastic modulus and thus stiffness: Neoceram (NEG), and products from Corning and Ohara;
- glass-ceramics with extremely good weathering properties for architectural applications: Neoparies (NEG) and Cryston (Asahi Glass);
- biocompatible, bioactive glass-ceramics based on apatite and orthophosphate crystals for dental restoration or bone replacement in medicine: Cerabone (NEG), Bioverit (Vitron), Ceravital, IPS Empress, etc.;
- highly transparent glass-ceramics and glass-ceramics with specific dopings for temperature-resistant fiber optic components, high-temperature loaded color filters, and luminescent solar collectors.

An excellent overview and many details can be found in [4.4].

## 3.4.8 Glasses for Miscellaneous Applications

### 3.4.8.1 Sealing Glasses

Glasses are very well suited for the production of mechanically reliable, vacuum-tight fusion seals with metals, ceramics, and mica. Some particularly favorable properties are the viscosity behavior of glass and the direct wettability of many crystalline materials by glasses. As a result, the production technology for such seals is characterized by uncomplicated procedures with few, easily manageable, well-controllable process steps.

A necessary condition for the stability and mechanical strength of glass seals is the limitation of the mechanical stress in the glass component at temperatures encountered during production and use. To ensure "sealability" (which means that the thermal contractions of the two sealing components match each other below the transformation temperature of the glass), glasses of special compositions, called sealing glasses, have been developed. Apart from sealability, such glasses must very often fulfill other requirements such as high electrical insulation or special optical properties. The sealability can be tested and evaluated with sufficient accuracy and certainty by stress-optical measurements in the glass portion of a test seal (ISO 4790).

Apart from characteristic material values such as the coefficient of linear thermal expansion, transformation temperature, and elastic properties, the cooling rate (Fig. 3.4-31) and the shape can also have a considerable influence on the degree and distribution of seal stresses. The material combinations for sealing between metals and ceramics recommended for Schott glasses are shown in Fig. 3.4-32.

#### Types of Sealing Glasses

Sealing glasses may be classified by reference to the expansion coefficients of metals (e.g. tungsten and molybdenum) and alloys (Ni–Fe–Co, Ni–Fe–Cr, and other alloys) with which they are used. Hence sealing

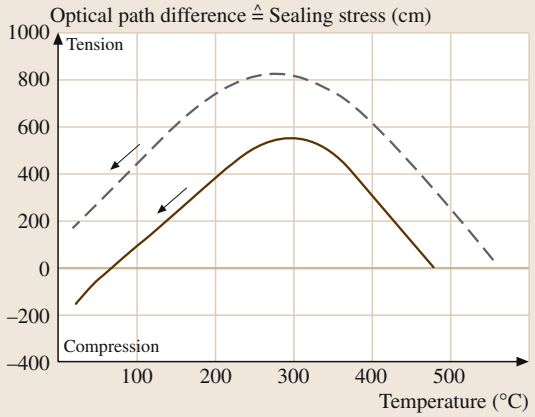


**Fig. 3.4-31** Influence of the cooling rate on the sealing stress in an 8516–Ni/Fe combination. The *lower curve* corresponds to a low cooling rate; the *upper curve* corresponds to a high cooling rate

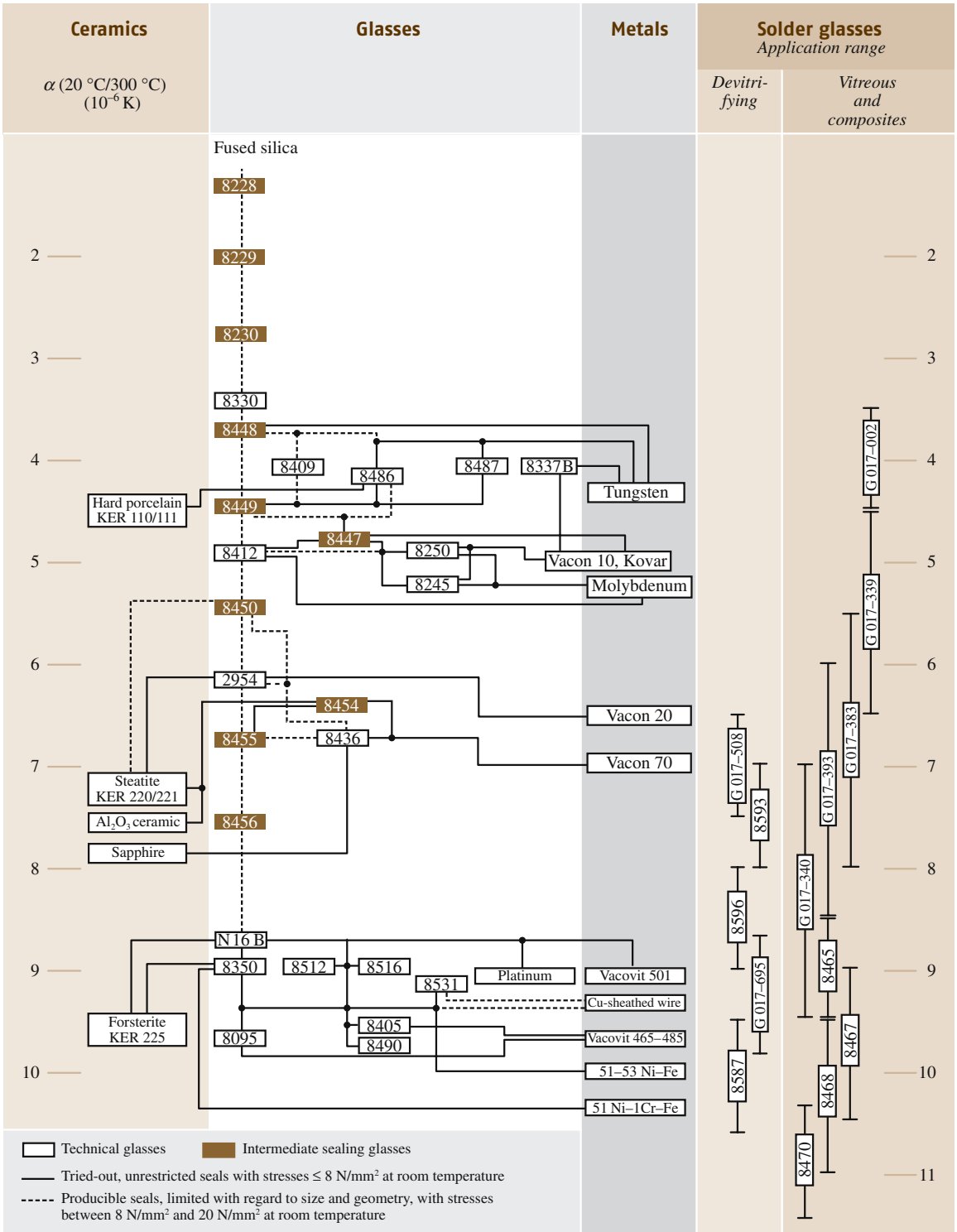


**Fig. 3.4-32** Recommended material combinations for "graded seals"

**Table 3.4-20** Special properties and principal applications of technically important sealing glasses, arranged according to their respective sealing partners

| Metal $\alpha_{20/300}$ ($10^{-6}$/K) | Glass number | Glass characteristics | Principal applications as sealing glass |
|---|---|---|---|
| Tungsten (4.4) | 8486 | Alkaline-earth borosilicate, high chemical resistance, high working temperature. Suprax® | Lamp bulbs |
| | 8487 | High boron content, low melting temperature | Discharge lamps, surge diverters |
| Molybdenum (5.2) | 8412 | Alkaline-earth borosilicate, high chemical resistance. Fiolax® clear | Lamp bulbs |
| | 8253 | Alkaline-earth aluminosilicate glass | Lamp interior structures, lamp bulbs |
| Molybdenum and 28Ni/18Co/Fe (5.1) | 8250 | High boron content, low melting temperature, high electrical insulation, low dielectric losses | Transmitter tubes, image converters, TV receiver tubes |
| | 8245 | High boron content, low melting temperature, low X-ray absorption | X-ray tubes |
| 28Ni/23Co/Fe (7.7) | 8454 | Alkali–alkaline-earth silicate, sealable with steatite and $Al_2O_3$ ceramics | Intermediate sealing glass |
| | 8436 | Alkali–alkaline-earth silicate, sealable with sapphire, resistant to Na vapor and alkalis | Special applications |
| 51Ni/1Cr/Fe (10.2) | 8350 | Soda–lime silicate glass. AR glass | Tubes |
| Cu-sheathed wire ($\alpha_{20/400}$ radial 99, $\alpha_{20/400}$ axial 72) | 8095 | Alkali–lead silicate, high electrical insulation | Lead glass, stem glass for electric lamps and tubes |
| | 8531 | Dense lead silicate, Na- and Li-free, low melting temperature | Low-temperature encapsulation of diodes |
| | 8532 | High electrical insulation | |
| 52–53Ni/Fe (10.2–10.5) | 8512 | Contains FeO for hot forming by IR, lead-free | Reed switches |
| | 8516 | Contains FeO for hot forming by IR, low volatilization, lead-free | Reed switches |

glasses may be referred to as "tungsten sealing glasses", "Kovar glasses", etc. (see Table 3.4-20).

Alkaline-earth borosilicate glasses (8486 and 8412) and aluminosilicate glasses (8252 and 8253) have the necessary sealability and thermal resistance to be particularly suitable for the tungsten and molybdenum seals frequently used in heavy-duty lamps.

Ni–Fe–Co alloys, which often substitute for molybdenum, require that the transformation temperature be limited to 500 °C maximum. Suitable glasses (8250 and 8245) characteristically contain relatively high amounts of $B_2O_3$. These glasses have additional special properties, such as high electrical insulation, low dielectric loss, and low X-ray absorption, and meet the most stringent requirements for vacuum-tube technology and electronic applications.

For Ni–Fe–(Cr) alloys, which are frequently used in technological applications, as well as for copper-sheathed wire, glass groups belonging to the soft-glass category are recommended. Such glasses usually meet

certain special requirements, such as high electrical insulation (e.g. alkali–lead silicate, 8095) or an exceptionally low working temperature (e.g. the dense-lead glasses 8531 and 8532).

FeO-containing glasses (8512 and 8516) are frequently used for hermetic encapsulation of electrical switches and electronic components in an inert gas. Hot forming and sealing are easily achieved by the absorption of IR radiation with an intensity maximum at 1.1 μm wavelength (Fig. 3.4-33). The presence of a proportion of $Fe_2O_3$ makes these glasses appear green. At appropriately high IR intensities, they require considerably shorter processing times than do flame-heated clear glasses.

### Compression Seals

A common feature of all compression seals is that the coefficient of thermal expansion of the external metal part is considerably higher than the thermal expansion coefficients of the sealing glass and the metallic inner partner (conductor). As a result, the glass body is under overall radial pressure after sealing. This prestressing protects the glass body against dangerous mechanical loads. Because the compressive stress of the glass is compensated by a tensile stress in the jacket, the jacket wall must be sufficiently thick (at least 0.5 mm, even for small seals) to be able to permanently withstand such tension. If the thermal expansion of the metallic inner partner is lower than that of the sealing glass, an additional prestressing of the glass body results.

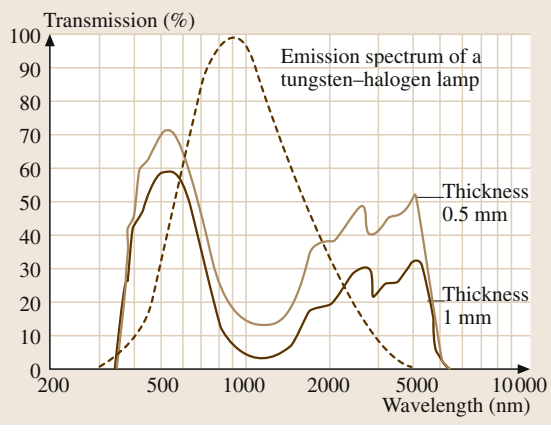


**Fig. 3.4-33** IR absorption of Fe-doped glasses compared with the emission of a tungsten–halogen lamp at 3000 K (in relative units). The transmission of reed glass 8516 with thicknesses 0.5 mm and 1 mm is shown

### Glasses for Sealing to Ceramics

Dielectrically superior, highly insulating ceramics such as hard porcelain, steatite, $Al_2O_3$ ceramics, and forsterite exhaust almost the complete expansion range offered by technical glasses. Hard porcelain can generally be sealed with alkaline-earth borosilicate glasses (for example 8486), which are also compatible with tungsten. Glass seals to $Al_2O_3$ ceramics and steatite are possible with special glasses such as 8454 and 8436, which will also seal to a 28Ni/18Co/Fe alloy. Soft glasses with thermal expansions around $9 \times 10^{-6}$ /K are suitable for sealing to forsterite.

### Intermediate Sealing Glasses

Glasses whose thermal expansion differs so widely from that of the partner component that direct sealing is impossible for reasons of stress must be sealed with intermediate sealing glasses. These glasses are designed in such a way that for the recommended combinations of glasses, the sealing stress does not exceed 20 $N/mm^2$ at room temperature (Table 3.4-21).

## 3.4.8.2 Solder and Passivation Glasses

*Solder glasses* are special glasses with a particularly low softening point. They are used to join glasses to other glasses, ceramics, or metals without thermally damaging the materials to be joined. Soldering is carried out in the viscosity range $10^4$–$10^6$ dPa s of the solder glass; this corresponds to a temperature range $T_{solder} = 350$–$700\,°C$.

One must distinguish between vitreous solder glasses and devitrifying solder glasses, according to their behavior during the soldering process.

Vitreous solder glasses behave like traditional glasses. Their properties do not change during soldering; upon reheating of the solder joint, the temperature dependence of the softening is the same as in the preceding soldering process.

Unlike vitreous solder glasses, devitrifying solder glasses have an increased tendency to crystallize. They change into a ceramic-like polycrystalline state during soldering. Their viscosity increases by several orders of magnitude during crystallization so that further flow is suppressed. An example of this time-dependent viscosity behavior is shown in Fig. 3.4-34 for a devitrifying solder glass processed by a specific temperature–time program. Crystallization allows a stronger thermal reloading of the solder joint, up to the temperature range of the soldering process itself (e.g. glass 8596 has a soldering temperature of approx-

**Table 3.4-21** Intermediate sealing glasses and the combinations of sealing partners in which they are used

| Glass no. | Sealing partners [a] | $\alpha_{20/300}$ ($10^{-6}$ /K) | Transformation temperature $T_g$ (°C) | Temperature at viscosity $10^{13}$ dPa s (°C) | $10^{7.6}$ dPa s (°C) | $10^{4}$ dPa s (°C) | Density $\varrho$ (g/cm$^3$) | $T_{k100}$ (°C) |
|---|---|---|---|---|---|---|---|---|
| **N16B** | KER 250, Vacovit 501, Platinum – N16B, 8456, (Red Line®) | 8.8 | 540 | 540 | 720 | 1045 | 2.48 | 128 |
| **2954** | KER 220, KER 221, Vacon 20 – 2954 | 6.3 | 600 | 604 | 790 | 1130 | 2.42 | 145 |
| **4210** | Iron–4210 | 12.7 | 450 | 455 | 615 | 880 | 2.66 | – |
| **8228** | Fused silica–8228–8229 | 1.3 | ~ 700 | 726 | 1200 | 1705 | 2.15 | 355 |
| **8229** | 8228–8229–8230 | 2.0 | 630 | 637 | 930 | 1480 | 2.17 | 350 |
| **8230** | 8229–8230–8330 | 2.7 | 570 | 592 | 915 | 1520 | 2.19 | 257 |
| **8447** | 8412–8447–Vacon 10 | 4.8 | 480 | 505 | 720 | 1035 | 2.27 | 271 |
| **8448** | 8330–8448–8449, 8486, 8487 | 3.7 | 510 | 560 | 800 | 1205 | 2.25 | 263 |
| **8449** | 8486, 8487 – 8449 – 8447, 8412 | 4.5 | 535 | 550 | 785 | 1150 | 2.29 | 348 |
| **8450** | 8412–8450 – KER 220 2954, 8436 | 5.4 | 570 | 575 | 778 | 1130 | 2.44 | 200 |
| **8454** | KER 221, $Al_2O_3$ – 8454 – Vacon 70 | 6.4 | 565 | 575 | 750 | 1070 | 2.49 | 210 |
| **8455** | 2954, 8436, 8454 – 8455–8456 | 6.7 | 565 | – | 740 | 1030 | 2.44 | – |
| **8456** | 8455–8456 – N16B, 8350 | 7.4 | 445 | – | 685 | 1145 | 2.49 | – |

[a] Type designation of ceramics according to DIN 40685; manufacturer of Vacon alloys Vacuumschmelze Hanau (VAC).

imately 450 °C and a maximum reload temperature of approximately 435 °C).

The development of solder glasses (Table 3.4-22) with very low soldering temperatures is limited by the fact that reducing the temperature generally means increasing the coefficient of thermal expansion. This effect is less pronounced in devitrifying solder glasses. It can be avoided even more effectively by adding inert (nonreacting) fillers with low or negative coefficients of thermal expansion (for example $ZrSiO_4$ or $\beta$-eucryptite). The resulting glasses are called *composite solder glasses*. As a rule, the coefficient of thermal expansion of a solder glass should be smaller than the expansion coefficients of the sealing partners by $\Delta\alpha = 0.5–1.0 \times 10^{-6}$ /K.

Up to their maximum service temperature, solder glasses are moisture- and gas-proof. Their good elec-

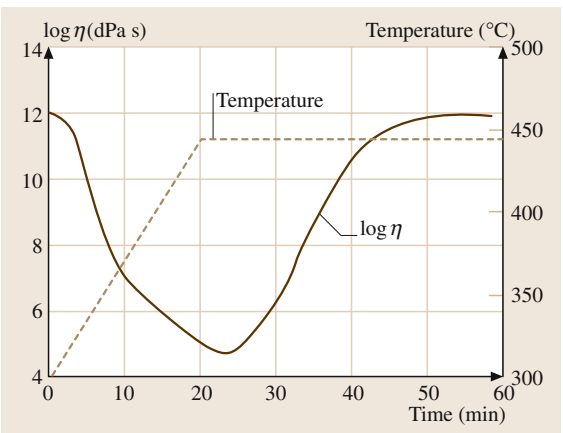


**Fig. 3.4-34** Variation of the viscosity of a crystallizing solder glass during processing

**Table 3.4-22** Schott solder glasses

| Glass number | $\alpha_{(20/300)}$ ($10^{-6}$/K) | $T_g$ (°C) | $T$ at viscosity $10^{7.6}$ dPa s (°C) | Firing conditions $T$ (°C) | Firing conditions $t_{hold}$ (min) | Density $\varrho$ (g/cm$^3$) | $T_{k100}$ (°C) | $\varepsilon_r$ | tan $\delta$ ($10^{-4}$) |
|---|---|---|---|---|---|---|---|---|---|
| **Vitreous and composite solder glasses** | | | | | | | | | |
| G017-002[a] | 3.6 | 540 | 650 | 700 | 15 | 3.4 | – | 6.8 | 37 |
| G017-339[a] | 4.7[b] | 325 | 370 | 450 | 30 | 4.0 | 320 | 11.5 | 19 |
| G017-383[a] | 5.7[b] | 325 | 370 | 430 | 15 | 4.7 | 325 | 13.0 | 15 |
| G017-393[a] | 6.5[b] | 320 | 370 | 425 | 15 | 4.8 | 305 | 11.6 | 15 |
| G017-340[a] | 7.0[b] | 315 | 360 | 420 | 15 | 4.8 | 320 | 13.4 | 14 |
| 8465 | 8.2 | 385 | 460 | 520 | 60 | 5.4 | 375 | 14.9 | 27 |
| 8467 | 9.1 | 355 | 420 | 490 | 60 | 5.7 | 360 | 15.4 | 29 |
| 8468 | 9.6 | 340 | 405 | 450 | 60 | 6.0 | 335 | 16.3 | 31 |
| 8470 | 10.0 | 440 | 570 | 680 | 60 | 2.8 | 295 | 7.7 | 15.5 |
| 8471 | 10.6[b] | 330 | 395 | 440 | 30 | 6.2 | – | 17.1 | 52 |
| 8472 | 12.0[b] | 310 | 360 | 410 | 30 | 6.7 | – | 18.2 | 47 |
| 8474 | 19.0[b] | 325 | 410 | 480 | 30 | 2.6 | 170 | 7.2 | 5 |
| **Devitrifying solder glasses** | | | | | | | | | |
| G017-508 | 6.5 | 365 | – | 530[c] | 60 | 5.7 | 340 | 15.6 | 206 |
| 8593 | 7.7 | 300 | – | 520[c] | 30 | 5.8 | 230 | 21.3 | 260 |
| 8596 | 8.7 | 320 | – | 450[c] | 60 | 6.4 | 280 | 17.4 | 58 |
| G017-695 | 8.9 | 310 | – | 425[c] | 45 | 5.7 | 275 | 15.4 | 54 |
| 8587 | 10.0 | 315 | – | 435[c] | 40 | 6.6 | 265 | 22.1 | 33 |

[a] Composite. [b] $\alpha_{20/250}$. [c] Heating rate 7–10 °C/min.

trical insulating properties are superior to those of many standard technical glasses. They are therefore also suitable as temperature-resistant insulators. The chemical resistance of solder glasses is generally lower than that of standard technical glasses. Therefore, solder glass seals can be exposed to chemically aggressive environments (e.g. acids or alkaline solutions) only for a limited time.

*Passivation glasses* are used for chemical and mechanical protection of semiconductor surfaces. They are generally zinc–borosilicate or lead–alumina–silicate glasses.

To avoid distortion and crack formation, the different coefficients of thermal expansion of the passivation glass and the semiconductor component must be taken into account. If the mismatch is too large, a network of cracks will originate in the glass layer during cooling or subsequent processing and destroy the hermetic protection of the semiconductor surface. There are three ways to overcome this problem:

- A thinner passivation glass layer. Schott recommends a maximum thickness for this layer.
- Slow cooling in the transformation range. As a rough rule, a cooling rate of 5 K/min is suitable for passivation layers in the temperature range $T_g \pm 50$ K.
- Use of composite glasses. Composites can be made with an inert filler such as a powdered ceramic with a very low or negative thermal expansion.

### Properties of Passivation Glasses

The electrical insulation, including the dielectric breakdown resistance, generally depends on the alkali content, particularly the $Na^+$ content. Typical contents are below 100 ppm for $Na_2O$ and $K_2O$, and below 20 ppm for $Li_2O$. Heavy metals which are incompatible with semiconductors are controlled as well. The CuO content, for example, is below 10 ppm.

Because the mobility of charge carriers increases drastically with increasing temperature, a temperature

limit, called the junction temperature $T_j$, is defined up to which glass-passivated components can be used in blocking operations.

Various types of passivation glasses are listed in Table 3.4-23.

### 3.4.8.3 Colored Glasses

In physics, color is a phenomenon of addition or subtraction of parts of the visible spectrum, due to selective absorption or scattering in a material. The light transmission through a sample of thickness $d$ at a wavelength $\lambda$ is described by Lambert's law,

$$\tau_i(\lambda) = \exp\left[-\sum\sum \varepsilon_n(\lambda, c_n, c_m)d\right], \qquad (4.42)$$

where $\varepsilon$ is the extinction coefficient, which depends on the wavelength and the concentration of the active agents. For low concentrations, $\varepsilon$ is additive and proportional to the concentration, and we obtain Beer's law,

$$\tau_i(\lambda) = \exp\left[-\sum \varepsilon_n(\lambda)c_n d\right], \qquad (4.43)$$

where $\varepsilon$ now depends only on the wavelength and the specific species or process $n$. In glasses, the extinction is caused by electronic and phononic processes in the UV and IR regions, respectively, and by absorption and scattering by ions, lattice defects, and colloids and microcrystals in the visible region. Different oxidation states of one atom, for example $Fe^{2+}$ and $Fe^{3+}$, must be treated as different species. Charge transfer and ligand fields are examples of multiatom mechanisms that modify the absorption characteristics. The position of the maximum-extinction peak depends on the refractive index of the base glass; for example, for Ag metal colloids the position of the peak shifts from $\lambda_{max} = 403$ nm in Duran®, with $n_d = 1.47$, to $\lambda_{max} = 475$ nm in SF 56, with $n_d = 1.79$.

**Table 3.4-23** Schott passivation glasses

| Glass number | Type | Typical applications | $\alpha_{(20/300)}$ ($10^{-6}$/K) | $T_g$ (°C) | Pb content (wt%) | Sealing temp. (°C) | Sealing time (min) | $T_j$ (°C) | Layer thickness (µm) |
|---|---|---|---|---|---|---|---|---|---|
| G017-057 | Zn–B–Si | Sintered glass diodes | 4.5 | 546 | 1–5 | 690 | 10 | 180 | – |
| G017-388 | Zn–B–Si composite | Thyristors, high-blocking rectifiers | 3.6 | 550 | 1–5 | 700 | 5 | 180 | ≤ 30 |
| G017-953 | Zn–B–Si composite | | 2.81 | [a] | 1–5 | 770 | 30 | 180 | – |
| G017-058 | Zn–B–Si | Sintered glass diodes | 4.5 | 543 | 1–5 | 690 | 10 | 180 | – |
| G017-002 | Zn–B–Si composite | Sintered glass diodes | 3.7 | 545 | 1–5 | 700 | 10 | 180 | – |
| G017-984 | Zn–B–Si | Stack diodes | 4.6 | 538 | 5–10 | 720 | 10 | 180 | – |
| G017-096R | Pb–B–Si | Sintered glass diodes, planar and mesa diodes | 4.8 | 456 | 10–50 | 680 | 5 | 160 | – |
| G017-004 | Pb–B–Si | Mesa diodes | 4.1 | 440 | 10–50 | 740 | 5 | 160 | ≤ 30 |
| G017-230 | Pb–B–Si composite | Power transistors | 4.2 | 440 | 10–50 | 700 | 5 | 160 | ≤ 25 |
| G017-725 | Pb–B–Si | Sintered glass diodes | 4.9 | 468 | 10–50 | 670 | 10 | 180 | – |
| G017-997 | Pb–B–Si composite | Wafers | 4.4 | 485 | 10–50 | 760 | 20 | 180 | – |
| G017-209 | Pb–Zn–B | ICs, transistors | 6.6 | 416 | 10–50 | 510 | 10 | 180 | ≤ 5 |
| G017-980 | Pb–Zn–B | Varistors | | | 10–50 | | | – | – |
| Vitreous | | | 6.5 | 393 | | 520 | 30 | – | – |
| Devitrified | | | 5.8 | [a] | | 620 | 30 | – | – |
| G018-088 | Pb–Zn–B composite | Varistors | 4.88 | 425 | 10–50 | 560 | 30 | – | – |

[a] Cannot be determined.

Colored glasses are thus technical or optical colorless glasses with the addition of coloring agents. A collection of data can be found in [4.17]. They are widely used as optical filters for various purposes, such as short-pass or long-pass edge filters, or in combinations of two or more elements as band-pass or blocking filters.

Owing to the absorbed energy, inhomogeneous heating occurs (between the front and rear sides, and, especially, in the radial direction), which results in internal stress via the thermal expansion under intense illumination. Precautions have to be taken in the mechanical mounting to avoid breakage. The application temperature $T$ should satisfy the conditions $T \leq T_g - 300\,°C$ in the long term and $T \leq T_g - 250\,°C$ for short periods. Prestressing may be necessary to improve the breaking strength in heavy-load applications.

The Schott filter glasses are classified into groups listed in Table 3.4-24:

**Table 3.4-24** Groups of Schott Filter glasses

| | |
|---|---|
| UG | Black and blue glasses, ultraviolet-transmitting |
| BG | Blue, blue–green, and multiband glasses |
| VG | Green glasses |
| OG | Orange glasses, IR transmitting |
| RG | Red and black glasses, IR-transmitting |
| NG | Neutral glasses with uniform attenuation in the visible |
| WG | Colorless glasses with different cutoffs in the UV, which transmit in the visible and IR |
| KG | Virtually colorless glasses with high transmission in the visible and absorption in the IR (heat protection filters) |
| FG | Bluish and brownish color temperature conversion glasses |

DIN has defined a nomenclature to allow one to see the main optical properties for a reference thickness $d$ from the identification symbol (see Table 3.4-25):
Multiband filters and color conversion filters are not specified by DIN.

### Ionically Colored Glasses

Ions of heavy metals or rare earths influence the color when in true solution. The nature, oxidation state, and quantity of the coloration substance, as well as the type of the base glass, determine the color (Figs. 3.4-35 – 3.4-38, and Table 3.4-26).

**Table 3.4-25** DIN nomenclature for optical filter glasses

| | |
|---|---|
| Band-pass filters | BP $\lambda_{max}/\Delta\lambda_{HW}$, where $\lambda_{max}$ = wavelength of maximum internal transmission, and $\Delta\lambda_{HW}$ = bandwidth at 50% internal transmission. |
| Short-pass filters | KP $\lambda_{50\%}$, where $\lambda_{50\%}$ = cutoff wavelength at 50% internal transmission. |
| Long-pass filters | LP $\lambda_{50\%}$, where $\lambda_{50\%}$ = cutoff wavelength at 50% internal transmission. |
| Neutral-density filters | N $\tau$, where $\tau$ = internal transmission at 546 nm. |

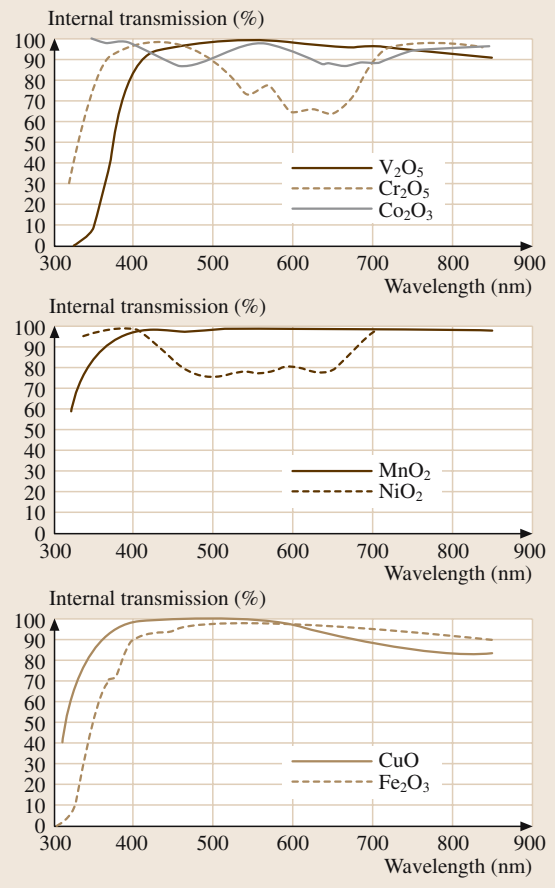


**Fig. 3.4-35** Spectral internal transmission of BK7, colored with various oxides; sample thickness 100 mm

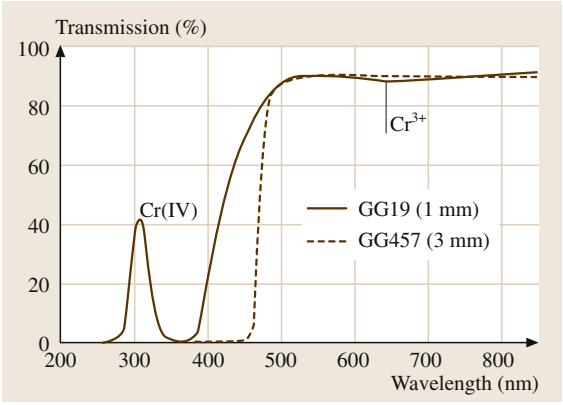


**Fig. 3.4-36** Transmission spectra of yellow glasses

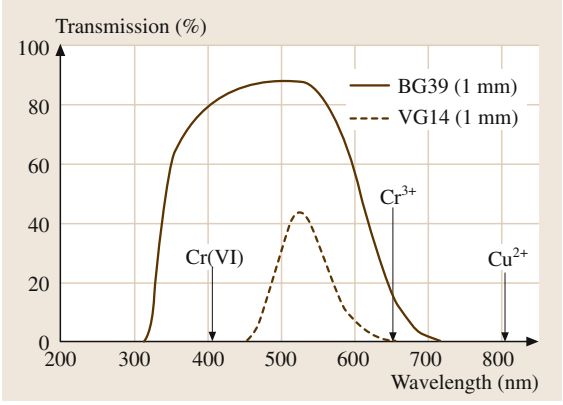


**Fig. 3.4-37** Transmission spectra of blue and green glasses

**Table 3.4-26** Colors of some ions in glasses

| Element | Valency | Color |
|---|---|---|
| Fe | 2+ | Green, sometimes blue |
| Fe | 3+ | Yellowish brown |
| Cu | 2+ | Light blue, turquoise |
| Cr | 3+ | Green |
| Cr | 6+ | Yellow |
| Ni | 2+ | Violet (tetrahedral coordination) |
| Ni | 2+ | Yellow (octahedral coord.) |
| Co | 2+ | Intense blue |
| Co | 3+ | Green |
| Mn | 2+ | Pale yellow |
| Mn | 3+ | Violet |
| V | 3+ | Green (silicate), brown (borate) |
| Ti | 3+ | Violet (reducing melt) |
| Pr | 3+ | Light green |
| Nd | 3+ | Reddish violet |
| Er | 3+ | Pale red |

**Fig. 3.4-39** Transmission spectra of red glasses

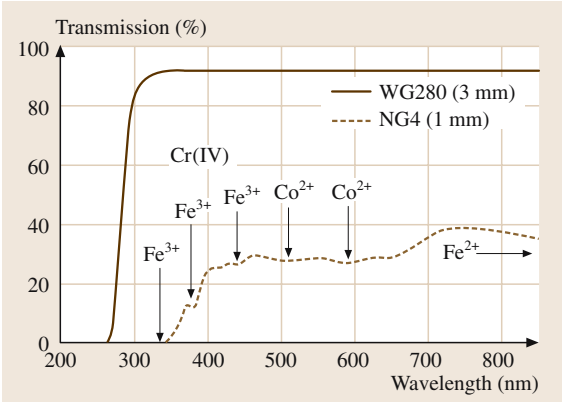


**Fig. 3.4-38** Transmission spectra of gray and white glasses

### Colloidally Colored Glasses

The colorants of these glasses are, in most cases, rendered effective by a secondary heat treatment (striking) of the initially nearly colorless glass. Particularly important glasses of this type are the yellow, orange, red, and black filter glasses, with their steep absorption edges. As with ionic coloration, the color depends on the type and concentration of the additives, on the type of the base glass, and on the thermal history, which determines the number and diameter of the precipitates (Fig. 3.4-39 and Table 3.4-27).

**Table 3.4-27** Colors of some metal colloids

| Element | Peak position (nm) | $n_d$ | Color |
|---|---|---|---|
| Ag | 410 | 1.5 | Yellow |
| Cu | 530–560 | ? | Red |
| Au | 550 | 1.55 | Red |
| Se | 500 | ? | Pink |

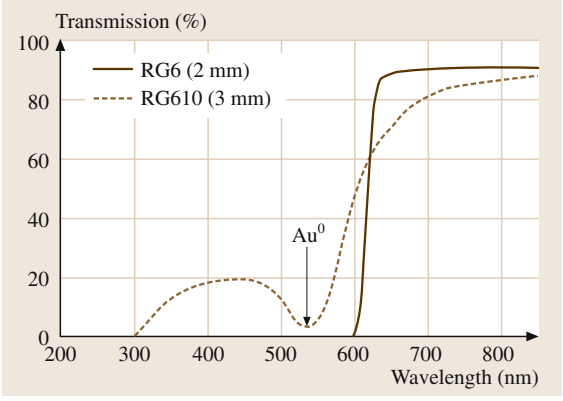

Doping with semiconductors results in microcrystalline precipitates which have band gap energies in the range 1.5–3.7 eV, corresponding to wavelengths in the range 827–335 nm. The preferred materials are ZnS, ZnSe, ZnTe, CdS, CdSe, and CdTe, which also form solid solutions. By mixing these dopants, any cutoff wavelength between 350 nm and 850 nm can be achieved (Table 3.4-30).

### 3.4.8.4 Infrared-Transmitting Glasses

The transmission in the infrared spectral region is limited by phonons and by local molecular vibrations and their overtones. The vibration frequencies decrease with increasing atomic mass. This intrinsic absorption has extrinsic absorption caused by impurities and lattice defects, such as hydroxyl ions, dissolved water, and microcrystals, superimposed on it. An overview can be found in [4.12].

#### Oxide Glasses

The transmission is determined by the vibrations of the common network formers [4.19] (Fig. 3.4-40). The vibrations of the network modifiers are found at longer wavelengths.

The heavy-metal oxide (HMO) glasses are transparent up to approximately 7 µm for a 1 mm thickness. But often they show a strong tendency toward devitrification, which very much limits the glass-forming compositions. The transmission of some commercial glasses is shown in Fig. 3.4-41.

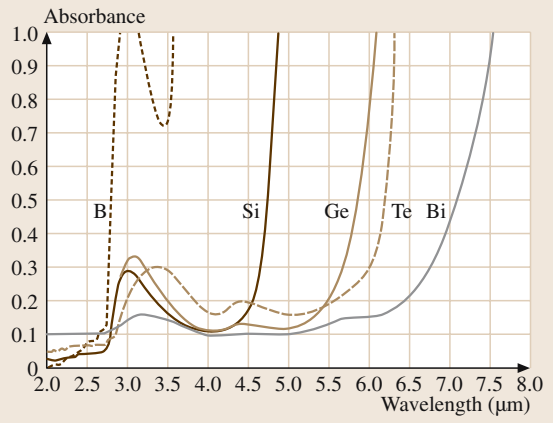


**Fig. 3.4-40** Infrared absorbance of analogous oxide glasses with different network-forming cations [4.18]; sample thickness 1.85 mm, except for Bi, where the thickness was 2.0 mm

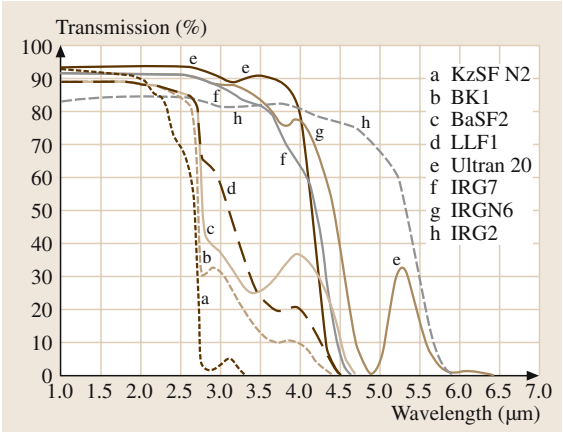


**Fig. 3.4-41** Infrared transmission spectra of some Schott optical and special IR glasses; thickness 2.5 mm. The OH absorption of the glasses may vary owing to differences in the raw materials and the melting process

#### Halide Glasses

These glasses use F, Cl, Br, and I (halogens) as anions instead of oxygen. The transmission range is extended up to approximately 15 µm [4.20]. The oldest halide glasses are $BeF_2$, $ZnCl_2$, and $AlF_3$, which, however, have limited application owing to their toxicity, tendency toward crystallization, and hygroscopic behavior.

Some new glasses use $ZrF_4$, $HfF_4$, and $ThF_4$ as glass formers, and $BaF_2$, $LaF_3$ (heavy-metal flourides, HMFs) as modifiers. They are often named after their cation composition; for example, a glass with a cation composition $Zr_{55}Ba_{18}La_6Al_4Na_{17}$ would be called a ZBLAN glass.

#### Chalcogenide Glasses

These glasses use S, Se, and Te (chalcogens) as anions instead of oxygen. The transmission range is extended up to approximately 30 µm. Stable glass-forming regions are found in the Ge–As–S, Ge–As–Se, and Ge–Sb–Se systems; an example of a commercial glass is $Ge_{30}As_{15}Se_{55}$.

A combination of chalcogenides with halides is found in the TeX glasses, for example $Te_3Cl_2S$ and $Te_2BrSe$.

The main properties of infrared-transmitting glasses are compiled in Tables 3.4-29 and 3.4-30.

**Table 3.4-28** Properties of Schott filter glasses

| Glass type | DIN identification | Reference thickness $d_r$ (mm) | Density $\varrho$ (g/cm$^3$) | Refractive index $n_d$ | Chemical resistance | | | Transformation temperature $T_g$ (°C) | Thermal expansion | | Temp. coeff. $T_K$ (nm/K) |
|---|---|---|---|---|---|---|---|---|---|---|---|
| | | | | | Stain FR | Acid SR | Alkali AR | | $\alpha_{-30/+70\,°C}$ ($10^{-6}$/K) | $\alpha_{20/300\,°C}$ ($10^{-6}$/K) | |
| UG1 | BP 351/78 | 1 | 2.77 | 1.54 | 0 | 1.0 | 1.0 | 603 | 7.9 | 8.9 | – |
| UG5 | BP 318/173 | 1 | 2.85 | 1.54 | 0 | 3.0 | 2.0 | 462 | 8.1 | 9.4 | – |
| UG11 | BP 324/112 + BP 720/57 | 1 | 2.92 | 1.56 | 0 | 3.0 | 2.0 | 545 | 7.8 | 9 | – |
| BG3 | BP 378/185 | 1 | 2.56 | 1.51 | 0 | 1.0 | 1.0 | 478 | 8.8 | 10.2 | – |
| BG4 | BP 378/165 | 1 | 2.66 | 1.53 | 0 | 1.0 | 1.0 | 536 | 7.7 | 9 | – |
| BG7 | BP 466/182 | 1 | 2.61 | 1.52 | 0 | 1.0 | 1.0 | 468 | 8.5 | 19.9 | – |
| BG12 | BP 409/140 | 1 | 2.58 | 1.52 | 0 | 1.0 | 1.0 | 480 | 8.6 | 10.1 | – |
| BG18 | BP 480/250 + KP 605 | 1 | 2.68 | 1.54 | 0 | 2.0 | 2.0 | 459 | 7.4 | 8.8 | – |
| BG20 | Multiband | – | 2.86 | 1.55 | 0 | 1.0 | 1.0 | 561 | 8.3 | 9.3 | – |
| BG23 | BP 459/232 + KP 575 | 1 | 2.37 | 1.52 | 0 | 1.0 | 1.0 | 483 | 8.9 | 10.2 | – |
| BG24A | BP 342/253 | 1 | 2.72 | 1.53 | 0 | 3.0 | 1.0 | 460 | 8.5 | 9.7 | – |
| BG25 | BP 401/156 | 1 | 2.56 | 1.51 | 0 | 1.0 | 1.0 | 487 | 8.7 | 10.1 | – |
| BG26 | – | 1 | 2.56 | 1.51 | 0 | 1.0 | 1.0 | 494 | 8.8 | 10.3 | – |
| BG28 | BP 436/156 + KP 514 | 1 | 2.60 | 1.52 | 0 | 1.0 | 1.0 | 474 | 8.7 | 10 | – |
| BG34 | Color conversion | 2 | 3.23 | 1.59 | 0 | 1.0 | 1.0 | 441 | 9.9 | 10.7 | – |
| BG36 | Multiband | – | 3.62 | 1.69 | 1 | 52.2 | 1.2 | 660 | 6.1 | 7.2 | – |
| BG38 | BP 487/334 + KP 654 | 1 | 2.62 | 1.53 | 0 | 2.0 | 2.0 | 466 | 7.5 | 8.9 | – |
| BG39 | BP 475/269 + KP 609 | 1 | 2.73 | 1.54 | 0 | 5.1 | 3.0 | 321 | 11.6 | 13.1 | – |
| BG40 | BP 482/318 + KP 641 | 1 | 2.67 | 1.53 | 0 | 5.1 | 3.0 | 305 | 11.9 | 13.7 | – |
| BG42 | BP 478/253 + KP 604 | 1 | 2.69 | 1.54 | 0 | 2.0 | 2.0 | 477 | 7.3 | 8.7 | – |
| VG6 | BP 523/160 | 1 | 2.90 | 1.55 | 0 | 1.0 | 1.0 | 470 | 9.1 | 10.6 | – |
| VG9 | BP 530/114 | 1 | 2.87 | 1.55 | 0 | 1.0 | 1.0 | 470 | 9.2 | 10.6 | – |
| VG14 | BP 52487 | 1 | 2.89 | 1.56 | 0 | 1.0 | 1.0 | 470 | 9.2 | 10.6 | – |
| GG385 | LP 385 | 3 | 3.22 | 1.58 | 0 | 2 | 2.3 | 459 | 7.7 | 8.8 | 0.07 |
| GG395 | LP 395 | 3 | 3.61 | 1.62 | 0 | 1 | 2.3 | 438 | 7.7 | 8.6 | 0.08 |
| GG400 | LP 400 | 3 | 2.75 | 1.54 | 3 | 4.4 | 1.0 | 595 | 9.6 | 10.5 | 0.07 |
| GG420 | LP 420 | 3 | 2.76 | 1.54 | 3 | 4.4 | 1.0 | 586 | 9.6 | 10.5 | 0.07 |

**Table 3.4-28** Properties of Schott filter glasses, cont.

| | | | | | | | | | | | |
|---|---|---|---|---|---|---|---|---|---|---|---|
| GG435 | LP 435 | 3 | 2.75 | 1.54 | 3 | 4.4 | 1.0 | 605 | 9.5 | 10.5 | 0.07 |
| GG455 | LP 455 | 3 | 2.75 | 1.54 | 3 | 4.4 | 1.0 | 600 | 9.7 | 10.5 | 0.08 |
| GG475 | LP 475 | 3 | 2.75 | 1.54 | 3 | 4.4 | 1.0 | 594 | 9.8 | 10.6 | 0.09 |
| GG495 | LP 495 | 3 | 2.75 | 1.54 | 3 | 4.4 | 1.0 | 600 | 9.6 | 10.6 | 0.10 |
| OG515 | LP 515 | 3 | 2.76 | 1.54 | 3 | 4.4 | 1.0 | 597 | 9.7 | 10.6 | 0.11 |
| OG530 | LP 530 | 3 | 2.75 | 1.54 | 3 | 4.4 | 1.0 | 595 | 9.7 | 10.6 | 0.12 |
| OG550 | LP 550 | 3 | 2.75 | 1.54 | 3 | 4.4 | 1.0 | 597 | 9.6 | 10.7 | 0.13 |
| OG570 | LP 570 | 3 | 2.75 | 1.54 | 3 | 4.4 | 1.0 | 596 | 9.7 | 10.7 | 0.14 |
| OG590 | LP 590 | 3 | 2.75 | 1.54 | 3 | 4.4 | 1.0 | 599 | 9.8 | 10.6 | 0.15 |
| RG9 | BP 885307 + LP 731 | 3 | 2.76 | 1.54 | 3 | 4.4 | 1.0 | 581 | 9.8 | 10.7 | 0.07 |
| RG610 | LP 610 | 3 | 2.75 | 1.54 | 3 | 4.4 | 1.0 | 595 | 9.8 | 10.7 | 0.16 |
| RG630 | LP 630 | 3 | 2.76 | 1.54 | 3 | 4.4 | 1.0 | 597 | 9.6 | 10.7 | 0.17 |
| RG645 | LP 645 | 3 | 2.76 | 1.54 | 3 | 4.4 | 1.0 | 597 | 9.6 | 10.7 | 0.17 |
| RG665 | LP 665 | 3 | 2.75 | 1.54 | 3 | 4.4 | 1.0 | 592 | 9.8 | 10.8 | 0.17 |
| RG695 | LP 695 | 3 | 2.76 | 1.54 | 3 | 3 | 1.0 | 599 | 9.6 | 10.6 | 0.18 |
| RG715 | LP 715 | 3 | 2.75 | 1.54 | 3 | 3 | 1.0 | 589 | 9.8 | 10.7 | 0.18 |
| RG780 | LP 780 | 3 | 2.9 | 1.56 | 5 | 52.4 | 1.0 | 571 | 9.7 | 10.7 | 0.22 |
| RG830 | LP 830 | 3 | 2.94 | 1.56 | 5 | 53.4 | 1.0 | 569 | 9.5 | 10.5 | 0.23 |
| RG850 | LP 850 | 3 | 2.93 | 1.56 | 5 | 53.4 | 1.0 | 571 | 9.5 | 10.5 | 0.24 |
| RG1000 | LP 1000 | 3 | 2.75 | 1.55 | 0 | 1 | 1.2 | 478 | 9.2 | 9.9 | 0.38 |
| NG1 | N 10-4 | 1 | 2.49 | 1.52 | 1 | 2.2 | 1.0 | 466 | 6.6 | 7.2 | – |
| NG3 | N 0.09 | 1 | 2.44 | 1.51 | 1 | 2.2 | 1.0 | 462 | 6.5 | 7.3 | – |
| NG4 | N 0.27 | 1 | 2.43 | 1.51 | 1 | 3.2 | 2.0 | 483 | 6.7 | 7.2 | – |
| NG5 | N 0.54 | 1 | 2.43 | 1.5 | 1 | 3.2 | 2.0 | 474 | 6.6 | 7.3 | – |
| NG9 | N 0.04 | 1 | 2.44 | 1.51 | 1 | 3.2 | 2.0 | 487 | 6.4 | 7.3 | – |
| NG10 | N 0.004 | 1 | 2.47 | 1.52 | 1 | 3.2 | 2.0 | 468 | 6.4 | 7.2 | – |
| NG11 | N 0.72 | 1 | 2.42 | 1.5 | 1 | 3.4 | 2.0 | 473 | 6.9 | 7.5 | – |
| NG12 | N 0.89 | 1 | 2.34 | 1.49 | 4 | 51.4 | 2.0 | 460 | 5.9 | 6.4 | – |
| WG225 | LP 225 | 2 | 2.17 | 1.47 | 3 | 51.3 | 3.3 | 437 | 3.8 | 4.1 | 0.02 |
| WG280 | LP 280 | 2 | 2.51 | 1.52 | 0 | 1 | 2.0 | 563 | 7.0 | 8.3 | 0.04 |
| WG295 | LP 295 | 2 | 2.51 | 1.52 | 0 | 1 | 2.0 | 557 | 7.1 | 8.3 | 0.06 |
| WG305 | LP 305 | 2 | 2.59 | 1.52 | 0 | 1 | 1.0 | 546 | 8.2 | 9.6 | 0.06 |
| WG320 | LP 320 | 2 | 3.22 | 1.58 | 0 | 1 | 2.3 | 413 | 9.1 | 10.6 | 0.06 |
| KG1 | KP 751 | 2 | 2.53 | 1.52 | 0 | 2.0 | 3.0 | 599 | 5.3 | 6.1 | – |
| KG2 | KP 814 | 2 | 2.52 | 1.51 | 0 | 2.0 | 3.0 | 605 | 5.4 | 6.3 | – |
| KG3 | KP 708 | 2 | 2.52 | 1.51 | 0 | 2.0 | 4.0 | 581 | 5.3 | 6.1 | – |
| KG4 | KP 868 | 2 | 2.53 | 1.51 | 0 | 2.0 | 3.0 | 613 | 5.4 | 6.2 | – |
| KG5 | KP 689 | 2 | 2.53 | 1.51 | 0 | 3.0 | 4.0 | 565 | 5.4 | 6.2 | – |
| FG3 | Color conversion | 2 | 2.37 | 1.5 | 0 | 1.0 | 1.0 | 564 | 5.4 | 6 | – |
| FG13 | Color conversion | 2 | 2.78 | 1.56 | 1 | 3.4 | 1.0 | 556 | 9.6 | 10.5 | – |

**Table 3.4-29** Property ranges of various infrared-transmitting glass types

| Glass type | Transparency range[a] (μm) | Refractive index $n_d$ | Abbe value $\nu_d$ | Thermal expansion $\alpha$ ($10^{-6}$/K) | Microhardness HV | Transformation temperature $T_g$ (°C) | Density $\varrho$ (g/cm$^3$) |
|---|---|---|---|---|---|---|---|
| Fused silica | 0.17–3.7 | 1.46 | 67 | 0.51 | 800 | 1075 | 2.2 |
| Oxide glasses | 0.25–6.0 | 1.45–2.4 | 20–100 | 3–15 | 330–700 | 300–700 | 2–8 |
| Fluorophosphate glasses | 0.2–4.1 | 1.44–1.54 | 75–90 | 13–17 | – | 400–500 | 3–4 |
| Fluoride glasses | 0.3–8.0 | 1.44–1.60 | 30–105 | 7–21 | 225–360 | 200–490 | 2.5–6.5 |
| Chalcogenide glasses | 0.7–25 | 2.3–3.1[b] | 105–185[c] | 8–30 | 100–270 | 115–370 | 3.0–5.5 |

[a] 50% internal transmission for 5 mm path length.
[b] Infrared refractive index at 10 μm.
[c] Infrared Abbe value $\nu_{8-12} = (n_{10} - 1)/(n_8 - n_{12})$.

**Table 3.4-30** Commercial infrared-transmitting glasses

| Glass type | Glass name | Transparency range[a] (μm) | Refractive index $n$ | Density $\varrho$ (g/cm$^3$) | Thermal expansion $\alpha$ ($10^{-6}$/K) | Transformation temperature $T_g$ (°C) | Manufacturer |
|---|---|---|---|---|---|---|---|
| Fused silica | $SiO_2$ | 0.17–3.7 | 1.4585[b] | 2.20 | 0.51 | 1075 | Corning, Heraeus, General Electric, Quartz et Silice, Schott Lithotec |
| Silicates | IRG7 | 0.32–3.8 | 1.5644[b] | 3.06 | 9.6 | 413 | Schott |
| | IRG15 | 0.28–4.0 | 1.5343[b] | 2.80 | 9.3 | 522 | Schott |
| | IRG3 | 0.40–4.3 | 1.8449[b] | 4.47 | 8.1 | 787 | Schott |
| Fluorophosphate | IRG9 | 0.36–4.2 | 1.4861[b] | 3.63 | 16.1 | 421 | Schott |
| Ca aluminate | 9753[c] | 0.40–4.3 | 1.597[d] | 2.80 | 6.0 | 830 | Corning |
| | IRG N6[c] | 0.35–4.4 | 1.5892[b] | 2.81 | 6.3 | 713 | Schott |
| | WB37A[c] | 0.38–4.7 | 1.669[b] | 2.9 | 8.3 | 800 | Sasson |
| | VIR6 | 0.35–5.0 | 1.601[b] | 3.18 | 8.5 | 736 | Corning France |
| | IRG11 | 0.38–5.1 | 1.6809[b] | 3.12 | 8.2 | 800 | Schott |
| | BS39B | 0.40–5.1 | 1.676[b] | 3.1 | 8.4 | – | Sasson |
| Germanate | 9754 | 0.36–5.0 | 1.664[b] | 3.58 | 6.2 | 735 | Corning |
| | VIR3 | 0.49–5.0 | 1.869[b] | 5.5 | 7.7 | 490 | Corning France |
| | IRG2 | 0.38–5.2 | 1.8918[b] | 5.00 | 8.8 | 700 | Schott |
| Heavy-metal oxide | EO | 0.5–5.8 | 2.31[d] | 8.2 | 11.1 | 320 | Corning |
| Heavy-metal fluoride | ZBLA | 0.30–7.0 | 1.5195[b] | 4.54 | 16.8 | 320 | Verre Fluoré |
| | Zirtrex | 0.25–7.1 | 1.50[b] | 4.3 | 17.2 | 260 | Galileo |
| | HTF-1 | 0.22–8.1 | 1.517[d] | 3.88 | 16.1 | 385 | Ohara |

**Table 3.4-30** Commercial infrared-transmitting glasses, cont.

| Glass type | Glass name | Transparency range[a] (μm) | Refractive index $n$ | Density $\varrho$ (g/cm$^3$) | Thermal expansion $\alpha$ ($10^{-6}$/K) | Transformation temperature $T_g$ (°C) | Manufacturer |
|---|---|---|---|---|---|---|---|
| Chalcogenide | AMTIR1 | 0.8–12 | 2.5109[e] | 4.4 | 12 | 362 | Amorph. Materials |
| | IG1.1 | 0.8–12 | 2.4086[e] | 3.32 | 24.6 | 150 | Vitron |
| | AMTIR3 | 1.0–13 | 2.6173[e] | 4.7 | 13.1 | 278 | Amorph. Materials |
| | IG6 | 0.9–14 | 2.7907[e] | 4.63 | 20.7 | 185 | Vitron |
| | IG2 | 0.9–15 | 2.5098[e] | 4.41 | 12.1 | 368 | Vitron |
| | IG3 | 1.4–16 | 2.7993[e] | 4.84 | 13.4 | 275 | Vitron |
| | $As_2S_3$ | 1.0–16 | 2.653[e] | 4.53 | 30 | 98 | Corning France |
| | IG5 | 1.0–16 | 2.6187[e] | 4.66 | 14.0 | 285 | Vitron |
| | IG4 | 0.9–16 | 2.6183[e] | 4.47 | 20.4 | 225 | Vitron |
| | 1173 | 0.9–16 | 2.616[e] | 4.67 | 15 | 300 | Texas Instruments |

[a] 50% internal transmission for 5 mm path length.
[b] Refractive index at 0.587 μm.
[c] This glass contains $SiO_2$.
[d] Refractive index at 0.75 μm.
[e] Refractive index at 5 μm.



## References


4.1 S. R. Elliott: *Physics of Amorphous Materials* (Longman, Harlow 1990)
4.2 H. Bach, D. Krause (Eds.): *Analysis of the Composition and Structure of Glass and Glass Ceramics* (Springer, Berlin, Heidelberg 1999) 2nd printing
4.3 H. Bach (Ed.): *Low Thermal Expansion Glass Ceramics* (Springer, Berlin, Heidelberg 1995)
4.4 W. Höland, G. Beall: *Glass Ceramic Technology* (American Ceramic Society, Westerville 2002)
4.5 N. P. Bansal, R. H. Doremus: *Handbook of Glass Properties* (Academic Press, Orlando 1986)
4.6 O. V. Mazurin, M. V. Streltsina, T. P. Shvaiko-Shvaikovskaya: *Handbook of Glass Data*, Part A, *Silica Glass and Binary Silicate Glasses*; Part B, *Single Component and Binary Non-silicate Oxide Glasses*; Part C, *Ternary Silicate Glasses*, Physical Sciences Data Series, Vol. 15, (Elsevier, Amsterdam 1983–1987)
4.7 R. Blachnik (Ed.): *Taschenbuch für Chemiker und Physiker*, D'Ans-Lax, Vol. 3, 4th edn. (Springer, Berlin, Heidelberg 1998)
4.8 *MDL SciGlass*, Version 4.0 (Elsevier, Amsterdam)
4.9 *INTERGLAD* (International Glass Database), Version 5, New Glass Forum
4.10 S. English, W. E. S. Turner: Relationship between chemical composition and the thermal expansion of glasses, J. Am. Ceram. Soc. **10**, 551 (1927); J. Am. Ceram. Soc. **12** (1929) 760
4.11 A. Paul: *Chemistry of Glasses* (Chapman and Hall, New York 1982)
4.12 H. Bach, N. Neuroth (Eds.): *The Properties of Optical Glass*, Schott Series on Glass and Glass Ceramics, 2nd printing (Springer, Berlin, Heidelberg 1998)
4.13 A. Winckelmann, F. O. Schott: Über thermische Widerstandskoeffizienten verschiedener Gläser in ihrer Abhängigkeit von der chemischen Zusammensetzung, Ann. Phys. (Leipzig) **51**, 730–746 (1894)
4.14 H. Scholze: *Glass* (Vieweg, Braunschweig 1965)
4.15 Schott: *Schott Technical Glasses* (Schott Glas, Mainz 2000)
4.16 H. R. Philipp: Silicon dioxide ($SiO_2$) (glass). In: *Handbook of Optical Constants of Solids*, ed. by E. D. Palik (Academic Press, New York 1985) pp. 749–763
4.17 C. R. Bamford: *Colour Generation and Control in Glass* (Elsevier, Amsterdam 1977)
4.18 W. H. Dumbaugh: Infrared-transmitting oxide glasses, Proc. SPIE **618**, 160–164 (1986)
4.19 N. Neuroth: Zusammenstellung der Infrarotspektren von Glasbildnern und Gläsern, Glastechn. Ber. **41**, 243–253 (1968)
4.20 J. Lucas, J.-J. Adam: Halide glasses and their optical properties, Glastechn. Ber. **62**, 422–440 (1989)
W. Vogel: *Glass Chemistry* (Springer, Berlin, Heidelberg 1994)

# Part 4 Functional

## Part 4 Functional Materials


**1 Semiconductors**
Werner Martienssen, Frankfurt/Main, Germany

**2 Superconductors**
Claus Fischer, Dresden, Germany
Günter Fuchs, Dresden, Germany
Bernhard Holzapfel, Dresden, Germany
Barbara Schüpp-Niewa, Dresden, Germany
Hans Warlimont, Dresden, Germany

**3 Magnetic Materials**
Hideki Harada, Higashikaya, Fukaya, Saitama, Japan
Manfred Müller, Dresden, Germany
Hans Warlimont, Dresden, Germany

**4 Dielectrics and Electrooptics**
Gagik G. Gurzadyan, Garching, Germany
Pancho Tzankov, Berlin, Germany

**5 Ferroelectrics and Antiferroelectrics**
Toshio Mitsui, Takarazuka, Japan

# 4.1. Semiconductors



The organization of this section follows a two-step approach. The first step corresponds to searching for the substance of interest, that is, the relevant group of substances. The second step corresponds to the physical property of interest.

This section has three subsections, characterized by the groups of the Periodic Table that the constituent elements belong to. The first subsection, Sect. 4.1.1, deals with the elements of Group IV of the Periodic Table and semiconducting binary compounds between elements of this group (IV–IV compounds). The second subsection, Sect. 4.1.2, treats the semiconducting binary compounds between the elements of Groups III and V (III–V compounds); Sect. 4.1.3 treats compounds between the elements of Groups II and VI (II–VI compounds). These two subsections are subdivided further according to the first element in the formula of the compound.

The elements and compounds treated in Sect. 4.1.1 (Group IV and IV–IV compounds) are treated as one group; the data in the tables are given for the whole group in all cases. In Sects. 4.1.2 (III–V compounds) and 4.1.3 (II–VI compounds), data are given separately for each subdivision of those subsections.

For each group of substances, the physical properties are organized into four classes. These are

A. Crystal structure, mechanical and thermal properties.
B. Electronic properties.
C. Transport properties.
D. Electromagnetic and optical properties.

These property classes, finally, are subdivided into individual properties, which are described in the text, tables, and figures.


4.1.1 **Group IV Semiconductors and IV–IV Compounds** ..... 578

4.1.2 **III–V Compounds** ..... 604
4.1.2.1 Boron Compounds ..... 604
4.1.2.2 Aluminium Compounds ..... 610
4.1.2.3 Gallium Compounds ..... 621
4.1.2.4 Indium Compounds ..... 638

4.1.3 **II–VI Compounds** ..... 652
4.1.3.1 Beryllium Compounds ..... 652
4.1.3.2 Magnesium Compounds ..... 655
4.1.3.3 Oxides of Ca, Sr, and Ba ..... 660
4.1.3.4 Zinc Compounds ..... 665
4.1.3.5 Cadmium Compounds ..... 676
4.1.3.6 Mercury Compounds ..... 686

**References** ..... 691

This section deals with the physical properties of semiconductors. Semiconductors are substances which, like metals, are electronic conductors. In contrast to metals, however, the density of freely mobile charge carriers in semiconductors is, under normal conditions, smaller by orders of magnitude than it is in metals. Therefore, in semiconductors, a *small change* in the absolute value of the charge carrier density can induce a *large relative change* in this carrier density and in the electrical conductivity. In metals, on the other hand, the carrier density is so high from the beginning that it is practically impossible to produce a reasonable relative change by small changes of the absolute value of the carrier density. In conclusion, we can say that in semiconductors, and only in semiconductors, is it possible to *manipulate* the electronic conduction by small changes of the carrier density.

Such changes can be effected by a number of techniques, for instance by chemical doping, by temperature changes, by the application of an electric field, or by light. The electronic conductivity of a semiconductor can be changed *intentionally* by these techniques by orders of magnitude; some techniques allow stationary changes, and some techniques also allow time-dependent changes on a very short timescale.

Semiconducting materials are functional materials thanks to the above properties: they can be used as very small, robust, energy-efficient devices to control the current in electrical networks, either on the basis of external driving or on the basis of their internal, tailor-made device characteristics.

During the last 50 years, a tremendous amount of knowledge and experience has been collected worldwide in research and development laboratories in the field of semiconductor physics, semiconductor engineering, and semiconductor chemistry. During this time, semiconductor technology laid the foundations for the development of data processing and of communication technology and, more generally, for the establishment of the information society. Today, semiconductor technology is a basic technology of our economy, business practice, and daily life with its modern comforts.

We can give an account of only a very small part of the empirical knowledge about semiconductors in this Handbook. Thus, a very limited selection of semiconducting substances and of physical properties is treated here. Only three major groups of substances are considered. These are, first, the elements of the fourth group of the Periodic Table, C, Si, Ge, and Sn, and binary compounds between these (IV–IV compounds); second, binary compounds between one element from the third group of the Periodic Table, namely B, Al, Ga, or In, and one element from the fifth group of the Periodic Table, N, P, As, or Sb, the so-called III–V semiconductors; and third, binary compounds between one element from the second group of the Periodic Table, namely Mg, Ca, Sr, Ba, Zn, Cd, or Hg, and one element from the sixth group of the Periodic Table O, S, Se, or Te, the so-called II–VI semiconductors.

In fact, these three major groups form a kind of basic set for the physical understanding of semiconductor phenomena and for the wide field of semiconductor applications. It has to be kept in mind, however, that ternary and higher compounds play a very important role in many semiconductor applications and, furthermore, that a large number of semiconducting substances containing elements other than those mentioned above have been developed for special applications.

The limited number of pages of this Handbook has forced us, furthermore, to be even more restrictive with regard to the properties of semiconductors, which are considered as being of first-order importance for this data collection. So, semiconductor chemistry is beyond the scope of this Handbook. The very broad and important field of semiconductor technology could not be included at all. Also, the wide field of the influence of chemical doping, impurities, and defects on the properties of semiconductors had to be left out. The Handbook's emphasis is on the physical properties of a restricted number of most important pure semiconducting materials.

All the data have been compiled from Landolt–Börnstein, *Numerical Data and Functional Relationships in Science and Technology*, New Series, Group III, Vol. 41, *Semiconductors*, published in eight subvolumes between 1998 and 2003 [1.1].

The CD-ROM and the online version of the Landolt–Börnstein volume present a completely revised and supplemented version of the older Landolt–Börnstein volumes III/17 and III/22 on semiconductors. The printed edition of Vol. III/41 contains only a supplement to the earlier Volumes III/17 and III/22, but nevertheless the printed version of Vol. III/41 extends to more than 4000 pages in the eight subvolumes. If, in addition to the data in this Handbook, further or more detailed information is needed, the reader is recommended to consult [1.1].

Only a very restricted number of references is given in this chapter to the original publications in journals.

A very large number of references to all the original papers are given, however, in the Landolt–Börnstein volume mentioned above [1.1] (see also [1.2]).

The data are presented mainly in tables, which always cover data concerning one or a few related properties for a full group of substances. It is felt that this synoptic presentation will provide an immediate overview of the data for the group of substances. This might be especially helpful if one is interested in development or modeling of materials.

In many cases, functional relationships, in particular temperature dependences, are of the utmost importance in condensed-matter physics and materials science. Therefore a large number of figures have been included, in addition to short sections of text and the numerical data in the tables. Figures in the form of graphs allow one to see the general features of a functional relationship at a glance; they also, of course, present information in a very condensed form.

The physical properties of semiconductors treated in this section are the following:

A. Crystal structure, mechanical and thermal properties:

- Crystal structure (space group, crystal system, and structure type) (tables and figures).
- Lattice parameters $a$ and $c$, given in nm.
- Density $\varrho$, given in $\mathrm{g/cm^3}$.
- Elastic constants $c_{ik}$, given in GPa.
- Melting point $T_\mathrm{m}$, given in K.
- Temperature dependence of the lattice parameters, i. e. the functional relationships $a(T)$ and $c(T)$.
- Linear thermal expansion coefficient $\alpha$, given in $10^{-6}\,\mathrm{K^{-1}}$.
- Heat capacity $c_p$, given in J/mol K.
- Debye temperature $\Theta_\mathrm{D}$, given in K.
- Phonon wavenumbers $\tilde{\nu}$, frequencies $\nu$, energies $E_\mathrm{phon}$ at symmetry points, given in $\mathrm{cm^{-1}}$, THz, and eV, respectively.
- Phonon dispersion relations, i. e. wavenumber $\bar{\nu}$ versus wave vector $\boldsymbol{q}$.

B. Electronic properties:

- First Brillouin zone (figures).
- Band structure (text and figures).
- Energy gap, given in eV.
- Exciton binding energies, given in eV.
- Spin–orbit splitting energies, given in eV.
- Effective masses, in units of the electron mass $m_0$.
- $g$-factor $g_\mathrm{c}$ of conduction electrons.

C. Transport properties:

- Electronic transport, general description.
- Intrinsic carrier concentrations, $n$ and $p$, given in $\mathrm{cm^{-3}}$.
- Electrical conductivity $\sigma$, given in $\Omega^{-1}\,\mathrm{cm^{-1}}$.
- Electron and hole mobilities $\mu_\mathrm{n}$ and $\mu_\mathrm{p}$, given in $\mathrm{cm^2/V\,s}$.
- Thermal conductivity, given in W/cm K.

D. Electromagnetic and optical properties:

- Dielectric constant $\varepsilon$.
- Refractive index $n$.
- Spectral dependence of the optical constants (tables and figures).

The data given in this Handbook, if not stated otherwise, are numerical data valid at room temperature (RT) and at normal pressure (100 kPa). If the material crystallizes in different modifications, the data given, if not stated otherwise, concern the phase which is stable under normal conditions (i. e. RT and 100 kPa).

# 4.1.1 Group IV Semiconductors and IV–IV Compounds

## A. Crystal Structure, Mechanical and Thermal Properties

Tables 4.1-1 – 4.1-10.

**Table 4.1-1** Crystal structures of Group IV semiconductors and IV–IV compounds

| Crystal | | Space group | | Crystal system | Structure type | Figure |
|---|---|---|---|---|---|---|
| Diamond | C | $O_h^7$ | $Fd3m$ | fcc | Diamond | Fig. 4.1-1 |
| Silicon | Si | $O_h^7$ | $Fd3m$ | fcc | Diamond | Fig. 4.1-1 |
| Germanium | Ge | $O_h^7$ | $Fd3m$ | fcc | Diamond | Fig. 4.1-1 |
| Gray tin[a] | $\alpha$-Sn | $O_h^7$ | $Fd3m$ | fcc | Diamond | Fig. 4.1-1 |
| Silicon carbide[b] | 3C-SiC [c] | $T_d^2$ | $F\bar{4}3m$ | fcc | Zinc blende | Fig. 4.1-2 |
| | 2H-SiC [c] | $C_{6v}^4$ | $P6_3mc$ | Hexagonal | Wurtzite | Fig. 4.1-3 |
| Silicon–germanium alloys [d] | | $O_h^7$ | $Fd3m$ | fcc | Diamond | Fig. 4.1-1 |

[a] Below 290 K (17 °C) and at ambient pressure.

[b] Silicon carbide is said to be polytypic because it crystallizes in more than one hundred different modifications. This is due to the small energy differences between the different structures.

[c] The labels "3C", "2H", etc. indicate the stacking order along the $c$ axis in a hexagonal system; the cubic form can be considered as fitting into this system by taking the [111] direction as the "$c$ axis".

[d] Silicon and germanium form a continuous series of solid solutions with gradually varying properties.

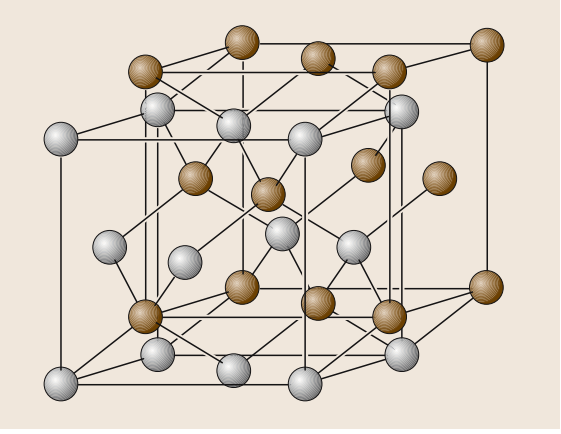

**Fig. 4.1-1** The diamond lattice. The elementary cubes of the two face-centered cubic lattices are shown. In the diamond lattice all the atoms in the two elementary cubes are identical, they are atoms from the same chemical element. Each atom in this lattice is surrounded tetrahedrally by four nearest neighbour atoms

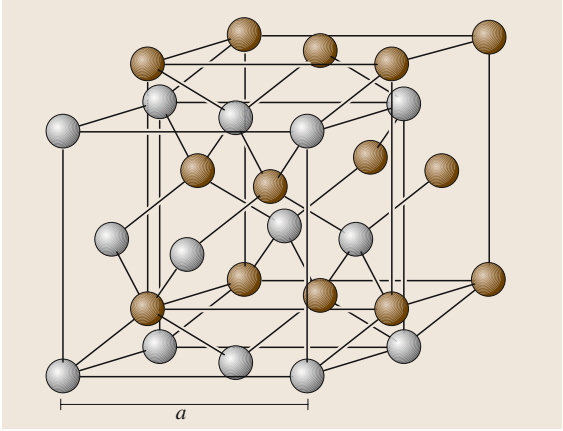


**Fig. 4.1-2** The zinc blende lattice ($a$ is the lattice parameter). This is a diamond lattice in which the two elementary cubes are occupied by different atomic species, for example by Zn-ions and by S-ions of opposite charge. Each Zn-ion is surrounded tetrahedrally by four nearest neighbour S-atoms and vice versa

**Table 4.1-2** Lattice parameters of Group IV semiconductors and IV–IV compounds

| Crystal | | Lattice parameters (nm) | Temperature (K) | Remarks |
|---|---|---|---|---|
| Diamond | C | $a = 0.356685$ | 298 | X-ray diffraction |
| Silicon | Si | $a = 0.543102018\ (34)$ | 295.7 | High-purity single crystal, vacuum |
| Germanium | Ge | $a = 0.56579060$ | 298.15 | Single crystal |
| Gray tin | $\alpha$-Sn | $a = 0.64892\ (1)$ | 293.15 | X-ray diffraction |
| Silicon carbide | 3C-SiC | $a = 0.43596$ | 297 | Debye–Scherrer method |
| | 2H-SiC | $a = 0.30763\ (10)$ | 300 | Laue and Weissenberg patterns |
| | | $c = 0.50480\ (10)$ | | |
| Silicon–germanium alloys | | There is a small deviation from Vegard's law (Fig. 4.1-4) | | |

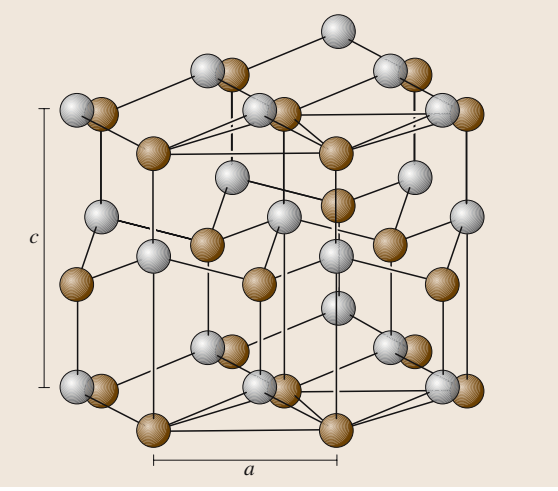


**Fig. 4.1-3** The wurtzite lattice ($a$ and $c$ are the lattice parameters)

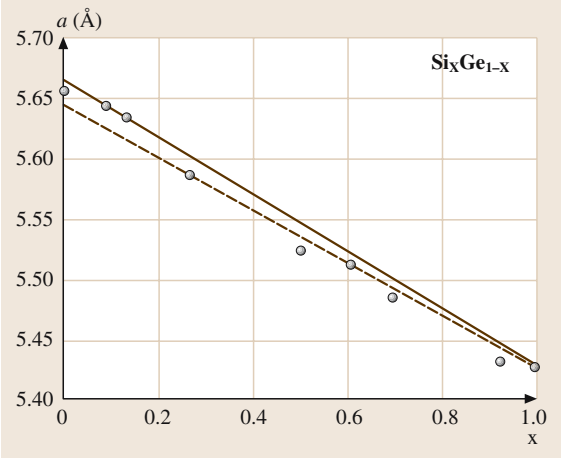


**Fig. 4.1-4** $Si_xGe_{1-x}$. Compositional dependence of the lattice parameter. *Circles*, experimental results from X-ray diffraction; *dashed curve*, calculated by Vegard's law from the values for pure Ge and Si; *solid curve*, experimental results from [1.3]

**Table 4.1-3** Densities of Group IV semiconductors and IV–IV compounds

| Crystal | | Density (g/cm$^3$) | Temperature (K) | Remarks |
|---|---|---|---|---|
| Diamond | C | 3.51537 (5) | 298 | Flotation, type Ia |
| | | 3.51506 (5) | 298 | Flotation, type IIb |
| Silicon | Si | 2.329002 | 298.15 | High-purity crystal, hydrostatic weighing |
| Germanium | Ge | 5.3234 | 298 | Hydrostatic weighing |
| Gray tin | $\alpha$-Sn | 7.285 | 291 | |
| Silicon carbide | 3C-SiC | 3.166 | 293 | Polycrystalline sample |
| | 6H-SiC | 3.211 | 300 | |

**Table 4.1-4** Elastic constants $c_{ik}$ of Group IV semiconductors and IV–IV compounds

| Crystal | | $c_{11}$ (GPa) | $c_{12}$ (GPa) | $c_{33}$ (GPa) | $c_{44}$ (GPa) | Temperature (K) | Remarks |
|---|---|---|---|---|---|---|---|
| Diamond | C | 1076.4 (2) | 125.2 (2.3) | | 577.4 (1.4) | 296 | Brillouin scattering |
| Silicon | Si | 165.77 | 63.93 | | 79.62 | 298 | Ultrasound measurement [a] |
| Germanium | Ge | 124.0 | 41.3 | | 68.3 | 298 | Ultrasound measurement |
| Gray tin | $\alpha$-Sn | 69.0 | 29.3 | | 36.2 | | [b] |
| Silicon carbide | 3C-SiC | 289 | 234 | | 55.4 | 300 | |
| | 4H-SiC | 507 (6) | 108 (8) | 547 (6) | 159 (7) | RT | Brillouin scattering |

[a] p-type sample, $\rho = 410\,\Omega\,\text{cm}$.
[b] Calculated from an 11-parameter shell model fitted to experimental data.

**Table 4.1-5** Melting point $T_m$ of Group IV semiconductors and IV–IV compounds

| Crystal | | Melting point (K) | Remarks |
|---|---|---|---|
| Diamond | C | 4100 | Diamond–graphite–liquid eutectic at $p = 12.5\,\text{GPa}$ |
| Silicon | Si | 1687 | The coordination number changes from 4 in the diamond phase to 6.4 in the liquid phase with an increase in bond length from 0.235 to 0.25 nm. The liquid phase shows metallic conduction |
| Germanium | Ge | 1210.4 | |
| Gray tin | $\alpha$-Sn | | Transforms into metallic $\beta$-Sn slightly below RT |
| Silicon carbide | 3C-SiC | 3103 (40) | Peritectic decomposition temperature at $p = 35\,\text{bar}$ |

**Table 4.1-6** Temperature dependence of the lattice parameters of Group IV semiconductors and IV–IV compounds

| Crystal | | Temperature dependence of lattice parameter |
|---|---|---|
| Diamond | C | Fig. 4.1-5 |
| Silicon | Si | Fig. 4.1-6 [a] |
| Germanium | Ge | Fig. 4.1-7 |
| Gray tin | $\alpha$-Sn | $da/dT = 3.1\times10^{-6}$ nm/K; temperature range −130 to 25 °C |
| Silicon carbide | 3C-SiC | Fig. 4.1-8 |
| | 6H-SiC | Fig. 4.1-9 |

[a] The lattice parameter $a$ of high-purity Si can be approximated in the range 20–800 °C by $a(T) = 5.4304 + 1.8138\times10^{-5}(T - 298.15\,\text{K}) + 1.542\times10^{-9}(T - 298.15\,\text{K})^2$.

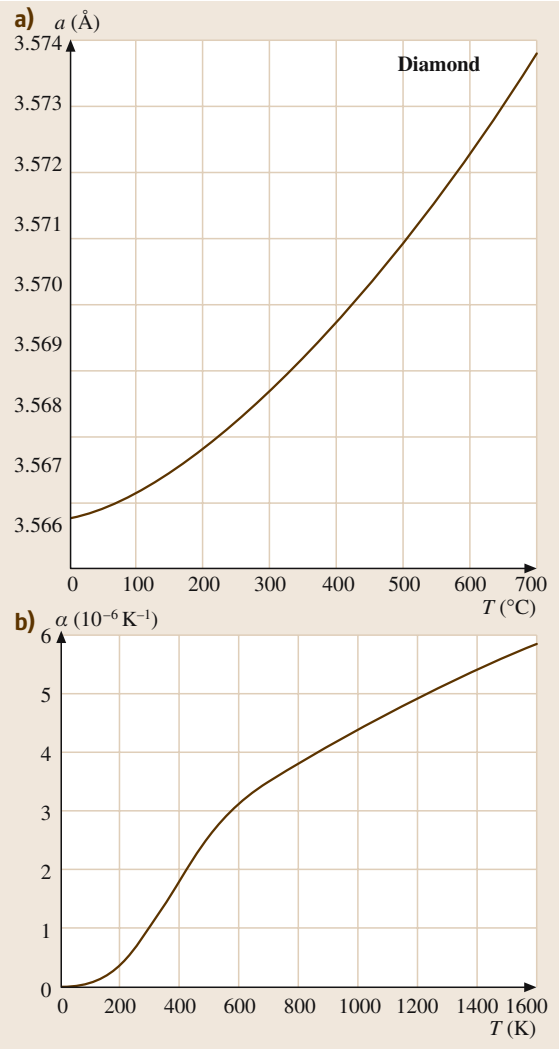


**Fig. 4.1-5a,b** Diamond. (**a**) Lattice parameter vs. temperature [1.4]; (**b**) linear thermal expansion coefficient vs. temperature [1.5]

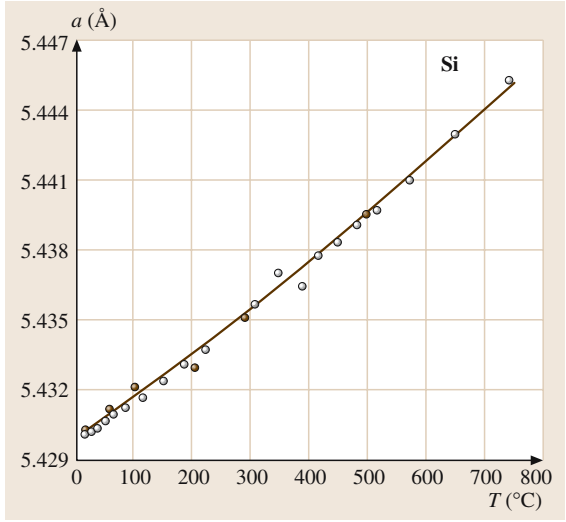


**Fig. 4.1-6** Si. Lattice parameter vs. temperature in the range 20–740 °C, measurements on various samples [1.6]

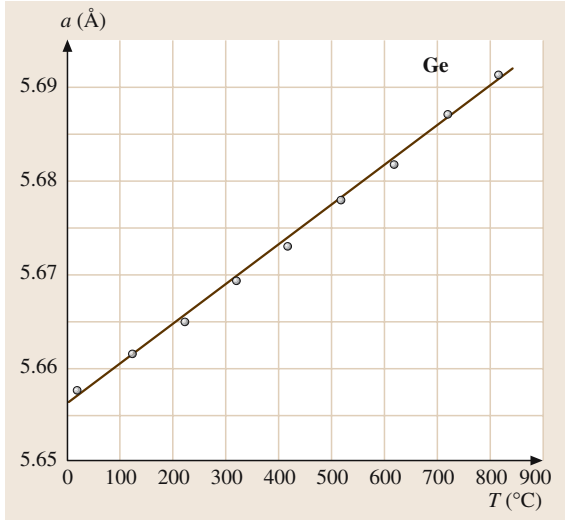


**Fig. 4.1-7** Ge. Lattice parameter vs. temperature [1.7]

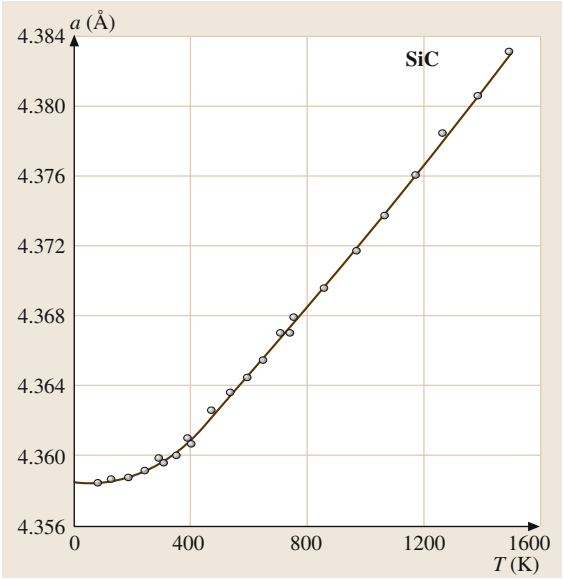


**Fig. 4.1-8** SiC (3C). Lattice parameter vs. temperature [1.8]

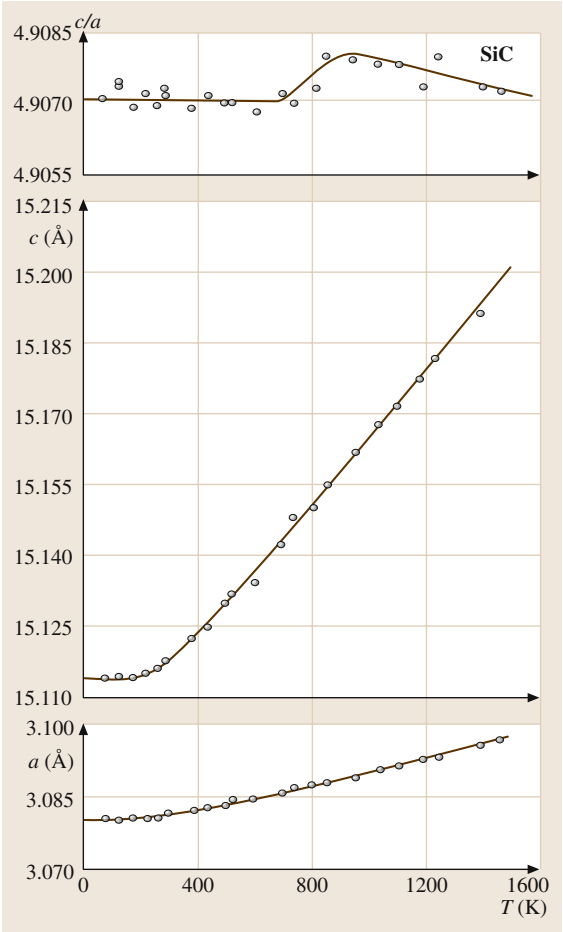


**Fig. 4.1-9** SiC (6H). Lattice parameters vs. temperature [1.8]

**Table 4.1-7** Linear thermal expansion coefficient $\alpha$ of Group IV semiconductors and IV–IV compounds and its temperature dependence

| Crystal | | Expansion coefficient $\alpha$ ($K^{-1}$) | Temperature (K) | Remarks |
|---|---|---|---|---|
| Diamond | C | $1.0\times10^{-6}$ | 300 | See Fig. 4.1-5 for temperature dependence |
| Silicon | Si | $2.92\,(6)\times10^{-6}$ | 293 | See Fig. 4.1-10 for temperature dependence[a] |
| Germanium | Ge | $5.90\times10^{-6}$ | 300 | See Fig. 4.1-11 for temperature dependence |
| Gray tin | $\alpha$-Sn | $4.7\times10^{-6}$ | 293 | See Fig. 4.1-12 for temperature dependence |
| Silicon carbide | 3C-SiC | $2.77\,(42)\times10^{-6}$ | 300 | See Fig. 4.1-13 for temperature dependence |

[a] The linear thermal expansion coefficient $\alpha$ of Si can be approximated in the temperature range 120–1500 K by $\alpha(T) = \left(3.725\left\{1-\exp[-5.88\times10^{-3}(T-124)]\right\}+5.548\times10^{-4}T\right)\times10^{-6}\,(K^{-1})$ ($T$ measured in K)

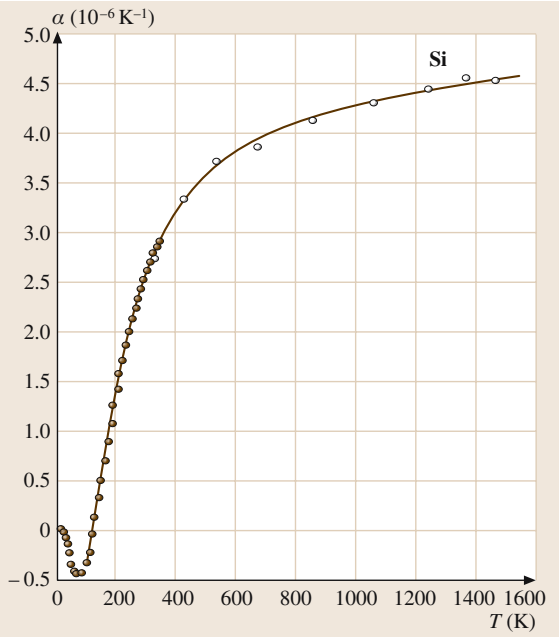


**Fig. 4.1-10** Si. Linear thermal expansion coefficient vs. temperature. Experimental data from [1.9] (*filled circles*) and [1.10] (*open circles*)

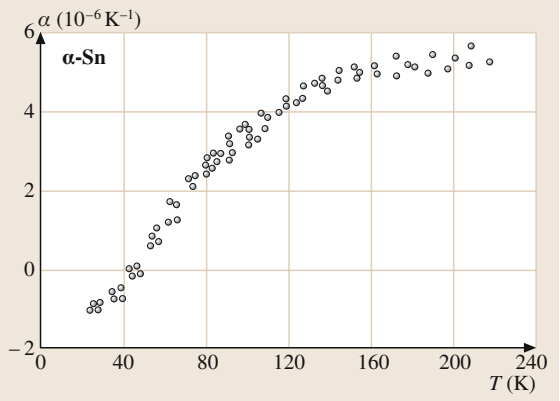


**Fig. 4.1-12** $\alpha$-Sn. Coefficient of linear thermal expansion vs. temperature [1.12, 13]

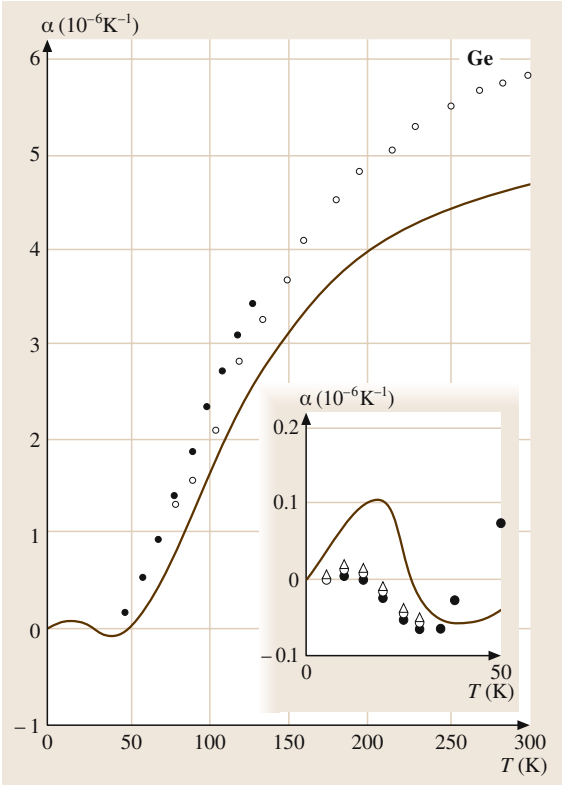


**Fig. 4.1-11** Ge. Linear thermal expansion coefficient vs. temperature. Experimental data from various authors (*symbols*) and theoretical results (*solid line*) [1.11]

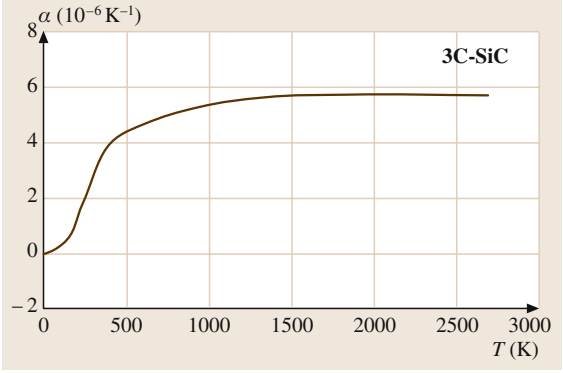


**Fig. 4.1-13** 3C-SiC. Recommended linear thermal expansion coefficient vs. temperature according to an analysis of data from nine references [1.5]

**Table 4.1-8** Heat capacities and Debye temperatures of Group IV semiconductors and IV–IV compounds

| Crystal | | Heat capacity $c_p$ (J/mol K) | Debye temperature $\Theta_D$ | Temperature (K) | Remarks |
|---|---|---|---|---|---|
| Diamond | C | 6.195 | 1860 (10) | 300 | See Fig. 4.1-14 for temperature dependence of $c_p$, $c_V$ |
| Silicon | Si | 45.358<br>45.882 | 636 | 77<br>298 | See Fig. 4.1-15 for temperature dependence of $c_V$ |
| Germanium | Ge | 51.88 | 374 | 298 | See Fig. 4.1-16 for temperature dependence of $c_V$ |
| Gray tin | $\alpha$-Sn | 19.09 | 220 | 100 | See Fig. 4.1-17 for temperature dependence of $c_V$ |
| Silicon carbide | 3C-SiC | 28.5 | 1270 (20) | 293 | Polycrystalline sample |

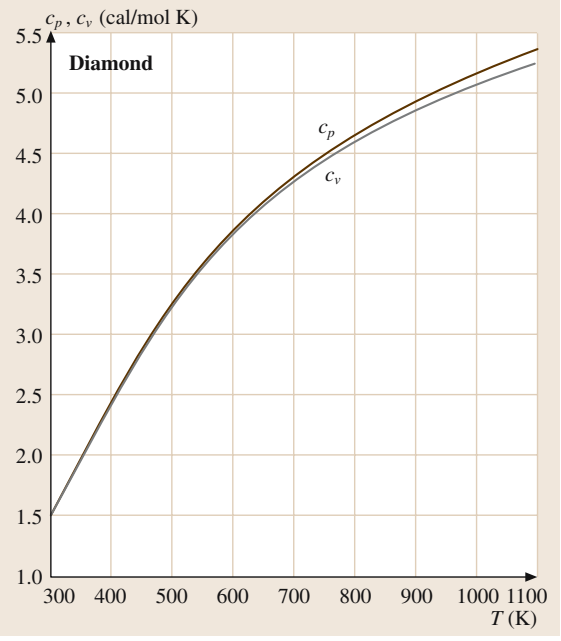


**Fig. 4.1-14** Diamond. Molar heat capacity vs. temperature [1.14]

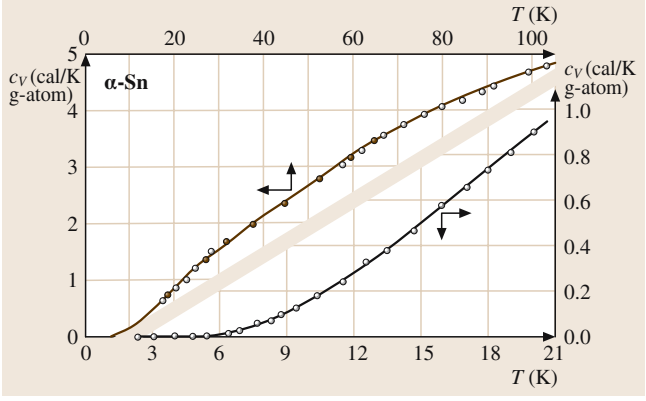


**Fig. 4.1-17** $\alpha$-Sn. Heat capacity $c_v$ vs. temperature. *Lower curve*, temperature range 0–20 K; *upper curve*, temperature range 0–105 K [1.15]

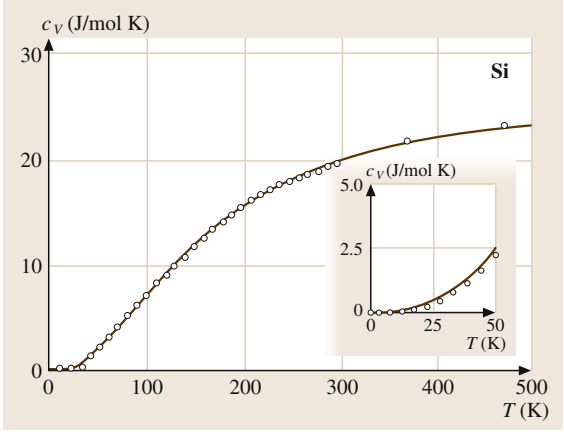


**Fig. 4.1-15** Si. Heat capacity at constant volume vs. temperature. Figure from [1.11]

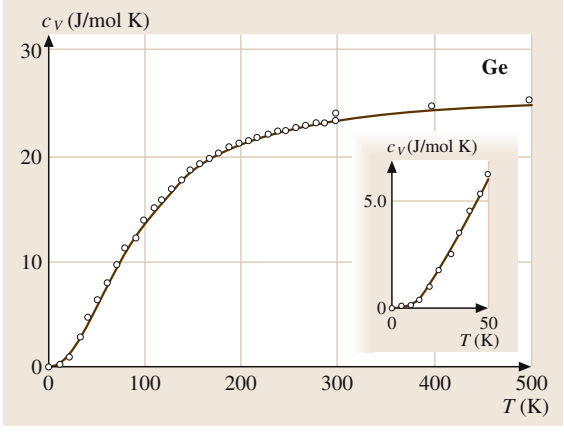


**Fig. 4.1-16** Ge. Heat capacity at constant volume vs. temperature

**Table 4.1-9** Phonon frequencies at symmetry points. Diamond (C) ($\nu$ in THz, 300 K, from Raman spectroscopy); silicon (Si) ($\nu$ in THz, 296 K, from inelastic neutron scattering); germanium (Ge) ($\nu$ in THz, 300 K, from coherent inelastic neutron scattering); gray tin ($\alpha$-Sn) ($\nu$ in THz, 90 K, from inelastic thermal neutron scattering); silicon carbide (3C-SiC) (phonon wavenumbers $\tilde{\nu}$ in $cm^{-1}$, RT, from Raman spectroscopy); silicon carbide (6H-SiC) ($\nu$ in THz, derived from photoluminescence data)

| Diamond (C) | | Silicon (Si) | | Germanium (Ge) | | Gray tin (Sn) | | Silicon carbide (3C-SiC) | |
|---|---|---|---|---|---|---|---|---|---|
| $\nu_{TO/LO}(\Gamma_{25'})$ | 39.9 | $\nu_{LTO}(\Gamma_{25'})$ | 15.53 (23) | $\nu_{LTO}(\Gamma_{25'})$ | 9.02 (2) | $\nu_{TO/LO}(\Gamma_{25'})$ | 6.00 (6) | $\tilde{\nu}_{TA}(L)$ | 266 |
| $\nu_{TA}(L_3)$ | 16.9 | $\nu_{TA}(X_3)$ | 4.49 (6) | $\nu_{TA}(X_3)$ | 2.38 (2) | $\nu_{TA}(L_3)$ | 1.00 (4) | $\tilde{\nu}_{LA}(L)$ | 610 |
| $\nu_{LA}(L_1)$ | 30.2 | $\nu_{LAO}(X_1)$ | 12.32 (20) | $\nu_{LAO}(X_1)$ | 7.14 (2) | $\nu_{LA}(L_1)$ | 4.15 (4) | $\tilde{\nu}_{TO}(L)$ | 766 |
| $\nu_{LO}(L_{2'})$ | 37.5 | $\nu_{TO}(X_4)$ | 13.90 (30) | $\nu_{TO}(X_4)$ | 8.17 (3) | $\nu_{LO}(L_{2'})$ | 4.89 (8) | $\tilde{\nu}_{LO}(L)$ | 838 |
| $\nu_{TO}(L_{3'})$ | 36.2 | $\nu_{TA}(L_3)$ | 3.43 (5) | $\nu_{TA}(L_{3'})$ | 1.87 (2) | $\nu_{TO}(L_{3'})$ | 5.74 (12) | $\tilde{\nu}_{TA}(X)$ | 373 |
| $\nu_{TA}(X_3)$ | 24.2 | $\nu_{LA}(L_2)$ | 11.35 (30) | $\nu_{LA}(L_2)$ | 6.63 (4) | $\nu_{TA}(X_3)$ | 1.25 (6) | $\tilde{\nu}_{LA}(X)$ | 640 |
| $\nu_{LA/LO}(X_1)$ | 35.5 | $\nu_{LO}(L_1)$ | 12.60 (32) | $\nu_{TO}(L_3)$ | 8.55 (3) | $\nu_{LA/LO}(X_1)$ | 4.67 (6) | $\tilde{\nu}_{TO}(X)$ | 761 |
| $\nu_{TO}(X_4)$ | 32.0 | $\nu_{TO}(L_3)$ | 14.68 (30) | $\nu_{TO}(L_1)$ | 7.27 (2) | $\nu_{TO}(X_4)$ | 5.51 (8) | $\tilde{\nu}_{LO}(X)$ | 829 |

**Table 4.1-9** Phonon frequencies at symmetry points, cont.

| Silicon carbide (6H-SiC) | | | | | | | |
|---|---|---|---|---|---|---|---|
| $\nu_{TA}$ | 8.1 | 8.8 | 9.5 | 9.8 | 10.6 | 11.2 | 12.9 |
| $\nu_{LA}$ | 12.2 | 12.9 | 16.2 | 16.7 | 18.6 | | |
| $\nu_{TO}$ | 22.9 | 23.1 | 23.7 | | | | |
| $\nu_{LO}$ | 25.2 | 25.5 | 25.9 | | | | |

**Table 4.1-10** Phonon dispersion relations of Group IV semiconductors and IV–IV compounds

| Crystal | | Phonon dispersion curves |
|---|---|---|
| Diamond | C | Fig. 4.1-18 |
| Silicon | Si | Fig. 4.1-19 |
| Germanium | Ge | Fig. 4.1-20 |
| Gray tin | $\alpha$-Sn | Fig. 4.1-21 |
| Silicon carbide | 3C-SiC | Fig. 4.1-22 |
| | 6H-SiC | |

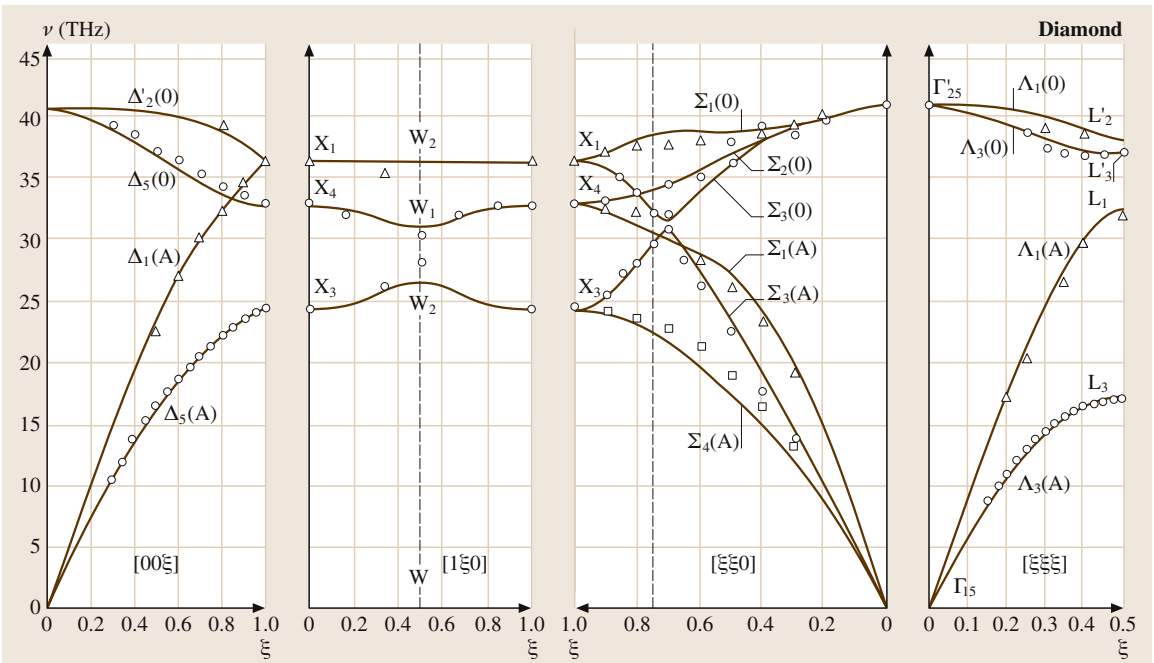


**Fig. 4.1-18** Diamond. Phonon dispersion curves. *Symbols*, experimental data from neutron scattering; *solid curves*, shell model calculation [1.16]

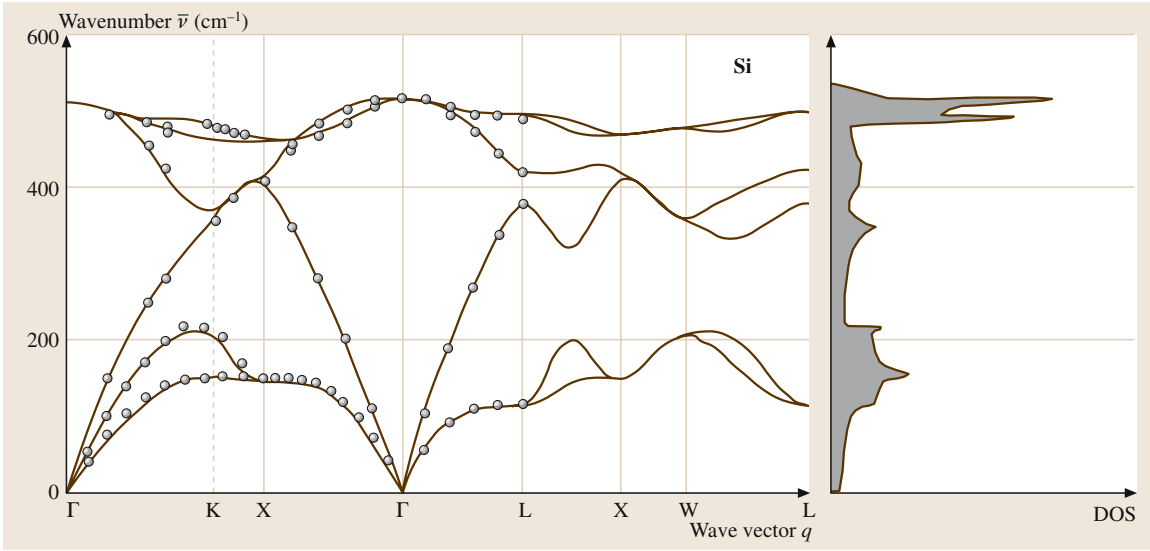


**Fig. 4.1-19** Si. Phonon dispersion curves (*left panel*) and phonon density of states (*right panel*) [1.16]. Experimental data points [1.17, 18] and ab initio calculations [1.16]

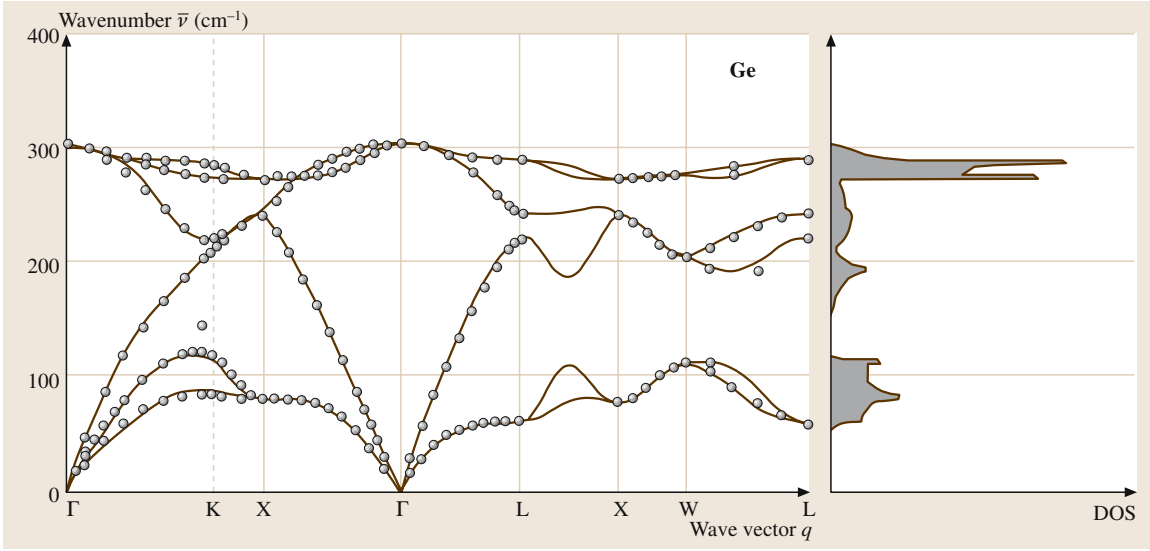


**Fig. 4.1-20** Ge. Phonon dispersion curves (*left panel*) and phonon density of states (*right panel*) [1.16]. Experimental data points [1.19] and ab initio calculations [1.16]

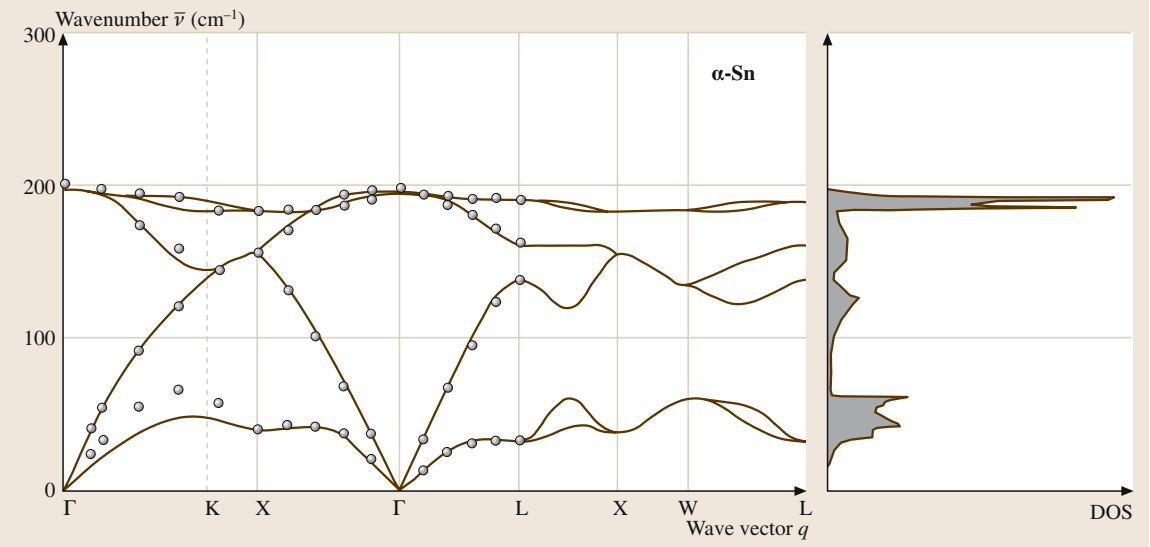


**Fig. 4.1-21** $\alpha$-Sn. Phonon dispersion curves (*left panel*) and phonon density of states (*right panel*) [1.20]. Experimental data points from inelastic neutron scattering at 90 K [1.21]. *Solid lines*, ab initio pseudopotential calculation [1.20]

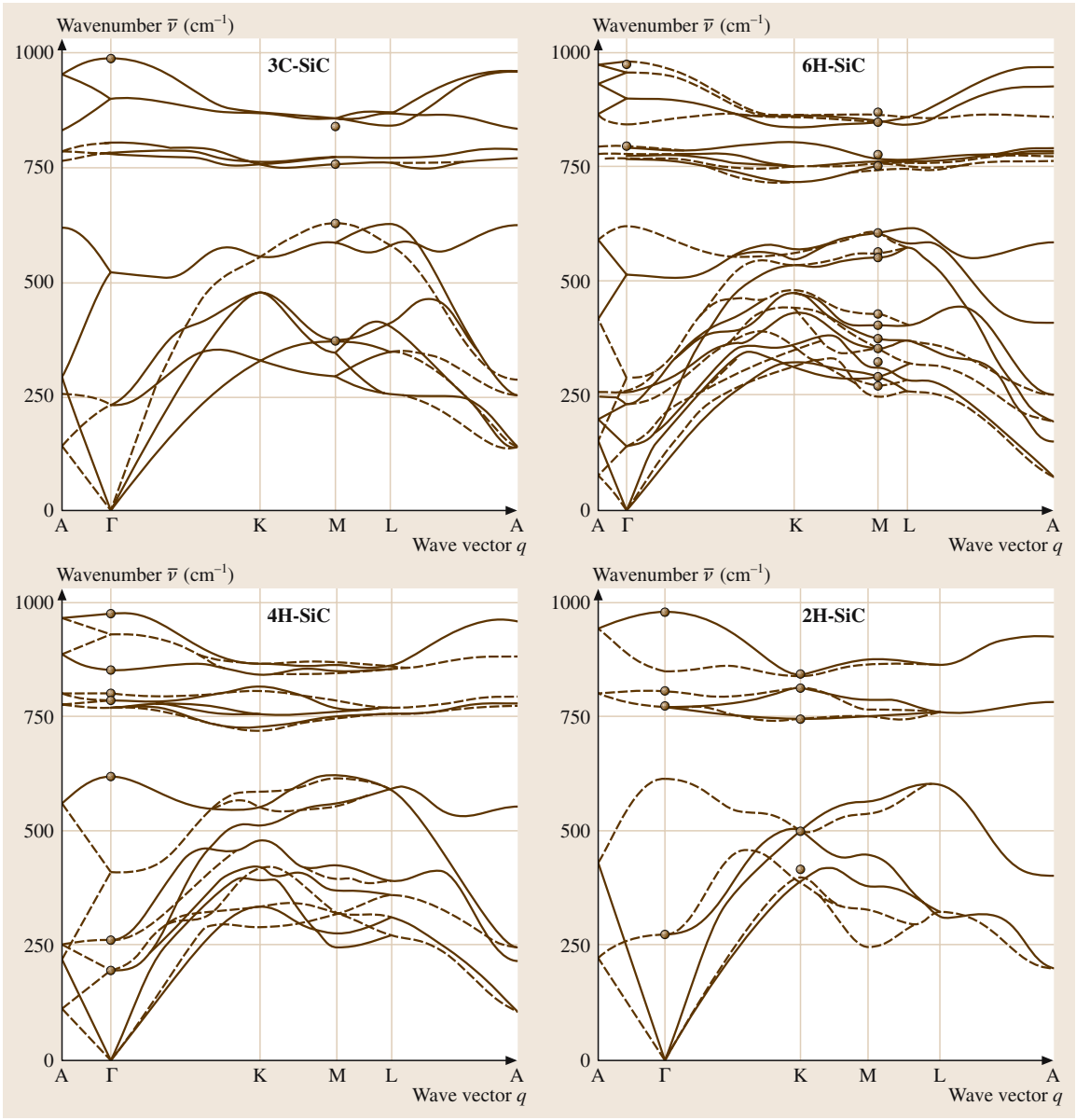


**Fig. 4.1-22** SiC. Phonon dispersion curves for the 3C, 2H, 4H, and 6H modifications obtained from a bond-charge model calculation [1.22]. *Symbols* represent experimental data. The different types of *lines* indicate different polarization states

### B. Electronic Properties

Tables 4.1-11 – 4.1-18.

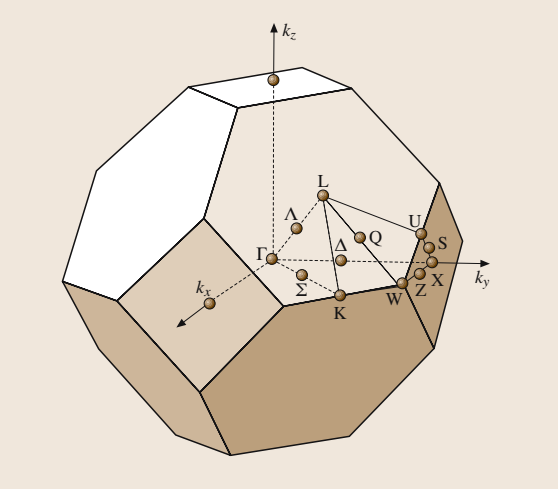


**Fig. 4.1-23** Brillouin zone of the diamond and of the zinc blende lattice

**Table 4.1-11** First Brillouin zones of Group IV semiconductors and IV–IV compounds

| Crystal | | Figures |
|---|---|---|
| Diamond | C | Fig. 4.1-23 |
| Silicon | Si | Fig. 4.1-23 |
| Germanium | Ge | Fig. 4.1-23 |
| Gray tin | $\alpha$-Sn | Fig. 4.1-23 |
| Silicon carbide | 3C-SiC | Fig. 4.1-23 |
| | 2H-SiC | Fig. 4.1-24 |

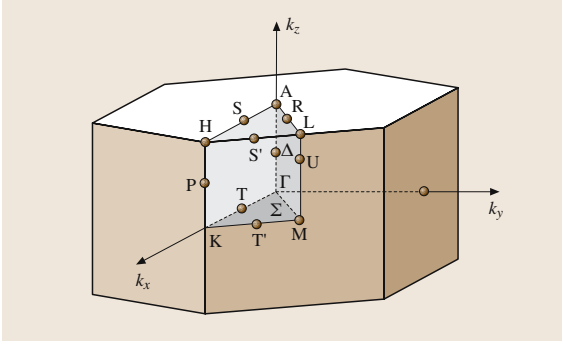


**Fig. 4.1-24** Brillouin zone of the Wurtzite lattice

**Table 4.1-12** Band structures of Group IV semiconductors and IV–IV compounds

**Diamond (C) (Fig. 4.1-25)**

Diamond is an indirect-gap semiconductor, the lowest minima of the conduction band being located along the Δ axes. The valence band has the structure common to all group IV semiconductors, namely three bands degenerate at Γ. The spin–orbit splitting of these bands is negligible.

**Silicon (Si) (Fig. 4.1-26)**

The conduction band is characterized by six equivalent minima along the [100] axes of the Brillouin zone located at about $k_0 = 0.85(2\pi/a)$ (symmetry $\Delta_1$). The surfaces of constant energy are ellipsoids of revolution with their major axes along [100]. Higher minima are located at Γ and along the [111] axes about 1 eV above the [100] minima.

The valence band has its maximum at the Γ point (symmetry $\Gamma_8$), the light- and heavy-hole bands being degenerate at this point. Both bands show warping. The third, spin–orbit split-off band has $\Gamma_7$ symmetry. The spin–orbit splitting energy at Γ is small compared with most interband energy differences. Thus, spin–orbit interaction is mostly neglected in band structure calculations and the notation of the single group is used to denote the symmetry of a band state.

**Table 4.1-12** Band structures of Group IV semiconductors and IV–IV compounds, cont.

**Germanium (Ge) (Fig. 4.1-27)**

The conduction band is characterized by eight equivalent minima at the end points L of the [111] axes of the Brillouin zone (symmetry $L_6$). The surfaces of constant energy are ellipsoids of revolution with their major axes along [111]. Higher energy minima of the conduction band are located at the Γ point and (above these) on the [100] axes.

The valence band has its maximum at the Γ point (symmetry $\Gamma_8$), the light- and heavy-hole bands being degenerate at this point. Both bands are warped. The third, spin–orbit split-off band has $\Gamma_7$ symmetry. In contrast to silicon the spin–orbit splitting energies are considerable. Thus, the symmetry notation of the double group of the diamond lattice is mostly used for Ge.

**Gray tin (α-Sn) (Fig. 4.1-28)**

The band structure of gray tin (α-Sn) is qualitatively different from those of the other Group IV elements. The s-like $\Gamma_7$ conduction band edge, which decreases drastically with atomic number in the sequence C → Si → Ge, is situated below the p-like $\Gamma_8$ valence band edge in α-Sn. This causes an inversion of the curvature of the $\Gamma_8$ light-hole band. Consequently, α-Sn is a zero-gap semiconductor, with its lowest conduction band and its highest valence band being degenerate at Γ (symmetry $\Gamma_8$). A second conduction band, with minima at $L_6$, follows at a slightly higher energy. This second hand determines the properties of n-type samples for $n > 10^{17}$ cm$^{-3}$ ($T > 77$ K for intrinsic samples).

**Silicon carbide**

Band structure calculations show that the conduction band minima are situated along the cubic axes at the border of the Brillouin zone. The band structure of 3C-SiC is shown in Fig. 4.1-29, and that of 2H-SiC in Fig. 4.1-30.

**Silicon–germanium alloys**

The band structure is characterized by a crossover in the lowest conduction band edge from Ge-like [111] symmetry to Si-like [100] symmetry at the composition $x = 0.15$. The shape of the band edge (and hence the effective masses) varies only slightly as a function of composition.

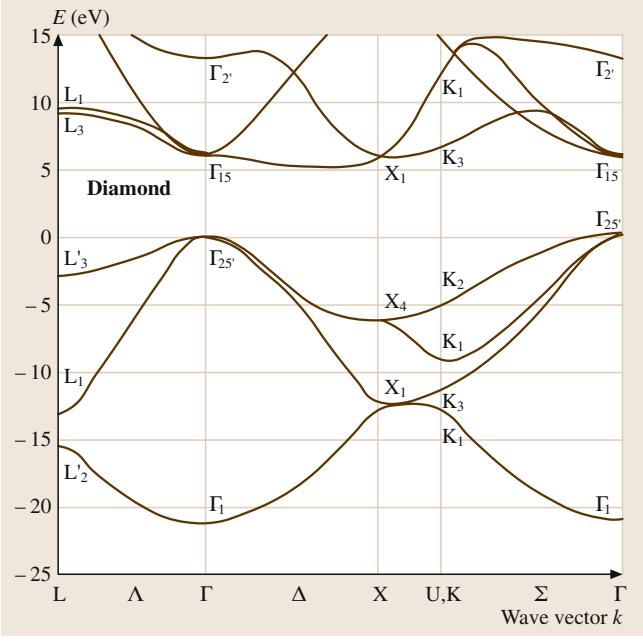


**Fig. 4.1-25** Band structure of diamond

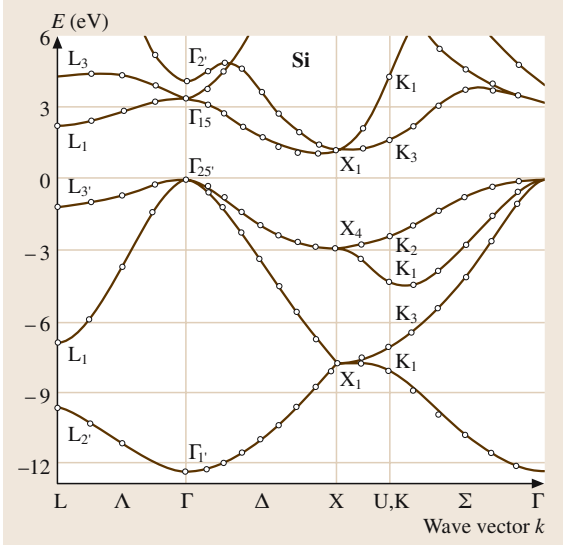


**Fig. 4.1-26** Band structure of silicon

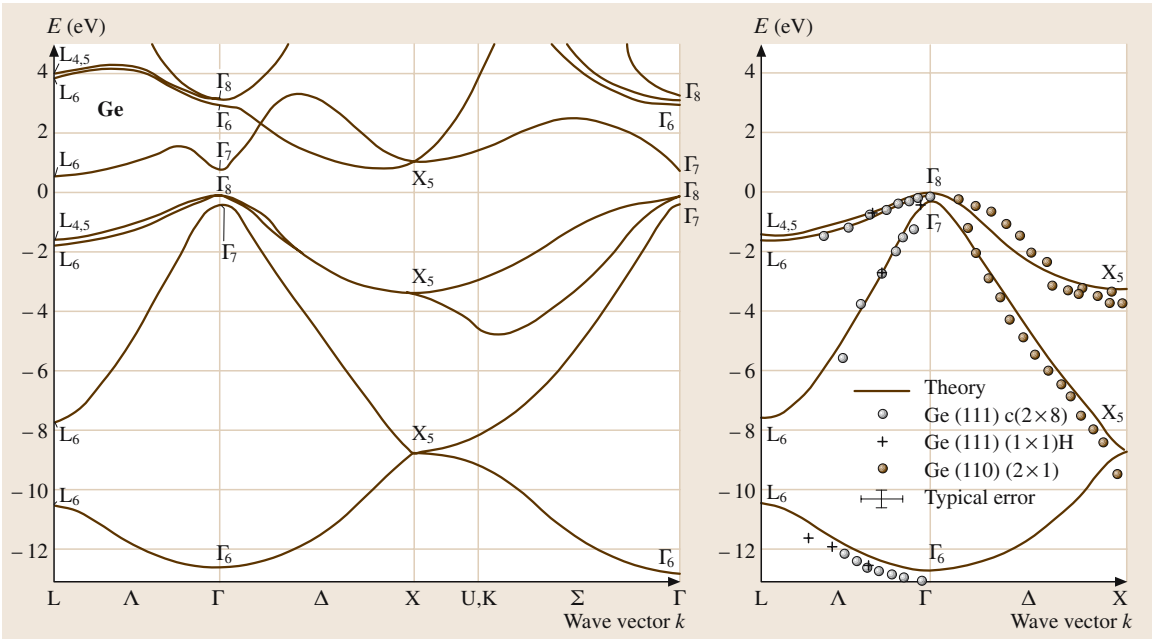


**Fig. 4.1-27** Band structure of germanium

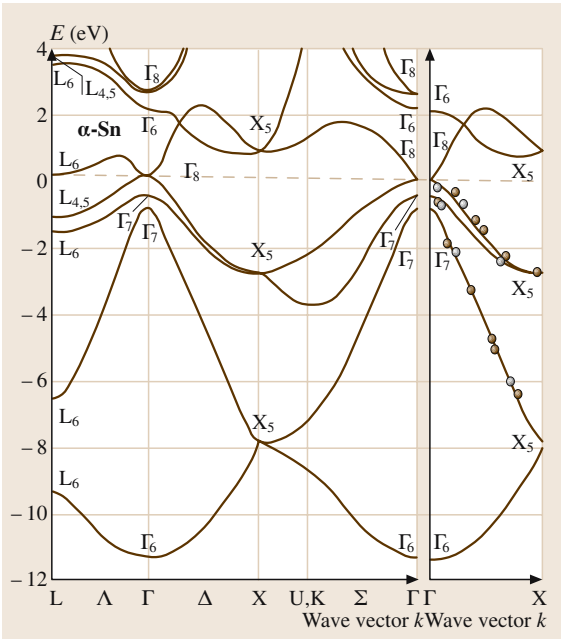


**Fig. 4.1-28** Band structure of gray tin

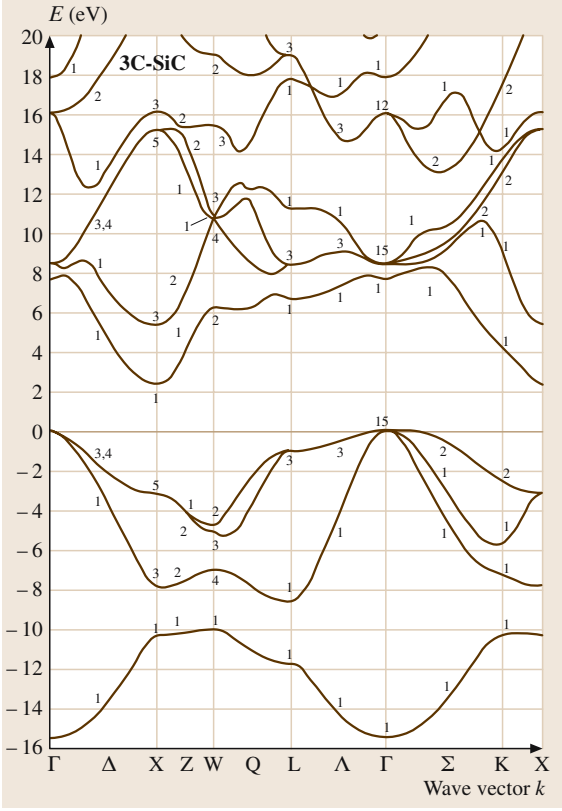


**Fig. 4.1-29** Band structure of 3C silicon carbide

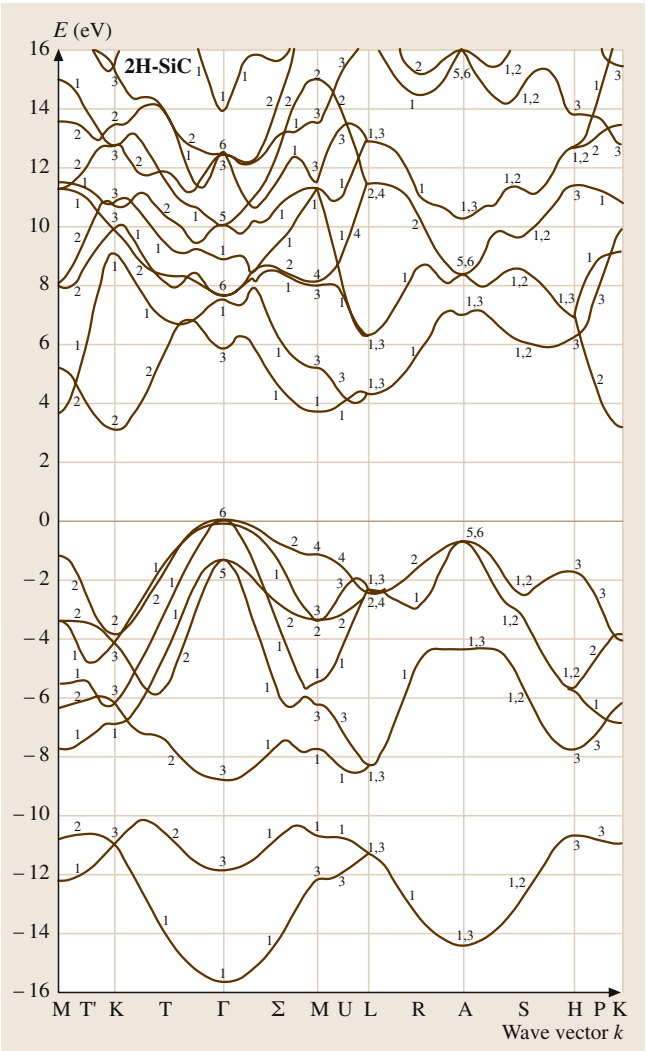


**Fig. 4.1-30** Band structure of 2H silicon carbide

**Table 4.1-13** Energy gaps of Group IV semiconductors and IV–IV compounds

| Crystal | | Between bands | Gap | Energy (eV) | Temperature (K) | Remarks |
|---|---|---|---|---|---|---|
| Diamond | C | $\Gamma_{25'v}$ and $\Delta_{1c}$ | $E_{g,\,indir}$ | 5.50 (5) | RT | Quantum photoyield |
| | | | $E_{gx,\,indir}$ | 5.416 (2) | 100 | Indirect exciton gap with lower valence band |
| | | | | 5.409 (2) | | Indirect exciton gap with upper valence band |
| Silicon | Si | $\Gamma_{25'v}$ and $\Delta_{1c}$ | $E_{g,\,ind}$ | 1.1700 | 0 | Extrapolated, wavelength-modulated transmission |
| | | | | 1.1242 | 300 | Wavelength-modulated transmission |
| | | | $E_{g,\,th}$ | 1.205 | 0 | Extrapolated from temperature dependence of conductivity above 200 K |
| | | $\Gamma_{25'v}$ and $\Gamma_{2'c}$ | $E_{g,\,dir}$ | 4.185 (10) | 4.2 | Electroreflection |
| | | | | 4.135 | 190 | |

**Table 4.1-13** Energy gaps of Group IV semiconductors and IV–IV compounds, cont.

| Crystal | | Between bands | Gap | Energy (eV) | Temperature (K) | Remarks |
|---|---|---|---|---|---|---|
| Germanium | Ge | $\Gamma_{8v}$ and $L_{6c}$ | $E_{g,\,ind}$ | 0.744 (1) | 1.5 | Magnetotransmission |
| | | | | 0.664 | 291 | Optical absorption |
| | | | $E_{g,\,th}$ | 0.785 | 0 | Extrapolated from temperature dependence of intrinsic conductivity |
| | | $\Gamma_{8v}$ and $\Gamma_{7c}$ | $E_{g,\,dir}$ | 0.898 (1) | 1.5 | Magnetoabsorption |
| | | | | 0.805 (1) | 293 | |
| Silicon carbide | 3C-SiC | $\Gamma_{15v}$ and $X_{1c}$ | $E_{g,\,ind}$ | 2.417 (1) | 2 | Wavelength-modulated absorption |
| | | | | 2.2 | 300 | Optical absorption |
| | | | $E_{g,\,dir}$ | 6.0 | 300 | Optical absorption |
| | | | $E_{gx}$ | 2.390 | 2 | Excitonic energy gap, wavelength-modulated absorption |
| Silicon carbide | 2H-SiC | | $E_{gx}$ | 3.330 | 4 | Excitonic energy gap; optical absorption |
| Silicon carbide | 6H-SiC | | $E_{g,\,ind}$ | 2.86 | 300 | Optical absorption |
| | | | $E_{gx}$ | 3.023 | 4 | |

**Table 4.1-14** Exciton energies of Group IV semiconductors and IV–IV compounds ($E_b$ = exciton binding energy)

| Crystal | Quantity | State | Exciton energy (eV) | Temperature (K) | Remarks |
|---|---|---|---|---|---|
| Diamond | $E_b(1S)$ | | 0.19 (15) | | 1S core exciton |
| | $E_b$ | | 0.07 | | Indirect exciton binding energy |
| Silicon | $E(1S)$ | | 1.1552 (3) | 1.8 | Wavelength-modulated absorption |
| | $E_b$ | | 0.01412 | 4.2 | Calculated binding energy |
| Germanium | $E(1S)$ | $1S_{3/2}^{3/2}$ ($L_4+L_5$) | 0.74046 (3) | 2.1, 5.1 | Optical absorption at 2.1 K and luminescence at 5.1 K |
| | | $1S_{1/2}^{3/2}$ ($L_6$) | 0.74158 (3) | | |
| | $E_b$ | $1S_{3/2}^{3/2}$ ($L_4+L_5$) | 0.00418 | | |
| | | $1S_{1/2}^{3/2}$ ($L_6$) | 0.00317 | | |
| Silicon carbide (3C-SiC) | $E_b$ | | 0.027 | 2 | Wavelength-modulated absorption |

**Table 4.1-15** Spin–orbit splitting energies of Group IV semiconductors and IV–IV compounds

| Crystal | Quantity | Bands | Splitting energy (eV) | Temperature (K) | Remarks |
|---|---|---|---|---|---|
| Diamond | $\Delta(\Gamma_{25'v})$ | | 0.006 (1) | | Cyclotron resonance |
| Silicon | $\Delta_0(\Gamma_{25'v})$ | | 0.0441 (3) | 1.8 | Wavelength-modulated absorption |
| Germanium | $\Delta_0$ | $\Gamma_{7v}$ to $\Gamma_{8v}$ | 0.297 | 10 | Electroreflectance |
| | | $\Gamma_{6v}$ to $\Gamma_{8c}$ | 0.200 | | |
| Silicon carbide (3C-SiC) | $\Delta_0$ | | 0.010 | 2 | Wavelength-modulated absorption |

**Table 4.1-16** Effective masses of electrons (in units of the electron mass $m_0$) for Group IV semiconductors and IV–IV compounds

| Crystal | Quantity | Value | Temperature (K) | Remarks |
|---|---|---|---|---|
| Diamond | $m_{n,\,parall}$ | 1.4 | | Field dependence of electron drift velocity |
| | $m_{n,\,perpend}$ | 0.36 | | |
| Silicon | $m_{n,\,parall}$ | 0.9163 (4) | 1.26 | Cyclotron resonance with uniaxial stress |
| | $m_{n,\,perpend}$ | 0.1905 (1) | | |

**Table 4.1-16** Effective masses of electrons for Group IV semiconductors and IV–IV compounds, cont.

| Crystal | Quantity | Value | Temperature (K) | Remarks |
|---|---|---|---|---|
| Germanium | $m_{n,\,perpend}(L_6)$ | 0.0807 (8) | 30–100 | Cyclotron resonance magnetophonon resonance |
| | | 0.0823 | 120 | |
| | $m_{n,\,parall}(L_6)$ | 1.57 (3) | 30–100 | Cyclotron resonance magnetophonon resonance |
| | | 1.59 | 120 | |
| | $m_n(\Gamma_7)$ | 0.0380 (5) | 30 | Piezomagnetoreflectance |
| Gray tin | $m_{n,\,light}(\Gamma_8)$ | 0.0236 (2) | 1.3 | Density-of-states mass |
| | $m_{n,\,heavy}(L_6)$ | 0.21 | 4.2 | |
| Silicon carbide (3C-SiC) | $m_{n,\,parall}$ | 0.677 (15) | 45 | Cyclotron resonance |
| | $m_{n,\,perpend}$ | 0.247 (11) | | |
| Silicon carbide (6H-SiC) | $m_{n,\,parall}$ | 3–6 | | Cyclotron resonance |
| | $m_{n,\,perpend}$ | 0.48 (2) | | |

**Table 4.1-17** Effective masses of holes (in units of the electron mass $m_0$) for Group IV semiconductors and IV–IV compounds

| Crystal | Quantity | Value | Temperature (K) | Field direction | Remarks |
|---|---|---|---|---|---|
| Diamond | $m_{p,\,heavy}$ | 1.08 | | | Calculated from valence band parameters |
| | $m_{p,\,light}$ | 0.36 | | | |
| | $m_{spin\text{–}orbit\ split}$ | 0.15 | | | |
| | $m_{p,\,dens\ stat}$ | 0.75 | 300 | | Hall effect |
| Silicon | $m_{p,\,heavy}$ | 0.537 | 4.2 | | Cyclotron resonance |
| | $m_{p,\,light}$ | 0.153 | | | |
| | $m_{spin\text{–}orbit\ split}$ | 0.234 | | | |
| | $m_{p,\,dens\ stat}$ | 0.591 | | | Density-of-states mass |
| Germanium | $m_{p,\,light}$ | 0.0438 (3) | 4 | $\boldsymbol{B}$ parallel to [100] | Cyclotron resonance |
| | | 0.0426 (2) | | $\boldsymbol{B}$ parallel to [111] | |
| | | 0.0430 (3) | | $\boldsymbol{B}$ parallel to [110] | |
| | $m_{p,\,heavy}$ | 0.284 (1) | | $\boldsymbol{B}$ parallel to [100] | |
| | | 0.376 (1) | | $\boldsymbol{B}$ parallel to [111] | |
| | | 0.352 (4) | | $\boldsymbol{B}$ parallel to [110] | |
| | $m_{spin\text{–}orbit\ split}$ | 0.095 (7) | 30 | | Piezomagnetoabsorption |
| Gray tin | $m_p(\Gamma_8)$ | 0.195 | | | Interband magnetoreflection |
| | $m_p(\Gamma_7)$ | 0.058 | | | |
| Silicon carbide (3C-SiC) | $m_p$ | 0.45 | 45 | | High-field cyclotron resonance |
| Silicon carbide (6H-SiC) | $m_{p,\,parall}$ | 1.85 (3) | | | Cyclotron resonance |
| | $m_{p,\,perpend}$ | 0.66 (2) | | | |

**Table 4.1-18** $g$-factor $g_c$ of conduction electrons for Group IV semiconductors

| Crystal | $g_c$ | Temperature (K) | Remarks |
|---|---|---|---|
| Diamond | 2.0030 (3) | 140–300 | Electron spin resonance |
| Silicon | 1.99893(28) | | Electron spin resonance |
| Germanium | −3.0 (2) | 30 | Piezomagnetoabsorption |

### C. Transport Properties

Tables 4.1-19 – 4.1-21.

*Electronic Transport, General Description.*

*Diamond (C).* Owing to the large band gap, most diamonds are insulators at room temperature, and so electronic transport is extrinsically determined and therefore strongly dependent on the impurity content. Natural (type IIb) and synthetic semiconducting diamonds are always p-type. The electron mobility can be derived only from photoconductivity experiments.

**Table 4.1-19** Intrinsic carrier concentration $n_i$ and electrical conductivity $\sigma_i$ of Group IV semiconductors and IV–IV compounds

| Crystal | $n_i$ ($cm^{-3}$) | $\sigma_i$ ($\Omega^{-1}cm^{-1}$) | $T$ (K) | Temperature dependence |
|---|---|---|---|---|
| Silicon | $1.02\times10^{10}$ | $3.16\times10^{-2}$ | 300 | Fig. 4.1-31 [a] |
| Germanium | $2.33\times10^{13}$ | $2.1\times10^{-2}$ | 300 | Figs. 4.1-32 and 4.1-33 |
| 3C-SiC | | | | Fig. 4.1-34 |
| Si–Ge alloys | Composition dependence of intrinsic conductivity: Fig. 4.1-36<br>Composition dependence of the mobilities: Figs. 4.1-35 and 4.1-37 | | | |

[a] The intrinsic conductivity of Si up to 1273 K is given by the phenomenological expression $\log_{10}\sigma_i = 4.247 - 2.924\times10^3 T^{-1}$ ($\sigma_i$ in $\Omega^{-1}cm^{-1}$, $T$ in K).

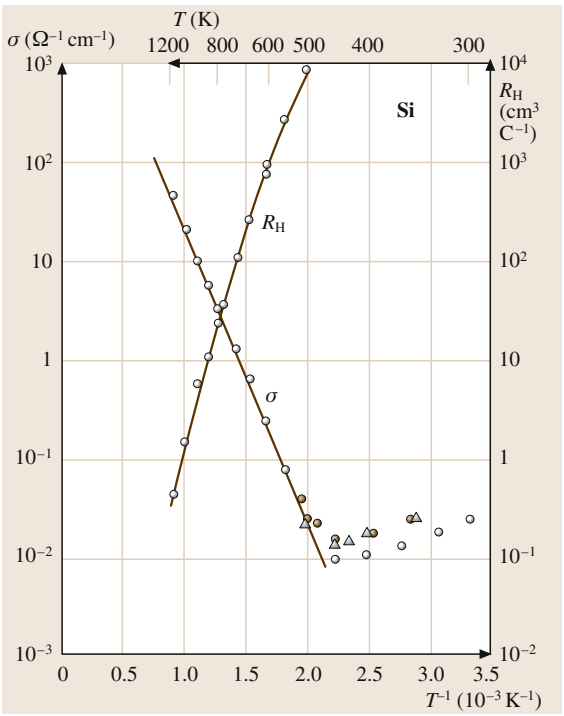


**Fig. 4.1-31** Si. Conductivity and Hall coefficient vs. reciprocal temperature in the range of intrinsic conduction; n- and p-type samples with doping concentrations of $1.7\times10^{14}\,cm^{-3}$ and above [1.23]. The different *symbols* show results from different samples

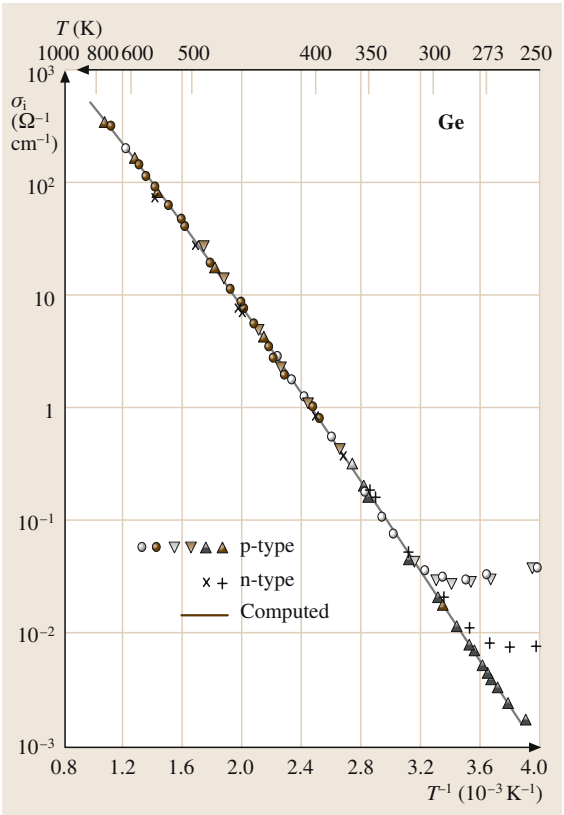


**Fig. 4.1-32** Ge. Conductivity vs. reciprocal temperature in the range of intrinsic conduction [1.24]

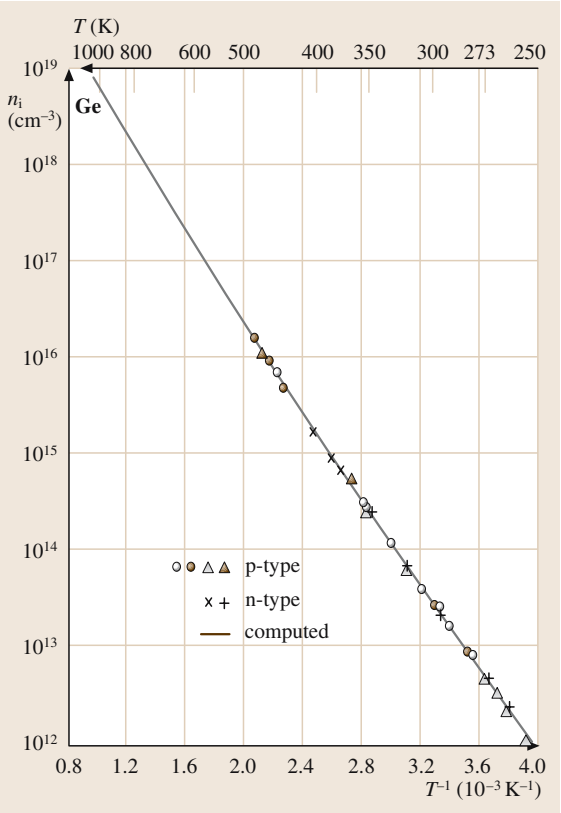


**Fig. 4.1-33** Ge. Intrinsic carrier concentration vs. reciprocal temperature [1.24]

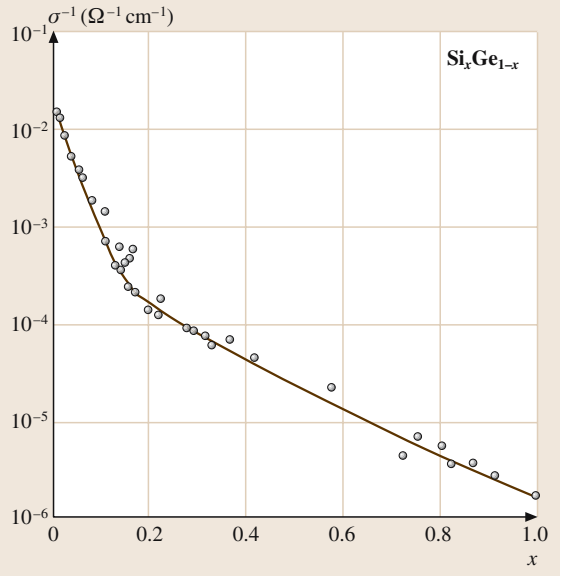


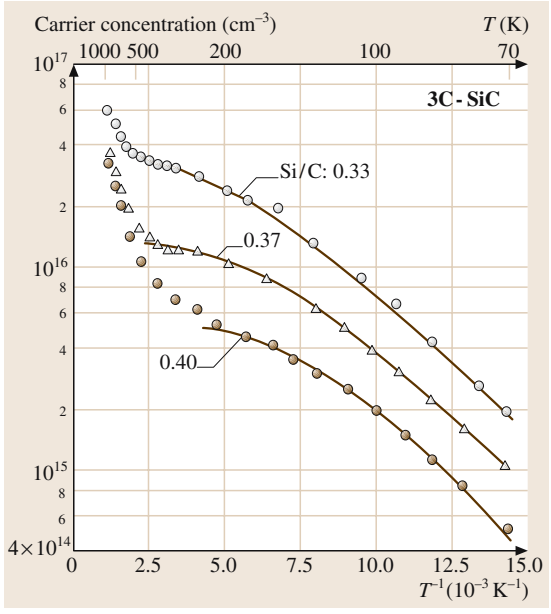


**Fig. 4.1-34** 3C-SiC. Temperature dependence of carrier concentration for n-type films grown by CVD on Si(100) substrates [1.25]. *Solid lines*, calculated values. Si/C = ratio of source gases

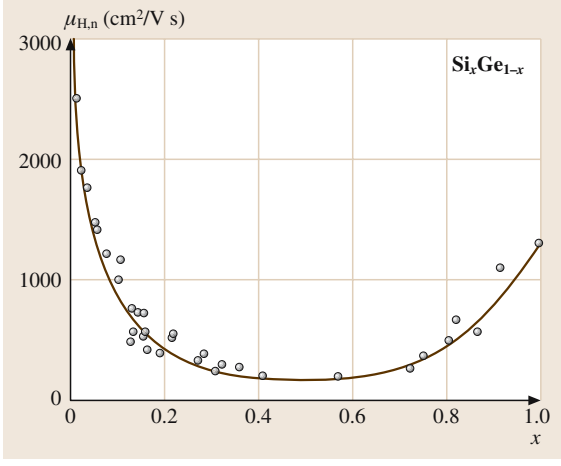


**Fig. 4.1-35** $Si_xGe_{1-x}$. Composition dependence of the electron Hall mobility at room temperature [1.26]

**Fig. 4.1-36** $Si_xGe_{1-x}$. Composition dependence of the intrinsic conductivity at room temperature [1.26]

**Table 4.1-20** Electron mobilities $\mu_n$ and hole mobilities $\mu_p$ of Group IV semiconductors and IV–IV compounds

| Crystal | $\mu_n$ ($cm^2/V\,s$) | $\mu_p$ ($cm^2/V\,s$) | $T$ (K) | Remarks |
|---|---|---|---|---|
| Diamond | 2000 | 2100 | 293 | See Figs. 4.1-38 and 4.1-39 for temperature dependence |
| Silicon | 1450 | 370<br>$2\times10^5$ | 300<br>20 | See Figs. 4.1-40 and 4.1-41 for temperature dependence |
| Germanium | 3800 | 1800 | 300 | See Figs. 4.1-33 and 4.1-42 for temperature dependence |
| Gray tin | $\mu_n(\Gamma_8)\ 0.12\times10^6$<br>$\mu_n(L_6)\ 1.6\times10^3$ | $10\times10^3$ | 100 | From Hall and magnetoresistance data, via conductivity and Hall coefficient |
| Silicon carbide (3C-SiC) | 510 | 15–21 | 296 | Epitaxial film grown on Si(100) |

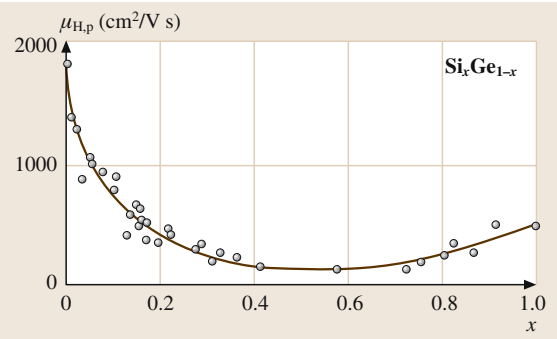


**Fig. 4.1-37** $Si_xGe_{1-x}$. Composition dependence of the hole Hall mobility at room temperature [1.26]

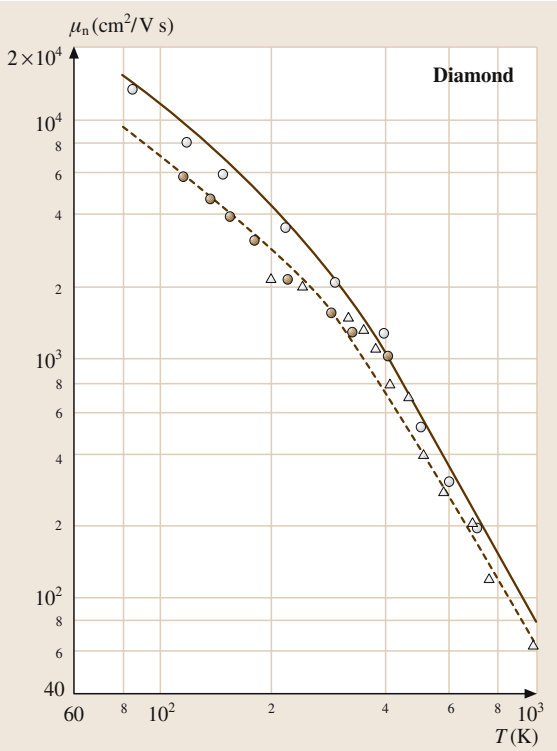


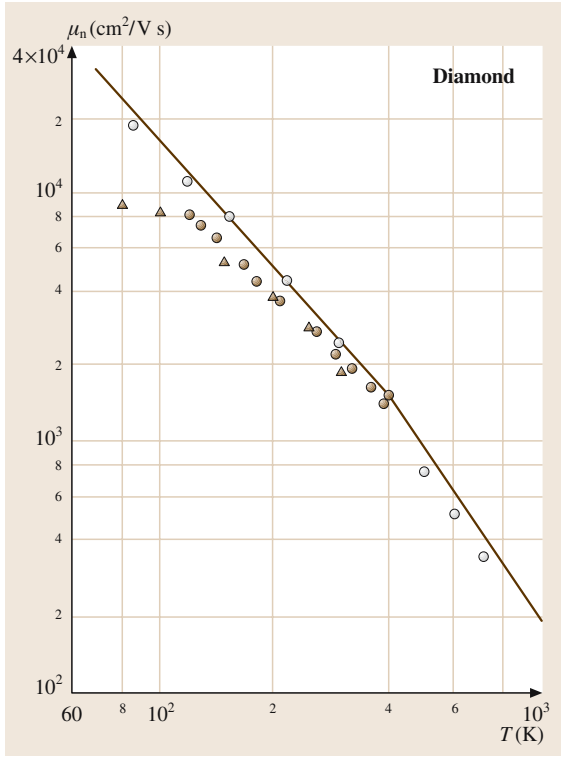


**Fig. 4.1-38** Diamond. Electron mobility vs. temperature. *Open circles*, drift mobility data from [1.27]; *filled triangles* and *filled circles*, Hall mobility data from [1.28] and [1.29, 30], respectively. *Continuous curve*, theoretical drift mobility [1.27]

**Fig. 4.1-39** Diamond. Hole mobility vs. temperature. *Open circles*, drift mobility data from [1.31]; *filled circles* and *filled triangles*, Hall mobility data from [1.29, 30] and [1.32], respectively. *Solid* and *dashed curves*: calculated drift and Hall mobilities, respectively [1.33]

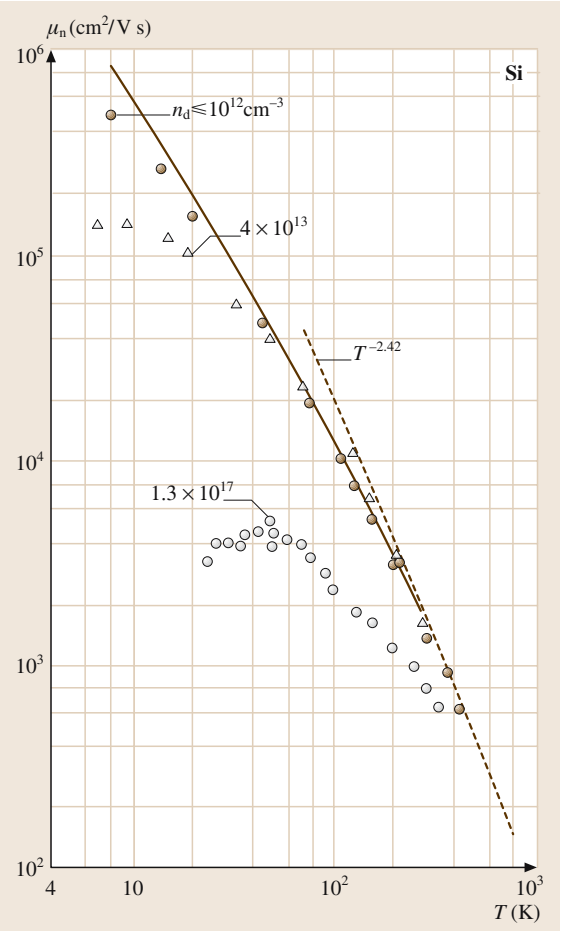


**Fig. 4.1-40** Si. Electron mobility vs. temperature [1.34]. Data points for $n_d \leq 10^{12}\,\mathrm{cm}^{-3}$ obtained by time-of-flight technique [1.35]. Other experimental values taken from [1.36] ($4 \times 10^{13}\,\mathrm{cm}^{-3}$) and [1.23] ($1.3 \times 10^{17}\,\mathrm{cm}^{-3}$). *Continuous line*, theoretical lattice mobility, after [1.35]. *Dash–dotted line*, $T^{-2.42}$ dependence of $\mu_n$ around room temperature

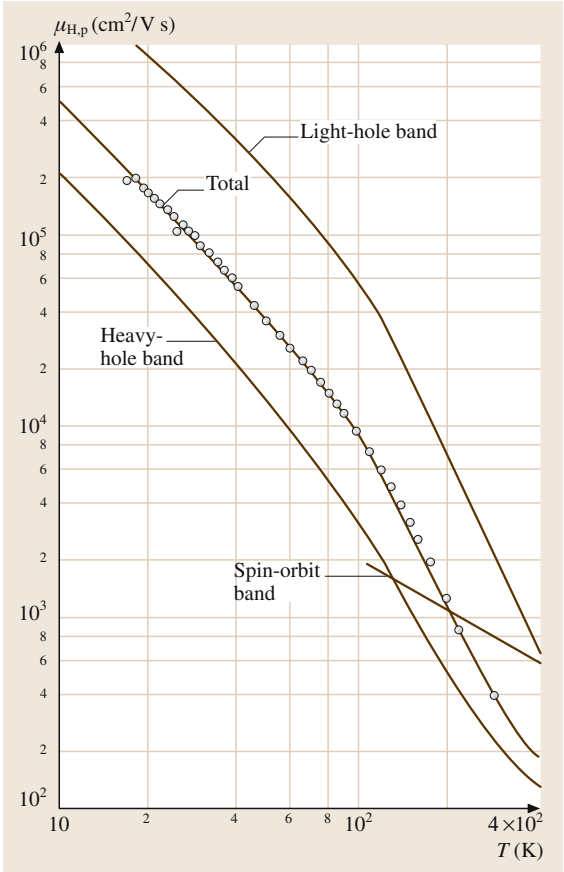


**Fig. 4.1-41** Si. (b) Hall hole mobility vs. temperature; *circles* from [1.37], *solid lines* calculated contributions from the three valence bands

*Silicon (Si).* The electronic transport is due exclusively to electrons in the [100] conduction band minima and holes in the two uppermost (heavy and light) valence bands. In samples with impurity concentrations below $10^{12}\,\mathrm{cm}^{-3}$, the mobilities are determined by pure lattice scattering down to temperatures of about 10 K (n-type) or 50 K (p-type), for electrons and holes, respectively. Higher impurity concentrations lead to deviations from the lattice mobility at corresponding higher temperatures. For electrons, the lattice mobility below 50 K is dominated by deformation-potential coupling to accoustic phonons. At higher temperatures, intervalley scattering between the six equivalent minima of the conduction band is added to the intravalley process, modifying the familiar $T^{-1.5}$ dependence of the acoustic-mode-dominated mobility to $T^{-2.42}$. At temperatures below 100 K, the lattice mobility of holes is dominated by acoustic scattering, but does not follow a $T^{-1.5}$ law, owing to the nonparabolicity of the valence bands. The proportionality of $\mu_p$ to $T^{-2.2}$ around room temperature is a consequence of optical-phonon scattering.

*Germanium (Ge).* Low-field electronic transport is provided by electrons in the $L_6$ minima of the conduction band and holes near the $\Gamma_8$ point in the valence bands. At room temperature, the mobility of samples with impurity concentrations below $10^{15}\,\mathrm{cm}^{-3}$ is limited essentially by lattice scattering; higher donor or acceptor concen-

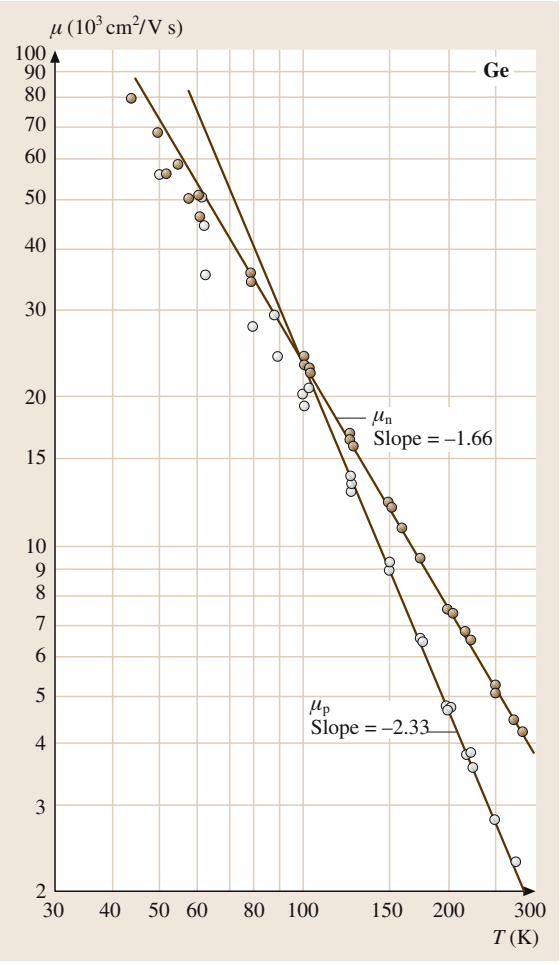


**Fig. 4.1-42** Ge. Electron and hole mobilities vs. temperature for a constant carrier concentration (high-purity samples) [1.38]

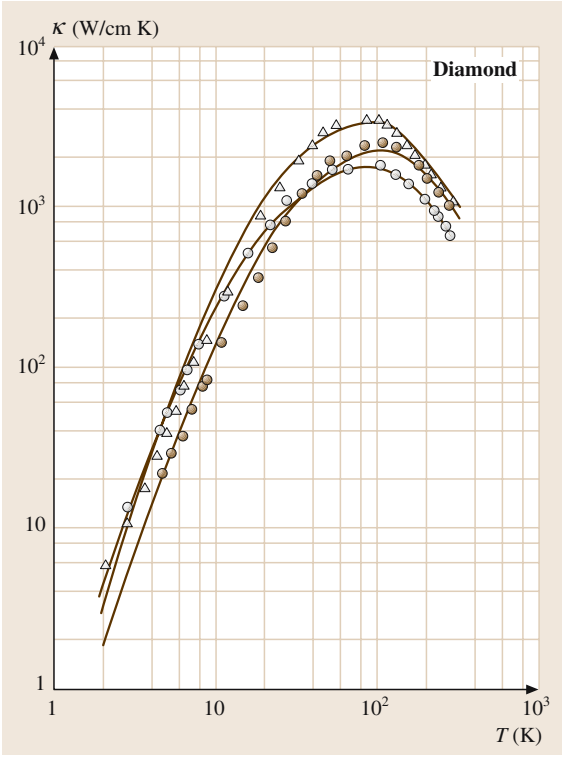


**Fig. 4.1-43** Diamond. Thermal conductivity vs. temperature for three type Ia diamonds [1.39]

trations result in an increasing influence of impurity scattering. At 77 K, even for doping concentrations below $10^{13}$ cm$^{-3}$, the mobilities depend on the impurity concentration. Low temperatures and high concentrations lead to the replacement of free-carrier conduction by impurity conduction.

*Gray Tin (α-Sn).* In intrinsic samples, light electrons and holes in the $\Gamma_8$ bands determine the transport properties. When the Fermi level crosses the energy of the $L_6$ minima, heavy electrons have an influence. This leads, for example, to a screening enhancement of the light-electron mobility and, in heavily doped n-type samples, to a dominant role of the L electrons. Consequently,

**Table 4.1-21** Thermal conductivity $\kappa$ of Group IV semiconductors and IV–IV compounds

| Crystal | | $\kappa$ (W/cm K) | Temperature (K) | Remarks |
|---|---|---|---|---|
| Diamond | C | 6–10 | 293 | See Fig. 4.1-43 for temperature dependence |
| Silicon | Si | 1.56 | 300 | See Fig. 4.1-44 for temperature dependence |
| Germanium | Ge | | | See Fig. 4.1-46 for temperature dependence |
| Silicon carbide | 3C-SiC | | | |
| | 6H-SiC | 4.9 | 300 | Perpendicular to *c* axis; See Fig. 4.1-45 for temperature dependence |

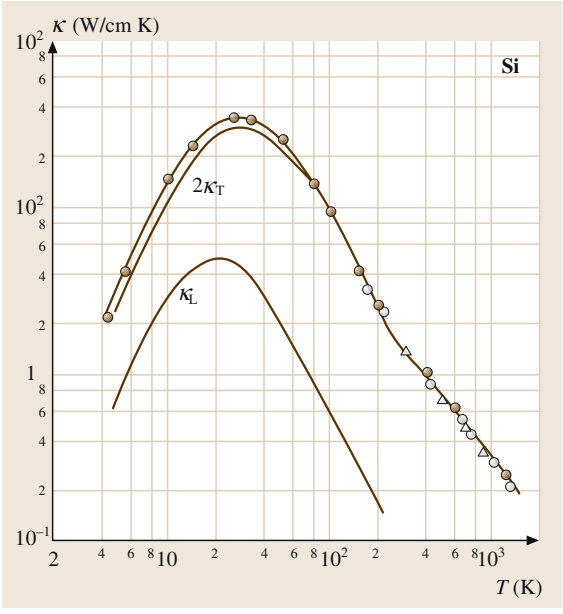


**Fig. 4.1-44** Si. Lattice thermal conductivity vs. temperature, according to [1.40] (*filled circles*), [1.41] (*open circles*), and [1.42] (*triangles*). The *curves* marked $\kappa_L$ and $2\kappa_T$ represent the contributions of the longitudinal and transverse phonons, respectively [1.43]

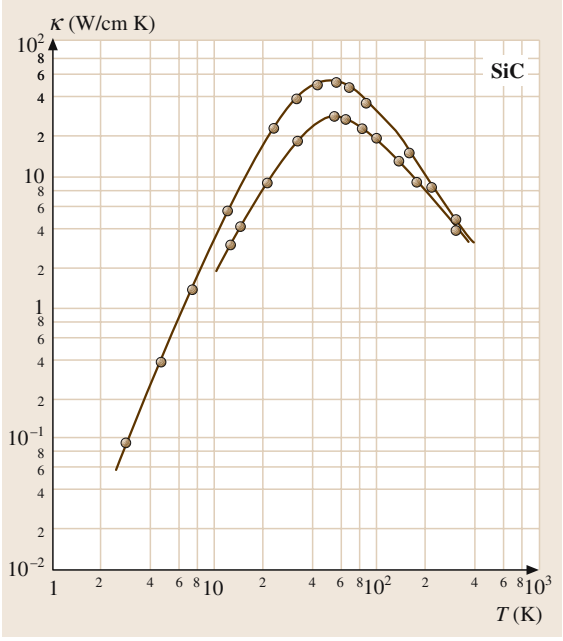


**Fig. 4.1-45** 6H-SiC. Thermal conductivity ($\perp c$ axis) vs. temperature for two different samples [1.44]

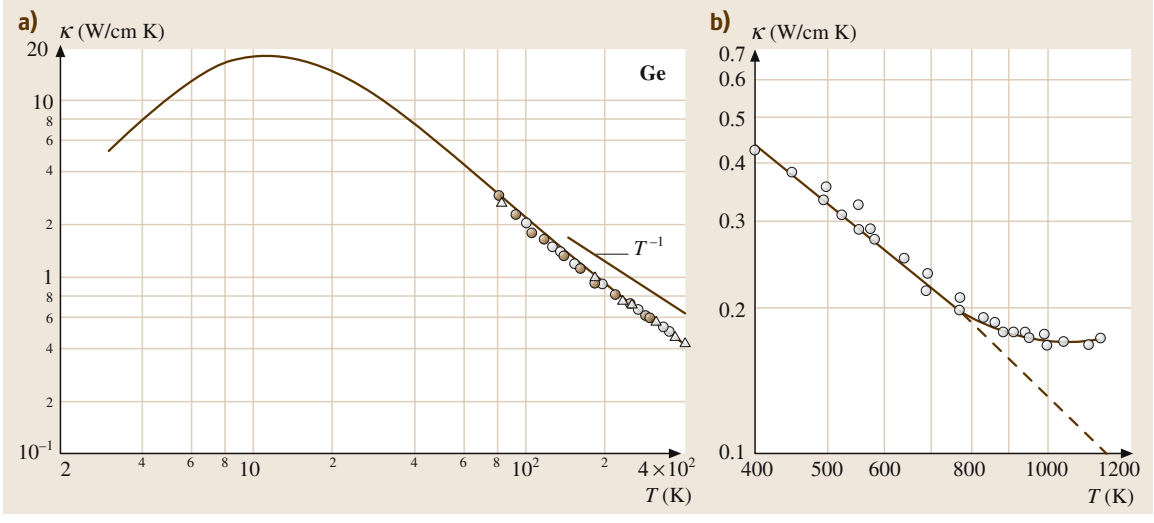


**Fig. 4.1-46a,b** Ge. Thermal conductivity vs. temperature. **(a)** 3–400 K, **(b)** 400–1200 K. *Solid curve* in **(a)** and data in **(b)** from [1.40]; experimental data in **(a)** from [1.45]. *Dashed line* in **(b)**, extrapolated lattice component

heavily doped n-type samples behave as indirect-gap semiconductors with an $E_g$ of about 0.09 eV.

*Silicon–Germanium Alloys ($Si_xGe_{1-x}$).* The transport properties have been investigated mostly on single crystals. The mobility is influenced by alloy scattering, which makes a contribution $\mu_{alloy} \propto T^{0.8} x^{-1}(1-x)^{-1}$. Near the band crossover ($x = 0.15$), intervalley scattering has to be taken into account.

### D. Electromagnetic and Optical Properties

Tables 4.1-22 – 4.1-25.

**Table 4.1-22** High-frequency dielectric constant $\varepsilon$ (real part of the complex dielectric constant) of Group IV semiconductors and IV–IV compounds

| Crystal | | $\varepsilon$ | $T$ (K) | Frequency | Method |
|---|---|---|---|---|---|
| Diamond | C | 5.70 (5) | 300 | 1 – 10 kHz | Capacitance bridge |
| Silicon | Si | 12.1 | 4.2 | 750 MHz | Capacitance bridge |
| | | 11.97 | 300 | | |
| Germanium | Ge | 16.5 | 4.2 | 750 MHz | Capacitance bridge |
| | | 16.0 | 4.2 | 9200 MHz | Microwave measurement |
| | | 16.2 | 300 | | |
| | | 15.8 | 77 | 1 MHz | Capacitance bridge |
| Gray tin | $\alpha$-Sn | 24 | 300 | Infrared | Infrared reflectance measurement |
| Silicon carbide | 3C-SiC | 9.52 | 300 | Low frequency | Infrared transmission |
| | | 6.38 | | High frequency | |
| Silicon carbide | 6H-SiC | 9.66 | 300 | Low frequency | $\varepsilon_{perp}$ |
| | | 10.03 | | | $\varepsilon_{parall}$ |
| | | 6.52 | 300 | High frequency | $\varepsilon_{perp}$ |
| | | 6.70 | | | $\varepsilon_{parall}$ |

*Optical Constants.* The real part ($\varepsilon_1$) and imaginary part ($\varepsilon_2$) of the dielectric constant at optical frequencies were measured by spectroscopic ellipsometry. The refractive index $n$, the extinction coefficient $k$, the absorption coefficient $K$, and the reflectivity $R$ have been calculated from $\varepsilon_1$ and $\varepsilon_2$. The frequency dependences of $\varepsilon_1$, $\varepsilon_2$, $n$, and $K$ are shown in Figs. 4.1-48 and 4.1-47.

*Diamond.* The refractive index $n$ is equal to 3.5 at $\lambda = 177.0$ nm. The spectral dependence of the refractive index $n$ can be approximated by the empirical formula

$$n^2 - 1 = a\lambda^2 / \left(\lambda^2 - \lambda_1^2\right) + b\lambda^2 / \left(\lambda^2 - \lambda_2^2\right) ,$$

with the parameters $a = 0.3306$, $b = 4.3356$, $\lambda_1 = 175.0$ nm, and $\lambda_2 = 106.0$ nm.

*Silicon.* (See Table 4.1-23).

*Germanium.* (See Fig. 4.1-48).

*Gray Tin ($\alpha$-Sn).* The index of refraction $n$, extinction coefficient $k$, and absorption coefficient $K$ versus photon energy are shown in Fig. 4.1-47.

*Silicon Carbide (SiC).*

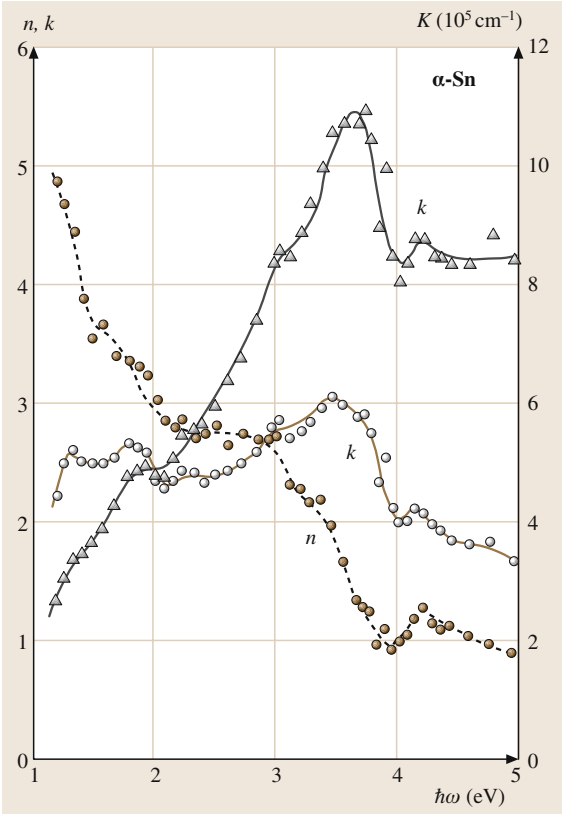


**Fig. 4.1-47** $\alpha$-Sn. Index of refraction $n$, extinction coefficient $k$, and absorption coefficient $K$ vs. photon energy [1.46]

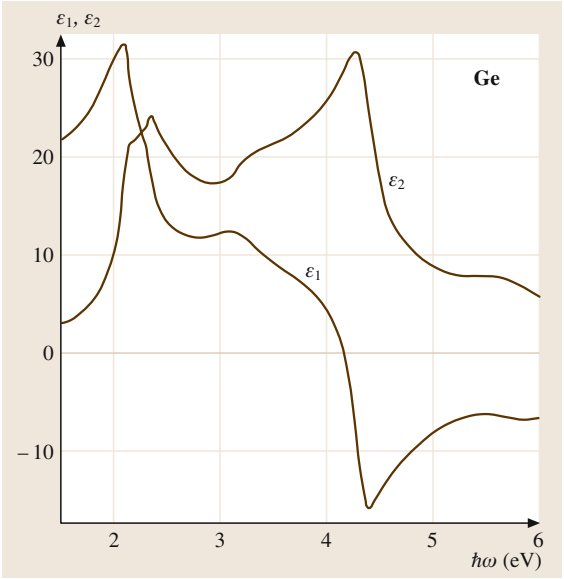


**Fig. 4.1-48** Ge. Real and imaginary parts of the dielectric constant vs. photon energy [1.47]

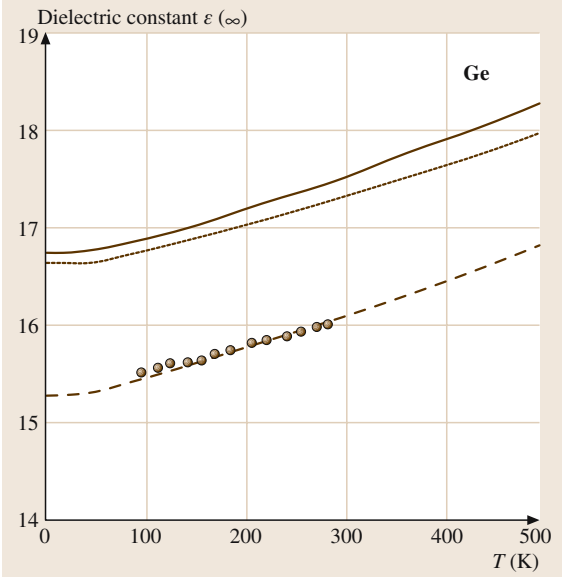


**Fig. 4.1-49** Ge. Temperature dependence of the high-frequency dielectric constant [1.48]. Experimental data points [1.49] and ab initio calculations (*solid line*); the *dotted line* is the theoretical result without the effect of thermal expansion, and the *dashed line* is the *solid line* shifted to match the experimental data

**Table 4.1-23** Optical constants of silicon

| $h\nu$ (eV) | $\varepsilon_1$ | $\varepsilon_2$ | $n$ | $k$ | $K$ ($10^3$/cm) | $R$ |
|---|---|---|---|---|---|---|
| 1.5 | 13.488 | 0.038 | 3.673 | 0.005 | 0.78 | 0.327 |
| 2.0 | 15.254 | 0.172 | 3.906 | 0.022 | 4.47 | 0.351 |
| 2.5 | 18.661 | 0.630 | 4.320 | 0.073 | 18.48 | 0.390 |
| 3.0 | 27.197 | 2.807 | 5.222 | 0.269 | 81.73 | 0.461 |
| 3.5 | 22.394 | 33.818 | 5.610 | 3.014 | 1069.19 | 0.575 |
| 4.0 | 12.240 | 35.939 | 5.010 | 3.586 | 1454.11 | 0.591 |
| 4.5 | −19.815 | 24.919 | 2.452 | 5.082 | 2317.99 | 0.740 |
| 5.0 | −10.242 | 11.195 | 1.570 | 3.565 | 1806.67 | 0.675 |
| 5.5 | −9.106 | 8.846 | 1.340 | 3.302 | 1840.59 | 0.673 |
| 6.0 | −7.443 | 5.877 | 1.010 | 2.909 | 1769.27 | 0.677 |

**Table 4.1-24** Optical constants of germanium

| $h\nu$ (eV) | $\varepsilon_1$ | $\varepsilon_2$ | $n$ | $k$ | $K$ ($10^3$/cm) | $R$ |
|---|---|---|---|---|---|---|
| 1.5 | 21.560 | 2.772 | 4.653 | 0.298 | 45.30 | 0.419 |
| 2.0 | 30.361 | 10.427 | 5.588 | 0.933 | 189.12 | 0.495 |
| 2.5 | 13.153 | 20.695 | 4.340 | 2.384 | 604.15 | 0.492 |
| 3.0 | 12.065 | 17.514 | 4.082 | 2.145 | 652.25 | 0.463 |
| 3.5 | 9.052 | 21.442 | 4.020 | 2.667 | 946.01 | 0.502 |
| 4.0 | 4.123 | 26.056 | 3.905 | 3.336 | 1352.55 | 0.556 |
| 4.5 | −14.655 | 16.782 | 1.953 | 4.297 | 1960.14 | 0.713 |
| 5.0 | −8.277 | 8.911 | 1.394 | 3.197 | 1620.15 | 0.650 |
| 5.5 | −6.176 | 7.842 | 1.380 | 2.842 | 1584.57 | 0.598 |
| 6.0 | −6.648 | 5.672 | 1.023 | 2.774 | 1686.84 | 0.653 |

**Table 4.1-25** Optical constants of silicon carbide

| Crystal | Refractive index | Wavelength range (nm) |
|---|---|---|
| 3C-SiC | $n(\lambda) = 2.55378 + 3.417 \times 10^4/\lambda^2$ | 467–691 |
| 6H-SiC | $n_o(\lambda) = 2.5531 + 3.34 \times 10^4/\lambda^2$<br>$n_e(\lambda) = 2.5852 + 3.68 \times 10^4/\lambda^2$ | |

## 4.1.2 III–V Compounds

### 4.1.2.1 Boron Compounds

A. Crystal Structure, Mechanical and Thermal Properties

Tables 4.1-26 – 4.1-32.

**Table 4.1-26** Crystal structures of boron compounds

| Crystal | | Space group | | Crystal system | Structure type | Remarks | Figure |
|---|---|---|---|---|---|---|---|
| Boron nitride, hexagonal | $BN_{hex}$ | | $P6_3/mmc$ | hex | h-BN | Stable under normal conditions | Fig. 4.1-50 |
| Boron nitride, cubic | $BN_{cub}$ | $T_d^2$ | $F\bar{4}3m$ | fcc | Zinc blende | Metastable under normal conditions | Fig. 4.1-2 |
| Boron nitride, wurtzite | $BN_w$ | $C_{6v}^4$ | $P6_3mc$ | hex | Wurtzite | Metastable under all conditions | Fig. 4.1-3 |
| Boron phosphide | BP | $T_d^2$ | $F\bar{4}3m$ | fcc | Zinc blende | Stable under normal conditions | Fig. 4.1-2 |
| Boron arsenide | BAs | $T_d^2$ | $F\bar{4}3m$ | fcc | Zinc blende | Stable in presence of As vapor up to 920 °C | Fig. 4.1-2 |
| Boron antimonide | BSb | $T_d^2$ | $F\bar{4}3m$ | fcc | Zinc blende | Stable under normal conditions | Fig. 4.1-2 |

**Table 4.1-27** Lattice parameters of boron compounds

| Crystal | | Lattice parameters (nm) | Temperature (K) | Remarks |
|---|---|---|---|---|
| Boron nitride, cubic | $BN_{cub}$ | $a = 0.36160\,(3)$ | RT | X-ray diffraction |
| Boron nitride, hexagonal | $BN_{hex}$ | $a = 0.25072\,(1)$ | 297 | Prepared from amorphous BN in |
| | | $c = 0.687\,(1)$ | 297 | $N_2$ atmosphere at room temperature |
| Boron phosphide | BP | $a = 0.45383\,(4)$ | 297 | |
| Boron arsenide | BAs | $a = 0.4777$ | | |
| Boron antimonide | BSb | $a = 0.512$ | | Ab initio pseudopotential calculation |

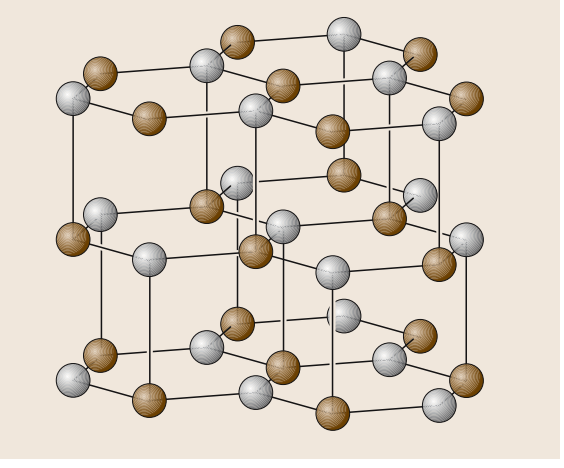

**Fig. 4.1-50** The hexagonal lattice of h-BN ($BN_{hex}$)

**Table 4.1-28** Densities of boron compounds

| Crystal | | Density ($g/cm^3$) | Remarks |
|---|---|---|---|
| Boron nitride, cubic | $BN_{cub}$ | 3.4863 | X-ray diffraction |
| Boron nitride, hexagonal | $BN_{hex}$ | 2.279 | X-ray density |
| Boron phosphide | BP | | |
| Boron arsenide | BAs | 5.22 | |

**Table 4.1-29** Melting point $T_m$ or decomposition temperature of boron compounds

| Crystal | | Melting point $T_m$ (K) | Remarks |
|---|---|---|---|
| Boron nitride, cubic | $BN_{cub}$ | > 3246 | |
| Boron nitride, hexagonal | $BN_{hex}$ | 3200–3400 | $N_2$ ambient; pyrometric measurement |
| Boron phosphide | BP | 1400 | Decomposition temperature |

**Table 4.1-30** Linear thermal expansion coefficient $\alpha$ of boron compounds

| Crystal | | Expansion coefficient $\alpha$ ($K^{-1}$) | Remarks |
|---|---|---|---|
| Boron nitride, cubic | $BN_{cub}$ | $1.15 \times 10^{-6}$ | X-ray measurement |
| Boron nitride, hexagonal | $BN_{hex}$ | $40.6\,(4) \times 10^{-6}$ | |
| Boron phosphide | BP | $3.65 \times 10^{-6}$ | At 400 K |
| Boron arsenide | BAs | $4.1 \times 10^{-6}$ | Calculated |

**Table 4.1-31** Heat capacities and Debye temperatures of boron compounds

| Crystal | | Debye temperature $\Theta_D$ (K) | Remarks |
|---|---|---|---|
| Boron nitride, cubic | $BN_{cub}$ | 1730 (70) | See Fig. 4.1-51 for temp. dependence of $c_p$ |
| Boron nitride, hexagonal | $BN_{hex}$ | 598 (7) | Calorimetry |
| Boron phosphide | BP | 985 | See Fig. 4.1-52 for temp. dependence of $c_p$ |
| Boron arsenide | BAs | 800 | |

**Table 4.1-32** Phonon wavenumbers/frequencies of boron compounds. Values for hexagonal boron nitride ($BN_{hex}$) obtained from infrared reflectivity; values for boron phosphide (BP) from ab initio pseudopotential calculations

| Crystal | | Phonon wavenumbers ($cm^{-1}$) | | | | Remarks |
|---|---|---|---|---|---|---|
| Boron nitride, cubic | $BN_{cub}$ | $\tilde{\nu}_{LO}$ | 1305 (1) | $\tilde{\nu}_{TO}$ | 1054.7 (6) | RT; Raman scattering |
| Boron arsenide | BAs | $\tilde{\nu}_{LO}$ (Γ) | 714 | $\tilde{\nu}_{TO}$ (Γ) | 695 | Raman scattering |

**Table 4.1-32** Phonon wavenumbers/frequencies, cont.

| $BN_{hex}$ | |
|---|---|
| **Phonon branch** | **Wavenumber ($cm^{-1}$)** |
| $\tilde{\nu}_{TO1}$ | 783 |
| $\tilde{\nu}_{LO1}$ | 828 |
| $\tilde{\nu}_{TO2}$ | 1510 |
| $\tilde{\nu}_{LO2}$ | 1595 |
| $\tilde{\nu}_{TO1}$ | 767 |
| $\tilde{\nu}_{LO1}$ | 778 |
| $\tilde{\nu}_{TO2}$ | 1367 |
| $\tilde{\nu}_{LO2}$ | 1610 |

**Table 4.1-32** Phonon wavenumbers/frequencies, cont.

| BP | |
|---|---|
| **Phonon branch** | **Frequency (THz)** |
| $\nu_{TO}$ (Γ) | 24.25 |
| $\nu_{LO}$ (X) | 24.00 |
| $\nu_{TO}$ (X) | 15.81 |
| $\nu_{LO}$ (X) | 21.04 |
| $\nu_{TO}$ (X) | 9.20 |
| $\nu_{LO}$ (L) | 22.91 |
| $\nu_{TO}$ (L) | 15.18 |

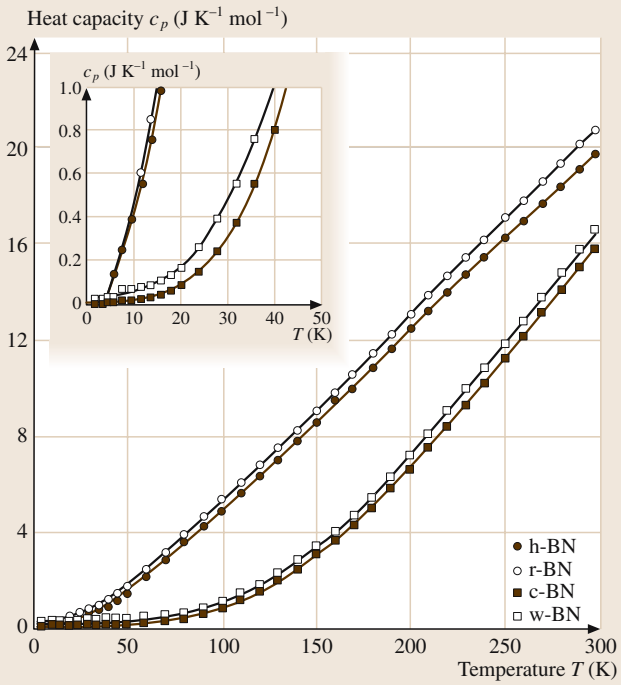


**Fig. 4.1-51** BN. Heat capacities for four polymorphic boron nitride modifications. Data taken from [1.50]

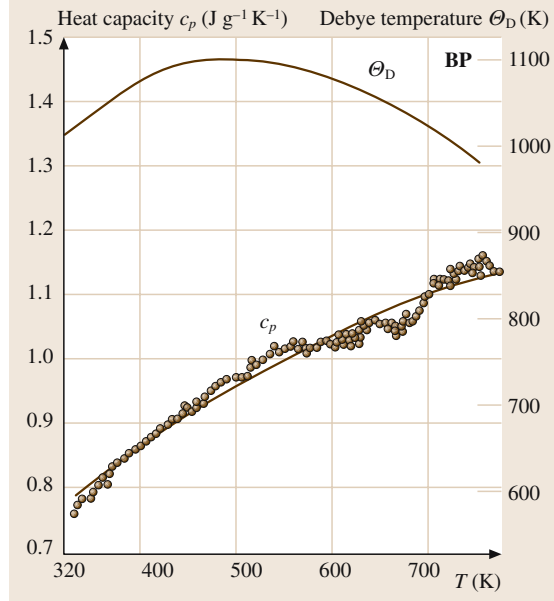


**Fig. 4.1-52** BP. Temperature dependence of specific heat capacity and Debye temperature [1.51]

### B. Electronic Properties

Tables 4.1-33 – 4.1-35.

*Band Structures of Boron Compounds.*

*Boron Nitride, Cubic ($BN_{cub}$).* All band structure calculations lead to an indirect-gap structure (Fig. 4.1-53).

*Boron Nitride, Hexagonal ($BN_{hex}$).* All recent band structure calculations yield an indirect gap (Fig. 4.1-54). The conduction band minimum is located at P.

*Boron Phosphide (BP).* BP is an indirect-gap semiconductor (Fig. 4.1-55).

*Boron Arsenide (BAs).* The calculated band structure shows an indirect (Γ–X) gap of a few eV. The conduction

**Table 4.1-33** First Brillouin zones of boron compounds

| Crystal | | Figure |
|---|---|---|
| Boron nitride, cubic | $BN_{cub}$ | Fig. 4.1-23 |
| Boron nitride, hexagonal | $BN_{hex}$ | Fig. 4.1-24 |
| Boron phosphide | BP | Fig. 4.1-23 |
| Boron arsenide | BAs | Fig. 4.1-23 |

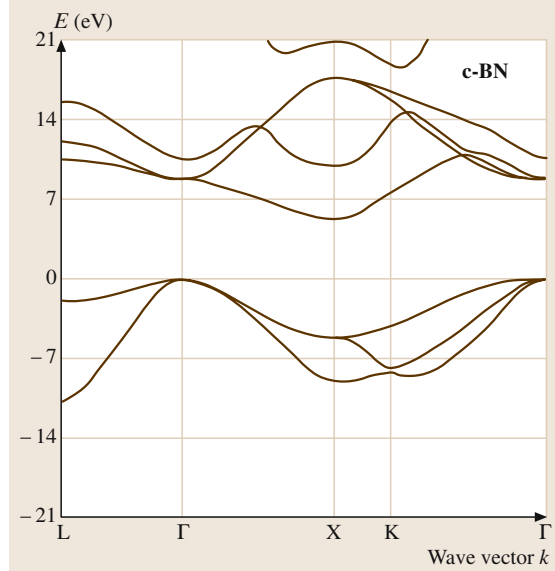


**Fig. 4.1-53** Band structure of cubic boron nitride

**Table 4.1-34** Energy gaps of boron compounds

| Crystal | | Quantity | Bands | Energy (eV) | Remarks |
|---|---|---|---|---|---|
| Boron nitride, cubic | $BN_{cub}$ | $E_{g,\,ind}$ | $\Gamma_{15v}$ to $X_{1c}$ | 6.2 | Soft-X-ray emission spectroscopy |
| | | $E_{g,\,dir}$ | $\Gamma_{15v}$ to $\Gamma_{1c}$ | 14.5 | Reflectivity |
| Boron nitride, hexagonal | $BN_{hex}$ | $E_g$ | | 5.9 (1) | Inelastic electron scattering |
| | | $E_{g,\,th}$ | | 7.1 (1) | Temperature dependence of electrical resistivity |
| Boron phosphide | BP | $E_{g,\,ind}$ | | 2.1 | X-ray emission and absorption |
| | | $E_{g,\,dir}$ | $\Gamma$ | 4.4 | |
| | | | X | 6.5 | |
| | | | L | 6.5 | |
| Boron arsenide | BAs | $E_{g,\,ind}$ | | 0.67 | Absorption |
| | | $E_{g,\,dir}$ | | 1.46 | |
| Boron antimonide | BSb | $E_g$ | $\Gamma$ to $\Delta$ | 0.527 | Calculated |

**Table 4.1-35** Effective masses of electrons ($m_n$) and holes ($m_p$) for cubic boron nitride (in units of the electron mass $m_0$)

| Crystal | | $m_n$ | $m_{p,\,heavy}$ | $m_{p,\,light}$ | Remarks |
|---|---|---|---|---|---|
| Boron nitride, cubic | $BN_{cub}$ | 0.752 | | | Calculated from band structure data |
| | | | 0.375 | 0.150 | Parallel to [100] |
| | | | 0.926 | 0.108 | Parallel to [111] |

band minimum is on the $\Delta$ axis close to the X point. As in silicon, the $\Gamma_{15c}$ level is below the $\Gamma_{1c}$ level (Fig. 4.1-56). *Boron Antimonide (BSb)*. Boron antimonide is an indirect-gap semiconductor (Fig. 4.1-57).

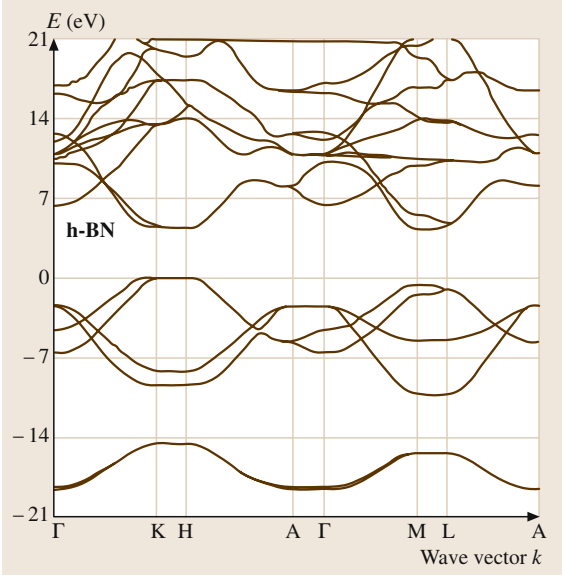


**Fig. 4.1-54** Band structure of hexagonal boron nitride

**Fig. 4.1-55** Band structure of boron phosphide ▶

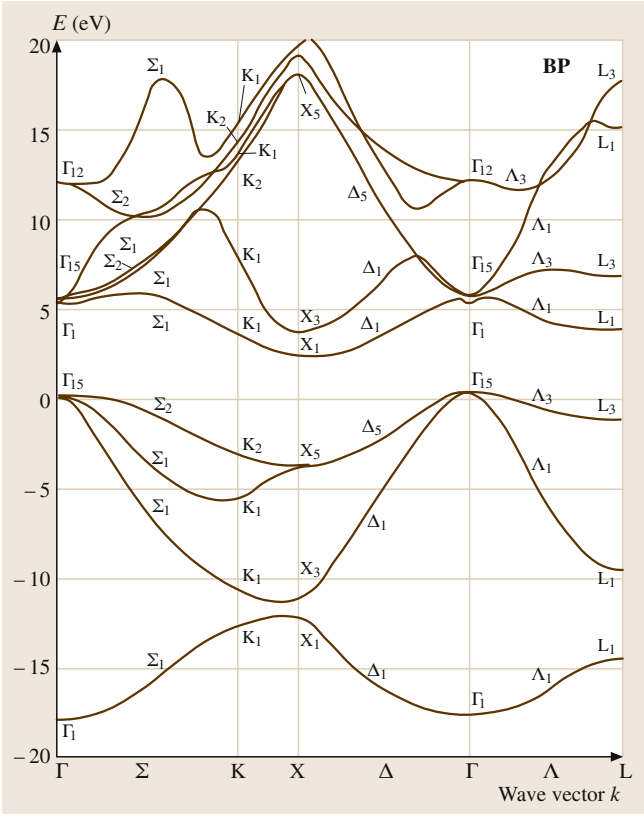

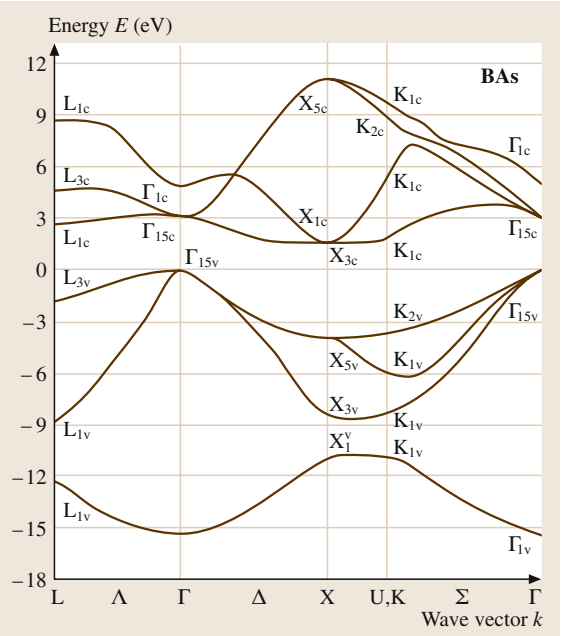


**Fig. 4.1-56** Band structure of boron arsenide

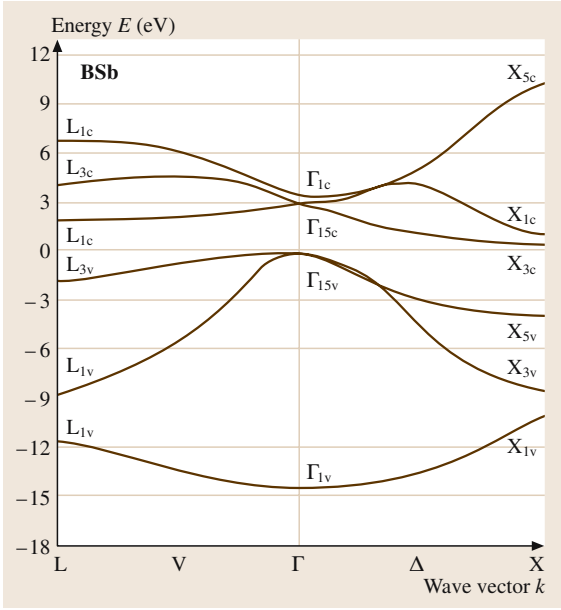


**Fig. 4.1-57** Band structure of boron antimonide

### C. Transport Properties

*Electronic Transport, General Description.* *Boron Nitride, Cubic ($BN_{cub}$).* Owing to the large gap, all literature data refer to extrinsic conduction. For the temperature dependence of the conductivity, see Fig. 4.1-58. Hall measurements on nominally undoped thin films yield values of the carrier mobility of around 500 $cm^2/V\,s$.

*Boron Nitride, hexagonal ($BN_{hex}$).* Figure 4.1-59 shows the temperature dependence of the electrical resistivity at high temperatures. In an undoped nanocrystalline film, resistivity values of the order of $2 \times 10^{11}\ \Omega\,cm$ have been found.

*Boron Phosphide (BP).* Boron phosphide is extrinsic at room temperature, and the transport is limited by impurity scattering. Figure 4.1-60 shows the temperature dependence of the conductivity, carrier concentration, and Hall mobility of several samples. In n-doped single crystals, electron mobilities of the order of 30–40 $cm^2/V\,s$ have been found at 300 K; in p-doped single crystals, mobilities around 500 $cm^2/V\,s$ have been measured at 300 K.

*Boron Arsenide (BAs).* There is almost no information about the semiconducting properties of BAs.

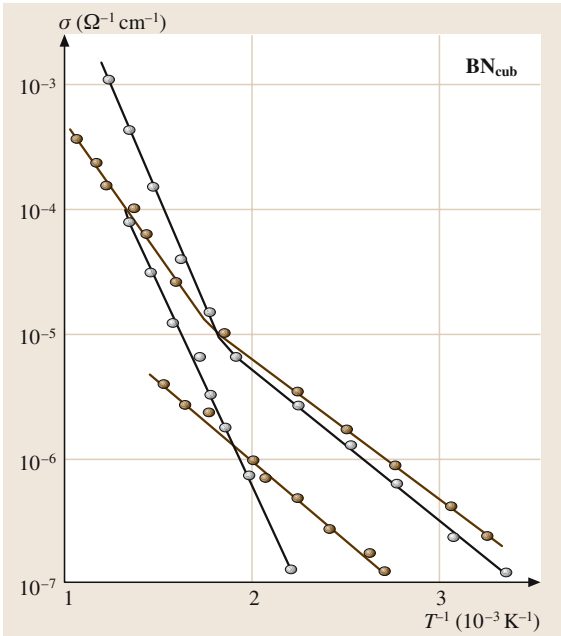


**Fig. 4.1-58** c-BN ($BN_{cub}$). Electrical conductivity vs. reciprocal temperature for several different polycrystalline samples above RT [1.52, 53]

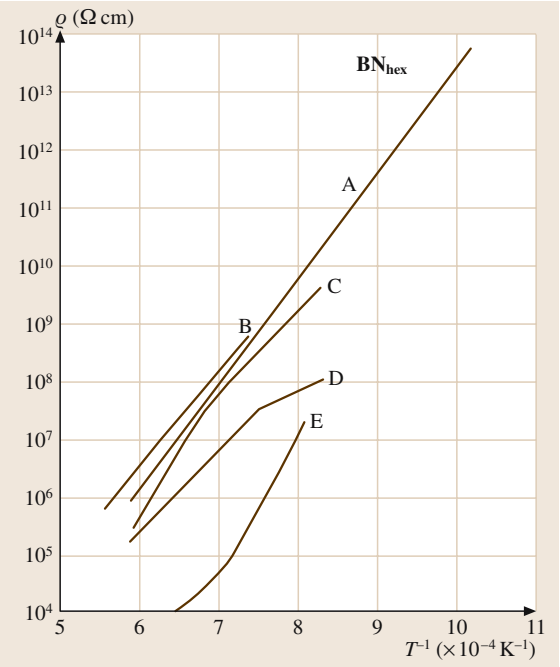


**Fig. 4.1-59** h-BN ($BN_{hex}$). Resistivity vs. temperature above 700 °C. A, from bulk resistance of a disk measured in the *c* direction; B – E, earlier literature data for comparison [1.54]

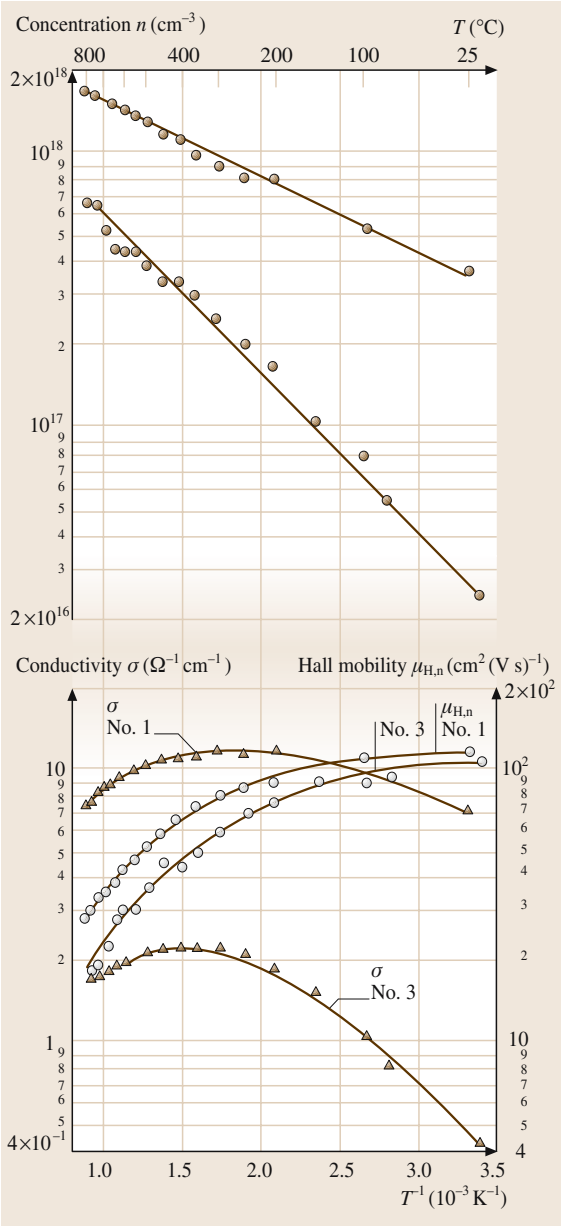


**Fig. 4.1-60** Temperature dependence of the conductivity $\sigma_i$, the carrier concentration $n$, and the mobility $\mu_{H,n}$ of n-type BP(100) wafers [1.55]. Sample No. 1 contains autodoped Si with a concentration of $5 \times 10^{18}$ atoms/cm$^3$ and sample No. 3 contains $5 \times 10^{19}$ atoms/cm$^3$

#### D. Electromagnetic and Optical Properties

Table 4.1-36.

**Table 4.1-36** Dielectric constant $\varepsilon$ and refractive index $n$ of boron compounds

| Crystal | | Temperature (K) | $\varepsilon(0)$ | $\varepsilon(\infty)$ | $n$ at $\lambda$ (nm) | Remarks |
|---|---|---|---|---|---|---|
| Boron nitride, cubic | $BN_{cub}$ | 300 | 7.1 | | 2.097 712.5 | IR reflectivity |
| Boron nitride, hexagonal | $BN_{hex}$ | 300 | 5.09<br>7.04 | 4.10<br>4.95 | 2.13<br>1.65 | Parallel to $c$ axis, IR reflectivity<br>Perpendicular to $c$ axis, IR reflectivity |
| Boron phosphide | BP | 300<br>RT | 11 | 7.8 | <br>3.34 (5) 454.5<br>3.34 (5) 458<br>3.32 (5) 488<br>3.30 (5) 496<br>3.26 (5) 514.5<br>3.00 (5) 632.8 | Schottky barrier reflectance<br>Brewster angle method |

### 4.1.2.2 Aluminium Compounds

#### A. Crystal Structure, Mechanical and Thermal Properties

Tables 4.1-37 – 4.1-44.

**Table 4.1-37** Crystal structures of aluminium compounds

| Crystal | | Space group | | Crystal system | Structure type | Remarks | Figure |
|---|---|---|---|---|---|---|---|
| Aluminium nitride | AlN I<br>AlN II | $C_{6v}^4$<br>$O_h^5$ | $P6_3mc$<br>$Fm\bar{3}m$ | hex<br>fcc | Wurtzite<br>NaCl structure | At normal pressure<br>At 21 GPa (shock compression) | Fig. 4.1-3 |
| Aluminium phosphide | AlP I<br>AlP II | $T_d^2$<br>$O_h^5$ | $F\bar{4}3m$<br>$Fm\bar{3}m$ | fcc<br>fcc | Zinc blende<br>NaCl structure | At normal pressure<br>High-pressure phase | Fig. 4.1-2 |
| Aluminium arsenide | AlAs | $T_d^2$ | $F\bar{4}3m$ | fcc | Zinc blende | Transition to NiAs structure at high pressure | Fig. 4.1-2 |
| Aluminium antimonide | AlSb I<br>AlSb II | $T_d^2$ | $F\bar{4}3m$<br>$Cmcm$ | fcc | Zinc blende<br>Orthorhombic | At normal pressure<br>At high pressure | Fig. 4.1-2 |

**Table 4.1-38** Lattice parameters of aluminium compounds

| Crystal | | Lattice parameters (nm) | Temperature | Remarks |
|---|---|---|---|---|
| Aluminium nitride | AlN | $a = 0.31111$<br>$c = 0.49788$ | 300 K | X-ray diffraction on ultrafine powder |
| Aluminium phosphide | AlP | $a = 0.54635$ (4) | 25 °C | Epitaxial film on GaP |
| Aluminium arsenide | AlAs | $a = 0.566139$ | 291 K | High-resolution X-ray diffraction |
| Aluminium antimonide | AlSb | $a = 0.61355$ (1) | 291.15 K | Powder, X-ray measurement |

**Table 4.1-39** Densities of aluminium compounds

| Crystal | | Density (g/cm$^3$) | Temperature (K) | Remarks |
|---|---|---|---|---|
| Aluminium nitride | AlN | 3.255 | | X-ray diffraction |
| Aluminium phosphide | AlP | 2.40 (1) | | |
| Aluminium arsenide | AlAs | 3.760 | | Calculated from lattice parameter |
| Aluminium antimonide | AlSb | 4.26 | 293 | |

**Table 4.1-40** Elastic constants $c_{ik}$ of aluminium compounds

| Crystal | | $c_{11}$ (GPa) | $c_{12}$ (GPa) | $c_{13}$ (GPa) | $c_{33}$ (GPa) | $c_{44}$ (GPa) | Remarks |
|---|---|---|---|---|---|---|---|
| Aluminium nitride | AlN | 296 (18) | 130 (11) | 158 (06) | 267 (18) | 241 (20) | [a] |
| Aluminium phosphide | AlP | 140.50 (28) | 62.03 (24) | | | 70.33 (7) | Ultrasound ($f = 10$ and 30 MHz) |
| Aluminium arsenide | AlAs | 190 (1) | 53.8 (1) | | | 59.5 (1) | $T = 300$ K |
| | | 122.1 (3) | 56.6 (3) | | | 59.9 (1) | $T = 77$ K |
| | | 112.6 | 57.1 | | | 60.0 | $T = 0$ K; extrapolated data |
| Aluminium antimonide | AlSb | 88.34 | 40.23 | | | 43.22 | $T = 296$ K; ultrasound |

[a] Calculated from the mean square displacement of the lattice atoms measured by X-ray diffraction.

**Table 4.1-41** Melting point $T_m$ of aluminium compounds

| Crystal | | Melting point $T_m$ (K) |
|---|---|---|
| Aluminium nitride | AlN | 3025 |
| Aluminium phosphide | AlP | 2823 |
| Aluminium arsenide | AlAs | 2013 (20) |
| Aluminium antimonide | AlSb | 1327 (1) |

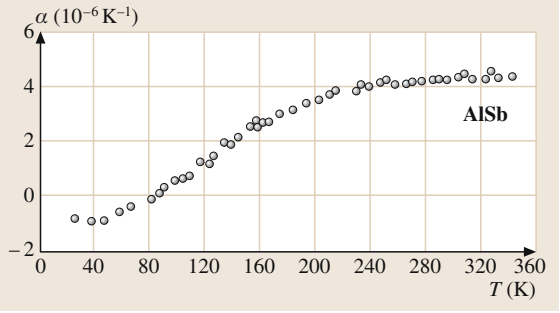


**Fig. 4.1-61** AlSb. Coefficient of linear thermal expansion vs. temperature [1.56, 57]

**Table 4.1-42** Linear thermal expansion coefficient $\alpha$ of aluminium compounds

| Crystal | | Expansion coefficient $\alpha$ (K$^{-1}$) | Temperature | Remarks |
|---|---|---|---|---|
| Aluminium nitride | AlN | $\alpha_{perpend}$ $4.35 \times 10^{-6}$<br>$\alpha_{parallel}$ $3.48 \times 10^{-6}$ | 300 K | Powder; X-ray diffraction |
| Aluminium phosphide | AlP | | | |
| Aluminium arsenide | AlAs | $5.20\,(5) \times 10^{-6}$ | 15–840 °C | X-ray diffraction |
| Aluminium antimonide | AlSb | | | Fig. 4.1-61 |

**Table 4.1-43** Phonon wavenumbers of aluminium compounds: aluminium nitride (300 K, from Raman scattering); aluminium Phosphide (from Raman spectroscopy); aluminium arsenide (from Raman spectroscopy; 0.5 μm layer of AlAs on GaAs; $T = 37$ K); aluminium antimonide (from Raman spectroscopy)

| AlN | | AlP | | | AlAs | | AlSb | |
|---|---|---|---|---|---|---|---|---|
| Symmetry point, polarization | Wave-number ($cm^{-1}$) | Symmetry point, polarization | Wave-number ($cm^{-1}$) | Temperature (K) | Symmetry point, polarization | Wave-number ($cm^{-1}$) | Symmetry point, polarization | Wave-number ($cm^{-1}$) |
| $\tilde{\nu}\ (E_2^{(1)})$ | 248.6 | $\tilde{\nu}_{LO}\ (\Gamma)$ | 504.5 (4) | 5 | $\tilde{\nu}_{LO}\ (\Gamma)$ | 404 (1) | $\tilde{\nu}_{LO}\ (\Gamma)$ | 334 [a] |
| $\tilde{\nu}_{TO}\ (A_1)$ | 611.0 | $\tilde{\nu}_{LO}\ (\Gamma)$ | 501.0 (2) | 300 | $\tilde{\nu}_{TO}\ (\Gamma)$ | 361 (1) | $\tilde{\nu}_{TO}(\Gamma)$ | 316 [a] |
| $\tilde{\nu}\ (E_2^{(2)})$ | 657.4 | $\tilde{\nu}_{TO}\ (\Gamma)$ | 442.5 (2) | 5 | $\tilde{\nu}_{LO}\ (X)$ | 403 (8) | $\tilde{\nu}_{TA}\ (X)$ | 64 [a] |
| $\tilde{\nu}_{TO}\ (E_1)$ | 670.8 | $\tilde{\nu}_{TO}\ (\Gamma)$ | 439.4 (2) | 300 | $\tilde{\nu}_{TO}\ (X)$ | 335 (8) | $\tilde{\nu}_{LA}\ (X)$ | 153 [a] |
| $\tilde{\nu}_{LO}\ (A_1)$ | 890.0 | | | | $\tilde{\nu}_{TA}\ (X)$ | 109 (8) | $\tilde{\nu}_{TO}\ (X)$ | 290 [a] |
| $\tilde{\nu}_{LO}\ (E_1)$ | 912.0 | | | | $\tilde{\nu}_{LA}\ (X)$ | 222 (12) | $\tilde{\nu}_{LO}\ (X)$ | 343 [a] |

**Table 4.1-43** Wavenumbers of aluminium compounds, cont.

| AlSb | |
|---|---|
| Symmetry point, polarization | Wave-number ($cm^{-1}$) |
| $\tilde{\nu}_{TA}\ (L)$ | 49 [a] |
| $\tilde{\nu}_{LA}\ (K)$ | 149 [a] |
| $\tilde{\nu}_{TO}\ (L)$ | 306 [a] |
| $\tilde{\nu}_{LO}\ (L)$ | 327 [a] |
| $\tilde{\nu}_{LO}\ (\Gamma)$ | 340.0 (7) [b] |
| $\tilde{\nu}_{TO}\ (\Gamma)$ | 318.7 (7) [b] |

[a] Ab initio pseudopotential calculation.
[b] First-order Raman scattering.

**Table 4.1-44** Phonon dispersion curves of aluminium compounds

| Crystal | | Figure |
|---|---|---|
| Aluminium nitride | AlN | Fig. 4.1-62 |
| Aluminium phosphide | AlP | Fig. 4.1-63 |
| Aluminium arsenide | AlAs | Fig. 4.1-64 |
| Aluminium antimonide | AlSb | Fig. 4.1-65 |

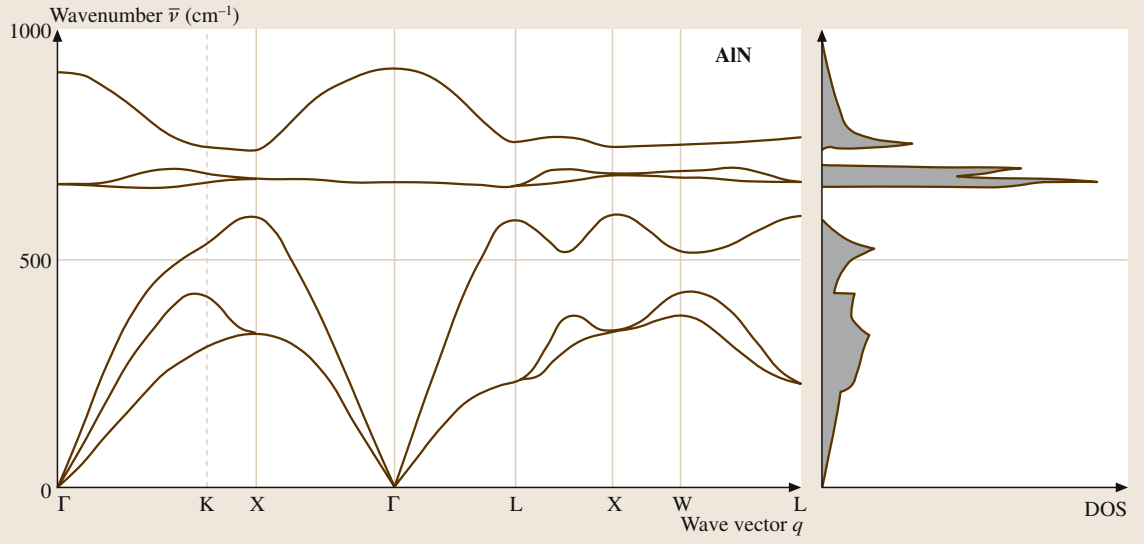


**Fig. 4.1-62** AlN (wurtzite structure). Phonon dispersion curves (*left panel*) and phonon density of states (*right panel*), from a rigid-ion model calculation [1.58, 59]

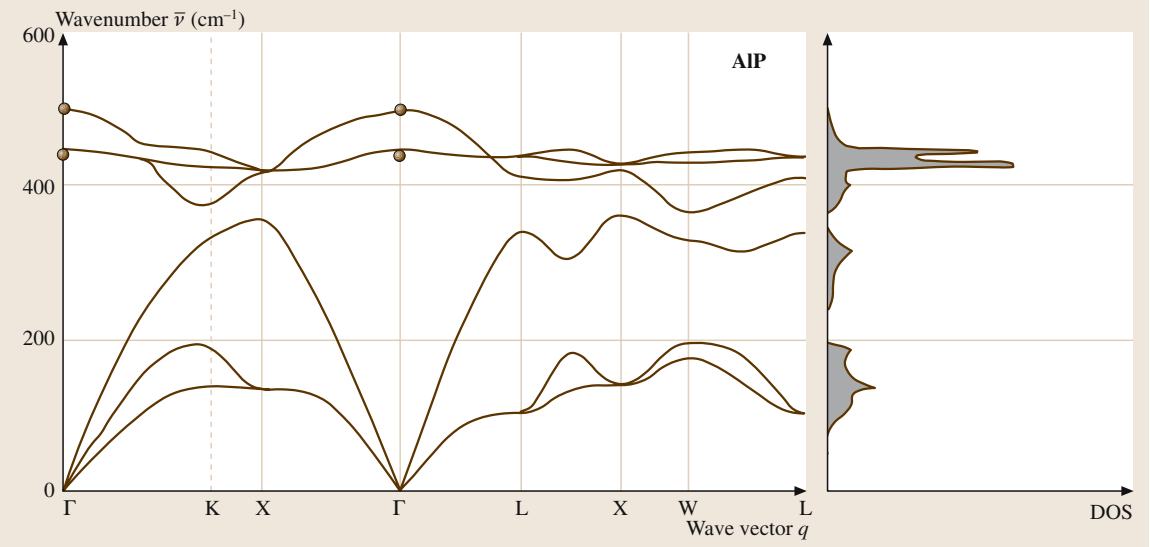


**Fig. 4.1-63** AlP. Phonon dispersion curves (*left panel*) and phonon density of states (*right panel*), from ab initio calculations [1.60]. The data points were obtained from Raman scattering [1.61]

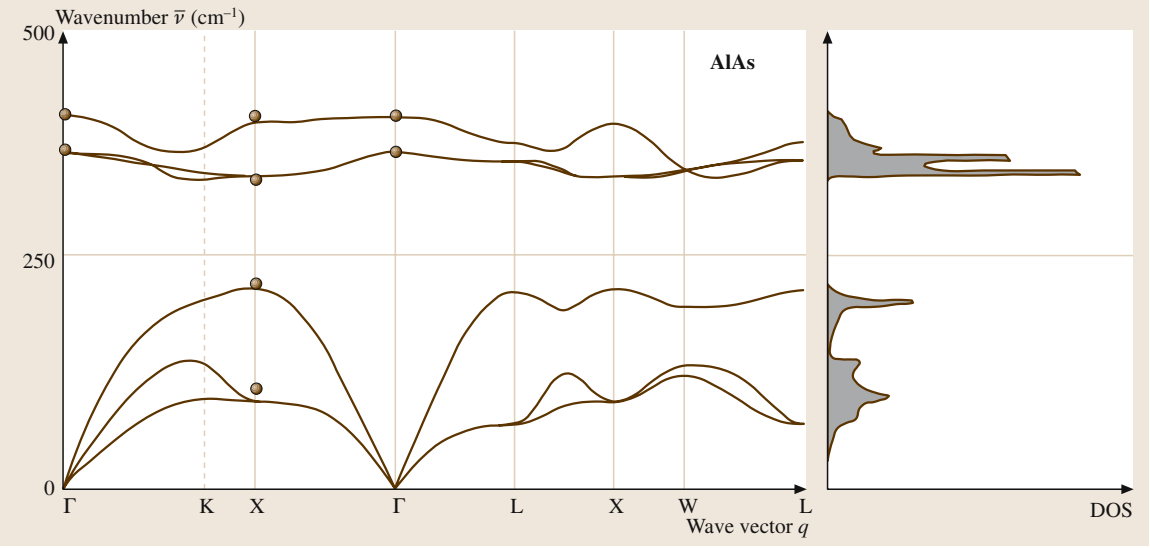


**Fig. 4.1-64** AlAs. Phonon dispersion curves (*left panel*) and phonon density of states (*right panel*). Experimental data points [1.61, 62] and ab initio calculations [1.16]. From [1.16]

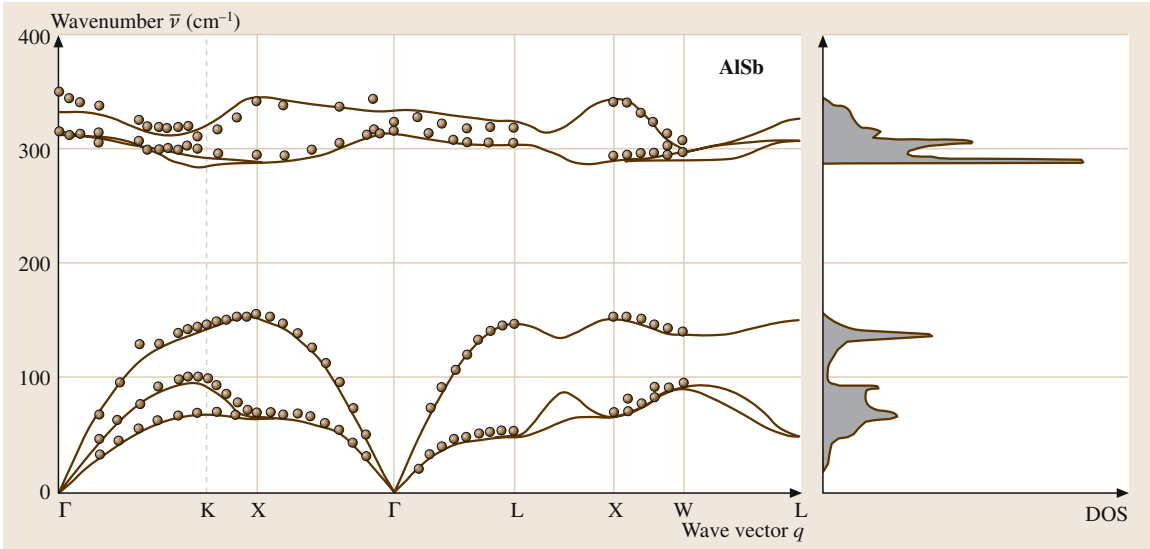


**Fig. 4.1-65** AlSb. Phonon dispersion curves (*left panel*) and phonon density of states (*right panel*). Experimental data points [1.63] and ab initio calculations [1.16]. From [1.16]

## B. Electronic Properties

Tables 4.1-45 – 4.1-48.

*Band Structures of Aluminium Compounds. Aluminium Nitride (AlN).* Aluminium nitride is a direct-gap semiconductor. Since it crystallizes in the wurtzite structure, the band structure (Fig. 4.1-66) differs from that of most of the other III–V compounds.

*Aluminium Phosphide (AlP).* Aluminium phosphide is an indirect, wide-gap semiconductor. The minima of the conduction bands are located at the X point of the Brillouin zone. The top of the valence band has the structure common to all zinc blende semiconductors (Fig. 4.1-67).

*Aluminium Arsenide (AlAs).* Aluminium arsenide is a wide-gap semiconductor with a band structure (Fig. 4.1-68) similar to that of AlP. Measurements have revealed a camel's back structure near X.

**Table 4.1-45** First Brillouin zones of aluminium compounds

| Crystal | | Figure |
|---|---|---|
| Aluminium nitride | AlN | Fig. 4.1-24 |
| Aluminium phosphide | AlP | Fig. 4.1-23 |
| Aluminium arsenide | AlAs | Fig. 4.1-23 |
| Aluminium antimonide | AlSb | Fig. 4.1-23 |

*Aluminium Antimonide (AlSb).* Aluminium antimonide (like AlAs) is an indirect-gap semiconductor with camel's back conduction band minima near X (Fig. 4.1-69).

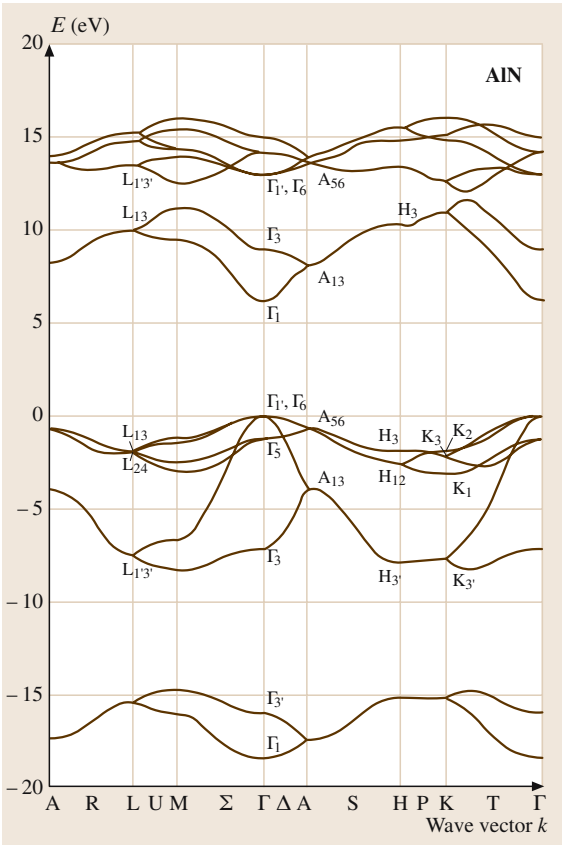


**Fig. 4.1-66** AlN. Band structure calculated by a semiempirical tight-binding method [1.64]

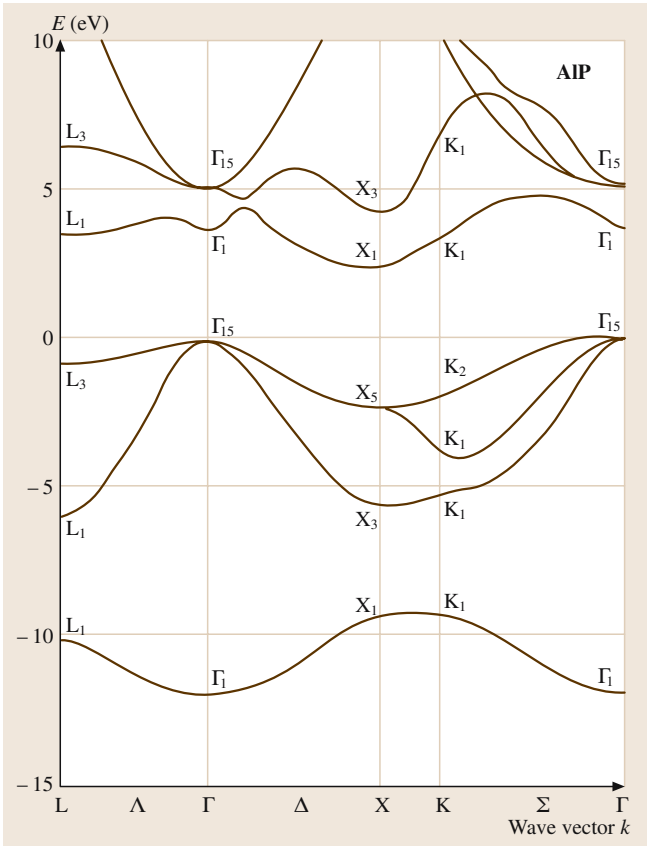


**Fig. 4.1-67** AlP. Band structure calculated by an orthogonalized LCAO method [1.65]

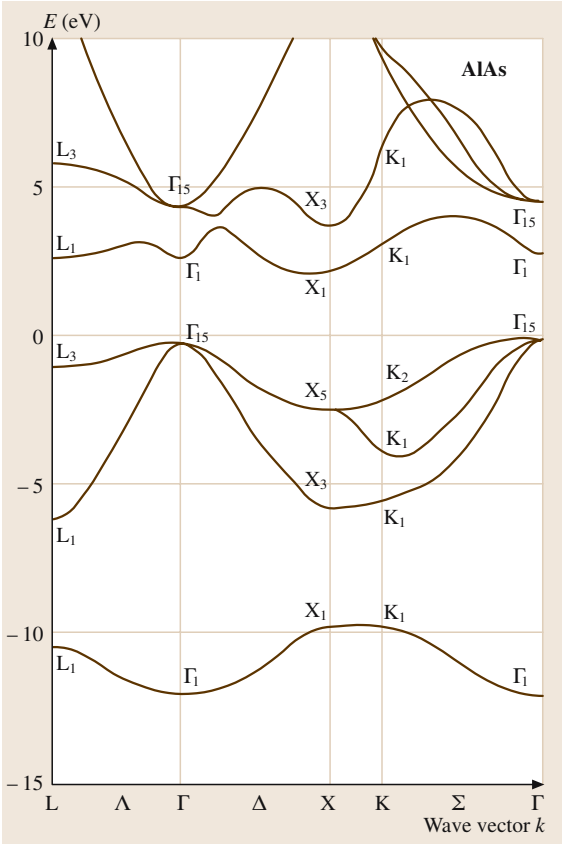


**Fig. 4.1-68** AlAs. Band structure calculated by an orthogonalized LCAO method [1.65]

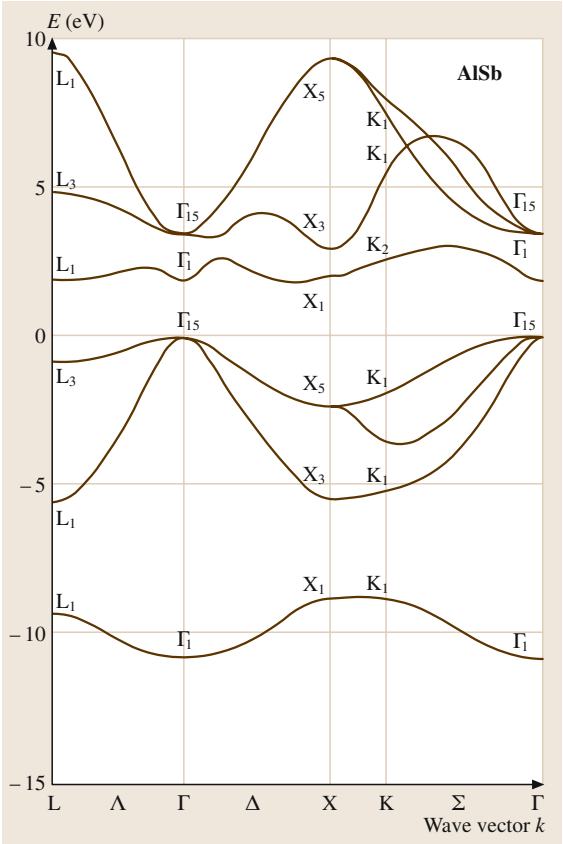


**Fig. 4.1-69** Band structure of aluminium antimonide

**Table 4.1-46** Energy gaps of aluminium compounds

| Crystal | | Quantity | Bands | Energy (eV) | Temperature (K) | Remarks |
|---|---|---|---|---|---|---|
| Aluminium nitride | AlN | $E_{g,\,dir}$ | | 6.19 | 7 | Optical absorption |
| | | | | 6.13 | 300 | |
| Aluminium phosphide | AlP | $E_{g,\,ind}$ | $\Gamma_{15v}$ to $X_{1c}$ | 2.5 (1) | 2 | Excitonic gap; |
| | | | | 2.45 | 300 | Absorption |
| | | $E_{g,\,dir}$ | $\Gamma_{15v}$ to $\Gamma_{1c}$ | 3.63 (2) | 4 | Excitonic gap; |
| | | | | 3.62 (2) | 77 | Photoluminescence |
| Aluminium arsenide | AlAs | $E_{g,\,ind}$ | $\Gamma_{15v}$ to $X_{1c}$ | 2.229 (1) | 4 | Excitonic gap; |
| | | | | 2.153 (2) | 300 | Photoluminescence |
| | | $E_{g,\,ind}$ | $\Gamma_{15v}$ to $L_{1c}$ | 2.363 | 295 | Transport |
| | | $E_{g,\,dir}$ | $\Gamma_{15v}$ to $\Gamma_{1c}$ | 3.13 (1) | 4 | Excitonic gap; |
| | | | | 3.03 (1) | 300 | Photoluminescence |
| | | | | 3.14 (1) | 300 | Transmission |
| Aluminium antimonide | AlSb | $E_{g,\,ind}$ | $\Gamma_{15v}$ to $\Delta_{1c}$ | 1.615 (3) | 300 | Excitonic gap |
| | | | | 1.686 (1) | 27 | |
| | | $E_{g,\,ind}$ | $\Gamma_{15v}$ to $L_{1c}$ | 2.211 | 295 | Electroreflectance |
| | | | | 2.327 | 35 | |
| | | $E_{g,\,dir}$ | $\Gamma_{15v}$ to $\Gamma_{1c}$ | 2.300 | 295 | Electroreflectance |
| | | | | 2.384 | 25 | |

**Table 4.1-47** Spin–orbit splitting energies of aluminium compounds

| Crystal | Spin–orbit splitting | Symmetry points | Energy (eV) | Temperature (K) | Remarks |
|---|---|---|---|---|---|
| AlAs | $\Delta_0$ | $\Gamma_{15v}$ | 0.275 | 300 | Electroreflectance |
| | $\Delta_1$ | $L_{15v}$ | 0.20 | | |
| | $\Delta_0'$ | $\Gamma_{15c}$ | 0.15 | | |
| AlSb | $\Delta_0$ | $\Gamma_{8v}$ to $\Gamma_{7v}$ | 0.673 | 295 | Splitting of $\Gamma_{15v}$ |
| | $\Delta_1$ | $L_{4,5v}$ to $L_{6v}$ | 0.426 | | Splitting of $L_{3v}$ |

**Table 4.1-48** Effective masses of electrons ($m_n$) and holes ($m_p$) for aluminium compounds (in units of the electron mass $m_0$). Aluminium nitride (AlN), calculated values; aluminium phosphide (AlP), calculated from band structure; aluminium arsenide (AlAs), calculated from band structure data; Aluminium antimonide (AlSb), theoretical estimates

| AlN | | AlP | | AlAs | | AlSb | |
|---|---|---|---|---|---|---|---|
| $m_{n,\,parall}$ | 0.33 | $m_{n,\,parall}$ | 3.67 | $m_{n,\,parall}$ (X) | 1.1[a] | $m_{n,\,perpend}$ ($\Delta_1$) | 0.26 estimated |
| $m_{n,\,perpend}$ | 0.25 | $m_{n,\,perpend}$ | 0.212 | $m_{n,\,perpend}$ (X) | 0.19[a] | $m_{n,\,parall}$ ($\Delta_1$) | 1.0 |
| $m_{p,\,A,\,parall}$ | 3.53 | $m_{p,\,heavy}$ | 0.513 parallel to [100] | $m_{n,\,parall}$ (L) | 1.32 | $m_{p,\,heavy}$ | 0.336 parallel to [100] |
| $m_{p,\,A,\,perpend}$ | 11.14 | $m_{p,\,heavy}$ | 1.372 parallel to [111] | $m_{n,\,perpend}$ (L) | 0.15[b] | $m_{p,\,heavy}$ | 0.872 parallel to [111] |
| $m_{p,\,B,\,parall}$ | 3.53 | $m_{p,\,light}$ | 0.211 parallel to [100] | $m_{p,\,heavy}$ | 0.409 parallel to [100] | $m_{p,\,light}$ | 0.123 parallel to [100] |
| $m_{p,\,B,\,perpend}$ | 0.33 | $m_{p,\,light}$ | 0.145 parallel to [111] | $m_{p,\,heavy}$ | 1.022 parallel to [111] | $m_{p,\,light}$ | 0.091 parallel to [111] |
| $m_{p,\,C,\,parall}$ | 0.26 | | | $m_{p,\,light}$ | 0.153 parallel to [100] | | |
| $m_{p,\,C,\,perpend}$ | 4.05 | | | $m_{p,\,light}$ | 0.109 parallel to [111] | | |

[a] Effective masses at X, neglecting camel's back structure.

[b] Effective masses at L.

### C. Transport Properties

Tables 4.1-49 and 4.1-50.

*Electronic Transport, General Description.* *Aluminium Nitride (AlN).* Owing to the large energy gap, transport is always extrinsic. Typical numerical values for the electrical conductivity of undoped single crystals lie in the range $10^{-13}\,\Omega^{-1}\,cm^{-1} < \sigma < 10^{-11}\,\Omega^{-1}\,cm^{-1}$.

*Aluminium Phosphide (AlP).* At room temperature, electrical conductivities $\sigma$ of bulk crystals and layers between 1 and $10^5\,\Omega^{-1}\,cm^{-1}$ have been measured. For the temperature dependence of the electrical conductivity, see Fig. 4.1-70.

*Aluminium Arsenide (AlAs).* Only a small amount of reliable data exists on the transport properties of AlAs. Most results are extrapolations from data obtained from the technologically more important solid solutions of type $Al_xGa_{1-x}As$. At roomtemperature, values of the electrical conductivity of around $10\,\Omega^{-1}\,cm^{-1}$ have been found.

*Aluminium Antimonide (AlSb).* Aluminium antimonide grown without intentional doping is p-type and becomes intrinsic at about 1000 K. For the temperature dependence of the electrical conductivity, see Fig. 4.1-71.

**Table 4.1-49** Electron and hole mobilities $\mu_n$ and $\mu_p$ of aluminium compounds

| Crystal | | Temperature (K) | $\mu_n$ (cm$^2$/V s) | $\mu_p$ (cm$^2$/V s) | Remarks |
|---|---|---|---|---|---|
| Aluminium nitride | AlN | 290 | | 14 | Doped single crystal |
| Aluminium phosphide | AlP | 298 | 10–80 | | Single crystals |
| Aluminium arsenide | AlAs | 300 | 293–75 | 105 | Single crystal layers, MBE-grown, Be-doped |
| Aluminium antimonide | AlSb | 295 | 200 | | Single crystal, Te-doped, |
| | | 77 | 700 | | $n = 4.7 \times 10^{16}$ cm$^{-3}$ |
| | | 300 | | 400 | Single crystal, $p = 10^{16}$ cm$^{-3}$ |
| | | 77 | | 2000 | |

**Table 4.1-50** Thermal conductivity $\kappa$ of aluminium compounds

| Crystal | | Temperature (K) | $\kappa$ (W/cm K) | Remarks |
|---|---|---|---|---|
| Aluminium nitride | AlN | 300 | 3.19 | See Fig. 4.1-72 |
| Aluminium phosphide | AlP | 300 | 0.9 | |
| Aluminium arsenide | AlAs | 300 | 0.91 | |
| Aluminium antimonide | AlSb | | | See Fig. 4.1-73 |

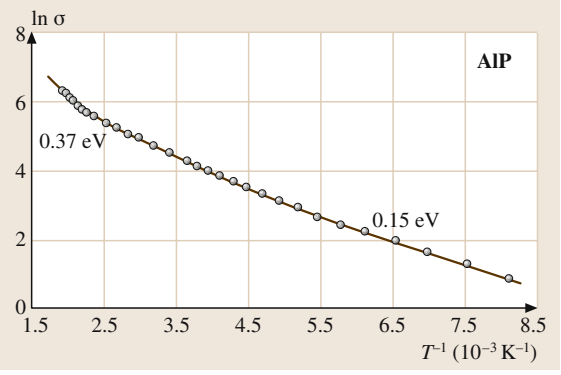


**Fig. 4.1-70** AlP. Natural logarithm of electrical conductivity vs. reciprocal temperature for an undoped sample [1.66]. $\sigma$ in $\Omega^{-1}$ cm$^{-1}$. Activation energies are also shown

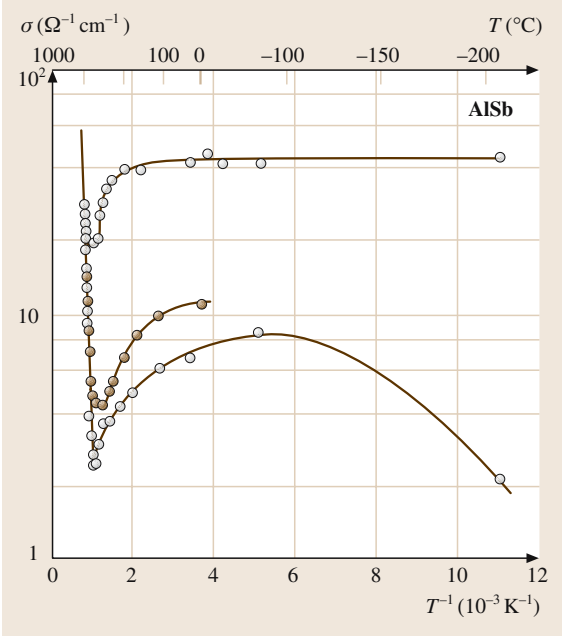


**Fig. 4.1-71** AlSb. Electrical conductivity vs. reciprocal temperature for three different polycrystalline p-type samples [1.67]

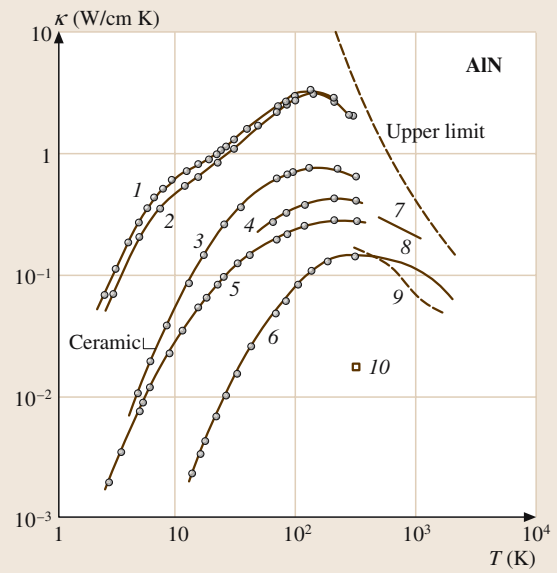


**Fig. 4.1-72** AlN. Temperature dependence of the thermal conductivity for two single crystals (*curves 1* and *2*) and several ceramic samples (*curves 3–6*). Other published results are included (*curves 7–10*), as well as a theoretical estimate of the upper limit [1.68]

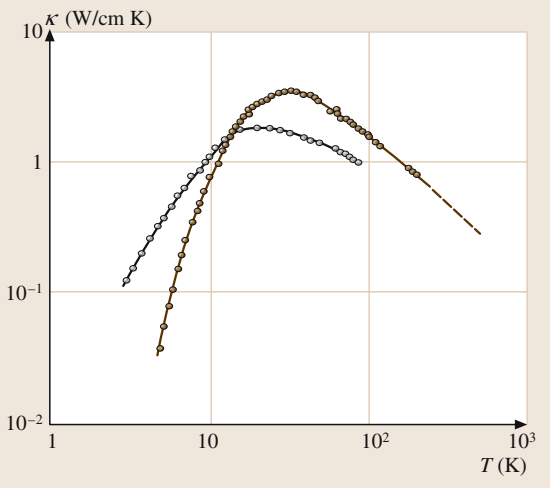


**Fig. 4.1-73** AlSb. Thermal conductivity vs. temperature for an n-type and a p-type sample, low-temperature range [1.69, 70]

### D. Electromagnetic and Optical Properties

Table 4.1-51.

**Table 4.1-51** Dielectric constant $\varepsilon$ and refractive index $n$ of aluminium compounds

| Crystal | | Temperature (K) | $\varepsilon(0)$ | $\varepsilon(\infty)$ | $n$ at | λ (μm) | Remarks |
|---|---|---|---|---|---|---|---|
| Aluminium nitride | AlN | 300 | 9.14 | $\varepsilon_{perpend}$ 4.71 (22)<br>$\varepsilon_{parall}$ 4.93 (22) | 2.17–2.34<br>2.04–2.18 | 0.25<br>0.30 | Reflectivity and optical interferometry, λ = 589.0 nm, CVD films [a] |
| Aluminium phosphide | AlP | | 9.8 | 7.5 | | | From refractive index [b] |
| Aluminium arsenide | AlAs | | 10.1 | 8.2 | | | From infrared reflectivity [c] |
| Aluminium antimonide | AlSb | 300<br>300 | 121.04 | 10.24 | <br>3.652<br>2.995<br>2.080<br>3.100<br>3.182<br>3.300<br>3.445 | <br>40<br>20<br>15<br>10<br>4<br>2<br>1.1 | IR reflectance, transmission and reflectance [d] |

[a] See Fig. 4.1-74 for the spectral dependence of the refractive index.
[b] See Fig. 4.1-75 for the spectral dependence of the refractive index.
[c] See Fig. 4.1-76 for the spectral dependence of the refractive index.
[d] See Fig. 4.1-77 for the spectral dependence of the refractive index.

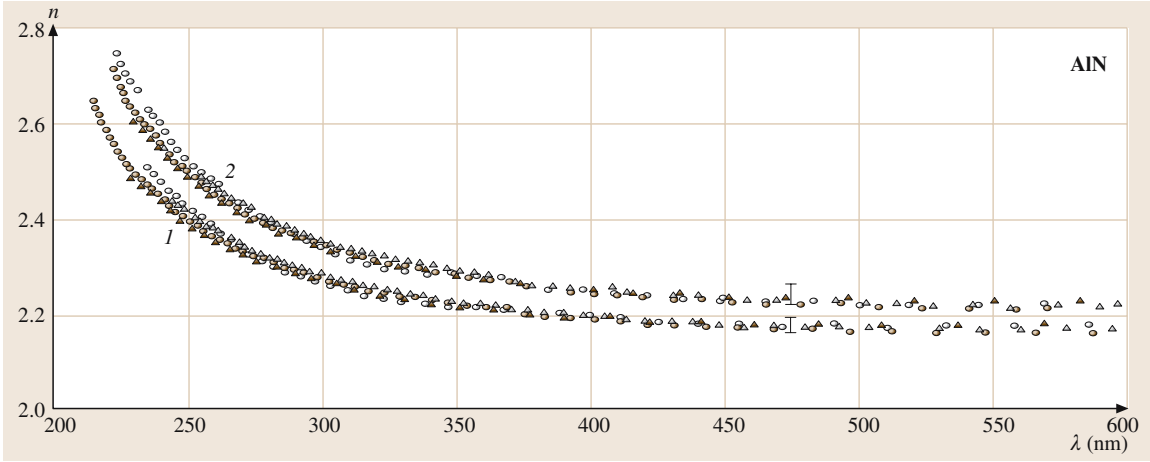


**Fig. 4.1-74** AlN. Spectral dependence of the refractive index (*1*, ordinary ray; *2*, extraordinary ray) [1.71]

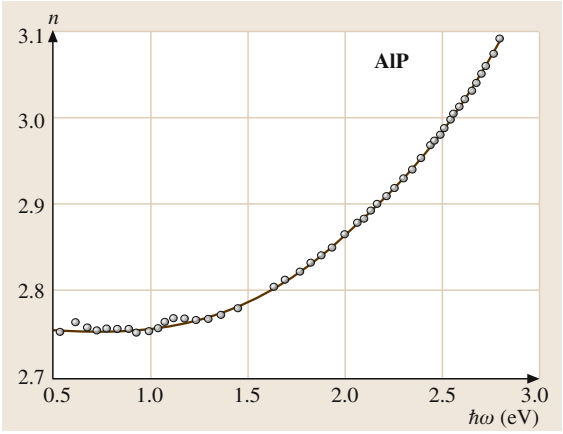


**Fig. 4.1-75** AlP. Refractive index vs. photon energy at 300 K [1.72]

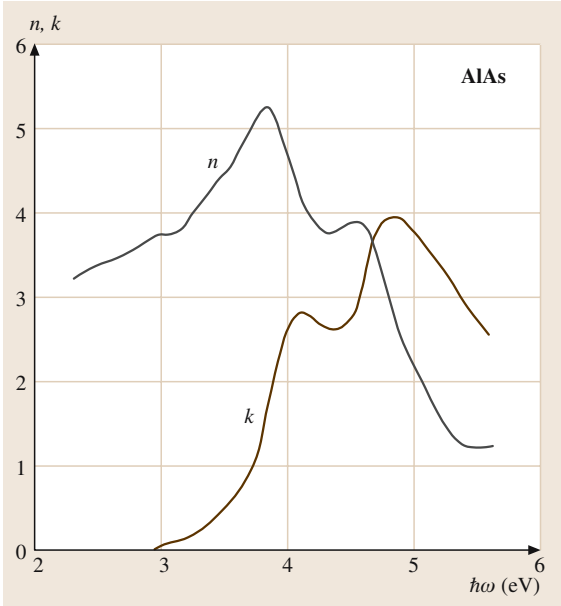


**Fig. 4.1-76** AlAs. Spectral variation of the complex refractive index calculated from the dielectric function [1.73]

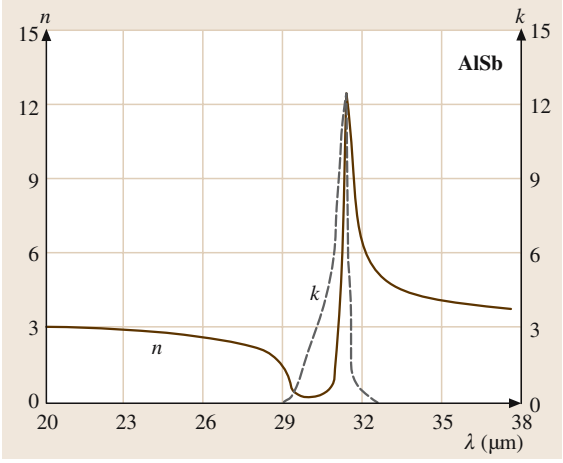


**Fig. 4.1-77** AlSb. Refractive index $n$ and extinction coefficient $k$ vs. wavelength in the region of lattice absorption [1.74]

### 4.1.2.3 Gallium Compounds

A. Crystal Structure, Mechanical and Thermal Properties

Tables 4.1-52 – 4.1-60.

**Table 4.1-52** Crystal structures of gallium compounds

| Crystal | | Space group | | Crystal system | Structure type | Remarks | Figure |
|---|---|---|---|---|---|---|---|
| Gallium nitride | GaN | $C_{6v}^4$<br>$T_d^2$ | $P6_3mc$<br>$F\bar{4}3m$ | hex<br>fcc | Wurtzite<br>Zinc blende | Stable at ambient pressure<br>Epitaxial growth on cubic substrate | Fig. 4.1-3<br>Fig. 4.1-2 |
| Gallium phosphide | GaP | $T_d^2$<br>$D_{4h}^{19}$ | $F\bar{4}3m$<br>$I4_1/amd$ | fcc | Zinc blende<br>$\beta$-tin structure | Stable at normal pressure<br>Pressure > 21 – 30 GPa | Fig. 4.1-2 |
| Gallium arsenide | GaAs I<br>GaAs II | $T_d^2$ | $F\bar{4}3m$ | fcc | Zinc blende<br>Orthorhombic | Stable at normal pressure<br>Pressure > 17 GPa | Fig. 4.1-2 |
| Gallium antimonide | GaSb I<br>GaSb II | $T_d^2$<br>$D_{4h}^{19}$ | $F\bar{4}3m$<br>$I4_1/amd$ | fcc | Zinc blende<br>$\beta$-tin structure | Stable at normal pressure<br>Pressure > 8 – 10 GPa | Fig. 4.1-2 |

**Table 4.1-53** Lattice parameters of gallium compounds

| Crystal | | Lattice parameters (nm) | Temperature (K) | Remarks |
|---|---|---|---|---|
| Gallium nitride | GaN | $a = 0.3190\ (1)$<br>$c = 0.5189\ (1)$ | | X-ray diffraction, monocrystal |
| Gallium phosphide | GaP | $a = 0.54506\ (4)$ | RT | Single crystal |
| Gallium arsenide | GaAs | $a = 0.565359$ | RT | |
| Gallium antimonide | GaSb | $a = 0.609593\ (4)$ | 298.15 | X-ray powder diffraction |

**Table 4.1-54** Densities of gallium compounds

| Crystal | | Density ($g/cm^3$) | Temperature (K) |
|---|---|---|---|
| Gallium nitride | GaN | 6.07 | |
| Gallium phosphide | GaP | 4.138 | 300 |
| Gallium arsenide | GaAs | 5.3161 (2) | 298.15 |
| Gallium antimonide | GaSb | 5.6137 (4) | 300 |

**Table 4.1-55** Elastic constants $c_{ik}$ of gallium compounds

| Crystal | | $c_{11}$ (GPa) | $c_{12}$ (GPa) | $c_{13}$ (GPa) | $c_{33}$ (GPa) | $c_{44}$ (GPa) | Temperature (K) | Remarks |
|---|---|---|---|---|---|---|---|---|
| Gallium nitride | GaN | 377 | 160 | 114 | 209 | 81.4 | 300 | Ultrasound resonance technique |
| Gallium phosphide | GaP | 140.50 (28) | 62.03 (24) | – | – | 70.33 (7) | | Ultrasound ($f = 10$ and 30 MHz) |
| Gallium arsenide | GaAs | 119 (1)<br>112.6 | 53.8 (1)<br>57.1 | –<br>– | –<br>– | 59.5 (1)<br>60.0 | 300<br>0 | <br>Extrapolated data |
| Gallium antimonide | GaSb | 88.34 | 40.23 | – | – | 43.22 | 296 | Ultrasound |

**Table 4.1-56** Melting point $T_m$ of gallium compounds

| Crystal | | Melting point $T_m$ (K) | Remarks |
|---|---|---|---|
| Gallium nitride | GaN | 2791 | GaN sublimes without decomposition around 800 °C |
| Gallium phosphide | GaP | 1749 | |
| Gallium arsenide | GaAs | 1511 | |
| Gallium antimonide | GaSb | 991 (1) | |

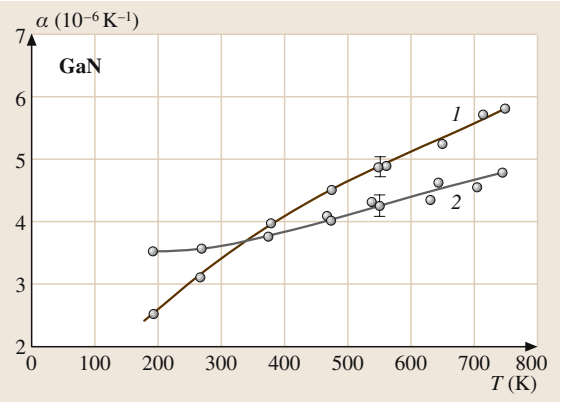


**Fig. 4.1-78** GaN. Coefficient of linear thermal expansion vs. temperature (*curve 1*, $\alpha_\perp$; *curve 2*, $\alpha_\parallel$) [1.75]

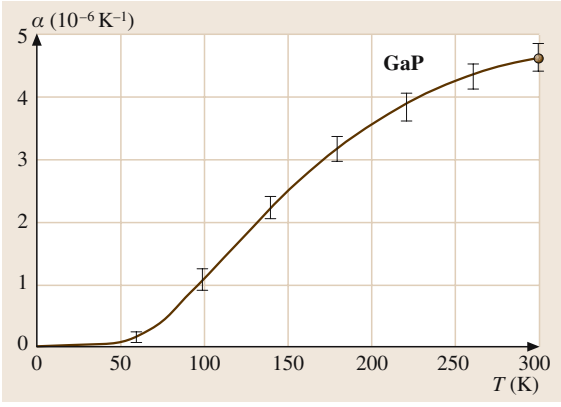


**Fig. 4.1-79** GaP. Linear thermal expansion coefficient vs. temperature between 0 K and 300 K [1.76]

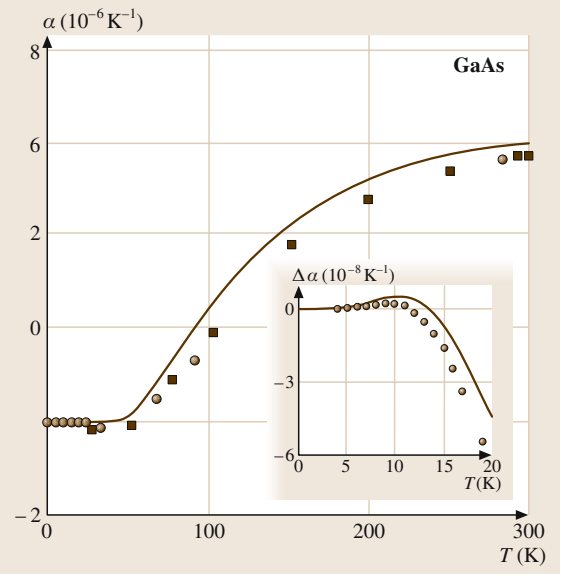


**Fig. 4.1-80** GaAs. Coefficient of linear thermal expansion. Experimental data points, and curves from an ab initio pseudopotential calculation [1.77]

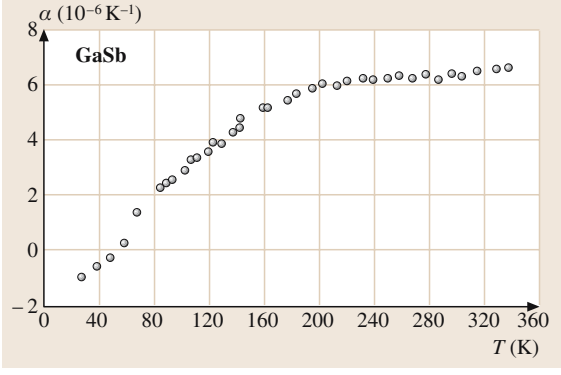


**Fig. 4.1-81** GaSb. Linear thermal expansion coefficient vs. temperature measured with a quartz dilatometer. High-temperature range [1.56, 57]

**Table 4.1-57** Linear thermal expansion coefficient $\alpha$ of gallium compounds

| Crystal | | Expansion coefficient $\alpha$ ($10^{-6}$ K$^{-1}$) | | Remarks | Temperature dependence |
|---|---|---|---|---|---|
| Gallium nitride | GaN | $\alpha_{parall}$<br>$\alpha_{perpend}$ | 5.59<br>3.17 | X-ray diffraction | Fig. 4.1-78 |
| Gallium phosphide | GaP | | 4.65 | 300 K | Fig. 4.1-79 |
| Gallium arsenide | GaAs | | 5.87 | 300 K | Fig. 4.1-80 |
| Gallium antimonide | GaSb | | 7.75 (50) | Around 300 K; X-ray diffraction | Fig. 4.1-81 |

**Table 4.1-58** Heat capacity $c_p$ and Debye temperature $\Theta_D$ of gallium compounds

| Crystal | | Heat capacity (J/mol K) | Temperature (K) | Debye temperature (K) | Remarks |
|---|---|---|---|---|---|
| Gallium nitride | GaN | | | 600 | Estimated |
| Gallium phosphide | GaP | 49.65 | 800 | 445 | |
| Gallium arsenide | GaAs | 46.90 | 300 | 344 | |
| Gallium antimonide | GaSb | | | 266 | |

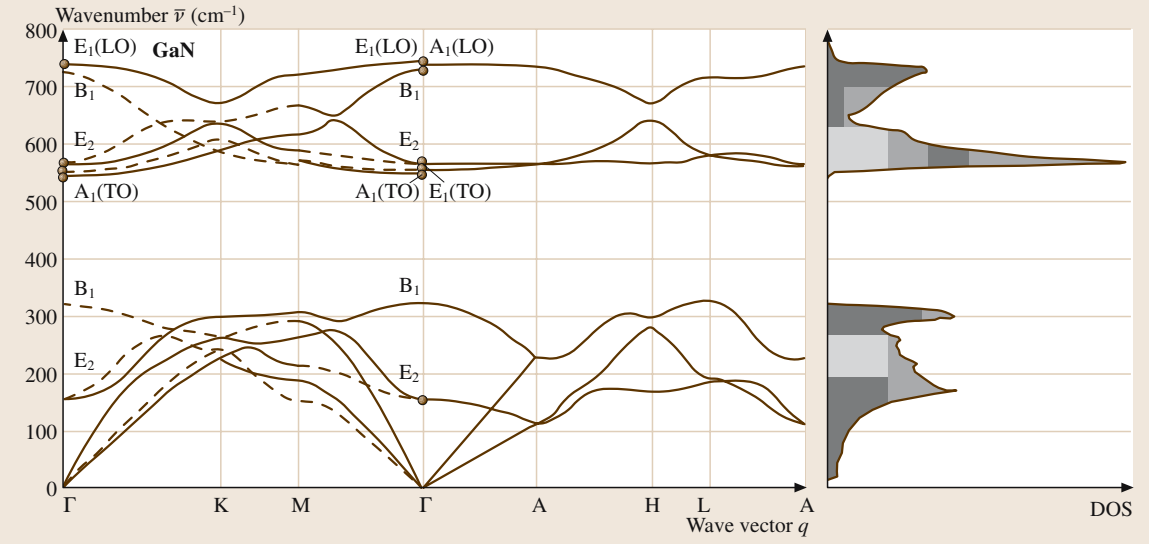


**Fig. 4.1-82** GaN (wurtzite structure). Phonon dispersion curves (decomposed according to different irreducible representations along the main symmetry directions) and density of states, from a model-potential calculation. The *circles* show Raman data from [1.78]. From [1.79]

**Table 4.1-59** Phonon wavenumbers of gallium compounds. Gallium nitride (GaN), $T = 300\,\mathrm{K}$, from Raman spectroscopy; gallium phosphide (GaP), RT, from an analysis of Raman, neutron, luminescence, and absorption data; gallium arsenide (GaAs), $T = 296\,\mathrm{K}$, from coherent inelastic neutron scattering; gallium antimonide (GaSb), $T = 300\,\mathrm{K}$, from second-order Raman effect

| GaN | | | GaP | | |
|---|---|---|---|---|---|
| Symmetry point | Branch | Wavenumber ($cm^{-1}$) | Symmetry point | Branch | Frequency (THz) |
| $\tilde{\nu}_{low}$ ($E_2$) | | 145 | $\nu$ ($\Gamma$) | TO | 10.95 (1) |
| $\tilde{\nu}$ ($A_1$) | TO | 533 | | LO | 12.06 (1) |
| $\tilde{\nu}$ ($E_1$) | TO | 560 | $\nu$ (X) | TA | 3.13 (3) |
| $\tilde{\nu}_{high}$ ($E_2$) | | 567 | | LA | 7.46 (6) |
| $\tilde{\nu}$ ($A_1$) | LO | 735 | | TO | 10.58 (3) |
| $\tilde{\nu}$ ($E_1$) | LO | 742 | | LO | 11.09 (6) |
| | | | $\nu$ (L) | TA | 2.58 (3) |
| | | | | LA | 6.45 (3) |
| | | | | TO | 10.64 (3) |
| | | | | LO | 11.24 (3) |

| GaAs | | | GaSb | | |
|---|---|---|---|---|---|
| Symmetry point | Branch | Frequency (THz) | Symmetry point | Branch | Wavenumber ($cm^{-1}$) |
| $\nu$ ($\Gamma_{15}$) | LO | 8.55 (20) | $\tilde{\nu}$ (L) | TA | 46 |
| | TO | 8.02 (8) | $\tilde{\nu}$ (X) | TA | 56 |
| $\nu$ ($X_1$) | TA | 2.36 (2) | $\tilde{\nu}$ (W) | TA | 75 |
| | LO | 7.22 (15) | $\tilde{\nu}$ (L) | LA | 155 |
| $\nu$ ($X_3$) | LA | 6.80 (6) | | LO | 204 |
| $\nu$ ($X_5$) | TO | 7.56 (8) | $\tilde{\nu}$ (X) | LO | 210 |
| $\nu$ ($L_1$) | LA | 6.26 (10) | $\tilde{\nu}$ (L, X, $\Sigma$) | TO | 218 |
| | LO | 7.15 (7) | | | |
| $\nu$ ($L_3$) | TA | 1.86 (2) | | | |
| | TO | 7.84 (12) | | | |

**Table 4.1-60** Phonon dispersion curves of gallium compounds

| Crystal | | Figure |
|---|---|---|
| Gallium nitride | GaN | Fig. 4.1-82 |
| Gallium phosphide | GaP | Fig. 4.1-83 |
| Gallium arsenide | GaAs | Fig. 4.1-84 |
| Gallium antimonide | GaSb | Fig. 4.1-85 |

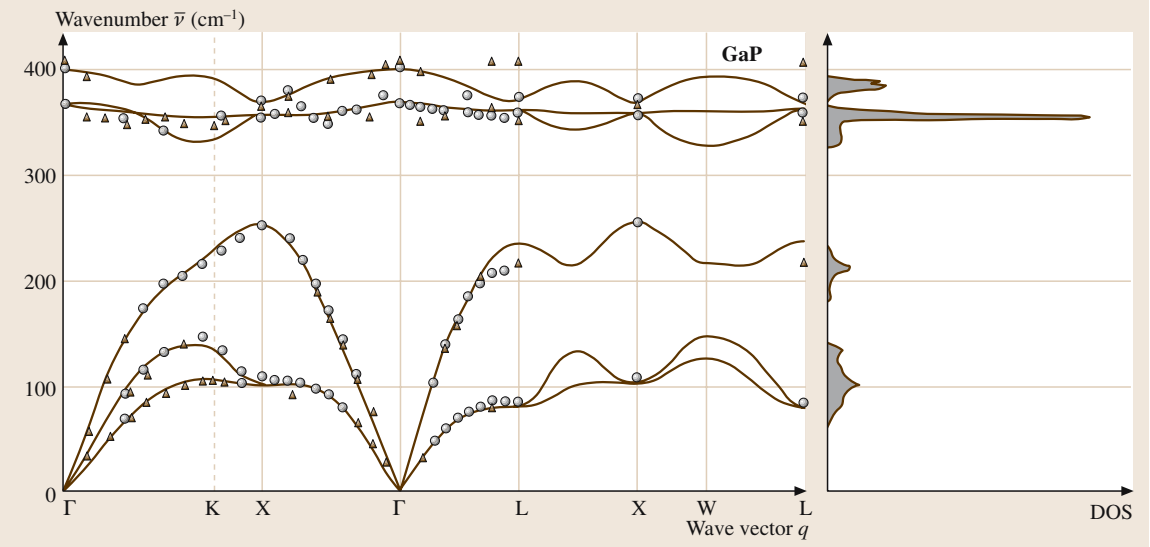


**Fig. 4.1-83** GaP. Phonon dispersion curves (*left panel*) and density of states (*right panel*). Experimental data points from [1.80] (*open symbols*) and from [1.81] (*filled symbols*) and theoretical curves from ab initio calculations [1.82]. From [1.82]

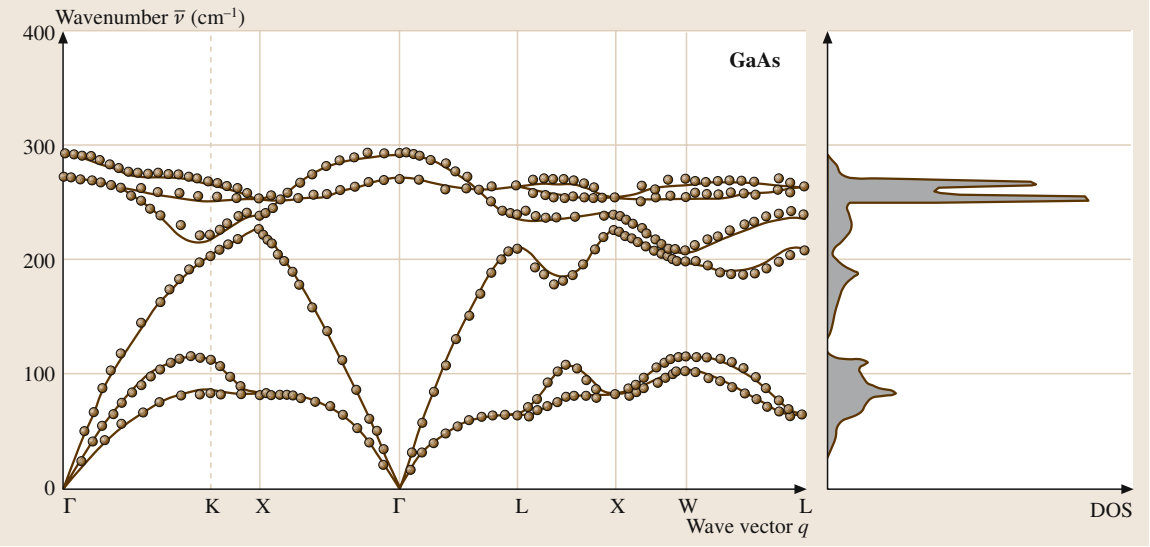


**Fig. 4.1-84** GaAs. Phonon dispersion curves (*left panel*) and phonon density of states (*right panel*) [1.16]. Experimental data points [1.83] and ab initio calculations [1.16].

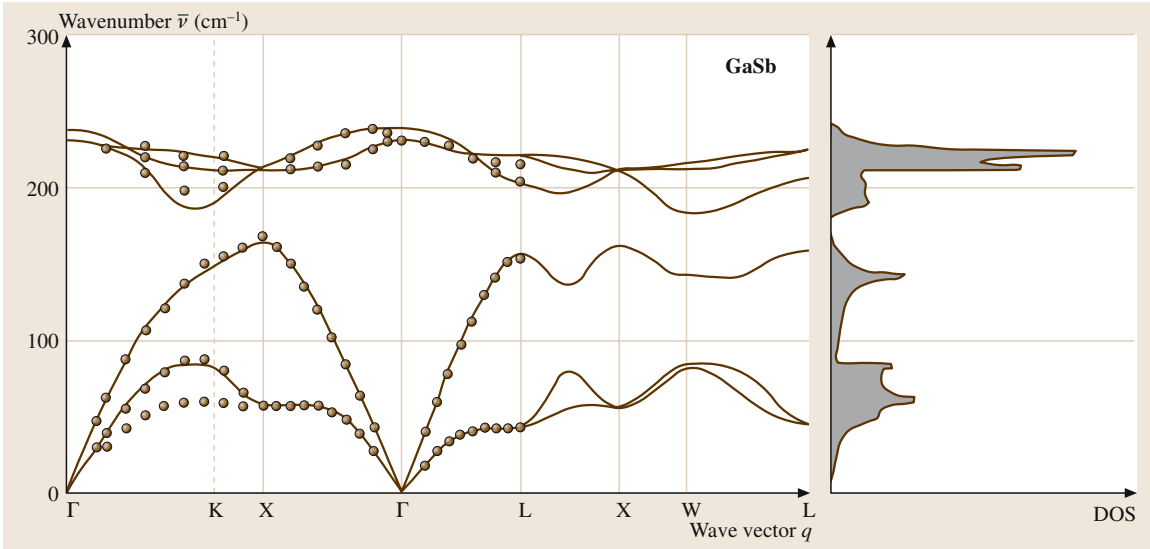


**Fig. 4.1-85** GaSb. Phonon dispersion curves (*left panel*) and phonon density of states (*right panel*) [1.16]. Experimental data points [1.84] and ab initio calculations [1.16]

### B. Electronic Properties

Tables 4.1-61 – 4.1-66.

*Band Structures of Gallium Compounds.* *Gallium Nitride (GaN).* The band structure is shown in Fig. 4.1-87. Owing to spin–orbit interaction, the two top valence bands ($\Gamma_6$ and $\Gamma_1$) are split into three spin-degenerate bands, one with quantum number $J_z = 3/2(\Gamma_9)$ and two with $Jz = 1/2(\Gamma_7)$'. For convenience, the notation A, B, C is used for these bands.

*Gallium Phosphide (GaP).* Gallium phosphide is an indirect-gap semiconductor. The lowest set of conduction bands shows a camel's back structure; the band minima are located on the $\Delta$ axes near the zone boundary. The valence bands show the usual structure characteristic of zinc blende semiconductors.

The spin–orbit splitting of the top of the valence band is negligible compared with most other energy separations in the band structure. Therefore, Fig. 4.1-86 shows the band structure calculated without inclusion of spin–orbit splitting; the symmetry symbols of the high-symmetry band states are symbols of the single group of the zinc blende structure.

*Gallium Arsenide (GaAs).* Gallium arsenide is a direct-gap semiconductor. The minimum of the lowest conduction band is located at Γ; higher sets of minima at L and near X (about 10% away from the zone boundary) are also important for the optical and transport properties. The minimum near X most probably has a camel's back-like structure similar to that of GaP, AlAs, and AlSb. The valence bands have the usual structure characteristic of zinc blende crystals (Fig. 4.1-88).

*Gallium Antimonide (GaSb).* The conduction band of GaSb is characterized by two types of minima, the lowest minimum at Γ and slightly higher minima at the L points at the surface of the Brillouin zone. A third set of minima at the X points has been detected in optical experiments. The valence bands show the usual structure common to zinc blende semiconductors (Fig. 4.1-89).

**Table 4.1-61** First Brillouin zones of gallium compounds

| Crystal | | Figure |
|---|---|---|
| Gallium nitride | GaN | Fig. 4.1-24 |
| Gallium phosphide | GaP | Fig. 4.1-23 |
| Gallium arsenide | GaAs | Fig. 4.1-23 |
| Gallium antimonide | GaSb | Fig. 4.1-23 |

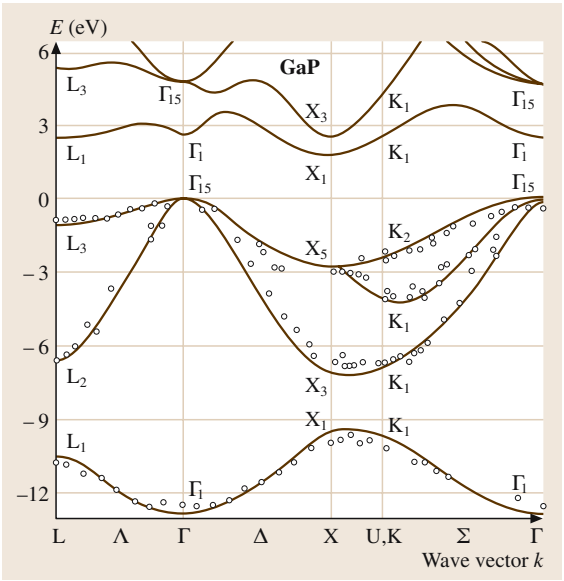


**Fig. 4.1-86** Band structure of gallium phosphide

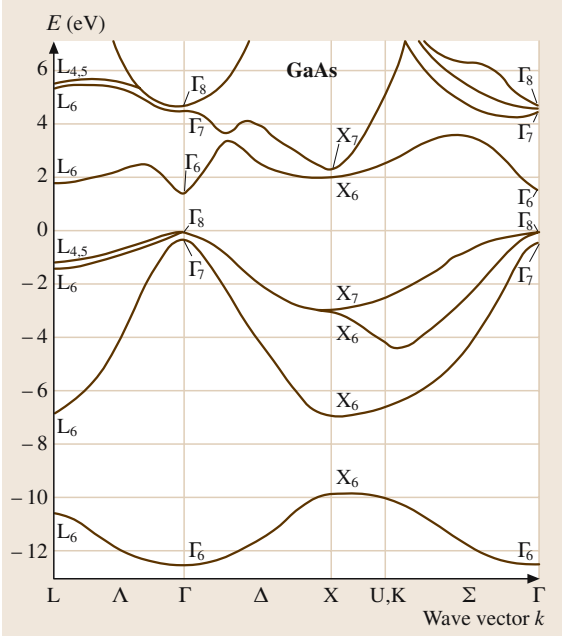


**Fig. 4.1-88** Band structure of gallium arsenide

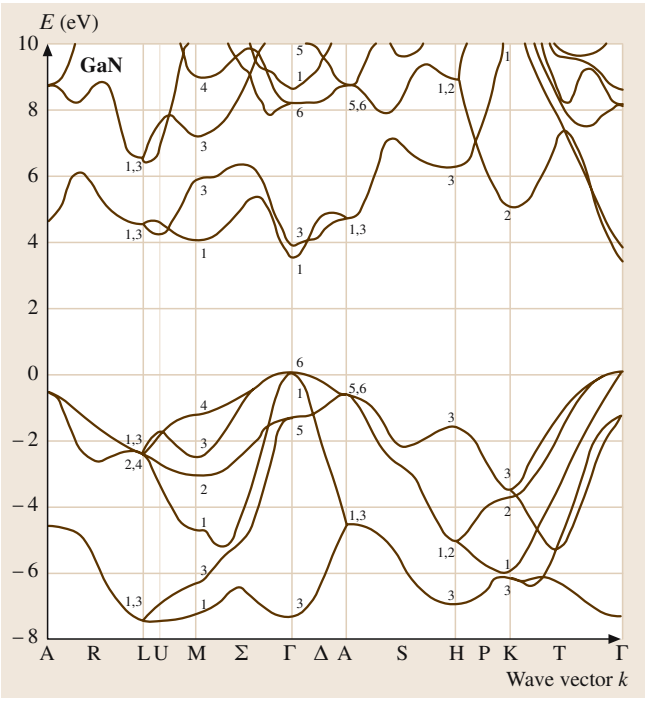


**Fig. 4.1-87** Band structure of gallium nitride

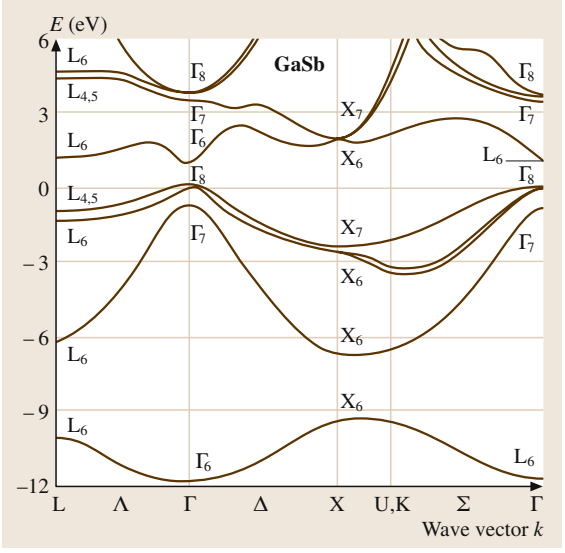


**Fig. 4.1-89** Band structure of gallium antimonide

**Table 4.1-62** Energy gaps of gallium compounds

| Crystal | | Quantity | Bands | Energy (eV) | Temperature (K) | Remarks |
|---|---|---|---|---|---|---|
| Gallium nitride | GaN | $E_{g,\,dir}$ | | 3.503 (2) | 1.6 | Photoluminescence |
| | | | A exciton | 3.4751 (5) | | Transition from $\Gamma_{9v}$ |
| | | | B exciton | 3.4815 (10) | | Transition from upper $\Gamma_{7v}$ |
| | | | C exciton | 3.493 (5) | | Transition from lower $\Gamma_{7v}$ |
| Gallium phosphide | GaP | $E_{g,\,ind}$ | $\Gamma_{8v}$ to $\Delta_{5c}$ | 2.350 (1) | 0 | Extrapolated, from exciton data |
| | | | | 2.272 | 300 | |
| | | $E_{g,\,ind}$ | $\Gamma_{15v}$ to $L_{1c}$ | 2.637 (10) | 78 | Electroabsorption |
| Gallium arsenide | GaAs | $E_{g,\,dir}$ | $\Gamma_{8v}$ to $\Gamma_{6c}$ | 1.51914 | 0 | Extrapolated, photoluminescence |
| | | | | 1.424 (1) | 300 | Differentiated reflectivity |
| | | $E_{g,\,th}$ | | 1.604 | 0 | Extrapolated, intrinsic carrier concentration |
| Gallium antimonide | GaSb | $E_{g,\,dir}$ | $\Gamma_{8v}$ to $\Gamma_{6c}$ | 0.822 | 0 | Extrapolated, electroreflectance |
| | | | | 0.75 | 300 | |

**Table 4.1-63** Exciton binding energies of gallium compounds

| Crystal | | Quantity | Energy (meV) | Remarks |
|---|---|---|---|---|
| Gallium nitride | GaN | $E_b^A$ | 20 | A exciton, photoreflectance |
| | | $E_b^B$ | 18.5 | B exciton, photoreflectance |
| | | $E_b^C$ | 22.4 | C exciton, photoluminescence |
| Gallium antimonide | GaSb | $E_b$ | 1.6 | Calculated ground-state binding energy |

**Table 4.1-64** Spin–orbit splitting energies of gallium compounds

| Crystal | | Quantity | Bands | Energy (meV) | Temperature (K) | Remarks |
|---|---|---|---|---|---|---|
| Gallium nitride | GaN | $\Delta_1$ | | 9.8 | | Epitaxial films, reflectance measurements |
| | | $\Delta_2$ | | 5.6 | | |
| | | $\Delta_3$ | | 5.6 | | |
| Gallium phosphide | GaP | $\Delta_0$ | $\Gamma_{8v}$ to $\Gamma_{7v}$ | 80 (3) | 100–200 | Splitting of $\Gamma_{15v}$ into $\Gamma_{8v}$ (upper level) and $\Gamma_{7v}$ (lower level) |
| Gallium arsenide | GaAs | $\Delta_0$ | $\Gamma_{15v}$ | 346.4 (5) | 1.7 | Splitting of $\Gamma_{15v}$ valence band state into $\Gamma_{7v}$ and $\Gamma_{8v}$, magnetoabsorption splitting of $\Gamma_{15}$ conduction band state into $\Gamma_{7c}$ and $\Gamma_{8c}$, electroreflectance |
| | | $\Delta_0'$ | $\Gamma_{15c}$ | 171 (15) | 4.2 | |
| Gallium antimonide | GaSb | $\Delta_0$ | $\Gamma_{8v}$ to $\Gamma_{7v}$ | 756 (15) | 10 | Electroreflectance |
| | | $\Delta_0'$ | $\Gamma_{7c}$ to $\Gamma_{8c}$ | 213 (10) | | |
| | | $\Delta_1$ | $L_{4,5v}$ to $L_{6v}$ | 430 (10) | | |
| | | $\Delta_1'$ | $L_{4,5c}$ to $L_{6c}$ | 130 | | |

**Table 4.1-65** Effective masses of electrons ($m_n$) and holes ($m_p$) for gallium compounds (in units of the electron mass $m_0$)

| GaN | | | | GaP | | | | |
|---|---|---|---|---|---|---|---|---|
| $m_n$ | 0.22 | 6 K | Cyclotron resonance, polaron mass | $m_{n,\,parall}$ | Near $\Delta_{min}$ | 7.25 | 1–20 K | At bottom of camel's back |
| $m_{n,\,parall}$ | 0.20 (6) | | From reflectance spectrum | $m_{n,\,perp}$ | Near $\Delta_{min}$ | 0.21 | | Luminescence |
| $m_{n,\,perp}$ | 0.20 (2) | | | $m_{n,\,parall}$ | Away from $\Delta_{min}$ | 2.2 | | High above bottom of camel's back |
| $m_p^{(A)}$ | 1.01 | 7 K | Estimated from binding energies | $m_{p,\,heavy}$ | Parallel to [111] | 0.67 (4) | 1.6 | Cyclotron resonance at 1.6 K |
| $m_p^{(B)}$ | 1.1 | | | $m_{p,\,light}$ | Parallel to [111] | 0.17 (1) | Parallel to [111] | |
| $m_p^{(C)}$ | 1.6 | | | $m_{p,\,so}$ | | 0.4649 | 0 | Spin–orbit mass, calculated from $\boldsymbol{k}\cdot\boldsymbol{p}$ model |

| GaAs | | | | |
|---|---|---|---|---|
| $m_n$ ($\Gamma$) | | 0.0662 (2) | 1.6 | Cyclotron resonance |
| $m_{p,\,heavy}$ | Parallel to [100]<br>Parallel to [111] | 0.34<br>0.75 | 10 K | Electronic Raman scattering |
| $m_{p,\,light}$ | Parallel to [100]<br>Parallel to [111] | 0.094<br>0.082 | | |

| GaSb | | | | |
|---|---|---|---|---|
| $m_n$ ($\Gamma$) | 0.039 (5) | 2 K | | Optically detected cyclotron resonance |
| $m_n$ ($L_{6c}$) | 0.11<br>0.95<br>0.226 | | | Transverse mass<br>Longitudinal mass<br>Density-of-states mass |
| $m_{p,\,heavy}$ | 0.29 (9)<br>0.36 (13)<br>0.40 (16) | 30 K | $\boldsymbol{B}$ parallel to [100]<br>$\boldsymbol{B}$ parallel to [110]<br>$\boldsymbol{B}$ parallel to [111] | Stress-modulated magnetoreflectance |
| $m_{p,\,light}$ | 0.042 (2) | | | |

**Table 4.1-66** Electron $g$-factor $g_c$ of gallium antimonide

| Crystal | | $g_c$ | Temperature (K) | Remarks |
|---|---|---|---|---|
| Gallium antimonide | GaSb | −9.1 (2) | 4.2–50 | Magnetoluminescence |

### C. Transport Properties

Tables 4.1-67 and 4.1-68.

*Electronic Transport, General Description. Gallium Nitride (GaN).* Undoped GaN is normally an n-type conductor. Carrier concentrations in undoped films can vary from $5\times10^{19}\,cm^{-3}$ to $5\times10^{16}\,cm^{-3}$ because of unintentional incorporation of extrinsic impurities, mainly silicon and oxygen. In the purest $\alpha$-GaN material ($n = 10^{17}\,cm^{-3}$), conductivities of the order of 10 Ω cm have been found at 300 K. For the temperature dependence of the electrical resistivity, see Fig. 4.1-90.

*Gallium Phosphide (GaP).* Even in high-purity samples, intrinsic conduction occurs in gallium phosphide only above 500 °C. Thus, the transport properties are in general determined by the properties of impurities and lattice defects. The data for the electrical conductivity $\sigma$ of pure n-type material are found to lie around 0.5 Ω cm at 300 K.

As in the case of GaAs, semi-insulating GaP can be obtained by doping with shallow donors and acceptors and with deep centers. Resistivities at room temperature are of the order of $10^8 - 10^{11}\ \Omega$ cm. Typical data at high temperatures are shown in Fig. 4.1-91.

*Gallium Arsenide (GaAs).* At low fields, the electrons are in the $\Gamma_6$ minima at the zone center. The dominating scattering process at room temperature is polar optical scattering, while below 60 K the most important contribution to the lattice mobility is from piezoelectric potential scattering. At room temperature, the hole mobility of samples with $p < 5 \times 10^{15}$ cm$^{-3}$ is governed by lattice scattering alone. An intrinsic carrier concentration of $n_i = 2.1 \times 10^6$ cm$^{-3}$ has been found at $T = 300$ K (Fig. 4.1-92).

Owing to the very low intrinsic carrier concentration, the electrical conductivity of GaAs at 300 K is determined by charge carriers provided by impurities. Only under certain doping conditions (e.g. compensation of shallow acceptor levels by donor impurities and overcompensation by deep Cr levels) can the Fermi level be pinned in the middle of the energy gap and nearly intrinsic conduction achieved (semi-insulating GaAs, $\rho = 10^5 - 10^9\ \Omega$ cm).

*Gallium Antimonide (GaSb).* Transport in n-type GaSb is complicated by the contribution of three sets of conduction bands with minima located at Γ, L, and X. The data on transport coefficients can be consistently explained by a three-band model, the X bands contributing to transport above 180 °C. Intrinsic carrier concentrations $n_i$ of the order of $10^{14}$ cm$^{-3}$ have been estimated for a temperature $T = 365$ K.

In p-type GaSb, a multiellipsoidal model has to be used at low temperatures, taking into account the shift of the heavy- and light-hole bands away from $k = 0$. At high temperatures, a warped-sphere model (as in the case of Si and Ge) is adequate.

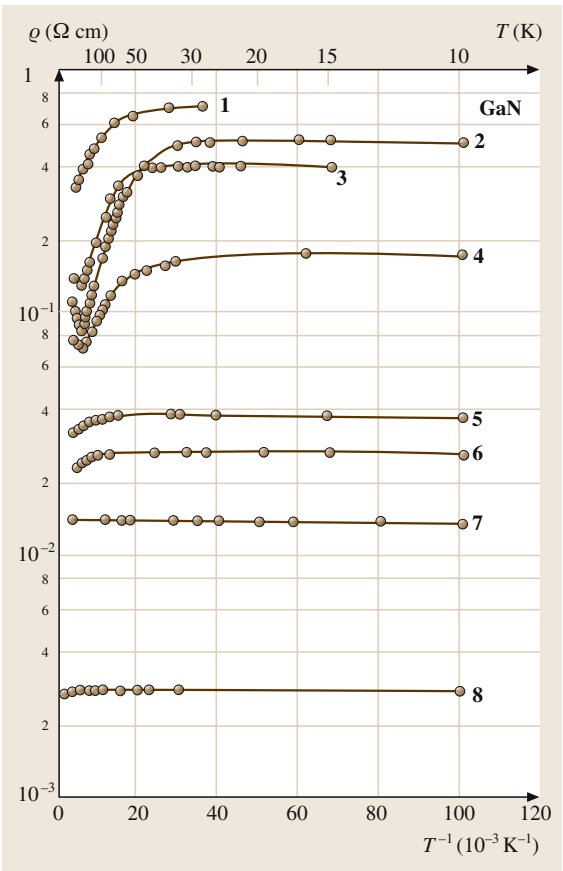


**Fig. 4.1-90** GaN. Resistivity of several undoped samples (1 – 7) and a Zn-doped sample (8) vs. reciprocal temperature [1.85]

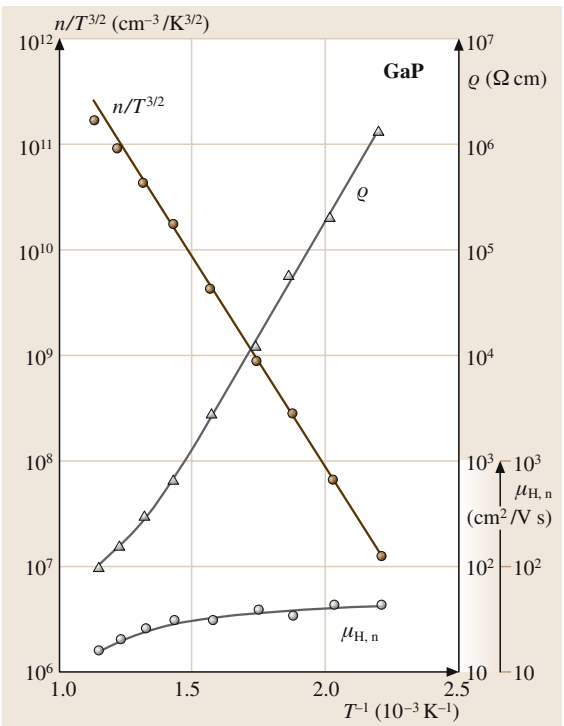


**Fig. 4.1-91** GaP. Resistivity, Hall mobility, and electron concentration (divided by $T^{-3/2}$) vs. temperature for a semi-insulating sample [1.86]

**Table 4.1-67** Electron and hole mobilities $\mu_n$ and $\mu_p$ of gallium compounds

| Crystal | Temperature (K) | Carrier concentration ($cm^{-3}$) | $\mu_n$ ($cm^2/V\,s$) | $\mu_p$ ($cm^2/V\,s$) | Remarks |
|---|---|---|---|---|---|
| Gallium nitride | 300 | $n = 3\times10^{16}$<br>$p = 5\times10^{13}$ | 900 | <br>350 | Hall mobility [a]<br>$\beta$-GaN, Hall mobility |
| Gallium phosphide | RT | | 160 | 135 | Thin films, Hall mobility, maximum mobility [b] |
| Gallium arsenide | 300<br>300 | | 2400–3300 | <br>400 | Bulk GaAs, Hall mobility [c]<br>Hall mobility |
| Gallium antimonide | 300<br>300 | $n = 1.2\times10^{16}$ | 7620 | <br>680 | MBE-grown on GaSb substrates<br>Hall mobility |

[a] See Fig. 4.1-93 for the temperature dependence of the electron mobility in GaN.
[b] See Figs. 4.1-94a,b for the temperature dependence of the electron and hole mobilities in GaP.
[c] See Figs. 4.1-95 and 4.1-96 for the temperature dependences of the electron and hole mobilities in GaAs.

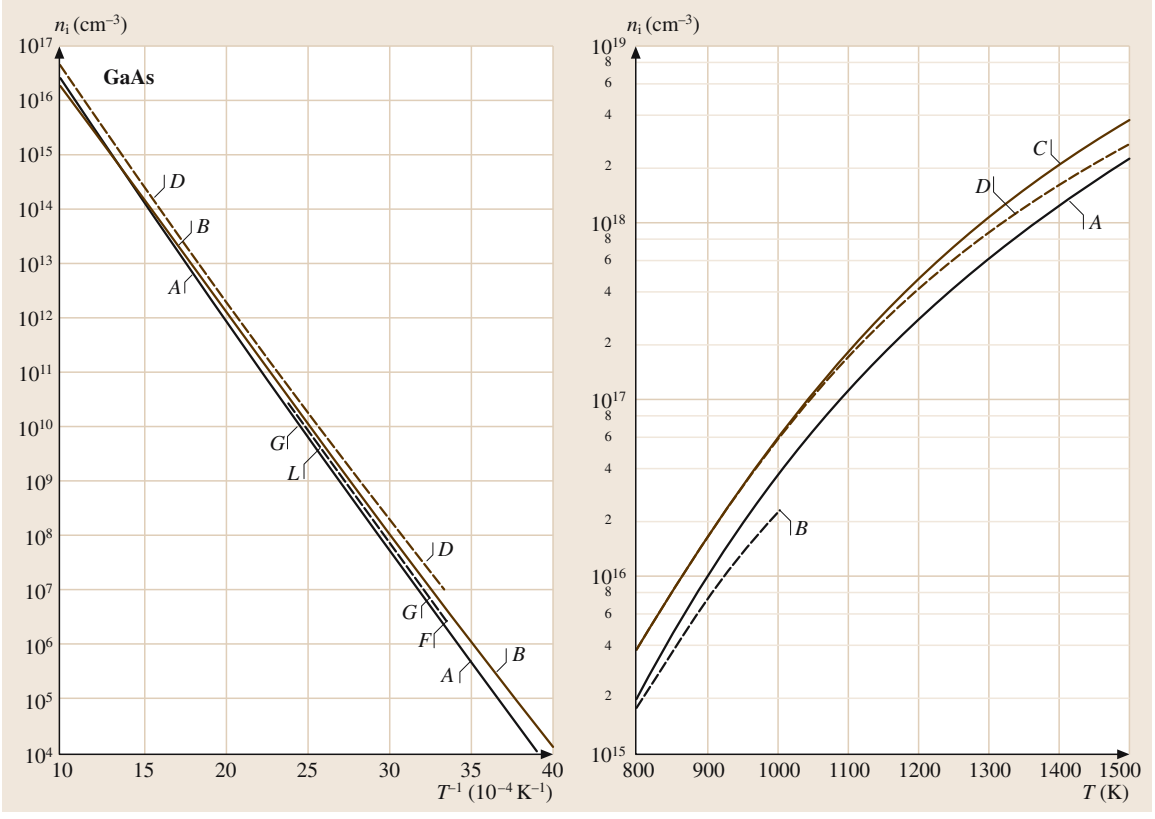


**Fig. 4.1-92** GaAs. Intrinsic carrier concentration vs. reciprocal temperature for the range 250–1000 K and vs. temperature for the range 800–1500 K. The *solid curves* (A) are the result of a critical discussion of the literature data. The other curves (B – G) represent data from other sources [1.87]

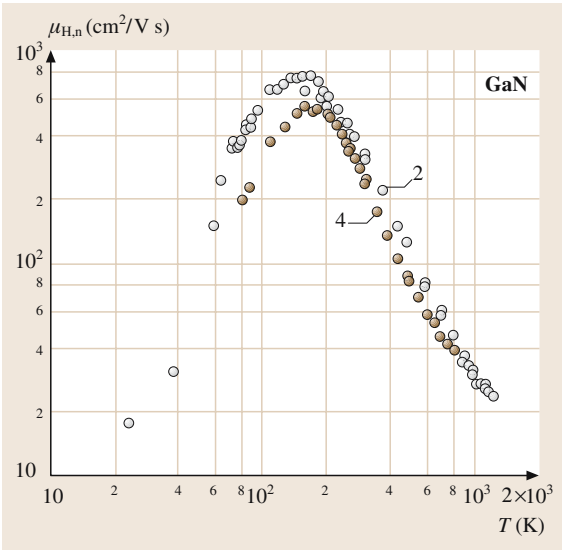


**Fig. 4.1-93** GaN. Electron Hall mobility vs. temperature for two samples [1.85]

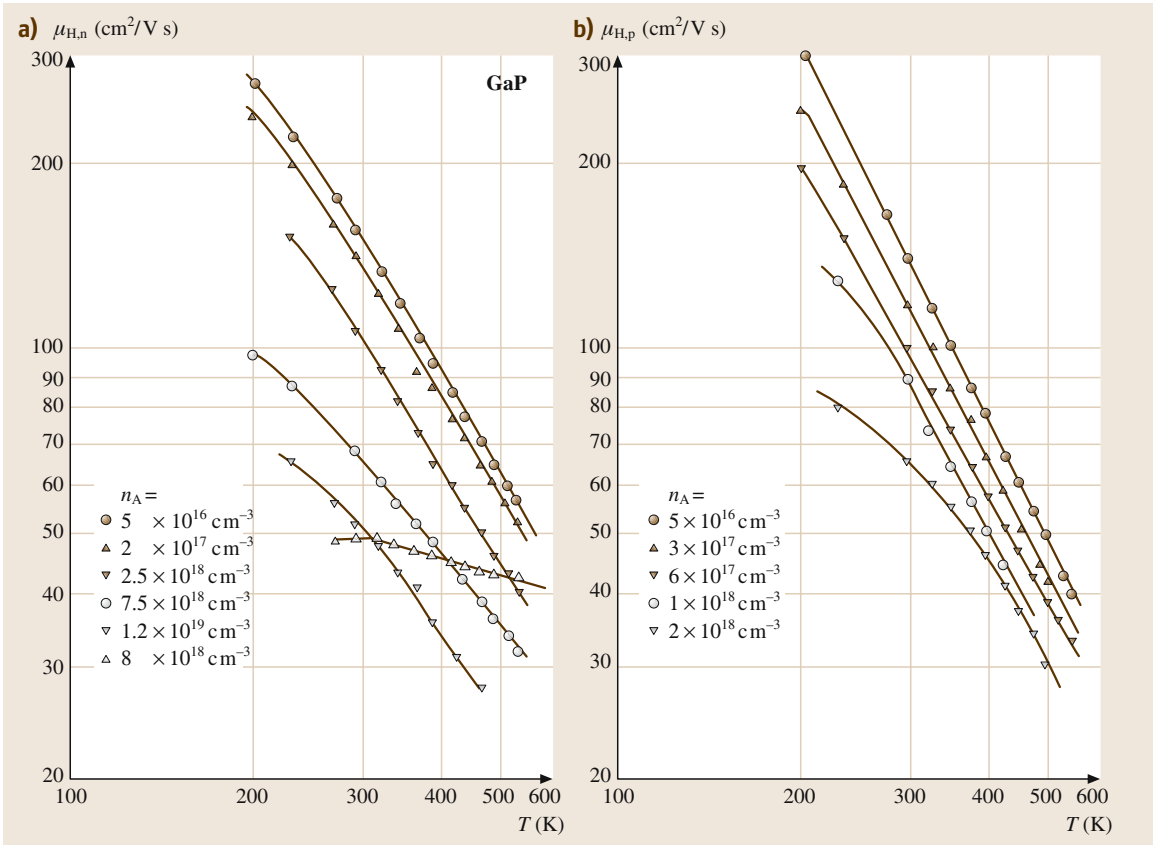


**Fig. 4.1-94a,b** GaP. Hall mobility in n-type **(a)** and p-type **(b)** LPE-grown layers vs. temperature [1.86]

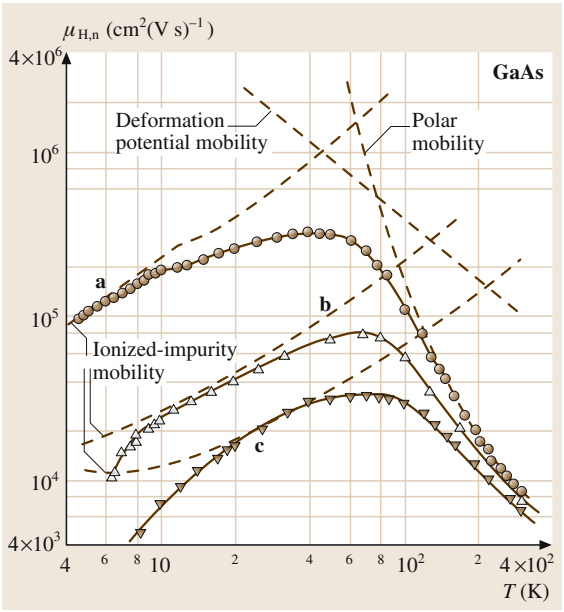


**Fig. 4.1-95** GaAs. Temperature variation of Hall mobility at 5 kG for three n-GaAs samples. In the temperature range from 300 K to 77 K, the electron mobility of sample a is dominated by polar optical scattering. Samples b and c show increased effects of ionized-impurity scattering [1.88]

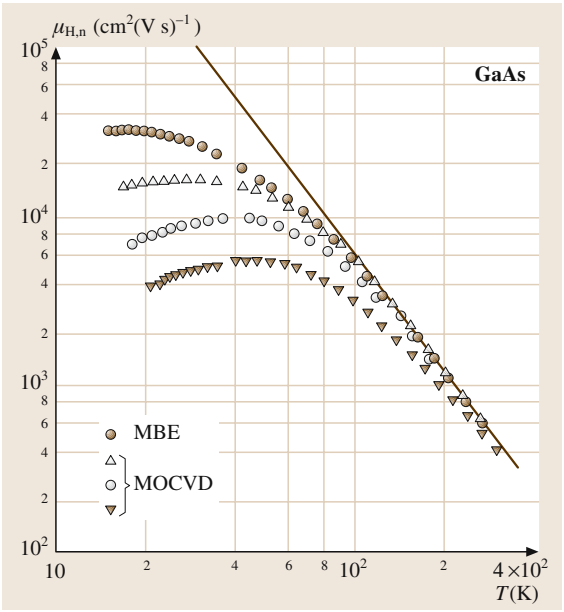


**Fig. 4.1-96** GaAs. Hall mobility of holes vs. temperature for MBE- and MOCVD-grown samples. The *solid line* represents the empirical relation $\mu_{H,n} = 450 \times (300/T)^{2.3}$ [1.89]

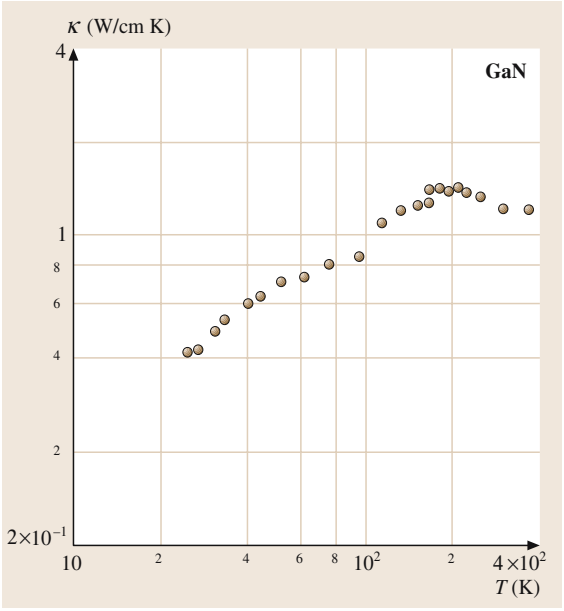


**Fig. 4.1-97** GaN. Thermal conductivity along the *c* axis vs. temperature [1.90]

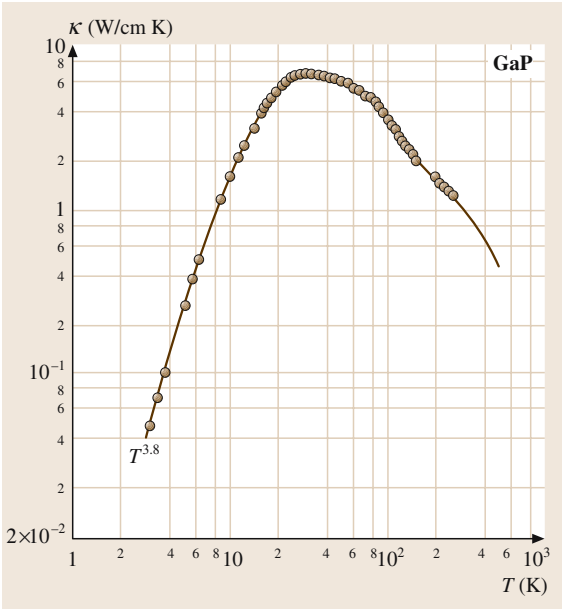


**Fig. 4.1-98** GaP. Thermal conductivity vs. temperature for a p-type sample [1.69, 70]

**Table 4.1-68** Thermal conductivity $\kappa$ of gallium compounds

| Crystal | $\kappa$ (W/cm K) | Temperature (K) | Remarks |
|---|---|---|---|
| Gallium nitride | 1.3 | 300 | See Fig. 4.1-97 for temperature dependence. |
| Gallium phosphide | 0.77 | 300 | See Fig. 4.1-98 for temperature dependence. |
| Gallium arsenide | 0.455 | 300 | See Fig. 4.1-99 for temperature dependence. |
| Gallium antimonide | | | See Fig. 4.1-100 for temperature dependence. |

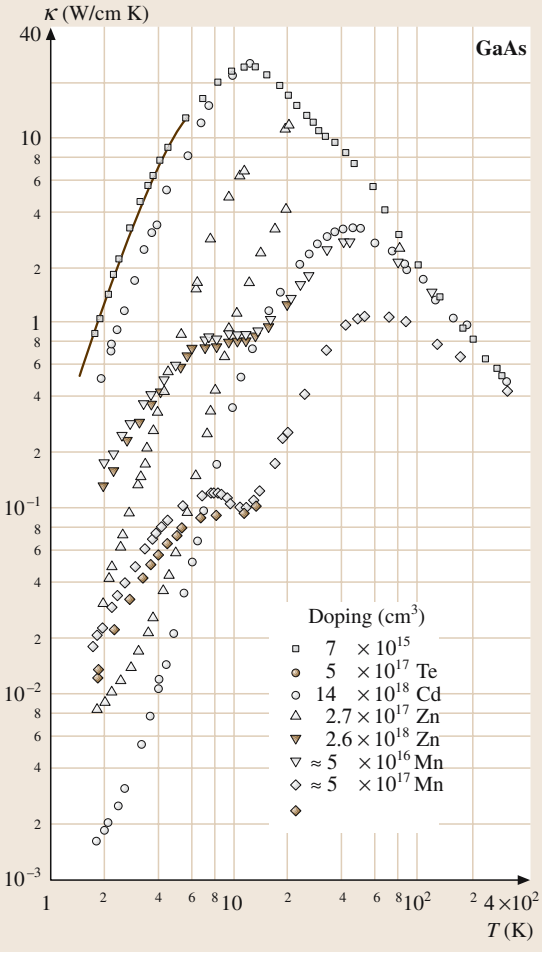


**Fig. 4.1-99** GaAs. Thermal conductivity vs. temperature for seven samples with impurity concentrations between $7\times10^{15}$ cm$^{-3}$ and $2.6\times10^{18}$ cm$^{-3}$ [1.91]

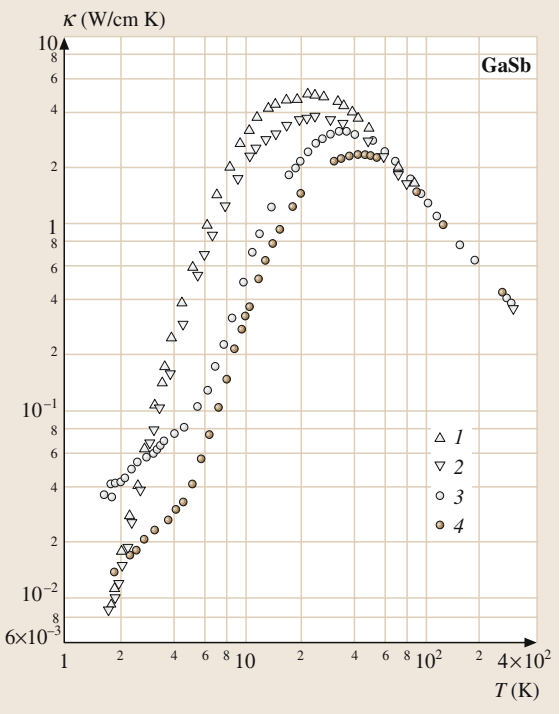


**Fig. 4.1-100** GaSb. Thermal conductivity of two n-type samples with impurity contents of $4\times10^{18}$ cm$^{-3}$ (1) and $1.4\times10^{18}$ cm$^{-3}$ (2) and of two p-type samples with impurity contents of $1\times10^{17}$ cm$^{-3}$ (3) and $2\times10^{17}$ cm$^{-3}$ (4) [1.92]

### D. Electromagnetic and Optical Properties

Tables 4.1-69 – 4.1-72 and Figs. 4.1-101 – 4.1-105.

**Table 4.1-69** Dielectric constant $\varepsilon$ and refractive index $n$ of gallium compounds

| Crystal | | Temperature (K) | $\varepsilon(0)$ | $\varepsilon(\infty)$ | $n$ at or $\lambda$ (nm) $h\nu$ (eV) | Remarks | Figure |
|---|---|---|---|---|---|---|---|
| Gallium nitride | GaN | 300 | 9.5 (3) | | | $\boldsymbol{E}$ perpendicular to $c$ | Fig. 4.1-101 |
| | | | 10.4 (3) | | | $\boldsymbol{E}$ parallel to $c$ | |
| | | | | 5.8 (4) | | $\boldsymbol{E}$ parallel to $c$ | |
| | | | | 5.35 (20) | | $\boldsymbol{E}$ perpendicular to $c$ | |
| | | | | | 2.29 (5) 500 nm | Optical interference | |
| Gallium phosphide | GaP | 300 | 11.11 | | | Low-frequency capacitance measurements | Fig. 4.1-103 |
| | | 75.7 | 10.86 | | | Derived from refractive index | |
| | | 300 | | 9.11 | | | |
| | | | | | 3.334 2.0 eV | Spectroscopic ellipsometry | |
| Gallium arsenide | GaAs | 300 | 12.80 (5) | | | Microwave technique | Fig. 4.1-102 |
| | | | | 10.86 | | Optical-transmission interference | |
| | | | | | 3.878 2.0 eV | Spectroscopic ellipsometry | |
| Gallium antimonide | GaSb | 300 | 15.7 | | | Reflectance and oscillator fit | Fig. 4.1-105 |
| | | | | 14.44 | | | |
| | | | | | 5.239 2.0 eV | Spectroscopic ellipsometry | |

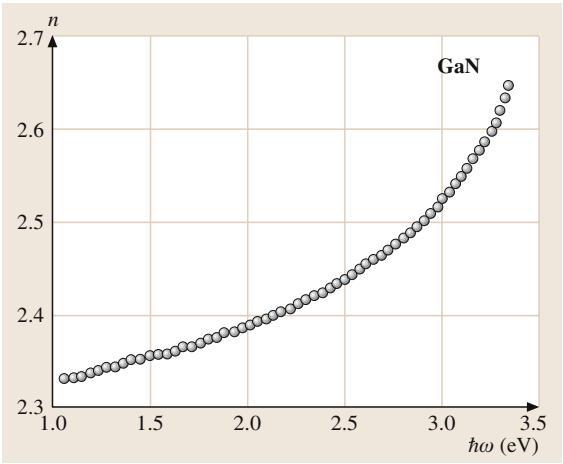


**Fig. 4.1-101** GaN. Refractive index vs. photon energy at 300 K; $\boldsymbol{E} \perp c$ [1.93]

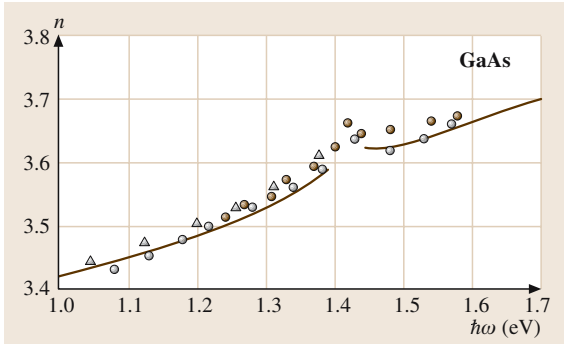


**Fig. 4.1-102** GaAs. Refractive index vs. photon energy in the range 1.0 – 1.7 eV [1.94]. *Solid line*, calculated; *symbols*, experimental data from three sources

**Table 4.1-70a** Optical constants of gallium phosphide

| $h\nu$ (eV) | $\varepsilon_1$ | $\varepsilon_2$ | $n$ | $k$ | $R$ | $K$ ($10^3$ cm$^{-1}$) |
|---|---|---|---|---|---|---|
| 1.5 | 10.102 | 0.000 | 3.178 | 0.000 | 0.272 | 0.00 |
| 2.0 | 11.114 | 0.000 | 3.334 | 0.000 | 0.290 | 0.00 |
| 2.5 | 12.996 | 0.046 | 3.605 | 0.006 | 0.320 | 1.63 |
| 3.0 | 16.601 | 1.832 | 4.081 | 0.224 | 0.369 | 68.26 |
| 3.5 | 24.833 | 8.268 | 5.050 | 0.819 | 0.458 | 290.4 |
| 4.0 | 9.652 | 16.454 | 3.790 | 2.171 | 0.452 | 880.1 |
| 4.5 | 11.073 | 17.343 | 3.978 | 2.180 | 0.461 | 994.3 |
| 5.0 | 0.218 | 26.580 | 3.661 | 3.631 | 0.580 | 1840 |
| 5.5 | −10.266 | 10.974 | 1.543 | 3.556 | 0.677 | 1983 |
| 6.0 | −5.521 | 7.041 | 1.309 | 2.690 | 0.583 | 1636 |

**Table 4.1-71** Optical constants of gallium arsenide

| $h\nu$ (eV) | $\varepsilon_1$ | $\varepsilon_2$ | $n$ | $k$ | $R$ | $K$ ($10^3$ cm$^{-1}$) |
|---|---|---|---|---|---|---|
| 1.5 | 13.435 | 0.589 | 3.66 | 0.080 | 0.327 | 12.21 |
| 2.0 | 14.991 | 1.637 | 3.878 | 0.211 | 0.349 | 42.79 |
| 2.5 | 18.579 | 3.821 | 4.333 | 0.441 | 0.395 | 111.7 |
| 3.0 | 16.536 | 17.571 | 4.509 | 1.948 | 0.472 | 592.5 |
| 3.5 | 8.413 | 14.216 | 3.531 | 2.013 | 0.425 | 714.2 |
| 4.0 | 9.279 | 13.832 | 3.601 | 1.920 | 0.421 | 778.7 |
| 4.5 | 6.797 | 22.845 | 3.913 | 2.919 | 0.521 | 1331 |
| 5.0 | −11.515 | 18.563 | 2.273 | 4.084 | 0.688 | 2070 |
| 5.5 | −6.705 | 8.123 | 1.383 | 2.936 | 0.613 | 1637 |
| 6.0 | −4.511 | 6.250 | 1.264 | 2.472 | 0.550 | 1503 |

**Table 4.1-72a** Optical constants of gallium antimonide

| $h\nu$ (eV) | $\varepsilon_1$ | $\varepsilon_2$ | $n$ | $k$ | $R$ | $K$ ($10^3$ cm$^{-1}$) |
|---|---|---|---|---|---|---|
| 1.5 | 19.135 | 3.023 | 4.388 | 0.344 | 0.398 | 52.37 |
| 2.0 | 25.545 | 14.442 | 5.239 | 1.378 | 0.487 | 279.4 |
| 2.5 | 13.367 | 19.705 | 4.312 | 2.285 | 0.484 | 579.1 |
| 3.0 | 9.479 | 15.838 | 3.832 | 2.109 | 0.444 | 641.2 |
| 3.5 | 7.852 | 19.267 | 3.785 | 2.545 | 0.485 | 902.8 |
| 4.0 | −1.374 | 25.138 | 3.450 | 3.643 | 0.583 | 1477 |
| 4.5 | −8.989 | 10.763 | 1.586 | 3.392 | 0.561 | 1547 |
| 5.0 | −5.693 | 7.529 | 1.369 | 2.751 | 0.585 | 1394 |
| 5.5 | −5.527 | 5.410 | 1.212 | 2.645 | 0.592 | 1475 |
| 6.0 | −4.962 | 4.520 | 0.935 | 2.416 | 0.610 | 1469 |

**Table 4.1-70b** GaP. Refractive index in the infrared

| Wavelength (μm) | Refractive index $n$ | Remarks |
|---|---|---|
| 20 | 2.529 | Reflectance and transmission at 300 K |
| 10 | 2.90 | |
| 5 | 2.94 | |
| 2 | 3.02 | |
| 1 | 3.17 | |

**Table 4.1-72b** GaSb. Refractive index in the infrared

| Wavelength (μm) | Refractive index $n$ | Temperature (K) | Remarks |
|---|---|---|---|
| 14.9 | 3.880 | 300 | Reflectance and transmission |
| 10 | 3.843 | | |
| 4 | 3.833 | | |
| 2 | 3.789 | | Prism method |
| 1.9 | 3.802 | | |
| 1.8 | 3.820 | | |

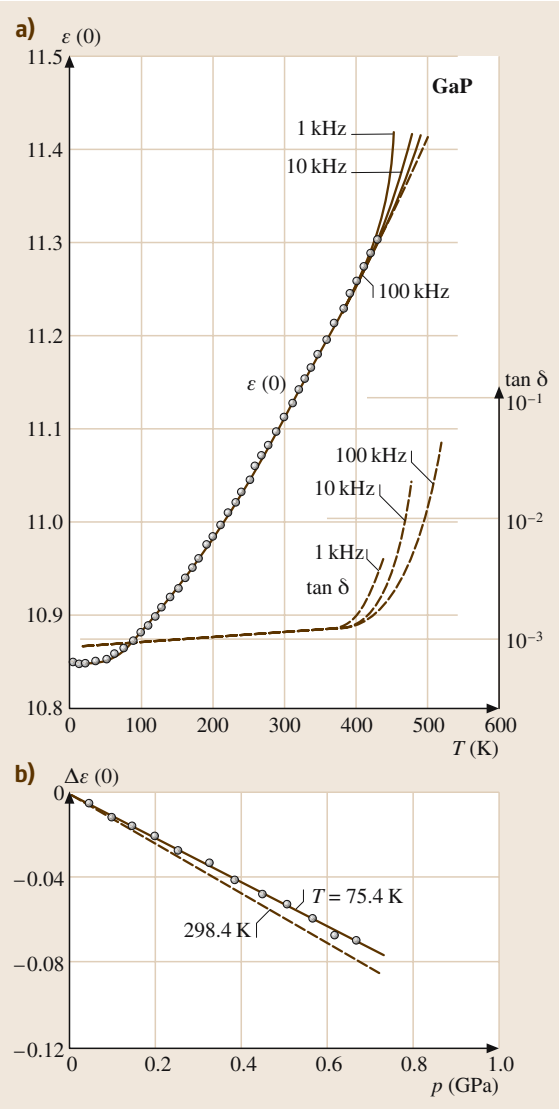


**Fig. 4.1-103a,b** GaP. **(a)** Static dielectric constant $\varepsilon(0)$ and dielectric loss $\tan\delta$ vs. temperature, obtained from low-frequency capacitance measurements. For clarity, the actual data points at only one frequency (100 kHz) are shown. The data have been corrected for dimensional changes due to thermal expansion. **(b)** Change in static dielectric constant vs. pressure at two temperatures [1.95]

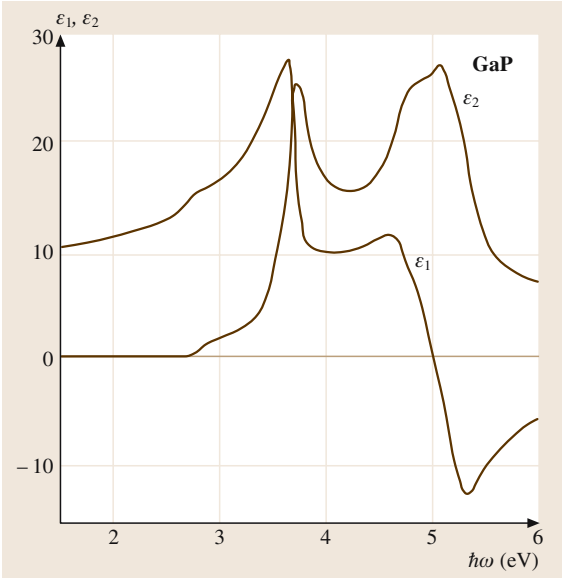


**Fig. 4.1-104** GaP. Real and imaginary parts of the dielectric constant vs. photon energy [1.47]

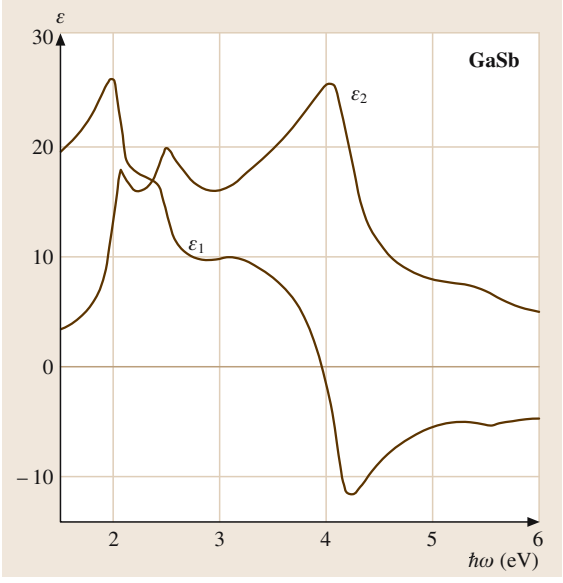


**Fig. 4.1-105** GaSb. Real and imaginary parts of the dielectric constant vs. photon energy [1.47]

### 4.1.2.4 Indium Compounds

A. Crystal Structure, Mechanical and Thermal Properties

Tables 4.1-73 – 4.1-81.

**Table 4.1-73** Crystal structures of indium compounds

| Crystal | | Space group | | Crystal system | Structure type | Remarks | Figure |
|---|---|---|---|---|---|---|---|
| Indium nitride | InN | $C_{6v}^4$ | $P6_3mc$ | hex | Wurtzite | Phase transition to NaCl structure under pressure | Fig. 4.1-3 |
| Indium phosphide | InP I | $T_d^2$ | $F\bar{4}3m$ | fcc | Zinc blende | Stable at normal pressure | Fig. 4.1-2 |
| | InP II | $O_h^5$ | $Fm3m$ | fcc | NaCl | Pressure > 34 GPa | |
| Indium arsenide | InAs I | $T_d^2$ | $F\bar{4}3m$ | fcc | Zinc blende | Stable at normal pressure | Fig. 4.1-2 |
| | InAs II | $O_h^5$ | $Fm3m$ | fcc | NaCl | Pressure > 4 GPa, RT | |
| Indium antimonide | InSb I | $T_d^2$ | $F\bar{4}3m$ | fcc | Zinc blende | Stable at normal pressure [a] | Fig. 4.1-2 |

[a] Quite a number of phase transitions have been observed at high pressures (> 2.1 GPa).

**Table 4.1-74** Lattice parameters of indium compounds

| Crystal | | Lattice parameters (nm) | Temperature (K) | Remarks |
|---|---|---|---|---|
| Indium nitride | InN | $a = 0.35446$<br>$c = 0.57034$ | | Epitaxial layers, X-ray diffraction |
| Indium phosphide | InP | $a = 0.58687\ (10)$ | 291.15 | Powder, X-ray diffraction |
| Indium arsenide | InAs | $a = 0.60583$ | 298.15 | |
| Indium antimonide | InSb | $a = 0.647937$ | 298.15 | Powder, X-ray diffraction |

**Table 4.1-75** Densities of indium compounds

| Crystal | | Density (g/cm$^3$) | Temperature (K) | Remarks |
|---|---|---|---|---|
| Indium nitride | InN | 6.78 (5) | | Pycnometric |
| Indium phosphide | InP | 4.81 | | |
| Indium arsenide | InAs | 5.667 | 300 | X-ray diffraction |
| Indium antimonide | InSb | 5.7747 (4) | 300 | X-ray diffraction |

**Table 4.1-76** Elastic constants $c_{ik}$ (in GPa) of indium compounds

| Crystal | | $c_{11}$ | $c_{12}$ | $c_{13}$ | $c_{33}$ | $c_{44}$ | Remarks |
|---|---|---|---|---|---|---|---|
| Indium nitride | InN | 190 (7) | 104 (3) | 121 (7) | 182 (6) | 9.9 (11) | Calculated from the mean square displacements of the lattice atoms measured by X-ray diffraction |
| Indium phosphide | InP | 101.1 | 56.1 | – | – | 45.6 | Ultrasonic-wave transit times, RT |
| Indium arsenide | InAs | 83.29 | 45.26 | – | – | 39.59 | Ultrasound, $f = 15$ MHz, n-type, RT |
| Indium antimonide | InSb | 69.18 | 37.88 | – | – | 31.32 | $T = 0$ K, extrapolated from 4.2 K, ultrasound, $f = 10$ MHz |

**Table 4.1-77** Melting point $T_m$ of indium compounds

| Crystal | | Melting point $T_m$ (K) | Remarks |
|---|---|---|---|
| Indium nitride | InN | 1900 | Estimated; at 80 kbar $N_2$ |
| Indium phosphide | InP | 1327 | Optimized |
| Indium arsenide | InAs | 1221 (1) | |
| Indium antimonide | InSb | 800 (1) | Drop calorimetry |

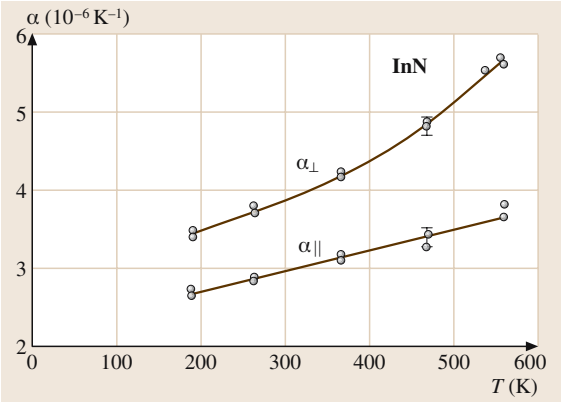


**Fig. 4.1-106** InN. Coefficient of linear thermal expansion vs. temperature [1.75]

**Table 4.1-78** Linear thermal expansion coefficient $\alpha$ of indium compounds

| Crystal | | Expansion coefficient $\alpha$ ($10^{-6}$ $K^{-1}$) | | Temperature (K) | Temperature dependence | Remarks |
|---|---|---|---|---|---|---|
| Indium nitride | InN | $\alpha_a$<br>$\alpha_c$ | 3.6 (2)<br>2.6 (3) | 100–673 | Fig. 4.1-106 | X-ray diffraction |
| Indium phosphide | InP | | 4.75 (10) | 298 | Fig. 4.1-107 | |
| Indium arsenide | InAs | | 4.52 | 20–250 | Fig. 4.1-108 | Average value, X-ray diffraction |
| Indium antimonide | InSb | | 5.37 (50) | 283–343 | Fig. 4.1-109 | X-ray diffraction |

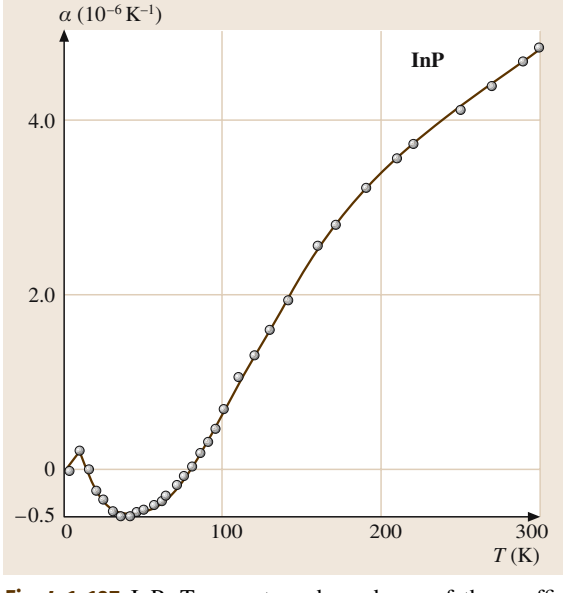


**Fig. 4.1-107** InP. Temperature dependence of the coefficient of linear thermal expansion, obtained by the Bond method [1.96]

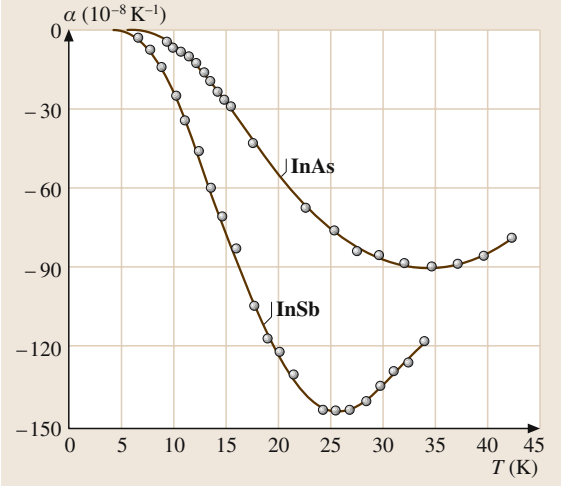


**Fig. 4.1-108** InAs, InSb. Linear thermal expansion coefficient vs. temperature, measured with a variable-transformer dilatometer [1.97]

**Table 4.1-79** Heat capacity $c_p$ and Debye temperature $\Theta_D$ of indium compounds

| Crystal | | Heat capacity (J/mol K) | Temperature (K) | Debye temperature (K) | Remarks |
|---|---|---|---|---|---|
| Indium nitride | InN | 41.74 | 300 | 660 | Calorimetry |
| Indium phosphide | InP | | | 321 | |
| Indium arsenide | InAs | | | 247 | |
| Indium antimonide | InSb | | | 206 | Average value |

**Table 4.1-80** Phonon wavenumbers of indium compounds. Indium nitride (InN), $T = 300$ K; indium phosphide (InP), RT, from coherent inelastic neutron scattering, carrier concentration $n = 10^{12}$ cm$^{-3}$; indium arsenide (InAs), from Raman scattering; indium antimonide (InSb), $T = 300$ K, from inelastic neutron scattering, carrier concentration $n = 8 \times 10^{13}$ cm$^{-3}$

| InN | | | | | InP | | |
|---|---|---|---|---|---|---|---|
| Symmetry point | Branch | Wave-number (cm$^{-1}$) | Temperature (K) | Remarks | Symmetry point | Branch | Frequency (THz) |
| $\tilde{\nu}$ ($\Gamma$) | TO | 478 | 300 | Reflectivity, Kramers–Kronig analysis | $\nu$ (111)(0.05) | LO | 10.3 (3) |
| | LO | 694 | | Reflectivity, Kramers–Kronig analysis | $\nu$ ($\Gamma_{15}$) | TO | 9.2 (2) |
| $\tilde{\nu}$ ($A_1$) | TO | 400 | | Experimental data | $\nu$ ($X_5$) | TA | 2.05 (10) |
| $\tilde{\nu}$ ($E_1$) | TO | 484 | | | $\nu$ ($X_3$) | LA | 5.8 (3) |
| | LO | 570 | | | $\nu$ ($X_5$) | TO | 9.70 (10) |
| $\tilde{\nu}$ ($E_2^{(1)}$) | TO | 190 | | | $\nu$ ($X_1$) | LO | 9.95 (20) |
| $\tilde{\nu}$ ($E_2^{(2)}$) | TO | 590 | | | $\nu$ ($L_3$) | TA | 1.65 (2) |
| | | | | | $\nu$ ($L_1$) | LA | 5.00 (10) |
| | | | | | $\nu$ ($L_3$) | TO | 9.50 (15) |
| | | | | | $\nu$ ($L_1$) | LO | 10.2 (3) |

| InAs | | | | InSb | | |
|---|---|---|---|---|---|---|
| Symmetry point | Branch | Wave-number (cm$^{-1}$) | Temperature (K) | Symmetry point | Branch | Frequency (THz) |
| $\tilde{\nu}$ ($\Gamma$) | TO | 217.3 | 300 | $\nu$ ($\Gamma_{15}$) | LO | 5.90 (25) |
| | LO | 238.6 | | | TO | 5.54 (5) |
| $\tilde{\nu}$ (X) | TA | 53 | | $\nu$ ($X_5$) | TA | 1.12 (5) |
| | LA | 160 | | $\nu$ ($X_3$) | LA | 4.30 (10) |
| | TO | 216 | | $\nu$ ($X_1$) | LO | 4.75 (20) |
| | LO | 203 | 100 | $\nu$ ($X_5$) | TO | 5.38 (17) |
| $\tilde{\nu}$ (L) | TA | 44 | 300 | $\nu$ ($L_3$) | TA | 0.98 (5) |
| | LA | 139.5 | | $\nu$ ($L_1$) | LA | 3.81 (6) |
| | TO | 216 | | | LO | 4.82 (10) |
| | LO | 203 | 100 | $\nu$ ($L_3$) | TO | 5.31 (6) |

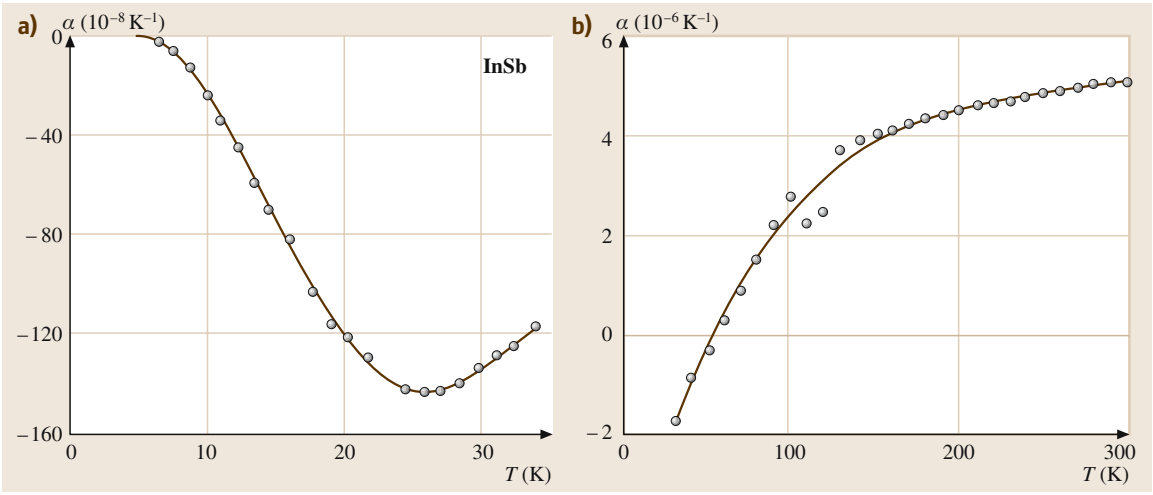


**Fig. 4.1-109a,b** InSb. Linear thermal expansion coefficient vs. temperature: **(a)** low-temperature region [1.97], **(b)** high-temperature region [1.98]

**Table 4.1-81** Phonon dispersion curves of indium compounds

| Crystal | | Figure |
|---|---|---|
| Indium phosphide | InP | Fig. 4.1-110 |
| Indium arsenide | InAs | Fig. 4.1-111 |
| Indium antimonide | InSb | Fig. 4.1-112 |

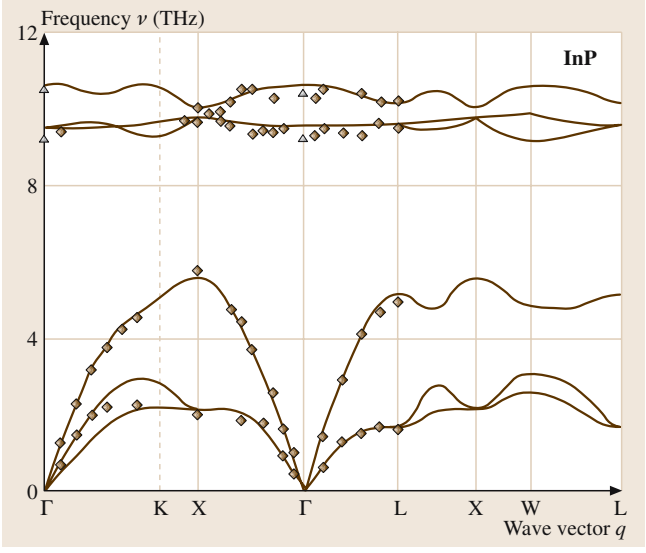


**Fig. 4.1-110** InP. Phonon dispersion curves. Experimental neutron data (*diamonds*) [1.99] and Raman data (*triangles*) [1.100] and ab initio pseudopotential calculations (*solid curves*) [1.101]. From [1.101]

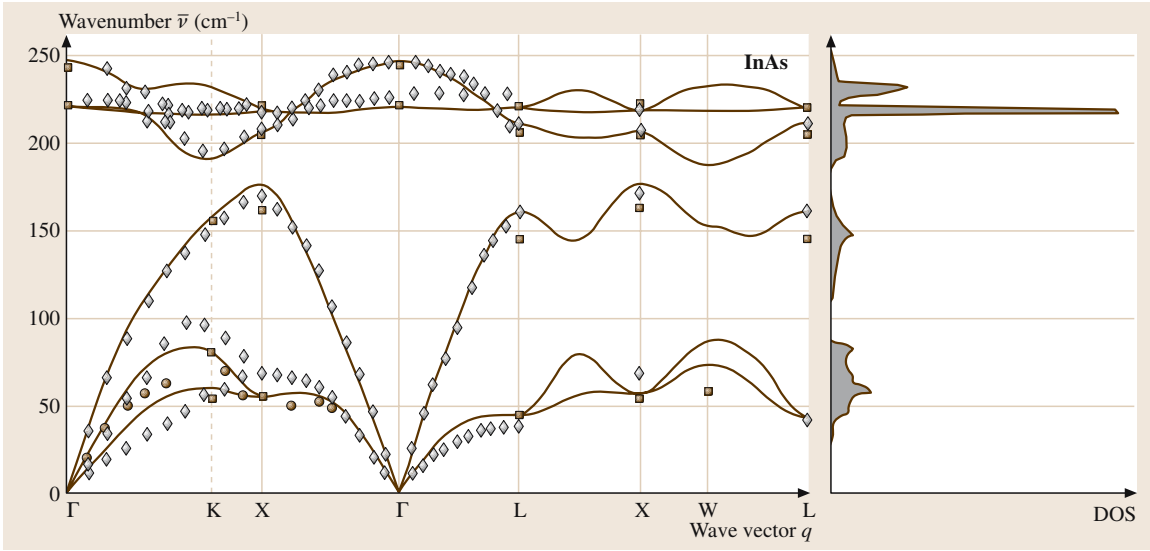


**Fig. 4.1-111** InAs. Phonon dispersion curves (*left panel*) and density of states (*right panel*) [1.82]. Experimental neutron data (*circles*, $T = 300$ K) [1.102], thermal-diffuse-scattering X-ray data (*diamonds*, $T = 80$ K) [1.102], Raman data (*squares*, $T = 330$ K) [1.103], and ab initio calculations (*solid curves* [1.82]). From [1.82]

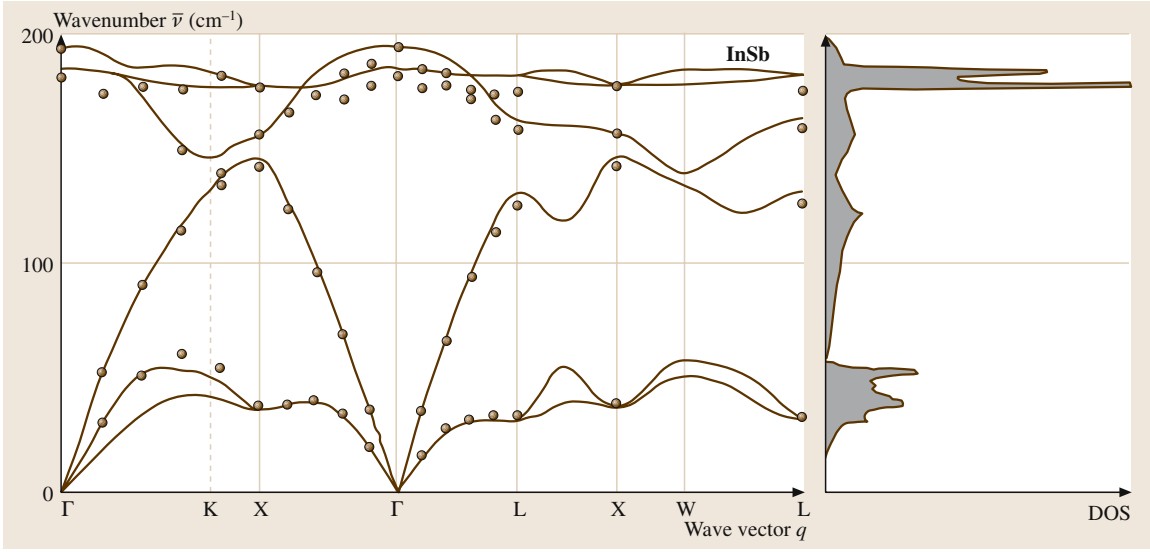


**Fig. 4.1-112** InSb. Phonon dispersion curves (*left panel*) and density of states (*right panel*). Experimental neutron data (*circles*) [1.21] and ab initio pseudopotential calculations (*solid curves*) [1.60]. From [1.60]

## B. Electronic Properties

Tables 4.1-82 – 4.1-87.

*Band Structures of Indium Compounds. Indium Nitride (InN).* The band structure (Fig. 4.1-114) shows a direct gap at Γ very similar to that of GaN. A low-lying many-valley conduction band leading to an indirect gap has been suggested.

*Indium Phosphide (InP).* Indium phosphide is a direct-gap semiconductor. The conduction band minimum is situated at Γ. Higher conduction band minima at L and X have been detected in optical experiments. The X-band minima show no camel's back structure, in contrast to most other III–V compounds with the zinc blende structure. The valence band has the structure common to all zinc blende-type semiconductors (Fig. 4.1-113).

*Indium Arsenide (InAs).* Indium arsenide resembles InSb in its band structure, having only a slightly larger energy gap and a smaller spin–orbit splitting of the top of the valence band. The conduction band minimum ($\Gamma_6$) is situated in the center of the Brillouin zone. Near the minimum, $E(k)$ is isotropic but nonparabolic. The valence band shows the usual structure common to all zinc blende-type III–V compounds (Fig. 4.1-116).

**Table 4.1-82** First Brillouin zones of indium compounds

| Crystal | | Figure |
|---|---|---|
| Indium nitride | InN | Fig. 4.1-24 |
| Indium phosphide | InP | Fig. 4.1-23 |
| Indium arsenide | InAs | Fig. 4.1-23 |
| Indium antimonide | InSb | Fig. 4.1-23 |

*Indium Antimonide (InSb).* Indium antimonide is a direct-gap semiconductor. The minimum of the conduction band ($\Gamma_6$) is located in the center of the Brillouin zone. Near the minimum, $E(k)$ is isotropic but nonparabolic. Thus the effective mass of the electrons is scalar and depends strongly on the electron concentration. Higher band minima (about 0.63 eV above the lowest minimum) seem to have been established by transport measurements in heavily doped n-InSb. The valence band shows the structure common to all zinc blende semiconductors, i. e. two subbands degenerate at $\Gamma_8$ and one spin-split band at $\Gamma_7$ (Fig. 4.1-115).

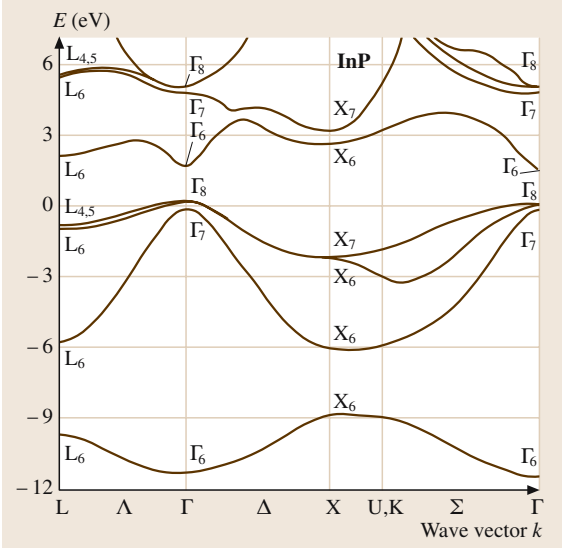


**Fig. 4.1-113** Band structure of indium phosphide

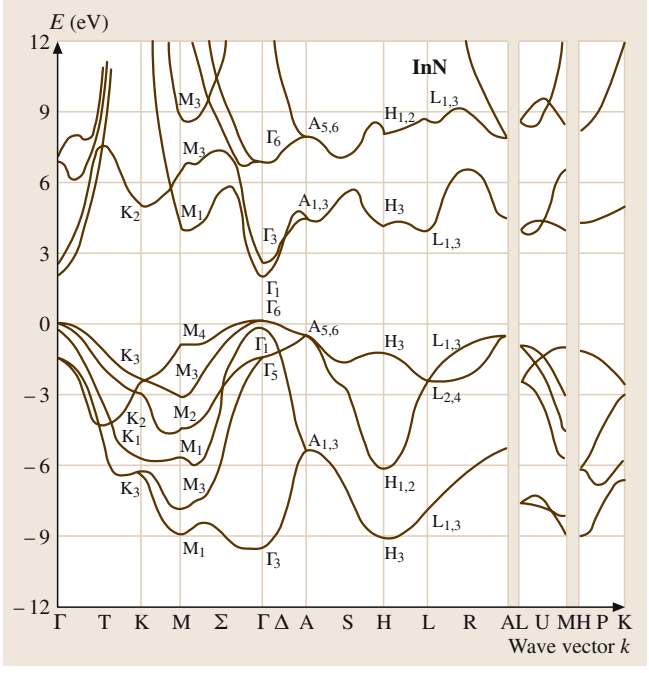


**Fig. 4.1-114** Band structure of indium nitride

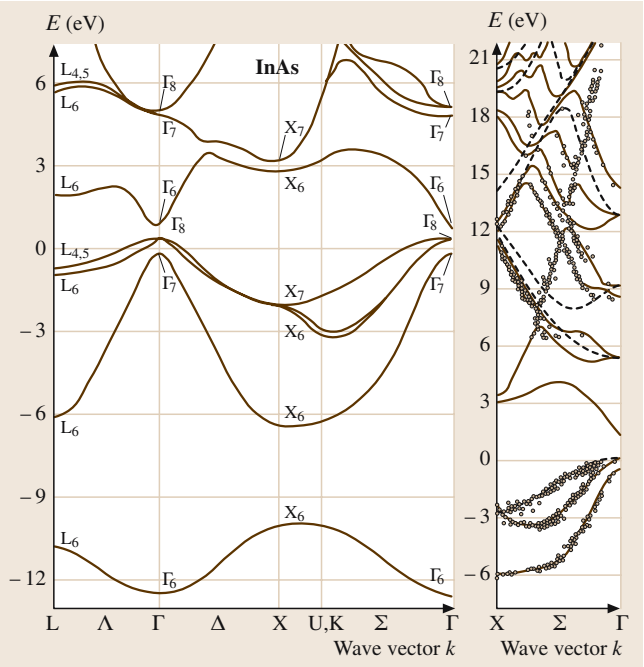


Fig. 4.1-116 Band structure of indium arsenide

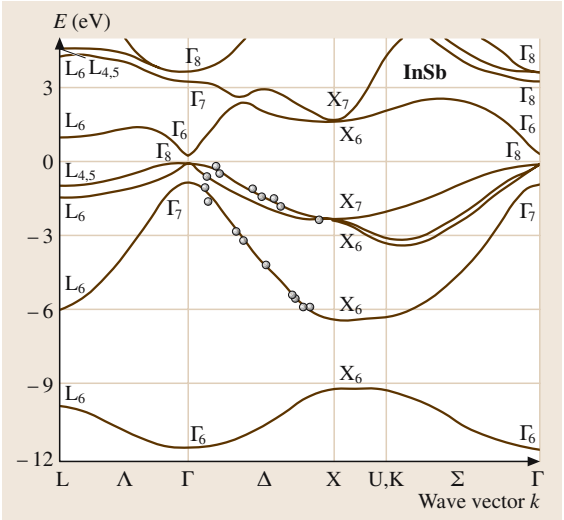


Fig. 4.1-115 Band structure of indium antimonide

**Table 4.1-83** Energy gaps of indium compounds

| Crystal | | Quantity | Bands | Energy (eV) | Temperature (K) | Remarks |
|---|---|---|---|---|---|---|
| Indium nitride | InN | $E_{g,\,dir}$ | | 1.95 | 300 | Polycrystalline film, absorption edge |
| Indium phosphide | InP | $E_{g,\,dir}$ | $\Gamma_{8v}$ to $\Gamma_{6c}$ | 1.4236 (1) | 1.6 | From excitonic gap |
| | | | | 1.344 | 300 | Absorption, photoluminescence |
| Indium arsenide | InAs | $E_{g,\,dir}$ | $\Gamma_{8v}$ to $\Gamma_{6c}$ | 0.4180 (5) | 4.2 | Magnetotransmission |
| | | | | 0.354 (3) | 295 | Electroreflectance |
| | | $E_{g,\,x}$ | | 0.41565 (1) | 1.4 | Excitonic band gap, photoluminescence |
| Indium antimonide | InSb | $E_{g,\,dir}$ | $\Gamma_{8v}$ to $\Gamma_{6c}$ | 0.2352 | 1.7 | Emission spectra, from exciton data |
| | | | | 0.180 | 300 | Reflectance, magnetoabsorption |

**Table 4.1-84** Spin–orbit splitting energies of indium compounds

| Crystal | | Spin–orbit splitting | Bands | Numerical value (eV) | Temperature (K) | Remarks |
|---|---|---|---|---|---|---|
| Indium phosphide | InP | $\Delta_0$ | $\Gamma_{8v}$ to $\Gamma_{7v}$ | 0.108 (8) | 4.2 | Wavelength-modulated photovoltaic effect |
| | | $\Delta_1$ | $\Lambda_{4,5v}$ to $\Lambda_{6v}$ | 0.13 | 77 | Thermoreflectance |
| | | | | 0.15 (5) | 300 | Electroreflectance |
| | | $\Delta_0'$ | $\Gamma_{8c}$ to $\Gamma_{7c}$ | 0.07 | 300 | Electroreflectance |
| Indium arsenide | InAs | $\Delta_0$ | $\Gamma_{8v}$ to $\Gamma_{7v}$ | 0.38 (1) | 1.5 | Magnetoelectroreflectance |
| | | $\Delta_1$ | $L_{4,5v}$ to $L_{6v}$ | 0.267 | 5 | Wavelength-modulated reflectance |
| Indium antimonide | InSb | $\Delta_0$ | $\Gamma_{8v}$ to $\Gamma_{7v}$ | 0.81 (1) | 1.5 | Magnetoelectroreflectance |
| | | $\Delta_0'$ | $\Gamma_{7v}$ to $\Gamma_{8c}$ | 0.39 | 5 | Wavelength-modulated reflectance |
| | | $\Delta_1$ | $\Lambda_{4,5v}$ to $\Lambda_{6v}$ | 0.495 | | |

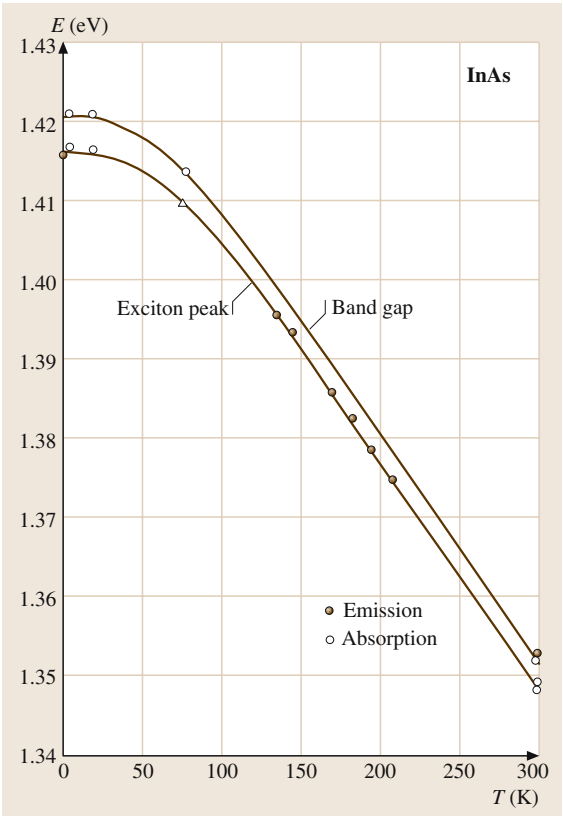


**Fig. 4.1-117** InP. Energy gap and exciton peak energy vs. temperature from absorption and emission data [1.104]

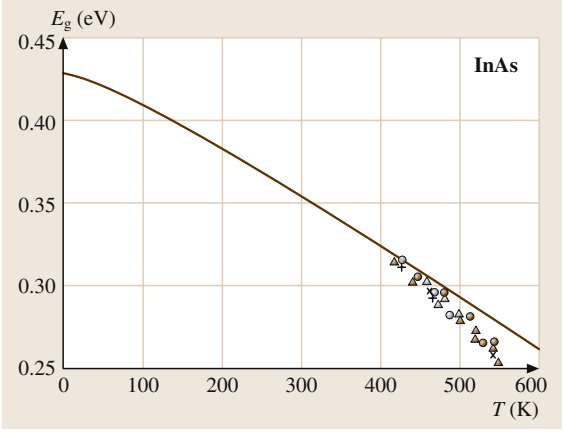


**Fig. 4.1-118** InAs. Band gap vs. temperature. *Solid line*, optical band gap calculated from parameters used for fitting various transport data; *symbols*, thermal band gap of six samples, obtained from conductivity and Hall coefficient [1.105]

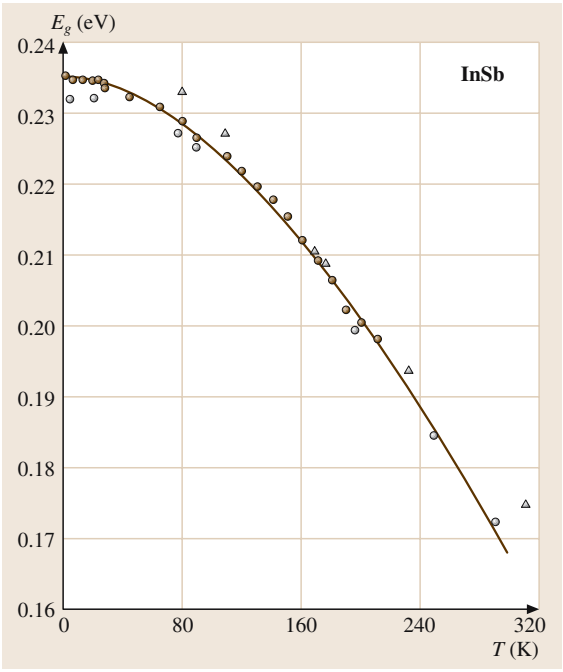


**Fig. 4.1-119** InSb. Energy gap vs. temperature below RT, measured by resonant two-photon photo-Hall effect (*filled circles*); the *open circles* and *triangles* show earlier literature data for comparison. *Solid curve*: fit by Varshni's formula [1.106]

**Table 4.1-85** Temperature dependence of the energy gaps of indium compounds

| Crystal | | Figure |
|---|---|---|
| Indium phosphide | InP | Fig. 4.1-117 |
| Indium arsenide | InAs | Fig. 4.1-118 |
| Indium antimonide | InSb | Fig. 4.1-119 |

**Table 4.1-86** Effective masses of electrons ($m_n$) and holes ($m_p$) for indium compounds (in units of the electron mass $m_0$)

| | | | |
|---|---|---|---|
| **InN** | | | |
| $m_n$ | 0.11 | 300 K | Optical mass, plasma edge |
| $m_{n,\,calc}$ | 0.12 | | Calculated effective mass |
| $m_{p,\,heavy}$ | 0.5 | | |
| $m_{p,\,light}$ | 0.17 | | |
| **InP** | | | |
| $m_n$ | 0.0808(10) | 0 K | Magnetophonon resonance |
| | 0.073 | 300 K | Faraday rotation |
| $m_{p,\,heavy}$ | 0.45 (5) | 4.2 K | Piezomodulated photovoltaic effect |
| $m_{p,\,light}$ | 0.12 (1) | 4.2 K | |
| $m_{p,\,so}$ | 0.121 (1) | 110 K | ***B*** parallel to [111] and [100] |
| **InAs** | | | |
| $m_n$ | 0.0265 | 4.2 K | |
| | 0.023 | 300 K | |
| $m_{p,\,heavy}$ | 0.57 | 300 K | |
| $m_{p,\,[100]}$ | 0.35 | | |
| $m_{p,\,[111]}$ | 0.85 | | |
| **InSb** | | | |
| $m_n$ ($\Gamma_{6c}$) | 0.01359 (3) | 4.2 K | Faraday effect, $n = 4.6 \times 10^{13}$ cm$^{-3}$ |
| | 0.0118 | 300 K | Cyclotron resonance |
| $m_{p,\,heavy}$ | 0.44 | 20 K | Parallel to [111], magnetoabsorption, Faraday rotation |
| | 0.42 | | Parallel to [110] |
| | 0.32 | | Parallel [100] |
| $m_{p,\,light}$ | 0.016 | 20 K | Magnetoabsorption, Faraday rotation |

**Table 4.1-87** Electron $g$-factor $g_c$ of indium compounds

| Crystal | $g_c$ | Temperature (K) | Remarks |
|---|---|---|---|
| Indium phosphide | 1.48 (5) | 4.2 | Modulated photovoltaic effect |
| Indium arsenide | −15.3 (2) | 1.4 | Magnetoluminescence |
| Indium antimonide | −51.31 (1) | 1.4 | Electron spin resonance |

### C. Transport Properties

Tables 4.1-88 – 4.1-90.

*Electronic Transport, General Description. Indium Phosphide (InP).* The transport properties are determined mainly by the electrons in the $\Gamma_{6c}$ minimum. Above 800 K, multivalley conduction, where the $L_{6c}$ minimum is involved, becomes important.

*Indium Arsenide (InAs).* The transport properties are determined mainly by the electrons in the $\Gamma_6$ minimum. Pure material with intrinsic conduction down to 450 K is available.

*Indium Antimonide (InSb).* The transport properties are mainly determined by the extremely high mobility of the electrons in the $\Gamma_6$ minimum of the conduction band. Pure material with intrinsic conduction down to 200 K is available. At low temperatures and in doped material, impurity scattering limits the electron mobility.

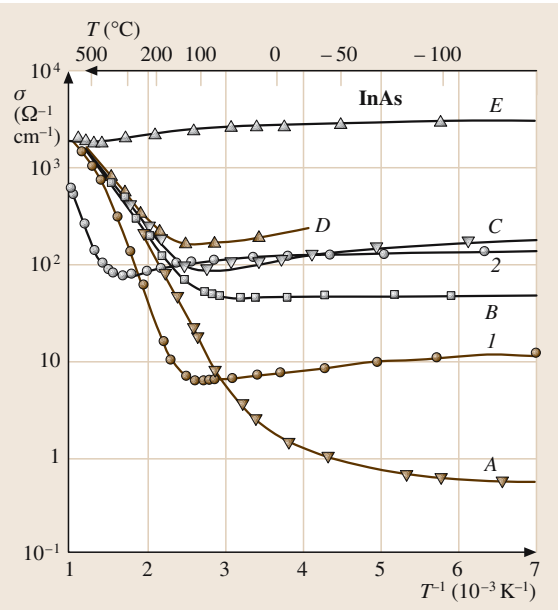


**Fig. 4.1-120** InAs. Electrical conductivity vs. reciprocal temperature [1.107]. *A*, $n = 1.2\times10^{15}$ cm$^{-3}$; *B*, $n = 1.7\times10^{16}$ cm$^{-3}$; *C*, $n = 4\times10^{16}$ cm$^{-3}$; *D*, $n = 7\times10^{16}$ cm$^{-3}$; *E*, $n = 2\times10^{18}$ cm$^{-3}$; 1, $p = 2\times10^{17}$ cm$^{-3}$; 2, $p = 7\times10^{18}$ cm$^{-3}$

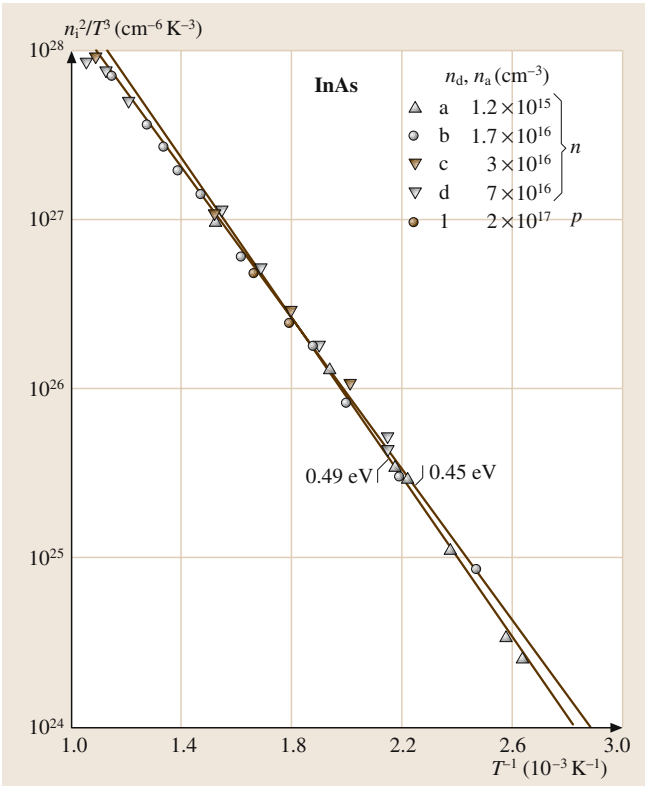


**Fig. 4.1-121** InAs. Square of the intrinsic carrier concentration divided by $T^3$ vs. reciprocal temperature for several different samples [1.107]

**Table 4.1-88** Carrier concentrations $n_i$ and electrical conductivity $\sigma$ of indium compounds

| Crystal | | Temperature (K) | Carrier concentration $n_i$ (cm$^{-3}$) | Conductivity $\sigma$ ($\Omega^{-1}$ cm$^{-1}$) | Remarks |
|---|---|---|---|---|---|
| Indium nitride | InN | 300 | | $2-3\times10^2$ | Temperature coefficient of resistivity $3.7\times10^{-3}$ K$^{-1}$ at 200–300 K for pressed powder |
| Indium phosphide | InP | 300 | $6.3\times10^{15}$ | 4–5 | n-type pure material |
| Indium arsenide | InAs | 300 | | 50 | See Fig. 4.1-120 for temperature dependence |
| Indium antimonide | InSb | 300 | $1.9\times10^{16}$ | 220 | See Fig. 4.1-122 for temperature dependence |

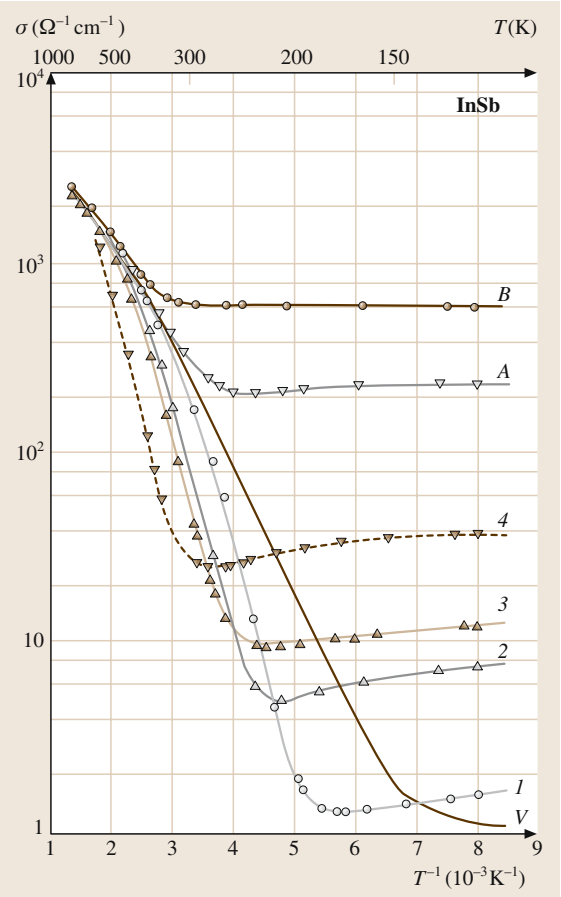


**Fig. 4.1-122** InSb. Electrical conductivity vs. reciprocal temperature [1.108]. *Curve V*, $n \approx 10^{13}\,cm^{-3}$; *A*, $n = 1.3\times10^{16}\,cm^{-3}$; *B*, $n = 1\times10^{16}\,cm^{-3}$; 1, $p = 4\times10^{15}\,cm^{-3}$; 2, $p = 2.2\times10^{16}\,cm^{-3}$; 3, $p = 6\times10^{16}\,cm^{-3}$; 4, $p = 2\times10^{17}\,cm^{-3}$

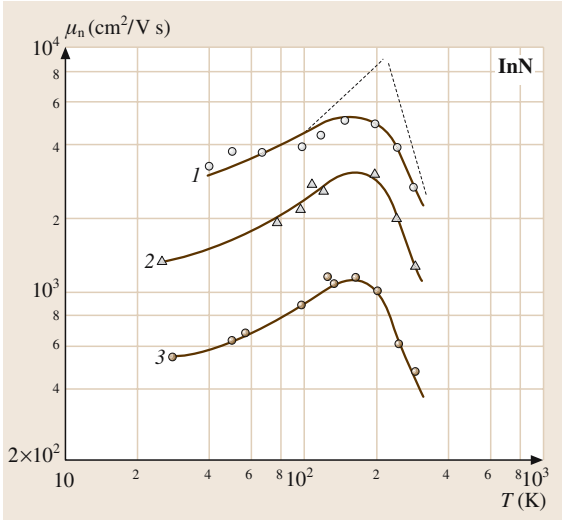


**Fig. 4.1-123** InN. Electron mobility vs. temperature for three samples with RT carrier concentrations of $5.3\times10^{16}$ (1), $7.5\times10^{16}$ (2), and $1.8\times10^{17}\,cm^{-3}$ (3). *Left broken line*, calculated ionized-impurity-scattering mobility; *right broken line*, empirical high-temperature mobility ($\mu \propto T^{-3}$) for sample 1. *Solid lines*, total mobility calculated for each sample [1.109]

**Table 4.1-89** Electron and hole mobilities $\mu_n$ and $\mu_p$ of indium compounds

| Crystal | Temperature (K) | Carrier concentration ($cm^{-3}$) | $\mu_n$ ($cm^2/V\,s$) | $\mu_p$ ($cm^2/V\,s$) | Remarks | Temperature dependence of mobilities |
|---|---|---|---|---|---|---|
| Indium nitride | 300<br>300 | $5–18\times10^{16}$ | 250 (50)<br>20 | | | Fig. 4.1-123 |
| Indium phosphide | 300<br>77<br>300 | $n = 0.5–1\times10^{16}$<br>$n = 6\times10^{13}$ | $4–5.4\times10^3$<br>$130\times10^3$ | <br><br>190 | Pure material,<br>Hall mobilities | Fig. 4.1-124<br><br>Fig. 4.1-125 |
| Indium arsenide | 300<br>77<br>300 | $n \sim 10^{16}$ | $2–3.3\times10^4$<br>$0.8–1\times10^5$ | <br><br>100–450 | Pure material | Fig. 4.1-121 |
| Indium antimonide | 300<br>300 | | $70\times10^3$ | <br>850 | Hall mobilities | Fig. 4.1-126<br>Fig. 4.1-127 |

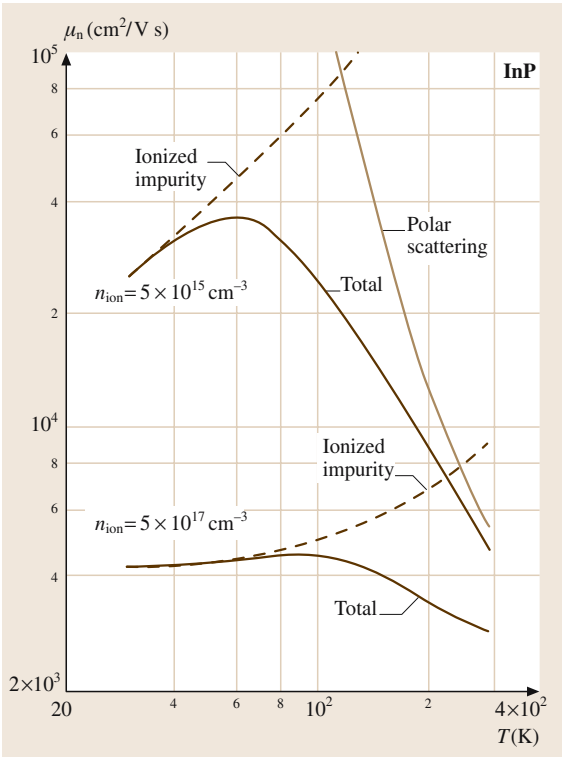


**Fig. 4.1-124** InP. Electron mobility vs. temperature, calculated for two concentrations of ionized impurities [1.110]

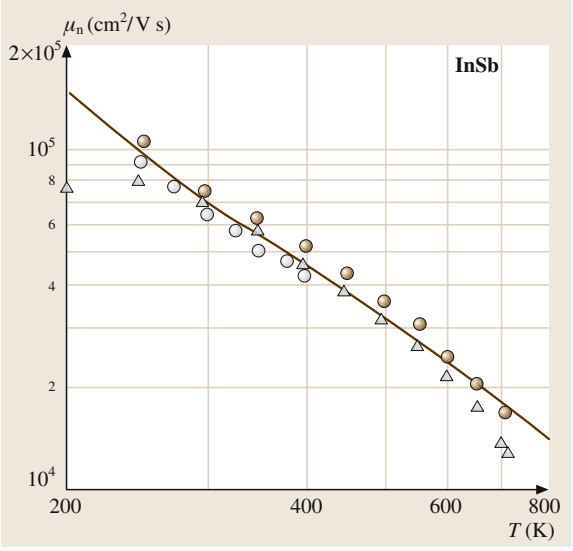


**Fig. 4.1-126** InSb. Electron mobility vs. temperature. The experimental data are Hall mobilities. *Triangles*, [1.112]; *filled circles* [1.113]; *open circles*, [1.114, 115]; *solid line*, calculated drift mobility [1.116]

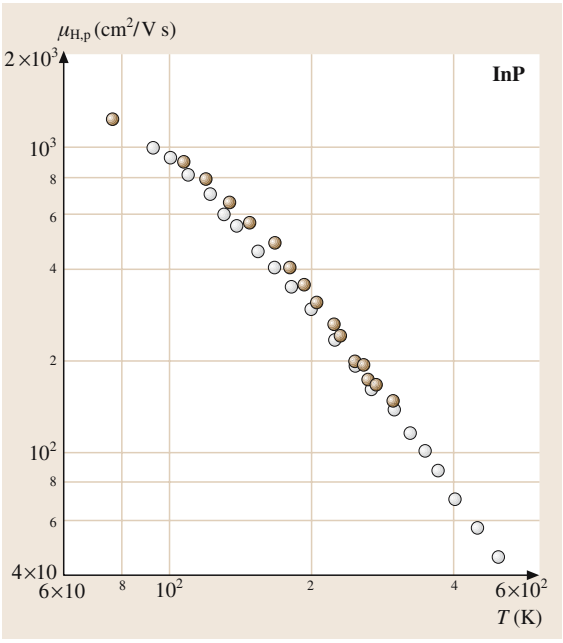


**Fig. 4.1-125** InP. Hole Hall mobility vs. temperature for pure p-type samples, after [1.111]

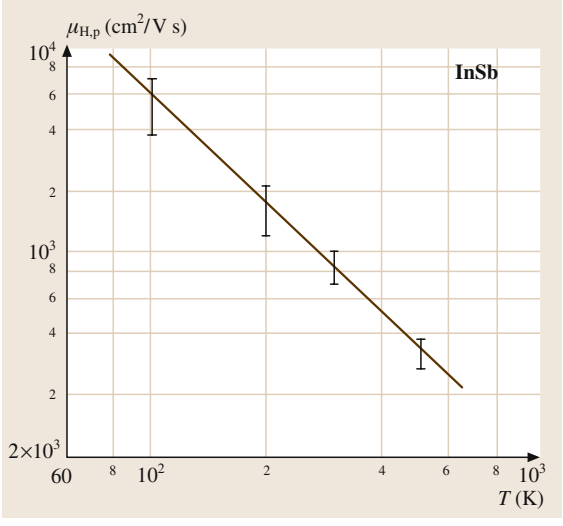


**Fig. 4.1-127** InSb. Hole Hall mobility vs. temperature [1.111]. The *vertical bars* indicate the ranges of the experimental values. The *solid line* has a slope –1.8

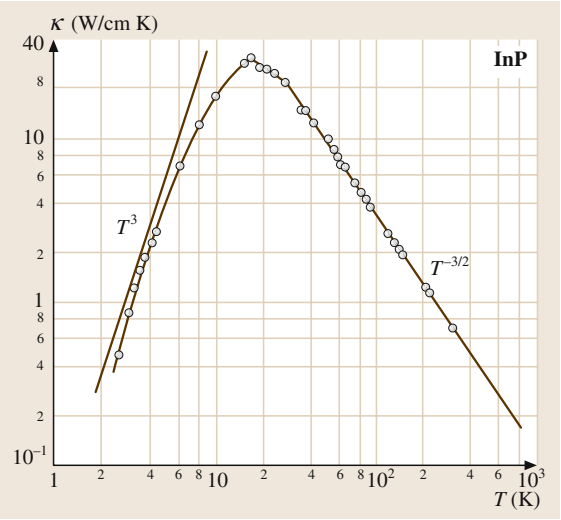


**Fig. 4.1-128** InP. Thermal conductivity vs. temperature [1.117, 118]

**Table 4.1-90** Thermal conductivity $\kappa$ of indium compounds

| Crystal | | $\kappa$ (W/m K) | Remarks |
|---|---|---|---|
| Indium nitride | InN | 38.4 | |
| Indium phosphide | InP | | See Fig. 4.1-128 |
| Indium arsenide | InAs | | |
| Indium antimonide | InSb | | See Fig. 4.1-129 |

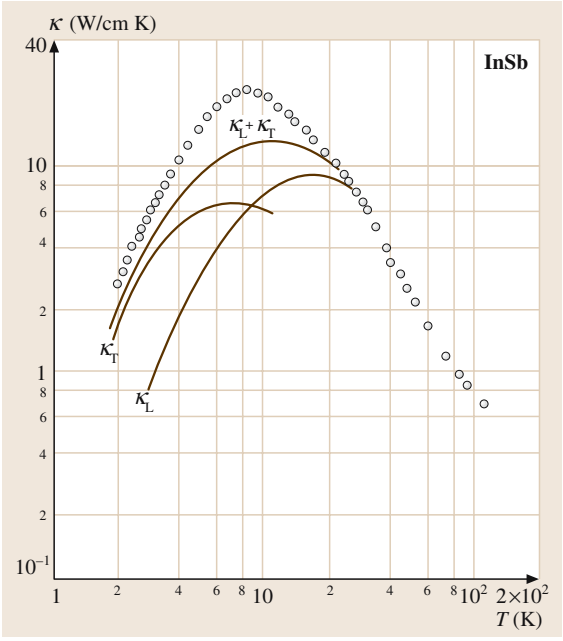


**Fig. 4.1-129** InSb. Thermal conductivity vs. temperature for an n-type sample, and theoretical curve showing the contributions of the longitudinal and transverse phonons [1.119]

## D. Electromagnetic and Optical Properties

Tables 4.1-91 – 4.1-93.

**Table 4.1-91** Dielectric constant $\varepsilon$ and refractive index $n$ of indium compounds

| Crystal | | Temperature (K) | $\varepsilon(0)$ | $\varepsilon(\infty)$ | $n$ at $\lambda$ (μm) | Remarks |
|---|---|---|---|---|---|---|
| Indium nitride | InN | | 9.3 | 8.4 | 2.56 1.0 μm<br>2.93 0.82 μm<br>3.12 0.66 μm | Infrared reflectivity, heavily doped film<br>Interference method, $n = 3 \times 10^{20}$ cm$^{-3}$ |
| Indium phosphide | InP | 300<br>77<br>297 | 12.56 (20)<br>11.93 (20) | 10.9 (10) | Table 4.1-92 | Capacitance measurements<br>Film interference |
| Indium arsenide | InAs | 300 | 15.15 | 12.37 | Table 4.1-92 | Infrared reflectance and oscillator fit |
| Indium antimonide | InSb | | 16.8 (2) | 15.68 | Table 4.1-92 | Gyroscopic sphere resonance, infrared reflectance, and oscillator fit |

**Table 4.1-92** Wavelength dependence of refractive index $n$ of indium compounds at $T = 300\,\mathrm{K}$

| InP | | | InAs | | | InSb | | |
|---|---|---|---|---|---|---|---|---|
| λ (μm) | $n$ | Remarks | λ (μm) | $n$ | Remarks | λ (μm) | $n$ | Remarks |
| 14.85 | 3.03 | Transmission and reflectance | 25 | 3.26 | Interference | 45 | 2.57 | Reflectance and transmission, $n = 6\times10^{15}$ cm$^{-3}$ |
| 5 | 3.08 | | 10 | 3.42 | | 21.15 | 3.814 | |
| 2 | 3.134 | Prism method | 3.74 | 3.52 | | 19.98 | 3.826 | Interference technique, $n = 2\times10^{16}$ cm$^{-3}$ |
| 1 | 3.327 | | 1.38 | 3.516 | Reflectance and dispersion relations | 10.06<br>7.87 | 3.953<br>4.001 | |
| 0.652 | 3.410 | Reflectance and dispersion relations | 0.517 | 4.558 | | 2.07 | 4.03 | Reflectance and dispersion relations |
| 0.399 | 4.100 | | 0.282 | 3.800 | | 0.689 | 5.13 | |
| 0.200 | 1.525 | | 0.049 | 1.139 | | 0.062 | 1.17 | |
| 0.062 | 0.793 | | | | | | | |

**Table 4.1-93** Energy dependence of optical constants of indium compounds. Real and imaginary parts of the complex dielectric constant measured by spectroscopic ellipsometry; $n$, $k$, $R$, $K$ calculated from these data

| InP | | | | | | |
|---|---|---|---|---|---|---|
| $h\nu$ (eV) | $\varepsilon_1$ | $\varepsilon_2$ | $n$ | $k$ | $R$ | $K$ ($10^3$ cm$^{-1}$) |
| 1.5 | 11.904 | 1.400 | 3.456 | 0.203 | 0.395 | 30.79 |
| 2.0 | 12.493 | 2.252 | 3.549 | 0.317 | 0.317 | 64.32 |
| 2.5 | 14.313 | 3.062 | 3.818 | 0.511 | 0.349 | 129.56 |
| 3.0 | 17.759 | 10.962 | 4.395 | 1.247 | 0.427 | 379.23 |
| 3.5 | 5.400 | 12.443 | 3.193 | 1.948 | 0.403 | 691.21 |
| 4.0 | 6.874 | 10.871 | 3.141 | 1.730 | 0.376 | 701.54 |
| 4.5 | 8.891 | 16.161 | 3.697 | 2.186 | 0.449 | 996.95 |
| 5.0 | −7.678 | 14.896 | 2.131 | 3.495 | 0.613 | 1771.5 |
| 5.5 | −4.528 | 7.308 | 1.426 | 2.562 | 0.542 | 1428.1 |
| 6.0 | −2.681 | 5.644 | 1.336 | 2.113 | 0.461 | 1285.1 |
| **InAs** | | | | | | |
| $h\nu$ (eV) | $\varepsilon_1$ | $\varepsilon_2$ | $n$ | $k$ | $R$ | $K$ ($10^3$ cm$^{-1}$) |
| 1.5 | 13.605 | 3.209 | 3.714 | 0.432 | 0.337 | 65.69 |
| 2.0 | 15.558 | 5.062 | 3.995 | 0.634 | 0.370 | 128.43 |
| 2.5 | 15.856 | 15.592 | 4.364 | 1.786 | 0.454 | 452.64 |
| 3.0 | 6.083 | 13.003 | 3.197 | 2.034 | 0.412 | 618.46 |
| 3.5 | 5.973 | 10.550 | 3.008 | 1.754 | 0.371 | 622.13 |
| 4.0 | 7.744 | 11.919 | 3.313 | 1.799 | 0.393 | 729.23 |
| 4.5 | −1.663 | 22.006 | 3.194 | 3.445 | 0.566 | 1571.2 |
| 5.0 | −5.923 | 8.752 | 1.524 | 2.871 | 0.583 | 1455.3 |
| 5.5 | −3.851 | 6.008 | 1.282 | 2.344 | 0.521 | 1306.6 |
| 6.0 | −2.403 | 6.005 | 1.434 | 2.112 | 0.448 | 1284.2 |
| **InSb** | | | | | | |
| $h\nu$ (eV) | $\varepsilon_1$ | $\varepsilon_2$ | $n$ | $k$ | $R$ | $K$ ($10^3$ cm$^{-1}$) |
| 1.5 | 19.105 | 5.683 | 4.418 | 0.643 | 0.406 | 97.79 |
| 2.0 | 14.448 | 14.875 | 4.194 | 1.773 | 0.443 | 359.46 |
| 2.5 | 7.811 | 15.856 | 3.570 | 2.221 | 0.447 | 562.77 |
| 3.0 | 7.354 | 13.421 | 3.366 | 1.994 | 0.416 | 606.27 |
| 3.5 | 5.995 | 17.673 | 3.511 | 2.517 | 0.474 | 892.82 |
| 4.0 | −6.722 | 19.443 | 2.632 | 3.694 | 0.608 | 1497.8 |
| 4.5 | −6.297 | 8.351 | 1.443 | 2.894 | 0.598 | 1320.2 |
| 5.0 | −4.250 | 6.378 | 1.307 | 2.441 | 0.537 | 1237.0 |
| 5.5 | −4.325 | 4.931 | 1.057 | 2.333 | 0.563 | 1300.6 |
| 6.0 | −3.835 | 3.681 | 0.861 | 2.139 | 0.572 | 1300.9 |

## 4.1.3 II–VI Compounds

### 4.1.3.1 Beryllium Compounds

A. Crystal Structure, Mechanical and Thermal Properties

Tables 4.1-94 – 4.1-99.

**Table 4.1-94** Crystal structures of beryllium compounds

| Crystal | | Space group | | Crystal system | Structure type | Figure |
|---|---|---|---|---|---|---|
| Beryllium oxide | BeO | $C_{6v}^4$ | $P6_3mc$ | hex | Wurtzite | Fig. 4.1-130 |
| Beryllium sulfide | BeS | $T_d^2$ | $F\bar{4}3m$ | fcc | Zinc blende | Fig. 4.1-131 |
| Beryllium selenide | BeSe | $T_d^2$ | $F\bar{4}3m$ | fcc | Zinc blende | Fig. 4.1-131 |
| Beryllium telluride | BeTe | $T_d^2$ | $F\bar{4}3m$ | fcc | Zinc blende | Fig. 4.1-131 |

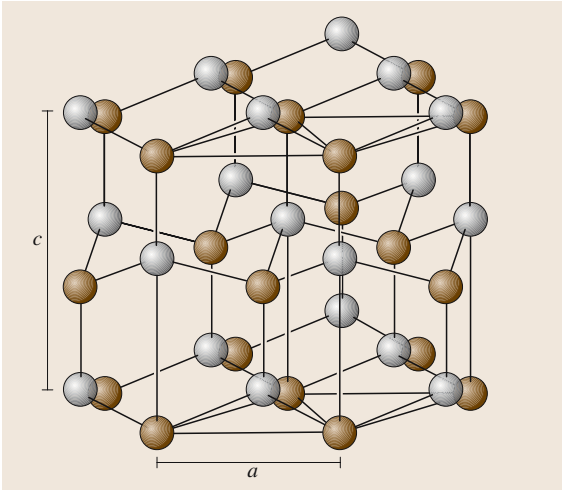


**Fig. 4.1-130** The wurtzite lattice ($a$ and $c$ are the lattice parameters)

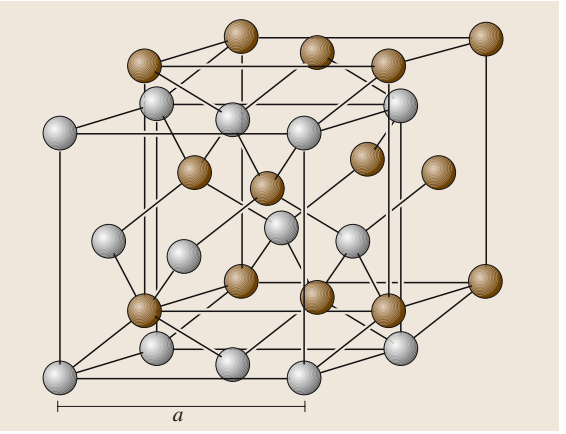


**Fig. 4.1-131** The zinc blende lattice ($a$ is the lattice parameter)

**Table 4.1-95** Lattice parameters of beryllium compounds

| Crystal | | Lattice parameters (nm) | Temperature (K) | Remarks |
|---|---|---|---|---|
| Beryllium oxide | BeO | $a = 0.26979$<br>$c = 0.4380$ | | X-ray diffraction |
| Beryllium sulfide | BeS | $a = 0.48630\,(5)$ | RT | X-ray diffraction |
| Beryllium selenide | BeSe | $a = 0.51520\,(23)$ | RT | Epitaxial film, X-ray diffraction |
| Beryllium telluride | BeTe | $a = 0.56270\,(15)$ | 300 | Epitaxial film, X-ray diffraction |

**Table 4.1-96** Elastic constants $c_{ik}$ (in GPa) of beryllium oxide

| Crystal | | $c_{11}$ | $c_{12}$ | $c_{13}$ | $c_{33}$ | $c_{44}$ | Remarks |
|---|---|---|---|---|---|---|---|
| Beryllium oxide | BeO | 460.6 | 126.5 | 88.5 | 491.6 | 147.7 | Ultrasonic data, RT |

**Table 4.1-97** Densities of beryllium compounds

| Crystal | | Density (g/cm$^3$) |
|---|---|---|
| Beryllium oxide | BeO | 3.01 |
| Beryllium sulfide | BeS | 2.36 |

**Table 4.1-98** Melting point $T_m$ of beryllium oxide

| Crystal | | Melting point $T_m$ |
|---|---|---|
| Beryllium oxide | BeO | 2507 °C |

**Table 4.1-99** Linear thermal expansion coefficient $\alpha$ of beryllium compounds

| Crystal | | Expansion coefficient $\alpha$ (K$^{-1}$) | Temperature (K) |
|---|---|---|---|
| Beryllium oxide | BeO | $9.7\times10^{-6}$ | 373 |
| Beryllium telluride | BeTe | $7.66\,(21)\times10^{-6}$ | 300 |

## B. Electronic Properties

Tables 4.1-100 – 4.1-102.

**Table 4.1-100** First Brillouin zones of beryllium compounds

| Crystal | | Figures |
|---|---|---|
| Beryllium oxide | BeO | Fig. 4.1-132 |
| Beryllium sulfide | BeS | Fig. 4.1-133 |
| Beryllium selenide | BeSe | Fig. 4.1-133 |
| Beryllium telluride | BeTe | Fig. 4.1-133 |

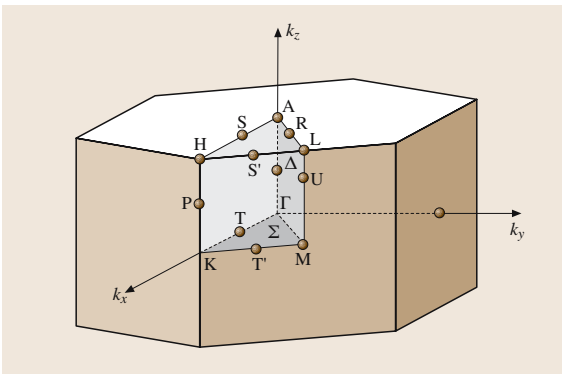


**Fig. 4.1-132** The Brillouin zone of the wurtzite lattice

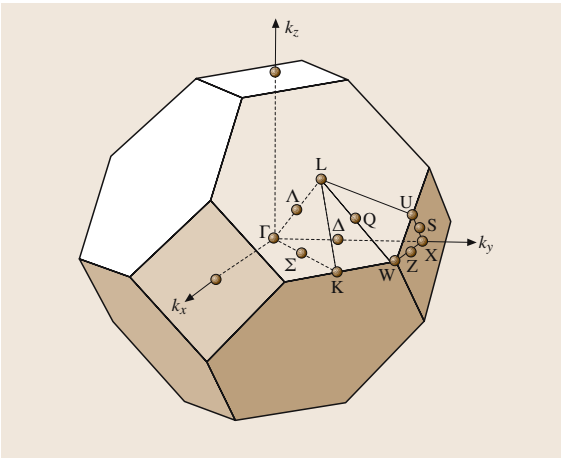


**Fig. 4.1-133** The Brillouin zone of the zinc blende and rock salt lattices

**Table 4.1-101** Band structures of beryllium compounds

| Crystal | | Figure | Remarks |
|---|---|---|---|
| Beryllium oxide | BeO | Fig. 4.1-135 | |
| Beryllium sulfide | BeS | Fig. 4.1-134 | a |
| Beryllium selenide | BeSe | Fig. 4.1-136 | b |
| Beryllium telluride | BeTe | Fig. 4.1-137 | |

[a] According to theory, BeS is an indirect-gap material with the highest valence band edge at Γ and the lowest conduction band edge at X.

[b] According to theory, BeSe is an indirect-gap material with the highest valence band edge at Γ and the lowest conduction band edge at X.

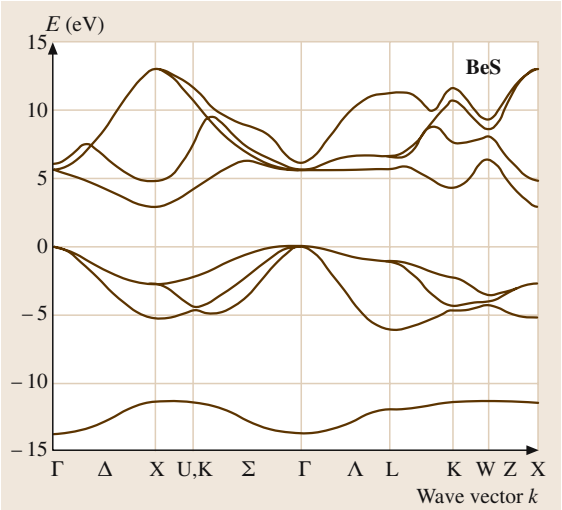


**Fig. 4.1-134** Band structure of beryllium sulfide

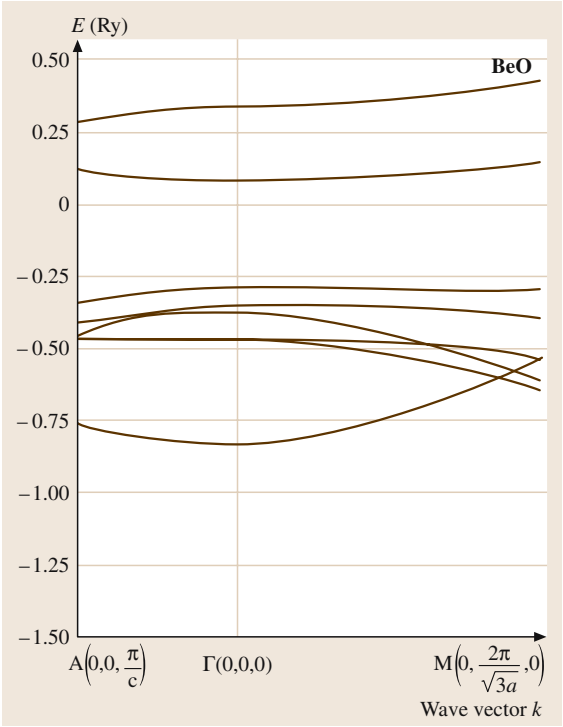


**Fig. 4.1-135** Band structure of beryllium oxide

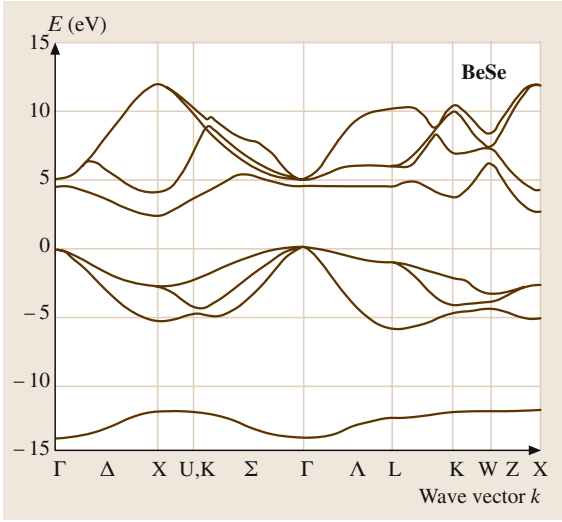


**Fig. 4.1-136** Band structure of beryllium selenide

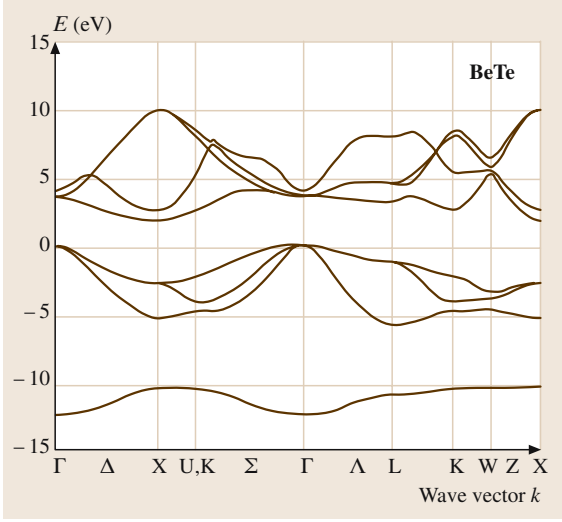


**Fig. 4.1-137** Band structure of beryllium telluride

**Table 4.1-102** Energy gaps of beryllium compounds

| Crystal | | Band gap | | Remarks |
|---|---|---|---|---|
| Beryllium oxide | BeO | 10.585 eV | | |
| Beryllium sulfide | BeS | >5.5 eV | | Absorption |
| Beryllium selenide | BeSe | 5.6 eV | | RT |
| Beryllium telluride | BeTe | $E_{g,\,ind}$ 2.8 eV | $E_{g,\,dir}$ 4.1 eV | 300 K optical reflection, ellipsometry |

### C. Transport Properties

Table 4.1-103.

**Table 4.1-103** Electronic transport in beryllium compounds, general description

| Crystal | | Transport properties |
|---|---|---|
| Beryllium oxide | BeO | BeO, synonym beryllia, is an electrical insulator like a ceramic, but conducts heat like a metal. The electrical resistivity is larger than $10^{16}\,\Omega\,\mathrm{cm}$ |
| Beryllium sulfide | BeS | The electrical conductivity of polycrystalline BeS disks was found to be p-type. This is attributed to Be vacancies or S interstitials |
| Beryllium telluride | BeTe | BeTe, like ZnTe, tends towards p-type conductivity. Using plasma-assisted nitrogen doping during molecular-beam epitaxy, very high p-type concentrations above $10^{20}\,\mathrm{cm}^{-3}$ could be achieved; n-type doping of BeTe has not yet been reported |

### D. Electromagnetic and Optical Properties

Table 4.1-104.

**Table 4.1-104** Dielectric constants $\varepsilon$ of beryllium compounds

| Crystal | | Temperature (K) | $\varepsilon(0)$ | $\varepsilon(\infty)$ | Method | Remarks |
|---|---|---|---|---|---|---|
| Beryllium oxide | BeO | 300 | $\varepsilon_{\mathrm{parall}}$ 7.65 $\varepsilon_{\mathrm{perpend}}$ 6.94 | | Reflectance | Crystalline BeO[a] |
| Beryllium selenide | BeSe | 300 | | | | [b] |
| Beryllium telluride | BeTe | RT | | 7 | Infrared reflection | [c] |

[a] BeO is transparent up to 9.4 eV (vacuum UV) and quite resistant to UV damage.

[b] The interest in BeSe originates from the fact that ternary BeZnSe and quaternary BeMgZnSe alloys can be lattice-matched to silicon substrates and can also be used as base materials for blue–green-emitting ZnSe-based laser diodes grown on GaAs. The ternary alloy has a band gap of approximately 4 eV if lattice-matched to silicon.

[c] BeTe is used in efficient pseudomorphic p-contacts for ZnSe laser diodes.

## 4.1.3.2 Magnesium Compounds

### A. Crystal Structure, Mechanical and Thermal Properties

Tables 4.1-105 – 4.1-111.

**Table 4.1-105** Crystal structures of magnesium compounds

| Crystal | | Space group | | Crystal system | Structure type | Figure |
|---|---|---|---|---|---|---|
| Magnesium oxide | MgO | $O_h^5$ | $Fm3m$ | fcc | NaCl | Fig. 4.1-138 |
| Magnesium sulfide | MgS | $O_h^5$ | $Fm3m$ | fcc | NaCl | Fig. 4.1-138 |
| Magnesium selenide | MgSe | $O_h^5$ | $Fm3m$ | fcc | NaCl | Fig. 4.1-138 |
| Magnesium telluride | MgTe | $C_{6v}^4$ | $P6_3mc$ | hex | Wurtzite | Fig. 4.1-130 |

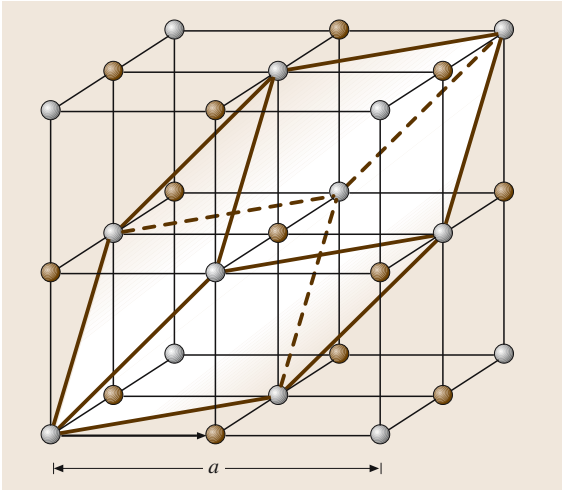


**Fig. 4.1-138** The rock salt lattice

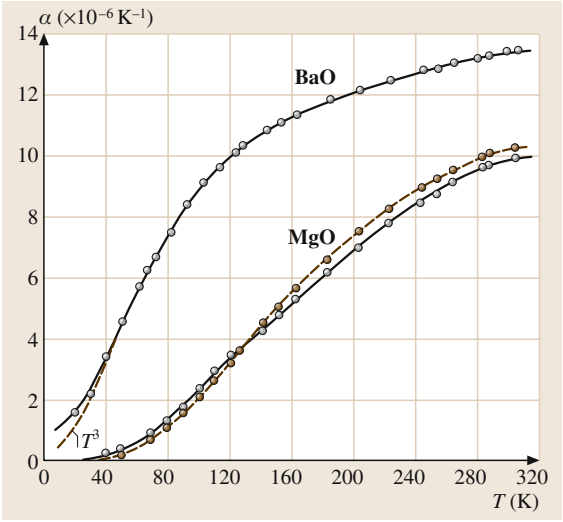


**Fig. 4.1-139** MgO, BaO. Linear thermal expansion coefficient $\alpha$ vs. temperature. *Open circles*, [1.120]; *filled circles*, [1.121]

**Table 4.1-106** Lattice parameters of magnesium compounds

| Crystal | | Lattice parameters (nm) | Temperature (K) | Remarks |
|---|---|---|---|---|
| Magnesium oxide | MgO | $a = 0.4216$ | 298 | X-ray diffraction, powder samples |
| Magnesium sulfide | MgS | $a = 0.5203$ | 300 | X-ray diffraction |
| Magnesium selenide | MgSe | $a = 0.546$ | 300 | X-ray diffraction |
| Magnesium telluride | MgTe | $a = 0.45303$<br>$c = 0.74056$ | 300 | |

**Table 4.1-107** Densities of magnesium compounds

| Crystal | | Density ($g/cm^3$) | Temperature (K) |
|---|---|---|---|
| Magnesium oxide | MgO | 3.576 | 298 |
| Magnesium sulfide | MgS | 2.86 | |
| Magnesium selenide | MgSe | 4.21 | |
| Magnesium telluride | MgTe | | |

**Table 4.1-108** Melting point $T_m$ of magnesium oxide

| Crystal | | Melting point $T_m$ |
|---|---|---|
| Magnesium oxide | MgO | 2827 °C |

**Table 4.1-109** Elastic constants $c_{ik}$ (in $10^{12}$ dyn/cm$^2$) of magnesium oxide

| Crystal | | $c_{11}$ | $c_{12}$ | $c_{44}$ | Temperature (K) | Remarks |
|---|---|---|---|---|---|---|
| Magnesium oxide | MgO | 2.971 (6) | 0.965 (7) | 1.557 (2) | 293 | Single crystals |

**Table 4.1-110** Linear thermal expansion coefficient $\alpha$ of magnesium oxide

| Crystal | | Expansion coefficient $\alpha$ ($K^{-1}$) | Temperature (K) | Remarks |
|---|---|---|---|---|
| Magnesium oxide | MgO | $9.84 \times 10^{-6}$ | 283 | Capacitance cell [a] |

[a] See Fig. 4.1-139 for the temperature dependence.

**Table 4.1-111** Phonon frequencies/wavenumbers of magnesium compounds

| Crystal | | $\nu_{TO}$ (THz) | $\nu_{LO}$ (THz) | $\tilde{\nu}_{TO}$ ($cm^{-1}$) | $\tilde{\nu}_{LO}$ ($cm^{-1}$) | Temperature (K) | Symmetry point | Remarks |
|---|---|---|---|---|---|---|---|---|
| Magnesium oxide | MgO | 12.05 | 21.52 | | | 300 | Γ | Thin films, polarized reflectance |
| Magnesium telluride | MgTe | | | 235 | 292 | 300 | | Raman spectroscopy |

## B. Electronic Properties

Tables 4.1-112 – 4.1-114.

**Table 4.1-112** First Brillouin zones of magnesium compounds

| Crystal | | Figure |
|---|---|---|
| Magnesium oxide | MgO | Fig. 4.1-133 |
| Magnesium sulfide | MgS | Fig. 4.1-133 |
| Magnesium selenide | MgSe | Fig. 4.1-133 |
| Magnesium telluride | MgTe | Fig. 4.1-132 |

**Table 4.1-113** Band structures of magnesium compounds

| Crystal | | Figure |
|---|---|---|
| Magnesium oxide | MgO | Fig. 4.1-140 [a] |
| Magnesium sulfide | MgS | Fig. 4.1-141 |
| Magnesium selenide | MgSe | Fig. 4.1-142 |
| Magnesium telluride | MgTe | Fig. 4.1-143 |

[a] Disagreement exists about the position of the minimum of the lowest conduction band. Some authors place the minimum at $\Gamma_1$ and anticipate a direct gap; others claim that the minimum is at $X_3$, indicating an indirect gap.

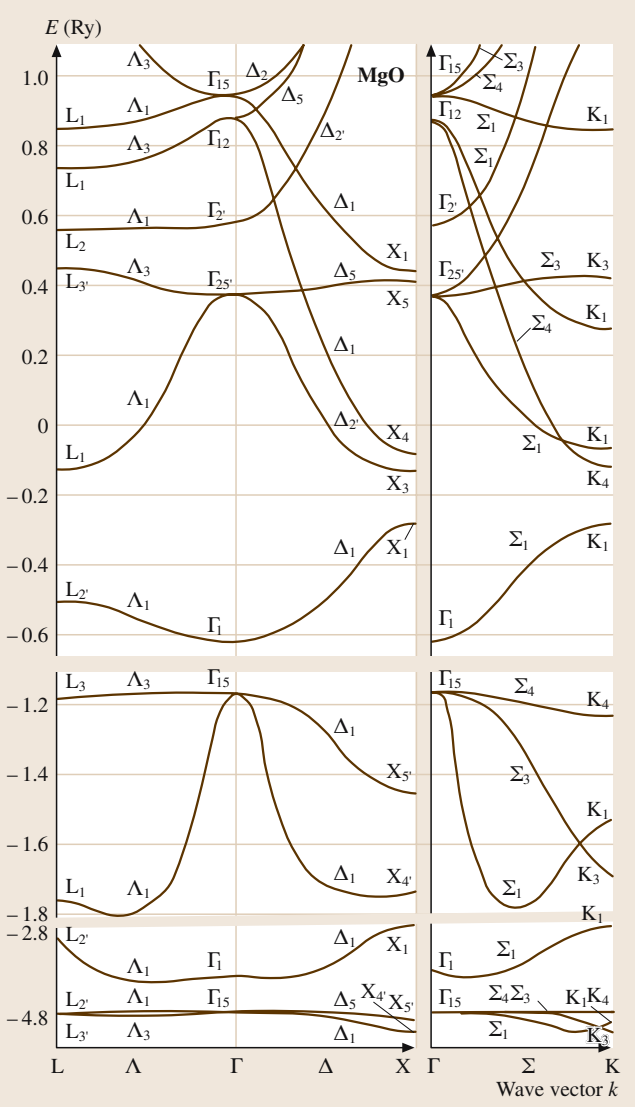


**Fig. 4.1-140** Band structure of magnesium oxide

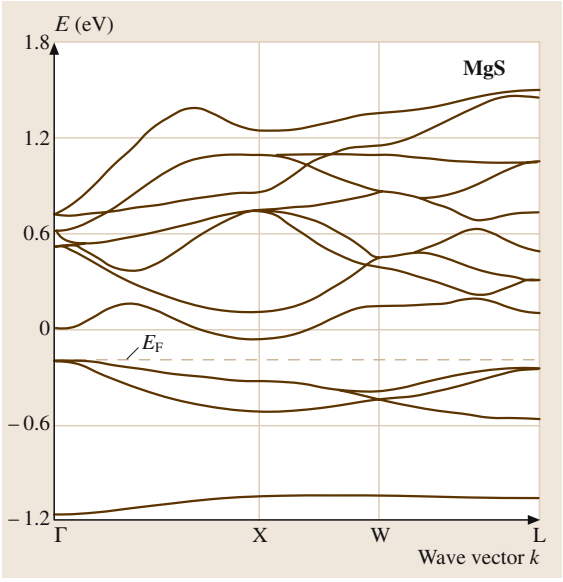


**Fig. 4.1-141** Band structure of magnesium sulfide, rock salt structure

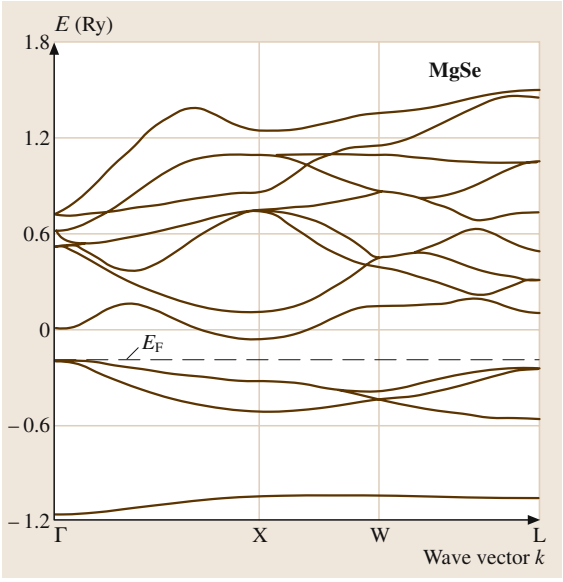


**Fig. 4.1-142** Band structure of magnesium selenide, rock salt structure

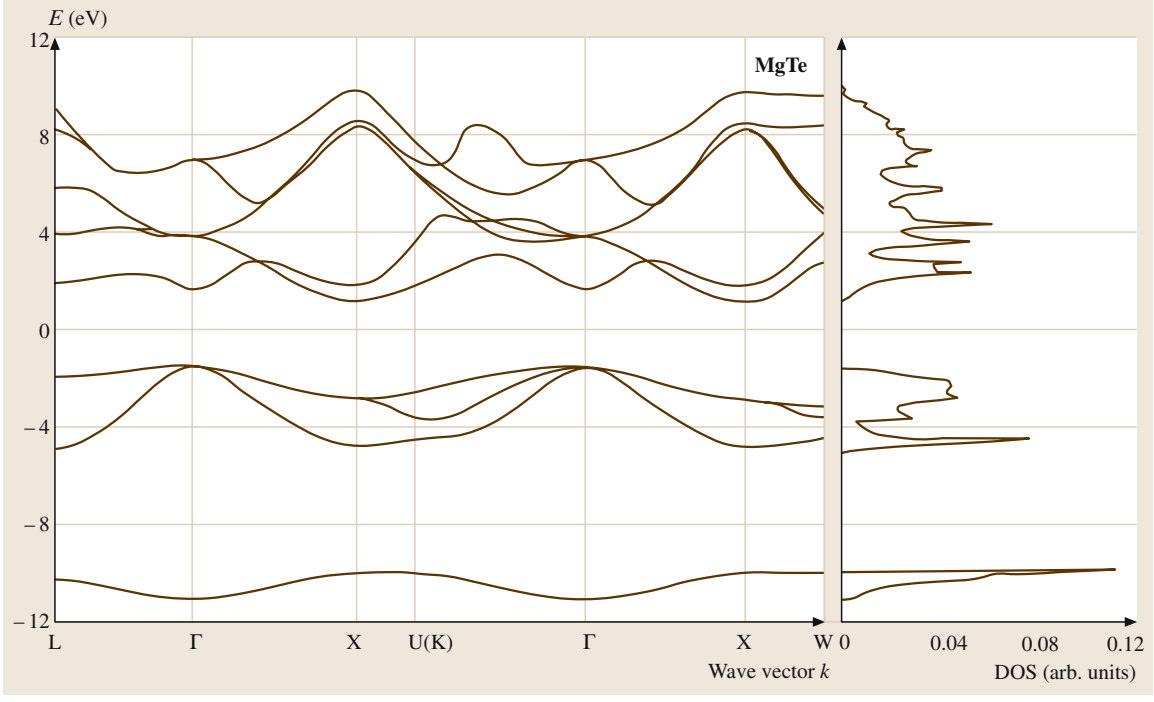


**Fig. 4.1-143** Band structure of magnesium telluride

**Table 4.1-114** Energy gaps of magnesium compounds

| Crystal | | Band gap (eV) | | Temperature (K) | Remarks |
|---|---|---|---|---|---|
| Magnesium oxide | MgO | $E_{gx,\,dir}$ | 7.672 (10) | 85 | Exciton states |
| | | $E_{g,\,theor}$ | 7.9 (7) | 0 | Temperature dependence of microwave conductivity |
| Magnesium sulfide | MgS | 4.5 | | 77 | Zinc blende structure |
| Magnesium selenide | MgSe | 4.05 | | 300 | Zinc blende structure |
| Magnesium telluride | MgTe | 3.49 | | RT | Epitaxial films, photoluminescence, zinc blende structure |

### C. Transport Properties

*Electronic Transport, General Description. Magnesium Oxide (MgO).* Electrical transport measurements on alkaline earth oxides encounter several difficulties, such as high resistance at low temperatures, a strong influence of surface layers, and high-temperature thermionic emission. The partly contradictory results depend considerably on the purity and nature of the samples (pressed porous powders, sintered samples, polycrystals, and single crystals) and on the experimental conditions.

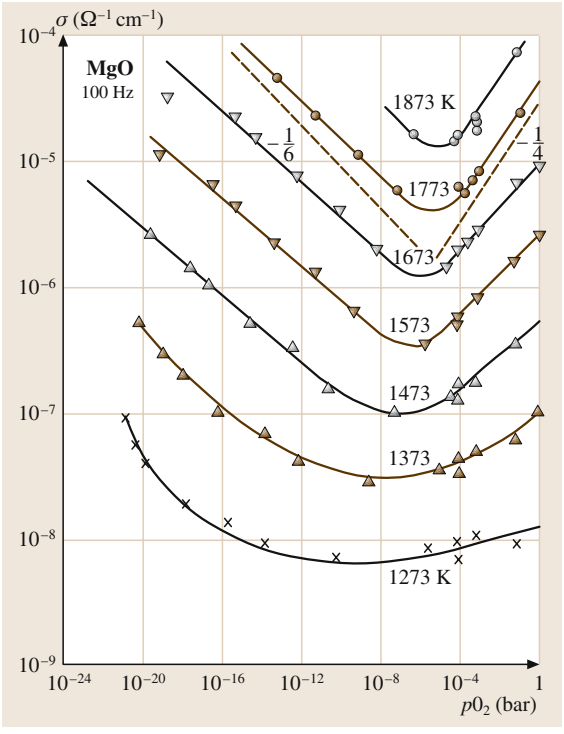


**Fig. 4.1-144** MgO. Electrical conductivity $\sigma$ of a high-purity single crystal at various temperatures vs. oxygen partial pressure $p_{O_2}$ [1.122]. The numbers between the curves for 1673 K and 1773 K indicate the slopes of the *dashed* straight lines

As in several semiconducting oxides, the conductivity and the type of conduction are determined by the oxygen partial pressure of the ambient atmosphere. In high-purity MgO crystals, temperatures below 1600 K favor ionic conduction, whereas at temperatures above 2000 K, electronic conduction is increasingly predominant. At low oxygen pressures ($< 10^{-3}$ mbar) the conduction is n-type; at high pressures ($> 10^{-1}$ mbar) ionic and electronic hole conduction seem to be superimposed.

See Fig. 4.1-144 for the temperature dependence of the electrical conductivity of MgO and Fig. 4.1-145 for the thermal conductivity of MgO.

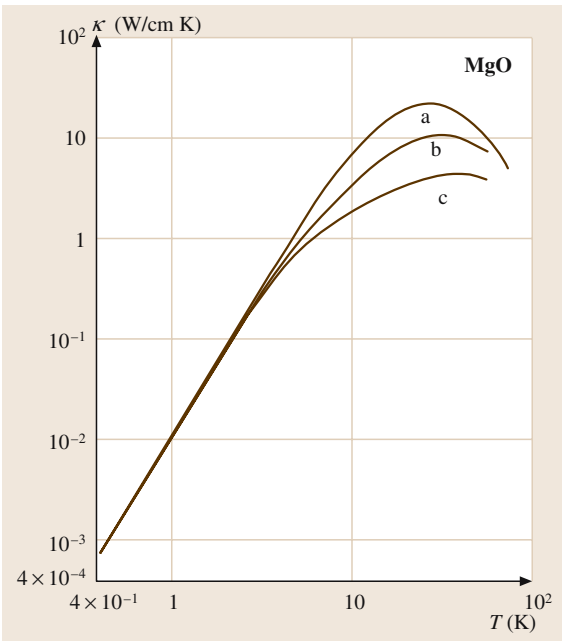


**Fig. 4.1-145** MgO. Thermal conductivity $\kappa$ vs. temperature [1.123]. *Curve* a, high-purity crystal; b, after additive coloration in Mg vapor; c, after subsequent bleaching with UV light

D. Electromagnetic and Optical Properties

Table 4.1-115.

**Table 4.1-115** Dielectric constant $\varepsilon$ of magnesium compounds

| Crystal | | $\varepsilon(0)$ | $\varepsilon(\infty)$ | Temperature (K) | Remarks |
|---|---|---|---|---|---|
| Magnesium oxide | MgO | 9.830 | 2.944 | 300 | Single crystals |
| Magnesium sulfide | MgS | | | | |
| Magnesium selenide | MgSe | | 3.8 | RT | Zinc blende structure, Raman scattering |
| Magnesium telluride | MgTe | | | | |

## 4.1.3.3 Oxides of Ca, Sr, and Ba

A. Crystal Structure, Mechanical and Thermal Properties

Tables 4.1-116–4.1-123.

**Table 4.1-116** Crystal structures of oxides of Ca, Sr, and Ba

| Crystal | | Space group | | Crystal system | Structure type | Figure |
|---|---|---|---|---|---|---|
| Calcium oxide | CaO | $O_h^5$ | $Fm3m$ | fcc | NaCl | Fig. 4.1-138 |
| Strontium oxide | SrO | $O_h^5$ | $Fm3m$ | fcc | NaCl | Fig. 4.1-138 |
| Barium oxide | BaO | $O_h^5$ | $Fm3m$ | fcc | NaCl | Fig. 4.1-138 |

**Table 4.1-117** Lattice parameters of oxides of Ca, Sr, and Ba

| Crystal | | Lattice parameters (nm) | Temperature (K) | Remarks |
|---|---|---|---|---|
| Calcium oxide | CaO | $a = 0.48110\,(2)$ | 297 | Single crystal, X-ray diffraction |
| Strontium oxide | SrO | $a = 0.5159$ | | Semiempirical calculation |
| Barium oxide | BaO | $a = 0.55363\,(8)$ | 300 | Powder samples, negligible oxygen pressure |

**Table 4.1-118** Densities of oxides of Ca, Sr, and Ba

| Crystal | | Density (g/cm$^3$) |
|---|---|---|
| Calcium oxide | CaO | 3.335 |
| Strontium oxide | SrO | 4.75 |
| Barium oxide | BaO | 5.68 |

**Table 4.1-119** Melting point $T_m$ of oxides of Ca, Sr, and Ba

| Crystal | | Melting point $T_m$ (K) |
|---|---|---|
| Calcium oxide | CaO | 2900 |
| Strontium oxide | SrO | 2930 (30) |
| Barium oxide | BaO | 2290 (30) |

**Table 4.1-120** Elastic constants $c_{ik}$ of oxides of Ca, Sr, and Ba

| Crystal | | $c_{11}$ (GPa) | $c_{12}$ (GPa) | $c_{44}$ (GPa) | Temperature (K) | Remarks |
|---|---|---|---|---|---|---|
| Calcium oxide | CaO | 221.89 (60) | 57.81 (66) | 80.32 (10) | 298 | Calculated from sound velocities |
| Strontium oxide | SrO | 175.47 (37) | 49.08 (35) | 55.87 (13) | 298 | |
| Barium oxide | BaO | 126.14 (66) | 50.03 (60) | 33.68 (30) | 298 | |

**Table 4.1-121** Linear thermal expansion coefficient $\alpha$ of oxides of Ca, Sr, and Ba

| Crystal | | Expansion coefficient $\alpha$ (K$^{-1}$) | Temperature (K) | Remarks |
|---|---|---|---|---|
| Calcium oxide | CaO | $15.2 \times 10^{-6}$ | | Single crystal, X-ray diffraction |
| Strontium oxide | SrO | $13.72 \times 10^{-6}$ | 293–593 | Mean value, X-ray diffraction |
| Barium oxide | BaO | $12.8\,(9) \times 10^{-6}$ | 200–400 | Powder samples, X-ray diffraction |

**Table 4.1-122** Heat capacity and Debye temperature of oxides of Ca, Sr, and Ba

| Crystal | | Heat capacity $c_p$ (J/mol K) | Debye temperature $\Theta_D$ (K) | Remarks |
|---|---|---|---|---|
| Calcium oxide | CaO | 14.70 at 100 K<br>42.21 at 300 K | 605 (2) | $\Theta_D(0)$ from heat capacity at low temperatures |
| Strontium oxide | SrO | | 446 (5) | $\Theta_D$ from heat capacity at very high temperatures |
| Barium oxide | BaO | 47.28 at 298 K | 370 (4) | $\Theta_D$ from heat capacity at very high temperatures |

**Table 4.1-123** Phonon frequencies at symmetry points for oxides of Ca, Sr, and Ba. Calcium oxide (CaO), 293 K; strontium oxide (SrO), 300 K; barium oxide (BaO), 300 K. All data from inelastic thermal-neutron scattering

| CaO | | | SrO | | | BaO | | |
|---|---|---|---|---|---|---|---|---|
| Mode | Symmetry point | Frequency (THz) | Mode | Symmetry point | Frequency (THz) | Mode | Symmetry point | Frequency (THz) |
| $\tilde{\nu}_{LO}$ | $q/q_{max} = 0.2$ | 16.40 (25) | $\tilde{\nu}_{TO}$ | Γ | 7.02 (10) | $\tilde{\nu}_{TO}$ | Γ | 4.32 (6) |
| $\tilde{\nu}_{TO}$ | Γ | 8.8 (4) | $\tilde{\nu}_{LO}$ | Γ | 14.47 (15) | $\tilde{\nu}_{LO}$ | Γ | 13.02 (3) |
| $\tilde{\nu}_{LO}$ | X | 12.00 (22) | $\tilde{\nu}_{TA}$ | L | 3.33 (5) | $\tilde{\nu}_{TA}$ | L | 1.99 (7) |
| $\tilde{\nu}_{TO}$ | X | 9.4 (5) | $\tilde{\nu}_{LA}$ | L | 7.14 (10) | $\tilde{\nu}_{LA}$ | L | 4.88 (27) |
| $\tilde{\nu}_{TA}$ | X | 6.48 (11) | $\tilde{\nu}_{TO}$ | L | 8.35 (12) | $\tilde{\nu}_{TO}$ | L | 6.58 (9) |
| | | | $\tilde{\nu}_{LO}$ | L | 12.94 (24) | | | |

## B. Electronic Properties

Tables 4.1-124 – 4.1-127.

**Table 4.1-124** First Brillouin zones of oxides of Ca, Sr, and Ba

| Crystal | | Figure |
|---|---|---|
| Calcium oxide | CaO | Fig. 4.1-133 |
| Strontium oxide | SrO | Fig. 4.1-133 |
| Barium oxide | BaO | Fig. 4.1-133 |

**Table 4.1-125** Energy gaps of oxides of Ca, Sr, and Ba

| Crystal | | Band gap (eV) | | Temperature (K) | Remarks |
|---|---|---|---|---|---|
| Calcium oxide | CaO | $E_{g,\,dir}$ | 6.931 (6) | 85 | Exciton states |
| | | $E_{g,\,theor}$ | 7.8 | 0 | |
| Strontium oxide | SrO | $E_{g,\,opt}$ | 5.22 | 300 | |
| | | $E_{g,\,theor}$ | 6.4 | 0 | Estimated from temperature dependence of conductivity |
| Barium oxide | BaO | $E_{g,\,theor}$ | 4.4 | 0 | Estimated from temperature dependence of conductivity |

**Table 4.1-126** Effective masses of electrons for oxides of Ca, Sr, and Ba (in units of the electron mass $m_0$)

| Crystal | | Quantity | Mass | Temperature (K) | Remarks |
|---|---|---|---|---|---|
| Calcium oxide | CaO | $m_n$ | 0.50 | 700 | From Hall mobility |
| | | $m_{n,\,polaron}$ | 0.68 | 700–800 | Polaron mass, Hall mobility |
| Strontium oxide | SrO | $m_n$ | 0.54 | 600–700 | From Hall mobility |
| | | $m_{n,\,polaron}$ | 0.77 | | Polaron mass, Hall mobility |
| Barium oxide | BaO | $m_n$ | 0.59 | 600 | From Hall mobility |
| | | $m_{n,\,polaron}$ | 0.86 | 500–700 | Polaron mass, Hall mobility |

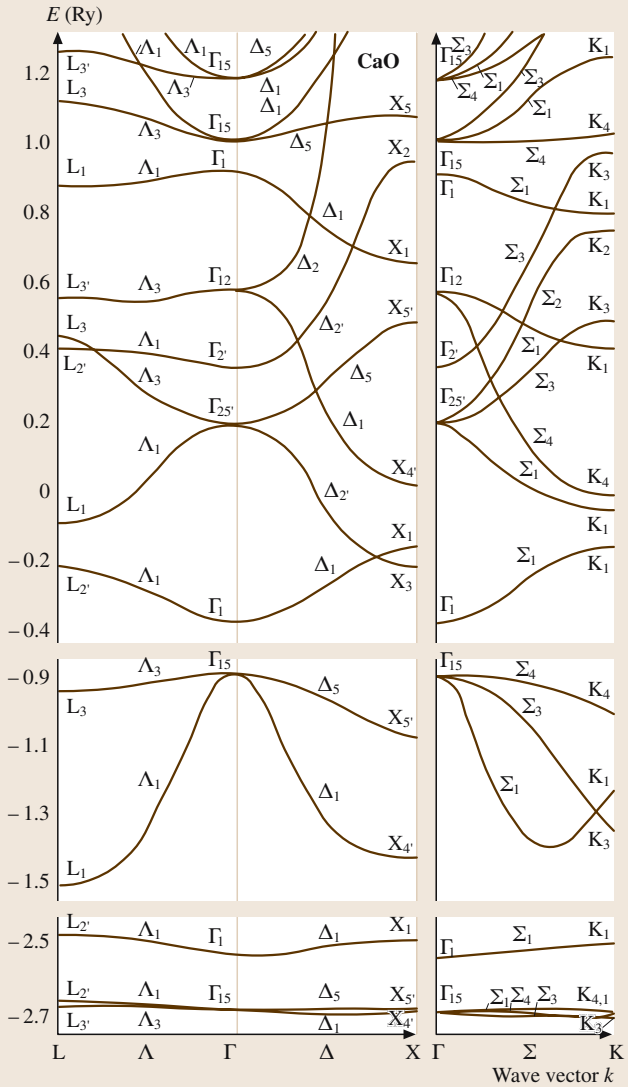


**Fig. 4.1-146** Band structure of calcium oxide

**Table 4.1-127** Band structure of calcium oxide

| Crystal | | Figure | Remarks |
|---|---|---|---|
| Calcium oxide | CaO | Fig. 4.1-146 | [a] |

[a] Some controversy exists in the literature about the positions of the lowest conduction band minima. One result shows the lowest minimum at $\Gamma_1$ and the minimum of the d states at $X_3$, below some s states but above $\Gamma_1$. Other results claim the symmetry point of the conduction band bottom is at $X_3$ instead of $\Gamma_1$, whereas according to other authors $\Gamma_1$ and $X_3$ are nearly degenerate.

### C. Transport Properties

Tables 4.1-128 – 4.1-130.

**Table 4.1-128** Electronic transport in oxides of Ca, Sr, and Ba, general description

| Crystal | | Transport properties |
|---|---|---|
| Calcium oxide | CaO | For general remarks, see the comments on the transport properties of MgO on p. 659. The transport of charge carriers in CaO has been discussed in various models, e.g. polaron band conduction and hopping conduction through compensated semiconducting samples, and also a considerable contribution from ionic conductivity has been taken into account. From measurements of the oxygen pressure dependence of the conductivity of undoped CaO, it is concluded that n-type conduction occurs at low pressures ($< 10^{-2}$ – $10^{-4}$ mbar) and that p-type conduction occurs at higher pressures ($> 10^{-2}$ – 1 mbar). In some cases this conclusion is confirmed by Hall and thermoelectric measurements. For intermediate pressures, it is supposed that the lattice disorder (presumably of Schottky type) gives rise to predominantly ionic conduction |
| Strontium oxide | SrO | The transport of charge carriers has been discussed in various models as in the case of CaO (see above). It is supposed that the dominating scattering mechanism is optical-mode scattering |
| Barium oxide | BaO | The electrical transport has been discussed mainly on the assumption that it is due to electronic conduction. The ionic contribution is small. Polaron conduction and predominant optical-mode scattering are assumed |

**Table 4.1-129** Electrical conductivity $\sigma$ and electron mobility $\mu_n$ of oxides of Ca, Sr, and Ba

| Crystal | | Conductivity | Electron mobility | | | Remarks |
|---|---|---|---|---|---|---|
| | | | $\mu_n$ ($cm^2/V\,s$) | at temperature (K) | at $O_2$ pressure (mbar) | |
| Calcium oxide | CaO | | 8 | 700 | $< 10^{-6}$ | Single crystals, Hall mobility |
| Strontium oxide | SrO | | 5 | 700 | $< 10^{-6}$ | Single crystals, Hall mobility |
| Barium oxide | BaO | Fig. 4.1-148 | 5 | 600 | $< 10^{-6}$ | Polycrystals, Hall mobility |

**Table 4.1-130** Thermal conductivity $\kappa$ of oxides of Ca, Sr, and Ba

| Crystal | | Temperature (K) | $\kappa$ (W/cm K) | Remarks |
|---|---|---|---|---|
| Calcium oxide | CaO | 300 | 0.3 | See Fig. 4.1-147 for temperature dependence |
| Strontium oxide | SrO | 300 | 0.1 | See Fig. 4.1-147 for temperature dependence |
| Barium oxide | BaO | 300 | 0.03 | See Fig. 4.1-147 for temperature dependence |

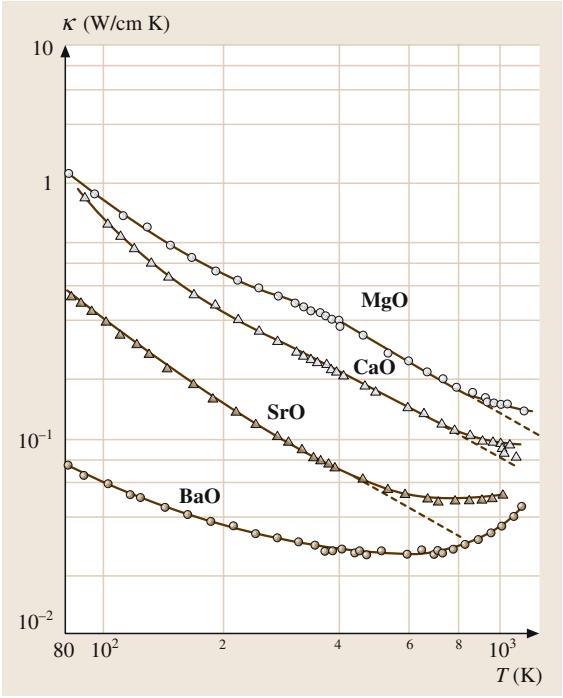


**Fig. 4.1-147** MgO, CaO, SrO, BaO. Temperature dependence of the thermal conductivity $\kappa$ of single crystals [1.124]. *Dashed lines*, $\kappa \propto T^{-1}$

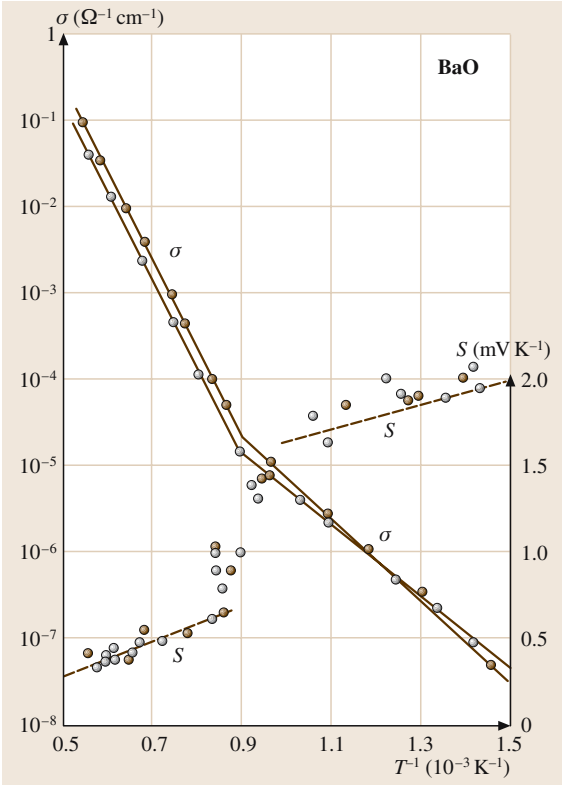


**Fig. 4.1-148** BaO. Electrical conductivity $\sigma$ (*solid lines*) and thermoelectric power $S$ (*dashed lines*) of two crystals vs. $1/T$ [1.125]. $p_{O_2} = 3 \times 10^{-5}$ mbar. n-type conduction at temperatures below the discontinuity

## D. Electromagnetic and Optical Properties

Table 4.1-131.

**Table 4.1-131** Dielectric constant $\varepsilon$ of oxides of Ca, Sr, and Ba

| Crystal | | Temperature (K) | $\varepsilon(0)$ | $\varepsilon(\infty)$ | Remarks |
|---|---|---|---|---|---|
| Calcium oxide | CaO | 273 | 12.01 (10) | 3.27 | Capacitance measurement at 1 kHz and 10 kHz<br>Compilation |
| Strontium oxide | SrO | | | | |
| Barium oxide | BaO | 296 | 3.903–4.197 | | Calculated from refractive-index values in the spectral range 624–436 nm |

### 4.1.3.4 Zinc Compounds

A. Crystal Structure, Mechanical and Thermal Properties

Tables 4.1-132 – 4.1-139.

**Table 4.1-132** Crystal structures of zinc compounds

| Crystal | | Space group | | Crystal system | Structure type | Figure |
|---|---|---|---|---|---|---|
| Zinc oxide | ZnO | $C_{6v}^4$ | $P6_3mc$ | hex | Wurtzite | Fig. 4.1-130 |
| Zinc sulfide | ZnS | $T_d^2$ | $F\bar{4}3m$ | fcc | Zinc blende | Fig. 4.1-131[a] |
| Zinc selenide | ZnSe | $T_d^2$ | $F\bar{4}3m$ | fcc | Zinc blende | Fig. 4.1-131 |
| Zinc telluride | ZnTe | $T_d^2$ | $F\bar{4}3m$ | fcc | Zinc blende | Fig. 4.1-131 |

[a] At room temperature, ZnS bulk material consists predominantly of the cubic phase, often with hexagonal inclusions, leading to polytypic material. Epitaxial ZnS has mostly been grown on GaAs and thus has pseudomorphically assumed the cubic structure of the substrate material. In this section, all data refer to the cubic modification unless explicitly stated otherwise.

**Table 4.1-133** Lattice parameters of zinc compounds

| Crystal | | Lattice parameters (nm) | Temperature | Remarks |
|---|---|---|---|---|
| Zinc oxide | ZnO | $a = 0.3249\ (6)$<br>$c = 0.52042\ (20)$ | | X-ray diffraction |
| Zinc sulfide | ZnS | $a = 0.54053$ | RT | X-ray diffraction |
| Zinc selenide | ZnSe | $a = 0.5667\ (4)$ | 300 K | X-ray diffraction |
| Zinc telluride | ZnTe | $a = 0.60882$ | RT | X-ray diffraction |

**Table 4.1-134** Densities of zinc compounds

| Crystal | | Density (g/cm$^3$) | Temperature | Remarks |
|---|---|---|---|---|
| Zinc oxide | ZnO | 5.67526 (19) | 293 K | Hydrostatic weighing |
| Zinc sulfide | ZnS | Cubic: 4.088<br>Hexagonal: 4.087 | RT<br>RT | |
| Zinc selenide | ZnSe | 5.266 | | Shock wave experiment |
| Zinc telluride | ZnTe | 5.636 | 298 K | |

**Table 4.1-135** Elastic constants $c_{ik}$ (in GPa) of zinc compounds

| Crystal | | $c_{11}$ (GPa) | $c_{13}$ (GPa) | $c_{33}$ (GPa) | $c_{44}$ (GPa) | $c_{66}$ (GPa) | Remarks |
|---|---|---|---|---|---|---|---|
| Zinc oxide | ZnO | 206 (4) | 118 (10) | 211 (4) | 44.3 (10) | 44.0 (10) | ZnO film on Si substrate, Brillouin scattering |

**Table 4.1-135** Elastic constants $c_{ik}$ (in GPa) of zinc compounds, cont.

| Crystal | | $c_{11}$ (GPa) | $c_{12}$ (GPa) | $c_{44}$ (GPa) | Temperature | Remarks |
|---|---|---|---|---|---|---|
| Zinc sulfide | ZnS | 103.2 (5) | 64.6 (5) | 46.2 (4) | 293 K | Resonance method |
| Zinc selenide | ZnSe | 90.3 (19) | 53.6 (23) | 39.4 (12) | | Brillouin scattering |
| Zinc telluride | ZnTe | 72.2 (2) | 40.9 (6) | 30.8 (3) | RT | Brillouin scattering |

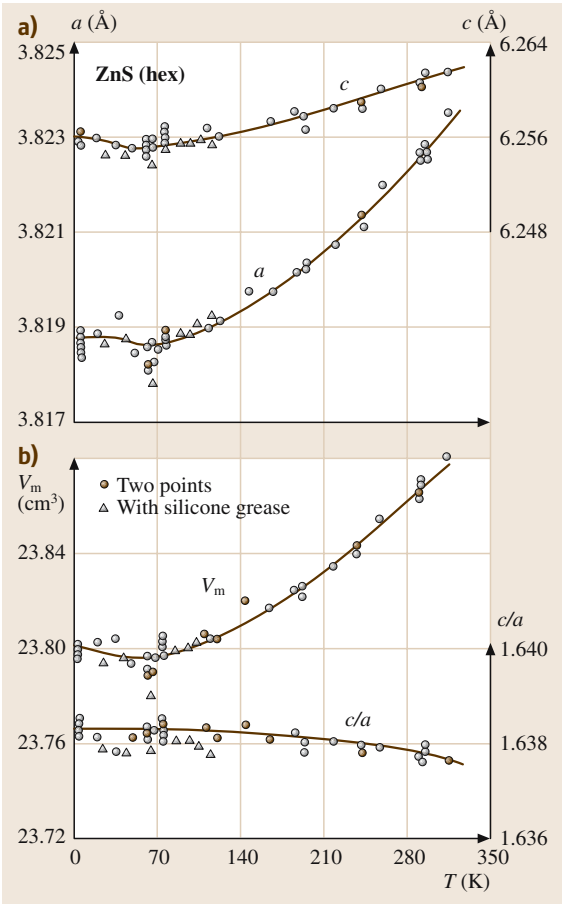


**Fig. 4.1-149a,b** ZnS, hexagonal. **(a)** Lattice parameters $a$ and $c$ vs. temperature; **(b)** molar volume and $c/a$ ratio vs. temperature [1.126]

**Table 4.1-136** Melting point $T_m$ of zinc compounds

| Crystal | | Melting point $T_m$ (K) | Remarks |
|---|---|---|---|
| Zinc oxide | ZnO | 2242 (5) | |
| Zinc sulfide | ZnS | 1991 | Under normal pressure, ZnS sublimes before melting |
| Zinc selenide | ZnSe | 1799 | |
| Zinc telluride | ZnTe | 1563 (8) | |

**Table 4.1-137** Linear thermal expansion coefficient $\alpha$ of zinc compounds

| Crystal | | Expansion coefficient $\alpha$ ($K^{-1}$) | Temperature (K) | Remarks |
|---|---|---|---|---|
| Zinc oxide | ZnO | $\alpha_{\text{parall } c}$: $2.92 \times 10^{-6}$<br>$\alpha_{\text{perpend } c}$: $4.75 \times 10^{-6}$ | 399<br>300 | Interferometric and capacitance methods |
| Zinc sulfide | ZnS | See Fig. 4.1-149 | | |
| Zinc selenide | ZnSe | $7.4 \times 10^{-6}$ | 300 | Polycrystal, capacitance dilatometer |
| Zinc telluride | ZnTe | $0.083 \times 10^{-6}$ | 300 | |

**Table 4.1-138** Heat capacities and Debye temperatures of zinc compounds

| Crystal | | Heat capacity $c_p$ (J/mol K) | Debye temperature $\Theta_D$ (K) | Temperature (K) | Remarks |
|---|---|---|---|---|---|
| Zinc oxide | ZnO | | 440 (25) | 300 | Calorimetric data |
| Zinc sulfide | ZnS | 45.358 | 352 | 77 | Zinc blende lattice, $\Theta_D$ calculated from $c_p$ |
| | | 45.882 | 351 | 298 | Wurtzite lattice; $\Theta_D$ calculated from $c_p$ |
| Zinc selenide | ZnSe | 51.88 | 339 (2) | 298 | |
| Zinc telluride | ZnTe | | 180 (6) | 93–298 | $\Theta_D$ from X-ray intensities from powders |

**Table 4.1-139** Phonon frequencies/wavenumbers at symmetry points for zinc compounds. Zinc oxide (ZnO), fundamental optical modes, $T = 300$ K, from Raman spectroscopy; zinc sulfide (ZnS), $T = 300$ K; zinc selenide (ZnSe), from Raman spectroscopy and luminescence; zinc telluride (ZnTe), RT, from neutron scattering

| ZnO Mode | Symmetry point | Wavenumber ($cm^{-1}$) | ZnS Mode | Symmetry point | Wavenumber ($cm^{-1}$) |
|---|---|---|---|---|---|
| $\tilde{\nu}$ | $E_2$ | 101 | $\tilde{\nu}_{LO}$ | Γ | 350 |
| $\tilde{\nu}$ | $E_2$ | 437 | $\tilde{\nu}_{TO}$ | Γ | 274 |
| $\tilde{\nu}_{TO}$ | $E_{1,\ perp\ c}$ | 407 | $\tilde{\nu}_{LO}$ | X | 332 (1) |
| $\tilde{\nu}_{TO}$ | $A_{1,\ parall\ c}$ | 380 | $\tilde{\nu}_{TO}$ | X | 318 (1) |
| $\tilde{\nu}_{LO}$ | $E_{1,\ perp\ c}$ | 583 | $\tilde{\nu}_{LA}$ | X | 212 (1) |
| $\tilde{\nu}_{LO}$ | $A_{1,\ parall\ c}$ | 574 | $\tilde{\nu}_{TA}$ | X | 88 (1) |
| | | | $\tilde{\nu}_{LO}$ | L | 334 (1) |
| | | | $\tilde{\nu}_{TO}$ | L | 298 (1) |
| | | | $\tilde{\nu}_{LA}$ | L | 192 (1) |
| | | | $\tilde{\nu}_{TA}$ | L | 72 (1) |

| ZnSe Mode | Symmetry point | Phonon energy (meV) | ZnTe Mode | Symmetry point | Frequency (THz) |
|---|---|---|---|---|---|
| $h\nu_{LO}$ | $\Gamma_1$ | 30.99 | $\nu_{LO}$ | Γ | 6.20 (5) |
| $h\nu_{TO}$ | $\Gamma_{15}$ | 25.17 | $\nu_{TO}$ | Γ | 5.30 (7) |
| $h\nu_{LA}$ | Γ | 19.8 | $\nu_{LO}$ | X | 5.51 (10) |
| $h\nu_{TA}$ | Γ | 8.0 | $\nu_{TO}$ | X | 5.21 (10) |
| $h\nu_{LO}$ | X | 27.64 | $\nu_{LA}$ | X | 4.29 (5) |
| $h\nu_{TO}$ | | 25.54 | $\nu_{TA}$ | X | 1.62 (2) |
| $h\nu_{LA}$ | | 23.55 | $\nu_{LO}$ | L | 5.39 (5) |
| $h\nu_{LO}$ | L | 27.77 | $\nu_{TO}$ | L | 5.20 (9) |
| $h\nu_{TO}$ | | 25.54 | $\nu_{LA}$ | L | 4.06 (5) |
| $h\nu$ | $W_3$ | 24.9 | $\nu_{TA}$ | L | 1.25 (2) |
| $h\nu$ | $W_1$ | 18.59 | | | |
| $h\nu$ | $W_2'$ | 11.53 | | | |
| $h\nu$ | $W_2''$ | 26.53 | | | |
| $h\nu$ | $W_4'$ | 14.26 | | | |
| $h\nu$ | $W_4''$ | 26.41 | | | |

## B. Electronic Properties

Tables 4.1-140 – 4.1-145.

*Band Structures of Zinc Compounds.*

*Zinc oxide (ZnO) (Fig. 4.1-150)*

The topmost valence band ($\Gamma_5 + \Gamma_1$) is split owing to crystal-field splitting and spin–orbit coupling into three spin-degenerate states ($\Gamma_7$, $\Gamma_9$, $\Gamma_7$). The exciton states formed with holes in these valence band states are referred to as the A, B, and C excitons, respectively. Owing to the negative spin–orbit coupling (there is a contribution from Zn 3d states), the positions of the edges of the two highest valence band states are reversed as compared with other II–VI compounds with the wurtzite structure.

The conduction band edge, originating from the 4s states of Zn, possesses $\Gamma_7$ symmetry.

*Zinc sulfide ZnS (Fig. 4.1-150)*

Cubic ZnS is a direct-gap semiconductor with the smallest energy gap at the center of the Brillouin zone ($\Gamma$). When spin–orbit splitting is taken into account, the topmost valence band state $\Gamma_{15v}$ splits into $\Gamma_{8v}$ and $\Gamma_{7v}$; further splitting into A, B, and C levels is caused by the crystal field.

**Table 4.1-140** First Brillouin zones of zinc compounds

| Crystal | | Figure |
|---|---|---|
| Zinc oxide | ZnO | Fig. 4.1-132 |
| Zinc sulfide | ZnS | Fig. 4.1-133 |
| Zinc selenide | ZnSe | Fig. 4.1-133 |
| Zinc telluride | ZnTe | Fig. 4.1-133 |

*Zinc selenide ZnSe (Fig. 4.1-151)*

Zinc selenide is a direct-gap semiconductor with the smallest energy gap at the center of the Brillouin zone ($\Gamma$). The topmost valence band ($\Gamma_{15}$) is split owing to spin–orbit coupling into a fourfold ($\Gamma_8$) and a twofold ($\Gamma_7$) state.

*Zinc telluride ZnTe (Fig. 4.1-152)*

Zinc telluride is a direct-gap semiconductor with the smallest energy gap at the center of the Brillouin zone ($\Gamma$). The topmost valence band ($\Gamma_{15}$) is split owing to spin–orbit coupling into a fourfold ($\Gamma_8$) and a twofold ($\Gamma_7$) state.

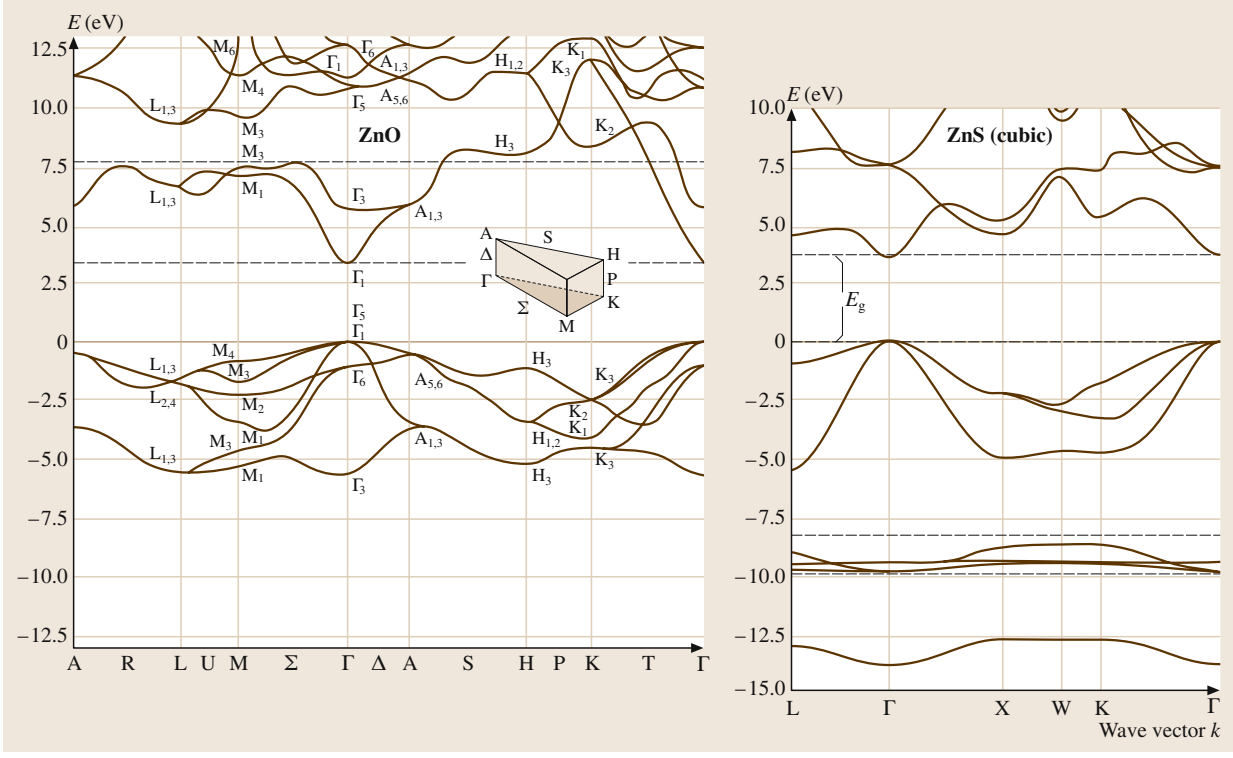


**Fig. 4.1-150** Band structure of zinc oxide and cubic zinc sulfide

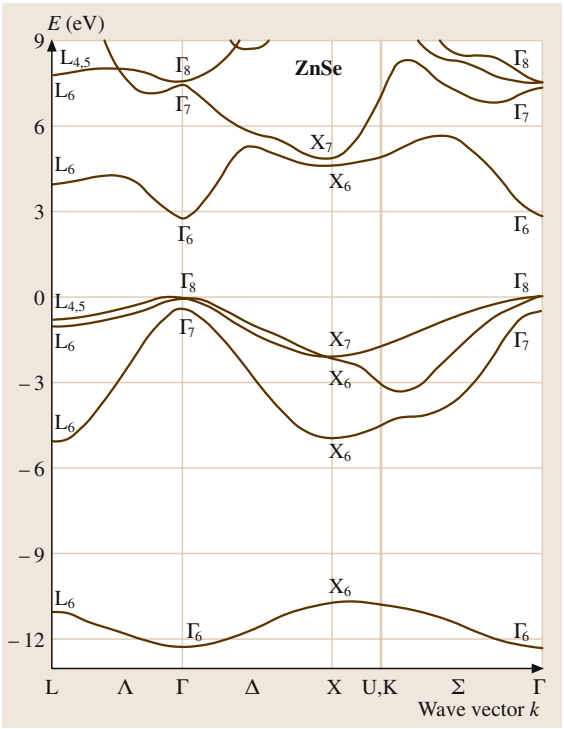


Fig. 4.1-151 Band structure of zinc selenide

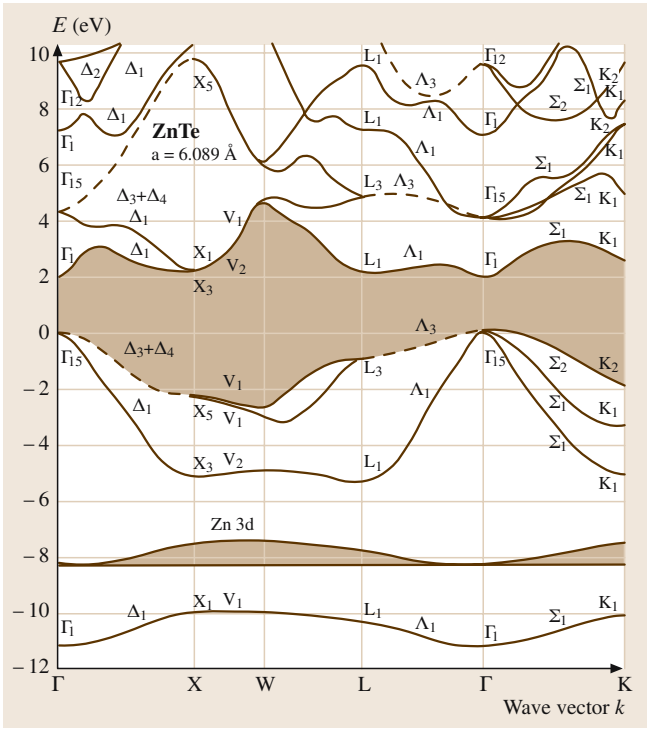


Fig. 4.1-152 Band structure of zinc telluride

**Table 4.1-141** Energy gaps of zinc compounds

| Crystal | | Band gap (eV) | | Between bands | Temperature (K) | Remarks |
|---|---|---|---|---|---|---|
| Zinc oxide | ZnO | $E_g^A$ | 3.4410 (1) | | 6 | Two-photon absorption, |
| | | $E_g^B$ | 3.4434 (1) | | | distance from A, B, and C valence bands |
| | | $E_g^C$ | 3.4817 (2) | | | to conduction band |
| Zinc sulfide | ZnS | $E_{g,\,dir}$ | 3.723 (1) | $\Gamma_{15v}$ and $\Gamma_{1c}$ | 300 | Luminescence; |
| | | $E_{g,\,dir}$ | 3.78 | $\Gamma_{8v}$ and $\Gamma_{6c}$ | 295 | For temperature dependence |
| | | $E_{g,\,dir}$ | 3.76 | $\Gamma_{7v}$ and $\Gamma_{6c}$ | 298 | see Fig. 4.1-162 |
| Zinc selenide | ZnSe | $E_{g,\,dir}$ | 2.8222 (1) | $\Gamma_{8v}$ and $\Gamma_{6c}$ | 6 | Two-photon spectroscopy |
| Zinc telluride | ZnTe | $E_{g,\,dir}$ | 2.3945 | $\Gamma_{8v}$ and $\Gamma_{6c}$ | < 2 | Transmission spectroscopy |
| | | | 2.35 | $\Gamma_{8v}$ and $\Gamma_{6c}$ | 300 | Reflectivity |

**Table 4.1-142** Exciton binding energies of zinc compounds

| Crystal | | Binding energy (meV) | | Temperature (K) | Remarks |
|---|---|---|---|---|---|
| Zinc oxide | ZnO | $E_b$(A) | 63.1 | 6 | Two-photon absorption, |
| | | $E_b$(B) | 50.4 | | |
| | | $E_b$(C) | 48.9 | | |
| Zinc sulfide | ZnS | $E_b$(1S) | 38 (1) | 10 | Absorption, |
| | | $E_b$(2S) | 10 (2) | | Heavy-hole exciton |
| Zinc selenide | ZnSe | $E_b$(1S) | 20.8 | 1.8 | Absorption, strained layers |
| | | $E_b(2P_{1/2})$ | 4.19 | 1.6 | Two-photon absorption |
| | | $E_b(2P_{5/2},\Gamma_7)$ | 4.80 | | |
| | | $E_b(2P_{5/2},\Gamma_8)$ | 5.15 | | |

**Table 4.1-143** Spin–orbit splitting energy $\Delta_{so}$ of zinc compounds

| Crystal | | Splitting energy | Bands | Temperature (K) | Remarks |
|---|---|---|---|---|---|
| Zinc oxide | ZnO | −3.5 (2) meV | | 6 | Two-photon absorption |
| Zinc sulfide | ZnS | 64 meV | $\Gamma_{8v}$ to $\Gamma_{7v}$ | 293 | Reflectivity |
| Zinc selenide | ZnSe | 0.42 eV | $\Gamma_{8v}$ to $\Gamma_{7v}$ | 295 | Reflectivity |
| | | 0.20 eV | $\Gamma_{4-5v}$ to $\Gamma_{6v}$ | 300 | |
| Zinc telluride | ZnTe | 0.97 eV | $\Gamma_{8v}$ to $\Gamma_{7v}$ | 80 | Reflectivity |

**Table 4.1-144** Effective masses of electrons (in units of the electron mass $m_0$) for zinc compounds

| Crystal | | Quantity | Mass | Temperature (K) | Remarks |
|---|---|---|---|---|---|
| Zinc oxide | ZnO | $m_{n}$ | 0.275 | 6 | Cyclotron resonance |
| | | $m_{n,\,polaron}$ | 0.3 | 80 | Polaron mass |
| Zinc sulfide | ZnS | $m_{n,\,polaron}$ | 0.22 | | Polaron mass, cyclotron resonance |
| Zinc selenide | ZnSe | $m_{n}$ | 0.160 (2) | 4.2 | Photoluminescence |
| Zinc telluride | ZnTe | $m_{n}$ | 0.122 (2) | 3.5 | Cyclotron resonance |
| | | $m_{n,\,polaron}$ | 0.124 (2) | 1.5 | Polaron mass |

**Table 4.1-145** Effective masses of holes (in units of the electron mass $m_0$) for zinc compounds

| Crystal | | Quantity | Mass | Temperature (K) | Remarks |
|---|---|---|---|---|---|
| Zinc oxide | ZnO | $m_{p,\,parall}$ | 0.59 | 1.6 | Magnetoreflection |
| | | $m_{p,\,perpend}$ | 0.59 | | Polaron mass |
| Zinc sulfide | ZnS | $m_{p,\,light}$ | 0.23 | | Calculated |
| | | $m_{p,\,heavy}$ | 1.76 | | |
| Zinc selenide | ZnSe | $m_{p}$ | 0.75 | 2.1–200 | Phonon-assisted exciton absorption |
| Zinc telluride | ZnTe | $m_{p}$ | 0.6 | | Estimated from hole mobility |

### C. Transport Properties

Table 4.1-146.

*Electronic Transport, General Description.*

*Zinc oxide (ZnO)*

The electronic conductivity of pure, stoichiometric ZnO is still unknown. The concentration of foreign admixtures in undoped crystals is of the order of $10^{15}$–$10^{16}$ cm$^{-3}$. Since $E_{g,\,opt} = 3.2$ eV and impurity ionization energies are about 0.01–0.1 eV at temperatures below 900 K, impurity conduction is always observed. At temperatures above 900 K, dissociation of the intrinsic material occurs.

The conductivity depends on the surrounding atmosphere (which my be $O_2$, Zn, or Ar). Nevertheless, it is possible to investigate the influence of intentional admixtures on the conductivity, the charge-carrier concentration, and the mobility as a function of temperature and current direction.

Data for the electrical resistivity vary between values of the order of $10^{8}$–$10^{9}$ Ω cm for ultrapure bulk single crystals to values of the order of $10^{-2}$–$10^{-4}$ Ω cm for doping concentrations of up to $10^{20}$ cm$^{-3}$. Data for the

**Table 4.1-146** Thermal conductivity $\kappa$ of zinc compounds

| Crystal | | $\kappa$ (W/cm K) | Temperature (K) | Temperature dependence | Remarks |
|---|---|---|---|---|---|
| Zinc oxide | ZnO | 0.54 | 300 | Fig. 4.1-154 | Steady-state heat flow |
| Zinc sulfide | ZnS | 0.27 | 300 | | Pulse method |
| | | 3.6 | 30 | | |
| Zinc selenide | ZnSe | 0.19 | 300 | Fig. 4.1-155 | |
| Zinc telluride | ZnTe | 0.18 | 300 | | |

electron mobility $\mu_n$ at room temperature range between 0.5 and 200 $cm^2/V\,s$. Figure 4.1-153 shows the electrical conductivity of a crystal without intentional admixtures.

*Zinc sulfide (ZnS)*

The (photo)conductivity of ZnS depends strongly on the growth conditions, dopants, doping characteristics, etc. Data for the electrical resistivity vary between $10^{-3}$ and $10^2\,\Omega\,cm$ depending on sample preparation. Values of the electron mobility around $100\,cm^2/V\,s$ and $600\,cm^2/V\,s$ have been found at room temperature, and values around $3000\,cm^2/V\,s$ have been found at 77 K. A value of $40\,cm^2/V\,s$ has been given for the hole mobility.

*Zinc selenide (ZnSe)*

The (photo)conductivity of ZnSe depends strongly on the growth conditions, dopants, doping characteristics, etc. In undoped material, values of the electrical resistivity between $10^5$ and a few $\Omega\,cm$ have been found. Values of the electron mobility at room temperature reach up to $400\,cm^2/V\,s$; for the hole mobility, $\mu_p = 110\,cm^2/V\,s$ has been calculated as an upper limit.

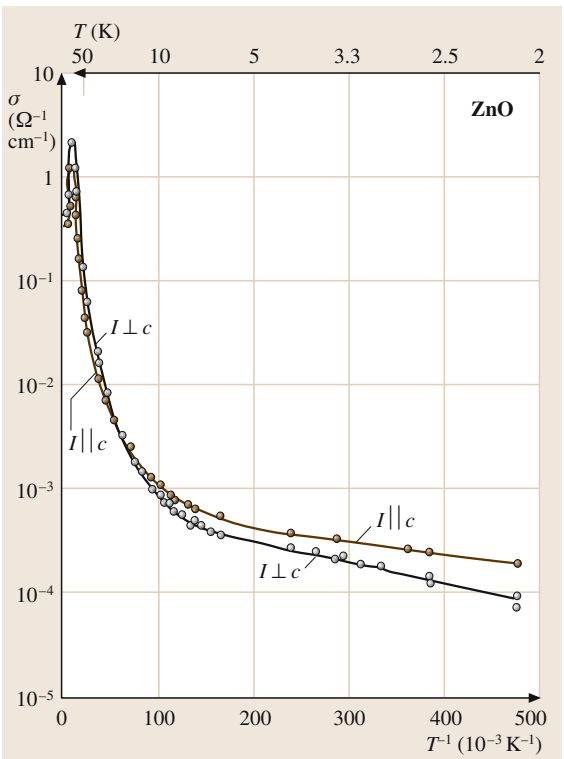


**Fig. 4.1-153** ZnO. Electronic conductivity parallel and perpendicular to the $c$ axis vs. temperature. Crystal grown in $Al_2O_3$ ceramic without intentional admixtures [1.127]

*Zinc telluride (ZnTe)*

ZnTe is a p-type conductor owing to deviations from stoichiometry when it is not intentionally doped; n-type doping is extremely difficult. The transport properties of ZnTe depend strongly on the growth conditions, dopants, doping characteristics, etc.

Typical data for the electrical resistivity at room temperature are of the order of a few times $10^4\,\Omega\,cm$; at temperatures around 77 K, values of a few times $10^6\,\Omega\,cm$ have been found. The experimental values of the electron and hole mobilities at room temperature range from 300 to $350\,cm^2/V\,s$.

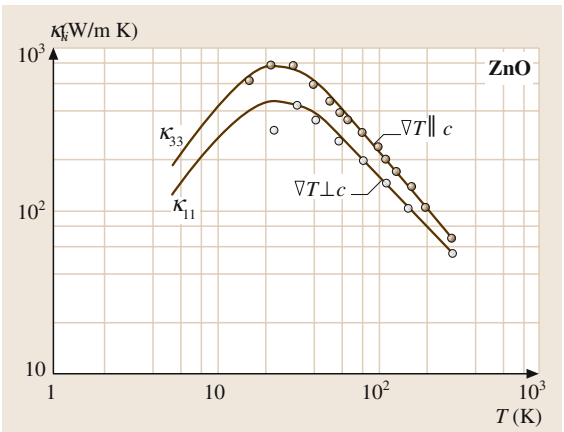


**Fig. 4.1-154** ZnO. Thermal conductivity (lattice contribution) vs. temperature. *Solid lines*, calculated values [1.128]

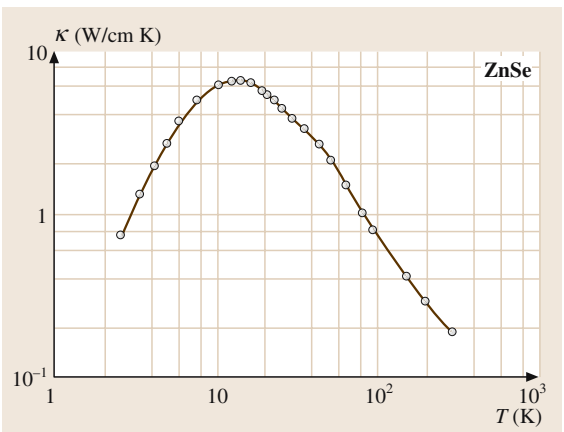


**Fig. 4.1-155** ZnSe. Thermal conductivity vs. temperature [1.129]

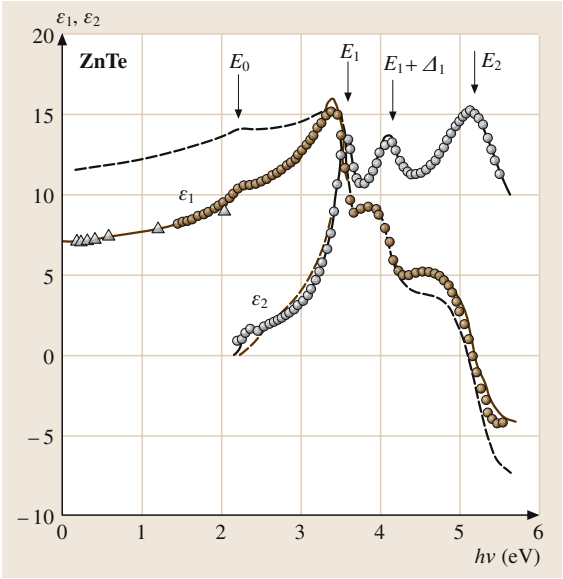


**Fig. 4.1-156** ZnTe. Dielectric-function spectrum $\varepsilon(\omega)$, measured by spectroscopic ellipsometry at RT (*filled* and *open circles*); the *solid* and *dashed lines* show calculated values [1.130]. The *triangles* are experimental data from [1.131]

## D. Electromagnetic and Optical Properties

Tables 4.1-147 – 4.1-149.

**Table 4.1-147** Dielectric constant $\varepsilon$ of zinc compounds

| Crystal | | $\varepsilon(0)$ | | $\varepsilon(\infty)$ | | Temperature (K) | Remarks |
|---|---|---|---|---|---|---|---|
| Zinc oxide | ZnO | $\varepsilon_{\text{parall } c}$<br>8.75 | $\varepsilon_{\text{perpend } c}$<br>7.8 | $\varepsilon_{\text{parall } c}$<br>3.75 | $\varepsilon_{\text{perpend } c}$<br>3.70 | 300 | |
| Zinc sulfide | ZnS | | | | | 300 | See Fig. 4.1-157 for spectral dependence and Fig. 4.1-158 for the temperature dependence |
| Zinc selenide | ZnSe | 8.6 | | 5.7 | | 300 | Ellipsometry |
| Zinc telluride | ZnTe | 10.3 | | <br>7.28 | | RT<br>300 | Reflectivity derived from refraction data<br>See Fig. 4.1-160 for spectral dependence |

**Table 4.1-148** Refractive index $n$ of zinc compounds

| Crystal | | Refractive index $n$ | | λ (nm) | Temperature (K) | Spectral dependence |
|---|---|---|---|---|---|---|
| Zinc oxide | ZnO | $n_{\text{parall } c}$<br>$n_{\text{perpend } c}$ | 2.151<br>2.137 | 436 | 293 | Fig. 4.1-161 |
| Zinc sulfide | ZnS | | | | 300 | |
| Zinc selenide | ZnSe | | | | 300 | Fig. 4.1-163 |
| Zinc telluride | ZnTe | | | | 300 | Fig. 4.1-164 |

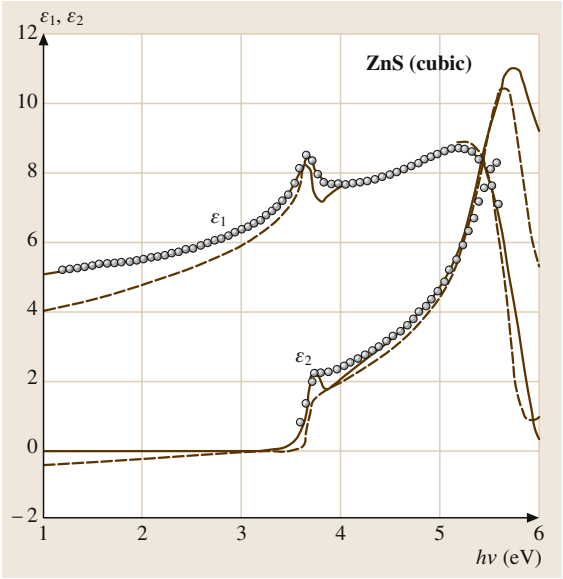


**Fig. 4.1-157** ZnS, cubic. Dielectric-function spectrum $\varepsilon(E)$, measured by spectroscopic ellipsometry at 300 K after chemomechanical polishing of the sample (*circles*). The *solid lines* show values calculated from a model dielectric function for interband critical points. The *dashed lines* represent the best-fit standard critical-point lineshapes [1.132]

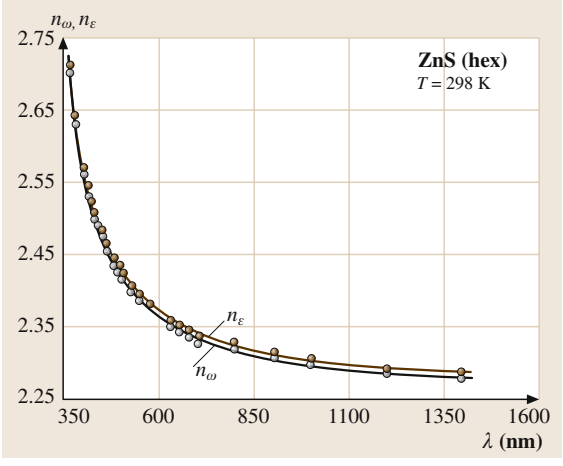


**Fig. 4.1-159** ZnS, hexagonal. Index of refraction vs. wavelength. $n_\omega$, ordinary ray; $n_\varepsilon$, extraordinary ray [1.134]

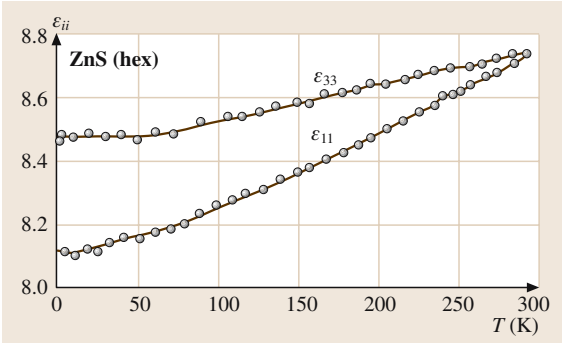


**Fig. 4.1-158** ZnS, hexagonal. Dielectric constant vs. temperature [1.133]. At 300 K, the dielectric constant of hexagonal ZnS is isotropic

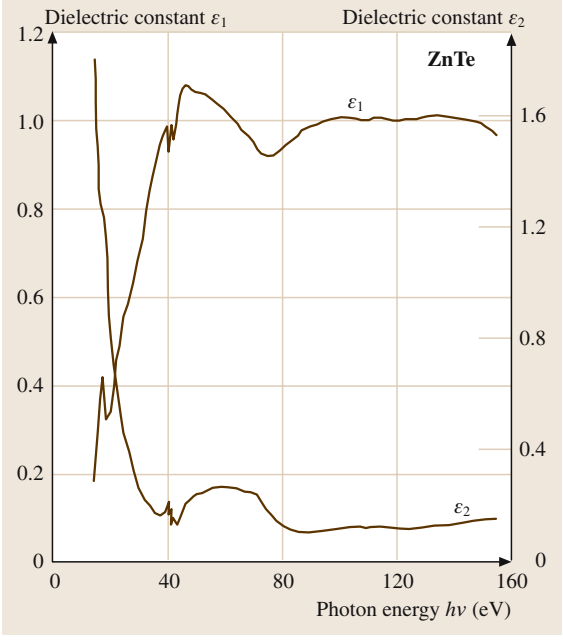


**Fig. 4.1-160** ZnTe. Spectral dependence of the real and imaginary parts of the complex dielectric constant, $\varepsilon_1$ and $\varepsilon_2$ [1.135]

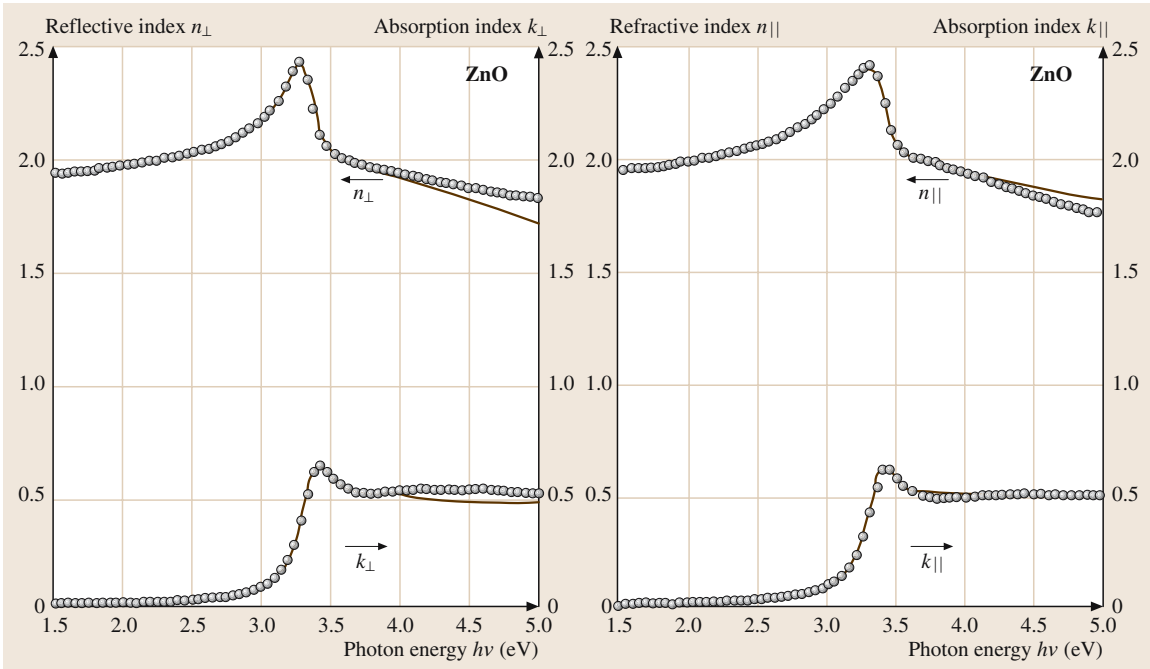


**Fig. 4.1-161** ZnO. Numerically calculated spectral dependence of the complex refractive index $n^* = n(E) + ik(E)$ for ZnO (*solid lines*). The *circles* represent experimental data at 300 K [1.136]

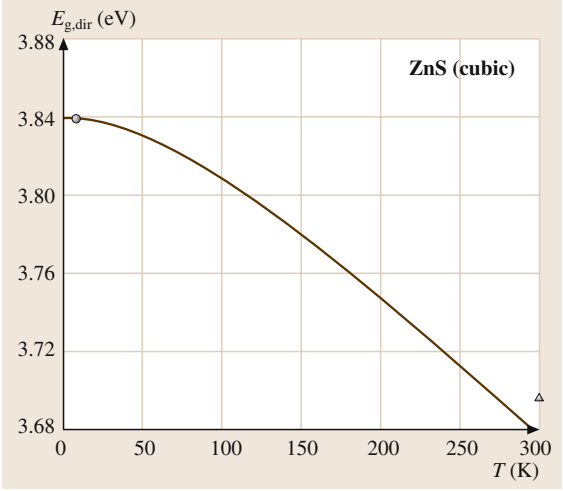


**Fig. 4.1-162** ZnS, cubic. Direct energy gap ($\Gamma_{15v}$ to $\Gamma_{1c}$) vs. temperature [1.137]. *Solid line*, theoretical result. *Circle*, experimental data from [1.138]. *Triangle*, experimental data from [1.139]

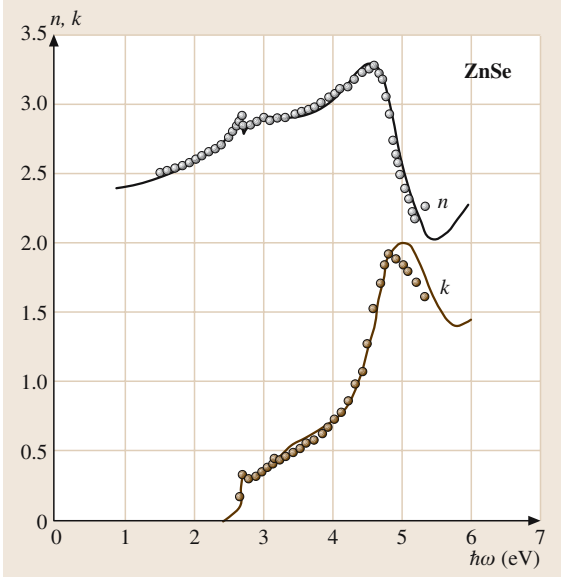


**Fig. 4.1-163** ZnSe. Numerically calculated spectral dependence of the real refractive index $n$ and the extinction coefficient $k$ (*solid lines*). The *filled circles* ($n$) and *open circles* ($k$) are experimental data [1.140]

**Table 4.1-149** Electro-optical constants of zinc compounds. Under the influence of an electric field, the refractive index changes in accordance to the nonlinearity of the dielectric polarization (Pockels effect). Crystals with hexagonal symmetry have three electro-optical constants $r_{31}$, $r_{33}$, $r_{51}$; crystals with cubic symmetry have only one electro-optical constant $r_{41}$

| Crystal | | Electro-optical constant ($10^{-9}$ cm/V) | | λ (nm) | Temperature (K) | Remarks |
|---|---|---|---|---|---|---|
| Zinc oxide | ZnO | $r_{13}, r_{33}$ | −1.4 | 400 | 295 | Electrotransmission |
| | | $r_{51}$ | −0.31 | | | |
| Zinc sulfide | ZnS | $r_{41}$ | 0.21 | 650 | | Retardation angle |
| Zinc telluride | ZnTe | $r_{41}$ | −4.71 | | | Calculated |

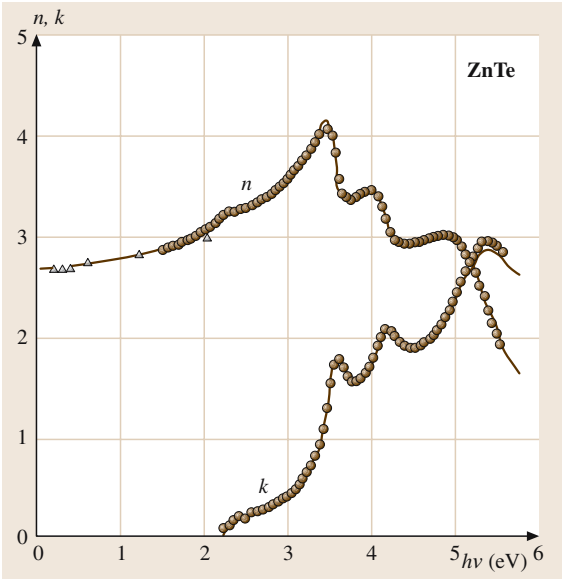


**Fig. 4.1-164** ZnTe. Numerically calculated spectral dependence of the complex refractive index ($n$ and $k$) (*solid lines*). The *circles* are measured ellipsometry data [1.130]. The *triangles* are experimental data taken from [1.131]

### 4.1.3.5 Cadmium Compounds

#### A. Crystal Structure, Mechanical and Thermal Properties

Tables 4.1-150 – 4.1-157.

**Table 4.1-150** Crystal structures of cadmium compounds

| Crystal | | Space group | | Crystal system | Structure type | Figure |
|---|---|---|---|---|---|---|
| Cadmium oxide | CdO | $O_h^5$ | $Fm3m$ | fcc | NaCl | Fig. 4.1-138[a] |
| Cadmium sulfide | CdS | $C_{6v}^4$ | $P6_3mc$ | hex | Wurtzite | Fig. 4.1-130[b] |
| Cadmium selenide | CdSe | $T_d^2$ | $F\bar{4}3m$ | fcc | Zinc blende | Fig. 4.1-131[c] |
| Cadmium telluride | CdTe | $T_d^2$ | $F\bar{4}3m$ | fcc | Zinc blende | Fig. 4.1-131 |

[a] Cadmium oxide is the only II–VI semiconductor which crystallizes in the NaCl structure at standard pressure.

[b] CdS crystallizes in several different structures. Besides the most common wurtzite structure, it is found also in the zinc blende structure and in the high-pressure NaCl structure. Epitaxial layers of CdS are frequently found in one of the cubic modifications.

[c] Under ambient conditions, CdSe crystallizes in the zinc blende structure. Ab initio calculations show that the energy of the zinc blende structure is lower than that of the wurtzite structure by 1.4 meV/atom. Under increasing pressure, the wurtzite structure transforms to the NaCl structure, the $\beta$-tin structure, and as yet unidentified structures. If not stated otherwise, the data in this section concern CdSe in the zinc blende structure.

**Table 4.1-151** Lattice parameters of cadmium compounds

| Crystal | | Lattice parameters (nm) | Remarks |
|---|---|---|---|
| Cadmium oxide | CdO | $a = 0.4689$ | |
| Cadmium sulfide | CdS | $a = 0.41348$<br>$c = 0.67490$ | X-ray diffraction |
| Cadmium selenide | CdSe | $a = 0.6077\ (5)$<br>$a = 0.6078\ (1)$ | Perpendicular to surface, X-ray diffraction<br>Parallel to surface |
| Cadmium telluride | CdTe | $a = 0.646$ | X-ray diffraction |

**Table 4.1-152** Densities of cadmium compounds

| Crystal | | Density (g/cm$^3$) | Temperature (K) | Remarks |
|---|---|---|---|---|
| Cadmium oxide | CdO | 8.15 | | X-ray crystal density method |
| Cadmium sulfide | CdS | 4.82 | 300 | |
| Cadmium selenide | CdSe | 5.81 | 300 | |
| Cadmium telluride | CdTe | 5.87 | 4 | |

**Table 4.1-153** Elastic constants $c_{ik}$ of cadmium compounds

| Crystal | | $c_{11}$ (GPa) | $c_{13}$ (GPa) | $c_{33}$ (GPa) | $c_{44}$ (GPa) | $c_{66}$ (GPa) | Remarks |
|---|---|---|---|---|---|---|---|
| Cadmium sulfide | CdS | 90.7 | 51.0 | 93.8 | 15.04 | | |
| Cadmium selenide | CdSe | 74.6 | 46.1 | 81.7 | 13.0 | 14.3 | Ultrasound measurements, RT |

**Table 4.1-153** Elastic constants $c_{ik}$ of cadmium compounds, cont.

| Crystal | | $c_{11}$ (GPa) | $c_{12}$ (GPa) | $c_{44}$ (GPa) | Temperature (K) |
|---|---|---|---|---|---|
| Cadmium telluride | CdTe | 53.8 | 37.4 | 20.18 | 298 |
| | | 56.2 | 39.4 | 20.61 | 77 |

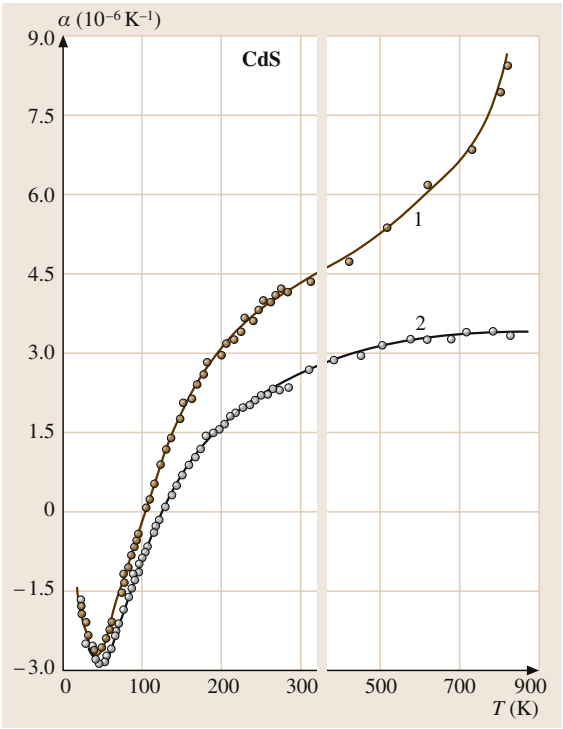


**Fig. 4.1-165** CdS, hexagonal. Temperature dependence of the linear thermal expansion coefficients $\alpha_\perp$ (perpendicular to the $c$ axis, *curve 1*) and $\alpha_\parallel$ (parallel to the $c$ axis, *curve 2*), measured by dilatometer experiments [1.141, 142]

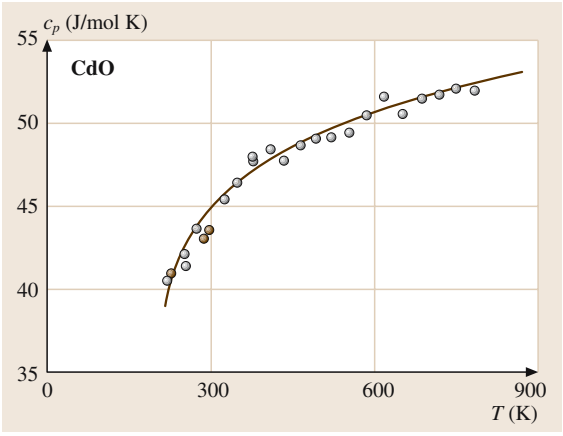


**Fig. 4.1-166** CdO. Heat capacity $c_p$ vs. temperature. Measurements from two authors [1.143]

**Table 4.1-154** Melting point $T_m$ of cadmium compounds

| Crystal | | Melting point $T_m$ (K) | Remarks |
|---|---|---|---|
| Cadmium oxide | CdO | >1773 | |
| Cadmium sulfide | CdS | 1750 | Under pressure $p > 3.85$ bar |
| Cadmium selenide | CdSe | 1537 | Assessed |
| Cadmium telluride | CdTe | 1366.6 (70) | Mean of experimental values |

**Table 4.1-155** Linear thermal expansion coefficient $\alpha$ of cadmium compounds

| Crystal | | Expansion coefficient $\alpha$ ($K^{-1}$) | Temperature (K) | Remarks |
|---|---|---|---|---|
| Cadmium oxide | CdO | $14 \times 10^{-6}$ | 300–770 | Dilatometer measurements |
| Cadmium sulfide | CdS | | | See Fig. 4.1-165 for temperature dependence |
| Cadmium selenide | CdSe | | | |
| Cadmium telluride | CdTe | $4.96 \times 10^{-6}$ | 20–420 | |

**Table 4.1-156** Heat capacity $c_p$ and Debye temperature $\Theta_D$ of cadmium compounds

| Crystal | | Heat capacity $c_p$ (J/mol K) | Temperature (K) | Debye temperature $\Theta_D$ (K) | Remarks |
|---|---|---|---|---|---|
| Cadmium oxide | CdO | 43.639 | 298.15 | 255 (6) | See Fig. 4.1-166 for temperature dependence<br>Calculated from X-ray diffraction measurements |
| Cadmium sulfide | CdS | 55.10 | 300 | 219.32 | $T = 298–1678$ K<br>From elastic constants |
| Cadmium selenide | CdSe | 49.58 | 300 | 181.7 | Monocrystalline sample, $T = 400–700$ K<br>$T = 0$ K |
| Cadmium telluride | CdTe | 25.63 | 300 | 140 (3) | Polycrystalline sample, $T = 300–530$ K<br>Single crystal, X-ray diffraction |

**Table 4.1-157** Phonon frequencies/wavenumbers at symmetry points for cadmium compounds. Cadmium oxide (CdO), Fundamental optical-mode frequencies; cadmium sulfide (CdS), 25 K; cadmium selenide (CdSe), 300 K, from infrared and Raman spectroscopy; cadmium telluride (CdTe), 300 K, from inelastic neutron scattering

| CdO Mode | Symmetry point | Frequency (THz) | Temperature (K) |
|---|---|---|---|
| $\tilde{\nu}_O$ | $\Gamma$ | 7.85 | 300 |
| $\tilde{\nu}_{\Lambda O}$ | $\Gamma$ | 15.83 | 300 |
| $\tilde{\nu}_{LO}$ | L | 14.4 | 2 |
| $\tilde{\nu}_{LO}$ | X | 15.6 | 2 |
| $\tilde{\nu}_{TO}$ | X | 7.2 | 2 |

| CdS Mode | Symmetry point | Wavenumber ($cm^{-1}$) |
|---|---|---|
| $\bar{\nu}_{LO}$ | $\Gamma_5$, perpendicular to $c$ | 307 |
| $\bar{\nu}_{LO,\,1}$ | $\Gamma_1$, parallel to $c$ | 305 |
| $\bar{\nu}_{TO,\,1}$ | $\Gamma_5$, perpendicular to $c$ | 242 |
| $\bar{\nu}_{TO,\,1}$ | $\Gamma_1$, parallel to $c$ | 234 |
| $\bar{\nu}_{LO,\,2}$ | $\Gamma_6$, perpendicular to $c$ | 256 |
| $\bar{\nu}_{TO,\,3}$ | $\Gamma_6$, perpendicular to $c$ | 43 |

| CdSe Mode | Symmetry point | Wavenumber ($cm^{-1}$) |
|---|---|---|
| $\bar{\nu}_{LO,\,1}$ | $\Gamma_1$, parallel to $c$ | 210 |
| $\bar{\nu}_{TO,\,1}$ | $\Gamma_5$, perpendicular to $c$ | 169 |
| $\bar{\nu}_{LO,\,2}$ | $\Gamma_5$, perpendicular to $c$ | 212 |
| $\bar{\nu}_{TO,\,2}$ | $\Gamma_1$, parallel to $c$ | 166 |
| $\bar{\nu}_{TA}$ | $A_3$ | 43.5 |

| CdTe Mode | Symmetry point | Frequency (THz) |
|---|---|---|
| $\nu_{LO}$ | $\Gamma$ | 5.08 (10) |
| $\nu_{TO}$ | $\Gamma$ | 4.20 (10) |
| $\nu_{LO}$ | X | 4.44 (6) |
| $\nu_{TA}$ | X | 1.05 (3) |
| $\nu_{LO}$ | L | 4.33 (6) |
| $\nu_{TAO}$ | L | 4.33 (7) |
| $\nu_{LA}$ | L | 3.25 (8) |
| $\nu_{TA}$ | L | 0.88 (3) |

## B. Electronic Properties

Tables 4.1-158 – 4.1-164.

**Table 4.1-158** First Brillouin zones of cadmium compounds

| Crystal | | Figure |
|---|---|---|
| Cadmium oxide | CdO | Fig. 4.1-133 |
| Cadmium sulfide | CdS | Fig. 4.1-132 |
| Cadmium selenide | CdSe | Fig. 4.1-133 |
| Cadmium telluride | CdTe | Fig. 4.1-133 |

**Table 4.1-159** Band structures of cadmium compounds

**Cadmium oxide (CdO) (Fig. 4.1-167)**

The lowest conduction band has its minimum at the $\Gamma_1$ point in the center of the Brillouin zone. Within an energy range of a few tenths of an electron volt above its bottom, the band is isotropic but highly nonparabolic. The nonparabolicity is revealed by the strong dependence of the optical electron mass on the electron concentration. The lowest conduction band is separated from the higher bands by a small gap. The valence band consists of several branches, with maxima at $L_3$ and $\Sigma$.

**Cadmium sulfide (CdS) (Fig. 4.1-168)**

Hexagonal CdS is a direct-gap semiconductor with the smallest energy gap at the center of the Brillouin zone ($\Gamma$). The topmost valence band ($\Gamma_5 + \Gamma_1$) is split owing to the crystal field and spin–orbit coupling into three spin-degenerate states. The exciton states formed with holes in these valence band states are referred to as the A, B, and C excitons, respectively.

**Cadmium selenide (CdSe)**

See Fig. 4.1-170.

**Cadmium telluride (CdTe) (Fig. 4.1-169)**

Cadmium telluride is a direct-gap semiconductor with the smallest energy gap at the center of the Brillouin zone ($\Gamma$). The topmost valence band is split owing to spin–orbit coupling into a fourfold ($\Gamma_8$) and a twofold ($\Gamma_7$) state.

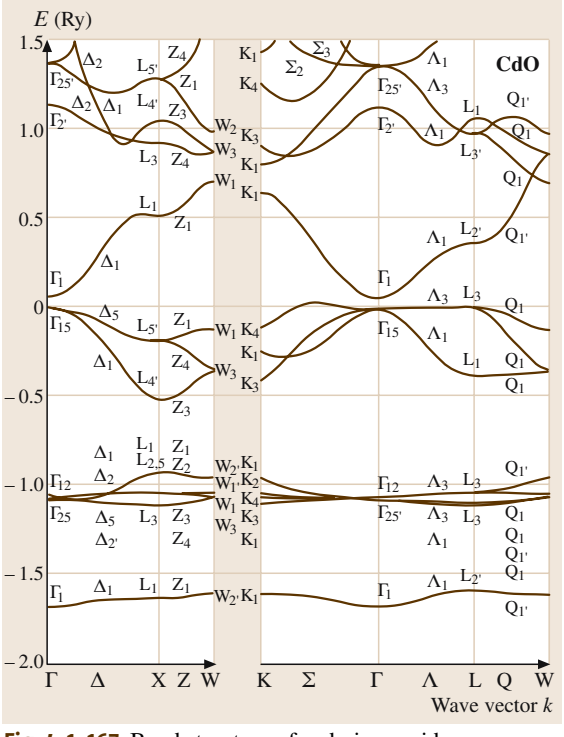


**Fig. 4.1-167** Band structure of cadmium oxide

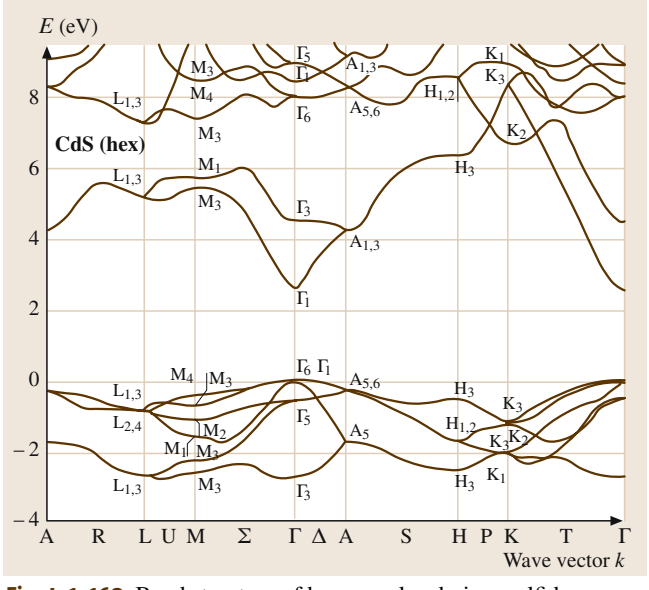


**Fig. 4.1-168** Band structure of hexagonal cadmium sulfide

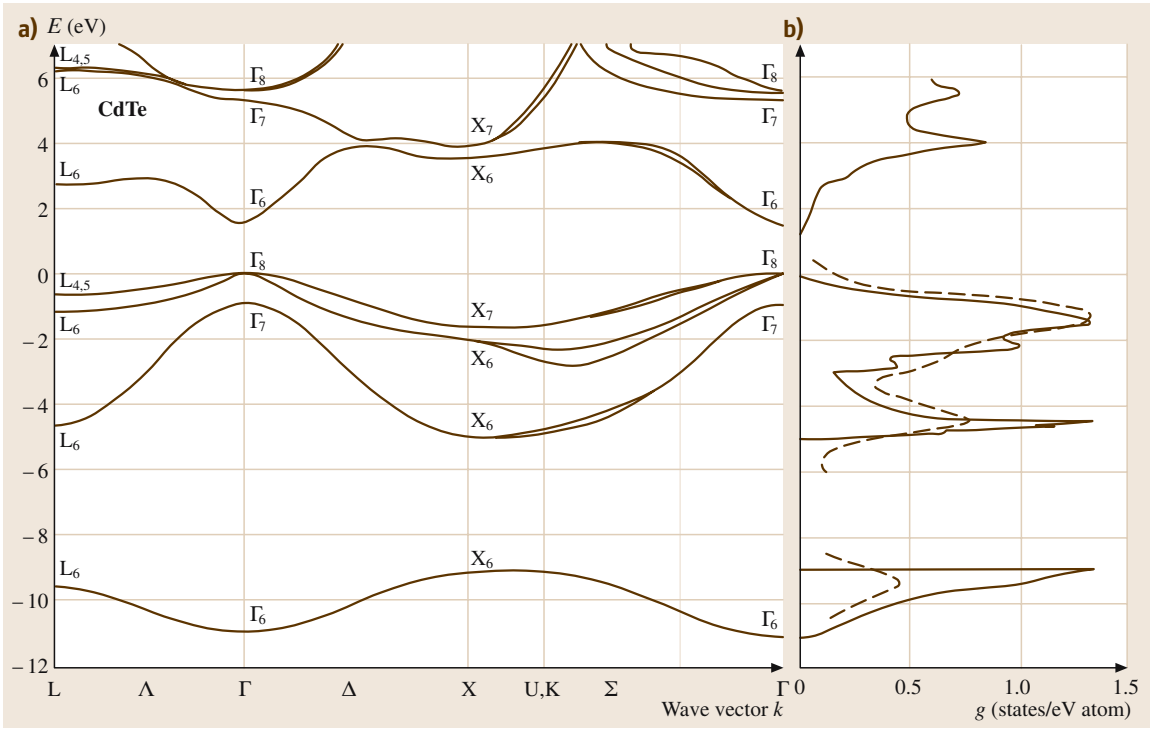


**Fig. 4.1-169a,b** CdTe. (**a**) Band structure and (**b**) electron density of states from a pseudopotential calculation [1.144]. *Dashed curve*: Experimental data

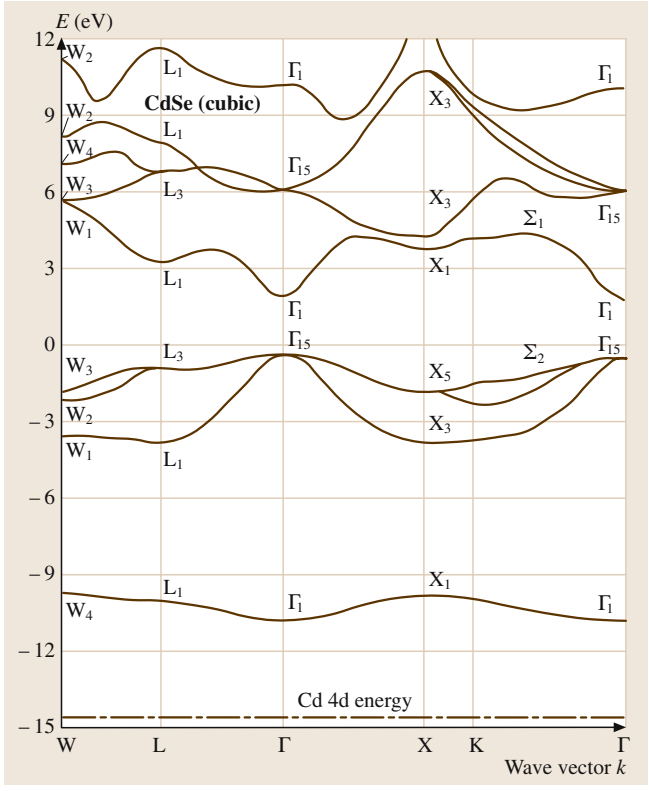


**Fig. 4.1-170** Band structure of cubic cadmium selenide

**Table 4.1-160** Energy gaps of cadmium compounds (for the letters A, B, C see CdS band structure, Fig. 4.1-168)

| Crystal | | Band gap (eV) | | Between bands | Temperature (K) | Remarks |
|---|---|---|---|---|---|---|
| Cadmium oxide | CdO | $E^{(1)}_{g,\,ind}$ | 1.09 (5) | $\Sigma_{3v}$ and $\Gamma_{1c}$ | 100 | Thermoreflectance |
| | | $E^{(2)}_{g,\,ind}$ | 0.84 | $L_{3v}$ and $\Gamma_{1c}$ | | |
| | | $E_{g,\,dir}$ | 2.28 | $\Gamma_{15v}$ and $\Gamma_{1c}$ | | |
| Cadmium sulfide | CdS | $E^{A}_{g,\,dir}$ | 2.482 | $\Gamma_{9v}$ and $\Gamma_{7c}$ | 300 | Band gaps of the three subbands; |
| | | $E^{B}_{g}$ | 2.496 | $\Gamma_{7v}$ and $\Gamma_{7c}$ | | Ellipsometry |
| | | $E^{C}_{g}$ | 2.555 | $\Gamma_{7v}$ and $\Gamma_{7c}$ | | |
| Cadmium selenide | CdSe | $E_{g,\,dir}$ | 1.74 | $E_0$ | 300 | Ellipsometry |
| Cadmium telluride | CdTe | $E_{g,\,dir}$ | 1.475 | $\Gamma_{8v}$ and $\Gamma_{6c}$ | RT | Photoelectrochemistry |

**Table 4.1-161** Spin–orbit splitting energy $\Delta_{so}$ of cadmium compounds

| Crystal | | Splitting energy (meV) | Bands | Temperature (K) | Remarks |
|---|---|---|---|---|---|
| Cadmium selenide | CdSe | 470 | | | Calculation |
| Cadmium telluride | CdTe | 950 (20) | $\Gamma_{7v}$ to $\Gamma_{78}$ | 300 | Photoemission |

**Table 4.1-162** Effective masses of electrons (in units of the electron mass $m_0$) for cadmium compounds

| Crystal | | Quantity | Mass | Temperature (K) | Remarks |
|---|---|---|---|---|---|
| Cadmium oxide | CdO | $m_n$ | 0.33–0.46 | 81 | Comparison of low-temperature mobilities, $n = 0.4–6.3 \times 10^{19}$ cm$^{-3}$ |
| Cadmium sulfide | CdS | $m_n$ | 0.25 | 300 | Thermoelectric power |
| Cadmium selenide | CdSe | $m_n$ | 0.12 | | Calculation |
| Cadmium telluride | CdTe | $m_n$ [110] | 0.096 (3) | 1.5 | Cyclotron resonance |
| | | $m_n$ [100] | 0.094 (4) | 1.8 | |
| | | $m_n$ [111] | 0.095 (4) | 1.8 | |

**Table 4.1-163** Effective masses of holes (in units of the electron mass $m_0$) for cadmium compounds

| Crystal | | Quantity | Mass | Temperature (K) | Remarks |
|---|---|---|---|---|---|
| Cadmium sulfide | CdS | $m^{A}_{p,\,perpend}$ | 0.7 (1) | 1.6 | Exciton magnetoabsorption |
| | | $m^{A}_{p,\,parall}$ | 5 | | |
| Cadmium selenide | CdSe | $m_{p,\,heavy}$ [111] | 2.14 | | Calculation |
| | | $m_{p,\,heavy}$ [100] | 0.9 | | |
| | | $m_{p,\,heavy}$ [110] | 1.7 | | |
| | | $m_{p,\,light}$ [111] | 0.16 | | |
| | | $m_{p,\,light}$ [100] | 0.18 | | |
| | | $m_{p,\,light}$ [110] | 0.16 | | |
| Cadmium telluride | CdTe | $m_{p,\,heavy}$ [110] | 0.81 (5) | 1.5 | Cyclotron resonance |
| | | $m_{p,\,light}$ [110] | 0.12 (2) | | |

**Table 4.1-164** $g$-factors in the conduction band ($g_c$) and valence band ($g_v$) for cadmium compounds

| Crystal | | Quantity | $g$-factor | Temperature (K) | Remarks |
|---|---|---|---|---|---|
| Cadmium oxide | CdO | $g_c$ | 1.806 (5) | 77 | Electron spin resonance measurements |
| Cadmium sulfide | CdS | $g_{c,\,perpend}$ | 1.78 (5) | 1.6 | Exciton absorption |
| | | $g_{c,\,parall}$ | 1.72 (10) | | (for the letters A, B, C see |
| | | $g^{A}_{v,\,parall}$ | 1.15 (5) | 16 | CdS band structure, Fig. 4.1-168) |
| | | $g^{B}_{v,\,perpend}$ | 0.8 | 1.8 | Lineshape analysis of excitonic polaron reflectivity |
| Cadmium selenide | CdSe | $g$ | 0.23 | | Calculation |
| Cadmium telluride | CdTe | $g_c$ | 1.652 | 1.5 | Spin-flip Raman measurements |

### C. Transport Properties

Tables 4.1-165 – 4.1-167.

**Table 4.1-165** Electronic transport, general description

**Cadmium oxide (CdO)**

Owing to a high degree of nonstoichiometry, CdO is generally a highly degenerate n-type semiconductor. The conductivity is related to an excess of Cd in the lattice. Usually the electron concentration is several times $10^{19}$ cm$^{-3}$. Values of the electrical resistivity at 300 K range from 1.2 to $1.5 \times 10^{-3}$ Ω cm.

**Cadmium sulfide (CdS)**

Electrical transport in CdS is performed by electrons in the $\Gamma_7$ conduction band and holes in the $\Gamma_9$ valence band. Because of compensation effects during the preparation of the samples and the large ratio $\mu_n/\mu_p > 10$, CdS is normally n-type conducting; p-type conductivity is observed only in a few special cases. The carrier concentration depends on the impurity or defect content and on temperature. Furthermore, the carrier concentration can be changed markedly by illumination: CdS is known to be a model substance for photoconductivity.

**Cadmium selenide (CdSe)**

Electrical transport in CdSe is governed by electrons in the $\Gamma_7$ conduction band and holes in the $\Gamma_9$ valence band. CdSe is mainly n-type conducting, owing to compensation effects during the preparation of the samples and to a ratio of the mobilities of electrons and holes of order 10. The carrier concentration depends on the impurity or defect content and on temperature. Furthermore, it depends strongly on irradiation. Photoconductivity in CdSe can be produced by electromagnetic illumination (photon energy > band gap) and by high-energy particles.

**Cadmium telluride (CdTe)**

CdTe bulk crystals can be doped to become n- or p-type conductive. High-resistivity crystals ($\rho > 10^9$ Ω cm) can be obtained under various growth and doping conditions.

**Table 4.1-166** Electron and hole mobilities $\mu_n$ and $\mu_p$ of cadmium compounds

| Crystal | | $\mu_n$ (cm$^2$/V s) | $\mu_p$ (cm$^2$/V s) | Temperature (K) | Remarks |
|---|---|---|---|---|---|
| Cadmium oxide | CdO | 180 | | 300 | Hall mobility, cold-pressed CdO, $n = 1.1 \times 10^{19}$ cm$^{-3}$ |
| Cadmium sulfide | CdS | 160 | | 300 | In-doped, $n = 5 \times 10^{19}$ cm$^{-3}$ |
| | | >10 000 | | 30–40 | Peak mobility, ultrapure crystals |
| | | | 15 | 300 | Highly resistive crystals |
| Cadmium selenide | CdSe | 660 | | 300 | Polycrystal and single-crystal material |
| | | 5000 | | 80 | Dc Hall effect |
| | | 200 | | 800 | |
| | | | 40 | 300 | N-doped epitaxial films |
| Cadmium telluride | CdTe | <110 000 | | 32 | Hall mobilities |
| | | | 60 | 300 | |
| | | | 1200 | 170 | |

**Table 4.1-167** Thermal conductivity $\kappa$ of cadmium compounds

| Crystal | | $\kappa$ (W/cm K) | Temperature (K) dependence | Temperature | Remarks |
|---|---|---|---|---|---|
| Cadmium sulfide | CdS | 0.20 | 300 | Fig. 4.1-171 | |
| Cadmium selenide | CdSe | 0.09 | 300 | | |
| Cadmium telluride | CdTe | 0.071 | 298 | Fig. 4.1-172 | Single crystal |
| | | 10 | 8 | | Theoretical maximum for a pure crystal |

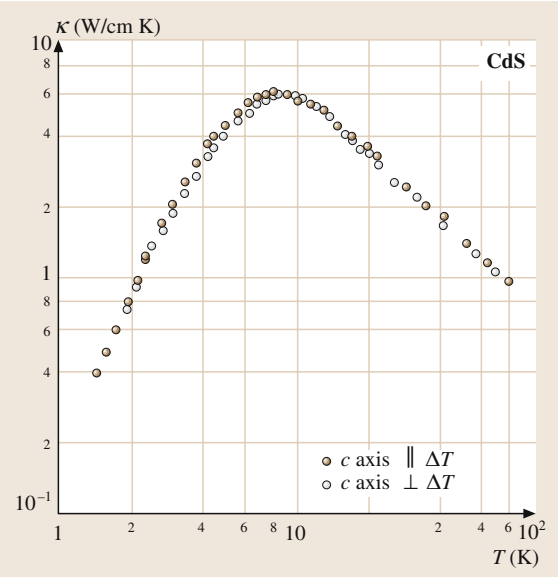


**Fig. 4.1-171** CdS. Thermal conductivity vs. temperature for $c$ axis parallel and perpendicular to the heat flow $\Delta T$ [1.145, 146]

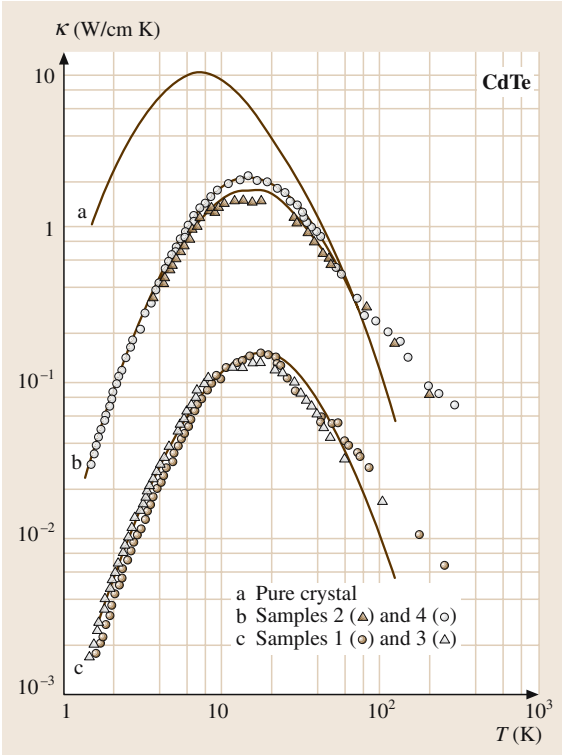


**Fig. 4.1-172** CdTe. Thermal conductivity of several different specimens vs. temperature. The results for specimens 1 and 3 have been plotted reduced by a factor of 10. The point defect concentrations of the samples are (1) $3.42\times10^{18}\,cm^{-3}$; (2) $3.99\times10^{18}\,cm^{-3}$; (3) $3.42\times10^{18}\,cm^{-3}$; (4) $2.66\times10^{18}\,cm^{-3}$ [1.147]

## D. Electromagnetic and Optical Properties

Tables 4.1-168 and 4.1-169.

**Table 4.1-168** Dielectric constant $\varepsilon$ of cadmium compounds

| Crystal | | $\varepsilon(0)$ | | $\varepsilon(\infty)$ | | Temperature (K) | Remarks |
|---|---|---|---|---|---|---|---|
| Cadmium oxide | CdO | | 21.9 | | | 300 | Infrared reflectivity |
| | | | | | 2.1 | 300 | Transmittance, absorption |
| Cadmium sulfide | CdS | $\varepsilon(0)_{perpend}$ | 8.28 | $\varepsilon(\infty)_{perpend}$ | 5.23 | 300 | Spectroscopic ellipsometry |
| | | $\varepsilon(0)_{parall}$ | 8.73 | $\varepsilon(\infty)_{parall}$ | 5.29 | | |
| Cadmium selenide | CdSe | $\varepsilon(0)_{perpend}$ | 9.29 | | | 300 | Infrared spectroscopy |
| | | | 9.15 | | | 100 | |
| | | $\varepsilon(0)_{parall}$ | 10.16 | | | 300 | |
| | | | 9.29 | | | 100 | |
| Cadmium telluride | CdTe | | 10.4 | | 7.1 (1) | 300 | |

**Table 4.1-169** Refractive index $n$ of cadmium compounds

| Crystal | | Refractive index $n$ | λ (nm) | Temperature (K) | Spectral dependence | Remarks |
|---|---|---|---|---|---|---|
| Cadmium oxide | CdO | 1.95–2.65 | 600 | | Fig. 4.1-173 | |
| Cadmium sulfide | CdS | $n_{\text{parall } c}$<br>$n_{\text{perpend } c}$ | | | Fig. 4.1-174 | |
| Cadmium selenide | CdSe | | | | Fig. 4.1-175 | |
| Cadmium telluride | CdTe | 2.70 | 2500 | 300 | | Prism refraction |

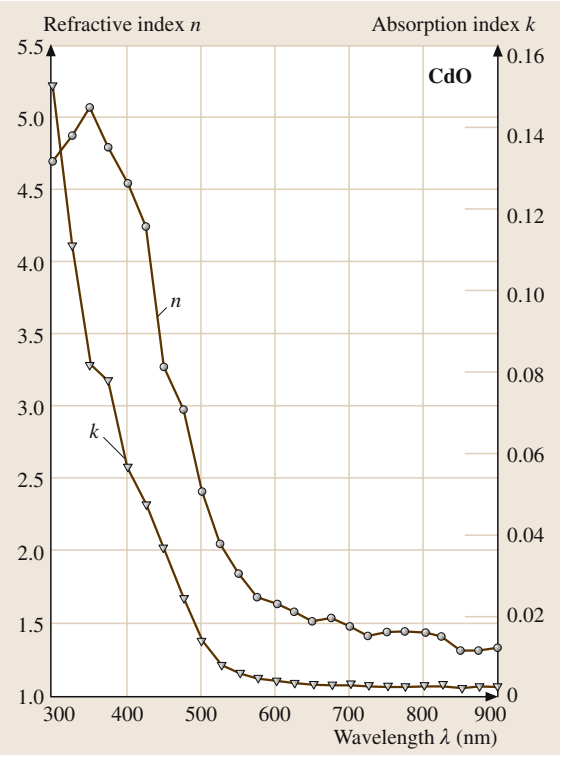


**Fig. 4.1-173** CdO. Dispersion of the optical constants $n$ and $k$ of a film [1.148]

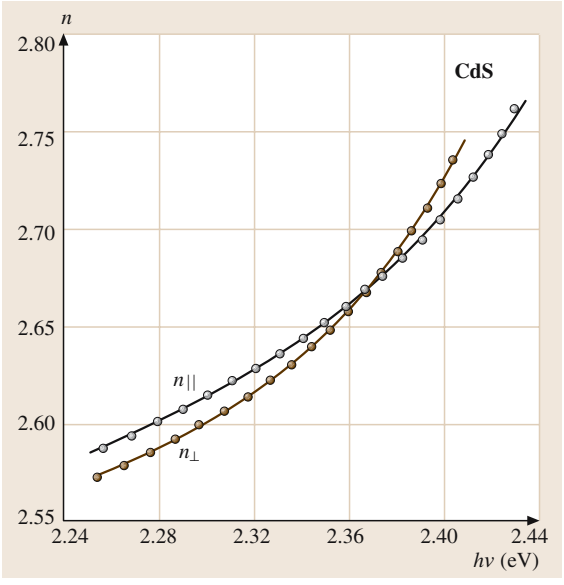


**Fig. 4.1-174** CdS, hexagonal. Dispersion of the refractive index. The *symbols* are experimental values and the *curves* correspond to polynomial fits [1.149]

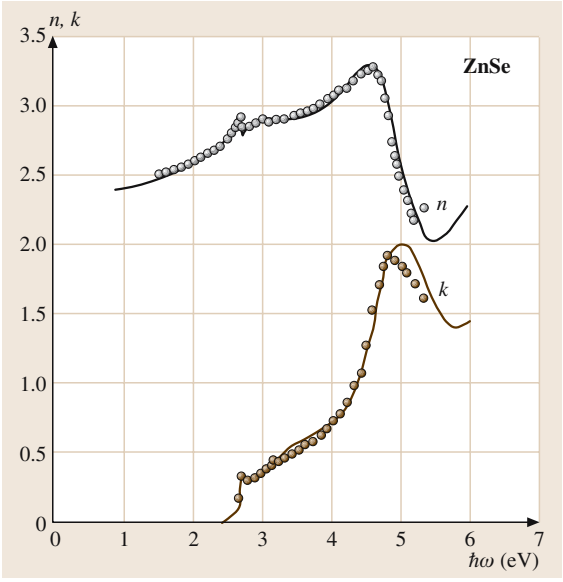


**Fig. 4.1-175** CdSe, hex, cub. The real refractive index $n(E)$ and the extinction coefficient $k(E)$, forming the complex refractive index $n*(E) = n(E) + \mathrm{i}k(E)$, for both hexagonal and cubic CdSe. The *circles* represent experimental data, the *solid lines* numerically calculated energy dependences [1.150]

### 4.1.3.6 Mercury Compounds

#### A. Crystal Structure, Mechanical and Thermal Properties

Tables 4.1-170 – 4.1-177.

**Table 4.1-170** Crystal structures of mercury compounds

| Crystal | | Space group | Crystal system | Structure type | Figure |
|---|---|---|---|---|---|
| Mercury oxide | HgO | $D_{2h}^{16}$ | Trigonal | | |
| Mercury sulfide | HgS | | | Red $\alpha$-HgS | |
| Mercury selenide | HgSe | $T_d^2$ $F\bar{4}3m$ | fcc | Zinc blende | Fig. 4.1-131 |
| Mercury telluride | HgTe | $T_d^2$ $F\bar{4}3m$ | fcc | Zinc blende | Fig. 4.1-131 |

**Table 4.1-171** Lattice parameters of mercury compounds

| Crystal | | Lattice parameters (nm) | Remarks |
|---|---|---|---|
| Mercury oxide | HgO | $a = 0.3577$<br>$b = 0.8681$<br>$c = 0.2427$ | X-ray diffraction |
| Mercury sulfide | HgS | $a = 0.414$<br>$b = 0.949$<br>$c = 0.2292$ | X-ray diffraction |
| Mercury selenide | HgSe | $a = 0.5997\,(5)$ | Angle-dispersion X-ray diffraction, pressure $p = 2.25$ GPa |
| Mercury telluride | HgTe | $a = 0.6453$ | Energy-dispersive X-ray diffraction |

**Table 4.1-172** Densities of mercury compounds

| Crystal | | Density (g/cm$^3$) |
|---|---|---|
| Mercury oxide | HgO | 11.080 |
| Mercury selenide | HgSe | 8.11 |
| Mercury telluride | HgTe | 8.21 |

**Table 4.1-173** Melting point $T_m$ of mercury compounds

| Crystal | | Melting point $T_m$ (K) | Remarks |
|---|---|---|---|
| Mercury sulfide | HgS | 1093 | Zinc blende structure |
| Mercury selenide | HgSe | 1072 | Assessed |
| Mercury telluride | HgTe | 943 | |

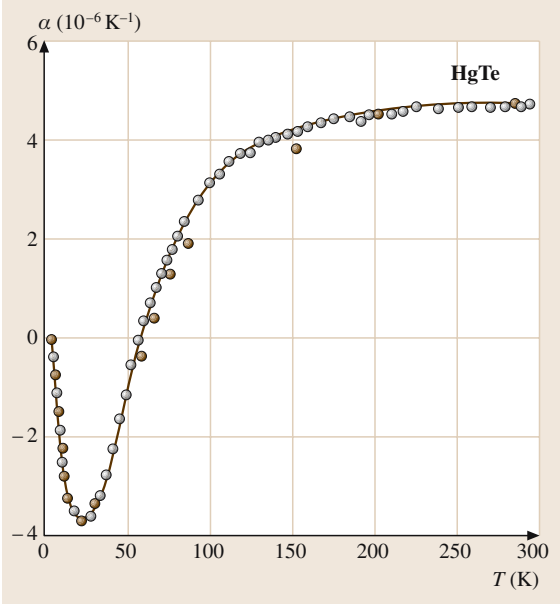


**Fig. 4.1-176** HgTe. Linear thermal expansion coefficient $\alpha$ vs. $T$. *Symbols*, experimental points; *solid line*, calculated values [1.151]

**Table 4.1-174** Elastic constants $c_{ik}$ of mercury compounds

| Crystal | | $c_{11}$ (GPa) | $c_{12}$ (GPa) | $c_{33}$ (GPa) | $c_{44}$ (GPa) | $c_{66}$ (GPa) | Remarks |
|---|---|---|---|---|---|---|---|
| Mercury sulfide | HgS | 35.0 (14) | | 48.6 (5) | | 13.0 (5) | 300 K |
| Mercury selenide | HgSe | 62.2 (1) | 46.4 | | 22.7 (1) | | 292 K, ultrasound measurements |
| Mercury telluride | HgTe | 53.6 | 36.6 | | 21.10 | | 300 K |
| | | 58.7 | 40.5 | | 22.3 | | 77 K |

**Table 4.1-175** Linear thermal expansion coefficient $\alpha$ of mercury compounds

| Crystal | | Linear thermal expansion coefficient $\alpha$ ($10^{-6}$ K$^{-1}$) | | Temperature | Remarks |
|---|---|---|---|---|---|
| Mercury sulfide | HgS | $\alpha_{parall}$ | 18.8 (8) | 20–200 °C | Parallel to $c$ axis |
| | | $\alpha_{perpend}$ | 18.1 (5) | | Perpendicular to $c$ axis, trigonal HgS |
| Mercury selenide | HgSe | | 28.61 | 30–380 °C | From temperatur dependence of lattice constant $a$ |
| Mercury telluride | HgTe | | 4.0 | 77–300 K | See Fig. 4.1-176 for temperature dependence |

**Table 4.1-176** Heat capacity $c_p$ and Debye temperature $\Theta_D$ of mercury compounds

| Crystal | | Heat capacity $c_p$ (J/mol K) | Temperature (K) | Debye temperature $\Theta_D$ (K) | Remarks |
|---|---|---|---|---|---|
| Mercury sulfide | HgS | 50.25 | 300 | 152 | $T = 0$ K, calorimetry, extrapolated |
| Mercury selenide | HgSe | 49.79 | 300 | 142 | $T = 0$ K, calorimetry, extrapolated |
| Mercury telluride | HgTe | 54.81 | 300 | 141.5 | |

**Table 4.1-177** Phonon frequencies/wavenumbers at symmetry points for mercury compounds. Mercury sulfide (HgS), 80 K, from infrared reflectance; mercury selenide (HgSe), RT, from resonance Raman scattering; mercury telluride (HgTe), 290 K, from neutron scattering

| HgS | | | HgSe | | HgTe | | |
|---|---|---|---|---|---|---|---|
| Mode | Symmetry point | Wavenumber (cm$^{-1}$) | Mode | Wavenumber (cm$^{-1}$) | Mode | Symmetry point | Phonon energy (meV) |
| $\bar{\nu}_{LO}$ | $E_1$ | 356 | $\bar{\nu}_{TO}$ | 130 | $h\nu_{LO}$ | $\Gamma$ | 14.86 (16) |
| $\bar{\nu}_{TO}$ | $E_1$ | 347.6 | $\bar{\nu}_{LO}$ | 174 | $h\nu_{TO}$ | $\Gamma$ | 14.63 (17) |
| $\bar{\nu}_{LO}$ | $E_2$ | 296 | | | $h\nu_{LO}$ | X | 16.86 (12) |
| $\bar{\nu}_{TO}$ | $E_2$ | 284.2 | | | $h\nu_{TO}$ | X | 16.64 (10) |
| $\bar{\nu}_{LO}$ | $E_3$ | 156 | | | $h\nu_{LA}$ | X | 10.56 (7) |
| $\bar{\nu}_{TO}$ | $E_3$ | 115.5 | | | $h\nu_{TA}$ | X | 1.97 (2) |
| $\bar{\nu}_{LO}$ | $E_4$ | 98 | | | $h\nu_{LO}$ | L | 18.07 (24) |
| $\bar{\nu}_{TO}$ | $E_4$ | 92 | | | $h\nu_{TO}$ | L | 15.86 (18) |
| $\bar{\nu}_{LO}$ | $E_5$ | 50 | | | $h\nu_{LA}$ | L | 9.97 (6) |
| $\bar{\nu}_{TO}$ | $E_5$ | 42 | | | $h\nu_{TA}$ | L | 2.28 (2) |

B. Electronic Properties

Tables 4.1-179 – 4.1-183.

**Table 4.1-178** Band structures of mercury compounds

**Mercury selenide (HgSe)**

Mercury selenide is a zero-gap material (semimetal). The lowest conduction band minimum and the top of the valence band are degenerate at the center of the Brillouin zone ($\Gamma_8$). The $\Gamma_6$ level, which for most cubic semiconductors is the conduction band minimum and has an energy larger than that of the $\Gamma_8$ state, is found to be below the $\Gamma_8$ state in HgSe ("negativ energy gap", inverted band structure).

**Mercury telluride (HgTe)**

Mercury telluride, like mercury selenide, is a zero-gap material (semimetal). The lowest conduction band minimum and the top of the valence band are degenerate at the center of the Brillouin zone ($\Gamma_8$). The $\Gamma_6$ level, which for most cubic semiconductors is the conduction band minimum and has an energy larger than that of the $\Gamma_8$ state, is found to be below the $\Gamma_8$ state in HgTe ("negativ energy gap", inverted band structure) (see Fig. 4.1-177).

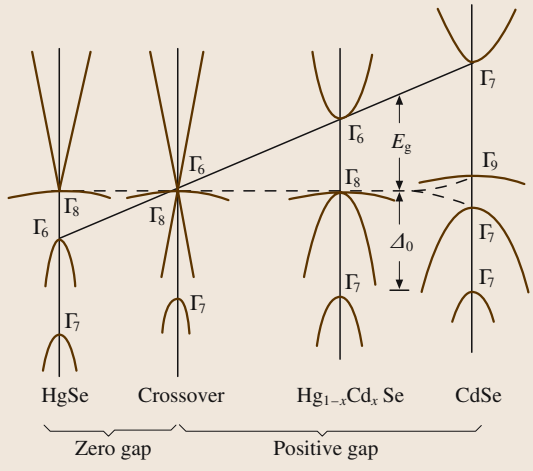


**Fig. 4.1-177** Schematic band structure of the Hg–Cd–Se system near the $\Gamma$ point [1.152]

**Table 4.1-179** First Brillouin zones of mercury compounds

| Crystal | | Figure |
|---|---|---|
| Mercury selenide | HgSe | Fig. 4.1-133 |
| Mercury telluride | HgTe | Fig. 4.1-133 |

**Table 4.1-180** Energy gaps of mercury compounds

| Crystal | | Band gap (eV) | Between bands | Temperature (K) | Remarks |
|---|---|---|---|---|---|
| Mercury oxide | HgO | 2.19<br>2.80 | | | Photoconductivity |
| Mercury sulfide | HgS | 2.03 | | 300 | Absorption |
| Mercury selenide | HgSe | −0.274<br>−0.061 | $\Gamma_{8v}$ and $\Gamma_{6c}$<br>$\Gamma_{8v}$ and $\Gamma_{6c}$ | 4.2<br>300 | Shubnikov–de Haas effect |
| Mercury telluride | HgTe | −0.304<br>−0.141 (13) | $\Gamma_{8v}$ and $\Gamma_{6c}$<br>$\Gamma_{8v}$ and $\Gamma_{6c}$ | 0<br>300 | Extrapolated optical and magneto-optical data |

**Table 4.1-181** Spin–orbit splitting energies $\Delta_{so}$ of mercury compounds

| Crystal | | Splitting energy (eV) | Bands | Temperature (K) | Remarks |
|---|---|---|---|---|---|
| Mercury selenide | HgSe | 0.383 (2) | $\Gamma_{8v}$ to $\Gamma_{7v}$ | 4.2 | Interband magnetoabsorption |
| | | 0.45 | $\Gamma_{15v}$ | 12 | Reflectivity |
| Mercury telluride | HgTe | 1.08 (2) | $\Gamma_{7v}$ to $\Gamma_{8c}$ | 300 | Electroreflectance |

**Table 4.1-182** Effective masses of electrons (in units of the electron mass $m_0$) for mercury compounds

| Crystal | | Quantity | Band | Mass | Temperature (K) | Remarks |
|---|---|---|---|---|---|---|
| Mercury selenide | HgSe | $m_n$ | | | | Strongly dependent on electron concentration |
| Mercury telluride | HgTe | $m_n$ | $\Gamma_8$ | 0.031 (1) | 4.4 | Interband magnetoabsorption |

**Table 4.1-183** Effective masses of holes (in units of the electron mass $m_0$) for mercury compounds

| Crystal | | Quantity | Band | Mass | Temperature (K) | Remarks |
|---|---|---|---|---|---|---|
| Mercury selenide | HgSe | $m_p$ | | 0.78 | | |
| Mercury telluride | HgTe | $m_p$ [100] | $\Gamma_8$ | 0.320 | 4.2 | Interband magnetoreflection |
| | | $m_p$ [110] | | 0.406 | | |
| | | $m_p$ [111] | | 0.445 | | |
| | | $m_p$ | $\Gamma_6$ | 0.3 | 4–100 | Transport measurements |
| | | | | 0.028 (1) | 4.4 | Interband magnetoabsorption |

### C. Transport Properties

Tables 4.1-184 and 4.1-185. See Fig. 4.1-179 for the thermal conductivity of mercury telluride.

**Table 4.1-184** Electronic transport, general description

**Mercury sulfide (HgS)**

In natural red cinnabar crystals ($\alpha$-HgS), carrier concentrations $n = 10^{10}$–$10^{12}\,cm^{-3}$ are found; in synthetic crystals, the values range from $10^{11}$ to $10^{12}\,cm^{-3}$. The observed values of the resistivity $\rho$ are: parallel to the $c$ axis, 6400 Ω cm at 77 K, and perpendicular to the $c$ axis, 3450 Ω cm at 300 K, both values being obtainded from natural crystals.

**Mercury selenide (HgSe)**

All HgSe samples show n-type conductivity. As-grown crystals have carrier concentrations of about $10^{17}$ electrons/$cm^3$.

**Mercury telluride (HgTe)**

See Fig. 4.1-178 for the temperature dependence of the electrical conductivity.

**Table 4.1-185** Electron mobilities $\mu_n$ of mercury compounds

| Crystal | | $\mu_n$ ($cm^2/V\,s$) | | Temperature (K) | Remarks |
|---|---|---|---|---|---|
| Mercury sulfide | HgS | $\mu_{parall}$ | 157 | 77 | Natural crystal, maximum values |
| | | | 30 | 300 | |
| | | $\mu_{perpend}$ | 49 | 77 | |
| | | | 10 | 300 | |
| Mercury selenide | HgSe | | $15\times10^3$ | 300 | All HgSe samples show n-type conductivity |
| | | | $55\times10^3$ | 95 | |
| Mercury telluride | HgTe | | $35\times10^3$ | 300 | Maximum mobility values |
| | | | $120\times10^3$ | 77 | |
| | | | $800\times10^3$ | 4.2 | |

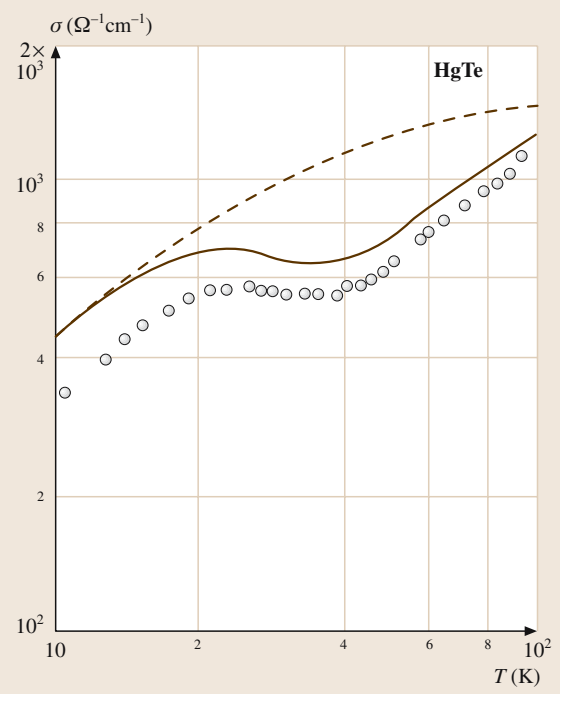


**Fig. 4.1-178** HgTe. Electrical conductivity vs. temperature. Experimental data (*circles*), in comparison with calculated curves assuming mixed scattering modes (*solid line*) and neglecting interband optical-phonon scattering (*broken line*) [1.153]

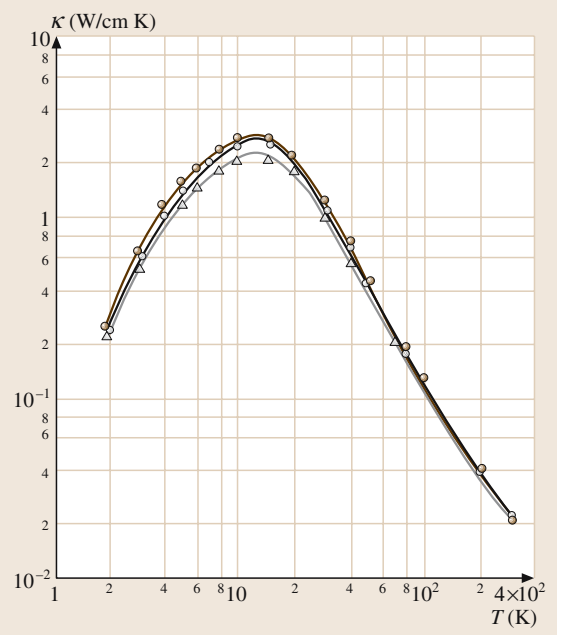


**Fig. 4.1-179** HgTe. Thermal conductivity vs. temperature for three different samples; the *solid lines* represent theoretical fits [1.154]

### D. Electromagnetic and Optical Properties

Tables 4.1-186 and 4.1-187.

**Table 4.1-186** Dielectric constant $\varepsilon$ of mercury compounds

| Crystal | | $\varepsilon(0)$ | | $\varepsilon(\infty)$ | | Temperature (K) | Remarks |
|---|---|---|---|---|---|---|---|
| Mercury sulfide | HgS | $\varepsilon(0)_{\text{perpend}}$ | 16.85 | $\varepsilon(\infty)_{\text{perpend}}$ | 5.38 | 80 | Synthetic crystal |
| | | | 18.2 | | 6.25 | 300 | |
| | | $\varepsilon(0)_{\text{parall}}$ | 21.5 | $\varepsilon(\infty)_{\text{parall}}$ | 7.4 | 80 | |
| | | | 23.5 | | 7.9 | 300 | |
| Mercury selenide | HgSe | | 25.6 | | 12–21 | | Reflectivity and Kramers–Kronig analysis of fits to data on plasmon–LO-phonon coupled mode |
| Mercury telluride | HgTe | | 21.0 | | 15.2 | 77 | Reflectance |

**Table 4.1-187** Refractive indices $n$ of mercury compounds

| Crystal | | Refractive index $n$ | | λ (nm) | Temperature (K) |
|---|---|---|---|---|---|
| Mercury oxide | HgO | | 2.5 | 550 | |
| Mercury sulfide | HgS | $n_o$ | 2.9028 | 620 | 298 |
| | | $n_e$ | 3.2560 | | |

## References


1.1 O. Madelung, U. Rössler, M. Schulz (Eds.): *Semiconductors*, Landolt–Börnstein, New Series III/41 (Springer, Berlin, Heidelberg 1998 – 2003)
1.2 O. Madelung (Ed.): *Semiconductors: Data Handbook*, 3rd edn. (Springer, Berlin, Heidelberg 2004)
1.3 E. R. Johnson, S. M. Christian: Phys. Rev. **95**, 560 (1954)
1.4 B. J. Skinner: Am. Mineral. **42**, 39 (1957)
1.5 G. A. Slack, S. F. Bartram: J. Appl. Phys. **46**, 89 (1975)
1.6 R. O. A. Hall: Acta Crystallogr. **14**, 1004 (1961)
1.7 H. P. Singh: Acta Crystallogr. **24a**, 469 (1968)
1.8 A. Taylor, R. M. Jones: *Silicon Carbide – A High Temperature Semiconductor*, ed. by J. R. O'Connor, J. Smiltens (Pergamon, Oxford 1960)
1.9 K. G. Lyon, G. L. Salinger, C. A. Swenson, G. K. White: J. Appl. Phys. **48**, 865 (1977)
1.10 Y. Okada, Y. Tokumaru: J. Appl. Phys. **56**, 314 (1984)
1.11 H.-M. Kagaya, T. Soma: Phys. Status Solidi (b) **127**, K5 (1985)
1.12 S. I. Novikova: Sov. Phys. Solid State (English Transl.) **2**, 2087 (1961)
1.13 S. I. Novikova: Fiz. Tverd. Tela **2** (1960)
1.14 A. C. Victor: J. Chem. Phys. **36**, 1903 (1962)
1.15 J. L. Warren, J. L. Yarnell, G. Dolling, R. A. Cowley: Phys. Rev. **158**, 805 (1967)
1.16 P. Giannozzi, S. de Gironcoli, P. Pavone, S. Baroni: Phys. Rev. B **43**, 7231 (1991)
1.17 G. Dolling: *Inelastic Scattering of Neutrons in Solids and Liquids*, Vol. 11 (International Atomic Energy Agency, Vienna 1963) p. 37
1.18 G. Nilsson, G. Nelin: Phys. Rev. B **6**, 3777 (1972)
1.19 G. Nilsson, G. Nelin: Phys. Rev. B **3**, 364 (1971)
1.20 P. Pavone, R. Bauer, K. Karch, O. Schütt, S. Vent, W. Windl, D. Strauch, S. Baroni, S. de Gironcoli: Physica B **219 & 220**, 439 (1996)
1.21 D. L. Price, J. M. Rowe, R. M. Nicklow: Phys. Rev. B **3**, 1268 (1971)
1.22 M. Hofmann, A. Zywietz, K. Karch, F. Bechstedt: Phys. Rev. B **50**, 13401 (1994)
1.23 F. J. Morin, J. P. Maita: Phys. Rev. **96**, 28 (1954)
1.24 F. J. Morin, J. P. Maita: Phys. Rev. **94**, 1525 (1954)
1.25 A. Suzuki, A. Uemoto, M. Shigeta, K. Furukawa, S. Nakajima: Appl. Phys. Lett. **49**, 450 (1986)
1.26 G. Busch, O. Vogt: Helv. Phys. Acta **33**, 437 (1960)
1.27 F. Nava, C. Canali, C. Jacoboni, L. Reggiani: Solid State Commun. **33**, 475 (1980)

1.28 A. G. Redfield: Phys. Rev. **94**, 526 (1954)
1.29 E. A. Konorova, S. A. Shevchenko: Sov. Phys. Semicond. (English Transl.) **1**, 299 (1967)
1.30 E. A. Konorova, S. A. Shevchenko: Fiz. Tekh. Poluprovodn. **1**, 364 (1967)
1.31 L. Reggiani, S. Bosi, C. Canali, F. Nava: Phys. Rev. B **23**, 3050 (1981)
1.32 P. J. Dean, E. C. Lightowlers, D. R. Wright: Phys. Rev. A **140**, 352 (1965)
1.33 L. Reggiani, D. Waechter, S. Zukotynski: Phys. Rev. B **28**, 3550 (1983)
1.34 C. Jacoboni, C. Canali, G. Ottaviani, A. Alberigi Quaranta: Solid State Electron. **20**, 77 (1977)
1.35 C. Canali, C. Jacoboni, F. Nava, G. Ottaviani, A. Alberigi Quaranta: Phys. Rev. B **12**, 2265 (1975)
1.36 P. Norton, T. Braggins, H. Levinstein: Phys. Rev. B **8**, 5632 (1973)
1.37 W. C. Mitchel, P. M. Hemenger: J. Appl. Phys. **53**, 6880 (1982)
1.38 F. J. Morin: Phys. Rev. **93**, 62 (1954)
1.39 R. Berman, M. Martinez: Diamond Res. (Suppl. Ind. Diamond, Rev.) **7** (1976)
1.40 C. J. Glassbrenner, G. A. Slack: Phys. Rev. **134**, A1058 (1964)
1.41 W. Fulkerson, J. P. Moore, R. K. Williams, R. S. Graves, D.L. McElroy: Phys. Rev. **167**, 765 (1968)
1.42 H. R. Shanks, P. D. Maycock, P. H. Sidles, G. C. Danielson: Phys. Rev. **130**, 1743 (1963)
1.43 Y. P. Joshi, G. S. Verma: Phys. Rev. B **1**, 750 (1970)
1.44 G. A. Slack: J. Appl. Phys. **35**, 3460 (1964)
1.45 S. R. Bakhchieva, N. P. Kekelidse, M. G. Kekua: Phys. Status Solidi (a) **83**, 139 (1984)
1.46 T. Hanyu: J. Phys. Soc. Jpn. **31**, 1738 (1971)
1.47 D. E. Aspnes, A. A. Studna: Phys. Rev. B **27**, 985 (1983)
1.48 S. Klotz, J. M. Besson, M. Braden, K. Karch, F. Bechstedt, D. Strauch, P. Pavone: Phys. Status Solidi (b) **198**, 105 (1996)
1.49 H. W. Icenogle, B. C. Platt, W. L. Wolfe: Appl. Opt. **15**, 2348 (1976)
1.50 V. L. Solozhenko: *Properties of Group III Nitrides*, ed. by J. H. Edgar (Inspec, London 1994) Chap. 2.1, p. 43
1.51 Y. Kumashiro: J. Mater. Res. **5**, 2933 (1990)
1.52 I. S. Ham, V. M. Davidenko, V. G. Sidorov, L. I. Fel'dgun, M. D. Skagalov, Y. K. Shalabutov: Sov. Phys. Semicond. (English Transl.) **10**, 331 (1976)
1.53 I. S. Ham, V. M. Davidenko, V. G. Sidorov, L. I. Fel'dgun, M. D. Skagalov, Y. K. Shalabutov: Fiz. Tekh. Poluprov. **10**, 554 (1976)
1.54 L. G. Carpenter, P. J. Kirby: J. Phys. D **15**, 1143 (1982)
1.55 Y. Kumashiro, M. Hirabayashi, T. Kosiro: J. Less-Common Metals **143**, 159 (1988)
1.56 S. I. Novikova, N. Kh. Abrikhosov: Sov. Phys. Solid State (English Transl.) **5**, 1558 (1963)
1.57 S. I. Novikova, N. Kh. Abrikhosov: Fiz. Tverd. Tela **5**, 2138 (1963)
1.58 J. C. Nipko, C. K. Loong: Phys. Rev. B **57**, 10550 (1998)
1.59 C. K. Loong: Gallium nitride and related materials, MRS Symposia Proceedings No. 395, ed. by F. A. Ponce, R. D. Dupuis, S. Nakamura, J. A. Edmond (Materials Research Society, Pittsburgh 1996) 423
1.60 T. Pletl, P. Pavone, U. Engel, D. Strauch: Physics B **263/264**, 392 (1999)
1.61 A. Onton: Proceedings of the 10th International Conference on the Physics of Semiconductors, Cambridge 1970 (USAEC, Oak Ridge 1970) 107
1.62 B. Monemar: Phys. Rev. B **8**, 5711 (1973)
1.63 D. Strauch, B. Dorner, K. Karch: *Phonons 89*, ed. by S. Hunklinger, W. Ludwig, G. Weiss (World Scientific, Singapore 1990) p. 82
1.64 A. Kobayashi, O. F. Sankey, S. M. Volz, J. D. Dow: Phys. Rev. B **28**, 935 (1983)
1.65 M. Huang, W. Y. J. Ching: Phys. Chem. Solids **46**, 977 (1985)
1.66 H. G. Grimmeiss, W. Kischio, A. Rabenau: J. Phys. Chem. Solids **16**, 302 (1960)
1.67 H. Welker: Z. Naturforsch. **5a**, 248 (1953)
1.68 G. A. Slack: J. Phys. Chem. Solids **34**, 321 (1973)
1.69 V. M. Muzhdaba, A. Ya. Nashel'skii, P. V. Tamarin, S. S. Shalyt: Sov. Phys. Solid State (English Transl.) **10**, 2265 (1969)
1.70 V. M. Muzhdaba, A. Ya. Nashel'skii, P. V. Tamarin, S. S. Shalyt: Fiz. Tverd. Tela **10**, 2866 (1968)
1.71 J. Pastrnak, L. Roskovcova: Phys. Status Solidi **14**, K5 (1966)
1.72 B. Monemar: Solid State Commun. **8**, 1295 (1970)
1.73 S. Adachi: *GaAs and Related Materials: Bulk Semiconducting and Superlattice Properties* (World Scientific, Singapore 1994)
1.74 W. J. Turner, W. E. Reese: Phys. Rev. **127**, 126 (1962)
1.75 A. U. Sheleg, V. A. Savastenko: Vesti Akad. Nauk BSSR, Ser. Fiz. Mat. Nauk **3**, 126 (1976)
1.76 T. Soma: Solid State Commun. **34**, 375 (1980)
1.77 A. Debernardi, M. Cardona: Phys. Rev. B **54**, 11305 (1996)
1.78 T. Azuhata, T. Matsunaga, K. Shimada, K. Yoshida, T. Sota, K. Suzuki, S. Nakamura: Physica B **219 & 220**, 493 (1996)
1.79 V. Yu. Davydov, Yu. E. Kitaev, I. N. Goncharuk, A. N. Smirnov, J. Graul, O. Semchinova, D. Uffmann, M. B. Smirnov, A. P. Mirgorodsky, R. A. Evarestov: Phys. Rev. B **58**, 12899 (1998)
1.80 J. L. Yarnell, J. L. Warren, R. G. Wenzel, P. J. Dean: *Neutron Inelastic Scattering* (International Atomic Energy Agency, Vienna 1968) p. 301
1.81 P. H. Borcherds, K. Kunc, G. F. Alfrey, R. L. Hall: J. Phys. C: Solid State Phys. **12**, 4699 (1979)
1.82 C. Eckl, P. Pavone, J. Fritsch, U. Schröder: *The Physics of Semiconductors*, Vol. 1, ed. by M. Scheffler, R. Zimmermann (World Scientific, Singapore 1996) p. 229
1.83 D. Strauch, B. Dorner: J. Phys. Condens. Matter **2**, 1457 (1990)
1.84 M. K. Farr, J. G. Traylor, S. K. Sinha: Phys. Rev. B **11**, 1587 (1975)
1.85 M. Ilegems, H. C. Montgomery: J. Phys. Chem. Solids **34**, 885 (1972)
1.86 Y. C. Kao, O. Eknoyan: J. Appl. Phys. **54**, 2468 (1983)

1.87 J. S. Blakemore: J. Appl. Phys. **53**, R123 (1982)
1.88 R. A. Stradling, R. A. Wood: J. Phys. C **3**, L94 (1970)
1.89 M. H. Kim, S. S. Bose, B. J. Skromme, B. Lee, G. E. Stillman: J. Electron. Mater. **20**, 671 (1991)
1.90 E. K. Sichel, J. I. Pankove: J. Phys. Chem. Solids **38**, 330 (1977)
1.91 M. G. Holland: Proc. 7th Int. Conf. Phys. Semiconductors, Paris 1964 (Dunod, Paris 1964) 1161
1.92 M. G. Holland: Proc. Int. Conf. Phys. Semiconductors, Paris 1964 (Dunod, Paris 1964) 713
1.93 E. Ejder: Phys. Status Solidi (a) **6**, K39 (1971)
1.94 B. Clerjaud, C. Naud, B. Deveaud, B. Lambert, B. Plot, C. Bremond, C. Benjeddou, G. Guillot, A. Nouailhat: J. Appl. Phys. **58**, 4207 (1985)
1.95 G. A. Samara: Phys. Rev. B **27**, 3494 (1983)
1.96 K. Haruna, H. Maeta, K. Ohashi, T. Koike: J. Phys. C: Solid State Phys. **20**, 5275 (1987)
1.97 P. W. Sparks, C. A. Swenson: Phys. Rev. **163**, 779 (1967)
1.98 D. F. Gibbons: Phys. Rev. **112**, 779 (1958)
1.99 P. H. Borcherds, G. F. Alfrey, D. H. Saunderson, A. D. B. Woods: J. Phys. C **8**, 2022 (1975)
1.100 A. Mooradian, G. B. Wright: Solid State Commun. **4**, 431 (1966)
1.101 J. Fritsch, P. Pavone, U. Schröder: Phys. Rev. B **52**, 11326 (1995)
1.102 N. S. Orlova: Phys. Status Solidi (b) **119**, 541 (1983)
1.103 R. Carles, N. Saint-Cricq, J. B. Renucci, M. A. Renucci, A. Zwick: Phys. Rev. B **22**, 4804 (1980)
1.104 W. J. Turner, W. E. Reese, G. D. Pettit: Phys. Rev. **136**, A1467 (1964)
1.105 Y. J. Jung, B. H. Kim, H. J. Lee, J. C. Wolley: Phys. Rev. **26**, 3151 (1982)
1.106 S. Logothetidis, L. Vina, M. Cardona: Phys. Rev. B **31**, 947 (1985)
1.107 O. G. Folberth, O. Madelung, H. Weiss: Z. Naturforsch. **9a**, 954 (1954)
1.108 O. Madelung, H. Weiss: Z. Naturforsch. **9a**, 527 (1954)
1.109 T. L. Tansley, C. P. Foley: Electron. Lett. **20**, 1087 (1984)
1.110 W. Walukiewicz, J. Lagowski, L. Jastrzebski, P. Rava, M. Lichtensteiger, C. H. Gatos, H.Ċ. Gatos: J. Appl. Phys. **51**, 2659 (1980)
1.111 J. D. Wiley: *Semiconductors and Semimetals*, Vol. 10, ed. by R. K. Willardson, A. C. Beer (Academic Press, New York 1975)
1.112 U. Busch, E. Steigmeier: Helv. Phys. Acta **34**, 1 (1961)
1.113 H. J. Hrostowski, F. J. Morin, T. H. Geballe, G. H. Wheatley: Phys. Rev. **100**, 1672 (1955)
1.114 N. I. Volokobinskaya, V. V. Galavanov, D. N. Nasledov: Sov. Phys. Solid State (English Transl.) **1**, 687 (1959)
1.115 N. I. Volokobinskaya, V. V. Galavanov, D. N. Nasledov: Fiz. Tverd. Tela **1**, 756 (1959)
1.116 D. L. Rode: Phys. Rev. **3**, 3287 (1971)
1.117 S. A. Aliev, A. Ya. Nashelskii, S. S. Shalyt: Sov. Phys. Solid State (English Transl.) **7**, 1287 (1965)
1.118 S. A. Aliev, A. Ya. Nashelskii, S. S. Shalyt: Fiz. Tverd. Tela **7**, 1590 (1965)
1.119 H. Katzman, J. Moss, W. F. Libby: J. Phys. Chem. Solids **32**, 2786 (1971)
1.120 K.-Oh Park, J. M. Sivertsen: J. Am. Ceram. Soc. **62**, 218 (1979)
1.121 G. K. White, O. L. Anderson: J. Appl. Phys. **37**, 430 (1966)
1.122 C. M. Osburn, R. W. Vest: J. Am. Ceram. Soc. **54**, 428 (1971)
1.123 D. S. Kupperman, H. Weinstock, Y. Chen: J. Low Temp. Phys. **14**, 277 (1974)
1.124 O. Kamada, T. Takizawa, T. Sakurai: Jpn. J. Appl. Phys. **10**, 485 (1971)
1.125 N. N. Kovalev, M. V. Krasin'kova: Sov. Phys. Solid State **16**, 1960 (1975)
1.126 R. R. Reeber, G. W. Powell: J. Appl. Phys. **38**, 1531 (1967)
1.127 R. Helbig, P. Wagner: J. Phys. Chem. Solids **35**, 327 (1974)
1.128 P. Wagner: Ph.D Thesis (Erlangen-Nürnberg 1978)
1.129 G. A. Slack: *Physics and Chemistry of II–VI Compounds*, ed. by M. Aven, J. S. Prener (1967) p. 557
1.130 K. Sato, S. Adachi: J. Appl. Phys. **73**, 926 (1993)
1.131 L. Ward: *Handbook Optical Constants Solids*, Vol. 2, ed. by E. D. Palik (Academic Press, New York 1991) p. 737
1.132 S. Ozaki, S. Adachi: Jpn. J. Appl. Phys. **32**, 5008 (1993)
1.133 T. B. Kobyakov, G. S. Pado: Sov. Phys. Solid State (English Transl.) **9**, 1707 (1968)
1.134 T. M. Bieniewski, S. J. Czyzak: J. Opt. Soc. Am. **53**, 496 (1963)
1.135 Q. Guo, M. Ikejira, M. Nishio, H. Ogawa: Solid State Commun. **100**, 813 (1996)
1.136 H. Yoshikawa, S. Adachi: Jpn. J. Appl. Phys. **36**, 6237 (1997)
1.137 Y. F. Tsay, S. S. Mitra, J. F. Vetelino: J. Phys. Chem. Solids **34**, 2167 (1973)
1.138 J. L. Birman, H. Samelson, A. Lempicki: G.T. & E. Res. Dev. J. **1**, 1 (1961)
1.139 M. Cardona, G. Harbeke: Phys. Rev. A **137**, 1467 (1965)
1.140 S. Adachi, T. Taguchi: Phys. Rev B **43**, 9569 (1991)
1.141 V. S. Oskotskii, I. B. Kobyakov, A. V. Solodukhin: Fiz. Tverd. Tela **22**, 1479 (1980)
1.142 V. S. Oskotskii, I. B. Kobyakov, A. V. Solodukhin: Sov. Phys. Solid State (English Transl.) **22**, 861 (1980)
1.143 K. C. Mills: High Temp. High Press. **4**, 371 (1972)
1.144 J. R. Chelikowsky, M. L. Cohen: Phys. Rev. B **14**, 556 (1976)
1.145 G. E. Moore, M. V. Klein: Phys. Rev. **179**, 722 (1969)
1.146 J. L. Beene, G. Contwell: J. Appl. Phys. **57**, 1171 (1985)
1.147 M. S. Kushwaha, S. S. Kushwaha: Can. J. Phys. **58**, 351 (1980)
1.148 A. J. Varkey, A. F. Fort: Thin Solid Films **239**, 211 (1994)
1.149 J. Oberlé, B. Kippelen, A. Daunois, J.-B. Grun: Opt. Commun. **90**, 339 (1992)
1.150 S. Ninomiya, S. Adachi: J. Appl. Phys. **78**, 4681 (1995)
1.151 D. Bagot, R. Granger, S. Rolland: Phys. Status Solidi (b) **177**, 295 (1993)

1.152 C. R. Whitsett, J. G. Broerman, C. J. Summers: *Semiconductors and Semimetals*, Vol. 16, ed. by R. K. Willardson, A. C. Beer (Academic Press, New York 1981) p. 54
1.153 J. J. Dubowski, T. Dietl, W. Szymanska, R. R. Galazka: J. Phys. Chem. Solids **42**, 351 (1981)
1.154 A. Noguera, S. M. Wasim: Phys. Rev. B **32**, 8046 (1985)

# 4.2. Superconductors




4.2.1 **Metallic Superconductors** ..... 696
4.2.1.1 Elements ..... 696
4.2.1.2 Practical Metallic Superconductors ..... 704

4.2.2 **Non-Metallic Superconductors** ..... 711
4.2.2.1 Oxide Superconductors ..... 711
4.2.2.2 Superconductors Based on the Y–Ba–Cu–O System ..... 720
4.2.2.3 Superconductors Based on the Bi–Sr–Ca–Cu–O System .. 736
4.2.2.4 Carbides, Borides, Nitrides ..... 744

**References** ..... 749


Superconductors are characterized by an anomalous temperature dependence of the electrical resistivity. Below a critical temperature $T_c$, their resistivity drops by more than a factor of $10^{10}$. In superconductors the magnetic flux density $B = \mu_r B_a$ induced by an externally applied field $H_a$ is zero, like in ideal diamagnets with $\mu_r = 0$ (Meißner–Ochsenfeld effect). If $H_a$ exceeds a critical value $H_c$ the superconductor becomes normal conducting. But the magnetic induction $B$ decreases from $B_a$ at the free surface to $B = 0$ in the interior through a layer of finite thickness characterized by the Landau penetration depth $\lambda$. The critical field varies with temperature as $H_c(T) = H_c(0)[1-(T/T_c)^2]$, where $H_c(0) = H_c(T = 0\,\mathrm{K})$. According to the isothermal field dependence of the magnetization $I(H_a) = -\mu_0 H_a$, two types of superconductors may be differentiated, as shown in Fig. 4.2-1:

- Type I superconductors such as Pb with a sudden drop of $-I$, at $H_c$; all pure metallic elements and their dilute solid solutions belong to this group;
- Type II superconductors such as Pb–In15 which are characterized by a lower critical field $H_{c1}$ at which the drop of $-I$ sets in and an upper critical field $H_{c2}$ at which $-I$ reaches 0.

In Type I superconductors, the transition from the fully superconducting to the fully normal conducting state as a function of the applied magnetic field $H_a$ passes through an intermediate, mixed state in which the total volume decomposes into lamellae in the superconducting and the normal conducting state. At their interface, the transition from the superconducting lamellae of the maximum density of electron pairs (Cooper pairs) $n_e$, which carry the superconducting current, to the normal conducting lamellae where $n_e = 0$ occurs through a transition layer characterized by the coherence length $\xi$. In terms of the microscopic theory of superconductivity, $\xi$ is the size of the Cooper pairs which is of the order of 1 μm in pure metals. The coherence length $\xi$ as well as the penetration depth $\lambda$ can be highly anisotropic in compounds with crystal structures of low symmetry, which is the case in low-$T_c$ oxide superconductors (see Sect. 4.2.2.1).

Since superconductivity is caused by electron–phonon interaction, the upper critical field $H_{c2}$ depends on the mean free path of the electrons, and thus on the electrical resistivity $\rho$ in the normal conducting state, and on the electronic specific heat $\gamma$ as

$$\mu_0 H_{c2}(0) = 3.11\,\rho\gamma T_c \,.$$

As both $\rho$ and $T_c$ are affected by impurities and structural defects, $H_{c2}$ depends not only on composition and structure but also on structural defects accordingly.

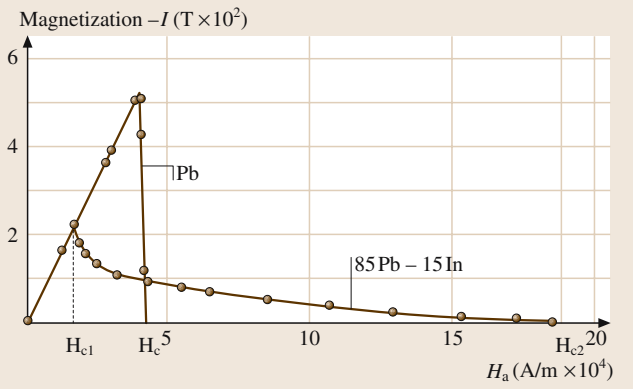


**Fig. 4.2-1** $-I(H_a)$ curves for pure Pb as a Type I and the Pb–In15 alloy as a Type II superconductor [2.1]

Type II superconductors in a magnetic field of intermediate strength $H_{c1} < H_a < H_{c2}$ are in a mixed state (Shubnikow phase) consisting of a superconducting matrix through which magnetic flux "lines" of finite thickness, also termed fluxoids or vortices are penetrating, each carrying a quantum of magnetic flux $\Phi = h/2e$. The movement of these flux lines may be pinned by point defects, dislocations, and interfaces due to various modes of interaction. Deliberate introduction of pinning defects is the basis of increasing the critical magnetic field such that the materials – termed non-ideal Type II, Type III or hard superconductors – can bear an increased critical external field and/or critical current at a given temperature. High-field superconducting materials are developed on this basis of microstructural design.

Practical superconductors are mainly applied to generate high magnetic fields in wound magnet coils. Accordingly they are produced as wires or cables. The materials used are based on non-ideal Type II superconductors with a specially optimized microstructure such that strong flux line pinning persists up to a high critical current density $J_c(T)$. A second field of application are superconducting electronic devices, most frequently based on the Josephson effect. The present practical superconductors for high field applications are highly complex composite materials, based essentially on two groups of superconducting alloy phases, the intermetallic phase $Nb_3Sn$ and the solid solution phase Nb−Ti. Recent developments have also led to high field oxide high-$T_c$ superconductors for practical applications in wire, electronic device, and massive form, the latter serving as high field permanent magnets.

Superconducting substances of fundamental as well as practical interest may be divided into 3 main groups which are dealt with in the subsequent sections:

- Metallic superconductors
- Superconducting oxides
- Superconducting carbides, nitrides and borides

An extensive listing of individual publications containing data of both metallic and non-metallic superconductors is given in [2.2]. An encyclopaedic survey of all essential aspects of superconductivity may be found in [2.3].

## 4.2.1 Metallic Superconductors

The basic superconducting properties of metals and alloys have been compiled comprehensively in [2.1, 2]. While the superconducting properties of all pure metals have been determined, the studies of alloys have been concentrated on those of the elements with the highest critical temperatures, i. e., Pb ($T_c = 7.2$ K), V ($T_c = 5.5$ K), Nb ($T_c = 9.3$ K), and Tc ($T_c = 7.7$ K).

### 4.2.1.1 Elements

Table 4.2-1 lists $T_c$ and $H_c$ of the superconducting metallic elements along with their relevant thermodynamic properties, the Debye temperature $\Theta_D$ and the Sommerfeld constant $\gamma$ which determines the electronic specific heat in the superconducting state $C_{p,el} = 9.17\,\gamma T_c \exp(-1.5T_c/T)$. Table 4.2-2 lists the pressure dependence of $T_c$.

#### Pb Alloys

Ready availability and easy alloy formation of Pb have led to extensive studies of superconductivity of Pb alloys results of which are given in Tables 4.2-3 and 4.2-4, and Figs. 4.2-1 and 4.2-2.

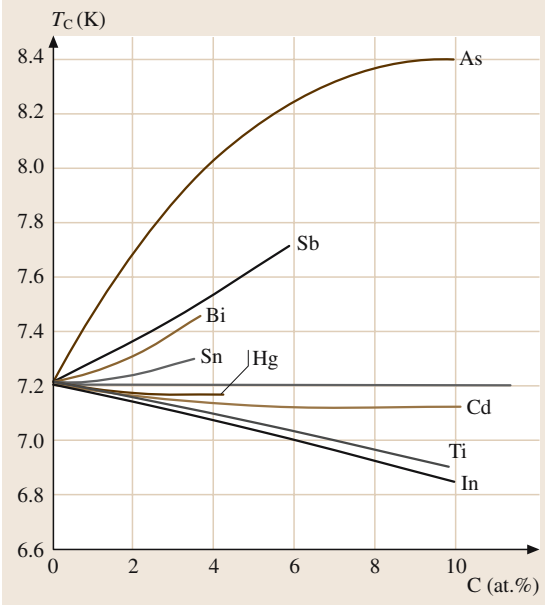


**Fig. 4.2-2** Composition dependence of $T_c$ in Pb solid solution alloys [2.1]

**Table 4.2-1** Superconducting properties of metallic elements [2.1]

| Element | Purity (%) | Residual resistivity ratio $\rho_{293\,K}/\rho_{4.2\,K}$ | $T_c$ (K) | $\mu_0 H_c$ (mT) | $\Theta_D$ (K) | $\gamma$ (mJ mol$^{-1}$ K$^{-2}$) |
|---|---|---|---|---|---|---|
| Al | | 2000–4100 | 1.175 | 10.49 | 420 | 1.35 |
| Am | | | 0.6 | | | |
| Be | 99.996 | | 0.026 | | 1390 | 0.21 |
| Cd | | >38 000 | 0.517 | 2.805 | 209 | 0.69 |
| Ga | | 46 500 | 1.0833 | 5.93 | 325 | 0.60 |
| Hf | | 80 | 0.128 | 1.27 | 256 | 2.21 |
| Hg | 99.9999 | | 4.154 | 41.1 | 87 | 1.81 |
| In | | 9000 | 3.4087 | 28.15 | 109 | 1.672 |
| Ir | | >2000 | 0.1125 | 1.6 | 425 | 3.19 |
| La | >99.9 | | 4.87 | 9.8 | 151 | 9.8 |
| Lu | | 15 | 0.1 | 35.0 | 210 | 10.2 |
| Mo | | 17 000 | 0.916 | 9.686 | 460 | 1.83 |
| Nb | | 500–16 500 | 9.25 | 206 | 276 | 7.80 |
| Os | | | 0.66 | 7.0 | 500 | 2.35 |
| Pa | | | 1.4 | | | |
| Pb | | 15 000 | 7.196 | 80.34 | 105 | 3.36 |
| Re | | 1700 | 1.697 | 20.1 | 415 | 2.35 |
| Ru | | | 0.493 | 6.9 | 580 | 2.8 |
| Sn | | | 3.722 | 30.55 | 195 | 1.78 |
| Ta | | 29–120 | 4.47 | 82.9 | 258 | 6.15 |
| Tc | | 80–100 | 7.77 | 141 | 411 | 6.28 |
| Th | | 1200 | 1.374 | 16.0 | 165 | 4.32 |
| Ti | >99.9 | | 0.40 | 5.6 | 415 | 3.3 |
| Tl | | 53 | 2.38 | 17.65 | 87.5 | 1.47 |
| V | | 24–430 | 5.46 | 140 | 383 | 9.82 |
| U | | | 0.68 | 10.0 | 206 | 10.60 |
| W | | 57 000 | 0.0154 | 0.115 | 383 | 0.90 |
| Zn | 99.9999 | | 0.857 | 5.41 | 310 | 0.66 |
| Zr | 99.9 | | 0.63 | 4.7 | 290 | 2.77 |

**Table 4.2-2** Pressure dependence of the superconductivity of metals [2.1]

| Metal | Pressure range[a] ($10^2$ MPa) | $T_c$ (K) | $T_{c(max)}/p$[a] (K $10^{-2}$ MPa$^{-1}$) | $\delta T_c/\delta p$ ($10^{-4}$ K MPa$^{-1}$) |
|---|---|---|---|---|
| Al | 0–62 | 2.1–1.7 | 2.1/0 | −4.5 |
| As I | <100 | <0.1 | | |
| As II | 100–140 | 0.2–0.25 | 0.25/100 | >0 |
| As III | 140–220 | 0.31–0.5 | 0.5/140 | <0 |
| Ba I | 0–55 | <1 | | |
| Ba II | 55–85 | 1–1.8 | 1.8/83 | 100 |
| Ba III | 85–144 | 1.8–5 | 5.0/100 | −15 |
| Ba IV | 144–192 | 4.5–5.4 | 5.4/175 | 1.3 |
| Bi II | 25–27 | ≦3.9 | 3.9/25 | <0 |

**Table 4.2-2** Pressure dependence of the superconductivity of metals [2.1], cont.

| Metal | Pressure range [a] ($10^2$ MPa) | $T_c$ (K) | $T_{c(max)}/p$ [a] (K $10^{-2}$ MPa$^{-1}$) | $\delta T_c/\delta p$ ($10^{-4}$ K MPa$^{-1}$) |
|---|---|---|---|---|
| Bi II′ | 25–30 | ≦8.2 | 8.2/30 | −3.2 |
| Bi III | 27–37 | 6.55–7.25 | 7.25/27 | −4.0 |
| Bi VI | 80–200 | ≦8.55 | 8.55/90 | −2.3 |
| Cd | 0–28 | ≦0.52 | 0.52/0 | <0 |
| Ce ($\alpha$) | 20–35 | 0.020–0.045 | 0.045/35 | >0 |
| Ce ($\alpha$)′ | 45–125 | 1.9–1.3 | 1.9/45 | <0 |
| Cs V | 125–150 | 1.5–1.6 | 1.6/125 | <0 |
| Ga II | 30–38 | 6.24–6.38 | 6.38/35 | −3 |
| Ga II′ | ≧ 35 | 7.5 | | |
| Ge | 115–120 | ≦ 5.35 | 5.35/115 | <0 |
| Hf | 0–160 | 0–0.25 | 0.25/160 | 0.06 |
| $\alpha$-Hg | >10 | 4.2–3.9 | 4.156/0 | −3.47 |
| $\beta$-Hg | >10 | 4.0–3.9 | 4.017/0 | −4.48 |
| $\alpha$-La | 0–23 | 4.9–8.2 | 8.2/23 | 14.1 |
| | 0–225 | 4.8–11.5 | 11.5/225 | |
| $\beta$-La | 23–250 | 5.5–12.9 | 12–12.9/140–200 | 11.3 |
| Lu | 45–190 | 0.024–1 | 1.0/180 | 1.2 |
| Nb | 0–24 | 7–9.2 | 9.214/0 | −0.25 |
| | 25–250 | 9.7 | 9.7/250 | 2.6 |
| P | 0–260 | 5.8–3.6 | 5.8/170 | <0 |
| Pb I | 0–110 | ≈7.2–4.2 | 7.2/0 | −4.9 |
| Pb II | 135–200 | 3.55–2.9 | 3.55/160 | −2.2 |
| Re<br>Re II | 0–20 | ≦1.7<br>≦2.3 | 1.7/0 | Minimum at 700 MPa |
| Sb | 0–120 | 2.6–2.7 | | |
| Sb III | 85–150 | 3.40–3.55 | 3.55/85 | <0 |
| Sb II | 0–130 | 6.75–6.95 | 6.95/130 | <0 |
| Si | 120–130 | 6.7–7.1 | 7.1/120 | <0 |
| Sn I | 0–113 | ≦3.7 | 3.7/0 | 0 |
| Sn II | 125–160 | 5.2–4.85 | 5.2/125 | −5.04 |
| Sn III | 113–270 | ≦5.3 | 5.3/113 | −4.95 |
| Ta | 0–250 | ≦4.3 | 4.3/0 | −0.26 |
| Tc | 0–15 | 8.0–7.8 | 8.0/15 | |
| Te II | 39–70 | 2.5–3.9 | 3.9/70 | 7.7–8.5 |
| Te III | 68–80 | 4.28–4.15 | 4.3/70 | −0.3–1.7 |
| Bi IV | 43–62 | 6–8.7 | 8.7/43 | −4.6 |
| Bi V | 68–81 | 6.7–8.3 | 6.7/81 | −3.0 |
| Te IV | 80–260 | 4.3–2.8 | 4.3/80 | −4.2 |
| Th | 0–170 | 1.4–0.64 | 1.4/0 | Minimum at 700 MPa |
| Ti | 0–25 | – | – | 0.06 |
| TI II | 0–35 | | 2.395/2 | −1.0 |
| TI III | 35–50 | | 1.45/35 (bcc) | −4.95 |

**Table 4.2-2** Pressure dependence of the superconductivity of metals [2.1], cont.

| Metal | Pressure range[a] ($10^2$ MPa) | $T_c$ (K) | $T_{c(max)}/p$[a] (K $10^{-2}$ MPa$^{-1}$) | $\delta T_c/\delta p$ ($10^{-4}$ K MPa$^{-1}$) |
|---|---|---|---|---|
| TI IV | 40–60 | | 2.32/40 (fcc) | −2.0 |
| $\alpha$-U | 10–85 | 2.4–0.4 | 2.4/10 | |
| $\beta$-U | 0–12 | | 1.15/95 | >0 |
| U | 90–160 | <0.35 | | |
| V | 0–250 | 5.5–7.15 | | 0.7 |
| Y | 110–170 | 2.7–1.7 | 2.7/160 | 3.7 |
| Zn | 0–26 | ≦0.87 | 0.87/0 | <0 |
| $\alpha$-Zr | 0–45 | | 0.69/45 | 0.35–0.8 |
| $\omega$-Zr | 60–130 | 1.7 | 1.17/130 | 0.77 |

[a] 0 = ambient pressure

**Table 4.2-3** Critical temperature of superconductivity of binary Pb compounds [2.1]

| Compound | Crystal structure | $T_c$ (K) | Compound | Crystal structure | $T_c$ (K) |
|---|---|---|---|---|---|
| PbLi[a] | Cub. B2 | 7.2 | $Pb_3Th$ | Cub. | 5.5 |
| $Pb_3Na$[a] | Cub. | 5.62 | $PbZr_3$ | Cub. A15 | 0.76 |
| $PbMg_2$ | C1 | 5.6 | $PbZr_5$ | Hex. $D8_8$ | 4.6 |
| $Pb_3Ca$ | Cub. $L1_2$ | 0.84 | $PbV_3$[c] | Cub. A15 | <4.2 |
| $Pb_3Sr$ | Tetr. $L1_2$[b] | 1.85 | $PbNb_3$[c] | Cub. A15 | 9.6 |
| $Pb_3Y$ | Cub. $L1_2$ | 4.72 | $PbTa_3$[c] | Cub. A15 | 17 |
| $Pb_3La_5$ | | <4.2[b] | $PbRh_2$ | | <0.32 |
| $Pb_3La_4$ | | <4.2 | $Pb_2Rh$[a] | Tetr. C16 | 2.66–1.32 |
| $Pb_4La_5$ | | <4.2 | $PbPd_3$ | Cub. $L1_2$ | <0.10 |
| $Pb_{10}La_{11}$ | | <4.2 | $Pb_2Pd$ | Tetr. C16 | 3.01–2.95 |
| $Pb_4La_3$ | | <4.2 | $Pb_4Pt$ | Tetr. C16 | 2.80 |
| $Pb_2La$ | | <4.2 | $PbAu_2$ | C15 | 1.18 |
| $Pb_3La$ | Cub. $L1_2$ | 4.10–4.05 | $Pb_2Au$ | Tetr. C16 | 3.15 |
| $PbSm_3$ | | <4.2 | $Pb_3Au$ | | 4.4 |
| $Pb_3Sm_5$ | | <4.2 | $PbIn_3(\alpha)$ | Hex. | 6.05–5.65 |
| $Pb_4Sm_5$ | | <4.2 | $Pb_2Bi(\epsilon)$[a] | $A3_3$ | 8.2–8.5 |
| $Pb_{10}Sm_{11}$ | | <4.2 | $PbO_2$ | | <1.02 |
| $Pb_2Sm$ | | 6.7 | PbS | B1 | <1.0 |
| $Pb_3Sm$ | Cub. $L1_2$ | <4.2 | PbSe | B1 | <1.26 |
| $Pb_3Yb$ | Cub. $L1_2$ | 0.23 | PbP | | 7.8 |

[a] Compound has a range of homogeneity

[b] No superconductivity is observed above 4.2 K

[c] Compound is formed under high pressure and high temperature

**Table 4.2-4** Critical magnetic field $\mu_0 H_{c2}$ of binary Pb alloys

| Material [a] | $\mu_0 H_{c2}$ (mT) | Temperature (K) |
|---|---|---|
| Pb–1.6–8.6% Na | 205–600 | 4.2 |
| Pb–3–5% Ag | 82 | 0 [b] |
| Pb–~ 25% Cd | 135 | 0 |
| Pb–5–15% Hg | 230–> 900 | 4.2 |
| Pb–2–30% In | 98–390 | 4.2 |
| Pb–14% Sn | 100 | |
| Pb–12.9–64% Sn | 110–204 | 1.3 |
| Pb–30% Tl | 280 | 4.2 |
| Pb–0.8–40% Tl | 70–290 | 4.2 |
| Pb–2–50% Bi | 73–190 | 4.2 |
| Pb–30% Bi(ε) | 3500 | 0 |
| Pb–30–45 nm [c] | 2200 | 4.2 |
| 200–700 nm [c] | 80–110 | 4.2 |
| Pb pore diameter 3.2–5.8 nm [d] | 5500–9600 | 0 |
| Pb–25% Bi, 126 nm [c] | 14 500 | 4.2 |
| Pb–40% Bi, 2–5 nm [d] | 12 500–11 300 | 4.2 |

[a] At.%
[b] Extrapolated to 0 K
[c] Layer thickness
[d] Particle diameter in porous glass

### V Alloys

Table 4.2-5 and Fig. 4.2-3 contain $T_c$ data of binary V alloys. Even though $V_3Ga$ with its cubic A15 structure has a $T_c \leq 16.8$ K and was, therefore, studied extensively, it has never been considered as a practical superconducting material seriously because of the cost and difficulties of handling of Ga.

**Table 4.2-5** Critical temperature $T_c$ of superconductivity of V compounds [2.1]

| Compound | Crystal structure | $T_c$ (K) | Compound | Crystal structure | $T_c$ (K) |
|---|---|---|---|---|---|
| $V_3Al$ [a] | Cub. A15 [b] | 9.6–11.65 | $V_2O_5$ | Rhomb. | <4.2 |
| $V_5Al_8$ [a] | Cub. $D8_2$ | <1.2 [c] | $V_3Os_2$ [a] | Cub. B2 | <0.37 |
| $VAl_3$ | Tetr. $D0_{22}$ | <4.2 | VOs [a] | Cub. A15 | 5.7–3.0 |
| $V_4Al_{23}$ | Hex. | <4.2 | $V_3P$ | Tetr. | 0.07 |
| $V_7Al_{45}$ | Monocl. | <4.2 | VP [a] | Hex. $B8_1$ | <1.02 |
| $VAl_{11}$ [a] | Fcc | <4.2 | $VP_2$ | Monocl. | <0.035 |
| $V_3As$ [a] | Cub. A15 | <1.0 | $V_3Pb$ [a] | Cub. A15 [a] | <4.2 |
| VAs [a] | Rhomb. | <1.0 | $V_3Pd$ [a] | Cub. A15 | 0.082 |
| $VAs_2$ | Monocl. | <0.33 | VPd | Tetr. | – [e] |
| $V_3Au$ | Cub. A15 | 3.22–0.015 | $VPd_2$ | Tetr. | – |
| $VAu_2$ [a] | Rhomb. | <1.2 | $VPd_3$ | Tetr. | – |
| $VAu_4$ | Tetr. | <1.2 | $V_3Pt$ [a] | Cub. A15 | 3.62–0.98 |
| $V_3B_2$ | Tetr. | <0.1 | VPt [a] | Cub. $L1_0$ | – |
| VB | Rhomb. $B_f$ | 1.2 | $VPt_2$ [a] | Tetr. | 1.02 |

**Table 4.2-5** Critical temperature $T_c$ of superconductivity of V compounds [2.1], cont.

| Compound | Crystal structure | $T_c$ (K) | Compound | Crystal structure | $T_c$ (K) |
|---|---|---|---|---|---|
| $V_3B$ | Rhomb. | <4.2 | $VPt_3$ | Tetr. [h] | 0.07 |
| $VB_2$ [a] | Hex. C32 | <1.2 | | Cub. $L1_2$ [i] | 0.07 |
| $V_2B_5$ [b] | Hex. | – [e] | $V_3Re_7$ | Cub. A15 | 8.4–7.6 |
| $VBe_2$ | Hex. C14 | <4.2 | $VRe_3$ [a] | Tetr. $D8_b$ | 6.26–4.52 |
| $VBe_{12}$ | Tetr. | – | $V_3Rh$ [a] | Cub. A15 | 1.075 [g] – < 0.015 |
| $V_3Bi$ | Cub. A15 [b] | <4.2 | | | |
| $V_2C$ [a] | Hex. | <1.2 | $VRh$ [a] ($\alpha_1$) | – | – |
| $V_2C_3$ [a] | Fcc | – | $VRh$ [a] ($\alpha_2$) | Tetr. $L1_0$ | – |
| VC [a] | Cub. B1 | <0.03 | $VRh$ [a] ($\alpha_3$) | Rhomb. | – |
| $V_3Cd$ [a] | Cub. A15 [b] | <4.2 | $V_3Rh_5$ [a] | Rhomb. | – |
| $V_3Co$ [a] | Cub. A15 | 0.015 | $VRh_3$ [a] | Cub. $L1_2$ | 1.2 |
| VCo | Tetr. $D8_b$ | <4.2 | VRu | Cub. B2 | 5 [g] – < 0.14 |
| $VCo_3$ [a] | Hex. | <4.2 | $V_3S$ | Tetr. | <1.15 |
| VFe [a] | Tetr. $D8_b$ | <0.3 | $V_5S_4$ | Tetr. | <4.2 |
| VFe | Cub. B2 [b] | <4.2 | VS [a] | Hex. $B8_1$ | <4.2 |
| $V_3Ga$ [a] | Cub. A15 | 16.8–14.2 | $V_2Sb_3$ [a] | Hex. | <4.2 |
| $V_5Ga_3$ | Hex. $D8_8$ [f] | <4.2 | $V_3Sb$ | Cub. A15 | 0.80 |
| $V_6Ga_5$ | Hex. | <4.2 | $V_5Sb_4$ | Tetr. | <4.2 |
| $V_6Ga_7$ [a] | Cub. $D8_2$ | 4.2 | VSb | Hex. $B8_1$ | <4.2 |
| $V_2Ga_5$ | Tetr. | 2.1–4.07 | $VSb_2$ | Tetr. C16 | <0.06 |
| $VGa_4$ | Tetr. | <4.2 | $V_5Se_4$ | Tetr. | – |
| $V_3Ge$ [a] | Cub. A15 | 6.3–5.88 (7.5–11.2) [b] | VSe [a] | Hex. $B8_1$ | – |
| $V_5Ge_3$ [a] | Tetr. T1 | <4.2 | $V_2Se_3$ | Low | – |
| | Hex. $D8_8$ [f] | <1.02 | | Sym. | |
| | | | $V_3Si$ [a] | Cub. A15 | 17.2–17 |
| | | | | | |
| $V_{11}Ge_8$ | Rhomb. | <1.2 | $V_5Si_3$ | Tetr. T1 | <0.30 |
| $V_{17}Ge_{31}$ | Tetr. | <1.2 | $V_5Si_3$ | Hex. $D8_8$ [f] | <0.30 |
| $V_2H$ [a] | Tetr. $L_{2b}$ | <1.02 | $V_5Si_4$ | Tetr. | <1.2 |
| VH | Cub. | <4.2 | $VSi_2$ | Hex. C40 | <1.2 |
| $V_2Hf$ [a] | Cub. C15 | 9.4–9.0 | $V_3Sn$ [a] | Cub. A15 | 7.0–3.8 |
| $V_3In$ [a] | Cub. A15 [b] | 13.9 | | | (12.3–17.9) [b] |
| $V_3Ir$ [a] | Cub. A15 | 1.71 [g] – < 0.015 | $V_2Sn_3$ | Rhomb. | <1.15 |
| | | | $V_2Ta$ [a] | Hex. C14 [i] | 10.0 |
| VIr($\alpha$) [a] | Rhomb. | <1.6 | VTc [a] | Cub. C15 [h] | 3.6 |
| $\beta-V_{1-x}Ir_{1+x}$ | Tetr. $L1_0$ | <1.36 | | Cub. B2 | <1.39 |
| $VIr_3$ [a] | Cub. $L1_2$ | <4.2 | $V_2Tc_3$ [a] | – | – |
| $VMn_4$ | Tetr. $D8_b$ | <4.2 | $VTc_3$ [a] | Cub. | 7.8–4.0 |
| $V_3N$ [a] | Hex. | <1.2 | $V_4Te$ [a] | – | – |
| VN | Cub. B1 | 8.5–7.5 | VTe [a] | Hex. $B8_1$ | – |
| $V_3Ni$ [a] | Cub. A15 | <0.35 | $VTe_3$ | Monocl. | <1.13 |
| $V_2Ni_3$ [a] | Tetr. $D8_b$ | <4.2 | $VTe_2$ | Monocl. | <0.05 |

**Table 4.2-5** Critical temperature $T_c$ of superconductivity of V compounds [2.1], cont.

| Compound | Crystal structure | $T_c$ (K) | Compound | Crystal structure | $T_c$ (K) |
|---|---|---|---|---|---|
| $VNi_2$ [a] | Rhomb. | <4.2 | $V_3Ti$ [a] | Cub. A15 [b] | <4.2 |
| $VNi_3$ | Tetr. $DO_{22}$ | <4.2 | $V_4Zn_5$ | Tetr. | <4.2 |
| $V_4O$ [a] | Tetr. | <4.2 | $VZn_3$ | Cub. $L1_2$ | <4.2 |
| $V_2O$ [a] | Hex. | <4.2 | $VZn_{16}$ [d] | – | – |
| VO [a] | Cub. B1 | <0.07 | $V_2Zr$ [d] | Cub. C15 | 8.8–6.5 |
| $V_2O_3$ | Rhomb. | <1.28 | | Rhomb. [j] | 8.5 |

[a] Compound with a range of homogeneity
[b] Metastable phase
[c] "<" means that no superconductivity was found above the temperature indicated
[d] Supposed compound
[e] Superconducting properties not investigated
[f] Unstable in the absence of carbon
[g] Non-stoichiometric composition
[h] Low-temperature modification
[i] High-temperature modification
[j] Formed by martensitic transformation

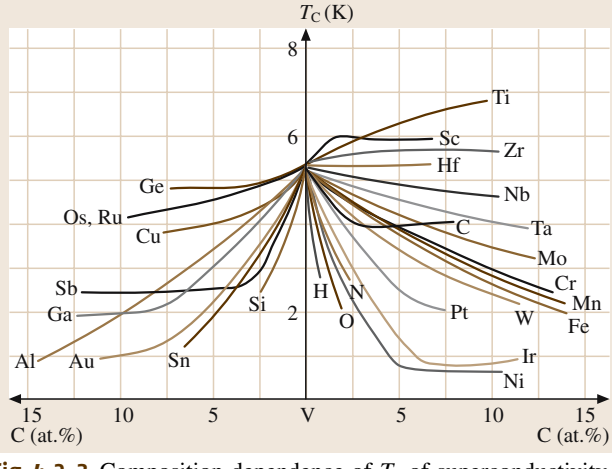


**Fig. 4.2-3** Composition dependence of $T_c$ of superconductivity in V solid solution alloys [2.1]

### Nb Alloys

Based on its highest $T_c$ among all elements Nb has been considered the most likely base metal for superconducting materials from the beginning and its alloys and intermetallic compounds have been investigated most extensively. Table 4.2-6 shows $T_c$ values for binary Nb compounds, where $Nb_3Al$, $Nb_3Ga$, $Nb_3Ge$, and $Nb_3Sn$ with the cubic A15 type crystal structure stand out for their particularly high $T_c$. Of these, $Nb_3Sn$ has been developed into a high-field superconducting material (see Sect. 4.2.1.2). Figure 4.2-4 shows the effect of alloying additions on $T_c$ in Nb solid solutions. The Nb–Ti alloys have, finally, been selected to form the most versatile and widely applied high-field superconducting material for present applications (see Sect. 4.2.1.2).

**Table 4.2-6** Superconductivity of Nb compounds [2.1]

| Compound | Crystal structure | $T_c$ (K) | Compound | Crystal structure | $T_c$ (K) |
|---|---|---|---|---|---|
| $Nb_3Al$ | Cub. A15 | 18.8–15.0 | $Nb_3Os$ | Cub. A15 | 1.5–0.5 |
| NbOAl | Tetr. $D8_b$ | 0.74 | $Nb_3Os_2$ | Tetr. $D8_b$ | 1.86–1.40 |
| $NbAl_3$ | Tetr. $D0_{22}$ | 0.64 | $NbOs_2$ | Cub. A12 | 2.86[d]–2.52 |
| $Nb_3As$ | Tetr. $Ti_3P$ | 0.31 | $Nb_3P$ | Tetr. $Ti_3P$ | 2–1.83 |
| | | | | | (7.5–6.0)[g] |
| $NbAs_2$ | Monocl. | <0.012[a] | $Nb_3Pb$[e] | Cub. A15 | 9.6<1.5 |
| $Nb_3Au$ | Cub. A15 | 11.5–8.99 | $Nb_3Pd_2$ | Cub. A12 | 2.47–1.7 |
| $Nb_3B_2$ | Tetr. | <1.0 | NbPd | Tetr. $D8_b$ | 2.0 |
| NbB[b] | Rhomb. $B_f$ | 8.25 | $Nb_3Pt$ | Cub. A15 | 10.9–6.0 |
| NbB[c] | – | <0.05 | $Nb_2Pt$ | Tetr. $D8_b$ | 4.2–3.73 |
| $Nb_3B_4$ | Rhomb. $D7_b$ | <1.28 | NbPt(α) | Rhomb. B19 | 2.4–<1.39 |
| $NbB_2$ | Hex. C32 | 6.4[d]–<1.0 | $NbPt_2$ | Rhomb. | <1.46 |
| $Nb_3Be_2$ | Tetr. | 2.3 | $Nb_7Re_9$ | Tetr. $D8_b$ | 3.8–2.5 |
| $NbBe_2$ | Cub. A15 | 2.15 | $NbRe_4$ | Cub. A12 | 2.45–9.7 |
| $NbBe_3$ | Rhomb. | <1.15 | $Nb_3Rh$ | Cub. A15 | 2.64–2.4 |
| $Nb_2Be_{17}$ | Rhomb. | 1.47–<1.38 | $Nb_5Rh_3$ | Tetr. $D8_b$ | 4.1–4.04 |
| | | | | | 10.2[g] |
| $NbBe_{12}$ | Tetr. | <1.38 | NbRh(γ) | Tetr. $L1_o$ | 3.76 |
| $Nb_3Bi$[e] | Cub. A15 | 3.05 (4.2–2) | NbRh(γ) | Rhomb. | 3.07 |
| $Nb_2C$ | Hex. | 9.11– < 1.98 | NbRh(ε) | Rhomb. B19 | 3.00 |
| NbC | Cub. B1 | 11.7– < 1.15 (14[f]) | $Nb_3Rh_5$(ξ) | Monocl. Sm | 2.7 |
| $Nb_3Ga$ | Cub. A15 | 16.8–14.1 (20.7)[g] | $NbRh_3$ | Cub. $L1_3$ | <1.43 |
| $Nb_5Ga_3$ | Tetr. | 1.35 | $Nb_3Ru_2$ | Tetr. | 1.2 |
| $Nb_3Ga_2$[h] | Tetr. | <2 | $Nb_2Ru_3$ | | 1.2 |
| $Nb_5Ga_4$ | Hex. | <2 | NbS | Hex. $B8_1$ | <1.28 (3.3–3.8)[g] |
| NbGa[h] | – | <2 | $NbS_2$[i] | Hex. C7 | 6.15–5.4 |
| $Nb_2Ga_3$ | – | <2 | $Nb_3Sb$ | Cub. A15 | 1.95–0.2 |
| $Nb_5Ga_{13}$ | Rhomb. | <2 | $Nb_3Sb_2$ | | <1.02 |
| $NbGa_3$ | Rhomb. | <2 | NbSb | Hex. $B8_1$ | <4.2 |
| $Nb_3Ge$ | Cub. A15 | 6.91 (23.2)[g] | $Nb_4Sb_5$ | Tetr. | 4.2–<1.15 |
| $Nb_3Ge$ | Tetr. $Ti_3P$ | <0.2 | $NbSb_2$ | Monocl. | 4.2–<1.15 |
| $Nb_2Ge$ | Hex. $D8_8$ | 1.90 | $Nb_3Se_4$ | Hex. | 1.61 |
| $Nb_5Ge_3$ | Tetr. | <1.02 | $NbSe_2$ | Hex. C7 | 7.5–5.4 (8.5–9)[g] |
| $NbGe_2$ | Hex. C40 | 2.23–2.09 | $NbSe_3$ | Monocl. | <1.0 |
| NbH | Cub. | <1.30 | $Nb_4Si$[h] | Hex. ε – $Fe_3N$ | <1.5 |
| $NbH_2$ | Cub. | <0.47 | $Nb_3Si$ | Tetr. | 0.29(5.45)[e] |
| $Nb_3In$ | Cub. A15 | 9.2–4 | $Nb_3Si$[e] | Cub. A15 | 19–13 |
| $Nb_3Ir$ | Cub. A15 | 1.76–1.63 | $Nb_5Si_3$(α) | Tetr.[b] | <1.02 |
| $Nb_5Ir_3$ | Tetr. $D8_b$ | 9.8[i]–2.4[d] | $Nb_5Si_3$ | Hex. $D8_8$ | <1.02 |
| $NbIr_{1+x}$ | Tetr. $L1_o$ | 4.75 | $NbSi_2$ | Hex. C40 | <1.20 |
| $Nb_2Ir(\alpha_2)$ | Rhomb. | 4.6 | $Nb_3Sn$ | Cub. A15 | 18.5–4.0 |
| $NbIr_3$ | Cub. $L1_2$ | <1.2 | $Nb_6Sn_5$ | Rhomb. | 2.07 |

**Table 4.2-6** Superconductivity of Nb compounds [2.1], cont.

| Compound | Crystal structure | $T_c$ (K) | Compound | Crystal structure | $T_c$ (K) |
|---|---|---|---|---|---|
| $Nb_2N(\beta)$ | Hex. | 9.5–<1.2 | $NbSn_2$ | Rhomb. | 2.68 |
| $Nb_4N_3(\gamma)$ | Tetr. | 12.2–7.8 | $NbTc_3$ | Cub. A12 | 12.9–10.5 |
| $NbN(\delta')$ | Tetr. | 7.2 | $Nb_3Te$ [g] | Cub. A15 | <2.5 |
| $NbN(\delta)$ | Cub. B1 | 16.5–9.7 | $Nb_5Te_4$ | – | <1.1 |
| $NbN(\varepsilon)$ | Hex. | <1.20 | $Nb_3Te_4$ | Hex. | 1.49 |
| $Nb_5N_6$ | Hex. | <1.77 | $NbTe_2$ | Hex. C7 | 0.74–0.5 |
| $Nb_4N_5$ | Tetr. | 8.0–8.5 | $NbTe_4$ | – | <0.025 |
| NbO | Cub. B1 | 1.61–1.38 | $Nb_3Tl$ [b] | Cub. A15 | 9.0 |
| $NbO_2$ | Tetr. | <1.2 | $NbZn_3$ | Cub. $L1_2$ | <1.02 |

[a] "<" means that no superconductivity was found above the temperature indicated
[b] Low-temperature modification
[c] High-temperature modification
[d] Non-stoichiometric composition
[e] Metastable phase
[f] Extrapolated maximum $T_c$
[g] Under extreme conditions
[h] Stabilized by adding interstitial elements
[i] Phase is stable at >850 °C only

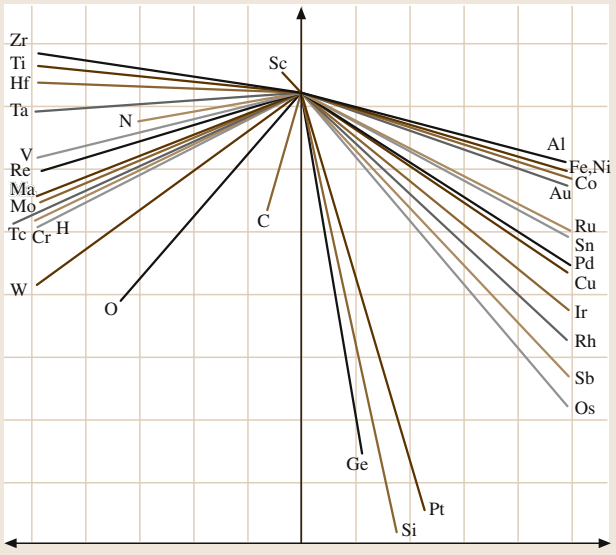


**Fig. 4.2-4** Composition dependence of $T_c$ of superconductivity in Nb solid solution alloys [2.1]

### Tc Alloys

Since Tc is rare and difficult to prepare in the alloy form, its superconducting properties have been studied to a limited extent only (see Table 4.2-7 and Fig. 4.2-5).

## 4.2.1.2 Practical Metallic Superconductors

Practical metallic superconductors for DC or AC applications are invariably composite wires with superconducting filaments which are embedded in a normal conducting matrix, usually Cu. They have a high longitudinal conductivity and may contain further components such as low conductivity barriers consisting of a Cu–Ni alloy, or diffusion barriers of Nb or Ta. Accounts of combining the aspects of the physics of superconductivity, materials science and technology, and electrical and mechanical performance criteria which have to be taken into account and are mastered in producing superconducting wires are given in [2.4–8].

**Table 4.2-7** $T_c$ of superconductivity of Tc compounds [2.1]

| Compound | Crystal structure | $T_c$ (K) | Compound | Crystal structure | $T_c$ (K) |
|---|---|---|---|---|---|
| $Tc_3As_7$ | Cub. $D8_f$ | <0.3 [a] | $Tc_6Ti$ [b] | Cub. A12 | 8.10–7.73 |
| TcBe | Cub. | 5.21 | TcTi | Cub. B2 | <1.7 |
| $TcBe_{22}$ | Cub. $ZrZn_{22}$ | 5.25 | $Tc_2Th$ | Hex. C14 | 5.3 [c] |
| TcC | Cub. | 3.85 | $Tc_3V(\delta)$ | Cub. | 7.8–4.0 |
| $Tc_2Hf$ | Hex. C14 | 5.6 | $TcV(\varepsilon)$ | Cub. B2 | <1.39 |
| $Tc_7Mo_3$ | Tetr. $D8_b$ | 15.8–14.7 | $Tc_3W_2$ | Tetr. $D8_b$ | 7.88–8.35 |
| $Tc_2Mo_3$ | Cub. A15 | 14–12 | $Tc_6Zr$ | Cub. A12 | 9.7 |
| $Tc_3Nb$ | Cub. A12 | 12.9–10.5 | $Tc_2Zr$ | Hex. C14 | 7.6 |
| $Tc_3SN$ [d] | Hex. | 5.92 | | | |

[a] "<" means that no superconductivity was found above the temperature indicated
[b] Formed as an ordered phase by extended annealing of the solid solution phase
[c] Non-stoichiometric composition
[d] Compound not determinded definitely; $T_c$ may be related to the solid solution

Only two superconducting metallic phases are used routinely in superconducting wires for applications: the Nb−Ti solid solution phase and the $Nb_3Sn$ intermetallic phase. Due to the difference of their intrinsic superconducting properties $T_c$ and $B_{c2}$, they have different ranges of application as indicated in Table 4.2-8.

The critical current density $J_c(T, B)$ obtained by applying optimal microstructural pinning of the flux lines in conductors of different composition and at different temperatures is shown in Fig. 4.2-6. Two factors of influence may be applied to obtain a higher critical current density $J_c(T, B)$ through effects of the intrinsic properties: either a decrease in temperature of application, e.g., from 4.2 to 1.8 K, or an increase of $B_{c2}$ by alloying as shown for (Nb, Ta, Ti)$_3$Sn in both Table 4.2-8 and Fig. 4.2-6. It should be noted that the intrinsic properties are affected only marginally by differences in processing of the conductors.

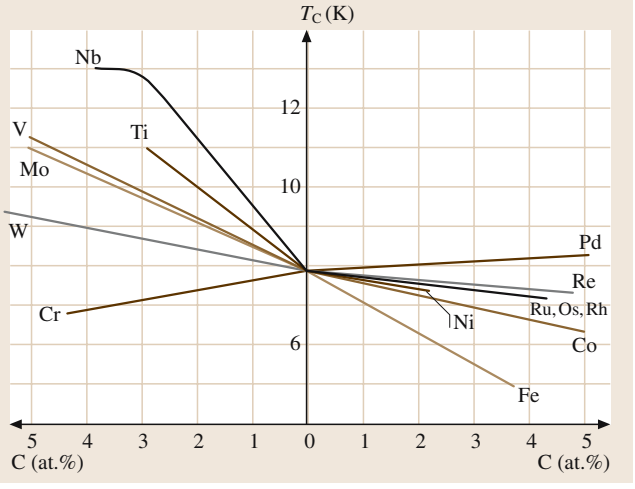


**Fig. 4.2-5** Composition dependence of $T_c$ of superconductivity in Tc solid solution alloys [2.1]

**Table 4.2-8** Characteristic properties of practical metallic superconductors (After [2.8])

| Superconducting phase | Composition | $T_c$(K) | $B_{c2}$(T) | Magnetic field in application $B$(T) |
|---|---|---|---|---|
| Nb−Ti | 46–52 wt% Ti,<br>≈ 47 wt% Ti optimal | ≈ 10 | ≈ 10.5 (4.2 K) | ≤ 9 (4.2 K)<br>> 9 (1.8 K) |
| $Nb_3Sn$<br>(Nb, Ta, Ti)$_3$Sn | 25 at.% Sn,<br>≤ 7.5 wt% Ta,<br>≤ 0.2 wt% Ti | ≈ 18 | ≈ 23 (4.2 K):<br>≈ 26–29 (4.2 K) | ≤ 20 T (4.2 K)<br>several T (< 4.2 K) |

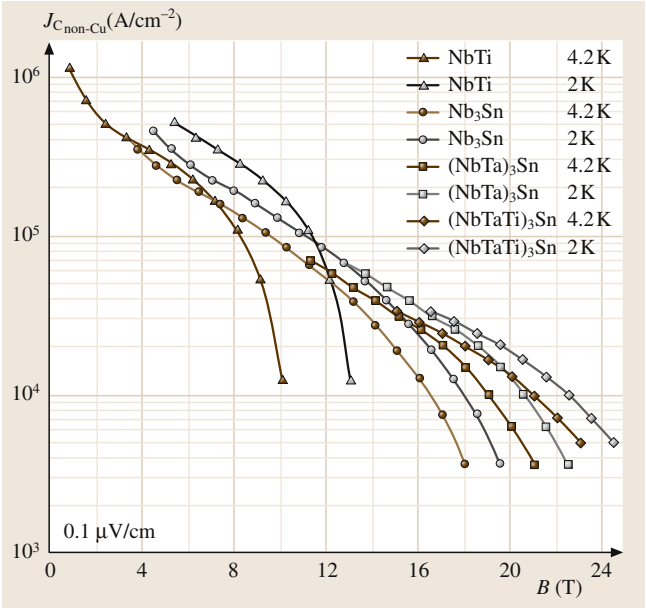


**Fig. 4.2-6** Non-Cu $J_c$ versus $B$ characteristics of Nb−Ti, binary $Nb_3Sn$, alloyed $(Nb, Ta)_3Sn$, and alloyed $(Nb, Ta, Ti)_3Sn$ multifilamentary superconductors [2.8]

### Nb−Ti Superconductors

Extensive accounts are given in [2.4, 6, 7]. The Nb−Ti alloy phase diagram combined with the low-temperature $T_c(c_{Ti})$ and $B_{c2}(c_{Ti})$ relations of the superconducting $\beta$ phase (Fig. 4.2-7a and b), provide the basic features of both the intrinsic superconducting properties of the $\beta$ phase and of the potential for flux pinning by precipitation of the $\alpha$ phase induced by suitable heat treatment in the $\alpha + \beta$ two-phase range.

The subsequent characteristic data are taken from systematic treatments and measurements of a Cu stabilized Nb–46.5 wt% Ti superconductor [2.9] which is in the range of optimum composition according to Table 4.2-8 and Fig. 4.2-7b. The processing of the composite consists essentially of a succession of deformation treatments, usually by wire drawing to different strains (true strain $\varepsilon_t = 2\ln(d_i/d)$, where $d_i$ is the initial rod diameter and $d$ is the filament diameter at the drawing strain considered), followed by heat treatments for 20 h to 40 h, mainly at temperatures in the range 360 to 380 °C, but also up to 420 °C. The first stage of deformation of the homogeneous metastable $\beta$ phase leads to the formation of a high density of dislocations, thus providing a high density of heterogeneous nucleation sites for the precipitation of a fine dispersion of $\alpha$ phase particles during the first heat treatment. During the subsequent cycles of deformation and heat treatment the $\alpha$ particles previously formed are elongated and partially broken up. Additional particles may be newly formed along dislocation cell walls and subgrain boundaries. The particle spacing transverse to the drawing direction is reduced. These variations of the dispersion are strongly affecting the pinning behavior and, thus, the $J_c$ values obtained, referring to a composite resistivity of $10^{-14}\ \Omega$ m.

The diagrams of Fig. 4.2-8a–e show $J_c$ as a function of the true drawing strain $\varepsilon_t$. The parameters are different thermal treatments, and different conditions (magnetic field, temperature) of measurement.

From measurements such as those shown in Fig. 4.2-8e, the effective bulk pinning force $F_p$ can be evaluated as shown in Fig. 4.2-9.

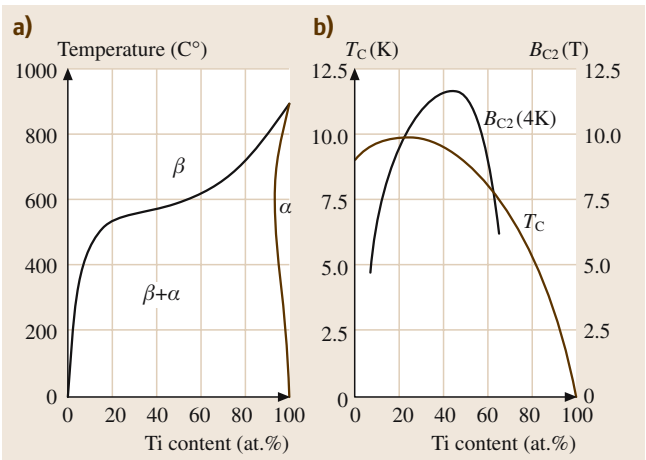


**Fig. 4.2-7a,b** Phase relations and superconducting properties in the Nb−Ti alloy system. **(a)** Nb−Ti phase diagram in the solid state. **(b)** $T_c$ and $B_{c2}$ (4 K) of the metastable $\beta$ phase

**Fig. 4.2-8a–e** ▶ Critical current variations as a function of different thermal treatments, final drawing strain and field of measurement, respectively, of an Nb–46.5 wt%Ti superconductor at 4.2 K [2.9]. **(a)** □ 160 h at 405 °C, ○ 80 h at 405 °C; ×40 h at 375 °C. — $B = 5$ T, --- $B = 8$ T. **(b)** All treatments for 80 h: 375 °C, ○ 405 °C, △ 420 °C, ◇ 435 °C. — $B = 5$ T, --- $B = 8$ T. **(c)** All treatments at 420 °C: ×160 h, 80 h, ○ 40 h, △ 10 h, ◇ 5 h. $B = 5$ T. **(d)** 160 h at 420 °C: ○ two heat treatments, three heat treatments. $B = 5$ T. **(e)** Full field optimum: ×80 h at 420 °C, 40 h at 375 °C, ○ 5 h at 405 °C

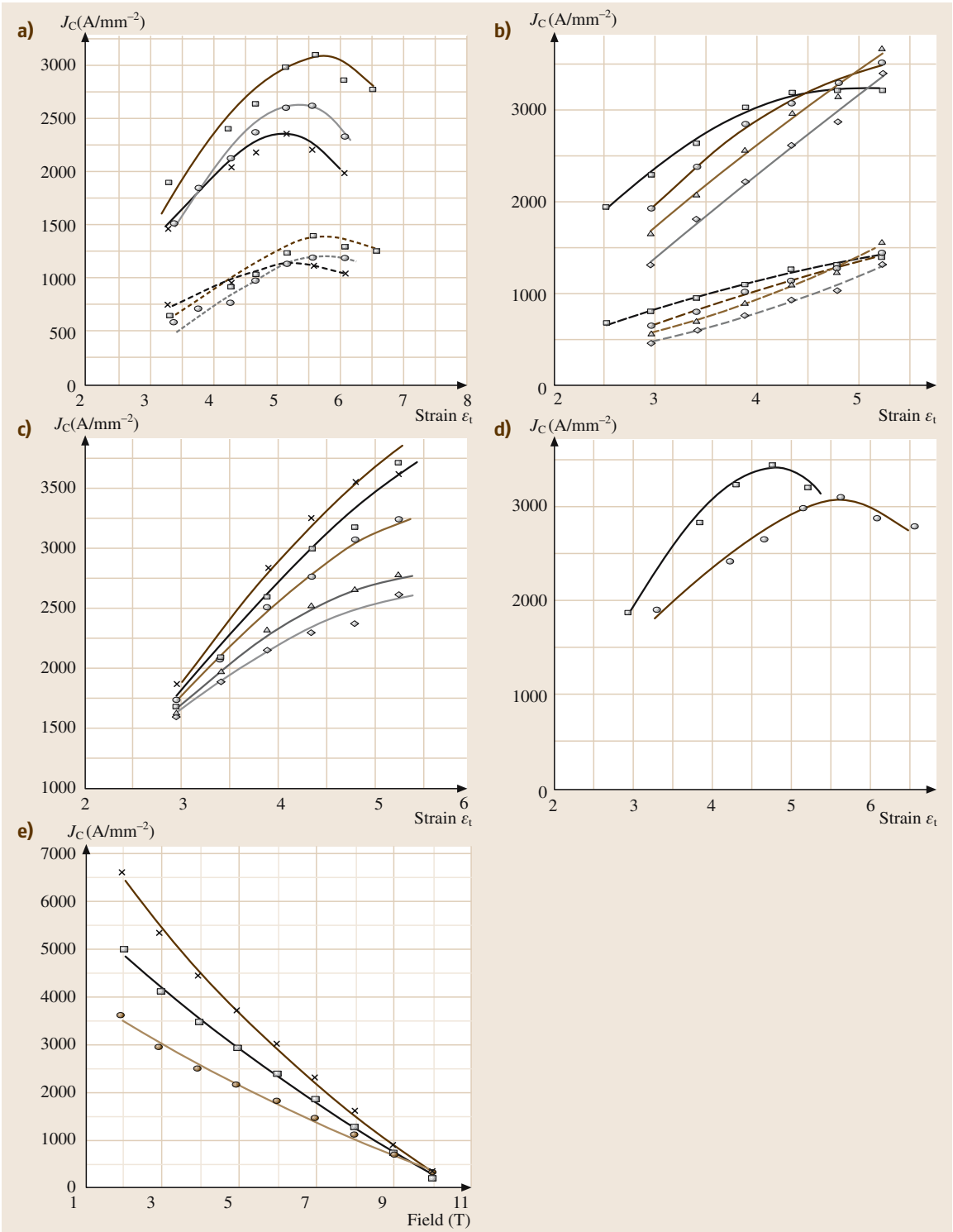
a)
$J_C$(A/mm$^{-2}$)
3000
2500
2000
1500
1000
500
0
2
3
4
5
6
7
8
Strain $\varepsilon_t$
b)
$J_C$ (A/mm$^{-2}$)
3000
2000
1000
0
2
3
4
5
Strain $\varepsilon_t$
c)
$J_C$(A/mm$^{-2}$)
3500
3000
2500
2000
1500
1000
2
3
4
5
6
Strain $\varepsilon_t$
d)
$J_C$ (A/mm$^{-2}$)
3000
2000
1000
0
2
3
4
5
6
Strain $\varepsilon_t$
e)
$J_C$ (A/mm$^{-2}$)
7000
6000
5000
4000
3000
2000
1000
0
1
3
5
7
9
11
Field (T)

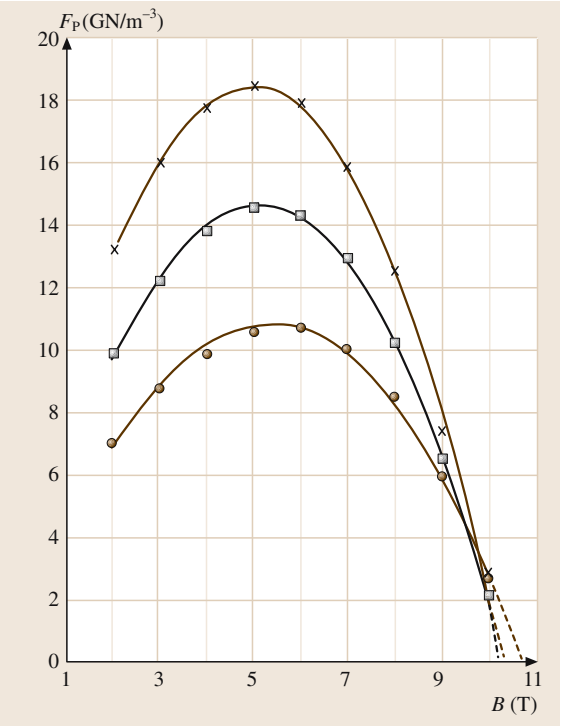


**Fig. 4.2-9** Bulk pinning force $F_p$ versus magnetic field, corresponding to the $J_c$ data shown in Fig. 4.2-8e. Typical particle spacings for the optimum $J_c$ is $d \approx 20$ nm and $d \approx 3-5$ nm, respectively [2.9]

Based on systematic variations and optimizations such as those shown in Fig. 4.2-8, commercial Nb−Ti superconducting composite wires are provided for a wide range of specifications. Figure 4.2-10 shows a typical wire cross section and Table 4.2-9 lists some characteristic data.

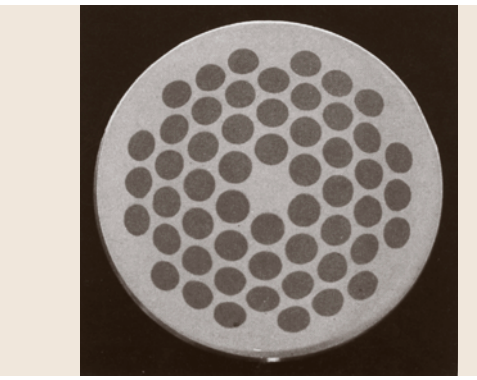

**Fig. 4.2-10** Typical cross section of a Cu-stabilized Nb−Ti superconducting wire

### $Nb_3Sn$ Superconductors

The production of superconductors based on $Nb_3Sn$ as the superconducting phase [2.7, 8] is hampered by the brittle behavior of this intermetallic phase which cannot be deformed by wire drawing. Consequently the conductors are produced by composing ductile components first, reducing the cross section of the composite into the final wire form by extrusion and drawing processes, and finally forming the $Nb_3Sn$ phase by a diffusion–reaction treatment after the specified wire diameter has been obtained. Five routes of processing have been developed:

1. *Bronze process:* The initial rod composite contains Nb rods surrounded by Cu−Sn alloy rods (13–15 wt% Sn) in a suitable arrangement such that after processing into wire form the diffusion–reaction treatment leads to the formation of $Nb_3Sn$ at the interface of Nb and Cu−Sn. The initial composite, if composed in a suitable configuration, has excellent deformation properties such that a geo-

**Table 4.2-9** Characteristic data at 4.2 K of commercial Nb−Ti superconductors, round wires

| Filaments | $A_{Cu}/A_{NbTi}$ [a] | Wire diameter (mm) | Filament diameter (μm) | Critical current $J_c$, (A) at $\mu_0 H$ (T) | | | |
|---|---|---|---|---|---|---|---|
| | | | | 3 T | 5 T | 7 T | 9 T |
| 54 | 1.35 | 0.3 | 27 | 100 | 70 | 45 | – |
| 54 | 1.35 | 0.6 | 53 | 380 | 265 | 170 | – |
| 54 | 1.35 | 0.85 | 75 | – | 480 | 310 | 140 |
| 45 | 1.8 | 0.4 | 36 | 150 | 105 | 70 | – |
| 45 | 1.8 | 0.7 | 62 | 420 | 295 | 185 | – |

[a] Ratio of cross sectional area
[b] Data extracted from a commercial brochure of Vacuumschmelze GmbH (9/1990)

**Table 4.2-10** Characteristic data at 4.2 K of commercial $Nb_3Sn$ superconductors produced according to the bronze process; filament diameters 4 to 6 μm

| Stabilization | Filament material | Wire diameter (mm) | Critical current density $I_c$ (A) at $\mu_0 H =$ | | | | Code[a] |
|---|---|---|---|---|---|---|---|
| | | | 8 T | 10 T | 12 T | 14 T | |
| None | Nb | 0.5 | 202 | 136 | 78 | – | NS 4500 (0.5) |
| None | Nb | 0.7 | 374 | 252 | 144 | – | NS 6000 (0.7) |
| None | Nb | 1.0 | 753 | 504 | 289 | – | NS 10 000 (1.0) |
| None | Nb–Ta | 0.5 | 171 | 123 | 86 | 58 | HNST 4500 (0.5) |
| None | Nb–Ta | 0.7 | 316 | 228 | 159 | 107 | HNST 6000 (0.7) |
| None | Nb–Ta | 1.0 | 636 | 456 | 321 | 215 | HNST 10 000 (1.0) |
| Cu/Ta core | Nb | 0.7 | 305 | 204 | 117 | – | NS 6000 (0.7) Ta I |
| Cu/Ta core | Nb | 1.0 | 623 | 417 | 239 | – | NS 10 000 (1.0) Ta I |
| Cu/Ta core | Nb | 1.25 | 973 | 652 | 373 | – | NS 13 000 (1.25) Ta I |
| Cu/Ta core | Nb–Ta | 0.7 | 258 | 185 | 130 | 87 | HNST 6000 (0.7) Ta I |
| Cu/Ta core | Nb–Ta | 1.0 | 526 | 378 | 266 | 178 | HNST 10 000 (1.0) Ta I |
| Cu/Ta core | Nb–Ta | 1.25 | 822 | 591 | 416 | 279 | HNST 13 000 (1.25) Ta I |

[a] According to the VACRYFLUX® designations of Vacuumschmelze GmbH (1990); the figures without parentheses indicate the approximate number of filaments

metrically well controlled wire results, in which decoupling of the filaments can be optimized and no bridging of filaments occurs. Table 4.2-10 shows the characteristic data of commercial $Nb_3Sn$ superconductors produced according to the bronze process.

2. *External* Sn *diffusion process:* Nb filaments in a Cu matrix are produced from a mechanical composite of rods by processing into wire form; at its final diameter the wire is coated with Sn; during a series of heat treatments with increasing temperature, Sn and Cu react to form a Cu–Sn alloy and this alloy reacts with the Nb filaments to form $Nb_3Sn$. This process is limited to wire with diameters $\leq 0.2$ mm.
3. *Internal* Sn *diffusion process:* Pure Sn or dilute Sn alloys with Cu or Mg are incorporated in the initial rod composite: after processing into wire form the $Nb_3Sn$ phase is formed by a diffusion–reaction process with the Nb filaments. However, due to the low melting point of Sn and its low yield stress, the processing cannot use hot extrusion and the drawing processes can readily lead to inhomogeneous deformation and mechanical instabilities.
4. *Jelly roll process:* Nb foil or mesh and Cu foil are wound into a roll as a starting rod which yields an Nb filament bundle after processing into wire form. In combination with the bronze or internal-Sn process this results in $Nb_3Sn$ filaments with extremely low diameter. It is difficult to scale the process to large quantities and wire cross-sections.

The four processes mentioned require a final diffusion–reaction treatment at 650 to 700 °C for 50 to 200 h. Since the stabilizing Cu constituent in the composite must not be exposed to Sn interdiffusion in order to maintain its high conductivity, a diffusion barrier is incorporated in the composite which usually consists of Ta in the form of a tube.

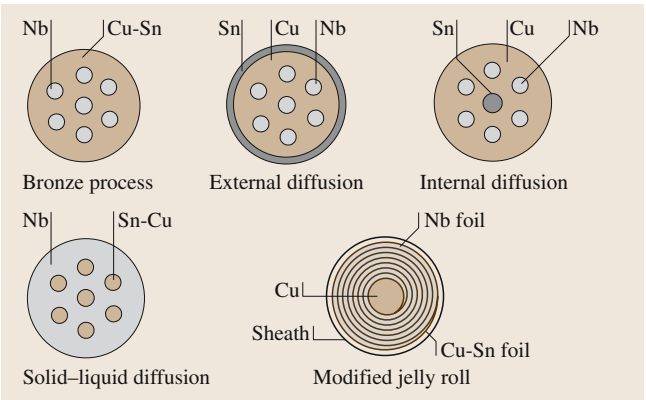


**Fig. 4.2-11** Processing routes of $Nb_3Sn$ superconductors [2.7]

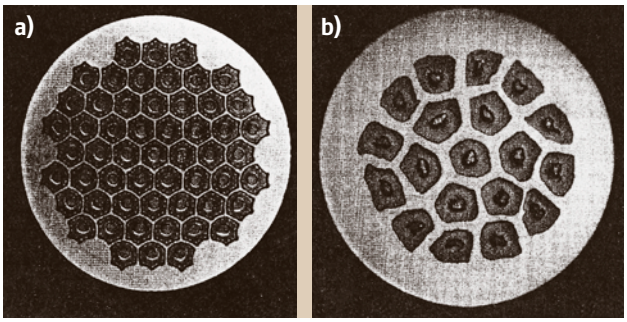


**Fig. 4.2-12a,b** Examples of cross sections of superconductors produced by the internal-Sn ((**a**) 0.8 mm diameter) and Nb-tube ((**b**) 0.5 mm diameter) processes [2.8]

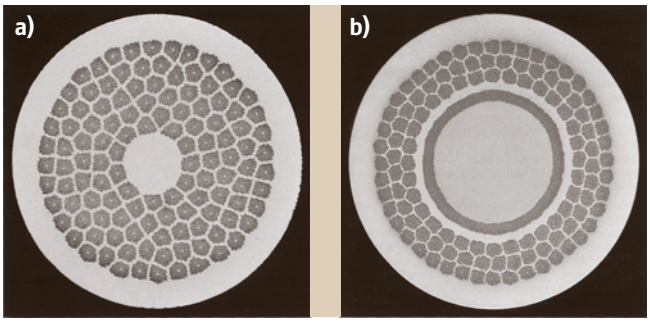


**Fig. 4.2-13a,b** Superconductors produced according to the bronze process (Vacuumschmelze). (**a**) Non-stabilized, 10 080 Nb filaments in a Cu−Sn matrix. (**b**) Internally stabilized by Cu in a Ta tube, 6156 Nb filaments in a Cu−Sn matrix

5. Nb-*tube process*: The need of an extra barrier element can be avoided by using Nb tubes, filled with Sn or with a Sn compound such as $NbSn_2$, embedded in a Cu matrix. During heat treatment, a $Nb_3Sn$ layer is formed inside the tube while its outer part acts as a diffusion barrier. This processing route leads to wires with high critical current densities but is difficult to scale up for industrial production.

Schematic drawings of the composites according to these five processing routes are shown in Fig. 4.2-11.

Examples of cross sections of superconductors produced by the internal-Sn, bronze, and Nb-tube processes are shown in Figs. 4.2-12 and 4.2-13.

In $Nb_3Sn$ superconductors the flux lines are pinned by the grain boundaries in the $Nb_3Sn$ filaments. The dependence of the effective volume pinning force $F_p$ on the grain size is shown in Fig. 4.2-14. This leads to the requirement that the reaction temperature is optimized not only regarding the rate of the diffusion–reaction process but also regarding the resulting grain size.

Moreover, the critical current density depends strongly on the state of strain in $Nb_3Sn$, in particular close to $B_{c2}$. Figure 4.2-15 shows the strain sensitiv-

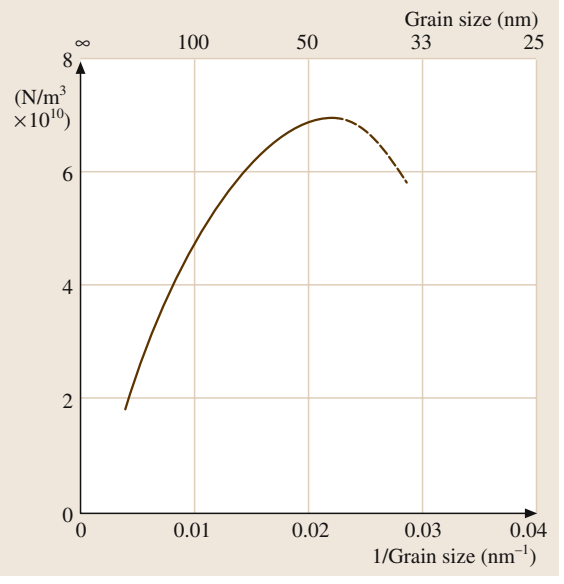


**Fig. 4.2-14** Dependence of the volume pinning force $F_p$ in $Nb_3Sn$ on the grain size

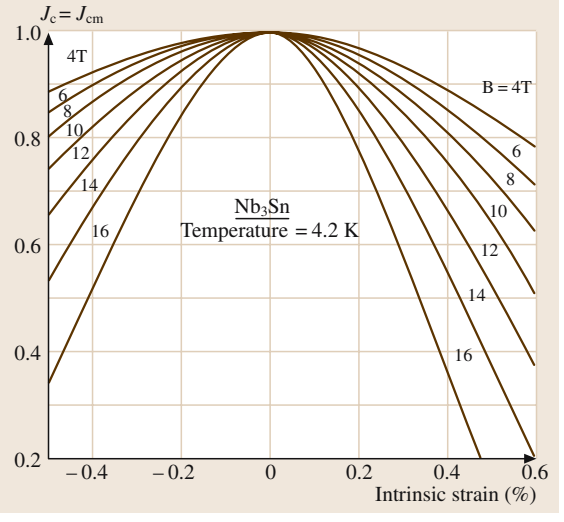


**Fig. 4.2-15** Strain sensitivity $J_c(\varepsilon)$ of $Nb_3Sn$ superconductors [2.10]

ity $J_c(\varepsilon)$ for binary $Nb_3Sn$ under uniaxial longitudinal strain. In its state of formation, i. e., in the absence of an externally applied strain, the $Nb_3Sn$ phase as formed has an intrinsic compressive strain of $\varepsilon_i = 0.2–0.3\%$, depending on the conductor design and processing parameters. Thus, applying a tensile strain will first lead to an increase in $J_c$. However, degradation sets in irreversibly if strains of a few tenths of one per cent are exceeded due to crack formation in the brittle $Nb_3Sn$ phase.

Table 4.2-10 lists characteristic data of commercial $Nb_3Sn$ superconductors.



## 4.2.2 Non-Metallic Superconductors

### 4.2.2.1 Oxide Superconductors

#### Low-$T_c$ Superconducting Oxides

Only a few oxides with critical temperatures above the boiling temperature of liquid helium (4.2 K) were known up to 1986. Their $T_c$ did not exceed 14 K. The stoichiometric composition of nearly all of these compounds ($T_c > 4.2$ K) is related to one of the formulas:

$$BaPb_{1-x}Bi_xO_3,\ Li_{1+x}Ti_{2-x}O_4,\quad \text{or}$$

$$A_yWO_3 (y < 0.5;\ A = Cs;\ Rb)\ .$$

Relatively high $T_c$ values of the Ba–Pb–Bi–O compounds were also observed after substitution of small amounts of K and Sr for Ba, respectively, and after substitution of Sn for Pb (Table 4.2-11).

**Table 4.2-11** Electrical and structural data of selected low-$T_c$ oxide superconductors

| Compound | Structure<br>Lattice parameters<br>$a, b, c$ (nm) | $T_c$ (K) | $\mu_0 H_{c2}$ (T) | $\mu_0 H_{c1}$ (mT) |
|---|---|---|---|---|
| $BaPb_{1-x}Bi_xO_3$<br>$x = 0.2–0.3$[a] | | 8–12 | | |
| Polycrystalline | Orthorhombic ($x = 0.30$)<br>$a = 0.6075$, $b = 0.610$,<br>$c = 0.857$<br>Tetragonal ($x = 0.275$)<br>$a = 0.6055$, $c = 0.8633$ | | For $x = 0.25$:<br>5.4 (1.8 K)<br>2.3 (8 K)<br>For $x = 0.2$:<br>7.0 (1.15 K)<br>2.3 (6 K) | For $x = 0.25$:<br>23 (4.2 K) |
| Single crystal | Orthorhombic ($x \approx 0.25$)<br>$a = 0.6058$, $b = 0.6081$,<br>$c = 0.8552$<br>Tetragonal ($x \approx 0.25$)<br>$a = 0.6045$, $b = 0.8613$ | | For $x = 0.27$:<br>3.8 (1.5 K)<br><br>For $x = 0.2$:<br>1.75 (3.5 K) | |
| $Ba_{0.9}K_{0.1}Pb_{0.75}–Bi_{0.25}O_3$ | | 11.5 | | |
| $BaSn_{0.01}Pb_{0.74–0.69}–Bi_{0.25–0.3}O_3$ | | 10–11 | | |
| $Li_{1...1.3}Ti_{2–1.67}O_4$ | Cubic<br>$a = 0.841–0.836$ | 9.6–12 | 3.3 (0 K) | |
| $Li_{2.6}Ti_{1.5–2.7}O_4$ | Cubic | 10.9–11.4 | 9.6–16.2 (4.2 K) | |
| $Rb_{0.3}WO_3$ | Hexagonal | 7.5–0.6 | | |
| $Cs_{0.1}WO_{2.9}F_{0.1}$<br>(Single crystal) | Hexagonal<br>$a = 0.74$; $c = 0.76$ | $\approx 4.9$ | 0.13–0.36<br>(dependent on temperature and crystal orientation relative to H) | |

[a] The electrical and structural data of $BaPb_{1-x}Bi_xO_3$ are values of different authors published in [2.2]

An extensive compilation of the oxide superconductors of the class called low-$T_c$ superconductors is given in [2.11]. Some data, which are relevant to bulk materials revealing relatively high $T_c$ values are summarized in Table 4.2-11.

For metallic superconductors the electron–phonon interaction accounts for the superconductivity of low-$T_c$ oxide conductors. For all of these materials the electrical parameters indicated in Table 4.2-11 depend on the electron mean free path, and thus on the resistivity $\rho$, of the material in the normal state. The quantitative relation for $H_{c2}$ is given by

$$\mu_0 H_{c2}(0) = 3.11\, \rho\gamma\, T_c\ ,$$

where $\gamma$ is the electronic specific heat. As a consequence of the influence of $\rho$ on $T_c$ and $H_c$, both parameters depend not only on the stoichiometric composition of the multi-component oxides but also on impurities and lattice defects introduced by the preparation. Accordingly, in the literature the electrical parameters are not all identical to those of Table 4.2-11. For $BaPb_{1-x}Bi_xO_3$ compounds the following values of coherence length $\xi_0$ and London penetration depth $\lambda$ were published: $\xi_0 = 2400, 250, 50$ nm, $\lambda = 0.5, 0.7, 1.5$ nm for $x = 0,\ 0.12$ and 0.3, respectively [2.11].

### High-$T_c$ Superconducting Oxides

*Chemical Composition.* Bednorz and Müller carried out a series of investigations aiming to enhance the electron–phonon interaction in superconducting oxides. As a result, they found superconductivity at around 30 K in the Ba−La−Cu−O system [2.12]. These compounds were the first ones of the class of cuprates called high-$T_c$ superconductors.

After this discovery many new compounds revealing $T_c$ values up to 138 K under ambient pressure were detected. The stoichiometric compositions of most high-$T_c$ cuprates can be assigned to one of the formulas presented in Table 4.2-12. A similar classification is given by [2.13]. The A-elements as well as the E-elements can be partially substituted by one ore more other metallic elements as shown in Table 4.2-13.

The partial substitution of oxygen by non-metallic elements, such as fluorine or chlorine, is also possible for some compounds. Sometimes this even leads to a slight enhancement of $T_c$. The introduction of rows of carbonate groups between two $CuO_2$ layers (see structure principles below) leads to superconducting layered oxy-carbonates with the formulation $(A_2CO_3)_mCa_{n-m}(CuO_2)_n$. The "$m = 1,\ n = 2$" and "$m = 1,\ n = 3$" members with A = Ba are considered as the basic high-$T_c$ compounds of this class [2.14].

*The Structure of the Superconducting Compounds.* In Fig. 4.2-16, which shows the crystal structure of the $Bi_mSr_2Ca_{n-1}Cu_nO_{2n+m+2}$ homologous series, the structural principles of most of the superconducting high-$T_c$ cuprates are indicated. The structure element carrying the mobile charges is a stack of a certain number $n$ ($n = 1, 2, 3$ in Fig. 4.2-16) of $CuO_2$ monolayers, which are separated by intermediate monolayers of alkaline earth elements E (E = Ca in Fig. 4.2-16) or monolayers of lanthanide elements L (in $LBa_2Cu_3O_{7-x}$, Table 4.2-12). These stacks of $CuO_2$/E and $CuO_2$/L, re-

**Table 4.2-12** General chemical formulas of high-$T_c$ cuprates

| Formula | Examples A-elements | Stoichiometric coefficients $m$ | $n$ | Examplary E-elements |
|---|---|---|---|---|
| $A_mE_2Ca_{n-1}Cu_nO_{2n+m+2}$ | Tl | 1–2 | 1–4 | Ba, Sr |
| | Bi | 1–2 | 1–4 | |
| | (Bi,Pb) | 1–2 | 1–4 | |
| | Hg | 1–2 | 1–6 | |
| | Cu | 1–2 | 3–5 | |
| | B | 1 | 3–5 | |
| | Pb | 1 | 1–2 | |
| | Au | 1 | 2 | |
| $LBa_2Cu_3O_7$ | Y, La, Pr, Nd, Sm, Eu, Gd, Tb, Dy, Ho, Er, Tm, Yb, Lu | | | |
| $A_2CuO_4$ | La, Pr, Nd, Sm, Eu | | | |
| $AE_2CuO_{4-5}$ | Hg, Tl | | | Ba, Sr |
| $A_2Ca_{n-1}Cu_nO_{2n+2}$ | Ba, La | | 2–4 | |

**Table 4.2-13** Electrical data of high-$T_c$ cuprates

| Compound | $T_c$ (K) | $\Delta T_c$ (K) | $\rho(0)$; $\rho(T_c)$ ($\mu\Omega$ cm) | $H_{c2}(0)$ (T) | $\lambda_{ab}(0)$ (nm) | Ref. |
|---|---|---|---|---|---|---|
| **$A_2CuO_4$ family** | | | | | | |
| $Sr_2CuO_4$ | 25 | | | | | [2.13] |
| $La_{1.9}Sr_{0.1}CuO_4$ | 33 | 6.5 | | | $320 \pm 16$ | [2.15] |
| $La_{1.875}Sr_{0.125}CuO_4$ | 36 | 4.5 | | | $270 \pm 13.5$ | [2.15] |
| $La_{1.85}Sr_{0.15}CuO_4$ | 39 | 2 | 0; $33 \pm 6$ | $45 \pm 10$ | $218.5 \pm 10$ | [2.15] |
| $La_{1.775}Sr_{0.225}CuO_4$ | 29 | 7.5 | | | | [2.15] |
| $La_{1.725}Sr_{0.275}CuO_4$ | 22 | 10 | | | | [2.15] |
| $Eu_{2-x}Ce_xCuO_4$ | 23 | | | | | [2.13] |
| $(Nd_{2-x}Ce_x)CuO_4$ | 24<br>30 | 2 | 250; 250 | | | [2.13, 16] |
| $Pr_{2-x}Ce_xCuO_4$ | 24 | | | | | [2.13] |
| $Sm_{2-x}Ce_xCuO_4$ | 22 | | | | | [2.13] |
| **$ABa_2Cu_3O_7$ family** | | | | | | |
| $YBa_2Cu_3O_{6.67}$ | 60 | 1 | $x$; $63 \pm 8$ | 87 | $255 \pm 12.5$ | [2.15] |
| $YBa_2Cu_3O_7$ | 92 | 1 | 0; $40 \pm 5$ | $140 \pm 30$ | $141.5 \pm 1$ | [2.15] |
| $(Y_{0.95}Pr_{0.05})Ba_2Cu_3O_7$ | 90 | 1.8 | 50; 100 | | $150 \pm 7.5$ | [2.15] |
| $(Y_{0.9}Pr_{0.1})Ba_2Cu_3O_7$ | 86 | 2.2 | 50; 100 | | $173 \pm 8.5$ | [2.15] |
| $(Y_{0.8}Pr_{0.2})Ba_2Cu_3O_7$ | 78 | 3.2 | 100; 140 | | $198 \pm 10$ | [2.15] |
| $(Y_{0.7}Pr_{0.3})Ba_2Cu_3O_7$ | 60 | 7.5 | 250; 280 | | $215 \pm 10$ | [2.15] |
| $(Y_{0.6}Pr_{0.4})Ba_2Cu_3O_7$ | 40 | 13.2 | 300; 335 | | $290 \pm 15$ | [2.15] |
| $YBa_2(Cu_{0.99}Fe_{0.01})_3O_7$ | 91 | 1.3 | | | | [2.15] |
| $YBa_2(Cu_{0.975}Fe_{0.025})_3O_7$ | 85 | 3 | | | | [2.15] |
| $YBa_2(Cu_{0.95}Fe_{0.05})_3O_7$ | 75 | 5 | | | | [2.15] |
| $YBa_2(Cu_{0.99}Zn_{0.01})_3O_7$ | 78 | 1 | | | | [2.15] |
| $YBa_2(Cu_{0.975}Zn_{0.025})_3O_7$ | 62 | 1 | 150; 200 | | | [2.15] |
| $YBa_2(Cu_{0.95}Zn_{0.05})_3O_7$ | 36 | 1.5 | 240; 300 | | | [2.15] |
| $HoBa_2Cu_3O_7$ | 92 | 1 | | | | [2.15] |
| $NdBa_2Cu_3O_7$ | 96 | | | | | [2.13] |
| $GdBa_2Cu_3O_7$ | 94 | | | | | [2.13] |
| $ErBa_2Cu_3O_7$ | 92 | | | | | [2.13] |
| $YbBa_2Cu_3O_7$ | 89 | | | | | [2.13] |
| **$A_mE_2Ca_{n-1}Cu_nO_{2n+m+2}$ family** | | | | | | |
| $Bi_2Sr_2CaCu_2O_7$ | 107 | | | | | [2.13] |
| $Bi_2Sr_2CuO_6$ | 34 | | | | | [2.13] |
| $Bi_2(Sr_{1.6}La_{0.4})CuO_{6+x}$ | 23.5 | | 320; 360 | | | [2.15] |
| $(Bi, Pb)_2(Sr_{1.75}La_{0.25})CuO_6$ | 24 | | | | | [2.15] |
| $Bi_2Sr_2CaCu_2O_8$ (no anneal) | 90 | 1 | 0; $38 \pm 2$ | 107 | $250 \pm 50$ | [2.15] |
| $Bi_2Sr_2CaCu_2O_{8+x}$ ($O_2$-annealed) | 75 | 1 | | | | [2.15] |
| $Bi_2Sr_2Ca_2Cu_3O_{10}$ | 107<br>110 | 10 | 0; <60 | | | [2.13, 15] |
| $(Bi_{1.6}Pb_{0.4})Sr_2Ca_2Cu_3O_{10}$ | 110 | 1 | 0; $x$ | 184 | $253 \pm 30$ | [2.15] |
| $Bi_2Sr_2Ca_3Cu_4O_{12}$ | 110 | | | | | [2.13] |
| $PbSr_2CaCu_2O_7$ | 70 | | | | | [2.13] |
| $Pb_2Sr_2Ca_{0.5}Ln_{0.5}Cu_3O_8$ | 70 | | | | | [2.16] |
| $PbSr_2Ca_2Cu_3O_9$ | 122 | | | | | [2.13] |
| $AuBa_2CaCu_2O_7$ | 82 | | | | | [2.13] |

**Table 4.2-13** Electrical data of high-$T_c$ cuprates, cont.

| Compound | $T_c$ (K) | $\Delta T_c$ (K) | $\rho(0)$; $\rho(T_c)$ ($\mu\Omega$ cm) | $H_{c2}(0)$ (T) | $\lambda_{ab}(0)$ (nm) | Ref. |
|---|---|---|---|---|---|---|
| **$A_mE_2Ca_{n-1}Cu_nO_{2n+m+2}$ family** | | | | | | |
| $Tl_2Ba_2CuO_6$ | 85<br>90 | | 40; 100 | | $170 \pm 10$ | [2.13, 15] |
| $Tl_2Ba_2CaCu_2O_8$ | 99<br>110<br>119 | | $0 \pm 20$;<br>$300 \pm 80$ | 99 | $221 \pm 10$ | [2.13, 15, 16] |
| $Tl_2Ba_2Ca_2Cu_3O_{10}$ | 125<br>128 | | 20;83 | 75 | $196 \pm 10$ | [2.13, 15] |
| $Tl_2Ba_2Ca_3Cu_4O_{12}$ | 119 | | | | | [2.13] |
| $TlBa_2CaCu_2O_7$ | 82<br>103 | | | | | [2.13, 16] |
| $TlBa_2Ca_2Cu_3O_9$ | 135<br>110 | | | | | [2.13, 16] |
| $TlBa_2Ca_3Cu_4O_{11}$ | 127 | | | | | [2.13] |
| $(Tl_{0.5}Pb_{0.5})Sr_2CaCu_2O_7$ | 80 | | | | $182 \pm 9$ | [2.15] |
| $(Tl_{0.5}Pb_{0.5})Sr_2(Ca_{0.8}Y_{0.2})Cu_2O_7$ | 107 | | 0;250 | | | [2.15] |
| $(Tl_{0.5}Pb_{0.5})Sr_2Ca_2Cu_3O_9$ | 122 | | | | $158 \pm 8$ | [2.15] |
| $TlSr_2Ca_{0.5}Y_{0.5}Cu_2O_7$ | 90 | | | | | [2.16] |
| $CuBa_2Ca_2Cu_3O_9$ | 60 | | | | | [2.13] |
| $CuBa_2Ca_3Cu_4O_{11}$ | 117 | | | | | [2.13] |
| $Cu_2Ba_2Ca_2Cu_3O_{10}$ | 67 | | | | | [2.13] |
| $Cu_2Ba_2Ca_3Cu_4O_{12}$ | 113 | | | | | [2.13] |
| $BSr_2Ca_2Cu_3O_9$ | 75 | | | | | [2.13] |
| $BSr_2Ca_3Cu_4O_{11}$ | 110 | | | | | [2.13] |
| $BSr_2Ca_4Cu_5O_{13}$ | 85 | | | | | [2.13] |
| $Pb_2(Y_{1-x}Ca_x)Sr_2Cu_3O_8$ | 80 | | 50;250 | | | [2.15] |
| $HgBa_2CaCu_2O_7$ | 128 | | | | | [2.13] |
| $HgBa_2Ca_2Cu_3O_9$ | 135 | | | | | [2.13] |
| $HgBa_2Ca_3Cu_4O_{11}$ | 127 | | | | | [2.13] |
| $HgBa_2Ca_4Cu_5O_{13}$ | 110 | | | | | [2.13] |
| $HgBa_2Ca_5Cu_6O_{15}$ | 107 | | | | | [2.13] |
| $Hg_2Ba_2CaCu_2O_7$ | 44 | | | | | [2.13] |
| $Hg_2Ba_2Ca_2Cu_3O_9$ | 45 | | | | | [2.13] |
| $Hg_2Ba_2Ca_3Cu_4O_{12}$ | 114 | | | | | [2.13] |
| **$AE_2CuO_{4-5}$ family** | | | | | | |
| $HgBa_2CuO_5$ | 97 | | | | | [2.13] |
| $TlBa_2CuO_5$ | 50 | | | | | [2.13] |
| $(Hg_{0.8}V_{0.2})Ba_2CuO_{4.3}$ | 89 | | | | | [2.14] |
| $(Hg_{0.8}Mo_{0.2})Ba_2CuO_{4.4}$ | 66 | | | | | [2.14] |
| $(Hg_{0.9}Mo_{0.1})Ba_2CuO_{4.2}$ | 68 | | | | | [2.14] |
| $(Hg_{0.8}W_{0.2})Ba_2CuO_{4.4}$ | 37 | | | | | [2.14] |
| $(Hg_{0.9}W_{0.1})Ba_2CuO_{4.2}$ | 83 | | | | | [2.14] |
| $(Hg_{0.8}Ru_{0.2})Ba_2CuO_{4.2}$ | 91 | | | | | [2.14] |
| $(Hg_{0.7}Cr_{0.3})Sr_2CuO_{4.15}$ | 60 | | | | | [2.14] |
| $(Hg_{0.8}Mn_{0.2})Ba_2CuO_{4.2}$ | 90 | | | | | [2.14] |
| $(Hg_{0.8}Nb_{0.2})Ba_2CuO_{4.3}$ | 78 | | | | | [2.14] |

**Table 4.2-13** Electrical data of high-$T_c$ cuprates, cont.

| Compound | $T_c$ (K) | $\Delta T_c$ (K) | $\rho(0)$; $\rho(T_c)$ ($\mu\Omega$ cm) | $H_{c2}(0)$ (T) | $\Lambda_{ab}(0)$ (nm) | Ref. |
|---|---|---|---|---|---|---|
| **$AE_2CuO_{4-5}$ family** | | | | | | |
| $(Hg_{0.8}Mo_{0.2})Sr_2CuO_x$ | 78 | | | | | [2.14] |
| $(Hg_{0.9}Re_{0.1})Sr_2CuO_x$ | 70 | | | | | [2.14] |
| **$A_2Ca_{n-1}Cu_nO_{2n+2}$ family** | | | | | | |
| $Ba_2CaCu_2O_6$ | 90 | | | | | [2.13] |
| $Ba_2Ca_2Cu_3O_8$ | 120 | | | | | [2.13] |
| $Ba_2Ca_3Cu_4O_{10}$ | 105 | | | | | [2.13] |
| $Ba_2Ca_4Cu_5O_{12}$ | 90 | | | | | [2.13] |
| $La_{1.6}Sr_{0.4}CaCu_2O_6$ | 60 | 10 | | | | |
| **Other compounds** | | | | | | |
| $YBa_2Cu_4O_8$ | 80 | 2 | | | $196 \pm 10$ | [2.15] |
| $HoBa_2Cu_4O_8$ | 80 | 5 | 100; 400 | | $161 \pm 8$ | [2.15] |
| $Bi_2Sr_2(Ln_{1-x}Ce_x)_2Cu_2O_{10}$ | 25 | | | | | [2.16] |
| $Ca_{1-x}Sr_xCu_2O_2$ | 110 | | | | | [2.16] |
| $(Pb, Cu)Sr_2(Ln, Ca)Cu_2O_7$ | 50 | | | | | [2.16] |
| $(Pb, Cu)(Sr, Eu)(Eu, Ce)Cu_2O_x$ | 25 | | | | | [2.16] |
| $Sr_{1-x}Nd_xCuO_2$ | 40 | | | | | [2.16] |
| $Tl(Ba, La)CuO_5$ | 40 | | | | | [2.16] |
| $Tl(Sr, La)CuO_5$ | 40 | | | | | [2.16] |
| $(Tl_{0.5}Pb_{0.5})Sr_2CuO_6$ | 40 | | | | | [2.16] |
| $(Tl_{0.7}Cd_{0.3})BaLaCuO_5$ | 48 | | | | | [2.15] |

spectively, are sandwiched between insulating blocks consisting of $m$ monolayers of A-oxide ($m = 2$ and A = Bi in Fig. 4.2-16) and two monolayers of E-oxide (E = Sr in Fig. 4.2-16). These blocks can act as electronically active charge-reservoirs for hole or electron donation to the copper-oxygen layers.

*Superconducting Properties.* By means of flux quantization and Josephson tunneling experiments, it has been firmly established that superconductivity in the cuprate compounds is based on electron pairs similar to that of conventional Bardeen–Cooper–Schreiffer (BCS) superconductors. However, there are currently widely differing views as to the pairing mechanism and no consensus exists on a proper microscopic theory. In addition

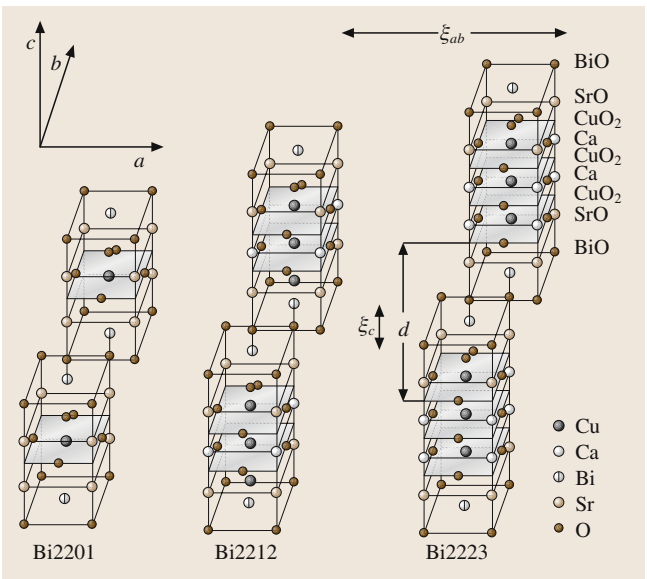


**Fig. 4.2-16** Schematic crystal structures of the homologous series of $Bi_2Sr_2Ca_{n-1}Cu_nO_{2n+4}$ superconductors with $n = 1$ ($Bi_2Sr_2CuO_6$, abbreviated as Bi2201), $n = 2$($Bi_2Sr_2CaCu_2O_8$ – Bi2212) and $n = 3$($Bi_2Sr_2Ca_2Cu_3O_{10}$ – Bi2223). The coherence length in the $c$-direction, $\xi_c$, is compared to that perpendicular to the $c$-direction, $\xi_{ab}$, and to the distance $d$ between the superconducting $CuO_2$/Ca stacks

to the conventional electron–phonon interaction other explanations have been proposed [2.17].

Compared to the conventional superconductors, the superconducting cuprate compounds exhibit significantly higher values of $T_c$, much smaller coherence lengths $\xi$, and a high anisotropy of the electronic transport properties. The anisotropy is caused by the layered structure of the cuprates (Fig. 4.2-16) and by the fact, concluded from both experiments and theoretical considerations, that superconductivity is essentially confined to the $CuO_2$-planes. The superconductive coupling between the $CuO_2$ layers within a $CuO_2$/E stack and within a $CuO_2$/L stack, respectively, is much weaker than the coupling within the $CuO_2$ layers. This is demonstrated qualitatively in Fig. 4.2-16 by the coherence lengths $\xi_{ab}$ and $\xi_c$ within the $CuO_2$ plane and in the $c$-direction, respectively, for the compound $Bi_2Sr_2Ca_2Cu_3O_{10}$, $\xi_c$ is of the order of the distance between two $CuO_2$ layers within the $CuO_2$/Ca stack. The coupling between neighboring $CuO_2$/Ca stacks separated by the BiO- and SrO-layers is even weaker. This coupling can be described as Josephson type. For the two compounds $YBa_2Cu_3O_{7-\delta}$ and Pb doped $Bi_2Sr_2Ca_2Cu_3O_{10-x}$, which are the most promising high-$T_c$ conductors for technical applications, the anisotropy of the superconducting properties caused by the quasi 2-dimensional nature of superconductivity in high-$T_c$ conductors is demonstrated and compared to the typical low temperature superconductor $Nb_3Sn$ in Table 4.2-14; $\gamma$ is the anisotropic parameters defined as $\gamma = \xi_{ab}/\xi_c \equiv \lambda_c/\lambda_{ab}$. The identity is derived from the anisotropic Ginzburg–Landau equations. Here $\lambda_{ab}$ and $\lambda_c$ are the London penetration depths for a magnetic field in the $c$-direction and parallel to the $ab$-plane, respectively. Considerably different values have been published for the parameters of the high-$T_c$ compounds given in Table 4.2-14. For more details and references see Sects. 4.2.2.2 and 4.2.2.3.

All high-$T_c$ cuprate compounds are Type II superconductors. While a microscopic theory which can describe the high-$T_c$ superconductivity sufficiently is missing, an understanding of this field is reached on the basic assumption that the phenomenological theories [2.18] of London and of Ginsburg and Landau also hold for high-$T_c$ superconductors. Following these theories, the critical fields can be expressed through the corresponding values of the coherence length $\xi$ and the London penetration depth $\lambda$. The lower critical field is given by

$$H_{c1||} = \frac{\Phi_0}{4\pi\lambda_{ab}^2}\left(\ln\frac{\lambda_{ab}}{\xi_{ab}} + 0.5\right)$$

and

$$H_{c1^\perp} = \frac{\Phi_0}{4\pi\lambda_{ab}\lambda_c}\left[\ln\left(\frac{\lambda_{ab}\lambda_c}{\xi_{ab}\xi_c}\right)^{1/2} + 0.5\right],$$

and the relations for the upper critical fields are

$$H_{c2||} = \frac{\Phi_0}{2\pi\xi_{ab}^2}$$

and

$$H_{c2^\perp} = \frac{\Phi_0}{2\pi\xi_{ab}\xi_c}.$$

$H_{c|}$ and $H_{c^\perp}$ are the critical fields along the $c$ axis and along the $ab$-plane, respectively; $\Phi_0 = hc/2e$ is the flux quantum.

Magnetic fields $\geq H_{c1}$ penetrate into bulk superconductors in the form of vortices. The structure of the vortices in layered superconducting cuprates is quite different from that in low-$T_{ic}$ conductors. Within conventional low-$T_{ic}$ superconductors the vortices are always line-like Abrikosov vortices (vortex lines). Each of them carries one flux quantum. In principle, it is a tube with the radius of the London penetration depth $\lambda$ in which superconducting screening currents circulate around a small non-superconducting core of the radius of the coherence length $\xi$. But the structure of the vortices in high-$T_c$ superconductors depends on the anisotropy of the compounds and the angle of the applied field

**Table 4.2-14** Critical temperature $T_c$, anisotropy coefficients and coherence lengths of three superconducting compounds

| | $Nb_3Sn$ | $YBa_2Cu_3O_{7-\delta}$ | $Bi_2Sr_2Ca_2Cu_3O_{10-x}$ |
|---|---|---|---|
| $T_c$ (K) | 18 | 92 | 110 |
| $\gamma$ | 1 | $\approx 5$ | $\approx 50$ |
| $\xi$ | 3 (0 K) | | |
| $\xi_{ab}$ (nm) | | 2.5 (0 K) | 2 (0 K) |
| $\xi_c$ (nm) | | 0.5 (0 K) | 0.05 (0 K) |

with regard to the crystal planes. In a field parallel to the *c*-direction in cuprates of low anisotropy such as $YBa_2Cu_3O_{7-\delta}$ the structure of the vortices is similar to that of conventional superconductors. However, in compounds of large anisotropy, in which the distance, *d*, between the $Cu_2$-stacks is larger than two times the coherence length, $\xi_c$, the vortex lines tend to disintegrate into stacks of vortices in different layers that are shaped like pancakes, due to the low Cooper pair density (Fig. 4.2-17).

Only a weak attractive interaction occurs between the pancake vortices of different layers, the strength of which depends on the magnetic field and the temperature. Therefore the pancake vortices are much more flexible than the continuous, relatively rigid vortex lines in conventional superconductors.

An external field parallel to the superconducting *ab*-planes penetrates into the sample in the form of so-called Josephson vortices. They differ from Abrikosov ones by the absence of a vortex core. The superconducting shielding currents are strongly confined to the *ab*-planes. In fields occurring at a small angle to the *ab*-plane the vortices have a step-like character (Fig. 4.2-18). They consist of a periodic sequence of parts parallel (Josephson vortices) and perpendicular (Abrikosov vortices) to the *ab*-planes, respectively. The distance between the "Abrikosov-parts" depends on $\Theta$.

For large-scale applications of the superconducting cuprate phases, an effective pinning of the vortices is an indispensable precondition. Pinning centers can be small defects of the crystal structure such as oxygen vacancies, dislocation loops, screw dislocations (e.g., in thin films), stacking faults, precipitates, and substitutional atoms of foreign elements in the superconducting compound. In a magnetic field parallel to the *ab*-planes, an intrinsic pinning is effective due to the interaction of the Josephson vortices with the periodic potential originating from the $CuO_2$ planes. This kind of pinning is much stronger than that caused by crystal defects.

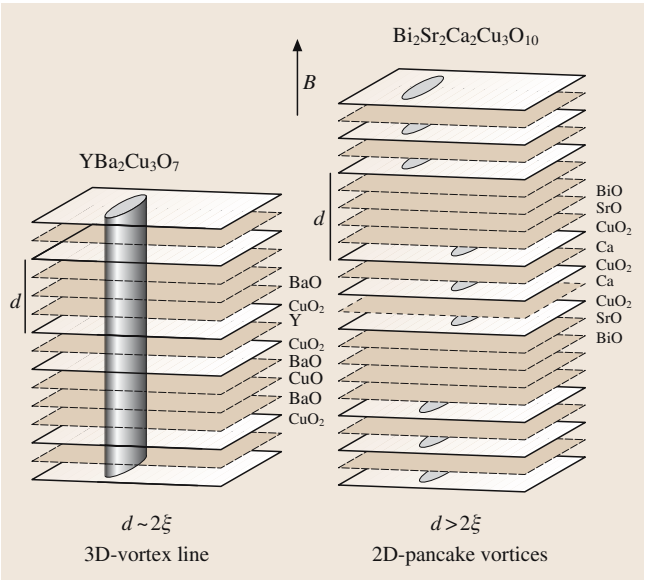


**Fig. 4.2-17** Vortex line in $YBa_2Cu_3O_7$ (*left-hand picture*) and pancake vortices in $Bi_2Sr_2Ca_2Cu_3O_{10}$ (*right-hand picture*); the $Cu_2$-planes are drawn with *bold lines* and the isolating planes with *broken lines*

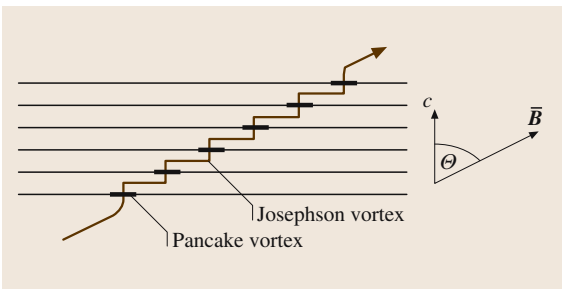


**Fig. 4.2-18** Vortex line caused by an external field exhibiting an angle $\Theta$ to the *ab*-planes

In contrast to conventional superconductors, thermal fluctuations of the vortex positions become very important in high-$T_c$ materials, in particular close to $H_{c2}(T)$. This is a consequence of both the small coherence length $\xi_c$ and the fact that the pinning centers in the cuprates are mainly provided by point defects.

In view of the thermal fluctuation and pinning, the behavior of the vortices determining the resistivity of the system can be demonstrated by the $H$–$T$ phase diagram proposed by [2.19]. A schematic representation is given in Fig. 4.2-19.

An important new feature compared to conventional superconductors is the existence of new vortex phases: a vortex glass phase and a vortex liquid. In cuprates without vortex pinning, a vortex lattice exists in place of the vortex glass. The presence of pinning centers leads to the destruction of the translational long-range order of the vortices, forming the vortex glass phase in which the resistivity is exponentially small. A truly superconducting state with essentially zero resistivity, $\rho(J \to 0) \to 0$ ($J$ = current density) exists only for this phase. Upon increasing the temperature and magnetic field, respec-

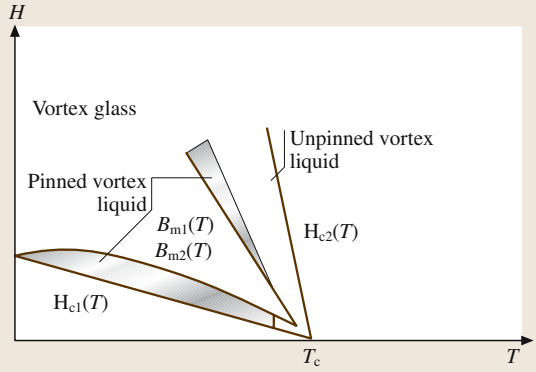


**Fig. 4.2-19** Schematic phenomenological phase diagram for the high-$T_c$ superconductors, including the effects of thermal fluctuations and pinning

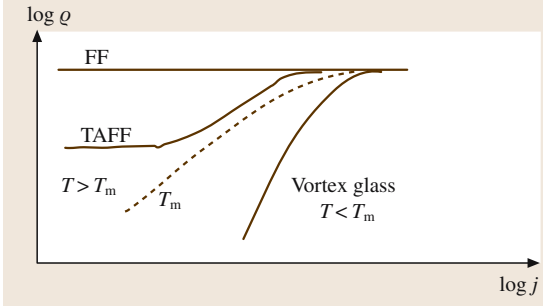


**Fig. 4.2-20** Schematic representation of the resistivity $\rho$ and its dependence on the current density $j$ for three different regions in the phenomenological phase diagram ($T_m$ is the melting line) [2.19]

tively, crossing the "melting line" $B_{m1}(T)$, the coupling between the vortices vanishes completely (i. e., the shear modulus $c_{66}$ of the vortex system becomes zero) and the vortex glass "melts", forming the vortex liquid. Close to $B_{m1}(T)$ the vortex liquid is in the pinned regime because the activation energy $U$ of the vortex motion is still large compared to the thermal energy $k_B T$($k_B$ = Boltzmann constant). However, in this field-temperature region the resistivity is not zero and its temperature dependence $P = E_0/J_c^0\, U/k_B T\, \exp[-U/k_B T]$ for small $J$ follows an Arrhenius law, i. e., the system is in a thermally activated flux flow (TAFF) regime where $E_0$ is the electrical field in the absence of energy barriers and $J_c^0$ the critical current density at $T = 0$ K [2.20]. When $U$ is considerable larger then $k_B T$ ($U/k_B T \geq 10$) a measurable "flux creep" is observed. Closer to the upper critical field $H_{c2}(T)$ the activation energy $U$ is small, $U < k_B T$, and the vortex liquid cannot be pinned. The system is in the flux flow (FF) regime. With increasing temperature in this $H$–$T$ region $\rho$ varies smoothly to the resistivity of the normal state.

The existence of a characteristic irreversibility line $B_{irr}(T)$, which is the boundary between the reversible and irreversible magnetization of the superconductor, is closely related to the vortex glass/vortex liquid transition. By crossing this line from lower to higher $B$ values, the critical current density goes to zero. It should be noted that the vortex glass melts not only on crossing $B_{m1}(T)$ but also with decreasing magnetic field near $H_{c1}(T)$ crossing the line $B_{m2}(T)$, as shown in Fig. 4.2-19. As the field decreases, the distance between the vortices increases and eventually exceeds the London penetration depth $\lambda$. In this case, the vortex–vortex interaction is exponentially small, and consequently the shear modulus $c_{66}$ decays rapidly, leading to a "melting" of the vortex glass.

For each vortex state a specific resistivity–current relation exists, as schematically shown in Fig. 4.2-20. A linear relation occurs for the "flux flow" regime only. Therefore a voltage criterion for the critical current has to be defined. The one generally used is 1 $\mu$V cm$^{-1}$. Extensive reviews of the structure and behavior of vortices in high-$T_c$ superconductors are given in [2.19, 20].

A significant limitation to the critical current density $J_c$ of high-$T_c$ materials is given by the grain boundaries which act as strong resistive barriers to current flow. Figure 4.2-21 shows that the critical current density $J_c$ of $YBa_2Cu_3O_{7-x}$ exhibits an exponential dependence on the misorientation angle $\theta$ between the neighboring crystallites [2.21]. Similar angular dependencies of the grain boundary critical current density were observed for all other high-$T_c$ superconductors [2.21].

This weak link (current obstruction) behavior results from the fact that the width of the disturbed crystal lattice region at the grain boundary is on the order of the coherence length. Therefore, for higher angles, a grain boundary becomes a Josephson weak link due to the local suppression of the superconducting order parameter. The reasons which may be responsible for the suppression of the order parameter leading to the strong dependence of $J_c$ on $\theta$ are discussed extensively in [2.21].

*Applications.* The advantage of high-$T_c$ superconductors is that superconductivity is achieved at temperatures above 77 K where liquid nitrogen can be used as a coolant. However, for many potential applications,

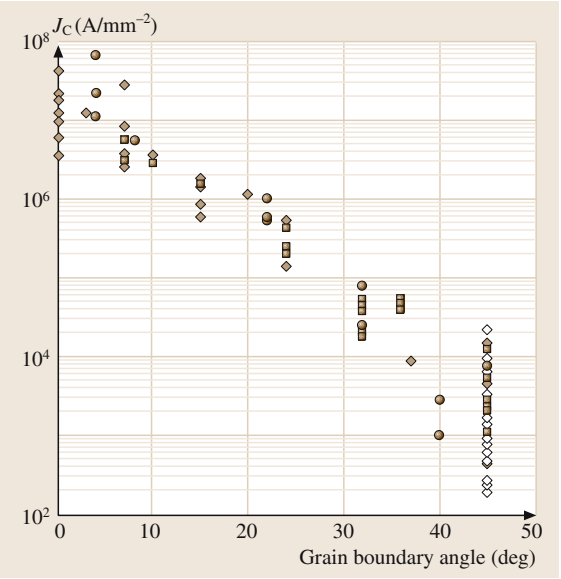


**Fig. 4.2-21** Critical current densities of [001] tilt grain boundaries in $YBa_2Cu_3O_{7-x}$ films as a function of tilt angle. The data published by different authors were compiled by [2.21]

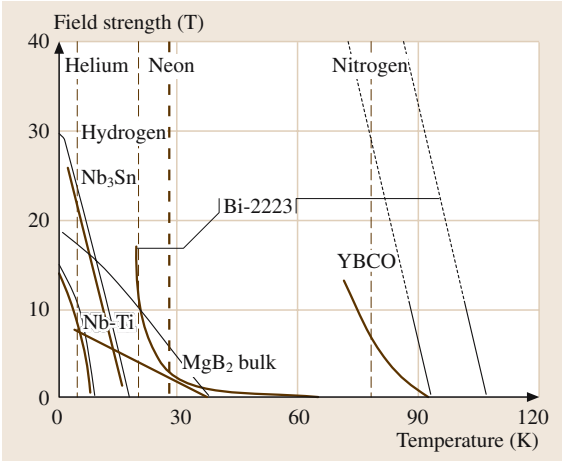


**Fig. 4.2-22** Magnetic field strength versus temperature diagram for various superconducting materials. The upper critical field $H_{c2}$ is indicated by *thin lines*, while the irreversibility field *thick lines* indicate $H_{irr}$

round or flat wires (tapes) with a high critical current density in strong magnetic fields are required. This is true in particular for the use of high-$T_c$ materials in electric power utility devices. Some performance requirements for various electric power applications are summarized in Table 4.2-15 [2.22].

Two main problems discussed above have to be overcome in order to achieve high $J_c$ values. The first one is the current barrier behavior of the grain boundaries, which can be solved by texturing of the crystalline microstructure of the superconducting phase. The second one is the flux flow and flux creep particularly in highly anisotropic materials which have to be avoided and minimized, respectively, in order to obtain a low-loss conductor. Considerable efforts are directed towards flux pinning by the creation of effective pinning centers for the improvement of $J_c$ in high fields at 77 K.

A measurable parameter characterizing the pinning behavior is $H_{irr}(T)$ as mentioned above. In Fig. 4.2-22 this parameter is plotted for the two high-$T_c$ materials $Yba_2Cu_3O_x$ (YBCO) and $(Bi, Pb)_2Sr_2Ca_2Cu_3O_x$ (Bi-2223), which have the most promising $H_{irr}$ characteristics for large scale applications in comparison with $H_{irr}$ of conventional superconductors.

**Table 4.2-15** Requirements for industrial wire performance in various utility device applications

| Application | $J_c$ (A/cm$^2$) | Prevailing field strength (T) | Temperature (K) | $J_c$ (A) | Wire length (m) | Strain (%) | Band radius (m) |
|---|---|---|---|---|---|---|---|
| Fault current limiter | $10^4$–$10^5$ | 0.1–3 | 20–77 | $10^3$–$10^4$ | 1000 | 0.2 | 0.1 |
| Large motor | $10^5$ | 4–5 | 20–77 | 500 | 1000 | 0.2–0.3 | 0.05 |
| Generator | $10^5$ | 4–5 | 20–50 | >1000 | 1000 | 0.2 | 0.1 |
| SMES [a] | $10^5$ | 5–10 | 20–77 | $\approx 10^4$ | 1000 | 0.2 | 1 |
| Transmission cable | $10^4$–$10^5$ | <0.2 | 65–77 | 100 per strand | 100 | 0.4 | 2 (cable) |
| Transformer | $10^5$ | 0.1–0.5 | 65–77 | $10^2$–$10^3$ | 1000 | 0.2 | 1 |

[a] SMES: superconducting magnetic-energy storage

At present, the only high-$T_c$ conductor produced in the form of long wires and tapes is Ag-sheathed Bi-2223. However, a shortcoming of this conductor is the fact, shown in Fig. 4.2-22, that it exhibits an enormous suppression of $H_{irr}(T)$ to the very low value of 0.2 T due to the large anisotropy. Although this does not preclude the use of Bi-2223 for power cables, there is not much scope for use at 77 K in any magnetic field of significant magnitude. This shortcoming of Bi-2223 is an important driving force for the development of a technology based on YBCO, for which $H_{irr}(77\,K) \approx 7\,T$.

Specific properties of superconductors at 77 K may be used for electronic applications, e.g., for passive microwave devices such as transmission lines and high-quality resonators. YBCO is widely used in active devices such as SQUIDs and detectors based on Josephson and quasi-particle tunnelling. A further field of application is the use for high-quality reliable and reproducible high-$T_c$ Josephson junctions. A more extensive account of real and potential large-scale applications, respectively, is given in [2.23].

*Electrical and Structural Data of High-$T_c$ Superconductors.* In Tables 4.2-13 and 4.2-16 electrical and structural data, respectively, of selected high-$T_c$ cuprates are summarized. The data were compiled on the basis of review articles [2.13–16]. In many cases the real stoichiometric coefficients of oxygen are a few tenths higher or lower than the one-digit numbers indicated in the formulas of the tables. The value $\Delta T_c$ is the difference between the temperatures at which the resistance reached 90% and 10% of the normal state resistance, respectively, during cooling of the sample; $\rho(0)$ is the residual resistivity expressed by the formula $\rho(T > T_c) = \rho(0) + \beta(T)$ with $\beta = d\rho/dT$.

**Table 4.2-16** Structural data of high-$T_c$ cuprates

| Compound | Space Group | *a* (nm) | *b* (nm) | *c* (nm) | Ref. |
|---|---|---|---|---|---|
| **$A_2CuO_4$ family** | | | | | |
| $La_{1.9}Sr_{0.1}CuO_4$ | I4/mmm | 0.37839 | 0.37839 | 1.3211 | [2.15] |
| $La_{1.875}Sr_{0.125}CuO_4$ | I4/mmm | 0.37784 | 0.37784 | 1.3216 | [2.15] |
| $La_{1.85}Sr_{0.15}CuO_4$ | | | | | |
| $La_{1.85}Sr_{0.15}CuO_4$ | I4/mmm | 0.37793 | 0.37793 | 1.32260 | [2.15] |
| $La_{1.775}Sr_{0.225}CuO_4$ | I4/mmm | 0.37708 | 0.37708 | 1.3247 | [2.15] |
| $La_{1.725}Sr_{0.275}CuO_4$ | I4/mmm | 0.37666 | 0.37666 | 1.3225 | [2.15] |
| $(Nd_{2-x}Ce_x)CuO_4$ | I4/mmm | 0.39469 | 0.39469 | 1.20776 | [2.15, 16] |
| | I4/mmm | 0.395 | | 1.207 | |
| **$LBa_2Cu_3O_{7-x}$ family** | | | | | |
| $YBa_2Cu_3O_{6.67}$ | Pmmm | 0.3831 | 0.3889 | 1.1736 | [2.15] |
| $YBa_2Cu_3O_7$ | Pmmm | 0.38198 | 0.38849 | 1.16762 | [2.15] |
| $(Y_{0.95}Pr_{0.05})Ba_2Cu_3O_7$ | Pmmm | | | | [2.15] |
| $(Y_{0.9}Pr_{0.1})Ba_2Cu_3O_7$ | Pmmm | | | | [2.15] |
| $(Y_{0.8}Pr_{0.2})Ba_2Cu_3O_7$ | Pmmm | | | | [2.15] |
| $(Y_{0.7}Pr_{0.3})Ba_2Cu_3O_7$ | Pmmm | | | | [2.15] |
| $(Y_{0.6}Pr_{0.4})Ba_2Cu_3O_7$ | Pmmm | | | | [2.15] |
| $YBa_2(Cu_{0.99}Fe_{0.01})_3O_7$ | Pmmm | | | | [2.15] |
| $YBa_2(Cu_{0.975}Fe_{0.025})_3O_7$ | Pmmm | | | | [2.15] |
| $YBa_2(Cu_{0.95}Fe_{0.05})_3O_7$ | Pmmm | | | | [2.15] |
| $YBa_2(Cu_{0.99}Zn_{0.01})_3O_7$ | Pmmm | | | | [2.15] |
| $YBa_2(Cu_{0.975}Zn_{0.025})_3O_7$ | Pmmm | 0.3820 | 0.3890 | 1.1673 | [2.15] |
| $YBa_2(Cu_{0.95}Zn_{0.05})_3O_7$ | Pmmm | 0.3820 | 0.38851 | 1.1671 | [2.15] |
| $HoBa_2Cu_3O_7$ | Pmmm | 0.38460 | 0.3881 | 1.1640 | [2.15] |

**Table 4.2-16** Structural data of high-$T_c$ cuprates, cont.

| Compound | Space Group | *a* (nm) | *b* (nm) | *c* (nm) | Ref. |
|---|---|---|---|---|---|
| **$A_mE_2Ca_{n-1}Cu_nO_{2n+m+2}$ family** | | | | | |
| $Bi_2(Sr_{1.6}La_{0.4})CuO_{6+x}$ | Cmmm | 0.5370 | 0.5400 | 0.2450 | [2.15] |
| $(Bi, Pb)_2(Sr_{1.75}La_{0.25})CuO_6$ | Cmmm | 0.5282 | 0.5410 | 2.462 | [2.15] |
| $Bi_2Sr_2CaCu_2O_8$ (no-anneal) | Fmmm | 0.5413 | 0.5411 | 3.091 | [2.15] |
| $Bi_2Sr_2CaCu_2O_{8+x}$ ($O_2$-annealed) | Fmmm | 0.5408 | 0.5413 | 3.081 | [2.15] |
| $Bi_2Sr_2Ca_2Cu_3O_{10}$ | Fmmm | 0.539 | 0.539 | 3.71 | [2.15] |
| $(Bi_{1.6}Pb_{0.4})Sr_2Ca_2Cu_3O_{10}$ | Fmmm | 0.5413 | 0.5413 | 3.7100 | [2.15] |
| $Pb_2Sr_2Ca_{0.5}Ln_{0.5}Cu_3O_8$ | C/mmm | 0.5435 | 0.5463 | 1.5817 | [2.16] |
| $Tl_2Ba_2CuO_6$ | I4/mmm | 0.3866 | 0.38662 | 2.3239 | [2.15] |
| $Tl_2Ba_2CaCu_2O_8$ | I4/mmm | 0.38550 | 0.38550 | 2.9318 | [2.15, 16] |
| $Tl_2Ba_2Ca_2Cu_3O_{10}$ | I4/mmm | 0.38503 | 0.38503 | 3.588 | [2.15] |
| $TlBa_2Ca_2Cu_3O_9$ | P4/mmm | 0.3853 | | 1.5913 | [2.16] |
| $(Tl_{0.5}Pb_{0.5})Sr_2CaCu_2O_7$ | P4/mmm | 0.38023 | 0.38023 | 1.2107 | [2.15] |
| $(Tl_{0.5}Pb_{0.5})Sr_2(Ca_{0.8}Y_{0.2})Cu_2O_7$ | P4/mmm | 0.38075 | 0.38075 | 1.2014 | [2.15] |
| $(Tl_{0.5}Pb_{0.5})Sr_2Ca_2Cu_3O_9$ | P4/mmm | 0.38206 | 0.38206 | 1.5294 | [2.15] |
| $TlSr_2Ca_{0.5}Y_{0.5}Cu_2O_7$ | P4/mmm | 0.380 | | 1.210 | [2.16] |
| $Pb_2(Y_{1-x}Ca_x)Sr_2Cu_3O_8$ | Cmmm | 0.53933 | 0.54311 | 1.57334 | [2.15] |
| **$AE_2CuO_{4-5}$ family** | | | | | |
| $(Hg_{0.8}V_{0.2})Ba_2CuO_{4.3}$ | | 0.38860 | | 0.9338 | [2.14] |
| $(Hg_{0.8}Mo_{0.2})Ba_2CuO_{4.4}$ | | 0.3882 | | 0.9378 | [2.14] |
| $(Hg_{0.9}Mo_{0.1})Ba_2CuO_{4.2}$ | | 0.3875 | | 0.9435 | [2.14] |
| $(Hg_{0.8}W_{0.2})Ba_2CuO_{4.4}$ | | 0.3871 | | 0.9416 | [2.14] |
| $(Hg_{0.9}W_{0.1})Ba_2CuO_{4.2}$ | | 0.3875 | | 0.9450 | [2.14] |
| **$AE_2CuO_{4-5}$ family** | | | | | |
| $(Hg_{0.8}Ru_{0.2})Ba_2CuO_{4.2}$ | | 0.3879 | | 0.9473 | [2.14] |
| $(Hg_{0.7}Cr_{0.3})Sr_2CuO_{4.15}$ | | 0.3845 | | 0.8683 | [2.14] |
| $(Hg_{0.8}Mn_{0.2})Ba_2CuO_{4.2}$ | | 0.3890 | | 0.9343 | [2.14] |
| $(Hg_{0.8}Nb_{0.2})Ba_2CuO_{4.3}$ | | 0.3885 | | 0.9461 | [2.14] |
| $(Hg_{0.8}Mo_{0.2})Sr_2CuO_x$ | | 0.3797 | | 0.8818 | [2.14] |
| $(Hg_{0.9}Re_{0.1})Sr_2CuO_x$ | | 0.3783 | | 0.8883 | [2.14] |
| **$A_2Ca_{n-1}Cu_nO_{2n+2}$ family** | | | | | |
| $La_{1.6}Sr_{0.4}CaCu_2O_6$ | I4/mmm | 0.38208 | 0.38208 | 1.95993 | [2.15] |
| **Other Compounds** | | | | | |
| $YBa_2Cu_4O_8$ | Ammm | 0.386 | 0.386 | 2.724 | [2.15] |
| $HoBa_2Cu_4O_8$ | Ammm | 0.3855 | 0.3874 | 2.7295 | [2.15] |
| $Bi_2Sr_2(Ln_{1-x}Ce_x)_2Cu_2O_{10}$ | P4/mmm | 0.3888 | | 1.728 | [2.16] |
| $YBa_2(Cu_{0.99}Fe_{0.01})_3O_7$ | Pmmm | | | | [2.15] |
| $YBa_2(Cu_{0.975}Fe_{0.025})_3O_7$ | Pmmm | | | | [2.15] |
| $YBa_2(Cu_{0.95}Fe_{0.05})_3O_7$ | Pmmm | | | | [2.15] |
| $YBa_2(Cu_{0.99}Zn_{0.01})_3O_7$ | Pmmm | | | | [2.15] |
| $YBa_2(Cu_{0.975}Zn_{0.025})_3O_7$ | Pmmm | 0.3820 | 0.3890 | 1.1673 | [2.15] |
| $YBa_2(Cu_{0.95}Zn_{0.05})_3O_7$ | Pmmm | 0.3820 | 0.38851 | 1.1671 | [2.15] |
| $HoBa_2Cu_3O_7$ | Pmmm | 0.38460 | 0.3881 | 1.1640 | [2.15] |

**Table 4.2-16** Structural data of high-$T_c$ cuprates, cont.

| Compound | Space Group | *a* (nm) | *b* (nm) | *c* (nm) | Ref. |
|---|---|---|---|---|---|
| **$A_mE_2Ca_{n-1}Cu_nO_{2n+m+2}$ family** | | | | | |
| $Bi_2(Sr_{1.6}La_{0.4})CuO_{6+x}$ | Cmmm | 0.5370 | 0.5400 | 0.2450 | [2.15] |
| $(Bi, Pb)_2(Sr_{1.75}La_{0.25})CuO_6$ | Cmmm | 0.5282 | 0.5410 | 2.462 | [2.15] |
| $Bi_2Sr_2CaCu_2O_8$ (no-anneal) | Pmmm | 0.5413 | 0.5411 | 3.091 | [2.15] |
| $Bi_2Sr_2CaCu_2O_{8+x}$ ($O_2$-annealed) | Pmmm | 0.5408 | 0.5413 | 3.081 | [2.15] |
| $Bi_2Sr_2Ca_2Cu_3O_{10}$ | Pmmm | 0.539 | 0.539 | 3.71 | [2.15] |
| $(Bi_{1.6}Pb_{0.4})Sr_2Ca_2Cu_3O_{10}$ | Pmmm | 0.5413 | 0.5413 | 3.7100 | [2.15] |
| $Pb_2Sr_2Ca_{0.5}Ln_{0.5}Cu_3O_8$ | C/mmm | 0.5435 | 0.5463 | 1.5817 | [2.16] |
| $Tl_2Ba_2CuO_6$ | I4/mmm | 0.3866 | 0.38662 | 2.3239 | [2.15] |
| $Tl_2Ba_2CaCu_2O_8$ | I4/mmm | 0.38550 | 0.38550 | 2.9318 | [2.15, 16] |
| $Tl_2Ba_2Ca_2Cu_3O_{10}$ | I4/mmm | 0.38503 | 0.38503 | 3.588 | [2.15] |
| $TlBa_2Ca_2Cu_3O_9$ | P4/mmm | 0.3853 | | 1.5913 | [2.16] |
| $(Tl_{0.5}Pb_{0.5})Sr_2CaCu_2O_7$ | P4/mmm | 0.38023 | 0.38023 | 1.2107 | [2.15] |
| $(Tl_{0.5}Pb_{0.5})Sr_2(Ca_{0.8}Y_{0.2})Cu_2O_7$ | P4/mmm | 0.38075 | 0.38075 | 1.2014 | [2.15] |
| $(Tl_{0.5}Pb_{0.5})Sr_2Ca_2Cu_3O_9$ | P4/mmm | 0.38206 | 0.38206 | 1.5294 | [2.15] |
| $TlSr_2Ca_{0.5}Y_{0.5}Cu_2O_7$ | P4/mmm | 0.380 | | 1.210 | [2.16] |
| $Pb_2(Y_{1-x}Ca_x)Sr_2Cu_3O_8$ | Cmmm | 0.53933 | 0.54311 | 1.57334 | [2.15] |
| **$AE_2CuO_{4-5}$ family** | | | | | |
| $(Hg_{0.8}V_{0.2})Ba_2CuO_{4.3}$ | | 0.38860 | | 0.9338 | [2.14] |
| $(Hg_{0.8}Mo_{0.2})Ba_2CuO_{4.4}$ | | 0.3882 | | 0.9378 | [2.14] |
| $(Hg_{0.9}Mo_{0.1})Ba_2CuO_{4.2}$ | | 0.3875 | | 0.9435 | [2.14] |
| $(Hg_{0.8}W_{0.2})Ba_2CuO_{4.4}$ | | 0.3871 | | 0.9416 | [2.14] |
| $(Hg_{0.9}W_{0.1})Ba_2CuO_{4.2}$ | | 0.3875 | | 0.9450 | [2.14] |
| $(Hg_{0.8}Ru_{0.2})Ba_2CuO_{4.2}$ | | 0.3879 | | 0.9473 | [2.14] |
| $(Hg_{0.7}Cr_{0.3})Sr_2CuO_{4.15}$ | | 0.3845 | | 0.8683 | [2.14] |
| $(Hg_{0.8}Mn_{0.2})Ba_2CuO_{4.2}$ | | 0.3890 | | 0.9343 | [2.14] |
| $(Hg_{0.8}Nb_{0.2})Ba_2CuO_{4.3}$ | | 0.3885 | | 0.9461 | [2.14] |
| $(Hg_{0.8}Mo_{0.2})Sr_2CuO_x$ | | 0.3797 | | 0.8818 | [2.14] |
| $(Hg_{0.9}Re_{0.1})Sr_2CuO_x$ | | 0.3783 | | 0.8883 | [2.14] |
| **$A_2Ca_{n-1}Cu_nO_{2n+2}$ family** | | | | | |
| $La_{1.6}Sr_{0.4}CaCu_2O_6$ | I4/mmm | 0.38208 | 0.38208 | 1.95993 | [2.15] |
| **Other Compounds** | | | | | |
| $YBa_2Cu_4O_8$ | Ammm | 0.386 | 0.386 | 2.724 | [2.15] |
| $HoBa_2Cu_4O_8$ | Ammm | 0.3855 | 0.3874 | 2.7295 | [2.15] |
| $Bi_2Sr_2(Ln_{1-x}Ce_x)_2Cu_2O_{10}$ | P4/mmm | 0.3888 | | 1.728 | [2.16] |
| $Ca_{1-x}Sr_xCu_2O_2$ | P4/mmm | 0.3902 | | 0.335 | [2.16] |
| $(Pb, Cu)Sr_2(Ln, Ca)Cu_2O_7$ | P4/mmm | 0.3820 | | 1.1826 | [2.16] |
| $(Pb, Cu)(Sr, Eu)(Eu, Ce)Cu_2O_x$ | I4/mmm | 0.3837 | 2.901 | | [2.16] |
| $Sr_{1-x}Nd_xCuO_2$ | P4/mmm | 0.3942 | | 0.3393 | [2.16] |
| $Tl(Ba, La)CuO_5$ | P4/mmm | 0.383 | | 0.955 | [2.16] |
| $Tl(Sr, La)CuO_5$ | P4/mmm | $\approx 0.37$ | | $\approx 0.9$ | [2.16] |
| $(Tl_{0.5}Pb_{0.5})Sr_2CuO_6$ | | | | | [2.16] |
| $(Tl_{0.7}Cd_{0.3})BaLaCuO_5$ | P4/mmm | 0.3844 | 0.38440 | 0.916 | [2.15] |

### 4.2.2.2 Superconductors Based on the Y–Ba–Cu–O System

The first superconducting compound with $T_c$ above the boiling point of liquid nitrogen ($T \approx 77$ K) was discovered as a mixed copper oxide representative of the system Y–Ba–Cu–O at ambient pressure by *Wu* et al. in 1987 [2.25], and marked the beginning of the worldwide high-temperature superconductor (HTSC) research. Since then, $YBa_2Cu_3O_{7-\delta}$ is one of the compounds studied most frequently. It is often abbreviated as "Y-123" or "YBCO".

#### Structural Properties

*Crystal Structure.* The crystal structure of $YBa_2Cu_3O_{7-\delta}$ has been analysed by diffraction studies and high resolution electron microscopy. The structure is of an orthorhombic perovskite type with oxygen deficiency and an ordered arrangement of the cations Y and Ba (Fig. 4.2-23). Compared with octahedral coordination in the perovskite type structure, 2/9 of the oxygen sites in YBCO are unoccupied, leading to coordination numbers $CN = 5$ and $CN = 4$ for two different Cu sites, respectively. For $\delta = 0$ the unit cell contains one Cu atom in the oxidation state +3 and two Cu atoms in the oxidation state +2. The latter Cu atoms are coordinated by five O atoms forming a square-pyramidal coordination sphere (4 shorter Cu–O bonds, $d$(Cu–O) < 2 Å; one longer bond to the apex of the pyramid, $d \approx 2.29$ Å), while the remaining Cu atom shows a fourfold, nearly square-planar coordination ($d$(Cu–O) < 2 Å). These rectangles are connected via vertices forming chains along the *b* axis [010]. The pyramids are also connected via vertices forming a two-dimensional arrangement within the *ab*-plane. The O–Cu–O angles within the layers are smaller than 180°, thus distorting the planar character of the layers. Ba atoms are coordinated by ten O atoms whereas Y atoms show $CN = 8$.

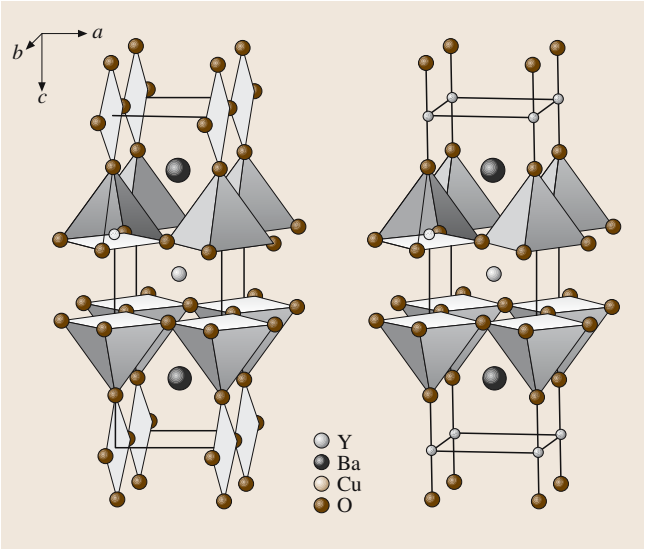


**Fig. 4.2-23** Crystal structure of $YBa_2Cu_3O_7$ ($\delta = 0$, *left*) and $YBa_2Cu_3O_6$ ($\delta = 1$, *right*)

The high-$T_c$ compound $YBa_2Cu_3O_{7-\delta}$ crystallizes in the orthorhombic space group *Pmmm* (No. 47) with $T_c \approx 91$ K for $0 \leq \delta \leq 0.2$ (Table 4.2-17). The superconducting properties depend on the oxygen content $7 - \delta$. Oxygen loss on the 1*e* site [O(1) in $YBa_2Cu_3O_7$] leads to a destruction of the Cu–O chains. For $\delta = 1$ only linear coordinated Cu(1) atoms are present.

**Table 4.2-17** Crystal structure data of orthorhombic $YBa_2Cu_3O_7$ at $T = 300$ K [2.24]

| **Formula** | | **$YBa_2Cu_3O_7$** | | |
|---|---|---|---|---|
| **Space group** | | ***Pmmm* (No. 47)** | | |
| **Lattice parameters** | | ***a* = 3.8206(1) Å** | | |
| | | ***b* = 3.8851(1) Å** | | |
| | | ***c* = 11.6757(4) Å** | | |
| Atom | Site | *x* | *y* | *z* |
| Y | 1*h* | 1/2 | 1/2 | 1/2 |
| Ba | 2*t* | 1/2 | 1/2 | 0.1841(4) |
| Cu(1) | 1*a* | 0 | 0 | 0 |
| Cu(2) | 2*q* | 0 | 0 | 0.3549(3) |
| O(1) | 1*e* | 0 | 1/2 | 0 |
| O(2) | 2*q* | 0 | 0 | 0.1581(4) |
| O(3) | 2*r* | 0 | 1/2 | 0.3777(5) |
| O(4) | 2*s* | 1/2 | 0 | 0.3779(4) |

**Table 4.2-18** Crystal structure data of tetragonal $YBa_2Cu_3O_6$ [2.26]

| **Formula**<br>**Space group**<br>**Lattice parameters** | | **$YBa_2Cu_3O_6$**<br>***P4/mmm* (No. 123)**<br>**$a = 3.865(1)$ Å**<br>**$c = 11.852(3)$ Å** | | |
|---|---|---|---|---|
| Atom | Site | $x$ | $y$ | $z$ |
| Y | 1*d* | 1/2 | 1/2 | 1/2 |
| Ba | 2*h* | 1/2 | 1/2 | 0.1951(2) |
| Cu(1) | 1*a* | 0 | 0 | 0 |
| Cu(2) | 2*g* | 0 | 0 | 0.3609(1) |
| O(1) | 2*g* | 0 | 0 | 0.1521(5) |
| O(2) | 4*i* | 0 | 1/2 | 0.3793(3) |

The non-superconducting $YBa_2Cu_3O_{7-\delta}$ phase with $0.5 \leq \delta \leq 1$, an antiferromagnetic insulator, crystallizes in a tetragonal unit cell, space group $P4/mmm$ (No. 123) (Table 4.2-18).

The temperature dependence of the lattice parameters of orthorhombic $YBa_2Cu_3O_{6.91}$ (see Fig. 4.2-24) was determined [2.27] in the range $5\,K \leq T \leq 320\,K$. With decreasing temperature the lattice contracts mainly along [001] perpendicular to the Cu−O layers. Small anomalies of the lattice parameters occur at 90 K.

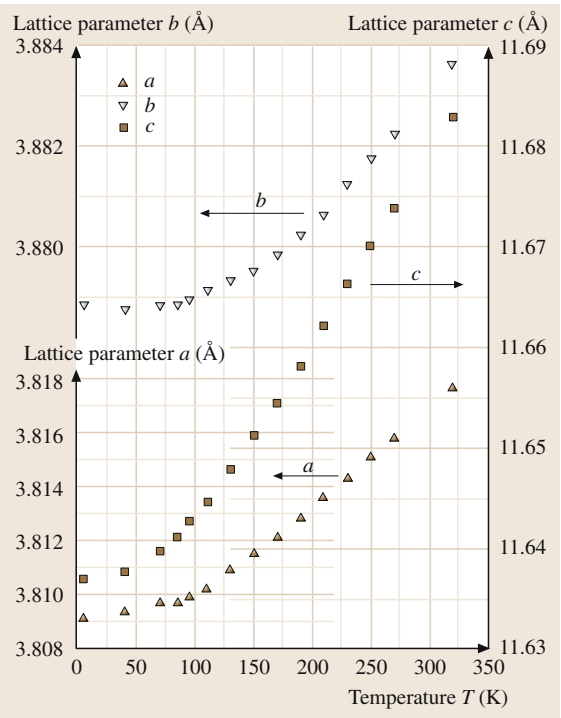


**Fig. 4.2-24** Lattice parameters of $YBa_2Cu_3O_{6.91}$ as function of the temperature [2.27].

*Oxygen Content in $YBa_2Cu_3O_{7-\delta}$.* The oxygen content of $YBa_2Cu_3O_{7-\delta}$ depends on temperature and oxygen partial pressure. $YBa_2Cu_3O_7$ can be prepared at $T < 400\,°C$ in an oxygen atmosphere. The oxygen content can be controlled by annealing in an inert atmosphere or vacuum, or by O-gettering with Zr or Ti. The lower the O partial pressure during annealing of $YBa_2Cu_3O_7$, the larger is the weight loss (Table 4.2-19, Fig. 4.2-25).

Increasing O loss leads to an increase of the lattice parameters $a$ and $c$, whereas $b$ decreases. At the phase transformation from the orthorhombic to the tetragonal symmetry ($7 - \delta \approx 6.35$) a discontinuious length change

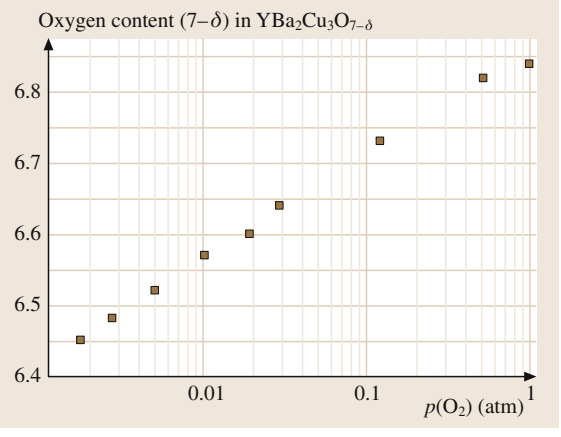


**Fig. 4.2-25** Oxygen content $(7 - \delta)$ of $YBa_2Cu_3O_{7-\delta}$ determined by weight loss, annealing conditions: $T = 520\,°C$, $t$ between 21 h and 27 h at different oxygen partial pressures $p(O_2)$ [2.28]

**Table 4.2-19** Annealing conditions according to [2.28] for oxygen-deficient samples $YBa_2Cu_3O_{7-\delta}$, $T = 520\,°C$

| Annealing conditions | | Oxygen content $(7-\delta)$ |
|---|---|---|
| $p(O_2)$(atm) | $t$(h) | Weight loss |
| 1.00 | 21 | 6.84 |
| 0.515 | 25 | 6.82 |
| 0.12 | 22 | 6.73 |
| 0.29 | 27 | 6.64 |
| 0.019 | 23 | 6.60 |
| 0.010 | 21 | 6.57 |
| 0.005 | 22 | 6.52 |
| 0.0027 | 21 | 6.48 |
| 0.00175 | 22 | 6.45 |
| 0.00107 | 21 | 6.40 |
| 0.001 | 22 | 6.40 |
| 0.000415 | 23 | 6.34 |

in the $c$ axis occurs, whereas $a$ and $b$ become equal (Table 4.2-20, Fig. 4.2-26).

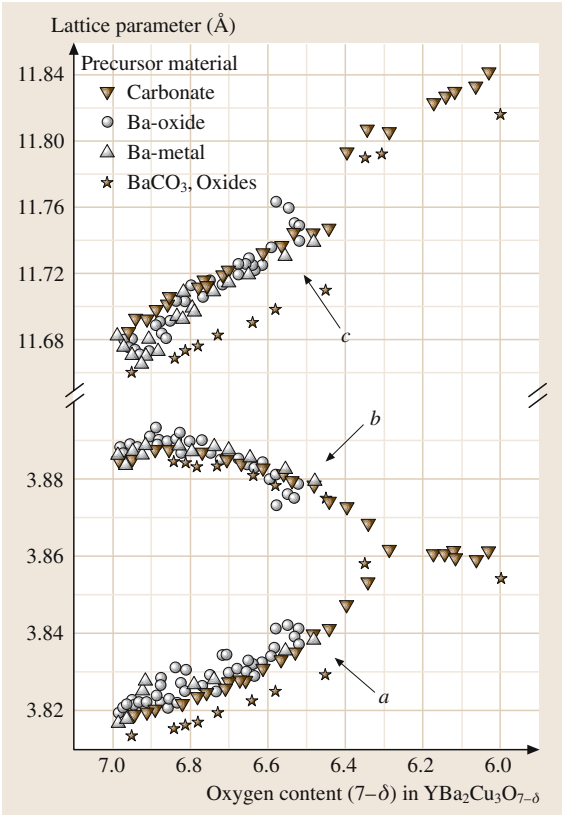


**Fig. 4.2-26** Lattice parameters of $YBa_2Cu_3O_{7-\delta}$ as a function of the oxygen content $7-\delta$; samples prepared from different precursor materials ▼ [2.29]; ∘ [2.29]; △ [2.29]; ∗ [2.30]

*Chemical Substitution. $RBa_2Cu_3O_{7-\delta}$: R = Y and Rare-earth Metals; $7-\delta = 6$ and 7.* The substitution of Y by trivalent rare earth metals has been studied extensively. The materials Ce and Tb do not form the orthorhombic 123-phase, and $PmBa_2Cu_3O_7$ has not been synthesized due to the short lifetime of radioactive Pm. The Lu compound is unstable in the polycrystalline ceramic form, but can be prepared as thin films.

For $RBa_2Cu_3O_{7-\delta}$ ($7-\delta = 6$ and 7), the lattice parameters as well as a large number of interatomic distances show linear dependence on the ionic radius of the trivalent rare earth metal according to the lanthanide contraction, except for $PrBa_2Cu_3O_7$ which is semiconducting, antiferromagnetic and shows no superconductivity. The superconducting transition temperature reaches a maximum for the Nd phase (Tables 4.2-21–4.2-22, Figs. 4.2-27–4.2-29).

*Further Substitutions.* Calcium atoms can substitute Y. The higher the Ca content, the lower is $T_c$. Substitution on the Ba site is reported for La, Sr, Nd, as well as for Na and K. Copper atoms can be substituted by transition metals $M$ (e.g. $M$ = Ti, V, Cr, Mn, Fe, Co, Ni, Zn, Pd, Ag) and main group metals (e.g. Li, Mg, Al, Ga). Concerning the substitution of oxygen, only fluorine has

**Table 4.2-20** Dependence of the lattice parameters and $T_c$ on the oxygen content [2.30] (n.d. = not determined)

| Oxygen content $(7-\delta)$ in $YBa_2Cu_3O_{7-\delta}$ | $T_c$ (K) | $a$ (Å) | $b$ (Å) | $c$ (Å) | $V$ (Å$^3$) |
|---|---|---|---|---|---|
| 6.95 | 90 | 3.8136 | 3.8845 | 11.6603 | 172.73 |
| 6.84 | 88 | 3.8153 | 3.8848 | 11.6692 | 172.96 |
| 6.81 | 86 | 3.8163 | 3.8845 | 11.6739 | 173.06 |
| 6.78 | n.d. | 3.817 | 3.8836 | 11.6768 | 173.09 |
| 6.73 | 69 | 3.8193 | 3.8835 | 11.6832 | 173.29 |
| 6.64 | 59 | 3.8224 | 3.8811 | 11.6912 | 173.44 |
| 6.58 | 56 | 3.8252 | 3.8786 | 11.6987 | 173.57 |
| 6.45 | 56 | 3.8293 | 3.875 | 11.7101 | 173.76 |
| 6.35 | – | 3.858 | 3.858 | 11.7913 | 175.50 |
| 6 | – | 3.8544 | 3.8544 | 11.8175 | 175.57 |

**Table 4.2-21** Lattice parameters of $RBa_2Cu_3O_{7-\delta}$ (orthorhombic, *Pmmm*) according to *Guillaume* et al. [2.32] at $T = 10$ K, superconducting transition temperature $T_c$ [2.32] and structural phase transformation temperature orthorhombic → tetragonal $T_{trans}$ [2.33]; ionic radii according to *Shannon* [2.34]

| Atom $R$ | Ionic radius $r$ of $R^{3+}$ (Å), $CN = 8$ | $a$ (Å) | $b$ (Å) | $c$ (Å) | $V$ (Å$^3$) | Oxygen content $(7-\delta)$ | $T_c$ (K) | $T_{trans}$ (K) |
|---|---|---|---|---|---|---|---|---|
| Y | 1.019 | 3.817(1) | 3.883(1) | 11.637(1) | 172.48 | 7.00 | 90(1) | 959 |
| La | 1.160 | 3.903(1) | 3.920(1) | 11.735(1) | 179.54 | 7.06(5) | 50(3) | 620 |
| Ce | 1.143 | | | | | | | |
| Pr | 1.126 | 3.863(1) | 3.918(1) | 11.650(1) | 176.33 | 6.98(3) | 0 | |
| Nd | 1.109 | 3.856(1) | 3.912(1) | 11.719(1) | 176.78 | 6.98(3) | 96(1) | 839 |
| Pm | 1.093 | | | | | | | |
| Sm | 1.079 | 3.844(1) | 3.901(1) | 11.692(1) | 175.33 | 6.98(3) | 94(1) | 888 |
| Eu | 1.066 | 3.836(1) | 3.897(1) | 11.682(1) | 174.63 | 6.98(3) | 95(1) | 906 |
| Gd | 1.053 | 3.831(1) | 3.893(1) | 11.667(1) | 174.00 | 6.99(3) | 94(1) | 914 |
| Tb | 1.040 | | | | | | | |
| Dy | 1.027 | 3.820(1) | 3.885(1) | 11.646(1) | 172.83 | 6.98(3) | 92(1) | 945 |
| Ho | 1.015 | 3.815(1) | 3.882(1) | 11.635(1) | 172.31 | 7.02(3) | 90(1) | 964 |
| Er | 1.004 | 3.810(1) | 3.879(1) | 11.625(1) | 171.81 | 7.02(3) | 90(1) | 972 |
| Tm | 0.994 | 3.805(1) | 3.876(1) | 11.616(1) | 171.31 | 7.02(3) | 90(1) | 979 |
| Yb | 0.985 | 3.800(1) | 3.872(1) | 11.607(1) | 170.78 | 7.02(3) | 90(1) | 954 |
| Lu | 0.977 | | | | | | 92 | |

**Table 4.2-22** Lattice parameters of $RBa_2Cu_3O_{7-\delta}$ (tetragonal, $P4/mmm$) according to *Guillaume* et al. [2.32] at $T = 10$ K, ionic radii according to *Shannon* [2.34]

| Atom $R$ | Ionic radius $r$ of $R^{3+}$ (Å), $CN = 8$ | $a$ (Å) | $c$ (Å) | $V$ (Å$^3$) | Oxygen content $(7-\delta)$ |
|---|---|---|---|---|---|
| Y | 1.019 | 3.856(1) | 11.793(1) | 175.35 | 6.11(3) |
| La | 1.160 | 3.915(1) | 11.850(1) | 181.63 | 6.04(3) |
| Ce | 1.143 | | | | |
| Pr | 1.126 | 3.900(1) | 11.832(1) | 179.96 | 6.15(3) |

**Table 4.2-22** Lattice parameters of $RBa_2Cu_3O_{7-\delta}$ (tetragonal, $P4/mmm$) according to *Guillaume* et al. [2.32] at $T = 10$ K, ionic radii according to *Shannon* [2.34], cont.

| Atom $R$ | Ionic radius $r$ of $R^{3+}$ (Å), $CN = 8$ | $a$ (Å) | $c$ (Å) | $V$ (Å$^3$) | Oxygen content $(7-\delta)$ |
|---|---|---|---|---|---|
| Nd | 1.109 | 3.893(1) | 11.830(1) | 179.29 | 6.12(3) |
| Pm | 1.093 | | | | |
| Sm | 1.079 | 3.880(1) | 11.815(1) | 177.87 | 6.11(3) |
| Eu | 1.066 | 3.879(1) | 11.811(1) | 177.72 | 6.13(3) |
| Gd | 1.053 | 3.872(1) | 11.807(1) | 177.02 | 6.06(3) |
| Tb | 1.040 | | | | |
| Dy | 1.027 | 3.860(1) | 11.796(1) | 175.76 | 6.12(3) |
| Ho | 1.015 | 3.855(1) | 11.792(1) | 175.24 | 6.10(3) |
| Er | 1.004 | 3.850(1) | 11.789(1) | 174.74 | 6.08(3) |
| Tm | 0.994 | 3.843(1) | 11.785(1) | 174.05 | 6.10(3) |
| Yb | 0.985 | 3.839(1) | 11.781(1) | 173.63 | 6.14(3) |
| Lu | 0.977 | | | | |

been studied intensively. $T_c$ decreases with increasing substitution nearly without exception (see "Superconducting transition temperature"). For additional partial substitution possibilities and advanced literature: [2.31].

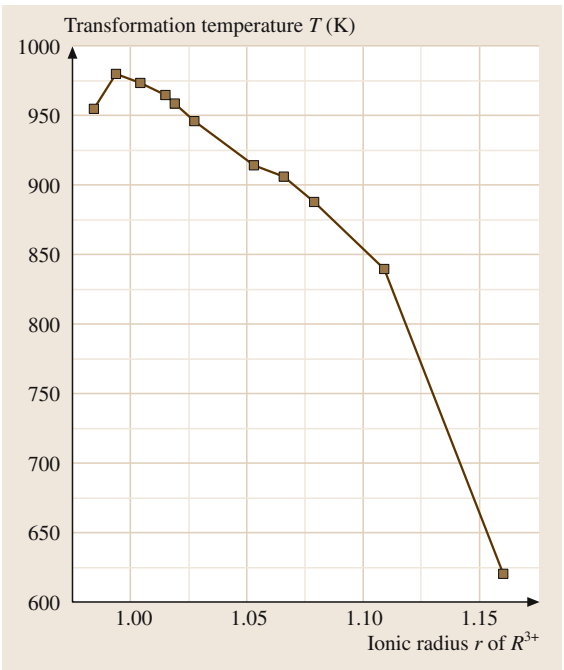


**Fig. 4.2-27** Orthorhombic to tetragonal transformation temperature $T_{trans}$ at an oxygen partial pressure of $p = 1$ atm as a function of the ionic radii of the $R^{3+}$ ions ($CN = 8$)

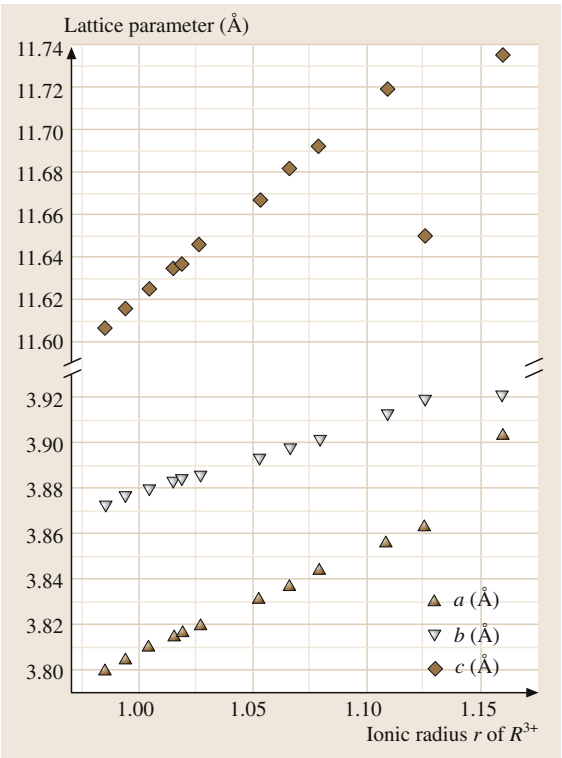


**Fig. 4.2-28** Lattice parameters of $RBa_2Cu_3O_7$ (orthorhombic, $Pmmm$) [2.32] at $T = 10$ K, with ionic radii according to *Shannon* [2.34]. Note the large deviation of the lattice parameter $c$ of non-superconducting $PrBa_2Cu_3O_7$

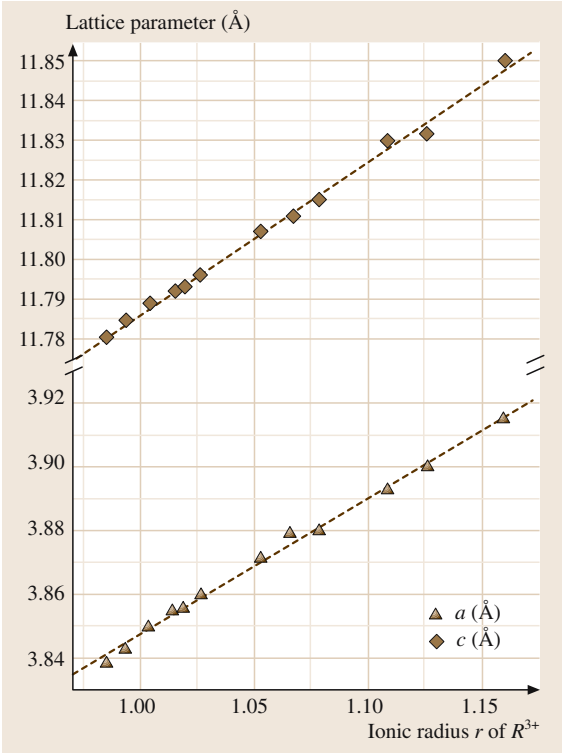


**Fig. 4.2-29** Lattice parameters of $R Ba_2Cu_3O_6$ (tetragonal, $P4/mmm$) [2.32] at $T = 10\,K$, ionic radii according to *Shannon* [2.34]

*Microstructural Features.* Crystal defects in YBCO grown from the melt may be grouped into crystal defects which are associated with the solidification process and those which are influenced by volume fraction and the size of the secondary phase $Y_2BaCuO_5$ particles, the so-called 211-phase. *Diko* [2.37] specified the groups of crystal defects as follows:

Crystal defects associated with crystallization from the melt:

- Porosity
- Subgrains
- 211-particles and their inhomogeneity in the sample
- Shape change of the sample
- High angle grain boundaries
- Macrocracks
- Secondary phases

Crystal defects influenced by the volume fraction and size of 211-particles:

- Residual dilation stresses around 211 particles
- Microcracks in *a*-*b* planes
- Twin structures

*211-Particles.* Non-superconducting 211-particles may be formed as a dispersion in the 123-phase as the matrix. These particles have a strong pinning effect on the magnetic flux lines. In agreement with theory $J_c$ increases proportionally to $V_f/d$, where $V_f$ is the volume fraction of the 211-phase particles and $d$ is their average size, as shown in Fig. 4.2-30.

*Macrocracks.* The stresses arising between the 123-grains on cooling lead to the formation of macrocracks. These stresses stem from the anisotropy of the thermal expansion of the lattice of the 123-phase. The $c$ axis contracts to a higher degree than the $a$ and $b$ axes and the residual stresses puts $c$-grain boundaries under tension. Data of the temperature dependence of the thermal expansion coefficient $\alpha = d[\ln L(T)]/dT$ at low temperatures are plotted for all three axes in Fig. 4.2-31 according to [2.38]. For further studies on Y-123 up to $T = 500\,K$ and for $YBa_2Cu_3O_{7-\delta}$, $\delta = 0$, and $\delta = 0.05$, see [2.39].

As an important microstructural feature twinning domains have to be considered. These twinning domains occur at oxygen-rich compositions. The formation of twins arises as a strain relief effect during the structural

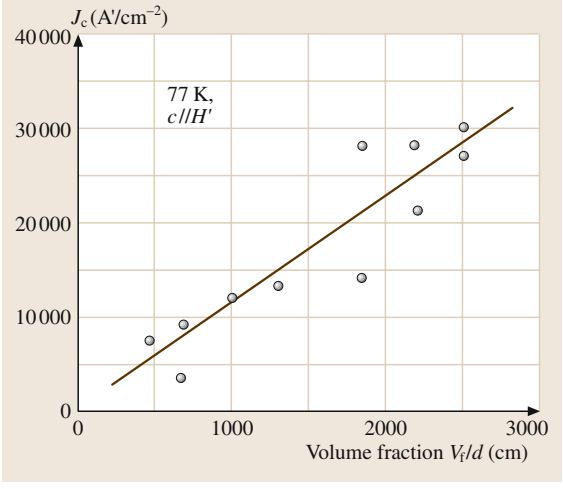


**Fig. 4.2-30** Critical current density as a function of $V_f/d$ of the 211-phase particles for melt-processed samples [2.35, 36]

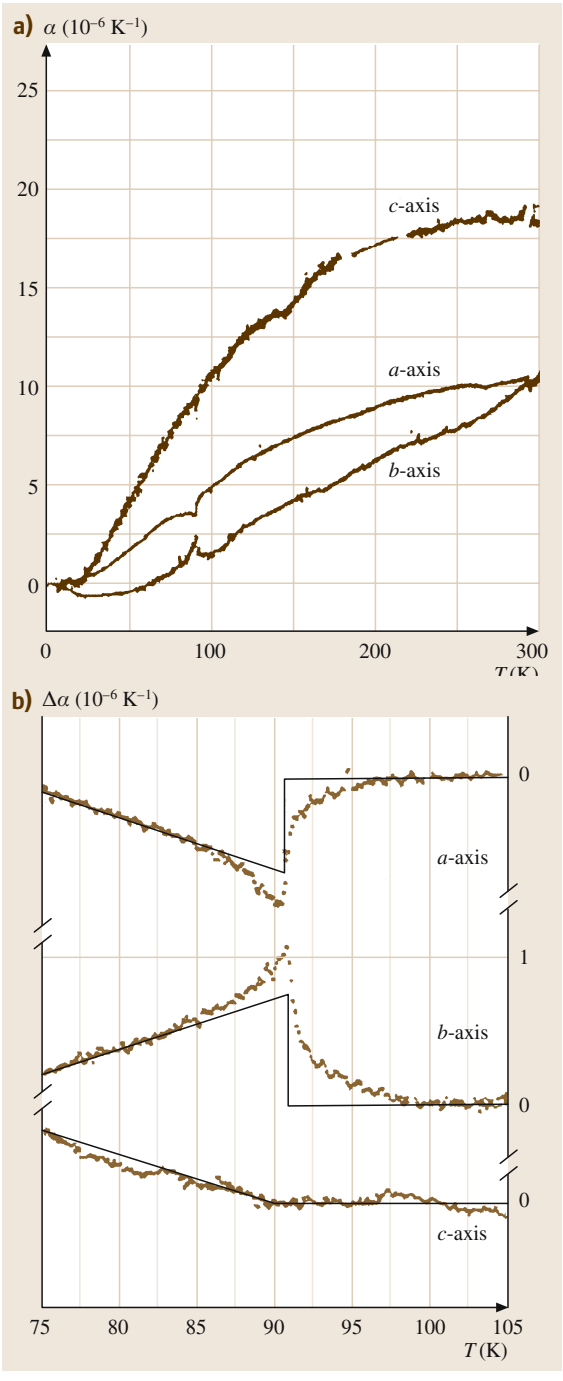


**Fig. 4.2-31** Coefficient of thermal expansion $\alpha$ of $YBa_2Cu_3O_{7-\delta}$ at $T \leq 300\,K$ **(a)** and **(b)** expanded view of the change in expansivity $\Delta\alpha$ near the transition temperature $T_c$ obtained by subtracting a linear fit above $T_c$ from the data

*Grain Boundaries.* The critical current density as a function of the magnetic field strength for a typical sintered polycrystalline sample and for a single crystal film is shown in Fig. 4.2-32. The critical current densities of polycrystalline samples are more sensitive to applied magnetic fields than those of single crystalline materials. Furthermore, the maximum critical current densities measured on epitaxial films exceed $10^6\,A\,cm^{-2}$, which is some $10^3$–$10^4$ times larger than for bulk polycrystalline samples. The critical current density of polycrystalline samples is controlled by the weak link effect of the grain boundaries. This detrimental effect of

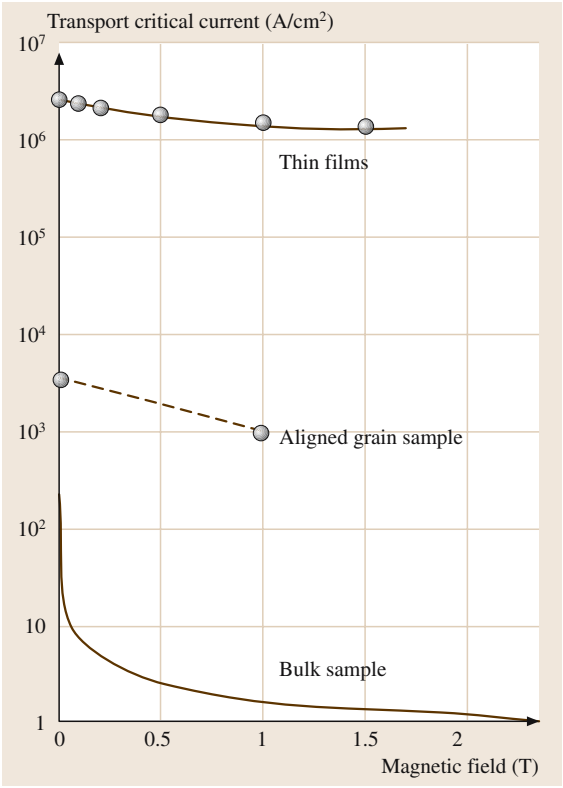


**Fig. 4.2-32** Critical current density on dependence on the applied magnetic field for a single crystal film and a sintered sample [2.40]

phase transformation from tetragonal to orthorhombic symmetry.

the grain boundaries is also evidenced by the occurrence of a rapid decrease in $J_c$ with an applied field (a field of few mT will reduce $J_c$ to zero), whereas such fields do not lower the $J_c$ values of single crystals significantly.

*High-Angle Grain Boundaries.* The critical current density across a grain boundary decreases exponentially with increasing grain-boundary misorientation angle. At low misorientation angles between 2° and 5°, a plateau without observable reduction of $J_c$ is suggested [2.44, 45]. Possible mechanisms could be connected with the reduction of the current-carrying cross-section by local suppression of the order parameter at the grain boundaries or by insulating dislocation cores. Figure 4.2-21 shows the critical current densities of [001]-tilt grain boundaries in YBCO films [2.21].

*Electrical Resistivity.* According to the crystal structure the electrical resistivity of YBCO is anisotropic. Figure 4.2-33 shows the temperature dependence of $\rho$ for a twin-free YBCO single crystal along the orthorhombic axes. Resistivity measurements on sintered $YBa_2Cu_3O_{7-\delta}$ samples with various oxygen deficiencies show a large increase in resistivity with increasing $\delta$ [2.42, 43] (Fig. 4.2-34).

*Resistivity as a Function of Temperature and Oxygen Content.* The in-plane ($\rho_a$) as well as the out-of-plane ($\rho_c$) resistivity of detwinned YBCO crystals

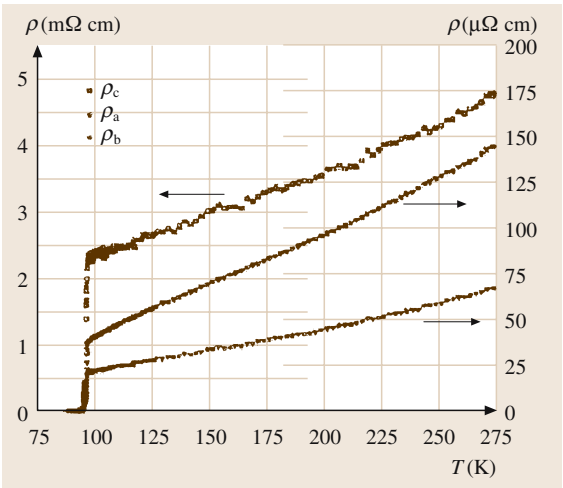


**Fig. 4.2-33** Anisotropic resistivity of YBCO for a twin-free single crystal along the orthorhombic axes [2.41]

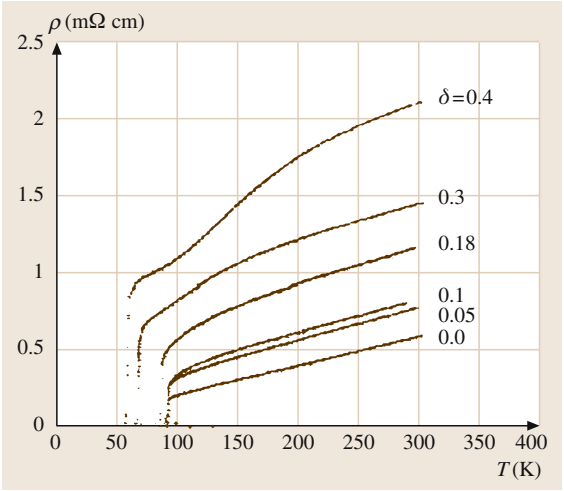


**Fig. 4.2-34** Temperature dependence of the resistivity of $YBa_2Cu_3O_{7-\delta}$ [2.42, 43]

decrease with increasing oxygen content. Moreover, the out-of-plane resistivity shows a crossover from high-temperature metallic behavior ($d\rho_c/dT > 0$) to low-temperature semiconducting behavior ($d\rho_c/dT < 0$). The in-plane resistivity (perpendicular to the CuO chain) deviates in the low-temperature region from linear temperature dependence (Fig. 4.2-35).

*Thermal Conductivity.* The thermal conductivity $\kappa(T)$ shows a maximum in the temperature range $40\,\mathrm{K} \leq T \leq 90\,\mathrm{K}$ and a change of the slope at $T_c$, as shown in Fig. 4.2-36. The experimental data depend on the sample microstructure, the oxygen content, crystalline borders and the admixture.

*Phase Diagram.* Figure 4.2-37 shows a schematic partial phase diagram for $YBa_2Cu_3O_{7-\delta}$ as a function of the oxygen content $7-\delta$. At $7-\delta = 6$ the compound is an antiferromagnetic insulator with $T_N \approx 500\,\mathrm{K}$. At high $\delta$ values two antiferromagnetic phases are marked, with only Cu spins in the plane layers ordered (AFM), or Cu spins in the chain layers also ordered ($AFM_c$). With decreasing $\delta$ the hole concentration increases, while $T_N$ decreases. At $7-\delta \approx 6.45$, antiferromagnetism disappears and superconductivity occurs at low temperatures. For $7-\delta \approx 6.75$, a plateau at $T_c \approx 60\,\mathrm{K}$ is reached which corresponds to a partial ordering of oxygen atoms. At high temperatures or at high oxygen content the compounds are paramagnetic.

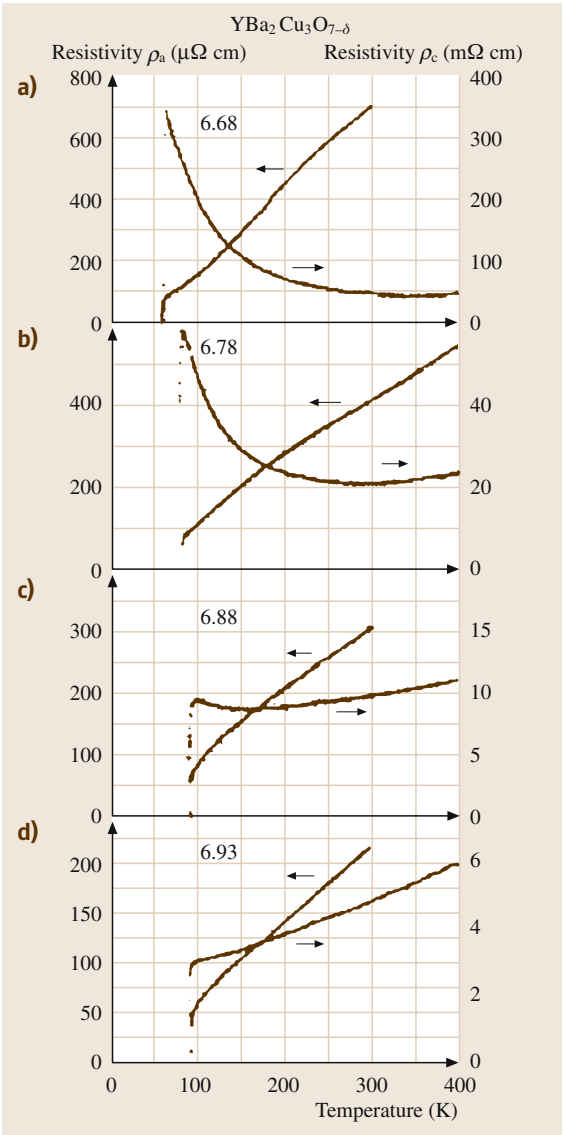


**Fig. 4.2-35a–d** In-plane ($\rho_a$) and out-of-plane ($\rho_c$) resistivity of $YBa_2Cu_3O_{7-\delta}$ as a function of the temperature for various oxygen contents [2.46]

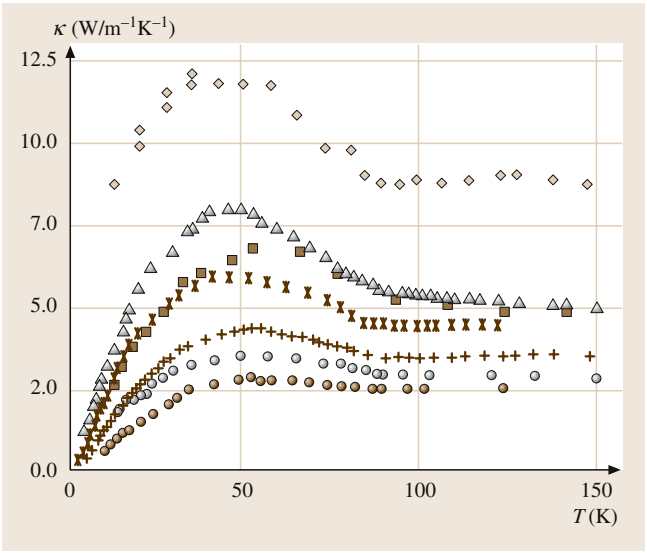


**Fig. 4.2-36** Thermal conductivity of different $YBa_2Cu_3O_{7-\delta}$ samples (◇ single crystals, others: polycrystalline samples) according to [2.47]

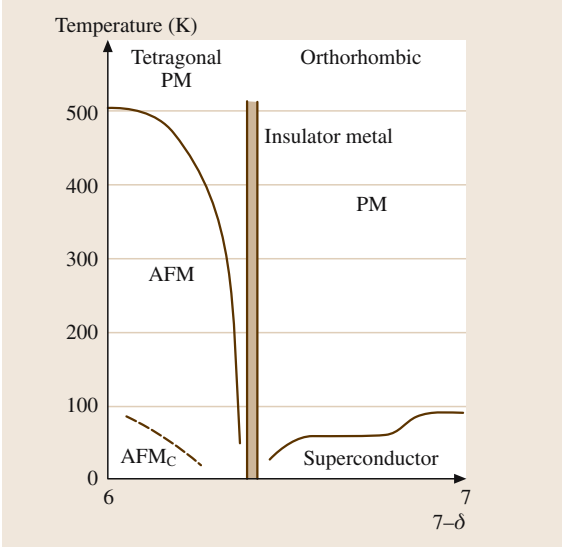


**Fig. 4.2-37** Schematic phase diagram for YBCO ($YBa_2Cu_3O_{7-\delta}$) in dependence of the oxygen content $7-\delta$ [2.48]

### Superconducting Properties

The intrinsic superconducting properties which are independent of the microstructure are the lower and the upper critical field, $H_{c1}$ and $H_{c2}$, respectively and the superconducting transition temperature $T_c$. These superconducting properties depend on the composition, especially the oxygen content (Table 4.2-23). Further parameters such as the effective coherence length $\xi$, the magnetic penetration depth $\lambda$, and the Ginzburg–Landau parameter that is dependent on the microstructure.

**Table 4.2-23** Typical properties of sintered YBCO according to [2.49]

| | |
|---|---|
| Flexural strength (MPa) | $216 \pm 16$ |
| Young's modulus (GPa) | 141.8 ($\varrho = 87\%$); 180–200 ($\varrho = 100\%$) |
| Fracture toughness, K1c (MPa $m^{1/2}$) | $1.07 \pm 0.18$ |
| Critical flow size (μm) | 15 |
| Thermal expansion, 50–450 °C ($\times 10^{-6}$ $K^{-1}$) | 11.5 |
| Specific heat at 82% theoretical density (J $kg^{-1}$ $K^{-1}$)) | 431 |
| Thermal conductivity (W $m^{-1}$ $K^{-1}$)) 300 K | 2.67 ($\varrho = 85\%$) |
| 77 K | 1 ($\varrho = 85\%$) |
| Resistivity (μΩ cm) 300 K | 670 |
| 100 K | 220 |
| $T_c$ (K) | 92 (width 1 K) |
| $J_c$(77 K, $H = 0$) (A $cm^{-2}$) | 500–1000 ($\varrho = 85\%$) |
| $\varrho$ : bulk density | |

**Table 4.2-24** Superconducting properties (transition temperature $T_c$, coherence length $\xi$, penetration depth $\lambda$, GL coefficient $\kappa$, lower critical field $H_{c1}$, upper critical field $H_{c2}$) for YBCO [2.54]

| | | | |
|---|---|---|---|
| $T_c$ (K) | | 92 | [2.25] |
| Coherence length (nm) | $\xi_0^{\parallel}$ | 0.6 | [2.50] |
| | | 0.4 | [2.51] |
| | $\xi_0^{\perp}$ | 2.7 | [2.50] |
| | | 3.1 | [2.51] |
| Penetration depth (nm) | $\lambda_L^{\parallel}$ | 26 | [2.52] |
| | | 90 | [2.51] |
| | | 130 | [2.53] |
| | $\lambda_L^{\perp}$ | 125 | [2.52] |
| | | 800 | [2.51] |
| | | 450 | [2.53] |
| GL coefficient | $\kappa^{\parallel}$ | 7.6 | [2.54] |
| | $\kappa^{\perp}$ | 37 | [2.54] |
| $H_{c1}$ (T) | $H_{c1}^{\parallel}$ | 53 | [2.55] |
| | $H_{c1}^{\perp}$ | 520 | [2.55] |
| $H_{c2}$ (T) | $H_{c2}^{\parallel}$ | 140 | [2.52] |
| | $H_{c2}^{\perp}$ | 650 | [2.52] |

**Table 4.2-25** Basic material and critical current density relevant parameters for YBCO according to *Larbalestier* et al. [2.22]

| | |
|---|---|
| Material | YBCO |
| Anisotropy | 7 |
| $T_c$ | 92 K |
| $H_{c2}$ | > 100 T (4 K) |
| $H^*$ | 5–7 T (77 K) |
| In-plane coherence length $\xi(0)$ | 1.5 nm |
| In-plane penetration depth $\lambda(0)$ | 150 nm |
| Depairing current density | $3 \times 10^8$ A $cm^{-2}$ (4.2 K) |
| Critical current density | $\approx 10^7$ A $cm^{-2}$ |
| $\rho(T_c)$ | ≈ 40–60 μΩ cm |

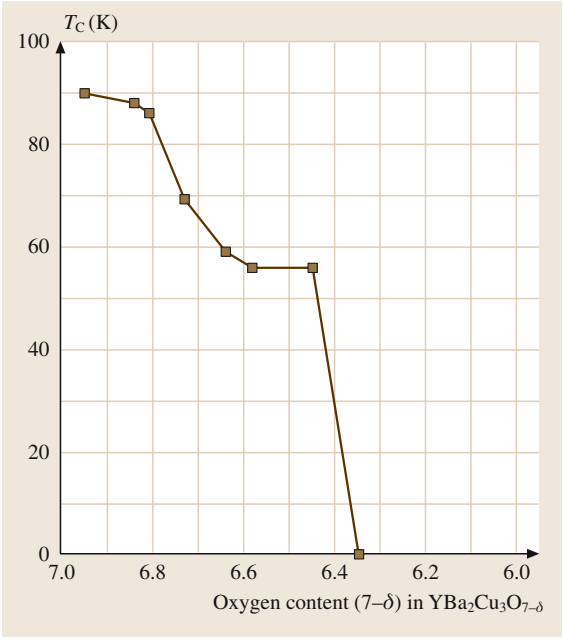


**Fig. 4.2-38** Critical temperature $T_c$ versus oxygen content $7-\delta$ [2.30]

*Superconducting Transition Temperature.* For the $T_c$ versus oxygen-content behavior, a two plateau dependence is observed (first plateau: $6.8 < 7-\delta < 7$, $T_c$ not actually constant, slight decrease in $T_c$ with decreasing $(7-\delta)$; second plateau: $6.55 < 7-\delta < 6.65$, $T_c \approx 56$ K) (Fig. 4.2-38). Complete substitution of yttrium by rare-earth metals do not show a significant change for the value of $T_c$, with the exception of the lanthanum ($T_c = 50$ K) and praseodym compounds (not superconducting) (Table 4.2-21). Other dopants on the different atomic sizes as a general rule show decreasing $T_c$ values with increasing substitution rates. Selected examples are shown in Fig. 4.2-39.

*Critical Current Density.* The critical current density $J_c(B)$ of YBCO thin films at three different temperatures as a function of the magnetic field $B_{\perp c}$ and $B_{\parallel c}$ is given in Fig. 4.2-40. At temperatures $T \leq 60$ K the maximum of $J_c(B)$ occurs when the magnetic field is aligned along the film plane. At $T = 77$ K *Roas* et al. [2.61] observed higher $J_c$ values at $B < 2$ T and a crossover of the curves perpendicular and parallel to the film plane. The crossover seems to depend on microstructural features, e.g., defect concentration, twin-boundary distance etc.

*Hole Concentration.* The oxygen content of YBCO ($YBa_2Cu_3O_{7-\delta}$) determines the hole concentration in the $CuO_2$-planes. As shown by *Breit* et al. [2.62] the maximum value of $T_c$ is achieved at an oxygen content of $7-\delta = 6.94$ (see Fig. 4.2-41). This maximum is due

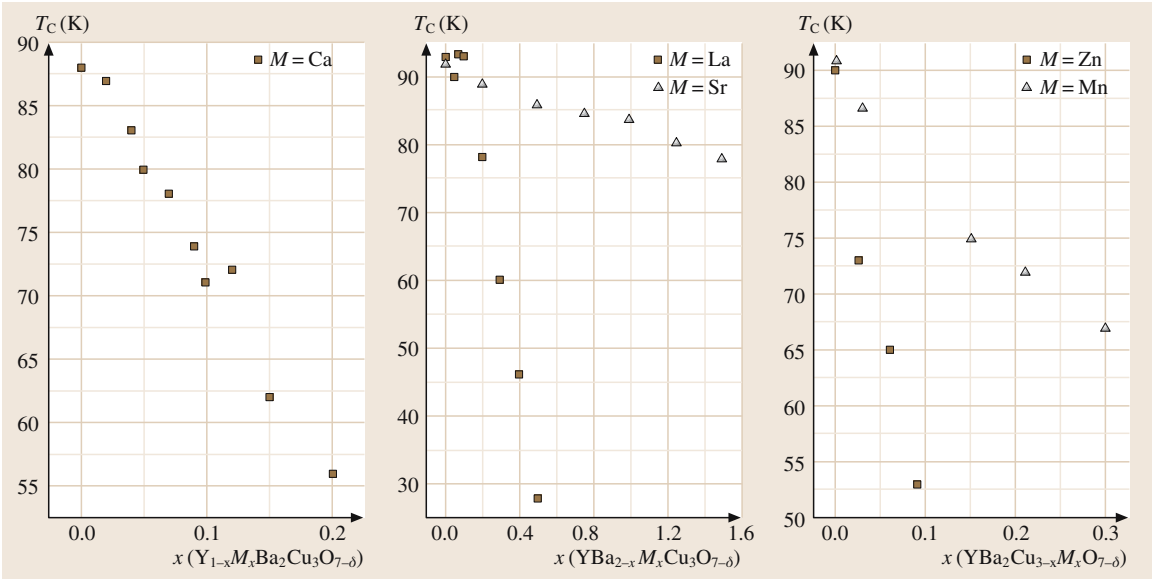


**Fig. 4.2-39** $T_c$ as a function of the substitution of the cations Y, Ba and Cu by selected cations $M$ according to [2.56–60]

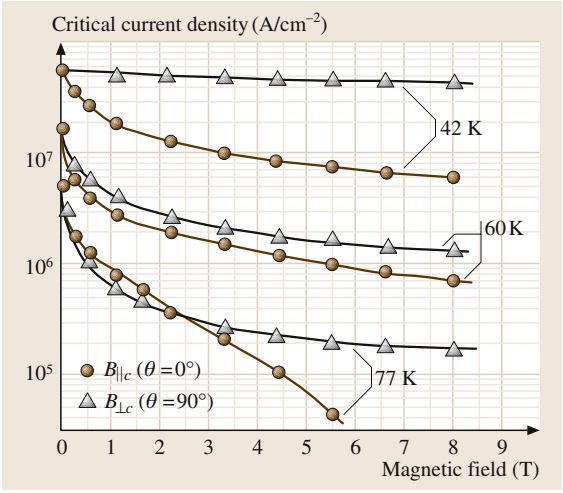


**Fig. 4.2-40** Critical current density with $B_{\perp c}$ and $B_{\parallel c}$ at various temperatures in magnetic fields up to 8 T according to [2.61]

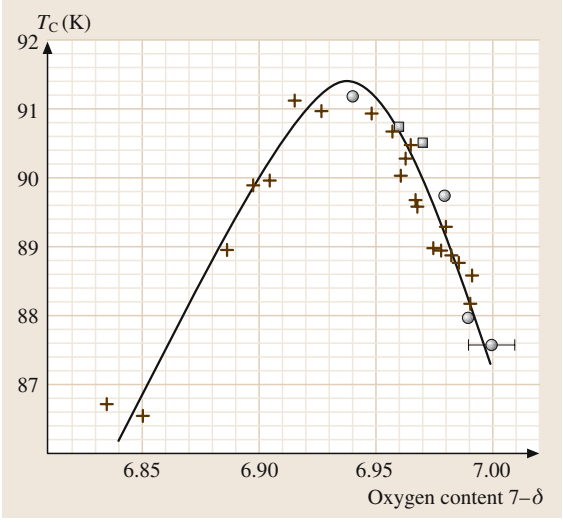


**Fig. 4.2-41** $T_c$ as a function of the oxygen content $7-\delta$ in $YBa_2Cu_3O_{7-\delta}$ according to [2.62] (data from neutron scattering experiments: ○ [2.62], □ [2.63]; data from normal-state resistivity: + [2.64, 65]). The line is a guide to the eyes

to an optimum hole doping of the $CuO_2$ planes. At an overdoped state $7-\delta > 6.94$, $T_c$ decreases as the holes in the planes exceed the optimum concentration.

*Lower Critical Field.* Figure 4.2-42 presents the temperature dependence of the lower critical field $H_{c1}$ parallel

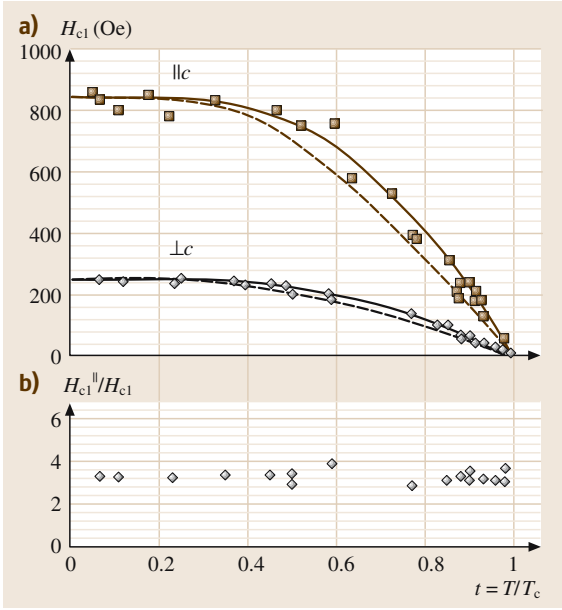


**Fig. 4.2-42a,b** Temperature dependence of $H_{c1}$ **(a)** and of the anisotropy ratio $H_{c1}^{||}/H_{c1}^{\perp}$ **(b)** according to [2.66]

and perpendicular to $c$. The anisotropy of the $H_{c1}$ is temperature-independent. The temperature dependence of $H_{c1}$ is in good agreement with BCS calculations (*solid lines* in Fig. 4.2-42a) as shown by *Wu* and *Shridhar* [2.66]. The authors obtained $H_{c1}^{||}(0) = 850 \pm 40$ Oe and $H_{c1}^{\perp}(0) = 250 \pm 20$ Oe.

*Upper Critical Field.* The upper critical fields $H_{c2}$ in high-$T_c$ superconductors give information about microscopic parameters, e.g., the coherence length and their anisotropies in the superconducting state. The temperature dependence of the upper critical field $H_{c2}(T)$ for $H_{\perp c}$ and $H_{\parallel c}$ measured on a polydomain sample [2.67] is given in Fig. 4.2-44. A linear dependence is observed for both directions with slopes of the critical field of $-1.9$ and $-10.5\,\mathrm{T\,K^{-1}}$ for $H_{\parallel c}$ and $H_{\perp c}$, respectively. The same dependence measured by the resistivity method is shown by the dashed lines. Corresponding to these measurements one can calculate: $H_{c2}^{||}(T = 0\,\mathrm{K}) = 122\,\mathrm{T}$, $H_{c2}^{\perp}(T = 0\,\mathrm{K}) = 674\,\mathrm{T}$, $\xi_0^{||} = 3.0$ Å, and $\xi_0^{\perp} = 16.4$ Å.

In low magnetic fields a region of nonlinear dependence of the upper critical field is observed, which could not be reproduced in monodomain crystals.

*Pinning Mechanisms.* In high $J_c$ value melt-processed YBCO samples, many defects – such as twin planes,

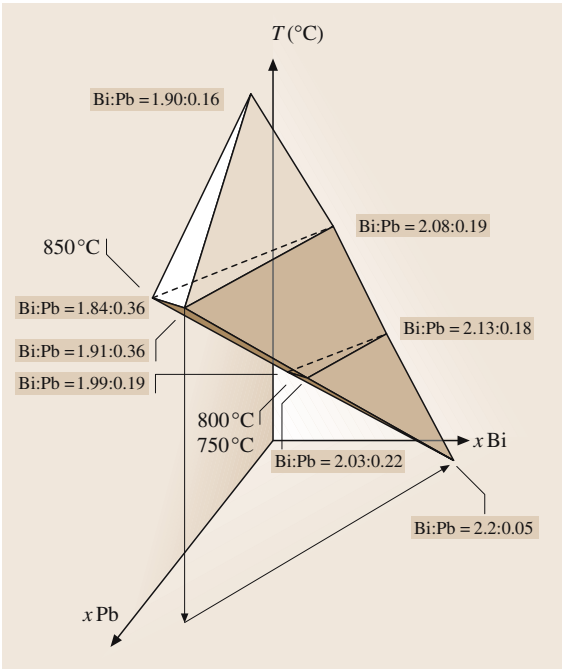


**Fig. 4.2-43** Schematical three-dimensional representation of the single-phase region of the Bi2223 phase, the variables being the temperature and the Bi and Pb contents [2.68]

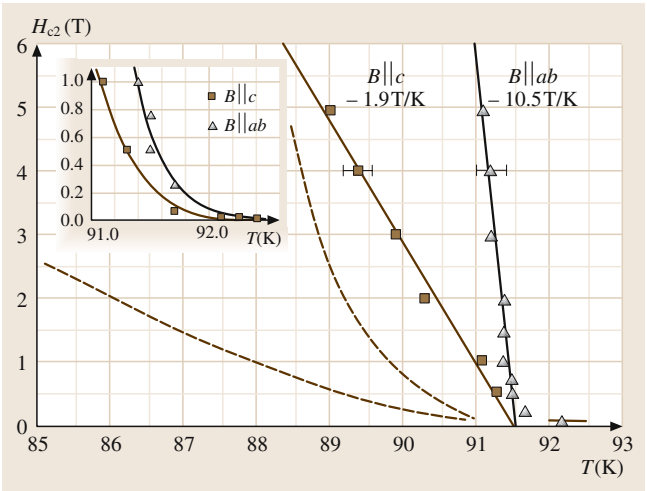


**Fig. 4.2-44** Temperature dependence of the upper critical field (*solid line*: magnetization measurements, *dashed line*: resistive measurements) [2.67]

stacking faults, grain boundaries, cracks, oxygen defects, dislocations or non-superconducting particles – can act as pinning centers.

*Twin planes* are usually introducted into YBCO crystals at the transformation from tetragonal to orthorhombic symmetry. The twin planes only act as effective pinning centers, when the fluxoids are aligned parallel to the twin plane while the Lorentz force acts perpendicular to the plane. Twin planes are not dominant pinning centers in melt-processed YBCO samples.

*Stacking faults.* If extra CuO layers are inserted adjacent to the chain plane of YBCO, this tends to a local structure of the defects resembling that of the so-called Y124 phase. These may act as important pinning centers for $H_{\perp c}$, but are not important for $H_{\parallel c}$. From a practical point of view these are not suitable pinning centers as it is no possible to prepare samples with or without stacking faults.

*Oxygen defects.* Däumling et al. observed a peak in the magnetization hysteresis in oxygen-deficient single crystals at an intermediate field, which they ascribed to flux pinning. This kind of pinning center is not the most important one.

*Cracks.* As mentioned above, the tetragonal to orthorhombic phase transition associated with oxygen addition causes stresses in YBCO samples leading to cracks in the *c*-direction. These cracks can contribute in flux pinning as in the case of twin planes or stacking faults.

*Dislocations.* In as-grown thin films, many screw dislocations may occur, which can act as pinning centers.

*Nonsuperconducting inclusions* in YBCO may be effective in flux pinning. Especially the influence of the 211-phase (or 422-phase in the case of Nd-123) is discussed. Such inclusions are stable and can be dispersed in a controlled pattern.

*Application of YBCO Superconductors.* Applications of YBCO high-$T_c$ superconductors are superconducting quantum interference devices (SQUIDS), magnetic shielding devices, infrared sensors, analog signal processing devices, microwave devices, and medical imaging systems. Since melt-textured bulk YBCO material shows magnetic pinning properties, a possible application may be high-field permanent magnets. For flexible tape conductors the YBCO material is coated onto metallic carrier tapes. Conductors coated with YBCO are studied intensively, because of the potentially high $J_c$ values in high magnetic fields at $T = 77$ K. Typical architectures of these coated conductors are sequences of polycrystalline metallic substrate or biaxially-textured metallic substrate – biaxially-textured

**Table 4.2-26** Present status of Y based coated conductors according to *Yamada* and *Shiohara* [2.69] (IBAD: Ion-beam-assisted deposition, RABiTS: Rolling assisted bi-axially textured substrates, PLD: Pulsed laser deposition, TFA-MOD: Trifluoroacetate–metal organic deposition)

| | |
|---|---|
| Material | YBCO |
| Typical Process | IBAD, RABiTS, PLD, TFA-MOD |
| Structure | Hastelloy (SUS) / oxide buffer / YBCO layer, monofilament |
| $J_c$ | 1–2 MA cm$^{-2}$ |
| $I_c$ | −100 A (77 K, 0 T) |
| Non-SC/SC ratio | 100 |
| Length achieved | 46 m (reported by Fujikura, Japan AS, Jan. 2003) |
| Wire configuration | Flat tape with thin YBCO layer |
| Reinforcement | Hastelloy, SUS substates |
| Application Tested | – |
| Remarks | R&D stage for 77 K, high field |

buffer layer – biaxially-textured superconducting YBCO layer – Ag stabilizer. The texturing is achieved by rolling and recrystallization.

Wafers of YBCO thin films are prepared for microwave applications. Thermal coevaporation is used as the commercial deposition method. With this method substrates of about $20 \times 20\,cm^2$ can be coated at rates of 20–30 nm/min. A double-sided deposition can be achieved in two deposition steps. The sol–gel method as well as the chemical solution deposition method are promising with respect to lower production costs. Detailed information on applications is given in [2.81] (Table 4.2-26)

### 4.2.2.3 Superconductors Based on the Bi–Sr–Ca–Cu–O System

#### General Properties

Three superconducting phases exist in the Bi−Sr−Ca−Cu−O (BSCCO) system: $Bi_2Sr_2Ca_2Cu_3O_{10}$ (abbreviated using the stoichiometric coefficients as Bi2223), $Bi_2Sr_2CaCu_2O_8$ (Bi2212), and $Bi_2Sr_2CuO_6$ (Bi2201). A review about phase diagram studies in the system Bi−Pb−Sr−Ca−Cu−O, particularly in view of the superconducting compounds, is given in [2.68]. The Bi2212 phase is thermodynamically stable over a relatively wide temperature range. By contrast, the

**Table 4.2-27** Structural data of superconducting compounds in the Bi−Sr−Ca−Cu−O system and of Pb substituted Bi2223 [2.15]

| Compound | Space group | Lattice parameters | | |
|---|---|---|---|---|
| | | *a* (nm) | *b* (nm) | *c* (nm) |
| $Bi_2Sr_2CuO_6$ | Cmmm | 0.5361 | 0.5370 | 2.4369 |
| $Bi_2Sr_2CaCu_2O_8$ | Fmmm | 0.5408 | 0.5413 | 3.081 |
| $Bi_2Sr_2Ca_2Cu_3O_{10}$ | Fmmm | 0.539 | 0.539 | 3.71 |
| $(Bi_{1.6}Pb_{0.4})Sr_2Ca_2Cu_3O_{10}$ | Fmmm | 0.5413 | 0.5413 | 3.7100 |

**Table 4.2-28** Maximum $T_c$ and a compilation of several values of the coherence lengths, London penetration depths and upper critical fields at $T = 0$ K for superconducting compounds of the Bi−Sr−Ca−Cu−O system

| Parameter | Bi2201 | Bi2212 | Bi2223 | Pb-doped Bi2223 |
|---|---|---|---|---|
| $T_c$ (K) | 34 [2.70][a] | 90 [2.71][a] | 110.4 [2.72][d] | 109 [2.73][c] |
| $\xi_{ab}(0)$ (nm) | 3.5–4.5 [2.74][b]<br>4.0 [2.75][a] | ≥1.09 [2.76][a]–3.8 [2.77][a] | 2.9 [2.78][c] | 2.9 [2.73][c]<br>≈ 1 [2.79, 80][e] |

**Table 4.2-28** Maximum $T_c$ and a compilation of several values of the coherence lengths, London penetration depths and upper critical fields at $T = 0$ K for superconducting compounds of the Bi−Sr−Ca−Cu−O system, cont.

| Parameter | Bi2201 | Bi2212 | Bi2223 | Pb-doped Bi2223 |
|---|---|---|---|---|
| $\xi_c(0)$ (nm) | 1.5 [2.74] [b] | 0.16 [2.77] [a] | 0.093 [2.78] [c] | 0.02 [2.80] [e] |
| $\lambda_{ab}(0)$ (nm) | 310 [2.82] 438 [2.75] [a] | 180 [2.83] [a]–310 [2.84] [a] | 165–230 [2.72] [d] | ≈ 250 [2.73] [c], [2.15] 194 [2.79] [e] |
| $\lambda_c(0)$ (nm) | | $1\times10^4$–$4\times10^4$ [2.85] | | |
| $B_{c2(ab)}$ (0) (T) | 43 [2.74] [b] | 533 [2.77] [a] | 1210 [2.78] [c] | |
| $B_{c2(c)}$ (0) (T) | 20.2 [2.75] [a] 16–27 [2.74] [b] | 60 [2.86] [a]; 70 [b] | 39 [2.78] [c] | 297 [2.79] [e] |

Types of the investigated samples
[a] Single crystal
[b] Overdoped single crystal
[c] Whisker
[d] Thin film
[e] Textured Ag-sheathed tape

Bi2223 phase is stable only over a narrow temperature and concentration range. Considering the preparation of Bi2223 materials, it has to be noted that small variations in concentration and/or temperature can result in quite different phase compositions and in a significant decrease of the volume content of the Bi2223 phase. The latter exhibits an excess of the Bi content of about $Bi_{2.5}$. The formation of the Bi2223 phase is significantly promoted by partial substitution of 20–30% Pb for Bi. Figure 4.2-43 represents the single-phase region of the BiPb2223 phase schematically. The BiPb2223 phase contains an excess of Bi + Pb concentration of about $(Bi, Pb)_{2.2}$. A review of the synthesis of bismuth cuprates is given in [2.16].

As shown in Fig. 4.2-16 of Sect. 4.2.1, the Bi superconductors have a layered perovskite structure which is composed of superconducting $CuO_2$/Ca stacks (one stack in Bi2201, two stacks in Bi2212, and three in Bi2223) sandwiched between insulating BiO and SrO planes. The structural data of the compounds are presented in Table 4.2-27.

Due to this layered structure, the compounds exhibit a more or less pronounced anisotropy of the electrical parameters (Table 4.2-28).

Here, $\lambda_{ab}$ and $\lambda_c$ are the London penetration depths for a magnetic field in the $c$-direction and parallel to the $ab$-plane, respectively. $B_{c2(c)}$ and $B_{c2(ab)}$ are approximate upper critical fields aligned in the $c$-direction and parallel to the $ab$-plane, respectively; $\xi_c$ and $\xi_{ab}$ are the coherence lengths in $c$-direction and in the $ab$ plane, respectively. Considerably different values have been reported for the parameters listed in Table 4.2-28. This is true in particular for $H_{c2}$ and also for $\xi$, which is usually

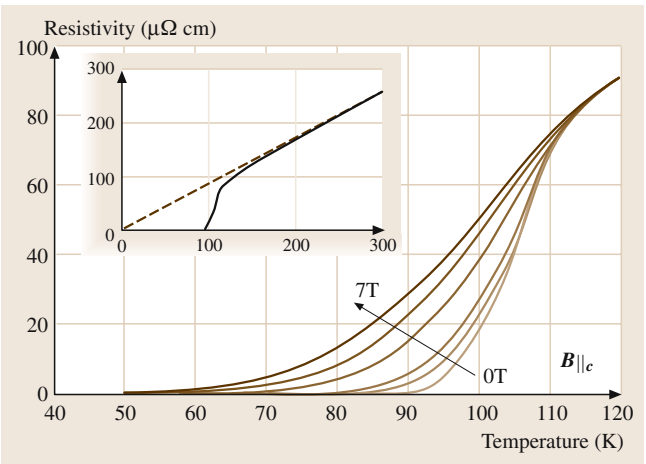


**Fig. 4.2-45** Resistivity of a Bi2223 film as a function of the magnetic field aligned parallel to the $c$ axis [2.87]

derived from $H_{c2}$. The scatter may be partly due to different chemical composition (doping) and type of samples (e.g., thin film, single crystal, polycrystalline textured bulk material). Furthermore, different methods of measuring, e.g., in the case of $H_{c2}$, magnetization $M(T)$ and resistive measurements $\rho(T)$, respectively, were used and various theoretical models were applied for the determination of the parameters at $T = 0$ K. Different criteria were also used for the resistive determination of $H_{c2}$: $\rho(T) = 0$ and $\rho(T) = 0.5\rho_n$, respectively. Here $\rho_n$ is the normal state resistivity near $T_c$. So values of $B_{c2(ab)}(0)$ were determined to 533 T using the criterion $\rho(T) = 0$ and to 2640 T using the criterion $\rho(t) = 0.5\rho_n$ for one and the same sample [2.77]. These high values

are questionable in general, as has been shown in [2.88]. A further compilation of data is given in [2.89].

### Thin Films, Single and Bi-Crystals

There are essentially four methods of preparation supplying high quality BSCCO films:

- Liquid phase epitaxy (LPE) [2.92]
- Chemical vapor deposition (CVD) [2.93]
- Ion sputtering [2.94]
- Pulsed laser deposition (PLD) [2.90]

Epitaxial deposition on monocrystalline ceramic substrates such as $Sr_2TiO_3$ or MgO is used to prepare monocrystalline films. Investigation on the influence of grain boundaries on the superconducting properties of the films' artificial grain boundaries within the films have been carried out using bi-crystalline substrates.

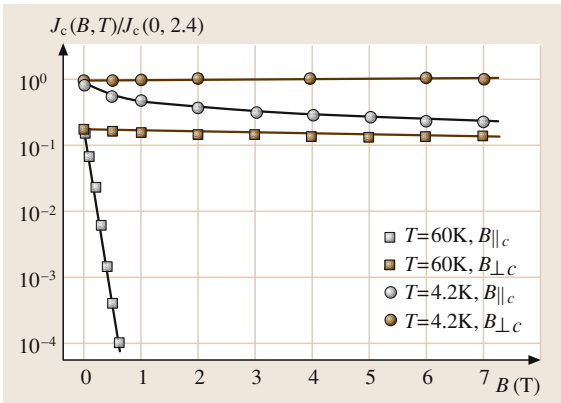


**Fig. 4.2-46** Magnetic field dependence of the critical current density of an epitaxial Bi2212 film for the $B_{\| c}$ and $B_{\perp c}$ directions at 4.2 K and 60 K, respectively. $J_c(0, 4.2)$ is the critical current density at 4.2 K in zero field [2.90]

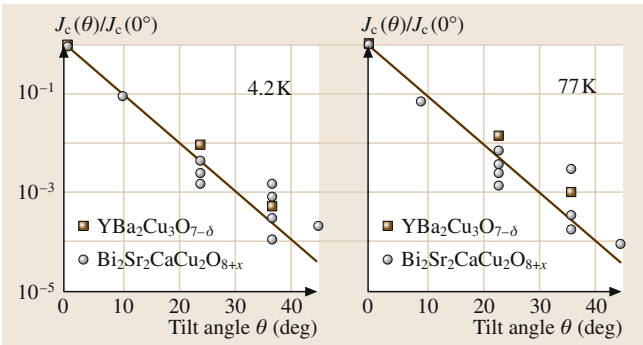


**Fig. 4.2-48** Ratio of the intergrain, $J_c(\theta)$ and intragrain critical current densities, $J_c(0)$, as a function of the misorientation angle $\theta$ for bicrystalline [001]-tilt Bi2223 (*circles*) and $YBa_2Cu_3O_{7-x}$ films (*squares*) [2.91]

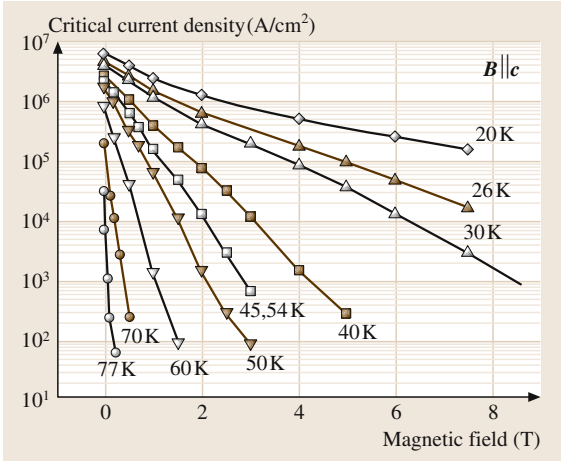


**Fig. 4.2-47** Critical current density $J_c$ of an epitaxial Bi2223 film as a function of the magnetic field aligned parallel to the $c$ axis for the temperature range of 20–77 K [2.87]

Critical temperatures up to 91 K [2.91] and 110.4 K [2.72] were measured on Bi2212 and Bi2223 films, respectively. Typical thickness values of such films are 200–400 nm. An example for the magnetic-field dependence of $T_c$ is given in Fig. 4.2-45 [2.87]. In contrast to the conventional low-$T_c$ conductors, the onset temperature of the superconducting transition practically does not depend on the field and a characteristic enhancement of the transition width with increasing field is observed.

Critical current densities on the order of $10^5$ A cm$^{-2}$ at 77 K in zero field were measured on BSCCO thin films. In Fig. 4.2-46 the field dependence of $J_c$ of a Bi2212 film is shown for two temperatures [2.90] and Fig. 4.2-47 demonstrates the $J_c(B, T)$ dependence of a Bi2223 film [2.87]. In magnetic fields aligned parallel to the plane of the film, that is perpendicular to the $c$ axis of the crystal structure, $J_c$ is practically independent on the field strength, even at higher temperatures such as 60 K. The reasons for this behavior are discussed below in connection with the $J_c(B, T)$ correlation of wires and tapes.

In connection with the manufacturing of real conductors of large length the influence of grain boundaries on the critical current density is of great importance. Investigations of BSCCO bi-crystalline thin films have shown that tilt boundaries act as weak links, causing an exponential dependence of $J_c$ on the misorientation angle, $\theta$,

similar to the $J_c(\theta)$ dependence of tilt grain boundaries in YBCO films as shown in Fig. 4.2-48 (compare also with Fig. 4.2-54 of Sect. 4.2.2.1).

Much effort has been expended to grow BSCCO single crystals using several methods, such as crystal growth from the melt, fused-salt reactions in alkali-halide and alkali-carbonate fluxes, respectively, solid-state reaction, and growth in a gaseous phase. Very high quality bulk single Bi2212 crystals with a size of a few mm along the *a* axis and *b* axis and about 0.1 mm along the *c* axis were prepared by the travelling solvent floating zone technique [2.95] or by slow cooling of the melt below the melting temperature and subsequent removing of single crystal fragments from the ingot by crashing [2.96]. Maximum $T_c$ values of 90 K were measured on these crystals. The critical current densities of such crystals were very small, on the order of 100 A cm$^{-2}$ at 77 K in zero field probably due to the small density of crystal defects. After irradiation of the crystals with 2.2-G eV Au ion beams directed along the *c* axis at a fluence of $1.0 \times 10^{11}$ cm$^{-2}$, an essential increase of the irreversibility line were observed at temperatures $< 70$ K. An enhancement of $J_c$ by a few orders of magnitude was also measured at low temperatures of about 30 K in a field of 9 T directed parallel to the *c* axis [2.97]. These effects can be attributed to columnar tracks within the crystal lattice.

It is much more difficult to grow Bi2223 than Bi2212 single crystals. Very small crystals with a phase purity of 97% Bi2223 and dimensions of 0.1 mm along the *a* and *b* axes and 0.001–0.01 mm along the *c* axis could be prepared by the fused-salt reaction method using a KCl flux [2.98]. The onset temperature of the superconducting transition was determined by dc magnetization measurement to 110 K and the transition width to 5 K. Using the measured magnetization curves and the "Bean" model, the zero field critical shielding-current density in the *ab*-plane of the crystal has been determined to be $1 \times 10^6$ A cm$^{-2}$ at 5 K.

The preparation of bulk Bi2212 bi-crystals provided the possibility to study the influence of [001] twist boundaries (*c* axis twist boundaries) on the superconducting properties of Bi2212 conductors [2.95, 96]. Assuming the results can be applied to Bi2223 tapes too, pieces of single crystals were cleaved. One cleave was rotated through an angle about the *c* axis with respect to the other, and placed atop it. The boundary was formed in a controlled sintering process. Results showed that the transition temperature of a bicrystal agreed with that of the single crystal (the twist angle is not noted [2.96]) and the ratio of critical current densities at $T/T_c \geq 0.9$ across the twist junction to that across the single crystal was unity, independent of the twist angle. However, it has to be noted that in these experiments the critical current densities were very low and it is not clear whether the true $J_c$ values of the grain boundaries could not be measured due to the current limiting $J_c$ of the single crystals. Bicrystals with an enhanced critical current density after irradiation with Au-ion beams revealed, at low temperatures, a more than one order of magnitude higher critical current across the single crystal than that across the 45° twist grain boundary [2.97].

### Practical Conductors

*Fabrication of Wires and Tapes.* The most common approach used to fabricate practical BSCCO conductors is the so called "Powder-in-Tube" (PIT) method. As a first step of PIT precursor, powders of appropriate chemical and phase compositions are produced. In the case of Bi2212 conductors, usually a mixture of $Bi_2O_3$, $SrCaO_3$, CaO or $CaCO_3$, and CuO with the ratio Bi:Sr:Ca:Cu equal to 2:2:1:2 is calcined at 800–850 °C to remove the residual carbon content. The mixture of oxides and carbonates can be obtained by alternatively applying mechanical mixing (e.g. milling), or a sol–gel process, a co-precipitation method, or spray freeze drying technique. Beside the oxide/carbonate mixture, a powder produced by spray pyrolysis of a metal-nitrate solution with subsequent calcination is often used as an alternate precursor for BiPb2223 conductors. Typical BPSCCO(2223) precursor powders exhibit the concentration ratio of Bi:Pb:Sr:Ca:Cu equal to (1.7–1.8):(0.3–0.4):(1.9–2.0):(2.0–2.1):3.0, and consist of the Bi2212 phase (major phase, about 70%) and other phases such as $Ca_2PbO_4$, $(Pb, Bi)_3Sr_3Ca_2CuO_x$, alkali earth cuprates, $(Ca, Sr)_{14}Cu_{24}O_x$, or CuO, depending on the preparation conditions (particularly on the final heat treatment of the precursor). The chemical and phase compositions of the precursor have a strong influence on the final properties of the wires and tapes [2.99].

The further steps of PIT excluding the thermal and thermomechanical treatments, respectively, are illustrated in Fig. 4.2-49. The as-produced powders are filled into an Ag tube and then swaged and drawn into wires. Mostly the conductors are produced as multifilamentary (MF) wires due to their more uniform superconducting properties and superior behavior with respect to the mechanical properties compared to monofilamentary conductors. When making MF conductors, pieces of the monofilamentary wire are bundled into a second Ag tube and then this composite is swaged and drawn

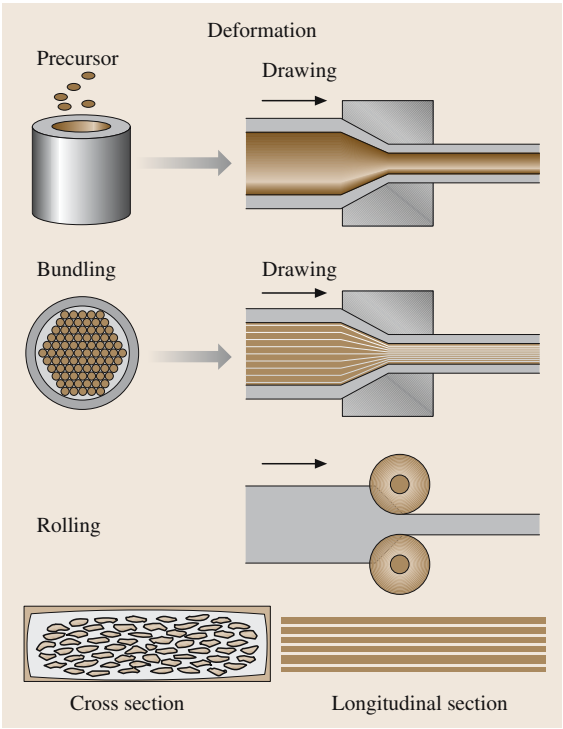


**Fig. 4.2-49** Scheme of the "powder-in-tube" method, excluding the thermal and thermomechanical treatments

into wires again. In most cases the wires are finally rolled into tapes since a higher critical current density can be achieved for tape-like conductors than for round wires.

After completion of the deformation process the Bi2212/Ag and BiPb2223/Ag composites have to be subjected to a thermal and thermomechanical process, respectively, in order to transform the Ag-sheathed precursors into superconducting phases and to realize an optimal microstructure of the superconducting phase with respect to high critical current densities. The Bi2212 composites are heated up slightly above the temperature of partial melting (880–900 °C, depending on the oxygen partial pressure of the annealing atmosphere) and then slowly cooled at a rate of 5–10 K $h^{-1}$ to about 830–860 °C, followed by holding the composites at this temperature for a few hours. During this process the Bi2212 phase crystallizes from the melt as platelets with the crystal *c* axes aligned perpendicular to the wide surface of the platelets. The microstructure reveals a pronounced degree of texture with the *c* axes perpendicular to the filament/sheath interface.

A more complicated thermomechanical process that usually contains three steps is needed in the case of the BiPb2223/Ag composites. At least the first annealing is performed in a temperature range where a transient melt occurs, accelerating the conversion of the precursor into the superconducting phase. The optimum temperature and dwell time strongly depend on the composition of the precursor and oxygen content of the $N_2/O_2$ annealing atmosphere. At a lower $O_2$-content compared to air, lower temperatures and shorter dwell times are suitable and less dependence of $J_c$ on the annealing temperature has been observed. For annealing atmospheres consisting of the inert nitrogen with an $O_2$ content of 7–21%, the optimal temperature is in the range of 820–835 °C, depending on the composition of the precursor. X-ray diffraction (XRD) investigations of tapes quenched from different states of the annealing process as well as in-situ measurements by means of high-energy synchrotron X-ray diffraction [2.100] and neutron diffraction [2.101], [2.102], respectively, have shown that during heating up and dwelling at the reaction temperature, several reactions such as the incorporation of Pb into the Bi2212 phase, the formation of transient compounds (e.g., $(Ca, Sr)_{14}Cu_{24}O_{41}$ and $Pb_3(Sr, Bi)_3Ca_2CuO_y$) and of a liquid phase mentioned above precede the real conversion of the Bi2212 into Bi2223. These reactions are accompanied by the recrystallization of the Bi2212 phase and improvement of its original texture degree, which was caused by the deformation of the composite into wires and tapes.

During the reaction annealing the density of the BiPb2223 filaments decreases. Therefore the tapes are densified after annealing by a compressive treatment, whereby the electrical connectivity and degree of texture of the grains are enhanced. Uniaxial pressing is the most effective method with respect to $J_c$. If long tapes are produced, however, the uniaxial pressing has to be replaced by rolling. The lower $J_c$ after rolling, compared to that after pressing, is probably due to additional microcracks induced by rolling and can not be recovered completely by the subsequent annealing which has to be performed after rolling as well as pressing. Mostly, a further increase of $J_c$ can be achieved after a second compressive treatment and subsequent third annealing.

Figure 4.2-50 shows the longitudinal cross-section of a BiPb2223 filament embedded in silver. The microstructure of the superconducting phase in contact with the Ag sheath reveals a higher density and degree of texture compared to areas in the middle of the filament. Obviously, Ag influences the conversion reaction of Bi2212 into BiPb2223. It is known that Ag

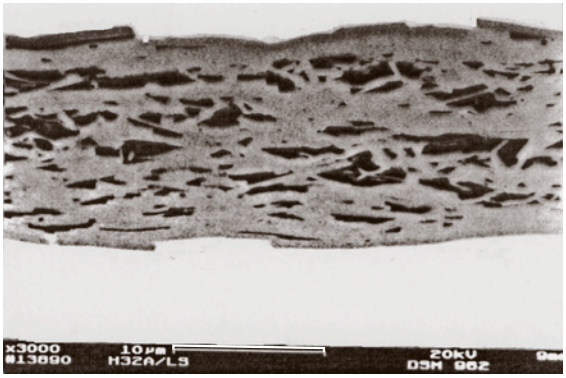


**Fig. 4.2-50** Longitudinal cross section of a BiP2223 filament embedded in silver

decreases the solidus temperature of Bi2212 [2.103] and accelerates the BiPb2223 formation process. However, the reaction mechanism has not yet been fully understood. Two different mechanisms have been proposed: the nucleation and growth of the BiPb2223 phase from the melt [2.104] and the formation of the BiPb2223 phase from the Bi2212 grains by intercalation of Ca, Cu, and O [2.105]. In connection with the first-mentioned mechanism beside the homogeneous nucleation, the heterogeneous one is discussed in [2.102]. In the frame of the intercalation process, the occurrence of a transient liquid phase also seems to be an important feature.

In order to improve the tensile strength of the conductors, Ag can be replaced by Ag alloys, such as Ag−Mg and Ag−Mn alloys as sheath material containing a few tenths wt% of the alloying element. Ternary alloys such as Ag−Ni−Mg are also used. Due to the respective internal oxidation of Mg and Mn, during the long-term annealing necessary to form the superconducting phase, the tensile stress which can be applied to the tapes without $J_c$ degradation could be enhanced from 40 MPa for BiPb2223/Ag tapes to 90 MPa [2.107] and 130 MPa [2.108] for AgMn- and AgMg-sheathed tapes, respectively. A high tensile strength protects the conductor against damages by handling and hoop stresses acting on the conductor due to the Lorentz force in magnetic coils. Silver and its alloys are indispensable since no other materials have been found so far which meet the following requirements necessary for the construction of practical conductors: high workability; resistance against oxidation at high temperatures; oxygen permeability since an exchange of oxygen between the precursor and ambient atmosphere during the heat treatment is necessary; no detrimental reaction with elements of the superconducting phase at high temperatures; and sufficiently high tensile strength.

*Superconducting Properties.* The largest efforts with respect to the production of practical conductors in long length have been made with BiPb2223 tapes since they are the most promising conductors for electric power applications at present. Figure 4.2-51 shows the critical current density, $J_c$, of the superconducting phase of BiPb2223 tapes, at 77 K in self-field versus the tape length achieved by various manufacturers [2.106]. With respect to application, the so-called engineering critical current density, $J_e$, defined by the critical current, $I_c$, divided by the whole transverse cross-section area (superconductor + sheath) is of great importance. An example of the performance of long tapes is given in Fig. 4.2-52, showing $J_e$ values at 77 K in self-field for 200-m long tapes produced in one 17 000-m manufacturing run [2.109]. Much higher critical current densities were measured on experimental short samples and still higher $J_c$ values were observed locally in tapes, demonstrating the potential of BiPb2223 conductors. In Fig. 4.2-53 the steady improvement of $J_c$ of short multifilamentary samples in the 1990s is shown [2.110]. Values of about 75 kA cm$^{-2}$ at 77 K and 0 T were achieved [2.111]. Magnetooptical investigations on a monofilamentary tape with an average $J_c$ (77 K, 0 T) = 35 kA cm$^{-2}$ revealed some small local regions carrying up to 180 kA cm$^{-2}$ (77 K, 0 T) [2.22].

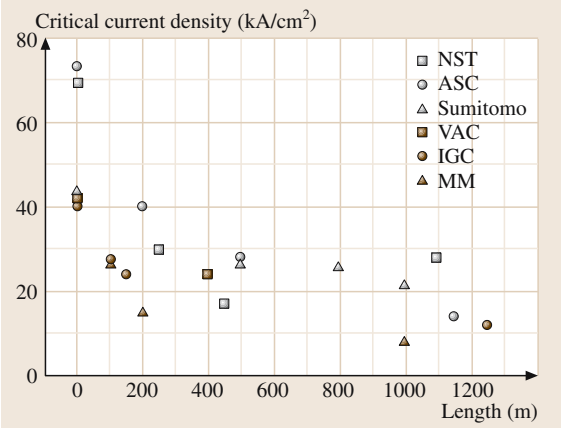


**Fig. 4.2-51** Critical current densities $J_c$ of long multifilamentary BiPb2223/Ag tapes produced by various manufacturers as a function of the length (NST = Nordic Superconductor Technologies, ASC = American Superconductor Corporation, VAC = Vacuumschmelze, IGC = Intermagnetics General Corporation [2.106])

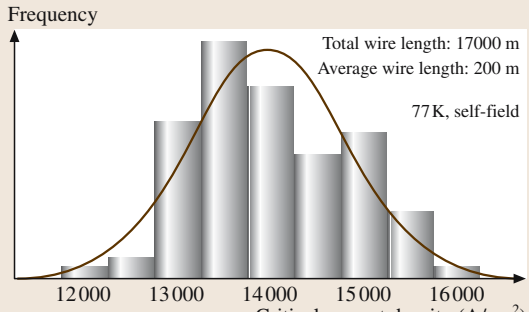


**Fig. 4.2-52** Distribution of the engineering critical current density $J_e$ at 77 K in self-field for 200-m long BiPb2223/Ag tapes produced in one 17 000-m manufacturing run [2.109]

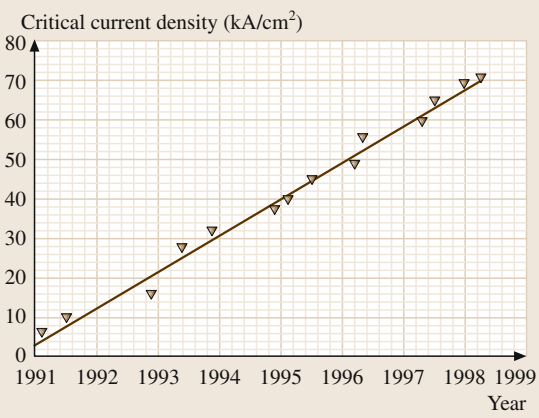


**Fig. 4.2-53** Critical current density $J_c$ for short length multifilamentary BiP2223/Ag tapes versus year of production [2.110]

The development of Bi2212 conductors has also reached a level in recent years which allows the manufacture of long-length wires and tapes. For instance, 70-m long wires with an average critical current density, $J_c$, of 200 kA cm$^{-2}$ at 4.2 K in self-field were produced [2.112]. On tapes of 0.1 to 0.3 mm thickness, $J_c$ values of up to 35 kA cm$^{-2}$ at 77 K and 0 T were measured.

The field dependence of $J_c$ at 77 K is strongly anisotropic for both BiP2222 and Bi2212 conductors. In Fig. 4.2-54a, the $J_c(B, T)$ correlations are demonstrated for BiPb2223 tapes in magnetic fields, $H_{\parallel c}$, aligned perpendicularly to the wide plane of the tape, that is parallel to the crystallographic $c$ axis. At temperatures near 77 K, $J_c$ already drops at $B \approx 0.1$ T to very small values. This tendency, which is also observed in Bi2212 (Fig. 4.2-46) and Bi2223 thin films (Fig. 4.2-47), respectively, is attributed to the thermally activated motion of the pancake vortices near the temperature of liquid nitrogen (see Sect. 4.2.2.1). At 4.2 K, the activation energy of vortex motion is large compared to the thermal energy, $k_B T$, and therefore a much weaker dependence of $J_c$ on $B$ is observed. Figure 4.2-54b represents the $J_c(B, T)$ dependence of BiPb2223 tapes in fields, $H_{\perp c}$, aligned parallel to the plane of the tape (parallel to the crystal $ab$-plane). A comparison of Fig. 4.2-54b with Fig. 4.2-54a shows that $J_c$ is less dependent on $B$ for $H_{\perp c}$ than for $H_{\parallel c}$ (also at 77 K). This can be attributed to the strong intrinsic pinning of Josephson vortices.

Even the highest $J_c$ values observed for the Ag-sheathed tapes are about one order of magnitude lower than those of monocrystalline thin films. These results pose the question of which microstructural features are responsible for this discrepancy. One cause might be different densities of the flux pinning centers. The flux–pinning interactions in BSCCO superconductors are not well known. In particular, due to the small coherence length of the high-$T_c$ superconductors, it is generally expected that even atomic-sized point defects can pin vortices. It could be shown experimentally that single-atomic impurities of Zn and Ni in Bi2212 [2.113] or line defects such as edge [2.114] and screw dislocations [2.115] in $YBa_2Cu_3O_{7-x}$ can effectively pin pancake vortices.

The essential reason for the much lower $J_c$ of the BSCCO tapes compared to monocrystalline films stems from the existence of grain boundaries, which act as barriers to current flow as discussed above. Considering the importance of grain boundaries in a frame of mechanism of the supercurrent flow in BiPb2223 tapes, two models were proposed, the "brick-wall" [2.116] and "railway-switch" [2.117] models, which were combined afterwards within the "freeway" model [2.118].

The models were based on microstructural investigations. Figure 4.2-55 shows the cross-sectional detail of a BiPb2223/Ag tape and reveals a platelet-like microstructure of the superconducting phase. Each platelet called "colony", with a typical diameter of 10–20 μm and a thickness of about 1 μm, consists of a group of single crystal grains sharing a common $c$ axis. The grains inside the colony have random $ab$-orientations, with planar twist basal grain boundaries (BGB's) lying along the $ab$-planes (Fig. 4.2-56a). Using transmission electron microscopy, the dominant colony-boundaries schematically depicted in Fig. 4.2-56b–c were observed. Considering these microstructural details, the main fea-

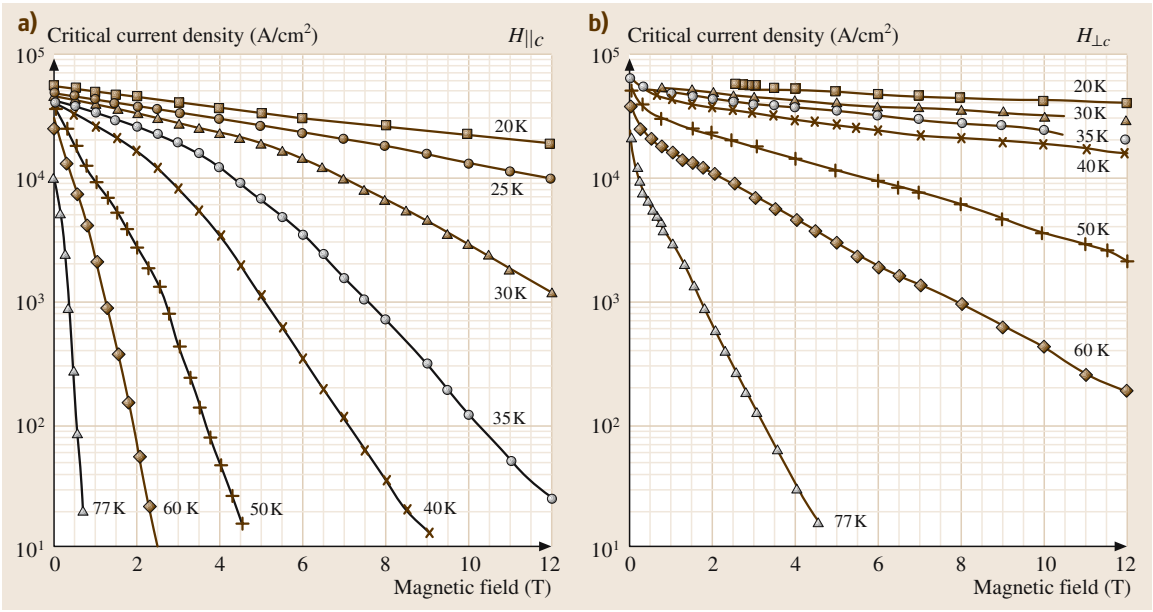


**Fig. 4.2-54a,b** Critical current density $J_c$ of BiP2223/Ag-alloy tapes as a function of the temperature and magnetic field aligned parallel **(a)** and perpendicular to the to the $c$ axis **(b)** [2.119]

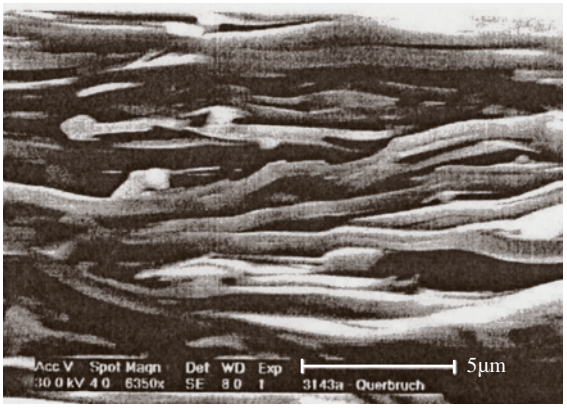


**Fig. 4.2-55** REM micrograph of the cross-sectional detail of a BiP2223/Ag tape [2.119]

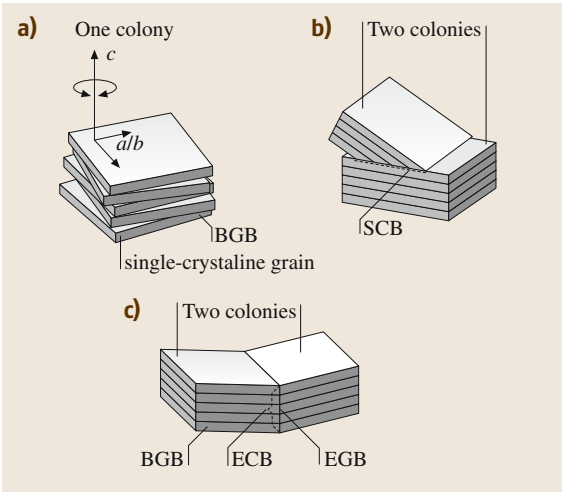


**Fig. 4.2-56a–c** Scheme of colony and single-crystal grain boundaries proposed for the "railway-switch model" [2.117] and in a modified picture for the "freeway model" [2.118]

tures of the "freeway" model can be summarized as follows:

- The "freeway" represents current flow along *ab*-planes.
- The current flows primarily across edge colony boundaries (ECB) rather than small-angle colony boundaries (SCB).
- The relative twist orientation of the *ab* axes across the ECB of adjacent colonies is considered as the dominant factor in the current flow limiting the critical current density.
- Misorientation angles of the *ab*-axes that are less than 10° are required to achieve strong superconducting links across the edge crystal grain

boundaries (EGB) within an edge colony boundary (ECB) of adjacent colonies.

- The probability of overlap of the *ab*-axes at the boundary of adjacent colonies within the 10° criterion is about 1/9 for any one grain inside the colony. Thus the colony structure can carry a current flow ($I$) at a fraction $f_{ECB} \approx 1/9$ of what a single crystal with the *ab*-plane parallel to the current direction ($I$) could carry. The ECB current is expected to be on the scale of the *ab*-current flow.
- An important assumption required for this mechanism is the possibility that high current can shift along the *c* axis between different *ab*-planes, otherwise the strongly coupled *ab*-planes cannot be accessed. This possibility is controversial, since the current must cross many *c* axes boundaries (BGB) inside the colony and the dependence of $J_c$ on the twist angle is not clear yet, as discussed above.

From the model one can derive opportunities to increase $J_c$ of Bi2223 tapes, e.g., through biaxial texturing of the colony grains and increasing the critical current density of the grains. Furthermore, the model provides a coherent explanation of a variety of data observed on Bi2223 tapes such as the $J_c(B, T)$ dependence discussed above.

#### 4.2.2.4 Carbides, Borides, Nitrides

Superconductivity is found in many carbides, nitrides, and borides. Several of these compounds contain transition metals $T$, forming a close-packed lattice with the small atoms, $X =$ C, N, or B, in the interstices of the lattice. The simplest compound of the form $TX$ has a cubic lattice of the NaCl-type. Compounds of $TX$ with $T =$ Nb, V, Mo, etc., are generally very hard, corrosion-resistant, and of high thermal stability. These desirable properties are understood to arise from strong covalent bonding. According to the BCS theory, superconductivity in these and related compounds can be explained by high-frequency phonon modes of the light $X$ atoms combined with a high density of states of the conduction electrons at the Fermi level. A further precondition for high superconducting transition temperatures (which is not included in the BCS theory) is a strong coupling of the phonon modes to the electrons. Recently, a supercon-

**Table 4.2-29** Structure and $T_c$ of carbides

| | $T_c$ (K) | Structure type | Ref. |
|---|---|---|---|
| $Rb_3C_{60}$ | 28 | $BiF_3$ | [2.120] |
| BEDT-TTF-based salt | 12.8 (HP) | organic | [2.120] |
| $MoC_{1-x}$ | 14.3 | NaCl | [2.121] |
| NbC | 12 | NaCl | [2.121] |
| TaC | 10 | NaCl | [2.121] |
| $Mo_2C$ | 12.2 | orthorh. | [2.120] |
| LaBrC | 7.1 | $Gd_2C_2I_2$ | [2.120] |
| YIC | 10 | $Gd_2C_2I_2$ | [2.120] |
| Y(Br, I)C | 7.1 | $Gd_2C_2I_2$ | [2.120] |
| $Mo_3Al_2C$ | 10 | $\beta$-Mn | [2.120] |
| $MgNi_3C$ | 8.5 | $SrTiO_3$ | [2.122] |
| $Nb_2SC$ | 5 | $Tm_2SC$ | [2.123] |
| $Nb_2S_2C$ | 7.6 | $Tm_2S_2C$ | [2.124] |
| $LaC_2$ | 1.6 | $CaC_2$ | [2.121] |
| $LuC_2$ | 3.3 | $CaC_2$ | [2.121] |
| $YC_2$ | 4.0 | $CaC_2$ | [2.120] |
| (La, Th)$NiC_2$ | 7.9 | $CeNiC_2$ | [2.120] |
| $U_2PtC_2$ | 1.5 | $U_2IrC_2$ | [2.121] |
| $La_2C_3$ | 11 | $Pu_2C_3$ | [2.120] |
| $Y_2C_3$ | 8.2 | $Pu_2C_3$ | [2.121] |
| $Th_2C_3$ | 4.1 | $Pu_2C_3$ | [2.121] |
| $(Y, Th)_2C_3$ | 17 | $Pu_2C_3$ | [2.120] |

**Table 4.2-30** Structure and $T_c$ of boron and borides [2.120]

| | $T_c$ (K) | Structure type |
|---|---|---|
| B | 11.2 (at 250 GPa) | |
| NbB | 8.3 | CrB |
| TaB | 4.0 | CrB |
| $Mo_2B$ | 5.1 | $CuAl_2$ |
| $Re_3B$ | 4.7 | $Re_3B$ |
| $MgB_2$ | 39 | $AlB_2$ |
| $ReB_2$ | 6.3 | $AlB_2$ |
| $YB_6$ | 7.1 | $CaB_6$ |
| $LaB_6$ | 5.7 | $CaB_6$ |
| $Yb_{12}$ | 4.7 | $UB_{12}$ |
| $ZrB_{12}$ | 5.8 | $UB_{12}$ |
| $YRUB_2$ | 7.8 | $LuRuB_2$ |
| $LuRuB_2$ | 10.0 | $LuRuB_2$ |
| $YOs_3B_2$ | 6.0 | $CeCo_3B_2$ |
| $LuOs_3B_2$ | 4.7 | $CeCo_3B_2$ |
| $ErRh_4B_4$ | 8–9 | $CeCo_4B_4$ |
| $YRh_4B_4$ | 10–11 | $CeCo_4B_4$ |
| $LuRh_4B_4$ | 8–12 | $CeCo_4B_4$ |

ducting transition temperature $T_c = 39$ K was found in $MgB_2$ [2.125], essentially metallic boron bonded by covalent B−B and ionic B−Mg bonds. This is the highest $T_c$ of binary compounds and close to or above the theoretical value predicted by the BCS theory. The material $MgB_2$ has been known since the early 1950s, but its transport and magnetic properties have not been investigated until recently despite an intensive search for higher values of $T_c$ in the family of binary compounds. The $T_c$ of 23 K obtained for the intermetallic A15 compound $Nb_3Ge$ in the early seventies could not be exceeded until the discovery of the high-$T_c$ superconductors in 1986. Since 1994, there has been a renewed interest in intermetallic superconductors which incorporate light elements such as boron due to the discovery of the new class of quaternary rare-earth transition metal borocarbides $RT_2$ $B_2C$ ($R$ = Y, Lu, or rare-earth metals; $T$ = Ni, Pt, or Pd) [2.126, 127]. These compounds are interesting with regard to the strong interplay between magnetism and superconductivity, including magnetic pair-breaking and the coexistence of superconductivity and magnetism.

### Carbides

Several carbon-containing superconductors are listed in Table 4.2-29. Superconductivity in the fullerenes can be achieved by alkali metal intercalation, resulting in electronically-doped bulk material. This was at first demonstrated by *Rosseinsky* et al. [2.128] who found superconductivity in $Rb_3C_{60}$ at 28 K. Among the superconductors in Table 4.2-29 that have not been mentioned so far are: a) organic compounds, e.g., in BEDT-TTF in which superconductivity is induced by high pressure (HP), b) the layered rare-earth carbide halides with $Gd_2C_2I_2$ structure, c) the niobium carbosulfides with $Tm_2SC$ and $Tm_2S_2C$ structure, d) the lanthanoid dicarbides which crystallize in the body-centered tetragonal $CaC_2$ structure, e) the lanthanoid (and actinide) sesquicarbides with $Pu_2C_3$ structure, and f) the intermetallic compound $MgNi_3C$ with cubic perovskite structure in which superconductivity was found very recently [2.122]. Not included in Table 4.2-29 are the rare-earth transition metal borocarbides RT2B2C, which will be described in more detail later.

### Borides

The superconducting transition temperatures of boron and selected borides are listed in Table 4.2-30. Boron itself, which is an isolator at ambient pressure, was recently found to become superconducting under high pressure [2.129]. The boron atoms in transition metal borides can form chains, nets, and three-dimensional networks. In this respect the borides differ markedly from other interstitial compounds such as carbides

**Table 4.2-31** Superconducting parameters (ranges of experimental and derived data) of $MgB_2$ [2.130]

| Parameter | | Values reported |
|---|---|---|
| Superconducting transition temperature | $T_c$ | 39–40 K |
| Lattic parameters | | $a = 0.3086$ nm, $b = 0.3524$ nm |
| Theoretical density | | 2.55 g cm$^{-3}$ |
| Resistivity near $T_c$ | $\rho(40\,\mathrm{K})$ | 0.4–360 μΩ cm |
| "Residual" resistance ratio | $\mathrm{RRR} = \rho(300\,\mathrm{K})/\rho(40\,\mathrm{K})$ | 1–27 |
| Coherence lengths | $\xi_{ab}$ | 4–12 nm |
| | $\xi_c$ | 1.6–3.6 nm |
| Penetration depths | $\lambda(0)$ | 85–180 nm |
| Upper critical fields | $H_{c2(ab)}(0)$ | 14–40 T |
| | $H_{c2(c)}(0)$ | 2–24 T |
| Anisotropy parameter | $H_{c2(ab)}(0)/H_{c2(c)}(0)$ | 2–13 |
| Lower critical fields | $H_{c1}(0)$ | 27–48 mT |
| Irreversibility fields | $H_{irr}(0)$ | 6–35 T |

and nitrides. Among the transition metal orthorhombic monoborides, NbN and TaN which crystallize in the CrB structure are superconductors. Some properties of $MgB_2$, which has the highest $T_c$ among the borides, are presented in the next section.

### $MgB_2$

The boride $MgB_2$ crystallizes in the simple hexagonal $AlB_2$-type structure and contains graphite-type boron layers which are separated by hexagonal close-packed layers of magnesium (see Fig. 4.2-57). $MgB_2$ has not only an attractively high transition temperature, but, in contrast to high-$T_c$ superconductors, the advantage of strongly-linked grains.

Therefore, high currents can flow across the grain boundaries of bulk polycrystalline $MgB_2$. This is due to the relatively large coherence length $\xi$ of this superconductor (Table 4.2-31). On the other hand, this large coherence length is responsible for the relatively low values of the upper critical field $H_{c2} \propto \xi^{-2}$ observed, especially for clean $MgB_2$ single crystals in a magnetic field parallel to the $c$ axis. Studies of the electronic structure of $MgB_2$ revealed two relevant bands which have to be taken into account in order to explain the magnitude and temperature dependence of the upper critical field $H_{c2}(T)$. Considerably higher upper critical fields than for bulk and single-crystalline $MgB_2$ can be achieved in thin films by the introduction of impurities to decrease the mean free path. In such films, enhanced resistivity, reduced values of $T_c$, and upper critical fields up to 40 T have been reported. One of the open questions concerns the anisotropy of $H_{c2}$. Reported values of $H_{c2}(ab)$ and $H_{c2}(c)$ range between 2 and 13.

### Borocarbides

Table 4.2-32 gives an overview of superconducting borocarbides. Most of them belong to the family of quaternary rare-earth transition metal borocarbides $RT_2B_2C$ ($R$ = Y, Lu, or other rare-earth metals; $T$ = Ni, Pt, or Pd). In this table the superconducting transition temperature $T_c$ and the magnetic ordering temperature $T_N$ are listed. The $LuNi_2B_2C$-type structure of these compounds can be considered as the $ThCr_2Si_2$-type (space group $I4/mmm$) interstitially modified by carbon. They consist of alternating sheets of $T_2B_2$ tetrahedra and $RC$ layers as shown in Fig. 4.2-58 for $RNi_2B_2C$. The

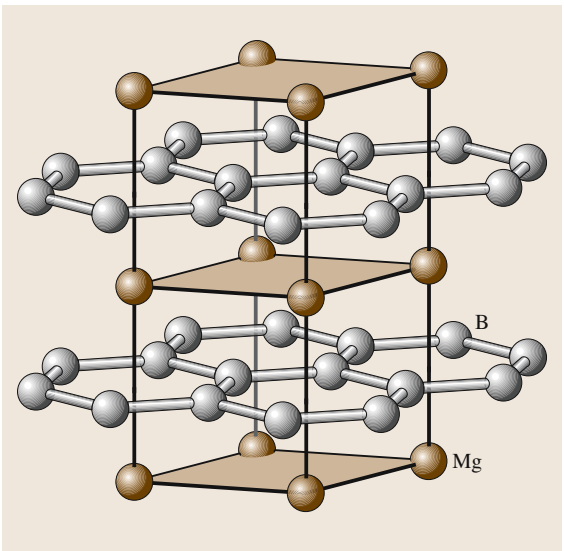


**Fig. 4.2-57** Structure of $MgB_2$

**Table 4.2-32** Borocarbide superconductors [2.120]

| | $T_c$ (K) | $T_N$ (K) | Structure type |
|---|---|---|---|
| $LuB_2C_2$ | 2.4 | – | $LaB_2C_2$ |
| $YB_2C_2$ | 3.6 | – | $LaB_2C_2$ |
| $Mo_2BC$ | 7.5 | – | $Mo_2BC$ |
| $LuNi_2B_2C$ | 16 | – | $LuNi_2B_2C$ |
| $YNi_2B_2C$ | 15.5 | – | $LuNi_2B_2C$ |
| $ScNi_2B_2C$ | 15.5 | – | $LuNi_2B_2C$ |
| $ThNi_2B_2C$ | 15 | – | $LuNi_2B_2C$ |
| $CeNi_2B_2C$ | 0.1 | – | $LuNi_2B_2C$ |
| $TmNi_2B_2$ | 11 | 1.5 | $LuNi_2B_2C$ |
| $ErNi_2B_2C$ | 10.5 | 6.8 | $LuNi_2B_2C$ |
| $HoNi_2B_2C$ | 7.5–8 | 5.8 | $LuNi_2B_2C$ |
| $DyNi_2B_2C$ | 6.2–6.4 | 11 | $LuNi_2B_2C$ |
| $YRu_2B_2C$ | 9.7 | – | $LuNi_2B_2C$ |
| $YPd_2B_2C$ | 23 | – | $LuNi_2B_2C$ |
| $ThPd_2B_2C$ | 14.5 | – | $LuNi_2B_2C$ |
| $LaPd_2B_2C$ | 1.8 | – | $LuNi_2B_2C$ |
| $YPt_2B_2C$ | 10–11 | – | $LuNi_2B_2C$ |
| $LaPd_2B_2C$ | 10–11 | – | $LuNi_2B_2C$ |
| $ThPt_2B_2C$ | 6.5 | – | $LuNi_2B_2C$ |
| $PrPt_2B_2C$ | 6 | – | $LuNi_2B_2C$ |

structure of $RNi_2B_2C$ is highly anisotropic with a $c/a$ ratio of about 3. Nevertheless, these compounds have a three-dimensional globally isotropic structure, but due to the complicated shape of the Fermi surface there is a pronounced dispersion in the Fermi velocity. This peculiarity of the electronic structure is important for the upper critical field $H_{c2}(T)$ because these superconductors are in the clean limit, i. e., their coherence length is smaller than the mean free path. The magnitude of $H_{c2}$ at low temperatures and an unusual positive curvature of $H_{c2}(T)$ observed near $T_c$, especially for the nonmagnetic $RNi_2B_2C$ ($R = Y, Lu$) compounds, can be understood by taking their two-band electronic structure into account.

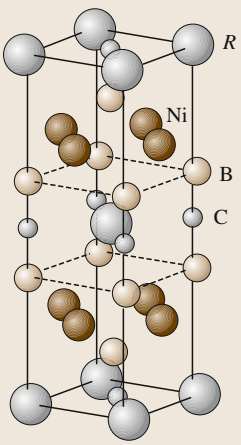


**Fig. 4.2-58** Structure of the rare-earth nickel borocarbides

The superconducting transition temperature of nonmagnetic $RNi_2B_2C$ compounds ($R = Sc, Lu, Y, Th, La$) strongly depends on the lattice parameter $a$, as shown in Fig. 4.2-59. The highest $T_c$ is obtained for $LuNi_2B_2C$, which has an optimum lattice parameter corresponding to a maximum density of states at the Fermi level. In Fig. 4.2-59, magnetic $R$ elements (Tm, Er, Ho, Dy, Yb, Tb, Gd, Eu, Nd, Pr) are also included. The $T_c$ of the superconducting compounds among the magnetic $RNi_2B_2C$ compounds ($R = Tm$, Er, Ho, and Dy) scales roughly with the de Gennes factor $dG = (g-1)^2 J(J+1)$ of the $R^{3+}$ Hund's-rule ground state, where $g$ is the Landé factor and $J$ the total angular momentum. Such so-called de Gennes scaling is observed for both $T_c$ and the magnetic or-

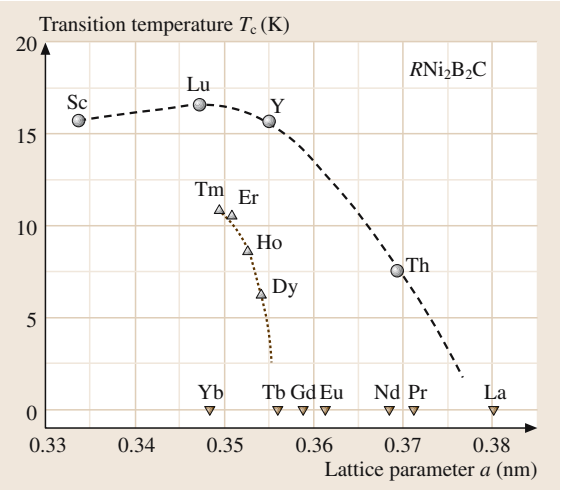


**Fig. 4.2-59** Transition temperature $T_c$ and lattice parameter $a$ for $RNi_2B_2C$ compounds for non-magnetic (*circles*) and magnetic (*triangles*) $R$ elements [2.131]

dering temperature $T_N$ as shown in Fig. 4.2-60. The reason is that both effects, i. e., antiferromagnetism and the suppression of superconductivity, are governed by the exchange interaction of conduction electrons with $R$ 4f electrons.

A striking feature distinguishing the superconducting $RNi_2B_2C$ compounds from other magnetic superconductors is their high magnetic ordering temperature $T_N$ being comparable with $T_c$. Therefore, the interplay between superconductivity and magnetism in these compounds is particularly pronounced. In particular, $DyNi_2B_2C$ is the unique member of the $RNi_2B_2C$ series which becomes superconducting in the antiferromagnetically ordered state.

### Nitrides

The refractory transition metal nitrides with NaCl-type crystal structure have been widely studied in the past. The basic features of superconductivity in these compounds indicate a standard BCS mechanism. The highest $T_c$ among these compounds was found for NbN (see Table 4.2-32). Niobium nitride which can easily prepared as a thin film is a promising material for the application in various cryogenic devices such as high resolution X-ray detectors or superconducting quantum mixers. For NbN thin films, very high upper critical fields up to 30 T and high critical currents, e.g.,

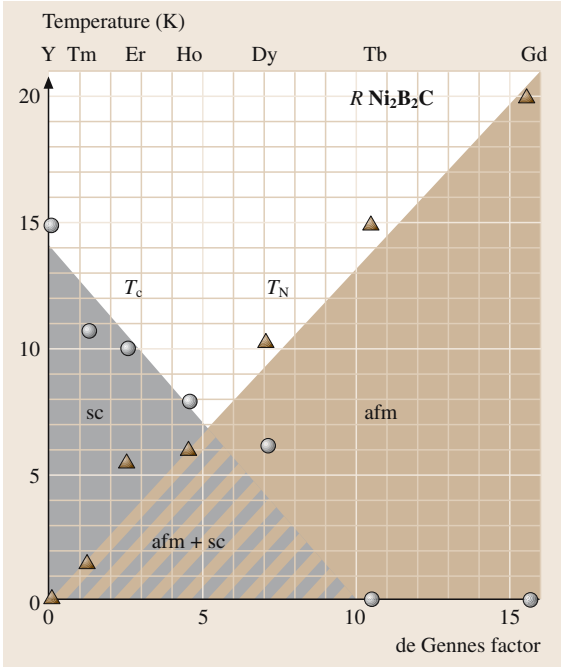


**Fig. 4.2-60** Superconducting transition temperature $T_c$ and antiferromagnetic ordering temperature $T_N$ for $RNi_2B_2C$ compounds, with $R$ = Lu, Tm, Er, Dy, Tb, and Gd as functions of the de Gennes factor (see text). (afm = antiferromagnetic, sc = superconducting, afm + sc = coexistence of superconductivity and antiferromagnetism)

$10^5$ A cm$^{-2}$ at 4.2 K in fields of 19 T [2.132] were reported. For MoN with the NaCl structure, $T_c$ = 29 K was predicted [2.133], although this structure does not appear in the equilibrium phase diagram of the Mo–N system. Attempts have been made to prepare it by techniques leading to non-equilibrium states. In single-phase films with the NaCl structure, $T_c$ = 12.5 K was found [2.134]. This unexpectedly low $T_c$ was explained by the presence of nitrogen vacancies and interstitial defects. The transition metal nitrides crystallize in several other structures, too. Some of these compounds are superconducting and have similar $T_c$ values as the corresponding NaCl-type compounds (see Table 4.2-33). Recently, a new route of preparation was developed for lithium intercalated metal nitride chloride. Superconductivity with $T_c$ = 14 K and even 25 K was reported for $Li_{0.16}ZrNCl$ and $Li_{0.48}(THF)_yHfNCl$, respectively [2.135,136], where THF = tetrahydrofuran.

**Table 4.2-33** Nitrides superconductors

| | $T_c$ (K) | Structure type | Reference |
|---|---|---|---|
| TiN | 6.5 | NaCl | 2.121 |
| ZrN | 10.6 | NaCl | 2.121 |
| HfN | 8.3 | NaCl | 2.121 |
| Vn | 8.8 | NaCl | 2.121 |
| NbN | 17.3 | NaCl | 2.121 |
| NbN | 9 | W | 2.132 |
| NbN | 15 | Fcc | 2.121 |
| TaN | 10.4 | NaCl | 2.121 |
| TaN | 10.8 | Fcc | 2.137 |
| MoN | 12.5 | NaCl | 2.121 |
| MoN | 13.2 | Hexagonal | 2.134 |
| ReN | 5 | NaCl | 2.121 |
| $Nb_2N$ | 8.6 | Hexagonal | 2.132 |
| $Ta_2N$ | 10.6 | Hexagonal | 2.137 |
| $Mo_2N$ | 6–7 | Fcc | 2.134 |
| $Li_{0.16}$ZrNCL | 14 | | 2.135 |
| $Li_{0.48}$(THF)HFNCl | 25.5 | | 2.136 |

## References


2.1 O. Henkel, E. M. Sawitzkij (Eds.): *Supraleitende Werkstoffe* (VEB Deutscher Verlag für Grundstoffindustrie, Leipzig 1982) (in German)

2.2 R. Flükiger, W. Klose (Eds.): *Superconductors*, Landolt–Börnstein, New Series III/21 (Springer, Berlin, Heidelberg 1997)

2.3 J. Evetts (Ed.): *Concise Encyclopedia of Magnetic & Superconducting Materials* (Pergamon Press, Oxford, New York, Seoul, Tokyo 1992)

2.4 H. Hillmann: Superconductor Materials Science. In: *Metallurgy, Fabrication, Applications*, ed. by S. Foner, B. B. Schwartz (Plenum, New York 1981)

2.5 D. C. Larbalastier: Superconductor Materials Science. In: *Metallurgy, Fabrication, Applications*, ed. by S. Foner, B. B. Schwartz (Plenum, New York, London 1981)

2.6 E. W. Collings (Ed.): *A Source Book of Titanium Alloy Superconductivity* (Plenum, New York 1983)

2.7 K. Osamura (Ed.): *Composite Superconductors* (Marcel Dekker, Basel, New York, Hong Kong 1994)

2.8 H. Krauth: *Conductors for d.c. Applications*, Handbook of Applied Superconductivity, ed. by B. Seeber (Institute of Physics Publishing, Bristol, Philadelphia 1998)

2.9 C. Li, D. C. Larbalastier: Development of high critical current densities in niobium 46.5 wt% titanium, Cryogenics **27**, 171 (1987)

2.10 J. Ekin: *Materials at Low Temperature*, ed. by P. R. Reed, F. C. Clark (American Society for Metals, Metals Park OH 1983)

2.11 R. Flükiger, W. Klose (Eds.): *Superconductors*, Landolt–Börnstein, New Series III/21 (Springer, Berlin, Heidelberg 1997) pp. 1–11

2.12 J. G. Bednorz, K. A. Müller: Possible high-$T_c$ superconductivity in the Ba–La–Cu–0 system, Z. Phys. **B 64**, 189 (1986)

2.13 R. Hott: *High Temperature Superconductivity, 1: Materials*, ed. by A. V. Narlikar (Springer, Berlin, Heidelberg, New York 2004) p. 1

2.14 B. Raveau: In: *High-$T_c$ superconductivity: Ten Years after the Discovery*, NATO ASI Ser. E: Applied Sciences, Vol. 343, ed. by E. Kaldis, E. Liarokapis, K. A. Müller (Kluwer 1997) p. 109

2.15 D. R. Harshman, A. P. Mills Jr.: Concerning the nature of high-$T_c$ superconductivity: Survey of experimental properties and implications for interlayer coupling, Phys. Rev. **B 45**, 10684 (1992)

2.16 C. N. R. Rao, R. Nagarajan, R. Vijayaraghavan: Synthesis of cuprate superconductors, Supercond. Sci. Technol. **6**, 1 (1993)

2.17 N. M. Plakida: *High-Temperature Superconductivity* (Springer, Berlin, Heidelberg 1995)

2.18 M. Tinkham: *Theory of Superconductivity* (McGraw-Hill, New York 1975)

2.19 G. Blatter, M. V. Feigelmann, V. B. Geschkenbein, A. I. Larkin, V. M. Vinokur: Vortices in high-$T_c$ superconductors, Rev. Mod. Phys. **66**, 1125 (1994)

2.20 K. H. Fischer: Vortices in high-$T_c$ superconductors, Superconductivity Rev. **1**, 153 (1995)

2.21 H. Hilgenkamp, J. Mannhart: Grain boundaries in high-$T_c$ superconductors, Rev. Mod. Phys. **74**, 485 (2002)2

2.22 D. Larbalestier, A. Gurevich, D. M. Feldmann, A. Polyanskii: High-$T_c$ superconducting materials for electric power applications, Nature **414**, 368 (2001)

2.23 B. Seeber (Ed.): *Handbook of Applied Superconductivity*, Vol. 2 (Institut of Physics Publishing, Bristol, Philadelphia 1998)

2.24 J. J. Capponi, C. Chaillout, A. W. Hewat, P. Lejay, M. Marezio, N. Nguyen, B. Raveau, J. L. Soubeyroux, J. L. Tholence, R. Tournier: Structure of the 100 K superconductor $Ba_2YCu_3O_7$ between (5 – 300) K by neutron powder diffraction, Europhys. Lett. **3**, 1301–1307 (1987)

2.25 M. K. Wu, J. R. Ashburn, C. J. Torng, P. H. Hor, R. L. Meng, L. Gao, Z. J. Huang, Y. Q. Wang, C. W. Chu: Superconductivity at 93 K in a new mixed-phase Y—Ba—Cu—O compound system at ambient pressure, Phys. Rev. Lett. **58**, 908–910 (1987)

2.26 N. L. Ross, R. J. Angel, L. W. Finger, R. M. Hazen, C. T. Prewitt: Oxygen-defect perovskites and the 93-K superconductor, American Chemical Society: Symposium Series **351**, Chemistry of high-temperature superconductors, New Orleans 1987, ed. by E. D. Nelson, M. S. Wittingham, T. F. George (American Chemical Society, New Orleans 1987) 164–172

2.27 M. François, A. Junod, K. Yvon, A. W. Hewat, J. J. Capponi, P. Strobel, M. Marezio, P. Fischer: A study of the Cu—O chains in the high $T_c$ superconductor $YBa_2Cu_3O_7$ by high resolution neutron powder diffraction, Solid State Comm. **66**, 1117–1125 (1988)

2.28 J. D. Jorgensen, B. W. Veal, A. P. Paulikas, L. J. Nowicki, G. W. Crabtree, H. Claus, W. K. Kwok: Structural properties of oxygen-deficient $YBa_2Cu_3O_{7-\delta}$, Phys. Rev. B **41**, 1863–1877 (1990)

2.29 E. Kaldis: Oxygen nonstoichiometry and lattice effects in $YBa_2Cu_3O_x$. In: *Handbook on the Physics and Chemistry of Rare Earths*, High-Temperature Superconductors II., Vol. 31, ed. by K. A. Gschneidner Jr., L. Eyring, M. B. Maple (Elsevier, Amsterdam, London, New York, Oxford, Paris, Shannon, Tokyo 2001) Chap. 195, pp. 1–186

2.30 R. J. Cava, A. W. Hewat, E. A. Hewat, B. Batlogg, M. Marezio, K. M. Rabe, J. J. Krajewski, W. F. Peck Jr., L. W. Rupp Jr.: Structural anomalies, oxygen ordering and superconductivity in oxygen deficient $Ba_2YCu_3O_x$, Physica C **165**, 419–433 (1990)

2.31 J. M. S. Shakle: Crystal chemical substitution and doping of $YBa_2Cu_3O_x$ and related superconductors, Mat. Sci. Engineering R **23**, 1–40 (1998)

2.32 M. Guillaume, P. Allenspach, W. Henggeler, J. Mesot, B. Roessli, U. Staub, P. Fischer, A. Furrer, V. Trounov: A systematic low-temperature neutron diffraction study of the $RBa_2Cu_3O_x$ (R = yttrium and rare earths; $x = 6$ and 7) compounds, J. Phys.: Condens. Matter **6**, 7963–7976 (1994)

2.33 Y. Nakabayashi, Y. Kubo, T. Manato, J. Tabuchi, A. Ochi, K. Utsumi, H. Igarashi, M. Yonezawa: The orthorhombic-tetragonal phase transformation an doxygen deficiency in $LnBa_2Cu_3P_{7-\delta}$, Jpn. J. Appl. Phys. **27**, L64–L66 (1988)

2.34 R. D. Shannon: Revised effective ionic radii and systematic studies of interatomic distances in halides and chalcogenides, Acta Crystallogr. A **32**, 751–767 (1976)

2.35 L. J. Masur, J. Kellers, C. M. Pegrum, D. A. Cardwell: Fundamentals of superconductivity: Applied properties of superconducting materials. In: *Handbook of Superconducting Materials*, Superconductivity, Materials and Processes, Vol. I, ed. by D. A. Cardwell, D. S. Ginley (IOP Publishing, Bristol, Philadelphia 2003) pp. 27–52

2.36 M. Murakami: Processing of bulk YBaCuO, Supercond. Sci. Technol. **5**, 185–203 (1992)

2.37 P. Diko: Characterization techniques: Optical microscopy. In: *Handbook of Superconducting Materials*, Characterization, Applications and Cryogenics, Vol. II, ed. by D. A. Cardwell, D. S. Ginley (IOP Publishing, Bristol 2003) pp. 1147–1175

2.38 C. Meingast, O. Kraut, T. Wolf, H. Wühl, A. Erb, G. Müller-Vogt: Large *a*-*b* anisotropy of the expansivity anomaly at $T_c$ in untwinned $YBa_2Cu_3O_{7-\delta}$, Phys. Rev. Lett. **67**, 1634–1637 (1991)

2.39 P. Nagel, V. Pasler, C. Meingast, A. I. Rykov, S. Tajima: Anomalously large oxygen-ordering contribution to the thermal expansion of untwinned $YBa_2Cu_3O_{6.95}$ single crystals: A glasslike transition near room temperature, Phys. Rev. Lett. **85**, 2376–2379 (2000)

2.40 D. Dimos, D. R. Clarke: Surfaces, Inferfaces of Ceramic Materials, NATO ASI series: E173, Proceedings of the NATO Advanced Study Institute on Surfaces and Interfaces of Ceramic Materials, CAES-CNRS, Ile d'Oléron, France 1988, ed. by L. C. Dufour, others (Kluwer Academic, Dordrecht 1989) 301–318

2.41 T. A. Friedmann, M. W. Rabin, J. Giapintzakis, J. P. Rice, D. M. Ginsberg: Direct measurement of the anisotropy of the resistivity in the *a*-*b* plane of twin-free single-crystal, superconducting $YBa_2Cu_3O_{7-\delta}$, Phys. Rev. B **42**, 6217–6221 (1990)

2.42 J. R. Cooper, S. D. Obertelli, A. Carrington, J. W. Loram: Effect of oxygen depletion on th etransport properties of $YBa_2Cu_3O_{7-\delta}$, Phys. Rev. B **44**, 12086–10289 (1991)

2.43 A. Carrington, D. J. C. Walker, A. P. Mackenzie, J. R. Cooper: Hall effect and resistivity of oxygen-deficient $YBa_2Cu_3O_{7-\delta}$ thin films, Phys. Rev. B **48**, 13051–13059 (1993)

2.44 D. T. Verebelyi, D. K. Christen, R. Feenstra, C. Cantoni, A. Goyal, D. F. Lee, M. Paranthaman, P. N. Arendt, R. F. DePaula, J. R. Groves, C. Prouteau: Low angle grain boundary transport in $YBa_2Cu_3O_{7-\delta}$ coated conductors, Appl. Phys. Lett. **76**, 1755–1757 (2000)

2.45 B. Holzapfel, D. Verebelyi, C. Cantoni, M. Paranthaman, B. Sales, R. Feenstra, D. Christen, D. P. Norton: Low angle grain boundary transport properties of undoped and doped Y123 thin film bicrystals, Physica C **341**, 1431–1434 (2000)

2.46 K. Takenaka, K. Mizuhashi, H. Takagi, S. Uchida: Interplane charge transport in $YBa_2Cu_3O_{7-y}$: Spin-gab effect on in-plane and out-of-plane resistivity, Phys. Rev. B **50**, 6534–6537 (1994)

2.47 M. D. Nunez Regueiro, D. Castello: Thermal conductivity of high temperature superconductors, Int. J. Mod. Phys. B **5**, 2003–2035 (1991)

2.48 W.-H. Li, J. W. Lynn, Z. Fisk: Magnetic order of the Cu planes and chains in $RBa_2Cu_3O_{7+x}$, Phys. Rev. B **41**, 4098–4111 (1990)

2.49 J. S. Abell, T. W. Button: Processing: Sintering techniques for YBCO. In: *Handbook of Superconducting Materials*, Superconductivity, Materials and Processes, Vol. I, ed. by D. A. Cardwell, D. S. Ginley (IOP Publishing, Bristol 2003) pp. 251–258

2.50 M. Hikita, Y. Tajima, A. Katsui, Y. Hidaka, S. Iwata, S. Tsurumi: Electrical properties of high-$T_c$ superconducting single-crystal $Eu_1Ba_2Cu_3O-y$, Phys. Rev. B **36**, 7199–7202 (1987)

2.51 W. J. Gallagher: Studies at IBM on anisotropy in single crystals of the high-temperature oxide superconductor $Y_1Ba_2Cu_3O_{7-\delta}$, J. Appl. Phys. **63**, 4216–4219 (1988), invited

2.52 T. K. Worthington, W. J. Gallagher, T. R. Dinger: Anisotropic nature of high-temperature superconductivity in single-crystal $Y_1Ba_2Cu_3O_{7-\delta}$, Phys. Rev. Lett. **59**, 1160–1163 (1987)

2.53 D. Feinberg, C. Villard: Intrinsic pinning and lock-in transition of flux lines in layered type-II superconductors, Phys. Rev. Lett. **65**, 919–922 (1990)

2.54 A. Koblischka-Veneva, N. Sakai, S. Tajima, M. Murakami: *High temperature superconductors: YBCO*, Superconductivity, Materials and Processes, Vol. I, ed. by D. A. Cardwell, D. S. Ginley (IOP Publishing, Bristol, Philadelphia 2003) pp. 893–945

2.55 T. R. Dinger, T. K. Worthington, W. J. Gallagher, R. L. Sandstrom: Direct observation of electronic anisotropy in single-crystal $Y_1Ba_2Cu_3O_{7-x}$, Phys. Rev. Lett. **58**, 2687–2690 (1987)

2.56 G. Böttger, I. Mangelschots, E. Kaldis, P. Fischer, C. Krüger, F. Fauth: The influence of Ca doping on the crystal structure and superconductivity of orthorhombic $YBa_2Cu_3O_{7-\delta}$, J. Phys.: Condens. Matter **8**, 8889–8905 (1996)

2.57 J. R. Grasmeder, M. T. Weller, P. C. Lanchester, C. E. Meats: Superconductivity in the Y–La–Ba–Cu–O system, Solid State Ionics **32/33**, 1115–1124 (1989)

2.58 F. Licci, A. Gauzzi, M. Marezio, G. P. Radaelli, R. Masini, C. Chaillout-Bougerol: Structural and electronic effects of Sr substitution for Ba in $Y(Ba_{1-x}Sr_x)Cu_3O_w$, Phys. Rev. B **58**, 15208–15217 (1998)

2.59 E. Kim, I.-S. Yang: Structural analysis of Y–Zn 123 superconductor using X-ray powder diffraction, New Physics (Korean Physical Society) **32**, 839–846 (1992)

2.60 N. L. Saini, K. B. Garg, H. Rajagopal, A. Sequeira: Neutron diffraction and Hall effect measurements on Y–Ba–Cu(Mn)–O, Solid State Comm. **82**, 895–899 (1992)

2.61 B. Roas, L. Schultz, G. Saemann-Ischenko: Anisotropy of the critical current density in epitaxial $YBa_2Cu_3O_x$ films, Phys. Rev. Lett. **64**, 479–482 (1990)

2.62 V. Breit, P. Schweiss, R. Hauff, H. Wühl, H. Claus, H. Rietschel, A. Erb, G. Müller-Vogt: Evidence for chain superconductivity in near-stoichiometric $YBa_2Cu_3O_x$ single crystals, Phys. Rev. **B 52**, R15727–R15730 (1995)

2.63 P. Schweiss, W. Reichardt, M. Braden, G. Collin, G. Heger, H. Claus, A. Erb: Static and dynamic displacement in $RBa_2Cu_3O_{7-\delta}$ ($R$ = Y, Ho; $\delta = 0.05, 0.5$): A neutron-diffraction study on single crystals, Phys. Rev. B **49**, 1387–1396 (1994)

2.64 H. Claus, M. Braun, A. Erb, K. Röhberg, B. Runtsch, H. Wühl, G. Bräuchle, P. Schweib, G. Müller-Vogt, H. v. Löhneysen: The "90 K" plateau of oxygen deficient of $YBa_2Cu_3O_{7-\delta}$ single crystals, Physica C **198**, 42–46 (1992)

2.65 H. Claus, U. Gebhard, G. Linker, K. Röhberg, S. Riedling, J. Franz, T. Ishida, A. Erb, G. Müller-Vogt, H. Wühl: Phase separation in $YBa_2Cu_3O_{7-\delta}$ single crystals near $\delta = 0$, Physica C **200**, 271–276 (1992)

2.66 D.-H. Wu, S. Sridhar: Pinning forces and lower critical fields in $YBa_2Cu_3O_y$ crystals: Temperature dependence and anisotropy, Phys. Rev. Lett. **65**, 2074–2077 (1990)

2.67 U. Welp, W. K. Kwok, G. W. Crabtree, K. G. Vandervoort, J. Z. Liu: Magnetic measurements of the upper critical field of $YBa_2Cu_3O_{7-\delta}$ single crystals, Phys. Rev. Lett. **62**, 1908–1911 (1989)

2.68 P. Majewski: Phase diagram studies in the system Bi–Pb–Sr–Ca–Cu–O–Ag, Supercond. Sci. Technol. **10**, 453 (1997)

2.69 Y. Yamada, Y. Shiohara: Progress of high-$T_c$ wires and its application. In: *High Temperature Superconductivity, 1: Materials*, ed. by A. V. Narlikar (Springer, Berlin, Heidelberg, New York 2004) pp. 291–337

2.70 D. L. Feng, A. Damascelli, K. M. Chen, N. Motoyama, D. H. Lu, H. Eisaki, K. Shimizu, J. Shimoyama, K. Kishio, N. Kaneko, M. Greven, G. D. Gu, X. J. Zhou, C. Kim, F. Ronning, N. P. Armitage, Z.-X. Shen: Electronic structure of the trilayer cuprate superconductor $Bi_2Sr_2Ca_2Cu_3O_{10+\delta}$, Phys. Rev. Lett. **88**, 107001–1 (2002)

2.71 A. Maeda, T. Shibauchi, N. Kondo, K. Uchinokura, M. Kobayashi: Magnetic-field penetration depth

and lower critical field of quasi-two-dimensional superconductor $Bi_2Sr_2Ca_2Cu_2O_y$, Phys. Rev. B **46**, 14234 (1992)

2.72 L. Miu, P. Wagner, U. Frey, A. Hadish, D. Miu, H. Adrian: Vortex unbinding and layer decoupling in epitaxial $Bi_2Sr_2Ca_2Cu_3O_{10+\delta}$ films, Phys. Rev. B. **52**, 4553 (1995)

2.73 I. Matsubara, R. Funahashi, K. Ueno, H. Yamashita, T. Kawai: Lower critical field and reversible magnetization of $(Bi,Pb)_2Sr_2Ca_2Cu_3O_x$ superconducting whiskers, Physica C **256**, 33 (1996)

2.74 S. I. Vedeneev, A. G. M. Jansen, E. Haanappel, P. Wyder: Temperature dependence of the upper critical field of $Bi_2Sr_2CuO_x$ single crystals, Phys. Rev. B **60**, 12467 (1999)

2.75 M. Akamatsu, L. X. Chen, H. Ikeda, R. Yoshizaki: Physica C **235–240**, 1619 (1994)

2.76 D. C. Johnston, J. H. Cho: Magnetic-susceptibility anisotropy of single-crystal $Bi_2Sr_2CaCu_2O_8$, Phys. Rev. B **42**, 8710 (1990)

2.77 T. T. M. Palstra, B. Batlogg, L. F. Scheemeyer, R. B. van Dover, J. Waszczak: Angular dependence of the upper critical field of $Bi_{2.2}Sr_2Ca_{0.8}Cu_2O_{8+\delta}$, Phys. Rev. B **38**, 5102 (1988)

2.78 I. Matsubara, H. Tanigawa, T. Ogura, H. Yamashita, M. Kinoshita, T. Kawai: Upper critical field and anisotropy of the high-$T_c$ $Bi_2Sr_2CaCu_2O_x$ phase, Phys. Rev. B **45**, 7414 (1992)

2.79 Q. Li, M. Suenaga, J. Gohng, D. K. Finnemore, T. Hikata, K. Sato: Reversible magnetic properties of c-axis-oriented superconducting $Bi_2Sr_2Ca_2Cu_{10}$, Phys. Rev. B **46**, 3195 (1992)

2.80 Q. Li, M. Suenaga, T. Hikata, K. Sato: Two-dimensional fluctuations in the magnetization of $Bi_2Sr_2Ca_2Cu_3O_{10}$, Phys. Rev. B **46**, 5857 (1992)

2.81 A. V. Narlikar (Ed.): *High Temperature Superconductivity, 1: Materials, 2: Engineering Applications* (Springer, Berlin, Heidelberg, New York 2004)

2.82 S. Martin, A. T. Fiory, R. M. Fleming, L. E. Schneemeyer, J. V. Waszczak: Normal-state transport properties of $Bi_{2+x}Sr_{2-y}CuO_{6\pm\delta}$ crystals, Phys. Rev. B **41**, 846 (1990)

2.83 T. W. Li, A. A. Menovski, J. J. M. Franse, P. H. Kes: Flux pinning in Bi-2212 single crystals with various oygen contents, Physica **C 257**, 179 (1996)

2.84 D. R. Harshman, R. N. Kleiman, M. Inui, G. P. Espinosa, D. B. Mitzi, A. Kapitulnik, T. Pfiz, D. L. Williams: Magnetic penetration depth and flux dynamics in single crystal $Bi_2Sr_2CaCu_2O_{8-\delta}$, Phys. Rev. Lett. **67**, 3152 (1991)

2.85 H. Enriquez, N. Bontemps, A. A. Zhukov, D. V. Shovkun, M. R. Trunin, A. Buzdin, M. Daumens, T. Tamegai: A compilation of references considering $\lambda_c(0)$, Phys. Rev. B **63**, 144 (2001)

2.86 Y. Ando, G. S. Boebinger, A. Passner, L. F. Schneemeyer, T. Kimura, M. Okuya, S. Watauchi, J. Shimoyama, K. Kishio, K. Tamsaku, N. Ichikawa, S. Uchida: Upper critical fields and irreversibility lines of optimal doped high-$T_c$ cuprates, Phys. Rev. **B 60**, 12475 (1999)

2.87 A. Attenberger: Elektrische Transportmessungen über definierte Korngrenzen-Strukturen in epitaktischen Bi2223-Schichten. Ph.D. Thesis (Technische Universität Dresden, Dresden 2000)

2.88 I. L. Landau, H. R. Ott: Temperature dependence of the upper critical field of type-II superconductors from isothermal magnetization data: Application to high-temperature superconductors, Phys. Rev. B **66**, 144506 (2002)

2.89 R. Wesche: *High-Temperature Superconductors: Materials, Properties, and Applications* (Kluwer, Boston, Dordrecht, London 1998)

2.90 P. Schmitt, P. Kummeth, L. Schultz, G. Saemann-Ischenko: Two-dimensional behavior and critical-current anisotropy in epitaxial $Bi_2Sr_2CaCu_2O_{8+x}$ thin films, Phys. Rev. Lett. **67**, 267 (1991)

2.91 T. Amrein, L. Schultz, B. Kabius, K. Urban: Orientation dependence of grain-boundary critical current densities in high-$T_c$ bicrystals, Phys. Rev. B **51**, 6792 (1995)

2.92 G. Balestrino, M. Marinelli, E. Milani, L. Reggiani, R. Vaglio, A. A. Varlamov: Exess conductivity in 2:2:1:2-phase Bi–Sr–Ca–Cu–O epitaxial thin films, Phys. Rev. B **46**, 14919 (1992)

2.93 K. Endo, H. Yamasaki, S. Misawa, S. Yoshida, K. Kajimura: Lett. Nature **355**, 327 (1992)

2.94 P. Wagner, F. Hillmer, U. Frey, H. Adrian, T. Steinborn, L. Ranno, A. Elschner, I. Heyvaert, Y. Bruynseraede: Preparation and structural characterisation of thin epitaxial $Bi_2Sr_2CaCu_2O_{8+\delta}$ films with $T_c$ in the 90 K range, Physica C **215**, 123 (1993)

2.95 Q. Li, Y. N. Tsay, M. Suenaga, R. A. Klemm, G. D. Gu, N. Koshizuka: $Bi_2Sr_2CaCu_2O_{8+\delta}$ bicrystal c-axis twist Josephson junktions: A new phase sensitive test of order parameter symmetry, Phys. Rev. Lett. **83**, 4160 (1999)

2.96 N. Tomita, Y. Takahashi, Y. Ishida: Preparation of bicrystal in a Bi–Sr–Ca–O superconductor, Jpn. J. Appl. Phys. **29**, 1 (1990)L 30

2.97 Q. Li, Y. N. Tsay, M. Suenaga, G. Wirth, G. D. Du, N. Koshizuka: Superconducting transport properties of 2.2-GeV Au-ion irradiated c-axis twist $Bi_2Sr_2CaCu_2O_{8+\delta}$ bicrystals, Appl. Phys. Lett. **74**, 1323 (1999)

2.98 S. Chu, M. E. McHenry: Growth and characterization of $(Bi,Pb)_2Sr_2Ca_2Cu_3O_x$ single crystals, J. Mater. Res. **13**, 589 (1998)3

2.99 B. Sailer, F. Schwaigerrer, K. Gibson, H.-J. Meyer, M. Lehmann, L. Woodall, M. Gerards: Effect of precursor powder properties on magnetic and electrical transport properties of (Bi,Pb)-2223-tapes, IEEE Trans. Appl. Supercond. **11**, 2975 (2001)

2.100 H. F. Poulsen, L. Gottschalck Andersen, T. Frello, S. Prantontep, N. H. Andersen, S. Garbe, J. Madsen, A. Abrahamsen, M. D. Bentzon, M. von Zimmermann: In situ study of equilibrium phenomena

and kinetics in a BSCCO/Ag tape, Physica C **315**, 254 (1999)
2.101 E. Giannini, E. Bellingeri, R. Passerini, R. Flükiger: Direct observation of the Bi,Pb (2223) phase formation inside Ag-sheathed tapes and quantitative secondary phase analysis by means of in situ high-temperature neutron diffraction, Physica C **315**, 185 (1999)
2.102 T. Fahr, H. P. Trinks, R. Schneider, C. Fischer: Investigation of the formation of the Bi-2223/Ag tapes by in situ high temperature neutron diffraction, IEEE Trans. Appl. Supercond. **11**, 3399 (2001)
2.103 T. Lang, B. Heeb, D. Buhl, L. J. Gaukler: Proc. of the Forth Intern. Conf. And Exhibition, World Congress on Supercoductivity, June 27–July 1, 1994, Orlando (Florida), Vol. 2, ed. by K. Krishen, C. Burnham, p. 753
2.104 J. C. Grivel, R. Flükiger: Visualization of the formation of the $(Bi,Pb)_2Sr_2Ca_2Cu_3O_{10+\delta}$ phase, Supercond. Sci. Technol. **9**, 555 (1996)
2.105 L. Y. Wang, W. Bian, Y. Zhu, Z. X. Cai, D. O. Welch, R. L. Sabatini, T. R. Thurston, M. Suenaga: A kinetic mechanism for the formation of aligned $(Bi,Pb)_2Sr_2Ca_2Cu_3O_{10}$ in a powder-in-tube processed tape, Appl. Phys. Lett. **69**, 580 (1996)
2.106 G. W. Wang, M. D. Bentzon, P. Vase: High critical current and detect free km long Bi-2223/Ag-alloy multifilament tapes, Proceedings of EUCAS 1999, ed. by X. Obradors, F. Sandiumenge, J. Fontcuberta, Institut of Physics Conference Ser. Number 167, Vol. 1, p. 459
2.107 C. Fischer, T. Fahr, A. Hütten, U. Schläfer, M. Schubert, C. Rodig, H. P. Trinks: Technology of Bi,Pb-2223 tape fabrication with Ag and Ag alloy sheaths for electric power systems, Supercond. Sci. Technol. **11**, 995 (1998)
2.108 P. Vase, R. Flükiger, M. Leghissa, B. Glowcki: Current status of high-$T_c$ wire, Supercond. Sci. Technol. **13**, R.71 (2000)
2.109 L. Masur: Adv. Cryog. Eng. **46**, 871 (2000)
2.110 P. M. Grant: IEEE Trans. Appl. Supercond. **7**, 7 (1997)
2.111 A. P. Malozemoff, W. Carter, S. Fleshler, L. Fritzemeier, Q. Li, L. Masue, P. Miles, D. Parker, R. Parella, E. Podtburg, G. N. Riley Jr., M. Rupich, J. Scudiere, W. Zhang: HTS wire at commercial levels, IEEE Trans. Appl. Supercond. **9**, 2469 (1999)
2.112 T. Hasegawa, N. Ohtani, T. Koizumi, Y. Aoki, S. Nagaya, N. Hirano, L. Motowidlo et al.: Improvement of superconducting properties of B-2212 round wire and primary test results of large capacity Rutherford cable, IEEE Trans. Appl. Supercond. **11**, 3034 (2001)
2.113 H. S. Pan, E. W. Hudson, K. M. Lang, H. Elsaki, S. Uchida, J. C. Davis: Imaging the effects of individual zinc impurity atoms on superconductivity in $Bi_2Sr_2CaCu_2O_{8+\delta}$, Nature **403**, 746 (2000)
2.114 A. Diaz, L. Mechin, P. Berghuis, J. E. Evetts: Evidence for vortex pinning by dislocations in $YBa_2Cu_3O_{7-\delta}$ low-angle grain boundaries, Phys. Rev. Lett. **80**, 3855 (1998)
2.115 B. Dam, J. L. Huijbregtse, F. C. Klaassen, R. C. F. van der Geest, G. Doornbos, J. H. Rector, A. M. Testa, S. Freisem, J. C. Martinez, B. Stäuble-Pümpin, R. Griessen: Origin of high critical currents in $YBa_2Cu_3O_{7-\delta}$ superconducting films, Nature **399**, 439 (1999)
2.116 L. Bulaevskij, L. Daemen, M. Maley, J. Coulter: Limits to the critical current in high-$T_c$ superconducting tapes, Phys. Rev. B **48**, 13798 (1993)
2.117 B. Hensel, G. Grasso, R. Flükiger: Limits to the critical transport current in superconducting $(Bi,Pb)_2Sr_2Ca_2Cu_3O_{10}$ silver sheathed tapes: The railway-switch model, Phys. Rev. B **51**, 15456 (1995)
2.118 G. N. Riley, A. P. Malozemoff, Q. Li, S. Fleshler, T. G. Holesinger: The freeway model: New concepts in understanding supercurrent transport in Bi-2223 tapes, JOM 49 **10**, 24 (1997)
2.119 T. Staiger: Stromtransport in supraleitenden $(Bi,Pb)_2Sr_2Ca_2Cu_3O_x$/Ag-Bändern. Ph.D. Thesis (Technische Universität Dresden, Dresden 1998)
2.120 K-H. Müller, G. Drechsler, S-L. Fuchs, V. N. Narozhnyi: *Magnetic, superconducting properties of rare earth borocarbides of the type* $RNi_2B_2C$, Handbook of Magnetic Materials, Vol. 14, ed. by K. H. J. Buschow (Elsevier, Amsterdam 2002) pp. 199–306
2.121 R. Flükiger, W. Klose (Eds.): *Superconductors*, Landolt–Börnstein, New Series III/21 (Springer, Berlin, Heidelberg 1990)
2.122 T. Q. Huang He, A. P. Ramirez, Y. Wang, K. A. Regan, N. Rogado, M. A. Hayward, M. K. Haas, J. I. Slusky, K. Inumara, H. W. Zandbergen, N. P. Ong, R. J. Cava: Nature **411**, 54 (2001)
2.123 K. Sakamaki, H. Wada, H. Nozaki, Y. Onuki: Solid State Commun. **112**, 323 (1999)
2.124 K. Sakamaki, H. Wada, H. Nozaki, Y. Onuki: Solid State Commun. **118**, 113 (2001)
2.125 J. Nagamatsu, N. Nakagawa, T. Muranaka, Y. Zenitani, J. Akimitsu: Nature **410**, 63 (2001)
2.126 R. Nagarajan, C. Mazumdar, Z. Hossain, S. K. Dhar, K. V. Gopalakrishnan, L. C. Gupta, C. Godart, B. C. Padalia, R. Vijayaraghavan: Phys. Rev. Lett. **72**, 274 (1994)
2.127 R. J. Cava, H. Takagi, H. W. Zandbergen, J. J. Krajewski, W. F. Peck Jr., T. Siegrist, B. Batlogg, R. B. van Dover, R. J. Felder, K. Mizuhashi, J. O. Lee, S. Uchida: Nature **367**, 252 (1994)
2.128 Rosseinsky et al.: Superconductivity at 28 K in $Rb_xC_{60}$, Phys. Rev. Lett. **60** (1991)
2.129 M. I. Eremets, V. V. Struzhkin, H.-K. Mao, R. J. Hemley: Science **293**, 272 (2001)
2.130 C. Buzea, T. Yamashita: Supercond. Sci. Technol. **14**, 115 (2001)
2.131 C. C. Lai, M. S. Lin, Y. B. You, H. C. Ku: Phys. Rev. B **51**, 420 (1995)

2.132 R. Flükiger, W. Klose (Eds.): *Superconductors*, Landolt–Börnstein, New Series III/21 (Springer, Berlin, Heidelberg 1994)
2.133 Z. Xou-xiang, H. Shou-an: Solid State Commun. **45**, 281 (1983)
2.134 H. Ihara, Y. Kimura, K. Senzaki, H. Kezuka, M. Hirabayashi: Phys. Rev. B **31**, 3177 (1985)
2.135 S. Yamanaka, H. Kawaji, K. Hotehama, M. Ohashi: Adv. Mater. **8**, 771 (1996)
2.136 S. Yamanaka, K. Hotehama, H. Kawaji: Nature **392**, 580 (1998)
2.137 R. Flükiger, W. Klose (Eds.): *Superconductors*, Landolt–Börnstein, New Series III/21 (Springer, Berlin, Heidelberg 1998)

# 4.3. Magnetic Materials

Magnetic materials consist of a wide variety of metals and oxides. Their effective properties are given by a combination of two property categories: *intrinsic* properties which are the atomic moment per atom $p_{at}$, Curie temperature $T_c$, magnetocrystalline anisotropy coefficients $K_i$, and magnetostriction coefficients $\lambda_i$; and *extrinsic* properties which are essentially their coercivity $H_c$ and their magnetisation $M$ or magnetic Induction $J$ as a function of the applied magnetic field $H$. Moreover, the effective properties are depending decisively on the microstructural features, texture and, in most cases, on the external geometric dimensions such as thickness or shape of the magnetic part. In some cases non-magnetic inorganic and organic compounds serve as binders or magnetic insulators in multiphase or composite magnetic materials.

4.3.1 **Basic Magnetic Properties** ..... 755
4.3.1.1 Atomic Moment ..... 755
4.3.1.2 Magnetocrystalline Anisotropy .. 756
4.3.1.3 Magnetostriction ..... 757
4.3.2 **Soft Magnetic Alloys** ..... 758
4.3.2.1 Low Carbon Steels ..... 758
4.3.2.2 Fe-based Sintered and Composite Soft Magnetic Materials ..... 759
4.3.2.3 Iron–Silicon Alloys ..... 763
4.3.2.4 Nickel–Iron-Based Alloys ..... 769
4.3.2.5 Iron–Cobalt Alloys ..... 772
4.3.2.6 Amorphous Metallic Alloys ..... 772
4.3.2.7 Nanocrystalline Soft Magnetic Alloys ..... 776
4.3.2.8 Invar and Elinvar Alloys ..... 780
4.3.3 **Hard Magnetic Alloys** ..... 794
4.3.3.1 Fe–Co–Cr ..... 795
4.3.3.2 Fe–Co–V ..... 797
4.3.3.3 Fe–Ni–Al–Co, Alnico ..... 798
4.3.3.4 Fe–Nd–B ..... 800
4.3.3.5 Co–Sm ..... 803
4.3.3.6 Mn–Al–C ..... 810
4.3.4 **Magnetic Oxides** ..... 811
4.3.4.1 Soft Magnetic Ferrites ..... 811
4.3.4.2 Hard Magnetic Ferrites ..... 813
**References** ..... 814



## 4.3.1 Basic Magnetic Properties

Basic magnetic properties of metallic systems and materials are treated by *Gignoux* in [3.1]. Extensive data on magnetic properties of metals can be found in [3.2]. Magnetic properties of ferrites are treated by *Guillot* in [3.3]. Extensive data on magnetic and other properties of oxides and related compounds can be found in [3.4] and [3.5].

### 4.3.1.1 Atomic Moment

The suitability of a metal or oxide to be used as a magnetic material is determined by its mean atomic moment ($p_{at}$). For metals the Bethe–Slater–Pauling curves, Fig. 4.3-1, indicate how $p_{at}$ depends on the average number ($n$) of 3d and 4s electrons per atom, and on the crystal structure, i. e., face-centered cubic (fcc) or body-centered cubic (bcc) structure. Alloys based on Fe, Co, and Ni are most suitable from this point of view, corresponding to their actual use. The characteristic temperature dependence of the spontaneous magnetization $I_s(T)$, shown for Fe in Fig. 4.3-2, the Curie temperature $T_c$ and the spontaneous magnetization at room temperature $I_s$ (see Table 4.3-1), are the ensuing properties.

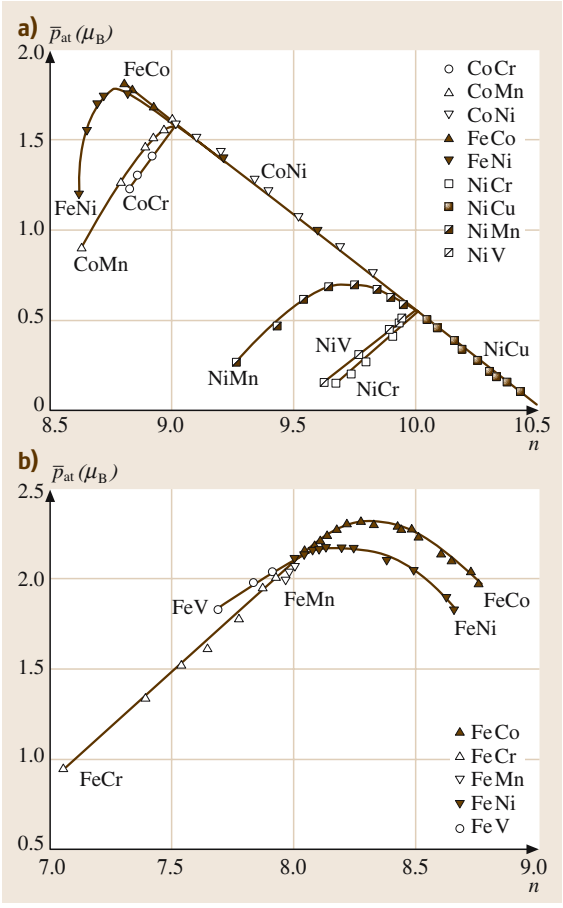


**Fig. 4.3-1a,b** Bethe–Slater–Pauling relation indicating the dependence of the mean magnetic moment per atom $p_{at}$ on the average number $n$ of 3d and 4s electrons per atom for binary alloys with **(a)** fcc structure and **(b)** bcc structure [3.6]

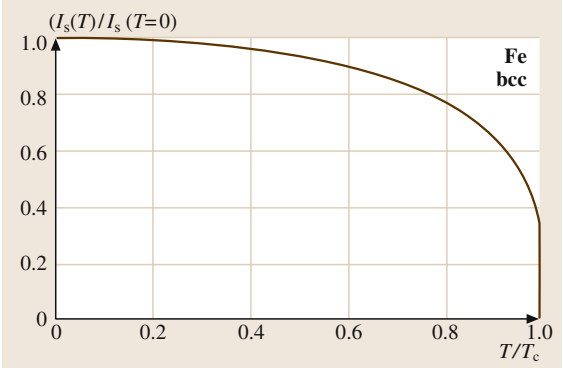


**Fig. 4.3-2** Reduced spontaneous magnetization $I_s(T)/I_s$ $(T = 0)$ vs. reduced temperature $T/T_c$ for Fe [3.6]

### 4.3.1.2 Magnetocrystalline Anisotropy

Since the magnetic moment arises from the exchange coupling of neighboring ions, it is also, coupled to their positions in the crystal structures. Basically this is the origin of the magnetocrystalline anisotropy which plays a major role as an intrinsic property for the optimization of both soft and hard magnetic materials because it determines the crystallographic direction and relative magnitude of easy magnetization. As an example, Fig. 4.3-3a shows the magnetization curves for a single crystal of Fe in the three major crystallo-

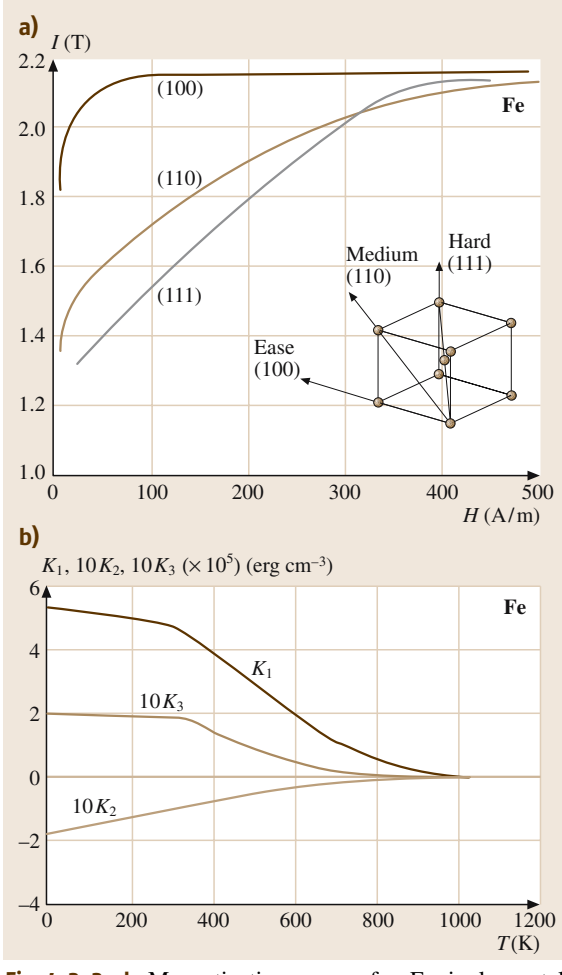


**Fig. 4.3-3a,b** Magnetization curves of an Fe single crystal indicting the typical characteristics of **(a)** magnetocrystalline anisotropy and **(b)** the temperature dependence of the magnetocrystalline anisotropy constants $K_i$ of Fe [3.6]

**Table 4.3-1** Curie temperatures and intrinsic magnetic properties at room temperature

| Element | $T_c$ (K) | $I_s$ (T) | $K_1$ ($10^4$ J m$^{-3}$) | $K_2$ ($10^4$ J m$^{-3}$) | $K_3$ ($10^4$ J m$^{-3}$) | $\lambda_{100}$ ($10^{-6}$) | $\lambda_{111}$ ($10^{-6}$) | $\lambda_{0001}$ ($10^{-6}$) | $\lambda_{10\bar{1}0}$ ($10^{-6}$) | $\lambda_s$ ($10^{-6}$) |
|---|---|---|---|---|---|---|---|---|---|---|
| Fe, bcc | 1044 | 2.15 | 4.81 | 0.012 | −0.012 | 22.5 | −18.8 | – | – | −4 |
| Co, hcp | 1388 | 1.62 | 41 | 120 | – | – | – | −4 | −22 | −71 |
| Ni, fcc | 624 | 0.55 | −0.57 | −0.23 | 0 | −46 | −24.3 | – | – | −34 |

graphic directions of the body-centered cubic crystal structure.

The anisotropy constants $K_1$, $K_2$, ... are defined for cubic lattices, such as Fe and Ni, by expressing the free energy of the crystal anisotropy per unit volume as

$$E_a = K_0 + K_1 S + K_2 P + K_3 S^2 + K_4 SP + \dots ,$$

with

$$S = \alpha_1^2\alpha_2^2 + \alpha_2^2\alpha_3^2 + \alpha_3^2\alpha_1^2 \quad \text{and} \quad P = \alpha_1^2\alpha_2^2\alpha_3^2 ,$$

where $\alpha_i$, $\alpha_j$, and $\alpha_k$ are the direction cosines of the angle between the magnetization vector and the crystallographic axes. Corresponding definitions pertain to the anisotropy constants for other crystal lattices.

In practice it can be important to know not only the room temperature value of the magnetocrystalline anisotropy constants $K_i$ but also their temperature dependence, which is shown for Fe in Fig. 4.3-3b. For many technical considerations it suffices to take the dominating anisotropy constant $K_1$ into account.

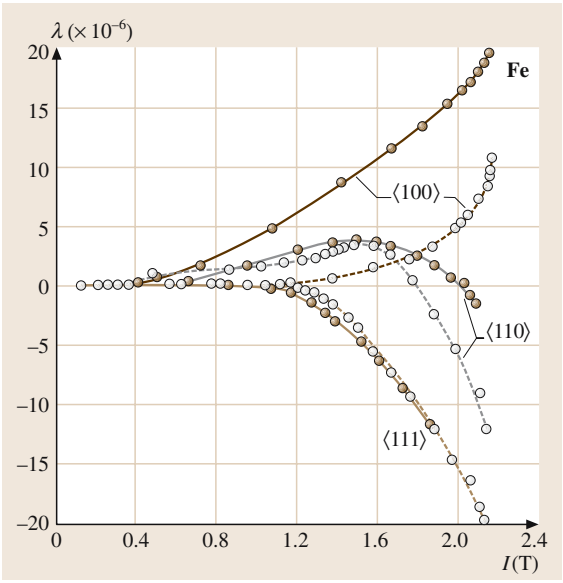


**Fig. 4.3-4** Dependence of the magnetostrictive elongation on the magnetization intensity in three different crystallographic directions of Fe single crystals according to two different sources (*open* and *closed circles*) [3.7]

### 4.3.1.3 Magnetostriction

Magnetostriction is the intrinsic magnetic property which relates spontaneous lattice strains to magnetization. It is treated extensively by *Cullen* et al. in [3.3]. As a crystal property magnetostriction is purely intrinsic. The phenomenon of macroscopic magnetostrictive strains of a single or polycrystalline sample is due to the presence of magnetic domains whose reorientation occurs under the influence of magnetic fields or applied stresses and, thus, is a secondary property which has to be distinguished.

Magnetostriction plays a role in determining a number of different effects:

- As a major factor of influence on the coercivity of soft magnetic materials because it determines the magnitude of interaction of internal stresses of materials with the movement of magnetic domain walls. These boundaries are associated with strains themselves unless the material is free of magnetostriction altogether. This is practically impossible because the components of this property vary with the applied magnetic field, as shown for the example of Fe in Fig. 4.3-4. Moreover, they vary with temperature and alloy composition.
- As a decisive variable determining the properties of invar and elinvar alloys (Sect. 4.3.2.8).
- As a property of anomalously high magnitude in cubic Laves phase compounds of rare earth metals such as $Fe_2(Tb_{0.3}Dy_{0.7})$, which are the basis of magnetostrictive materials serving as magnetostrictive transducers and sensors [3.3].

## 4.3.2 Soft Magnetic Alloys

The basic suitability of a metal or alloy as a soft magnetic material is provided if its Curie temperature $T_c$ and saturation polarization $I_s$ at room temperature are sufficiently high. The main goal in developing soft magnetic materials is to reduce the magnetocrystalline anisotropy constants $K_i$, in particular $K_1$, and the magnetostriction constants $\lambda_i$, to a minimum. This leads to a minimum energy requirement for magnetization reversal. The appropriate combination of the intrinsic magnetic properties can be achieved by alloying additions and, in some cases, by annealing treatments which induce atomic ordering and, thus, an additional variation of $K_1$ and/or $\lambda_i$. Surveys and data of soft magnetic alloys are given in [3.8].

### 4.3.2.1 Low Carbon Steels

Low carbon steels are the most widespread magnetic metallic materials for use in electric motors and inductive components such as transformers, chokes, and a variety of other AC applications which require high magnetic induction at moderate to low losses. This is mainly due to the high intrinsic saturation polarization of the base element Fe, $J_s = 2.15$ T, and to the low cost of mass produced steels.

Main processing effects on achieving materials with a high relative permeability is the minimization of the formation of particles (mainly carbides and sulfides) which may impede domain boundary motion, and induc-

**Table 4.3-2** Standard IEC specification for non-alloyed magnetic steel sheet. The conventional designation of the different grades (first column) comprises the following order: (1) 100 times the maximum specified loss ($W\,kg^{-1}$) at 1.5 T; (2) 100 times the nominal sheet thickness in (mm); (3) the characteristic letter "D"; (4) one tenth of the frequency in Hz at which the magnetic properties are specified. The materials are delivered in the semi-processed state. The magnetic properties apply to test specimens heat-treated according to manufacturer's specifications

| Grade | Nominal thickness (mm) | Maximum specific total loss for peak induction ($W\,kg^{-1}$) | | | Minimum induction in a direct or alternating field at field strength given (T) | | | Stacking factor | Conventional density ($kg\,dm^{-3}$) |
|---|---|---|---|---|---|---|---|---|---|
| | | 1.5 T at at 50 Hz | 1.0 T at at 50 Hz | 1.5 T at at 60 Hz | at 2500 A/m | at 5000 A/m | at 10 000 A/m | | |
| 660-50-D5 | 0.50 | 6.60 | 2.80 | 8.38 | 1.60 | 1.70 | 1.80 | 0.97 | 7.85 |
| 890-50-D5 | 0.50 | 8.90 | 3.70 | 11.30 | 1.58 | 1.68 | 1.79 | 0.97 | 7.85 |
| 1050-50-D5 | 0.50 | 10.50 | 4.30 | 13.34 | 1.55 | 1.65 | 1.78 | 0.97 | 7.85 |
| 800-65-D5 | 0.65 | 8.00 | 3.30 | 10.16 | 1.60 | 1.70 | 1.80 | 0.97 | 7.85 |
| 1000-65-D5 | 0.65 | 10.00 | 4.20 | 12.70 | 1.58 | 1.68 | 1.79 | 0.97 | 7.85 |
| 1200-65-D5 | 0.65 | 12.00 | 5.00 | 15.24 | 1.55 | 1.65 | 1.78 | 0.97 | 7.85 |

**Table 4.3-3** Standard IEC specifictaion for cold rolled magnetic alloyed steel strip delivered in the semi-processed state. The conventional designation of the different grades comprises the following order (first column): (1) 100 times the maximum specified loss at 1.5 T peak induction in ($W\,kg^{-1}$); (2) 100 times the nominal strip thickness, in (mm); (3) the characteristic letter "E"; (4) one tenth of the frequency in Hz, at which the magnetic properties are specified. the magnetic properties apply to test specimens subjected to a reference heat treatment

| Grade | Nominal thickness (mm) | Reference treatment temperature (°C) | Maximum specific total loss for peak induction ($W\,kg^{-1}$) | | Minimum induction in a direct or alternating field at field strength given (T) | | | Conventional density ($10^3\,kg\,m^{-3}$) |
|---|---|---|---|---|---|---|---|---|
| | | | 1.5 T | 1.0 T | 2500 $Am^{-1}$ | 5000 $Am^{-1}$ | 10 000 $Am^{-1}$ | |
| 340-50-E5 | 0.50 | 840 | 3.40 | 1.40 | 1.52 | 1.62 | 1.73 | 7.65 |
| 390-50-E5 | 0.50 | 840 | 3.90 | 1.60 | 1.54 | 1.64 | 1.75 | 7.70 |
| 450-50-E5 | 0.50 | 790 | 4.50 | 1.90 | 1.55 | 1.65 | 1.76 | 7.75 |
| 560-50-E5 | 0.50 | 790 | 5.60 | 2.40 | 1.56 | 1.66 | 1.77 | 7.80 |

ing a texture – by suitable combinations of deformation and recrystallization – with a preponderance of ⟨100⟩ and ⟨110⟩ components, while suppressing the ⟨111⟩ and ⟨211⟩ components, such that the operating induction can be aligned most closely to the easiest direction of magnetization ⟨100⟩. More details are given by *Rastogi* in [3.9]. Tables 4.3-2 and 4.3-3 show characteristic data of non-alloyed magnetic steel sheet and cold rolled magnetic alloyed steel strip, respectively.

### 4.3.2.2 Fe-based Sintered and Composite Soft Magnetic Materials

Iron-based sintered and composite soft magnetic materials are treated and listed extensively in [3.10]. Iron and Fe based alloys are used as sintered soft magnetic materials because of the particular advantages of powder metallurgical processing in providing net-shaped parts economically. The sintering process serves to achieve diffusion-bonding of the powder particles with a uniform distribution of the alloying elements. The metallic bond and degree of particle contact determine the magnetic properties in each alloy system.

The operating frequency in an application is limited by the resistivity of the material, which is increased beyond that of pure and dense Fe, primarily by varying the type and concentration of alloying elements. Density and crystal structure have a major impact on the magnetic properties, but only a minor effect on the resistivity. The sintered materials have a resistivity ranging from 10 to 80 μΩ cm and are applicable in DC and very low frequency fields. The sintered materials comprise Fe and Fe−P, Fe−Si, Fe−Si−P, Fe−Sn−P, Fe−Ni, Fe−Cr, and Fe−Co alloys. Characteristic data are listed in Tables 4.3-4 to 4.3-11 [3.10].

It is useful to note that the evaluation of a large number of test data of sintered soft magnetic materials yields consistent empirical relations. For sintered Fe products these are:

$$B_{15}[\mathrm{T}] = 4.47\varrho - 10.38\,,$$

$$B_{\mathrm{r}}[\mathrm{T}] = 3.87\varrho - 17.23\,,$$

$$H_{\mathrm{c}}[\mathrm{A/m}] = 11.47L^{-0.59}\,,$$

$$\rho[\mu\Omega\,\mathrm{cm}] = -4.34\varrho + 44.77\,,$$

and

$$\mu_{\max} = 0.21L^{0.68} \times 10^3\,,$$

where $\varrho$ = density ($\mathrm{g\,cm^{-3}}$) and $L$ = grain diameter (average intercept length) (μm).

Dust core materials consist of Fe or Fe alloy particles which are insolated by an inorganic high resistivity barrier. They are applied in the 1 kHz to 1 MHz range. These are to be distinguished from soft magnetic Fe composite materials, which consist of pure Fe particles separated by an insolating organic barrier, providing a medium to high bulk resistance. Compositions and magnetic properties of Fe based composite materials are listed in Tables 4.3-12 and 4.3-13. These materials are applicable in the frequency range from 50 Hz to 1 kHz.

**Table 4.3-4** Magnetic properties of sintered Fe products in relation to density [3.10]

| Density ϱ ($\mathrm{g\,cm^{-3}}$) | Sintering conditions temp. (°C), atm. | Induction at 1200 A $\mathrm{m^{-1}}$ (T) | Coercitivity $H_{\mathrm{c}}$ (A $\mathrm{m^{-1}}$) | Remanence $B_{\mathrm{r}}$ (T) | Max. rel. permeability $\mu_{\max}$ |
|---|---|---|---|---|---|
| 6.6 | 1120, DA | 0.90 | 170[a] | 0.78[a] | 1700 |
| 6.6 | 1120, $H_2$/Vac. | 0.95 | 140[a] | 0.82[a] | 1800 |
| 6.6 | 1260, $H_2$/Vac. | 1.05 | 120[a] | 0.85[a] | 2800 |
| 6.9 | 1120, DA | 1.05 | 170[a] | 0.90[a] | 2100 |
| 6.9 | 1120, $H_2$/Vac. | 1.05 | 140[a] | 0.97[a] | 2300 |
| 6.9 | 1260, $H_2$/Vac. | 1.20 | 120[a] | 1.0[a] | 3300 |
| 7.2 | 1120, DA | 1.20 | 170[a] | 1.05[a] | 2700 |
| 7.2 | 1120, $H_2$/Vac. | 1.20 | 140[a] | 1.10[a] | 2900 |
| 7.2 | 1260, $H_2$/Vac. | 1.30 | 120[a] | 1.15[a] | 3800 |
| 7.4 | | 1.25 | 136 | 1.20 | 3500 |
| 7.4 | | 1.30 | 112 | 1.30 | 5500 |
| 7.6 | | 1.50 | 80 | 1.40 | 6000 |

[a] Measured from a maximum applied magnetic field strength of 1200 A/m.

**Table 4.3-5** Magnetic properties of sintered Fe–0.8 wt% P products in relation to density [3.10]

| Density ϱ ($g\,cm^{-3}$) | Sintering conditions temp. (°C), atm. | Induction at 1200 $A\,m^{-1}$ (T) | Coercitivity $H_c$ ($A\,m^{-1}$) | Remanence $B_r$ (T) | Max. rel. permeability $\mu_{max}$ |
|---|---|---|---|---|---|
| 6.8 | 1120, DA | 1.05 | 120 [a] | 1.00 [a] | 3500 |
| 7.0 | 1120, $H_2$/Vac. | 1.20 | 100 [a] | 1.05 [a] | 4000 |
| 7.2 | 1260, $H_2$/Vac. | 1.25 | 95 [a] | 1.15 [a] | 4000 |
| 7.0 | 1120, DA | 1.20 | 120 [a] | 1.10 [a] | 4000 |
| 7.2 | 1120, $H_2$/Vac. | 1.25 | 100 [a] | 1.15 [a] | 4500 |
| 7.4 | 1260, $H_2$/Vac. | 1.30 | 95 [a] | 1.20 [a] | 4500 |
| 7.0 | 1120, DA | 1.25 | 120 [a] | 1.20 [a] | 4500 |
| 7.2 | 1120, $H_2$/Vac. | 1.30 | 100 [a] | 1.30 [a] | 5000 |
| 7.4 | 1260, $H_2$/Vac. | 1.35 | 95 [a] | 1.25 [a] | 5000 |

[a] Measured from a maximum applied magnetic field strength of 1200 A/m .

**Table 4.3-6** Magnetic properties of sintered Fe–3 wt% Si products in relation to density[a] [3.10]

| Density ϱ ($g\,cm^{-3}$) | Sintering conditions temp. (°C), time, atm. | Coercitivity $H_c$ ($A\,m^{-1}$) | Remanence $B_r$ (T) | Sat. induction $B_s$ (T) | Max. rel. permeability $\mu_{max}$ |
|---|---|---|---|---|---|
| 7.3 | | 64 | 1.15 | 1.90 | 8000 |
| 7.5 | | 48 | 1.25 | 2.00 | 9500 |
| 7.2 | 1250, 30 min, $H_2$ [b] | 80 | 1.0 | | 4300 |
| 7.01 | 1120, 60 min, $H_2$ [b] | 117 [d] | | | 2800 |
| 7.19 | 1200, 60 min, $H_2$ [b] | 88 [d] | | | 4200 |
| 7.40 | 1200, 60 min, $H_2$ [c] | 79 [d] | 1.25 | | 5600 |
| 7.43 | 1300, 60 min, $H_2$ | 56 [d] | | | 8400 |
| 7.55 | 1371, DA [e] | 51 | 1.21 | 1.50 | |
| 7.55 | 1371, DA [e] | 57 | 1.07 | 1.45 | |

[a] Measured according to ASTM A 596
[b] Conventional compacting at 600 MPa
[c] Warm compacted at 600 MPa
[d] Defined as coercive force i. e. magnetized to a field strength well below saturation
[e] Formed by MIM

**Table 4.3-7** Magnetic properties of sintered Fe−S−P in relation to density[a] [3.10]

| Density ϱ ($g\,cm^{-3}$) | Sintering conditions temp. (°C), atm. | Coercitivity $H_c$ ($A\,m^{-1}$) | Remanence $B_r$ (T) | Sat. induction $B_s$ (T) | Max. rel. permeability $\mu_{max}$ |
|---|---|---|---|---|---|
| 7.3 [b] | | 45 [b] | 1.30 [b] | 1.90 [b] | 10 800 [b] |
| 7.55 [c] | | 33 [c] | | 2.00 [c] | 12 500 [c] |
| 7.3 [c] | 1250 30 min, $H_2$ | 60 [c] | 1.1 [c] | | 6100 [c] |
| 6.8 [d] | 1120 30 min, $H_2$ | 100 [d] | 0.6 [d] | | 2200 [d] |

[a] Measured according to ASTM A 596
[b] Fe/3 wt% Si/0.45 wt% P
[c] Fe/2 wt% Si/0.45 wt% P
[d] Fe/4 wt% Si/0.45 wt% P

**Table 4.3-8** Magnetic properties of sintered Fe−Sn−P in relation to density [3.10]

| Density ϱ ($g\,cm^{-3}$) | Sintering temp. (°C), time, atm. | Coercitivity $H_c$ ($A\,m^{-1}$) | Remanence $B_r$ (T) | Max. rel. permeability $\mu_{max}$ |
|---|---|---|---|---|
| 7.2 [a] | 1120 30 min, $H_2$ [b] | 80 [a] | 1.1 [a] | 4800 [a] |
| 7.4 [b] | 1250 30 min, $H_2$ [b] | 37 [b] | 1.0 [b] | 9700 [b] |

[a] Fe/5 wt% Sn/0.45 wt% P
[b] Fe/5 wt% Sn/0.5 wt% P

**Table 4.3-9** Magnetic properties of sintered Fe−Ni in relation to density[a] [3.10]

| Density ϱ ($g\,cm^{-3}$) | Sintering temp. (°C), time atm. | Coercitivity $H_c$ ($A\,m^{-1}$) | Remanence $B_r$ (T) | Sat. induction $B_s$ (T) | Max. rel. permeability $\mu_{max}$ |
|---|---|---|---|---|---|
| 8.0 [b] | | 24 [b] | 0.25 [b] | 1.55 [b] | 6000 [b] |
| 8.0 [c] | | 13 [c] | 0.85 [c] | 1.60 [c] | 30 000 [c] |
| 8.5 [d] | | 2 [d] | 0.40 [d] | 0.80 [d] | 74 900 [d] |
| 6.99 [e] | 1260, $H_2$/Vac. | 20 [e] | 0.75 [e] | | |
| 6.99 [f] | | 24 [f] | 0.76 [f] | | 7800 [f] |
| 7.30 [e] | 1260, $H_2$/Vac. | 19 [e] | 0.90 [e] | | |
| 7.30 [f] | | 32 [f] | 0.85 [f] | | 8700 [f] |
| 7.50 [e] | 1260, $H_2$/Vac. | 16 [e] | 0.94 [e] | | 21 000 [e] |
| 7.50 [f] | | 32 [f] | 0.90 [f] | | 9100 [f] |
| 7.4 [c] | 1250, 30 min, $H_2$ | 25 [c] | 0.8 [c] | | 13 000 [c] |
| 7.66 | 1371, DA [f] | 16 | 0.42 | 1.27 | |

[a] Measured according to ASTM A 596
[b] Fe/35–40 wt% Ni
[c] Fe/45–50 wt% Ni
[d] Fe/72–82 wt% Ni/3–5 wt% Mo
[e] Fe/47–50 wt% Ni
[f] Formed by MIM

**Table 4.3-10** Magnetic properties of sintered Fe−Cr in relation to density[a] [3.10]

| Density ϱ ($g\,cm^{-3}$) | Coercitivity $H_c$ ($A\,m^{-1}$) | Remanence $B_r$ (T) | Sat. induction $B_s$ (T) | Max. rel. permeability $\mu_{max}$ |
|---|---|---|---|---|
| 7.1 [b] | 200 [b] | 0.50 [b] | | 1200 [b] |
| 7.45 [c] | 100 [c] | | 1.70 [c] | 2500 [c] |
| 7.35 [d] | 100 [d] | | 1.55 [d] | 1900 [d] |

[a] Measured according to ASTM A 596
[b] Fe/16–18 wt% Cr/0.5–1.5 wt% Mo
[c] Fe/12 wt% Cr/0.2 wt% Ni/0.7 wt% Si
[d] Fe/17 wt% Cr/0.9 wt% Mo/0.2 wt% Ni/0.8 wt% Si

**Table 4.3-11** Magnetic properties of sintered Fe–Co products in relation to density[a] [3.10]

| Density ϱ ($g\,cm^{-3}$) | Coercitivity $H_c$ ($A\,m^{-1}$) | Remanence $B_r$ (T) | Sat. induction $B_s$ (T) | Max. rel. permeability $\mu_{max}$ |
|---|---|---|---|---|
| 7.9[b] | 136[b] | 1.10[b] | 2.25[b] | 3900[b] |

[a] Measured according to ASTM A 596
[b] Fe/47–50 wt% Co/1–3 wt% V

**Table 4.3-12** Magnetic properties of composite Fe products in relation to density and insulation [3.10]

| Density ϱ ($g\,cm^{-3}$) | Insulation | Curing (°C) (min) | Coercitivity $H_c$ ($A\,m^{-1}$) | Induction at 3183 $A\,m^{-1}$ (T) | Max. rel. permeability $\mu_{max}$ |
|---|---|---|---|---|---|
| 5.7–7.26 | Polymer | | 263–374 | 0.33–0.83 | 97–245 |
| 7.2 | Oxide + 0.75 Polymer | | 374 | 0.77 | 210 |
| 7.4–7.45 | 0.75–0.6 % Polymer | | 381–374 | 1.09–1.12 | 400–425 |
| 7.54 | Oxide | | | | 630 |
| 7.04 | Inorganic (LCM™) | | | | 305 |
| 7.0 | 0.5 % Phenolic resin[a] | 150, 60 | 400 | | 270 |
| 7.13–6.84[b] | 0.4–1.8 % Phenolic[a] | 160.30 | | | 325–175[c] |
| 7.2[b] | 0.8 % Phenolic[a] | 150–500.30 | 445–310 | | 270–390 |
| 6.6 | 3 % resin | | | | 200 |
| 6.7–7.0 | Inorganic & 2 % resin | ?–500 | | | 200–400 |
| 7.4 | Inorganic (Somaloy™500) | 500 | | | 600 |

[a] Dry Mixing or wet mixing with phenolic resin
[b] Compacted at 620 MPa and 65 °C
[c] AC permeability at 60 Hz and 1.0 T

**Table 4.3-13** Core loss of composite Fe products in relation to lubricant and heat treatment [3.10]

| Lubricant | Heat treatment (°C) | (min.) | (Atm.) | Density ϱ ($g\,cm^{-3}$) | Total loss at 100 Hz, 1.5 T ($W\,kg^{-1}$) | Total loss at 1000 Hz, 1.5 T ($W\,kg^{-1}$) |
|---|---|---|---|---|---|---|
| 0.1 % Kenolube™[d] | 500 | 30 | air | 7.40[b] | 29 | |
| 0.5 % Kenolube™ | 500 | 30 | air | 7.20[a] | 32 | 450 |
| 0.5–0.8 % Kenolube™ | 500 | 30 | air | 7.36–7.26[b] | 29–31 | 330–450 |
| 0.5 % Kenolube™ | 500 | 30 | nitrogen | 7.35[b] | 31 | 350 |
| 0.5 % Kenolube™ | 250–580 | 30 | steam | 7.35[b] | 30–70 | |
| 0.6 % LBI™ | 275 | 60 | air | 7.27[b] | | 700 |
| 0.5 % Kenolube™ | 500 | 30 | air | 7.20[a] | 35 | 480 |
| 0.5 % Kenolube™ | 500 | 30 | air | 7.34[a] | 34 | 420 |

[a] Conventional compacting at 600 MPa
[b] Conventional compacting at 800 MPa
Water atomized iron powder, particle size > 150 µm < 400 µm, low inorganic insulation thickness, (Somatoy™ 550)

### 4.3.2.3 Iron–Silicon Alloys

The physical basis of the use of Fe–Si alloys, commonly called silicon steels, as soft magnetic materials is the fact that both the magnetocrystalline anisotropy $K_1$ and the magnetostriction parameters $\lambda_{100}$ and $\lambda_{111}$ of Fe approach zero with increasing Si content (see Fig. 4.3-5a). The lower the magnitude of these two intrinsic magnetic properties is, the lower are the coercivity $H_c$ and the AC magnetic losses $p_{Fe}$. The total losses $p_{Fe}$ consist of the static hysteresis losses $p_h$ and the dynamic eddy current losses $p_w$ which may be subdivided into a classical $p_{wc}$ and an anomalous $p_{wa}$ eddy current loss term,

$$\begin{aligned} p_{Fe} &= p_h + p_{wc} + p_{wa} \\ &= c_h(f) H_c B f \\ &\quad + c_{wc}(\pi d B f)^2/6\rho\gamma + c_{wa}(\alpha_R/\rho)(Bf)^{3/2} , \end{aligned}$$

where $c_h(f)$ is a form factor of the hysteresis which depends on the frequency $f$, $H_c$ is the coercivity of the material, $B$ is the peak operating induction, $c_{wc}$ and $c_{wa}$ are terms taking the wave form of the applied field into account, $d$ is the sheet thickness, $\rho$ is the resistivity, $\gamma$ is the density of the material, and $\alpha_R$ is the Raleigh constant. These are the factors to be controlled to obtain minimal losses. The increase in electrical resistivity with Si content (Fig. 4.3-5b) adds to lowering the eddy current losses as shown by the relation above.

The Fe–Si equilibrium diagram shows a very small stability range of the $\gamma$ phase, indicating that the ferromagnetic $\alpha$ phase can be heat-treated in a wide temperature range without interference of a phase transformation which would decrease the magnetic softness of the material by the lattice defects induced.

Next to low-carbon steels, Fe–Si steels are the most significant group of soft magnetic materials (30% of the world market). A differentiation is made between non-oriented, isotropic (NO), and grain-oriented (GO) silicon steels. Non-oriented steels are mainly applied in rotating machines where the material is exposed to varying directions of magnetic flux. Grain-oriented steels with GOSS-texture (110) ⟨001⟩ are used predominantly as core material for power transformers.

Since Fe–Si steels are brittle above about 4.0 wt% Si, conventional cold rolling is impossible at higher Si contents.

#### Non-oriented Silicon Steels (NO)

NO laminations are usually produced with thicknesses between 0.65 mm and 0.35 mm, and Si concentrations up to 3.5 wt%. According to their grade, NO silicon steels are classified in low grade (low Si content) alloys employed in small devices and high-grade (high Si content) alloys for large machines (motors and generators). Suitable microstructural features (optimum grain size) and a low level of impurities are necessary for optimum magnetic properties. Critical factors in processing are the mechanical behavior upon punching of laminations, the application of insulating coatings, and the build-up of stresses in magnetic cores. Table 4.3-14 lists the ranges of typical processing parameters.

In the case of low Si steels (< 1 wt% Si), the last two annealing steps are applied by the user after lamination punching (semi-finished sheet). Table 4.3-15 lists the specifications, including all relevant properties for non-oriented magnetic steel sheet.

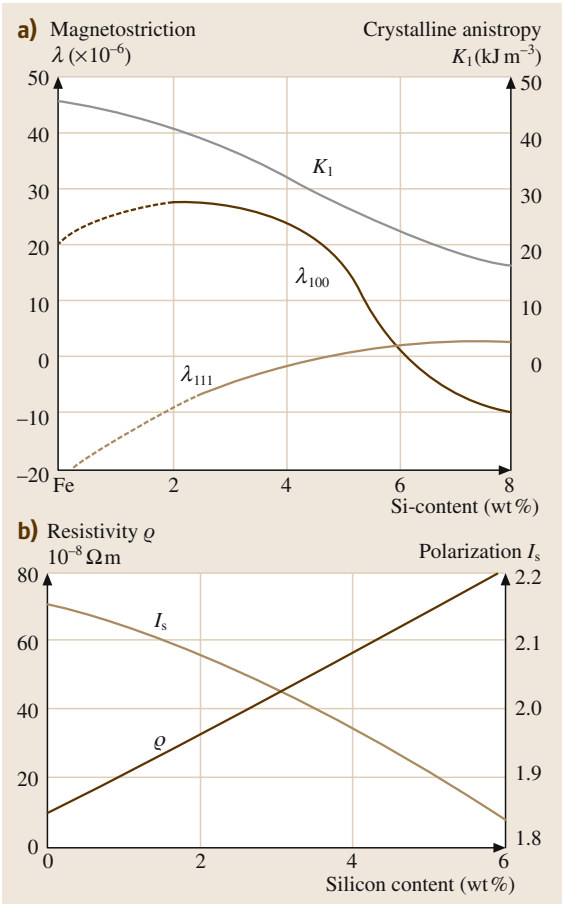


**Fig. 4.3-5 (a)** Magnetostriction $\lambda_{100}$ and $\lambda_{111}$ and magneto-crystalline anisotropy energy $K_1$. **(b)** Electrical resistivity $\rho$ and saturation polarization $I_s$, as a function of the Si content in Fe–Si alloys

| |
|---|
| Composition (wt%) Si: 0.9–3.4, Al: 0.2–0.6, Mn: 0.1–0.3 |
| Melting, degassing, continous casting |
| Hot rolling to 1.8–2.3 mm (1000–1250 °C) |
| Cold rolling to intermediate gauge |
| Annealing (750–900 °C) |
| Cold rolling to final gauge (0.65–0.35 mm) |
| Decarburizing anneal (830–900 °C, wet $H_2$) |
| Recrystallization |
| Grain growth anneal (830–1100 °C) |
| Coating |

**Table 4.3-14** Schematic of NO silicon steel processing. Addition of small quantities (50–800 wt ppm) of Sb, Sn, or rare earth metals can be made to improve texture and/or control the morphology of the precipitates. Cold reduction in a single stage repesents a basic variant of the above scheme. The final grain growth annealing aims at an optimum grain size, leading to minimum losses. Coating provides the necessary interlaminar electrial insulation. Phosphate- or chromate-based coatings are applied, which ensure good lamination punchability [3.7]



**Table 4.3-15** Standard IEC specification for nonoriented magnetic steel sheet delivered in the final sate. The conventional designation of the different grades comprises the following order (first column): (1) 100 times the maximum specified loss at 1.5 T peak induction in ($W\,kg^{-1}$); (2) 100 times the nominal sheet thickness; (3) the characteristic letter "A"; (4) one tenth of the frequency in Hz, at which the magnetic properties are specified. The anisotropy of loss, $T$, is specified at 1.5 T peak induction according to the formula $T = (P_1 - P_2)/(P_1 + P_2)100$, with $P_1$ and $P_2$ the power losses of samples cut perpendicular and parallel to the rolling direction, respectively [3.7]

| Quality | Nominal thickness (mm) | Maximum specific total loss ($W\,kg^{-1}$) at peak induction | | Minimum magnetic flux density (T) in direct or alternating field at field strength | | | Maximum anisotropy of loss (%) | Minimum stacking factor | Minimum number of bends | Conventional density ($10^3\,kg\,m^{-3}$) |
|---|---|---|---|---|---|---|---|---|---|---|
| | | 1.5 T | 1.0 T | 2500 $Am^{-1}$ | 5000 $Am^{-1}$ | 10 000 $Am^{-1}$ | | | | |
| 250-35-A5 | 0.35 | 2.50 | 1.00 | 1.49 | 1.60 | 1.71 | | | 2 | 7.60 |
| 270-35-A5 | 0.35 | 2.70 | 1.10 | 1.49 | 1.60 | 1.71 | ±18 | 0.95 | 2 | 7.65 |
| 300-35-A5 | 0.35 | 3.00 | 1.20 | 1.49 | 1.60 | 1.71 | | | 3 | 7.65 |
| 330-35-A5 | 0.35 | 3.30 | 1.30 | 1.49 | 1.60 | 1.71 | | | 3 | 7.65 |
| 270-50-A5 | 0.50 | 2.70 | 1.10 | 1.49 | 1.60 | 1.71 | | | 2 | 7.60 |
| 290-50-A5 | 0.50 | 2.90 | 1.15 | 1.49 | 1.60 | 1.71 | ±18 | | 2 | 7.60 |
| 310-50-A5 | 0.50 | 3.10 | 1.25 | 1.49 | 1.60 | 1.71 | | | 3 | 7.65 |
| 330-50-A5 | 0.50 | 3.30 | 1.35 | 1.49 | 1.60 | 1.71 | ±14 | | 3 | 7.65 |
| 350-50-A5 | 0.50 | 3.50 | 1.50 | 1.50 | 1.60 | 1.71 | | | 5 | 7.65 |
| 400-50-A5 | 0.50 | 4.00 | 1.70 | 1.51 | 1.61 | 1.72 | | 0.97 | 5 | 7.65 |
| 470-50-A5 | 0.50 | 4.70 | 2.00 | 1.52 | 1.62 | 1.73 | | | | 7.70 |
| 530-50-A5 | 0.50 | 5.30 | 2.30 | 1.54 | 1.64 | 1.75 | | | | 7.70 |
| 600-50-A5 | 0.50 | 6.00 | 2.60 | 1.55 | 1.65 | 1.76 | ±12 | | 10 | 7.75 |
| 700-50-A5 | 0.50 | 7.00 | 3.00 | 1.58 | 1.68 | 1.76 | | | | 7.80 |
| 800-50-A5 | 0.50 | 8.00 | 3.60 | 1.58 | 1.68 | 1.78 | | | | 7.80 |
| 350-65-A5 | 0.65 | 3.50 | 1.50 | 1.49 | 1.60 | 1.71 | | | 2 | 7.65 |
| 400-65-A5 | 0.65 | 4.00 | 1.70 | 1.50 | 1.60 | 1.71 | | | 2 | 7.65 |
| 470-65-A5 | 0.65 | 4.70 | 2.00 | 1.51 | 1.61 | 1.72 | ±14 | | 5 | 7.65 |
| 530-65-A5 | 0.65 | 5.30 | 2.30 | 1.52 | 1.62 | 1.73 | | 0.97 | 5 | 7.70 |
| 600-65-A5 | 0.65 | 6.00 | 2.60 | 1.54 | 1.64 | 1.75 | | | | 7.75 |
| 700-65-A5 | 0.65 | 7.00 | 3.00 | 1.55 | 1.65 | 1.76 | ±12 | | 10 | 7.75 |
| 800-65-A5 | 0.65 | 8.00 | 3.60 | 1.58 | 1.68 | 1.76 | | | | 7.80 |
| 1000-65-A5 | 0.65 | 10.00 | 4.40 | 1.58 | 1.68 | 1.78 | | | | 7.80 |

### Grain-Oriented Silicon Steels (GO)

Grain-oriented (GO) silicon steel is used mainly as core material for power transformers. Worldwide production is about 1.5 million tons per year. The increasing demand for energy-efficient transformers requiring still lower loss materials has led to continuous improvements of the magnetic properties over the years, where a decrease in the deviation from the ideal Goss texture (110)[001] has played a decisive role. Moreover, the eddy current losses have been reduced by decreasing the lamination thickness from 0.35 mm through 0.30 mm and 0.27 mm to 0.23 mm. Surface treatments of the laminations by mechanical scratching or laser scribing have been introduced. They increase the number of mobile Bloch walls and, thus, decrease the spacing between them, i. e., the domain size. Accordingly, the anomalous eddy current losses were reduced. The reduction of the total losses of grain oriented electrical steel due to these improvements is illustrated in Fig. 4.3-6.

The GO steels are classified in two categories: conventional grain-oriented (CGO) and high permeability (HGO) steels. The latter are characterized by a sharp crystallographic texture, with average misorientation of the [001] axes of the individual crystallites around the rolling direction (RD) on the order of 3°. For CGO the misorientation is about 7°. The relation between the angular deviation of grain orientation and the total loss reduction for HGO material is shown in Fig. 4.3-7.

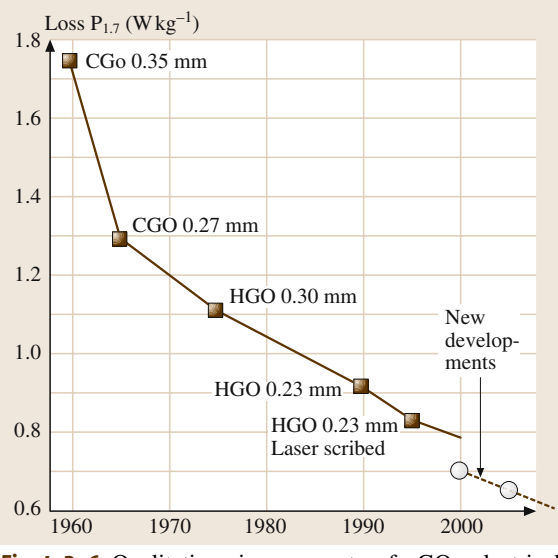


**Fig. 4.3-6** Qualitative improvment of GO electrical steel [3.11]

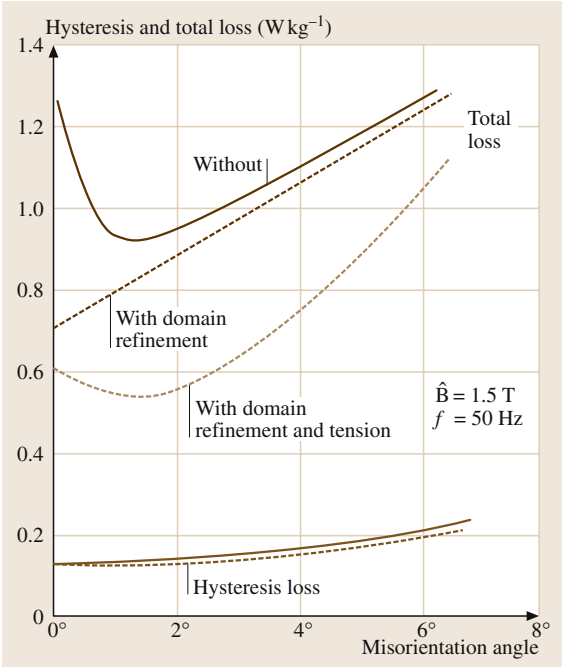


**Fig. 4.3-7** Relation between grain orientation and power loss reduction for highly grain-oriented material (single crystal) (*Bölling* and *Hastenrath*) [3.12, 13]

The (GO) manufacturing route is an extraordinarily long sequence of hot and cold processing steps. The final magnetic properties are highly sensitive to even small parameter variations throughout this route. Some of these processes, their microstructure, and the inhibitor element influence are given in Table 4.3-16.

A key factor is the controlled development of the (110)[001] texture during secondary recrystallization. It requires the presence of large Goss textured grains in the surface layers of the annealed hot band, the presence of inhibitors as finely dispersed second-phase particles which strongly impede normal grain growth during primary recrystallization and a primary recrystallized texture having a suitable orientation relationship with respect to the Goss texture. This can be obtained through carefully-controlled chemistry and a precisely-defined sequence of thermomechanical treatments. Abnormal grain growth during secondary recrystallization may increase the size of magnetic domains and consequently greater energy dissipation under dynamic conditions. Refining the domain structure by laser or mechanical scribing core as mentioned above reduces the losses. Standard IEC specifications for grain-oriented magnetic

**Table 4.3-16** Summary of the processing of grain-oriented silicon steel. The first column relates to the conventional grain-oriented (CGO) laminations. Process for three different types of high permeability (HGO) steels are outlined in columns 2–4. They basically differ for the type of grain growth inhibitors, the cold-rolling sequence, and the annealing temperatures. The processes CGO and HGO-1 adopt a two-stage cold reduction, with intermediate annealing, while HGO-2 and HGO-3 steels are reduced to the final thickness in a single step. Growth inhibition of the primary recrystallized grains is obtained by MnS precipitates in the CGO process. MnSe particles + solute Sb operate in process HGO-1, MnS + AlN particles in HGO-2, and solute B + N + S in HGO-3. Abnormal growth of (110)[001] grains occurs by final box annealing, which also promotes the dissolution of the precipitates [3.7]

| Type of Steel | | | | | | | |
|---|---|---|---|---|---|---|---|
| **CGO** | | **HGO-1** | | **HGO-2** | | **HGO-3** | |
| | | Composition | | (wt%) | | | |
| 3–3.2 | Si | 2.9–3.3 | Si | 2.9–3.3 | Si | 3.1–3.3 | Si |
| 0.04–0.1 | Mn | 0.05 | Mn | 0.03 | Al | 0.02 | Mn |
| 0.02 | S | 0.02 | Se | 0.015 | N | 0.02 | S |
| 0.03 | C | 0.04 | Sb | 0.07 | Mn | 0.001 | B |
| balance | Fe | 0.03–0.07 | C | 0.03 | S | 0.005 | N |
| | | balance | Fe | 0.05–0.07 | C | 0.03–0.05 | C |
| | | | | balance | Fe | balance | Fe |
| | | Inhibitors | | | | | |
| MnS | | MnSe + Sb | | MnS + AlN | | B + N + S | |
| | | Melting, degassing and continuous casting | | | | | |
| | | Reheating - hot rolling | | | | | |
| 1320 °C | | 1320 °C | | 1360 °C | | 1250 °C | |
| | | Annealing | | | | | |
| 800–1000 °C | | 900 °C | | 1100 °C | | 870–1020 °C | |
| | | Cold rolling | | | | | |
| 70 % | | 60–70 % | | 87 % | | 80 % | |
| Annealing | | | | | | | |
| 800–1000 °C | | | | | | | |
| Cold rolling | | | | | | | |
| 55 % | | 65 % | | | | | |
| | | Decarburizing anneal | | | | | |
| | | 800–850 °C (wet $H_2$) | | | | | |
| | | MgO coating and coiling | | | | | |
| | | Box-annealing | | | | | |
| 1200 °C | | 820–900 °C | | 1200 °C | | 1200 °C | |
| | | + 1200 °C | | | | | |
| | | Phospate coating and thermal flattening | | | | | |

steel sheets are listed in Table 4.3-17. Basic properties of grain-oriented Fe–3.2 wt% Si alloys are given in Table 4.3-18.

A recent technology development in the production of GO electrical steel is the combination of thin slab casting, direct hot rolling, and acquired inhibitor formation. This practice combines the advantages of low temperatures, process-shortening, microstructural homogeneity, improved strip geometry, and better surface condition of the products. The slab thickness is on the order of 50–70 mm. Another future technology with remarkable process shortening is to produce (GO) hot strip in the thickness range of about 2–3 mm by direct casting from the steel melt using a twin-roll casting method. In pilot line tests, good workability and good magnetic properties have been achieved.

Further potential for cost and time saving is expected from replacing box annealing at the end of the cold process by short-time continuous annealing.

**Table 4.3-17** Standard IEC specification for grain-oriented magnetic steel sheet: **(a)** normal material; **(b)** material with reduced loss; **(c)** high-permeability material. The conventional designation of the various grades (first column) includes, from left to right, (1) 100 times the maximum power loss, in ($W\,kg^{-1}$), at 1.5 T **(a)** or 1.7 T **(b,c)** peak induction; (2) 100 times the nominal sheet thickness, in (mm); (3) the letter "N" for the nominal material **(a)**, or "S" for material with reduced loss **(b)**, or "P" for high-permeability material **(c)**; (4) one tenth of the frequency in Hz, at which the magnetic properties are specified [3.7]

| a) Grade | Thickness (mm) | Maximum specific total loss ($W\,kg^{-1}$) at peak induction 1.5 T | 1.7 T | Minimum magnetic flux density (T) for $H = 800\,Am^{-1}$ | Minimum stacking factor |
|---|---|---|---|---|---|
| 089-27-N 5 | 0.27 | 0.89 | 1.40 | 1.75 | 0.950 |
| 097-30-N 5 | 0.30 | 0.97 | 1.50 | 1.75 | 0.955 |
| 111-35-N 5 | 0.35 | 1.11 | 1.65 | 1.75 | 0.960 |

| b) Grade | Thickness (mm) | Maximum specific total loss ($W\,kg^{-1}$) at 1.7 T peak induction | Minimum magnetic flux density (T) for $H = 800\,Am^{-1}$ | Minimum stacking factor |
|---|---|---|---|---|
| 130-27-S 5 | 0.27 | 1.30 | 1.78 | 0.950 |
| 140-30-S 5 | 0.30 | 1.40 | 1.78 | 0.955 |
| 155-35-S 5 | 0.35 | 1.55 | 1.78 | 0.960 |

| c) Grade | Thickness (mm) | Maximum specific total loss ($W\,kg^{-1}$) at 1.7 T peak induction | Minimum magnetic flux density (T) for $H = 800\,Am^{-1}$ | Minimum stacking factor |
|---|---|---|---|---|
| 111-30-P 5 | 0.30 | 1.11 | 1.85 | 0.955 |
| 117-30-P 5 | 0.30 | 1.17 | 1.85 | 0.955 |
| 125-35-P 5 | 0.35 | 1.25 | 1.85 | 0.960 |
| 135-35-P 5 | 0.35 | 1.35 | 1.85 | 0.960 |

**Table 4.3-18** Basic properties of grain-oriented Fe–3.2 wt% Si alloys [3.7]

| Property | Value |
|---|---|
| Density | $7.65 \times 10^3\,kg\,m^{-3}$ |
| Thermal concuctivity | $16.3\,W\,°C^{-1}\,kg\,m^{-3}$ |
| Electrical resistivity | $48 \times 10^{-8}\,\Omega\,m$ |
| **Young's modulus** | |
| Single crystals | |
| [100] direction | 120 GPa |
| [110] direction | 216 GPa |
| [111] direction | 295 GPa |
| (110)[001] texture | |
| Rolling direction (RD) | 122 GPa |
| 45° to RD | 236 GPa |
| 90° to RD | 200 GPa |
| **Yield strength** | |
| (110)[001] texture | |
| Rolling direction | 324 MPa |
| **Tensile strength** | |
| (110)[001] texture | |
| Rolling direction | 345 MPa |
| Saturation induction | 2.0 T |

**Table 4.3-18** Basic properties of grain-oriented Fe–3.2 wt% Si alloys [3.7], cont.

| Property | Value |
|---|---|
| Curie temperature | 745 °C |
| Magnetocrystalline anisotropy | $3.6\times10^{4}$ J m$^{-3}$ |
| **Magnetostriction constants** | |
| $\lambda_{100}$ | $23\times10^{-6}$ |
| $\lambda_{111}$ | $-4\times10^{-6}$ |

### Rapidly Solidified Fe–Si Alloys

The Fe–6.5 wt% Si alloy exhibits good high-frequency soft magnetic properties due to a favorable combination of low values of the saturation magnetostriction $\lambda_s$, as well as the low values of the magnetocrystalline anisotropy energy $K_1$, and a high electrical resistivity. But as mentioned above, Fe−Si alloys which contain more than about 4 wt% Si are brittle and thin sheets cannot be manufactured by rolling. Therefore, Fe–6.5 wt% Si sheets and ribbons are manufactured via two different routes by which the adverse mechanical properties are circumvented: a continuous "siliconizing" process in commercial scale production and a rapid quenching process.

In the siliconizing process Fe–3 wt% Si sheet reacts with a Si-containing gas at 1200 °C. The sheet is held at 1200 °C in order to increase and homogenize the Si content by diffusion. After this treatment the ductility of Fe–6.5 wt% Si sheets amounts to about 5% elongation to fracture.

By rapid quenching from the melt, the formation of the B2 and $D0_3$ type ordered structures, based on conventional cooling after casting of Fe–6.5 wt% Si alloys, may be suppressed. Thus, the ensuing material brittleness can be overcome. The ribbons formed by the rapid quenching process are about 20 to 60 μm thick and are ductile, with a microcrystalline structure. By means of an annealing treatment above 1000 °C fol-

**Table 4.3-19** Physical and magnetic properties of rapidly quenched Fe–6.5 wt% Si alloys [3.7]

| Property | Value |
|---|---|
| Density | $7.48\times10^{3}$ kg m$^{-3}$ |
| Thermal conductivity (31 °C) | 4.5 cal m$^{-1}$ °C$^{-1}$ s$^{-1}$ |
| Specific heat (31 °C) | 128 cal °C$^{-1}$ kg$^{-1}$ |
| Coefficient of thermal expansion (150 °C) | $11.6\times10^{-6}$ °C$^{-1}$ |
| Electrical resistivity | $82\times10^{-8}$ Ω m |
| Tensile strength (rapidly-quenched ribbons 60 μm thick) | 630 MPa |
| Saturation magnetization | 1.8 T |
| Curie temperature | 700 °C |
| Saturation magnetostriction | $0.6\times10^{-6}$ |

**Table 4.3-20** Magnetic properties of 30–40 μm thick, rapidly-quenched ribbons of Fe–6.5 wt% Si, in the as-quenched state and after 24 h annealing at various temperatures [3.7]

| Annealing temperature (°C) | $H_c$ (A m$^{-1}$) | $H_{10}$ (T) | $B_r/B_{10}$ | $\mu_{max}/\mu_0$ |
|---|---|---|---|---|
| As-quenched | 112 | 1.25 | 0.70 | 3100 |
| 500 | 100 | 1.27 | 0.93 | 4300 |
| 700 | 72 | 1.32 | 0.90 | 5400 |
| 800 | 45 | 1.31 | 0.92 | 9400 |
| 850 | 37.5 | 1.28 | 0.94 | 10 000 |
| 900 | 33 | 1.30 | 0.77 | 12 500 |
| 1000 | 21 | 1.31 | 0.83 | 17 000 |
| 1100 | 18 | 1.30 | 0.84 | 18 000 |
| 1200 | 20 | 1.32 | 0.87 | 22 000 |

lowed by rapid cooling to restrain $D0_3$ type ordering, large-grain-sized, recrystalllized (100) ⟨0vw⟩ textured material with good ductility and good soft magnetic properties is obtained, as characterized in Tables 4.3-19 and 4.3-20. Figures 4.3-8 and 4.3-9 show the loss behavior as a function of magnetizing frequency and ribbon thickness.

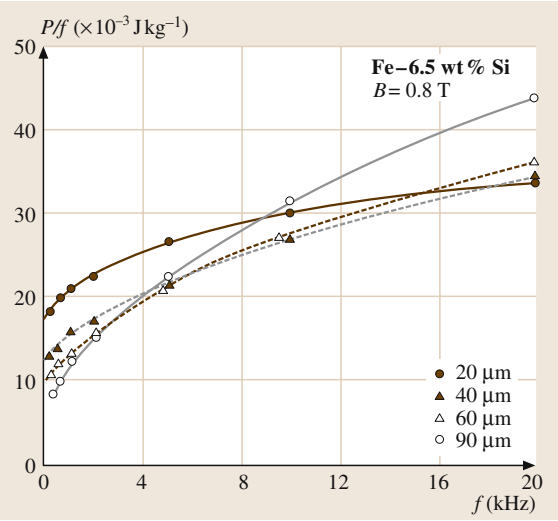


**Fig. 4.3-8** Power loss per cycle vs. magnetizing frequency for rapidly quenched Fe–6.5 wt% Si ribbons of various thicknesses [3.7]

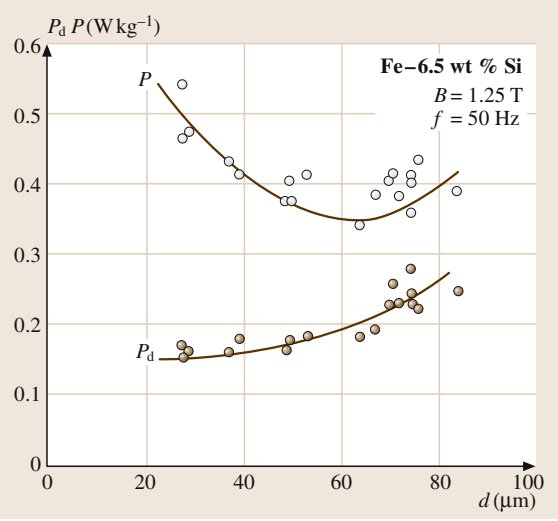


**Fig. 4.3-9** Total and dynamic loss at 1.25 T peak induction and 50 Hz vs. ribbon thickness for rapidly quenched Fe–6.5 wt% Si ribbons characterized by a strong (100) [0uv] grain texture induced by vacuum annealing [3.7]

### 4.3.2.4 Nickel–Iron-Based Alloys

The fcc phase in the Ni–Fe alloy system and the formation of the ordered $Ni_3Fe$ phase provide a wide range of structural and magnetic properties for developing soft magnetic materials with specific characteristics for different applications. The phase diagram is shown in Sect. 3.1.5. Before amorphous and nanocrystalline soft magnetic alloys were introduced, the Ni–Fe materials

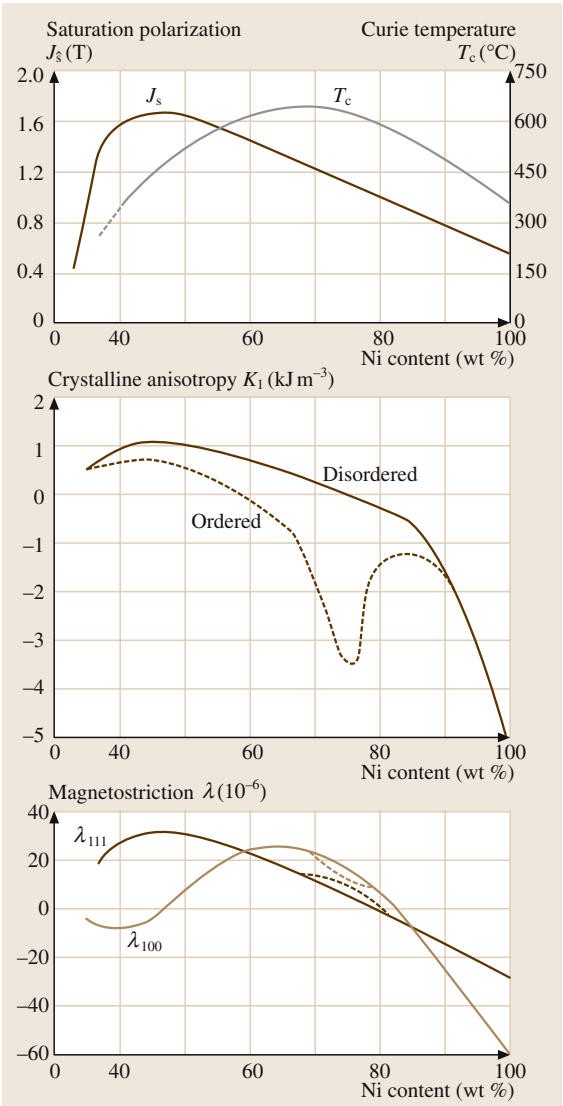


**Fig. 4.3-10** The dependence of the intrinsic magnetic parameters $I_s$, $T_c$, $K_1$, λ of Ni–Fe alloys on the Ni concentration [3.12]

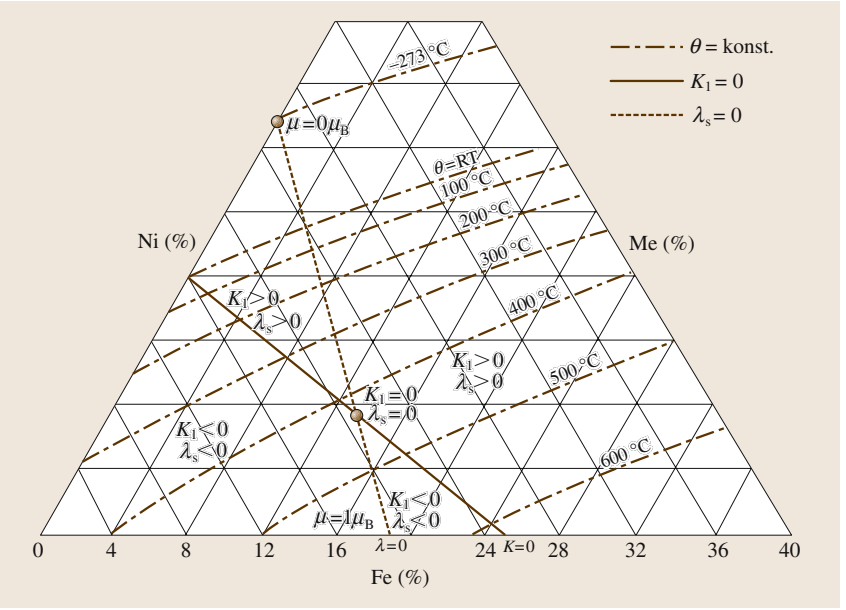


**Fig. 4.3-11** Zero lines for $K_1 = 0$ and $\lambda_s = 0$ in the Ni–Fe–Me system [3.14, 15]

containing about 72 to 83 wt% Ni with additions of Mo, Cu, and/or Cr were the magnetically softest materials available.

Based on the low magnetocrystalline anisotropy $K_1$ and low saturation magnetostriction $\lambda_s$, the alloys containing about 80 wt% Ni where $K_1$ and $\lambda_s$ pass through zero attain the lowest coercivity $H_c \approx 0.5\ \mathrm{A\,m^{-1}}$ and the highest initial permeability $\mu_i \approx 200\,000$. Figure 4.3-10 shows the variation of the decisive intrinsic magnetic parameters $I_s$, $T_c$, $K_1$, $\lambda_{100}$, and $\lambda_{111}$ of binary Ni–Fe alloys with the Ni concentration. The strong effect of structural ordering on the magnitude of $K_1$ should be noted because it permits control of this intrinsic magnetic property by heat treatment.

In the binary Ni–Fe system, $K_1 = 0$ at about 76 wt% Ni and $\lambda_s = 0$ at about 81 wt% Ni. Small additions of Cu lower the Ni content for which $\lambda_s = 0$ while Mo additions increase the Ni content for $K_1 = 0$. Thus different alloy compositions around 78 wt% Ni are available which have optimal soft magnetic properties. General relations of the effect of alloying elements in Ni–Fe-based alloys on $K_1$, $\lambda_s$, and on the permeability have been developed in [3.14, 15]. Figure 4.3-11 shows the position of the lines for $K_1 = 0$ and $\lambda_s = 0$ in the disordered Ni–Fe–Me system, where Me = Cu, Cr, Mo, W, and V. High permeability regions in the Ni–Fe–Me system with a different valence of Me are delineated in Fig. 4.3-12.

The main fields of application of high permeability Ni–Fe alloys are fault-current circuit breakers, LF and HF transformers, chokes, magnetic shielding, and high sensitivity relays.

It should be noted that annealing treatments in a magnetic field of specified direction induce atomic rearrangements which provide an additional anisotropy termed uniaxial anisotropy $K_u$. It can be used to modify the field dependence of magnetic induction in such a way that the hysteresis loop takes drastically different forms, as shown in Fig. 4.3-13.

The extremes of a steep loop (Z type) and a skewed loop (F type) are obtained by field annealing with the direction of the field (during annealing) longitudinal and transverse to the operating field of the product, respectively. Materials with Z and F loops produced by magnetic field annealing are used in magnetic amplifiers, switching and storing cores, as well as for pulse and instrument transformers and chokes.

Combined with small alloy variations, primary treatments and field annealing treatments, a wide variety of annealed states can be realized to vary the induction behavior. The field dependence of the permeability of some high-permeability Ni–Fe alloys (designations according to Vacuumschmelze GmbH) are shown in Fig. 4.3-14 [3.16].

Alloys of Ni–Fe in the range of 54–68 wt% Ni combine relatively high permeability with high saturation

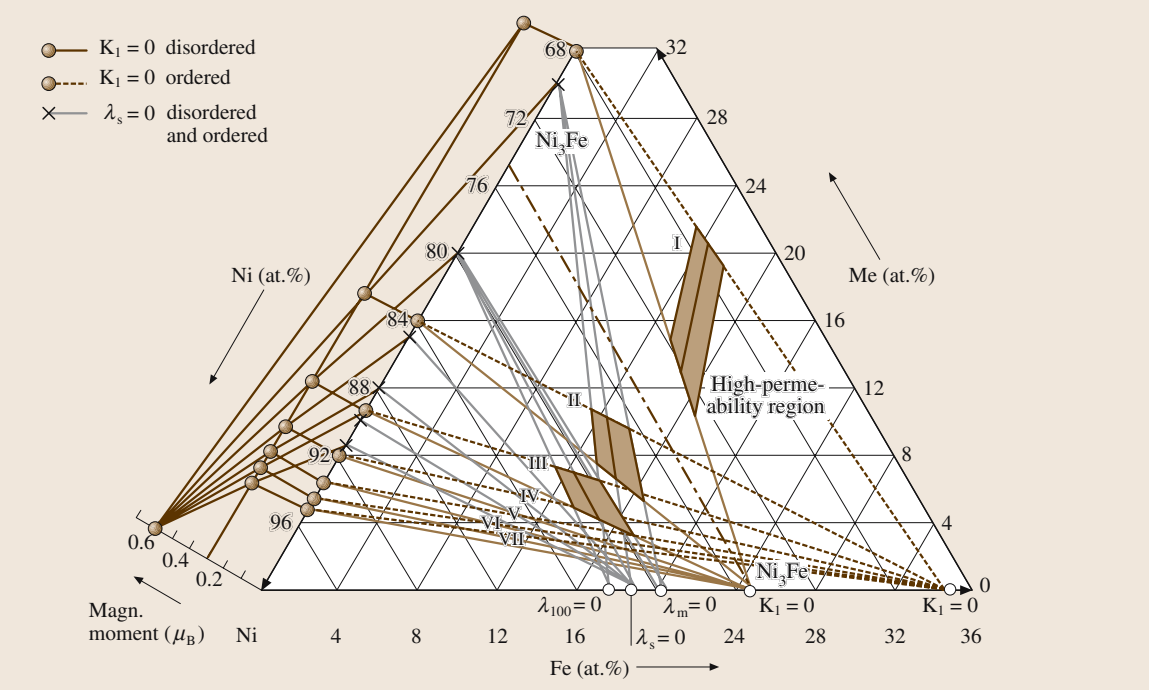


**Fig. 4.3-12** Schematic representation of high-permeability regions in the ternary system Ni−Fe−Me by means of the zero curves $K_1$, $\lambda_{100} = 0$ and $\lambda_{111} = 0$ for additives with valence I–VIII [3.15]

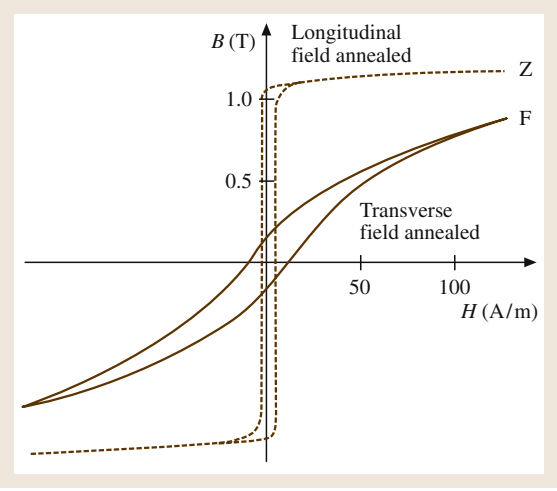


**Fig. 4.3-13** Alloy of the 54–68 wt% NiFe-group with Z- and F-loop [3.12]

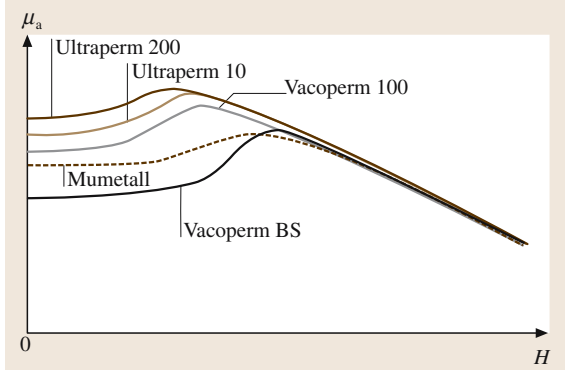


**Fig. 4.3-14** Permeability versus field strength for high permeability high Ni-content Ni−Fe-alloys of Vacuumschmelze Hanau

polarization. Magnetic field annealing of these alloys provides a particularly high uniaxial anisotropy with ensuing Z and F type loops [3.12].

Alloys containing 45 to 50 wt% Ni reach maximum saturation polarization of about 1.6 T. Under suitable rolling and annealing conditions a cubic texture with an ensuing rectangular hysteresis loop and further loop variants over a wide range can be realized. The microstructure may vary from fine grained to coarsely grained.

Alloys containing 35 to 40 wt% Ni show a small but constant permeability, $\mu_r = 2000–8000$, over a wide range of magnetic field strength. Moreover,

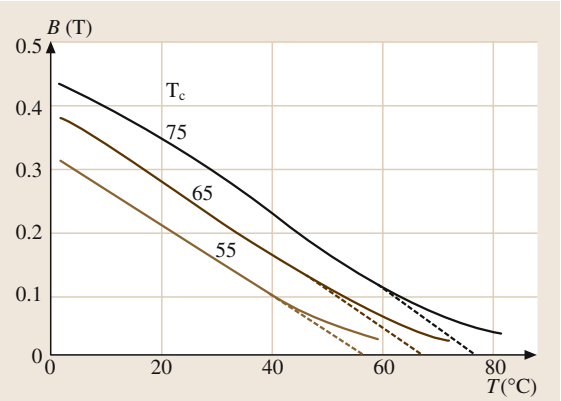


**Fig. 4.3-15** Induction vs. temperature of Fe−Ni alloys with approximately 30% Ni as a function of Curie temperature [3.17]

they have the highest resistivity of all Ni−Fe alloys and a saturation polarization between 1.3 and 1.5 T.

The Curie temperature of the alloys with about 30 wt% Ni is near room temperature. Accordingly, the magnetization is strongly temperature-dependent in this vicinity (see Fig. 4.3-15). By slight variation of the Ni content (a composition increase of 0.1 wt% Ni gives rise to an increase of $T_c$ by 10 K) $T_c$ can be varied between 30 °C and 120 °C. These alloys are used mainly for temperature compensation in permanent magnet systems, measuring systems, and temperature sensitive switches [3.16].

### 4.3.2.5 Iron–Cobalt Alloys

Of all known magnetic materials, Fe−Co alloys with about 35 wt% Co have the highest saturation polarization $I_s = 2.4$ T at room temperature and the highest Curie temperature of nearly 950 °C. The intrinsic magnetic properties $I_s$, $T_c$, $K_1$, and $\lambda_{hkl}$ as a function of Co content are shown in Fig. 4.3-16.

Since $K_1$ and $\lambda_s$ have minima at different Co contents, different compositions for different applications have been developed. A Fe–49 wt% Co–2 wt% V composition is commonly used. The V addition reduces the brittleness by retarding the structural ordering transformation, improves the rolling behavior, and increases the electrical resistivity. The workability of Co−Fe alloys is difficult altogether. Two further alloy variants containing 35 wt% Co and 27 wt% Co, respectively, are of technical interest. They are applied where highest flux density is required, e.g., in magnet yokes, pole

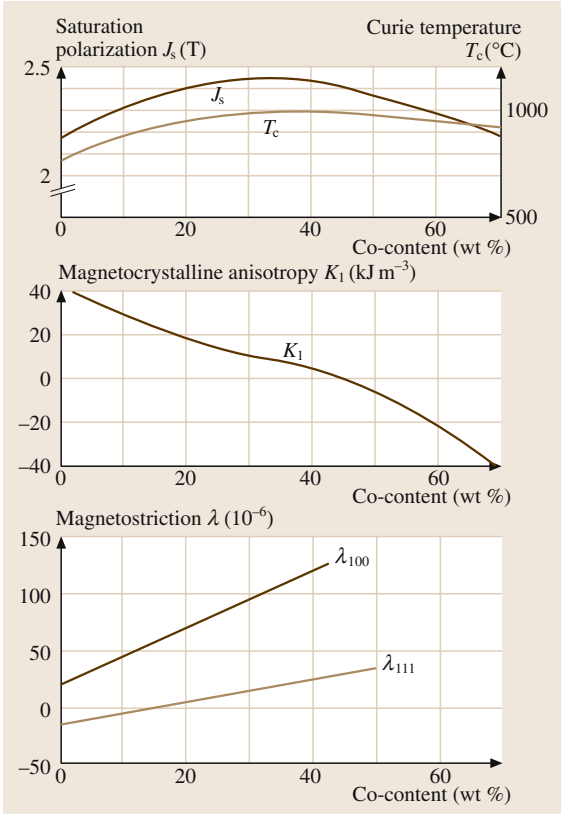


**Fig. 4.3-16** The dependence of intrinsic magnetic parameters $I_s$, $T_c$, $K_1$ and $\lambda$ of Co−Fe alloys on the Co content [3.12]

shoes, and magnetic lenses. The high $T_c$ makes Fe−Co based alloys applicable as high temperature magnet material.

### 4.3.2.6 Amorphous Metallic Alloys

By rapid quenching of a suitable alloy from the melt at a cooling rate of about $10^{-5}$–$10^{-6}$ K/s, an amorphous metallic state will be produced where crystallization is suppressed. Commonly, casting through a slit nozzle onto a rotating copper wheel is used to form a ribbon-shaped product. The thickness of the ribbons is typically between 20 and 40 μm.

From the magnetic point of view amorphous alloys have several advantages compared to crystalline alloys: they have no magnetocrystalline anisotropy, they combine high magnetic softness with high mechanical hardness and yield strength, their low ribbon thickness and their high electrical resistivity (100–150 μΩ cm)

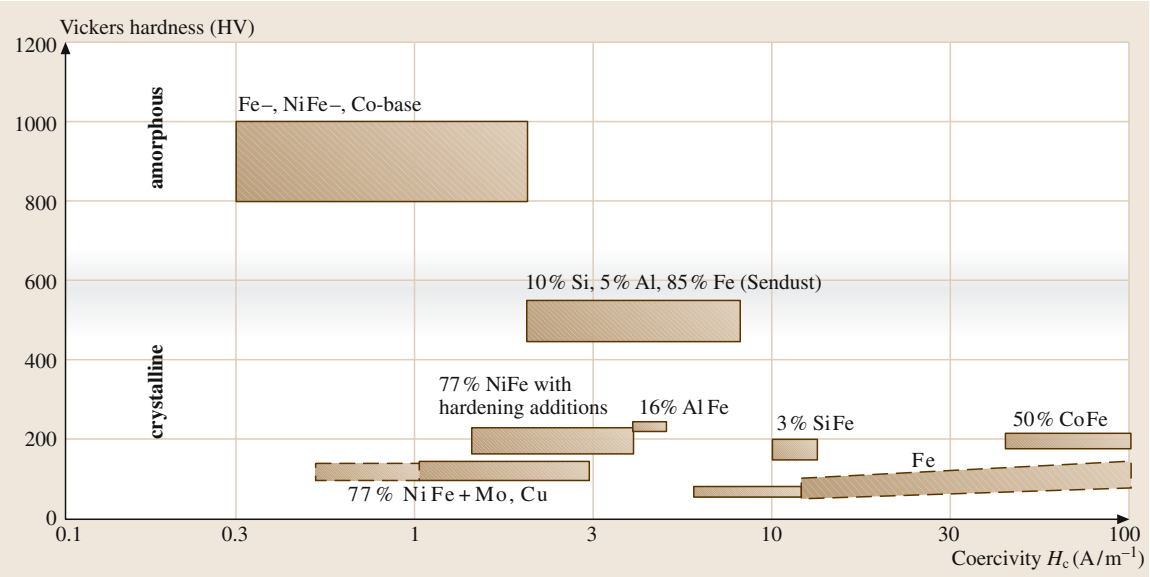


**Fig. 4.3-17** Vickers hardness and coercivity of crystalline and amorphous alloys [3.12]

provide excellent soft magnetic material properties for high frequency applications, in particular low losses. A plot of Vickers hardness (HV) vs. coercivity ($H_c$) for crystalline and amorphous alloys is shown in Fig. 4.3-17 and indicates that a particularly favorable combination for soft magnetic amorphous alloys applies: being magnetically soft and mechanically hard.

The soft magnetic properties of amorphous alloys depend essentially on alloy composition, focusing on a low saturation magnetostriction $\lambda_s$, high glass forming ability required for ribbon preparation at technically accessible cooling conditions, and annealing treatments which provide structural stability and field-induced anisotropy $K_u$.

The soft magnetic amorphous alloys are based on the ferromagnetic elements Fe, Co, and Ni with additions of metalloid elements, the so-called glass forming elements Si, B, C, and P. The most stable alloys contain about 80 at.% transition metal (TM) and 20 at.% metalloid (M) components.

Depending on their base metal they exhibit characteristic differences of technical significance. Accordingly they are classified into three groups: Fe-based alloys, Co-based alloys, and Ni-based alloys. The characteristic variation of their intrinsic magnetic properties saturation polarization $I_s$, saturation magnetostriction $\lambda_s$, and the maximum field induced magnetic anisotropy energy $K_u$, as functions of alloy concentration is shown in Figures 4.3-18 to 4.3-20.

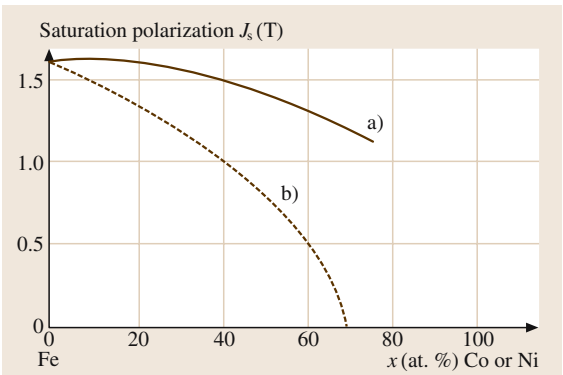


**Fig. 4.3-18a,b** Saturation polarization $J_s$ of Fe-based amorphous alloys depending on Co and Ni content: **(a)** $Fe_{80-x}Co_xB_{20}$ (*O'Handley*, 1977) [3.18]. **(b)** $Fe_{80-x}Ni_xB_{20}$ (*Hilzinger*, 1980) [3.12, 19]

### Iron–Based Amorphous Alloys

Of all amorphous magnetic alloys, the iron-rich alloys on the basis $Fe_{\sim 80}(Si, B)_{\sim 20}$ have the highest saturation polarization of 1.5–1.8 T. Because of their relatively high saturation magnetostriction ($\lambda_s$) of around $30 \times 10^{-6}$, their use as soft magnetic material is limited. The application is focused on transformers at low and

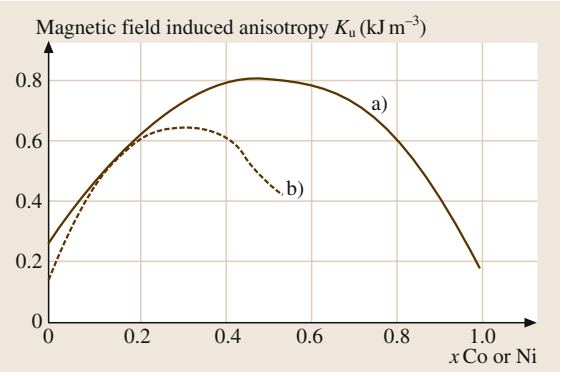


**Fig. 4.3-19a,b** Field induced anisotropy $K_u$ of FeCo-based and FeNi-based amorphous alloys: **(a)** $(Fe_{1-x}Co_x)_{77}Si_{10}B_{13}$ (*Miyazaki* et al., 1972) [3.20]. **(b)** $(Fe_{1-x}Ni_x)_{80}B_{20}$ (*Fujimori* et al., 1976) [3.12, 21]

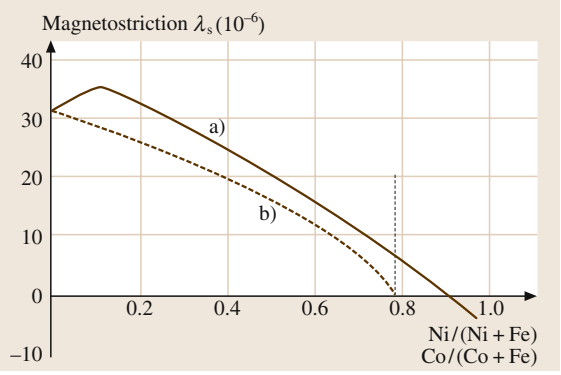


**Fig. 4.3-20a,b** Magnetostriction $\lambda_s$ of FeCo-based and FeNi-based amorphous alloys depending on Co and Ni Content: **(a)** $(FeCo)_{80}B_{20}$ [3.18]. **(b)** $(FeNi)_{80}B_{20}$ [3.12, 18]

medium frequencies in electric power distribution systems.

Compared to grain-oriented silicon steels the iron-rich amorphous alloys show appreciably lower coercivity and consequently lower total losses.

The physical and magnetic properties of a characteristic commercial Fe-rich Metglas amorphous alloy are shown in Fig. 4.3-21 and Table 4.3-21 [3.22].

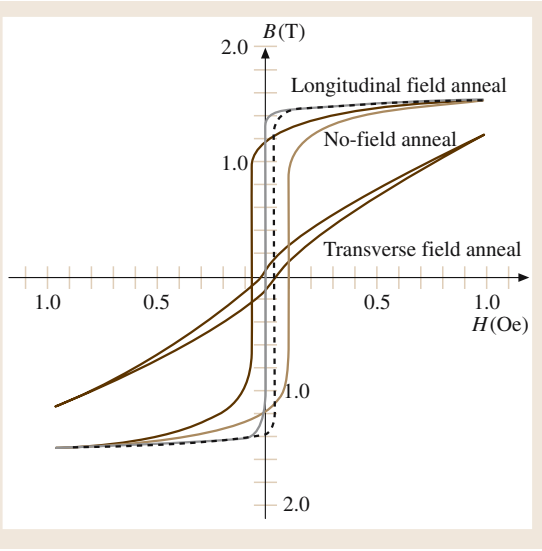


**Fig. 4.3-21** Typical dc hysteresis loop of Fe-rich METGLAS alloy SA 1 [3.22]

### Cobalt–Based Amorphous Alloys

In the $(Fe_xCo_{1-x})_{\sim 80}B_{\sim 20}$ system the saturation magnetostriction $\lambda_s$ passes through zero. Along with a proper selection of alloy composition this behavior gives rise to a particularly low coercivity, the highest permeability of all amorphous magnetic alloys, low stress sensitivity, and extremely low total losses.

The saturation polarization ranging from 0.55 to 1.0 T is lower than in Fe-rich amorphous alloys but comparable to the ~ 80 wt% Ni crystalline permalloy materials. By applying magnetic field annealing, well-controlled Z-type and F-type loops can be realized.

### Nickel–Based Amorphous Alloys

A typical composition of this amorphous alloy group is $Fe_{40}Ni_{40}(Si, B)_{20}$, with a saturation polarization $I_s$ of 0.8 T and a saturation magnetostriction $\lambda_s$ of $10 \times 10^{-6}$. The latter is causing magnetoelastic anisotropy which can be applied to design magnetoelastic sensors where a change in the state of applied stress causes a change in permeability and loop shape, respectively. Upon annealing, Fe–Ni-based alloys will have an R-(round) type

**Table 4.3-21** Physical and magnetic properties of Fe-rich METGLAS alloy SA 1 [3.22]

| Property | Value |
|---|---|
| Ribbon Thickness (μm) | 25 |
| Density (g/cm$^3$) | 7.19 |
| Thermal Expansion (ppm/°C) | 7.6 |
| Crystallization Temperature (°C) | 550 |
| Curie Temperature (°C) | 415 |
| Countinuous Service Temperature (°C) | 155 |
| Tensile Strength (MN/m$^2$) | 1–1.7 k |
| Elastic Modulus (GN/m$^2$) | 100–110 |
| Vicker's Hardness (50 g load) | 860 |
| Saturation Flux Density (Tesla) | 1.56 |
| Permeability (depending on gap size) | Variable |
| Saturation Magnetostriction (ppm) | 27 |
| Electrical Resistivity (μΩ cm) | 137 |

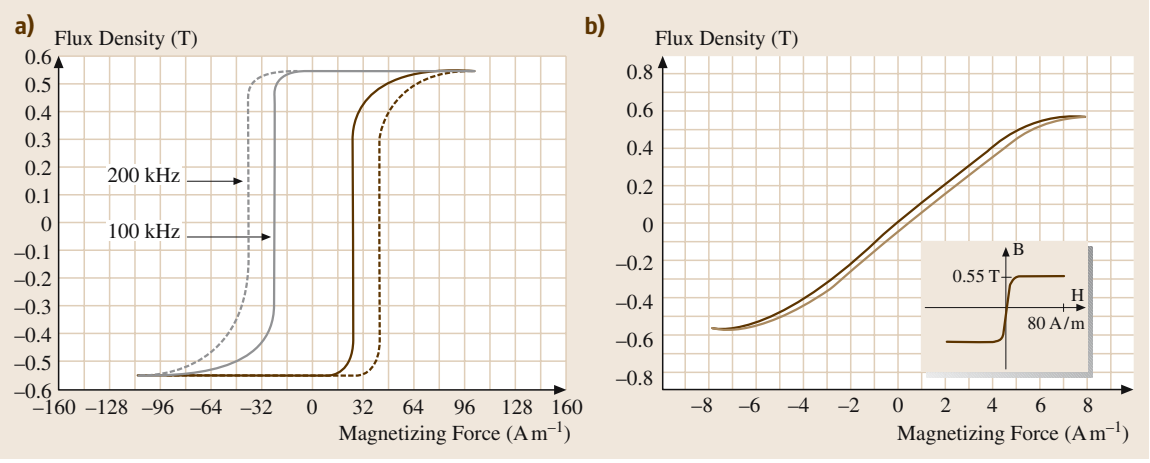


**Fig. 4.3-22a,b** Typical dc hysteresis loop of Co-based METGLAS alloy: (a) alloy 2714 AS (Z-loop) and (b) alloy 2714 AF (F-loop) [3.22]

**Table 4.3-22** Physical and magnetic properties of the cobalt-based amorphous alloy METGLAS alloy 2714 AF [3.22]

| Property | Value |
|---|---|
| Ribbon Thickness (μm) | 18 |
| Density (g/cm$^3$) | 7.59 |
| Thermal Expansion (ppm/°C) | 12.7 |
| Crystallization Temperature (°C) | 560 |
| Curie Temperature (°C) | 225 |
| Countinuous Service Temperature (°C) | 90 |
| Tensile Strength (MN/m$^2$) | 1–1.7 k |
| Elastic Modulus (GN/m$^2$) | 100–110 |
| Vicker's Hardness (50 g load) | 960 |
| Saturation Flux Density (Tesla) | 0.55 |
| Permeability ($\mu$@1 kHz, 2.0 mA/cm) | 90 000±20% |
| Saturation Magnetostriction (ppm) | $\ll 1$ |
| Electrical Resistivity (μΩ cm) | 142 |

**Table 4.3-23** Survey of soft magnetic amorphous and nanocrystalline alloys. Some amorphous alloy of METGLAS (Allied Signal Inc., Morristown/NJ) and VITROVAC (Vacuumschmelze GmbH, Hanau, Germany) have been selected from commercially available alloys [3.12]

| Composition | Typical properties | | | | | | |
|---|---|---|---|---|---|---|---|
| | Saturation polarization in (T) | Curie temperature in (°C) | Saturation magnetostriction in $10^{-6}$ | Coercivity (dc) in ($A\,m^{-1}$) | Permeability [a] at $H = 4\,mA\,m^{-1}$ $\times 10^3$ | Density in ($g\,cm^{-3}$) | Specific electrical resistivity [b] in ($\Omega\,mm^2\,m^{-1}$) |
| Amorphorus | | | | | | | |
| Fe-based: | | | | | | | |
| $Fe_{78}Si_9B_{13}$ | 1.55 | 415 | 27 | 3 | 8 | 7.18 | 1.37 |
| $Fe_{67}Co_{18}Si_1B_{14}$ | 1.80 | ~550 [c] | 35 | 5 | 1.5 | 7.56 | 1.23 |
| FeNi-based: | | | | | | | |
| $Fe_{39}Ni_{39}Mo_2Si_{12}B_8$ | 0.8 | 260 | +8 | 2 | 20 | 7.4 | 1.35 |
| Co-based: | | | | | | | |
| $Fe_{67}Fe_4Mo_1Si_{17}B_{11}$ | 0.55 | 210 | < 0.2 | 0.3 | 100 | 7.7 | 1.35 |
| $Fe_{74}Fe_2Mn_4Si_{11}B_9$ | 1.0 | 480 [c] | < 0.2 | 1.0 | 2 | 7.85 | 1.15 |
| Nanocristalline | | | | | | | |
| $Fe_{73.5}Cu_1Nb_3Si_{13.5}B_9$ | 1.25 | 600 | +2 | 1 | 100 | 7.35 | 1.35 |

[a] Materials with round (R) or flat loops (F), $f = 50\,Hz$

[b] $1\,\Omega\,mm^2/m = 10^{-4}\,\Omega\,cm$

[c] Extrapolated values ($T_c > T_x$, $T_x$: crystallization temperature)



hysteresis loop associated with high initial permeability, or an F-type loop with low losses.

Table 4.3-23 gives a survey of the magnetic and physical properties of several soft magnetic amorphous alloys

### 4.3.2.7 Nanocrystalline Soft Magnetic Alloys

Nanocrystalline soft magnetic alloys are a rather recent class of soft magnetic materials with excellent magnetic properties such as low losses, high permeability, high saturation polarization up to 1.3 T, and near-zero magnetostriction. The decisive structural feature of this alloy type is its ultra-fine microstructure of bcc $\alpha$-Fe−Si nanocrystals, with grain sizes of 10–15 nm which are embedded in an amorphous residual phase. Originally, this group of materials was discovered in the alloy system Fe−Si−B−Cu−Nb with the composition $Fe_{73.5}Si_{15.5}B_7Cu_1Nb_3$. This material is prepared by rapid quenching like an amorphous Fe−Si−B alloy with a subsequent annealing treatment and comparatively high temperature in the range of 500 to 600 °C which leads to partial crystallization.

The evolution of the nanocrystalline state during annealing occurs by partial crystallization into randomly oriented, ultrafine bcc $\alpha$-Fe−Si grains that are 10–15 nm in diameter. The residual amorphous matrix phase forms a boundary layer that is 1–2 nm thick. This particular nano-scaled microstructure is the basis for ferromagnetically-coupled exchange interaction of and through these phases, developing excellent soft magnetic properties: $\mu_a \approx 10^5$, $H_c < 1\,A\,m^{-1}$. Annealing above 600 °C gives rise to the precipitation of the borides $Fe_2B$ and/or $Fe_3B$ with grain sizes of 50–100 nm. At higher annealing temperatures, grain coarsening arises. Both of these microstructural changes are leading to a deterioration of the soft magnetic properties.

The influence of the annealing temperature on grain size, $H_c$, and $\mu_i$ of a nanocrystalline type alloy is shown in Fig. 4.3-23 [3.23].

The small additions of Cu and Nb favor the formation of the nanocrystalline structure. Copper is thought to increase the rate of nucleation of $\alpha$-Fe−Si grains by a preceding cluster formation, and Nb is supposed to lower the growth rate because of its partitioning effect and decrease of diffusivity in the amorphous phase. Figure 4.3-24 illustrates the formation of the nanocrystalline structure schematically.

It is useful to note the influence of the atomic diameter of alloying additions on the grain size of the $\alpha$-Fe−Si phase starting from the classical alloy composition $Fe_{73.5}Si_{15.5}B_7Cu_1Nb_3$. This effect is shown for

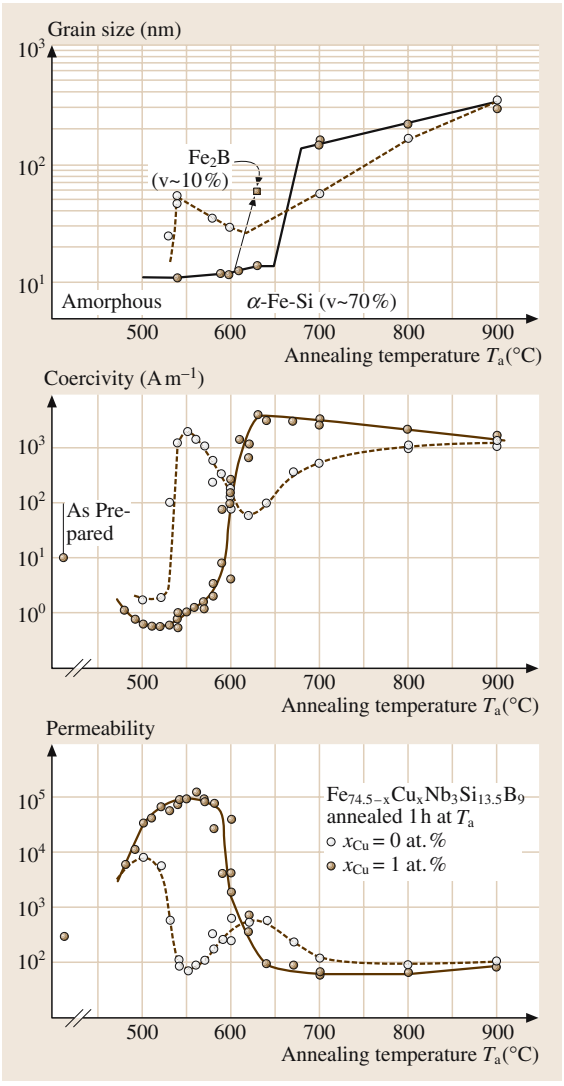


**Fig. 4.3-23** Average grain size, coercivity and initial permeability of a nanocrystalline soft magnetic alloy as a function of the annealing temperature [3.23]

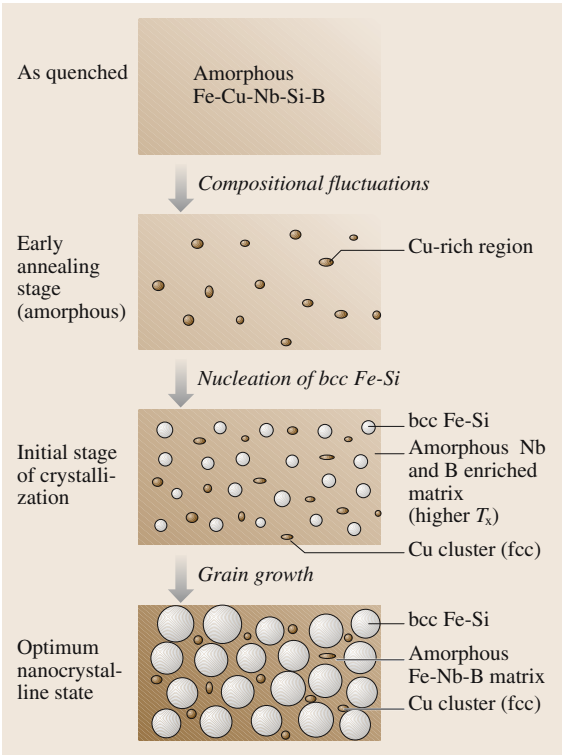


**Fig. 4.3-24** Schematic illustration of the formation of the nanocrystalline structure in Fe−Cu−Nb−Si−B alloys, based on atom probe analysis results and transmission electron microscopy observations by *Hono* et al. [3.23, 24]

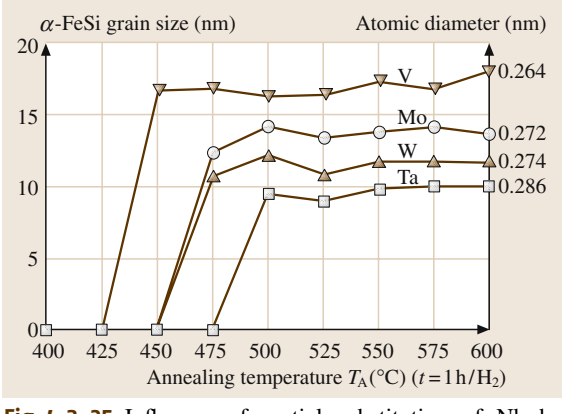


**Fig. 4.3-25** Influence of partial substitution of Nb by the refractory elements R = *V*, Mo, W and Ta on the α-FeSi grain size during annealing of the alloy $Fe_{73.5}Si_{15.5}B_7Cu_1Nb_3R_2$ [3.25]

partial substitution of Nb by V, Mo, W, and Ta (2 at.% each) in Fig. 4.3-25. The larger the atomic diameter, the smaller the resulting grain size. The elements Nb and Ta have the same atomic diameter. Furthermore, the smaller the atomic diameter of the alloying element, the sooner the crystallization of the α-Fe-Si phase begins.

One of the decisive requirements for excellent soft magnetic properties is the absence of magnetostriction. Amorphous Fe−Si−B−Cu−Nb alloys have a saturation

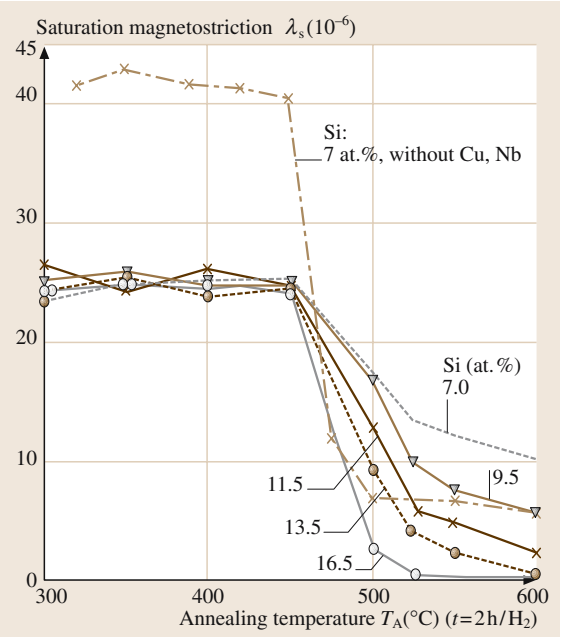


**Fig. 4.3-26** Influence of the Si-content on the saturation magnetostriction $\lambda_s$ during annealing of the nanocrystalline alloys $Fe_{(75-73.5)}Si_{(7-16.5)}B_{(14-6)}Cu_1Nb_3$ [3.26]

magnetostriction $\lambda_s \approx 24\times10^{-6}$, with a magnetoelastic anisotropy energy $K_\sigma \approx 50\,\mathrm{J\,m^{-3}}$. With partial crystallization of the $\alpha$-Fe−Si phase during annealing, $\lambda_s$ varies significantly. At higher Si contents it decreases strongly and passes through zero at about 16 at.% Si, as shown in Fig. 4.3-26.

This behavior is caused by the compensation of the negative saturation magnetostriction $\lambda_s$ of the $\alpha$-Fe−Si phase $\lambda_s \approx -8\times10^{-6}$ and the positve values of $\lambda_s$ of the residual amorphous phase of $\lambda_s \approx +24\times10^{-6}$.

The superposition of the local magnetostrictive strains to an effective zero requires a large crystalline volume fraction of about 70 vol.% to compensate the high positive value of the amorphous residual phase of about 30 vol.%. By anealing at about 550 °C this relation can be realized. The second requirement for superior soft magnetic properties is a small or vanishing magnetocrystalline anisotropy energy $K_1$.

By developing a particular variant of the random anisotropy model, it was shown [3.27] that for grain diameters $D$ smaller than the magnetic exchange length $L_0$, the averaged anisotropy energy density $\langle K\rangle$ is given by

$$\langle K\rangle \approx v_{cr}^2 K_1 (D\,L_0^{-1})^6 = v_{cr}^2 D^6 K_1^4 A^{-3}\,,$$

where $v_{cr}$ = crystallized volume, $K_1$ = intrinsic crystal anisotropy energy of $\alpha$-Fe−Si, $L_0 = \sqrt{A\,K_1^{-1}}$, and $A$ = exchange stiffness constant. A schematic representation of this model is given in Fig. 4.3-27. The basic effect of decreasing the grain size consists of local averaging of the magnetocrystalline anisotropy energy $K_1$ for $D = 10-15$ nm at $L_0 = 30-50$ nm (about equal to

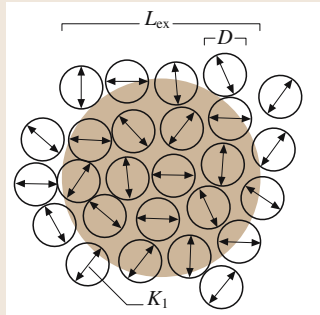


$$N = v_{cr}\,(L_{ex}/D)^3$$

$$\langle K\rangle = \frac{v_{cr}\times K_1}{\sqrt{N}}$$

**Fig. 4.3-27** Schematic representation of the random anisotropy model for grains embedded in an ideally soft ferromagnetic matrix. The *double arrows* indicate the randomly fluctuating anisotropy axis; the *dark* area represents the ferromagnetic correlation volume determined by the exchange length $L_{ex} = (A/\langle K\rangle)^{1/2}$ [3.23]

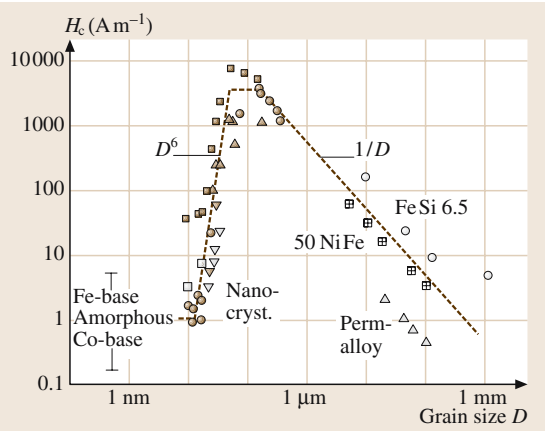


**Fig. 4.3-28** Coercivity, $H_c$, vs. grain size, $D$, for various soft magnetic metallic alloys [3.27]: Fe−Nb−Si−B (*solid up triangles*) [3.28], Fe−Cu−Nb−Si−B (*solid circles*) [3.29, 30], Fe−Cu−V−Si−B (*solid* and *open down triangles*) [3.31], Fe−Zr−B (*open squares*) [3.32], Fe−Co−Zr (*open diamonds*) [3.33], NiFe-alloys (+ *center squares* and *open up triangles*) [3.34], and Fe−Si(6.5 wt%) (*open circles*) [3.35]

**Table 4.3-24** Typical values of grain size $D$, saturation magnetization $J_s$, saturation magnetostriction $\lambda_s$, coercivity $H_c$, initial permeability $\mu_i$, electrical resistivity $\rho$, core losses $P_{Fe}$ at 0.2 T, 100 kHz and ribbon thickness $t$ for nanocrystalline, amorphous, and crystalline soft magnetic ribbons

| Alloy | $D$ (nm) | $J_s$ (T) | $\lambda_s$ ($10^{-6}$) | $H_c$ (A m$^{-1}$) | $\mu_i$ (1 kHz) | $\rho$ (μΩ cm) | $P_{Fe}$ (W kg$^{-1}$) | $t$ (μm) | Ref |
|---|---|---|---|---|---|---|---|---|---|
| $Fe_{73.5}Cu_1NB_3Si_{13.5}B_9$ | 13 | 1.24 | 2.1 | 0.5 | 100 000 | 118 | 38 | 18 | [a] |
| $Fe_{73.5}Cu_1NB_3Si_{15.5}B_7$ | 14 | 1.23 | ~ 0 | 0.4 | 110 000 | 115 | 35 | 21 | [b] |
| $Fe_{84}NB_7B_9$ | 9 | 1.49 | 0.1 | 8 | 22 000 | 58 | 76 | 22 | [c] |
| $Fe_{86}Cu_1Zr_7B_6$ | 10 | 1.52 | ~ 0 | 3.2 | 48 000 | 56 | 116 | 20 | [c] |
| $Fe_{91}Zr_7B_3$ | 17 | 1.63 | − 1.1 | 5.6 | 22 000 | 44 | 80 | 18 | [c] |
| $Co_{68}Fe_4(MoSiB)_{28}$ | amorphous | 0.55 | ~ 0 | 0.3 | 150 000 | 135 | 35 | 23 | [b] |
| $Co_{72}(FeMn)_5(MoSiB)_{23}$ | amorphous | 0.8 | ~ 0 | 0.5 | 3000 | 130 | 40 | 23 | [b] |
| $Fe_{76}(SiB)_{24}$ | amorphous | 1.45 | 32 | 3 | 8000 | 135 | 50 | 23 | [b] |
| 80 % Ni−Fe (permalloys) | ~100 000 | 0.75 | < 1 | 0.5 | 100 000 [d] | 55 | >90 [e] | 50 | [b] |
| 50–60 % Ni−Fe | ~100 000 | 1.55 | 25 | 5 | 40 000 [d] | 45 | >200 [e] | 70 | [b] |

[a] [3.36]
[b] Typical commercial grades for low remanence hysteresis loops, Vacuumschmelze GmbH 1990, 1993
[c] [3.37, 38]
[d] 50 Hz-values
[e] Lower bound due to eddy currents

the domain wall thickness), which leads to the extreme variation of $\langle K \rangle$ with the sixth power of grain size. These relations were confirmed experimentally and result in an anomalous variation of the coercivity with grain size, as shown in Fig. 4.3-28.

Another type of nanocrystalline soft magnetic materials is based on Fe−Zr−B−Cu alloys [3.37, 38]. A typical composition is $Fe_{86}Zr_7B_6Cu_1$. As Zr provides high glass-forming ability, the total content of glass-forming elements can be set to $\ll 20$ at.%. As a consequence the Fe content is higher, which implies higher saturation polarization. The nanocrystalline microstructure consists of a crystalline $\alpha$-Fe phase with grain sizes of about 10 nm embedded in an amorphous residual phase. After annealing at 600 °C, an optimum combination of magnetic properties is obtained: $I_s \geq 1.5$ T, $H_c \approx 3$ A m$^{-1}$, $\lambda_s \approx 0$. Because of the high reactivity of Zr with oxygen the preparation of this type of alloy is difficult. The production of these materials on an industrial scale has not yet succeeded.

Table 4.3-24 shows the magnetic and physical properties of some commercially-available nanocrystalline alloys for comparison to amorphous and Ni−Fe-based crystalline soft magnetic alloys. Magnetic field annealing allows the shape of the hysteresis loops of

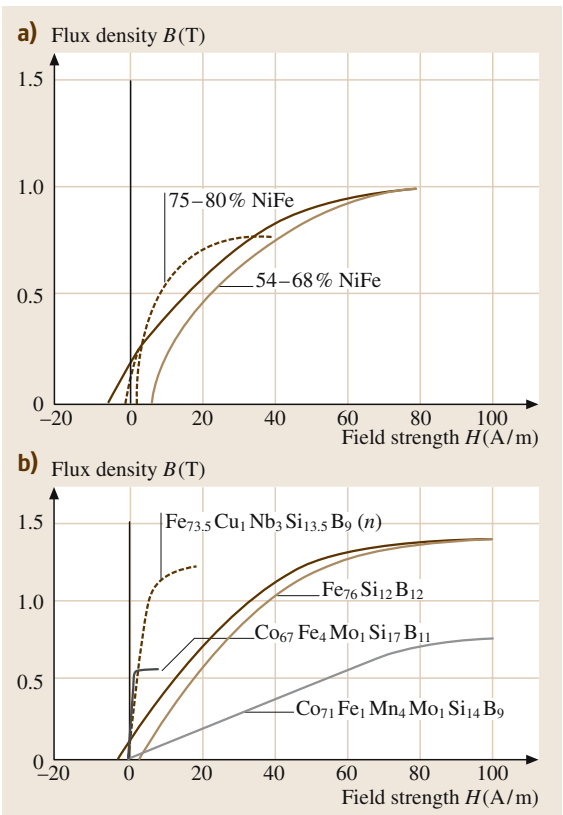


**Fig. 4.3-29a,b** Soft magnetic alloys with flat hysteresis loops: **(a)** Crystalline. **(b)** Amorphous and nanocrystalline (curve indicated by $n$) [3.12]

nanocrystalline soft magnetic alloys to be varied according to the demands of the users. Accordingly, different shapes of hystesis loops (Z, F, or R type) may be achieved. For comparison several characteristic hysteresis loops of crystalline, amorphous, and nanocrystalline soft magnetic alloys are shown in Figs. 4.3-29a,b and 4.3-30a,b.

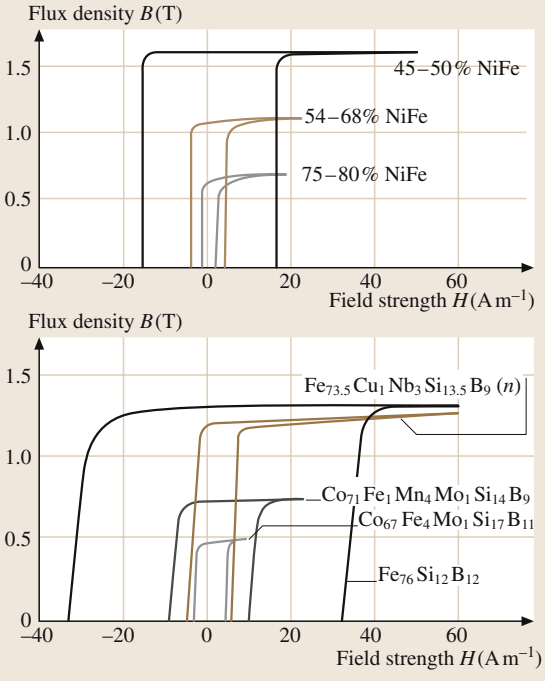


**Fig. 4.3-30a,b** Soft magnetic alloys with rectangular hysteresis loops: **(a)** Crystalline. **(b)** amorphous and nanocrystalline (curve indicated by $n$) [3.12]

A survey of the field dependence of the amplitude permeability of various crystalline, amorphous, and nanocrystalline soft magnetic alloys is given in Fig. 4.3-31 [3.12]. Figure 4.3-32 [3.23] represents the frequency behavior of the permeability $|\mu|$ of different soft magnetic materials for comparison.

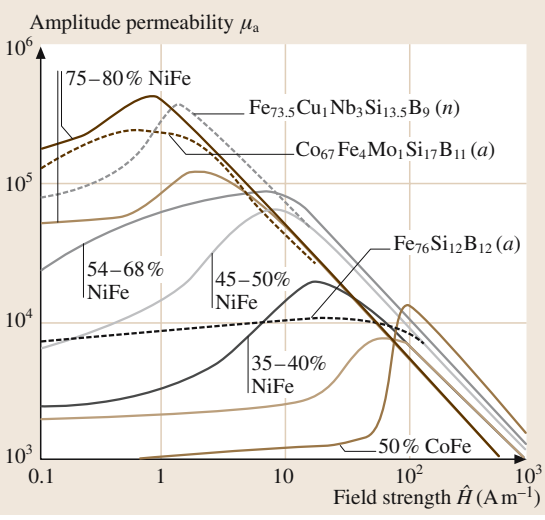


**Fig. 4.3-31** Amplitude permeability–field strength curves of soft magnetic alloys ($f = 50$ Hz): amorphous ($a$); nanocrystalline ($n$) [3.12]

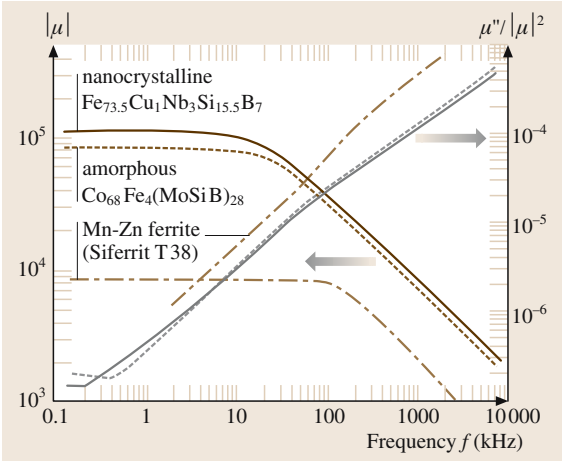


**Fig. 4.3-32** Frequency dependence of permeability, $|\mu|$, and the relative loss factor, $\mu''/|\mu|^2$, for nanocrystalline $Fe_{73.5}Cu_1Nb_3Si_{15.5}B_7$ and comparable, low remanence soft magnetic materials used for common mode choke cores [3.23]

## 4.3.2.8 Invar and Elinvar Alloys

The term invar alloys is used for some groups of alloys characterized by having temperature-invariant properties, either temperature-independent volume (invar) or temperature-independent elastic properties (elinvar) in a limited temperature range. A comprehensive survey of the physics and applications of invar alloys is given in [3.17].

### Invar Alloys

With the discovery of an Fe–36 wt% Ni alloy with an uncommonly low thermal expansion coefficient (TEC) around room temperature and called "Invar" by Guil-

laume in the 1890s, the history of invar and elinvar type alloys began. Below the magnetic transition temperature, Curie temperature $T_c$ or Néel temperature $T_N$ of ferromagnetic or antiferromagnetic materials, a spontaneous volume magnetostriction $\omega_s$ sets in. With some alloy compositions, $\omega_s$ is comparable in magnitude to the linear thermal expansion but opposite in sign. As a result the coefficient of linear thermal expansion may become low and even zero.

The linear ($\alpha$) and volumetric ($\beta$) thermal expansion coefficients (TECs) are defined as:

$$\alpha = (1/l)(\Delta l/\Delta T)_P \quad [K^{-1}]$$

and

$$\beta = (1/V)(\Delta V/\Delta T)_P \quad [K^{-1}] ,$$

with $l$ = length, $V$ = volume, and $T$ = temperature. If the alloys are isotropic the volumetric thermal expansion coefficient is equal to three times the linear TEC:

$$\beta = 3\alpha .$$

The spontaneous volume magnetostriction $\omega_s$ is in a first approximation:

$$\omega_s = \kappa C M_s^2 ,$$

with $\kappa$ = compressibility, $C$ = magnetovolume coupling constant, and $M_s$ = spontaneous magnetization. Figure 4.3-33 [3.42] illustrates schematically the temperature-dependent behavior of thermal expansion, $\omega_s$ and $M_s$, which give rise to a small linear expansion coefficient.

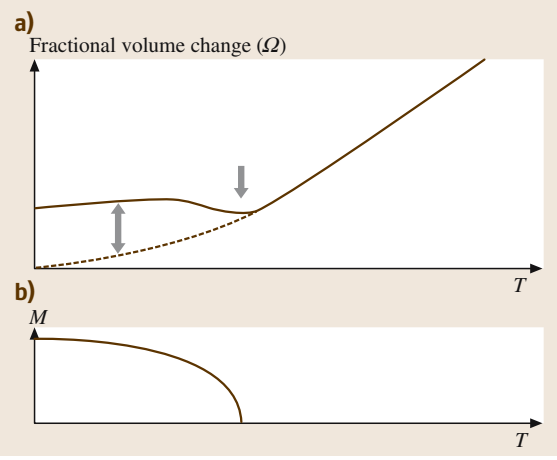


**Fig. 4.3-33** **(a)** Schematic diagram of invar-type thermal-expansion anomaly. The *dashed curve* indicates thermal expansion for hypothetical paramagnetic state. The difference between the two curves corresponds to the spontaneous volume magnetostriction, $\omega_s$. **(b)** Temperature dependence of the spontaneous magnetization

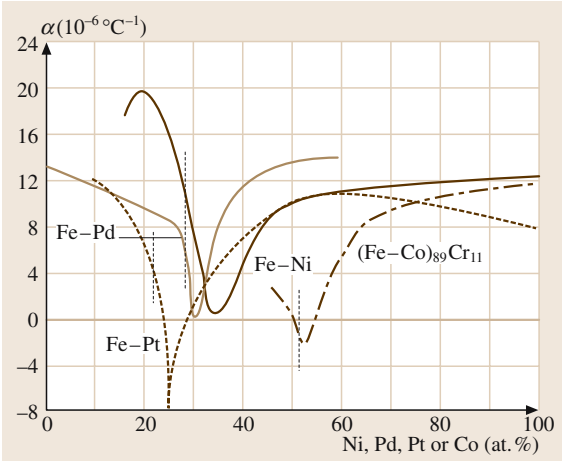


**Fig. 4.3-34** Temperature coefficient of linear thermal expansion $\alpha$ at room temperature as a function of the composition in typical invar alloy systems: Fe−Ni [3.39], Fe−Pt [3.40], Fe−Pd [3.40], and Fe−Co−Cr [3.39]. *Vertical dotted lines* show boundary between bcc and fcc phases

Crystalline invar alloys are essentially based on 4 binary alloy systems: Fe−Ni, Fe−Pt, Fe−Pd, and Fe−Co, containing a few percent of Cr. Figure 4.3-34 [3.17] shows the thermal expansion coefficient of these invar type alloy systems. The invar alloy in each system is fcc

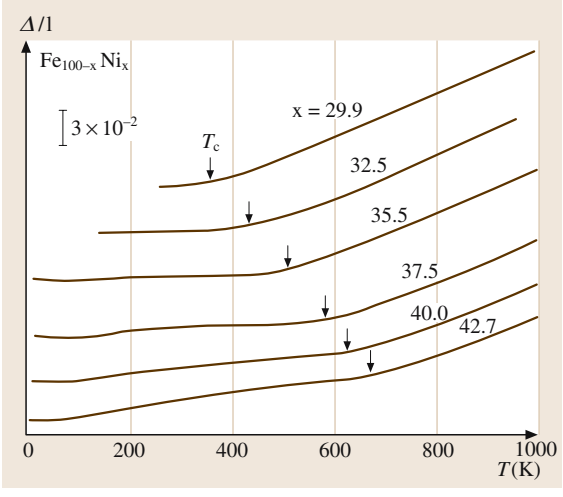


**Fig. 4.3-35** Thermal expansion curves of Fe−Ni alloys annealed at 1323 K for 5 days [3.41]

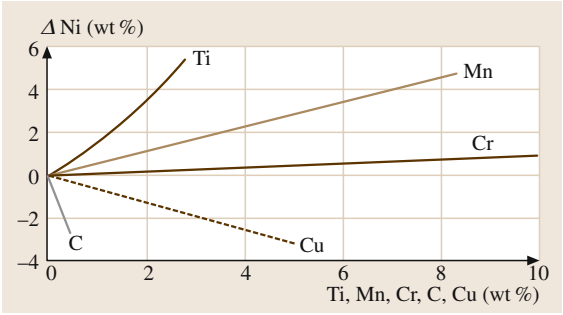


**Fig. 4.3-36** Displacement of the composition corresponding to the minimum thermal expansion coefficient of Fe−Ni alloys by the addition of Ti, Mn, Cr, Cu, and C [3.17]

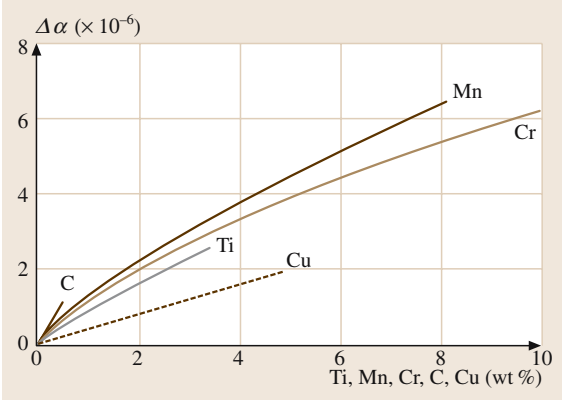


**Fig. 4.3-37** Increase of the minimum value of thermal expansion coefficient of Fe−Ni alloys by the addition of Ti, Mn, Cr, Cu, and C [3.17]

and its composition is near the boundary between the bcc and fcc phase fields.

*Fe–Ni–Based Invar Alloys.* An iron alloy containing 34 to 36.5 wt% Ni is well known as a commercial invar material. The materials C < 0.12 wt%, Mn < 0.50 wt%, and Si < 0.50 wt% are generally added for metallurgical purposes. Figure 4.3-35 [3.41] shows the thermal expansion curves of some Fe−Ni alloys.

The thermal expansion of invar alloys is affected significantly by the addition of third elements,

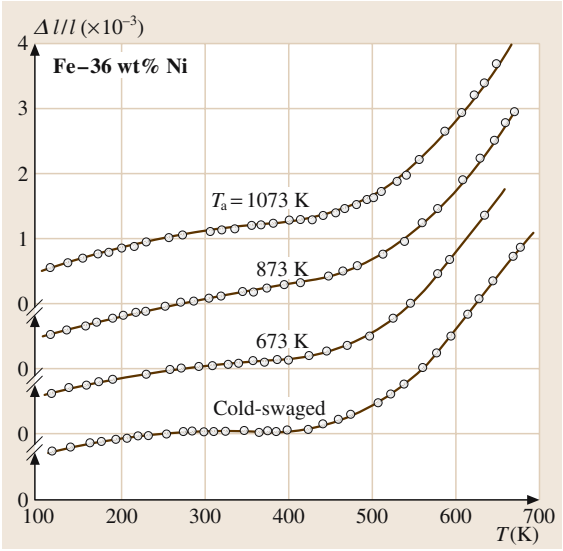


**Fig. 4.3-38** Effect of thermal annealing at a temperature $T_a$ and of mechanical treatment on the thermal expansion of Fe–36 at.% Ni invar alloy [3.41]

by cold working and by thermal treatment as shown in Fig. 4.3-36 [3.17], Fig. 4.3-37 [3.17] and Fig. 4.3-38 [3.41].

Invar is an austenitic alloy and cannot be hardened by heat treatment. The effect of heat treatment on the TEC $\alpha$ depends on the method of cooling after annealing. Air cooling or water quenching from the annealing temperature results in a reduction of $\alpha$ but at the same time $\alpha$ becomes unstable. In order to stabilize the material, annealing at low temperature and slow cooling to room temperature are necessary.

Following heat treatments for an optimum and stable magnitude of $\alpha$ are recommended: 830 °C, 1/2 h, water quenching; 315 °C, 1 h, air cooling; 95 °C, 20 h, air cooling. Cold working reduces $\alpha$. But before use in high precision instruments a stress-relief anneal at 320 to 370 °C for 1 h followed by air cooling is required.

The mechanical properties of some invar-type alloys are listed in Table 4.3-25 [3.42].

**Table 4.3-25** Thermal expansion coefficient, $\alpha$ and mechanical properties of invar alloys for practical use [3.42]

| | Composition (wt%) | $\alpha$ at RT ($10^{-6}$ K$^{-1}$) | Vickers hardness | Tensile stress (MPa) |
|---|---|---|---|---|
| Invar | Fe–36Ni | <2 | 150–200 | 500–750 |
| Super Invar[a] | Fe–32Ni–4Co | <0.5 | 150–200 | 500–800 |
| Stainless Invar[b] | Fe–54Co–9Cr | <0.5 | | |
| High strength Invar | Fe–Ni–Mo–C[c] | <4 | | 1250 |
| | Fe–Ni–Co–Ti[d] | <4 | 300–400 | 1100–1400 |

[a] Masumoto, 1931
[b] Masumoto, 1934
[c] Yokota et al., 1982
[d] Yahagi et al., 1980

**Table 4.3-26** Thermal expansion coeffcient of invar 36 and free-cut invar [3.17]

| Temperature | $\alpha$ ($\times 10^{-6}$ K$^{-1}$) | | | |
|---|---|---|---|---|
| | As annealed | | As cold-drawn | |
| (°C) | Invar 36 | Free-cut Invar 36 | Invar 36 | Free-cut Invar 36 |
| 25–100 | 11.18 | 1.60 | 0.655 | 0.89 |
| 25–200 | 1.72 | 2.91 | 0.956 | 1.62 |
| 25–300 | 4.92 | 5.99 | 2.73 | 3.33 |
| 25–350 | 6.60 | 7.56 | 3.67 | 4.20 |
| 25–400 | 7.82 | 8.88 | 4.34 | 4.93 |
| 25–450 | 8.82 | 9.80 | 4.90 | 5.45 |
| 25–500 | 9.72 | 10.66 | 5.40 | 5.92 |
| 25–600 | 11.35 | 12.00 | 6.31 | 6.67 |
| 25–700 | 12.70 | 12.90 | 7.06 | 7.17 |
| 25–800 | 13.45 | 13.60 | 7.48 | 7.56 |
| 25–900 | 13.85 | 14.60 | 7.70 | 8.12 |

**Table 4.3-27** Some physical properties of invar alloys [3.17]

| Property | Value | |
|---|---|---|
| Melting point | 1.425 °C | 2600 °F |
| Density | 8 g cm$^{-3}$ (8.0–8.13) | 500 lb ft$^{-3}$ |
| Thermal electromotive force to copper (0–96 °C) | 9.8 μV/K | |
| Specific resistance (Annealed) | $82 \times 10^{-6}$ Ω cm (81–88) | 495 Ω circ. mil/ft |
| Temperature coefficient of electric resistivity | $1.21 \times 10^{-3}$ K$^{-1}$ | $0.67 \times 10^{-3}$ °F$^{-1}$ |
| Specific heat | 0.123 cal/g K (25–100 °C) | 0.123 Btu/lb °F (77–212 °F) |
| Thermal conductivity | 0.0262 cal/sec cm K (22–100 °C) | 72.6 Btu in./hr ft$^2$ °F (68–212 °F) |
| Curie temperature | 277 °C (277–280 °C) | 530 °F |
| Inflection temperature | 191 °C | 375 °F |
| Modulus of elasticity (in tension) | $15.0 \times 10^{10}$ Pa | $21.4 \times 10^6$ lb in.$^{-2}$ |
| Temperature coefficient of elastic modulus | $+50 \times 10^{-5}$ K$^{-1}$ (16–50 °C) | $+27 \times 10^{-5}$ °F$^{-1}$ (60–122 °F) |
| Modulus of rigidity | $5.7 \times 10^{10}$ Pa | $8.1 \times 10^6$ lb in.$^{-2}$ |
| Temperature coefficient of rigidity modulus | $+58 \times 10^{-5}$ K$^{-1}$ | $+30 \times 10^{-5}$ °F$^{-1}$ |
| Posson's ratio | 0.290 | |

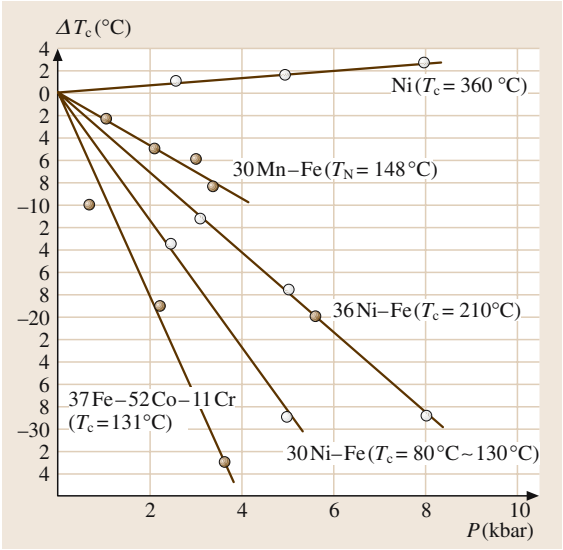


**Fig. 4.3-39** The displacement of the Curie point $\Delta T_c$ vs. pressure in Fe−Ni invar alloys [3.43] and in Fe−Co−Cr invar alloy [3.44]. The results for Ni [3.43] and for a 30Mn−Fe alloy [3.44] are also shown for comparison. Numerical values in parentheses show the Curie or Néel point at atmospheric pressure

Invar-type alloys show large effects of pressure on magnetization and on the Curie temperature, which suggests a high sensitivity to the interatomic spacing, as shown in Fig. 4.3-39 [3.17].

Thermal expansion coefficients of invar 36 and free-cut invar 36 (containing S and P, or Se) between 25 and 900 °C are listed in Table 4.3-26 [3.17]. Some physical properties of Invar alloys are given in Table 4.3-27 [3.17].

Low thermal expansion coefficients are observed at ternary and quaternary Fe-alloy systems, too. The composition Fe–32 wt% Ni–4 wt% Co was the starting point of superinvar, whose TEC $\alpha$ is in the order of $10^{-7}$ $K^{-1}$. The thermal expansion curves of different variants are shown in Fig. 4.3-40 [3.17].

In order to improve the corrosion resistance of invar alloys, "stainless invar" was developed. The basic composition is Fe–54 wt% Co–9.5 wt% Cr. Stainless invar has the bcc structure at room temperature in the equilibrium state. As an invar material, it is used after quenching from a high temperature to retain the fcc structure [3.17].

To improve the mechanical properties two types of high strength invar materials were developed: a work-hardening type based on Fe−Ni−Mo−C, and a precipitation-hardening type Fe−Ni−Co−Ti alloy [3.17].

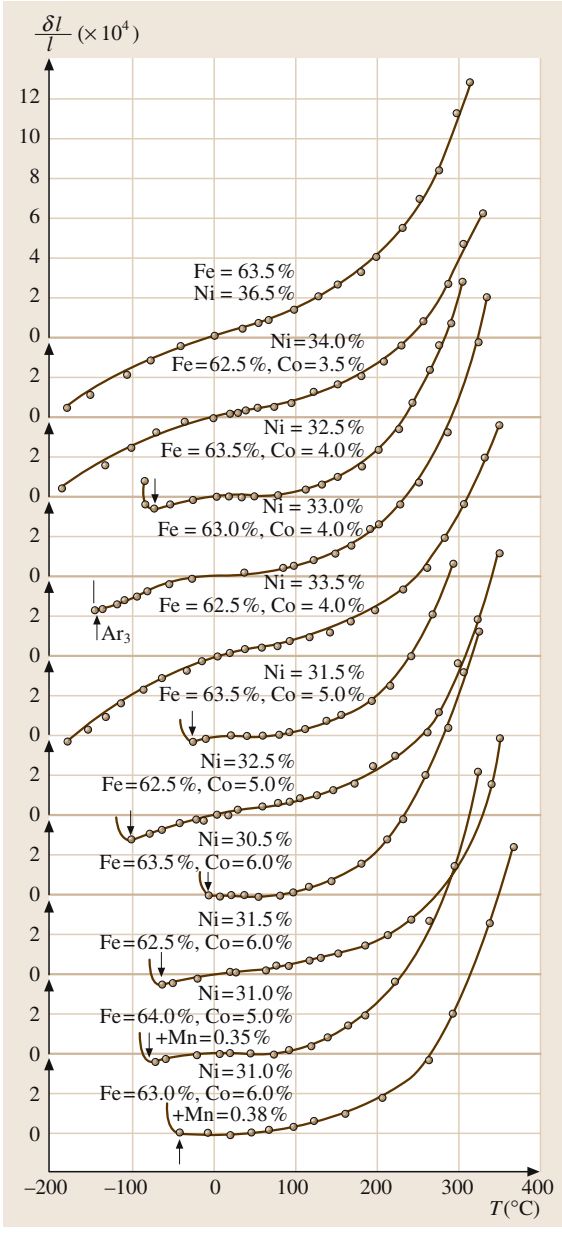


**Fig. 4.3-40** Thermal expansion curves of super invar alloys [3.17]

*Fe–Pt-Based Invar Alloys.* Among the ordered phases of the Fe−Pt system (Fig. 4.3-41 [3.17]), the $Fe_3Pt$ phase shows the invar type thermal expansion anomaly. In

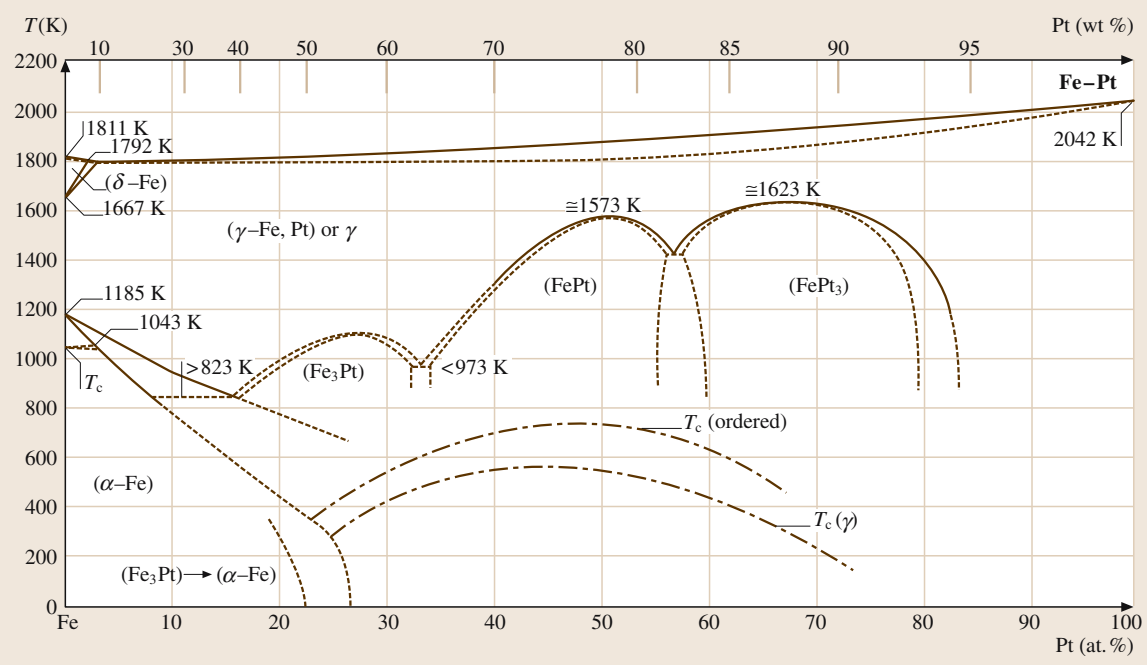


**Fig. 4.3-41** Fe−Pt phase diagram. *Dashed-dotted lines*: Curie temperature $T_c$

order to obtain a well ordered state, a long annealing time is necessary (600 °C, 160 h). Disordered fcc alloys which show invar anomalies, too, may be obtained by rapid quenching from above the order–disorder transformation temperature. The Curie temperature of the disordered state is lower than that of the ordered state. A high negative value of $\alpha$ is observed just below the Curie temperature, particularly for disordered alloys. Annealed alloys containing 52 to 54 wt% Pt have small TEC and those containing 52.5 to 53.5 wt% Pt show negative values of $\alpha$, Fig. 4.3-42 [3.17].

*Fe–Pd–Based Invar Alloys.* Alloys of Fe−Pd (see Fig. 4.3-43) containing 28 to 31 at.% Pd show invar characteristics, as seen in Fig. 4.3-44 [3.41]. In order to obtain invar behavior, the alloys are quenched from the high temperature $\gamma$ phase field such that phase transformations at lower temperatures are suppressed. As shown in Fig. 4.3-45 [3.41], the thermal expansion is strongly decreased by cold deformation, i. e., by disordering, lattice defects, and internal stresses. After cold working, an instability of the invar property is observed.

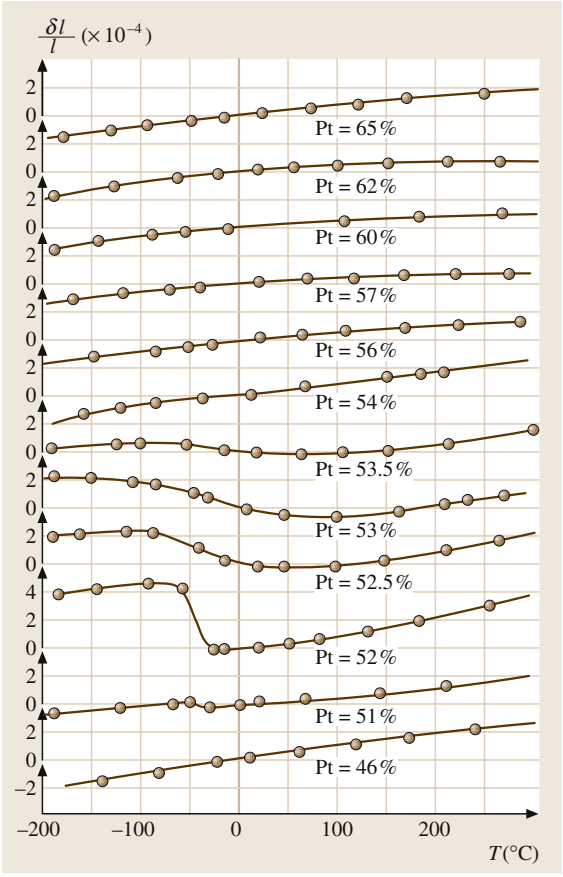


**Fig. 4.3-42** Thermal expansivity curves of Fe−Pt alloys [3.17]

*Other Alloy Systems with Invar Behavior.* Beyond the invar-type alloys mentioned, many other Fe-based alloy systems show invar behavior, for instance, Fe−Ni−Cr, Fe−Ni−V, Fe−Pt−Re, Fe−Ni−Pt, Fe−Ni−Pd, Fe−Pt−Ir, Fe−Cu−Ni, and Fe−Mn−Ni. Some amorphous melt/quenched alloy systems show invar characteristics too, e.g., $Fe_{83}B_{17}$, $Fe_{85}P_{15}$, $Fe_{79}Si_9B_{12}$. Similarly, amorphous alloys prepared by sputtering show invar characteristics: $Fe_{75}Zr_{25}$, $Fe_{72}Hf_{28}$. Some antiferromagnetic Mn- and Cr-based alloys also exhibit a remarkable anomaly of thermal expansion due to magnetic ordering: $Pd_{64.5}Mn_{35.5}$, $Mn_{77}Ge_{23}$, $Cr_{92.5}Fe_{4.3}Mn_{0.5}$, $Cr_{96.5}Si_3Mn_{0.5}$.

### Elinvar Alloys

Elinvar or constant-elastic-modulus alloys are based on work by *Guillaume* [3.45] and *Chevenard* [3.46]. They show a nearly temperature-independent behavior of the Young's modulus ($E$). For technical applications, elinvar alloys are designed to show the anomaly in the range of their operating temperature, usually close to room temperature. Since the resonance frequency $f_0$ of an oscillating body is related to its $E$ modulus by $f_0 \sim \sqrt{E/\varrho}$ ($\varrho$ =density), the thermoelastic properties of elinvar alloys are utilized for components in oscillating systems of the precision instrument industry. In these applications highly constant resonance frequencies are required. Typical examples are: resonators in magnetomechanical filters; balance springs in watches, tuning forks; helical springs in spring balances or seismographs, as well as in pressure or load cells. The condition for temperature compensation of the Young's modulus $E$ is:

$$2\Delta f/f\Delta T = \Delta E/E\Delta T + \alpha \approx 0\,,$$

with $T$ = temperature and $\alpha$ = linear thermal expansion coefficient. Elinvar characteristics also refer to the temperature independence of the shear modulus $G$, which is related to the $E$ modulus via

$$3/E = 1/G + 1/3B$$

and

$$E = 2(1+\nu)G = 3(1-\nu)B\,,$$

with $B$ = bulk modulus and $\nu$ = Poisson's ratio.

In ordinary metallic materials, $E$ decreases with increasing temperature according to the variation of the elastic constants with temperature according to the anharmonicity in the phonon energy term. The temperature compensation of the $E$-modulus in ferromagnetic and antiferromagnetic elinvar alloys is caused by an anomaly in its temperature behavior ($\Delta E$ effect). As a consequence in ferromagnetic alloys, the $E$ modulus in the demagnetized state is different from that in the magnetized state. The $\Delta E$ effect with ferromagnetic elinvar alloys consists of three parts [3.47]:

$$\Delta E = \Delta E_\lambda + \Delta E_\omega + \Delta E_A\,.$$

A schematic description of the components of the $\Delta E$ effect in ferromagnetic elinvar alloys is given in Fig. 4.3-46.

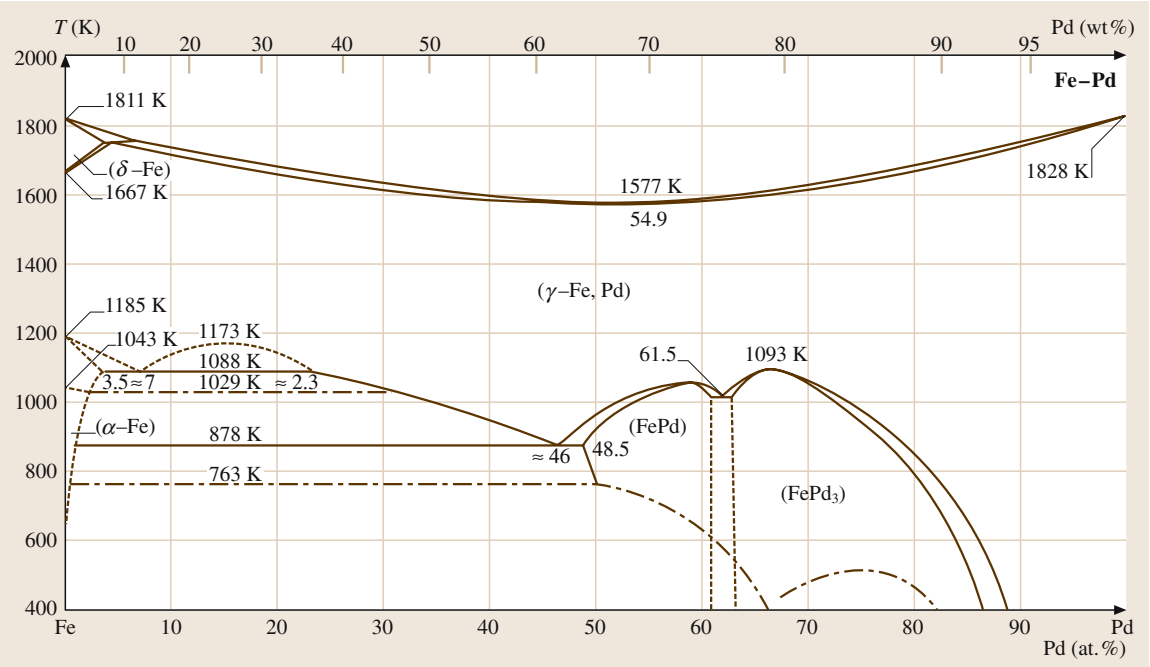


**Fig. 4.3-43** Fe−Pd phase diagram. *Dashed-dotted lines*: Curie temperature $T_c$

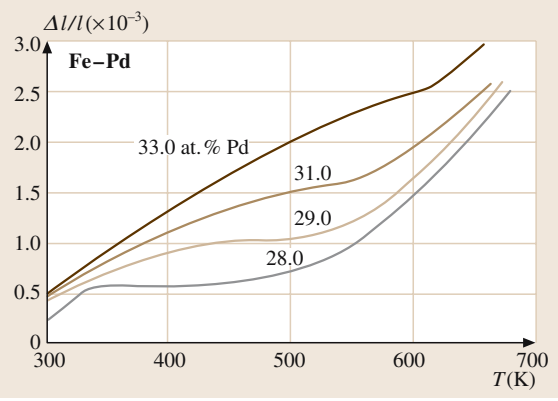


**Fig. 4.3-44** Thermal expansion curves of Fe−Pd alloys rapidly cooled from high temperature [3.41]

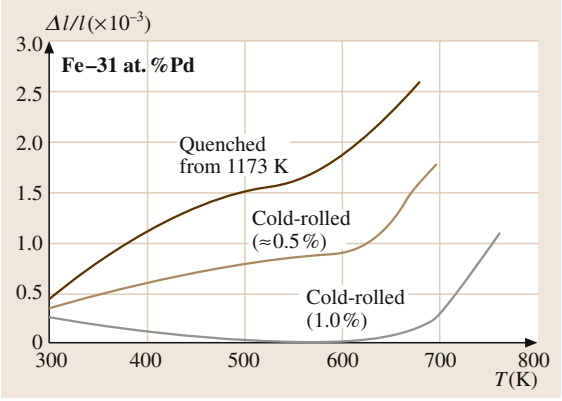


**Fig. 4.3-45** Thermal expansion curves of cold-worked Fe–31 at.% Pd alloy. The rolling ratio is given by percentage

These components are attributable to the following relations:

$$\Delta E_\lambda = -2/5 E^2 \lambda_s/\sigma_i \,,$$

where $\Delta E_\lambda$ is attributed to the shape magnetostriction ($\lambda_s$) that changes the direction of the spontaneous magnetization, owing to domain wall motion and rotation processes as a consequence of the influence of mechanical stresses ($\sigma_i$) or magnetic fields on the unsaturated state of material [3.48]. The value $\Delta E_\omega$ is caused by forced volume magnetostriction ($\omega$) as a consequence of changes of the interatomic distances induced by stress or very high magnetic fields, which lead to a change of the magnetic interaction [3.49]:

$$\Delta E_\omega = -1/9 E^2 [(\partial\omega/\partial H)^2/\partial J/\partial H] \,,$$

where $\partial\omega/\partial H =$ forced volume magnetostriction and $\partial J/\partial H =$ para-susceptibility. The value $\Delta E_A$ takes the

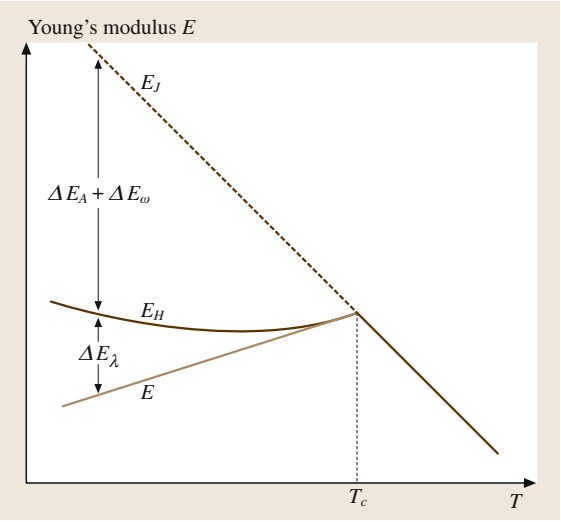


**Fig. 4.3-46** Young's modulus $E$ as a function of temperature of ferromagnetic elinvar alloys: $E = E$ modulus in the absence of a magnetic field, $E_H = E$ modulus measured in a magnetic field $H$, $E_J = E$ modulus at constant polarization $J$

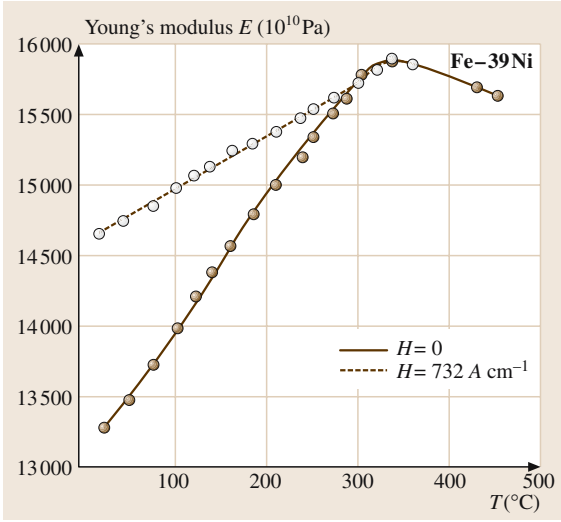


**Fig. 4.3-47** $E$ modulus and its dependence on the temperature of an annealed Fe–39 wt% Ni alloy, with and without influence of a magnetic field $H$ [3.51]

role of the exchange energy into account [3.50]:

$$\Delta E_A \sim -\omega_s \sim J_s^2 \,,$$

where $\omega_s =$ volume magnetostriction and $J_s =$ saturation polarization. It originates from the spontaneous volume magnetostriction $\omega_s$ as a function of the change of exchange energy with temperature due to the variation of magnetic ordering up to the Curie temperature.

*Ferromagnetic Elinvar Alloys.* The development of ferromagnetic elinvar alloys is based on affecting the shape magnetostriction $\lambda_s$ by control of internal stresses resulting from deformation and/or precipitation hardening. But this requires a zero or negative temperature coefficient of the $E_H$ modulus. Based on an Fe–39 wt% Ni alloy, it can be shown how this behavior is achievable. Alloys of Fe−Ni with 36 to 45 wt% Ni have a positive sign of the temperature coefficient of the $E_H$ modulus (see Fig. 4.3-47 [3.51]).

By addition of 7 wt% Cr this coefficient is reduced to zero or to slightly negative values. By a deformation it can be influenced furthermore while the absolute value

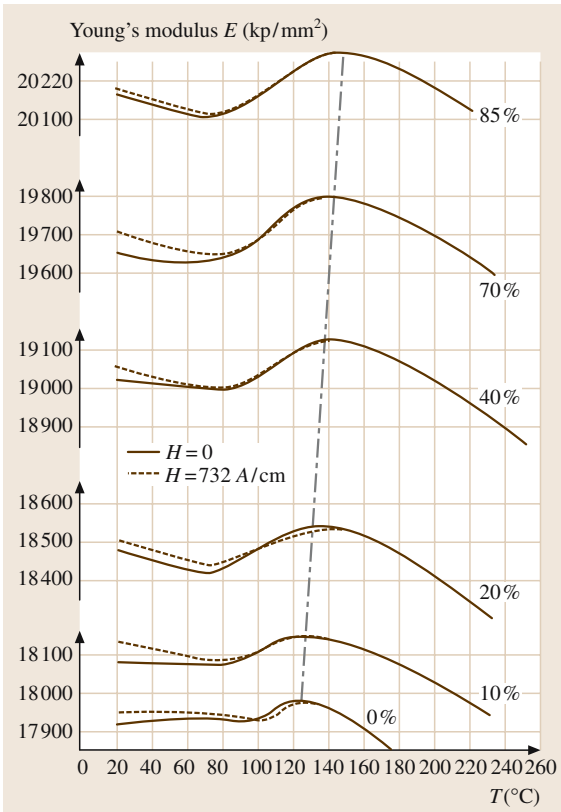


**Fig. 4.3-48** Young's modulus $E$ of an Fe−39Ni−7Cr−0.8Be−1.0Ti (wt%) alloy as a function of temperature, degree of cold deformation $\eta$ (%) with and without a magnetic field $H$ [3.51]

and 1.0 wt% Ti on the $E = f(T)$ characteristic. Cold deformation causes the Curie temperature to rise.

The final processing steps consist of solution annealing at 1150 °C, water quenching, cold deformation, and a final precipitation annealing at about 600 °C. Accordingly commercial elinvar alloys are produced, such as those listed in Tables 4.3-28, 4.3-29, and 4.3-30.

Apart from the well-tried Fe−Ni−Cr−(Be, Ti)-based elinvar-type alloys, Fe−Ni−Mo-based alloys have gained technical application. Addition of Mo improves the elastic properties, lowers the Curie temperature, and increases the resistance to corrosion. While in Europe and the USA, Fe−Ni-based elinvar-type alloys mainly were developed, in Japan Co−Fe-based elinvar alloys were discovered. Ternary Co−Fe−Cr alloys and quaternary alloys containing Ni (Co-elinvar) attained significant technical relevance. Distinguishing marks worth mentioning include: higher Young's modulus than Fe−Ni-based alloys, corrosion resistance, wide range of temperature compensating of $E$ modulus, and easy hardening by cold-working.

*Antiferromagnetic Elinvar Alloys.* In antiferromagnetic alloys no domains are formed and no $\Delta E_\lambda$ effect occurs. With antiferromagnetic ordering the $\Delta E_A$ effect can only be exploited in combination with a pronounced cubic to tetragonal lattice distortion associated with antiferromagnetic ordering. This requires methods to develop temperature compensating elastic behavior which are different from those for ferromagnetic thermoelastic materials. The development of antiferromagnetic alloys with Elinvar properties has been concentrated on Mn−Cu, Mn−Ni, and Fe−Mn base alloys. In [3.52] the distinct anomalies of Young's modulus at the Néel



**Table 4.3-28** Compositions in (wt%) of Fe−Ni-based elinvar alloys [3.17]

| | Bal. Fe | | | | | | | | | | | | | | | |
|---|---|---|---|---|---|---|---|---|---|---|---|---|---|---|---|---|
| | C | Ni | Cr | Ti | Mo | W | Mn | Si | Al | Be | Nb | Cu | V | Co | P | S |
| Durinal | 0.1 | 42 | | 2.1 | | | 2 | | 2 | | | | | | | |
| Elinvar Extra | 0.04 | 43 | 5 | 2.75 | | | 0.6 | 0.5 | 0.3 | | | | | 0.35 | | |
| | 0.6 | 42 | 5.5 | 2.5 | | | 0.5 | 0.5 | 0.6 | | | | | | | |
| Elinvar New | 1 | 35 | 5 | | | 2 | 1 | | | | | | | | | |
| Elinvar Original | | 36 | 12 | | | | | | | | | | | | | |
| | 0.5–2 | 33–35 | 21–5 | | | 1–3 | 0.5–2 | 0.5–2 | | | | | | | | |
| | 0.71 | 33.5 | 8.4 | | | 2.98 | 2.4 | 0.33 | | | | | | | 0.018 | 0.01 |
| Iso-elastic | | 36 | 8 | | 0.5 | (other small constituents) | | | | | | | | | | |
| | 0.1 | 36 | 7.5 | | 0.5 | | 0.6 | 0.5 | | | | 0.2 | | | | |
| Isoval | 0.6 | 30 | | | 2.2 | 3.2 | 0.15 | 0.2 | | | 3.8 | | 4.2 | | | |
| Métélinvar | 0.6 | 40 | 6 | | 1.5 | 3 | 2 | | | | | | | | | |
| Ni-Span C | 0.03 | 42.2 | 5.3 | 2.5 | | | 0.4 | 0.4 | 0.4 | | | 0.05 | | | <0.04 | <0.04 |
| Ni-Span C 902 | <0.06 | 42 | 5.2 | 2.3 | | | <0.8 | <0.1 | 0.5 | | | | | | | |
| Nivarox CT | 0.02 | 37 | 8 | 1 | | | 0.8 | 0.2 | | 0.8 | | | | | | |
| Nivarox CTC | 0.2 | 38 | 8 | 1 | | | | | | 1 | | | | | | |
| Nivarox M | 0.03 | 31 | | | 6 | | 0.7 | 0.1 | | 0.7 | | | | | | |
| Nivarox M30 | | 30 | | | 9 | | | | | 1 | | | | | | |
| Nivarox M40 | | 40 | | | 9 | | | | | 1 | | | | | | |
| Nivarox W | | 36 | | 1 | | | | | | 1 | | | | | | |
| Sumi-Span 1 | | 36 | 9 | | | | | | | | | | | | | |
| Sumi-Span 2 | 0.4 | 38 | 11 | | | | | | | | | | | | | |
| Sumi-Span 3 | | 42.5 | 5.5 | 2.4 | | | | | | | | | | | | |
| Thermelast 4009 | | 40 | | | 9 | | | | | 0.5 | | | | | | |
| Thermelast 5409 | | 40 | | | 9 | | | | | 0.5 | | | | | | |
| Vibralloy | | 39 | | | 9 | | | | | | | | | | | |
| | | 40 | | | 10 | | | | | | | | | | | |
| YNiC | 0.03 | 41–43 | 5.1–5.5 | 2.2–3 | | | | | 0.5–0.6 | | | | | | | |

**Table 4.3-29** Fe–Ni-based commercial elinvar-type alloys and the corresponding values of: density $d$, melting point $T_m$, Curie temperature $T_c$, electrical resistivity $\rho$, thermal expansion coefficient $\alpha$, Young's modulus $E$, its temperature coefficient $e$, and shear modulus $G$ [3.17]

| | $d$ ($g\,cm^{-3}$) | $T_m$ (°C) | $T_c$ (°C) | $\rho$ ($\mu\Omega$ cm) | $\alpha$ ($10^{-6}\,K^{-1}$) | $E$ ($10^{10}$ Pa) | $e$ ($10^{-5}\,K^{-1}$) | $G$ ($10^{10}$ Pa) |
|---|---|---|---|---|---|---|---|---|
| Durinal | | | 90 | | | | −1.0–1.0 | |
| Elinvar | | 1420–1450 | −100 | | 8 | 7.8–8.3 | −0.3–0.3 | |
| Elinvar Extra [a] | 8.15 | | | | 6.5 | 18.9 | 0 | 6.9 |
| Iso-elastic | | | | 88 | 6.7 | 18.0 | −3.3–2.5 | 6.4 |
| Métélinvar | | | 260, 295 | | | | 0 | |
| Ni-Span C | 8.15 | 1450–1480 | | 80 | 7.1 | 18.9 | −1.7–1.7 | |
| Ni-Span C 902 [a] | 8.14 | 1460–1480 | 160–190 | 100–120 | 8.1 | 17.7–19.6 | | 6.9–7.4 |
| Nivarox CT | 8.3 | | 80 | 97 | 7.5 | 18.6 | −2.5–2.5 | |
| Sumi-Span 1 | 8.15 | | −140 | 100 | −10 | 18.1 | 0–2.5 | |
| Sumi-Span 2 | 8.08 | | −190 | 105 | −10 | 18.1 | −1.5–0 [b] | |
| Sumi-Span 3 [a] | 8.05 | | −190 | 110 | ≈8 | 19.2 | −1.0–1.0 | 7.8 |
| Thermelast 4002 [a] | 8.3 | | | 100 | 8.5 | 18.6 | | 6.4 |
| Thermelast 4005 [a] | 8.3 | | | 100 | 8.3 | 17.2 | | 6.4 |
| Thermelast 5405 [a] | 8.3 | | | 100 | 8.0 | 18.6 | | 6.4 |
| Thermelast 5429 [a] | 8.3 | | | 100 | 8.0 | 18.6 | | 6.4 |
| Vibralloy [a] | 8.3 | | 300 | | 8 | 17.4 | 0 | |
| YNiC | 8.15 | | 90–180 | | 8.1 | 19.6 | −1.8–1.5 | 6.5–6.8 |

[a] Properties in the fully aged state

[b] Temperature coefficient of the frenquency of proper vibration

**Table 4.3-30** Co–Fe-based elinvar-type alloys (annealed state). Composition, thermal expansion coefficient $\alpha$, Young's modulus $E$ and shear modulus $G$, and their respective temperature coefficients, $e$ and $g$ [3.17]

| | Composition in wt% | | | | | | | | $\alpha$ [a] ($10^{-6}\,K^{-1}$) | $E$ [b] ($10^{10}$ Pa) | $e$ [c] ($10^{-5}\,K^{-1}$) | $G$ [b] ($10^{10}$ Pa) | $g$ [c] ($10^{-5}\,K^{-1}$) |
|---|---|---|---|---|---|---|---|---|---|---|---|---|---|
| | Co | Fe | Cr | V | Mo | W | Mn | Ni | | | | | |
| Co-elinvar | 60.0 | 30.0 | 10.0 | | | | | | 5.1 | 17.07 | | 6.91 | −0.2 |
| | 51.5 | 38.5 | 10.0 | | | | | | 8.7 | 18.84 | −1.0 | 7.55 | |
| | 47.3 | 34.5 | 9.1 | | | | | 9.1 | 7.8 | | | 6.61 | 0.2 |
| | 27.7 | 39.2 | 10.0 | | | | | 23.1 | 8.1 | | | 6.48 | −0.3 |
| | 26.7 | 50.8 | 5.8 | | | | | 16.7 | 7.8 | | | 4.99 | 0.3 |
| | 17.9 | 42.8 | 10.7 | | | | | 28.6 | 8.3 | | | 6.74 | 0.9 |
| Elcolloy | 40.0 | 35.0 | 5.0 | | | 5.0 | | 15.0 | 5.0 | | | | −0.2 |
| | 35.0 | 36.0 | 5.0 | | 4.0 | 4.0 | | 16.0 | 9.0 | | | | 0.5 |
| Mangelinvar | 38.0 | 37.0 | | | | | 15.0 | 10.0 | 9.7 | 18.0 | −1.0 | | |
| Moelinvar | 50.0 | 32.5 | | | 17.5 | | | | 9.6 | | | 7.36 | −0.2 |
| | 45.0 | 35.0 | | | 10.0 | | | 10.0 | 8.5 | | | 6.15 | 0.7 |
| | 20.0 | 40.0 | | | 20.0 | | | 20.0 | 8.4 | | | 7.70 | 0.9 |
| | 10.0 | 45.0 | | | 15.0 | | | 30.0 | 9.8 | | | 7.85 | −0.4 |
| Tungelinvar | 50.0 | 28.5 | | | | 21.5 | | | 7.4 | | | 6.45 | −0.7 |
| | 39.0 | 32.0 | | | | 19.0 | | 10.0 | 7.8 | | | 8.13 | 0.4 |

**Table 4.3-30** Co–Fe-based elinvar-type alloys (annealed state). Composition, thermal expansion coefficient $\alpha$, cont.

| | Composition in wt% | | | | | | | | $\alpha$ [a] | $E$ [b] | $e$ [c] | $G$ [b] | $g$ [c] |
|---|---|---|---|---|---|---|---|---|---|---|---|---|---|
| | Co | Fe | Cr | V | Mo | W | Mn | Ni | ($10^{-6}$ K$^{-1}$) | ($10^{10}$ Pa) | ($10^{-5}$ K$^{-1}$) | ($10^{10}$ Pa) | ($10^{-5}$ K$^{-1}$) |
| Velinvar | 60.0 | 30.0 | | 10.0 | | | | | 8.1 | | | 6.53 | 0.0 |
| | 50.0 | 31.8 | | 8.2 | | | | 9.1 | 11.0 | | | 6.70 | 1.0 |
| | 37.5 | 35.5 | | 7.0 | | | | 20.0 | 11.1 | | | 6.45 | −0.6 |
| | 22.5 | 43.5 | | 4.0 | | | | 30.0 | 12.3 | | | 5.66 | −0.3 |

[a] For the temperature range 10–50 °C
[b] At 20 °C
[c] For the temperature range 0–50 °C

temperature of Mn–Ni- and Mn–Cu-based alloys were modified by additions of Cr, Fe, Ni, Mo, and W as well as by suitable technological treatment in such a way that useful thermoelastic coefficients could be reached. However, the mechanical workability, the sensitivity of elastic properties to the degree of cold-working, the unsufficient spring properties as well the low corrosion resistance and high mechanical damping could not satisfy the conditions of technical application. Figures 4.3-49 and 4.3-50 [3.17] indicate the temperature dependence of $E$ of some Mn–Ni- and Mn–Cu-based alloys. Table 4.3-31 [3.17] lists the compositions and the thermoelastic and mechanical properties of this group of alloys.

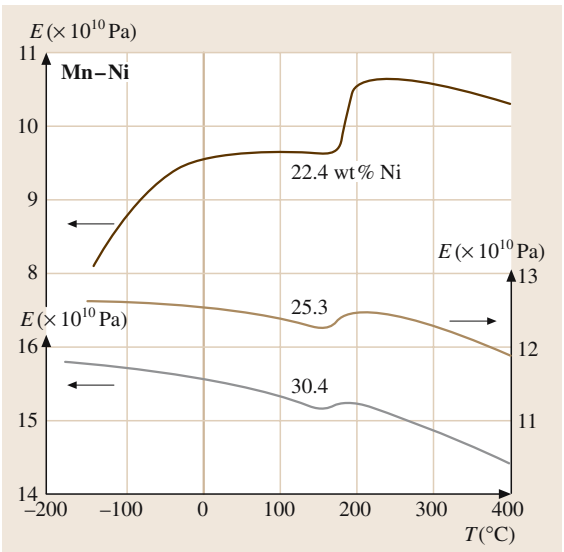


**Fig. 4.3-49** Mn–Ni binary alloys. Young's modulus $E$ vs. temperature for alloys annealed at 1223 K for 1 h after cold-working [3.17]

By optimization of the chemical composition and the processing technology, an Fe–24Mn–8Cr–7Ni–0.8Be

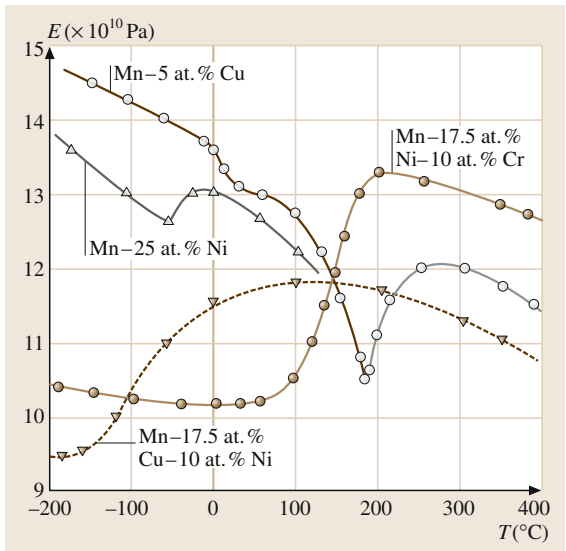


**Fig. 4.3-50** Temperature dependence of Young's modulus $E$ [3.17] for various Mn-based alloys annealed at 1223 K for 1 h and then quenched

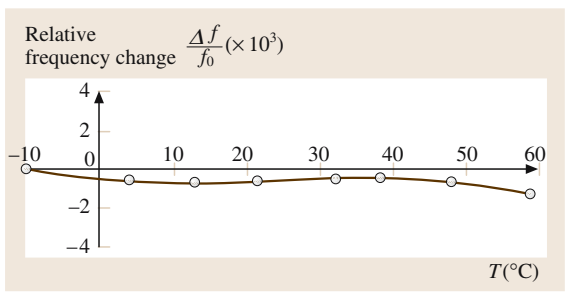


**Fig. 4.3-51** Temperature dependence of the frequency of a screw spring [3.53]

**Table 4.3-31** Nonferromagnetic Mn-based elinvar-type alloys. Composition, thermal expansion coefficient $\alpha$, Young's modulus $E$ and shear modulus $G$, and their respective temperature coefficients, $e$ and $g$ and hardness HV [3.17]

| Composition in wt% | | | | | | | | | $\alpha$ [a] | $E$ | $e$ [a] | $G$ | $g$ [a] | HV |
|---|---|---|---|---|---|---|---|---|---|---|---|---|---|---|
| Mn | Cu | Ni | Cr | Fe | Co | Mo | W | Ge | ($10^{-6}$ K$^{-1}$) | ($10^{10}$ Pa) | ($10^{-5}$ K$^{-1}$) | ($10^{10}$ Pa) | ($10^{-5}$ K$^{-1}$) | |
| 87 | | 10 | | 3 | | | | | 23.7 | 12.3 | 1.25 | 5.18 | 1.05 | 121 |
| 82 | | 15 | | | | | 3 | | 23.0 | 12.1 | 0.55 | 5.07 | 0.78 | 149 |
| 80 | | 16 | | | 4 | | | | 21.1 | 12.2 | −0.13 | 4.63 | −0.75 | 150 |
| 80 | | 9 | | | | 11 | | | 20.3 | 11.9 | 0.05 | 5.00 | 1.10 | 380 |
| 80 | | | | | | | | 20 | 12.3 | 9.0 | 1.5 | | | 255 |
| 79 | | 21 | | | | | | | | 9.8 | −2.5 | 3.60 | −2.7 | 235 |
| 67 | 20 | 13 | | | | | | | 22.4 | 14.4 | 0.21 | 4.55 | 0.29 | 125 |
| 59 | | 16 | 25 | | | | | | 21.6 | 16.2 | 0.85 | 5.21 | 0.83 | 250 |
| 49 | 41 | | | 10 | | | | | 22.4 | 13.5 | −0.97 | 5.53 | −0.20 | 250 |
| 44 | 55 | | 1 | | | | | | 22.1 | 13.2 | 0.11 | 5.03 | 0.08 | 145 |
| 43 | 57 | | | | | | | | 23.6 | 11.2 | 0.3 | 4.2 | −0.9 | 131 |
| 43 | 55 | | | | 2 | | | | 22.9 | 8.50 | −1.11 | 4.02 | −2.57 | 135 |
| 42 | 55 | | | | | 3 | | | 23.0 | 15.2 | 2.30 | 6.77 | 1.88 | 149 |
| 39 | 56 | | | | | | 5 | | 23.2 | 12.0 | −0.25 | 5.05 | −0.56 | 140 |

[a] For the temperature range 0–40 °C
[b] At 20 °C

**Table 4.3-32** Properties of an antiferromagnetic Fe−24Mn−8Cr−7Ni−0.8Be elinvar alloy [3.53]

| Property | Value |
|---|---|
| Young's modulus $E$ | 165–195 GPa |
| Thermoelastic coefficient TKE | (1–10) MK$^{-1}$ |
| Compensation range of $E$ | 0–50 °C |
| Shear modulus $G$ | 74–82 GPa |
| Coefficient of thermal expansion $\alpha$ (20–100 °C) | 13 MK$^{-1}$ |
| Tensile strength $\sigma_B$ | 1200–1800 MPa |
| Yield point $\sigma_s$ | 1100–1650 MPa |
| Elongation $\delta$ | 12–2 % |
| Vicker's Hardness HV 10 | 420–540 HV |
| Quality factor $Q$ | 20 000–10 000 |
| Specific electrical resistance $\rho$ | 80 μΩ cm |
| Density $\gamma$ | 7.6 g cm$^{-3}$ |
| Electrochemical breahdown potential $\epsilon_D$ | −0.25 V |
| Melting temperature $T_s$ | 1450–1480 °C |

antiferromagnetic elinvar alloy was developed which fulfills the complex requirements for an antiferromagnetic, corrosion resistant, temperature compensating thermoelastic spring material for applications near room temperature, Fig. 4.3-51 [3.53]. The thermoelastic, mechanical and physical properties are summarized in Table 4.3-32 [3.53].

*Other Nonmagnetic Elinvar-Type Alloys.* In general, the elastic constants decrease with increasing tem-

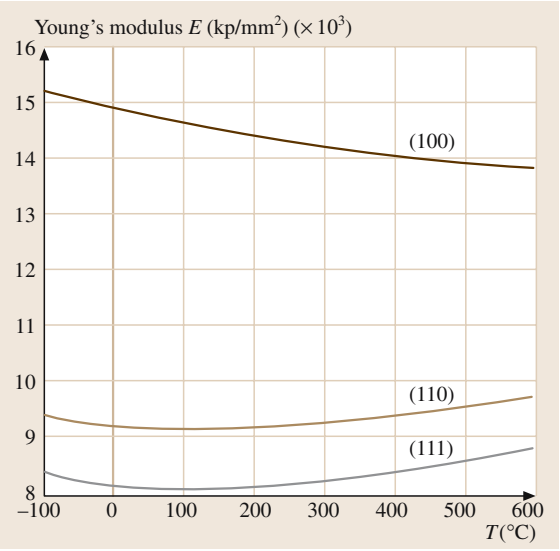


**Fig. 4.3-52** Thermoelastic behavior of single crystalline Nb in the major lattice directions [3.54]

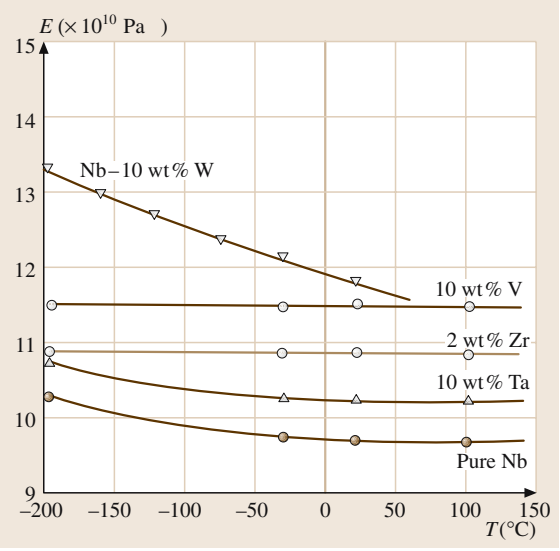


**Fig. 4.3-53** Young's modulus $E$ vs. temperature. Samples annealed at 1400 °C for 4 h [3.41] of pure Nb and Nb-based binary alloys

perature. The temperature dependence of the elastic properties of Nb shows highly anisotropic anomalies (see Fig. 4.3-52) [3.54]. In a randomly oriented polycrystal, Nb becomes an elinvar-type material, Fig. 4.3-53 [3.41]. This plot of Young's modulus vs. temperature also shows the influence of alloying elements.

Elinvar behavior is, also, found in concentrated Nb–Zr and Nb–Ti alloys. Furthermore, some amorphous alloys, e.g., in the Fe–B-, Fe–P-, and Fe–Si–B-based systems, show elinvar behavior. Examples for amorphous Fe–B alloys are shown in Fig. 4.3-54.

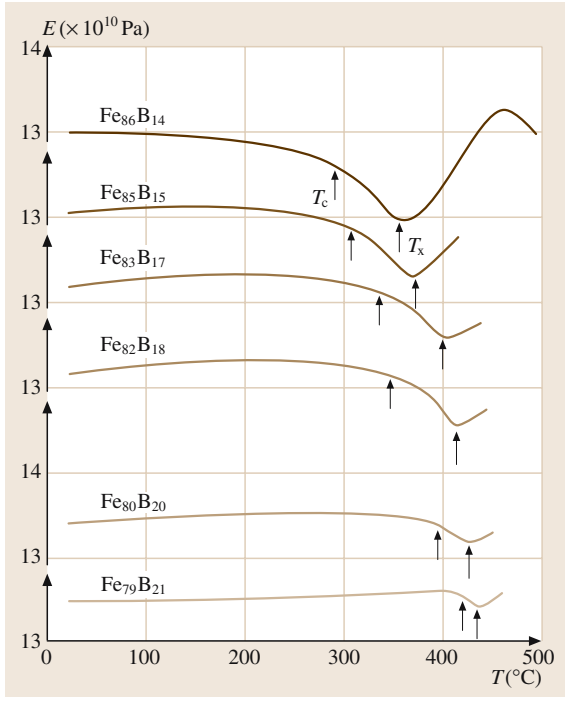


**Fig. 4.3-54** Fe–B alloys. Temperature dependence of Young's modulus $E$ for amorphous alloys annealed at 200 °C for 2 h. $T_x$ and $T_c$ show the crystallization and the Curie temperature, respectively [3.41]

## 4.3.3 Hard Magnetic Alloys

Permanent or hard magnetic materials comprise traditionally some special steels but consist essentially of multiphase alloys and intermetallic and ceramic compounds today. Relatively few magnetic alloys and compounds fulfill the requirement of combining high magnetic efficiency and competitive cost: Fe−Ni−Al−Co (Alnico), Fe−Cr−Co, Mn−Al−C, hard ferrites, and rare-earth transition metal compounds of the Co−Sm, Fe−Nd−B and Fe−Sm−N alloy systems. Surveys may be found in handbooks [3.1, 3, 55] and data collections [3.10, 56]. A survey of permanent magnetic materials is given in Table 4.3-33. The metallic hard magnets are treated in this chapter, the oxidic hard magnetic materials are dealt with in Sect. 4.3.4.

All of the hard magnetic materials are based on choosing a base alloy with a sufficiently high saturation magnetization $M_s$ and a high magnetocrystalline anisotropy constant $K_1$, and tailoring the microstructure to exploit this crystal anisotropy. In some cases, shape anisotropy is generated in addition. This microstructural control is achieved by

1. Inducing a texture by processing in such a way that a macroscopic direction in the material, e.g., the rolling direction of a sheet or the pressing direction in a sintered material, is an easy direction, and processing at 90°, i. e., the transverse direction, is a hard direction for magnetization. This is the basic magnetic hardening mechanism of hard magnetic steels which have lost their importance in present technology; but it is the basis of producing the more recent high energy magnets made from intermetallic compounds such as $Co_5Sm$ and ferrites.
2. Inducing a two-phase microstructure by coherent precipitation or decomposition and promoting, by suitable magnetic field annealing procedures, the alignment of the elongated precipitates in one direction of easy magnetization, i. e., inducing both

**Table 4.3-33** Survey commercially used permanent magnetic materials. Survey

| Material | Fe, Co content (wt%) | $B_r$[a] (T) | $_JH_c$ (kA m$^{-1}$) | $(BH)_{max}$ (kJ m$^{-3}$) | appr. $T_c$ (°C) | $T_{max}$[b] (°C) | Process[c] |
|---|---|---|---|---|---|---|---|
| Dense magnets | | | | | | | |
| 3.5Cr steel | 94–95 | 0.95 | 5 | 2.3 | 745 | | C[d] |
| 6W steel | 92–93 | 0.95 | 6 | 2.6 | 760 | | C |
| 36Co steel | 90–91 | 0.95 | 19 | 7.4 | 890 | | C |
| Alnico | 67–74 | 0.52–1.4 | 40–135 | 13–69 | 810–900 | 450–550 | C, P[d] |
| Fe−Cr−Co | 65–73 | 1.1–1.4 | 40–65 | 25–55 | 670 | 500 | C |
| hard ferrite | 58–63 | 0.37–0.45 | 160–400 | 26–40 | 460 | 250 | P |
| Pt-Co | 23.3 | 0.64 | 430 | 73 | 480 | 350 | C, P |
| MnAlC | – | 0.55 | 250 | 44 | 500 | 300 | P |
| $Co_5Sm$ | 63–65 | 0.85–1 | >1600 | 140–200 | 730 | 250 | P |
| $TM_{17}Sm_2$ | 61–68 | 0.95–1.15 | 480–2000 | 190–220 | 810 | 330–550 | P |
| Fe−Nd−B | 66–72 | 1.05–1.5 | 950–2700 | 240–400 | 320 | 60–180 | P |
| Bonded magnets | | | | | | | |
| hard ferrite | 58–63 | 0.1–0.31 | 180–300 | 2–18 | | 140 | P |
| $TM_{17}Sm_2$ | 61–68 | | | 70–120 | | 150 | P |
| $Fe_{14}Nd_2B$ | 70–72 | 0.47–0.69 | 600–1200 | 35–80 | | 80–110 | P |
| $Fe_{17}Sm_2N_3$ | | 0.77 | 650 | 105 | | 100 | P |

[a] $B_r$ values are for magnets operated at load lines $B/H \gg 1$

[b] The maximum operating temperature of bonded magnets is determined by the organic binder used

[c] Magnets are manufactured either by a casting/heat treatment technique or by a powder metallurgical process. Powder metallurgy is applied for small magnets where small and intricate shapes to precise tolerances are required

[d] C: magnets produced by cast and heat treatment; P: magnets produced by means of powder metallurgical techniques

magnetocrystalline and shape anisotropy. This is termed magnetic shape anisotropy and is employed in the Alnico and Fe−Co−Cr hard magnetic materials.

3. Inducing a fine grained microstructure with a magnetically insulating phase at the grain boundaries so that the grains are magnetically decoupled and, as a consequence, the nucleation of reverse magnetization is requiring an extremely high nucleation energy. This is applied, for example, to $TM_{17}Sm_2$, $Fe_{14}Nd_2B$ and bonded magnets.

In some of the hard magnetic materials two of these variants of microstructural design are combined.

### 4.3.3.1 Fe–Co–Cr

Hard magnetic materials made of ternary Fe−Co−Cr alloys are based on the high atomic moment of Fe−Co alloys and the miscibility gap occurring when Cr is added. Intrinsic magnetic properties are compiled in [3.6]. Extensive magnetic materials data are found in [3.56]. Figure 4.3-55 shows the relevant metastable phase relations in the ternary equilibrium diagram. If an alloy is homogenized in the solid solution range above the solvus surface with $T_{max} > 700\,°C$ first and annealed in the miscibility gap subsequently, coherent decomposition occurs, which results in a two-phase microstructure on the nanometer scale. The $\alpha_1$ phase is rich in Fe and Co and ferromagnetic while the $\alpha_2$ phase is rich in Cr and antiferromagnetic. This two-phase microstructure on the nm scale has hard magnetic properties which can be varied by adjusting the alloy composition and heat treatment. The term spinodal decomposition is frequently applied to all kinds of coherent decomposition, e.g., in [3.56]. But it is used correctly only if referring to a special mode of compositional evolution associated with particular kinetics in the initial stage of decomposition within the spinodal of a miscibility gap.

Three groups of materials have been developed, differing essentially in the Co content (< 5, 10–15, 23–25 wt% Co), while the Cr content ranges from 22 to 40 wt% Cr. Table 4.3-34 lists data obtained by varying composition, mode of manufacturing, and heat treatment systematically for the group characterized by < 5 wt% Co as an example. The variation of the magnetic properties is determined by the intrinsic properties of the decomposed phases $\alpha_1$ and $\alpha_2$ and their microstructural array.



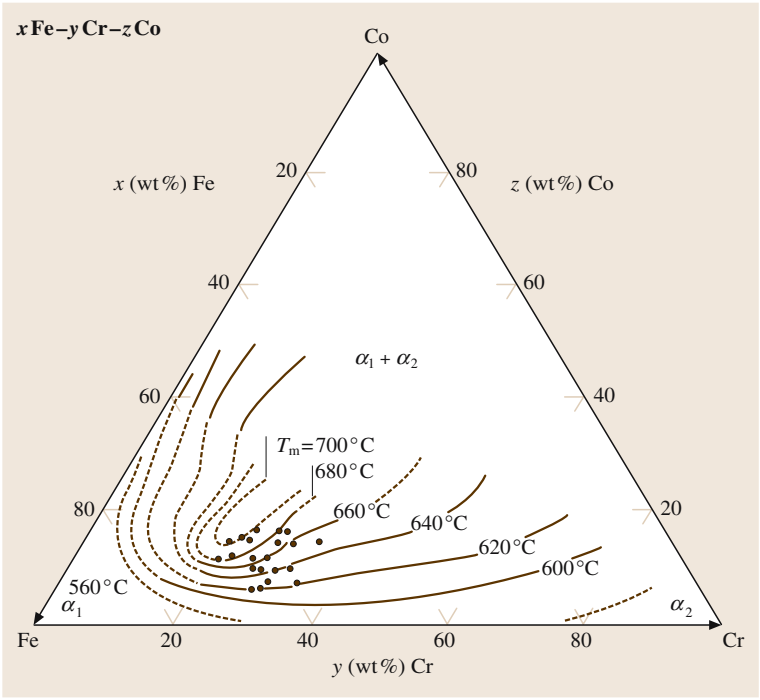


**Fig. 4.3-55** The miscibility gap ($\alpha_1 + \alpha_2$) of the bcc $\alpha$-phase in the Fe−Co−Cr phase diagram [3.56]

**Table 4.3-34** Survey of magnetic properties of Fe−Cr−Co (≤ 5 wt% Co) alloys in relation to the composition, mode of manufacturing and heat treatment [3.56]

| Alloy components (wt%) | | | Mode of manufacturing and heat treatment | Magnetic properties | | | | | |
|---|---|---|---|---|---|---|---|---|---|
| | | | | $B_r$ | | $_BH_c$ | | $(BH)_{max}$ | |
| Cr | Co | others | | (T) | (kG) | (kA m$^{-1}$) | (kOe) | kJ m$^{-3}$ | (MGOe) |
| 33 | 2 | 1 Hf | H(700, 15):MCL > $T_s$, R, 500):FCL | 1.25 | 12.5 | 16.2 | 0.203 | 14.0 | 1.76 |
| 32 | 3 | | As above | 1.29 | 12.9 | 35.9 | 0.449 | 32.4 | 4.08 |
| 32 | 4 | 0.5 Ti | As above | 1.26 | 12.6 | 42.7 | 0.534 | 40.1 | 5.06 |
| 28 | 5 | | As above | 1.38 | 13.8 | 29.0 | 0.362 | 27.9 | 3.52 |
| 30 | 5 | | As above | 1.34 | 13.4 | 42.2 | 0.528 | 42.1 | 5.31 |
| 33 | 5 | | As above | 1.22 | 12.2 | 40.8 | 0.51 | 36.3 | 4.58 |
| 35 | 5 | | As above | 1.15 | 11.5 | 37.0 | 0.462 | 29.3 | 3.69 |
| 30 | 5 | 0.1 B | As above | 1.31 | 13.1 | 42.0 | 0.525 | 40.2 | 5.07 |
| 30 | 5 | 0.25 B | As above | 1.29 | 12.9 | 39.8 | 0.498 | 34.8 | 4.39 |
| 30 | 5 | 0.1 C | As above | 1.31 | 13.1 | 42.2 | 0.527 | 38.8 | 4.89 |
| 30 | 5 | 0.8 Ge | As above | 1.32 | 13.2 | 24.8 | 0.31 | 39.1 | 4.93 |
| 30 | 5 | 0.25 Ti | As above | 1.34 | 13.4 | 27.2 | 0.34 | 40.2 | 5.07 |
| 30 | 5 | 0.5 Ti | As above | 1.30 | 13.0 | 41.4 | 0.518 | 40.1 | 5.06 |
| 30 | 5 | 1.5 Ti | As above | 1.27 | 12.7 | 40.8 | 0.51 | 38.1 | 4.81 |
| 30 | 5 | 0.25 Hf | As above | 1.32 | 13.2 | 43.0 | 0.537 | 41.2 | 5.2 |
| 30 | 5 | 0.5 Hf | As above | 1.29 | 12.9 | 43.9 | 0.549 | 41.4 | 5.22 |
| 30 | 5 | 1 Hf | As above | 1.30 | 13.0 | 43.0 | 0.537 | 40.4 | 5.1 |
| 30 | 5 | 3 Hf | As above | 1.24 | 12.4 | 41.5 | 0.519 | 34.8 | 4.39 |
| 23 | 2 | 1 Hf | MCL(> $T_s$, 550): CCL (550, 500) | 1.24 | 12.4 | 36.8 | 0.46 | 34.1 | 4.3 |
| 32 | 3 | | As above | 1.25 | 12.5 | 40.0 | 0.5 | 34.1 | 4.3 |
| 30 | 5 | | As above | 1.34 | 13.4 | 42.4 | 0.53 | 42.0 | 5.3 |
| 32 | 4 | 0.5 Ti | As above | 1.26 | 12.6 | 42.8 | 0.535 | 40.4 | 5.1 |
| 28 | 5 | 4 Ni | As above | 1.27 | 12.7 | 29.6 | 0.37 | 30.1 | 3.8 |
| 28 | 7 | | As above | 1.25 | 12.5 | 40.8 | 0.51 | 41.2 | 5.2 |
| 27 | 9 | | MCL: CCL (as above) | 1.30 | 13.0 | 46.4 | 0.58 | 49.2 | 6.2 |
| 33 | 5 | | CL(680, 40 K/h):HW(D:67%):H (600): CCL (15–4 K/h, 500)[a] | 1.15 | 11.5 | 24.8 | 0.31 | 19.0 | 2.4 |
| 33 | 7 | 2 Cu | As above | 1.19 | 11.9 | 38.8 | 0.485 | 26.2 | 3.3 |
| 33 | 7 | | As above | 1.18 | 11.8 | 42.0 | 0.525 | 33.3 | 4.2 |
| 33 | 9 | | As above | 1.24 | 12.4 | 46.4 | 0.58 | 32.5 | 4.1 |
| 28 | 7 | | CL(> $T_s$, 60 ($T_s$ = 645 °C)) | 0.97 | 9.7 | 26.4 | 0.33 | 11.1 | 1.4 |
| 31 | 5 | | (Sintered 1400 °C, 4 h; $H_2$)[b]:WQ: H (700, 30): FCL (700, 640):MCL (640, 0.9 K/h, 500) | 1.23 | 12.3 | 40.0 | 0.5 | 34.9 | 4.4 |

[a] For the deformation aging process the initially aged state corresponds to an overaged state

[b] Sintering ST

Commercial materials are characterized by the fact that they can be quenched from temperatures above the miscibility gap first, which results in mechanical properties amenable to forming by conventional processes such as rolling, stamping, drilling. The final annealing treatment in the miscibility gap results in the magnetically hard state. This is associated with a drastic decrease in ductility. If the annealing treatment is carried out in a magnetic field, the final product has an anisotropic behavior. Table 4.3-35 shows the property range of commercial Fe−Cr−Co materials.

### 4.3.3.2 Fe−Co−V

Magnetic materials based on the Fe−Co−V alloy system were the first ductile magnets. The intrinsic magnetic properties may be found in [3.6] while extensive magnetic materials data are treated in [3.56]. The optimum magnetic behavior is obtained for alloy compositions around Fe–55 wt% Co–10 wt% V. As the isothermal sections of the Fe−Co−V phase diagram Fig. 4.3-56a and Fig. 4.3-56b show, this alloy is mainly in the fcc $\gamma$-phase (austenite) state at 900 °C,

**Table 4.3-35** Commercial Fe−Cr−Co magnetic materials

| Composition nominal wt% | Variant | Remanence (T) | Coercivity (kA m$^{-1}$) | Energy density (kJ m$^{-3}$) | Curie temperature (°C) | Maximum application temperature (°C) | Hardness HV | Commercial designation[a] |
|---|---|---|---|---|---|---|---|---|
| Fe−27Cr−11Co−Mo | isotropic | 0.85–0.95 | 36–42 | 13 | 640 | 480 | 480 | 12/160 |
| Fe−28Cr−16Co−Mo | isotropic | 0.80–0.90 | 39–45 | 15 | 640 | 480 | 480 | 16/160 |
| Fe−27Cr−11Co−Mo | anisotropic | 1.15–1.25 | 47–55 | 35 | 640 | 480 | 480 | 12/500 |
| Fe−28Cr−16Co−Mo | anisotropic | 1.10–1.20 | 53–61 | 37 | 640 | 480 | 480 | 16/550 |

[a] Designation of CROVAC® by Vacuumschmelze, Hanau, Germany

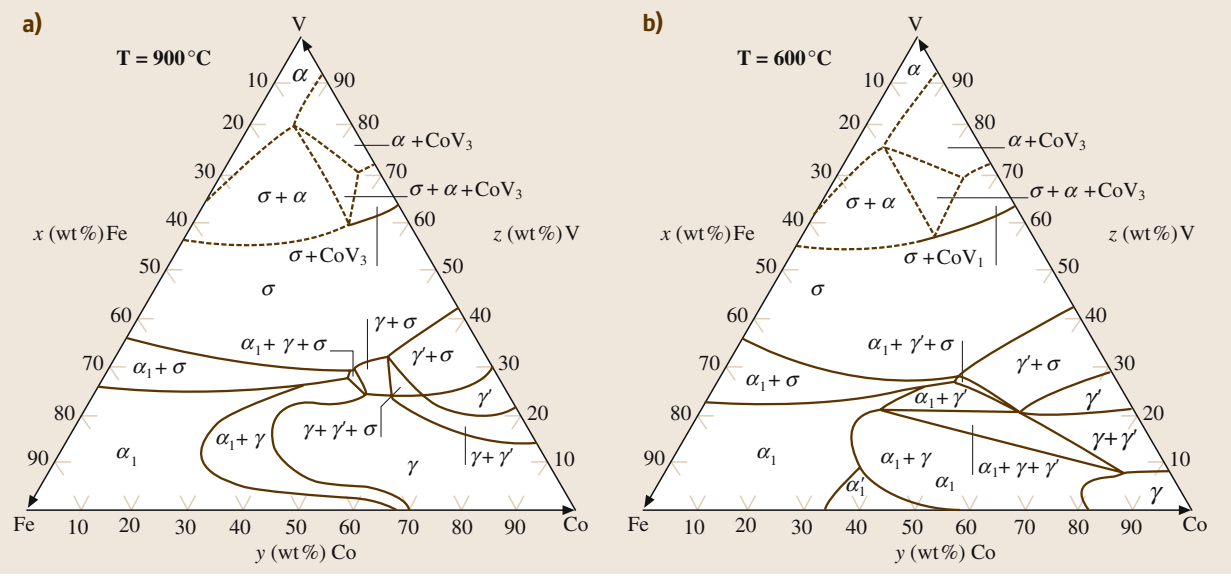


**Fig. 4.3-56a,b** Isothermal sections of the Fe−Co−V phase diagram at 900 °C (**a**) and 600 °C (**b**). $\alpha$: bcc disordered; $\alpha_1$: bcc ordered (CsCl type); $\gamma$: fcc disordered (austenite); $\gamma'$: fcc ordered ($Au_3Cu$ type) [3.56]

**Table 4.3-36** Commercial Fe−Co−V-based magnetic materials

| Composition nominal (wt%) | Remanence (T) | Coercivity (kA m$^{-1}$) | Energy density (kJ m$^{-3}$) | Curie temperature (°C) | Maximum application temperature (°C) | Hardness (HV) As rolled | Hardness (HV) Heat treated | Alloy code[a] |
|---|---|---|---|---|---|---|---|---|
| 34Fe−52Co−13V | 0.80–0.90 | 25–30 | 12 | 700 | 500 | 480 | 900 | 35U |
| 34Fe−53Co−8.5V−3.5Cr | 1.00–1.10 | 30–35 | 20 | 700 | 500 | 520 | 950 | 93 |

[a] Designation of MAGNETOFLEX® by Vacuumschmelze, Hanau, Germany

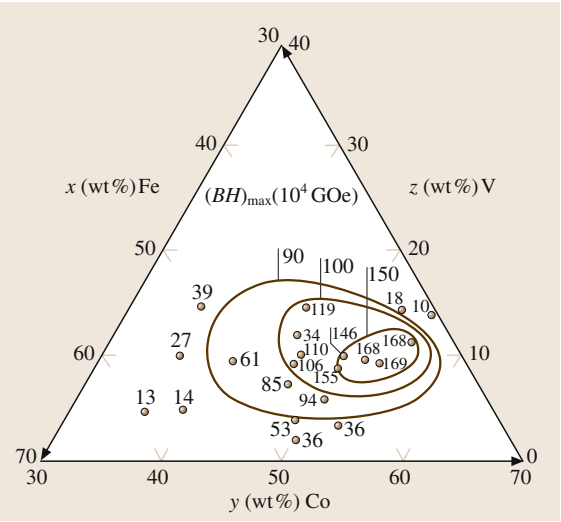


**Fig. 4.3-57** Contour map of $(BH)_{max}$ of Fe−Co−V alloys in the optimum annealed state. It is obtained by annealing in the temperature range $T_a = 555–750\,°C$ in the magnetically preferred direction of the anisotropic sample [3.56]

while it decomposes into the bcc ordered $\alpha_1 + \gamma$ state upon annealing at lower temperature such as 600 °C. In combinations of heat treatment with plastic deformation (also serving to form the product, e.g., wire) an optimum anisotropic hard magnetic state can be realized.

If quenched from the $\gamma$-phase state, the alloy can be deformed. By a judicious choice of annealing temperatures in the range of 555 to 750 °C the maximum energy product as a function of alloy composition, as shown in Fig. 4.3-57, may be obtained. This annealing treatment is associated with a drastic increase in hardness, as indicated in Table 4.3-36, and a concomitant loss in ductility.

Based on these interrelations of phase equilibria and thermomechanical treatments as well as by optimization through further alloying additions, commercial magnetic materials such as those listed with their properties in Table 4.3-36 have been developed.

### 4.3.3.3 Fe–Ni–Al–Co, Alnico

The term Alnico refers to two-phase hard magnetic materials based on the Fe−Ni−Al system (Fig. 4.3-58). The intrinsic magnetic properties may be found in [3.6], while extensive magnetic materials data are treated in [3.56]. Table 4.3-37 lists some of the magnetic properties of Alnico type magnets. The magnetically optimized microstructure consists essentially of elongated ferromagnetic Fe-rich precipitates ($\alpha_1$-phase, bcc disordered) in a non-magnetic matrix of NiAl ($\alpha_2$-phase, bcc ordered, CsCl type). The remanence $B_r$ is increased significantly by adding Co, which leads to the formation of precipitates rich in Fe−Co. The coercivity $H_c$ is optimized by adding Ti and Cu. The two-phase state is obtained by a homogenization at about 1300 °C, followed by annealing treatments which lead to decomposition into structurally coherent phases on the nanometer scale. The particles are aligned preferentially along the ⟨100⟩ directions of the bcc lattice. This decomposition microstructure is the essential microstructural feature. Higher remanence and coercivity prevails in chill-cast magnets with a columnar microstructure and ⟨100⟩ fiber texture, providing additional magnetocrystalline anisotropy. More extensive treatments and data may be found in [3.10, 56, 57].

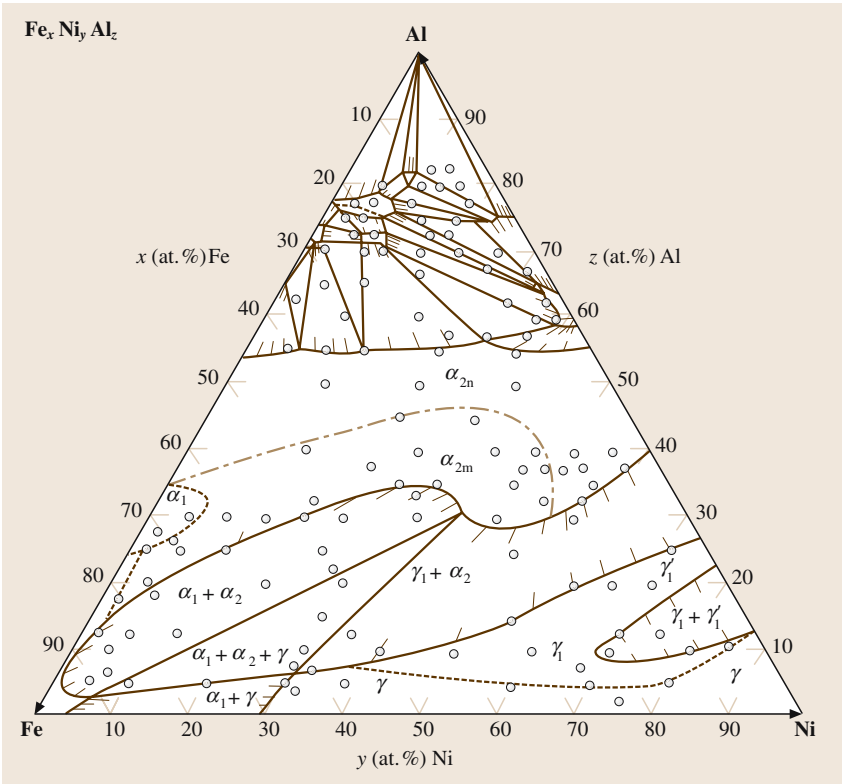


**Fig. 4.3-58** Effective $Fe_xNi_yAl_z$ phase diagram after cooling from the melt at 10 K/h. *Broken lines* indicate superlattice phase boundaries; the *point-dash line* the magnetic phase boundary in the Ni(Al,Fe) phase field. $\alpha_1$: bcc; $\alpha_1'$: $Fe_3Al$-type superlattice phase; $\alpha_2$: (Fe,Ni)Al-type superlattice phase; $\gamma$: fcc; $\gamma_1$: $Ni_3Al$-type superlattice phase; $\gamma_1'$ : as $\gamma_1$ but with the larger lattice spacing. The indices m and n indicate magnetic and non-magnetic phases, respectively

**Table 4.3-37** Magnetic properties of Alnico type magnets

| Designation according to DIN 17410 [a] | Remanence $B_r$ (mT) | (G) | Coercivity $_BH_c$ (kA m$^{-1}$) | (Oe) | $_JH_c$ (kA m$^{-1}$) | (Oe) | Energy density $(BH)_{max}$ (kJ m$^{-3}$) | (MGOe) | Alloy code [b] |
|---|---|---|---|---|---|---|---|---|---|
| AlNiCo 9/5i | 550 | 5500 | 54 | 679 | 57 | 716 | 10.3 | 1.3 | 130 |
| AlNiCo 12/6i | 650 | 6500 | 57 | 716 | 60 | 754 | 13.5 | 1.7 | 160 |
| AlNiCo 19/11i | 640 | 6400 | 105 | 1319 | 115 | 1433 | 22.3 | 2.8 | 260 |
| AlNiCo 15/6a | 750 | 7500 | 60 | 54 | 62 | 57 | 16.7 | 2.1 | 190 |
| AlNiCo 28/6a | 1100 | 11 000 | 64 | 804 | 65 | 817 | 31.8 | 4.0 | 400 |
| AlNiCo 39/12a | 880 | 8800 | 115 | 1445 | 119 | 1495 | 43.8 | 5.5 | 450 |
| AlNiCo 37/5a | 1240 | 12 400 | 51 | 641 | 51 | 641 | 41.4 | 5.2 | 500 |
| AlNiCo 39/15a | 740 | 7400 | 150 | 1855 | 160 | 2011 | 43.8 | 5.5 | 1800 |

[a] i = isotropic; a = anisotropic

[b] Commercial designations of Koerzit® by WIDIA Magnettechnik

**Table 4.3-38** Intrinsic properties of $Fe_{14}RE_2B$ at $T = 300\,K$

| RE | $K_1$ ($10^7$ erg cm$^{-3}$) | $4\pi M_s$ (T) | $H_a = 2K_1/M_s$ (MA m$^{-1}$) | $T_c$ (K) |
|---|---|---|---|---|
| Ce | 1.7 | 1.28 (4) | 3.0 | 430 (6) |
| Pr | 4.5 | 1.59 (8) | 6.3 | 563 (3) |
| Nd | 4.8 (3) | 1.68 (9) | 5.7 | 590 (5) |
| Sm | plane | 1.55 (10) | | 618 |
| Gd | 1.0 | 0.94 (2) | 2.3 | 665 (4) |
| Tb | | 0.72 (5) | 11.1 [a] | 639 |
| Dy | 4.1 | 0.75 (5) | 12.6 | 597 (5) |
| Ho | | 0.84 (12) | 5.7 [a] | 576 |
| Er | plane | 1.02 (12) | | 556 (3) |
| TM | | 1.25 (2) | | 543 (2) |
| Lu | | – | 2.1 [a] | 538 |
| La | | – | | 543 |
| Y | 1.1(1) | 1.40(5) | 2.2 | 566 (2) |

[a] Data taken from [3.58]. $H_a$ value obtained directly by extrapolation of the magnetization curves for the easy and the hard direction. The average value is given where more than one reference is available; the number in parentheses indicates the standard deviation in the last figure

### 4.3.3.4 Fe–Nd–B

The most powerful permanent magnets presently available consist essentially of the tetragonal $Fe_{14}Nd_2B$ phase. The intrinsic magnetic properties may be found in [3.6] while extensive magnetic materials treatments and data may be found in [3.1, 10, 56]. Two different production routes are used to prepare dense anisotropic magnets: conventional powder metallurgy and a rapid quenching process to produce flake-shaped powder particles with a nanocrystalline microstructure as a starting material. The flakes are then processed further into dense isotropic or anisotropic magnets by means of a combination of cold pre-forming, hot pressing, and hot deformation steps.

The $Fe_{14}RE_2B$ phase is formed with all rare earth (RE) elements with the exception of Eu. Their intrinsic properties have been investigated extensively. They are listed in Table 4.3-38. Neodymium shows the highest permanent magnet potential based on its combination of high values of $K_1$ and $M_s$.

#### Conventional Powder Metallurgical Processing

Figure 4.3-59 shows the approximate phase relations of Fe–Nd–B at room temperature. According to the phase diagram of the Fe–Nd–B system the $Fe_{14}Nd_2B$ phase forms at 1180 °C. In powder metallurgical processing of the magnets, sintering at 1050 °C leads to the formation of $Fe_{14}Nd_2B$ in equilibrium with a Nd-rich liquid and with the $Fe_4NdB_4$ boride phase. The liquid phase solidifies below the ternary eutectic at 630 °C. The resulting non-magnetic Nd-rich solid phase spreads along

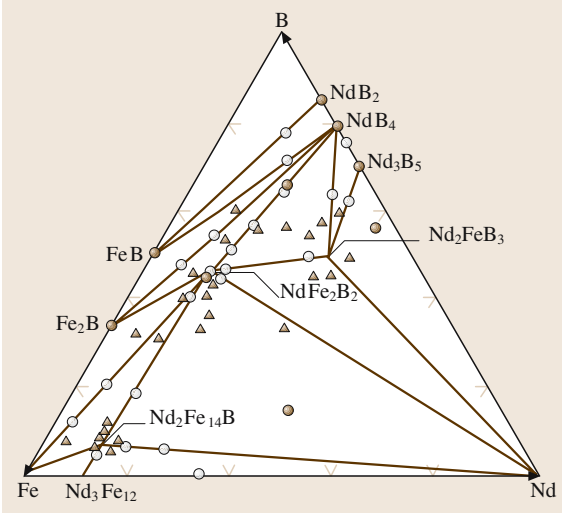


**Fig. 4.3-59** Approximate phase relations of Fe–Nd–B at room temperature

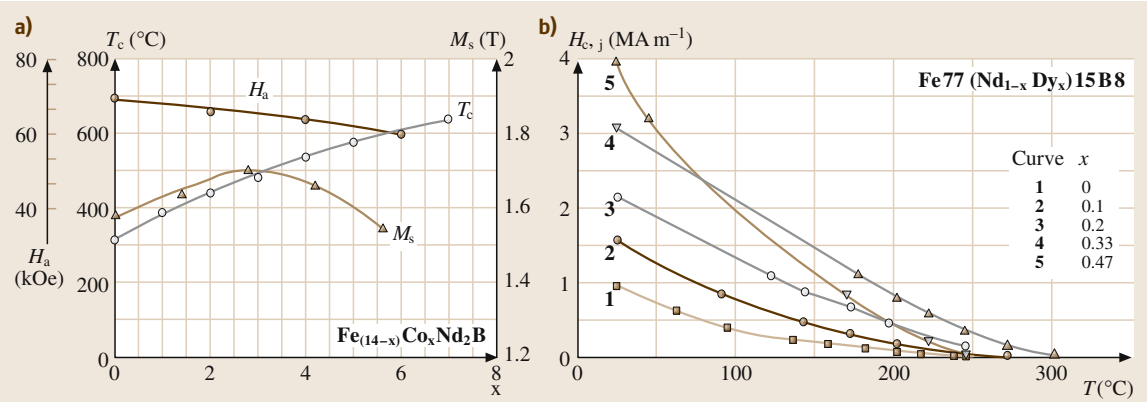


**Fig. 4.3-60a,b** Influence of substitutional elements on $Fe_{14}Nd_2B$ type magnets. **(a)** Influence of the Co content on the intrinsic properties at room temperature. Data for the magnetization $M_s$, for the anisotropy field $H_a$, and for the Curie temperature $T_c$. **(b)** Influence of the Dy content on the temperature dependence of the coercivity $_JH_c$ of sintered magnets. There is an approximately linear increase of $_JH_c$ at room temperature. The temperature dependence increases with increasing Dy content

the grain boundaries and provides the magnetic decoupling of the $Fe_{14}Nd_2B$ grains, thus providing the basic coercivity of the sintered magnet.

Additions of Dy and Al are increasing the coercivity. Dysprosium enters the RE sites in the $Fe_{14}Nd_2B$ structure, increasing the magnetocrystalline anisotropy but decreasing the magnetic remanence $B_r$. At compositions of $> 2$ at.% Al, the anisotropy field $H_a$ decreases linearly at a rate of 0.13 MA m$^{-1}$ per at.% Al. Nevertheless the coercivity increases significantly due to an optimization of the microstructure: Al is enriched in the Nd grain boundary phase which is spreading more uniformly around the magnetic grains, thus leading to better decoupling of exchange interactions. This is a basic condition for the increase in coercivity.

As indicated by Fig. 4.3-60a, Co addition leads to a strong increase of the Curie temperature. However, the anisotropy field $H_a$ is reduced by Co, and the decrease of the coercive field is even larger than expected from this decrease in $H_a$. On the other hand, there is only a small increase in the magnetic saturation with a maximum at 20 at.% Fe substituted by Co. Accordingly the alloying is limited to 20 at.% Co.

The vulnerability of RE compounds to corrosion is a problem. The corrosion behavior of Fe−Nd−B magnets has been improved by adding elements which influence the electrochemical properties of the Nd-rich grain boundary phase. Additions of small amounts of more noble elements such as Cu, Co, Ga, Nb, and V result in the formation of compounds which replace the highly corrosive Nd-rich phase. Table 4.3-39 lists some of the elements used for manufacturing Fe−Nd−B magnets.

A multitude of grades of Fe−Nd−B magnets is produced by varying chemical composition and processing, such as the press technique applied in order to satisfy the different specifications required for the different fields of application. A maximum remanence is needed, for instance, for disc drive systems in personal computers and for background field magnets in magnetic resonance imaging systems. On the other hand, straight line demagnetization curves up to operating temperatures of 150 °C are specified for application in highly dynamic motors. This requires very high coercive fields at room temperature. Magnetic remanence values of $B_r > 1.4$ T as well as $_JH_c$ values of $> 2500$ kA/m can be achieved. However, high $B_r$ values are attainable only with lowering the $_JH_c$ value and the operating temperature, and vice versa. Possible combinations of $B_r$ and $_JH_c$ for a given manufacturing process (pressing technique), can be rep-

**Table 4.3-39** Elements used for manufacturing Fe−Nd−B magnets

| Element | Fe | Nd | B | Dy | Co | Al | Ga | Nb, V |
|---|---|---|---|---|---|---|---|---|
| wt% | balance | 15–33 | 0.8–1 | 0–15 | 0–15 | 0.5–2 | 0–2 | 0–4 |

**Table 4.3-40** Physical properties of sintered Nd–Fe–B magnets [a]

| Density ($g\,cm^{-3}$) | Curie temperature (K) | Electrical resistivity ($\Omega\,mm^2\,m^{-1}$) | Specific heat ($J\,kg^{-1}\,K^{-1}$) | Thermal conductivity ($W\,m^{-1}\,K^{-1}$) | Thermal expansion coefficient ∥-*c* axis ($10^{-6}\,K^{-1}$) | Thermal expansion coefficient ⊥-*c* axis ($10^{-6}\,K^{-1}$) | Young's modulus ($kN\,mm^{-2}$) | Flexural strength ($N\,mm^{-2}$) | Compression strength ($N\,mm^{-2}$) | Vickers Hardness |
|---|---|---|---|---|---|---|---|---|---|---|
| 7.5 (0.05) | 580–605 | 1.50 (0.10) | 430 (10) | 9 | 4.4 (0.6) | −1 | 155 (5) | 260 (10) | 930 (170) | 580 (10) |

[a] All values are for 300 K. The values are the averages taken from the companies brochures of: VAC Vacuumschmelze, Hanau, Germany; MS Magnetfabrik Schramberg, Schramberg, Germany; Ugimag Inc, Valparaiso, USA; Neorem Magnets Oy, Ulvila, Finland; TDK Corporation, Tokyo, Japan; Hitachi Metals Ltd, Tokyo, Japan. The numbers in parentheses indicate the maximum deviation



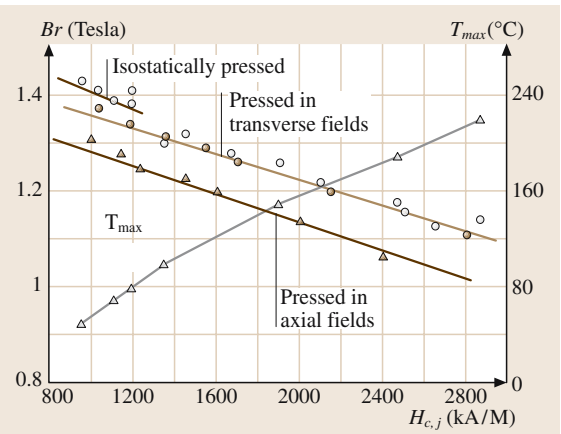


**Fig. 4.3-61** Sintered Nd–Fe–B magnets. Possible combinations of $B_r$ and $_JH_c$

resented by a straight line, as shown in Fig. 4.3-61. The physical properties of sintered Nd–Fe–B magnets are given in Table 4.3-40.

### Magnets Processed by the Rapid Quenching/Hot Working Technique

This alternative technology uses isotropic or amorphous material processed by a rapid quench technique involving melt spinning the molten alloy through a nozzle on to a rotating wheel. Flakes that are about 30 µm thick are obtained. Their microstructure shows typically an average grain size of 50 to 60 nm. The material is subjected to controlled deformation at elevated temperatures, which gives rise to a texture oriented perpendicular to the direction of mass flow during deformation. Hot working processes applied are the die-upset method and indirect extrusion. The major steps of the process are: alloy preparation, melt spinning, cold forming, hot working, coating, and magnetizing. The first step of the hot working procedure is pressing to 100% density at temperatures between 700 and 800 °C. Isotropic magnets are obtained. The isotropic parts are deformed at about 800 °C by using the die-upset technique. Constant strain rates have to be applied. Typically, the strain rate is about 0.1 $sec^{-1}$. The strain rate and the degree of deformation determine the alignment factor of the final magnet. A maximum value for the magnetic remanence $B_r$ of about 1.35 T may be achieved under economically reasonable conditions. The relationship between the degree of deformation and $B_r$ is shown in Fig. 4.3-62. Properties of commercially availabe magnets are included in Table 4.3-41. The application of the magnets is limited to special fields where complicated shapes would otherwise require expensive machining

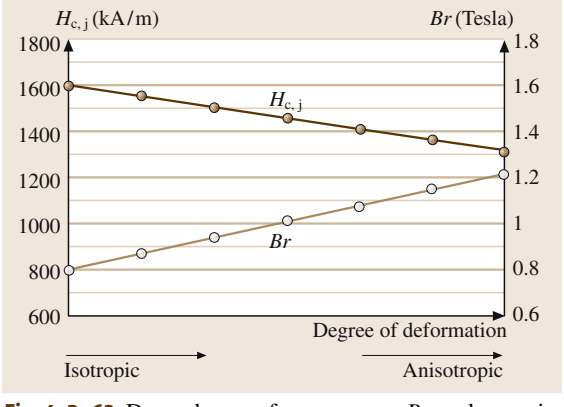


**Fig. 4.3-62** Dependence of remanence $B_r$ and coercivity $_JH_r$ of dense magnets, manufactured by the hot pressing/hot working technique, on the degree of deformation. Data provided and authorized for publication by Magnequench Int., Tübingen

**Table 4.3-41** Magnetic properties of $Fe_{14}Nd_2B$-based magnetic materials at room temperature. Typical values of commercially available magnets

| Remanence | Coercivity | | Energy density | Temperature coefficients | | Max. operation temperature [a] | Product code [b] |
|---|---|---|---|---|---|---|---|
| (T) | (kA m$^{-1}$) | | (kJ m$^{-3}$) | (% K$^{-1}$) | | (°C) | |
| $B_r$ | $_BH_c$ | $_JH_c$ | $(BH)_{max}$ | $TC(B_r)$ | $TC(_JH_c)$ | $T_{max}$ | |
| Sinter Route | | | | | | | |
| 1.47 | 915 | 955 | 415 | −0.115 | −0.77 | 50 | VD722HR |
| 1.44 | 1115 | 1195 | 400 | −0.115 | −0.73 | 70 | VD745HR |
| 1.35 | 1040 | 1430 | 350 | −0.095 | −0.65 | 110 | VD633HR |
| 1.30 | 980 | 1035 | 325 | −0.115 | −0.80 | 70 | VD335HR |
| 1.18 | 915 | 2465 | 270 | −0.085 | −0.55 | 190 | VD677HR |
| 1.43 | 915 | 9550 | 395 | −0.115 | −0.77 | 50 | VD722TP |
| 1.41 | 1090 | 1195 | 385 | −0.115 | −0.73 | 70 | VD745TP |
| 1.32 | 1020 | 1430 | 335 | −0.095 | −0.65 | 110 | VD633TP |
| 1.25 | 965 | 1195 | 300 | −0.115 | −0.75 | 70 | VD335TP |
| 1.14 | 885 | 2865 | 250 | −0.080 | −0.51 | 220 | VD688TP |
| 1.32 | 965 | 1115 | 335 | −0.115 | −0.73 | 80 | VD510AP |
| 1.26 | 965 | 1510 | 305 | −0.095 | −0.64 | 120 | VD633AP |
| 1.22 | 900 | 1195 | 285 | −0.115 | −0.75 | 80 | VD335AP |
| 1.08 | 830 | 2865 | 225 | −0.080 | −0.51 | 230 | VD688AP |
| Hot Working | | | | | | | |
| 0.83 | 575 | 1400 | 120 | −0.10 | −0.50 | 180 | MQ2-E15 |
| 1.28 | 907 | 995 | 302 | −0.10 | −0.60 | 125 | MQ3-E38 |
| 1.25 | 915 | 1313 | 287 | −0.09 | −0.60 | 150 | MQ3-F36 |
| 1.31 | 979 | 1274 | 334 | −0.09 | −0.60 | 150 | MQ3-F42 |
| 1.16 | 876 | 1592 | 255 | −0.09 | −0.06 | 200 | MQ3-G32SH |

[a] Maximum operating temperature is defined by a straight demagnetization line up to an operation point of the magnet of $B/\mu_0 H = -2$

[b] VD = Vacodym, trade name of Vacuumschmelze GmbH for NdFeB based magnets; HR grades = isostatically pressed, TP grades = transverse field pressed, AP grades = axial field pressed. MQ2, MQ3 = trade names of Magnequench International Inc. for hot pressed - hot deformed magnets

work, as for instance screwed arcs for non-cogging motors.

Typical technical alloys and their properties are listed in Table 4.3-41. Characteristic demagnetization curves are shown in Fig. 4.3-63.

### 4.3.3.5 Co–Sm

Numerous magnetic, binary, rare earth (RE) transition metal (TM) compounds exist, of which the $Co_5RE$ and $Co_{17}RE_2$ phases form the basis for materials with excellent permanent magnetic properties. They combine high saturation magnetization $M_s$ with high crystal anisotropy $K_1$ and high Curie temperature $T_c$. The intrinsic magnetic properties of the $Co_5RE$ and $Co_{17}RE_2$ phases are summarized in Tables 4.3-42 and 4.3-43, respectively ($Co_5RE$ and $Co_{17}RE_2$ are, also, referred to as 5/1 and 17/2 phases). It is obvious that $Co_5Sm$ and $Co_{17}Sm_2$ have the best potential for manufacturing permanent magnetic materials.

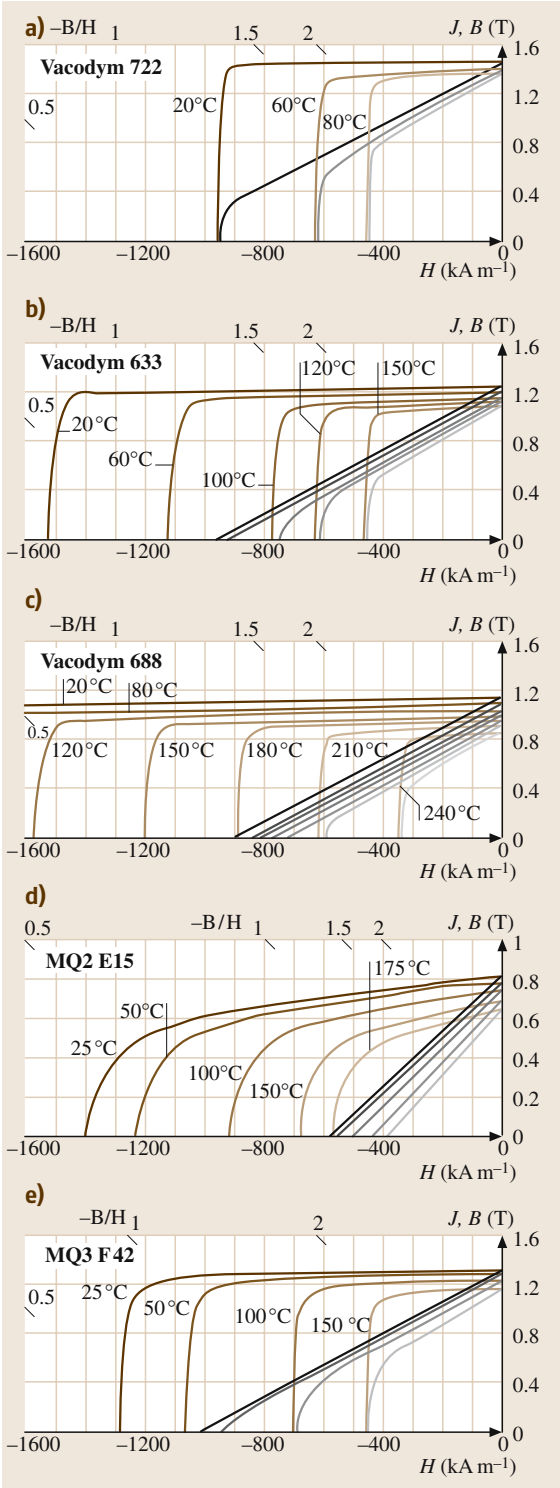


**Fig. 4.3-63a–e** $Fe_{14}Nd_2B$-based commercial magnets [3.10]. **(a)** Top grade magnet with highest remanence $B_r$. Isostatically pressed, designed to meet exceptional requirements for maximum energy density at operating temperatures up to 60 °C. **(b)** Magnet, axially pressed, with an optimum combination of high coercivity and energy product **(c)** Magnet, axially pressed, with a very high coercivity; exceptionally well suited for use in highly dynamic servo motor applications. **(d)** Isotropic dense magnet made from rapidly quenched powder by means of the hot pressing technique. **(e)** Magnet made from rapidly quenched powder by means of the hot pressing and hot deforming technique; especially well suited for complicated shaped magnets, such as scewed arcs in special motor applications

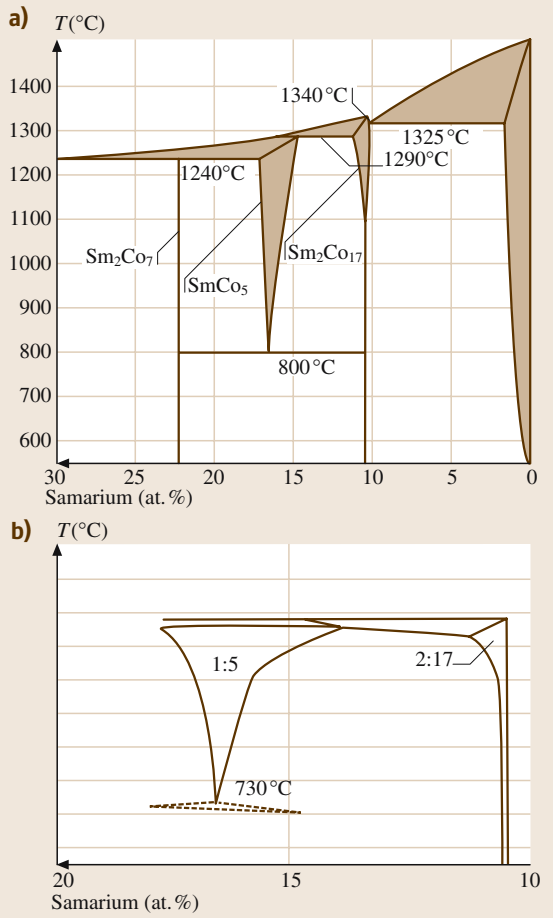


**Fig. 4.3-64** **(a)** Part of the Co–Sm phase diagram. **(b)** Section of the Co–Sm–Cu phase diagram at 10 at.% Cu [3.10]

**Table 4.3-42** $Co_5RE$ alloys. Room temperature intrinsic magnetic properties, the crystal anisotropy constant $K_1$, the magnetic saturation $M_s$, the anisotropy field $H_a = 2K_1/M_s$, and the Curie temperature, $T_c$ [3.10]

| RE [a] | $K_1$ [b] ($10^7$ erg cm$^{-3}$) | $4\pi M_s$ [b] (T) | $H_a$ (MA m$^{-1}$) | $T_c$ [b] (K) |
|---|---|---|---|---|
| Ce | 5.3 (6) | 0.83 | 13 | 660 (20) |
| Pr | 8.1 (9) | 1.29 | 12.5 | 900 (10) |
| Nd | 0.7 (5) | 1.34 | 1.1 | 910 (2) |
| Sm | 17.2 (9) | 1.12 (3) | 31 | 990 (10) |
| Gd | 4.6 (5) | 0.35 (3) | 26 | 1035 |
| Tb | NC | | | 973 |
| Dy | NC | | | 961 |
| Ho | 3.6 (3) | 0.52 | 13.8 | 996 |
| Er | 4.2 (4) | 0.4 | 14.6 | 983 |
| La | 5.9 (5) | 0.91 | 10.6 | 834 |
| Y | 5.2 (4) | 1.11 | 9.3 | 980 |

[a] No data are available for the RE elements Tm, Yb, and Lu

[b] The mean value is given where more than one reference is available; the number in parentheses indicates the standard deviation in the last figure. NC: non-collinear spin structure

**Table 4.3-43** Room temperature intrinsic magnetic properties, of $Co_{17}RE_2$ alloys [3.10]

| RE [a] | $K_1$ [b] ($10^7$ erg cm$^{-3}$) | $4\pi M_s$ [b] (T) | $H_a$ (MA m$^{-1}$) | $T_c$ [b] (K) |
|---|---|---|---|---|
| Ce | −0.6 | 1.15 | | 1068 (10) |
| Pr | −0.6 | 1.38 | | 1160 (10) |
| Nd | −1.1 | 1.39 | | 1160 (3) |
| Sm | 3.3 (1) | 1.25 (3) | 5.3 (1) | 1196 (1) |
| Gd | −0.5 | 0.73 | | 1212 (6) |
| Tb | −3.3 (6) | 0.67 | | 1189 (4) |
| Dy | −2.6 (5) | 0.69 | | 1173 (8) |
| Ho | −1.0 (2) | 0.85 | | 1177 (1) |
| Er | 0.41 (3) | 1.05 (5) | 0.75 | 1175 (15) |
| TM | 0.50 (5) | 1.21 | 0.83 | 1179 (2) |
| Yb | −0.38 | 1.35 | | 1180 |
| Lu | −0.20 (5) | 1.41 | | 1202 (6) |
| Y | −0.34 (2) | 1.27 | | 1199 (13) |

[a] La does not form the 17/2 phase. The 17/2 phases with Sm, Er, and Tm show uniaxial anisotropy while all others have easy plane anisotropy

[b] The mean value is given where more than one reference is available; the number in parentheses indicates the standard deviation in the last figure

### Phase Equilibria of Co–RE Systems

The phase diagrams of Co–RE systems are very similar. Figure 4.3-64 shows the magnetically relevant part of the Co–Sm phase diagram. The features to note are: Co and $Co_{17}Sm_2$ form a eutectic, while $Co_5Sm$ forms as a result of a peritectic reaction between $Co_{17}Sm_2$ and liquid. Both $Co_5Sm$ and $Co_{17}Sm_2$ show a significant range of homogeneity at elevated temperatures. The compound $Co_5Sm$ is unstable at room temperature and decomposes via an eutectoid reaction into $Co_7Sm_2$ and $Co_{17}Sm_2$.

Iron and Cu are two important substitutional elements for Co–RE alloys with respect to manufacturing

permanent magnets. In $Co_5RE$ compounds, Fe may substitute up to 5 at.% Co while complete solubility occurs in $(Co_{1-x}Fe_x)_{17}RE_2$. Copper is essential in $Co_{17}Sm_2$ type alloys. The different solubility of Cu in 5/1 and 17/2 is used to form precipitates in the 17/2 phase, resulting in a microstructure which provides high coercivity.

### Co–Sm-Based Permanent Magnets

*Powder Metallurgical Processing.* Cobalt–Samarium magnets are produced using powder metallurgical techniques. Alloys are prepared by an inductive melting process or a Ca reduction process. The starting alloys are crushed and pulverized to single crystalline particles 3–4 μm in diameter. The powders are compacted in a magnetic field to obtain anisotropic magnets: by uniaxial compaction in magnetic fields, either parallel or transverse to the direction of the applied force; or by isostatic compaction of powders in elastic bags after subjecting the filled bags to a pulsed field. The magnetically aligned green compacts are sintered in an inert atmosphere to achieve an optimum combination of high density and high coercive field.

*5/1 Type Magnets.* Binary $Co_5Sm$ is the basis of 5/1 type magnets. Table 4.3-44 lists some of the magnetic properties at room temperature and Table 4.3-45 lists the physical properties of sintered $Co_5Sm$ magnets. Partial substitution of Sm by Pr increases $B_s$ while still yielding sufficiently high ${}_JH_c$. The microstructure of $Co_5Sm$ magnets consists of single domain grains. Magnetization reversal starts by nucleation of domains in a demagnetizing field. The domain wall moves easily through the particle.

The application of permanent magnets in measuring devices or in devices in aircraft or space systems requires a small temperature coefficient (TC) of $B_r$. The combination of $Co_5Sm$ which has a negative TC, with $Co_5Gd$, which has a positive TC, yields magnets with reduced temperature dependence of $B_r$, reaching about

**Table 4.3-44** $Co_5Sm$-based magnetic materials. Magnetic properties at room temperature, typical values [3.10]

| $B_r$ (T) | ${}_BH_c$ (kA m$^{-1}$) | ${}_JH_c$ (kA m$^{-1}$) | $(BH)_{max}$ (kJ m$^{-3}$) | Press mode [a] | Material | Producer code [b] |
|---|---|---|---|---|---|---|
| 1.01 | 755 | 1500 | 200 | Iso | $Co_5Sm$ | Vacomax 200 |
| 0.95 | 720 | 1800 | 180 | TR | $Co_5Sm$ | Vacomax 170 |
| 1.0 | 775 | 2400 | 200 | Iso | $Co_5Sm$ | Recoma 25 |
| 0.94 | 730 | 2400 | 175 | TR | $Co_5Sm$ | Recoma 22 |
| 0.9 | 700 | 2400 | 160 | A | $Co_5Sm$ | Recoma 20 |
| 0.73 | 570 | >2400 | 105 | A | $Co_5Sm_{0.8}Gd_{0.2}$ | EEC 1.5TC-13 |
| 0.61 | 480 | >2400 | 70 | A | $Co_5Sm_{06}Gd_{0.4}$ | EEC 1.5TC-9 |

[a] Iso: isostatically pressed; TR: uniaxially pressed in transverse oriented aligning fields; A: uniaxially pressed in axially oriented aligning fields
[b] Vacomax: Trademark of Vacuumschmelze GmbH, Germany; Recoma: Trademark of Ugimag AG, Switzerland; EEC: Trademark of EEC Electron Energy Corporation, USA

**Table 4.3-45** Physical properties of sintered $Co_5Sm$ magnets [a] [3.10]

| Density (g cm$^{-3}$) | Curie temperature (K) | Electrical resistivity (Ω mm$^2$ m$^{-1}$) | Specific heat (J kg$^{-1}$ K$^{-1}$) | Thermal conductivity (W m$^{-1}$ K$^{-1}$) | Thermal expansion coefficient ∥ $c$ axis ($10^{-6}$ K$^{-1}$) | Thermal expansion coefficient ⊥ $c$ axis ($10^{-6}$ K$^{-1}$) | Young's modulus (kN mm$^{-2}$) | Flexural strength (N mm$^{-2}$) | Compression strength (N mm$^{-2}$) | Vickers Hardness |
|---|---|---|---|---|---|---|---|---|---|---|
| 8.40 (0.10) | 990 (10) | 0.53 (0.03) | 372 (3) | 11.5 (1.0) | 6.0 (1.5) | 12.5 (0.5) | 150 (40) | 125 (35) | 900 (300) | 580 (50) |

[a] All values for 300 K. Average values are taken from the companies brochures of: VAC Vacuumschmelze, Hanau, Germany; MS Magnetfabrik Schramberg, Schramberg, Germany; Ugimag AG, Lupfig, Switzerland; EEC Electron Energy Corporation, Landisville, USA; TDK Corporation, Tokyo Japan; Hitachi Metals Ltd, Tokyo, Japan. The numbers in parentheses indicate the standard deviation

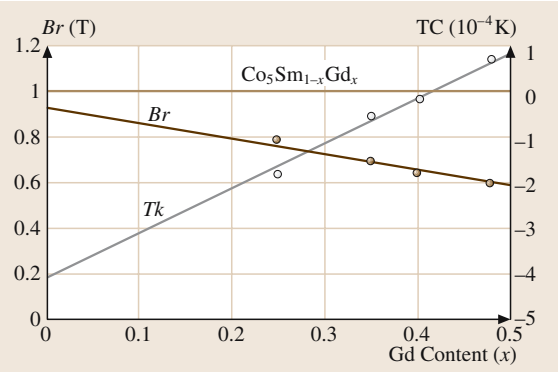


**Fig. 4.3-65** Temperature coefficient TC of $Co_5Sm_{1-x}Gd_x$ magnets in the temperature range between 20 and 200 °C. The coercivity of these ternary magnets is comparable to that of binary $Co_5Sm$ magnets due to the high anisotropy field of $Co_5Gd$ $H_a = 24\,MA\,m^{-1}$ while for $Co_5Sm$, $H_a = 31\,MA\,m^{-1}$ [3.10]

zero for $Co_5Sm_{0.6}Gd_{0.4}$ between room temperature and 200 °C (Fig. 4.3-65).

Tables 4.3-44 and 4.3-45 list the magnetic properties of typical $Co_5Sm$ based magnets and their physical properties, respectively. Figures 4.3-66a,b show characteristic demagnetisation curves.

*17/2 Type Magnets.* The permanent magnetic potential of the binary phase $Co_{17}Sm_2$ is increased by partially substituting Co by other transition metals. The general chemical composition of commercial magnets corresponds to $(Co_{bal}Fe_vCu_yZr_x)_zSm$. Copper is the essential addition. Its solubility in the 17/2 phase is strongly temperature-dependent, and this is used for precipitation hardening of 17/2 magnets.

The influence of Fe on the intrinsic magnetic properties is summarized in Fig. 4.3-67. Both Zr and Hf increase coercivity. Figures 4.3-67a,b show the combined effects of Fe, Cu, and Zr additions and the Co/Sm ratio on the temperature dependence of coercivity $_JH_c$. The magnets are sintered between 1200 and 1220 °C. A single phase with $Zn_{17}Th_2$ structure is obtained by homogenization at temperatures between 1160 and 1190 °C. After rapid cooling the magnets are finally annealed between 800 and 850 °C, followed by cooling to 400 °C. The microstructure leading to high coercivity $_JH_c$ consists of 17/2 matrix grains, a 5/1 boundary phase enriched in Cu, and platelet-shaped precipitates enriched in Fe and Zr. The coercivity of these magnets

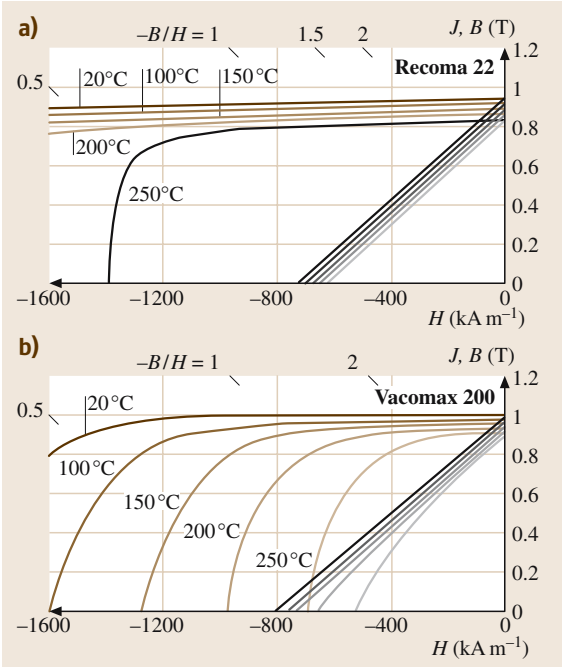


**Fig. 4.3-66a,b** $Co_5Sm$ magnets. Demagnetization curves of typical commercially available magnets [3.10]. **(a)** Magnet with high intrinsic coercivity $_JH_c$ up to 300 °C, uniaxially pressed in a transverse aligning field; Recoma: trademark of Ugimag AG, Switzerland. **(b)** Magnet with highest energy density obtained by cutting from isostatically pressed block; Vacomax: trademark of Vacuumschmelze GmbH, Germany

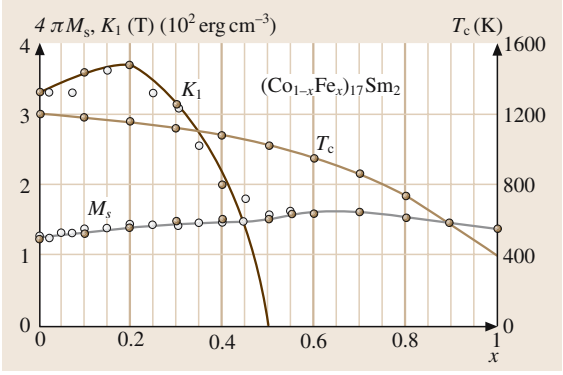


**Fig. 4.3-67** $(Co_{1-x}Fe_x)_{17}Sm_2$. Dependence $K_1$, $4\pi M_s$, and $T_c$ on the Fe content $x$ [3.10]

is based on pinning of the Bloch walls at the 5/1 grain boundary phase.

**Table 4.3-46** Chemical composition of commercial high energy 17/2 magnets [3.10]

| Element | Sm [a] | Co | Cu | Fe | Zr |
|---|---|---|---|---|---|
| wt% | 25–27 | balance | 4.5–8 | 14–20 | 1.5–3 |

[a] The Sm content includes the fraction of Sm which is present as $Sm_2O_3$, typically 2.5 wt%

**Table 4.3-47** Annealing treatments for 17/2 type magnets [3.10]

| | Isothermal ageing | Cooling rate to 400 °C | ${}_{\mathrm{J}}H_{\mathrm{c}}$ (kA m$^{-1}$) | Magnetizing field $H_{\mathrm{m}}$ (kA m$^{-1}$) |
|---|---|---|---|---|
| high ${}_{\mathrm{J}}H_{\mathrm{c}}$ | 850 °C/10 hours | 1 K/min | > 2000 | 5000 |
| low ${}_{\mathrm{J}}H_{\mathrm{c}}$ | 800 °C/30 min. | 5 K/min | 500–800 | 1500 |



**Table 4.3-48** High energy $TM_{17}Sm_2$ magnets for applications up to 300 °C, typical values [3.10]

| $B_{\mathrm{r}}$ (T) | ${}_{\mathrm{B}}H_{\mathrm{c}}$ (kA m$^{-1}$) | ${}_{\mathrm{J}}H_{\mathrm{c}}$ (kA m$^{-1}$) | $(BH)_{\max}$ (kJ m$^{-3}$) | Press mode [a] | Material | Producer code [b] |
|---|---|---|---|---|---|---|
| 1.14 | 670 | 800 | 247 | Iso | $TM_{17}Sm_2$ | Hicorex -30CH |
| 1.12 | 730 | 800 | 240 | Iso | $TM_{17}Sm_2$ | Vacomax 240HR |
| 1.05 | 720 | 800 | 210 | A | $TM_{17}Sm_2$ | Vacomax 240 |
| 1.10 | 820 | 2070 | 225 | Iso | $TM_{17}Sm_2$ | Vacomax 225HR |
| 1.07 | 800 | 2000 | 215 | TR | $TM_{17}Sm_2$ | Recoma 28 |
| 1.04 | 760 | 2070 | 205 | A | $TM_{17}Sm_2$ | Vacomax 225 |
| 0.9 | 654 | > 2000 | 150 | A | $TM_{17}(Sm_{0.8}, Gd_{0.2})_2$ | EEC2:17TC-18 |
| 0.8 | 575 | > 2000 | 115 | A | $TM_{17}(Sm_{0.6}, Gd_{0.4})_2$ | EEC2:17TC-15 |

[a] Iso: isostatically pressed; TR: uniaxially pressed in transverse oriented aligning fields; A: uniaxially pressed in parallel oriented aligning fields

[b] Hicorex: Trademark of Hitachi Metals Ltd., Japan; Vacomax: Trademark of Vacuumschmelze GmbH, Germany; Recoma: Trademark of Ugimag AG, Switzerland; EEC: Trademark of EEC Electron Energy Corporation, USA

**Table 4.3-49** Composition of 17/2 magnets for operating up to 550 °C [3.10]

| Element | Sm | Co | Cu | Fe | Zr |
|---|---|---|---|---|---|
| wt% | 26.5–29 | balance | 6–12 | 7 | 2.5–6 |

**Table 4.3-50** Physical properties of sintered $TM_{17}Sm_2$ magnets [a] [3.10]

| Density (g cm$^{-3}$) | Curie temperature (K) | Electrical resistivity (Ω mm$^2$ m$^{-1}$) | Specific heat (J kg$^{-1}$ K$^{-1}$) | Thermal conductivity (W m$^{-1}$ K$^{-1}$) | Thermal expansion coefficient ∥-$c$ axis (10$^{-6}$ K$^{-1}$) | Thermal expansion coefficient ⊥-$c$ axis (10$^{-6}$ K$^{-1}$) | Young's modulus (kN mm$^{-2}$) | Flexural strength (kN mm$^{-2}$) | Compression strength (kN mm$^{-2}$) | Vickers hardness |
|---|---|---|---|---|---|---|---|---|---|---|
| 8.38 (0.08) | 1079 (8) | 0.86 (0.05) | 355 (30) | 10.5 (1.5) | 8.4 (1) | 11.5 (0.5) | 160 ( 40) | 130 (15) | 760 (150) | 600 (50) |

[a] All values are for 300 K. The values are the average of values taken from company brochures

*High Energy Magnets for Applications at Temperatures up to 300 °C.* The compositional parameters $v$, $y$, $x$, and $z$ of the 17/2 type magnets are normally optimized for highest $(BH)_{max}$ between room temperature and 300 °C. The range of chemical compositions of these high energy magnets is given in Table 4.3-46.

Tables 4.3-48 and 4.3-50 list the magnetic properties of typical $Co_{17}Sm_2$ based magnets and their physical properties, respectively. Figures 4.3-69a–c show characteristic demagnetization curves.

Two modifications of 17/2 magnets can be obtained from identical chemical compositions according to the annealing treatment applied (see Table 4.3-47). 17/2 magnets with reduced TC of $B_r$ are obtained by substituting part of Sm by Gd. Table 4.3-45 shows some typical values of the magnetic properties of high energy $TM_{17}Sm_2$ magnets.

*Magnets for High Temperature Applications.* Special applications in aircraft and spacecraft require magnets with linear demagnetization curves up to 550 °C. Suitable high temperature magnets are obtained by increasing Sm and Cu and decreasing Fe. Data are given in Table 4.3-49 and Fig. 4.3-69a.

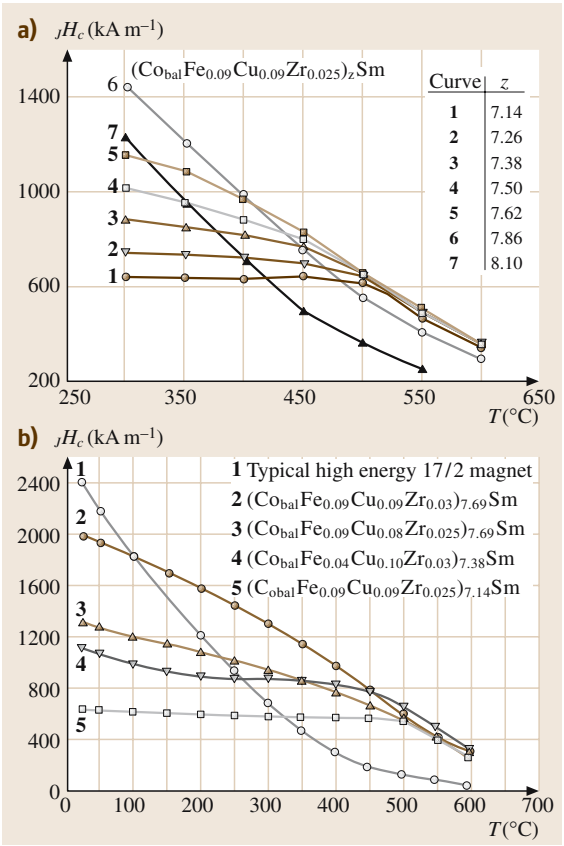


**Fig. 4.3-68a,b** Temperature dependence of $_JH_c$ for $(Co_{bal}Fe_vCu_yZr_x)_z$ as varied by the concentration of the substitutional elements and of Sm [3.10] **(a)** Dependence on the TM/Sm ratio; **(b)** Dependence on other variations in chemical composition

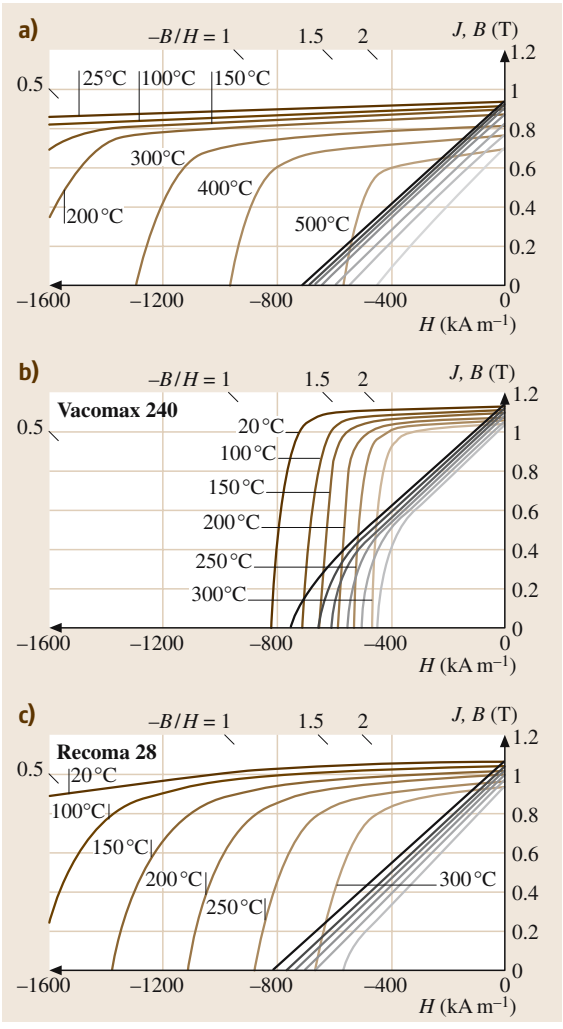


**Fig. 4.3-69a–c** $TM_{17}Sm_2$ magnets. Demagnetization curves [3.10] **(a)** Magnet may be used up to 500 °C. Coating is needed for protection against oxidation > 300 °C. **(b)** Low coercivity, easy-to-magnetize magnet. **(c)** High energy, high coercivity magnet

### 4.3.3.6 Mn–Al–C

In the binary Mn–Al system the ferromagnetic, metastable $\tau$-Mn–Al phase containing 55 wt% Mn is obained by annealing at 923 K, or by controlled cooling of the stable $\varepsilon$ phase from $\geq$ 1073 K. The $\tau$ phase has a high magnetocrystalline anisotropy $K_1 \cong 10^6\,\mathrm{J\,m^{-3}}$ and $I_s = 0.6\,\mathrm{T}$. The magnetic easy axis is the $c$ axis. The $\tau$ phase can be stabilized by adding 0.5 wt% C. Hot deformation at about 973 K permits formation of anisotropic magnets. Figure 4.3-70 shows schematically the 873 K isotherm of the Mn–Al–C phase diagram.

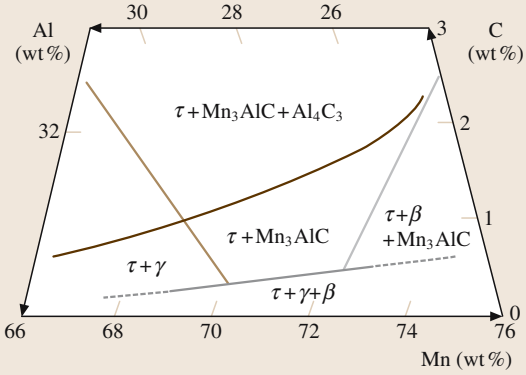


**Fig. 4.3-70** Schematic representation of the phase relations of Mn–Al–C at 873 K [3.10]

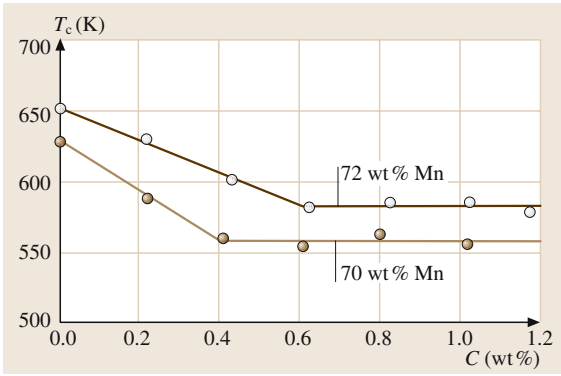


**Fig. 4.3-71** Dependence of Curie temperature of $\tau$-Mn–Al–C on the carbon concentration [3.10]

Carbides coexist with the metallic ferromagnetic phases. This is unfavorable for the mechanical properties. The Curie temperature of the $\tau$ phase decreases with increasing C content to a constant value (see Fig. 4.3-71) according to the phase diagram.

An alternative process to form $\tau$-Mn–Al–C magnets is to use gas-atomized powder which is canned

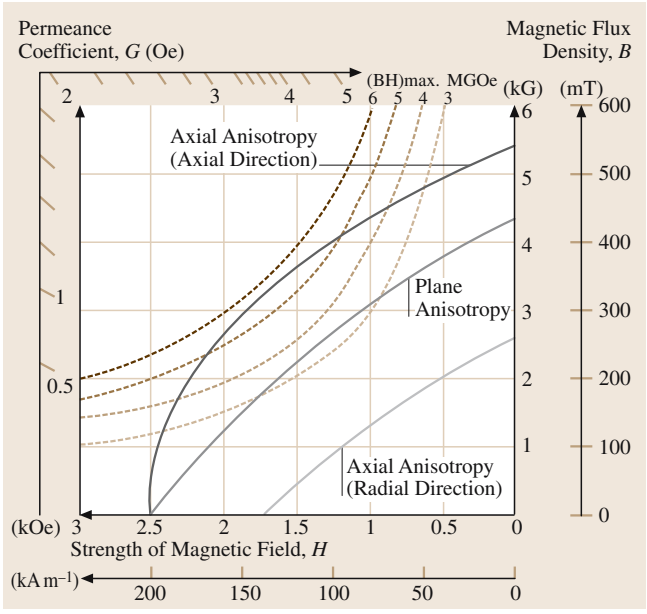


**Fig. 4.3-72** Magnetic properties of an extruded Mn–Al–C magnet [3.10]

**Table 4.3-51** Properties of a Mn−Al−C magnet [3.10]

| | | Axial Anisotropy | | Plane anisotropy |
|---|---|---|---|---|
| | | Axial direction | Radial direction | |
| Maximum energy product $(BH)_{max}$ | $(kJ\,m^{-3})$ | 44 | 10 | 28 |
| Residual magnetic flux density $B_r$ | (mT) | 550 | 270 | 440 |
| Coercivity $H_c$ | $(kA\,m^{-1})$ | 200 | 144 | 200 |
| Optimum permeance coefficient | $(\mu H\,m^{-1})$ | 1.9 | 1.9 | 1.9 |
| Average reversal permeability | $(\mu H\,m^{-1})$ | 1.4 ~ 1.6 | 1.4 ~ 1.6 | 1.4 ~ 1.6 |
| Temperature coefficient of $B_r$ | $(\%\,K^{-1})$ | −0.11 | −0.11 | −0.11 |
| Curie point $T_c$ | (K) | 573 | 573 | 573 |
| Maximum operating temperature | (K) | 773 | 773 | 773 |
| Density | $(kg\,m^{-3})$ | 5100 | 5100 | 5100 |
| Hardness | $(HR_c)$ | 49 ~ 56 | 49 ~ 56 | 49 ~ 56 |
| Tensile strength $R_m$ | $(N\,m^{-2})$ | $> 290\times10^6$ | $> 290\times10^6$ | $> 290\times10^6$ |
| Compression strength | $(N\,m^{-2})$ | $> 2000\times10^6$ | $> 2000\times10^6$ | $> 2000\times10^6$ |

and extruded at 973 K. By atomizing, the powder is rapidly quenched and consists of the high temperature $\varepsilon$ phase. During hot extrusion it transforms to the axially anisotropic $\tau$ phase. Repeated die pressing results in plane anisotropy. The magnetic properties are shown in Fig. 4.3-72 and listed in Table 4.3-51.

## 4.3.4 Magnetic Oxides

The magnetic properties of oxides and related compounds have been tabulated in comprehensive data collections [3.4]. A review of the basic magnetic properties of garnets $\{A_3\}[B_2](Si_3)O_{12}$ and spinel ferrites $MeOFe_2O_3$ or $Me^{II}Fe_2^{III}O_4$ is given by *Guillot* in [3.3].

### 4.3.4.1 Soft Magnetic Ferrites

Both MnZn and NiZn ferrites are the common designations of the two main groups of soft magnetic oxide materials. A more extensive account is given in [3.10]. The chemical formula of MnZn and NiZn ferrites is $M^{2+}Fe_2O_4$ and they have spinel structures. The divalent ions ($M^{2+}$) are elements such as Mn, Fe, Co, Ni, Cu, Mg, Zn, and Cd. They are located at tetrahedral or octahedral sites of the spinel structures. Ceramic processing methods are applied to produce the magnetic parts such as ring-shaped cores for inductive components.

The use of different types of MnZn and NiZn ferrite materials varies with the operating frequency in the application concerned. Figure 4.3-73 and Table 4.3-52 indicate the typical ranges of use and the magnetic properties of characteristic materials. Typically, MnZn ferrites are used in the range of several MHz. Table 4.3-53 lists the major applications with the pertinent operating frequencies. Since a phase shift occurs in an ac-excited magnetic field, the permeability $\mu$ is expressed as a complex number, $\mu' - i\mu''$. The imaginary

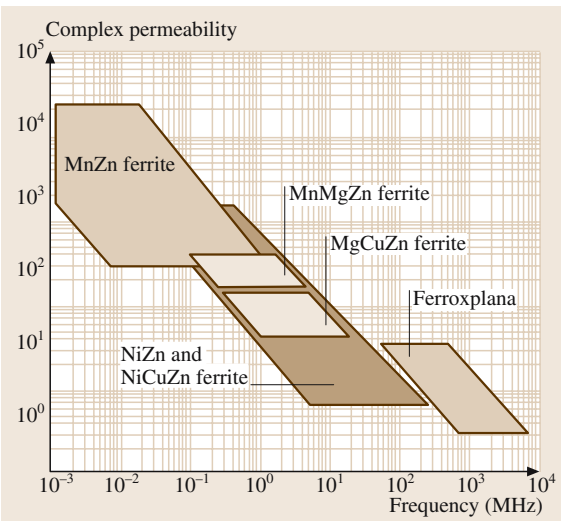


**Fig. 4.3-73** Relationships between frequency and complex permeability of groups of characteristic soft magnetic ferrites [3.10]

**Table 4.3-52** Typical magnetic properties of characteristic materials [3.10]

| Type | MnZn ferrite | | | | | NiCuZn ferrite | | |
|---|---|---|---|---|---|---|---|---|
| Designation | PC40 | PC44 | PC45 | PC50 | H5C4 | L7H | HF70 | L6 |
| $\mu_i$ | 2300 | 2400 | 2500 | 1400 | 12 000 | 800 | 1300 | 1500 |
| $B_s$ (mT) at 25 °C | 510 | 510 | 530 | 470 | 380 | 390 | 270 | 280 |
| $H_c$ (A m$^{-1}$) at 25 °C | 14 | 13 | 12 | 37 | 4 | 16 | 16 | 16 |
| $T_c$ (°C) | >215 | >215 | >230 | >240 | >110 | >180 | >110 | >110 |
| $\rho_v$ (m) | 6.5 | | | | | $10^6$ | $10^6$ | $10^6$ |
| Pcv (kW m$^{-3}$) | 410 | 300 | 250 | 80[a] | | | | |
| At 100 kHz, 200 mT | (100 °C) | (100 °C) | (75 °C) | (100 °C) | | | | |

[a] At 500 kHz, 50 mT

**Table 4.3-53** Ferrite applications [3.10]

| Application | Frequency | Ferrite material |
|---|---|---|
| Communication coils | 1 kHz ~ 1 MHz<br>0.5 ~ 80 MHz | MnZn<br>NiZn |
| Pulse transformers | | MnZn, NiZn |
| Transformers | ~ 300 kHz | MnZn |
| Flyback transformers | 15.75 kHz | MnZn |
| Deflection yoke cores | 15.75 kHz | MnZn, MnMgZn, NiZn |
| Antennas | 0.4 ~ 50 MHz | NiZn |
| Intermediate frequency transformers | 0.4 ~ 200 MHz | NiZn |
| Magnetic heads | 1 kHz ~ 10 MHz | MnZn |
| Isolators | | MnMgAl |
| Circulators | 30 MHz ~ 30 GHz | YIG |
| Splitters | | YIG |
| Temperature responsive switches | | MnCuZn |

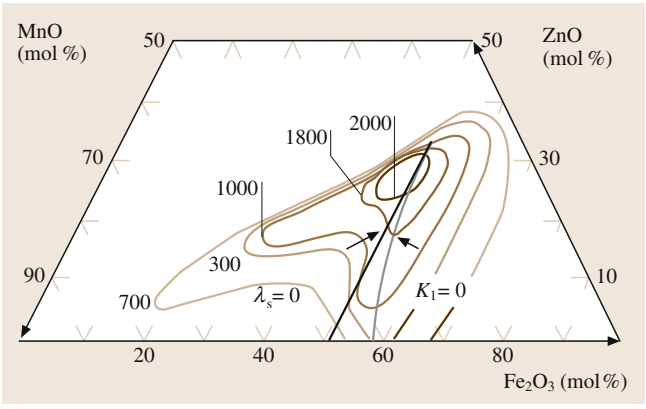


**Fig. 4.3-74** Relationship between composition and complex permeability in MnZn ferrites [3.10]

part, $\mu''$, is related to magnetic losses and is high at the resonance frequency. For a specific composition range, the values of magnetic anisotropy and magnetostriction are reduced to near zero leading to a maximum in complex permeability, as shown in Fig. 4.3-74. By suitable control of the microstructure it is possible to favor the formation and mobility of fast-moving domain walls. Consequently, the permeability of MnZn ferrite is the highest among the ferrites with spinel structure. However, the increase of the loss factor is considerably enhanced with increasing frequency because of the lower resistivity of MnZn ferrites compared to other ferrite materials.

The properties of NiZn and NiCuZn ferrites are designed for applications in the radio wave band. Figure 4.3-75 shows the effect of the Zn content on

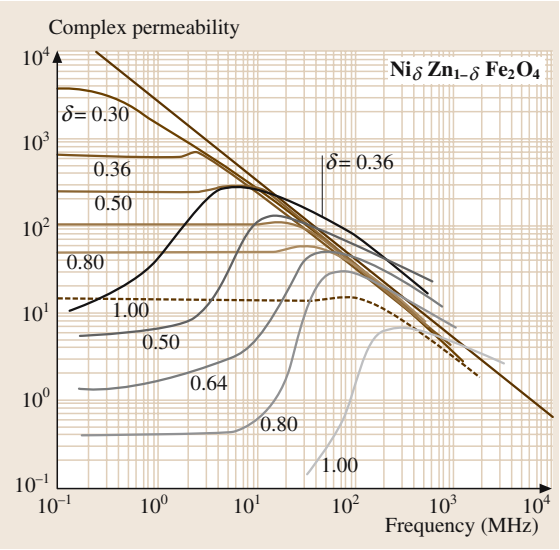


**Fig. 4.3-75** Frequency dependence of the complex permeability in NiZn ferrites. *Solid* and *dashed lines* refer to the real and the imaginary part, respectively [3.10]

the complex permeability spectra of NiZn ferrites. In general, the high-permeability materials cause lower resonance frequencies.

### 4.3.4.2 Hard Magnetic Ferrites

A hard magnetic ferrite, also called ferrite magnet, is a magnetic material based on iron oxide. The composition of the typical hard magnetic ferrite compounds is shown in Table 4.3-54. M type material is used most widely and BaO can be replaced by SrO.

Figure 4.3-76 shows the quasi-binary phase diagram $BaO–Fe_2O_3$. The composition of the actual industrial hard magnetic ferrite is selected to deviate slightly from the stoichiometric composition in order to provide easy wetting and permit liquid-phase sintering. The ferromagnetic phase $SrO{\cdot}6Fe_2O_3$ has a higher magnetocrystalline anisotropy constant $K_1$ and, thus, a higher intrinsic coercive force ${}_JH_c$ than the BaO-based compound.

Table 4.3-55 shows the basic magnetic properties of hard magnetic ferrites. The properties of actual products are shown in Fig. 4.3-77. The demagnetization curves of type YBM-9B, which have the best magnetic properties, are shown in Fig. 4.3-78.

Comparing hard ferrites and rare earth magnets, the ratio of remanence $B_r$ is about 1 : 3, that of the coercivity ${}_JH_c$ is also about 1 : 3, such that the ratio of the energy product $(BH)_{max}$ is about 1 : 10. From the cost/performance point of view, the rare earth magnets are used where weight and size are essential.

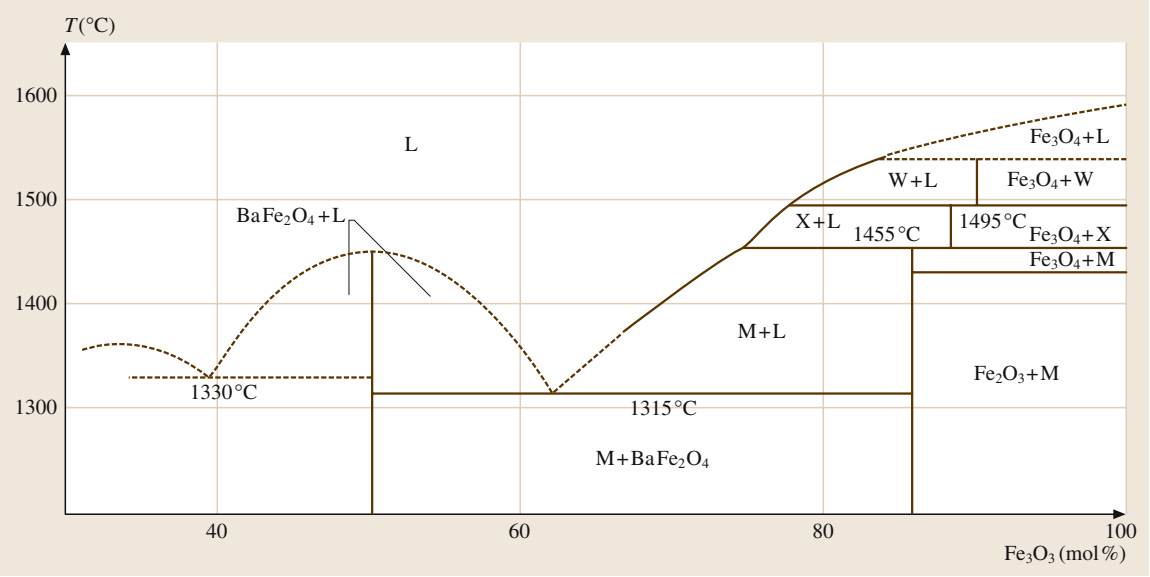


**Fig. 4.3-76** Quasi-binary phase diagram $BaO–Fe_2O_3$. $p(O_2) = 1$ atm; X = $BaO{\cdot}FeO{\cdot}7Fe_2O_3$; W = $BaO{\cdot}2FeO{\cdot}8Fe_2O_3$. *van Hook* 1964 [3.10,59]

**Table 4.3-54** $BaO-MeO-Fe_2O_3$ hexagonal magnetic compounds and their technical designations as hard ferrite materials 3.10

| Designation symbol | Molecular formula | Chemical composition (mol%) | | |
|---|---|---|---|---|
| | | MeO | BaO | $Fe_2O_3$ |
| M | $BaO \cdot 6Fe_2O_3$ | – | 14.29 | 85.71 |
| W | $2MeO{\cdot}BaO{\cdot}8Fe_2O_3$ | 18.18 | 9.09 | 72.71 |
| Y | $2MeO{\cdot}2BaO{\cdot}6Fe_2O_3$ | 20 | 20 | 60 |
| Z | $2MeO{\cdot}3BaO{\cdot}12Fe_2O_3$ | 11.76 | 17.65 | 70.59 |

**Table 4.3-55** Magnetic properties of hard ferrites 3.10

| Composition | $\sigma_s$ ($10^{-4}$ Wb m kg$^{-1}$) | (emu g$^{-1}$) | $\sigma_o$ ($10^{-4}$ Wb m kg$^{-1}$) | (emu g$^{-1}$) | $J_s$ (wb m$^{-3}$) | $T_c$ (K) | $K_1$ ($10^3$ J m$^{-2}$) | $H_a$ (kA m$^{-1}$) | $D_c$ (μm) |
|---|---|---|---|---|---|---|---|---|---|
| $BaFe_{17}O_{19}$ | 0.89 | 71 | 1.257 | 100 | 47.8 | 723 | 3.2 | 1.350 | 0.90 |
| $SrFe_{17}O_{19}$ | 0.905 | 72 | 1.357 | 108 | 47.8 | 735 | 3.5 | 1.590 | 0.94 |



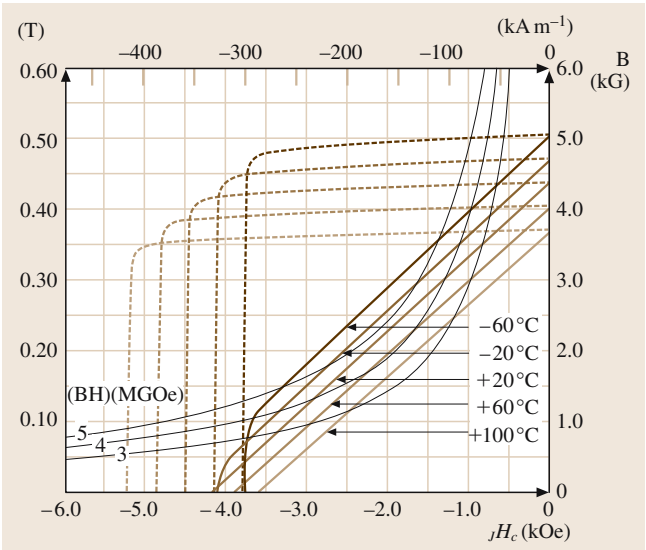


**Fig. 4.3-78** Demagnetization behavior and its temperature dependence of a hard ferrite YBM9B (Hitachi Metals) 3.10

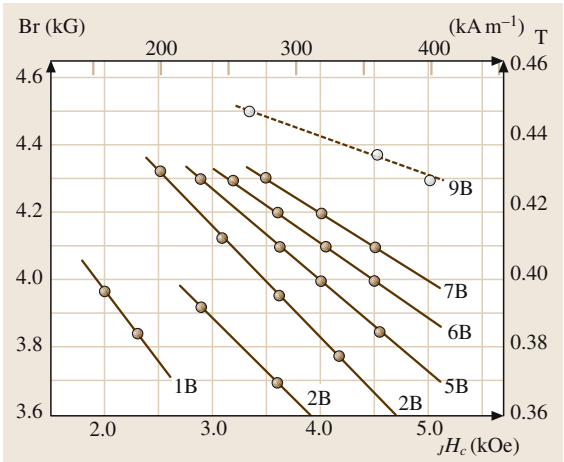


**Fig. 4.3-77** Magnetic properties of ferrite magnets (Hitachi Metals series YBM 1B-9B) 3.10

## References


3.1 K. H. J. Buschow: Electronic and Magnetic Properties of Metals and Ceramics, Part I. In: *Materials Science and Technology*, Vol. 3, ed. by R. W. Cahn, P. Haasen, E. J. Kramer (VCH, Weinheim 1991)

3.2 H. P. J. Wijn (Ed.): *Magnetic Properties of Metals*, Landolt–Börnstein, New Series III/19, 32 (Springer, Berlin, Heidelberg 1986–2001)

3.3 K. H. J. Buschow: Electronic and Magnetic Properties of Metals and Ceramics, Part II. In: *Materials Science and Technology*, Vol. 3, ed. by R. W. Cahn, P. Haasen, E. J. Kramer (VCH, Weinheim 1994)

3.4 K.-H. Hellwege, A. M. Hellwege (Eds.): *Magnetic and Other Properties of Oxides and Related Compounds*, Landolt–Börnstein, New Series III/4, 12 (Springer, Berlin, Heidelberg 1970–1982)

3.5 H. P. J. Wijn (Ed.): *Magnetic Properties of Non-Metallic Inorganic Compounds Based on Transition Metals*, Landolt–Börnstein, New Series III/27 (Springer, Berlin, Heidelberg 1988–2001)

3.6 K. Adachi, D. Bonnenberg, J. J. M. Franse, R. Gersdorf, K. A. Hempel, K. Kanematsu, S. Misawa, M. Shiga, M. B. Stearns, H. P. J. Wijn: *Magnetic*

*Properties of Metals: 3d, 4d, 5d Elements, Alloys, Compounds*, Landolt–Börnstein, New Series III/19 (Springer, Berlin, Heidelberg 1986)
3.7 G. Bertotti, A. R. Ferchmin, E. Fiorello, K. Fukamichi, S. Kobe, S. Roth: *Magnetic Alloys for Technical Applications. Soft Magnetic Alloys, Invar, Elinvar Alloys*, Landolt–Börnstein, New Series III/19, ed. by H. P. J. Wijn (Springer, Berlin, Heidelberg 1994)
3.8 R. Boll: *Soft Magnetic Materials* (Heyden & Son, London 1979)
3.9 J. Evetts: Concise Encyclopedia of Magnetic & Superconducting Materials. In: *Advances in Materials Science, Engineering* (Pergamon Press, Oxford 1992)
3.10 P. Beiss, R. Ruthardt, H. Warlimont (Eds.): *Advanced Materials, Technologies: Materials: Powder Metallurgy Data: Metals, Magnets*, Landolt–Börnstein, New Series VIII/2 (Springer, Berlin, Heidelberg 2003)
3.11 K. Günther: SMM Conference 2003
3.12 R. Boll: Soft Magnetic Metals and Alloys. In: *Materials Science and Technology*, Vol. 3B, ed. by K. H. J. Buschow (VCH, Weinheim 1994) pp. 399–450
3.13 Bölling and Hastenrath
3.14 G. Rassmann, U. Hofmann: Magnetismus, Struktur und Eigenschaften magnetischer Festkörper. In: (VEB Deutscher Verlag für Grundstoffindustrie, Leipzig 1967) pp. 176–198
3.15 G. Rassmann, U. Hofmann: J. Appl. Phys. **39**, 603 (1968)
3.16 R. Boll: *Weichmagnetische Werkstoffe*, 4 edn. (Vacuumschmelze, 1990)
3.17 H. Saito (Ed.): *Physics and Application of Invar Alloys* (Maruzen Company, Ltd., Tokyo 1978)
3.18 O'Handley 1977
3.19 Hilzinger 1980
3.20 Miyazaki 1972
3.21 Fujimori 1976
3.22 Allied Signal: Technical Bulletin 9 (1998)
3.23 H. Herzer: Nanocrystalline Soft Magnetic Alloys. In: *Handbook of Magnetic Materials*, ed. by K. H. J. Buschow (Elsevier, Amsterdam 1997) pp. 416–462
3.24 Hono and Sakurai 1995
3.25 M. Müller, N. Mattern, L. Illgen, H. R. Hilzinger, G. Herzer: Key Eng. Mater. **81–83**, 221–228 (1991)
3.26 M. Müller, N. Mattern, L. Illgen: Z. Metallkunde **82**, 895–901 (1991)
3.27 G. Herzer: IEEE Trans. Magn. Mag. **26**, 1397 (1990)
3.28 *Herzer* 1990
3.29 *Herzer* 1990–1995
3.30 *Herzer* and *Warlimont* 1992
3.31 *Sawa* and *Takahashi* 1990
3.32 *Suzuki* et al. 1991
3.33 *Guo* et al. 1991
3.34 *Pfeifer* and *Radeloff* 1980
3.35 *Arai* et al. 1984
3.36 Y. Yoshizawa, S. Oguma, K. Yamauchi: J. Appl. Phys. **64**, 6044 (1988)
3.37 K. Suzuki, A. Makino, N. Kataoka, A. Inoue, T. Masumoto: Mater. Trans. Japn. Inst. Met. (JIM) **32**, 93 (1991)
3.38 K. Suzuki, A. Makino, N. Kataoka, A. Inoue, T. Masumoto: J. Appl. Phys. **74**, 3316 (1993)
3.39 *Masumoto*
3.40 *Kussmann* and *Jessen*
3.41 K. Fukamichi: *Magnetic Properties of Metal*, Landolt–Börnstein, New Series III/19, ed. by H. P. J. Wijn (Springer, Berlin, Heidelberg 1994) pp. 193–238
3.42 M. Shiga: Invar Alloys. In: *Materials Science and Technology*, Vol. 3B, ed. by K. H. J. Buschow (VCH, Weinheim 1994) pp. 161–207
3.43 *Patrick*
3.44 *Fujimori* and *Kaneko*
3.45 C. E. Guillaume: C.R. hebd. Séances Acad. Sci. **1244**, 176–179 (1897)
3.46 P. Chevenard, X. Waché, A. Villechon: Ann. France Chronométrie , 259–294 (1937)
3.47 M. Müller: . Ph.D. Thesis (Akademie der Wissenschaften der DDR, Berlin 1977)
3.48 M. Kersten: Z. Phys. **85**, 708 (1933)
3.49 R. Becker, W. Döring: *Ferromagnetismus* (Springer, Berlin 1939) p. 340
3.50 G. Hausch: Phys. Stat. Sol. (a) **15**, 501 (1973) **16 (1973), 371**
3.51 M. Müller: . Ph.D. Thesis (Technische Universität Dresden, Dresden 1969)
3.52 H. Masumoto, S. Sawaya, M. Kikuchi: J. Japn. Inst. Met. (JIM) **35**, 1143, 1150 (1971) **36 (1972), 57, 176, 492, 498, 881, 886, 1116**
3.53 M. Müller: J. Magn. Magn. Mater. **78**, 337 (1989)
3.54 P. E. Armstrong, J. M. Dickinson, A. L. Brown: Trans. AIME **236**, 1404 (1966)
3.55 E. P. Wohlfahrt: Hard Magnetic Materials. Advances in Physics, Phil. Mag. **A8** (1959)
3.56 D. Bonnenberg, K. Burzo, K. Fukamichi, H. P. Kirchmayr, T. Nakamichi, H. P. J. Wijn: *Magnetic Properties of Metals: Magnetic Alloys for Technical Applications. Hard Magnetic Alloys*, Landolt–Börnstein, New Series III/19 (Springer, Berlin, Heidelberg 1992)
3.57 WIDIA Magnettechnik, Gesinterte Dauermagnete Koerzit und Koerox, d.2000.D.5
3.58 C. Abache, H. Oesterreicher: J. Appl. Phys. **57**, 4112 (1985)
3.59 *van Hook* 1964

# 4.4. Dielectrics and Electrooptics

The present section describes the physical properties of dielectrics and includes the following data:

1. *low-frequency properties*, i. e. density and Mohs hardness, thermal conductivity, static dielectric constant, dissipation factor (loss tangent), elastic stiffness and elastic compliance, and piezoelectric strain;
2. *high-frequency (optical) properties*, i. e. elastooptic and electrooptic coefficients, optical transparency range, two-photon absorption coefficient, refractive indices and their temperature variation, dispersion relations (Sellmeier equations), and second and/or third-order nonlinear dielectric susceptibilities.


4.4.1 **Dielectric Materials: Low-Frequency Properties** ..... 822
4.4.1.1 General Dielectric Properties ..... 822
4.4.1.2 Static Dielectric Constant (Low-Frequency) ..... 823
4.4.1.3 Dissipation Factor ..... 823
4.4.1.4 Elasticity ..... 823
4.4.1.5 Piezoelectricity ..... 824

4.4.2 **Optical Materials: High-Frequency Properties** ..... 824
4.4.2.1 Crystal Optics: General ..... 824
4.4.2.2 Photoelastic Effect ..... 824
4.4.2.3 Electrooptic Effect ..... 825
4.4.2.4 Nonlinear Optical Effects ..... 825

4.4.3 **Guidelines for Use of Tables** ..... 826

4.4.4 **Tables of Numerical Data for Dielectrics and Electrooptics** ..... 828
Isotropic Materials ..... 828
Cubic, Point Group $m3m$ ($O_h$) Materials ..... 828
Cubic, Point Group $\bar{4}3m$ ($T_d$) Materials ..... 834
Cubic, Point Group 23 ($T$) Materials ..... 838
Hexagonal, Point Group $\bar{6}m2$ ($D_{3h}$) Materials ..... 838
Hexagonal, Point Group $6mm$ ($C_{6v}$) Materials ..... 840
Hexagonal, Point Group 6 ($C_6$) Materials ..... 842
Trigonal, Point Group $\bar{3}m$ ($D_{3d}$) Materials ..... 844
Trigonal, Point Group 32 ($D_3$) Materials ..... 844
Trigonal, Point Group $3m$ ($C_{3v}$) Materials ..... 848
Tetragonal, Point Group $4mmm$ ($D_{4h}$) Materials ..... 852
Tetragonal, Point Group $4/m$ ($C_{4h}$) Materials ..... 854
Tetragonal, Point Group 422 ($D_4$) Materials ..... 854
Tetragonal, Point Group $\bar{4}2m$ ($D_{2d}$) Materials ..... 856
Tetragonal, Point Group $4mm$ ($C_{4v}$) Materials ..... 864
Orthorhombic, Point Group $mmm$ ($D_{2h}$) Materials ..... 866
Orthorhombic, Point Group 222 ($D_2$) Materials ..... 866
Orthorhombic, Point Group $mm2$ ($C_{2v}$) Materials ..... 872
Monoclinic, Point Group 2 ($C_2$) Materials ..... 884

**References** ..... 890


A large amount of the information in this section is taken from the compilations of low- and high-frequency properties of dielectric crystals in Landolt–Börnstein, Group III, Vols. 29 and 30, especially Vol. 30b. Since 1992–1993, the date of publication of the first of these volumes, a large amount of new data on the physical properties of dielectrics has appeared in the literature. In particular, various linear and nonlinear optical properties of new crystals in the borate family (BBO, LBO, CBO, and CLBO) and of new organic crystals (DLAP, MNMA, etc.) have been (re)measured in recent years. This situation has encouraged us to "refresh" the knowledge about these crystals by adding new data from publications from the last decade. We have also included the most commonly used isotropic materials. The criteria for the selection of 124 dielectrics out of several hundred were their wide range of application and the availability of most of the above-mentioned data.

One of our aims was to produce a "reader-friendly" compilation. For this purpose, all data on dielectrics

are presented in a unified form in tables that are similar for both isotropic materials and crystals of various symmetry classes. Moreover, *all* data for each particular material are collected together in one place. Sections 4.4.1–4.4.2 serve as a brief introduction to the various physical phenomena and to the definitions, symbols, and abbreviations used. All numerical data are presented in Sect. 4.4.4. The tables in this section are arranged according to piezoelectric classes in order of decreasing symmetry. Guidelines for searching for (and finding!) the required parameter in these tables can be found in Sect. 4.4.3.

The following table presents a list of the 124 different substances which have been selected to be described in Sect. 4.4.4.

**Alphabetical List of Described Crystals and Isotropic Dielectrics**

| Name of material | Formula | Symbol | Page |
|---|---|---|---|
| $\alpha$-Aluminium oxide (sapphire) | $Al_2O_3$ | | 844 |
| Aluminium phosphate (berlinite) | $AlPO_4$ | | 844 |
| Ammonium dideuterium phosphate | $ND_4D_2PO_4$ | AD*P or DADP | 856 |
| Ammonium dihydrogen arsenate | $NH_4H_2AsO_4$ | ADA | 856 |
| Ammonium dihydrogen phosphate | $NH_4H_2PO_4$ | ADP | 856 |
| Ammonium sulfate | $(NH_4)_2SO_4$ | | 872 |
| $\beta$-Barium borate | $BaB_2O_4$ | BBO | 848 |
| Barium fluoride | $BaF_2$ | | 828 |
| Barium formate | $Ba(COOH)_2$ | | 866 |
| Barium magnesium fluoride | $BaMgF_4$ | BMF | 872 |
| Barium nitrite monohydrate | $Ba(NO_2)_2 \cdot H_2O$ | | 842 |
| Barium sodium niobate (“banana”) | $Ba_2NaNb_5O_{15}$ | | 872 |
| Barium titanate | $BaTiO_3$ | | 864 |
| Beryllium oxide (bromellite) | $BeO$ | | 840 |
| Bismuth germanium oxide | $Bi_{12}GeO_{20}$ | BGO | 838 |
| Bismuth silicon oxide (sillenite) | $Bi_{12}SiO_{20}$ | BSO | 838 |
| Bismuth triborate | $BiB_3O_6$ | BIBO | 884 |
| BK7 Schott glass | | BK7 | 828 |
| Cadmium germanium arsenide | $CdGeAs_2$ | | 856 |
| Cadmium germanium phosphide | $CdGeP_2$ | | 856 |
| Cadmium selenide | $CdSe$ | | 840 |
| Cadmium sulfide (greenockite) | $CdS$ | | 840 |
| Cadmium telluride (Irtran-6) | $CdTe$ | | 834 |
| Calcite (calcspar, Iceland spar) | $CaCO_3$ | | 844 |
| Calcium fluoride (fluorite, fluorspar, Irtran-3) | $CaF_2$ | | 828 |
| Calcium tartrate tetrahydrate | $Ca(C_4H_4O_6) \cdot 4H_2O$ | L-CTT | 874 |
| Cesium dideuterium arsenate | $CsD_2AsO_4$ | CD*A or DCDA | 856 |
| Cesium dihydrogen arsenate | $CsH_2AsO_4$ | CsDA or CDA | 858 |

| Name of material | Formula | Symbol | Page |
|---|---|---|---|
| Cesium lithium borate | $CsLiB_6O_{10}$ | CLBO | 858 |
| Cesium triborate | $CsB_3O_5$ | CBO | 868 |
| *m*-Chloronitrobenzene | $ClC_6H_4NO_2$ | CNB | 875 |
| Copper bromide | CuBr | | 834 |
| Copper chloride (nantokite) | CuCl | | 834 |
| Copper gallium selenide | $CuGaSe_2$ | | 858 |
| Copper gallium sulfide | $CuGaS_2$ | | 858 |
| Copper iodide | CuI | | 834 |
| 2-Cyclooctylamino-5-nitropyridine | $C_{13}H_{19}N_3O_2$ | COANP | 874 |
| Deuterated L-arginine phosphate | $(ND_xH_{2-x})_2^+(CND)(CH_2)_3CH(ND_yH_{3-y})^+COO^- \cdot D_2PO_4^- \cdot D_2O$ | DLAP | 884 |
| Diamond | C | | 830 |
| 4-(*N*1*N*-Dimethylamino)-3-acetamido-nitrobenzene (*N*-[2-(dimethylamino)-5-nitrophenyl]-acetamide) | $C_{10}H_{13}N_3O_3$ | DAN | 884 |
| *N*, 2-Dimethyl-4-nitrobenzenamine | $C_8H_{10}N_2O_2$ | MNMA | 874 |
| Dipotassium tartrate hemihydrate | $K_2C_4H_4O_6 \cdot 0.5H_2O$ | DKT | 886 |
| Gadolinium molybdate | $Gd_2(MoO_4)_3$ | GMO | 876 |
| Gallium antimonide | GaSb | | 834 |
| Gallium arsenide | GaAs | | 834 |
| Gallium nitride | GaN | | 840 |
| Gallium phosphide | GaP | | 834 |
| Gallium selenide | GaSe | | 838 |
| Gallium sulfide | GaS | | 838 |
| Germanium | Ge | | 830 |
| Indium antimonide | InSb | | 836 |
| Indium arsenide | InAs | | 836 |
| Indium phosphide | InP | | 836 |
| $\alpha$-Iodic acid | $HIO_3$ | | 868 |
| Lead molybdate | $PbMoO_4$ | | 854 |
| Lead titanate | $PbTiO_3$ | | 864 |
| Lithium fluoride | LiF | | 830 |
| Lithium formate monohydrate | $LiCOOH \cdot H_2O$ | LFM | 876 |
| Lithium gallium oxide (lithium metagallate) | $LiGaO_2$ | | 876 |
| $\alpha$-Lithium iodate | $LiIO_3$ | | 842 |
| Lithium niobate | $LiNbO_3$ | | 848 |

| Name of material | Formula | Symbol | Page |
|---|---|---|---|
| Lithium niobate (MgO-doped) | $MgO:LiNbO_3$ | | 848 |
| Lithium sulfate monohydrate | $Li_2SO_4 \cdot H_2O$ | | 886 |
| Lithium tantalate | $LiTaO_3$ | | 848 |
| Lithium tetraborate | $Li_2B_4O_7$ | | 864 |
| Lithium triborate | $LiB_3O_5$ | LBO | 878 |
| Magnesium fluoride | $MgF_2$ | | 852 |
| Magnesium oxide | MgO | | 830 |
| Magnesium silicate (forsterite) | $Mg_2SiO_4$ | | 866 |
| $\alpha$-Mercurie sulfide (cinnabar) | HgS | | 846 |
| 3-Methyl 4-nitropyridine 1-oxide | $C_6N_2O_3H_6$ | POM | 868 |
| *m*-Nitroaniline (3-nitrobenzenamine, meta-nitroaniline) | $C_6H_4(NO_2)NH_2$ | mNA | 878 |
| Poly(methyl methacrylate) (Plexiglas®) | $(C_5H_8O_2)_n$ | PMMA | 828 |
| Potassium acid phthalate | $KH(C_8H_4O_4)$ | | 878 |
| Potassium bromide | KBr | | 830 |
| Potassium chloride (sylvine, sylvite) | KCl | | 830 |
| Potassium dideuterium arsenate | $KD_2AsO_4$ | KD*A or DKDA | 858 |
| Potassium dideuterium phosphate | $KD_2PO_4$ | KD*P or DKDP | 858 |
| Potassium dihydrogen arsenate | $KH_2AsO_4$ | KDA | 860 |
| Potassium dihydrogen phosphate | $KH_2PO_4$ | KDP | 860 |
| Potassium fluoroboratoberyllate | $KBe_2BO_3F_2$ | KBBF | 846 |
| Potassium iodide | KI | | 830 |
| Potassium lithium niobate | $K_3Li_2Nb_5O_{15}$ | KLINBO | 864 |
| Potassium niobate | $KNbO_3$ | | 880 |
| Potassium pentaborate tetrahydrate | $KB_5O_8 \cdot 4H_2O$ | KB5 | 880 |
| Potassium sodium tartrate tetrahydrate (Rochelle salt) | $KNa(C_4H_4O_6) \cdot 4H_2O$ | | 870 |
| Potassium titanate (titanyl) phosphate | $KTiOPO_4$ | KTP | 880 |
| Potassium titanyl arsenate | $KTiOAsO_4$ | KTA | 880 |
| Rubidium dideuterium arsenate | $RbD_2AsO_4$ | RbD*A, RD*A, or DRDA | 860 |
| Rubidium dideuterium phosphate | $RbD_2PO_4$ | RbD*P, RD*P, or DRDP | 860 |
| Rubidium dihydrogen arsenate | $RbH_2AsO_4$ | RbDA or RDA | 860 |
| Rubidium dihydrogen phosphate | $RbH_2PO_4$ | RbDP or RDP | 862 |
| Rubidium titanate (titanyl) phosphate | $RbTiOPO_4$ | RTP | 882 |

| Name of material | Formula | Symbol | Page |
|---|---|---|---|
| D(+)-Saccharose (sucrose) | $C_{12}H_{22}O_{11}$ | | 888 |
| Silicon | Si | | 830 |
| $\alpha$-Silicon carbide | SiC | | 840 |
| $\alpha$-Silicon dioxide (quartz) | $SiO_2$ | | 846 |
| Silicon dioxide (fused silica) | $SiO_2$ | | 828 |
| Silver antimony sulfide (pyrargyrite) | $Ag_3SbS_3$ | | 850 |
| Silver arsenic sulfide (proustite) | $Ag_3AsS_3$ | | 850 |
| Silver gallium selenide | $AgGaSe_2$ | | 862 |
| Silver gallium sulfide (silver thiogallate) | $AgGaS_2$ | | 862 |
| Sodium ammonium tartrate tetrahydrate (ammonium Rochelle salt) | $Na(NH_4)C_4H_4O_6 \cdot 4H_2O$ | | 870 |
| Sodium chlorate | $NaClO_3$ | | 838 |
| Sodium chloride (rock salt, halite) | NaCl | | 832 |
| Sodium fluoride | NaF | | 832 |
| Sodium nitrite | $NaNO_2$ | | 882 |
| Strontium fluoride | $SrF_2$ | | 832 |
| Strontium titanate | $SrTiO_3$ | | 832 |
| Tellurium | Te | | 846 |
| Tellurium dioxide (paratellurite) | $TeO_2$ | | 854 |
| Thallium arsenic selenide | $Tl_3AsSe_3$ | TAS | 850 |
| Titanium dioxide (rutile) | $TiO_2$ | | 852 |
| Tourmaline | $(Na, Ca)(Mg, Fe)_3B_3Al_6Si_6(O, OH, F)_{31}$ | | 850 |
| Triglycine sulfate | $(CH_2NH_2COOH)_3 \cdot H_2SO_4$ | TGS | 888 |
| Urea | $(NH_2)_2CO$ | | 862 |
| Yttrium aluminate | $YAlO_3$ | YAP or YALO | 866 |
| Yttrium aluminium garnet | $Y_3Al_5O_{12}$ | YAG | 832 |
| Yttrium lithium fluoride | $YLiF_4$ | YLF | 854 |
| Yttrium vanadate | $YVO_4$ | YVO | 852 |
| Zinc germanium diphosphide | $ZnGeP_2$ | | 862 |
| Zinc oxide (zincite) | ZnO | | 840 |
| Zinc selenide | ZnSe | | 836 |
| $\alpha$-Zinc sulfide (wurtzite) | ZnS | | 842 |
| Zinc telluride | ZnTe | | 836 |

The physical quantities used to describe the properties of the dielectric substances are drawn up as follows.

| Used Physical Qunatities, their Symbols and their Units | | |
|---|---|---|
| $B_{ij}$ $(B_m)$ | relative dielectric impermeability | dimensionless |
| $C$ | capacitance C/V | |
| $c_{ijkl}$ $(c_{mn})$ | elastic stiffness tensor | $10^9$ Pa = GPa |
| $D$ | electric displacement field (or electric flux density) | $C/m^2$ |
| $d_{ijk}$ $(d_{in})$ | piezoelectric strain tensor | $10^{-12}$ C/N |
| $E$ | electric field | V/m |
| $n$ | refractive index | dimensionless |
| $P$ | polarization (dipole moment per unit volume of matter) | $C/m^2$ |
| $p_{ijkl}$ $(p_{mn})$ | elastooptic tensor | dimensionless |
| $q_{ijkl}$ $(q_{mn})$ | piezooptic tensor | $10^{-9}\,Pa^{-1} = (GPa)^{-1}$ |
| $r_{ijk}$ $(r_{mk})$ | electrooptic coefficient | $10^{-12}$ m/V = pm/V |
| $r^{\mathbf{S}}_{mk}$, $r^{\mathbf{T}}_{mk}$ | electrooptic coefficient at constant strain or stress, respectively | $10^{-12}$ m/V = pm/V |
| $S_{ij}$ $(S_m)$ | strain tensor | dimensionless |
| $s_{ijkl}$ $(s_{mn})$ | elastic compliance tensor | $10^{-12}\,Pa^{-1} = (TPa)^{-1}$ |
| $T_{ij}$ $(T_m)$ | stress tensor | $10^9$ Pa = GPa |
| $\tan\delta$ | dissipation factor (loss tangent) | dimensionless |
| $\varrho$ | density | $g/cm^3$ |
| $\varepsilon_0$ | dielectric constant (or permittivity) of free space (vacuum), | $8.854\times10^{-12}$ C/V m |
| $\varepsilon$ | relative dielectric constant (permittivity) | dimensionless |
| $\kappa_{ij}$ | thermal conductivity | W/m K |
| $v^{\mathrm{s}}_{mn}$ | sound velocity in the direction $mn$ | m/s |
| $\chi_{ij}$ $\left(\chi^{(1)}_{ij}\right)$ | linear dielectric susceptibility | dimensionless |
| $\chi^{(2)}_{ijk}$, $d_{ijk}$ $(d_{im})$ | second-order nonlinear dielectric susceptibility | $10^{-12}$ m/V = pm/V |
| $\chi^{(3)}_{ijkl}$ | third-order nonlinear dielectric susceptibility | $10^{-22}\,m^2/V^2$ |



## 4.4.1 Dielectric Materials: Low-Frequency Properties

### 4.4.1.1 General Dielectric Properties

#### Density

The density of a substance is defined as the mass per unit volume of the substance:

$$\varrho = \frac{m}{V}\,, \tag{4.1}$$

where $V$ is the volume occupied by a mass $m$. The density is thus a measure of the volume concentration of mass.

#### Mohs Hardness Scale

In 1832, Mohs introduced a hardness scale ranging from 1 to 10, based on ten minerals:

1. talc, $Mg_3H_2SiO_{12}$;
2. gypsum, $CaSO_4 \cdot 2H_2O$;
3. iceland spar, $CaCO_3$;
4. fluorite, $CaF_2$;
5. apatite, $Ca_5F(PO_4)_3$;
6. orthoclase, $KAlSi_3O_8$;

7. quartz, $SiO_2$;
8. topaz, $Al_2F_2SiO_4$;
9. corundum, $Al_2O_3$;
10. diamond, C.

#### Thermal Conductivity

A temperature gradient between different parts of a solid causes a flow of heat. In an isotropic medium, the heat flux of thermal energy $h$ (i. e. the heat transfer rate per unit area normal to the direction of heat flow) is given by

$$h = -\kappa \operatorname{grad} T \,, \tag{4.2}$$

where $\kappa$ is the thermal conductivity. In a crystal, this expression is replaced by

$$h_i = -\kappa_{ij} \frac{\partial T}{\partial x_j} \,. \tag{4.3}$$

Here $\kappa_{ij}$ is the thermal-conductivity tensor. Note that other notations are also used in the literature, e.g. $\kappa \equiv \lambda$ or $\kappa \equiv k$.

### 4.4.1.2 Static Dielectric Constant (Low-Frequency)

In isotropic and cubic dielectric materials, the electric displacement field $D$, the electric field $E$, and the polarization $P$ are connected by the relation

$$D = \varepsilon_0 E + P = \varepsilon_0 (1 + \chi) E \,, \tag{4.4}$$

where $\varepsilon_0 = 8.854 \times 10^{-12}\,\mathrm{C/V\,m}$ is the dielectric constant (or permittivity) of free space (vacuum), and $\chi$ is the *dielectric susceptibility*. The relative dielectric constant of the material is defined as

$$\varepsilon = 1 + \chi \,, \tag{4.5}$$

and therefore (4.4) becomes

$$D = \varepsilon_0 \varepsilon E \,. \tag{4.6}$$

In anisotropic crystals, these equations should be written in tensor form:

$$D_i = \varepsilon_0 \varepsilon_{ij} E_j \,, \quad \varepsilon_{ij} = 1 + \chi_{ij} \,. \tag{4.7}$$

The following relations are valid:

$$\varepsilon_{ij} = \varepsilon_{ji} \,, \quad \chi_{ij} = \chi_{ji} \,. \tag{4.8}$$

Note that other notations are also used in the literature, e.g. $\varepsilon \equiv \varepsilon_\mathrm{r}$, or $\varepsilon \equiv \kappa$ and $\varepsilon_0 \equiv \kappa_0$.

### 4.4.1.3 Dissipation Factor

The capacitance $C$ of a capacitor filled with a dielectric is

$$C = \frac{\varepsilon_0 \varepsilon A}{d} \,, \tag{4.9}$$

where $A$ is the area of the two parallel plates and $d$ is the spacing between them. For a lossy dielectric, the relative dielectric constant $\varepsilon$ can be represented in a complex form,

$$\varepsilon = \varepsilon' - \mathrm{i}\varepsilon'' \,. \tag{4.10}$$

The imaginary part is the frequency-dependent conductivity

$$\sigma(\omega) = \omega \varepsilon_0 \varepsilon'' \,, \tag{4.11}$$

where $\omega$ is the frequency. The dissipation factor (or loss tangent) is defined as

$$\tan\delta = \varepsilon''/\varepsilon' \,. \tag{4.12}$$

and in anisotropic crystals

$$\tan\delta_1 = \frac{\varepsilon''_{11}}{\varepsilon'_{11}} \,; \quad \tan\delta_2 = \frac{\varepsilon''_{22}}{\varepsilon'_{22}} \,; \quad \tan\delta_3 = \frac{\varepsilon''_{33}}{\varepsilon'_{3}} \,; \tag{4.13}$$

The quality factor $Q$ of the dielectric is the reciprocal of the dissipation factor:

$$Q = 1/\tan\delta \,. \tag{4.14}$$

### 4.4.1.4 Elasticity

Hooke's law states that for sufficiently small deformations the strain is directly proportional to the stress. Thus the strain tensor $\mathbf{S}$ and the stress tensor $\mathbf{T}$ obey the relation

$$S_{ij} = s_{ijkl} T_{kl} \,, \tag{4.15}$$

where $s_{ijkl}$ is called the *elastic compliance constant* (or compliance, or elastic constant). The *elastic stiffness constant* (or stiffness, or Young's modulus) is the reciprocal tensor

$$c_{ijkl} = s^{-1}_{ijkl} \,, \tag{4.16}$$

**Table 4.4-1** The relations between $ij$ (tensor notation) and $m$ (matrix notation), $jk$ and $n$, and $kl$ and $n$

| Tensor notation | 11 | 22 | 33 | 23 or 32 | 31 or 13 | 12 or 21 |
|---|---|---|---|---|---|---|
| Matrix notation | 1 | 2 | 3 | 4 | 5 | 6 |

and for the stress tensor we have

$$T_{ij} = c_{ijkl} S_{kl} \,. \tag{4.17}$$

In the matrix notation for the elastic compliance and stiffness, we have

$$S_m = s_{mn} T_n \text{ and } T_m = c_{mn} S_n \,, \tag{4.18}$$

where

$$\begin{aligned} s_{ijkl} &= s_{mn} && \text{when both } m \text{ and } n \text{ are 1, 2, or 3 ,} \\ 2s_{ijkl} &= s_{mn} && \text{when either } m \text{ or } n \text{ is 4, 5, or 6} \\ 4s_{ijkl} &= s_{mn} && \text{when both } m \text{ and } n \text{ are 4, 5, or 6 ,} \\ c_{ijkl} &= c_{mn} && \text{for all } m \text{ and } n \text{ ;} \end{aligned} \tag{4.19}$$

and

$$\begin{aligned} S_{ij} &= S_m && \text{when } m \text{ is 1, 2, or 3 ,} \\ S_{ij} &= \frac{1}{2} S_m && \text{when } m \text{ is 4, 5, or 6 ,} \\ T_{ij} &= T_m && \text{for all } m \,. \end{aligned} \tag{4.20}$$

For relations between tensor and matrix notation, see Table 4.4-1. The sound velocity $v^{\mathrm{s}}_{mn}$ in the direction $mn$ in a crystal is given by

$$v^{\mathrm{s}}_{mn} = \sqrt{c_{mn}/\varrho} \,. \tag{4.21}$$

#### 4.4.1.5 Piezoelectricity

The phenomenon of the development of an electric moment $P_i$ if a stress $T_{jk}$ is applied to a crystal is called the direct piezoelectric effect:

$$P_i = d_{ijk} T_{jk} \,, \tag{4.22}$$

where $d_{ijk}$ is the piezoelectric strain tensor (or the piezoelectric moduli). The relation $d_{ijk} = d_{ikj}$ reduces the number of independent tensor components to 18. The matrix notation is introduced for the piezoelectric strain as follows:

$$\begin{aligned} d_{ijk} &= d_{in} && \text{when } n = 1, 2, \text{ or } 3 \,, \\ 2d_{ijk} &= d_{in} && \text{when } n = 4, 5, \text{ or } 6 \,, \end{aligned} \tag{4.23}$$

and thus

$$P_i = d_{in} T_n \,. \tag{4.24}$$

The relations between $jk$ and $n$ are presented in Table 4.4-1.

The converse piezoelectric effect is described by

$$S_{jk} = d_{ijk} E_i \tag{4.25}$$

and, correspondingly,

$$S_n = d_{in} E_i \,. \tag{4.26}$$

## 4.4.2 Optical Materials: High-Frequency Properties

#### 4.4.2.1 Crystal Optics: General

The dielectric properties of a medium at optical frequencies are given by

$$D = \varepsilon_0 \varepsilon E \,, \tag{4.27}$$

where $\varepsilon_0$ is the dielectric constant of free space and $\varepsilon$ is the relative dielectric constant of the material. From Maxwell's equations, the velocity of propagation of electromagnetic waves through the medium is given by

$$v = c/\sqrt{\varepsilon} \,, \tag{4.28}$$

where $c$ is the velocity in vacuum (the relative magnetic permeability is taken as 1). The refractive index $n = c/v$ is therefore $n = \sqrt{\varepsilon}$.

In an anisotropic medium,

$$D_i = \varepsilon_0 \varepsilon_{ij} E_j \,. \tag{4.29}$$

In this general case, two waves of different velocity may propagate through the crystal. The relative dielectric impermeabilities are defined as the reciprocals of the principal dielectric constants:

$$B_i = 1/\varepsilon_i = 1/n_i^2 \,. \tag{4.30}$$

#### 4.4.2.2 Photoelastic Effect

The photoelastic effect is the effect in which a change of the refractive index is caused by stress. The changes

in the relative dielectric impermeabilities are

$$\Delta B_{ij} = q_{ijkl} T_{kl} \,, \tag{4.31}$$

where the $q_{ijkl}$ are the piezooptic coefficients. The photoelastic effect can also be expressed in terms of the stress:

$$\Delta B_{ij} = p_{ijrs} S_{rs} \,, \tag{4.32}$$

where the $p_{ijrs} = q_{ijkl} c_{klrs}$ are the (dimensionless) elastooptic coefficients. In matrix notation,

$$\Delta B_m = q_{mn} T_n \quad \text{and} \quad \Delta B_m = p_{mn} S_n \,. \tag{4.33}$$

Note that $q_{mn} = q_{ijkl}$ when $n = 1, 2$, or 3 and $q_{mn} = 2q_{ijkl}$ when $n = 4, 5$, or 6; $p_{mn} = p_{ijrs}$ (see Table 4.4-1).

### 4.4.2.3 Electrooptic Effect

The electrooptic effect is the effect in which a change in the refractive index of a crystal is produced by an electric field:

$$n = n_0 + aE_0 + bE_0^2 + \dots \,, \tag{4.34}$$

where $a$ and $b$ are constants and $n_0$ is the refractive index at $E_0 = 0$. The linear electrooptic effect (Pockels effect) is due to the first-order term $aE_0$. In isotropic dielectrics and in crystals with a center of symmetry, $a = 0$, and only the second-order term $bE_0^2$ and higher even-order terms exist (Kerr effect).

The changes in the relative dielectric impermeabilities are

$$\Delta B_{ij} = r_{ijk} E_k \,, \tag{4.35}$$

where the $r_{ijk}$ are the electrooptic coefficients. Since $r_{ijk} = r_{jik}$, the number of independent tensor components is 18, and the above formula can be written in matrix notation (see Table 4.4-1):

$$\Delta B_m = r_{mk} E_k \quad (m = 1, 2, \dots, 6,\ k = 1, 2, 3) \,. \tag{4.36}$$

### 4.4.2.4 Nonlinear Optical Effects

The dielectric polarization $\boldsymbol{P}$ is related to the electromagnetic field $\boldsymbol{E}$ at optical frequencies by the material equation of the medium:

$$\boldsymbol{P}(\boldsymbol{E}) = \varepsilon_0 \left( \chi^{(1)} \boldsymbol{E} + \chi^{(2)} \boldsymbol{E}^2 + \chi^{(3)} \boldsymbol{E}^3 + \dots \right) \,, \tag{4.37}$$

where $\chi^{(1)} = n^2 - 1$ is the linear dielectric susceptibility, and $\chi^{(2)}$, $\chi^{(3)}$, etc. are the nonlinear dielectric susceptibilities.

The Miller delta formulation is

$$\varepsilon_0 E_i(\omega_3) = \delta_{ijk} P_j(\omega_1) P_k(\omega_2) \,, \tag{4.38}$$

where the Miller coefficient,

$$\delta_{ijk} = \frac{1}{2\varepsilon_0} \frac{\chi^{(2)}_{ijk}(\omega_3)}{\chi^{(1)}_{ii}(\omega_1) \chi^{(1)}_{jj}(\omega_2) \chi^{(1)}_{kk}(\omega_3)} \,, \tag{4.39}$$

has a small dispersion and is almost constant for a wide range of crystals.

For anisotropic media, the coefficients $\chi^{(1)}$ and $\chi^{(2)}$ are, in general, second- and third-rank tensors, respectively. In practice, the tensor

$$d_{ijk} = (1/2)\chi_{ijk} \tag{4.40}$$

is used instead of $\chi_{ijk}$. Usually the "plane" representation of $d_{ijk}$ in the form $d_{il}$ is used; the relations between $jk$ and $l$ are presented in Table 4.4-1.

The Kleinman symmetry conditions

$$\begin{aligned} &d_{21} = d_{16}, \quad d_{23} = d_{34}, \quad d_{14} = d_{25} = d_{36}, \\ &d_{26} = d_{12}, \quad d_{31} = d_{15}, \quad d_{32} = d_{24}, \quad d_{35} = d_{13} \end{aligned} \tag{4.41}$$

are valid in the case of no dispersion of the electronic nonlinear polarizability.

The following three-wave interactions in crystals with a square nonlinearity ($\chi^{(2)} \neq 0$) are possible:

- second-harmonic generation (SHG), $\omega + \omega = 2\omega$;
- sum frequency generation (SFG) or up-conversion, $\omega_1 + \omega_2 = \omega_3$;
- difference frequency generation (DFG) or down-conversion, $\omega_3 - \omega_2 = \omega_1$;
- optical parametric oscillation (OPO), $\omega_3 = \omega_2 + \omega_1$.

For efficient frequency conversion, the phase-matching condition $\boldsymbol{k}_1 + \boldsymbol{k}_2 = \boldsymbol{k}_3$, where the $\boldsymbol{k}_i$ are the wave vectors for $\omega_1$, $\omega_2$, and $\omega_3$, respectively, must be satisfied. Two types of phase matching can be defined:

type I: o + o → e or e + e → o ;

and

type II: o + e → e or o + e → o .

These can be represented with a shortened notation as follows:

ooe: o + o → e or e → o + o ;

eeo: e + e → o or o → e + e ;

eoe: e + o → e or e → e + o ;

oeo: o + e → o or o → e + o .

In the shortened notation (ooe, eoe, ... ), the frequencies satisfy the condition $\omega_1 < \omega_2 < \omega_3$, i. e. the first symbol refers to the longest-wavelength radiation, and the last symbol refers to the shortest-wavelength radiation. Here the ordinary beam, or o-beam is the beam with its polarization normal to the principal plane of the crystal, i. e. the plane containing the wave vector $\boldsymbol{k}$ and the crystallophysical axis $Z$ (or the optical axis, for uniaxial crystals). The extraordinary beam, or e-beam is the beam with its polarization in the principal plane. The third-order term $\chi^{(3)}$ is responsible for the optical Kerr effect.

### Uniaxial Crystals

For uniaxial crystals, the difference between the refractive indices of the ordinary and extraordinary beams, the birefringence $\Delta n$, is zero along the optical axis (the crystallophysical axis $Z$) and maximum in a direction normal to this axis. The refractive index for the ordinary beam does not depend on the direction of propagation. However, the refractive index for the extraordinary beam $n^{\mathrm{e}}(\theta)$, is a function of the polar angle $\theta$ between the $Z$ axis and the vector $\boldsymbol{k}$:

$$n^{\mathrm{e}}(\theta) = n_{\mathrm{o}} \left( \frac{1 + \tan^2 \theta}{1 + (n_{\mathrm{o}}/n_{\mathrm{e}})^2 \tan^2 \theta} \right)^{1/2} , \qquad (4.42)$$

where $n_{\mathrm{o}}$ and $n_{\mathrm{e}}$ are the refractive indices of the ordinary and extraordinary beams, respectively in the plane normal to the $Z$ axis, and are termed the *principal values*. If $n_{\mathrm{o}} > n_{\mathrm{e}}$ the crystal is called *negative*, and if $n_{\mathrm{o}} < n_{\mathrm{e}}$ it is called *positive*. For the o-beam, the indicatrix of the refractive indices is a sphere with radius $n_{\mathrm{o}}$, and for the e-beam it is an ellipsoid of rotation with semiaxes $n_{\mathrm{o}}$ and $n_{\mathrm{e}}$. In the crystal, in general, the beam is divided into two beams with orthogonal polarizations; the angle between these beams $\rho$ is the *birefringence* (or *walk-off*) angle.

Equations for calculating phase-matching angles in uniaxial crystals are given in [4.1–4].

### Biaxial Crystals

For biaxial crystals, the optical indicatrix is a bilayer surface with four points of interlayer contact, which correspond to the directions of the two optical axes. In the simple case of light propagation in the principal planes $XY$, $YZ$, and $XZ$, the dependences of the refractive indices on the direction of light propagation are represented by a combination of an ellipse and a circle. Thus, in the principal planes, a biaxial crystal can be considered as a uniaxial crystal; for example, a biaxial crystal with $n_Z > n_Y > n_X$ in the $XY$ plane is similar to a negative uniaxial crystal with $n_{\mathrm{o}} = n_Z$

$$n^{\mathrm{e}}(\varphi) = n_Y \left( \frac{1 + \tan^2 \varphi}{1 + (n_Y/n_X)^2 \tan^2 \varphi} \right)^{1/2} , \qquad (4.43)$$

where $\varphi$ is the azimutal angle. Equations for calculating phase-matching angles for propagation in the principal planes of biaxial crystals are given in [4.3–6].

## 4.4.3 Guidelines for Use of Tables

Tables 4.4-3 – 4.4-21 are arranged according to piezoelectric classes in order of decreasing symmetry (see Table 4.4-2), and alphabetically within each class. They contain a number of columns placed on two pages, even and odd. The following properties are presented for each dielectric material: density $\varrho$, Mohs hardness, thermal conductivity $\kappa$, static dielectric constant $\varepsilon_{ij}$, dissipation factor $\tan\delta$ at various temperatures and frequencies, elastic stiffness $c_{mn}$, elastic compliance $s_{mn}$ (for isotropic and cubic materials only), piezoelectric strain tensor $d_{in}$, elastooptic tensor $p_{mn}$, electrooptic coefficients $r_{mk}$ (the latter two at 633 nm unless otherwise stated), optical transparency range, temperature variation of the refractive indices $dn/dT$, refractive indices $n$ (the latter two at 1.064 µm unless otherwise stated), dispersion relations (Sellmeier equations), second-order nonlinear dielectric susceptibility $d_{ij}$, and third-order nonlinear dielectric susceptibility $\chi^{(3)}_{ijk}$ (for isotropic and cubic materials only) (the latter two at 1.064 µm unless otherwise stated). For isotropic materials, the two-photon absorption coefficient $\beta$ is also included

The numerical values of the elastic and elastooptic constants are often averages of three or more measurements, as presented in [4.7–11]. In such cases, the corresponding Landolt–Börnstein volume is cited together with the most reliable (latest) reference. The standard deviation of the averaged value is given in parentheses. Vertical bars ‖ mean the modulus of the corresponding quantity. The absolute scale for the second-order nonlinear susceptibilities of crystals is based on [4.12–14]. The second-order susceptibilities for all crystals measured relative to a standard crystal have been recalculated accordingly. In particular,

all previous measurements relative to KDP and quartz have been normalized to $d_{36}(\mathrm{KDP}) = 0.39\,\mathrm{pm/V}$ and $d_{11}(\mathrm{SiO_2}) = 0.30\,\mathrm{pm/V}$. These data lead to an accurate, self-consistent set of absolute second-order nonlinear coefficients [4.14]. All numerical data are for room temperature (300 K) and in SI units.

**Table 4.4-2** Number of independent components of the various property tensors

| Symmetry point group | Dielectric tensor[a] $\varepsilon_{ij}$ | Elastic tensor $c_{mn}$ or $s_{mn}$ | Piezoelectric tensor $d_{imn}$ | Elasto-optic tensor $p_{mn}$ or $q_{mn}$ | Electro-optic tensor $r_{mk}$ | Nonlinear susceptibility tensors[b] $\chi^{(2)}$ | $\chi^{(3)}$ | Table number |
|---|---|---|---|---|---|---|---|---|
| Isotropic | 1(1) | 2 | 0 | 2 | 0 | 0(0) | 1(1) | 4.4-3 |
| Cubic: | | | | | | | | |
| 432 ($O$) | 1(1) | 3 | 0 | 3 | 0 | 0(0) | 2(2) | |
| $m3m$ ($O_h$) | 1(1) | 3 | 0 | 3 | 0 | 0(0) | 2(2) | 4.4-4 |
| $\bar{4}3m$ ($T_d$) | 1(1) | 3 | 1 | 3 | 1 | 1(1) | 2(2) | 4.4-5 |
| 23 ($T$) | 1(1) | 3 | 1 | 4 | 1 | 1(1) | 3(2) | 4.4-6 |
| Hexagonal: | | | | | | | | |
| $6/mmm$ ($D_{6h}$) | 2(2) | 5 | 0 | 6 | 0 | 0(0) | 4(3) | |
| $6/m$ ($C_{6h}$) | 2(2) | 5 | 0 | 8 | 0 | 0(0) | 6(3) | |
| 622 ($D_6$) | 2(2) | 5 | 1 | 6 | 1 | 1(1) | 4(3) | |
| $\bar{6}m2$ ($D_{3h}$) | 2(2) | 5 | 1 | 6 | 1 | 1(1) | 4(3) | 4.4-7 |
| $\bar{6}$($C_6$) | 2(2) | 5 | 2 | 8 | 2 | 2(2) | 6(3) | |
| $6mm$ ($C_{6v}$) | 2(2) | 5 | 3 | 6 | 3 | 3(2) | 4(3) | 4.4-8 |
| 6 ($C_6$) | 2(2) | 5 | 4 | 8 | 4 | 4(3) | 6(3) | 4.4-9 |
| Trigonal: | | | | | | | | |
| $\bar{3}m$ ($D_{3d}$) | 2(2) | 6 | 0 | 8 | 0 | 0(0) | 5(4) | 4.4-10 |
| $\bar{3}$ ($C_{3i}$) | 2(2) | 7 | 0 | 12 | 0 | 0(0) | 10(5) | |
| 32 ($D_3$) | 2(2) | 6 | 2 | 8 | 2 | 2(2) | 5(4) | 4.4-11 |
| 3m ($C_{3v}$) | 2(2) | 6 | 4 | 8 | 4 | 4(3) | 5(4) | 4.4-12 |
| 3 ($C_3$) | 2(2) | 7 | 6 | 12 | 6 | 6(5) | 10(5) | |
| Tetragonal: | | | | | | | | |
| $4/mmm$ ($D_{4h}$) | 2(2) | 6 | 0 | 7 | 0 | 0(0) | 5(4) | 4.4-13 |
| $4/m$ ($C_{4h}$) | 2(2) | 7 | 0 | 10 | 0 | 0(0) | 8(6) | 4.4-14 |
| 422 ($D_4$) | 2(2) | 6 | 1 | 7 | 1 | 1(1) | 5(4) | 4.4-15 |
| $\bar{4}2m$ ($D_{2d}$) | 2(2) | 6 | 2 | 7 | 2 | 2(1) | 5(4) | 4.4-16 |
| $4mm$ ($C_{4v}$) | 2(2) | 6 | 3 | 7 | 3 | 3(2) | 5(4) | 4.4-17 |
| $\bar{4}$($S_4$) | 2(2) | 7 | 4 | 10 | 4 | 4(2) | 8(6) | |
| 4 ($C_4$) | 2(2) | 7 | 4 | 10 | 4 | 4(3) | 8(6) | |
| Orthorhombic: | | | | | | | | |
| $mmm$ ($D_{2h}$) | 3(3) | 9 | 0 | 12 | 0 | 0(0) | 9(6) | 4.4-18 |
| 222 ($D_2$) | 3(3) | 9 | 3 | 12 | 3 | 3(1) | 9(6) | 4.4-19 |
| $mm2$ ($C_{2v}$) | 3(3) | 9 | 5 | 12 | 5 | 5(3) | 9(6) | 4.4-20 |
| Monoclinic: | | | | | | | | |
| $2/m$ ($C_{2h}$) | 4(3) | 13 | 0 | 20 | 0 | 0(0) | 16(9) | |
| 2 ($C_2$) | 4(3) | 13 | 8 | 20 | 8 | 8(4) | 16(9) | 4.4-21 |
| $m$ ($C_s$) | 4(3) | 13 | 10 | 20 | 10 | 10(6) | 16(9) | |
| Triclinic: | | | | | | | | |
| $\bar{1}$ ($C_i$) | 9(3) | 21 | 0 | 36 | 0 | 0(0) | 30(15) | |
| 1 ($C_1$) | 9(3) | 21 | 18 | 36 | 18 | 18(10) | 30(15) | |

[a] The number of principal refractive indices $n_i$ is given in parentheses.

[b] The number of independent components for the case of Kleinman symmetry conditions is given in parentheses.

## 4.4.4 Tables of Numerical Data for Dielectrics and Electrooptics

**Table 4.4-3** Isotropic materials

| | General | Static dielectric constant | Dissipation factor | Elastic stiffness tensor | Elastic compliance tensor | Elastooptic tensor | |
|---|---|---|---|---|---|---|---|
| Material | $\varrho$ (g/cm$^3$)<br>Mohs hardness<br>$\kappa$ (W/m K) | $\varepsilon_{11}^{S}$<br>$\varepsilon_{11}^{T}$ | $\tan\delta_1$<br>($f$ (Hz)) | $c_{11}$<br>$c_{12}$<br>($10^9$ Pa) | $s_{11}$<br>$s_{12}$<br>($10^{-12}$ Pa$^{-1}$) | $p_{11}$<br>$p_{12}$ | |
| BK7 Schott glass | 2.510<br>–<br>1.114<br>[4.17] | | | 92.325 (145)<br>–<br>[4.15] | 12[b]<br>−2[b]<br>[4.16] | –<br>0.198 (22)<br>[4.15] | |
| Poly(methylmethacrylate), $(C_5H_8O_2)_n$ (PMMA, Plexiglas) | 1.190<br>2–3<br>0.2 [4.19] | 3.65 (19)[a]<br>[4.18] | 0.06<br>(50 Hz)<br>[4.18] | 9.282 (30)<br>–<br>[4.15] | 300[b]<br>8.9[b] [4.18] | | |
| Silicon dioxide, $SiO_2$ (Fused silica, fused quartz, vitreous quartz) | 2.202<br>5–6<br>1.38<br>[4.21] | 3.5[a]<br>[4.20] | $14\,(5)\times10^{-4}$<br>(1 MHz)<br>[4.20] | 77.806 (185)<br>–<br>[4.15] | 14[b]<br>−2.1[b]<br>[4.20] | –<br>0.243 (17)<br>[4.15] | |

[a] This value for $\varepsilon_{11}$ is neither at constant stress nor at constant strain.

[b] The elastic compliances are at constant electric field $(s^E)$ and have been calculated from the Young's modulus via $Y_0 = 1/s^E$ and from the shear modulus via $G = \left[2\left(s_{11}^E - s_{12}^E\right)\right]^{-1}$.

**Table 4.4-4** Cubic, point group $m3m$ ($O_h$) materials

| | General | Static dielectric constant | Dissipation factor | Elastic stiffness tensor | Elastic compliance tensor | Elastooptic tensor | |
|---|---|---|---|---|---|---|---|
| Material | $\varrho$ (g/cm$^3$)<br>Mohs hardness<br>$\kappa$ (W/m K) | $\varepsilon_{11}$ | $\tan\delta_1$<br>($f$ (Hz)) | $c_{11}$<br>$c_{44}$<br>$c_{12}$<br>($10^9$ Pa) | $s_{11}$<br>$s_{44}$<br>$s_{12}$<br>($10^{-12}$ Pa$^{-1}$) | $p_{11}$<br>$p_{12}$<br>$p_{44}$<br>$p_{11} - p_{12}$ | |
| Barium fluoride, $BaF_2$ | 4.89<br>3<br>11 [4.21, 22] | 7.33 [4.21] | | 91.1(10)<br>25.3(4)<br>41.2(15)<br>[4.7] | 15.2(1)<br>39.6(7)<br>−4.7(1)<br>[4.7] | 0.11<br>0.26<br>0.02<br>−0.14<br>(589–633 nm)<br>[4.23–25] | |
| Calcium fluoride, $CaF_2$ (fluorite, fluorspar, Irtran-3) | 3.179<br>4.0<br>9.71 [4.21, 22] | 7.4 [4.26] | | 165(2)<br>33.9(3)<br>47(3)<br>[4.7] | 6.93(14)<br>29.5(3)<br>−1.52(11)<br>[4.7] | 0.027<br>0.198<br>0.02<br>−0.17<br>(550–650 nm)<br>[4.23, 24, 27] | |

**Table 4.4-3** Isotropic materials, cont.

| General optical properties<br>Transparency range (μm)<br>$dn/dT$ ($10^{-5}$ K$^{-1}$) | Refractive index<br>$n$ | Two-photon absorption coefficient $\beta$<br>($10^{-9}$ cm/W) | Nonlinear dielectric susceptibility $\chi^{(3)}_{1111}$<br>($10^{-22}$ m$^2$/V$^2$) |
|---|---|---|---|
| 0.35–2.8 [4.16, 28]<br>0.28 (0.546 μm) [4.16] | **1.5067** [4.16]<br>For dispersion relation, see[c] [4.28] | 0.006 (351 nm) [4.29]<br>0.0029 (532 nm) [4.31] | 2.7 ± 0.2 [4.30] |
| 0.27–1.1<br>– | **1.503** (0.436 μm)<br>**1.493** (0.546 μm)<br>**1.489** (0.633 μm)<br>**1.481** (1.052 μm)<br>[4.32] | | |
| 0.17–4.0 [4.22]<br>1.5 (0.21 μm)<br>1.0 (0.4 μm)<br>1.2 (2.0 μm)<br>1.0 (3.7 μm)<br>[4.39] | **1.5343** (0.2139 μm)<br>**1.4872** (0.3022 μm)<br>**1.4601** (0.5461 μm)<br>**1.4494** (1.083 μm)<br>**1.4372** (2.0581 μm)<br>**1.3994** (3.7067 μm)<br>For dispersion relation, see [d] [4.39] | 0.75 (212.8 nm) [4.33]<br>0.5 (216 nm) [4.35]<br>0.08 (248 nm) [4.37]<br>0.045 (266 nm) [4.38] | 1.8 [4.34]<br>1.7 ± 0.3 [4.36] |

[cd] Dispersion relations (λ (μm), $T = 20\,^{\circ}$C):

[c] $$n^2 = 1 + \frac{1 + 1.03961212\lambda^2}{\lambda^2 - 0.00600069867} + \frac{0.2317923444\lambda^2}{\lambda^2 - 0.0200179144} + \frac{1.01046945\lambda^2}{\lambda^2 - 103.560653};$$

[d] $$n^2 = 1 + \frac{1 + 0.6961663\lambda^2}{\lambda^2 - (0.0684043)^2} + \frac{0.4079426\lambda^2}{\lambda^2 - (0.1162414)^2} + \frac{0.8974794\lambda^2}{\lambda^2 - (9.896161)^2}.$$

**Table 4.4-4** Cubic, point group $m3m$ ($O_h$) materials, cont.

| General optical properties | Refractive index[a] | | Nonlinear dielectric susceptibility |
|---|---|---|---|
| Transparency range (μm)<br>$dn/dT$ ($10^{-5}$ K$^{-1}$) | $n$<br>$A$<br>$B$<br>$C$ | $D$<br>$E$<br>$F$<br>$G$ | $\chi^{(3)}_{1111}$<br>$\chi^{(3)}_{1122}$<br>$\chi^{(3)}_{1133}$<br>($10^{-22}$ m$^2$/V$^2$) |
| 0.14–12.2 [4.40]<br>−1.60 (0.633 μm) [4.41]<br><br>−0.6 (0.150 μm)<br>−1.0 (0.590 μm)<br>−1.1 (15.0 μm) [4.43] | **1.678** (0.150 μm)<br>**1.557** (0.200 μm)<br>**1.5118** (0.266 μm)<br>**1.4744** (0.590 μm)<br>**1.4683** (1.05 μm)<br>**1.4441** (6.00 μm) | **1.4027** (9.00 μm)<br>**1.3865** (11.0 μm)<br>**1.305** (15.0 μm)<br>dispersion relations, see [4.43][a] | 1.548 ± 0.17<br>–<br>0.636 ± 0.06<br>(0.575; 0.613 μm)<br>[4.42] |
| 0.135–9.4 [4.40]<br>−1.04 (0.633 μm) [4.44]<br><br>−0.1 (0.150 μm)<br>−1.5 (0.590 μm)<br>−1.0 (12.0 μm) | **1.577** (0.150 μm)<br>**1.495** (0.200 μm)<br>**1.4621** (0.266 μm)<br>**1.4338** (0.590 μm)<br>**1.4286** (1.05 μm)<br>**1.3856** (6.00 μm) | **1.3268** (9.00 μm)<br>**1.268** (11.0 μm)<br>**1.230** (12.0 μm)<br>dispersion relations, see [4.43][b] | 0.8 ± 0.24<br>0.36 ± 0.1<br>(0.575; 0.613 μm)<br>[4.42] |

**Table 4.4-4** Cubic, point group $m3m$ ($O_h$) materials, cont.

| | General | Static dielectric constant | Dissipation factor | Elastic stiffness tensor | Elastic compliance tensor | Elastooptic tensor | |
|---|---|---|---|---|---|---|---|
| Material | $\varrho$ (g/cm$^3$)<br>Mohs hardness<br>$\kappa$ (W/m K) | $\varepsilon_{11}$ | $\tan\delta_1$<br><br>($f$ (Hz)) | $c_{11}$<br>$c_{44}$<br>$c_{12}$<br>($10^9$ Pa) | $s_{11}$<br>$s_{44}$<br>$s_{12}$<br>($10^{-12}$ Pa$^{-1}$) | $p_{11}$<br>$p_{12}$<br>$p_{44}$<br>$p_{11}-p_{12}$ | |
| Diamond, C | 3.52<br>10<br>660 (0 °C)<br>[4.22,45] | 5.5–10.0<br>[4.26] | | 1077(2)<br>577(1)<br>124.7(6)<br>[4.7] | 0.951(2)<br>1.732(3)<br>−0.0987(6)<br>[4.7] | −0.25<br>0.04<br>0.17<br>−0.30(1)<br>(514–633 nm) [4.46] | |
| Germanium, Ge | 5.33<br>6<br>58.61 [4.21] | 16.6 [4.21] | | 129(3)<br>67.1(5)<br>48(3) [4.7] | 9.73(5)<br>14.90(12)<br>−2.64(11)<br>[4.7] | | |
| Lithium fluoride, LiF | 2.639<br>4<br>4.01<br>[4.21] | 9.1 [4.21] | | 112(2)<br>63.5(6)<br>46(3)<br>[4.7] | 11.6(1)<br>15.8(2)<br>−3.35(13)<br>[4.7] | 0.02<br>0.13<br>−0.04(1)<br>−0.10<br>(589–633 nm)<br>[4.27,47] | |
| Magnesium oxide, MgO | 3.58<br>–<br>42 [4.21] | 9.7 [4.26] | 0.009<br>(10 GHz)<br>[4.48] | 294(6)<br>155(3)<br>93(5) [4.7] | 4.01(4)<br>6.46(12)<br>−0.96(2)<br>[4.7] | −0.25<br>−0.01<br>−0.10<br>−0.24 (589 nm)<br>[4.27,49] | |
| Potassium bromide, KBr | 2.753<br>1.5<br>4.816 [4.21] | 4.9 [4.21] | | 34.5(3)<br>5.1(2)<br>5.5(4)<br>[4.7] | 30.3(6)<br>196(6)<br>−4.2(3)<br>[4.7] | 0.22<br>0.17 (546–600 nm)<br>[4.50]<br>0.02<br>0.04 (488–600 nm)<br>[4.51] | |
| Potassium chloride, KCl (sylvine, sylvite) | 1.99<br>2<br>6.53 [4.21] | 4.6 [4.26] | | 40.5(4)<br>6.27(6)<br>6.9(3)<br>[4.7] | 25.9(1)<br>159(1)<br>−3.8(3)<br>[4.7] | 0.23<br>0.17<br>0.02<br>0.05 (546–600 nm)<br>[4.50–53] | |
| Potassium iodide, KI | 3.12<br>–<br>2.1 [4.21] | 5.6 [4.26] | | 27.4(5)<br>3.70(4)<br>4.3(2)<br>[4.7] | 38.2(8)<br>270(3)<br>−5.2(3)<br>[4.7] | 1.21<br>0.15<br>−0.031 [4.41]<br>– | |
| Silicon, Si | 2.329<br>7<br>163.3 [4.21] | 11.0–12.0<br>[4.26] | | 165(2)<br>79.1(6)<br>63(1)<br>[4.7] | 7.73(8)<br>12.70(9)<br>−2.15(4)<br>[4.7] | −0.094<br>0.017<br>−0.051<br>−0.111 (3390 nm)<br>[4.54–57] | |

**Table 4.4-4** Cubic, point group $m3m$ ($O_h$) materials, cont.

| | **General optical properties** | **Refractive index**[a] | | **Nonlinear dielectric susceptibility** |
|---|---|---|---|---|
| | Transparency range (μm)<br>$dn/dT$ $(10^{-5}\,\mathrm{K}^{-1})$ | $n$<br>$A$<br>$B$<br>$C$ | $D$<br>$E$<br>$F$<br>$G$ | $\chi^{(3)}_{1111}$<br>$\chi^{(3)}_{1122}$<br>$\chi^{(3)}_{1133}$<br>$(10^{-22}\,\mathrm{m^2/V^2})$ |
| | 0.24–27<br>1.01 (0.546 μm)<br>0.96 (30 μm)<br>[4.59, 60] | **2.7151** (0.2265 μm)<br>**2.4190** (0.578 μm)<br>**2.3914** (1.064 μm) | For dispersion relation, see[c] [4.58] | $\chi^{(3)}_{1122} = 4.87(12)$<br>$\chi^{(3)}_{1111} + 3\chi^{(3)}_{1122} = 30 \pm 0.8$<br>(both at 0.407 μm) [4.42]<br>$\chi^{(3)}_{1111} + 3\chi^{(3)}_{1133} = 65 \pm 20$<br>(0.53 μm) [4.61] |
| | 1.8–15 [4.62]<br>– | **4.0038** (10.6 μm)<br>9.28156<br>6.72880<br>0.44105 | 0.21307<br>3870.1<br>0<br>0 [4.63][d] | $56\,000 \pm 28\,000$<br>$34\,000 \pm 1200$<br>–<br>(10.6 and 9.5 μm) [4.64] |
| | 0.120–6.60<br>– | **1.387**<br>1<br>0.9259<br>0.005441 | 6.96747<br>1075<br>0<br>0 [4.65][d] | 1.12(24)<br>0.50<br>–<br>(0.6943 and 0.7456 μm)<br>[4.66] |
| | 0.35–6.8 [4.67]<br>1.95 (0.365 μm)<br>1.65 (0.546 μm)<br>1.36 (0.768 μm)<br>[4.68] | **1.7217**<br>1<br>1.111033<br>0.00507606 | 0.8460085<br>0.01891186<br>7.808527<br>723.2345<br>[4.69][d] | +1.4(2)<br>–<br>+0.77(15)<br>(0.6943 and 0.7456 μm)<br>[4.66] |
| | 0.200–30 [4.40]<br>−3.93 (0.458 μm)<br>−4.19 (1.15 μm)<br>−4.11 (10.6 μm) [4.41] | **1.5435**<br>For dispersion relation, see[e] [4.65] | | 15.7 [4.70]<br>5.8 [4.71]<br>6.2 (0.6943 and 0.7456 μm)<br>[4.66] |
| | 0.18–23.3 [4.40]<br>−3.49 (0.458 μm)<br>−3.62 (1.15 μm)<br>−3.48 (10.6 μm) [4.41] | **1.4792**<br>For dispersion relation, see[f] [4.65] | | 6.7 [4.70]<br>1.9 [4.71]<br>0.8 (0.6943 and 0.7456 μm)<br>[4.66] |
| | 0.32–42 [4.21]<br>−4.15 (0.458 μm)<br>−4.47 (1.15 μm)<br>−3.08 (30 μm) [4.41] | **1.6393**<br>For dispersion relation, see[g] [4.65] | | $1.4 \pm 0.3$ (0.6943 and 0.7456 μm)<br>[4.66]<br>–<br>– |
| | 1.1–6.5 [4.62]<br>– | **3.4176** (10.6 μm)<br>1<br>10.6684293<br>0.09091219 | 0.003043475<br>1.2876602<br>1.54133408<br>1 218 820 [4.73][d]<br>[4.74] | 24 300 [4.72]<br>–<br>33 000 [4.71] at 10.6 and 11.8 μm<br>$\chi^{(3)}_{1111} = 2800$<br>$\chi^{(3)}_{1122} = 1340$ [4.75] |

**Table 4.4-4** Cubic, point group $m3m$ ($O_h$) materials, cont.

| | General | Static dielectric constant | Dissipation factor | Elastic stiffness tensor | Elastic compliance tensor | Elastooptic tensor | |
|---|---|---|---|---|---|---|---|
| Material | $\varrho$ $(g/cm^3)$<br>Mohs hardness<br>$\kappa$ (W/m K) | $\varepsilon_{11}$ | $\tan\delta_1$<br><br>($f$ (Hz)) | $c_{11}$<br>$c_{44}$<br>$c_{12}$<br>($10^9$ Pa) | $s_{11}$<br>$s_{44}$<br>$s_{12}$<br>$(10^{-12}\,Pa^{-1})$ | $p_{11}$<br>$p_{12}$<br>$p_{44}$<br>$p_{11}-p_{12}$ | |
| Sodium chloride, NaCl<br>(rock salt, halite) | 2.17<br>2<br>1.15 [4.21] | 5.9 [4.26] | | 49.1(5)<br>12.8(1)<br>12.8(1)<br>[4.7] | 22.9(5)<br>78.3(8)<br>−4.8(1)<br>[4.7] | 0.128<br>0.171<br>−0.01<br>−0.04 (589–633 nm)<br>[4.52, 53, 76] | |
| Sodium fluoride, NaF | 2.558<br>–<br>3.746 [4.21] | 6 [4.21] | | 97.0(4)<br>28.1(3)<br>24.2(10)<br>[4.7] | 11.50(6)<br>35.6(4)<br>−2.30(7)<br>[4.7] | 0.03<br>0.14<br>–<br>−0.10 (589–633 nm)<br>[4.76–78] | |
| Strontium fluoride, $SrF_2$ | 4.24<br>–<br>1.42 [4.21] | 7.69 [4.21] | | 124(1)<br>31.8(3)<br>44(1)<br>[4.7] | 9.86(4)<br>31.5(3)<br>−2.57(5)<br>[4.7] | 0.080<br>0.269<br>0.018<br>−0.189 [4.23, 24] | |
| Strontium titanate,<br>$SrTiO_3$ | 5.12<br>6–6.5<br>12 [4.79] | 300 [4.48] | 0.02<br>(10 GHz)<br>[4.48] | 316(2)<br>123(1)<br>102(1)<br>[4.7] | 3.75(3)<br>8.15(8)<br>−0.92(1)<br>[4.7] | \|0.15\|<br>\|0.095\|<br>\|0.072\|<br>–<br>[4.80] | |
| Yttrium aluminium<br>garnet, $Y_3Al_5O_{12}$<br>(YAG) | 4.56<br>8–8.5<br>13.4 [4.81] | | | 333(3)<br>114(1)<br>111(3)<br>[4.7] | 3.61(4)<br>8.74(4)<br>−0.90(2)<br>[4.7] | −0.029<br>0.0091<br>−0.0615<br>−0.038 [4.82] | |

[a] The refractive index is given in **bold** type to distinguish it from the constants $A$, $B$, etc. in the dispersion relation.

[abcdefghij] Dispersion relations ($\lambda$ (μm), $T = 20\,°C$):

[a] $$\mathbf{n^2} = 1.33973 + \frac{0.81070\lambda^2}{\lambda^2 - 0.10065^2} + \frac{0.19652\lambda^2}{\lambda^2 - 29.87^2} + \frac{4.52469\lambda^2}{\lambda^2 - 53.82^2};$$

[b] $$\mathbf{n^2} = 1.33973 + \frac{0.69913\lambda^2}{\lambda^2 - 0.09374^2} + \frac{0.11994\lambda^2}{\lambda^2 - 21.18^2} + \frac{4.35181\lambda^2}{\lambda^2 - 38.46^2};$$

[c] $$\mathbf{n^2} = 2.37553 + \frac{0.0336440\lambda^2}{\lambda^2 - 0.028} - \frac{0.0887524}{(\lambda^2 - 0.028)^2} - 2.40455\times10^{-6}\lambda^2 + 2.21390\times10^{-9}\lambda^4;$$

[d] $$\mathbf{n^2} = A + \frac{B\lambda^2}{\lambda^2 - C} + \frac{D\lambda^2}{\lambda^2 - E} + \frac{F\lambda^2}{\lambda^2 - G};$$

[e] $$\mathbf{n^2} = 1.39408 + \frac{0.79221\lambda^2}{\lambda^2 - 0.0213} + \frac{0.01981\lambda^2}{\lambda^2 - 0.0299} + \frac{0.15587\lambda^2}{\lambda^2 - 0.0350} + \frac{0.17673\lambda^2}{\lambda^2 - 3674} + \frac{2.0621\lambda^2}{\lambda^2 - 7695}.$$

**Table 4.4-4** Cubic, point group $m3m$ ($O_h$) materials, cont.

| | General optical properties | Refractive index | | Nonlinear dielectric susceptibility |
|---|---|---|---|---|
| | Transparency range (μm)<br>$dn/dT$ $(10^{-5}\,\mathrm{K}^{-1})$ | $n$<br>$A$<br>$B$<br>$C$ | $D$<br>$E$<br>$F$<br>$G$ | $\chi^{(3)}_{1111}$<br>$\chi^{(3)}_{1122}$<br>$\chi^{(3)}_{1133}$<br>$(10^{-22}\,\mathrm{m^2/V^2})$ |
| | 0.2–16 [4.40]<br>−3.42 (0.458 μm)<br>−3.54 (0.633 μm)<br>−3.63 (3.39 μm) [4.41] | **1.5313**<br>For dispersion relation, see[h] [4.65] | | 6.7 [4.70]<br>2.78 [4.71]<br>at 0.6943 and 0.7456 μm<br>–<br>$\chi^{(3)}_{1111} = 9.5 \pm 2$,<br>$\chi^{(3)}_{1133} = 4.0 \pm 1.2$ [4.66] |
| | 0.135–11.2 [4.83]<br>−1.19 (0.458 μm)<br>−1.32 (0.633 μm)<br>−1.25 (3.39 μm) [4.41] | **1.32**<br>1.41572<br>0.32785<br>0.0137 | 3.18248<br>1646<br>0<br>0 [4.65][d] | 1.4 [4.70]<br>–<br>– |
| | 0.13–11<br>−0.9 (0.150 μm)<br>−1.2 (0.590 μm)<br>−0.4 (14.0 μm)<br>[4.43] | **1.59** (0.150 μm)<br>**1.50** (0.200 μm)<br>**1.47** (0.266 μm)<br>**1.4380** (0.590 μm)<br>**1.433** (1.05 μm)<br>**1.404** (6.00 μm) | **1.37** (9.00 μm)<br>**1.33** (11.0 μm)<br>**1.25** (14.0 μm)<br>dispersion relations, see [4.43][i] | $0.82 \pm 0.2$<br>–<br>$0.56 \pm 0.8$<br>(0.575; 0.613 μm)<br>[4.42] |
| | 0.41–5.1 [4.84, 85]<br>– | **2.3104**<br>1<br>3.042143<br>0.02178287 | 1.170065<br>0.08720717<br>30.83326<br>1101.3146 [4.86][d] | ≈ 2000<br>–<br>≈ 1000<br>(0.6943 and 0.7456 μm) [4.66] |
| | 0.21–5.3 [4.87]<br>0.905 [4.87] | **1.8422** (0.5 μm)<br>**1.8258** (0.7 μm)<br>**1.8186** (0.9 μm)<br>**1.8152** (1.05 μm)<br>**1.8149** (1.064 μm) | For dispersion relation, see[j] [4.88] | |

[f] $n^2 = 1.26486 + \frac{0.30523\lambda^2}{\lambda^2 - 0.0100} + \frac{0.41620\lambda^2}{\lambda^2 - 0.0172} + \frac{0.18870\lambda^2}{\lambda^2 - 0.0262} + \frac{2.6200\lambda^2}{\lambda^2 - 4959}$;

[g] $n^2 = 1.47285 + \frac{0.16512\lambda^2}{\lambda^2 - 0.0166} + \frac{0.41222\lambda^2}{\lambda^2 - 0.0306} + \frac{0.44163\lambda^2}{\lambda^2 - 0.0350} + \frac{0.16076\lambda^2}{\lambda^2 - 0.0480} + \frac{0.33571\lambda^2}{\lambda^2 - 4822} + \frac{1.92474\lambda^2}{\lambda^2 - 9612}$;

[h] $n^2 = 1.00055 + \frac{0.19800\lambda^2}{\lambda^2 - 0.00250} + \frac{0.48398\lambda^2}{\lambda^2 - 0.0100} + \frac{0.38696\lambda^2}{\lambda^2 - 0.0164} + \frac{0.25998\lambda^2}{\lambda^2 - 0.0250} + \frac{0.08796\lambda^2}{\lambda^2 - 1640} + \frac{3.17064\lambda^2}{\lambda^2 - 3719} + \frac{0.30038\lambda^2}{\lambda^2 - 14482}$;

[i] $n^2 = 1.33973 + \frac{0.7097\lambda^2}{\lambda^2 - 0.09597^2} + \frac{0.1788\lambda^2}{\lambda^2 - 26.03^2} + \frac{3.8796\lambda^2}{\lambda^2 - 45.60^2}$;

[j] $n^2 = 3.2968230 - 0.0166197\lambda^2 + 0.0126503\lambda^{-2} + 0.0069986\lambda^{-4} - 0.0013968\lambda^{-6} + 0.0001088\lambda^{-8}$.

**Table 4.4-5** Cubic, point group $\overline{4}3m$ ($T_d$) materials

| | General | Static dielectric constant | Dissipation factor | Elastic stiffness tensor | Piezoelectric strain tensor | Elastooptic tensor | |
|---|---|---|---|---|---|---|---|
| Material | $\varrho$ (g/cm$^3$)<br>Mohs hardness<br>$\kappa$ (W/m K) | $\varepsilon_{11}^{S}$<br>$\varepsilon_{11}^{T}$ | $\tan\delta_1$<br><br>($f$ (Hz)) | $c_{11}$<br>$c_{44}$<br>$c_{12}$<br>($10^9$ Pa) | $d_{14}$<br>($10^{-12}$ C/N) | $p_{11}$<br>$p_{12}$<br>$p_{44}$<br>$p_{11}-p_{12}$ | |
| Cadmium telluride, CdTe (Irtran-6) | 5.855<br>3<br>6.28 [4.79] | 9.65 (−196 °C)<br>[4.89]<br>11.00 (23 °C)<br>[4.90] | | 53.5(2)<br>20.2(2)<br>36.9(3)<br>[4.7] | 1.68(8)<br>(−196 °C)<br>[4.89] | −0.152<br>−0.017<br>−0.057<br>−0.135 (10 600 nm)<br>[4.91] | |
| Copper bromide, CuBr | | 7.9(8) (22 °C) [4.92]<br>6.6 (−193 °C) [4.93] | | 43.5<br>14.7<br>34.9<br>[4.95] | 16(1)<br>[4.94] | 0.072<br>0.195<br>−0.083<br>−0.123 [4.96] | |
| Copper chloride, CuCl (nantokite) | 4.136<br>–<br>– | 8.3(5)<br>9.2(5) [4.97, 98] | | 45.4<br>13.6[a]<br>36.3<br>[4.99] | 27.2(5)<br>[4.94] | 0.120<br>0.250<br>−0.082<br>−0.130 [4.96] | |
| Copper iodide, CuI | 5.60<br>–<br>– | –<br>6.5 (−269 °C) [4.93] | | 45.1<br>18.2[a]<br>30.7<br>[4.93] | 7(1)<br>[4.94] | 3.032<br>0.151<br>−0.068<br>−0.119 [4.96] | |
| Gallium antimonide, GaSb | 5.614<br>4.5<br>32 [4.101] | 15 [4.100]<br>15.7[b] [4.101] | | 88.4(9)<br>43.4(9)<br>40.3(8) [4.7] | −2.9 [4.100] | | |
| Gallium arsenide, GaAs | 5.3169<br>4.5<br>46.05 [4.16] | 12.95(10) [4.102]<br>13.08 [4.90] | 0.001<br>(2.5–10 GHz)<br>[4.103] | 118(1)<br>59.4(2)<br>53.5(5) [4.7] | −2.7 [4.100] | −0.16<br>−0.13<br>−0.05<br>−0.03 (1150 nm)<br>[4.96, 104] | |
| Gallium phosphide, GaP | 4.138<br>5<br>110 [4.101] | 11.1[b] [4.105] | | 141(3)<br>71.2(21)<br>62.4(12) [4.7] | | −0.151<br>−0.082<br>−0.074<br>−0.069 [4.82] | |

**Table 4.4-5** Cubic, point group $\overline{4}3m$ ($T_d$) materials, cont.

| | Electrooptic tensor | General optical properties | Refractive index | Nonlinear dielectric susceptibility Second order | Third order |
|---|---|---|---|---|---|
| | $r_{41}^{T}$ ($10^{-12}$ m/V) | Transparency range (μm)<br>$dn/dT$ ($10^{-5}$ K$^{-1}$) | ***n***<br>*A*<br>*B*<br>*C*<br>*D*<br>*E* | $d_{14}$ ($10^{-12}$ m/V) | $\chi^{(3)}_{1111}$<br>$\chi^{(3)}_{1122}$<br>$\chi^{(3)}_{1133}$<br>($10^{-22}$ m$^2$/V$^2$) |
| | 6.8 (10.6 μm)<br>[4.106] | 0.85–29.9 [4.85]<br>For temperature-dependent dispersion relations, see [4.110] | **2.693** (14 μm)<br>1<br>6.1977889<br>0.100533<br>3.2243821<br>5193.55 [4.111][c] | 170 ± 60 (10.6 μm)<br>60 ± 24 (28 μm)<br>[4.107–109] | |
| | −2.5(5) [4.112][f] | 0.50–20 [4.113]<br>– | **2.3365** (0.4358 μm)<br>**2.152** (0.532 μm)<br>**2.045** (1.064 μm)<br>**2.025** (10.6 μm)<br>[4.92, 113, 114] | −6.5 ± 1.3 (1.064 μm) [4.114]<br>−5.0 ± 1.5 (10.6 μm) [4.113] | |
| | −4.97(50) [4.115] | 0.45–15 [4.113]<br>– | **1.9216**<br>3.580<br>0.03162<br>0.1642<br>0.09288<br>0 [4.116][c] | −5.7 ± 1.1 (1.064 μm) [4.114]<br>−4.15 ± 1.2 (10.6 μm) [4.113] | |
| | 18 [4.117, 118][g] | 0.50–20 [4.113]<br>– | **2.5621** (0.4358 μm)<br>**2.378** (0.532 μm)<br>**2.245** (1.064 μm)<br>[4.113, 114] | −4.7 ± 1.0 (1.064 μm) [4.114]<br>−5.0 ± 1.5 (10.6 μm) [4.113] | |
| | | 1.8–20 [4.22, 85]<br>– | **3.820** (1.8 μm)<br>**3.898** (3.0 μm)<br>**3.824** (5.0 μm)<br>**3.843** (10 μm) [4.121] | +628 ± 63 (10.6 μm)<br>[4.119, 120] | |
| | 1.43(7) (1.15 μm)<br>1.24(4) (3.39 μm)<br>1.51(5) (10.6 μm)<br>[4.126] | 0.900–17.3 [4.122]<br>25 (1.15 μm)<br>20 (3.39 μm)<br>20 (10.6 μm) [4.127] | **3.5072**<br>3.5<br>7.497<br>0.167<br>1.935<br>1382 [4.129][c] | $d_{36} = 170$ (1.064 μm)<br>[4.13, 14, 123, 124]<br>$d_{36} = 83$ (10.6 μm)<br>[4.12, 14, 128] | 6700 [4.64]<br>1400 [4.125]<br>1700 [4.64]<br>(all at 10.6 μm) |
| | −0.76(3) [4.130] | 0.54–10.5<br>20 (0.546 μm)<br>16 (0.633 μm)<br>[4.131] | **3.1057**<br>For dispersion relation, see [4.132][d] | 100 [4.105, 131]<br>58 (10.6 μm) [4.131] | |

**Table 4.4-5** Cubic, point group $\overline{4}3m$ ($T_d$) materials, cont.

| | General | Static dielectric constant | Dissipation factor | Elastic stiffness tensor | Piezoelectric strain tensor | Elastooptic tensor | |
|---|---|---|---|---|---|---|---|
| Material | $\varrho$ (g/cm$^3$)<br>Mohs hardness<br>$\kappa$ (W/m K) | $\varepsilon_{11}^{\mathbf{S}}$<br>$\varepsilon_{11}^{\mathbf{T}}$ | $\tan\delta_1$<br><br>($f$ (Hz)) | $c_{11}$<br>$c_{44}$<br>$c_{12}$<br>($10^9$ Pa) | $d_{14}$<br>($10^{-12}$ C/N) | $p_{11}$<br>$p_{12}$<br>$p_{44}$<br>$p_{11}-p_{12}$ | |
| Indium antimonide, InSb | 5.78<br>–<br>18 [4.101] | 16.8[b] [4.101]<br>17 [4.100] | | 66.2(7)<br>30.2(3)<br>35.9(22) [4.7] | −2.35 [4.100] | 0.46<br>0.58<br>0.064 (10.6 µm)<br>–<br>[4.133, 134] | |
| Indium arsenide, InAs | 5.70<br>3.8<br>27 [4.101] | 15.5[b] [4.101]<br>14.5 [4.100] | | 84.4(17)<br>39.6(1)<br>46.4(19) [4.7] | −1.14 [4.100] | | |
| Indium phosphide, InP | 4.78<br>–<br>68 [4.101] | 12.56(20)[b] | See [4.135] | 101.1<br>45.6<br>56.1 [4.136] | | | |
| Zinc selenide, ZnSe | 5.26<br>3–4<br>19 [4.137] | 9.12<br>9.12 [4.89] | | 86.4(39)<br>40.2(18)<br>51.5(34) [4.7] | 1.1(1) [4.89] | \|0.100\|<br>\|0.065\|<br>\|0.065\| (633 nm)<br>[4.138]<br>−0.10 (10 600 nm)<br>[4.139] | |
| Zinc telluride, ZnTe | 6.34<br>6<br>18 [4.140] | 10.10<br>10.10 [4.89] | | 71.5(6)<br>31.1(3)<br>40.8(1) [4.7] | 0.91(5) [4.89] | −0.144<br>−0.094<br>−0.046 [4.141]<br>−0.040 [4.142] | |

[a] The elastic stiffness was measured at constant electric field ($c^E$).

[b] This value for $\varepsilon_{11}$ is neither at constant stress nor at constant strain.

[cde] Dispersion relations ($\lambda$ (µm), $T = 20\,^\circ$C):

[c] $n^2 = A + \dfrac{B\lambda^2}{\lambda^2 - C} + \dfrac{D\lambda^2}{\lambda^2 - E}$.

[d] $n^2 = 1 + \dfrac{1.390\lambda^2}{\lambda^2 - 0.0296} + \dfrac{4.131\lambda^2}{\lambda^2 - 0.05476} + \dfrac{2.570\lambda^2}{\lambda^2 - 0.1190} + \dfrac{2.056\lambda^2}{\lambda^2 - 757.35}$.

**Table 4.4-5** Cubic, point group $\overline{4}3m$ ($T_d$) materials, cont.

| | Electrooptic tensor | General optical properties | Refractive index | Nonlinear dielectric susceptibility Second order | Third order |
|---|---|---|---|---|---|
| | $r_{41}^{T}$ ($10^{-12}$ m/V)<br>– | Transparency range (μm)<br>$dn/dT$ ($10^{-5}$ K$^{-1}$)<br>– | ***n***<br>*A*<br>*B*<br>*C*<br>*D*<br>*E* | $d_{14}$ ($10^{-12}$ m/V) | $\chi^{(3)}_{1111}$<br>$\chi^{(3)}_{1122}$<br>$\chi^{(3)}_{1133}$<br>($10^{-22}$ m$^2$/V$^2$) |
| | | 8–30 [4.85]<br>– | **3.904** (14 μm)<br>**3.745** (28 μm) [4.107] | 660 [4.123]<br>2280 ± 270 (10.6 μm) [4.145]<br>580 (28 μm) [4.107] | See [4.143, 144] |
| | | 3.9–20 [4.85]<br>50 (4 μm)<br>40 (6 μm)<br>30 (10 μm) [4.127] | **3.49** (10.6 μm)<br>11.1<br>0.71<br>6.5076<br>2.75<br>2084.8 [4.146][c] | 346 (1.058 μm) [4.123]<br>249 (10.6 μm) [4.119, 120] | ≈ 25 000 (10.6 and 9.5 μm) [4.64] |
| | 1.45 (1.06 μm) [4.149] | 0.98–20 [4.147]<br>8.3 (5 μm)<br>8.2 (10.6 μm)<br>7.7 (20 μm) [4.150] | **3.44**<br>7.255<br>2.316<br>0.39225<br>2.765<br>1084.7 [4.151, 152][c] | 136 (1.058 μm) [4.148]<br>105 ± 11 (10.6 μm) [4.145] | |
| | 1.8 [4.153, 154]<br>2.2 (10.6 μm) [4.155] | 0.47–19 [4.122]<br>– | **2.48**<br>For dispersion relation, see [4.41][e] | +103 [4.122]<br>+80 (10.6 μm) [4.109, 156] | $1.05 \times 10^7$ (0.4606 μm)<br>2650 (0.532 μm)<br>1680 (1.064 μm)<br>(all for $\lvert\chi^{(3)}\rvert$) [4.157] |
| | 4.27 (0.616 μm) [4.153, 154] | 0.59–25 [4.14]<br>– | **2.69** (10.6 μm)<br>4.27<br>3.01<br>0.142<br>0<br>0 [4.158][c] | 3.47 [4.122]<br>+90 (10.6 μm) [4.108, 109] | |

[e] $n^2 = 1 + \frac{4.2980149\lambda^2}{\lambda^2 - 0.03688810} + \frac{0.62776557\lambda^2}{\lambda^2 - 0.14347626} + \frac{2.8955633\lambda^2}{\lambda^2 - 2208.4920}$.

[f] $r_{41}^{S}$.

[g] $n^3 r_{41}$.

**Table 4.4-6** Cubic, point group 23 ($T$) materials

| | General | Static dielectric constant | Dissipation factor | Elastic stiffness tensor | Piezoelectric strain tensor | Elastooptic tensor | |
|---|---|---|---|---|---|---|---|
| Material | $\varrho$ (g/cm$^3$)<br>Mohs hardness<br>$\kappa$ (W/m K) | $\varepsilon_{11}^{\mathbf{S}}$<br>$\varepsilon_{11}^{\mathbf{T}}$ | $\tan\delta_1$<br><br>($f$ (Hz)) | $c_{11}$<br>$c_{44}$<br>$c_{12}$<br>($10^9$ Pa) | $d_{14}$<br>($10^{-12}$ C/N) | $p_{11}$<br>$p_{12}$<br>$p_{44}$<br>$p_{11}-p_{12}$ | |
| Bismuth germanium oxide, $Bi_{12}GeO_{20}$ (BGO) | 9.239<br>5 [4.159]<br>– | 38.0(4)<br>[4.160]<br>40 [4.161] | 0.0035<br>[4.161] | 126.0<br>26.9<br>34.2 [4.163] | 37.58(4)<br>[4.162] | 0.12<br>0.10<br>0.09(1)<br>0.01 [4.164–169] | |
| Bismuth silicon oxide, $Bi_{12}SiO_{20}$ (BSO, sillenite) | 9.2<br>5 [4.159]<br>– | 42(1) [4.170]<br>64(2) [4.171] | 0.0004<br>($>1$ MHz)<br>[4.171] | 129(2)<br>24.7(2)<br>29.4(12) [4.7] | | 0.16<br>0.13<br>0.12<br>0.015 [4.172, 173] | |
| Sodium chlorate, $NaClO_3$ | 2.488<br>–<br>– | 4.8<br>5.85 [4.175] | | 49.6(5)<br>11.6(2)<br>14.7(6) [4.7] | −1.74 [4.174] | 0.162<br>0.24<br><br>−0.0198<br>−0.078<br>[4.176] | |

**Table 4.4-7** Hexagonal, point group $\overline{6}m2$ ($D_{3h}$) materials

| | General | Static dielectric tensor | Elastic stiffness tensor | Elastooptic tensor | |
|---|---|---|---|---|---|
| Material | $\varrho$ (g/cm$^3$)<br>Mohs hardness<br>$\kappa \perp c$<br>$\kappa \parallel c$<br>(W/m K) | $\varepsilon_{11}^{\mathbf{S}}$<br>$\varepsilon_{33}^{\mathbf{S}}$<br>$\varepsilon_{11}^{\mathbf{T}}$<br>$\varepsilon_{33}^{\mathbf{T}}$ | $c_{11}$<br>$c_{33}$<br>$c_{44}$<br>$c_{12}$<br>$c_{13}$<br>($10^9$ Pa) | $p_{11}$<br>$p_{12}$<br>$p_{13}$<br>$p_{31}$<br>$p_{33}$<br>$p_{44}$ | |
| Gallium selenide, GaSe | 5.0<br>2<br>9.0 ($\perp c$)<br>8.25 ($\parallel c$)<br>[4.178] | 7.45[a]<br>7.1[a]<br>9.80[a]<br>8.0(3)<br>[4.179] | 106.4(37)<br>35.8(15)<br>10.2(5)<br>30.0(25)<br>12.1(4) [4.7] | $\lvert p_{12}/p_{13}\rvert < 0.05$<br>[4.177] | |
| Gallium sulfide, GaS | 3.86<br>2<br>–<br>– | | 127(19)<br>42(11)<br>12.0(73)<br>35.7(45)<br>14.3(81) [4.7] | | |

[a] From IR measurements. "$\varepsilon^{\mathbf{S}}$" is $\varepsilon$ at optical frequencies.

**Table 4.4-6** Cubic, point group 23 ($T$) materials, cont.

| | **Electrooptic tensor** | **General optical properties** | **Refractive index** | **Nonlinear dielectric susceptibility** |
|---|---|---|---|---|
| | $r_{41}^{\mathbf{T}}$<br>($10^{-12}$ m/V) | Transparency range (μm)<br>$dn/dT$ ($10^{-5}$ K$^{-1}$) | $\boldsymbol{n}$<br>$A$<br>$B$<br>$C$<br>$D$<br>$E$ | $d_{14}$<br>($10^{-12}$ m/V) |
| | 4.1(1) | 0.385–7 [4.159, 180]<br>– | **2.55** (0.633 μm) [4.159] | |
| | 4.25–5.0<br>[4.181–183] | 0.390–6 [4.159, 180]<br>– | **2.54** (0.633 μm) [4.159] | |
| | 0.36 (0.4 μm)<br>0.39 (0.59 μm)<br>[4.185] | | **1.512** (0.6943 μm)<br>For dispersion relation, see [4.186][a] | 0.43 (0.6943 μm)<br>[4.184] |

[a] Dispersion relation (λ (μm), $T = 20\,^{\circ}$C):
$n^2 = A + \frac{B\lambda^2}{\lambda^2 - C} + \frac{D\lambda^2}{\lambda^2 - E} + \frac{F\lambda^2}{\lambda^2 - G}$.

**Table 4.4-7** Hexagonal, point group $\overline{6}m2$ ($D_{3h}$) materials, cont.

| | **Electrooptic tensor** | **General optical properties** | **Refractive index** | | **Nonlinear dielectric susceptibility** |
|---|---|---|---|---|---|
| | $r_{13}^{\mathbf{T}}$<br>$r_{33}^{\mathbf{T}}$<br>$r_{41}^{\mathbf{T}}$<br>$r_{51}^{\mathbf{T}}$<br>($10^{-12}$ m/V)<br>at λ = 633 nm | Transparency range (μm) | $\boldsymbol{n}_{\mathrm{o}}$<br>$A$<br>$B$<br>$C$<br>$D$<br>$E$<br>$F$ | $\boldsymbol{n}_{\mathrm{e}}$<br>$A$<br>$B$<br>$C$<br>$D$<br>$E$<br>$F$ | $d_{31}$<br>$d_{33}$<br>($10^{-12}$ m/V) |
| | 22 ($n_{\mathrm{o}}^3 r_{11}$)<br>[4.188, 189] | 0.62–20 [4.187] | **2.9082**<br>7.443<br>0.4050<br>0.0186<br>0.0061<br>3.1485<br>2194 [4.193][b] | **2.5676**<br>5.76<br>0.3879<br>0.2288<br>0.1223<br>1.8550<br>1780 [4.193][b] | $d_{22} = 54$ pm/V (10.6 μm)<br>[4.190–192] |
| | | 0.420– | | | $d_{16} = 84$ pm/V (0.6943 μm)<br>[4.194] |

[b] Dispersion relations (λ (mm), $T = 20\,^{\circ}$C):
$n^2 = A + \frac{B}{\lambda^2} + \frac{C}{\lambda^4} + \frac{D}{\lambda^6} + \frac{E\lambda^2}{\lambda^2 - F}$.

**Table 4.4-8** Hexagonal, point group $6mm$ ($C_{6v}$) materials

| | General | Static dielectric tensor | Elastic stiffness tensor | Piezoelectric tensor | Elastooptic tensor | |
|---|---|---|---|---|---|---|
| Material | $\varrho$ (g/cm$^3$)<br>Mohs hardness<br>$\kappa \perp c$<br>$\kappa \parallel c$<br>(W/m K) | $\varepsilon_{11}^{\mathbf{S}}$<br>$\varepsilon_{33}^{\mathbf{S}}$<br>$\varepsilon_{11}^{\mathbf{T}}$<br>$\varepsilon_{33}^{\mathbf{T}}$ | $c_{11}$<br>$c_{33}$<br>$c_{44}$<br>$c_{12}$<br>$c_{13}$<br>($10^9$ Pa) | $d_{31}$<br>$d_{33}$<br>$d_{15}$<br>$d_{\mathrm{h}}$<br>($10^{-12}$ C/N) | $p_{11}$<br>$p_{12}$<br>$p_{13}$<br>$p_{31}$<br>$p_{33}$<br>$p_{44}$ | |
| Beryllium oxide, BeO<br>(bromellite) | 3.010<br>–<br>370<br>–<br>[4.45] | 6.82[a]<br>7.62[a]<br>[4.195] | 460.6<br>491.6<br>147.7<br>126.5<br>88.4 [4.196] | −0.12(3)<br>+0.24(6)<br>–<br>–<br>[4.197] | | |
| Cadmium selenide, CdSe | 5.67<br>3.25<br>6.2 ($\perp c$)<br>6.9 ($\parallel c$)<br>[4.200] | 9.53<br>10.20<br>9.70<br>10.65<br>[4.89] | 74.1<br>83.6<br>13.17<br>45.2<br>39.3 [4.89][b] | −3.80(11)<br>7.81(23)<br>−10.1(4)<br>–<br>[4.201, 202] | See [4.198, 199] | |
| Cadmium sulfide, CdS<br>(greenockite) | 4.82<br>3–3.5<br>14 ($\perp c$)<br>16 ($\parallel c$)<br>[4.200] | 8.67(7)<br>9.53(7)<br>8.92(7)<br>10.20(7)<br>[4.203, 204] | 88.4(47)<br>95.2(22)<br>15.0(3)<br>55.4(39)<br>48.0(22)<br>[4.7, 205] | −5.09(9)<br>[4.203, 204]<br>+9.71(29)<br>[4.203, 204]<br>−11.91(39)<br>[4.203, 204]<br><0.05 [4.8] | −0.142<br>−0.066<br>−0.057<br>−0.041<br>−0.20<br>≈\|0.054\|<br>[4.82, 206] | |
| Gallium nitride, GaN | 6.15<br>–<br>1300<br>–<br>[4.208] | 9.5(3)<br>10.4(3)<br>[4.207][a] | 296<br>267<br>24.1<br>130<br>158 [4.209] | | | |
| $\alpha$-Silicon carbide, SiC | 3.217<br>–<br>490 [4.45]<br>– | $\varepsilon_{33} = 6.65$<br>[4.213] | 502<br>565<br>169<br>95<br>56 [4.214] | | See [4.210–212] | |
| Zinc oxide, ZnO<br>(zincite) | 5.605<br>–<br>29 [4.45]<br>– | 8.33(8)<br>8.81(10)<br>8.67(9)<br>11.26(12)<br>[4.215, 216] | 207.0<br>209.5<br>44.8<br>117.7<br>106.1<br>[4.215, 216][b] | −5.12(6)<br>[4.215, 216]<br>12.3(2)<br>[4.215, 216]<br>−8.3(3)<br>[4.215, 216]<br><0.2 [4.8] | \|0.221\|<br>\|0.099\|<br>−0.090<br>\|0.089\|<br>−0.263<br>−0.061 [4.90] | |

**Table 4.4-8** Hexagonal, point group $6mm$ ($C_{6v}$) materials, cont.

| | Electrooptic tensor | General optical properties | Refractive index | | Nonlinear dielectric susceptibility |
|---|---|---|---|---|---|
| | $r_{13}^{\mathbf{T}}$<br>$r_{33}^{\mathbf{T}}$<br>$r_{51}^{\mathbf{T}}$<br>($10^{-12}$ m/V)<br>at $\lambda = 633$ nm | Transparency range (μm)<br>$dn_o/dT$ ($10^{-5}$ K$^{-1}$)<br>$dn_e/dT$ ($10^{-5}$ K$^{-1}$) | $n_o$<br>$A$<br>$B$<br>$C$<br>$D$<br>$E$ | $n_e$<br>$A$<br>$B$<br>$C$<br>$D$<br>$E$ | $d_{31}$<br>$d_{33}$<br>$d_{15}$<br>($10^{-12}$ m/V) |
| | 1.33 ($r_{51}^{\mathbf{T}}$)<br>[4.218, 219] | 0.21–7, 15–25 [4.217]<br>0.818 [4.220]<br>1.34 [4.220] | **1.7055**<br>1<br>1.92274<br>0.0062536<br>1.24209<br>94.344 [4.222][c] | **1.7204**<br>1<br>1.96939<br>0.0073788<br>1.24209<br>109.82 [4.222][c] | 0.23<br>0.32<br>–<br>[4.156, 221] |
| | 1.8 ($r_{13}^{\mathbf{S}}$)<br>4.3 ($r_{33}^{\mathbf{S}}$)<br>[4.225] | 0.75–20 [4.223, 224]<br>–<br>– | **2.5375**<br>4.2243<br>1.768<br>0.227<br>3.12<br>3380 [4.227][c] | **2.5572**<br>4.2009<br>1.8875<br>0.2171<br>3.6461<br>3629 [4.227][c] | −29 (10.6 μm) [4.109]<br>+55 (10.6 μm) [4.109]<br>23 ± 3 (1.054 mm) [4.226] |
| | 2.45(8)<br>2.75(8)<br>1.7(3)<br>(all at 10.6 μm)<br>[4.126] | 0.53–16 [4.122]<br>5.86 (10.6 μm)<br>6.24 (10.6 μm)<br>[4.229] | **2.212** (10.6 μm)<br>5.235<br>−0.1819<br>0.1651<br>0 [4.230][d]<br>– | **2.225** (10.6 μm)<br>5.239<br>0.2076<br>0.1651<br>0 [4.230][d]<br>– | 16 [4.228]<br>32 [4.228]<br>18 [4.228]<br>−16 ($d_{31}$, 10.6 μm) [4.12, 14]<br>−16 ($d_{32}$, 10.6 μm) [4.12, 14]<br>32 ($d_{33}$, 10.6 μm) [4.12, 14] |
| | 0.57 ± 0.11 ($r_{31}$)<br>1.91 ± 0.35 ($r_{33}$)<br>[4.231] | 0.37–<br>–<br>– | **2.33**<br>3.60<br>1.75<br>0.0655<br>4.1<br>319 [4.207] | **2.35**<br>5.35<br>5.08<br>315.4<br>0 [4.207]<br>– | 21<br>44<br>25.5<br>[4.232] |
| | | 0.51–4<br>–<br>– | **2.5830**<br>1<br>5.5515<br>0.026406<br>0 [4.213][c]<br>– | **2.6225**<br>1<br>5.7382<br>0.028551<br>0 [4.213][c]<br>– | 5<br>50 [4.233]<br>– |
| | −1.4 ($r_{13}^{\mathbf{S}}$)<br>+2.6 ($r_{33}^{\mathbf{S}}$)<br>[4.225, 234, 235]<br>−3.1 ($r_{51}^{\mathbf{T}}$)<br>at 396 nm<br>[4.236] | 0.38–6.0<br>–<br>– | **1.939**<br>2.81418<br>0.87968<br>0.09254<br>0.00711 [4.222][e]<br>– | **1.955**<br>2.80333<br>0.94470<br>0.09024<br>0.00714 [4.222][e]<br>– | +1.7 ± 0.15<br>−5.6 ± 0.15<br>1.8 ± 0.15<br>[4.156, 228] |

**Table 4.4-8** Hexagonal, point group $6mm$ ($C_{6v}$) materials, cont.

| | General | Static dielectric tensor | Elastic stiffness tensor | Piezoelectric tensor | Elastooptic tensor | |
|---|---|---|---|---|---|---|
| Material | $\varrho$ (g/cm$^3$)<br>Mohs hardness<br>$\kappa \perp c$<br>$\kappa \parallel c$<br>(W/m K) | $\varepsilon_{11}^{\mathbf{S}}$<br>$\varepsilon_{33}^{\mathbf{S}}$<br>$\varepsilon_{11}^{\mathbf{T}}$<br>$\varepsilon_{33}^{\mathbf{T}}$ | $c_{11}$<br>$c_{33}$<br>$c_{44}$<br>$c_{12}$<br>$c_{13}$<br>($10^9$ Pa) | $d_{31}$<br>$d_{33}$<br>$d_{15}$<br>$d_{\mathrm{h}}$<br>($10^{-12}$ C/N) | $p_{11}$<br>$p_{12}$<br>$p_{13}$<br>$p_{31}$<br>$p_{33}$<br>$p_{44}$ | |
| $\alpha$-Zinc sulfide, $\alpha$-ZnS<br>(wurtzite, zinc blende) | 4.09<br>–<br>27 [4.45]<br>– | 8.58<br>8.52<br>8.60(5)<br>8.57(7)<br>[4.239, 240] | 122.0<br>140.2<br>28.5<br>58.0<br>46.8<br>[4.239, 240][b] | −1.1(0)<br>+3.2(1)<br>−2.8(1)<br>+1.0 [4.237, 238] | −0.115<br>0.017<br>0.025<br>0.0271<br>−0.13<br>−0.0627 [4.241] | |

[a] These values for $\varepsilon_{ij}$ are neither at constant stress nor at constant strain.
[b] The elastic stiffness constant were measured at constant electric field $(c^E)$.

**Table 4.4-9** Hexagonal, point group 6 ($C_6$) materials

| | General | Static dielectric tensor | Elastic stiffness tensor | Piezoelectric strain tensor | Elastooptic tensor | |
|---|---|---|---|---|---|---|
| Material | $\varrho$ (g/cm$^3$)<br>Mohs hardness<br>$\kappa \perp c$<br>$\kappa \parallel c$<br>(W/m K) | $\varepsilon_{11}^{\mathbf{S}}$<br>$\varepsilon_{33}^{\mathbf{S}}$<br>$\varepsilon_{11}^{\mathbf{T}}$<br>$\varepsilon_{33}^{\mathbf{T}}$ | $c_{11}$<br>$c_{33}$<br>$c_{44}$<br>$c_{12}$<br>$c_{13}$<br>($10^9$ Pa) | $d_{31}$<br>$d_{33}$<br>$d_{14}$<br>$d_{15}$<br>($10^{-12}$ C/N) | $p_{11}$<br>$p_{12}$<br>$p_{13}$<br>$p_{16}$<br>$p_{31}$<br>$p_{33}$<br>$p_{44}$<br>$p_{45}$ | |
| Barium nitrite monohydrate,<br>$Ba(NO_2)_2 \cdot H_2O$ | 3.179<br>–<br>–<br>–<br>– | –<br>–<br>7.56(8)<br>6.78(7)<br>[4.242] | 54.2<br>29.9<br>11.2<br>27.5<br>17.8<br>[4.242][b] | −1.73(17)<br>+3.27(16)<br>+0.47(9)<br>−1.03(10)<br>[4.242] | | |
| $\alpha$-Lithium iodate, $LiIO_3$ | 4.490<br>4<br>1.27 ($\perp c$)<br>0.65 ($\parallel c$)<br>[4.247, 248] | 7.9(4) (−20 °C)<br>[4.245]<br>5.9(3) (−20 °C)<br>[4.245]<br>8.25[a] (0 °C)<br>[4.246]<br>6.53[a] (0 °C)<br>[4.246] | 82.5(8)<br>55.9(23)<br>18.0(3)<br>31.9(8)<br>20.8(87)<br>[4.7, 249][b] | 3.5 [4.8, 243, 244]<br>48.5<br>[4.8, 243, 244]<br>73(7) [4.246]<br>55.5 [4.8, 243, 244] | \|0.32\|<br>–<br>\|0.24\|<br>\|0.03\|<br>\|0.41\|<br>\|0.23\| [4.250]<br>–<br>– | |

[a] The values for $\varepsilon_{ij}$ are neither at constant stress nor at constant strain.
[b] The elastic stiffness constants were measured at constant electric field $(c^E)$.

**Table 4.4-8** Hexagonal, point group $6mm$ ($C_{6v}$) materials, cont.

| | Electrooptic tensor | General optical properties | Refractive index | | Nonlinear dielectric susceptibility |
|---|---|---|---|---|---|
| | $r_{13}^{\mathrm{T}}$<br>$r_{33}^{\mathrm{T}}$<br>$r_{51}^{\mathrm{T}}$<br>($10^{-12}$ m/V)<br>at $\lambda = 633$ nm | Transparency range (μm)<br>$dn_o/dT$ ($10^{-5}$ K$^{-1}$)<br>$dn_e/dT$ ($10^{-5}$ K$^{-1}$) | $\boldsymbol{n}_o$<br>$A$<br>$B$<br>$C$<br>$D$<br>$E$ | $\boldsymbol{n}_e$<br>$A$<br>$B$<br>$C$<br>$D$<br>$E$ | $d_{31}$<br>$d_{33}$<br>$d_{15}$<br>($10^{-12}$ m/V) |
| | 0.92<br>1.85 [4.234, 235]<br>– | 0.35–23 [4.122]<br>–<br>– | **2.213** (10.6 μm)<br>3.4175<br>1.7396<br>0.07166<br>0 [4.222][e]<br>– | **2.219** (10.6 μm)<br>3.4264<br>1.7491<br>0.07150<br>0 [4.222][e]<br>– | $-18.9 \pm 6.3$<br>$+37.3 \pm 12.6$<br>$21.4 \pm 8.4$<br>(all at 10.6 μm)<br>[4.109, 251] |

[cde] Dispersion relations (λ (mm), $T = 20\,^{\circ}\mathrm{C}$):

[c] $n^2 = A + \dfrac{B\lambda^2}{\lambda^2 - C} + \dfrac{D\lambda^2}{\lambda^2 - E}$.

[d] $n^2 = A + \dfrac{B}{\lambda^2 - C} - D\lambda^2$.

[e] $n^2 = A + \dfrac{B\lambda^2}{\lambda^2 - C} - D\lambda^2$.

**Table 4.4-9** Hexagonal, point group 6 ($C_6$) materials, cont.

| | Electrooptic tensor | General optical properties | Refractive index | | Nonlinear dielectric susceptibility |
|---|---|---|---|---|---|
| | $r_{13}^{\mathrm{T}}$<br>$r_{33}^{\mathrm{T}}$<br>$r_{41}^{\mathrm{T}}$<br>$r_{51}^{\mathrm{T}}$<br>($10^{-12}$ m/V)<br>at $\lambda = 633$ nm | Transparency range (μm)<br>$dn_o/dT$ ($10^{-5}$ K$^{-1}$)<br>$dn_e/dT$ ($10^{-5}$ K$^{-1}$) | $\boldsymbol{n}_o$<br>$A$<br>$B$<br>$C$<br>$D$ | $\boldsymbol{n}_e$<br>$A$<br>$B$<br>$C$<br>$D$ | $d_{31}$<br>$d_{33}$<br>($10^{-12}$ m/V) |
| | +3.47(10)<br>+3.31(13)<br>−0.85(21)<br>−0.41(10)<br>[4.242] | 0.4–2 [4.252]<br>–<br>– | **1.6266** (0.5 μm)<br>1.99885<br>0.542910<br>0.04128<br>0.01012 [4.252][c] | **1.5238** (0.5 μm)<br>1.48610<br>0.775625<br>0.01830<br>0.00090 [4.252][c] | 1.14 [4.252]<br>– |
| | 6.4<br>4.2<br>3.1<br>7.9 ($r_{51}^{\mathrm{S}}$)<br>[4.256, 257] | 0.3–6.0 [4.253, 254]<br>−9.38 [4.255]<br>−8.25 [4.255] | **1.8571**<br>3.415716<br>0.047031<br>0.035306<br>0.008801 [4.258][c] | **1.7165**<br>2.918692<br>0.035145<br>0.028224<br>0.003641 [4.258][c] | 4.4<br>4.5 [4.12, 14] |

[c] Dispersion relation (λ (mm), $T = 20\,^{\circ}\mathrm{C}$):

$n^2 = A + \dfrac{B}{\lambda^2 - C} - D\lambda^2$.

**Table 4.4-10** Trigonal, point group $\overline{3}m$ ($D_{3d}$) materials

| | General | Static dielectric tensor | Dissipation factor | Elastic stiffness tensor | Elastic compliance tensor | Elastooptic tensor | |
|---|---|---|---|---|---|---|---|
| Material | $\varrho$ (g/cm$^3$)<br>Mohs hardness<br>$\kappa \perp c$<br>$\kappa \parallel c$<br>(W/m K) | $\varepsilon_{11}^{\mathbf{S}}$<br>$\varepsilon_{33}^{\mathbf{S}}$<br>$\varepsilon_{11}^{\mathbf{T}}$<br>$\varepsilon_{33}^{\mathbf{T}}$ | $\tan\delta_1$<br>$\tan\delta_3$ | $c_{11}$<br>$c_{33}$<br>$c_{44}$<br>$c_{12}$<br>$c_{13}$<br>$c_{14}$<br>($10^9$ Pa) | $s_{11}$<br>$s_{33}$<br>$s_{44}$<br>$s_{12}$<br>$s_{13}$<br>$s_{14}$<br>($10^{-12}$ Pa$^{-1}$) | $p_{11}$<br>$p_{12}$<br>$p_{13}$<br>$p_{14}$<br>$p_{31}$<br>$p_{33}$<br>$p_{41}$<br>$p_{44}$ | |
| $\alpha$-Aluminium oxide, $Al_2O_3$ (sapphire) | 3.98<br>9<br>33 ($\perp c$)<br>35 ($\parallel c$)<br>[4.259] | 9.4<br>11.5 [4.48][a] | 0.0001<br>[4.48]<br>– | 496(3)<br>499(4)<br>146(3)<br>159(10)<br>114(3)<br>−23(1)<br>[4.7, 260] | 2.35<br>2.17<br>6.95<br>−0.70<br>−0.38<br>0.46<br>[4.260] | −0.23<br>−0.03<br>0.02<br>0.00<br>0.04<br>−0.20<br>0.01<br>−0.10 (644 nm) [4.261] | |
| Calcite, $CaCO_3$ (calcspar, Iceland spar) | 2.71<br>3<br>3.00 ($\perp c$)<br>3.40 ($\parallel c$)<br>(50 °C)<br>[4.262] | 8.0[ab]<br>[4.26] | | 144(3)<br>84.3(26)<br>33.5(7)<br>54.2(47)<br>51.2(34)<br>−20.5(2)<br>[4.7, 263] | 11.4(2)<br>17.3(5)<br>41.4(12)<br>−4.0(4)<br>4.5(4)<br>9.5(5)<br>[4.7] | 0.062<br>0.147<br>0.186<br>−0.011<br>0.241<br>0.139<br>−0.036<br>−0.058 (514 nm) [4.264] | |

[a] These values for $\varepsilon_{11}$ are neither at constant stress nor at constant strain.
[b] It is not clear which relative dielectric constant $\varepsilon_{ij}$ is specified.

**Table 4.4-11** Trigonal, point group 32 ($D_3$) materials

| | General | Static dielectric tensor | Elastic stiffness tensor | Piezoelectric tensor | Elastooptic tensor | |
|---|---|---|---|---|---|---|
| Material | $\varrho$ (g/cm$^3$)<br>Mohs hardness<br>$\kappa \perp c$<br>$\kappa \parallel c$<br>(W/m K) | $\varepsilon_{11}^{\mathbf{S}}$<br>$\varepsilon_{33}^{\mathbf{S}}$<br>$\varepsilon_{11}^{\mathbf{T}}$<br>$\varepsilon_{33}^{\mathbf{T}}$ | $c_{11}$<br>$c_{33}$<br>$c_{44}$<br>$c_{12}$<br>$c_{13}$<br>$c_{14}$<br>($10^9$ Pa) | $d_{11}$<br>$d_{14}$<br>($10^{-12}$ C/N) | $p_{11}$<br>$p_{12}$<br>$p_{13}$<br>$p_{14}$<br>$p_{31}$<br>$p_{33}$<br>$p_{41}$<br>$p_{44}$ | |
| Aluminium phosphate, $AlPO_4$ (berlinite) | 2.620<br>6.5<br>≈6 [4.45]<br>– | 5.88<br>[4.8, 265]<br>–<br>4.73<br>4.62<br>[4.268, 269] | 67.0(26)<br>87.2(10)<br>42.9(4)<br>9.3(14)<br>13.1(21)<br>−12.7(5)<br>[4.7, 270][a] | −3.0<br>1.3<br>[4.266, 267] | | |

**Table 4.4-10** Trigonal, point group $\bar{3}m$ ($D_{3d}$) materials, cont.

| | General optical properties | Refractive index | |
|---|---|---|---|
| | Transparency range (μm)<br>$dn_o/dT$ ($10^{-5}$ K$^{-1}$)<br>$dn_e/dT$ ($10^{-5}$ K$^{-1}$) | $n_o$<br>$A$<br>$B$<br>$C$<br>$D$<br>$E$<br>$F$ | $n_e$<br>$A$<br>$B$<br>$C$<br>$D$<br>$E$<br>$F$ |
| | 0.147–5.2 [4.87]<br>–<br>– | **1.7655** (0.7 μm)<br>1.077<br>0.0033<br>1.025<br>0.0114<br>5.04<br>151.2 [4.271][cd] | **1.7573** (0.7 μm)<br>1.041<br>0.0004<br>1.030<br>0.0141<br>3.55<br>123.8 [4.271][cd] |
| | 0.2–2.3<br>0.21 (0.633 μm)<br>1.19 (0.633 μm) [4.22] | **1.6428** (1.042 μm) [4.272] | **1.4799** (1.042 μm) [4.272] |

[c] Dispersion relation (λ (μm), $T = 20\,°C$):
$$n^2 = 1 + \frac{A\lambda^2}{\lambda^2 - B} + \frac{C\lambda^2}{\lambda^2 - D} + \frac{E\lambda^2}{\lambda^2 - F}.$$
[d] For crystals grown by heat exchanger method (HEM).

**Table 4.4-11** Trigonal, point group 32 ($D_3$) materials, cont.

| | Electrooptic tensor | General optical properties | Refractive index | | Nonlinear dielectric susceptibility |
|---|---|---|---|---|---|
| | $r_{11}^T$<br>$r_{41}^T$<br>($10^{-12}$ m/V)<br>at λ = 633 nm | Transparency range (μm)<br>$dn_o/dT$ ($10^{-5}$ K$^{-1}$)<br>$dn_e/dT$ ($10^{-5}$ K$^{-1}$) | $n_o$<br>$A$<br>$B$<br>$C$<br>$D$<br>$E$ | $n_e$<br>$A$<br>$B$<br>$C$<br>$D$<br>$E$ | $d_{11}$<br>($10^{-12}$ m/V) |
| | | | **1.5161** (1 μm) [4.273] | **1.5285** (1 μm) [4.273] | 0.53 [4.228]<br>$d_{14} = 0.013$ [4.228] |

**Table 4.4-11** Trigonal, point group 32 ($D_3$) materials, cont.

| | General | Static dielectric tensor | Elastic stiffness tensor | Piezoelectric tensor | Elastooptic tensor | |
|---|---|---|---|---|---|---|
| Material | $\varrho$ (g/cm$^3$)<br>Mohs hardness<br>$\kappa \perp c$<br>$\kappa \parallel c$<br>(W/m K) | $\varepsilon_{11}^{S}$<br>$\varepsilon_{33}^{S}$<br>$\varepsilon_{11}^{T}$<br>$\varepsilon_{33}^{T}$ | $c_{11}$<br>$c_{33}$<br>$c_{44}$<br>$c_{12}$<br>$c_{13}$<br>$c_{14}$<br>($10^9$ Pa) | $d_{11}$<br>$d_{14}$<br>($10^{-12}$ C/N) | $p_{11}$<br>$p_{12}$<br>$p_{13}$<br>$p_{14}$<br>$p_{31}$<br>$p_{33}$<br>$p_{41}$<br>$p_{44}$ | |
| $\alpha$-Mercuric sulfide, HgS (cinnabar) | 8.05<br>2–2.5<br>–<br>– | 14.0(3)<br>25.5(5)<br>15.0(3)<br>25.5(5)<br>[4.275] | 35.36<br>50.92<br>21.40<br>7.02<br>8.66<br>11.3<br>[4.277][b] | 19.1<br>≈\|1.7\|<br>[4.8, 274] | –<br>–<br>\|0.445\|<br>–<br>–<br>\|0.115\| [4.276]<br>–<br>– | |
| Potassium fluoroboratoberyllate, $KBe_2BO_3F_2$ (KBBF) | | | | | | |
| $\alpha$-Silicon dioxide, $SiO_2$ (quartz) | 2.6485<br>7<br>6.5 ($\perp c$)<br>11.7 ($\parallel c$)<br>[4.200] | 4.435<br>4.640<br>4.520<br>4.640 [4.280] | 86.6(3)<br>106.4(12)<br>58.0(7)<br>6.7(9)<br>12.4(16)<br>17.8(3) [4.7][a] | +2.3<br>−0.67<br>[4.278, 279] | 0.16<br>0.27<br>0.27<br>−0.030<br>0.29<br>0.10<br>−0.047<br>−0.079 (589 nm)<br>[4.281] | |
| Tellurium, Te | 6.25<br>2–2.5<br>2.0 ($\perp c$)<br>3.4 ($\parallel c$)<br>[4.285] | 33 [4.282]<br>53 [4.282]<br>–<br>37 [4.284] | 33(1)<br>71(3)<br>31.8(25)<br>9.1(7)<br>24.5(15)<br>(−)12.4(15)<br>[4.7] | +55<br>+50 [4.283] | 0.164<br>0.138<br>0.146<br>−0.04<br>−0.086<br>0.038<br>0.28<br>0.14 (10.6 µm) [4.286] | |

[a] These values are approximately the constant-field values $c^E$.

[b] $c^E$ at constant electric field.

[cde] Dispersion relations ($\lambda$ (µm), $T = 20\,^\circ$C):

[c] $n^2 = A + \frac{B\lambda^2}{\lambda^2 - C} + \frac{D\lambda^2}{\lambda^2 - E}$.

**Table 4.4-11** Trigonal, point group 32 ($D_3$) materials, cont.

| | Electrooptic tensor | General optical properties | Refractive index | | Nonlinear dielectric susceptibility |
|---|---|---|---|---|---|
| | $r_{11}^{\mathbf{T}}$<br>$r_{41}^{\mathbf{T}}$<br>($10^{-12}$ m/V)<br>at $\lambda = 633$ nm | Transparency range (μm)<br>$dn_o/dT$ ($10^{-5}$ K$^{-1}$)<br>$dn_e/dT$ ($10^{-5}$ K$^{-1}$) | $n_o$<br>$A$<br>$B$<br>$C$<br>$D$<br>$E$ | $n_e$<br>$A$<br>$B$<br>$C$<br>$D$<br>$E$ | $d_{11}$<br>($10^{-12}$ m/V) |
| | 3.1<br>1.55 [4.289] | 0.63–13.5 [4.287]<br>–<br>– | **2.7041**<br>4.1506<br>2.7896<br>0.1328<br>1.1378<br>705 [4.227][c] | **2.9909**<br>4.0101<br>4.3736<br>0.1284<br>1.5604<br>705 [4.227][c] | 50 (10.6 μm) [4.288] |
| | | 0.155–3.5 [4.290]<br>–<br>– | **1.487** (0.4 μm)<br>1<br>1.169725<br>0.00624<br>0.009904 [4.290][d]<br>– | **1.410** (0.4 μm)<br>1<br>0.956611<br>0.0061926<br>0.027849 [4.290][d]<br>– | 0.76 [4.290] |
| | −0.445(10)<br>+0.1904(50)<br>[4.293] | 0.15–4.5 [4.262]<br>−0.62 (546 nm)<br>−0.7 (546 nm) [4.68] | **1.5350** (1 μm)<br>For dispersion relation, see [4.68][e] | **1.5438** (1 μm)<br>For dispersion relation, see [4.68][e] | 0.30<br>[4.12–14, 128, 291, 292] |
| | | 3.8–32 [4.85]<br>–<br>– | **4.7979** (10.6 μm)<br>18.5346<br>4.3289<br>3.9810<br>3.78<br>11.813 [4.227][c] | **6.2483** (10.6 μm)<br>29.5222<br>9.3068<br>2.5766<br>9.235<br>13.521 [4.227][c] | 598 (10.6 μm) [4.294] |

[d] $n^2 = A + \dfrac{B\lambda^2}{\lambda^2 - C} - D\lambda^2$ .

[e] $n_o^2 = 1 + \dfrac{0.663044\lambda^2}{\lambda^2 - 0.0036} + \dfrac{0.517852\lambda^2}{\lambda^2 - 0.0112} + \dfrac{0.175912\lambda^2}{\lambda^2 - 0.0142} + \dfrac{0.565380\lambda^2}{\lambda^2 - 78.216} + \dfrac{1.675299\lambda^2}{\lambda^2 - 430.23}$ ;

$n_e^2 = 1 + \dfrac{0.665721\lambda^2}{\lambda^2 - 0.0036} + \dfrac{0.503511\lambda^2}{\lambda^2 - 0.0112} + \dfrac{0.214792\lambda^2}{\lambda^2 - 0.0142} + \dfrac{0.539173\lambda^2}{\lambda^2 - 77.30} + \dfrac{1.807613\lambda^2}{\lambda^2 - 390.85}$.

**Table 4.4-12** Trigonal, point group $3m$ ($C_{3v}$) materials

| | General | Static dielectric tensor | Dissipation factor | Elastic stiffness tensor | Piezoelectric tensor | Elastooptic tensor |
|---|---|---|---|---|---|---|
| Material | $\varrho$ (g/cm$^3$)<br>Mohs hardness<br>$\kappa \perp c$<br>$\kappa \parallel c$<br>(W/m K) | $\varepsilon_{11}^{S}$<br>$\varepsilon_{33}^{S}$<br>$\varepsilon_{11}^{T}$<br>$\varepsilon_{33}^{T}$ | $\tan\delta_1$<br>$\tan\delta_3$<br><br>($f$ (kHz)) | $c_{11}$<br>$c_{33}$<br>$c_{44}$<br>$c_{12}$<br>$c_{13}$<br>$c_{14}$<br>($10^9$ Pa) | $d_{22}$<br>$d_{31}$<br>$d_{33}$<br>$d_{15}$<br>$d_h$<br>($10^{-12}$ C/N) | $p_{11}$<br>$p_{12}$<br>$p_{13}$<br>$p_{14}$<br>$p_{31}$<br>$p_{33}$<br>$p_{41}$<br>$p_{44}$ |
| $\beta$-Barium borate, $BaB_2O_4$ (BBO) | 3.849<br>4<br>1.2 ($\perp c$)<br>1.6 ($\parallel c$)<br>[4.200] | –<br>–<br>6.7<br>8.1 [4.295] | $< 10^{-3}$<br>$< 10^{-3}$<br>(10–50 °C,<br>1–100 kHz)<br>[4.295] | 123.8<br>53.3<br>7.8<br>60.3<br>49.4<br>12.3 [4.295] | | |
| Lithium niobate, $LiNbO_3$ | 4.628<br>5–5.5<br>4.6 [4.137] | 43.9(22) [4.296]<br>23.7(12) [4.296]<br>85.2 [4.298]<br>28.7 [4.298] | 0.0015(4)<br>0.0011(3)<br>(1 GHz)<br>[4.296] | 202(2)<br>244(5)<br>60.2(6)<br>55(2)<br>72(5)<br>8.5(7) [4.7][a] | 20.7(1) [4.297]<br>−0.86(2) [4.297]<br>+16.2(1) [4.297]<br>74.0(3) [4.297]<br>6.310(14) [4.299] | −0.031(9)<br>0.082(9)<br>0.135(7)<br>−0.076(15)<br>0.170(14)<br>0.069(5)<br>−0.150(10)<br>0.147(100) [4.11][b] |
| Lithium niobate (5% MgO-doped) MgO:$LiNbO_3$ | | | | | | |
| Lithium tantalate, $LiTaO_3$ | 7.45<br>5.5 | 42.6<br>42.8<br>53.6<br>43.4 [4.298] | 0.0013(4)<br>0.0007(3)<br>(1 GHz)<br>[4.296] | 230(2)<br>276(6)<br>96(1)<br>42(6)<br>79(4)<br>−11(1)<br>[4.7, 301, 302] | 8.5 [4.300]<br>−3.0 [4.300]<br>9.2 [4.300]<br>26 [4.300]<br>2.000(12) [4.299] | −0.081<br>0.081<br>0.093<br>−0.026<br>0.089<br>−0.044<br>−0.085<br>0.028 [4.303, 304] |

**Table 4.4-12** Trigonal, point group $3m$ ($C_{3v}$) materials, cont.

| | Electrooptic tensor | General optical properties | Refractive index | | Nonlinear dielectric susceptibility |
|---|---|---|---|---|---|
| | $r_{13}^{\mathbf{T}}$<br>$r_{22}^{\mathbf{T}}$<br>$r_{33}^{\mathbf{T}}$<br>$r_{51}^{\mathbf{T}}$<br>($10^{-12}$ m/V)<br>at $\lambda = 633$ nm | Transparency range (μm)<br>$dn_o/dT$ ($10^{-5}$ K$^{-1}$)<br>$dn_e/dT$ ($10^{-5}$ K$^{-1}$) | $\boldsymbol{n}_o$<br>$A$<br>$B$<br>$C$<br>$D$<br>$E$<br>$F$ | $\boldsymbol{n}_e$<br>$A$<br>$B$<br>$C$<br>$D$<br>$E$<br>$F$ | $d_{31}$<br>$d_{33}$<br>$d_{22}$<br>$d_{15}$<br>($10^{-12}$ m/V) |
| $\beta$-Barium borate, $BaB_2O_4$ (BBO) | +0.27(2)<br>−2.41(3)<br>+0.29(3)<br>+1.7(1) [4.310] | 0.189–3.5<br>[4.295, 305–308]<br>−1.66 [4.295]<br>−0.93 [4.295] | **1.6551**<br>2.7359<br>0.01878<br>0.01822<br>0.01471<br>0.0006081<br>0.0000674 [4.311][h] | **1.5426**<br>2.3753<br>0.01224<br>0.01667<br>0.01627<br>0.0005716<br>0.00006305 [4.311][h] | 2.16 ± 0.08 ($d_{22}$)<br>[4.12, 14, 309] |
| Lithium niobate, $LiNbO_3$ | +9.6<br>+6.8<br>+30.9<br>+32.6<br>[4.315, 316] | 0.33–5.5 [4.312]<br>$dn_o/dT = 0.141$ [4.313][f]<br>$dn_o/dT = 2.0$ [4.314][g]<br>$dn_e/dT = 3.85$ [4.313][f]<br>$dn_e/dT = 7.6$ [4.314][g] | **2.2340**<br>4.91296<br>0.116275<br>0.048398<br>0.0273 [4.313][i]<br>–<br>– | **2.1554**<br>4.54528<br>0.091649<br>0.046079<br>0.0303 [4.313][i]<br>–<br>– | −4.6<br>−25 [4.13, 14]<br>–<br>– |
| Lithium niobate (5% MgO-doped) MgO:$LiNbO_3$ | 11.2(5)<br>–<br>36.0(5)<br>–<br>(for 10.7% MgO)<br>[4.320] | 0.4–5 [4.317–319]<br>–<br>– | **2.2272**<br>4.9017<br>0.112280<br>0.049656<br>0.039636 [4.317, 318][i]<br>–<br>– | **2.1463**<br>4.5583<br>0.091806<br>0.048086<br>0.032068 [4.317, 318][i]<br>–<br>– | −4.69 [4.309]<br>\|25\| [4.13]<br>–<br>– |
| Lithium tantalate, $LiTaO_3$ | 4.5<br>0.3<br>27<br>15<br>(all for $r^{\mathbf{S}}$ at 3.39 μm) [4.323] | 0.4–5.5<br>–<br>– | **2.1366** (1.058 μm)<br>[4.321] | **2.1406** (1.058 μm)<br>[4.321] | −1.0 ± 0.2<br>−16 ± 2<br>+1.7 ± 0.2 [4.156, 322]<br>– |

**Table 4.4-12** Trigonal, point group $3m$ ($C_{3v}$) materials, cont.

| | General | Static dielectric tensor | Dissipation factor | Elastic stiffness tensor | Piezoelectric tensor | Elastooptic tensor | |
|---|---|---|---|---|---|---|---|
| Material | $\varrho$ (g/cm$^3$)<br>Mohs hardness<br>$\kappa \perp c$<br>$\kappa \parallel c$<br>(W/m K) | $\varepsilon_{11}^{\mathbf{S}}$<br>$\varepsilon_{33}^{\mathbf{S}}$<br>$\varepsilon_{11}^{\mathbf{T}}$<br>$\varepsilon_{33}^{\mathbf{T}}$ | $\tan\delta_1$<br>$\tan\delta_3$<br><br>($f$ (kHz)) | $c_{11}$<br>$c_{33}$<br>$c_{44}$<br>$c_{12}$<br>$c_{13}$<br>$c_{14}$<br>($10^9$ Pa) | $d_{22}$<br>$d_{31}$<br>$d_{33}$<br>$d_{15}$<br>$d_h$<br>($10^{-12}$ C/N) | $p_{11}$<br>$p_{12}$<br>$p_{13}$<br>$p_{14}$<br>$p_{31}$<br>$p_{33}$<br>$p_{41}$<br>$p_{44}$ | |
| Silver antimony sulfide,<br>$Ag_3SbS_3$ (pyrargyrite) | 5.83<br>2–2.5<br>–<br>– | –<br>–<br>21.7(7)<br>24.7(7)<br>[4.324] | | 52.7<br>35.6<br>11.6<br>26.3<br>28.0<br>−0.4<br>[4.324, 327][c] | 16.2<br>−19.5<br>62.2<br>31.6<br>–<br>[4.325, 326] | | |
| Silver arsenic sulfide,<br>$Ag_3AsS_3$ (proustite) | 5.63<br>2–2.5<br>–<br>– | 20.2(2)<br>20.2(2)<br>21.5<br>22.0 [4.324] | | 56.76<br>37.0<br>9.12<br>30.4<br>30.4<br>−0.16 [4.324] | 12.1<br>−13.8<br>30<br>−20 [4.324]<br>– | \|0.056\|<br>\|0.082\|<br>\|0.068\|<br>–<br>\|0.103\|<br>\|0.100\|<br>$\lvert \approx 0.01 \rvert$ (1150 nm)<br>–<br>[4.328, 329] | |
| Thallium arsenic selenide,<br>$Tl_3AsSe_3$ (TAS) | 7.83<br>2–3<br>–<br>– | | | See [4.330] | | See [4.330] | |
| Tourmaline,<br>$(Na, Ca)(Mg, Fe)_3B_3Al_6Si_6(O, OH, F)_{31}$ | 3.0–3.2<br>7–7.5<br>3.03 ($\perp c$)<br>2.92 ($\parallel c$)<br>(125 °C)<br>[4.332][d] | 6.3[e] [4.278]<br>7.1[e] [4.278]<br>8.2 [4.331]<br>7.5 [4.331] | | 277(19)<br>163(11)<br>64(3)<br>65(24)<br>32(20)<br>−6.9(25)<br>[4.7] | −0.3 [4.331]<br>−0.34 [4.331]<br>−1.8 [4.331]<br>−3.6 [4.331]<br>4.00(6)<br>[4.333, 334]<br>[4.333, 334] | | |

[a] These values are approximately the constant-field values $c^{\boldsymbol{E}}$.
[b] $p^{\boldsymbol{E}}$ at constant electric field.
[c] $c^{\boldsymbol{E}}$ at constant electric field.
[d] The thermal conductivities have been interpolated from $\kappa(\perp c) = 0.108 \times T^{0.556}$ and $\kappa(\parallel c) = 0.492 \times T^{0.297}$, valid for temperature ranges of 398.2–723.2 K and 393.2–729.2 K, respectively [4.332].
[e] These values for $\varepsilon_{ij}$ are neither at constant stress nor at constant strain.
[f] Fabricated by vapor transport equilibration (VTE).
[g] Stoichiometric melt.

**Table 4.4-12** Trigonal, point group $3m$ ($C_{3v}$) materials, cont.

| | Electrooptic tensor | General optical properties | Refractive index | | Nonlinear dielectric susceptibility |
|---|---|---|---|---|---|
| | $r_{13}^{\mathbf{T}}$<br>$r_{22}^{\mathbf{T}}$<br>$r_{33}^{\mathbf{T}}$<br>$r_{51}^{\mathbf{T}}$<br>($10^{-12}$ m/V)<br>at $\lambda = 633$ nm | Transparency range (μm)<br>$dn_o/dT$ ($10^{-5}$ K$^{-1}$)<br>$dn_e/dT$ ($10^{-5}$ K$^{-1}$) | $\boldsymbol{n}_o$<br>$A$<br>$B$<br>$C$<br>$D$<br>$E$<br>$F$ | $\boldsymbol{n}_e$<br>$A$<br>$B$<br>$C$<br>$D$<br>$E$<br>$F$ | $d_{31}$<br>$d_{33}$<br>$d_{22}$<br>$d_{15}$<br>($10^{-12}$ m/V) |
| | | 0.7–14 [4.335]<br>–<br>– | **2.9458**<br>1<br>6.585<br>0.16<br>0.1133<br>225 [4.335][j]<br>– | **2.7956**<br>1<br>5.845<br>0.16<br>0.0202<br>225 [4.335][j]<br>– | 7.8 (10.6 μm)<br>–<br>8.2 (10.6 μm)<br>–<br>[4.3, 4, 294, 336] |
| | 2.0 [4.337, 338]<br>1.05(4) [4.340]<br>0.22 [4.337, 338]<br>3.4(5) [4.340] | 0.6–13 [4.339]<br>–<br>– | **2.8163**<br>9.220<br>0.4454<br>0.1264<br>1733<br>1000 [4.341][k]<br>– | **2.5822**<br>7.007<br>0.3230<br>0.1192<br>660<br>1000 [4.341][k]<br>– | 10.4 (10.6 μm)<br>–<br>16.6 (10.6 μm)<br><br>10.8 (10.6 μm)<br>[4.339, 342] |
| | | 1.28–17 [4.343]<br>−4.52 [4.344]<br>+3.55 [4.344] | **3.331** (11 μm)<br>1<br>10.210<br>0.197136<br>0.522<br>625 [4.344][j]<br>– | **3.152** (11 μm)<br>1<br>8.993<br>0.197136<br>0.308<br>625 [4.344][j]<br>– | $d_{\text{eff}}$ SHG 10.6 μm:<br>67.5 [4.342, 343]<br>36.5 [4.294, 343]<br>29 [4.345]<br>20 [4.346] |
| | $r_{13}^{\mathbf{S}} = 1.7$ [4.347]<br>$r_{22}^{\mathbf{T}} = 0.3$ (589 nm) [4.348]<br>$r_{33}^{\mathbf{S}} = 1.7$ [4.347] | | **1.6274**<br>1<br>1.6346<br>0.010734<br>0 [4.349][j]<br>–<br>– | **1.6088**<br>1<br>1.57256<br>0.011346<br>0 [4.349][j]<br>–<br>– | 0.13(3)<br>0.47(6)<br>0.07(1)<br>0.23(4) [4.321] |

[hijk] Dispersion relations (λ (μm), $T = 20\,^{\circ}$C):

[h] $n^2 = A + \dfrac{B}{\lambda^2 - C} - D\lambda^2 + E\lambda^4 - F\lambda^6$.

[i] $n^2 = A + \dfrac{B}{\lambda^2 - C} - D\lambda^2$.

[j] $n^2 = A + \dfrac{B\lambda^2}{\lambda^2 - C} + \dfrac{D\lambda^2}{\lambda^2 - E}$.

[k] $n^2 = A + \dfrac{B}{\lambda^2 - C} + \dfrac{D}{\lambda^2 - E}$.

**Table 4.4-13** Tetragonal, point group $4/mmm$ ($D_{4h}$) materials

| | General | Static dielectric tensor | Dissipation factor | Elastic stiffness tensor | Elastic compliance tensor | Elastooptic tensor | |
|---|---|---|---|---|---|---|---|
| Material | $\varrho$ $(g/cm^3)$<br>Mohs hardness<br>$\kappa \perp c$<br>$\kappa \parallel c$<br>(W/m K) | $\varepsilon_{11}^{S}$<br>$\varepsilon_{33}^{S}$<br>$\varepsilon_{11}^{T}$<br>$\varepsilon_{33}^{T}$ | $\tan\delta_1$ | $c_{11}$<br>$c_{33}$<br>$c_{44}$<br>$c_{66}$<br>$c_{12}$<br>$c_{13}$<br>($10^9$ Pa) | $s_{11}$<br>$s_{33}$<br>$s_{44}$<br>$s_{66}$<br>$s_{12}$<br>$s_{13}$<br>$(10^{-12}\,Pa^{-1})$ | $p_{11}$<br>$p_{12}$<br>$p_{13}$<br>$p_{31}$<br>$p_{33}$<br>$p_{44}$<br>$p_{66}$ | |
| Magnesium fluoride, $MgF_2$ | 3.177<br>6<br>21 ($\perp c$)<br>30 ($\parallel c$)<br>[4.200] | 5.85<br>4.87 [4.21][a] | | 138(7)<br>201(10)<br>56.5(5)<br>96(2)<br>88(7)<br>62(4) [4.7] | 12.6(1)<br>6.0(3)<br>17.7(2)<br>10.5(2)<br>−7.2(2)<br>−1.7(1) [4.7] | 0.041<br>0.119<br>0.078<br>−0.099<br>0.014<br>–<br>−0.0475 [4.350] | |
| Titanium dioxide, $TiO_2$ (rutile) | 4.26<br>6–6.5<br>8.8 ($\perp c$)<br>(40 °C)<br>12.6 ($\parallel c$)<br>[4.262] | 85<br>190 [4.79][a] | 0.017 [4.79]<br>– | 269(3)<br>480(5)<br>124(1)<br>192(2)<br>177(4)<br>146(6) [4.7] | 6.8(3)<br>2.60(1)<br>8.06(5)<br>5.21(5)<br>−4.0(3)<br>−0.85(3) [4.7] | 0.012(4)<br>0.162(16)<br>−0.157(12)<br>−0.092(9)<br>−0.059(3)<br>0.020<br>−0.060 [4.351] | |
| Yttrium vanadate, $YVO_4$ (YVO) | 4.22<br>5<br>5.32 ($\perp c$)<br>5.10 ($\parallel c$)<br>[4.48] | | | | | | |

[a] These values for $\varepsilon_{ij}$ are neither at constant stress nor at constant strain.

**Table 4.4-13** Tetragonal, point group $4mmm$ ($D_{4h}$) materials, cont.

| | General optical properties | Refractive index | | Nonlinear dielectric susceptibility |
|---|---|---|---|---|
| | Transparency range (μm)<br>$dn_o/dT$ ($10^{-5}$ K$^{-1}$)<br>$dn_e/dT$ ($10^{-5}$ K$^{-1}$) | $n_o$<br>$A$<br>$B$<br>$C$<br>$D$<br>$E$ | $n_e$<br>$A$<br>$B$<br>$C$<br>$D$<br>$E$ | $\chi^{(3)}$ |
| | 0.12–7.5<br>0.17 (0.4 μm)<br>0.23 (0.4 μm) [4.21] | **1.48** (0.150 μm)<br>**1.423** (0.200 μm)<br>**1.3776** (0.590 μm)<br>**1.373** (1.05 μm)<br>**1.32** (6.00 μm)<br>**1.29** (7.50 μm)<br>dispersion relations, see [4.43][b] | **1.49** (0.150 μm)<br>**1.437** (0.200 μm)<br>**1.3894** (0.590 μm)<br>**1.385** (1.05 μm)<br>**1.33** (6.00 μm)<br>**1.30** (7.50 μm)<br>dispersion relations, see [4.43][b] | [4.21] |
| | 0.42–4.0 [4.84]<br>0.4 (0.4 μm) [4.353]<br>−0.9 (0.4 μm) [4.353] | **2.4851**<br>5.913<br>0.2441<br>0.0803<br>0 [4.353][c]<br>– | **2.7488**<br>7.197<br>0.3322<br>0.0843<br>0 [4.353][c]<br>– | See [4.352] |
| | 0.4–5<br>0.85<br>0.3 [4.354] | **1.9573**<br>3.77834<br>0.069736<br>0.04724<br>0.0108133 [4.354][d]<br>– | **2.1652**<br>4.59905<br>0.110534<br>0.04813<br>0.0122676 [4.354][d]<br>– | |

[bcd] Dispersion relations (λ (μm), $T = 20\,^{\circ}$C):

[b] $n_o^2 = 1.27620 + \frac{0.60967\lambda^2}{\lambda^2 - 0.08636^2} + \frac{0.0080\lambda^2}{\lambda^2 - 18.0^2} + \frac{2.14973\lambda^2}{\lambda^2 - 25.0^2}$;

$n_e^2 = 1.25385 + \frac{0.66405\lambda^2}{\lambda^2 - 0.088504^2} + \frac{1.0899\lambda^2}{\lambda^2 - 22.2^2} + \frac{0.1816\lambda^2}{\lambda^2 - 24.4^2} + \frac{2.1227\lambda^2}{\lambda^2 - 40.6}$;

[c] $n^2 = A + \frac{B\lambda^2}{\lambda^2 - C} + \frac{D\lambda^2}{\lambda^2 - E}$;

[d] $n^2 = A + \frac{B}{\lambda^2 - C} - D\lambda^2$.

**Table 4.4-14** Tetragonal, point group $4/m$ ($C_{4h}$) materials

| | General | Elastic stiffness tensor | Elastic compliance tensor | Elastooptic tensor |
|---|---|---|---|---|
| Material | $\varrho$ (g/cm$^3$)<br>Mohs hardness<br>$\kappa \perp c$<br>$\kappa \parallel c$<br>(W/m K) | $c_{11}$<br>$c_{33}$<br>$c_{44}$<br>$c_{66}$<br>$c_{12}$<br>$c_{13}$<br>$c_{16}$<br>($10^9$ Pa) | $s_{11}$<br>$s_{33}$<br>$s_{44}$<br>$s_{66}$<br>$s_{12}$<br>$s_{13}$<br>$s_{16}$<br>($10^{-12}$ Pa$^{-1}$) | $p_{11}$<br>$p_{12}$<br>$p_{13}$<br>$p_{16}$<br>$p_{31}$<br>$p_{33}$<br>$p_{44}$<br>$p_{45}$<br>$p_{61}$<br>$p_{66}$ |
| Lead molybdate, $PbMoO_4$ | 6.95<br>2.5–3<br>150 ($\perp c$)<br>150 ($\parallel c$)<br>[4.355] | 107.2(19)<br>93.2(13)<br>26.4(3)<br>34.8(8)<br>61.9(55)<br>52.0(8)<br>−15.8(18)<br>[4.7] | 20.8(2)<br>16.3(8)<br>37.9(4)<br>42.3(20)<br>−11.8(6)<br>−5.0(5)<br>14.8(12)<br>[4.356] | 0.253(23)<br>0.253(23)<br>0.273(43)<br>0.015(4)<br>0.163(20)<br>0.298(12)<br>0.04(0)<br>−0.01(0)<br>0.025(21)<br>0.046(5)<br>(477–633 nm) [4.357] |
| Yttrium lithium fluoride, $YLiF_4$ (YLF) | 3.995<br>4–5<br>7.2 ($\perp c$)<br>5.8 ($\parallel c$)<br>[4.358] | 121<br>156<br>40.9<br>17.7<br>60.9<br>52.6<br>−7.7 [4.359] | 12.8<br>7.96<br>24.4<br>63.6<br>−6.0<br>−2.3<br>8.16 [4.359] | |

[a] Dispersion relation ($\lambda$ (μm), $\lambda > 0.5$ μm, $T = 20$ °C):
$n^2 = A + \frac{B\lambda^2}{\lambda^2 - C}$ .

**Table 4.4-15** Tetragonal, point group 422 ($D_4$) materials

| | General | Static dielectric tensor | Dissipation factor | Elastic stiffness tensor | Piezoelectric tensor | Elastooptic tensor |
|---|---|---|---|---|---|---|
| Material | $\varrho$ (g/cm$^3$)<br>Mohs hardness<br>$\kappa \perp c$<br>$\kappa \parallel c$<br>(W/m K) | $\varepsilon_{11}^{\mathbf{S}}$<br>$\varepsilon_{33}^{\mathbf{S}}$<br>$\varepsilon_{11}^{\mathbf{T}}$<br>$\varepsilon_{33}^{\mathbf{T}}$ | $\tan\delta_1$<br>$\tan\delta_3$<br>($f$ (kHz)) | $c_{11}$<br>$c_{33}$<br>$c_{44}$<br>$c_{66}$<br>$c_{12}$<br>$c_{13}$<br>($10^9$ Pa) | $d_{14}$<br>($10^{-12}$ C/N) | $p_{11}$<br>$p_{12}$<br>$p_{13}$<br>$p_{31}$<br>$p_{33}$<br>$p_{44}$<br>$p_{66}$ |
| Tellurium dioxide, $TeO_2$ (paratellurite) | 5.99<br>4<br>3.0(3) [4.362]<br>– | 22.7 [4.360]<br>24.9[a] [4.361]<br>22.9(10) [4.360]<br>24.7(15) [4.360] | 0.0011<br>0.012<br>(100 kHz)<br>[4.360] | 55.9(2)<br>105.5(4)<br>26.7(2)<br>66.3(4)<br>51.6(3)<br>23.9(22) [4.7] | 8.13(70)<br>[4.360] | 0.007<br>0.187<br>0.340<br>0.091<br>0.240<br>−0.17<br>−0.046 [4.363] |

[a] This value for $\varepsilon_{33}$ is neither at constant stress nor at constant strain.

**Table 4.4-14** Tetragonal, point group $4/m$ ($C_{4h}$) materials, cont.

| General optical properties | Refractive index | |
|---|---|---|
| Transparency range (μm)<br>$dn_o/dT$ ($10^{-5}$ K$^{-1}$)<br>$dn_e/dT$ ($10^{-5}$ K$^{-1}$) | $\boldsymbol{n}_o$<br>$A$<br>$B$<br>$C$ | $\boldsymbol{n}_e$<br>$A$<br>$B$<br>$C$ |
| 0.42–5.5 [4.364]<br>$-(3.0 \pm 0.2)\boldsymbol{n}_o$<br>$-(1.8 \pm 0.2)\boldsymbol{n}_e$ [4.355] | **2.38** (633 nm) [4.364]<br>1<br>4.0650407<br>0.0536585 [4.355][a] | **2.25** (633 nm) [4.364]<br>1<br>3.7037037<br>0.0400000 [4.355][a] |
| 0.18–6.7<br>−0.2<br>−0.43 [4.354] | **1.448**<br>1.38757<br>0.70757<br>0.00931<br>0.18849<br>50.99741 [4.354][c] | **1.470**<br>1.31021<br>0.84903<br>0.00876<br>0.53607<br>134.9566 [4.354][c] |

[c] $n^2 = A + \frac{B\lambda^2}{\lambda^2 - C} + \frac{D\lambda^2}{\lambda^2 - E}$.

**Table 4.4-15** Tetragonal, point group 422 ($D_4$) materials, cont.

| Electrooptic tensor | General optical properties | Refractive index | | Nonlinear dielectric susceptibility |
|---|---|---|---|---|
| $r_{41}^{\mathbf{T}}$<br>($10^{-12}$ m/V)<br>at λ = 633 nm | Transparency range (μm)<br>$dn_o/dT$ ($10^{-5}$ K$^{-1}$)<br>$dn_e/dT$ ($10^{-5}$ K$^{-1}$) | $\boldsymbol{n}_o$<br>$A$<br>$B$<br>$C$<br>$D$<br>$E$ | $\boldsymbol{n}_e$<br>$A$<br>$B$<br>$C$<br>$D$<br>$E$ | $d_{14}$<br>($10^{-12}$ m/V) |
| 0.62 [4.365] | 0.35–6 [4.366]<br>0.9 (0.644 μm)<br>0.8 (0.644 μm) [4.368] | **2.2005**<br>1<br>2.584<br>0.0180<br>1.157<br>0.0696 [4.368][b] | **2.3431**<br>1<br>2.823<br>0.0180<br>1.542<br>0.0692 [4.368][b] | 0.39 [4.367] |

[b] Dispersion relation (λ (μm), $T = 20\,°C$):
$n^2 = A + \frac{B\lambda^2}{\lambda^2 - C} + \frac{D\lambda^2}{\lambda^2 - E}$

**Table 4.4-16** Tetragonal, point group $\overline{4}2m$ ($D_{2d}$) materials

| | General | Static dielectric tensor | Dissipation factor | Elastic stiffness tensor | Piezoelectric tensor | Elastooptic tensor | |
|---|---|---|---|---|---|---|---|
| Material | $\varrho$ (g/cm$^3$)<br>Mohs hardness<br>$\kappa \perp c$<br>$\kappa \parallel c$<br>(W/m K) | $\varepsilon_{11}^{S}$<br>$\varepsilon_{33}^{S}$<br>$\varepsilon_{11}^{T}$<br>$\varepsilon_{33}^{T}$ | $\tan\delta_1$<br>$\tan\delta_3$<br><br>($f$ (kHz)) | $c_{11}$<br>$c_{33}$<br>$c_{44}$<br>$c_{66}$<br>$c_{12}$<br>$c_{13}$<br>($10^9$ Pa) | $d_{14}$<br>$d_{36}$<br>($10^{-12}$ C/N) | $p_{11}$<br>$p_{12}$<br>$p_{13}$<br>$p_{31}$<br>$p_{33}$<br>$p_{44}$<br>$p_{66}$ | |
| Ammonium dideuterium phosphate, $ND_4D_2PO_4$ (AD*P, DADP) | 1.885<br>[4.370, 371]<br>–<br>–<br>– | 70[a] [4.369]<br>26[a] [4.369]<br>72 [4.372]<br>22 [4.372] | 0.003<br>0.015<br>(1 kHz)<br>[4.369] | 62.1<br>29.9<br>9.1<br>6.1<br>–5<br>14 [4.372][b] | 10<br>75 [4.372] | –<br>–<br>–<br>–<br>–<br>–<br>0.04 [4.373, 374] | |
| Ammonium dihydrogen arsenate, $NH_4H_2AsO_4$ (ADA) | 2.310<br>–<br>–<br>– | 74 [4.375]<br>13 [4.375]<br>75 [4.376]<br>14 [4.376] | | 67.5<br>30.2<br>6.85<br>6.39<br>–10.6<br>16.5 [4.379] | 36.5<br>27.5<br>[4.377, 378] | | |
| Ammonium dihydrogen phosphate, $NH_4H_2PO_4$ (ADP) | 1.80<br>2.0<br>1.26 ($\perp c$)<br>0.71 ($\parallel c$)<br>(315 K)<br>[4.262] | 55.5(15)<br>15.0(5)<br>56.0(15)<br>15.5(5)<br>[4.97, 98] | 0.001<br>0.004<br>(1 kHz)<br>[4.369] | 67.3(27)<br>33.7(7)<br>8.6(2)<br>6.02(6)<br>5.0(13)<br>19.8(6) [4.7] | 1.76<br>48.31 [4.380] | 0.302(12)<br>0.252(17)<br>0.204(33)<br>0.191(6)<br>0.219(49)<br>–0.058<br>–0.088(17)<br>(589–633 nm) [4.381] | |
| Cadmium germanium arsenide, $CdGeAs_2$ | 5.60<br>3.5–4<br>4.18 [4.140]<br>– | | | 98.0<br>86.6<br>43.2<br>42.3<br>60.5<br>59.6 [4.382] | | | |
| Cadmium germanium phosphide, $CdGeP_2$ | | | | | | | |
| Cesium dideuterium arsenate, $CsD_2AsO_4$ (CD*A, DCDA) | | –<br>–<br>74<br>61 [4.369][cd] | 0.57<br>0.38<br>(1 kHz)<br>[4.369][cd] | | 10.5<br>125.4<br>[4.383][c] | 0.223<br>0.271<br>0.160<br>0.206<br>0.133<br>–0.061 [4.384, 385]<br>– | |

**Table 4.4-16** Tetragonal, point group $\overline{4}2m$ ($D_{2d}$) materials, cont.

| | Electrooptic tensor | General optical properties | Refractive index | | Nonlinear dielectric susceptibility |
|---|---|---|---|---|---|
| | $r_{41}^{\mathrm{T}}$<br>$r_{63}^{\mathrm{T}}$<br>($10^{-12}$ m/V) | Transparency range (μm)<br>$dn_o/dT$ ($10^{-5}$ K$^{-1}$)<br>$dn_e/dT$ ($10^{-5}$ K$^{-1}$) | $n_o$<br>$A$<br>$B$<br>$C$<br>$D$<br>$E$ | $n_e$<br>$A$<br>$B$<br>$C$<br>$D$<br>$E$ | $d_{36}$<br>($10^{-12}$ m/V) |
| | | 0.22–1.7<br>[4.386–389]<br>–<br>– | **1.5049**<br>2.279481<br>1.215879<br>57.97555433<br>0.010761<br>0.013262977 [4.386][e] | **1.4659**<br>2.151161<br>1.199009<br>126.6005279<br>0.009652<br>0.009712103 [4.386][e] | 0.43 (0.6943 μm)<br>[4.390, 391] |
| | 33.5 (550 nm)<br>9.2 (550 nm)<br>[4.284, 369] | 0.22–1.2 [4.386]<br>−4.56 [4.392]<br>1.25 [4.392] | **1.5550**<br>2.443449<br>2.017752<br>57.83514282<br>0.016757<br>0.018272821 [4.386][e] | **1.5081**<br>2.275962<br>1.59826<br>126.8851303<br>0.014296<br>0.016560859 [4.386][e] | 0.43 [4.386] |
| | 26.0 (633 nm)<br>8.7 (633 nm) | 0.18–1.53 [4.386, 393]<br>−4.93 [4.392]<br>0 [4.392] | **1.5065**<br>2.302842<br>15.102464<br>400<br>0.011125165<br>0.013253659 [4.394][e] | **1.4681**<br>2.163510<br>5.919896<br>400<br>0.009616676<br>0.012989120 [4.394][e] | 0.47 [4.12, 14] |
| | | 2.5–15 [4.395]<br>–<br>– | **3.5046** (10.6 μm)<br>10.1064<br>2.2988<br>1.0872<br>1.6247<br>1370 [4.227][f] | **3.5911** (10.6 μm)<br>11.8018<br>1.2152<br>2.6971<br>1.6922<br>1370 [4.227][f] | 282 (10.6 μm)<br>[4.395, 396] |
| | | 0.9–12 [4.396]<br>–<br>– | **3.1422** (10.6 μm)<br>5.9677<br>4.2286<br>0.2021<br>1.6351<br>671.33 [4.397][f] | **3.1563** (10.6 μm)<br>6.1573<br>4.0970<br>0.2330<br>1.4925<br>671.33 [4.397][f] | 100 (10.6 μm)<br>[4.396] |
| | –<br>38.8 (700 nm)<br>[4.399] | 0.27–1.66 [4.398]<br>−2.33 [4.392]<br>−1.67 [4.392] | **1.5499**<br>2.40817<br>2.2112173<br>126.871163<br>0.015598<br>0.019101728 [4.386][e] | **1.5341**<br>2.345809<br>0.651843<br>127.3304614<br>0.015141<br>0.016836101 [4.386][e] | 0.402 [4.398] |

**Table 4.4-16** Tetragonal, point group $\overline{4}2m$ ($D_{2d}$) materials, cont.

| | General | Static dielectric tensor | Dissipation factor | Elastic stiffness tensor | Piezoelectric tensor | Elastooptic tensor | |
|---|---|---|---|---|---|---|---|
| Material | $\varrho$ (g/cm$^3$)<br>Mohs hardness<br>$\kappa \perp c$<br>$\kappa \parallel c$<br>(W/m K) | $\varepsilon_{11}^{S}$<br>$\varepsilon_{33}^{S}$<br>$\varepsilon_{11}^{T}$<br>$\varepsilon_{33}^{T}$ | $\tan\delta_1$<br>$\tan\delta_3$<br><br>($f$ (kHz)) | $c_{11}$<br>$c_{33}$<br>$c_{44}$<br>$c_{66}$<br>$c_{12}$<br>$c_{13}$<br>($10^9$ Pa) | $d_{14}$<br>$d_{36}$<br>($10^{-12}$ C/N) | $p_{11}$<br>$p_{12}$<br>$p_{13}$<br>$p_{31}$<br>$p_{33}$<br>$p_{44}$<br>$p_{66}$ | |
| Cesium dihydrogen arsenate, $CsH_2AsO_4$ (CsDA, CDA) | 3.53<br>–<br>–<br>– | 58.0[a] [4.400][d]<br>34.0[a] [4.400][d]<br>61 [4.369][d]<br>29 [4.369][d] | 15<br>13<br>(1 kHz)<br>[4.369] | 51.6<br>39.9<br>6.66<br>1.7<br>0.56<br>1.33<br>[4.403, 404] | 5.6(10)<br>123(8) [4.401, 402] | 0.238(58)<br>0.225(0)<br>0.211(19)<br>0.200(4)<br>0.220(12)<br>−0.042<br>\|0.065\| (633 nm)<br>[4.384, 385] | |
| Cesium lithium borate, $CsLiB_6O_{10}$ (CLBO) | –<br>4<br>–<br>– | | | | | | |
| Copper gallium selenide, $CuGaSe_2$ | | | | | | | |
| Copper gallium sulfide, $CuGaS_2$ | 4.45<br>–<br>–<br>– | 9.3[a]<br>10[a] [4.112] | | | | | |
| Potassium dideuterium arsenate, $KD_2AsO_4$ (KD*A, DKDA) | 2.890 [4.405][c]<br>–<br>–<br>– | 71[a]<br>33[ad] [4.369]<br>(≈ 90% deuterated) | 0.02<br>0.20<br>(1 kHz)<br>[4.369][d]<br>(≈ 90% deuterated) | 74.6<br>69.3<br>9.88<br>6.17<br>12.4<br>33.9 [4.406] | 22.5<br>24.8 [4.406]<br>(≈ 90% deuterated) | | |
| Potassium dideuterium phosphate, $KD_2PO_4$ (KD*P, DKDP) | 2.355<br>2.5<br>2.09 ($\perp c$)<br>1.86 ($\parallel c$)<br>[4.386] | 47.1(24)[a]<br>[4.177][c]<br>48 [4.375][c]<br>–<br>50(2) [4.407][c] | 0.0068(17)<br>0.0072(18)<br>(1 GHz)<br>[4.296][c] | 67.4<br>54.5<br>12.6<br>5.94<br>−5.8<br>12.2 [4.408] | –<br>58 [4.407][c] | 0.241<br>0.247<br>0.245<br>0.236<br>0.245<br>−0.035<br>−0.072 [4.409, 410] | |

**Table 4.4-16** Tetragonal, point group $\overline{4}2m$ ($D_{2d}$) materials, cont.

| | Electrooptic tensor | General optical properties | Refractive index | | Nonlinear dielectric susceptibility |
|---|---|---|---|---|---|
| | $r_{41}^{\mathbf{T}}$<br>$r_{63}^{\mathbf{T}}$<br>($10^{-12}$ m/V) | Transparency range (μm)<br>$dn_o/dT$ ($10^{-5}$ K$^{-1}$)<br>$dn_e/dT$ ($10^{-5}$ K$^{-1}$) | $\boldsymbol{n}_o$<br>*A*<br>*B*<br>*C*<br>*D*<br>*E* | $\boldsymbol{n}_e$<br>*A*<br>*B*<br>*C*<br>*D*<br>*E* | $d_{36}$<br>($10^{-12}$ m/V) |
| | –<br>19.1 (700 nm)<br>[4.284] | 0.26–1.43 [4.398]<br>−2.87 [4.392]<br>−2.21 [4.392] | **1.5514**<br>2.420405<br>1.403336<br>57.82416181<br>0.016272<br>0.018005614 [4.386]e | **1.5356**<br>2.350262<br>0.685328<br>127.2688578<br>0.015645<br>0.014820871 [4.386]e | 0.402 [4.398] |
| | | 0.18–2.75 [4.411]<br>$-0.104\lambda^2+0.035\lambda-1.291$<br>[4.412]<br>$0.331\lambda^2-0.243\lambda-0.84$<br>[4.412] | **1.4854**<br>2.2145<br>0.00890<br>0.02051<br>0.01413 [4.412]g<br>– | **1.4352**<br>2.0588<br>0.00866<br>0.01202<br>0.00607 [4.412]g<br>– | 0.86 [4.411] |
| | | 0.73–17 [4.413]<br>–<br>– | **2.8358** (1.0 μm)<br>**2.7430** (2.0 μm)<br>**2.7133** (6.0 μm) [4.413] | **2.8513** (1.0 μm)<br>**2.7510** (2.0 μm)<br>**2.7192** (6.0 μm)<br>[4.413] | 27 (10.6 μm) [4.413] |
| | 1.76 (633 nm)<br>–<br>[4.112] | 0.52–12 [4.414]<br>5.9 [4.415]<br>6.0 [4.415] | **2.4360** (10.6 μm)<br>4.0984<br>2.1419<br>0.1225<br>1.5755<br>738.43 [4.414]f | **2.4201** (10.6 μm)<br>4.4834<br>1.7316<br>0.1453<br>1.7785<br>738.43 [4.414]f | 9.0 (10.6 μm)<br>[4.414] |
| | –<br>18.2 (550 nm)<br>[4.284] | 0.22–2.3 [4.416]<br>–<br>– | | | 0.39 [4.386] |
| | 8.8(4) (546 nm)<br>[4.418]<br>25.8 (633 nm)<br>[4.419] | 0.2–2.1 [4.387,417]<br>−3.1 [4.392]<br>−2.1 [4.392] | **1.4928**<br>1.661145<br>0.586015<br>0.016017<br>0.691194<br>30 [4.397]f | **1.4555**<br>1.687499<br>0.44751<br>0.017039<br>0.596212<br>30 [4.397]f | 0.37 [4.12, 14] |

**Table 4.4-16** Tetragonal, point group $\overline{4}2m$ ($D_{2d}$) materials, cont.

| | General | Static dielectric tensor | Dissipation factor | Elastic stiffness tensor | Piezoelectric tensor | Elastooptic tensor | |
|---|---|---|---|---|---|---|---|
| Material | $\varrho$ (g/cm$^3$)<br>Mohs hardness<br>$\kappa \perp c$<br>$\kappa \parallel c$<br>(W/m K) | $\varepsilon_{11}^{S}$<br>$\varepsilon_{33}^{S}$<br>$\varepsilon_{11}^{T}$<br>$\varepsilon_{33}^{T}$ | $\tan\delta_1$<br>$\tan\delta_3$<br><br>($f$ (kHz)) | $c_{11}$<br>$c_{33}$<br>$c_{44}$<br>$c_{66}$<br>$c_{12}$<br>$c_{13}$<br>($10^9$ Pa) | $d_{14}$<br>$d_{36}$<br>($10^{-12}$ C/N) | $p_{11}$<br>$p_{12}$<br>$p_{13}$<br>$p_{31}$<br>$p_{33}$<br>$p_{44}$<br>$p_{66}$ | |
| Potassium dihydrogen arsenate, $KH_2AsO_4$ (KDA) | 2.87<br>–<br>–<br>– | 53 [4.420]<br>18 [4.420]<br>53.7 [4.421]<br>21.0 [4.421] | 0.007<br>0.008<br>(10 GHz)<br>[4.420] | 64.8<br>48.2<br>10.75<br>6.63<br>0.77<br>13.6 [4.422] | 17.1<br>19.1 [4.406] | –<br>–<br>–<br>–<br>–<br>–<br>0.020 [4.373, 374] | |
| Potassium dihydrogen phosphate, $KH_2PO_4$ (KDP) | 2.3383<br>2.5<br>1.34 ($\perp c$)<br>(42 °C)<br>1.21 ($\parallel c$)<br>[4.262] | 42.5(15)<br>20.0(5)<br>43.2(15)<br>20.8(5)<br>[4.97, 98] | 0.004<br>(9.2 GHz)<br>[4.423]<br>0.0005<br>(1 GHz)<br>[4.97, 98] | 71.2(14)<br>57(1)<br>12.6(4)<br>6.2(1)<br>−5.0(11)<br>14.1(14) [4.7] | 3.5(15)<br>22.4(10)<br>[4.401, 402] | 0.256(18)<br>0.254(19)<br>0.224(34)<br>0.227(8)<br>0.200(54)<br>−0.265(10)<br>−0.063(6)<br>(589–633 nm)<br>[4.409, 410] | |
| Rubidium dideuterium arsenate, $RbD_2AsO_4$ (RbD*A, RD*A, DRDA) | 3.333<br>–<br>–<br>– | 72[a]<br>41[ac] [4.369] | 1.6<br>2.3<br>(1 kHz)<br>[4.369][c] | 49.3<br>38.6<br>9.48<br>4.08<br>−19.3<br>4.9 [4.424] | 14.6<br>45.8[c]<br>[4.424] | | |
| Rubidium dideuterium phosphate, $RbD_2PO_4$ (RbD*P, RD*P, DRDP) | | –<br>72[a]<br>[4.425, 426] | | See [4.427, 428][c] | 3.3(3)<br>52(1) | | |
| Rubidium dihydrogen arsenate, $RbH_2AsO_4$ (RbDA, RDA) | 3.28<br>–<br>–<br>– | 54.5[a]<br>28.5[a] [4.429] | 2.1<br>5.2 [4.429] | 51.0<br>39.2<br>10.4<br>4.31<br>−18.9<br>2.3 [4.424] | 9.9<br>28.5<br>[4.400, 424] | 0.227<br>0.239<br>0.200<br>0.205<br>0.182 [4.430, 431]<br>–<br>0.023 [4.373, 374] | |

**Table 4.4-16** Tetragonal, point group $\overline{4}2m$ ($D_{2d}$) materials, cont.

| | **Electrooptic tensor** | **General optical properties** | **Refractive index** | | **Nonlinear dielectric susceptibility** |
|---|---|---|---|---|---|
| | $r_{41}^{T}$<br>$r_{63}^{T}$<br>($10^{-12}$ m/V) | Transparency range (μm)<br>$dn_o/dT$ ($10^{-5}$ K$^{-1}$)<br>$dn_e/dT$ ($10^{-5}$ K$^{-1}$) | $n_o$<br>$A$<br>$B$<br>$C$<br>$D$<br>$E$ | $n_e$<br>$A$<br>$B$<br>$C$<br>$D$<br>$E$ | $d_{36}$<br>($10^{-12}$ m/V) |
| | 12.5 (550 nm)<br>10.9 (550 nm)<br>[4.369, 399] | 0.216–1.67<br>[4.386, 387, 390, 391]<br>−3.95 [4.392]<br>−2.27 [4.392] | **1.5509**<br>2.424647<br>3.742954<br>126.9036045<br>0.015841<br>0.018624061 [4.386][e] | **1.5059**<br>2.262579<br>0.769288<br>127.0537007<br>0.013461<br>0.016165851 [4.386][e] | 0.41 [4.228] |
| | −8.277(7)<br>(589 nm)<br>+10.22<br>(589 nm) [4.433] | 0.174–1.57<br>[4.393, 417, 432]<br>−3.4 [4.392]<br>−2.87 [4.392] | **1.4938**<br>2.259276<br>0.01008956<br>0.012942625<br>13.00522<br>400 [4.434, 435][f] | **1.4599**<br>2.132668<br>0.008637494<br>0.012281043<br>3.2279924<br>400 [4.434, 435][f] | 0.39 [4.12, 14] |
| | –<br>21.4 (550 nm)<br>[4.399] | 0.26–1.7 [4.386]<br>–<br>– | **1.5392**<br>2.373255<br>1.979528<br>126.9867549<br>0.01543<br>0.015836964 [4.386][e] | **1.5091**<br>2.270806<br>0.275372<br>58.08499107<br>0.013592<br>0.01596609 [4.386][e] | 0.31 [4.386] |
| | | 0.22–1.5 [4.386, 436]<br>–<br>– | **1.4913**<br>2.235596<br>0.010929<br>0.001414783<br>2.355322<br>126.8547185 [4.386][e] | **1.4681**<br>2.152727<br>0.010022<br>0.001379157<br>0.691253<br>127.0144778 [4.386][e] | 0.38 [4.386] |
| | 13.5 (550 nm)<br>[4.369]<br>14.8 (550 nm)<br>[4.399] | 0.26–1.46 [4.437]<br>−3.37 [4.392]<br>−2.21 [4.392] | **1.5405**<br>2.390661<br>3.487176<br>126.7648558<br>0.015513<br>0.018112315 [4.386][e] | **1.5105**<br>2.27557<br>0.720099<br>126.6309092<br>0.013915<br>0.01459264 [4.386][e] | 0.4 (0.694 μm)<br>[4.438, 439] |

**Table 4.4-16** Tetragonal, point group $\overline{4}2m$ ($D_{2d}$) materials, cont.

| | General | Static dielectric tensor | Dissipation factor | Elastic stiffness tensor | Piezoelectric tensor | Elastooptic tensor | |
|---|---|---|---|---|---|---|---|
| Material | $\varrho$ (g/cm$^3$)<br>Mohs hardness<br>$\kappa \perp c$<br>$\kappa \parallel c$<br>(W/m K) | $\varepsilon_{11}^{S}$<br>$\varepsilon_{33}^{S}$<br>$\varepsilon_{11}^{T}$<br>$\varepsilon_{33}^{T}$ | $\tan\delta_1$<br>$\tan\delta_3$<br><br>($f$ (kHz)) | $c_{11}$<br>$c_{33}$<br>$c_{44}$<br>$c_{66}$<br>$c_{12}$<br>$c_{13}$<br>($10^9$ Pa) | $d_{14}$<br>$d_{36}$<br>($10^{-12}$ C/N) | $p_{11}$<br>$p_{12}$<br>$p_{13}$<br>$p_{31}$<br>$p_{33}$<br>$p_{44}$<br>$p_{66}$ | |
| Rubidium dihydrogen phosphate, $RbH_2PO_4$ (RbDP, RDP) | 2.805<br>–<br>–<br>– | 42.0<br>26.5<br>41.4<br>27<br>[4.440, 441] | 0.034<br>0.051<br>(38.6 GHz)<br>[4.440, 441] | 63(7)<br>50.0(55)<br>10.6(7)<br>3.56(7)<br>−6.0(6)<br>10.6(72) [4.7] | 4.0(3)<br>37(1)<br>[4.427, 428] | 0.247<br>0.265<br>0.248<br>0.229<br>0.248<br>−0.032<br>−0.032 [4.409, 410] | |
| Silver gallium selenide, $AgGaSe_2$ | 5.71<br>3–3.5<br>1.1 ($\perp c$)<br>1.0 ($\parallel c$)<br>[4.200] | –<br>–<br>10.5<br>12.0 [4.442] | | | 9.0<br>3.7 [4.442] | | |
| Silver gallium sulfide (silver thiogallate), $AgGaS_2$ | 4.58<br>3–3.5<br>1.5 ($\perp c$)<br>1.4 ($\parallel c$)<br>[4.200] | 10<br>14 [4.443][a] | | 87.9<br>75.8<br>24.1<br>30.8<br>58.4<br>59.2<br>[4.444, 445] | | | |
| Urea, $(NH_2)_2CO$ | 1.318<br><2.5<br>–<br>– | 5–8[a] [4.26] | | 23.5<br>51.0<br>6.2<br>0.50<br>−0.50<br>7.5 [4.446] | | | |
| Zinc germanium diphosphide, $ZnGeP_2$ | 4.12<br>5.5<br>35 ($\perp c$)<br>36 ($\parallel c$)<br>[4.200] | 15<br>12 [4.112][a] | | | | See [4.447, 448] | |

[a] These values for $\varepsilon_{ij}$ are neither at constant stress nor at constant strain.
[b] The elastic stiffness constants were measured at constant electric field $(c^E)$.
[c] May be only partially deuterated.
[d] *Adhav* and *Vlassopoulous* [4.369] measured arsenates with low resistivity ($\approx 10^8\ \Omega$ cm), and as a result their $\tan\delta$ values are high and $\varepsilon$ may also be high. The data for RDA in [4.369] are incorrectly labeled ADA (remarks of the compiler).

**Table 4.4-16** Tetragonal, point group $\overline{4}2m$ ($D_{2d}$) materials, cont.

| | Electrooptic tensor | General optical properties | Refractive index | | Nonlinear dielectric susceptibility |
|---|---|---|---|---|---|
| | $r_{41}^{\mathbf{T}}$<br>$r_{63}^{\mathbf{T}}$<br>($10^{-12}$ m/V) | Transparency range (μm)<br>$dn_o/dT$ ($10^{-5}$ K$^{-1}$)<br>$dn_e/dT$ ($10^{-5}$ K$^{-1}$) | $\boldsymbol{n}_o$<br>$A$<br>$B$<br>$C$<br>$D$<br>$E$<br>$F$ | $\boldsymbol{n}_e$<br>$A$<br>$B$<br>$C$<br>$D$<br>$E$<br>$F$ | $d_{36}$<br>($10^{-12}$ m/V) |
| | 10.3<br>14.3 [4.449, 450] | 0.22–1.5 [4.386, 436]<br>−3.74 [4.392]<br>−2.73 [4.392] | **1.4926**<br>2.249885<br>0.01056<br>0.007780475<br>3.688005<br>127.1998253 [4.386]e<br>– | **1.4700**<br>2.159913<br>0.009515<br>0.00847799<br>0.988431<br>127.692938 [4.386]e<br>– | 0.36 [4.438] |
| | 4.5 (1.15 μm)<br>3.9 (1.15 μm)<br>[4.453] | 0.71–18 [4.451]<br>4.5 (3.39 μm) [4.452]<br>7.6 (3.39 μm) [4.452] | **2.7008**<br>4.6453<br>2.2057<br>0.1879<br>1.8377<br>1600 [4.227]f<br>– | **2.6800**<br>5.2912<br>1.3970<br>0.2845<br>1.9282<br>1600 [4.227]f<br>– | 33 (10.6 μm) [4.12, 14] |
| | 4.0(2)<br>3.0(1) [4.455] | 0.47–13 [4.454]<br>For $dn/dT$, see [4.456, 457] | **2.4540**<br>3.40684<br>2.40065<br>0.09311<br>2.06248<br>950 [4.457]f<br>– | **2.4012**<br>3.60728<br>1.94792<br>0.11066<br>2.24544<br>1030.7 [4.457]f<br>– | 17.5 (1.06 μm) [4.12, 14]<br>11.2 (10.6 μm) [4.12, 14] |
| | +1.03 (633 nm)<br>−0.75 (633 nm)<br>[4.460] | 0.2–1.8 [4.458]<br>–<br>– | **1.4811**<br>2.1823<br>0.0125<br>0.03<br>0 [4.461]h<br>–<br>– | **1.5825**<br>2.51527<br>0.0240<br>0.03<br>0.0202<br>1.52<br>0.08771 [4.461]h | 1.18 (0.6 μm) [4.458, 459] |
| | 1.8 (5 μm)<br>–<br>[4.463] | 0.74–12 [4.462]<br>21.18 [4.415]<br>23.01 [4.415] | **3.2324**<br>4.4733<br>5.26576<br>0.13381<br>1.49085<br>662.55 [4.464, 465]f<br>– | **3.2786**<br>4.63318<br>5.34215<br>0.14255<br>1.45785<br>662.55 [4.464, 465]f<br>– | 69 (10.6 μm) [4.12, 462] |

efgh Dispersion relations (λ (μm), $T = 20\,°C$):

e $n^2 = A + \frac{B\lambda^2}{\lambda^2 - C} + \frac{D}{\lambda^2 - E}$ .

f $n^2 = A + \frac{B\lambda^2}{\lambda^2 - C} + \frac{D\lambda^2}{\lambda^2 - E}$ .

g $n^2 = A + \frac{B}{\lambda^2 - C} - D\lambda^2$ .

h $n^2 = A + \frac{B}{\lambda^2 - C} + \frac{D(\lambda^2 - E)}{(\lambda^2 - E) + F}$ .

**Table 4.4-17** Tetragonal, point group $4mm$ ($C_{4v}$) materials

| | General | Static dielectric tensor | Dissipation factor | Elastic stiffness tensor | Piezoelectric tensor | Elastooptic tensor | |
|---|---|---|---|---|---|---|---|
| Material | $\varrho$ (g/cm$^3$)<br>Mohs hardness<br>$\kappa \perp c$<br>$\kappa \parallel c$<br>(W/m K) | $\varepsilon_{11}^{S}$<br>$\varepsilon_{33}^{S}$<br>$\varepsilon_{11}^{T}$<br>$\varepsilon_{33}^{T}$ | $\tan\delta_1$<br>$\tan\delta_3$<br><br>($f$ (kHz)) | $c_{11}$<br>$c_{33}$<br>$c_{44}$<br>$c_{66}$<br>$c_{12}$<br>$c_{13}$<br>($10^9$ Pa) | $d_{31}$<br>$d_{33}$<br>$d_{15}$<br>$d_h$<br>($10^{-12}$ C/N) | $p_{11}$<br>$p_{12}$<br>$p_{13}$<br>$p_{31}$<br>$p_{33}$<br>$p_{44}$<br>$p_{66}$ | |
| Barium titanate, $BaTiO_3$[a] | 6.02<br>–<br>1.34 [4.45]<br>– | 1970<br>109<br>2920<br>168 [4.468] | 0.13<br>–<br>(24 GHz)<br>[4.469] | 243<br>147.9<br>54.9<br>120<br>128<br>123 [4.467][b] | −33.4<br>+68.5<br>647.0 [4.467]<br>– | See [4.443, 466] | |
| Lead titanate, $PbTiO_3$ | 7.9<br>–<br>–<br>– | 102(3)<br>33.5(10)<br>130–140<br>105–110<br>[4.472] | 0.02–0.05<br>0.02–0.05<br>(0.1 GHz)<br>[4.472] | $s_{11}^{E} = 7.2$<br>$s_{33}^{E} = 32.5$<br>$s_{44}^{E} = 12.2$<br>$s_{66}^{E} = 7.9$<br>$s_{12}^{E} = -2.1$<br>[4.470, 471][c] | −25<br>+117<br>61 [4.470, 471]<br>– | | |
| Lithium tetraborate, $Li_2B_4O_7$ | 2.44<br>5<br>–<br>– | 78.80<br>71.45<br>82.61<br>87.92 [4.473] | | 130.9(42)<br>55.4(11)<br>57.3(14)<br>46.4(7)<br>1.5(12)<br>30(4) [4.7] | | | |
| Potassium lithium niobate, $K_3Li_2Nb_5O_{15}$ (KLINBO) | 4.3<br>–<br>–<br>– | 271<br>83<br>306<br>115<br>(405 °C)<br>[4.474][d] | | 220<br>109<br>68<br>70<br>74<br>59 [4.474][bd] | −14<br>57<br>68 [4.474][d]<br>– | | |

[a] Top-seeded solution grown (TSSG) $BaTiO_3$.

[b] The elastic stiffness constants were measured at constant electric field ($c^E$).

[c] Units not specified in original, but probably $10^{-12}$ Pa$^{-1}$.

[d] The stoichiometry was $K_{2.89}Li_{1.55}Nb_{5.11}O_{15}$ instead of $K_3Li_2Nb_5O_{15}$.

**Table 4.4-17** Tetragonal, point group $4mm$ ($C_{4v}$) materials, cont.

| | Electrooptic tensor | General optical properties | Refractive index | | Nonlinear dielectric susceptibility |
|---|---|---|---|---|---|
| | $r_{13}^{\mathrm{T}}$<br>$r_{33}^{\mathrm{T}}$<br>$r_{51}^{\mathrm{T}}$<br>($10^{-12}$ m/V)<br>at $\lambda = 633$ nm | Transparency range (μm)<br>$dn_o/dT$ ($10^{-5}$ K$^{-1}$)<br>$dn_e/dT$ ($10^{-5}$ K$^{-1}$) | $n_o$<br>$A$<br>$B$<br>$C$<br>$D$<br>$E$<br>$F$ | $n_e$<br>$A$<br>$B$<br>$C$<br>$D$<br>$E$<br>$F$ | $d_{31}$<br>$d_{33}$<br>($10^{-12}$ m/V) |
| | 8<br>105<br>1300 [4.477] | 0.14–10<br>–<br>– | **2.3218**<br>1<br>4.195<br>0.04964<br>0 [4.478][e]<br>–<br>– | **2.2894**<br>1<br>4.073<br>0.04456<br>0 [4.478][e]<br>–<br>– | −14.4<br>−5.4 [4.475, 476] |
| | 13.8 ($r_{13}^{\mathrm{S}}$)<br>5.9 ($r_{33}^{\mathrm{S}}$) [4.480] | 0.6–6 [4.479]<br>–<br>– | **2.5715**<br>1<br>5.359<br>0.0502<br>0 [4.479][e]<br>–<br>– | **2.5690**<br>1<br>5.365<br>0.0471<br>0 [4.479][e]<br>–<br>– | +35.3<br>−7.0 [4.479] |
| | +3.74<br>+3.67<br>−0.11 [4.484] | 0.17–3.5 [4.481, 482]<br>≈ 0.1 [4.482]<br>≈ 0.3 [4.482] | **1.5968** (1.1 μm)<br>2.564310<br>0.012337<br>0.013103<br>0.019075 [4.482][f]<br>–<br>– | **1.5422** (1.1 μm)<br>2.386510<br>0.010664<br>0.012878<br>0.012813 [4.482][f]<br>–<br>– | 0.12<br>0.93 [4.483] |
| | 8.9 [4.485, 486]<br>78 [4.485, 486]<br>80 [4.488] | 0.4–5 [4.485–487]<br>–<br>– | **2.208**<br>1<br>3.708<br>0.04601<br>0 [4.321][e]<br>–<br>– | **2.112**<br>1<br>3.349<br>0.03564<br>0 [4.321][e]<br>–<br>– | 11.8 (0.8 μm) [4.487]<br>10.5 [4.485, 486] |

[ef] Dispersion relations (λ (μm), $T = 20\,^{\circ}$C):

[e] $n^2 = A + \dfrac{B}{\lambda^2 - C} - D\lambda^2$ .

[f] $n^2 = A + \dfrac{B}{\lambda^2 - C} + \dfrac{D(\lambda^2 - E)}{(\lambda^2 - E) + F}$ .

**Table 4.4-18** Orthorhombic, point group *mmm* ($D_{2h}$) materials

| | General | Static dielectric tensor | Dissipation factor | Elastic stiffness tensor | Elastic compliance tensor | Piezooptic tensor |
|---|---|---|---|---|---|---|
| Material | $\varrho$ (g/cm$^3$)<br>Mohs hardness<br>$\kappa$ (W/m K) | $\varepsilon_{11}$<br>$\varepsilon_{22}$<br>$\varepsilon_{33}$ | $\tan\delta_1$ | $c_{11}$<br>$c_{22}$<br>$c_{33}$<br>$c_{44}$<br>$c_{55}$<br>$c_{66}$<br>$c_{12}$<br>$c_{13}$<br>$c_{23}$<br>($10^9$ Pa) | $s_{11}$<br>$s_{22}$<br>$s_{33}$<br>$s_{44}$<br>$s_{55}$<br>$s_{66}$<br>$s_{12}$<br>$s_{13}$<br>$s_{23}$<br>($10^{-12}$ Pa$^{-1}$) | |
| Magnesium silicate, $Mg_2SiO_4$ (forsterite) | 3.217<br>7<br>5.12 [4.332] | 6.2[a] [4.26] | | 328.5(13)<br>200.0(1)<br>235.3(7)<br>66.9(6)<br>81.3(1)<br>80.9(2)<br>68.0(16)<br>68.7(7)<br>72.8(6) [4.7] | 3.37<br>5.84<br>4.93<br>15.0<br>12.3<br>12.4<br>−0.85<br>−0.71<br>−1.56 [4.7] | $q_{11}+q_{12}+q_{13}=0.16$<br>$q_{21}+q_{22}+q_{23}=0.20$<br>$q_{31}+q_{32}+q_{33}=0.27$<br>(589 nm) [4.489] |
| Yttrium aluminate, $YAlO_3$ (YAP, YALO) | 5.35<br>8.5<br>11 [4.259] | 16–20[a] [4.48] | 0.001 [4.48] | | | |

[a] It is not clear which relative dielectric constant $\varepsilon_{ij}$ is specified.

**Table 4.4-19** Orthorhombic, point group 222 ($D_2$) materials

| | General | Static dielectric tensor | Elastic stiffness tensor | Piezoelectric tensor | Elastooptic tensor |
|---|---|---|---|---|---|
| Material | $\varrho$ (g/cm$^3$) | $\varepsilon_{11}^{\mathbf{S}}$<br>$\varepsilon_{22}^{\mathbf{S}}$<br>$\varepsilon_{33}^{\mathbf{S}}$<br>$\varepsilon_{11}^{\mathbf{T}}$<br>$\varepsilon_{22}^{\mathbf{T}}$<br>$\varepsilon_{33}^{\mathbf{T}}$ | $c_{11}$<br>$c_{22}$<br>$c_{33}$<br>$c_{44}$<br>$c_{55}$<br>$c_{66}$<br>$c_{12}$<br>$c_{13}$<br>$c_{23}$<br>($10^9$ Pa) | $d_{14}$<br>$d_{25}$<br>$d_{36}$<br>($10^{-12}$ C/N) | $p_{11}$<br>$p_{12}$<br>$p_{13}$<br>$p_{21}$<br>$p_{22}$<br>$p_{23}$<br>$p_{31}$<br>$p_{32}$<br>$p_{33}$<br>$p_{44}$<br>$p_{55}$<br>$p_{66}$ |
| Barium formate, $Ba(COOH)_2$ | 3.261 | 6.9[a] [4.490, 491]<br>6.7[a] [4.490, 491]<br>5.2[a] [4.490, 491]<br>7.9 [4.331]<br>5.9 [4.331]<br>7.5 [4.331] | $s_{44}^{\mathbf{E}}=78.5$<br>$s_{55}^{\mathbf{E}}=60$<br>$s_{66}^{\mathbf{E}}=82.5$<br>[4.331] | −5.6(5)<br>−10.2(10)<br>+1.9(1)<br>[4.8, 492] | |

**Table 4.4-18** Orthorhombic, point group $mmm$ ($D_{2h}$) materials, cont.

| **General optical properties** | **Refractive index** | | |
|---|---|---|---|
| Transparency range (μm)<br>$dn_X/dT$ ($10^{-5}\,K^{-1}$)<br>$dn_Y/dT$ ($10^{-5}\,K^{-1}$)<br>$dn_Z/dT$ ($10^{-5}\,K^{-1}$) | $\boldsymbol{n}_X$<br>$A$<br>$B$<br>$C$ | $\boldsymbol{n}_Y$<br>$A$<br>$B$<br>$C$ | $\boldsymbol{n}_Z$<br>$A$<br>$B$<br>$C$ |
| 0.27–5.9 [4.87]<br>1.45 [4.493]<br>–<br>0.98 [4.493] | **1.9111** (1 μm)<br>1<br>2.61960<br>0.012338 [4.494][b] | **1.9251** (1 μm)<br>1<br>2.67171<br>0.012605 [4.494][b] | **1.9337** (1 μm)<br>1<br>2.70381<br>0.012903 [4.494][b] |

[b] Dispersion relation (λ (μm), $T = 20\,°C$):
$n^2 = A + \dfrac{B\lambda^2}{\lambda^2 - C}$ .

**Table 4.4-19** Orthorhombic, point group 222 ($D_2$) materials, cont.

| **Electrooptic tensor** | **General optical properties** | **Refractive index** | | | **Nonlinear dielectric susceptibility** |
|---|---|---|---|---|---|
| $r_{41}^{\mathbf{T}}$<br>$r_{52}^{\mathbf{T}}$<br>$r_{63}^{\mathbf{T}}$<br>($10^{-12}$ m/V) | Transparency range (μm)<br>$dn_X/dT$ ($10^{-5}\,K^{-1}$)<br>$dn_Y/dT$ ($10^{-5}\,K^{-1}$)<br>$dn_Z/dT$ ($10^{-5}\,K^{-1}$) | $\boldsymbol{n}_X$<br>$A$<br>$B$<br>$C$<br>$D$ | $\boldsymbol{n}_Y$<br>$A$<br>$B$<br>$C$<br>$D$ | $\boldsymbol{n}_Z$<br>$A$<br>$B$<br>$C$<br>$D$ | $d_{14}$<br>$d_{25}$<br>$d_{36}$<br>($10^{-12}$ m/V) |
| +1.81(18)<br>−2.03(20)<br>+0.48(10) [4.492] | 0.245–2.2,<br>4.8–5.1 [4.495]<br>–<br>–<br>– | **1.6214**<br>2.619<br>0.0177<br>0.039<br>0 [4.495][b] | **1.5819**<br>2.491<br>0.0184<br>0.035<br>0 [4.495][b] | **1.5585**<br>2.421<br>0.016<br>0.042<br>0 [4.495][b] | 0.10<br>0.11<br>0.11 [4.495] |

**Table 4.4-19** Orthorhombic, point group 222 ($D_2$) materials, cont.

| | General | Static dielectric tensor | Elastic stiffness tensor | Piezoelectric tensor | Elastooptic tensor |
|---|---|---|---|---|---|
| Material | $\varrho$ $(g/cm^3)$ | $\varepsilon_{11}^{S}$<br>$\varepsilon_{22}^{S}$<br>$\varepsilon_{33}^{S}$<br>$\varepsilon_{11}^{T}$<br>$\varepsilon_{22}^{T}$<br>$\varepsilon_{33}^{T}$ | $c_{11}$<br>$c_{22}$<br>$c_{33}$<br>$c_{44}$<br>$c_{55}$<br>$c_{66}$<br>$c_{12}$<br>$c_{13}$<br>$c_{23}$<br>($10^9$ Pa) | $d_{14}$<br>$d_{25}$<br>$d_{36}$<br>($10^{-12}$ C/N) | $p_{11}$<br>$p_{12}$<br>$p_{13}$<br>$p_{21}$<br>$p_{22}$<br>$p_{23}$<br>$p_{31}$<br>$p_{32}$<br>$p_{33}$<br>$p_{44}$<br>$p_{55}$<br>$p_{66}$ |
| Cesium triborate, $CsB_3O_5$ (CBO) | 3.357 | | | | |
| $\alpha$-Iodic acid, $HIO_3$ | 4.64 | 7.5<br>12.4<br>8.1 [4.331][a] | 57(2)<br>43(1)<br>30.0(3)<br>21(1)<br>16(1)<br>17.8(13)<br>6(3)<br>15(2)<br>11.5(5) [4.7] | −26(1)<br>−18(1)<br>+28(1)<br>[4.8, 496] | 0.418(16)<br>0.308(330)<br>0.313(56)<br>0.304(36)<br>0.322(31)<br>0.307(57)<br>0.527(48)<br>0.340(31)<br>0.377(103)<br>−0.077(66)<br>0.107(12)<br>0.092(8) [4.11] |
| 3-Methyl 4-nitropyridine 1-oxide, $C_6N_2O_3H_6$ (POM) | 1.55 | 3.77<br>5.41<br>3.77 [4.497][a] | 13.29<br>18.14<br>12.20<br>7.8<br>5.2<br>5.4<br>4.9<br>−2.6<br>10.6 [4.498] | | 0.45<br>0.53<br>0.49<br>0.53<br>0.57<br>0.42<br>0.36<br>0.70<br>0.64<br>−0.078<br>−0.074<br>−0.046 (514.5 nm)<br>[4.498] |

**Table 4.4-19** Orthorhombic, point group 222 ($D_2$) materials, cont.

| Electrooptic tensor | General optical properties | Refractive index | | | Nonlinear dielectric susceptibility |
|---|---|---|---|---|---|
| $r_{41}^{\mathbf{T}}$<br>$r_{52}^{\mathbf{T}}$<br>$r_{63}^{\mathbf{T}}$<br>($10^{-12}$ m/V) | Transparency range (μm)<br>$dn_X/dT$ ($10^{-5}$ K$^{-1}$)<br>$dn_Y/dT$ ($10^{-5}$ K$^{-1}$)<br>$dn_Z/dT$ ($10^{-5}$ K$^{-1}$) | $\boldsymbol{n}_X$<br>$A$<br>$B$<br>$C$<br>$D$ | $\boldsymbol{n}_Y$<br>$A$<br>$B$<br>$C$<br>$D$ | $\boldsymbol{n}_Z$<br>$A$<br>$B$<br>$C$<br>$D$ | $d_{14}$<br>$d_{25}$<br>$d_{36}$<br>($10^{-12}$ m/V) |
| | 0.170–3.0 [4.499]<br>–<br>–<br>– | **1.5194**<br>2.3035<br>0.01378<br>0.01498<br>0.00612 [4.500][b] | **1.5505**<br>2.3704<br>0.01528<br>0.01581<br>0.00939 [4.500][b] | **1.5781**<br>2.4753<br>0.01806<br>0.01752<br>0.01654 [4.500][b] | 1.5 [4.499]<br>–<br>– |
| 6.6(3)<br>7.0(5)<br>6.0(3) [4.502, 503] | 0.35–1.6 $E \parallel a$<br>0.35–2.2 $E \parallel c$<br>[4.504, 505]<br>–<br>– | **1.8129**<br>2.5761<br>0.6973<br>0.05550736<br>0.0201 [4.505][c] | **1.9273**<br>2.4701<br>1.2054<br>0.05044516<br>0.0152 [4.505][c] | **1.9500**<br>2.6615<br>1.1316<br>0.05202961<br>0.0398 [4.505][c] | 8.3 [4.501]<br>–<br>– |
| \|3.6(6)\|<br>\|5.1(4)\|<br>\|2.6(3)\| [4.507] | 0.4–3.3 [4.506]<br>–<br>–<br>– | **1.625**<br>2.4529<br>0.1641<br>0.128<br>0 [4.506][c] | **1.668**<br>2.4315<br>0.3556<br>0.1276<br>0.0579 [4.506][c] | **1.829**<br>2.5521<br>0.7962<br>0.1289<br>0.0941 [4.506][c] | 5.3–6.0 [4.506]<br>–<br>– |

**Table 4.4-19** Orthorhombic, point group 222 ($D_2$) materials, cont.

| | General | Static dielectric tensor | Elastic stiffness tensor | Piezoelectric tensor | Elastooptic tensor |
|---|---|---|---|---|---|
| Material | $\varrho$ $(g/cm^3)$ | $\varepsilon_{11}^{S}$<br>$\varepsilon_{22}^{S}$<br>$\varepsilon_{33}^{S}$<br>$\varepsilon_{11}^{T}$<br>$\varepsilon_{22}^{T}$<br>$\varepsilon_{33}^{T}$ | $c_{11}$<br>$c_{22}$<br>$c_{33}$<br>$c_{44}$<br>$c_{55}$<br>$c_{66}$<br>$c_{12}$<br>$c_{13}$<br>$c_{23}$<br>($10^9$ Pa) | $d_{14}$<br>$d_{25}$<br>$d_{36}$<br>($10^{-12}$ C/N) | $p_{11}$<br>$p_{12}$<br>$p_{13}$<br>$p_{21}$<br>$p_{22}$<br>$p_{23}$<br>$p_{31}$<br>$p_{32}$<br>$p_{33}$<br>$p_{44}$<br>$p_{55}$<br>$p_{66}$ |
| Potassium sodium tartrate tetrahydrate, $KNa(C_4H_4O_6)\cdot 4H_2O$ (Rochelle salt) | 1.767 | 245<br>–<br>–<br>1100<br>11.1<br>9.2 [4.331] | 40(16)<br>55(25)<br>63(23)<br>11.9(38)<br>3.1(2)<br>10.0(16)<br>24(29)<br>32(20)<br>23.8(438)<br>[4.7] | 2300<br>−56<br>11.8 [4.331] | 0.35<br>0.41<br>0.42<br>0.37<br>0.28<br>0.34<br>0.36<br>0.35<br>0.36<br>−0.030<br>0.0046<br>−0.025 (589 nm) [4.508] |
| Sodium ammonium tartrate tetrahydrate, $Na(NH_4)C_4H_4O_6\cdot 4H_2O$ (Ammonium Rochelle salt) | | 10(1)[a]<br>10(1)[a]<br>10(1)[a] [4.509]<br>9.0<br>8.9<br>10.0 [4.331] | 36.8<br>50.9<br>55.4<br>10.6<br>3.03<br>8.70<br>27.2<br>30.8<br>34.7 [4.331] | ≈ 13<br>38<br>≈ 7<br>[4.510,511] | −0.48<br>−0.61<br>−0.68<br>−0.55<br>−0.76<br>−0.83<br>−0.44<br>−0.57<br>−0.71<br>0.0077<br>0.013<br>−0.0026 (589 nm)<br>[4.512] |

**Table 4.4-19** Orthorhombic, point group 222 ($D_2$) materials, cont.

| Electrooptic tensor | General optical properties | Refractive index | | | Nonlinear dielectric susceptibility |
|---|---|---|---|---|---|
| $r_{41}^{\mathrm{T}}$<br>$r_{52}^{\mathrm{T}}$<br>$r_{63}^{\mathrm{T}}$<br>($10^{-12}$ m/V) | Transparency range (μm)<br>$dn_X/dT$ ($10^{-5}$ K$^{-1}$)<br>$dn_Y/dT$ ($10^{-5}$ K$^{-1}$)<br>$dn_Z/dT$ ($10^{-5}$ K$^{-1}$) | $\boldsymbol{n}_X$<br>$A$<br>$B$<br>$C$<br>$D$ | $\boldsymbol{n}_Y$<br>$A$<br>$B$<br>$C$<br>$D$ | $\boldsymbol{n}_Z$<br>$A$<br>$B$<br>$C$<br>$D$ | $d_{14}$<br>$d_{25}$<br>$d_{36}$<br>($10^{-12}$ m/V) |
| 8.3 [4.513, 514]<br>–<br>– | <250 to >850 nm<br>−6.54 [4.515, 516]<br>−5.57 [4.515, 516]<br>−6.00 [4.515, 516] | **1.49540**<br>(585 nm) [4.517]<br>**1.5622**<br>(260 nm)<br>[4.515, 516] | **1.49183**<br>(585 nm) [4.517]<br>**1.5576**<br>(260 nm)<br>[4.515, 516]<br>$A = 1$<br>$B = 1.1851057$<br>$C = 0.0113636$<br>$D = 0$<br>[4.515, 516][c] | **1.49001**<br>(585 nm) [4.517]<br>**1.5566**<br>(260 nm)<br>[4.515, 516] | $\chi^{(3)}_{zzzz}$<br>$= 0.8 \times 10^{-22}$ V$^{-2}$ m$^2$<br>$\chi^{(3)}_{xxxx}$<br>$= 0.4 \times 10^{-22}$ V$^{-2}$ m$^2$<br>(at 576.8 and 627 nm)<br>[4.518] |
| $r_{52} = 2.1$<br>[4.519, 520] | | **1.4984**<br>(589 nm)<br>[4.521, 522] | **1.4996**<br>(589 nm)<br>[4.521, 522] | **1.4953**<br>(589 nm)<br>[4.521, 522] | |

[a] The relative dielectric constant $\varepsilon_{ij}$ was measured neither at constant stress nor at constant strain.

[bc] Dispersion relations (λ (μm), $T = 20\,^{\circ}$C):

[b] $n^2 = A + \dfrac{B}{\lambda^2 - C} - D\lambda^2$ .

[c] $n^2 = A + \dfrac{B\lambda^2}{\lambda^2 - C} - D\lambda^2$ .

**Table 4.4-20** Orthorhombic, point group $mm2$ ($C_{2v}$) materials

| | General | Static dielectric tensor | Dissipation factor | Elastic stiffness tensor | Piezoelectric tensor | Elastooptic tensor |
|---|---|---|---|---|---|---|
| Material | $\varrho$ (g/cm$^3$)<br>Mohs hardness<br>$\kappa$ (W/m K) | $\varepsilon^{\mathbf{S}}_{11}$<br>$\varepsilon^{\mathbf{S}}_{22}$<br>$\varepsilon^{\mathbf{S}}_{33}$<br>$\varepsilon^{\mathbf{T}}_{11}$<br>$\varepsilon^{\mathbf{T}}_{22}$<br>$\varepsilon^{\mathbf{T}}_{33}$ | $\tan\delta_1$<br>$\tan\delta_2$<br>$\tan\delta_3$<br>($T$ (°C),<br>$f$ (kHz)) | $c_{11}$<br>$c_{22}$<br>$c_{33}$<br>$c_{44}$<br>$c_{55}$<br>$c_{66}$<br>$c_{12}$<br>$c_{13}$<br>$c_{23}$<br>($10^9$ Pa) | $d_{31}$<br>$d_{32}$<br>$d_{33}$<br>$d_{15}$<br>$d_{24}$<br>$d_h$<br>($10^{-12}$ C/N) | $p_{11}$<br>$p_{12}$<br>$p_{13}$<br>$p_{21}$<br>$p_{22}$<br>$p_{23}$<br>$p_{31}$<br>$p_{32}$<br>$p_{33}$<br>$p_{44}$<br>$p_{55}$<br>$p_{66}$ |
| Ammonium sulfate, $(NH_4)_2SO_4$ | | –<br>–<br>8[a] (−60 °C)<br>[4.526, 527] | | 35.2<br>29.7<br>36.0<br>9.5<br>7.0<br>10.3<br>14.1<br>15.7<br>17.3 [4.525] | | 0.26 [4.523, 524]<br>\|0.27\| [4.525]<br>\|0.26\| [4.525]<br>\|0.23\| [4.525]<br>≈ \|0.27\| [4.525]<br>\|0.25\| [4.525]<br>\|0.23\| [4.525]<br>≈ \|0.26\| [4.525]<br>≈ 0.26 [4.525]<br>0.02 [4.525]<br>≤ \|0.02\| [4.525]<br>≈ 0.01 [4.11, 525] |
| Barium magnesium fluoride, $BaMgF_4$ (BMF) | | 14 [4.528]<br>8 [4.528]<br>8.5 [4.528]<br>14.75(74)[a]<br>8.24(41)[a]<br>8.40(42)[a]<br>[4.529] | | 104<br>81<br>130<br>32.1<br>55.1<br>24.7<br>28.7<br>63.7<br>35.8 [4.529] | +2.5(3)<br>−4.1(4)<br>+8.0(2)<br>−5.3(5)<br>−1.2(1) [4.529]<br>– | |
| Barium sodium niobate, $Ba_2NaNb_5O_{15}$ ("banana") | 5.41<br>–<br>3.5 [4.532] | 215<br>205<br>20<br>238(5)<br>228(5)<br>430 [4.534][b] | 0.0068(17)<br>–<br>0.0024(6)<br>(25 °C, 1 GHz)<br>[4.296] | 239<br>247<br>135<br>65<br>66<br>76<br>104<br>50<br>52 [4.535][c] | −6.8<br>−6.9<br>34<br>32<br>45 [4.533]<br>– | $p_{66} = 0.0021$<br>[4.530, 531] |

**Table 4.4-20** Orthorhombic, point group $mm2$ ($C_{2v}$) materials, cont.

| | **Electrooptic tensor** | **General optical properties** | **Refractive index** | | | **Nonlinear dielectric susceptibility** |
|---|---|---|---|---|---|---|
| | $r_{13}^{\mathbf{T}}$<br>$r_{23}^{\mathbf{T}}$<br>$r_{33}^{\mathbf{T}}$<br>$r_{42}^{\mathbf{T}}$<br>$r_{51}^{\mathbf{T}}$<br>($10^{-12}$ m/V) | Transparency range (μm)<br>$dn_X/dT$ ($10^{-5}$ K$^{-1}$)<br>$dn_Y/dT$ ($10^{-5}$ K$^{-1}$)<br>$dn_Z/dT$ ($10^{-5}$ K$^{-1}$) | $\boldsymbol{n}_X$<br>*A*<br>*B*<br>*C*<br>*D*<br>*E*<br>*F* | $\boldsymbol{n}_Y$<br>*A*<br>*B*<br>*C*<br>*D*<br>*E*<br>*F* | $\boldsymbol{n}_Z$<br>*A*<br>*B*<br>*C*<br>*D*<br>*E*<br>*F* | $d_{31}$<br>$d_{32}$<br>$d_{33}$<br>$d_{15}$<br>$d_{24}$<br>($10^{-12}$ m/V) |
| Ammonium sulfate, $(NH_4)_2SO_4$ | $r_c = 0.4$<br>[4.536] | | | | | 0.27<br>0.29<br>0.50 [4.537]<br>–<br>– |
| Barium magnesium fluoride, $BaMgF_4$ | | 0.185–10 [4.495] | **1.4436**<br>2.077<br>0.0076<br>0.0079<br>0 [4.495][h]<br>–<br>– | **1.4604**<br>2.1238<br>0.0086<br>0<br>0 [4.495][h]<br>–<br>– | **1.4674**<br>2.1462<br>0.00736<br>0.009<br>0 [4.495][h]<br>–<br>– | 0.022<br>0.033<br>0.009<br>–<br>0.024 [4.495] |
| Barium sodium niobate, $Ba_2NaNb_5O_{15}$ (“banana”) | 15(1)<br>13(1)<br>48(2)<br>92(4)<br>90(4) [4.534] | 0.37–5 [4.534, 538, 539]<br>−2.5 [4.534]<br>–<br>8 [4.534] | **2.2573**<br>1<br>3.9495<br>0.04038894<br>0 [4.534][i]<br>–<br>– | **2.2571**<br>1<br>3.9495<br>0.04014012<br>0 [4.534][i]<br>–<br>– | **2.1694**<br>1<br>3.6008<br>0.03219871<br>0 [4.534][i]<br>–<br>– | −12<br>−12<br>−16.5<br>12<br>11.4 [4.534] |

**Table 4.4-20** Orthorhombic, point group $mm2$ ($C_{2v}$) materials, cont.

| | General | Static dielectric tensor | Dissipation factor | Elastic stiffness tensor | Piezoelectric tensor | Elastooptic tensor |
|---|---|---|---|---|---|---|
| Material | $\varrho$ (g/cm$^3$)<br>Mohs hardness<br>$\kappa$ (W/m K) | $\varepsilon^{\mathbf{S}}_{11}$<br>$\varepsilon^{\mathbf{S}}_{22}$<br>$\varepsilon^{\mathbf{S}}_{33}$<br>$\varepsilon^{\mathbf{T}}_{11}$<br>$\varepsilon^{\mathbf{T}}_{22}$<br>$\varepsilon^{\mathbf{T}}_{33}$ | $\tan\delta_1$<br>$\tan\delta_2$<br>$\tan\delta_3$<br>($T$ (°C),<br>$f$ (kHz)) | $c_{11}$<br>$c_{22}$<br>$c_{33}$<br>$c_{44}$<br>$c_{55}$<br>$c_{66}$<br>$c_{12}$<br>$c_{13}$<br>$c_{23}$<br>($10^9$ Pa) | $d_{31}$<br>$d_{32}$<br>$d_{33}$<br>$d_{15}$<br>$d_{24}$<br>$d_{\mathrm{h}}$<br>($10^{-12}$ C/N) | $p_{11}$<br>$p_{12}$<br>$p_{13}$<br>$p_{21}$<br>$p_{22}$<br>$p_{23}$<br>$p_{31}$<br>$p_{32}$<br>$p_{33}$<br>$p_{44}$<br>$p_{55}$<br>$p_{66}$ |
| Calcium tartrate tetrahydrate, $Ca(C_4H_4O_6)\cdot 4H_2O$ (L-CTT) | | 14.3<br>10<br>20 [4.540][a] | 0.9<br>–<br>–<br>(30 °C, 100 Hz)<br>[4.540, 541] | | | |
| *m*-Chloronitrobenzene, $ClC_6H_4NO_2$ (CNB) | | | | | | |
| 2-Cyclooctylamino-5-nitropyridine, $C_{13}H_{19}N_3O_2$ (COANP) | 1.24<br>–<br>– | | | | | |
| *N*, 2-Dimethyl-4-nitrobenzenamine, $C_8H_{10}N_2O_2$ (MNMA) | | | | | | |

**Table 4.4-20** Orthorhombic, point group $mm2$ ($C_{2v}$) materials, cont.

| Electrooptic tensor | General optical properties | Refractive index | | | Nonlinear dielectric susceptibility |
|---|---|---|---|---|---|
| $r_{13}^{T}$<br>$r_{23}^{T}$<br>$r_{33}^{T}$<br>$r_{42}^{T}$<br>$r_{51}^{T}$<br>($10^{-12}$ m/V) | Transparency range (μm)<br>$dn_X/dT$ ($10^{-5}$ K$^{-1}$)<br>$dn_Y/dT$ ($10^{-5}$ K$^{-1}$)<br>$dn_Z/dT$ ($10^{-5}$ K$^{-1}$) | $n_X$<br>$A$<br>$B$<br>$C$<br>$D$<br>$E$<br>$F$ | $n_Y$<br>$A$<br>$B$<br>$C$<br>$D$<br>$E$<br>$F$ | $n_Z$<br>$A$<br>$B$<br>$C$<br>$D$<br>$E$<br>$F$ | $d_{31}$<br>$d_{32}$<br>$d_{33}$<br>$d_{15}$<br>$d_{24}$<br>($10^{-12}$ m/V) |
| | 0.28–1.4 [4.542]<br>–<br>–<br>– | **1.5125**<br>1<br>1.26<br>0.0127273<br>0 [4.542]$^{i}$<br>–<br>– | **1.5220**<br>1<br>1.30<br>0.0121495<br>0 [4.542]$^{i}$<br>–<br>– | **1.5477**<br>1<br>1.38<br>0.0094521<br>0 [4.542]$^{i}$<br>–<br>– | <0.015<br>0.20<br>0.14<br>1.73<br>0.90 [4.542] |
| | | **1.6557**<br>2.4882<br>0.2384<br>0.1070<br>0.0091 [4.543]$^{i}$<br>–<br>– | **1.6626**<br>2.5411<br>0.2148<br>0.1122<br>0.0135 [4.543]$^{i}$<br>–<br>– | **1.624**<br>2.2469<br>0.3722<br>0.0810<br>0.0092 [4.543]$^{i}$<br>–<br>– | 4.6<br>4<br>7.8 [4.543]<br>–<br>– |
| 0.63 [4.544]<br>–<br>–<br>–<br>– | 0.41– . . . [4.545]<br>–<br>–<br>– | **1.6100**<br>2.3320<br>0.2215<br>0.1686<br>0 [4.545]$^{i}$<br>–<br>– | **1.6383**<br>2.3994<br>0.2469<br>0.1500<br>0 [4.545]$^{i}$<br>–<br>– | **1.7170**<br>2.5104<br>0.3689<br>0.1780<br>0 [4.545]$^{i}$<br>–<br>– | 11.3<br>24<br>10.8 [4.546, 547]<br>–<br>– |
| 8 ± 2<br>–<br>7.5 ± 2 [4.548]<br>–<br>– | 0.5–2 [4.548]<br>–<br>–<br>– | **1.936**<br>1.6797<br>1.7842<br>0.1571<br>0 [4.548]$^{i}$<br>–<br>– | | **1.506**<br>2.1798<br>0.0736<br>0.1757<br>0 [4.548]$^{i}$<br>–<br>– | 13<br>–<br>2.6<br>12 [4.548]<br>– |

**Table 4.4-20** Orthorhombic, point group $mm2$ ($C_{2v}$) materials, cont.

| | General | Static dielectric tensor | Dissipation factor | Elastic stiffness tensor | Piezoelectric tensor | Elastooptic tensor | |
|---|---|---|---|---|---|---|---|
| Material | $\varrho$ (g/cm$^3$)<br>Mohs hardness<br>$\kappa$ (W/m K) | $\varepsilon_{11}^{S}$<br>$\varepsilon_{22}^{S}$<br>$\varepsilon_{33}^{S}$<br>$\varepsilon_{11}^{T}$<br>$\varepsilon_{22}^{T}$<br>$\varepsilon_{33}^{T}$ | $\tan\delta_1$<br>$\tan\delta_2$<br>$\tan\delta_3$<br>($T$ (°C),<br>$f$ (kHz)) | $c_{11}$<br>$c_{22}$<br>$c_{33}$<br>$c_{44}$<br>$c_{55}$<br>$c_{66}$<br>$c_{12}$<br>$c_{13}$<br>$c_{23}$<br>($10^9$ Pa) | $d_{31}$<br>$d_{32}$<br>$d_{33}$<br>$d_{15}$<br>$d_{24}$<br>$d_h$<br>($10^{-12}$ C/N) | $p_{11}$<br>$p_{12}$<br>$p_{13}$<br>$p_{21}$<br>$p_{22}$<br>$p_{23}$<br>$p_{31}$<br>$p_{32}$<br>$p_{33}$<br>$p_{44}$<br>$p_{55}$<br>$p_{66}$ | |
| Gadolinium molybdate, $Gd_2(MoO_4)_3$ (GMO) | | –<br>–<br>9.6<br>–<br>–<br>10.2 [4.550] | | 55(4)<br>71(3)<br>101(3)<br>25.2(8)<br>25.8(2)<br>33.1(3)<br>12.8(46)<br>23.5(45)<br>27.2(76) [4.7][c] | 1.5 [4.549]<br>0.2 [4.8]<br>0.5 [4.549]<br>–<br>–<br>– | 0.19<br>0.31<br>0.175<br>0.215<br>0.235<br>0.175<br>0.185<br>0.23<br>0.115<br>−0.033<br>−0.028<br>0.035 [4.551]<br>(515–633 nm) | |
| Lithium formate monohydrate, $LiCOOH \cdot H_2O$ (LFM) | 1.46<br>–<br>– | 3.24 [4.552, 553]<br>–<br>–<br>4.5(5)[a] [4.554, 555]<br>5.0(5)[a] [4.554, 555]<br>6.0(3)[a] [4.554, 555] | | 19.15<br>33.55<br>41.98<br>15.02<br>5.31<br>4.89<br>8.62<br>8.40<br>22.77<br>[4.552, 553][c] | −2.1(2)<br>−6.7(5)<br>+9.2(7)<br>−15.0(10)<br>+1.2(2)<br>[4.554–557] | | |
| Lithium gallium oxide, $LiGaO_2$ (lithium metagallate) | 4.187<br>7.5<br>– | 7.0 [4.8]<br>6.0 [4.8]<br>8.3 [4.558]<br>7.18 [4.8]<br>6.18 [4.8]<br>8.78 [4.8] | | 140<br>120<br>140<br>57.1<br>47.4<br>69.0<br>14<br>28<br>31 [4.558][c] | −2.5 [4.558]<br>−4.7 [4.558]<br>+8.6 [4.558]<br>−6.9 [4.558]<br>−6.0 [4.558]<br>+0.9 [4.8, 274] | | |

**Table 4.4-20** Orthorhombic, point group $mm2$ ($C_{2v}$) materials, cont.

| | Electrooptic tensor | General optical properties | Refractive index | | | Nonlinear dielectric susceptibility |
|---|---|---|---|---|---|---|
| | $r_{13}^{\mathrm{T}}$<br>$r_{23}^{\mathrm{T}}$<br>$r_{33}^{\mathrm{T}}$<br>$r_{42}^{\mathrm{T}}$<br>$r_{51}^{\mathrm{T}}$<br>($10^{-12}$ m/V) | Transparency range (μm)<br>$dn_X/dT$ ($10^{-5}$ K$^{-1}$)<br>$dn_Y/dT$ ($10^{-5}$ K$^{-1}$)<br>$dn_Z/dT$ ($10^{-5}$ K$^{-1}$) | $\boldsymbol{n}_X$<br>$A$<br>$B$<br>$C$<br>$D$<br>$E$<br>$F$ | $\boldsymbol{n}_Y$<br>$A$<br>$B$<br>$C$<br>$D$<br>$E$<br>$F$ | $\boldsymbol{n}_Z$<br>$A$<br>$B$<br>$C$<br>$D$<br>$E$<br>$F$ | $d_{31}$<br>$d_{32}$<br>$d_{33}$<br>$d_{15}$<br>$d_{24}$<br>($10^{-12}$ m/V) |
| | +2.15(16)<br>−2.31(16)<br>+0.123(15)<br>–<br>–<br>[4.560, 561] | | **1.8141**<br>1<br>2.2450<br>0.022693<br>0 [4.321]$^{i}$<br>–<br>– | **1.8145**<br>1<br>2.24654<br>0.0226803<br>0 [4.321]$^{i}$<br>–<br>– | **1.8637**<br>1<br>2.41957<br>0.0245458<br>0 [4.321]$^{i}$<br>–<br>– | −2.3<br>+2.3<br>−0.04<br>−4.1<br>+4 [4.156, 559] |
| | −1.0(1)<br>+3.2(2)<br>−2.6(2)<br>+1.0(2)<br>+2.4(2)<br>[4.554–557] | 0.23–1.2 [4.562, 563]<br>–<br>–<br>– | **1.3595** (1 μm)<br>1.4376<br>0.4045<br>0.01692601<br>0.0005 [4.564]$^{i}$<br>–<br>– | **1.4694** (1 μm)<br>1.6586<br>0.5006<br>0.023409<br>0.0127 [4.564]$^{i}$<br>–<br>– | **1.5055** (1 μm)<br>1.6714<br>0.5928<br>0.02534464<br>0.0153 [4.564]$^{i}$<br>–<br>– | 0.13<br>−0.60<br>+0.94 [4.12]<br>–<br>– |
| | | 0.3–5 [4.251, 565]<br>–<br>–<br>– | **1.7477**<br>(0.5 μm) [4.566] | **1.7768**<br>(0.5 μm) [4.566] | **1.7791**<br>(0.5 μm) [4.566] | +0.066<br>−0.14<br>+0.57 [4.156, 565]<br>–<br>– |

**Table 4.4-20** Orthorhombic, point group $mm2$ ($C_{2v}$) materials, cont.

| | General | Static dielectric tensor | Dissipation factor | Elastic stiffness tensor | Piezoelectric tensor | Elastooptic tensor | |
|---|---|---|---|---|---|---|---|
| Material | $\varrho$ (g/cm$^3$)<br>Mohs hardness<br>$\kappa$ (W/m K) | $\varepsilon^{\mathbf{S}}_{11}$<br>$\varepsilon^{\mathbf{S}}_{22}$<br>$\varepsilon^{\mathbf{S}}_{33}$<br>$\varepsilon^{\mathbf{T}}_{11}$<br>$\varepsilon^{\mathbf{T}}_{22}$<br>$\varepsilon^{\mathbf{T}}_{33}$ | $\tan\delta_1$<br>$\tan\delta_2$<br>$\tan\delta_3$<br>($T$ (°C),<br>$f$ (kHz)) | $c_{11}$<br>$c_{22}$<br>$c_{33}$<br>$c_{44}$<br>$c_{55}$<br>$c_{66}$<br>$c_{12}$<br>$c_{13}$<br>$c_{23}$<br>($10^9$ Pa) | $d_{31}$<br>$d_{32}$<br>$d_{33}$<br>$d_{15}$<br>$d_{24}$<br>$d_{\mathrm{h}}$<br>($10^{-12}$ C/N) | $p_{11}$<br>$p_{12}$<br>$p_{13}$<br>$p_{21}$<br>$p_{22}$<br>$p_{23}$<br>$p_{31}$<br>$p_{32}$<br>$p_{33}$<br>$p_{44}$<br>$p_{55}$<br>$p_{66}$ | |
| Lithium triborate, $LiB_3O_5$ (LBO) | 2.47<br>6<br>3.5 [4.200] | | | | | | |
| *m*-Nitroaniline; (3-nitrobenzenamine, meta-nitroaniline), $C_6H_4(NO_2)NH_2$ (mNA) | | 3.9<br>4.2<br>4.6 [4.567][a] | | | | | |
| Potassium acid phthalate, $KH(C_8H_4O_4)$ | | 6.00(2)<br>3.87(2)<br>4.34(2)<br>[4.568, 569]<br>–<br>–<br>4.34[a] [4.570] | | 17.6<br>13.3<br>17.0<br>4.86<br>7.59<br>6.23<br>7.4<br>10.4<br>5.0<br>[4.568, 569] | −15.3(0)<br>+8.8(0)<br>+5.5(0)<br>−7.1(0)<br>+4.3(0)<br>[4.568, 569]<br>– | −0.61<br>−0.25<br>−0.52<br>−0.58<br>−0.36<br>−0.60<br>−0.84<br>−0.36<br>−0.90<br>−0.26<br>−0.63<br>−0.13 (589 nm)<br>[4.571] | |

**Table 4.4-20** Orthorhombic, point group $mm2$ ($C_{2v}$) materials, cont.

| | Electrooptic tensor | General optical properties | Refractive index | | | Nonlinear dielectric susceptibility |
|---|---|---|---|---|---|---|
| | $r_{13}^{T}$<br>$r_{23}^{T}$<br>$r_{33}^{T}$<br>$r_{42}^{T}$<br>$r_{51}^{T}$<br>($10^{-12}$ m/V) | Transparency range (μm)<br>$dn_X/dT$ ($10^{-5}$ K$^{-1}$)<br>$dn_Y/dT$ ($10^{-5}$ K$^{-1}$)<br>$dn_Z/dT$ ($10^{-5}$ K$^{-1}$) | $n_X$<br>$A$<br>$B$<br>$C$<br>$D$<br>$E$<br>$F$ | $n_Y$<br>$A$<br>$B$<br>$C$<br>$D$<br>$E$<br>$F$ | $n_Z$<br>$A$<br>$B$<br>$C$<br>$D$<br>$E$<br>$F$ | $d_{31}$<br>$d_{32}$<br>$d_{33}$<br>$d_{15}$<br>$d_{24}$<br>($10^{-12}$ m/V) |
| | | 0.16–2.6 [4.572]<br>−18 [4.573]<br>−136 [4.573]<br>−(63 + 21λ) [4.573] | **1.5656**<br>2.4542<br>0.01125<br>0.01135<br>0.01388<br>0<br>0 [4.575][j] | **1.5905**<br>2.5390<br>0.01277<br>0.01189<br>0.01849<br>$4.3025\times10^{-5}$<br>$2.9131\times10^{-5}$<br>[4.575][j] | **1.6055**<br>2.5865<br>0.01310<br>0.01223<br>0.01862<br>$4.5778\times10^{-5}$<br>$3.2526\times10^{-5}$<br>[4.575][j] | −0.67<br>0.85<br>0.04<br>[4.12, 14, 572–574]<br>–<br>– |
| | 7.4(7)<br>0.1(6)<br>16.7(2) [4.578]<br>–<br>– | 0.5–2 [4.576, 577]<br>–<br>–<br>– | **1.631**<br>2.469<br>0.1864<br>0.16<br>0.0199 [4.579][i]<br>–<br>– | **1.678**<br>2.6658<br>0.1626<br>0.1719<br>0.0212 [4.579][i]<br>–<br>– | **1.719**<br>2.8102<br>0.1524<br>0.175<br>0.0294 [4.579][i]<br>–<br>– | 20<br>1.6<br>21 [4.543]<br>–<br>– |
| | $r_b \approx 1.8$ [4.570] | 0.3–1.7<br>with a narrow absorption band at 1.14 μm [4.580]<br>–<br>–<br>– | **1.63**<br>(1.1 μm) [4.580] | **1.64**<br>(1.1 μm) [4.580] | **1.48**<br>(1.1 μm) [4.580] | 0.21 ($d_{31}$, 1.15 μm)<br>0.06 ($d_{32}$, 1.15 μm)<br>0.65 ($d_{31}$, 0.63 μm)<br>0.15 ($d_{32}$, 0.63 μm)<br>–<br>[4.580] |

**Table 4.4-20** Orthorhombic, point group $mm2$ ($C_{2v}$) materials, cont.

| | General | Static dielectric tensor | Dissipation factor | Elastic stiffness tensor | Piezoelectric tensor | Elastooptic tensor | |
|---|---|---|---|---|---|---|---|
| Material | $\varrho$ (g/cm$^3$)<br>Mohs hardness<br>$\kappa$ (W/m K) | $\varepsilon_{11}^{S}$<br>$\varepsilon_{22}^{S}$<br>$\varepsilon_{33}^{S}$<br>$\varepsilon_{11}^{T}$<br>$\varepsilon_{22}^{T}$<br>$\varepsilon_{33}^{T}$ | $\tan\delta_1$<br>$\tan\delta_2$<br>$\tan\delta_3$<br>($T$ (°C),<br>$f$ (kHz)) | $c_{11}$<br>$c_{22}$<br>$c_{33}$<br>$c_{44}$<br>$c_{55}$<br>$c_{66}$<br>$c_{12}$<br>$c_{13}$<br>$c_{23}$<br>($10^9$ Pa) | $d_{31}$<br>$d_{32}$<br>$d_{33}$<br>$d_{15}$<br>$d_{24}$<br>$d_h$<br>($10^{-12}$ C/N) | $p_{11}$<br>$p_{12}$<br>$p_{13}$<br>$p_{21}$<br>$p_{22}$<br>$p_{23}$<br>$p_{31}$<br>$p_{32}$<br>$p_{33}$<br>$p_{44}$<br>$p_{55}$<br>$p_{66}$ | |
| Potassium niobate, $KNbO_3$ | 4.617<br>–<br>>3.5 [4.581] | 37(2)<br>780(50)<br>24(2)<br>160(10)<br>1000(80)<br>55(5)<br>(25 °C)<br>[4.583] | 0.003<br>0.002<br>0.01<br>(25 °C)<br>[4.583] | 226<br>270<br>280<br>74.3<br>25.0<br>95.5<br>96 [4.583]<br>–<br>– | +9.8(7)<br>−19.5(20)<br>+24.5(15)<br>[4.582]<br>215(5)<br>159(5)<br>[4.583]<br>– | \|0.197\|[d]<br>\|0.115\|[d]<br>\|0.109\|[e]<br>\|0.130\|[d]<br>\|0.234\|[d]<br>\|0.005\|[e]<br>\|0.64\|[d]<br>\|0.153\|[d]<br>\|0.075\|[e]<br>\|0.57\|[d]<br>\|0.45\|[d] [4.584]<br>– | |
| Potassium pentaborate tetrahydrate, $KB_5O_8 \cdot 4H_2O$ (KB5) | 1.74<br>2.5<br>– | 5.5<br>4.6<br>4.5 [4.585]<br>–<br>–<br>– | | 58.2<br>35.9<br>25.5<br>16.4<br>4.63<br>5.7<br>22.9<br>17.4<br>23.1 [4.585] | −0.35<br>−2.3<br>+5.5<br>+4.7<br>+20.3 [4.586]<br>– | | |
| Potassium titanyl arsenate, $KTiOAsO_4$ (KTA) | 3.45<br>3<br>– | –<br>–<br>–<br>12(1)<br>12(1)<br>18(1)<br>[4.587, 588] | | | | | |
| Potassium titanate (titanyl) phosphate, $KTiOPO_4$ (KTP) | 3.02<br>5<br>2 (‖ $X$)<br>3 (‖ $Y$)<br>3.3 (‖ $Z$)<br>[4.590] | 11.6(2)<br>11.0(2)<br>15.4(3)<br>11.9(2)<br>11.3(2)<br>≥17.5(4)<br>[4.591] | $\lesssim 0.004$<br>$\leq 0.004$<br>$< 0.005$<br>(10–10$^3$ MHz)<br>$\approx 0.017$<br>0.017<br>$\approx 0.35$<br>(100 kHz)<br>[4.591] | 159<br>154<br>175 [4.589]<br>–<br>–<br>–<br>–<br>–<br>– | | | |

**Table 4.4-20** Orthorhombic, point group $mm2$ ($C_{2v}$) materials, cont.

| | **Electrooptic tensor** | **General optical properties** | **Refractive index** | | | **Nonlinear dielectric susceptibility** |
|---|---|---|---|---|---|---|
| | $r_{13}^{\mathrm{T}}$<br>$r_{23}^{\mathrm{T}}$<br>$r_{33}^{\mathrm{T}}$<br>$r_{42}^{\mathrm{T}}$<br>$r_{51}^{\mathrm{T}}$<br>($10^{-12}$ m/V) | Transparency range (μm)<br>$dn_X/dT$ ($10^{-5}$ K$^{-1}$)<br>$dn_Y/dT$ ($10^{-5}$ K$^{-1}$)<br>$dn_Z/dT$ ($10^{-5}$ K$^{-1}$) | $n_X$<br>$A$<br>$B$<br>$C$<br>$D$<br>$E$<br>$F$ | $n_Y$<br>$A$<br>$B$<br>$C$<br>$D$<br>$E$<br>$F$ | $n_Z$<br>$A$<br>$B$<br>$C$<br>$D$<br>$E$<br>$F$ | $d_{31}$<br>$d_{32}$<br>$d_{33}$<br>$d_{15}$<br>$d_{24}$<br>($10^{-12}$ m/V) |
| | 34(2)<br>6(1)<br>63.4(10)<br>450(30)<br>120(10) [4.584] | 0.4–4.5 [4.386]<br>For temperature-dependent dispersion relations, see [4.592] | **2.2576**<br>1<br>1.44121874<br>0.07439136<br>2.54336918<br>0.01877036<br>0.02845018<br>[4.594][k] | **2.2195**<br>1<br>1.33660410<br>0.06664629<br>2.49710396<br>0.01666505<br>0.02517432<br>[4.594][k] | **2.1194**<br>1<br>1.04824955<br>0.06514225<br>2.37108379<br>0.01433172<br>0.01943289<br>[4.594][k] | +11 [4.12–14]<br>−13 [4.12–14]<br>−19.5 [4.12–14]<br>16 [4.593]<br>17 [4.593] |
| | | 0.165–1.4 [4.595]<br>–<br>–<br>– | **1.4917** (0.5 μm)<br>1<br>1.1790826<br>0.0087815<br>0 [4.596, 597][i]<br>–<br>– | **1.4380** (0.5 μm)<br>1<br>1.0280852<br>0.0090222<br>0 [4.596, 597][i]<br>–<br>– | **1.4251** (0.5 μm)<br>1<br>0.9919090<br>0.0093289<br>0 [4.596, 597][i]<br>–<br>– | 0.04<br>0.003<br>0.05<br>(all at 0.5 μm)<br>–<br>–<br>[4.12, 598, 599] |
| | 15(1)<br>21(1)<br>40(1)<br>–<br>–<br>[4.587, 588] | 0.35–5.3<br>[4.587, 588, 600]<br>–<br>–<br>– | **1.782**<br>1.90713<br>1.23552<br>0.0387775<br>0.01025 [4.601][i]<br>–<br>– | **1.790**<br>2.15912<br>1.00099<br>0.0477160<br>0.01096 [4.601][i]<br>–<br>– | **1.868**<br>2.14786<br>1.29559<br>0.0516153<br>0.01436 [4.601][i]<br>–<br>– | 2.9<br>5.2<br>12.0<br>–<br>–<br>[4.12, 14, 602–604][l] |
| | +9.5(5)<br>+15.7(8)<br>+36.3(18)<br>9.3(9)<br>7.3(7) [4.591] | 0.35–4.5 [4.605, 606]<br>0.61 [4.607][m]<br>0.83 [4.607][m]<br>1.45 [4.607][m] | **1.7381**<br>3.0065<br>0.03901<br>0.04251<br>0.01327 [4.608][hm]<br>–<br>– | **1.7458**<br>3.0333<br>0.04154<br>0.04547<br>0.01408 [4.608][hm]<br>–<br>– | **1.8302**<br>3.3134<br>0.05694<br>0.05658<br>0.01682 [4.608][hm]<br>–<br>– | 2.2<br>3.7<br>14.6<br>1.9<br>3.7 [4.13][l] |

**Table 4.4-20** Orthorhombic, point group $mm2$ ($C_{2v}$) materials, cont.

| | General | Static dielectric tensor | Dissipation factor | Elastic stiffness tensor | Piezoelectric tensor | Elastooptic tensor | |
|---|---|---|---|---|---|---|---|
| Material | $\varrho$ (g/cm$^3$)<br>Mohs hardness<br>$\kappa$ (W/m K) | $\varepsilon_{11}^{\mathbf{S}}$<br>$\varepsilon_{22}^{\mathbf{S}}$<br>$\varepsilon_{33}^{\mathbf{S}}$<br>$\varepsilon_{11}^{\mathbf{T}}$<br>$\varepsilon_{22}^{\mathbf{T}}$<br>$\varepsilon_{33}^{\mathbf{T}}$ | $\tan\delta_1$<br>$\tan\delta_2$<br>$\tan\delta_3$<br>($T$ (°C),<br>$f$ (kHz)) | $c_{11}$<br>$c_{22}$<br>$c_{33}$<br>$c_{44}$<br>$c_{55}$<br>$c_{66}$<br>$c_{12}$<br>$c_{13}$<br>$c_{23}$<br>($10^9$ Pa) | $d_{31}$<br>$d_{32}$<br>$d_{33}$<br>$d_{15}$<br>$d_{24}$<br>$d_h$<br>($10^{-12}$ C/N) | $p_{11}$<br>$p_{12}$<br>$p_{13}$<br>$p_{21}$<br>$p_{22}$<br>$p_{23}$<br>$p_{31}$<br>$p_{32}$<br>$p_{33}$<br>$p_{44}$<br>$p_{55}$<br>$p_{66}$ | |
| Rubidium titanate (titanyl) phosphate, $RbTiOPO_4$ (RTP) | | 23[f]<br>(25 °C)<br>[4.609–611] | | 143<br>142<br>175<br>33<br>40<br>57 [4.589]<br>–<br>–<br>– | | | |
| Sodium nitrite, $NaNO_2$ | 2.168<br>–<br>– | 8 [4.612]<br>5.2 [4.612]<br>4.18 [4.612]<br>7.4 [4.614]<br>5.5 [4.614]<br>5.0 [4.614] | 0.004<br>0.006<br>0.015<br>(3.3 GHz)<br>[4.612] | 30.6(3)<br>56(2)<br>64(2)<br>12(1)<br>9.9(1)<br>5.0(3)<br>12.5(1)<br>15.6(53)<br>14.6(48) [4.7] | −1.1<br>−2.8<br>+1.6<br>+9.3<br>−20.2<br>–<br>[4.8,614] | \|0.44\| [4.613]<br>\|0.37\| [4.613]<br>\|0.36\| [4.613]<br>\|0.39\| [4.613]<br>\|0.33\| [4.613]<br>\|0.27\| [4.613]<br>\|0.18\| [4.613]<br>\|0.19\| [4.613]<br>\|0.15\| [4.613]<br>−0.050[g] [4.615]<br>−0.30 [4.615]<br>−0.10[g] [4.615] | |

[a] These values for $\varepsilon_{ij}$ are neither at constant stress nor at constant strain.

[b] Stoichiometric crystal.

[c] $c^{\boldsymbol{E}}$ at constant electric field.

[d] $p^{\boldsymbol{E}}$ at constant electric field.

[e] $p_{i3}^{*} = p_{i3}^{\boldsymbol{E}} - r_{i3}^{\mathbf{S}} e_{333}/\varepsilon_0 \varepsilon_{33}^{\mathbf{S}}$, where $r_{i3}^{\mathbf{S}}$ is the electrooptic-tensor element $i3$ at zero strain, $e_{333}$ is the piezoelectric-tensor element 333, and $\varepsilon_{33}^{\mathbf{S}}$ is the relative-dielectric-constant element 33 at constant strain.

[f] Element of $\varepsilon$ unspecified, but probably $\varepsilon_{11}$ or $\varepsilon_{33}$.

**Table 4.4-20** Orthorhombic, point group $mm2$ ($C_{2v}$) materials, cont.

| | **Electrooptic tensor** | **General optical properties** | **Refractive index** | | | **Nonlinear dielectric susceptibility** |
|---|---|---|---|---|---|---|
| | $r_{13}^{\mathbf{T}}$<br>$r_{23}^{\mathbf{T}}$<br>$r_{33}^{\mathbf{T}}$<br>$r_{42}^{\mathbf{T}}$<br>$r_{51}^{\mathbf{T}}$<br>($10^{-12}$ m/V) | Transparency range (μm)<br>$dn_X/dT$ ($10^{-5}$ K$^{-1}$)<br>$dn_Y/dT$ ($10^{-5}$ K$^{-1}$)<br>$dn_Z/dT$ ($10^{-5}$ K$^{-1}$) | $\boldsymbol{n}_X$<br>$A$<br>$B$<br>$C$<br>$D$<br>$E$<br>$F$ | $\boldsymbol{n}_Y$<br>$A$<br>$B$<br>$C$<br>$D$<br>$E$<br>$F$ | $\boldsymbol{n}_Z$<br>$A$<br>$B$<br>$C$<br>$D$<br>$E$<br>$F$ | $d_{31}$<br>$d_{32}$<br>$d_{33}$<br>$d_{15}$<br>$d_{24}$<br>($10^{-12}$ m/V) |
| | +9.7(9)<br>+10.8(9)<br>+22.5(9)<br>+14.9(9)<br>−7.6(9)<br>[4.618–620] | 0.35–4.5 [4.616, 617]<br>–<br>–<br>– | **1.7569**<br>2.56666<br>0.53842<br>0.06374<br>0.01666 [4.617][i]<br>–<br>– | **1.7730**<br>2.34868<br>0.77949<br>0.05449<br>0.0211 [4.617][i]<br>–<br>– | **1.8540**<br>2.77339<br>0.63961<br>0.08151<br>0.02237 [4.617][i]<br>–<br>– | 3.3<br>4.1<br>17.3 [4.603]<br>–<br>– |
| | $r_{42} = -3.0(2)$<br>$r_{51} = -1.9(2)$<br>(at 546 nm) [4.623] | 0.35–3.4 and 5–8<br>[4.621, 622]<br>–<br>–<br>– | **1.3395**<br>1<br>0.727454<br>0.0118285<br>0 [4.621][i]<br>–<br>– | **1.4036**<br>1<br>0.978108<br>0.0112296<br>0 [4.621][i]<br>–<br>– | **1.6365**<br>1<br>1.616683<br>0.0222073<br>0 [4.621][i]<br>–<br>– | 0.11<br>2.9<br>0.14<br>0.11<br>2.8 [4.624] |

[g] $p_{ijkl}^{\text{eff}} = p_{ijkl}^{\boldsymbol{E}} - r_{ijm}^{\mathbf{S}} a_m a_n e_{nkl} / \boldsymbol{a} \cdot \boldsymbol{\varepsilon} \cdot \boldsymbol{a}$, where $r^{\mathbf{S}}$ is the electrooptic tensor, $\boldsymbol{a}$ is a unit acoustic-wave propagation vector, and $\boldsymbol{\varepsilon}$ is the dielectric-constant tensor at the frequency of the acoustic wave.

[hijk] Dispersion relations (λ (μm), $T = 20\,^{\circ}\text{C}$):

[h] $n^2 = A + \dfrac{B}{\lambda^2 - C} - D\lambda^2$ .

[i] $n^2 = A + \dfrac{B\lambda^2}{\lambda^2 - C} - D\lambda^2$ .

[j] $n^2 = A + \dfrac{B}{\lambda^2 - C} - D\lambda^2 + E\lambda^4 - F\lambda^6$ .

[k] $n^2 = A + \dfrac{B\lambda^2}{\lambda^2 - C} + \dfrac{D\lambda^2}{\lambda^2 - E} - F\lambda^2$ .

[l] Note reversals between $d_{31}$ and $d_{32}$ (also between $d_{15}$ and $d_{24}$) for KTA and KTP given in [4.12] and [4.13].

[m] For flux-grown crystals.

**Table 4.4-21** Monoclinic, point group 2 ($C_2$) materials

| | General | Static dielectric tensor | Dissipation factor | Elastic stiffness tensor | Piezoelectric tensor | Elastooptic tensor | |
|---|---|---|---|---|---|---|---|
| Material | $\varrho$ $(g/cm^3)$<br>Mohs hardness<br>$\kappa$ (W/m K) | $\varepsilon^{S}_{11}$<br>$\varepsilon^{S}_{22}$<br>$\varepsilon^{S}_{33}$<br>$\varepsilon^{S}_{13}$<br>$\varepsilon^{T}_{11}$<br>$\varepsilon^{T}_{22}$<br>$\varepsilon^{T}_{33}$<br>$\varepsilon^{T}_{13}$ | $\tan\delta_1$<br>$\tan\delta_2$<br>$\tan\delta_3$<br><br>($f$ (kHz)) | $c_{11}$<br>$c_{22}$<br>$c_{33}$<br>$c_{44}$<br>$c_{55}$<br>$c_{66}$<br>$c_{12}$<br>$c_{13}$<br>$c_{23}$<br>$c_{15}$<br>$c_{25}$<br>$c_{35}$<br>$c_{46}$<br>($10^9$ Pa) | $d_{21}$<br>$d_{22}$<br>$d_{23}$<br>$d_{14}$<br>$d_{16}$<br>$d_{25}$<br>$d_{34}$<br>$d_{36}$<br>$d_h$<br>($10^{-12}$ C/N) | $p_{11}$<br>$p_{12}$<br>$p_{13}$<br>$p_{15}$<br>$p_{21}$<br>$p_{22}$<br>$p_{23}$<br>$p_{25}$<br>$p_{31}$<br>$p_{32}$<br>$p_{33}$<br>$p_{35}$<br>$p_{44}$<br>$p_{46}$<br>$p_{51}$<br>$p_{52}$<br>$p_{53}$<br>$p_{55}$<br>$p_{64}$<br>$p_{66}$ | |
| Bismuth triborate, $BiB_3O_6$ (BIBO) | 4.9 [4.625]<br>–<br>– | | | | | | |
| Deuterated L-arginine phosphate, $(ND_xH_{2-x})_2^+(CND)(CH_2)_3CH(ND_yH_{3-y})^+COO^- \cdot D_2PO_4^- \cdot D_2O$ (DLAP) | ≈ 1.5<br>3<br>– | | | 17.477(111)<br>31.996(89)<br>31.575(72)<br>–<br>–<br>–<br>–<br>–<br>–<br>–<br>–<br>–<br>–<br>[4.15] | | | |
| 4-($N1N$-Dimethylamino)-3-acetamidonitrobenzene ($N$-[2-(dimethylamino)-5-nitrophenyl]-acetamide, DAN) | | | | | | | |

**Table 4.4-21** Monoclinic, point group 2 ($C_2$) materials, cont.

| | **Electrooptic tensor** | **General optical properties** | **Refractive index** | | | **Nonlinear dielectric susceptibility** |
|---|---|---|---|---|---|---|
| | $r_{12}^{\mathbf{T}}$<br>$r_{22}^{\mathbf{T}}$<br>$r_{32}^{\mathbf{T}}$<br>$r_{41}^{\mathbf{T}}$<br>$r_{43}^{\mathbf{T}}$<br>$r_{52}^{\mathbf{T}}$<br>$r_{61}^{\mathbf{T}}$<br>$r_{63}^{\mathbf{T}}$ ($10^{-12}$ m/V)<br>(at $\lambda = 633$ nm) | Transparency range (μm)<br>$dn_X/dT$ ($10^{-5}$ K$^{-1}$)<br>$dn_Y/dT$ ($10^{-5}$ K$^{-1}$)<br>$dn_Z/dT$ ($10^{-5}$ K$^{-1}$) | $\boldsymbol{n}_X$<br>$A$<br>$B$<br>$C$<br>$D$ | $\boldsymbol{n}_Y$<br>$A$<br>$B$<br>$C$<br>$D$ | $\boldsymbol{n}_Z$<br>$A$<br>$B$<br>$C$<br>$D$ | $d_{21}$<br>$d_{22}$<br>$d_{23}$<br>$d_{25}$<br>($10^{-12}$ m/V) |
| | | 0.27–6.25 [4.625]<br>–<br>–<br>– | **1.9190**<br>3.6545<br>0.0511<br>0.0371<br>0.0226 [4.626][a] | **1.7585**<br>3.0740<br>0.0323<br>0.0316<br>0.01337 [4.626][a] | **1.7854**<br>3.1685<br>0.0373<br>0.0346<br>0.01750 [4.626][a] | 2.3(2)<br>2.53(8)<br>1.3(1)<br>2.3(2) [4.626]<br>(see also [4.627]) |
| | | 0.25–1.3 [4.628]<br>−3.64<br>−5.34<br>−6.69<br>(all at 532 nm [4.629]) | **1.4960**<br>2.2352<br>0.0118<br>0.0146<br>0.00683 [4.628][a] | **1.5584**<br>2.4313<br>0.0151<br>0.0214<br>0.0143 [4.628][a] | **1.5655**<br>2.4484<br>0.0172<br>0.0229<br>0.0115 [4.628][a] | 0.48<br>0.685<br>−0.80<br>−0.22<br>[4.12, 14, 628] |
| | | 0.485–2.27 [4.630]<br>–<br>–<br>– | **1.517**<br>2.1390<br>0.147408<br>0.3681 [4.630][b]<br>– | **1.636**<br>2.3290<br>0.307173<br>0.3933 [4.630][b]<br>– | **1.843**<br>2.5379<br>0.719557<br>0.4194 [4.630][b]<br>– | 1.1<br>3.9<br>37.5<br>1.1 [4.630, 631] |

**Table 4.4-21** Monoclinic, point group 2 ($C_2$) materials, cont.

| | General | Static dielectric tensor | Dissipation factor | Elastic stiffness tensor | Piezoelectric tensor | Elastooptic tensor | |
|---|---|---|---|---|---|---|---|
| Material | $\varrho$ (g/cm$^3$)<br>Mohs hardness<br>$\kappa$ (W/m K) | $\varepsilon^{\mathbf{S}}_{11}$<br>$\varepsilon^{\mathbf{S}}_{22}$<br>$\varepsilon^{\mathbf{S}}_{33}$<br>$\varepsilon^{\mathbf{S}}_{13}$<br>$\varepsilon^{\mathbf{T}}_{11}$<br>$\varepsilon^{\mathbf{T}}_{22}$<br>$\varepsilon^{\mathbf{T}}_{33}$<br>$\varepsilon^{\mathbf{T}}_{13}$ | $\tan\delta_1$<br>$\tan\delta_2$<br>$\tan\delta_3$<br><br>($f$ (kHz)) | $c_{11}$<br>$c_{22}$<br>$c_{33}$<br>$c_{44}$<br>$c_{55}$<br>$c_{66}$<br>$c_{12}$<br>$c_{13}$<br>$c_{23}$<br>$c_{15}$<br>$c_{25}$<br>$c_{35}$<br>$c_{46}$<br>($10^9$ Pa) | $d_{21}$<br>$d_{22}$<br>$d_{23}$<br>$d_{14}$<br>$d_{16}$<br>$d_{25}$<br>$d_{34}$<br>$d_{36}$<br>$d_h$<br>($10^{-12}$ C/N) | $p_{11}$<br>$p_{12}$<br>$p_{13}$<br>$p_{15}$<br>$p_{21}$<br>$p_{22}$<br>$p_{23}$<br>$p_{25}$<br>$p_{31}$<br>$p_{32}$<br>$p_{33}$<br>$p_{35}$<br>$p_{44}$<br>$p_{46}$<br>$p_{51}$<br>$p_{52}$<br>$p_{53}$<br>$p_{55}$<br>$p_{64}$<br>$p_{66}$ | |
| Dipotassium tartrate hemihydrate, $K_2C_4H_4O_6 \cdot 0.5H_2O$ (DKT) | 1.987<br>–<br>– | 6.44<br>5.80<br>6.49<br>0.005 [4.331][d]<br>–<br>–<br>–<br>– | | 35.7(86)<br>39(17)<br>62(10)<br>9.0(5)<br>11.7(19)<br>8.3(1)<br>17.8(9)<br>22.5(99)<br>13.5(37)<br>1.8<br>1.2(1)<br>5.9(27)<br>0.54(18) [4.7] | −0.8<br>4.5<br>−5.3<br>7.9<br>3.4<br>−6.4<br>−12.2<br>−23.2<br>1.6 [4.632] | | |
| Lithium sulfate monohydrate, $Li_2SO_4 \cdot H_2O$ | –<br>–<br>≈ 4 [4.635] | 5.16[d]<br>[4.633, 634]<br>10.3[d]<br>[4.633, 634]<br>4.95[d]<br>[4.633, 634]<br>–<br>5.6 [4.331]<br>10.3 [4.331]<br>6.5 [4.331]<br>0.07 [4.331] | | 54.9<br>70.5<br>61.8<br>14.0<br>24.2<br>27.0<br>26.3<br>11.4<br>17.1<br>6.5<br>15.7<br>−5.2<br>−26.5 [4.331][e] | −3.6<br>+16.3<br>+1.7<br>+0.7<br>−2.0<br>−5.0<br>−2.13<br>−4.2<br>14.4 [4.632] | | |

**Table 4.4-21** Monoclinic, point group 2 ($C_2$) materials, cont.

| | **Electrooptic tensor** | **General optical properties** | **Refractive index** | | | **Nonlinear dielectric susceptibility** |
|---|---|---|---|---|---|---|
| | $r_{12}^{\mathbf{T}}$<br>$r_{22}^{\mathbf{T}}$<br>$r_{32}^{\mathbf{T}}$<br>$r_{41}^{\mathbf{T}}$<br>$r_{43}^{\mathbf{T}}$<br>$r_{52}^{\mathbf{T}}$<br>$r_{61}^{\mathbf{T}}$<br>$r_{63}^{\mathbf{T}}$ ($10^{-12}$ m/V)<br>(at $\lambda = 633$ nm) | Transparency range (μm)<br>$dn_X/dT$ ($10^{-5}$ K$^{-1}$)<br>$dn_Y/dT$ ($10^{-5}$ K$^{-1}$)<br>$dn_Z/dT$ ($10^{-5}$ K$^{-1}$) | $\boldsymbol{n}_X$<br>$A$<br>$B$<br>$C$<br>$D$ | $\boldsymbol{n}_Y$<br>$A$<br>$B$<br>$C$<br>$D$ | $\boldsymbol{n}_Z$<br>$A$<br>$B$<br>$C$<br>$D$ | $d_{21}$<br>$d_{22}$<br>$d_{23}$<br>$d_{25}$<br>($10^{-12}$ m/V) |
| | | | **1.4832**<br>(1.014 μm)<br>[4.636] | **1.5142**<br>(1.014 μm)<br>[4.636] | **1.5238**<br>(1.014 μm)<br>[4.636] | $d_{21} = 0.11$<br>$d_{22} = 3.9$<br>$d_{14} = 0.17$<br>(all at 0.6943 μm)<br>[4.637] |
| | +8.5(4)<br>+6.5(4)<br>+4.5(5)<br>0<br>−1.2(7)<br>−0.7(2)<br>+0.41(2)<br>+0.8(6) [4.638] | | **1.4521** [4.321] | **1.4657** [4.321] | **1.4752** [4.321] | $d_{22} = 0.38 \pm 0.06$<br>$d_{23} = 0.27 \pm 0.04$<br>$d_{34} = 0.23 \pm 0.04$<br>[4.321] |

**Table 4.4-21** Monoclinic, point group 2 ($C_2$) materials, cont.

| | General | Static dielectric tensor | Dissipation factor | Elastic stiffness tensor | Piezoelectric tensor | Elastooptic tensor | |
|---|---|---|---|---|---|---|---|
| Material | $\varrho$ (g/cm$^3$)<br>Mohs hardness<br>$\kappa$ (W/m K) | $\varepsilon^{\mathbf{S}}_{11}$<br>$\varepsilon^{\mathbf{S}}_{22}$<br>$\varepsilon^{\mathbf{S}}_{33}$<br>$\varepsilon^{\mathbf{S}}_{13}$<br>$\varepsilon^{\mathbf{T}}_{11}$<br>$\varepsilon^{\mathbf{T}}_{22}$<br>$\varepsilon^{\mathbf{T}}_{33}$<br>$\varepsilon^{\mathbf{T}}_{13}$ | $\tan\delta_1$<br>$\tan\delta_2$<br>$\tan\delta_3$<br><br>($f$ (kHz)) | $c_{11}$<br>$c_{22}$<br>$c_{33}$<br>$c_{44}$<br>$c_{55}$<br>$c_{66}$<br>$c_{12}$<br>$c_{13}$<br>$c_{23}$<br>$c_{15}$<br>$c_{25}$<br>$c_{35}$<br>$c_{46}$<br>($10^9$ Pa) | $d_{21}$<br>$d_{22}$<br>$d_{23}$<br>$d_{14}$<br>$d_{16}$<br>$d_{25}$<br>$d_{34}$<br>$d_{36}$<br>$d_h$<br>($10^{-12}$ C/N) | $p_{11}$<br>$p_{12}$<br>$p_{13}$<br>$p_{15}$<br>$p_{21}$<br>$p_{22}$<br>$p_{23}$<br>$p_{25}$<br>$p_{31}$<br>$p_{32}$<br>$p_{33}$<br>$p_{35}$<br>$p_{44}$<br>$p_{46}$<br>$p_{51}$<br>$p_{52}$<br>$p_{53}$<br>$p_{55}$<br>$p_{64}$<br>$p_{66}$ | |
| D(+)-Saccharose,<br>$C_{12}H_{22}O_{11}$<br>(sucrose) | –<br>> 2.5<br>– | | | | 1.47<br>−3.41<br>0.73<br>1.25<br>−2.41<br>−0.87<br>−4.21<br>0.423 [4.639]<br>– | | |
| Triglycine sulfate,<br>$(CH_2NH_2COOH)_3 \cdot H_2SO_4$<br>(TGS) | | 9.38[d] [4.640]<br>20[d] [4.643]<br>6.00[d] [4.640]<br>1.17(2)[d] [4.640]<br>9 [4.644]<br>40 [4.644]<br>6.6 [4.644] | 0.043<br>–<br>–<br>(9.6 GHz) [4.643] | 41.7<br>32.1<br>33.6<br>9.40<br>9.39<br>6.31<br>17.3<br>18.1<br>20.7<br>4.1<br>−0.6<br>7.7<br>−0.6<br>[4.646–648] | 23.5(0)<br>7.9(1)<br>25.3(0)<br>2.7(0)<br>−4.5(0)<br>24.3(1)<br>−3.20(1)<br>2.8(0)<br>–<br>[4.646, 647] | \|0.204\| [4.641, 642]<br>\|0.162\| [4.641, 642]<br>\|0.175\| [4.641, 642]<br>–<br>\|0.172\| [4.641, 642]<br>\|0.208\| [4.641, 642]<br>\|0.150\| [4.641, 642]<br>\|0.083\| [4.645]<br>\|0.204\| [4.641, 642]<br>\|0.169\| [4.641, 642]<br>\|0.151\| [4.641, 642]<br>–<br>\|0.273\| [4.645]<br>\|0.276\| [4.645]<br>–<br>\|0.075\| [4.645]<br>–<br>–<br>\|0.075\| [4.645]<br>– | |

**Table 4.4-21** Monoclinic, point group 2 ($C_2$) materials, cont.

| | **Electrooptic tensor** | **General optical properties** | **Refractive index** | | | **Nonlinear dielectric susceptibility** |
|---|---|---|---|---|---|---|
| | $r^{\mathbf{T}}_{12}$<br>$r^{\mathbf{T}}_{22}$<br>$r^{\mathbf{T}}_{32}$<br>$r^{\mathbf{T}}_{41}$<br>$r^{\mathbf{T}}_{43}$<br>$r^{\mathbf{T}}_{52}$<br>$r^{\mathbf{T}}_{61}$<br>$r^{\mathbf{T}}_{63}$ ($10^{-12}$ m/V)<br>(at $\lambda = 633$ nm) | Transparency range (μm)<br>$dn_X/dT$ ($10^{-5}$ K$^{-1}$)<br>$dn_Y/dT$ ($10^{-5}$ K$^{-1}$)<br>$dn_Z/dT$ ($10^{-5}$ K$^{-1}$) | $\boldsymbol{n_X}$<br>$A$<br>$B$<br>$C$<br>$D$ | $\boldsymbol{n_Y}$<br>$A$<br>$B$<br>$C$<br>$D$ | $\boldsymbol{n_Z}$<br>$A$<br>$B$<br>$C$<br>$D$ | $d_{21}$<br>$d_{22}$<br>$d_{23}$<br>$d_{25}$<br>($10^{-12}$ m/V) |
| | | 0.192–1.35 [4.649]<br>–<br>–<br>– | **1.5278**<br>1.8719<br>0.466<br>0.0214<br>0.0113 [4.649][c] | **1.5552**<br>1.9703<br>0.4502<br>0.0238<br>0.0101 [4.649][c] | **1.5592**<br>2.0526<br>0.3909<br>0.252<br>0.0187 [4.649][c] | See [4.649, 650] |
| | 70 [4.651, 652]<br>–<br>54 [4.651, 652]<br>–<br>–<br>1 [4.654, 655]<br>–<br>– | | | | | $d_{23} = 0.3$<br>at 0.6943 μm [4.653] |

[abc] Dispersion relations (λ (μm), $T = 20\,^{\circ}$C):

[a] $n^2 = A + \dfrac{B}{\lambda^2 - C} - D\lambda^2$ .

[b] $n^2 = A + \dfrac{B\lambda^2}{\lambda^2 - C}$ .

[c] $n^2 = A + \dfrac{B\lambda^2}{\lambda^2 - C} - D\lambda^2$ .

[d] These values for $\varepsilon_{ij}$ are neither at constant stress nor at constant strain.

[e] The elastic stiffness constant were measured at constant electric field $(c^E)$.

## References


4.1 D. N. Nikogosyan, G. G. Gurzadyan: Kvantovaya Elektron. **13**, 2519–2520 (1986)
4.2 D. N. Nikogosyan, G. G. Gurzadyan: Sov. J. Quantum Electron. [English Transl.] **16**, 1663–1664 (1986)
4.3 V. G. Dmitriev, G. G. Gurzadyan, D. N. Nikogosyan: *Handbook of Nonlinear Optical Crystals*, 2nd edn. (Springer, Berlin, Heidelberg 1997)
4.4 V. G. Dmitriev, G. G. Gurzadyan, D. N. Nikogosyan: *Handbook of Nonlinear Optical Crystals*, 3rd edn. (Springer, Berlin, Heidelberg 1999)
4.5 D. N. Nikogosyan, G. G. Gurzadyan: Kvantovaya Elektron. **14**, 1529–1541 (1987)
4.6 D. N. Nikogosyan, G. G. Gurzadyan: Sov. J. Quantum Electron. [English Transl.] **17**, 970–977 (1987)
4.7 A. G. Every, A. K. McCurdy: *Second and Higher Order Elastic Constants*, Landolt–Börnstein, New Series III/29, ed. by D. F. Nelson, O. Madelung (Springer, Berlin, Heidelberg 1992)
4.8 W. R. Cook Jr.: *Piezoelectric, Electrostrictive, Dielectric Constants, Electromechanical Coupling Factors*, Landolt–Börnstein, New Series III/29, ed. by D. F. Nelson, O. Madelung (Springer, Berlin, Heidelberg 1993)
4.9 W. R. Cook Jr.: *Electrooptic Coefficients*, Landolt–Börnstein, New Series III/30, ed. by D. F. Nelson (Springer, Berlin, Heidelberg 1996)
4.10 D. F. Nelson: *Piezooptic, Electrooptic Constants of Crystals*, Landolt–Börnstein, New Series III/30, ed. by D. F. Nelson (Springer, Berlin, Heidelberg 1996)
4.11 K. Vedam: *Piezooptic, Elastooptic Coefficients*, Landolt–Börnstein, New Series III/30, ed. by D. F. Nelson (Springer, Berlin, Heidelberg 1996)
4.12 D. A. Roberts: IEEE J. Quantum Electron. **28**, 2057 (1992)
4.13 I. Shoji, T. Kondo, A. Kitamoto, M. Shirane, R. Ito: J. Opt. Soc. Am. B **14**, 2268 (1997)
4.14 F. Charra, G. G. Gurzadyan: *Nonlinear Dielectric Susceptibilities*, Landolt–Börnstein, New Series III/30, ed. by D. F. Nelson (Springer, Berlin, Heidelberg 2000)
4.15 G. W. Faris, L. E. Jusinski, A. P. Hickman: J. Opt. Soc. Am. B **3**, 587–599 (1993)
4.16 Opto-Technological Laboratory: Data sheet – Catalog of optical materials (Opto-Technological Laboratory, St. Petersburg 2003)
4.17 Layertec: Data sheet – Material data (Layertec GmbH, Mellingen 2003)
4.18 Röhm Plexiglas: Data sheet – Technical data (Röhm Plexiglas, Darmstadt 2003)
4.19 D. G. Cahill, R. O. Pohl: Phys. Rev. B **35**, 4067–4073 (1987)
4.20 Schott Lithotec: Data sheet – Products and applications (Schott Lithotec AG, Jena 2003)
4.21 Crystran: Data sheet – Materials (Crystran Ltd., Poole 2002)
4.22 D. E. Gray: *American Institute of Physics Handbook* (McGraw-Hill, New York 1972)
4.23 O. V. Shakin, M. F. Bryzhina, V. V. Lemanov: Fiz. Tverd. Tela **13**, 3714–3716 (1971)
4.24 O. V. Shakin, M. F. Bryzhina, V. V. Lemanov: Sov. Phys. Solid State [English Transl.] **13**, 3141–3142 (1972)
4.25 E. D. D. Schmidt, K. Vedam: J. Phys. Chem. Solids **27**, 1563–1566 (1966)
4.26 ASI Instruments: Data sheet – Dielectric constant reference guide (ASI Instruments, Inc., Houston 2003)
4.27 R. Waxler: IEEE J. Quantum Electron. **7**, 166–167 (1971)
4.28 Melles Griot: Data sheet – Optics: Windows and optical flats (Melles Griot, Rochester 2003)
4.29 W. L. Smith: Optical materials, Part I. In: *CRC Handbook of Laser Science and Technology*, Vol. 3, ed. by M. J. Weber (CRC Press, Boca Raton 1986) pp. 229–258
4.30 D. Milam, M. J. Weber: J. Appl. Phys. **47**, 2497–2501 (1976)
4.31 W.T. White III, M. A. Henesian, M. J. Weber: J. Opt. Soc. Am. B **2**, 1402–1408 (1985)
4.32 I. D. Nikolov, C. D. Ivanov: Appl. Opt. **39**, 2067–2070 (2000)
4.33 Yu. A. Repeyev, E. V. Khoroshilova, D. N. Nikogosyan: J. Photochem. Photobiol. B **12**, 259–274 (1992)
4.34 R. Adair, L. L. Chase, S. A. Payne: Phys. Rev. B **39**, 3337–3349 (1989)
4.35 G. G. Gurzadyan, R. K. Ispiryan: Int. J. Nonlin. Opt. Phys. **1**, 533–540 (1992)
4.36 R. DeSalvo, A. A. Said, D. J. Hagan, E. W. Van Stryland, M. Sheik-Bahae: IEEE J. Quantum Electron. **32**, 1324–1333 (1996)
4.37 T. Tomie, I. Okuda, M. Yano: Appl. Phys. Lett. **55**, 325–327 (1989)
4.38 P. Liu, W. L. Smith, H. Lotem, J. H. Bechtel, N. Bloembergen, R. S. Adhav: Phys. Rev. B **17**, 4620–4632 (1978)
4.39 I. H. Malitson: J. Opt. Soc. Am. **55**, 1205–1209 (1965)
4.40 A. Smakula: *Harshaw Optical Crystals* (Harshaw Chemical Co., Cleveland 1967)
4.41 A. Feldman, D. Horowitz, R. M. Waxier, M. J. Dodge: Natl. Bur. Stand. (USA) Techn. Note **993** (1979) erratum (see also [4.656])
4.42 M. D. Levenson, N. Bloembergen: Phys. Rev. B **10**, 4447–4463 (1974)
4.43 H. H. Li: J. Phys. Chem. Ref. Data **9**, 161–289 (1980)
4.44 I. H. Malitson: Appl. Opt. **2**, 1103–1107 (1963)
4.45 S. S. Ballard, J. S. Browder: Thermal properties. In: *Optical Materials, CRC Handbook of Laser Science and Technology*, Vol. 4, Subvol. 2, ed. by M. J. Weber (CRC, Boca Raton 1987) pp. 49–54
4.46 A. D. Papadopoulos, E. Anastassakis: Phys. Rev. B **43**, 9916–9923 (1991)
4.47 H. Braul, C. A. Plint: Solid State Commun. **38**, 227–230 (1981)

4.48 MarkeTech: Data sheet – Non-metallic crystals (MarkeTech International Inc., Port Townsend 2002)
4.49 K. V. Krishna Rao, V. G. Krishna Murty: Acta Crystallogr. **17**, 788–789 (1964)
4.50 K. Vedam, E. D. D. Schmidt, W. C. Schneider: *Optical Properties of Highly Transparent Solids*, ed. by S. S. Mitra, B. Bendow (Plenum, New York 1975) pp. 169–175
4.51 J. P. Szczesniak, D. Cuddeback, J. C. Corelli: J. Appl. Phys. **47**, 5356–5359 (1976)
4.52 V. M. Maevskii, A. B. Roitsin: Fiz. Tverd. Tela **31**, 294–296 (1989)
4.53 V. M. Maevskii, A. B. Roitsin: Sov. Phys. Solid State [English Transl.] **31**, 1448–1449 (1989)
4.54 D. K. Biegelsen: Phys. Rev. Lett. **32**, 1196–1199 (1974)
4.55 D. K. Biegelsen: Erratum, Phys. Rev. Lett. **33**, 51 (1974)
4.56 A. A. Berezhnoi, V. M. Fedulov, K. P. Skornyakova: Fiz. Tverd. Tela **17**, 2785–2787 (1975)
4.57 A. A. Berezhnoi, V. M. Fedulov, K. P. Skornyakova: Sov. Phys. Solid State [English Transl.] **17**, 1855–1856 (1975)
4.58 D. F. Edwards, E. Ochoa: J. Opt. Soc. Am. **71**, 607 (1981)
4.59 G. N. Ramachandran: Proc. Indian Acad. Sci. A **25**, 266–279 (1947)
4.60 J. Fontanella, R. L. Johnston, J. H. Colwell, C. Andeen: Appl. Opt. **16**, 2949–2951 (1977)
4.61 M. D. Levenson, C. Flytzanis, N. Bloembergen: Phys. Rev. B **6**, 3962–3965 (1972)
4.62 D. E. McCarthy: Appl. Opt. **2**, 591–603 (1963)
4.63 N. P. Barnes, M. S. Piltch: J. Opt. Soc. Am. **69**, 178–180 (1979)
4.64 J. J. Wynne: Phys. Rev. **178**, 1295–1303 (1969)
4.65 H. H. Li: J. Phys. Chem. Ref. Data **5**, 329–528 (1976)
4.66 P. D. Maker, R. W. Terhune: Phys. Rev. **137**, A801–A818 (1965)
4.67 A. J. Moses: *Optical Materials Properties*, Handbook of Electronic Materials, Vol. 1 (IFI/Plenum, New York 1971)
4.68 T. Radhakrishnan: Proc. Indian Acad. Sci. A **33**, 22–34 (1951)
4.69 R. F. Stephens, I. H. Malitson: Natl. Bur. Stand. J. Res. **49**, 249 (1952)
4.70 C. C. Wang, E. L. Baardsen: Phys. Rev. **185**, 1079–1082 (1969)
4.71 W. K. Burns, N. Bloembergen: Phys. Rev. B **4**, 3437–3450 (1971)
4.72 N. Bloembergen, W. K. Burns, M. Matsukoda: Opt. Commun. **1**, 195 (1969)
4.73 B. Tatian: Appl. Opt. **23**, 4477–4485 (1984)
4.74 D. F. Edwards, E. Ochoa: Appl. Opt. **19**, 4130 (1980)
4.75 J. J. Wynne, G. D. Boyd: Appl. Phys. Lett. **12**, 191–192 (1968)
4.76 W. Kucharczyk: Physica B **172**, 473–490 (1991)
4.77 A. V. Pakhnev, M. P. Shaskol'skaya, S. S. Gorbach: Izv. Vyssh. Uchebn. Zaved., Fiz. **12**, 28–34 (1975)
4.78 A. V. Pakhnev, M. P. Shaskol'skaya, S. S. Gorbach: Sov. Phys. J. [English Transl.] **18**, 1662 (1975)
4.79 Princeton Scientific: Data sheet – Crystalline materials (Princeton Scientific Corp., Princeton 2003)
4.80 J. Reintjes, M. B. Schulz: J. Appl. Phys. **39**, 5254–5258 (1968)
4.81 S. Musikant: *Optical Materials: An Introduction to Selection and Application* (Marcel Dekker, New York 1985)
4.82 R. W. Dixon: J. Appl. Phys. **38**, 5149–5153 (1967)
4.83 P. Billard: Acta Electron. **6**, 75–169 (1962)
4.84 M. D. Beals, L. Merker: Mater. Des. Eng. **51**, 12–13 (1960)
4.85 D. E. McCarthy: Appl. Opt. **7**, 1997 (1968)
4.86 M. O. Manasreh, D. O. Pederson: Phys. Rev. B **30**, 3482–3485 (1984)
4.87 L. G. DeShazer, S. C. Rand, B. A. Wechsler: Laser crystals. In: *Optical Materials, CRC Handbook of Laser Science and Technology*, Vol. 5, Subvol. 3, ed. by M. J. Weber (CRC, Boca Raton 1987) pp. 281–338
4.88 K. L. Ovanesyan, A. G. Petrosyan, G. O. Shirinyan, A. A. Avetisyan: Izv. Akad. Nauk SSSR, Ser. Neorg. Materiali [in Russian] **17**, 459–462 (1981)
4.89 D. Berlincourt, H. Jaffe, L. R. Shiozawa: Phys. Rev. **129**, 1009–1017 (1963)
4.90 H. Sasaki, K. Tsoubouki, N. Chubachi, N. Mikoshiba: J. Appl. Phys. **47**, 2046–2049 (1976)
4.91 R. Weil, M. J. Sun: Proc. Int. Symp. Cadmium Telluride Materials Gamma-Ray Detectors, Tech. Dig., Strasbourg 1971, pages XIX-1 to XIX-6
4.92 E. H. Turner, I. P. Kaminow, C. Schwab: Phys. Rev. B **9**, 2524–2529 (1974)
4.93 R. C. Hanson, J. R. Hallberg, C. Schwab: Appl. Phys. Lett. **21**, 490–492 (1972)
4.94 A. Boese, E. Mohler, R. Pitka: J. Mater. Sci. **9**, 1754–1758 (1974)
4.95 B. Prevot, C. Carabatos, C. Schwab, B. Hennion, F. Moussa: Solid State Commun. **13**, 1725–1727 (1973)
4.96 D. K. Biegelsen, J. C. Zesch, C. Schwab: Phys. Rev. B **14**, 3578–3582 (1976)
4.97 L. M. Belyaev, G. S. Belikova, G. F. Dobrzhanskii, G. B. Netesov, Yu. V. Shaldin: Fiz. Tverd. Tela **6**, 2526–2528 (1964)
4.98 L. M. Belyaev, G. S. Belikova, G. F. Dobrzhanskii, G. B. Netesov, Yu. V. Shaldin: Sov. Phys. Solid State [English Transl.] **6**, 2007–2008 (1965)
4.99 R. C. Hanson, K. Helliwell, C. Schwab: Phys. Rev. B **9**, 2649–2654 (1974)
4.100 G. Arlt, P. Quadflieg: Phys. Status Solidi **25**, 323–330 (1968)
4.101 Ioffe Institute: Database (Ioffe Institute, St. Petersburg 2003)
4.102 K. S. Champlin, R. J. Erlandson, G. H. Glover, P. S. Hauge, T. Lu: Appl. Phys. Lett. **11**, 348–349 (1967)
4.103 T. E. Walsh: RCA Rev. **27**, 323–335 (1966)
4.104 A. Feldman, R. M. Waxler: J. Appl. Phys. **53**, 1477–1483 (1982)
4.105 D. R. Nelson, E. H. Turner: J. Appl. Phys. **39**, 3337–3343 (1968)

4.106 J. E. Kiefer, A. Yariv: Appl. Phys. Lett. **15**, 26–27 (1969)
4.107 G. H. Sherman, P. D. Coleman: J. Appl. Phys. **44**, 238 (1973)
4.108 R. C. Miller, W. A. Nordland: Phys. Rev. B **5**, 4931–4934 (1972)
4.109 J. Pastrnak, L. Roskovcova: Phys. Status Solidi **14**, K5–K8 (1966)
4.110 N. P. Barnes, M. S. Piltch: J. Opt. Soc. Am. **67**, 628 (1977)
4.111 A. G. DeBell, E. L. Dereniak, J. Harvey, J. Nissley, J. Palmer, A. Selvarajan, W. L. Wolfe: Appl. Opt. **18**, 3114–3115 (1979)
4.112 E. H. Turner, E. Buehler, H. Kasper: Phys. Rev. B **9**, 558–561 (1974)
4.113 D. S. Chemla, P. Kupecek, C. Schwartz, C. Schwab, A. Goltzene: IEEE J. Quantum Electron. **7**, 126 (1971)
4.114 R. C. Miller, W. A. Nordland, S. C. Abrahams, J. L. Bernstein, C. Schwab: J. Appl. Phys. **44**, 3700 (1973)
4.115 E. Mohler, B. Thomas: Phys. Status Solidi (b) **79**, 509–517 (1977)
4.116 A. Feldman, D. Horowitz: J. Opt. Soc. Am. **59**, 1406–1408 (1969)
4.117 T. G. Okroashvili: Opt. Spektrosk. **47**, 798–800 (1979)
4.118 T. G. Okroashvili: Opt. Spectrosc. [English Transl.] **47**, 442–443 (1979)
4.119 J. J. Wynne, N. Bloembergen: Phys. Rev. **188**, 1211 (1969)
4.120 J. J. Wynne, N. Bloembergen: Erratum, Phys. Rev. B **2**, 4306 (1970)
4.121 B. O. Seraphin, H. E. Bennett: *Semiconductors and Semimetals 3*, ed. by R. K. Willard, R. C. Beer (Academic Press, New York 1967)
4.122 R. A. Soref, H. W. Moos: J. Appl. Phys. **35**, 2152 (1964)
4.123 R. K. Chang, J. Ducuing, N. Bloembergen: Phys. Rev. Lett. **15**, 415–418 (1965)
4.124 W. D. Johnston Jr., I. P. Kaminow: Phys. Rev. **188**, 1209–1211 (1969)
4.125 E. Yablonovitch, C. Flytzanis, N. Bloembergen: Phys. Rev. Lett. **29**, 865–868 (1972)
4.126 M. Sugie, K. Tada: Jpn. J. Appl. Phys. **15**, 421–430 (1976)
4.127 M. Bertolotti, V. Bogdanov, A. Ferrari, A. Jascow, N. Nazorova, A. Pikhtin, L. Schirone: J. Opt. Soc. Am. B **7**, 918–922 (1990)
4.128 B. F. Levine, C. G. Bethea: Appl. Phys. Lett. **20**, 272–274 (1972)
4.129 A. H. Kachare, W. G. Spitzer, J. E. Fredrickson: J. Appl. Phys. **47**, 4209 (1976)
4.130 Yu. Berezashvili, S. Machavariani, A. Natsvlishvili, A. Chirakadze: J. Phys. D **22**, 682–686 (1989)
4.131 M. M. Choy, R. L. Byer: Phys. Rev. B **14**, 1693–1705 (1976)
4.132 D. F. Parsons, P. D. Coleman: Appl. Opt. **10**, 1683–1685 (1971)
4.133 Yu. X. Ilisavskii, L. A. Kutakova: Fiz. Tverd. Tela **23**, 3299–3307 (1981)
4.134 Yu. X. Ilisavskii, L. A. Kutakova: Sov. Phys. Solid State [English Transl.] **23**, 1916–1920 (1981)
4.135 L. G. Meiners: J. Appl. Phys. **59**, 1611–1613 (1986)
4.136 D. N. Nichols, D. S. Rimai, R. J. Sladek: Solid State Commun. **36**, 667–669 (1980)
4.137 A. A. Blistanov, V. S. Bondarenko, N. V. Perelomova, F. N. Strizhevskaya, V. V. Tchakalova, M. P. Shaskolskaya: *Acoustic Crystals* [in Russian] (Nauka, Moscow 1982)
4.138 E. Käräjämäki, R. Laiho, T. Levola: Physica **429**, 3–18 (1982)
4.139 G. R. Mariner, K. Vedam: Appl. Opt. **20**, 2878–2879 (1981)
4.140 A. V. Novoselova (Ed.): *Physical-Chemical Properties of Semiconductors – Handbook* [in Russian] (Nauka, Moscow 1979)
4.141 M. Yamada, K. Yamamoto, K. Abe: J. Phys. D **10**, 1309–1313 (1977)
4.142 S. Adachi, C. Hamaguchi: J. Phys. Soc. Jpn. **43**, 1637–1645 (1977)
4.143 C. K. N. Patel, R. E. Slusher, P. A. Fleury: Phys. Rev. Lett. **17**, 1011–1014 (1966)
4.144 H. McKenzie, D. J. Hagan, H. A. Al-Attar: IEEE J. Quantum Electron. **22**, 1328 (1986)
4.145 C. C. Lee, H. Y. Fan: Phys. Rev. B **9**, 3502 (1974)
4.146 O. G. Lorimor, W. G. Spitzer: J. Appl. Phys. **36**, 1841–1844 (1965)
4.147 T. S. Moss: *Optical Properties of Semiconductors* (Academic Press, New York 1959) p. 224
4.148 R. Braunstein, N. Ockman: *Interactions of Coherent Optical Radiation with Solids*, Final Report, Office of Naval Research (Department of Navy, Washington, DC 1964) ARPA Order No. 306-362
4.149 K. Tada, N. Suzuki: Jpn. J. Appl. Phys. **19**, 2295–2296 (1980)
4.150 Y. Tsay, B. Bendow, S. S. Mitra: Phys. Rev. B **5**, 2688–2696 (1972)
4.151 J. Stone, M. S. Whalen: Appl. Phys. Lett. **41**, 1140–1142 (1982)
4.152 A. N. Pikhtin, A. D. Yas'kov: Sov. Phys. Semicond. **12**, 622–626 (1978)
4.153 I. I. Adrianova, A. A. Berezhnoi, K. K. Dubenskii, V. A. Sokolov: Fiz. Tverd. Tela **12**, 2462–2464 (1970)
4.154 I. I. Adrianova, A. A. Berezhnoi, K. K. Dubenskii, V. A. Sokolov: Sov. Phys. Solid State [English Transl.] **12**, 1972–1973 (1970)
4.155 C. Kojima, T. Shikama, S. Kuninobu, A. Kawabata, T. Tanaka: Jpn. J. Appl. Phys. **8**, 1361–1362 (1969)
4.156 R. C. Miller, W. A. Nordland: Phys. Rev. B **2**, 4896–4902 (1970)
4.157 A. Chergui, J. L. Deiss, J. B. Grun, J. L. Loison, M. Robino, R. Besermann: Appl. Surf. Sci. **96**, 874 (1996)
4.158 D. T. F. Marple: J. Appl. Phys. **35**, 539 (1964)
4.159 Alkor Technologies: Data sheet – Optical crystals (Alkor Technologies, St. Petersburg 2002)
4.160 E. A. Kraut, B. R. Tittman, L. J. Graham, T. C. Lim: Appl. Phys. Lett. **17**, 271–272 (1970)

4.161 R. E. Aldrich, S. L. Hou, M. L. Harvill: J. Appl. Phys. **42**, 493–494 (1971)
4.162 J. Zelenka: Czech. J. Phys. B **28**, 165–169 (1978)
4.163 M. Krzesinska: Ultrasonics **24**, 88–92 (1986)
4.164 V. V. Kucha, V. I. Mirgorodskii, S. V. Peshin, A. T. Sobolev: Pis'ma Zh. Tekh. Fiz. **10**, 124–126 (1984)
4.165 V. V. Kucha, V. I. Mirgorodskii, S. V. Peshin, A. T. Sobolev: Sov. Tech. Phys. Lett. [English Transl.] **10**, 51–52 (1984)
4.166 A. Reza, G. Babonas, D. Senuliene: Liet. Fiz. Rinkinys. **26**, 41–47 (1986)
4.167 A. Reza, G. Babonas, D. Senuliene: Sov. Phys. Collection [English Transl.] **26**, 33–38 (1986)
4.168 P. I. Ropot: Opt. Spektrosk. **70**, 371–375 (1991)
4.169 P. I. Ropot: Opt. Spectrosc. [English Transl.] **70**, 217–220 (1991)
4.170 H. Schweppe, P. Quadflieg: IEEE Trans. Sonics Ultrason. **21**, 56–57 (1974)
4.171 Y. R. Reddy, L. Sirdeshmukh: Phys. Status Solidi (a) **103**, K157–K160 (1987)
4.172 G. A. Babonas, A. A. Reza, E. I. Leonov, V. I. Shandaris: Zh. Tekh. Fiz. **55**, 1203–1205 (1985)
4.173 G. A. Babonas, A. A. Reza, E. I. Leonov, V. I. Shandaris: Sov. Phys. Tech. Phys. [English Transl.] **30**, 689–690 (1985)
4.174 R. Bechmann: Proc. R. Phys. Soc. (London) B **64**, 323–337 (1951)
4.175 A. D. Prasad Rao, P. da R. Andrade, S. P. S. Porto: Phys. Rev. B **9**, 1077–1084 (1974)
4.176 T. S. Narasimhamurty: Proc. Indian Acad. Sci. A **40**, 167–175 (1954)
4.177 M. Tanaka, M. Yamada, C. Hamaguchi: J. Phys. Soc. Jpn. **38**, 1708–1714 (1975)
4.178 Eksma: Data sheet – Optics and optomechanics (Eksma Co., Vilnius 2003)
4.179 P. C. Leung, G. Andermann, W. G. Spitzer, C. A. Mead: J. Phys. Chem. Solids **27**, 849–855 (1966)
4.180 V. M. Skorikov, I. S. Zakharov, V. V. Volkov, E. A. Spirin: Inorgan. Mater. **38**, 172–178 (2002)
4.181 F. Vachss, L. Hesselink: Opt. Commun. **62**, 159–165 (1987)
4.182 P. Bayvel, M. McCall, R. V. Wright: Opt. Lett. **13**, 27–29 (1988)
4.183 P. Bayvel: Sensors Actuators **16**, 247–254 (1989)
4.184 H. J. Simon, N. Bloembergen: Phys. Rev. **171**, 1104 (1968)
4.185 H.-J. Weber: Acta Crystallogr. A **35**, 225–232 (1979)
4.186 S. Chandrasekhar: Proc. R. Soc. A **259**, 531 (1961)
4.187 K. L. Vodopyanov, L. A. Kulevskii, V. G. Voevodin, A. I. Gribenyukov, K. R. Allakhverdiev, T. A. Kerimov: Opt. Commun. **83**, 322–326 (1991)
4.188 V. I. Sokolov, V. K. Subashiev: Fiz. Tverd. Tela **14**, 222–228 (1972)
4.189 V. I. Sokolov, V. K. Subashiev: Sov. Phys. Solid State [English Transl.] **14**, 178–183 (1972)
4.190 G. B. Abdullaev, L. A. Kulevsky, A. M. Prokhorov, A. D. Saleev, E. Yu. Salaev, V. V. Smirnov: Pisma Zh. Eksp. Teor. Fiz. **16**, 130 (1972)
4.191 G. B. Abdullaev, L. A. Kulevsky, A. M. Prokhorov, A. D. Saleev, E. Yu. Salaev, V. V. Smirnov: JETP Lett. [English Transl.] **16**, 90–92 (1972)
4.192 P. J. Kupecek, E. Batifol, A. Kuhn: Opt. Commun. **11**, 291–295 (1974)
4.193 K. L. Vodopyanov, I. A. Kulevskii: Opt. Commun. **118**, 375 (1995)
4.194 G. A. Akundov, A. A. Agaeve, V. M. Salmanov, Yu. P. Sharorov, I. D. Yaroshetskii: Sov. Phys. Semicond. **7**, 826–827 (1973)
4.195 C. A. Arguello, D. L. Rousseau, S. P. S. Porto: Phys. Rev. **181**, 1351–1363 (1969)
4.196 C. F. Cline, H. L. Dunegan, G. W. Henderson: J. Appl. Phys. **38**, 1944 (1967)
4.197 S. B. Austerman, D. A. Berlincourt, H. H. A. Krueger: J. Appl. Phys. **34**, 339–341 (1963)
4.198 A. A. Reza, G. A. Babonas: Fiz. Tverd. Tela **16**, 1414–1418 (1974)
4.199 A. A. Reza, G. A. Babonas: Sov. Phys. Solid State [English Transl.] **16**, 909–911 (1974)
4.200 J. D. Beasley: Appl. Opt. **33**, 1000–1003 (1994)
4.201 E. F. Tokarev, G. S. Pado, L. A. Chernozatonskii, V. V. Drachev: Fiz. Tverd. Tela **15**, 1593–1595 (1973)
4.202 E. F. Tokarev, G. S. Pado, L. A. Chernozatonskii, V. V. Drachev: Sov. Phys. Solid State [English Transl.] **15**, 1064–1065 (1973)
4.203 I. A. Dan'kov, G. S. Pado, I. B. Kobyakov, V. V. Berdnik: Fiz. Tverd. Tela **21**, 2570–2575 (1979)
4.204 I. A. Dan'kov, G. S. Pado, I. B. Kobyakov, V. V. Berdnik: Sov. Phys. Solid State [English Transl.] **21**, 1481–1483 (1979)
4.205 I. B. Kobyakov, V. M. Arutyunova: Zh. Tekh. Fiz. [in Russian] **58**, 983 (1988)
4.206 K. Vedam, T. A. Davis: Phys. Rev. **181**, 1196–1201 (1969)
4.207 A. S. Barker, M. Ilegems: Phys. Rev. B **7**, 743–750 (1973)
4.208 E. K. Sichel, J. I. Pankove: J. Phys. Chem. Solids **38**, 330 (1977)
4.209 V. A. Savastenko, A. U. Sheleg: Phys. Status Solidi (a) **48**, K135 (1978)
4.210 M. Gospodinov, P. Sveshtarov, N. Petkov, T. Milenov, V. Tasev, A. Nikolov: Bulg. J. Phys. **16**, 520–522 (1989)
4.211 S. A. Geidur: Opt. Spektrosk. **49**, 193–195 (1980)
4.212 S. A. Geidur: Opt. Spectrosc. [English Transl.] **49**, 105–106 (1980)
4.213 S. Singh, J. R. Potopowicz, L. G. Van Uitert, S. H. Wemple: Appl. Phys. Lett. **19**, 53–56 (1971)
4.214 G. Arlt, G. R. Schodder: J. Acoust. Soc. Am. **37**, 384 (1965)
4.215 E. E. Tokarev, I. B. Kobyakov, I. P. Kuz'mina, A. N. Lobachev, G. S. Pado: Fiz. Tverd. Tela **17**, 980–986 (1975)
4.216 E. E. Tokarev, I. B. Kobyakov, I. P. Kuz'mina, A. N. Lobachev, G. S. Pado: Sov. Phys. Solid State [English Transl.] **17**, 629–632 (1975)
4.217 R. J. Morrow, H. W. Newkirk: Rev. Int. Hautes Temp. Refract. **6**(2), 99–104 (1969)

4.218 D. A. Belogurov, T. G. Okroashvili, Yu. V. Shaldin, V. A. Maslov: Opt. Spektrosk. **54**, 298–301 (1983)
4.219 D. A. Belogurov, T. G. Okroashvili, Yu. V. Shaldin, V. A. Maslov: Opt. Spectrosc. [English Transl.] **54**, 177–179 (1983)
4.220 H. W. Newkirk, D. K. Smith, J. S. Kahn: Am. Mineral. **51**, 141–151 (1966)
4.221 J. Jerphagnon, H. W. Newkirk: Appl. Phys. Lett. **18**, 245–247 (1971)
4.222 M. Bass (Ed.): *Handbook of Optics*, Vol. 2 (McGraw-Hill, New York 1995)
4.223 A. A. Davydov, L. A. Kulevsky, A. M. Prokhorov, A. D. Savelev, V. V. Smirnov: Pisma Zh. Eksp. Teor. Fiz. **15**, 725 (1972)
4.224 A. A. Davydov, L. A. Kulevsky, A. M. Prokhorov, A. D. Savelev, V. V. Smirnov: JETP Lett. [English Transl.] **15**, 513 (1972)
4.225 S. H. Wemple, M. DiDomenico Jr.: Appl. Solid State Sci. **3**, 263–283 (1972)
4.226 A. Penzkofer, M. Schaffner, X. Bao: Opt. Quantum Electron. **22**, 351 (1990)
4.227 G. C. Bhar: Appl. Opt. **15**, 305 (1976)
4.228 R. C. Miller: Appl. Phys. Lett. **5**, 17–19 (1964)
4.229 R. Weil, D. Neshmit: J. Opt. Soc. Am. **67**, 190–195 (1977)
4.230 S. J. Czyzak, W. M. Baker, R. C. Crane, J. B. Howe: J. Opt. Soc. Am. **47**, 240 (1957)
4.231 X. C. Long, R. A. Myers, S. R. J. Brueck, R. Ramer, K. Zheng, S. D. Hersee: Appl. Phys. Lett. **67**, 1349–1351 (1995)
4.232 I. Ishidate, K. Inone, M. Aoki: Jpn. J. Appl. Phys. **19**, 1641–1645 (1980)
4.233 P. M. Lundquist, W. P. Lin, G. K. Wong, M. Razeghi, J. B. Ketterson: Appl. Phys. Lett. **66**, 1883–1885 (1995)
4.234 I. P. Kaminow, E. H. Turner: Appl. Opt. **5**, 1612–1628 (1966)
4.235 I. P. Kaminow, E. H. Turner: Proc. IEEE **54**, 1374–1390 (1966)
4.236 O. W. Madelung, E. Mollwo: Z. Phys. **249**, 12–30 (1971)
4.237 L. B. Kobyakov: Kristallografiya **11**, 419–421 (1966)
4.238 L. B. Kobyakov: Sov. Phys. Crystallogr. [English Transl.] **11**, 369–371 (1966)
4.239 I. A. Dan'kov, I. B. Kobyakov, S. Yu. Davydov: Fiz. Tverd. Tela **24**, 3613–3620 (1982)
4.240 I. A. Dan'kov, I. B. Kobyakov, S. Yu. Davydov: Sov. Phys. Solid State [English Transl.] **24**, 2058–2063 (1982)
4.241 N. Uchida, S. Saito: J. Appl. Phys. **43**, 971–976 (1972)
4.242 S. Haussühl: Acta Crystallogr. A **34**, 547–550 (1978)
4.243 N. A. Zakharov, A. V. Egorov, N. S. Kozlova, O. G. Portnov: Fiz. Tverd. Tela **30**, 3166–3168 (1988)
4.244 N. A. Zakharov, A. V. Egorov, N. S. Kozlova, O. G. Portnov: Sov. Phys. Solid State [English Transl.] **30**, 1823–1824 (1988)
4.245 S. Haussühl: Acustica **23**, 165–169 (1970)
4.246 S. Haussühl: Phys. Status Solidi **29**, K159–K162 (1968)
4.247 Ya. V. Burak, K. Ya. Borman, I. S. Girnyk: Fiz. Tverd. Tela **26**, 3692–3694 (1984)
4.248 Ya. V. Burak, K. Ya. Borman, I. S. Girnyk: Sov. Phys. Solid State [English Transl.] **26**, 2223–2224 (1984)
4.249 J. Wang, H. Li, L. Zhang, R. Wang: Acta Acust. (China) **11**, 338 (1986)
4.250 A. W. Warner, D. A. Pinnow, J. G. Bergman Jr, G. R. Crane: J. Acoust. Soc. Am. **47**, 791–794 (1970)
4.251 R. C. Miller, S. C. Abrahams, R. L. Barns, J. L. Bernstein, W. A. Nordland, E. H. Turner: Solid State Commun. **9**, 1463–1465 (1971)
4.252 A. A. Abdullaev, A. V. Vasil'eva, G. F. Dobrzhanskii, Yu. N. Polivanov: Sov. J. Quantum Electron. **7**, 56–59 (1977)
4.253 G. Nath, H. Nehmanesch, M. Gsänger: Appl. Phys. Lett. **17**, 286–288 (1970)
4.254 S. V. Bogdanov (Ed.): *Lithium Iodate – Growth, Properties and Applications* [in Russian] (Nauka, Novosibirsk 1980)
4.255 D. J. Gettemy, W. C. Harker, G. Lindholm, N. P. Barnes: IEEE J. Quantum Electron. **24**, 2231 (1988)
4.256 O. G. Vlokh, I. A. Velichko, L. A. Laz'ko: Kristallografiya **20**, 430–432 (1975)
4.257 O. G. Vlokh, I. A. Velichko, L. A. Laz'ko: Sov. Phys. Crystallogr. [English Transl.] **20**, 263–264 (1975)
4.258 K. Kato: IEEE J. Quantum Electron. **21**, 119 (1985)
4.259 M. J. Weber: Insulating crystal lasers. In: *CRC Handbook of Lasers with Selected Data on Optical Technology*, ed. by R. J. Pressley (Chemical Rubber Co., Cleveland 1971) pp. 371–417
4.260 T. Goto, O. L. Anderson, I. Ohno, S. Yamamoto: J. Geophys. Res. **94**, 7588 (1989)
4.261 R. M. Waxler, E. N. Farabaugh: J. Res. Natl. Bur. Stand. A **74**, 215–220 (1970)
4.262 E. M. Voronkova, B. N. Grechushnikov, G. I. Distler, I. P. Petrov: *Optical Materials for the Infrared Technique* [in Russian] (Nauka, Moscow 1965)
4.263 N. N. Khromova: Izv. Akad. Nauk SSSR, Ser. Neorg. Materiali [in Russian] **23**, 1500 (1987)
4.264 D. F. Nelson, P. D. Lazay, M. Lax: Phys. Rev. B **6**, 3109–3120 (1972)
4.265 Z. P. Chang, G. R. Barsch: IEEE Trans. Sonics Ultrason. **23**, 127–135 (1976)
4.266 I. M. Sil'vestrova, Yu. V. Pisarevskii, O. V. Zvereva, A. A. Shternberg: Kristallografiya **32**, 792–794 (1987)
4.267 I. M. Sil'vestrova, Yu. V. Pisarevskii, O. V. Zvereva, A. A. Shternberg: Sov. Phys. Crystallogr. [English Transl.] **32**, 467–468 (1987)
4.268 I. M. Sil'vestrova, O. A. Aleshko-Ozhevskii, Yu. V. Pisarevskii, A. A. Shternberg, G. S. Mironova: Fiz. Tverd. Tela **29**, 3454–3456 (1987)
4.269 I. M. Sil'vestrova, O. A. Aleshko-Ozhevskii, Yu. V. Pisarevskii, A. A. Shternberg, G. S. Mironova: Sov. Phys. Solid State [English Transl.] **29**, 1979–1980 (1987)
4.270 H. A. A. Sidek, G. A. Saunders, H. Wang, B. Xu, J. Han: Phys. Rev. B **36**, 7612 (1987)
4.271 A. C. DeFranzo, B. G. Pazol: Appl. Opt. **32**, 2224–2234 (1993)
4.272 E. Carvallo: Compte Rendus **126**, 950 (1898)
4.273 W. L. Bond: J. Appl. Phys. **36**, 1674–1677 (1965)

4.274 H. Jaffe, D. A. Berlincourt: Proc. IEEE **53**, 1372–1386 (1965)
4.275 J. Sapriel, R. Lancon: Proc. IEEE **61**, 678–679 (1973)
4.276 J. Sapriel: Appl. Phys. Lett. **19**, 533–535 (1971)
4.277 I. M. Silvestrova, V. A. Kuznetsov, N. A. Moiseeva, E. P. Efremova, Yu. V. Pisarevskii: Fiz. Tverd. Tela [in Russian] **28**, 180 (1986)
4.278 W. G. Cady: *Piezoelectricity* (McGraw-Hill, New York 1946)
4.279 P. H. Carr: J. Acoust. Soc. Am. **41**, 75–83 (1967)
4.280 R. Bechmann: Phys. Rev. **110**, 1060–1061 (1958)
4.281 T. S. Narasimhamurty: J. Opt. Soc. Am. **59**, 682–686 (1969)
4.282 H. Wagner: Z. Phys. **193**, 218–234 (1966)
4.283 P. Grosse: *Die Festkörpereigenschaften von Tellur*, Springer Tracts in Modern Physics, No. 48 (Springer, Berlin, Heidelberg 1969) p. 65
4.284 G. Arlt, P. Quadflieg: Phys. Status Solidi **32**, 687–689 (1969)
4.285 I. S. Grigoriev, E. Z. Melikhov (Eds.): *Physical Quantities Handbook* [in Russian] (Emergoatomizdat, Moscow 1991)
4.286 D. Souilhac, D. Billeret, A. Gundjan: Appl. Opt. **28**, 3993–3996 (1989)
4.287 W. L. Bond, G. D. Boyd, H. L. Carter Jr.: J. Appl. Phys. **38**, 4090–4091 (1967)
4.288 G. D. Boyd, T. J. Bridges, E. G. Burkhardt: IEEE J. Quantum Electron. **4**, 515 (1968)
4.289 E. H. Turner: IEEE J. Quantum Electron. **3**, 695 (1967)
4.290 C. Chen, Z. Xu, D. Deng, J. Zhang, G. K. L. Wong, B. Wu, N. Ye, D. Tang: Appl. Phys. Lett. **68**, 2930–2932 (1996)
4.291 J. Jerphagnon, S. K. Kurtz: Phys. Rev. B **1**, 1739 (1970)
4.292 F. Hache, A. Zeboulon, G. Gallot, G. M. Gale: Opt. Lett. **20**, 1556–1558 (1995)
4.293 A. J. Rogers: Proc. R. Soc. London A **353**, 177–192 (1977)
4.294 J. H. McFee, G. D. Boyd, P. H. Schmidt: Appl. Phys. Lett. **17**, 57–59 (1970)
4.295 D. Eimerl, L. Davis, S. Velsko, E. K. Graham, A. Zalkin: J. Appl. Phys. **62**, 1968–1983 (1987)
4.296 J. R. Teague, R. R. Rice, R. Gerson: J. Appl. Phys. **46**, 2864–2866 (1975)
4.297 T. Yamada, N. Niizeki, H. Toyoda: Jpn. J. Appl. Phys. **6**, 151–155 (1967)
4.298 R. T. Smith, F. S. Welsh: J. Appl. Phys. **42**, 2219–2230 (1971)
4.299 R. A. Graham: Ferroelectrics **10**, 65–69 (1976)
4.300 T. Yamada, H. Iwasaki, N. Niizeki: Jpn. J. Appl. Phys. **8**, 1127–1132 (1969)
4.301 I. Tomeno, N. Hirano: J. Phys. Soc. Jpn. **50**, 1809 (1981)
4.302 I. Tomeno, N. Hirano: J. Phys. Soc. Jpn. **51**, 339 (1982)
4.303 L. P. Avakyants, D. F. Kiselev, N. N. Shchitov: Fiz. Tverd. Tela **18**, 2129–2130 (1976)
4.304 L. P. Avakyants, D. F. Kiselev, N. N. Shchitov: Sov. Phys. Solid State [English Transl.] **18**, 1242–1243 (1976)
4.305 C. Chen, B. Wu, A. Jiang, G. You: Sci. Sin. B **28**, 235 (1985)
4.306 L. J. Bromley, A. Guy, D. C. Hanna: Opt. Commun. **67**, 316–320 (1988)
4.307 G. G. Gurzadyan, A. S. Oganesyan, A. V. Petrosyan, R. O. Sharkhatunyan: Zh. Tekh. Fiz. **61**, 152–154 (1991)
4.308 G. G. Gurzadyan, A. S. Oganesyan, A. V. Petrosyan, R. O. Sharkhatunyan: Sov. Phys. Tech. Phys. [English Transl.] **36**, 341–342 (1991)
4.309 R. C. Eckardt, H. Masuda, Y. X. Fan, R. L. Byer: IEEE J. Quantum Electron. **26**, 922–933 (1990)
4.310 L. Bohaty, J. Liebertz: Z. Kristallogr. **192**, 91–95 (1990)
4.311 D. Zhang, Y. Kong, J.-Y. Zhang: Opt. Commun. **184**, 485–491 (2000)
4.312 M. V. Hobden, J. Warner: Phys. Lett. **22**, 243 (1966)
4.313 D. H. Jundt, M. M. Fejer, R. L. Byer: IEEE J. Quantum Electron. **26**, 135–138 (1990)
4.314 J. E. Midwinter: J. Appl. Phys. **39**, 3033–3038 (1968)
4.315 K. F. Hulme, P. H. Davies, V. M. Cound: J. Phys. C **2**, 855–857 (1969)
4.316 J. D. Zook, D. Chen, G. N. Otto: Appl. Phys. Lett. **11**, 159–161 (1967)
4.317 A. L. Aleksandrovskii, G. I. Ershova, G. Kh. Kitaeva, S. P. Kulik, I. I. Naumova, V. V. Tarasenko: Kvantovaya Elektron. **18**, 254–256 (1991)
4.318 A. L. Aleksandrovskii, G. I. Ershova, G. Kh. Kitaeva, S. P. Kulik, I. I. Naumova, V. V. Tarasenko: Sov. J. Quantum Electron. [English Transl.] **21**, 225–227 (1991)
4.319 Y. Chang, J. Wen, H. Wang, B. Li: Chin. Phys. Lett. **9**, 427–430 (1992)
4.320 R. J. Holmes, Y. S. Kim, C. D. Brandle, D. M. Smyth: Ferroelectrics **51**, 41–45 (1983)
4.321 S. Singh: Nonlinear optical materials. In: *CRC Handbook of Lasers with Selected Data on Optical Technology*, ed. by R. J. Pressley (Chemical Rubber Co., Cleveland 1971) pp. 489–525
4.322 R. C. Miller, A. Savage: Appl. Phys. Lett. **9**, 169–171 (1966)
4.323 E. H. Turner: Meeting Opt. Soc. Am., Tech. Dig. Paper A13, San Francisco 1966
4.324 C. O'Hara, N. M. Shorrocks, R. W. Whatmore, O. Jones: J. Phys. D **15**, 1289–1299 (1982)
4.325 Ya. M. Olikh: Fiz. Tverd. Tela **25**, 2222–2225 (1983)
4.326 Ya. M. Olikh: Sov. Phys. Solid State [English Transl.] **25**, 1282–1283 (1983)
4.327 Ya. M. Olikh: Phys. Status Solidi (a) **80**, K81 (1983)
4.328 I. I. Zubrinov, V. I. Semenov, D. V. Sheloput: Fiz. Tverd. Tela **15**, 2871–2873 (1973)
4.329 I. I. Zubrinov, V. I. Semenov, D. V. Sheloput: Sov. Phys. Solid State [English Transl.] **15**, 1921–1922 (1974)
4.330 V. V. Lomanov: *Acoustooptical Radioelectronic System Devices* [in Russian] (Nauka, Leningrad 1988) pp. 48–61
4.331 W. P. Mason: *Piezoelectric Crystals and their Applications to Ultrasonics* (Van Nostrand, New York 1950)
4.332 Y. S. Touloukian, R. W. Powell, C. Y. Ho, P. G. Klemens: *Thermal Conductivity, Non-Metallic Solids*, Thermal Properties of Matter, Vol. 2 (IFI/Plenum, New York 1970)

4.333 I. S. Zheludev, M. M. Tagieva: Kristallografiya **7**, 589–592 (1962)
4.334 I. S. Zheludev, M. M. Tagieva: Sov. Phys. Crystallogr. [English Transl.] **7**, 473–475 (1963)
4.335 J. D. Feichtner, R. Johannes, G. W. Roland: Appl. Opt. **9**, 1716–1717 (1970)
4.336 W. B. Gandrud, G. D. Boyd, J. H. McFee, F. H. Wehmeier: Appl. Phys. Lett. **16**, 59–61 (1970)
4.337 I. V. Kityk: Fiz. Tverd. Tela **33**, 1826–1833 (1991)
4.338 I. V. Kityk: Sov. Phys. Solid State [English Transl.] **33**, 1026–1030 (1991)
4.339 K. F. Hulme, O. Jones, P. H. Davies, M. V. Hobden: Appl. Phys. Lett. **10**, 133–135 (1967)
4.340 J. Warner: Brit. J. Appl. Phys. II **1**, 949–950 (1968)
4.341 R. F. Lucy: Appl. Opt. **11**, 1329 (1972)
4.342 D. S. Chemla, P. J. Kupecek, C. A. Schwartz: Opt. Commun. **7**, 225–228 (1973)
4.343 J. D. Feichtner, G. W. Roland: Appl. Opt. **11**, 993–998 (1972)
4.344 M. D. Ewbank, P. R. Newman, N. L. Mota, S. M. Lee, W. L. Wolfe, A. G. DeBell, W. A. Harrison: J. Appl. Phys. **51**, 3848–3852 (1980)
4.345 R. C. Y. Auyeung, D. M. Zielke, B. J. Feldman: Appl. Phys. B **48**, 293 (1989)
4.346 D. R. Suhre: Appl. Phys. B **52**, 367–370 (1991)
4.347 I. P. Kaminow, E. H. Turner: *CRC Handbook of Lasers with Selected Data on Optical Technology*, ed. by R. J. Pressley (Chemical Rubber Co., Cleveland 1971) pp. 447–459
4.348 F. Pockels: Abhandl. Ges. Wiss. Göttingen **39**, 1–204 (1894)
4.349 M. J. Weber (Ed.): *Handbook of Laser Science and Technology*, Vol. 3 (CRC, Boca Raton 1986)
4.350 S. Chang, H. R. Carleton: *Basic Optical Properties of Materials*, National Bureau of Standards Special Publication 574, ed. by A. Feldman (National Bureau of Standards, Boulder 1980) pp. 213–216
4.351 M. H. Grimsditch, A. K. Ramdas: Phys. Rev. B **22**, 4094–4096 (1980)
4.352 H. J. Eichler, H. Fery, J. Knof, J. Eichler: Z. Phys. B **28**, 297–306 (1977)
4.353 J. R. DeVore: J. Opt. Soc. Am. **41**, 416–419 (1951)
4.354 Bluelightning Optics: Data sheet – Product (Bluelightning Optics Co., Ltd., Beijing 2002)
4.355 G. C. Coquin, D. A. Pinnow, A. W. Warner: J. Appl. Phys. **42**, 2162–2168 (1971)
4.356 K. Wu, W. Hua: Acta. Acust. (China) **12**, 64 (1987)
4.357 I. L. Chistyi, L. Csillag, V. F. Kitaeva, N. Kroo, N. N. Sobolev: Phys. Status Solidi (a) **47**, 609–615 (1978)
4.358 B. W. Woods, S. A. Payne, J. E. Marion, R. S. Hughes, L. E. Davis: J. Opt. Soc. Am. B **8**, 970–977 (1991)
4.359 P. Blanchfield, G. A. Saunders: J. Phys. C **12**, 4673 (1979)
4.360 Y. Ohmachi, N. Uchida: J. Appl. Phys. **41**, 2307–2311 (1970)
4.361 G. Arlt, H. Schweppe: Solid State Commun. **6**, 783–784 (1968)
4.362 A. W. Warner, D. L. White, W. A. Bonner: J. Appl. Phys. **11**, 4489–4495 (1972)
4.363 Y. Ohmachi, N. Uchida: Rev. Electr. Commun. Lab. (Tokyo) **20**, 529–541 (1972)
4.364 Almaz Optics Inc.: Data sheet – Optical components (Almaz Optics Inc., Marlton 2002)
4.365 M. D. Ewbank, F. R. Newman: J. Appl. Phys. **53**, 1150–1153 (1982)
4.366 G. H. Sherman, P. D. Coleman: IEEE J. Quantum Electron. **9**, 403–409 (1973)
4.367 Y. Fujii, S. Yoshida, S. Misawa, S. Mackawa, T. Sakudo: Appl. Phys. Lett. **31**, 815–816 (1977)
4.368 N. Uchida: Phys. Rev. **4**, 3736 (1971)
4.369 R. S. Adhav, A. D. Vlassopoulos: IEEE J. Quantum Electron. **10**, 688 (1974)
4.370 E. N. Volkova, A. N. Izrailenko: Kristallografiya **28**, 1217–1219 (1983)
4.371 E. N. Volkova, A. N. Izrailenko: Sov. Phys. Crystallogr. [English Transl.] **28**, 716–717 (1983)
4.372 W. P. Mason, B. T. Matthias: Phys. Rev. **88**, 477–479 (1952)
4.373 A. S. Vasilevskaya, A. S. Sonin: Kristallografiya **14**, 713–716 (1969)
4.374 A. S. Vasilevskaya, A. S. Sonin: Sov. Phys. Crystallogr. [English Transl.] **14**, 611–613 (1970)
4.375 Clevite Corp.: *Reference Data on Linear Electro-Optic Effects* (Clevite Corp., Cleveland 1967)
4.376 H. Jaffe: Meeting Opt. Soc. Am., Tech. Dig., Cleveland 1950
4.377 G. K. Afanaseva: Kristallografiya **13**, 1024 (1968)
4.378 G. K. Afanaseva: Sov. Phys. Crystallogr. [English Transl.] **13**, 1024 (1968)
4.379 R. S. Adhav: J. Acoust. Soc. Am. **43**, 835 (1968)
4.380 F. Hoff, B. Stadnik: Electron. Lett. **2**, 293 (1966)
4.381 T. S. Narasimhamurty, K. Veerabhadra Rao, H. E. Pettersen: J. Mater. Sci. **8**, 577–580 (1973)
4.382 T. Hailing, G. A. Saunders, W. A. Lambson: Phys. Rev. B **26**, 5786 (1982)
4.383 R. S. Adhav: 76th Annual Meeting Acoust. Soc. Am., Tech. Dig. Paper No. 79, Cleveland 1968
4.384 B. A. Strukov, T. P. Spiridonov, N. N. Tkachev, K. A. Minaeva, M. Yu. Kozhevnikov: Izv. Akad. Nauk SSSR Ser. Fiz. **53**, 1320–1326 (1989)
4.385 B. A. Strukov, T. P. Spiridonov, N. N. Tkachev, K. A. Minaeva, M. Yu. Kozhevnikov: Bull. Acad. Sci. USSR, Phys. Ser. [English Transl.] **53**, 86–92 (1989)
4.386 D. Eimerl: Ferroelectrics **72**, 95–139 (1987)
4.387 A. S. Sonin, A. S. Vasilevskaya: *Electrooptic Crystals* [in Russian] (Atomizdat, Moscow 1971)
4.388 A. S. Vasilevskaya, E. N. Volkova, V. A. Koptsik, L. N. Rashkovich, T. A. Regulskaya, I. S. Rez, A. S. Sonin, V. S. Suvorov: Kristallografiya **12**, 518 (1967)
4.389 A. S. Vasilevskaya, E. N. Volkova, V. A. Koptsik, L. N. Rashkovich, T. A. Regulskaya, I. S. Rez, A. S. Sonin, V. S. Suvorov: Sov. Phys. Crystallogr. [English Transl.] **12**, 446 (1967)

4.390 V. S. Suvorov, A. S. Sonin, I. S. Rez: Zh. Eksp. Teor. Fiz. **53**, 491 (1967)
4.391 V. S. Suvorov, A. S. Sonin, I. S. Rez: Sov. Phys. JETP [English Transl.] **26**, 23 (1967)
4.392 N. P. Barnes, D. J. Gettemy, R. S. Adhav: J. Opt. Soc. Am. **72**, 895 (1982)
4.393 F. M. Johnson, J. A. Duardo: Laser Focus **11**, 31 (1967)
4.394 F. Zernike: J. Opt. Soc. Am. **55**, 91 (1965)
4.395 R. L. Byer, H. Kildal, R. S. Feigelson: Appl. Phys. Lett. **19**, 237–240 (1971)
4.396 G. D. Boyd, E. Buehler, F. G. Storz, J. H. Wernick: IEEE J. Quantum Electron. **8**, 419–426 (1972)
4.397 G. C. Ghosh, G. C. Bhar: IEEE J. Quantum Electron. **18**, 143 (1982)
4.398 K. Kato: IEEE J. Quantum Electron. **10**, 616 (1974)
4.399 R. S. Adhav: J. Opt. Soc. Am. **59**, 414–418 (1969)
4.400 R. S. Adhav: J. Appl. Phys. **46**, 2808 (1975)
4.401 M. P. Zaitseva, Yu. I. Kokorin, A. M. Sysoev, I. S. Rez: Kristallografiya **27**, 146–151 (1982)
4.402 M. P. Zaitseva, Yu. I. Kokorin, A. M. Sysoev, I. S. Rez: Sov. Phys. Crystallogr. [English Transl.] **27**, 86–89 (1982)
4.403 A. T. Anistratov, V. G. Martynov, L. A. Shabanova, I. S. Rez: Fiz. Tverd. Tela **21**, 1354 (1979)
4.404 A. T. Anistratov, V. G. Martynov, L. A. Shabanova, I. S. Rez: Sov. Phys. Solid State [English Transl.] **21** (1979)
4.405 C. W. Fairall, W. Reese: Phys. Rev. B **6**, 193–199 (1972)
4.406 R. S. Adhav: J. Appl. Phys. **39**, 4091 (1968)
4.407 T. R. Sliker, S. R. Burlage: J. Appl. Phys. **34**, 1837–1840 (1963)
4.408 L. A. Shuvalov, A. V. Mnatsakanyan: Kristallografiya **11**, 222 (1966)
4.409 L. P. Avakyants, D. F. Kiselev, N. V. Perelomova, V. I. Sugrei: Fiz. Tverd. Tela **25**, 580–582 (1983)
4.410 L. P. Avakyants, D. F. Kiselev, N. V. Perelomova, V. I. Sugrei: Sov. Phys. Solid State [English Transl.] **25**, 329–330 (1983)
4.411 Y. Mori, I. Kuroda, S. Nakajima, T. Sasaki, S. Nakai: Appl. Phys. Lett. **67**, 1818–1820 (1995)
4.412 N. Umemura, K. Kato: Appl. Opt. **36**, 6794 (1997)
4.413 G. D. Boyd, H. M. Kasper, J. H. McFee, F. G. Storz: IEEE J. Quantum Electron. **8**, 900–908 (1972)
4.414 G. D. Boyd, H. Kasper, J. M. McFee: IEEE J. Quantum Electron. **7**, 563–573 (1971)
4.415 G. C. Bhar, G. Ghosh: J. Opt. Soc. Am. **69**, 730–733 (1979)
4.416 R. S. Adhav: J. Appl. Phys. **39**, 4095–4098 (1968)
4.417 R. Danelyus, A. Piskarskas, V. Sirutkaitis, A. Stabinis, Ya. Yasevichyute: *Parametric Generators of Light and Picosecond Spectroscopy* [in Russian] (Mokslas, Vilnius 1983)
4.418 J. H. Ott, T. R. Sliker: J. Opt. Soc. Am. **54**, 1442–1444 (1964)
4.419 M. I. Zugrav, A. Dumitrica, A. Dumitras, N. Comaniciu: Cryst. Res. Technol. **17**, 475–480 (1982)
4.420 I. P. Kaminow: Phys. Rev. A **138**, 1539–1543 (1965)
4.421 D. A. Berlincourt, D. R. Curran, H. Jaffe: *Physical Acoustics*, Vol. 1A, ed. by W. P. Mason (Academic Press, New York 1964) pp. 1169–1270
4.422 S. Haussühl: Z. Kristallogr. **120**, 401 (1964)
4.423 I. P. Kaminow, G. O. Harding: Phys. Rev. **129**, 1562–1566 (1963)
4.424 R. S. Adhav: J. Phys. D **2**, 171–175 (1969)
4.425 E. N. Volkova, B. M. Berezhnoi, A. N. Izrailenko, A. V. Mishchenko, L. N. Rashkovich: Izv. Akad. Nauk SSSR, Ser. Fiz. **35**, 1858–1861 (1971)
4.426 E. N. Volkova, B. M. Berezhnoi, A. N. Izrailenko, A. V. Mishchenko, L. N. Rashkovich: Bull. Acad. Sci. USSR, Phys. Ser. [English Transl.] **35**, 1690–1693 (1971)
4.427 L. A. Shuvalov, I. S. Zheludev, A. V. Mnatsakanyan, Ts.-Zh. Ludupov, I. Fiala: Izv. Akad. Nauk SSSR, Ser. Fiz. **31**, 1919–1922 (1967)
4.428 L. A. Shuvalov, I. S. Zheludev, A. V. Mnatsakanyan, Ts.-Zh. Ludupov, I. Fiala: Bull. Acad. Sci. USSR, Phys. Ser. [English Transl.] **31**, 1963–1966 (1967)
4.429 R. S. Adhav: J. Phys. D **2**, 177–182 (1969)
4.430 K. S. Aleksandrov, A. T. Anistratov, A. R. Zamkov, I. S. Rez: Fiz. Tverd. Tela **19**, 1863–1866 (1977)
4.431 K. S. Aleksandrov, A. T. Anistratov, A. R. Zamkov, I. S. Rez: Sov. Phys. Solid State [English Transl.] **19**, 1090–1091 (1977)
4.432 W. L. Smith: Appl. Opt. **6**, 1798 (1977)
4.433 K. Veerabhadra Rao, T. S. Narasimhamurty: J. Phys. C **11**, 2343–2347 (1978)
4.434 F. Zernike: J. Opt. Soc. Am. **54**, 1215 (1964)
4.435 F. Zernike: Erratum, J. Opt. Soc. Am. **55**, 210 (1965)
4.436 K. Kato, A. J. Alcock, M. C. Richardson: Opt. Commun. **11**, 5 (1974)
4.437 K. Kato: Opt. Commun. **13**, 93 (1975)
4.438 J. E. Pearson, G. A. Evans, A. Yariv: Opt. Commun. **4**, 366–367 (1972)
4.439 K. Kato: IEEE J. Quantum Electron. **10**, 622 (1974)
4.440 I. S. Zheludev, Ts.-Zh. Ludupov: Kristallografiya **10**, 764–766 (1965)
4.441 I. S. Zheludev, Ts.-Zh. Ludupov: Sov. Phys. Crystallogr. [English Transl.] **10**, 645–646 (1966)
4.442 H. Horinaka, H. Nozuchi, H. Sonomura, T. Miyauchi: Jpn. J. Appl. Phys. **22**, 546 (1983)
4.443 V. M. Cound, P. H. Davies, K. F. Hulme, D. Robertson: J. Phys. C **3**, L83–L84 (1970)
4.444 M. H. Grimsditch, G. D. Holah: Phys. Rev. B **12**, 4377 (1975)
4.445 M. H. Grimsditch, G. D. Holah: J. Phys. (Paris) **36**, Suppl. C, C3–C185 (1975)
4.446 A. Yoshihara, E. R. Bernstein: J. Chem. Phys. **77**, 5319 (1982)
4.447 G. Ambrazevicius, G. Babonas: Liet. Fiz. Sbornik. **18**, 765–774 (1978)
4.448 G. Ambrazevicius, G. Babonas: Sov. Phys. Collection [English Transl.] **18**, 52–59 (1978)
4.449 Yu. K. Shaldin, D. A. Belogurov: Opt. Spektrosk. **35**, 693–701 (1973)
4.450 Yu. K. Shaldin, D. A. Belogurov: Opt. Spectrosc. [English Transl.] **35**, 403–407 (1973)

4.451 R. L. Byer, M. M. Choy, R. L. Herbst, D. S. Chemla, R. S. Feigelson: Appl. Phys. Lett. **24**, 65–68 (1974)
4.452 N. P. Barnes, D. J. Gettemy, J. R. Hietanen, R. A. Iannini: Appl. Opt. **28**, 5162–5168 (1989)
4.453 H. Horinaka, H. Sonomura, T. Migauchi: Jpn. J. Appl. Phys. **21**, 1485–1488 (1982)
4.454 D. S. Chemla, P. J. Kupecek, D. S. Robertson, R. C. Smith: Opt. Commun. **3**, 29 (1971)
4.455 M. G. Cohen, M. DiDomenico Jr., S. H. Wemple: Phys. Rev. B **1**, 4334–4337 (1970)
4.456 G. C. Bhar, D. K. Ghosh, P. S. Ghosh, D. Schmitt: Appl. Opt. **22**, 2492 (1983)
4.457 J. J. Zondy, D. Touahri: J. Opt. Soc. Am. B **14**, 1331 (1997)
4.458 J. M. Halbout, S. Blit, W. Donaldson, C. L. Tang: IEEE J. Quantum Electron. **15**, 1176–1180 (1979)
4.459 K. Betzler, H. Hesse, P. Loose: J. Mol. Struct. **47**, 393–396 (1978)
4.460 L. Bohaty: Z. Kristallogr. **163**, 307–309 (1983)
4.461 M. J. Rosker, K. Cheng, C. L. Tang: IEEE J. Quantum Electron. **21**, 1600 (1985)
4.462 G. D. Boyd, E. Buehler, F. G. Storz: Appl. Phys. Lett. **18**, 301–304 (1971)
4.463 S. R. Sashital, R. R. Stephens, J. F. Lotspeich: J. Appl. Phys. **59**, 757–760 (1986)
4.464 G. C. Bhar, L. K. Samanta, D. K. Ghosh, S. Das: Kvantovaya Elektron. **14**, 1361 (1987)
4.465 G. C. Bhar, L. K. Samanta, D. K. Ghosh, S. Das: Sov. J. Quantum Electron. [English Transl.] **17**, 860 (1987)
4.466 K. Tada, K. Kikuchi: Jpn. J. Appl. Phys. **19**, 1311–1315 (1980)
4.467 A. Schaefer, H. Schmitt, A. Dörr: Ferroelectrics **69**, 253–266 (1986)
4.468 D. Berlincourt, H. Jaffe: Phys. Rev. **111**, 143–148 (1958)
4.469 W. J. Merz: Phys. Rev. **76**, 1221–1225 (1949)
4.470 V. G. Gavrilyachenko, E. G. Fesenko: Kristallografiya **16**, 640–641 (1971)
4.471 V. G. Gavrilyachenko, E. G. Fesenko: Sov. Phys. Crystallogr. [English Transl.] **16**, 549–550 (1971)
4.472 A. V. Turik, N. B. Shevchenko, V. G. Gavrilyachenko, E. G. Fesenko: Phys. Status Solidi (b) **94**, 525–528 (1979)
4.473 Molecular Technology: Data sheet – World of crystals (Molecular Technology GmbH, Berlin 2002)
4.474 M. Adachi, A. Kawabata: Jpn. J. Appl. Phys. **17**, 1969–1973 (1978)
4.475 R. C. Miller, D. A. Kleinman, A. Savage: Phys. Rev. Lett. **11**, 146–149 (1963)
4.476 R. C. Miller, W. A. Nordland: Opt. Commun. **1**, 400–402 (1970)
4.477 M. Zgonik, P. Bernasconi, M. Duelli, R. Schlesser, P. Günter, M. H. Garrett, D. Rytz, Y. Zhu, X. Wu: Phys. Rev. B **50**, 5941–5949 (1994)
4.478 S. H. Wemple, M. DiDomenico Jr., I. Camlibel: J. Phys. Chem. Solids **29**, 1797–1803 (1968)
4.479 S. Singh, J. P. Remeika, J. R. Potopowicz: Appl. Phys. Lett. **20**, 135–137 (1972)
4.480 E. H. Turner: unpublished work (quoted in [4.225, 347])
4.481 R. Komatsu, T. Sugawara, K. Sassa, N. Sarukura, Z. Liu, S. Izumida, Y. Segawa, S. Uda, T. Fukuda, K. Yamanouchi: Appl. Phys. Lett. **70**, 3492–3494 (1997)
4.482 T. Sugawara, R. Komatsu, S. Uda: Solid State Commun. **107**, 233 (1998)
4.483 S. I. Furusawa, O. Chikagawa, S. Tange, T. Ishidate, H. Orihara, Y. Ishibashi, K. Miwa: J. Phys. Soc. Jpn. **60**, 2691–2693 (1991)
4.484 L. Bohaty, S. Haussühl, J. Liebertz: Cryst. Res. Technol. **24**, 1159–1163 (1989)
4.485 L. G. Van Uitert, S. Singh, H. J. Levinstein, J. E. Geusic, W. A. Bonner: Appl. Phys. Lett. **11**, 161–163 (1967)
4.486 L. G. Van Uitert, S. Singh, H. J. Levinstein, J. E. Geusic, W. A. Bonner: Erratum, Appl. Phys. Lett. **12**, 224 (1968)
4.487 J. J. E. Reid: Appl. Phys. Lett. **62**, 19–21 (1993)
4.488 M. Adachi, T. Shiosaki, A. Kawabata: Ferroelectrics **27**, 89–92 (1980)
4.489 J. L. Kirk, K. Vedam: J. Phys. Chem. Solids **33**, 1251–1255 (1972)
4.490 R. Kiriyama: Science (Tokyo) **17**, 239–240 (1947)
4.491 R. Kiriyama: Chem. Abstr. **45**, 2278c (1951)
4.492 M. S. Madhava, S. Haussühl: Z. Kristallogr. **141**, 25–30 (1975)
4.493 M. J. Dodge: Refractive index. In: *Optical Materials*, CRC Handbook of Laser Science and Technology, Vol. 4, Subvol. 2, ed. by M. J. Weber (CRC, Boca Raton 1987) pp. 21–47
4.494 K. W. Martin, L. G. DeShazer: Appl. Opt. **12**, 941–943 (1973)
4.495 P. S. Bechthold, S. Haussühl: Appl. Phys. **14**, 403–410 (1977)
4.496 S. Haussühl: Acta Crystallogr. A **24**, 697–698 (1968)
4.497 P. Günter: Ferroelectrics **75**, 5–23 (1987)
4.498 J. Sapriel, R. Hierle, J. Zyss, M. Bossier: Appl. Phys. Lett. **55**, 2594–2596 (1989)
4.499 Y. Wu, T. Sasaki, S. Nakai, A. Yokotani, H. Tang, C. Chen: Appl. Phys. Lett. **62**, 2614–2615 (1993)
4.500 K. Kato: IEEE J. Quantum Electron. **31**, 169–171 (1995)
4.501 G. R. Crane: J. Chem. Phys. **62**, 3571 (1975)
4.502 E. N. Volkova, V. A. Dianova, A. L. Zuev, A. N. Izrailenko, A. S. Lipatov, V. N. Parygin, L. N. Rashkovich, L. E. Chirkov: Kristallografiya **16**, 346–349 (1971)
4.503 E. N. Volkova, V. A. Dianova, A. L. Zuev, A. N. Izrailenko, A. S. Lipatov, V. N. Parygin, L. N. Rashkovich, L. E. Chirkov: Sov. Phys. Crystallogr. [English Transl.] **16**, 284–286 (1971)
4.504 S. K. Kurtz, T. T. Perry, J. G. Bergman Jr.: Appl. Phys. Lett. **12**, 186–188 (1968)
4.505 H. Naito, H. Inaba: Optoelectronics **4**, 335 (1972)
4.506 J. Zyss, D. S. Chemla, J. F. Nicoud: J. Chem. Phys. **74**, 4800–4811 (1981)
4.507 M. Sigelle, R. Hierle: J. Appl. Phys. **52**, 4199–4204 (1981)
4.508 T. S. Narasimhamurty: Phys. Rev. **186**, 945–948 (1969)

4.509 Y. Takagi, Y. Makita: J. Phys. Soc. Jpn. **13**, 272–277 (1958)
4.510 V. V. Gladkii, V. K. Magataev, V. A. Kirikov: Fiz. Tverd. Tela **19**, 1102–1106 (1977)
4.511 V. V. Gladkii, V. K. Magataev, V. A. Kirikov: Sov. Phys. Solid State [English Transl.] **19**, 641–644 (1977)
4.512 M. S. Khan, T. S. Narasimhamurty: Solid State Commun. **43**, 941–943 (1982)
4.513 A. T. Anistratov, S. X. Mel'nikova: Kristallografiya **17**, 149–152 (1972)
4.514 A. T. Anistratov, S. X. Mel'nikova: Sov. Phys. Crystallogr. [English Transl.] **17**, 119–121 (1972)
4.515 N. A. Romanyuk, A. M. Kostetskii: Fiz. Tverd. Tela **18**, 1489–1491 (1976)
4.516 N. A. Romanyuk, A. M. Kostetskii: Sov. Phys. Solid State [English Transl.] **18**, 867–869 (1976)
4.517 J. Valasek: Phys. Rev. **20**, 639–664 (1922)
4.518 G. B. Hadjichristov, P. P. Kircheva, N. Kirov: J. Mol. Struct. **382**, 33–37 (1996)
4.519 I. V. Berezhnoi, R. O. Vlokh: Fiz. Tverd. Tela **30**, 2223–2225 (1988)
4.520 I. V. Berezhnoi, R. O. Vlokh: Sov. Phys. Solid State [English Transl.] **30**, 1282–1284 (1988)
4.521 N. R. Ivanov, D. Khusravov, L. A. Shuvalov, N. M. Shchagina: Izv. Akad. Nauk SSSR, Ser. Fiz. **43**, 1691–1701 (1979)
4.522 N. R. Ivanov, D. Khusravov, L. A. Shuvalov, N. M. Shchagina: Bull. Acad. Sci. USSR, Phys. Ser. [English Transl.] **43**, 121–129 (1979)
4.523 V. G. Martynov, K. S. Aleksandrov, A. T. Anistratov: Fiz. Tverd. Tela **15**, 2922–2926 (1973)
4.524 V. G. Martynov, K. S. Aleksandrov, A. T. Anistratov: Sov. Phys. Solid State [English Transl.] **15**, 1950–1952 (1974)
4.525 Y. Luspin, G. Hauret: C. R. Hebd. Seances Acad. Sci. (Paris), Ser. B **274**, 995 (1972)
4.526 A. T. Anistratov, V. G. Martynov: Kristallografiya **15**, 308–312 (1970)
4.527 A. T. Anistratov, V. G. Martynov: Sov. Phys. Crystallogr. [English Transl.] **15**, 256–260 (1970)
4.528 M. Eibschütz, H. J. Guggenheim, S. H. Wemple, I. Camlibel, M. DiDomenico Jr.: Phys. Lett. A **29**, 409–410 (1969)
4.529 K. Recker, F. Wallrafen, S. Haussühl: J. Cryst. Growth **26**, 97–100 (1974)
4.530 R. O. Vlokh, I. P. Skab: Fiz. Tverd. Tela **34**, 3250–3255 (1992)
4.531 R. O. Vlokh, I. P. Skab: Sov. Phys. Solid State [English Transl.] **34**, 1739–1741 (1992)
4.532 J. D. Barry, C. J. Kennedy: IEEE J. Quantum Electron. **11**, 575–579 (1975)
4.533 T. Yamada, H. Iwasaki, N. Niizeki: J. Appl. Phys. **41**, 4141–4147 (1970)
4.534 S. Singh, D. A. Draegert, J. E. Geusic: Phys. Rev. B **2**, 2709–2724 (1970)
4.535 A. W. Warner, G. A. Coquin, J. L. Fink: J. Appl. Phys. **40**, 4353 (1969)
4.536 J. Fousek, C. Konak: Ferroelectrics **12**, 185–187 (1976)
4.537 K. Suzuki, K. Inoue, M. Shibuya: J. Phys. Soc. Jpn. **43**, 1457–1458 (1977)
4.538 J. E. Geusic, H. J. Levinstein, J. J. Rubin, S. Singh, L. G. Van Uitert: Appl. Phys. Lett. **11**, 269–271 (1967)
4.539 J. E. Geusic, H. J. Levinstein, J. J. Rubin, S. Singh, L. G. Van Uitert: Erratum, Appl. Phys. Lett. **12**, 224 (1968)
4.540 S. K. Gupta, H. B. Gon, K. V. Rao: Ferroelectr. Lett. **7**, 15–19 (1987)
4.541 S. K. Gupta, H. B. Gon, K. V. Rao: J. Mater. Sci. Lett. **6**, 4–6 (1987)
4.542 C. Medrano, P. Günter, H. Arend: Phys. Status Solidi **143**, 749–754 (1987)
4.543 A. Carenco, J. Jerphagnon, A. Perigaud: J. Chem. Phys. **66**, 3806–3813 (1977)
4.544 M. Y. Antipin, T. V. Timofeeva, R. D. Clark, V. N. Nesterov, F. M. Dolgushin, J. Wu, A. J. Leyderman: Mater. Chem. **11**, 351–358 (2001)
4.545 C. Bosshard, K. Sutter, P. Günter, G. Chapuis, R. J. Twieg, D. Dobrowolsky: Proc. SPIE **1017**, 207–211 (1988)
4.546 P. Günter, C. Bosshard, K. Sutter, H. Arend, G. Chapuis, R. J. Twieg, D. Dobrowolski: Appl. Phys. Lett. **50**, 486–488 (1987)
4.547 C. Bosshard, K. Sutter, P. Günter: Ferroelectrics **92**, 387–393 (1989)
4.548 K. Sutter, C. Bosshard, M. Ehrensperger, P. Günter, R. J. Twieg: IEEE J. Quantum Electron. **24**, 2362–2366 (1988)
4.549 C. Scheiding, G. Schmidt, H. D. Kürsten: Krist. Tech. **8**, 311–321 (1973)
4.550 L. E. Cross, A. Fouskova, S. E. Cummins: Phys. Rev. Lett. **21**, 812–814 (1968)
4.551 J. Sapriel, R. Vacher: J. Appl. Phys. **48**, 1191–1194 (1977)
4.552 M. P. Zaitseva, L. A. Shabanova, B. I. Kidyarov, Yu. I. Kokorin, S. I. Burkov: Kristallografiya **28**, 741–744 (1983)
4.553 M. P. Zaitseva, L. A. Shabanova, B. I. Kidyarov, Yu. I. Kokorin, S. I. Burkov: Sov. Phys. Crystallogr. [English Transl.] **28**, 439–440 (1983)
4.554 A. L. Aleksandrovskii, A. N. Izrailenko, L. N. Razhkovich: Kvantovaya Elektron. **1**, 1261–1264 (1974)
4.555 A. L. Aleksandrovskii, A. N. Izrailenko, L. N. Razhkovich: Sov. J. Quantum Electron. [English Transl.] **4**, 699–700 (1974)
4.556 A. L. Aleksandrovskii: Prib. Tekh. Eksp. **1**, 205–206 (1974)
4.557 A. L. Aleksandrovskii: Instrum. Exp. Tech., USSR [English Transl.] **17**, 234–235 (1974)
4.558 S. Nanamatsu, K. Doi, M. Takahashi: Jpn. J. Appl. Phys. **11**, 816–822 (1972)
4.559 R. C. Miller, W. A. Nordland, K. Nassau: Ferroelectrics **2**, 97–99 (1971)
4.560 Yu. V. Shaldin, D. A. Belogurov, T. M. Prokhortseva: Fiz. Tverd. Tela **15**, 1383–1387 (1973)
4.561 Yu. V. Shaldin, D. A. Belogurov, T. M. Prokhortseva: Sov. Phys. Solid State [English Transl.] **15**, 936–938 (1973)

4.562 S. Singh, W. A. Bonner, J. R. Potopowicz, L. G. Van Uitert: Appl. Phys. Lett. **17**, 292–294 (1970)
4.563 F. B. Dunning, F. K. Tittel, R. F. Stebbings: Opt. Commun. **7**, 181 (1973)
4.564 H. Naito, H. Inaba: Optoelectronics **5**, 256 (1973)
4.565 R. C. Miller, W. A. Nordland, E. D. Kolb, W. L. Bond: J. Appl. Phys. **41**, 3008–3011 (1970)
4.566 P. V. Lenzo, E. G. Spencer, J. P. Remeika: Appl. Opt. **4**, 1036–1037 (1965)
4.567 K. Araki, T. Tanaka: Jpn. J. Appl. Phys. **11**, 472–479 (1972)
4.568 L. M. Belyaev, G. S. Belikova, A. B. Gilvarg, I. M. Silvestrova: Kristallografiya **14**, 645–651 (1969)
4.569 L. M. Belyaev, G. S. Belikova, A. B. Gilvarg, I. M. Silvestrova: Sov. Phys. Crystallogr. [English Transl.] **14**, 544–549 (1970)
4.570 A. Miniewicz, A. Samoc, J. Sworakowski: J. Mol. Electron. **4**, 25–29 (1988)
4.571 M. S. Khan, T. S. Narasimhamurty: J. Mater. Sci. Lett. **1**, 268–270 (1982)
4.572 C. Chen, Y. Wu, A. Jiang, B. Wu, G. You, R. Li, S. Lin: J. Opt. Soc. Am. B **6**, 616–621 (1989)
4.573 S. P. Velsko, M. Webb, L. Davis, C. Huang: IEEE J. Quantum Electron. **27**, 2182–2192 (1991)
4.574 S. Lin, Z. Sun, B. Wu, C. Chen: J. Appl. Phys. **67**, 634 (1990)
4.575 K. Kato: IEEE J. Quantum Electron. **30**, 2950–2952 (1994)
4.576 B. L. Davydov, L. G. Koreneva, E. A. Lavrovsky: Radiotekh. Elektron. **19**, 1313 (1974)
4.577 B. L. Davydov, L. G. Koreneva, E. A. Lavrovsky: Radio Eng. Electron. Phys. [English Transl.] **19**(6), 130 (1974)
4.578 J. L. Stevenson: J. Phys. D **6**, L13–L16 (1973)
4.579 S. K. Kurtz, J. Jerphagnon, M. M. Choy: *Elastic, Piezoelectric, Pyroelectric, Piezooptic, Electrooptic Constant, and Nonlinear Dielectric Susceptibilities of Crystals*, Landolt–Börnstein, New Series III/11, ed. by K. H. Hellwege (Springer, Berlin, Heidelberg 1979) pp. 671–743
4.580 G. S. Belyaev, G. S. Belikova, A. G. Gilvarg, M. P. Golovei, I. N. Kalinkina, G. I. Kosourov: Opt. Spectr. (USSR) [English Transl.] **29**, 522 (1970)
4.581 Y. Uematsu, T. Fukuda: Jpn. J. Appl. Phys. **12**, 841–844 (1973)
4.582 P. Günter: Jpn. J. Appl. Phys. **16**, 1727–1728 (1977)
4.583 E. Wiesendanger: Ferroelectrics **6**, 263–281 (1974)
4.584 M. Zgonik, R. Schlesser, I. Biaggio, I. Voit, J. Tscherry, P. Günter: J. Appl. Phys. **74**, 1287–1297 (1993)
4.585 W. R. Cook Jr., H. Jaffe: Acta Crystallogr. **10**, 705–707 (1957)
4.586 T. Krajewski, Z. Tylczynski, T. Breczewski: Acta Phys. Polonica A **47**, 455–466 (1975)
4.587 J. D. Bierlein, H. Vanherzeele, A. A. Ballman: Appl. Phys. Lett. **54**, 783–785 (1989)
4.588 J. D. Bierlein, H. Vanherzeele, A. A. Ballman: Erratum, Appl. Phys. Lett. **61**, 3193 (1992)
4.589 V. V. Aleksandrov, T. S. Velichkina, V. I. Voronkova, L. V. Koltsova, I. A. Yakovlev, V. K. Yanovskii: Solid State Commun. **69**, 877 (1989)
4.590 J. D. Bierlein, H. Vanherzeele: J. Opt. Soc. Am. B **6**, 622–633 (1989)
4.591 J. D. Bierlein, C. B. Arweiler: Appl. Phys. Lett. **49**, 917–919 (1986)
4.592 D. H. Jundt, P. Günter, B. Zysset: Nonlin. Opt. **4**, 341–345 (1993)
4.593 Y. Uematsu: Jpn. J. Appl. Phys. **13**, 1362–1368 (1974)
4.594 B. Zysset, I. Biaggio, P. Günter: J. Opt. Soc. Am. B **9**, 380–386 (1992)
4.595 J. A. Paisner, M. L. Spaeth, D. C. Gerstenberger, I. W. Ruderman: Appl. Phys. Lett. **32**, 476–478 (1978)
4.596 W. R. Cook, L. H. Hubby Jr.: J. Opt. Soc. Am. **66**, 72 (1976)
4.597 F. B. Dunning, R. G. Stickel Jr.: Appl. Opt. **15**, 3131 (1976)
4.598 H. J. Dewey: IEEE J. Quantum Electron. **12**, 303 (1976)
4.599 Y. Wu, C. Chen: Wuli Xuebao (Acta Phys. Sin.) **35**, 1–6 (1986)
4.600 A. H. Kung: Appl. Phys. Lett. **65**, 1082–1084 (1994)
4.601 D. L. Fenimore, K. L. Schepler, U. B. Ramabadran, S. R. McPherson: J. Opt. Soc. Am. B **12**, 794–796 (1995)
4.602 L. T. Cheng, L. K. Cheng, J. D. Bierlein, F. C. Zumsteg: Appl. Phys. Lett. **63**, 2618–2620 (1993)
4.603 L. K. Cheng, L. T. Cheng, J. Galperin, P. A. M. Hotsenpiller, J. D. Bierlein: J. Cryst. Growth **137**, 107–115 (1994)
4.604 K. Kato: IEEE J. Quantum Electron. **30**, 881–883 (1994)
4.605 A. C. Aleksandrovsky, S. A. Akhmanov, V. A. Dyakov, N. I. Zheludev, V. I. Pryalkyn: Kvantovaya Elektron. **12**, 1333 (1985)
4.606 A. C. Aleksandrovsky, S. A. Akhmanov, V. A. Dyakov, N. I. Zheludev, V. I. Pryalkyn: Sov. J. Quantum Electron. [English Transl.] **15**, 885 (1985)
4.607 W. Wiechmann, S. Kubota, T. Fukui, H. Masuda: Opt. Lett. **18**, 1208–1210 (1993)
4.608 K. Kato: IEEE J. Quantum Electron. **QE-27**, 1137–1140 (1991)
4.609 V. K. Yanovskii, V. I. Voronkova, A. P. Leonov, S. Yu. Stefanovich: Fiz. Tverd. Tela **27**, 2516–2517 (1985)
4.610 V. K. Yanovskii, V. I. Voronkova, A. P. Leonov, S. Yu. Stefanovich: Sov. Phys. Solid State [English Transl.] **27**, 1508–1509 (1985)
4.611 V. K. Yanovskii, V. I. Voronkova: Phys. Status Solidi (a) **93**, 665–668 (1980)
4.612 E. Nakamura: J. Phys. Soc. Jpn. **17**, 961–966 (1962)
4.613 H. Shimizu, M. Tsukamoto, Y. Ishibashi, Y. Takagi: J. Phys. Soc. Jpn. **38**, 195–201 (1975)
4.614 K. Hamano, K. Negishi, M. Marutake, S. Nomura: Jpn. J. Appl. Phys. **2**, 83–90 (1963)
4.615 G. Hauret, J. P. Chapelle, L. Taurel: Phys. Status Solidi (a) **11**, 255–261 (1972)
4.616 F. C. Zumsteg, J. D. D. Bierlein, T. E. Gier: J. Appl. Phys. **47**, 4980 (1976)

4.617 Yu. S. Oseledchik, A. I. Pisarevsky, A. L. Prosvirin, V. N. Lopatko, L. E. Kholodenkov, E. F. Titkov, A. A. Demidovich, A. P. Shkadarevich: Proc. of Laser Optics Conf. [in Russian], (Leningrad Univ. Press, Leningrad 1990)
4.618 J. Y. Wang, Y. G. Liu, J. Q. Wei, L. P. Shi, M. Wang: Z. Kristallogr. **191**, 231–238 (1990)
4.619 J. Y. Wang, Y. G. Liu, J. Q. Wei, L. P. Shi, M. Wang: Guisuanyan Xuebao **18**, 165–170 (1990)
4.620 J. Y. Wang, Y. G. Liu, J. Q. Wei, L. P. Shi, M. Wang: Chem. Abstr. **114** (1991) No. 154040x
4.621 K. Iio: J. Phys. Soc. Jpn. **34**, 138 (1973)
4.622 D. S. Chemla, E. Batifol, R. L. Byer, R. L. Herbst: Opt. Commun. **11**, 57 (1974)
4.623 A. R. Johnston, T. Nakamura: J. Appl. Phys. **40**, 3656–3658 (1969)
4.624 K. Inoue, T. Ishidate: Ferroelectrics **7**, 105–106 (1974)
4.625 B. Teng, J. Wang, Z. Wang, H. Jiang, X. Hu, R. Song, H. Liu, Y. Liu, J. Wei, Z. Shao: J. Cryst. Growth **224**, 280–283 (2001)
4.626 H. Hellwig, J. Liebertz, L. Bohaty: J. Appl. Phys. **88**, 240 (2000)
4.627 Z. Lin, Z. Wang, C. Chen, M.-H. Lee: J. Appl. Phys. **90**, 5585 (2001)
4.628 D. Eimerl, S. Velsko, L. Davis, F. Wang, G. Loiacono, G. Kennedy: IEEE J. Quantum Electron. **25**, 179–193 (1989)
4.629 C. E. Barker, D. Eimerl, S. P. Velsko: J. Opt. Soc. Am. B **8**, 2481–2492 (1991)
4.630 P. Kerkoc, M. Zgonik, K. Sutter, C. Bosshard, P. Günter: J. Opt. Soc. Am. B **7**, 313–319 (1990)
4.631 I. Biaggio, P. Kerkoc, L.-S. Wu, P. Günter, B. Zysset: J. Opt. Soc. Am. B **9**, 507–517 (1992)
4.632 R. Bechmann: *Elastic, Piezoelectric, Piezooptic and Electrooptic Constants of Crystals*, Landolt–Börnstein, New Series III/1 (Springer, Berlin, Heidelberg 1966) pp. 40–123
4.633 C. S. Brown, R. C. Kell, R. Taylor, L. A. Thomas: Proc. Inst. Elec. Eng. (London) B **109**, 99–114 (1962)
4.634 C. S. Brown, R. C. Kell, R. Taylor, L. A. Thomas: IRE Trans. Compon. Parts **9**, 193–211 (1962)
4.635 B. M. Suleiman, A. Lundén, E. Karawacki: Solid State Ionics **136–137**, 325–330 (2000)
4.636 M. V. Hobden: J. Appl. Phys. **38**, 4365 (1967)
4.637 A. Sonin, A. A. Filimonov, S. V. Suvorov: Sov. Phys. Solid State **10**, 1481 (1968)
4.638 L. Bohaty, S. Haussühl, G. Nohl: Z. Kristallogr. **139**, 33–38 (1974)
4.639 W. F. Holman: Ann. Phys. **29**, 160–178 (1909)
4.640 G. Brosowki, G. Luther, H. E. Muser: Phys. Status Solidi (a) **14**, K15–K17 (1972)
4.641 B. A. Strukov, K. A. Minaeva: Prib. Tekh. Eksp. **29**, 157–160 (1986)
4.642 B. A. Strukov, K. A. Minaeva: Instrum. Exp. Tech. (USSR) [English Transl.] **29**, Part II, 1413–1416 (1986)
4.643 P. P. Craig: Phys. Lett. **20**, 140–142 (1966)
4.644 F. Jona, G. Shirane: *Ferroelectric Crystals* (MacMillan, New York 1962)
4.645 J. Berdowski, A. Opilski, J. Szuber: J. Tech. Phys. (Poland) **18**, 211–217 (1977)
4.646 V. P. Konstantinova, I. M. Silvestrova, K. S. Aleksandrov: Kristallografiya **4**, 69–73 (1959)
4.647 V. P. Konstantinova, I. M. Silvestrova, K. S. Aleksandrov: Sov. Phys. Crystallogr. [English Transl.] **4**, 63–67 (1960)
4.648 S. Haussühl, J. Albers: Ferroelectrics **15**, 73 (1977)
4.649 J. M. Halbout, C. L. Tang: IEEE J. Quantum Electron. **18**, 410–415 (1982)
4.650 M. J. Rosker, C. L. Tang: IEEE J. Quantum Electron. **20**, 334 (1984)
4.651 N. R. Ivanov, S. Ya. Benderskii, L. A. Shuvalov: Kristallografiya **22**, 115–125 (1977)
4.652 N. R. Ivanov, S. Ya. Benderskii, L. A. Shuvalov: Sov. Phys. Crystallogr. [English Transl.] **22**, 64–69 (1977)
4.653 A. S. Sonin, V. S. Suvorov: Sov. Phys. Solid State **9**, 1437 (1967)
4.654 N. R. Ivanov, L. A. Shuvalov: Kristallografiya **11**, 760–765 (1966)
4.655 N. R. Ivanov, L. A. Shuvalov: Sov. Phys. Crystallogr. [English Transl.] **11**, 648–651 (1967)
4.656 A. Feldman, R. M. Waxler: Phys. Rev. Lett. **45**, 126–129 (1980)

# 4.5. Ferroelectrics and Antiferroelectrics

Ferroelectric crystals (especially oxides in the form of ceramics) are important basic materials for technological applications in capacitors and in piezoelectric, pyroelectric, and optical devices. In many cases their nonlinear characteristics turn out to be very useful, for example in optical second-harmonic generators and other nonlinear optical devices. In recent decades, ceramic thin-film ferroelectrics have been utilized intensively as parts of memory devices. Liquid crystal and polymer ferroelectrics are utilized in the broad field of fast displays in electronic equipment.

This chapter surveys the nature of ferroelectrics, making reference to the data presented in the Landolt–Börnstein data collection *Numerical Data and Functional Relationships in Science and Technology*, Vol. III/36, *Ferroelectrics and Related Substances* (LB III/36). The data in the figures in this chapter have been taken mainly from the Landolt–Börnstein collection. The Landolt–Börnstein volume mentioned above consists of three subvolumes: Subvolume A [5.1, 2], covering oxides; Subvolume B [5.3], covering inorganic crystals other than oxides; and Subvolume C [5.4], covering organic crystals, liquid crystals, and polymers.

4.5.1 **Definition of Ferroelectrics and Antiferroelectrics** ..... 903
4.5.2 **Survey of Research on Ferroelectrics** ..... 904
4.5.3 **Classification of Ferroelectrics** ..... 906
4.5.3.1 The 72 Families of Ferroelectrics 909
4.5.4 **Physical Properties of 43 Representative Ferroelectrics** ..... 912
4.5.4.1 Inorganic Crystals Oxides [5.1, 2] 912
4.5.4.2 Inorganic Crystals Other Than Oxides [5.3] ..... 922
4.5.4.3 Organic Crystals, Liquid Crystals, and Polymers [5.4] ..... 930
**References** ..... 936



Matter consists of electrons and nuclei. Most of the electrons generally are tightly bound to the nuclei, but some of the electrons are only weakly bound or are freely mobile in a lattice of ions. The physical properties of matter can be considered as being split into two categories. The properties in the first category are determined directly by the electrons and by the interaction of the electrons with lattice vibrations. Examples are the metallic, magnetic, superconductive, and semiconductive properties. The properties in the second category are only indirectly related to the electrons and can be discussed as being due to interaction between atoms, ions, or molecules. In this category we have, for example, the dielectric, elastic, piezoelectric, and pyroelectric properties; we have the dispersion relations of the lattice vibrations; and we have most of the properties of liquid crystals and polymers. The important properties of ferroelectrics are linked to all the latter properties, and they exhibit diverse types of phase transitions together with anomalies in these properties. These specific modifications convey information about cooperative interactions among ions, atoms, or molecules in the condensed phase of matter.

## 4.5.1 Definition of Ferroelectrics and Antiferroelectrics

A ferroelectric crystal is defined as a crystal which belongs to the pyroelectric family (i. e. shows a spontaneous electric polarization) and whose direction of spontaneous polarization can be reversed by an electric field. An antiferroelectric crystal is defined as a crystal whose structure can be considered as being composed of two sublattices polarized spontaneously in antiparallel directions and in which a ferroelectric phase can

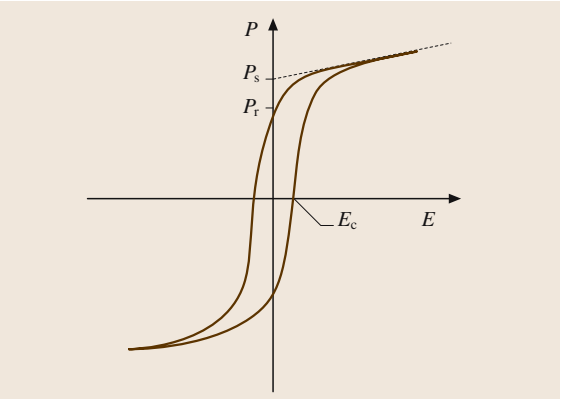


**Fig. 4.5-1** Ferroelectric hysteresis loop. $P_s$, spontaneous polarization; $P_r$, remanent polarization; $E_c$, coercive field

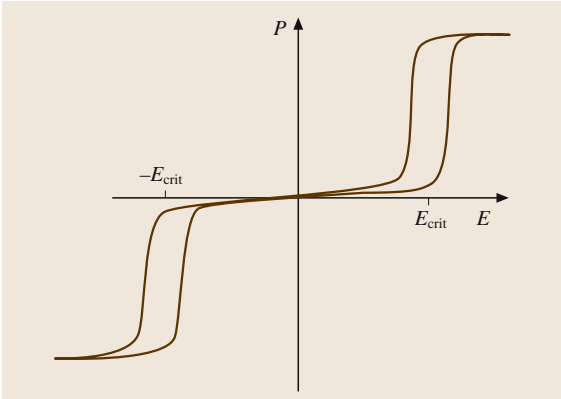


**Fig. 4.5-2** Antiferroelectric hysteresis loop. $E_{crit}$, critical field

be induced by applying an electric field. Experimentally, the reversal of the spontaneous polarization in ferroelectrics is observed as a single hysteresis loop (Fig. 4.5-1), and the induced phase transition in antiferroelectrics as a double hysteresis loop (Fig. 4.5-2), when a low-frequency ac field of a suitable strength is applied.

The spontaneous polarization in ferroelectrics and the sublattice polarizations in antiferroelectrics are analogous to their magnetic counterparts. As described above, however, these polarizations are a necessary but not sufficient condition for ferroelectricity or antiferroelectricity. In other words, ferroelectricity and antiferroelectricity are concepts based not only upon the crystal structure, but also upon the dielectric behavior of the crystal. It is a common dielectric characteristic of ferroelectrics and antiferroelectrics that, in a certain temperature range, the dielectric polarization is observed to be a two-valued function of the electric field.

The definition of ferroelectric liquid crystals needs some comments; see remark *l* in Sect. 4.5.3.1.



## 4.5.2 Survey of Research on Ferroelectrics

The ferroelectric effect was discovered in 1920 by *Valasek*, who obtained hysteresis curves for Rochelle salt analogous to the *B*–*H* curves of ferromagnetism [5.5], and studied the electric hysteresis and piezoelectric response of the crystal in some detail [5.6]. For about 15 years thereafter, ferroelectricity was considered as a very specific property of Rochelle salt, until Busch and Scherrer discovered ferroelectricity in $KH_2PO_4$ and its sister crystals in 1935. During World War II, the anomalous dielectric properties of $BaTiO_3$ were discovered in ceramic specimens independently by Wainer and Solomon in the USA in 1942, by Ogawa in Japan in 1944, and by Wul and Goldman in Russia in 1946. Since then, many ferroelectrics have been discovered and research activity has rapidly increased. In recent decades, active studies have been made on ferroelectric liquid crystals and high polymers, after ferroelectricity had been considered as a characteristic property of solids for more than 50 years.

Figures 4.5-3, 4.5-4, and 4.5-5 demonstrate how ferroelectric research has developed. Figure 4.5-3 indicates the number of ferroelectrics discovered each year for oxide (Fig. 4.5-3a) and nonoxide ferroelectrics (Fig. 4.5-3b). Figure 4.5-4 gives the total number of ferroelectrics known at the end of each year. At present more than 300 ferroelectric substances are known. Figure 4.5-5 indicates the number of research papers on ferroelectrics and related substances published each year.

Advanced experimental methods (e.g. inelastic neutron scattering and hyper-Raman scattering) have been applied effectively to studies of ferroelectrics, and several new concepts (e.g. soft modes of lattice vibrations and the dipole glass) have been introduced to understand the nature of ferroelectrics. Ferroelectric crystals have been widely used in capacitors and piezoelectric devices. Steady developments in crystal growth and in the preparation of ceramics and ceramic thin

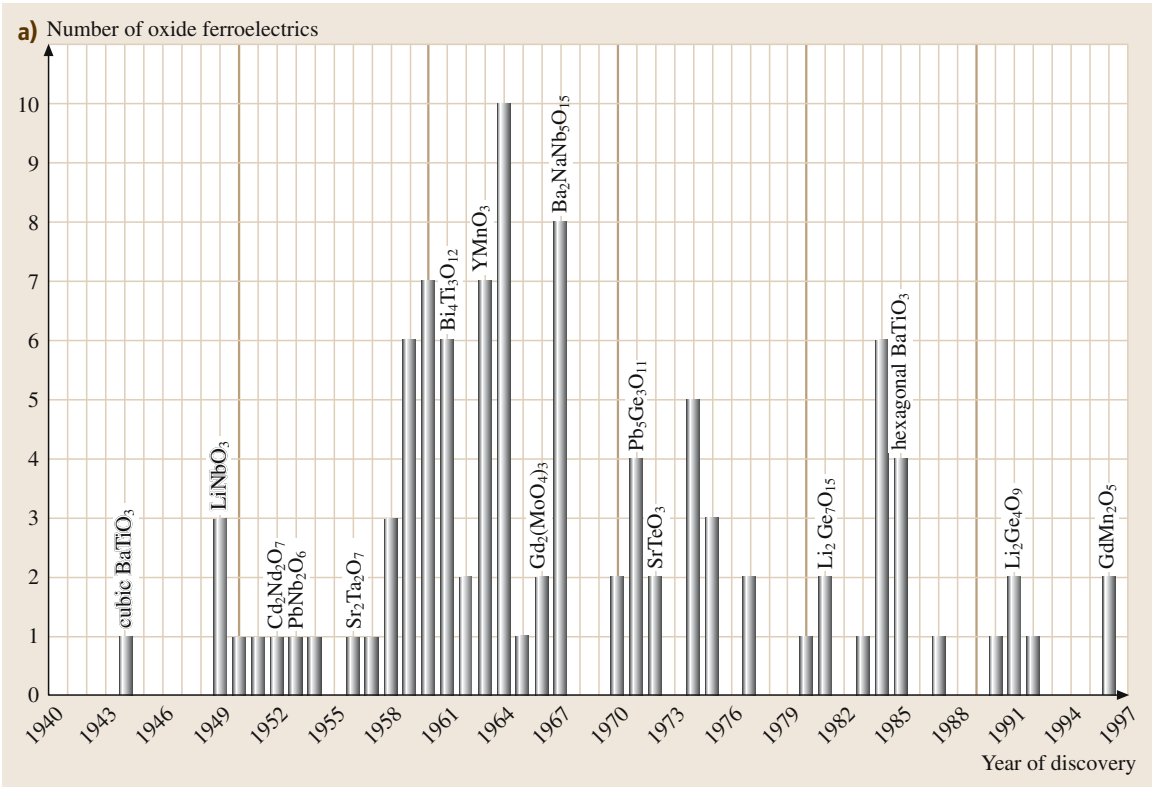


**Fig. 4.5-3a,b** Number of ferroelectric substances discovered in each year. Representative ferroelectrics are indicated at their year of discovery. **(a)** Oxide ferroelectrics. Only pure compounds are taken into account. **(b)** Nonoxide ferroelectrics. *Gray bars* stand for nonoxide crystals, counting each pure compound as one unit. *Brown bars* stand for liquid crystals and polymers, counting each group of homologues (cf. Chaps. 71 and 72 in [5.4]) as one unit. The figure was prepared by Prof. K. Deguchi using data from LB III/36

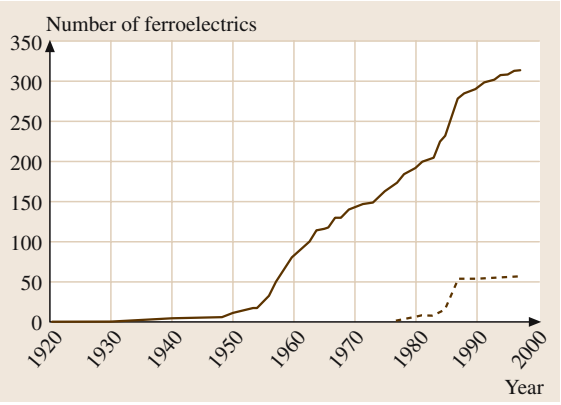


**Fig. 4.5-4** Number of ferroelectric substances known at the end of each year. The *solid line* represents all ferroelectrics, including liquid crystals and polymers. For liquid crystals and polymers, each group of homologues is counted as one substance. The *dashed line* represents ferroelectric liquid crystals and polymers alone. Figure prepared by Prof. K. Deguchi

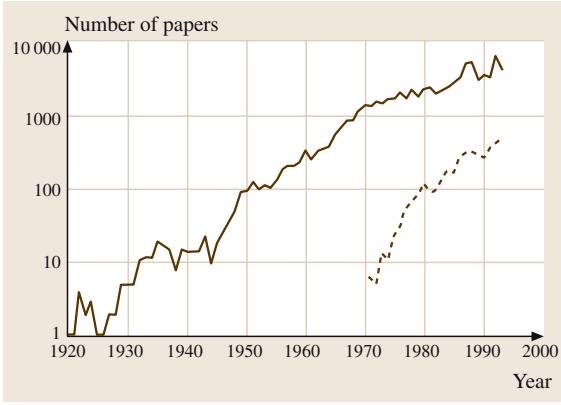


**Fig. 4.5-5** Number of research papers on ferroelectrics and related substances published in each year. The *solid line* indicates the number of papers concerning all ferroelectrics (crystals + liquid crystals + polymers). The *dashed line* indicates the number of papers concerning liquid crystals and polymers alone. Prepared by Prof. K. Deguchi

films have opened the way to various other applications (e.g. second-harmonic generation and memory devices). Liquid crystals and high-polymer ferroelectrics are very useful as fast display elements.

Corresponding to this intense development, many textbooks, monographs, and review articles have been published on ferroelectric research during recent years. Some of them, arranged according to the various research fields, are listed here:

- Introduction to ferroelectrics: [5.7–10]
- Applications in general: [5.10, 11]
- Piezoelectricity: [5.12–14]
- Structural phase transitions: [5.15–17]
- Incommensurate phases: [5.18]
- Soft-mode spectroscopy: [5.19]
- Inelastic neutron scattering studies of ferroelectrics: [5.20]
- Raman and Brillouin scattering: [5.21]
- Ceramic capacitors: [5.22]
- Dipole glasses: [5.23]
- Relaxors: [5.24]
- Second-harmonic generation (SHG): [5.25–28]
- Ferroelectric ceramics: [5.29]
- Thin films: [5.30–35]
- Acoustic surface waves (ASWs): [5.36–39]
- Ferroelectric transducers and sensors: [5.40]
- Memory applications: [5.35]
- Ferroelectric liquid crystals: [5.41–47]
- Ferroelectric polymers: [5.48–51]

## 4.5.3 Classification of Ferroelectrics

Ferroelectricity is caused by a cooperative interaction of molecules or ions in condensed matter. The transition to ferroelectricity is characterized by a phase transition. Depending on the mechanism of how the molecules or ions interact in the material, we can classify the ferroelectric phase transitions and also the ferroelectric materials themselves into three categories: (I) order–disorder type, (II) displacive type, and (III) indirect type. In the order–disorder type (I), the spontaneous polarization is caused by orientational order of dipolar molecules, which is best visualized by the Ising model. The dielectric constants of order–disorder type ferroelectrics increase markedly in the vicinity of the Curie point. In the displacive type (II), the spontaneous polarization results from softening of the transverse optical modes of the lattice vibrations at the origin of the Brillouin zone; again, a marked increase of the dielectric constants is observed near the Curie temperature. The

indirect type (III) is further classified into $III_{op}$ and $III_{ac}$. In type $III_{op}$, the phase transition is originally caused by softening of the optical modes at the Brillouin zone boundary; a coupling of the soft modes with the electric polarization (through a complex mechanism) causes the spontaneous polarization (e.g. substance 18, GMO, in Sect. 4.5.4.1); only a very slight anomaly of the dielectric constants is observed above the Curie point (see Fig. 4.5-6). In type $III_{ac}$, softening of the acoustic modes (decrease of the tangent of the dispersion relation) takes place at the origin of the Brillouin zone, and a piezoelectric coupling between the soft modes and the polarization results in the spontaneous polarization (e.g. substance 40, LAT, in Sect. 4.5.4.3). No dielectric-constant anomaly appears above the Curie temperature when the crystal is clamped so that elastic deformation is prohibited (see Fig. 4.5-7). Most of the nonoxide ferroelectrics are of the order–disorder type and most of the oxide ferroelectrics are of the displacive type, while a few ferroelectrics are of the indirect type.

It might be expected that the dielectric dispersion would be dissipative and occur at relatively low frequency (e.g. in the microwave region) in the order–disorder ferroelectrics, while the dispersion would be of the resonance type and occur in the millimeter or infrared region in the displacive ferroelectrics. Actually, however, the situation is more complex owing to phonon–phonon coupling and cluster formation near the Curie temperature. Phonon–phonon coupling is inevitable in displacive ferroelectrics because their ferroelectricity is closely related to the anharmonic term of the ion potential, as first pointed out by *Slater* (see [5.7]). Accordingly, the resonance-type oscillation tends to be overdamped. High dielectric constants

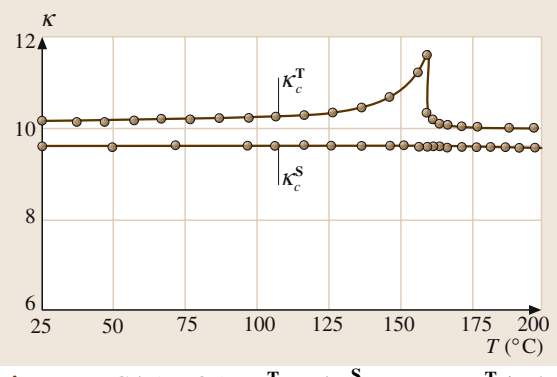


**Fig. 4.5-6** $Gd_2(MoO_4)_3$. $\kappa_c^{\mathbf{T}}$, and $\kappa_c^{\mathbf{S}}$ versus $T$. $\kappa_c^{\mathbf{T}}$ is the free dielectric constant $\kappa_c$ measured at 1 kHz, and $\kappa_c^{\mathbf{S}}$ is the clamped dielectric constant $\kappa_c$ measured at 19 MHz

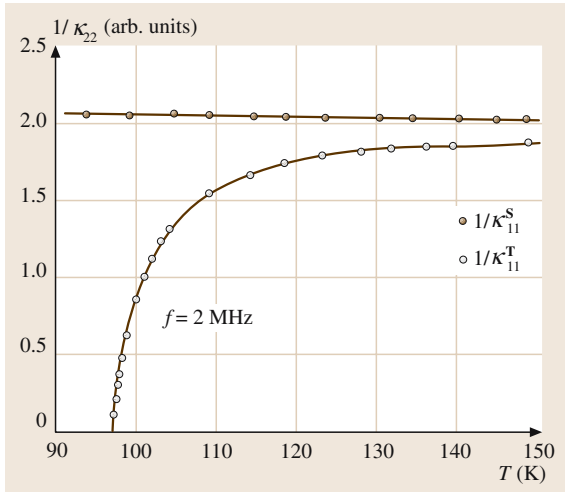


**Fig. 4.5-7** $LiNH_4C_4H_4O_6 \cdot H_2O$. $1/\kappa_{22}^{\mathbf{S}}$, and $1/\kappa_{22}^{\mathbf{T}}$ versus $T$. $\kappa_{22} = \kappa_b$. $f = 2$ MHz. $\kappa_{22}^S$ is $\kappa_{22}$ of the clamped crystal. $\kappa_{22}^{\mathbf{T}}$ is $\kappa_{22}$ of the free crystal

tend to induce the formation of clusters in which unit cell polarizations are aligned, similarly to the domains in the ferroelectric phase, but the boundaries of these clusters fluctuate thermally. Inelastic neutron, hyper-Raman, and hyper-Rayleigh scattering, etc. indicate the existence of such clusters in several displacive ferroelectrics. It is known that a ferromagnetic domain wall can move to follow an ac magnetic field and contribute to the magnetic susceptibility, while a ferroelectric domain wall usually cannot follow an ac electric field and in practice does not contribute to the dielectric constant. The cluster boundaries, however, fluctuate thermally and hence will be able to follow an ac electric field and contribute to the dielectric constant. This contribution will be dissipative in its character. Accordingly, it is possible that dielectric dispersion occurs as a combination of an overdamped-resonance dispersion and a dissipative dispersion in most displacive ferroelectrics.

In second-order or nearly second-order phase transitions, the dielectric dispersion is observed to show a critical slowing-down: a phenomenon in which the response of the polarization to a change of the electric field becomes slower as the temperature approaches the Curie point. Critical slowing-down has been observed in the GHz region in several order–disorder ferroelectrics (e.g. Figs. 4.5-8 and 4.5-9) and displacive ferroelectrics (e.g. Fig. 4.5-10). The dielectric constants at the Curie point in the GHz region are very small in order–disorder

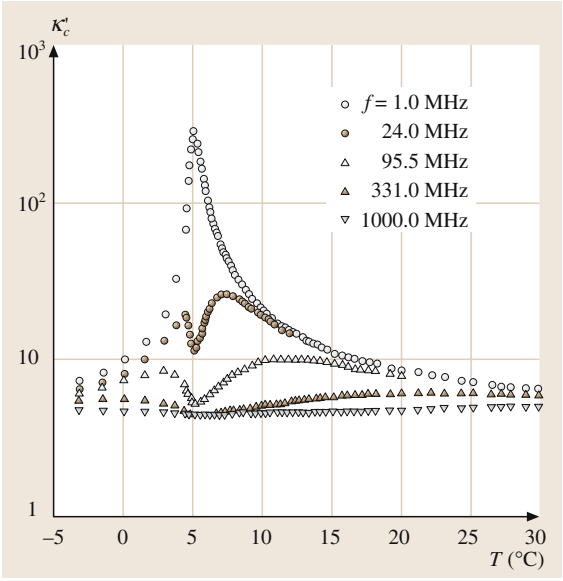


**Fig. 4.5-8** $Ca_2Sr(CH_3CH_2COO)_6$. $\kappa'_c$ versus $T$. Parameter: $f$

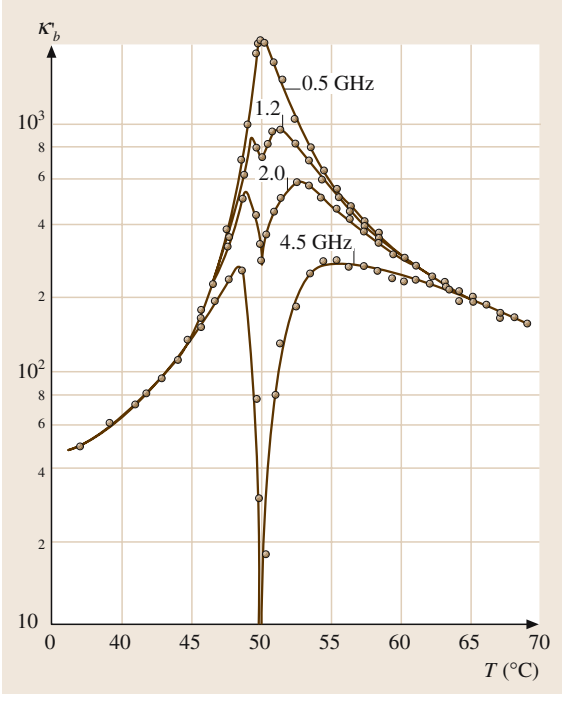


**Fig. 4.5-9** $(NH_2CH_2COOH)_3 \cdot H_2SO_4$. $\kappa'_b$ versus $T$ relation, showing critical slowing-down. Parameter: $f$

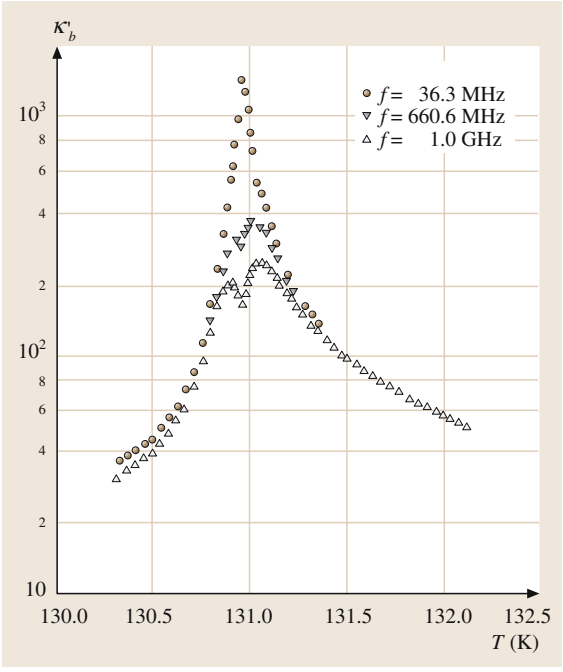


**Fig. 4.5-10** $(CH_3NHCH_2COOH)_3 \cdot CaCl_2$. $\kappa'_b$ versus $T$. Parameter: $f$. Critical slowing-down takes place

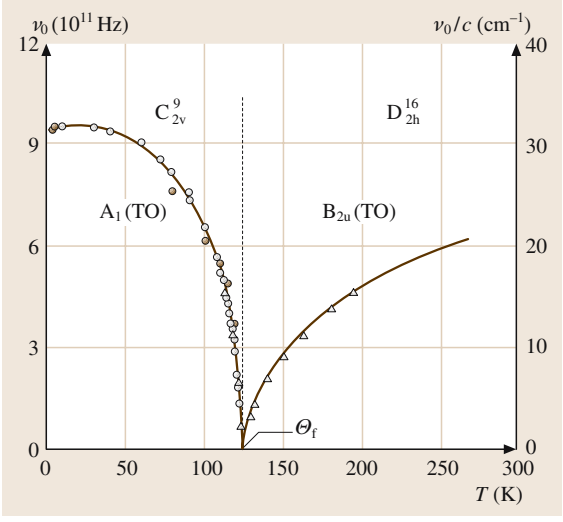


**Fig. 4.5-11** $(CH_3NHCH_2COOH)_3 \cdot CaCl_2$. $\nu_0$ versus $T$. $\nu_0$ is the phonon mode frequency. *Triangles*: measured by millimeter spectroscopy. *Brown circles*: measured from far-infrared spectra. *Gray circles*: measured from electric-field-induced Raman spectra. In the paraelectric phase ($T > \Theta_f$), $\nu_0$ decreases as the temperature decreases toward $\Theta_f$, that is, the phonon mode softens

ferroelectrics, as seen in Figs. 4.5-8 and 4.5-9. The dielectric constant at the Curie point at 1 GHz is not so small in displacive ferroelectrics, as seen in Fig. 4.5-10, where the critical slowing-down seems to be related to cluster boundary motion, and the dielectric constant at the Curie point at 1 GHz contains a contribution from the soft phonon as observed in millimeter spectroscopy (Fig. 4.5-11).

### 4.5.3.1 The 72 Families of Ferroelectrics

In the Landolt–Börnstein data collection, ferroelectric and antiferroelectric substances are classified into 72 families according to their chemical composition and their crystallographic structure. Some substances which are in fact neither ferroelectric nor antiferroelectric but which are important in relation to ferroelectricity or antiferroelectricity, for instance as an end material of a solid solution, are also included in these families as related substances. This subsection surveys these 72 families of ferroelectrics presented in Landolt–Börnstein Vol. III/36 (LB III/36). Nineteen of these families concern oxides [5.1, 2], 30 of them concern inorganic crystals other than oxides [5.3], and 23 of them concern organic crystals, liquid crystals, and polymers [5.4]. Table 4.5-1 lists these families and gives some information about each family. Substances classified in LB III/36 as miscellaneous crystals (outside the families) are not included.

In the following, remarks are made on 13 of the families, labeled by the letters a – m in Table 4.5-1. The corresponding family numbers are repeated in the headings.

*a. Perovskite-Type Family (Family Number 1).* The name of this group is derived from the mineral perovskite ($CaTiO_3$). The perovskite-type oxides are cubic (e.g. $CaTiO_3$ above 1260 °C and $BaTiO_3$ above 123 °C) or pseudocubic with various small lattice distortions (e.g. $CaTiO_3$ below 1260 °C and $BaTiO_3$ below 123 °C). Ceramics made from solid solutions of perovskite-type oxides are the most useful ferroelectrics in high-capacitance capacitors, piezoelectric elements, and infrared sensors. Ceramic thin films are useful in memory devices.

The pure compounds are divided into simple perovskite-type oxides and complex perovskite-type oxides. Simple perovskite-type oxides have the chemical formula $A^{1+}B^{5+}O_3$ or $A^{2+}B^{4+}O_3$. Complex perovskite-type oxides have chemical formulas expressed by $(A^{1+}_{1/2}A'^{3+}_{1/2})BO_3$, $A^{2+}(B^{2+}_{1/2}B''^{6+}_{1/2})O_3$, $A^{2+}(B^{3+}_{1/2}B'^{5+}_{1/2})O_3$, $A^{2+}(B^{2+}_{1/3}B'^{5+}_{2/3})O_3$, $A^{2+}(B^{3+}_{2/3}B''^{6+}_{1/3})O_3$, $A(B, B', B'')O_3$, or $(A, A')(B, B')O_3$. Among the complex perovskite-type oxides, most of the $Pb(B, B')O_3$-type oxides show a diffuse phase transition such that the transition point is smeared out over a relatively wide temperature range and exhibits a characteristic dielectric relaxation; these materials therefore are called "relaxors".

*b. $LiNbO_3$ Family (Family Number 2).* This family contains $LiNbO_3$ and $LiTaO_3$. Their chemical formulas are similar to those of the simple perovskite oxides, but their structures are trigonal, unlike the perovskite oxides.

*c. Stibiotantalite Family (Family Number 5).* The members of this family are isomorphous with the mineral stibiotantalite $Sb(Ta, Nb)O_4$. They have the common chemical formula $ABO_4$, where A stands for Sc, Sb, or Bi and B for Ta, Nb, or Sb.

*d. Tungsten Bronze-Type Family (Family Number 6).* The tungsten bronzes are a group of compounds having the chemical formula $M_xWO_3$, where M stands for an alkali metal, an alkaline earth metal, Ag, Tl, etc. (e.g. $Na_xWO_3$, where $x = 0.1–0.95$). Most of them exhibit a bronze-like luster. The tungsten bronze-type oxides consist of crystals isomorphous with tungsten bronze, including a simple type (e.g. $Pb_{1/2}NbO_3$) and a complex type (e.g. $Ba_2NaNb_5O_{15}$). Single crystals (not ceramics) are used for technological applications.

*e. Pyrochlore-Type Family (Family Number 7).* The members of this family are isomorphous with the mineral pyrochlore, $CaNaNb_2O_6F$. Most of the members have the general chemical formula $A_2B_2O_7$ or $A_2B_2O_6$ (anion-deficient compounds), where A stands for Cd, Pb, Bi, etc. and B for Nb, Ta, etc.

*f. $Sr_2Nb_2O_7$ Family (Family Number 8).* This family contains high-temperature ferroelectrics such as $Nb_2Ti_2O_7$ and $La_2Ti_2O_7$. Their Curie points are higher than 1500 °C.

*g. Layer-Structure Family (Family Number 9).* The common chemical formula of these oxides is $(Bi_2O_2)(A_{n-1}B_nO_{3n-1})$, where A stands for Ca, Sr, Ba, Pb, Bi, etc., B stands for Ti, Nb, Ta, Mo, W, etc., and $n$ varies from 1 to 9. The crystal structure is a repeated stacking of a layer of $(Bi_2O_2)^{2+}$ and a layer of $(A_{n-1}B_nO_{3n-1})^{2-}$, which can be approximately repre-

| Inorganic Crystals Oxides [5.1,2] | | Inorganic Crystals other than Oxides [5.3] | | Organic Crystals, Liquid Crystals, and Polymers [5.4] | |
|---|---|---|---|---|---|
| Family Nr. | Name | Family Nr. | Name | Family Nr. | Name |
| 1 | Perovskite-type family (90, 40; 11) a | 20 | SbSI family (11, 4; 1) | 50 | $SC(NH_2)_2$ family (1, 1; 1) |
| 2 | $LiNbO_3$ family (2, 2; 1) b | 21 | TlS family (1, 1; 0) | 51 | $CCl_3CONH_2$ family (1, 1; 0) |
| 3 | $YMnO_3$ family (6, 6; 0) | 22 | $TlInS_2$ family (5, 2; 0) | 52 | $Cu(HCOO)_2 \cdot 4H_2O$ family (1, 1; 0) |
| 4 | $SrTeO_3$ family (1, 1; 1) | 23 | $Ag_3AsS_3$ family (2, 1; 0) | 53 | $N(CH_3)_4HgCl_3$ family (6, 5; 0) |
| 5 | Stibiotantalite family (7, 6; 0) c | 24 | $Sn_2P_2S_6$ family (2, 2; 0) | 54 | $(CH_3NH_3)_2AlCl_5 \cdot 6H_2O$ family (3, 2; 0) |
| 6 | Tungsten bronze-type family (141, 21; 2) d | 25 | $KNiCl_3$ family (3, 3; 0) | 55 | $[(CH_3)_2NH_2]_2CoCl_4$ family (3, 2; 0) |
| 7 | Pyrochlore-type family (19, 2; 0) e | 26 | $BaMnF_4$ family (6, 6; 1) | 56 | $[(CH_3)_2NH_2]_3Sb_2Cl_9$ family (5, 5; 0) |
| 8 | $Sr_2Nb_2O_7$ family (6, 5; 1) f | 27 | HCl family (2, 2; 1) | 57 | $(CH_3NH_3)_5Bi_2Cl_{11}$ family (2, 2; 0) |
| 9 | Layer-structure family (36, 16; 0) g | 28 | $NaNO_2$ family (2, 2; 1) | 58 | DSP $(Ca_2Sr(CH_3CH_2COO)_6)$ family (3, 3; 1) |
| 10 | $BaAl_2O_4$-type family (1, 1; 0) | 29 | $CsCd(NO_2)_3$ family (2, 2; 0) | 59 | $(CH_2ClCOO)_2H \cdot NH_4$ family (2, 2; 0) |
| 11 | $LaBGeO_5$ family (1, 1; 0) | 30 | $KNO_3$ family (4, 3; 1) | 60 | TGS $((NH_2CH_2COOH)_3 \cdot H_2SO_4)$ family (3, 3; 1) |
| 12 | $LiNaGe_4O_9$ family (2, 2; 0) | 31 | $LiH_3(SeO_3)_2$ family (7, 5; 0) | 61 | $NH_2CH_2COOH \cdot AgNO_3$ family (1, 1; 0) |
| 13 | $Li_2Ge_7O_{15}$ family (1, 1; 1) | 32 | $KIO_3$ family (3, 3; 0) | 62 | $(NH_2CH_2COOH)_2 \cdot HNO_3$ family (1, 1; 0) |
| 14 | $Pb_5Ge_3O_{11}$ family (1,1; 0) | 33 | KDP $(KH_2PO_4)$ family (12, 12; 3) | 63 | $(NH_2CH_2COOH)_2 \cdot MnCl_2 \cdot 2H_2O$ family (1, 1; 0) |
| 15 | $5PbO \cdot 2P_2O_5$ family (1, 1; 0) (exact chemical formula unknown) | 34 | $PbHPO_4$ family (2, 2; 1) | 64 | $(CH_3NHCH_2COOH)_3 \cdot CaCl_2$ family (2, 2; 1) |
| 16 | $Ca_3(VO_4)_2$ family (2, 2; 0) | 35 | $KTiOPO_4$ family (23, 15; 0) | 65 | $(CH_3)_3NCH_2COO \cdot H_3PO_4$ family (3, 3; 0) |
| 17 | GMO $(Gd_2(MoO_4)_3)$ family (5, 5; 1) | 36 | $CsCoPO_4$ family (5, 5; 0) | 66 | $(CH_3)_3NCH_2COO \cdot CaCl_2 \cdot 2H_2O$ family (1, 1; 1) |
| 18 | Boracite-type family (28, 14; 1) h | 37 | $NaTh_2(PO_4)_3$ family (2, 2; 0) | 67 | Rochelle salt $(NaKC_4H_4O_6 \cdot 4H_2O)$ family (3, 2; 1) |
| 19 | $Rb_3MoO_3F_3$ family (4.4; 0) | 38 | $Te(OH)_6 \cdot 2NH_4H_2PO_4 \cdot (NH_4)_2HPO_4$ family (1, 1; 0) | 68 | $LiNH_4C_4H_4O_6 \cdot H_2O$ family (3, 2; 1) k |
| | | 39 | $(NH_4)_2SO_4$ family (22, 21; 1) | 69 | $C_5H_6NBF_4$ family (1, 1; 0) |
| | | 40 | $NH_4HSO_4$ family (9, 4; 1) | 70 | $3C_6H_4(OH)_2 \cdot CH_3OH$ family (1, 1; 0) |
| | | 41 | $NH_4LiSO_4$ family (9, 6; 1) | 71 | Liquid crystal family (97, 90; 2) l |
| | | 42 | $(NH_4)_3H(SO_4)_2$ family (2, 2; 1) | 72 | Polymer family (5, 5; 1) m |
| | | 43 | Langbeinite-type family (16, 5; 1) i | | |
| | | 44 | Lecontite $(NaNH_4SO_4 \cdot 2H_2O)$ family (2, 2; 0) | | |
| | | 45 | Alum family (16, 15; 0) j | | |
| | | 46 | GASH $(C(NH_2)_3Al(SO_4)_2 \cdot 6H_2O)$ family (9, 9; 0) | | |
| | | 47 | Colemanite $(Ca_2B_6O_{11} \cdot 5H_2O)$ family (1, 1; 0) | | |
| | | 48 | $K_4Fe(CN)_6 \cdot 3H_2O$ family (4, 4; 0) | | |
| | | 49 | $K_3BiCl_6 \cdot 2KCl \cdot KH_3F_4$ family (1, 1; 0) | | |

◀ **Table 4.5-1** The 72 families of ferroelectric materials. The number assigned to each family corresponds to the number used in LB III/36. The numbers in parentheses ($N_{Sub}$, $N_{F+A}$; $n$) after the family name serve the purpose of conveying some information about the size and importance of the family. The numbers indicate the following: $N_{Sub}$, the number of pure substances (ferroelectric, antiferroelectric, and related substances) which are treated as members of this family in LB III/36; $N_{F+A}$, the number of ferroelectric and antiferroelectric substances which are treated as members of this family in LB III/36; $n$, the number of representative substances from this family whose properties are surveyed in Sect. 4.5.4. For some of these families, additional remarks are needed: for instance, because the perovskite-type oxide family has many members and consists of several subfamilies; because the liquid crystal and polymer families have very specific properties compared with crystalline ferroelectrics; and because the traditional names of some families are apt to lead to misconceptions about their members. Such families are marked by letters a–m following the parentheses, and remarks on these families are given under the corresponding letter in the text in Sect. 4.5.3.1

sented by a chain of $n$ perovskite-type units of $ABO_3$ perpendicular to the layer.

*h. Boracite-Type Family (Family Number 18).* Boracite is a mineral, $Mg_3B_7O_{13}Cl$. The boracite-type family contains crystals isomorphous with the mineral, and has the chemical formula $M_3^{2+}B_7O_{13}X^{1-}$, where $M^{2+}$ stands for a divalent cation of Mg, Cr, Mn, Fe, Co, Ni, Cu, Zn, or Cd, and $X^{1-}$ stands for an anion of Cl, Br, or I.

*i. Langbeinite-Type Family (Family Number 43).* This family consists of crystals which are basically isomorphous with $K_2Mg_2(SO_4)_3$ (langbeinite), and have the common chemical formula $M_2^{1+}M_2^{2+}(SO_4)_3$, where $M^{1+}$ stands for a monovalent ion of K, Rb, Cs, Tl, or $NH_4$, and $M^{2+}$ stands for a divalent ion of Mg, Ca, Mn, Fe, Co, Ni, Zn, or Cd.

*j. Alum Family (Family Number 45).* The alums are compounds with the chemical formula $M^{1+}M^{3+}(SO_4)_2 \cdot 12\,H_2O$, where $M^{1+}$ is a monovalent cation and $M^{3+}$ is a trivalent cation. Ferroelectricity has been found for the monovalent cations of $NH_4$, $CH_3NH_3$, etc. and the trivalent cations of Al, V, Cr, Fe, In, and Ga. This family contains a few isomorphous selenates, $M^{1+}M^{3+}(SeO_4)_2 \cdot 12\,H_2O$.

*k. $LiNH_4C_4H_4O_6 \cdot H_2O$ Family (Family Number 68).* This family contains two ferroelectrics, $LiNH_4C_4H_4O_6 \cdot H_2O$ and $LiTlC_4H_4O_6 \cdot H_2O$. The polar directions of the two ferroelectrics are different from each other.

*l. Liquid Crystals (Family Number 71).* Ferroelectric and antiferroelectric liquid crystals are very useful as fast display elements.

A. *Ferroelectric liquid crystals (family number 71A).* Ferroelectric liquid crystals are defined as liquid crystals which exhibit a ferroelectric hysteresis loop like that shown in Fig. 4.5-1. Unlike ferroelectric crystals, however, ferroelectric liquid crystals generally have no spontaneous polarization in the bulk state. The chiral smectic phase denoted by Sm C* (e.g. of DOBAMBC) consists of many layers, each of which has a spontaneous polarization parallel to the layer plane, but the spontaneous polarization varies helically in different directions from layer to layer, so that the bulk has no spontaneous polarization as a whole. A sufficiently strong electric field causes a transition from the helical phase to a polar phase. Under an alternating electric field, the helical structure does not have a chance to build up owing to the delay in the transition. Instead, a direct transition occurs between the induced polar phases, resulting in a hysteresis loop of the type shown in Fig. 4.5-1. Accordingly, the hysteresis loop may be regarded as one in which the linear part of the antiferroelectric hysteresis shown in Fig. 4.5-2 is eliminated. It should be noted, however, that the helical structure disappears and two stable states with parallel and antiparallel polarizations appear, similar to the domain structure of a ferroelectric crystal, when a liquid crystal is put in a cell which is thinner than the helical pitch [5.52].

B. *Antiferroelectric liquid crystals (family number 71B).* The phase denoted by Sm $C_A^*$ (e.g. of MHPOBC) exhibits a double hysteresis of the type shown in Fig. 4.5-2, and a liquid crystal showing this phase is called antiferroelectric [5.53].

*m. Polymers (Family Number 72).* Polyvinylidene fluoride $(CH_2CF_2)_n$ and its copolymers with trifluoroethylene $(CHFCF_2)_n$, etc. are ferroelectric. Ferroelectric polymers are usually prepared as thin films in which crystalline and amorphous regions coexist. The ferroelectric hysteresis loop originates from reversal of the

spontaneous polarization in the crystalline regions. The electric-field distribution is expected to be complex in the thin film because of the interposition of the amorphous regions. A ferroelectric hysteresis loop can be observed when the ratio of the volume of the crystalline regions to the total volume is relatively large (e.g. more than 50%). The coercive field is larger (e.g. $> 50\,\mathrm{MV/m}$) than that of solid ferroelectrics (usually a few MV/m or smaller). The ferroelectric properties depend sensitively upon the details of sample preparation, for example the use of melt quenching or melt extrusion, the annealing temperature, or the details of the poling procedure. Polymer ferroelectrics are useful for soft transducers.

## 4.5.4 Physical Properties of 43 Representative Ferroelectrics

This section surveys the characteristic properties of 43 representative ferroelectrics with the aim of demonstrating the wide variety in the behavior of ferroelectrics. The 43 representative ferroelectrics are selected from 29 of the above-mentioned families. The presentation is mainly graphical. Most of the figures are reproduced from LB III/36, where the relevant references can be found. Table 4.5-2 summarizes the meaning of the symbols frequently used in the figure captions and indicates the units in which the data are given.

To facilitate to get more information on each representative substance in LB II/36, the number assigned to the substance in LB III/36 is given in parenthesis following its chemical formula, e.g., $KNbO_3$ (LB number 1A-2).

### 4.5.4.1 Inorganic Crystals Oxides [5.1, 2]

#### Perovskite-Type Family

*$KNbO_3$ (LB Number 1A-2).* This crystal is ferroelectric below about 418 °C. Further phase transitions take place at about 225 °C and about −10 °C, retaining ferroelectric activity. The crystal has large electromechanical coupling constants and is useful in lead-free piezoelectric elements and SAW (surface acoustic wave) filters in communications technology (Fig. 4.5-13,4.5-14).

**Table 4.5-2** Symbols and units frequently used in the figure captions

| | |
|---|---|
| $\boldsymbol{a}, \boldsymbol{b}, \boldsymbol{c}$ | unit cell vector, units Å |
| $\boldsymbol{a}^*, \boldsymbol{b}^*, \boldsymbol{c}^*$ | unit cell vector in reciprocal space, units $Å^{-1}$ |
| $E_c$ | coercive field, units V/m |
| $f$ | frequency, units $Hz = 1/s$ |
| $P_s$ | spontaneous polarization, units $C/m^2$ |
| $T$ | temperature, units K or °C |
| $\kappa$ | dielectric constant (or relative permittivity) $= \varepsilon/\varepsilon_0$, where $\varepsilon$ is the permittivity of the material and $\varepsilon_0$ is the permittivity of a vacuum. $\kappa$ is a dimensionless number |
| $\kappa', \kappa''$ | real and imaginary parts of the complex dielectric constant $\kappa^* = \kappa' + i\kappa''$. $\kappa'$ and $\kappa''$ are both dimensionless numbers |
| $\kappa_{ij}$ | component of dielectric-constant tensor; dimensionless numbers |
| $\kappa_a, \kappa_b, \kappa_c$ | $\kappa$ measured along $a$, $b$, $c$ axes; dimensionless numbers |
| $\kappa_{(hkl)}$ | $\kappa$ measured perpendicular to the $(hkl)$ plane; dimensionless number |
| $\kappa_{[uvw]}$ | $\kappa$ measured parallel to the $[uvw]$ direction; dimensionless number |
| $\kappa^{\mathbf{T}}$ | $\kappa$ of free crystal, i. e. $\kappa$ measured at constant stress $\mathbf{T}$; dimensionless number |
| $\kappa^{\mathbf{S}}$ | $\kappa$ of clamped crystal, i. e. $\kappa$ measured at constant strain $\mathbf{S}$; dimensionless number |
| $\Theta_f$ | ferroelectric transition temperature, units K or °C |

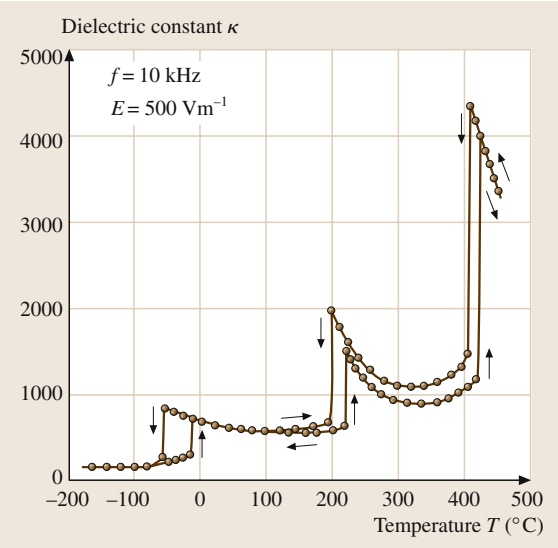


**Fig. 4.5-12** $KNbO_3$. Dielectric constant $\kappa$ versus temperature $T$

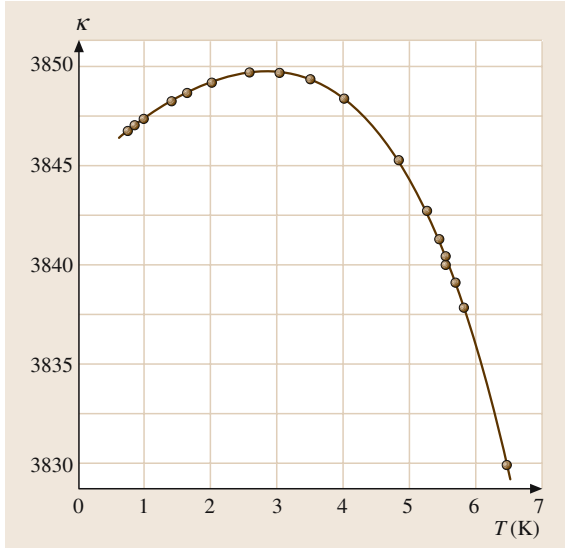


**Fig. 4.5-14** $KTaO_3$. Real part of dielectric constant $\kappa'$ versus $T$. $f = 1$ kHz

*$KTaO_3$ (LB Number 1A-5).* $KTaO_3$ is cubic at all temperatures, and its dielectric constant becomes very large at low temperatures without a phase transition (Fig. 4.5-14). It is generally believed that this behavior is related to the zero-point lattice vibrations. Replacement of Nb by Ta generally lowers drastically the ferroelectric Curie temperature , as seen by comparing Fig. 4.5-14 with Fig. 4.5-12. (This effect is well demonstrated later in Figs. 4.5-39 and 4.5-40).

*$SrTiO_3$ (LB Number 1A-8).* This crystal is cubic at room temperature and slightly tetragonal below 105 K. The phase transition at 105 K is caused by softening of the lattice vibration mode at the (1/2, 1/2, 1/2) Brillouin zone corner (Fig. 4.5-15) without an appreciable dielectric anomaly. At very low temperatures, the dielectric constants become extraordinarily high without a phase transition (Fig. 4.5-16), owing to softening of the optical phonon at the origin of the Brillouin zone (Fig. 4.5-17). It is generally believed that the absence of a low-temperature transition is related to zero-point lat-

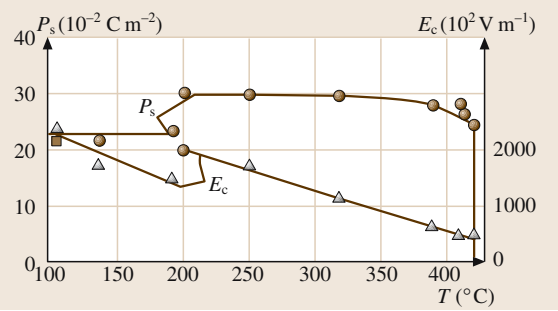


**Fig. 4.5-13** $KNbO_3$. $P_s$ and $E_c$ versus $T$. Measurements were made by applying the electric field parallel to the pseudocubic [100] direction

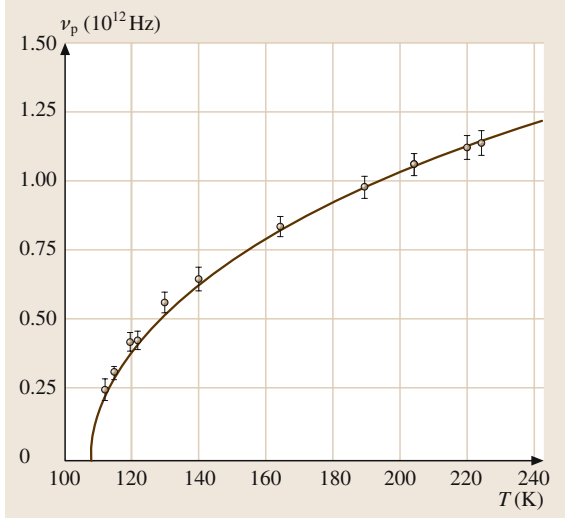


**Fig. 4.5-15** $SrTiO_3$. $\nu_P$ versus $T$. $\nu_P$ is the frequency of the $R_{25}$ ($\Gamma_{25}$) optical phonon

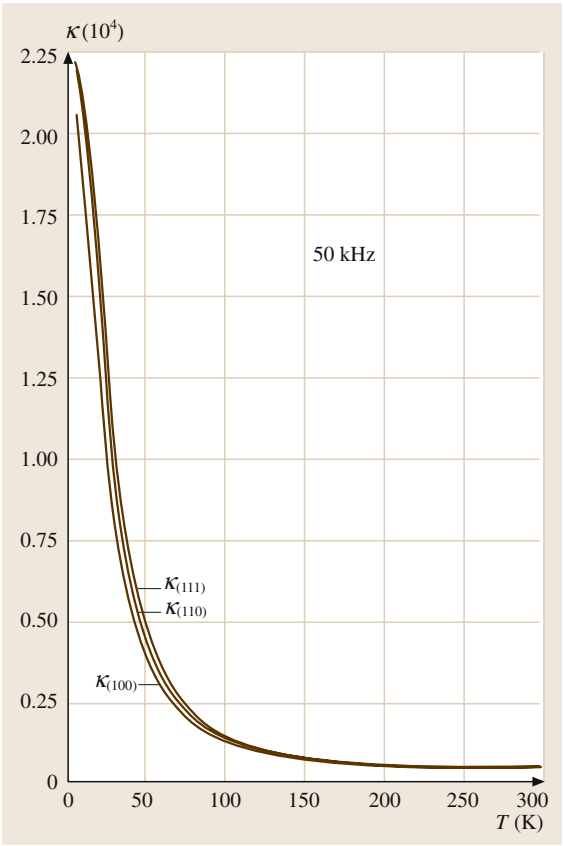


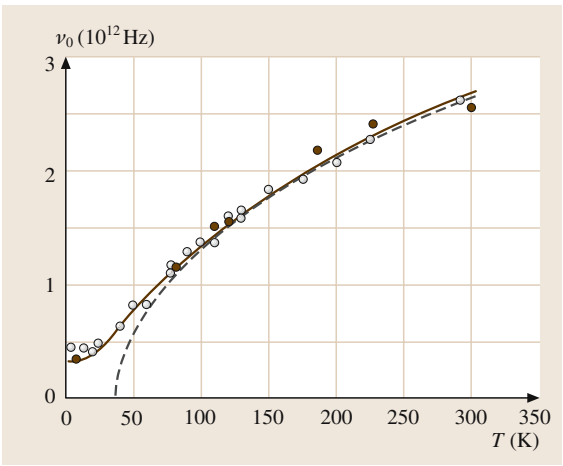


**Fig. 4.5-17** $SrTiO_3$. $\nu_0$ versus $T$. $\nu_0$ is the frequency of the soft phonon at $q = 0$. *Open circles*: inelastic neutron scattering. *Filled circles*: Raman scattering. The *solid curve* is $194.4\,\kappa^{1/2}$ and the *dashed curve* is $0.677(T - T_0)^{1/2}$, with $T_0 = 38$ K

**Fig. 4.5-16** $SrTiO_3$. $\kappa_{(111)}$, $\kappa_{(110)}$, and $\kappa_{(100)}$ versus $T$ at $f = 50$ kHz. $\kappa_{(111)}$, $\kappa_{(110)}$, and $\kappa_{(100)}$ are slightly different from each other in the tetragonal phase

tice vibrations as in $KTaO_3$. Solid solutions of $SrTiO_3$ are useful as ceramic thin films in memory devices.

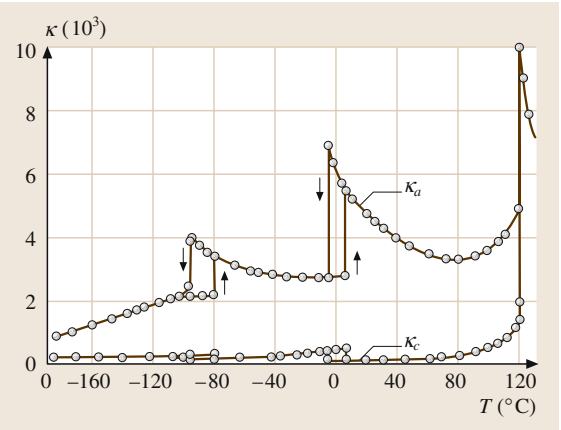


**Fig. 4.5-18** $BaTiO_3$. $\kappa_a$ and $\kappa_b$ versus $T$. $\kappa_a$ and $\kappa_b$ are the values of $\kappa$ along the $a$ and $b$ axes, respectively, of the tetragonal phase

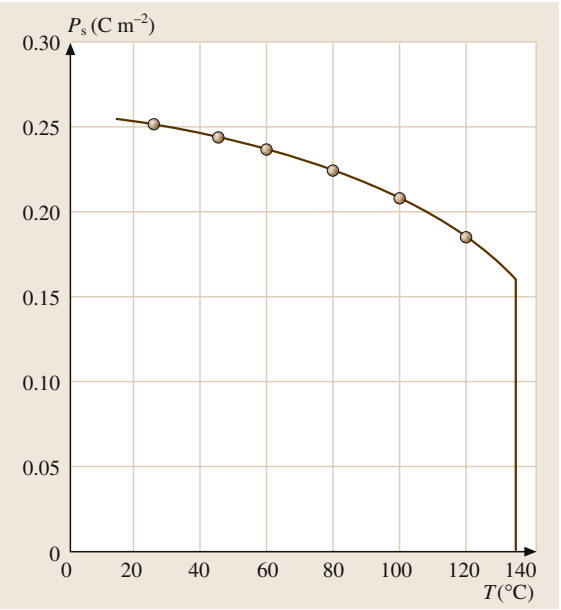


**Fig. 4.5-19** $BaTiO_3$. $P_s$ versus $T$ in the tetragonal phase. $P_s$ is parallel to the $c$ axis

*$BaTiO_3$ (LB Number 1A-10).* $BaTiO_3$ is the most extensively studied ferroelectric crystal. It is ferroelectric below about 123 °C, where the crystal symmetry changes from cubic to tetragonal. Further phase transitions take place from tetragonal to orthorhombic at about 5 °C and to rhombohedral at about −90 °C (Figs. 4.5-18 to 4.5-20). It is believed that the ferroelectric transition

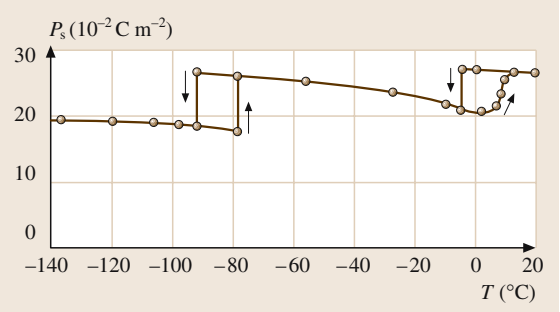


**Fig. 4.5-20** $BaTiO_3$. $P_{s[001]}$ versus $T$ below 20 °C, where $P_{s[001]}$ is the component of the spontaneous polarization parallel to the $c$ axis in the tetragonal phase

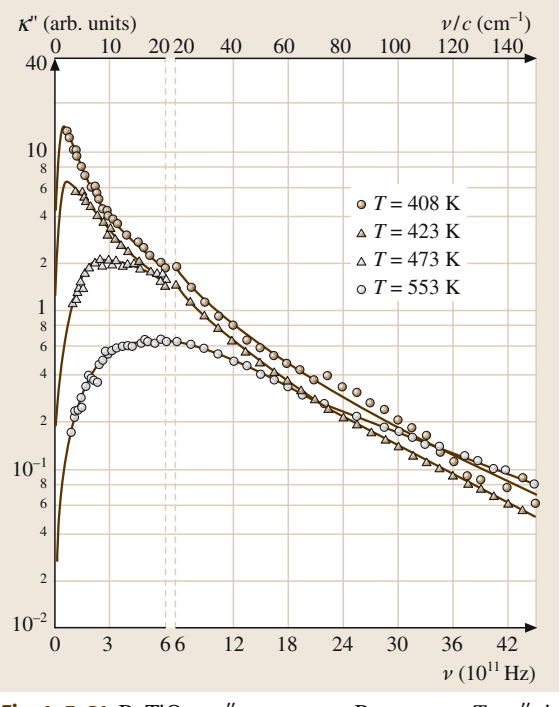


**Fig. 4.5-21** $BaTiO_3$. $\kappa''$ versus $\nu$. Parameter: $T$. $\kappa''$ is the imaginary part of $\kappa$ obtained from the hyper-Raman spectrum. *Curves*: calculations based upon the classical dispersion oscillator model. $c$: light velocity

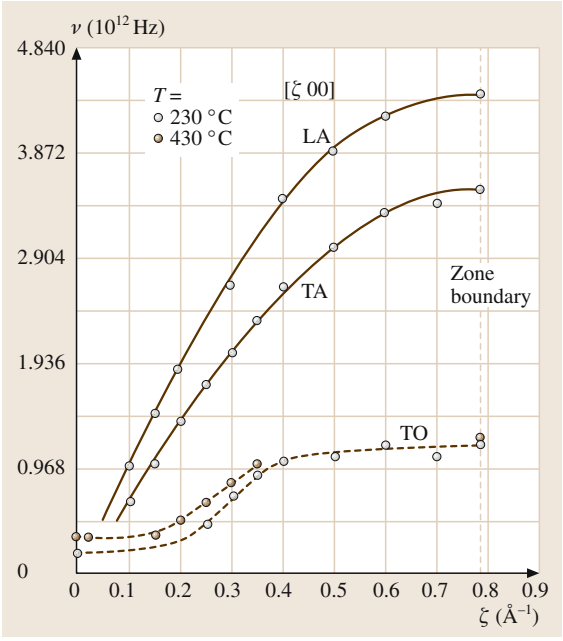


**Fig. 4.5-22** $BaTiO_3$. Phonon dispersion relation determined by neutron scattering along the [100] direction in the cubic phase. $\nu$ is the phonon frequency. LA, longitudinal acoustic branch; TA, transverse acoustic branch; TO, transverse optical branch. The frequency of the TO branch is lower (softer) at 230 °C than at 430 °C, indicating mode softening

is caused by softening of an optical mode at the center of the Brillouin zone. Hyper-Raman scattering studies support this model (Figs. 4.5-21 and 4.5-22). The results of neutron scattering studies favor this model (Fig. 4.5-23), but the measurement was not easy owing to the intense elastic peaks (Fig. 4.5-24a). These elastic peaks indicate marked cluster formation in the vicinity of the Curie point. As discussed in Sect. 4.5.3, there seem to be two components contributing to the dielectric constant measured in the vicinity of the Curie point: a component due to the soft mode and another one due to the motion of the cluster boundaries. Presumably the two components suggested by infrared and hyper-Raman scattering data correspond to these two components. For theoretical studies of the phase transitions, readers should refer to [5.7]. Solid solutions of $BaTiO_3$ are the most useful ferroelectrics in ceramic condensers and as thin films in memory devices.

When the temperature is raised above 1460 °C, cubic $BaTiO_3$ performs another phase transition to a hexagonal structure. This hexagonal phase can be quenched

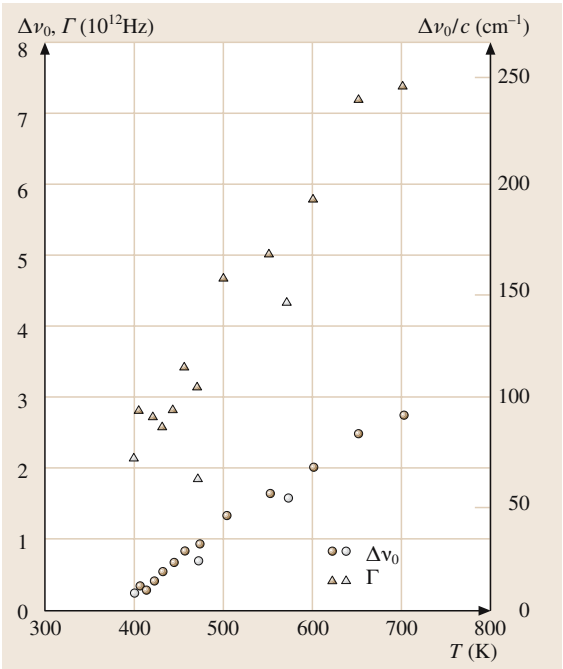


**Fig. 4.5-23** $BaTiO_3$. $\Delta\nu_0$ and $\Gamma$ versus $T$, obtained from hyper-Raman scattering in the cubic phase. $\Delta\nu_0$ and $\Gamma$ are the optical mode frequency and damping constant, respectively. The different symbols (*brown* and *gray*) show results from different authors. $\Delta\nu_0$ decreases as the temperature decreases to the Curie point, showing the presence of mode softening. $c$: ligth velocity

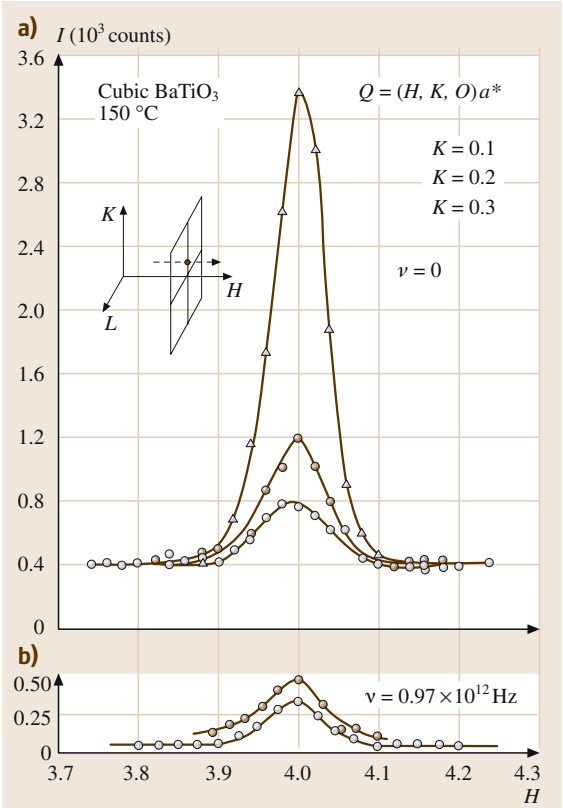


**Fig. 4.5-24a,b** $BaTiO_3$. Triple-axis neutron spectrometer scans at constant frequency across the sheet of diffuse scattering at 150 °C. The path of the scans is shown in the *inset*. **(a)** shows the elastic scan ($\nu = 0$), where the high background level is due to nuclear incoherent scattering. **(b)** Ineleastic scan ($\nu = 0.97 \times 10^{12}$ Hz)

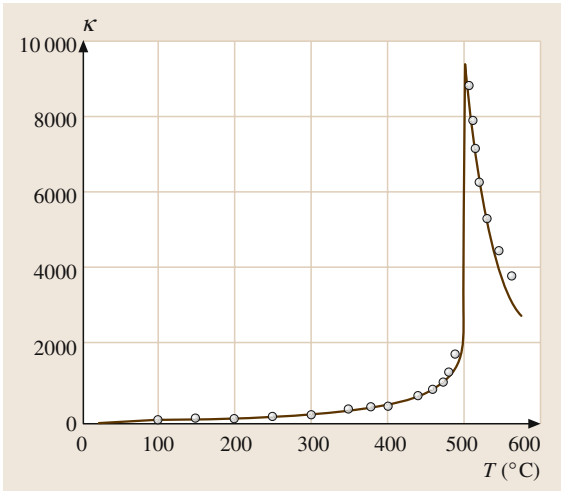


**Fig. 4.5-25** $PbTiO_3$. $\kappa$ versus $T$

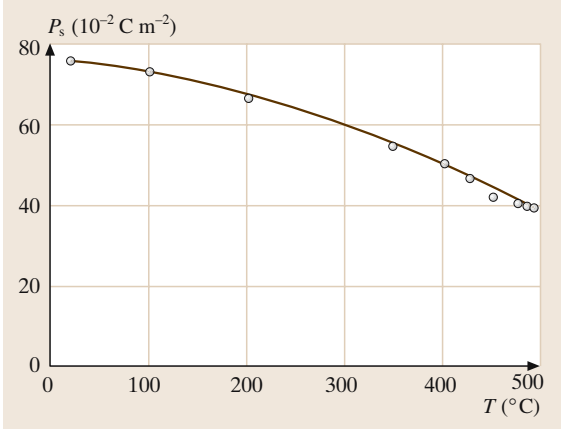


**Fig. 4.5-26** $PbTiO_3$. $P_s$ versus $T$

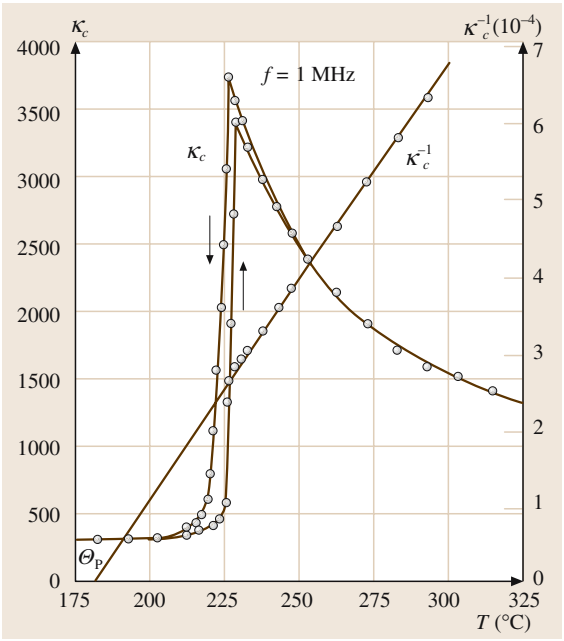


**Fig. 4.5-27** $PbZrO_3$ (single crystal). $\kappa_c$ and $\kappa_c^{-1}$ versus $T$

to room temperature by relatively rapid cooling. This hexagonal $BaTiO_3$ also shows ferroelectric activity below −199 °C.

*$PbTiO_3$ (LB Number 1A-11).* This crystal is ferroelectric below about 500 °C (Figs. 4.5-25, 4.5-26). The spontaneous polarization is large (Fig. 4.5-26) and thus the pyroelectric coefficient is large, which makes the crystal useful in infrared sensors. Solid solutions with other perovskite-type oxides provide good dielectric and piezoelectric materials (see PZT, PLZT, and $(PbTiO_3)_x(Pb(Sc_{1/2}Nb_{1/2})O_3)_{1-x}$ below).

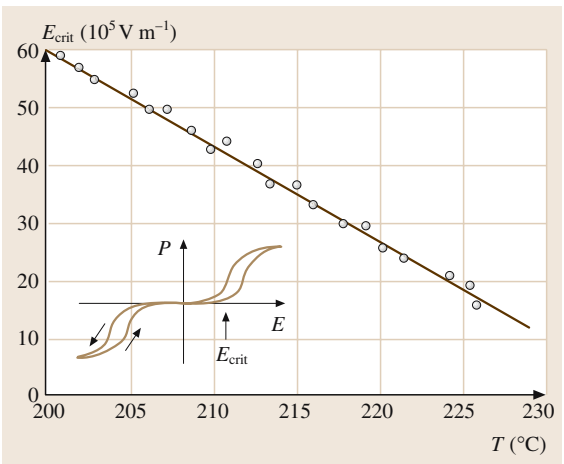


**Fig. 4.5-28** $PbZrO_3$. $E_{crit}$ versus $T$. $E_{crit}$ is the critical field of the antiferroelectric hysteresis loop

*$PbZrO_3$ (LB Number 1A-15).* This crystal is antiferroelectric below about 230 °C (Fig. 4.5-27), exhibiting a typical antiferroelectric hysteresis loop (Fig. 4.5-28). Solid solutions of this substance are very important in technological applications (see PZT and PLZT below).

*$Pb(Mg_{1/3}Nb_{2/3})O_3$ (LB Number 1B-d4).* This crystal exhibits a broad ferroelectric phase transition with an average transition temperature of −8 °C determined by the maximum of the low-frequency dielectric constant. A marked frequency dispersion of the

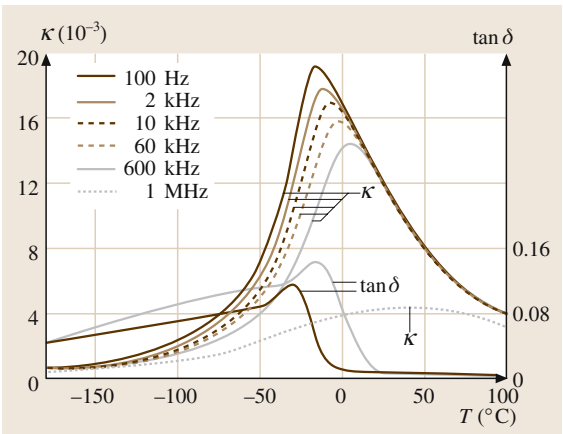


**Fig. 4.5-29** $Pb(Mg_{1/3}Nb_{2/3})O_3$ (ceramic). $\kappa$ and tan $\delta$ versus $T$. Parameter: $f$

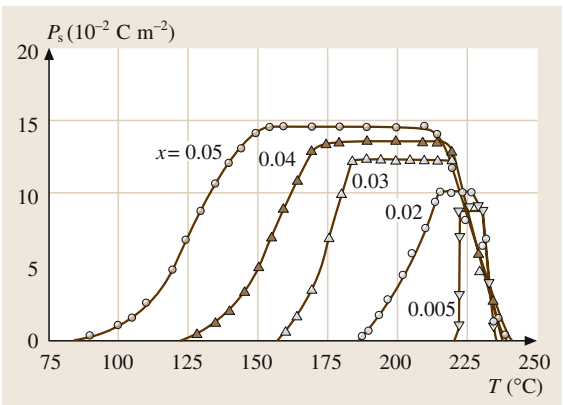


**Fig. 4.5-30** $Pb(Zr_{1-x}Ti_x)O_3$ (ceramic). $P_s$ versus $T$. Parameter: $x$

dielectric constant occurs around the transition temperature. These is a typical behavior of a relaxor (Fig. 4.5-29).

*$Pb(Zr,Ti)O_3$ (LB Number 1C-a62).* $PbZrO_3$ is antiferroelectric, as described above, while a small addition of $PbTiO_3$ induces a ferroelectric phase (Fig. 4.5-30).

*PZT (LB Number 1C-a63).* Solid solutions $Pb(Ti_{1-x}Zr_x)O_3$ with $x = 0.5–0.6$ are commonly called PZT. They have very large electromechanical coupling constants and are widely utilized as piezoelectric elements. Thin ceramic films are useful in memory devices (Fig. 4.5-31).

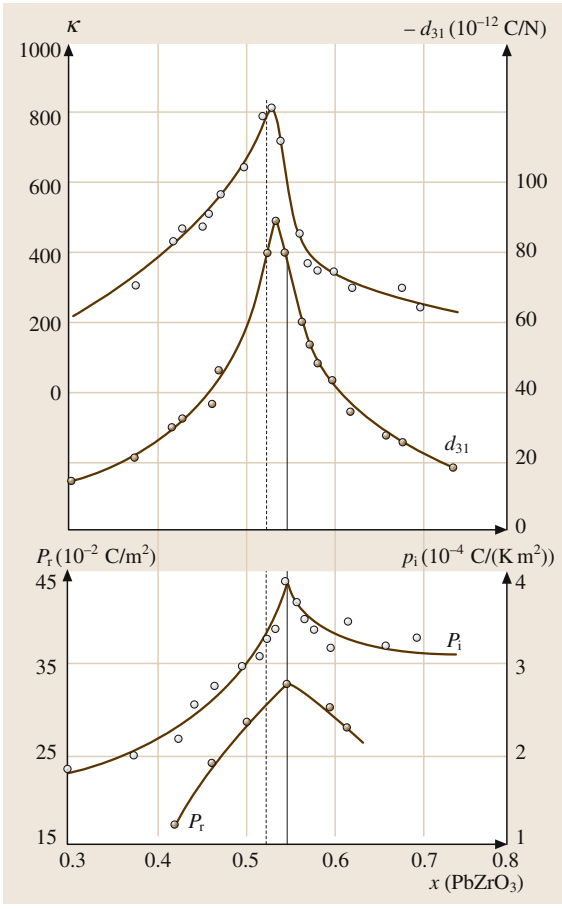


**Fig. 4.5-31** $Pb(Ti_{1-x}Zr_x)O_3$ 2% $Zr(Mn_{1/3}Bi_{2/3})O_3$ as an additive (ceramic). $\kappa$, $p_i$, $d_{31}$, and $P_r$ versus $x$. $p_i$ is the pyroelectric coefficient, $d_{31}$ is the piezoelectric strain constant, and $P_r$ is the remanent polarization (see Fig. 4.5-1)

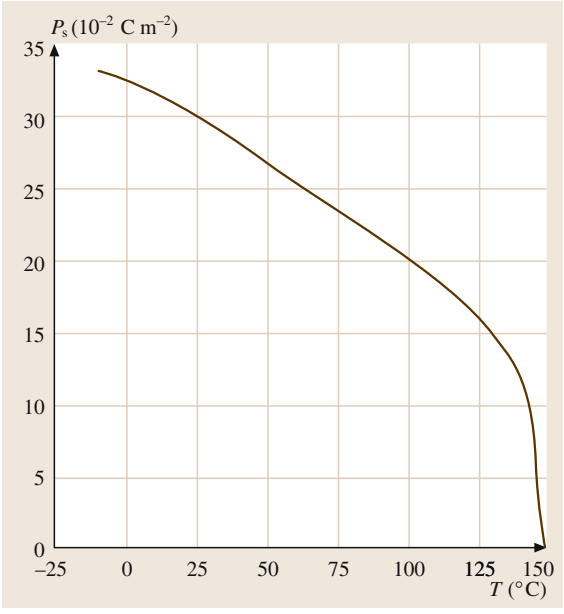


**Fig. 4.5-32** $(Pb_{0.92}La_{0.08})(Zr_{0.40}Ti_{0.60})_{0.98}O_3$ (PLZT). $P_s$ versus $T$

*PLZT (LB Number 1C-c66).* The acronym PLZT means La-modified PZT. Hot-pressed ceramic PLZT is transparent and useful for optical switches and similar devices (Fig. 4.5-32).

*$(PbTiO_3)_x(Pb(Sc_{1/2}Nb_{1/2})O_3)_{1-x}$ (LB Number 1C-b34).* These solid solutions have very large electromechan-

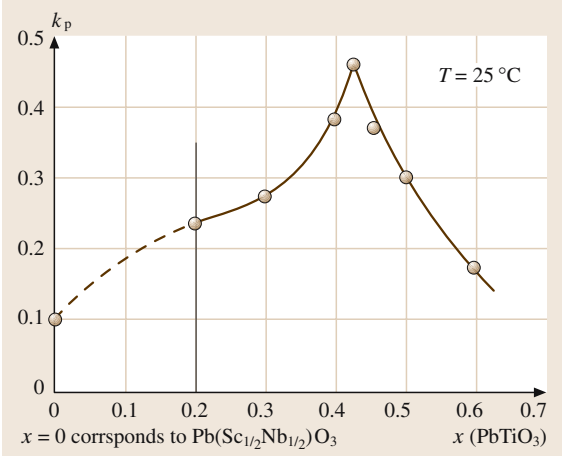


**Fig. 4.5-33** $(PbTiO_3)_x(Pb(Sc_{1/2}Nb_{1/2})O_3)_{1-x}$ (ceramic). $k_p$ versus $x$. $k_p$ is the planar electromechanical coupling factor

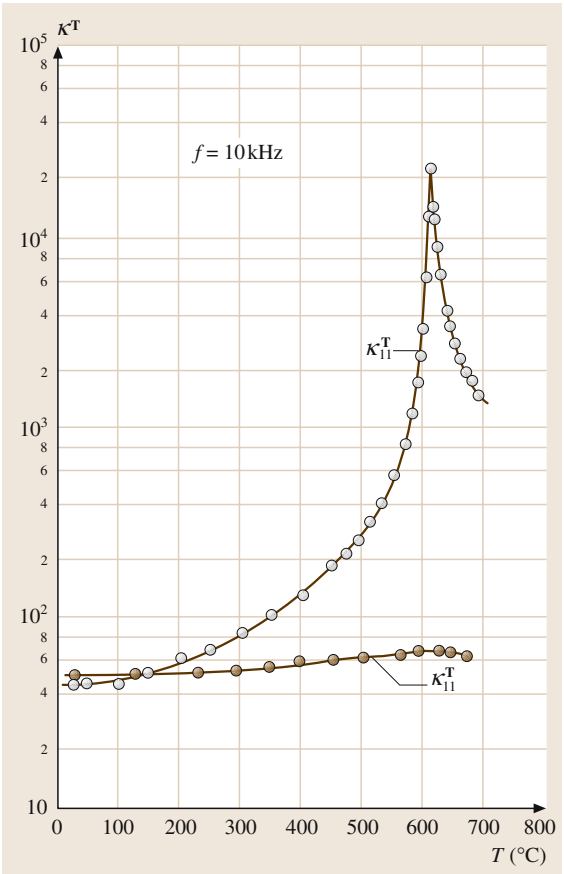


**Fig. 4.5-34** $LiTaO_3$. $\kappa_{11}^{\mathbf{T}}$ and $\kappa_{33}^{\mathbf{T}}$ versus $T$. $f = 10\,\text{kHz}$

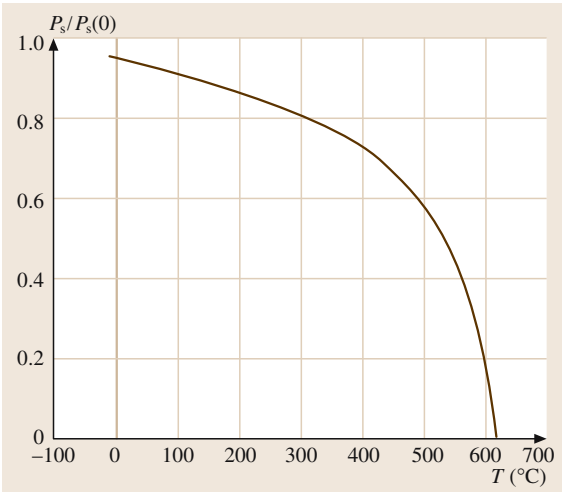


**Fig. 4.5-35** $LiTaO_3$. $P_s/P_s(0)$ versus $T$. $P_s(0)$ is the value of $P_s$ at 0 K (about $0.5\,\text{C m}^{-2}$)

ical coupling factors, and are utilized for piezoelectric actuators and similar devices (Fig. 4.5-33).

### $LiNbO_3$ Family

*$LiTaO_3$ (LB Number 2A-2).* This crystal is ferroelectric below 620 °C. The coercive field is large. The crystal is useful for piezoelectric elements, for linear and nonlinear optical elements, and for SAW filters in communications technology (Figs. 4.5-34 and 4.5-35).

### $SrTeO_3$ Family

*$SrTeO_3$ (LB Number 4A-1).* This crystal is ferroelectric between 312 and 485 °C (Figs. 4.5-36 and 4.5-37).

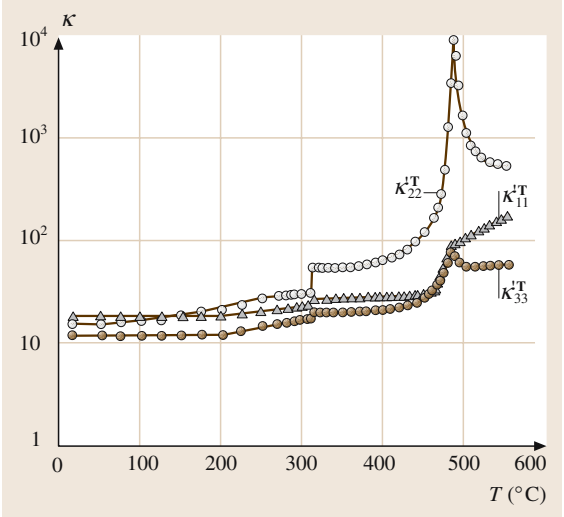


**Fig. 4.5-36** $SrTeO_3$. $\kappa$ versus $T$. $f = 10\,\text{kHz}$

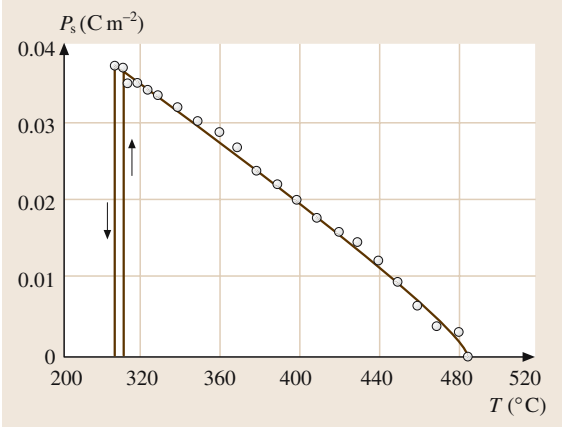


**Fig. 4.5-37** $SrTeO_3$. $P_s$ versus $T$

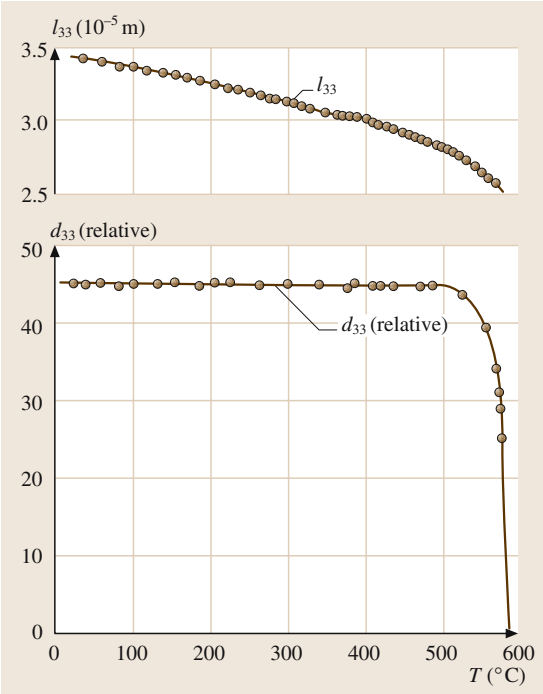


**Fig. 4.5-38** $Ba_2NaNb_5O_{15}$. $d_{33}$ and $l_{33}$ versus $T$. $d_{33}$ is the nonlinear optical susceptibility (relative value), and $l_{33}$ is the coherence length

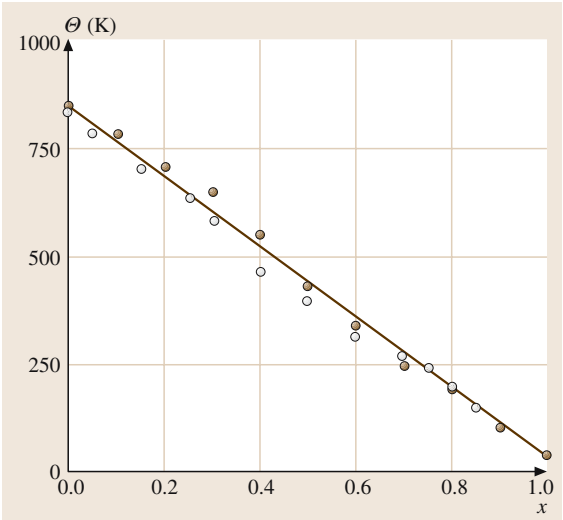


**Fig. 4.5-39** $Ba_2Na(Nb_{1-x}Ta_x)_5O_{15}$. Ferroelectric transition temperature $\Theta$ versus $x$. *Brown circles* and *gray circles* represent data measured by different authors

### Tungsten Bronze-Type Family

*$Ba_2NaNb_5O_{15}$ (BNN) (LB Number 6B-a7).* This crystal is ferroelectric below about 580 °C. The crystal structure is modulated below 300 °C. This material is utilized for optical second-harmonic generation and in optical parametric oscillators (Fig. 4.5-38).

*$Ba_2Na(Nb_{1-x}Ta_x)_5O_{15}$ (BNNT) (LB Number 6C-b30).* The transition temperature varies over a wide temperature range as $x$ varies from 0 to 1.0 (Fig. 4.5-39).

### $Sr_2Nb_2O_7$ Family

*$Sr_2(Nb_{1-x}Ta_x)_2O_7$ (LB Number 8B-6).* These solid solutions can be made over the whole range of $x = 0-1.0$, and the Curie point varies over a wide temperature range from 1342 °C to −107 °C (Fig. 4.5-40). The solid solutions are very useful as high-temperature dielectric materials, especially because they do not contain Pb, which is volatile at high temperatures.

### $Li_2Ge_7O_{15}$ Family

*$Li_2Ge_7O_{15}$ (LB Number 13A-1).* This crystal is ferroelectric below 283.5 K. The sign of the spontaneous polarization is reversed around 130 K (Figs. 4.5-41 and 4.5-42).

### GMO ($Gd_2(MoO_4)_3$) Family

*$Gd_2(MoO_4)_3$ (GMO) (LB Number 17A-3).* Three crystal structures of GMO are known, $\alpha$, $\beta$, and $\gamma$. The $\beta$ structure is stable above 850 °C but can be obtained at room temperature as a metastable state by

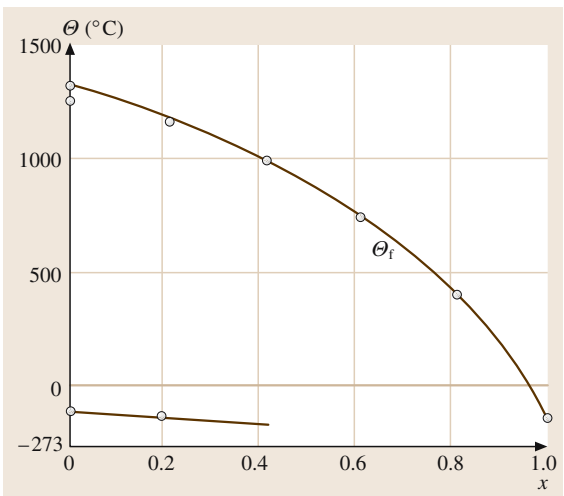


**Fig. 4.5-40** $Sr_2(Nb_{1-x}Ta_x)_2O_7$. Ferroelectric transition temperature $\Theta_f$ versus $x$. The *lower curve* shows another phase transition temperature

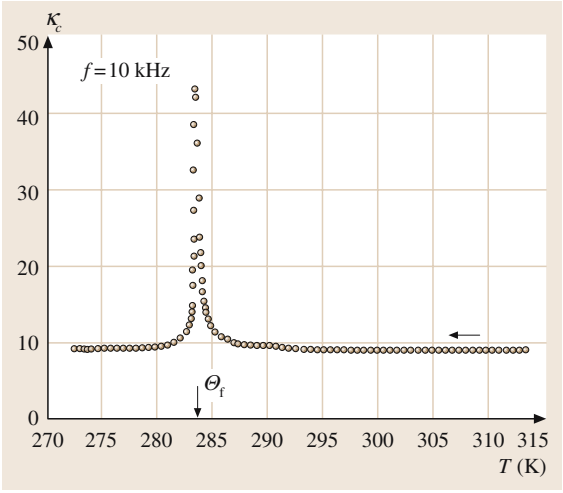


**Fig. 4.5-41** $Li_2Ge_7O_{15}$. $\kappa_c$ versus $T$. $f = 10$ kHz

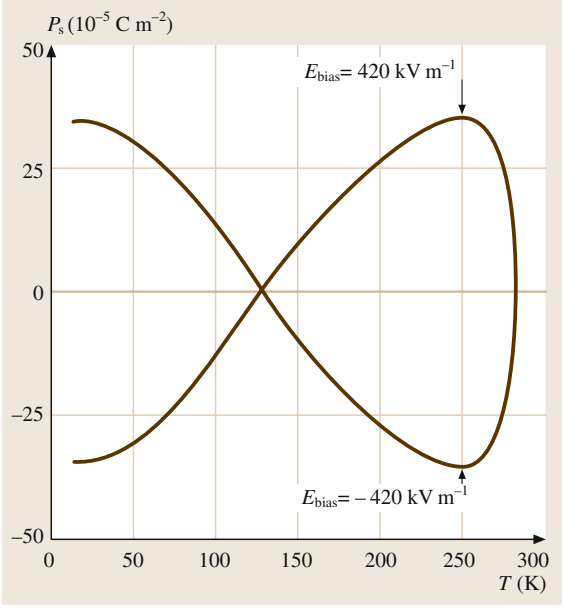


**Fig. 4.5-42** $Li_2Ge_7O_{15}$. $P_s$ versus $T$. $P_s$ was determined by pyroelectric-charge measurement

rapid cooling. Ferroelectric activity takes place in this metastable $\beta$-GMO below 159 °C. The phase transition is the indirect type $III_{op}$ discussed in Sect. 4.5.3. The dielectric constant of the clamped crystal ($\kappa_c^S$ in Fig. 4.5-6) shows no anomaly at the transition point. The ferroelectric phase results from a phonon instability at the (1/2, 1/2, 0) Brillouin zone corner of the parent tetragonal phase. Anharmonic coupling to the

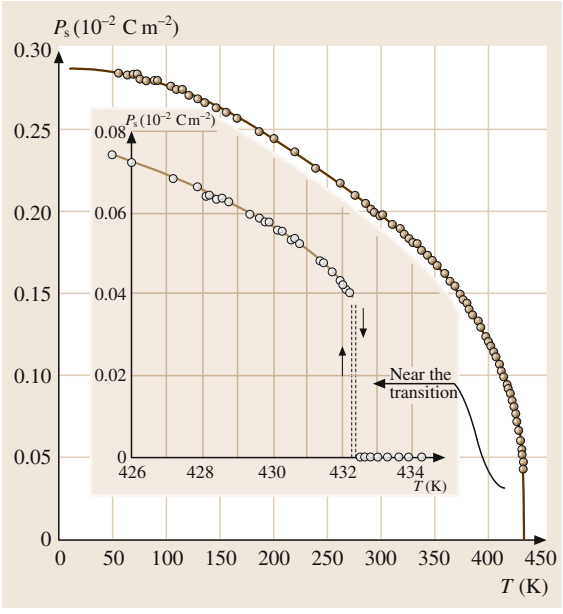


**Fig. 4.5-43** $Gd_2(MoO_4)_3$. $P_s$ versus $T$

resulting antiparallel displacements produces a spontaneous strain, which in turn causes a spontaneous polarization through the normal piezoelectric coupling (Fig. 4.5-43).

### Boracite-Type Family

*$Ni_3B_7O_{13}I$ (LB Number 18A-23).* This crystal is ferroelectric and ferromagnetic below about 60 K (Figs. 4.5-44, 5-45, 5-46): a rare example where both ferroelectric and ferromagnetic spontaneous polarizations

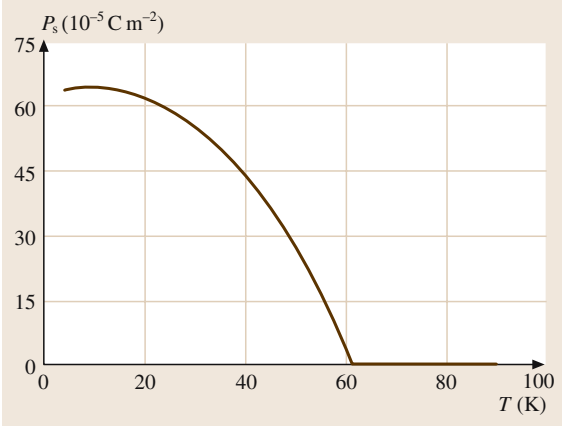


**Fig. 4.5-44** $Ni_3B_7O_{13}I$. $P_s$ versus $T$. $P_s$ was measured with the specimen parallel to the cubic (001) plane

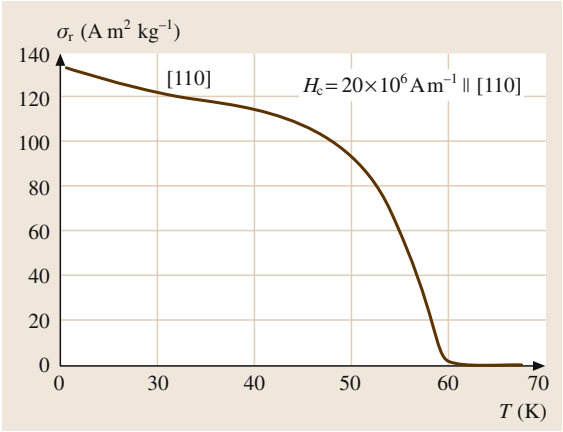


**Fig. 4.5-45** $Ni_3B_7O_{13}I$. $\sigma_r$ versus $T$. $\sigma_r$ is the remanent magnetization. The sample was cooled down to 4.2 K in a magnetic field of $1.6\times10^6$ A/m parallel to [100] prior to the measurement

take place simultaneously. There is a magnetoelectric effect, where the magnetic polarization is reversed by reversal of the electric polarization and vice versa.

### 4.5.4.2 Inorganic Crystals Other Than Oxides [5.3]

#### SbSI Family

*SbSI (LB Number 20A-7).* SbSI is ferroelectric below 20 °C. The phase transition is of the displacive type, a relatively rare characteristic in nonoxide materials. The crystal is photoconductive (Figs. 4.5-47 and 4.5-48).

#### $BaMnF_4$ Family

*$BaMnF_4$ (LB Number 26A-2).* This crystal exhibits a dielectric anomaly at about 242 K (Fig. 4.5-49). The coercive field is very large. The crystal is antiferromagnetic below 25 K (Fig. 4.5-50). The dielectric constant varies depending upon the magnetic field at low temperatures (Fig. 4.5-51).

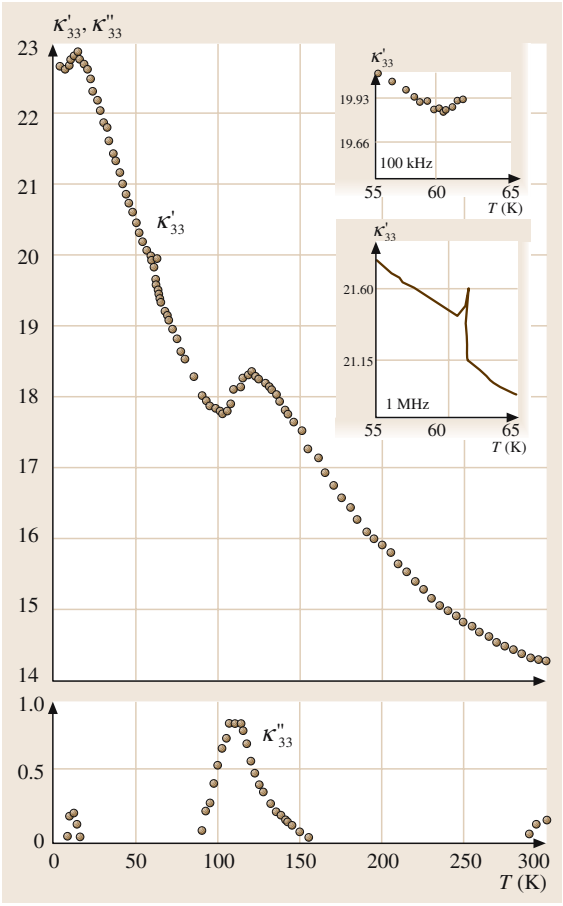


**Fig. 4.5-46** $Ni_3B_7O_{13}I$. $\kappa'_{33}$ and $\kappa''_{33}$ versus $T$. $f =$ 100 kHz. The *insets* show details of $\kappa'_{33}$ versus $T$ at 100 kHz and 1 MHz around $\Theta_f$

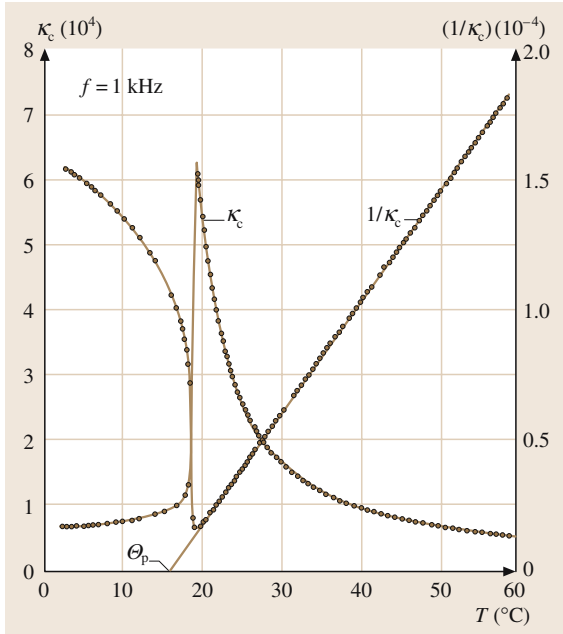


**Fig. 4.5-47** SbSI. $\kappa_c$ and $1/\kappa_c$ versus $T$

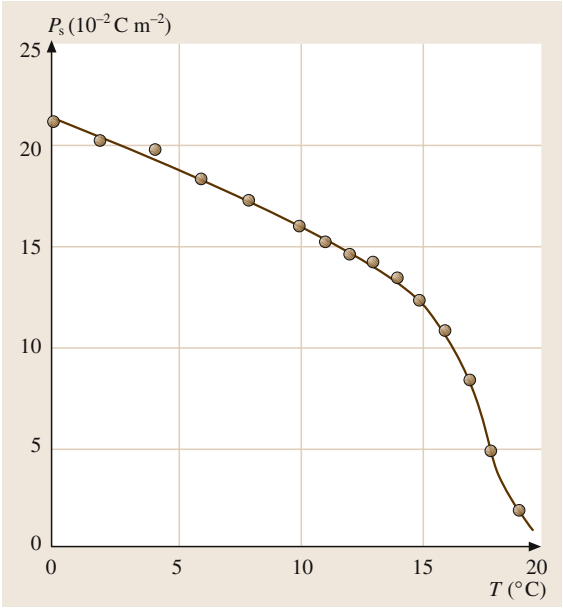


**Fig. 4.5-48** SbSI. $P_s$ versus $T$

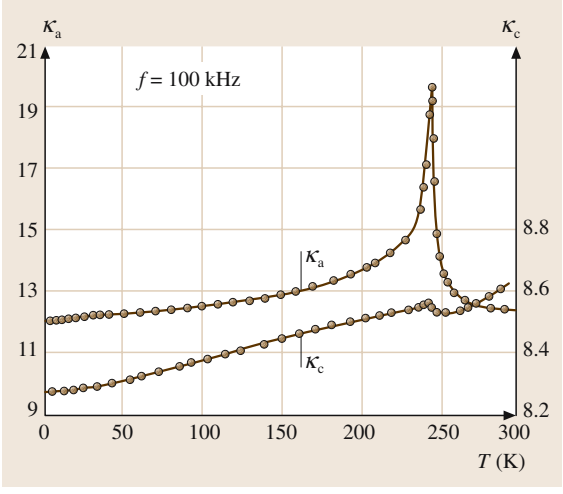


**Fig. 4.5-49** $BaMnF_4$. $\kappa_a$ and $\kappa_c$ versus $T$

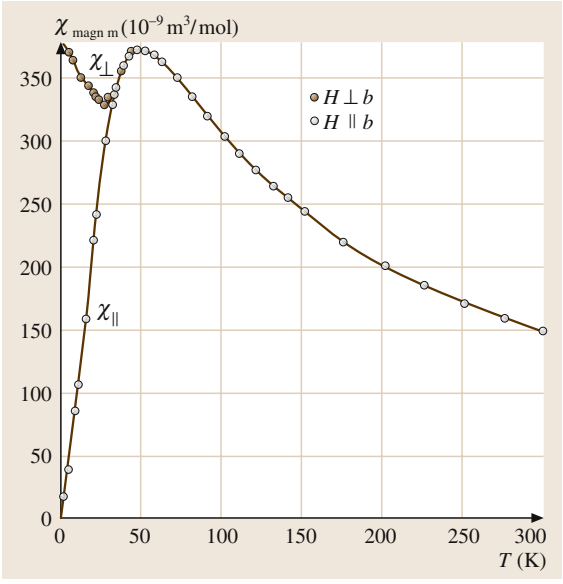


**Fig. 4.5-50** $BaMnF_4$. $\chi_{magn\ m}$ versus $T$. $\chi_{magn\ m}$ is the magnetic susceptibility, and $\chi_\perp$ and $\chi_\parallel$ are the magnetic susceptibilities measured perpendicular and parallel, respectively, to the $b$ axis

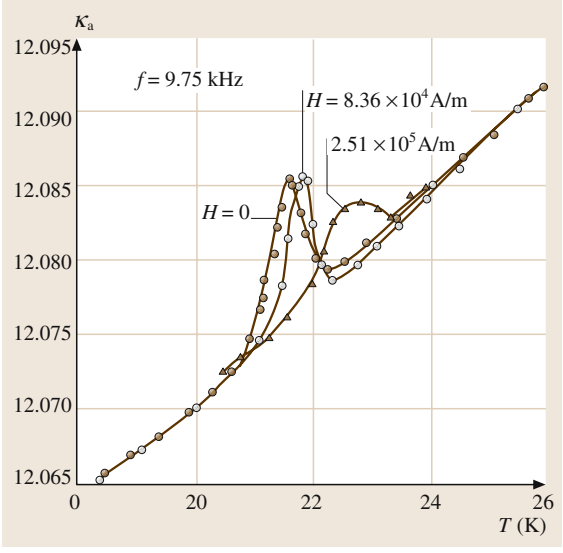


**Fig. 4.5-51** $BaMnF_4$. $\kappa_a$ versus $T$. Parameter: magnetic field $H$. $f = 9.75$ kHz

### HCl Family

*HCl (LB Number 27A-1).* This crystal is ferroelectric below 98 K. The chemical formula is the simplest one among all known ferroelectrics. The coercive field is large (Figs. 4.5-52 and 4.5-53).

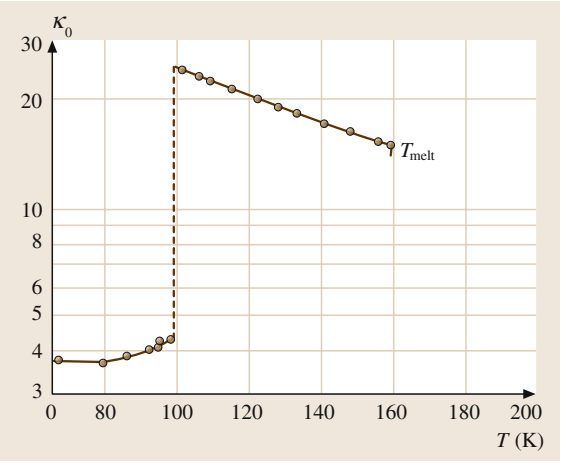


**Fig. 4.5-52** HCl (polycrystalline). $\kappa_0$ versus $T$. $\kappa_0$ is the static dielectric constant

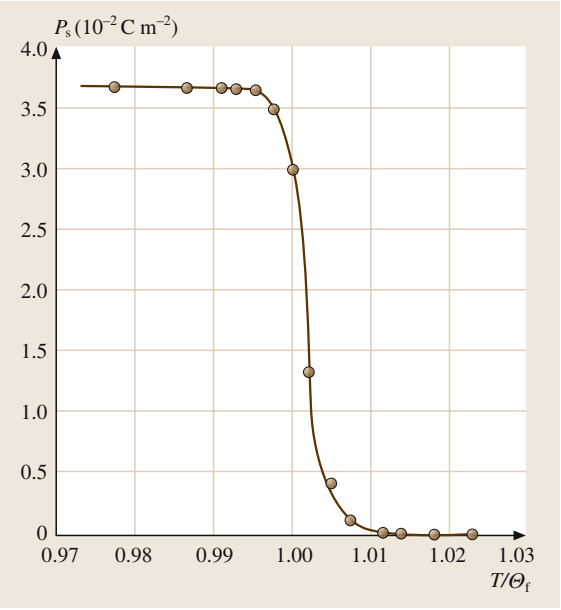


**Fig. 4.5-53** HCl. $P_s$ versus $T/\Theta_f$ obtained from pyroelectric-current measurement. $\Theta_f = 98$ K

**Fig. 4.5-55** $NaNO_2$. $P_s$ versus $T$, determined by pyroelectric-charge measurement

### $NaNO_2$ Family

*$NaNO_2$ (LB Number 28A-1).* This crystal is ferroelectric below 163.9 °C (Figs. 4.5-54 and 4.5-55). The spontaneous polarization results from orientational order of the $NO_2^-$ ions. Between 163.9 and 165.2 °C, the crystal structure is incommensurately modulated with a wave vector $\delta \boldsymbol{a}^*$, where $\delta$ varies from 0.097 to 0.120 with increasing temperature.

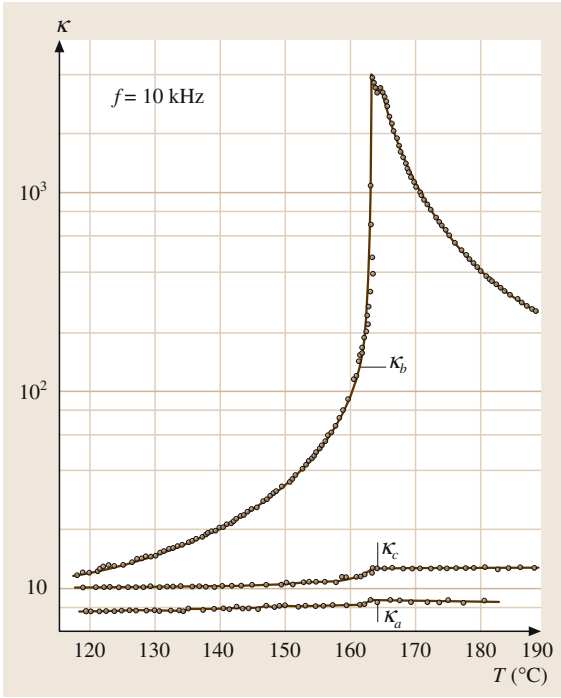


**Fig. 4.5-54** $NaNO_2$. $\kappa_a$, $\kappa_b$, and $\kappa_c$ versus $T$

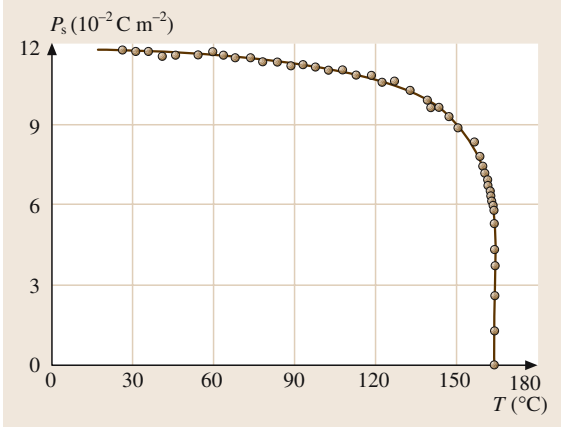

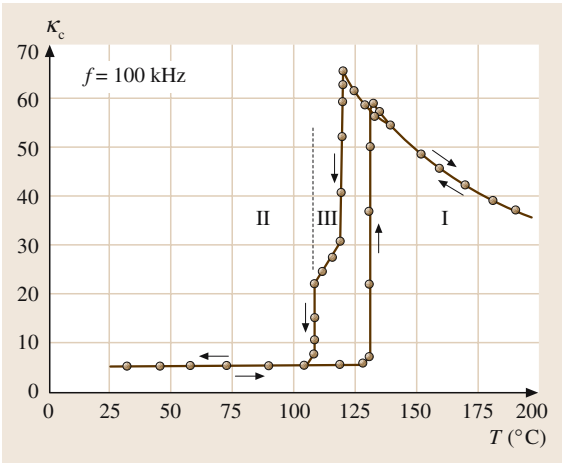


**Fig. 4.5-56** $KNO_3$. $\kappa_c$ versus $T$

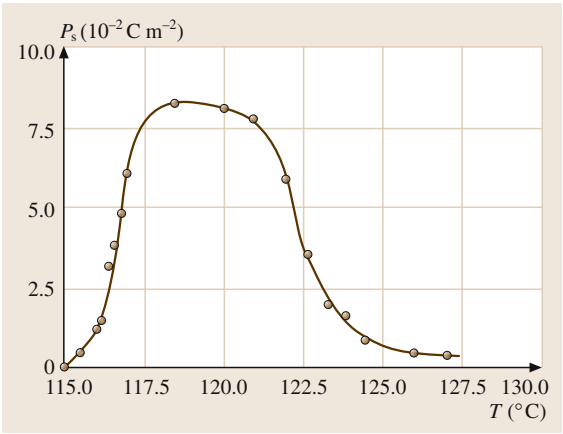


**Fig. 4.5-57** $KNO_3$. $P_s$ versus $T$

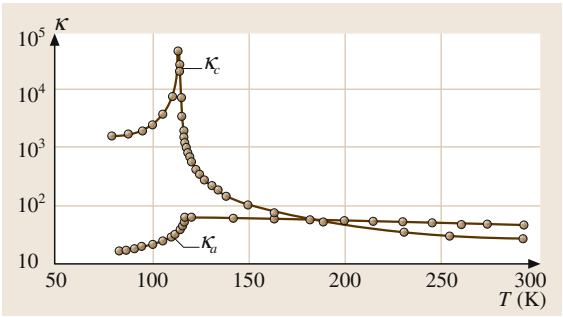


**Fig. 4.5-58** $KH_2PO_4$. $\kappa_a$ and $\kappa_c$ versus $T$. $f = 800$ Hz

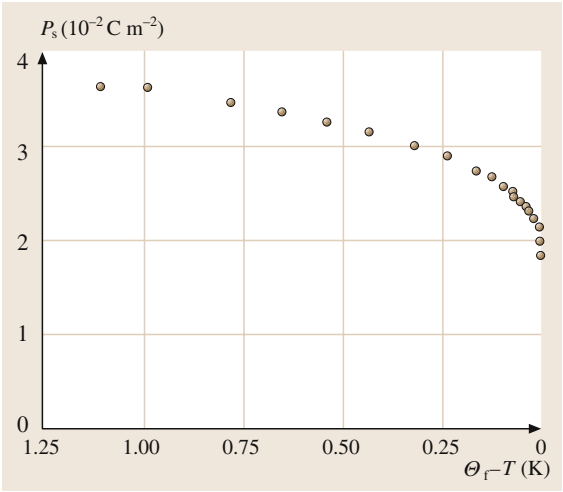


**Fig. 4.5-59** $KH_2PO_4$. $P_s$ versus $(\Theta_f - T)$. $\Theta_f = 123$ K

### $KNO_3$ Family

*$KNO_3$ (LB Number 30A-2).* This crystal is ferroelectric between about 115 and 125 °C in a metastable phase III which appears on cooling. Hydrostatic pressure stabilizes this phase (Figs. 4.5-56 and 4.5-57).

### KDP ($KH_2PO_4$) Family

*$KH_2PO_4$ (KDP) (LB Number 33A-1).* $KH_2PO_4$ is a classical and extensively studied ferroelectric crystal. It is ferroelectric below 123 K (Figs. 4.5-58 and 4.5-59). The transition is a typical ferroelectric phase transition, related to a configuration change in a three-dimensional hydrogen-bond network. Figures 4.5-61 and 4.5-60 demonstrate changes in the proton configuration associated with the phase transition. The transitions related to hydrogen atom rearrangement in the hydrogen-bond network are characterized by sensitivity to deuteration and hydrostatic pressure, as demonstrated in Figs. 4.5-62 and 4.5-63, respectively. For theoretical studies of the phase transition, readers should refer to [5.7]. The crystal is useful in nonlinear optical devices.

*$CsH_2PO_4$ (LB Number 33A-3).* This crystal is ferroelectric below about 151.5 K. The crystal system of its paraelectric phase (monoclinic) is different from that of $KH_2PO_4$ (tetragonal). The temperature dependence of the dielectric constant above the Curie point deviates considerably from the Curie–Weiss law, suggesting that the transition is related to one-dimensional ordering of hydrogen atoms in a hydrogen-bond network. Deuteration changes the transition temperature from 151.5 to 264.7 K (Fig. 4.5-64).

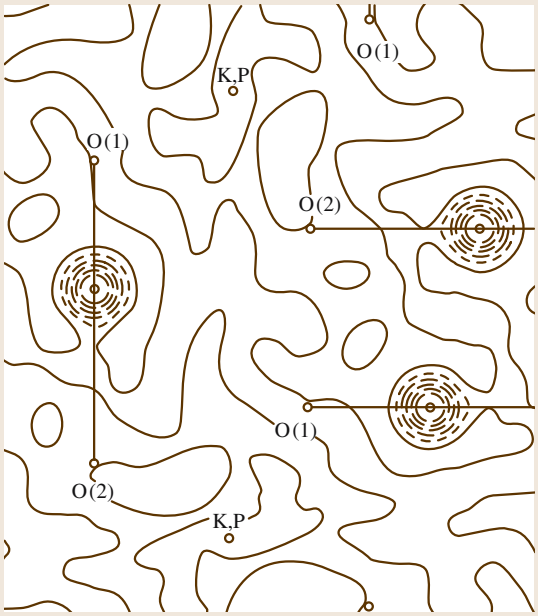


**Fig. 4.5-60** $KH_2PO_4$. Fourier map of the projection of the proton distribution on (001) in the ferroelectric phase (77 K), determined by neutron diffraction. The proton distribution lies approximately on a line joining two oxygen atoms O(1) and O(2) and closer to O(1)

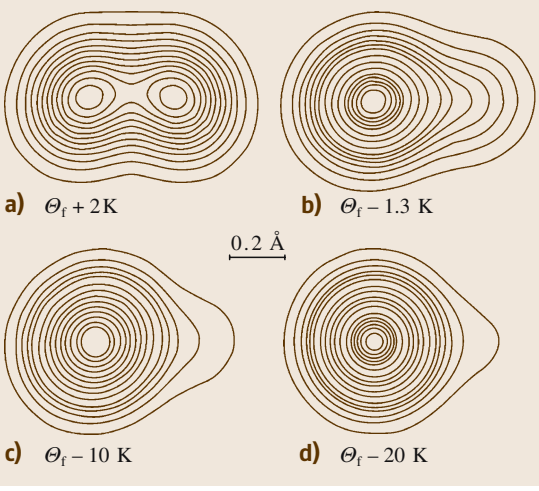


**Fig. 4.5-61a–d** $KH_2PO_4$. Change of proton distribution above and below the Curie point $\Theta_f$, determined by neutron diffraction. Contours are all equally spaced. **(a)** $\Theta_f + 2$ K; **(b)** $\Theta_f - 1.3$ K; **(c)** $\Theta_f - 10$ K; **(d)** $\Theta_f - 20$ K

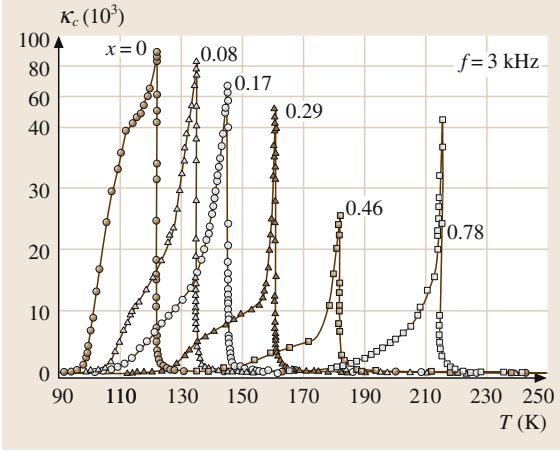


**Fig. 4.5-62** $KH_{2(1-x)}D_{2x}PO_4$. $\kappa_c$ versus $T$. Parameter: $x$

*$RbH_2PO_4$–$NH_4H_2PO_4$ (LB Number 33B-5).* The mixed crystals $Rb_{1-x}(NH_4)_xH_2PO_4$, where $0.2 < x < 0.8$, show a characteristic temperature dependence of the dielectric constants, suggesting that at low temperatures

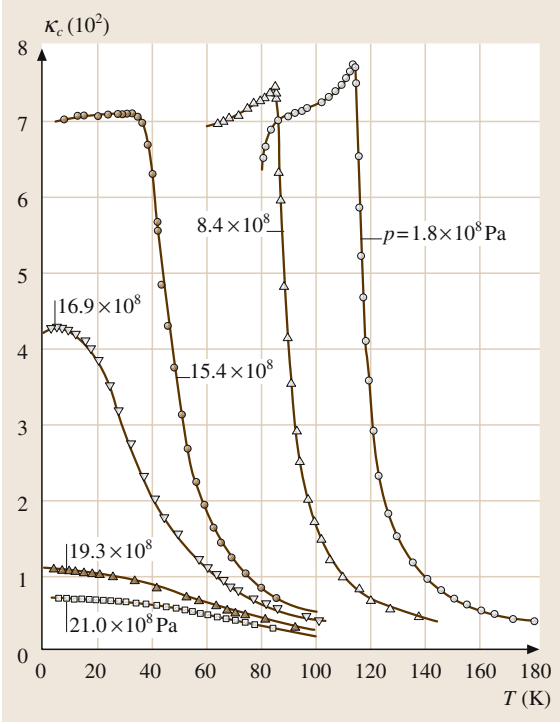


**Fig. 4.5-63** $KH_2PO_4$. $\kappa_c$ versus $T$. Parameter: hydrostatic pressure $p$

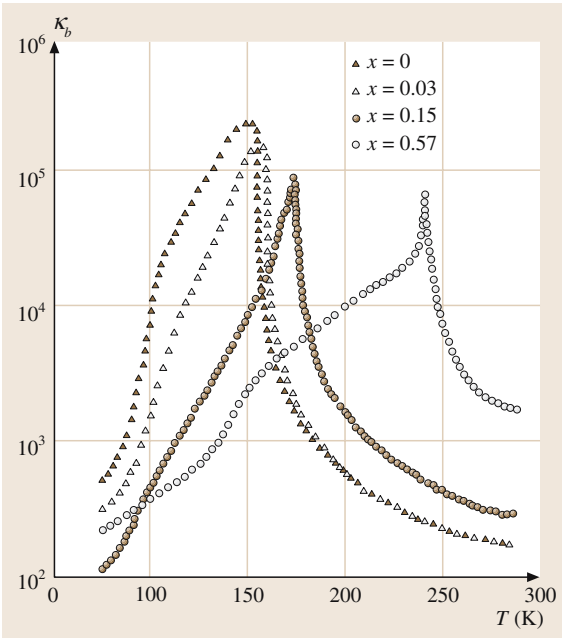


**Fig. 4.5-64** $CsH_2PO_4$ and $CsH_{2(1-x)}D_{2x}PO_4$. $\kappa_b$ versus $T$. Parameter: $x$

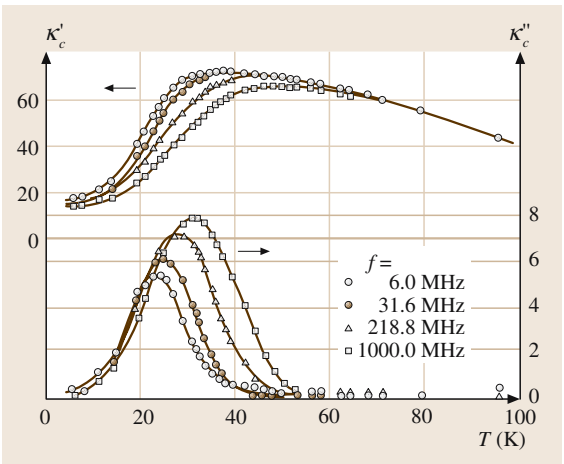


**Fig. 4.5-65** $Rb_{0.65}(NH_4)_{0.35}H_2PO_4$. $\kappa'_c$ and $\kappa''_c$ versus $T$. Parameter: $f$

a local order becomes predominant in a configuration of hydrogen atoms without definite long-range order, i. e. a dipole glass state develops (Fig. 4.5-65).

### $PbHPO_4$ Family

*$PbHPO_4$ (LB Number 34A-1).* This crystal is ferroelectric below 37 °C (Figs. 4.5-66 and 4.5-67). It exhibits

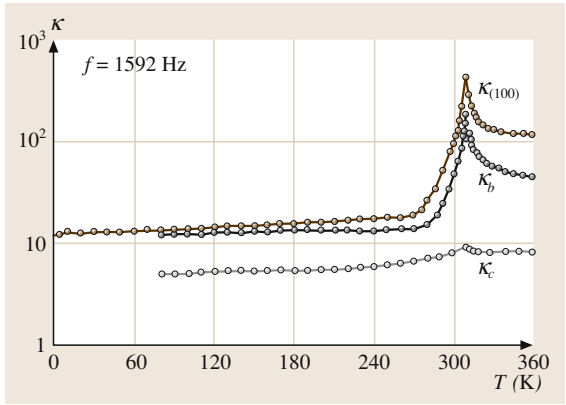


**Fig. 4.5-66** $PbHPO_4$. $\kappa_{(100)}$, $\kappa_b$, and $\kappa_c$ versus $T$. $\kappa_{(100)}$ is the dielectric constant perpendicular to the (100) plane

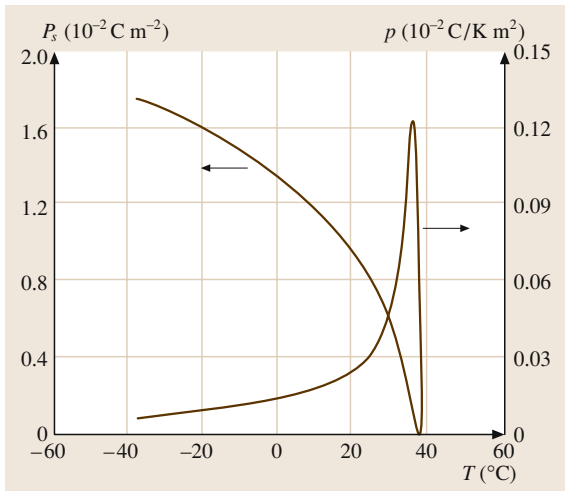


**Fig. 4.5-67** $PbHPO_4$. $P_s$ and $p$ versus $T$, measured on (100) planar specimen. $p = -dP_s/dT$ is the pyroelectric coefficient

characteristic critical phenomena, suggesting that the spontaneous polarization results from an ordered arrangement of hydrogen atoms in a one-dimensional array of hydrogen bonds.

### $(NH_4)_2SO_4$ Family

*$(NH_4)_2SO_4$ (LB Number 39A-1).* This crystal is ferroelectric below −49.5 °C. The dielectric constant is practically independent of temperature above the Curie point (Fig. 4.5-68). The spontaneous polarization changes its sign at about −190 °C (Fig. 4.5-69), suggesting a ferrielectric mechanism for the spontaneous polarization.

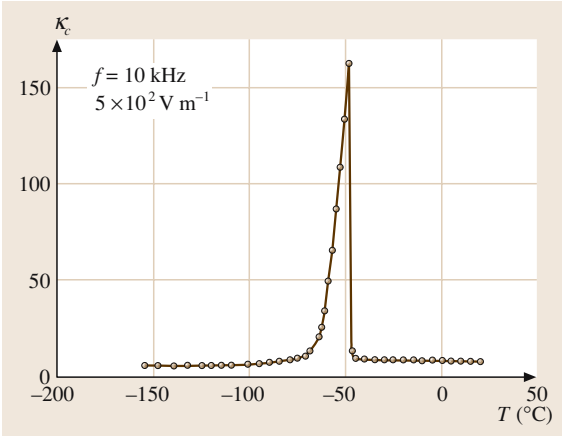


**Fig. 4.5-68** $(NH_4)_2SO_4$. $\kappa_c$ versus $T$

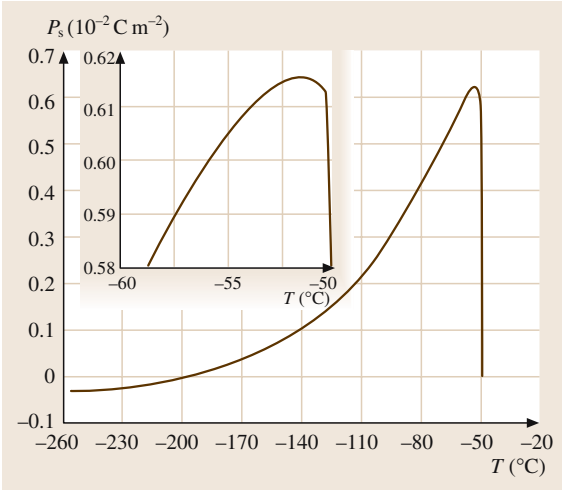


**Fig. 4.5-69** $(NH_4)_2SO_4$. $P_s$ versus $T$

### $(NH_4)HSO_4$ Family

*$(NH_4)HSO_4$ (LB Number 40A-5).* This crystal is ferroelectric in the temperature range between −119 and −3 °C (Figs. 4.5-70 and 4.5-71).

### $(NH_4)LiSO_4$ Family

*$(NH_4)LiSO_4$ (LB Number 41A-5).* This crystal is ferroelectric in the temperature range between 10 and 186.5 °C (Figs. 4.5-72 and 4.5-73).

### $(NH_4)_3H(SO_4)_2$ Family

*$(NH_4)_3H(SO_4)_2$ (LB Number 42A-1).* This crystal is ferroelectric in its phase VII below −211 °C. Another

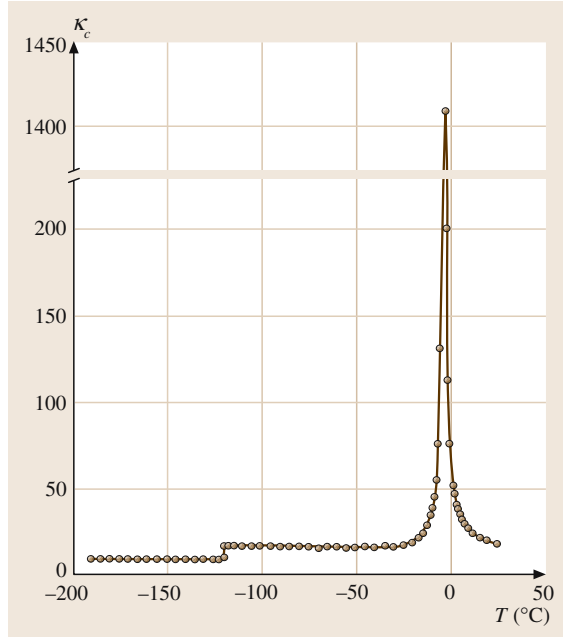


**Fig. 4.5-70** $NH_4HSO_4$. $\kappa_c$ versus $T$. $f = 10$ kHz

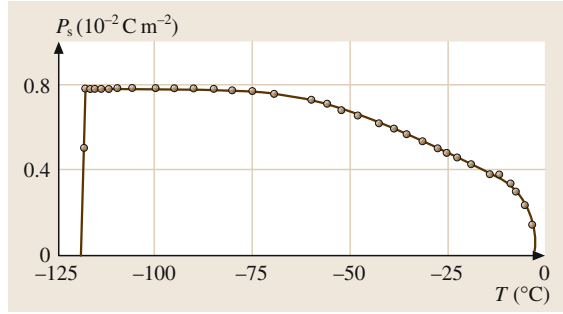


**Fig. 4.5-71** $NH_4HSO_4$. $P_s$ versus $T$

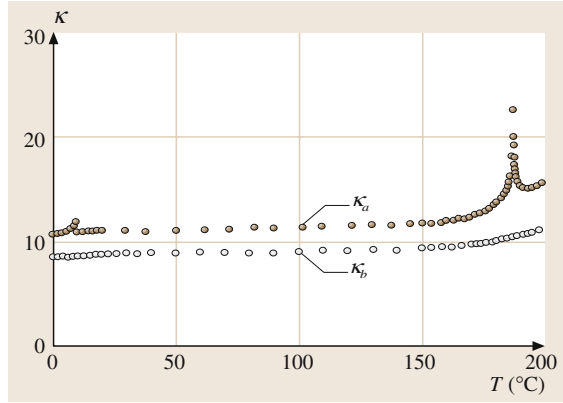


**Fig. 4.5-72** $NH_4LiSO_4$. $\kappa_a$ and $\kappa_b$ versus $T$. $f = 3$ kHz

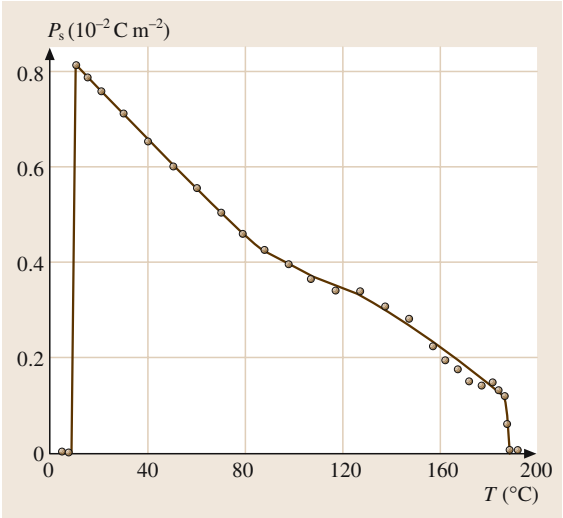


**Fig. 4.5-73** $NH_4LiSO_4$. $P_s$ versus $T$

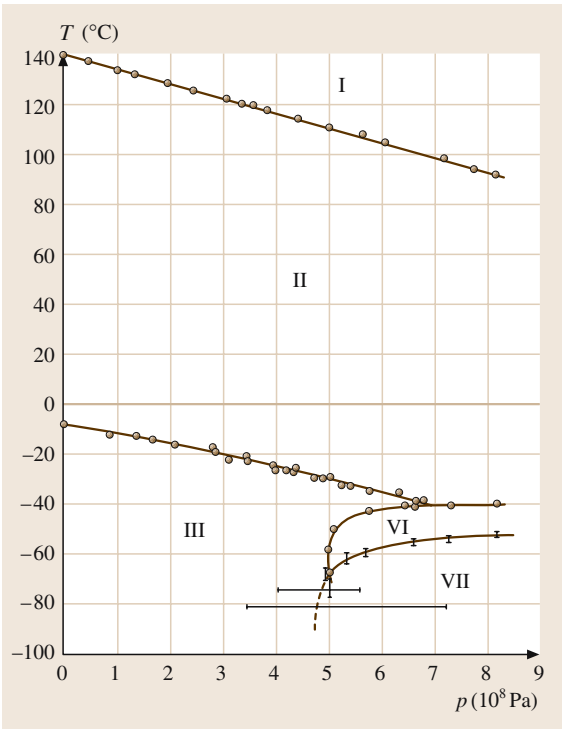


**Fig. 4.5-74** $(NH_4)_3H(SO_4)_2$. $T$ versus $p$ phase diagram. $p$ is the hydrostatic pressure. Phases VI and VII are ferroelectric

**Fig. 4.5-76** $(NH_4)_2Cd_2(SO_4)_3$. $\kappa'_{[100]}$ and $\kappa''_{[100]}$ versus $T$

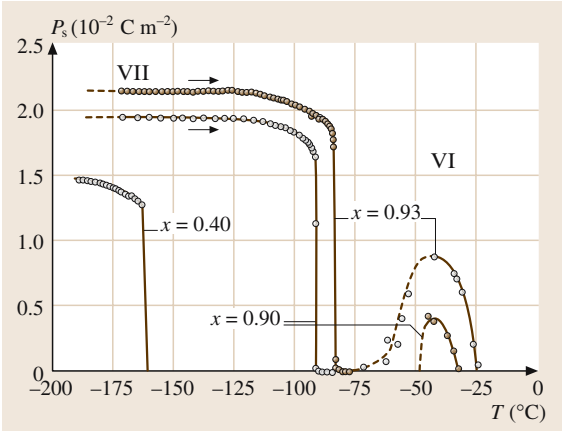


**Fig. 4.5-75** $((NH_4)_3H)_{1-x}((ND_4)_3D)_x(SO_4)_2$. $P_s$ versus $T$. Parameter: $x$. *Gray circles* (for Phase VI), determined by pyroelectric measurements. *Brown circles* (for phase VII), determined by hysteresis loop measurements

ferroelectric phase, VI, is induced by hydrostatic pressure (Fig. 4.5-74). When H is substituted by D, phase VI appears at atmospheric pressure and the temperature of the transition to phase VII becomes higher. Figure 4.5-75

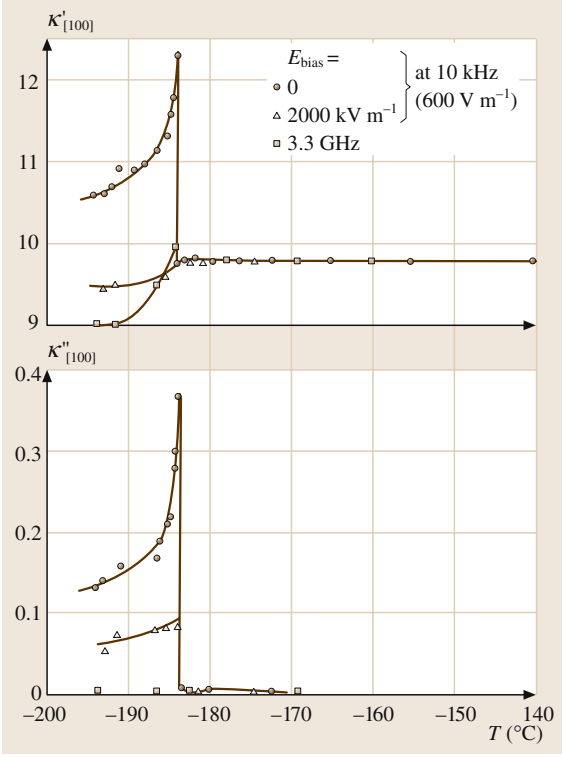

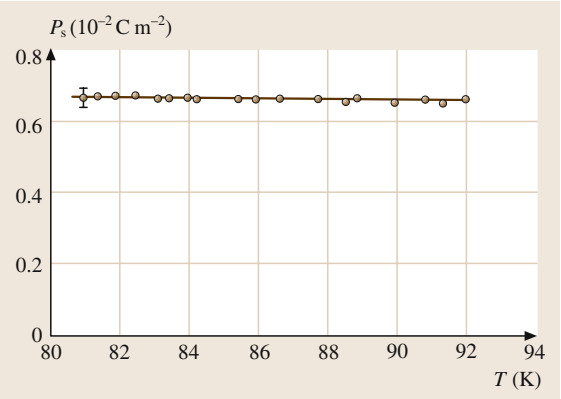


**Fig. 4.5-77** $(NH_4)_2Cd_2(SO_4)_3$. $P_s$ versus $T$

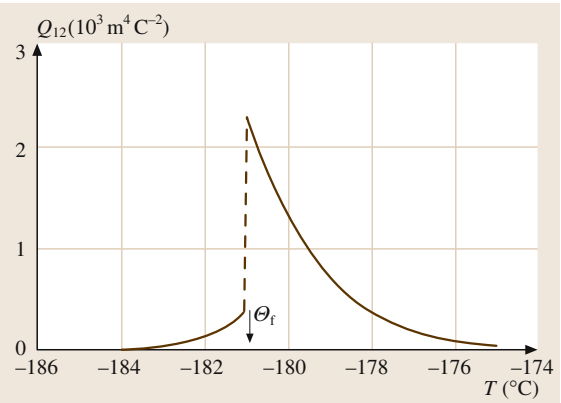


**Fig. 4.5-78** $(NH_4)_2Cd_2(SO_4)_3$. $Q_{12}$ versus $T$. $Q_{12}$ is the electrostrictive constant

shows temperature dependence of $P_s$ for three values of $x$ in $((NH_4)_3H)_{1-x}((ND_4)_3D)_x(SO_4)_2$.

#### Langbeinite-Type Family

*$(NH_4)_2Cd_2(SO_4)_3$ (LB Number 43A-13).* This crystal is ferroelectric below about −184 °C. The dielectric constants are insensitive to temperature above the transition point (Fig. 4.5-76), and the spontaneous polarization does not depend upon temperature (Fig. 4.5-77). The electrostrictive constant $Q_{12}$, however, exhibits an anomaly at the transition point (Fig. 4.5-78).

### 4.5.4.3 Organic Crystals, Liquid Crystals, and Polymers [5.4]

#### $SC(NH_2)_2$ Family

*$SC(NH_2)_2$ (LB Number 50A-1).* This crystal exhibits at least five phases, I, II, III, IV, and V (Figs. 4.5-79

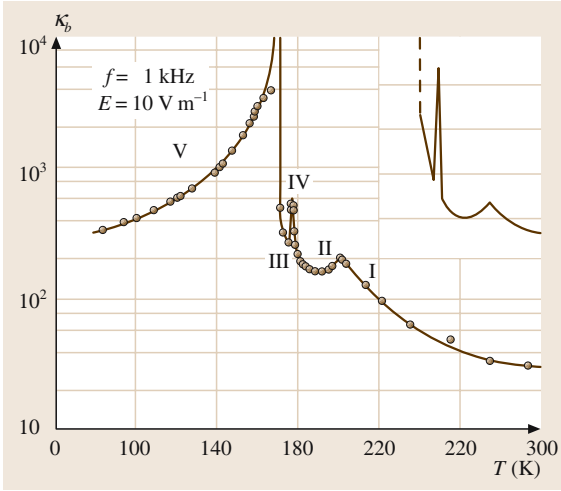


**Fig. 4.5-79** $SC(NH_2)_2$. $\kappa_b$ versus $T$

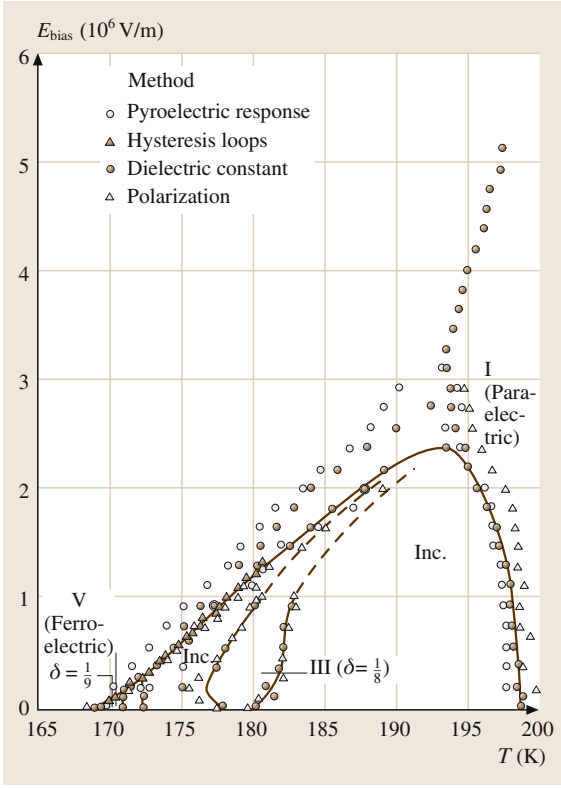


**Fig. 4.5-80** $SC(NH_2)_2$. $E_{bias}$ versus $T$ phase diagram. The value of $\delta$ means that the phase is commensurately modulated with a vector of wavenumber $\delta c^*$. Inc., incommensurate phase

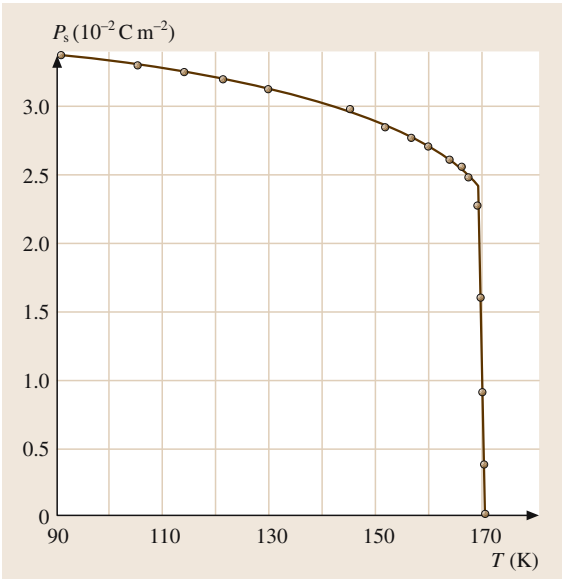


**Fig. 4.5-81** $SC(NH_2)_2$. $P_s$ versus $T$ for phase V

and 4.5-80). The crystal is ferroelectric in phase V (Fig. 4.5-81), and slightly ferroelectric with a very small spontaneous polarization in phase III. The crystal structure is modulated commensurately or incommensurately except for phases I and V, as indicated in Fig. 4.5-80.

### DSP ($Ca_2Sr(CH_3CH_2COO)_6$) Family

*$Ca_2Sr(CH_3CH_2COO)_6$ (DSP) (LB Number 58A-1).* This crystal is ferroelectric below about 4 °C (Fig. 4.5-82). The Curie–Weiss constant is small (60 K). Critical slowing-down (see Sect. 4.5.3) takes place (Fig. 4.5-8).

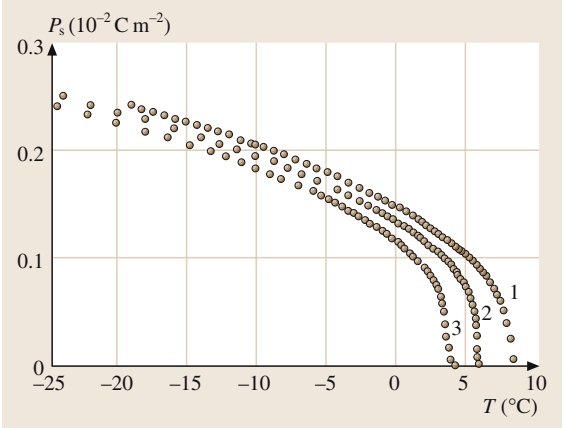


**Fig. 4.5-82** $Ca_2Sr(CH_3CH_2COO)_6$. $P_s$ versus $T$. The three curves show the effect of annealing: 1, unannealed; 2, annealed at 330 °C for 60 h; 3, annealed at 330 °C for 60 h and at 390 °C for 5 h

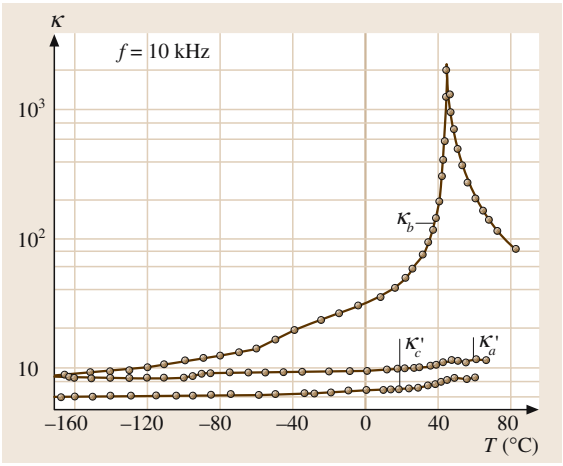


**Fig. 4.5-83** $(NH_2CH_2COOH)_3 \cdot H_2SO_4$. $\kappa_{a'}$, $\kappa_{b'}$, and $\kappa_{c'}$ versus $T$. These quantities are referred to the unit cell vectors: $\boldsymbol{a}' = \boldsymbol{a} + \boldsymbol{c}$, $\boldsymbol{b}' = -\boldsymbol{b}$, and $\boldsymbol{c}' = -\boldsymbol{c}$

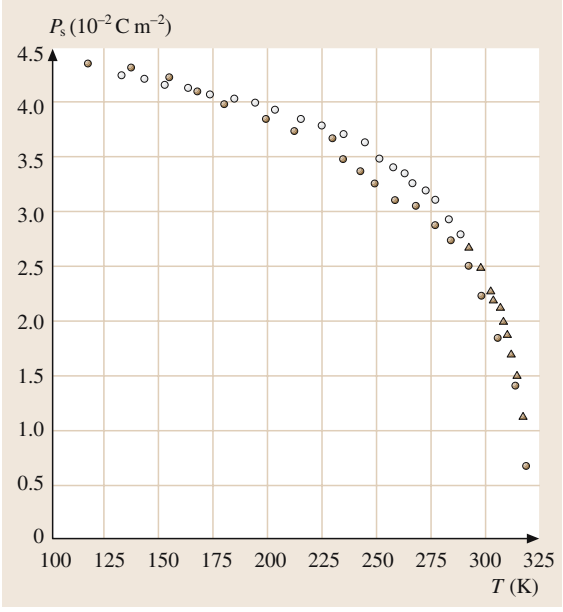


**Fig. 4.5-84** $(NH_2CH_2COOH)_3 \cdot H_2SO_4$. $P_s$ versus $T$. $P_s$ is parallel to the $b$ axis. *Gray circles*: values determined by pyroelectric measurements. *Triangles* and *brown circles*: determined from hysteresis loop by different authors

### TGS ($(NH_2CH_2COOH)_3 \cdot H_2SO_4$) Family

*$(NH_2CH_2COOH)_3 \cdot H_2SO_4$ (TGS) (LB Number 60A-1).* This crystal is ferroelectric below 49.4 °C (Figs. 4.5-83 and 4.5-84). Critical slowing-down takes place (Fig. 4.5-9).

### $(CH_3NHCH_2COOH)_3 \cdot CaCl_2$ Family

*$(CH_3NHCH_2COOH)_3 \cdot CaCl_2$ (LB Number 64A-1).* This crystal is ferroelectric below 127 K (Figs. 4.5-85 and 4.5-86). The Curie–Weiss constant is small (40 K). As discussed in Sect. 4.5.3, two components are expected in the dielectric constants of displacive-type ferroelectrics: one contribution from the soft optical phonon and one contribution from cluster boundary motion. This crystal provides a good example of this situation. Softening of the optical phonon mode $B_{2u}$ occurs (Fig. 4.5-11), indicating that the transition is of the displacive type, while critical slowing-down takes place in the GHz region (Fig. 4.5-10); this seems to take place in the contribution from cluster boundary motion. The value of the dielectric constant at the Curie point at 1.0 GHz seems to contain a contribution from the optical phonon mode.

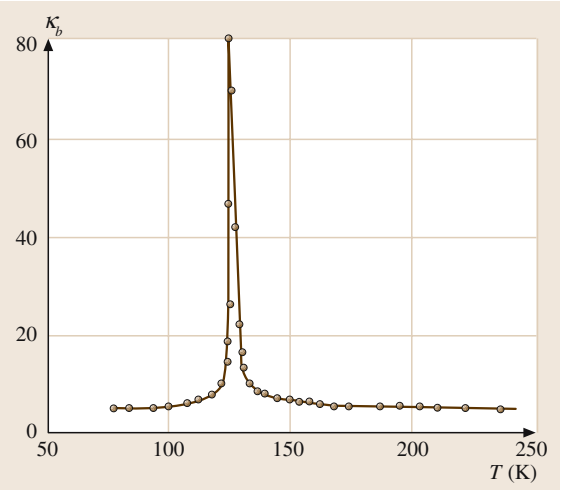


**Fig. 4.5-85** $(CH_3NHCH_2COOH)_3 \cdot CaCl_2$. $\kappa_b$ versus $T$. $f = 10$ kHz

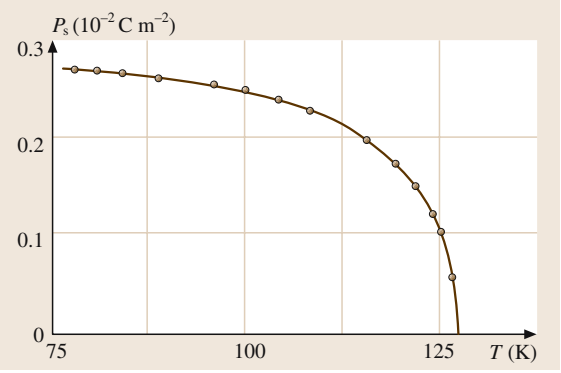


**Fig. 4.5-86** $(CH_3NHCH_2COOH)_3 \cdot CaCl_2$. $P_s$ versus $T$

### $(CH_3)_3NCH_2COO \cdot CaCl_2 \cdot 2H_2O$ Family

*$(CH_3)_3NCH_2COO \cdot CaCl_2 \cdot 2H_2O$ (LB Number 66A-1).* This crystal is ferroelectric below 46 K. It exhibits at least ten phase transitions (eight can be recognized in Fig. 4.5-87), and the crystal structure is commensurately or incommensurately modulated between 46 and 164 K, with a feature known as a devil's staircase. Multiple hysteresis loops are observed in the modulated phases, as shown in Fig. 4.5-88.

### Rochelle Salt ($NaKC_4H_4O_6 \cdot 4H_2O$) Family

*$NaKC_4H_4O_6 \cdot 4H_2O$ (Rochelle Salt, RS) (LB Number 67A-1).* Rochelle salt was the first ferroelectric crystal to be discovered. It is ferroelectric between −18 and 24 °C (Figs. 4.5-89 and 4.5-90). It is rare that an ordered ferroelectric phase of lower symmetry ($P2_1$ in this case) appears in an intermediate temperature range between disordered phases of the same higher symmetry ($P2_12_12$). Figure 4.5-91 shows X-ray evidence for such space group changes. For theoretical studies, readers should refer to [5.7].

### LAT ($LiNH_4C_4H_4O_6 \cdot H_2O$) Family

*$LiNH_4C_4H_4O_6 \cdot H_2O$ (LAT) (LB Number 68A-1).* Ferroelectric activity appears along the $b$ axis below 106 K (Fig. 4.5-92). The dielectric constant of the clamped

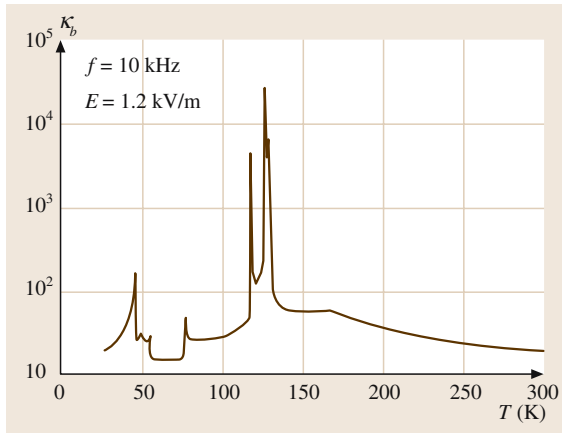


**Fig. 4.5-87** $(CH_3)_3NCH_2COO \cdot CaCl_2 \cdot 2H_2O$. $\kappa_b$ versus $T$

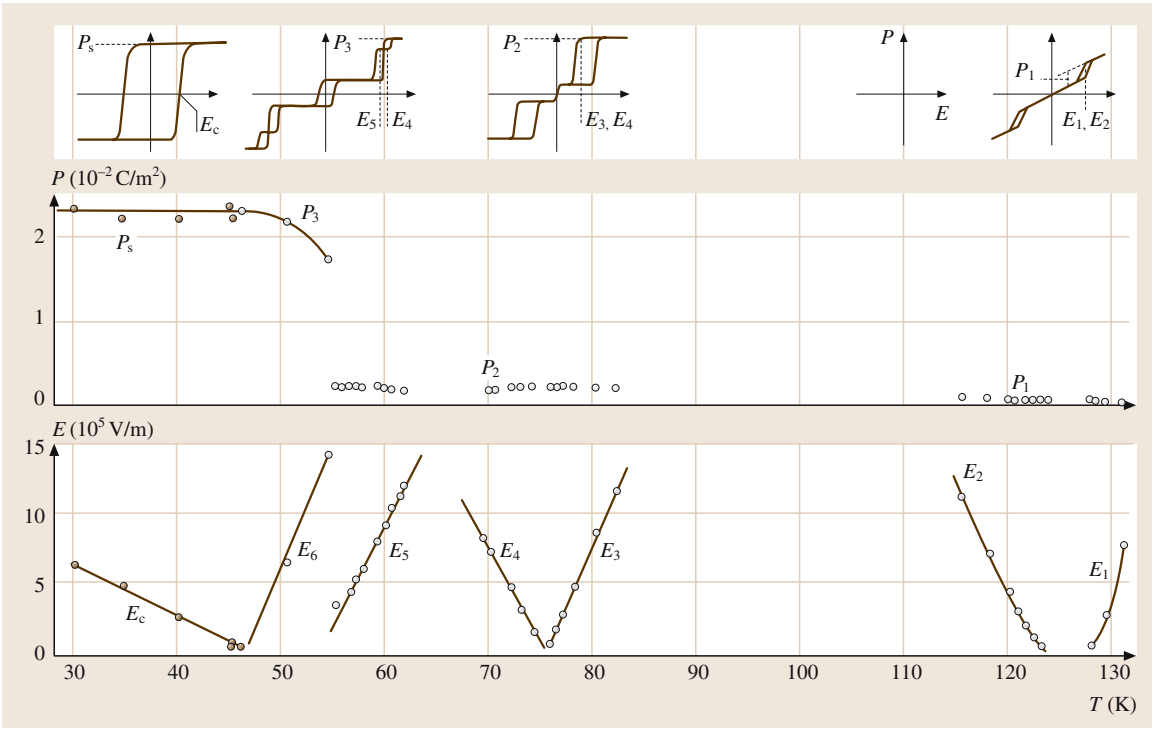


**Fig. 4.5-88** $(CH_3)_3NCH_2COO \cdot CaCl_2 \cdot 2H_2O$. $P_s$, $E_c$, $P_i$, and $E_i$ versus $T$. Definitions of $P_i$ $(i = 1, 2, 3)$ and $E_i$ are shown in the *top figure*

crystal $\left(\kappa_{22}^{S}\right)$ shows no anomaly at the transition temperature (Fig. 4.5-7), while the elastic compliances exhibit a pronounced anomaly (Fig. 4.5-93). These data indicate that the ferroelectric phase transition is of the indirect type $III_{ac}$ triggered by an elastic anomaly (see Sect. 4.5.3). The crystal is piezoelectric in the paraelec-

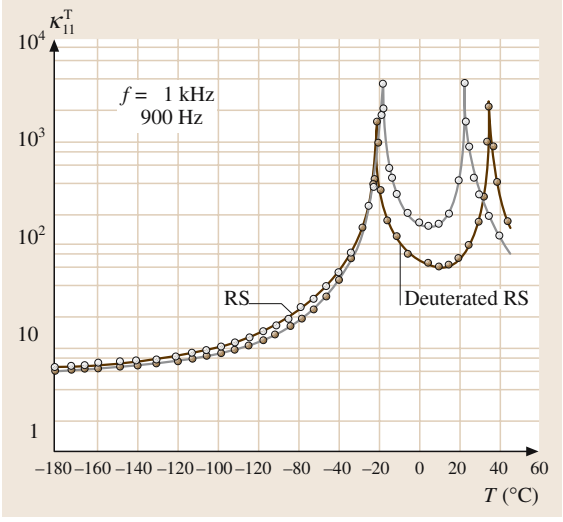


**Fig. 4.5-89** $NaKC_4H_4O_6 \cdot 4H_2O$ (RS) and $NaKC_4H_2D_2O_6 \cdot 4D_2O$ (deuterated RS). $\kappa_{11}^{T}$ versus $T$

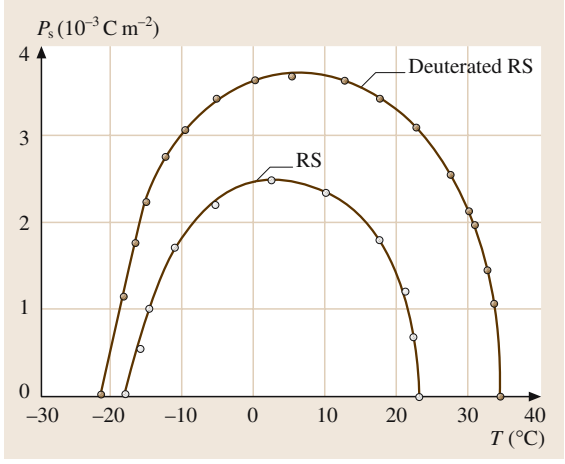


**Fig. 4.5-90** $NaKC_4H_4O_6 \cdot 4H_2O$ (RS) and $NaKC_4H_2D_2O_6 \cdot 4D_2O$ (deuterated RS). $P_s$ versus $T$

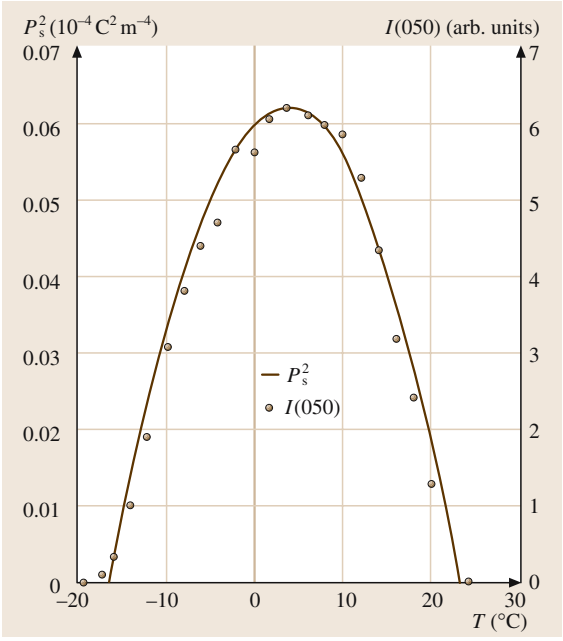


**Fig. 4.5-91** $NaKC_4H_4O_6 \cdot 4H_2O$. $I_{(050)}$ versus $T$. $I_{(050)}$ is the integrated intensity of the X-ray (050) reflection, which should disappear in the space group $P2_12_12$ below −18 °C and above 23 °C. The *solid line* is $P_s^2$ normalized to fit to $I_{(050)}$

tric phase and the elastic anomaly causes a dielectric anomaly in the free crystal ($\kappa_b$ in Fig. 4.5-92 and $\kappa_{22}^{\mathbf{T}}$ in Fig. 4.5-7), but no dielectric anomaly in the clamped crystal ($\kappa_{22}^{\mathbf{S}}$ in Fig. 4.5-7).

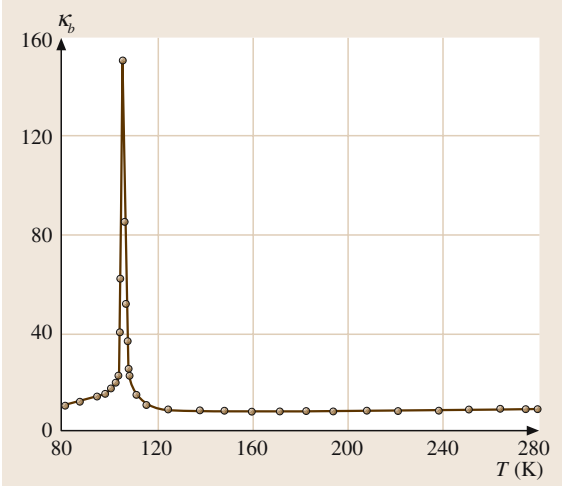


**Fig. 4.5-92** $LiNH_4C_4H_4O_6 \cdot H_2O$. $\kappa_b$ versus $T$

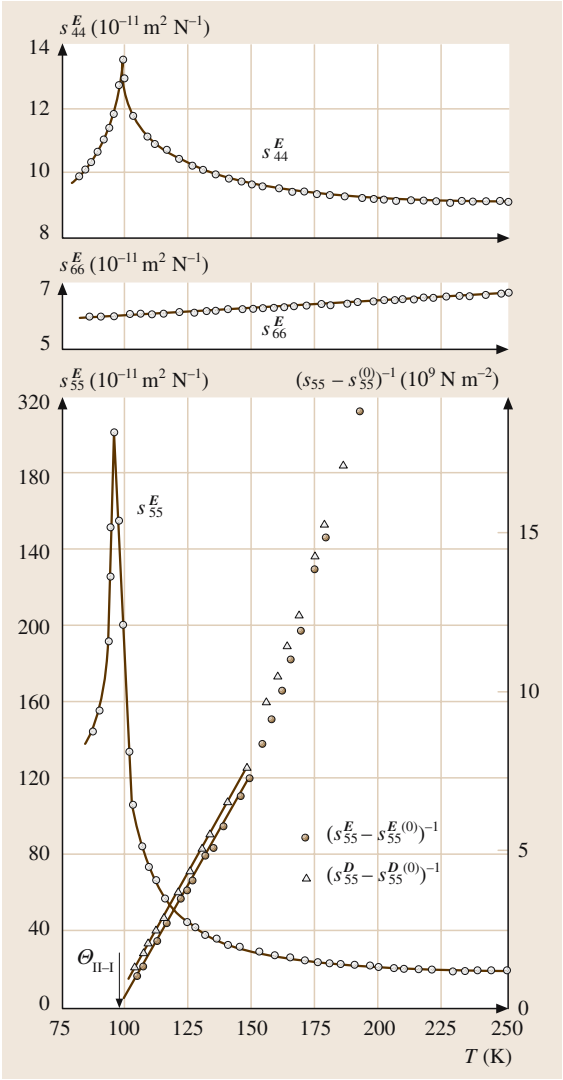


**Fig. 4.5-93** $LiNH_4C_4H_4O_6 \cdot H_2O$. $s_{44}^E$, $s_{55}^E$, and $s_{66}^E$ versus $T$. $s_{44}^E$, $s_{55}^E$, and $s_{66}^E$ are the shear components of the elastic compliance tensor at constant electric field. The two *straight lines* show $\left[s_{55}^E - s_{55}^E(0)\right]^{-1}$ and $\left[s_{55}^D - s_{55}^D(0)\right]^{-1}$, where $s_{55}^D$ is $s_{55}$ at constant electric displacement, $s_{55}^E(0) = 18.0\,\mathrm{m^2\,N^{-1}}$, and $s_{55}^D(0) = 17.0\,\mathrm{m^2\,N^{-1}}$

### Liquid Crystal Family

*DOBAMBC, p-decyloxybenzylidene p′-amino 2-methylbutyl cinnamate (LB Number 71A-1 (A)) (Liquid Crystal).* This liquid crystal is ferroelectric in the smectic C* phase between about 76 and 92 °C on heating. On cooling, the C* phase is transformed into a smectic H*

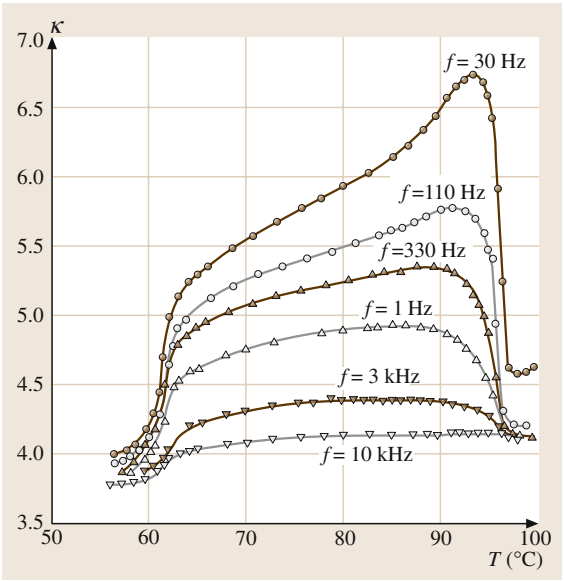


**Fig. 4.5-94** DOBAMBC. $\kappa$ versus $T$. Parameter: $f$. Sample cell thickness = 2.3 μm

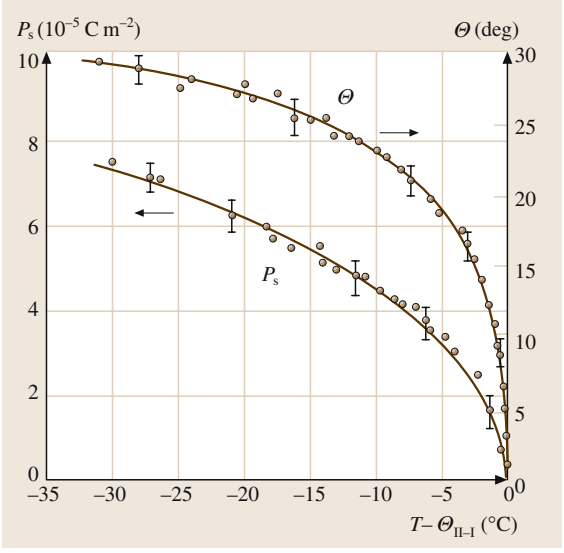


**Fig. 4.5-95** DOBAMBC. $P_s$ and $\theta$ versus $T - \Theta_{II-I}$. $\theta$ is the apparent tilt angle, and $\Theta_{II-I}$ is the ferroelectric transition temperature

**Fig. 4.5-96a,b** MHPOBC. $D - E$ hysteresis loops obtained from switching-current measurements. $D$ is the electric displacement. Sample cell thickness = 3 μm. **(a)** Double hysteresis loop at 2 Hz. **(b)** Single hysteresis loop at 100 Hz

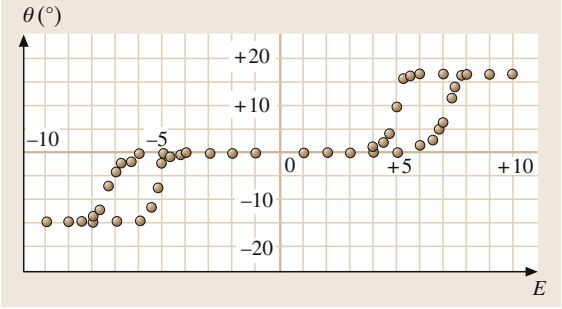


**Fig. 4.5-97** MHPOBC. $\theta$ versus $E$. $\theta$ is the apparent tilt angle. Sample cell thickness = 3 μm

phase at about 63 °C, retaining the ferroelectric activity (Figs. 4.5-94 and 4.5-95).

*MHPOBC, 4-(1-methylheptyl oxycarbonyl)phenyl 4′-octyloxybiphenyl-4-carboxylate (LB Number 71B-1 (A)) (Liquid Crystal).* Seven phases are known for this liquid crystal. It exhibits an antiferroelectric hysteresis loop at low frequency, as shown in Fig. 4.5-96a, between

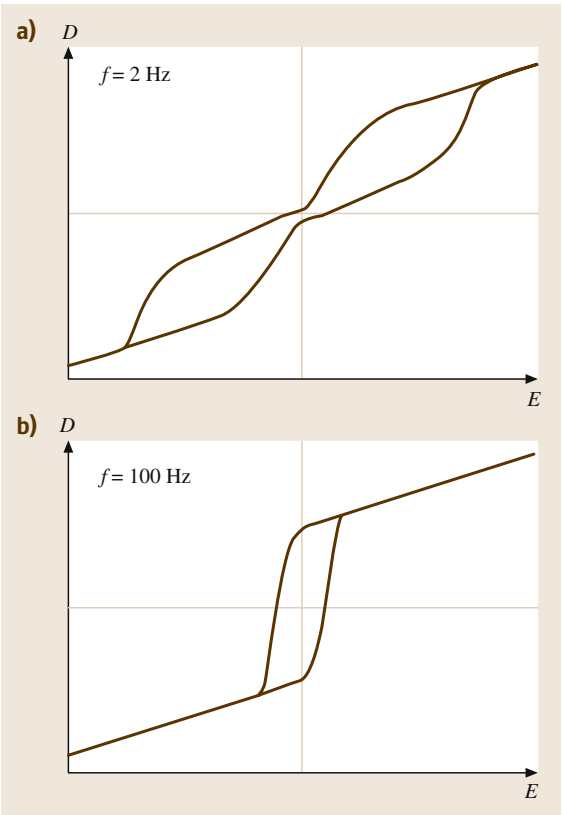

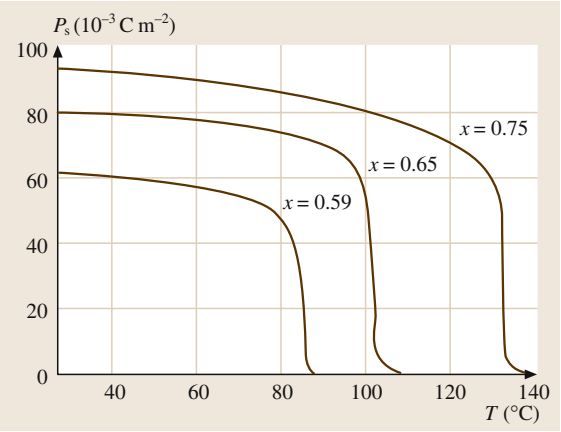


**Fig. 4.5-98** $((CH_2CF_2)_x(CF_2CHF)_{1-x})_n$. $P_s$ versus $T$. Parameter: $x$. Thickness of specimen film = 50 µm

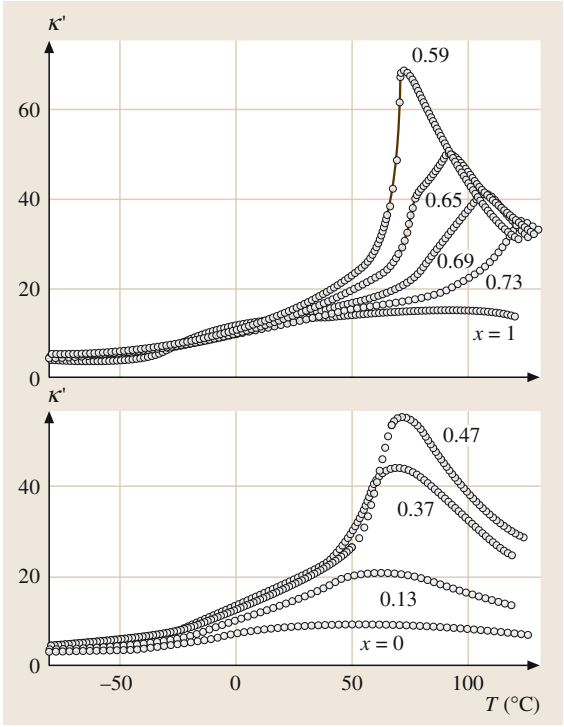


**Fig. 4.5-99** $((CH_2CF_2)_x(CF_2CHF)_{1-x})_n$. $\kappa'$ versus $T$. Parameter: $x$. $f = 1$ kHz. Thickness of specimen film = 50 µm

65 and 119.7 °C. The antiferroelectric behavior can be best demonstrated by measuring the apparent tilt angle, as shown in Fig. 4.5-97. The hysteresis loop turns into a triple one between 119.7 and 120.6 °C, and into a normal ferroelectric hysteresis loop between 120.6 and 122.1 °C. The phase exhibiting the triple hysteresis loop is called "ferrielectric" by several authors.

### Polymer Family

*$((CH_2CF_2)_x(CF_2CHF)_{1-x})_n$, Vinylidene fluoride–trifluoroethylene Copolymer, $((VDF)_x(TrFE)_{1-x})_n$ (LB Number 72-2) (Polymer).* Random polymers $(CH_2CF_2)_x(CF_2CHF)_{1-x}$ exhibit a ferroelectric hysteresis loop for $x > 0.5$ (Figs. 4.5-98 and 4.5-99). Ferroelectric activity is preserved up to the melting point for $x > 0.8$.



## References


5.1 Y. Shiozaki, E. Nakamura, T. Mitsui (Eds.): *Ferroelectrics and Related Substances: Oxides: Perovskite-Type Oxides and* $LiNbO_3$ *Family*, Landolt–Börnstein, New Series III/36 (Springer, Berlin, Heidelberg 2001)

5.2 Y. Shiozaki, E. Nakamura, T. Mitsui (Eds.): *Ferroelectrics and Related Substances: Oxides: Oxides Other Than Perovskite-Type Oxides and* $LiNbO_3$ *Family*, Landolt–Börnstein, New Series III/36 (Springer, Berlin, Heidelberg 2002)

5.3 Y. Shiozaki, E. Nakamura, T. Mitsui (Eds.): *Ferroelectrics and Related Substances: Inorganic Crystals Other Than Oxides*, Landolt–Börnstein, New Series III/36 (Springer, Berlin, Heidelberg 2004)

5.4 Y. Shiozaki, E. Nakamura, T. Mitsui (Eds.): *Ferroelectrics and Related Substances: Organic Crystals, Liquid Crystals and Polymers*, Landolt–Börnstein, New Series III/36 (Springer, Berlin, Heidelberg 2005) in preparation

5.5 J. Valasek: Piezoelectric and Allied Phenomena in Rochelle Salt, Phys. Rev. **15**, 537 (1920)

5.6 J. Valasek: Piezo-Electric and Allied Phenomena in Rochelle Salt, Phys. Rev. **17**, 475 (1921)

5.7 T. Mitsui, E. Nakamura, I. Tatsuzaki: *An Introduction to the Physics of Ferroelectrics* (Gordon and Breach, New York 1976)

5.8 F. Jona, G. Shirane: *Ferroelectric Crystals* (Dover Publications, New York 1993)

5.9 B. A. Strukov, A. P. Levanyuk: *Ferroelectric Phenomena in Crystals: Physical Foundations* (Springer, Berlin, Heidelberg 1998)

5.10 M. E. Lines, A. M. Glass: *Principles and Applications of Ferroelectrics and Related Materials* (Clarendon, Oxford 1979)

5.11 Y. Xu: *Ferroelectric Materials and Their Applications* (North-Holland, Amsterdam 1991)
5.12 B. Jaffe, W. R. Cook Jr., H. Jaffe: *Piezoelectric Ceramics* (Academic Press, London 1971)
5.13 J. Zelenka: *Piezoelectric Resonators and Their Applications* (Elsevier, Amsterdam 1986)
5.14 T. Ikeda: *Fundamentals of Piezoelectricity* (Oxford Univ. Press, Oxford 1990)
5.15 R. A. Cowley: *Structural Phase Transitions* (Consultant Bureau, New York 1980)
5.16 K. A. Miller, H. Thomas (Eds.): *Structural Phase Transitions I*, Topics in Current Physics, Vol. 23 (Springer, Berlin, Heidelberg 1981)
5.17 M. Fujimoto: *The Physics of Structural Phase Transitions* (Springer, Berlin, Heidelberg 1997)
5.18 R. Blinc, A. P. Levanyuk (Eds.): *Incommensurate Phases in Dielectrics*, Modern Problems in Condensed Matter Science 14 (Elsevier, Amsterdam 1986)
5.19 F. J. Scott: Soft-mode spectroscopy: Experimental studies of structural phase transitions, Rev. Mod. Phys. **46**, 83 (1974)
5.20 G. Shirane: Neutron scattering studies of structural phase transitions, Rev. Mod. Phys. **46**, 437 (1974)
5.21 C. H. Wang: Raman and Brillouin scattering spectroscopy of phase transitions in solids. In: *Vibrational Spectroscopy of Phase Transitions*, ed. by Z. Iqbal, F. J. Owens (Academic Press, Orlando 1984) pp. 153–207
5.22 J. M. Herbert: *Ceramic Dielectrics and Capacitors*, Electrocomp. Sci. Mon., Vol. 6 (Gordon and Breach, New York 1985)
5.23 B. E. Vugmeister, M. D. Glinchuk: Dipole glass and ferroelectricity in random-site electric dipole systems, Mod. Phys. **62**, 993 (1990)
5.24 L. E. Cross: Relaxor ferroelectrics, Ferroelectrics **76**, 241 (1987)
5.25 S. Singh: Nonlinear optical materials. In: *Handbook of Lasers with Selected Data on Optical Technology*, ed. by R. J. Pressley (The Chemical Rubber Co., Cleveland 1971) pp. 489–525
5.26 V. G. Dmitriev, G. G. Gurzadyan, D. N. Nikogosyan: *Handbook of Nonlinear Optical Crystals*, Springer Series in Optical Science, Vol. 64, ed. by A. E. Siegman (Springer, Berlin, Heidelberg 1991)
5.27 P. Yeh: *Introduction to Photorefractive Nonlinear Optics* (Wiley, New York 1993)
5.28 G. Rosenman, A. Skliar, A. Arie: Ferroelectric domain engineering for quasi-phase-matched nonlinear optical devices, Ferroelectr. Rev. **1**, 263 (1999)
5.29 N. Setter, E. L. Colla: *Ferroelectric Ceramics* (Birkhäuser, Basel 1993)
5.30 B. A. Tuttle, S. B. Desu, R. Ramesh, T. Shiosaki: *Ferroelectric Thin Films IV* (Materials Research Society, Pittsburgh 1995)
5.31 C. P. Araujo, J. F. Scott, G. W. Taylor (Eds.): *Ferroelectric Thin Films: Synthesis and Basic Properties* (Gordon and Breach, New York 1996)
5.32 R. Ramesh (Ed.): *Thin Film Ferroelectric Materials and Devices*, Electronic Materials Science and Technology, Vol. 3 (Kluwer, Dordrecht 1997)
5.33 J. F. Scott: The physics of ferroelectric ceramic thin films for memory applications, Ferroelectr. Rev. **1**, 1 (1998)
5.34 D. Damjanovic: Ferroelectric, dielectric and piezoelectric properties of ferroelectric thin films and ceramics, Rep. Prog. Phys. **62**, 1267 (1998)
5.35 J. F. Scott: *Ferroelectric Memories*, Springer Series in Advanced Microelectronics, Vol. 3 (Springer, Berlin, Heidelberg 2000)
5.36 R. M. White: Surface elastic waves, Proc. IEEE **58**, 1238 (1970)
5.37 G. W. Farnell, E. L. Adler: Acoustic Wave Propagation in Thin Layers. In: *Physical Acoustics*, Vol. 9, ed. by W. P. Mason, R. N. Thurston (Academic Press, New York 1972) pp. 35–127
5.38 A. A. Oliner (Ed.): *Acoustic Surface Waves* (Springer, Berlin, Heidelberg 1978)
5.39 K.-Y. Hashimoto: *Surface Acoustic Wave Devices in Telecommunications, Modeling and Simulation* (Springer, Berlin, Heidelberg 2000)
5.40 J. M. Herbert: *Ferroelectric Transducers and Sensors*, Electrocomp. Sci. Mon., Vol. 3 (Gordon and Breach, New York 1982)
5.41 W. H. de Jeu: *Physical Properties of Liquid Crystalline Materials* (Gordon and Breach, New York 1980)
5.42 J. W. Goodby, R. Blinc, N. A. Clark, S. T. Lagerwall, M. A. Osipov, S. A. Pikin, T. Sakurai, K. Yoshino, B. Zeks: *Ferroelectric Liquid Crystals: Principles, Properties and Applications*, Ferroelectrics and Related Phenomena, Vol. 7 (Gordon and Breach, New York 1991)
5.43 G. W. Taylor (Ed.): *Ferroelectric Liquid Crystals: Principles, Preparations and Applications* (Gordon and Breach, New York 1991)
5.44 L. M. Blinov, V. G. Chigrinov: *Electric Effects in Liquid Crystal Materials* (Springer, Berlin, Heidelberg 1994)
5.45 A. Fukada, Y. Takanishi, T. Isozaki, K. Ishikawa, H. Takezoe: Antiferroelectric Chiral Smectic Liquid Crystals, J. Mater. Chem. **4**, 997 (1994)
5.46 P. J. Collings, J. S. Patel (Eds.): *Handbook of Liquid Crystal Research* (Oxford Univ. Press, Oxford 1997)
5.47 S. T. Lagerwall: *Ferroelectric and Antiferroelectric Liquid Crystals* (Wiley VCH, Weinheim 1999)
5.48 T. Furukawa: Ferroelectric Properties of Vinylidene Fluoride Copolymers, Phase Transitions **18**, 143 (1989)
5.49 D. K. Das-Gupta (Ed.): *Ferroelectric Polymer and Ceramic-Polymer Composites* (Trans Tech Publications, Aedermannsdorf 1994)

5.50 H. S. Nalva (Ed.): *Ferroelectric Polymers: Chemistry, Physics and Applications* (Marcel Dekker, New York 1995)
5.51 H. Kodama, Y. Takahashi, T. Furukawa: Effects of Annealing on the Structure and Switching Characteristics of VDF/TrFE Copolymers, Ferroelectrics **205**, 433 (1997)
5.52 N. A. Clark, S. T. Lagerwall: Submicrosecond Bistable Electro-Optic Switching in Liquid Crystals, Appl. Phys. Lett. **36**, 899 (1980)
5.53 A. D. L. Chandani, E. Gorecka, Y. Ouchi, H. Takezoe, A. Fukuda: Antiferroelectric Chiral Smectic Phases Responsible for the Tristable Switching in MHPOBC, Jpn. J. Appl. Phys. **28**, L1265 (1989)

# Part 5 Special Structures


**1 Liquid Crystals**
Sergei Pestov, Moscow, Russia
Volkmar Vill, Hamburg, Germany

**2 The Physics of Solid Surfaces**
Gianfranco Chiarotti, Roma, Italy

**3 Mesoscopic and Nanostructured Materials**
Fabrice Charra, Gif-sur-Yvette, France
Susana Gota-Goldmann, Fontenay aux Roses, France

# 5.1. Liquid Crystals

Liquid crystals (LCs) are widely used in information-processing devices, for optical visualization of physical influences (heat, IR, high-frequency radiation, pressure, etc.), for nondestructive testing, and for thermography.


5.1.1 **Liquid Crystalline State** ..... 941
5.1.1.1 Chemical Requirements ..... 943
5.1.1.2 Physical Properties of Liquid Crystals ..... 943
5.1.1.3 Applications of Liquid Crystals ... 944
5.1.1.4 List of Abbreviations ..... 944
5.1.1.5 Conversion Factors ..... 945

5.1.2 **Physical Properties of the Most Common Liquid Crystalline Substances** ..... 946
5.1-2 Acids ..... 946
5.1-3 Two-ring Systems without Bridges ..... 947
5.1-4 Two-ring Systems with Bridges . 955
5.1-5 Three and Four-ring Systems .... 964
5.1-6 Ferroelectric Liquid Crystals ..... 967
5.1-7 Cholesteryl (cholest-5-ene) Substituted Mesogens ..... 968
5.1-8 Discotic Liquid Crystals ..... 972
5.1-9 Liquid Crystal Salts ..... 973

5.1.3 **Physical Properties of Some Liquid Crystalline Mixtures** ..... 975
5.1-10 Nematic Mixtures ..... 975
5.1-11 Ferroelectric Mixtures ..... 975

**References** ..... 977


## 5.1.1 Liquid Crystalline State

Liquid crystals represent an intermediate state of order (mesophase) between crystals and liquids. Crystals have a three-dimensional long-range order of both position and orientation (Fig. 5.1-1a). Liquids, in contrast, do not show any long-range order (Fig. 5.1-1b). In plastic crystals (disordered crystals, Fig. 5.1-1c), positional order is maintained, but orientational order is lost. In mesophases, imperfect long-range order is observed, and thus they are situated between crystals and liquids. The reasons for the formation of a mesophase can be the molecular shape or a microphase separation of amphiphilic compounds.

More than 100 000 individual liquid crystals have been prepared until now [1.1–4]. About 2000 of them have been tested for physical properties and technical applications [1.5–14]. These materials can be classified by chemical structures and physical characteristics (see Table 5.1-1).

Generally, molecules of liquid crystalline substances have the following shapes:

- rod-like molecules, which form calamitic liquid crystals (nematicand smectic phases);
- disk-like molecules, which form discotic liquid crystals (discoid nematic and discotic phases);
- amphiphilic compounds, which form layered columnar or cubic phases in the pure state and in solution.

The simplest and most widespread liquid crystalline phase is the nematic phase. The molecules are statistically distributed within the medium, but the long axes are orientated in one direction, the director (Fig. 5.1-2a). A special class of nematic phases is the cholesteric phase

**Table 5.1-1** Classifications of liquid crystals

| | | |
|---|---|---|
| Shape | Rod-like molecules | Disk-like molecules |
| Phase structure | Calamitic liquid crystals | Discotic liquid crystals |
| Mesophase units | Thermotropic liquid crystals | Lyotropic liquid crystals |
| Mesophase origin | Amphiphilic liquid crystals | Monophilic liquid crystals |

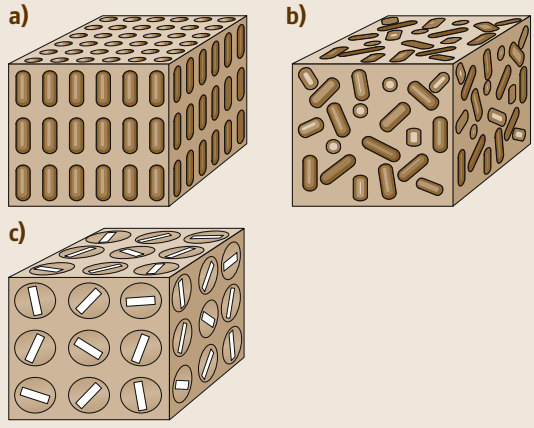


**Fig. 5.1-1a–c** Types of states: (**a**) crystal, (**b**) isotropic liquid, (**c**) plastic crystal

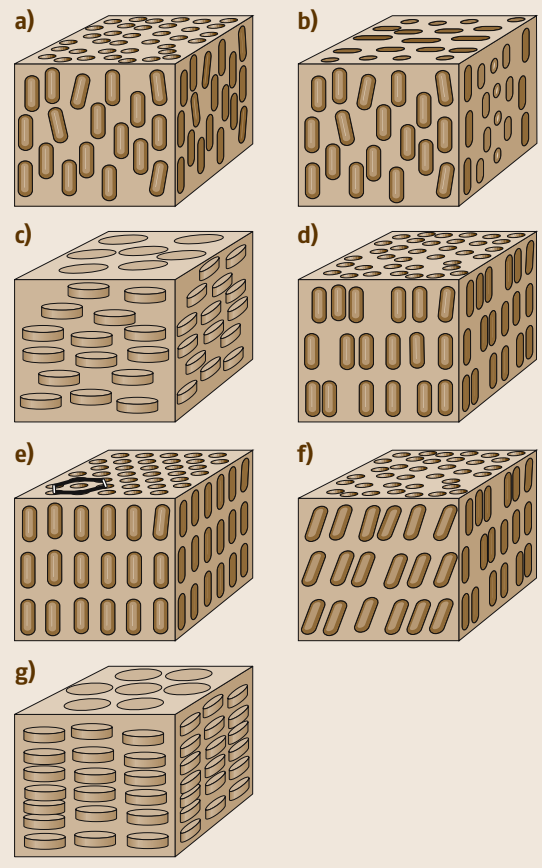


**Fig. 5.1-2a–g** Types of mesophase: (**a**) nematic, (**b**) cholesteric, (**c**) discoid nematic, (**d**) smectic A, (**e**) smectic B, (**f**) smectic C, (**g**) discotic

(Fig. 5.1-2b). Here the orientation of the director does not apply to the whole medium but rather to a virtual layer. Perpendicular to this layer, the director follows a helix with a certain pitch. In the case of the blue phases, such a helical structure is formed not in one but in all three dimensions. Thus, highly complex arrangements, with chiral cubic symmetry in most cases, are generated. Not only rod-like but also disk-like molecules can form nematic phases. The discoid nematic phase is shown in Fig. 5.1-2c.

Rod-like molecules arranged in layers form smectic phases. They are subdivided into a considerable number of different species. These classifications result from various arrangements of the molecules within the layers and different restrictions on their movement. The smectic A phase, the simplest smectic phase, can be regarded as a two-dimensional liquid. The molecules are arranged normal to the layers (Fig. 5.1-2d). The smectic B phase can be interpreted as the closest packing of rod-like molecules, so that within a layer each molecule has a hexagonal environment (Fig. 5.1-2e). The smectic A phase and the smectic C phase are similar, except that in the latter the molecules are tilted within the layers by a tilt angle (Fig. 5.1-2f). A particular case of smectic C is the chiral smectic C* phase, where the tilt angle varies from layer to layer, forming a helical structure. For discussion of other smectic phases, as well as their further subclassification, the reader should consult the references [1.15, 16].

In discotic phases, the disk-like molecules are arranged in columns. In this group, again various phases are possible, depending of the orientation of

the molecules within the columns and the order between the columns. The simplest phase is the hexagonal columnar discotic phase. It can be regarded as a one-dimensional liquid. The columns have a hexagonal order (Fig. 5.1-2g).

Lyotropic liquid crystals are formed by aggregation of micelles. They are multicomponent systems. Normally they consist of an amphiphilic substance and a solvent. In contrast, thermotropic liquid crystals are individual compounds.

Enantiotropic LC phases are formed during both the heating and the cooling process. Monotropic LC phases exist only in the supercooled state below the melting point. Thus, these phases are observed during cooling only.

### 5.1.1.1 Chemical Requirements

A liquid crystalline compound can be divided into the mesogenic group and the side groups. The mesogenic group is subdivided into fragments of rings and bridges. The side groups are subdivided into links and terminal groups.

Many other types of liquid crystalline compounds exist besides those with rod-like molecules e.g. compounds with disk-shaped, banana-shaped, and bowl-shaped molecules. However, over 80% of all liquid crystals have a rod-like form (e.g. the molecule shown in Fig. 5.1-3).

### 5.1.1.2 Physical Properties of Liquid Crystals

The order parameter $S = 0.5(3\langle\cos^2\Theta\rangle - 1)$ characterizes the long-range order of molecules in a mesophase, where $\Theta$ is the momentary angle between the long axis of the molecule and the director. In an ideal crystal the order parameter $S$ equals 1, and it equals 0 in an isotropic liquid. In a nematic phase the order parameter lies in the range 0.5–0.7.

One of the most useful properties for the application of liquid crystals is the anisotropy of their refractive index $\Delta n = n_e - n_o$, where $n_e$ is the extraordinary and $n_o$ is the ordinary refractive index. For nematics, $n_e$ corresponds to $n_\parallel$ and $n_o = n_\perp$. For $n_\perp$ the vibration vector of plane-polarized light is perpendicular to the optical axis, i. e. the director, while for $n_\parallel$ the vibration vector of plane-polarized light is parallel to the director. For the majority of LCs the value of $\Delta n$ is positive, but cholesteryl-substituted compounds are optically negative ($\Delta n < 0$). On increasing the wavelength, $\Delta n$ usually decreases. For homologues $\Delta n$ decreases as the length of the alkyl chains increases.

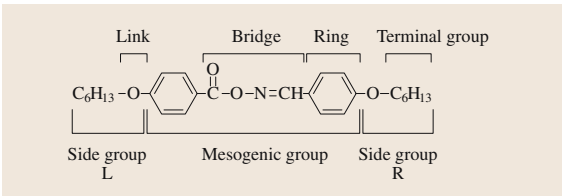


**Fig. 5.1-3** Structure of a calamitic mesogenic compound

The orientation of molecules in an electric field is determined by the sign of the dielectric anisotropy ($\Delta\varepsilon = \varepsilon_\parallel - \varepsilon_\perp$); $\varepsilon_\parallel$ and $\varepsilon_\perp$ are the dielectric constants measured parallel and perpendicular to the director. Some nematic LCs can change their sign of $\Delta\varepsilon$ depending upon the frequency of the applied field.

The majority of mesogens are diamagnetic. The diamagnetic anisotropy ($\Delta\chi$) characterizes the behavior of a LC under the influence of a magnetic field; $\Delta\chi = \chi_\parallel - \chi_\perp$, where $\chi_\parallel$ and $\chi_\perp$ are the diamagnetic susceptibilities parallel and perpendicular to the director.

The basic methods for the determination of phase transition temperatures ($T^{tr}$) are DSC (differential scanning calorimetry), DTA (differential thermal analysis), and polarization microscopy. Every method has its advantages and restrictions. DSC allows one to determine the enthalpies of phase transitions ($\Delta H^{tr}$). Microscopy allows one both to determine the phase transition temperatures and to identify the type of mesophase. DTA gives reliable results for melting temperatures of LCs that show solid-state polymorphism, and of LC mixtures. The differences in $T^{tr}$ that can be found in publications by different authors arise from different measurement techniques and the presence of impurities. We have selected the data with the higher $T^{tr}$ values in such cases.

The temperature dependence of the density ($\varrho$) is practically linear, with the exception of jumps near phase transitions. The volume changes are 3–9%, 0.1–0.4%, and 0.01–0.2% for the crystal–mesophase, nematic–isotropic, and smectic A–nematic transitions, respectively.

The kinematic and dynamic viscosities $\nu$ and $\eta$, respectively, can be determined by a capillary viscometer of the Ubbelohde or Ostwald type ($\nu = \eta/\varrho$).

The surface tension ($\gamma_{LV}$) influences the angle between the surface and the nematic-phase director. It plays an important role in the selection of coatings for the creation of homeotropic alignment (where the molecules are perpendicular to the cell surfaces) or planar alignment (where the molecules are parallel to the surfaces) of LCs. The Friedel–Creagh–Kmetz rule states that if

$\gamma_L$ (energy of LC–surface interaction ) > $\gamma_S$ (solid surface energy), then a homeotropic alignment is induced; otherwise, a parallel alignment is induced.

### 5.1.1.3 Applications of Liquid Crystals

The main requirements on LC materials (LCMs) for electro-optics are a high clearing temperature ($T^{N\text{-}Is}$) and low melting temperature, i. e. a wide temperature range of definite liquid crystalline phases, and a low viscosity for reducing the switching time of electro-optical effects. Wide usage of LCMs in displays became possible after the discovery of mesogenic cyanobiphenyls. At present many of homologous LCs are synthesized for display applications. Phenylcyclohexane- and bicyclohexane-substituted LCs are used as components in LCMs; they have low viscosity and, accordingly, fast switching. Fluorinated three-ring LCs containing two cyclohexane rings and a phenyl ring are used in LCMs with high dielectric anisotropy, which are used at low voltages. For the application of a LCM as a material in LC displays, many properties have to correspond to rigid specifications. For this reason LCMs consist typically of 7 to 15 components. Sometimes LCMs contain non-mesogenic additives, e.g. to reduce the viscosity of the mixture.

In the twist structure, the molecules are parallel to the cell surfaces and the angle between the boundary directors is 90°. In the S effect (Frederics effect), a planar structure is transformed to a homeotropic one, and in the B effect, a homeotropic structure is transformed to a planar one. In the twist effect (or twisted nematic, TN, effect) a twist structure turns into a homeotropic one. The disadvantage of the TN effect is the necessity to use polarizers. The "dynamic scattering mode" of use of LCs depends on the influence of an electric current on the orientation of the molecules. At a high enough voltage, transparent nematic cells becomes turbid. A disadvantage of this effect is that the lower the voltage, the longer the time of switching. One of the modern uses of this effect is use of the dynamic scattering mode for data storage. After the applied voltage is switched off, the mode of the planar cell does not return to its initial state. The cell can be stored in the turbid state for a long time (from some minutes to some months).

The host–guest effect results from a reorientation of dye dopants (1–2% in the LC matrix) in an electric field. In this case the wavelength of maximum absorption of light is shifted and the color of the LC cell changes.

The sign of the dielectric anisotropy of a LCM determines the type of electro-optical effect. LCMs with $\Delta\varepsilon > 0$ are used for the TN (twisted nematic), STN (supertwisted nematic), and TFT (thin-film transistor) effects. LCMs with low negative values of $\Delta\varepsilon$ were formerly used for the dynamic scattering mode. Now LCMs with negative anisotropy $\Delta\varepsilon$ are utilized for MVA-TFT (multidomain vertical-alignment thin-film transistor) displays. The higher the value of $\Delta\varepsilon > 0$, the smaller the working voltage.

Electric current leads to degradation of a LCM and reduces the lifetime of the display. Impurities influence the stability of the material and accelerate electrodegradation. Therefore a multistage purification, consisting for example of recrystallization, and column chromatography, to remove conducting impurities (intermediate products, water, and $CO_2$), is necessary. Usually the specific conductivity of a LCM is lower than $10^{-11}$–$10^{-12}$ C m/cm and corresponds to the intrinsic conductivity.

The elastic constants ($K_i$) determine the switching time of the electro-optical effects. The elastic constant $K_1$ corresponds to the S effect, $K_3$ to the B effect, and $K_2$ to the TN effect; here $K_1$ corresponds to splaying $K_2$ to twisting, and $K_3$ to bending [1.11, 12].

Cholesteryl compounds were the first materials that found application in thermography.

A huge number of other applications exist, where the chemical and physical requirements are totally different. These applications include reflectors, temperature measurement with thermochromic materials, nonlinear optics, polymer materials, SAMs (self-assembled monolayers) and LB (Langmuir–Blodgett) films, the use of liquid crystals in template synthesis of porous materials, drug delivery, and many more.

### 5.1.1.4 List of Abbreviations

| | |
|---|---|
| Cr, Cr′ | crystalline phases |
| S | smectic |
| A, B, C, E, F, G, H | specific smectic mesophases |
| C* | chiral smectic C (ferroelectric) |
| D | discotic |

| | |
|---|---|
| Dh, Dho, Dhd | hexagonal columnar discotic (ordered or disordered) |
| Dr, Dt | rectangular, tilted columnar discotic |
| N | nematic |
| N* | cholesteric |
| Is | isotropic |

Examples

| | |
|---|---|
| Cr 95.0 C 99.0 N 107.5 Is | Crystals melt at 95 °C, smectic C transforms to nematic at 99 °C and to isotropic liquid at 107.5 °C. |
| Cr′ 5.0 Cr 67.3 (N 30.3) Is | Crystals melt at 67.3 °C. Compound has a monotropic nematic phase on cooling below 30.3 °C and polymorphism (solid–solid transition) at 5 °C. |

| | |
|---|---|
| (extra) | Data were extrapolated from 10–20 wt% solution in nematic mixture. |
| dec | Substance decomposes on heating. |

Common names are historical names, and trade names of BDH, Licristal® Merck, and Hoffmann-La Roche [1.8, 9, 17].

| | |
|---|---|
| CAS-RN | Registration number of the Chemical Abstract Service (CAS) |
| $T^{tr}$ | temperatures of phase transitions |
| $T^{N–Is}$ | temperature of nematic–isotropic transition (in Kelvin) |

Relative temperatures (e.g. $T = 0.977T^{N–Is}$) are assumed to be in K only. Inverse temperatures are always given in 1/Kelvin (e.g. $1000/T = 2.4$).
Some data are given for supercooled mesophases ($T < T_{melting}$).

| | |
|---|---|
| $\Delta H^{tr}$ | enthalpies of phase transitions (kJ/mol) |
| $C_p$ | heat capacity at constant pressure (J/(mol K)) |
| $v$ | sound velocity (m/s) |
| $p$ | helix pitch (for N* phase) (μm) |
| $\Delta n$ | anisotropy of the refractive index ($n_e - n_o$) |
| $\Delta\varepsilon$ | dielectric anisotropy |
| $P_s$ | spontaneous polarization (for ferroelectric LC) (nC/cm$^2$) |
| $D$ | diffusion coefficient (m$^2$/s) |
| $C_6H_{12}$ | cyclohexane |

### 5.1.1.5 Conversion Factors

| | |
|---|---|
| Molar mass | $1\ \text{g/mol} = 1\times10^{-3}\ \text{kg/mol}$ |
| Dipole moment ($\mu$) | $1\ \text{D (Debye)} = 3.33564\times10^{-30}\ \text{Cm (Coulomb meter)}$ |
| Density $\varrho$ | $1\ \text{g/cm}^3 = 1\times10^3\ \text{kg/m}^3$ |
| Temperatures of phase transitions $T^{tr}$ | $T(°\text{C}) = T(\text{K}) - 273.15$ |
| Dynamic viscosity $\eta$ | $1\ \text{mPa s} = 1\times10^{-3}\ \text{Pa s} = 1\ \text{cP (centi-Poise)}$ |
| Kinematic viscosity $\nu = \eta/\varrho$ | $1\ \text{mm}^2/\text{s} = 1\times10^{-6}\ \text{m}^2/\text{s} = 1\ \text{cSt (centi-Stokes)}$ |
| Diamagnetic anisotropy $\Delta\chi$ | $1\ \text{m}^3/\text{kg} = 1\times10^3\ \text{cm}^3/\text{g (CGS unit)}$ |
| Thermal conductivity | $1\ \text{W/(m K)} = 1\times10^{-2}\ \text{W/(cm K)}$ |

## 5.1.2 Physical Properties of the Most Common Liquid Crystalline Substances

The compounds are arranged in the tables on the basis of the number and priority of fragments. The order principles for mesogenic groups are the number of rings and bridges, and the priority of rings, bridges, and side groups.

Priority of rings:

benzene > cyclohexane > heterocycles > halogen-substituted benzenes .

Priority of bridges:

$C_nH_m$ > CH=N > N=N > N=N(O) > COO .

Homologues are arranged in order of increasing number of carbon atoms in the alkyl chains.

We have attempted to include all of the most common liquid crystals, from the traditional "model substances" (e.g. 5CB, MBBA, and PAA) to substances used in modern applications.

**Table 5.1-2** Acids

| Number/common name | 1 | 2 | 3 |
|---|---|---|---|
| Substance | 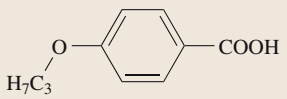 | 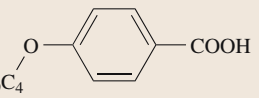 | 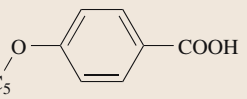 |
| Formula | $C_{10}H_{12}O_3$ | $C_{11}H_{14}O_3$ | $C_{12}H_{16}O_3$ |
| Molar mass (g/mol) | 180.205 | 194.232 | 208.26 |
| CAS-RN | 5438-19-7 | 1498-96-0 | 15872-41-0 |
| Temperatures of phase transitions $T^{tr}$ (°C) | Cr 146.0 N 156.0 Is | Cr 147.5 N 161.0 Is | Cr 124.4 N 151.4 Is |
| Enthalpies of phase transitions $\Delta H^{tr}$ (kJ/mol) | 16.7 (Cr–N), 2.5 (N–Is) | 19.7 (Cr–N), 2.4 (N–Is) | 18.0 (Cr–N), 1.8 (N–Is) |
| Crystallographic space group | $P2_1/c$ | $P\bar{1}$ | $P2_1$ |
| Order parameter $S$ | 0.533 (149 °C) | 0.538 (154 °C) | 0.587 (137 °C) |
| Density $\varrho$ (g/cm$^3$) | 1.0095 (N, 150 °C), 1.0008 (Is, 159 °C) | 1.0079 (N, 150 °C), 0.9883 (Is, 165 °C) | 0.9945 (N, 145 °C), 0.9721 (Is, 155 °C) |
| Refractive index $n$ | $n_e$ 1.632, $n_o$ 1.457 (N, 546 nm, 140.5 °C) | $n_e$ 1.615, $n_o$ 1.449 (N, 589 nm, 149 °C) | $n_e$ 1.602, $n_o$ 1.456 (N, 546 nm, 140.5 °C) |
| Dielectric anisotropy $\Delta\varepsilon$ | – | 0.079 ($T = 0.977\,T^{N–Is}$) | 0.042 ($T = 0.977\,T^{N–Is}$) |
| Dynamic viscosity $\eta$ (mPa s) | 1.81 (149 °C), 2.63 (159 °C) | 1.88 (151 °C), 2.62 (165 °C) | 2.37 (145 °C), 3.30 (155 °C) |
| Diffusion coefficient $D$ (m$^2$/s) | – | $D_\perp = 4\times10^{-10}$, $D_\parallel = 14\times10^{-10}$ ($1000/T = 2.38$) | $D_\perp = 4\times10^{-10}$, $D_\parallel = 12\times10^{-10}$ ($1000/T = 2.45$) |
| **Number/common name** | **4** | **5 (HOBA)** | **6 (OOBA)** |
| Substance | 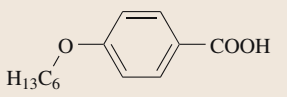 | 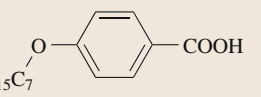 | 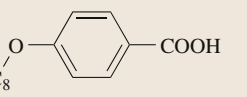 |
| Formula | $C_{13}H_{18}O_3$ | $C_{14}H_{20}O_3$ | $C_{15}H_{22}O_3$ |
| Molar mass (g/mol) | 222.287 | 236.314 | 250.341 |
| CAS-RN | 1142-39-8 | 15872-42-1 | 2493-84-7 |
| Temperatures of phase transitions $T^{tr}$ (°C) | Cr′ 75 Cr 105.4 N 153.2 Is | Cr 94.0 C 102.0 N 147.5 Is | Cr 100.5 C 107.5 N 147.0 Is |
| Enthalpies of phase transitions $\Delta H^{tr}$ (kJ/mol) | 13.8 (Cr–N), 3.3 (N–Is), 6.7 (Cr′–Cr) | 19.2 (Cr–C), 2.5 (N–Is) | 12.7 (Cr–C), 1.1 (C–N), 2.1 (N–Is) |

**Table 5.1-2** Acids, cont.

| Number/common name | 4 | 5 (HOBA) | 6 (OOBA) |
|---|---|---|---|
| Crystallographic space group | $P2_1/c$ (Cr), $P1$ (Cr′) | $P\bar{1}$ | $P\bar{1}$ |
| Order parameter $S$ | 0.611 (129 °C) | 0.626 (123 °C) | 0.615 (128 °C) |
| Density $\varrho$ (g/cm$^3$) | 0.983 (N, 146 °C), 0.969 (Is, 156 °C) | 0.970 (N, 140 °C), 0.959 (Is, 150 °C) | 0.961 (N, 140 °C), 0.945 (Is, 150 °C) |
| Refractive index $n$ | $n_e$ 1.595, $n_o$ 1.453 (546 nm, N, 142.5 °C) | $n_e$ 1.580, $n_o$ 1.452 (546 nm, N, 137.5 °C) | $n_e$ 1.578, $n_o$ 1.450 (546 nm, N, 138.5 °C) |
| Dielectric anisotropy $\Delta\varepsilon$ | 0.052 ($T = 0.977\,T^{N–Is}$) | 0.038 ($T = 0.977\,T^{N–Is}$) | 0.037 ($T = 0.977\,T^{N–Is}$) |
| Dynamic viscosity $\eta$ (mPa s) | 2.61 (146 °C), 3.46 (157 °C) | 3.02 (137 °C), 3.95 (150 °C) | 3.19 (140.5 °C), 3.97 (151 °C) |
| Thermal conductivity (W/(m K)) | 0.137 (N, 115 °C), 0.159 (Is, 157 °C) | 0.146 (N, 130 °C), 0.162 (Is, 159 °C) | – |
| Sound velocity $v$ (m/s) | 972 (3.36 GHz, 141 °C) | 1021 (3.40 GHz, 135 °C) | 1050 (3.63 GHz, 137 °C) |
| Diffusion coefficient $D$ (m$^2$/s) | $D_\perp = 2\times10^{-10}$, $D_\parallel = 8\times10^{-10}$ (1000/$T$ = 2.45) | – | – |
| **Number/common name** | **7** | **8** | **9** |
| Substance | 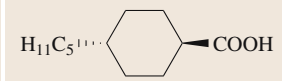 | 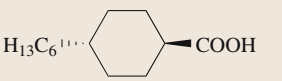 | 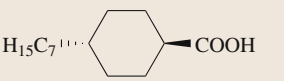 |
| Formula | $C_{12}H_{22}O_2$ | $C_{13}H_{24}O_2$ | $C_{14}H_{26}O_2$ |
| Molar mass (g/mol) | 198.308 | 212.335 | 226.362 |
| CAS-RN | 32829-29-1 | 38289-30-4 | 32829-31-5 |
| Temperatures of phase transitions $T^{tr}$ (°C) | Cr 53.0 (B 45.0) N 105.0 Is | Cr 31.7 B 47.2 N 96.4 Is | Cr′ 31.0 Cr 54.0 B 77.0 N 104.0 Is |
| Enthalpies of phase transitions $\Delta H^{tr}$ (kJ/mol) | 20.9 (Cr–N), 1.1 (N–Is) | 15.7 (Cr–B), 1.0 (B–N), 0.5 (N–Is) | 13.4 (Cr′–Cr), 5.2 (Cr–B), 2.3 (B–N), 1.1 (N–Is) |
| $\Delta\varepsilon$ (N, 90 °C, 500 kHz) | 0.05 | – | 0.05 |

**Table 5.1-3** Two-ring systems without bridges

| Number/common name | 10 (2CB, K6, RO-CM-5106) | 11 (3CB, K9, RO-CM-5109) | 12 (4CB, K12, RO-CM-5112) |
|---|---|---|---|
| Substance | 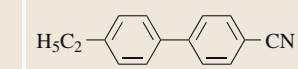 | 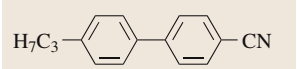 | 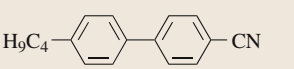 |
| Formula | $C_{15}H_{13}N$ | $C_{16}H_{15}N$ | $C_{17}H_{17}N$ |
| Molar mass (g/mol) | 207.278 | 221.305 | 235.332 |
| CAS-RN | 58743-75-2 | 58743-76-3 | 52709-83-8 |
| Temperatures of phase transitions $T^{tr}$ (°C) | Cr 75.0 (N 22.0) Is | Cr 67.3 (N 30.3) Is | Cr 48.0 (N 16.5) Is |
| Enthalpies of phase transitions $\Delta H^{tr}$ (kJ/mol) | 17.2 (Cr–Is) | 26.8 (Cr–Is), 0.3 (N–Is) | 23.0 (Cr–Is) |
| Crystallographic space group | – | $P2_1/c$ | $P2_1/c$ |
| Anisotropy of refractive index $\Delta n$ | 0.206 | 0.211 | 0.202 |
| Dielectric constant $\varepsilon$ | $\Delta\varepsilon$ +18.9 | $\varepsilon_\parallel$ 25.8, $\varepsilon_\perp$ 6.9 (20 °C) | $\Delta\varepsilon$ +17 |
| Kinematic viscosity $\nu$ (mm$^2$/s) | 5 (70 °C) | 23 (extra, 20 °C), 7 (70 °C) | 7.5 (70 °C) |
| Dipole moment $\mu$ (D), 25 °C | 4.81 ($CCl_4$), 4.96 ($C_6H_{14}$), 4.90 ($C_6H_{12}$), 5.01 ($C_6H_6$) | 4.72 ($CCl_4$), 5.02 ($C_6H_{14}$), 4.93 ($C_6H_{12}$), 4.93 ($C_6H_6$) | 4.73 ($CCl_4$), 5.04 ($C_6H_{14}$), 4.94 ($C_6H_{12}$), 4.99 ($C_6H_6$) |

**Table 5.1-3** Two-ring systems without bridges, cont.

| Number/common name | 13 (5CB, K15, RO-CM-5115) | 14 (6CB, K18, RO-CM-5118) | 15 (7CB, K21, RO-CM-5121) |
|---|---|---|---|
| Substance | 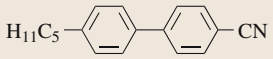 | 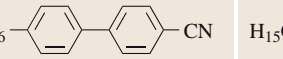 | 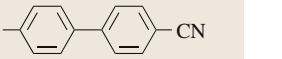 |
| Formula | $C_{18}H_{19}N$ | $C_{19}H_{21}N$ | $C_{20}H_{23}N$ |
| Molar mass (g/mol) | 249.359 | 263.386 | 277.413 |
| CAS-RN | 40817-08-1 | 41122-70-7 | 41122-71-8 |
| Temperatures of phase transitions $T^{tr}$ (°C) | Cr 24.0 N 35.3 Is | Cr 14.3 N 30.1 Is | Cr′ 15.0 Cr 30.0 N 42.8 Is |
| Enthalpies of phase transitions $\Delta H^{tr}$ (kJ/mol) | 17.2 (Cr–N), 0.4 (N–Is) | 24.3 (Cr–N), 0.4 (N–Is) | 25.9 (Cr–N), 0.9 (N–Is) |
| Crystallographic space group | $P2_1/a$ | $P1$ | $P1$ |
| Order parameter $S$ | 0.64 (24 °C) | – | 0.65 (29 °C) |
| Density $\varrho$ (g/cm$^3$) | 1.022 (N, 24 °C), 1.016 (N, 30 °C) | 1.017 (N, 20 °C), | 1.001 (N, 29 °C), 0.991 (N, 39 °C) |
| Refractive index $n$ (589 nm) | $n_e$ 1.716, $n_o$ 1.533 (N, 24 °C, 589 nm) | $n_e$ 1.687, $n_o$ 1.531 (N, 20 °C, 633 nm) | $n_e$ 1.679, $n_o$ 1.522 (N, 32 °C, 589 nm) |
| Dielectric constant $\varepsilon$ | $\varepsilon_\parallel$ 20, $\varepsilon_\perp$ 7 (25 °C, 1.5 kHz) | $\varepsilon_\parallel$ 14.45, $\varepsilon_\perp$ 7.2 (28 °C, 1 kHz) | $\varepsilon_\parallel$ 13.55, $\varepsilon_\perp$ 6.8 (41 °C, 1 kHz) |
| Viscosity | $\eta$ 28 mPa s (25 °C) | $\nu$ 46 mm$^2$/s (20 °C) | $\nu$ 26 mm$^2$/s (20 °C) |
| Surface tension (mN/m) | 33 (N, 20 °C), 28 (N, 30 °C), 28.3 (Is, 40 °C) | 27.4 (N, 22 °C), 28.0 (Is, 32 °C) | 26.3 (N, 37 °C), 27.5 (Is, 47 °C) |
| Thermal conductivity (W/(m K)) (N, 25 °C) | $k_\perp$ 0.124, $k_\parallel$ 0.242 | $k_\perp$ 0.126, $k_\parallel$ 0.223 | $k_\perp$ 0.127, $k_\parallel$ 0.269 |
| Magnetic susceptibility $\Delta\chi$ (m$^3$/kg) ($\times 10^{-12}$) | 113.5 (25.6 °C) | 101.5 (20 °C) | 102.0 (33 °C) |
| Sound velocity $v$ (m/s) | $v_\parallel$ 1740, $v_\perp$ 1680 (14.75 GHz, 30 °C) | $v_\parallel$ 1776, $v_\perp$ 1712 (14.75 GHz, 25 °C) | $v_\parallel$ 1675, $v_\perp$ 1640 (14.75 GHz, 38 °C) |
| Diffusion coefficient $D$ (m$^2$/s) | $D_\perp$ $6.8\times10^{-8}$, $D_\parallel$ $12.7\times10^{-8}$ (25 °C) | $D_\perp$ $6.4\times10^{-8}$, $D_\parallel$ $10.9\times10^{-8}$ (25 °C) | $D_\perp$ $6.8\times10^{-8}$, $D_\parallel$ $14.4\times10^{-8}$ (25 °C) |
| Dipole moment $\mu$ (D), 25 °C | 4.85 ($CCl_4$), 5.08 ($C_6H_{14}$), 4.95 ($C_6H_{12}$), 4.93 ($C_6H_6$) | 4.83 ($CCl_4$), 5.09 ($C_6H_{14}$), 5.01 ($C_6H_{12}$), 4.98 ($C_6H_6$) | 4.74 ($CCl_4$), 5.11 ($C_6H_{14}$), 4.94 ($C_6H_{12}$), 4.97 ($C_6H_6$) |
| **Number/common name** | **16 (8CB, K24)** | **17 (9CB, K27)** | **18 (10CB, K30)** |
| Substance | 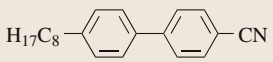 | 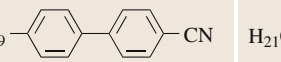 | 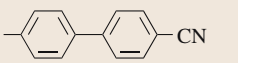 |
| Formula | $C_{21}H_{25}N$ | $C_{22}H_{27}N$ | $C_{23}H_{29}N$ |
| Molar mass (g/mol) | 291.44 | 305.467 | 319.494 |
| CAS-RN | 52709-84-9 | 52709-85-0 | 59454-35-2 |
| Temperatures of phase transitions $T^{tr}$ (°C) | Cr 21.5 A 33.5 N 40.5 Is | Cr 42.0 A 48.0 N 49.5 Is | Cr 44.0 A 54.5 Is |
| Enthalpies of phase transitions $\Delta H^{tr}$ (kJ/mol) | 28.3 (Cr–A), 0.2 (A–N), 0.7 (N–Is) | 33.5 (Cr–A), 0.6 (A–N), 1.7 (N–Is) | 33.1 (Cr–A), 2.8 (N–Is) |
| Crystallographic space group | $P2_1/n$ | $P\bar{1}$ | $P2_1/n$ |
| Density $\varrho$ (g/cm$^3$) | 0.991 (A, 32.5 °C), 0.981 (N, 40 °C), 0.978 (Is, 41 °C) | 0.973 (A, 47.7 °C), 0.968 (N, 49.5 °C) | – |
| Refractive index $n$ (589 nm) | $n_e$ 1.657, $n_o$ 1.524 (N, 37.4 °C) | $n_e$ 1.638, $n_o$ 1.519 (N, 49 °C) | – |
| Dielectric constant $\varepsilon$ (1 kHz) | $\varepsilon_\parallel$ 12.8, $\varepsilon_\perp$ 5.3 (N, 34 °C), $\varepsilon_\parallel$ 12.4, $\varepsilon_\perp$ 4.8 (A, 28 °C) | $\varepsilon_\parallel$ 12.5, $\varepsilon_\perp$ 5.1 (44 °C) | $\varepsilon$ 8.8 (Is, 64.5 °C) |
| Dynamic viscosity $\eta$ (mPa s) | 35 (N, 33.5 °C) | – | – |

**Table 5.1-3** Two-ring systems without bridges, cont.

| Number/common name | 16 (8CB, K24) | 17 (9CB, K27) | 18 (10CB, K30) |
|---|---|---|---|
| Surface tension (mN/m) | 25.5 (N, 35 °C), 26.2 (Is, 41 °C) | – | – |
| Thermal conductivity (W/(m K)) | $k_\perp$ 0.130, $k_\parallel$ 0.276 (A, 30 °C), $k_\perp$ 0.132, $k_\parallel$ 0.254 (N, 35 °C) | $k_\perp$ 0.130, $k_\parallel$ 0.310 (40 °C) | – |
| Magnetic susceptibility $\Delta\chi$($m^3$/kg) ($\times10^{-12}$) | 88 (35 °C) | 88.5 (48.9 °C) | – |
| Sound velocity $v$ (m/s) | $v_\parallel$ 1596, $v_\perp$ 1545 (14.75 GHz, 39 °C) | $v_\parallel$ 1740, $v_\perp$ 1680 (14.75 GHz, 44.5 °C) | – |
| Diffusion coefficient $D$ ($m^2$/s) | $D_\perp$ $6\times10^{-8}$, $D_\parallel$ $12\times10^{-8}$ (A, 30 °C), $D_\perp$ $5.8\times10^{-8}$, $D_\parallel$ $10\times10^{-8}$ (N, 35 °C) | $D_\perp$ $6.6\times10^{-8}$, $D_\parallel$ $15.2\times10^{-8}$ (A, 40 °C) | – |
| Dipole moment $\mu$ (D), 25 °C | 4.78 ($CCl_4$), 5.12 ($C_6H_{14}$), 4.93 ($C_6H_{12}$), 5.00 ($C_6H_6$) | 4.73 ($CCl_4$), 5.11 ($C_6H_{14}$), 4.94 ($C_6H_{12}$), 4.94 ($C_6H_6$) | 4.76 ($CCl_4$), 5.10 ($C_6H_{14}$), 5.00 ($C_6H_{12}$), 5.00 ($C_6H_6$) |
| **Number/common name** | **19 (3OCB, M9, RO-CM-5309)** | **20 (4OCB, M12)** | **21 (5OCB, M15, RO-CM-5315)** |
| Substance | 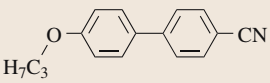 | 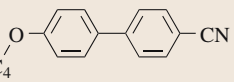 | 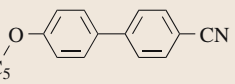 |
| Formula | $C_{16}H_{15}NO$ | $C_{17}H_{17}NO$ | $C_{18}H_{19}NO$ |
| Molar mass (g/mol) | 237.304 | 251.331 | 265.368 |
| CAS-RN | 52709-86-1 | 52709-87-2 | 52364-71-3 |
| Temperatures of phase transitions $T^{tr}$ (°C) | Cr 71.5 (N 64.0) Is | Cr 78.0 (N 75.5) Is | Cr′ 48.0 Cr 53.0 N 68.0 Is |
| Enthalpies of phase transitions $\Delta H^{tr}$ (kJ/mol) | 19.2 (Cr–Is) | 23.4 (Cr–Is) | 28.9 (Cr–N), 0.2 (N–Is) |
| Crystallographic space group | $P2_1/c$ | $Pca2_1$ | $P2_1/n$ |
| Order parameter $S$ | – | – | 0.63 (55 °C) |
| Density $\varrho$ (g/$cm^3$) | 1.19 (Cr) | 1.14 (Cr) | 1.042 (N, 61.5 °C), 1.029 (Is, 70 °C) |
| Refractive index $n$ (589 nm) | – | – | $n_e$ 1.697, $n_o$ 1.528 (N, 55 °C) |
| Dielectric constant $\varepsilon$ (1 kHz) | – | $\Delta\varepsilon$ +28.7, $\varepsilon_\perp$ +7.5 (20 °C, extra) | $\Delta\varepsilon$ +8.5, $\varepsilon_\parallel$ 16.7 ($T = 0.98T^{N–Is}$) |
| Kinemamic viscosity $\nu$ ($mm^2$/s) | 10 (Is, 80 °C) | 10 (75 °C) | 20 (53 °C), 10 (85 °C) |
| Surface tension (mN/m) | – | – | 33.2 (N, 51 °C), 31.9 (Is, 70 °C) |
| Magnetic susceptibility $\Delta\chi$ ($m^3$/kg) ($\times10^{-12}$) | – | – | 87 (58 °C), 98 (50 °C) |
| Dipole moment $\mu$ (D) | – | 5.1 | – |
| **Number/common name** | **22 (6OCB, M18)** | **23 (7OCB, M21)** | **24 (8OCB, M24, RO-CM-5324)** |
| Substance | 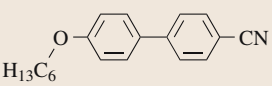 | 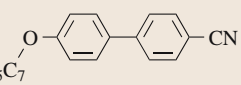 | 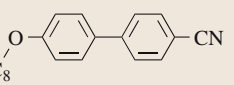 |
| Formula | $C_{19}H_{21}NO$ | $C_{20}H_{23}NO$ | $C_{21}H_{25}NO$ |
| Molar mass (g/mol) | 279.385 | 293.412 | 307.44 |
| CAS-RN | 41424-11-7 | 52364-72-4 | 52364-73-5 |
| Temperatures of phase transitions $T^{tr}$ (°C) | Cr′ 44.0 Cr 57.0 N 75.5 Is | Cr′ 45.5 Cr 53.5 N 75.0 Is | Cr′ 46.0 Cr′ 51.0 Cr 54.5 A 67.0 N 80.0 Is |
| Enthalpies of phase transitions $\Delta H^{tr}$ (kJ/mol) | 29.7 (Cr–N), 0.8 (N–Is) | 28.9 (Cr–N), 0.6 (N–Is) | 28.5 (Cr–A), 0.1 (A–N), 0.8 (N–Is) |

**Table 5.1-3** Two-ring systems without bridges, cont.

| Number/common name | 22 (6OCB, M18) | 23 (7OCB, M21) | 24 (8OCB, M24, RO-CM-5324) |
|---|---|---|---|
| Crystallographic space group | – | $P2_1/c$, $P\bar{1}$ | $P\bar{1}$ |
| Order parameter $S$ | – | 0.61 (63 °C) | |
| Density $\varrho$ (g/cm$^3$) | 1.017 (N, 71 °C),<br>1.025 (N, 63 °C) | 1.0051 (N, 63 °C),<br>0.9869 (Is, 79.5 °C) | 0.990 (N, 75 °C),<br>0.977 (Is, 85 °C) |
| Refractive index $n$ (589 nm) | $n_e$ 1.72, $n_o$ 1.50 (60 °C) | $n_e$ 1.6734, $n_o$ 1.5155 (60 °C) | $n_e$ 1.647, $n_o$ 1.509 (71 °C) |
| Dielectric constant $\varepsilon$ (1 kHz) | $\Delta\varepsilon$ +8.0,<br>$\varepsilon_\parallel$ 15.8 ($T = 0.98T^{N–Is}$) | $\Delta\varepsilon$ +7.5,<br>$\varepsilon_\parallel$ 15.0 ($T = 0.98T^{N–Is}$) | $\Delta\varepsilon$ +8.0 (N, 74 °C) |
| Kinematic viscosity $\nu$ (mm$^2$/s) | 17 (60 °C), 12 (85 °C) | 10 (70 °C), 30 (50 °C) | 16 (70 °C), 12 (85 °C) |
| Surface tension (mN/m) | – | – | 36.5 (A, 60), 35.4 (N, 70),<br>30.5 (Is, 80) |
| Magnetic susceptibility $\Delta\chi$ (m$^3$/kg) (×10$^{-12}$) | 88 (67 °C), 80 (71 °C) | 71 (70 °C), 87.5 (60 °C) | 83 (70.6 °C) |
| Dipole moment $\mu$ (D) | 5.2 | 4.9 | 5.2 ($CCl_4$) |
| **Number/common name** | **25 (PCH-3)** | **26 (PCH-4)** | **27 (PCH-5)** |
| Substance | 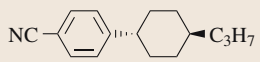 | 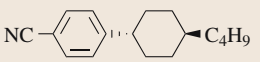 | 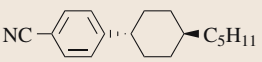 |
| Formula | $C_{16}H_{21}N$ | $C_{17}H_{23}N$ | $C_{18}H_{25}N$ |
| Molar mass (g/mol) | 227.352 | 241.38 | 255.407 |
| CAS-RN | 61203-99-4 | 61204-00-0 | 61204-01-1 |
| Temperatures of phase transitions $T^{tr}$ (°C) | Cr 42.7 N 45.9 Is | Cr 41.0 N 39.0 Is | Cr 30.0 N 55.0 Is |
| Enthalpies of phase transitions $\Delta H^{tr}$ (kJ/mol) | 19.0 (Cr–N), 0.7 (N–Is) | 22.2 (Cr–Is) | 18.0 (Cr–N), 0.9 (N–Is) |
| Crystallographic space group | $C2/c$ | $P2_1/c$, $P\bar{1}$ | – |
| Order parameter $S$ | 0.64 (43 °C) | – | 0.54 (43 °C) |
| Density $\varrho$ (g/cm$^3$) | 0.9672 (N, 43 °C),<br>0.9571 (Is, 46.5 °C) | 0.962 (N, 35 °C),<br>0.951 (Is, 43 °C) | 0.967 (N, 25 °C),<br>0.932 (Is, 60 °C) |
| Refractive index $n$ (589 nm) | $n_e$ 1.582, $n_o$ 1.492 (N, 43 °C) | $n_e$ 1.579, $n_o$ 1.498 (N, 37 °C) | $n_e$ 1.600, $n_o$ 1.492 (N, 40 °C) |
| Dielectric constant $\varepsilon$ (1 kHz) | $\varepsilon_\parallel$ 19.3, $\varepsilon_\perp$ 5.5 ($T = 0.95T^{N–Is}$) | $\Delta\varepsilon$ +11 (20 °C) | $\varepsilon_\parallel$ 14.4, $\varepsilon_\perp$ 5.2 (39 °C) |
| Viscosity (20 °C) | $\eta$ 19.2 mPa s | $\nu$ 23 mm$^2$/s | $\nu$ 23 mm$^2$/s |
| Dipole moment $\mu$ (D) | 3.9 | – | 4.1 |
| **Number/common name** | **28 (PCH-7)** | **29 (PCH-8)** | **30 (PCH-32, RO-CM-4232, ZLI-1484)** |
| Substance | 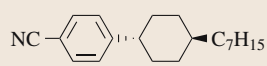 | 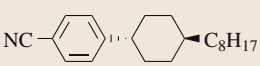 | 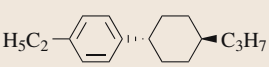 |
| Formula | $C_{20}H_{29}N$ | $C_{21}H_{31}N$ | $C_{17}H_{26}$ |
| Molar mass (g/mol) | 283.461 | 297.488 | 230.397 |
| CAS-RN | 61204-03-3 | 83626-40-8 | 82991-47-7 |
| Temperatures of phase transitions $T^{tr}$ (°C) | Cr 30.0 N 57.8 Is | Cr 37.0 N 55.0 Is | Cr −1 Is |

**Table 5.1-3** Two-ring systems without bridges, cont.

| Number/common name | 28 (PCH-7) | 29 (PCH-8) | 30 (PCH-32, RO-CM-4232, ZLI-1484) |
|---|---|---|---|
| Enthalpies of phase transitions $\Delta H^{tr}$ (kJ/mol) | 25.5 (Cr–N), 1.0 (N–Is) | – | 18.4 (Cr–Is) |
| Crystallographic space group | – | $P2_1/c$, $P\bar{1}$ (Cr′) | – |
| Order parameter $S$ | 0.47 (47 °C) | – | – |
| Density $\varrho$ (g/cm$^3$) | 0.952 (N, 30 °C), 0.915 (Is, 67 °C) | 0.941 (N, 37 °C), 0.915 (Is, 62 °C) | 0.909 (20 °C) |
| Refractive index $n$ (589 nm) | $n_e$ 1.590, $n_o$ 1.482 (47 °C) | – | 1.514 (20 °C) |
| Dielectric constant $\varepsilon$ (1 kHz) | $\varepsilon_\parallel$ 12.9, $\varepsilon_\perp$ 4.2 (31 °C) | – | $\varepsilon$ 2.293, $\Delta\varepsilon$ +0.5 (20 °C, extra) |
| Kinematic viscosity $\nu$ (mm$^2$/s) | 28 (extra, 20 °C) | – | 4 (extra, 20 °C) |
| **Number/common name** | **31 (PCH-301, ZLI-2446)** | **32 (PCH-302, ZLI-1476)** | **33 (PCH-304, ZLI-1477)** |
| Substance | 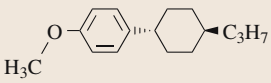 | 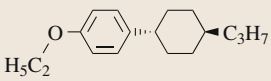 | 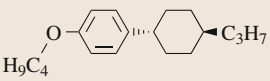 |
| Formula | $C_{16}H_{24}O$ | $C_{17}H_{26}O$ | $C_{19}H_{30}O$ |
| Molar mass (g/mol) | 232.369 | 246.396 | 274.45 |
| CAS-RN | 81936-32-5 | 80944-44-1 | 79709-84-5 |
| Temperatures of phase transitions $T^{tr}$ (°C) | Cr 32.0 (N 10.0) Is | Cr 40.8 (N 37.8) Is | Cr 35.5 (N 33.0) Is |
| Enthalpies of phase transitions $\Delta H^{tr}$ (kJ/mol) | 17.6 (Cr–Is) | 26.4 (Cr–Is), 0.7 (N–Is) | 30.6 (Cr–Is), 0.5 (N–Is) |
| Anisotropy of refractive index $\Delta n$ (20 °C, 589 nm) | 0.09 (extra) | 0.09 (extra) | 0.09 (extra) |
| Dielectric anisotropy $\Delta\varepsilon$ (20 °C, 1 kHz) | −0.5 (extra) | −0.5 (extra) | −0.5 (extra) |
| Kinematic viscosity $\nu$ (mm$^2$/s) | 6 (extra, 20 °C) | 7 (extra, 20 °C) | 10 (extra, 20 °C) |
| **Number/common name** | **34 (H33, ZLI-1305)** | **35** | **36** |
| Substance | 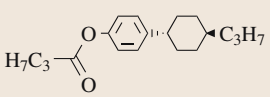 | 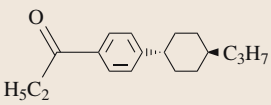 | 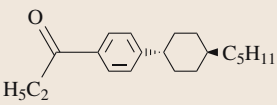 |
| Formula | $C_{19}H_{28}O_2$ | $C_{18}H_{26}O$ | $C_{20}H_{30}O$ |
| Molar mass (g/mol) | 288.434 | 258.407 | 286.462 |
| Temperatures of phase transitions $T^{tr}$ (°C) | Cr 11.0 B 26.1 N 30.3 Is | Cr 49.2 N 56.5 Is | Cr 56.6 N 68.8 Is |
| Enthalpies of phase transitions $\Delta H^{tr}$ (kJ/mol) | 16.4 (Cr–B), 4.9 (B–N), 0.4 (N–Is) | – | – |
| Refractive index $n$ (589 nm) | $\Delta n$ 0.09 (20 °C) | $n_e$ 1.589, $n_o$ 1.497 ($T = 0.95T^{N–Is}$) | $n_e$ 1.574, $n_o$ 1.487 ($T = 0.95T^{N–Is}$) |
| Dielectric constant $\varepsilon$ (1 kHz) | $\Delta\varepsilon$ −1.5 (20 °C) | $\varepsilon_\parallel$ 9.0, $\varepsilon_\perp$ 7.6 ($T = 0.95T^{N–Is}$) | $\varepsilon_\parallel$ 8.3 $\varepsilon_\perp$ 6.9 ($T = 0.95T^{N–Is}$) |
| Viscosity $\nu$ (20 °C) | 15 mm$^2$/s (extra) | – | – |
| Diamagnetic anisotropy $\Delta\chi$ (m$^3$/mol) (×10$^{-12}$) | – | 25.3 | 26.1 |
| Dipole moment $\mu$ (D) | – | 3.02 | 3.1 |

**Table 5.1-3** Two-ring systems without bridges, cont.

| Number/common name | 37 | 38 | 39 |
|---|---|---|---|
| Substance | 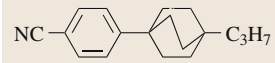 | 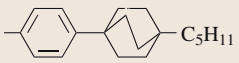 | 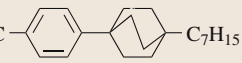 |
| Formula | $C_{18}H_{23}N$ | $C_{20}H_{27}N$ | $C_{22}H_{31}N$ |
| Molar mass (g/mol) | 253.391 | 281.445 | 309.499 |
| CAS-RN | – | 74385-67-4 | – |
| Temperatures of phase transitions $T^{tr}$ (°C) | Cr 66.5 N 88.0 Is | Cr 62.0 N 100.0 Is | Cr 61.0 N 95.0 Is |
| Enthalpies of phase transitions $\Delta H^{tr}$ (kJ/mol) | 17.4 (Cr–N) | 20.7 (Cr–N) | 32.7 (Cr–N) |
| Density $\varrho$ (g/cm$^3$) | 1.007 (N, 66 °C) | 0.993 (N, 60 °C) | 0.975 (N, 65 °C) |
| Refractive index $n$ (633 nm) | $n_e$ 1.614, $n_o$ 1.492 (66 °C) | $n_e$ 1.616, $n_o$ 1.490 (60 °C) | $n_e$ 1.598, $n_o$ 1.489 (65 °C) |
| Dielectric constant $\varepsilon$ (10 kHz) | $\varepsilon_\perp$ 5.2, $\varepsilon_\parallel$ 15.4 (66 °C) | $\varepsilon_\perp$ 4.6, $\varepsilon_\parallel$ 13.1 (60 °C) | $\varepsilon_\perp$ 4.4, $\varepsilon_\parallel$ 12.0 (65 °C) |
| Viscosity $\nu$ (mm$^2$/s) | – | 7.8 (70 °C) | – |
| Dipole moment $\mu$ (D) | – | 4.1 | – |
| **Number/common name** | **40 (CCH-3)** | **41 (CCH-5)** | **42 (CCH-7)** |
| Substance | 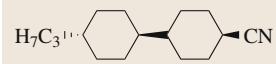 | 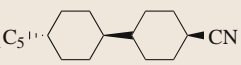 | 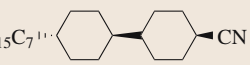 |
| Formula | $C_{16}H_{27}N$ | $C_{18}H_{31}N$ | $C_{20}H_{35}N$ |
| Molar mass (g/mol) | 233.4 | 261.454 | 289.509 |
| CAS-RN | 65355-35-3 | 65355-36-4 | 65355-37-5 |
| Temperatures of phase transitions $T^{tr}$ (°C) | Cr 58.0 (S 18.0 S 44.0 S 48.0 B 57.0) N 80.0 Is | Cr′ 59.2 Cr 63.4 (S 40.5 B 49.1) N 86.4 Is | Cr 71.0 N 83.0 Is |
| Enthalpies of phase transitions $\Delta H^{tr}$ (kJ/mol) | 26.8 (Cr–N), 1.1 (N–Is) | 26.8 (Cr–N), 1.3 (N–Is) | 33.9 (Cr–N), 0.9 (N–Is) |
| Crystallographic space group | $P\bar{1}$ | $P2_1/c$, $P2_12_12_1$ (Cr′) | $P2_12_12_1$ |
| Density $\varrho$ (g/cm$^3$) | 0.902 (N, 73 °C), 0.885 (Is, 87 °C) | 0.902 (N, 72 °C) | 0.893 (N, 70 °C) |
| Order parameter $S$ | 0.53 (73 °C) | 0.62 (72 °C) | 0.52 (71 °C) |
| Refractive index $n$ (589 nm) | $n_e$ 1.4930, $n_o$ 1.4553 (N, 73 °C) | $n_e$ 1.5061, $n_o$ 1.4568 (N, 72 °C) | $n_e$ 1.502, $n_o$ 1.456 (N, 70 °C) |
| Dielectric constant $\varepsilon$ (1 kHz) | $\varepsilon_\perp$ 5.5, $\varepsilon_\parallel$ 10.0 (73 °C) | $\varepsilon_\perp$ 4.75, $\varepsilon_\parallel$ 9.25 (73 °C) | $\varepsilon_\perp$ 3.89, $\varepsilon_\parallel$ 7.17 (74 °C) |
| Viscosity $\nu$ (mm$^2$/s) (20 °C) | 63 (extra) | 66 (extra) | 78 (extra) |
| Dipole moment $\mu$ (D) | – | 3.8 (xylene) | – |
| **Number/common name** | **43 (RO-CM-4513)** | **44 (RO-CM-4535)** | **45 (CCH-301)** |
| Substance | 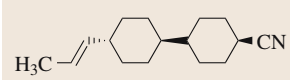 | 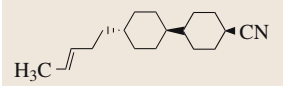 | 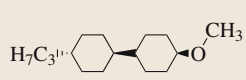 |
| Formula | $C_{16}H_{25}N$ | $C_{18}H_{29}N$ | $C_{16}H_{30}O$ |
| Molar mass (g/mol) | 231.384 | 259.439 | 238.417 |
| CAS-RN | 122705-86-6 | – | – |

**Table 5.1-3** Two-ring systems without bridges, cont.

| **Number/common name** | **43 (RO-CM-4513)** | **44 (RO-CM-4535)** | **45 (CCH-301)** |
|---|---|---|---|
| Temperatures of phase transitions $T^{tr}$ (°C) | Cr 64.9 N 99.7 Is | Cr 79.5 (A 45.0) N 100.0 Is | Cr 10.0 N 17.0 Is |
| Enthalpies of phase transitions $\Delta H^{tr}$ (kJ/mol) | – | – | 18.8 (Cr–N) |
| Refractive index $n$ (589 nm) | $\Delta n$ 0.066, $n_o$ 1.457 (89.7 °C) | $\Delta n$ 0.065, $n_o$ 1.456 (89.7 °C) | – |
| Dielectric constant $\varepsilon$ (1 kHz) | $\varepsilon_\perp$ 4.35, $\Delta\varepsilon$ +5.03 (89.7 °C) | $\varepsilon_\perp$ 4.12, $\Delta\varepsilon$ +4.61 (89.7 °C) | $\Delta\varepsilon$ −0.3 (20 °C) |
| Viscosity $\nu$ (mm²/s) (20 °C) | – | – | 7 (extra) |
| Dipole moment $\mu$ (D) | 3.76 | 3.83 | – |
| **Number/common name** | **46 (CCN55, ZLI-2395)** | **47 (C33)** | **48 (C35)** |
| Substance | 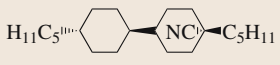 | 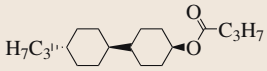 | 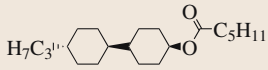 |
| Formula | $C_{23}H_{41}N$ | $C_{19}H_{34}O_2$ | $C_{21}H_{38}O_2$ |
| Molar mass (g/mol) | 331.59 | 294.482 | 322.536 |
| CAS-RN | 88510-89-8 | – | – |
| Temperatures of phase transitions $T^{tr}$ (°C) | Cr 25.0 B 30.0 N 66.0 Is | Cr 41.0 B 69.0 N 73.0 Is | Cr 44.0 S 46.0 N 74.0 Is |
| Enthalpies of phase transitions $\Delta H^{tr}$ (kJ/mol) | 22.6 (Cr–S) | 22.6 (Cr–S) | 23.8 (Cr–S) |
| Anisotropy of refractive index $\Delta n$ (extra, 20 °C, 589 nm) | 0.03 | 0.04 | 0.03 |
| Dielectric anisotropy $\Delta\varepsilon$ (20 °C, 1 kHz) | −8.4 (extra) | −1.6 (extra) | −0.8 (extra) |
| Viscosity $\nu$ (mm²/s) (20 °C) | 67 (extra) | 11 (extra) | 13 (extra) |
| **Number/common name** | **49** | **50 (RO-CM-7035)** | **51 (RO-CM-7037, RO-CP-7037)** |
| Substance | 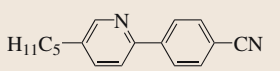 | 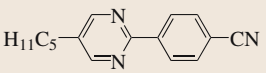 | 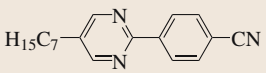 |
| Formula | $C_{17}H_{18}N_2$ | $C_{16}H_{17}N_3$ | $C_{18}H_{21}N_3$ |
| Molar mass (g/mol) | 250.346 | 251.334 | 279.388 |
| CAS-RN | 77782-82-2 | 59855-05-9 | 59854-97-6 |
| Temperatures of phase transitions $T^{tr}$ (°C) | Cr 33.6 N 43.5 Is | Cr 71.0 (N 52.0) Is | Cr 45.0 N 51.0 Is |
| Enthalpies of phase transitions $\Delta H^{tr}$ (kJ/mol) | 20.9 (Cr–N) | – | 0.4 (N–Is) |
| Density $\varrho$ (g/cm³) | 1.0483 (N, 30.0 °C) | – | – |
| Anisotropy of refractive index $\Delta n$ | 0.176 ($T = 0.95T^{N–Is}$) | 0.220 (extra, 20 °C) | 0.2098 |
| Dielectric constant $\varepsilon$ | $\varepsilon_\parallel$ 28.7, $\Delta\varepsilon$ +17.8 (27.7 °C) | $\Delta\varepsilon$ +21.3, $\varepsilon_\parallel$ 31.3 ($T = 0.98T^{N–Is}$, 1.592 kHz) | $\Delta\varepsilon$ +16.0, $\varepsilon_\parallel$ 24.6 ($T = 0.98T^{N–Is}$) |
| Viscosity | $\nu$ 50 mm²/s (extra, 20 °C) | $\nu$ 55 mm²/s (extra, 20 °C) | $\eta$ 25 mPa s (38 °C) |
| Diamagnetic anisotropy $\Delta\chi$ (m³/kg) (×10⁻¹²) | – | – | 90.7 ($T = 0.98T^{N–Is}$) |
| Dipole moment $\mu$ (D) | 6.0 | 6.0 | 6.7 |

**Table 5.1-3** Two-ring systems without bridges, cont.

| Number/common name | 52 (PYP605, ZLI-2543) | 53 (PYP606, ZLI-2303) | 54 (PYP607, ZLI-2304) |
|---|---|---|---|
| Substance | 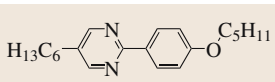 | 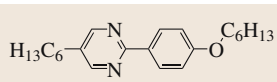 | 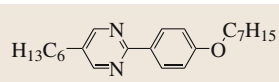 |
| Formula | $C_{21}H_{30}N_2O$ | $C_{22}H_{32}N_2O$ | $C_{23}H_{34}N_2O$ |
| Molar mass (g/mol) | 326.486 | 340.513 | 354.54 |
| CAS-RN | 57202-28-5 | 51518-75-3 | 57202-29-6 |
| Temperatures of phase transitions $T^{tr}$ (°C) | Cr 43.0 N 53.0 Is | Cr 30.5 N 60.8 Is | Cr 35.5 N 58.3 Is |
| Enthalpies of phase transitions $\Delta H^{tr}$ (kJ/mol) | 29.4 (Cr–N), 1.2 (N–Is) | 19.2 (Cr–N), 1.4 (N–Is) | 32.7 (Cr–N), 1.5 (N–Is) |
| Density $\varrho$ (g/cm$^3$) | 0.9899 (N, 48.0 °C), 0.9673 (Is, 68.0 °C) | 0.9857 (N, 48.0 °C), 0.9618 (Is, 68.0 °C) | 0.9806 (N, 48.0 °C), 0.9562 (Is, 68.0 °C) |
| Refractive index $n$ (589 nm) | $n_e$ 1.6217, $n_o$ 1.5042 (48 °C) | $n_e$ 1.6435, $n_o$ 1.4939 (48 °C) | $n_e$ 1.6305, $n_o$ 1.4940 (48 °C) |
| Dielectric constant (1 kHz) | $\Delta\varepsilon$ +1.2 (extra, 20 °C) | $\varepsilon_\parallel$ 3.92, $\varepsilon_\perp$ 3.14 ($T = 0.97T^{N–Is}$) | $\varepsilon_\parallel$ 3.79, $\varepsilon_\perp$ 3.10 ($T = 0.97T^{N–Is}$) |
| Viscosity $\nu$ (mm$^2$/s) (20 °C) | 50 (extra) | 43 (extra) | 49 (extra) |
| **Number/common name** | **55 (PYP609, ZLI-2306)** | **56 (PYP707, ZLI-2710)** | **57 (PYP909, ZLI-2713)** |
| Substance | 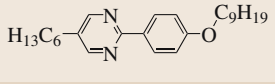 | 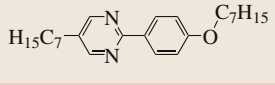 | 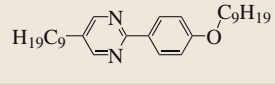 |
| Formula | $C_{25}H_{38}N_2O$ | $C_{24}H_{36}N_2O$ | $C_{28}H_{44}N_2O$ |
| Molar mass (g/mol) | 382.594 | 368.567 | 424.676 |
| CAS-RN | 51462-26-1 | – | 99895-85-9 |
| Temperatures of phase transitions $T^{tr}$ (°C) | Cr 35.0 N 61.0 Is | Cr 44.0 C 44.0 A 49.0 N 68.0 Is | Cr 34.0 C 61.0 A 75.0 Is |
| Enthalpies of phase transitions $\Delta H^{tr}$ (kJ/mol) | 35.1 (Cr–N), 1.7 (N–Is) | 35.5 (Cr–A), 2.0 (N–Is) | 35.1 (Cr–C) |
| Density $\varrho$ (g/cm$^3$) | 0.9707 (N, 48.0 °C), 0.9454 (Is, 68.0 °C) | – | 0.9650 (C, 48.0 °C), 0.9494 (N, 68.0 °C) |
| Refractive index $n$ (589 nm) | $n_e$ 1.6191, $n_o$ 1.4886 (48 °C) | $\Delta n$ 0.14 (20 °C) | $\Delta n$ 0.13 (20 °C) |
| Dielectric anisotropy $\Delta\varepsilon$ | +0.49 (56.0 °C) | +1.1 (extra, 20 °C) | +0.9 (extra, 20 °C) |
| Viscosity $\nu$ (mm$^2$/s) (20 °C) | 63 (extra) | 53 (extra) | 110 (extra) |
| **Number/common name** | **58 (PDX3, ZLI-1906)** | **59 (PDX5, ZLI-1908)** | **60 (PDX7, ZLI-1910)** |
| Substance | 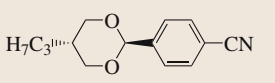 | 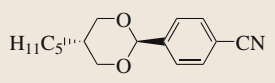 | 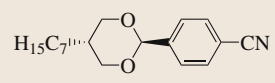 |
| Formula | $C_{14}H_{17}NO_2$ | $C_{16}H_{21}NO_2$ | $C_{18}H_{25}NO_2$ |
| Molar mass (g/mol) | 231.397 | 259.351 | 287.405 |
| CAS-RN | – | – | 97128-75-1 |
| Temperatures of phase transitions $T^{tr}$ (°C) | Cr 52.9 (N 39.3) Is | Cr 56.0 (N 49.0) Is | Cr 54.0 (N 53.0) Is |
| Enthalpies of phase transitions $\Delta H^{tr}$ (kJ/mol) | 20.9 (Cr–Is) | 21.0 (Cr–Is), 0.4 (N–Is) | 26.4 (Cr–Is), 0.8 (N–Is) |

**Table 5.1-3** Two-ring systems without bridges, cont.

| Number/common name | 58 (PDX3, ZLI-1906) | 59 (PDX5, ZLI-1908) | 60 (PDX7, ZLI-1910) |
|---|---|---|---|
| Crystallographic space group | – | – | $P2_12_12_1$ |
| Anisotropy of refractive index $\Delta n$ (589 nm, 20 °C) | 0.13 | 0.14 | 0.13 |
| Dielectric constant $\varepsilon$ (1 kHz) | $\Delta\varepsilon$ +32 (20 °C) | $\Delta\varepsilon$ +29.6, $\varepsilon_\perp$ 8.2 (20 °C) | $\Delta\varepsilon$ +32 (20 °C), $\Delta\varepsilon$ +7.9 ($T = 0.98T^{N–Is}$) |
| Kinematic viscosity $\nu$ (mm$^2$/s) | 33 (20 °C) | 29.4 (25 °C) | 34.7 (25 °C) |
| Dipole moment $\mu$ (D) | 4.1 | 6.2 ($C_6H_{12}$) | 6.2 ($C_6H_{12}$) |

**Table 5.1-4** Two-ring systems with bridges

| Number/common name | 61 | 62 | 63 (RO-CM-3952) |
|---|---|---|---|
| Substance | 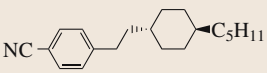 | 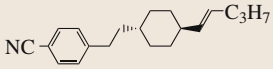 | 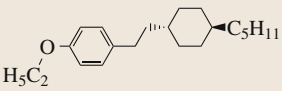 |
| Formula | $C_{20}H_{29}N$ | $C_{20}H_{27}N$ | $C_{21}H_{34}O$ |
| Molar mass (g/mol) | 283.461 | 281.445 | 302.505 |
| Temperatures of phase transitions $T^{tr}$ (°C) | Cr 31.0 N 52.5 Is | Cr 25.1 N 47.5 Is | Cr 27.0 (B 8.0) N 47.0 Is |
| Enthalpies of phase transitions $\Delta H^{tr}$ (kJ/mol) | 14.6 (Cr–N), 2.0 (N–Is) | 15.2 (Cr–N) | – |
| Dielectric constant $\varepsilon$ (1 kHz) | $\varepsilon_\perp$ 4.98, $\Delta\varepsilon$ +9.77 (42.5 °C) | $\varepsilon_\perp$ 4.61, $\Delta\varepsilon$ +11.13 (22 °C) | $\Delta\varepsilon$ −0.24, $\varepsilon_\perp$ 2.98 |
| Dynamic viscosity $\eta$ (mPa s) | $\eta$ 22.4 (22 °C) | $\eta$ 22.8 (22 °C) | $\eta$ 12.0 (22 °C) |
| **Number/common name** | **64** | **65** | **66** |
| Substance | 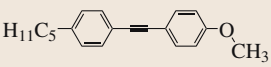 | 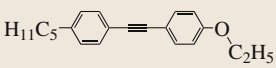 | 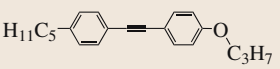 |
| Formula | $C_{20}H_{22}O$ | $C_{21}H_{24}O$ | $C_{24}H_{30}O$ |
| Molar mass (g/mol) | 278.398 | 292.425 | 334.506 |
| Temperatures of phase transitions $T^{tr}$ (°C) | Cr 47.0 N 58.0 Is | Cr 60.0 N 80.0 Is | Cr 41.0 N 65.0 Is |
| Enthalpies of phase transitions $\Delta H^{tr}$ (kJ/mol) | 18.0 (Cr–N), 0.6 (N–Is) | 23.2 (Cr–N), 1.0 (N–Is) | 22.6 (Cr–N), 0.9 (N–Is) |
| Refractive index $n$ (589 nm) | $n_e$ 1.735, $n_o$ 1.526 (44.5 °C) | $n_e$ 1.726, $n_o$ 1.517 (70 °C) | $n_e$ 1.683, $n_o$ 1.510 (60 °C) |
| Dielectric constant $\varepsilon$ (1 kHz) | $\varepsilon_\perp$ 3.58, $\Delta\varepsilon$ −0.11 (50 °C) | $\Delta\varepsilon$ +0.2, (extra, 20 °C) | $\varepsilon_\perp$ 3.67, $\Delta\varepsilon$ −0.18 (55 °C) |
| Kinematic viscosity (mm$^2$/s) | – | $\nu$ 20 (extra, 20 °C) | – |
| Surface tension (mN/m) | 25 (22 °C) | – | – |
| **Number/common name** | **67 (MBBA)** | **68 (EBBA)** | **69 (CBOOA)** |
| Substance | 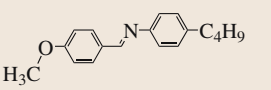 | 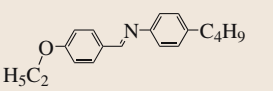 | 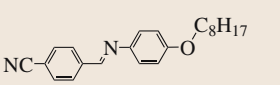 |
| Formula | $C_{18}H_{21}NO$ | $C_{19}H_{23}NO$ | $C_{22}H_{26}N_2O$ |
| Molar mass (g/mol) | 267.374 | 281.401 | 334.465 |
| CAS-RN | 26227-73-6 | 29743-08-6 | 65756-96-9 |

**Table 5.1-4** Two-ring systems with bridges, cont.

| Number/common name | 67 (MBBA) | 68 (EBBA) | 69 (CBOOA) |
|---|---|---|---|
| Temperatures of phase transitions $T^{tr}$ (°C) | Cr 22.0 N 48.0 Is | Cr 36.5 N 79.8 Is | Cr 73.1 A 83.3 N 107.9 Is |
| Enthalpies of phase transitions $\Delta H^{tr}$ (kJ/mol) | 15.1 (Cr–N), 0.4 (N–Is) | 17.2 (Cr–N), 0.6 (N–Is) | 27.6 (Cr–N), 0.7 (N–Is) |
| Crystallographic space group | – | $P2_1/c$ | $P2_1/c$ |
| Order parameter $S$ | 0.55 (25 °C) | 0.39 (55 °C) | – |
| Density $\varrho$ (g/cm$^3$) | 1.042 (N, 25 °C), 1.015 (Is, 60 °C) | 1.020 (N, 40 °C), 0.988 (Is, 80 °C) | 1.009 (A, 83 °C), 1.003 (N, 90 °C), 0.981 (Is, 110 °C) |
| Refractive index $n$ | $n_e$ 1.764, $n_o$ 1.549 (589 nm, 25 °C) | $n_e$ 1.763, $n_o$ 1.524 (578 nm, N, 43.5 °C) | – |
| Dielectric constant $\varepsilon$ | $\varepsilon_\parallel$ 4.72, $\varepsilon_\perp$ 5.31 (30 °C, 1.6 kHz) | $\varepsilon_\parallel$ 4.37, $\varepsilon_\perp$ 4.50 (73.8 °C) | $\varepsilon_\parallel$ 14.4, $\varepsilon_\perp$ 7.5 (95 °C, 1 kHz) |
| Dynamic viscosity $\eta$ (mPa s) | 23 (N, 30 °C) | 11 (N, 69 °C) | 13 (N, 84 °C) |
| Surface tension (mN/m) | 34.0 (N, 22 °C), 32.6 (Is, 50 °C) | 23.8 (N, 45 °C), 23.3 (Is, 80 °C) | 26.1 (A, 80 °C), 26.7 (N, 90 °C), 26.6 (Is, 110 °C) |
| Thermal conductivity (W/(m K)) | 0.125 (N, 20 °C), 0.128 (N, 30 °C), 0.145 (N, 50 °C) | 0.135 (N, 125 °C), 0.157 (Is, 140 °C) | – |
| Heat capacity $C_p$ (J/(mol K)) | 509 (N, 37 °C), 507 (Is, 49 °C) | 540 (N, 37 °C), 590 (Is, 82 °C) | 401 (A, 80 °C), 474 (N, 100 °C), 514 (Is, 120 °C) |
| Magnetic susceptibility $\Delta\chi$ (m$^3$/kg) (×10$^{-12}$) | 116 (N, 23 °C) | 47 ($T = T^{N–Is}$) | – |
| Sound velocity $v$ (m/s) | 1200 (N, 33 °C) | 1375 (N, 73 °C, 4.8 GHz) | 1340 (N, 90 °C, 2 MHz) |
| Diffusion coefficient $D$ (m$^2$/s) | $D_\perp$ $8\times10^{-10}$, $D_\parallel$ $13\times10^{-10}$ ($1000/T = 3.3$) | $D$ $2.5\times10^{-10}$ (Is, 89 °C) | $D_\perp$ $6.6\times10^{-8}$, $D_\parallel$ $13.5\times10^{-8}$ (N, 88 °C) |
| Dipole moment $\mu$ (D) | 3.2 (22 °C) | $\mu_\parallel$ 1.28, $\mu_\perp$ 1.35 (73.8 °C) | 5.21 ($C_6H_6$, 25 °C) |
| **Number/common name** | **70 (BBBA)** | **71 (HBT)** | **72 (OBT)** |
| Substance | 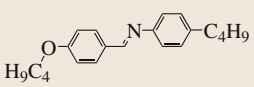 | 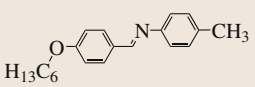 | 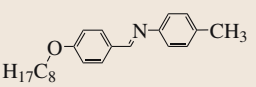 |
| Formula | $C_{21}H_{27}NO$ | $C_{20}H_{25}NO$ | $C_{22}H_{29}NO$ |
| Molar mass (g/mol) | 309.455 | 295.428 | 323.483 |
| CAS-RN | 29743-09-7 | 25959-51-7 | – |
| Temperatures of phase transitions $T^{tr}$ (°C) | Cr 8.0 G 41.0 B 45.0 A 45.5 N 75.0 Is | Cr 58.0 (G 44.0 B 53.0) N 76.0 Is | Cr 70.0 (B 61.5 A 69.0) N 78.5 Is |
| Enthalpies of phase transitions $\Delta H^{tr}$ (kJ/mol) | 3.3 (Cr–G), 0.7 (G–B), 2.9 (B–A), 0.4 (A–N), 0.9 (N–Is) | 29.3 (Cr–N), 5.4 (B–N), 1.0 (N–Is) | – |
| Crystallographic space group | – | – | $P\bar{1}$ |
| Order parameter $S$ | 0.36 (52 °C) | – | – |
| Density $\varrho$ (g/cm$^3$) | 1.007 (B, 40 °C), 0.990 (N, 50 °C), 0.964 (Is, 75 °C) | 0.985 (N, 70 °C), 0.976 (Is, 77 °C) | 0.9714 (N, 71 °C), 0.9576 (Is, 81 °C) |
| Refractive index $n$ (589 nm) | $n_e$ 1.670, $n_o$ 1.527 (52 °C) | $n_e$ 1.692, $n_o$ 1.525 (71 °C) | $n_e$ 1.688, $n_o$ 1.500 (72.5 °C) |

**Table 5.1-4** Two-ring systems with bridges, cont.

| Number/common name | 70 (BBBA) | 71 (HBT) | 72 (OBT) |
|---|---|---|---|
| Dielectric constant $\varepsilon$ (68 °C) | $\varepsilon_\parallel$ 3.99, $\varepsilon_\perp$ 4.01 (1 MHz) | $\varepsilon_\parallel$ 4.41, $\varepsilon_\perp$ 4.25 (10 kHz) | – |
| Dynamic viscosity $\eta$ (mPa s) | 18 (N, 57 °C) | 6.5 (N, 70 °C), 7.0 (Is, 80 °C) | 8.6 (N, 71 °C), 8.3 (Is, 80 °C) |
| Heat capacity $C_p$ (J/(mol K)) | – | 689 (N, 67 °C), 624 (Is, 90 °C) | – |
| Magnetic susceptibility $\Delta\chi$ ($m^3$/kg) ($\times 10^{-12}$) | 49 ($T = T^{N–Is}$) | – | – |
| Sound velocity $v$ (m/s) | 1467 (G, 40 °C), 1405 (N, 60 °C) (2 MHz) | 1358 (N, 70 °C), 1328 (Is, 82 °C) (2 MHz) | 1360 (N, 70 °C), 1332 (Is, 80 °C) (2 MHz) |
| **Number/common name** | **73** | **74** | **75** |
| Substance | 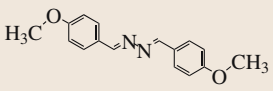 | 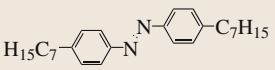 | 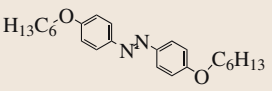 |
| Formula | $C_{16}H_{16}N_2O_2$ | $C_{26}H_{38}N_2$ | $C_{24}H_{34}N_2O_2$ |
| Molar mass (g/mol) | 268.318 | 378.606 | 382.551 |
| CAS-RN | 2299-73-2 | 37592-97-5 | 10225-93-1 |
| Temperatures of phase transitions $T^{tr}$(°C) | Cr 173.0 N 186.0 Is | Cr 40.0 (A 21.4) N 47.3 Is | Cr 102.6 N 116.2 Is |
| Enthalpies of phase transitions $\Delta H^{tr}$ (kJ/mol) | 38.7 (Cr–N), 1.6 (N–Is) | 24.4 (Cr–N), 1.1 (N–Is) | 39.0 (Cr–N), 1.5 (N–Is) |
| Crystallographic space group | *Cc* | – | – |
| Order parameter $S$ | 0.656 (154.2 °C), 0.410 (180 °C) | – | 0.676 (105.7 °C) |
| Density $\varrho$ (g/$cm^3$) | 1.044 (N, 178 °C), 1.023 (Is, 195 °C) | 0.9430 (40.6 °C) | 0.9493 (Is, 115 °C) |
| Refractive index $n$ (589 nm) | $n_e$ 1.791, $n_o$ 1.549 (178 °C) | $n_o$ 1.5095, $\Delta n$ 0.191 (40.3 °C) | – |
| Dielectric constant $\varepsilon$ | −0.124 (172.5 °C, 0.8 MHz) | $\varepsilon_\parallel$ 2.8, $\varepsilon_\perp$ 2.5 (23 °C, extra) | $\varepsilon_\parallel$ 3.254, $\varepsilon_\perp$ 3.219 (106 °C, 650 kHz) |
| Dynamic viscosity $\eta$ (mPa s) | 130 (N, 175 °C), 170 (Is, 197 °C) | – | – |
| Surface tension (mN/m) | 34.6 (N, 180 °C), 32.9 (Is, 190 °C) | – | – |
| Heat capacity $C_p$ (J/(mol K)) | 572 (N, 180 °C), 606 (Is, 220 °C) | – | – |
| Diamagnetic anisotropy $\Delta\chi$ ($10^{-11}$ $m^3$/kg) | – | 10.0 (N, 35 °C) | – |
| Diffusion coefficient $D$ ($m^2$/s) | $1.3\times10^{-9}$(N), $2.0\times10^{-9}$ ($1000/T = 2.15$) (Is) | – | – |
| Dipole moment $\mu$ (D) | – | – | 1.87 ($C_6H_6$) |

**Table 5.1-4** Two-ring systems with bridges, cont.

| Number/common name | 76 (PAA) | 77 (PAP) | 78 |
|---|---|---|---|
| Substance | 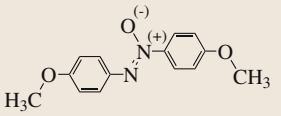 | 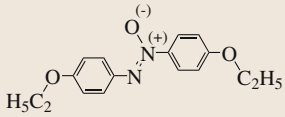 | 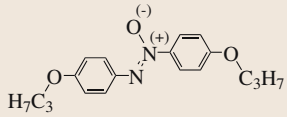 |
| Formula | $C_{14}H_{14}N_2O_3$ | $C_{16}H_{18}N_2O_3$ | $C_{18}H_{22}N_2O_3$ |
| Molar mass (g/mol) | 258.279 | 286.333 | 314.388 |
| CAS-RN | 51437-65-1 | 51437-64-0 | 104746-32-9 |
| Temperatures of phase transitions $T^{tr}$ (°C) | Cr 119.5 N 136.5 Is | Cr 136.8 N 168.4 Is | Cr 118.3 N 124.0 Is |
| Enthalpies of phase transitions $\Delta H^{tr}$ (kJ/mol) | 29.6 (Cr–N), 0.6 (N–Is) | 26.9 (Cr–N), 1.5 (N–Is) | 26.9 (Cr–N), 0.7 (N–Is) |
| Crystallographic space group | $P2_1/c$ | $Cc$ | $P2_1/n$ |
| Order parameter $S$ | 0.50 (N, 122 °C) | 0.57 ($T = 0.90 \times T^{N–Is}$) | 0.605 ($T = 0.90 \times T^{N–Is}$) |
| Density $\varrho$ (g/cm$^3$) | 1.165 (N, 120 °C),<br>1.140 (Is, 140 °C) | 1.096 (N, 142 °C),<br>1.032 (Is, 198 °C) | 1.067 (N, 114 °C),<br>1.046 (Is, 134 °C) |
| Refractive index $n$ | $n_e$ 1.804, $n_o$ 1.572<br>(589 nm, N, 130 °C) | $n_e$ 1.784, $n_o$ 1.522<br>(589 nm, N, 160 °C) | $n_o$ 1.534 (N, 114 °C, 546 nm) |
| Dielectric constant $\varepsilon$ | $\varepsilon_\parallel$ 5.53, $\varepsilon_\perp$ 5.69 (126 °C) | $\varepsilon_\parallel$ 4.77, $\varepsilon_\perp$ 4.97<br>(160 °C, 1.2 MHz) | $\Delta\varepsilon$ −0.22 (118.4 °C, 0.8 MHz) |
| Dynamic viscosity $\eta$ (mPa s) | 2.5 (N, 120 °C), 2.5 (151 °C) | 5.2 (N, 164.6 °C) | 9.6 (N, 121.2 °C) |
| Surface tension (mN/m) | 38.8 (N, 126 °C),<br>38.0 (Is, 136 °C) | 29.7 (N, 159 °C),<br>28.8 (Is, 170 °C) | – |
| Thermal conductivity (W/(m K)) | 0.135 (N, 125 °C),<br>0.157 (Is, 140 °C) | – | – |
| Heat capacity $C_p$ (J/(mol K)) | 399 (Cr, 100 °C),<br>507 (N, 120 °C),<br>508 (Is, 150 °C) | 548 (Cr, 126 °C),<br>682 (N, 160 °C),<br>643 (Is, 169 °C) | 609 (Cr, 100 °C),<br>696 (N, 117 °C),<br>665 (Is, 128 °C) |
| Diamagnetic anisotropy $\Delta\chi$ ($10^{-11}$ m$^3$/kg) | 9.7 (130.8 °C) | 13.7 (N, 136 °C) | 10.8 (N, 112 °C) |
| Sound velocity $v$ (m/s) | 1240 (N, 130 °C, 3 MHz) | 1128 (N, 160 °C, 4.2 MHz) | 1247 (N, 121 °C, 3.1 MHz) |
| Diffusion coefficient $D$ (m$^2$/s) | $D_\perp$ $5.5 \times 10^{-10}$, $D_\parallel$ $9 \times 10^{-10}$<br>($1000/T = 2.55$) | $D_\perp$ $7.5 \times 10^{-10}$, $D_\parallel$ $12 \times 10^{-10}$<br>($1000/T = 2.45$) | $D_\perp$ $4 \times 10^{-10}$, $D_\parallel$ $7 \times 10^{-10}$<br>($1000/T = 2.60$) |
| Dipole moment $\mu$ (D) | 2.3 | 2.42 | 2.41 |
| **Number/common name** | **79** | **80** | **81** |
| Substance | 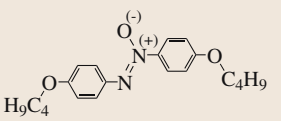 | 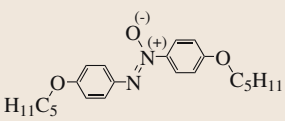 | 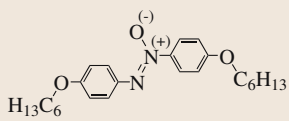 |
| Formula | $C_{20}H_{26}N_2O_3$ | $C_{22}H_{30}N_2O_3$ | $C_{24}H_{34}N_2O_3$ |
| Molar mass (g/mol) | 342.442 | 370.496 | 398.55 |
| CAS-RN | 113787-54-5 | 107266-21-7 | 122055-52-1 |

**Table 5.1-4** Two-ring systems with bridges, cont.

| Number/common name | 79 | 80 | 81 |
|---|---|---|---|
| Temperatures of phase transitions $T^{tr}$ (°C) | Cr 105.8 N 136.6 Is | Cr′ 68.0 Cr 76.0 N 124.0 Is | Cr 81.0 (C 74.0) N 129.0 Is |
| Enthalpies of phase transitions $\Delta H^{tr}$ (kJ/mol) | 20.9 (Cr–N), 1.0 (N–Is) | 14.6 (Cr–N), 0.7 (N–Is) | 41.4 (Cr–N), 1.0 (N–Is) |
| Crystallographic space group | – | $P\bar{1}$ | – |
| Order parameter $S$ | 0.590 around ($T = 0.90 \times T^{N–Is}$) | 0.590 around ($T = 0.90 \times T^{N–Is}$) | 0.610 around ($T = 0.90 \times T^{N–Is}$) |
| Density $\varrho$ (g/cm$^3$) | 1.031 (N, 127 °C),<br>1.007 (Is, 147 °C) | 1.072 (N, 120 °C),<br>1.063 (Is, 123 °C) | 0.990 (N, 125 °C),<br>0.979 (Is, 132 °C) |
| Refractive index $n$ (589 nm) | $n_o$ 1.516 (127 °C) | $n_e$ 1.812, $n_o$ 1.518 (103.3 °C) | $n_e$ 1.731, $n_o$ 1.505 (107.5 °C) |
| Dielectric anisotropy $\Delta\varepsilon$ | – 0.38 (110 °C, 0.8 MHz) | – 0.29 (105 °C) | – 0.65 (99.5 °C, 0.8 MHz) |
| Dynamic viscosity $\eta$ (mPa s) | 6.9 (N, 131.7 °C) | 13.5 (N, 120 °C) | 10.5 (N, 128.1 °C) |
| Surface tension (mN/m) | 32.0 (N, 110 °C),<br>29.4 (Is, 140 °C) | 30.9 (N, 120 °C),<br>30.6 (Is, 140 °C) | 28.4 (N, 120 °C),<br>27.4 (Is, 140 °C) |
| Heat capacity $C_p$ (J/(mol K)) | 759 (N, 120 °C),<br>761 (Is, 143 °C) | 718 (Cr, 70 °C),<br>808 (N, 100 °C),<br>854 (Is, 125 °C) | 828 (Cr, 69 °C),<br>978 (N, 120 °C),<br>917 (Is, 155 °C) |
| Diamagnetic anisotropy $\Delta\chi$ ($10^{-11}$ m$^3$/kg) | 10.2 (N, 122 °C) | 8.9 (N, 112 °C) | 9.5 (N, 109 °C) |
| Sound velocity $v$ (m/s) | 1235 (N, 125 °C, 3.1 MHz) | 1205 (N, 122 °C, 3.1 MHz) | 1160 (N, 125 °C, 3.1 MHz) |
| Diffusion coefficient $D$ (m$^2$/s) | $D_\perp$ $5.5 \times 10^{-8}$, $D_\parallel$ $12 \times 10^{-8}$ (N, 117.6 °C) | $D_\perp$ $6.0 \times 10^{-8}$, $D_\parallel$ $12 \times 10^{-8}$ (N, 110 °C) | $D_\perp$ $6.0 \times 10^{-8}$, $D_\parallel$ $13 \times 10^{-8}$ (N, 113.6 °C) |
| Dipole moment $\mu$ (D) | 2.38 | 2.35 | 2.35 |
| **Number/common name** | **82** | **83 (EPAB)** | **84 (N-4)** |
| Substance | 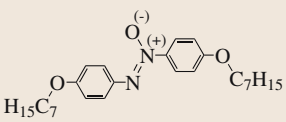 | 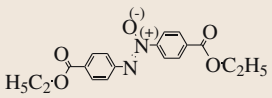 | 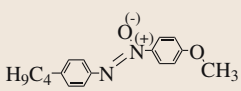 |
| Formula | $C_{26}H_{38}N_2O_3$ | $C_{18}H_{18}N_2O_5$ | $C_{17}H_{20}N_2O_2$ |
| Molar mass (g/mol) | 426.604 | 342.355 | 284.361 |
| CAS-RN | 70906-50-2 | 6421-04-1 | 102135-46-6 |
| Temperatures of phase transitions $T^{tr}$ (°C) | Cr 74.4 C 95.4 N 124.2 Is | Cr′ 102.0 Cr 115.8 A 123.1 Is | Cr 16.0 N 76.0 Is |
| Enthalpies of phase transitions $\Delta H^{tr}$ (kJ/mol) | 40.9 (Cr–C), 1.6 (C–N),<br>1.0 (N–Is) | 19.7 (Cr–A), 5.0 (A–Is) | – |
| Crystallographic space group | $P\bar{1}$ | $C2/c$, $P\bar{1}$ (Cr′) | – |
| Order parameter $S$ | 0.615 ($T = 0.90 \times T^{N–Is}$) | – | 0.65 (19 °C) |
| Density $\varrho$ (g/cm$^3$) | 0.994 (C, 94 °C),<br>0.985 (N, 105 °C) | 1.146 (Is, 123 °C),<br>1.138 (Is, 135 °C) | 1.1217 (N, 20 °C),<br>1.1067 (N, 40 °C) |
| Refractive index $n$ | $n_e$ 1.673, $n_o$ 1.512<br>(589 nm, N, 117 °C) | – | $\Delta n$ 0.45 (450 nm), 0.34 (550 nm),<br>0.30 (650 nm) (20 °C) |
| Dynamic viscosity $\eta$ (mPa s) | 15.1 (N, 123.5 °C) | – | – |
| Surface tension (mN/m) | – | 26.0 (A, 120 °C),<br>26.3 (Is, 160 °C) | 37.3 (N, 23 °C),<br>35 (N, 76 °C) |

**Table 5.1-4** Two-ring systems with bridges, cont.

| Number/common name | 82 | 83 (EPAB) | 84 (N-4) |
|---|---|---|---|
| Heat capacity $C_p$ (J/(mol K)) | 887 (C, 77 °C), 1004 (N, 102 °C), 987 (Is, 127 °C) | 675 (A, 116.2 °C), 676 (Is, 130 °C) | 511 (N, 61 °C) |
| Diamagnetic anisotropy $\Delta\chi$ | $7.5\times10^{-11}$ m$^3$/kg (116 °C) | – | $6.9\times10^{-10}$ m$^3$/mol (75.3 °C) |
| Sound velocity $v$ (m/s) | 1300 (80 °C), 1250 (100 °C) (12 MHz) | 1276 (2 MHz, 117.4 °C) | – |
| Diffusion coefficient $D$ (m$^2$/s) | $D_\perp$ $3.7\times10^{-10}$, $D_\parallel$ $6\times10^{-10}$ ($1000/T = 2.60$) | – | – |
| Dipole moment $\mu$ (D) | 2.36 | – | – |
| **Number/common name** | **85 (RO-CM-1500)** | **86 (RO-CM-1530)** | **87 (RO-CM-1510)** |
| Substance | 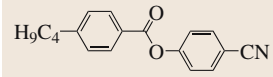 | 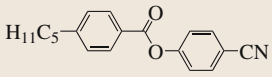 | 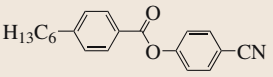 |
| Formula | $C_{18}H_{17}NO_2$ | $C_{19}H_{19}NO_2$ | $C_{20}H_{21}NO_2$ |
| Molar mass (g/mol) | 279.342 | 293.369 | 307.396 |
| CAS-RN | 38690-77-6 | 49763-64-6 | 50793-85-6 |
| Temperatures of phase transitions $T^{tr}$ (°C) | Cr 67.1 (N 42.6) Is | Cr 64.4 (N 55.4) Is | Cr 44.4 N 48.6 Is |
| Enthalpies of phase transitions $\Delta H^{tr}$ (kJ/mol) | 28.0 (Cr–Is) | 25.1 (Cr–Is) | 40.2 (Cr–N) |
| Crystallographic space group | – | $P2_1/n$ | – |
| Density $\varrho$ (g/cm$^3$) | 1.095 (N, 40 °C), 1.061 (Is, 80 °C) | 1.076 (N, 47.4 °C), 1.053 (Is, 67.4 °C) | 1.064 (N, 36.6 °C), 1.043 (Is, 56.6 °C) |
| Refractive index $n$ | $n_e$ 1.639, $n_o$ 1.525 (589 nm, N, 39 °C) | $n_e$ 1.669, $n_o$ 1.512 (546 nm, N, 47.4 °C) | $n_e$ 1.657, $n_o$ 1.514 (546 nm, N, 36.6 °C) |
| Dielectric constant $\varepsilon$ (1.592 kHz, $T = 0.98T^{N-Is}$) | $\varepsilon_\parallel$ 34.3, $\varepsilon_\perp$ 12.0 | $\varepsilon_\parallel$ 30.2, $\varepsilon_\perp$ 10.2 | $\varepsilon_\parallel$ 29.3, $\varepsilon_\perp$ 9.7 |
| Surface tension (mN/m) | – | 28.2 (N, 38 °C), 30.7 (53 °C) | – |
| Dipole moment $\mu$ (D) | 5.77 | – | – |
| **Number/common name** | **88 (RO-CM-1540)** | **89** | **90** |
| Substance | 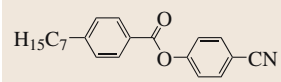 | 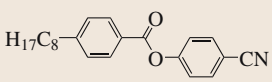 | 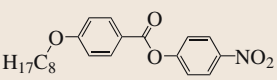 |
| Formula | $C_{21}H_{23}NO_2$ | $C_{22}H_{25}NO_2$ | $C_{21}H_{25}NO_5$ |
| Molar mass (g/mol) | 321.423 | 335.45 | 371.437 |
| CAS-RN | 38690-76-5 | 50793-86-7 | 52910-78-8 |
| Temperatures of phase transitions $T^{tr}$ (°C) | Cr 44.0 N 56.5 Is | Cr 47.0 N 55.0 Is | Cr′ 47.5 Cr 50.5 A 61.4 N 68.1 Is |
| Enthalpies of phase transitions $\Delta H^{tr}$ (kJ/mol) | 31.5 (Cr–N), 1.0 (N–Is) | 38.5 (Cr–N) | 18.4 (Cr–A), 0.2 (A–N), 0.4 (N–Is) |
| Crystallographic space group | $P2_1/n$ | – | $P2_1/c$ |
| Order parameter $S$ | 0.574 (44 °C), 0.42 (56 °C) | – | 0.605 (A, 44 °C), 0.31 (N, 66 °C) |

**Table 5.1-4** Two-ring systems with bridges, cont.

| Number/common name | 88 (RO-CM-1540) | 89 | 90 |
|---|---|---|---|
| Density $\varrho$ (g/cm$^3$) | 1.050 (N, 48 °C),<br>1.034 (Is, 60 °C) | 1.042 (N, 45.8 °C),<br>1.021 (Is, 65.8 °C) | 1.123 (A, 52 °C),<br>1.110 (N, 66 °C), 1.106 (Is, 70 °C) |
| Refractive index $n$ | $n_e$ 1.649, $n_o$ 1.505<br>(546 nm, N, 45 °C) | $n_e$ 1.627, $n_o$ 1.508<br>(546 nm, N, 50.8 °C) | $n_e$ 1.644, $n_o$ 1.504<br>(589 nm, N, 55 °C) |
| Dielectric constant $\varepsilon$ | $\varepsilon_\parallel$ 26.4, $\varepsilon_\perp$ 8.7<br>(1.592 kHz, $T = 0.98T^{N–Is}$) | $\varepsilon_\parallel$ 24.3, $\varepsilon_\perp$ 8.5<br>(1.592 kHz, $T = 0.98T^{N–Is}$) | $\Delta\varepsilon$ 11.1 (60 °C), $\Delta\varepsilon$ 11.4 (65 °C)<br>(1 kHz) |
| Dynamic viscosity $\eta$ (mPa s) | 22 (50 °C), 22 (60 °C) | – | – |
| Surface tension (mN/m) | 27 (22 °C), 25.4 (45 °C) | 19.6 (43 °C), 22.5 (58 °C) | – |
| Sound velocity $v$ (m/s) | 1235 (N, 125 °C, 3.1 MHz) | – | 1372 (58 °C, 4.74 GHz) |
| Dipole moment $\mu$ (D) | 6.1 ($CCl_4$) | – | 6.04 |
| **Number/common name** | **91** | **92** | **93** |
| Substance | 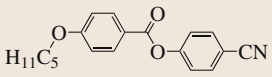 | 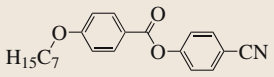 | 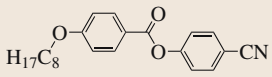 |
| Formula | $C_{19}H_{19}NO_3$ | $C_{21}H_{23}NO_3$ | $C_{22}H_{25}NO_3$ |
| Molar mass (g/mol) | 309.368 | 337.422 | 351.449 |
| CAS-RN | 50649-73-5 | 50793-88-9 | 50793-89-0 |
| Temperatures of phase transitions $T^{tr}$ (°C) | Cr 87.0 (N 78.0) Is | Cr 71.5 N 82.0 Is | Cr 75.6 N 88.0 Is |
| Enthalpies of phase transitions $\Delta H^{tr}$ (kJ/mol) | 32.2 (Cr–Is) | 34.3 (Cr–N) | 40.6 (Cr–N) |
| Crystallographic space group | *Pnam* | $P2_1/a$ | $P\bar{1}$ |
| Density $\varrho$ (g/cm$^3$) | 1.093 (N, 69 °C),<br>1.075 (Is, 85.5 °C) | 1.061 (N, 73 °C),<br>1.045 (Is, 88 °C) | 1.044 (N, 79 °C),<br>1.028 (Is, 94 °C) |
| Refractive index $n$ (546 nm) | $n_e$ 1.662, $n_o$ 1.513 (76.7 °C) | $n_e$ 1.633, $n_o$ 1.508 (73.3 °C) | $n_e$ 1.627, $n_o$ 1.502 (79 °C) |
| Dielectric constant $\varepsilon$ | $\varepsilon_\parallel$ 27.8, $\varepsilon_\perp$ 11.7 (71.8 °C) | | |
| Surface tension (mN/m) | 29.1 (76 °C), 26.4 (91 °C) | 25.0 (73 °C), 22.9 (88 °C) | 23.2 (76 °C), 21.1 (91 °C) |
| Sound velocity $v$ (m/s) | 1359 (83 °C, 2 MHz) | – | – |
| Dipole moment $\mu$ (D) | 6.6 ($CCl_4$) | – | – |
| **Number/common name** | **94 (ME105, ZLI-0245)** | **95 (ME605, ZLI-1004)** | **96** |
| Substance | 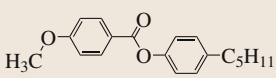 | 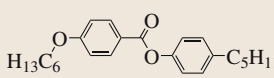 | 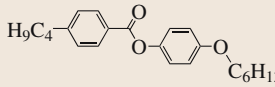 |
| Formula | $C_{19}H_{22}O_3$ | $C_{24}H_{32}O_3$ | $C_{23}H_{30}O_3$ |
| Molar mass (g/mol) | 298.385 | 368.521 | 354.494 |
| CAS-RN | – | 38444-15-4 | 38454-28-3 |
| Temperatures of phase transitions $T^{tr}$ (°C) | Cr 29.5 N 43.5 Is | Cr 50.0 N 63.0 Is | Cr 31.3 N 48.6 Is |
| Enthalpies of phase transitions $\Delta H^{tr}$ (kJ/mol) | 17.6 (Cr–N), 0.6 (N–Is) | 21.9 (Cr–N) | 17.6 (Cr–N) |

**Table 5.1-4** Two-ring systems with bridges, cont.

| Number/common name | 94 (ME105, ZLI-0245) | 95 (ME605, ZLI-1004) | 96 |
|---|---|---|---|
| Density $\varrho$ (g/cm$^3$) | 1.078 (N, 31 °C),<br>1.061 (Is, 45 °C) | 1.019 (N, 50 °C),<br>1.001 (Is, 65 °C) | 1.020 (N, 41 °C),<br>1.006 (Is, 53 °C) |
| Refractive index $n$ (589 nm) | $n_e$ 1.639, $n_o$ 1.515 (35 °C) | $n_e$ 1.613, $n_o$ 1.490 (47.4 °C) | $n_e$ 1.599, $n_o$ 1.498 (41 °C) |
| Dielectric anisotropy $\Delta\varepsilon$ | +0.11 (38 °C) | +0.1 (20 °C, 1 kHz) | – |
| Kinematic viscosity $\nu$ (mm$^2$/s) | 38 (20 °C) | 87 (20 °C) | – |
| Surface tension (mN/m) | 24.5 (20 °C) | – | 27.5 (41.5 °C) |
| Dipole moment $\mu$ (D) | $\mu_\parallel$ 2.18, $\mu_\perp$ 2.15 (38 °C) | – | 2.3 ($CCl_4$) |
| **Number/common name** | **97** | **98** | **99** |
| Substance | 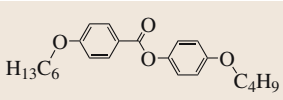 | 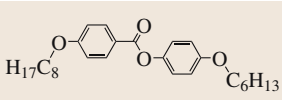 | 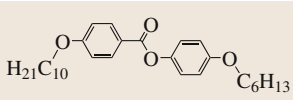 |
| Formula | $C_{23}H_{30}O_4$ | $C_{27}H_{38}O_4$ | $C_{29}H_{42}O_4$ |
| Molar mass (g/mol) | 370.493 | 426.602 | 454.656 |
| CAS-RN | 38454-24-9 | 54963-63-2 | 68162-09-4 |
| Temperatures of phase transitions $T^{tr}$ (°C) | Cr 66.0 N 89.5 Is | Cr 55.0 C 66.0 N 89.0 Is | Cr 62.5 (E 38.0 B 44.5)<br>C 77.5 A 83.3 N 88.9 Is |
| Enthalpies of phase transitions $\Delta H^{tr}$ (kJ/mol) | 35.0 (Cr–N), 1.3 (N–Is) | 38.0 (Cr–C), 0.4 (C–N),<br>2.1 (N–Is) | 45.3 (Cr–C), 4.7 (B–C),<br>0.7 (A–N), 2.1 (N–Is) |
| Order parameter $S$ | 0.49 (84 °C) | 0.49 (84.5 °C) | 0.51 (84 °C) |
| Density $\varrho$ (g/cm$^3$) | 1.015 (N, 88 °C) | 0.9821 (N, 83 °C) | 0.9735 (N, 84.9 °C) |
| Refractive index $n$ | $n_e$ 1.518, $n_o$ 1.394<br>(80 °C, 650 nm) | $n_e$ 1.5811, $n_o$ 1.4828<br>(83.5 °C, 589 nm) | – |
| Dielectric constant $\varepsilon$ (1 kHz) | $\Delta\varepsilon$ −0.27 (79 °C) | $\Delta\varepsilon$ −0.20 (84 °C) | $\varepsilon_\parallel$ 3.85, $\varepsilon_\perp$ 4.05 (85 °C) |
| Dynamic viscosity $\eta$ (mPa s) | – | 11.4 (80 °C) | – |
| Sound velocity $v$ (m/s) | – | 1383 (83 °C, 0.36 MHz) | 1285 (80 °C, 0.36 MHz) |
| Dipole moment $\mu$ (D), 25 °C | 2.67 ($CCl_4$) | 2.86 ($C_6H_6$) | 3.31 ($CCl_4$) |
| **Number/common name** | **100 (D55, ZLI-1497)** | **101 (D301, ZLI-2469)** | **102 (D302, ZLI-1496)** |
| Substance | 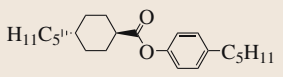 | 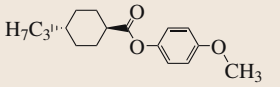 | 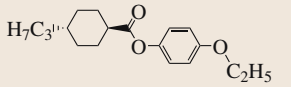 |
| Formula | $C_{23}H_{36}O_2$ | $C_{17}H_{24}O_3$ | $C_{18}H_{26}O_3$ |
| Molar mass (g/mol) | 344.542 | 276.379 | 290.406 |
| CAS-RN | 67589-72-4 | – | 67589-39-3 |
| Temperatures of phase transitions $T^{tr}$ (°C) | Cr 36.0 (A 29.0) N 48.0 Is | Cr 55.5 N 62.5 Is | Cr 49.0 N 79.8 Is |
| Enthalpies of phase transitions $\Delta H^{tr}$ (kJ/mol) | 28.9 (Cr–N), 0.55 (N–Is) | 28.0 (Cr–N) | 27.6 (Cr–N) |
| Order parameter $S$ | 0.67 (39 °C) | – | 0.71 (60 °C) |
| Density $\varrho$ (g/cm$^3$) | 0.9508 (N, 36 °C) | – | 1.0118 (51 °C) |
| Refractive index $n$ (589 nm) | $n_e$ 1.5304, $n_o$ 1.4730 (36 °C) | $\Delta n$ 0.09 (20 °C) | $n_e$ 1.5304, $n_o$ 1.4684 (60 °C) |
| Dielectric constant $\varepsilon$ (1 kHz) | $\varepsilon_\parallel$ 2.958, $\varepsilon_\perp$ 3.396 (40 °C) | $\Delta\varepsilon$ −1.8 (20 °C) | $\varepsilon_\parallel$ 3.28, $\varepsilon_\perp$ 4.54 (51 °C) |
| Kinematic viscosity $\nu$ (mm$^2$/s) 20 °C | 13 (extra) | 12 (extra) | 14 (extra) |
| Dipole moment $\mu$ (D) | 1.99 | – | 2.17 |

**Table 5.1-4** Two-ring systems with bridges, cont.

| **Number/common name** | **103 (D401, ZLI-2470)** | **104 (D402, RO-CM-1942, ZLI-1563)** | **105 (D501, RO-CM-1951, ZLI-1495)** |
|---|---|---|---|
| Substance | 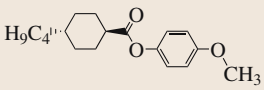 | 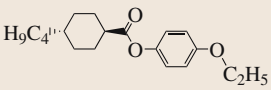 | 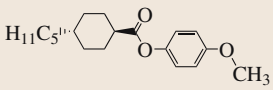 |
| Formula | $C_{18}H_{26}O_3$ | $C_{19}H_{28}O_3$ | $C_{19}H_{28}O_3$ |
| Molar mass (g/mol) | 290.406 | 304.433 | 304.433 |
| CAS-RN | 67589-46-2 | 67589-47-3 | 67589-52-0 |
| Temperatures of phase transitions $T^{tr}$ (°C) | Cr 42.0 N 59.0 Is | Cr 36.3 N 74.6 Is | Cr 40.9 N 71.3 Is |
| Enthalpies of phase transitions $\Delta H^{tr}$ (kJ/mol) | 23.0 (Cr–N) | 21.4 (Cr–N) | 21.0 (Cr–N), 0.5 (N–Is) |
| Order parameter $S$ | – | 0.73 (40 °C) | 0.71 (50 °C) |
| Density $\varrho$ (g/cm$^3$) | – | 1.059 (40 °C) | 1.050 (48 °C) |
| Refractive index $n$ (589 nm) | $\Delta n$ 0.09 (20 °C) | $n_e$ 1.5508, $n_o$ 1.4730 (40 °C) | $n_e$ 1.5389, $n_o$ 1.4742 (50 °C) |
| Dielectric constant $\varepsilon$ (1 kHz) | $\Delta\varepsilon$ −1.8 (20 °C) | $\varepsilon_\perp$ 4.20, $\Delta\varepsilon$ −0.91 (65.4 °C) | $\varepsilon_\parallel$ 3.37, $\varepsilon_\perp$ 4.28 (51 °C) |
| Viscosity | $\nu$ 14 mm$^2$/s (20 °C) | $\eta$ 20 mPa s (22 °C) | – |
| Diamagnetic anisotropy $\Delta\chi$ ($10^{-11}$ m$^3$/kg) | – | 3.0 (52 °C) | 3.0 (52.5 °C) |
| Dipole moment $\mu$ (D) | – | 2.08 ($C_6H_6$) | 2.23 ($C_6H_6$) |
| **Number/common name** | **106 (OS33, RO-CM-1633, ZLI-2155)** | **107 (OS53, RO-CM-1653, ZLI-2256)** | **108 (OS55, ZLI-2495)** |
| Substance | 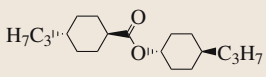 | 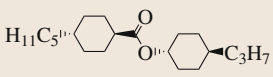 | 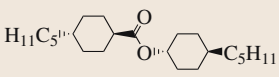 |
| Formula | $C_{19}H_{34}O_2$ | $C_{21}H_{38}O_2$ | $C_{23}H_{42}O_2$ |
| Molar mass (g/mol) | 294.482 | 322.536 | 350.59 |
| CAS-RN | 73255-62-6 | 73255-65-9 | – |
| Temperatures of phase transitions $T^{tr}$ (°C) | Cr 22.8 N 36.6 Is | Cr 24.5 B 37.5 N 52.0 Is | Cr 52.0 B 72.0 Is |
| Enthalpies of phase transitions $\Delta H^{tr}$ (kJ/mol) | – | 29.3 (Cr–S) | 31.0 (Cr–S) |
| Anisotropy of refractive index $\Delta n$ (589 nm) | 0.036 (25 °C) | 0.05 (extra, 20 °C) | – |
| Dielectric anisotropy $\Delta\varepsilon$ (1 kHz) | −1.1 (25 °C) | −1.5 (20 °C) | −1.6 (20 °C) |
| Kinematic viscosity $\nu$ (mm$^2$/s) (20 °C) | 11 | 14 | 15 |
| **Number/common name** | **109** | **110** | **111** |
| Substance | 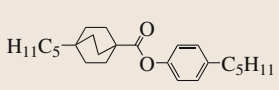 | 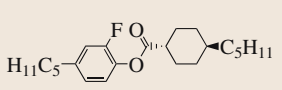 | 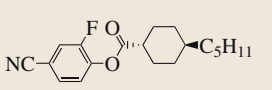 |
| Formula | $C_{25}H_{38}O_2$ | $C_{23}H_{35}FO_2$ | $C_{19}H_{24}FNO_2$ |

**Table 5.1-4** Two-ring systems with bridges, cont.

| Number/common name | 109 | 110 | 111 |
|---|---|---|---|
| Molar mass (g/mol) | 370.58 | 362.533 | 317.407 |
| Temperatures of phase transitions $T^{tr}$ (°C) | Cr 31.0 N 64.5 Is | Cr 19.0 N 37.9 Is | Cr 75.5 N 93.5 Is |
| Enthalpies of phase transitions $\Delta H^{tr}$ (kJ/mol) | 29.8 (Cr–N) | 33.5 (Cr–N) | – |
| Refractive index $n$ | $n_e$ 1.5337, $n_o$ 1.4770 ($T = 0.97 \times T^{N–Is}$, 633 nm) | $\Delta n$ 0.0608, $n_e$ 1.5273 ($T = 0.97 \times T^{N–Is}$, 633 nm) | $\Delta n$ 0.093 ($T = 0.95 \times T^{N–Is}$, 589 nm) |
| Dielectric constant $\varepsilon$ (1 kHz) | $\varepsilon_\parallel$ 2.79, $\varepsilon_\perp$ 3.18 ($T = 0.97 \times T^{N–Is}$) | – | $\Delta\varepsilon$ +4.4 ($T = 0.95 \times T^{N–Is}$) |
| Viscosity (20 °C) | $\eta$ 35 mPa s (extra) | $\nu$ 16 mm$^2$/s (extra) | – |

**Table 5.1-5** Three and four-ring systems

| Number/common name | 112 (RO-CM-5515, T15) | 113 | 114 |
|---|---|---|---|
| Substance | 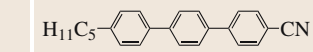 | 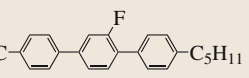 | 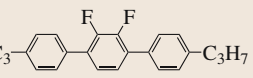 |
| Formula | $C_{24}H_{23}N$ | $C_{24}H_{22}FN$ | $C_{24}H_{24}F_2$ |
| Molar mass (g/mol) | 325.458 | 343.448 | 350.456 |
| CAS-RN | 54211-46-0 | – | – |
| Temperatures of phase transitions $T^{tr}$ (°C) | Cr′ 80.0 Cr′ 115.0 Cr 131.0 N 240.0 Is | Cr 97.0 N 189.0 Is | Cr 95.0 N 131.0 Is |
| Enthalpies of phase transitions $\Delta H^{tr}$ (kJ/mol) | 17.2 (Cr–N), 0.9 (N–Is) | – | 24.3 (Cr–N) |
| Anisotropy of refractive index $\Delta n$ (extra, 20 °C, 589 nm) | 0.30 | 0.343 | 0.24 |
| Dielectric anisotropy $\Delta\varepsilon$ (1 kHz) | +13, $\varepsilon_\parallel$ 16.0 ($T = 0.75 \times T^{N–Is}$) | +10, (20 °C, extra) | – 1.7, (20 °C, extra) |
| Kinematic viscosity $\nu$ (mm$^2$/s) | 86 (extra, 20 °C) | 195 (extra, 20 °C) | 31 (extra, 20 °C) |
| **Number/common name** | **115 (BCH5, ZLI-1131)** | **116 (BCH32, ZLI-1639)** | **117 (BCH52, ZLI-1409)** |
| Substance | 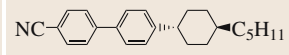 | 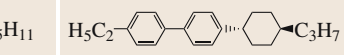 | 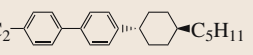 |
| Formula | $C_{24}H_{29}N$ | $C_{23}H_{30}$ | $C_{25}H_{34}$ |
| Molar mass (g/mol) | 331.505 | 306.496 | 334.55 |
| Temperatures of phase transitions $T^{tr}$ (°C) | Cr 96.0 N 222.0 Is | Cr 66.0 S 134.0 N 166.0 Is | Cr 34.0 B 146.0 N 164.0 Is |
| Enthalpies of phase transitions $\Delta H^{tr}$ (kJ/mol) | 21.1 (Cr–N), 0.7 (N–Is) | – | 18.5 (Cr–B), 6.8 (B–N), 0.5 (N–Is) |
| Crystallographic space group | $P2_1/c$ | – | $C2/c$ |
| Density $\varrho$ (g/cm$^3$) | 1.196 (101 °C) | – | – |
| Refractive index $n$ | $n_e$ 1.734, $n_o$ 1.515 (101 °C, 546 nm) | $\Delta n$ 0.18 (20 °C, 589 nm) | $\Delta n$ 0.18 (20 °C, 589 nm) |
| Dielectric constant $\varepsilon$ (1 kHz) | $\varepsilon_\parallel$ 16.8, $\varepsilon_\perp$ 4.9 (20 °C, extra) | $\Delta\varepsilon$ +0.5 (20 °C, extra) | $\Delta\varepsilon$ +0.4 (20 °C, extra) |
| Kinematic viscosity $\nu$ (mm$^2$/s) | 90 (extra, 20 °C) | 20 (extra, 20 °C) | 20 (extra, 20 °C) |

**Table 5.1-5** Three and four-ring systems, cont.

| Number/common name | 118 (BCH52F) | 119 | 120 |
|---|---|---|---|
| Substance | 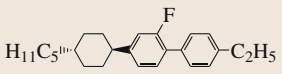 | 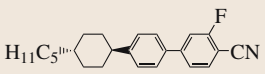 | 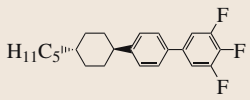 |
| Formula | $C_{25}H_{33}F$ | $C_{24}H_{28}FN$ | $C_{23}H_{27}F_3$ |
| Molar mass (g/mol) | 352.54 | 349.496 | 360.467 |
| CAS-RN | – | – | 137019-95-5 |
| Temperatures of phase transitions $T^{tr}$ (°C) | Cr 37.0 N 117.0 Is | Cr 84.0 N 175.4 Is | Cr 30.4 N 58.0 Is |
| Enthalpies of phase transitions $\Delta H^{tr}$ (kJ/mol) | 23.0 (Cr–N) | – | 18.0 (Cr–N), 0.2 (N–Is) |
| Refractive index $n$ | $\Delta n$ 0.096 (633 nm) ($T = 0.97 \times T^{N-Is}$) | $\Delta n$ 0.201 (20 °C, extra, 589 nm) | $\Delta n$ 0.134 (25 °C, extra, 589 nm) |
| Dielectric constant $\varepsilon$ (1 kHz) | $\varepsilon_\parallel$ 2.97, $\varepsilon_\perp$ 2.85 ($T = 0.97 \times T^{N-Is}$) | $\Delta\varepsilon$ +20.3 (20 °C, extra) | $\Delta\varepsilon$ +11.3 (20 °C, extra) |
| Viscosity (20 °C, extra) | $\nu$ 27 mm$^2$/s | $\nu$ 110 mm$^2$/s | $\eta$ 32.1 mPa s |
| **Number/common name** | **121** | **122 (BCN55, ZLI-2769)** | **123** |
| Substance | 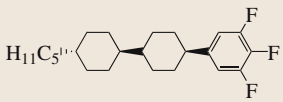 |  | 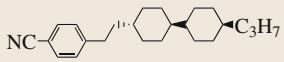 |
| Formula | $C_{23}H_{33}F_3$ | $C_{29}H_{51}N$ | $C_{24}H_{35}N$ |
| Molar mass (g/mol) | 366.515 | 413.737 | 337.553 |
| Temperatures of phase transitions $T^{tr}$ (°C) | Cr 87.3 N 101.2 Is | Cr 33.0 B 176.0 A 185.0 N 198.7 Is | Cr 69.0 N 196.0 Is |
| Enthalpies of phase transitions $\Delta H^{tr}$ (kJ/mol) | 26.4 (Cr–N), 0.6 (N–Is) | 17.6 (Cr–B) | – |
| Anisotropy of refractive index $\Delta n$ (589 nm) | 0.085 (25 °C, extra) | 0.06 (20 °C, extra) | 0.17 (20 °C, extra) |
| Dielectric anisotropy $\Delta\varepsilon$ (extra, 20 °C, 1 kHz) | +7.8 | −4.7 | +12 |
| Kinematic viscosity $\nu$ (mm$^2$/s) | 20 (extra, 20 °C) | 110 (extra, 20 °C) | 75 (extra, 20 °C) |
| **Number/common name** | **124 (I32)** | **125 (I35)** | **126 (I52)** |
| Substance | 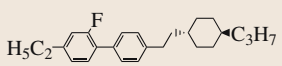 | 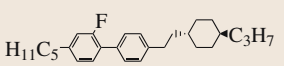 | 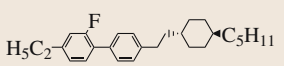 |
| Formula | $C_{25}H_{33}F$ | $C_{28}H_{39}F$ | $C_{27}H_{37}F$ |
| Molar mass (g/mol) | 352.54 | 394.621 | 380.594 |
| CAS-RN | | 100497-33-4 | 95379-18-3 |
| Temperatures of phase transitions $T^{tr}$ (°C) | Cr 27.0 N 97.0 Is | Cr 30.0 N 106.0 Is | Cr 24.0 (B 14.0) N 103.0 Is |
| Enthalpies of phase transitions $\Delta H^{tr}$ (kJ/mol) | – | – | 14.2 (Cr–N), 1.3 (N–Is) |
| Density $\varrho$ (g/cm$^3$) | 1.0156 (N, 25 °C) | 0.9975 (N, 25 °C) | 1.003 (N, 25 °C) |
| Refractive index $n$ ($T = 0.95 \times T^{N-Is}$, 633 nm) | $n_e$ 1.6108, $n_o$ 1.4893 | $n_e$ 1.6021, $n_o$ 1.4851 | $n_e$ 1.6013, $n_o$ 1.4824 |

**Table 5.1-5** Three and four-ring systems, cont.

| Number/common name | 124 (I32) | 125 (I35) | 126 (I52) |
|---|---|---|---|
| Dielectric constant $\varepsilon$ | $\varepsilon_\parallel$ 2.94, $\varepsilon_\perp$ 2.93 ($T = 0.95 \times T^{N-Is}$, 0.5 kHz) | $\varepsilon_\parallel$ 2.92, $\varepsilon_\perp$ 2.89 ($T = 0.95 \times T^{N-Is}$, 0.5 kHz) | $\Delta\varepsilon$ −0.06, $\varepsilon_\parallel$ (25 °C, 1 kHz) 2.964, $\varepsilon_\perp$ 3.024 |
| Kinematic viscosity $\nu$ ($mm^2/s$) | 19 (20 °C) | 24.5 (20 °C) | 25.1 (25 °C) |
| **Number/common name** | **127 (HP5N, ZLI-1226)** | **128 (HP33, ZLI-1222)** | **129 (HP35, ZLI-2429)** |
| Substance | 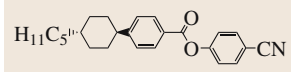 | 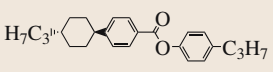 | 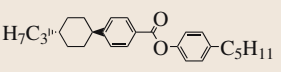 |
| Formula | $C_{25}H_{29}NO_2$ | $C_{25}H_{32}O_2$ | $C_{27}H_{36}O_2$ |
| Molar mass (g/mol) | 375.515 | 364.533 | 392.587 |
| Temperatures of phase transitions $T^{tr}$ (°C) | Cr′ 82.0 Cr 111.5 N 226.0 Is | Cr 87.0 N 186.0 Is | Cr 83.0 (S 79.0) N 175.0 Is |
| Enthalpies of phase transitions $\Delta H^{tr}$ (kJ/mol) | 5.4 (Cr–Cr′), 19.0 (Cr–N), 1.4 (N–Is) | 20.9 (Cr–N) | 22.0 (Cr–N) |
| Density $\varrho$ ($g/cm^3$) | – | 1.141 (N, 99.5 °C) | – |
| Refractive index $n$ | $\Delta n$ 0.16 (20 °C, 589 nm) | $n_e$ 1.655, $n_o$ 1.509 (99.5 °C, 546 nm) | $\Delta n$ 0.14 (20 °C, 589 nm) |
| Dielectric constant $\varepsilon$ (1 kHz) | $\varepsilon_\parallel$ 24.4, $\varepsilon_\perp$ 7.5 (156.0 °C) | $\Delta\varepsilon$ +0.4 (20 °C) | $\Delta\varepsilon$ +0.6 (20 °C) |
| Kinematic viscosity $\nu$ ($mm^2/s$) | 220 (extra, 20 °C) | 60 (extra, 20 °C) | 41 (extra, 20 °C) |
| **Number/common name** | **130 (HH33, ZLI-1224)** | **131 (HH53, ZLI-1223)** | **132 (HD34, ZLI-1749)** |
| Substance | 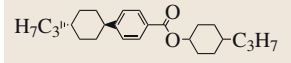 | 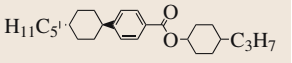 | 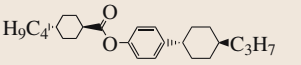 |
| Formula | $C_{25}H_{38}O_2$ | $C_{27}H_{42}O_2$ | $C_{26}H_{40}O_2$ |
| Molar mass (g/mol) | 370.58 | 398.635 | 384.63 |
| Temperatures of phase transitions $T^{tr}$ (°C) | Cr 94.0 N 158.0 Is | Cr 67.0 (S 43.0 A 55.0) N 155.0 Is | Cr 64.0 S 97.0 S 116.0 N 189.0 Is |
| Enthalpies of phase transitions $\Delta H^{tr}$ (kJ/mol) | 18.1 (Cr–N) | 21.8 (Cr–N) | 13.5 (Cr–S) |
| Crystallographic space group | $P\bar{1}$ | $P\bar{1}$ | |
| Anisotropy of refractive index $\Delta n$ (extra, 589 nm) | 0.19 (20 °C) | 0.092 (N, 80 °C) | 0.11 (20 °C) |
| Dielectric anisotropy $\Delta\varepsilon$ (20 °C, 1 kHz) | −1 | −1 | −1.4 |
| Kinematic viscosity $\nu$ ($mm^2/s$) | 130 (extra, 20 °C) | 119 (extra, 20 °C) | 40 (extra, 20 °C) |
| **Number/common name** | **133 (CH33)** | **134 (CH35)** | **135 (CH45)** |
| Substance | 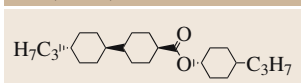 | 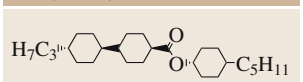 | 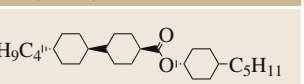 |
| Formula | $C_{25}H_{44}O_2$ | $C_{27}H_{48}O_2$ | $C_{28}H_{50}O_2$ |
| Molar mass (g/mol) | 376.628 | 404.682 | 418.71 |
| Temperatures of phase transitions $T^{tr}$ (°C) | Cr 58.0 S 155.0 N 189.0 Is | Cr 53.0 S 169.0 N 188.0 Is | Cr 38.0 S 181.0 N 186.0 Is |
| Enthalpies of phase transitions $\Delta H^{tr}$ (kJ/mol) | 24.3 (Cr–S) | 30.1 (Cr–S) | 22.2 (Cr–S) |
| Anisotropy of refractive index $\Delta n$ (extra, 589 nm) | 0.06 (20 °C) | 0.06 (20 °C) | 0.05 (20 °C) |

**Table 5.1-5** Three and four-ring systems, cont.

| Number/common name | 133 (CH33) | 134 (CH35) | 135 (CH45) |
|---|---|---|---|
| Dielectric anisotropy $\Delta\varepsilon$ (20 °C, 1 kHz) | − 1.8 | − 1.6 | − 1.7 |
| Kinematic viscosity $\nu$ ($mm^2/s$) | 31 (extra, 20 °C) | 34 (extra, 20 °C) | 37 (extra, 20 °C) |
| **Number/common name** | **136 (CBC53, ZLI-1544)** | **137 (CBC33, ZLI-1987)** | **138** |
| Substance | 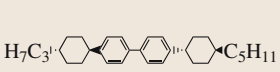 | 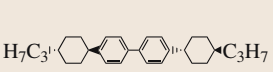 | 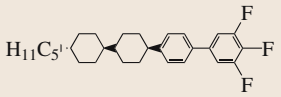 |
| Formula | $C_{32}H_{46}$ | $C_{30}H_{42}$ | $C_{29}H_{37}F_3$ |
| Molar mass (g/mol) | 430.723 | 402.669 | 442.613 |
| CAS-RN | 80955-71-1 | 85600-56-2 | – |
| Temperatures of phase transitions (°C) | Cr′ 54.0 Cr 58.0 B 232.0 A 251.0 N 311.0 Is | Cr′ 108.0 Cr′ 127.0 Cr 155.0 B 210.0 A 220.0 N 325.0 Is | Cr 87.8 N >250.0 Is |
| Enthalpies of phase transitions $\Delta H^{tr}$ (kJ/mol) | 5.1 (Cr–Cr′), 1.4 (Cr–B), 6.1 (B–A), 0.5 (A–N), 1.1 (N–Is) | 12.0 (Cr–B), 5.2 (B–A), 1.2 (N–Is) | – |
| Anisotropy of refractive index $\Delta n$ (extra, 589 nm) | 0.19 (20 °C) | 0.19 (20 °C) | 0.144 (25 °C) |
| Dielectric anisotropy $\Delta\varepsilon$ (extra, 20 °C, 1 kHz) | + 0.4 | + 0.5 | + 11.3 |
| Viscosity (extra, 20 °C) | $\nu$ 42 $mm^2/s$ | $\nu$ 53 $mm^2/s$ | $\eta$ 51.1 mPa s |

**Table 5.1-6** Ferroelectric liquid crystals

| Number/common name | 139 (DOBAMBC) | 140 (C-7) | 141 (MHPOBC) |
|---|---|---|---|
| Substance | 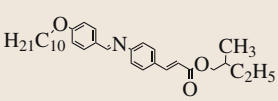 | 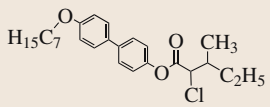 | 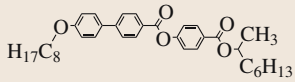 |
| Formula | $C_{31}H_{43}NO_3$ | $C_{25}H_{33}ClO_3$ | $C_{36}H_{46}O_5$ |
| Molar mass (g/mol) | 477.693 | 416.993 | 558.765 |
| CAS-RN | 97335-57-4 | 100497-43-6 | 103376-72-3 |
| Temperatures of phase transitions $T^{tr}$ (°C) | Cr 74.6 (I* 62.0) C* 94.0 A 117.0 Is | Cr 55.0 C* 55.0 A 62.0 Is | Cr 84.0 CA* 118.4 C$\gamma$ 119.2 C* 120.9 C$\alpha$ 122.0 A 148.0 Is |
| Enthalpies of phase transitions $\Delta H^{tr}$ (J/mol) | $2.58\times10^4$ (Cr–C*), $1.67\times10^3$ (I–C*), $5.15\times10^3$ (A–Is) | – | 14.6 (C*–C$\alpha$), 16.4 (CA*–C$\gamma$), 18.8 (C$\alpha$–C*), 288 (C$\alpha$–A), 6420 (A–Is) |
| Density $\varrho$ ($g/cm^3$) | 0.994 (C*, 92 °C), 0.985 (A, 100 °C), 0.959 (Is, 120 °C) | – | – |
| Refractive index $n$ | $n_e$ 1.700, $n_o$ 1.490 (A, 110 °C, 633 nm) | – | – |
| Dynamic viscosity $\eta$ (mPa s) | 6.7 (90 °C) | – | – |
| Spontaneous polarization $P_s$ ($nC/cm^2$) | + 4.75 (65 °C) | +260 (45 °C) | +70 (139.5 °C) |

**Table 5.1–7** Cholesteryl (cholest-5-ene) substituted mesogens

| Number/common name | 142 (CC) | 143 | 144 |
|---|---|---|---|
| Substance | 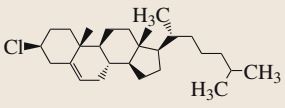 | 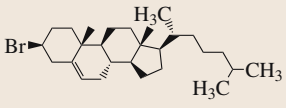 | 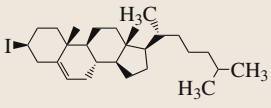 |
| Formula | $C_{27}H_{45}Cl_1$ | $C_{27}H_{45}Br$ | $C_{27}H_{45}I$ |
| Molar mass (g/mol) | 405.113 | 449.569 | 496.564 |
| CAS-RN | 910-31-6 | 516-91-6 | 2930-80-5 |
| Temperatures of phase transitions $T^{tr}$ (°C) | Cr 95.7 (N* 67.3) Is | Cr 100 (N* 69) Is | Cr 106.5 (N* 95) Is |
| Enthalpies of phase transitions $\Delta H^{tr}$ (kJ/mol) | 54.4 (Cr–Is), 0.38 (N*–Is) | – | – |
| Crystallographic space group | $P2_1$ | $P2_1$ | – |
| Density $\varrho$ (g/cm$^3$) | 0.98 | – | – |
| Dielectric constant $\varepsilon$ (10 kHz) | 3.52 (60 °C), 5.02 (90 °C) | – | – |
| Dipole moment $\mu$ (D) | 2.36 ($CCl_4$), 2.48 ($C_6H_6$) | 2.68 ($CCl_4$), 2.40 ($C_6H_6$) | – |
| **Number/common name** | **145** | **146** | **147 (CP)** |
| Substance | 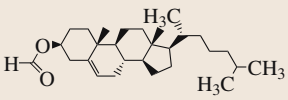 | 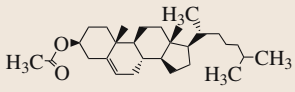 | 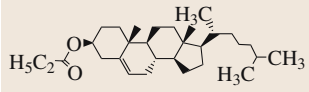 |
| Formula | $C_{28}H_{46}O_2$ | $C_{29}H_{48}O_2$ | $C_{30}H_{50}O_2$ |
| Molar mass (g/mol) | 414.678 | 428.705 | 442.732 |
| CAS-RN | 4351-55-7 | 604-35-3 | 633-31-8 |
| Temperatures of phase transitions $T^{tr}$ (°C) | Cr 97.5 (N* 60.5) Is | Cr 116.5 (N* 94.5) Is | Cr 101.6 N* 115.2 Is |
| Enthalpies of phase transitions $\Delta H^{tr}$ (kJ/mol) | 22.6 (Cr–Is) | 20.1 (Cr–Is), 0.3 (N*–Is) | 23.0 (Cr–N*), 0.5 (N*–Is) |
| Crystallographic space group | – | $P2_1$ | – |
| Density $\varrho$ (g/cm$^3$) | – | 0.951 (100 °C), 0.898 (130 °C) | 0.919 (110 °C), 0.901 (130 °C) |
| Refractive index $n$ | – | $n_e$ 1.482, $n_o$ 1.499 (N*, 95 °C) | $n_e$ 1.472, $n_o$ 1.489 (N*, 589 nm, 107.5 °C) |
| Dielectric constant $\varepsilon$ (10 kHz) | 2.45 (80 °C), 3.40 (100 °C) | 2.35 (90 °C), 2.90 (130 °C) | 2.22 (80 °C), 2.79 (120 °C) |
| Viscosity | $\eta$ 44 (71 °C), 25 (100 °C) (mPa s) | $\eta$ 53 (105 °C), 17 (125 °C) (mPa s) | $\nu$ 22.1 mm$^2$/s (117 °C) |
| Surface tension (mN/m) | 28.5 (70 °C) | 26.6 (110 °C) | 24.7 (110 °C) |
| Sound velocity $v$ (m/s) (2 MHz) | 1030 (95 °C), 990 (100 °C) | 1107 (100 °C), 1042 (130 °C) | 1245 (113 °C), 1228 (120 °C) |
| Pitch $p$ (µm) | – | – | 0.289 (110 °C) |
| Dipole moment $\mu$ (D) | 2.50 ($CCl_4$), 2.55 ($C_6H_6$) | 2.08 ($CCl_4$), 1.98 ($C_6H_6$) | 2.30 ($CCl_4$), 2.16 ($C_6H_6$) |

**Table 5.1-7** Cholesteryl (cholest-5-ene) substituted mesogens, cont.

| Number/common name | 148 | 149 | 150 |
|---|---|---|---|
| Substance | 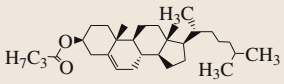 | 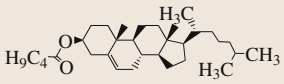 | 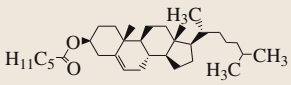 |
| Formula | $C_{31}H_{52}O_2$ | $C_{32}H_{54}O_2$ | $C_{33}H_{56}O_2$ |
| Molar mass (g/mol) | 456.759 | 470.786 | 484.813 |
| CAS-RN | 521-13-1 | 7726-03-6 | 1062-96-0 |
| Temperatures of phase transitions $T^{tr}$ (°C) | Cr 102.0 N* 113.0 Is | Cr 93.0 N* 101.5 Is | Cr 99.5 N* 101.5 Is |
| Enthalpies of phase transitions $\Delta H^{tr}$ (kJ/mol) | 22.0 (Cr–N*), 0.6 (N*–Is) | 22.0 (Cr–N*), 0.6 (N*–Is) | 30.0 (Cr–N*), 0.7 (N*–Is) |
| Crystallographic space group | $P2_1$ | $P2_12_12_1$ | $P2_1$ |
| Density $\varrho$ (g/cm$^3$) | 0.992 (110 °C), 0.984 (120 °C) | 0.893 (99 °C), 0.853 (119 °C) | – |
| Refractive index $n$ (589 nm) | $n_e$ 1.4716, $n_o$ 1.4865 (N*, 589 nm, 107.0 °C) | $n_e$ 1.4763, $n_o$ 1.4905 (N*, 589 nm, 92.5 °C) | $n_e$ 1.4735, $n_o$ 1.4880 (N*, 589 nm, 95 °C) |
| Kinematic viscosity $\nu$ (mm$^2$/s) | 22.3 (117 °C) | 39.8 (97.3 °C) | – |
| Surface tension (mN/m) | 24.6 (110 °C) | 24.6 (110 °C) | 25.0 (100 °C) |
| Pitch $p$ (µm) | 0.260 (109 °C) | 0.2588 (96.2 °C) | 0.247 (97 °C) |
| Dipole moment $\mu$ (D) | 2.21 ($CCl_4$), 2.12 ($C_6H_6$) | 2.34 ($CCl_4$), 2.48 ($C_6H_6$) | 1.86 (45 °C, $C_6H_6$) |
| **Number/common name** | **151** | **152** | **153 (CN)** |
| Substance | 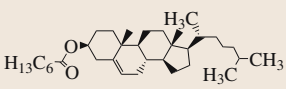 | 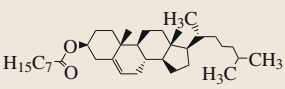 | 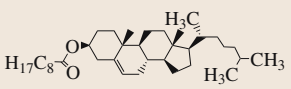 |
| Formula | $C_{34}H_{58}O_2$ | $C_{35}H_{60}O_2$ | $C_{36}H_{62}O_2$ |
| Molar mass (g/mol) | 498.84 | 512.867 | 526.894 |
| CAS-RN | 1182-07-6 | 1182-42-9 | 1182-66-7 |
| Temperatures of phase transitions $T^{tr}$ (°C) | Cr 114.0 (S <92.5 N* 95.5) Is | Cr 110.0 (S 69.5 N* 96.5) Is | Cr 80.5 (S 77.5) N* 92.0 Is |
| Enthalpies of phase transitions $\Delta H^{tr}$ (kJ/mol) | 32.2 (Cr–Is), 0.5 (N*–Is) | 34.1 (Cr–Is), 0.7 (N*–Is) | 23.4 (Cr–N*), 0.7 (N*–Is), 0.5 (S–N*) |
| Crystallographic space group | $P2_1$ | $P2_1$ | $P2_1$ |
| Refractive index $n$ (589 nm) | – | – | $n_e$ 1.4728, $n_o$ 1.4895 (N*, 85 °C), $n_e$ 1.5173, $n_o$ 1.4734 (S, 75.5 °C) |
| Dielectric constant $\varepsilon$ | – | – | 2.78 (90 °C, 600 kHz) |
| Dynamic viscosity $\eta$ (mPa s) | – | 31 (90 °C) | 98 (N*, 90.2 °C) |
| Surface tension (mN/m) | 20.4 (120 °C) | 21.0 (110 °C) | 24 (80 °C), 25 (90 °C) |
| Sound velocity $v$ (m/s) (2 MHz) | 1250 (105 °C), 1208 (120 °C) | – | – |
| Pitch $p$ (µm) | – | – | 0.231 (90 °C) |
| Dipole moment $\mu$ (D), 45 °C | 1.78 ($C_6H_6$) | 1.79 ($C_6H_6$) | 1.73 ($C_6H_6$) |

**Table 5.1-7** Cholesteryl (cholest-5-ene) substituted mesogens, cont.

| Number/common name | 154 | 155 | 156 (CM) |
|---|---|---|---|
| Substance | 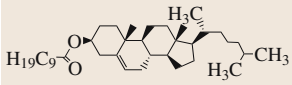 | 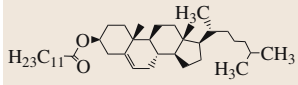 | 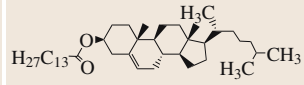 |
| Formula | $C_{37}H_{64}O_2$ | $C_{39}H_{68}O_2$ | $C_{41}H_{72}O_2$ |
| Molar mass (g/mol) | 540.921 | 568.976 | 597.03 |
| CAS-RN | 1183-04-6 | 1908-11-8 | 1989-52-2 |
| Temperatures of phase transitions $T^{tr}$ (°C) | Cr 85.5 (S 81.5) N* 92.5 Is | Cr 92.4 (A 80.2 N* 88.9) Is | Cr 73.6 A 80.0 N* 85.6 Is |
| Enthalpies of phase transitions $\Delta H^{tr}$ (kJ/mol) | 31.0 (Cr–N*), 0.8 (N*–Is), 0.6 (S–N*) | 37.9 (Cr–Is), 0.9 (N*–Is), 0.6 (S–N*) | 46.9 (Cr–A), 1.0 (N*–Is), 1.3 (S–N*) |
| Crystallographic space group | $P2_1$ | $P2_1$ | $P2_1$ |
| Density $\varrho$ (g/cm$^3$) | – | 0.932 (N*, 86 °C), 0.941 (A, 79 °C) | 0.896 (A, 74 °C), 0.890 (N*, 82 °C), 0.885 (Is, 86 °C) |
| Refractive index $n$ (589 nm) | $n_e$ 1.4724, $n_o$ 1.4863 (N*, 90 °C), $n_e$ 1.5151, $n_o$ 1.4713 (S, 80 °C) | $n_e$ 1.4715, $n_o$ 1.4878 (N*, 85 °C), $n_e$ 1.5148, $n_o$ 1.4705 (S, 80 °C) | $n_e$ 1.4717, $n_o$ 1.4876 (N*, 81 °C), $n_e$ 1.5152, $n_o$ 1.4704 (S, 76 °C) |
| Dielectric constant $\varepsilon$ (10 kHz) | – | 2.33 (80 °C) | 4.72 (70 °C) |
| Dynamic viscosity $\eta$ (mPa s) | | 40 (90.4 °C), 43 (82 °C) | 41 (88 °C), 126 (79.6 °C) |
| Heat capacity $C_p$ (J/(mol K)) | 1300 (N*, 90 °C) | $C_p = 1008 + 3.67 \times T$ (S, $T$ (°C) = 69–80) | $C_p = 1033 + 4.84 \times T$ (S, $T$ (°C) = 66–71) |
| Surface tension (mN/m) | 24.7 (100 °C), 24.5 (90 °C) | 24.7 (100 °C), 24.4 (90 °C) | 23.9 (82 °C), 25.0 (94 °C) |
| Sound velocity $v$ (m/s) | – | 1348 (85 °C), 1335 (100 °C) (2 MHz) | 1345 (84 °C), 1316 (90 °C) |
| Diffusion coefficient $D$ (m$^2$/s) | – | – | $1.88 \times 10^{-10}$ (Is, 90 °C), $1.75 \times 10^{-10}$ (N*, 80 °C) |
| Pitch $p$ (µm) | 0.225 (90 °C) | 0.2125 (82 °C) | 0.1994 (83 °C) |
| Dipole moment $\mu$ (D), 45 °C | 1.74 ($C_6H_6$) | 1.73 ($C_6H_6$) | – |
| **Number/common name** | **157** | **158** | **159 (CB)** |
| Substance | 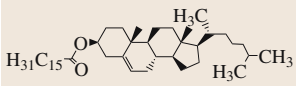 | 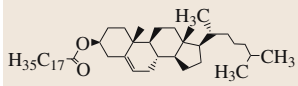 | 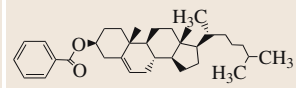 |
| Formula | $C_{43}H_{76}O_2$ | $C_{45}H_{80}O_2$ | $C_{34}H_{50}O_2$ |
| Molar mass (g/mol) | 625.084 | 653.138 | 490.776 |
| CAS-RN | 601-34-3 | 35602-69-8 | 604-32-0 |
| Temperatures of phase transitions $T^{tr}$ (°C) | Cr 79.0 (S 78.5) N* 83.0 Is | Cr 83.0 (S 75.5 N* 79.5) Is | Cr 150.5 N* 182.6 Is |
| Enthalpies of phase transitions $\Delta H^{tr}$ (kJ/mol) | 59.4 (Cr–N*), 1.3 (N*–Is), 1.7 (S–N*) | 67.5 (Cr–Is), 1.7 (N*–Is), 1.8 (S–N*) | 22.2 (Cr–N*), 0.6 (N*–Is) |
| Crystallographic space group | $A2$ | $P2_1$ | $P2_12_12_1$ |
| Density $\varrho$ (g/cm$^3$) | 0.917 (N*, 80 °C), 0.909 (Is, 100 °C) | 0.855 (Is, 90 °C) | 0.9574 (N*, 159.2 °C), 0.9354 (Is, 185.4 °C) |

**Table 5.1-7** Cholesteryl (cholest-5-ene) substituted mesogens, cont.

| Number/common name | 157 | 158 | 159 (CB) |
|---|---|---|---|
| Refractive index $n$ (589 nm) | $n_e$ 1.4752, $n_o$ 1.4881 (N*, 78 °C) | – | $n_e$ 1.4813, $n_o$ 1.5656 (N*, 160 °C) |
| Dielectric constant $\varepsilon$ (10 kHz) | – | 2.36 (70 °C) | – |
| Dynamic viscosity $\eta$ (mPa s) | 47 (85 °C), 68 (76.6 °C) | 78.4 (80 °C), 85.2 (78 °C), 117 (74 °C) | 35.5 (170 °C), 25.8 (180 °C) |
| Surface tension (mN/m) | 25.0 (90 °C), 24.2 (80 °C) | 25.6 (Is, 80 °C), 25.2 (N*, 75 °C), 25.3 (S, 70 °C) | 21.8 (Is, 210 °C), 23.8 (N*, 147.4 °C), 22.9 (N*, 177 °C) |
| Sound velocity $v$ (m/s) (2 MHz) | – | 1343 (77 °C), 1332 (85 °C) | 1093 (170 °C), 1087 (190 °C) |
| Pitch $p$ (µm) | 0.2215 (77 °C) | – | – |
| Dipole moment $\mu$ (D) | 1.69 (45 °C, $C_6H_6$) | 1.62 (45 °C, $C_6H_6$) | 2.08 ($CCl_4$), 2.11 ($C_6H_6$) |
| **Number/common name** | **160 (CO)** | **161 (COC)** | **162** |
| Substance | 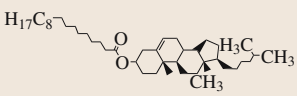 | 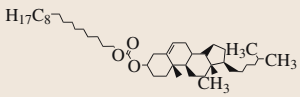 | 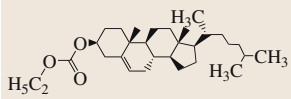 |
| Formula | $C_{45}H_{78}O_2$ | $C_{46}H_{80}O_3$ | $C_{30}H_{50}O_3$ |
| Molar mass (g/mol) | 651.122 | 681.149 | 458.731 |
| CAS-RN | 303-43-5 | 17110-51-9 | 23836-43-3 |
| Temperatures of phase transitions $T^{tr}$ (°C) | Cr 51 (A 42 N* 47.5) Is | Cr 26.7 (A 20) N* 34 Is | Cr 83.9 N* 105.8 Is |
| Enthalpies of phase transitions $\Delta H^{tr}$ (kJ/mol) | 29.0 (Cr–Is), 0.84 (N*–Is), 1.3 (S–N*) | 27.3 (Cr–N*), 0.8 (N*–Is), 0.8 (S–N*) | 21.1 (Cr–N*), 0.7 (N*–Is) |
| Crystallographic space group | $P2_1$ | – | $P2_1$ |
| Density $\varrho$ (g/cm$^3$) | 1.084 (N*, 40 °C), 1.072 (Is, 50 °C) | 0.972 (N*, 20 °C), 0.962 (Is, 32 °C) | – |
| Refractive index $n$ (589 nm) | $n_e$ 1.505, $n_o$ 1.521 (A, 20 °C) | $n_e$ 1.4947, $n_o$ 1.5101 (N*, 25 °C) | $n_e$ 1.472, $n_o$ 1.490 (N*, 90 °C) |
| Dielectric constant $\varepsilon$ (10 kHz) | – | 2.44 (A, 3 °C), 2.41 (Is, 40 °C) | – |
| Sound velocity $v$ (m/s) (10 MHz) | 1459 (45 °C), 1406 (58 °C) | – | – |
| Pitch $p$ (nm) | – | – | 232.3 (90 °C) |
| Dipole moment $\mu$ (D) | – | 1.14 (45 °C, $C_6H_{12}$) | – |

**Table 5.1-8** Discotic liquid crystals

| Number/common name | 163 | 164 | 165 (H10TX) |
|---|---|---|---|
| Substance | 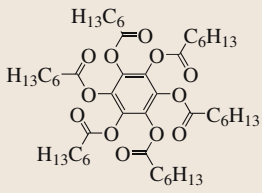 | 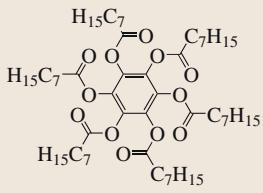 | 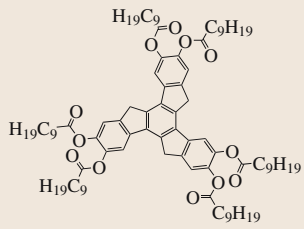 |
| Formula | $C_{48}H_{78}O_{12}$ | $C_{54}H_{90}O_{12}$ | $C_{87}H_{126}O_{12}$ |
| Molar mass (g/mol) | 847.15 | 931.312 | 1363.967 |
| CAS-RN | 65201-70-9 | 65201-71-0 | 86108-14-7 |
| Temperatures of phase transitions $T^{tr}$ (°C) | Cr 81.2 D 87.0 Is | Cr′ 28.8 Cr 82.0 D 84.0 Is | Cr 68 N 85 Drd 138 Dho 280 Is |
| Enthalpies of phase transitions $\Delta H^{tr}$ (kJ/mol) | 32.2 (Cr–D), 21.5 (D–Is) | 46.1 (Cr–D), 19.2 (D–Is), 49.0 (Cr′–Cr) | 21.3 (Cr–N), 1.0 (N–D) |
| Refractive index $n$ | – | – | $n_o$ 1.531, $n_e$ 1.454 ($T = 0.999T^{N-D}$) |
| **Number/common name** | **166 (HAT5)** | **167 (HAT6)** | **168 (HAT8)** |
| Substance | 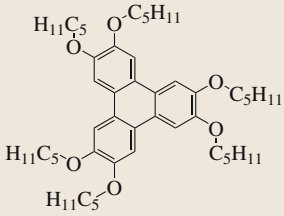 | 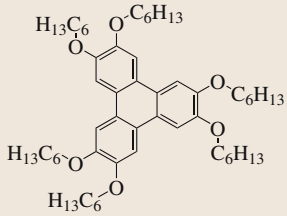 | 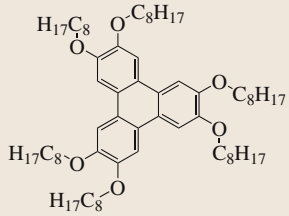 |
| Formula | $C_{48}H_{72}O_6$ | $C_{54}H_{84}O_6$ | $C_{66}H_{108}O_6$ |
| Molar mass (g/mol) | 745.105 | 829.268 | 997.593 |
| CAS-RN | 69079-52-3 | 70351-86-9 | 70351-87-0 |
| Temperatures of phase transitions $T^{tr}$ (°C) | Cr 69.0 Dho 122.0 Is | Cr 68.0 Dho 97.0 Is | Cr 67.0 Dho 86.0 Is |
| Enthalpies of phase transitions $\Delta H^{tr}$ (kJ/mol) | 32.6 (Cr–D), 8.1 (D–Is) | 36.4 (Cr–D), 3.6 (D–Is) | 83.3 (Cr–D), 4.2 (D–Is) |
| **Number/common name** | **169** | **170 (HAT11)** | **171** |
| Substance | 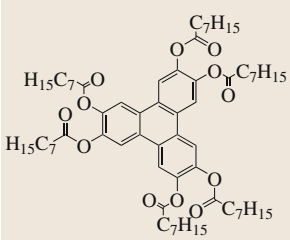 | 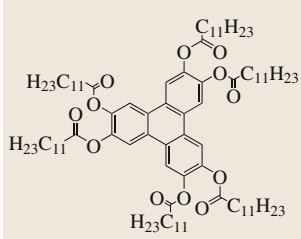 | 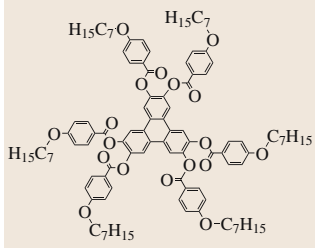 |
| Formula | $C_{66}H_{96}O_{12}$ | $C_{90}H_{144}O_{12}$ | $C_{102}H_{120}O_{18}$ |
| Molar mass (g/mol) | 1081.494 | 1418.144 | 1634.083 |
| CAS-RN | 70351-94-9 | 70187-34-7 | 75747-38-5 |

**Table 5.1-8** Discotic liquid crystals, cont.

| Number/common name | 169 | 170 (HAT11) | 171 |
|---|---|---|---|
| Temperatures of phase transitions $T^{tr}$ (°C) | Cr 66.0 D 126.0 Is | Cr 80.0 Dh 93.0 Dt 111.0 Dh 122.3 Is | Cr′ 117.8 Cr′ 130.9 Cr 169.1 N 253.1 Is |
| Enthalpies of phase transitions $\Delta H^{tr}$ (kJ/mol) | 19.7 (Cr–D), 2.8 (D–Is) | 59.4 (Cr–D), 2.4 (D–Is) | 9.4 (Cr–D) |
| Anisotropy of refractive index $\Delta n$ | – | – | – 0.09 (200 °C, 633 nm) |
| Dielectric constant $\varepsilon$ | – | – | $\varepsilon_{\parallel}$ 3.78, $\varepsilon_{\perp}$ 3.33 (230 °C) |
| Dynamic viscosity $\eta$ (mPa s) | – | – | 350 (230 °C) |

**Table 5.1-9** Liquid crystal salts

| $Na^+$ | Temperatures of phase transitions (°C) | $Tl^+$ | Temperatures of phase transitions (°C) |
|---|---|---|---|
| $C_3H_7-COO-$ | Cr 251.0 S 327.0 Is | $C_4H_9-COO-$ | Cr 80.4 S 180.0 A 214.3 Is |
| $C_4H_9-COO-$ | Cr 241.0 A 344.0 Is | $C_5H_{11}-COO-$ | Cr 124.4 S 137.2 S 148.5 A 227.1 Is |
| $C_5H_{11}-COO-$ | Cr 210.0 S 235.0 A 361.0 Is | $C_6H_{13}-COO-$ | Cr 140.5 A 226.0 Is |
| $C_6H_{13}-COO-$ | Cr 198.0 S 242.0 A 363.0 Is | $C_7H_{15}-COO-$ | Cr 135.0 A 221.0 Is |
| $C_7H_{15}-COO-$ | Cr 189.0 S 243.0 A 360.0 Is | $C_8H_{17}-COO-$ | Cr 39.5 S 55.8 S 136.5 A 217.9 Is |
| $C_8H_{17}-COO-$ | Cr 185.0 S 243.0 A 355.0 Is | $C_9H_{19}-COO-$ | Cr 30.2 S 49.8 S 128.4 A 207.6 Is |
| $C_9H_{19}-COO-$ | Cr 140.0 S 181.0 S 245.0 S 348.0 Is | $C_{10}H_{21}-COO-$ | Cr 35.8 S 47.0 S 74.4 S 128.7 A 201.6 Is |
| $C_{10}H_{21}-COO-$ | Cr 115.0 S 145.0 S 167.0 S 187.0 S 242.0 A 337.0 Is | $C_{11}H_{23}-COO-$ | Cr 36.0 S 73.8 S 122.3 A 196.8 Is |
| $C_{11}H_{23}-COO-$ | Cr 100.0 S 141.0 S 182.0 S 220.0 S 255.0 A 336.0 Is | $C_{12}H_{25}-COO-$ | Cr 53.8 S 58.6 S 97.0 S 125.3 A 192.5 Is |
| $C_{12}H_{25}-COO-$ | Cr 121.0 S 162.0 S 187.0 S 200.0 S 217.0 S 248.0 A 323.0 Is | $C_{13}H_{27}-COO-$ | Cr 36.5 S 42.0 S 94.8 S 118.9 A 184.4 Is |
| $C_{13}H_{27}-COO-$ | Cr 113.0 S 138.0 S 171.0 S 215.0 S 246.0 A 311.0 Is | $C_{14}H_{29}-COO-$ | Cr 66.9 S 111.6 S 120.4 A 179.6 Is |
| $C_{14}H_{29}-COO-$ | Cr 121.0 S 160.0 S 187.0 S 203.0 S 251.0 S 277.0 A 307.0 Is | $C_{15}H_{31}-COO-$ | Cr 54.0 S 114.4 S 116.4 A 175.5 Is |
| $C_{15}H_{31}-COO-$ | Cr 117.0 S 136.0 S 168.0 S 212.0 S 251.0 A 302.0 Is | $C_{16}H_{33}-COO-$ | Cr 75.3 S 119.4 A 171.5 Is |
| $C_{16}H_{33}-COO-$ | Cr 130.0 S 205.0 S 260.0 A 290.0 Is | $C_{17}H_{35}-COO-$ | Cr 62.1 S 118.4 A 168.1 Is |
| $C_{17}H_{35}-COO-$ | Cr 117.0 S 132.0 S 167.0 S 198.0 S 257.0 A 288.0 Is | $C_{19}H_{39}-COO-$ | Cr 70.2 S 120.5 A 158.2 Is |
| $C_{18}H_{37}-COO-$ | Cr 118.0 S 133.0 S 146.0 S 193.0 S 202.0 S 258.0 A 283.0 Is | $C_{21}H_{43}-COO-$ | Cr 67.2 S 76.8 S 121.8 A 151.8 Is |
| $C_{19}H_{39}-COO-$ | Cr 110.0 S 131.0 S 163.0 S 200.0 A 262.0 Is | $C_{25}H_{51}-COO-$ | Cr 114.0 S 125.0 Is |

**Table 5.1-9** Liquid crystal salts, cont.

| $Li^+$ | Temperatures of phase transitions (°C) | $K^+$ | Temperatures of phase transitions (°C) |
|---|---|---|---|
| $C_{11}H_{23}-COO-$ | Cr 229.0 S 239.0 Is | $C_3H_7-COO-$ | Cr 353.0 S 404.0 Is |
| $C_{12}H_{25}-COO-$ | Cr 224.0 S 232.0 Is | $C_4H_9-COO-$ | Cr 313.4 S 443.0 Is |
| $C_{13}H_{27}-COO-$ | Cr 210.0 S 231.0 S 239.0 Is | $C_5H_{11}-COO-$ | Cr 308.5 S 452.0 Is |
| $C_{14}H_{29}-COO-$ | Cr 206.0 S 229.0 Is | $C_6H_{13}-COO-$ | Cr 298.1 S 449.0 Is |
| $C_{15}H_{31}-COO-$ | Cr 197.0 S 215.0 S 223.0 Is | $C_7H_{15}-COO-$ | Cr 287.0 S 439.0 Is |
| $C_{17}H_{35}-COO-$ | Cr 190.0 S 215.0 S 229.0 Is | $C_8H_{17}-COO-$ | Cr 276.0 S 434.0 Is |
| $C_{19}H_{39}-COO-$ | Cr 189.0 S 226.0 Is | $C_9H_{19}-COO-$ | Cr 271.0 S 423.0 Is |
| $Cs^+$ | Temperatures of phase transitions (°C) | $C_{10}H_{21}-COO-$ | Cr 268.0 S 418.0 Is |
| $C_5H_{11}-COO-$ | Cr 359.0 S 399.0 Is | $C_{11}H_{23}-COO-$ | Cr 268.0 S 406.0 Is |
| $C_6H_{13}-COO-$ | Cr 345.0 S 421.0 Is | $C_{12}H_{25}-COO-$ | Cr 89.9 S 397.6 Is |
| $C_7H_{15}-COO-$ | Cr 334.0 S 425.0 Is | $C_{13}H_{27}-COO-$ | S 271.0 A 375.0 Is |
| $C_8H_{17}-COO-$ | Cr 325.0 S 424.0 Is | $C_{14}H_{29}-COO-$ | Cr 64.0 S 388.5 Is |
| $C_9H_{19}-COO-$ | Cr 314.0 S 415.0 Is | $C_{15}H_{31}-COO-$ | Cr 195.0 S 269.0 A 362.0 Is |
| $C_{11}H_{23}-COO-$ | Cr 278.0 S 355.0 Is | $C_{17}H_{35}-COO-$ | Cr 170.0 S 238.0 S 264.0 S 356.0 Is |
| $C_{13}H_{27}-COO-$ | Cr 287.0 S 386.0 Is | $C_{19}H_{39}-COO-$ | Cr 74.1 S 339.9 Is |
| $Rb^+$ | Temperatures of phase transitions (°C) | $Cu^{2+}$ | Temperatures of phase transitions (°C) |
| $C_4H_9-COO-$ | Cr 367.0 S 430.0 Is | $C_3H_7-COO-$ | Cr 195.0 D > 200.0 dec |
| $C_5H_{11}-COO-$ | Cr 342.2 S 450.0 Is | $C_4H_9-COO-$ | Cr 111.0 D > 200.0 dec |
| $C_6H_{13}-COO-$ | Cr 327.0 S 451.0 Is | $C_5H_{11}-COO-$ | Cr 95.0 D > 200.0 dec |
| $C_7H_{15}-COO-$ | Cr 312.0 A 440.0 Is | $C_6H_{13}-COO-$ | Cr 93.0 D > 200.0 dec |
| $C_8H_{17}-COO-$ | Cr 300.0 A 439.0 Is | $C_7H_{15}-COO-$ | Cr 88.0 D > 200.0 dec |
| $C_9H_{19}-COO-$ | Cr 291.0 A 429.0 Is | $C_8H_{17}-COO-$ | Cr 102.0 D > 200.0 dec |
| $C_{11}H_{23}-COO-$ | Cr 300.0 A 400.0 Is | $C_9H_{19}-COO-$ | Cr 106.9 D 210.0 dec |
| $C_{13}H_{27}-COO-$ | Cr 212.4 S 217.9 S 240.3 S 277.6 S 394.0 Is | $C_{15}H_{31}-COO-$ | Cr 122.0 D 220.0 dec |

**Table 5.1-9** Liquid crystal salts, cont.

| 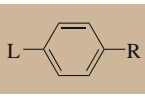 | | | 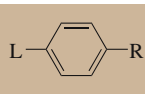 | | |
|---|---|---|---|---|---|
| H− | $-C_3H_6-COO-Tl$ | Cr 58.4 A 62.4 Is | $C_5H_{11}-O-$ | −COO−Tl | Cr 160.0 S 294.0 A 344.0 Is |
| H− | $-C_5H_{10}-COO-Tl$ | Cr 34.0 A 93.0 Is | $C_6H_{13}-O-$ | −COO−Tl | Cr 27.0 S 114.0 S 284.0 A 343.0 Is |
| H− | $-C_7H_{14}-COO-Tl$ | Cr 39.0 A 107.5 Is | $C_7H_{15}-O-$ | −COO−Tl | Cr 36.0 S 57.0 S 121.0 S 274.0 A 334.0 Is |
| H− | $-C_9H_{18}-COO-Tl$ | Cr 51.0 A 114.0 Is | $C_8H_{17}-O-$ | −COO−Tl | Cr 30.0 S 43.0 S 131.0 S 269.0 A 330.0 Is |
| $C_6H_{13}-$ | −COO−Tl | Cr 118.0 S 264.0 A 334.0 Is | $C_9H_{19}-O-$ | −COO−Tl | Cr 57.0 S 62.0 S 135.0 S 264.0 A 322.0 Is |

## 5.1.3 Physical Properties of Some Liquid Crystalline Mixtures

**Table 5.1-10** Nematic mixtures

| Mixture | E49 (Merck) | ZLI-2857 (Merck) | ZLI-3086 (Merck) |
|---|---|---|---|
| Components | Cyanobiphenyls | | |
| Temperatures of phase transitions $T^{tr}$ (°C) | Cr −9 N 100 Is | Cr −19 N 82.3 Is | N 72.0 Is |
| Anisotropy of refractive index $\Delta n$ (20 °C) | 0.251 | 0.0776 | 0.1131 |
| Dielectric anisotropy $\Delta\varepsilon$ (20 °C) | | −1.4 | 0.1 |
| Kinematic viscosity ($mm^2/s$) (20 °C) | 46.5 | 20 | |
| **Mixture** | **E7 (Merck)** | **ZLI-1132 (Merck)** | **ZLI-4792 (Merck)** |
| Components | Cyanobiphenyls | Phenylcyclohexanes | Fluorinated LCs |
| Temperatures of phase transitions $T^{tr}$ (°C) | Cr <−30 N 58 Is | Cr −6 N 71 Is | Cr <−40 N 92 Is |
| Anisotropy of refractive index $\Delta n$ (589 nm, 20 °C) | 0.2253 | 0.1396 | 0.0969 |
| Extraordinary refractive index $n_e$ (589 nm, 20 °C) | 1.7464 | 1.6326 | 1.5763 |
| Dielectric anisotropy $\Delta\varepsilon$ (1 kHz, 20 °C) | 13.8 | 13.1 | 5.2 |
| $\varepsilon_\parallel$ (1 kHz, 20 °C) | 19.0 | 17.7 | 8.3 |
| Kinematic viscosity ($mm^2/s$) | 39 (20 °C), 145 (0 °C) | 28 (20 °C), 110 (0 °C) | 15 (20 °C), 40 (0 °C) |
| Surface tension (mN/m) | 29.3 (22 °C), $\sigma_\perp$ 14.5, $\sigma_\parallel$ 23.7 | 31.0 (22 °C), $\sigma_\perp$ 13.6, $\sigma_\parallel$ 26.0 | – |
| Elastic-constants ratio $K_3/K_1$ (20 °C) | 1.54 | 1.95 | 1.39 |
| $V_{10}$ (V) threshold | 1.41 | 1.77 | 2.00 |
| $V_{50}$ (V) | 1.63 | 2.05 | 2.47 |
| $V_{90}$ (V) saturation | 1.99 | 2.49 | 3.15 |

Data have been taken from [1.5]. ZLI-4792 is an SFM (superfluorinated material); it is recommended for VIP (viewing-independent panel) twisted nematic displays. Mixtures E7 and ZLI-1132 are recommended for usage in calculators, wristwatches, and measuring instruments. $V_{10}$, $V_{50}$, and $V_{90}$ are voltages at 10, 50, and 90%, respectively, of the maximum absorption at 0° viewing angle and 20 °C.

**Table 5.1-11** Ferroelectric mixtures

| Mixture | CS1024 | CS2004 | CS4000 |
|---|---|---|---|
| CAS-RN | 123967-01-1 | 135976-66-8 | 150260-44-9 |
| Temperatures of phase transitions $T^{tr}$ (°C) | Cr −12 C* 62 A 82 N* 90 Is | Cr <20 C* 62 N* 71 Is | Cr −10 CA 70.5 C$\gamma$ 72.5 C* 74.6 C$\alpha$ 75.6 A 100 Is |
| Spontaneous polarization $P_s$ (25 °C) ($nC/cm^2$) | −46.9 | – | – |
| Tilt $\Theta$ (25 °C) | 25 | 44 | – |
| Pitch (μm) | >20 | – | – |

**Table 5.1–11** Ferroelectric mixtures, cont.

| **Mixture** | **Felix-015-100** | **SCE8** | **SCE9** |
|---|---|---|---|
| CAS-RN | 211365-96-7 | 145380-16-1 | 126879-69-4 |
| Temperatures of phase transitions $T^{tr}$ (°C) | Cr −12 C* 72 A 83 N* 86 Is | Cr <20 C 59 A 79 N 100 Is | Cr <20 C* 61 A 91 N* 115 Is |
| Spontaneous polarization $P_s$ (25 °C) (nC/cm$^2$) | +33 | +630 | – |
| Tilt $\Theta$ (25 °C) | 25.5 | – | – |
| Switching time $\tau$ (25 °C) | – | 294 µs | – |
| **Mixture** | **SCE10** | **SCE13** | **TKF 8617** |
| CAS-RN | 134499-04-0 | 133758-42-6 | 114899-67-1 |
| Temperatures of phase transitions $T^{tr}$ (°C) | Cr <20 C* 61 N* 109 Is | Cr <0 C* 61 A 86 N* 103 Is | Cr 4 C* 54 A 65 Is |
| Spontaneous polarization $P_s$ (20 °C) (nC/cm$^2$) | 19.5 | 30.6 | – |
| Tilt $\Theta$ (20 °C) | – | 29 | – |
| Pitch (µm) | – | 10–12 | – |
| **Mixture** | **W22** | **ZhKS-309C** | **ZLI-3654** |
| CAS-RN | 137988-43-3 | 205599-65-1 | 116580-90-6 |
| Temperatures of phase transitions $T^{tr}$ (°C) | Cr 4 C* 51 A 82 N* 92 Is | Cr −1 C* 42 A 91 Is | Cr −30 C* 62 A 76 N 86 Is |
| Spontaneous polarization $P_s$ (20 °C) (nC/cm$^2$) | – | +50.8 | −29 |
| Tilt $\Theta$ (20 °C) | – | 26 | – |
| Pitch (µm) | – | 0.4 | 3 |
| **Mixture** | **ZLI-4655-000** | **ZLI-4851-100, Felix-M-4851-100** | **ZLI-5014-100** |
| CAS-RN | 139352-77-5 | 158854-82-1 | 172452-16-3 |
| Temperatures of phase transitions $T^{tr}$ (°C) | Cr <10 C* 60 A 69 N* 72 Is | Cr <−20 C* 67 A 71 N* 76 Is | Cr <−10 C* 65 A 70 N* 72 Is |
| Spontaneous polarization $P_s$ (20 °C) (nC/cm$^2$) | +7 | +22.8 | −20 |
| Tilt $\Theta$ (20 °C) | – | 30.5 | – |
| Pitch (µm) | – | – | 10 |
| Switching time $\tau$ (20 °C) | – | 38 µs | 3 µs |

## References


1.1 D. Demus, H. Demus, H. Zaschke: *Flüssige Kristalle in Tabellen I* (VEB Deutscher Verlag Grundstoffindustrie, Leipzig 1974)

1.2 D. Demus, H. Zaschke: *Flüssige Kristalle in Tabellen II* (Deutscher Verlag Grundstoffindustrie, Leipzig 1982)

1.3 V. Vill: *Liquid Crystals*, Landolt–Börnstein, New Series IV/7 (Springer, Berlin, Heidelberg 1992 – 1995)

1.4 V. Vill: Liqcryst 4.3 - Database of liquid crystalline compounds, http://liqcryst.chemie.uni-hamburg.de/ (2003)

1.5 Merck: Product information, liquid crystal mixtures for electro-optic displays (Merck, Darmstadt 1992)

1.6 H. Kelker, R. Hatz: *Handbook of Liquid Crystals* (Verlag Chemie, Weinheim 1980)

1.7 A. Beguin, J. C. Dubois, P. Le Barny, J. Billard, F. Bonamy, J. M. Buisine, P. Cuvelier: Sources of thermodynamic data on mesogens, Mol. Cryst. Liq. Cryst. **115**, 1 (1984)

1.8 BDH Chemical: Product information (BDH, Poole 1986)

1.9 E. Merck: Product information (Merck, Darmstadt 1986)

1.10 S. Chandrasekhar: *Liquid Crystals* (Cambridge Univ. Press, Cambridge 1992)

1.11 D. Demus, J. Goodby, G. W. Gray, H.-W. Spiess, V. Vill (Eds.): *Handbook of Liquid Crystals*, Vol. I – III (Wiley-VCH, Weinheim 1998)

1.12 D. Demus, J. Goodby, G. W. Gray, H.-W. Spiess, V. Vill (Eds.): *Physical Properties of Liquid Crystals* (Wiley-VCH, Weinheim 1999)

1.13 V. G. Chigrinov: *Liquid Crystal Devices: Physics and Applications* (Artech House, Boston 1999)

1.14 S. Pestov: *Physical Properties of Liquid Crystals*, Landolt–Börnstein, New Series VIII/5 (Springer, Berlin, Heidelberg 2003)

1.15 D. Demus, R. Richter: *Textures of Liquid Crystals* (Verlag Chemie, Weinheim 1978)

1.16 G. W. Gray, J. W. G. Goodby: *Smectic Liquid Crystals – Textures and Structures* (Hill, Glasgow 1984)

1.17 Hoffmann-La Roche: Product information (Hoffmann-La Roche, Basel 1988)

# 5.2. The Physics of Solid Surfaces



The data compiled in this chapter refer to so-called "clean surfaces", i. e. crystalline surfaces that are atomically clean and well characterized. Data on interfaces are dealt with only marginally, in connection with MOS devices.

The values reported in the tables are mainly averages from several different authors. In such cases the errors are given as standard deviations. Reference to the individual measurements and to the original papers is made by referring to larger compilations (mainly the four volumes of Landolt–Börnstein III/24, *Physics of Solid Surfaces*, [2.1] or the single articles therein [2.2–16]). On the other hand, the figures are fully referenced.


5.2.1 **The Structure of Ideal Surfaces** ..... 979
5.2.1.1 Diagrams of Surfaces [2.2] ..... 979
5.2.1.2 Crystallographic Formulas ..... 986

5.2.2 **Surface Reconstruction and Relaxation** ..... 986
5.2.2.1 Definitions and Notation ..... 986
5.2.2.2 Metals ..... 987
5.2.2.3 Semiconductors ..... 987

5.2.3 **Electronic Structure of Surfaces** ..... 996
5.2.3.1 Metals ..... 997
5.2.3.2 Semiconductors ..... 1003
5.2.3.3 Magnetic Surfaces ..... 1007

5.2.4 **Surface Phonons** ..... 1012
5.2.4.1 Metals ..... 1012
5.2.4.2 Semiconductors and Insulators ..... 1017
5.2.4.3 Atom–Surface Potential ..... 1019

5.2.5 **The Space Charge Layer at the Surface of a Semiconductor** ..... 1020
5.2.5.1 Definitions and Notation ..... 1020
5.2.5.2 Useful Formulas and Numerical Values ..... 1022
5.2.5.3 Surface Conductivity ..... 1023

5.2.6 **Most Frequently Used Acronyms** ..... 1026

**References** ..... 1029


## 5.2.1 The Structure of Ideal Surfaces

An ideal surface is a surface of a half-crystal in which the atoms are held in their original positions. The structure of an ideal surface is identical to that of a parallel crystallographic plane in the bulk. For a 2-D lattice, the elementary Bravais cell can have only one of the five structures shown in Fig. 5.2-1.

### 5.2.1.1 Diagrams of Surfaces [2.2]

Figure 5.2-2 gives diagrams of ideal surfaces for some common faces of the fcc (face-centered cubic), bcc (body-centered cubic), diamond, and zinc blende systems, as well as the coordinates of the atoms of the first layers of the half-crystal. The atoms are drawn as solid balls with diameters appropriate to close-packed stacking.

Atoms in the surface layer are labeled by O, A, B, C, . . . . Atoms in the first, second, third, etc. sublayer are labeled by 1, 2, 3, . . . . When two classes of atoms are present (for example in diamond-like structures), the atoms of the second class are indicated by primed symbols. In such a case, the division of an ideal crystal by a geometrical plane may expose different types of surfaces. A well-known example is the (111) face of NaCl-type crystals, which may be either anion- or cation-terminated.

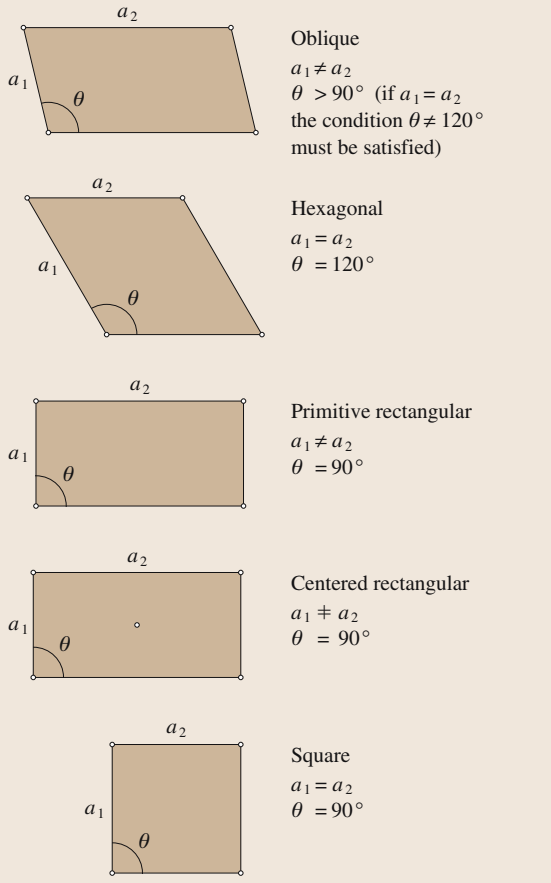


**Fig. 5.2-1** Elementary Bravais cells for a 2D lattice

A parameter $\delta$, $0 \leq \delta < 1$, is introduced to specify the distance from the dividing plane to the nearest plane through lattice points.

Coordinates are referred either to crystal axes (O$xyz$) or to a system O$XYZ$, in which $XY$ are axes in the surface plane; $X$ is parallel to a side of the 2-D Bravais cell and $Z$ is perpendicular to the surface.

Coordinates are always given in terms of $a/2$, $a$ being the lattice parameter.

A more detailed discussion of the structure of ideal surfaces and many other diagrams of surfaces can be found in [2.2].

**a)**

fcc (100)

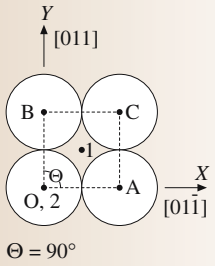


| Atom | Atomic positions: Coordinates | | | | | |
|---|---|---|---|---|---|---|
| | Relative to cubic axes | | | Relative to O*XYZ* | | |
| A | 0 | 1 | −1 | $\sqrt{2}$ | 0 | 0 |
| B | 0 | 1 | 1 | 0 | $\sqrt{2}$ | 0 |
| 1 | −1 | 1 | 0 | $\frac{\sqrt{2}}{2}$ | $\frac{\sqrt{2}}{2}$ | −1 |
| 2 | −2 | 0 | 0 | 0 | 0 | −2 |

fcc (110)

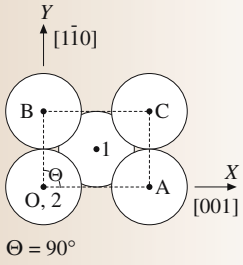


| Atom | Atomic positions: Coordinates | | | | | |
|---|---|---|---|---|---|---|
| | Relative to cubic axes | | | Relative to O*XYZ* | | |
| A | 0 | 0 | 2 | 2 | 0 | 0 |
| B | 1 | −1 | 0 | 0 | $\sqrt{2}$ | 0 |
| 1 | 0 | −1 | 1 | 1 | $\frac{\sqrt{2}}{2}$ | $\frac{-\sqrt{2}}{2}$ |
| 2 | −1 | −1 | 0 | 0 | 0 | $-\sqrt{2}$ |

fcc (111)

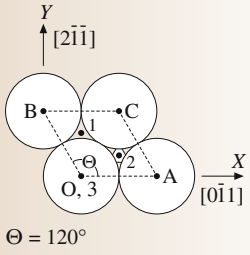


| Atom | Atomic positions: Coordinates | | | | | |
|---|---|---|---|---|---|---|
| | Relative to cubic axes | | | Relative to O*XYZ* | | |
| A | 0 | −1 | 1 | $\sqrt{2}$ | 0 | 0 |
| B | 1 | 0 | −1 | $\frac{-\sqrt{2}}{2}$ | $\frac{3}{\sqrt{6}}$ | 0 |
| 1 | 0 | −1 | −1 | 0 | $\frac{2}{\sqrt{6}}$ | $\frac{-2}{\sqrt{3}}$ |
| 2 | −1 | −2 | −1 | $\frac{\sqrt{2}}{2}$ | $\frac{1}{\sqrt{6}}$ | $\frac{-4}{\sqrt{3}}$ |
| 3 | −2 | −2 | −2 | 0 | 0 | $\frac{-6}{\sqrt{3}}$ |

**Fig. 5.2-2** **(a)** Surface diagrams: face-centered cubic (fcc) positions given in terms of $a/2$ [2.2] **(b)** Surface diagrams: body-centered cubic (bcc) positions given in terms of $a/2$ [2.2] **(c)** Surface diagrams: diamond, GaAs (positions given in terms of $a/2$) Ga atoms are denoted by *unprimed symbols*; As atoms by *primed symbols* and *shaded circles* [2.2]

**b)**

bcc (100)

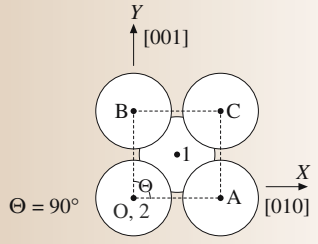


| Atom | Atomic positions | | | | | |
|---|---|---|---|---|---|---|
| | Coordinates | | | | | |
| | Relative to cubic axes | | | Relative to O*XYZ* | | |
| A | 0 | 2 | 0 | 2 | 0 | 0 |
| B | 0 | 0 | 2 | 0 | 2 | 0 |
| 1 | −1 | 1 | 1 | 1 | 1 | −1 |
| 2 | −2 | 0 | 0 | 0 | 0 | −2 |

bcc (110)

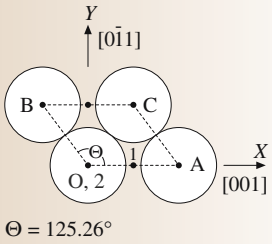


| Atom | Atomic positions | | | | | |
|---|---|---|---|---|---|---|
| | Coordinates | | | | | |
| | Relative to cubic axes | | | Relative to O*XYZ* | | |
| A | 0 | 0 | 2 | 2 | 0 | 0 |
| B | 1 | −1 | −1 | −1 | $\sqrt{2}$ | 0 |
| 1 | −1 | −1 | 1 | 1 | 0 | $-\sqrt{2}$ |
| 2 | −2 | −2 | 0 | 0 | 0 | $-2\sqrt{2}$ |

bcc (111)

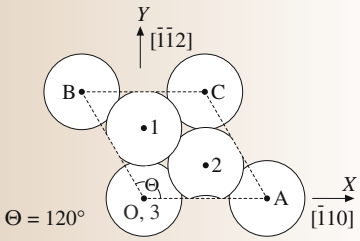


| Atom | Atomic positions | | | | | |
|---|---|---|---|---|---|---|
| | Coordinates | | | | | |
| | Relative to cubic axes | | | Relative to O*XYZ* | | |
| A | −2 | 2 | 0 | $2\sqrt{2}$ | 0 | 0 |
| B | 0 | −2 | 2 | $-\sqrt{2}$ | $\frac{6}{\sqrt{6}}$ | 0 |
| 1 | −1 | −1 | 1 | 0 | $\frac{4}{\sqrt{6}}$ | $\frac{-1}{\sqrt{3}}$ |
| 2 | −2 | 0 | 0 | $\sqrt{2}$ | $\frac{2}{\sqrt{6}}$ | $\frac{-2}{\sqrt{3}}$ |
| 3 | −1 | −1 | −1 | 0 | 0 | $\frac{-3}{\sqrt{3}}$ |

**Fig. 5.2-2b** Surface diagrams: body-centered cubic (bcc) positions given in terms of $a/2$ [2.2]

**c)**

| Atomic positions | | | | | | |
|---|---|---|---|---|---|---|
| Atom | Coordinates | | | | | |
| | Relative to cubic axes | | | Relative to O*XYZ* | | |
| A | 0 | 1 | –1 | $\sqrt{2}$ | 0 | 0 |
| B | 0 | 1 | 1 | 0 | $\sqrt{2}$ | 0 |
| 1' | $-\frac{1}{2}$ | $\frac{1}{2}$ | $-\frac{1}{2}$ | $\frac{\sqrt{2}}{2}$ | 0 | $-\frac{1}{2}$ |
| 2 | –1 | 1 | 0 | $\frac{\sqrt{2}}{2}$ | $\frac{\sqrt{2}}{2}$ | –1 |
| 3' | $\frac{-3}{2}$ | $\frac{1}{2}$ | $\frac{1}{2}$ | 0 | $\frac{\sqrt{2}}{2}$ | $\frac{-3}{2}$ |
| 4 | –2 | 0 | 0 | 0 | 0 | –2 |

Diamond and GaAs (100) $0 \leq \delta < 1/4;\ 1/2 \leq \delta < 3/4$

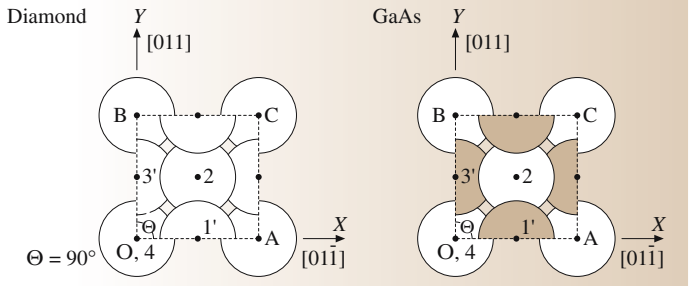


| Atomic positions | | | | | | |
|---|---|---|---|---|---|---|
| Atom | Coordinates | | | | | |
| | Relative to cubic axes | | | Relative to O'*XYZ* | | |
| A' | 0 | 1 | –1 | $\sqrt{2}$ | 0 | 0 |
| B' | 0 | 1 | 1 | 0 | $\sqrt{2}$ | 0 |
| 1 | $-\frac{1}{2}$ | $\frac{1}{2}$ | $\frac{1}{2}$ | 0 | $\frac{\sqrt{2}}{2}$ | $-\frac{1}{2}$ |
| 2' | –1 | 1 | 0 | $\frac{\sqrt{2}}{2}$ | $\frac{\sqrt{2}}{2}$ | –1 |
| 3 | $-\frac{3}{2}$ | $\frac{1}{2}$ | $-\frac{1}{2}$ | $\frac{\sqrt{2}}{2}$ | 0 | $\frac{-3}{2}$ |
| 4' | –2 | 0 | 0 | 0 | 0 | –2 |

Diamond and GaAs (100) $1/4 \leq \delta < 1/2;\ 3/4 \leq \delta < 1$

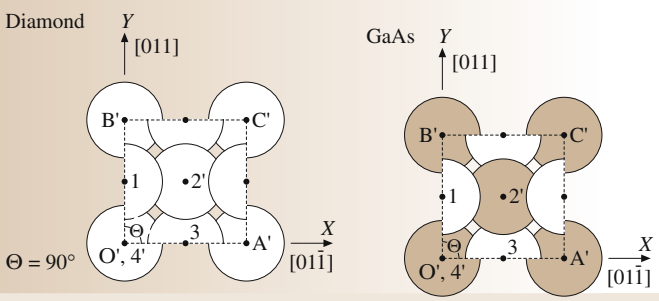


| Atomic positions | | | | | | |
|---|---|---|---|---|---|---|
| Atom | Coordinates | | | | | |
| | Relative to cubic axes | | | Relative to O*XYZ* | | |
| A | 0 | –1 | 1 | $\sqrt{2}$ | 0 | 0 |
| B | 0 | 1 | 1 | 0 | $\sqrt{2}$ | 0 |
| 1' | $\frac{1}{2}$ | $\frac{1}{2}$ | $\frac{1}{2}$ | 0 | $\frac{\sqrt{2}}{2}$ | $-\frac{1}{2}$ |
| 2 | 1 | 0 | 1 | $\frac{\sqrt{2}}{2}$ | $\frac{\sqrt{2}}{2}$ | –1 |
| 3' | $\frac{3}{2}$ | $-\frac{1}{2}$ | $\frac{1}{2}$ | $\frac{\sqrt{2}}{2}$ | 0 | $-\frac{3}{2}$ |
| 4 | 2 | 0 | 0 | 0 | 0 | –2 |

Diamond and GaAs ($\bar{1}$00) $0 \leq \delta < 1/4;\ 1/2 \leq \delta < 3/4$

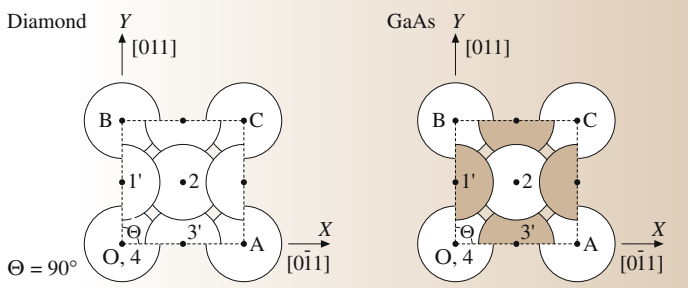


**Fig. 5.2-2c** Surface diagrams: diamond, GaAs (positions given in terms of $a/2$) Ga atoms are denoted by *unprimed symbols*; As atoms by *primed symbols* and *shaded circles* [2.2]

## c) (cont.)

Atomic positions

| Atom | Coordinates | | | | | |
|---|---|---|---|---|---|---|
| | Relative to cubic axes | | | Relative to OXYZ | | |
| A' | 0 | –1 | 1 | $\sqrt{2}$ | 0 | 0 |
| B' | 0 | 1 | 1 | 0 | $\sqrt{2}$ | 0 |
| 1 | $\frac{1}{2}$ | $-\frac{1}{2}$ | $\frac{1}{2}$ | $\frac{\sqrt{2}}{2}$ | 0 | $\frac{-1}{2}$ |
| 2' | 1 | 0 | 1 | $\frac{\sqrt{2}}{2}$ | $\frac{\sqrt{2}}{2}$ | –1 |
| 3 | $\frac{3}{2}$ | $\frac{1}{2}$ | $\frac{1}{2}$ | 0 | $\frac{\sqrt{2}}{2}$ | $\frac{-3}{2}$ |
| 4' | 2 | 0 | 0 | 0 | 0 | –2 |

Diamond and GaAs ($\bar{1}00$) $1/4 \leq \delta < 1/2;\ 3/4 \leq \delta < 1$

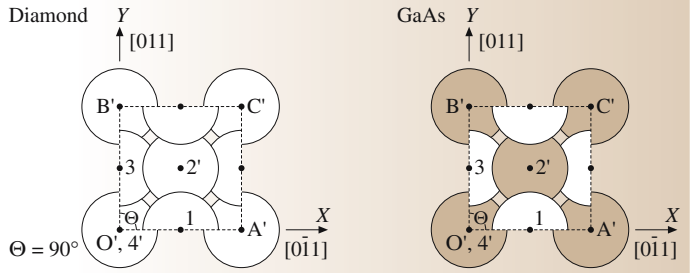


Diamond and GaAs (110)

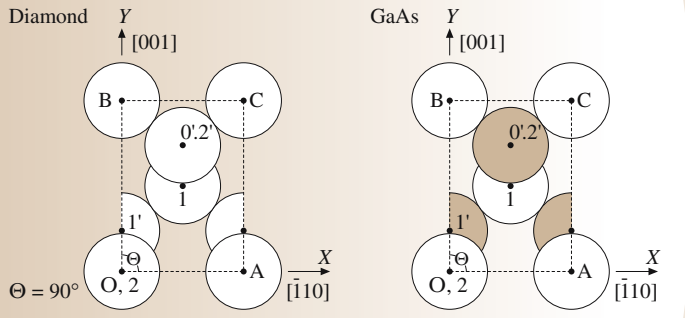


Atomic positions

| Atom | Coordinates | | | | | |
|---|---|---|---|---|---|---|
| | Relative to cubic axes | | | Relative to OXYZ | | |
| A | –1 | 1 | 0 | $\sqrt{2}$ | 0 | 0 |
| B | 0 | 0 | 2 | 0 | 2 | 0 |
| 0' | $-\frac{1}{2}$ | $\frac{1}{2}$ | $\frac{3}{2}$ | $\frac{\sqrt{2}}{2}$ | $\frac{3}{2}$ | 0 |
| 1 | –1 | 0 | 1 | $\frac{\sqrt{2}}{2}$ | 1 | $\frac{-\sqrt{2}}{2}$ |
| 1' | $-\frac{1}{2}$ | $-\frac{1}{2}$ | $\frac{1}{2}$ | 0 | $\frac{1}{2}$ | $\frac{-\sqrt{2}}{2}$ |
| 2 | –1 | –1 | 0 | 0 | 0 | $-\sqrt{2}$ |
| 2' | $-\frac{3}{2}$ | $-\frac{1}{2}$ | $\frac{3}{2}$ | $\frac{\sqrt{2}}{2}$ | $\frac{3}{2}$ | $-\sqrt{2}$ |

Atomic positions

| Atom | Coordinates | | | | | |
|---|---|---|---|---|---|---|
| | Relative to cubic axes | | | Relative to OXYZ | | |
| A | –1 | 1 | 0 | $\sqrt{2}$ | 0 | 0 |
| B | 0 | –1 | 1 | $\frac{-\sqrt{2}}{2}$ | $\frac{3}{\sqrt{6}}$ | 0 |
| 1' | $-\frac{1}{2}$ | $-\frac{1}{2}$ | $\frac{1}{2}$ | 0 | $\frac{2}{\sqrt{6}}$ | $-\frac{1}{2\sqrt{3}}$ |
| 4 | –1 | –1 | 0 | 0 | $\frac{2}{\sqrt{6}}$ | $\frac{-2}{\sqrt{3}}$ |
| 5' | $-\frac{3}{2}$ | $-\frac{1}{2}$ | $-\frac{1}{2}$ | $\frac{\sqrt{2}}{2}$ | $\frac{1}{\sqrt{6}}$ | $-\frac{5}{2\sqrt{3}}$ |
| 8 | –2 | –1 | –1 | $\frac{\sqrt{2}}{2}$ | $\frac{1}{\sqrt{6}}$ | $\frac{-4}{\sqrt{3}}$ |
| 9' | $-\frac{3}{2}$ | $-\frac{3}{2}$ | $-\frac{3}{2}$ | 0 | 0 | $-\frac{9}{2\sqrt{3}}$ |

Diamond and GaAs (111) $0 \leq \delta < 3/4$

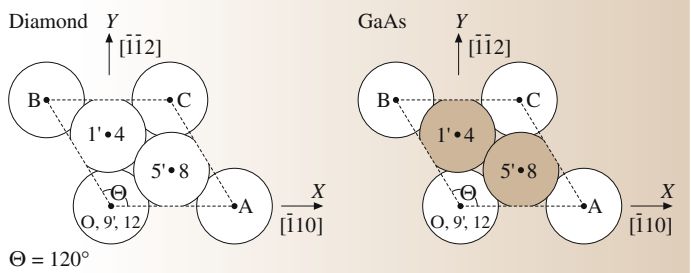


**Fig. 5.2-2c** cont.

**c) (cont.)**

Atomic positions

| Atom | Coordinates | | | | | |
|---|---|---|---|---|---|---|
| | Relative to cubic axes | | | Relative to O'*XYZ* | | |
| A' | $-1$ | $1$ | $0$ | $\sqrt{2}$ | $0$ | $0$ |
| B' | $0$ | $-1$ | $1$ | $\frac{-\sqrt{2}}{2}$ | $\frac{3}{\sqrt{6}}$ | $0$ |
| 3 | $-\frac{1}{2}$ | $-\frac{1}{2}$ | $-\frac{1}{2}$ | $0$ | $0$ | $-\frac{3}{2\sqrt{3}}$ |
| 4' | $-1$ | $-1$ | $0$ | $0$ | $\frac{2}{\sqrt{6}}$ | $-\frac{2}{\sqrt{3}}$ |
| 7 | $-\frac{3}{2}$ | $-\frac{3}{2}$ | $-\frac{1}{2}$ | $0$ | $\frac{2}{\sqrt{6}}$ | $-\frac{7}{2\sqrt{3}}$ |
| 8' | $-2$ | $-1$ | $-1$ | $\frac{\sqrt{2}}{2}$ | $\frac{1}{\sqrt{6}}$ | $\frac{-4}{\sqrt{3}}$ |
| 11 | $-\frac{5}{2}$ | $-\frac{3}{2}$ | $-\frac{3}{2}$ | $\frac{\sqrt{2}}{2}$ | $\frac{1}{\sqrt{6}}$ | $-\frac{11}{2\sqrt{3}}$ |

Diamond and GaAs (111) $3/4 \leq \delta < 1$

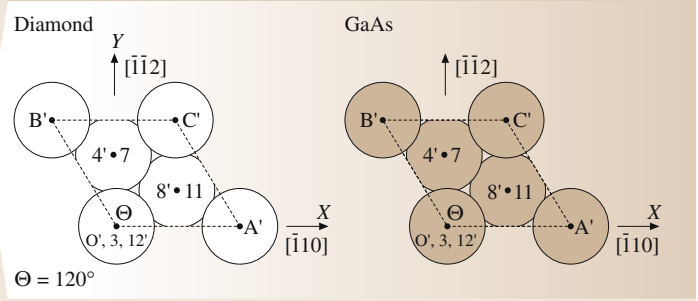


Atomic positions

| Atom | Coordinates | | | | | |
|---|---|---|---|---|---|---|
| | Relative to cubic axes | | | Relative to O*XYZ* | | |
| A | $1$ | $-1$ | $0$ | $\sqrt{2}$ | $0$ | $0$ |
| B | $-1$ | $0$ | $1$ | $\frac{-2}{\sqrt{2}}$ | $\frac{3}{\sqrt{6}}$ | $0$ |
| 3' | $\frac{1}{2}$ | $\frac{1}{2}$ | $\frac{1}{2}$ | $0$ | $0$ | $-\frac{3}{2\sqrt{3}}$ |
| 4 | $1$ | $0$ | $1$ | $\frac{\sqrt{2}}{2}$ | $\frac{1}{\sqrt{6}}$ | $\frac{-2}{\sqrt{3}}$ |
| 7' | $\frac{3}{2}$ | $\frac{1}{2}$ | $\frac{3}{2}$ | $\frac{\sqrt{2}}{2}$ | $\frac{1}{\sqrt{6}}$ | $-\frac{7}{2\sqrt{3}}$ |
| 8 | $1$ | $1$ | $2$ | $0$ | $\frac{2}{\sqrt{6}}$ | $\frac{-4}{\sqrt{3}}$ |
| 11' | $\frac{3}{2}$ | $\frac{3}{2}$ | $\frac{5}{2}$ | $0$ | $\frac{2}{\sqrt{6}}$ | $-\frac{11}{2\sqrt{3}}$ |

Diamond and GaAs $(\bar{1}\bar{1}\bar{1})$ $0 \leq \delta < 1/4$

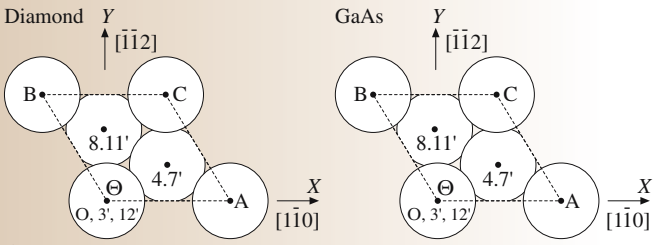


Atomic positions

| Atom | Coordinates | | | | | |
|---|---|---|---|---|---|---|
| | Relative to cubic axes | | | Relative to O'*XYZ* | | |
| A' | $1$ | $-1$ | $0$ | $\sqrt{2}$ | $0$ | $0$ |
| B' | $-1$ | $0$ | $1$ | $\frac{-\sqrt{2}}{2}$ | $\frac{3}{\sqrt{6}}$ | $0$ |
| 1 | $\frac{1}{2}$ | $-\frac{1}{2}$ | $\frac{1}{2}$ | $\frac{\sqrt{2}}{2}$ | $\frac{1}{\sqrt{6}}$ | $-\frac{1}{2\sqrt{3}}$ |
| 4' | $1$ | $0$ | $1$ | $\frac{\sqrt{2}}{2}$ | $\frac{1}{\sqrt{6}}$ | $-\frac{2}{\sqrt{3}}$ |
| 5 | $\frac{1}{2}$ | $\frac{1}{2}$ | $\frac{3}{2}$ | $0$ | $\frac{2}{\sqrt{6}}$ | $-\frac{5}{2\sqrt{3}}$ |
| 8' | $1$ | $1$ | $2$ | $0$ | $\frac{2}{\sqrt{6}}$ | $-\frac{4}{\sqrt{3}}$ |
| 9 | $\frac{3}{2}$ | $\frac{3}{2}$ | $\frac{3}{2}$ | $0$ | $0$ | $-\frac{9}{2\sqrt{3}}$ |

Diamond and GaAs $(\bar{1}\bar{1}\bar{1})$ $1/4 \leq \delta < 1$

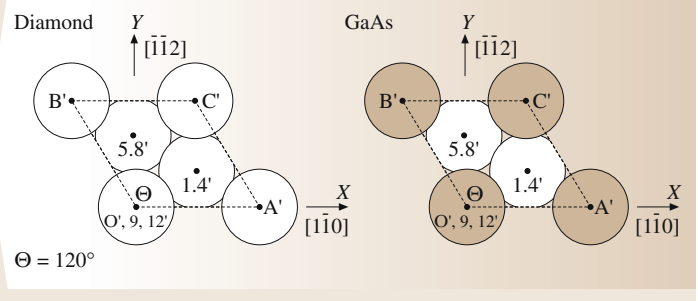


**Fig. 5.2-2c** cont.

### 5.2.1.2 Crystallographic Formulas

Some useful crystallographic formulas are listed in Table 5.2-1.

**Table 5.2-1** Some useful crystallographic formulas

| | Cubic system | | Hexagonal system |
|---|---|---|---|
| Lattice parameter(s) | $a$ | | $a, c$ |
| Plane | $(hkl)$ | | $[hkil]$ |
| Plane normal, $\boldsymbol{n}$ | $[hkl]$ | | $[hkil/\lambda^2]$<br>$\lambda = \sqrt{2/3}\, c/a$ |
| Cosine of the angle between planes with normals $\boldsymbol{n}_1, \boldsymbol{n}_2$ | $\dfrac{h_1h_2+k_1k_2+l_1l_2}{(h_1^2+k_1^2+l_1^2)^{1/2}(h_2^2+k_2^2+l_2^2)^{1/2}}$ | | $\dfrac{h_1h_2+k_1k_2+i_1i_2+l_1l_2/\lambda^2}{(h_1^2+k_1^2+i_1^2+l_1^2/\lambda^2)^{1/2}(h_2^2+k_2^2+i_2^2+l_2^2/\lambda^2)^{1/2}}$ |
| Interlayer distance | fcc<br>$(a/Q)(h^2+k^2+l^2)^{-1/2}$<br>$Q = 1$, except that $Q = 2$ if at least one of $hkl$ is even | bcc<br>$(a/Q)(h^2+k^2+l^2)^{-1/2}$<br>$Q = 1$, except that $Q = 2$ if $h+k+l$ is odd | $(c/\lambda)(h^2+k^2+i^2+l^2/\lambda^2)^{-1/2}$ |
| Volume of the primitive cell | $\frac{1}{4}a^3$ | $\frac{1}{2}a^3$ | $\frac{1}{2}a^2c\sqrt{3}$ |
| Area of the surface primitive cell | $\frac{1}{4}a^2Q(h^2+k^2+l^2)^{1/2}$ | $\frac{1}{2}a^2Q(h^2+k^2+l^2)^{1/2}$ | $ac[(h^2+k^2+i^2+l^2/\lambda^2)/2]^{1/2}$ |

## 5.2.2 Surface Reconstruction and Relaxation

The structure of a real (clean) surface may differ from that of an ideally truncated crystal. Two types of deviation are possible: relaxation and reconstruction.

Relaxation consists of a rigid inward or outward displacement of the uppermost planes of the surface, the symmetry in the surface plane being maintained. In contrast, in the case of reconstruction, the displacements, of atoms alter the 2-D symmetry of the surface.

### 5.2.2.1 Definitions and Notation

If $\boldsymbol{a}$ and $\boldsymbol{b}$ are the basis vectors of an ideally terminated surface and $\boldsymbol{A}$ and $\boldsymbol{B}$ those of the reconstructed surface, then

$$\boldsymbol{A} = m_{11}\boldsymbol{a} + m_{12}\boldsymbol{b}\,,$$
$$\boldsymbol{B} = m_{21}\boldsymbol{a} + m_{22}\boldsymbol{b}\,.$$

The matrix

$$\begin{pmatrix} m_{11} & m_{12} \\ m_{21} & m_{22} \end{pmatrix}$$

characterizes the reconstruction. If all the $m_{ij}$ are integers the reconstruction is said to be commensurate. If at least one of the $m_{ij}$ is irrational, the reconstruction is said to be incommensurate. The term "incommensurate", however, is often extended to rational noninteger numbers. For example the reconstruction of Mo(100),

$$\begin{pmatrix} 2 & 0 \\ 0 & 2 \end{pmatrix},$$

is called incommensurate.

If the angle between $\boldsymbol{A}$ and $\boldsymbol{B}$ is the same as that between $\boldsymbol{a}$ and $\boldsymbol{b}$, a simpler notation introduced by *Wood* [2.17] can be used, namely:

$$\mathrm{p}(u\times v)\mathrm{R}\Phi \quad \text{or} \quad \mathrm{c}(u\times v)\mathrm{R}\Phi\,,$$

where $u = \boldsymbol{A}/\boldsymbol{a}$, $v = \boldsymbol{B}/\boldsymbol{b}$; p and c stand for *primitive* and centered, respectively, and R$\Phi$ means a rotation of $\Phi$ of the cell $(\boldsymbol{A},\boldsymbol{B})$ with respect to $(\boldsymbol{a},\boldsymbol{b})$. When $\Phi = 0$, R$\Phi$ is omitted. Also, the prefix p and the rotation symbol R are often omitted.

Figure 5.2-3 shows a few examples of reconstruction for a layer of adatoms on top of a substrate. The matrix and Wood notations are compared. It can be seen from the figure that (i) the elementary cell is not uniquely

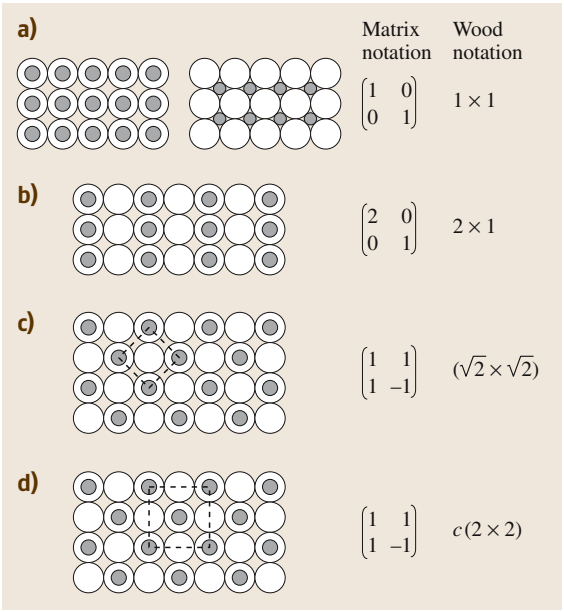


**Fig. 5.2-3a–d** Examples of reconstruction for a layer of adatoms (*small shaded circles*) on top of a square lattice substrate (*large empty circles*). Matrix and Wood notations are compared. Notice that (c) and (d) differ only for the choice of the unit cell

defined (as in 3-D), and (ii) the symmetry alone does not define unequivocally the reconstruction. In practice this means that LEED (low-energy electron diffraction) patterns are not enough to define a model for a reconstruction and that other techniques (including dynamical LEED) are necessary.

The energies associated with reconstruction are $\sim 10^{-2}$ eV/atom in metals and $\sim 10^{-1}$ eV/atom in semiconductors. Metals are therefore seldom reconstructed, while semiconductors are very often reconstructed.

A detailed discussion of the various problems connected to relaxation and reconstruction are found in [2.3–8]

### 5.2.2.2 Metals

Table 5.2-2 summarizes the essential features of reconstruction or relaxation at metal surfaces. Vertical relaxations (in % of the bulk interlayer distances) are given in Table 5.2-3.

#### Reconstruction Models

In Figs. 5.2-4 and 5.2-6, some accepted models of reconstructed surfaces of metals are shown. Table 5.2-4 gives the parameters for the $2\times1$ missing-row reconstruction of Au(110), Ir(110), and Pt(110). The missing-row reconstruction stabilizes the surface by relieving the elastic stress.

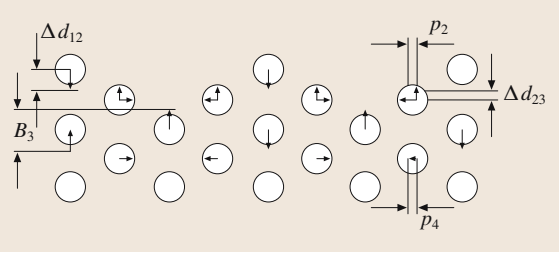


**Fig. 5.2-4** Side view of the atomic positions in the $2\times1$ missing-row reconstruction of the (110) face of Au, Ir, and Pt, and definition of parameters used in Table 5.2-4

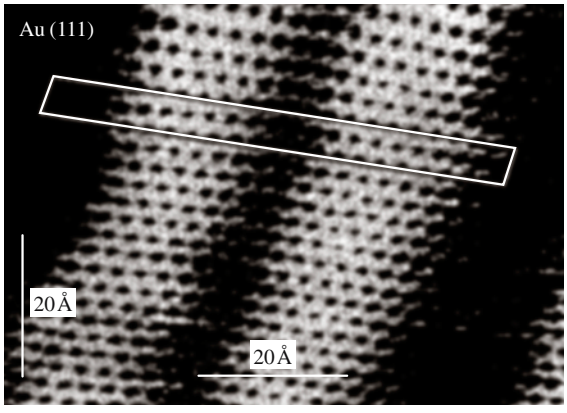


**Fig. 5.2-5** STM image of the $23\times1$ reconstruction of Au(111) [2.18]

**Table 5.2-2** Reconstruction and relaxation of metals [1]

| Metal | Structure | Face | Reconstruction | Remarks |
|---|---|---|---|---|
| Ag | fcc | (100) | $1\times1$ | Unrelaxed |
| | | (110) | $1\times1$ | Relaxed |
| | | (111) | $1\times1$ | Unrelaxed |
| Al | fcc | (100) | $1\times1$ | Unrelaxed |
| | | (110) | $1\times1$ | Relaxed |
| | | (111) | $1\times1$ | Relaxed |

**Table 5.2-2** Reconstruction and relaxation of metals [1], cont.

| Metal | Structure | Face | Reconstruction | Remarks |
|---|---|---|---|---|
| Au | fcc | (100) | 5×20 | $T < 700$ K. Reconstruction model: incommensurate hexagonal layer |
| | | | 6×6 | $700 < T < 820$ K |
| | | (110) | 1×2 | Reconstruction model: missing-row (Fig. 5.2-4 and Table 5.2-4). Reversible phase transition to 1×1 at $T \cong 690$ K |
| | | (111) | 1×23 | Reconstruction model: see Fig. 5.2-5 (observed by STM) |
| Co | hcp<br>cubic phase | (0001) | 1×1 | Unrelaxed |
| | | (100) | 1×1 | Relaxed |
| | | (111) | 1×1 | Unrelaxed |
| Cu | fcc | (100) | 1×1 | Relaxed |
| | | (110) | 1×1 | Relaxed |
| | | (111) | 1×1 | Essentially unrelaxed |
| Fe | bcc | (100) | 1×1 | Relaxed |
| | | (110) | 1×1 | Essentially unrelaxed |
| | | (111) | 1×1 | Relaxed |
| Ir | fcc | (100) | 1×5 | $T < 2000$ K. Reconstruction model: hexagonal layer with buckling. A metastable 1×1 phase is also observed |
| | | (110) | 1×2 | Reconstruction model: missing-row (Fig. 5.2-4 and Table 5.2-4). A metastable 1×1 phase is also observed |
| | | (111) | 1×1 | Essentially unrelaxed |
| Mo | bcc | (100) | 2.2×2.2 | $T < 300$ K, incommensurate |
| | | | 1×1 | $T > 300$ K, relaxed |
| | | (110) | 1×1 | Relaxed |
| Ni | fcc | (100) | 1×1 | Relaxed (results controversial) |
| | | (110) | 1×1 | Relaxed |
| | | (111) | 1×1 | Unrelaxed |
| Pb | fcc | (110) | 1×1 | Relaxed; annealing at $T > 340$ K gives a c(2×4) reconstruction |
| Pd | fcc | (100) | 1×1 | Essentially unrelaxed |
| | | (110) | 1×1 | Relaxed |
| | | (111) | 1×1 | Unrelaxed |
| Pt | fcc | (100) | 1×5 | $77\text{ K} < T < 1900$ K. Reconstruction model: hexagonal layer slightly rotated. Other metastable superstructures, 1×1 and 5×20, are observed |
| | | (110) | 1×2 | Reconstruction model: missing-row (Fig. 5.2-4 and Table 5.2-4). Reversible transition to 1×1 at $T = 1100$ K |
| | | (111) | 1×1 | Essentially unrelaxed |
| Rh | fcc | (100) | 1×1 | Essentially unrelaxed |
| | | (110) | 1×1 | Relaxed |
| | | (111) | 1×1 | Relaxed |
| Ta | bcc | (100) | 1×1 | Relaxed |
| Th | fcc | (111) | 1×1 | After annealing at $T \approx 1000$ K becomes 9×9 |
| V | bcc | (100) | 1×1 | Relaxed |
| | | (110) | 1×1 | Essentially unrelaxed |
| W | bcc | (100) | c(2×2) | $T < 400$ K. Reconstruction model: see Fig. 5.2-6 |
| | | | 1×1 | $T > 400$ K. Relaxed |
| | | (110) | 1×1 | Unrelaxed |

[1] Reference to the original papers is given in [2.3]

**Table 5.2-3** Vertical relaxation of metals. Data are given as a percentage of the bulk interlayer distance $d_{bulk}$. The data are average values from various authors.[1] Errors are expressed as standard deviations from the average. The + sign corresponds to expansion. LEIS, low-energy ion scattering; HEIS, high-energy ion scattering; MEIS: medium-energy ion scattering

| Crystal | Face | $d_{bulk}$ (Å) | $\Delta d_{12}$ (%) | $\Delta d_{23}$ (%) | $\Delta d_{34}$ (%) | Technique |
|---|---|---|---|---|---|---|
| Ag | (110) | 1.445 | −7.5 (13) | +1.6 (6) | −2 (2) | LEED |
| | | | −8.6 (8) | +5.1 (8)[2] | – | LEIS, MEIS |
| Al | (100) | 2.025 | 0 (5) | – | – | LEED |
| | | | −2.4 (24) | – | – | HEIS |
| | (110) | 1.427 | −7 (2) | +5.0 (2) | −1.6 | LEED |
| | (111) | 2.329 | +1.5 (6) | – | – | LEED |
| Cu | (100) | 1.807 | −1.1 | +1.7 | <1 | LEED |
| | | | −2.3 (2) | – | – | MEIS |
| | (110) | 1.278 | −8.3 (9) | +2.3 | −0.9 | LEED |
| | | | −7 (3) | +2.9 (4) | – | LEIS, MEIS, HEIS |
| | (111) | 2.087 | +0.8 (2) | – | – | LEED |
| Fe | (100) | 1.433 | −1.4 (30) | – | – | LEED |
| | (110) | 2.027 | +0.5 (20) | – | – | LEED |
| | | | +1 (2) | – | – | MEIS |
| | (111) | 0.827 | −16.9 (30) | −9.8 (30) | +4.2 (36) | LEED |
| | | | −29 (7) | +7 (5)[2] | – | MEIS |
| Ir | (100) 1×1 metastable | 1.920 | +5.2 | – | – | LEED |
| Mo | (100) | 1.574 | −9 (2) | +0.25 (175) | +0.5 (30) | LEED |
| | (110) | 2.225 | −1.6 | – | – | LEED |
| | (111) | 0.909 | −18 | +4 | – | LEED |
| | | | −16 | +4 | – | LEIS |
| Ni | (110) | 1.245 | −7 (2) | +3.3 (3) | −0.5 (7) | LEED |
| | | | −6.9 (21) | +3.0 (6) | – | MEIS, HEIS |
| Pb | (110) | 1.750 | −17.6 (13) | +3.8 (10) | −5.9 (13) | LEED |
| | | | −15.8 | +7.9 | −6.8 | MEIS |
| Pd | (110) | 1.375 | −5.6 (4) | +1.5 (10) | – | LEED |
| Rh | (100) | 1.902 | +0.5 (10) | 0 (15) | – | LEED |
| | (110) | 1.345 | −3.5 (25) | – | – | LEED |
| | (111) | 2.196 | −1 | – | – | LEED |
| Ta | (100) | 1.653 | −11 | +1 | – | LEED |
| | | | −10.5 | – | – | PED |
| V | (100) | 1.514 | −6.8 (2) | +1 | – | LEED |
| W | (100) | 1.583 | −6.2 (14) | +1 | – | LEED |
| | high-$T$ phase | | −5.6 | – | – | X-ray |

[1] References to the original papers and individual errors are given in [2.3–5]

[2] Inconsistency between LEED and ion scattering data

**Table 5.2-4** Structural parameters of the 1×2 reconstruction of the (110) face of Au, Ir, and Pt (average values from various authors[1]). Errors are expressed as standard deviations from the average. An illustration of the model and parameters is given in Fig. 5.2-4. The bulk interlayer spacings are 1.445 Å for Au, 1.358 Å for Ir, and 1.387 Å for Pt

| Crystal | $\Delta d_{12}$ (Å) | $\Delta d_{23}$ (Å) | $p_2$ (Å) | $p_4$ (Å) | $B_3$ (Å) | Technique |
|---|---|---|---|---|---|---|
| Au | −0.25 (3) | 0.03 | 0.07 | – | 0.24 | LEED |
| | −0.20 (4) | 0.06 | < 0.1 | – | 0.20 | LEIS, MEIS |
| | −0.32 | – | 0.05 | 0.05 | – | X-ray |
| Ir | −0.17 | −0.16 | 0.04 | – | 0.23 | LEED |
| | −0.13 | – | – | – | – | MEIS |
| Pt | −0.30 (5) | −0.04 (10) | 0.06 (2) | 0.08 (3) | 0.22 (7) | LEED, RHEED |
| | −0.22 (4) | 0.06 (4) | < 0.04 | – | 0.10 | MEIS |
| | −0.27 | −0.11 | 0.05 | 0.04 | – | X-ray |

[1] References to the original papers and individual errors are given in [2.3]

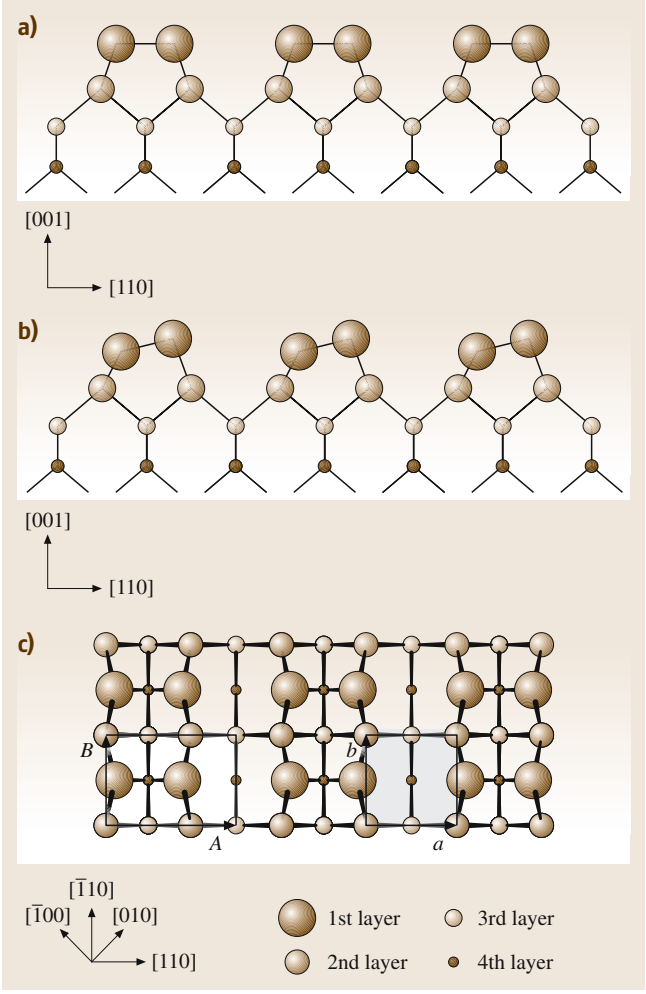


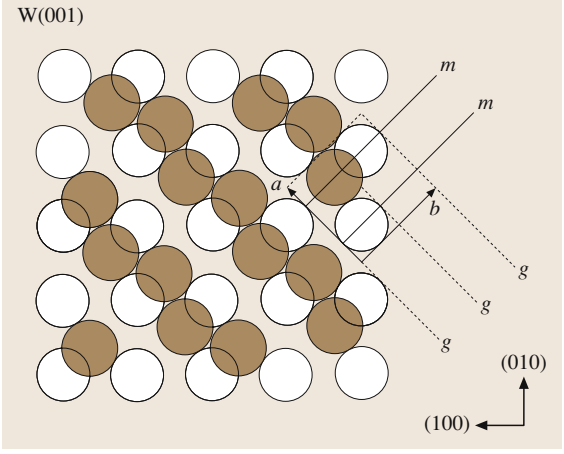


**Fig. 5.2-6** Top view of the c(2×2) reconstruction of the W(001) face. *g*, glide plane; *m*, mirror plane. *Shaded circles*, surface atoms; *empty circles*, second-layer atoms [2.19]

### 5.2.2.3 Semiconductors

The essential features of reconstruction and relaxation of semiconductor surfaces are given in Table 5.2-5, together with indications of the methods of preparation and remarks on pecularities of the specific surfaces.

**Fig. 5.2-7a–c** Dimer models for the 2×1 reconstruction of Si and Ge(100) faces, with **(a)** symmetric and **(b)** buckled dimers (side views). **(c)** Top view of the symmetric case. Ideal (*shaded*) and reconstructed unit cells are shown

### Reconstruction Models

In semiconductors, directional bonds are present that are unsaturated at the surface. The driving force for reconstruction is the tendency to minimize the number of such dangling bonds (DBs).

In $sp^3$-bonded crystals, the energy associated with the angles between the bonds is rather small. In contrast, the energy associated with the length of the bonds is large. Accordingly, reconstruction of covalent (or moderately ionic) semiconductors occurs through dis-

**Table 5.2-5** Reconstruction and relaxation of semiconductors. IBA, ion bombardment and annealing; MBE, molecular-beam epitaxy; DAS, dimer–adatom–stacking fault. References are given in [2.3]

| Crystal | Face | Reconstruction symmetry | Preparation | Model | Remarks |
|---|---|---|---|---|---|
| Diamond | (100) | 2×1 | Annealing $T > 1300$ K | Symmetric dimers | |
| | (110) | 1×1 | Annealing | Truncated bulk | |
| | (111) | 2×1 | Annealing $T > 1200$ K | $\pi$-bonded chains | |
| Si | (100) | 2×1 | IBA or MBE | Symmetric and/or buckled dimers (Fig. 5.2-7) | |
| | | p(2×2) | Same as above | Ordered arrangement of buckled dimers (Fig. 5.2-8) | Present locally (~ 5 %) |
| | | c(4×2) | Same as above | Ordered arrangement of buckled dimers (Fig. 5.2-10) | Present locally (~ 5 %) |
| | (110) | 16×2 | Annealing $T > 1300$ K | Dimers + adatoms + terraces (?) | Other superstructures (probably stabilized by impurities) are observed: 4×5, 5×1, 2×1 |
| | | 32×2 | Same as above | Same as above | |
| | (111) | 2×1 | Cleaving | $\pi$-bonded chains (Fig. 5.2-11, Table 5.2-6) | Transforms irreversibly into 7×7 at $T \simeq 550$ K |
| | | 7×7 | Cleaving + annealing at 550 K or Annealing at 900 K or MBE | DAS + vacancies (Fig. 5.2-13) | Equilibrium reconstruction |
| | | 5×5 | Same as above | Same as above | Present locally near steps |
| Ge | (100) | 2×1 | IBA or MBE | Symmetric and/or buckled dimers | |
| | | p(2×2) | Same as above | Ordered arrangement of buckled dimers | Present locally |
| | | c(4×2) | Same as above | Same as above | Same as above |
| | (111) | 2×1 | Cleaving at $40 < T < 400$ K | $\pi$-bonded chains | Transforms irreversibly into c(2×8) at $T \simeq 400$ K |
| | | c(2×8) | Annealing $T > 400$ K | Adatoms (Fig. 5.2-16) | Equilibrium reconstruction |
| GaAs | (100) | c(2×8) | IBA $T \simeq 850$ K | Ga (or As) dimers (?) | As coverage 0.22–0.52 |
| | | c(4×4) | MBE + annealing $T \simeq 670$ K | | As coverage 1–1.25 |
| | | 4×6 | IBA $T \simeq 770$–$850$ K | | As coverage 0.27–0.31 |
| | (110) | 1×1 | Cleaving, IBA | Rotation/relaxation (Fig. 5.2-17, Table 5.2-8) | |
| | (111)Ga | 2×2 | IBA or MBE | Ga vacancies | |
| | $(\bar{1}\bar{1}\bar{1})$As | 2×2 | Same as above | As trimers | |
| GaP | (110) | 1×1 | Cleaving, IBA | Rotation/relaxation (Fig. 5.2-17, Table 5.2-8) | |
| GaSb | (110) | 1×1 | Cleaving | Same as above | |

**Table 5.2-5** Reconstruction and relaxation of semiconductors, cont.

| Crystal | Face | Reconstruction symmetry | Preparation | Model | Remarks |
|---|---|---|---|---|---|
| InAs | (110) | 1×1 | Same as above | Same as above | |
| InSb | (110) | 1×1 | Same as above | Same as above | |
| CdS | (0001)Cd | 1×1 | IBA | | |
| CdSe | $(10\bar{1}0)$ | 1×1 | Cleaving | Rotation/relaxation (Fig. 5.2-17, Table 5.2-8) | Results controversial |
| ZnO | (0001)Zn | 1×1 | Cleaving, IBA | | |

placements of atoms that conserve the lengths of the bonds but not their relative angles.

Figures 5.2-7 – 5.2-17 give the accepted reconstruction models for a selection of covalent and polar semiconductors, together with STM (scanning tunneling microscopy) images of some of the surfaces. Tables 5.2-6, 5.2-7, and 5.2-8 give the positions of the atoms in reconstructed Si(111) 2×1 and Si (111)7×7 surfaces and the parameters of the rotation/relaxation model of polar semiconductors.

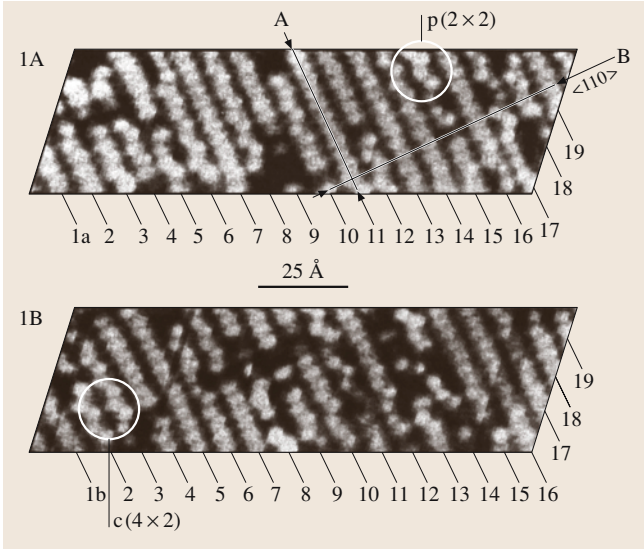


**Fig. 5.2-9** STM image of the Si(100) surface showing coexistence of 2×1, p(2×2), and c(4×2) reconstructions [2.20]

**Fig. 5.2-10** Ordered arrangement of buckled dimers that gives rise to c(4×2) reconstruction of the (100) face of Si and Ge (*top views*). Ideal (*shaded*) and reconstructed unit cells are shown

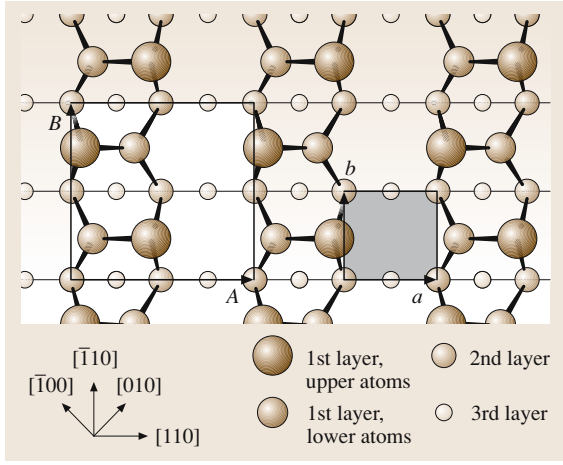


**Fig. 5.2-8** Ordered arrangement of buckled dimers that gives rise to p(2×2) reconstruction of the (100) face of Si and Ge (*top views*). Ideal (*shaded*) and reconstructed unit cells are shown

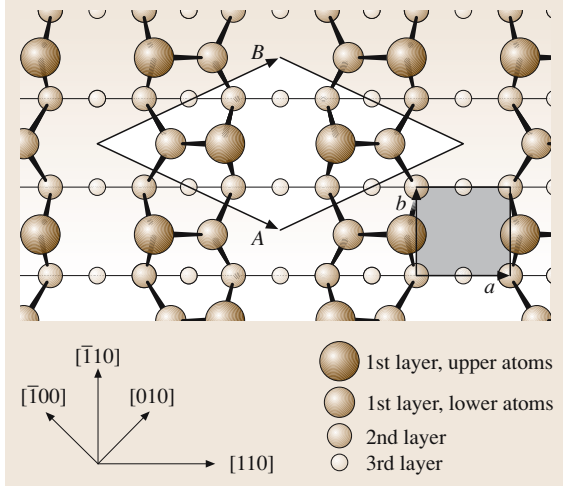

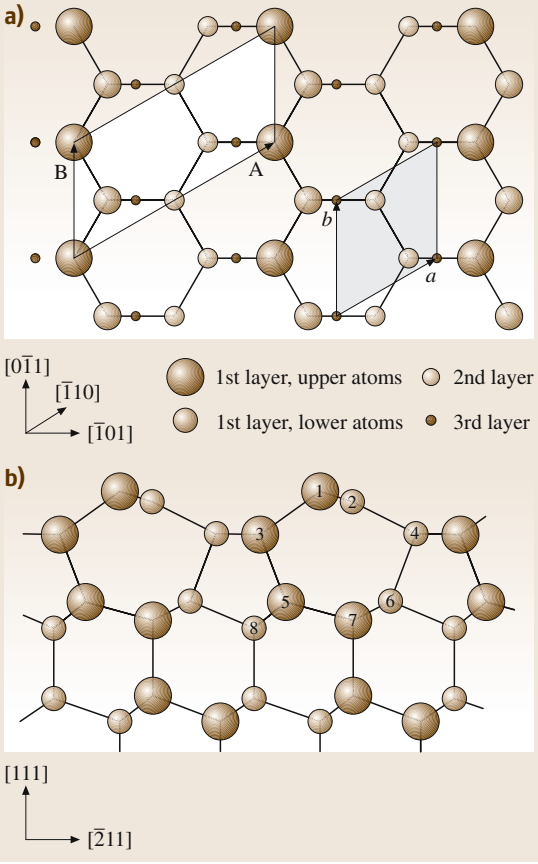


**Fig. 5.2-11** **(a)** top view and **(b)** side view of the Pandey's $\pi$-bonded chain model for the $2\times1$ reconstruction of the (111) face of diamond, Si and Ge [2.21]. In **(a)** the ideal (*shaded*) and $2\times1$ unit cells are shown. The numeration of atoms in **(b)** refers to the positions given in Table 5.2-6

**Table 5.2-6** Coordinates of the atoms of the uppermost layers of Si(111) $2\times1$ ($\pi$-bonded chain geometry). The atoms are labeled as in Fig. 5.2-11b. The origin is at atom 1; the $XYZ$ axes are in the directions [$\bar{1}\bar{1}\bar{1}$], [1$\bar{1}$0], and [$\bar{1}\bar{1}$2], respectively[1]

| Atom | $X$ (Å) | $Y$ (Å) | $Z$ (Å) |
|---|---|---|---|
| 1 | 0.0 | 0.0 | 0.0 |
| 2 | 0.34 | 1.92 | 1.12 |
| 3 | 1.32 | 0.0 | −1.98 |
| 4 | 1.23 | 1.92 | 3.28 |
| 5 | 3.51 | 0.0 | −1.14 |
| 6 | 3.40 | 1.92 | 2.35 |
| 7 | 4.09 | 0.0 | 1.16 |
| 8 | 4.35 | 1.92 | −2.18 |

[1] Data are average values from various authors. References to the original papers are given in [2.3]

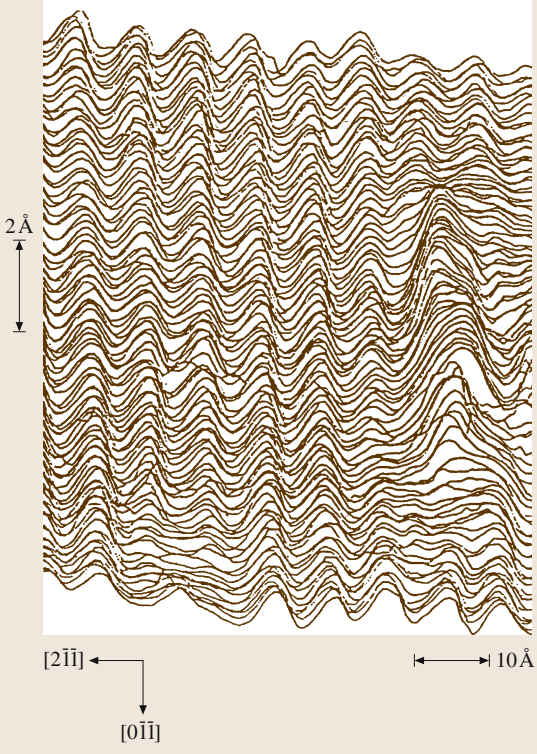


**Fig. 5.2-12** STM image of Si(111) $2\times1$, showing the great anisotropy of the surface, in agreement with the model of Fig. 5.2-11. Optical SDR spectra (see Fig. 5.2-41) show the same anisotropy [2.22]

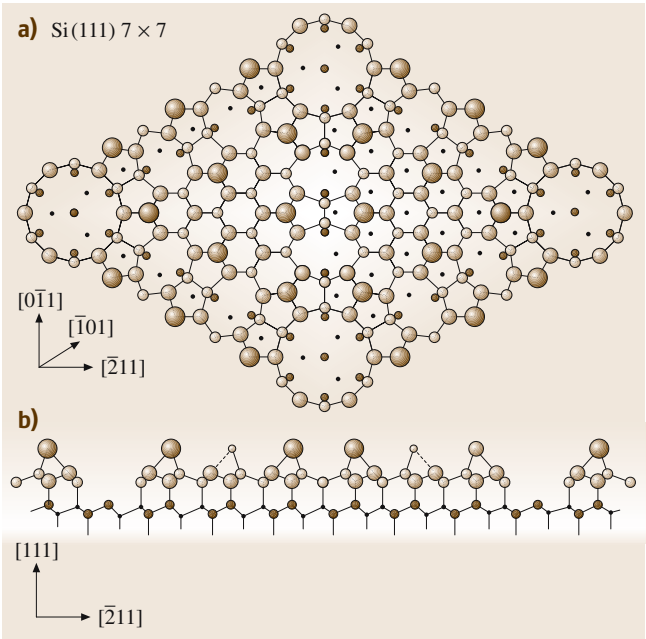


**Fig. 5.2-13a,b** DAS (dimers, adatoms, and stacking faults) + vacancy model of Takayanagi et al. for Si(111) 7×7. **(a)** Top view; **(b)** side view. In **(a)**, the unit cell could be drawn by joining the centers of the four vacancies. The faulted area is the triangular half-cell on the left. The rotation associated with the stacking fault hides atoms in deep unreconstructed layers, which, in contrast, are visible in the unfaulted right-hand side [2.23]

**Fig. 5.2-14a–d** Symmetry-reduced unit cell for Si(111) 7×7 (DAS model). In **(a)**, the unit cell (two triangular halves, one faulted (*hatched*) and one unfaulted) is reduced to smaller subunits and recomposed into a c-hexagonal cell. The atoms are drawn and numbered in **(b)** – **(d)**. The numbering is the same as in Table 5.2-7; the origin of the coordinates is at atom 103. **(b)** The four adatoms; **(c)** the first- and second-layer atoms; **(d)** the third- and fourth-layer atoms [2.24, 25]

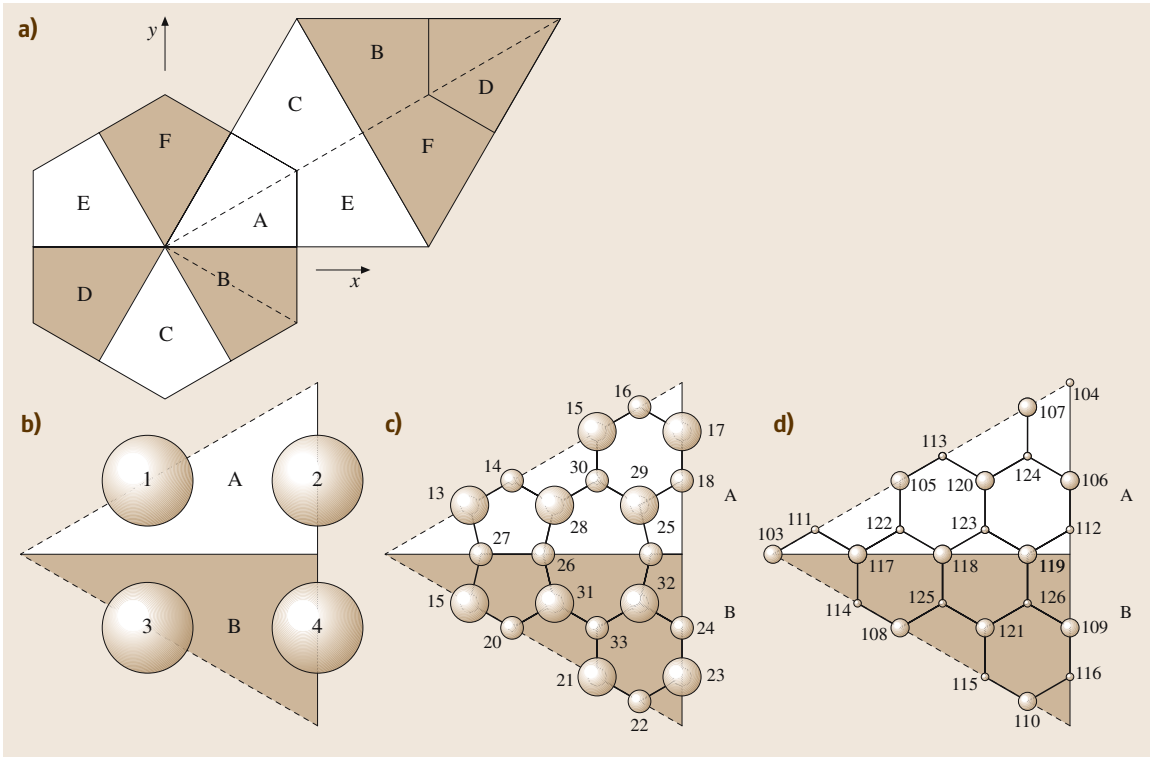

**Table 5.2-7** Coordinates of the adatoms and four uppermost layer atoms in the symmetry-reduced unit cell of Si(111) 7×7 (see Fig. 5.2-14 for the numbering of the atoms). The origin is taken at atom 103[1]. X-ray data give a value of 2.11 Å for the adatom–back atom projected bond length (between atoms 1 and 13 and between atoms 1 and 28 in the table) and a value of 2.49 Å for the dimer bond length (betweens atoms 26 and 27 in the table) [2.24–26]

| Atom no. | $x$ (Å) | $y$ (Å) | $z$ (Å) | Atom no. | $x$ (Å) | $y$ (Å) | $z$ (Å) |
|---|---|---|---|---|---|---|---|
| 1 | 5.76 | 3.33 | −4.21 | 103 | 0.00 | 0.00 | −0.05 |
| 2 | 13.44 | 3.33 | −4.17 | 104 | 13.44 | 7.76 | 0.73 |
| 3 | 5.76 | −3.33 | −4.29 | 105 | 5.76 | 3.33 | 0.45 |
| 4 | 13.44 | −3.33 | −4.25 | 106 | 13.44 | 3.33 | 0.45 |
| 13 | 4.01 | 2.32 | −2.94 | 107 | 11.52 | 6.65 | −0.07 |
| 14 | 5.76 | 3.33 | −1.68 | 108 | 5.76 | −3.33 | 0.45 |
| 15 | 9.60 | 5.54 | −3.11 | 109 | 13.44 | −3.33 | 0.45 |
| 16 | 11.55 | 6.67 | −2.41 | 110 | 11.52 | −6.65 | −0.07 |
| 17 | 13.44 | 5.32 | −2.98 | 111 | 1.92 | 1.11 | 0.74 |
| 18 | 13.44 | 3.33 | −1.68 | 112 | 13.44 | 1.11 | 0.87 |
| 19 | 4.01 | −2.32 | −2.99 | 113 | 7.68 | 4.43 | 0.80 |
| 20 | 5.76 | −3.33 | −1.73 | 114 | 3.84 | −2.22 | 0.85 |
| 21 | 9.60 | −5.54 | −3.16 | 115 | 9.60 | −5.54 | 0.73 |
| 22 | 11.55 | −6.67 | −2.46 | 116 | 13.44 | −5.54 | 0.80 |
| 23 | 13.44 | −5.32 | −3.03 | 117 | 3.84 | 0.00 | 0.00 |
| 24 | 13.44 | −3.33 | −1.73 | 118 | 7.68 | 0.00 | 0.00 |
| 25 | 12.21 | 0.00 | −2.24 | 119 | 11.52 | 0.00 | 0.00 |
| 26 | 6.98 | 0.00 | −2.24 | 120 | 9.60 | 3.33 | −0.07 |
| 27 | 4.53 | 0.00 | −2.24 | 121 | 9.60 | −3.33 | −0.07 |
| 28 | 7.49 | 2.33 | −2.98 | 122 | 5.76 | 1.11 | 0.87 |
| 29 | 11.71 | 2.33 | −2.98 | 123 | 9.60 | 1.11 | 0.72 |
| 30 | 9.60 | 3.29 | −2.41 | 124 | 11.52 | 4.43 | 0.80 |
| 31 | 7.49 | −2.33 | −3.03 | 125 | 7.68 | −2.22 | 0.83 |
| 32 | 11.71 | −2.33 | −3.03 | 126 | 11.52 | −2.22 | 0.83 |
| 33 | 9.60 | −3.29 | −2.46 | | | | |

[1] A table of the atomic positions for the full 7×7 cell is given in [2.25]. The results were obtained by LEED analysis [2.24]

**Table 5.2-8** Surface relaxation and rotation parameters for polar semiconductors as defined in Fig. 5.2-17[1]

| Crystal | $\omega$ (°) | $\Delta_{1\perp}$ (Å) | $\Delta_{2\perp}$ (Å) | $\Delta_{1y}$ (Å) | $d_{12\perp}$ (Å) | $d_{12y}$ (Å) | $d_{23\perp}$ (Å) |
|---|---|---|---|---|---|---|---|
| GaAs | 27.4 | 0.65 | −0.12 | 4.39 | 1.43 | 3.31 | 2.06 |
| GaP | 27.5 | 0.63 | 0.0 | 4.24 | 1.44 | 3.20 | 1.93 |
| GaSb | 30 | 0.77 | 0.0 | 4.79 | 1.61 | 3.27 | 2.16 |
| InAs | 36.5 | 0.78 | −0.15 | 4.98 | 1.50 | 3.60 | 2.21 |
| InP | 28 | 0.69 | 0.0 | 4.57 | 1.59 | 3.45 | 2.07 |
| InSb | 28.8 | 0.78 | −0.18 | 5.06 | 1.60 | 3.82 | 2.38 |
| CdSe | 21.3 | 1.03 | 0.0 | 4.60 | 0.45 | 4.10 | 2.48 |

[1] The data were obtained by dynamical LEED analysis. References to the original papers are given in [2.3, 4]

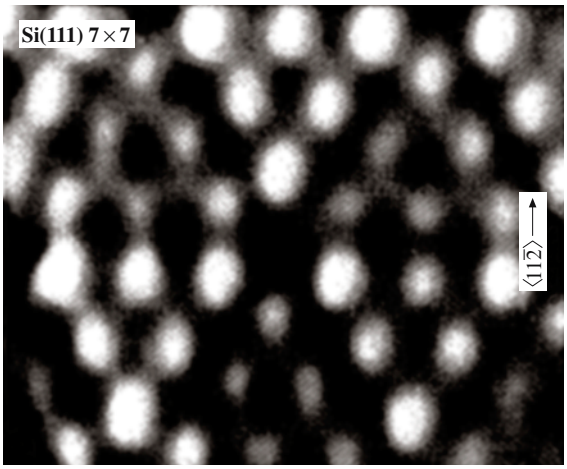


**Fig. 5.2-15** STM image of the Si(111)7×7 surface. The picture gives evidence to the 12 adatoms, the 4 vacancies, and the asymmetry between the two triangular half cells of Fig. 5.2-13 [2.7, 27]

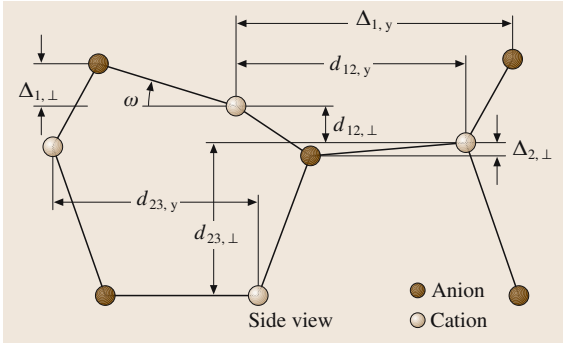


**Fig. 5.2-17** Side view of the relaxed cell of a GaAs-type crystal, with parameters occurring in the relaxation/rotation model of the (110) face used in Table 5.2-8

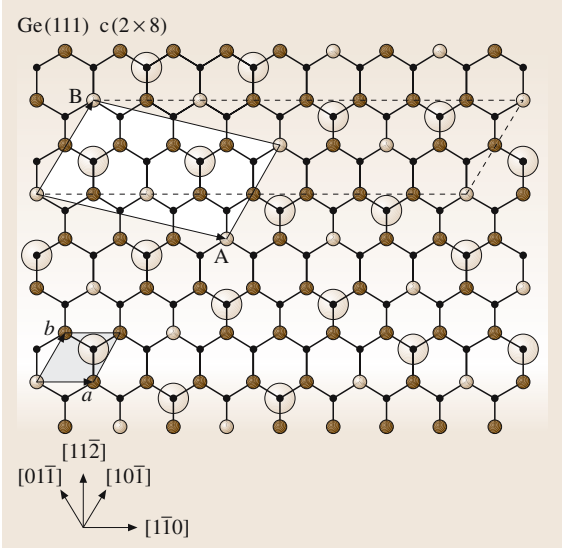


**Fig. 5.2-16** Top view of Ge(111)c(2×8) simple adatom model. Large and small empty circles represent adatoms and "rest" atoms respectively. Both ideal (*shaded*) and c(2×8) unit cells are shown [2.28]

## 5.2.3 Electronic Structure of Surfaces

The truncation of the lattice and/or the reconstruction and relaxation cause the electronic states at the surface or in the uppermost layers to be distinctly different from those of the bulk. Such new states are called surface states. Their wave functions decay exponentially on both sides of the surface. Since their $k_\perp$ is imaginary, the surface band structure is defined in the surface Brillouin zone (SBZ), which is the projection of the 3-D Brillouin zone onto the surface plane. The projection of the bulk bands onto the SBZ is called the projected band structure. When the energy of a surface state is localized in a gap of the projected bulk structure (either an absolute gapp, i. e. one that extends throughout the whole SBZ, or a *partial* gap), one speaks of a true (or bona fide) surface state. When there is degeneracy (both in energy and $\boldsymbol{k}$) with the bulk bands, one speaks of a surface resonance.

The SBZs, of the most common faces of fcc and bcc crystals are shown in Fig. 5.2-18.

The potential felt by an electron outside the surface (though sufficiently far from it) is the classical image potential: $(-e^2/4z)(\varepsilon-1)/(\varepsilon+1)$, $\varepsilon$ being the dielectric function of the crystal. From a microscopic point of view, the image potential arises from the charge density fluctuations induced in the solid by the outside electron. An important consequence of the Coulomb-like image potential is the occurrence of image states in the potential well outside the solid (especially in metals). In surface structure calculations done with the local-density approximation (LDA), such image states are not present,

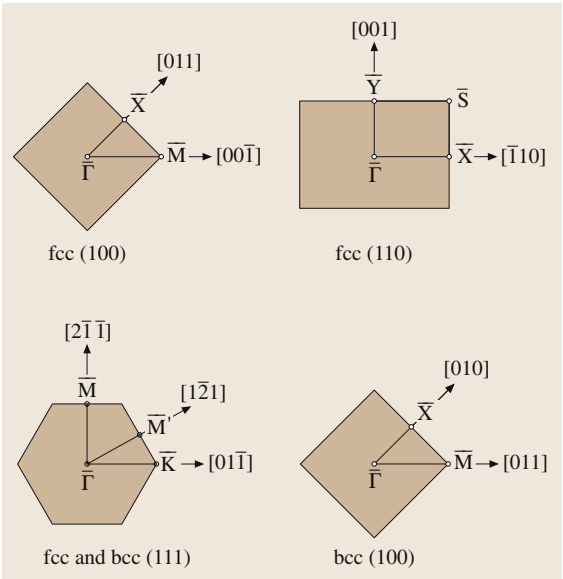


**Fig. 5.2-18** Surface Brillouin zones of fcc (100), (110), and (111), bcc (100) and (111) faces

since the potential decays exponentially on the vacuum side. Nonlocal forms of the exchange correlation energies that give the correct long-range potential have been introduced to overcome this difficulty.

Surface states were first detected by optical techniques in semiconductors and are now studied mainly by ARUPS, KRIPES, STM, SDR, and reflectance anisotropy spectroscopy (RAS).

Data, in the form of tables and figures, are presented separately for metals (including jellium), semiconductors, and magnetic surfaces.

### 5.2.3.1 Metals

The data are ordered alphabetically according to the chemical symbol. Where necessary, introductory remarks are given. A more detailed discussion is given in [2.9, 11].

#### Work Function Data

Work function data are listed in Table 5.2-9 with the specification of the method of measurement.

**Table 5.2-9** Work functions $\Phi$ of metals (average values from various authors; references to the original papers are given in [2.9, 16]). P, photoelectric threshold; A, angle-resolved photoemission spectroscopy; T, thermionic emission; F, field emission; th, theory

| Metal | Face | $\Phi$ (eV) | Technique |
|---|---|---|---|
| Ag | (100) | 4.18 | P |
| | | 4.38 | A |
| | | 4.2 | th |
| | (111) | 4.46 | P |
| | | 4.50 | A |
| Al | (100) | 4.30 | P |
| | (110) | 4.17 | P |
| | (111) | 4.23 | P |
| | | 4.5 | th |
| Au | (100) | 5.22 | A |
| | (110) | 5.20 | A |
| | (111) | 5.26 | A |
| Co | (0001) | 5.2 | A |
| Cu | (100) | 4.59 | P |
| | | 4.63 | A |
| | | 5.10 | F |
| | | 4.5 | th |
| | (110) | 4.48 | P |
| | | 4.5 | A |
| | (111) | 4.85 | P |
| | | 4.5 | A |
| Fe | (100) | 4.67 | P |
| | (110) | 5.05 | A |
| | (111) | 4.81 | P |
| Ir | (110) | 5.42 | F |
| | (111) | 5.76 | F |
| Mo | (100) | 4.53 | P |
| | (110) | 4.95 | P |
| | (111) | 4.55 | P |
| Ni | (100) | 4.89 | T |
| | | 5.53 | F |
| | | 5.1 | th |
| | (110) | 4.64 | T |
| | (111) | 5.22 | T |
| Pb | (111) | 4.05 | A |
| Pd | (111) | 5.58 | A |
| | | 5.8 | th |
| Pt | (100) | 5.84 | P |
| | | 5.84 | F |
| | (111) | 5.82 | A |
| | | 5.93 | F |
| Rh | (100) | 5.1 | th |
| | (111) | 5.35 | th |
| Ta | (100) | 4.15 | T |
| | (110) | 4.80 | T |
| | (111) | 4.00 | T |
| W | (100) | 4.66 | F |
| | | 4.5 | th |
| | (110) | 5.57 | F |
| | (111) | 4.46 | F |

### Surface Core Level Shifts (SCLS)

A shift in the energy of the core levels is caused by charge transfer between surface and bulk atoms. A positive SCLS means a larger binding energy. It is generally assumed that in metals the change in the width of the band and its position with respect to the Fermi energy are the important factors. Data are shown in Table 5.2-10.

### Jellium Model

The jellium model of a metal surface takes into account, in a simplified though significant way, the problem of electron–electron interaction. The atomic potential is smeared out into a uniform positive background extending over the region $z \leq 0$. The electron density is taken into account by a dimensionless parameter $r_s$, defined by the equation

$$(4/3)\pi(r_s a_0)^3 n = 1 \,,$$

where $a_0$ is the Bohr radius and $n$ the bulk electron density.

Figure 5.2-19 shows the charge density as a function of $z$ for $r_s = 2$ and $r_s = 5$, corresponding roughly to Al and K. Table 5.2-11 gives the values of the work function $\Phi$ for various values of $r_s$ and compares the

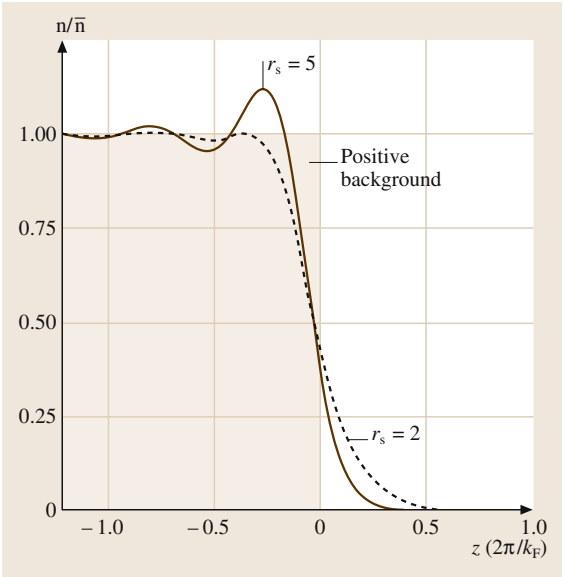


**Fig. 5.2-19** Charge density near a jellium surface, for $r_s = 2$ and $r_s = 5$ as a function of $z$ [2.29]

**Table 5.2-10** Surface core level shift data. The data are from various authors. References to the original papers are given in [2.9]

| Metal | Surface | Core level | SCLS (eV) | Remarks |
|---|---|---|---|---|
| Al | (100) | 2p | −0.057 | Photoemission (partial yield) |
| | | | −0.120 | Theory |
| | (110) and (111) | | 0.0 | UPS |
| Au | (100) 1×1 | 4f | −0.35 | UPS |
| | (100) 5×20 | | −0.28 | UPS |
| | (111) | | −0.35 | UPS, no distinct results for (111) 23×1 |
| Cu | (100) | 3s | −0.36 | Theory |
| | | 2p | −0.27 | UPS |
| Ir | (100) 1×5 | 4f | −0.49 | |
| | (111) | | −0.50 | |
| Pt | (110) 1×2 | 4f | −0.21 | UPS, evidence for nonequivalent atoms |
| | | | −0.55 | |
| | (111) | | −0.40 | UPS |
| Rh | (100) | 4d | −0.75 1st layer | Theory |
| | | | −0.05 2nd layer | |
| | (111) | | −0.46 1st layer | |
| | | | −0.05 2nd layer | |
| W | (110) | 4f | −0.30 | UPS |
| | | | −0.30 1st layer | Theory |
| | | | −0.02 2nd layer | |

**Table 5.2-11** Work functions for the jellium model. References to the original papers are given in [2.9]

| $r_s$ | $\Phi_{jellium}$ (eV) | Element | $\Phi_{exp}$ (eV) |
|---|---|---|---|
| 2 | 3.89 | Al ($r_s = 2.08$) | 4.25 |
| 2.5 | 3.72 | | |
| 3 | 3.50 | Ag ($r_s = 3.02$) | 4.35 |
| 3.5 | 3.26 | | |
| 4 | 3.06 | Na ($r_s = 3.93$) | 2.45 |
| 4.5 | 2.87 | | |
| 5 | 2.73 | K ($r_s = 4.86$) | 2.3 |

results with experimental values for metallic elements of comparable densities. Figure 5.2-20 gives some useful insight into the problem of the potential near a metallic surface.

### Image States

Image states are confined to the region of space between the crystal surface and the image potential which describes the electrostatic force acting on an electron close to the surface. Figure 5.2-21 illustrates the occurrence of image states in Ag(100). The figure shows (i) the electron potential inside and outside the crystal, (ii) the image state levels $n = 1$ and $n = 2$ and the corresponding wave functions, and (iii) the bulk band structure

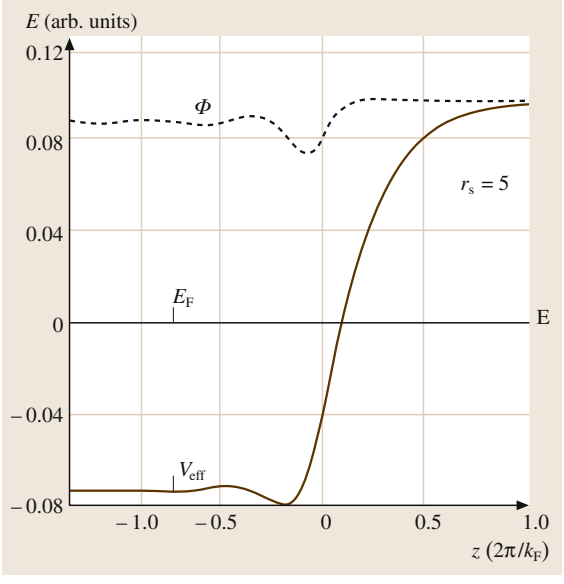


**Fig. 5.2-20** Effective one-electron potential $V_{eff}$ (*continuous line*) and its electrostatic part (*dashed line*) near a jellium surface for $r_s = 5$. Notice the characteristic oscillations (Friedel oscillations) [2.29]

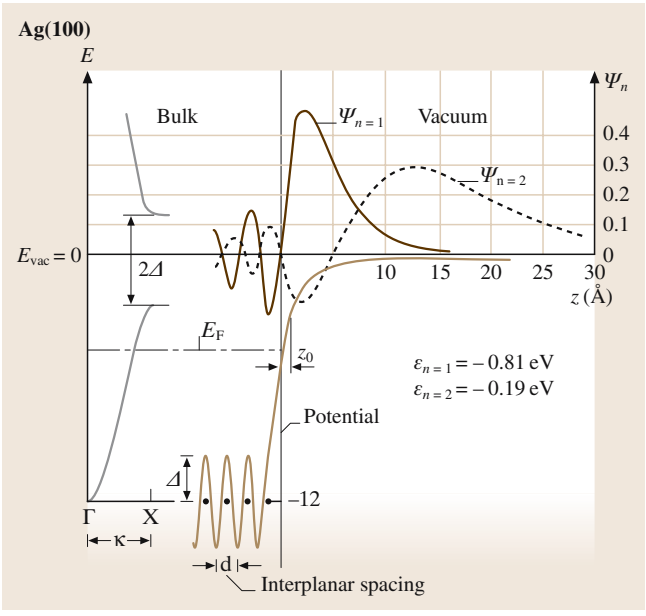


**Fig. 5.2-21** Schematic drawing of energy versus distance at the surface of Ag(100), illustrating the origin of the image states. Wave functions for $n = 1$ and $n = 2$ are also displayed in the right part of the figure, corresponding to the levels in the potential well. On the left side of the figure the bulk energy bands as a function of $\boldsymbol{k}$ are also shown. Notice that the image state energies occur in the band gap of the bulk. This allows confinement of the image state electron [2.30, 31]

with an energy gap of width $2\Delta$. It can be seen that the image state levels have energies corresponding to the bulk gap so that the electron cannot penetrate the crystal [2.32].

Figure 5.2-22 shows the dispersion curves $E(\boldsymbol{k}_\parallel)$ for the (111) faces of Ni, Cu, and Ag. Image states ($S_1$) and surface and resonance states ($S_2$, $S_3$), together with the projected bulk bands (hatched regions), are shown. Table 5.2-12 gives average values of the binding energies $E_b$ (measured downward from the vacuum level) and effective masses $m^*/m_0$ for some image states.

### Surface Dispersion Curves $E(\boldsymbol{k}_\parallel)$

Dispersion curves are given as a function of $\boldsymbol{k}_\parallel$ along symmetry lines of the SBZ in Figs. 5.2-23 – 5.2-30. Where possible, a comparison with theoretical results and the projected bulk band structure has been presented.

Most of the experimental data were obtained by ARUPS (for filled states) and KRIPES (for empty states). Since the component $\boldsymbol{k}_\parallel$ is conserved across the

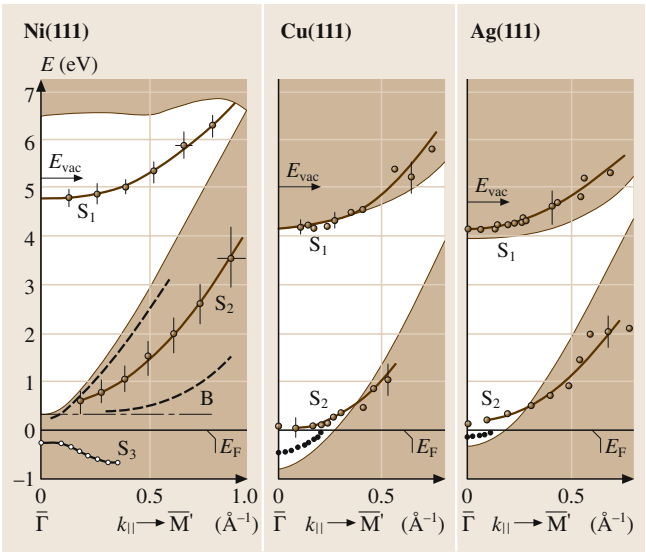


**Fig. 5.2-22** Dispersion curves $E(\boldsymbol{k}_\parallel)$ for the empty states of the (111) face of Ni, Cu and Ag, showing image states ($S_1$), surface states and resonances ($S_2$, $S_3$). Experimental data by KRIPES [2.33]

**Table 5.2-12** Image state parameters. The data are from various authors. References to the original papers are given in [2.9]

| Crystal | Face | $E_b$ (eV) | $m^*/m_0$ |
|---|---|---|---|
| Ag | (100) | 0.51 | 1.32 |
| | | 0.16 ($n = 2$) | |
| | (111) | 0.69 | 1.35 |
| | | 0.23 ($n = 2$) | |
| Au | (100) | 0.63 | 1.0 |
| | (111) | 0.42 | |
| Cu | (100) | 0.65 | 1.13 |
| | | 0.18 ($n = 2$) | |
| | (110) | 0.48 | |
| | (111) | 0.82 | 1.07 |
| Ni | (100) | 0.4 | 1.2 |
| | (110) | 0.6 | 1.7 |
| | (111) | 0.74 | 1.3 |
| | | 0.25 ($n = 2$) | |
| | | 0.10 ($n = 3$) | |
| Pt | (111) | 0.63 | |

**Fig. 5.2-25** Energy dispersion curves $E(\boldsymbol{k}_\parallel)$ around $\overline{\Gamma}$ point of the SBZ for Ag(111). Experimental data from ARUPS are fitted with a parabolic band with $m^*/m_0 = 0.53$ [2.36]

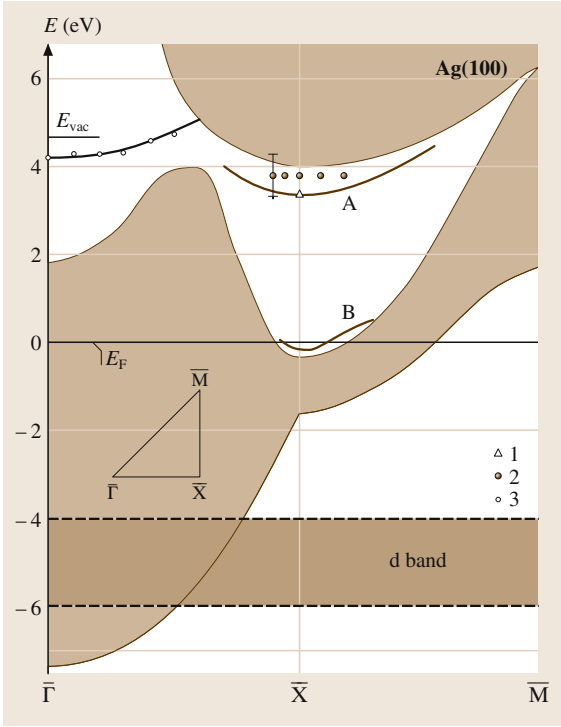


**Fig. 5.2-24** Energy dispersion curves $E(\boldsymbol{k}_\parallel)$ around $\overline{X}$ of the SBZ for Ag(100). Projected bands and surface state features A and B are the same as in Fig. 5.2-8a. Experimental points are obtained by: electroreflectance (1) and KRIPES (2 and 3). Curve (3) represents image states [2.34, 35]

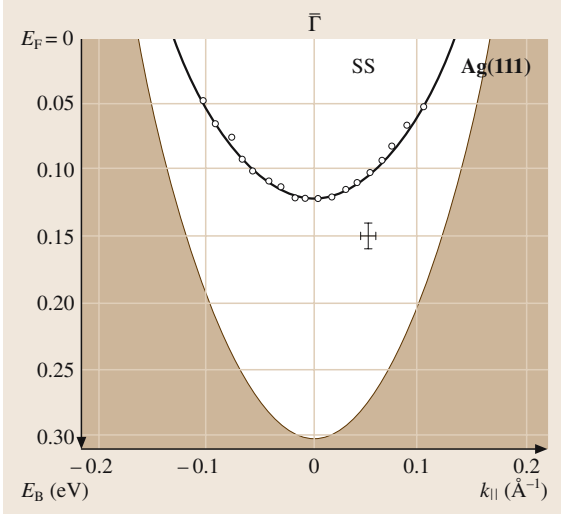

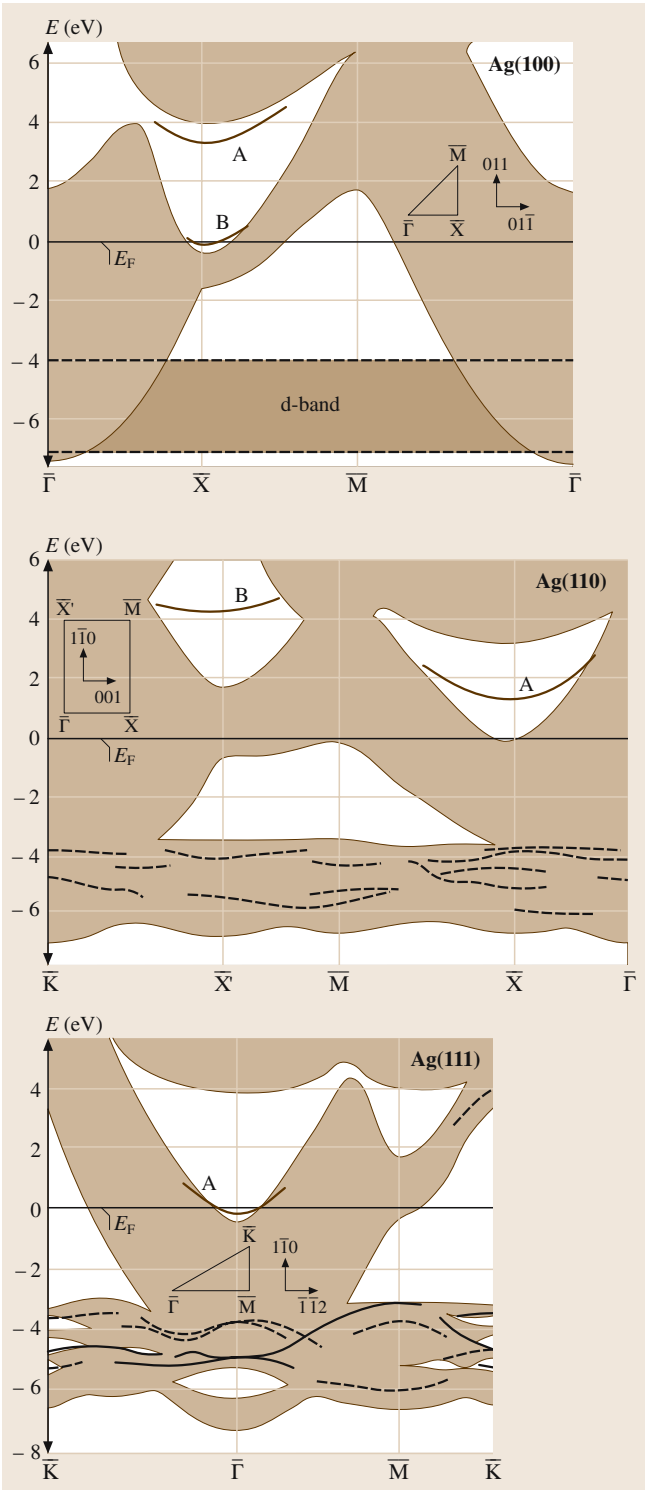


**Fig. 5.2-23** Theoretical projected band structures (*shaded areas*) along symmetry lines of the SBZ for Ag(100), Ag(110) and Ag(111). Surface states (*solid lines*) and resonances (*dashed lines*) are shown. SBZ in the *insets* [2.37–39]

surface, the determination of the direction of the emitted or incident electron in ARUPS or KRIPES, respectively, and its energy allows the determination of the dispersion curve through the relation

$$\boldsymbol{k}_{\parallel} = (2mE_{\mathrm{kin}}/\hbar^2)^{1/2} \sin\theta \,,$$

where $E_{\mathrm{kin}}$ is the kinetic energy of the emitted or incident electron and $\theta$ the angle of emission or incidence with respect to the surface normal.

Because of the large amount of data available for metals, only a few significant examples have been given. For more detailed information, the reader is referred to [2.9, 11].

### Surface Plasmons

Surface plasmons are self-sustained oscillations that decay exponentially on both sides of the surface plane. They occur at the poles of the loss function, i. e. for $\varepsilon_1 = 0$ in the bulk and $\varepsilon_1 = -1$ at the surface, $\varepsilon_1$ being the real part of the dielectric function. The surface plasmon is shifted to lower energies with respect to the bulk.

Table 5.2-13 gives some of the parameters of surface plasmons for various metals. $d_\perp(\omega)$ is, in the jellium model, the distance of the centroid of the induced charge from the surface plane. $d_\perp > 0$ means that the centroid is outside the edge of the jellium. Figure 5.2-31 shows the dispersion curves of surface plasmons for Al(111). For a more detailed discussion see [2.12].

**Table 5.2-13** Surface plasmon parameters. The data are from various authors. References to the original papers are given in [2.12]

| Metal | Surface plasmon energy (eV) | Bulk plasmon energy (eV) | $d_\perp(\omega_{\mathrm{sp}})$ (Å) |
|---|---|---|---|
| Al | 10.3 | 15 | |
| Mg | 7.38 | 10.4 | 0.82 |
| Li | 4.3 | 7.12 | 0.48 |
| Na | 3.98 | 5.72 | 0.73 |
| K | 2.73 | 3.72 | 0.73 |
| Rb | | 3.41 | |
| Cs | 1.99 | 2.90 | 0.88 |

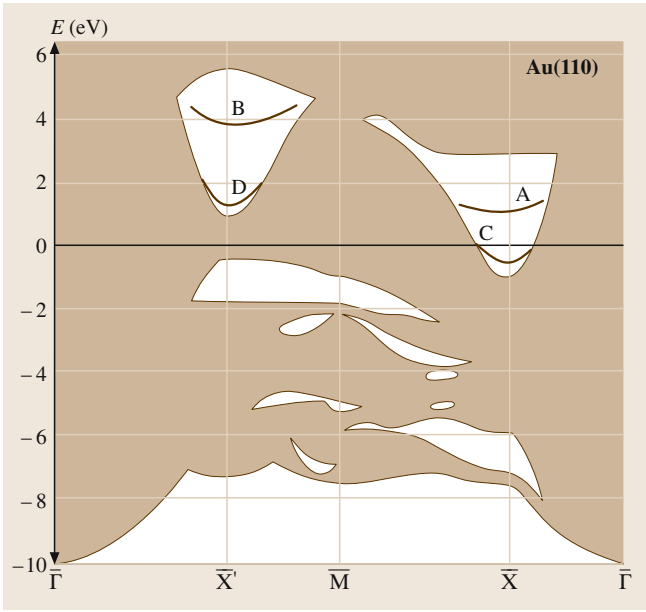


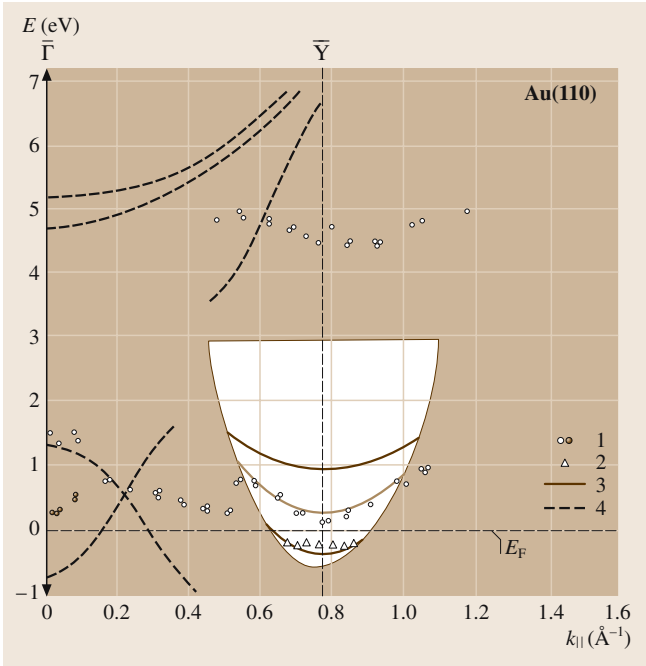


**Fig. 5.2-27** Comparison of experimental results [obtained by KRIPES for the empty states (*dots*) and by ARUPS for the initial states (*triangles*)] with the theoretical calculations of Fig. 5.2-26. Notice the splitting of the state near $\overline{Y}(\overline{X}')$ probably due to the $2\times1$ reconstruction [2.40, 41]

**Fig. 5.2-26** Theoretical projected band structure for the unreconstructed Au(110) surface. Note that in the notation of this figure, $\overline{X}'$ and $\overline{M}$ correspond to $\overline{Y}$ and $\overline{S}$, respectively, in the SBZ of Fig. 5.2-18 [2.39]

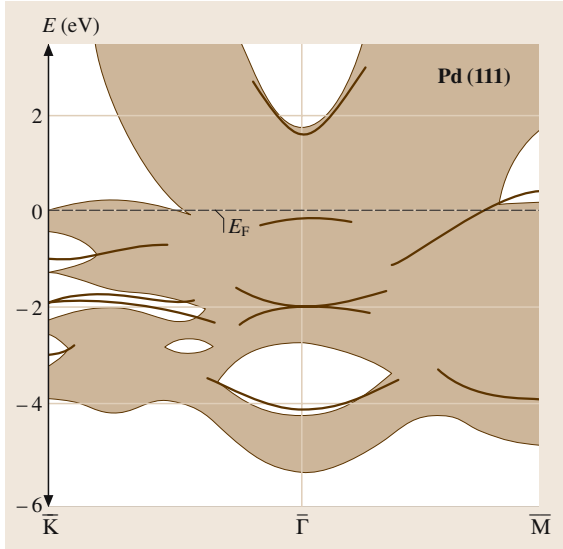


**Fig. 5.2-28** Theoretical projected band structure (*shaded area*) for Pd(111), showing an empty surface state (near $\overline{\Gamma}$) and various occupied surface states and resonances [2.42]

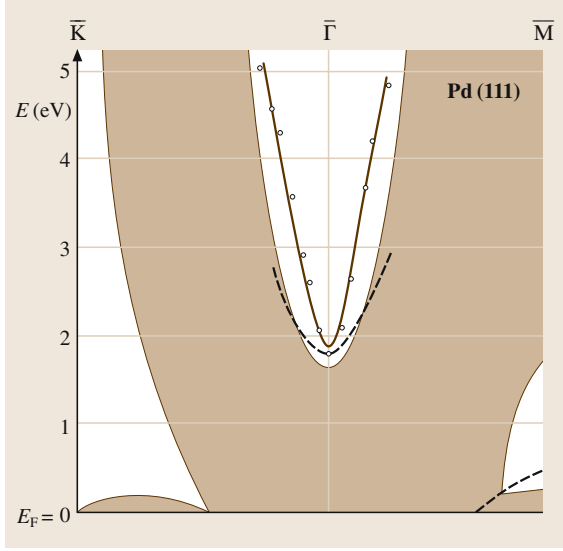


**Fig. 5.2-29** Comparison of the dispersion of the empty surface state of Fig. 5.2-28 with experimental results obtained by KRIPES [2.43]

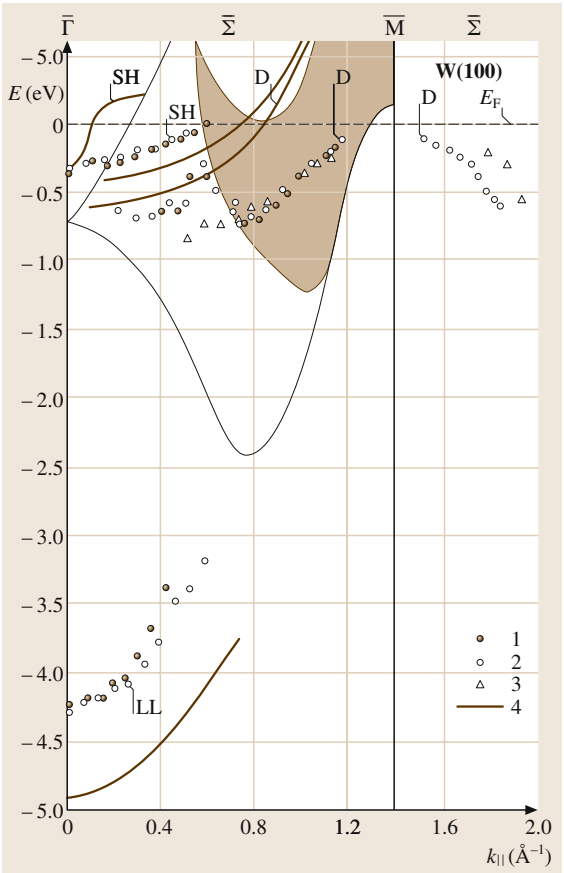


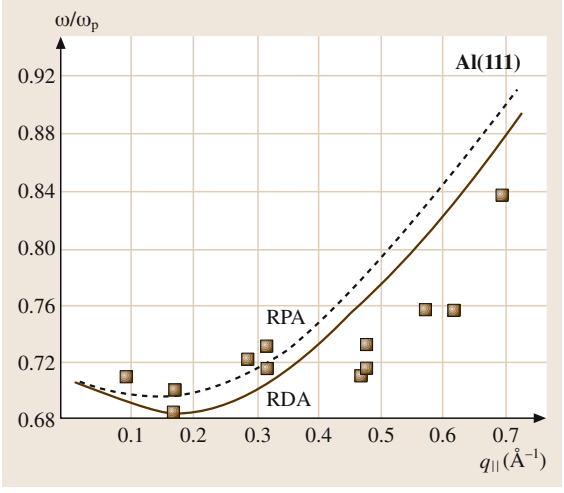


**Fig. 5.2-31** Experimental dispersion of the surface plasmon in Al(111) as a function of $q_{\parallel}$ (*squares*) and comparison with theoretical results obtained with two different approximations [2.46]

**Fig. 5.2-30** Dispersion of surface states for W(100) along the $\overline{\Gamma M}$ line obtained by ARUPS and comparison with theory [2.44, 45]

### 5.2.3.2 Semiconductors

The data on elemental semiconductors (including diamond) are ordered according to the atomic number. They are followed by data on some of the compound semiconductors. For a more detailed discussion of the various subjects, the reader may consult [2.8, 10, 11] or the books [2.47, 48].

#### Surface Ionization Energies

The *ionization energy* is defined as the distance of the top of the valence band at the surface from the vacuum level. At low impurity concentrations, the ionization energy is independent of doping and should, preferably, be measured in place of the work function. Table 5.2-14 reports the ionization energies for a number of semiconductors.

#### Surface Core Level Shifts

In semiconductors, core levels are shifted because of charge transfer between surface atoms. Table 5.2-15

**Table 5.2-14** Ionization energies at semiconductor surfaces[1]

| Crystal | Face | Reconstruction | Ionization energy (eV) |
|---|---|---|---|
| Diamond | (111) | 2×1 | 6.25 (25) |
| Si | (100) | 2×1 | 5.33 |
| | (111) | 2×1 | 5.24 (9) |
| | | 7×7 | 5.30 |
| Ge | (111) | 2×1 | 4.77 (2) |
| | | c(2×8) | 4.70 |
| GaP | (110) | 1×1 | 5.98 (3) |
| GaAs | (100) | c(2×8) | 5.40 (7) |
| | | c(4×4) | 5.34 (5) |
| | | 4×6 | 5.05 |
| | (110) | 1×1 | 5.48 (6) |
| GaSb | (110) | 1×1 | 4.79 (9) |
| InP | (110) | 1×1 | 5.77 (8) |
| InAs | (110) | 1×1 | 5.37 (6) |
| InSb | (110) | 1×1 | 4.84 (6) |
| CdS | (110) | 1×1 | 6.7 (6) |
| CdSe | (110) | 1×1 | 6.62 |
| CdTe | (110) | 1×1 | 5.79 (1) |

[1] Data are average values from various authors. Errors are standard deviations. References to the original papers and individual errors are given in [2.47]

**Table 5.2-15** Surface core level shifts for elemental semiconductors[1]

| Crystal | Face | Reconstruction | Core level | Surface shifts (eV) | | | |
|---|---|---|---|---|---|---|---|
| | | | | $S_1$ | $S_2$ | $S_3$ | $S_4$ |
| Diamond | (111) | 2×1 | 1s | −0.8 | | | |
| Si | (100) | 2×1 | 2p | −0.49 (3) | −0.230 | 0.062 | 0.29 (5) |
| | | c(2×4) | | −0.485 | −0.205 | 0.062 | 0.22 |
| | (111) | 2×1 | | −0.46 (9) | −0.14 | 0.23 (6) | 0.64 |
| | | 7×7 | | −0.74 (5) | −0.07 (5) | 0.30 (6) | 0.52 (3) |
| Ge | (100) | 2×1 | 3d | −0.49 (7) | −0.21 (3) | | |
| | | c(4×2) | | −0.60 | −0.24 | | |
| | (111) | 2×1 | | −0.49 (8) | | 0.44 | |
| | | c(2×8) | | −0.73 (3) | −0.24 (3) | | |

[1] Data are average values from various authors. Errors are standard deviations. References to original papers and individual errors are given in [2.47]

**Table 5.2-16** Surface core level shifts at Ga and As sites in GaAs[1]

| Face | Reconstruction | Surface shift (eV) | |
|---|---|---|---|
| | | Ga(3d) | As(3d) |
| (100) | c(4×4) | +0.49 | −0.285 (5) |
| | | | +0.55 |
| | c(2×8) | +0.3 | −0.26 (1) |
| | | | +0.55 (0) |
| | 4×6 | +0.4 | −0.45 (16) |
| | | −0.21 | |
| (110) | 1×1 | +0.28 (0) | −0.373 (5) |

[1] Data are average values from various authors. Errors are standard deviations. References to the original papers and individual errors are given in [2.47]

**Table 5.2-17** Surface core level shifts at (110) surfaces of III–V compounds[1]

| Crystal | Surface shifts (eV) | |
|---|---|---|
| | Cation | Anion |
| AlSb | +0.38 | −0.38 |
| GaP | +0.31 (2) | −0.41 (0) |
| GaAs | +0.28 (0) | −0.370 (5) |
| GaSb | +0.30 | −0.36 |
| InP | +0.30 (2) | −0.30 (1) |
| InAs | +0.27 (1) | −0.30 (0) |
| InSb | +0.23 (1) | −0.29 (1) |

[1] Data are average values from various authors. Errors are standard deviations. References to the original papers and individual errors are given in [2.47]

gives the shifts for the C(1s), Si(2p), and Ge(3d) levels for various faces and reconstructions. The surface shifts of the 3d levels at the Ga and As sites of GaAs (110) and (100) faces are given in Table 5.2-16.

The p and d levels are spin–orbit split and give rise to doublets. Nonequivalent atoms increase further the number of surface shifts. Up to four components are observed in Si and Ge and up to two in GaAs.

Unresolved surface shifts for various III–V compounds are given in Table 5.2-17.

### Surface State Bands

The origin and nature of surface states have been discussed in the introduction to Sect. 5.2.3. Here the energy versus $\boldsymbol{k}_\parallel$ along significant directions of the SBZ and/or the density of states are reported for various reconstructed/relaxed surfaces. The experimental data were obtained mainly with ARUPS and KRIPES or by optical, energy loss, and STM techniques.

Because of the large amount of available data, only a selection of dispersion curves and surfaces has been given. For more detailed information, the reader is referred to [2.10, 11].

The rearrangement of unsaturated dangling bonds at the surface is considered to be the driving force for reconstruction of semiconductors. An example of DBs is shown in Fig. 5.2-32a,b that give contours of the charge density for the filled (P) and empty (Ga) surface states on the (110) surface of GaP. In Fig. 5.2-32c, a comparison is made with an STM image taken with a bias voltage that allows the observation of filled and empty states.

Figures 5.2-33 – 5.2-36 and 5.2-38 – 5.2-40 give the $E(\boldsymbol{k}_\parallel)$ curves for selected surfaces of diamond, Si, Ge,

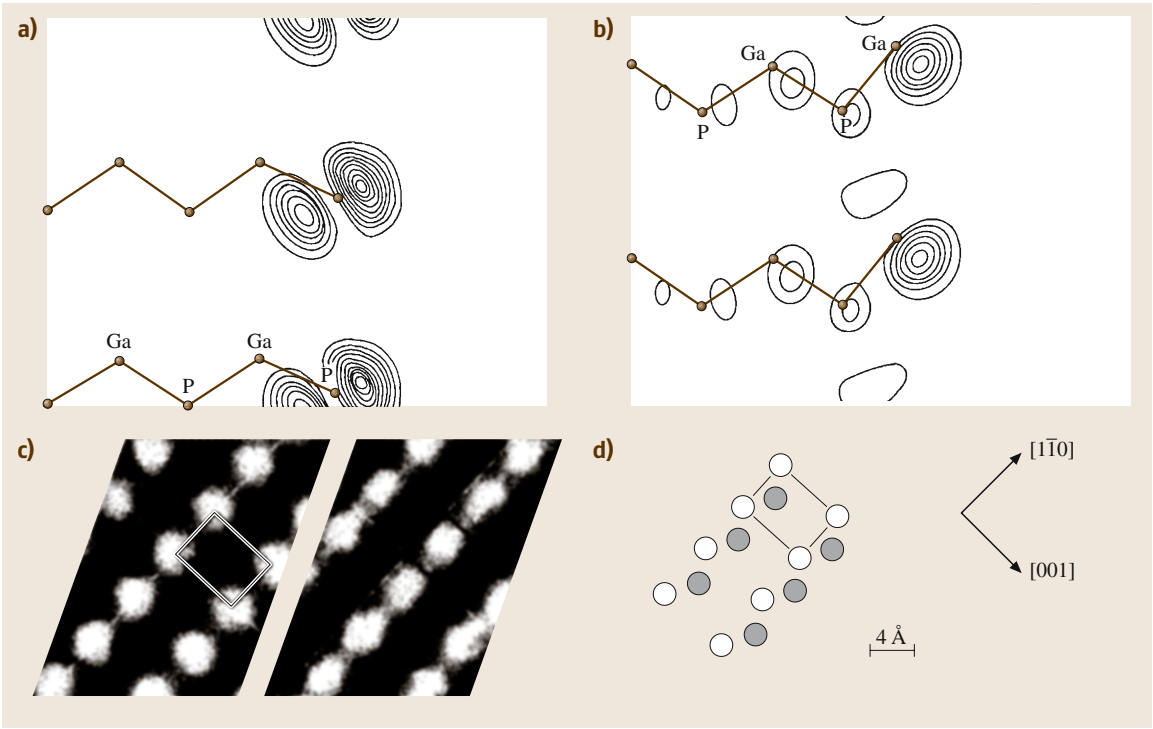


**Fig. 5.2-32** **(a)** Theoretical charge density contours for the filled DB states at P sites on the relaxed GaP(110) surface, **(b)** the same for the Ga site empty states, **(c)** comparison with constant current STM images for GaAs(110). The two STM images refer to filled (As) states (*left*) and empty (Ga) states (*right*). The two images are obtained with positive (*left*) and negative (*right*) bias. The rectangular unit cell is in the same (absolute) position. **(d)** Schematic representation of the unit cell. As atoms are shown as *empty circles*; Ga atoms as *black circles* [2.49, 50]

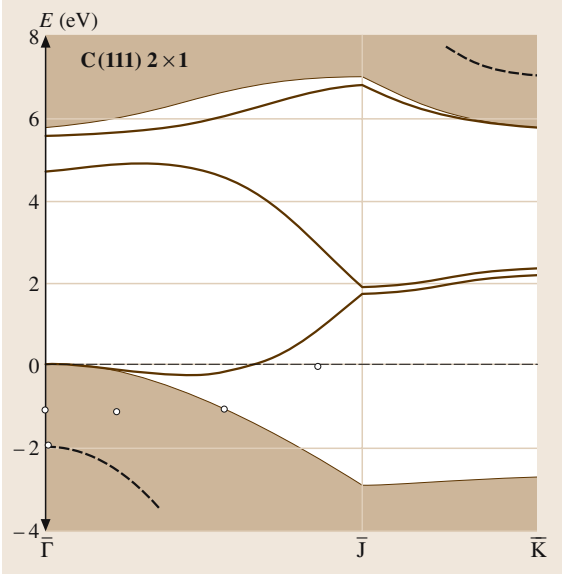


GaAs, and CdSe. The local density of states for Si(111) 7×7 as obtained from ARUPS and STM spectroscopy is shown in Fig. 5.2-37.

### Transitions Between Surface States

Transitions between surface state levels give rise to optical absorption and electron energy loss. Such transitions have been observed by SDR, RAS, ellipsometry, and EELS. As an example, the arrows in Figs. 5.2-36 and 5.2-38 show the transitions observed in Si and Ge(111)2×1. Notice the high joint density of states caused by the quasi-parallelism of the bands along $\overline{JK}$.

**Fig. 5.2-33** Theoretical surface state bands (*full lines*) and resonances (*dashed lines*) for a relaxed $\pi$-bonded chain model of diamond(111)2×1. Comparison with experimental results (*open circles*) obtained by ARUPS along the $\overline{\Gamma J}$ line [2.51, 52]

**Fig. 5.2-35** Dispersion curves of Si(100)2×1 observed by ARUPS at 21.2 eV. Prominent peaks are indicated by *open circles*, while weak peaks and shoulders by *dots*. S and B peaks have surface and bulk characters. The experimental bands should be compared with the surface structures of Fig. 5.2-34. No optical transition clearly associated to $S_1$, $S_2$ (or $D_{down}$, $D_{up}$ in Fig. 5.2-34) has been observed in spite of the essential parallelism of the two bands (meaning a high JDOS) [2.54, 55] ▶

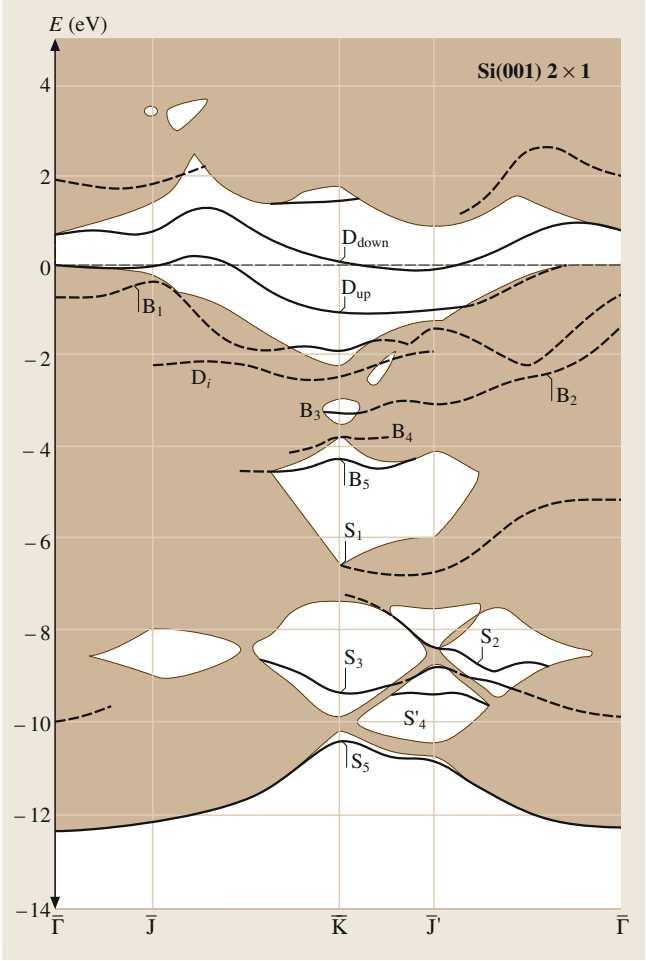


**Fig. 5.2-36** Surface band structure of Si(111)2×1. Comparison between theoretical structure based on pseudopotential calculations for the $\pi$-bonded chain model (see Sect. 5.2.2.3, Fig. 5.2-11) and experimental results from ARUPS. Photoemission from the excited surface states (around the B point in the figure) is obtained by using highly doped samples. *Arrows* indicate optical transitions observed in SDR and EELS (see Figs. 5.2-41 and 5.2-43) [2.56, 57] ▶

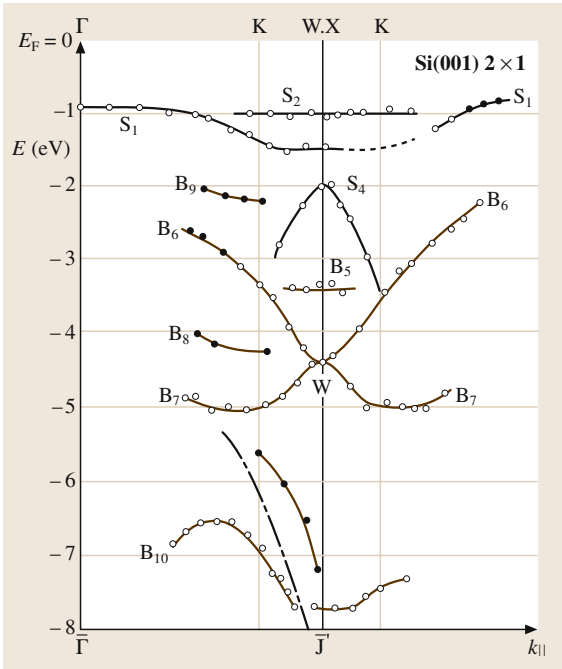


◀ **Fig. 5.2-34** Theoretical surface band structure of Si (100)2×1, obtained with the asymmetric dimer model (see Sect. 5.2.2.3, Fig. 5.2-7). $D_{down}$ and $D_{up}$ refer to the DB bands at the down and up atoms. The bands labeled $S_1 - S_5$ and $B_1 - B_5$ are back-bond states (modified by the surface) [2.53]

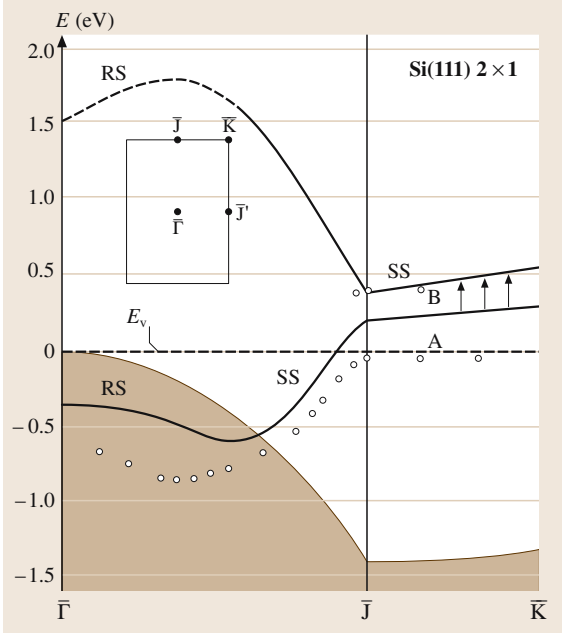

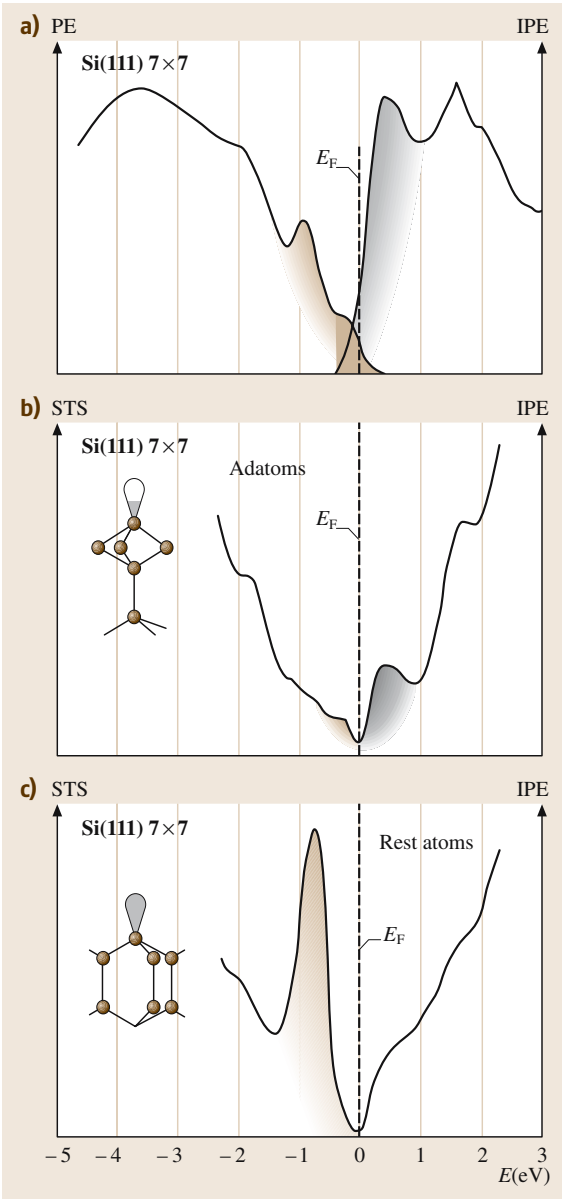


**Fig. 5.2-37a–c** Density of states associated with the dangling bonds (on the adatoms and "rest atoms") of the Si(111) 7×7 surface (see Fig. 5.2-13), obtained **(a)** by ARUPS (integrated over all atoms), and **(b)** and **(c)** by STM spectroscopy. Notice that the gap (if present) occurs at the Fermi energy [2.57–59]

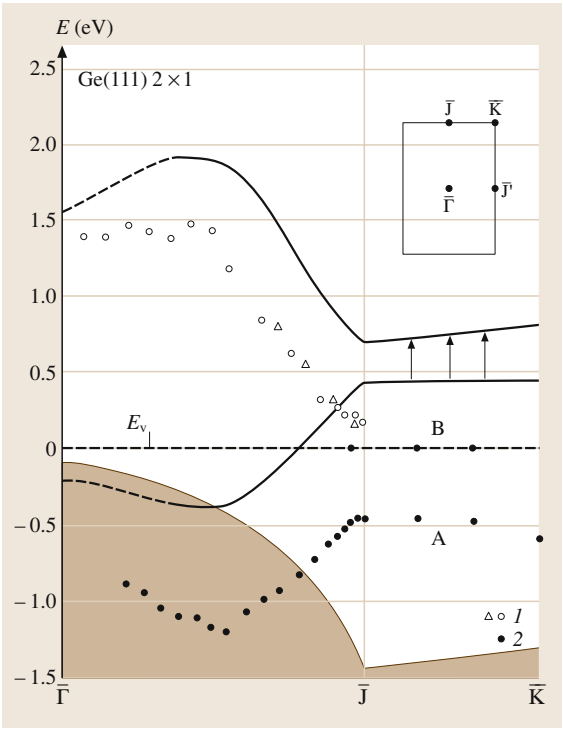


**Fig. 5.2-38** Surface band structure of Ge(111)2×1. Comparison between theoretical structure (in the frame of the chain model) and experimental results obtained with KRIPES (*open dots* and *triangles*) and ARUPS (*black dots*). Photoemission from excited states has been reached by using highly doped Ge. *Arrows* indicate optical transitions observed in SDR and EELS (see Figs. 5.2-42 and 5.2-44) [2.60–62]

In the dielectric theory of the surface response, the transition probability is proportional to $-\mathrm{Im}\,\hat{\varepsilon} = \varepsilon''$ in the optical absorption and to $\mathrm{Im}[1/1+\hat{\varepsilon}] = \varepsilon''/[(1+\varepsilon')^2+\varepsilon''^2]$ in EELS, $\hat{\varepsilon} = \varepsilon' - \mathrm{i}\varepsilon''$ being the dielectric function of the surface layer. The two techniques give essentially the same results, as shown in Fig. 5.2-45.

The great anisotropy of some reconstructed surfaces, as shown in Figs. 5.2-41 and 5.2-42, is reflected in second-harmonic generation, which is specially sensitive to the symmetry of the surface, being forbidden for centrosymmetric media (see Fig. 5.2-46 for Si(111)2×1).

Surface anisotropy has given rise to the technique of reflectance anisotropy spectroscopy (RAS), in which linearly polarized light is modulated between two principal directions (of the surface tensor) and the difference

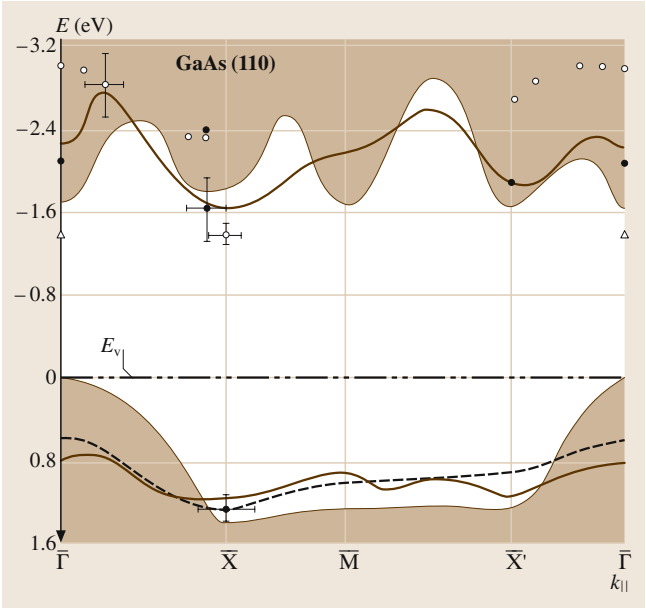


**Fig. 5.2-39** Surface band structure of GaAs(110). Comparison between theoretical structure (*continous brown line*) and experimental determinations: KRIPES (*filled* and *open circles*), ARUPS (*dashed line*), and two-step photoemission (*triangles*). It can be noticed that the surface states nearly coincide with the band edges of the projected bulk band structure [2.63–67]

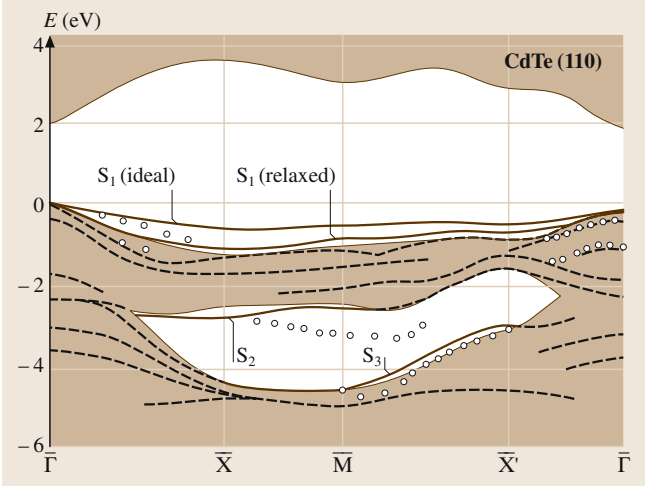


**Fig. 5.2-40** Electronic band structure of the CdTe(110) surface. The *open circles* show experimental points obtained by ARUPS. Theoretical surface states and resonances are shown by *solid* and *dashed lines*, respectively [2.68, 69]

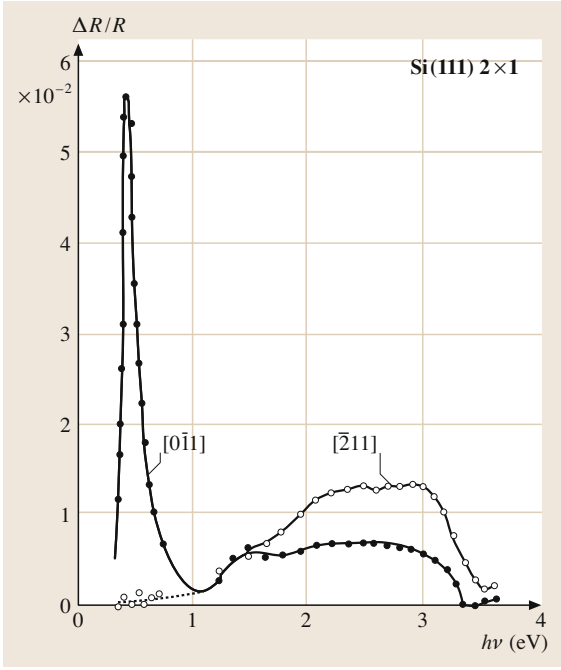


**Fig. 5.2-41** Surface differential reflectivity (SDR) spectra for Si(111)2×1, obtained with two polarizations: with the electric vector parallel ([0$\bar{1}$1], *filled circles*) and perpendicular ([$\bar{2}$11], *open circles*) to the chains of the $\pi$-bonded chain model. For the transitions shown by *arrows* in Fig. 5.2-36 ($h\nu < 1$ eV) the change in reflectivity can be observed only with the electric vector parallel to the chains. The spectrum for $h\nu > 1$ eV is associated to transitions along $\overline{\Gamma J}$ in the SBZ. The change of anisotropy at approximately 1.2 eV is conform to the "sum rule": $\int \varepsilon_x \omega d\omega = \int \varepsilon_y \omega d\omega$ [2.70]

in the reflected light is recorded. Figure 5.2-47 gives an example of RAS spectra for GaAs(100).

### 5.2.3.3 Magnetic Surfaces

The magnetic moments of atoms near the surface plane, $p_n$ ($n = 1$ for the surface), differ from those for the bulk, $p_b$. The total incremental moment at the surface is defined as

$$\Delta p_{sb} = \sum_{n=1}^{\infty} (p_n - p_b) \,.$$

Table 5.2-18 gives the values of $p_b$, $p_n$, and $\Delta p_{sb}$ for various ferromagnetic surfaces.

Temperature is more effective in destroying the magnetic order at the surface than in the bulk. This

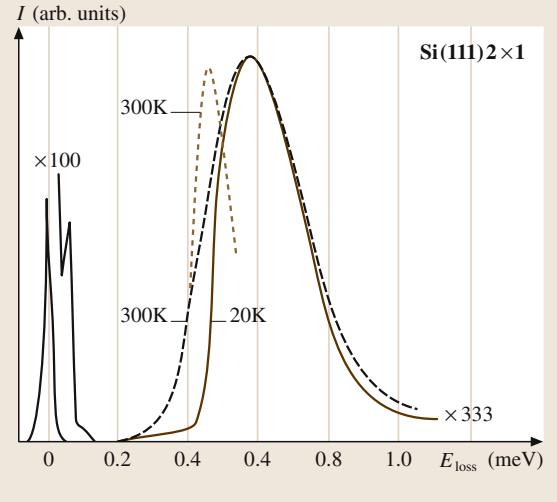


**Fig. 5.2-43** EELS spectra at $T = 20\,\mathrm{K}$ and $300\,\mathrm{K}$ for Si(111)2×1 (*full* and *dashed lines*) compared with the results of SDR of Fig. 5.2-41 (*brown dashed line*). The peak of EELS is slightly displaced towards higher energies because of the energy dependence of the factor in front of the loss function $\mathrm{Im}\left(1/\hat{\varepsilon}+1\right)$ [2.70, 71]

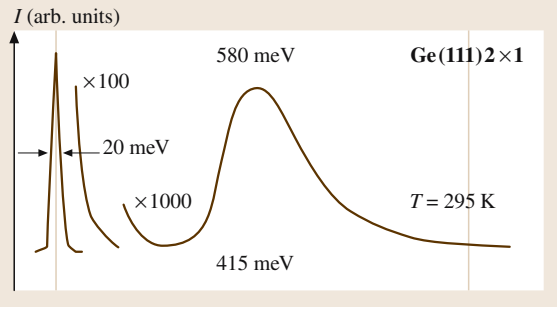


**Fig. 5.2-44** EELS spectrum of Ge(111)2×1 at room temperature. The same considerations done in the caption of Fig. 5.2-43 hold also here [2.73]

effect is shown in Fig. 5.2-48, where the ratio of the polarization $P$ at a given temperature to that at absolute zero is plotted versus temperature. The Curie temperature at the surface $T_{CS}$ is approximately equal to that of the bulk ($T_C$) in most cases. Table 5.2-19 reports the ratio $T_{CS}/T_C$ for a number of materials.

A more detailed discussion of the magnetic properties of surfaces is given in [2.13].

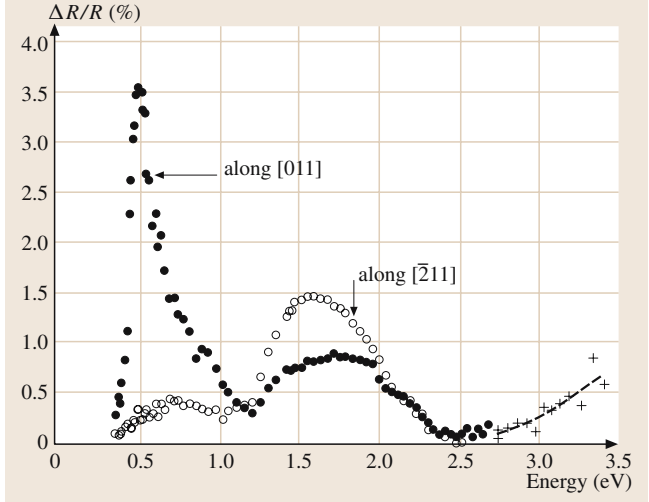


**Fig. 5.2-42** Surface differential reflectivity versus energy for Ge(111)2×1 with polarization parallel and perpendicular to the chains of the $\pi$-bonded model. The anisotropy for $h\nu < 1\,\mathrm{eV}$ is smaller than for Si(111)2×1. The same considerations done in the caption of Fig. 5.2-41 hold also here [2.72]

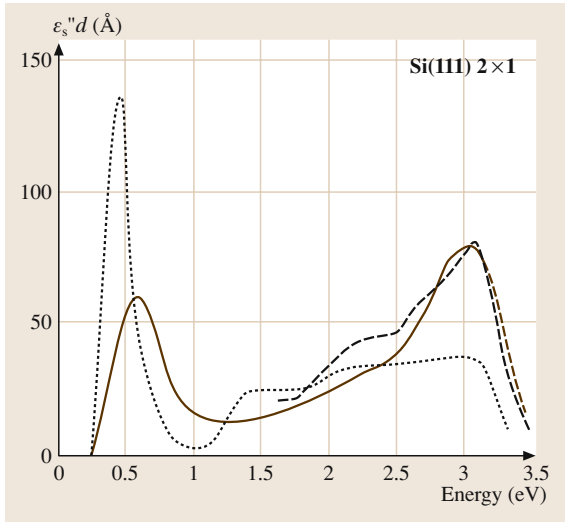


**Fig. 5.2-45** Comparison of SDR (*dotted line*) [2.70, 74], EELS (*solid line*) [2.75] and ellipsometry (*dashed line*) [2.76] spectra for Si(111)2×1. The qualitative agreement is remarkable [2.70, 74–76]

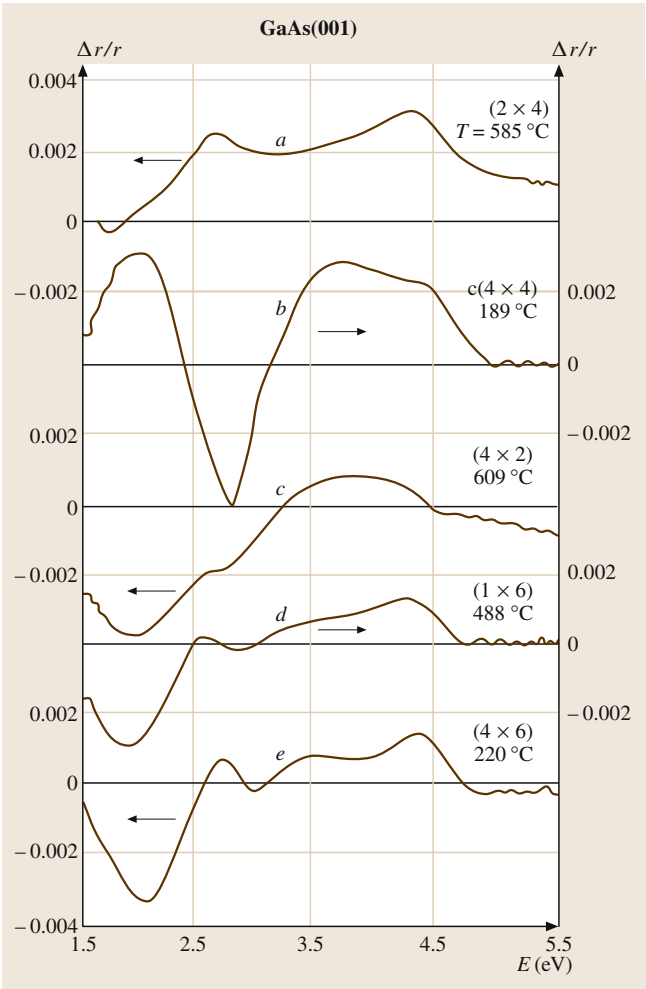


**Fig. 5.2-47** Reflectance anisotropy spectra for GaAs(100) grown by MBE at different substrate temperatures in an $As_4$ flux of $2.8 \times 10^{-6}$ torr. The corresponding reconstructions (as determined by RHEED) are also reported [2.78]

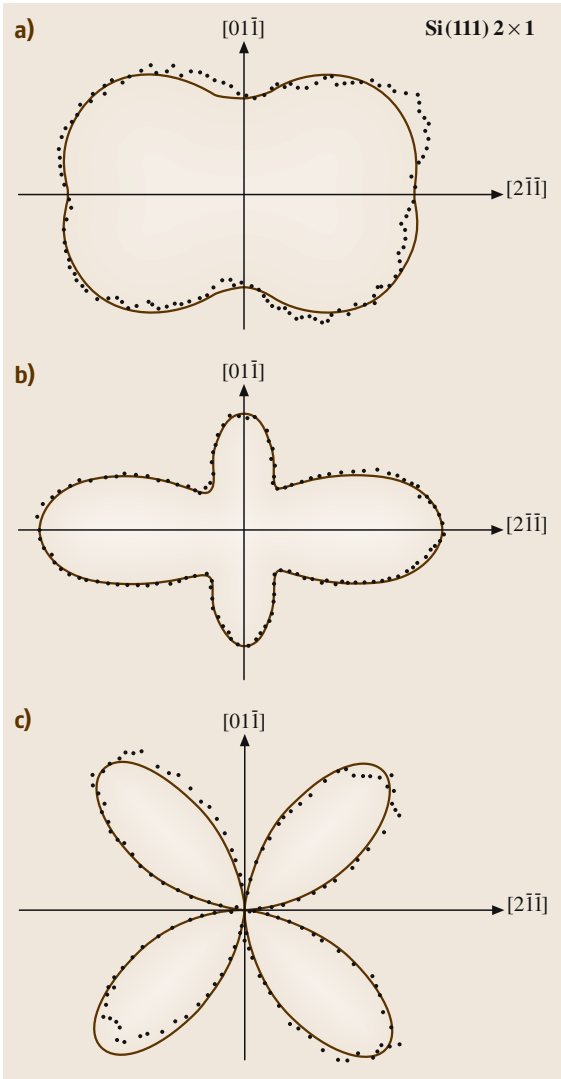


**Fig. 5.2-46a–c** Intensity of the second harmonic (SH) generation signal as a function of polarization of the incidence pump beam (1.17 eV), for Si(111)2×1. **(a)** total SH signal; **(b)** SH component polarized along [2$\bar{1}\bar{1}$]; **(c)** SH component polarized along [01$\bar{1}$] [2.77]

**Table 5.2-18** Surface magnetizations at given temperatures. The theoretical values are averages from various authors (obtained with linearized-augmented-plane-wave or tight-binding methods). References to original papers are given in [2.13]

| Crystal | Face | $T$ (K) | Magnetic moment (Bohr magnetons) | | | | | Technique |
|---|---|---|---|---|---|---|---|---|
| | | | $p_b$ | $p_1$ | $p_2$ | $p_3$ | $\Delta p_{sb}$ | |
| Fe | (100) | 0 | 2.25 | 2.96 | 2.34 | 2.45 | 1.0 | Theory |
| | (110) | 0 | 2.22 | 2.60 | 2.37 | 2.28 | 0.66 | Theory |
| | | 300 | 2.2 | 2.9 (3) | | | 0.7 (3) | SPLEED |
| Ni | (100) | 0 | 0.57 | 0.67 | 0.59 | 0.60 | 0.13 | Theory |
| | | 300 | | | | | 0.03 (3) | SPLEED |
| | (110) | 0 | 0.62 | 0.63 | 0.64 | 0.58 | 0.11 | Theory |
| | (111) | 0 | 0.58 | 0.63 | 0.64 | 0.58 | 0.11 | Theory |
| | | 300 | | | | | 0.06 (12) | SPLEED |

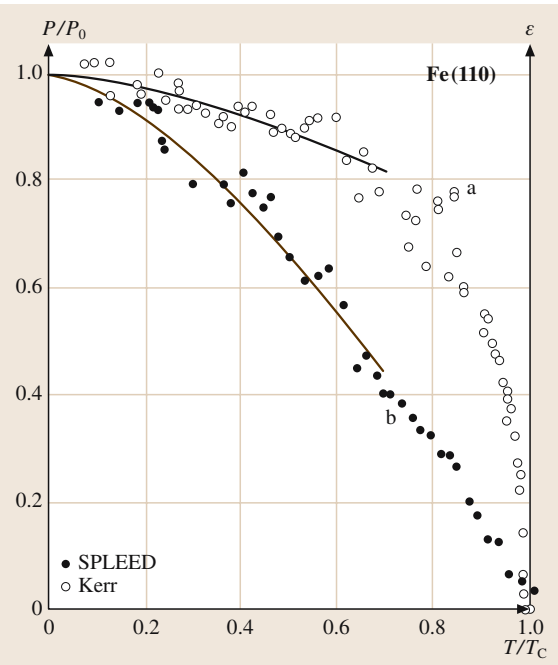


**Fig. 5.2-48** Temperature dependence of magnetic ordering. Kerr ellipticity (representing bulk magnetization) and normalized polarization $P/P_0$ of scattered electrons in SPLEED (representing surface magnetization) as a function of $T/T_C$. The *solid curves* are fits to a Bloch law: $m_1(0) - m_1(T) = bT^{3/2}$, $m_1$ being the magnetization of the first layer [2.79]

**Table 5.2-19** Surface Curie temperatures ($T_{CS}$). References to original papers are given in [2.13]

| Crystal | Face | $T_C$ (K) | $T_{CS}/T_C$ | Technique |
|---|---|---|---|---|
| Ni | (100) | 630 | 1 | SPLEED |
| | (110) | 630 | 1 | SPLEED |
| | (111) | 630 | 1 | ECS |
| Fe | (100) | 1040 | 1 | SPARPES |
| | (110) | 1040 | 1 | Spin-polarized secondary electrons |
| EuS | (111) | 16.71 (5) | 1.000 (4) | SPLEED |
| Gd | (0001) | 293 | 1.05–1.07 | SPLEED |
| Tb | (0001) | 220 | 1.14 | ECS |

## 5.2.4 Surface Phonons

The lattice dynamics is strongly perturbed by the presence of the surface. The elements of the force constant matrix connecting two atoms at or near the surface differ from those for the bulk. The number of neighbors is also different at the surface. Vibrational frequencies are generally expected to be lower than in the bulk.

Phonon bands occur in the SBZ, similarly to the surface states discussed in Sect. 5.2.3. When the frequency of a surface mode corresponds to a gap in the bulk spectrum, the mode is localized at the surface and is called a surface phonon. If degeneracy with bulk modes exists, one speaks of surface resonances. Surface phonon modes are labeled $S_j$ ($j = 1, 2, 3, \ldots$), and surface resonances by $R_j$; when strong mixing with bulk modes is present, the phonon is labeled $MS_j$. The lowest mode that is desired from the (bulk) acoustic band is often called the Rayleigh mode, after Lord Rayleigh, who first predicted (in 1887) the existence of surface modes at lower frequencies than in the bulk.

The experimental results have been obtained mainly through atom and electron scattering, HATOF and EELS.

### 5.2.4.1 Metals

Surface phonon bands along symmetry lines of the SBZ are given for fcc metals in Figs. 5.2-49 – 5.2-55 and in Table 5.2-20. In all figures the horizontal axis is the reduced wave vector, expressed as the ratio to its value at the zone boundary. Table 5.2-21 gives the surface Debye temperatures for some fcc and bcc metals, as well as the amplitudes of thermal vibrations of atoms in the first layer: $\rho_1$ as compared with those of the bulk: $\rho_b$. In the harmonic approximation, the root mean square displacement of the atoms is proportional to the inverse of the Debye temperature.

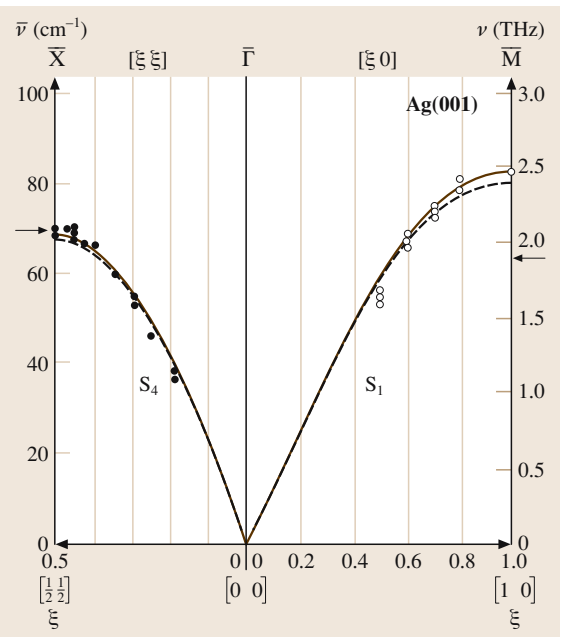


**Fig. 5.2-49** Surface phonon dispersion curves for Ag(100) measured by EELS. The *filled* and *open circles* refer to different electron energies. The *full* and *dashed lines* are theoretical fits. Energies are given in cm$^{-1}$. 1 cm$^{-1}$ = 0.1240 meV [2.80]

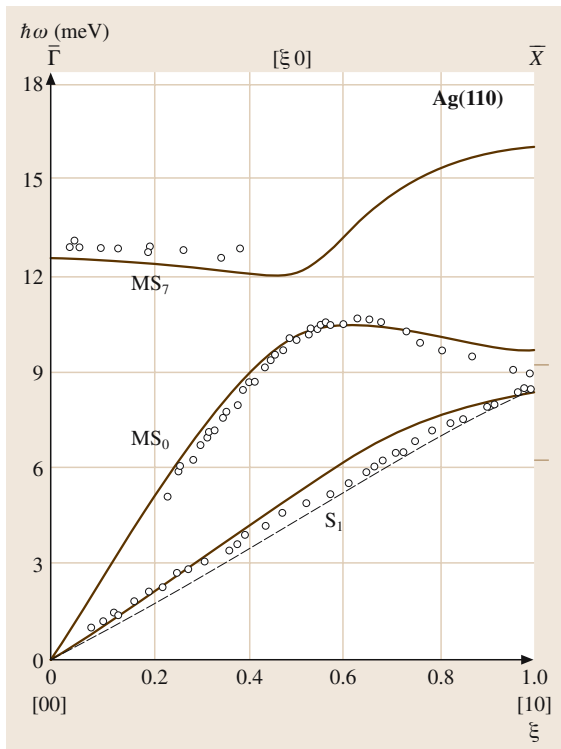


**Fig. 5.2-50** Surface phonon dispersion curves for Ag(110) measured by HATOF. The *solid curves* are theoretical fits [2.81]

**Table 5.2-20** Surface phonon energies of fcc metals. References to the original articles are given in the figure captions and/or in [2.14, 15]

| Metal | Face | Energy (meV) and mode | | | | Figure | Technique |
|---|---|---|---|---|---|---|---|
| | | $S_1$ | $S_2$ | $S_3$ | $S_4$ | | |
| Ag | (100) | 10.2 ($\overline{M}$) | | | 8.6 ($\overline{X}$) | Fig. 5.2-49 | EELS |
| | (110) | 8.15 ($\overline{X}$) | | | | Fig. 5.2-50 | HATOF |
| | | 5.0 ($\overline{Y}$) | | 7.7 ($\overline{Y}$) | | | |
| | (111) | 8.7 ($\overline{M}$) | | | | Fig. 5.2-51 | HATOF |
| | | 9.1 ($\overline{K}$) | | | | | |
| Al | (100) | | | | 15.1 ($\overline{X}$) | | EELS |
| | (110) | 14.6 ($\overline{X}$) | | | | Fig. 5.2-52 | HATOF |
| | | 8.9 ($\overline{Y}$) | | 13.5 ($\overline{Y}$) | | | |
| | (111) | 17 ($\overline{M}$) | | | | | HATOF |
| | | 18.6 ($\overline{K}$) | | | | | |
| Au | (110) $2\times1$ | | | | | Fig. 5.2-53 | EELS |
| | (111) | 7.5 ($\overline{M}$) | | | | | HATOF |
| | | 7.5 ($\overline{K}$) | | | | | |
| Cu | (100) | 16.7 ($\overline{M}$) | 20.2 ($\overline{M}$) | | | Fig. 5.2-54 | EELS |
| | | | 14.1 ($\overline{X}$) | | 13.6 ($\overline{X}$) | | |
| | (110) | $\cong$ 14 ($\overline{X}$) | | 13 ($\overline{Y}$) | | | HATOF |
| | | 7.5 ($\overline{Y}$) | | | | | |
| | (111) | 13.3 ($\overline{M}$) | 26.1 ($\overline{M}$) | | | | EELS, HATOF |
| | | 14.0 ($\overline{K}$) | | | | | |
| Ni | (100) | 19.2 ($\overline{M}$) | | | 16.1 ($\overline{X}$) | Fig. 5.2-55 | EELS, HATOF |
| | (110) | 17 ($\overline{X}$) | | 15.8 | | | EELS |
| | | 9.9 ($\overline{Y}$) | | | | | |
| | (111) | 17.2 ($\overline{M}$) | 32.2 ($\overline{M}$) | | | | EELS |
| Pd | (110) | 11 ($\overline{X}$) | | | | | HATOF |
| | | 6.7 ($\overline{Y}$) | 9 ($\overline{Y}$) | | | | |
| Pt | (111) | 10.8 ($\overline{M}$) | | | | | HATOF |
| | | 11.1 ($\overline{K}$) | | | | | |

**Table 5.2-21** Surface Debye temperatures of metals. References to the original articles are given in [2.4, 6]

| Crystal | Bulk $\Theta_D$ (K) | Face | Surface $\Theta_D$ (K) | $\rho_1/\rho_b$ | Technique |
|---|---|---|---|---|---|
| Ag | 225 | (100) | 104 | | LEED |
| | | (110) | 150–190 | | LEED |
| | | | | 1.5 | LEIS |
| | | | | 1.65 | MEIS |
| | | | | 1.44 | HEIS |
| | | (111) | $\perp$ surface 155 | | LEED |
| | | | $\parallel$ surface 226 | | |
| | | | 247 | | HAS |
| Al | 428 | (100) | 200 | | LEED |
| | | | | 1.25 | HEIS |
| | | (110) | 140 | | LEED |
| | | (111) | 200 | | LEED |

**Table 5.2–21** Surface Debye temperatures of metals, cont.

| Crystal | Bulk $\Theta_D$ (K) | Face | Surface $\Theta_D$ (K) | $\rho_1/\rho_b$ | Technique |
|---|---|---|---|---|---|
| Au | 165 | (100) | 82 | | LEED |
| | | (110) 2×1 | 83 | | LEED |
| | | | 127 | | LEIS |
| | | | | 1.55 | HEIS |
| | | (111) | 83 | | LEED |
| Cu | 343 | (100) | 230 | | LEED |
| | | | 260 | | LEIS |
| | | | | 1.5 | MEIS |
| | | (110) | 260 (150) | 1.5 | LEIS |
| | | | | 1.55 | MEIS |
| | | | | 1.27 | HEIS |
| | | (111) | 245 | | LEED |
| Fe | 467 | (111) | | 1.18 | MEIS |
| Ir | 420 | (110) | 150 | | LEED |
| | | | 160 | | LEIS |
| | | (111) | 170 | | LEED |
| Mo | 450 | (100) | 239 | | LEED |
| Ni | 450 | (100) | | 1.46 | MEIS |
| | | | | 1.35 | HEIS |
| | | (110) | ⊥ surface 216 | | LEED |
| | | | ∥ surface 344 | | |
| | | | 395 | | MEIS |
| | | | | 1.15 | HEIS |
| | | (111) | ⊥ surface 208 | | LEED |
| | | | ∥ surface 348 | | |
| | | | | 1.20 | HEIS |
| Pt | 240 | (100) | 118 | | LEED |
| | | (110) | 107 | | LEED |
| | | | | 1.6 | MEIS |
| | | (111) | 111 | | LEED |
| | | | | 1.3 | MEIS |
| Rh | 480 | (111) | 197 | | LEED |
| V | 380 | (100) | 250 | | LEED |
| W | 400 | (100) 1×1 | 210 | | LEED |
| | | (100) c2×2 | 400 (200) | | LEED |
| | | | | 1.5 | HEIS |
| | | (110) | 190–235 | | LEED |
| | | | | 2.6, 1 | HEIS |

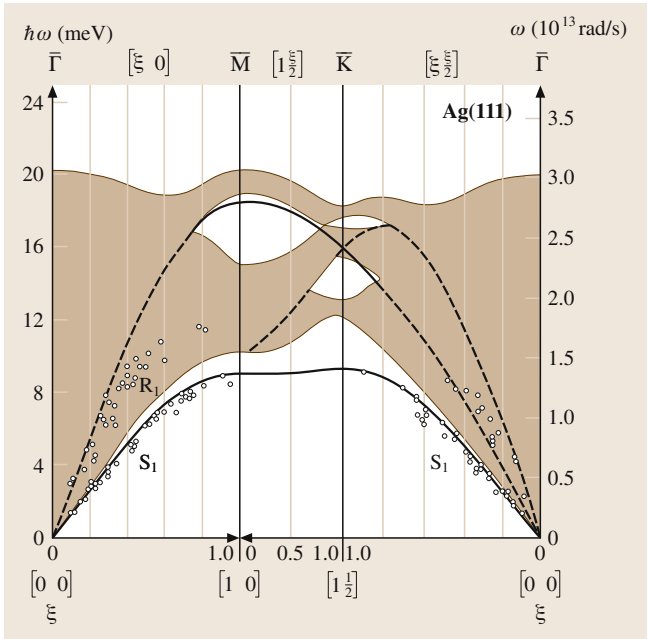


**Fig. 5.2-51** Surface phonon dispersion curves for Ag(111) measured by HATOF. *Cirles* are experimental points; *solid* and *dashed lines* theoretical calculations. The *hatched area* represents the projected band structure [2.82].
Very similar plots hold for Au(111) and Cu(111). For appropriate energy parameters see Table 5.2-20

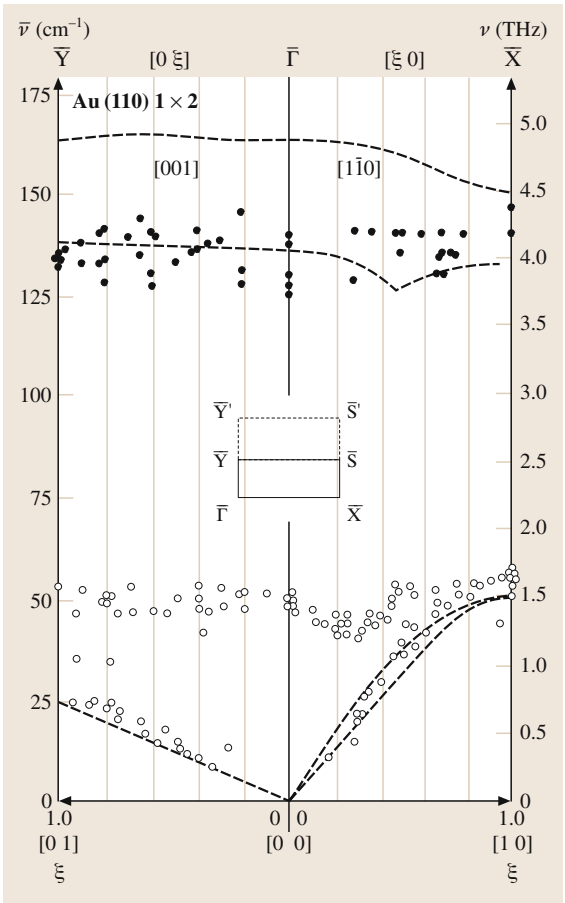


**Fig. 5.2-53** Surface phonon dispersion curves along two directions of the SBZ for reconstructed Au(110) 2×1, measured by EELS. The *dashed lines* are theoretical results. In the *inset*, the SBZ shows the folding due to the 2×1 reconstruction that introduces the optical bands. Energies are given in $cm^{-1}$. $1\,cm^{-1} = 0.1240$ meV [2.84]

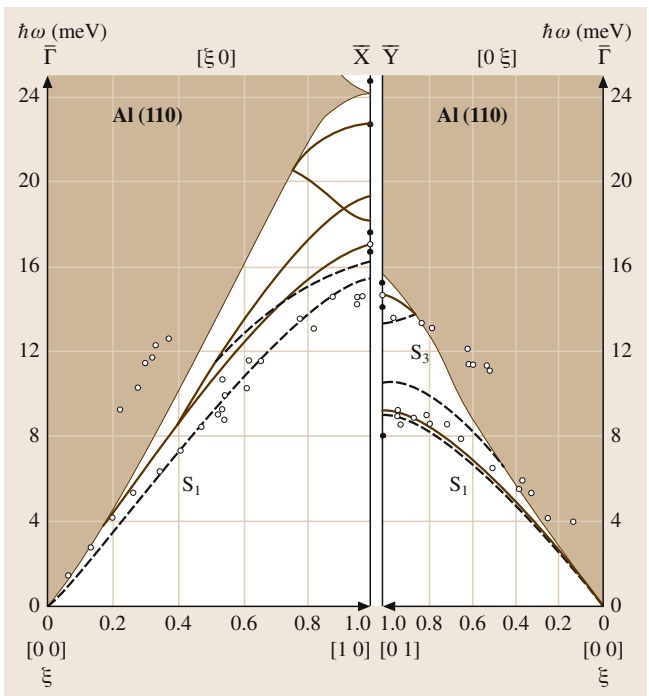


**Fig. 5.2-52** Surface phonon dispersion curves for Al(110). The experimental results (*circles*) were obtained by HATOF. The *solid* and *dashed lines* are theoretical fits. The *shaded regions* represent the projected bulk modes [2.83]

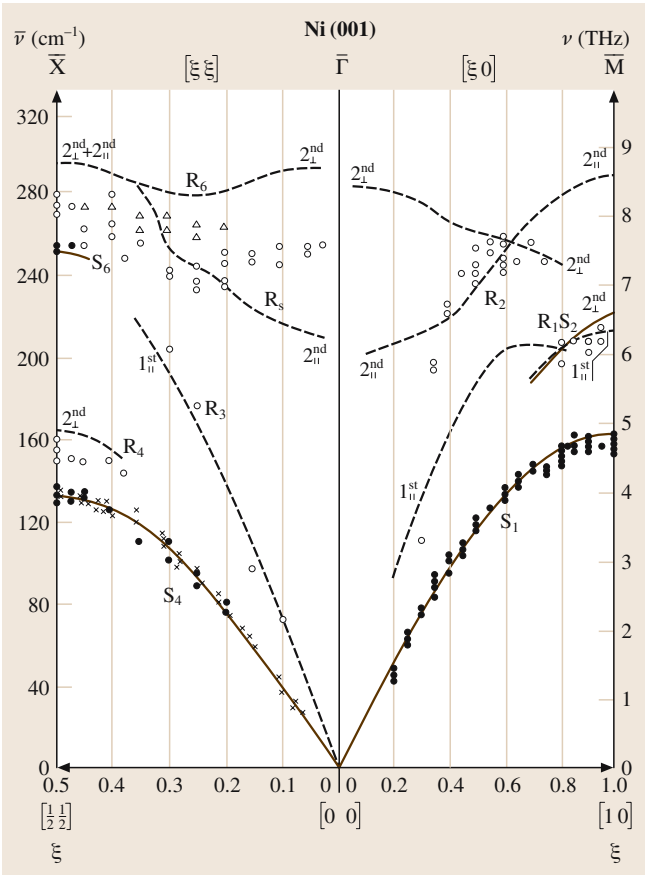


**Fig. 5.2-55** Surface phonon dispersion curves of Ni(100) obtained by EELS. $S_j$, surface phonons; $R_j$, surface resonances. Energies are given in cm$^{-1}$. 1 cm$^{-1}$ = 0.1240 meV [2.86]

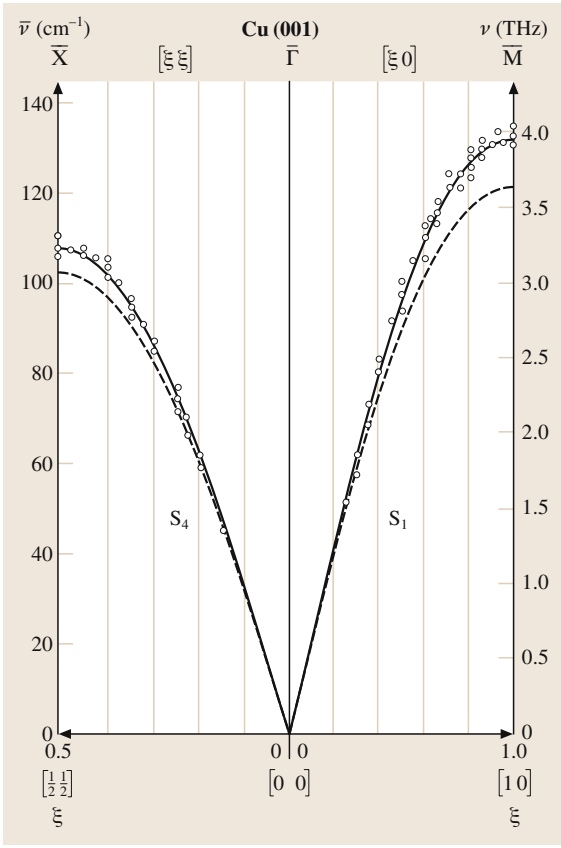


**Fig. 5.2-54** Surface phonon dispersion curves for Cu(100) measured by EELS. The *solid* and *dashed lines* are theoretical fits. Energies are given in cm$^{-1}$. 1 cm$^{-1}$ = 0.1240 meV [2.85]

### 5.2.4.2 Semiconductors and Insulators

Phonon surface bands of some insulators and semiconductors are given in Figs. 5.2-56 – 5.2-58. Surface phonon energies of alkali halide crytals are summarized in Table 5.2-23. Since insulators and semiconductors have in general more than one atom per unit cell, they display both acoustical and optical branches. Surface Debye temperatures of some semiconductors are given in Table 5.2-22.

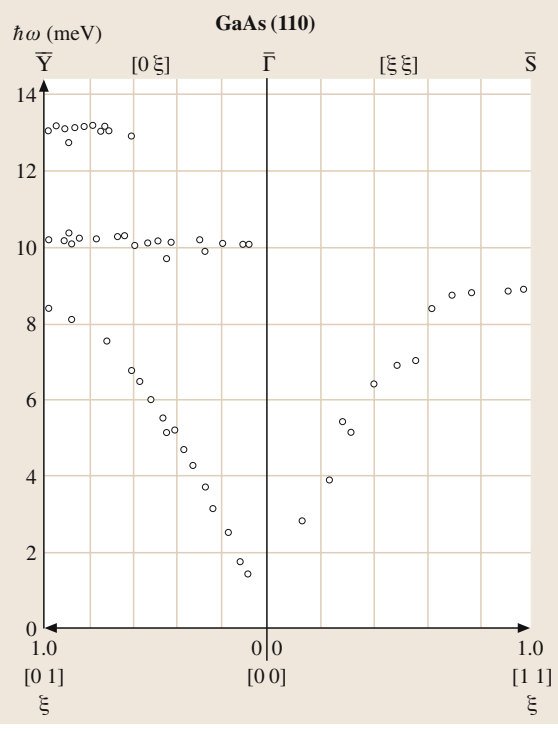


**Fig. 5.2-56** Surface phonon dispersion curves for GaAs(110) measured by HATOF (*open circles*). The energies at symmetry points are: Y, 8.3, 10.2, and 13.0 meV; Γ, 10.0 meV; S, 8.9 meV [2.87]

**Table 5.2-23** Surface phonon energies of alkali halides. References to the original articles are given in [2.14, 15]

| Crystal | Face | Energy of mode $S_1$ (meV) | Technique |
|---|---|---|---|
| LiF | (100) | 22.9 ($\overline{M}$) | HATOF |
| NaF | (100) | 16.0 ($\overline{M}$)<br>18.5 ($\overline{X}$) | HATOF |
| NaCl | (100) | 9.9 ($\overline{M}$)<br>11 ($\overline{X}$) | HATOF |
| NaI | (100) | 4.1 ($\overline{M}$)<br>4.9 ($\overline{X}$) | HATOF |
| KCl | (100) | 7.2 ($\overline{M}$) | HATOF |
| RbCl | (100) | 4.7 ($\overline{M}$)<br>$\cong$ 5.7 ($\overline{X}$) | HATOF |

**Table 5.2-22** Surface Debye temperatures of semiconductors. References to the original articles are given in [2.4, 6]

| Crystal | Bulk $\Theta_D$ (K) | Face | Surface $\Theta_D$ (K) | $\rho_1/\rho_b$ | Technique |
|---|---|---|---|---|---|
| GaSb | 265 | (110) | | 1.57 | MEIS |
| InAs | 249 | (110) | | 1.65 | MEIS |
| Si | 640 | (100) | 430–475 | | HEED |
| | | | | 1.4 | HEED, LEED |
| | | (111) 2×1 | | 1.45, 2.1 | MEIS |
| | | | 300 | | HEIS |

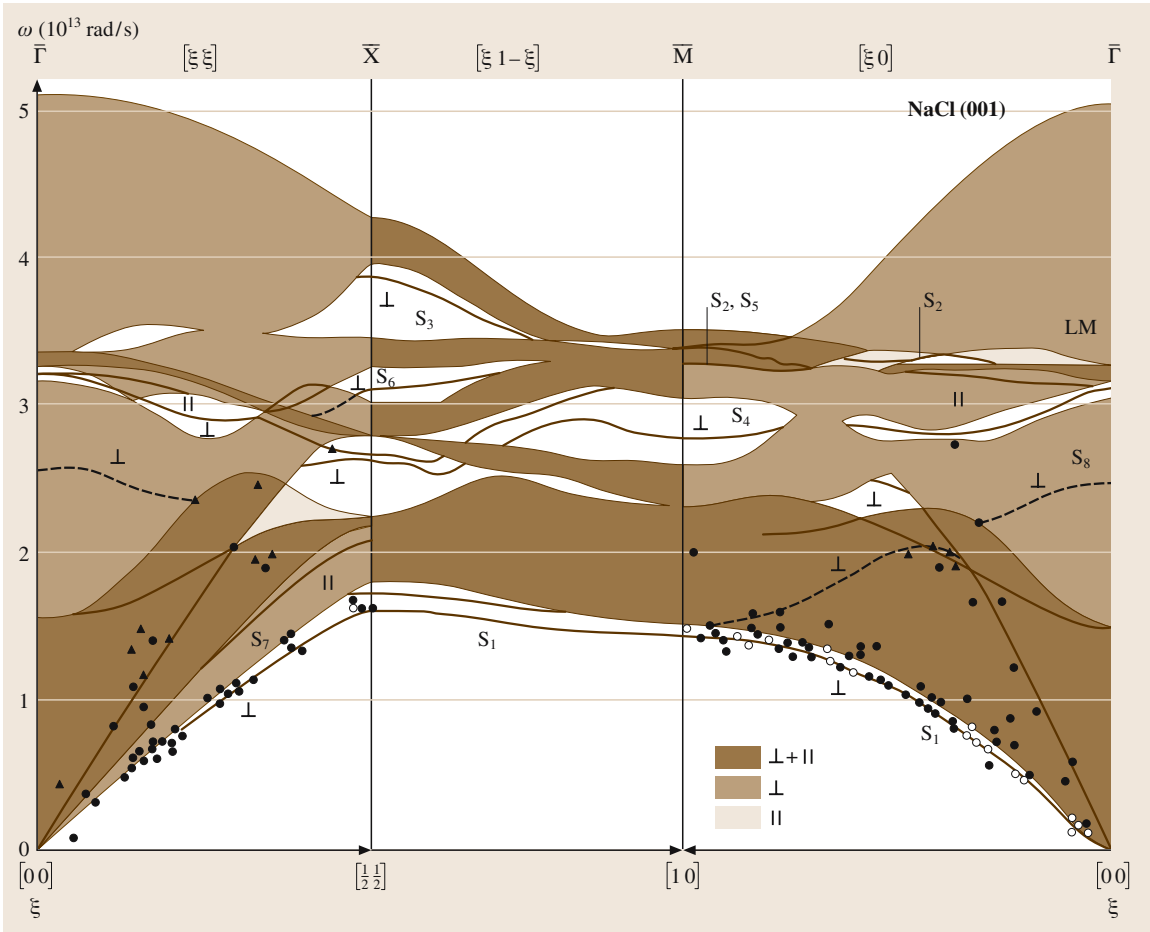


**Fig. 5.2-57** Surface phonon dispersion curves for NaCl(100). Theoretical projected band structure (*hatched*) and experimental points (*dots*) measured by HATOF. *Solid* and *dashed lines* represent theoretical surface states and resonances. Ordinates are given in units of $10^{13}$ rad/s = 6.586 meV [2.88, 89]

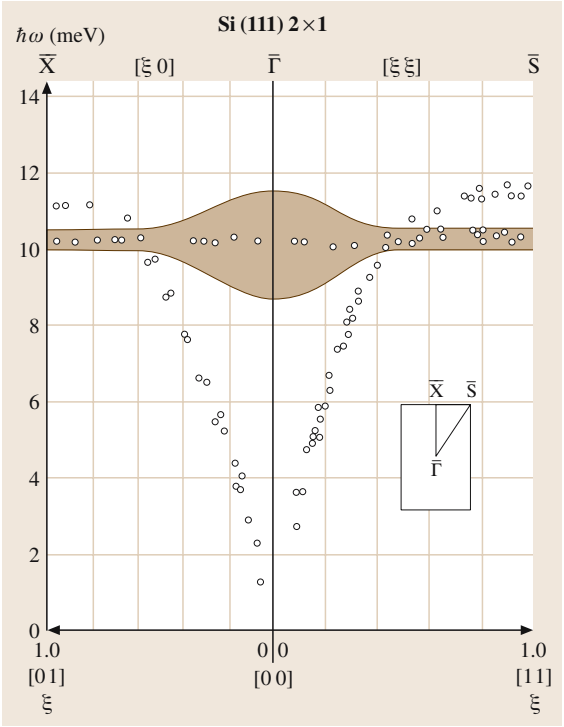


**Fig. 5.2-58** Surface phonon dispersion curves for Si(111) 2×1 measured by HATOF. Energies at symmetry points: X, 10.2 and 11.1 meV; S, 10.5 and 11.6 meV. The flat phonon mode at 10.5 meV is associated with the 2×1 reconstruction. The surface mode couples with transverse bulk phonons near the center of the SBZ, giving rise to considerable broadening. The *shaded area* corresponds to the width of the 10.5 meV peak [2.90]. The energy of the optical mode (not shown in the figure) is 56.0 meV [2.91]

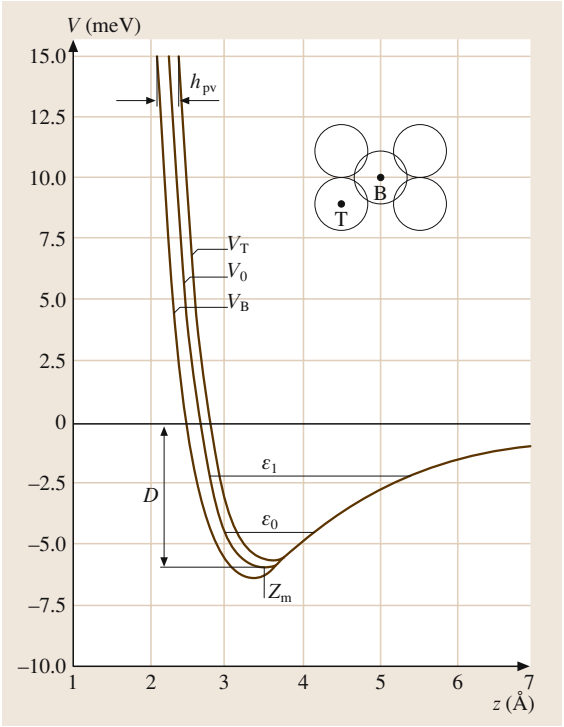


**Fig. 5.2-59** Typical atom–surface potential, with definitions of the main interaction parameters. The surface unit cell is shown in the *inset*. The numbers on the axes refer to He–Ag(110) [2.92]. $V_0$: surface averaged potential; $V_T$: potential at the top position; $V_B$: potential at the bottom position

### 5.2.4.3 Atom–Surface Potential

Many results on surface phonon dispersions are obtained through atomic (mainly He) scattering.

The interaction of an incident atom with a surface is described by the atom–surface potential (Fig. 5.2-59), which consists of a hard repulsive part at short distances and a weak van der Waals attraction at larger distances.

The attractive contribution is often assumed in to be the form

$$V_{\text{att}} = -\frac{C_3}{(z - z_{\text{vW}})^3} \,.$$

In the potential well between the van der Waals potential and the hard repulsive potential, quantized energy levels $\varepsilon_n$ exist (see Fig. 5.2-59). Table 5.2-24 summarizes the parameters of the atom–surface potentials for a number of surfaces and impinging atoms (or molecules). A more extended discussion is given in [2.14, 15].

**Table 5.2-24** Parameters of the atom–surface potential. Values of $\varepsilon_n$ are given in the order $n = 0, 1, 2, 3 \ldots$. References to the original papers are given in [2.15]

| Crystal | Face | Atom/ molecule | $D$ (meV) | $z_m$ (Å) | $z_{vW}$ (Å) | $C_3$ (meV Å$^3$) | $\varepsilon_n$ (meV) |
|---|---|---|---|---|---|---|---|
| Ag | (110) | $H_2$ | 31.7 | 3.27 | 0.755 | 714 | 25.3, 16.4, 9.7, 5.3, 2.5, 1.1 |
| | | He | 6.0 | | 0.755 | 249 | 4.44, 2.18, 0.92, 0.31, 0.1 |
| | (111) | $H_2$ | 32.5 | 2.5 | 0.2 | 714 | 25.5, 16.6, 9.9, 5.4, 2.5, 1.1 |
| Al | (110) | He | 5.2 | 4.47 | 1.71 | 202 | 3.65 |
| Au | (111) | He | 8.0 | 3.98 | 1.34 | 274 | 5.91 |
| Cu | (110) | He | 6.27 | 3.65 | 1.21 | 235 | 4.52, 2.2, 1.0, 0.3 |
| GaAs | (110) | He | (7) | (3.5) | (−0.2) | (473) | (4.2) |
| NaCl | (100) | He | 6.1 | 3.49 | 1.03 | 106 | 4.1, 1.5, 0.31 |
| LiF | (100) | He | 8.5 | 2.98 | 0.79 | 93 (137) | 5.9, 2.46, 0.78, 0.21 |
| | | Ne | 13.5 | | | 192 | 11.7 |
| Ni | (100) | He | 4.2 (theory) | 3.76 (theory) | | 218 | |
| Pd | (110) | He | 8.05 | 3.60 | | 211 | 6.42 |
| Pt | (110) 2×1 | He | 8.8 | | | 251 | 7.4, 5.1, 3.1, 1.5 |
| Si | (100) | He | | | | 174 | |
| W | (110) | He | | | | 265 | 5.6 |

## 5.2.5 The Space Charge Layer at the Surface of a Semiconductor

Surface states in the gap of a semiconductor may trap or loose electrons. The localized charge in surface states is neutralized by a macroscopic space charge layer of opposite sign, caused by accumulation or depletion of the bulk carriers. The potential associated with the space charge gives rise to a band bending of the bulk bands at the surface. Band bending alters various properties of semiconductor surfaces and is crucial for many applications, such as chemisorption, catalysis, corrosion, and, most significantly, channel conductivity in MOS field-effect transistors. For this reason, the problem of the surface space charge layer is treated extensively in the following sections.

### 5.2.5.1 Definitions and Notation

Figure 5.2-60 shows the main parameters that characterize the space charge layer. With reference to the figure, the following definitions can be given:

- $E_i(z)$ is the *intrinsic level*: this level runs parallel to the band edges and coincides, in the bulk, with the intrinsic Fermi level $E_{ib}$:

$$E_{ib} = \frac{E_c + E_v}{2} + \frac{1}{2} k_B T \ln \frac{N_v}{N_c} .$$

- The following quantities related to band bending:

$$u(z) \equiv \frac{E_F - E_i(z)}{k_B T} ,$$

$$v(z) = u(z) - u_b \equiv \frac{E_{ib} - E_i(z)}{k_B T} , \qquad (2.1)$$

where $v_s$, $u_s$, and $u_b$ are the values of $v(z)$, and $u(z)$ at the surface and the value of $u(z)$ in the bulk; $u_b > 0$ for n-type semiconductors and $u_b < 0$ for p-type semiconductors. If $v_s > 0$ the band bends downward; if $v_s < 0$ the band bends upward. $v_s = 0$ is the condition for flat bands, and $u_s = 0$ the condition for an intrinsic surface.

An accumulation layer exists if $v_s$ and $u_b$ have the same sign (as in Fig. 5.2-60).

An depletion layer exists if $v_s$ and $u_b$ have opposite signs and $u_s$ and $u_b$ have the same sign.

An inversion layer exists if both of the pairs $v_s$, $u_b$ and $u_s$, $u_b$ have opposite signs.

- Debye length:

$$L_D = \sqrt{\frac{\varepsilon_0 \varepsilon_b k_B T}{q^2 (n_b + p_b)}} , \qquad (2.2)$$

where $n_b$ and $p_b$ are the bulk carrier concentrations and $q$ is the elementary charge. For small

**Table 5.2-25** Intrinsic Debye lengths for various semiconductors

| | Si | Ge | GaAs | InP | InAs | InSb |
|---|---|---|---|---|---|---|
| Intrinsic Debye length (cm) | $2.9\times10^{-3}$ | $7.0\times10^{-5}$ | $2.0\times10^{-1}$ | $2.7\times10^{-2}$ | $8.6\times10^{-6}$ | $2.4\times10^{-6}$ |

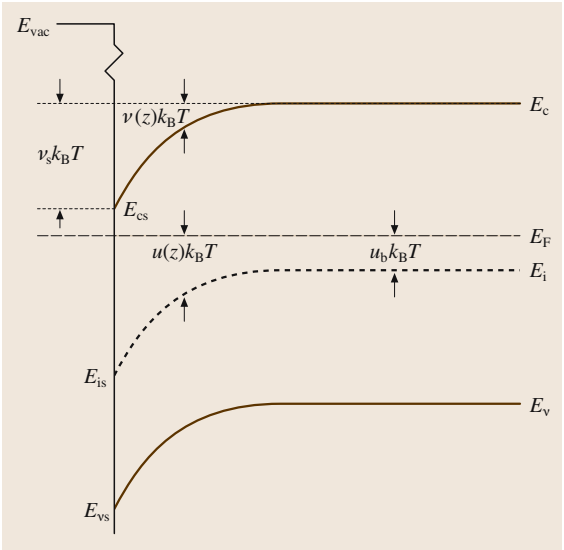


**Fig. 5.2-60** Schematic behavior of the bands at the surface of a semiconductor and definition of the main parameters. Notice that band bending $v(z)$ is positive when the band bends downward

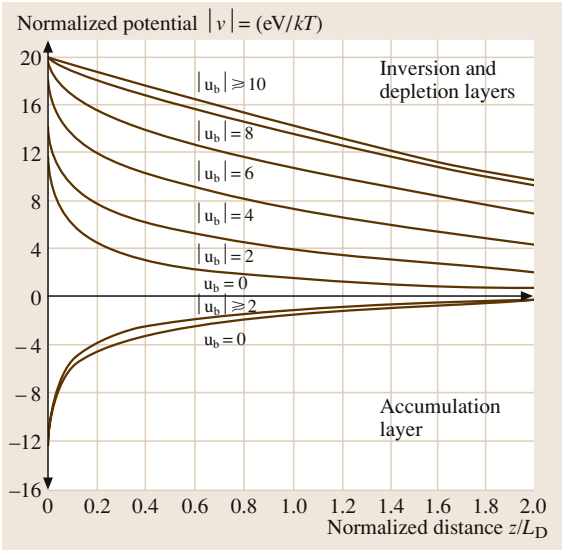


**Fig. 5.2-61** Profile of the potential $|v(z)|$ as a function of $z/L_D$ plotted for $|v_s| = 20$ and various values of $|u_b|$. The behavior for other values of $|v_s|$ can be obtained by drawing the parallel to the abscissa through the new value $|v_s'|$ and translating the origin of the abscissa at the value of the interception [2.48, p. 329]

bending ($< k_BT$), the surface barrier decays as $v(z) = v_s e^{-z/L_D}$. For larger bending, the shape of the potential cannot be given in analytic form, though the thickness of the space charge layer is still on the order of the Debye length (see Fig. 5.2-61). Values of the intrinsic Debye length for various semiconductors are given in Table 5.2-25. Figures 5.2-62 and 5.2-63 give $L_D$ as a function of the carrier density and bulk resistivity for various semiconductors.

- $Q_{sc}$ is the space charge density (per unit area), $Q_{ss}$ is the charge density (per unit area) in surface states, and

$$Q_{total} = Q_{sc} + Q_{ss}\,; \qquad (2.3)$$

$Q_{total} = 0$ in the absence of an external electric field. In the presence of an external field, $Q_{total}$ is the charge density on the field electrode (the gate in a MOSFET).

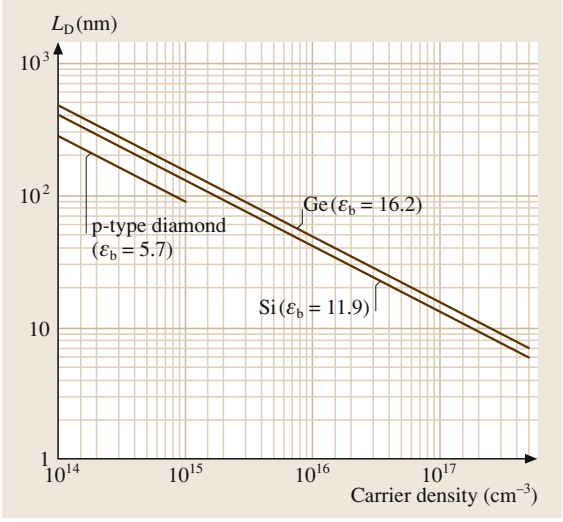


**Fig. 5.2-62** Debye length as a function of carrier concentration for Si, Ge and p-type diamond

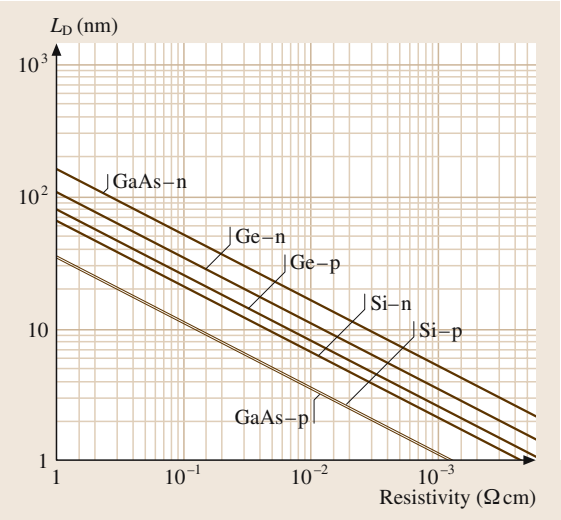


**Fig. 5.2-63** Debye length as a function of resistivity for n-type and p-type Si, Ge, GaAs

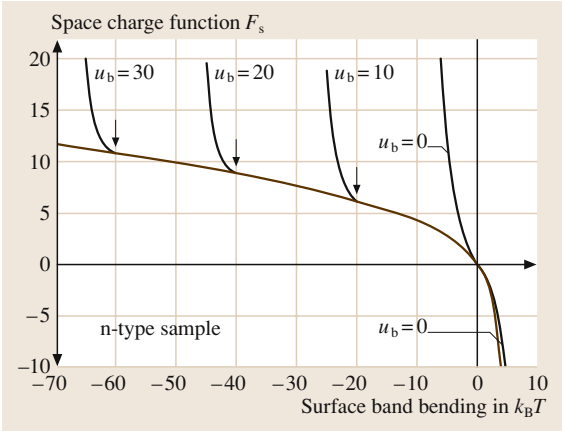


**Fig. 5.2-64** The space charge function $F_s(v_s, u_b)$ for n-type semiconductors ($u_b > 0$) plotted versus band bending $v_s k_B T$. The function for p-type semiconductors ($u_b < 0$) may be obtained from the relation: $F(u_b, -v_s) = F(-u_b, v_s)$ [2.47, p. 25]

### 5.2.5.2 Useful Formulas and Numerical Values

The space charge density and surface potential can be obtained by solving Poisson's equation for the one-dimensional problem at the surface [2.93, 94]. For nondegenerate conditions, one obtains

$$Q_{sc} = \mp q(n_b + p_b) L_D F_s(u_b, v_s) \tag{2.4}$$

(minus sign if $v_s > 0$), where

$$F(u_b, v) = \sqrt{2}\left(\frac{\cosh(u_b + v)}{\cosh u_b} - v \tanh u_b - 1\right)^{1/2} . \tag{2.5}$$

The function $F_s$ is plotted in Fig. 5.2-64 as a function of $k_B T v_s$ for various values of $u_b > 0$.

To obtain values for $u_b < 0$, the following relation can be used:

$$F(u_b, -v) = F(-u_b, v) . \tag{2.6}$$

The profile of the potential barrier $v(z)$ can be obtained from

$$\frac{z}{L_D} = \int_{v_s}^{v} \frac{dv}{\mp F_s(u_b, v)} , \tag{2.7}$$

which can be solved numerically.

Figure 5.2-61 shows $v(z)$ as a function of $z/L_D$ for accumulation and depletion/inversion layers and various values of $u_b$. The profiles are plotted for $|v_s| = 20$. The behavior, however, has a universal character, since

$$\frac{z'}{L_D} - \frac{z' - z}{L_D} = \int_{v_s}^{v'} \frac{dv}{\mp F_s} + \int_{v'}^{v} \frac{dv}{\mp F_s} , \tag{2.8}$$

so that curves can be scaled for different values of $v_s$ simply by translating the origin.

The charge $Q_{ss}$ in the surface states can be calculated once their energy in the gap and their donor or acceptor character is known. (A surface state is called a *donor* if it is neutral when filled with electrons, and an *acceptor* if it is neutral when empty.)

For a discrete distribution of surface states of densities $N_i^d$ and $N_j^a$, where the superscripts "d" and "a" refer to donors and acceptors, respectively,

$$Q_{ss} = -q \sum_j N_j^a(E_j) f(E_j - E_F) + q \sum_i N_i^d(E_i)[1 - f(E_i - E_F)] , \tag{2.9}$$

where $f$ is the Fermi function. A similar expression holds for a continuous distribution of states. If we define a reduced surface state energy

$$u_j \equiv \frac{E_j - E_{is}}{k_B T} , \tag{2.10}$$

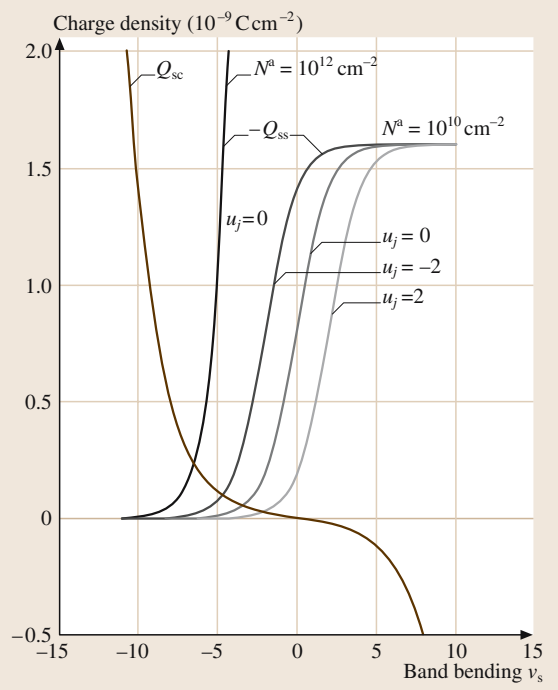


**Fig. 5.2-65** Sketch of the graphical solution of the equation $Q_{sc} + Q_{ss} = 0$, for an intrinsic semiconductor ($u_b = 0$) with a single acceptor surface level at reduced energy $u_j$. Two values of acceptor densities $N^a$ are shown. In case of $u_b \neq 0$, the curves $-Q_{ss}$ should be translated rigidly towards the new origin $v_s = -u_b$. When, on the other hand, $Q_{total} \neq 0$, the $Q_{ss}$ curves should be translated vertically by $Q_{total}$. The actual band bending is at the intersection of the two sets of curves

where $E_{is}$ is the intrinsic level at the surface, the Fermi function can be written as

$$f(E_j - E_F) = \frac{1}{e^{u_j - v_s - u_b} + 1} \,. \tag{2.11}$$

It is then possible to solve (2.1) numerically to obtain the band bending $v_s$. A graphical solution (valid in the absence of an external field) is sketched in Fig. 5.2-65 for an intrinsic semiconductor ($u_b = 0$) with a single surface acceptor level and various values of $u_j$ and $N_j^a$. For extrinsic semiconductors ($u_b \neq 0$) the procedure is similar, provided the origin is translated to $v_s = -u_b$ and the appropriate function for $Q_{sc}$ is chosen. The same procedure can also be used in the presence of an external field by translating the origin of the coordinates.

### 5.2.5.3 Surface Conductivity

The excess carrier densities, defined as

$$\Delta N = \int_0^\infty (n - n_b)\, dz \,, \tag{2.12}$$

excess electron density (per unit area) at the surface, and

$$\Delta P = \int_0^\infty (p - p_b)\, dz \,, \tag{2.13}$$

the excess hole density (per unit area) at the surface, can also be obtained from the function $F_s$:

- for majority carriers in accumulation layers:

$$\Delta N = n_b L_D G^+(u_b, v_s) \;\; (u_b > 0,\; v_s > 0) \,,$$
$$\Delta P = p_b L_D G^+(u_b, v_s) \;\; (u_b < 0,\; v_s < 0) \,;$$

- for majority carriers in depletion/inversion layers:

$$\Delta N = n_b L_D G^-(u_b, v_s) \;\; (u_b > 0,\; v_s < 0) \,,$$
$$\Delta P = p_b L_D G^-(u_b, v_s) \;\; (u_b < 0,\; v_s > 0) \,;$$

- for minority carriers in accumulation layers:

$$\Delta N = p_b L_D g^-(u_b, v_s) \;\; (u_b < 0,\; v_s < 0) \,,$$
$$\Delta P = n_b L_D g^-(u_b, v_s) \;\; (u_b > 0,\; v_s > 0) \,;$$

- for minority carriers in depletion/inversion layers:

$$\Delta N = p_b L_D g^+(u_b, v_s) \;\; (u_b < 0,\; v_s > 0) \,,$$
$$\Delta P = n_b L_D g^+(u_b, v_s) \;\; (u_b > 0,\; v_s < 0) \,.$$

The four functions $G^+$, $G^-$, $g^+$, $g^-$ are defined as

$$G^+ = \int_0^{|v_s|} \frac{e^v - 1}{F(|u_b|, v)}\, dv \,,$$
$$G^- = \int_0^{|v_s|} \frac{e^{-v} - 1}{F(-|u_b|, v)}\, dv \,, \tag{2.14}$$
$$g^+ = e^{-2|u_b|} \int_0^{|v_s|} \frac{e^v - 1}{F(-|u_b|, v)}\, dv \,,$$
$$g^- = e^{-2|u_b|} \int_0^{|v_s|} \frac{e^{-v} - 1}{F(|u_b|, v)}\, dv \,. \tag{2.15}$$

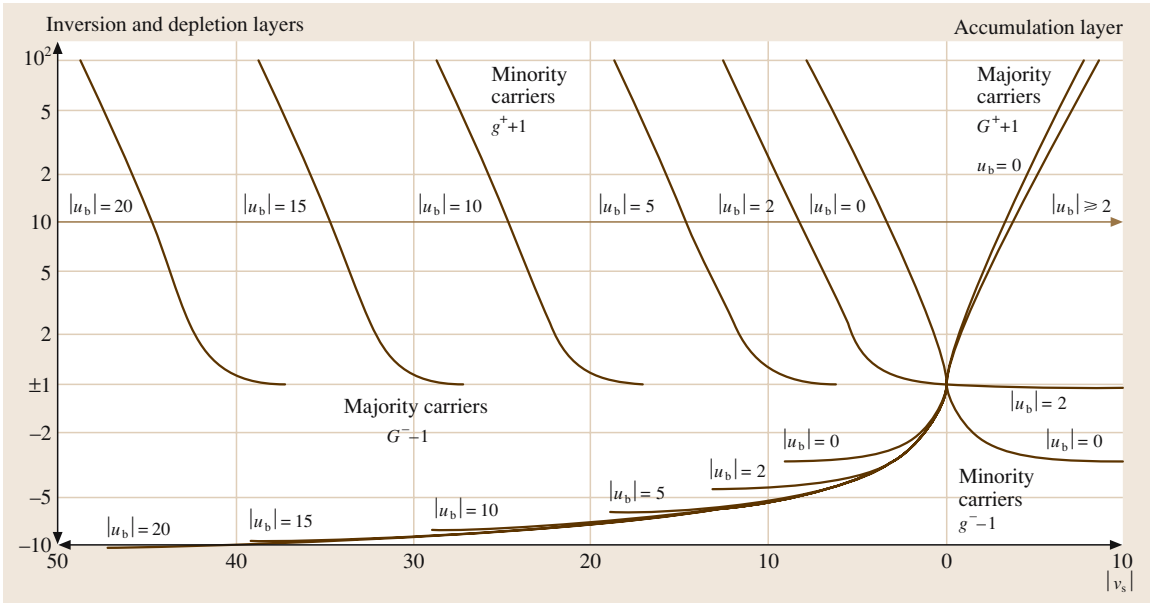


**Fig. 5.2-66** Dependence of the functions $G^+$, $G^-$, $g^+$, $g^-$ on $|v_s|$ for various values of $|u_b|$. The functions defined in (2.14), (2.15) can be used to obtain the excess carrier densities for majority and minority carriers in accumulation and depletion/inversion layers [2.93, p. 151]

**Table 5.2-26** Field-effect mobilities of semiconductors. References to original papers are given in [2.47]

| Semiconductor | Face | Reconstruction | Field-effect mobility ($cm^2\,V^{-1}\,s^{-1}$) |
|---|---|---|---|
| Si | (111) | 2×1 | −(1 ± 0.5) |
| | | 7×7 (?) [1] | −(0.01 ± 0.003) |
| Ge | (111) | 2×1 | −(100 ± 50) |
| | | c(2×8) | −(200 ± 50) |

[1] Surface prepared in situ by IBA

The superscripts of the functions indicate the signs of the respective integrals. The above functions are plotted in Fig. 5.2-66 as a function of $|v_s|$ and, in greater detail, in Fig. 5.2-67 for an inversion layer (as in a MOSFET). Tabulations are given in [2.94].

The surface excess conductivity is defined as

$$\Delta\sigma = q(\mu_{ns}\,\Delta N + \mu_{ps}\,\Delta P)\,, \qquad (2.16)$$

where $\Delta N$ and $\Delta P$ are given above. The surface mobilities $\mu_{ns}$ and $\mu_{ps}$ are in general different from the mobilities in the bulk, because of excess scattering at the surface.

The surface field-effect mobility can be defined as

$$\mu_{fe}(u_b, v_s) = \frac{d\Delta\sigma}{dQ_{total}}\,. \qquad (2.17)$$

The presence of surface states, which may capture the carriers, decreases the surface field-effect mobility. Values of $\mu_{fe}$ for some surfaces are presented in Table 5.2-26.

The very low field effect mobilities reported in Table 5.2-26, show that the Fermi level is pinned in the gap because of the large concentration of surface states. Pinning positions of the Fermi level with respect to the top of the valence band at the surface are given in Table 5.2-27 for various semiconductors.

In a MOSFET, the surface conductance of the inversion layer channel between the source and the drain (Fig. 5.2-68) is controlled by the gate potential. The above formulas for the surface conductivity are applicable to MOSFETs under equilibrium conditions (low frequency and low voltage). Here the interface states play the role of surface states at the free surface. The density of interface states should be kept to a minimum for optimal performance. Figure 5.2-69 shows the den-

| Crystal | Face | Reconstruction | $E_F - E_{VS}$ (eV) |
|---|---|---|---|
| Diamond | (111) | 2×1 | 1.5 |
| Si | (100) | 2×1 | 0.32 (1) |
| | (111) | 2×1 | 0.38 (2) |
| | | 7×7 | 0.69 (3) |
| Ge | (111) | 2×1 | 0.01 (2) |
| | | c(2×8) | 0.12 (2) |
| GaAs | (100) | c(2×8) | 0.47 (7) |
| | | c(4×4) | 0.47 (7) |
| | | 4×6 | 0.49 |
| | (110) | 1×1 | Flat bands |
| GaSb | (110) | 1×1 | Flat bands |
| GaP | (110) | 1×1 | Flat bands |
| InAs | (110) | 1×1 | Flat bands |

**Table 5.2-27** Pinning position of the Fermi level at semiconductor surfaces. Data are average values from various authors. Errors are given as standard deviations. References to the original papers and individual errors are given in [2.47]

sity of interface states in the gap of Si for two different orientations.

Channel mobilities are generally lower than bulk mobilities. An example is reported for n- and p-type carriers at the silicon–silicon oxide interface in Fig. 5.2-70.

A more extended discussion of the space charge layer may be found in [2.47, 48, 93, 94].

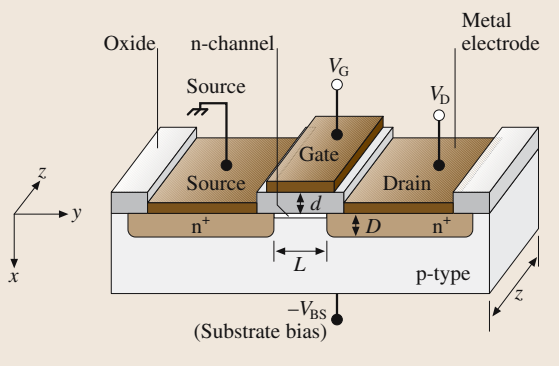


**Fig. 5.2-68** Schematic drawing of a MOSFET. The n-inversion layer is obtained with a positive bias of the gate with respect to the source [2.48, p. 345]

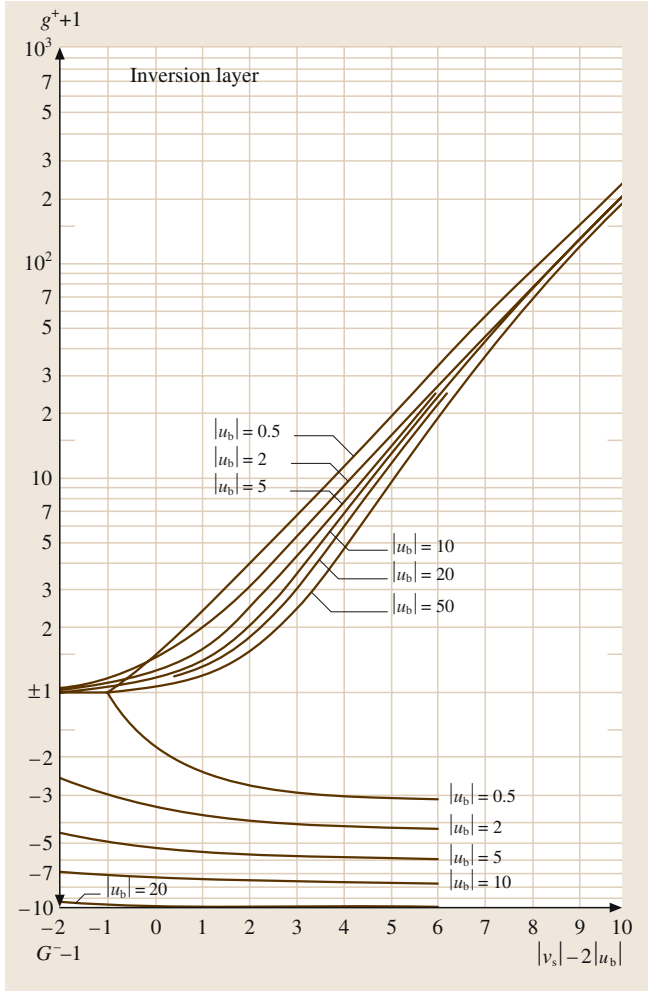


**Fig. 5.2-67** More detailed plots of the functions $G^-$, $g^+$ for inversion layers. Notice the change of the abscissa to $|v_s| - 2|u_b|$ [2.93, p. 155]

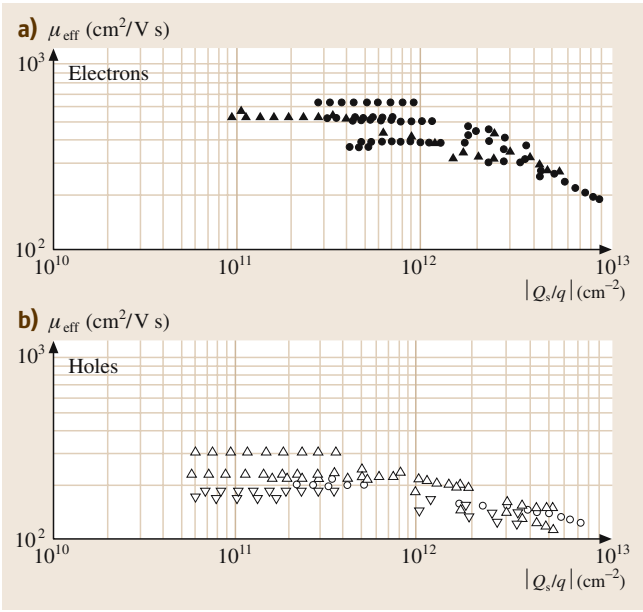


**Fig. 5.2-70** Effective mobility of electrons and holes in MOSFET's inversion channel. $Q_s = Q_{total}$ is the charge on the gate electrode. It is seen that mobility decreases at high transverse electric fields. For comparison, bulk mobilities are: $\mu_n = 1600$, $\mu_p = 600\,cm^2/V\,s$ [2.96]

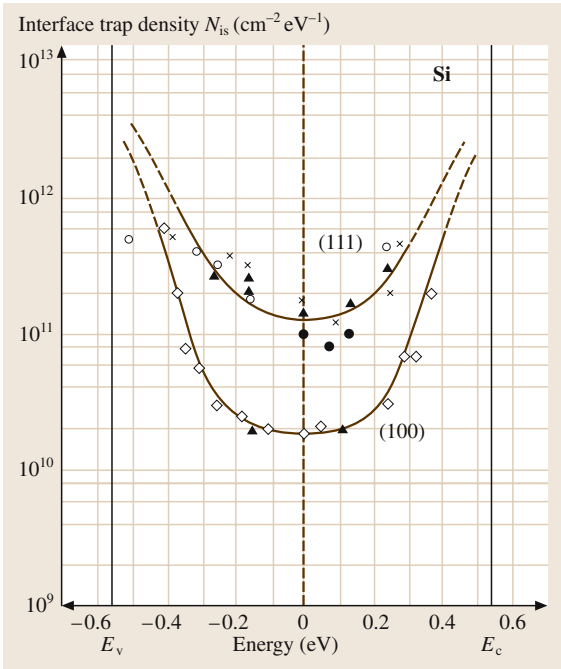


**Fig. 5.2-69** Interface state density in thermally oxidized silicon for two different orientations. Notice the low density around mid-gap [2.95, after [2.48] p. 340]

## 5.2.6 Most Frequently Used Acronyms

Surface physics, like many other fields, is plagued by the use of acronyms. The acronyms used in this chapter, as well as those most frequently found in the literature, are listed below:

| | |
|---|---|
| AES | Auger electron spectroscopy |
| AFM | atomic force microscope/microscopy |
| APS | appearance potential spectroscopy |
| ARUPS | angle-resolved ultraviolet photoemission spectroscopy |
| ARXPS | angle-resolved X-ray photoemission spectroscopy |
| ATR | attenuated total reflection |
| BB | back bond |
| BBZ | bulk Brillouin zone |
| BEP | beam-equivalent pressure |
| bl | blocking |
| BZ | Brillouin zone |
| CB | conduction band |
| CBM | conduction band minimum |
| CCV | core–core valence Auger transition |
| chan | channeling |
| CISS | collision ion scattering spectroscopy |

| | |
|---|---|
| CITS | current imaging tunneling spectroscopy |
| CMA | cylindrical mirror analyzer |
| CVD | chemical vapor deposition |
| CVV | core valence–valence Auger transition |
| DAS | dimer–adatom–stacking fault |
| DB | dangling bond |
| 2D BZ | 2-dimensional Brillouin zone |
| DOS | density of states |
| DR | differential reflectivity |
| ECS | electron capture spectroscopy |
| EDC | energy distribution curve |
| EELS | electron-energy loss spectroscopy |
| ELEED | elastic low-energy electron diffraction |
| ESA | electrostatic analyzer |
| ESD | electron-stimulated desorption |
| EXAFS | extended X-ray absorption fine structure |
| FEED | field emission energy distribution |
| FEM | field emission microscope/microscopy |
| FIM | field ion microscope/microscopy |
| FLAPW | full-potential linearized augmented plane wave |
| HAS | helium atom scattering |
| HATOF | helium atom time-of-flight spectroscopy |
| HEED | high-energy electron diffraction |
| HEIS | high-energy ion scattering/high-energy ion scattering spectroscopy |
| HREELS | high-resolution electron energy loss spectroscopy |
| HR-LEED | high-resolution LEED |
| HR-RHEED | high-resolution RHEED |
| IB | ion bombardment |
| IBA | ion bombardment and annealing |
| ICISS | impact ion scattering spectroscopy |
| IPE | inverse photoemission |
| IPES | inverse photoemission spectroscopy |
| IS | image state |
| ISS | ion scattering spectroscopy |
| JDOS | joint density of states |
| KRIPES | K-resolved inverse photoelectron spectroscopy |
| LAPW | linearized augmented-plane-wave method |
| LDA | local-density approximation |
| LDOS | local density of states |
| LEED | low-energy electron diffraction |
| LEED-I/V | LEED intensity/voltage measurements |
| LEIS | low-energy ion scattering/low-energy ion scattering spectroscopy |
| LEPD | low-energy positron diffraction |
| MBE | molecular-beam epitaxy |

| | |
|---|---|
| MD | molecular dynamics |
| MEED | medium-energy electron diffraction |
| MEIS | medium-energy ion scattering/medium-energy ion scattering spectroscopy |
| ML | monolayer |
| MOKE | magneto-optical Kerr effect |
| MR | missing row |
| NICISS | neutral impact collision ion scattering spectroscopy |
| PBBS | projected bulk band structure |
| PDS | photothermal displacement spectroscopy |
| PED | photoelectron diffraction |
| PES | photoemission spectroscopy, photoelectron spectroscopy |
| PLAP | pulsed laser atom probe |
| 2P-PES | 2-photon photoemission spectroscopy |
| RAS | reflectance anisotropy spectroscopy |
| REM | reflection electron microscope/microscopy |
| RHEED | reflection high-energy electron diffraction |
| RPA | random-phase approximation |
| SAM | scanning Auger microscope/microscopy |
| SARS | scattering and recoiling ion spectroscopy |
| SBZ | surface Brillouin zone |
| SCLS | surface core level shift |
| SDR | surface differential reflectivity |
| SEM | scanning electron microscope |
| sh | shadowing |
| SHG | second-harmonic generation |
| SIMS | secondary-ion mass spectroscopy |
| SPARPES | spin-polarized angle-resolved photoemission spectroscopy |
| SPIPES | spin-polarized inverse photoemission spectroscopy |
| SPLEED | spin-polarized LEED |
| SPV | surface photovoltage spectroscopy |
| SS | surface state |
| STM | scanning tunneling microscope/microscopy |
| STS | scanning tunneling spectroscopy |
| SXRD | surface X-ray diffraction |
| TEM | transmission electron microscope/microscopy |
| TOF | time of flight |
| TOM | torsion oscillation magnetometry |
| TRS | truncation rod scattering |
| UHV | ultra-high vacuum |
| UPS | ultraviolet photoemission spectroscopy |
| VB | valence band |
| VBM | valence band maximum |
| VLEED | very low-energy electron diffraction |
| XPS | X-ray photoemission spectroscopy |

## References


2.1 G. Chiarotti (Ed.): *The Physics of Solid Surfaces*, Landolt–Börnstein, New Series III/24 (Springer, Berlin, Heidelberg 1993 – 1996)

2.2 J. F. Nicholas: *The Structure of Ideal Surfaces*, Landolt–Börnstein, New Series III/24, ed. by G. Chiarotti (Springer, Berlin, Heidelberg 1993) p. 29

2.3 A. Fasolino, A. Selloni, A. Shkrebtii: *Surface Reconstruction and Relaxation*, Landolt–Börnstein, New Series III/24, ed. by G. Chiarotti (Springer, Berlin, Heidelberg 1993) p. 125

2.4 E. Zanazzi: *Elastic Scattering and Diffraction of Electrons and Positrons*, Landolt–Börnstein, New Series III/24, ed. by G. Chiarotti (Springer, Berlin, Heidelberg 1995) p. 29

2.5 R. Colella: *X-ray Diffraction of Surface Structures*, Landolt–Börnstein, New Series III/24, ed. by G. Chiarotti (Springer, Berlin, Heidelberg 1996) p. 312

2.6 P. Alkemade: *Elastic and Inelastic Scattering of Ions*, Landolt–Börnstein, New Series III/24, ed. by G. Chiarotti (Springer, Berlin, Heidelberg 1995) p. 176

2.7 R. J. Hamers, R. M. Tromp, J. E. Demuth: Phys. Rev. Lett. **56**, 1972 (1986)

2.8 P. Chiaradia: *Optical Properties of Surfaces*, Landolt–Börnstein, New Series III/24, ed. by G. Chiarotti (Springer, Berlin, Heidelberg 1996) p. 29

2.9 K. Jacobi: *Electronic Structure of Surfaces: Metals*, Landolt–Börnstein, New Series III/24, ed. by G. Chiarotti (Springer, Berlin, Heidelberg 1994) p. 29

2.10 C. Calandra, F. Manghi: *Electronic Structure of Surfaces: Semiconductors*, Landolt–Börnstein, New Series III/24, ed. by G. Chiarotti (Springer, Berlin, Heidelberg 1994) p. 352

2.11 A. M. Bradshaw, R. Hemmen, D. E. Ricken, T. Schedel-Niedrig: *Photoemission and Inverse Photoemission*, Landolt–Börnstein, New Series III/24, ed. by G. Chiarotti (Springer, Berlin, Heidelberg 1996) p. 70

2.12 M. Rocca: *Inelastic Scattering of Electrons*, Landolt–Börnstein, New Series III/24, ed. by G. Chiarotti (Springer, Berlin, Heidelberg 1995) p. 113

2.13 U. Gradmann: *Magnetic Properties of Single Crystal Surfaces*, Landolt–Börnstein, New Series III/24, ed. by G. Chiarotti (Springer, Berlin, Heidelberg 1994) p. 506

2.14 R. F. Wallis, S. Y. Tong: *Surface Phonons*, Landolt–Börnstein, New Series III/24, ed. by G. Chiarotti (Springer, Berlin, Heidelberg 1994) p. 433

2.15 V. Celli: *Interaction of Atoms with Surfaces*, Landolt–Börnstein, New Series III/24, ed. by G. Chiarotti (Springer, Berlin, Heidelberg 1995) p. 278

2.16 G. L. Kellog: *Field Emission, Field Ionization and Field Desorption*, Landolt–Börnstein, New Series III/24, ed. by G. Chiarotti (Springer, Berlin, Heidelberg 1996) p. 342

2.17 W. A. Wood: J. Appl. Phys. **35**, 1306 (1963)

2.18 J. V. Barth, H. Brune, G. Ertl, R. J. Behm: Phys. Rev. B **42**, 9307 (1990)

2.19 M. K. Debe, D. A. King: Phys. Rev. Lett. **39**, 708 (1977)

2.20 R. M. Tromp, R. J. Hamers, J. E. Demuth: Phys. Rev. Lett. **55**, 1303 (1985)

2.21 K. C. Pandey: Phys. Rev. Lett. **47**, 1913 (1981)

2.22 R. M. Feenstra, W. A. Thompson, A. P. Fein: Phys. Rev. Lett. **56**, 608 (1986)

2.23 K. Takayanagi, Y. Tanishiro, M. Takahashi, S. Takahashi: J. Vac. Sci. Technol. A **3**, 1502 (1985)

2.24 H. Huang, S. Y. Tong, W. E. Packard, M. B. Webb: Phys. Lett. A **130**, 166 (1988)

2.25 S. Y. Tong, H. Huang, C. M. Wei, W. E. Packard, F. K. Men, G. Glander, M. B. Webb: J. Vac. Sci. Technol. A **6**, 615 (1988)

2.26 I. K. Robinson, W. K. Waskiewics, P. H. Fuoss, L. J. Norton: Phys. Rev. B **37**, 4325 (1988)

2.27 R. J. Hamers: *Scanning Tunneling Microscopy*, Landolt–Börnstein, New Series III/24, ed. by G. Chiarotti (Springer, Berlin, Heidelberg 1996) p. 363

2.28 W. S. Yang, F. Jona: Phys. Rev. B **29**, 899 (1984)

2.29 N. D. Lang, W. Kohn: Phys. Rev. B **1**, 4555 (1970)

2.30 H. Eckardt, L. Fritsche: J. Phys. F **14**, 97 (1984)

2.31 N. Garcia, B. Reihl, K. H. Frank, A. R. Williams: Phys. Rev. Lett. **54**, 591 (1985)

2.32 M. Echenique, J. B. Pendry: Progr. Surf. Sci. **32**, 111 (1990)

2.33 A. Goldmann, V. Dose, G. Borstel: Phys. Rev. B **32**, 1971 (1985)

2.34 D. M. Kolb, W. Boeck, K.-M. Ho, S. H. Liu: Phys. Rev. Lett. **47**, 1921 (1981)

2.35 B. Reihl, K. H. Frank, R. R. Schlittler: Phys. Rev. B **30**, 7328 (1984)

2.36 S. D. Kevan, R. H. Gaylord: Phys. Rev. B **36**, 5809 (1987)

2.37 K. M. Ho, C. L. Liu, D. M. Kolb, G. Piazza: J. Electroanal. Chem. **150**, 235 (1983)

2.38 K. M. Ho, B. N. Harmon, S. H. Liu: Phys. Rev. Lett. **44**, 1531 (1980)

2.39 S. H. Liu, C. Hinnen, C. Nguyen Van Huong, N. R. De Tacconi, K. M. Ho: J. Electroanal. Chem. **176**, 325 (1984)

2.40 R. A. Bartynski, T. Gustafsson: Phys. Rev. B **33**, 6588 (1986)

2.41 P. Heimann, H. Miosga, H. Neddermeyer: Phys. Rev. Lett. **42**, 801 (1979)

2.42 S. G. Louie: Phys. Rev. Lett. **40**, 1525 (1978)

2.43 P. D. Johnson, N. V. Smith: Phys. Rev. Lett. **49**, 290 (1982)

2.44 M. I. Holmes, T. Gustafsson: Phys. Rev. Lett. **47**, 443 (1981)

2.45 M. Posternak, H. Krakauer, A. J. Freeman, D. D. Koelling: Phys. Rev. B **21**, 5601 (1980)

2.46 K. D. Tsuei, E. W. Plummer, A. Liebsch, E. Pehlke, K. Kempa, P. Bakshi: Surf. Sci. **247**, 302 (1991)

2.47 W. Mönch: *Semiconductor Surfaces and Interfaces* (Springer, Berlin, Heidelberg 1995)
2.48 H. Lüth: *Surfaces and Interfaces of Solid Materials* (Springer, Berlin, Heidelberg 1995)
2.49 F. Manghi, C. M. Bertoni, C. Calandra, E. Molinari: Phys. Rev. B **24**, 6029 (1981)
2.50 J. A. Stroscio, R. M. Feenstra, D. M. Newns, A. P. Fein: J. Vac. Sci. Technol. A **6**, 499 (1988)
2.51 V. Vanderbilt, S. G. Louie: Phys. Rev. B **30**, 6118 (1984)
2.52 F. J. Himpsel, D. E. Eastman, P. Heimann, J. F. van der Veen: Phys. Rev. B **24**, 7270 (1981)
2.53 P. Kruger, A. Mazur, G. Wolfgarten: Phys. Rev. Lett. **57**, 1468 (1986)
2.54 P. Koke, A. Goldmann, W. Monch, G. Wolfgarten, J. Polmann: Surf. Sci. **152/153**, 1001 (1985)
2.55 A. Goldmann, P. Koke, W. Monch, G. Wolfgarten, J. Polmann: Surf. Sci. **169**, 438 (1986)
2.56 J. E. Northrup, M. L. Cohen: Phys. Rev. Lett. **49**, 1349 (1982)
2.57 P. Martensson, A. Cricenti, G. V. Hansson: Phys. Rev. B **32**, 6959 (1985)
2.58 F. J. Himpsel, T. Fauster: J. Vac. Sci. Technol. A **2**, 815 (1984)
2.59 R. Wolkov, P. Avouris: Phys. Rev. Lett. **60**, 1049 (1988)
2.60 J. M. Nicholls, B. Reihl: Surf. Sci. **218**, 237 (1989)
2.61 J. M. Nicholls, P. Martensson, G. V. Hansson: Phys. Rev. Lett. **54**, 2363 (1985)
2.62 J. E. Northrup, M. L. Cohen: Phys. Rev. B **27**, 6553 (1983)
2.63 D. Straub, M. Skibowski, F. J. Himpsel: Phys. Rev. B **32**, 5237 (1985)
2.64 B. Reihl, T. Riesterer, M. Tschudy, P. Perfetti: Phys. Rev. B **38**, 13456 (1988)
2.65 J. Henk, W. Shattke, H. P. Hanneschеidt, C. Janowitz, R. Manzke, M. Skibowski: Phys. Rev. B **39**, 13286 (1989)
2.66 A. Huijser, J. van Laar, T. L. van Roy: Phys. Lett. A **65**, 337 (1978)
2.67 Zhu, S. B. Zhang, S. G. Louie, M. L. Cohen: Phys. Rev. Lett. **63**, 2112 (1989)
2.68 K. O. Magnusson, S. A. Flodstrom, P. E. S. Persson: Phys. Rev. B **38**, 5384 (1988)
2.69 Y. R. Wang, C. B. Duke, K. O. Magnusson, S. A. Flodström: Surf. Sci., **205**, 2760 (1988)
2.70 S. Selci, P. Chiaradia, F. Ciccacci, A. Cricenti, N. Sparvieri, G. Chiarotti: Phys. Rev. B **31**, 4096 (1985)
2.71 N. J. DiNardo, J. E. Demuth, W. A. Thompson, P. Avouris: Phys. Rev. B **31**, 4077 (1985)
2.72 G. Chiarotti, P. Chiaradia, E. Faiella, C. Goletti: Surf. Sci. **453**, 112 (2000)
2.73 J. E. Demuth, R. Imbihl, W. A. Thompson: Phys. Rev. B **34**, 1330 (1986)
2.74 G. Chiarotti, S. Nannarone, R. Pastore, P. Chiaradia: Phys. Rev. B **4**, 3398 (1971)
2.75 H. Froitzheim, H. Ibach, D. L. Mills: Phys. Rev. B **11**, 4980 (1975)
2.76 M. K. Kelly, S. Zollner, M. Cardona: Surf. Sci. **285**, 282 (1993)
2.77 T. F. Heinz, M. M. T. Loy, W. A. Thompson: Phys. Rev. Lett. **54**, 63 (1985)
2.78 I. Kamiya, D. E. Aspness, L. J. Florez, J. P. Harbison: Phys. Rev. B **46**, 15894 (1992)
2.79 M. Taborelli, O. Paul, O. Zuger, M. Landolt: J. Phys. (Paris) Colloq. **8**, 1659 (1988)
2.80 P. Moretto, M. Rocca, U. Valbusa, J. E. Black: Phys. Rev. B **41**, 12905 (1990)
2.81 G. Bracco, R. Tatarek, F. Tommasini, U. Linke, M. Persson: Phys. Rev. B **36**, 2928 (1987)
2.82 U. Harten, J. P. Toennies, Ch. Woll: Faraday Discuss. Chem. Soc. **80**, 137 (1985)
2.83 J. P. Toennies, C. Wöll: Phys. Rev. B **36**, 4475 (1987)
2.84 B. Voigtlander, S. Lehwald, H. Ibach, K. P. Bohnen, K. M. Ho: Phys. Rev. B **40**, 8068 (1989)
2.85 M. Wuttig, R. Franchy, H. Ibach: Z. Phys. B **65**, 71 (1986)
2.86 M. Rocca, S. Lehwald, H. Ibach, T. S. Rahman: Surf. Sci. **171**, 632 (1986)
2.87 U. Harten, J. P. Toennies: Europhys. Lett. **4**(7), 833 (1987)
2.88 A. Safron, W. P. Brug, G. Chern, J. Duan, J. G. Skofronick: J. Vac. Sci. Technol. A **8**, 2627 (1990)
2.89 G. Benedek, G. Brusdeylins, R. B. Doak, J. G. Skofronick, J. P. Toennies: Phys. Rev. B **28**, 2104 (1983)
2.90 U. Harten, J. P. Toennies, C. Woll: Phys. Rev. Lett. **57**, 2947 (1986)
2.91 H. Ibach: Phys. Rev. Lett. **27**, 253 (1971)
2.92 D. Eichenauer, U. Harten, J. P. Toennies, V. Celli: J. Chem. Phys. **86**, 3693 (1987)
2.93 A. Many, Y. Goldstein, N. B. Grove: *Semiconductor Surfaces* (North-Holland, Amsterdam 1965)
2.94 D. R. Frankl: *Electrical Properties of Semiconductor Surfaces* (Pergamon, Oxford 1967)
2.95 M. H. White, J. R. Cricchi: IEEE Trans. Electron Dev. **19**, 1280 (1972)
2.96 O. Leistiko, A. S. Grove, C. T. Sah: IEEE Trans. Electron Dev. **12**, 248 (1965)

# 5.3. Mesoscopic and Nanostructured Materials

This chapter addresses the properties of nanostructured materials considered as statistical ensembles of nanostructures. Emphasis is put on size and confinement effects, although enhancements in surface and interface properties are mentioned. After a survey and a summary of basic definitions and concepts in the introductory Sect. 5.3.1, the properties associated with electronic confinement are addressed in Sect. 5.3.2. Electronic confinement affects the spectral properties, i. e. light absorption and luminescence, mainly through quantum size effects, and the electrical conduction properties through the Coulomb blockade. Both two-dimensional systems (quantum wells) and zero-dimensional systems (quantum dots) are reviewed. Particular attention is drawn to semiconductor-doped matrices. The effects associated with confinement of electromagnetic fields are treated in Sect. 5.3.3. Numerical relationships and data for plasmon excitations of various metal nanoparticles can be found in this section. Magnetic nanostructures are addressed in Sect. 5.3.4. The two main applications of nanostructured magnetic materials, namely spin electronics, or spintronics, and ultrahigh-density data storage media, are treated. Finally, we list and briefly describe in Sect. 5.3.5 some generic techniques for the preparation of nanostructured materials, organized into the following groups of methods: molecular-beam epitaxy (MBE), metal-organic chemical vapor deposition (MOCVD), nanolithography, nanocrystal growth in matrices, and ex-situ synthesis of clusters.

5.3.1 **Introduction and Survey** ..... 1031
5.3.1.1 Historical Review ..... 1031
5.3.1.2 Definitions ..... 1032
5.3.1.3 Specific Properties ..... 1034
5.3.1.4 Organization of this Chapter ..... 1034

5.3.2 **Electronic Structure and Spectroscopy** ... 1035
5.3.2.1 Electronic Quantum Size Effects . 1035
5.3.2.2 Breakdown of the Momentum Conservation Rule ..... 1036
5.3.2.3 Excitons in Quantum-Confined Systems .. 1036
5.3.2.4 Vibrational Modes and Electron–Phonon Coupling . 1040
5.3.2.5 Electron Transport Phenomena . 1042

5.3.3 **Electromagnetic Confinement** ..... 1044
5.3.3.1 Nanoparticle-Doped Materials .. 1044
5.3.3.2 Periodic Electromagnetic Lattices ..... 1048

5.3.4 **Magnetic Nanostructures** ..... 1048
5.3.4.1 Spin Electronics ..... 1049
5.3.4.2 Ultrahigh-Density Storage Media in Hard Disk Drives ..... 1060

5.3.5 **Preparation Techniques** ..... 1063
5.3.5.1 Molecular-Beam Epitaxy ..... 1063
5.3.5.2 Metal-Organic Chemical Vapor Deposition (MOCVD) ..... 1064
5.3.5.3 Lithography ..... 1064
5.3.5.4 Nanocrystals in Matrices ..... 1064
5.3.5.5 Ex Situ Synthesis of Clusters ..... 1065

**References** ..... 1066



## 5.3.1 Introduction and Survey

### 5.3.1.1 Historical Review

Except in the life sciences, there are only a few examples of materials that are naturally structured on scales of the order of a few to a few hundred nanometers. One can cite, however, the natural zeolites, which constitute a group of hydrated crystalline aluminosilicates containing regularly shaped pores with sizes from 1 nm to several nanometers. This provides them the ability to reversibly adsorb and desorb specific molecules.

They were named "zeolite" ("boiling stone") in 1756 by Cronstedt, a Swedish mineralogist, who observed their emission of water vapor when heated. At the other size limit, opals constitute another example of a naturally occurring nanostructured material. These gems are made up mainly of spheres of amorphous silica with sizes ranging from 150 nm to 300 nm. In precious opals, these spheres are of approximately equal size and can thus be arranged in a three-dimensional periodic lattice. The optical interferences produced by this periodic index modulation are the origin of the characteristic iridescent colors (opalescence).

Apart from these few examples, most nanostructured materials are synthetic. Empirical methods for the manufacture of stained glasses have been known for centuries. It is now well established that these methods make use of the diffusion-controlled growth of metal nanoparticles. The geometrical constraints on the electron motion and the electromagnetic field distribution in noble-metal nanoparticles lead to the existence of a particular collective oscillation mode, called the plasmon oscillation, which is responsible for the coloration of the material. It has been noticed recently that the beautiful tone of Maya blue, a paint often used in Mesoamerica, involves simultaneously metal nanoparticles and a superlattice organization [3.1].

The chemistry and color changes of colloidal gold solutions were observed by Faraday during the 19th century [3.2]. These properties were due to highly size-dispersed gold nanoparticles.

Improvements in the diffusion-controlled growth technique opened up the possibility of growing nanocrystallites with better-controlled sizes and densities and permitted its extension to various semiconductors. The fabrication of colored long-wavelength-pass glasses and of photochromic glasses provides well-known examples of commercial technologies based on such methods developed decades ago. Various techniques for the production and assembly of cluster- and nanoparticle-based materials are currently under intense study.

More recently, important technological efforts have been made, driven by the increasing needs of the electronics industry, in order to understand and control the growth of semiconductors at the atomic level. The development of molecular-beam epitaxy (MBE) permitted the control of atomic-layer-by-atomic-layer growth of semiconductors. It has become possible to create structures made up of an alternation of different layers, each of which is only a few atomic layers thick. The first observation of the quantization of energy levels in a quantum well in 1974 [3.3] opened the way to the tailoring of the electronic wave function in one dimension on the nanometer scale, leading to the production of new electronic and also magnetic materials. A new trend in surface science is work aimed at the control of in-plane nanostructuring, such as the formation of wire or dot shapes, through self-organization.

In parallel to developments in the field of electronics, nanostructured materials have been developed by materials scientists and chemists also. The concept of nanocrystalline structures emerged in the field of materials science, and polycrystals with ultrafine grain sizes in the nanometer range have been produced. These "nanophase materials" have been shown to have significant modifications of their mechanical properties compared with the coarse-grain equivalent materials. The huge surface area of nanoporous materials has attracted much attention for applications in chemistry such as molecular sieves, catalysis, and gas sensing. This has motivated intense research aimed at the fabrication of materials with a well-controlled composition and nanoscale structure, such as synthetic zeolites.

The scientific and technological domains of research on nanostructured materials cover a range of disciplines, from biology to physics and chemistry. However, their convergent aspects, as well as, to some extent, a common type of approach, have been recognized recently in the realm of nanoscience and nanotechnology, under the term "nanostructured materials", or simply "nanomaterials".

For an extended review on nanotechnology see the recently published Handbook of Nanotechnology [3.4].

### 5.3.1.2 Definitions

In their broadest definition, nanostructured materials show structural features with sizes in the range from 1 nm to a few hundred nanometers in at least one dimension. This very general criterion actually includes very diverse physical situations.

First, as is apparent from the previous section, each nanostructured material is associated with a specific novel property or a significant improvement in a specific property resulting from the nanoscale structuring. As a consequence, the type of nanostructuring used must be based on a spatial dependence of some parameter related to the property under consideration. This parameter could be, for example, the material density, transport parameters, or the dielectric constant. Another consequence is that the upper size limit of the structural features varies depending on the property considered,

from a molecular size for molecular-sieve properties up to the wavelength of light for the optical properties.

Second, in addition to the nanometer-scale structuring, a larger-scale ordering of the unit patterns may be necessary for the existence of the property sought. For example, the particular optical properties of opals mentioned above require the silica nanospheres to show a long-range order with a coherence length well beyond a micron. The same considerations hold for quantum-well superlattices, for example. In other cases, the nanosized building blocks do not need long-range order to provide a specific property, but still require some degree of short-range organization. For example, an electrical conductivity appears only above a critical percolation density of conducting particles. Finally, some properties of nanostructured materials simply reflect a corresponding intrinsic property of their individual building blocks. This is the case, for instance, in nanoparticles embedded in glass or polymer matrices for optical-filtering applications.

Two main technological approaches may be defined:

- The top-down manufacturing paradigm consists in downscaling the patterning of materials to nanometer sizes. This allows the generation of materials which are coherently and continuously ordered from macroscopic down to nanoscopic sizes.
- The bottom-up paradigm is based on the atomically precise fabrication of entities of increasing size. It is the domain of macromolecular and supramolecular chemistry (dendrimers, engineered DNA, etc.) and of cluster and surface physics (epitaxy, self-assembly, etc.).

Mesoscopic materials form the subset of nanostructured materials for which the nanoscopic scale is large compared with the elementary constituents of the material, i. e. atoms, molecules, or the crystal lattice. For the specific property under consideration, these materials can be described in terms of continuous, homogeneous media on scales less than that of the nanostructure. The term "mesoscopic" is often reserved for electronic transport phenomena in systems structured on scales below the phase-coherence length $\Lambda_\Phi$ of the carriers.

Most of the common nanomaterials can be classified in terms of dimensionality, according to the number of orthogonal directions $X$, $Y$, $Z$ in which the structural patterns referred to above have dimensions $L_{X,Y,Z}$ smaller than the nanoscopic limit $L_0$. This leads to the classical definitions of dimensionality summarized in Table 5.3-1. However, it should be noted that experimental situations



**Table 5.3-1** Examples of reduced-dimensional material geometries, and definitions of their dimensionality and of the associated type of confinement

| | | | | |
|---|---|---|---|---|
| $L_{X,Y,Z} > L_0$ | No nanostructures | No confinement | Bulk material | 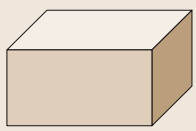 |
| $L_{X,Y} > L_0 > L_Z$ | Two-dimensional (2-D) nanostructures | One-dimensional (1-D) confinement | Wells | 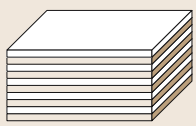 |
| $L_X > L_0 > L_{Y,Z}$ | One-dimensional (1-D) nanostructures | Two-dimensional (2-D) confinement | Wires | 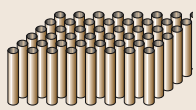 |
| $L_0 > L_{X,Y,Z}$ | Zero-dimensional (0-D) nanostructures | Three-dimensional (3-D) confinement | Dots | 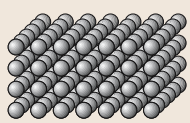 |

can be encountered in which the dimensionality may not be so obviously defined. For instance, the structural patterns may be formed by nonrectilinear wires which occupy a surface or a volume or may be branched.

The structure of the density of states (DOS) in nanostructures is strongly dependent on the dimensionality. A free 3-D motion yields a band characterized by three wave vectors $k_x, k_y, k_z$. The corresponding DOS depends smoothly on the energy $E$, as $(E - E^0)^{1/2}$, where $E^0$ is the energy of the bottom of the band. Confinement into a 2-D system splits the band into subbands, and leaves only two continuously varying wave vectors $k_x, k_y$ in each subband. The DOS for each subband is then constant above the energy $E_N^0$ of its bottom state. The overall DOS is discontinuous, with a stepwise structure that is characteristic of quantum wells (Fig. 5.3-1). Confinement in one additional dimension splits each 2-D subband further into a set of 1-D subbands. Each 1-D subband is characterized by only one continuously varying wave vector $k_x$, and two quantum numbers $N, M$. The DOS corresponding to the subband $N, M$ has a variation of the form $(E - E_{N,M}^0)^{-1/2}$, with a divergence at the bottom of the subband $E_{N,M}^0$. The DOS of a quantum wire thus has a more pronounced structure than does a 2-D well, with a larger number of subbands, each one starting as a peak (Fig. 5.3-1). Finally, confinement in all three dimensions creates a completely discrete, atom-like set of states. The DOS of a quantum dot thus consists of a series of $\delta$-functions (not represented in Fig. 5.3-1). The sharpening of the DOS at specific energies induced by quantum confinement is the origin of many improvements in the properties of nanostructured materials compared with bulk materials. This spectral concentration enhances all resonant effects and increases the energy selectivity. The preservation of these effects when one is dealing with an ensemble of quantum-confined systems requires a high homogeneity.

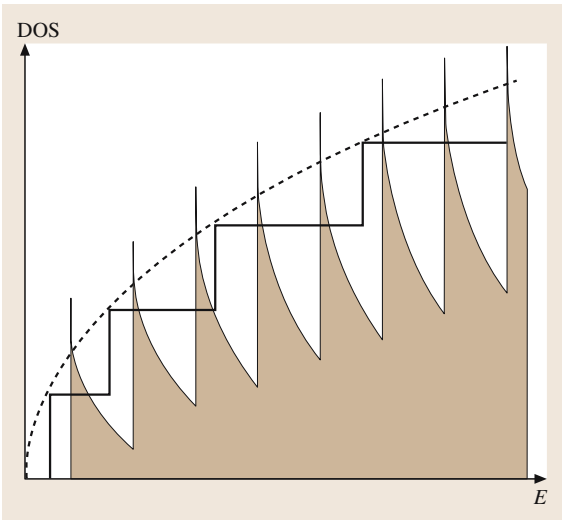


**Fig. 5.3-1** Schematic illustration of the density of states for 3-D motion of a free electron (*dashed line*), a 2-D quantum well (*solid line*), and a 1-D quantum wire (*shaded area*) as a function of energy

### 5.3.1.3 Specific Properties

The specific properties of nanostructured materials can have two different possible origins:

- Size effects, which result from the spatial confinement of a physical entity inside an element of the nanoscale structural pattern. Such an element is called a low-dimensional system. An example is the confinement of electron wave functions inside a region whose size is smaller than the electron mean free path. This class of effects may give birth to completely new properties.
- Boundary effects, which are a consequence of the significant volume fraction of matter located near surfaces, interfaces, or domain walls. Processes that take place only at such locations may be highly favored, and properties specific to structural boundaries may also be greatly enhanced.

For a recent comprehensive review of the basic principles of the origin of the properties of nanostructured materials, see [3.5].

### 5.3.1.4 Organization of this Chapter

Many classification schemes for nanostructured materials exist. These may be based on their chemical composition, on the technique for their manufacture, or on their dimensionality. These schemes, however, are often suitable only for a subset of materials. Moreover, they generally address only one particular scientific or technological approach and its associated community of specialists. Since, as noted above, most nanostructured materials are associated with a specific property, we have chosen a presentation based on properties. This scheme allows us to include all nanostructured materials and is accessible to the largest possible readership.

Consistently with the materials approach of this chapter and with its limited size, only the properties of statistical ensembles of nanostructures will be considered. The specific behaviors of individual nano-

sized objects or devices are not included. Since surface and interface properties are treated in another section, emphasis will be put here on size effects. Properties related to electronic confinement and its consequences for spectral properties are addressed in Sect. 5.3.2. Effects of the confinement of electromagnetic fields are treated in Sect. 5.3.3. Magnetic size effects are addressed in Sect. 5.3.4. Finally, we list and briefly describe in Sect. 5.3.5 some generic methods for preparation of nanostructured materials.

## 5.3.2 Electronic Structure and Spectroscopy

### 5.3.2.1 Electronic Quantum Size Effects

Confined electronic systems are quantum systems in which carriers, either electron or holes, are free to move only in a restricted number of dimensions. In the confined dimension, the sizes of the structural elements are of the order of a few de Broglie wavelengths of the carriers or less. Depending on their dimensionality, these structures can be quantum dots (0-D), quantum wires (1-D), or quantum wells (2-D). Quantum wells are typically produced by the alternate epitaxial growth of two or more different semiconductors. Quantum wires are less commonly encountered, since their fabrication procedures are much more complicated (Sect. 5.3.4).

One of the most dramatic effects, called the quantum size effect, consists in a redistribution of the energy spectrum of the system, the density of states becoming discrete along the confinement direction. In the most simple "particle in a box" model of a quantum well, the energies of the corresponding eigenstates are

$$E_{N,k_x,k_y} = N^2 \frac{\pi^2 \hbar^2}{2md^2} + \left(k_x^2 + k_y^2\right) \frac{\hbar^2}{2m} , \qquad (3.1)$$

where $m$ is the effective mass of the carrier, $d$ is the confinement dimension, and $N$ is a quantum number. The first term appears because of the quantized motion in the $z$ direction, whereas the second term represents the energy of the free $x, y$ motion, characterized by wave vectors $k_x, k_y$. Each value of $N$ defines a semi-infinite subband of energy levels. Although the "particle in a box" model is simplistic compared with real systems, this limiting case is often successful in describing the essential features of quantum size effects [3.6].

The importance of the quantum size effect is mainly determined by the energy differences $E_{N+1} - E_N$. Quantum size effects become observable when this separation exceeds the thermal energy of the carriers, so that adjacent subbands are differently populated. Since the energy difference $E_{N+1} - E_N$ increases with $N$, it could be anticipated that quantization effects would be more important for processes involving higher subbands. However, the practical observation of such effects in systems with a large Fermi energy ($E_F \gg E_1$), i. e. in metals, is often made difficult because of contributions from many levels and the appearance of collective phenomena such as plasmon oscillations, which wash out quantization effects. Most of the spectral data revealing quantum well states in metal films a few monolayers thick have been obtained by angle-resolved photoemission for Cs on Cu(111) [3.7] and for Ag on Au(111) [3.8]. The Fabry–Perot-like regularly-spaced spectrum of energy levels appears particularly clearly in a study of Ag films on Fe(100) for thicknesses up to more than 100 monolayers (Fig. 5.3-2). The superposition at half-integer coverages (27.5 and 42.5 monolayers) of two sets of peaks corresponding to the two closest integer thicknesses emphasizes the extreme sensitivity to surface homogeneity. Quantitatively, the characteristic roughness of well barriers must be much below the de Broglie wavelength of the quantum states observed. This is another reason why quantum size effects have been observed mainly in semiconductor nanostructures, which have large Fermi wavelengths, rather than in metals, which have Fermi wavelengths comparable to a few crystal lattice periods.

The existence of discrete electronic states of electrons confined in a small metal cluster has been observed to influence the thermodynamic stability of the system, in particular during the production of sodium clusters in supersonic beams composed of the metal vapor and an inert gas. The statistics of the relative abundances of different particle sizes reveal the existence of "magic numbers" for the number of atoms in the cluster, $N = 8, 20, 40, 58, 92, \ldots$ [3.9]. This has been interpreted in terms of the existence of degenerate energy levels in a spherical well with infinite-potential walls. Particularly stable structures are obtained when the number of valence electrons is such that it leads to a closed-shell electronic structure, i. e. a structure with a completely filled energy level and an empty up-

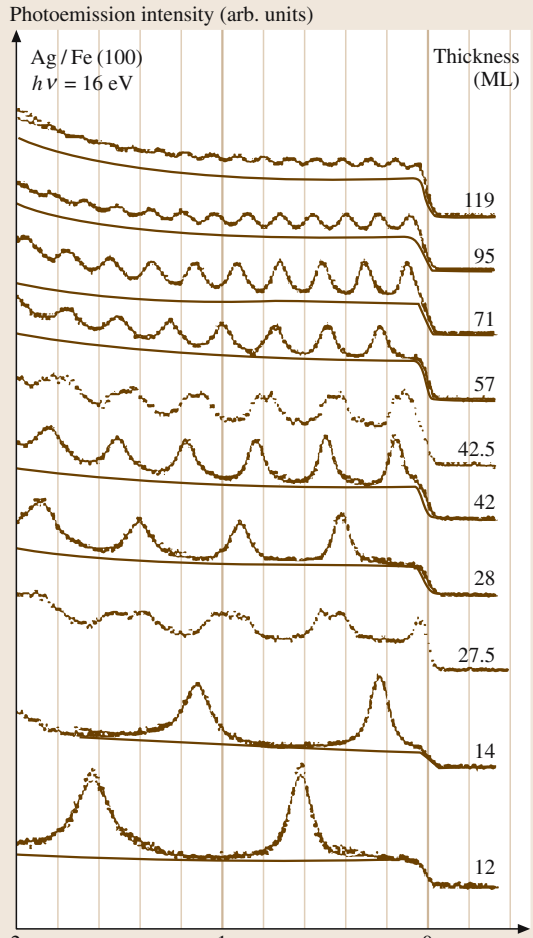


**Fig. 5.3-2** *Dots*: experimental normal photoemission spectra for Ag quantum wells deposited on Fe(100), with various thicknesses. *Solid curves*: fits and background functions. (After [3.12])

per level. The electronic shell structure induces similar size dependences in the work function and the electron density, through Friedel-like oscillations [3.10]. The series of "magic numbers" is discernible up to $N = 1430$. For larger particles, the relative abundance of different sizes is controlled instead by the stability and relative sizes of the various facets of the surface of the particle. It is noteworthy that 2-D quantum well states are also predicted to produce oscillatory variations of the energetics of a film as a function of thickness, with similar "magic numbers" for the number of deposited monolayers [3.11].

### 5.3.2.2 Breakdown of the Momentum Conservation Rule

As a result of the Heisenberg uncertainty principle, localization of carriers in a confinement volume spreads their wave functions in reciprocal space. The possible overlap in $k$ space of electron and hole wave functions breaks the rule of conservation of crystal momentum. In other words, the momentum needed for a transition at a different $k$ may be provided by scattering from the boundaries. This consequence of quantum confinement is particularly meaningful for nanostructures based on indirect-band-gap semiconductors, for which luminescence from recombination of the lowest-energy electrons and holes is forbidden in the bulk material, but becomes increasingly possible for systems of decreasing size, with a scaling law of $d^{-6}$ for dots [3.13]. The observation of bright luminescence from nanoporous silicon samples [3.14] was, from the start, interpreted in terms of quantum confinement into silicon nanowires [3.14, 15]. This observation triggered an important research activity motivated by the industrial prospect of being able to incorporate silicon photonic elements into the current silicon technology. Although it has been shown that other phenomena such as surface effects and phonon modes (discussed later) come into the play, and that more complicated geometries including both quantum dots and quantum wires have to be considered, the role of quantum confinement in the luminescence of porous silicon is generally considered to be central, at least for the "red" part of the luminescence. The studies of nanostructure-induced luminescence have been extended to porous GaP [3.16,17] and SiC [3.18], two other semiconductors with an indirect band gap, and the results parallel those for porous silicon. Quantum-confined luminescence has been observed in indirect-gap semiconductor nanostructures with well-controlled geometries such as silicon and germanium 2-D wells [3.19] and quantum dots (see e.g. [3.20]), which may possibly be integrated into light-emitting devices [3.21]. The observation of optical gain in silicon nanocrystals [3.22] opens up new prospects for the creation of silicon-based lasers [3.23].

### 5.3.2.3 Excitons in Quantum-Confined Systems

A very general effect of quantum confinement in semiconductors is a widening of their optical band gap. For the model system of an infinite-barrier 2-D quantum well, (3.1) shows that the lowest energy ($N = 1$) of a con-

duction electron is increased compared with the bottom of the conduction band. A similar consideration applies to the lowest energy of a hole in the valence band. Both effects contribute to an increase in the minimum excitation energy of the system compared with the bulk band gap. This blueshift has a comparable magnitude in 2-D and 0-D structures [3.24]. This constitutes the leading contribution to the characteristic blueshifts in the optical spectra of strongly quantum-confined semiconductor systems. However, the confinement of oppositely charged carriers at reduced separations also has dramatic effects on the electron–hole Coulomb energy and thus on exciton formation.

Two regimes of exciton confinement must be distinguished, depending on the confinement size $d$ compared with the Bohr radius $a_0^*$ of the Mott–Wannier exciton in the bulk semiconductor [3.25]. The weak-confinement regime corresponds to sizes such that $d \geq 4a_0^*$. In this regime, the relative electron–hole motion, and in particular its binding energy, is essentially left unchanged. The exciton can still be considered as a quasiparticle, but its center-of-mass translational motion becomes quantized. A simple model [3.26] of a single-point quasiparticle with mass $M_{\mathrm{Ex}}$ equal to the total mass of the exciton, $M_{\mathrm{Ex}} = m_{\mathrm{e}}^* + m_{\mathrm{h}}^*$, explains the observed frequency shifts. The translational state with the lowest energy, $N = 1$, which is the only optically allowed state, has a nonzero kinetic energy. Compared with an infinite-sized system, the lowest excitation energy in the weak-confinement regime is thus increased by

$$\Delta E_{\mathrm{Weak}} = \frac{\pi^2 \hbar^2}{2 M_{\mathrm{Ex}} d^2} \,. \tag{3.2}$$

Like that for electron states, this shift has comparable magnitudes for various dimentionalities. In the weak-confinement regime, the exciton wave function still involves combinations of several conduction-band electron states and valence-band hole states, and not only the lowest-energy states. The quantization of carrier states does not change significantly the average energy of all of the states involved in exciton formation. As a consequence, in the weak-confinement regime, the exciton energy is not affected by the band gap increase which results from the increase in the energy levels of the lowest electron and hole states discussed above. The weak-confinement model is very suitable for describing spectral variations in nanoparticles of semiconductors with low exciton Bohr radii, such as CuCl (Table 5.3-2), as shown in Fig. 5.3-3.

The strong-confinement regime corresponds to the opposite limit, $d \leq 2a_0^*$. In that case the relative electron–hole motion is strongly affected by the barriers. In the direction of restricted motion, the kinetic energies of the lowest-energy electron and hole states determined by the quantum confinement are larger than the Coulomb

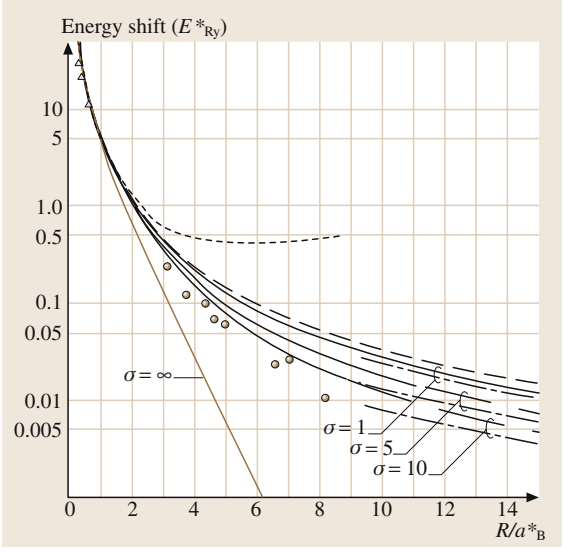


**Fig. 5.3-3** Observed values of energy shifts in the luminescence peak of CuCl nanocrystals in NaCl (*circles*) and in the absorption peak of CdS nanocrystals in silicate glass (*triangles*), compared with theoretical models: weak-confinement model (*dashed-dotted lines*), strong confinement model (*short-dashed line*); $\sigma = m_{\mathrm{h}}^*/m_{\mathrm{e}}^*$ is considered as a fixed parameter. (After [3.25])

**Table 5.3-2** 1s exciton Bohr radius for various semiconductors

| **Direct-band-gap semiconductors** | | | | | | | |
|---|---|---|---|---|---|---|---|
| Semiconductor | CuCl | Diamond | CdTe | CdS | GaN | CdSe | GaAs |
| $a_{\mathrm{B}}^*$ (nm) | 0.7 | 0.85 | 2.8 | 2.9 | 3.6 | 5.6 | 12 |
| **Indirect-band-gap semiconductors** | | | | | | | |
| Semiconductor | GaP | SiC | Si | Ge | | | |
| $a_{\mathrm{B}}^*$ (nm) | 1.17 | 2.7 | 4.9 | 17.7 | | | |

attraction. The exciton states are thus formed from uncorrelated electron and hole states of the "particle in a box" model in the confinement direction, whereas spatially correlated electron–hole bound states can still be formed in the unrestricted directions. This yields 2-D, 1-D, and 0-D excitons in quantum wells, quantum wires, and quantum dots, respectively. The binding energy of a 2-D exciton can be deduced from the two-dimensional hydrogen atom problem [3.27]. The exciton Rydberg series changes from $E^*_{\text{3-D}} = -R^*/n^2$ in the 3-D case to $E^*_{\text{3-D}} = -R^*/(n-1/2)^2$ in the 2-D case, where $R^*$ is the Rydberg constant for the exciton. This effect is opposed by the increased energy required for the creation of an electron–hole pair owing to the confinement of the carrier motion. The variation of the excitation energy of the first 1s-like exciton state in the regime of strong 1-D confinement is then

$$\Delta E^{\text{2-D}}_{\text{Strong}} = \frac{\pi^2\hbar^2}{2\mu d^2} - 3R^* \,, \tag{3.3}$$

where $\mu$ is the electron–hole reduced mass, such that $\mu^{-1} = m_{\text{e}}^{*-1} + m_{\text{h}}^{*-1}$. The first term is larger than the term due to the weak confinement of exciton motion (3.2) because of the difference between $\mu$ and $M_{\text{Ex}}$. The 0-D case is treated in detail in [3.25]. The variation of the minimum excitation energy in the regime of strong 3-D confinement is

$$\Delta E^{\text{0-D}}_{\text{Strong}} = \frac{\pi^2\hbar^2}{2\mu d^2} - 1.786\frac{e^2}{4\pi\varepsilon d} - 0.248R^* \,. \tag{3.4}$$

The divergence as $d^{-1}$ of the second term for small sizes results from the increased Coulomb interaction in this restricted geometry compared with the 2-D case. As could be expected, the case of a 1-D exciton in a quantum wire is intermediate between 0-D and 2-D, with a divergent Coulomb interaction which is sublinear in $d^{-1}$ [3.28]. For all dimensionalities, in the strong-confinement regime, the increased kinetic energy of quantum-confined carriers is dominant, and a blueshift of the optical gap is observed that varies continuously between the weak- and the strong-confinement regimes. However, the considerably increased exciton binding energy in strongly confined systems yields more pronounced exciton effects. For the most widely used semiconductors, excitonic effects are not discernible in room temperature spectra without quantum-confinement. However, in strongly confined geometries of any dimensionality, many semiconductors exhibit well-resolved excitonic peaks since the exciton binding energy can then exceed the thermal excitation energy $k_{\text{B}}T$. Both the blueshift of the spectra and the increasingly pronounced excitonic absorption are very evident in II–VI semiconductor nanoparticles, as exemplified in Fig. 5.3-4 for CdSe [3.29]. Semiconductor-doped glasses, formed from a dispersion of II–VI semiconductor crystallites in a silicate glass matrix, are the basis for some commercially available yellow-to-red long-wavelength-pass optical filters [3.30]. The glasses with a cutoff wavelength in the visible contain $CdS_{1-x}Se_x$ nanocrystallites, and the glasses used in the infrared filters contain essentially CdTe nanocrystallites. Their abrupt absorption band edge can be tuned by adjusting the composition, the size [3.31], and, as will be discussed later, the concentration of the particles. In other widely used semiconductors, such as Si, Ge, and III–V compounds, the valence bands may have complex features and contain light- and heavy-hole branches. The two corresponding types of excitons will have different characteristics, such as different binding energies.

The second important consequence of the squeezing of excitons in the strong-confinement regime is an increase in the optical matrix element associated with their excitation. A detailed discussion of this effect can be found in [3.32]. Its origin is the stronger overlap of electron and hole wave functions in reduced-dimensional excitons. This effect, associated with the concentration of oscillator strength into a few discrete transitions, has found many applications in optoelectronic devices. Certainly the most important is the fabrication of electrically powered multiple-quantum-well (MQW) lasers in $In_xGa_{1-x}As$ and $Al_xGa_{1-x}As$ (infrared), and $Al_xGa_yIn_{1-x-y}P$ (red). These systems are widely used today in data storage systems, bar code scanners, laser pointers, and printers. The physics and technology of MQW lasers are far beyond the scope of this section. Details may be found in [3.33], for example. 1-D and 0-D systems are also of interests for laser systems [3.34]. Laser applications of quantum-confined systems exploit the enhanced stimulated-emission coefficients that result from the increased transition matrix elements and spectral sharpening in quantum-confined systems. Besides MBE-grown devices, optical gain in chemically synthesized CdSe nanocrystal quantum dots has been achieved [3.35]. The operation of an optically pumped solid-state distributed-feedback (DFB) laser based on a CdSe-doped titania matrix gain medium has been demonstrated [3.36]. The output color of this laser can be selected by choosing appropriately sized nanocrystals and tuning the DFB period accordingly (see Fig. 5.3-5).

Another consequence of the large oscillator strengths associated with confined-exciton transitions is the

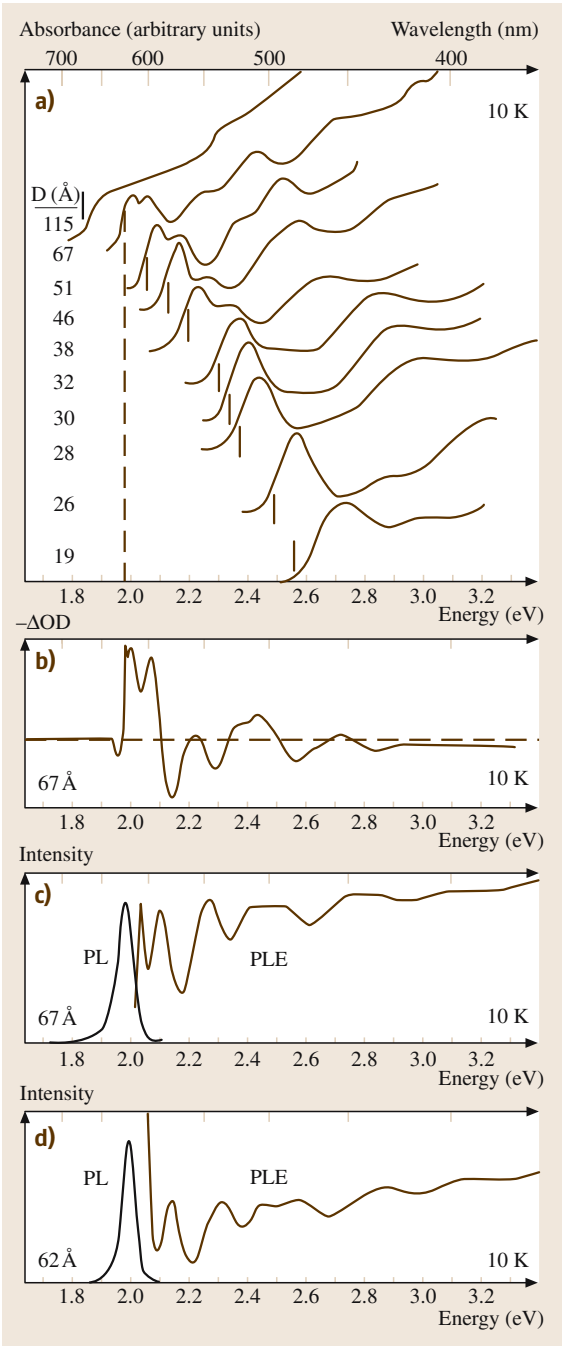


**Fig. 5.3-4** **(a)** Low-temperature (10 K) absorption spectra of CdSe dots dispersed in a polymer matrix, for various mean diameters. **(b)** Nanosecond saturated-absorption spectra for 67 Å dots. The pump beam had a 7 ns FWHM. The excitation photon energy, 1.984 eV, is prolonged as a *dashed vertical line* from **(a)** for easier comparison. The *horizontal dashed line* corresponds to $\Delta OD = 0$. **(c)**,**(d)** Photoluminescence(PL) and photoluminescence-excitation(PLE, observed at 2.022 eV) spectra for 67 Å dots **(c)** and for 62 Å dots **(d)**. (After [3.29])

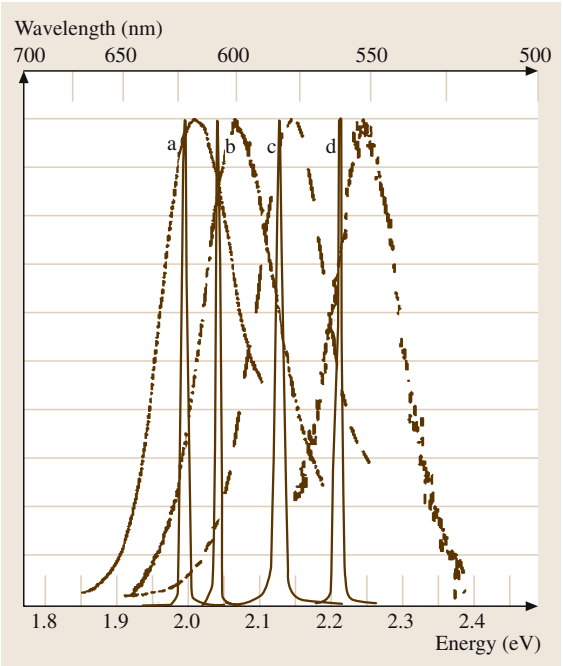


**Fig. 5.3-5** The photoluminescence emission spectra of CdSe nanocrystals with different radii (*dashed* and *dotted lines*, for radii of 2.7 nm, 2.4 nm, and 2.1 nm) and of 1.7 nm CdSe/ZnS core–shell nanocrystals (the radii are given in order of increasing photon energy) at low pump power, and at a pump power above the laser threshold (*solid lines*). The nanocrystals were dispersed in a titania film used in a distributed-feedback laser configuration at 80 K. (After [3.36])

enhancement of nonlinear optical and electrooptical coefficients. Nonlinear absorption and electroabsorption correspond to changes in absorption coefficients induced by high-intensity optical fields and large DC electric fields, respectively. Exciton–exciton interactions increase the energy of doubly excited states in quantum dots, which results in large saturable absorption effects (see Fig. 5.3-4b). The absorption saturation intensities may be as low as those of saturable dye solutions, but these systems have an increased robustness and the possibility of including them in solid-state media.

PbS-nanocrystal-doped glasses with an absorption saturation intensity of 0.2 MW/cm have been realized [3.37] and used as intracavity passive $Q$-switches in picosecond [3.37] and femtosecond [3.38] pulsed near-infrared lasers. The Frantz–Keldysh effect is also strongly enhanced in quantum-confined systems [3.39]. Moreover, the well-resolved excitonic transition shows quantum-confined Stark effects (QCSEs) with particularly large magnitudes. In quantum wells, this effect usually consists of a redshift of the absorption and a strong decrease of its oscillator strength, and has been exploited for the realization of fast, low-drive-voltage electrooptic modulators [3.40], which could possibly be integrated with semiconductor lasers [3.41].

### 5.3.2.4 Vibrational Modes and Electron–Phonon Coupling

The description in terms of phonons of the vibrational properties of solids assumes a translational invariance. It can be used only inside domains of homogeneous mechanical properties with sizes larger than the spatial extension of the phonon considered, typically given by its wavelength $\lambda_{ph}$. Similarly to the case of vibrational modes of impurities in crystals [3.43], the confinement of phonons in structures smaller than $\lambda_{ph}$ leads to the localization and the quantization of the vibrational modes. For typical solids, the phonon frequencies affected by confinement sizes on the 1–100 nm scale have frequencies on the order of 0.1–10 THz, i. e. thermal phonon energies and higher, and both acoustic and optical phonons are affected. The frequencies of the quantized modes, as well as their damping rates, depend on the size, shape, and nature of the environment of the nanostructure and its interfaces. The electron–phonon coupling may be strongly modified by phonon confinement, with manifestations in the transport properties and in the optical absorption and luminescence.

In 2-D systems, two-dimensional phonons appear, with properties and consequences similar to those of surface phonons. The role of in-plane propagating phonons in electron–phonon scattering rates has been demonstrated in metal films [3.44] and in Si/Ge quantum wells [3.45]. Phonon propagation perpendicular to a quantum-well superlattice produces Bragg-like selective transmission [3.46]. The formation of phonon band gaps results from the zone folding of the LA and TA phonons propagating perpendicular to the layers, and is well described by a mesoscopic model of a periodic series of homogeneous layers [3.47].

When we move to 0-D systems, the phonon spectrum changes to a set of size-dependent discrete lines. As in the case of 2-D systems, most data on the various vibrational modes of metal nanoparticles [3.48] and semiconductor nanocrystals (see e.g. [3.49] and references therein) embedded in solid matrices have been obtained by spontaneous-Raman-scattering spectroscopy. The lowest frequencies are well described by the simple Lamb theory [3.50] of the vibration of a homogeneous, elastic sphere. The breathing mode, the mode of lowest energy, is usually the best resolved one. A detailed calculation of the mesoscopic acoustic modes in quantum dots of various compositions embedded in various matrices can be found in [3.51]. The availability of ultrafast pulsed lasers, with a pulse duration shorter than the period of an acoustic vibration mode, offers the possibility to monitor the vibrations in the time domain rather than the frequency domain, as shown in Fig. 5.3-6 for 3 nm PbS quantum dots in a polymer matrix. Similar experiments have been performed on Ag particles of various sizes in a glass matrix [3.52]. These experiments offer a unique opportunity to analyze the damping of these vibrations, which is generally attributed to radiation of acoustic waves into the matrix.

The modes excited by ultrafast laser pulses are usually not the same as those detected by spontaneous-Raman spectroscopy, mainly for symmetry reasons [3.53] (see Fig. 5.3-7). Moreover, the symmetry selection rules depend on the mechanism of excitation by the laser pulse. A thermal mechanism provokes

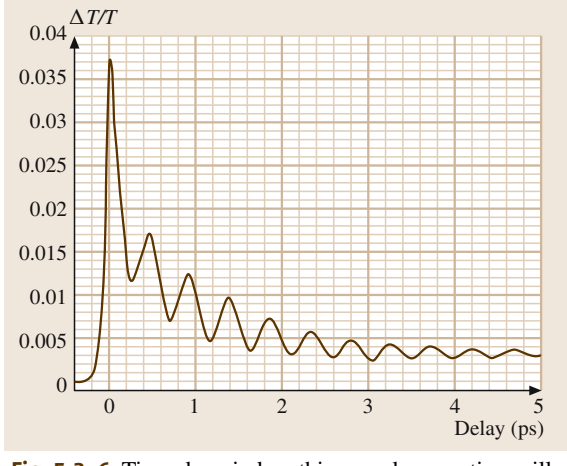


**Fig. 5.3-6** Time-domain breathing-mode acoustic oscillations in 3 nm PbS quantum dots embedded in a polymer matrix, observed by transient saturated absorption. (After [3.42])

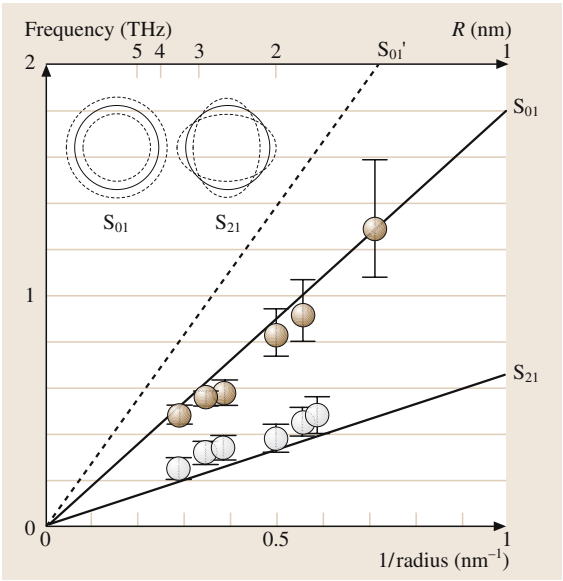


**Fig. 5.3-7** Frequency of the coherent-phonon and Raman peaks as function of PbSe dot size. The *solid lines* represent the calculation on the assumption that the stress at the dot boundary is zero, and the *dashed line* represents the calculation with a rigid boundary condition. The matrix was a phosphate glass. The *inset* represents the displacement in the $S_{01}$ and $S_{21}$ spheroidal modes. The coherent-phonon and Raman frequencies are assigned to the $S_{01}$ and $S_{21}$ modes, respectively. (After [3.53])

breathing-mode ($S_{01}$) oscillations, whereas electrostrictive excitation excites the elongation mode ($S_{12}$). Figure 5.3-7 also illustrates the parallel dependences of the modes excited by Raman scattering and by ultrafast laser-pulse on particle size. These dependences are consistent with a Lamb model with boundary conditions corresponding to the absence of stress.

The confinement also influences the electron–phonon coupling. For example, in GaAs, each quantized optical-phonon mode produces a Huang–Rhys ladder in the phonon sidebands in the spectrum of the exciton transition [3.55]. A scaling law in $d^{-3}$ is predicted for the effective coupling strength [3.55]. It has been shown that the luminescence spectra of silicon nanocrystals exhibit not only a no-phonon peak but also TO- and TA-phonon-assisted peaks. Hence, besides the breakdown of the momentum conservation rule discussed above, an increased electron–phonon interaction also favors luminescence in this indirect-band-gap semiconductor. This coupling prevails for moderate confinement energies, below 0.7 eV [3.56]. The enhanced electron–phonon coupling results not from phonon quantization but rather from an increased overlap factor [3.57].

In metal particles, the main consequence of changes in the electron–phonon couplings is a variation of the electron relaxation rates. This effect depends strongly on the intensity regime of the excitation, but experiments carried out at weak excitation on Ag and Au nanoparticles in various matrices show a strong increase of the relaxation rate, i. e. a decrease of the electron–lattice energy exchange time, with quantum confinement (see Fig. 5.3-8) [3.54]. In this case also, the increased

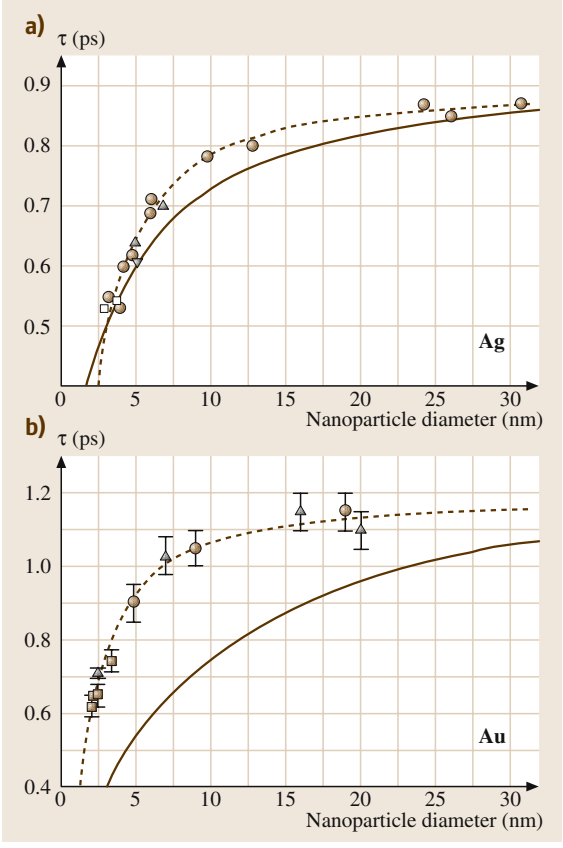


**Fig. 5.3-8** **(a)** Size dependence of the measured electron-lattice energy exchange time $\tau_{e-ph}$ for silver clusters in $BaO-P_2O_5$ (*circles*), in $Al_2O_3$ (*open squares*), in $MgF_2$ (*diamond*), in a polymer (*up triangles*), and deposited on a glass substrate (*down triangle*). The *solid line* is the result of the theoretical model proposed by the authors of [3.54]. The *dashed line* is a guide to the eye. **(b)** As **(a)**, for gold clusters in $Al_2O_3$ (*squares*), in colloidal solutions prepared using a radiolysis technique (*triangles*), and in commercially available colloidal solutions (*circles*). (After [3.54])

electron–phonon coupling is attributed not to phonon confinement but to a reduction of the screening of the electron–ion interaction following electron confinement.

### 5.3.2.5 Electron Transport Phenomena

The charge transport properties in the direction of free-carrier motion in a restricted-dimensional system have important consequences for the magnetotransport effects. This is treated in Sect. 5.3.4. For disordered systems, when the Mott variable-range hopping mechanism [3.58] dominates the conductivity, the temperature scaling law depends on the dimensionality: the 3-D conductivity $\sigma_{3\text{-D}}$ varies with temperature following the law $\log \sigma_{3\text{-D}} \propto T^{-4}$, whereas the 2-D conductivity varies as $\log \sigma_{2\text{-D}} \propto T^{-3}$. The transition from 3-D to 2-D behavior has been demonstrated for films of amorphous Ge at a thickness $d$ of 50 nm, as illustrated in Fig. 5.3-9 [3.54].

A vertical conductance, i. e. perpendicular to the free-motion direction, is necessary in quantum wells in many device applications. This requires a finite barrier in order for one to have a continuum of unbound states, in addition to one or a few bound states, as illustrated in Fig. 5.3-10. Practical realizations of such structures are formed from an n-type low-band-gap well, usually GaAs, sandwiched between barrier layers of an intrinsic semiconductor with larger band gap, such as $Al_xGa_{1-x}Al$. The conduction electron states form a structure of the type shown in Fig. 5.3-10. The choice of the well width and barrier height (through the composition $x$ of the barrier) permits one to adjust the number and energy of bound states, and the n-type doping of the well controls their population.

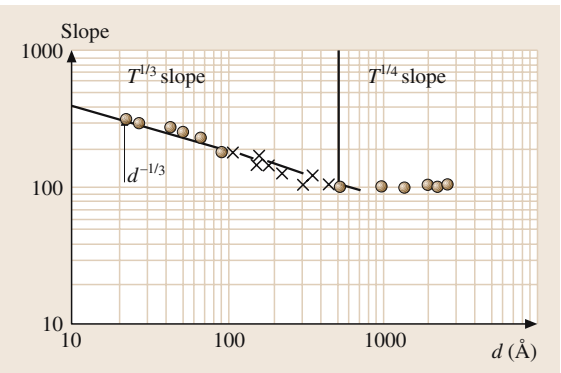


**Fig. 5.3-9** Plot of the experimental power-law dependence of the conductivity on temperature for films of amorphous Ge of various thicknesses $d$. The transition from a 3-D ($T^{-1/4}$) behavior (region marked as $T^{1/4}$ slope) to a 2-D ($T^{-1/3}$) behavior (region marked as $T^{1/3}$ slope), as expected for the variable-range hopping mechanism, is clearly observed $d = 500$ Å (*vertical bar*). (After [3.54])

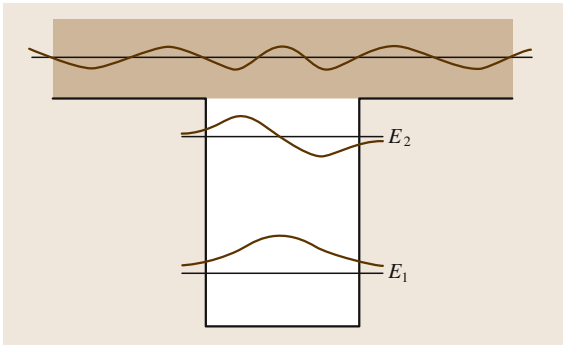


**Fig. 5.3-10** Schematic view of the electron states in a finite-barrier quantum well. States with energies below the barrier are bound to the well, and states with energies above the barrier are extended outside the well and form a continuum of conduction states

An important example of a device based on such a structure is the quantum-well infrared photodetector (QWIP) [3.59]. The energy difference $E_1 - E_2$ between the subbands matches the energy of the photons to be detected. $E_2$ is close to the top of the barrier. Excitation of the intersubband transition by absorption of an IR photon results in the population of the second subband. If an electric field is applied, the excited electron can tunnel through the small remaining barrier towards the continuum and move away from the well under the influence of the electric field. This gives rise to a photocurrent, which can either constitute the signal of the detector or feed a visible-light-emitting junction in order to achieve IR-to-visible conversion. To increase the collection efficiency in practical devices, several quantum wells are associated in a periodic stack. For a large enough bias, once an electron has reached the continuum it is accelerated by the electric field and has a high probability of crossing subsequent wells without being trapped in a bound state.

In applications such as IR detection, the conductivity is obtained by populating the continuum. In that case, the interwell spacing is large enough to prevent direct coupling between neighboring wells, and each well can be considered as isolated. Such systems are usually called multiple quantum wells.

A nonzero conductivity in the ground state can be obtained by reducing the width of the barriers, as originally proposed in [3.60]. Then, the subband states of neighboring wells interact through the evanescent parts

of their wave functions in the barrier. The ensemble of bound states consisting of the subband levels from all of the coupled quantum wells forms a band in the confinement direction called a miniband. The periodic set of coupled quantum wells is called a superlattice. At very low applied voltages, a band-type conduction governs the electron transport. However, above a threshold voltage, the conduction mechanism becomes highly complicated. This results in highly nonlinear behaviors, with the appearance of negative differential resistance and oscillations at low temperatures [3.61]. These effects are attributed to the localization of the electron states when the voltage drop between neighboring wells induces an energy difference larger than the coupling energy between them. At even higher fields, the voltage drop spontaneously localizes on one single well [3.61]. A particularly spectacular manifestation of this effect has been observed in weakly coupled wells at low temperature, as shown in Fig. 5.3-11 [3.62].

Electrical conduction is also very important for many devices that exploit the huge area of surface or interface per unit volume in zero-dimensional nanostructured materials such as nanoporous materials, granular materials, nanocomposites, and nanoparticle assemblies. Examples of such devices are chemiresistor-type sensors, solar cells, light-emitting diodes, and energy-storage cells. From the point of view of electron transport, these materials can often be modeled as a dense assembly of metal or semiconductor quantum dots dispersed in an insulating matrix. As in noncrystalline materials [3.63], the elementary mechanism of conduction is phonon-assisted electron tunneling from one dot to another, or hopping. Above a threshold temperature, the limiting factor for the hopping probability is the spatial proximity of two dots. Below this threshold, the weak thermal energy available imposes a strong selection of sites with a low energy difference, tunneling to such sites at larger distances becomes dominant, and the variable-range hopping regime is obtained [3.58]. The temperature dependence of the conductance $\sigma$ changes from $-\log(\sigma) \propto T^{-\alpha}$ with $1/2 < \alpha < 1$ for nearest-neighbor hopping to $-\log(\sigma) \propto T^{-1/4}$ for variable-range hopping [3.64]. However, in contrast to noncrystalline semiconductors, the sites in such granular materials are spatially expanded to the particle size, and the tunnel gap between neighboring particles is usually much smaller than this size. As a consequence, the threshold temperature is very low and a $T^{\alpha}$ law with $\alpha \approx 1/2$ is observed over a wide temperature range.

Another important factor comes into play in nanoparticle-based conductors compared with 2-D well systems. The addition of an electron to an initially electrically neutral nanoparticle requires an energy $e^2/2C$, where $C$ is the capacitance between the nanoparticle

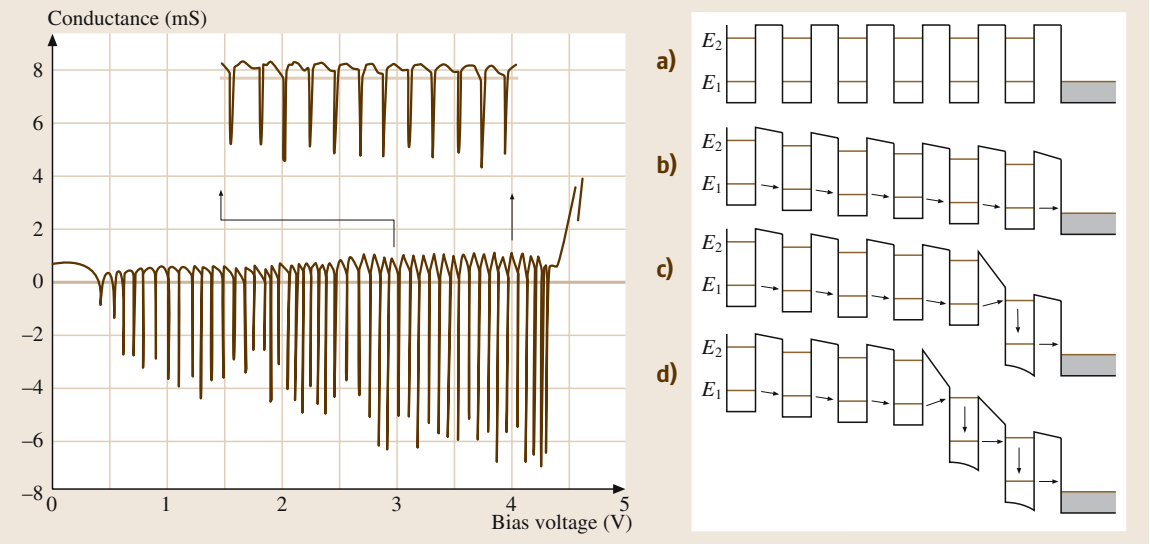


**Fig. 5.3-11** *Left*: differential conductance as a function of the applied voltage for a 49-period superlattice at 20 K. *Right*: schematic model to explain the 48 negative peaks in the differential conductance. **(a)** Zero bias; **(b)** ground-state resonant-tunneling conduction; **(c)** first field localization, where resonant tunneling between the ground state and an adjacent excited state takes place; **(d)** expansion of the high-field region by one additional quantum well. (After [3.62])

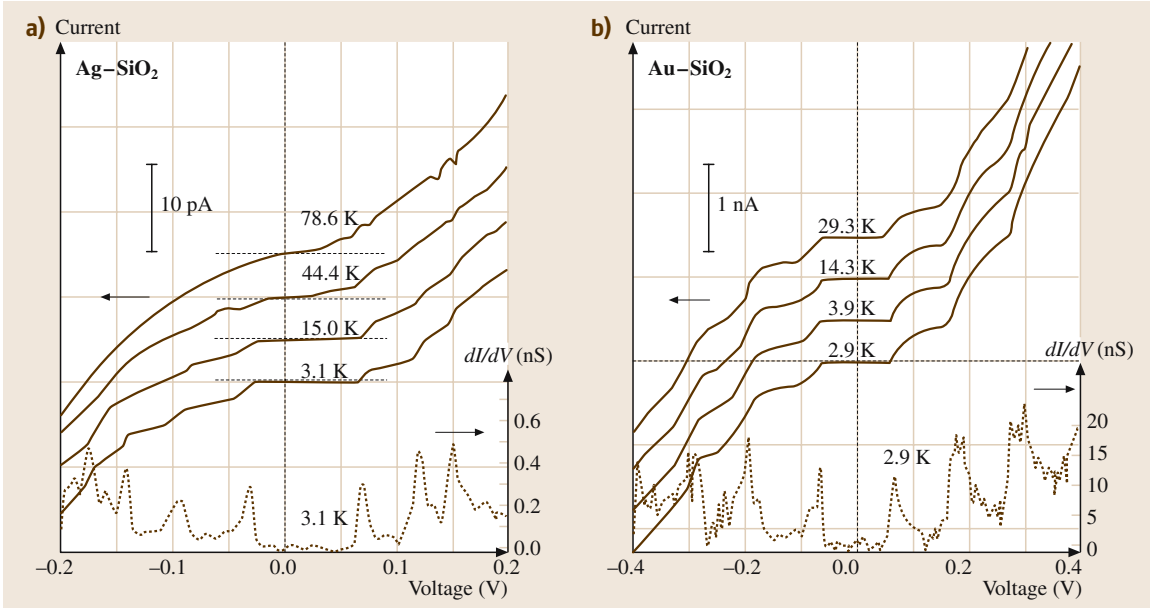


**Fig. 5.3-12a,b** Temperature dependence of $I/V$ characteristics of films of **(a)** Ag nanoparticles dispersed in $SiO_2$ (sizes $3.8 \pm 1.0$ nm, volume fraction 1.5%, film thickness 12 nm) and **(b)** Au nanoparticles dispersed in $SiO_2$ (sizes 2.9 nm, film thickness 9 nm). In both cases the electrode area was $100 \times 100\,\mu m^2$. (After [3.68])

and its surroundings. Typical values of $C$ can be in the region of $10^{-17}$ F or less, so that the charging energy approaches or is larger than the thermal energy at room temperature. This produces the Coulomb blockade effect: conduction through a single nanoparticle requires a minimum voltage to overcome the cost in charging energy. The conduction may even show a stepwise dependence on the bias, called a Coulomb staircase, which has been observed for a single nanoparticle at room temperature [3.65]. Extension to three-terminal devices has led to the realization of mesoscopic devices such as single-electron transistors, where the charge state of a confined electron pool is controlled by a gate voltage [3.66]. The influence of the single-electron charging energy on the conductivity of a mesoscopic material made of an assembly of dots has not yet been completely elucidated. It is predicted to reinforce the $T^{\alpha}$ law with $\alpha \approx 1/2$ for the conductivity [3.67]. However, the most prominent experimental effect is the appearance of remnants of the single-particle blockade effect when the conducting path involves only a few particles, which occurs mainly for the perpendicular conductivity in very thin films with a low particle volume fraction (see Fig. 5.3-12) [3.68, 69]. There are some indications that a regular ordering also favors Coulomb blockade effects [3.70].

## 5.3.3 Electromagnetic Confinement

### 5.3.3.1 Nanoparticle-Doped Materials

The polarizability $\alpha(\omega)$ of a spherical inclusion of volume $V$ with a dielectric constant $\varepsilon(\omega)$ at an optical frequency $\omega$, in a matrix with a dielectric constant $\varepsilon_M(\omega)$, is given by

$$\alpha = 9\varepsilon_0 V \frac{\varepsilon - \varepsilon_M}{\varepsilon + 2\varepsilon_M}\,, \tag{3.5}$$

where the explicit frequency dependence of $\alpha$, $\varepsilon$, and $\varepsilon_M$ has been dropped in the notation. When the medium is subjected to a propagating optical field, the polarizability of the particle will produce both absorption and elastic scattering of light. The corresponding cross sections, $\sigma_A$ and $\sigma_S$, respectively, are

$$\sigma_A = \frac{18\pi V}{\lambda_M} \frac{\varepsilon_0 \varepsilon''}{(\varepsilon' + 2\varepsilon_M)^2 + \varepsilon''^2} \tag{3.6}$$

and

$$\sigma_S = \frac{6\varepsilon_0^2 V^2}{\varepsilon_M^2 \lambda_0^3 \lambda_M} \frac{(\varepsilon' - \varepsilon_M)^2 + \varepsilon''^2}{(\varepsilon' + 2\varepsilon_M)^2 + \varepsilon''^2} , \quad (3.7)$$

where $\lambda_0$ and $\lambda_M$ are the wavelengths of the light in vacuum and in the matrix, respectively, and $\varepsilon = \varepsilon' + i\varepsilon''$, with $\varepsilon'$ and $\varepsilon''$ real. The dependence of $\sigma_A$ and $\sigma_S$ on the volume shows that for nanoparticles with diameters much smaller than the optical wavelength, absorption effects, when present, are preponderant over scattering.

### Low-Concentration Systems

For semiconductor particles, the absorption spectrum is changed only slightly compared with the bulk. The scattering losses, present even in the nonabsorbing region, have been studied in detail, in view of their waveguiding applications and account has been taken of the size dependence of the refractive index [3.71]. Some results are reproduced in Fig. 5.3-13.

In contrast, metals often show negative values of $\varepsilon'$. In that case both the absorption and the scattering show resonances when $\varepsilon' + 2\varepsilon_M = 0$, which corresponds to the dipolar plasmon oscillation mode, and a peak appears in the absorption spectrum; this is observed especially clearly with alkali and noble metals (Fig. 5.3-14). For most metals, the plasmon peak shifts towards longer wavelengths and becomes sharper for matrices with a larger refractive index. This is clearly observed for the alkali metals in Fig. 5.3-14; for a computation of matrix-dependent spectra for various metals, see [3.72]. Higher-multipolar-order plasmon modes exist [3.73] but cannot be excited optically in the quasi-static regime. However, they have a nonnegligible influence on the optical absorption spectra of larger particles, as shown in Fig. 5.3-15, and can be excited by, for example, electron beams. From the Mie theory, the frequency of the $L$th-order plasmon mode of a small particle of a Drude-model metal, with $\varepsilon(\omega) = \varepsilon_0(1 - \omega_p^2/\omega^2)$, where $\omega_p$ is the plasma frequency, is given by [3.73]

$$\omega_L = \sqrt{\frac{\omega_p}{1 + (\varepsilon_M/\varepsilon_0)(1 + 1/L)}} . \quad (3.8)$$

A continuous tuning of the positions of the plasmon absorption peak by alloy formation has been demonstrated. The dependence of the absorption spectra of Au–Ag alloy nanoparticles on the composition is reproduced in Fig. 5.3-16 [3.74].

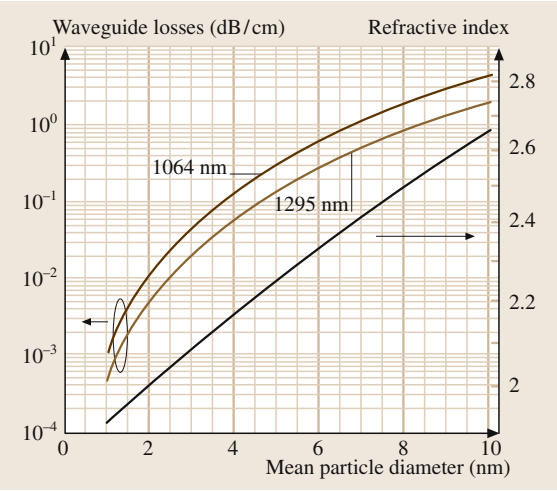


**Fig. 5.3-13** Scattering losses of a 5% PbS nanoparticle-doped silica–titania waveguide as a function of the nanoparticle diameter at wavelengths of 1064 nm and 1295 nm (After [3.71])

### Local-Field Effects

In the quasi-static approximation, the electric field inside a nanoparticle is changed compared with the field outside by a local-field factor $f$, given by

$$f(\omega) = \frac{3\varepsilon_M(\omega)}{\varepsilon(\omega) + 2\varepsilon_M(\omega)} . \quad (3.9)$$

This factor is taken into account in (3.5)–(3.8) above, but it can have an even greater importance in nonlinear effects, since the second-order and third-order nonlinear optical coefficients, $\chi^{(2)}$ and $\chi^{(3)}$, respectively, are affected by factors $f^2$ and $f^3$, respectively, as compared with the bulk material of the nanoparticle. Hence, for large $f$, a nanostructured material can have a larger optical nonlinearity than its bulk constituents. For typical semiconductor-doped matrices, $\varepsilon > \varepsilon_M$ and $f < 1$. However, particularly strong local-field enhancements are observed for metal nanoparticles in the vicinity of the plasmon resonance [3.75].

### Electromagnetic Concentration Effects

For larger particle concentrations, the interactions between particles influence the electromagnetic properties. For interparticle distances much smaller than the wavelength, the Maxwell–Garnett model applies and leads to the Lorentz–Lorenz relation for the effective dielectric constant $\varepsilon_{eff}$ of the composite medium, which takes the form

$$\varepsilon_{eff} = \varepsilon_M \frac{\varepsilon(\omega)(1 + 2p) + 2\varepsilon_0(1 - p)}{\varepsilon(\omega)(1 - p) + \varepsilon_0(2 + p)} , \quad (3.10)$$

where $p$ is the volume fraction. This usually leads to a redshift of absorption peaks. In particular, the frequency of the dipole ($L = 1$) plasmon mode of a particle

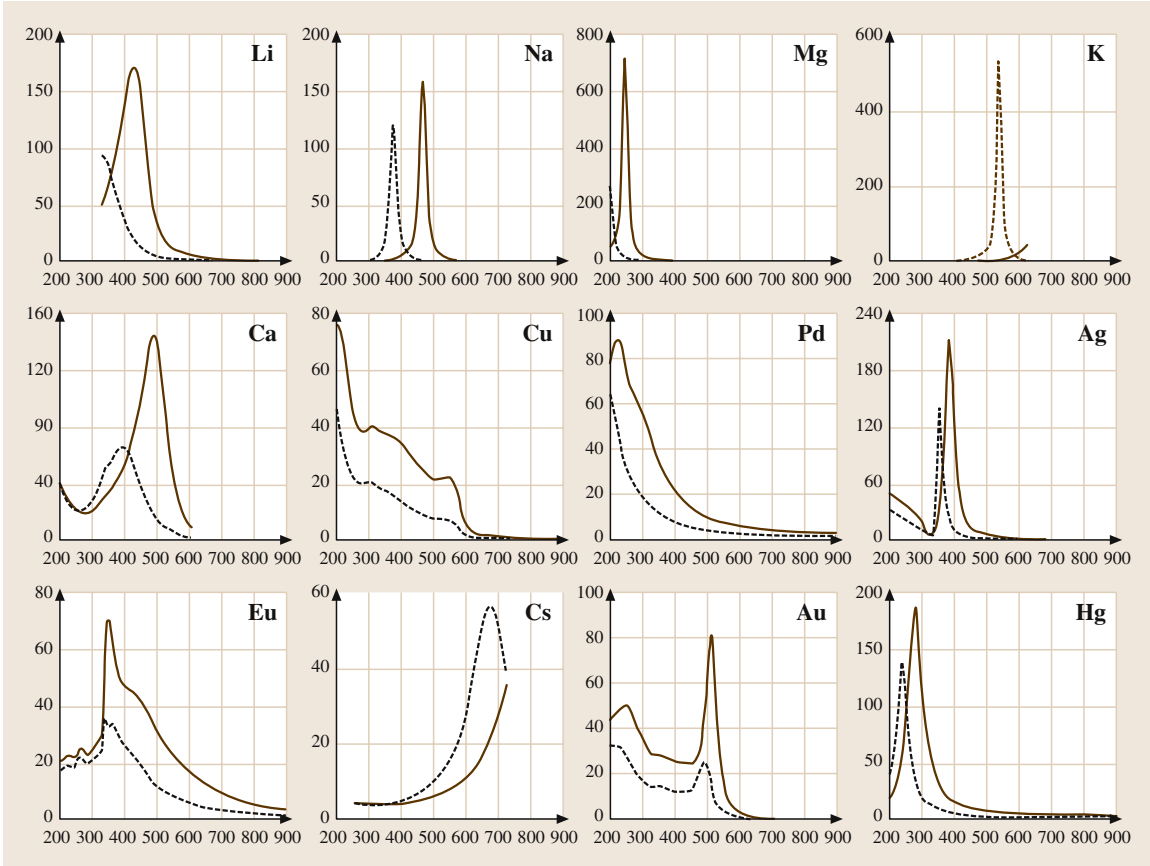


**Fig. 5.3-14** Absorption spectra, represented by the dimensionless function $C\lambda/V$ where $C$ is the cross section, $\lambda$ the wavelength, and $V$ the particle volume, of 10 nm diameter spherical particles of selected metallic elements, as calculated from their frequency-dependent dielectric constant, in vacuum (*dashed lines*) and in a matrix with a refractive index equal to that of water, 1.33 (*solid lines*). Horizontal scale: $\lambda$ (nm). (After [3.77])

**Fig. 5.3-15** Absorption spectra of spherical particles of various materials, as calculated from their frequency-dependent dielectric constant, in vacuum for various particle radii. (After [3.72]) ▶

**Fig. 5.3-16** Effect of formation of a gold–silver alloy on the surface plasmon absorption: measured UV–VIS absorption spectra of spherical Au−Ag alloy nanoparticles of various compositions. The gold mole fraction $x_{Au}$ varies between 1 and 0.27. The plasmon absorption maximum is blueshifted with decreasing $x_{Au}$. (After [3.74])

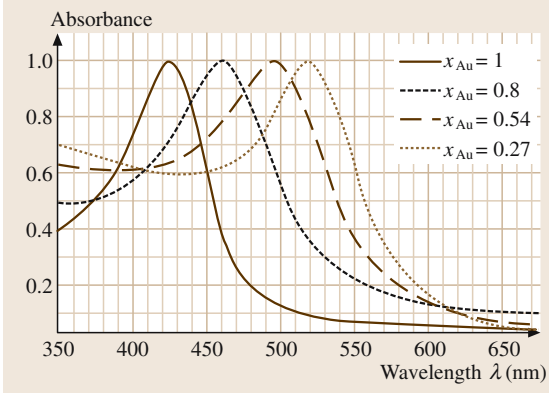


in the Drude model is $\omega_{L=1} = \sqrt{(1-p)/3}\omega_p$ instead of $\omega_p/\sqrt{3}$, the value in the low-concentration limit ($p \approx 0$).

This effect has found applications in sensing, in particular the selective colorimetric detection of nucleotides based on aggregation of gold nanoparticles [3.76]. The electromagnetic concentration effect is also used,

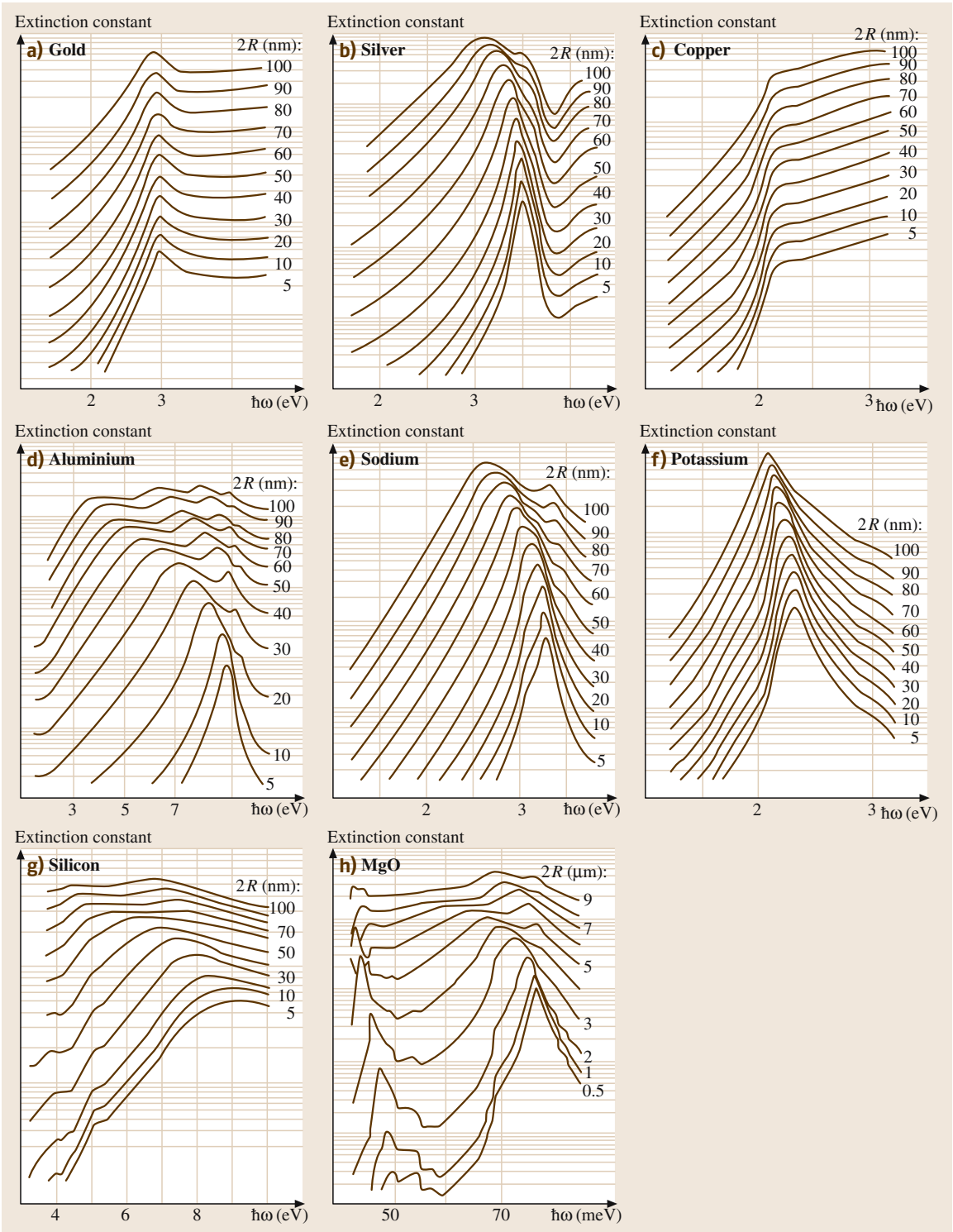
Extinction constant
a) Gold
2R (nm):
100
90
80
70
60
50
40
30
20
10
5
2
3
ħω (eV)
Extinction constant
b) Silver
2R (nm):
100
90
80
70
60
50
40
30
20
10
5
2
3
ħω (eV)
Extinction constant
c) Copper
2R (nm):
100
90
80
70
60
50
40
30
20
10
5
2
3
ħω (eV)
Extinction constant
d) Aluminium
2R (nm):
100
90
80
70
60
50
40
30
20
10
5
3
5
7
ħω (eV)
Extinction constant
e) Sodium
2R (nm):
100
90
80
70
60
50
40
30
20
10
5
2
3
ħω (eV)
Extinction constant
f) Potassium
2R (nm):
100
90
80
70
60
50
40
30
20
10
5
2
3
ħω (eV)
Extinction constant
g) Silicon
2R (nm):
100
70
50
30
10
5
4
6
8
ħω (eV)
Extinction constant
h) MgO
2R (μm):
9
7
5
3
2
1
0.5
50
70
ħω (meV)

in addition to quantum size effects (Sect. 5.3.2), to tune the absorption band edge of semiconductor-doped glasses.

### 5.3.3.2 Periodic Electromagnetic Lattices

#### Coupled Plasmon Modes

The coupling between the plasmon modes of several closely packed nanoparticles yields new electromagnetic eigenmodes and spectroscopic properties. The electromagnetic eigenmodes of some few-particle systems, such as Ag and Au pairs and triplets with various geometries, have been computed, for instance in [3.72, Sect. 2.3.4], and have been observed directly by e-beam excitation [3.78]. For the lowest eigenmodes, a large field enhancement is observed in the small gap between the particles.

Coupled plasmon modes have been observed experimentally in regularly spaced linear chains of gold nanoparticles [3.79] and in 2-D hexagonal arrays of silver nanoparticles [3.80]. The controlled propagation of plasmon excitations in tailored metal nanoparticle structures is a new domain of application, sometimes called "plasmonics" [3.81].

#### Opals and Photonic-Band-Gap Materials

3-D ordered arrays of nanostructures with periods of the order of a fraction of the optical wavelength may show intense Bragg diffraction for specific wavelengths and diffraction angles. This phenomenon is the origin of the iridescent colors (opalescence) of opals. Opals consist of an fcc-like array of silica nanoparticles with sizes in the range 150–900 nm [3.82], with a size dispersion below 5% [3.83].

For nanoscale objects with large scattering strengths and particular geometries, spectral intervals where no propagating mode is allowed in any direction appear, thus forming "photonic band gaps". The idea of exploiting this phenomenon in optoelectronic devices has been suggested [3.84,85]. However, up to now, this phenomenon has been realized only in the infrared and microwave regions. Application in the visible, which would require 3-D nanostructured materials, is still under active development.

## 5.3.4 Magnetic Nanostructures

The driving force for the research on magnetic nanostructures is the possibility of their incorporation into future generations of information storage devices. This could lead to a real technological breakthrough, and a huge economic impact is foreseen. As always, the key question is whether any potential benefit of such technology will be worth the production costs. Overall, the current effort in this research field is considerable. The study of the magnetism of nanoscale objects is characterized by the closeness between fundamental research and applications. What is more, a number of magnetic devices are currently in commercial use without a full understanding of the basic magnetic phenomena underlying them. An instructive example is the following: spin electronic phenomena have been applied rapidly since the first observation of giant magnetoresistance (GMR) was reported in 1988, and magnetic sensors and read heads based on this effect have been available since 1994 and 1997, respectively.

Most digital information is stored in the form of tiny magnetized regions or "bits" within thin magnetic layers on disks. The size of a magnetic bit determines the information storage capacity of a magnetic disk drive. The magnetic storage media used in today's commercial hard disks consist of homogeneous polycrystalline magnetic films. Owing to continuous improvements in both the magnetic properties of the media and the read/write heads, the storage density of hard disk drives has increased considerably during recent years, as shown in Fig. 5.3-17. Since 1990, the storage capacity of disk drives has increased at a 60%

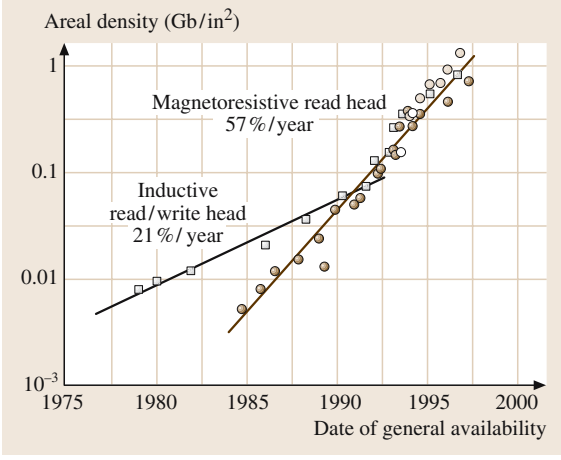


**Fig. 5.3-17** Evolution of areal storage density of hard disk drives (data from IBM, Almaden)

annual compound growth rate. The changes of the head technology first from thin-film heads to magnetoresistive heads and then to read heads based on the GMR effect [3.86, 87] have enabled enormous increases in volumetric storage capacity.

The overall gain in areal density has been achieved by scaling the complete disk drive system. The medium has to accommodate smaller bit dimensions and smaller transition widths between written bits. However, the optimization also includes more sensitive read/write heads, improving the signal processing and coding, and improving the head–disk tribology. A good discussion of these aspects can be found in [3.88].

Progress in this field would not be possible without the maturity of growth techniques such as electron- or ion-beam lithography, and molecular-beam epitaxy and the ability to manufacture devices on a nanometric scale by nanoimprinting lithography. Another essential point has been the addition of magnetic contrast to near-field microscopy and electron microscopy (magnetic-force and Lorentz microscopy, respectively). These new tools permit us to establish a link between magnetism and structure on the atomic scale.

We have selected here some examples to illustrate the state of the art in nanometric nanostructures, keeping as the main idea the impact of the underlying technological breakthrough. We focus our attention on two very active fields: magnetoresistive nanometric multilayers for spin electronics, and magnetic dots for ultrahigh-density storage media.

### 5.3.4.1 Spin Electronics

Conventional electronic devices are based on charge transport, and their performance is limited by the speed of the carriers (electrons) and the dissipation of their energy. Conventional electronics has ignored the spin of the electron. Nevertheless, in every wire or device, approximately 50% of the conducting electrons are generally spin-up and the remainder spin-down (where "up" or "down" relate to some locally induced quantization axis). *Spin electronics*, or *spintronics*, is a new field of electronics which relies on the different transport properties of majority-spin and minority-spin electrons. *Mott* postulated the basis of spin electronics in the mid-1930s: he attributed certain anomalies in the electrical transport behavior of metallic ferromagnets to the fact that the spin-up and spin-down conduction electrons are two *independent* families of charge carriers, each with its own distinct transport properties [3.89].

#### The Concepts of Spin Accumulation and Spin Diffusion Length

The other necessary ingredient of this model is that the two families contribute very differently to the electrical transport processes. This may be because the number densities of the carrier types are different, or it may because they have different mobilities. In either case, the asymmetry which makes spin-up electrons behave differently from spin-down ones arises because the ferromagnetic exchange field causes a splitting between the spin-up and spin-down conduction bands, leaving different band structures evident at the Fermi surface. In nonmagnetic materials, the two spin channels are equivalent because they have the same density of states (DOS) at the Fermi energy. In a magnetic material, the *spin polarization* is defined as the ratio of the difference between the populations in the up and down spin channels to the total number of carriers at the Fermi level,

$$SP = \frac{N_\uparrow - N_\downarrow}{N_\uparrow + N_\downarrow} \,. \tag{3.11}$$

Clearly, if there is a nonzero spin polarization, the numbers of electrons participating in the conduction process are different for the two spin channels. More subtly, this implies that the susceptibilities to scattering of the two spin types are different, and this in turn leads to different mobilities [3.90].

Let us consider two spin channels of different mobility. When an electric field is applied to the metal, there is a shift in momentum space $\Delta k$ of the spin-up and spin-down Fermi surfaces in accordance with the equation

$$F = eE = \hbar \frac{dk}{dt} = \hbar \frac{\Delta k}{\tau} \,, \tag{3.12}$$

where $F$ is the force on the carrier, $E$ is the electric field, $e$ is the electronic charge, and $\tau$ is the electron scattering time. Since the channels have different mobilities, this shift is different for the spin-up and spin-down Fermi surfaces, as illustrated in Fig. 5.3-18.

As a consequence, if a current is passed from such a spin-asymmetric material, for example cobalt, into a paramagnetic material such as silver (which has no spin asymmetry between spin channels), there is a net influx into the silver of up-spins over down-spins. Thus, a surplus of up-spins appears in the silver, and with it a small associated magnetic moment per unit volume. This surplus is known as a *spin accumulation*. Evidently, for a constant current flow, the spin accumulation cannot increase indefinitely. The spin-up electrons injected across

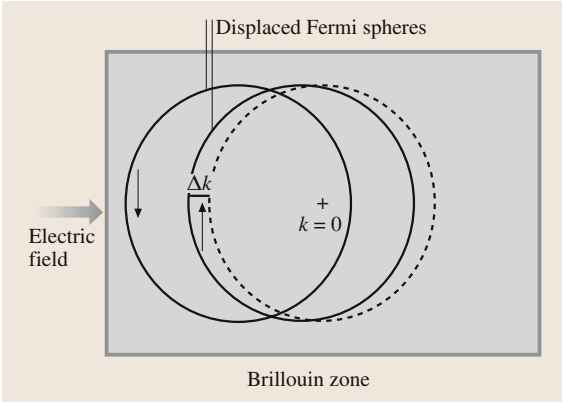


**Fig. 5.3-18** Schematic illustration of the shift in the Fermi surface when an electric field is applied to a ferromagnet. The *solid circles* represent the Fermi spheres of up- and down-spin electrons in the field, and the *dashed circle* represents the Fermi sphere in zero external field. (After [3.90])



the cobalt–silver interface are converted into spin-down electrons by spin-flip process, which we have hitherto ignored. So now we have a dynamic equilibrium between an influx of up-spins and their destruction by spin-flipping. This in turn defines a characteristic length scale that describes how far the spin accumulation extends into the silver. In the present description, we have assumed that both the spin-up and spin-down electrons are present in the ferromagnetic material in equal numbers but that their mobilities are different. Nevertheless, we can produce spin accumulation either as a direct consequence of an asymmetric density of states or as an indirect consequence via asymmetry in the electron mobility.

It follows from the above discussion that the spin accumulation decays exponentially away from the interface, on a length scale called the *spin diffusion length* ($\lambda_{sd}$). This concept is crucial for realizing a link between spin electronics and magnetic nanostructures. In this section, we shall not go further into this concept, but we shall do a rough calculation to see how large $\lambda_{sd}$ is and on what parameters it depends. We use the following expression from [3.90]:

$$\lambda_{sd} = \sqrt{\frac{\lambda v_F \tau_{\uparrow\downarrow}}{3}} , \qquad (3.13)$$

where $v_F$ is the Fermi velocity, $\tau_{\uparrow\downarrow}$ is the spin-flip time, and $\lambda$ is the mean free path. This relationship highlights the critical role of the impurity concentration in determining the spin diffusion length. If the impurity level is increased in the nonmagnetic material, $\lambda_{sd}$ drops because $\lambda$ is shortened. This relation also allows us to estimate values for the spin diffusion length. Taking silver as an example, $\lambda_{sd}$ can vary between several microns for very pure silver to the order of 10 nm for silver with 1% gold impurity. In a realistic material, $\lambda_{sd}$ is of the order of 10–100 nm. This is the reason why the experimental observation of spin-dependent transport phenomena has been possible when researchers have controlled the growth of nanometric multilayers. It is obvious that the layer thickness has to be small on the scale of the spin diffusion length.

### The Discovery of Giant Magnetoresistance

The era of spin electronics began with the discovery of a magnetoresistance effect in a magnetic multilayer consisting of a sequence of thin magnetic layers separated by equally thin nonmagnetic metallic layers: the electric current is strongly influenced by the relative orientation of the magnetizations of the magnetic layers. This experimental observation was made almost simultaneously by two research groups: Albert Fert's group in Orsay [3.86] and Peter Grünberg's group in Jülich [3.87, 91].

In fact, it was found that the resistance of the overall multilayer is low when the magnetizations of all the magnetic layers are parallel (ferromagnetic coupling), but it becomes much higher when the magnetizations of neighboring magnetic layers are antiparallel (antiferromagnetic coupling).

Figure 5.3-19 shows the magnetoresistance curves at 4.2 K of Fe/Cr (magnetic/nonmagnetic) multilayers with thicknesses of the individual layers of the order of 1 nm (from [3.86]). In these multilayers, for certain thicknesses of the Cr interlayer, the magnetizations of adjacent Fe layers are oriented antiparallel by an antiferromagnetic interlayer exchange coupling [3.87]. When a magnetic field is applied, the resistance of the multilayer decreases drastically as the magnetizations of the two layers progressively align in the direction of the field. The GMR ratio is usually defined as

$$\text{GMR} = \frac{R^{AP} - R^{P}}{R^{P}} , \qquad (3.14)$$

where $R^P$ and $R^{AP}$ are the resistances in the parallel and the antiparallel state, respectively. In the case of Fe/Cr multilayers, the GMR is 80% at liquid-helium temperature and 20% at room temperature when the thickness of the Cr is 9 Å.

The relative change of the resistance can be larger than 200% [3.92], and that is the reason why the effect is called "giant" magnetoresistance. GMR effects

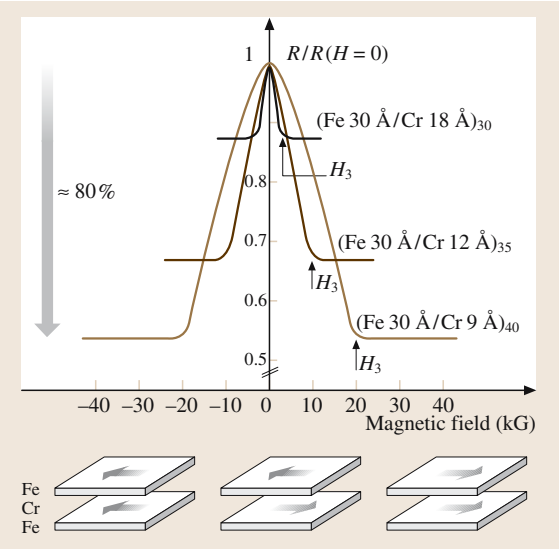


**Fig. 5.3-19** Magnetoresistance curves at 4.2 K of Fe/Cr multilayers. (After [3.86])

have been reported in a large number of systems combining ferromagnetic transition metals or alloys with nonmagnetic metals (for a review, see [3.93]). The most commonly used combinations of magnetic and nonmagnetic layers are Co/Cu and Fe/Cr, but multilayers based on permalloy as the magnetic component are also frequently used.

The second key ingredient was discovered by *Parkin* and *Mauri* [3.94]. These authors discovered that the orientation of the magnetic moments of two neighboring magnetic layers depends on the thickness of the intervening nonmagnetic layer. In fact, the orientation of the magnetic moments oscillates between parallel and antiparallel as a function of the thickness of the nonmagnetic layer [3.96]. This phenomenon is referred to as an oscillatory exchange coupling. Figure 5.3-20 shows the results of the original experiment of Parkin and Mauri. Oscillations of the GMR as a function of the Cr thickness occur because the magnetoresistive effect is only measurable for those thicknesses of Cr for which the interlayer coupling aligns the magnetic moments of all the Fe layers so that they are antiparallel.

GMR effects have been obtained in two geometries. In the first one, the current is applied in the plane of the layer (hereafter denoted by CIP), as in the experiments for which results are shown in Figs. 5.3-19 and 5.3-20, while in the second one, the current flows perpendicular to the plane of the layers (hereafter denoted by CPP). The first measurements in the CPP configuration were

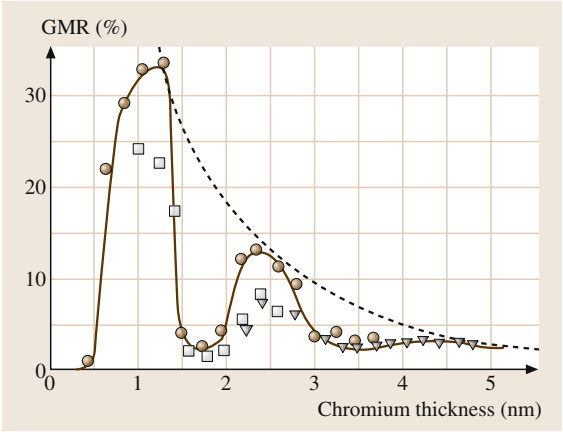


**Fig. 5.3-20** Dependence of the GMR ratio of an Fe/Cr multilayer on Cr thickness. (After [3.94])

obtained by sandwiching the multilayer between two superconducting Nb layers [3.97]. A CPP-GMR configuration has also been obtained in nanowires, namely multilayers electrodeposited in the pores of a nuclear-track-etched polycarbonate membrane [3.98], and by oblique deposition on a prestructured substrate [3.99]. The CPP-GMR effect is definitely larger than the CIP-GMR effect and occurs at much larger thicknesses.

The mechanism of the GMR effect is illustrated in Fig. 5.3-21 for $\alpha = (\rho_\downarrow/\rho_\uparrow) > 1$, where $\rho_\downarrow$ and $\rho_\uparrow$ are

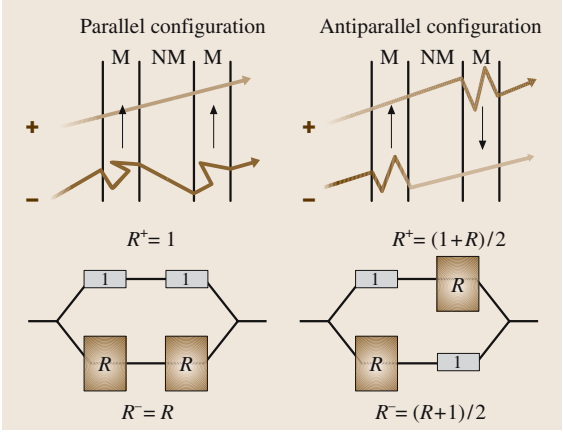


**Fig. 5.3-21** Schematic picture of the GMR mechanism. The electron trajectories between two scatterings are represented by *straight lines* and the scatterings by abrupt changes in the direction. The *signs* + and − are for spins $S_z = 1/2$ and $S_z = -1/2$, respectively. The *arrows* represent the majority-spin direction in the magnetic layers. M = magnetic, NM = nonmagnetic. (After [3.95])

the resistivities for spins parallel and antiparallel, respectively, to the magnetization direction; $\alpha > 1$ means that the resistivity is smaller for the majority spins. In the parallel configuration, the spin$^+$ (up) electrons are always the majority-spin electrons and are always weakly scattered in all layers, resulting in a resistance $r$ for this channel that is smaller than the resistance $R$ for the spin$^-$ (down) channel. The shorting of the current by this fast electron channel makes the resistivity low in the parallel state ($R^{\mathrm{P}} = r$). In the antiparallel configuration, each of the spin directions is alternately the majority and the minority one. The resistance is averaged for each channel, and the overall resistance $R^{\mathrm{AP}} = (r + R)/4$ is larger than in the parallel state. The GMR ratio is then

$$\mathrm{GMR} = \frac{R^{\mathrm{AP}} - R^{\mathrm{P}}}{R^{\mathrm{P}}} = \frac{(r-R)^2}{4rR} \,. \qquad (3.15)$$

This picture holds in both the CIP and the CPP geometries.

An antiparallel configuration can also be obtained in multilayers in which consecutive magnetic layers have different coercivities [3.101], or by combining hard and soft magnetic layers.

### Spin Valves

The best known structure for obtaining an antiparallel arrangement is the *spin valve* structure, originally proposed by *Dieny* et al. [3.100] (Fig. 5.3-22). A spin valve has two ferromagnetic layers (alloys of Ni, Fe, and Co) sandwiching a thin nonmagnetic metal (usually Cu), with one of the two magnetic layers being "pinned", i. e. the magnetization in this layer is relatively insensitive to moderate magnetic fields. The other magnetic layer is called the "free layer" and its magnetization can be changed by application of a relatively small magnetic field.

As the alignment of the magnetizations in the two layers changes from parallel to antiparallel, the resistance of the spin valve typically rises by 5–10%. The goal is to obtain the result that the magnetization of the free layer reverses in a very small field (a few oersteds), while the magnetization of the pinned layer remains

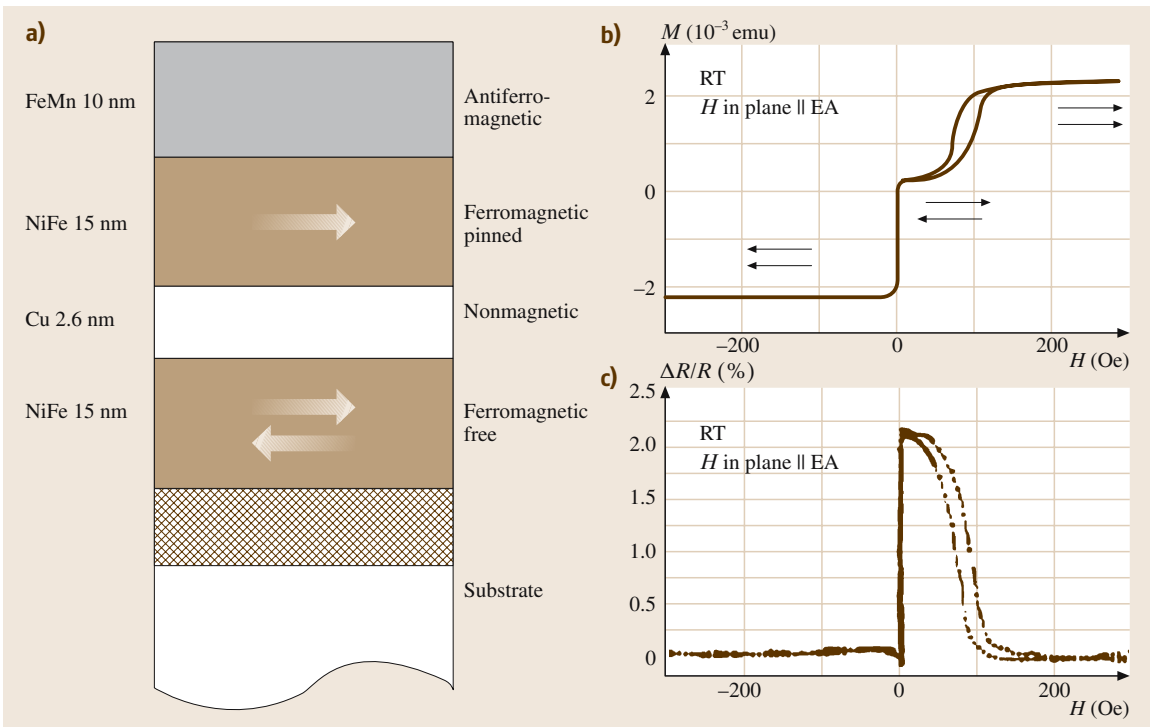


**Fig. 5.3-22** **(a)** Schematic illustration of the spin valve multilayer originally proposed by Dieny et al. (15 nm NiFe/2.6 nm Cu/15 nm NiFe/10 nm FeMn). **(b)** Magnetization curve, and **(c)** relative change in resistance. The magnetic field is applied parallel to the exchange anisotropy (EA) field created by the FeMn layer. The current flows perpendicular to this direction. (After [3.100])

fixed. Pinning is usually accomplished by using an antiferromagnetic layer, such as FeMn, that is in close contact with the pinned magnetic layer. The resultant spin valve response is given by $\Delta R \propto \cos(\theta_1 - \theta_2)$, where $\theta_1$ and $\theta_2$ are the angles of the magnetization directions respectively of the free layer and of the pinned layer with respect to the direction parallel to the plane of the magnetization of the medium whose magnetization is being sensed, as shown in Fig. 5.3-23.

The discovery of the GMR effect has created great expectations, since this effect has important applications, particularly in magnetic information storage technology. The use of spin valve multilayers in hard-disk read heads was first proposed by IBM in 1994 [3.102]. The principle of operation of a magnetic read head will be detailed in the section on 'Applications' below. Because the GMR effect is so important for industrial applications, there have been many improvements in recent years. The simplest type of pinned layer has been replaced by a synthetic antiferromagnet (two magnetic layers separated by a very thin (1 nm) nonmagnetic conductor, usually ruthenium) [3.94]. The magnetizations in the two magnetic layers are strongly coupled so as to make them antiparallel, and are thus effectively immune to outside magnetic fields. The second innovation is the nano-oxide layer (NOL), which is formed on the outside surface of the soft magnetic layer. This NOL reduces the resistance due to surface scattering, thus reducing the background resistance and thereby increasing the percentage change in the magnetoresistance of the structure [3.103].

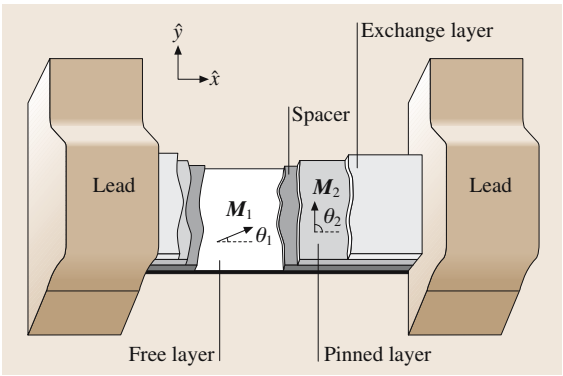


**Fig. 5.3-23** Schematic illustration of an IBM GMR spin valve sensor used in read heads. $\boldsymbol{M}_1$ and $\boldsymbol{M}_2$ are magnetizations,and $\theta_1$ and $\theta_2$ are angles from the longitudinal direction. The read head moves perpendicular to the $xy$ plane. (After [3.102])

### Magnetic Tunnel Junctions

Tunneling belongs to a class of electron transport phenomena known as *quantum transport*, "quantum" because they cannot be explained unless the wave nature of electrons is invoked. In the quantum mechanical picture, an electron is associated with a wave function $\psi$ related to the probability $\Psi$ that the electron can be found in a volume $dv$: by $\Psi = \psi\psi^* dv$. Quantum theory predicts that a particle has a nonzero probability of penetrating through a classically forbidden region separating two classically allowed regions of configuration space, by the process of *tunneling*.

The concept of tunneling has found applications in a vast number of domains in modern physics and chemistry; the particular case of interest here is tuneling in heterostructures consisting of metallic and insulator films, leading to innovative electronic devices. In a metal–insulator–metal (M–I–M) heterostructure, the potential barrier arises from the microscopic interactions between the metals and the insulator layer. By means of tunneling, an electron with an energy lower than the potential barrier can be transferred from one metal to the other, under the condition that the thickness of the potential barrier is not too large compared with the electron's wavelength (Fig. 5.3-24).

For a long period, up to the 1970s, the spin of the electron was neglected in tunnel transport. In 1971, *Tedrow* and *Meservey* [3.104] conducted tunneling measurements on junctions between a very thin superconducting Al film and a ferromagnetic Ni film, through an $Al_2O_3$ barrier, in a high magnetic field. They showed

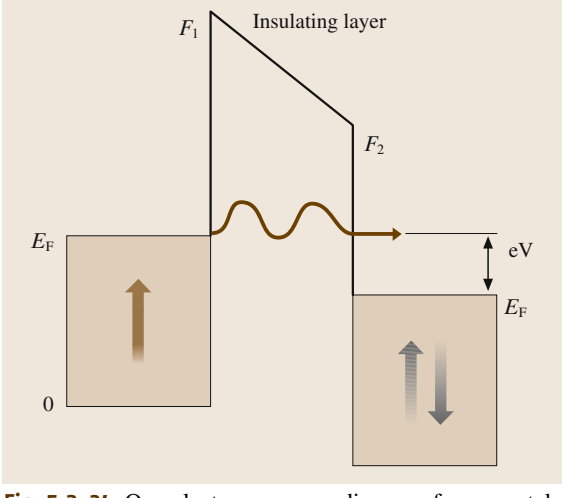


**Fig. 5.3-24** One-electron energy diagram for a metal–insulator–metal tunnel junction

that the tunneling current was spin-dependent. The spin splitting of the quasiparticle density of states of the superconductor caused by the application of the magnetic field was used to analyze the spin polarization of the tunneling current for Ni. The same method was used by the same authors to measure the spin polarization of electrons tunneling from a variety of ferromagnetic films: Fe, Co, Ni, and Gd [3.105]. A positive spin polarization was obtained in all cases; +44% was found for Fe, +34% for Co, +11% for Ni, and +4.3% for Gd. These results demonstrated that the tunneling process preserves the character of the electronic spin and inaugurated the exciting research field of spin-dependent tunnel transport. The large amount of progress in recent years in this particular domain has led to the construction of innovative spintronic devices, at the heart of which we find the magnetic tunnel junction (MTJ).



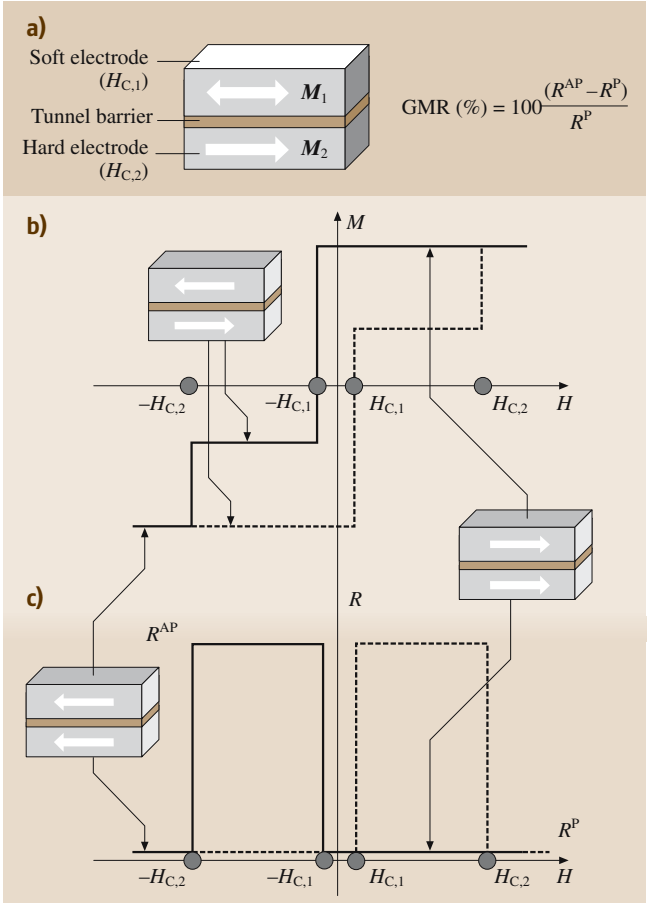


**Fig. 5.3-25a–c** Schematic representation of a magnetic tunnel junction (**a**) and its magnetization loop (**b**). The resistance of the MTJ is determined by the relative orientation of the magnetizations of the ferromagnetic electrodes of the junction, giving rise to low- and high-resistance states for parallel and antiparallel alignments, respectively (**c**). (After [3.106])

An MTJ behaves as a spin valve. However, it is a hybrid system comprising at least two ferromagnetic metals of different coercivities $H_{C,1}$ and $H_{C,2}$ ($H_{C,1} < H_{C,2}$), separated by a *thin insulator* (Fig. 5.3-25a) instead of a nonmagnetic metallic spacer as in classic spin valves. In Fig. 5.3-25b, the magnetization loop of a magnetic tunnel junction is schematically shown. In such a device, the current flowing perpendicular to the film plane (CPP geometry) depends on the relative orientation of the magnetizations $\boldsymbol{M}_1$ and $\boldsymbol{M}_2$ of the two ferromagnetic electrodes of the junction, reaching extreme values for parallel and antiparallel alignment (we assume that the magnetization lies in the plane of the ferromagnetic layers). For an applied magnetic field parallel to the plane of the films with a value $H \geq |H_{C,2}|$, the magnetizations of the two electrodes are aligned parallel to each other, giving rise to a low-resistance state ($R^{P}$) for the junction (Fig. 5.3-25c). In the magnetic-field window $|H_{C,1}| < H < |H_{C,2}|$, the electrodes' magnetizations are aligned antiparallel to each other, corresponding to a high-resistance state ($R^{AP}$) for the junction.

High tunnel magnetoresistance (TMR) at room temperature was discovered in magnetic tunnel junctions in the mid-1990s in $Fe/Al_2O_3/Fe$ junctions [3.107], $Fe/Al_2O_3/Ni_{1-x}Fe_x$ junctions [3.108], and CoFe/$\alpha$-$Al_2O_3$/Co and NiFe [3.109] junctions, although the first measurements at low temperature were performed in 1975 [3.110]. The tunneling resistance is modulated by the magnetic field in the same way as in a spin valve, but the advantage over a "classical" spin valve is that it has been shown to exhibit a significantly higher GMR ratio (50% or more), while requiring a saturation magnetic field equal to or somewhat less than that required for a spin valve. It was proposed that these MTJs would have potential uses as low-power field sensors and memory elements. Because the tunneling current density is usually small, MTJ devices tend to have high resistances. The resistance of an MTJ depends exponentially on the thickness of the insulating layer. Uniformity over the insulating layer is crucial to device operation. In addition, reproducibility from MTJ element to MTJ element is important for the proper working of arrays of such devices.

An example of such an effect is shown in Fig. 5.3-26, for a $Co/Al_2O_3/NiFe$ junction. When the magnetizations of the Co and NiFe layers go from an antiparallel

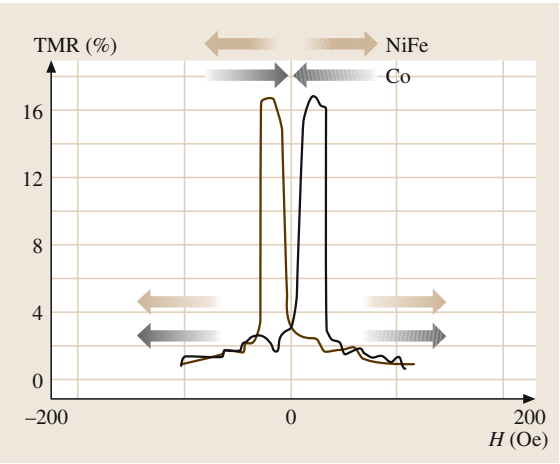


**Fig. 5.3-26** Tunnel magnetoresistance curve at room temperature of a $Co/AL_2O_3/NiFe$ junction. (After [3.111])

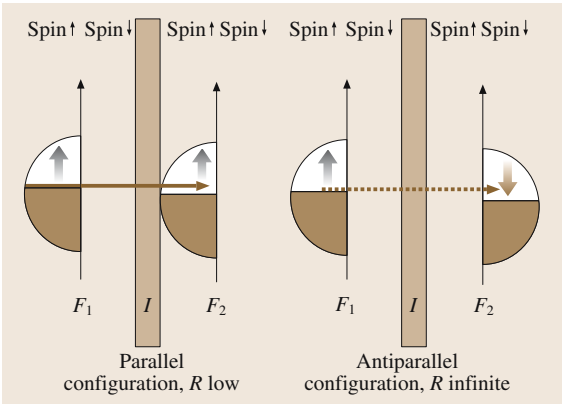


**Fig. 5.3-27** Schematic picture of the TMR effect in the case of two half-metallic electrodes. The transmission of the electrons from one layer to the other is only possible in the parallel state, resulting in a 100% TMR effect. (Courtesy of A. Bartélémy)

to a parallel arrangement, the resistance of the junction decreases. In this example, the effect is 16% at room temperature [3.111]. Most of the measurements reported in the literature have been performed using an alumina (oxidized aluminium) barrier.

In Jullière's model [3.110], the TMR ratio is expressed as a function of the spin polarizations $SP_1$ and $SP_2$ of the two magnetic electrodes by

$$\text{GMR} = \frac{R^{\text{AP}} - R^{\text{P}}}{R^{\text{P}}} = \frac{2\text{SP}_1\text{SP}_2}{1+\text{SP}_1\text{SP}_2}\,,$$

$$\text{where} \quad \text{SP}_i = \frac{N_\uparrow(E_\text{F}) - N_\downarrow(E_\text{F})}{N_\uparrow(E_\text{F}) + N_\downarrow(E_\text{F})}\,. \qquad (3.16)$$

A structure analogous to the spin valve described above may be made by making the two metallic electrodes from a half-metallic ferromagnet (HMF, SP = 100%) and separating them with a thin layer of insulator. Now, if the magnetizations of the electrodes are opposite, no current can flow across the junction, since the electrons which might tunnel have no density of final states on the far side to receive them. However, if the electrode magnetizations are parallel, a tunneling current may flow as usual. This can be explained simply by the schematic picture in Fig. 5.3-27, which represents the case of two half-metals (with only one spin direction at the Fermi level) separated by a thin insulating barrier.

We thus have a spin-electronic switch whose operation mirrors that of a pair of crossed optical polarizers, and which may be switched "on" and "off" by the application of an external magnetic field. If the electrodes are not ideal HMFs, then the on/off conductance ratio is finite and reflects the majority and minority densities of states of the ferromagnet concerned. In the case of an ideal HMF, in the antiparallel configuration, transmission from one electrode to the other is not allowed, and the resistance of the junction is infinite. In contrast, in the parallel state, transmission occurs, and the resistance is finite. This gives, for half-metallic electrodes, a spin polarization equal to 1 and a maximum TMR effect of 100%. In the case of a transition metal, the effect is more complex to analyze owing to the presence of s and d bands at the Fermi level with majority and minority spin directions. For transition metals, the TMR ratio is limited to 40% at liquid-helium temperature and 29% at room temperature. This is a demonstration of how the properties of metallic systems are controlled exclusively by the "mafia" of electrons at or very near the Fermi surface, whose band-structure properties the metal reflects.

The spin tunnel junctions described above depend for their operation only on the density of states, and not on the carrier mobility. Unlike fully metallic systems, they have a lower conductance per unit area of device, and hence larger signal voltages (of the order of millivolts or more) are realizable for practical values of the operating current. Moreover, the device characteristics, such as the size of the "on" resistance, the current density, the operating voltage, and the total current, may be tuned by varying with device cross section, the barrier height, and the barrier width. This is just one reason why spin tunnel junctions are very promising candidates for the spin injector stages of future spin-

electronic devices. They will also be the basis of the next generation of MRAMs, as illustrated later in this section.

Large TMR effects have been obtained using HMFs as electrodes, as can be seen in Fig. 5.3-28 in the case of a junction with $La_{0.7}Sr_{0.3}MnO_3$ (LSMO) electrodes and a $SrTiO_3$ (STO) barrier [3.112, 113]. The spin polarization deduced from this measurement is 83% if one assumes the same polarization for the two magnetic electrodes. With a polarization of 100%, half-metallic compounds would allow true on/off operations, and would be appropriate for gates of nonvolatile logic devices.

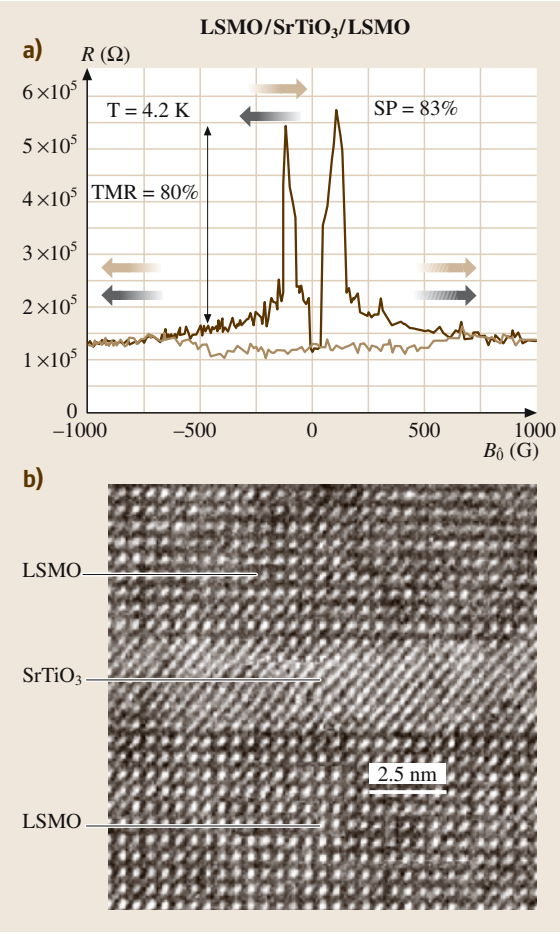


**Fig. 5.3-28** **(a)** TMR curve of an LSMO/STO/LSMO junction at 4.2 K. The spin polarization of the LSMO layer is 83%. After [3.112, 113]. **(b)** High-resolution transmission electron microscopy (HRTEM) image of an LSMO/STO/LSMO junction (courtesy of J. L. Maurice)

Recently, *Bowen* et al. [3.114] reported a TMR ratio of more than 1800% at $T = 4.2$ K in LSMO/$SrTiO_3$/LSMO fully epitaxial MTJs, from which they deduce a spin polarization of least 95% for the LSMO layer. This large TMR value arises both from preserving the quality of the LSMO/STO interfaces during the upgraded patterning process and from the use of junctions of small size ($5.6 \times 5.6\ \mu m^2$) (Fig. 5.3-29). The TMR extends to temperatures of about 280 K, an improvement compared with previous results in the literature [3.115].

The temperature dependence of the TMR is plotted in Fig. 5.3-30a,b for two junctions using $R(H)$ loops measured at $V_{dc} = 10$ mV. The TMR decreases rather quickly with increasing $T$, but vanishes only at temperatures of about 280 K for the $2 \times 6\ \mu m^2$ junction. TMR ratios of 30% (Fig. 5.3-30c) and 12% are obtained at 250 and 270 K, respectively. This represents a sizable improvement with respect to previous results [3.112, 113] obtained from heterostructures grown under identi-

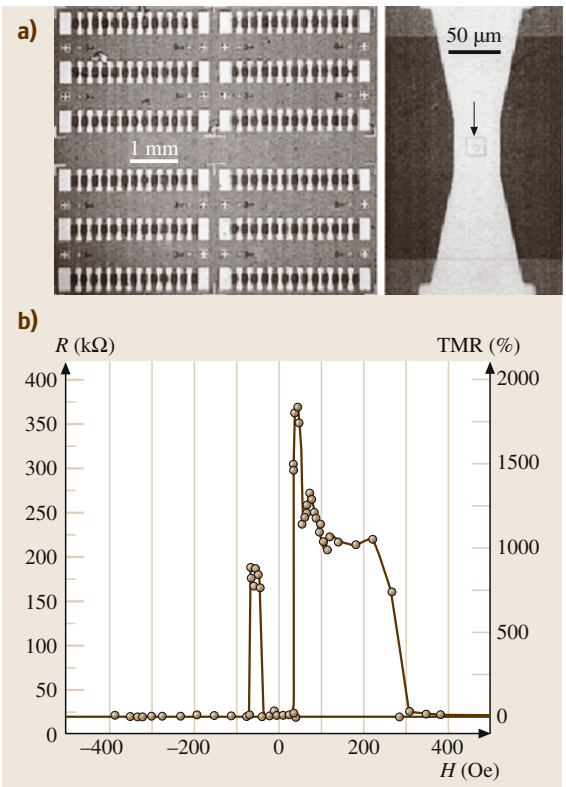


**Fig. 5.3-29** **(a)** Optical images of a processed sample of small-size LSMO/STO/LSMO magnetic tunnel junctions. **(b)** $R(H)$ loop for a $5.6 \times 5.6\ \mu m^2$ junction measured at 4.2 K. (After [3.114])

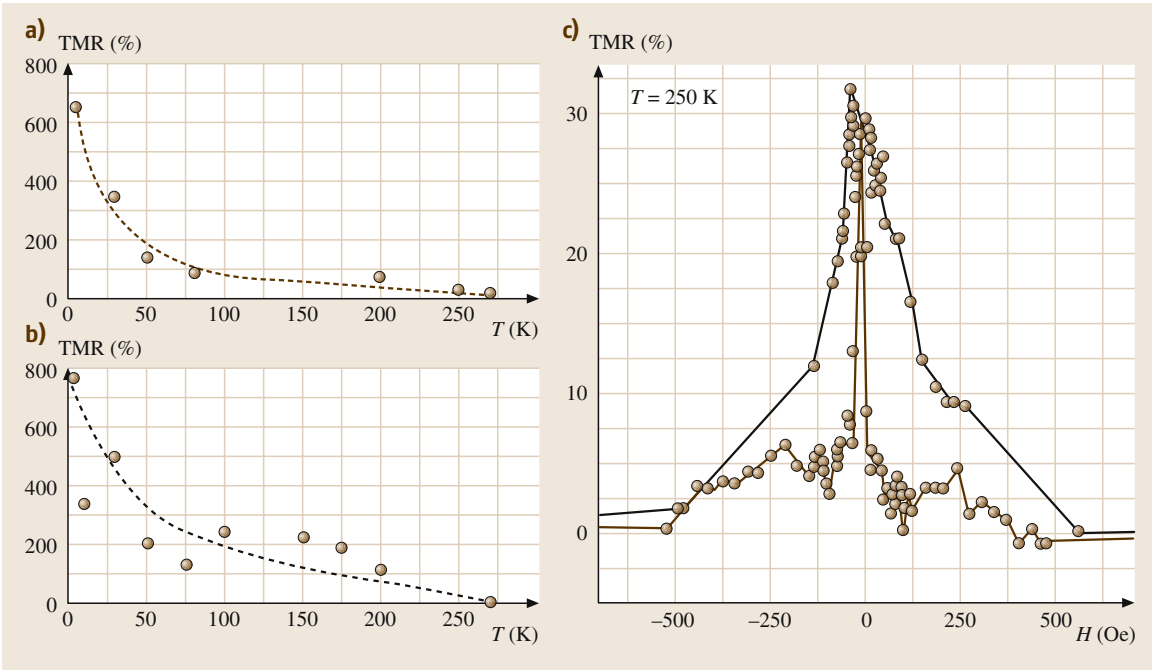


**Fig. 5.3-30a–c** Temperature dependence of the TMR measured with $V_{dc} = 510\,\text{mV}$ for two junctions: $2\times6\,\mu\text{m}^2$ **(a)** and $1.4\times4.2\,\mu\text{m}^2$ **(b)** (the *dashed lines* are guides to the eye). **(c)** $R(H)$ loop at $T = 250\,\text{K}$ and $V_{dc} = 10\,\text{mV}$, showing 30% TMR. (After [3.114])

cal conditions. Since the results shown in Fig. 5.3-30 were obtained from LSMO/STO/LSMO junctions with a fully strained crystallographic structure, these measurements prove that strain is not a limiting factor in the potential production of manganite-based MTJs with sizable TMR values at relatively high temperatures. High-quality interfaces that limit the disruption of the properties of the manganite are a more important requirement.

This example illustrates fairly well that progress in spin electronics would not be possible without the improvement in the manufacturing of devices on the nanometric scale.

Another promising HMF is $Fe_3O_4$, because this oxide exhibits the highest Curie temperature ($T_c = 858\,\text{K}$). Consequently, one can expect that its HMF character will remain significant at room temperature. Figure 5.3-31 shows a cross-sectional high-

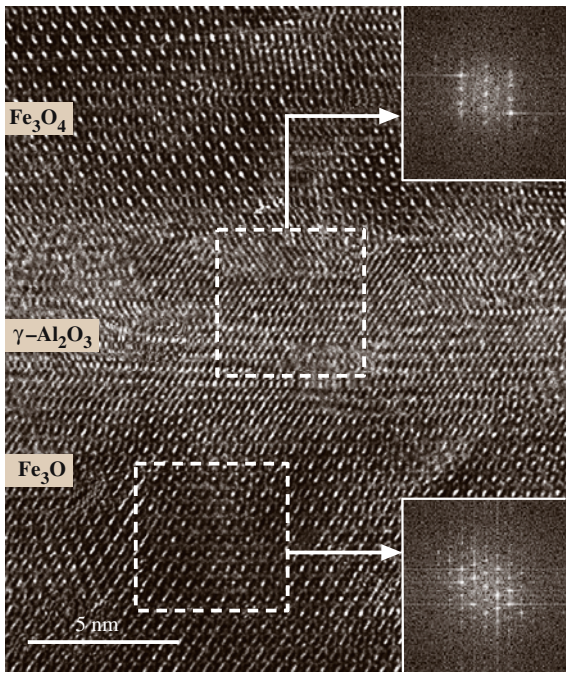


**Fig. 5.3-31** HRTEM image of a fully epitaxial $Fe_3O_4/Al_2O_3/Fe_3O_4$ MTJ grown by MBE. The Fourier transform of the barrier region of the micrograph shows the high crystalline quality of this region. (Courtesy of P. Bayle Guillemaud and P. Warin)

resolution transmission electron micrograph of a fully epitaxial $Fe_3O_4/Al_2O_3/Fe_3O_4$ MJT, grown by MBE assisted by atomic oxygen [3.116]. The interest in this result is that the growth of the interfaces was performed without exposing the surface layers to air, limiting the disruption of the bulk properties. The Fourier transform of the barrier region of the micrograph shows the high crystalline quality of this region. The use of crystalline barriers in MTJs opens the way to investigation of tunnel transport in periodic barriers, which will permit a better understanding of the underlying fundamental physics.

The record for magnetoresistance values has recently been obtained by *Van Dijken* et al. [3.117]. These authors report a large magnetic-field sensitivity of the collector current in a three-terminal magnetic tunnel transistor device with spin-valve metallic base layers. Giant magnetocurrents exceeding 3400% result from strong spin-dependent filtering of electrons traversing perpendicular to the spin-valve layers at energies well above the Fermi energy. With its giant magnetocurrent and reasonable output current, the magnetic tunnel transistor is a promising candidate for future magnetoelectronic devices.



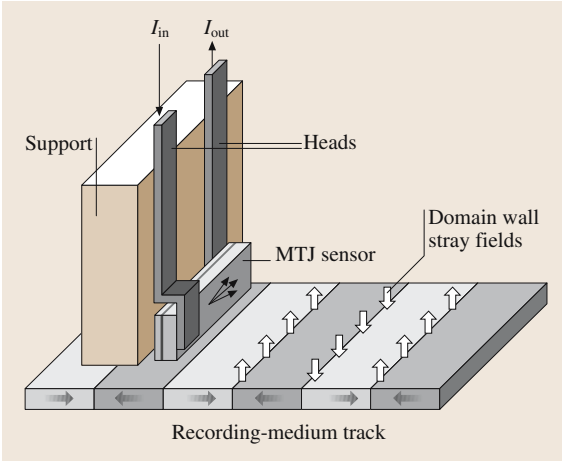


**Fig. 5.3-32** Schematic illustration of an MR read head. A spin valve ("all-metal" or MTJ) is used as an ultrasensitive sensor for the very low magnetic field strength generated by the small magnetic domains (bits). When a weak magnetic field, such as from a bit on a hard disk, passes beneath the read head, the magnetic orientation of the free layer changes its direction relative to the pinned layer, generating a change in electrical resistance due to the GMR effect. (After [3.106])

### Applications

*Magnetic Read Heads and Sensors.* Information is stored on a magnetic disk in small magnetic domains arranged in concentric tracks. The conventional read head used to be an induction coil, which sensed the rate of change of the magnetic field as the disk rotated. The signal and hence the density of magnetized bits were thus limited by the speed of rotation of the disk. Magnetoresistive sensors do not suffer from this defect, since they sense the strength of the field rather than its rate of change. They are, therefore, capable of reading disks with a much higher density of magnetic bits. Magnetoresistive read heads are commercially available and will be the leading technology beyond the year 2004.

When two oppositely magnetized domains meet, a domain wall appears, with a characteristic width of 100–1000 Å, depending on the magnetic properties of the material. Although there is no magnetic field emanating from the uniformly magnetized domains themselves, uncompensated magnetic poles at the domain walls emanate stray fields that extend out of the medium. Magnetic read heads contain a GMR or MTJ sensor element, which is sensitive to these domain wall stray fields. A schematic illustration of a GMR read head is shown in Fig. 5.3-32. The element is fabricated in such a way that the magnetization of the free layer is parallel to the plane of the medium. Every time the magnetic head passes over a domain wall, the magnetic field emanating from the wall pushes the magnetization of the free layer upwards or downwards, resulting in a change in the resistance of the MTJ device (the magnetization of the pinned layer is fixed). The design goal is to obtain the maximum rate of change in the resistance for a change in the magnetic field.

The concept used in read heads is also applied in another type of magnetic sensors, with which we can sense the operation of a piece of machinery when a magnetic field is applied, as illustrated in Fig. 5.3-33. A gear made of ferrous metal can be arranged so that it perturbs the magnetic fringing field originating from a permanent magnet close to the rotating gear and the sensor MTJ element. The MTJ element is sensitive to the changing orientation of the magnetic flux as gear teeth pass by the magnet. Thus, the readout resistance is related to the angular position of the rotating gear. Such an arrangement is used to monitor the engine speed in an automobile.

*Magnetic Random Access Memories (MRAMs).* Anisotropic-magnetoresistance elements were the first to be used for MRAM applications, approximately ten years ago. However, they provided a very small mag-

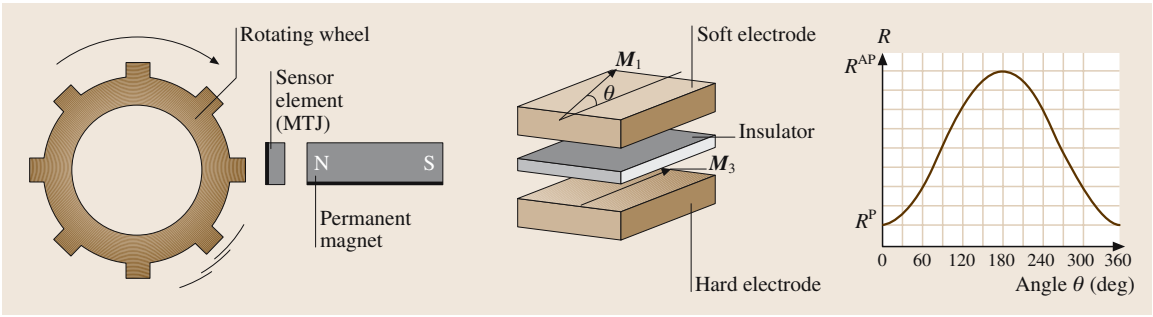


**Fig. 5.3-33** Principle of operation of a magnetic sensor using an MTJ element

netoresistive effect of about 2%, making their use disadvantageous in comparison with semiconductor memories in terms of read access time (> 250 ns). The density and cost of this kind of MRAMs were also not competitive with standard semiconductor memories. A major breakthrough in MRAM technology came with the use of GMR multilayers. The magnetoresistive signal is much higher – rising up to 18% – but the resistance of the all-metal GMR element is too small compared with the complementary metal–oxide–semiconductor (CMOS) transistor serving as the diode in an integrated structure. For this reason, a number of GMR cells have to be connected in series with the CMOS transistor, thereby decreasing the effective magnetoresistive signal. This is a serious drawback in the design of a fast-access memory. MTJs are the best candidates for MRAMs, as they provide a high magnetoresistive effect of 20–50% depending on the spin polarization of the magnetic electrodes, combined with a modifiable resistance, which depends on the thickness of the insulator and its degree of oxidation. This permits the utilisation of a single MTJ cell in series with a CMOS transistor (Fig. 5.3-34). This high-density architecture is suitable for fast-memory applications. The idea of the MRAM is to use the magnetization direction of the free magnetic layer for information storage, and the resulting resistance for readout. The resistance of the memory bit is either low or high, depending on the relative orientation (parallel or antiparallel) of the magnetization of the free layer with respect to the pinned layer. An applied magnetic field can switch the free layer between the two states. In an MRAM array, orthogonal lines pass under and over each memory bit, carrying the current which produces the switching magnetic field. The idea is that the current in one line is not sufficient to switch the memory cell; the bit will switch only if current is flowing through both of the lines that cross at the selected

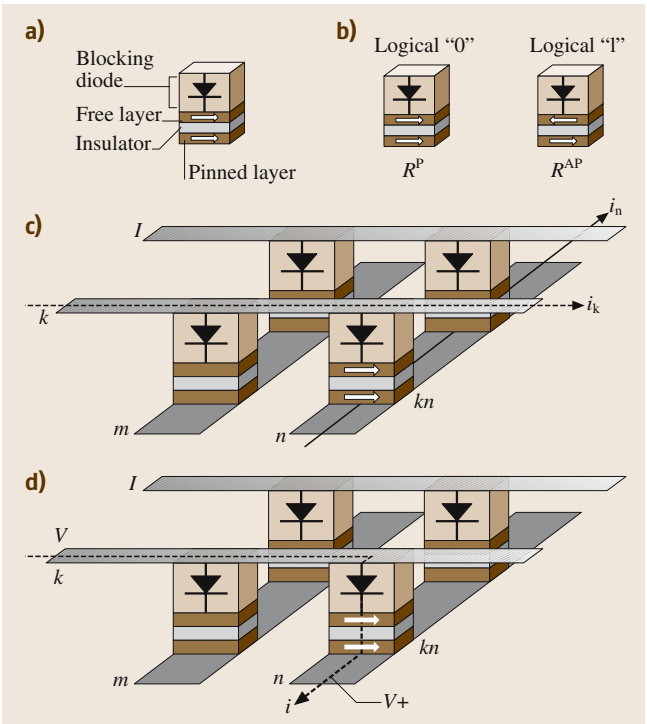


**Fig. 5.3-34** **(a)** Schematic representation of an MRAM cell containing a single MTJ and a blocking diode (CMOS transistor), allowing current flow in only one direction, in series. **(b)** Representation of a logical "0" by the low-resistance state $R^P$ and of a logical "1" by the high-resistance state $R^{AP}$. **(c)** The process of writing information on bit *kn* situated at the crossing of word lines *k* and *n*. The existence of the two currents $i_n$ and $i_k$ is necessary to switch the magnetization of the free layer. For example, in the memory cell *km*, which is influenced by a single current $i_k$, no information is stored. **(d)** The process of reading information from cell *kn*. A bias is applied between the word lines *k* and *n* and the current through the bit cell is measured and compared with a reference value. The determination of the magnetic state of the junction, which can then be related to logical "0" or "1", is thus possible

bit. The readout of the stored information in the selected bit is done by applying a bias between the lines that cross it and measuring the current that flows through it.

For the successful realization of MRAM devices using MTJs, two very critical components – the tunnel barrier and the free layer – have to be optimized. The tunnel barrier needs to show large-scale uniformity over the wafer, in addition to the more or less obvious prerequisites of being pinhole-free and extremely smooth. This is because the tunnel resistance depends exponentially on the barrier thickness and the absolute value of the MTJ resistance is compared with a reference cell during the read operation. As far as the free layer is concerned, its thickness is directly related to the value of the magnetic field or current required for switching a bit. A free layer less than 5 nm thick is desirable, since it results in a low switching field and, as a consequence, low power consumption.

A number of difficulties have to be resolved to create successful devices. These include efficient spin injection into semiconductors and heterostructures, and a search for new spin-polarized materials. Other effects potentially important for spintronic devices include optical and electrical manipulation of ferromagnetism, current-induced switching and precessing of magnetization, and the possibility of a long coherence time for optically excited spins in semiconductors. For a good overview of the issues in spin electronics, including the prospects for spintronic quantum devices, see [3.118].

### 5.3.4.2 Ultrahigh-Density Storage Media in Hard Disk Drives

#### The Limits of the Present Technology

In the current storage technology, which uses continuous polycrystalline thin-film media, the signal-to-noise ratio (SNR) of the medium is directly related to the number of grains per bit. At storage densities on the order of 80 Gb/in$^2$, the grain size of the CoCrPtX alloys (X = Ta, P, etc.) used in the current media is on the order of 8 nm, the number of grains per bit is about 100, and the bit size is on the order of 250 nm × 30 nm. A further reduction in the number of grains per bit below 100 would lead to a strong decrease in the SNR. To continue decreasing the bit cell size in continuous media (while keeping the SNR constant), it is necessary to reduce the grain size further. However, there is a physical limit to how small the grain size can be before thermal variations can affect the stability of the magnetization. This is known as the superparamagnetic limit. In CoCrPt alloys, the minimum grain size for which the criterion for magnetic stability can be satisfied is about 8 nm, which is the grain size used in today's media. Further reducing the grain size requires the use of other materials as FePt, SmCo, and FeNdB alloys. However, this implies that larger write fields will be needed to switch the magnetization of the grains. This would necessitate the development of new materials which are not yet known. In the short term, the use of antiferromagnetically coupled media has allowed the superparamagnetic limit to be extended in combination with GMR read heads [3.119].

#### The Promise of Perpendicular Media

It is foreseen that within two or three years, magnetic recording will switch to perpendicular discontinuous media for several reasons. In perpendicular media, as opposed to longitudinal granular media, the smaller the bit size, the smaller the effect of the demagnetizing field on each bit is. In addition, the efficiency of the writer can be greatly improved, and higher-anisotropy materials can be used. Both effects contribute to a better thermal stability at small size grain size as compared with longitudinal media. This should help us to reach densities of the order of 200–400 Gb/in$^2$. However, to progress beyond these densities, a totally different approach will be required, which may consist of using patterned media, i. e. media made of arrays of nanometer-scale individual dots, in which each dot carries a bit of information. The significant advantage of this type of medium is that the shape and edge of each bit are not determined by the grain size as in continuous media, but are determined by the patterning process used to make the dots. Consequently, each dot can be made of a single magnetic domain (1 grain per bit instead of the 100 grains per bit in a continuous medium). The volume of a grain can therefore be much larger in a patterned medium so that the superparamagnetic limit is no longer a problem, at least up to several terabits per square inch. Of course, the use of patterned media raises other questions such as fabrication at low cost, tracking, and reproducibility.

Various techniques have been developed to prepare arrays of submicrometer magnetic dots: optical, electron-beam, or X-ray lithography followed by etching of the magnetic material; patterning using a focused beam [3.120]; and self-organization of nanoparticles [3.121]. So far, however, none of these techniques seems to be able to combine the criteria of low cost, and rapid patterning of large areas (several square inches) down to 25 nm pitch.

*Nanoimprinting.* Nanoimprinting is a promising method of nanopatterning proposed recently for solving the above-mentioned drawbacks. Nanoimprint lithography is a major breakthrough in nanopatterning because it can produce sub-10 nm feature sizes over a large area with a high throughput and low cost, a feat impossible with current, conventional lithography.

Basically, the process of nanoimprinting starts by first making a mold by electron-beam lithography. This may take a long time, but this mold can be subsequently used a large number of times to imprint layers of resists on almost any kind of flat substrate. The patterned layer of resist is next used as an etching mask to transfer the pattern to the substrate by direct reactive ion etching (RIE) (Fig. 5.3-35a). The original approach to preparing arrays of magnetic dots starts from prepatterned wafers, on top of which a ferromagnetic material is deposited. In that case the nanopatterning of the magnetic material results directly from its deposition on a prepatterned wafer (Fig. 5.3-35b).

*Moritz* and coworkers have studied the coupling between the dots obtained by deposition of Co/Pt multilayers on prepatterned Si substrates [3.122, 123]. Two patterning process were compared: (a) electron-beam lithography followed by direct RIE [3.124], and (b) nanoimprint lithography followed by lift-off and dry RIE of silicon [3.125, 126]. Subsequent deposition of a magnetic material (Co−Pt) leads to arrays of single-domain dots with a perpendicular magnetization.

By nanoimprinting, a dot size down to 30 nm in diameter with a pitch of 60 nm has been obtained. This represents a density of 200 Gb/in$^2$. After the nanoimprinting of the Si substrate, a magnetic material was deposited on the prepatterned wafer by sputtering or by some other relatively directional physical deposition process. The magnetic material then covered the top of the dots, the bottom of the trenches separating the dots, and, to a lesser extent, the sidewalls of the dots [3.122].

Corresponding atomic and magnetic images are shown in Fig. 5.3-36.

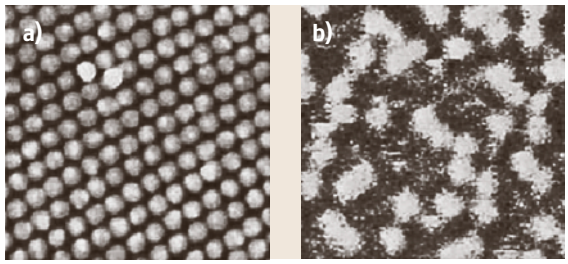


**Fig. 5.3-36** Structural (a) and magnetic (b) images of an array of single-domain dots with a 60 nm pitch prepared by nanoimprinting and coating with a (Pt/Co) multilayer. Images obtained by atomic and magnetic force microscopy

*Influence of the Angle of Deposition.* In order for one to be able to use these arrays of magnetic dots as recording media, the dots should be weakly coupled so that the magnetization of one dot can be switched without affecting the magnetization of the neighboring dots. In the present example, the sputtered species

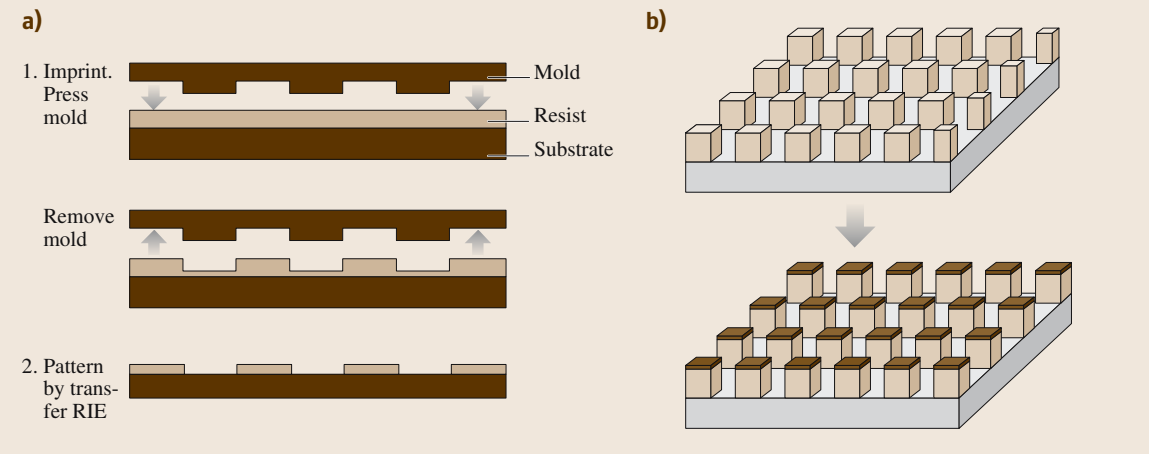


**Fig. 5.3-35a,b** Schematic principle of (a) the successive technological steps of pattern transfer by imprinting, and (b) the deposition of a magnetic material on a prepatterned substrate. The magnetic deposit covers the top of the dots, the bottom of the trenches, and, to a lesser extent, the sidewalls of the dots

(Co and Pt) were directed onto the substrate at either normal or oblique (37° from the normal) incidence (Fig. 5.3-37) [3.123].

When the substrate consists of an array of silicon pillars, the structural and magnetic properties obtained with the two deposition modes are quite different, as illustrated in Figs. 5.3-37 and 5.3-38 [3.123]. With normal deposition, a rough deposit made of Co, Pt, and CoPt alloy grains is observed (Fig. 5.3-37a), which induces a ferromagnetic coupling between adjacent dots (Fig. 5.3-38a) via the sidewalls and the magnetic deposit in the bottom of the trenches [3.122].

In contrast, when the Pt is deposited at oblique incidence, one sidewall of the dots is coated with antiferromagnetic CoO, whereas the other side consists of a Pt-rich PtCo alloy, which is nonmagnetic (Fig. 5.3-37b). In this latter case, no direct coupling between the top of the dots and the bottom of the trenches takes place, resulting on no direct ferromagnetic coupling between adjacent dots. A checkerboard-like pattern of single-domain dots with a perpendicular magnetization is observed (Fig. 5.3-38b) [3.122, 123, 126]. This second situation is favorable if one wishes to use this type of array of dots as a discrete recording medium.

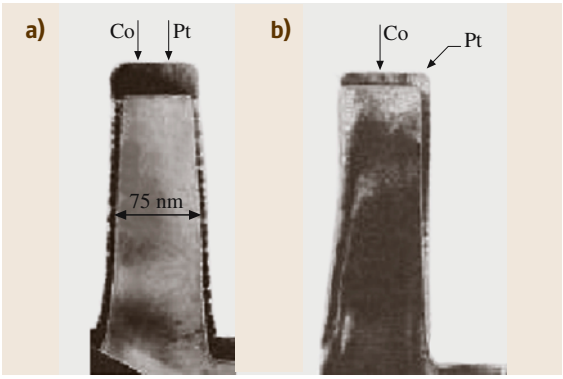


**Fig. 5.3-37a,b** Cross-sectional TEM views of dots prepared by electron-beam lithography followed by Si RIE and covering by (Pt/Co) multilayers. In **(a)**, both Co and Pt were deposited at normal incidence. In **(b)**, Co was deposited at normal incidence, whereas Pt was deposited at oblique incidence. The width of the dots in both cases is 75 nm. (From [3.123])

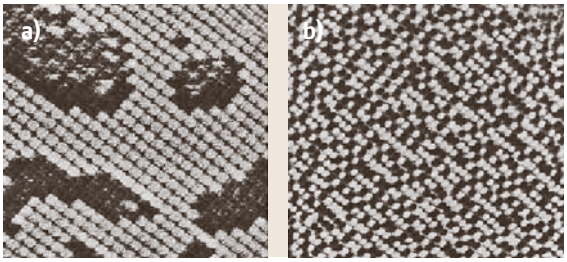


**Fig. 5.3-38a,b** 8 μm MFM images of domain patterns in arrays of (Pt/Co) dots deposited at normal incidence **(a)**, and oblique incidence **(b)**. (Courtesy of B. Dieny)

*Storing the Information on the Sidewalls of the Dots.* So far, the magnetic deposit on the top of the dots carries the recorded information. An alternative method would be to deposite the material on the sidewalls of the dots. This can be achieved by performing a codeposition of Cr at normal incidence and Co at oblique incidence. Thereby, a nonmagnetic Cr-rich CoCr alloy forms on top of the dots, whereas the sidewalls are coated with almost pure magnetic Co. The information can be stored by setting the magnetization of these "vertical nanomagnets" to be up or down on the sidewalls.

Figure 5.3-39 compares the magnetic contrast measured by magnetic force microscopy (MFM) in two arrays of dots of the same geometry, one coated on the top of the dots with a (Pt/Co) multilayer, the other coated on the sidewalls with Co. Clearly the stray fields are much more localized and intense in the second case. It should be pointed out that the sidewalls are not single-domain here, but this can be fixed by using materials with higher coercivity ($Co_{80}Cr_{20}$ alloys for instance). Another advantage of this approach is that two opposite sidewalls can be used per dot, which allows one to double the areal density for the same geometry.

*Manipulating the Magnetization of Individual Dots.* Two techniques have been developed to manipulate the magnetization of each dot individually. The first one is a thermomagnetic technique, which consists of us-

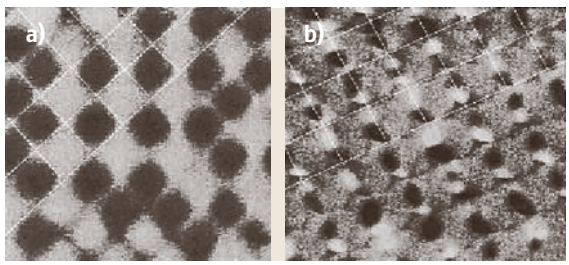


**Fig. 5.3-39a,b** MFM domain patterns in as-deposited arrays of 400×400 nm dots **(a)** coated on the top by a (Pt/Co) multilayer and **(b)** coated on the sidewall by 5 nm thick Co deposit. (Courtesy of B. Dieny)

ing a conductive atomic force microscope (AFM) tip to locally heat a given dot by passing a pulse of current between the tip and the dot [3.127]. The temperature rise leads to a decrease in the switching field of the magnetization of the addressed dot. Simultaneously, a static field of −200 Oe is applied to the whole sample. This field is large enough to switch the magnetization of the heated dot in the desired direction but low enough not to switch the magnetization of the other dots [3.123]. This is illustrated in Fig. 5.3-40. These experiments are preliminary, but impressive and highly encouraging. The main difficulty was irreproducibility in the contact resistance.

A second technique has also been developed to manipulate the magnetization of individual dots; this technique is based on the use of write heads developed by Headway Inc. The array of dots is mounted on a piezoelectric stage, which allows displacement of the sample over an area of 120 μm × 120 μm. The head is in contact with the surface of the sample. A write current of 30 mA was used in the writer. An example of controlled writing of a line of dots is shown in Fig. 5.3-41 [3.123].

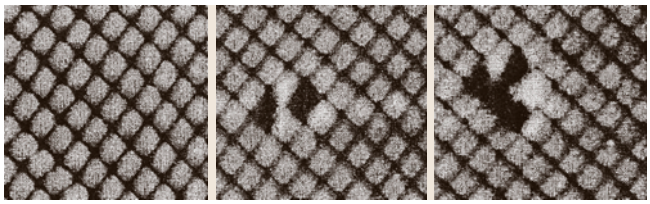

**Fig. 5.3-40** MFM images of an array of dots covered by a multilayer of composition Pt 20 nm/(Co 0.5 nm/Pt 1.8 nm). The dots are 400 nm in size, with an edge-to-edge spacing of 100 nm. A controlled switching of individual dots has been achieved by passing a pulse of current from a metallic AFM tip to the dot and simultaneously applying a uniform field of −200 Oe over the whole sample. (From [3.123])

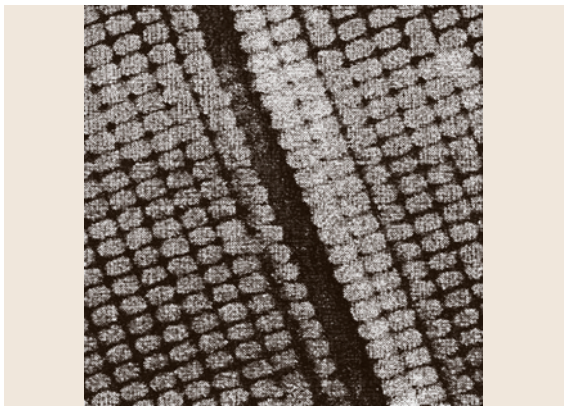

**Fig. 5.3-41** 4 μm × 4 μm MFM image of a line written on an array of rectangular dots 100 nm × 200 nm in size with an edge-to-edge spacing of 100 nm. The writing was performed using a commercial inductive write head provided by Headway Inc. (From [3.123])



## 5.3.5 Preparation Techniques

Various strategies have been developed for the manufacture of nanostructured materials. They follow essentially two approaches:

- The *top-down* manufacturing paradigm is that of the existing electronic technologies. It consists in downscaling the pattern size in lithographically structured materials.
- The *bottom-up* paradigm of nanosciences consists in the fabrication of atomically precise structures of increasing size, up to the mesoscopic scale.

Many preparation techniques are very specific to one particular type of material: for instance, many different chemical and physical techniques are used to produce porous silicon. Hence, we list and briefly describe below only the most common and generic methods for the synthesis and fabrication of nanostructured materials. For a more detailed, recent, comprehensive description and discussion of the following production techniques, see [3.5, 128].

### 5.3.5.1 Molecular-Beam Epitaxy

#### 2-D Structures

An atomic or molecular beam of Ga, As, Al, and/or other elements is created thermally in a ultrahigh-vacuum chamber and directed at a specific, well-defined, atomically flat facet of a single-crystal substrate. A very low deposition rate, associated with a precisely controlled substrate temperature and various real-time techniques for monitoring the state of the surface, permit one to find growth conditions that preserve a coherent crystalline order or minimize the density of structural

defects. Because of the atomic layer-by-layer deposition, MBE is the technique that allows the best control over the thickness of a 2-D film down to the subatomic level. This has motivated a huge number of research studies on the mechanism of MBE growth. MBE is used when the highest thickness accuracy, abrupt interfaces, the highest purity, and/or the lowest density of surface defects is needed. Its main applications are for semiconductor quantum wells, since the band gap of $Al_xGa_{1-x}As$ can be tuned continuously through the composition $x$ of the ternary alloy without inducing too large a lattice mismatch (see e.g. [3.32]).

#### 1-D Structures

Quantum wires are less commonly encountered, since their fabrication procedures are even more complicated: one method exploits the step-flow growth of vicinal surfaces [3.129].

Self-assembly in specific MBE-type situations leads to the formation of wire structures. Thus, straight atomic lines of Si have been grown on a $\beta$-SiC(100) surface [3.130].

#### 0-D Structures

MBE was primarily designed for the growth of 2-D nanostructures. However, it has been observed that the combination of two lattice-mismatched materials can lead to the formation of self-assembled size-monodispersed clusters or dots during growth in the Stranski–Krastanov (SK) mode. The most studied system is that of InAs deposited on a GaAs(100) substrate [3.131]. In that case, the lattice mismatch is 7%, and the nanocluster size is $20\,\text{nm} \pm 10\%$. The average nanocluster size and density are tunable over a narrow range through the choice of growth parameters. Moreover, various cluster shapes are obtained with different substrate faces. More complicated systems have been produced, such as 2-D core–shell magnetic dots [3.132]. Finally, the use of a high-index substrate (such as GaAs(311)) can lead to a lateral ordering of the nanocluster distribution [3.133].

Clusters of various metals can be formed by use of a dewetting (Vollmer–Weber) type of epitaxial growth; this has been done mainly on highly oriented pyrolytic graphite (HOPG). Formation of 3-D islands has been reported for Cu, Ag, Au [3.134], Pt [3.135], Co [3.136], Mo, [3.137], and Pd [3.138].

In some specific situations, a 3-D stacking of quantum dot layers has been achieved [3.139].

### 5.3.5.2 Metal-Organic Chemical Vapor Deposition (MOCVD)

This type of growth takes place in a reaction chamber in which the substrate is heated to a very high temperature (500 °C to 1000 °C). A combination of metal-organic and metal hydride vapors (e.g. triethylgallium, $Ga(C_2H_5)_3$, and arsine, $AsH_3$, for GaAs formation) is then brought into contact with the substrate by use of a laminar flow of a carrier gas (typically $N_2$ or $H_2$). The desired atoms are deposited layer by layer through a chemical reaction taking place at the substrate surface. MOCVD can be adapted to large-scale, long, continuous runs. Today, it is thus the most conventional industrial manufacturing technique for semiconductor heterostructures.

### 5.3.5.3 Lithography

The lateral patterning in large-scale integrated electronic circuits is produced by projection photolithography. The resolution is limited not by the resists themselves but by optical diffraction during exposure, the minimum line spacing being of the order of $\lambda/\text{NA}$, where $\lambda$ is the wavelength and NA the numerical aperture of the projection system. Today, the deep-UV technology is used; this is based on ArF excimer laser sources ($\lambda = 193\,\text{nm}$), the numerical aperture is of the order of 0.8, and image enhancement techniques such as phase-shift masks are used [3.140]. This technique achieves typical line spacings close to 100 nm. To achieve higher resolution, alternative radiation sources and/or exposure techniques have been used and are summarized in Table 5.3-3.

### 5.3.5.4 Nanocrystals in Matrices

#### Diffusion-Controlled Growth

The growth of clusters from ions dissolved in a glass can be kinetically controlled by tuning the temperature between the glass transition temperature and the melting temperature. Empirical methods for the growth of metal clusters for use in stained-glass windows have been known for centuries. This technique is now mainly used for the fabrication of color cutoff filters using II–VI compounds. The main compound used is $CdS_xSe_{1-x}$, and such filters are made by Schott in Germany, Corning in the USA, and Hoya in Japan. It is also used for photochromic glasses based on I–VII compounds (mainly AgBr).

**Table 5.3-3** Radiation sources and exposure techniques for higher resolution

| Radiation source | Energy |
|---|---|
| Deep UV | 6.4 eV |
| X-rays | 2 keV |
| Electrons | 20 keV |
| Ions | 100 keV |

| Exposure techniques | Comments |
|---|---|
| Contact printing | The resolution is the limited by the optical skin depth of the mask material. |
| Proximity printing | The resolution is limited by diffraction, with a minimum line spacing of $\sqrt{g\lambda}$, where $g$ is the mask–surface distance. Proximity printing techniques have been used mainly in conjunction with X-ray radiation sources. |
| Nanoimprinting | A master stamp is used directly for hot embossing of a substrate, usually made of a polymer. This allows the stamp to produce many patterned substrates. Although there is no diffraction limit here, hot embossing has been applied mainly for low-resolution applications, in various fields such as miniaturized total-analysis Systems (μTAS), microfluidics, and microoptics.<br>UV–nanoimprint lithography corresponds to contact printing with UV exposure. |
| **Scanned-source techniques** | |
| Electron and ion beams | Scanning electron beam lithography is the most widely used technique for nanostructuring surfaces beyond the optical resolution limit. The resist used is polymethylmethacrylate (PMMA). |
| Near-field scanning optical microscope (NSOM) | This is the scanned-source equivalent of contact and proximity printing. |
| Scanning tunneling microscope (STM) | In contrast to electron-beam lithography, the mechanism of STM lithography is generally an inelastic electron tunneling process, with energy quanta of an electron volt. STM can also be used for single-atom or single-molecule manipulations for the fabrication of individual nanostructures. |

#### Sol–Gel Synthesis

Cold chemical synthesis of nanoporous glasses by the sol–gel technique allows the embedding of temperature-sensitive clusters such as organic nanocrystals. Moreover, it often permits one to achieve larger densities of semiconductor nanocrystals than in diffusion-controlled growth.

#### Zeolites

Zeolites constitute a group of hydrated crystalline aluminosilicates containing regularly shaped pores with sizes from 1 nm to several nanometers. This provides them with the ability to reversibly adsorb and desorb specific molecules. Chemical synthesis of semiconductors inside such pores permits the fabrication of regularly distributed, highly size-monodispersed nanocrystal arrays. This has been applied to CdS, $PbI_2$, and Ge.

### 5.3.5.5 Ex Situ Synthesis of Clusters

As an alternative to in situ growth, nanocrystals can be synthesized either in solution (e.g. by colloidal synthesis) or in the gas phase, prior to dispersion in a matrix or deposition or self-assembly onto a substrate.

#### Colloidal Synthesis

Although gold colloids were known and studied very early [3.2], the synthesis technique has been much studied and greatly improved during the past few decades. The two-phase approach permits the fabrication of thiol-covered noble-metal nanoparticles [3.141]. The thiol layer prevents coalescence of the metal particles, thus stabilizing the colloid and preserving the size distribution. Motivated by the self-ordering properties of layers of nanoparticles with a narrow size distribution,

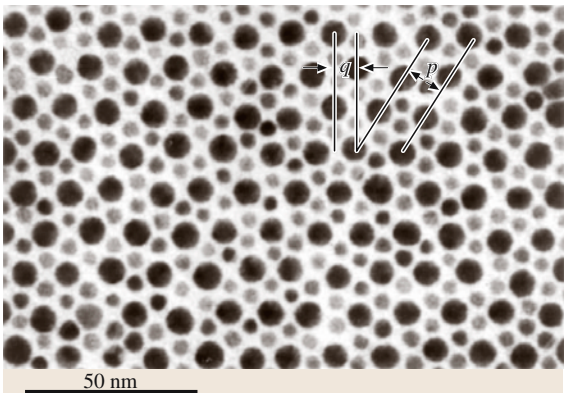


**Fig. 5.3-42** TEM image showing a superlattice of thiol-passivated Au clusters with a bimodal size distribution (~4.5 and 7.8 nm diameter). The 2-D supracrystallization shows a regular self-organized bimodal packing. (After 3.144)

researchers have developed various size-selection techniques [3.142, 143]. As shown in Fig. 5.3-42, relatively complex self-organized structures are now achievable through self-assembly of size-selected thiol-capped nanoparticles obtained from colloidal synthesis [3.144], including mixtures of particles of different chemical nature (Au and Ag, [3.145]).

This technique has been extended to transition metals. 6 nm trioctylphosphine-coated Co particles have been synthesized using a reverse-micelle approach and assembled as a hexagonal self-organized superlattice [3.146]. 3-D self-assembled superlattices of FePt nanoparticles have also been produced [3.121].

Ligand-stabilization techniques have led to macromolecular complexes consisting of a metal core containing a fixed number of atoms surrounded by a precise number of organic ligand molecules. Following the synthesis of $Au_{55}(P(C_6H_5)_3)_{12}Cl_3$ clusters [3.147], a number of such macromolecules of various sizes and compositions have been studied, such as giant ligand-stabilized clusters containing 561 Pd atoms [3.148].

Variations of the colloidal-synthesis and size selection techniques have also been developed in parallel for the preparation of semiconductor nanoparticles, particularly II–VI compounds such as CdSe [3.149], from which self-assembled superlattices can be grown [3.150]. GaAs nanocrystals have been produced similarly [3.151].

### Gas-Phase Production

Several techniques have been applied for the production of "preformed" clusters in the gas phase, prior to their deposition onto a substrate. The low-energy cluster beam deposition technique was developed especially for the deposition of small clusters of transition metals (Ni, Fe, Co, etc.) [3.152]. An extensive review of this vast subject can be found in [3.153].

## References


3.1 M. José-Yacaman, L. Rendon, J. Arenas, M. C. S. Puche: Maya blue paint: An ancient nanostructured material, Science **273**, 223–225 (1996)

3.2 M. Faraday: Experimental relations of gold (and other metals) to light, Phil. Trans. R. Soc. **147**, 145–181 (1857)

3.3 R. Dingle, W. Wiegmann, C. H. Henry: Quantum states of confined carriers in very thin $Al_xGa_{1-x}As$–GaAs–$Al_xGa_{1-x}As$ heterostructures, Phys. Rev. Lett. **33**, 827–830 (1974)

3.4 B. Bhushan (Ed.): *Springer Handbook of Nanotechnology* (Springer, Berlin, Heidelberg 2004)

3.5 P. Moriarty: Nanostructured materials, Rep. Prog. Phys. **64**, 297–381 (2001)

3.6 M. Milun, P. Pervan, D. P. Woodruff: Quantum well structures in thin metal films: Simple model physics in reality?, Rep. Prog. Phys. **65**, 99–141 (2002)

3.7 S. A. Lindgren, S. Valden: Electron-energy-band determination by photoemission from overlayer states, Phys. Rev. Lett. **61**, 2894–2897 (1988)

3.8 T. Miller, A. Samsavar, G. E. Franklin, T.-C. Chiang: Quantum-well states in a metallic system: Ag on Au(111), Phys. Rev. Lett. **61**, 1404–1407 (1988)

3.9 S. Bjornholm, J. Borggren, O. Echt, K. Hansen, J. Pedersen, H. D. Rasmussen: The influence of shells, electron thermodynamics, and evaporation on the abundance spectra of large sodium metal clusters, Z. Phys. D **19**, 47 (1991)

3.10 W. Ekardt: Work function of small metal particles: Self-consistent spherical jellium-background model, Phys. Rev. B **29**, 1558–1564 (1984)

3.11 J. H. Cho, K. S. Kim, C. T. Chan, Z. Y. Zhang: Oscillatory energetics of flat Ag films on MgO(001), Phys. Rev. B **63**, 113408 (2001)

3.12 J. J. Paggel, T. Miller, T. C. Chiang: Quantum-well states as Fabry-Perot modes in a thin-film electron interferometer, Science **283**, 1709–1711 (1999)

3.13 M. S. Hybertsen: Mechanism for light emission from nanoscale silicon. In: *Porous Silicon Science and Technology*, ed. by J.-C. Vial, J. Derrien (Les éditions de physique, Les Ulis 1995) p. 67

3.14 L.T. Canham: Silicon quantum wire array fabrication by electrochemical and chemical dissolution of wafers, Appl. Phys. Lett. **57**, 1046–1048 (1990)

3.15 V. Lehmann, U. Gösele: Porous silicon formation: A quantum wire effect, Appl. Phys. Lett. **58**, 856–858 (1990)

3.16 A. I. Belogorokhov, V. A. Karavanskii, A. N. Obraztsov, V. Y. Timoshenko: Intense photoluminescence in porous gallium-phosphide, JETP Lett. **60**, 274–279 (1994)

3.17 A. Anedda, A. Serpi, V. A. Karavanski, I. M. Tiginyanu, V. M. Ichizli: Time-resolved blue and ultraviolet photoluminescence in porous GaP, Appl. Phys. Lett. **67**, 3316–3318 (1995)

3.18 J. S. Shor, L. Bemis, A. D. Kurtz, I. Grimberg, B. Z. Weiss, M. F. Macmillian, W. J. Choyke: Characterization of nanocrystallites in porous p-type 6H-SiC, J. Appl. Phys. **76**, 4045–4049 (1994)

3.19 D. J. Lockwood, Z. H. Lu, J.-M. Baribeau: Quantum confined luminescence in $Si/SiO_2$ superlattices, Phys. Rev. Lett. **76**, 539–541 (1996)

3.20 R. W. Collins, P. M. Fauchet, I. Shimizu, J.-C. Vial, T. Shimada, A. P. Alivisatos (Eds.): *Advances in Microcrystalline and Nanocrystalline Semiconductors*, Vol. 452 (Materials Research Society, Pittsburgh 1997)

3.21 N. M. Park, T. S. Kim, S. J. Park: Band gap engineering of amorphous silicon quantum dots for light-emitting diodes, Appl. Phys. Lett. **78**, 2575–2577 (2001)

3.22 L. Pavesi, L. Dal Negro, C. Mazzoleni, G. Franzo, F. Priolo: Optical gain in silicon nanocrystals, Nature **408**, 440–444 (2000)

3.23 P. Ball: Let there be light, Nature **409**, 974–976 (2001)

3.24 L. E. Brus: Electron–electron and electron–hole interactions in small semiconductor crystallites: The size dependence of the lowest excited electronic state, J. Chem. Phys. **80**, 4403–4409 (1984)

3.25 Y. Kayanuma: Quantum-size effects of interacting electrons and holes in semiconductor microcrystals with spherical shape, Phys. Rev. B **38**, 9797–9805 (1988)

3.26 Al. L. Efros, A. L. Efros: Interband absorption of light in a semiconductor sphere, Sov. Phys. Semicond. **16**, 772–775 (1982)

3.27 A. Shik: *Quantum Wells, Physics and Electronics of Two-Dimensional Systems* (World Scientific, Singapore 1997) Chap. 4.4

3.28 S. Glutsch, D. S. Chemla: Transition to one-dimensional behavior in the optical absorption of quantum-well wires, Phys. Rev. B **53**, 15902–15908 (1996)

3.29 D. J. Norris, A. Sacra, C. B. Murray, M. G. Bawendi: Measurement of the size-dependent hole spectrum in CdSe quantum dots, Phys. Rev. Lett. **72**, 2612–2615 (1994)

3.30 G. Banfi, V. Degiorgio: Neutron scattering investigation of the structure of semiconductor-doped glasses, J. Appl. Phys. **74**, 6925–6935 (1993)

3.31 M. H. Yukselici: Growth kinetics of CdSe nanoparticles in glass, J. Phys.: Condens. Matter **14**, 1153–1162 (2002)

3.32 C. Weisbuch, B. Vinter: *Quantum Semiconductor Structures* (Academic Press, Boston 1991) Chap. 3

3.33 B. Zhao, A. Yariv: Quantum well semiconductor lasers. In: *Semiconductor Lasers I: Fundamentals*, ed. by E. Kapon, P. L. Kelley (Academic Press, San Diego 1999) Chap. 1

3.34 E. Kapon: Quantum wire and quantum dot lasers. In: *Semiconductor Lasers I: Fundamentals*, ed. by E. Kapon, P. L. Kelley (Academic Press, San Diego 1999) Chap. 4

3.35 V. I. Klimov, A. A. Mikhailovsky, S. Xu, A. Malko, J. A. Hollingsworth, C. A. Leatherdale, H. J. Eisler, M. G. Bawendi: Optical gain and stimulated emission in nanocrystal quantum dots, Science **290**, 314–317 (2000)

3.36 H. J. Eisler, V. C. Sundar, M. G. Bawendi, M. Walsh, H. I. Smith, V. Klimov: Color-selective semiconductor nanocrystal laser, Appl. Phys. Lett. **80**, 4614–4616 (2002)

3.37 P. T. Guerreiro, S. Ten, N. F. Borrelli, J. Butty, G. E. Jabbour, N. Peyghambarian: PbS quantum-dot doped glasses as saturable absorbers for mode locking of a Cr:forsterite laser, Appl. Phys. Lett. **71**, 1595–1597 (1997)

3.38 K. Wundke, S. Potting, J. Auxier, A. Schulzgen, N. Peyghambarian, N. F. Borrelli: PbS quantum-dot-doped glasses for ultrashort-pulse generation, Appl. Phys. Lett. **76**, 10–12 (2000)

3.39 S. Schmitt-Rink, D. S. Chemla, D. A. B. Miller: Linear and nonlinear optical properties of semiconductor quantum wells, Adv. Phys. **38**, 89–188 (1989)

3.40 F. Devaux, F. Dorgeuille, A. Ougazzaden, F. Huet, M. Carre, A. Carenco, M. Henry, Y. Sorel, J.-F. Kerdiles, E. Jeanney: 20 Gbit/s operation of a high-efficiency InGaAsP/InGaAsP MQW electroabsorption modulator with 1.2-V drive voltage, IEEE Photonics Tech. Lett. **5**, 1288–1990 (1993)

3.41 D. Delprat, A. Ramdane, A. Ougazzaden, H. Nakajima, M. Carre: Integrated multiquantum well distributed feedback laser-electroabsorption modulator with a negative chirp for zero bias voltage, Electron. Lett. **33**, 53–55 (1997)

3.42 T. D. Krauss, F. W. Wise: Coherent acoustic phonons in a semiconductor quantum dot, Phys. Rev. Lett. **79**, 5102–5105 (1997)

3.43 D. Donovan, J. F. Andress: *Lattice Vibrations* (Chapman and Hall, London 1971)

3.44 J. F. DiTusa, K. Lin, M. Park, M. S. Isaacson, J. M. Parpia: Role of phonon dimensionality on electron–phonon scattering rates, Phys. Rev. Lett. **68**, 1156–1159 (1992)

3.45 S. H. Song, W. Pan, D. C. Tsui, Y. H. Xie, D. Monroe: Energy relaxation of two-dimensional carriers in strained $Ge/Si_{0.4}Ge_{0.6}$ and $Si/Si_{0.7}Ge_{0.3}$ quan-

tum wells: Evidence for two-dimensional acoustic phonons, Appl. Phys. Lett. **70**, 3422–3424 (1997)
3.46 V. Narayanamurti, H. L. Störmer, M. A. Chin, A. C. Gossard, W. Wiegmann: Selective transmission of high-frequency phonons by a superlattice: The dielectric phonon filter, Phys. Rev. Lett. **43**, 2012–2016 (1979)
3.47 P. V. Santos, L. Ley, J. Mebert, O. Koblinger: Frequency gaps for acoustic phonons in a-Si:H/a-$SiN_x$:H superlattices, Phys. Rev. B **36**, 4858–4867 (1987)
3.48 M. Fujii, T. Nagareda, S. Hayashi, K. Yamamoto: Low-frequency Raman scattering from small silver particles embedded in $SiO_2$ thin films, Phys. Rev. B **44**, 6243–6248 (1991)
3.49 L. Saviot, B. Champagnon, E. Duval, A. I. Ekimov: Size-selective resonant Raman scattering in CdS doped glasses, Phys. Rev. B **57**, 341–346 (1998)
3.50 H. Lamb: On the vibrations of an elastic sphere, Proc. Math. Soc. London **13**, 187 (1882)
3.51 S. Rufo, M. Dutta, M. A. Stroscio: Acoustic modes in free and embedded quantum dots, J. Appl. Phys. **93**, 2900–2905 (2003)
3.52 N. Del Fatti, C. Voisin, F. Chevy, F. Vallee, C. Flytzanis: Coherent acoustic mode oscillation and damping in silver nanoparticles, J. Chem. Phys. **110**, 11484–11487 (1999)
3.53 M. Ikezawa, T. Okuno, Y. Masumoto, A. A. Lipovskii: Complementary detection of confined acoustic phonons in quantum dots by coherent phonon measurement and Raman scattering, Phys. Rev. B **64**, 201315 (2001)
3.54 A. Arbouet, C. Voisin, D. Christofilos, P. Langot, N. Del Fatti, F. Vallee, J. Lerme, G. Celep, E. Cottancin, M. Gaudry, M. Pellarin, M. Broyer, M. Maillard, M.-P. Pileni, M. A. Treguer: Electron–phonon scattering in metal clusters, Phys. Rev. Lett. **90**, 177401 (2003)
3.55 S. Schmitt-Rink, D. A. B. Miller, D. S. Chemla: Theory of the linear and nonlinear optical properties of semiconductor microcrystallites, Phys. Rev. B **35**, 8113–8125 (1987)
3.56 D. Kovalev, H. Heckler, M. Ben-Chorin, G. Polisski, M. Schwartzkopff, F. Koch: Breakdown of the *k*-conservation rule in Si nanocrystals, Phys. Rev. Lett. **81**, 2803–2806 (1998)
3.57 M. S. Hybertsen: Absorption and emission of light in nanoscale silicon structures, Phys. Rev. Lett. **72**, 1514–1517 (1994)
3.58 N. F. Mott: Conduction in non-crystalline materials III. Localized states in a pseudogap and near extremities of conduction and valence bands, Philos. Mag. **19**, 835–852 (1969)
3.59 B. F. Levine: Quantum-well infrared photodetectors, J. Appl. Phys. **74**, R1–81 (1993)
3.60 L. Esaki, R. Tsu: Superlattice and negative differential conductivity in semiconductors, IBM J. Res. Devel. **14**, 61–65 (1970)
3.61 L. Esaki, L. L. Chang: New transport phenomenon in a semiconductor superlattice, Phys. Rev. Lett. **33**, 495–498 (1974)
3.62 K. K. Choi, B. F. Levine, R. J. Malik, J. Walker, C. G. Bethea: Periodic negative conductance by sequential resonant tunneling through an expanding high-field superlattice domain, Phys. Rev. B **35**, 4172–4175 (1987)
3.63 N. F. Mott: *Conduction in Non-Crystalline Materials*, Oxford Science Publications, 2nd edn. (Clarendon, Oxford 1993)
3.64 P. Sheng, J. Klafter: Hopping conductivity in granular disordered systems, Phys. Rev. B **27**, 2583–2586 (1983)
3.65 R. P. Andres, T. Bein, M. Dorogi, S. Feng, J. I. Henderson, C. P. Kubiak, W. Mahoney, R. G. Osifchin, R. Reifenberger: Coulomb staircase at room temperature in a self-assembled molecular nanostructure, Science **272**, 1323–1325 (1996)
3.66 M. A. Kastner: The single-electron transistor, Rev. Mod. Phys. **64**, 849–858 (1992)
3.67 A. L. Efros, B. I. Shklovskii: Coulomb gap and low-temperature conductivity of disordered systems, J. Phys. C: Solid State Phys. **8**, L49–51 (1975)
3.68 M. Fujii, T. Kita, S. Hayashi, K. Yamamoto: Current-transport properties of Ag–$SiO_2$ and Au–$SiO_2$ composite films: Observation of single-electron tunnelling and random telegraph signals, J. Phys.: Condens. Matter **9**, 8669–8677 (1997)
3.69 P. E. Trudeau, A. Escorcia, A. A. Dhirani: Variable single electron charging energies and percolation effects in molecularly linked nanoparticle films, J. Chem. Phys. **119**, 5267–5273 (2003)
3.70 A. Taleb, F. Silly, A. O. Gusev, F. Charra, M.-P. Pileni: Electron transport properties of nanocrystals: Isolated, and "supra"-crystalline phases, Adv. Mater. **12**, 633–637 (2000)
3.71 J. Fick, A. Martucci, M. Guglielmi, J. Shell: Nonlinear optical properties of semiconductor-doped sol–gel waveguides, Fiber Integrated Opt. **19**, 43–56 (2000)
3.72 U. Kreibig, M. Vollmer: *Optical Properties of Metal Clusters* (Springer, Berlin, Heidelberg 1995) p. 50
3.73 K. Kolwas, S. Demianiuk, M. Kolwas: Optical excitation of radius-dependent plamon resonances in large metal clusters, J. Phys. B **29**, 4761–4770 (1996)
3.74 S. Link, Z. L. Wang, M. A. El-Sayed: Alloy formation on gold–silver nanoparticles and the dependence of the plasmon absorption on their composition, J. Phys. Chem. B **103**, 3529–3533 (1999)
3.75 F. Hache, D. Ricard, C. Flytzanis: Optical nonlinearities of small metal nanoperticles: Surface-mediated resonance and quantum size effects, J. Opt. Soc. Am. B **3**, 1647–1655 (1986)
3.76 R. Elghanian, J. J. Storhoff, R. C. Mucic, R. L. Letsinger, C. A. Mirkin: Selective colorimetric detection of polynucleotides based on the distance-dependent optical properties of gold nanoparticles, Science **277**, 1078–1081 (1997)

3.77 J. A. Creighton, D. G. Eadon: Ultraviolet–visible spectra of the colloidal metallic elements, J. Chem. Soc. Faraday Trans. **87**, 3881–3891 (1991)

3.78 P. E. Batson: Surface plasmon coupling in clusters of small spheres, Phys. Rev. Lett. **49**, 936–940 (1982)

3.79 J. R. Krenn, A. Dereux, J. C. Weeber, E. Bourillot, Y. Lacroute, J. P. Goudonnet, G. Schider, W. Gotschy, A. Leitner, F. R. Aussenegg, C. Girard: Squeezing the optical near-field zone by plasmon coupling of metallic nanoparticles, Phys. Rev. Lett. **82**, 2590–2593 (1999)

3.80 F. Silly, A. O. Gusev, A. Taleb, F. Charra, M. P. Pileni: Coupled plasmon modes in an ordered hexagonal monolayer of metal nanoparticles: A direct observation, Phys. Rev. Lett. **84**, 5840–5843 (2000)

3.81 S. A. Maier, M. L. Brongersma, P. G. Kik, S. Meltzer, A. A. G. Requicha, H. A. Atwater: Plasmonics – a route to nanoscale optical devices, Adv. Mater. **13**, 15 (2001)

3.82 R. Mayoral, J. Requena, J. S. Moya, C. Lopez, A. Cintas, H. Miguez, F. Meseguer, L. Vazquez, M. Holgado, A. Blanco: 3D long-range ordering in an $SiO_2$ submicrometer-sphere sintered superstructure, Adv. Mater. **9**, 257–260 (1997)

3.83 J. V. Sanders: Colour of precious opal, Nature **204**, 1151–1153 (1964)

3.84 E. Yablonovitch: Inhibited spontaneous emission in solid-state physics and electronics, Phys. Rev. Lett. **58**, 2059–2062 (1987)

3.85 S. John: Strong localization of photons in certain disordered dielectric superlattices, Phys. Rev. Lett. **58**, 2486–2489 (1987)

3.86 M. N. Baibich, J. M. Broto, A. Fert, F. Nguyen Van Dau, F. Petroff, P. Etienne, G. Creuzet, A. Friederich, J. Chazelas: Giant magnetoresistance of (001)Fe/(001)Cr magnetic superlattices, Phys. Rev. Lett. **61**, 2472 (1988)

3.87 P. Grünberg, R. Shreiber, Y. Pang, M. B. Brodsky, H. Sowers: Layered magnetic structures: Evidence for antiferromagnetic coupling of Fe layers across Cr interlayers, Phys. Rev. Lett. **57**, 2442 (1986)

3.88 R. L. Comstock: *Introduction to Magnetism and Magnetic Recording* (Wiley, New York 1999)

3.89 N. F. Mott: The electrical conductivity of transition metals, Proc. R. Soc. **153**, 699 (1935)

3.90 J. F. Gregg: Introduction to spin electronics. In: *Spin Electronics*, Lecture Notes in Physics, No. 569, ed. by M. Ziese, M. J. Thornton (Springer, Berlin, Heidelberg 2001) Chap. 1

3.91 G. Binasch, P. Grünberg, F. Saurenbach, W. Zinn: Enhanced magnetoresistance in layered magnetic structures with antiferromagnetic interlayer exchange, Phys. Rev. B **39**, 4828 (1989)

3.92 R. Schad, C. D. Potter, P. Beliën, G. Verbanck, V. V. Moshchalkov, Y. Bruynseraede: Giant magnetoresistance in Fe/Cr superlattices with very thin Fe layers, Appl. Phys. Lett. **64**, 3500 (1994)

3.93 A. Bartélémy, A. Fert, F. Petroff: Giant magnetoresistance in magnetic multilayers. In: *Handbook of Magnetic Materials*, Vol. 12, ed. by K. H. J. Buschow (Elsevier, Amsterdam 1999) Chap. 1, pp. 1–96

3.94 S. S. P. Parkin, D. Mauri: Spin engineering: Direct determination of the Ruderman–Kittel–Kasuya–Yosida far-field range function in ruthenium, Phys. Rev. B **44**, 7131 (1991)

3.95 A. Barthélémy, A. Fert, J-P. Contour, M. Bowen, V. Cros, J. M. De Teresa, A. Hamzic, J. C. Faini, J. M. George, J. Grollier, F. Montaigne, F. Pailloux, F. Petroff, C. Vouille: Magnetoresistance and spin electronics, J. Magn. Magn. Mater. **242–245**, 68 (2002)

3.96 D. H. Mosca, F. Petroff, A. Fert, P. A. Schroeder, W. P. Pratt, R. Loloee: Oscillatory interlayer coupling and giant magnetoresistance in Co/Cu multilayers, J. Magn. Magn. Mater. **94**, L1 (1991)

3.97 W. P. Pratt, S. F. Lee, J. M. Slaughter, R. Loloee, P. A. Schroeder, J. Bass: Perpendicular giant magnetoresistances of Ag/Co multilayers, Phys. Rev. Lett. **66**, 3060 (1991)

3.98 A. Fert, L. Piraux: Magnetic nanowires, J. Magn. Magn. Mater. **200**, 338 (1999) (Special issue)

3.99 M. A. M. Gijs, M. T. Johnson, A. Reinders, P. E. Huisman, R. J. M. van de Veerdonk, S. K. J. Lenczowski, R. M. Gansewinkel: Perpendicular giant magnetoresistance of Co/Cu multilayers deposited under an angle on grooved substrates, Appl. Phys. Lett. **66**, 1839 (1995)

3.100 B. Dieny, V. S. Speriosu, S. S. Parkin, B. A. Gurney, D. R. Wilhoit, D. Mauri: Giant magnetoresistance in soft ferromagnetic multilayers, Phys. Rev. B **43**, 1297 (1991)

3.101 J. Barnas, A. Fuss, R. E. Camley, P. Grünberg, W. Zinn: Novel magnetoresistance effect in layered magnetic structures: Theory and experiment, Phys. Rev. B **42**, 8110 (1990)

3.102 C. Tsang, D. E. Heim, R. E. Fontana, V. S. Speriosu, B. A. Gurney, M. L. Williams: Design, fabrication and testing of spin-valve read heads for high density recording, IEEE Trans. Magn. **30**, 3801 (1994)

3.103 W. F. Egelhoff Jr, P. J. Chen, C. J. Powell, D. Parks, G. Serpa, R. D. McMichael, D. Martien, A. E. Berkowitz: Specular electron scattering in metallic thin films, J. Vac. Sci. Technol. B **17**, 1702 (1999)

3.104 P. M. Tedrow, R. Meservey: Spin-dependent tunneling into ferromagnetic nickel, Phys. Rev. Lett. **26**, 192 (1971)

3.105 P. M. Tedrow, R. Meservey: Spin polarization of electrons tunneling from films of Fe, Co, Ni, and Gd, Phys. Rev. B **7**, 318 (1973)

3.106 T. Dimopoulos: Spin polarised tunnel transport in magnetic tunnel junctions: The role of metal/oxide interfaces in the tunnel process. Ph.D. Thesis (University Louis Pasteur, Strasbourg 2002)

3.107 T. Miyazaki, N. Tezuka: Giant magnetic tunneling effect in Fe/$Al_2O_3$/Fe junction, J. Magn. Magn. Mater. **139**, L231 (1995)

3.108 N. Tezuka, T. Miyazaki: Magnetic tunneling effect in Fe/$Al_2O_3$/$Ni_{1-x}Fe_x$ junctions, J. Appl. Phys. **79**, 6262 (1996)

3.109 J. S. Moodera, L. R. Kinder, T. M. Wong, R. Meservey: Large magnetoresistance at room temperature in ferromagnetic thin film tunnel junctions, Phys. Rev. Lett. **74**, 3273 (1995)

3.110 M. Jullière: Tunneling between ferromagnetic films, Phys. Lett. **54**, 225 (1975)

3.111 J. Nassar, M. Hehn, A. Vaures, F. Petroff, A. Fert: Magnetoresistance of ferromagnetic tunnel junctions with $Al_2O_3$ barriers formed by rf sputter etching in Ar/$O_2$ plasma, Appl. Phys. Lett. **73**, 698 (1998)

3.112 M. Viret, M. Drouet, J. Nassar, J. P. Contour, C. Fermon, A. Fert: Low-field colossal magnetoresistance in manganite tunnel spin valves, Europhys. Lett. **39**, 545 (1997)

3.113 J. Nassar, M. Viret, M. Drouet, J. P. Contour, C. Fermon, A. Fert: Low-field colossal magnetoresistance in manganite tunnel junctions, Mater. Res. Soc. Symp. Proc. **494**, 231 (1998)

3.114 M. Bowen, M. Bibes, A. Barthélémy, J.-P. Contour, A. Anane, Y. Lemaître, A. Fert: Nearly total spin polarization in $La_2O_3Sr_1O_3MnO_3$ from tunneling experiments, Appl. Phys. Lett. **82**, 233 (2003)

3.115 T. Obata, T. Manako, Y. Shimakawa, Y. Kubo: Tunneling magnetoresistance at up to 270 K in $La_{0.8}Sr_{0.2}MnO_3$/$SrTiO_3$/$La_{0.8}Sr_{0.2}MnO_3$ junctions with 1.6-nm-thick barriers, Appl. Phys. Lett. **74**, 290 (1999)

3.116 S. Gota, J. B. Moussy, M. Henriot, M. J. Guittet, M. Gautier-Soyer: Atomic-oxygen-assisted MBE growth of $Fe_2O_4$(111) on $\alpha$-$Al_2O_3$(0001), Surf. Sci. **482–485**, 809–816 (2001)

3.117 S. Van Dijken, X. Jiang, S. S. P. Parkin: Giant magnetocurrent exceeding 3400% in magnetic tunnel transistors with spin-valve base layers, Appl. Phys. Lett. **83**, 951 (2003)

3.118 S. A. Wolf, A. Y. Chtchenlkanova, D. M. Treger: Spintronics: Spin based electronics. In: *Handbook of Nanoscience, Engineering and Technology*, Electrical Engineering Textbook Series, Vol. 27, ed. by W. A. Goddard III, D. W. Brenner, S. E. Lyshevski, G. J. Iafrate (CRC, Boca Raton 2003) Chap. 8

3.119 E. E. Fullerton, D. T. Margulies, M. E. Schabes, M. Carey, B. Gurney, A. Moser, M. Best, G. Zeltzer, K. Rubin, H. Rosen, M. Doerner: Antiferromagnetically coupled magnetic media layers for thermally stable high-density recording, Appl. Phys. Lett. **77**, 3806 (2000)

3.120 C. Fermon: Micro- and nanofabrication techniques. In: *Spin Electronics*, Lecture Notes in Physics, No. 569, ed. by M. Ziese, M. J. Thornton (Spinger, Berlin, Heidelberg 2001) Chap. 16

3.121 S. H. Sun, C. B. Murray, D. Weller, L. Folks, A. Moser: Monodisperse FePt nanoparticles and ferromagnetic FePt nanocrystal superlattices, Science **287**, 1989–1992 (2000)

3.122 J. Moritz, B. Dieny, J. P. Nozières, S. Landis, A. Lebib, Y. Chen: Domain structure in magnetic dots prepared by nanoimprinting and E-beam lithography, J. Appl. Phys. **91**, 7314 (2002)

3.123 J. Moritz, S. Landis, J. C. Toussaint, P. Bayle-Guillemaud, B. Rodmacq, G. Casali, A. Lebib, Y. Chen, J. P. Nozières, B. Dieny: Patterned media made from pre-etched wafers: A promising route toward ultrahigh-density magnetic recording, IEEE Trans. Magn. **38**, 1731 (2002)

3.124 S. Landis, B. Rodmacq, B. Dieny, B. Dal'Zotto, S. Tedesco, M. Heitzmann: Domain structure of magnetic layers deposited on patterned silicon, Appl. Phys. Lett. **75**, 2473 (1999)

3.125 A. Lebib, Y. Chen, F. Carcenac, E. Cambril, L. Manin, L. Couraud, H. Launois: Tri-layer systems for nanoimprint lithography with an improved process latitude, Microelectron. Eng. **53**, 175 (2000)

3.126 S. Landis, B. Rodmacq, B. Dieny: Magnetic properties of Co/Pt multilayers deposited on silicon dot arrays, Phys. Rev. B **62**, 12271 (2000)

3.127 X. G. Binning, M. Despont, U. Drechsler, W. Häberle, M. Lutwyche, P. Vettiger, H. J. Mamin, B. W. Chui, T. W. Kenny: Ultrahigh-density atomic force microscopy data storage with erase capability, Appl. Phys. Lett. **74**, 1329 (1999)

3.128 J. L. Marin, R. Riera, R. A. Rosas: Confined systems and nanostructured materials. In: *Nanomaterials*, Handbook of Advanced Electronic and Photonic Materials and Devices, Vol. 9, ed. by H. S. Nalwa (Elsevier, Amsterdam 2000) p. 55

3.129 J. M. Hartmann, M. Charleux, J. L. Rouviere, H. Mariette: Growth of CdTe/MnTe tilted and serpentine lattices on vicinal surfaces, Appl. Phys. Lett. **70**, 1113–1115 (1997)

3.130 P. Soukiassian, F. Semond, A. Mayne, G. Dujardin: Highly stable Si atomic line formation on the beta-SiC(100) surface, Phys. Rev. Lett. **79**, 2498–2501 (1997)

3.131 D. Leonard, K. Pond, P. M. Petroff: Critical layer thickness for self-assembled InAs islands on GaAs, Phys. Rev. B **50**, 11687–11692 (1994)

3.132 S. Rusponi, T. Cren, N. Weiss, M. Epple, P. Buluschek, L. Claude, H. Brune: The remarkable difference between surface and step atoms in the magnetic anisotropy of two-dimensional nanostructures, Nature Mater. **2**, 546–551 (2003)

3.133 R. Nötzel, T. Fukui, H. Hasegawa, J. Temmyo, T. Tamamura: Atomic-force microscopy study of strained InGaAs quantum disks self-organizing on GaAs(*n*11) substrates, Appl. Phys. Lett. **65**, 2854–2856 (1994)

3.134 E. Ganz, K. Sattler, J. Clarke: Scanning tunneling microscopy of the local atomic structure of two-dimensional gold and silver islands on graphite, Phys. Rev. Lett. **60**, 1856–1859 (1988)

3.135 G. W. Clark, L. L. Kesmodel: Ultrahigh vacuum scanning tunneling microscopy studies of platinum on graphite, J. Vac. Sci. Technol. B **11**, 131–136 (1993)

3.136 H. Xu, K. Y. S. Ng: Scanning tunneling microscopy investigation of Co cluster growth and induced surface morphology changes on highly oriented pyrolitic graphite, J. Vac. Sci. Technol. B **13**, 2160–2165 (1995)

3.137 H. Xu, K. Y. S. Ng: Surface process and interaction of Mo clusters on highly oriented pyrolytic graphite observed by scanning tunneling microscopy, J. Vac. Sci. Technol. B **15**, 186–191 (1997)

3.138 A. Piednoir, E. Perrot, S. Granjeaud, A. Humbert, C. Chapon, C. R. Henry: Atomic resolution on small three-dimensional metal clusters by STM, Surf. Sci. **391**, 19–26 (1997)

3.139 G. Springholz, V. Holy, M. Pinczolits, G. Bauer: Self-organized growth of three-dimensional quantum-dot crystals with fcc-like stacking and a tunable lattice constant, Science **282**, 734–737 (1998)

3.140 M. D. Levenson, N. S. Viswanathan, R. A. Simpson: Improving resolution in photolithography with a phase-shifting mask, IEEE Trans. Electron Devices **ED-29**, 1812–1836 (1982)

3.141 M. Brust, M. Walker, D. Bethell, D. J. Schiffrin, R. Whyman: Synthesis of thiol-derivatized gold nanoparticles in a 2-phase liquid–liquid system, J. Chem. Soc., Chem. Commun. **1994**, 801–802 (1994)

3.142 R. P. Andres, J. D. Bielefeld, J. I. Henderson, D. B. Janes, V. R. Kolagunta, C. P. Kubiak, W. J. Mahoney, R. G. Osifchin: Self-assembly of a two-dimensional superlattice of molecularly linked metal clusters, Science **273**, 1690–1693 (1996)

3.143 A. Taleb, C. Petit, M. P. Pileni: Synthesis of highly monodisperse silver nanoparticles from AOT reverse micelles: A way to 2D and 3D self-organization, Chem. Mater. **9**, 950–959 (1997)

3.144 C. J. Kiely, J. Fink, M. Brust, D. Bethell, D. J. Schiffrin: Spontaneous ordering of bimodal ensembles of nanoscopic gold clusters, Nature **396**, 444–446 (1998)

3.145 C. J. Kiely, J. Fink, J. G. Zheng, M. Brust, D. Bethell, D. J. Schiffrin: Ordered colloidal nanoalloys, Adv. Mater. **12**, 640 (2000)

3.146 C. Petit, A. Taleb, M.-P. Pileni: Self-organization of magnetic nanosized cobalt particles, Adv. Mater. **10**, 259–261 (1998)

3.147 G. Schmid, R. Pfeil, R. Boese, F. Bandermann, S. Meyer, S. G. Calis, J. W. A. Van Der Velden: Au55[P(C6H5)]12Cl6 ein Goldcluster ungewöhnlicher Größe, Chem. Ber. **114**, 3634–3642 (1981)

3.148 V. Oleshko, V. Volkov, R. Gijbels, W. Jacob, M. Vargaftik, I. Moiseev, G. Vantendeloo: High-resolution electron-microscopy and electron-energy-loss spectroscopy of giant palladium clusters, Z. Phys. **D34**, 283–291 (1995)

3.149 C. B. Murray, D. B. Norris, M. G. Bawendi: Synthesis and characterization of nearly monodisperse CdE (E=S, Se, Te) semiconductor nanocrystallites, J. Am. Chem. Soc. **115**, 8706–8715 (1993)

3.150 C. B. Murray, C. R. Kagan, M. G. Bawendi: Self-organization of CdSe nanocrystallites into 3-dimensional quantum-dot superlattices, Science **270**, 1335–1338 (1995)

3.151 M. A. Olshavsky, A. N. Goldstein, A. P. Alivisatos: Organometallic synthesis of GaAs crystallites exhibiting quantum confinement, J. Am. Chem. Soc. **112**, 9438–9439 (1990)

3.152 C. Binns: Nanoclusters deposited on surfaces, Surf. Sci. Rep. **44**, 1–49 (2001)

3.153 W. A. De Heer: The physics of simple metal clusters: Experimental aspects and simple models, Rev. Mod. Phys. **65**, 611 (1993)

# Acknowledgements


## 2.1 The Elements

***by Werner Martienssen***

We thank Dr. G. Leichtfried, Plansee AG, A-6600 Reutte/Tirol for recently determined new data on the refractory metals Nb, Ta, and Mo, W.

## 4.1 Semiconductors

***by Werner Martienssen***

In selecting the "most important information" from the huge data collection in Landolt–Börnstein, the author found great help in the new *Semiconductors: Data Handbook* [1]. Again, the data in this Springer Handbook of Condensed Matter and Materials Data represent only a small fraction of the information given in *Semiconductors: Data Handbook*, which is about 700 pages long. I am much indebted to my colleague O. Madelung for kindly presenting me the manuscript of that Handbook prior to publication.

[1] O. Madelung (Ed.): *Semiconductors: Data Handbook*, 3rd Edn. (Springer, Berlin, Heidelberg 2004)

## 4.5 Ferroelectrics and Antiferroelectrics

***by Toshio Mitsui***

The author of this subchapter thanks the coauthors of LB III/36 for their helpful discussions and suggestions. Especially, he is much indebted to Prof. K. Deguchi for his kind support throughout the preparation of the manuscript.

# About the Authors





**Wolf Assmus**

Johann Wolfgang Goethe-University
Physics Department
Frankfurt am Main, Germany
*assmus@physik.uni-frankfurt.de*
*http://www.rz.uni-frankfurt.de/piweb/kmlab/Leiter.html*

Chapter 1.3

Dr. Wolf Assmus (Kucera Professor) is Professor of Physics at the University of Frankfurt and Dean of the Physics-Faculty. He is a solid state physicist, especially interested in materials research and crystal growth. His main research fields are: materials with high electronic correlation, quasicrystals, materials with extremely high melting temperatures, magnetism, and superconductivity.



**Stefan Brühne**

Johann Wolfgang Goethe-University
Physics Department
Frankfurt am Main, Germany
*bruehne@physik.uni-frankfurt.de*

Chapter 1.3

Dr. Stefan Brühne, née Mahne, a chemist by education in Germany and England, received his PhD in 1994 from Dortmund University, Germany, on giant cell crystal structures in the Al–Ta system. Following a post doc position at the Materials Department (Crystallography) at ETH Zurich he spent seven years in the ceramics industry. His main activity was R&D of glasses, frits and pigments for high-temperature applications, thereby establishing design of experiment (DoE) techniques. Since 2002, at the Institute of Physics at Frankfurt University he has been investigated X-ray structure determination of quasicrystalline, highly complex and disordered intermetallic materials.



**Fabrice Charra**

Commissariat à l'Énergie Atomique,
Saclay
Département de Recherche sur l'État Condensé, les Atomes et les Molécules
Gif-sur-Yvette, France
*fabrice.charra@cea.fr*
*http://www-drecam.cea.fr/spcsi/*

Chapter 5.3

Fabrice Charra conducts researche in the emerging field of nanophotonics, in the surface physics laboratory of CEA/Saclay. The emphasis of his work is on light emission and absorption form single nanoscale molecular systems. His area of expertise also extends to nonlinear optics, a domain to which he contributed several advances in the applications of organic materials.



**Gianfranco Chiarotti**

University of Rome "Tor Vergata"
Department of Physics
Roma, Italy
*chiarotti@roma2.infn.it*

Chapter 5.2

Gianfranco Chiarotti is Professor Emeritus, formerly Professor of General Physics, Fellow of the American Physical Society, fellow of the Italian National Academy (Accademia Nazionale dei Lincei). He was Chairman of the Physics Committee of the National Research Council (1988–1994), Chair Franqui at the University of Liège (1975), Assistant Professor at the University of Illinois (1955–1957), Editor of the journal Physics of Solid Surfaces, and Landolt–Börnstein Editor of Springer-Verlag from 1993 through 1996. He has worked in several fields of solid state physics, namely electronic properties of defects, modulation spectroscopy, optical properties of semiconductors, surface physics, and scanning tunnelling microscopy (STM) in organic materials.



**Claus Fischer**

Formerly Institute of Solid State and Materials Research (IFW)
Dresden, Germany
*A_C.FischerDD@t-online.de*

Chapter 4.2

Claus Fischer recieved his PhD from the Technical University Dresden (Since his retirement in 2000 he continues to work as a foreign scientist of IFW in the field of high-$T_c$ superconductors.) His last position at IFW was head of the Department of Superconducting Materials. The main areas of research were growth of metallic single crystals in particular of magnetic materials, developments of hard magnetic materials, of materials for thick film components of microelectronics and of low-$T_c$ and high-$T_c$ superconducting wires and tapes. Many activities were performed in cooperation with industrial manufacturers.

**Günter Fuchs**

Leibniz Institute for Solid State and Materials Research (IFW) Dresden
Magnetism and Superconductivity in the Institute of Metallic Materials
Dresden, Germany
*fuchs@ifw-dresden.de*
*http://www.ifw-dresden.de/imw/21/*



Chapter 4.2

Dr. Günter Fuchs studied physics at the Technical University of Dresden, Germany, and received his PhD in 1980 on the pinning mechanism in superconducting NbTi alloys. Since 1969 he has been at the Institute of Solid State and Materials Research (IFW) in Dresden. His activities are in superconductivity (HTSC, $MgB_2$, intermetallic borocarbides) and the applications of superconductors. He received the PASREG Award for outstanding scientific achievements in the field of bulk cuprate superconductors in high magnetic fields in 2003.

**Frank Goodwin**

International Lead Zinc Research Organization, Inc.
Research Triangle Parc, NC, USA
*fgoodwin@ilzro.org*
*http://www.ilzro.org/Contactus.htm*



Chapter 3.1

Frank Goodwin received his Sc.D. from the Massachusetts Institute of Technology in 1979 and is responsible for all materials science research at International Lead Zinc Research Organization, Inc. where he has conceived and managed numerous projects on lead and zinc-containing products. These have included lead in acoustics, cable sheathing, nuclear waste management and specialty applications, together with zinc in coatings, castings and wrought forms.



**Susana Gota-Goldmann**

Commissariat à l'Energie Atomique (CEA)
Direction de la Recherche Technologique (DRT)
Fontenay aux Roses, France
*susana.gota-goldmann@cea.fr*

Chapter 5.3

Dr. Susana Gota-Goldmann received her PhD in Materials Science form the Université Pierre et Marie Curie (Paris V) in 1993. After her PhD, she was engaged as a researcher in the Materials Science Division of the CEA (Commissariat à l'Energie Atomique, France). She has focused her scientific activity on the growth and characterisation of nanometric oxide layers with applications in spin electronics and photovoltaics. In parallel she has developed the use of synchrotron radiation techniques (X-ray absorption magnetic dicroism, photoemission, resonant reflectivity) for the study of oxide thin layers. Recently she has moved from fundamental to technological research. Dr. Gota-Goldmann is now working as a project manager at the scientific affairs direction of the Technology Research Division (CEA/DRT).



**Sivaraman Guruswamy**

University of Utah
Metallurgical Engineering
Salt Lake City, UT, USA
*sguruswa@mines.utah.edu*
*http://www.mines.utah.edu/metallurgy/MML*

Chapter 3.1

Dr. Guruswamy is a Professor of Metallurgical Engineering at the University of Utah. He obtained his Ph.D. degree in Metallurgical Engineering from the Ohio State University in 1984. He has made significant contributions in several areas including magnetic materials development, deformation of compound semiconductors, and lead alloys. His current work focuses on magnetostrictive materials and hybrid thermionic/thermoelectric thermal diodes.

**Gagik G. Gurzadyan**

Technical University of Munich
Institute for Physical and Theoretical Chemistry
Garching, Germany
*gurzadyan@ch.tum.de*
*http://zentrum.phys.chemie.tu-muenchen.de/gagik*



Chapter 4.4

Gagik G. Gurzadyan, Ph.D., Dr. Sci., has extensive experience in nonlinear optics and crystals, laser photophysics and spectroscopy. He has authored several books including the Handbook of Nonlinear Optical Crystals published by Springer-Verlag. He worked in the Institute of Spectroscopy (USSR), CEA/Saclay (France), Max-Planck-Institute of Radiation Chemistry (Germany). At present he works at the Technical University of Munich with ultrafast lasers in the fields of nonlinear photochemistry of biomolecules and femtosecond spectroscopy.

**Hideki Harada**

High Tech Association Ltd.
Higashikaya, Fukaya,Saitama, Japan
*khb16457@nifty.com*
*http://homepage1.nifty.com/JABM*



Chapter 4.3

Dr. Hideki Harada is chief advisor of magnetic materials and their application and President of High Tech Association Ltd., Saitama, Japan. He is Chairman of the Japan Association of Bonded Magnet Industries (JABM) and received his Ph.D. in 1987 with a work on electrostatic ferrite materials. He worked in research and development of magnetic materials and cemented carbide tools at Hitachi Metals where he also was on the Board of Directors. He received the Japanese National Award for Industries Development Contribution.



**Bernhard Holzapfel**

Leibniz Institute for Solid State and Materials Research Dresden – Institute of Metallic Materials
Superconducting Materials
Dresden, Germany
*B.Holzapfel@ifw-dresden.de*
*http://www.ifw-dresden.de/imw/26/*

Chapter 4.2

Dr. Bernhard Holzapfel is head of the superconducting materials group at the Leibniz Institute for Solid State and Materials Research (IFW) Dresden, Germany. His main area of research is pulsed laser deposition of functional thin films and superconductivity. Currently he works on the development of HTSC high $J_c$ coated conductors using ion beam assisted deposition or highly textured metal substrates. His work is supported by a number of national and European founded research projects.



**Karl U. Kainer**

GKSS Research Center Geesthacht
Institute for Materials Research
Geesthacht, Germany
*karl.kainer@gkss.de*
*http://www.gkss.de*

Chapter 3.1

Professor Kainer is director of Institute for Materials Research at GKSS-Research Center, Geesthacht and Professor of Materials Technology at the Technical University of Hamburg-Harburg. He obtained his Ph.D. in Materials Science at the Technical University of Clausthal in 1985 and his Habilitation in 1996. In 1988 he received the Japanese Government Research Award for Foreign Specialists. His current research activities are the development of new alloys and processes for magnesium materials.

**Catrin Kammer**

METALL – Intl. Journal for Metallurgy
Goslar, Germany
*Kammer@metall-news.com*
*http://www.giesel-verlag.de*



Chapter 3.1

Catrin Kammer received her Ph.D. in materials sciences from the Technical University Bergakademie Freiberg, Germany, in 1989. She has been working in the field of light metals and is author of several handbooks about aluminium and magnesium. She is working as author for the journal ALUMINIUM and is teaching in material sciences. Since 2001 she is editor-in-chief of the journal METALL, which deals with all non-ferrous metals.

**Wolfram Knabl**

Plansee AG
Technology Center
Reutte, Austria
*wolfram.knabl@plansee.com*
*http://www.plansee.com*



Chapter 3.1

Dr. Wolfram Knabl studied materials science at the Mining University of Leoben, Austria and received his Ph.D. at the Plansee AG focusing on the development of oxidation protective coatings for refractory metals. Between 1996 and 2002 he was responsible for the test laboratories at Plansee AG and since October 2002 he is working in the field of refractory metals, especially material and process development in the technology center of Plansee AG.



**Alfred Koethe**

Leibniz-Institut für Festkörper- und Werkstoffforschung
Institut für Metallische Werkstoffe
(retired)
Dresden, Germany
*alfred.koethe@web.de*

Chapter 3.1

Dr. Alfred Koethe is physicist and professor of Materials Science. He retired in 2000 from his position as head of department in the Institute of Metallic Materials at the Leibniz Institute of Solid State and Materials Research in Dresden, Germany. His main research activities were in the fields of preparation and properties of ultrahigh-purity refractory metals and, especially, of steels (stainless steels, high strenght steels, thermomechanical treatment, microalloying, relations chemical composition/microstructure/properties).



**Dieter Krause**

Schott AG
Research and Technology-Development
Mainz, Germany
*dieter.krause@schott.com*

Chapter 3.4

Dieter Krause studied physics at the universities of Erlangen and Munich, Germany, where he received his Ph.D. for work on magnetism and metal physics. He was professor in Tehran, Iran, lecturer in Munich and Mainz, Germany. As scientist and director of Schott's corporate research and development centre he was involved in research on optical and mechanical properties of amorphous materials, thin films, and optical fibres. Now he is consultant, chief scientist, and the editor of the "Schott Series on Glass and Glass Ceramics – Science, Technology, and Applications" published by Springer.

**Manfred D. Lechner**

Universität Osnabrück
Institut für Chemie – Physikalische Chemie
Osnabrück, Germany
*lechner@uni-osnabrueck.de*
*http://www.chemie.uni-osnabrueck.de/pc/index.html*



Chapter 3.3

Professor Lechner has a PhD in chemistry from the University of Mainz, Germany. Since 1975 he is Professor of Physical Chemistry at the Institute of Chemistry of the University of Osnabrück, Germany. His scientific work concentrates on the physics and chemistry of polymers. In this area he is mainly working on the influence of high pressure on polymer systems, polymers for optical storage and waveguides as well as synthesis and properties of superabsorbers from renewable resources.

**Gerhard Leichtfried**

Plansee AG
Technology Center
Reutte, Austria
*gerhard.leichtfried@plansee.com*
*http://www.plansee.com*



Chapter 3.1

Dr. Gerhard Leichtfried received his Ph.D from the Montanuniversität Leoben and is qualified for lecturing in powder metallurgy. For 20 years he has been working in various senior positions for the Plansee Aktiengesellschaft, a company engaged in refractory metals, composite materials, cemented carbides and sintered iron and steels.



**Werner Martienssen**

Universität Frankfurt/Main
Physikalisches Institut
Frankfurt/Main, Germany
*Martienssen@Physik.uni-frankfurt.de*

Chapters 1.1, 1.2, 2.1, 4.1

Werner Martienssen studied physics and chemistry at the Universities of Würzburg and Göttingen, Germany. He obtained his Ph.D. in Physics with R.W. Pohl, Göttingen, and holds an honorary doctorate at the University of Dortmund. After a visiting-professorship at the Cornell University, Ithaca, USA in 1959 to 1960 he taught physics at the University of Stuttgart and since 1961 at the University of Frankfurt/Main. His main research fields are condensed matter physics, quantum optics and chaotic dynamics. Two of his former students and coworkers became Nobel-laureates in Physics, Gerd K. Binnig for the design of the scanning tunneling microscope in 1986 and Horst L. Störmer for the discovery of a new form of quantum-fluid with fractionally charged excitations in 1998. Werner Martienssen is a member of the Deutsche Akademie der Naturforscher Leopoldina, Halle and of the Akademie der Wissenschaften zu Göttingen. Since 1994 he is Editor-in-Chief of the data collection Landolt–Börnstein published by Springer, Heidelberg.



**Toshio Mitsui**

Osaka University
Takarazuka, Japan
*t-mitsui@jttk.zaq.ne.jp*

Chapter 4.5

Toshio Mitsui is an emeritus professor of Osaka University. He studied solid state physics and biophysics at Hokkaido University, Pennsylvania State University, Brookhaven National Laboratory, the Massachusetts Institute of Technology, Osaka University and Meiji University. He was the first to observe the ferroelectric domain structure in Rochelle salt with a polarization microscope. He proposed various theories on ferroelectric effects and biological molecular machines.



**Manfred Müller**

Dresden University of Technology
Institute of Materials Science
Dresden, Germany
*m.mueller33@t-online.de*

Chapter 4.3

Dr.-Ing. habil. Manfred Müller is a Professor emeritus of Special Materials at the Institute of Materials Science of the Dresden University of Technology. Before his retirement he was for many years head of department for special materials at the Central Institute for Solid State Physics and Materials Research of the Academy of Sciences in Dresden, Germany. His main field was the research and development of metallic materials with emphasis on special physical properties, such as soft and hard magnetic, electrical and thermoelastic properties. His last field of research was amorphous and nanocrystalline soft magnetic alloys. He is a member of the German Society of Materials Science (DGM) and was a member of the Advisary Board of DGM.



**Sergei Pestov**

Moscow State Academy of Fine Chemical Technology
Department of Inorganic Chemistry
Moscow, Russia
*pestovsm@yandex.ru*

Chapter 5.1

Dr. Pestov is a docent of the Inorganic Chemistry Department and a head of group on liquid crystals (LC) at the Moscow State Academy of Fine Chemical Technology. He earned his Ph.D. in physical chemistry in 1992. His research is focused on thermal analysis and thermodynamics of systems containing LC and physical properties of LC. He is an author of a Landolt–Börnstein volume and two books devoted to liquid crystals.



**Günther Schlamp**

Metallgesellschaft Ffm and Degussa
Demetron (retired)
Steinbach/Ts, Germany

Chapter 3.1

Günther Schlamp received his Ph.D. from the Johann-Wolfgang-Goethe University of Frankfurt/Main, Germany, in Physical Chemistry. His industrial activities in research include the development and production of refractory material coatings, high purity materials and parts for electronics, and sputter targets for the reflection-enhancing coating of glas. He has contributed to several Handbooks with repoprts on properties and applications of noble metals and their alloys.



**Barbara Schüpp-Niewa**

Leibniz-Institute for Solid State and Materials Research Dresden
Institute for Metallic Materials
Dresden, Germany
*b.schuepp@ifw-dresden.de*
*http://www.ifw-dresden.de*

Chapter 4.2

Barbara Schüpp-Niewa studied chemistry in Gießen and Dortmund where she received her Ph.D. in 1999. Since 2000 she has been a scientist at the Leibniz-Institute for Solid State and Materials Research Dresden with a focus on crystal structure investigations of oxometalates with superconducting or exciting magnetic ground states. Her current research activities include coated conductors.

**Roland Stickler**

University of Vienna
Department of Chemistry
Vienna, Austria
*roland.stickler@univie.ac.at*

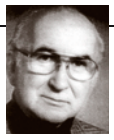

Chapter 3.1

Professor Stickler received his master and Dr. degree from the Technical University in Vienna. From 1958 to 1972 he was manager of physical metallurgy with the Westinghouse Research Laboratory in Pittsburgh, Pa. In 1972 he accepted a full professorship at the University of Vienna heading a materials science group in the Institute of Physical Chemistry, and from 1988 he was head of this institute until his retirement as professor emeritus in 1998. He was involved in research and engineering work on superalloys, semiconductor materials and high melting point materials, investigating the relationship between microstructure and mechanical behavior, in particular fatigue and fracture mechanics properties. He was leader of a successful project on brazing under microgravity conditions in the Spacelab-Mission. Further activities included the participation in European COST projects, in particular as chairman of actions on powder metallurgy and light metals. He has authored and coauthored more than 250 publications in scientific journals and proceedings.

**Pancho Tzankov**

Max Born Institute for Nonlinear Optics
and Short Pulse Spectroscopy
Berlin, Germany
*tzankov@mbi-berlin.de*
*http://staff.mbi-berlin.de/tzankov/*



Chapter 4.4

Pancho Tzankov studied laser physics at Sofia University, Bulgaria, and received his Ph.D. in physical chemistry from the Technical University of Munich, Germany. He is now a postdoctoral fellow at the Max Born Institute in Berlin, Germany. His research activities involve development of new nonlinear optical parametric sources of ultrashort pulses and their application for time-resolved spectroscopy.



**Volkmar Vill**

University of Hamburg
Department of Chemistry, Institute of
Organic Chemistry
Hamburg, Germany
*vill@chemie.uni-hamburg.de*
*http://liqcryst.chemie.uni-hamburg.de/*

Chapter 5.1

Professor Volkmar Vill received his Diploma in Chemistry in 1986, his Diploma in Physics in 1988 and his Ph.D. in Chemistry in 1990 from the University of Münster, Germany. In 1997 he earned his Habilitation in Organic Chemistry from the University of Hamburg where he is Professor of Organic Chemistry since 2002. He is the author of the LiqCryst – Database of Liquid Crystals and the Editor of the Handbook of Liquid Crystals, of Landolt–Börnstein, Organic Index, and Vol. VIII/5a, Physical Properties of Liquid Crystals.



**Hans Warlimont**

DSL Dresden Material-Innovation GmbH
Dresden, Germany
*warlimont@ifw-dresden.de*

Chapters 3.1, 3.2, 4.2, 4.3

Hans Warlimont is a physical metallurgist and has worked on numerous topics in several research institutions and industrial companies. Among them were the Max-Planck-Institute of Metals Research, Stuttgart, and Vacuumschmelze, Hanau. He was Scientific Director of the Leibniz-Institute of Solid State and Materials Research Dresden and Professor of Materials Science at Dresden University of Technology. Recently he has established DSL Dresden Material-Innovation GmbH to industrialise his invention of electroformed battery grids.

# Detailed Contents

**List of Abbreviations** ..... XV

## Part 1 General Tables

1 **The Fundamental Constants**
*Werner Martienssen* ..... 3
1.1 What are the Fundamental Constants and Who Takes Care of Them? ..... 3
1.2 The CODATA Recommended Values of the Fundamental Constants ..... 4
1.2.1 The Most Frequently Used Fundamental Constants ..... 4
1.2.2 Detailed Lists of the Fundamental Constants in Different Fields of Application ..... 5
1.2.3 Constants from Atomic Physics and Particle Physics ..... 7
**References** ..... 9

2 **The International System of Units (SI), Physical Quantities, and Their Dimensions**
*Werner Martienssen* ..... 11
2.1 The International System of Units (SI) ..... 11
2.2 Physical Quantities ..... 12
2.3 The SI Base Units ..... 13
2.3.1 Unit of Length: the Meter ..... 13
2.3.2 Unit of Mass: the Kilogram ..... 14
2.3.3 Unit of Time: the Second ..... 14
2.3.4 Unit of Electric Current: the Ampere ..... 14
2.3.5 Unit of (Thermodynamic) Temperature: the Kelvin ..... 14
2.3.6 Unit of Amount of Substance: the Mole ..... 14
2.3.7 Unit of Luminous Intensity: the Candela ..... 15
2.4 The SI Derived Units ..... 16
2.5 Decimal Multiples and Submultiples of SI Units ..... 19
2.6 Units Outside the SI ..... 20
2.6.1 Units Used with the SI ..... 20
2.6.2 Other Non-SI Units ..... 20
2.7 Some Energy Equivalents ..... 24
**References** ..... 25

3 **Rudiments of Crystallography**
*Wolf Assmus, Stefan Brühne* ..... 27
3.1 Crystalline Materials ..... 28
3.1.1 Periodic Materials ..... 28
3.1.2 Aperiodic Materials ..... 33
3.2 Disorder ..... 38

3.3 Amorphous Materials ..... 39
3.4 Methods for Investigating Crystallographic Structure ..... 39
**References** ..... 41

## Part 2 The Elements

1 **The Elements**
*Werner Martienssen* ..... 45
1.1 Introduction ..... 45
1.1.1 How to Use This Section ..... 45
1.2 Description of Properties Tabulated ..... 46
1.2.1 Parts A of the Tables ..... 46
1.2.2 Parts B of the Tables ..... 46
1.2.3 Parts C of the Tables ..... 48
1.2.4 Parts D of the Tables ..... 49
1.3 Sources ..... 49
1.4 Tables of the Elements in Different Orders ..... 49
1.5 Data ..... 54
1.5.1 Elements of the First Period ..... 54
1.5.2 Elements of the Main Groups and Subgroup I to IV ..... 59
1.5.3 Elements of the Main Groups and Subgroup V to VIII ..... 98
1.5.4 Elements of the Lanthanides Period ..... 142
1.5.5 Elements of the Actinides Period ..... 151
**References** ..... 158

## Part 3 Classes of Materials

1 **Metals**
*Frank Goodwin, Sivaraman Guruswamy, Karl U. Kainer, Catrin Kammer, Wolfram Knabl, Alfred Koethe, Gerhard Leichtfried, Günther Schlamp, Roland Stickler, Hans Warlimont* ..... 161
1.1 Magnesium and Magnesium Alloys ..... 162
1.1.1 Magnesium Alloys ..... 163
1.1.2 Melting and Casting Practices, Heat Treatment ..... 168
1.1.3 Joining ..... 169
1.1.4 Corrosion Behavior ..... 169
1.1.5 Recent Developments ..... 170
1.2 Aluminium and Aluminium Alloys ..... 171
1.2.1 Introduction ..... 171
1.2.2 Production of Aluminium ..... 171
1.2.3 Properties of Pure Al ..... 172
1.2.4 Aluminium Alloy Phase Diagrams ..... 174
1.2.5 Classification of Aluminium Alloys ..... 179
1.2.6 Structure and Basic Mechanical Properties of Wrought Work-Hardenable Aluminium Alloys ..... 180

1.2.7 Structure and Basic Mechanical Properties of Wrought Age-Hardenable Aluminium Alloys ..... 182
1.2.8 Structure and Basic Mechanical Properties of Aluminium Casting Alloys ..... 184
1.2.9 Technical Properties of Aluminium Alloys ..... 186
1.2.10 Thermal and Mechanical Treatment ..... 194
1.2.11 Corrosion Behavior of Aluminium ..... 202
1.3 Titanium and Titanium Alloys ..... 206
1.3.1 Commercially Pure Grades of Ti and Low-Alloy Ti Materials ..... 207
1.3.2 Ti-Based Alloys ..... 208
1.3.3 Intermetallic Ti–Al Materials ..... 209
1.3.4 TiNi Shape-Memory Alloys ..... 216
1.4 Zirconium and Zirconium Alloys ..... 217
1.4.1 Technically-Pure and Low-Alloy Zirconium Materials ..... 217
1.4.2 Zirconium Alloys in Nuclear Applications ..... 218
1.4.3 Zirconium-Based Bulk Glassy Alloys ..... 218
1.5 Iron and Steels ..... 221
1.5.1 Phase Relations and Phase Transformations ..... 222
1.5.2 Carbon and Low-Alloy Steels ..... 227
1.5.3 High-Strength Low-Alloy Steels ..... 240
1.5.4 Stainless Steels ..... 240
1.5.5 Heat-Resistant Steels ..... 257
1.5.6 Tool Steels ..... 262
1.5.7 Cast Irons ..... 268
1.6 Cobalt and Cobalt Alloys ..... 272
1.6.1 Co-Based Alloys ..... 272
1.6.2 Co-Based Hard-Facing Alloys and Related Materials ..... 274
1.6.3 Co-Based Heat-Resistant Alloys, Superalloys ..... 274
1.6.4 Co-Based Corrosion-Resistant Alloys ..... 276
1.6.5 Co-Based Surgical Implant Alloys ..... 277
1.6.6 Cemented Carbides ..... 277
1.7 Nickel and Nickel Alloys ..... 279
1.7.1 Commercially Pure and Low-Alloy Nickels ..... 279
1.7.2 Highly Alloyed Ni-Based Materials ..... 279
1.7.3 Ni-Based Superalloys ..... 284
1.7.4 Ni Plating ..... 288
1.8 Copper and Copper Alloys ..... 296
1.8.1 Unalloyed Coppers ..... 296
1.8.2 High Copper Alloys ..... 297
1.8.3 Brasses ..... 298
1.8.4 Bronzes ..... 298
1.8.5 Copper–Nickel and Copper–Nickel–Zinc Alloys ..... 300
1.9 Refractory Metals and Alloys ..... 303
1.9.1 Physical Properties ..... 306
1.9.2 Chemical Properties ..... 308
1.9.3 Recrystallization Behavior ..... 311
1.9.4 Mechanical Properties ..... 314

1.10 Noble Metals and Noble Metal Alloys ..... 329
1.10.1 Silver and Silver Alloys ..... 330
1.10.2 Gold and Gold Alloys ..... 347
1.10.3 Platinum Group Metals and Alloys ..... 363
1.10.4 Rhodium, Iridium, Rhutenium, Osmium, and their Alloys ..... 386
1.11 Lead and Lead Alloys ..... 407
1.11.1 Pure Grades of Lead ..... 407
1.11.2 Pb–Sb Alloys ..... 411
1.11.3 Pb–Sn Alloys ..... 414
1.11.4 Pb–Ca Alloys ..... 416
1.11.5 Pb–Bi Alloys ..... 419
1.11.6 Pb–Ag Alloys ..... 420
1.11.7 Pb–Cu, Pb–Te, and Pb–Cu–Te Alloys ..... 421
1.11.8 Pb–As Alloys ..... 421
1.11.9 Lead Cable Sheathing Alloys ..... 421
1.11.10 Other Lead Alloys ..... 421
**References** ..... 422

2 **Ceramics**
*Hans Warlimont* ..... 431
2.1 Traditional Ceramics and Cements ..... 432
2.1.1 Traditional Ceramics ..... 432
2.1.2 Cements ..... 432
2.2 Silicate Ceramics ..... 433
2.3 Refractory Ceramics ..... 437
2.4 Oxide Ceramics ..... 437
2.4.1 Magnesium Oxide ..... 444
2.4.2 Alumina ..... 445
2.4.3 Al–O–N Ceramics ..... 447
2.4.4 Beryllium Oxide ..... 447
2.4.5 Zirconium Dioxide ..... 447
2.4.6 Titanium Dioxide, Titanates, etc. ..... 450
2.5 Non-Oxide Ceramics ..... 451
2.5.1 Non-Oxide High-Temperature Ceramics ..... 451
2.5.2 Borides ..... 451
2.5.3 Carbides ..... 458
2.5.4 Nitrides ..... 467
2.5.5 Silicides ..... 473
**References** ..... 476

3 **Polymers**
*Manfred D. Lechner* ..... 477
3.1 Structural Units of Polymers ..... 480
3.2 Abbreviations ..... 482
3.3 Tables and Figures ..... 483
3.3.1 Polyolefines ..... 483
3.3.2 Vinyl Polymers ..... 489

Detailed Cont.

3.3.3 Fluoropolymers ..... 492
3.3.4 Polyacrylics and Polyacetals ..... 497
3.3.5 Polyamides ..... 501
3.3.6 Polyesters ..... 503
3.3.7 Polysulfones and Polysulfides ..... 506
3.3.8 Polyimides and Polyether Ketones ..... 508
3.3.9 Cellulose ..... 509
3.3.10 Polyurethanes ..... 511
3.3.11 Thermosets ..... 512
3.3.12 Polymer Blends ..... 515
**References** ..... 522

4 **Glasses**
*Dieter Krause* ..... 523
4.1 Properties of Glasses – General Comments ..... 526
4.2 Composition and Properties of Glasses ..... 527
4.3 Flat Glass and Hollowware ..... 528
4.3.1 Flat Glass ..... 528
4.3.2 Container Glass ..... 529
4.4 Technical Specialty Glasses ..... 530
4.4.1 Chemical Stability of Glasses ..... 530
4.4.2 Mechanical and Thermal Properties ..... 533
4.4.3 Electrical Properties ..... 537
4.4.4 Optical Properties ..... 539
4.5 Optical Glasses ..... 543
4.5.1 Optical Properties ..... 543
4.5.2 Chemical Properties ..... 549
4.5.3 Mechanical Properties ..... 550
4.5.4 Thermal Properties ..... 556
4.6 Vitreous Silica ..... 556
4.6.1 Properties of Synthetic Silica ..... 556
4.6.2 Gas Solubility and Molecular Diffusion ..... 557
4.7 Glass-Ceramics ..... 558
4.8 Glasses for Miscellaneous Applications ..... 559
4.8.1 Sealing Glasses ..... 559
4.8.2 Solder and Passivation Glasses ..... 562
4.8.3 Colored Glasses ..... 565
4.8.4 Infrared-Transmitting Glasses ..... 568
**References** ..... 572

## Part 4 Functional Materials

1 **Semiconductors**
*Werner Martienssen* ..... 575
1.1 Group IV Semiconductors and IV–IV Compounds ..... 578
1.2 III–V Compounds ..... 604

1.2.1 Boron Compounds ..... 604
1.2.2 Aluminium Compounds ..... 610
1.2.3 Gallium Compounds ..... 621
1.2.4 Indium Compounds ..... 638
1.3 II–VI Compounds ..... 652
1.3.1 Beryllium Compounds ..... 652
1.3.2 Magnesium Compounds ..... 655
1.3.3 Oxides of Ca, Sr, and Ba ..... 660
1.3.4 Zinc Compounds ..... 665
1.3.5 Cadmium Compounds ..... 676
1.3.6 Mercury Compounds ..... 686
**References** ..... 691

2 **Superconductors**
*Claus Fischer, Günter Fuchs, Bernhard Holzapfel, Barbara Schüpp-Niewa, Hans Warlimont* ..... 695
2.1 Metallic Superconductors ..... 696
2.1.1 Elements ..... 696
2.1.2 Practical Metallic Superconductors ..... 704
2.2 Non-Metallic Superconductors ..... 711
2.2.1 Oxide Superconductors ..... 711
2.2.2 Superconductors Based on the Y–Ba–Cu–O System ..... 720
2.2.3 Superconductors Based on the Bi–Sr–Ca–Cu–O System ..... 736
2.2.4 Carbides, Borides, Nitrides ..... 744
**References** ..... 749

3 **Magnetic Materials**
*Hideki Harada, Manfred Müller, Hans Warlimont* ..... 755
3.1 Basic Magnetic Properties ..... 755
3.1.1 Atomic Moment ..... 755
3.1.2 Magnetocrystalline Anisotropy ..... 756
3.1.3 Magnetostriction ..... 757
3.2 Soft Magnetic Alloys ..... 758
3.2.1 Low Carbon Steels ..... 758
3.2.2 Fe-based Sintered and Composite Soft Magnetic Materials ..... 759
3.2.3 Iron–Silicon Alloys ..... 763
3.2.4 Nickel–Iron-Based Alloys ..... 769
3.2.5 Iron–Cobalt Alloys ..... 772
3.2.6 Amorphous Metallic Alloys ..... 772
3.2.7 Nanocrystalline Soft Magnetic Alloys ..... 776
3.2.8 Invar and Elinvar Alloys ..... 780
3.3 Hard Magnetic Alloys ..... 794
3.3.1 Fe–Co–Cr ..... 795
3.3.2 Fe–Co–V ..... 797
3.3.3 Fe–Ni–Al–Co, Alnico ..... 798
3.3.4 Fe–Nd–B ..... 800

3.3.5 Co–Sm ... 803
3.3.6 Mn–Al–C ... 810
3.4 Magnetic Oxides ... 811
3.4.1 Soft Magnetic Ferrites ... 811
3.4.2 Hard Magnetic Ferrites ... 813
**References** ... 814

4 **Dielectrics and Electrooptics**
*Gagik G. Gurzadyan, Pancho Tzankov* ... 817
4.1 Dielectric Materials: Low-Frequency Properties ... 822
4.1.1 General Dielectric Properties ... 822
4.1.2 Static Dielectric Constant (Low-Frequency) ... 823
4.1.3 Dissipation Factor ... 823
4.1.4 Elasticity ... 823
4.1.5 Piezoelectricity ... 824
4.2 Optical Materials: High-Frequency Properties ... 824
4.2.1 Crystal Optics: General ... 824
4.2.2 Photoelastic Effect ... 824
4.2.3 Electrooptic Effect ... 825
4.2.4 Nonlinear Optical Effects ... 825
4.3 Guidelines for Use of Tables ... 826
4.4 Tables of Numerical Data for Dielectrics and Electrooptics ... 828
Isotropic Materials ... 828
Cubic, Point Group $m3m$ ($O_h$) Materials ... 828
Cubic, Point Group $\overline{4}3m$ ($T_d$) Materials ... 834
Cubic, Point Group 23 ($T$) Materials ... 838
Hexagonal, Point Group $\overline{6}m2$ ($D_{3h}$) Materials ... 838
Hexagonal, Point Group $6mm$ ($C_{6v}$) Materials ... 840
Hexagonal, Point Group 6 ($C_6$) Materials ... 842
Trigonal, Point Group $\overline{3}m$ ($D_{3d}$) Materials ... 844
Trigonal, Point Group 32 ($D_3$) Materials ... 844
Trigonal, Point Group $3m$ ($C_{3v}$) Materials ... 848
Tetragonal, Point Group $4mmm$ ($D_{4h}$) Materials ... 852
Tetragonal, Point Group $4/m$ ($C_{4h}$) Materials ... 854
Tetragonal, Point Group 422 ($D_4$) Materials ... 854
Tetragonal, Point Group $\overline{4}2m$ ($D_{2d}$) Materials ... 856
Tetragonal, Point Group $4mm$ ($C_{4v}$) Materials ... 864
Orthorhombic, Point Group $mmm$ ($D_{2h}$) Materials ... 866
Orthorhombic, Point Group 222 ($D_2$) Materials ... 866
Orthorhombic, Point Group $mm2$ ($C_{2v}$) Materials ... 872
Monoclinic, Point Group 2 ($C_2$) Materials ... 884
**References** ... 890

5 **Ferroelectrics and Antiferroelectrics**
*Toshio Mitsui* ... 903
5.1 Definition of Ferroelectrics and Antiferroelectrics ... 903
5.2 Survey of Research on Ferroelectrics ... 904

5.3 Classification of Ferroelectrics ..... 906
5.3.1 The 72 Families of Ferroelectrics ..... 909
5.4 Physical Properties of 43 Representative Ferroelectrics ..... 912
5.4.1 Inorganic Crystals Oxides [3.1, 2] ..... 912
5.4.2 Inorganic Crystals Other Than Oxides [3.3] ..... 922
5.4.3 Organic Crystals, Liquid Crystals, and Polymers [3.4] ..... 930
**References** ..... 936

## Part 5 Special Structures

1 **Liquid Crystals**
*Sergei Pestov, Volkmar Vill* ..... 941
1.1 Liquid Crystalline State ..... 941
1.1.1 Chemical Requirements ..... 943
1.1.2 Physical Properties of Liquid Crystals ..... 943
1.1.3 Applications of Liquid Crystals ..... 944
1.1.4 List of Abbreviations ..... 944
1.1.5 Conversion Factors ..... 945
1.2 Physical Properties of the Most Common Liquid Crystalline Substances 946
1.3 Physical Properties of Some Liquid Crystalline Mixtures ..... 975
**References** ..... 977

2 **The Physics of Solid Surfaces**
*Gianfranco Chiarotti* ..... 979
2.1 The Structure of Ideal Surfaces ..... 979
2.1.1 Diagrams of Surfaces [3.2] ..... 979
2.1.2 Crystallographic Formulas ..... 986
2.2 Surface Reconstruction and Relaxation ..... 986
2.2.1 Definitions and Notation ..... 986
2.2.2 Metals ..... 987
2.2.3 Semiconductors ..... 987
2.3 Electronic Structure of Surfaces ..... 996
2.3.1 Metals ..... 997
2.3.2 Semiconductors ..... 1003
2.3.3 Magnetic Surfaces ..... 1007
2.4 Surface Phonons ..... 1012
2.4.1 Metals ..... 1012
2.4.2 Semiconductors and Insulators ..... 1017
2.4.3 Atom–Surface Potential ..... 1019
2.5 The Space Charge Layer at the Surface of a Semiconductor ..... 1020
2.5.1 Definitions and Notation ..... 1020
2.5.2 Useful Formulas and Numerical Values ..... 1022
2.5.3 Surface Conductivity ..... 1023
2.6 Most Frequently Used Acronyms ..... 1026
**References** ..... 1029

3 **Mesoscopic and Nanostructured Materials**
*Fabrice Charra, Susana Gota-Goldmann* ..... 1031
3.1 Introduction and Survey ..... 1031
3.1.1 Historical Review ..... 1031
3.1.2 Definitions ..... 1032
3.1.3 Specific Properties ..... 1034
3.1.4 Organization of this Chapter ..... 1034
3.2 Electronic Structure and Spectroscopy ..... 1035
3.2.1 Electronic Quantum Size Effects ..... 1035
3.2.2 Breakdown of the Momentum Conservation Rule ..... 1036
3.2.3 Excitons in Quantum-Confined Systems ..... 1036
3.2.4 Vibrational Modes and Electron–Phonon Coupling ..... 1040
3.2.5 Electron Transport Phenomena ..... 1042
3.3 Electromagnetic Confinement ..... 1044
3.3.1 Nanoparticle-Doped Materials ..... 1044
3.3.2 Periodic Electromagnetic Lattices ..... 1048
3.4 Magnetic Nanostructures ..... 1048
3.4.1 Spin Electronics ..... 1049
3.4.2 Ultrahigh-Density Storage Media in Hard Disk Drives ..... 1060
3.5 Preparation Techniques ..... 1063
3.5.1 Molecular-Beam Epitaxy ..... 1063
3.5.2 Metal-Organic Chemical Vapor Deposition (MOCVD) ..... 1064
3.5.3 Lithography ..... 1064
3.5.4 Nanocrystals in Matrices ..... 1064
3.5.5 Ex Situ Synthesis of Clusters ..... 1065
**References** ..... 1066

**Acknowledgements** ..... 1073
**About the Authors** ..... 1075
**Detailed Contents** ..... 1081
**Subject Index** ..... 1091

# Subject Index


$\pi$-bonded chain geometry 993
$\pi$-bonded chain model
– diamond(111)2×1 1005
$\alpha = 0$ glass-ceramics 558
$(CH_3NHCH_2COOH)_3 \cdot CaCl_2$ family 932
5CB
– liquid crystals 948
8CB
– liquid crystals 948
8OCB
– liquid crystals 949

## A

Abbe value
– glasses 543, 548
Abrikosov vortices 717
absorption and fluorescence spectra of CdSe 1039
absorption coefficient
– two-photon 826
absorption spectra of spherical particles 1046
Ac actinium 84
acceptor surface level 1023
acceptor surface state 1022
accumulation layer 1020
accuracy 4
acids
– liquid crystals 946
acoustic band 1012
acoustic surface wave 906
acronyms
– solid surface 1026
actinium Ac
– elements 84
adatom 995
adopted numerical values for selected quantities 23
Ag silver 65
Ag-based materials 344
age hardening 198
AISI (American Iron and Steel Institute) 221
Al aluminium 78
Al bronzes 298
alkali aluminium silicates
– electrical properties 434
– mechanical properties 434
– thermal properties 434
alkali halides
– surface phonon energy 1017
alkali–alkaline-earth silicate glasses 530
alkali–lead silicate glasses 530
alkaline-earth aluminium silicates
– electrical properties 436
– glasses 530
– mechanical properties 435
– thermal properties 436
allotropic and high-pressure modifications
– elements 46
alloy
– cast irons 270
– cobalt 272
– elinvar 780
– invar 780
– lead, battery grid 413
– lead–antimony 412
– lead–tin 415
– magnesium 163
– $Ti_3Al$-based 210
– TiAl-based 213
– titanium 206
– wear resistant 274
alloy systems 296
Allred 46
Alnico 798
Al–O–N ceramics
– dielectric properties 447
– optical properties 447
alum family 911
– ferroelectrics 911
alumina
– electrical properties 446
– mechanical properties 445
– properties 445
– thermal properties 446
aluminium Al
– aluminium alloys 171
– aluminium production 171
– chemical properties 172
– cold working 195
– corrosion behavior 204
– elements 78
– hot working 195
– mechanical properties 172
– mechanical treatment 195
– surface layers 204
– work hardening 195
aluminium alloy
– abrasion resistance 190
– aging 198
– behavior in magnetic fields 194
– binary Al-based systems 174
– classification of aluminium alloys 179
– coefficient of thermal expansion 192
– creep behavior 187
– elastic properties 194
– electrical conductivity 194
– hardness 186
– homogenization 198
– machinability 192
– mechanical properties 180, 182
– nuclear properties 194
– optical properties 194
– physical properties 192, 193
– sheet formability 190
– soft annealing 197
– specific heat 194
– stabilization 197
– stress-relieving 198
– structure 182
– technical property 186
– technological properties 190
– tensile strength 186
– thermal softening 195
– work-hardenable 180
aluminium antimonide
– crystal structure, mechanical and thermal properties 610
– electromagnetic and optical properties 619
– electronic properties 616
– transport properties 618
aluminium arsenide
– crystal structure, mechanical and thermal properties 610
– electromagnetic and optical properties 619
– electronic properties 616
– transport properties 618
aluminium casting alloys
– mechanical properties 184
– structure 184
aluminium compounds
– crystal structure, mechanical and thermal properties 610

– electromagnetic and optical properties 619
– electronic properties 614
– mechanical properties 610
– phonon dispersion curves 612
– thermal conductivity 618
– thermal properties 610
– transport properties 617
aluminium nitride
– crystal structure, mechanical and thermal properties 610
– electromagnetic and optical properties 619
– electronic properties 616
– transport properties 618
aluminium phase diagram
– aluminium alloy phase diagram 174
aluminium phosphide
– crystal structure, mechanical and thermal properties 610
– electromagnetic and optical properties 619
– electronic properties 616
– transport properties 618
aluminothermy 174
Al–Ni phase diagram 285
Am americium 151
americium Am
– elements 151
amorphous alloys
– cobalt–based 774
– iron–based 773
– nickel–based 774
amorphous materials 27, 39
amorphous metallic alloys 772
amount of substance
– definition 14
ampere
– SI base unit 14
amphiphilic compound 941
amphiphilic liquid crystal 942
anisotropic magnetoresistance 1058
annealing coefficient
– glasses 548
annealing of steel 223
antiferroelectric crystal 903
antiferroelectric hysteresis loop 904
antiferroelectric liquid crystal 911
antiferroelectrics
– definition 903
– dielectric properties 903
– elastic properties 903
– pyroelectric properties 903
antimony Sb
– elements 98
aperiodic crystals 27
aperiodic materials 33
apparent tilt angle 935
Ar argon 128
area of surface primitive cell
– crystallographic formulas 986
argon Ar
– elements 128
arsenic As
– elements 98
ARUPS 997
As arsenic 98
astatine At
– elements 118
ASTM 241, 242
ASTM (American Society for Testing and Materials) 330
ASW 906
At astatine 118
atomic moment 755
atomic number $Z$
– elements 45
atomic radius
– elements 46
atomic scattering 1019
atomic, ionic, and molecular properties
– elements 46
atomically clean crystalline surface 979
atom–surface potential
– surface phonons 1019–1020
Au gold 65
austenitizing 224

## B

B boron 78
Ba barium 68
back-bond state 1006
bainite 223
$BaMnF_4$ family 922
band bending
– solid surfaces 1023
band gap *see* energy gap 592
band pass filters
– glasses 566
band structure
– aluminium compounds 614
– beryllium compounds 653
– boron compounds 606
– cadmium compounds 679
– group IV semiconductors and IV–IV compounds 589–592
– indium compounds 643
– magnesium compounds 657
– mercury compounds 688
– oxides of Ca, Sr, and Ba 662
– zinc compounds 668
barium Ba
– elements 68
barium oxide
– crystal structure, mechanical and thermal properties 660
– electromagnetic and optical properties 664
– electronic properties 661
– transport properties 663
barium titanate 915
base quantities 12
– ISO 13
base unit
– SI 13
basis
– crystal structure 28
$BaTiO_3$ 915
bcc positions
– surface diagrams 982
Be beryllium 68
becquerel
– SI unit of activity 19
benzene 946
berkelium Bk
– elements 151
beryllium Be
– elements 68
beryllium compounds 652
– crystal structure, mechanical and thermal properties 652
– electromagnetic and optical properties 655
– electronic properties 653
– mechanical and thermal properties 652
– optical properties 655
– thermal properties 652
– transport properties 655
beryllium oxide 447
– crystal structure, mechanical and thermal properties 652
– electrical properties 448
– electronic properties 653
– mechanical properties 447
– thermal properties 448
beryllium selenide
– crystal structure, mechanical and thermal properties 652
– electronic properties 653
beryllium sulfide
– crystal structure, mechanical and thermal properties 652

– electronic properties 653
beryllium telluride
– crystal structure, mechanical and thermal properties 652
– electronic properties 653
Bethe–Slater–Pauling relation 755, 756
Bh Bohrium 124
Bi bismuth 98
biaxial crystals 826
binding energy 998
– metal 999
Bioverit
– glasses 559
BIPM (Bureau International des Poids et Mesures) 3, 11, 12
bismuth Bi
– elements 98
Bi – Sr – Ca – Cu – O (BSCCO) 736
Bi–Sr–Ca–Cu–O
– coherence lengths 736
– London penetration depths 736
– maximum $T_c$ 736
– structural data 736
– superconducting properties 741
– upper critical fields 736
BK 7
– glasses 537
Bk berkelium 151
blue phase 942
BNN
– ferroelectric material 920
Bohrium Bh
– elements 124
boiling temperature
– elements 47
Bondi 46
boracite-type family 911, 921
borides
– physical properties 452
Borofloat
– glasses 528, 529
boron antimonide
– crystal structure, mechanical, and thermal properties 604
– electromagnetic and optical properties 610
– electronic properties 607
– transport properties 608
boron arsenide
– crystal structure, mechanical, and thermal properties 604
– electromagnetic and optical properties 610
– electronic properties 606
– transport properties 608
boron B
– elements 78
boron compounds
– crystal structure, mechanical and thermal properties 604
– electromagnetic and properties 610
– electronic properties 606
– mechanical properties 604
– thermal properties 604
– transport properties 608
boron nitride
– crystal structure, mechanical, and thermal properties 604
– electromagnetic and optical properties 610
– electronic properties 606
– transport properties 608
boron phosphide
– crystal structure, mechanical, and thermal properties 604
– electromagnetic and optical properties 610
– electronic properties 606
– transport properties 608
borosilicate glasses 529, 530
Br bromine 118
Bragg equation 40
brasses 298
Bravais cell 979
– 2D lattice 980
Bravais lattice 32
– elements 47
breathing-mode acoustic oscillations 1040
Brillouin scattering 906
Brillouin zone 913
– aluminium compounds 614
– beryllium compounds 653
– boron compounds 606
– cadmium compounds 678
– gallium compounds 626
– group IV semiconductors and IV–IV compounds 589
– indium compounds 643
– magnesium compounds 657
– mercury compounds 688
– oxides of Ca, Sr, and Ba 661
– zinc compounds 668
Brillouin zone corner 921
bromine Br
– elements 118
bronzes 298
BSCCO
– films 738
– single crystal 739
– tapes 739
– wires 739
buckled dimer 991
bulk electron density 998
bulk glassy alloys 217, 218
bulk mobility 1026
bulk modulus
– elements 47

## C

C carbon 88
Ca calcium 68
cadmium Cd
– elements 73
cadmium compounds
– crystal structure, mechanical and thermal properties 676
– electromagnetic and optical properties 683
– electronic properties 678
– mechanical and thermal properties 676
– optical properties 683
– thermal properties 676
– transport properties 682
cadmium oxide
– crystal structure, mechanical and thermal properties 676
– electromagnetic and optical properties 683
– electronic properties 678
– transport properties 682
cadmium selenide
– crystal structure, mechanical and thermal properties 676
– electromagnetic and optical properties 683
– electronic properties 678
– transport properties 682
cadmium sulfide
– crystal structure, mechanical and thermal properties 676
– electromagnetic and optical properties 683
– electronic properties 678
– transport properties 682
cadmium telluride
– crystal structure, mechanical and thermal properties 676
– electromagnetic and optical properties 683
– electronic properties 678
– transport properties 682
calamitic liquid crystal 941, 942

calcium Ca
– elements 68
calcium oxide
– crystal structure, mechanical and thermal properties 660
– electromagnetic and optical properties 664
– electronic properties 661
– transport properties 663
californium Cf
– elements 151
candela
– SI base unit 15
capacitor 903
capillary viscometer 943
carat 23
carbide
– cemented 277
– electrical properties 466
– mechanical properties 466
– physical properties 458
– thermal properties 466
carbon C
– elements 88
carbon equivalent (CE) 268
carbon fibers
– physical properties 477
carbon steels 230
carrier concentration $n_i$
– gallium compounds 631
– indium compounds 647
cast
– classification 268
cast iron 268
– grades 268
– mechanical properties 270
casting technology 170
catalysis 1020
Cd cadmium 73
Ce cerium 142
cell surface 943
cellulose 481, 509
– cellulose acetate (CA) 509, 510
– cellulose acetobutyrate (CAB) 509, 510
– cellulose propionate (CP) 509, 510
– ethylcellulose (EC) 509, 510
– polymers 509
– vulcanized fiber (VF) 509, 510
cement 432
cemented carbides 277
centering types
– crystal structure 28
centrosymmetric media 1007
Cerabone
– glasses 559
ceramic capacitor 906
ceramic thin film 914
– ferroelectrics 903
ceramics 345, 431
– Al–O–N 447
– applications 432
– non-oxide 451
– oxide 437
– properties 432
– refractory 437
– silicon 433
– technical 437
– traditional 432
Ceran®
– glasses 559
– linear thermal expansion 558
Ceravital
– glasses 559
cerium Ce
– elements 142
cesium Cs
– elements 59
Cf californium 151
CGPM (Conférence Générale des Poids et Mesures) 11, 12
CGS
– electromagnetic system 21
– electrostatic system 21
– Gaussian system 21
cgs definitions of magnetic susceptibility 48
chalcogenide glasses 568, 571
channel conductivity 1020
characterization of optical glasses 547
Charpy impact strength 478
– polymers 478
chemical disorder 38
chemical stability
– glasses 530, 531
– optical glasses 550
chemical symbols
– element 45
chemisorption 1020
chiral smectic C
– liquid crystals 944
chlorine Cl
– elements 118
cholesteric phase 942
cholesteryl (cholest-5-ene) substituted mesogens
– liquid crystals 968
cholesteryl compound 944
chromium Cr
– elements 114
CIP (current in the plane of layer) 1051
CIPM (Comité International des Poids et Mesures) 3, 11
Cl chlorine 118
clamped crystal 907, 921, 934
clamped dielectric constant 907
classifications of liquid crystals 942
climatic influences
– glasses 550
cluster boundaries 907
cluster formation 907
CM
– liquid crystals 970
Cm curium 151
CMOS (complementary metal-oxide-semiconductor) 1059
Co cobalt 135
$Co_{17}RE_2$ 805
$Co_5RE$ 805
coating 943
cobalt
– alloys 272
– applications 273
– hard-facing alloy 274
– mechanical properties 277
– superalloys 274
– surgical implant alloys 277
cobalt Co
– elements 135
cobalt corrosion-resistant alloys 276
cobalt-based corrosion-resistant alloys 276
CODATA (Committee on Data for Science and Technology) 4
coefficient of expansion 478
– polymers 478
coefficient of thermal expansion
– glasses 526
coercive field 904
coherence length 920
coherent phonon and Raman spectra 1041
colloidal synthesis
– nanostructured materials 1065
colored glasses
– colorants 567
– glasses 565
columnar phase 941
commensurate reconstruction 986
commercially pure titanium (cp-Ti) 206
communication technology 912

compacted (vermicular) graphite (CG) 268
complex perovskite-type oxide 909
complex refractive index
– zinc compounds 674
composite medium 1045
– dielectric constant 1045
composite solder glasses
– glasses 563
composite structures
– crystallography 34
compound semiconductor 1003
compressibility 478
– polymers 478
compression modulus
– elements 47
condensed matter 27
– classification 28
conductivity
– frequency-dependent 823
conductivity tensor
– elements 47
conductor
– nanoparticle-based 1043
confined electronic systems
– nanostructured materials 1035
confinement effect
– nanostructured materials 1031
constants
– fundamental 3
container glasses 529
continuous distribution of states 1022
continuous-cooling-transformation (CCT) diagram 238
controlled rolling 240
Convention du Mètre 12
conventional system
– ISO 13
conversion factor 945
– density 945
– diamagnetic anisotropy 945
– dipole moment 945
– dynamic viscosity 945
– kinematic viscosity 945
– molar mass 945
– temperatures of phase transitions 945
– thermal conductivity 945
cooperative interactions 903
coordination number
– elements 46, 47
copolymers
– physical properties 477, 483
copper
– unalloyed 297
copper alloys 296, 297
copper Cu
– elements 65
copper–nickel 300
copper–nickel–zinc 300
Co–RE
– phase equilibria 805
corrosion 1020
– resistance 218
Coulomb blockade
– nanostructured materials 1031, 1044
coupled plasmon modes 1048
Co−Sm 803
CPP (current flows perpendicular to the plane of the layer) 1051, 1054
Cr chromium 114
creep modulus 478
– polymers 478
critical field 904
critical slowing-down 907, 908
critical temperature
– elements 47, 48
– Pb alloys 699
CrNi steels 252
Cronstedt, swedish mineralogist 1032
crystal axes 980
crystal morphology 30
crystal optics 824
crystal structure
– beryllium compounds 652
– cadmium compounds 676
– group IV semiconductors 578
– III–V compounds 610
– indium compounds 638
– IV–IV compound semiconductors 578
– magnesium compounds 655
– mercury compounds 686
– oxides of Ca, Sr, and Ba 660
– zinc compounds 665
crystal structure, mechanical and thermal properties
– III–V compounds 621, 638
– III–V semiconductors 604
– II–VI compounds 652, 655, 660, 665, 676, 686
crystal symmetry
– elements 47
– ferroelectrics 915
crystalline ferroelectric 911
crystalline materials
– definition 27
crystalline surface
– atomically clean 979
crystallization
– glasses 524
crystallographic formulas 986
crystallographic properties
– elements 46, 47
crystallographic space group 946–952, 955–961, 964, 966, 968–971
crystallographic structure
– methods to investigate 39
crystallography
– concepts and terms 27
– rudiments of 27
crystals
– biaxial 826
– cubic 826
– isotropic 826
– uniaxial 826
Cryston
– glasses 559
Cs cesium 59
CS2004
– liquid crystals 975
Cu copper 65
cubic
– dielectrics 828, 838
cubic $BaTiO_3$ 916
cubic boron nitride 451
cubic crystal 47
cubic system 986
Curie point 906
Curie temperature 906
– surface 1009
Curie–Weiss constant 931, 932
curium Cm
– elements 151
current/voltage characteristics of films 1044
Cu−Ni
– electrical conductivity 302
– thermal conductivity 303
Cu−Zn
– electrical conductivity 302
– thermal conductivity 303
Cu−Zn phase diagram 299
cyclohexane 946
cycloolefine copolymer (COC) 486, 487
cyclosilicate 433

## D

D deuterium 54
damping constant
– optical mode frequency 916
dangling bonds (DBs) 991

DAS 991
data storage media
– nanostructured materials 1031
Db dubnium 105
de Broglie wavelength 1035
Debye length
– solid surfaces 1020
Debye temperature $\Theta_D$
– boron compounds 605
– cadmium compounds 678
– gallium compounds 623
– group IV semiconductors 584
– indium compounds 640
– IV–IV compound semiconductors 584
– mercury compounds 687
– metal surfaces 1013
– oxides of Ca, Sr, and Ba 661
– solid surfaces 1014
– surface phonons 1012
– zinc compounds 667
decimal multiples of SI units 19
degree Celsius
– unit of temperature 14
density $\varrho$ 478, 945–954, 956–971
– aluminium compounds 611
– beryllium compounds 653
– boron compounds 604
– cadmium compounds 676
– elements 47
– gallium compounds 621
– group IV semiconductors and IV–IV compounds 579
– indium compounds 638
– magnesium compounds 656
– mercury compounds 686
– oxides of Ca, Sr, and Ba 660
– polymers 478
– temperature dependence 943
– zinc compounds 665
density of electronic states
– magnesium compounds 658
density of electronic states *see also* density of states 658
density of phonon states *see also* density of states 658
density of states (DOS)
– nanostructure 1034
dentistry 330
depletion layer 1020
– solid surfaces 1024
derived quantities 12
– ISO 13
derived units
– SI 16
– special names and symbols 16
deuteration 925
deuterium D
– elements 54
devices
– optical 903
– piezoelectric 903
– pyroelectric 903
devil's staircase 932
devitrifying solder glasses 562
DFB (distributed feedback) 1038
DFG (difference frequency generation) 825
diamagnetic anisotropy 943, 945
diamond
– crystal structure, mechanical and thermal properties 578–588
– electromagnetic and optical properties 601
– electronic properties 589–594
– transport properties 595
diamond positions
– surface diagrams 983
diamond-like structure 979
Dicor
– glasses 559
dielectric
– constant (low-frequency) 823
– dissipation factor 823
– elasticity 823
– general properties 822
– lossy 823
– low-frequency materials 822
– stiffness constant 823
dielectric anisotropy 943, 946, 947
dielectric anomaly 922, 934
dielectric constant $\varepsilon$ 907, 947–958, 960–966, 968–971, 973, 1045
– aluminium compounds 619
– beryllium compounds 655
– boron compounds 610
– cadmium compounds 683
– elements 46
– gallium compounds 635, 637
– group IV semiconductors and IV–IV compounds 601–603
– indium compounds 650
– magnesium compounds 660
– mercury compounds 691
– oxides of Ca, Sr, and Ba 664
– zinc compounds 672
dielectric dispersion 907
dielectric dissipation factor
– glasses 538
dielectric function 1001
– surface layer 1007
dielectric loss tan $\delta$
– gallium compounds 635
dielectric material
– properties 826
dielectric polarization 825
dielectric properties
– glasses 538
dielectric strength
– glasses 539
dielectric tensor 827
dielectrics
– $\alpha$-iodic acid, $\alpha$-$HIO_3$ 868
– $\alpha$-mercuric sulfide, $\alpha$-HgS 846
– $\alpha$-silicon carbide, SiC 840
– $\alpha$-silicon dioxide, $\alpha$-$SiO_2$ 846
– $\alpha$-zinc sulfide, $\alpha$-ZnS 842
– $\beta$-barium borate, $\beta$-$BaB_2O_4$ 848
– 2-cyclooctylamino-5-nitropyridine, $C_{13}H_{19}N_3O_2$ 874
– 3-methyl 4-nitropyridine 1-oxide, $C_6N_2O_3H_6$ 868
– 3-nitrobenzenamine, $C_6H_4(NO_2)NH_2$ 878
– 4-(*N*1*N*-dimethylamino)-3-acetamidonitrobenzene 884
– ADA 856
– ADP 856
– aluminium oxide, $\alpha$-$Al_2O_3$ 844
– aluminium phosphate $AlPO_4$ 844
– ammonium dideuterium phosphate, $ND_4D_2PO_4$ 856
– ammonium dihydrogen arsenate, $NH_4H_2AsO_4$ 856
– ammonium dihydrogen phosphate, $NH_4H_2PO_4$ 856
– ammonium Rochelle salt 870
– ammonium sulfate, $(NH_4)_2SO_4$ 872
– "banana" 872
– barium fluoride, $BaF_2$ 828
– barium formate, $Ba(COOH)_2$ 866
– barium magnesium fluoride, $BaMgF_4$ 872
– barium nitrite monohydrate, $Ba(NO_2)_2 \cdot H_2O$ 842
– barium sodium niobate, $Ba_2NaNb_5O_{15}$ 872
– Barium titanate, $BaTiO_3$ 864
– BBO 848
– berlinite 844
– beryllium oxide, BeO 840
– BGO 838
– BIBO 884
– bismuth germanium oxide, $Bi_{12}GeO_{20}$ 838

– bismuth silicon oxide, $Bi_{12}SiO_{20}$ 838
– bismuth triborate, $BiB_3O_6$ 884
– BK7 Schott glass 828
– BMF 872
– BSO 838
– cadmium germanium arsenide, $CdGeAs_2$ 856
– cadmium germanium phosphide, $CdGeP_2$ 856
– cadmium selenide, CdSe 840
– cadmium sulfide, CdS 840
– cadmium telluride, CdTe 834
– calcite, $CaCO_3$ 844
– calcium fluoride, $CaF_2$ 828
– calcium tartrate tetrahydrate, $Ca(C_4H_4O_6)\cdot 4H_2O$ 874
– CBO 868
– CDA 858
– cesium dideuterium arsenate, $CsD_2AsO_4$ 856
– cesium dihydrogen arsenate, $CsH_2AsO_4$ 858
– cesium lithium borate, $CsLiB_6O_{10}$ 858
– cesium triborate, $CsB_3O_5$ 868
– cinnabar 846
– CLBO 858
– CNB 874, 875
– COANP 874
– copper bromide, CuBr 834
– copper chloride, CuCl 834
– copper gallium selenide, $CuGaSe_2$ 858
– copper gallium sulfide, $CuGaS_2$ 858
– copper iodide, CuI 834
– cubic $m3m$ ($O_h$) 828
– cubic $\overline{4}3m$ ($T_d$) 834
– cubic, 23 ($T$) 838
– D(+)-saccharose, $C_{12}H_{22}O_{11}$ 888
– DADP 856
– DAN 884
– DCDA 856
– deuterated L-arginine phosphate, $(ND_xH_{2-x})_2^+(CND)(CH_2)_3CH(ND_yH_{3-y})^+COO^-\cdot D_2PO_4^-\cdot D_2O$ 884
– diamond, C 830
– dipotassium tartrate hemihydrate, $K_2C_4H_4O_6\cdot 0.5H_2O$ 886
– DKDA 858
– DKDP 858
– DKT 886
– DLAP 884, 886
– DRDA 860
– DRDP 860
– fluorite 828
– fluorspar 828
– forsterite 866
– gadolinium molybdate, $Gd_2(MoO_4)_3$ 876
– gallium antimonide, GaSb 834
– gallium arsenide, GaAs 834
– gallium nitride, GaN 840
– gallium phosphide, GaP 834
– gallium selenide, GaSe 838
– gallium sulfide, GaS 838
– germanium, Ge 830
– GMO 876
– greenockite 840
– halite 832
– hexagonal, 6 ($C_6$) 842
– hexagonal, $\overline{6}mm$ ($C_{6v}$) 840
– hexagonal, $\overline{6}m2$ ($D_{3h}$) 838
– high-frequency (optical) properties 817
– Iceland spar 844
– indium antimonide, InSb 836
– indium arsenide, InAs 836
– indium phosphide, InP 836
– Irtran-3 828
– Irtran-6 834
– isotropic 828
– KB5 880
– KBBF 846
– KDA 860
– KDP 860
– KLINBO 864
– KTA 880
– KTP 880
– LBO 878
– L-CTT 874
– lead molybdate, $PbMoO_4$ 854
– lead titanate, $PbTiO_3$ 864
– LFM 876
– list of described substances 818
– lithium fluoride, LiF 830
– lithium formate monohydrate, $LiCOOH\cdot H_2O$ 876
– lithium gallium oxide, $LiGaO_2$ 876
– lithium iodate, $\alpha$-$LiIO_3$ 842
– lithium metagallate 876
– lithium niobate (5% MgO-doped), MgO:$LiNbO_3$ 848
– lithium niobate, $LiNbO_3$ 848
– lithium sulfate monohydrate, $Li_2SO_4\cdot H_2O$ 886
– lithium tantalate, $LiTaO_3$ 848
– lithium tetraborate, $Li_2B_4O_7$ 864
– lithium triborate, $LiB_3O_5$ 878
– low-frequency properties 817
– magnesium fluoride, $MgF_2$ 852
– magnesium oxide, MgO 830
– magnesium silicate, $Mg_2SiO_4$ 866
– Maxwell's equations 824
– $m$-chloronitrobenzene, $ClC_6H_4NO_2$ 874, 875
– mNA 878
– $m$-nitroaniline 878
– MNMA 874
– monoclinic, 2 ($C_2$) 884
– $N$,2-dimethyl-4-nitrobenzenamine, $C_8H_{10}N_2O_2$ 874
– $N$-[2-(dimethylamino)-5-nitrophenyl]-acetamide 884
– nantokite 834
– numerical data 818, 828
– orthorhombic, 222 ($D_2$) 866
– orthorhombic, $mm2$ ($C_{2v}$) 872
– orthorhombic, $mmm$ ($D_{2h}$) 866
– paratellurite 854
– physical properties 817
– PMMA (Plexiglas) 828
– POM 868
– potassium acid phthalate, $KH(C_8H_4O_4)$ 878
– potassium bromide, KBr 830
– potassium chloride, KCl 830
– potassium dideuterium arsenate, $KD_2AsO_4$ 858
– potassium dideuterium phosphate, $KD_2PO_4$ 858
– potassium dihydrogen arsenate, $KH_2AsO_4$ 860
– potassium dihydrogen phosphate, $KH_2PO_4$ 860
– potassium fluoroboratoberyllate, $KBe_2BO_3F_2$ 846
– potassium iodide, KI 830
– potassium lithium niobate, $K_3Li_2Nb_5O_{15}$ 864
– potassium niobate, $KNbO_3$ 880
– potassium pentaborate tetrahydrate, $KB_5O_8\cdot 4H_2O$ 880
– potassium sodium tartrate tetrahydrate, $KNa(C_4H_4O_6)\cdot 4H_2O$ 870
– potassium titanate (titanyl) phosphate, $KTiOPO_4$ 880
– potassium titanyl arsenate, $KTiOAsO_4$ 880
– proustite 850
– pyragyrite 850
– quartz 846

– RDA 860
– RDP 862
– Rochelle salt 870
– rock salt 832
– RTP 882
– rubidium dideuterium arsenate, $RbD_2AsO_4$ 860
– rubidium dideuterium phosphate, $RbD_2PO_4$ 860
– rubidium dihydrogen arsenate, $RbH_2AsO_4$ 860
– rubidium dihydrogen phosphate, $RbH_2PO_4$ 862
– rubidium titanate (titanyl) phosphate, $RbTiOPO_4$ 882
– rutile 852
– sapphire 844
– Silicon dioxide, $SiO_2$ 828
– silicon, Si 830
– silver antimony sulfide, $Ag_3SbS_3$ 850
– silver arsenic sulfide, $Ag_3AsS_3$ 850
– silver gallium selenide, $AgGaSe_2$ 862
– silver thiogallate, $AgGaS_2$ 862
– sodium ammonium tartrate tetrahydrate, $Na(NH_4)C_4H_4O_6 \cdot 4H_2O$ 870
– sodium chlorate, $NaClO_3$ 838
– sodium chloride, NaCl 832
– sodium fluoride, NaF 832
– sodium nitrite, $NaNO_2$ 882
– strontium fluoride, $SrF_2$ 832
– strontium titanate, $SrTiO_3$ 832
– sucrose 888
– sylvine 830
– sylvite 830
– TAS 850
– tellurium dioxide, $TeO_2$ 854
– tellurium, Te 846
– tetragonal, $4/m$ ($C_{4h}$) 854
– tetragonal, $4/mmm$ ($D_{4h}$) 852
– tetragonal, 422 ($D_4$) 854
– tetragonal, $4mm$ ($C_{4v}$) 864
– tetragonal, $\bar{4}2m$ ($D_{2d}$) 856
– TGS 888
– thallium arsenic selenide, $Tl_3AsSe_3$ 850
– titanium dioxide, $TiO_2$ 852
– tourmaline, $(Na,Ca)(Mg,Fe)_3B_3Al_6Si_6(O,OH,F)_{31}$ 850
– triglycine sulfate, $(CH_2NH_2COOH)_3 \cdot H_2SO_4$ 888
– trigonal, 32 ($D_3$) 844
– trigonal, $3m$ ($C_{3v}$) 848
– trigonal, $\bar{3}m$ ($D_{3d}$) 844
– urea, $(NH_2)_2CO$ 862
– wurtzite 842
– YAG 832
– YAP 866
– YLF 854
– yttrium aluminate, $YAlO_3$ 866
– yttrium aluminium garnet, $Y_3Al_5O_{12}$ 832
– yttrium lithium fluoride, $YLiF_4$ 854
– yttrium vanadate, $YVO_4$ 852
– YVO 852
– zinc blende 842
– zinc germanium diphosphide, $ZnGeP_2$ 862
– zinc oxide, ZnO 840
– zinc selenide, ZnSe 836
– zinc telluride, ZnTe 836
– zincite 840
difference frequency generation (DFG) 825
differential conductance as function of voltage 1043
diffraction method 39
diffusion coefficient 946–949, 956–960, 970
diffusion-controlled growth
– nanostructured materials 1064
dimensionality
– nanostructured materials 1033
dimensions
– physical quantities 4, 13
dimer bond length 995
dioxide
– zirconium 448
dipole glass 906
dipole moment 945, 947–953, 955–963, 968–971
direct gap
– group IV semiconductors and IV–IV compounds 592
direct piezoelectric effect 824
director 943
discotic liquid crystal 941, 942, 972
– physical properties 972
disk-like molecule 942
disordered materials 38
dispersion
– glasses 543
dispersion curves
– electronic structure of surfaces 999
dispersion hardening 329
displacement of atoms
– surface phonons 1012
displacive disorder 38
displacive ferroelectrics 907
display lifetime 944
dissipation factor 826, 828
dissipative dispersion 907
dissociation energy of molecule
– elements 46
DOBAMBC (liquid crystal) 934
domain pattern
– perpendicular magnetization 1062
domain wall
– ferroelectric 907
– ferromagnetic 907
donor surface state 1022
doping
– chemical 576
DOS (density of states) 330, 1049
– nanostructured materials 1034
drain 1024
Drude-model metal 1045
drug delivery 944
DSP family 931
DTA (differential thermal analysis) 39
dubnium Db
– elements 105
ductile iron 269
Duran
– glasses 527, 531, 537
Dy dysprosium 142
dye dopant 944
dynamic viscosity 945–948, 955–959, 961, 962, 967, 969–971, 973
dysprosium Dy
– elements 142


## E


E7
– liquid crystals 975
ECS 1011
EDX (energy-dispersive analysis of X-rays) 39
EELS 1013
effect of solute elements conductivity of Cu 297
effective masses
– aluminium compounds 617
– boron compounds 607
– cadmium compounds 681
– group IV semiconductors and IV–IV compounds 593
– indium compounds 646
– mercury compounds 689

– oxides of Ca, Sr, and Ba 661
– zinc compounds 670
effective masses $m_n$ and $m_p$
– gallium compounds 629
einsteinium Es
– elements 151
elastic compliance 828
elastic compliance tensor 934
– elements 47
elastic constant $c_{ik}$ 823
– aluminium compounds 611
– beryllium compounds 652
– cadmium compounds 676
– gallium compounds 621
– group IV semiconductors and IV–IV compounds 580
– indium compounds 638
– magnesium compounds 656
– mercury compounds 687
– oxides of Ca, Sr, and Ba 660
– zinc compounds 665
elastic modulus 478, *see* elastic constant 580
– elements 46, 47
– polymers 478
elastic stiffness 828
– elements 47
elastic tensor 827
elastooptic coefficient 825
elastooptic constant 828
elastooptic tensor 827
electric strength 478
– polymers 478
electrical conductivity
– aluminium compounds 618
– boron compounds 608
– elements 46
– group IV semiconductors and IV–IV compounds 595
electrical conductivity *see also* electrical resistivity 659
electrical conductivity $\sigma$
– indium compounds 647
– magnesium compounds 659
– mercury compounds 690
– oxides of Ca, Sr, and Ba 663
electrical resistivity
– boron compounds 609
– elements 48
– gallium compounds 630
electrical steel 766
electroforming 288
electromagnetic and optical properties
– group IV semiconductors and IV–IV compounds 601
– III–V compounds 610, 619, 635, 650
– II–VI compounds 655, 660, 664, 672, 683, 691
electromagnetic concentration effect 1046
electromagnetic confinement
– nanostructured materials 1044
electromechanical coupling constant 912, 918
electron affinity
– elements 46
electron and hole mobilities
– aluminium compounds 618
electron density of states 1034
– cadmium compounds 680
electron diffraction 41
electron effective mass $m_n$ 593, *see* effective mass 661
electron $g$-factor $g_c$
– gallium compounds 629
– indium compounds 646
electron microscope image
– magnetic tunneling junction 1057
electron microscopy 1049
electron mobility $\mu_n$ 663, *see* mobility $\mu$ 682
– elements 48
– gallium compounds 631
– indium compounds 648
– mercury compounds 690
– oxides of Ca, Sr, and Ba 663
electron transport phenomena
– nanostructured materials 1042
electron tunneling
– phonon-assisted 1043
electronegativity
– elements 46
electronic band gap
– elements 48
electronic conductivity $\sigma$
– zinc compounds 671
electronic configuration
– elements 46
electronic dispersion curves 1000
electronic ground state
– elements 46
electronic properties
– group IV semiconductors and IV–IV compounds 589–594
– III–V compounds 606, 614, 626, 643
– II–VI compounds 653, 657, 661, 668, 678, 688
electronic structure
– solid surfaces 996
electronic transport, general description
– aluminium compounds 617
– beryllium compounds 655
– boron compounds 608
– cadmium compounds 682
– gallium compounds 629
– group IV semiconductors and IV–IV compounds 595
– indium compounds 647
– magnesium compounds 659
– mercury compounds 689
– oxides of Ca, Sr, and Ba 663
– zinc compounds 670
electronic work function
– elements 48
electronic, electromagnetic, and optical properties
– elements 46
electron–phonon coupling 1040, 1041
electrooptic coefficients 826
electrooptic modulators
– nanostructured materials 1040
electrooptic tensor 827
electro-optical constants
– zinc compounds 675
electro-optical effect 944
electrostrictive constant 930
elemental semiconductor 1003
elements 45
– allotropic modifications 48
– atomic properties 46
– electromagnetic properties 48
– electronic properties 48
– high-pressure modifications 48
– ionic properties 46
– macroscopic properties 46
– materials data 46
– molecular properties 46
– optical properties 48
– ordered according to the Periodic table 52
– ordered by their atomic number 51
– ordered by their chemical symbol 50
– ordered by their name 49
elinvar alloys 786
– antiferromagnetic 789
elinvar-type alloys
– nonmagnetic 792
energy bands *see* band structure 590

energy diagram for a MIM tunnel junction 1053
energy dispersion curve 1000
energy equivalents 24
energy equivalents in different units 24
energy exchange time $\tau_{e-ph}$ 1041
energy gap
– aluminium compounds 616
– beryllium compounds 654
– cadmium compounds 681
– gallium compounds 628
– group IV semiconductors 592, 593
– indium compounds 644
– IV–IV compound semiconductors 592, 593
– magnesium compounds 659
– mercury compounds 688
– oxides of Ca, Sr, and Ba 661
– zinc compounds 669
energy gaps
– boron compounds 607
energy shifts in the luminescence peaks 1037
energy-storage cell 1043
engineering critical current density 741
enthalpies of phase transitions 946–973
enthalpy change
– elements 47
enthalpy of combustion 477
– polymers 477
enthalpy of fusion 477
– polymers 477
entropy of fusion 477
– polymers 477
Er erbium 142
erbium Er
– elements 142
Es einsteinium 151
Eu europium 142
europium Eu
– elements 142
EXAFS (extended X-ray atomic fine-structure analysis) 39
excess carrier density 1023
excitation energy
– nanostructured materials 1038
exciton binding energy
– gallium compounds 628
– zinc compounds 669
exciton Bohr radii
– semiconductors 1037
exciton energy
– group IV semiconductors and IV–IV compounds 593
exciton peak energy
– indium compounds 645
exciton Rydberg series 1038
excitons
– nanostructured materials 1036
external forces 46
external-field dependence 46
extinction coefficient *k*
– gallium compounds 635
– zinc compounds 674

## F

F fluorine 118
F2
– optical glasses 551
F5
– glasses 537
facets
– crystallography 27
Fahrenheit 48
families of ferroelectrics 909
fast displays 903
fcc positions
– surface diagrams 981
Fe iron 131
$Fe_{14}Nd_2B$
– commercial magnets 804
– magnetic materials 803
Fe–C(-X)
– carbide phases 224
Fe–Cr alloy 226
Fe–Mn alloys 226
Fe–Ni alloys 225
Fermi energy 998
Fermi function 1022
Fermi level pinning 1025
Fermi surface
– nanostructured materials 1055
Fermi surface shift in an electric field 1050
Fermi surfaces
– nanostructured materials 1049
Fermi wavelength
– nanostructured materials 1035
fermium Fm
– elements 151
ferrielectric triple hysteresis loop 936
ferrielectricity 927
ferrite
– applications 812
– hard magnetic 813
– MnZn 812
– NiZn 813
– soft magnetic 811
ferroelectric ceramics 906
ferroelectric hysteresis loop 904
ferroelectric liquid crystal 906, 911, 945, 967
– physical properties 967
ferroelectric mixtures
– liquid crystals 975
– physical properties 975
ferroelectric phase transition 906, 933
ferroelectric polymers 906
ferroelectric transducer 906
ferroelectrics
– classification 906
– definition 903
– dielectric properties 903
– displacive type 906
– elastic properties 903
– families 909, 911
– general properties 906
– indirect type 906
– inorganic crystals 903
– inorganic crystals other than oxides 922
– inorganic crystals oxides 912
– liquid crystals 903, 930
– order–disorder type 906
– organic crystals 903, 930
– phase transitions 903
– piezoelectric properties 903
– polymers 903, 930
– pyroelectric properties 903
– symbols and units 912
ferromagnetic surface 1008
Fe−Co−Cr 795
Fe−Co−V 797
Fe−Nd−B 800
– phase relations 800
Fe−Ni−Al−Co 798
Fe−Si alloys
– rapidly solidified 768
Fibonacci sequence 35
field-effect mobility 1024
– solid surfaces 1024
first Brillouin zone *see* Brillouin zone 657
flat glasses 528
flat-band condition 1020
fluorinated three-ring LC 944
fluorine F
– elements 118

fluoropolymers 480, 496
– poly(ethylene-co-chlorotrifluoroethylene) (ECTFE) 496, 497
– poly(ethylene-co-tetrafluoroethylene) (ETFE) 496, 497
– poly(tetrafluoroethylene-co-hexafluoropropylene) (FEP) 496, 497
– polychlorotrifluoroethylene (PCTFE) 496, 497
– polytetrafluoroethylene (PTFE) 496, 497
flux flow (FF) 718
Fm fermium 151
formation curve
– glasses 524
formulas
– crystallographic 986
Fotoceram
– glasses 559
Fotoform
– glasses 559
Foturan
– glasses 559
Fourier map 926
four-ring system 964
Fr francium 59
francium Fr
– elements 59
Frantz–Keldysh effect 1040
free dielectric constant 907
frequency conversion 825
Fresnel reflectivity
– glasses 549
Friedel–Creagh–Kmetz rule 943
fundamental constants 3
– 2002 adjustment 4
– alpha particle 9
– atomic physics and particle physics 7
– CODATA recommended values 4
– electromagnetic constants 6
– electron 7
– meaning 4
– most frequently used 4
– neutron 8
– proton 8
– recommended values 3, 4
– thermodynamic constants 6
– units of measurement 3
– universal constants 5
– what are the fundamental constants? 3
fused silica
– glasses 534, 537

## G

Ga gallium 78
GaAs positions
– surface diagrams 983
gadolinium Gd
– elements 142
gallium antimonide
– crystal structure, mechanical and thermal properties 621
– electromagnetic and optical properties 635
– electronic properties 626
– transport properties 631
gallium arsenide
– crystal structure, mechanical and thermal properties 621
– electromagnetic and optical properties 635
– electronic properties 626
– transport properties 631
gallium compounds
– crystal structure, mechanical and thermal properties 621
– electromagnetic and optical properties 635
– electronic properties 626
– mechanical and thermal properties 621
– thermal conductivity 634
– thermal properties 621
– transport properties 629
gallium Ga
– elements 78
gallium nitride
– crystal structure, mechanical and thermal properties 621
– electromagnetic and optical properties 635
– electronic properties 626
– transport properties 631
gallium phosphide
– crystal structure, mechanical and thermal properties 621
– electromagnetic and optical properties 635
– electronic properties 626
– transport properties 631
gamma titanium aluminides 213
gas permeation 478
– polymers 478
Gd gadolinium 142
Ge germanium 88
germanium
– band structure 590
– crystal structure, mechanical and thermal properties 578–588
– electromagnetic and optical properties 601
– electronic properties 589–594
– transport properties 598
germanium Ge
– elements 88
*g*-factor
– cadmium compounds 681
*g*-factor, conduction electrons
– group IV semiconductors and IV–IV compounds 594
glass designation 544
glass formers 527
glass matrix 1040
glass number 8nnn 534, 537
glass number nnnn
– sealing glasses 563
glass structure
– sodium silicate glasses 524
glass temperature
– glasses 524
glass transition temperature 477
– polymers 477
glass-ceramics 525, 526, 558
– density 558
– elastic properties 558
– manufacturing process 558
glasses 523
– Abbe value 547
– abbreviating glass code 543
– acid attack 532
– acid classes 533
– alkali attack 532
– alkali classes 533
– alkali–alkaline-earth silicate 530
– alkali–lead silicate 530
– alkaline-earth aluminosilicate 530
– amorphous metals 523
– armor plate glasses 529
– automotive applications 529
– band pass filters 566
– Borofloat 528, 529
– borosilicate 529, 530
– borosilicate glasses 529
– brittleness 536
– chemical constants 553
– chemical properties 549
– chemical resistance 549
– chemical stability 530, 531
– chemical vapor deposition 523
– color code 554
– composition 527

– compound glasses 529
– container glasses 528, 529
– crack effects 536
– density 528
– dielectric properties 538
– Duran® 531
– elasticity 536
– electrical properties 537
– engineering material 523
– fire protecting glasses 529
– flat 528
– fracture toughness 537
– frozen-in melt 533
– halide glasses 568
– hydrolytic classes 533
– infrared transmitting glasses 568
– infrared-transmitting 571
– inhomogeneous 525
– internal transmission 554
– linear thermal expansion 536, 556
– long pass filters 566
– major groups 526
– manufacturers, preferred optical glasses 545
– melting range 533
– mixtures of oxide compounds 524
– neutral density filters 566
– optical 551
– optical characterization 547
– optical glasses 543
– optical properties 539, 543
– oxide glasses 568
– passivation glasses 562
– physical constants 553
– plate glasses 528
– properties 526
– quasi-solid melt 533
– refractive index 539
– Schott filter glasses 569
– sealing glasses 559
– short pass filters 566
– silicate based 526
– soda–lime type 528
– solder glasses 562
– strength 534
– stress behavior 535
– stress rate 535
– stress-induced birefringence 539
– supercooled melt 533
– surface (cleaning and etching) 533
– surface modification 532
– surface resistivity 538
– technical 530
– tensile strength 536
– thermal conductivity 556
– thermal strength 537
– transmittance 539
– viscosity 534
– vitreous silica 556
– volume resistivity 537
– wear-induced surface defects 535
glasses, colored
– nomenclature 566
– optical filter 566
glasses, sealing
– ceramic 562
– principal applications 561
– recommended material combinations 560
– special properties 561
glasses, solder and passivation
– composite 563
– properties 564
glassy state
– crystallography 39
GMO family
– ferroelectrics 920
GMR (giant magnetoresistance) 1049, 1050
– mechanism 1051
– thickness dependence 1051
GMR ratio 1050
gold
– alloys 347
– applications 347
– chemical properties 361
– electrical properties 356
– electrical resistivity 356
– intermetallic compounds 350
– magnetic properties 358
– mechanical properties 352
– optical properties 359
– phase diagrams 347
– production 347
– special alloys 361
– thermal properties 359
– thermochemical data 347
– thermoelectric properties 358
gold Au
– elements 65
golden mean 35
granular materials 1043
gray
– SI unit of absorbed dose 19
gray iron 269
gray tin
– band structure 590
– crystal structure, mechanical and thermal properties 578–588
– electromagnetic and optical properties 601
– electronic properties 589–594
– transport properties 599
Griffith flaw
– glasses 534
Group IV semiconductors 576, 578–603
– electron mobility 597
– hole mobility 597
Group IV semiconductors and IV–IV compounds
– crystal structure 578
– electromagnetic and optical properties 601
– electronic properties 589–594
– mechanical properties 578
– thermal properties 578
– transport properties 595–601
groups of elements (Periodic table) 45

## H

H hydrogen 54
hafnium Hf
– elements 94
Haigh Push-Pull test 408
Hall coefficient
– elements 48
– group IV semiconductors and IV–IV compounds 595
Hall mobility
– group IV semiconductors and IV–IV compounds 596, 597
Hall mobility *see also* mobility $\mu$ 596
halogen-substituted benzene 946
hard disk drive 1060
– limits 1060
– technology 1060
hard ferrites
– magnetic properties 814
hard magnetic alloys 794
hardenability 237
hardmetals 277
hassium Hs
– elements 131
Hatfield steel 226
HATOF 1013
HCl family 924
He helium 54
heat capacities $c_p$, $c_V$
– boron compounds 605
– group IV semiconductors 584

– IV–IV compound semiconductors 584
heat capacity 477, 956–960, 970
– cadmium compounds 678
– gallium compounds 623
– indium compounds 640
– mercury compounds 687
– oxides of Ca, Sr, and Ba 661
– polymers 477
– zinc compounds 667
heat-resistant steels 258
HEIS (high-energy ion scattering) 989, 1013
helical structure 942
helium He
– elements 54
Hermann–Mauguin symbols 30
hertz
– SI unit of frequency 19
heterocycles 946
hexagonal $BaTiO_3$ 917
Hf hafnium 94
Hg mercury 73
high copper alloy 297
high-$T_c$ superconductors
– lower critical 716
– upper critical 716
high-frequency dielectric constant $\varepsilon$ *see also* dielectric constant $\varepsilon$ 601
high-Ni alloys 281
high-pressure die casting (HPDC) 168
high-pressure modifications 48
high-strength low-alloy 240
hip implants 277
HMF (half-metallic ferromagnet) 1055
Ho holmium 142
hole effective mass $m_p$ 594, *see* effective mass 661
hole mobility $\mu_p$ *see* mobility $\mu$ 682
– elements 48
– gallium compounds 631
– indium compounds 648
hollow-ware
– glasses 528
holmium Ho
– elements 142
holohedry
– crystallography 30
homeotropic alignment 943
Hooke's law 47, 823
hopping mechanism
– nanostructured materials 1043
host–guest effect 944
hot forming
– glasses 524
Hoya code
– glasses 544
HPDC (high-pressure die casting) 168
HRTEM (high-resolution transition electron microscopy) 39
Hs hassium 131
Hume-Rothery phase 333, 350
Hume-Rothery phases 296
hydrogen H
– elements 54
hydrostatic pressure 926
hyper-Raman scattering 915

## I

I iodine 118
IBA 991, 1024
ICSU (International Council of the Scientific Unions) 4
ideal surface 979
III–V compound semiconductors 604
II–VI semiconductor compounds 652
image potential 996
image state 996, 997, 999
– effective mass 999
impact strength 478
– polymers 478
impurity elements 206
impurity scattering
– group IV semiconductors and IV–IV compounds 599
In indium 78
incommensurate phase 930
incommensurate phases 906
incommensurate reconstruction 986
index of refraction
– complex 674
indirect gap
– group IV semiconductors and IV–IV compounds 589
indium antimonide
– crystal structure, mechanical and thermal properties 638
– electromagnetic and optical properties 650
– electronic properties 643
– transport properties 647
indium arsenide
– crystal structure, mechanical and thermal properties 638
– electromagnetic and optical properties 650
– electronic properties 643
– transport properties 647
indium compounds
– crystal structure, mechanical and thermal properties 638
– electromagnetic and optical properties 650
– electronic properties 643
– mechanical and thermal properties 638
– optical properties 650
– thermal properties 638
– transport properties 647
indium In
– elements 78
indium nitride
– crystal structure, mechanical and thermal properties 638
– electromagnetic and optical properties 650
– electronic properties 643
– transport properties 647
indium phosphide
– crystal structure, mechanical and thermal properties 638
– electromagnetic and optical properties 650
– electronic properties 643
– transport properties 647
induced phase transition 904
inelastic neutron scattering 906
infrared-transmitting glasses 568, 571
inorganic ferroelectrics 903
inorganic ferroelectrics other than oxides 922
inosilicates 433
insulator
– surface phonon 1017
intercritical annealing 240
interface state density
– solid surface 1026
interlayer distance
– crystallographic formulas 986
International Annealed Copper Standard (IACS) 296
international system of units 11
international tables for crystallography 31
International Union of Pure and Applied Chemistry (IUPAC) 15
International Union of Pure and Applied Physics (IUPAP) 14
internuclear distance
– elements 46
intrinsic carrier concentration

– group IV semiconductors and IV–IV compounds 595, 596
intrinsic charge carrier concentration
– elements 48
intrinsic Debye length 1021
intrinsic Fermi level 1020
invar alloys
– Fe−Ni-based 782
– Fe−Pd base 785
– Fe−Pt-based 784
Invar effect 385
inversion center 30
inversion layer 1020
– solid surfaces 1024
inversion layer channel 1024
iodine I
– elements 118
ionic radius
– elements 46, 49
ionization energy
– elements 46
Ir iridium 135
iridium 393
– alloys 393
– applications 393
– chemical properties 398
– diffusion 398
– electrical properties 397
– lattice parameter 394
– magnetic properties 397
– mechanical properties 395
– optical properties 398
– phase diagram 393
– production 393
– thermal properties 398
– thermoelectrical properties 397
iridium Ir
– elements 135
iron and steels 221
iron Fe
– elements 131
iron miscibility gap 226
iron phase diagram 226
iron-carbon alloys 222
iron-cobalt alloys 772
iron–silicon alloys 763
Ising model 906
ISO (International Organization for Standardization) 12
isothermal transformation (IT) diagram 238
isotropic
– dielectrics 828
isotropic liquid 943
IV–IV compound semiconductors 576, 578–603
– electron mobility 597
– hole mobility 597

## J

JDOS 1006
jellium 997
jellium model 998
– work functions 999
jewellery 330
joint density of states 1005
jominy apparatus 238
Josephson vortices 717
joule
– SI unit of energy 19

## K

K 50
– glasses 537
K potassium 59
K10
– optical glasses 551
K7
– optical glasses 551
katal
– SI unit of catalytic activity 19
KDP family 925
kelvin 48
– SI base unit 14
Kerr effect 825
– optical 826
Kerr ellipticity 1011
$KH_2PO_4$ family 925
kilogram
– SI base unit 14
kinematic viscosity 945, 947, 950, 951, 955, 962, 964–967, 969, 975
Kleinman symmetry conditions 825
$KNbO_3$ 913
knee joint replacements 277
$KNO_3$ family 925
Knoop hardness
– optical glasses 550
Kr krypton 128
KRIPES 997
Kroll process 206
krypton Kr
– elements 128
$KTaO_3$ 913

## L

LA
– phonon spectra 915
La lanthanum 84
Lamb theory of elastic vibrations 1040
lamellar (flake) graphite (FG) 268
langbeinite-type family 911, 930
lanthanum La
– elements 84
LASF35
– optical glasses 551
LAT family 932
lattice concept
– crystallography 28
lattice constants *see* lattice parameters 656
lattice dynamics 1012
lattice parameter 980
– aluminium compounds 610
– beryllium compounds 652
– boron compounds 604
– cadmium compounds 676
– gallium compounds 621
– group IV semiconductors and IV–IV compounds 579
– indium compounds 638
– magnesium compounds 656
– mercury compounds 686
– oxides of Ca, Sr, and Ba 660
– zinc compounds 665
lattice scattering
– group IV semiconductors and IV–IV compounds 598
lattice vibration 906
lattices
– planes and directions 28
Laue images 41
lawrencium Lr
– elements 151
layer-structure family 909
LB (Langmuir–Blodgett) film 944
LC display 944
LC materials (LCMs) 944
LC–surface interaction 944
lead 407
– antimony 412
– arsenic alloys 421
– battery grid alloys 413
– bearing alloys 415
– bismuth 419
– cable sheathing alloys 421
– calcium–tin 417
– calcium–tin, battery grid 418
– coper alloys 421
– corrosion 408
– corrosion classification 411
– fusible alloys 420
– gamma-ray mass-absorption 412
– grades 407

– internal friction 408
– low-melting alloys 419
– mechanical properties 408
– quaternary eutectic alloy 420
– recrystallization 409
– silver alloys 420
– solder alloys 415
– solders 416
– tellurium alloys 421
– ternary alloys 413
– tin alloy 415
lead glasses 527
lead Pb
– elements 88
lead–antimony
– phase diagram 413
LEED (low-energy electron diffraction) 987, 1013
LEIS (low-energy ion scattering) 989, 1013
LF5
– optical glasses 551
Li lithium 59
$Li_2Ge_7O_{15}$ family 920
$LiBaO_3$ 919
light transmittance
– glasses 539
light-emitting diode 1043
$LiNbO_3$ family 909, 919
linear thermal expansion
– optical glasses 556
linear thermal expansion coefficient $\alpha$
– aluminium compounds 611
– beryllium compounds 653
– boron compounds 605
– cadmium compounds 677
– gallium compounds 623
– group IV semiconductors 582, 583
– indium compounds 639
– IV–IV compound semiconductors 582, 583
– magnesium compounds 656
– mercury compounds 687
– oxides of Ca, Sr, and Ba 660
– zinc compounds 666
$LiNH_4C_4H_4O_8$ family 911
liquid crystal
– anisotropy 943
– refractive index 943
– rod-like 943
liquid crystal family 911, 934
liquid crystal ferroelectrics 903
liquid crystal material (LCM)
– degradation 944
liquid crystal salts 973
– physical properties 973
liquid crystal two-ring systems with bridges
– physical properties 955
liquid crystal two-ring systems without bridges
– physical properties 947
liquid crystalline acids
– physical properties 946
liquid crystalline compound 943
– mesogenic group 943
– side group 943
– terminal group 943
liquid crystalline mixtures
– physical properties 975
liquid crystals
– ferroelectric properties 905
liquid crystals (LCs) 941
list of described physical properties 822
lithium Li
– elements 59
lithium niobate 919
lithography
– nanostructured materials 1064
Lithosil™ 551
LLF1
– optical glasses 551
local-field effect 1045
long pass filters
– glasses 566
longitudinal acoustic branch 915
long-range order 39, 927
– glasses 524
long-range order of molecules 943
losses
– dynamic eddy current 763
– hysteresis 763
low dielectric loss glasses 527
low-dimensional system
– nanostructured materials 1034
low-frequency dielectric constant 917
low-temperature annealing 298
Lr lawrencium 151
LSMO ($La_{0.7}Sr_{0.3}MnO_3$) 1056
Lu lutetium 142
lumen
– non-SI unit in photometry 15
luminescence
– nanostructured materials 1036
luminous flux
– photometry 15
luminous intensity $I_v$
– photometry 15
lutetium Lu
– elements 142
lyotropic liquid crystals 942

## M

M. Faraday 1032
Macor
– glasses 559
magnesium alloys 163
– corrosion behavior 169
– heat treatments 169
– joining 169
– mechanical properties 168
– nominal composition 165
– solubility data 163
– tensile properties 167
– tensile property 166
magnesium compounds
– crystal structure, mechanical and thermal properties 655
– electromagnetic and optical properties 660
– electronic properties 657
– mechanical and thermal properties 655
– optical properties 660
– thermal properties 655
– transport properties 659
magnesium Mg
– casting practices 168
– elements 68
– magnesium alloys 162
– melting practices 168
magnesium oxide 444
– applications 444
– crystal structure, mechanical and thermal properties 655
– electrical properties 444
– electromagnetic and optical properties 660
– electronic properties 657
– mechanical properties 444
– thermal properties 444
– transport properties 659
magnesium selenide
– crystal structure, mechanical and thermal properties 655
– electromagnetic and optical properties 660
– electronic properties 657
– transport properties 659
magnesium silicate
– electrical properties 435, 436
– mechanical properties 435, 436
– thermal properties 435, 436
magnesium sulfide

– crystal structure, mechanical and thermal properties 655
– electromagnetic and optical properties 660
– electronic properties 657
– transport properties 659
magnesium telluride
– crystal structure, mechanical and thermal properties 655
– electromagnetic and optical properties 660
– electronic properties 657
– transport properties 659
magnet
– Mn−Al−C 811
magnetic domain 1058
magnetic dots
– nanostructured materials 1049
magnetic dots, arrays of 1061
magnetic field constant
– fundamental constant 14
magnetic layers 1048, 1050
– spin valve 1052
magnetic materials 755
– $Co_5Sm$ based 806
– hard 794
– permanent 794
magnetic nanostructures 1031, 1048, 1050
– information storage 1048
– read heads 1048
– sensors 1048
magnetic oxides 811
magnetic periodic structures 33
magnetic reading head 1053, 1058
magnetic recording
– perpendicular discontinuous media 1060
magnetic sensors 1048, 1058
magnetic surface 1008
magnetic susceptibility 948–950, 956, 957
– elements 46, 48
magnetic tunnel junction 1054
– manganite-based 1057
magnetic tunneling junctions (MTJ) 1056
magnetization
– elements 48
magnetocrystalline anisotropy 756
magnetoelectronic devices 1058
magnetoresistance effect 1050
magnetoresistance of Fe/Cr multilayers 1051
magnetostriction 757
magnets
– 17/2 type 807
– 5/1 type 806
– $TM_{17}Sm_2$ 808
majority carriers 1023
malleable irons 270
manganese Mn
– elements 124
manipulating the dot magnetization 1062
manufacturing
– Fe−Nd−B magnets 801
manufacturing process
– glasses 525
martensite 223
martensitic transformation 225, 226
mass magnetic susceptibility
– elements 48
mass susceptibility
– elements 48
mass-production glasses 526
materials
– semiconductors 576
materials data
– elements 46
material-specific parameters 46
matrix composites 170
Maxwell–Garnett model 1045
Maya blue color 1032
MBBA
– liquid crystals 955
MBE (molecular-beam epitaxy) 991, 1032, 1049, 1063
– 0-D structures 1064
– 1-D structures 1064
– 2-D structures 1063
Md mendelevium 151
mechanical and thermal properties
– III–V compounds 621, 638
– II–VI compounds 652, 655, 660, 665, 676, 686
mechanical properties
– elements 46, 47
– group IV semiconductors 578–588
– III–V compounds 610
– III–V semiconductors 604
– IV–IV compound semiconductors 578–588
– optical glasses 550
– technical glasses 533
MEIS (medium-energy ion scattering) 989, 1013
meitnerium Mt
– elements 135
melt viscosity 478
– polymers 478
melting point $T_m$
– aluminium compounds 611
– beryllium compounds 653
– boron compounds 605
– cadmium compounds 677
– gallium compounds 622
– group IV semiconductors and IV–IV compounds 580
– indium compounds 639
– magnesium compounds 656
– mercury compounds 686
– oxides of Ca, Sr, and Ba 660
– zinc compounds 666
melting temperature 477
– elements 47, 48
– polymers 477
memory devices 903
mendelevium Md
– elements 151
mercury compounds
– crystal structure, mechanical and thermal properties 686
– electromagnetic and optical properties 691
– electronic properties 688
– mechanical and thermal properties 686
– thermal properties 686
– transport properties 689
mercury Hg
– elements 73
mercury oxide
– crystal structure, mechanical and thermal properties 686
– electromagnetic and optical properties 691
– electronic properties 688
– transport properties 689
mercury selenide
– crystal structure, mechanical and thermal properties 686
– electromagnetic and optical properties 691
– electronic properties 688
– transport properties 689
mercury sulfide
– crystal structure, mechanical and thermal properties 686
– electromagnetic and optical properties 691
– electronic properties 688
– transport properties 689
mercury telluride
– crystal structure, mechanical and thermal properties 686

– electromagnetic and optical properties 691
– electronic properties 688
– transport properties 689
mesogen 943
mesogenic group 943
mesophase 941
mesoscopic material
– conductivity 1044
– nanoparticle doped 1044
– waveguide applications 1045
mesoscopic materials 1031, 1033
– manufacturing 1033
mesoscopic system
– quantum size effect 1035
– thermodynamic stability 1035
metal
– nanoparticle 1040
– resonance state 999
– surface 987
– surface core level shifts (SCLS) 998
– surface Debye temperature 1013
– surface phonon 1012
– surface state 999
– work function 997
metal surface 987
– jellium model 998
metals 997
– vertical relaxation 989
meter
– SI base unit 13
metrologica, international journal 12
MFM image of a written line on an array of dots 1063
MFM image of arrays of dots 1063
MFM image of domain pattern 1062
– sidewalls 1062
Mg magnesium 68
MHPOBC (liquid crystal) 935, 967
microphase separation 941
Mie theory 1045
Miller delta 825
Miller indices 28
M–I–M (metal–insulator–metal) heterostructure 1053
minority carriers 1023
missing-row reconstruction 987
Mn manganese 124
Mn−Al−C 810
– phase relations 810
Mo molybdenum 114
Mo-based alloys 317
mobility $\mu$
– aluminium compounds 618
– cadmium compounds 682
– group IV semiconductors and IV–IV compounds 597–599
– indium compounds 648
MOCVD (metal-organic chemical vapor deposition) 1064
modulated crystal structure 924
modulated structures
– crystallography 34
moduli *see* elastic constant 580
Mohs hardness 822, 826
– elements 47
molar enthalpy of sublimation
– elements 47
molar entropy
– elements 47
molar heat capacity
– elements 47
molar magnetic susceptibility
– elements 48
molar mass 945–972
– glasses 527
molar susceptibility
– elements 48
molar volume
– elements 47
mole
– definition 14
– SI base unit 14
mole fraction
– glasses 527
molecular architecture 477
molybdenum Mo
– elements 114
momentum-conservation rule 1036
monocrystalline material 47
monolithic alloys 170
monophilic liquid crystal 942
MOS devices 979
MOS field-effect transistor 1020
MOSFET
– electron and hole mobility 1025
– equilibrium condition 1024
– schematic drawing 1025
Mott–Wannier exciton 1037
MQW (multiple quantum well) 1038
MRAM (magnetic random access memories) 1058
MRAM cell
– schematic diagram 1059
Mt meitnerium 135
MTJ (magnetic tunnel junction) 1053, 1054
MTJ sensor
– operation principle 1059
multi-component alloys 219
multiphase (MP) alloys 276
multiple hysteresis loops 932
multiple quantum wells 1042
MVA-TFT (multidomain vertical-alignment thin-film transistor) 944

## N

N nitrogen 98
N16B
– glasses 537
– sealing glasses 563
N-4
– liquid crystals 959
Na sodium 59
$NaNO_2$ family 924
nanocrystal 1038
nanoimprint lithography 1061
nanoimprinted single domain dots
– images 1061
nanoimprinting 1061
nanolithography 1031
nanomaterial 1032
nanometric multilayers 1049
nanoparticle 1031
– doped material 1045
– local-field 1045
nanopatterning 1061
nanophase materials 1032
nanoporous materials 1032, 1043
nanoscience 1032
nanostructured material 1031, 1032
– classification scheme 1034
– conductance 1043
– definition 1032
– electrical conductivity 1043
– manufacturing 1063
– preparation 1031, 1035
– zeolites 1065
nanostructures
– magnetic 1048
nanotechnology 1032
Nb niobium 105
N-BAF10
– optical glasses 551
N-BAF52
– optical glasses 551
N-BAK4
– optical glasses 551
N-BALF4
– optical glasses 551
N-BASF64
– optical glasses 551

Nb-based alloys 318
N-BK7
– glasses 548
– optical glasses 551
Nd neodynium 142
Nd–Fe–B
– physical properties 802
Ne neon 128
near field microscopy 1049
nematic mixtures
– liquid crystals 975
– physical properties 975
nematic phase
– liquid crystals 941
nematic–isotropic transition 945
nematic-phase director 943
Neoceram
– glasses 559
neodynium Nd
– elements 142
neon Ne
– elements 128
Neoparies
– glasses 559
neptunium Np
– elements 151
nesosilicate 433
neutral density filters
– glasses 566
neutron diffraction 41, 926
neutron scattering 915
neutron spectrometer scan 916
new rheocast process (NRC) 170
newton meter
– SI unit of moment of force 19
N-FK51
– glasses 548
– optical glasses 551
N-FK56
– optical glasses 551
$(NH_4)_2SO_4$ family 927
$(NH_4)_3H(SO_4)_2$ family 928
$(NH_4)HSO_4$ family 928
$(NH_4)LiSO_4$ family 928
Ni nickel 139
Ni superalloys 294
nickel
– alloys 279
– application 279
– carbides 285
– low-alloy 279
– mechanical properties 280
– plating 288
nickel Ni
– elements 139
nickel-based superalloys 284
nickel–iron alloys 769
nickel-silvers 300
NIMs (National Institutes for Metrology 4
niobium Nb
– elements 105
nitride
– electrical properties 467
– mechanical properties 467
– thermal properties 467
nitrides
– physical properties 468
nitrogen N
– elements 98
N-KF9
– optical glasses 551
N-KZFS2
– optical glasses 551
N-LAF2
– optical glasses 551
N-LAK33
– optical glasses 551
N-LASF31
– optical glasses 551
No nobelium 151
nobelium No
– elements 151
noble metals 329
– Ag 329
– alloys 329
– applications 330
– Au 329
– catalysts 330
– corrosion resistance 329
– hardness 329
– Ir 329
– optical reflectivity 330
– Os 329
– Pd 329
– Pt 329
– Rh 329
– Ru 329
– vapour pressure 330
NOL (nano-oxide layer) 1053
noncrystallographic diffraction symmetries 36
nondestructive testing 941
nonlinear field-dependent properties 46
nonlinear optical coefficients
– nanostructured materials 1039
nonlinear optical device 903, 925
nonlinear optical susceptibility 920
nonlinear susceptibility tensors 827
non-oxide ferroelectrics 905
non-SI units 11, 20
normalizing 224
Np neptunium 151
N-PK51
– optical glasses 551
N-PSK57
– optical glasses 551
N-SF1
– optical glasses 551
N-SF56
– optical glasses 551
N-SF6
– glasses 548
– optical glasses 551
N-SK16
– optical glasses 551
N-SSK2
– optical glasses 551
nuclear incoherent scattering 916
nuclear reactor 218

## O

O oxygen 108
occupied electron shells
– elements 46
Ohara code
– glasses 544
one-dimensional liquid 943
one-electron potential 999
opal
– nanostructured materials 1032
opals 1048
OPO (optical parametric oscillation) 825
optical constants
– gallium compounds 635
– group IV semiconductors and IV–IV compounds 601–603
– indium compounds 651
optical constants *n* and *k*
– cadmium compounds 684
optical glasses 526, 543
– thermal properties 556
optical materials
– high-frequency properties 824
optical mode frequency 916
optical parametric oscillation (OPO) 825
optical parametric oscillator 920
optical phonon scattering
– group IV semiconductors and IV–IV compounds 598
optical phonon scattering *see also* phonon scattering 598
optical phonon softening 913
optical properties

– group IV semiconductors and IV–IV compounds 601
– III–V compounds 610, 619, 635, 650
– II–VI compounds 655, 660, 664, 672, 683, 691
optical second-harmonic generator 903
optical transparency range 826
optical visualization 941
optoelectronic devices
– nanostructured materials 1038
order parameter 946–952, 956–960, 962, 963
order parameter, $S$ 943
order principle for mesogenic groups 946
organic ferroelectrics 903
orientational order 941
Os osmium 131
osmium Os
– alloys 402
– applications 402
– cathodes 404
– chemical properties 406
– electrical properties 404
– elements 131
– lattice parameter 402
– magnetic properties 405
– mechanical properties 404
– phase diagrams 402
– production 402
– thermal properties 405
– thermoelectric properties 404
outer-shell orbital radius
– elements 46
over-aging 201
oxidation states
– elements 46
oxide 437
– beryllium 447
– magnesium 444
– physical properties 438
oxide ceramics
– production of 444
oxide ferroelectrics 903, 905
oxide superconductors
– low-$T_c$ oxide 711
oxides of Ca, Sr, and Ba
– crystal structure, mechanical and thermal properties 660
– electromagnetic and optical properties 664
– electronic properties 661
– mechanical and thermal properties 660
– thermal properties 660
– transport properties 663
oxygen O
– elements 108

## P

P phosphorus 98
Pa protactinium 151
PAA
– liquid crystals 958
pair distribution function
– crystallography 40
palladium Pd
– alloys 364
– applications 364
– electrical properties 370
– elements 139
– lattice parameters 366
– magnetic properties 372
– mechanical properties 368
– phase diagrams 364
– production 364
– thermoelectric properties 370
parabolic band 1000
Parkes process 330
partially stabilized zirconia (PSZ)
– electrical properties 449
– mechanical properties 449
– thermal properties 449
particle in a box model 1035
particle intensity $I_p$
– radiometry 15
passivation glasses 562, 564
– glasses 565
– properties 564
pattern transfer by imprinting 1061
Pauling 46
Pb lead 88
$PbHPO_4$ family 927
$PbTiO_3$ 916
$PbZrO_3$ 918
Pb–Ca–Sn
– battery grid alloys 418
PCH-7
– liquid crystals 950
Pd palladium 139
pearlite 222
Pearson symbol
– elements 47
percolation density
– nanostructured materials 1033
periodes of elements (Periodic table) 45
Periodic table
– elements 45
Periodic table of the elements 53
permanent magnets
– Co–Sm 806
perovskite-type family 909, 911, 912
perovskite-type oxide 909
phase diagram
– Fe–C 222
– Fe–Cr 226
– Fe–Mn 225
– Fe–Ni 225
– Fe–Si 227
– Ti–Al 210
– Zr–Nb 218
– Zr–O 218
phase separation
– glasses 525
phase transition temperature 943
phase-matching angle 826
phase-matching condition 825
phonon confinement
– nanostructured materials 1042
phonon density of states
– gallium compounds 623, 625
– indium compounds 642
phonon dispersion
– surface phonons 1012
phonon dispersion curve
– aluminium compounds 612
– gallium compounds 623–625
– indium compounds 641
– surface phonons 1015–1026
phonon dispersion relation
– group IV semiconductors 585–587
– IV–IV compound semiconductors 585, 588
phonon energies
– nanostructured materials 1040
– solid surfaces 1013
phonon frequencies $\nu$
– cadmium compounds 678
– gallium compounds 624
– group IV semiconductors 585
– indium compounds 640
– IV–IV compound semiconductors 585
– magnesium compounds 657
– mercury compounds 687
– oxides of Ca, Sr, and Ba 661
– zinc compounds 667
phonon frequencies $\nu$ *see also* phonon wavenumbers $\tilde{\nu}$ 605
phonon instability 921
phonon mode frequency 908
phonon scattering

– group IV semiconductors and IV–IV compounds 598
phonon wavenumbers $\tilde{\nu}$ *see also* phonon frequencies $\nu$ 605
– aluminium compounds 612
– cadmium compounds 678
– gallium compounds 624
– indium compounds 640
– magnesium compounds 657
– mercury compounds 687
– zinc compounds 667
phonon wavenumbers $\tilde{\nu}$/frequencies $\nu$
– boron compounds 605
phonon–phonon coupling 907
phosphorus P
– elements 98
photochromic glasses
– nanostructured materials 1032
photoconductive crystal 922
photoelastic effect 824
photoemission spectra for Ag quantum wells 1036
photoluminescence spectra of CdSe 1039
photometry
– intensity measurements 15
photonic band-gap materials 1048
phyllosilicate 433
physical properties
– liquid crystals 943
physical quantities 12
– base 11, 12
– data 13
– definition 12
– derived 11, 12
– general tables 4
piezoelectric
– element 918
– material 917
– strain constant 918
– strain tensor 824
– tensor 827
piezoelectricity 824, 906
piezooptic coefficient 825
planar alignment 943
planar electromechanical coupling factor 918
Planck radiator 15
plasmon excitations
– nanostructured materials 1031
plasmon oscillation
– nanostructured materials 1032
plasmon peak
– metals 1045
plasmon resonance 1045
plastic crystal 941
platinum group metals (PGM) 363
– alloys 363
platinum Pt
– alloys 376
– applications 376
– catalysis 385
– chemical properties 385
– electrical properties 381
– elements 139
– magnetical properties 384
– mechanical properties 378
– optical properties 385
– phase diagrams 376
– production 376
– thermal properties 385
– thermoelectric properties 382
plutonium Pu
– elements 151
PLZT
– ceramic material 918
Pm promethium 142
Po polonium 108
Pockels effect 825
point groups
– crystallography 30
Poisson equation 1022
Poisson number
– elements 47
Poisson's ratio 478
– optical glasses 550
– polymers 478
polarization microscopy 943
polonium Po
– elements 108
poly(4-methylpentene-1) (PMP) 488, 489
poly(ethylene-co-acrylic acid) (EAA) 486, 487
poly-(ethylene-co-norbornene) 486, 487
poly(ethylene-co-vinyl acetate) (EVA) 486, 487
poly(vinyl chloride) 492, 495
– plastisized (60/40) (PVC-P2) 492, 495
– plastisized (75/25) (PVC-P1) 492, 495
– unplastisized (PVC-U) 492, 494–496
polyacetals 480, 497
– poly(oxymethylene) (POM-H) 497–500
– poly(oxymethylene-co-ethylene) (POM-R) 497, 498, 500
polyacrylics 480, 497
– Poly(methyl methacrylate) (PMMA) 497–499
polyamides 480, 501
– polyamide 11 (PA11) 501
– polyamide 12 (PA12) 501
– polyamide 6 (PA6) 501, 502
– polyamide 610 (PA610) 501, 502
– polyamide 66 (PA66) 501, 502
polybutene-1 (PB) 488, 489
polyesters 481, 503
– poly(butylene terephthalate) (PBT) 503–505
– poly(ethylene terephthalate) (PET) 503–505
– poly(phenylene ether) (PPE) 504–506
– polycarbonate (PC) 503, 504
polyether ketones 481, 508
– poly(ether ether ketone) (PEEK) 508, 509
polyethylene 483–486
– high density (HDPE) 483–486
– linear low density (LLDPE) 484–486
– low density (LDPE) 484–486
– medium density (MDPE) 484–486
– ultra high molecular weight (UHMWPE) 484–486
polyethylene ionomer (EIM) 486, 487
polyimides 481, 508
– poly(amide imide) (PAI) 508
– poly(ether imide) (PEI) 508, 509
– polyimide (PI) 508
polyisobutylene (PIB) 488, 489
polymer
– physical properties 483
polymer blend 515
– physical properties 477, 483
– poly(acrylonitrile-co-butadiene-co-acrylester) + polycarbonate (ASA + PC) 515–517
– poly(acrylonitrile-co-butadiene-co-styrene) + polyamide (ABS + PA) 515–517
– poly(acrylonitrile-co-butadiene-co-styrene) + polycarbonate (ABS + PC) 515–517
– poly(butylene terephthalate) + poly(acrylonitrile-co-butadiene-co-acrylester) (PBT + ASA) 517, 521
– poly(butylene terephthalate) + polystyrene (PBT + PS) 515, 519, 520

– poly(ethylene terephthalate) + polystyrene (PET + PS) 515, 519, 520
– poly(phenylene ether) + polyamide 66 (PPE + PA66) 517, 521
– poly(phenylene ether) + polystyrene (PPE + PS) 520, 521
– poly(styrene-co-butadiene) (PPE + SB) 517, 520, 521
– poly(vinyl chloride) + chlorinated polyethylene (PVC + PE-C) 515, 518
– poly(vinyl chloride) + poly(acrylonitrile-co-butadiene-co-acrylester) (PVC + ASA) 515, 518
– poly(vinyl chloride) + poly(vinyl chloride-co-acrylate) (PVC + VC/A) 515, 518
– polycarbonate + liquid crystal polymer (PC + LCP) 515, 519, 520
– polycarbonate + poly(butylene terephthalate) (PC + PBT) 515, 519, 520
– polycarbonate + poly(ethylene terephthalate) (PC + PET) 515, 519, 520
– polypropylene + ethylene/propylene/diene rubber (PP + EPDM) 515, 516
– polysulfone + poly(acrylonitrile-co-butadiene-co-styrene) (PSU + ABS) 517, 521
polymer family 911, 936
polymer ferroelectrics 903
polymer matrix 1040
polymers 477
– abbreviations 482
– Charpy impact strength 478
– coefficient of expansion 478
– compressibility 478
– creep modulus 478
– crystallinity 477
– density 478
– elastic modulus 478
– electric strength 478
– enthalpy of combustion 477
– enthalpy of fusion 477
– entropy of fusion 477
– ferroelectric properties 905
– gas permeation 478
– glass transition temperature 477
– heat capacity 477
– impact strength 478
– melt viscosity 478
– melting temperature 477
– physical properties 477
– physicochemical properties 477
– Poisson's ratio 478
– refractive index 478
– relative permittivity 478
– shear modulus 478
– shear rate 478
– Shore hardness 478
– sound velocity 478
– steam permeation 478
– stress 478
– stress at 50% strain (elongation) 478
– stress at fracture 478
– stress at yield 478
– structural units 479–481
– surface resistivity 478
– thermal conductivity 478
– Vicat softening temperature 477
– viscosity 478
– volume resistivity 478
polyolefines 480, 483–486
polypropylene (PP) 488, 489
polysulfides 481, 506
– poly(phenylene sulfide) (PPS) 506, 507
polysulfones 481, 506
– poly(ether sulfone) (PES) 506, 507
– polysulfone (PSU) 506, 507
polyurethanes 481, 511
– polyurethane (PUR) 511, 512
– thermoplastic polyurethane elastomer (TPU) 511, 512
polyvinylidene fluoride
– ferroelectrics 911
porous aluminium silicates
– electrical properties 436
– mechanical properties 436
– thermal properties 436
Portland cement
– ASTM types 433
– chemical composition 432
positional order 941
potassium K
– elements 59
potential barrier 1022
powder-composite materials 277
Powder-in-Tube (PIT) 739
power-law dependence of conductivity on film thickness 1042
Pr praseodymium 142
practical superconductors
– characteristic properties 705
praseodynium Pr
– elements 142
prefixes
– decimal multiples of units 19
primitive cell
– crystal structure 28
projected band structure 996
projected bond length 995
promethium Pm
– elements 142
property tensor 46
– independent components 827
protactinium Pa
– elements 151
proton distribution 926
pseudopotential calculation 1006
Pt platinum 139
p-type diamond
– Debye length 1021
Pu plutonium 151
pulsed infrared lasers 1040
pyrochlore-type family 909
pyroelectric coefficient 917
pyroelectric measurement 931
PZT
– piezoelectric material 917

## Q

quantum confinement 1036
– nanostructured materials 1042
quantum dots
– nanostructured materials 1031, 1035
quantum size effect
– nanostructured materials 1031, 1035
quantum transport
– nanostructured materials 1053
quantum well
– coupled 1043
– nanostructured materials 1031, 1035
quantum wires
– nanostructured materials 1035
quantum-well superlattices 1033
quasicrystals 34
QWIP (quantum well infrared photodetector) 1042

## R

Ra radium 68
radiant intensity $I_e$
– radiometry 15

radiation sources and exposure techniques in lithography 1065
radiometric and photometric quantities 16
radiometry
– intensity measurements 15
radium Ra
– elements 68
radon Rn
– elements 128
Raman scattering 906
Raman scattering spectroscopy 1040
Raman spectrum 908
RAS 997
Rayleigh mode 1012
Rb rubidium
– elements 59
Re rhenium
– elements 124
real and imaginary parts $\varepsilon_1$ and $\varepsilon_2$ of the dielectric constant *see* dielectric constant $\varepsilon$ 602
– gallium compounds 637
reconstruction model 987
– solid surfaces 991
reconstruction of semiconductors 991
reconstruction of surface 986
– metals 987
recording media
– arrays of magnetic dots 1061
reduced surface state energy 1022
reduced wave vector 1012
reduced-dimensional material geometries 1033
references
– solid surfaces 1029
reflectance anisotropy spectroscopy (RAS) 1007
refractive index 478, 829, 946–972
– elements 48
– glasses 539, 543
– polymers 478
– Sellmeier dispersion formula 547
– temperature dependence 548
refractive index $n$ 619
– boron compounds 610
– cadmium compounds 684
– gallium compounds 635
– group IV semiconductors and IV–IV compounds 601–603
– indium compounds 650
– mercury compounds 691
– zinc compounds 672
refractories
– boride-based 452
– carbide-based 458
– nitride-based 468
– oxide-based 438
– silicide-based 472
refractory ceramics 437
refractory metals 303
– alloys 303
compositions 305
dispersion-strengthened 304
– annealing 311
– chemical properties 308
– crack growth behavior 325
– creep elongation 316
– creep properties 327
– dynamic properties 318
– evaporation rate 307
– fatigue data 321
– flow stress 316
– fracture mechanics 322
– grain boundaries 314
– high-cycle fatigue properties 319
– linear thermal expansion 306
– low-cycle fatigue properties 320
– mechanical properties 314
– metal loss 308
– microplasticity 318
– oxidation behavior 308
– physical properties 306
– production routes 304
– recrystallization 311
– resistance against gaseous media 309
– resistance against metal melts 309
– specific electrical resistivity 307
– specific heat 307
– static mechanical properties 315
– stress–strain curves 320
– thermal conductivity 306
– thermomechanical treatment 314
– vapor pressure 307
– Young's modulus 307
refractory metals alloys
– application 306
– products 306
refractory production
– raw materials 444
relative permittivity 478
– polymers 478
relaxation of semiconductors 991
relaxation of surface 986
– metals 987
relaxor 906, 909, 918
remanent magnetization 922
remanent polarization 918
residual resistance ratio (RRR) 397
residual resistivity ratio (RRR) 338
resistivity
– gallium compounds 630
response of material 46
Rf rutherfordium 94
Rh rhodium
– elements 135
RHEED (reflection high-energy electron diffraction) 990
rhenium Re
– elements 124
rhodium
– alloys 386
– applications 386
– chemical properties 392
– electrical properties 390
– magnetical properties 391
– mechanical properties 387
– optical properties 392
– phase diagrams 386
– production 386
– thermal properties 392
– thermoelectrical properties 391
rhodium Rh
– elements 135
ribbon silicates 433
RIE (reactive ion etching) 1061
Rn radon 128
Rochelle salt 904
Rochelle salt family 932
rod-like molecule 942
RT (room temperature) 49
RTP (room temperaure and standard pressure) 49
Ru ruthenium 131
rubidium Rb
– elements 59
ruthenium Ru
– alloys 399
– applications 399
– chemical properties 402
– electrical properties 401
– elements 131
– lattice parameter 400
– magnetic properties 401
– mechanical properties 400
– optical properties 402
– phase diagrams 399
– production 399
– thermal properties 402
– thermoelectric properties 401
rutherfordium Rf
– elements 94
RW (weighted sound reduction) 409

## S


S sulfur 108
SAE (Society of Automotive Engineers) 221
SAM (self-assembled monolayer) 944
samarium Sm
– elements 142
SAW (surface acoustic wave ) 912
Sb antimony 98
SbSI family 922
Sc scandium 84
$SC(NH_2)_2$ family 930
scandium Sc
– elements 84
scattering
– nanoscale objects 1048
scattering losses of a waveguide 1045
Schoenflies symbol 30
– elements 47
Schott AG 523
Schott code
– glasses 544
Schott filter glasses
– glasses 569
Schott glasses 8nnn 540, 541
SDR 997
Se selenium 108
seaborgium Sg
– elements 114
sealing glasses 527
– glasses 559
second
– SI base unit 14
secondary hardening 263
second-harmonic generation (SHG) 825, 906
second-order elastic constants *see* elastic constant 580
second-order phase transition 907
selenium Se
– elements 108
Sellmeier dispersion formula
– glasses 547
Sellmeier equations 826
SEM (scanning electron microscopy) 39
semiconductor 1003
– covalent 992
– field-effect mobility 1024
– III–V compounds 1004
– intrinsic Debye length 1021
– nanocrystal 1040
– polar 992
– quantum confinement 1036
– reconstruction 1004
– reconstruction model 991
– surface 990
– surface core level shift 1003
– surface Debye temperature 1017
– surface phonon 1017
– surface shift 1004
semiconductor band bending 1020
semiconductor nanostructures 1035
semiconductor surface
– Fermi level pinning 1025
– ionization energy 1003
semiconductors
– aluminium compounds 610
– boron compounds 604
– cadmium compounds 676
– chemical doping 576
– gallium compounds 621
– group IV semiconductors and IV–IV compounds 578–603
– III–V compounds 576, 604
– II–VI compounds 576, 652
– indium compounds 638
– introduction 575
– IV–IV compounds 576
– magnesium compounds 655
– mercury compounds 686
– oxides of Ca, Sr, and Ba 660
– physical properties 577
– table of contents 575
– zinc compounds 665
semi-solid metal processing (SSMP) 170
sensor
– chemiresistor-type 1043
SF1
– optical glasses 551
SF11
– optical glasses 551
SF2
– optical glasses 551
SF6
– glasses 537, 548
– optical glasses 551
SF66
– optical glasses 551
SFG (sum frequency generation) 825
SFM (superfluorinated material) 975
Sg seaborgium 114
shape memory 298
– nickel 279
shape-memory alloys
– TiNi 216
shear modulus 478
– elements 47
– polymers 478
shear rate 478
– polymers 478
SHG (second-harmonic generation) 825, 906
Shore hardness 478
– polymers 478
short pass filters
– glasses 566
short-range order 39
– glasses 524
Shubnikov groups
– crystallography 33
SI (Système International d'Unités) 3, 11
SI (the International System of Units) 12
SI base unit 13
SI definitions of magnetic susceptibility 48
SI derived units 16, 17
– with special names 17, 18
SI prefixes 19
Si silicon 88
SI units
– base quantities 13
– base units 13
$Si_3N_4$ ceramics 451
$Si_3N_4$ powders 472
SiC ceramics 451
side group 943
sievert
– SI unit of dose equivalent 19
silica
– glasses 524
silicate 433
silicate based glasses 526
silicide 473
– physical properties 472
silicon
– electromagnetic and optical properties 601
– electronic properties 589–594
– transport properties 598
silicon carbide
– band structure 590
– crystal structure, mechanical and thermal properties 578–588
– electromagnetic and optical properties 601

– electronic properties 589–594
– transport properties 595
silicon nitride 467
silicon Si
– crystal structure, mechanical and thermal properties 578–588
– elements 88
silicon steels
– grain-oriented 765
– non-oriented 763
silicon technology 1036
silicon-based lasers 1036
silicon–germanium alloys
– band structure 590
– transport properties 601
silicon-germanium alloys
– crystal structure, mechanical and thermal properties 578–588
– electromagnetic and optical properties 601
silicon–silicon oxide interface 1025
silver 330
– alloys 330
– application 330
– chemical properties 344
– crystal structures 333
– diffusion 342
– electrical properties 338
– intermetallic phases 333
– magnetic properties 339
– mechanical properties 335
– optical properties 341
– phase diagrams 331
– production 330
– ternary alloys 345
– thermal properties 340
– thermodynamic data 331
– thermoelectric properties 339
silver Ag
– elements 65
simple perovskite-type oxide 909
single hysteresis loop 904
$SiO_2$
– glasses 524
SK51
– optical glasses 551
Sm samarium
– elements 142
smectic $C^*$ phase 934
smectic phase 942
Sn tin 88
SNR (signal-to-noise ratio) 1060
soda lime glasses 528, 529, 534
sodium Na
– elements 59
soft annealing 224
soft magnetic alloys 758
– nanocrystalline 776
soft magnetic materials
– composite 759
– sintered 759
soft-mode spectroscopy 906
solar cell 1043
solder alloy 345
solder glasses 562
sol–gel synthesis
– nanostructured materials 1065
solid material
– structure 27
solid material, structure 27
solid surface energy 944
solid-state polymorphism 943
sorosilicate 433
sound velocity 478, 947–949, 956–962, 968–971
– elements 47
– polymers 478
source 1024
$sp^3$-bonded crystal 991
space charge function
– solid surfaces 1022
space charge layer
– semiconductor surface 1020
– solid surfaces 1020
space groups
– crystallography 31
SPARPES 1011
speed of light
– fundamental constant 13
spheroidal (nodular) graphite (SG) 268
spheroidite 223
spin accumulation 1049
spin diffusion length 1050
spin electronics
– applications 1057
– nanostructured materials 1031, 1049
spin polarization 1055
– nanostructured materials 1049
spin valve multilayers 1052
spin valve read head
– schematic diagram 1058
spin valve sensor 1053
spin-asymmetric material 1049
spinel structure
– crystallography 33
spin-electronic switch 1055
spin–orbit splitting energy $\Delta_{so}$
– aluminium compounds 617
– cadmium compounds 681
– gallium compounds 628
– group IV semiconductors and IV–IV compounds 593
– indium compounds 644
– mercury compounds 689
– zinc compounds 670
spintronics
– nanostructured materials 1031, 1049
SPLEED 1011
spontaneous electric polarization 903
spontaneous polarization 917, 945
Sr strontium 68
$Sr_2Nb_2O_7$ family 920
SRI (sound reduction index) 409
$SrNb_2O_7$ family 909
$SrTeO_3$ family 919
$SrTiO_3$ 913
stabilized zirconia (PSZ) 448
stacking faults
– crystallography 41
stain resistance
– optical glasses 550
stainless steels 240
– austenitic 252
– duplex 257
– ferritic 246
– martensitic 250
– martensitic-ferritic 250
standard electrode potential
– elements 46
standard entropy
– elements 47
standard temperature and pressure (STP) 46
Stark effect
– nanostructured materials 1040
static dielectric constant 826
– elements 48
static dielectric constant 828–889
STC (sound transmission classification) 409
steam permeation 478
– polymers 478
steel
– austenitic 259
– carbon 227
– ferritic 258
– ferritic austenitic 259
– hardening 237
– heat-resistant 258, 261
– high-strength low-alloy (HSLA) 240

– low-alloy carbon steel 227
– mechanical properties 237
– stainless 240
– tool 262
stibiotantalite family 909
stiffness constant *see* elastic constant 580
STM (scanning tunneling microscopy) 988, 992, 997
STM spectroscopy 1005
STN (supertwisted nematic) effect 944
STO ($SrTiO_3$) 1056
storage capacity of hard disks 1048
storage density evolution of hard disk drives 1048
storage media 1060
– arrays of nanometer-scale dots 1060
– limits 1060
– technology 1060
storing information on the sidewalls of the dots 1062
strain
– polymers 478
strength
– glasses 534
stress 478
– polymers 478
stress at 50% strain (elongation) 478
– polymers 478
stress at fracture 478
stress at yield 478
– polymers 478
stress birefringence
– glasses 539, 549
stress intensity factor
– glasses 534
strong-confinement regime
– nanostructured materials 1037, 1038
strontium oxide
– crystal structure, mechanical and thermal properties 660
– electromagnetic and optical properties 664
– electronic properties 661
– transport properties 663
strontium Sr
– elements 68
strontium titanate 913
structural parameters 990
structural phase transitions 906
structure
– diamond-like 979
structure type
– crystallography 33
*Strukturbericht* type 47
sublattice 903
sublattice polarization 904
submicrometer magnetic dots 1060
substituted mesogens (liquid crystals)
– physical properties 968
sulfur S
– elements 108
sum frequency generation (SFG) 825
superalloys
– Ni-based cast 288
– nickel 294
superconducting high-$T_c$
– crystal structure 712
superconducting oxides
– high-$T_c$ chemical composition 712
superconductivity
– elements 48
superconductor 695
– borides 745
– borocarbides 746, 747
– carbides 745
– commercial $Nb_3Sn$ 709
– critical temperature 699
– crystal structure 712
– Debye temperature 696
– device applications 719
– high-$T_c$ cuprates 712, 713, 720
– industrial wire performance 719
– metallic 696
– Nb alloys 702
– non-metallic 712
– Pb alloys 696
– pinning 717
– practical metallic 704
– production $Nb_3Sn$ 708
– Sommerfeld constant 696
– SQUIDs 720
– structural data 720
– thermodynamic properties 696
– Type I 695
– Type II 695
– V alloys 700
– vortex lines 717
– Y−Ba−Cu−O 723
supercooled liquid
– glasses 524
supercooled mesophase 945
superstructures
– crystallography 41
supertwisted nematic (STN) effect 944
Supremax
– glasses 527
surface
– Curie temperature 1009
– diagram 979
– ionization energy 1003
– magnetic 1008
– semiconductor 990
– structure of an ideal 979
surface band structure 996
surface Brillouin zone (SBZ) 996
surface conductivity
– solid surfaces 1024
surface core level shifts (SCLS) 998
– solid surfaces 1003, 1004
surface differential reflectivity (SDR) 1008
surface excess conductivity 1024
surface magnetization 1011
surface mobility 1024
surface of diamond 1004
surface phonon 1012
– dispersion 1019
– metal 1013
– mode 1012
surface plasmon
– absorption of nanoparticles 1046
– dispersion curve 1001
surface resistivity 478
– polymers 478
surface resonance 996
– phonons 1012
surface response
– dielectric theory 1007
surface state
– acceptor 1022
– band 1005
– donor 1022
– transitions 1005
surface state bands
– solid surfaces 1004
surface states 996
surface tension 948–950, 955–962, 968–971, 975
– elements 47
surface tension ($\gamma_{LV}$) 943
surfaces 979
surgical implant alloys
– cobalt-based 277
susceptibility

– magnetic 48
– mass 48
– molar 48
– nonlinear dielectric 825, 829
– second-order nonlinear dielectric 826
– third-order nonlinear dielectric 826
SV (spin valve) 1052
symmetry elements of point groups 30
synthesis of clusters
– gas-phase production 1066
– nanostructured materials 1065
synthetic silica
– glasses 557

## T

T tritium 54
TA
– phonon spectra 915
Ta tantalum 105
Ta-based alloys 318
tailoring of the electronic wave function 1032
tantalum Ta
– elements 105
Tb terbium 142
TC 12 (Technical Committee 12 of ISO) 12
Tc technetium 124
Te tellurium 108
technetium Tc
– elements 124
technical ceramics 437
technical coppers 297
technical glasses 527, 530
technical specialty glasses 526
tellurium Te
– elements 108
TEM (transmission electron microscopy) 39
TEM image of a superlattice of Au clusters 1066
TEM views of single dots 1062
temper graphite (TG) 268
temperature dependence of carrier concentration
– group IV semiconductors and IV–IV compounds 596
temperature dependence of electrical conductivity
– indium compounds 647
temperature dependence of electronic mobilities
– indium compounds 649
temperature dependence of energy gap
– indium compounds 645
temperature dependence of linear thermal expansion coefficient
– cadmium compounds 677
– magnesium compounds 656
temperature dependence of the lattice parameters
– group IV semiconductors and IV–IV compounds 580–582
temperature dependence of thermal conductivity
– group IV semiconductors and IV–IV compounds 599, 600
– indium compounds 650
temperatures of phase transitions 946–976
tempering of steel 223
template synthesis 944
tensile strength
– elements 47
tensor
– elastooptic 826
– piezoelectric strain 826
terbium Tb
– elements 142
terminal group 943
ternary alloys 298
terne steel coatings 415
TFT (thin-film transistor) 944
TGS family 932
Th thorium 151
thallium Tl
– elements 78
thermal and thermodynamic properties
– elements 46
thermal conductivity $\kappa$ 478, 945, 947–949, 956, 958
– aluminium compounds 618
– cadmium compounds 682
– elements 46, 47
– gallium compounds 634
– group IV semiconductors and IV–IV compounds 599
– indium compounds 650
– magnesium compounds 659
– mercury compounds 690
– oxides of Ca, Sr, and Ba 663
– polymers 478
– zinc compounds 670
thermal expansion
– glasses 526
thermal expansion coefficient, linear
– elements 47
thermal gap
– indium compounds 645
thermal properties
– group IV semiconductors 578–588
– III–V compounds 610, 621, 638
– III–V semiconductors 604
– II–VI compounds 652, 655, 660, 665, 676, 686
– IV–IV compound semiconductors 578–588
– technical glasses 533, 536
thermal vibrations
– surface phonons 1012
thermal work function
– elements 48
thermally activated flux flow (TAFF) 718
thermochromic material 944
thermodynamic properties
– elements 47
thermoelectric coefficient
– elements 48
thermoelectric power
– oxides of Ca, Sr, and Ba 664
thermography 941, 944
thermomechanical treatment (TMT) 314
thermosets 481, 512
– diallyl phthalate (DAP) 512, 514
– epoxy resin (EP) 514, 515
– melamine formaldehyde (MF) 512, 513
– phenol formaldehyde (PF) 512, 513
– polymers 512
– silicone resin (SI) 514, 515
– unsaturated polyester (UP) 512–514
– urea formaldehyde (UF) 512, 513
thermotropic liquid crystal 942
thin film 906
thin-film transistor (TFT) 944
thixomolding 170
thorium Th
– elements 151
three and four-ring systems
– liquid crystals 964
three-dimensional long-range order 941
three-ring system 964
three-wave interactions
– in crystals 825
thulium Tm
– elements 142

Ti titanium 94
time-temperature-transformation (TTT) diagram 238
tin Sn
– elements 88
titanates 450
titanium 206
– commercially pure grades 207
– creep behavior 208
– creep strength 210
– hardness 207
– high-temperature phase 206
– intermetallic materials 210
– phase transformation 206
– sponge 207
– superalloys 210
– titanium alloys 206
titanium alloys 209
– applications 209
– chemical composition 209
– chemical properties 213
– mechancal properties 213
– mechanical properties 209
– physical properties 213
– polycrystalline 213
– single crystalline 213
– thermal expansion coefficient 214
titanium dioxide
– mechanical properties 450
– thermal properties 450
titanium oxide
– phase diagram 206
titanium Ti
– elements 94
Tl thallium 78
Tm thulium 142
TMR (tunnel magnetoresistance) 1054, 1055
TN (twisted nematic)
– liquid crystals 944
TO 915
tool steels 262
torsional modulus
– optical glasses 550
total losses 763
transformation temperature
– glasses 524
transition range
– glasses 524
transition temperature
– glasses 525
transitions
– surface states 1005
transmission spectra
– colored glasses 566, 567
transmission window
– glasses 524
transmittance
– glasses 548
transmittance of glasses
– color code 549
transport properties
– group IV semiconductors and IV–IV compounds 595–601
– III–V compounds 608, 617, 629, 647
– II–VI compounds 655, 659, 663, 670, 682, 689
transverse acoustic branch 915
transverse optical branch 915
transverse optical mode 906
triple point of water 48
tritium T
– elements 54
truncated crystal 986
tungsten bronze-type family 909, 920
tungsten W
– elements 114
tunnel junction
– magnetic 1053
tunnel magnetoresistance
– function of field and temperature 1057
tunnel magnetoresistance as a function of magnetic field 1055
tunneling
– nanostructured materials 1053
tunneling mechanism
– nanostructured materials 1043
twisted nematic (TN) effect 944
two-dimensional liquid 942
two-photon absorption coefficient 829
two-ring systems with bridges
– liquid crystals 955
two-ring systems without bridges
– liquid crystals 947
Type II superconductors
– anisotropy coefficients 716
– coherence lengths 716
– high-$T_c$ cuprate compounds 716
type metals 414

## U

U uranium 151
ultrahigh density storage media 1049, 1060
unalloyed coppers 296
uniaxial crystals 826
Unified Numbering System for Metals and Alloys (UNS) 296
unit cell of Si(111) 7×7 995
units
– amount of substance 14
– atomic 21
– atomic units (a.u.) 22
– candela 15
– CGS units 21
– coherent set of 20
– crystallography 21
– electric current 14
– general tables 4
– length 13
– luminous intensity 15
– mass 14
– natural 21
– natural units (n.u.) 21
– non-SI 22
– non-SI units 20, 21
– other non-SI units 23
– temperature 14
– the international system of 11
– time 14
– used with the SI 20
– X-ray-related units 22
units of physical quantities
– fundamental constants 3
units outside the SI 20
UNS (Unified Numbering System) 221
UPS 998
uranium U
– elements 151
UTS – ultimate tensile strength 219

## V

V vanadium 105
van der Waals attraction 1019
vanadium V
– elements 105
vertical nanomagnets 1062
vertical relaxation of metals 989
VFT (Vogel, Fulcher, Tammann) equation
– glasses 533
Vicat softening temperature 477
– polymers 477
Vickers hardness
– elements 47

vinylpolymers 480, 489–492
– poly(acrylonitrile-co-butadiene-co-styrene) (ABS) 492–494
– poly(acrylonitrile-co-styrene-co-acrylester) (ASA) 492–494
– poly(styrene-co-acrylnitrile) (SAN) 489, 490, 492
– poly(styrene-co-butadiene) (SB) 489–491
– poly(vinyl carbazole) (PVK) 492, 493
– polystyrene (PS) 489–491
VIP (viewing-independent panel) 975
viscosity 478, 948, 950–954, 963–965, 967, 968, 975
– dynamic 943
– elements 47
– glasses 524
– kinematic 943
– optical glasses 556
– polymers 478
– technical glasses 533
– temperature dependence 525
viscosity of glasses
– temperature dependence 534
vitreous silica
– electrical properties 557
– gas solubility 557
– glasses 526, 556
– molecular diffusion 557
– optical constants 557
vitreous solder glasses 562
Vitronit
– glasses 559
volume compressibility
– elements 47
volume magnetization
– elements 48
volume of primitive cell
– crystallographic formulas 986
volume resistivity 478
– polymers 478
volume–temperature dependence
– glasses 524
Vycor™
– glasses 527

## W

W tungsten 114
wavelength dependence of refractive index *n*
– indium compounds 651
WDX (wavelength-dispersive analysis of X-rays) 39
weak-confinement regime
– nanostructured materials 1037, 1038
wear-induced surface defects
– glasses 535
Weibull distribution
– glasses 535
weight fraction
– glasses 527
Wood's metal 420
work function $\Phi$
– metal 997
– solid surfaces 997
work hardening wrought copper alloys 300
wrought alloys 298
wrought magnesium alloys 164
wrought superalloys 284
wtppm (weight part per million) 407
Wyckoff position
– crystallography 32

## X

Xe xenon 128
xenon Xe
– elements 128
X-ray diffraction 39
X-ray interferences
– crystallography 27

## Y

Y yttrium 84
Yb ytterbium 142
Young's modulus 823
– elements 47
– optical glasses 550
YS – yield stress 219
ytterbium Yb
– elements 142
yttrium Y
– elements 84
Y−Ba−Cu−O
– critical current density 733
– crystal defects 728
– crystal structure 723
– electric resistivity 730
– grain boundaries 730
– hole concentration 733
– lattice parameters 726
– lower critical field 734
– oxygen content 724
– pinning 735
– substitutions 725
– superconducting properties 731
– thermal conductivity 730
– transition temperature 733
– upper critical field 734

## Z

zeolites
– nanostructured materials 1031, 1065
Zerodur®
– glasses 558
– linear thermal expansion 558
zinc compounds
– crystal structure, mechanical and thermal properties 665
– effective hole mass 670
– electromagnetic and optical properties 672
– electronic properties 668
– mechanical and thermal properties 665
– optical properties 672
– thermal properties 665
– transport properties 670
zinc oxide
– crystal structure, mechanical and thermal properties 665
– electromagnetic and optical properties 672
– electronic properties 667
– transport properties 670
zinc selenide
– crystal structure, mechanical and thermal properties 665
– electromagnetic and optical properties 672
– electronic properties 667
– transport properties 670
zinc sulfide
– crystal structure, mechanical and thermal properties 665
– electromagnetic and optical properties 672
– electronic properties 667
– transport properties 670
zinc telluride
– crystal structure, mechanical and thermal properties 665
– electromagnetic and optical properties 672
– electronic properties 667
– transport properties 670

zinc Zn
– elements 73
zircaloy 219
– irradiation effect 219
zirconium
– alloys 217
– bulk glassy alloys 218
– bulk glassy behavior 220
– low alloy materials 217
– nuclear applications 218
– technically-pure materials 217
zirconium dioxide 448
zirconium Zr
– elements 94
ZLI-1132
– liquid crystals 975
Zn zinc 73
Zr zirconium 94